Digitized by the Internet Archive
in 2023

https://archive.org/details/transactions-society-of-petroleum-engineers_1961_222

TN
1
A5
Vol. 222
NIC

TRANSACTIONS

of the

SOCIETY OF PETROLEUM ENGINEERS

of the

American Institute of Mining, Metallurgical, and Petroleum Engineers, Inc.

VOLUME 222

1961

PAPERS AND DISCUSSIONS INCLUDED HAVE BEEN APPROVED FOR PUBLICATION BY THE SOCIETY OF PETROLEUM ENGINEERS TRANSACTIONS EDITORIAL COMMITTEE. THEY WERE SELECTED FROM PAPERS PRESENTED BEFORE THE SOCIETY AT MEETINGS HELD IN DALLAS, TEX., OCT. 4-7, 1959; SAN FRANCISCO, CALIF., DEC. 6-9, 1959; WICHITA FALLS, TEX., MAY 2-3, 1960; TULSA, OKLA., SEPT. 25-28, 1960; DENVER, COLO., OCT. 2-5, 1960; PASADENA, CALIF., OCT. 20-21, 1960; HOUSTON, TEX., NOV. 21-22, 1960; DHAHRAN, SAUDI ARABIA, MARCH 27-29, 1961; DALLAS, TEX., OCT. 8-11, 1961; BAKERSFIELD, CALIF., NOV. 2-3, 1961; AND PAPERS NOT PRESENTED AT THESE MEETINGS BUT OFFERED TO THE SOCIETY OF PETROLEUM ENGINEERS OF AIME FOR PUBLICATION.

PUBLISHED BY THE INSTITUTE

AT THE OFFICE OF THE SOCIETY OF PETROLEUM ENGINEERS

6300 NORTH CENTRAL EXPRESSWAY

DALLAS, TEXAS

Headquarters of the Institute are at 345 East 47th Street, New York 17, N. Y.

1961 SOCIETY OF PETROLEUM ENGINEERS OF AIME
TRANSACTIONS EDITORIAL COMMITTEE

H. J. Ramey, Jr., *Chairman*
Mobil Oil Co.
Los Angeles, Calif.

Irving Fatt, *Vice-chairman*
University of California
Berkeley, Calif.

Ronald H. Newman
Long Beach Oil Development Co.
Long Beach, Calif.

R. L. Jewett
Shell Oil Co.
Los Angeles, Calif.

R. L. Perrine
University of California
Los Angeles, Calif.

T. D. Mueller
Standard Oil Co. of California
San Francisco, Calif.

James W. Wilson
Union Oil Co. of California
Brea, Calif.

The primary function of the Transactions Editorial Committee is to receive the papers tendered for publication by the Society of Petroleum Engineers, and to select from them those papers that shall be published in the Transactions Section of Journal of Petroleum Technology and in Society of Petroleum Engineers Journal. This selection shall be based on the merit of such papers in the light of existing standards.

TRANSACTIONS

The Transactions are considered the basic form of contribution to the published professional literature of the Society of Petroleum Engineers. Manuscripts should present completed original work embodying the results of extensive field, plant, laboratory, or theoretical investigations of a fundamental engineering nature, or new interpretive concepts on old but important technical problems. Also, shorter papers are invited which present results of conclusions arising in the course of an investigation which the author wishes to present prior to completion of investigation. Previously such contributions were referred to as Technical Notes, but this designation is no longer used.

Copyright, 1962, by the
Society of Petroleum Engineers
of AIME

Printed in the United States of America

Storm Printing Company, Dallas, Texas

FOREWORD

AN IMPORTANT milestone in the history of SPE took place in March, 1961, with the publication of the first issue of SOCIETY OF PETROLEUM ENGINEERS JOURNAL. In introducing this quarterly journal, the Society is now providing a second prestige publication for the recording of the most important literature in the fields of drilling and production of oil and gas. "SPEJ" presents noteworthy advancements in petroleum research, including the more complex mathematical and theoretical papers which are of special interest to a vital portion of our membership.

The new Journal started with a 66-page issue, but the influx of good technical material required the size to be increased to 68 pages in June, 104 pages in September and 92 pages in December. The number of papers attracted to the new SPEJ far exceeded our expectations—and this is indicative of the excellent response we have received to the new publication.

The introduction of SOCIETY OF PETROLEUM ENGINEERS JOURNAL is partially responsible for the 1961 volume being the largest TRANSACTIONS volume ever published by SPE. The nearly 700 pages printed here need only to be compared to the 332 pages published in the 1953 volume to see how our literature has grown over the years.

The introduction of the new Journal has prompted several changes which will be immediately obvious in the use of this TRANSACTIONS volume. Even the name on the cover is different, in that the volume is called the "Transactions of the Society of Petroleum Engineers of AIME".

The volume is now divided into two parts: Part I is Transactions material reprinted from JOURNAL OF PETROLEUM TECHNOLOGY; Part II contains all papers printed during the year in SOCIETY OF PETROLEUM ENGINEERS JOURNAL. The folio (which is the line at the bottom of each page listing the name of the publication and the page number) no longer says "Trans., AIME", but the standard reference to papers printed here will be their original publication—either "*Jour. Pet. Tech.*" or "*Soc. Pet. Eng. Jour.*".

Even the appearance of the paper changes as you progress from Part I to Part II of this volume. This is because our editors have found it more economical to print one portion by the "letterpress method" and the second part by the "offset method".

Still other differences are apparent. Page numbers are skipped in Part I—rather than the continuous page numbering system which has been offered in past years. The special committee which planned our SOCIETY OF PETROLEUM ENGINEERS JOURNAL felt that the TRANSACTIONS volume is a summation of our monthly and quarterly publications, and that it is more important for a simple numbering system to be used in those periodicals than it is in this one. Consequently, the double numbering system has been eliminated in "JPT" this year. To lessen the confusion in the 1961 volume, footnotes have been provided immediately after each skip to indicate the pages which have been intentionally omitted.

Another "first" in this volume is a listing on page 308 of Part II of "Available Papers Not Published by the Society of Petroleum Engineers". Space does not permit the SPE to print all papers that are presented before our meetings, and this list is designed to make known the names of papers that are available from the authors. The list is not all inclusive, for some authors stated a preference that we not include their papers in this record.

Turning to other SPE matters, we have had a healthy year financially as our income and expense have balanced at approximately one-half million dollars. This money is used to run our book publishing business, our magazine publishing business, our selling of advertising and our handling of some rather large conventions. Through new innovations carried out this year we have further improved the management of our Society's business activities and funds.

The most serious problem of the year has been the continued loss of members. After years of dynamic growth we have slowed to the point where our new members gained during 1961 barely offset our losses for the year. We are taking steps to encourage our members to continue their affiliation and we hope that this trend can be reversed in 1962.

A highlight of the year was the Fall Meeting program of some 100 papers, by far the largest in our history. Included in this program was a special joint symposium of SPE and the American Institute of Chemical Engineers. Special attention was given at this meeting to natural gas engineering, a growing and most important part of our technology.

As evidenced by the improvements in this TRANSACTIONS volume, and the introduction of SOCIETY OF PETROLEUM ENGINEERS JOURNAL, the SPE is dedicated to progress. Each year brings innovations which are intended to increase the value of the Society to its members. We firmly believe that the Society will continue to grow and prosper as long as we are willing to change and adjust to meet the needs of our members.

EARL M. KIPP, President
Society of Petroleum Engineers of AIME, 1961

OFFICERS AND STAFF OF THE AIME

(For the Year Ending February, 1962)

PRESIDENT and DIRECTOR

R. R. McNaughton

VICE-PRESIDENTS and DIRECTORS

John S. Bell
A. B. Cummins
Wayne E. Glenn
Carleton C. Long
J. S. Smart, Jr.
J. W. Woomer

DIRECTORS

J. B. Austin
Herbert F. Beardmore
John Chipman
Richard C. Cole
R. H. Feierabend
K. L. Fetters
Robert B. Gilmore
James C. Gray
Earl M. Kipp
Richard A. Morse
W. B. Stephenson
C. L. Wilson

DIRECTOR, TREASURER, and CONTROLLER

George I. Brigden

STAFF OF THE INSTITUTE

GENERAL SECRETARY

E. O. Kirkendall

ASSISTANT SECRETARIES

Joe B. Alford
H. Newell Appleton
John C. Fox
Clifford J. Hicks
R. W. Shearman

ASSISTANT TREASURER

John F. Lynch

STAFF OF SOCIETY OF PETROLEUM ENGINEERS IN DALLAS

Joe B. Alford
EXECUTIVE SECRETARY

R. W. Taylor
EDITOR, *JOURNAL OF PETROLEUM TECHNOLOGY*

Maurice D. Bratt
ADVERTISING MANAGER, *JOURNAL OF PETROLEUM TECHNOLOGY*

David L. Riley
ASSOCIATE EDITOR, *JOURNAL OF PETROLEUM TECHNOLOGY*

Don A. Williams
ACTIVITIES MANAGER

Hattie Hight
ASSISTANT SECRETARY

John C. Cargile
BUSINESS MANAGER

Ann Gibson
ASSISTANT EDITOR, *JOURNAL OF PETROLEUM TECHNOLOGY*

SOCIETY OF PETROLEUM ENGINEERS OFFICERS AND COMMITTEE CHAIRMEN

(For the Year Ending February, 1962)

PRESIDENT

EARL M. KIPP
Standard Oil Co. of California
San Francisco, Calif.

VICE-PRESIDENTS

MILTON E. LOY
Schlumberger Well Surveying Corp.
New Orleans, La.

L. P. WHORTON
The Atlantic Refining Co.
Dallas, Tex.

TREASURER

EVERETT G. TROSTEL
DeGolyer & MacNaughton
Dallas, Tex.

BOARD OF DIRECTORS

EARL M. KIPP

MILTON E. LOY

EVERETT G. TROSTEL

L. P. WHORTON

R. A. MORSE
SPE President-Elect
Gulf Research & Development Co.
Pittsburgh, Pa.

R. L. HOSS
Consultant
Denver, Colo.

H. M. KRAUSE, JR.
Humble Oil & Refining Co.
Houston, Tex.

H. J. MAIERS
Mobil Oil Co. de Venezuela
Caracas, Venezuela

R. G. PARKER
Continental Oil Co.
Fort Worth, Tex.

WAYNE E. GLENN
SPE Past-President
Continental Oil Co.
Houston, Tex.

JOHN A. RODGERS
Gulf Oil Corp.
Columbia, Miss.

JAMES E. RUSSELL
Russell Engineering
Abilene, Tex.

ROY H. SMITH
Pan American International Oil Co.
New York, N. Y.

HAL M. STANIER
Sunray Mid-Continent Oil Co.
Bakersfield, Calif.

SIDNEY B. RICHARDS
Pan American Petroleum Corp.
Calgary, Alta., Canada

COMMITTEE CHAIRMEN

ADMISSIONS

B. M. GOTTLIEB
Sun Oil Co.
Dallas, Tex.

ADVERTISING AND EXHIBITS

BERNARD F. KLEIN
Ralph M. Parsons Co.
Los Angeles, Calif.

AIChE-SPE JOINT SYMPOSIA

V. J. BERRY, JR.
Sinclair Research, Inc.
Tulsa, Okla.

CARLL AWARD

T. A. ATKINSON
Douglas Oil Co. of California
Los Angeles, Calif.

CERTIFICATE OF SERVICE

CLAUDE R. HOCOTT
Humble Oil & Refining Co.
Houston, Tex.

DISTINGUISHED LECTURER

RAY S. OUSTERHOUT
Dowell Div. of The Dow Chemical Co.
Dallas, Tex.

EDUCATION

E. T. GUERRERO
U. of Tulsa
Tulsa, Okla.

FERGUSON MEDAL

CHARLES F. WEINAUG
U. of Kansas
Lawrence, Kans.

GENERAL EDITORIAL

GENE L. SCHEIRMAN
Shell Oil Co.
Houston, Tex.

LUCAS MEDAL

CHARLES H. PISHNY
Pishny & Atkinson
Fort Worth, Tex.

MEMBERSHIP

H. A. NEDOM
Amerada Petroleum Corp.
Tulsa, Okla.

NOMINATING

WAYNE E. GLENN
Continental Oil Co.
Houston, Tex.

PRODUCTION REVIEW

GEORGE ALLMAN, JR.
National Bank of Commerce
Houston, Tex.

PROGRAM

T. M. GEFFEN
Pan American Petroleum Corp.
Tulsa, Okla.

TRANSACTIONS EDITORIAL

H. J. RAMEY, JR.
Mobil Oil Co.
Los Angeles, Calif.

CONTENTS

1961 Society of Petroleum Engineers Transactions Editorial Committee ii

Foreword by Earl M. Kipp iii

Officers and Staff of AIME iv

Society of Petroleum Engineers Officers and Committee Chairmen v

The John Franklin Carll Award ix

The Anthony F. Lucas Medal x

The Cedric K. Ferguson Medal xi

Society of Petroleum Engineers Certificate of Service xii

Local Section Officers for 1961 xiii

Index, Petroleum Transactions, Volume 222 . . . . . II-300

Available Papers Not Published by the Society of Petroleum Engineers II-308

TECHNICAL PAPERS

(This volume is divided into two parts: Part I reprinted from Journal of Petroleum Technology *and Part II reprinted from* Society of Petroleum Engineers Journal. *Papers listed here have a part number designation preceding the paper number.)*

DRILLING—EQUIPMENT, METHODS AND MATERIALS

Laboratory Drilling Performance of the Full-Scale Rock Bit by D. S. Rowley, R. J. Howe and F. H. Deily I-71

Maximum Permissible Dog-Legs in Rotary Boreholes by A. Lubinski I-175

Stresses Caused by Bit Loading at the Center of the Hole by J. B. Cheatham, Jr., and J. C. Wilhoit, Jr. II-177

Simplified Analysis Aids in Optimizing Drilling Factors for Minimum Cost by H. W. R. Wardlaw . I-475

Theory of Formation Cutting Using the Sand Erosion Process by R. W. Brown and J. L. Loper . . I-483

Experimental Stress Analysis of Tool Joints by J. F. Gormley I-496

Some Effects of Size Distribution on Particle Bridging in Lost Circulation and Filtration Tests by C. Gatlin and C. E. Nemir I-575

Wellbore Pressure Surges Produced by Pipe Movement by J. A. Burkhardt I-595

LOGGING AND LOG INTERPRETATION

A Sonic Method for Analyzing the Quality of Cementation of Borehole Casings by M. Grosmangin, F. P. Kokesh and P. Majani I-165

Velocity-Log Interpretation: Effect of Rock Bulk Compressibility by J. Geertsma II-235

The Significance of Particle Shape in Formation Resistivity Factor—Porosity Relationships by E. R. Atkins, Jr. and G. H. Smith I-285

An Electrodeless System for Measuring Electric Logging Parameters on Core and Mud Samples by I. Fatt I-292

Induced Nuclear Reaction Logging by W. A. Hoyer I-797

Further Discussion of the Significance of Particle Shape in Formation Resistivity Factor-Porosity Relationships by G. H. F. Gardner I-1057

The Effect of Coil Design on the Performance of the Induction Log by W. C. Duesterhoeft, Jr., R. E. Hartline and H. S. Thomsen I-1137

NATURAL GAS TECHNOLOGY

Nonequilibrium Gas Displacement Calculations by H. D. Attra II-130

Multiple Liquid Phases in a Natural-Gas System by L. Stroud, W. E. DeVaney and J. E. Miller . II-137

An Approximate Method for Computing Nonsteady-State Flow of Gases in Porous Media by L. G. Jones II-264

Study of Gas Reservoirs Subject to Water Drive on Electronic Differential Analyzer by H. D. Yoo, D. L. Katz and M. R. Tek II-287

Natural Gas Hydrates at Pressures to 10,000 psia by H. O. McLeod, Jr. and J. M. Campbell . . I-590

Equilibrium Ratios of Water in the Water-Triethylene Glycol-Natural Gas System by F. R. Scauzillo . I-697

Multiphase Flow of Water, Oil and Natural Gas Through Vertical Flow Strings by M. R. Tek . . I-1029

Unsteady-State Gas Flow Into Gas Wells by R. V. Smith I-1151

OPERATIONS RESEARCH

Application of Optimizing Techniques for Studying Field Producing Operations by H. D. Attra, W. B. Wise and W. M. Black I-82

PRODUCING—EQUIPMENT, METHODS AND MATERIALS

The Effect of Oil Production Rate Upon Performance of Wells Producing from More Than One Horizon by W. Tempelaar-Lietz II-26

Application of Optimizing Techniques for Studying Field Producing Operations by H. D. Attra, W. B. Wise and W. M. Black I-82
Sand Concentration for Maximum Fracture Capacity by A. Romero-Juarez II-119
A Sonic Method for Analyzing the Quality of Cementation of Borehole Casings by M. Grosmangin, F. P. Kokesh and P. Majani I-165
The Effect of Restricted Fluid Entry on Well Productivity by F. Brons and V. E. Marting . . . I-172
Fractures and Craters Produced in Sandstone by High-Velocity Projectiles by J. S. Rinehart and W. C. Maurer I-273
Improved Compositions for Cementing Wells with Extreme Temperatures by G. W. Ostroot and W. A. Walker I-277
Hydraulic Fracture—Field Tests to Determine Areal Extent and Orientation by J. J. Reynolds, J. B. Scott, J. L. Popham and H. F. Coffer I-371
The Evaluation of Vertical-Lift Performance in Producing Wells by R. V. McAfee I-391
Investigation of Abrasive-Laden-Fluid Method for Perforation and Fracture Initiation by F. C. Pittman, D. W. Harriman and J. C. St. John I-489
Propping Fractures with Aluminum Particles by L. C. Kern, T. K. Perkins and R. W. Wyant . . I-583
Use of Oxygen Scavengers to Control External Corrosion of Oil-String Casing by F. W. Schremp, J. W. Chittum and T. S. Arczynski I-703
Improved Bentonite Cements Through Partial Acceleration by H. J. Beach I-923
Widths of Hydraulic Fractures by T. K. Perkins and L. R. Kern I-937
Further Discussion of Fractures and Craters Produced in Sandstone by High-Velocity Projectiles by A. A. Venghiattis I-955
The Calculation of Pressure Gradients in High-Rate Flowing Wells by P. B. Baxendell and R. Thomas I-1023
Simultaneous Flow of Gas and Liquid as Encountered in Well Tubing by N. C. J. Ros I-1037
The Effect of Horizontal Hydraulic Fracturing on Well Performance by J. H. Hartsock and J. E. Warren I-1050

RESERVOIR ENGINEERING EQUIPMENT

Constant-Pressure Gas Porosimeter by A. H. Heim I-87
An Electrodeless System for Measuring Electric Logging Parameters on Core and Mud Samples by I. Fatt I-292
The Use of Alternating Flow to Characterize Porous Media Having Storage Pores by C. R. Stewart, A. Lubinski and K. A. Blenkarn I-383

RESERVOIR ENGINEERING—GENERAL

Stability Theory and Its Use to Optimize Solvent Recovery of Oil by R. L. Perrine II-9
The Development of Stability Theory for Miscible Liquid-Liquid Displacement by R. L. Perrine . . II-17
The Effect of Oil Production Rate Upon Performance of Wells Producing from More Than One Horizon by W. Tempelaar-Lietz II-26
Linear Water Flood with Gravity and Capillary Effects by S. A. Hovanessian and F. J. Fayers . . II-32
A Study of the Behavior of Bounded Reservoirs Composed of Stratified Layers by H. C. Lefkovits, P. Hazebroek, E. E. Allen and C. S. Matthews II-43
An Imbibition Model—Its Application to Flow Behavior and the Prediction of Oil Recovery by J. Naar and J. H. Henderson II-61
Microbial Flora in a Number of Oilfield Water-Injection Systems by V. Carlson, E. O. Bennett and J. A. Rowe, Jr. II-71
Injection Rates—The Effect of Mobility Ratio, Area Swept, and Pattern by J. C. Deppe . . . II-81
Application of Optimizing Techniques for Studying Field Producing Operations by H. D. Attra, W. B. Wise and W. M. Black I-82
A Scale-Model Study of Bottom-Water Drives by D. H. Henley, W. W. Owens and F. F. Craig, Jr. . I-90
Analysis of Gas-Cap or Dissolved-Gas Drive Reservoirs by H. L. Stone and A. O. Garder, Jr. . . II-92
Effect of Vertical Fractures on Reservoir Behavior—Incompressible-Fluid Case by M. Prats . . . II-105
A Potentiometric Study of the Effects of Mobility Ratio on Reservoir Flow Pattern by H. B. Bradley, J. P. Heller and A. S. Odeh II-125
Nonequilibrium Gas Displacement Calculations by H. D. Attra II-130
Multiple Liquid Phases in a Natural-Gas System by L. Stroud, W. E. DeVaney and J. E. Miller . II-137
The Calculated Performance of Solution-Gas-Drive Reservoirs by J. S. Levine and M. Prats II-142
Flow in Heterogeneous Porous Media by J. E. Warren and H. S. Price II-153
Pressure Drop in a Composite Reservoir by T. L. Loucks and E. T. Guerrero II-170
The Effect of Restricted Fluid Entry on Well Productivity by F. Brons and V. E. Marting . . . I-172
A Numerical Solution to the Unsteady-State Partial-Water-Drive Reservoir Performance Problem by W. L. Henson, P. L. Wearden and J. D. Rice II-184
Further Discussion on Experiments on Mixing During Miscible Displacement in Porous Media by J. P. Heller II-213
A Study of Flow in Stratified Reservoirs by Use of the Thermal Analogy by C. H. Pickering, N. T. Cotman and P. B. Crawford II-215
Pressure Studies in Bounded Reservoirs by S. A. Hovanessian II-223
Correlation of Surface and Interfacial Tension of Light Hydrocarbons in the Critical Region by E. W. Hough and G. L. Stegemeier II-259
An Approximate Method for Computing Nonsteady-State Flow of Gases in Porous Media by L. G. Jones II-264
An Approximate Method for Determining Areal Sweep Efficiency and Flow Capacity in Formations with Anisotropic Permeability by M. Mortada and G. W. Nabor II-277
Study of Gas Reservoirs Subject to Water Drive on Electronic Differential Analyzer by H. D. Yoo, D. L. Katz and M. R. Tek II-287
Further Discussion on the Development of Stability Theory for Miscible Liquid-Liquid Displacement by H. D. Outmans II-298
The Influence of Production Rate, Permeability Variation and Well Spacing on Solution-Gas-Drive Performance by G. J. Heuer, Jr., G. C. Clark and J. N. Dew I-469

Effects of Reservoir Environment on Water-Oil Displacement by J. R. Kyte, V. O. Naumann and C. C. Mattax I-579
Natural Gas Hydrates at Pressures to 10,000 psia by H. O. McLeod, Jr., and J. M. Campbell . . I-590
Determining Areal Permeability Distribution by Calculations by W. D. Kruger I-691
Equilibrium Ratios of Water in the Water-Triethylene Glycol-Natural Gas System by F. R. Scauzillo I-697
The Linear Displacement of Oil from Porous Media by Enriched Gas by H. J. Welge, E. F. Johnson, S. P. Ewing, Jr. and F. H. Brinkman I-787
A Simple Method for Correcting Spot Pressure Readings by F. Brons and W. C. Miller . . . I-803
Effect of Bank Size on Oil Recovery in the High-Pressure Gas-Driven LPG-Bank Process by J. W. Lacey, J. E. Faris and F. H. Brinkman I-806
Analysis of Gravity Drainage by H. N. Hall I-927
The Calculation of Pressure Gradients in High-Rate Flowing Wells by P. B. Baxendell and R. Thomas I-1023
Multiphase Flow of Water, Oil and Natural Gas Through Vertical Flow Strings by M. R. Tek . . I-1029
Simultaneous Flow of Gas and Liquid as Encountered in Well Tubing by N. C. J. Ros I-1037
Calculation of Differential Gas Liberation and Shrinkage by C. F. Weinaug I-1135
Unsteady-State Gas Flow Into Gas Wells by R. V. Smith I-1151

RESERVOIR ENGINEERING—LABORATORY RESEARCH

Experiments on Mixing During Miscible Displacement in Porous Media by W. E. Brigham, P. W. Reed and J. N. Dew II-1
Effect of Viscosity on Relative Permeability by J. Downie and F. E. Crane II-59
Microbial Flora in a Number of Oilfield Water-Injection Systems by V. Carlson, E. O. Bennett, and J. A. Rowe, Jr. II-71
A Potentiometric Study of the Effects of Mobility Ratio on Reservoir Flow Pattern by H. B. Bradley, J. P. Heller and A. S. Odeh II-125
Mechanism of Alcohol Displacement of Oil from Porous Media by J. J. Taber, I. S. K. Kamath and R. L. Reed II-195
A Study of Flow in Stratified Reservoirs by Use of the Thermal Analogy by C. H. Pickering, N. T. Cotman and P. B. Crawford II-215
Cellar Oil by M. H. Gaskell and D. C. Lindley I-377
Laboratory Studies of Oil Recovery by Injection by B. T. Willman, V. V. Valleroy, G. W. Runberg, A. J. Cornelius and L. W. Powers I-681
Model Studies of Oil Displacement from Thin Sands by Vertical Water Influx from Adjacent Shales by J. E. Bobek and P. T. Bail I-950

RESERVOIR ROCK CHARACTERISTICS

Thermal Conductivities of Porous Rocks Filled with Stagnant Fluid by D. Kunii and J. M. Smith . . II-37
Effect of Viscosity on Relative Permeability by J. Downie and F. E. Crane II-59
Constant-Pressure Gas Porosimeter by A. H. Heim I-87
Deflocculation of Fractionated Montmorillonite by Sodium Polyphosphates by F. W. Jessen and F. H. Turan II-229
Velocity-Log Interpretation: Effect of Rock Bulk Compressibility by J. Geertsma II-235
Additional Thermal Data for Porous Rocks—Thermal Expansion and Heat of Reaction by W. H. Somerton and M. A. Selim II-249
Three-Phase Imbibition Relative Permeability by J. Naar and R. J. Wygal II-254
The Significance of Particle Shape in Formation Resistivity Factor—Porosity Relationships by E. R. Atkins, Jr. and G. H. Smith I-285
The Use of Alternating Flow to Characterize Porous Media Having Storage Pores by C. R. Stewart, A. Lubinski and K. A. Blenkarn I-383
Further Discussion of the Significance of Particle Shape in Formation Resistivity Factor—Porosity Relationships by G. H. F. Gardner I-1057
Large-Scale Laboratory Investigation of Sand Consolidation Techniques by W. F. Hower and W. Brown I-1221
Characteristics of the Delaware Formation by R. E. Jenkins I-1230

SECONDARY RECOVERY AND PRESSURE MAINTENANCE

Experiments on Mixing During Miscible Displacement in Porous Media by W. E. Brigham, P. W. Reed and J. N. Dew II-1
Stability Theory and Its Use to Optimize Solvent Recovery of Oil by R. L. Perrine II-9
The Development of Stability Theory for Miscible Liquid-Liquid Displacement by R. L. Perrine . . II-17
Linear Water Flood with Gravity and Capillary Effects by S. A. Hovanessian and F. J. Fayers . . II-32
Microbial Flora in a Number of Oilfield Water-Injection Systems by V. Carlson, E. O. Bennett and J. A. Rowe, Jr. II-71
Injection Rates—The Effect of Mobility Ratio, Area Swept, and Pattern by J. C. Deppe II-81
Mechanism of Alcohol Displacement of Oil from Porous Media by J. J. Taber, I. S. K. Kamath and R. L. Reed II-195
Further Discussion on Experiments on Mixing During Miscible Displacement in Porous Media by J. P. Heller II-213
Pressure Studies in Bounded Reservoirs by S. A. Hovanessian II-223
Further Discussion on the Development of Stability Theory for Miscible Liquid-Liquid Displacement by H. D. Outmans II-298
Laboratory Studies of Oil Recovery by Injection by B. T. Willman, V. V. Valleroy, G. W. Runberg, A. J. Cornelius and L. W. Powers I-681
The Linear Displacement of Oil from Porous Media by Enriched Gas by H. J. Welge, E. F. Johnson, S. P. Ewing, Jr. and F. H. Brinkman I-787
Effect of Bank Size on Oil Recovery in the High-Pressure Gas-Driven LPG-Bank Process by J. W. Lacey, J. E. Faris and F. H. Brinkman I-806

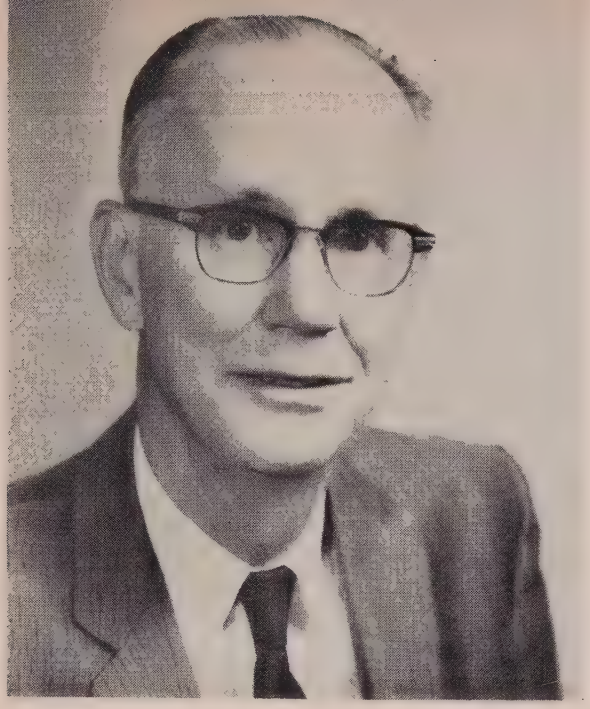

HALLAN N. MARSH

John Franklin Carll Award, 1961

"In recognition of his contributions to the art of petroleum engineering, his advancement of the professional status of the engineer in oil-producing operations, and his inspirational teaching and development of junior engineers—all accomplished through a dedicated adherence to the simple basic concepts of science, economics and professional integrity."

THE JOHN FRANKLIN CARLL AWARD

Established in 1956 and first presented in 1957, the John Franklin Carll Award is awarded "to recognize distinguished achievement in or contributions to petroleum engineering". The medal commemorates John Franklin Carll (1828-1904) whose ideas and writings first expressed principles of petroleum engineering which are now considered commonplace. Herbert C. Otis, Sr. was the first recipient of the award in 1957; Gen. E. O. Thompson in 1958; Eugene A. Stephenson, 1959; and Ralph J. Schilthuis, 1960. Members of the 1961 John Franklin Carll Award Committee are T. A. Atkinson, Chairman, Jack H. Beesley, Carrol M. Beeson, Lincoln F. Elkins, B. L. Francis and Robert H. McLemore. SPE President Earl M. Kipp is an ex officio member of the committee.

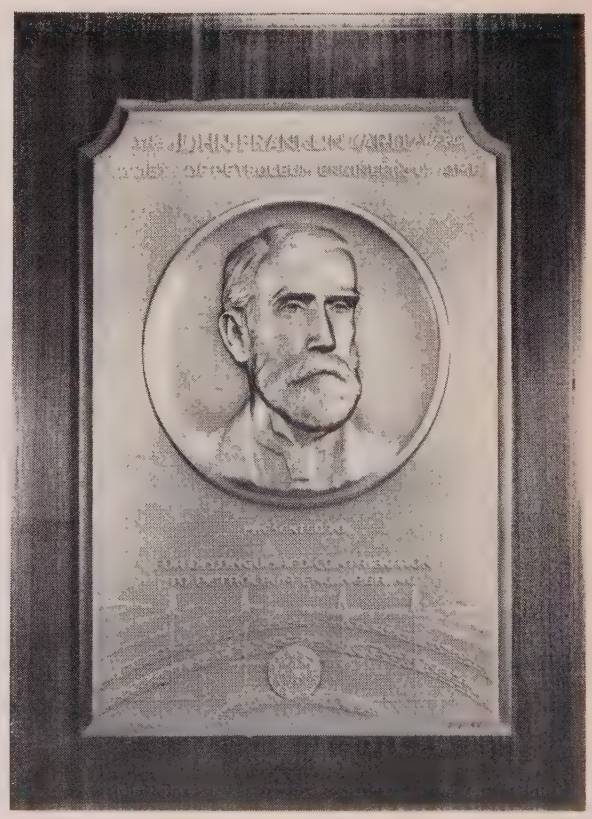

E. O. BENNETT
Lucas Medalist, 1961

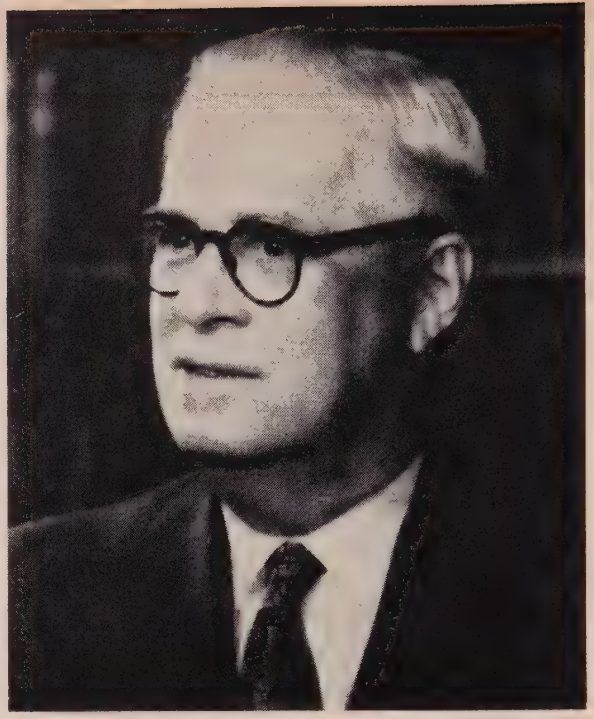

"For fostering the development of gas pressure maintenance in oil reservoirs; supervising the first field stabilization of high gravity crude oil; and developing the techniques of multiple zone completion of wells. For his pioneering in the design of high pressure gas cycling plants resulting in increased recovery of condensate from reservoirs."

THE ANTHONY F. LUCAS MEDAL

In 1936 the Institute established the Anthony F. Lucas Gold Medal, to be awarded from time to time "for distinguished achievement in improving the technique and practice of finding and producing petroleum". These awards are sponsored by the Society of Petroleum Engineers of AIME. Members of the Committee of Award of the Lucas Medal are: Charles H. Pishny, Chairman, Earl M. Kipp, Everett G. Trostel, L. B. Meaders, Gail F. Moulton, E. N. Van Duzee, E. C. Babson, George R. Gray, G. M. Stearns, Wilbur F. Cloud, John P. Hammond, Howard C. Pyle. Members Ex Officiis are: Marling J. Ankeny, USBM director; Frank M. Porter, API president; Ben H. Parker, AAPG president; and R. R. McNaughton, AIME president.

MEDALS AWARDED

J. Edgar Pew, 1937
Henry L. Doherty, 1938
E. DeGolyer, 1940
Conrad (Posthumously) and Marcel Schlumberger, 1941
John Robert Suman, 1943
Charles Van Ormer Millikan, 1944
James Ogier Lewis, 1946
William Noble Lacey, 1947
Wallace Everette Pratt, 1948
William Embry Wrather, 1950
Morris Muskat, 1953
Bruce H. Sage, 1954
Stuart E. Buckley, 1956
John Edward Brantly, 1957
Carl E. Reistle, Jr., 1958
John T. Hayward, 1959
A. C. Rubel, 1960

FRED H. BRINKMAN

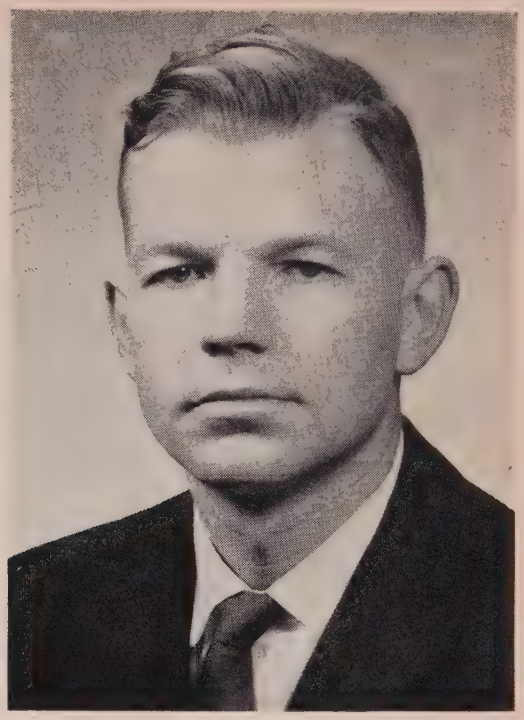

THE CEDRIC K. FERGUSON MEDAL

Fred H. Brinkman is the recipient of the 1961 Cedric K. Ferguson Medal. He was selected to receive this award for his paper "Equilibrium Ratios for Reservoir Studies by a Calculative Method", published in part in the Dec., 1960, issue of JOURNAL OF PETROLEUM TECHNOLOGY and appearing in the 1960 TRANSACTIONS volume. A co-author of this paper is J. N. Sicking, Jersey Production Research Co., an associate member of AIME. This was the seventh presentation of the Ferguson Medal, first awarded posthumously to Cedric K. Ferguson in 1954. Co-recipients in 1956 were William M. Campbell and the late John L. Martin. W. O. Brown received the medal in 1957. Jim Douglas, Jr., Philip M. Blair and R. J. Wagner were joint recipients in 1958. Henry J. Ramey, Jr., received the medal in 1959, and Charles B. Ammann, 1960.

The purpose of the medal is to recognize the writing of an outstanding technical paper by a young member or members (under 33 years of age) of the profession.

The medal is presented annually unless waived for lack of a worthy candidate. Members of the 1961 Cedric K. Ferguson Medal Committee are: Charles F. Weinaug, Chairman, William Hurst, and Joe S. Levine.

HAROLD F. WINHAM

"In recognition of his outstanding contribution in the field of student relations through 20 years of devoted service as student counselor and chairman of the Student Relations Committee for the Delta Section of AIME."

SOCIETY OF PETROLEUM ENGINEERS CERTIFICATE OF SERVICE

Established in 1948, the Society of Petroleum Engineers Certificate of Service is awarded to recognize and show appreciation for exceptional services of Members of the Society. Members of the 1961 Certificate of Service Award Committee were: Claude R. Hocott, Chairman, Fred L. Oliver and Burton Atkinson.

CERTIFICATES AWARDED

Eugene A. Stephenson, 1948
Fred B. Plummer, 1948 (Posthumously)
Earl Oliver, 1948
F. Julius Fohs, 1949
Joseph B. Umpleby, 1949
Stuart E. Buckley, 1952
Francis A. Collins, 1956
John E. Sherborne, 1959
Lloyd E. Elkins, 1959
Alfred H. Bell, 1960
Lawrence W. Chasteen, 1960
James Terry Duce, 1960
Herbert F. Beardmore, 1960
Raymond M. Larsen, 1960

LOCAL SECTION OFFICERS FOR 1961

APPALACHIAN PETROLEUM SECTION

Robert H. Edele, *Chairman*, United Carbon Co., Charleston, W. Va.; Robert Vutech, *Vice-Chairman*, Dowell, Charleston; Robert Tullis, *Vice-Chairman*, United Fuel Gas Co., Charleston; Frederick T. Solomon, *Secretary-Treasurer*, United Fuel Gas Co., Charleston.

BALCONES SECTION

Frank W. Jessen, *Chairman*, U. of Texas, Austin, Tex.; Gilbert M. Andreen, *Vice-Chairman*, Texstar Petroleum Co., San Antonio, Tex.; Lloyd N. Johnson, *Vice-Chairman*, Texas Petroleum Research Committee, Austin; W. C. Vercellino, *Secretary-Treasurer*, Lane-Wells Co., San Antonio.

BIG HORN BASIN SUBSECTION (WYO.)

B. E. Yester, *Chairman*, The Ohio Oil Co., Cody, Wyo.; Robert J. Woodhall, *Vice-Chairman*, Pan American Petroleum Corp., Powell, Wyo.; Herbert A. Koch, *Vice-Chairman*, Petroleum Service Co., Inc., Worland, Wyo.; Dean Costello, *Secretary*, Continental Oil Co., Powell, Wyo.; Thomas W. DeLong, *Treasurer*, The Ohio Oil Co., Cody, Wyo.

BILLINGS PETROLEUM SECTION

George O. Ellis, *Chairman*, Schlumberger, Billings, Mont.; Robert L. Spottswood, *Vice-Chairman*, Shell Oil Co., Billings; Robert M. Watkins, *Vice-Chairman*, Oil & Gas Conservation Committee, Billings; Joseph H. Bato, *Secretary-Treasurer*, McAlester Fuel Co., Billings.

CALGARY CIM-AIME SECTION

John J. Justen, *Chairman*, Mobil Oil of Canada, Calgary, Alta.; Al McLatchie, *Vice-Chairman*, Imperial Oil, Ltd., Calgary; Charles C. Fry, *Vice-Chairman*, Hudson's Bay Oil & Gas Co., Ltd., Calgary; George Welsh, *Secretary-Treasurer*, Dowell of Canada, Ltd., Calgary.

CALIFORNIA COASTAL SECTION

Kenneth Nugent, *Chairman*, McCullough Tool Co., Ventura, Calif.; Kurt F. Pilgram, *Vice-Chairman*, Shell Oil Co., Ventura; T. W. Simmons, *Secretary*, Texaco, Inc., Ventura; Gay Rieder, *Treasurer*, Welex, Inc., Ventura.

CARACAS SECTION

Harold L. Siegele, *Chairman*, Creole Petroleum Corp., Caracas, Venezuela; Harry D. Brown, *Vice-Chairman*, Schlumberger Surenco, Caracas; Robert E. Finken, *Vice-Chairman*, Phillips Petroleum Co., Caracas; G. V. Atkinson, *Secretary*, Mobil Oil Co. de Venezuela, Caracas; William A. Gatenby, *Treasurer*, Texas Petroleum Co., Caracas.

COASTAL BEND SECTION

James K. Evans, *Chairman*, Kaffie Lumber & Bulk Barites, Inc., Bay City, Tex.; F. L. Nelson, *Vice-Chairman*, Pan American Petroleum Corp., Bay City; Jimmy Powers, *Vice-Chairman*, Dowell, Bay City; Herbert H. Hill, *Secretary-Treasurer*, Texaco, Inc., El Campo, Tex.

COLORADO-NEBRASKA SUBSECTION (DENVER)

H. N. Rhodes, *Chairman*, Nebraska Oil & Gas Conservation Commission, Sidney, Nebr.; Bill Garber, *Vice-Chairman*, Nebraska Oil & Gas Conservation Commission, Sidney; Allen R. Livingston, *Vice-Chairman*, Ohio Oil Co., Sidney; Lloyd J. Harbert, *Secretary-Treasurer*, Continental Oil Co., Fort Morgan, Colo.

DALLAS SECTION

R. E. Vickrey, *Chairman*, Sun Oil Co., Dallas; Tom G. Calhoun, II, *Vice-Chairman*, DeGolyer & MacNaughton, Dallas; T. L. Kennerly, *Vice-Chairman*, Core Labs., Inc., Dallas; Sid H. Davis, *Secretary*, Atlantic Refining Co., Dallas; H. Edison Ellis, *Treasurer*, Republic National Bank, Dallas.

DELTA SECTION

George J. Decker, *Chairman*, Schlumberger, New Orleans, La.; Walter W. Poimboeuf, *Vice-Chairman*, Continental Oil Co., Harvey, La.; Charles A. Langner, *Vice-Chairman*, Humble Oil & Refining Co., New Orleans; Richard J. Goeken, *Secretary*, Gulf Oil Corp., New Orleans; John P. Everett, *Treasurer*, Hibernia National Bank, New Orleans.

DENVER PETROLEUM SECTION

Fred H. Poettmann, *Chairman*, Ohio Oil Co., Littleton, Colo.; William R. Smith, *Vice-Chairman*, Colorado State Oil & Gas Conservation Commission, Denver, Colo.; James C. Roe, *Vice-Chairman*, Lufkin Foundry & Machine Co., Denver; James A. Mullinax, *Secretary-Treasurer*, Schlumberger, Denver.

EAST KENTUCKY SUBSECTION

Phillip Jenkins, *Chairman*, Kentucky West Virginia Gas Co., Paintsville, Ky.; George Thomas, *Vice-Chairman*, United Fuel Gas Co., Paintsville; J. R. Price, *Vice-Chairman*, Dowell, Paintsville; Jerry V. George, *Secretary-Treasurer*, Texas-Canadian Oil Corp., Paintsville.

EAST TEXAS SECTION

C. M. Browning, *Chairman*, Lane-Wells, Tyler, Tex.; C. R. Olson, *Vice-Chairman*, Ohio Oil Co., Price, Tex.; B. J. Ingram, *Secretary-Treasurer*, Humble Oil & Refining Co., Hawkins, Tex.

EASTERN VENEZUELA SECTION

N. Howard Jorgensen, *Chairman*, Mobil Oil Co. de Venezuela, Caracas; Robert T. Mish, *Vice-Chairman*, Mene Grande Oil Co., Barcelona; John Bjordammen, *Vice-Chairman*, Texas Petroleum Co., Caracas; Jose Pernia, *Vice-Chairman*, Ministerio de Minas e Hidrocarburos, San Tome; Jack C. Thompson, *Secretary*, Dowell, El Tigre; Julio Perez-M, *Treasurer*, Mobil Oil Co. de Venezuela, Caracas.

EDMONTON CIM-AIME SECTION

A. E. Piper, *Chairman*, Pan American Petroleum Corp., Edmonton, Alta.; Bob Porteous, *Secretary*, Halliburton Co., Edmonton; Harry Webber, *Treasurer;* Oil & Gas Conservation Board, Edmonton.

EVANGELINE SECTION

C. E. Lohn, *Chairman*, Halliburton Co., Lafayette, La.; Earl F. Thomas, *Vice-Chairman*, Sun Oil Co., Lafayette; John T. Douglas, *Vice-Chairman*, Schlumberger, Lafayette; J. C. Landry, *Vice-Chairman*, Tuboscope Co., Lafayette; Don R. Atteberry, *Secretary-Treasurer*, Midwest Oil Corp., Lafayette.

FORT WORTH SECTION

Fred S. Reynolds, *Chairman*, Ralph H. Cummins Co., Fort Worth; Robert H. Vick, *Vice-Chairman*, Ambassador Oil Corp., Fort Worth; Charles J. Hoffman, *Vice-Chairman*, Champlin Oil & Refining, Fort Worth; Robert D. Cocanower, *Vice-Chairman*, Western Co., Fort Worth; Robert D. Lane, *Vice-Chairman*, Pan American Petroleum Corp., Fort Worth; Stanley G. Britton, *Secretary*, LaGorce Oil Co., Fort Worth.

FOUR CORNERS SECTION

Urban E. Johnson, *Chairman*, Texaco, Inc., Farmington, N. M.; Hal M. Stierwalt, *Vice-Chairman*, Sunray Mid-Continent Oil Co., Farmington; Alton R. Kendrick, *Vice-Chairman*, N. M. Oil Conservation Commission, Aztec, N. M.; Harold L. Kendrick, *Secretary-Treasurer*, El Paso Natural Gas Co., Farmington.

GOLDEN GATE SUBSECTION	George C. Wishart, *Chairman*, Honolulu Oil Corp., San Francisco, Calif.; Frank G. Miller, *Vice-Chairman*, Stanford U. Stanford, Calif.; Ralph V. Higgins, *Secretary-Treasurer*, USBM, San Francisco.
GREAT BEND SECTION	Edgar B. Krider, *Chairman*, National Cooperative Refining Association, Great Bend, Kans.; John E. McLeland, *Vice-Chairman*, Petroleum, Inc., Great Bend; Robert L. Waller, *Vice-Chairman*, Pan American Petroleum Corp., Ellinwood, Kans.; Charles H. Peterson, *Secretary-Treasurer*, Sunray Mid-Continent Oil Co., Great Bend.
GULF COAST SECTION	W. M. McCardell, *Chairman*, Humble, Houston, Tex.; Jack McWilliams, *Vice-Chairman*, Pan American Petroleum Corp., Houston; George Allman, Jr., *Secretary-Treasurer*, National Bank of Commerce of Houston, Houston.
HOBBS PETROLEUM SECTION	C. M. Bumpass, *Chairman*, Gulf Oil, Hobbs, N. M.; E. H. Furrey, *Vice-Chairman*, Cities Service, Hobbs; J. W. Meek, *Vice-Chairman*, Pan American Petroleum Corp., Hobbs; B. D. Ford, *Secretary-Treasurer*, Tidewater, Hobbs.
HUGOTON SECTION	Jerry L. Jenkins, *Chairman*, United Producing Co., Inc., Liberal, Kans.; E. N. Bennett, *Vice-Chairman*, Pan American Petroleum Corp., Liberal; Leslie E. Goodwin, *Vice-Chairman*, Panhandle Eastern Pipeline Co., Liberal; Barry C. Rist, Jr., *Secretary-Treasurer*, Panhandle Eastern Pipeline Co., Liberal.
ILLINOIS BASIN SECTION	Ray M. Dost, *Chairman*, Kingwood Oil Co., Mt. Vernon, Ill.; Joe A. McClure, *Vice-Chairman*, Dowell, Mt. Vernon; Bernard Podolsky, *Vice-Chairman*, petroleum engineer, Fairfield, Ill.; John W. Stephenson, *Secretary-Treasurer*, Tidewater, Robinson, Ill.
KANSAS SECTION	Tom G. Bush, *Chairman*, Lane-Wells Co., Wichita, Kans.;; R. S. Allison, *Vice-Chairman*, Kewanee Oil, Wichita; Frank Beach, *Vice-Chairman*, Cities Service Oil Co., El Dorado, Kans.; Carl W. Wilson, *Secretary*, Sunray Mid-Continent Oil Co., Wichita; Ed Blincoe, *Treasurer*, Texaco, Inc., Wichita.
LOS ANGELES BASIN SECTION	John I. Gates, *Chairman*, Shell Oil Co., Los Angeles, Calif.; Richard G. Crippen, *Vice-Chairman*, Texaco, Inc., Los Angeles; Edward H. Mayer, *Secretary*, Humble, Long Beach, Calif.; James T. Carriel, *Treasurer*, Signal Oil & Gas Co., Los Angeles.
LOU-ARK SECTION	James A. Latham, *Chairman*, Arkansas Fuel Oil Corp., Shreveport, La.; Richard M. Pitcher, *Vice-Chairman*, Carter Oil Co., Shreveport; James E. Carlton, Jr., *Vice-Chairman*, Magcobar, Shreveport; Loyle P. Miller, *Secretary-Treasurer*, Tennessee Gas & Oil Co., Shreveport.
MID-CONTINENT SECTION	H. A. Nedom, *Chairman*, Amerada Petroleum Corp., Tulsa, Okla.; Wayne E. Swearingen, *Vice-Chairman*, Swearingen Engineering Co., Tulsa; George C. Howard, *Vice-Chairman*, Pan American Petroleum Corp., Tulsa; Phillip L. Essley, Jr., *Secretary*, Skelly Oil Co., Tulsa; Brook D. Tarbel, *Treasurer*, Helmerich & Payne, Tulsa.
MISSISSIPPI SECTION	C. L. King, *Chairman*, Tri-State Tool, Laurel, Miss.; W. F. Ellis, *Vice-Chairman*, Union Producing Co., Jackson, Miss.; B. D. Meltzer, *Vice-Chairman*, California Co., Jackson; J. E. Vick, *Secretary-Treasurer*, Halliburton Co., Laurel, Miss.
THE NETHERLANDS SECTION	Elton P. Bresenham, *Chairman*, Aramco Overseas Co., The Hague; Dillard R. Thomas, *Vice-Chairman*, Reed Roller Bit, Leiden; C. R. Morgan, *Vice-Chairman*, Black, Sivalls & Bryson, The Hague; Bernard P. Planner, *Secretary-Treasurer*, The Hague.
NEW YORK PETROLEUM SECTION	Bryant C. Frihart, *Chairman*, Cities Service, New York City; Gerald E. Sherrod, *Vice-Chairman*, First National City Bank, New York City; Shannon L. Matheny, Jr., *Vice-Chairman*, Ideco, Inc., New York City; G. M. Mitchell, *Secretary*, Stone & Webster Service Corp., New York City; James W. Glanville, *Treasurer*, Lehman Bros., New York City.
NORTH TEXAS SECTION	Richard R. Newton, *Chairman*, Ryder-Scott Management Co., Wichita Falls, Tex.; Robert C. Thomas, *Vice-Chairman*, Tennessee Gas & Oil Co., Wichita Falls; Joe M. Foster, *Secretary*, Continental Oil Co., Wichita Falls; Ollie Blodgett, *Treasurer*, Pump Engineering, Wichita Falls.
NORTHERN OKLAHOMA SECTION	Henry F. Coffer, *Chairman*, Continental Oil Co., Ponca City, Okla.; Martin Felsenthal, *Vice-Chairman*, Continental Oil Co., Ponca City; Bill Edmiston, *Vice-Chairman*, Lane-Wells Co., Ponca City; Ted Cobb, *Secretary-Treasurer*, Continental Oil Co., Ponca City.
OKLAHOMA CITY SECTION	Robert W. Bashe, *Chairman*, Schlumberger, Oklahoma City; Homer G. Riley, *Vice-Chairman*, Pan American Petroleum Corp., Oklahoma City; Marvin Charles Respess, *Vice-Chairman*, The Western Co., Oklahoma City; Sidney D. Farrar, *Secretary*, Lone Star Producing Co., Oklahoma City; Carl House, *Treasurer*, Continental Oil Co., Oklahoma City.
PANHANDLE SECTION	Guy H. Tomlinson, Jr., *Chairman*, Colorado Interstate Gas Co., Amarillo, Tex.; Raymond D. Davidson, *Vice-Chairman*, Dowell, Amarillo; Edward M. McGuire, *Vice-Chairman*, Cities Service Petroleum, Pampa, Tex.; James C. Hamilton, *Secretary-Treasurer*, J. M. Huber Corp., Borger, Tex.
PERMIAN BASIN SECTION	William S. Davis, *Chairman*, Humble, Midland, Tex.; T. W. Kidd, *Vice-Chairman*, Gulf Oil Corp., Midland; Donald K. Lawrence, *Vice-Chairman*, Sun Oil Co., Odessa, Tex.; James F. Ormond, *Vice-Chairman*, Cardinal Chemical, Midland; Paul Crenshaw, *Secretary-Treasurer*, Dowell, Midland.
PITTSBURGH PETROLEUM SUBSECTION	David M. Ellington, *Chairman*, Manufacturers Light and Heat Co., Pittsburgh, Pa.; John L. Schweizer, *Vice-Chairman*, Gulf Oil Corp., Pittsburgh; James K. Gregg, *Vice-Chairman*, Sand Surveys, Inc., Apollo, Pa.; Tom L. Irby, *Secretary-Treasurer*, Gulf Research & Development Co., Pittsburgh.
ROSWELL PETROLEUM SECTION	John A. Queen, *Chairman*, Continental Oil Co., Roswell, N. M.; Vance Hendricks, *Vice-Chairman*, Gulf Oil Corp., Roswell; Vincent D. Foster, *Vice-Chairman*, Carper Drilling Co., Inc., Artesia, N. M.; R. A. Lowry, *Secretary-Treasurer*, Shell Oil Co., Roswell.

SAN JOAQUIN VALLEY SECTION

R. J. Fernandes, *Chairman*, Gulf Oil Corp of California, Bakersfield, Calif.; C. A. Champion, *Vice-Chairman*, Richfield Oil Corp., Bakersfield; K. J. Stracke, *Secretary*, Union Oil Corp., Bakersfield; W. G. Frailing, *Treasurer*, Standard Oil Co., Taft, Calif.

SAUDI ARABIA SECTION

Karl D. Romine, *Chairman*, Arabian American Oil Co., Dhahran, Saudi Arabia; J. P. Calligeros, *Vice-Chairman*, Aramco, Dhahran; S. F. Kiersznowski, *Vice-Chairman*, Aramco, Dhahran; H. P. Walter, *Secretary-Treasurer*, Aramco, Dhahran.

SNYDER SECTION

Bryan P. Dixon, *Chairman*, Standard Oil Co. of Texas, Snyder, Tex.; Jack D. Patchell, *Vice-Chairman*, Halliburton Co., Snyder; Cholly G. Howard, *Vice-Chairman*, McCullough Tool Co., Snyder; Joseph L. Black, Jr., *Secretary*, R. E. Smith Operator, Snyder; Eddie L. Epley, *Treasurer*, Mobil Oil Co., Snyder.

SOUTH PLAINS SECTION

James E. Thomas, *Chairman*, Pan American Petroleum Corp., Lubbock, Tex.; Jack C. Bendler, *Vice-Chairman*, Honolulu Oil Corp., Brownfield, Tex.; Donald R. Dodson, *Vice-Chairman*, Mobil Oil Co., Lubbock; Robert L. Hansen, *Secretary-Treasurer*, Pan American Petroleum Corp., Brownfield, Tex.

SOUTHWEST TEXAS SECTION

Carroll Hudson, *Chairman*, The Atlantic Refining Co., Corpus Christi, Tex.; Robert C. Miner, *Vice-Chairman*, Spartan Well Service, Corpus Christi; E. G. Wagenecht, *Vice-Chairman*, Pan American Petroleum Corp., Beeville, Tex.; Jack Culberson, *Secretary-Treasurer*, Republic Natural Gas., Corpus Christi.

SPINDLETOP SECTION

E. J. Noone, *Chairman*, Gulf Oil Corp., Beaumont, Tex.; Roy Anderson, *Vice-Chairman*, Humble, Beaumont; Donald W. Moore, *Secretary*, Pan American Petroleum Corp., Beaumont; Pat Turcotte, *Treasurer*, Ohio Oil Co., Orange, Tex.

SUMATRA PEROLEUM SECTION

Kenneth L. Atwood, *Chairman*, Standard Vacuum Oil Co., Pendopo, Sumatra; E. J. Zenker, *Vice-Chairman*, Standard Vacuum Oil Co., Pendopo; David K. Watson, *Vice-Chairman*, Standard Vacuum Oil Co., Lirik; Harold P. Dunn, *Vice-Chairman*, Standard Vacuum Oil Co., Pendopo; Robert L. Holman, *Secretary*, Standard Vacuum Oil Co., Pendopo.

UINTAH BASIN SUBSECTION

Glade Nielson, *Chairman*, McCullough Tool Co., Vernal, Utah; Frank J. Murphy, *Vice-Chairman*, The California Co., Rangely, Colo.; William T. Hayes, *Vice-Chairman*, Dowell, Vernal, Utah; Jerry D. Webb, *Secretary-Treasurer*, The California Co., Rangely, Colo.

WEST CENTRAL TEXAS SECTION

Lee D. Webster, *Chairman*, Katz Oil Co., Abilene, Tex.; Hollis W. Deats, *Vice-Chairman*, Texas Pacific Coal & Oil Co., Abilene; W. R. Sittig, *Vice-Chairman*, Shell Oil Co., Abilene; Bill R. Brogdon, *Secretary*, Halliburton Co., Abilene.

WESTERN VENEZUELA SECTION

N. Schwarz, *Chairman*, Cia. Shell de Venezuela, Maracaibo, Venezuela; U. R. Ceconi, *Vice-Chairman*, Creole Petroleum Corp., Maracaibo; W. K. Waters, *Vice-Chairman*, Servicios Tecnicos de Pozos Otis, Maracaibo; T. W. Morris, Jr., *Secretary*, Venezuelan Sun Oil Co., Maracaibo; R. D. Denson, *Treasurer*, The Superior Oil Co. de Venezuela, Maracaibo.

WILLISTON BASIN SECTION

Daniel E. Boone, *Chairman*, Amerada Petroleum Corp., Williston, N. D.; Dois D. Dallas, *Vice-Chairman*, Dallea Petroleum Co., Tioga, N. D.; John Fincher, *Vice-Chairman*, Lufkin Foundry & Machine Co., Sidney, Mont.; Ronald L. Erickson, *Secretary-Treasurer*, Amerada Petroleum Corp., Williston, N. D.

WYOMING PETROLEUM SECTION

Fred A. Haddenhorst, *Chairman*, Mobil Oil Co., Casper, Wyo.; K. W. Beaver, *Vice-Chairman*, Pan American Petroleum Corp., Casper; Bruce A. Landis, *Vice-Chairman*, Pan American Petroleum Corp., Casper; James Davis, *Secretary-Treasurer*, Continental Oil Co., Casper.

PART I

PETROLEUM TRANSACTIONS

Papers Reprinted from
JOURNAL OF PETROLEUM TECHNOLOGY

Laboratory Drilling Performance of the Full-Scale Rock Bit

D. S. ROWLEY
JUNIOR MEMBER AIME
R. J. HOWE
F. H. DEILY
MEMBERS AIME

JERSEY PRODUCTION RESEARCH CO.
TULSA, OKLA.

ABSTRACT

Laboratory drilling tests with 4¾-in. hard-formation rock bits were made under rock pressure and borehole fluid pressures simulating a 3,000-ft borehole. The effects of bit weight and rotary speed on drilling rate and bit rotary power were determined in a hard, impermeable dolomite. With added bit weight, the drilling rate and rotary power both increased at an increasing rate; but, with added rotary speed, the rate and power both increased at a decreasing rate. The rock volume removed per unit of energy increased as weight was raised or as rotary speed was reduced. Empiric quadratic equations for drilling rate and rotary power were obtained and bit mechanical efficiency was calculated.

INTRODUCTION

During the past three years, Jersey Production Research Co. has performed an extensive series of tests using roller cone, drag and diamond bits varying in size from 3¾ to 9⅞ in. These tests have been made under a wide range of drilling conditions in several types of rocks at both atmospheric pressure and elevated pressures simulating depths to 3,000 ft. This paper reports the effects of bit weight and rotary speed on the penetration rate of and power consumed by a 4¾-in. hard-formation rock bit drilling in impermeable dolomite.

The laboratory work reported here supplements and extends previously published data describing the effects of bit weight and rotary speed on drilling rate from tests made at atmospheric pressure.[1,2] Similarly, the effects of pressure have been previously investigated,[3-5] using 1¼-in. "microbits", and the effects on drilling rate of pressure and fluid environments have been reported. Several investigators[6,7] have also studied certain theoretical aspects of the roller-cone rock bit performance problem. Despite this work, however, there are no published data available on the performance of field-sized bits under controlled laboratory conditions which simulate the down-hole pressure environment. There also is very little information in the referenced papers on the amount of power consumed by the bit. Therefore, the purposes of this paper are (1) to present laboratory performance data on a field-sized bit to aid in the interpretation of field test results, and (2) to make data available on the rotary power at the bit. It is hoped that this information will stimulate industry studies of energy consumption in rotary drilling and lead to the improvement of drill-bit efficiency.

One of the newer concepts in the oil- and gas-well drilling industry today is the use of optimum variable bit weights and rotary speeds to obtain minimum drilling cost per foot.[8,9] The successful application of this concept depends on accurate bit performance data that can be used in applying mathematical relations to the field drilling situation. In particular, accurate data are needed on the effects of bit weight and rotary speed on the penetration rate of roller-cone rock bits.

Two recent papers[10,11] presented penetration rate data from a lengthy series of tests conducted by the AAODC. One conclusion reached was that, at best, the field data were difficult to interpret because of the influence of uncontrollable test variables. Similar problems were noted in another extensive study which was aimed at obtaining the best combination of constant bit weight, and constant rotary speed for minimum cost per foot drilling.[12]

Accurate field data are quite difficult to obtain because of the influence on drilling rate of many uncontrollable variables such as formation hardness, formation permeability, changing fluid properties, etc. But even this type data is often very costly because many runs must be made before a statistically significant result is obtained. Thus, by providing at least one standard of comparison from full-scale laboratory test results under simulated pressure conditions, this paper hopes to assist in answering the question "What happens if formation hardness, drilling fluid properties, formation permeability and bit dullness are all held constant?".

EXPERIMENTAL PROCEDURE

All tests were made with a laboratory drilling machine, which is shown in Fig. 1 drilling a dolomite quarry block at atmospheric pressure. This hydraulically driven drilling rig is capable of producing any combination of bit weights up to 50,000 lb

Original manuscript received in Society of Petroleum Engineers office July 29, 1960. Revised manuscript received Nov. 8, 1960. Paper presented at 35th Annual Fall Meeting of SPE, Oct. 2-5, 1960, in Denver.

Discussion of this and all following technical papers is invited. Discussion in writing (three copies) may be sent to the office of the *Journal of Petroleum Technology*. Any discussion offered after Dec. 31, 1961, should be in the form of a new paper. No discussion should exceed 10 per cent of the manuscript being discussed.

[1]References given at end of paper.

The *Petroleum Transactions, AIME*, begin with this page. The preced-

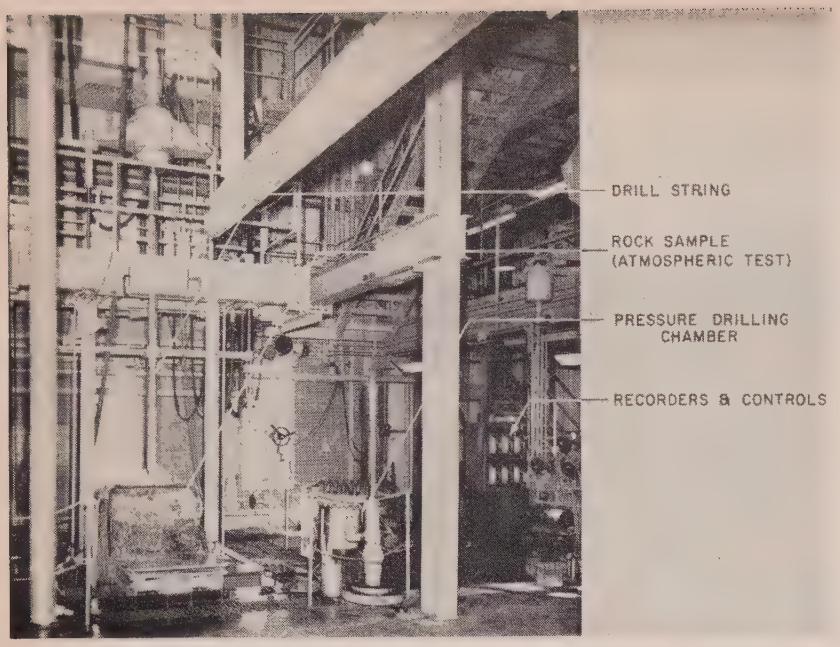

FIG. 1—LABORATORY DRILLING EQUIPMENT SET UP FOR TESTS AT ATMOSPHERIC PRESSURE.

and rotary speeds to 400 rpm. The torque capacity of the machine is 9,000 ft-lb. Bit sizes from 3¾ to 9⅞ in. have been used at various times. The rig is controlled from the console (at the right in Fig. 1), and the data are automatically recorded in a bank of electric strip-chart recorders.

A pressure chamber, shown schematically in Fig. 2A, is designed to hold octagonal rock samples (Fig. 2B) and permit application of simulated borehole and overburden pressures. Borehole (mud-column) pressure is simulated by holding a back pressure on the circulating fluid in the return flowline. The overburden pressure is applied by means of a near-zero fluid-loss "mud", located in the space around the sample as indicated in Fig. 2A. Bit weight is applied hydraulically by the two large vertical cylinders and is measured by a hydraulic jack located below the chamber. Torque applied to the rock is sensed by a hydraulic cylinder attached to the side of the chamber. Tare torque and tare weight readings are obtained after circulation and rotation have been established with the bit turning in the space just above the rock sample. Tare values are subtracted from the values indicated while drilling to obtain true bit weight and applied torque.

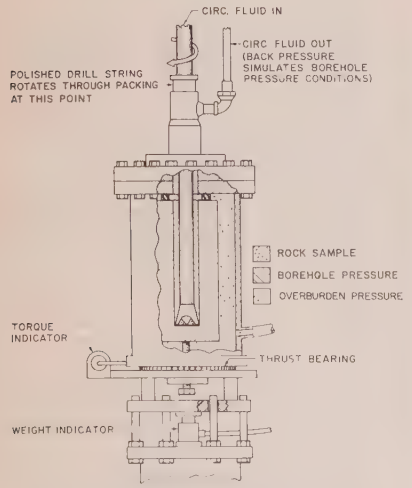

FIG. 2A—SCHEMATIC VIEW OF PRESSURE CHAMBER FOR EXPERIMENTAL DRILLING AT SIMULATED BOTTOM-HOLE CONDITIONS.

FIG. 2B—DOLOMITE SAMPLE FOR CHAMBER, USED IN 4¾-IN. DRILLING TEST.

TABLE 1—PRESSURE CONDITIONS USED IN EXPERIMENTS

Simulated Depth (Ft)	Overburden Pressure (psi)	Borehole Pressure (psi)
0	0	0
1000	1000	465
3000	3000	1395

The term "simulated depth" is used to describe a pressure condition where the overburden pressure is equal to 1.0 psi/ft of depth and the borehole pressure has a nominal hydrostatic value of 0.465 psi/ft of depth. The nominal values listed in Table 1 were used in the experiments.

The Beekmantown dolomite rock samples used for these tests were obtained from the Virginian Limestone Co. of Ripplemead, Va. This fine-grained rock consists mainly of dolomite rhombs about 0.01 mm in cross section. Many irregularly shaped dolomite grains ranging in size from about 0.01 to 0.05 mm are also present, as well as a small quantity of calcite and a trace of quartz. Tests of this rock at atmospheric pressure gave the principal physical properties listed in Table 2.

Bredthauer[14] made compressive tests on this rock at hydrostatic pressures of 0, 10,000 and 15,000 psi. He found failure of the rock sample was of the brittle-tensile type for all three pressures, with 2 per cent axial elastic strain before rupture in the 15,000-psi hydrostatic pressure tests.

The main advantages of the Beekmantown dolomite for these laboratory tests were considered to be (1) very great strength, (2) brittle-tensile rupture behavior within the drilling test pressure range, (3) availability, (4) uniformity and (5) lack of permeability. Zero permeability eliminated the effect on chip hold-down of flow across the borehole bottom face, and also made it unnecessary to introduce the additional variable of formation pore pressure. Since more than 50 per cent of all field drilling is done in low-permeability or impermeable shales, the impermeable quality of the dolomite test rock was considered representative of many field situations.

The octagonal rock samples for the

TABLE 2—PHYSICAL PROPERTIES OF BEEKMANTOWN DOLOMITE ROCK SAMPLE USED IN EXPERIMENTS.

Apparent Specific Gravity[13]	2.82 (± 1%)
Apparent Porosity[13]	5.0% (± 44%)
Compressive Strength[13]	46,000 psi (± 13%)
Tensile Strength[13]	14,000 psi (± 23%)
Young's Modulus[13]	11,140,000 psi (± 2%)
Permeability (Air)	0

pressure chamber were prepared by diamond-sawing large quarry blocks. Since the cost of preparing each sample is approximately $80, the quarry blocks were used for the tests at atmospheric pressure conditions (Fig. 1). In this case, the block rests on a special table that measures the torque. Owing to the good uniformity of the rock used and its great strength, which gave relatively low drilling rates, runs as short as 6 in. were found to be suitable for drilling data. For one set of drilling conditions, three to six such short runs were made in different rock samples and the resulting data were averaged. Therefore, each data point presented in this paper (Table 3) resulted from a minimum of about 18 in. and a maximum of about 36 in. of drilling. Actual data varied by about ± 5 to 10 per cent from the averaged values.

Since high bit loads were frequently imposed and the dolomite contained several per cent quartz, test bits were changed before any measurable wear had occurred. Bearings were kept clean and well lubricated. A standard, off-the-shelf hard-formation bit was used, and all bits had conventional watercourses. The circulating fluid was fresh water, circulated at 70 gal/min using a standard type of reciprocating slush pump. A separate series of drilling tests established that, at drilling rates of about 30 ft/hr (near maximum), circulation rates above 70 gal/min did not increase drilling rate when all other variables were held constant. All instruments and controls were regularly calibrated to insure accuracy.

ANALYSIS OF DATA

The data from the dolomite experiments are presented in Table 3. Each value represents the arithmetic average of three to six data runs. The data for each simulated depth were reduced with a digital computer using a least-squares quadratic surface-fitting procedure. The drilling rate and bit rotary power were expressed as empiric quadratic equations, in terms of bit weight and rotary speed, in the following forms.

$$R = a + bN + cN^2 + dW + eW^2 + fNW;$$

and

$$P = A + BN + CN^2 + DW + EW^2 + FNW$$

where

R = drilling rate, ft/hr,
P = bit rotary power, hp,
N = rotary speed, rpm,
W = bit weight, 1,000 lb,
$a, b, c, d, e, f,$ = drilling rate constants, and
$A, B, C, D, E, F,$ = bit rotary power constants.

These equations define three-dimensional weight-speed-rate and weight-speed-power surfaces that can be used conveniently to interpolate and extrapolate the data. The quadratic form of equation was chosen because it provides the minimum number of terms which were considered necessary to fit the experimental data accurately and permit limited extrapolation at high drilling rates. Depending upon the application, it may be possible to eliminate some terms or simplify the equations. For example, the reader can readily fit a power equation of the form ($R = KN^xW^y$) to the data.

The rate and power constants for three simulated depth conditions are presented in Tables 4 and 5 respectively. All of the graphs showing trends of drilling rate, bit rotary power and drilling effectiveness were prepared by calculation using the quadratic equations, rather than the actual data. A sample comparison of the actual data and the calculated curve is shown in Fig. 3. The agreement with the calculated curve in most cases was quite good. The agreement between calculated values and observed data is not good at low drilling rates (i.e., very low rotary speed, variable weight or very low bit weight, variable speed) where improved accuracy would have no field application in any event. The agreement at high drilling rates is good, however, and limited extrapolations are considered possible. The calculated trend is considered accurate because all drilling data at a particular depth were used to calculate the empirical equations. This technique made it possible to obtain a large amount of information from a small number of actual tests.

The drilling rate, bit rotary power and drilling effectiveness results will be discussed separately.

TABLE 3—DRILLING DATA FOR BEEKMANTOWN DOLOMITE
4¾-in. Bit

Bit Weight (lb)	Rotary Speed (rpm)	Simulated 0-ft Depth		Simulated 1000-ft Depth		Simulated 3000-ft Depth	
		Drlg. Rate (ft/hr)	Rot. Power (hp)	Drlg. Rate (ft/hr)	Rot. Power (hp)	Drlg. Rate (ft/hr)	Rot. Power (hp)
3,800	60	—	—	0.79	0.45	0.68	0.58
4,587	400	6.01	2.83	—	—	—	—
4,685	180	2.50	1.48	—	—	—	—
4,750	60	0.72	0.41	0.89	0.56	0.71	0.51
4,750	120	—	—	—	—	0.76	0.80
4,750	180	—	—	2.62	1.70	—	—
4,750	200	—	—	—	—	1.45	1.25
4,750	240	—	—	3.40	2.00	—	—
4,750	300	—	—	4.22	2.72	—	—
4,750	400	—	—	5.06	2.98	3.02	1.91
7,125	120	—	—	2.21	1.74	—	—
8,869	400	22.50	7.79	—	—	—	—
9,000	300	17.50	6.02	—	—	—	—
9,240	180	9.28	3.19	—	—	—	—
9,389	60	3.68	1.21	—	—	—	—
9,500	60	—	—	2.73	1.65	2.10	1.71
9,500	120	—	—	—	—	3.21	2.15
9,500	180	—	—	8.27	4.85	—	—
9,500	200	—	—	—	—	3.51	4.49
9,500	240	—	—	10.66	6.45	—	—
9,500	260	—	—	—	—	3.80	5.32
9,500	300	—	—	11.66	6.99	—	—
9,500	400	—	—	14.40	8.67	4.92	6.93
13,691	120	19.70	5.62	—	—	—	—
14,250	120	—	—	8.45	5.18	—	—
17,609	180	50.40	9.99	—	—	—	—
18,090	120	32.20	6.75	—	—	—	—
18,512	60	16.90	4.35	—	—	—	—
19,000	60	—	—	9.64	3.52	6.25	3.23
19,000	120	—	—	15.40	6.41	11.30	6.83
19,000	200	—	—	24.50	9.32	14.90	8.96
19,000	240	—	—	34.80	12.35	—	—
26,745	120	63.90	12.30	—	—	—	—
27,525	60	35.60	7.01	—	—	—	—
28,500	60	—	—	17.30	5.77	13.40	6.21
28,500	120	—	—	30.40	12.15	20.60	11.74
38,000	60	—	—	28.90	9.51	—	—

DRILLING RATE

Laboratory Results

Calculated trends from the equations in Table 4 are plotted in Fig. 4, which shows how variable bit weight, rotary speed and depth affect penetration rate. As shown by the curves, drilling rate increases at an increasing rate with bit weight, both at the surface pressure condition (0 ft) and at depth (simulated 3,000 ft). Conversely, drilling rate increases at a decreasing rate with

TABLE 4—DRILLING RATE IN TERMS OF BIT WEIGHT AND ROTARY SPEED

$$R = a + bN + cN^2 + dW + eW^2 + fNW$$

Where
R = Drilling Rate (Ft/Hr)
N = Bit Rotary Speed (rpm)
W = Bit Weight (1,000 lb)
a, b, c, d, e, f = Drilling Rate Constants

Conditions	a	b	c	d	e	f
4¾-in. bit drilling dolomite with water at 0-ft simulated depth	+ .111	-2.95×10^{-2}	-9.89×10^{-5}	-9.89×10^{-1}	$+5.53 \times 10^{-2}$	$+1.66 \times 10^{-2}$
4¾-in. bit drilling dolomite with water at 1000-ft simulated depth	+ .06	$-.782 \times 10^{-2}$	-4.82×10^{-5}	-3.42×10^{-1}	$+1.78 \times 10^{-2}$	$+.773 \times 10^{-2}$
4¾-in. bit drilling dolomite with water at 3,000-ft simulated depth	+ .052	$+.224 \times 10^{-2}$	-3.3×10^{-5}	-1.84×10^{-1}	$+1.87 \times 10^{-2}$	$+.292 \times 10^{-2}$

TABLE 5—BIT ROTARY POWER IN TERMS OF BIT WEIGHT AND ROTARY SPEED

$$P = A + BN + CN^2 + DW + EW^2 + FNW$$

Where
P = Bit Rotary Power (hp)
N = Rotary Speed (rpm)
W = Bit Weight (1,000 lb)
A, B, C, D, E, F = Bit Rotary Power Constants

Conditions	A	B	C	D	E	F
4¾-in. bit drilling dolomite with water at 0-ft simulated depth	$-.486 \times 10^{-2}$	-7.4×10^{-3}	$-.34 \times 10^{-5}$	-3.5×10^{-2}	$+4.71 \times 10^{-3}$	$+3.25 \times 10^{-3}$
4¾-in. bit drilling dolomite with water at 1,000-ft simulated depth	$-.672 \times 10^{-2}$	$+.504 \times 10^{-3}$	-1.44×10^{-5}	-4.78×10^{-2}	$+3.45 \times 10^{-3}$	$+2.84 \times 10^{-3}$
4¾-in. bit drilling dolomite with water at 3,000-ft simulated depth	$+3.32 \times 10^{-2}$	$-.436 \times 10^{-3}$	-1.75×10^{-5}	-7.52×10^{-2}	$+5.37 \times 10^{-3}$	$+2.66 \times 10^{-3}$

rotary speed, both at the surface and at depth. Finally, the drilling rate decreases with depth at a decreasing rate, and the most significant reduction in drilling rate due to pressure environment occurs within the first 1,000 ft.

The drilling rate trends show, as indicated in Fig. 4, that the drilling rate for constant rotary speed and variable weight would not be limited by inability of the bit to form chips. Rather, the limitation would be imposed by external factors, such as the weight capacity of the bit bearings and teeth, or by limitations on the bottom-hole cleaning capacity of the hydraulic jetting action.

On the other hand, the equations also show that, at constant weight and variable rotary speed, the drilling rate approaches a maximum for each value of bit weight. Although the quadratic equation predicts such maxima, none were reached experimentally—even at very low values of bit weight and high rotary speeds. It is possible that the discrepancy could be explained by considering that the rock bit tooth action includes both a chipping and a scraping action, even for so-called "hard-formation" rock bits. Scraping action is introduced by cone and by bit geometry and comes about because every cone has more than one rolling center. It seems reasonable to suspect that at progressively higher rotary speeds an increasing percentage of total chip volume is attributable to this scraping action, since the effectiveness of the impulse (chipping) per tooth contact is probably decreasing. This would lead to a condition at very high rotary speeds where almost no chipping was taking place and most of the chips were being produced by a drag action, shearing process. The accelerated rate of wear of rock bits at higher speeds, as discussed by Cunningham,[8] tends to confirm this viewpoint. Finally, then, since the tests reported here did not exceed 400 rpm rotary speed, it is possible that the drilling rate maxima are predicted from data which mainly include chipping action and do not adequately reflect the importance of scraping action on drilling rates at higher rotary speeds.

The concave downward trend of drilling rate vs rotary speed is more graphically demonstrated by plotting penetration per revolution (instead of drilling rate) against rotary speed, as shown in Fig. 5. Thus, the penetration per revolution decreases for all bit weights as rotary speed is increased, with greater percentage decreases occuring at high bit weight where the drilling rate is high. Although experiments cannot now be made at rotary speeds above 400 rpm with our equipment, the trends (as plotted in Fig. 5) agree with Shreiner and Chzhi-Tszyan's data,[15] which indicate that the penetration per revolution approaches zero asymptotically with rotary speed.

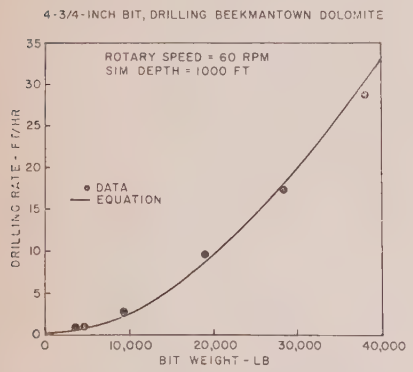

FIG. 3—A SAMPLE COMPARISON BETWEEN ACTUAL DRILLING DATA AND TREND CALCULATED FROM LEAST-SQUARES QUADRATIC SURFACE EQUATION.

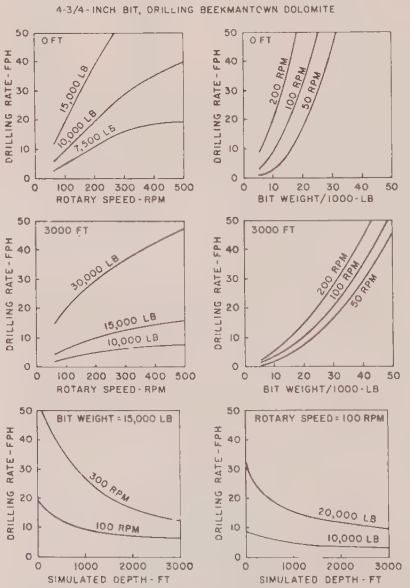

FIG. 4—SUMMARY OF WEIGHT AND SPEED EFFECTS ON PENETRATION RATE, PLOTTED FROM LEAST-SQUARES QUADRATIC EQUATIONS.

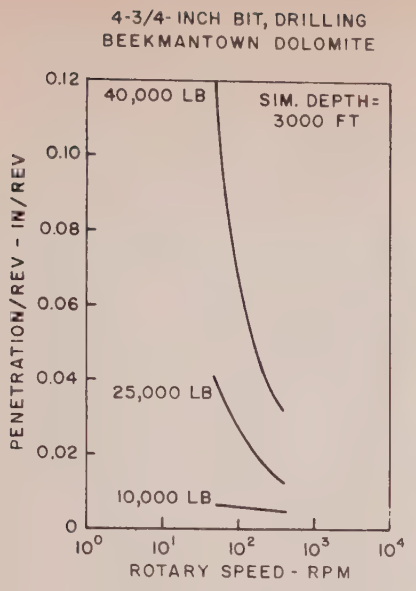

FIG. 5—EFFECT OF ROTARY SPEED ON PENETRATION PER REVOLUTION, PLOTTED FROM LEAST-SQUARES QUADRATIC EQUATIONS.

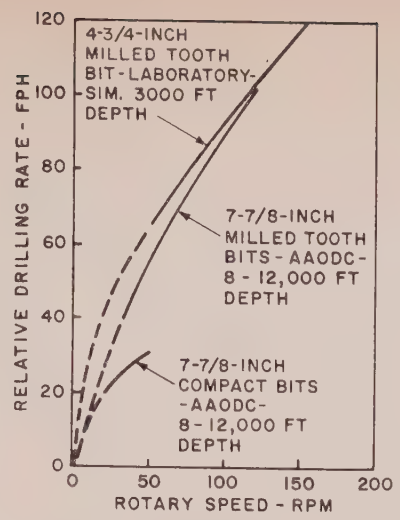

FIG. 6—COMPARISON OF LABORATORY AND FIELD RESULTS.

Field Results

Field testing has verified the concave upward curvature of drilling rate with added weight. Woods and Galle[10] show these results when using jet bits in a 7⅞-in. hole below 8,000 ft in West Texas. They approximated their data with the empirical result $R = KW^{1.2}$, where R is drilling rate, K is an arbitrary constant and W is the bit weight. On the other hand, the concave upward trend of drilling rate with bit weight at depth conflicts to some extent with the field data cited by Speer.[12] His data indicated that drilling rate was directly proportional to bit weight, as expressed in the equation $R = KN^xW$. K in this case is again an arbitrary constant, R is the drilling rate, W is the bit weight, N is the rotary speed and x is an exponent less than 1.0.

Field testing has also verified the concave downward curvature of drilling rate with added rotary speed. The comparison of laboratory and field results shown in Fig. 6 indicates that, under jet bit drilling conditions such as those in the AADC field tests in West Texas,[11] the drilling rate increases with rotary speed at a decreasing rate. The relative curvatures of the field tests and laboratory tests are similar. The penetration per revolution results in Fig. 5 are substantiated generally by Payne's[16] field data. Payne analyzed 156 bit runs, half of which were made with a turbodrill and half with conventional rotary. The data showed that, while the turbodrill bits averaged twice as many total revolutions, they only obtained half as much total footage. This meant that the penetration per revolution was four times greater for conventional rotary, as indicated by the data shown in Fig. 5.

Discussion

Interpretation of field drilling tests has always been difficult because of the usually adverse effects of loosely controlled and recorded variables. To determine true drilling rate effects under local conditions, the controllable factors such as mud weight, mud viscosity, fluid loss, fluid hydraulic impact and bit type must be adjusted carefully to bring about the best possible drilling rate response to bit weight and rotary speed. This information is needed to obtain optimum bit performance and reduce drilling costs.

The forces affecting chip holddown and ejection may partially explain why the field test results, like those shown by Speer,[12] do not generally reflect the concave upward curvature of drilling rate with added weight. In these laboratory tests, where an impermeable rock was drilled with clear water, there was no flow from the borehole to the formation pore space below, which tended to hold chips down. Further, the low viscosity of the water (relative to that of field drilling muds) permitted rapid communication of pressure along the fissures of chips being formed by the bit teeth.

Mud properties and bit hydraulics can be controlled in field drilling to improve the actual response of the formation to added bit weight. First, as shown by Moore and Gatlin,[17] there is an increase in drilling rate associated with increased "fluid loss". Among other things, fluid loss indicates a low-viscosity phase, such as clear water, is present in a drilling mud. Other than fluid loss effects, further increases are shown by various authors to result from lower mud weight and lower mud viscosity.[4,5,17] Thus, a high-fluid-loss mud of low weight and low viscosity should aid chip ejection by the drilling fluid and contribute to a concave upward drilling rate-vs-weight trend. Secondly, despite conclusive tests and widely reported economies, many drilling programs do not yet take full advantage of improved rates for jet bit drilling with high fluid impact. In this case, when weight is raised, the full effect of improved chip formation may not be realized because inadequate hydraulic impact is used to clean the hole bottom properly. Optimum use of hydraulic power is needed to cause rapid ejection of every chip formed by the teeth.

Interpretation of both field and laboratory results is also made more difficult by the lack of comprehensive theoretical studies. One physical interpretation of the response of the rock to added weight and speed may involve the force-time characteristics of the tooth impulses. The trends shown here might be interpreted to mean that in brittle rock, at least, faster drilling rate is attained both by increased magnitude of impulse (force × time) per tooth contact and by an increased number of impulses per unit of time. The data do not show how the impulse time duration changes, but added weight produces a greater effect on drilling rate than does the same per cent of added speed. Therefore, it would also seem that increasing the magnitude of impulse per tooth is more effective than an increased number of impulses. In other words, by raising weight with speed held constant, the average dynamic tooth force increases, while the time of force application is assumed to remain essentially constant. This is apparently more effective than raising speed, where average-force level remains about constant, where time of contact decreases but where the total number of tooth contacts increases. It remains for further analytical and experimental work to establish the characteristics of the most effective force-time function to accomplish rock failure under a given set of conditions.

APPLICATION

The general response of the formation to increase in bit weight and rotary speed shows a basic advantage to favoring higher bit weights over increased rotary speeds. More field data (correlating per-foot costs with weight-speed practices) are needed to prove the economic justification for this approach. For a specific field application situation, Graham and Muench[18] have shown that, for 7⅞-in. bits at depths approaching 6,000 ft, high weights of 50,000 to 95,000 lb are needed to minimize drilling costs when low rotary speeds of 50 to 100 rpm are used.

The rock responds in a complex manner to bit weight and rotary speed. Simplified drilling rate equations, such as those suggested by Woods and Galle[10] and Speer,[12] are not thought to be completely capable of reflecting these complex responses. The quadratic drilling rate equations of Table 4, however, provide a family of curves for each selected depth. By contrast, field test results at best provide only a very general curve. Such curves show the averaged results for all depths and, in some cases, weight and speed are considered separable variables. Using separable variables leads to considerable scatter when field data are plotted.

The more general quadratic form of equation has been applied with success to actual field drilling situations by multiplying all terms by an arbitrary constant. The arbitrary constant in this case is the ratio of the actual penetration rate to the drilling rate calculated from Table 4 for the depth under consideration. Accordingly, the ordinates in Fig. 4 can be adjusted by the same constant and the relative trends studied. Extrapolation to greater depths and other bit sizes is also possible by graphical means, using equations from Table 4 as a starting point.

BIT ROTARY POWER RESULTS

Table 5 lists the constants for the three bit rotary power equations, expressing power in terms of the bit weight and rotary speed. Calculated trends (plotted in Fig. 7) show a marked similarity to the drilling rate trends in Fig. 4. However, as indicated by the comparison in Fig. 8, the drilling rate is not in all cases directly proportional to the bit rotary power.

The bit rotary power in these experiments is calculated using the rotary speed and the torque reaction measured between the cones and the rock. This observed torque then includes the torque reaction exerted by the rock on the cones, which causes cones to rotate on their own axes, as well as the torque which overcomes rolling resistance on the rock itself. Thus, these power values include a certain amount of friction horsepower which is not actually used in doing work on the formation, but which is necessary to operate the bit. Example sources of friction power are cone bearing friction and frictional drag between the rotating cones and the circulating fluid. In a separate series of tests, it was determined that the bit friction power varied with bit loading in very nearly the same way as the bit drilling power, but that the friction power was only about 5 per cent of the total bit rotary power.

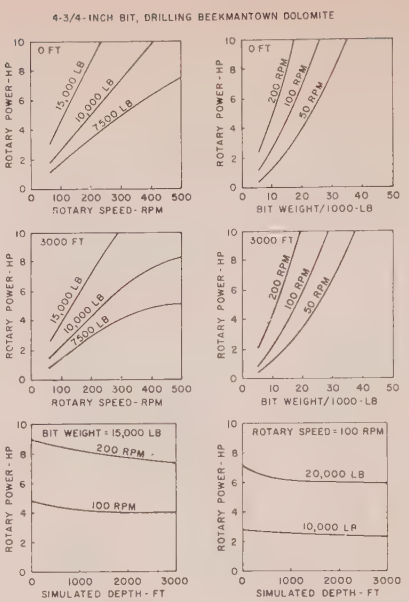

FIG. 7—SUMMARY OF WEIGHT AND SPEED EFFECTS ON BIT ROTARY POWER, PLOTTED FROM LEAST-SQUARES QUADRATIC EQUATIONS.

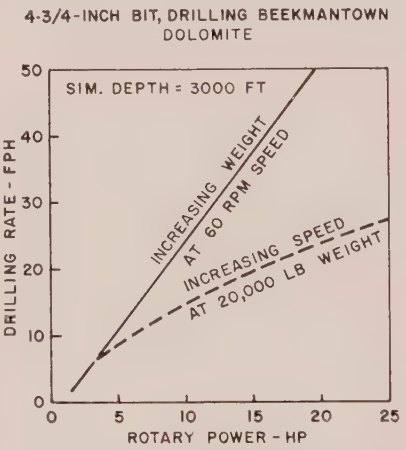
4-3/4-INCH BIT, DRILLING BEEKMANTOWN DOLOMITE
SIM. DEPTH = 3000 FT
INCREASING WEIGHT AT 60 RPM SPEED
INCREASING SPEED AT 20,000 LB WEIGHT
DRILLING RATE - FPH
ROTARY POWER - HP

FIG. 8—EFFECT OF ROTARY POWER ON DRILLING RATE, PLOTTED FROM LEAST-SQUARES QUADRATIC EQUATIONS.

Therefore, the bit rotary power reported here includes a small percentage of nonproductive power. The remainder exactly equals the power which the formation will accept for chip formation under the particular conditions of drilling. The thrust power due to bit weight ranged under test conditions from about 0.5 to 2 per cent of the measured bit rotary power and is, therefore, not included in the data. For a particular depth, formation and bit geometry, the results of the drilling experiments indicate no limit on the amount of power that might be dissipated into the formation to create chips, but the manner in which the power is applied does make a difference. As shown in Fig. 7, the bit rotary power increases at a decreasing rate with rotary speed. This means simply that the torque required to rotate the bit, when bit weight remains constant, decreases as rotary speed increases. This is shown in Fig. 9. From this result, it can be inferred that, besides tooth geometry, formation properties and the static state of stress at the hole bottom, the chip formation is dependent also on either the rate of loading during each tooth contact or on the time duration of tooth contact, or both.

Other than the relation of drilling rate to bit rotary power and the relation of torque to bit load, the low value of bit rotary power is also of interest. From Fig. 7, for example, the hard-formation type of bit at a simulated depth of 3,000 ft required only 7 hp, drilling 10 ft/hr at 200 rpm and 15,000 lb bit weight. How effective this amount of bit rotary power is can best be understood by combining power, penetration rate and hole area into a term called "drilling effectiveness".

DRILLING EFFECTIVENESS RESULTS

The drilling effectiveness is a measure of the energy required to fracture out a unit volume of rock and is defined in terms of cubic feet of rock removed per horsepower-hour of energy expended. The drilling effectiveness is calculated by multiplying drilling rate times bottom-hole area and dividing by bit rotary horsepower.

The effects of bit weight, rotary

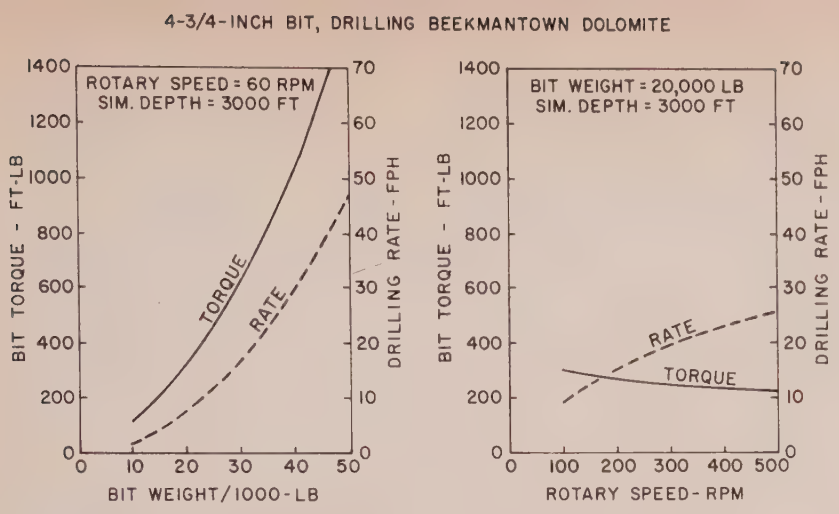

FIG. 9—SUMMARY OF BIT WEIGHT AND ROTARY SPEED EFFECTS ON TORQUE AT THE BIT, PLOTTED FROM LEAST-SQUARES QUADRATIC EQUATIONS.

speed and depth on drilling effectiveness are shown in summary form Fig. 10. Effectiveness is related to drilling rate in Fig. 11, for reference. The characteristic trends show that the drilling effectiveness decreases with added rotary speed, increases with added bit weight and decreases with greater depth.

It must be remembered, however, that maximum drilling effectiveness does not mean least drilling cost per foot. Minimizing the drilling cost per foot, the ultimate aim, naturally involves simultaneous consideration of many important factors such as drilling rate, bearing and tooth wear, rig costs and bit costs. The drilling effectiveness is only one measure of bit performance and is introduced here to aid understanding of how the rock bit utilizes energy.

Additional bit weight, or force, is an obvious way of increasing drilling effectiveness. Since it is not always possible to carry long strings of drill collars, additional means of applying bit force may have merit. Kellner and Roberts[19] recently disclosed such a means — a hydraulic wall-anchored drill collar. In areas having competent hole wall on which to anchor (as in hard formations which require greater weights), such a tool appears to have both a fundamental and an operational advantage.

The drilling effectiveness results also show that two important factors have adversely affected the operation of turbodrills when used at depth. First, since the turbodrill bit operates at rotary speeds beween 600 and 1,000 rpm, the drilling effectiveness is relatively low, probably due to a high rate of loading per tooth contact and to a short time duration of individual tooth contact. Second, as depth increases the formation becomes harder, and more energy is required per unit volume to maintain constant drilling rate. But, since the turbine rotor must operate within a certain speed range to maximize turbine output power, weight on bit cannot be arbitrarily raised to increase energy input to the formation without risk of exceeding turbine torque output. If output torque requirement is excessive, of course, the turbine stalls.

Under certain conditions where high bit weights cannot be maintained, it would be desirable to increase bit rotary power and the drilling rate by operating at moderate weights and at rotary speeds in the range of about 300 to 400 rpm. Such weight-speed practices are outside the range of normal rotary practices, mainly because of excessive wear and tear on the drill string at increased speeds. However, a turbodrill speed reducer would permit the turbine rotor to operate at the desired speed but would reduce bit rotary speed by about three times—into the range of 300 to 400 rpm.

In this regard, Bingman[20] recently suggested, "A tool having higher torque and lower speed (perhaps the same horsepower) should perform better with both diamond bits and rock bits than present turbodrills". Russia has already been experimenting with several kinds of speed reducers for turbodrills. At least one USSR experiment has been reported[21] where an 8-in. hole was drilled at 49.4 ft/hr using a turbodrill and speed reducer, compared to 34.6 ft/hr under comparable conditions with the standard turbodrill at higher rotary speeds.

DRILL BIT EFFICIENCY

Having the values of drilling effectiveness available, as shown in Fig. 10, an estimate of the efficiency of the roller-cone rock bit can be obtained and energy requirements in drilling compared to other means of destroying rock. Calculation of the theoretical energy required to drill rock with a roller-cone drill bit is complicated by the fact that two distinctly different jobs must be done. First, the bit must break down the formation into chips which can be lifted by the circulating fluid. Secondly, the bit must produce the geometry of a borehole. Plainly, it is one thing to break from a piece of rock a small cube which has three free faces (as Cube A in Fig. 12) and another thing to fracture out the same-sized cube having only one free face (Cube B, Fig. 12), as would be the case at the bottom of the borehole. Thus, in calculating the efficiency of the rock bit, the energy required to form the borehole geometry (one-free-face situation) must be considered in addition to the subsequent energy required to break down the unsupported rock (three-free-faces situation) into suitable-sized chips.

On this basis, then, a reasonable model can be proposed from which the drilling energy required at 100 per cent bit efficiency can be calculated and compared to actual energy requirements. It seems reasonable that the least possible energy expenditure per unit volume of rock removed would require that the drilling process first cut a very narrow, circular kerf at the hole periphery to form the required geometry; and, second, break down the core which remains standing in the center by using comminution methods.[22] In this hypothetical drilling process, the kerf could be cut using a very narrow, diamond coring bit or it could also be cut using a narrow, rolling cutter-type coring bit. The main volume of the formation drilled then would be broken down by comminution and circulated up the hole.

Consider the diamond coring-plus-comminution method first. Practical consideration of diamond drill design indicates that a kerf not narrower than about ⅛-in. might be cut.

Assume that a total of 1 cu ft of Beekmantown dolomite is to be removed from a 4¾-in. borehole at about 3,000 ft. The diamond-cut kerf would be 4.75-in. OD by 4.50-in. ID by 8.14-ft long and require 1,835,000 ft/lb of energy. The latter figure is based on laboratory data for the drilling effectiveness of a 4¾-in. full-hole diamond bit in the same rock. Following the methods of Charles,[22] only 128,000 ft/lb would be needed to reduce the core to ⅛-in. cubes. Thus, the hypothetical process of coring and comminution uses 1,963,000 ft/lb total to remove 1 cu ft. Using an effectiveness of 0.32 cu ft /hp-hr (Fig. 10) for the rock bit, drilling the same 1 cu ft would require 6,180,000 ft/lb. Thus, the rock bit efficiency is calculated as (1,963,000)/(6,180,000) = 31.8 per cent.

Similary, the material in the kerf could also be removed by a rolling cutter-type core drill with a minimum width of about ⅜-in. Assuming for lack of data that such a drill would cut at the same effectiveness as the full-hole rock bit (0.32 cu ft/hp-hr), the kerf would require 1,786,000 ft/lb and, again following the methods of Charles,[22] the core would require only 101,000 ft/lb. These figures yield a rock bit efficiency of (1,887,000)/(6,180,000) = 30.6 per cent, or about the same as before.

It is not considered realistic to assume that all the rock within the geometrical confines of the borehole can be broken down by the more efficient comminution methods alone. This type of calculation gives no credit to the bit for having formed the geometry of the borehole and leads to very pessimistic values for over-all bit efficiency.[23] On the other hand, efficiency on the order of 30 per cent still gives considerable incentive for continued research on improved drill bits and for development of more efficient means for rock attack.

To compare energy requirements for the rock bit with other common means for breaking down rock into small particles, Table 6 was prepared. Using the same basis of calculation, energy requirements for crushing, blasting and drilling are compared. Theoretical (but not practi-

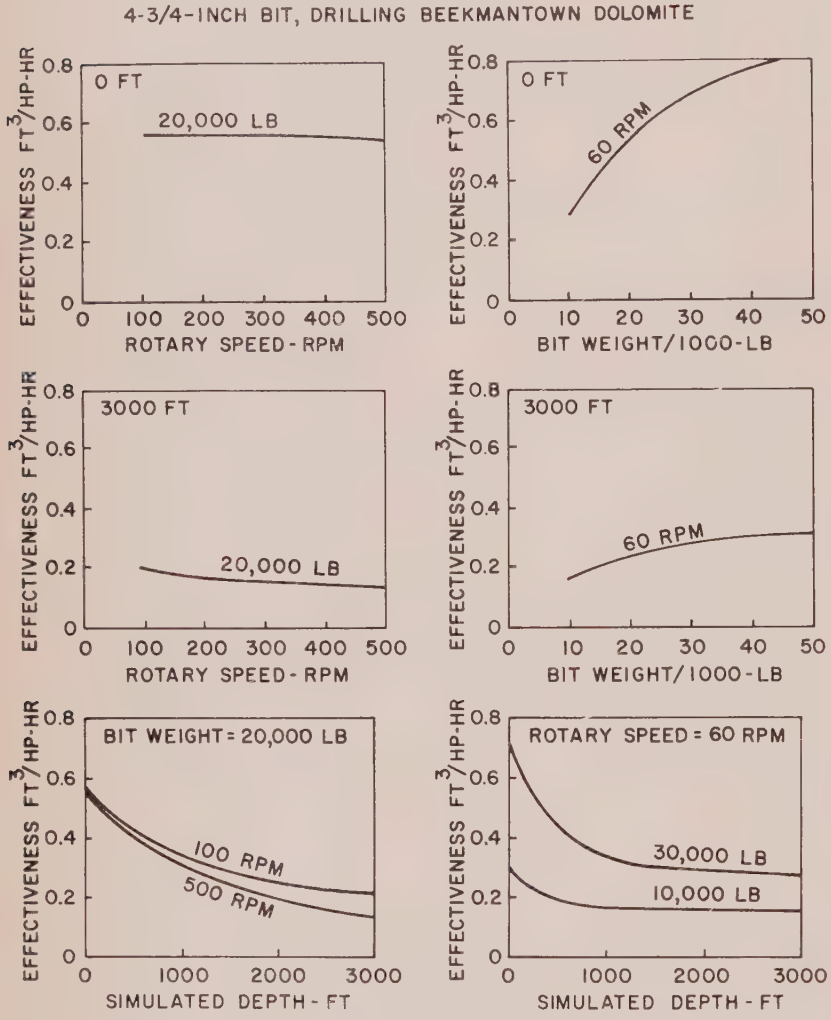

FIG. 10—SUMMARY OF BIT WEIGHT AND ROTARY SPEED EFFECTS ON DRILLING EFFECTIVENESS, PLOTTED FROM LEAST-SQUARES QUADRATIC EQUATIONS.

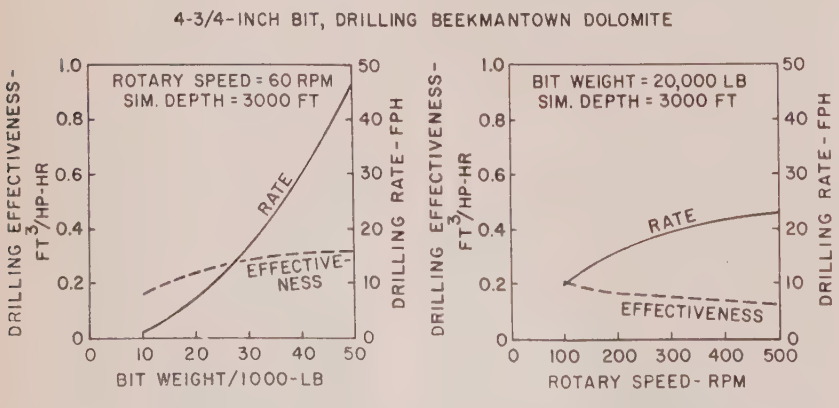

FIG. 11—SUMMARY OF BIT WEIGHT AND ROTARY SPEED EFFECTS ON DRILLING RATE AND EFFECTIVENESS, PLOTTED FROM LEAST-SQUARES QUADRATIC EQUATIONS.

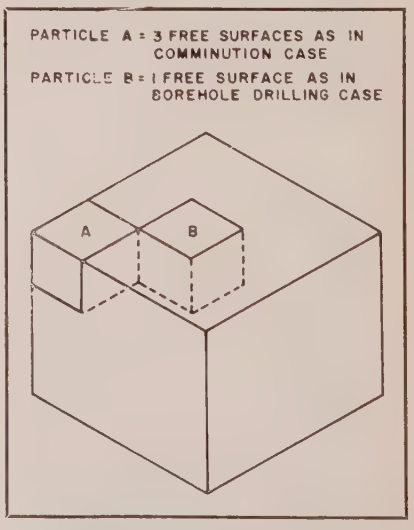

FIG. 12—DIFFERENCE IN CONSTRAINT FOR TWO ROCK PARTICLES.

TABLE 6—ENERGY REQUIRED PER CUBIC INCH TO REDUCE SIZE OF SIMILAR ROCKS TO 100 PER CENT FINER THAN 1 MM

Theoretically	
Surface Energy Relations	
E = 0.64 ft-lb/cu in. (Ref. Somerton[23])	
Experimentally (Approximate)	
Crushing (Comminution, 3 Free Faces)	
E = 230 to 805 ft-lb/cu in. (Ref. Charles,[22] Somerton[23])	
Blasting (2 Free Faces, Confined 1½-in. holes, 6 to 10-ft deep, 3-ft spacing)	
E = 4,760 to 8,030 ft-lb/cu in. (Ref. Bond[24])	
Drilling (full-scale, three-cone, 4¾-in. Roller Bit; 1 Free Face)	
E = 4,400 to 17,400 ft-lb/cu in.	
Drilling ("Microbit", Two-Cone, 1¼-in. Diameter, 1 Free Face)	
E = 6,000 to 30,000 ft-lb/cu in. (Ref. Somerton[23])	

cally applicable) surface energy requirements are shown for reference. In Table 6 it is seen that the least energy requirements for the three-cone, 4¾-in. bit are on the same order as energy requirements in blasting, where the more attractive situation of two free faces was available instead of one as in drilling. Also, it can be seen that the smaller diameter two-cone microbit is not so efficient as the full-scale bit, indicating that extrapolation of microbit test results to field drilling conditions may involve important limitations. Since a very hard rock and a short-toothed, hard-formation bit were used in the tests being reported here, the energy requirements indicated in Table 6 for the 4¾-in. rock bit probably represent upper limits. Suitable particle-size distributions for diamond, drag and percussion drilling chips were not available for comparative energy requirement calculations. Actual energy requirements for the three-cone rock bit would be 1,400 to 5,500 ft-lb/cu in., somewhat less than those shown in Table 6 because in the actual case not all particles were reduced to 1 mm.

CONCLUSIONS

Based upon full-scale laboratory testing at simulated depths to 3,000 ft using a 4¾-in. hard-formation type of roller-cone bit in impermeable Beekmantown dolomite, the following conclusions are drawn.

1. Added bit weight causes drilling rate and bit rotary power to increase at an increasing rate and causes drilling effectiveness (volume removed per unit of drilling energy) to increase at a decreasing rate.

2. Added rotary speed causes drilling rate and bit rotary power to increase at a decreasing rate and causes drilling effectiveness to decrease at a decreasing rate.

3. For the conditions studied, the following are representative values of bit performance characteristics: drilling rate, 5 to 40 ft per hour; bit torque, 150 to 750 ft-lb; bit rotary power, 4 to 20 hp; and drilling effectiveness, 0.2 to 0.9 cu ft/hp-hr.

4. In an impermeable formation, the energy required to drill a unit volume of rock increases with simulated depth. This is compatible with a similar increase of rock strength at increased depth.

5. Through a series of quadratic equations, means are available to predict the complex response of the rock to drill bit loading.

6. The mechanical efficiency of a rock bit is about 30 per cent. Full-scale rock bit efficiency is (1) greater than the efficiency of the microbit and (2) about the same as blasting with two free faces.

ACKNOWLEDGMENTS

For permission to publish this paper, the authors express appreciation to Jersey Production Research Co., the principal production, drilling and exploration research affiliate of Standard Oil Co. (N.J.).

Appreciation is also expressed to J. M. Camp and J. M. Kellner of Jersey Production Research, who designed and set up much of the experimental drilling equipment and to H. L. Hartman of Pennsylvania State U., for assistance with calculations for Table 6.

REFERENCES

1. Hughes Tool Co., Catalog 22, 1958, 2451.
2. Wardroup, W. R. and Cannon, G. E.: "How to Increase Your Drilling Rates", *Oil and Gas Jour.* (Apr. 30, 1956) **54,** No. 52, 204.
3. Moore, P. L.: "Five Factors That Affect Drilling Rate", *Oil and Gas Jour.* (Oct. 6, 1958) **56,** No. 40, 141.
4. Cunningham. R. A. and Eenink, J. G.: "Laboratory Study of Effect of Overburden, Formation and Mud Column Pressures on Drilling Rate of Permeable Formations", *Trans.*, AIME (1959) **216,** 9.
5. Murray, A. S. and Cunningham, R. A.: "Effect of Mud Column Pressure on Drilling Rate", *Trans.*, AIME (1955) **204,** 196.
6. Outmans, H. D.: "The Effect of Some Drilling Variables on the Instantaneous Rate of Penetration", *Trans.*, AIME (1960) **219,** 137.
7. Polyakov, V. S.: "Some Problems on the Mechanics of Cone Bit Operation", *Neftyanoe Khoz.* (1957) **35,** No. 9, 18.
8. Cunningham, R. A.: "How High Rotary Speed Shortens Bit Life, Increases Drilling Costs", *Oil and Gas Jour.* (July 11, 1960) **58,**, No. 28, 91.
9. McGhee, Ed: "What Weight and Speed Produce the Lowest Drilling Cost?", *Oil and Gas Jour.* (March 17, 1960) **58,** No. 10, 84.
10. Woods, H. B. and Galle, E. M.: "Effects of Weight on Penetration", *Drill. Contr.* (Oct. 1957) **13,** No. 6, 74.
11. Eckel, J. E. and Rowley, D. S.: "How Rotary Speed Affects Penetration", *Oil and Gas Jour.* (Nov. 25, 1957) **55,** No. 47, 86.
12. Speer, J. W.: "A Method for Determining Optimum Drilling Techniques", *Oil and Gas Jour.* (Mar. 31, 1958) **56,** No. 13, 90; (Apr. 7, 1958) No. 14, p. 148.
13. Dashiell, L. L.: "Physical Properties of Limestone from Virginian Limestone Co., Ripplemead, Virginia", R.I. E1-125, USBM (Feb. 28, 1957).
14. Bredthauer, R. O.: "Strength Characteristics of Rock Samples under Hydrostatic Pressure", *Trans.*, ASME (May, 1957) **79,** No. 4, 695.
15. Shreiner, L. A. and Chzhi-Tszyan, G.: "Effect of Rotational Speed on the Drilling Speed with Roller Bits", *Neftyanoe Khoz.* (1956) **34,** No. 12.
16. Payne, Lyle: Unpublished remarks at API Drilling Research Symposium, Biloxi, Miss. (Jan. 13, 1960).
17. Moore, P. L. and Gatlin, C.: "Six Variable Factors That Affect Penetration Rate", *Oil and Gas Jour.* (Apr. 11, 1960) **58,** No. 15, 118.
18. Graham, J. W. and Muench, N. L.: "Analytical Determination of Optimum Bit Weight and Rotary Speed Combinations", Paper 1349-G presented at 34th Annual Fall Meeting of SPE in Dallas (Oct. 5, 1959).
19. Kellner, J. M. and Roberts, A. P.: "Hydraulic Wall-Anchored Drill Collar", presented at ASME 15th Annual Pet. Mech. Engrg. Conf., New Orleans, La. (Sept. 18, 1960).
20. Bingman, W. E.: "Basic Changes Needed for Turbodrills", *Pet. Week*, (Mar. 4, 1959) **10,** No. 9, 34.
21. Ivanov, V.: "Rubber Padded Speed Reducer for Turbodrills", *Neftyanik* (Jan. 1959) **4,** No. 1, 19. (Refers to USSR Patent 107,287: G. A. Lyubimov.)
22. Charles, R. J.: "Energy Size Reduction Relationships in Comminution", *Min. Engrg.* (Jan. 1957) **9,** No. 1, 80.
23. Somerton, W. H.: "A Laboratory Study of Rock Breakage by Rotary Drilling", *Trans.*, AIME (1959) **216,** 92.
24. Bond, F. C. and Whitney, B. B.: "The Work Index in Blasting", *Qrtly. Colo. School of Mines* (July, 1959 **54,** No. 3, 77.

DISCUSSION

RALPH SIMON | BATTELLE MEMORIAL INSTITUTE
COLUMBUS, OHIO

W. H. Somerton[1] showed that the dimensionless parameter RD^2S/NW^2 is significant for the process of rotary drilling. The discussor[2] showed this parameter to be related to RD^2S/P, a significant parameter for all rock drilling methods employing concentrated mechanical loadings. The notations D and S are, respectively, the hole diameter and drilling strength; the other notations are the same as those of the authors.

R should vary approximately as NW^2 for the ranges of values of other pertinent parameters under which the Somerton parameter is reasonably constant. This is well substantiated by the authors' data of Table 3. $R/NW^2 = 7.8 \pm 0.8$, 4.0 ± 0.6 and 2.5 ± 0.5 for the simulated depths of 0, 1,000 and 3,000 ft, respectively, for all values of N and for all values of $W \geq 7{,}125$ lb, where R is given in ft/hr, N is 10^2 rpm and W is 10^4 lb. The $\pm$ variations are average deviations. For $W \leq 4{,}750$ lb, R/NW^2 increases rapidly with decrease in W for the 1,000- and 3,000-ft depths and reaches values of 9 and 8, respectively, at $W = 3{,}800$ lb. For the 0-ft simulated depth, R/NW^2 decreases for the smaller values of W but by an amount that may not be statistically significant.

These results may be demonstrated graphically by plotting R/NW^2 as a function of W for each simulated depth. No tendency is evident for the vertical ordering of the points at each value of W to vary in any systematic manner with N, with the exception of the 60-rpm points for 3,000-ft simulated depth. This exception is probably the main reason why the authors' least-squares match to their empirical quadratic equations led to the erroneous conclusion regarding the effects of increased rotary speed on the rate of penetration. On the contrary, the authors' data demonstrate the absence of any significant rate of loading effects in the range of rates of loading involved in rotary drilling into brittle rock, in agreement with the results of the discussor's concentrated loading experiments. This conclusion applies to all three simulated depths.

The primary cause or causes of the decreased penetration per revolution often experienced in field practice as the rotary speed is increased remain to be investigated. The effective force between the bit and the rock for producing fragmentation may differ appreciably from the force of gravity on the mass of elongated geometry (the drill collars) because of dynamic effects (coupled longitudinal, torsional and bending vibrations of the column generated at the bottom of the hole), which would increase with increased rotary speed. The force between the bit and the rock was obtained by hydraulic loading in the authors' experiments.

It is certainly within the authors' prerogative to use empirical relationships to fit their data if they choose not to be guided by existing theoretical considerations. However, empirical relationships must be chosen judiciously with due regard given to limiting conditions of the variables insofar as possible. Thus, R should vary at least as NW to obtain $R = 0$ for either $N = 0$ or $W = 0$, and higher-order terms should involve products of higher positive powers of N with higher positive powers of W. The approximate proportionality between R and NW^2 would have become evident. Furthermore, all conclusions based on empirical relationships developed from experimental data must be evaluated for statistical significance by well known methods; i. e., consideration must be given to the probability that each specific conclusion could have been the result of chance statistical fluctuations, in view of the limited amount of data, the number of variables involved and the accuracies of the measurements. Closeness of fit between the data and the empirical relationships is no criterion for the reliability of the resultant conclusions. Any finite amount of data, no matter how poor in experimental accuracy, can be fitted as accurately as desired with an empirical power law series by using a sufficient number of terms in the series.

The authors' data show that the value of $R/P = 2.0 \pm 0.5$ and 1.4 ± 0.3 ft/hr hp for the 1,000- and 3,000-ft simulated depths, respectively, for all values of N and W. Plots of R/P as a function of W seem to exhibit some small variation with W for these two simulated depths, but this variation may not be statistically significant. No variation with N is evident. The value of R/P for the 0-ft simulated depth rises from about two at low values of W to approach a constant value of about five at the higher values of W. The value of S for dry Beekmantown dolomite at atmospheric pressure is $27{,}000 \pm 8{,}000$ psi, based on the results of measurements performed by the discussor on a sample kindly furnished by the authors. The predicted value of R/P based on a value of 2.0 for the parameter RD^2S/P is 6.6 ft/hr hp. The efficiency of utilization of energy to break rock thus approaches 100 per cent for rotary drilling with sufficient weight on the bit, as previously pointed out by the discussor on the basis of the energy requirements for concentrated loadings.[2]

Consideration of the mechanisms of energy dissipation by concentrated loadings[3] shows that the energy required to drill a unit distance should consist of two additive terms, one proportional to the area of the bottom of the hole and another proportional to the wall area. The latter term becomes significantly large only for small-size bits and thus accounts for the lower efficiency of the microbit. The latter term is the predominant one when drilling out a narrow kerf around a core; hence, the energy required to drill out a unit volume of kerf material bears no direct relationship to that measured with a full-scale rock bit.

REFERENCES

1. Somerton, W. H.: "A Laboratory Study of Rock Breakage by Rotary Drilling", *Trans.*, AIME (1959) **216**, 92.

2. Simon, R.: "Discussion of A Laboratory Study of Rock Breakage", *Trans.*, AIME (1959) **216**, 361.

3. Simon, R.: "Fragmentation of Brittle Media by Concentrated Loadings", Paper 1532-G presented at 35th Annual Fall Meeting of SPE, Oct. 2-5, 1960 in Denver, Colo.

AUTHORS' REPLY TO R. SIMON

One of the main points of R. Simon's discussion is that our empirical least-squares equations for drilling rate and rotary power have ignored the existence of "significant dimensionless drilling parameters" developed by Simon and by Somerton. The possibilities for reducing our data through use of these and other dimensionless forms (with or without theoretical basis) have been previously evaluated by us. We concluded that, at this time, it would be impossible to prove or disprove the validity of any dimensionless parameters for full-scale bits from data in only one type of rock, as in our tests. When additional data from such tests have been provided, it will then be possible to test the validity of such dimensionless groups and perhaps gain an improved understanding of rock drilling processes. We noted that Somerton's dimensionless terms have been tested only against 1¼-in. diameter "microbit" data, and Simon's parameters have been tested only against single point drop chisel tests. Neither bears a proved similarity to full-scale roller bit dynamics or geometry. Thus, at this time, we could not agree with Simon that his parameter (RD^2S/P) applies without qualification as "a significant parameter for all rock drilling methods employing concentrated mechanical loadings".

In a related argument, Simon points out that our empirical relations do not furnish a statistically significant basis for drawing conclusions. It can be seen from the paper, however, that it is not necessary to extrapolate any of our equations beyond the test range in order to reach the conclusions drawn in the paper. Thus, the conclusions are based upon irrevocable trends as developed in the raw test data, later reduced to a few quadratic equations which are intended only to ease the job of interpreting and handling the data. Our interpretation of high rotary speed test results (i.e. by extrapolating the data) is also questioned by Simon. As we suggested in the paper, rate of tooth loading and time duration of contact effects may be operative. Drill collar inertial effects (discussed by Simon) and chip clearance effects[6] may also be important in determining high rotary speed behavior of the system. ★★★

Application of Optimizing Techniques for Studying Field Producing Operations

H. D. ATTRA
W. B. WISE
JUNIOR MEMBERS AIME
W. M. BLACK
MEMBER AIME

HUMBLE OIL & REFINING CO.
HOUSTON, TEX.

ABSTRACT

The purpose of this paper is to illustrate a comparatively new approach for solving a problem that has plagued oil producers for many years—how to make the most money with available field production capacity.

In a very basic operation such as a top-allowable one-well field, a computer and staff of engineers are not required to determine that the best operation is to produce that well at its maximum for as long a time as it will produce. However, as the problem becomes more complex and the number of wells and number of reservoirs increase, it probably will be a wise choice to devote some engineering thought and calculation time to determine the best way to operate that field on both an ultimate and day-to-day basis.

Continued developments in the field broadly referred to as "operations research" have led to a number of useful engineering analyses for optimizing field operational problems. One of these techniques, termed linear programing, is particularly interesting because of its potential applications to the study of complex oilfield operating problems. Linear programing is concerned with the problem of planning a complex set of interdependent activities in the best possible (optimal) fashion.

A field application of linear programing is being used to maximize daily income from a multi-reservoir producing operation. The initial results of this study indicate that the linear programing technique (1) can be applied effectively to field problems, (2) can be used to detect unsuspected avenues for improving operations and (3) can effect a significantly improved means of controlling field operations through the use of the high-speed computer.

INTRODUCTION

The usual approach for studying complex field operational problems has been to look in detail at several basic plans suggested by judgement and experience and, then, to choose the best plan from those investigated. This approach is entirely satisfactory provided: (1) that judgment and experience alone will reliably pick the best or near the best program as one of the plans to be investigated; and (2), and most important, that the factors which control field production will not change.

This paper deals with the large group of field operations which are at least one-step removed from a satisfactory solution using the conventional method of analysis. Problems such as pipeline- and gathering-system design, transportation studies, large field development projects and multi-reservoir producing operations fall in this latter category.

To find the best program for handling these problems when the best program is not obvious, a complete optimization study is required, and high-speed computers are required to continually update the program once it is selected. Operations of this type have an extremely large number of possible solutions. However, only one will result in maximum economic return and, more important, this one program must be re-evaluated and adjusted constantly to accomodate such changing field factors as the number of producing days, the price of crude, the discovery of new reserves, declining reservoir pressure with subsequent decline in production and a host of other factors which characterize specific operations.

One of the most widely used, direct methods of optimization is a numerical procedure termed "linear programing", which is designed to investigate systematically each of the possible solutions involved in a given problem, determining rapidly and uniquely the optimum answer. As implied by the name, linear programing requires that all field variables be either defined or expressed in a series of interdependent linear equalities or inequalities. These relationships are solved simultaneously, using a form of matrix solutions to determine the optimum values for each producing variable that will maximize net profits. The solution techniques used in a recent field case study is termed the "simplex method" and is discussed in full detail in Ref. 1.

Original manuscript received in Society of Petroleum Engineers office July 17, 1959. Revised manuscript received Oct. 28, 1960. Paper presented at 34th Annual Fall Meeting of SPE, Oct. 4-7, 1959, in Dallas.

[1]Reference at end of paper.

Although the primary purpose of this paper is to illustrate the application of linear programing to the field case study, a very brief discussion outlining the basic mechanics of the simplex method of linear programing solutions is deemed necessary. (A complete background of the method should be obtained by consulting Ref. 1).

The use of the first-order algebraic approximations is basic in the simplex method of linear programing solutions. These can be applied to nearly all kinds of scheduling and optimizing problems in engineering. The method is adaptable to hand or machine computation. It is simpler, although more tedious, than the methods used for least-squares or correlation calculations. No operation more complex than division, multiplication, subtraction or addition is required. Although selection and construction of the mathematical model of the problem is somewhat of an art, the solutions are reduced to a mechanically routine calculation.

The simplex method of linear programing consists essentially of the following.

1. *Restriction relationships*—a series of *inequality* statements that describe all of the conditions of the problem that must be kept within certain limits.
2. *Definitional relationships*—a series of *equations* that define the conditions of the problem that can be stated as equalities.
3. *Combination of the restrictional and definitional relational relations (requirements vector)*—a series of inequalities that encompasses all of the restrictional and definitional conditions.
4. *"Slack" variables*—a set of values introduced into the relationships outlined in Item 3 to reduce the inequality statements to equations.
5. *Maximal function*—considering slack variables, the problem has more unknowns than equations, which result generally in an infinite number of solutions. At this point it is necessary to introduce a functional that will minimize or maximize a set of conditions in the problem under consideration. This is usually a net profit, maximum production or minimum error equation.
6. *Simplex matrix*—the solutions to the equations derived are solved using matrix algebra so that the maximal function is satisfied.

FIELD HISTORY

Producing operations in the example field are characteristic of most large multi-reservoir fields, with the exception that there are no regulatory restrictions. Fig. 1 is a schematic drawing of the producing operation on which the optimization program was based. There currently are four major reservoirs, with some 40 oil- and gas-producing wells. Three of the reservoirs (Zones A, B and C) are producing under gas-injection operations, with Zone D serving as a source for a portion of the make-up gas. Normally, total field gas production is injected into Zones A, B and C, and no gas is sold except upon emergency shut-down of the compressor station.

To provide an adequate supply of extraneous gas for conducting the conservation programs, a "borrow-return" agreement was negotiated with the connecting gas company. Under terms of the agreement, "storage" gas is supplied to the field during the warmer months, with a lesser volume of gas being returned to the gas company during brief periods of peak demand. Both the field gas production and "borrowed" gas are compressed at the central plant for injection into Zones A, B and C. A portion of the field gas is used to supply lease fuel and a high-pressure gas-lift system.

The field produces into a four-pressure gathering system of 50, 250, 950 and 2,000 psi. Five compressors with 13 stages of compression are used to compress the gas from each of the gathering systems to reservior injection pressure. While the total horsepower available from each compressor is fixed, the capacity available for any of the four gathering systems can be adjusted by changing the clearance in the 13 stages of compression through common manifolding.

BASIC ANALYSIS

The economic justification for each of the secondary

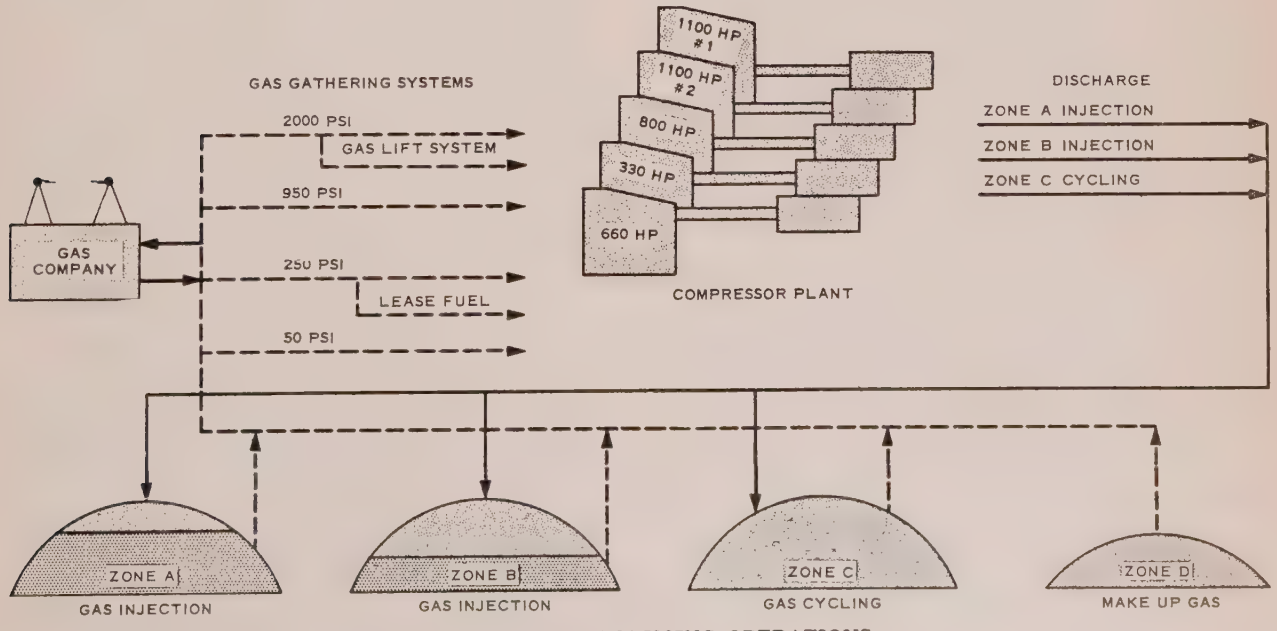

FIG. 1 — FIELD PRODUCING OPERATIONS.

recovery programs was determined from separate reservoir studies. The problem to be solved by the optimization study is to maintain maximum net income on a day-to-day basis while complying with the following restrictions.

1. Do not exceed the maximum economic productivity of oil- and gas-producing wells. (The capacity at which operating difficulty such as freezing will not be encountered.)

2. Maintain the injection requirements for each of the secondary recovery programs so as to realize the ultimate economics indicated by the reservoir study.

3. Do not exceed the permissible working pressure of the gathering systems or compressors but still handle the total gas production of the field.

4. Predict in advance the changes required in producing schedules and compressor cylinder sizing to maintain most efficient use of the gas plant throughout the life of the field.

5. Meet the gas contractural obligations and individual lease requirements.

6. Distribute gas-lift gas in such a way as to maximize production from this system without overloading the plant.

In the past, the conventional methods of analysis discussed earlier were used to maintain control of the over-all field operation. However, changing characteristics of the field have altered the basic plan of operation and have indicated that constant re-evaluation would be necessary to retain maximum economics on a day-to-day basis. Factors such as changing well and reservoir pressures have necessitated redistributions of compressor horsepower capacity to make more efficient use of the plant. Increasing gas-oil ratios due to gas breakthrough have resulted in the overloading of some of the gathering systems and the underloading of others. Changing prices of crude and condensate have shifted the emphasis of production among the four major reservoirs. The addition of new wells and new oil reserves has changed the over-all operation of the field, and most important the variable supply-and-demand requirements of the connecting gas markets are effecting the total amount of gas that can be produced to and handled by the central plant.

Because all of these factors are interdependent, an excess of engineering time was being required to maintain control; this fact indicated that a more powerful, and certainly more efficient, method of studying the field would be needed. The desired control has been achieved through the combination of linear programing and high-speed computers.

BASIC CALCULATION PHASE

In applying the linear programing technique, it was necessary to express all of the relevant factors in terms of linear equalities and inequalities. Formulation of these relationships was the most critical and time-consuming portion of the optimization study because every factor which has an influence on field operations must be included and must express the correct meaning. *If one factor is omitted or stated improperly*, the entire study can be ineffective. Once the linear restraints and definitional relations properly express the field program, optimization analyses are performed routinely with only the addition of new field data.

Table 1 illustrates the basic linear equalities and inequalities required for the field case study. Each relationship defines or expresses the restrictions governing a *group* of field variables; although there are only eight relationships shown, the actual study involves more than 100. To illustrate the meaning of these relationships, consider the following.

Restriction 1 states that the daily production of any oil or gas-condensate well in the field must not exceed the well's producing capacity. Well tests indicating the maximum producing capabilities in barrels per day are obtained from each well in the field. These tests are designed to express the economic maximum for each well so that operating difficulties will not be encountered and reservoir damage will not occur from excessive production.

Restrictions 2a through 2d pertain to the reservoir injection requirements for Zones A, B and C. These requirements were defined by separate reservoir studies to state the following.

1. Gas injection into Zone A must equal 100 per cent of the reservoir withdrawals to obtain maximum oil recovery from this reservoir.

2. An independently determined percentage of the total free gas produced from Zone B must be replaced to prevent gas-cap shrinkage and loss of recoverable oil.

3. Injection into Zone C, the gas-condensate reservoir, must be at least 5,000 Mcf/D to repressure and regain liquid lost from retrograde condensation.

4. The total high-pressure gas available from the plant must be equal to or greater than the total injection requirements of Zones A, B and C.

TABLE 1—STATEMENT OF FIELD PROBLEMS FOR LINEAR PROGRAMING SOLUTION

(x) Well test data [y] Field data or compressor data
{ } Optimum value solved for

1. Daily Production of Each Well:
   {Well production} $\leq$ (Maximum well capability) STB/D
2. Reservoir Injection Requirements—Mcf/D (Each Reservoir):
   (a) Σ {Well production Zone A} $\left[\frac{1}{B_o B_g} + R_p - R_s + \frac{\Delta W_p}{\Delta N_p}\frac{1}{B_g}\right]$ = {Zone A injection}
   (b) Σ {Well production Zone B}$[R_p - R_s]_B$ [0.95] = {Zone B injection}
   (c) [5,000] $\leq$ Zone C injection
   (d) {Zone A injection} + {Zone B injection} + [Zone C injection] $\leq$ (Σ optimum high-pressure-stage capacity)
3. Optimum Low Compressor Stage Capacity:
   (a) Σ {Well production} (Low-pressure R_p) − [Lease fuel] + (Borrowed gas) = (Low-pressure gas handled by plant)
   (b) [Σ Maximum Mcf capacity of low stage of 800 hp + 660 hp + 2(1,100 hp)] $\leq$ (Low-pressure gas handled by plant)
4. Optimum Intermediate Compressor Stage Capacity:
   (a) Σ (Well capacity) (Intermediate separator R_p) + (Total low-pressure gas) = (Intermediate-pressure gas handled by plant)
   (b) {Intermediate gas handled by plant} $\leq$ [Σ Maximum Mcf capacity of intermediate stage of 800 hp + 660 hp + 2(1,100 hp)]
5. Optimum High-Pressure Compressor Stage Capacity:
   (a) Σ {Well capacity} (High pressure R_p) + {Total intermediate-pressure gas} − {Gas-lift gas} = {High-pressure gas handled by plant}
   (b) {High-pressure gas handled by plant} $\leq$ [Σ Maximum Mcf capacity of high-pressure stage of 800 hp + 330 hp + 2(1,100 hp)]
6. Total Plant Capacity Horsepower (One for Each Compressor):
   (Optimum low-pressure gas volume) [hp/Mcf] + (Optimum intermediate-gas volume) [hp/Mcf] + {Optimum high-pressure gas volume} [hp/Mcf] $\leq$ [Total compressor hp]
7. Special Lease Requirements:
   {Well production} = (Maximum STB/D)
8. Gas-lift Requirements—Mcf/D:
   Σ {Well production} (input GOR) $\leq$ Σ {Well production} (R_p 2,000-psi separator)
9. Fulfillment Vector:
   Net profit = Σ {Well production} [Net $/bbl worth of crude]

Restrictions 3a and 3b state that sufficient stage capacity, must be available from the 800-, 660- and two 1,100-hp compressors to handle the low-pressure field gas production minus lease fuel plus borrowed gas volumes. Restrictions 4 (a and b) and 5 (a and b) state similar relationships for the intermediate and high-stage capacity. An average horsepower-per-thousand cubic feet factor was obtained for each of the 13 compressors and used in Restriction 6 to limit the capacity available from each individual stage within a given compressor. A restraint relationship of this form is written for each compressor and states that the volume of gas through the stage multiplied by the average horsepower-per-thousand cubic feet factor (total horsepower required for each pressure stage) must be equal to or less than the total horsepower capacity of the compressor.

Restriction 7 illustrates the special lease requirement that a given well be produced at maximum allowable, regardless of the effects of this well's production on the optimized program. Restriction 8 pertains to limitations on the volume of the gas-lift gas available and states that the total field gas-lift requirements must be equal to or less than the 2,000-psi field gas production.

The last relationship refers to the net profit, or the factor which is to be maximized. Because all produced gas is used in conducting the conservation programs, the production of gas has no value from a sales consideration; hence, gas does not contribute to the net profit. The lifting cost and royalty associated with each well are deducted from the oil value of that well to effect a net dollar-per-barrel worth of the specific crude. This factor, multiplied by the optimum production for each well, represents maximum daily profits for the field.

It should be noted that all of the linear equalities or inequalities listed in Table 1 contain one or more of the field variables so that all factors are related through common restraint relationships.

Once the basic relationships were properly stated, they were reduced to the form of a simplex matrix, as described in Ref. 1, and solved using the linear programing technique and the high-speed computer. The results of the optimization analysis are in the form of the optimum (1) barrels-per-day producing schedule for every well in the field, (2) clearance settings for each stage of compression, (3) produced gas volume into each gathering system, (4) gas-injection requirements for Zones A, B and C, (5) volume of gas to be handled by each compressor, (6) gathering-system pressure for each well, (7) volume of gas required for the gas lift system and (8) maximum daily profits resulting from the calculated producing schedule.

BASIC DATA REQUIREMENTS

The basic data required to conduct a linear program analysis consist primarily of the following.

1. The well test showing gas-oil ratio and maximum stock-tank barrels of oil production for each well in the field.

2. The voidage replacement for each of the reservoirs in fraction of total withdrawals for Zones A and B and minimum injection volume for Zone C.

3. The available compressor horsepower in terms of the number of compressors and maximum capacity of each stage of the compressors (compressor curves of thousand cubic feet per day vs horsepower).

4. The upper and lower limits on the volume of borrowed gas, the proposed disposition of this gas and its properties in terms of standard thousand cubic feet per barrel of reservoir voidage. Volumetric demands for return of borrowed gas also must be entered into the program.

The last category pertaining to basic data input for the optimization program is concerned with the flow diagram covering the compressor plant. Fig. 2 illustrates the gathering systems, the common manifolding among compressors and the flexibility available at the plant. This diagram is used as the basis for determining the available compressor horsepower for each of the gathering systems and for determining the gas available for injection into each of the three major reservoirs.

It should be noted that estimates of the producing capabilities of shut-in wells are included in the optimization program. Although the high gas-oil ratio or the apparent inefficiency of shut-in wells may indicate that it would be uneconomical to produce them, all producing possibilities should be included under a complete optimization study for the purpose of determining otherwise-unnoted avenues for improving operations.

FUTURE ANALYSES

The linear programing calculation used for the field case study is designed to be run on a frequent and routine basis so that maximum control can be maintained over producing operations. Future analyses will include new field variables such as condensate yields from contemplated gas-processing facilities, blending of the crude oil and condensate, and the effects of deferred income. The only data that will be required are maximum well tests conducted periodically for each of the wells, the addition of new wells as they are acquired and the varying supply-and-return requirements of the gas company.

CONCLUSIONS

The foregoing field case study is just one example of a new application of linear programing and optimization. As far as the oil industry is concerned, the technique has been used for several years in refining and transportation studies such as gasoline blending and product shipping. The calculation is also being extended into the areas of (1) optimum field development programs and (2) determining in advance the effect that unpredictable factors such as crude price, producing days and future markets will have on a given operation. These effects can be determined quickly and efficiently by selecting a range for each factor and evaluating its effect on the over-all program.

During the 12 months the example field has been studied, four machine runs have been made to determine optimized conditions. Initially, several significant changes were indicated in compressor stage settings. However, subsequent changes in field conditions have been somewhat gradual, and calculated optimum conditions have paralleled field conditions. Using the IBM 705 computer, a total field study can be performed in 1½ hours; thus, a significant amount of engineering time can be made available by virtue of the efficiency

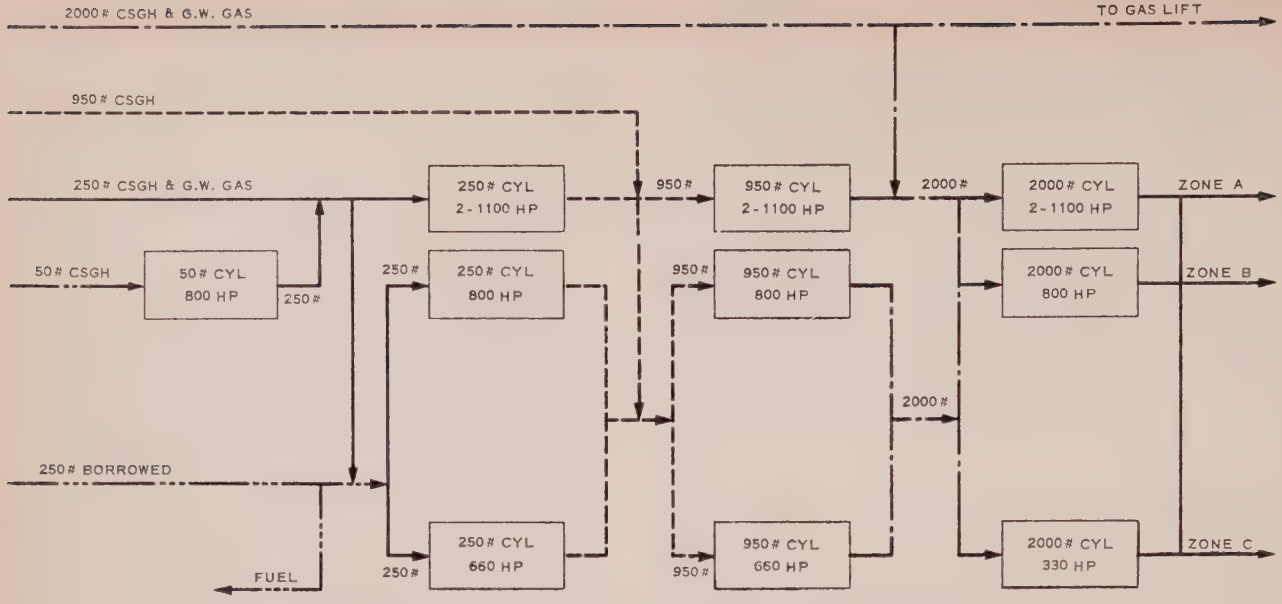

FIG. 2 — SIMPLIFIED FLOW DIAGRAM OF CENTRAL COMPRESSOR STATION.
(CSGH = Casinghead and G.W. = Gas Well.)

of the computer study. As the secondary recovery programs progress, the optimized course will become less readily discernible because relevant factors will vary to a greater degree, and material improvements in producing capacity should accrue. Further, there is assurance that the need for major equipment revisions will be recognized in time to realize their full benefit.

Based on the favorable results obtained from the field case study, it is concluded that a field problem of this type can be reduced to a series of linear relationships without seriously reducing accuracy. This technique is being applied in other areas for the solution of a large multi-well gas gathering and deliverability problem, and initial results also appear favorable. In fields where producing capacity is being controlled primarily by regulatory bodies, optimization routines should be used to minimize operating and lifting costs and, thereby to miximize net profits.

REFERENCE

1. Charnes, Cooper and Henderson: *An Introduction to Linear Programming*, John Wiley and Sons, Inc., N. Y. (1953). ★★★

Constant-Pressure Gas Porosimeter

A. H. HEIM
MEMBER AIME

SCHLUMBERGER WELL SURVEYING CORP.
RIDGEFIELD, CONN.

ABSTRACT

A method and apparatus for measuring gas porosities of rocks are described. The apparatus can be assembled from commercially available components. In principle, measurements are made by volume substitution at constant pressure. The maximum error is not more than 0.3 porosity per cent. Typical results are given.

INTRODUCTION

Determining the porosity of rock samples is one of the most important and yet most varied types of measurement in core analysis. Among the many techniques devised are the so-called "gas porosity" methods. An old and well known example is the Washburn-Bunting method.[1] The U. S. Bureau of Mines[2-4] described and later improved the apparatus for a now widely used method generally known as the "Boyle's law" method.

In the present form of the Washburn-Bunting method,[5] the volume of air in the pores of a rock sample at atmospheric pressure is extracted and then collected in a graduated burette at atmospheric pressure. The volume of air is read directly as the pore volume of the sample. The absolute error in reading the collected volume of gas is independent of the total volume; thus, the relative error is larger when the volume is small, as it is for rocks of low porosity. In addition, the sample after measurement contains mercury, which limits its use for other analyses.

The Bureau of Mines (or Boyle's law) method measures directly the solids volume of a sample from which the pore volume and porosity are derived, using a separate measurement of the bulk volume. Gas at a few atmospheres pressure is introduced into a sample chamber of known volume containing the rock sample. The pressure is accurately measured. Following, the gas is expanded into a burette at 1 atm, and the gas volume is read directly. From the initial pressure p_1 and the final pressure p_2 and volume v_2, the initial gas volume v_1 is calculated using Boyle's law; that is, $p_1v_1 = p_2v_2$. Volume v_1 minus the volume of the empty sample chamber is the solids volume of the sample. The accuracy of the method is limited, unless corrections are made, by deviations of the gas from the "ideal" gas-law behavior assumed in the simple form of Boyle's law.

Original manuscript received in Society of Petroleum Engineers office July 13, 1959. Revised manuscript received Nov. 14, 1960.
[1]Referer ces given at end of paper.

The purpose of the present paper is to describe a method for measuring the gas porosity of a rock which avoids many of these difficulties. Gas volumes are measured directly with the same accuracy as the bulk volumes. Pressures of at least an order of magnitude larger than those of previous methods are employed to insure rapid penetration of the gas into the sample. While special equipment may be built to apply the method, the porosimeter may be constructed as well from commercially available components. For simplicity, the apparatus described will be referred to as the "Constant-Pressure gas porosimeter".

THE CONSTANT-PRESSURE METHOD

Fig. 1 shows schematically the arrangement of components comprising the present Constant-Pressure porosimeter. Briefly, the method is one of *volume substitution* and may be considered a *null* measurement.

Omitting (for the present) some of the operational details, the method of measurement consists of the following three steps.

1. After evacuation, the volume of the measuring system (a ballast chamber, a manifold, two gauges and their connections) up to the sample chamber is filled with gas to a high pressure ($\sim$ 1,000 psi). A sample of the gas at this pressure is trapped in one side of a sensitive differential pressure gauge to serve as the reference pressure for subsequent steps.

2. The evacuated sample chamber containing the rock sample is opened to the measuring system. As the gas expands into the chamber, the resulting decrease in pressure unbalances the differential pressure gauge.

3. The pressure is restored by means of a mercury volumetric pump. The volume of mercury injected exactly equals the free or void volume of the sample chamber (volume of empty chamber minus the solids volume of the rock within). From the injected volume and the known empty chamber volume, the solids volume is obtained and the porosity calculated.

The pressure and the volume occupied by the gas are the same before and after opening the sample chamber. Expansion and compression of the gas are incidental operations and do not enter into the calculation of porosity. By the pressure balancing or nulling, the free volume of the sample chamber is merely substituted by an equal and measured volume of mercury. Since the measurements are at constant pressure, there are no compressibility corrections necessary for the sample chamber.

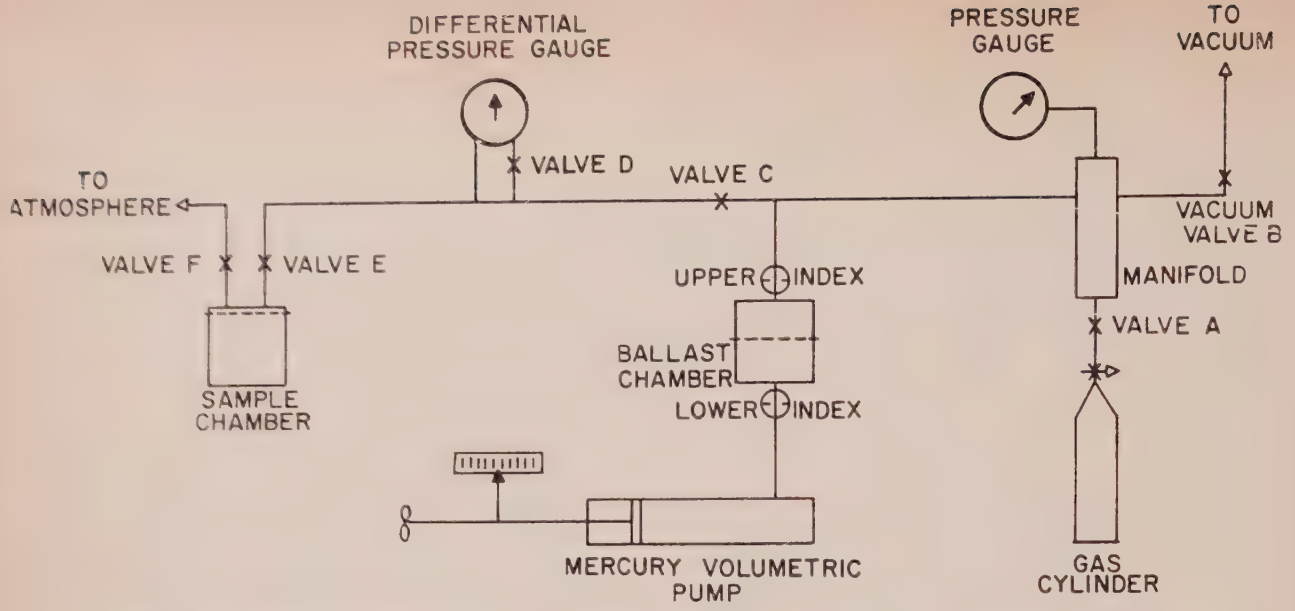

FIG. 1—SCHEMATIC REPRESENTATION OF THE CONSTANT-PRESURE GAS POROSITY METHOD.

DETAILS OF THE CONSTANT-PRESSURE POROSIMETER CONSTRUCTION*

The porosimeter presently being used (Fig. 2) utilizes a mercury capillary-pressure apparatus for all of the assembly of Fig. 1 to the right of Valve C. The differential gauge is a diaphragm differential pressure indicator. For the sample chamber, the sub-assembly of a mercury porometer or pycnometer assembly is used. Valve F is an integral part of this unit. All connections except two are made with swaged stainless-steel fittings and ⅛-in. OD stainless-steel capillary tubing. The connectors at the left of Valve C and between Valve E and the sample chamber are quick-disconnect O-ring types. The connection at Valve C must be broken to open the ballast chamber for measuring bulk volumes (described later). Valves C, D and E are stainless-steel toggle valves. Valve C is not necessary for porosity measurements; it is incorporated solely to permit the continued use of the apparatus for measuring capillary pressures.

OPERATION OF THE POROSIMETER

The rock sample is placed in the sample chamber and the system is evacuated to a static 20 to 30 μ of mercury pressure with Valves F and A closed. The sample chamber is isolated by closing Valve E. Then Vacuum Valve B is closed, Valve A opened and the manifold, ballast chamber and gauges are pressurized to about 1,000 psi with argon from the gas cylinder (the exact value of this pressure is not important). The mercury level is then placed at the lower index of the ballast chamber by adjusting the mercury volumetric pump, and the volume scale of the pump is set to zero. The system is now isolated from the gas cylinder by closing Valve A. A sample of the existing pressure is "captured" in one side of the differential pressure gauge by closing Valve D. Care must be taken that the gauge does not become unbalanced due to the slight compression when the valve is closed.

Valve E is opened and the gas in the measure system is allowed to expand into the sample chamber and sample pores. There is an accompanying decrease in pressure and an unbalance of the differential gauge. The mercury level in the ballast chamber is raised by means of the volumetric pump until the differential gauge is again balanced to indicate that the original pressure has been restored. The volume of mercury injected is read directly on the scale of the pump and is equal to the total volume added to the system on opening Valve E.

The same sequence of operations is repeated with the sample chamber empty. The difference between the volumes of the chamber with and without the rock sample is the *solids volume* of the sample.

With the system now open to the atmosphere, the volume of mercury necessary to raise its level from the lower to the upper index of the ballast chamber is measured. The measurement is repeated with the sample in the ballast chamber. The difference between the two volume measurements is the *bulk volume* of the sample.

From the solids volume V_s and the bulk volume V_b, the porosity is calculated,

$$\phi = \frac{V_b - V_s}{V_b} \times 100. \quad \ldots\ldots\ldots \quad (1)$$

MEASUREMENT PRECISION

The smallest division of the volume scale on the volumetric pump is .01 cc. Since this division is about ⅛-in. long, the volume could be estimated to at least one fourth of a division, or .0025 cc.

Although the differential gauge has contact screws graduated for pressure measurement, it is used solely as a null device. Changes as small as 0.1 psi at 2,000 psi can be determined. To make the gauge less sensitive to vibrations and valve operations, however, the contacts are opened slightly. For this reason it becomes the least-precise measurement, and volume readings are not better than .01 cc.

Of the two chambers, the ballast chamber has the smaller diameter, 2.5 cm, and the sample chamber has

*Specific manufacturer names and component catalog numbers can be obtained from the author.

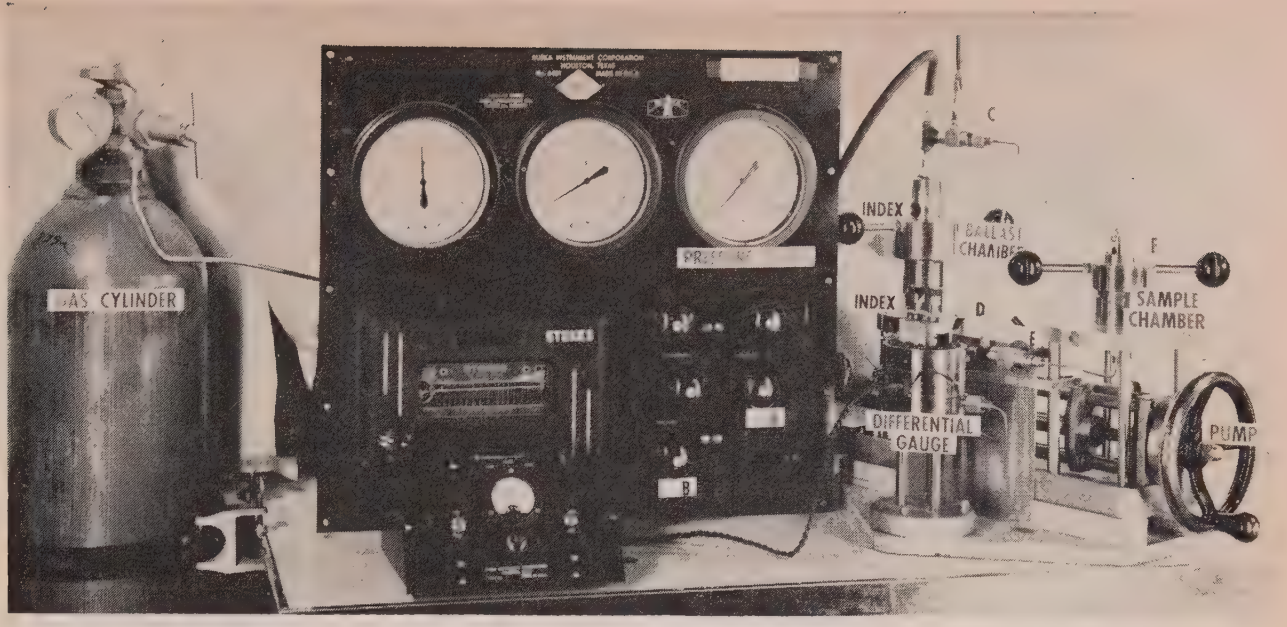

FIG. 2—CONSTANT-PRESSURE POROSIMETER ASSEMBLED.

the shorter height, 3.5 cm. These measurements limit the maximum sample size. The sample should fill as much as possible of the space of the sample chamber in order that the solids volume is not a small difference of two large numbers. Also, the empty volume of the sample chamber must be smaller than that of the ballast chamber between the two indexes because the latter must accept a volume of mercury at least equal to that of the sample chamber. A stainless-steel sleeve was fitted into the sample chamber to accept cylindrical rock samples 2 cm in diameter. A solid metal tare is added when the sample is much shorter than the length of the chamber.

Argon is used in preference to nitrogen to decrease the effect of gas adsorption on the sample. Helium would serve as well. No corrections are made for temperature changes. The mass of the metal parts is large, and the time necessary for recompression with the pump is sufficiently long for proper temperature equilibration.

The total gas volume of the porosimeter at null is about 100 cc, which at 1,000 psi gives a volume-to-pressure ratio of 0.1 cc/psi. If a pressure null error of 0.1 psi is made in each of the two determinations for the solids volume, the maximum possible error in V_S is .02 cc. In the measurement of bulk volume V_B, the repeatability of the ballast chamber volume is .005 cc, resulting in a possible error in V_B of .01 cc. The largest error possible in $(V_B - V_S)$ is then .03 cc. The magnitude of the resulting error in porosity is inversely proportional to V_B (for $V_B \gg \delta V_B$), but for the largest sample size of 11 cc for the described apparatus the maximum error is not more than 0.3 porosity per cent.

TABLE 1 — COMPARISON OF POROSITY PER CENT VALUES BY THE CONSTANT-PRESSURE METHOD WITH THOSE BY OTHER METHODS

Sample Description	Constant-Pressure Method		Density	Water Impregnation
	Argon	Nitrogen		
Vermont Marble				
No. 1	2.1	—	2.3	1.8
No. 2	2.6	2.7	1.8	1.6
Carthage Marble				
No. 1	3.0	4.1	3.1	2.2
No. 2	3.4	—	3.7	2.8
Shaly Chert	9.2	—	8.8	—
Ferruginous Shaly Sandstone	12.4	—	12.4	—
Berea Sandstone				
No. 1	17.9	—	17.6	17.9
No. 2	20.3	—	19.1	19.5
Siliceous Shale	46.6	—	47.1	—

TYPICAL RESULTS

Table 1 shows some typical measurements of porosity with the present system. The values are compared with those obtained from bulk and grain densities and vacuum impregnation with water. Values range from 2 to 47 per cent, and the samples include clean and shaly sands and carbonates. Gas porosities by the present method are shown slightly higher than water impregnation values, but they agree well with density values.

Argon gas values are generally lower than nitrogen values, but the differences are not important except in the low porosity ranges.

REFERENCES

1. Washburn, E. W. and Bunting, E. N.: "Determination of Porosity by the Method of Gas Expansion", *Jour. Am. Ceramic Soc.* (1922) **5**, 112, 527.
2. Taliaferro, D. B., Johnston, T. W. and DeWees, E. J.: "A Method of Determining Porosity: A List of Porosities of Oil Sands", R. I. 3352, USBM (1937).
3. Rall, C. G. and Taliaferro, D. B.: "A Bureau of Mines Method for Determining Porosity: A list of Porosities of Oil Sands", R. I. 4548, USBM (1949).
4. Rall, C. G., Hamontre, H. C. and Taliaferro, D. B.: "Determination of Porosity by a Bureau of Mines Method: A List of Porosities of Oil Sands", R. I. 5025, USBM (1954).
5. Muskat, M.: *The Flow of Homogeneous Fluids through Porous Media,* McGraw-Hill Book Publishing Co., Inc., N. Y. (1937), 116-117.

★★★

A Scale-Model Study of Bottom-Water Drives

D. H. HENLEY
JUNIOR MEMBER AIME
W. W. OWENS
F. F. CRAIG, JR.
MEMBERS AIME

PAN AMERICAN PETROLEUM CORP.
TULSA, OKLA.

ABSTRACT

The oil recovery performance of systems producing entirely by bottom-water encroachment has been experimentally determined in a series of scaled laboratory-model tests. The effects of well spacing, fluid mobilities, rate of production, capillary and gravity forces, well penetration and well completion techniques on the oil recovery performance have been investigated. The laboratory tests were performed using two uniform, unconsolidated sand-pack models. The models have ratios of the interwell distance to the formation thickness of 12 and 2, respectively. Tests at constant total fluid production rate were performed simulating a range of uniform reservoir characteristics and operating conditions encountered in field operations. The performance was determined by material balance and by observation of the encroachment of dyed fluids into the models. The results of the model tests agreed with those obtained mathematically when the conditions previously considered in theoretical studies were simulated, that is, when the oil and water are of equal density and no capillary forces exist.

The model study of bottom-water drive indicated that certain variables can affect the oil recovery performance to a greater degree than can be predicted by present analytical methods. In one comparison, the oil recovery at a water-oil ratio of 20 (obtained at a wide well spacing) varied as much as threefold, depending upon the system's properties and the production rate. Lesser effect of mobility ratio and no effect of capillary forces over the range studied were observed. The test results also showed that the deeper the well penetration into the oil column, the greater the total water production to a producing WOR of 20. However, the ultimate sweep efficiency, and so the oil recovery to this level of WOR, did not vary significantly with well penetration. Horizontal fractures at the top of the formation did not significantly change the sweep characteristics of the reservoir models when values of radius and fracture capacity encountered in actual reservoirs were used. Impermeable pancakes at the bottom of the well moderately increased the oil recovery efficiency both at water breakthrough and at high water-oil ratios. A method is outlined by which the oil recovery performance of other uniform bottom-water drive systems can be estimated from the information obtained in these model tests.

INTRODUCTION

When oil is produced from a well which partially penetrates an oil zone completely underlain by water, the water rises directly beneath the well in a symmetrical cone when the system is uniform. Two different flow mechanisms can cause the water cone to form—coning and bottom-water drive. In coning, the aquifer is relatively inactive and the cone is formed beneath the well by the pressure gradients associated with the oil flow to the well. The oil can be produced by a solution-gas drive, an edge-water drive or other driving forces in the interwell area. In a bottom-water drive, the driving force for oil production comes from an upward encroachment of the underlying active aquifer.

Two papers have analyzed the theoretical performance characteristics of bottom-water drive reservoirs. In the initial mathematical investigation, Muskat[1] established the equations which determine the pressure distribution in this type of reservoir and solved these equations for certain conditions. Specifically, it was assumed that the water and oil had equal mobilities and equal densities, there were no capillary forces, the pressure throughout the oil zone remained above the bubble-point pressure, a constant pressure existed at the initial water-oil contact and the oil was completely displaced by the encroaching water. These assumptions were used in obtaining analytical solutions. In general, Muskat found that the sweep efficiency to initial water breakthrough to the well was larger for the thicker oil zones, the closer well spacings, the lower ratios of vertical to horizontal permeabilities, the smaller the penetration of the well into the oil zone and the smaller the bore size of the well. The production history after water breakthrough was expressed as a volumetric sweep efficiency at a given producing water-oil ratio. The results indicated that cumulative oil production at producing water-oil ratios of 10 is less affected by the well spacing than is the water-free production history. Muskat studied well spacing which today would be regarded as close. The maximum value of his dimensionless well spacing (ratio of interwell distance to formation thickness) was 4.5. This would require the development of a 50-ft-thick oil sand on less than 10-acre spacing if the vertical and horizontal permeabilities were equal, with

Original manuscript received in Society of Petroleum Engineers office July 13, 1960. Revised manuscript received Nov. 14, 1960. Paper presented at 35th Annual Fall Meeting of SPE, Oct. 2-5, 1960 in Denver.

[1]References given at end of paper.

wider well spacing being simulated if the vertical permeability is less than the horizontal.

Hutchinson and Kemp[2] extended the mathematical methods of Muskat to include wider well spacings and added approximations to include the effect of gravity forces and non-unity mobility ratios. In their study, capillary forces were neglected. Mobility ratio was shown to influence the sweep efficiency at high producing water-oil ratios to a varying degree, depending on the well spacing studied. A maximum increase in the sweep efficiency of 40 per cent of the reservoir volume was found when the interwell distance was six times the formation thickness for mobility-ratio decreases from 2 to 0.33. They further concluded that gravity forces can affect the performance, but in most cases any significant improvement due to gravity effects will be realizable only at very low rates of oil production.

The results reported here were obtained from tests in scaled reservoir models in which several of the variables which were either not included or approximated in previous mathematical investigations can demonstrate their effect upon the performance. Non-zero fluid density difference, non-unity mobility ratios and the effect of capillary forces were evaluated at a wide and at a close well-spacing value for several degrees of well penetration into the oil zone.

MODEL SCALING METHODS

The use of dimensional and inspectional analysis to obtain physical and dynamic dimensionless groups which interrelate variables pertinent to fluid flow in porous media has received sufficient attention in the literature in recent years to obviate repeating the methods here.[3] It is desirable, however, to list the specific groups of variables which should control performance of bottom-water drive reservoirs. Inspectional analysis indicates the required inclusion of the geometric and dynamic parameters listed in Table 1.

Accepted model-scaling techniques require that the dimensionless groups listed in Table 1 be the same in the model and the prototype simulated. Inherent in the foregoing is the requirement that the relative-permeability and capillary-pressure curves be congruent functions of saturation in the model and reservoir. In general, reservoir models which are composed of unconsolidated sand will have relative-permeability and capillary-pressure curves different in shape and saturation range from most consolidated reservoir rock. However, these factors will affect the performance of models through their influence on the mobility ratio and the length and saturation distribution of the water-oil transition zone. Since for some types of reservoir flow behavior the performance in terms of the sweep efficiency has been shown to be dependent only on the mobility ratio, the difference in the relative permeability characteristics in model and prototype can be neglected so long as the mobility ratio is properly defined.[4] Frontal-drive calculations for the vertical flow of water into a preferentially water-wet reservoir have shown that over a wide range of rock and fluid characteristics the saturation of oil after passage of the stabilized transition zone is very close to the residual oil saturation. In calculating the mobility ratio, therefore, the relative permeabilities to oil in the unflooded region and to water after passage of the transition zone should be used. These calculations further indicate that the stabilized length of the transition zone existing at vertical flow rates of 1.0 to 0.001 ft/D will be, in many instances, less than 10 per cent of the length of the static transition zone.

TABLE 1 — BOTTOM-WATER DRIVE SCALING PARAMETERS

Geometrical Parameters	Possible Practical Range	This Investigation
Dimensionless Well Spacing $a_D = \frac{a}{h}\sqrt{\frac{k_v}{k_h}}$	2.0 to 20.0	2.0 to 12.0
Dimensionless Well Radius $r_{WD} = \frac{r_w}{h}\sqrt{\frac{k_v}{k_h}}$	8×10^{-5} to 2×10^{-1}	1.6×10^{-3} to 6.4×10^{-3}
Dimensionless Well Penetration $b_D = \frac{b}{h}$	0 to 1.0	.25 to 1.0
Rock- and Fluid-Property Parameters		
Mobility Ratio $M = \frac{k\mu_w}{k\mu_o}$	0.1 to 10.0	0.1 to 10.0
Cumulative-Production Parameter $R_2 = \frac{h\phi(1 - S_{or} - S_{wi})}{\frac{q}{A}t}$	Unity	Unity
Dynamic Parameters		
Gravity-to-Viscous Force Ratio $R_3 = \frac{kg\ \Delta\rho\ A}{q\ \mu_o}$	0 to 1,000	0.05 to 123
Capillary-to-Gravity Force Ratio $R_4 = \frac{\sigma\ \cos\ \Theta}{\sqrt{kg}\ \Delta\rho\ h}$	0 to 15	0 to 22

RESERVOIR MODELS

Two models were used to obtain the experimental information in this investigation. Each of the models represented a portion of the reservoir which surrounds a single well. Since the water invasion profiles at any well generally possess axial symmetry, the performance of a segment of any well yields information representative of the entire field if uniform well spacing and reservoir thickness exist. The models represented two values of the ratio of the interwell distance to the oil-zone thickness—2 and 12. The model simulating the closer well spacing was triangular and represented one-eighth of a square well-spacing pattern with a thickness of 12 in. and a drainage radius of 13.6 in. The model simulating the wide well spacing was a pie-shaped segment representing 1/24 of the drainage volume of a well with a thickness of 8.85 in. and a drainage radius of 60 in. A photograph of both models is shown in Fig. 1. Unconsolidated sand packs retained on sheets of artificially consolidated porous media served as bodies of the models. The bottom retaining sheet rested upon open channels which provided the means of maintaining a constant pressure over the entire bottom surface of the sand bodies. The sand packs used ranged from 30 to 250 darcies in permeability. Wells represented by slots 0.015-in. wide located at the corner of the models were installed to penetrate various depths into the sand packs. The sides of the models were made of Lucite which permitted both visual observation of the shape and location of the water-oil contact in the sand bodies and inspection of the sand-pack condition. The models were packed using vibration and flowing slurry techniques. A Neoprene sheet pressured from the out-

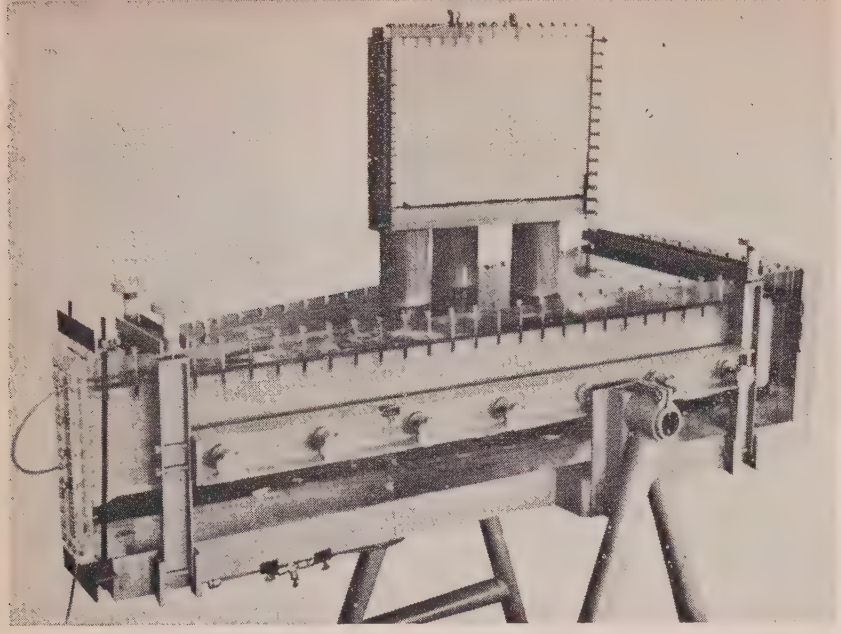

FIG. 1 — RESERVOIR MODELS.

side was used to maintain a tight seal across the top surface of the sand.

TEST METHODS AND INTERPRETATION

Tests on these models were conducted at constant injection and production rates. The aquifers or void spaces below the porous retaining sheets at the bottom of the sand-packed bodies were filled with the fluid, simulating the encroaching water, and the test started using a constant-rate injection pump. The volume of reservoir contacted by the invading front was determined by material balance for the tests where the fluids were miscible (100 per cent displacement) and by profile analysis and/or per cent of total recoverable oil for the immiscible fluid tests. In this way the volume contacted (that is, the volumetric sweep efficiency) was determined and related to other pertinent variables such as the producing water-oil ratio.

Various oil and water solutions were used to obtain the combination of fluid properties desired for a particular test. Additives used were barium bromide or chlorothene as weighting agents, ammonium chloride to alter the refractive index and glycerin or mineral oil to increase the viscosity. Interfacial tension between oil and water solutions were reduced in some cases by the addition of alcohol to both phases.

All tests using water and oil were made with a simulated connate or irreducible water saturation present in the model. This saturation was achieved by initially saturating a dry sand pack with the desired water and then displacing this water with the desired oil phase. In this manner an immobile or irreducible saturation exists which renders the sand pack spontaneously water-wet to the water encroaching during the test.

Production streams from the models were analyzed by refractive index in the case of miscible fluid tests and by graphical differentiation of cumulative-production curves for the immiscible fluid tests.

EXPERIMENTAL RESULTS AND DISCUSSION

THE WELL-SPACING PARAMETER

The discussion of model scaling methods indicated the relationship between the well spacing, formation thickness and the vertical-to-horizontal permeability ratio which specifies the dimensionless well-spacing parameter a_D. The results of the experimental variation of this well-spacing parameter indicate that the performance of the models generally agreed with the theoretical performance calculated by Muskat and by Hutchinson and Kemp, as the experimental conditions approached the conditions assumed in the calculations. Thus, in tests with miscible fluids, effective density difference approaching zero and a specified mobility ratio, the performance of the models approaches the theoretical performance. Fig. 2 shows results obtained from the close well-spacing model in which the gravity-to-viscous force ratio R_3 was successively decreased. The models were not designed to permit experimental operation with zero density difference, but the compatibility of the results with the theoretical ones at low density difference and at high flow rate is apparent. Similar results were obtained in the wide well-spacing model. These experimental results confirm the theoretical indication of the role of well spacing in the expected recoveries from bottom-water drive reservoirs.

RATE AND GRAVITY

The term interrelating the viscous and gravitational forces specified by the dimensionless ratio R_3 was used to study the effect of production rate on the performance of the models. The discussion of the effect of this term will be divided into its effect on the breakthrough sweep efficiency and on the after-breakthrough performance.

Fig. 3 shows the results of a number of tests in the model in which the interwell distance was twice the formation thickness. In all these tests, the well penetrated 25 per cent of the formation thickness. Tests at four mobility ratios (M) over a wide range of flow rates show the effect of these variables on the sweep efficiency of the reservoir at the time of initial water breakthrough. Higher sweep efficiencies at lower mobility ratios and lower rates are much as intuitively expected. The data at a mobility ratio of one can be observed to approach the theoretical value obtained by Muskat as the term R_3 approaches zero. The effect of rate appears to be greater for the higher mobility ratios. This is due to the increased tendency of the cone to cusp into the well at the unfavorable mobilities. A greater than twofold increase in oil recovery over the range of gravity-to-viscous force ratios studied

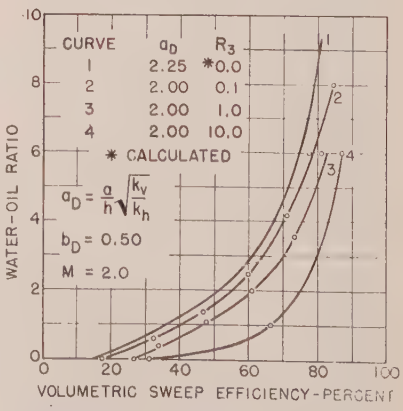

FIG. 2 — BOTTOM-WATER DRIVE PERFORMANCE FOR CLOSE WELL SPACING, EXPERIMENTAL AND CALCULATED.

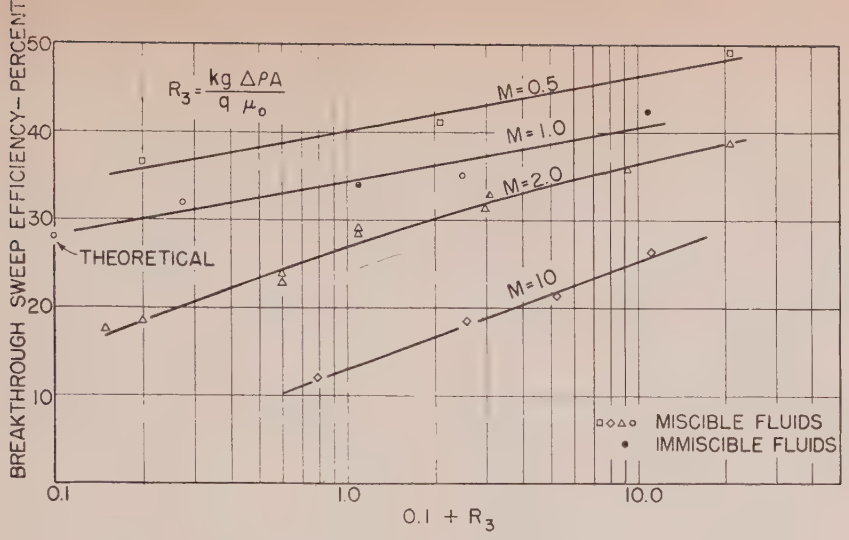

FIG. 3 — BREAKTHROUGH SWEEP EFFICIENCY FOR CLOSE WELL SPACING; ($a_D = 2$; $b_D = 0.25$).

was observed for the tests at a mobility ratio of two, with lesser increases over the same R_3 range as the mobility ratio used was more favorable.

The experimental results obtained from the wider well-spacing model with a 12:1 ratio of interwell distance to reservoir thickness did not exhibit the rate sensitivity on a percentage basis observed in the smaller model. The breakthrough sweep efficiency observed in all tests using the model having an interwell distance equal to 12 times the formation thickness was less than 1 per cent of the reservoir volume. The breakthrough sweep efficiency for this model can be found as that sweep efficiency at a water-oil ratio of zero on the several after-breakthrough performance curves shown throughout the paper. The absolute size and shape of the water-oil contact at water breakthrough was about the same in both models. For the same formation thickness, however, the reservoir volume drained by a well having a spacing-to-thickness ratio of 12 is 36 times that drained by a well having a spacing-to-thickness ratio of two. At water breakthrough, therefore, a volumetric sweep efficiency of 20 per cent in the smaller system would be equivalent to a sweep of less than 1 per cent in the larger system. No attempt was made to interrelate the effect of rate changes in the two models because sweep efficiency differences of less than 1 per cent in the large model were difficult to measure.

Fig. 4 shows the improvement in sweep efficiency which resulted in the wide well-spacing model from gravity forces and a favorable mobility ratio such as might normally be expected in bottom-water drives. At a mobility ratio of 0.5 and R_3 value of 123, an increase in the volumetric sweep efficiency from 23 to 86 per cent at a producing water-oil ratio of 20 resulted from the effect of gravitational forces on the invading water front. A prototype synthesized to match the conditions of the model test of Fig. 4 is shown in the legend of the figure. This prototype has properties that are within the range of those encountered in actual reservoirs and illustrates the favorable role of gravity in increasing the oil recovery in these systems. The higher sweep efficiency due to the inclusion of gravity effects would result in a higher oil recovery of over 1 million bbl/well for the prototype of Fig. 4. These results show that gravity effects must be considered in estimating oil recovery because they can be a major influence on performance.

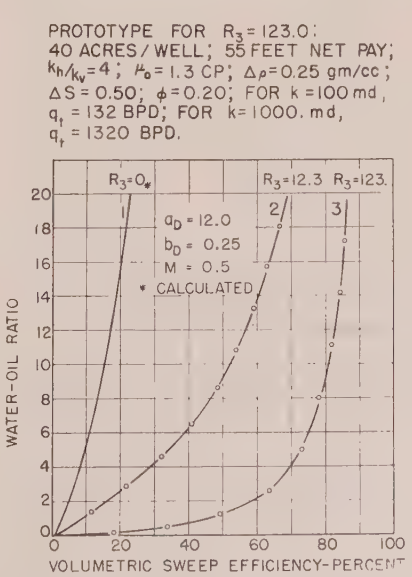

FIG. 4 — BOTTOM-WATER DRIVE PERFORMANCE FOR WIDE WELL SPACING, EFFECT OF PRODUCTION RATE

MOBILITY RATIO

The effect of lower mobility ratios for equal values of the gravity-to-viscous scaling term is shown in Fig. 5. For the wider well spacing, the increase in sweep efficiency as the mobility ratio decreased from 1.0 to 0.5 was found to be a higher percentage increase than was observed in the tests where the mobility ratio decreased from 2.0 to 1.0. Mobility ratios normally encountered in naturally water-driven fields generally will be less than unity. A wider range of mobilities was investigated in the close well-spacing model. Decreasing the mobility ratio by a hundred-fold increased the breakthrough sweep efficiency from 18 to 43 per cent. In these tests, the difference in the sweep efficiency observed at breakthrough for the different mobility ratios was observed to remain about the same percentage difference during the water-oil production period. This is noticeably different than the behavior observed in the wider-spacing model where differences in the breakthrough sweep efficiency of less than 1 per cent increased after breakthrough to as much as 20 per cent of the reservoir volume. As in other patterns of water encroachment toward wells, the more efficient oil recovery performance is obtained at lower values of the mobility ratio.

WELL PENETRATION

Well penetration into the oil zone of a bottom-water drive reservoir is commonly expressed as a fraction of

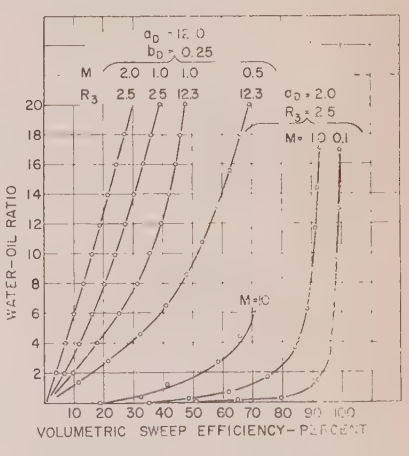

FIG. 5 — BOTTOM-WATER DRIVE PERFORMANCE FOR WIDE AND CLOSE WELL SPACING, EFFECT OF MOBILITY RATIO AND RATE.

the formation thickness. The effect of this variable was studied in both the wide and close well-spacing models. Fig. 6 shows the results of a pair of experimental tests in which the well first penetrated 25 per cent of the formation and a corresponding test in which the penetration was 100 per cent, which is the same as drilling and completing the well completely through the oil zone to the aquifer. In these tests, the difference in sweep efficiency at water breakthrough was 35 per cent of the reservoir volume. However, by the time a water-oil ratio of 11 was reached, the difference in sweep efficiency had decreased to less than four per cent. These results show that the ultimate recovery to producing water-oil ratios of about 20 does not depend upon the well penetration, although the volume of water produced to recover the oil increases with increasing well penetration. These test results further suggest that wells be completed over a sufficient fraction of the formation thickness to obtain the desired well productivity. Muskat[1] has shown the variation in well productivity for various degrees of well penetration.

CAPILLARY FORCES

The effect of capillary forces on the production performance of bottom-water drive reservoirs has been investigated to a limited degree. The breakthrough sweep efficiencies of two immiscible tests are shown on Fig. 3. Fig. 7 shows a comparison of miscible and immiscible after-breakthrough performance curves in the closer-spacing model. These tests indicated no difference in performance from initial water breakthrough to a producing water-oil ratio of 10. The absolute quantities of fluids produced in these tests were different because in the miscible test there was a 100 per cent displacement of the in-place fluid in the portion of the model invaded, while an initial irreducible water and a residual oil saturation existed in the immiscible test. The sweep efficiency performances, however, based on the per cent reservoir invaded were equal. The properties of the assumed prototype shown on Fig. 7 are those of a typical water-wet formation. The fact that the sweep efficiency was not influenced greatly by these capillary forces in this test (and in a limited number of additional tests with capillary-to-gravity force ratios R_4 up to 22) leads to the conclusion that over the range of conditions studied capillary forces do not affect the sweep efficiencies of bottom-water drive reservoirs.

SPECIAL TESTS

Several special tests were performed to determine what effect certain well treatments or production practices might have on the oil recovery performance of bottom-water drive reservoirs. Fractures, impermeable pancakes and intermittent production were evaluated with the models.

Fig. 8 shows the results of model tests in which fractures were placed in the wide well-spacing model at the top of the productive interval. The test in which the fracture radius of 25 per cent of the drainage radius of the formation and a flow capacity of four times the formation flow capacity indicated less than 2 per cent increase in the sweep efficiency. A fracture radius of 100 per cent of the drainage radius and capacity of 7,500 times the formation capacity were used to obtain the 95 per cent recovery at a water-oil ratio of one shown on the extreme right of Fig. 8. The first test indicates that many of the fractures which are produced today may not materially alter the sweep efficiency in a reservoir with bottom-water drive. The rate of production from wells in the reservoir can be greatly increased by fracturing, of course, but the sweep efficiency may not be greatly improved. The second test shows the greatly improved sweep efficiency with might be realized by large increases in fracture capacity and radius.

The close well-spacing model was used to evaluate the merit of placing an impermeable cement pancake at the bottom of the producing interval in an attempt to retard the cusping of water below the well. In the comparative tests shown in Fig. 9, a 7 per cent increase in the reservoir volume swept at water breakthrough was observed when an impermeable barrier with a radius of 25 per cent of the drainage radius of the model was placed immediately below the 25 per cent penetrating well. This improvement at breakthrough remained throughout the two-phase production period of the experiment. The increase in oil recovery at any producing water-oil ratio observed here on the basis of the absolute quantity of oil produced should be nearly independent of well spacings for the same-size pancake; the pancake should affect only the reservoir volume relatively near the well. This volume of increased oil production as

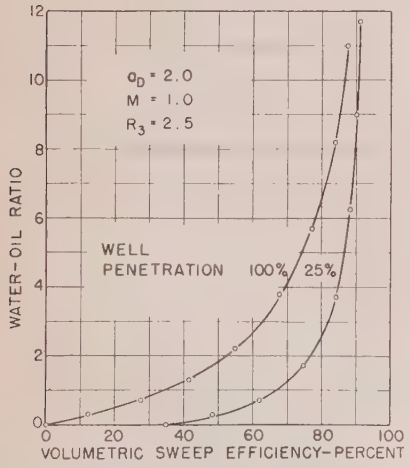

FIG. 6—BOTTOM-WATER DRIVE PERFORMANCE FOR CLOSE WELL SPACING, EFFECT OF WELL PENETRATION.

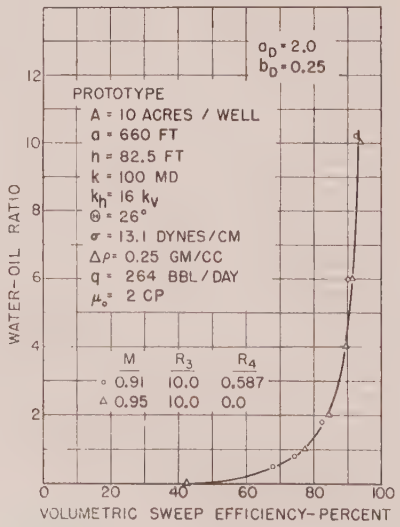

FIG. 7—BOTTOM-WATER DRIVE PERFORMANCE FOR CLOSE WELL SPACING, EFFECT OF CAPILLARY FORCES.

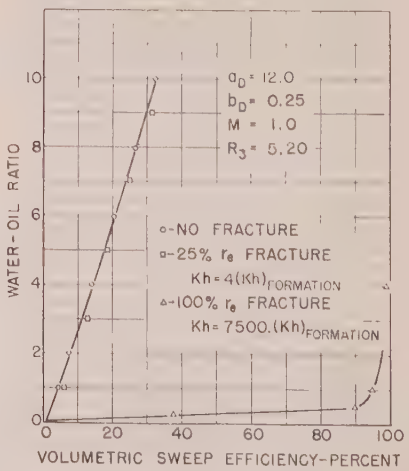

FIG. 8—BOTTOM-WATER DRIVE PERFORMANCE FOR WIDE WELL SPACING, EFFECT OF HORIZONTAL FRACTURE AT TOP OF FORMATION.

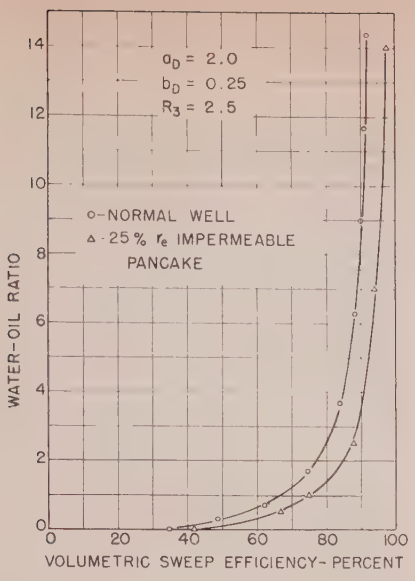

FIG. 9 — BOTTOM-WATER DRIVE PERFORMANCE FOR CLOSE WELL SPACING, EFFECT OF IMPERMEABLE PANCAKE AT BOTTOM OF PRODUCING INTERVAL.

a per cent of the total reservoir volume will be a much smaller improvement at wider well spacings where the basis for sweep efficiency will be a larger total quantity of oil.

To determine the effect that an intermittent production schedule might have on reservoir sweep efficiency, two tests shown in Fig. 10 were made. The constant-rate production test was performed in the same manner as the tests previously described. In the intermittent test, equal periods of production and shut-in were maintained, simulating production for 30 days followed by 30-day shut-in period. During the production period of the intermittent test, the flow rate was twice the flow rate during the constant production test so that the average rate in both tests over the total test time was the same. For the particular model configuration shown in Fig. 10, an increase of 12 per cent in reservoir volume swept was obtained by intermittent production to a producing water-oil ratio of 10. The improvement in sweep efficiency due to the intermittent flow condition appears to increase continually as higher water-oil ratios are reached.

As shown in Fig. 4, the value of the term R_3 (which includes flow rate) has a much greater effect on the after-breakthrough performance than on the sweep efficiency at water breakthrough. Furthermore, the volumetric sweep efficiency at any producing water-oil ratio does not vary linearly with the value of R_3. Therefore, it is expected that with

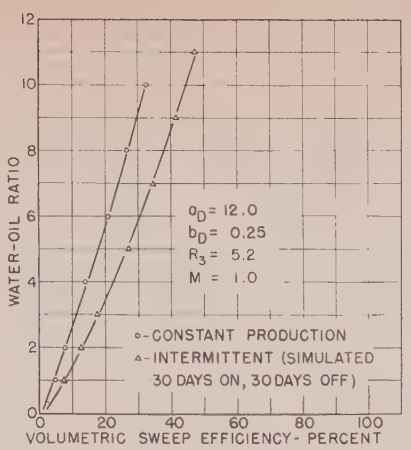

FIG. 10 — BOTTOM-WATER DRIVE PERFORMANCE FOR WIDE WELL SPACING, EFFECT OF INTERMITTENT FLOW.

periods of intermittent production the recovery performance would not be identical to that with continuous production at the average rate.

PERFORMANCE PREDICTION

The desired end product of a study such as the one described in this paper is a method of predicting the performance of any system which is producing by bottom-water encroachment. As has been discussed in previous paragraphs, many variables must be considered to completely describe all bottom-water drive systems. As an aid to estimation of the performance of any system which might come under consideration, a method of interpolation of some of the more pertinent variables is presented in the Appendix. This method will permit estimation of the performance as affected by well spacing, mobility ratio and production rate. The method was derived using the experimental variables presented in preceding sections, together with other experimental results and the theoretical results of Muskat and of Hutchinson and Kemp. This approximate method is proposed for use until a more formal method is developed.

The invasion pattern during downward encroachment of gas from a gas cap is analogous to that during upward encroachment of bottom water. While this prediction method was developed primarily from bottom-water drive systems, it can be used to predict the well performance during gas-cap encroachment.

CONCLUSIONS

For the range of conditions studied, the following conclusions about the performance characteristics of uniform bottom-water drive reservoirs have been reached.

1. The experimental results confirm previous mathematical work in showing that the ratio of the effective interwell distance to the effective oil-zone thickness is a factor of importance in determining the per cent of the available oil recovered to any given producing water-oil ratio.

2. Gravity effects must be considered in estimating oil recovery because they can be a major influence on performance.

3. As in other patterns of water encroachment toward wells, the more efficient oil recovery performance is obtained at lower values of mobility ratio.

4. The ultimate recovery at water-oil ratios of about 20 will not depend on the well penetration at a unit mobility ratio, although the volume of water produced increases with increasing well penetration.

5. Capillary forces do not affect the sweep efficiency of bottom-water drive reservoirs over the range of conditions studied.

6. Extremely high-capacity, large radius fractures at the top of the productive zone can result in greatly improved sweep efficiencies. However, fractures of the capacity and radius currently obtainable have little effect on over-all oil recovery. In another test an impermeable pancake at the bottom of the well moderately increased the oil recovery efficiency both at water breakthrough and at high water-oil ratios.

NOMENCLATURE*

a = interwell distance
b = well penetration
E_{vs} = volumetric sweep efficiency
k_v = vertical permeability
k_h = horizontal permeability
M, N = empirical constants
R = dimensionless ratios
θ = contact angle

SUBSCRIPTS
BT = breakthrough

REFERENCES

1. Muskat, M.: "Performance of Bottom-Water Drive Reservoirs", *Trans.*, AIME (1947) **170**, 81.
2. Hutchinson, T. S. and Kemp, C. E.: "An Extended Analysis of Bottom-Wa-

*For definitions of other symbols, see AIME Symbols List in *Trans.*, AIME (1956) **207**, 363.

ter Drive Reservoir Performance", *Trans.*, AIME (1956) **207**, 256.

3. Geertsma, J., Croes, G. A. and Schwarz, N.: "Theory of Dimensionally Scaled Models of Petroleum Reservoirs", *Trans.*, AIME (1956) **207**, 118.

4. Craig, F. F., Geffen, T. M. and Morse, R. A.: "Oil Recovery Performance of Pattern Gas or Water Injection Operations from Model Tests", *Trans.*, AIME (1955) **204**, 7.

APPENDIX

RESERVOIR PERFORMANCE PREDICTION

DIMENSIONLESS WELL SPACING PARAMETER

Both theory and experimentation have shown the wide variation in reservoir sweep efficiency which can result from various well spacings for a given thickness of reservoir. The importance of this parameter requires that careful estimation be made of the factors which comprise this grouping of variables. The two most important factors which must be estimated are the ratio of the vertical to horizontal permeabilities and the thickness of the oil-bearing zone.

Muskat's calculations of bottom-water drive performance provide two methods of estimating the ratio of vertical to horizontal permeabilities. Even if an indication of the value of this ratio is known from core data, confirmation by one of the following methods will be desirable because the gross properties of the reservoir must be evaluated. Muskat suggested that the quantity of oil produced at initial water breakthrough in conjunction with appropriate saturation changes be used to calculate a sweep efficiency which should be a direct function of the dimensionless well spacing. Comparison with theoretical spacing-to-thickness ratio will show the ratio of horizontal to vertical permeabilities which is required to equate the actual ratio to the one predicted from the performance. Hutchinson and Kemp replotted Muskat's productivity data to obtain a correlation which would permit estimation of the over-all ratio of vertical to horizontal permeabilities from well test information. Either or both of these methods should be used to obtain an estimate of this important parameter.

In conjunction with the well spacing and permeability ratio, the effective reservoir thickness must be known to completely specify bottom-water drive systems. This thickness should take into account the transition zone from the irreducible water saturation in the formation far removed from the initial water-oil contact to the residual oil saturation at the initial water-oil contact. Since capillary forces have been found not to alter greatly the sweep efficiency, a possible solution is to convert the transition zone to an equivalent thickness of reservoir containing the minimum water saturation.

OTHER SCALING FACTORS

The other scaling factors needed to determine the reservoir performance are the well penetration, the gravity-to-viscous force ratio and the mobility ratio. These factors have been listed in the model scaling discussion, and their calculation is straight-forward.

DETERMINATION AND USE OF THE PERFORMANCE CURVE

The desired performance curve for bottom-water drive reservoirs is the volumetric sweep efficiency as a function of the producing water-oil ratio. To determine the specific curve for any combination of reservoir conditions, two separate correlations will be used. First, an equation relating breakthrough sweep efficiency as a function of well spacing to well penetration when corrected for mobility ratio and rate effects will determine one end of the after-breakthrough curves. A separate correlation in which the after-breakthrough performance can be plotted as straight lines will be used to determine the water-oil ratio vs sweep efficiency from a water-oil ratio of 2 to 20. Using these two correlations, a plot of water-oil ratio vs sweep efficiency can be prepared from which water and oil production as a function of time can be determined.

Breakthrough Sweep Efficiency

As discussed earlier, the breakthrough sweep efficiency of a bottom-water drive reservoir varies with all the variables which control the system. However, the well spacing and well penetration have the greatest effect upon the volumetric sweep efficiency at initial water breakthrough. Muskat showed that for a given well penetration, the breakthrough sweep efficicency for a mobility ratio of one and for zero density difference varies inversely as the square of the dimensionless well spacing over certain ranges. In addition, the well penetration has a second, almost linear effect from a penetration of 20 to 80 per cent of the formation thickness. These effects can be combined into the following equation.

$$(E_{vs})_{BT} = (1.81 - 2.12\, b_D)\frac{1}{a_D^2} \quad \ldots\ldots\ldots (1)$$

when $a_D > 3.5$

$0.2 < b_D < 0.8$

$M = 1.0$

$\Delta\rho = 0.0$

This equation will predict breakthrough sweep efficiencies at most values of the well spacing which will be encountered in reservoirs. For values of a_D less than 3.5, reference to Muskat's work[1] should be made.

At this point, a discussion of the effect of mobility ratio and rate will be required to specify completely the volumetric sweep efficiency at water breakthrough. Experimental evidence of the effect of these variables is known only at the two spacings studied by the use of models. An effect of rate and a lesser effect of mobility ratio up to 40 and 10 per cent sweep efficiency, respectively, at water breakthrough may be

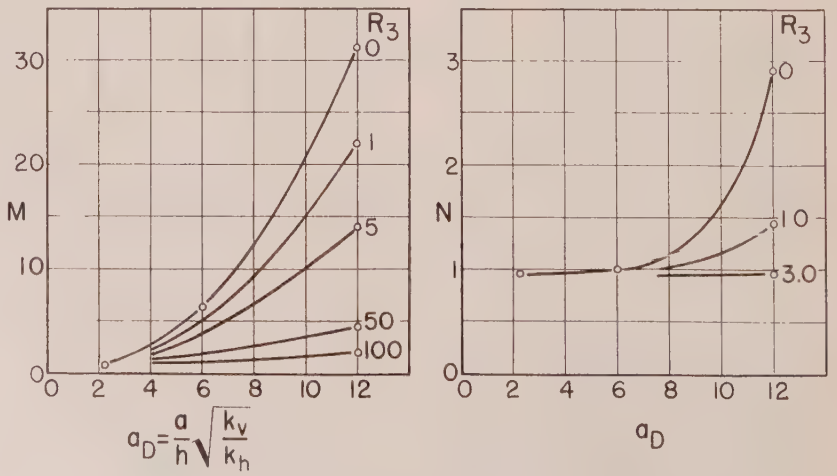

FIG. 11 — EMPIRICAL PERFORMANCE CONSTANTS, MOBILITY RATIO = .05.

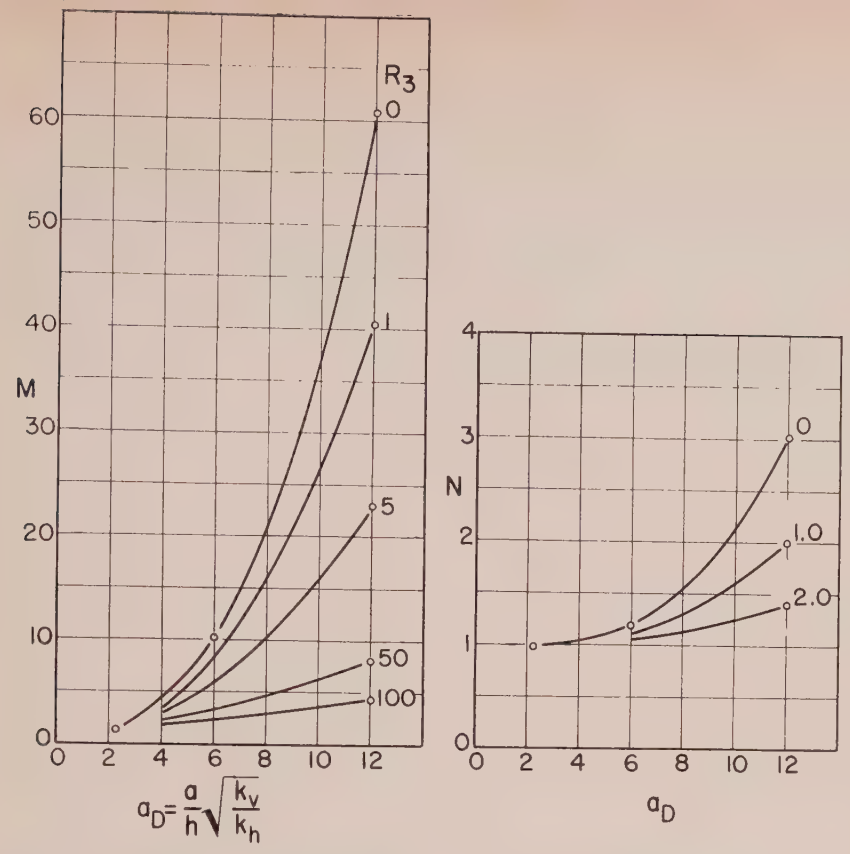

FIG. 12 — EMPIRICAL PERFORMANCE CONSTANTS, MOBILITY RATIO = 1.0.

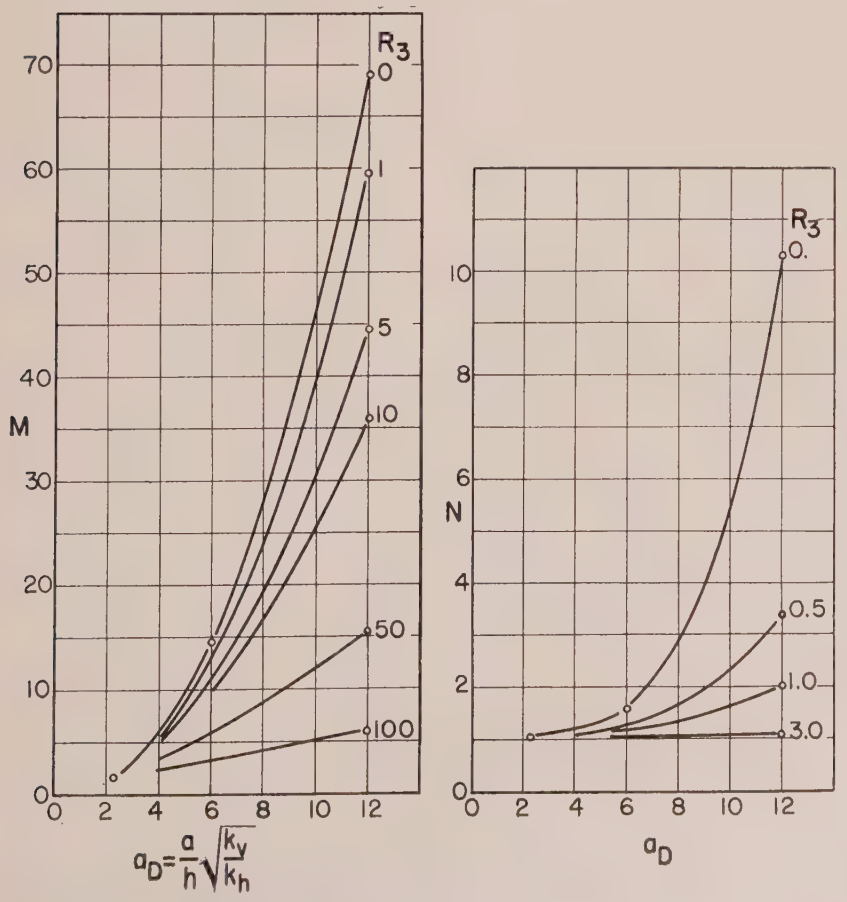

FIG. 13 — EMPIRICAL PERFORMANCE CONSTANTS, MOBILITY RATIO = 2.0.

expected at very close well spacings. At an a_D value of 12, the maximum change observed due to these variables was less than 1 per cent. The transition of these effects between a_D values of 2 and 12 cannot presently be quantitatively determined. However, the variables appear to affect the performance in areas which are near, or immediately below, the production well. Hence, a method of extrapolating the variations due to gravity and mobility ratio from $a_D = 2$ to higher values is proposed. The method simply involves changing the absolute value of the volume increase or decrease at $a_D = 2$ to an equivalent percentage of the wider spacings.

$$\frac{\Delta(a_D = x) = \Delta(a_D = 2)}{V(a_D = 2.0)} \cdot \cdot \cdot \cdot \cdot \quad (2)$$
$$V(a_D = x)$$

where Δ = a change in the volume of oil produced due to non-unity mobility ratio or finite gravity forces.

Testing this relation on the only available experimental information shows that a 10 per cent increase in sweep efficiency at $a_D = 2$ is equivalent to a 0.3 per cent increase at $a_D = 12$, which is the order of magnitude of the experimental results at this spacing.

After-Breakthrough Sweep Efficiency

The best method found for handling and interpolating the after-breakthrough sweep efficiency is an alternate plotting procedure in which most of the performance curves after breakthrough will occur as straight lines. It was found in the course of the analysis of the information obtained from these experiments that, if the water-oil ratio divided by the sweep efficiency was plotted as a function of the water-oil ratio, nearly straight lines were obtained between water-oil ratios of 2 and 20. This type of plot was used to correlate the data.

The first step in the method was to determine the slope and intercept of the curves in their rectified form. These slopes and intercepts then were cross-plotted as functions of the variables studied. The resulting curves are presented in Figs. 11, 12 and 13. A separate set of curves is provided for mobility ratios of 0.5, 1.0 and 2.0. The coefficients from these graphs then are used in the equation

$$E_{vs} = \frac{(\text{WOR})}{M + N\,(\text{WOR})} \cdot \cdot \cdot \cdot \cdot \cdot \cdot \cdot \cdot \quad (3)$$

A tabulation in which E_{vs} is cal-

culated as a function of WOR from this equation then can be replotted on rectangular paper to obtain the desired performance curves. The coefficients most appropriate to the reservoir under study should be selected from these graphs. Some care is required in this interpolation method. Normally, the coefficients M and N will be more correct at high water-oil ratios, but they may be used safely to a water-oil ratio as low as two. However, once the shape of the performance curve from 2 to 20 is obtained and the breakthrough sweep efficiency determined as previously described, a rectangular graph of E_{vs} vs water-oil ratio may be completed graphically between the known values. In addition, the coefficients should not be used to calculate performance curves for systems having a_D values less than about four.

When the performance in terms of the producing water-oil ratio as a function of the volumetric sweep efficiency is known, the actual quantities of water and oil produced can be calculated easily from the total reservoir size, porosity and saturation changes by using incremental material balances. These quantities can be related to production times by incorporating the desired or available production rate. The most-often-desired result is the total quantity of oil and water produced as a function of time. ★★★

A Sonic Method for Analyzing the Quality of Cementation of Borehole Casings

M. GROSMANGIN — SCHLUMBERGER SURENCO, S. A., CARACAS, VENEZUELA
F. P. KOKESH — SCHLUMBERGER WELL SURVEYING CORP., HOUSTON, TEX.
P. MAJANI — SCHLUMBERGER SURENCO, S. A., CARACAS, VENEZUELA
MEMBERS AIME

ABSTRACT

Determination of the quality of cementation of casing in oil wells in the past has involved inflow and circulation tests to insure that the producing zones were adequately sealed off from the adjacent zones. Existing logging methods, such as temperature and radioactivity surveys, may detect the presence of cement behind the casing. However, the qualities of the cement (i.e., its hardness and particularly its bond to the casing) are not indicated.

The new logging method described in this paper operates on the principle that the attenuation of a sonic pulse transmitted by a casing is greatly increased when that casing is bonded to an outer annulus of hard material (such as set cement) which has an appreciably smaller sonic-wave velocity than that of the casing.

The down-hole tool contains a source of recurrent sound pulses which are detected by a receiver spaced a few feet from the source The amplitude of the detected casing-borne pulse is measured, and the resulting signal is transmitted to the surface where it is recorded vs depth. Since amplitude is a function of attenuation, the log is readily interpreted.

Laboratory studies have shown straightforward relationship between attenuation and such variables as source-detector spacing and per cent of circumference bonded. It is shown that cement not set or not bonded to the casing has comparatively little attenuating effect. Field examples show not only the cement top, but also the variation in cementation quality below the top. Further, the increase of bonding with time and after squeeze cementation is depicted. The detection of poor cement jobs is confirmed by production tests and by formation-test results.

It is anticipated that the method will have wide application in evaluating cementation quality prior to formation testing in completions and recompletions. The analysis it affords may aid in further improving cementation techniques.

INTRODUCTION

The main purpose of oilwell cementing is to isolate a production zone from other undesirable zones. To investigate whether this purpose has been accomplished, several logging methods have been used such as temperature logs, radioactive tracer logs, etc. While these logs all respond to the presence of cement behind the casing, they do not indicate the degree of bonding of the cement to the casing.

Early in the application of sonic logging, it was noticed that considerable attenuation of sound signals takes place in cemented pipe and is often made evident on the standard Sonic log by cycle skipping.[1] The development of a circuit capable of continuously recording the amplitude of the casing-borne sound signal has made possible an extensive series of laboratory and field tests, which gave the following results.

The amplitude of a sound signal after it has traveled in a firmly cemented pipe is only a small fraction of that recorded by the same device in free pipe. This provides a wide spectrum of energy levels; for given local conditions, empirical values of the amplitude can be correlated with the quality of cementation. Interpretations made in this manner generally have been confirmed by production tests, circulation tests and squeeze cementation.

The purposes of this paper are to give a general description of the new logging method and to present some laboratory and field results.

CYCLE SKIPPING

Early attempts to study the quality of the cement behind the casing were performed with a standard Sonic log, which measures the transit time Δt, and were based on the well known phenomenon of cycle skipping.[1] Cycle skipping normally is interpreted as being a manifestation of weak signals at the receivers.

The log of Fig. 1 was run with the recording instrumentation adjusted to enhance cycle skipping. A mirror-image presentation was used for better visual interpretation. The transit time of sound in steel is about 58 microseconds/ft (corresponding to a velocity of 17,000 ft/sec), and the portions of the log where this value is recorded are interpreted as zones with no cement bond. Where cycle skipping produces a higher value of Δt, weak signals (or a high rate of attenuation) are indicated, and a good cement bond may be present.

The occurrence of cycle skipping, however, depends too much on instrument adjustment to give a uni-

Original manuscript received in Society of Petroleum Engineers office Sept. 9, 1960. Revised manuscript received Jan. 12, 1961. Paper presented at 35th Annual Fall Meeting of SPE, Oct. 2-5, 1960, in Denver.

[1] Tixier, M. P., Alger, R. P. and Doh, C. A.: "Sonic Logging", *Trans.*, AIME (1959) **216**, 109.

This page of *Petroleum Transactions, AIME* follows page 98. The intervening non-Transactions pages appeared in *Journal of Petroleum Technology.*

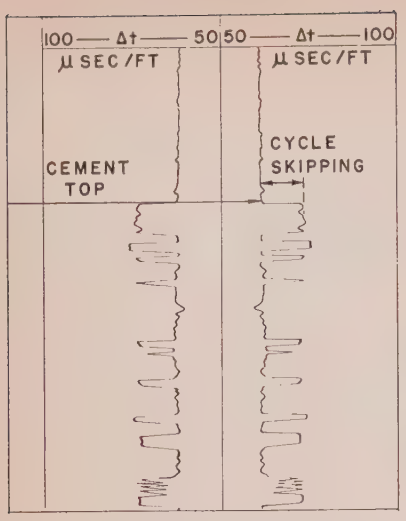

FIG. 1—EARLY ATTEMPT TO DETERMINE CEMENT TOP FROM CYCLE SKIPPING ON STANDARD SONIC LOG (3-FT SPAN).

formly reliable indication of signal strength. Cement quality, as revealed by attenuation of the signal, is presented much more effectively by continuously recording the amplitude of the signal.

DESCRIPTION OF LOGGING DEVICE

Sonic pulses in the Cement Bond logging tool, emitted by a transmitter at a repetititon rate of about 10/sec, are detected by a receiver located a few feet from the transmitter (Fig. 2). The sonic pulse wave is coupled by the drilling liquid into the casing through which the pulse-wave front travels with the compressional velocity of sound in steel. Some of the energy of the pulse wave is coupled back into the receiver by the borehole liquid. The ray path of the first arrival is shown in Fig. 2 by the arrowed solid line drawn from the transmitter, through the casing, to the receiver.

Typical transmitter pulses and casing-borne receiver signals are illustrated schematically in Fig. 3. In the present device, the ringing frequency of the transmitter is about 25 kilocycles/sec. Receiver output signals in unbonded casing and in casing bonded to a cement sheath are shown. The earliest arrivals at the receiver consist of relatively weak "forerunners" which are followed by oscillations of substantially larger amplitude. The forerunners generally drop below the threshold of detection in cement-bonded casing. Experience to date indicates that late arrivals are unpredictable in amplitude, probably because of distortions due to energy

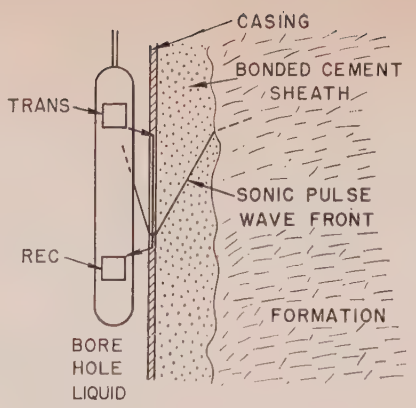

FIG. 2—SCHEMATIC DIAGRAM OF THE CEMENT BOND LOGGING TOOL.

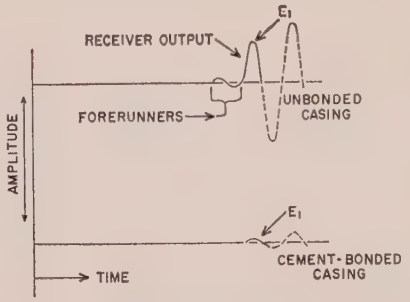

FIG. 3—COMPARISON OF TYPICAL RECEIVER SIGNAL IN UNBONDED CASING AND IN CEMENT-BONDED CASING.

which arrives by longer-time paths. The peak marked E_1 in Fig. 3 has been found to give the most reliable characterization of the amplitude of the casing-borne signal. In the present device, the amplitude of this peak is measured continuously, and the resulting indications are transmitted to the surface for recording.

Any attempt to describe the precise mechanics by which the sonic pulse is propagated through the casing, and by which the pulse is severely attenuated when bonded cement is present, is beyond the scope of the present paper. However, a superficial explanation of the mechanics of attenuation will be useful in understanding the operation of the device. Propagation of the sonic pulse through the casing results in a motion of the casing wall. Any solid material (e.g., set cement) located near and bonded to the casing will be carried along in this motion. Since the velocity in the cement is less than that in the casing, the imparting of motion to the cement can be brought about only by a continuous transfer of energy from the casing to the cement and the signal is thereby attenuated. If the material outside the casing is not solid or is not bonded to the casing, the motion of the casing is not impeded

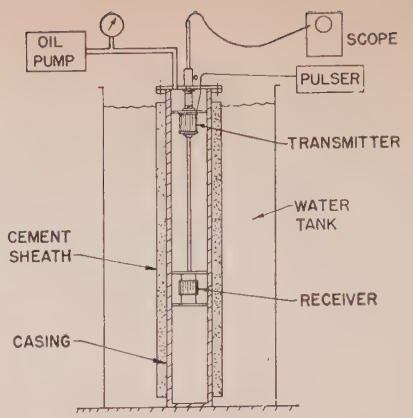

FIG. 4—CEMENT-BOND TEST SETUP USED IN LABORATORY STUDY.

appreciably; consequently, the loss of energy (i.e., the attenuation) is much less.

LABORATORY INVESTIGATIONS

Concurrent with the development of the logging tool, laboratory studies were undertaken to observe the effect of bonded cement on a casing-borne signal and to provide a basis for log interpretation. In the typical test setup shown in Fig. 4, a standard size of casing is immersed in a tank of water. A transmitter is fixed in position at the upper end while the spacing to the receiver can be varied at will. In this diagram, a cement sheath is shown bonded to the casing.

The relation between amplitude and transmitter-receiver spacing is shown in Fig. 5 for a 5½-in. OD, 23-lb/ft casing, both unbonded and also for the casing bonded to a 1¼-in. annulus of medium-density cement. The straight-line plots on a semilogarithmic grid show that the amplitude at a distance z from a reference point at the transmitter may be expressed as

$$\text{Amplitude} = A_o e^{-\alpha z} \quad . \quad . \quad . \quad (1)$$

where α is a composite attenuation factor.

The relation of Eq. 1 is not an unexpected result because, in a system of this kind, the rate of energy dissipation at a given point along the casing should be proportional to the energy level.

The attenuation is computed according to the conventional expression,

$$\text{Attenuation (in decibels/ft)} = \frac{20}{z} \log_{10} \frac{A_1}{A_2} \quad . \quad . \quad . \quad . \quad (2)$$

where A_1 and A_2 are the amplitudes at the beginning and the end, respectively, of a depth interval z.

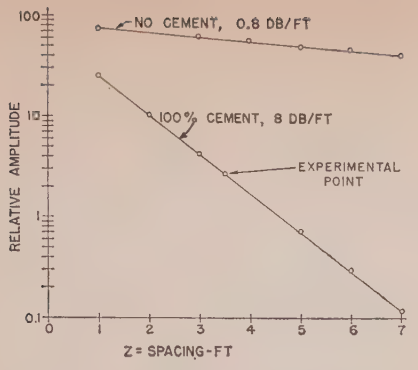

FIG. 5—PLOT OF RELATIVE AMPLITUDE VS TRANSMITTER-RECEIVER SPACING WITH THE SETUP SHOWN IN FIG. 4 (PLOT FOR THE SAME PIPE WITH NO CEMENT ALSO IS SHOWN).

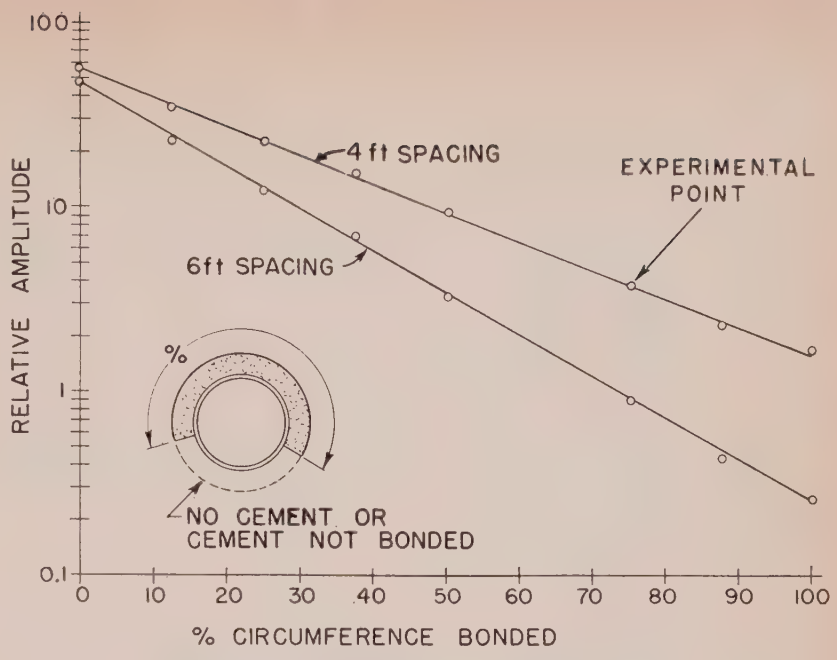

FIG. 6—RESULTS OF EXPERIMENT TO SIMULATE EFFECT OF CHANNELING ON THE RELATIVE AMPLITUDE.

For the typical case shown in Fig. 5, the 8-decibels/ft rate of attenuation in cement-bonded pipe is about 10 times greater than in unbonded pipe; the ratio of amplitudes (cement-bonded to unbonded), at a spacing of 4 ft between transmitter and receiver, is about 1:32.

Tests have shown that decreasing casing weight and increasing cement density both increase the attenuation. Rates as great as 14 decibels/ft have been encountered in 5½-in, 15-lb casing bonded to relatively dense cement.

Particularly interesting is the effect of vertical channels of no cement bonding on the signal amplitude. The bonded cement sheath of the casing sample of Fig. 5 was removed in vertical strips of increasing width. In Fig. 6, the casing is shown in cross-section, with the remaining cement expressed as per cent of full annulus. The channel is represented by the section which has no cement. The relation between amplitude and per cent of bonded cement again is a straight line on this presentation, the attenuation being greater for the 6-ft spacing than for the 4-ft spacing.

This evidence indicates that it might be possible to scale the readings of the Cement Bond log in terms of per cent bond. However, because of a number of variables such as cement type, setting time, thickness, and size and weight of pipe, it will be difficult to distinguish between 100 per cent bond and, say, 90 per cent bond. In applying the amplitude readings of a log for practical evaluation of the effectiveness of a shut-off, it will be necessary to take into account other factors such as the vertical extent of the bonded section.

Other laboratory tests show clearly that the mere presence of cement, soft or hard, is not the primary factor in signal attenuation. A hard cement sheath can be associated closely with a casing, but there is little attenuating effect if that sheath is not actually bonded to the casing. For instance, in a laboratory test where the bond of a cement sheath was broken without removal of the cement, the loss of bond became evident by a return of the attenuation to the uncemented rate. Therefore, it appears that the Cement Bond log can detect damage to cement jobs.

The thickness of the bonded cement sheath is relatively unimportant, provided that it is greater than about one-quarter wave length of the sonic pulse. For instance, the attenuation in a 5½-in. OD casing with a 2¼-in. cement sheath was not appreciably different from that with a 1¼-in. sheath. Therefore, it follows that, unless the cement annulus around a casing is relatively thin, the bond of the cement to the formation will not be expected to have a significant effect on the signal amplitude.

INTERPRETATION

Once the basic concept of amplitude attenuation as a result of loading the outside of the casing by solid material is recognized, the interpretation of Cement Bond logs for quality of cementation becomes relatively straightforward. Almost every log will extend over zones of no cement, or of no cement bond, which will be indicated by large-amplitude readings. Likewise, uniformly low-amplitude levels in sections of possible cement usually will correspond to zones where the cement bond is good in quality.

Fig. 7 shows a schematic Cement Bond log derived from laboratory measurements and field experience. The amplitude curve is presented at the right, with amplitude increasing to the right. Scaling, in terms of millivolts of amplitude of the casing-borne signal, is done arbitrarily for purposes of calibration. For the time being at least, it is subject to change with the particular type of instrumentation. The higher-amplitude levels, corresponding to completely free pipe, are of little interest; these are eliminated from the recording by al-

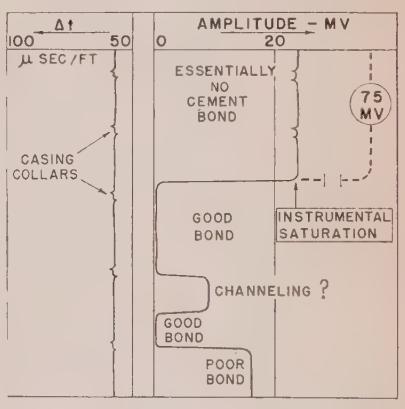

FIG. 7—SCHEMATIC CEMENT BOND LOG, DRAWN FROM LABORATORY MEASUREMENTS AND FIELD EXPERIENCE.

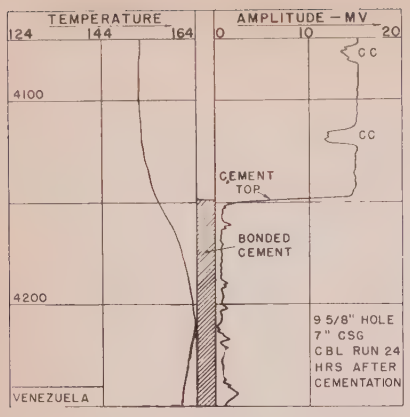

FIG. 8—COMPARISON OF TEMPERATURE LOG AND AMPLITUDE CURVE OF CEMENT BOND LOG IN DELINEATING A CEMENT TOP. NOTE CASING-COLLAR INDICATIONS ON THE AMPLITUDE CURVE.

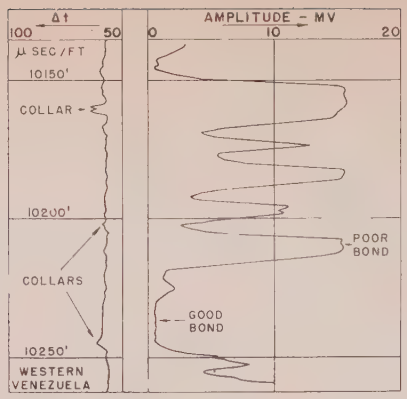

FIG. 9—FIELD EXAMPLE OF VARIOUS DEGREES OF BONDING BELOW THE CEMENT TOP IN A WESTERN VENEZUELA WELL.

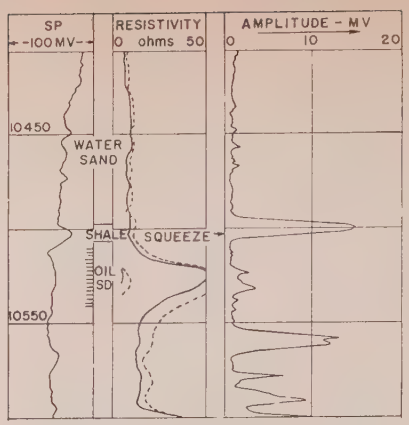

FIG. 10—CEMENT BOND LOG FOR WATER SHUT-OFF ANALYSIS.

lowing the circuit to saturate at a pre-set value, which generally corresponds to less than 40 per cent bond.

Low-amplitude readings usually indicate good cementation quality, while intermediate-amplitude levels correspond to zones of channeling or of poor bond.

The sonic-transit-time (Δt) curve is presented at the left on Fig. 7. Through appropriate instrumentation and operating technique, the Δt reading normally corresponds to the transit time of sound in steel (58 microseconds/ft), regardless of the amplitude.

In high-velocity formations, the Δt reading may differ from that of steel due to early signal arrivals through the formation. Such indications are expected to occur when the cement is bonded in some degree to both casing and formation. However, an estimation of the degree or percentage of bonding from transit-time readings will be very difficult to make because only a partial bond may result in detectable formation-borne arrivals.

Fig. 7 also shows typical shapes of the amplitude and Δt curves when the tool passes by a casing collar. This response, which has been verified in the laboratory, is complicated because of the discontinuities in the metallic path and varies widely with the type of casing collar. Generally, the casing collars can be clearly discerned on both the amplitude and the transit-time curves in free pipe. In cement-bonded sections, the casing-collar anomaly sometimes is obscured on the amplitude curve.

FIELD EXAMPLES

Field testing was started in April, 1959, and most of the early field logs were run in South Louisiana and Western Venezuela.

Fig. 8 shows a good cement job in a shallow well. The temperature log indicates the cement top to be somewhere between 4,120 and 4,150 ft, but the Cement Bond log pinpoints it at 4,148 ft. Above 4,148 ft, the amplitude curve reaches the saturation value. Two casing collars can be noted above the cement top. Below 4,148 ft, the curve stays mostly below the 1.5-mv level, indicating a good cement bond.

Fig. 9 shows a section of a Cement Bond log run in a deeper well. Here, intervals showing good, fair and poor bonding are found.

Fig. 10 shows an application of the Cement Bond log to water shut-off repairs. In this well, 7-in. casing was cemented in a 9⅝-in. hole at 10,695 ft, and the top of the cement was located by other means considerably above the top of the productive formations. When the well was brought into production (10,510 to 10,540-ft interval), it yielded only water. A Cement Bond log indicated a zone of poor bonding opposite the shale separating the productive sands from overlying water sands. A squeeze cementation was performed in the middle of the shale, after which the well produced clean oil.

The validity of the indications of the Cement Bond log also is proved by production tests. For instance, the log of Fig. 11 shows that there should be no communication between the two sets of perforations. As a matter of fact, the upper interval

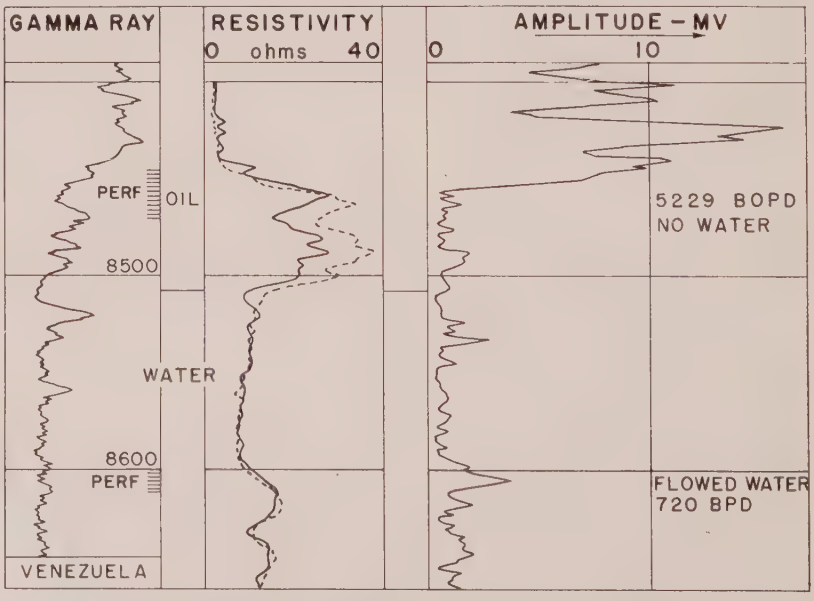

FIG. 11—GOOD CEMENT QUALITY INDICATED BY LOW AMPLITUDE THROUGHOUT THE SAND BODY IS CONFIRMED BY PRODUCTION TESTS.

produced clean oil and the lower one 100 per cent water.

Similarly, the Cement Bond log has proved to be useful in connection with the wireline formation tester in casing. Tests preferably should be attempted only where the Cement Bond log shows a good bond over an interval of several feet.

The Cement Bond log also can be used to check the effectiveness of a squeeze cementation. For instance, the first log (dashed amplitude curve) run in the well of Fig. 12 shows poor bonding over most of the section, particularly in front of the oil and gas sands. An attempt to complete in the oil sand had resulted in gas production. After a squeeze with 185 sacks of cement, the amplitude curve shows that the bond was greatly improved, especially opposite the gas sand; a subsequent recompletion produced oil.

Other field examples show that, while bonding generally is improved by a squeeze job, sometimes the original bond is destroyed. On Fig. 13, the first Cement Bond log run (solid curve) shows a poor cement job between 8,900 and 9,000 ft and an intermittent good-to-fair bond below 9,000 ft. The formation then was broken down with water, and two squeezes at 4,000 psi were performed. The second Cement Bond log run (dotted curve) shows a good bond between 8,900 and 9,000 ft, but the bond below 9,000 ft has been damaged.

Other problems for which the Cement Bond log provides additional information are the influence of down-hole conditions on the effectiveness of the cement job and the setting-up time of the cement. Fig. 14 shows a Cement Bond log run in a well where deep caving has occurred. The bond definitely is poorer in the washed-out sections (i.e., Section A), but even a true-to-gauge hole does not guarantee good cementation, as can be seen at Section B.

The cement bond often is poorer in a pay zone than in nearby water sands or shale sections. No completely satisfactory theory has been advanced to explain this phenomenon. An example appears in Fig. 15.

Fig. 16 shows a possible correlation between the quality of the cement bond and the use of scratchers.

During the course of field testing the Cement Bond log, systematic studies of bonding vs time were undertaken in several wells. Fig. 17 shows some of the results in a well where 9⅝-in. casing was cemented in a 12¼-in. hole at 9,157 ft. The

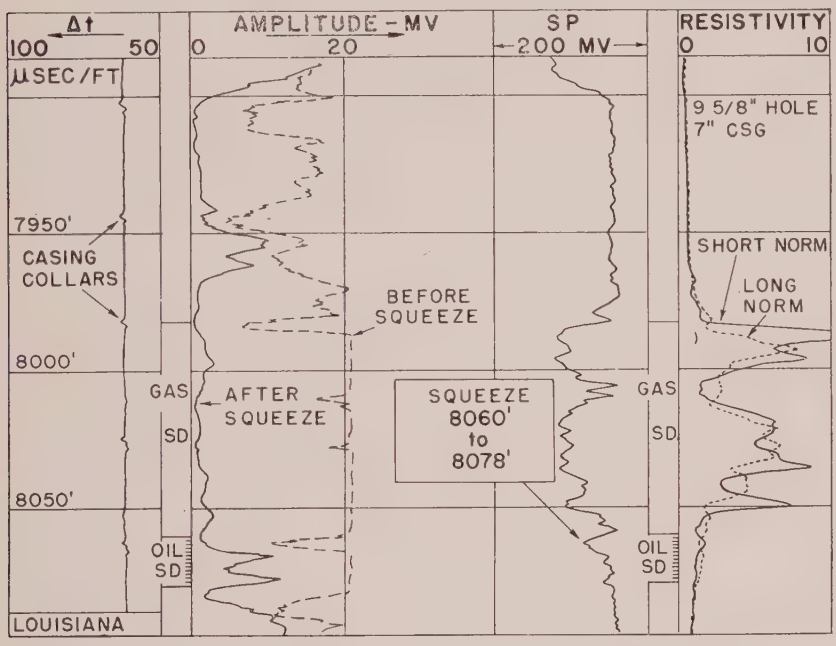

FIG. 12—"BEFORE-SQUEEZE" AND "AFTER-SQUEEZE" CEMENT-BOND CURVES INDICATE IMPROVEMENT IN CEMENTATION QUALITY RESULTING FROM SQUEEZE AT 8,060 TO 8,078 FT WITH 185 SACKS OF 14-LB/GAL SLURRY.

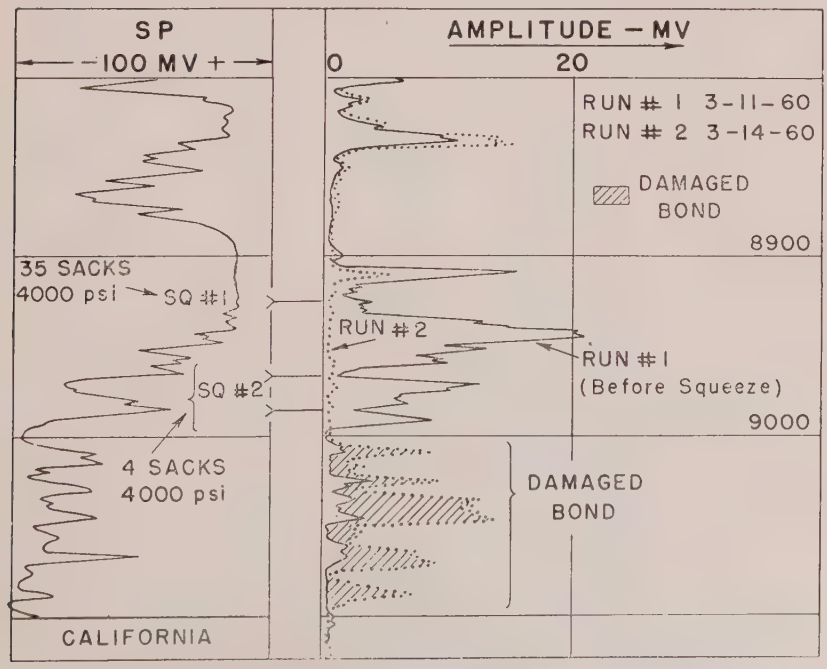

FIG. 13—DAMAGE TO BOND DUE TO SQUEEZE OPERATION.

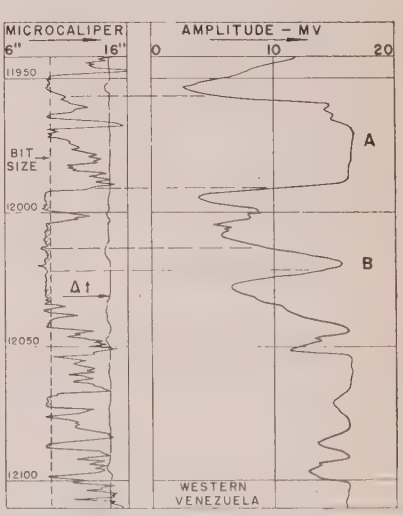

FIG. 14—GENERAL CORRELATION BETWEEN HOLE SIZE AND CEMENTATION QUALITY (7-IN. CASING CEMENTED IN 9⅝-IN. HOLE WITH 15.5-LB/GAL VENCEMOS CEMENT).

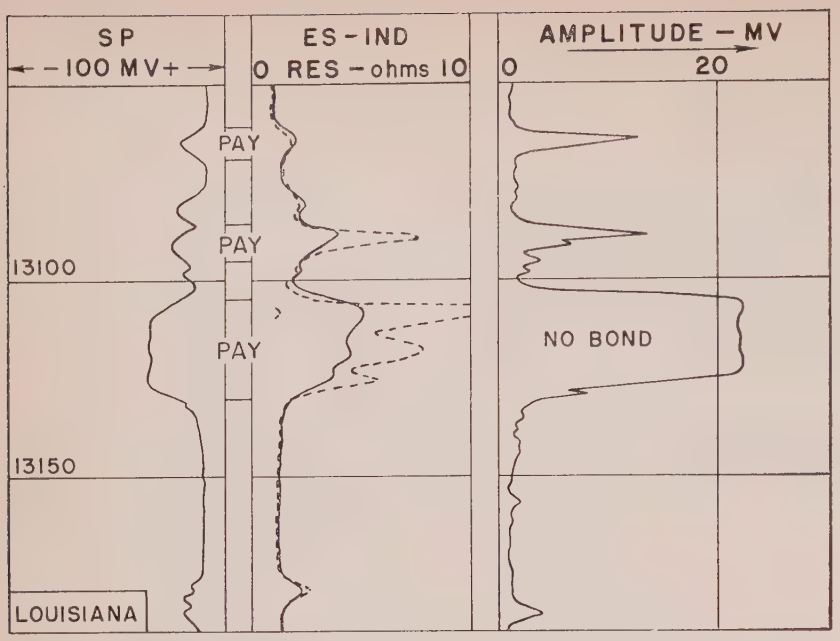

FIG. 15—EXAMPLE OF POOR BONDING FOUND OPPOSITE PAY SECTIONS (LOG RUN 11 DAYS AFTER CEMENTING).

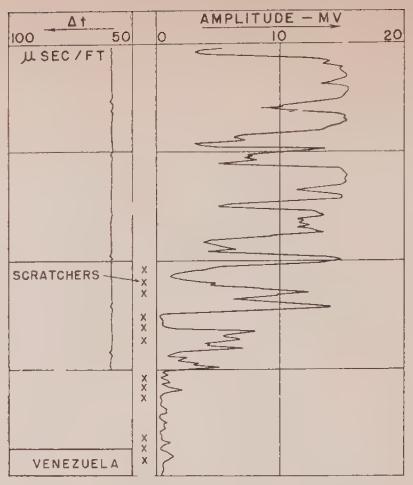

FIG. 16—GENERAL CORRELATION BETWEEN LOCATION OF SCRATCHERS AND CEMENTATION QUALITY (7-IN. CASING IN 12½-IN. HOLE; LOG RUN THREE DAYS AFTER CEMENTING).

cement used was designed for 14,000-ft wells and was retarded according to API schedules. Laboratory tests show that this type of cement may be expected to set completely within a period of 24 hours after cementation. When the cement is contaminated with 10 per cent quebracho mud, the setting time becomes 50 to 55 hours.

Seven Cement Bond logs were run 4, 5½, 18, 22, 28, 33 and 40 hours after cementation, four of which are shown in Fig. 17. A radioactive tracer log showed the top of the cement at 6,350 ft, above the section shown. In this section, bonding was nearly complete after 33 hours. It was complete throughout the section after 40 hours. However, there are differences in the development of bonding vs time. Opposite sand sections, bonding is complete after 18 to 22 hours, whereas opposite shales it takes about 12 hours longer. A possible explanation is that the cement loses water to the permeable sections and, thus, sets faster.

In the upper part of the cemented section below 6,350 ft, (not shown on the illustration), virtually no bonding occurred even after 40 hours, probably because the cement was contaminated by the mud.

Moderately low amplitudes have been found above the cement top in some wells. The most likely explanation is that the mud in the annulus has set up sufficiently to load the casing, that the formation has moved in to grip the casing, or that the pipe is wedged against the formation.

CONCLUSIONS

By the end of Nov., 1960, more than 500 Cement Bond logs had been run in North and South America. Not all of the logs were checked by circulation and production tests; however, whenever such tests were made, the success ratio of the Cement Bond log in assessing cementation quality has been extremely high.

The device responds to the attenuation of the casing-borne sound signal and is not expected, in the general case, to give an indication of cement-to-formation bond. Evaluation of formation bond by sonic methods is a most difficult problem involving such important variables as type and density of cement and transducer spacing. Assuming that a formation bond is required for good

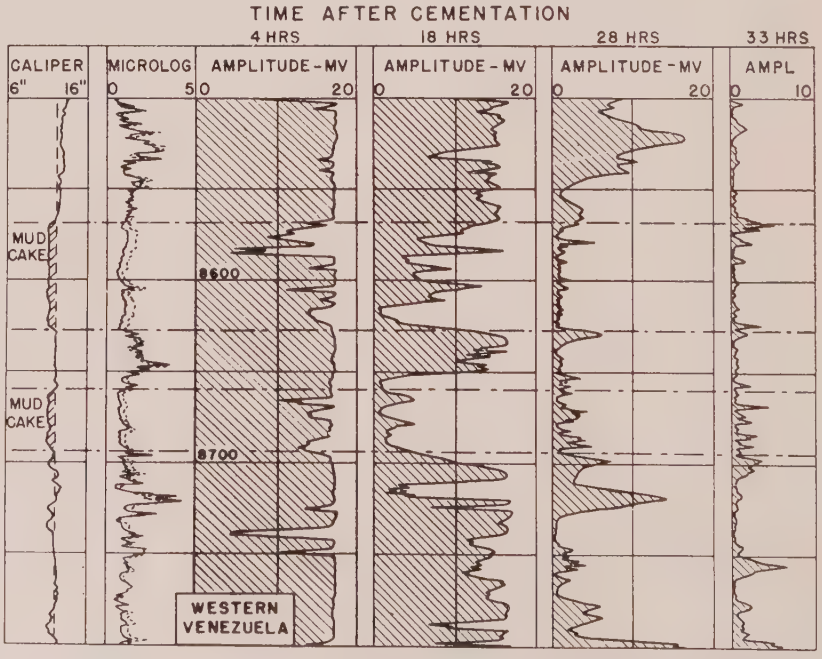

FIG. 17—TIME OF CEMENT SETTING STUDIED IN A WESTERN VENEZUELA WELL. CEMENT BOND DEVELOPED MORE QUICKLY OPPOSITE THE PERMEABLE FORMATIONS INDICATED ON MICROLOG-CALIPER CURVES AT LEFT.

cementation quality, the high success ratio of the present tool seems to indicate that a bond to the casing normally is accompanied by a bond to the formation; i.e., conditions favorable for one are generally favorable for the other.

It is concluded that this new tool can be used to evaluate the quality of the cement job around a casing string and, in many cases, that its use may eliminate the necessity of expensive inflow and circulation tests.

In addition, this new technique is particularly well adapted to the systematic investigation of down-hole cementation and the factors that affect it, including the following.

1. Time, temperature, pressure and depth.

2. Additives in the cement and in the mud.

3. Quantity of cement and rate of injection.

4. Reservoir and down-hole fluids.

5. Hole size and hole deviation.

6. Use of centralizers and scratchers.

7. Damage to cement bond by perforation and/or high-pressure squeezing.

It is to be expected that, when more results of basic research on cementation and on the propagation of sound through such discontinuities as occur in borehole configurations are available, the interpretation of the Cement Bond log can be made even more reliable.

ACKNOWLEDGMENTS

The authors are indebted to F. W. Zill and L. H. Gollwitzer, who were responsible for the logging-device development, and to R. H. Scanlan for the Cement Bond log laboratory study; to A. V. Rushton for important technical contributions; to J. C. Bouffard, who helped perform the field tests; to C. A. Doh for his constructive assistance in the preparation of the manuscript; to J. Arthur and R. A. Slotboom for their valuable suggestions; and to Cia. Shell de Venezuela, whose great interest sparked the development in its early stages. Release for publication of the field examples by the various oil companies is appreciated greatly.

★★★

The Effect of Restricted Fluid Entry on Well Productivity

F. BRONS
MEMBER AIME
V. E. MARTING*

SHELL OIL CO.
LOS ANGELES, CALIF.

INTRODUCTION

In the past, other authors[1, 2] have studied the influence of a skin effect on the productivity of a well. This skin effect, expressed by the skin factor S, is considered to be caused by a thin layer of impaired permeability immediately around the wellbore and extending vertically over the whole productive interval penetrated by the well. The skin factor S is defined as follows.

The pressure drop Δp in a well without skin is given by

$$\Delta p = \left(\frac{q\mu}{2\pi kh}\right) p_T \quad . \quad . \quad . \quad . \quad . \quad . \quad . \quad . \quad . \quad (1)$$

(For the meaning of the pressure function p_T see Ref. 3.)

The skin effect causes an increase in pressure drop described by

$$\Delta p = \frac{q\mu}{2\pi kh}(p_T + S) \quad . \quad . \quad . \quad . \quad . \quad . \quad . \quad . \quad . \quad (2)$$

where S is the skin factor, and $\left(\frac{q\mu}{2\pi kh}\right) S$ is the pressure drop in the skin.

Based on this, the impairment in productivity caused by a skin can be expressed by the fractional loss in productivity I, which is the loss in productivity divided by the total unimpaired productivity. For compressible flow in a stabilized well which drains a circular area of radius r_e, I is given by

$$I = \frac{S}{\ln r_e/r_w - 0.75 + S} \quad . \quad . \quad . \quad . \quad . \quad . \quad . \quad (3)$$

STATEMENT OF PROBLEM

The present paper deals with a different kind of productivity impairment. Consider a well in which part of the productive formation is blocked off completely, either by incomplete penetration or by exclusion of parts of the productive zone by blank casing.

In Fig. 1 (A, B and C), three examples are shown. Fig. 1(A) shows the situation where a well only partially penetrates the formation. This often is done to combat the actual or imagined danger of bottom-water coning. Fig. 1(B) shows a well producing from only the central portion of a productive interval. This type of completion is sometimes used where both water and gas coning are a problem. Although the case of a well producing through perforated casing cannot be treated in a manner similar to the previous two cases (where radial flow in the horizontal plane is assumed), Fig. 1(C) shows several intervals open to production and qualitatively describes this case (as will be discussed later).

To study the loss in productivity in all these cases, two parameters are introduced which fully determine the impairment. The first is the penetration ratio "b," i.e., the total interval open to fluid entry divided by the total thickness of the productive zone. The second is the ratio h/r_w. In this ratio, r_w is the wellbore radius. The definition of h is more cumbersome. In Fig. 1(A), h is the thickness of the total productive interval. The streamline configuration for this case of partial penetration is basic to the other two cases considered (Views B and C of Fig. 1). It will be obvious from Fig. 1(A) that the flow lines in the uppermost portion of the formation will be essentially horizontal, while those in the lower portion will curve upward toward the well. In Fig. 1(B), with only the middle portion of the zone open to production, the streamline configuration of the upper half will be an exact mirror image of that in the lower half of the zone. Hence, for the case illustrated in Fig. 1(B), h is defined as one-half the total sand thickness. It follows, then, that in Fig. 1(C) h is one-half the distance between corresponding points in adjacent intervals. (In gun-perforated casing, h would be one-half the distance between perforations.)

DISCUSSION OF RESULTS

In a paper by Nisle[4] and a paper given by the present authors[5], the mathematical theory was developed for the cases under consideration. In the present publication, the emphasis is put on the results of these studies; consequently, the equations derived in Refs. 4 and 5 will be omitted, for the most part.

The pressure drop Δp in a well producing from only a portion of the total formation thickness can, in analogy with Eq. 1, be expressed by

$$\Delta P = \frac{q\mu}{2\pi kh} p_T(b) \quad . \quad . \quad . \quad . \quad . \quad . \quad . \quad . \quad (4)$$

where

$$p_T(b) = \frac{1}{2b}\int_o^t F(\tau)\,d\tau \quad . \quad . \quad . \quad . \quad . \quad . \quad . \quad . \quad . \quad (5)$$

and $F(\tau)$ is a function given in Refs. 4 and 5.

Numerical solution of Eq. 5 by use of the IBM 650 leads to the following important conclusions. First, during a short period after starting production (usually on the order of a few minutes), the function $p_T(b)$ is given by

Original manuscript received in Society of Petroleum Engineers office July 14, 1959. Revised manuscript received Dec. 1, 1960. Paper presented at 34th Annual Fall Meeting of SPE, Oct. 4-7, 1959, in Dallas.

*Presently associated with International Business Machines Corp. in South Africa.

[1]References given at end of paper.

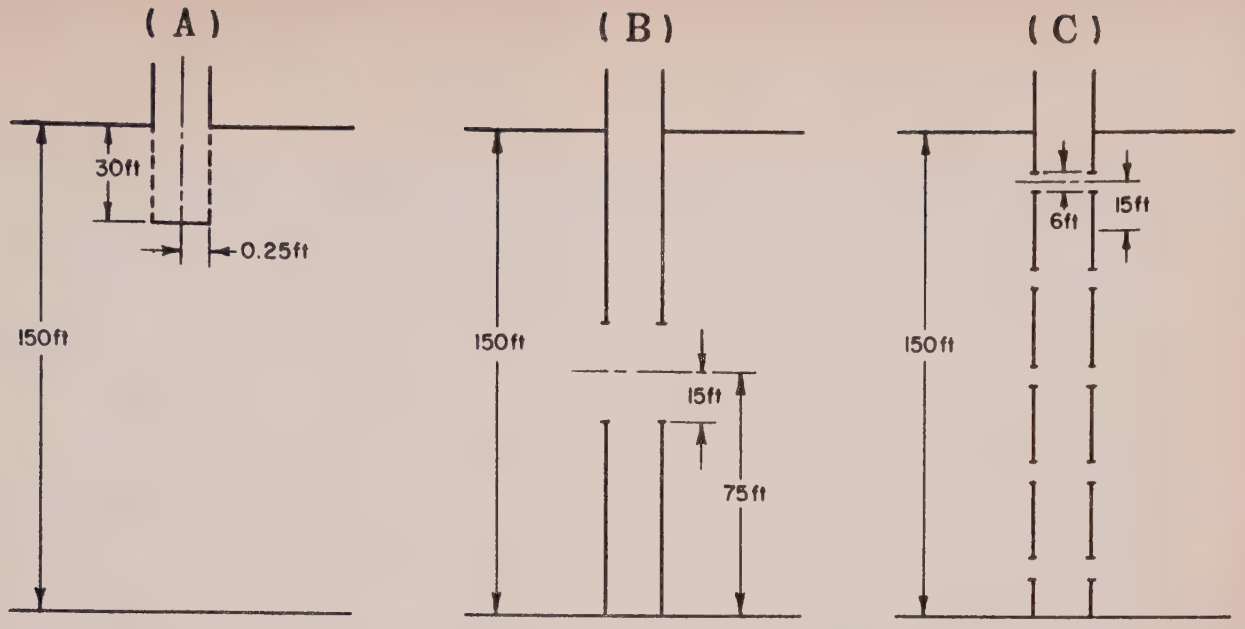

FIG. 1—EXAMPLES SHOW (A) WELL ONLY PARTIALLY PENETRATING FORMATION, (B) WELL PRODUCING FROM ONLY THE CENTRAL PORTION OF PRODUCTIVE INTERVAL, AND (C) WELL WITH SEVERAL INTERVALS OPEN TO PRODUCTION.

$$p_T(b) = \left(\frac{1}{b}\right) p_T \quad . \quad . \quad . \quad . \quad . \quad . \quad . \quad . \quad . \quad . \quad . \quad (6)$$

This means that the pressure drop during this very short initial period is expressed by

$$\Delta P = \frac{q\mu}{2\pi kbh} p_T \quad . \quad . \quad . \quad . \quad . \quad . \quad . \quad . \quad . \quad . \quad . \quad (7)$$

Compared to Eq. 1, this shows that during this time the well behaves as if the total sand thickness were equal to bh, i.e., the interval open to flow.

Secondly, after a short transition period, the pressure drop is given by

$$\Delta P = \frac{q\mu}{2\pi kh}\left[p_T + \frac{1-b}{b}\left(\ln\frac{h}{r_w} - G(b)\right)\right] \quad . \quad . \quad . \quad . \quad . \quad . \quad . \quad . \quad . \quad . \quad . \quad . \quad . \quad . \quad . \quad . \quad . \quad . \quad (8)$$

The second term in the bracketed expression is time independent, being a function only of b and h/r_w. This means that the restriction to fluid entry by virtue of only partial well penetration results in an additional pressure drop, independent of time, similar to that caused by a skin. In analogy with Eq. 2, a "pseudo" skin factor S_b is introduced and is defined by

$$S_b = \frac{1-b}{b}\left(\ln\frac{h}{r_w} - G(b)\right) \quad . \quad . \quad . \quad . \quad . \quad (9)$$

where $G(b)$ is a function of b. Since this function cannot be expressed analytically, it has been calculated numerically. In Table 1, $G(b)$ is given for a range of b values.

Based on Eq. 9 and Table 1, pseudo skin factors S_b were calculated for a range of values of h/r_w and b, as shown in Table 2 and Fig. 2. Note that Eq. 9 loses its validity for low values of h/r_w. This limitation can be explained by the fact that, for low values of h/r_w, r_w becomes of the same order of magnitude as h; consequently, the "point-source" solution on which the equations are based no longer applies. In such cases the exact solution, rather than the point-source solution, should be used.[5] The exact S_b values for low values of h/r_w are included in Table 2 and Fig. 2.

The fractional loss in productivity I is related to the skin factor S_b by Eq. 3. Based on this relation, I is given in Fig. 3 as a function of S_b, for $r_e = 660$ ft and $r_w = 3$ in. By comparison, Muskat[6] gives a solution for the case of incompressible flow. In Fig. 4, values of I based on Muskat's equations are compared with those calculated for depletion-type flow, for $h/r_w = 100$ and $h/r_w = 1{,}000$ and using the same values for r_e and r_w as shown in Fig. 3. This plot shows that the values for incompressible and depletion-type flow are quite close. However, Muskat's method is not applicable to low h/r_w values.

Considering again the conditions sketched in Fig. 1 (A, B and C), it is seen that in all cases the penetration ratio b is 0.2. However, h/r_w is 600, 300 and 60, respectively, in Views A, B and C of Fig. 1. It follows from Fig. 3 that, for $r_e = 660$ ft and $r_w = 3$ in., the loss in productivity I is 71, 68 and 56 per cent, respectively. From these results, we conclude that better productivity is obtained from an interval open in the

TABLE 1—$G(b)$ FOR RANGE OF b VALUES

b	$G(b)$
0.1	2.337
0.2	1.862
0.4	1.569
0.6	1.621
0.8	1.995

TABLE 2—PSEUDO SKIN FACTORS S_b FOR RANGE OF h/r_w AND b

h/r_w	b = 0.1	0.2	0.4	0.6	0.8
1	S_b = 0.6359	0.4474	0.2214	0.0938	0.0246
2	1.2384	0.8587	0.4197	0.1782	0.0474
5	2.8750	1.9210	0.9120	0.3893	0.1073
10	5.1589	3.2949	1.5146	0.6502	0.1867
20	8.6406	5.2130	2.3101	0.9982	0.3002
50	15.0060	8.3839	3.5562	1.548	0.4932
100	20.7013	11.0340	4.5669	1.9962	0.6571
200	26.7437	13.7617	5.5968	2.4535	0.8272
300	30.2995	15.3695	6.2011	2.7219	0.9272
500	34.9150	17.4159	6.9679	3.0628	1.0551
700	37.9347	18.7602	7.4723	3.2869	1.1391
1000	41.1398	20.1860	8.0071	3.5246	1.2282
10,000	61.8577	29.3953	11.4607	5.0596	1.8038

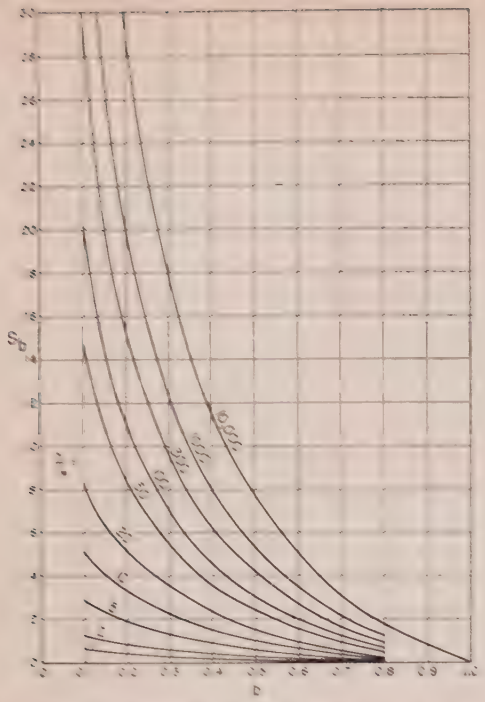

FIG. 2—PSEUDO SKIN FACTOR S_b AS A FUNCTION OF b AND h/r_w.

middle of a productive zone than from the same open interval located at either the top or bottom of the zone.

Additionally, we conclude that the larger the number of intervals for a given total-penetration ratio, the higher the productivity will be.

Although the case of a well producing through perforated casing is not covered by the present theory, which assumes radially symmetric flow in the horizontal plane, qualitatively speaking the foregoing may still be applied to this case. It supports the experience that, above a certain perforation density, the productivity is almost unimpaired although the fraction of the formation actually open to the wellbore may be small and, further, that above a certain density increasing the number of perforations per foot will add little to the productivity. To put these statements on a quantitative basis, the present theory must be modified to include this type of completion.

Finally, all previous statements are valid only for isotropic permeability distribution; any degree of horizontal stratification will lower the productivity until, for zero vertical permeability, I becomes equal to $1 - b$. See Fig. 3.

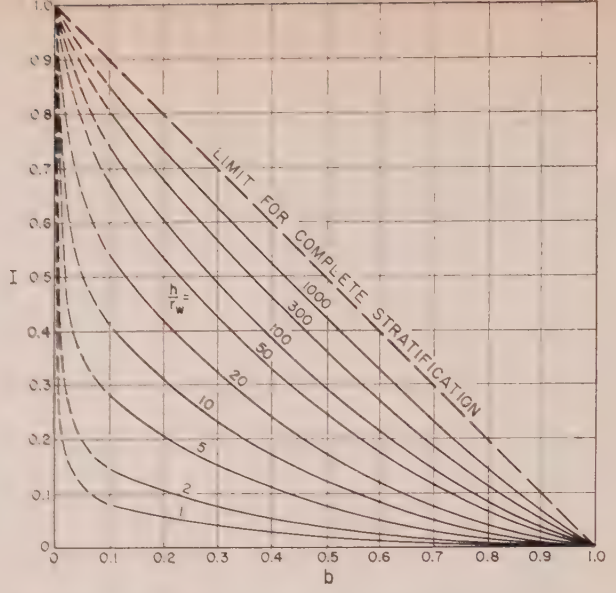

FIG. 3—FRACTIONAL LOSS OF PRODUCTIVITY I AS A FUNCTION OF b AND h/r_w FOR r_e = 660 FT AND r_w = 3 IN.

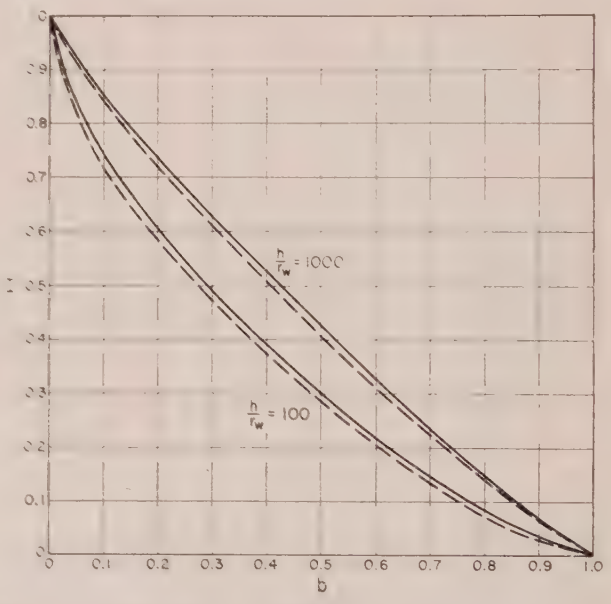

FIG. 4—COMPARISON BETWEEN FRACTIONAL LOSS OF PRODUCTIVITY I. (SOLID LINE REPRESENTS CALCULATIONS MADE BY THIS PAPER; DASHED LINE REPRESENTS COMPARISON MADE BY MUSKAT.[6])

REFERENCES

1. Van Everdingen, A. F.: "The Skin Effect and Its Influence on the Productive Capacity of a Well", *Trans.*, AIME (1953) **198**, 171.
2. Hurst, William: "Establishment of the Skin Effect and Its Impediment to Fluid Flow Into a Well Bore", *Pet. Engr.* (Oct., 1953).
3. Van Everdingen, A. F. and Hurst, W.: "The Application of the Laplace Transformation to Flow Problems in Reservoirs", *Trans.*, AIME (1949) **186**, 305.
4. Nisle, R. G.: "The Effect of Partial Penetration on Pressure Build-up in Oil Wells", *Trans.*, AIME (1958) **213**, 85.
5. Brons, F. and Marting, V. E.: "The Effect of Restricted Fluid Entry on Well Productivity", Preprint of paper 1322-G presented at 34th Annual Fall Meeting at SPE (Oct. 4-7, 1959) in Dallas.
6. Muskat, M.: *Physical Principles of Oil Production*, McGraw-Hill Book Co., Inc., N. Y. (1949) 211. ★★★

Maximum Permissible Dog-Legs in Rotary Boreholes

ARTHUR LUBINSKI
MEMBER AIME

PAN AMERICAN PETROLEUM CORP.
TULSA, OKLA.

ABSTRACT

In drilling operations, attention generally is given to hole angles rather than to changes of angle, in spite of the fact that the latter are responsible for drilling and production troubles. The paper presents means for specifying maximum permissible changes of hole angle to insure a trouble-free hole, using a minimum amount of surveys. It is expected that the paper will result in a decrease of drilling costs, not only by avoiding troubles, but also by removing the fear of such troubles.

SUMMARY, CONCLUSIONS AND RECOMMENDATIONS

Excessive dog-legs result in such troubles as fatigue failures of drill pipe, fatigue failures of drill-collar connections, worn tool joints and drill pipe, key seats, grooved casing, etc. Most of these detrimental effects greatly increase with the amount of tension to which drill pipe is subjected in the dog-leg. Therefore, the closer a dog-leg is to the total anticipated depth, the greater becomes its acceptable severity.

Very large collar-to-hole clearances will cause fatigue of drill-collar connections and shorten their life, even in very mild dog-legs. Another finding regarding fatiguing of collar connections in dog-legs is that rotating with the bit off bottom sometimes may be worse than drilling with the full weight of drill collars on the bit, mainly in highly inclined holes when the inclination decreases with depth in the dog-leg.

Means are given for specifying maximum dog-legs compatible with trouble-free holes. An inexpensive technique proposed is to take inclinometer or directional surveys far apart; then, if an excessive dog-leg is detected in some interval, intermediate close-spaced surveys are run in this interval.

The application of the findings should result in a decrease of drilling costs, not only by avoiding troubles, but mainly by removing the fear of such troubles. The result would be much more frequent drilling with heavy weights on bit, regardless of hole deviation.

Because of errors inherent to their use, presently available surveys are not very suitable for detecting dog-legs. There is a need for instruments especially adapted to dog-leg surveys.

Original manuscript received in Society of Petroleum Engineers office Aug. 29, 1960. Revised manuscript received Jan. 9, 1961. Paper presented at 35th Annual Fall Meeting of SPE, Oct. 2-5, 1960, in Denver.

INTRODUCTION

Crooked hole drilling rules should fall into two distinct categories—(1) those whose purpose is to bottom the hole as desired, and (2) those whose purpose is to insure a trouble-free hole. Three kinds of first-category rules in usage today are as follows.

1. A means to bottom the hole as desired is to prevent the bottom of the hole from being horizontally too far from the surface location; this may be achieved by keeping the hole inclination below some maximum permissible value such as, for instance, 5°.

2. Another means to achieve the same goal is to limit the rate at which the inclination is allowed to increase with depth. A frequently used rate is 1°/1,000 ft. In other words, a maximum deviation of 1° is allowed at 1,000 ft, 2° at 2,000 ft, 3° at 3,000 ft, etc.

3. Whenever application of the first two means precludes carrying the full weight on bit required for most economical drilling, then the best course is to take advantage of the natural tendency of the hole to drift updip, displace the surface location accordingly and impose a target area within which the hole should be bottomed. This method has already been successfully applied,[1,2] and its usage probably will become more frequent in the future. Means for calculating the amount of necessary surface location displacement are available.[3,5,6] If in high-dip formations the full weight on bit should result in unreasonably great deviations, the situation could be remedied by increasing the size of collars and (if needed) the size of both hole and collars,[3,5,6] or in some cases by using several stabilizers.[4]

Rules which would fall into the second category (i.e., rules whose purpose is to insure a trouble-free hole) are seldom specified today. It is vaguely believed that following Rules 1 and 2 of the first category will automatically prevent troubles. Actually, this is not true. If at some depth the only specified rule is that the hole inclination must be less than 4°, the hole may be lost if the deviation suddenly drops from 4 to 2°, or if the direction of the drift changes, etc.

Rule 3 of the first category is generally used in conjunction with a rule belonging to the second category, namely, that the hole curvature[7] (dog-leg severity) must not exceed the arbitrarily chosen value of 1½° /100 ft. Moreover, when using this rule, the industry is not clear over what depth intervals the hole curvature should be measured. All this results in a frequent fear

[1]References given at end of paper.

of letting the hole drift freely, in spite of the recognized fact that such a practice decreases drilling costs.

This situation prompted an investigation which resulted in this paper, the purpose of which is to propose rules (as lenient as possible pertaining to the change of hole inclination and drift) which will require the smallest possible number of surveys and still ensure a trouble-free hole.

The investigation was sponsored both by the Crooked Hole Subcommittee of the AAODC Rotary Drilling Committee and the API Mid-Continent Study Committee on Straight Hole Drilling.

FATIGUE FAILURES OF DRILL PIPE

GENERALITIES

Consider hole inclinations of 3° and 4¼° at two successive survey stations. If the direction of the deviation with respect to north is the same at the two stations, the change of angle between these stations is 1¼°. However, if the direction of the deviation changes, then the change of angle, called change of the over-all angle,[7] is greater than 1¼°; the reason is that this angle is a resultant of the 1¼° change in the vertical angle and some change in the horizontal angle. Means for calculating this resultant are available.[7] In this paper the expression "change of angle" must be understood to mean "change of the over-all angle" whenever surveys are directional.

In this paper two idealized, extreme kinds of dog-legs will be investigated—the gradual dog-leg shown in Fig. 1a, and the abrupt one shown in Fig. 1b.

Consider first the gradual dog-leg shown in Fig. 1a. The hole axis is an arc of circle. Such a dog-leg must be described in terms of a rate of change of angle with respect to the length, in degrees /100 ft. By saying that the rate of change, which is also called hole curvature (dog-leg severity),[7] is 3°/100 ft, it is not implied that the dog-leg is 100-ft long and its angle 3°. It is rather implied that, in every foot of dog-leg length (whichever this length might be), the hole turns by .03°.

The only gradual dog-legs which will be investigated here are those extending over several lengths of drill pipe. Such dog-legs will be called "gradual and long". Bending stress in the drill pipe in the vicinity of a tool joint will be considered for tool joints which are not located close to either the beginning or the end of a gradual and long dog-leg.

For zero tension, the pipe between two tool joints in a gradual and long dog-leg assumes the same shape as the hole, i.e., an arc of circle. As the tension increases, the bending at the vicinity of tool joints becomes greater, while the pipe partially straightens between tool joints, which is the situation shown in Fig. 1a. For even greater tension, drill pipe may contact the wall of the hole between tool joints. In all cases, however, the bending stress is the greatest at the immediate vicinity of tool joints. Consider as an example a bending stress of 10,000 psi. If the pipe is under a tension of 150,000 lb, i.e., under a tensile stress of 34,000 psi (150,000 lb. over 4.407 sq in. of wall cross-sectional area), then because of bending, the Point A in Fig. 1a is actually subjected to a tensile stress of 34,000 − 10,000 = 24,000 psi and the Point B to a tensile stress of 34,000 + 10,000 = 44,000 psi. Thus, because of rotation, the stress at the periphery of the pipe varies at every point between 24,000 and 44,000 psi. Such a repeated change of stress may cause a failure called "fatigue failure". Such failures sometimes, but not always, occur in the slip mark.[8] According to H. M. Hollins, Drilco Oil Tools, the most frequent fatigue failures in West Texas are at the upset fadeout on either end (box or pin) of the pipe.

GOODMAN DIAGRAM

The maximum reversed bending stress which will cause no fatigue failures depends upon the average tensile stress to which the pipe is subjected. The greater the average tensile stress, the smaller is the maximum bending stress which the pipe may withstand. The curve of the completely reversed bending stress vs the average tensile stress is called "Goodman diagram".

The usual Goodman diagram is a straight line, such as the dashed Line CD in Fig. 2. The intercept with the abscissa (Point D) is the tensile strength of steel, i.e., 100,000 psi for Grade E steel. The intercept with the ordinate (Point C) is obtained from repeated bending experiments conducted in the laboratory on pipe lengths subjected to no tension. Such experiments indicate a value of 22,000 psi at least.

The dashed straight Line CD was not used in this work. Instead, a curve drawn as a solid Line EF in Fig. 2 was adopted and called "modified Goodman diagram". Its intercept, E, with the ordinate is below the Point C (i.e., at 18,000 instead of 22,000 psi) to make allowance for slip marks and some wear of the pipe. On the other hand, for large tensions the Curve EF was chosen to be slightly above the straight Line CD.

The choice of Line EF is due to a recommendation by the engineering departments of the Hughes Tool Co.

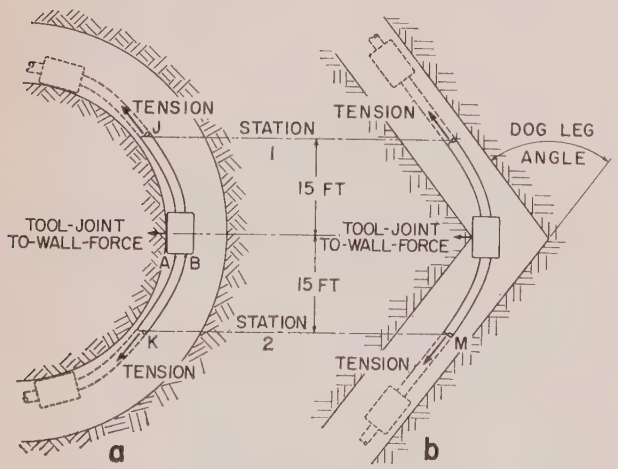

FIG. 1—(a) GRADUAL AND LONG DOG-LEG; (b) ABRUPT DOG-LEG (TOOL JOINT IN THE DOG-LEG).

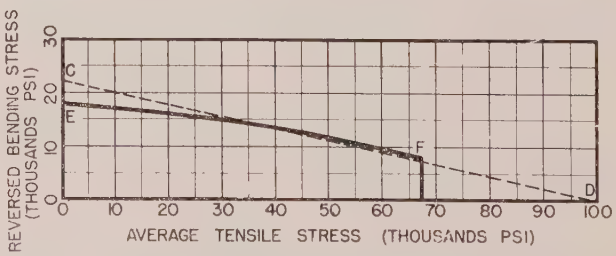

FIG. 2—MODIFIED GOODMAN DIAGRAM FOR GRADE "E" DRILL PIPE.

and is based upon their best available experience in the matter. Nevertheless, this choice may be considered only as an educated, but probably somewhat conservative, guess. The author could not argue with those who would prefer to make a somewhat different guess.

Theoretically, for conditions represented by points located below the Line EF in Fig. 2, the pipe will withstand an infinite number of stress reversals without failing. This, however, holds true only in noncorrosive muds. In a corrosive medium, the pipe will always fail after a finite number of stress reversals even if the bending stress is small. However, if the bending stresses were maintained within some fraction of these given by the modified Goodman diagram (Fig. 2), then drill-pipe life probably would be longer than with present practices. The value of this fraction depends on the corrosivity of the medium. A value of 0.6 is suggested for very severe conditions.

The greater the tension to which drill pipe is subjected, the smaller is the hole curvature which the pipe may stand without fatigue failures. The reasons for this are the two following already-explained facts.

1. The bending stress increases with tension.
2. As shown in Fig. 2, under greater tension the drill pipe will stand less bending.

GRADUAL AND LONG DOG-LEGS

Taking into account both these effects, a curve indicated "Fatigue of Grade E Drill Pipe" was plotted in Fig. 3,* which is for 4½-in. OD 16.6-lb/ft drill pipe. The abscissa is the hole curvature in degrees/100 ft. The ordinate is the tension to which the pipe is subjected in the dog-leg. There are two ordinate scales. One is in pounds and the other is in equivalent lengths of drill pipe in feet. The conversion of both scales was made assuming a buoyancy factor 0.847, i.e., a 10 lb/gal mud. In view of the fact that the tension in the drill pipe is due not only to its own weight, but also to the weight of drill collars, the ordinate scale in feet may be used only if the weight of drill collars is converted to an equivalent length of drill pipe to be added to the actual length of drill pipe.

*Means by which various curves of this paper were prepared are explained in the Appendix.

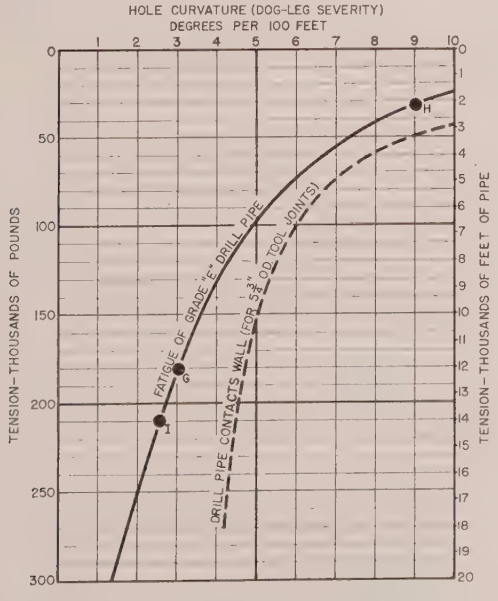
HOLE CURVATURE (DOG-LEG SEVERITY)
DEGREES PER 100 FEET
1 2 3 4 5 6 7 8 9 10
0 50 100 150 200 250 300
TENSION—THOUSANDS OF POUNDS
0 1 2 3 4 5 6 7 8 9 10 11 12 13 14 15 16 17 18 19 20
TENSION—THOUSANDS OF FEET OF PIPE
FATIGUE OF GRADE "E" DRILL PIPE
(FOR 4½" OD TOOL JOINTS)
DRILL PIPE CONTACTS WALL
G
H
I

FIG. 3—GRADUAL AND LONG DOG-LEG—HOLE CURVATURE (DOG-LEG SEVERITY) VS TENSION FOR 4½-IN. DRILL PIPE.

Fig. 3 shows that the influence of tension upon the maximum tolerable dog-leg angle is very large. As an example, consider first a tension of 180,000 lb, for which Point G in Fig. 3 indicates that hole curvature in a long and gradual dog-leg should not exceed 3° per 100 ft if fatigue failures are to be avoided. On the other hand, Point H shows that for a tension of 32,000 lb drill pipe could withstand curvatures up to 9°/100 ft.

The modified Goodman diagram (Fig. 2) was used in calculating the fatigue curve of Fig. 3. A good justification for the choice of the modified Goodman diagram is provided by the reasonableness of the results obtained from the fatigue curve. Eastman Oil Well Survey Co.'s experience indicates that a hole curvature of less than 3°/100 ft never causes any trouble.** Therefore, if Eastman's statement is valid for points higher than 10,000 ft above total depth (9,700 ft of drill pipe plus 300 ft of drill collars weigh about 180,000 lb), then the fatigue curve in Fig. 2 is on the conservative side. To explain this, consider for instance a dog-leg 13,000 ft above the total anticipated depth where the tension may be 210,000 lb. Fig. 3, obtained from Fig. 2, indicates at Point I that for such conditions hole curvature should be smaller than 2.6°/100 ft, while Eastman's experience would allow 3°/100 ft.

The dashed curve in Fig. 3 indicates the conditions for which 4½-in. drill pipe in a gradual and long dog-leg contacts the wall of the hole between tool joints. The meaning of the fact that the entire fatigue curve is located to the left of the dashed curve is as follows. If operations are conducted in such a manner that drill pipe is not subjected to fatigue, then in gradual and long dog-legs only the tool joints (and not the drill pipe) contact the wall of the hole.

ABRUPT DOG-LEGS

Consider the case of an abrupt dog-leg shown in Fig. 1b. The hole is geometrically straight (which does not mean vertical) both above and below the dog-leg. The angle by which the hole turns in the dog-leg will be referred to as "dog-leg angle".

In Fig. 1b, a tool joint is located in an abrupt dog-leg. The bending stress in the drill pipe is the greatest in the immediate vicinity of that tool joint. This greatest bending stress increases with the tension to which the pipe is subjected.

In Fig. 4 it is not a tool joint but, rather, the drill pipe between tool joints which is located in an abrupt dog-leg. In this case, drill pipe contacts the wall of the hole and the greatest bending, which is the same as in the previous case, does not occur at the vicinity of a tool joint. However, after an abrupt dog-leg is rounded out and becomes a gradual one, drill pipe generally loses its contact with the wall of the hole; the most severe bending then occurs only at the vicinity of tool joints.

There is a basic difficulty in the usage of surveys for the purpose of calculating the effects of dog-legs, namely, that the actual shape of a dog-leg between two successive survey stations is not known. However, one might

**According to a conversation in Long Beach, Calif., in Oct., 1956, with R. E. Wiley, John Weddle and Fay Brady, all with Eastman, a hole curvature between 3° and 5°/100 ft could cause trouble, but in hard formations only.

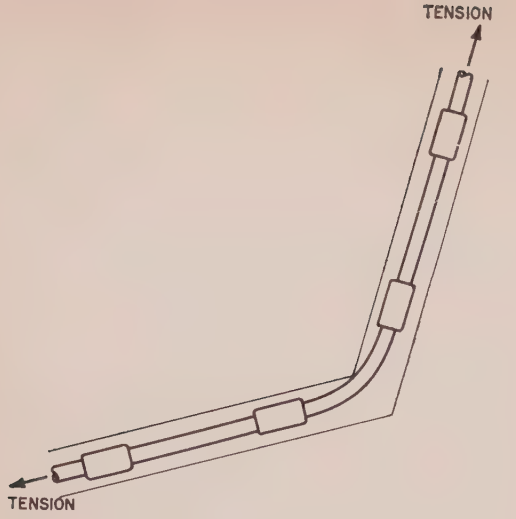

FIG. 4—ABRUPT DOG-LEG (DRILL PIPE IN THE DOG-LEG).

assume that either there is an abrupt dog-leg between the stations (as shown in Fig. 1b), or that the dog-leg is gradual and long (as shown in Fig. 1a). The method developed in this paper consists in choosing between the two stations. These stations are at J and K in Fig. 1a,

Consider a 30-ft survey spacing, i.e., a spacing equal to the distance between two tool joints. Furthermore, consider that a tool joint is located half-way between two stations. These stations are at J and K in Fig. 1a, and at L and M in Fig. 1b.

In the case of the gradual and long dog-leg, for reasons of symmetry, the pipe at J and K is parallel to the wall of the hole; therefore, the change of angle of pipe betwen J and K is the same as that of hole.

In the case of an abrupt dog-leg, the pipe is not parallel to the wall of the hole at L and M. Therefore, the change of angle of pipe between these points is somewhat smaller than the change of hole angle. However, except for very small tensions, the difference between the two is negligible; and, for all practical purposes, it may be stated that the pipe is parallel to the wall of the hole at L and M.

Thus, if the change of hole angle between the 30-ft stations is the same in Figs. 1a and 1b, then the pipe is subjected to exactly the same conditions in both cases—(1) only the tool joint (and not the drill pipe) is in contact with the wall of the hole, and (2) at 15 ft, both above and below the tool joint, the pipe is subjected to the same tensions in the same directions. In other words, for 30-ft spacing, assuming an abrupt dog-leg is neither more nor less exacting than assuming a gradual and long one.

Consider now the same change of hole angle as previously, but with a longer spacing, such as 45 ft. Then, assuming an abrupt dog-leg results in the same bending conditions as previously. On the other hand, assuming a gradual and long dog-leg results in less severe effects because the same change of angle occurs over a longer distance. Therefore, for spacings greater than 30 ft assuming an abrupt dog-leg results in more severe conditions than assuming a gradual and long one. Conversely, for spacings smaller than 30 ft, assuming an abrupt dog-leg results in less severe conditions than assuming a gradual and long one.

These conclusions hold true if, in the case of an abrupt dog-leg, only the tool joint in the dog-leg (and not the neighboring tool joints) contacts the wall of the hole and if, in the case of a gradual dog-leg, only the tool joint (and not drill pipe) contacts the wall. A study of drill-pipe behavior in abrupt dog-legs revealed that the first condition is fulfilled if drill pipe is not subjected to smaller tensions than the weight of drill collars. Moreover, it has already been explained that, for 4½-in. drill pipe, the second condition is fulfilled if the operations are conducted in such a manner that fatiguing of drill pipe is avoided. This also is the case for 5-in. drill pipe. On the other hand, such is not the case within some range of tensions for 3½-in. drill pipe. For such conditions the limiting value of survey spacing, above which an abrupt dog-leg is more exacting than a gradual one, is smaller than 30 ft. However, for the sake of simplicity, this fact will be disregarded in this paper and no survey spacing closer than 30 ft will be considered as far as drill pipe is concerned. Thus, the assumption of an abrupt dog-leg between two successive stations will be made.

Figs. 5, 6 and 7 are for three sizes of drill pipe. These graphs are similar to Fig. 3, but for abrupt instead of gradual dog-legs. The abscissa is the dog-leg angle, while the two ordinate scales are the same as in Fig. 3, i.e., tensions. Fatigue curves, the meaning of which is the same as in Fig. 3, are drawn in Figs. 5, 6 and 7.

These fatigue curves are valid only for noncorrosive muds. As already stated in this paper, in corrosive media, bending stresses to avoid fatigue failures of drill pipe must be reduced to a fraction of those of noncorrosive fluids. This is equivalent to reducing in the same proportion the maximum permissible dog-leg angle obtained from fatigue curves in Figs. 5, 6 and 7. Consider, for instance, 4½-in. drill pipe subjected to 79,000-lb tension. Point J in Fig. 6 indicates that the dog-leg angle should not exceed 1.67°. In corrosive and

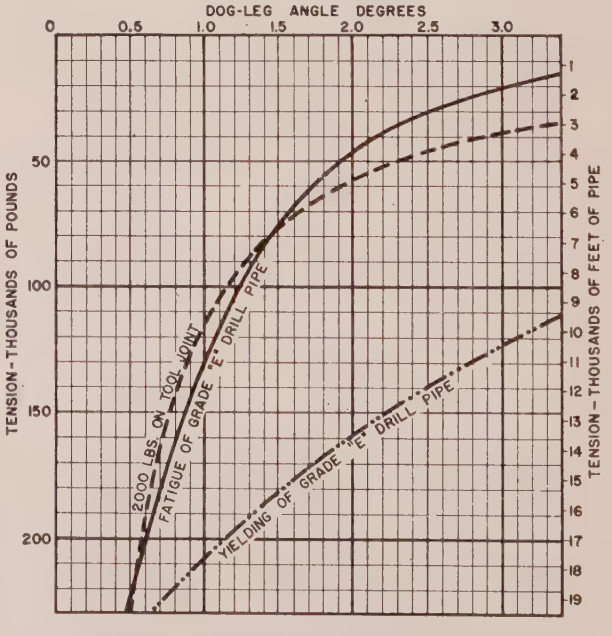

FIG. 5—ABRUPT DOG-LEG—DOG-LEG ANGLE VS TENSION FOR 3½-IN., 13.3-LB DRILL PIPE.

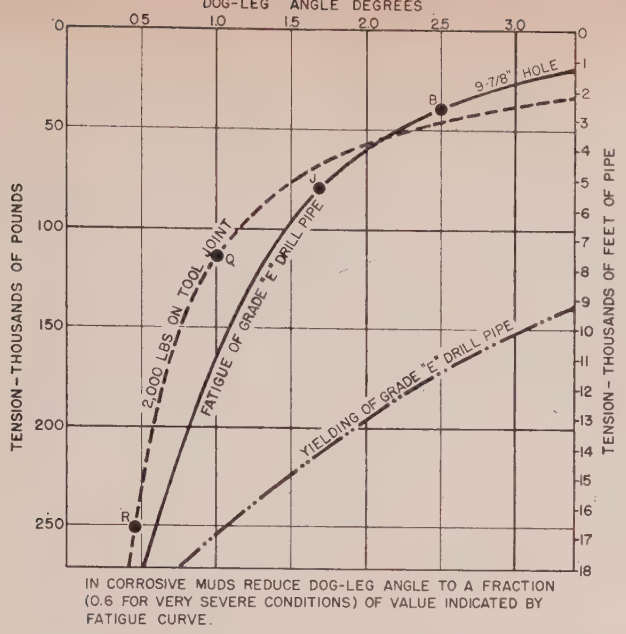

FIG. 6—ABRUPT DOG-LEG—DOG-LEG ANGLE VS TENSION FOR 4½-IN., 16.6-LB DRILL PIPE.

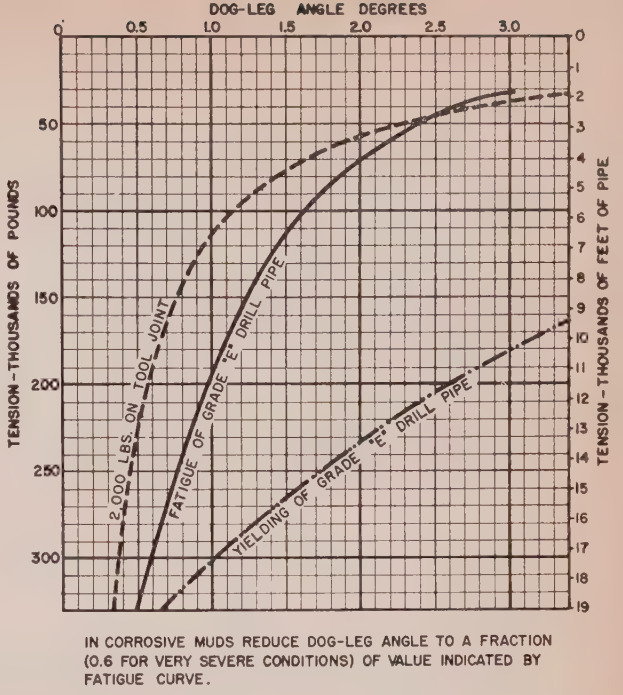
DOG-LEG ANGLE DEGREES
0.5
1.0
1.5
2.0
2.5
3.0
TENSION - THOUSANDS OF POUNDS
TENSION - THOUSANDS OF FEET OF PIPE
2,000 LBS. ON TOOL JOINT
FATIGUE OF GRADE "E" DRILL PIPE
YIELDING OF GRADE "E" DRILL PIPE
IN CORROSIVE MUDS REDUCE DOG-LEG ANGLE TO A FRACTION (0.6 FOR VERY SEVERE CONDITIONS) OF VALUE INDICATED BY FATIGUE CURVE.

FIG. 7—ABRUPT DOG-LEG—DOG-LEG ANGLE VS TENSION FOR 5-IN., 19.5-LB DRILL PIPE.

severe-corrosive conditions, one might reduce this value to $1.67 \times 0.8 = 1.34°$ and $1.67 \times 0.6 = 1.00°$ respectively.

In Figs. 5, 6 and 7 are also drawn curves indicated "Yielding of Grade E Drill Pipe". For conditions represented by points located to the right of these curves, the pipe would take a permanent set and would fail very quickly if rotated. These curves show that the greater the dog-leg angle, the smaller is the tensile load for which yielding will occur.

SURVEY ERRORS

Inclinometer and directional surveys generally are not run in the open hole but, rather, inside drill collars. Because of their stiffness, drill collars do not follow the hole contour exactly. For instance, the shape of collars bent in an abrupt dog-leg may be as shown in Figs. 8 or 9. Fig. 8 is for cases when hole inclination increases with depth and which will be referred to as "increasing dog-legs". Conversely, Fig. 9 is for "decreasing dog-legs".

In all cases if there is an abrupt dog-leg between two stations and if the distance between the stations is less than $2P$ (see Figs. 8 and 9), then the change of angle obtained from the two surveys will be less than the dog-leg angle. In other words, the condition might actually be more severe than indicated by surveys. For instance, if Fig. 6 indicates that dog-leg angles up to 1.69° could be tolerated, then a value somewhat less than 1.69°—namely, $f \times 1.69$ where f is a fraction—might have to be imposed for the maximum permissible dog-leg angle. The fraction f, which will be called "correction factor", depends upon the following parameters: collar size, survey spacing, dog-leg angle, collar-to-hole clearance and hole inclination; it also depends on whether the dog-leg is increasing or decreasing.

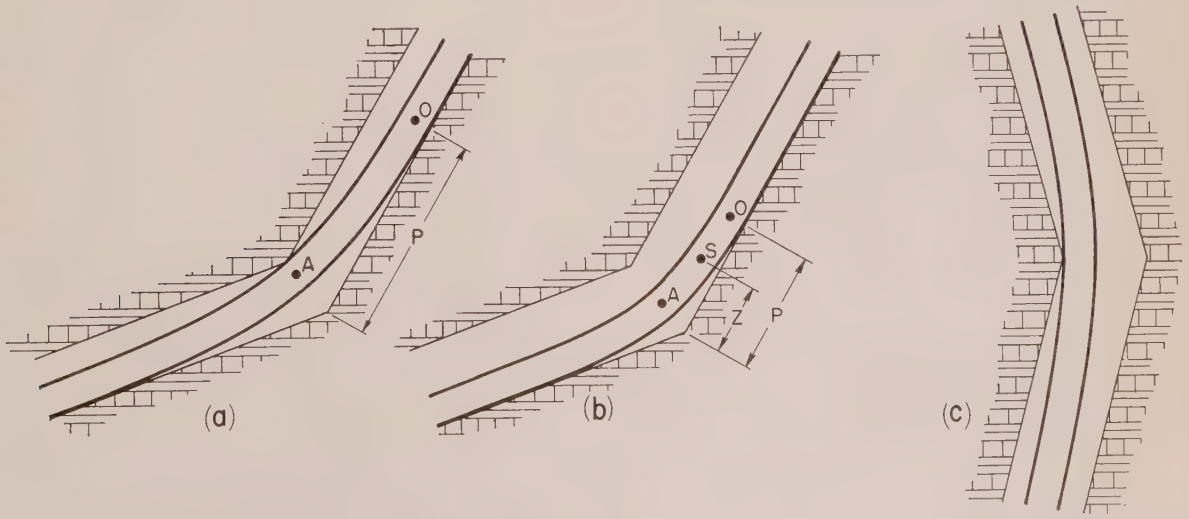

FIG. 8—ABRUPT INCREASING DOG-LEGS—(a) COMPRESSION WITH SMALL CLEARANCE OR TENSION WITH ANY CLEARANCE; (b) COMPRESSION WITH LARGE CLEARANCE; (c) TENSION WITH LARGE CLEARANCE IN NEARLY VERTICAL HOLE.

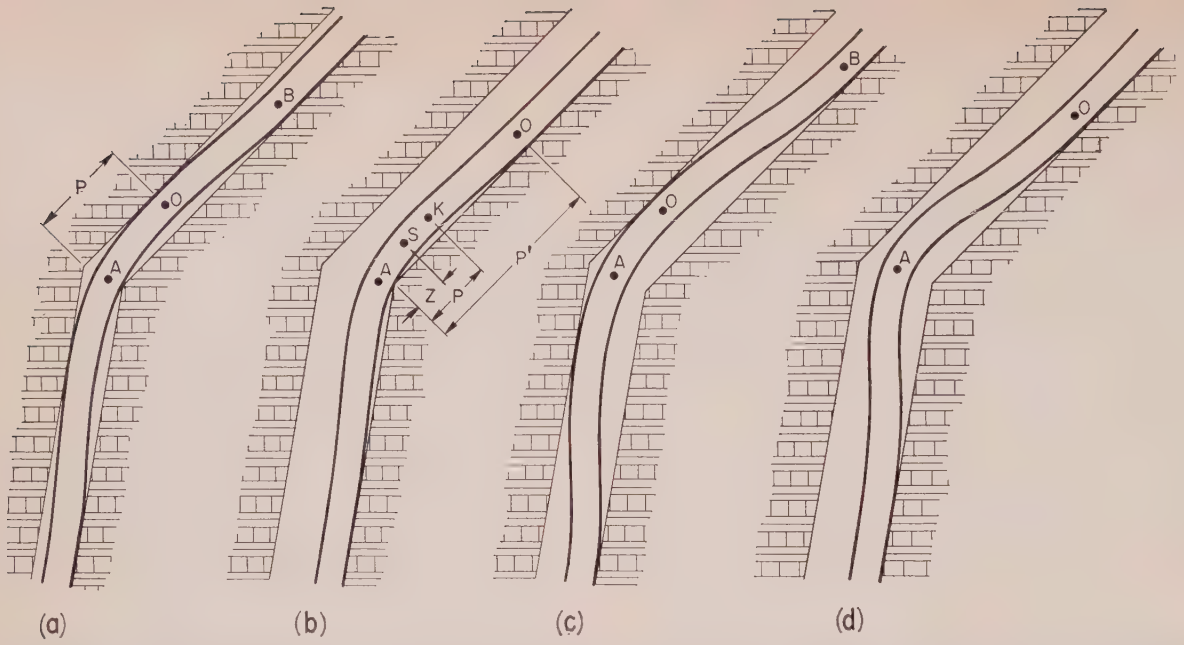

FIG. 9—ABRUPT DECREASING DOG-LEGS—(a) TENSION OR COMPRESSION WITH SMALL CLEARANCE; (b) TENSION OR COMPRESSION WITH LARGE CLEARANCE; (c) COMPRESSION WITH LARGE CLEARANCE; (d) COMPRESSION WITH LARGE CLEARANCE.

The values of the correction factor f for 30-ft spaced surveys are given in Figs. 10 through 13 for four sizes of drill collars. In all these graphs, f is plotted vs the dog-leg angle. Each figure contains three sections denoted a, b and c. Sections a and c must be used for increasing dog-legs, and Sections b and c for decreasing dog-legs.

Use of these graphs will be illustrated with the following example. It is desired to determine the maximum permissible change of angle between two 30-ft-apart surveys at a depth in which the tension in 4½ in. drill pipe could reach 79,000 lb. The drilling mud is not corrosive. At that depth, hole deviation is increasing with depth (the average deviation being 5° and surveys are made inside 6¼-in. drill collars in 7⅞-in. hole.

The problem is solved as follows. From Fig. 6, Point J (6¼-in. drill collars, 79,000 lb), we obtain 1.67° for the maximum permissible change of angle. From Fig. 11a, Point N (6¼-in. drill collars, 1.67°, hole inclination 5°, increasing with depth), we obtain $f = 0.46$. From Fig. 11c, Point P (6¼-in. drill collars, 1.67°, 7⅞-in. hole), we obtain $f = 0.80$. As explained in the Appendix, of the two obtained values 0.46 and 0.80, the largest must be used. Thus, the correction factor f is equal to 0.80, and the corrected value of the maximum permissible change of angle becomes $0.80 \times 1.67 = 1.34°$.* The surveying instruments indicate angles within ¼°. Thus, the value of 1.34° will be replaced by the closest multiple of ¼° smaller than 1.34°, i.e., by 1¼°.

As survey readings are made within more-or-less ± ⅛°, the difference of two readings (i.e., the change of angle between two surveys) is within ± ¼°. Therefore, in this example the obtained value of 1¼° becomes $1¼ - ¼ = 1°$. Thus, the maximum permissible change of angle between two 30-ft-apart survey stations is 1°.*

*These numbers are example numbers in the heavy rectangle in Table 1.

Repeating the same operations for several tensions and several hole inclinations, Table 1 was prepared. These tensions correspond to several depths between 4,000 ft and an assumed total depth of 12,000 ft. The tension at a depth is equal to the weight in 10 lb/gal mud of 810 ft of drill collars (62,000 lb) and the portion of drill pipe equipped with tool joints suspended below that depth after the hole reaches the total depth.

At the depth of 10,000 ft the tension is 79,000 lb, which is the value used in the preceding example. The results of the calculations set out in detail in that example are given in the heavy rectangle in Table 1. The upper line would contain a correction factor obtained from Fig. 11a, if this factor were greater than the factor $f = 0.80$ obtained from Fig. 11c, and written in the fourth column of the table.

In preparing the curves of the correction factor f in Figs. 10 through 13, it has been assumed that the drill collars are subjected to zero tension. In other words, the results are correct if the dog-leg is close to the bottom of the already-drilled hole. If, on the other hand, the dog-leg is located higher in the collar string and the instrument is run on a wire line, then the correction factors are somewhat greater than those indicated. In other words, in such cases Figs. 10 through 13 give somewhat conservative results.

Figs. 10 through 13 are for abrupt dog-legs. On the other hand, in long and gradual dog-legs there would be no correction factor; i.e., f would be equal to one. Therefore, in a somewhat rounded dog-leg the correction factors would be greater than in an abrupt dog-leg and, for this reason too, the graphs are on a conservative side.

In the event surveys are made inside drill pipe, then because of drill-pipe flexibility under tension, there is no need for a correction factor.

The smaller the correction factor f, the smaller is the maximum tolerable change of angle between two surveys. In other words, the conditions are better when

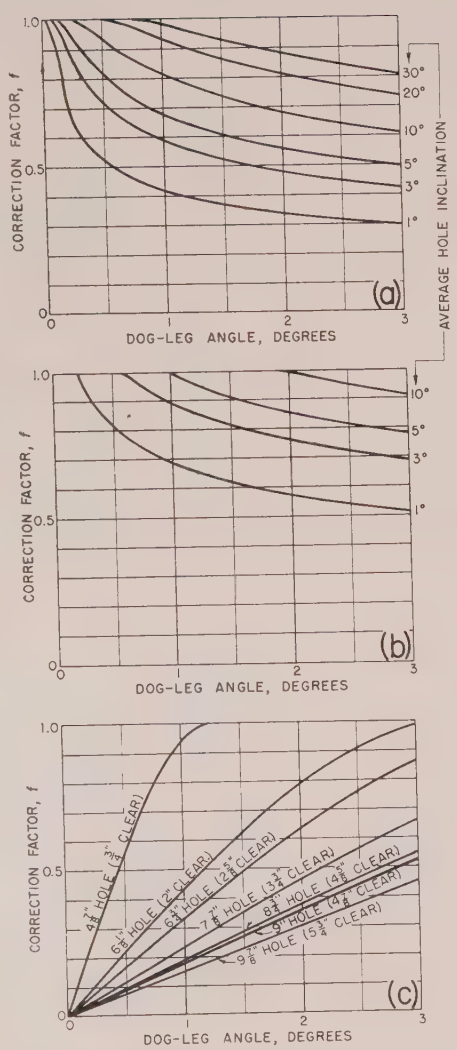

FIG. 10—CORRECTION FACTOR *f* FOR 4⅛-IN. DRILL COLLARS. 30-FT SPACING—(a) INCLINATIONS INCREASING WITH DEPTH; (b) INCLINATIONS DECREASING WITH DEPTH: (c) *f* FOR VARIOUS HOLE SIZES.

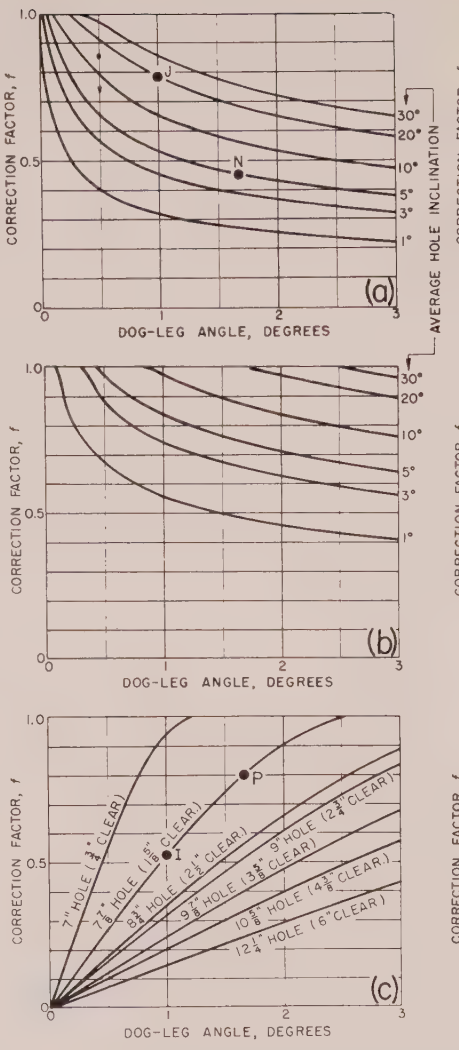

FIG. 11—CORRECTION FACTOR *f* FOR 6¼-IN. DRILL COLLARS, 30-FT SPACING—(a) INCLINATIONS INCREASING WITH DEPTH; (b) INCLINATIONS DECREASING WITH DEPTH; (c) *f* FOR VARIOUS HOLE SIZES.

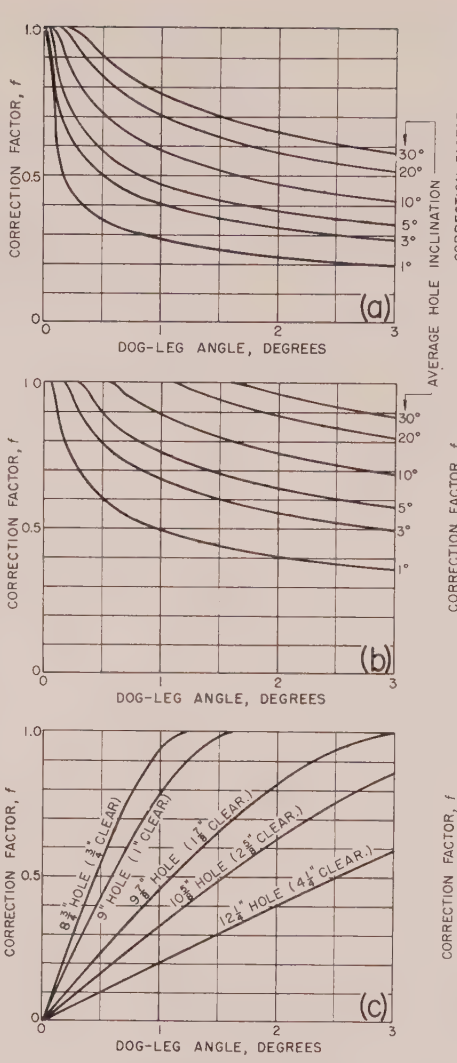

FIG. 12—CORRECTION FACTOR *f* FOR 8-IN. DRILL COLLARS, 30-FT SPACING—(a) INCLINATIONS INCREASING WITH DEPTH; (b) INCLINATIONS DECREASING WITH DEPTH; (c) *f* FOR VARIOUS HOLE SIZES.

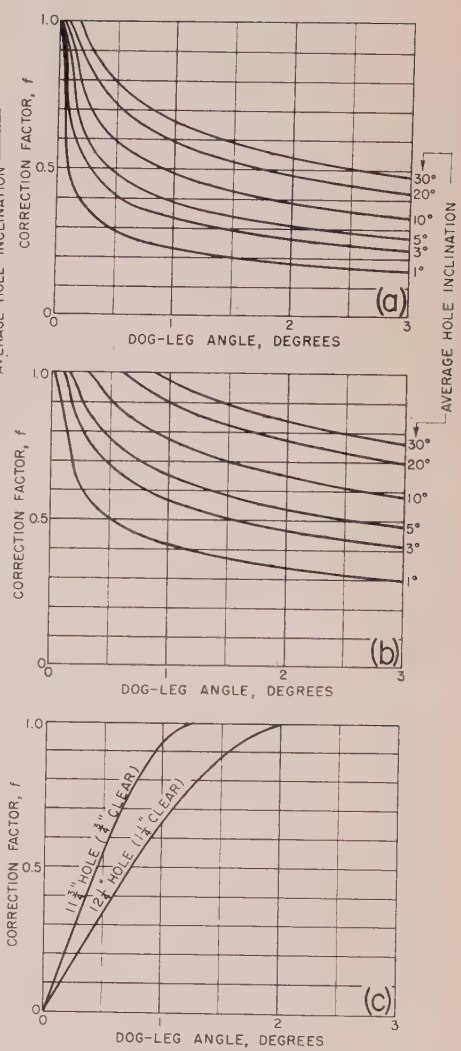

FIG. 13—CORRECTION FACTOR *f* FOR 11-IN. DRILL COLLARS, 30-FT SPACING—(a) INCLINATIONS INCREASING WITH DEPTH; (b) INCLINATIONS DECREASING WITH DEPTH; (c) *f* FOR VARIOUS HOLE SIZES.

TABLE 1—EXAMPLE OF CALCULATIONS OF THE MAXIMUM CHANGE OF ANGLE BETWEEN 30-FT SPACED SURVEYS TO PREVENT DRILL-PIPE FATIGUE FAILURES

4½-in., 16.6-lb/ft Drill Pipe. Total Depth 12,000 ft.
810 ft of 6¼-in. Drill Collars. 7⅞-in. Hole.

Depth (Ft)	Tension (Thous. Lb)	Readings for 4½-in. Drill Pipe From Fig. 6 (a)	Correction Factor f (Collar-to-Hole Clearance 1⅝-in.)	Average Inclination											
				Inclination Decreases With Depth						Inclination Increases With Depth					
				30°	20°	10°	5°	3°	1°	1°	3°	5°	10°	20°	30°
4,000	169	0.97	0.505	1 0.97 ½°	1 0.97 ½°	0.94 0.97 ½°	0.84 0.82 ½°	0.75 0.72 ½°	0.56 0.54 ½°	— 0.49 ½°	— 0.49 ½°	0.54 0.53 ½°	0.66 0.64 ½°	0.79 0.77 ½°	0.86 0.84 ½°
5,000	154	1.06	0.545	1 1.06 ¾°	1 1.06 ¾°	0.96 1.01 ¾°	0.83 0.88 ½°	0.73 0.77 ½°	0.55 0.58 ½°	— 0.58 ½°	— 0.58 ½°	— 0.58 ½°	0.65 0.69 ½°	0.78 0.82 ½°	0.85 0.90 ½°
6,000	139	1.15	0.59	1 1.15 ¾°	1 1.15 ¾°	0.94 1.08 ¾°	0.81 0.93 ½°	0.72 0.82 ½°	— 0.68 ½°	— 0.68 ½°	— 0.68 ½°	— 0.68 ½°	0.63 0.72 ½°	0.76 0.87 ½°	0.83 0.95 ½°
7,000	124	1.26	0.64	1 1.26 1°	1 1.26 1°	0.92 1.16 ¾°	0.79 1.00 ¾°	0.70 0.88 ½°	— 0.81 ½°	— 0.81 ½°	— 0.81 ½°	— 0.81 ½°	— 0.81 ½°	0.74 0.93 ½°	0.81 1.02 ¾°
8,000	109	1.37	0.685	1 1.37 1°	1 1.37 1°	0.91 1.24 ¾°	0.78 1.06 ¾°	— 0.94 ½°	— 0.94 ½°	— 0.94 ½°	— 0.94 ½°	— 0.94 ½°	— 0.94 ½°	0.73 1 ¾°	0.80 1.09 ¾°
9,000	94		0.74	1 1.51 1¼°	1 1.51 1¼°	0.89 1.34 1°	0.76 1.14 ¾°	— 1.12 ¾°	— 1.12 ¾°	— 1.12 ¾°	— 1.12 ¾°	— 1.12 ¾°	— 1.12 ¾°	— 1.12 ¾°	0.78 1.17 ¾°
10,000	79	1.67	0.80	1 1.67 1¼°	1 1.67 1¼°	0.87 1.45 1°	— 1.34 1°	— 1.34 1°	— 1.34 1°	— 1.34 1°	— 1.34 1°	— 1.34 1°	— 1.34 1°	— 1.34 1°	— 1.34 1°
11,000	64	1.91	0.87	1 1.91 1½°	0.97 1.86 1½°	— 1.66 1¼°	— 1.66 1¼°	— 1.66 1¼°	— 1.66 1¼°	— 1.66 1¼°	— 1.66 1¼°	— 1.66 1¼°	— 1.66 1¼°	— 1.66 1¼°	— 1.66 1¼°

*For the meaning of these numbers, see footnote on page 180.

f is as large as possible. Figs. 10 through 13 show that f is larger in packed than in nonpacked holes, in more-inclined than in less-inclined holes and, for equal inclinations, in holes whose inclination decreases rather than increases with depth.

FORCE ON TOOL JOINTS

Fatigue failures are not the only drilling troubles due to dog-legs. Another kind of trouble occurs due to the fact that in a dog-leg an appreciable force develops between the drilling string and the wall of the hole or casing (see Fig. 1). This force is responsible for the following troubles.

1. Wear of tool joints and drill pipe.
2. Keyseats in the wall of the hole.
3. Grooves in the casing made by tool joints during round trips. Such grooves decrease casing resistance to both collapse and burst, thus contributing to future failures. In some cases, the groove penetrates through the entire thickness of casing, causing failure before drilling is completed.

Curves indicated "2,000 lb on Tool Joint" are plotted in Fig. 5, 6 and 7. Point Q in Fig. 6 indicates (for instance) that for a 4½-in. drill pipe subjected to 114,000-lb tension, a 1° abrupt dog-leg results in a 2,000-lb force between the tool joint and the wall of the hole.

The force on tool joint is proportional to the dog-leg angle. Therefore, it would be easy to draw curves corresponding to any value of the force on tool joint.

It is difficult to assign some maximum tolerable value to the forces between the string and the wall. Such a value depends upon numerous factors such as abrasiveness of formation, abrasiveness of tool-joint surface, drilling rate, number of round trips, etc.

A tentative but rather conservative value of the maximum tolerable value of the tool joint-to-wall force will be determined in the following way. It is recognized that, below the surface casing, a hole curvature of 1.5°/100 ft never causes any trouble. This holds true even in deep wells such as 16,000- to 17,000-ft wells in the Carter-Knox field in Oklahoma in which, below the surface casing, 4½-in. drill pipe may be subjected to 250,000-lb tension. A hole curvature of 1.5°/100 ft corresponds to a 0.45° change of angle over a 30-ft interval. Point R in Fig. 6 shows that for such conditions the force between the tool joint and the wall is about 2,000 lb. Thus, it may be concluded that a force of 2,000 lb should be harmless. In most cases a greater force could be tolerated.

The National Supply Co. has provided us with reports describing six cases in which severe dog-legs have resulted in serious damage to tool joints. Metallurgical evidence indicated that these tool joints must have been subjected to heating by friction beyond 1,450°F. followed by quenching. All the cases occurred in the soft Gulf Coast formations in which the tool joints most likely buried themselves in the wall of the hole, thus making heat dissipation difficult. As directional surveys were taken, we were able to calculate the lateral force which developed in the dog-legs between the tool joints and the wall of the hole. In all cases, these forces were of the order of 5,000 or 6,000 lb. It is probable that the troubles would not have occurred had this force been no greater than 2,000 lb.

When the curve for a 2,000-lb force is used in preparing specifications of the maximum tolerable dog-leg angle, there is no need to use a correction factor which would take into account the fact that drill collars do not exactly conform with the hole geometry. Similarly, ¼° does not have to be subtracted to take into account surveying instrumental errors. The reason for this is that the acceptability of the 2,000-lb force has been deduced from the observed fact that hole curvatures up to 1.5°/100 ft do not cause trouble, such hole curvatures being measured with all the errors inherent to surveys.

Table 2 is similar to Table 1. It gives the maximum change of angle between 30-ft-apart surveys for which the force between the tool joints and the wall of the hole does not exceed 2,000 lb. The composition of the drilling string and the total depth are the same as in the example of Table 1. The readings from Fig. 6 are rounded to the closest smaller multiple of ¼°.

FATIGUE FAILURES OF DRILL-COLLAR CONNECTIONS

As already mentioned, numerous situations (shown in Figs. 8 and 9) may occur when drill collars are located in an abrupt dog-leg. These figures are for increasing and decreasing dog-legs, respectively.

For small collar-to-hole clearances, the situation is as shown in Fig. 8a (for increasing dog-legs) and in Fig. 9a (for decreasing dog-legs), regardless of whether the collars are subjected to tension or compression.

For large clearances and increasing dog-legs, the situation is as shown in Fig. 8a in the case of tension, and as in Fig. 8b in the case of compression.

For large clearances and decreasing dog-legs, the situation is as shown in Fig. 9b when drill collars are subjected to tension or to neither tension nor compression. On the other hand, in case of compression any of the situations illustrated in Figs. 9b, 9c and 9d may occur.

In all the cases described up to now, gravity pulls the string toward the low side of the hole. Therefore, starting at some distance below and above the dog-leg, the string lies on the low side of the hole. In a nearly vertical hole, however, the influence of gravity may be very weak; with drill collars under tension, a situation as shown in Fig. 8c rather than Fig. 8b may occur.

The situation of Fig. 8c for drill collars is the same as the situation of Figs. 1b and 4 for drill pipe. Drill pipe, however, is so much lighter and more flexible than collars that the effects of gravity are negligible, even in very inclined holes such as 30°. This is why the effect of dog-legs on drill pipe depends neither on hole inclinations nor on whether the dog-leg is increasing or decreasing. Hole inclination is not even indicated in Figs. 3, 5, 6 and 7, which pertain to drill pipe.

The weakest points in drill-collar string are connections. Reasonable estimates of the maximum bending moments to which drill collars of various sizes may be subjected without any fatigue were calculated from information obtained from the Hughes Tool Co. and are presented in Table 3.

Each connection was chosen to give a well balanced structure for the particular drill-collar diameter. The bending moments are based on a fatigue limit of 9,000 psi at the root of the pin thread ¾ in. from the shoulder. The 9,000-psi value was chosen as a result of numerous fatigue tests in which 13,000 psi was an average value but where some failures occurred as low as 9,000 psi.

As the drilling fluid has no access to the root of the pin, no corrosion considerations have to be taken into account.

TABLE 2—EXAMPLE OF CALCULATIONS OF THE MAXIMUM CHANGE OF ANGLE BETWEEN 30-FT SPACED SURVEYS TO MAINTAIN LESS THAN 2,000-LB FORCE ON TOOL JOINTS

4½-in., 16.6-lb/ft Drill Pipe. Total Depth 12,000 ft. 810 ft of 6¼-in. Drill Collars.

Depth (ft)	Tension (lb)	Maximum Change of Angle in Degrees From Fig. 6
4,000	169,000	½
5,000	154,000	¾
6,000	139,000	¾
7,000	124,000	¾
8,000	109,000	1
9,000	94,000	1
10,000	79,000	1¼
11,000	64,000	1¾

TABLE 3—ESTIMATES OF MAXIMUM BENDING MOMENTS TO WHICH DRILL COLLARS OF VARIOUS SIZES MAY BE SUBJECTED WITHOUT ANY CONNECTIONS FATIGUE

Drill-Collar OD (in.)	Size (in.) and Type Connection	Bending Moment for Fatigue (lb) Failure
11	8⅝ H-90	1,575,000
8	6⅝ Reg.	597,000
6¼	4½ Full Hole	284,000
4⅛	2⅞ I. F.	70,600

For each of these collar sizes, calculations were made of the abrupt dog-leg angle for which the connections are subjected to a bending moment causing fatigue failure. This dog-leg angle is a function of the following parameters: collar-to-hole clearance, amount of tension or compression to which the collars are subjected in the dog-leg, hole inclination and whether this inclination increases or decreases with depth.

As already explained in regard to the drill pipe, these calculated values of the dog-leg angle first must be multiplied by a correction factor f, and then decreased by ¼° to obtain the maximum difference of angle between two surveys for which no fatigue of drill-collar connections should occur.

This maximum difference of angle is plotted for four drill-collar sizes in Figs. 14 through 17 vs the average hole inclination at two 30-ft-apart stations, both for increasing and decreasing dog-legs. Each figure comprises several sections (denoted a, b, c, etc.) corresponding to different hole sizes. Various curves are for various values of tension or compression.*

Fig. 15a shows that in a packed hole the maximum difference of angle to avoid collar-connection fatigue failures is practically independent of whether the collars are under tension or compression and of the amount of tension or compression. This graph also shows that the phenomena are independent of hole inclination and of whether this inclination increases or decreases with depth in the dog-leg. In all cases, 6¼-in. drill collars may stand up to 1° difference of angle.

To investigate the effects of moderate drill collar-to-wall clearances, Fig. 15b (which is for a 1⅝-in. clearance) will be used. Starting from above, the five curves are listed in the following order—large compression, small compression, zero compression, small tension and large tension. This leads to the following conclusion. The greater the compression (i.e., the greater the weight on bit), the smaller become the odds of drill-collar-connection failures. This is rather unexpected. A visual although non-rigorous explanation is that the greater the compression, the easier it becomes for pipe to be bent around a corner. Another conclusion is that tension is worse than compression. When rotating with the bit off bottom, the upper portion of the drill-collar string is subjected to a tension equal to almost the entire weight of collars. If this portion is in a dog-leg, it suffers more from fatigue than any point on the collar string while drilling, regardless of dog-leg location. One should avoid rotating drill collars in a severe dog-leg under high tension. If, for instance, a severe dog-leg is located at the level of the upper portion of the collar string and it is necessary to rotate with the bit off bottom for any appreciable length of time, one should consider pulling

*The meaning of the word "tension" in this paper is the actual tension plus pa, where p is the static drilling-fluid pressure at the dog-leg depth, and a is the cross-sectional area of the collar wall. Similarly, the meaning of "compression" is the actual compression minus pa. The meaning of the expression "neither tension nor compression" is that the compression is equal to pa, which is the condition at the neutral point. It is proved in Refs. 9, 10 and 11 that bending depends upon tensions and compressions as defined herein.

the string several stands off bottom to decrease the tension in the dog-leg, thus prolonging drill-collar life.

In the right-hand half of Fig. 15b, the curves are almost horizontal, straight lines. This means that, in dog-legs in which the inclination increases with depth, dog-legs of equal angles have the same effect on fatigue of collar connections, regardless of hole inclination. In other words, a 1° dog-leg in a 20° inclined hole is no worse than a 1° dog-leg in a nearly vertical hole.

On the other hand, in the left-hand half of the graph, the curves corresponding to tension are sloping down to the left. This means that, in dog-legs in which the inclination decreases with depth, dog-legs of the same angle are worse in very inclined holes than in holes which are closer to vertical. The previously stated conclusion that tension is worse than compression, so far as dog-leg effects on drill-collar connections are concerned, holds true to an even greater extent for dog-legs in which the inclination decreases with depth than in holes in which the inclination builds up with depth.

Figs. 15c and 15f are used for greater collar-to-hole clearances, namely, 2¾ and 6 in., respectively. For 2¾-in. clearance, all the conclusions reached for a 1⅝-in. clearance still hold true except for very large compressions (i.e., for the 8,000-lb/in.-of-hole-diameter curve). For a 6-in. clearance, several other exceptions appear. It becomes very difficult to draw any conclusions except that, for both large tensions and large compressions, even small changes of angle result in fatigue of collar connections. Figs. 14e and 14f show that the situation is even much worse for small (4⅛-in.) collars. In any event, it is recommended that no drilling be done under such conditions. If it were necessary, however, to drill large holes with small collars, then the weight on bit and the weight of collars should be small.

It has been explained in the drill-pipe section of this paper that there is a limiting value of survey spacing such that, for any spacing greater than the limiting value, more severe conditions result from assuming an abrupt dog-leg rather than a long and gradual dog-leg. For drill-pipe, this limiting value was 30 ft due to tool

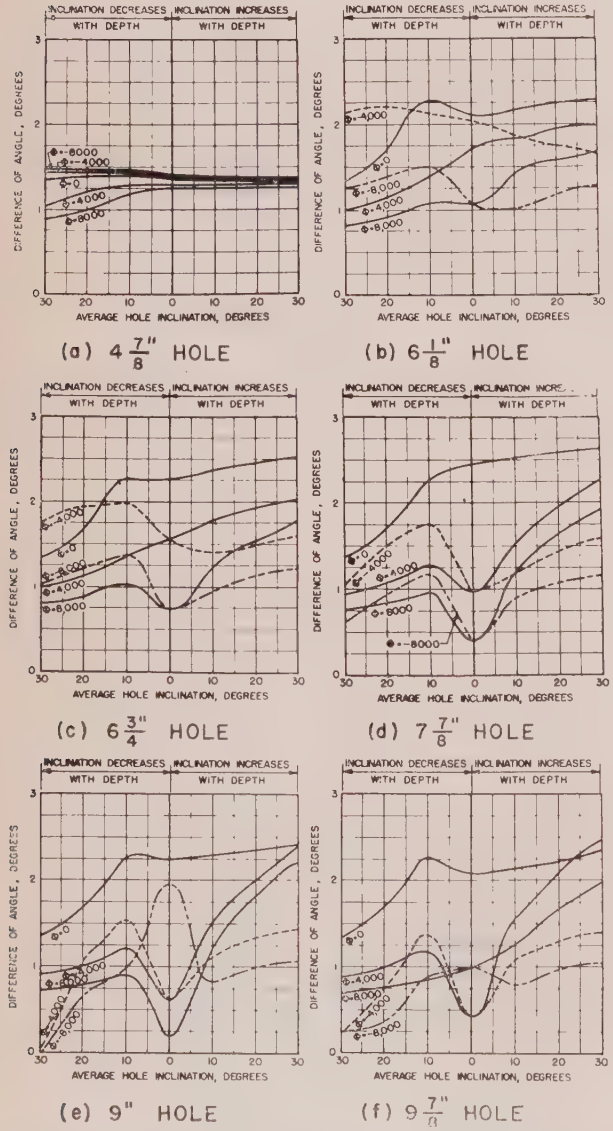

FIG. 14—MAXIMUM DIFFERENCE OF ANGLE OVER A 30-FT INTERVAL TO AVOID DRILL-COLLAR-CONNECTION FATIGUE FAILURES, 4⅛-IN. COLLARS. POSITIVE Φ = TENSION AND NEGATIVE Φ = COMPRESSION, BOTH IN POUNDS PER INCH OF HOLE DIAMETER.

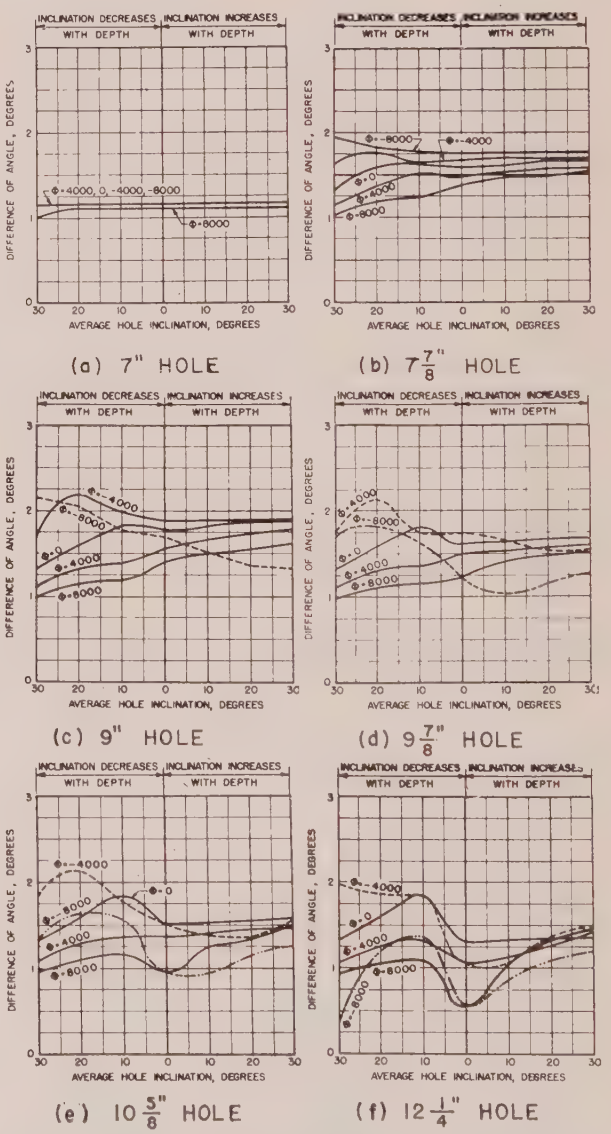

FIG. 15—MAXIMUM DIFFERENCE OF ANGLE OVER A 30-FT INTERVAL TO AVOID DRILL-COLLAR-CONNECTION FATIGUE FAILURES, 6¼-IN. COLLARS. POSITIVE Φ = TENSION AND NEGATIVE Φ = COMPRESSION, BOTH IN POUNDS PER INCH OF HOLE DIAMETER.

joint spacing. On the other hand, this limiting value is variable for drill collars and depends on the size of collars, size of hole, hole inclination, dog-leg angle and the amount of tension or compression. This limiting value is frequently less than 30 ft. Because it would not be practical to use a variety of spacings, computations of the maximum difference of angle to avoid collar-connection fatigue failures were made not only for 30-ft spacings, but also for 20- and 15-ft spacings. In the calculations either an abrupt or a gradual dog-leg was assumed, whichever corresponded to more severe effects.

In some cases, results such as the following have been obtained: maximum difference of angle for 30-ft spacing, 1°; for 20-ft, 1°; and for 15-ft, ¾°. In such an event, taking a shorter spacing than 30 ft could be useful. On the basis of a 30-ft interval, for instance, a difference of 1½° would be unacceptable. However, if an intermediate survey indicates that over each of the 15-ft sub-intervals the difference is only ¾°, the hole actually would be acceptable.

In other cases, results such as the following have been obtained: maximum difference of angle for 30-ft spacing, 1¾°; for 20-ft, 1°; and for 15-foot, ½°. In such case, a shorter spacing than 30 ft is not useful; consider, for instance, a 15-ft spacing. Two times ½° still is less than the 1¾° allowed over a 30-ft interval.

It has been found that spacings shorter than 30 ft are useful only for small collars (such as 4⅛ in.) and in packed holes for medium-size collars (such as 6¼ and 8 in.). For these cases, values of the maximum change of angle to avoid fatigue failures of drill-collar connections are given in Table 4 for 30-, 20- and 15-ft spacings.

Comparison of Figs. 14a, 15a, 16a and 17a shows that for equal clearances the maximum permissible difference of angle between two 30-ft surveys may be less for larger-diameter collars than for smaller ones. It should not be concluded, however, that large-diameter collars are less desirable. On the contrary, drilling with larger (i.e., stiffer) collars is better because it must actually result in less severe dog-legs.

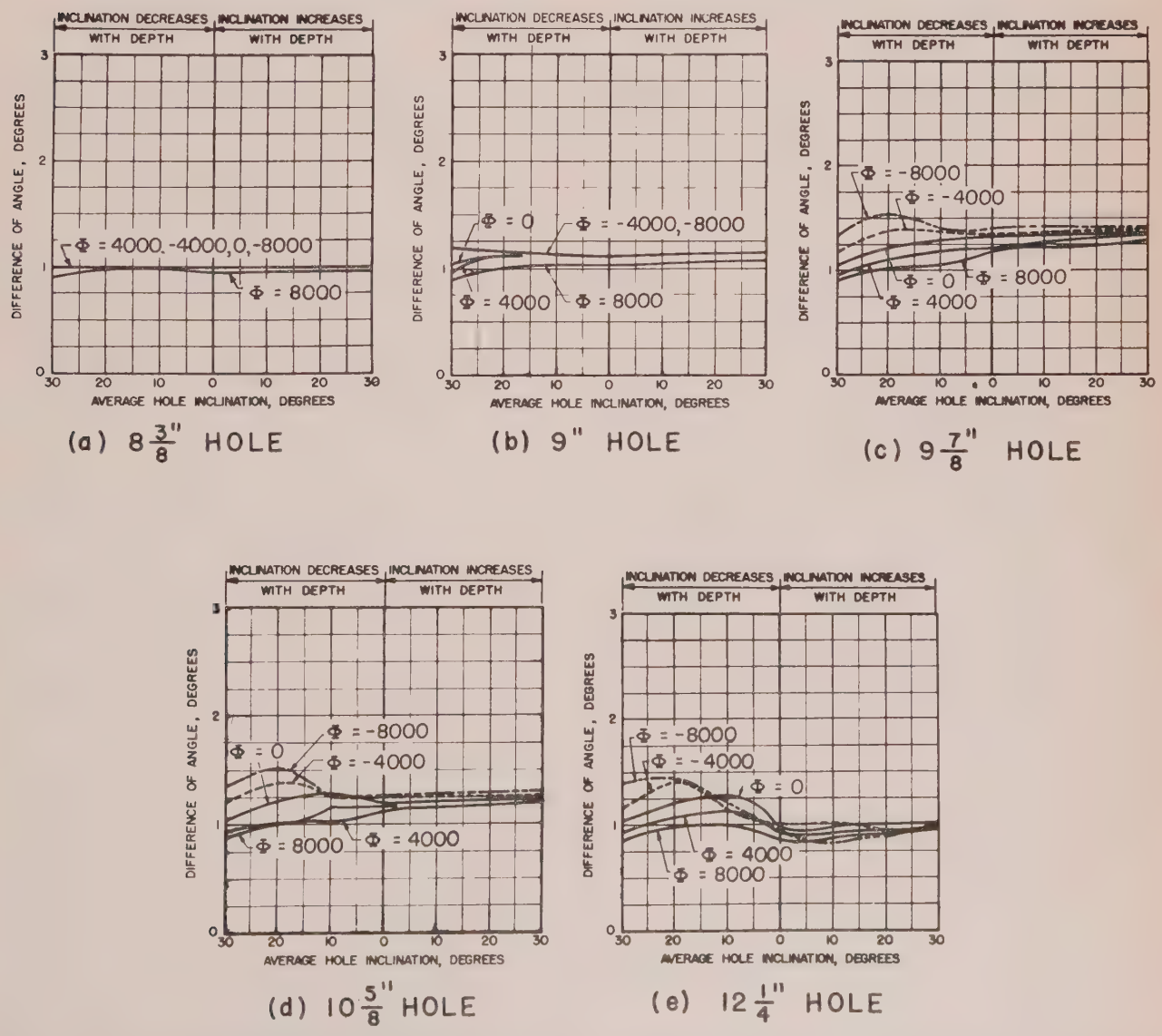

FIG. 16—MAXIMUM DIFFERENCE OF ANGLE OVER A 30-FT INTERVAL TO AVOID DRILL-COLLAR-CONNECTION FATIGUE FAILURES, 8-IN. COLLARS. POSITIVE Φ = TENSION AND NEGATIVE Φ = COMPRESSION, BOTH IN POUNDS PER INCH OF HOLE DIAMETER.

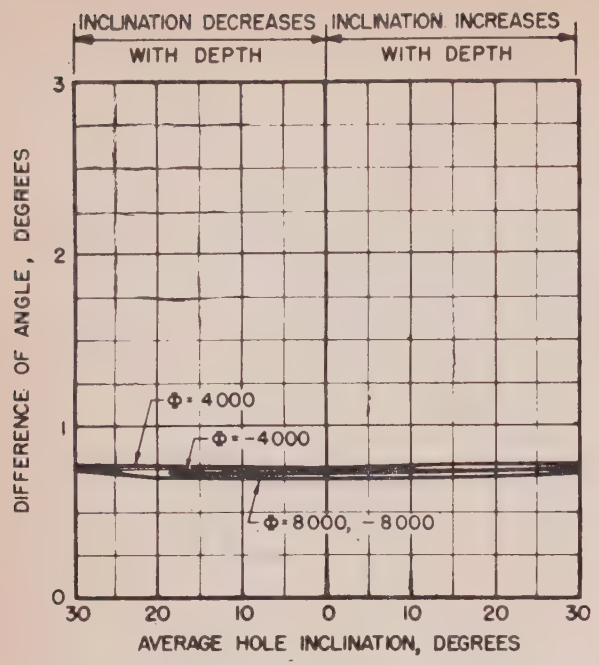

(a) 11¾-IN. HOLE

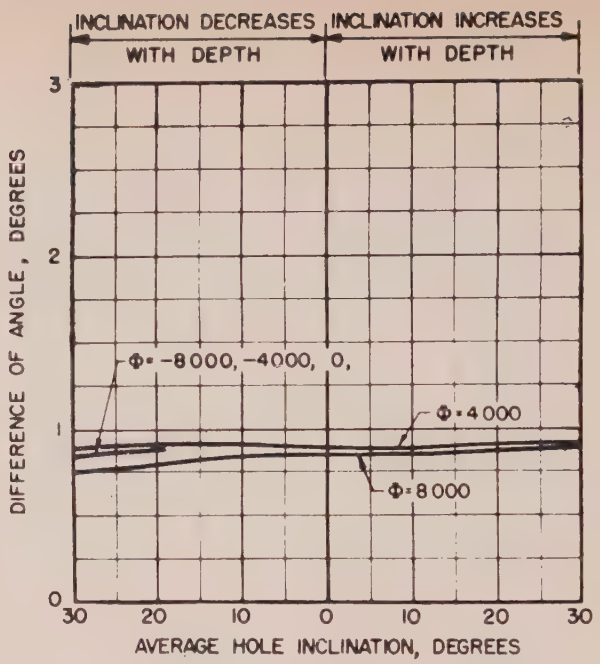

(b) 12¼-IN. HOLE

FIG. 17—MAXIMUM DIFFERENCE OF ANGLE OVER A 30-FT INTERVAL TO AVOID DRILL-COLLAR-CONNECTION FATIGUE FAILURES, 11-IN. COLLARS. POSITIVE Φ = TENSION AND NEGATIVE Φ = COMPRESSION, BOTH IN POUNDS PER INCH OF HOLE DIAMETER.

MAXIMUM PERMISSIBLE CHANGE OF ANGLE

The maximum permissible change of angle is obtained by choosing the smallest of the three following values: the one for drill-pipe fatigue, the one for 2,000-lb-on-tool-joint force or the one for fatigue of drill-collar connections.

Consider the example with which Table 1 for drill pipe has been prepared. Combining Tables 1 and 2 with Fig. 15b leads to the choice of several possible conclusions, two of which are given as follows.

1. Table 1 remains valid except that, for inclinations of 20° and 30° decreasing with depth, the values 1¼° and 1½° must be replaced by 1°.

2. Table 1 remains valid except that, for inclinations of 20° and 30° decreasing with depth, the values of 1½° must be replaced by 1¼°, and the following remark is added. "Whenever the change of angle over a 30-ft interval is greater than 1° in a hole whose inclination is greater than 10° and decreasing with depth, drill collars must not be rotated for any prolonged period of time under full tension in the dog-leg".

Using Method 2, the example in Table 5 of the maximum permissible change of angle over a 30-ft interval has been prepared.

Figs. 14, 15, 16 and 17 are for 4⅛-, 6¼-, 8- and 11-in. drill collars, respectively. Consider some other collar size such as, for instance, 7 in. Then, the best procedure first is to prepare tables similar to Table 5 for 6¼- and 8-in. collars and, thereafter using intermediate results, make a table for 7-in. collars.

Most of the maximum changes of angle in Table 5 were obtained from fatigue considerations. For greater changes of angle, either drill pipe or drill-collar connections are subjected to a certain number of revolutions, say a few tens of thousands, during which the steel is subjected to fatigue. However, fatigue failures generally occur after a much greater number of revolutions, say several million. Therefore, the detrimental effects of fatigue are not noticeable immediately. They simply result in shortening the life of either drill pipe or drill-collar connections. It is believed that the practices proposed in this paper should result in appreciable savings due to longer life of drill pipe and drill-collar connections.

For dog-legs which are far from the total anticipated depth, fatigue is more severe on drill pipe than on drill-collar connections. It should be realized, however, that pipe fatiguing occurs only when the drill pipe is under full tension, i.e., when drilling close to total depth. Therefore, one could contemplate accepting a greater change of angle than indicated in Tables 1 and 5 if some lengths of drill pipe (namely, those located in the dog-leg toward the end of drilling) were marked and later discarded from heavy-duty operations.

For dog-legs which are close to the total anticipated depth, the most fatigue occurs in drill-collar connections. In these cases, however, one could also accept greater changes of angle than indicated in Table 5, if drill collars are removed from the string after the dog-leg is found and later added one-by-one so as to have them rotating only below the dog-leg, as is done now in directional drilling.

If a greater change of angle than indicated in Tables 2 and 5 results in a tool joint-to-wall force greater than 2,000 lb, then (as already explained) this too could often be acceptable. Therefore, Table 5 should be considered as an ideal requirement, from which several exceptions might be tolerated.

TABLE 4—MAXIMUM CHANGE OF ANGLE BETWEEN SURVEY STATIONS TO AVOID FATIGUE FAILURES OF DRILL-COLLAR CONNECTIONS FOR 30-, 20- AND 15-FT SPACINGS*

Collar Size (In.)	Hole Size (In.)	Clear. (In.)	Tension (Pos.) or Compression (Neg.) (Thous. Lb/In. of Hole Diameter)	Average Inclination**															
				Inclination Decreases With Depth										Inclination Increases With Depth					
				30°			20°			10°			0°	10°			20°		30°
4⅛	4⅞	¾	8	¾ (¾) [¾]			1 (¾) [¾]			1 (1) [¾]			1¼ (1) [¾]	1¼ (1) [¾]			1¼ (1) [¾]		1¼ (1) [¾]
			4	1 (1) [¾]			1 (1) [¾]			1¼ (1) [¾]			1¼ (1) [¾]	1¼ (1) [¾]			1¼ (1) [1]		1¼ (1) [1]
			0	1¼ (1¼) [1]			1¼ (1¼) [1]			1¼ (1¼) [1]			1¼ (1¼) [1]	1¼ (1¼) [1]			1¼ (1¼) [1]		1¼ (1¼) [1]
			−4	1¼ (1¼) [1]			1¼ (1¼) [1]			1¼ (1¼) [1]			1¼ (1¼) [1]	1¼ (1¼) [1]			1¼ (1¼) [1]		1¼ (1¼) [1]
			−8	1¼ (1¼) [1]			1¼ (1¼) [1]			1¼ (1¼) [1]			1¼ (1¼) [1]	1¼ (1¼) [1]			1¼ (1¼) [1]		1¼ (1¼) [1]
4⅛	6⅛	2	8	¾ (¾) [½]			¾ (¾) [½]							1¼ (1)					
			4	1 (1) [¾]			1 (1) [¾]			1¼ (1) [¾]			1½ (1¼)					
			0	1¼ (1¼) [1]			1½ (1¼) [1]												
			−4	2 (1¾)			2 (1¾)												
			−8	1¼ (1¼) [1]			1¼ (1¼) [¾]												
4⅛	6¾	2⅝	8	¾ (¾) [½]			¾ (¾) [½]												
			4	¾ (¾) [¾]			1 (1) [¾]			1¼ (1) [¾]									
			0	1¼ (1¼) [1]			1½ (1¼) [1]												
			−4	1¾ (1½) [1]			1¾ (1½) [1]												
			−8	1 (1) [¾]			1 (1) [¾]			1¼ (1) [¾]									
4⅛	7⅞	3¾	8	¾ (¾) [½]			¾ (¾) [½]			¾ (¾) [½]									
			4	¾ (¾) [¾]			1 (1) [¾]			1¼ [¾]									
			0	1¼ (1¼) [1]			1½ (1¼) [1]												
			−4	1 (1) [¾]			1¼ (1¼) [1]												
			−8	½ (½) [½]			¾ (¾) [½]												
6¼	7	¾	8																
			4	1 (1) [¾]			1 (1) [¾]			1 (1) [¾]			1 (1) [¾]	1 (1) [¾]			1 (1) [¾]		1 (1) [¾]
			0	1 (1) [¾]			1 (1) [¾]			1 (1) [¾]			1 (1) [¾]	1 (1) [¾]			1 (1) [¾]		1 (1) [¾]
			−4	1 (1) [¾]			1 (1) [¾]			1 (1) [¾]			1 (1) [¾]	1 (1) [¾]			1 (1) [¾]		1 (1) [¾]
			−8	1 (1) [¾]			1 (1) [¾]			1 (1) [¾]			1 (1) [¾]	1 (1) [¾]			1 (1) [¾]		1 (1) [¾]
8	8¾	¾	8																
			4				¾ (¾)			¾ (¾)			¾ (¾)	¾ (¾)			¾ (¾)		¾ (¾)
			0				¾ (¾)			¾ (¾)			¾ (¾)	¾ (¾)			¾ (¾)		¾ (¾)
			−4	¾ (¾)			¾ (¾)						¾ (¾)	¾ (¾)			¾ (¾)		¾ (¾)
			−8	¾ (¾)			¾ (¾)			¾ (¾)			¾ (¾)	¾ (¾)			¾ (¾)		¾ (¾)

*For complete 30-ft Spacing Information, see Figs. 14, 15, 16 and 17.
**Numbers in parentheses ( ) are for 20-ft spacing; those in brackets [ ] are for 15-ft spacings.

For small tensions, the fatigue curve and the yielding curve in Figs. 5, 6 and 7 are far apart. The distance between these two curves decreases with increasing tension and becomes very small for large tensions. This means that, for very large tensions, failure should occur very fast if operating in conditions represented by points located to the right of the fatigue curve, and dog-legs causing drill-pipe fatigue should never be tolerated.

BEAM PUMPING TROUBLES DUE TO DOG-LEGS

Some beam pumping troubles probably are due to dog-legs. Frequently, however, troubles such as rod-on-tubing wear or excessive friction interfering with efficiency are attributed to crooked holes, while they are actually due to buckling of tubing.[12] In any event, it is believed that dog-legs should cause no beam pumping troubles if the changes of hole angle are within the limits recommended in this paper.

TABLE 5—EXAMPLE OF MAXIMUM CHANGE OF ANGLE BETWEEN 30-FT SPACED SURVEYS TO PREVENT FATIGUE FAILURES OF BOTH DRILL PIPE AND DRILL-COLLAR CONNECTIONS, AND TO KEEP THE TOOL JOINT-TO-WALL FORCE WITHIN 2,000 LB.

4½-in., 16.6-lb/ft Drill Pipe. Total Depth 12,000 ft.
810 ft of 6¼-in. Drill Collars. 7⅞-in. Hole.

Depth Interval (ft)	For Inclinations Increasing With Depth	For Inclinations Decreasing With Depth
4,000- 5,000	½°	½°
5,000- 6,000	½°	½° for Incins. up to 10° ¾° for Incins. betwn. 10° and 30°
6,000- 7,000	½°	½° for Incins. up to 10° ¾° for Incins. betwn. 10° and 30°
7,000- 8,000	½°	½° for Incins. up to 5° ¾° for Incins. betwn. 5° and 30°
8,000- 9,000	½° for inclinations up to 20° ¾° for inclinations betwn. 20° and 30°	½° for Incins. up to 5° ¾° for Incins. betwn. 5° and 20° 1° for Incins. betwn. 20° and 30°
9,000-10,000	¾°	¾° for Incins. up to 10° 1° for Incins. betwn. 10° and 30°
10,000-11,000	1°	1° for Incins. up to 20° 1¼°* for Incins. betwn. 20° and 30°
11,000-12,000	1¼°	1¼° for Incins. up to 10° 1¼°* for Incins. betwn. 10° and 30°

*For these conditions, drill collars must not be rotated for any prolonged period of time under full tension in the dog-leg.

SPACING BETWEEN SURVEYS

Let us now seek answers to the following frequently asked questions. How close should surveying stations be? Should surveys be directional?

With a very large survey spacing, such as 400 ft, some dog-legs could remain undetected because between surveys the hole inclination could first increase and then decrease. Similarly, nondirectional surveys could miss detecting dog-legs due to a change in the direction of the well, which often happens when drilling through an unconformity. On the other hand, such dog-legs would always be detected with 30-ft spaced directional surveys, but this is expensive. E. P. Rosser, Noble Drilling Co., pointed out at a recent API Mid-Continent Study Committee meeting that, in Central Oklahoma, surveying costs are often as high as $.50/ft for rig-time only. Therefore, the decision regarding the surveying interval and the fact of whether surveys should or should not be directional must be based on a compromise between a risk of trouble and the cost to prevent the trouble.

If no unconformities are expected, inclinometer surveys only (and not directional ones) should be taken. If past experience indicates that no dog-leg troubles should be expected and that bit footages are not extremely long, one survey per round trip could suffice.

On the other hand, if crooked hole formations are expected, directional surveys and/or more frequent surveys than one per round trip could be requested. However, it is hoped that one survey per round trip will suffice in most cases if used in conjunction with a practice proposed herein.

This practice consists of preparing in advance of

drilling a table such as the example Table 5, indicating the maximum permissible change of angle (or change of the over-all angle if surveys are directional) between two successive survey stations for various depths and other conditions. In the examples which follow, this maximum permissible change of angle will be 1° and the surveys will be nondirectional.

Consider first the following example of two successive surveys: at 10,100 ft, 13°; and at 10,280 ft, 14°. As the change of angle is only 1° (14−13), drilling may proceed.

Consider now the following example: at 10,100 ft, 13°; and at 10,280 ft, 14½°. This time, the change of angle is 1½° (14½−13), which is more than the maximum permissible value of 1°. However, this does not mean that the hole is necessarily unacceptable. Rather, it means that surveys at intermediate depths are needed. Assume first that with one intermediate survey the results are as follows: at 10,100 ft, 13°; at 10,190 ft, 14°; and at 10,280 ft, 14½°. Since the greatest change of angle between two successive surveys is 1° (14−13), drilling may proceed.

Second, assume that with one intermediate survey the results are: at 10,100 ft, 13°; at 10,190 ft, 14¼°; and at 10,280 ft, 14½°. Since the greatest change of angle is 1¼° (14¼−13), which is more than the maximum permissible value of 1°, additional surveys must be taken between 10,100 and 10,190 ft, the shortest interval generally being 30 ft. Assume first that the results are: at 10,100 ft, 13°; at 10,130 ft, 13¼°; at 10,160 ft, 14°; and at 10,190 ft, 14¼°. As the greatest change of angle between two successive surveys is ¾° (14−13¼), drilling may proceed.

Second, now assume that the results are: at 10,100 ft, 13°; at 10,130 ft, 14¼°; at 10,160 ft, 14½°; and at 10,190 ft, 14¼°.

Since this time the greatest change of angle between two successive surveys is 1¼° (14¼ − 13), which is too much, the hole must be considered unsatisfactory. It could be reamed and then surveyed again. In the event the unsatisfactory condition remains, the hole might have to be side-tracked.

As already explained in this paper, closer than 30-ft spacings may be necessary either when 4⅛-in. drill collars are used or in packed holes with larger collars.

An advantage of the technique explained in the aforementioned examples consists of savings in surveying costs because short-spaced surveys, such as 30-ft ones, would be taken only exceptionally.

SHORTCOMINGS OF THE PROPOSED TECHNIQUE

In the section "Survey Errors", a numerical example was given pertaining to prevention of drill-pipe fatigue failures. In that example, 4½-in. drill pipe was subjected to 79,000-lb tension, and the calculated maximum permissible change of angle between two stations 30-ft apart was 1°.

For larger tensions, calculated values as small as ¼° or even zero may be obtained. On the other hand, it has been shown in the section entitled "Force on Tool Joints" that according to field practice a change of angle of ½° (0.45° rounded here to ½°) between two 30-ft-apart surveys is generally harmless. One reason for this contradiction is that several simplifying assumptions were made, all on the safe side. Among them, one could mention that the Goodman diagram used is possibly too conservative; the tension to which drill pipe is subjected is assumed to be due not only to its own weight, but also to the weight of drill collars (actually, except when rotating off bottom, the weight of collars is applied to the bit); the survey correction factor due to drill collars' not conforming with hole geometry was calculated assuming zero tension in the drill collar at the survey level, which is not always the case.

Therefore, it seems that whenever a calculated result is smaller than ½° it may be replaced by ½°. By the same token, it seems that results which are larger than ½° are safe and should be used with confidence even if they are more lenient than present practices.

Use of presently available surveying methods is not very suitable for measuring changes of angle over close-spaced stations, because of inherent errors already explained in detail in this paper. Development of instruments especially adapted to that purpose could result in more leniency regarding the changes of hole angle than through use of the methods proposed in this paper, based on presently available instruments.

Present surveying methods cannot detect a so-called "ledge" in the hole (see Fig. 18), which might be as harmful as a dog-leg. On the other hand, in a hole in which the angle changes back and forth over short distances, the calculated conditions might be much more stringent than the actual situation.

ACKNOWLEDGMENT

The author wishes to thank Pan American Petroleum Corp. for having released this paper to the industry. He feels particularly grateful to his friends, H. B. Woods of Hughes Tool Co. and H. M. Rollins of Drilco Oil Tools, Inc., for their invaluable help and the appreciable time they were willing to devote to it. Information supplied by H. L. Willke, National Supply Co., is appreciated. Useful information used in the paper has been obtained from Eastman Oil Well Survey Co.

REFERENCES

1. Reedy, H. J.: "Drilling Controls Discarded in Steeply Dipping Formation", *World Oil* (Nov., 1958) **147**, No. 6, 115.
2. Rollins, H. M.: "Are 3° and 5° 'Straight Holes' Worth Their Cost?", *Oil and Gas Jour.* (Nov. 9, 1959) **57**, No. 46, 163.
3. Woods, H. B. and Lubinski, Arthur: "Practical Charts for Solving Problems on Hole Deviation", *Drill. and Prod. Prac.*, API (1954) 56.
4. Woods, H. B. and Lubinski, Arthur: "Use of Stabilizers in Controlling Hole Deviation", *Drill. and Prod. Prac.*, API (1955) 165.
5. Rollins, H. M.: "Studies of Straight-Hole Drilling Practices—1952 to 1956", *Drill. and Prod. Prac.*, API (1956) 37.
6. "Hole Inclination—Weight Tables", *AAODC Toolpusher's Manual*, 5th Printing (1960).
7. Lubinski, Arthur: "Chart for Determination of Hole Curvature (Dog-Leg Severity)", API Mid-Cont. Dist. Study Comm. on Straight-Hole Drilling (Oct. 31, 1956) Oklahoma City. Parts reprinted in: "How to Spot Dog-Legs

Early", *Oil and Gas Jour.* (Feb. 4, 1957) **55,** No. 5; "How to Determine Hole Curvature", *Pet. Eng.* (Feb., 1957) **29,** No. 2; "How Severe Is That Dog-Leg?", *World Oil* (Feb. 1, 1957) **144,** No. 2; "Dog-Leg Severity Can Be Determined by Use of a Chart", *Drilling* (Feb., 1957) **18,** No. 4. (Complete reprints available from author.)

8. Texter, H. G.: "Drill-Pipe Rejects Show Good Service Life", *Oil and Gas Jour.* (Nov. 10, 1952) **51,** No. 27, 100.
9. Lubinski, Arthur: "A Study of the Buckling of Rotary Drilling Strings", *Drill. and Prod. Prac.*, API (1950) 178.
10. Klinkenberg, A.: "The Neutral Zones in Drill Pipe and Casing and Their Significance in Relation to Buckling and Collapse", *Drill. and Prod. Prac.*, API (1951) 64.
11. Lubinski, Arthur: "Influence of Tension and Compression on Straightness and Buckling of Tubular Goods in Oil Wells", *Proc.*, API (1951) **31 (IV),** 31.
12. Lubinski, Arthur and Blenkarn, K. A.: "Buckling of Tubing in Pumping Wells, Its Effects and Means for Controlling It", *Trans.*, AIME (1957) **210,** 73.
13. Lubinski, Arthur and Woods, H. B.: "Fractors Affecting the Angle of Inclination and Dog-legging in Rotary Bore Holes", *Drill. and Prod. Prac.*, API (1953) 222.

APPENDIX

DIFFERENTIAL EQUATIONS AND THEIR SOLUTIONS

Let β denote the average hole inclination in a section containing a dog-leg. Let Q denote the weight in fluid per unit length of pipe. Q may be resolved into components $Q \cos \beta$ in the average direction of hole axis, and $Q \sin \beta$ in the perpendicular direction. The component $Q \sin \beta$ is a lateral load. The component $Q \cos \beta$ will be disregarded, which means that the pipe will be assumed to be subjected to a constant longitudinal force. Such an assumption is perfectly valid for large tensions or compressions, for which the variation of the longitudinal force over a short length under consideration is small compared to this force itself, On the other hand, for small tensions or compressions, the component $Q \cos \beta$ should be retained and the problems treated by the means used in Ref. 9. For the sake of simplicity, however, this was not done. It is felt that the results are sufficiently good for the purpose pursued here.

In tension, the elastic line is always a plane curve. In compression, on the other hand, the elastic line may either be a plane or a non-plane curve. However, in Ref. 13 it is shown that, in cases of geometrically straight but inclined holes (i.e., in presence of no dog-legs) in almost any actual situation encountered in drilling, the elastic line is a plane curve. It is believed that the same holds true in presence of dog-legs, and the elastic line will be assumed to be a plane curve.

Consider a Portion OA of a pipe shown in Fig. 19. Let O be the origin of co-ordinates and let the X-axis be parallel to the pipe at O. Let $Q \sin \beta$ be the lateral load per unit length, T the tension (both constant throughout the length of the pipe) and let S_o be the shear at O. Finally, let c_o be the curvature of the pipe at O.

The bending moment at any point along the pipe is

$$EIc_o + S_oX + TY - \int_o^x (Q \sin \beta) X \, dX,$$

where E is the Young's modulus of steel, and I is the moment of inertia of the pipe cross-section with respect to its diameter.

Performing the integration and equating this expression to $EI(d^2Y/dX^2)$, the following differential equation of the elastic line is obtained.

$$\frac{d^2Y}{dX^2} - K^2Y = c_o + \frac{S_o}{EI} X - \frac{Q \sin \beta}{2EI} X^2, \quad (1t)$$

in which

$$K = \sqrt{\frac{T}{EI}} \quad (2t)$$

It may be checked that the solution of Eq. 1, satisfying the boundary conditions at Point O, is

$$Y = \frac{1}{K^2}\left[c'_o (\cosh KX - 1) + s_o (\sinh KX - KX) + \frac{q}{2} (KX)^2 \right], \quad (3t)$$

in which

$$q = \frac{1}{K^2} \frac{Q \sin \beta}{EI}; \quad (4tc)$$

$$s_o = \frac{1}{K} \frac{S_o}{EI}; \quad (5tc)$$

and

$$c'_o = c_o - q. \quad (6t)$$

The rule regarding the signs of q and s_o is the same as that pertaining to $Q \sin \beta$ and S_o.

Following the same route, but for compression C instead of tension T, the following equations are obtained.

$$K = \sqrt{\frac{C}{EI}}; \quad (2c)$$

$$Y = \frac{1}{K^2}\left[c'_o (1 - \cos KX) + s_o (KX - \sin KX) - \frac{q}{2} (KX)^2 \right]; \quad (3c)$$

and

$$c'_o = c_o + q \quad (6c)$$

If the pipe is subjected to neither tension nor compression, then the term K^2Y is not present in the differential Eq. 1t, and its general solution becomes

$$Y = -\frac{q'}{24} X^4 + \frac{s'_o}{6} X^3 + \frac{c_o}{2} X^2, \quad (3n)$$

in which

$$q = \frac{Q \sin \beta}{EI}; \quad (4n)$$

and

FIG. 18 (LEFT)—LEDGE, UNDETECTABLE WITH SURVEYS.

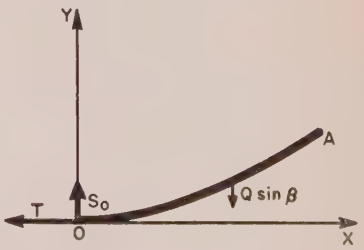

FIG. 19 (RIGHT).

$$s'_o = \frac{S_o}{EI} \quad \ldots\ldots\ldots\ldots \quad (5n)$$

In this first section of the Appendix, similar equations are denoted by the same numerals followed by letters "t", "c" or "n", respectively, for the cases of tension, compression, or neither tension nor compression. Both letters "t" and "c" are used to denote equations pertaining to both tension and compression, but not to the case of neither tension nor compression.

Further in this Appendix, reference will be made to these equations, but without any letter, for instance to Eq. 3. This will mean either Eq. 3t, 3c, or 3n, whichever may be the case.

DRILL PIPE UNDER TENSION IN GRADUAL AND LONG DOG-LEGS

Consider drill pipe under tension in an increasing gradual and long dog-leg shown in Fig. 20. The coordinate axes are so chosen that the equations derived from Fig. 19 remain valid. In these equations, the pipe curvature c_o may be considered as known because it easily can be obtained from Eq. 7.

$$c_o = \frac{2\sigma}{ED} \quad \ldots\ldots\ldots\ldots \quad (7)$$

where

D = the diameter of drill pipe, and
σ = the reversible bending stress obtained from the modified Goodman diagram (Fig. 2).

Let $2L$ denote the length of drill pipe between two tool joints. By reasons of symmetry, the pipe is parallel to the hole axis at $X = L$. Let α denote the angle by which the hole turns over the length L. If R is the radius of curvature, then $L = R\alpha$. Let c denote the hole curvature; i.e., $c = 1/R$.

Therefore,

$$\alpha = Lc \quad \ldots\ldots\ldots\ldots \quad (8)$$

Thus, a boundary condition of the elastic line is

$$\left(\frac{dY}{dX}\right)_{X=L} = Lc \quad \ldots\ldots\ldots\ldots \quad (9)$$

Assume that there is no pipe-to-wall contact at $X = L$. Then, because of symmetry, another boundary condition expresses the fact that the shear at $X = L$ is nil.

$$\left(\frac{d^3Y}{dX^3}\right)_{X=L} = O \quad \ldots\ldots\ldots\ldots \quad (10)$$

Substituting Eq. 3t into Eq. 10, we obtain

$$s_o = -\, c'_o \tanh KL \quad \ldots\ldots\ldots\ldots \quad (11)$$

Substituting Eqs. 3t and 11 into Eq. 9, we obtain

$$c' = c'_o \frac{\tanh KL}{KL} \quad \ldots\ldots\ldots\ldots \quad (12)$$

where

$$c' = c - q \quad \ldots\ldots\ldots\ldots \quad (13)$$

For every value of tension (i.e., of the ordinate in Fig. 3), σ is obtained from the modified Goodman diagram of Fig. 2; c_o is then calculated with Eq. 7; K with Eq. 2t; c'_o with Eqs. 4tc and 6t; c' with Eq. 12; and, finally, c is obtained from Eq. 13. c is the hole curvature in radians per inch. (1 radian/in. = 0.06876° /100 ft.) c is the abscissa in Fig. 3.

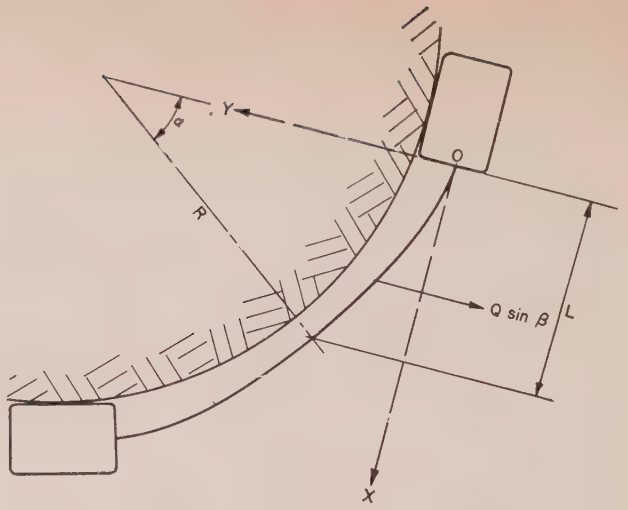

FIG. 20—INCREASING GRADUAL AND LONG DOG-LEG.

Fig. 21 is similar to Fig. 20, except that it is for a decreasing dog-leg. From these two figures it is self-evident that all the equations derived for increasing dog-legs hold true also for decreasing ones, if in numerical problems positive values are substituted for q in cases of increasing dog-legs, and negative values in cases of decreasing dog-legs.

If gravity forces are neglected, in the previous formulas $q = o$, $c' = c$ and $c'_o = c_o$. It has been found that in such a case, except for tensions which are less than the weight of drill collars, the effects of gravity are negligible. This is why they have been disregarded in calculating with Eq. 12 the fatigue curve of Fig. 3.

Eq. 12 holds true only if there is no contact at $X = L$. Conditions under which this contact occurs will now be investigated.

The amount by which drill pipe must be deflected at $X = L$ to contact the wall of the hole is a sum of two terms. One of these terms, denoted r_t, is

$$r_t = \frac{D_{T.J.} - D_{D.P.}}{2}$$

where $D_{T.J.}$ is tool-joint OD, and $D_{D.P.}$ is drill-pipe OD.

The other term, denoted U and shown in Fig. 22, is due to hole curvature. From this figure, we have

$$R^2 + L^2 = (R + U)^2;$$

i.e.,

$$L^2 = 2RU + U^2.$$

Neglecting the last term because U is small compared to R,

$$U = \frac{1}{2}\frac{1}{R}L^2 = \frac{cL^2}{2}.$$

Thus, the sought relation is

$$Y_{X=L} = r_t + \frac{cL^2}{2} \quad \ldots\ldots\ldots\ldots \quad (14)$$

Substituting Eq. 11 into Eq. 3t and the result into Eq. 14, we obtain in view of Eq. 13,

$$c' = 2c'_o \frac{KL \sinh KL - (\cosh KL - 1)}{(KL)^2 \cosh KL} - \frac{2r_t}{L^2} \quad \ldots\ldots\ldots\ldots \quad (15)$$

The yield curve in Fig. 3 has been calculated with Eq. 15.

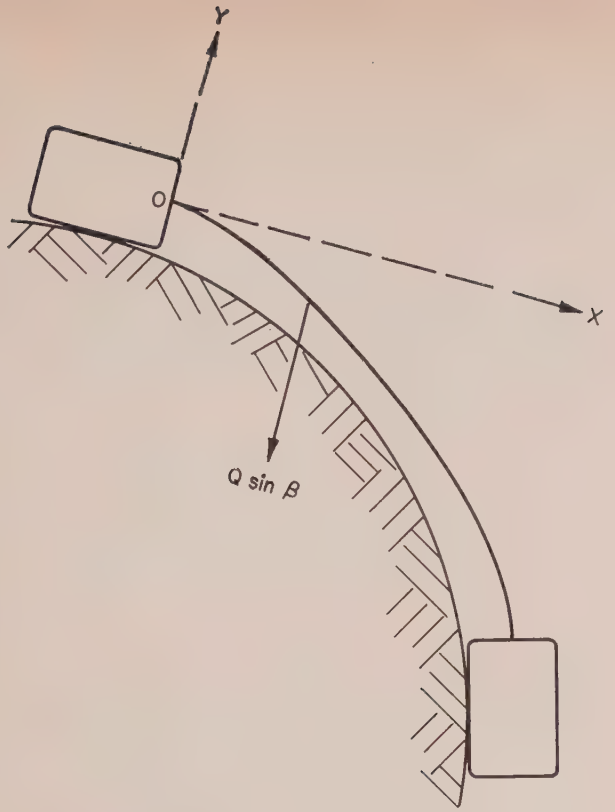

FIG. 21--DECREASING GRADUAL AND LONG DOG-LEG.

DRILL COLLARS IN ABRUPT DOG-LEGS

There are 18 cases of drill collars in abrupt dog-legs. These cases depend on: (1) whether the dog-leg is increasing (Fig. 8) or decreasing (Fig. 9); (2)—whether the collars are subjected to tension, compression or zero longitudinal force; and (3) the number of contacts with the wall of the hole.

The number of equations corresponding to such a large number of cases is far too great to be fully derived here. Instead of this, only the methods of derivation will be explained. The origin of co-ordinates was chosen at the Point 0 in Figs. 8 and 9, which is a point of contact with the wall of the hole at which the elastic line is parallel to the hole. In the event there are two such points, as in the cases of Figs. 9a and 9c, the origin is placed at the point which is closer to the middle Point A of the dog-leg. In all cases, the X and Y axes were chosen parallel and perpendicular to the hole, respectively. Therefore, the equations derived in the first section of the Appendix do apply.

Consider first the Sections OB in Figs. 9a and 9c where B is the point of contact with the low side of the hole. The following boundary conditions must be satisfied at Point B.

$$Y_B = r; \quad . \quad . \quad . \quad . \quad . \quad . \quad . \quad . \quad . \quad . \quad (16)$$

$$\left(\frac{dY}{dX}\right)_B = O; \quad . \quad . \quad . \quad . \quad . \quad . \quad . \quad . \quad . \quad . \quad (17)$$

and

$$\left(\frac{d^2Y}{dX^2}\right)_B = O \quad . \quad . \quad . \quad . \quad . \quad . \quad . \quad . \quad . \quad . \quad (18)$$

where r is the diametral collar-to-hole clearance. Using Eq. 3, the three unknowns c'_o (or c_o), s_o and the Distance OB are calculated with Eqs. 16, 17 and 18.

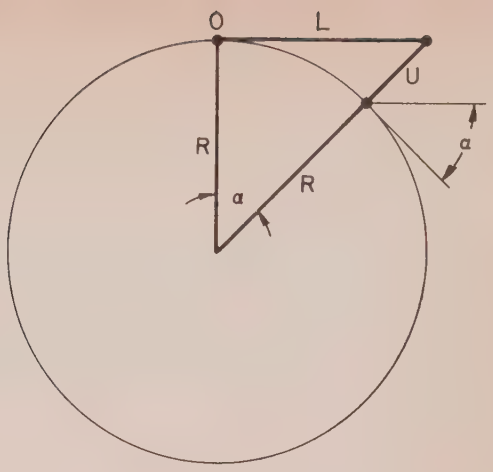

FIG. 22

Consider the Section OA in Figs. 9a and 9c. There is no discontinuity of the bending moment at Point O between the Sections OB and OA. Therefore, the curvature c_o at Point O is the same in both sections; and, in view of Eq. 6, c'_o is also the same. Thus, c'_o and c_o of the Section OA are known.

Consider now the Section OA in all the remaining cases of Figs. 8 and 9, except 8c which will be treated further in this paper. In all these cases $c_o = O$; therefore, c'_o is also known in view of Eq. 6.

In all the cases of Figs. 8 and 9, the following boundary condition must be satisfied at Point A.

$$\left(\frac{d^2Y}{dX^2}\right)_A = \frac{M}{EI} \quad . \quad . \quad . \quad . \quad . \quad . \quad . \quad . \quad . \quad (19)$$

where M is the bending moment for fatigure of drill-collars connections. Values of M for a few collar sizes were given in the body of the paper.

The second boundary condition at A depends on whether there is or there is not a collar-to-wall contact A. If there is contact, the boundary condition is

$$Y_A = r \quad . \quad . \quad . \quad . \quad . \quad . \quad . \quad . \quad . \quad . \quad . \quad (20)$$

and if there is no contact, in view of symmetry at A,

$$\left(\frac{d^3Y}{dX^3}\right)_A = O \quad . \quad . \quad . \quad . \quad . \quad . \quad . \quad . \quad . \quad . \quad (21)$$

Using Eq. 3, the two unknowns s_o and the Distance OA are calculated, either with Eqs. 19 and 20, or with Eqs. 19 and 21.

At the Point A, we also have

$$\left(\frac{dY}{dX}\right)_A = \alpha \quad . \quad . \quad . \quad . \quad . \quad . \quad . \quad . \quad . \quad . \quad (22)$$

where α is one-half the dog-leg angle in radians. Using Eq. 3, in which all the coefficients are either known or have already been calculated, α is calculated with Eq. 22.

In Figs. 8a, 9a and 9b, drill collars contact the wall at Point A, which is possible only if the reaction of the wall of the hole on the collar is positive and which, in turn, requires that

$$\left(\frac{d^3Y}{dX^3}\right)_A \geqslant O \quad . \quad . \quad . \quad . \quad . \quad . \quad . \quad . \quad . \quad . \quad (23)$$

Whenever Inequality 23 is not satisfied, calculations based on the assumption that there is contact at A must

be discarded, and calculations based upon the assumption that there is no such contact must be made.

In Figs. 9a and 9c, drill collars contact the wall at Point O, which is possible only if the reaction of the wall of the hole on the collar is positive and which, in turn, requires that

$$(s_o)_{\text{Section OA}} + (s_o)_{\text{Section OB}} \geqslant O \quad . \quad . \quad . \quad (24)$$

Whenever Inequality 24 is not satisfied, a case different from that of Figs. 9a and 9c must be assumed.

Consider now Fig. 8a in the case of tension and negligible gravity forces. The relationships presented symbolically as Eqs. 19, 20 and 22 greatly simplify and become

$$s_o \sinh KP = \frac{M}{EI}; \quad . \quad . \quad . \quad . \quad . \quad . \quad . \quad . \quad . \quad (25)$$

$$\frac{1}{K^2}\frac{M}{EI}\frac{\sinh KP - KP}{\sinh KP} = r; \quad . \quad . \quad . \quad . \quad (26)$$

and

$$\frac{s_o}{K}(\cosh KP - 1) = \alpha \quad . \quad . \quad . \quad . \quad . \quad . \quad (27)$$

where P is the Distance OA.

In absence of gravity ($\beta = q = O$) which pulls the string toward the low side of the hole, the collars may lose contact at Point O but not at A. This situation, which is shown in Fig. 8c, occurs for $KP = \infty$, i.e., in view of Eq. 26, for $r = M/(K^2EI)$. Thus, the case of Fig. 8c requires that the three following conditions be fulfilled—(1) no gravity forces; (2) tension; and (3)

$$r \geqslant \frac{1}{K^2}\frac{M}{EI} \quad . \quad . \quad . \quad . \quad . \quad . \quad . \quad . \quad . \quad (28)$$

In such case we obtain, eliminating s_o between Eqs. 25 and 27 and making $KP = \infty$,

$$\alpha = \frac{1}{K}\frac{M}{EI}, \quad . \quad . \quad . \quad . \quad . \quad . \quad . \quad . \quad . \quad (29)$$

with which α is calculated.

Using Eqs. 29 and 22 it has been found that, for drill collars in abrupt dog-legs, neglecting gravity forces is valid in holes which are nearly vertical.

As an example of the results obtained for drill collars in abrupt dog-legs, four figures for 6¼-in. collars have been prepared: Fig. 23a for a tension of 4,000 lb/in. of hole diameter; Fig. 23b for neither tension nor compression; and Figs. 23c and 23d for a compression of 4,000 lb/in. of hole diameter. The abscissa is the diametral collar-to-hole clearance r, and the ordinate is the dog-leg angle 2 α in degrees. Various curves are for various values of the average hole inclination β, either in increasing or in decreasing dog-legs.

Table 6 indicates to which cases of Figs. 8 and 9 correspond various curves in Figs. 23a, 23b, 23c and 23d.

Dog-leg angles 2 α at which fatigue of collar connections occurs were calculated for numerous other situations than those plotted in the afore-mentioned figures. The obtained values of 2 α were used in calculating the correction factor f with the equations derived in the next section. Finally, 2 $\alpha f - 0.25$ was plotted in Figs. 14, 15, 16 and 17, and some of the results also are given in Table 4.

DRILL COLLARS IN GRADUAL AND LONG DOG-LEGS

Since there are no tool joints in a drill-collar string, drill collars generally assume the same shape as the hole in a gradual and long dog-leg. Therefore, the hole curvature at which fatigue of connections occurs is

$$c = \frac{M}{EI} \quad . \quad . \quad . \quad . \quad . \quad . \quad . \quad . \quad . \quad . \quad . \quad (30)$$

The limiting value of survey spacing, above which assuming an abrupt dog-leg results in more severe conditions than assuming a gradual and long one, is equal to the ratio of 2 α calculated with Eq. 22 over c obtained with Eq. 30.

DRILL PIPE UNDER TENSION IN ABRUPT DOG-LEGS

In the case of drill pipe, Eq. 29 may be written

$$\alpha = \frac{c_o}{K} \quad . \quad . \quad . \quad . \quad . \quad . \quad . \quad . \quad . \quad . \quad . \quad (31)$$

in which c_o is known from Eq. 7.

Using Eqs. 31 and 22 in investigating drill pipe under tension in abrupt dog-legs, it has been found that (as for gradual dog-legs) neglecting gravity forces is justified even in very inclined holes, except for tensions which are smaller than the weight of drill collars.

Figs. 5, 6 and 7 were prepared with Eq. 31, in which c_o was obtained from Eq. 7. For fatigue curves, σ in Eq. 7 was obtained from the modified Goodman diagram (Fig. 2). For yielding curves, σ in Eq. 7 is the yield strength of Grade E steel, i.e., 75,000 psi.

The expression of the force F between a tool joint in an abrupt dog-leg and the wall of the hole is obtained from equilibrium considerations, α being small, this expression is

$$F = 2\,T\,\alpha \quad . \quad . \quad . \quad . \quad . \quad . \quad . \quad . \quad . \quad . \quad . \quad (32)$$

The 2,000-lb curves in Figs. 5, 6 and 7 were calculated with Eq. 32.

CORRECTION FACTOR f

INCREASING DOG-LEGS

Consider drill collars subjected to zero tension and located in an increasing dog-leg. Furthermore, consider first that the case is that of Fig. 8b and not 8a, i.e., that Eq. 23 is not satisfied. Instead of Eq. 23, however, we

TABLE 6—CORRELATION OF FIGURES

Curve	In Fig. No.	Corresponds to Case of Fig. No.
AB	23a	9a
BC	23a	9b
AD	23a	8a
DE	23a	8c
AF	23a	8a
GH	23b	9a
HI	23b	9b
GJ	23b	8a
KL	23d	9a
LM	23d	9c
KN	23d	9a
NO	23d	9c
OP	23d	9d
KQ	23d	9a
QR	23d	9b
KS	23c	8a
ST	23c	8b

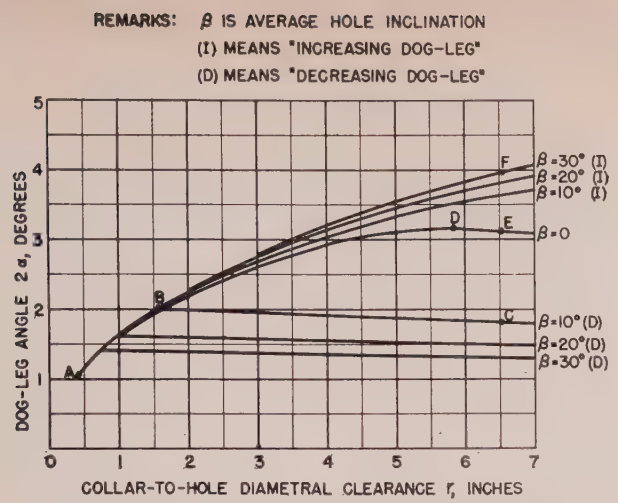

FIG. 23a—FATIGUE OF 6¼-IN. DRILL-COLLAR CONNECTIONS IN ABRUPT DOG-LEGS. TENSION = 4,000 LB/IN. OF HOLE DIAMETER.

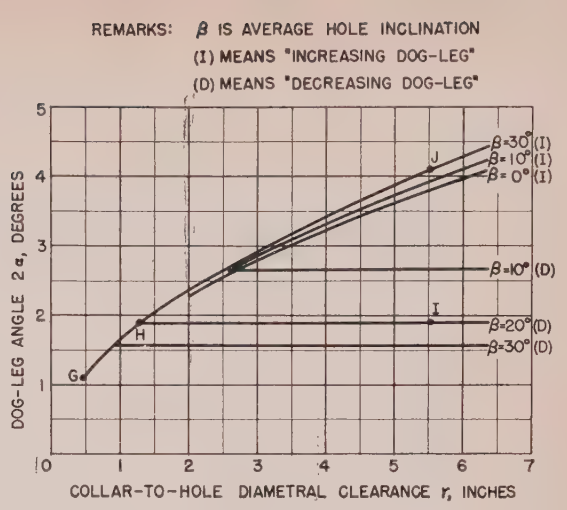

FIG. 23b—FATIGUE OF 6¼-IN. DRILL-COLLAR CONNECTIONS IN ABRUPT DOG-LEGS. CASE OF NEITHER TENSION NOR COMPRESSION.

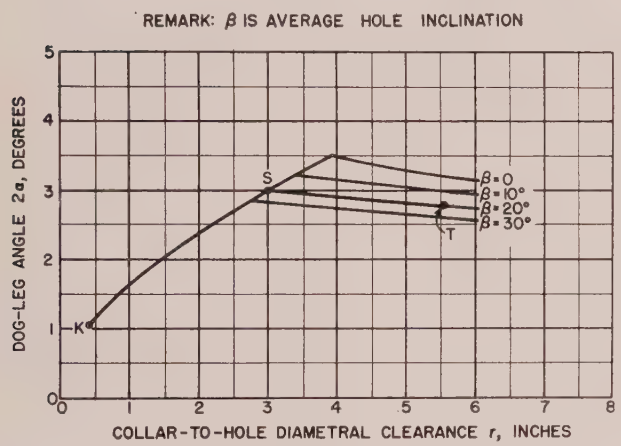

FIG. 23c—FATIGUE OF 6¼-IN. DRILL-COLLAR CONNECTIONS IN ABRUPT INCREASING DOG-LEGS. COMPRESSION = 4,000 LB/IN. OF HOLE DIAMETER.

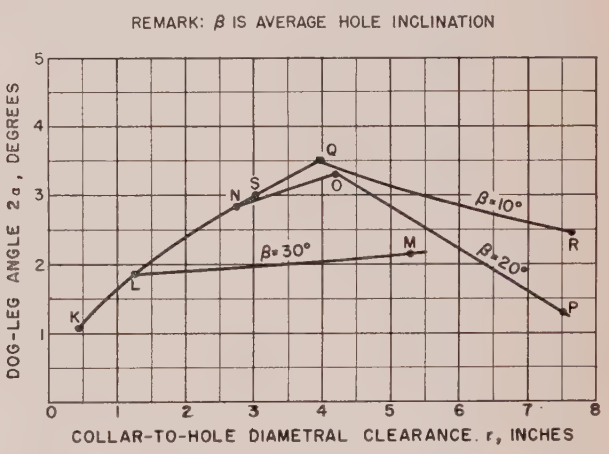

FIG. 23d—FATIGUE OF 6¼-IN. DRILL-COLLAR CONNECTIONS IN ABRUPT DECREASING DOG-LEGS. COMPRESSION = 4,000 LB/IN. OF HOLE DIAMETER.

shall now use the following condition which must hold true in the case of Fig. 8b.

$$r \geqslant r_{lim} \quad , \quad . \quad . \quad . \quad . \quad . \quad . \quad . \quad . \quad . \quad . \quad . \quad . \quad (33)$$

in which

$$r_{lim} = Y_A \quad . \quad . \quad . \quad . \quad . \quad . \quad . \quad . \quad . \quad . \quad . \quad . \quad (34)$$

where r is the collar-to-hole diametral clearance, and r_{lim} is the smallest value of r for which the case of Fig. 8b is possible.

Substituting Eq. 3n into Eqs. 21 and 22, eliminating s'_0 between them and solving for P,

$$P = \sqrt[3]{\frac{3\ \alpha}{q'}} \quad . \quad . \quad . \quad . \quad . \quad . \quad . \quad . \quad . \quad . \quad . \quad . \quad (35)$$

Substituting Eq. 3n into Eqs. 21 and 34, eliminating s'_0 between them, and substituting P from Eq. 35, we obtain

$$r_{lim} = \frac{3\sqrt[3]{3}}{8} \sqrt[3]{\frac{\alpha^4}{q'}} \quad . \quad . \quad . \quad . \quad . \quad . \quad . \quad . \quad . \quad . \quad (36)$$

Referring to Fig. 8b, let S be a survey station, the Point A being assumed to be halfway between two stations. Let Z denote the Distance AS, i.e., half the survey spacing. Then the expression of the correction factor f is

$$f = 1 - \frac{1}{\alpha}\left(\frac{dY}{dX}\right)_{X-P-z} \quad . \quad . \quad . \quad . \quad . \quad . \quad (37)$$

Substituting Eq. 3n into Eqs. 21, 22 and 34, solving for q', P and s'_0, and substituting these into Eq. 37, we obtain

$$f = 1 - (1 - W)^2\ (1 + 0.5\ W) \quad , \quad . \quad (38)$$

in which

$$W = \frac{3}{8}\frac{Z}{r_{lim}}\frac{\alpha}{} \quad . \quad . \quad . \quad . \quad . \quad . \quad . \quad . \quad . \quad . \quad . \quad (39)$$

Consider now the case of Fig. 8a. Substituting Eq. 3n into Eqs. 22 and 20 and eliminating s'_0 between them, we obtain

$$\frac{1}{72}\ q'\ P^4 + \frac{1}{3}\ \alpha\ P - r = O \quad . \quad . \quad . \quad . \quad (40)$$

Substituting Eq. 3n into Eqs. 22 and 20, solving for s'_0 and q', and substituting these into Eq. 37, we obtain

$$f = 1 - \left[4\left(\frac{3r}{\alpha P} - 1\right)\frac{Z}{P} + 1\right]\left(1 - \frac{Z}{P}\right)^3$$
$$. \quad . \quad . \quad . \quad . \quad . \quad . \quad . \quad . \quad . \quad . \quad . \quad . \quad . \quad . \quad . \quad . \quad . \quad (41)$$

Thus, to calculate f one must first obtain r_{lim} from Eq. 36. Then, if Inequality 33 is satisfied, f is calculated with Eqs. 38 and 39. On the other hand, if Eq. 33 is not

satisfied, Eq. 40 must be numerically solved for P and, thereafter, f calculated with Eq. 41.

In the first of these two cases, f depends on q', i.e., on β in view of Eq. 4n, but not on r. On the other hand, in the second case f depends on both r and q'. However, it has been found through numerical substitutions that, actually, f depends strongly on r and very little on q'. Furthermore, it has been found that a sufficiently good approximation consists of calculating the second case by the same means as the first one (i.e., by using Eq. 38); however, W is given by Eq. 42 instead of by Eq. 39.

$$W = \frac{3}{8}\frac{Z\alpha}{r} \quad \ldots\ldots\ldots\ldots \quad (42)$$

Consider the following example case: 30-ft survey spacing; 6¼-in. drill collars; 7⅞-in. hole; and average hole inclination $\beta = 20°$, increasing with depth. f has been calculated vs 2 α and plotted in Fig. 24.

For conditions represented by the straight Line CD, 2 α is very small and P (Fig. 8b) is less than 15 ft. Therefore, $f = 1$.

Curve DE corresponds to conditions of Fig. 8b, and Curve EF corresponds to conditions of Fig. 8a. The Curve EF has been calculated by the approximate method explained previously. Actually, there is a family of curves, such as EF, corresponding to various values of β; one of them corresponds to $\beta = 20°$, but these curves are all close to each other.

For conditions represented by the straight Line FG, P (Fig. 8a) is again less than 15 ft and $f = 1$.

The Curve DE is a portion of Curve DH in Fig. 24, which is the same as the curve for 7⅞-in. hole in Fig. inclination, increasing with depth, in Fig. 11a. Similarly, the Curve EF is a portion of the Curve OF in Fig. 24, which is the same as the curve for 7⅞-in. hole in Fig. 11c. Consider now, as an example, that 2 $\alpha = 1°$. In the method explained in the body of the report, f would have been obtained by reading the ordinate of Point J in Fig. 11a and the ordinate of Point I in Fig. 11c, retaining the larger of the two. This procedure is self-evident in view of the fact that in Fig. 24 the answer is obtained at J.

Figs. 10a, 11a, 12a, and 13a were prepared using Eqs. 38, 39 and 36. Figs. 10c, 11c, 12c and 13c were prepared using Eqs. 38 and 42. The same equations were used in calculating f, with which values of 2 αf − 0.25 were obtained and plotted in Figs. 14, 15, 16, 17 and Table 4.

DECREASING DOG-LEGS

Consider now the case of Fig. 9b. The origin of co-ordinates will be at Point O. The case of Fig. 9b requires that

$$r \geq r_{11m} \quad \ldots\ldots\ldots\ldots \quad (43)$$

in which

$$r_{11m} = Y_K \,|\, Y_{X=P'-P} \quad \ldots\ldots\ldots \quad (44)$$

K is the point of maximum deflection, i.e., the point at which

$$\left(\frac{dY}{dX}\right)_K - \left(\frac{dY}{dX}\right)_{X=P'-P} = O \quad \ldots \quad (45)$$

At Point A we have, in addition to Eq. 22,

$$Y_A = Y_{X=P'} = O \quad \ldots\ldots\ldots \quad (46)$$

Substituting Eq. 3n into Eqs. 46 and 22, eliminating s'_o between them and solving for P'

$$P' = \sqrt[3]{\frac{24\,\alpha}{(-q')}} \quad \ldots\ldots\ldots\ldots \quad (47)$$

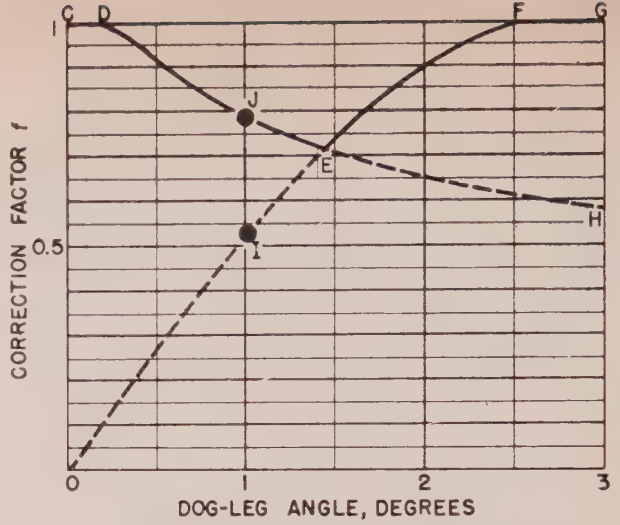

FIG. 24—CORRECTION FACTOR f FOR 6¼-IN. DRILL COLLAR, 7⅞-IN. HOLE, 20° AVERAGE HOLE INCLINATION, INCREASING WITH DEPTH, 30-FT SPACING.

Remember that in a decreasing dog-leg ($-q'$) is positive.

Substituting Eq. 3n into Eqs. 45 and 46 and eliminating s'_o, we obtain

$$P = -\frac{1}{4}P' \quad \ldots\ldots\ldots\ldots \quad (48)$$

Substituting Eq. 3n into Eqs. 45 and 44, eliminating s'_o between them and substituting P from Eq. 48 and P' from Eq. 47 into the result, we obtain

$$r_{11m} = \frac{27\sqrt{3}}{128}\sqrt[3]{\frac{\alpha^4}{(-q')}} \quad \ldots\ldots\ldots \quad (49)$$

The expression of the correction factor f, similar to Eq. 37, is (see Fig. 9b)

$$f = 1 - \frac{1}{\alpha}\left(\frac{dY}{dX}\right)_{X=P'-Z} \quad \ldots\ldots\ldots \quad (50)$$

Substituting Eq. 3n into Eqs. 45, 22 and 44, substituting in them P from Eq. 48, solving for q', P', and s'_o and substituting these into Eq. 50, we obtain

$$f = 1 - (1 - V)^2\,(1 - 4V) \quad \ldots \quad (51)$$

in which

$$V = \frac{27}{256}\frac{Z\alpha}{r_{11m}} \quad \ldots\ldots\ldots\ldots \quad (52)$$

Consider now the case of Fig. 9a. Proceeding in a similar way as for the case of Fig. 8a, it has been found that f depends very little on q' and that, for all practical purposes, one may still calculate f with Eq. 51; however, V is given by Eq. 53 instead of by Eq. 52.

$$V = \frac{27}{256}\frac{Z\alpha}{r} \quad \ldots\ldots\ldots\ldots \quad (53)$$

Furthermore, it has been found that the results are not very much different if f is calculated with Eqs. 38 and 42 instead of with Eqs. 51 and 53, except when $P < Z < P'$, in which case f calculated with Eqs. 51 and 53 is greater than one. As such results should not be used anyway, no figures were prepared with Eqs. 51 and 53, and Figs. 10c, 11c, 12c and 13c derived with Eqs. 38 and 42 are to be used for both increasing and decreasing dog-legs.

Eqs. 51, 52 and 49 were used in preparing both Figs. 10b, 11b, 12b and 13b (pertaining to drill pipe) and Figs. 14, 15, 16, 17 and Table 4 (pertaining to drill-collar connections). ★★★

Fractures and Craters Produced in Sandstone by High-Velocity Projectiles

JOHN S. RINEHART
WILLIAM C. MAURER

COLORADO SCHOOL OF MINES
GOLDEN, COLO.

ABSTRACT

The mechanics of impact crater formation in rock, particularly sandstone, has been sutdied, the velocity range being approximately that normally associated with oilwell gun perforators. The bullets were small steel spheres having diameters of 3/16, 9/32 and 7/16 in.; impact velocities ranged from 300 to 7,000 ft/sec. The craters have two distinct parts — a cylindrical hole (or burrow) with a diameter the same as that of the impacting sphere, and a wide-angle cup comprising most of the volume of the crater. The burrow is formed as material in front of the projectile is crushed and pushed aside, forming a cylindrical hole surrounded by a high-density zone. The cup forms as fractures are initiated in front of the projectile and propagate along logarithmic spirals, approximating maximum shear trajectories, to the free surface of the rock. A most significant observation (made for the first time) was that, below the base of the cup in one type of sandstone, there are a group of similar fractures, not extending to the surface, which are spaced uniformly a few millimeters apart. Each fracture follows roughly the contour of the base of the cup and appears to require a certain threshold impulse to initiate it. These fractures comprise a relatively high fraction of the total, newly exposed surface area. The volume of the material removed by crushing varies as the first power of the impact velocity and the volume removed by fracturing, as the second power of the impact velocity. Penetration varies linearly with the impact velocity and is inversely proportional to the specific acoustic resistance of the target material, the proportionality constant being dependent upon the shape of the projectile.

Original manuscript received in Society of Petroleum Engineers office June 27, 1960. Revised manuscript received Jan. 5, 1961. Paper presented at 35th Annual Fall Meeting of SPE, Oct. 2-5, 1960, in Denver.

Discussion of this and all following technical papers is invited. Discussion in writing (three copies) may be sent to the office of the *Journal of Petroleum Technology*. Any discussion offered after Dec. 31, 1961, should be in the form of a new paper. No discussion should exceed 10 per cent of the manuscript being discussed.

INTRODUCTION

Yield of oil from a producing well is frequently enhanced by firing bullets and shaped charges through the well casing into the oil-bearing rock, forming craters and fractures from which oil can flow more readily. The purpose of this investigation has been to develop a better understanding of the mechanics of impact crater formation in rock, particularly sandstone, the velocity range being approximately that normally associated with oilwell gun perforators.

FORCES OPERATIVE DURING IMPACT

When a projectile moving at considerable velocity strikes a massive target such as oil-bearing sandstone, intense and complex transient stress situations develop within both the projectile and the rock or sandstone against which it is striking. Usually the struck rock fails, the missile or projectile penetrating into the rock to some depth where it comes to rest or is forcibly ejected from its burrow by expansion of a plug of target material compressed in front of it. When the impact velocity is very high, the projectile itself may fail, breaking apart or becoming distorted; this situation is not considered here, the discussion being limited to nondeforming projectiles.

Many experimental studies[1-3] have been carried out to determine the nature of the mechanics of crater formation and the salient features of the forces coming into play, some of the earliest studies being the French Army experiments performed at Metz between 1835 and 1845.[4] The stratagem in most instances has been to make a post-mortem examination of the crater, measuring volume and depth of penetration and deducing force relationships from these observations rather than performing the more difficult (usually almost impossible) feat of measuring stresses during penetration.

In many materials, the force acting during penetration of the projectile is found to be the sum of two components—(1) a constant force, independent of the velocity, representing some inherent strength of the target material; and (2) a component, proportional to the square of the velocity, representing inertial forces. For such materials, the average force per unit area acting on the projectile at any instant while it is in motion and being decelerated may be written

$$F/A = a + bv^2 \quad . \quad . \quad . \quad (1)$$

where v is the velocity of the projectile at that instant, A is the cross-sectional area of the penetrating projectile taken normal to its trajectory, and a and b are constants which are dependent upon the target material and the shape of the projectile. It follows that the total penetration s is given by

$$s = (m/2bA) \log_e [1 + (b/a) v_o^2] \quad . \quad . \quad . \quad . \quad . \quad . \quad . \quad . \quad . \quad (2)$$

where v_o is the velocity of the projectile when it just strikes the target.

Values of a and b for spherical projectiles impacting in a loose sand-gravel mixture and compacted earth were obtained in the Metz experiments. For sand-gravel, a and b are 620 psi and 0.0115 (psi) $(ft/sec)^2$, respectively; and for compacted earthworks, a and b are 432 psi and 0.0008 (psi) $(ft/sec)^2$. Figs 1 and 2

[1]References given at end of paper.

This page of *Petroleum Transactions, AIME* follows page 194. The intervening non-Transactions pages appeared in *Journal of Petroleum Technology*.

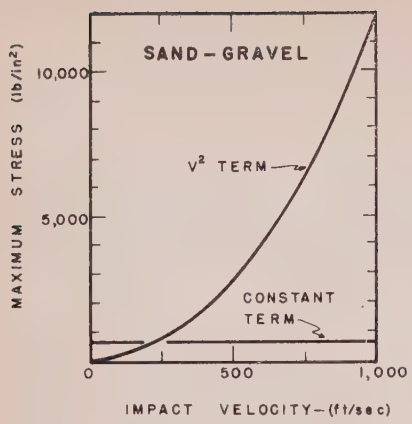

FIG. 1—RELATIVE VALUES OF VELOCITY-DEPENDENT AND VELOCITY-INDEPENDENT COMPONENTS OF FORCE RESISTING PENETRATION, 620 PSI AND 0.0115 (FT/SEC)² PSI, RESPECTIVELY. LOOSE SAND AND GRAVEL.

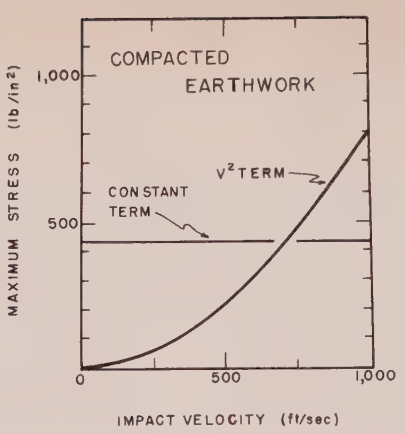

FIG. 2—RELATIVE VALUES OF VELOCITY-DEPENDENT AND VELOCITY-INDEPENDENT COMPONENTS OF FORCE RESISTING PENETRATION, 432 PSI AND 0.0008 (FT/SEC)² RESPECTIVELY. COMPACTED EARTHWORK.

show the average stresses which would be acting on spherical projectiles penetrating into sand-gravel and compacted earthwork, respectively, as a function of impact velocity broken down into its two components—velocity-independent and velocity-dependent. Note that for sand-gravel, in going from 100-ft/sec impact velocity to 1,000-ft/sec, the dominant-force term changes from a static term of 620 psi to a dynamic inertial term of 11,500 psi. In earthwork the transition takes place at a much higher velocity, illustrating that in hard compact materials the inertial velocity-dependent term does not become relatively significant until high velocities are reached. In steel, for example, it is negligible up to velocities of about 3,000 ft/sec. At very high velocities (thousands of feet per second), it is of paramount importance.

Experiments on rocks show clearly that the dominant force resisting penetration into those materials is neither constant nor a velocity-squared term, the principal force component being proportional to the first power of the velocity. In this case, the total penetration can be written

$$s = K_1 (m/A) (v_o - d) \quad . \quad . \quad (3)$$

where K_1 is a constant characteristic of the target material and the shape of the projectile, m is the mass of the projectile, A is its projected cross-sectional area and d is a small, frequently negligible, correction factor which is very complex in nature. During penetration, the instantaneous value of the force on the penetration projectile will be proportional to the velocity at that instant.

A force proportional to the first power of the velocity could arise in two ways—as an elastic compression or as a viscous or shearing drag. During elastic compression resulting from impact, the stress σ is given by

$$\sigma = \rho c v \quad . \quad . \quad . \quad . \quad . \quad (4)$$

where ρ is the density of the target material, c is the velocity of propagation of a longitudinal wave in it and v is the velocity of compression. The exact nature of the viscous or shearing drag is somewhat more difficult to understand. In the experiments to be discussed later, it was found that among several rocks the force resisting penetration correlates well with both shearing strength and the specific acoustic resistance, the product ρc of the rock. Progress through the material logically might proceed as a series of repeatable events in which the material is first compressed more-or-less elastically, generating a stress proportional to velocity which shears the material and exposes a new region for the process to repeat itself at a somewhat reduced stress level.

EXPERIMENTAL WORK

Recent tests at the mining research laboratory of the Colorado School of Mines, in which spherical steel projectiles were fired into rocks, have thrown considerable light on the mechanics of crater formation in rock and have uncovered some unexpected phemenonology having important relevance to the recovery of oil through use of bullet-firing guns.

Specifically, tests were run using 3/16-in. diameter 0.442-gm and 9/32-in. diameter 1.503-gm steel balls fired from 0.22- and 0.30-in. caliber guns, respectively, at velocities ranging from 300 to 7,000 ft/sec. The rock targets were sandstone (a poorly cemented, argillaceous, feldspathic sandstone, ranging from thinly bedded to massive structure), granite (a holo-crystalline, coarse-grained inequigranular, quartz-biotite granite), Carlsbad potash and Oak Springs tuff.

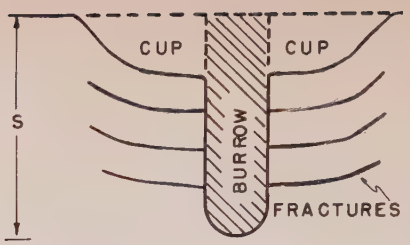

FIG. 3—PROFILE OF TYPICAL CRATER PRODUCED BY A SMALL STEEL SPHERE IMPACTING SANDSTONE, POTASH OR TUFF AT AN ANGLE OF 90° WITH THE SURFACE. s = TOTAL DEPTH OF PENETRATION.

The typical crater produced in sandstone, potash and tuff by a projectile fired at an impact angle of 90° is shown in Fig. 3.

The crater has two distinct parts — a cylindrical hole (or burrow) with diameter the same as that of the impacting sphere, and a wide-angle cup comprising most of the volume of the crater. The burrow is formed as material in front of the projectile is crushed and pushed aside, forming a cylindrical hole surrounded by a high-density zone. The cup forms as fractures are initiated in front of the projectile and propagate along logarithmic spirals, approximating maximum shear trajectories, to the free surface of the rock. In sandstone, but usually not in potash and tuff, a number of these fractures lie below the surface of the cup as illustrated in the drawing. In granite the burrow probably is also formed initially, but the chipping or stepwise fracturing process discussed later soon engulfs and obliterates it.

The penetration s was found to vary linearly with impact velocity v_o as can be seen in Figs. 4 through 7, in which penetration is plotted against striking velocity for four different rocks and for steel spheres of two different diameters.

It can be deduced from the sandstone and granite data, where spheres of two diameters are represented, that the data fit well the relationship previously given.

$$s = K_1 (m/A) (v_o - d) \quad . \quad (5)$$

A few additional firings with 7/16-in. diameter steel spheres also con-

firmed this relationship. It is assumed to be correct for potash and tuff where only one size of sphere was fired.

The applicability of this relationship implies at once that inertial forces are negligible, the instantaneous force F resisting the projectile being given by

$$F = (A/K_1)\ v, \quad . \quad . \quad . \quad (6)$$

and the instantaneous stress σ, average over the front surface of the projectile, by

$$\sigma = v/K_1 \quad . \quad . \quad . \quad . \quad . \quad (7)$$

Values for K_1 for the four rocks are listed in Table 1.

An attempt was made to relate the material constant K_1 to some measurable physical property of the rock. The shear strength and the acoustic resistance of each rock has been plotted against the reciprocal of the material constant in Figs. 8 and 9, respectively. It is evident from Fig. 8 that the correlation between shear strength and material constant is excellent. This correlation is significant and lends support to the theory that the rock fails in shear.

Furthermore, from Fig. 9 it appears that the material constant is inversely proportional to the specific acoustic resistance ρc of the target material, where ρ is its density and c is the velocity of propagation of the longitudinal stress wave in the material. Values of c were determined experimentally for the four rocks. That the stress σ is directly proportional to ρc is a logical result because in elastic impact, as indicated previously, the stress set up in the impactor and the target depends upon the relative acoustic resistance of the two. The projectile here is spherical so that a shape factor having a value of about 0.3 enters, the average particle velocity in front of the projectile being less than the velocity of the projectile. For a blunter projectile, the value of the shape factor should increase, almost reaching one for a right circular cylinder.

Experimentally, it was found that the projectile usually did not remain in the crater but bounced back out with a velocity of a few feet per second. It is easy to imagine that

TABLE 1—VALUES OF K_1 IN PENETRATION EQUATION, $s = K_4\ (m/A)\ (v_0 - d)$

Rock	K_1 (ft/sec/psi)
Carlsbad Potash	0.010
Granite	0.004
Sandstone	0.019
Oak Springs Tuff	0.016

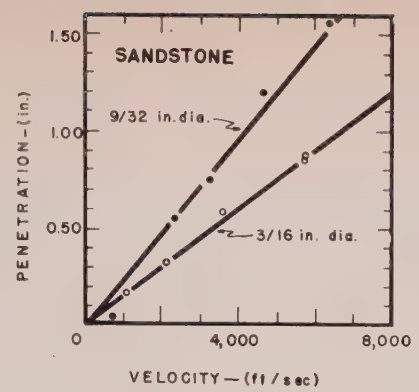

FIG. 4—PENETRATION VS STRIKING VELOCITY FOR NORMAL IMPACTS OF STEEL SPHERES AGAINST SANDSTONE.

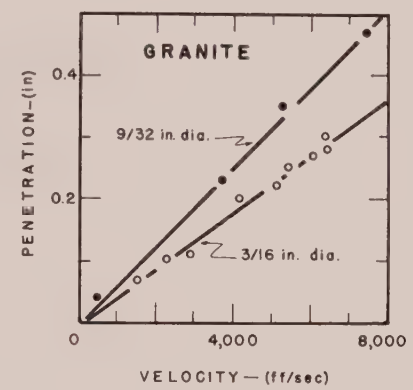

FIG. 5—PENETRATION VS STRIKING VELOCITY FOR NORMAL IMPACTS OF STEEL SPHERES AGAINST GRANITE.

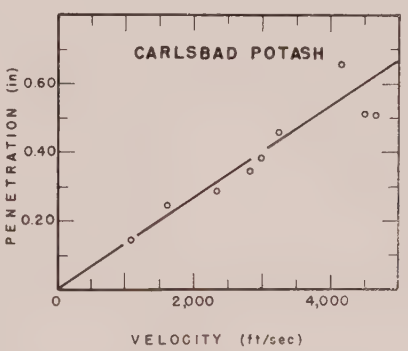

FIG. 6—PENETRATION VS STRIKING VELOCITY FOR NORMAL IMPACTS OF STEEL SPHERES AGAINST CARLSBAD POTASH.

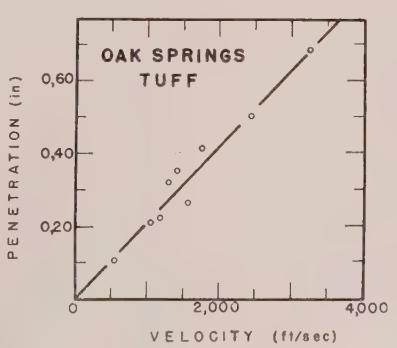

FIG. 7—PENETRATION VS STRIKING VELOCITY FOR NORMAL IMPACTS OF STEEL SPHERES AGAINST OAK SPRINGS TUFF.

ejection of the ball follows expansion of a compressed plug of rock, lying just ahead of the projectile when it comes to rest.

INITIATION AND PROPAGATION OF FRACTURES

A most significant observation (made for the first time) was that, below the base of the cup in one type of sandstone, there are a group of similar fractures, not extending to the surface, which are spaced uniformly a few millimeters apart. Each fracture follows roughly the contour of the base of the cup (Fig. 3) and appears to require a certain threshold impulse to initiate it. These fractures comprise a relatively high fraction of the total, newly exposed surface area.

They appear to be initiated in a step-like fashion as the projectile penetrates the rock, each fracture propagating along a logarithmic spiral[3] of maximum shear (Fig. 10). The shape of these spirals can be expressed mathematically by the equation,

$$r = r_0 \exp\ [\pm\ \theta \tan\ (45° + \phi/2)] \quad . \quad . \quad . \quad . \quad . \quad . \quad . \quad . \quad . \quad (8)$$

where r is a radius vector of the spiral, r_0 is the distance from the point of application of the load to the intersection of the logarithmic spiral and the horizontal boundary, θ is the polar angle from the nearest surface and ϕ is the angle of internal friction. In elastic media, the angle of internal friction is zero; therefore, the logarithmic spirals are equivalent to the trajectories of maximum shear.

The angles of internal friction were determined from specimens that had failed under static compressive loads and were approximately 0° for sandstone and 30° for granite. Because granite has a much larger angle of internal friction than sandstone, the granite craters have much more gently sloping sides.

The point of application of the force changes continuously, always being located at the projectile so that the stress field likewise is changing continuously; new sets of trajectories, similar in configuration to the original set, are continuously forming. Moreover, there is at all times a concentration of stress trajectories in the center of the crater which, because of the large cross-sectional area of the projectile, is obliterated by the projectile as it penetrates.

The uniformity of spacing of the

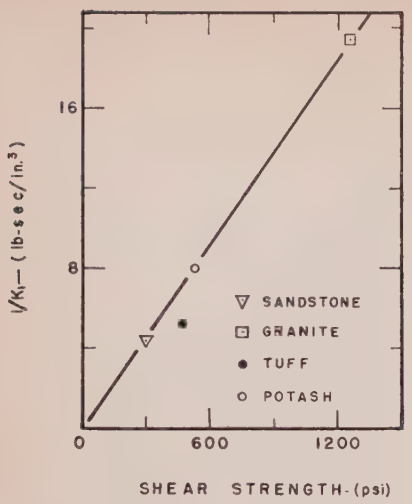

FIG. 8—THE MATERIAL PARAMETER $1/K_1$ VS SHEAR STRENGTH FOR THE FOUR ROCKS STUDIED.

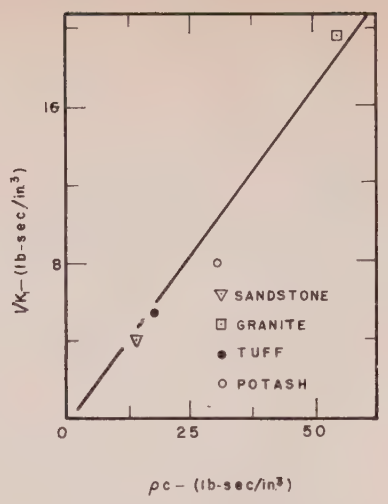

FIG. 9—THE MATERIAL PARAMETER $1/K_1$ VS SPECIFIC ACOUSTIC RESISTANCE ρc FOR THE FOUR ROCKS STUDIED.

lateral fractures implies that a constant impulse is required to initiate each successive fracture. Let the distance between two fractures be Δs. The time Δt that the projectile acts on a portion of the burrow of length Δs is

$$\Delta t = \Delta s/v \quad . \quad . \quad . \quad . \quad . \quad (9)$$

The impulse I, being given by

$$I = F\Delta t = (A/K_1)\,\Delta s, \quad . \quad (10)$$

is thus constant.

SUMMARY AND CONCLUSIONS

The craters formed in sandstone consist of two parts: (1) the burrow, which is a long cylindrical hole formed as the material is forced aside in front of the projectile; and (2) the cup, the blown-out part of the crater formed as a series of fractures, each initiated by a constant impulse and propagated along a logarithemic spiral to the surface of the rock. In granite, no burrow is formed.

The penetration of the projectile is directly proportional to its mass, to a material constant for the target material and to the difference between the impact velocity and the minimum velocity at which cratering takes place. Penetration is inversely proportional to the projected cross-sectional area of the projectile.

A close correlation has been found between the shear strengths of rocks and their material constants. The material constant appears to be inversely proportional to the specific acoustic resistance of the target material, the proportionality factor being dependent upon the shape of the projectile.

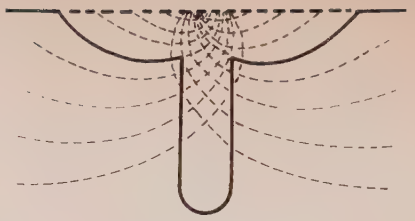

FIG. 10—SUPERPOSITION OF SET OF MAXIMUM SHEAR TRAJECTORIES UPON PROFILE OF TYPICAL CRATER PRODUCED BY A STEEL SPHERE STRIKING SANDSTONE NORMALLY.

The mechanics of impact crater formation in rocks should apply to other brittle materials subjected to impact velocities below the critical velocity at which the projectile begins to deform or break up.

REFERENCES

1. Rinehart, J. S. and Pearson, John: "Behavior of Metals Under Impulsive Loads", paper presented at ASME meeting in Cleveland (1954).
2. Livingston, C. W. and Smith, F. L.: "Report on Bomb Penetration Project", Colorado School of Mines Research Foundation, Inc. (June, 1951).
3. Maurer, W. C. and Rinehart, J. S.: "Impact Crater Formation in Rock", *Jour. Appl. Phys.* (July, 1960).
4. Helie, Felix: *Traite de Balistique Experimentale,* Dumain, Paris (1884). Translated by John S. Rinehart, NOTS RRB, 75 (May 1, 1950). ★★★

Improved Compositions for Cementing Wells with Extreme Temperatures

G. WARREN OSTROOT
MEMBER AIME
WAYNE A. WALKER

HALLIBURTON CO.
DUNCAN, OKLA.

ABSTRACT

An increase in the number of deep wells being drilled where extreme bottom-hole temperatures are encountered, and the anticipated drilling of wells where temperatures in the range of 500°F or higher may occur, has brought about a comprehensive investigation of cementing materials and of the techniques involved in their proper usage at these elevated temperatures.

Included are developments in cements, retarders, weighting materials and other cement additives which make it possible to formulate a variety of compositions to help resolve the cementing problems of these extreme well conditions. The problems associated with the selection and testing of cements are discussed, and a resume of field results is included.

Previous studies on strength retrogression indicate that caution should be exercised in the selection of a cementing composition for use in high-temperature wells. It now appears that, by the addition of silica flour as a stabilizing additive to certain cements, compositions covering a wide range of slurry densities can be designed to meet extreme well conditions without strength retrogression.

Improvements in cement retarders make it possible to produce a four-hour thickening time at static temperatures up to 500°F. This temperature is considerably higher than conditions presently being encountered in drilling and completion work. Inert weighting materials, used to produce 20-lb/gal or heavier cement slurries, are reviewed.

INTRODUCTION

As the search for oil continues, the number of wells being drilled to depths of 10,000 ft or below has continued to increase over the past decade. During 1959, there were 50,893 wells drilled in the United States for a total of 209 million ft of hole. Of this total, approximately 4.45 per cent were drilled below 10,000 ft and 0.30 per cent below 15,000 ft, with a record depth of 25,340 ft recorded (Table 1).

With the drilling of this record-shattering hole comes the question, "How deep can wells be drilled?".[2] Limitations with respect to equipment (surface and subsurface), cementing materials and techniques would cause some concern; however, a panel of experts have agreed that the U. S. oil industry has the equipment and know-how to drill a 50,000-ft hole. The greatest deterrent would be the 700°F temperature they would anticipate encountering at this depth.

Although the number of wells drilled under what is generally considered hot-hole conditions (230°F and higher) has been relatively high, each well often presents distinctly individual problems and requires separate consideration and selection of special materials, techniques and equipment. At the present time there are over 30 additives and special cements available for use in "tailoring" a cementing composition for a specific well. It is not uncommon to use three or four different additives with the basic cement to produce the desired slurry characteristics. A generally accepted procedure is to make laboratory tests on selected cementing compositions prior to pumping them into wells deeper than 12,000 ft, or where static temperatures are in the range of 260°F or higher. In some instances, it is recommended that laboratory tests be made where less severe well conditions are encountered.

Prior to selecting a cementing composition for a particular well, key personnel representing the operator, drilling contractor and service company should meet to determine that each individual is acquainted with every detail which might influence cementing results and to discuss the execution of the job. For cementing hot-holes, a number of factors must be evaluated before proceeding with the operation. Consideration must be given to the following.

1. Thickening time—The slurry must remain fluid for a sufficient length of time to allow displacement down the casing and up the annular space in a primary cementing job or, in squeeze-cementing, adequate thickening time for both the build-up of a satisfactory squeeze pressure and the reversing out of excess cement. The thickening time of standard retarded cements will often be too short under extreme temperature conditions, thus involving special formulations and requiring laboratory tests to determine the proper amount of additional retarder to obtain the desired pumpability.

TABLE 1—DEPTH CLASSIFICATION OF DEEP WELLS DRILLED IN THE UNITED STATES FROM 1950 THROUGH 1959[1]

	Well Depth (Thousand ft)			
Year	10 to12	12.5 to 15	Over 15	Over 10
1950	968	157	0	
1953	1579	408	32	
1956	1678	815	142	2635
1959	1580	634	151	2365
1965	—	—	—	4000*

*Of the estimated 4000 wells to be drilled below 10,000 ft, it is forecast that 82 of this number will be drilled below 18,000 ft.

Original manuscript received in Society of Petroleum Engineers office Aug. 31, 1960. Revised manuscript received Nov. 29, 1960. Paper presented at 35th Annual Fall Meeting of SPE, Oct. 2-5, 1960, in Denver.

[2]References given at end of paper.

2. Compressive Strength—Having been placed with suitable thickening time, the slurry should set and develop adequate compressive strength in a reasonable period of time to allow well completion or resumption of drilling operations.

Proper slurry formulation, to provide optimum pumpability and minimum waiting-on-cement (WOC) time, usually becomes a problem only when cementing exceptionally long intervals where the temperature differential from top to bottom may be as much as 100° to 140°F. Under extreme bottom-hole temperature conditions where a relatively high quantity of retarder will be necessary to provide adequate pumpability, the cement may be designed to set hard within 24 hours over the lower section of the cemented interval; but, the cement at the top of the interval may be soft. An additional WOC time of 12 to 24 hours may be necessary for the upper portion of the cement column to set.

3. Strength Retrogression—Some cementing compositions develop adequate compressive strength initially when exposed to conditions of extreme temperature but, over a period of time, will decrease in strength to the point of failure. Knowledge of the temperatures at which retrogression takes place for the various cements, and of the additives available to inhibit this action, is essential.

4. Permeability—Laboratory tests also indicate certain cementing compositions will show an increase in permeability when exposed to high temperatures. Various authors [3,5] state that the permeability of set cement increases as retrogression progresses.

There are inherent problems encountered during the cementing of any well, regardless of depth and temperature. Seemingly minute problems, however, are magnified many times in deep wells where extremely high temperatures and pressures are encountered. These problems can result in increased operational and service costs or in the eventual complete loss of the well. The purpose of this paper is not to provide a "cure-all" for hot-hole cementing operations. Rather, it is to review some of the problems that can be and are being encountered and to discuss the many modifications that can be made with readily available materials to help combat the adverse properties of some cementing compositions.

WEIGHTING MATERIALS

Slurry density for deep well cementing often varies from one extreme to the other, depending on the mud weight. Normally, it is desired that the density of the cement slurry be heavier than, or at least equal to, the density of the drilling mud, with the type of formations through which the slurry must pass being the governing factor as to the type of slurry that would be most satisfactory. Where high gas pressures are encountered, it is imperative that the slurry density be of such magnitude as to help prevent a blowout from occuring. This type of slurry requires an additive having a high specific gravity (Fig. 1).

If weak formations or zones of lost returns are prevalent, it then is necessary to use additives to reduce the slurry density. Recent data indicate slurry densities ranging from 10.8 to 22.75 lb/gal have been successfully used in cementing deep wells. Slurry densities of 17 to 19 lb/gal are quite commonly used in most areas of deep drilling.

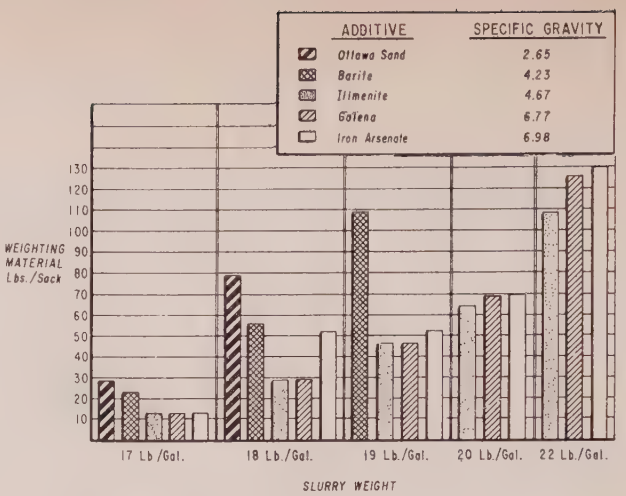

FIG. 1—API CLASS E CEMENT, SLURRY WEIGHT = 16.25 LB/GAL.

During the various stages in the development of heavyweight additives, many different materials have been tested. One of the first such additives to be blended with cement was barite, which was used almost exclusively at one time but which recently has given way to improved materials. One of the main disadvantages in using barite is the relatively large quantity required to produce the desired slurry weight. Barite, as well as other finely ground (powdered) weighting materials, requires additional water to maintain proper slurry viscosity. This additional water makes it necessary to use more weighting material than would be needed if the water requirements for the additive were zero. The water necessary to produce a pumpable slurry causes a reduction in compressive strength and, due to the dilution of the chemical retarder present in retarded (API Class E) cements, also shortens the thickening time. This reduced pumpability is especially critical at depths of 12,000 ft and below and may require the addition of more retarder with subsequent laboratory tests to insure adequate thickening time.

A coarse-ground barite was made available to the oil industry and was used successfully a number of times in the field. For a designated slurry weight a lesser amount of coarse barite was needed, due to the lower water requirements. Due to lack of control in grinding barite to a larger than 200-mesh particle size, the use of coarse-ground barite gradually diminished.

Illmenite ore, a relatively new type of weighting material, was introduced to the Gulf Coast area in 1957. Illmenite (iron sand) has many advantages over barite as a weighting material in cementing compositions. It has been possible to obtain a particle size distribution in the 30- to 100-mesh range. Due to the nature of the material and the particle size distribution, no additional water is necessary in the preparation of slurries with densities to 20 lb/gal. The combination of low water requirements and high specific gravity makes it possible to prepare high-density slurries with a minimum of weighting material. The amount of each weighting material necessary to produce various slurry weights with retarded (API Class E) cements is found in Fig. 1. Illmenite is an inert material and, as such, has very little effect on the physical properties of cementing compositions. It can be used in retarded cements, portland cements, pozzolan cements and pozzolan-lime cementing compositions.

Although Ottawa sand (20-40) is used extensively as an additive to produce a better cement upon which is set a whip-stock, it can also be used to increase slurry density. Other types of sand may be used; however, the sand should be clean (washed) to insure that no contamination occurs from foreign materials. Sand has a very low water requirement and is the most economical weighting material available; but, due to its low specific gravity (2.65), maximum slurry densities are restricted to 18 lb/gal when used in retarded cements. Most of the high-density, finely ground metallic minerals, which potentially could be used as weighting materials, will cause a reduction of the thickening time; therefore, it is essential that special laboratory tests under simulated well conditions be made prior to use of this type of material. An additional precaution to observe is uniformity of the specific gravity. Variations have been noted in some materials that could result in an error in excess of 1 lb/gal on slurry density when using a specific amount of material with each sack of cement.

Two of the highest-specific-gravity materials available for weighting cement slurries are galena and iron arsenate. These materials also are the most expensive of the heavyweight additives. It is possible to prepare cement slurries in the range of 25 lb/gal by using either of these materials. It will be noted in Fig. 1 that, to obtain a given slurry density, more galena and iron arsenate is required than illmenite. This is due to the variable water requirement of the galena and iron arsenate. Variations in grind can cause a change in the water requirement for either material. In turn, this will vary the amount of weighting material necessary for each specified slurry weight. Both materials cause a marked acceleration in the thickening time under high-temperature well conditions; now, however, through retarder research these slurries can be placed in wells having extremely high temperatures. Recent laboratory tests showed that a slurry, weighted with either galena or iron arsenate and retarded with a modified lignin-type retarder, would have a thickening time in excess of 4½ hours using a modified squeeze-cementing test schedule. For these tests, a cementing temperature of 300°F was reached in 43 minutes. As a result of these tests, an iron-arsenate cement slurry was used successfully in cementing a well.

Ferrophosphorus has been laboratory tested, and results indicate that high-density slurries can be produced using it as a weighting material. It also has the disadvantage of causing a marked decrease in thickening time. There is no knowledge of a ferrophosphorus-cement blend having been used in the field.

Further evaluation by laboratory testing and field usage will establish the versatility of these and other materials.

STRENGTH-STABILIZING ADMIXTURES

The problem of strength stability in cementing compositions was not given much consideration until 1954,[4] at which time it was disclosed that certain cementing compositions retrogressed in strength under high-temperature conditions. Prior to this, it was the general opinion that the compressive strength would increase with an increase in temperature. Ludwig[3] and others[5,6] found this to be true up to temperatures of approximately 230°F. The higher the temperature above 230°F, the more pronounced was retrogression. This phenomenon is prevalent in all portland-type cements. Retarded cements (API Class E) will lose in excess of 50 per cent of their 24-hour strength over an extended period of time when cured at a temperature of 320°F. The addition of high percentages of bentonite will cause the cement to retrogress to the point of failure under the same curing conditions. Laboratory tests indicated that maximum loss of strength takes place during the first 7 to 28 days, depending on the temperature.

As a result of the work by Smith and Carter,[5] an investigation by means of differential thermal analysis into the hydration products of various cementing compositions was instigated. Thermograms were prepared and evaluated on 16 different cementing compositions. These tests indicated the following.

1. The dicalcium silicate alpha-hydrate endotherm appears at 460° to 485°C.

2. The calcium hydroxide endotherm appears at 495° to 530°C.

3. The tobermorite group exotherm appears at 800° to 850°C.[7]

Initial tests were made on cementing compositions cured 7 and 180 days at a temperature of 260°F. Examination of the seven-day thermograms showed that, in most cases where strength-stabilizing additives were not used, the dicalcium silicate alpha-hydrate had not yet appeared and the compressive strengths in all cases were very good. After curing 180 days at 260°F, the dicalcium silicate alpha-hydrate appeared in moderate-to-large amounts; in all cases, there was a noticeable loss of compressive strength. Examination of more recent thermograms for cement compositions, cured at higher temperatures and not containing silica flour, indicated that some compositions contain the alpha-hydrate without calcium hydroxide. Others had a high alpha-hydrate to calcium hydroxide ratio. In each case, there was an accompanying decrease in compressive strength.

In earlier work on cement-silica systems at elevated temperatures, Kalousek[8] found that a portion of the silica first reacted with the calcium hydroxide from the cement to form dicalcium silicate alpha-hydrate. The remaining silica in turn reacted with the alpha-hydrates to form the tobermorite phase. Correlation of current data on reaction products with compressive strength and permeability data indicates that the tobermorite group of calcium silicate hydrates is a better cementing phase than the dicalcium silicate alpha-hydrate.

The development of cements which were not subject to retrogression or of additives that would inhibit strength reduction under high-temperature conditions was necessary as the problems of deep well cementing became more obvious. One of the first such cementing compositions, developed as a result of the need for a better material, was a blend of pozzolan, hydrated lime and set-control additives. Although neither the pozzolan nor the lime is cementitous in itself, in the presence of water both will react to form a cementitous material. The upper limits of this blend have not been investigated fully. It has been used in the field at temperatures in excess of 400°F (static), with compressive-strength determinations at a temperature of 500°F showing little tendency to retrogress. Laboratory tests together with reported field data indicate that the pozzolan-lime slurries are very uniform in performance. Also, they are very flexible in that they can be readily "tailored" to

meet individual well conditions pertaining to thickening time, compressive strength, slurry density, etc.

The most recent development along the line of additives to inhibit strength retrogression in retarded cements is silica flour (Fig. 2). The addition of 20 to 40 per cent silica flour will aid in stabilizing manufactured retarded cements (API Class E) against high-temperature strength retrogression (Fig. 3). Silica flour does not have too much effect on the thickening time of retarded cement except under extremely high temperatures. The optimum temperature range for using silica flour is from 260° to 400°F plus. Here again, it is recommended that the slurry be tested in the laboratory under simulated well conditions to insure adequate thickening time. These tests are essential, not only because of variations in the basic cement, but also because of the vast number of silica products available. Performance may vary, due to either chemical compositions (impurities present) or particle size, or both.

To determine the effect of silica flour on cement containing other additives, a series of accelerated tests were run. Test specimens composed of API Class A cement and 12 per cent bentonite were cured seven days at a temperature of 320°F. Without silica flour both the alpha-hydrate and calcium hydroxide were present, as indicated by differential thermal analysis. With 5 per cent silica flour, the calcium hydroxide disappeared, the alpha-hydrate had decreased and the phase responsible for the exothermic reaction (tobermorite) had started to appear. With 10 per cent silica flour, the alpha-hydrate had decreased considerably and the tobermorite phase had increased correspondingly. It also was noted that the compressive strength increased as the alpha-hydrate phase was decreased and the tobermorite increased by the addition of silica flour. Similar tests conducted on API Class A cement and diatomaceous earth, which is about 91 per cent silica, gave an excellent example of the reaction of silica with alpha-hydrate to yield the tobermorite phase, with a corresponding increase in compressive strength when adequate quantities were used.

Additional thermograms and X-ray patterns were run on API Class E cement containing 0, 20, 30 and 40 per cent silica flour (Fig. 4) after curing for 28 days at a temperature of 350°F. The thermograms on neat cement showed the presence of dicalcium silicate alpha-hydrate and considerable calcium hydroxide. With the addition of 20 per cent silica flour the calcium hydroxide has disappeared, the dicalcium silicate alpha-hydrate had diminished and the tobermorite phase appeared. The thermograms on specimens containing 30 and 40 per cent silica flour showed further reduction in the alpha-hydrate and a subsequent increase in the tobermorite phase.

Examination of the X-ray patterns further substantiates the differential thermal-analysis work and aids in pinpointing the hydration products. The presence of calcium hydroxide and dicalcium silicate alpha-hydrate in neat cement were also found by X-ray analysis. The X-ray patterns show the loss (by reaction with the silica) of calcium hydroxide, the reduction in the amount of the alpha-hydrate present and the indication of the formation of two new materials—namely, calcium silicate hydrate (1)[9] and calcium meta silicate hydrate (Xonotlite)[10]—when 20 per cent silica flour was added to retarded cement. X-ray analysis makes further identification as to compound classification possible. The pattern for the 30-per cent silica flour composition showed increased amounts of calcium meta silicate hydrate and calcium silicate hydrate (1) and the disappearance of the dicalcium silicate alpha-hydrate. The same two compounds were present in the 40-per cent silica-cement with some free silica also noted from the X-ray pattern. As with previous investigations, an increase in compressive strength was noted as the tobermorite phase increased (Fig. 3).

Identical tests made on the same compositions cured one day at 350°F indicate that hydration is not complete and that the final-reaction products are not the same as when cured 28 days.

Examination of the thermograms and X-ray patterns of cementing compositions composed of cement, blended with varying percentages of both silica flour and diatomaceous earth, indicates that the same hydration products are present as obtained with cement and silica flour only. The major differences noted were in the ultimate compressive strengths of the compositions containing diatomaceous earth. Even though the dicalcium silicate alpha-hydrate and calcium hydroxide were completely reacted with silica and the tobermorite phase was present, the compressive strengths were relatively low compared to silica flour-cement compositions. This reduction in strength undoubtedly was due to the high water requirement of the diatomaceous earth, which results in dilution of the cementitious compounds in the set material. Data reported previously[5] established the fact that retrogression occurs in the lower concentrations of diatomaceous earth with cement, but this does not take place with high concentrations or when used in combination with silica flour.

The addition of 30 to 40-per cent silica flour to bentonite cement systems, containing up to 8 per cent

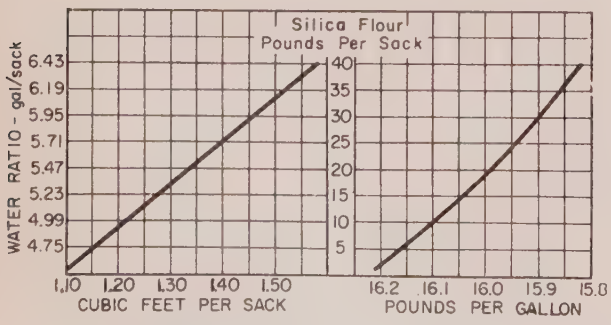

Fig. 2—Slurry Properties When Using Silica Flour (SSA No. 1) with API Class E Cement.

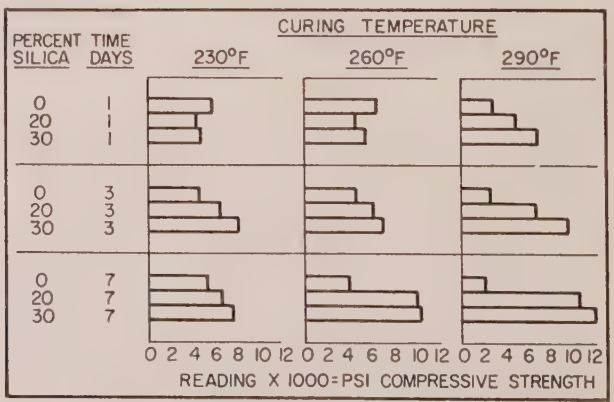

Fig. 3—Effect of Silica on API Class E Cement.

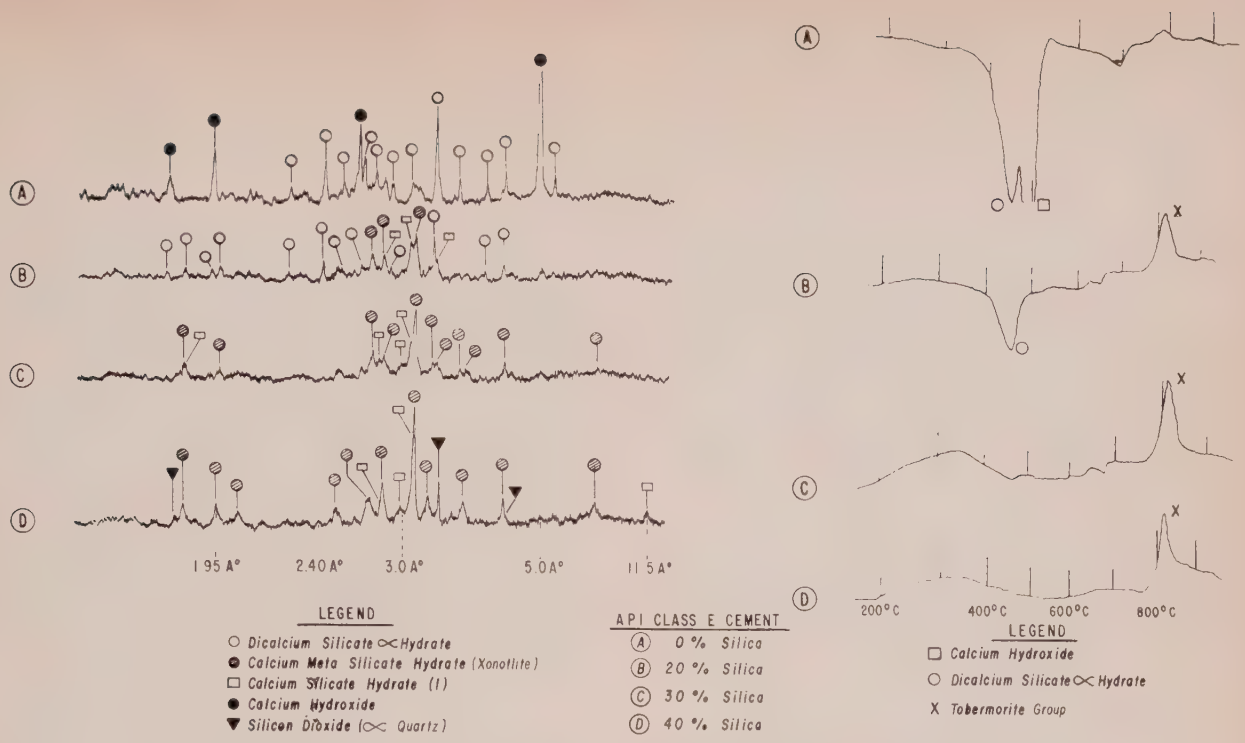

FIG. 4—X-RAY PATTERNS AND THERMOGRAMS OF HYDRATED CEMENT CURED 28 DAYS AT 350°F.

bentonite, will inhibit retrogression and produce adequate compressive strength at temperatures of 350°F. Gilsonite was added to these same compositions as a lost-circulation additive, and sufficient strength was recorded at the end of a 28-day curing period (350°F).

Permeability determinations made on 10 cementing compositions substantiate earlier tests, in that strength retrogression is accompanied by increased permeability (Table 2). Test specimens were cured 3 and 28 days at a temperature of 320°F (3,000-psi curing pressure). The permeability of retarded cement increased from 0.031 to 4.58 md as measured at 3 and 28 days, respectively. The addition of illmenite had little effect on permeability; however, when 4 per cent bentonite was added to retarded cement, the 28-day permeability increased to 9.72 md. When silica flour in concentrations of 30 and 40 per cent was added to the same compositions, the 28-day permeability decreased to less than 0.001 md.

CEMENT RETARDATION

Today very few cementing compositions are used to cement wells below 12,000 ft where static temperatures are more than 260°F, unless additional retarder is employed. Since most operators desire a three- to four-hour thickening time at these extreme depths and due to the effect of various additives, additional retarder must be used to achieve this pumpability. As stated before, adequate planning is necessary so that the proper cementing composition can be designed and tested before the job. On deep liners and squeeze jobs, samples of the cement, mixing water, retarder and other additives to be used on the job are commonly tested under modified thickening-time schedules to provide adequate pumpability.

TABLE 2—PERMEABILITY OF HYDRATED CEMENT, API CLASS E CEMENT

Per Cent			Permeability (md) at 320°F	
Silica	Bentonite	Illmenite	3 Day	28 Day
0	0	0	0.031	4.580
20	0	0	0.001	0.001*
30	0	0	0.001	0.001*
40	0	0	0.001*	0.001*
0	4	0	0.548	9.720
30	4	0	0.001*	0.001*
40	4	0	0.001*	0.001*
0	0	28	0.030	3.890
30	0	45	0.001*	0.001*
40	0	50	0.001*	0.001*

*Less than.

A survey of cementing compositions used on wells 10,000 ft and deeper indicates that a large number of the compositions used contain additives to modify the properties of the retarded oilwell cement and that these jobs range in volume from 2 to 4 Mcf of slurry. The rate at which the cement is mixed will average 40 to 50 cu ft/min, and it will be displaced at a rate of 60 to 80 cu ft/min. The total cementing time will vary with the volume of cement used, but the complete operation generally will require from 1½ to 2½ hours. This is the reason many operators specify a three- to four-hour thickening time because it gives a safety factor in placing the cement.

The selection of a retarder that will be compatible with the manufactured retarded cements, which in themselves contain a retarder, sometimes becomes a difficult task. Additives requiring additional mixing water have a diluting effect on the retarder, which makes it necessary to achieve a balance between the water, other additives and a retarder that is most compatible with the retarded cement to be used. When heavyweight slurries are being designed, retarded cements having a coarser grind, requiring less mixing water, and yielding a higher initial slurry density are generally preferred over common portland cement because they require less weight material.

For several years the lignin-type (calcium lignosulfonate) retarders have been used fairly successfully to

depths of approximately 14,000 to 16,000 ft, where static temperatures up to 300°F are encountered. These materials are quite effective when added to most cements, and good retardation of the composition can be obtained. There are instances, however, when the calcium lignosulfonate may not perform satisfactorily in conjunction with the retarder in the Class E cement, and higher concentrations actually will cause a reduction in the thickening time. This is particularly true at circulating temperatures around 350° and 400°F. Sometimes it has been necessary to go to special blends of retarders using a lignin blended with borax. In some cements, this gives additional retardation but involves compounding of the retarder and additional testing of the cement prior to the actual running of the job.

With the introduction of CMHEC[11] (carboxymethyl hydroxyethyl cellulose), relatively good retardation was achieved in most retarded-type cements, and its use in deep wells has been reasonably effective. Table 3 illustrates the added retarding effect of CMHEC on a manufactured cement containing a lignin retarder. However, it has been found that the CMHEC material, when used in concentrations in excess of 0.75 to 1.0 per cent, requires extra mixing water to produce a normal slurry viscosity. As this slurry is displaced into a well the temperature increase causes a decrease in viscosity, which is not considered objectionable except when weighting material has been added to increase slurry density. This reduction in viscosity enhances the possibility of the weighting material settling out during the job. While this factor apparently has not caused any extensive difficulty, it could be an objectionable feature where high concentrations of weight material are required. The abnormally high viscosity, obtained from cements containing high concentrations of CMHEC and mixed with API water-cement ratios, has the disadvantage of producing high frictional pressure drop as the slurry is displaced, thereby creating excessive wellhead pressure. This is born out in the field, as well as in the laboratory, where flow properties and pressure-drop calculations for cementing slurries were studied. When calculations were made to evaluate friction loss or to predict the flow velocity to approach turbulent flow, very little difference in frictional pressure drop was noted between slurries containing 0, 0.30 and 0.50 per cent CMHEC. However, when 0.70 per cent CMHEC or more was used, there was a notable increase in apparent viscosity, which indicates high-frictional pressure drop.

One major advantage of CMHEC is that it imparts low water-loss properties as well as retardation to the cementing composition to which it is added. While high temperatures will increase the water loss from slurries containing the usually recommended quantities of 0.3 to 0.5 per cent of this additive, it is possible to restore the low water-loss properties by using higher concentrations. It also is compatible with almost all of the commercial brands of cement but is somewhat more expensive than the lignin products.

Confronted with deep well cementing problems and the limitations associated with existing retarders, a research program was set up to improve retardation of all deep well cementing materials. The result of this program was the development of a modified lignin retarder,[12] which is fairly inexpensive, very effective with all types of cementing compositions and has the added advantage of being an excellent dispersant. The new

TABLE 3—THICKENING TIME OF API CLASS E CEMENT (LIGNIN RETARDER) WITH CMHEC ADDED, 15,000-FT LINER JOB, MODIFIED TESTING SCHEDULE, CIRCULATING TEMPERATURE = 250°F

Per Cent CMHEC	Thickening Time (hours:minutes)
0.5	2:43
0.7	2:48
1.0	2:55
1.25	3:43
1.50	4:00+

modified lignin gives exceptionally good performance with all types of retarded cements and is compatible with the existing retarders found in API Class D and E cements manufactured throughout the free world.

Relatively small concentrations are required, as can be seen from Fig. 5, which gives the approximate quantity required to obtain four-hour pumping times at the extreme temperatures listed. This curve shows the approximate percentage of retarder to add to any retarded cement over a temperature range from 200°F to approximately 400°F (circulating temperature). These data have been plotted from laboratory tests made with different retarded cements, some of which contained various percentages of weighting material and silica flour.

A resume of actual field jobs where modified lignin retarder was used with silica flour and illmenite in various basic cements is illustrated in Table 8. Retarded cements containing silica and modified lignin retarder exhibit excellent compressive strengths at temperatures ranging from 260° to 350°F (Fig. 6). It should be remembered that, while this curve (Fig. 5) represents the normally required concentrations of this particular retarder, variations in brands and batches of cement may yield slightly different results; it is recommended that tests be made prior to cementing a specific well.

Slurry properties and thickening times of API Class E cement blended with varying concentrations of silica, diatomaceous earth and modified lignin retarder are shown in Table 4. Here are shown the retarding properties of this new additive when used in a low-density, high-volume slurry. In contrast to what occurs when CMHEC is used, large concentrations of modified lignin retarder do not require additional mixing water; therefore, it is possible to produce designated slurry densities with lesser amounts of weighting material (Table 5). The modified lignin retarder does not exhibit low fluid-loss properties, nor does it inhibit these

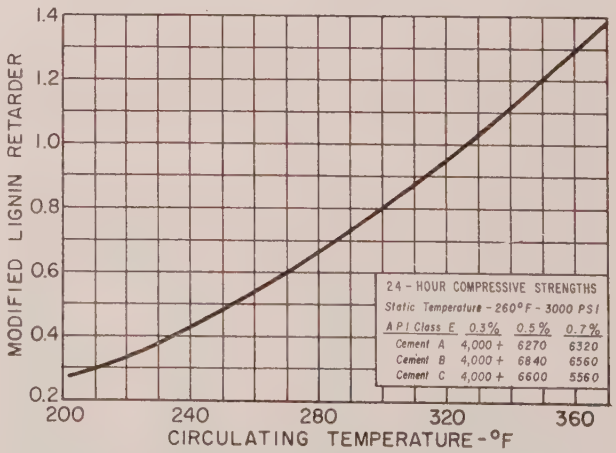

FIG. 5—PER CENT MODIFIED LIGNIN REQUIRED TO OBTAIN A FOUR-HOUR THICKENING TIME, API CLASS D OR E CEMENT.

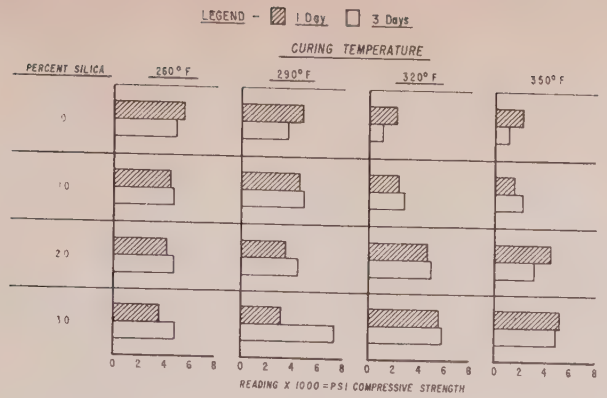

FIG. 6—EFFECT OF SILICA AND RETARDER ON API CLASS E CEMENT, THICKENING TIME = THREE TO FOUR HOURS (MODIFIED LIGNIN RETARDER).

properties when used in conjunction with CMHEC. The highest temperature at which the modified lignin has been used was a circulating temperature of approximately 400°F. In laboratory tests, using a pozzolan-lime composition at circulating temperatures to 410°F (450° to 460°F static), thickening times in excess of three hours have been obtained (Table 6).

Another unique feature of the modified lignin has been its compatibility with some of the very high-density materials such as the galena and iron arsenate discussed earlier. Prior tests with API Class E cements containing calcium lignosulfonate and either lead sulfide or iron arsenate indicated that sufficient thickening times could not be achieved. As shown in Table 7, it was possible to produce a cementing composition in excess of 22 lb/gal using an API Class E cement with either of these two weight materials and, with 300°F circulating temperature, obtain a four-hour thickening time using only 1 per cent of the modified lignin.

CONCLUSIONS

1. Strength retrogression is prevalent in most common cementing compositions after prolonged exposure to high-temperature conditions.

TABLE 4—API CLASS E CEMENT, MODIFIED LIGNIN-TYPE RETARDER

Per Cent Silica Flour	Per Cent Diatomaceous Earth	Per Cent Retarder	Slurry Properties: Water Ratio (gal/sack)	Slurry Weight (lb/gal)	Slurry Volume (cu ft/sack)
0.0	0.0	0.0	4.50	16.25	1.08
0.0	0.0	0.6	4.50	16.25	1.08
40.0	0.0	1.0	6.32	15.84	1.55
40.0	10.0	1.0	10.16	14.53	2.07
10.0	40.0	5.0	20.13	11.88	3.49
0.0	40.0	4.0	19.86	11.60	3.42

High-Pressure Thickening Time

Per Cent Silica Flour	Per Cent Diatomaceous Earth	Per Cent Retarder	Casing Cementing 18,000 Ft	Squeeze Cementing 16,000 Ft
0.0	0.0	0.6	3:30+	3:30+
40.0	0.0	1.0	3:30+	3:30+
40.0	10.0	1.0	3:30+	3:30+
10.0	40.0	5.0	3:30+	—
10.0	40.0	4.5	—	3:30+
0.0	40.0	4.0	3:17	3:30+

TABLE 5—API CLASS E CEMENT, SLURRY WEIGHT = 18.5 LB/GAL (138 LB/CU FT)

Water Ratio (gal/sack)	Temperature (°F) Static	Temperature (°F) Circulating	Per Cent Silica Flour	Ilmenite (lb/sack)	Per Cent Retarder	Thickening Time (hrs:min)
5.5	360	310	35	46	0.80*	2:30
5.5	360	310	35	46	1.00*	3:30
7.0	360	310	35	75	3.00**	3:28

*Modified Lignin
**Carboxymethyl Hydroxyethyl Cellulose

TABLE 6—POZZOLAN-LIME SLURRY, WELL DEPTH = 21,000 FT AND SLURRY WEIGHT = 18.5 LB/ GAL (138 LB/CU FT)

High-Pressure Thickening Time

Temperature (°F) Static	Temperature (°F) Circulating	Per Cent Retarder Type A*	Per Cent Retarder Type B**	Thickening Time (hrs:min)
380	330	3.25	—	3:56
380	330	—	1.0	3:21
400	350	4.0	—	3:13
410	360	—	1.25	3:12
410	360	—	1.50	4:25
420	370	4.4	—	3:00
440	390	—	3.0	3:06
440	390	—	5.0	5:00
460	410	—	3.5	3:05

*Type A—Calcium Lignosulfonate.
**Type B—Modified Lignin.

TABLE 7—API CLASS E CEMENT

Water Ratio (gal/sack)	Iron Arsenate (lb/sack)	Galena (lb/sack)	Lignin Retarder	Slurry Weight* (lb/gal)	Thickening Time (hrs:min)
6.46	135	0	1.0	22.75	4:30+
6.46	0	135	1.0	22.25	4:30+

*Measured weight.

2. High percentages of silica flour inhibit strength retrogression and will produce compressive strengths far in excess of the neat-cement capabilities.

3. High concentrations of diatomaceous earth in cement slurries inhibit strength retrogression, but the set cement does not attain the high ultimate strengh obtained as when silica flour is used; this is due to the high water ratio required of slurries containing diatomaceous earth.

4. Differential thermal analysis and X-ray diffraction analysis indicate that the hydration products, calcium hydroxide and dicalcium silicate alpha-hydrate, are the major compounds found in compositions where strength retrogression has occurred and that strength retrogression is inhibited by the formation of the tobermorite phase.

5. Permeability also is adversely affected during strength retrogression. The addition of silica flour to reduce strength retrogression also will reduce the permeability of the set cement.

6. Compositions containing various quantities of silica flour, diatomaceous earth, bentonite and/or Gilsonite can be retarded effectively for use in high-temperature wells.

7. The modified lignin-type retarder is more advantageous for use under extreme temperature conditions due to its being compatible with (1) retarders presently used in API Class E cements, (2) strength-stabilizing additives, (3) weighting materials and (4) pozzolan-lime compositions. Also, it is more economical; slurries for high-temperature wells can be designed with much greater ease and safety than previously has been possible with other types of cement retarders.

ACKNOWLEDGMENT

The authors wish to express their appreciation to Halliburton Co. for permission to prepare and publish this paper. Appreciation is also extended to those in this organization who offered suggestions for the preparation of this paper. Special thanks go to Dennis Gray, who helped obtain much of the data.

REFERENCES

1. *Oil and Gas Jour.*, Annual Reveiew and Forecast Issue.
2. "Could We Drill a 50,000 Foot Hole?", *Pet. Engr.* (March, 1958) B-44.
3. Ludwig, N. C. and Pence, S. A.: "Properties of Portland

TABLE 8—RESUME OF FIELD JOBS

	I	II	III	IV	V	VI	VII	VIII
Type of Job	Liner	Squeeze	Liner	Squeeze	Plug Back	Liner	Liner	Liner
Depth (ft)	17,000	17,500	15,300	14,000	15,494	13,000	14,500	14,500
Circulating Temp. (°F)	310	273	279	305	218	200	320	325
Time to Max. Temperature (Minutes)	70	45	40	50	30	30	34	38
Cement Brand	A	B	C	Poz.-Lime	C	C	D	D
Modified Lignin Retarder (per cent)	1.00	0.60	0.75	0.70	0.50	0.80	1.50	1.10
Silica Flour (per cent)	35	0	35	0	0	0	35	0
Slurry Weight	18.5*	18.5*	18.1*	17.2*	19.0*	16.2	15.5	16.2
Thickening Time	5:30+	3:00+	4:00+	4:15	3:00+	3:30+	8:15	4:46

*Ilmenite used as a weight material.

Cement Pastes Cured at Elevated Temperatures and Pressures", *Jour. of Am. Concrete Inst.* (Feb., 1956) **V-27**, No. 6.

4. Saunders, C. D. and Walker, W. A.: "Strength of Oil Well Cements and Additives Under High Temperature Well Conditions", Paper presented at AIME Petroleum Branch Meeting in San Antonio, Tex. (1954).
5. Carter, Greg and Smith, Dwight K.: "Properties of Cementing Compositions at Elevated Temperatures and Pressures", *Trans.*, AIME (1958) **213**, 20.
6. "Effects of High Temperatures and Pressures on the Strength of Oil Well Cements", Paper presented at 1954 Spring Meeting of API in Oklahoma City.
7. Kalousek, G. L.: "Tobermorite and Related Phases in the System $CaO-SiO_2-H_2O$", *Jour. of Am. Concrete Inst.* (June 1955) **V-26**, No. 10.
8. Kalousek, G. L.: "The Reactions of Cement Hydration at Elevated Temperatures", Paper No. 11 presented at Third Int. Sym. on Chem. of Cements (1952).
9. *X-Ray Powder Data File*, ASTM Card 9-210.
10. *X-Ray Powder Data File*, ASTM Card 3-0584.
11. *Technical Data Booklet No. D-22*, Drilling Specialties Co. (1959).
12. *HR-12 Super Cement Retarder for Deep Well Cementing*, Halliburton Co. Technical Data Sheet (April, 1960).★★★

The Significance of Particle Shape in Formation Resistivity Factor-Porosity Relationships

E. R. ATKINS, JR.
MEMBER AIME
G. H. SMITH

UNION OIL CO. OF CALIFORNIA
BREA, CALIF.

ABSTRACT

Results of laboratory tests are presented to show that the value of "m", in the Archie expression $\frac{1}{F} = \phi^m$, *is determined by the shapes of the particles in the system. The value of m, "the shape factor", is constant for a system of particles of a given shape for a range of* F - ϕ *values. Applying this concept, one can predict* F - ϕ *relationships for mixtures of particles with different shapes, and these predicted relationships are useful in electric log interpretation.*

It is suggested that an equation of the form $1/F = a\phi^m$ *can be used to describe the properties of natural formations containing varying amounts of sand and clay. From this work and values of "a" and "m" reported in the literature, it appears that in many cases rocks in the same geological horizon have a common primary porosity but contain varying amounts of a particular clay. It is concluded that the equation can be applied to a rock-water system only when values of "a" and "m" have been established for the particular system.*

INTRODUCTION

The petroleum literature contains many reports of the results obtained by determining formation resistivity factor F and porosity ϕ of rock samples from oil fields all over the world. The usual practice is to use data from a large number of samples from a number of fields to find an average relationship between F and ϕ. Several such average relationships have been advanced. In the absence of data on a particular formation or field, it has been the practice to use the average relationships to give a rough approximation of the F - ϕ relationship.

The purpose of this paper is to report on basic relationships that exist between F and ϕ for naturally occurring particles in water solutions. Other workers[1] have found the same relationships apply to the diffusion of hydrogen through packed beds of dry particles.

In the work discussed here, relationships for application to unconsolidated sands or shales containing mixtures of particle shapes are derived. These relationships, developed for unconsolidated formations, may apply to consolidated formations.

Original manuscript received in Society of Petroleum Engineers office July 13, 1960. Revised manuscript received Dec. 8, 1960. Paper presented at 35th Annual Fall Meeting of SPE Oct. 2-5, 1960, in Denver.

[1]References given at end of paper.

EXPERIMENTAL

To evaluate F-ϕ relationships for unconsolidated rocks, the results of laboratory measurements on simple slurries of clay or sand will be used. Such laboratory studies are concerned with the electrical behavior of water-containing rocks. The wet rock constituents are electrically similar in slurries and in rocks.

Archie[2] defined formation resistivity factor as

$$F = R_o/R_w \quad . \quad . \quad . \quad . \quad . \quad . \quad . \quad . \quad . \quad . \quad (1)$$

where R_o = resistivity of the formation 100 per cent wet with water of resistivity R_w.

In slurries of solid particles suspended in water or salt water, the formation resistivity factor concept can also apply. Thus,

$$F = R_{sl}/R'_w \quad . \quad . \quad . \quad . \quad . \quad . \quad . \quad . \quad . \quad . \quad (2)$$

where R_{sl} = resistivity of the slurry, and

R'_w = resistivity of the water phase in the slurry.

The resistivity of the water phase in the slurry, rather than the solution used to prepare the slurry, is used for R'_w. For dilute clay slurries, R'_w was determined by measurements on the supernatant layer.

Archie[2] also empirically determined an equation relating F to formation porosity.

$$\frac{1}{F} = \phi^m \quad . \quad . \quad . \quad . \quad . \quad . \quad . \quad . \quad . \quad . \quad . \quad (3)$$

where ϕ = fractional porosity of the formation, and

m = exponent relating F and ϕ.

This equation can be applied to slurries as well as formations. When used with slurries, ϕ is the volume fraction of the water phase in the slurry.

APPARATUS AND MATERIALS

All resistance measurements were made using a 1,000-cycle impedance bridge with an oscilloscope as the null detector.* The accuracy of this bridge was better than ± 0.15 per cent. For the particular apparatus employed, no additional reactance was required to achieve balance for samples with resistances between

*Manufacturers' names and model numbers for equipment used in research conducted in this paper can be obtained by contacting the author.

800 and 900 ohms. External reactance was required outside this range. The resistivity values for fluids and mobile slurries were measured using a micro dip cell with platinized platinum electrodes. For slurries that were too viscous to measure in the dip cell, a tube cell of Pyrex glass was used (Fig. 1). The cell constants for both cells were established over the entire salinity range using standard potassium-chloride solutions.

The stock clays used are described in Table 1, and the salt solutions employed were prepared by adding reagent-grade sodium chloride to conductivity water. The conductivity water employed in this work had a resistivity greater than 5×10^6 ohm-cm.

Preparation of the Slurries

The slurries were prepared by weighing clay into individual vials and adding a measured volume or weight of a salt solution having a known resistivity. The clay was dispersed by intermittent manual shaking. Under these conditions, little change in slurry resistivity was observed after four hours; however, final measurements were not taken until 16 to 24 hours had passed.

Special precautions were used to prepare slurries with resistivity values greater than 1,000 ohm-cm to avoid contamination by utensils and vessels. It was necessary to test the washings from the vials used for the dilute systems to prevent a significant contamination from occurring. The vials were tightly sealed to prevent the absorption of carbon dioxide from the air and evaporation from the solution.

Resistivity Measurements

Resistivities of the water phase were measured by immersing the dip cell in the clear supernatant layer or by decanting part of this layer into the dip cell. Slurry resistivities were measured by immersing the dip cell into the slurry immediately after shaking. Measurements were repeated in both the water phase and the slurries until the resistances were constant. These values were reproducible when the following precautions were observed.

1. Before any measurement, the dip cell was preconditioned in a solution of approximately the same salinity as the test solution.

2. Between measurements the dip cell was drained, rinsed and wiped, and any clay deposits were removed.

3. Measurements were made in a constant-temperature humidity cabinet at 25° ± 0.25°C.

4. Handling of the samples was minimized to prevent heating.

5. The vent hole at the top of the glass sleeve surrounding the electrodes of the dip cell was kept above the liquid level. When the vent hole was submerged, current could flow through the vent hole into the external liquid and return through the open dip-cell bottom. Variation in this current flow could be caused by partial blocking of either the vent hole or the open end of the cell and by a change in the size of the vessel containing the slurry. With the particular apparatus used in this study, failure to keep the vent hole above the liquid level could lead to a variation as great as 8 per cent of the total conductivity measured.

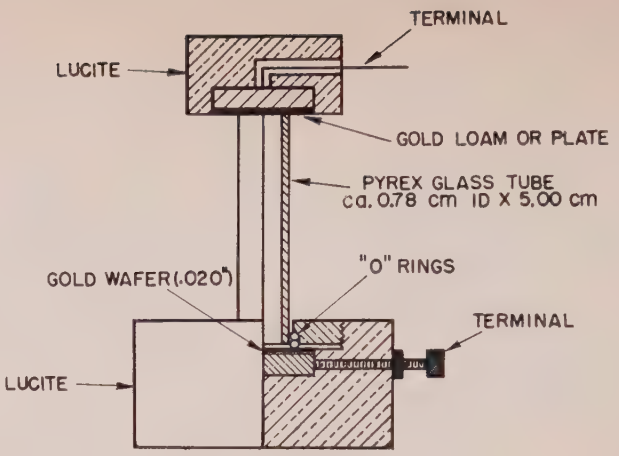

FIG. 1—TUBE CELL.

6. Cell constants were determined individually for each of the dip cells, and when not in use the cells were stored in conductivity water.

Results

Through use of the described procedure, the resistivity measurements contained in Table 2 were obtained. These results show that F is a constant for a given concentration of a particular clay. Measurements over a porosity range of 45 to 100 per cent are plotted logarithmically in Fig. 2 for three types of clay. The slopes of the straight lines in Fig. 2 show that each clay has a particular F-ϕ relationship. The slope of these lines are the respective values of the exponent m in Eq. 3 for each of these clays. For comparison, the data reported by Patnode[2] for sand have been plotted on the figure, and a line has been drawn corresponding to the reported value of 1.6 for m. It appears from the data in Fig. 2 that the Archie Eq. 3 with a given value of m holds for slurries and pastes or packs of particles having a given shape.

Shapes of sand and clay particles could readily ac-

TABLE 1—DESCRIPTION OF THE STOCK CLAYS

Clay	Designation	Source	Donor	Remarks
Sodium Montmorillonite	"Wyoming" Bentonite	Belle Fourche, South Dakota	Baroid Div., National Lead Co.	Minor amounts of quartz and feldspar. Base exchange capacity = 74 meq/100 gm
Calcium Montmorillonite	"Panther Creek" Bentonite	Northeastern Mississippi	American Colloid Co.	Does not form gels with fresh water. Base exchange capacity = 60.1 meq/100 gm
Illite	"Grundite"	Grundy County, Illinois	Illinois Clay Products Co.	Unrefined. Base exchange capacity = 16 meq/100 gm
Kaolinite	"Hydrite Clay" H223	Georgia	A. J. Lynch Co.	Base exchange capacity = 3 meq/100 gm
Attapulgite	"Georgia-Florida" Fuller's Earth	Georgia	Attapulgus Clay Co.	Colloidal fraction refined by removal of abrasive constituents
Muscovite	"Micro Mica" C-1000	N. Carolina	English Mica Co.	

count for a difference in the m value for sand and clay, respectively. Likewise, difference in the areal and thickness dimensions of the clay particles[4] can account for the variation in m value for the clays shown in Fig. 2. As the salinity of the water phase varies, the shape of the clay particles does not change, although the amount of water between the particles may change. Wyllie and Gregory[5] reported on F-ϕ data for particles of various shapes measured separately. In the paper by Wyllie and Gregory, no individual m values were associated with individual particle shapes other than the value 1.3 for systems of spheres. They point out that the value of 1.3 for the exponent in the Archie equation applies to their data obtained with spheres only over the porosity range of 10 to 25 per cent. Through use of techniques described previously, the value of $m = 1.3$ has been obtained repeatedly for stable systems of glass spheres (Superbrite beads) with a porosity of 38 per cent.

It is important to note that systems containing flat angular particles, such as sodium montmorillonite, are characterized by a larger value for the exponent m than that for systems of sand of intermediate sphericity. Such sand systems in turn are characterized by a larger value of m than the value of 1.3 reported for systems of perfect spheres. Thus, the value for the exponent m increases with particle angularity.

Shape factors have been determined for five clay minerals and one mica using the experimental techniques described. These results are listed in Table 3, together with Patnode's[3] value for sand.

TABLE 2—THE FORMATION FACTOR OF CLAYS SUSPENDED IN SODIUM-CHLORIDE SOLUTIONS

Clay Content in Slurry (% by wt)	Salt in the Clay (% by wt)	Resistivity (ohm-cm)			Slurry Resistivity Factor, **F
		Water*	Water Phase	Slurry	
Kaolinite					
0.1	0.016	7.94×10^2	7.94×10^2	7.91×10^2	1.00
1	0.016	7.94×10^2	7.98×10^2	8.00×10^2	1.00
2	0.016	7.94×10^2	8.04×10^2	8.12×10^2	1.01
5	0.016	7.94×10^2	8.10×10^2	8.36×10^2	1.03
10	0.016	7.94×10^2	7.91×10^2	8.55×10^2	1.08
0.1	0.016	1.195×10^1	1.19×10^1	1.193×10^1	1.00
1	0.016	1.195×10^1	1.19×10^1	1.20×10^1	1.01
2	0.016	1.195×10^1	1.195×10^1	1.21×10^1	1.01
5	0.016	1.22×10^1	1.226×10^1	1.27×10^1	1.04
10	0.016	1.195×10^1	1.195×10^1	1.28×10^1	1.07
5	0.016	8.21×10^3	1.04×10^4	1.07×10^4	1.03
5	0.34	7.68×10^2	6.03×10^2	6.17×10^2	1.02
5	0.34	1.195×10^1	1.18×10^1	1.22×10^1	1.03
5	3.1	7.68×10^2	2.42×10^2	2.48×10^2	1.03
5	3.1	9.07×10^1	7.41×10^1	7.65×10^1	1.03
5	3.1	5.41	5.36	5.53	1.03
10	0.016	8.21×10^3	1.085×10^4	1.16×10^1	1.07
10	0.34	9.21×10^3	8.73×10^1	9.29×10^3	1.07
10	0.34	1.22×10^1	1.22×10^1	1.29×10^1	1.06
10	3.1	9.21×10^1	6.31×10^1	6.75×10^1	1.07
10	3.1	1.22×10^1	1.18×10^1	1.26×10^1	1.07
Calcium Montmorillonite					
0.1	0.03	9.31×10^1	9.26×10^1	9.26×10^1	1.00
1	0.03	9.31×10^1	9.30×10^1	9.31×10^1	1.00
2	0.03	9.31×10^1	9.27×10^1	9.38×10^1	1.01
5	0.03	9.34×10^1	9.34×10^1	9.61×10^1	1.03
10	0.03	9.31×10^1	9.26×10^1	9.80×10^1	1.06
0.1	0.03	1.195×10^1	1.19×10^1	1.19×10^1	1.00
1	0.03	1.195×10^1	1.19×10^1	1.20×10^1	1.01
2	0.03	1.195×10^1	1.19×10^1	1.21×10^1	1.02
5	0.03	1.22×10^1	1.23×10^1	1.28×10^1	1.04
10	0.03	1.195×10^1	1.20×10^1	1.29×10^1	1.07
5	0.45	9.25×10^1	8.91×10^1	9.10×10^1	1.02
5	0.45	5.14	5.13	5.34	1.04
5	3.4	7.88×10^2	2.22×10^2	2.25×10^2	1.01
5	3.4	9.25×10^1	7.28×10^1	7.50×10^1	1.03
5	3.4	5.14	5.07	5.26	1.04
5	10.0	7.88×10^2	9.63×10^2	9.89×10^2	1.03
5	10.0	9.25×10^1	5.28×10^1	5.44×10^1	1.03
5	10.0	5.14	5.04	5.25	1.04
10	0.45	9.25×10^1	8.74×10^1	9.23×10^1	1.06
10	0.45	5.14	5.13	5.52	1.07
10	3.4	7.88×10^2	1.35×10^2	1.45×10^2	1.07
10	3.4	9.25×10^1	6.13×10^1	6.66×10^1	1.09
10	3.4	5.14	5.06	5.38	1.06
Sodium Montmorillonite					
0.1	0.24	9.31×10^1	9.25×10^1	9.22×10^1	1.00
1	0.24	9.31×10^1	9.25×10^1	9.39×10^1	1.01
2	0.24	9.31×10^1	9.43×10^1	9.57×10^1	1.02
5	0.24	9.31×10^1	———	1.03×10^2***	—
10	0.24	9.31×10^1	———	1.14×10^2***	—
0.1	0.24	1.195×10^1	1.19×10^1	1.19×10^1	1.00
1	0.24	1.195×10^1	1.19×10^1	1.21×10^1	1.02
2	0.24	1.195×10^1	1.19×10^1	1.22×10^1	1.02
5	0.24	1.195×10^1	1.186×10^1	1.27×10^1	1.07
10	0.24	1.195×10^1	1.175×10^1	1.35×10^1	1.15
5	2.7	1.19×10^1	1.16×10^1	1.21×10^1	1.04
5	4.1	1.19×10^1	1.15×10^1	1.21×10^1	1.05
10	2.7	1.22×10^1	1.17×10^1	1.29×10^1	1.10
10	4.1	1.22×10^1	1.16×10^1	1.29×10^1	1.11

*Most California formation waters fall within the range of 100 to 10 ohm-cm.

**F is calculated from $R_{sl} = F R'_w$.

***No solution was obtainable because these systems were thixotropic gels. The slurry reading was taken on the shaken fluidized gel.

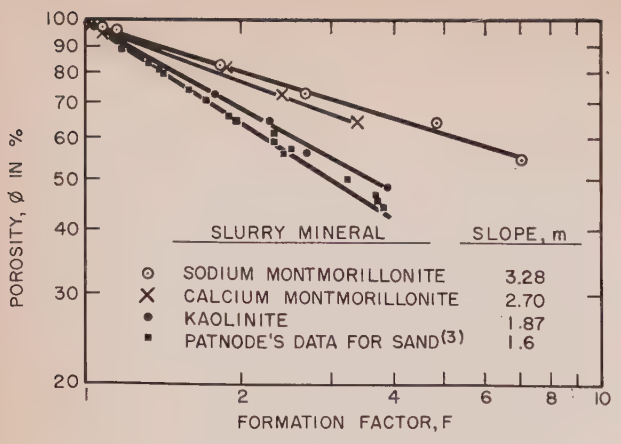

FIG. 2--MINERAL SLURRY F-ϕ MEASUREMENTS.

THEORY

The basic problem of relating F to ϕ for natural rock samples has been concerned with the fact that statistical analysis of samples from a single bed often suggests that the relationship should be[6-8]

$$1/F = a\phi^m \quad . \quad . \quad . \quad . \quad . \quad . \quad . \quad . \quad . \quad (4)$$

where a is not always unity. When a is not unity, the boundary condition $F = 1.0$ when $\phi = 1.0$ or 100 per cent apparently is not satisfied by Eq. 4. It is the main objective of this paper to show how the boundary conditions, $F = 1.0$ and $\phi = 100$ per cent, may be satisfied in such cases and the significance of a boundary value other than unity.

An unconsolidated sand may be thought of as a combination of one or more single-shaped particle systems. Consider an unconsolidated sand matrix with clay dispersed in the interstitial spaces. The sand particles usually will have similar shapes, although they may be of many different sizes. The clay particles will have a particular shape, as shown in Table 3, which is characteristic of the type of clay.

DEVELOPMENT OF EQUATIONS FOR UNCONSOLIDATED SANDS

By applying the Archie Eq. 3 sequentially for each of two components, we have found equations of the form of Eq. 4 which appear to describe the electrical and porosity characteristics of natural unconsolidated systems containing sand and clay. These equations are developed in the following paragraphs and illustrated in graphical form as applied to typical unconsolidated sand-clay rock systems. Variables involved in the development of the equations are as follows.

ϕ'' = primary porosity of the sand-grain matrix — the volume of the system that is not sand divided by the total volume of the system.

ϕ' = porosity of an equivalent clay slurry — the volume of the water in the system divided by the total volume of the water and the clay.

TABLE 3—SHAPE FACTORS FOR FIVE CLAYS AND ONE MICA

Mineral Particle	Shape Factor Exponent
Sodium Montmorillonite (NAM)	3.28
Calcium Montmorillonite (CAM)	2.70
Muscovite	2.46
Attapulgite	2.46
Illite (I)	2.11
Kaolinite (K)	1.87
Sand and Chalk[3]	1.60

ϕ = porosity of sand-clay-water system — space not occupied by clay or sand divided by the total volume of the system.

F'' = formation resistivity factor of a primary sand-water system having a porosity of ϕ''.

F' = formation resistivity factor of a clay slurry.

F = formation resistivity factor of the total sand-clay-water system.

m'' = shape factor exponent of the primary grains in a sand-water system having a porosity of ϕ''.

m' = shape factor exponent of clay particles in a clay-water slurry.

To develop the equations for a system made of two components, first consider the primary porosity of the sand grains.

$$\phi'' = \frac{v}{V} \quad . \quad . \quad . \quad . \quad . \quad . \quad . \quad . \quad . \quad . \quad . \quad (5)$$

where v = the volume of both clay and water in the interstices of the sand, also the volume of space not occupied by sand in the system, and

V = the total volume occupied by the system.

Then the porosity of the clay-water system would be

$$\phi' = \frac{u}{v} \quad . \quad . \quad . \quad . \quad . \quad . \quad . \quad . \quad . \quad . \quad . \quad (6)$$

where u = the net volume of water in the system.

Then,

$$\phi = \frac{u}{V} \quad . \quad . \quad . \quad . \quad . \quad . \quad . \quad . \quad . \quad . \quad . \quad (7)$$

Hence,

$$\phi = \frac{u}{v}\frac{v}{V} = \phi'\,\phi'' \quad . \quad . \quad . \quad . \quad . \quad . \quad . \quad . \quad (8)$$

As stated earlier, Archie's Eq. 3 applies to the F-ϕ relation of the sand system and the clay system separately, so

$$1/F'' = \phi''^{m''} \text{ and } \frac{1}{F'} = \phi'^{m'} \quad . \quad . \quad . \quad . \quad . \quad . \quad (9)$$

By considering the resistivities of simple and compound systems, the relation of F to F' and F'' can be developed. Applying Archie's relationship for formation resistivity factor to a dilute clay slurry (more water than clay) dispersed in sand,

$$F' = \frac{R_{sl}}{R'_w} \quad . \quad . \quad . \quad . \quad . \quad . \quad . \quad . \quad . \quad . \quad . \quad (10)$$

where

R_{sl} = resistivity of the clay slurry, and

R'_w = resistivity of the water phase.

This slurry is considered to be the material filling the primary porosity of the sand grains. To apply these equations to consolidated or unconsolidated rocks, it is assumed that the clay-water systems in such rocks carry electricity as though they were a clay slurry. Therefore,

$$F'' = \frac{R_o}{R_{sl}} \quad . \quad . \quad . \quad . \quad . \quad . \quad . \quad . \quad . \quad . \quad . \quad (11)$$

where R_o = resistivity of the system (clay and sand) 100 per cent saturated with water.

Then,

$$F = \frac{R_o}{R'_w} = \frac{R_o}{R_{sl}}\frac{R_{sl}}{R'_w} = F''\,F' \quad . \quad . \quad . \quad . \quad (12)$$

Combining Eqs. 9 and 12,

$$\frac{1}{F} = \frac{1}{F''}\frac{1}{F'} = \phi''^{m''}\,\phi'^{m'} \quad . \quad . \quad . \quad . \quad . \quad . \quad . \quad (13)$$

We usually are interested in a relationship between F and system porosity ϕ rather than F and the porosity components ϕ' and ϕ''. Using Eq. 8, Eq. 13 can be solved in terms of either ϕ and ϕ' or ϕ and ϕ''. Each solution is of interest.

$$\frac{1}{F} = \left(\frac{\phi}{\phi''}\right)^{m'} \phi''^{m''} = \phi''^{(m''-m')}\,\phi^{m'} \quad . \quad . \quad . \quad (14)$$

$$\frac{1}{F} = \left(\frac{\phi}{\phi'}\right)^{m''} \phi'^{m'} = \phi'^{(m'-m'')}\,\phi^{m''} \quad . \quad . \quad . \quad (15)$$

It will be noted that both Eqs. 14 and 15 have the general form of Eq. 4, suggested by Winsauer, *et al.*[6] The constant a in Eq. 4 is equivalent to $\phi''^{(m''-m')}$ and $\phi'^{(m'-m'')}$ in Eqs. 14 and 15, respectively. Previously, values of a were determined empirically. Eqs. 14 and 15 now provide a basis for understanding this practice. The significance of the constant a of Eq. 4 would be different in Eq. 14 than in Eq. 15, as would the exponent to ϕ.

Consider the systems described by Eqs. 14 and 15 separately. Two illustrative examples of how these equations apply to natural particles are described in the following discussions. Sand and sodium montmorillonite have been chosen because they represent the extremes of particle shapes which one usually should encounter in natural sandstones. If a plot of F vs ϕ is made on log-log paper, as in Fig. 3, the slope of the line for Eq. 14 would be m', the shape factor for the clay, which equals 3.28 when the clay is sodium montmorillonite. Sand, the primary grain, has a shape factor m'' of 1.6.

To illustrate the analogy between Fig. 3 and the physical model of a sand-clay system, first consider a cell full of water, $\phi = 100$ per cent. If the porosity in the cell (ϕ) is reduced by replacing water with sand, one obtains F and ϕ values along the dashed line of Fig. 3. In this example, the range of sand particle sizes is such that the packed sand matrix ultimately has a primary porosity of 40 per cent. The addition of clay to make a slurry in the primary pore space would cause a further reduction of rock porosity below 40 per cent, by displacing some of the interstitial water in the primary pore spaces of the sand. The solid line of Fig. 3 shows the $F - \phi$ relationship for varying amounts of sodium montmorillonite, dispersed in the water in a sand matrix, which had a primary porosity of 40 per cent. Although the value of F (when $\phi = 100$ per cent) obtained by the dotted extrapolation is useful for calculating ϕ'' by Eq. 14, the system just described never can have actual co-ordinates that lie on the dotted line. The dotted line, being an extension of the solid line, has the slope m' which applies only to systems containing clay. Over the porosity range of 40 to 100 per cent for the system illustrated in Fig. 3, there is no clay in the system—only sand; thus, the dotted line would not describe any part of the system being considered here.

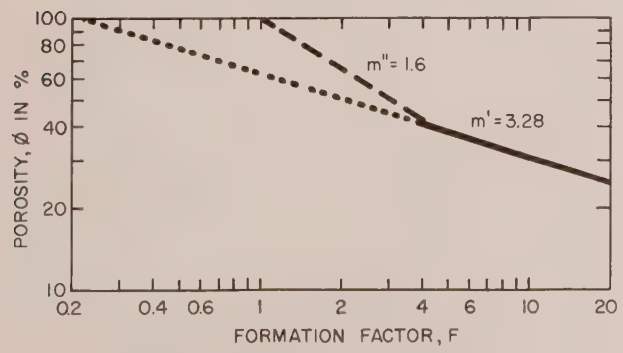

FIG. 3—F-ϕ RELATIONSHIP OF EQ. 14.

Eq. 15 can also be represented by a log-log plot. Such a plot is shown in Fig. 4. To illustrate the analogy between Fig. 4 and a sand-clay system, first consider a cell full of water where $\phi = 100$ per cent. If the porosity in the cell is reduced by replacing water with sodium montmorillonite clay, one obtains F and ϕ values along the dashed line of Fig. 4. In this example, addition of clay is ceased when the slurry porosity is reduced to 78.6 per cent. Further porosity reduction in this system is accomplished by addition of sand and corresponding displacement of clay-water slurry. The $F - \phi$ relationship caused by replacing slurry with sand would be described by the solid line in Fig. 4. Although the value of F (when $\phi = 100$ per cent) obtained by the dotted extrapolation is useful for calculating ϕ' by Eq. 15, the system just described can never have actual co-ordinates that lie on the dotted line. Thus, the proportion of clay to water would remain a constant along the solid line as both F and ϕ varied. The proportion of clay to sand would be different at every point on the solid line. The primary sand porosity ϕ'', which was a constant in the system of Fig. 3, is continually varying with F or ϕ in this system of Fig. 4.

From this description of Figs. 3 and 4, it is apparent that, although both Eqs. 14 and 15 are of the form $\frac{1}{F} = a\phi^m$, the value of a in Eq. 14 is greater than unity and that in Eq. 15 a is less than unity. Since the paper of Winsauer, *et al*,[6] several additional correlations of F-ϕ have been published.[5,7,8] Some of these correlations had a values greater than one, and others had a values less than one. The meaning of these various empirical formulas will be discussed later. Here it is of interest to note that equations like both Eqs. 14 and 15 are consistent with empirical data.

The first use of an equation of the form $1/F = a\phi^m$ caused serious misgivings among some log analysts because, when a was other than unity, the boundary condition that $F = 1.0$ when $\phi = 100$ per cent apparently was not satisfied by the equations. This discussion of Figs. 3 and 4 should help in understanding how equa-

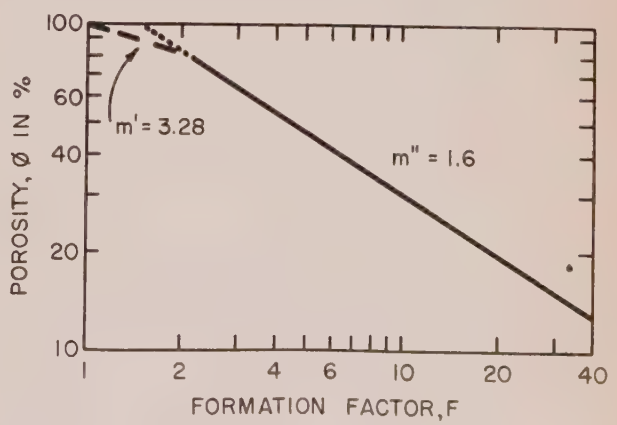

FIG. 4—F-ϕ RELATIONSHIP OF EQ. 15.

tions of the form $1/F = a\phi^m$ can apply to rocks of multiple-shaped particles, and yet the boundary condition, $F = 1.0$ when $\phi = 100$ per cent, still be satisfied.

Although this discussion has been concerned with rocks of one or two particle shapes, it is possible to write equations for mixtures of particles of three or more different shapes. Such equations could be developed as needed using the methods described for Eqs. 14 and 15. It should be noted that, where a particular shape is present as only a few volume per cent of the rock, very little precision will be sacrificed by neglecting its presence when developing an equation to describe the F-ϕ relationships of the rocks.

SUGGESTED APPLICATIONS

The equations derived previously herein are based upon measurements on unconsolidated systems. No experiments have been performed on natural sandstones or shales. However, applications of these equations to natural rock systems could be of value.

CORE MEASUREMENTS FROM THE LITERATURE

Many workers have applied statistical methods to collections of F-ϕ data and arrived at equations for "best" lines through their particular data. The data of Hill and Milburn[7] bear out their conclusion that such best lines give the least error only when applied to the particular reservoirs from which the data were obtained. Large errors may result if data from a group of diverse formations are applied to a particular formation.

If the reservoir engineer or log analyst could determine those factors which make a particular reservoir different from others, he might be expected to predict with less error the F-ϕ relationship which applies to that reservoir. Conversely, conventional F and ϕ data can be used to suggest special formation characteristics not normally available from such routine services. The data for Suite No. 2 of Hill and Milburn[7] will serve as an example. The equation for the best line for the data of Suite No. 2 is given by Hill and Milburn as

$$0.47/F = \phi^{2.23} \quad . \quad . \quad . \quad . \quad . \quad . \quad . \quad . \quad . \quad . \quad . \quad (16)$$

This is an average line resulting from data in which some points depart by as much as 25 per cent from the line. However, to the degree that Eq. 16 represents the formation, we can say the following.

1. The exponent value, 2.23, approximates that associated with illite in this work (Table 3). Other particles of similar shapes not studied in this work may be responsible for this value.

2. The equation is of the form suggested by Eq. 14; hence, a common primary sand porosity probably applies to this formation.

3. Examination of points on the plot gives a possible lower limit of the m value for sand as 1.54. If this sand shape factor is applied to the best line, the primary sand porosity is calculated to be 33.5 per cent.

EFFECTS OF OVERBURDEN PRESSURE

A more precise determination of porosity from log resistivity data might be made for formations containing little clay if an adjustment of the shape factor could be made as a function of depth. Several workers have shown that F increases with overburden pressure much faster than ϕ decreases.[8-11] Little data are available to describe how overburden pressure would affect shape factor for a particular reservoir rock. Overburden pressure could cause round particles to be flattened, thus giving a larger shape factor for the weight-bearing matrix of the rock. In view of this, it would seem reasonable to expect a change in shape factor with a change in overburden pressure on a sand matrix, either by distortion or by solution and overgrowth. It may be expected that some shaly sands have enough clay material between the sand grains so that the pressure would be transmitted by the clay particles. If actual displacement of the clay did not occur, overburden pressure should not cause much distortion of the flat clay particles nor, accordingly, much change of the shape factor exponent. As a corollary to this, it would be expected that formations characterized by small m values, approaching 1.3, would show the greatest effect of overburden pressure on m.

Glanville[9] studied two sandstones with and without overburden pressure. His resistivity data obtained parallel to the bedding planes can be interpreted to conform with the afore-mentioned suggestion. Fig. 5 shows these data. Note that the Tuscaloosa sand data show little change in m with increase of differential pressure on the sand. The Pennsylvanian sand data show a marked change in m with increase of differential pressure on the sand. More measurements of this kind on single- and multiple-component systems should be helpful in determining the relation between overburden pressure and shape factor.

CONSOLIDATED SANDS

It may be pertinent to suggest the influence which cementation would have on the value of the exponent m. The angularity of primary particles may change with cementation. If the angularity of the particles is increased by cementation, the m value will also increase, and vice versa. Of course, the porosity will be reduced as cementing increases. Thus, a particular m value would be associated with a particular amount of cementation added to a sand with a given primary porosity and grain shape.

It would be useful in log interpretation if there were a simple relationship between F and ϕ which applied to the variation of porosity found in a reservoir. From this discussion it appears that, for a reservoir of changing cementation, the simple Archie relationships[3] between F and ϕ will be accurate only if the primary sand porosity of the reservoir is known and if the relationship between decreasing porosity and changing m is known.

CONCLUSIONS

1. The clay-slurry resistivity factor can be determined if the resistivity of the water phase in the slurry can be measured or calculated.

2. For a given quantity of each particular clay studied, the slurry resistivity factor is a constant over a range of brine concentration of practical interest.

3. The Archie equation, $1/F = \phi^m$, applies to unconsolidated systems containing particles of a single shape.

4. The exponent m appears to be affected only by particle shape and has been referred to as the "shape factor" in this report. The shape factors for several minerals have been measured and are listed here.

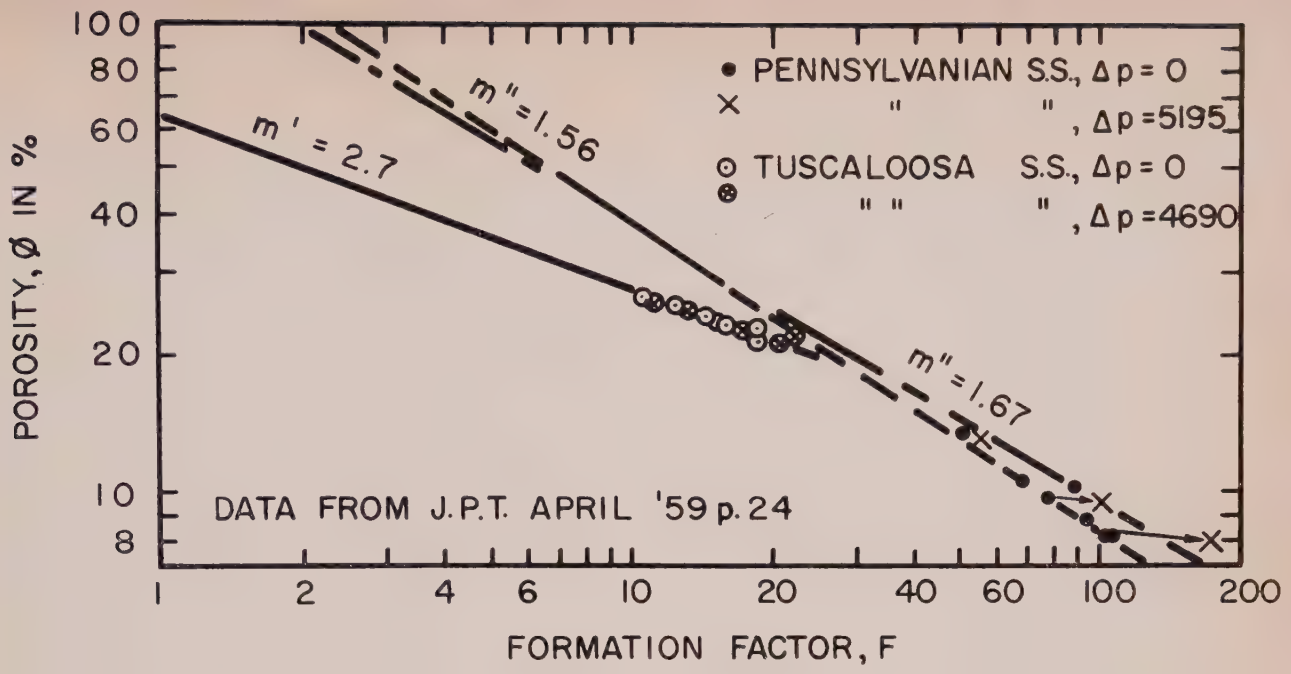

FIG. 5—GLANVILLE'S DATA SHOWING EFFECTS OF OVERBURDEN PRESSURE ON "m".

5. Equations having the general form, $1/F = a\phi^m$, are used to describe systems containing particles of more than one shape such as natural unconsolidated sandstones.

6. Equations were derived which show the relationship between the forms $1/F = \phi^m$ and $1/F = a\phi^m$. The derivation suggests how the boundary condition, $F = 1$ when $\phi = 1.0$ or 100 per cent, is satisfied as a system of particles of several shapes is built by a combination of systems each contributing particles of a different shape.

7. For greatest accuracy in finding F or ϕ from relationships that apply to natural sandstones, as also shown by others, data from only a single formation should be used to make the F-ϕ plots.

8. The equations developed here to describe systems containing particles of several shapes are shown to fit empirical data reported by others.

ACKNOWLEDGMENT

The authors wish to thank the management of the Union Oil Co. of California for permission to publish this paper.

REFERENCES

1. Currie, J. A.: "Gaseous Diffusion in Porous Media, Part 2, Dry Granular Materials", *Brit. Jour. Appl. Phys.* (1960) **11,** 318.

2. Archie, G. E.: "The Electrical Resistivity Log as an Aid in Determining Some Reservoir Characteristics", *Trans.*, AIME (1942) **146,** 54.

3. Patnode, H. W.: "Relationship of Drilling Mud Resistivity to Mud Filtrate Resistivity", *Trans.*, AIME (1949) **186,** 14.

4. Eirich, F. R.: *Rheology*, Academic Press (1960) **III,** Table IV, 277.

5. Wyllie, M. R. J. and Gregory, A. R.: "Formation Factors of Unconsolidated Porous Media: Influence of Particle Shape and Effect of Cementation", *Trans.*, AIME (1953) **198,** 103.

6. Winsauer, W. O., Shearin, H. M. Jr., Masson, P. H. and Williams, M.: "Resistivity of Brine-Saturated Sands in Relation to Pore Geometry", *Bull.*, AAPG (1952) **36,** 253.

7. Hill, H. J. and Milburn, J. D.: "Effect of Clay and Water Salinity on Electrochemical Behavior of Reservoir Rocks", *Trans.*, AIME (1956) **207,** 65.

8. Fatt, I.: "Effect of Overburden and Reservoir Pressure on Electric Logging Formation Factor", *Bull.*, AAPG (1957) **41,** 2456.

9. Glanville, C. R.: "Laboratory Study Indicates Significant Effect of Pressure on Resistivity of Reservoir Rocks", *Jour. Pet. Tech.* (April, 1959) **XI,** No. 4, 20.

10. Fatt I.: "Pore Volume Compressibilities of Sandstone Reservoir Rocks", *Trans.*, AIME (1958) **213,** 362.

11. Wyble, D. O.: "Effect of Applied Pressure on Conductivity, Porosity and Permeability of Sandstones", *Trans.*, AIME (1958) **213,** 430. ★★★

An Electrodeless System for Measuring Electric Logging Parameters on Cores and Mud Samples

IRVING FATT
MEMBER AIME

U. OF CALIFORNIA
BERKELEY, CALIF.

INTRODUCTION

A recently developed system for measuring electrical resistivity of liquids without use of electrodes offers some interesting possibilities in electric logging technology. The equipment as supplied by the manufacturer is satisfactory for continuous mud logging on a drilling rig or for measuring mud or filtrate resistivity in the laboratory. A simple modification of the commercially available instrument makes it suitable for measuring resistivity of core samples in the laboratory.

The continuous measurement of mud resistivity on a drilling rig is a convenient means for detecting mixing of formation water with the drilling mud. Such information is useful to the geologist, the mud engineer and the logging engineer. However, continuous mud resistivity logging by conventional electrode-type resistivity cells is beset with difficulties. The mud, sand and rock chips abrade the electrodes, thereby changing the cell constant and eventually destroying the cell. Also, additives and crude oil in the mud may poison the electrodes by coating them with a nonconductive material. An electrode-type resistivity cell, therefore, may give erroneous readings under certain conditions. Electric logging companies circumvent the electrode poisoning problem by using a four-electrode resistivity cell for measurement of mud resistivity. In this cell, change in electrode area does not change the cell constant. However, the four-electrode cell is difficult to adapt for continuous reading and does not solve completely the problem of electrode abrasion by the sand and cuttings in the mud.

The measurement of electric logging parameters on core samples in the laboratory encounters some of the same problems discussed in connection with mud logging. Ideally, the electrical resistivity of a core sample should be measured by placing platinum black electrodes in direct contact with the plane ends of a cylindrical or rectangular sample. Platinum black electrodes however, are much too fragile and easily abraded to be brought in contact with a rock sample. Also, oil or other constituents in the fluid contained in the sample will poison platinum black. In practice, gold-plated brass electrodes, in an AC bridge circuit operating at about 1,000 cps, are used for routine core analysis. For more precise work in research studies, a four-electrode scheme is used.[1,2] Preparation of the samples for the four-electrode method is much too involved for routine core analysis.

An apparatus for measuring resistivity of liquids without use of electrodes was described by Guthrie and Boys[3] in 1879. They suspended a beaker, containing the electrolyte, by a torsion wire and rotated a set of permanent bar magnets around the vessel. The eddy currents induced in the electrolyte reacted against the rotating magnetic field to develop a torque, which was measured as a deflection of the torsion wire. In 1879 this method could not be made precise or convenient because of the lack of strong permanent magnets. The writer described a very greatly improved apparatus similar to that of Guthrie and Boys, but it was not suitable for continuous measurements or core samples.[4]

Many electrodeless resistivity devices using radio frequency current are described in the literature.[5,6] These generally are suitable only for noting the end-point in a chemical titration. They do not measure resistivity, instead measuring a complex quantity which includes the dielectric constant and the magnetic permeability.

The first description of the apparatus to be discussed in this paper was given by Relis.[7] Improvements and modifications are described by Fielden,[8] Gupta and Hills,[9] and Eichholz and Bettens.[10]

DESCRIPTION OF APPARATUS

The apparatus used in this study is based on the principle that the solution under measurement can form a loop coupling two transformer coils, as shown in Fig. 1. For a fixed AC voltage applied across Coil A, the voltage appearing across Coil B is a function of the resistance of the liquid-filled loop. The details of the voltage generating and measuring circuits are given in Refs. 7, 8, 9 and 10. A block diagram of the equipment is given in Fig. 2. Special features worth mentioning are the operating frequency of 18,000 cps and the automatic temperature compensation which results in the given resistivity readings being automatically correlated to 25°C.

The liquid loop supplied by the manufacturer, shown in Figs. 1 and 2, was modified for use in core analysis (Fig. 3). The core sample under test is substituted for a section of the original loop. As shown in Fig. 3, the unit accepts only plastic-mounted cylindrical core specimens. A Hassler-type sleeve easily can be designed for the unit if unmounted cores are to be measured.

EXPERIMENTAL PROCEDURE

MUD LOGGING

A simulated mud line was set up in the laboratory.

Original manuscript received in Society of Petroleum Engineers office Aug. 24, 1960. Revised manuscript received Jan. 12, 1961. Paper presented at 31st Annual California Regional Meeting of SPE, Oct. 20-21, 1960, in Pasadena, Calif.

[1]References given at end of paper.

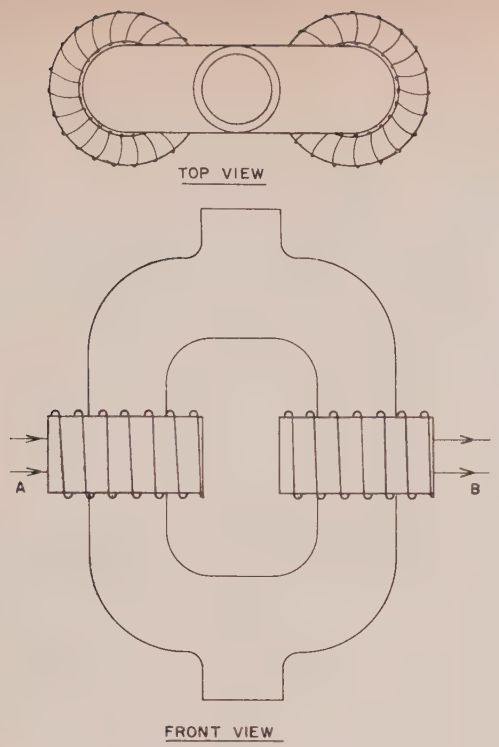

FIG. 1—SCHEMATIC SHOWING PRINCIPLE OF LIQUID-LOOP TRANSFORMER.

A typical water-base clay mud (Macco P-95, 18 per cent by weight) was circulated through the cell, shown in Figs. 1 and 2, from a 10-gal container. Mud resistivity was read on the panel meter of the electrodeless unit and also recorded continuously on a strip chart recorder. Mud resistivities were checked by: (1) a two-electrode cell using gold-plated electrodes and an AC bridge operating at 60 or 1,000 cps; and (2) a four-electrode cell consisting of a 1-in. in diameter cylinder 4-in. long, closed at each end by a stainless-steel plug and having two bands of stainless steel recessed into the inner surface. The four-electrode measurements were made with a circuit identical to that described by Dunlap, *et al*,[1] except that in this case the signal generator was a Heathkit Model AG-9A and the vacuum tube voltmeter was a Heathkit Model AV-3. Resistivities also were measured on several pure bentonite muds prepared in small quantities in a malted-milk mixer.

CORE ANALYSIS

Formation factors were measured on two unconsolidated sand packs and three consolidated sandstones. Measurements were made by the electrodeless unit, shown in Fig. 3, and checked by a two-electrode method and two separate four-electrode procedures.

Sand packs were prepared for the electrodeless unit by tamping the sand into a Lucite cylinder ¾-in. ID and 2-in. long. The sand was held in the cylinder by pieces of nylon mesh (women's hose) cemented over the ends. For the four-electrode measurements, the sand was packed into the same cell used for mud measurements described previously. The electrolyte saturating both sand packs and consolidated cores was 0.5-molar sodium chloride.

Formation factors of consolidated cores measured by the electrodeless unit were checked by a two-electrode

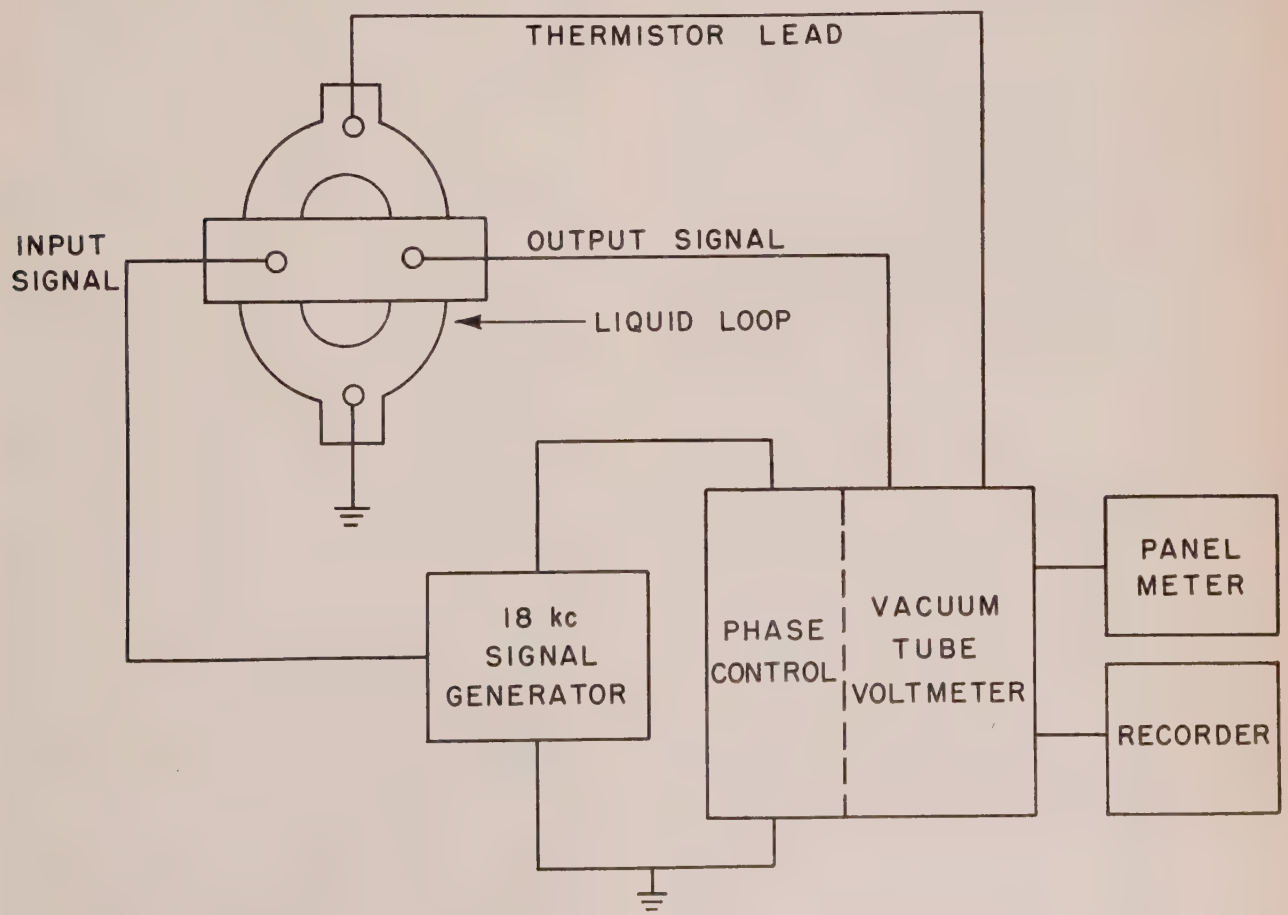

FIG. 2—BLOCK DIAGRAM OF ELECTRODELESS APPARATUS.

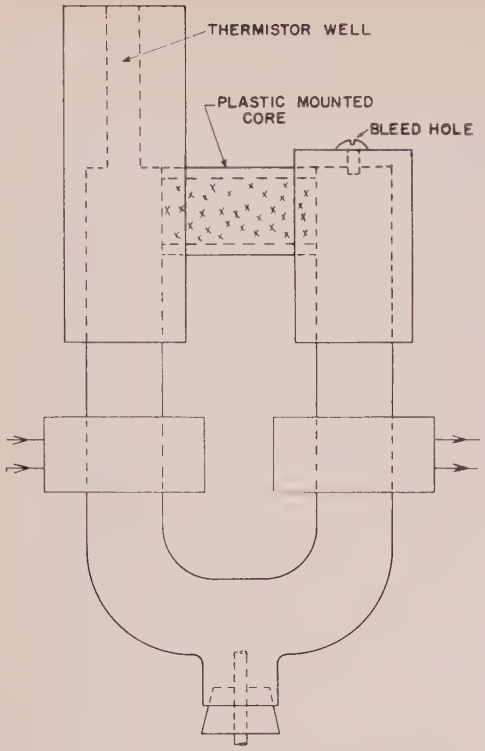

FIG. 3—ELECTRODELESS CELL MODIFIED TO TAKE CORE SAMPLES.

method and by Marshall and Madden's[2] four-electrode method. The cores were ¾-in. in diameter and 2-in. long mounted in epoxy resin.

The electrodeless unit was used as follows. A calibration curve was constructed by noting the resistivity readings on the panel meter of the electrodeless unit when a series of Lucite cylinders 2-in. long and with inner diameters ranging from ¾ to ⅛ in. were used as "cores". To avoid distortion of the electric flow lines at the ends of these cylinders, the ends were coated with conducting paint. When a sand pack or consolidated core was placed in the unit, its effective area could be read from the calibration curve. The bulk area divided by the effective area is then the formation factor because the electrolyte is always the same and the core is equal in length to the calibrating cylinders.

RESULTS

MUD LOGGING

Six water-base muds covering the resistivity range of 5 to 0.1 ohm-m were used in this study. The electrodeless unit was found to give an accurate and rapid indication of mud resistivity. The response time was completely dependent on the hydraulic system; the response time of the unit itself is of the order of milliseconds. The response time on the paper record depends upon the recorder characteristics. Agreement between mud resistivities measured on the electrodeless unit and those measured by the four-electrode method was ± 2 per cent for all muds. This included those muds which contained high concentrations of salt, surfactants, phosphates and crude oil (emulsified into the mud). Agreement also was obtained with a two-electrode mud cell for all muds, except for those containing emulsified crude oil. In the latter case, readings in the two-electrode cell were often erratic.

TABLE 1—MEASURED FORMATION FACTORS

Sample	Electrodeless	2-Electrode	4-Electrode
28-35 Mesh Ottawa Sand	4.0	—	4.18*
65-100 Mesh Ottawa Sand	3.8	—	3.94*
Brea***	20.6	19.4	20.0**
Boise***	13.3	13.0	15.0**
Bandera***	30.6	30.1	29.0**

*Measured in 4-electrode mud cell.
**Measured by Marshall and Madden's method (Ref. 2).
***Complete descriptions of these sandstones are given by Mann and Fatt (Ref. 11).

CORE ANALYSIS

The measured formation factors are given in Table 1.

CONCLUSIONS

The electrodeless resistivity unit described in this paper will give an accurate and instantaneous reading of drilling-mud resistivity in the resistivity range usually encountered. It is reliable and essentially foolproof. Adaptation to use on a drilling rig should be simple.

The electrodeless unit can be used in the laboratory for measurement of resistivity of core samples.

ACKNOWLEDGMENT

The author wishes to thank the Schlumberger Well Surveying Corp.. for donating the electrodeless unit. R. Rosenthal of Industrial Instruments, Inc., manufacturers of the unit, was very cooperative in designing a unit useful in electric logging technology. T. S. Purewal and N. Keevil gave technical assistance in obtaining the data. The Institute of Engineering Research, U. of California at Berkeley, provided support for this research.

REFERENCES

1. Dunlap, H. F., Bilhartz, H. L., Shuler, E. and Bailey, C. R.: "The Relation Between Electrical Resistivity and Brine Saturation in Reservoir Rocks", *Trans.*, AIME **186,** 259.
2. Marshall, D. J. and Madden, T. R.: "Induced Polarization, a Study of Its Causes", *Geophysics* (1959) **24,** 790.
3. Guthrie, F. and Boys, C. V.: *Phil. Mag.* (1879) **8,** 449; and (1880) **10,** 328.
4. Fatt, I.: "An Induction Method for Measuring Resistance of Electrolytes", *Rev. Sci. Inst.* (1952) **23,** 133.
5. Blake, C. G.: *Conductimetric Analysis at Radio-frequency*, Chapman and Hall Ltd., London (1950).
6. Reilly, C. N.: *New Instrumental Methods in Electrochemistry*, Edited by P. Delahay, Interscience Pub., Inc., N. Y. (1954) 319.
7. Relis, M. J.: "Method and Apparatus for Measuring Conductivity of an Electrolyte", U. S. Patent 2,542,057 (Feb. 20, 1951).
8. Fielden, J. E.: "Measurement of Conductivity of Liquids", U. S. Patent 2,709,785 (May 31, 1955) and Reissue No. Re 24,420 (Jan. 28, 1958).
9. Gupta, S. R. and Hills, G. J.: "A Precision Electrodeless Cell for Use at Audio Frequencies", *Jour. Sci. Inst.* (1956) **33,** 313.
10. Eichholz, G. G. and Bettens, A. H.: "Conductimetric Measurement and Control of Acid Concentration in Leach Pulps", *Trans.*, CIM (1960) **63,** 625.
11. Mann, R. L. and Fatt, I.: "Effect of Pore Fluids on the Elastic Properties of Sandstone", *Geophysics* (1960) **25,** 433.

★★★

Hydraulic Fracture—Field Test to Determine Areal Extent and Orientation

J. J. REYNOLDS
MEMBER AIME
J. B. SCOTT
J. L. POPHAM*
MEMBER AIME
H. F. COFFER
MEMBER AIME

CONTINENTAL OIL CO.
HOUSTON, TEX.

PONCA CITY, OKLA.

ABSTRACT

This paper concerns field experiments to define the areal extent, orientation and thickness of an artificial fracture in the Sacatosa field, Maverick County, Tex. The fracture was made by a sand-oil treatment of 176,000 gal of lease crude containing a fluid-loss additive and 270,000 lb of 20-40 mesh subangular Poteet sand. The well was perforated with a jet gun, consisting of six shots in a single plane.

Fourteen test holes were drilled at various locations around the fractured well. Drill-stem tests, Micro and Sonic Logs, coring and sampling of formation cuttings were used to determine the presence of the fracture in these holes. The test holes were drilled at distances up to 250 ft in a radial pattern around the fractured well. In addition to fracture areal extent and orientation, sand grain size before and after fracturing, erosion of perforations and fracture thickness were studied.

INTRODUCTION

The orientation,[1,2] areal extent[3,4] and thickness[5-9] of artificially induced fractures in reservoir rock by hydraulic means have been discussed in great detail in the oil industry in recent years. Methods for initiating vertical[10] and horizontal[11] fractures have been tested in the laboratory and the field. Although the methods used give successful well stimulation, good field data on the physical characteristics of the fracture are lacking in the literature. It is recognized generally that properties of a fracture, such as thickness, sand placement in the fracture[12] and shape, may vary from reservoir to reservoir.

This paper gives data on size, orientation and sand placement in a large fracture initiated in a single plane in Sacatosa field, Maverick County, Tex. It is not intended as a speculative study; rather, it is restricted to actual field data on fracture properties. No attempt is made to prove that the same type of fracture occurs in all wells.

The field procedure was to drill 14 test holes at various locations around the fractured well. By employing several different testing techniques, the presence of the fracture and some of its characteristics were determined. These techniques as well as the results obtained are discussed in detail in this paper.

DESCRIPTION OF FRACTURE TREATMENT

N. J. Chittim Well No. 37-1, completed in the San Miguel No. 1 sand, Sacatosa field, Maverick County, Tex., was chosen for the field study. The San Miguel sand is a tight, well consolidated sandstone with an average porosity of 23 per cent. The permeability ranges from 0.1 to 10 md, with a median permeability of 2.3 md. The sand thickness averages 23 ft and is located at depths of 1,150 to 1,700 ft throughout the field.[13] The fracture treatment performed on Well 37-1 was as follows.

1. The well was drilled to a depth of 1,438 ft with native mud, and 5½-in. casing was set and cemented to the surface.

2. The casing was perforated at 1,349 ft with a fracture-initiating jet gun. This gun consists of six shots, 7/16-in. diameter in a single horizontal plane. The jets were oriented in two groups of three, 180° opposed. The perforating device was designed to initiate a fracture perpendicular to the wellbore.

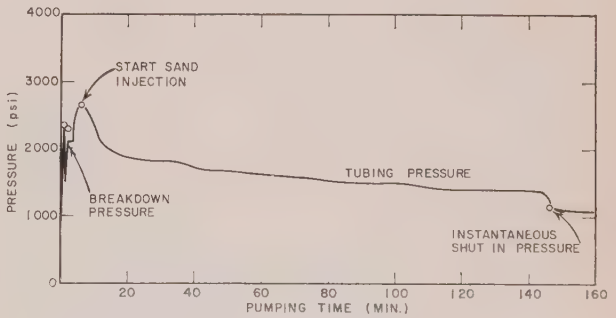

FIG. 1—PRESSURE CHART OF WELL NO. 37-1.

Original manuscript received in Society of Petroleum Engineers office Sept. 13, 1960. Revised manuscript received Feb. 13, 1961. Paper presented at 35th Annual Fall Meeting of SPE, Oct. 2-5, 1961, in Denver.

*Present address: Brown Oil Tools, Inc., Houston.

[1]References given at end of paper.

Discussion of this and all following technical papers is invited. Discussion in writing (three copies) may be sent to the office of the *Journal of Petroleum Technology*. Any discussion offered after Dec. 31, 1961, should be in the form of a new paper. No discussion should exceed 10 per cent of the manuscript being discussed.

This page of *Petroleum Transactions, AIME* follows page 294. The intervening non-Transactions pages appeared in *Journal of Petroleum Technology*.

3. Formation breakdown was obtained with lease crude oil at a pressure of 2,300 psi at the surface. Fracture pressures recorded during treatment are shown in Fig. 1.

4. After breakdown, a 1,000-gal blanket of fluid-loss-treated diesel oil was pumped ahead of the fracture fluid.

5. A mixture of 176,000 gal of diesel oil and lease crude oil treated with a fluid-loss agent was used as the treating fluid, and 270,000 lb of 20-40 mesh Poteet sand at a concentration of 1.5 lb/gal were added as the fracture propping agent.

6. Injection rates during treatment averaged 30 bbl/min.

FIELD TEST PROCEDURE

The test procedure used on the first 12 of the 14 test holes was to drill to the top of the San Miguel No. 1 sand with a native mud system. From this point to the bottom of the sand, either a rubber-sleeve core barrel or a conventional core barrel was used to core the producing sand. The formation cores obtained from this operation were examined for artificial fractures, presence of Poteet sand grains and stress areas resulting from the artificially induced fracture.

The Microlog and the Sonic log were run on several of the cored holes. The Microlog was run to obtain formation lithology data around Well 37-1. The Sonic log with the Amplitude curve was an experimental tool designed to pick up formation anomalies such as dense streaks and natural or artificial fractures.[14] This tool was run as an experimental test for correlation with other data indicating the presence of a fracture in the test holes.

During drilling and coring of each hole, samples of formation cuttings were taken from the mud stream at the surface. This test procedure was designed to obtain sand-grain data as the holes were drilled through the fracture. The sampling procedure consisted of screening the formation cuttings through a 20-40 mesh sieve, acid washing these cuttings with HCl and, then, examining the cuttings under a microscope for the presence of Poteet sand grains. A sand grain count of each sample was made, based on the number of grains of sand per gram of 20-40 mesh cuttings obtained from the screening.

The final test performed on each hole was to run a drill-stem test over the entire test zone. Initial flow pressures, final flow pressures and shut-in pressures were recorded on each well as another means of determining whether the fracture was present in the well. Fluid samples from the drill-stem test also were screened and analyzed for 20-40 mesh Poteet sand grains.

Core hole Nos. 13 and 14 were drilled to the top of the San Miguel sand, and 5½-in. casing was set at this point. The hole was loaded with lease crude oil, and drilling continued through the sand zone. While drilling with oil, samples of the formation cuttings were taken throughout the sand zone. Selected intervals of either 2 or 5 ft were drilled and all of the cuttings collected. This was accomplished by using a 40-mesh screen apparatus attached to the shale shaker. Cuttings larger than 10 mesh were caught from the shale-shaker 10-mesh screen. By flowing the effluent oil from the shale shaker upwards through the 40-mesh screen into the circulating pit, 10-40 mesh cuttings were retained in the apparatus. The 10-40 mesh cuttings were further screened down to 20-40 mesh and acid washed, dried and examined under the microscope for sand count as in previous tests.

FIELD RESULTS

PRESSURE CHART WELL 37-1

Fig. 1 shows the pressure recording of the fracture treatment in Well No. 37-1. The surface recorded pressure during breakdown was 2,300 psi. Since there was little fluid movement at this time, the hydrostatic pressure of 470 psi for lease crude oil added to this surface pressure gave a bottom-hole pressure of 2,770 psi at the perforations. The sudden increase in surface pressure on the tubing occurred when the 30-bbl blanket of low fluid-loss oil was injected ahead of the sand, and the pump rate was increased to 30 bbl/min.

After sand injection started, there was a sudden drop in treating pressure. Most of this drop in pressure may have been due to small enlargement or smoothing of the perforations by the sand. Either the pressure drop across the perforations changed as the treatment progressed or less pressure was needed for the fracture propagation as the area enlarged.

At the end of the treatment, an instantaneous shut-in pressure was recorded. The 300-lb drop in pressure was a measure of the pressure drop across the perforations. Calculating the treating pressure behind the perforations in the fracture gives a treating gradient of 1.16 psi/ft.

IMPRESSION BLOCK OF PERFORATIONS IN WELL 37-1

The perforations in this well, as described earlier, were made with a fracture-initiation gun consisting of six 7/16-in. diameter holes oriented in a single horizontal plane. The six shots are in two groups of three, each fired in opposite directions.

An oriented impression of the perforations was taken to determine (1) direction, (2) degree of erosion and (3) whether or not all perforations were open and taking fluid during the treatment. A casing-leak detector was used to obtain these impressions. This tool is an expandable rubber sleeve with a thin coating of plastic material. The tool was pressured up from the surface with a small hydraulic pump that inflated the rubber sleeve and pressured the plastic sleeve against the casing, thus taking an impression of the perforations.

Fig. 2 shows a photograph of a section of the plastic sleeve containing the six impressions.

Analysis of the plastic impressions shows: (1) all six holes penetrated the pipe, (2) only slight erosion or smoothing of the perforations took place during treatment, (3) no appreciable hole-size enlargement occurred and (4) the perforations were oriented in an east-west direction. With a pump rate of 30 bbl/min during the fracture treatment and a pumping time of 143 minutes, there was only a minor amount of perforation erosion. These results indicate that with the rate and volume used in most fracture jobs the perforations should remain relatively undamaged.

FRACTURES AND ANALYSIS

A large quantity of fracture sand was obtained on the drill-stem tests for Holes 13 and 3. Approximately 600 to 700 lb were recovered in 13, and samples of this sand were analyzed for mesh size and degree of crushing. Control tests were run also on Poteet sand

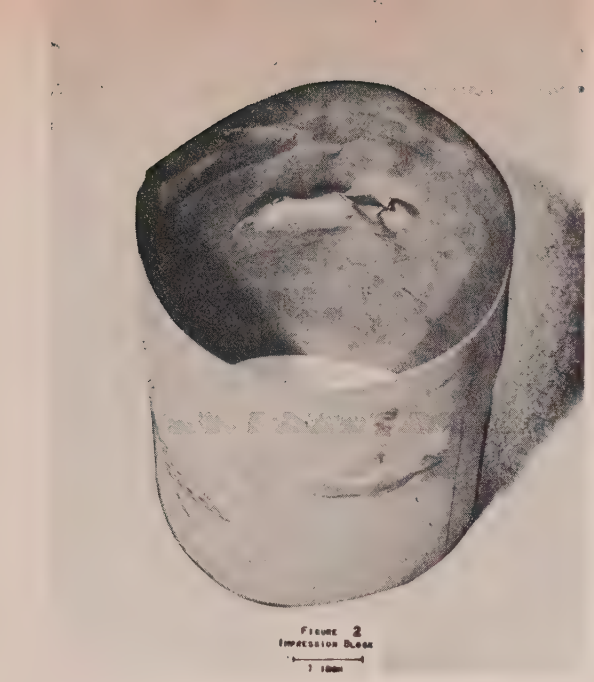

FIG. 2—IMPRESSION BLOCK.

before fracturing for correlation purposes.

Table 1 shows the results of the split sample tests of both Poteet sand before and after fracturing.

Slight variations are noted throughout the mesh range of all samples. The largest amount of crushing (7 per cent) was in the 20-40 mesh range. If crushing of sand does occur, one would expect the larger grains to be crushed first. This apparently is what happened, though the amount of crushing was only 7 per cent—much less than is often surmised. At what point during the treatment this crushing took place is not known, but there are several possibilities. Some crushing could have occurred in the pumps, while traveling down the annulus, while passing through the perforations, or in the fracture after the overburden settled down on the sand pack.

Judging from the large influx of sand into the wellbore during drill-stem testing, this portion could not have been held tightly in place by the overburden pressure. Therefore, the crushing that occurred probably was not due to the overburden pressure as much as to some other factor. In areas of the fracture where the

TABLE 1 — GRAIN-SIZE DISTRIBUTION OF POTEET SAND
20-40 MESH FRACTURE SAND

Mesh Size		Before Treatment	After Treatment
	20	1.38	1.05
20	40	88.79	81.28
40	60	7.58	13.23
60	80	1.74	2.33
80	100	0.25	.53
100	120	0.05	.22
120		0.22	1.29*

*Samples contain small amount of foreign matter from well.

sand pack is thinner and the sand grains are held more tightly by the overburden pressure, a greater degree of crushing may occur.

The ease with which 600 lb of sand flowed into the test hole 100-ft from the original well indicates that the sand probably is distributed unevenly in the fracture. This leads us to propose a "pillar-type" sand pack. The fracture is held open by "pillars" of sand. Other sand that is not held so tightly in place by the overburden is free to flow easily into the wellbore.

SONIC LOG EVALUATION

The Sonic log with the Amplitude curve was run on five of the 14 test holes as an experimental test tool. It has been observed that fractured zones sometimes cause "cycle skipping" on velocity of sound logs.[11] The cycle skippings that show up as sharp deflections to the left presumably result from absorption and reflections of a large part of the sonic energy by the fracture.

Fig. 3 shows the results of the five runs made and the depth at which an indication of a fracture was picked up. In all of the holes except Hole 7, there are definite indications of formation anomalies near the top of the San Miguel formation. These could be caused by a fracture. None of these data was used in establishing the location or depth of the fracture in the final conclusion of results in any of the test holes.

CORING

The coring operations on Holes 1 through 12 using the rubber sleeve and the conventional core barrel gave good core recovery. Numerous fractures were observed in the cores. Some of these breaks occurred during removal of the cores from the barrel. Other breaks could have been made during the drilling. A few could be correlated with sand-count data and Sonic logs and may have represented the actual fracture.

SAND-COUNT DATA

Table 2 shows the sand-count data on the 14 test wells. Also included are several development wells in

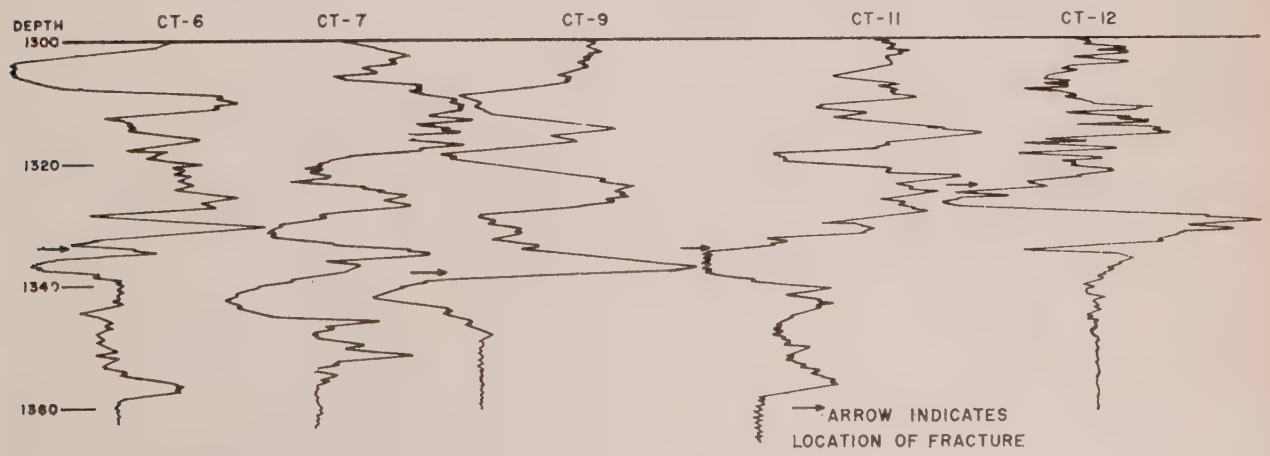

FIG. 3—SONIC LOG DATA.

TABLE 2—SAND-COUNT DATA

CT-1		CT-2		CT-3		CT-4		CT-5		CT-6	
Depth (ft)	Gr/Gm	Depth(ft)	Gr/Gm	Depth (ft)	Gr/Gm	Depth (ft)	Gr/Gm	Depth (ft)	Gr/Gm	Depth (ft)	Gr/Gm
1,329-53	Some grains but no quantitative est.	1,349-55	10 grains Poteet sand. No. grams unknown	DST circulation at 1,343	Large amount of Poteet	1,320-22	5	1,335 (C, D)	12	1,321-23 (C, D)	101
						1,322-24	5	1,336-37	13	1,325-26	46
						1,324-26	1	1,337-42	11	1,327-28	74
				1,341-43	Some Poteet	1,326-28	2	1,342-52	2	1,345-46	34
						1,328-30	2	1,352-55	10	1,353-54	20
						1,330-32	0	Circ. 1,355	10	DST	39
						1,332-34	0	DST 1,335-55	6		
						1,334-36	0				
						1,336-38	2				
						1,338-40	0				
						DST 1,322-40	80				

CT-7		CT-8		CT-9		CT-10		CT-11		CT-12	
1,332-32 (C, D)	119	1,306-08 (D)	310	DST	32	DST	62	1,322-23 (D)	85	1,318-20 (C)	8
1,333-36	55	1,312-13	276					1,328-29	93	1,323-25	23
1,336-40	61	1,321-22 (C)	106					1,334-35 (C)	71	1,325-27	14
1,340-43	37	1,324-26	105					1,336-38	19	1,330-32	6
1,343-46	35	DST 1,318-42	365					1,342 43	26	1,335-37	20
1,346-49	36							1,348-49	13	DST 1,317-42	27
1,349-52	85							1,351-52	21		
DST 1,333-52	160							1,353-54	24		
								DST Top	26		
								DST Bottom	55		

CT-13		CT-14		38-7		66-10		66-12	
1,310-15	41	1,334-36 (C)	2,550	1,348	16	778 (A)	34	348	13
1,315-20	21	1,336-38	1,515	1,358	8	848 (A)	11	723	27
1,320-30 (C)	11	1,338-40	335	1,368	4	1,481 (D)	22	807	23
1,330-32	9	1,340-42	175	1,378	20	1,491	65	1,418	23
1,332-34	5	1,342-44	100	1,388	16	1,516 (C)	10	1,433 (D)	52
1,334-36	3	1,344-46	25	1,398	0	1,522 (C)	9	1,443	46
1,336-38	6	1,346-48	60	1,408 (C)	12	1,527 (C)	9	1,453	16
1,338-40	4	1,348-50	65	1,468	6			1,463	8
1,340-42	5	1,350-54	13	1,478	0			1,476 (C)	12
1,342-44	0	1,354-58	13	1,343-53	14				
1,344-46	2	1,358-62	87	1,373-1,403	5				
1,346-48	0	1,362-66	12	1,403-33	7				
1,348-50	0	DST No. 1 1,331-46	2,900	1,433-63	0				
1,350-52	0								
1,352-56	0	DST No. 2 1,331-66	1,075						
1,356-61	1								
1,361-66	0								
1,366-71	8								
1,371-75	1,681								
DST No. 1	No solids								
DST No. 2	Large amt. of sand recovered								

(A) Olmos sand. (B) Bit change-circ. bottoms. (C) Son Miguel (first sample). (D) Top of core.

the Sacatosa field in which sand grain counts were made during drilling operations. This was done to establish a base count of Poteet-like sand grains obtained from the Olmos sand located at a depth of 600 to 900 ft. Since the Olmos sand grains are in the 20-40 mesh range and do resemble the subangular Poteet sand, this base count was necessary for a more accurate evaluation. Identification of the Poteet sand grains in the drilled solids collected in the sampling apparatus was made on the basis of shape or angularity, internal characteristics, inclusions, fracture planes and staining techniques. A comparison was made of the similarity of Poteet and San Miguel No. 1 sand grains. A distinct difference was noted in the size, shape and crystal facets of the San Miguel sand grains. All of the San Miguel sand grains are smaller than 40 mesh, with the large majority being in the 60-80 mesh range. They also are more angular in shape than the Poteet fracture sand.

A statistical average of the Poteet-like sand grains per gram of 20-40 mesh cuttings is *21*, and 95 per cent of the time the count should be below 65 grains/gm. These data from Table 2 have been used as one criterion in determining whether the fracture was or was not encountered in any specific well. Inspection of the table shows that Holes 3, 6, 7, 8, 11, 13 and 14 have high sand counts, indicating they are probably in the fracture.

FRACTURE ORIENTATION AND AREAL EXTENT

Fig. 5 is a location plot of the 14 test holes around the fractured Well 37-1. No pre-planned well-location sequence was made except for the first three holes. Test locations after these first three holes were based on the resulting data as the holes were drilled and tested. The primary purpose of this field study was to determine the direction or orientation of the fracture and its areal extent.

The shadowed holes plotted in Fig. 5 represent the holes in which sufficient data were obtained to place them in the fracture. As discussed in the general procedure earlier in this paper, several methods were used as criteria for determining whether or not the fracture was encountered. Holes 3, 4, 8, 13 and 14 are classified as in the fracture because of positive drill-stem tests. An example of a positive drill-stem test is shown in Fig. 4. Holes 6, 7 and 11 are classified as having at least one good positive test (sand count), which indicates that they penetrated the fracture.

Holes 1, 2, 5, 9, 10 and 12 gave no positive indications of being in the fracture system. That does not mean that small cracks might not have been in any or all of them. In many of the first 12 holes, a fracture could have been mudded-off easily during drilling, which would have a negative drill-stem test. It is interesting that the Sonic log indicated a fracture in Holes 9 and 12 while the other techniques gave negative results. It is also hard to accept a definite fracture in Hole 13 without assuming a probable fracture in Holes 1 and 5.

It can be seen readily from Fig. 5 that the fracture system is horizontal. Based on data to date, the major strike of the fracture is to the west. The complete fracture pattern has not been determined exactly. However, enough area has been determined positively to show as much as that calculated from the Howard

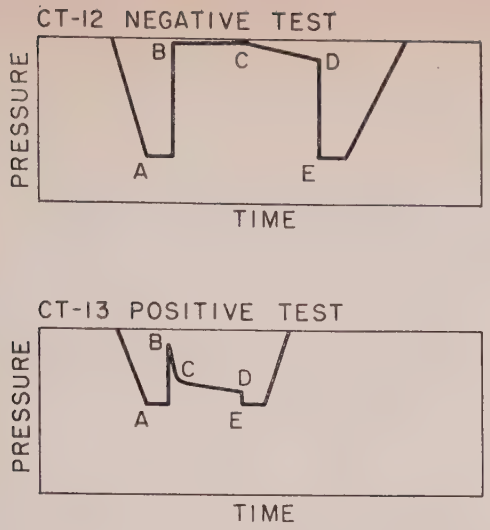

		CT-12	CT-13
A	Initial Hydrostatic Mud Pressure	711	438
B	Initial Flow Pressure	20	97
C	Final Flow Pressure	20	233
D	Final Closed In Pressure	105	380
E	Final Hydrostatic Mud Pressure	711	438

FIG. 4—COMPARISON OF POSITIVE AND NEGATIVE DRILL-STEM TEST.

FIG. 5—CHITTIM RANCH FRACTURE STUDY, MAVERICK COUNTY, TEX.: 1 IN. = 100 FT; 15° GRID.

and Fast Equation. Assuming a .2-in. fracture thickness and using fluid-loss data from actual formation cores, a fracture radius of 230 ft or a fracture area of 168,000 sq ft on one face was obtained. Further drilling might show that the fracture is considerably larger than that calculated by the equation.

Some contrasting data are noted on the wells in which the fracture was encountered. Hole 3 (located S 60° W 50 ft) and Hole 13 (N 15° W 100 ft from Well 37-1) produced large amounts of fracture sand during drill-stem testing. Holes 1 (N 50 ft) and 14 (E 100 ft) produced small quantities of sand. Since all four holes are in the fracture, the fracture width must vary, with some areas being thicker and containing a greater concentration of sand than others. Holes 1 and 3 were drilled through the sand interval with a conventional water-base mud, whereas Holes 13 and 14 were drilled through the sand with a lease crude oil. When drilling Hole 1, the fracture may have been mudded-off; and, as a result, no appreciable sand was obtained during drill-stem testing. However, in the case of Hole 3, the fracture is much wider with a higher concentration of sand grains and the drilling fluids could not plug-off this fracture as effectively. In the case of Holes 13 and 14 where the possibility of plugging-off the fracture was reduced, Hole 13 produced a large amount of sand during drill-stem testing and Hole 14 produced only a small quantity. Here again, we have the indication of a wider fracture in some areas and a thinner fracture in other areas.

DISCUSSION

Results of our test program show conclusively that the fracture formed was horizontal. It stayed within the San Miguel formation a horizontal distance of at least 250 ft.

The major portion of the fracture found thus far was west of Well 37-1. This is in the updip direction of the field and may indicate that the fracture preferentially heads toward the point of less overburden. An exception to this was in Hole 13 where the fracture definitely had traveled downward from the perforations and was in the bottom of the San Miguel formation. This was shown by the sand-count data and a drill-stem test made a few feet off bottom on this hole that also recovered a large quantity of Poteet sand.

The technique of setting casing on top of the sand to be tested and then completing open-hole was found to be very successful. This eliminated contamination from formations not under study. It also leaves a hole in position for further tests.

Pre-planning the fracture treatment will make identification much easier when drilling the test wells. Suggested techniques include using (1) radioactive sand or oil, (2) various types of propping agents that can be distinguished easily from formation sand (such as walnut shells, glass or plastic beads), (3) staining dye in the fracture fluid to color the formation sand and (4) injecting different-colored sand grains or propping agents at various intervals during treating to determine sand placement patterns and movement.

The authors would encourage further research based on these results and release of any other data that contribute to the present knowledge of fractures. An interesting subject for further research would be the orientation of a similarly created fracture at greater depth. If such a research program is undertaken, we would recommend that the fracture be prepared specifically prior to the field testing.

CONCLUSIONS

Although this paper has been limited to a presentation of the results of the tests described, the following conclusions can be made about the fracture in N. J. Chittim Well No. 37-1.

1. The fracture was horizontal.

2. The areal extent of fracture was at least as large as that calculated from the Howard and Fast equation.[4] It extended more than 250 ft from the wellbore.

3. The fracture was not uniform in all directions or in thickness.

4. The perforations were only slightly eroded during the fracturing job.

5. Fracturing sand was not changed appreciably during the fracturing job.

ACKNOWLEDGMENT

The authors wish to express their appreciation to K. H. Stimpson for the assistance given during the field tests and to R. J. Cavanaugh for his assistance in analyzing and collecting field data. Also, we wish to thank Continental Oil Co. for granting permission to publish this paper.

REFERENCES

1. Hubbert, M. King and Willis, David G.: "Mechanics of Hydraulic Fracture", *Trans.*, AIME (1957) **210,** 153.
2. McGuire, W. J., Jr., Harrison, Eugene and Kieschnick, W. F., Jr.: "The Mechanics of Formation Fracture Induction and Extension", *Trans.*, AIME (1954) **201,** 252.
3. Reynolds, J. J., Bocquet, P. E. and Coffer, Henry F.: "Conversion of Crude Oils to Low-Fluid-Loss Fracturing Fluids", *Drill. and Prod. Prac.*, API (1955).
4. Howard, George C. and Fast, C. R.: "Factors Controlling Fracture Extension", *Pet. and Nat. Gas Div.*, CIM Spring Meeting (May, 1957).
5. Davis, J. G., Reynolds, J. J. and Coffer, H. F.: "The Effect of Fluid Loss on Fracture Extension", Paper presented at SPE Fall Meeting (Oct., 1955) in New Orleans.
6. Halliburton Co.: *Fracture Guide.*
7. Dowell Div. of the Dow Chemical Co.: *Fracture Guide.*
8. The Western Co., Inc.: *Fracture Guide.*
9. Walther, H. C. and Kendig, R. L.: *Fracture Guide*, Continental Oil Co.
10. Clark, Roscoe C., Jr. and Reynolds, Jack J.: "Vertical Hydraulic Fracturing for Increasing Oil and Gas Production", *Drill. and Prod. Prac.*, API (1954).
11. Huitt. J. L.: "Hydraulic Fracturing with the Single-Point Entry Technique", *Jour. Pet. Tech.* (March, 1960) **XII,** No. 3, 11.
12. Darin, S. R. and Huitt, J. L.: "Effect of a Partial Monolayer of Propping Agent on Fracture Flow Capacity", *Trans.*, AIME (1960) **219,** 31.
13. Knutson, C. F., Timko, D. J., Bohor, B. F. and Conley, F. R.: "Characterization of the San Miguel Sandstone by a Coordinated Logging and Coring Program", Paper 1578-G presented at 35th Annual Fall Meeting of SPE (Oct. 2-5, 1960) in Denver.
14. Tixier, M. P., Alger, R. P. and Doh, C. A.: "Sonic Logging", *Trans.*, AIME (1959) **216,** 106. ★★★

Cellar Oil

M. H. GASKELL
MEMBER AIME
D. C. LINDLEY*
JUNIOR MEMBER AIME

HUMBLE OIL & REFINING CO.
HOUSTON, TEX.

INTRODUCTION

Small, steeply inclined reservoirs without natural water drives often are found associated with salt domes or other highly faulted structures. Frequently, only one well may be economically justified in these reservoirs, from which oil is produced by an expanding gas-cap drive or by a dissolved-gas drive. Although a large fraction of the oil upstructure from the well may be recovered during primary depletion, only a small fraction of the downdip oil can be produced because of gravity effects. This downdip oil has been defined as "cellar oil"[1] in contradistinction to "attic oil"[2] which is the oil above the structurally highest well in reservoirs where a natural water drive is present.

In this study, two methods of producing cellar oil by water flooding a one-well reservoir were investigated by means of a laboratory model. This model was scaled to represent a prototype reservoir having an area of 30 acres, a permeability of 500 md, and a thickness and dip of 30 ft and 30°, respectively.

One method considered, the *simultaneous injection of water and production of oil* from a single well, would require that the lower portion of the productive interval of a well be completed for water injection and the upper portion for oil production.

The other method considered, *intermittent injection,* would involve alternate injection of water into and production of oil from a single well. Injection of water into the formation would repressure the reservoir, causing gas to go back into solution. Since some of the injected water would flow updip from the well, water injection usually would be followed by a waiting period during which the water could drain from above the wellbore. Production of oil by gravity drainage and gas-cap drive could be initiated when water drainage became sufficiently complete. The amount of water produced along with the oil would naturally depend on how soon after water injection ceased that production was started. This process could be repeated in cycles until oil could no longer be produced economically.

Of these two methods, the intermittent injection technique would be simpler to put into operation since it does not require a dual completion. Also, it is probably more generally applicable than the simultaneous injection-production method. It is to be expected that in some reservoirs the rock and fluid properties would be such that practical oil-production rates could not be achieved by the simultaneous technique. However, in reservoirs where the simultaneous method will result in practical rates of oil production, it does have the advantage of permitting immediate, continuous oil production; whereas in the intermittent method, oil production is interrupted by periods of water injection and drainage.

It was the objective of this study to determine whether these two methods of cellar oil production are practical for the representative prototype investigated and to evaluate their relative merits.

DESIGN OF LABORATORY MODEL

SCALING REQUIREMENTS

The prototype reservoir and fluids were selected to have the dimensions and physical properties shown in Table 1. The laboratory model was then designed in accordance with well known scaling criteria, as discussed by Croes, *et al,*[2] except for one modification. According to Croes, *et al,* one requirement of scaling a laboratory model to a reservoir prototype is that both the relative permeabilities and dimensionless capillary pressure be the same functions of water saturation for the model and the prototype. Since unconsolidated sand packs are used in the laboratory model to represent the consolidated porous media of the prototype, it is virtually impossible to satisfy this requirement. Much of the difficulty stems from the fact that unconsolidated sands usually exhibit lower residual oil and connate-water saturations than do reservoir rocks. To satisfy the scaling requirement as nearly as possible, Perkins and Collins[4] have suggested that the relative permeabilities be re-defined as

$$k'_{rw} = \frac{k_w}{k_{wor}} \quad \text{and} \quad k'_{ro} = \frac{k_o}{k_{owr}}$$

where k'_{rw} = relative permeability to water,
k'_{ro} = relative permeability to oil,
k_{wor} = permeability to water at residual oil,
k_{owr} = permeability to oil at connate water,
k_w = effective permeability to water, and
k_o = effective permeability to oil.

A new water-saturation variable S'_w has been defined as

$$S'_w = \frac{S_w - S_{wr}}{1 - S_{or} - S_{wr}}$$

where S_w = water saturation,
S_{wr} = the connate-water saturation, and
S_{or} = the residual oil saturation.

Using these definitions, it can be shown that k'_{rw}, k'_{ro} and the dimensionless capillary pressure must be the same function of S'_w in both the model and the

Original manuscript received in Society of Petroleum Engineers office July 21, 1960. Revised manuscript received Jan. 31, 1961. Paper presented at 35th Annual Fall Meeting of SPE, Oct. 2-5, 1960, in Denver.

*Now at the U. of Houston.

[1]References given at end of paper.

TABLE 1—MODEL AND PROTOTYPE PROPERTIES

Property	Prototype	Model
Length	1,140 ft	36 in.
Thickness	30 ft	0.95 in.
Length/Thickness	38	38
Areal Extent	29.8 acres	9 sq ft
Dip	30°	30°
Porosity, per cent	30	37.9
Absolute Permeability	500 md	190 darcies
Oil Viscosity, cp	0.384	4.07
Water Viscosity, cp	0.4	4.24
Oil-to-Water Viscosity Ratio	0.960	0.960
Density Difference, gm/cc	0.346	0.4407
Interfacial Tension, dyne/cm	73	4.26
Connate Water, per cent	25	9.5
Residual Oil, per cent	15	15
Pore Volume	2,083,000 bbl	7,650 cc
Injection Rate	1,720 q (B/D)	q (cc/sec)
Time	t/241 months	t seconds

prototype. This requirement is more nearly satisfied than the requirement that conventional relative permeabilities and dimensionless capillary pressure be the same function of water saturation.

Other scaling requirements are (1) similar geometry, (2) similar initial and boundary conditions, and (3) the scaling groups

$$\frac{\mu_w k_{owr}}{\mu_o k_{wor}}, \frac{k_{wor}\,\sigma}{u\,\mu_w L}\left(\frac{\phi}{k}\right)^{\frac{1}{2}}, \text{ and } \frac{k_{wor}\,\Delta\rho g}{u\,\mu_w}$$

must have the same value in the model and prototype where

μ_w = water viscosity,
μ_o = oil viscosity,
σ = interfacial tension,
k = permeability,
ϕ = porosity,
u = a characteristic velocity,
L = a characteristic length, and
$\Delta\rho$ = the difference in density of the fluids.

Prototype and model times are related through the dimensionless group,

$$\frac{ut}{L(1 - S_{or} - S_{wr})\phi},$$

where t is time. This group must have equal values for both the model and the prototype at corresponding stages of the displacement.

These dimensionless groups are those necessary for scaling the simultaneous flow of oil and water through a porous medium. Although a gas cap was present in the experiments reported herein, as well as a residual gas saturation throughout the oil zone, the behavior of the gas phase was not scaled. In the model, as in the reservoir, the gas located in the oil zone was not free to flow and quickly went into solution in the oil when water injection caused the reservoir pressure to rise. The compressibility of the gas and the rate at which it went back into solution were not scaled to simulate reservoir behavior, but these effects are not deemed important insofar as a study of recovery of cellar oil by water flooding is concerned. Also, in the gas cap only gas was mobile and, hence, gas flow could affect the movement of oil only at the boundary between oil and gas. Because of the low viscosity and density of the gas as compared to the viscosity and density of the oil, both in the model and in the prototype, the properties of the gas phase should have little effect upon the movement of the oil boundary. Therefore, neglecting to scale gas viscosity and density, gas-oil interfacial tension and permeability to gas should have little effect upon the results.

MODEL DESCRIPTION

The model properties were chosen to satisfy the preceding scaling requirements as shown in Table 1. The clear Lucite model was a rectangular parallelepiped, 36-in. long, 36-in. wide and 0.95-in. thick. It was supported at a dip of 30° to the horizontal. With the model in this position, the well was drilled vertically through the geometric center of the sand. The model wellbore was scaled to represent a 9-in. wellbore and was perforated along the top and bottom third of its length; the middle third was plugged. The sand was a round-grained quartz (Ottawa), 20- to 30-mesh sand, packed to a permeability of 190 darcies and a porosity of 37.9 per cent. The oil phase was a white mineral oil with a density of 0.812 gm/cc and a viscosity of 4.07 cp.

The aqueous phase was a solution of sodium nitrate, glycerol, xylene sulfonate spent-caustic product and polyethylene glycol 300. The sodium nitrate was added to give a density of 1.253 gm/cc, glycerol was added to give a viscosity of 4.24 cp, and xylene sulfonate spent-caustic product and polyethylene glycol 300 were added to lower the interfacial tension to 4.26 dyne/cm. This interfacial tension only partially scaled the capillary effects, the prototype capillary effects being approximately two times as great as would be expected in a reservoir. It is believed that this lack of similitude had little effect on the gross displacement behavior. Flooding of a sand pack containing oil and connate aqueous solution with the aqueous solution resulted in a residual oil saturation of 15 per cent. Since this was the same saturation obtained in floods using ordinary water, it was concluded that this aqueous solution did not change the wettability of the sand.

INVESTIGATION OF SIMULTANEOUS INJECTION AND PRODUCTION PROCESS

For the simultaneous injection-production process, it was desired to find the effect that injection rate would have on the produced water-oil ratio. Ten experiments were performed, and in each the production rate was kept approximately equal to the injection rate. The range of rates studied was from 94 to 611 B/D for the prototype.

PREPARATION OF MODEL

At the end of each run, the sand nearest the bottom of the model had a high water saturation and a low oil saturation. Above this was a small region of sand with a high oil saturation and a low water saturation. The very top portion of the sand was predominantly saturated with gas, with low saturations of oil and water. The model was under vacuum because it had to be maintained at subatmospheric pressure at all times to prevent its being deformed.

The model was prepared for the next experiment without changing its 30° angle of dip by first withdrawing the mobile liquid from ports located along the bottom. The desired quantity of oil was then injected into these same ports. Carbon dioxide was next injected through the ports and flushed through the oil to simulate a gas saturation resulting from solution-gas drive, and the pressure was brought to approximately 7-in. Hg absolute. The oil was then allowed to drain until its final level reached the desired position. At this point the oil-rich zone contained both a connate-water saturation and residual-gas saturation, and the model was ready for the next experiment.

FLOODING PROCEDURE

The simultaneous injection and production process was carried out by injecting water into the bottom third

of the well, while oil or oil and water were produced from the top third. The production rate was controlled with a throttling valve, and the injection rate was adjusted to the same value with a constant-rate pump. The injection and production rates were controlled with a precision amounting to ±5 B/D in the prototype reservoir. When equal injection and production rates had been established, they were continued until the water-oil ratio stabilized. The model was re-prepared as described in the preceding section, and equilibrium production conditions were established at another injection rate.

RESULTS

As water was injected into the bottom third of the well, a bubble of water formed around the injection perforations and expanded upwards until it reached an equilibrium position. At very low rates, this bubble did not reach the top third of the well, which was the production interval; thus, only oil was produced. As the injection rate was increased, the bubble reached the production interval and water began to be produced. Further increases in the rate increased the water-oil ratio. The oil-production rate at first increased with increasing injection rate, but it eventually reached a maximum value and decreased thereafter.

The data from these experiments are presented in Fig. 1, in which both the water-oil ratio and the oil-production rate are shown as a function of injection rate. For the prototype studied, the first water was produced at a water-injection rate of about 125 B/D; the maximum oil-production rate, 275 B/D, occurred at an injection rate of 550 B/D.

INTERPRETATION OF RESULTS

The results of this study indicate that practical injection and production rates can be achieved in some reservoirs by the simultaneous injection-production process. In this process, there is a critical injection rate at which water is first produced and an injection rate which results in a maximum oil-production rate.

In applying this process, the optimum operating conditions would be most easily determined in the field. The field injection rate could be varied and the effect upon oil production and water-oil ratio could be observed. From the results of these tests, the most desirable injection and production rate could be selected.

INVESTIGATION OF INTERMITTENT INJECTION AND PRODUCTION PROCESS

One aspect of the intermittent injection process which was studied was the relationship between injection rate and the total time required for water injection and drainage of water away from the wellbore. Obviously, higher injection rates require less injection time. On the other hand, a high rate will cause the injected water to flow farther upstructure from the well and, hence, increase the time required for water drainage away from the wellbore. These two effects suggest the existence of an optimum rate, so a range of rates from 585 B/D to 2,340 B/D for the prototype was investigated. To determine if the optimum rate might vary with the volume of water injected, the volume injected into the prototype was varied from 2,120 to 619,000 bbl. These volumes may be compared to a total volume of floodable oil and residual gas of 650,000 bbl in the portion of the reservoir located below the well.

If it is desired to inject a given volume of water, this

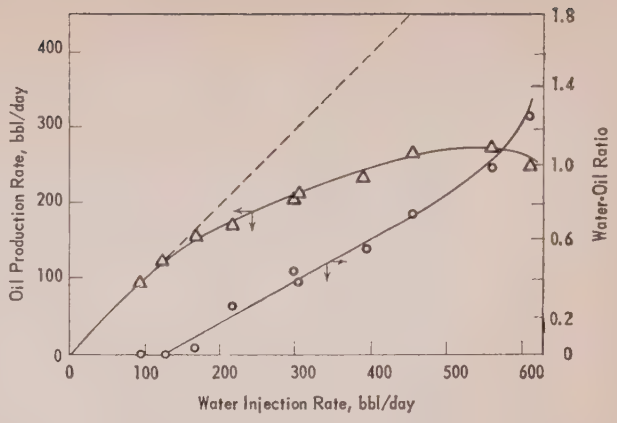

FIG. 1 — PROTOTYPE WATER-OIL RATIO AND OIL-PRODUCTION RATE VS WATER-INJECTION RATE.

injection may be accomplished in a single cycle of injection and production, or smaller volumes of water may be injected in multiple cycles. To investigate the optimum number of cycles, experiments were conducted with 1, 2 and 15 cycles.

In most of the work, it was assumed production should be deferred until the water had almost completely drained from the wellbore. In the field, it might be advantageous to start production at some earlier time. While this possibility was not systematically investigated, one experiment was conducted in which production was initiated before water drainage was complete.

FLOODING PROCEDURE

After the model was prepared for an experiment (as described previously in discussion of the simultaneous injection and production process), water was injected at a constant rate into both the upper and lower sections of the well. The pressure increased as injection progressed, causing the gas to dissolve. The pressure in the model always remained subatmospheric. After a given amount of water had been injected, the model was shut in and the water was allowed to drain into the downstructure part of the reservoir. In some experiments while the water was draining, short production tests were made to determine the water-oil ratio. When the water-oil ratio approached zero, or when the water-oil interface migrated below the bottom of the well, production was started from both the upper and lower intervals of the well. The movement of the front as a function of time and the amounts of oil and water produced were recorded. Production was continued until gas breakthrough; in some cases, the injection and production sequence was repeated.

RESULTS

The operating conditions and some of the results for the 10 experiments conducted are summarized in Table 2.

Typical patterns formed by the water injection into the well are shown in Fig. 2. The first water injected assumed an approximately circular shape around the well, but because of gravity the size of the circle on the bottom side of the model was larger than the one on the top, as shown in Fig. 2a. Initially, the centers of these circles were very near the well. As injection continued, the principal water flow was downward along the underside of the model, and oil flow was upward along the topside. When the injected water reached the

TABLE 2—SUMMARY OF RESULTS FOR INTERMITTENT INJECTION AND PRODUCTION

Experiment No.	Cycle	Injection Rate (B/D)	Injection Volume (bbl)	Injection Time (months)	Shut-in Time (months)	Production Time (months)	Production Water (bbl)	Production Oil (bbl)	Remarks
1	1	585	454,200	25.59	2.57	14.85	0	255,800	
2	1	1,015	440,800	14.32	3.94	11.12	200	308,400	
3	1	1,539	439,300	9.42	5.20	11.20	1,100	292,100	
4	1	1,575	440,200	9.22	0	11.63	79,000	235,200	Production started immediately after injection
5	1	1,929	222,200	3.80	4.93	6.55	1,100	125,900	Water-front movement not recorded
	2	1,954	223,100	3.77	5.43	9.85	1,500	187,600	
			445,300	7.57	10.36	16.40	2,600	313,500	
6	1	1,974	444,300	7.43	6.67	10.17	1,700	278,500	
7	1	2,087	619,300	9.79	12.61	345.81	41,100	539,700	Small gas leak in water injection line
8	1	2,000	599,400	9.89	10.33				No production recorded
9	1	2,342	543,800	7.66	8.74				No production recorded
				Time (days)	Time (days)	Time (days)			
10	1	1,342	2,121	1.58	19.67	10.67	129	1,818	
	2	750	2,986	3.98	19.02	7.95	216	2,749	
	3	939	2,986	3.18	17.98	10.21	238	2,575	
	4	747	2,986	4.00	18.59	9.86	129	2,814	
	5	1,239	2,986	2.41	19.97	9.00	216	2,727	
	6	1,650	2,986	1.81	20.95	9.02	346	2,640	Water reached lower limit of reservoir
	7	1,244	2,986	2.40	19.38	9.49	173	2,748	
	8	2,791	2,986	1.07	19.41	10.71	303	2,662	
	9	1,234	2,986	2.42	20.30	8.43	173	2,813	
	10	1,265	2,986	2.36	20.10	8.09	367	2,663	Water started upwards on top of sand
	11	1,736	2,986	1.72	21.94	6.30	346	2,510	
	12	2,045	2,986	1.46	22.71	6.14	281	2,467	Some production lost prior to measurement
	13	1,668	2,986	1.79	19.47	10.20	389	2,532	
	14	2,509	2,986	1.19	24.90	5.04	281	2,684	
	15	1,697	2,986	1.76	19.72	10.18	346	2,662	

lower boundary, it began filling the model from the bottom. The flow of oil updip caused a deformation of the originally circular water region around the top of the well. At the end of water injection, these effects resulted in a water pattern as shown in Fig. 2b. After injection ceased, the water continued to drain downstructure, and the oval water region disappeared from around the top of the well. This downdip drainage resulted in the pattern shown as Fig. 2c. Drainage eventually resulted in a horizontal water-oil boundary, but oil production was generally initiated before this condition was achieved.

Data shown in Fig. 3 describe for several experiments the movement of the water front above the well on the underside of the reservoir during the first cycle of operation. The ordinate in this figure is the scaled distance in the prototype reservoir from the bottom of the well to the updip water-oil contact, measured along the bottom of the reservoir. At the 585 and 1,015 prototype B/D injection rates, the water-oil boundary moved rapidly upwards a short distance above the well, but continued injection of water failed to move the boundary any higher. At greater injection rates, this stabilization of the boundary did not occur during the period of injection. As soon as injection ceased, the height of the boundary above the well began to decrease. The similar shapes of the curves after cessation of water injection show that the drainage velocity of the updip water-oil boundary was nearly independent of the location of the water-oil boundary when injection ceased. As will be shown later, this was not true for those experiments in which the total volume of water injected was almost equal to that required to flood the reservoir below the well, or those in which production was initiated before the water boundary had fallen below the wellbore.

Experiment 7 (Table 2) is an example in which the total volume of water injected (619,000 bbl) was only slightly less than that required to flood the reservoir below the well (650,000 bbl). The movement of the water-oil boundary for this experiment (2,087-B/D injection rate) is shown in Fig. 4. The solid curve is the observed experimental data, while the dashed curve is based on the boundary velocities of the runs plotted in Fig. 3. Comparison of these curves reveals that, when the volume of water injected was almost equal to the floodable volume of this reservoir, the water-oil boundary movement was slower than when smaller volumes were injected. This decrease in the boundary velocity was especially pronounced in the latter stages of the operation when almost all the reservoir below the well was full of water. Under these conditions, the water injected near the end of the injection period must flow away from the wellbore in an almost horizontal direction.

Experiment 4 is an example in which production was initiated immediately after injection was completed. The movement of the water-oil boundary for this test (1,575-B/D injection rate) is also shown in Fig. 4, along with a curve based on the boundary velocities from Fig. 3. The early initiation of production caused the boundary to fall to the bottom of the well three

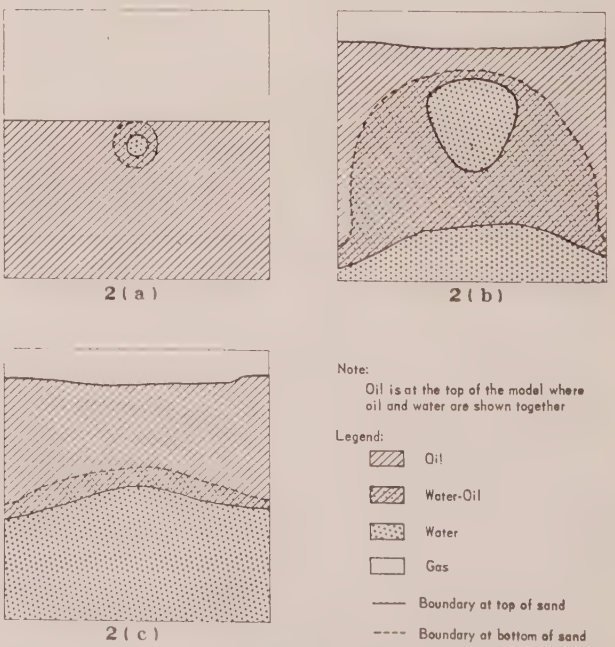

FIG. 2—DISTRIBUTION OF FLUIDS DURING INTERMITTENT INJECTION PROCESS.

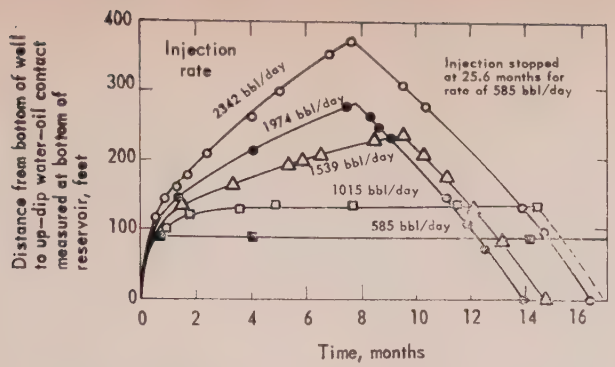
Distance from bottom of well to up-dip water-oil contact measured at bottom of reservoir, feet
Injection rate
2342 bbl/day
1974 bbl/day
1539 bbl/day
1015 bbl/day
585 bbl/day
Injection stopped at 25.6 months for rate of 585 bbl/day
Time, months

FIG. 3—WATER-FRONT MOVEMENTS ABOVE WELL.

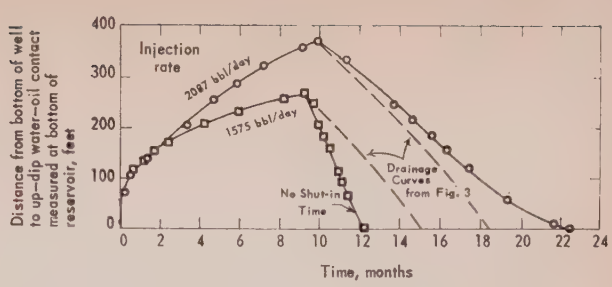
Distance from bottom of well to up-dip water-oil contact measured at bottom of reservoir, feet
Injection rate
2087 bbl/day
1575 bbl/day
Drainage Curves from Fig. 3
No Shut-in Time
Time, months

FIG. 4—WATER-FRONT MOVEMENTS ABOVE WELL.

months earlier than it would otherwise. However, about 18 per cent of the injected water was produced before the water level receded to the bottom of the well.

In Experiment 10, each cycle was completed in approximately one (prototype) month. In these cycles, the average prototype injection rate was 1,520 B/D and was continued for an average of 2.2 days/month. The well was shut in an average of 20.3 days/month to permit the injected water to drain downdip from the well, and the desired quantity of oil was produced at an average of 313 B/D. The monthly oil production, thus, was 2,740 bbl for the remaining 8.7 days in a 31-day month.

INTERPRETATION OF RESULTS

Optimum Injection Rate

In the experiments from which the data for Fig. 3 were taken, the maximum volume of water injected was 544,000 bbl, or 84 per cent of the floodable volume of the prototype reservoir. These data show that for this and smaller injection volumes the rate of movement of the water-oil boundary during drainage from above the wellbore was independent of the volume injected. From the movement of the boundary as determined from the data presented in Fig. 3, it was possible to determine the effect of injection rate on total time (injection plus shut-in) before production. This is shown in Fig. 5.

Note that the curves in Fig. 5 exhibit a minimum time at an "optimum" injection rate of about 2,050 B/D. This optimum rate is independent of the total volume of water injected, provided the volume injected is small enough that the velocity of the water-oil boundary is independent of injection volume. Note also that the injection plus shut-in time is not very sensitive to rate over the range of 1,500 to 2,340 B/D.

Effect of Volume Injected on Time For Injection Plus Shut-In

The effect of volume injected on rate of water drainage was studied by taking first-cycle data shown in Table 2 for Experiments 3, 5, 6, 7, 8, 9 and 10 and determining the minimum time for injection plus drainage per million bbl of water injection as a function of injected volume. The results of this determination are shown in Fig. 6. Although the injection rates for the points shown in Fig. 6 varied from 1,342 to 2,342 B/D, these rates are within the range (as discussed previously) where injection plus shut-in time was only slightly sensitive to rate. Hence, the effect of injection rate upon this time should only slightly affect the position of the curve. Note that the curve goes from relatively high values of time at small injection volumes to a minimum when about 84 per cent of the floodable volume of the reservoir had been injected, and then increases again with larger volumes of injection. Thus, the minimum injection plus shut-in time occurs when about 84 per cent of the floodable volume of the prototype reservoir is injected per cycle.

Effect of Average Production Rate on Number of Cycles

In some field cases, it may be necessary that a number of short injection and production cycles be used rather than one or two long cycles. For example, if the well is located high in the reservoir, the gas in the reservoir may have a smaller volume than the oil. In this case, the use of multiple cycles is required since the volume of water which can be injected per cycle is limited primarily by the volume of free gas present at the start of injection. In other situations, it may be advantageous to conduct the operation in a relatively large number of cycles to minimize any delay in production of oil and to achieve a maximum rate of return on the money invested in the project. However, when the operator has considerable freedom in selecting the number of cycles, the optimum number should be determined in each individual case. A few general comments may be made from the data obtained on the prototype studied.

The data taken during Experiment 10, shown in Table 2, represent a case in which the recovery process was carried out in a large number of monthly cycles. After allowing time for water injection and drainage, the production of 2,740 bbl of oil per month was near the maximum quantity that could be produced. Although only 15 cycles were actually completed, it is thought that the average results observed during the history studied can be applied to predict the future behavior until a volume of water injected approaches about 80 per cent of the floodable reservoir volume. By assuming that this extrapolation permits a reasonable estimate of the future injection and production behavior, 7.6 years would be required to produce 250,000 bbl of oil. In contrast, this same quantity of oil would have required 8.8 years to recover if the operation had been carried out by first injecting 439,000 bbl of water, as in Experiment 3, and then producing 2,740 bbl of oil per month. Thus, in the production of 2,740 bbl of oil per month, a large number of cycles may be preferred. This is also true for average production rates which are less than 2,740 bbl per month.

By a monthly injection, drainage and production cycle, it would not be possible to produce much more than 2,740 bbl of oil in any particular month. However, by the use of fewer cycles, an average production rate greater than 2,740 bbl of oil per month can be achieved. This is demonstrated by the data of Fig. 6

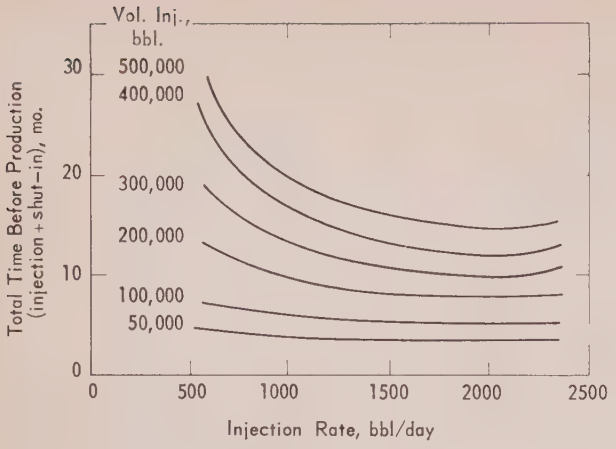

FIG. 5—EFFECT OF INJECTION RATE ON TOTAL TIME BEFORE PRODUCTION.

which show that total time for injection and shut-in decreases as the volume of water injected per cycle increases, as discussed in a previous section.

These results suggest that the number of cycles which may be optimum to recover the oil from a particular reservoir is dependent on the production schedule. If the allowable may be produced by injecting and producing each month, then this type of operation with the many cycles may be the preferred. On the other hand, if the highest average production rate is desired, then fewer and longer cycles are indicated.

COMPARISON OF SIMULTANEOUS AND INTERMITTENT INJECTION PROCESSES

Of these two methods, the intermittent injection technique is simpler to put into operation because it does not require a dual completion. It is also more generally applicable than the simultaneous injection-production method because in some reservoirs the rock and fluid properties would be such that practical oil-production rates could not be achieved by the simultaneous technique. In reservoirs where the simultaneous method would result in practical rates, this technique permits immediate oil production without delays caused by periods of water injection and drainage. Also, rock and fluid properties favorable for simultaneous injection and production would be favorable for short-cycle intermittent injection and production. Generally, the use of the intermittent process would be preferred to the simultaneous method.

CONCLUSIONS

On the basis of experiments performed on a laboratory model scaled to represent a cellar oil reservoir, the following conclusions have been reached for the *reservoir studied*.

1. In this reservoir cellar oil can be recovered from a single well by water injection using either simultaneous water injection and oil production or intermittent water injection and oil production.

2. In the simultaneous injection and production method, there is a critical injection rate below which no water is produced. As the injection rate is increased above the critical, the rate of oil production increases initially, but eventually an injection rate is reached at which maximum oil production is obtained.

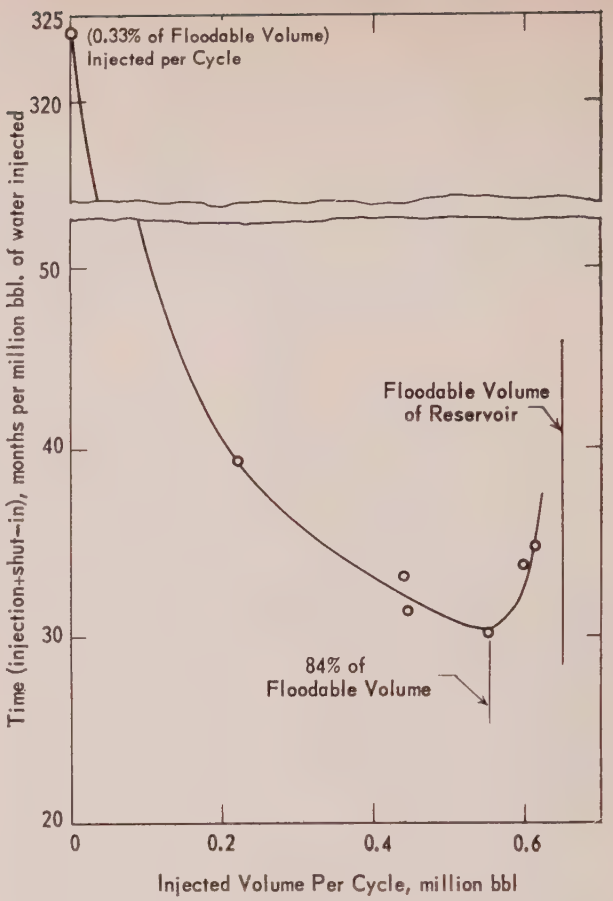

FIG. 6—EFFECT OF VOLUME INJECTED ON TIME FOR INJECTION AND DRAINAGE.

3. In the intermittent injection and production method, the minimum time (injection plus shut-in time) per million bbl of injected water occurs when the volume injected per cycle is equal to about 84 per cent of the floodable volume. For any given volume of water injected, the time for injection plus shut-in is insensitive to injection rate over a range of 1,500 to 2,340 B/D.

REFERENCES

1. McGhee, Ed: "Left-Over Oil 'Rescued' on Gulf Coast", *Oil and Gas Jour.* (1959) **57**, No. 17, 62.

2. van der Poel, C. and Killian, J. W.: "Attic Oil", Paper No. 919-G presented at 32nd Annual Fall Meeting of SPE in Dallas (Oct. 6-9, 1957).

3. Croes, G. A., Geertsma, J. and Schwarz, N.: "Theory of Dimensionally Scaled Models of Petroleum Reservoirs", *Trans.*, AIME (1956) **207**, 118.

4. Perkins, F. M. and Collins, R. E.: "Scaling Laws for Laboratory Flow Models of Oil Reservoirs", *Trans.*, AIME (1960) **219**, 67. ★★★

The Use of Alternating Flow to Characterize Porous Media Having Storage Pores

C. R. STEWART
A. LUBINSKI
K. A. BLENKARN
MEMBERS AIME

PAN AMERICAN PETROLEUM CORP.
TULSA, OKLA.

ABSTRACT

Storage porosity has been considered one of the important pore geometry characteristics of heterogeneous-porosity limestones. Storage pores are only containers for fluids, in contrast to flow channel pores which both contain fluids and provide continuity for fluid flow. The concept of another geometry characteristic, "porostriction", is presented as a second pertinent variable in describing limestone pore space. In simple terms, porostriction is a measure of the flow resistance between storage and flow channel pores.

Alternating-flow core-testing theory provides flow relationships which can be used to divide the pore space of heterogeneous-porosity media into flow channel and storage pores and to measure the "porostriction" of the latter. Experimental application of this theory to naturally occurring heterogeneous limestones shows that "porostriction" and the ratio of storage to flow channel pores can be estimated.

Porostriction and porosity ratio are microscopic characteristics which should influence oil-recovery efficiencies during certain types of displacement processes. A knowledge of pore geometry should be valuable in designing or selecting the most effective oil-recovery process for heterogeneous limestones containing storage porosity.

INTRODUCTION

The primary and secondary recovery of oil from limestone (carbonate) reservoirs has been and will continue to be a major source of the world's supply of petroleum. Oil recovery from this type of formation is strongly influenced by the size, shape and arrangement of the pore spaces which hold the formation fluids. Therefore, it is expected that better knowledge of pore geometry would lead to design of more effective recovery processes.

The concept of storage and flow channel pores has been presented as an important characteristic of limestone porosity.[1] In this concept, storage pores are only containers for fluids, whereas flow channel pores are those pores which both contain and transmit the fluids. The work reported herein involves the concept of an additional pore characteristic called "porostriction". This characteristic can be visualized as the flow resistance between the storage and flow channel pores. This resistance is an important pore geometry characteristic because it determines how easily gas and oil can replenish fluids removed from the flow channel pores.

Fatt and co-workers at the U. of California have studied the effect of storage porosity and a factor similar to porostriction on transient-flow response of models of porous media during a pressure build-up or drawdown test.[2-5] These models consisted of porous sandstone cores with artificially simulated storage pores. It is the purpose of this paper to describe tests which permit the storage porosity and porostriction of actual reservoir core samples to be estimated. The tests used for this purpose involved *not* transient tests but, rather, an alternating-flow technique in which pressure and flow are varied according to a sine-wave relationship. This technique may offer advantages over transient methods.

THE POROSTRICTION CONCEPT

Before discussing alternating-flow (A.F.) tests in core samples, it is necessary to define the porostriction parameter. For this purpose attention is focused upon an elemental volume v representative of a porous medium having both flow channel pores and restricted-access storage pores. For such an elemental volume, it is considered that the storage porosity is combined to form a single pore and that the access into the storage porosity may be represented by a single capillary tube connecting the single pore to the flow channels of the elemental volume. Let the radius of the capillary tube be designated as R_c and its length as L_c. When fluid flows into or out of the pore, the following equation (Poiseuille's law) relates flow rate q to pressure drop Δp, and the physical characteristics of the tube and the fluid of viscosity μ.

$$q = \Delta p \frac{\pi R_c^4}{8 \mu L_c} \quad . \quad . \quad . \quad . \quad . \quad . \quad . \quad . \quad . \quad . \quad . \quad (1)$$

The ratio q over Δp may be described as the fluid conductivity of the tube in the model corresponding to the rock volume v. The access into storage porosity in the medium can be described in terms of the conductivity per unit volume of medium, which may be expressed as

$$\frac{q}{v \Delta p} = \left(\frac{\pi R_c^4}{8 v L_c} \right) \frac{1}{\mu} = \frac{F}{\mu} \quad . \quad . \quad . \quad . \quad . \quad . \quad . \quad . \quad (2)$$

The factor in parentheses, designated F, is a dimension-

Original manuscript received in Society of Petroleum Engineers office Oct. 30, 1960. Revised manuscript received March 15, 1961.

[1]References given at end of paper.

less parameter depending only on properties of the medium and not upon the viscosity μ of the contained fluid. The parameter F is not, however, the most relevant measure of access to storage porosity. The A.F. flow behavior of a medium depends upon the ratio of conductivity in the flow channels to the conductivity from flow channels into storage pores. For example, if the conductivity of the flow channels (described in terms of permeability) is much lower than that to the storage pores, then one may see intuitively that conductivity to the storage pores will exercise little influence on the flow behavior of the medium. For a core of area A, length L and permeability k, the ratio of flow-channel conductivity to storage-pore-access conductivity is

$$\frac{\frac{kA}{\mu L}}{\frac{FLA}{\mu}} = \frac{k}{FL^2} = X \quad . \quad . \quad . \quad . \quad . \quad . \quad . \quad . \quad . \quad . \quad (3)$$

The dimensionless ratio X, the porostriction number which determines the flow behavior of a core, depends on the length of the core and, therefore, is not a property of the medium. On the other hand, the property XL^2 does not depend on the size of the core.

$$XL^2 = \frac{k}{F} = S \quad . \quad . \quad . \quad . \quad . \quad . \quad . \quad . \quad . \quad . \quad (4)$$

Property S is termed "porostriction" and is the fundamental property of the medium, defining the restriction of access into storage porosity. When S is large, access into storage pores is relatively restricted. When S is small, access is relatively free. It is noted that porostriction S has dimensions of length squared.

ALTERNATING FLOW IN A CORE SAMPLE

If the pressure at one end of an air-saturated core sample is alternately increased above and decreased below the pressure at the opposite end, air will flow back and forth between the ends of the sample. When such a pressure wave is applied to one end of a core and the resulting flow from the other end (or open end) of the core is observed, several facts are evident. Over a certain range of frequencies, a measurable quantity of air will flow out of and then into the open end of the core. The volume which moves at the open end of a given core sample will depend upon the frequency and the maximum pressures reached during the cycle. Also, the time at which maximum flow volume occurs will be somewhat later than the time of maximum pressure at the closed end. This time lag (see time lag, Fig. 1) will change as the frequency changes. For any particular value of pressure level and frequency applied, what happens at the open end will also depend upon certain core characteristics—that is, permeability, porosity, porostriction and the ratio M of storage porosity to total porosity.

The following equations define the A.F. response of a core sample in terms of measured quantities.

$$\text{Dimensionless Amplitude Response} = \rho = \frac{V_m}{2AL\phi} \times \frac{P_a}{P_m} \quad . \quad . \quad . \quad . \quad . \quad . \quad . \quad . \quad . \quad . \quad . \quad . \quad . \quad (5)$$

$$\text{Phase Response, degrees} = \Psi = \frac{\Delta T}{T} \times 360 \quad . \quad . \quad (6)$$

where ϕ = core porosity, fraction,
L = core length, cm,
A = core cross-sectional area, cm^2,

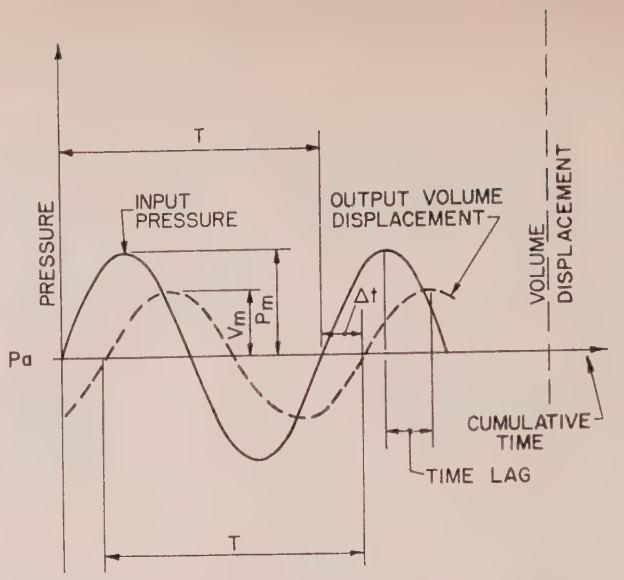

FIG. 1—ALTERNATING-FLOW CORE TESTING—INPUT PRESSURE VS OUTPUT CORE RESPONSE.

P_a = atmospheric pressure, atm,
P_m = maximum pressure above or below atmospheric, atm,
V_m = ½ of the volume of air moving out of or into the open end of the core sample, cc,
T = time for one complete pressure wave, called the *period*, seconds, and
ΔT = difference between the time at which zero pressure occurs at the closed core end and the time at which maximum velocity, or zero displacement, of air coming out of open end of core is reached. The time of zero pressure is the time at which the pressure cycle is changing from above to below atmospheric pressure.

The theoretical response equations for a hypothetical core can be derived for various proportions of flow-channel porosity and storage porosity and for various degrees of porostriction. Such equations, derived in the Appendix, have been solved for S/L^2 values of 0.2, 1.0, 2, 10 and 20, and M values of 0, 0.2, 0.4, 0.6, 0.8 and 1. Fig. 2 presents an example of the computed theoretical relationship between the dimensionless amplitude response ρ and Ψ for the previous M values at $S/L^2 = 0.2$.

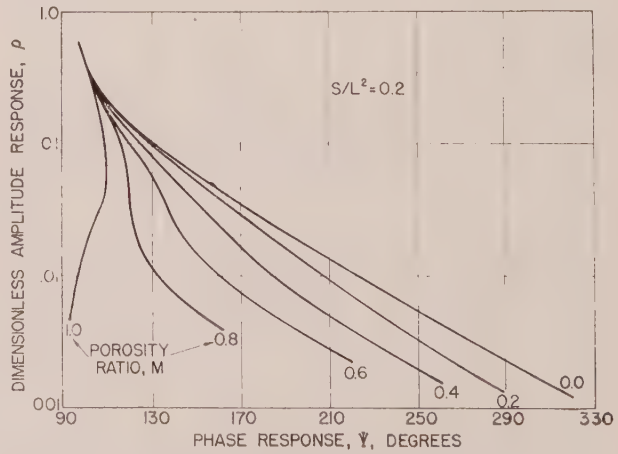

FIG. 2—ALTERNATING-FLOW CORE TESTING—THEORETICAL CORE RESPONSE.

EXPERIMENTAL APPARATUS AND PROCEDURE

Thirteen limestone core samples were selected for testing. These samples varied in diameter from 2 to 3½ in. and from 4 to 19 in. in length. The cores were taken from oil-producing formations, except for the Cordova outcrop sample. Six of the samples previously had been subjected to external and solution-gas-drive tests and showed differences between solution and external gas-drive performance. This difference in performance indicated the presence of storage porosity.[1]

Fig. 3 presents a schematic diagram of the test apparatus. Each sample was mounted in a rubber diaphragm and placed in a steel core cell where annulus pressure was applied for a seal. The pump which supplied the air pressure wave was a hydraulic cylinder containing an "O"-ring sealed piston. The frequency of the pressure wave was controlled by the use of a hydraulic drive. The Scotch yoke attached to the air pump was necessary to approximate a sine-wave relationship between pressure and time.

The open end of the core was connected to a calibrated glass tube containing a soap bubble. The tube, manometer and an electric timer were mounted together. The input pressure and output response of the core vs time thus could be observed visually or recorded by use of a motion picture camera.

To perform an A.F. test, the input pressure apparatus was started and adjusted to a predetermined time period or frequency. After a stabilized input pressure wave was obtained, the following data were observed and recorded: (1) position of the soap bubble in the calibrated tube vs time; (2) variation in pressure of the input system vs time; and (3) value of the maximum pressure reached, above and below atmospheric pressure.

The preceding data were obtained for a number of different pressure-wave periods covering a range of 3 to 2,000 seconds.

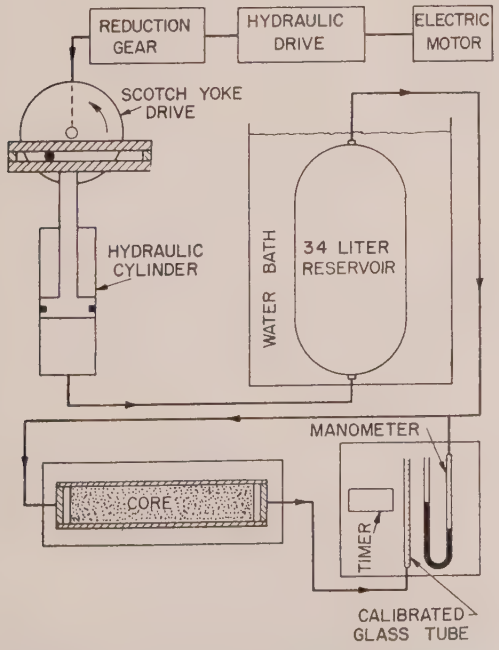

FIG. 3—ALTERNATING-FLOW CORE TESTING—SCHEMATIC DIAGRAM OF TESTING APPARATUS.

TEST RESULTS

The previously described test data were plotted as a function of cumulative time. Fig. 1 presents a schematic drawing typical of the test results. From such a pilot, the values of (1) period T in seconds, (2) displacement amplitude V_m in cubic centimeters, (3) pressure amplitude P_m in atmospheres and (4) time lag ΔT in seconds, were determined. Next, these basic data were used to calculate the dimensionless amplitude and the phase response (Eqs. 5 and 6). The relationship between amplitude and phase response for each sample then was expressed in graphical form. Typical results are shown in Fig. 4.

Porostriction number and porosity ratio for the core samples were estimated by comparing (using an overlay technique) the individual experimental curves of Fig. 4 with theoretical response curves such as those of Fig. 2. The estimates of these properties for six core samples are presented in Table 1. The other seven samples showed no measurable porostriction. Values of porostriction S shown in this table were calculated from the core length and porostriction number. These heterogeneous-porosity limestone core samples showed porosity ratios M varying from 0.25 to 0.6, porostriction numbers S/L^2 varying from 0.2 to 15, and porostrictions S varying from 12 to 6,000 cm².

DISCUSSION

The theory and experimental work presented in this paper pertain to conditions of single-phase flow in a core sample. Based upon the same concepts, the authors developed a radial alternating-flow theory to describe single-phase flow in a reservoir around a well. The following observation was made from study of the alternating-flow response of a well as predicted by this radial theory.

For permeabilities of the order of 0.1 md or greater, porostriction values less than 10,000 cm² do not influence the alternating-flow response of a well for alternating-flow periods greater than a few hours. But the producing performance of a well is described in terms of months or years and is closely related to alternating-flow responses having alternating-flow periods on the order of months or years. Thus, it seems that porostriction values measured on core samples, such as the

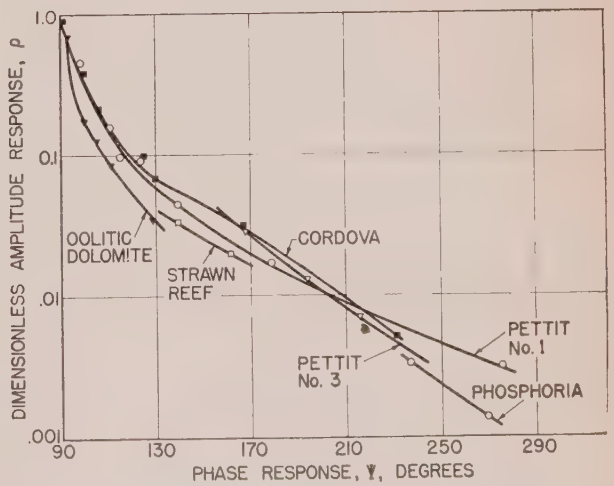

FIG. 4—ALTERNATING-FLOW CORE TESTING—EXPERIMENTAL CORE RESPONSE.

TABLE 1—ESTIMATION OF POROSTRICTION, POROSTRICTION NUMBER AND POROSITY RATIO BY COMPARISON OF EXPERIMENTAL RESPONSE WITH THEORETICAL RESPONSE

Core	Core Length (cm)	Air Perm. (md)	Porosity (per cent)	Porostriction No., S/L^2	Porostriction S (cm²)	Porosity Ratio, M
Cordova Shellstone*	24.5	36.0	26	10	6,000	0.30
Pettit Lime Wise No. 1	9.3	8.5	19	15	1,300	0.30
Pettit Lime No. 3	7.6	2.0	13	0.2	12	0.25
Oolitic Dolomite 3443-GA	12.6	33.8	11	10	1,600	0.60
Strawn Reef X-43	21.6	6.0	20	1.0	420	0.50
Phosphoria 3601-J	21.6	4.0	13	0.2	94	0.30

*Outcrop sample.

values in Table 1, cannot affect the single-phase producing performance of a well.

When considering two-phase flow, one can expect the microscopic porostriction and porosity-ratio characteristics measured on core samples to influence reservoir performance. Capillary forces influence the location and movement of fluids in two-phase flow, and these forces depend upon microscopic pore characteristics. Porosity ratio (a measure of the relative amount of restricted-access porosity) and porostriction (measure of the restriction) are characteristic of pore geometry and, therefore, are parameters which should be related to the microscopic oil-recovery efficiency during some types of two-phase displacement processes.

It is expected that a correlation connecting a given displacement process to porosity ratio and porostriction will provide useful insight into the nature of that process. At present, however, no definite relationship has been evident between porostriction or porosity ratio and laboratory oil-recovery perfomance. An unsuccessful attempt was made to correlate laboratory-observed differences in oil recovery by solution-gas drive as compared to external-gas drive[1] with porosity ratio and porostriction. This attempt was motivated by the speculation that increased oil recovery by solution-gas drive is due to formation and expansion of gas bubbles in the storage pores, such pores being by-passed during external-gas drive.

Although this described attempt at correlation was not successful, one might expect a correlation of other recovery processes with porosity ratio and porostriction measured on cores. For this reason, further attempts should be made to establish relations between recovery processes and the porosity ratio and porostriction combination.

For example, consider a water drive in a water-wet limestone which contains restricted-access storage pores.* Recovery of oil from this part of the porosity results when these pores imbibe water contained in the flow channel pores. If the rate of advance of water in the flow channel pores is equal to or less than the rate of advance in the storage pores, then the most favorable recovery conditions will exist. If the rate of water advance in the flow channel pores is greater than this imbibition rate, then some oil in the storage pores may be unrecoverable.

For this second case, the storage pores can become surrounded by water. Any further removal of oil by water imbibition into the storage pores will be opposed by countercurrent flow of oil into the flow channel pores. This type of oil-displacement process is much slower than for the first case where oil alone flows from the storage pores. It is believed that the rate of water imbibition into the storage pores will depend in some measure on the porostriction. Therefore, it would appear that the characteristics of porostriction and porosity ratio could determine the performance of a water flood.

This same line of reasoning also would predict that the performance of a wettability-reversal flood of an oil-wet formation, such as proposed by Wagner and Leach,[6] also could depend upon porostriction and porosity ratio. Intuitively, it also might be expected that the length of the mixing zone and, therefore, solvent requirements during a miscible-fluid injection program could be influenced by porostriction and porosity ratio.

Brigham, *et al*,[7] have observed differences in mixing during miscible floods in porous media. These investigators believe that these differences in mixing indirectly are a measure of the microscopic inhomogeneities of porous media. Therefore, since porostriction and porosity ratio are microscopic characteristics of inhomogeneous reservoir rock, they should influence mixing during a miscible-fluid drive. The larger the porostriction and porosity ratio, the larger should be the length of the mixing zone.

SUMMARY AND CONCLUSIONS

1. The proportion of storage porosity to total porosity and the porostriction of the storage porosity are considered to be two significant pore-geometry characteristics of heterogeneous limestones.

2. Alternating-flow core tests provide a method for estimating porostriction and the ratio of storage porosity to total porosity in reservoir-rock core samples.

3. Porostrictions and porosity ratios in samples from limestone producing formations varied from 12 to 1,600 cm² and from 0.25 to 0.6, respectively.

4. No correlation was found between the combination of porostriction and porosity ratio and laboratory gas-drive oil recoveries. However, further efforts should be made to establish correlations applicable to other recovery processes such as water drives or miscible-fluid injection.

NOMENCLATURE**

q = flow rate through capillary tube connecting storage pore to flow channel
Δp = pressure drop in capillary tube connecting storage pore to flow channel
R_c = radius of capillary tube connecting storage pore to flow channel
L_c = length of capillary tube connecting storage pore to flow channel
μ = fluid viscosity
v = a volume of rock
F = a dimensionless parameter
L = length of a core, cm
A = area of a core, cm²
k = permeability of a core
X = a dimensionless ratio

*In this example, the more realistic concept of a storage pore with many openings applies.

**Symbols defined here appear in the body of the paper, and appropriate dimensions are indicated in results which call for substitution of measured quantities. The meanings of symbols in the Appendix may best be understood from the context where they appear.

S = porostriction, cm²
M = the ratio of storage porosity to total porosity
ρ = dimensionless amplitude response
V_m = ½ of the volume of air moving out of or into the open end of a core sample, cc
ϕ = core porosity, dimensionless
P_a = atmospheric pressure, atm
P_m = maximum pressure above or below atmospheric, atm
Ψ = phase response, degrees
T = the period of a pressure wave, seconds
ΔT = the difference between the time at which zero pressure occurs at the closed end of the core and the time at which maximum velocity, or zero displacement, of air coming out of the core is reached, seconds

REFERENCES

1. Stewart, C. R., Hunt, E. B., Jr., Schneider, F. N., Geffen, T. M. and Berry, V. J., Jr.: "The Role of Bubble Formation in Oil Recovery by Solution Gas Drives in Limestones", *Trans.*, AIME (1954) **201**, 294.
2. Fatt, I.: "A Demonstration of the Effect of 'Dead-End' Volume on Pressure Transients in Porous Media", *Trans.*, AIME (1959) **216**, 449.
3. Goodknight, R. C.: "An Investigation of Pressure Transients in Porous Media with Sinks", MS Thesis, U. of California, Berkeley (January, 1960).
4. Goodknight, R. C., Klikoff, W. A., Jr. and Fatt, I.: "Non-Steady-State Fluid Flow and Diffusion in Porous Media Containing Dead-End Pore Volume", *Jour. Phys. Chem.* (Sept., 1960) **64**, 74.
5. Klikoff, W. A., Jr.: "Pressure Transients in Porous Media with 'Dead-End' Pore Volume", MS Thesis, U. of California, Berkeley (June, 1960).
6. Wagner, O. R. and Leach, R. O.: "Improving Oil Displacement Efficiency by Wettability Adjustment", *Trans.*, AIME (1959) **216**, 65.
7. Brigham, W. E., Reed, P. W. and Dew, J. N.: "Experiments on Mixing by Fluid Flow in Porous Media", *Soc. Pet. Eng. Jour.* (March, 1961) 1.
8. Kimbark, E. W.: *Electrical Transmission of Power and Signals*, John Wiley & Sons, Inc., N. Y. (1949).

APPENDIX

In deriving the theoretical equations for the alternating-flow (A.F.) response of porostricted core, the fluid-flow system is described in terms of the analogous alternating-current (A.C.) electrical transmission line. This is done because the mathematical techniques of transmission-line theory are well developed.*

The lumped-parameter model of an inductionless transmission line** is shown in Fig. 5(a) in which R represents the series resistance per unit length, G represents the shunt conductance per unit length, and C represents the shunt capacitance per unit length. The behavior of such a transmission line is described in terms of two parameters:

the *propagation constant* γ,

$$\gamma = \sqrt{RG + i\omega RC} \; ; \quad . \quad . \quad . \quad . \quad . \quad . \quad . \quad . \quad (7)$$

and the *characteristic impedance* Z_c,

$$Z_c = \sqrt{\frac{R}{G + i\omega C}} = \frac{R}{\gamma} \quad . \quad . \quad . \quad . \quad . \quad . \quad . \quad . \quad (8)$$

*See Chapter 6 of Ref. 8.

**An inductionless line is studied in anticipation of the neglection of fluid-inertia effects in the description of the flow system. Theoretical studies showed that, for all of the tests reported in this paper, such a neglection is reasonable.

The analogy of an A.F. core test is a transmission line of length L subjected to an A.C. steady-state voltage at the input or sending end, the output or receiving end being short-circuited. For such a line, the sending-end voltage E_S and the receiving-end current I_R are related, according to Eqs. 6 through 19 of Ref. 8, by the following equation.

$$\frac{I_R}{E_S} = \frac{2}{Z_c} \frac{1}{e^{\gamma L} - e^{-\gamma L}} = \frac{2}{RL} \frac{\gamma L}{e^{\gamma L} - e^{-\gamma L}} \quad . \quad . \quad (9)$$

It is convenient to separate γ into real and imaginary parts,

$$\gamma = \alpha + i\beta \quad . \quad . \quad . \quad . \quad . \quad . \quad . \quad . \quad . \quad . \quad . \quad (10)$$

Then, Eq. 9 becomes

$$\frac{I_R}{E_S} = \frac{1}{RL} \frac{\alpha L + i\beta L}{\sinh \alpha L \cos \beta L + i \cosh \alpha L \sin \beta L} \quad . \quad . \quad . \quad . \quad . \quad . \quad . \quad . \quad . \quad . \quad . \quad (11)$$

Written in terms of an amplitude ratio D and a phase angle δ, the response I_R/E_S becomes

$$\frac{I_R}{E_S} = \frac{D}{RL} e^{i\delta} \quad . \quad . \quad . \quad . \quad . \quad . \quad . \quad . \quad . \quad . \quad . \quad (12)$$

where

$$D = \sqrt{\frac{(\alpha L)^2 + (\beta L)^2}{\sinh^2 \alpha L \cos^2 \beta L + \cosh^2 \alpha L \sin^2 \beta L}} \; , \quad . \quad . \quad . \quad . \quad . \quad . \quad . \quad . \quad . \quad . \quad . \quad . \quad (13)$$

and

$$\cot \delta = \frac{\alpha L \sinh \alpha L \cos \beta L + \beta L \cosh \alpha L \sin \beta L}{\beta L \sinh \alpha L \cos \beta L - \alpha L \cosh \alpha L \sin \beta L} \quad . \quad . \quad . \quad . \quad . \quad . \quad . \quad . \quad . \quad . \quad . \quad . \quad (14)$$

The time-honored, lumped-parameter electrical analogy to flow through a permeable core is shown in Fig. 5(b). In that figure the series resistors represent the compressibility of fluid in the pores. Fig. 5(c) depicts

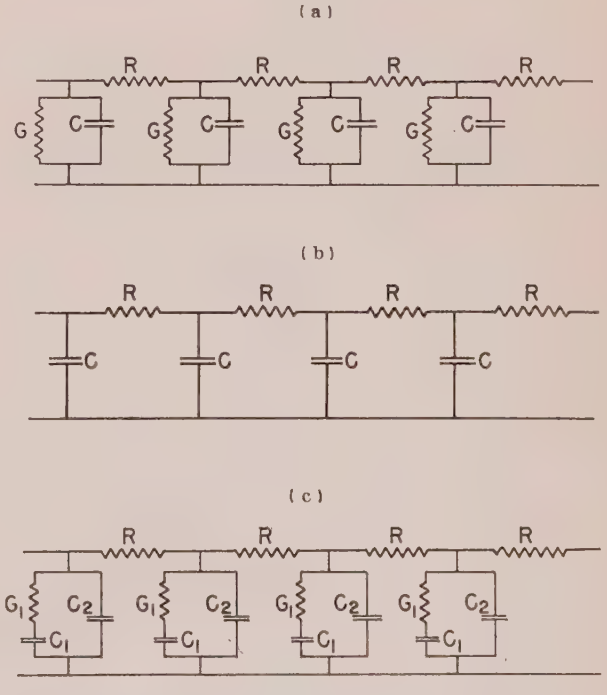

FIG. 5—(a) INDUCTIONLESS ELECTRICAL TRANSMISSION LINE; (b) CONVENTIONTIONAL ELECTRICAL ANALOGY TO FLUID FLOW IN A CORE; AND (c) ELECTRICAL ANALOGY TO FLUID FLOW IN A POROSTRICTED CORE.

the electrical analogy to flow in a core in which access to a part of the pore space is restricted, that is, where there is porostriction. Each characteristic lump in the network of Fig. 5(c) has two shunt capacitors. The capacitors designated C_2 represent the compressibility of fluid in the flow channel pores, and those designated C_1 represent the compressibility of fluid in restricted-access storage pores. The access into the storage pores is represented by the conductance G_1 of the resistors in series with capacitors C_1. If the lumped parameters are considered to relate to a unit length of a uniform transmission line, then the table of analogs (Table 2) may be compiled.

The last analog in Table 2 is obtained by noting that the total conductivity to porostricted porosity is FAL/μ. But from Eq. 4,

$$F = \frac{k}{S} \quad . \quad . \quad . \quad . \quad . \quad . \quad . \quad . \quad . \quad . \quad . \quad . \quad (15)$$

Hence, conductivity per unit length is

$$\frac{FAL/\mu}{L} = \frac{kAL/\mu S}{L} = \frac{kA}{\mu S} \quad . \quad . \quad . \quad . \quad . \quad . \quad (16)$$

In applying the response formulas (Eqs. 13 and 14) to the analog of interest, it must be recognized that the transmission line in Fig. 5(c) is not the same as that in Fig. 5(a). The line in Fig. 5(c), however, may be considered to be of the type in Fig. 5(a) if the parameters of the two systems are related by the following equations.

$$G = \frac{G_1}{1 + \left(\frac{G_1}{\omega C_1}\right)^2} \quad . \quad . \quad . \quad . \quad . \quad . \quad . \quad . \quad . \quad (17)$$

$$\omega C = \frac{G_1}{1 + \left(\frac{G_1}{\omega C_1}\right)^2} \left\{ \left(\frac{G_1}{\omega C_1}\right) + \frac{\frac{C_2}{C_1}}{\left(\frac{G_1}{\omega C_1}\right)} \left[1 + \left(\frac{G_1}{\omega C_1}\right)^2 \right] \right\} \quad . \quad . \quad . \quad . \quad . \quad . \quad . \quad (18)$$

The first step in transforming electrical response expressions to the A.F. core system is to note the following analogs.

$$\frac{C_2}{C_1} \sim \frac{1 - M}{M} \quad . \quad . \quad . \quad . \quad . \quad . \quad . \quad . \quad . \quad . \quad . \quad (19)$$

$$\frac{G_1}{\omega C_1} = \frac{G_1^*}{\frac{2\pi}{T} C_1} \sim \frac{\frac{Ak}{\mu S}}{\frac{2\pi}{T} \times \frac{AM\phi}{P_a}} = \frac{\tau L^2}{MS} \quad . \quad . \quad (20)$$

where dimensionless period τ has been defined as

$$\tau = \frac{Tk P_a}{2\pi L^2 \mu \phi} \quad . \quad . \quad . \quad . \quad . \quad . \quad . \quad . \quad . \quad . \quad (21)$$

Then Eqs. 19 and 20 may be substituted into Eqs. 17 and 18, and the resulting expression then may be substituted into Eq. 7 to find the analog of γ. Separation of γ into real and imaginary parts according to Eq. 10 leads to the following analogs for αL and βL.

$$\alpha L \sim \sqrt{\frac{M}{2\tau}} \sqrt{\frac{+\left(\frac{MS}{\tau L^2}\right) + \sqrt{\left(\frac{MS}{\tau L^2}\right)^2 + b^2}}{\left(\frac{MS}{\tau L^2}\right)^2 + 1}}, \quad . \quad . \quad . \quad . \quad . \quad . \quad . \quad . \quad . \quad . \quad . \quad (22)$$

and

$$\beta L \sim \sqrt{\frac{M}{2\tau}} \sqrt{\frac{-\left(\frac{MS}{\tau L^2}\right) + \sqrt{\left(\frac{MS}{\tau L^2}\right)^2 + b^2}}{\left(\frac{MS}{\tau L^2}\right)^2 + 1}} \quad . \quad . \quad . \quad . \quad . \quad . \quad . \quad . \quad . \quad . \quad . \quad (23)$$

where

$$b = 1 + \frac{1 - M}{M}\left[\left(\frac{MS}{\tau L^2}\right)^2 + 1\right] \quad . \quad . \quad (24)$$

Since $R \sim \frac{\mu}{kA}$, the A.F. response of a core may be written, according to Eq. 12.

$$\frac{Q_o}{P_i} = \frac{D}{\frac{\mu L}{kA}} e^{i\delta}, \quad . \quad . \quad . \quad . \quad . \quad . \quad . \quad . \quad . \quad . \quad (25)$$

or

$$Q_o = P_i \frac{D}{\frac{\mu L}{kA}} e^{i\delta} \quad . \quad . \quad . \quad . \quad . \quad . \quad . \quad . \quad . \quad . \quad (26)$$

The meaning of this complex equation is that instantaneous values of flow rate and pressure are related by the real part of this equation. Thus, if instantaneous pressure p is given by

$$p = P_m \cos \omega t = \text{real part of } (P_m e^{i\omega t}) \quad . \quad . \quad (27)$$

then instantaneous flow rate q is given by

$$q = \text{real part of } \left(P_m \frac{DAk}{\mu L} e^{i\omega t} e^{i\delta}\right)$$

$$q = \frac{DAk}{\mu L} P_m \cos(\omega t + \delta)$$

$$= Q_m \cos(\omega t + \delta) \quad . \quad . \quad . \quad . \quad . \quad . \quad (28)$$

in which we have defined

$$Q_m = \frac{DAk}{\mu L} P_m \quad . \quad . \quad . \quad . \quad . \quad . \quad . \quad . \quad . \quad . \quad (29)$$

But for measurement, it is more convenient to express the response in terms of flow volume rather than rate.

TABLE 2—TABLE OF ANALOGS

Current Flow in the Electrical Transmission Line of Fig. 5(c)	Fluid Flow in a Permeable Core with Porostriction
Sending-end A.C. voltage, (E_S)	Input A.F. pressure, (P_i)
Receiving-end A.C. current, (I_R)	Output A.F. flow rate, (Q_o)
Resistance per unit length, (R)	Flow resistance per unit length, $\left(\frac{\mu}{kA}\right)$
total shunt capacitance per unit length, ($C_1 + C_2$)	Total fluid compressibility per unit length, $\left(\frac{A\phi}{P_a}\right)^*$
Capacitance per unit length, (C_1)	Compressibility of fluid in porostricted porosity, $\left(\frac{AM\phi}{P_a}\right)$
Capacitance per unit length, (C_2)	Compressibility of fluid in flow channel porosity, $\left(\frac{A(1-M)\phi}{P_a}\right)$
Conductance per unit length, (G_1)	Access to porostricted porosity, $\left(\frac{Ak}{\mu S}\right)$

*This assumes that we may consider the compressibility of air as constant and equal to the isothermal compressibility of air at atmospheric pressure; i.e., $c = \frac{1}{P_a}$ The assumption is reasonable so long as P_m is small compared to P_a. For tests reported, P_m/P_a was of the order of 0.01.

*Here, frequency in radians per unit time has been expressed in terms of the period T of the signals.

The instantaneous value of flow volume, $v = V_m \cos(\omega t - \Psi)$, is related to flow rate as follows.

$$q = \frac{dv}{dt} = V_m \omega [-\sin(\omega t - \Psi)] \quad , \quad . \quad (30)$$

or

$$Q_m \cos(\omega t + \delta) = V_m \omega \cos\left(\omega t - \Psi + \frac{\pi}{2}\right). \quad . \quad . \quad . \quad . \quad . \quad . \quad . \quad . \quad . \quad . \quad . \quad . \quad . \quad (31)$$

From Eq. 31,

$$Q_m = V_m \omega = V_m \frac{2\pi}{T}, \quad . \quad . \quad . \quad . \quad . \quad . \quad . \quad (32)$$

and

$$\Psi = -\delta + \frac{\pi}{2} \quad . \quad . \quad . \quad . \quad . \quad . \quad . \quad . \quad . \quad . \quad (33)$$

so that

$$\tan \Psi = \cot \delta = \frac{\alpha L \sinh \alpha L \cos \beta L + \beta L \cosh \alpha L \sin \beta L}{\beta L \sinh \alpha L \cos \beta L - \alpha L \cosh \alpha L \sin \beta L}. \quad . \quad . \quad . \quad . \quad . \quad . \quad . \quad . \quad . \quad . \quad . \quad . \quad . \quad (34)$$

Note that phase angle Ψ is the phase angle by which output flow volume *lags* input pressure.

Substituting Eq. 32 into Eq. 29, multiplying the result by τ and re-arranging terms, one may obtain the following expression for dimensionless amplitude response ρ.

$$\frac{1}{2} \frac{V_m}{AL\phi} \frac{P_a}{P_m} = \frac{\tau}{2} D = \rho \quad , \quad . \quad . \quad . \quad . \quad . \quad . \quad (35)$$

in which, from Eq. 13,

$$\rho = \frac{\tau}{2} \sqrt{\frac{(\alpha L)^2 + (\beta L)^2}{\sinh^2 \alpha L \cos^2 \beta L + \cosh^2 \alpha L \sin^2 \beta L}}. \quad . \quad . \quad . \quad . \quad . \quad . \quad . \quad . \quad . \quad . \quad . \quad . \quad . \quad (36)$$

One sees that response ρ is indeed dimensionless since $\frac{V_m}{AL\phi}$ is the ratio of maximum output volume over the total pore volume in the core, and $\frac{P_a}{P_m}$ is the ratio of atmospheric pressure over the maximum input pressure amplitude. Of course, both volumes must be expressed in the same units, and both pressures must be expressed in the same units.

To determine the curve Ψ vs ρ for any given values of $\frac{S}{L^2}$ and M, one simply chooses various values of dimensionless period τ and calculates values of Ψ and ρ using Eqs. 22, 23, 24, 34 and 36. ★★★

The Evaluation of Vertical-Lift Performance in Producing Wells

R. V. McAFEE
MEMBER AIME

AXELSON-GARRETT DIV. OF U. S. INDUSTRIES, INC.
HOUSTON, TEX.

ABSTRACT

The fundamentals of vertical-lift performance are examined with the aid of computer-calculated flowing gradient charts.

Flowing and gas-lift well performance characteristics are determined from available well test data. The effect of tubing size, gas-liquid ratio and wellhead pressure is discussed for both flowing and gas-lift wells. The effect of gas-injection pressure, formation gas, bottom-hole pressure and valve spacing is also discussed for gas lift wells. From these studies conclusions may be reached for improving or prolonging natural flow, obtaining optimum lift efficiency when natural flow ceases and improving existing gas-lift systems.

The techniques perfected satisfy the requirement that the time involved to conduct an evaluation be practical for operating personnel.

INTRODUCTION

Flowing pressure gradients furnish the key to successful evaluation of vertical-lift performance in producing wells.

Command of multiphase flow gradients in some readily usable form is a necessity before operating personnel can competently include vertical-lift performance evaluation of both flowing and artificial-lift wells in their over-all consideration of production efficiency. A readily usable form cannot be overemphasized since most of the decisions which confront the production engineer with a problem well must be made quickly.

In moving a barrel of oil from the reservoir to the stock tank, the major portion of energy generally is expended in the vertical-lift phase. This may or may not be of concern during the flowing life of a well, depending upon the production requirements. It becomes of some concern when the flow performance of the well becomes erratic, and a conscious effort must be made to maintain natural flow. It is at this time that the first steps may be taken to modify existing conditions to relieve unnecessary limitations to proper flow.

When natural flow ceases and some form of artificial lift must be installed, the amount of energy expended in lifting liquids becomes quite obvious. It is at this time, if no other, that lifting efficiency becomes important because that part which must be supplied from an outside source is now related directly as a cost per barrel of oil produced.

Ten years ago, the majority of gas-lift wells were produced with gas-well gas. Today, the majority are produced by closed rotative gas-lift systems. This permits a direct evaluation of well performance in terms of horsepower requirements and has resulted in mixed conclusions as to the success of gas lift based upon the relative efficiency of a particular system. An increased awareness of the need to resolve vertical-lift performance on a readily usable, scientific basis was inevitable.

An indication of the need for better applied science in this field is the often-asked question of whether or not gas-lift can efficiently deplete a given well or reservoir. This question cannot possibly be answered without first evaluating reservoir, surface and vertical-lift performance both as encountered today and as anticipated throughout the life of the well or wells.

The technique presented in this paper was originally developed to upgrade gas-lift installation design from an applied art to an applied science. It has since been successfully used not only for this purpose, but also for the whole field of vertical-lift performance in its broadest sense. Lift efficiency should be considered important while the well is still flowing, as well as after natural flow ceases. Correct interpretation and proper modification of the vertical-lift performance of a producing well can provide dramatic improvement in production performance and/or efficiency.

STATEMENT OF THEORY AND DEFINITIONS

Fig. 1 illustrates the three divisions of production which will be used in this paper.

The terms are a modified version of those presented in the very fine paper by Gilbert.[1] The fields of reservoir and surface performance both have been greatly improved over the years. A study of those writings which may be found indicates that the field of vertical-lift performance has not progressed as well. There are two possible reasons for this lack of progress.

1. It has not been recognized as a scientific field in itself by the oil companies, as has reservoir engineering.

2. The equipment companies have confined their efforts to mechanical design research rather than the more basic study of vertical-lift performance of producing wells.

Both organizations must have an economic stimulus for doing research in this field, and most of the results obtained in past work has been so erratic as to arouse little enthusiasm.

The basic purpose of interpreting vertical-lift performance is to predict operating conditions below the surface of the ground from available data. The success of the interpretation depends upon the accuracy with

Original manuscript received in Society of Petroleum Engineers office Sept. 12, 1960. Revised manuscript received Jan. 30, 1961. Paper presented at 35th Annual Fall Meeting of SPE, Oct. 2-5, 1960, in Denver.

[1]References given at end of paper.

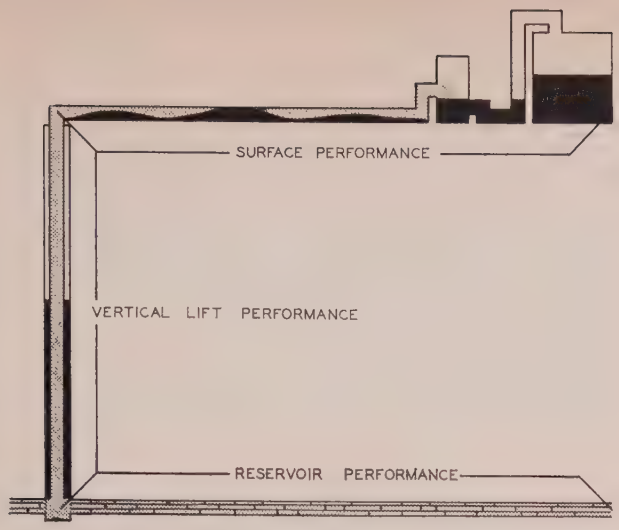

FIG. 1—THE THREE PHASES OF PRODUCTION.

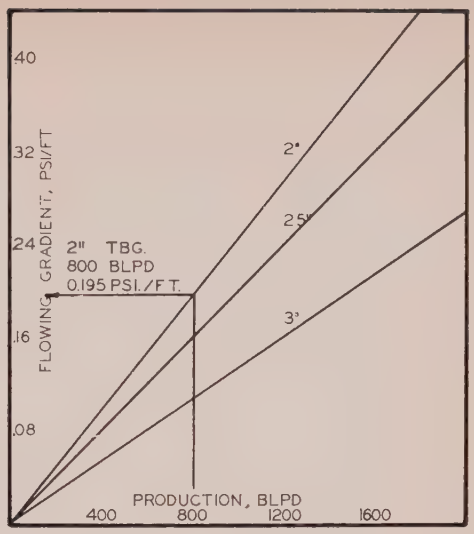

FIG. 2—PSI/FT GRADIENT CHART.

which the pressure gradient of the producing well can be predicted. The gas-lift industry elected to express this interpretation as a linear gradient for a given tubing size and rate of liquid flow, as shown in Fig. 2. Unfortunately, this is a completely invalid concept.

Fig. 3 shows the true nature of the gradients which exist in vertical flow. The gradient line marked "Liquid-Static" is a straight line since it is all liquid and may be expressed as a linear gradient in psi/ft. The line marked "Liquid-Flowing" is also a straight line since it too is all liquid. It differs from the static gradient because the liquid is in motion and flow resistance increases the pressure drop per unit of length. This gradient would ocur in artesian flow. It may also be expressed as a linear gradient in psi/ft.

A radical change takes place when gas is present with the liquid in the vertical column. This is shown in Fig. 3 as "Liquid and Gas-Flowing". The pressure gradient becomes less because of the presence of the gas. The gradient is no longer a straight line because the fluid is now a compressible mixture and the density increases with the increased pressure at increasing depths in the well. The latter is the key to all proper thinking with respect to flowing gradients.

A final point to be made is that the amount of gas per volume of liquid determines the density; variations in gas volume per volume of liquid will vary the density and, therefore, the flowing gradient. Thus, it can be seen that, at a given rate of liquid flow and other constant conditions, there must be a different depth-pressure gradient for each gas-liquid ratio.

Recognizing this to be true places a responsibility upon the individual to then seek a practical method of interpreting gradients in their true form as a curve and as a function of the volume of gas per volume of liquid. The most commonly accepted mathematical interpretation is that presented in the excellent paper by Poettmann and Carpenter.[2] Use of their mathematics was found to give an acceptable accuracy; however, it was time-consuming because the following 12 variables were taken into consideration for each calculation: tubing size, rate of liquid flow, gas-liquid ratio, flowing wellhead pressure, liquid composition, flowing friction factor, compressibility factor of gas, gas-liquid solubility, formation volume factor, average flowing temperature, gas gravity, and liquid gravity.

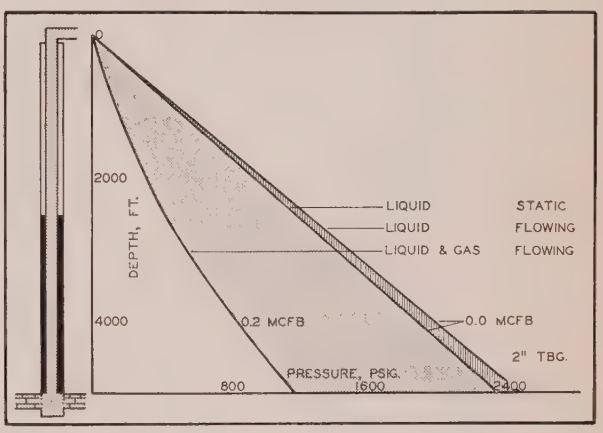

FIG. 3—ILLUSTRATION OF VARIOUS GRADIENTS.

It should also be noted that the viscosity was not considered to be of influence on the pressure gradient.

It was evident that an attempt should be made to resolve the mathematics to a language common to standard oilfield data, and to fewer significant variables. Gilbert[1] stated in his paper that " . . . there is a different depth pressure gradient for each size of pipe, each rate of liquid flow, and each gas-liquid ratio". In a footnote he further stated that, "Gradients presumably are also affected by many other factors including liquid surface tension, viscosity and gravity, flowing temperatures, gas gravity and gas-liquid solubilities".

"However, there is a reasonably close correspondence between results which have been obtained in the light-oil (25° to 40° API) fields of Long Beach, Santa Fe, Dominguez, Ventura, Canal and Ten Section, and several foreign fields without adjusting for such factors. Also, it has not been found necessary to correct gradients for water cuts. However, the gradients are inadquate to predict the effects of emulsions."

Using this philosophy, the listed variables of Poettmann and Carpenter were evaluated and the following was determined.

1. Liquid gravity, gas gravity and average flowing temperature could be fixed as a field constant without impairing the accuracy of the calculations from a practical-use standpoint.

2. The formation volume factor and gas-liquid solu-

bility are significant variables when oil is the liquid, but not when water is the liquid. These variables were taken into consideration in the oil calculations.

3. The flowing friction factor and the compressibility factor of gas are both significant, but they can be resolved at a given moment in the calculation.

4. The liquid composition is significant in the high flowing density range (low gas-liquid ratio) but becomes less significant as the flowing density decreases.

5. Tubing size, rate of liquid flow, gas-liquid ratio and flowing wellhead pressure are significant and must be considered individually with each problem.

The mathematics then could be resolved to four significant variables and plotted in a charted form for direct use.

An electronic computer program was set up to run the necessary calculations, and master charts were plotted as a pressure-depth relationship for tubing sizes of 1, 1¼, 1½, 2, 2½, 3 and 4-in.; rates of liquid flow from 50 to 10,000 B/D of liquid as applicable for each tubing size; and gas-liquid ratios from 0.0 to 4.0 Mcf/bbl. One complete set was plotted for 1.074 specific gravity water, and another for 32° API oil.

The calculations were run to a pressure of 4,000 psig. The published charts[3] are plotted to 2,800 psig. A set of charts plotted to 4,000 psig will be available, as will a set for 1¾-in. nominal tubing size. An example of the water and oil charts are shown in Figs. 4 and 5.

ACCURACY OF THE CURVES

The original accuracy checks run against the curves were based upon flowing bottom-hole pressures and related test data which permitted a flowing bottom-hole pressure correlation from the charts. It was found that the average error over all the checks made was 3.87 per cent. However, it should be pointed out that these checks were subject to the usual errors found in the measurement of gas (or reading thereof), measurement of water production involved and measurement of flowing wellhead pressure. These three variables are each significant and subject a chart interpretation to apparent error if any are, in themselves, in error. This is not intended to challenge testing practices so much as it is to point out the inherent weakness in single-point correlations. The most important checks that have been made are those that permit a multi-point correlation from the top to the bottom of a well. It is here that the actual slope of the pressure gradient can be correlated.

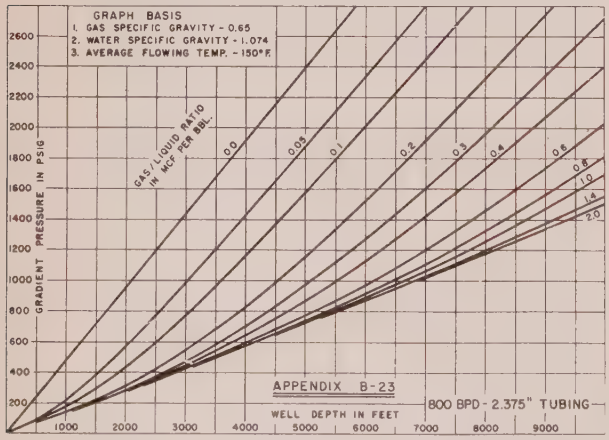

FIG. 4—FLOWING PRESSURE GRADIENTS AT VARIOUS GAS-LIQUID RATIOS—WATER.

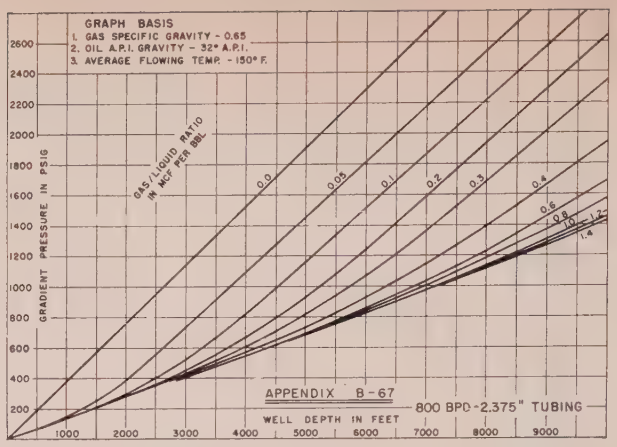

FIG. 5—FLOWING PRESSURE GRADIENTS AT VARIOUS GAS-LIQUID RATIOS—OIL.

This is of much greater importance than single pressure readings because a single reading does not provide an opportunity to determine the cause of any error. Usually, the pressure bomb reading and well test data are accepted as accurate and the calculated approach in question.

Fig. 6 shows one of the many "picture-book" correlations that have been made. The curvature of both flowing gradients is apparent, and the gradient lines drawn are the actual curves from the master charts for the corresponding tubing size and gas-liquid ratio using the 600 B/D of liquid water chart.

Fig. 7 shows a correlation which required an interpolation for gas-liquid ratio both above and below the point of gas injection. Again, the multi-point correlation is invaluable in determining the validity of the curves. This figure can be used to demonstrate the stated weakness in single-point correlations. If all conditions remained the same except that the formation gas-liquid ratio had been estimated or calculated to be 0.10 Mcf/bbl rather than the actual 0.066 Mcf/bbl, the error at 6,000 ft would have been 100 psig in 2,600 psig, or 3.85 per cent. The average error for single-point correlations was 3.87 per cent.

ADJUSTING FOR WELLHEAD PRESSURE

The method of adjusting for wellhead pressure is shown in Fig. 8. "A" and "B" represent two pressure gradients which have the same tubing size, rate of liquid flow and gas-liquid ratio. The fourth significant variable, wellhead pressure, requires an adjustment before a

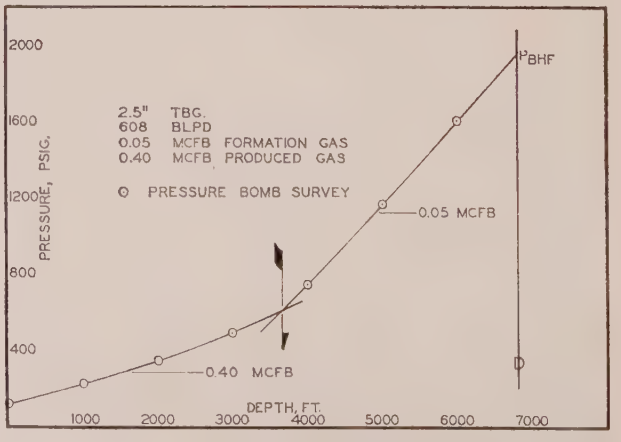

FIG. 6—CORRELATING PRESSURE SURVEYS.

correlation can be achieved. The correlation must be made along constant pressure planes. This is related to the flowing density of the fluid. The section of Gradient B from 300 psig to the surface has no correlative counterpart in Gradient A. The section of Gradient A from 1,600 psig to depth also has no correlative counterpart in Gradient B.

The remaining sections of the two gradients can be correlated by shifting one *laterally* to the other. This procedure applies to all wellhead pressure adjustments made on the master charts. These charts are designed for direct overlay with a graph work sheet, and all pressure adjustments are made by lateral shifting of the work sheet keeping the abscissas aligned. Having made the pressure adjustment, the desired segment of the pressure gradient is traced directly upon the work sheet.

EVALUATION OF FLOWING WELL PERFORMANCE

The effect of wellhead pressure upon flowing bottom-hole pressure is shown in Fig. 9. When the pressure is lowered 100 psig at the surface, the flowing bottom-hole pressure is reduced 330 psig. Again, this relates directly to flowing density and the over-all change in slope characteristic of the pressure gradient at the lower wellhead pressure. It should be noted that this evaluation is made at a constant rate of flow. In the field, any decrease in flowing bottom-hole pressure would normally result in an increase in production rate. This increase in rate might be considered the source of an offsetting increase in flowing bottom-hole pressure. However, so long as the change in rate occurs between the extremes of friction and slippage, no appreciable change in pressure gradient would occur at the increased rate at a given gas-liquid ratio.

For example, with a P.I. of 1.0 B/D of liquid/psi, the well in Fig. 9 would produce 330 B/D of liquid more, or a total of 930 B/D of liquid, at the decreased flowing bottom-hole pressure if no change occurred in the characteristic of the flowing gradient. Fig. 10 shows a plot of inflow performance against tubing intake performance for 160 psi and 60 psig. The well would actually produce 890 B/D of liquid at the reduced wellhead pressure. The example is based upon a constant gas-liquid ratio.

One particular production decline characteristic is pointed out since it is related to changes in gas-liquid ratio in the vertical column. Fig. 11 shows the progressive deterioration of well performance brought about by a change in water-oil ratio. None of the other conditions is allowed to vary. The change is not the presence of the heavier liquid but, rather, the change in total gas-liquid ratio as the produced gas declines with oil production. This is based on produced gas being solution gas only. To ensure a true relation to change in gas-liquid ratio, the 100 per cent water chart was used for all curves and no water-oil interpolation was made. The comparison including the water-oil interpolation would

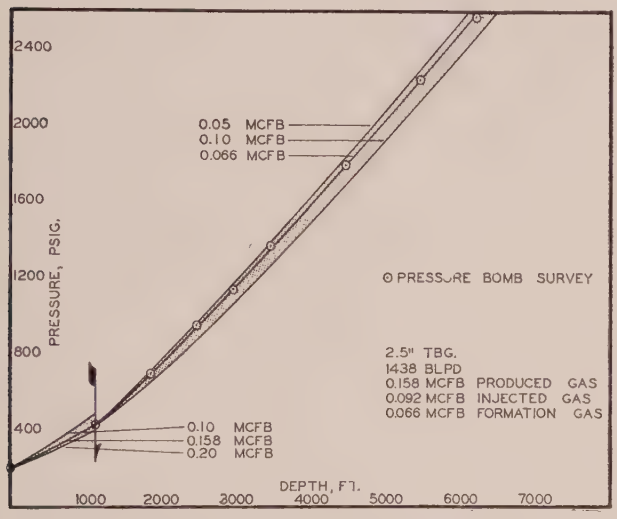

FIG. 7 — CORRELATION OF A PRESSURE SURVEY REQUIRING AN INTERPOLATION FOR THE MEASURED GAS-LIQUID RATIO.

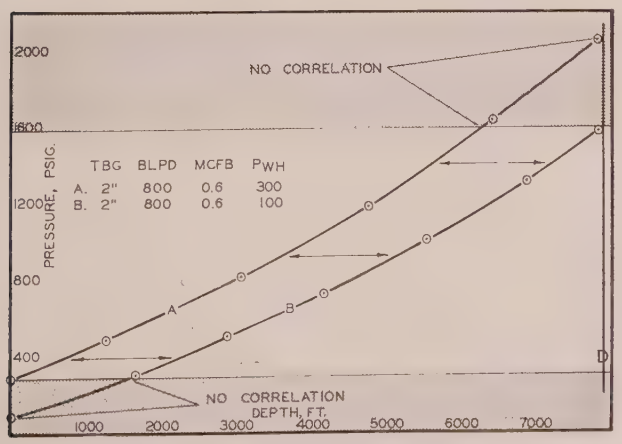

FIG. 8 — CORRELATION OF TWO PRESSURE SURVEYS SHOWING METHOD OF ADJUSTING FOR WELLHEAD PRESSURE.

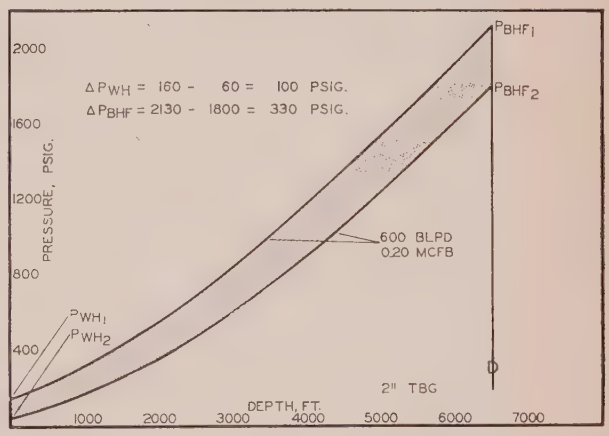

FIG. 9—EFFECT OF WELLHEAD PRESSURE UPON FLOWING BOTTOM-HOLE PRESSURE.

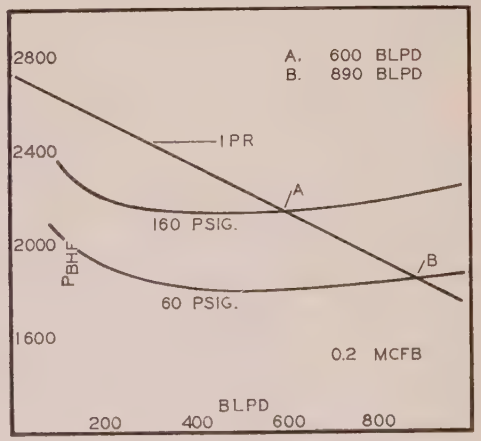

FIG. 10—PLOT OF 2.0-IN. TUBING PERFORMANCE AT 6,500 FT VS INFLOW PERFORMANCE OF WELL.

show the decline to be even more pronounced. Unless gas-liquid ratio is considered in vertical-lift performance evaluations, this occurrence would be overlooked.

The method of obtaining a P.I. from a given static bottom-hole pressure and well test data is shown in Fig. 12. The technique is used when a static bottom-hole pressure and well test information is all that is available. It is also used to check the results of a flowing pressure survey which was run to establish a P.I. For this check, well test data for a period of several weeks before or after the study are used in conjunction with the available static bottom-hole pressure. These well tests should include some that are under stable conditions and permit the calculation of a true producing P.I. The majority of the checks made to date show a calculated P.I. approximately one-half that obtained from the pressure survey. These were not permitted to reach their stabilized, flowing bottom-hole pressures before the bomb was pulled and readings were made.

Fig. 13 shows a method of obtaining a P.I. when no bottom-hole pressure survey information is available. The P.I. is based upon the change in flowing bottom-hole pressure at different rates of flow. When good test data were available, this method gave satisfactory results.

The P.I. of a well is not necessarily a constant, but can change with different rates of flow. The method outlined in Fig. 13 provides an economical way to obtain a flow performance curve, or IPR, by producing the well at several different rates and accurately measuring the necessary test data. This has also been successfully carried out on well data which had been obtained before cessation of natural flow, and the information obtained was used to design a proper gas-lift installation for re-starting and supplementing natural flow.

There is another method of using the charts when a flowing bottom-hole pressure reading is all that is needed. Instead of using a graph work sheet, the pressure reading is made directly from the master chart after first correcting for wellhead pressure. This correction is made by determining the depth from zero at which the wellhead pressure occurs for the given gas-liquid ratio, and adding that depth to the reference depth of the well. The flowing bottom-hole pressure point is then read from the applicable gas-liquid ratio curve at the corrected reference depth on the master chart.

EVALUATION OF GAS-LIFT WELL PERFORMANCE

The basic layout shown in Fig. 14 will be used throughout the gas-lift discussion. The design is predicated upon a knowledge of the productivity of the well. It will be shown that, if you are unable to determine the expected characteristics of a well, any degree of success can only be attributed to pure chance. Efficient supplementing of natural flow *must* be tailored to well performance characteristics.

Each illustration in this section is a study of the effect of one variable upon lift efficiency. This is done for two reasons: (1) the relative importance of each variable can be better resolved; and (2) questions arising in daily operations involve only one variable.

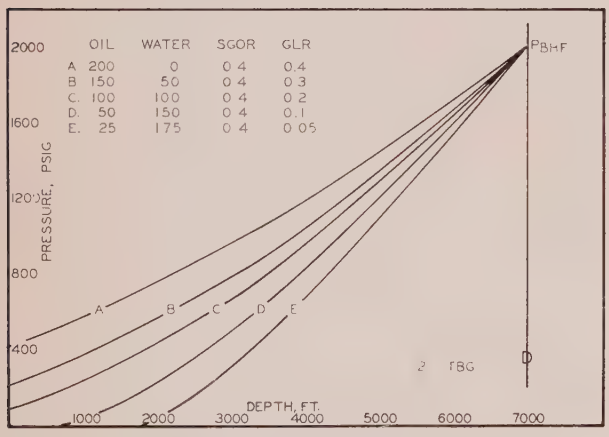

Fig. 11—Production Decline from Change in Water Cut.

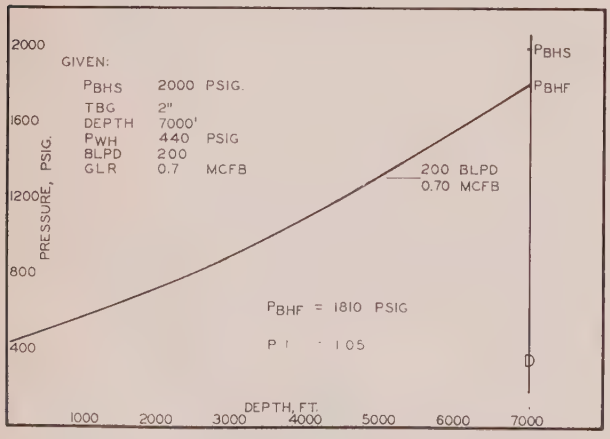

Fig 12—Obtaining Productivity Index from Static Bottom-Hole Pressure and Surface Test Data.

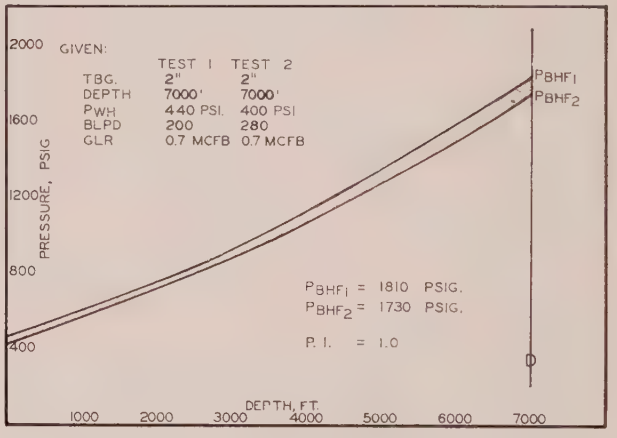

Fig. 13—Obtaining Productivity Index from Surface Test Data.

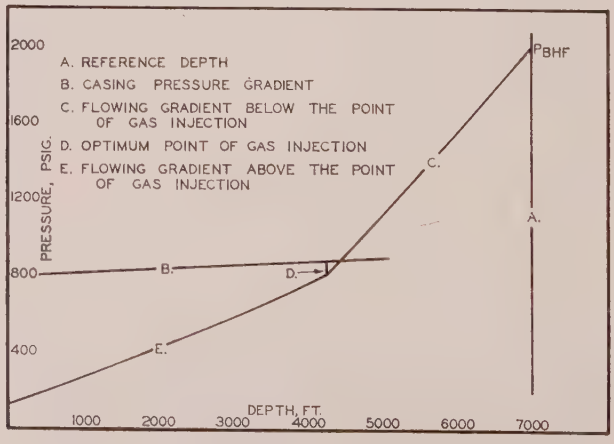

Fig 14—Fundamentals of Gas-Lift Design.

if the effect of more than one variable is involved in a particular problem, it may develop that the best economic solution lies not in making all possible corrections but, rather, in making only those which effect the major improvements in operation. Studying the problem with each individual variable provides such an opportunity.

The effect of the variables is expressed as horsepower requirements. The requirements are shown in block graph form and do not have a numerical value assigned. They have been scaled off very accurately and are designed to show the relative change in horsepower as the variable changes.

Fig. 15 shows the effect of wellhead pressure. This illustration is based upon a constant intake pressure at the compressor of 25 psig. The higher-than-necessary wellhead pressure would be the result of: (1) too long a flow line; (2) too small a flow line for the amount of fluid produced; (3) reduced ID from deposition or paraffination; (4) too many right angle turns, choke cages, chokes, restricted opening valves, or lack of streamlining at the tree; and (5) too high a separator pressure.

Over four times the horsepower would be required at 200-psig wellhead pressure as is required at 50 psig.

An alternate example is shown in Fig. 16. This figure is the same except that the compressor intake pressure is set at 15-psig less than wellhead pressure. Although the compression requirements are now less at the higher wellhead pressure, it still takes over four times the volume of gas to produce against the 200-psig wellhead pressure, and more horsepower is required to handle a larger volume of gas. More than twice the horsepower is still required to lift the fluid at 200-psig wellhead pressure as is required at 50 psig.

Fig. 17 shows the effect of tubing size upon horsepower requirements. As stated earlier, this would vary with rate of liquid flow and gas-liquid ratio, with the larger tubing sizes becoming even more favorable as the rate increases. There is not enough data available on flow performance in small tubing sizes (1 and 1¼ in.) to determine their relative value at lower rates of flow.

Particularly where depletion must be at high withdrawal rates, vertical-lift performance should be considered before wells are completed slim hole. In the example shown, five times the horsepower would be required for 1.5-in. tubing as for 2.5-in. tubing.

In addition to the relative efficiency of various tubing sizes, there are problems encountered where the desired production rate is either impossible or requires a high horsepower commitment for the given operating conditions. A larger tubing size often will permit the desired rate with reasonable horsepower requirements. In this manner, a well was successfully produced at 800 B/D of liquid and an injected gas-liquid ratio of 0.7 Mcf/bbl with 2½-in. tubing, when it could not be produced at over 400 B/D of liquid with 2-in. tubing installed.

Combination strings should not be overlooked when confronted with such problems as a well which will not produce the desired rate with 2-in. tubing but requires its use in the lower section of the well because of a liner. Swaging to 2½-in. tubing above the liner often will permit production of the desired rate. Whenever more than one size is used, a switch from one tubing gradient to the other is made at the depth where the change is to be made.

Gas-injection pressure has a definite effect upon lift efficiency. As shown in Fig. 18, a point of injection at 3,800 ft using 600-psig pressure would require four times the horsepower required at a point of injection at 6,800 ft using 1,700-psig pressure. By far the largest number of gas-lift systems in operation today are injecting in the 500- to 700-psig range.

Although no arbitrary control normally can be exerted upon the amount of formation gas produced, it too has a very definite effect upon gas-lift performance as shown in Fig. 19. It should never be ignored when

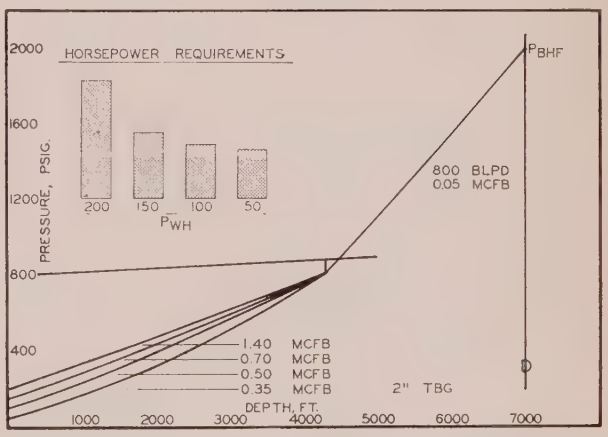

Fig. 16—Effect of Flowing Wellhead Pressure upon Horsepower Requirements—Compressor Intake = P_{WH} − 15 psig.

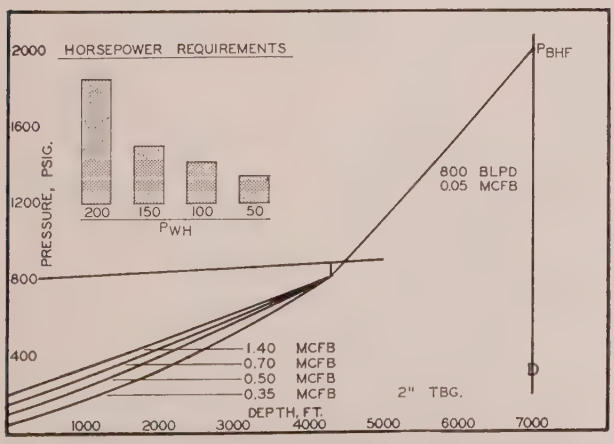

Fig. 15—Effect of Flowing Wellhead Pressure upon Horsepower Requirements—Compressor Intake = 25 psig.

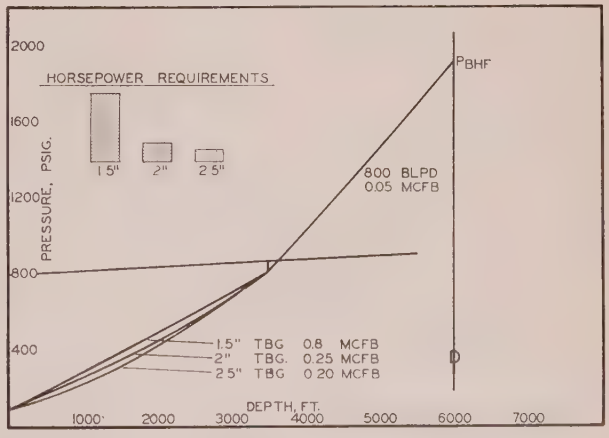

Fig. 17—Effect of Tubing Size upon Horsepower Requirements.

working out a design problem. It is one of several explanations why two installations in presumably "identical" wells will perform at widely divergent injected gas-liquid ratios.

The change in performance is affected by two factors. One is that the point of gas injection is not as deep for higher formation ratios. The other is that the formation gas is deducted from the total produced-gas requirement; the more the formation gas volume, the less the injected gas required. This is illustrated in the ultimate by the 0.3-Mcf/bbl curve. With that formation gas-liquid ratio, the well would be flowing naturally with a wellhead pressure of 150 psig.

The effect of flowing bottom-hole pressure is shown in Fig. 20. In many cases, nothing can be done except to anticipate the condition that actually exists in the well. This condition can range from some degree of satisfactory operation to the extreme of an impossible situation for the desired volume of liquid as P_{BHF4}.

Four times the horsepower would be required to produce at P_{BHF3} as would be required at P_{BHF1}. This change in P_{BHF} would be the result of either a normal decline in reservoir pressure or the necessity for increased drawdown at a constant reservoir pressure but deteriorating P.I. Thus, horsepower requirements would increase with time under these conditions.

The most interesting work done in connection with flowing bottom-hole pressure has been to obtain an improvement in productivity after producing wells at a higher withdrawal rate than any previous time in the life of the well. Using a reverse line of reasoning with Fig. 20, it may be shown that for a given well with producing conditions the same as P_{BHF3} an improvement in productivity that would permit withdrawal at the same rate at bottom-hole conditions the same as P_{BHF1} would reduce horsepower requirements to 26 per cent of the original requirements.

Table 1 lists the results for one particular well.

TABLE 1—RESULTS FOR ONE WELL

	Before	After
Tubing	2 in.	2.5 in.
B/D of Total Liquid	162	540
Oil	10%	14%
Injected Gas-Liquid Ratio	0.5 Mcf/bbl	0.09 Mcf/bbl
Lift Method	Intermittent	Continuous
P. I.	0.67	31.8

No other operating conditions such as wellhead and injection pressure changed. The combination of 2.5-in. tubing and continuous lift permitted a greater sustained downdraw across the sand face with the resultant change in productivity. Summarizing part of this data, the well is being produced at 3.3 times the previous rate of flow with 60 per cent of the original horsepower requirement. The measured flowing bottom-hole pressure at 540 B/D of liquid is now actually higher than the measured flowing pressure at 162 B/D of liquid.

Both P.I.'s were carefully obtained with bottom-hole pressure surveys and correlated with the master curves. The production is now held to 540 B/D of liquid for allowable reasons. To check the measured production potential, the well was opened up and produced at the rate of 1,460 B/D of liquid. This type of well response has been encountered many times in our work, and it has been discussed in various published papers. If it can be anticipated from a calculated P.I. using formation data that the actual producing P.I. is appreciably less than the formation P.I. of the well, steps can be taken to clean up the well and permit operation at greatly reduced horsepower requirements.

Fig. 21 shows the importance of correct valve placement with respect to horsepower requirements. If a point of injection were located at "A", the horsepower requirements would be over twice that required if it were located at "B". If the point were located at "C", injection would be impossible. Not only must the point of injection be properly located, but so also must any valves used to unload to the point of injection. All must be located in a manner which will accommodate the productivity of the well and achieve the desired point of injection. Any design which does not take well per-

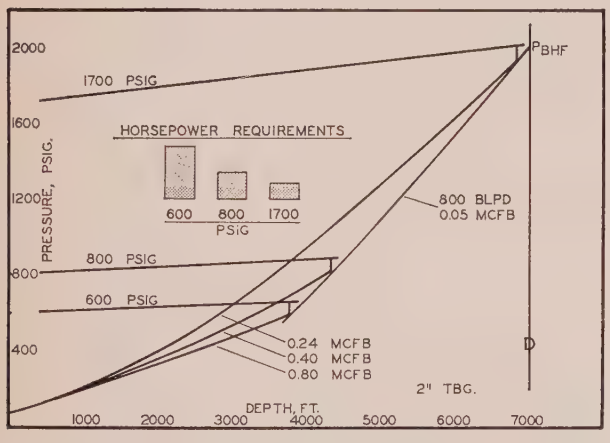

FIG. 18—EFFECT OF GAS-INJECTION PRESSURE UPON HORSEPOWER REQUIREMENTS.

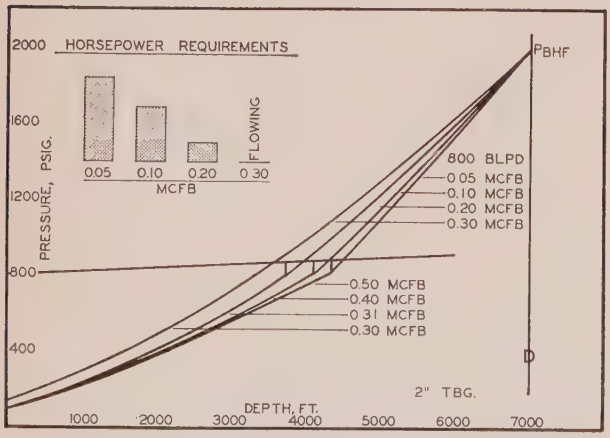

FIG. 19—EFFECT OF FORMATION GAS UPON HORSEPOWER REQUIREMENTS.

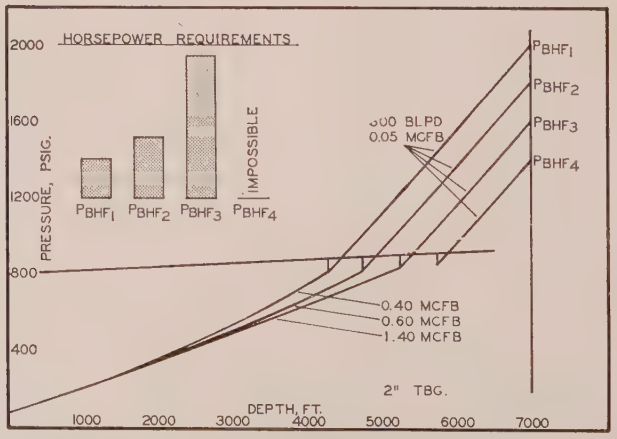

FIG. 20—EFFECT OF FLOWING BOTTOM-HOLE PRESSURE UPON HORSEPOWER REQUIREMENTS.

formance into consideration is relying upon pure chance that it will be successful.

NOTES ON SPECIAL DESIGN PROBLEMS

No attempt is made to demonstrate a method of installation design. Once the vertical-lift performance of a well has been evaluated, the design becomes a straightforward procedure to fulfill the requirements dictated by the well. However, the design of an installation both from the standpoint of valve spacing, pressure setting and gas throughput requirements should be based upon sound engineering principles to insure attaining the desired performance.

Fig. 22 shows the difficulty encountered in gas-lifting wells with formation ratios of 0.6 Mcf/bbl and higher. The change in flowing gradient created by adding gas does not have the dramatic effect which is encountered in low-ratio wells. In the example, more than doubling the amount of gas in the vertical column from 5,000 ft to the surface raises the flowing wellhead pressure from 40 to 100 psig. In contrast, a like injection of an additional 0.6 Mcf/bbl of gas at the same depth in a well with a formation gas-liquid ratio of 0.05 Mcf/bbl would raise the wellhead from 40 psig to 660 psig.

Higher-ratio wells, which can no longer flow on their own, present a more difficult artificial-lift problem than wells with low ratios.

The need for caution in designing an installation for a high-P.I. well is shown in Fig. 23. The point of injection which will produce the desired 800 B/D of liquid is very close to the static pressure gradient. All valves above this final point would unload static fluid, but none would sustain a drawdown in bottom-hole pressure. When the final point of injection is reached, the drawdown at bottom would increase from 0 to 100 psig, and the sustained production rate from 0 to 800 B/D of liquid. If the point of injection were located 50-ft higher in the hole, either through mis-design or mis-spacing, the well would only produce 480 B/D of liquid. Care should be exercised to prevent missing the correct evaluation of high-P.I. wells.

There is a distinction to be made between restarting a well and supplementing natural flow. In wells with little or no formation gas, this may be possible from the same injection point. When a well will produce with any appreciable formation gas, it must be re-started from one depth and supplemented at another. This is shown in Fig. 24. Formation Gradient A is the 0.0-Mcf/bbl curve with the well producing at the rate of of 600 B/D of liquid. The necessary point of injection is at 4,500 ft. When the normal 0.2-Mcf/bbl formation gas-liquid ratio returns to the vertical column, the point of injection will move up to 3,650 ft. Two completely separate points of injection are required for proper operation of the well.

The higher the formation gas-liquid ratio, the farther apart the two points. The extreme example of this condition is Fairbanks field where wells are unloaded to, and produced from, bottom until formation gas breaks in, at which time they will return to natural flow.

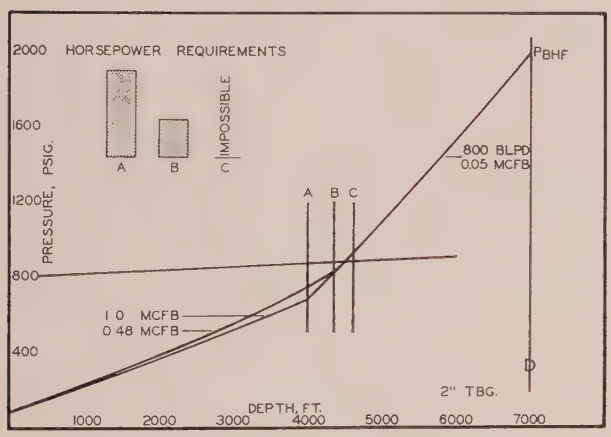

Fig. 21—Effect of Incorrect Valve Spacing upon Horsepower.

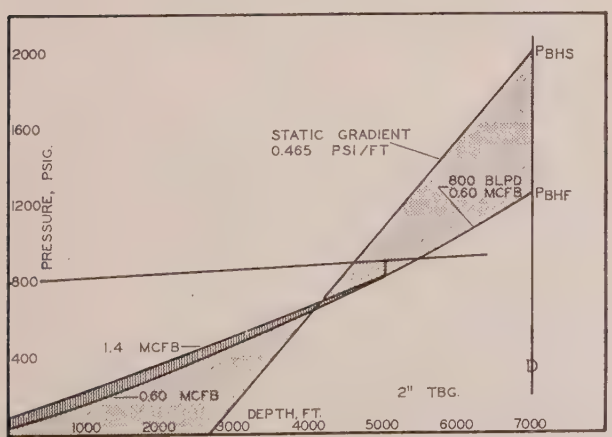

Fig. 22—Design Problem with Appreciable Formation Gas.

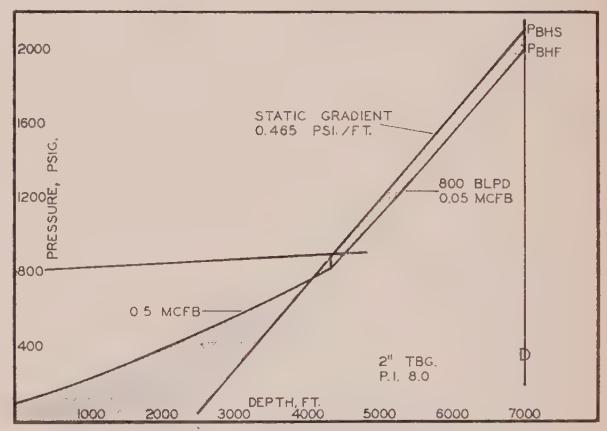

Fig. 23—Design Problem with a High-P. I. Well.

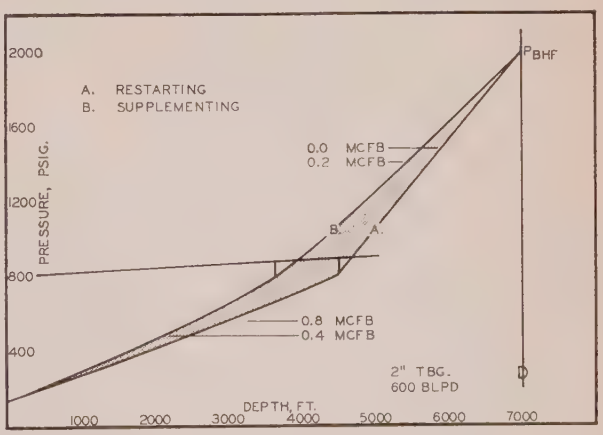

Fig. 24—Design Problem with Separate Points of Injection Required for Re-starting and Supplementing Flow.

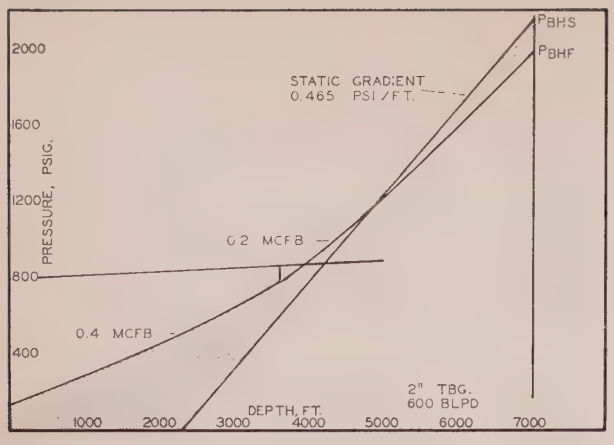

FIG. 25—DESIGN PROBLEM WITH FINAL POINT OF INJECTION ABOVE STATIC PRESSURE GRADIENT.

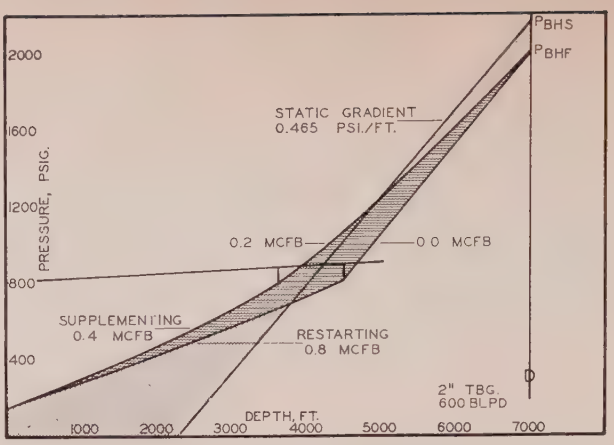

FIG. 26—SPECIAL RE-STARTING PROBLEM WITH FINAL POINT OF INJECTION ABOVE STATIC PRESSURE GRADIENT.

Fig. 25 illustrates a design problem with the final point of gas injection above the static pressure gradient. This is brought about by the 0.2-Mcf/bbl formation gas-liquid ratio creating a flowing gradient which crosses the static pressure gradient below the final point of gas injection. The final point of injection shown is not capable of creating sustained production from the formation until gas evolves; and, as discussed with Fig. 24, no formation gas can be counted upon until after formation fluid is produced.

Unless additional valves are run deeper to re-start formation flow, this well will not produce.

Fig. 26 is a composite of Figs. 24 and 25, illustrating re-starting below the static pressure gradient at 4,500 ft with a required injected gas-liquid ratio of 0.8 Mcf/bbl, finally supplementing at a point above the static pressure gradient with an injected gas-liquid ratio of 0.2 Mcf/bbl.

LIMITATIONS OF THE MASTER CHARTS

The following are the listed areas in which the curves are either unproven or suspect.

1. The 1- and 1¼-in. curves have not been verified because of the lack of available pressure survey data for these sizes.

2. The curves plotted for gas-liquid ratios above 2.0-Mcf/bbl have not correlated with pressure surveys at rates of flow of 400 B/D of liquid or less. It is believed that this point marks a transition from foam flow to mist flow and exceeds the mathematics of Poettman and Carpenter. The curves of Gilbert have given a good correlation when used in this range.

3. These curves are for continuous flow and will not provide suitable data for intermittent flow.

CONCLUSIONS

Some of the work accomplished to date on a practical approach to the evaluation of vertical-lift performance in producing wells is summarized. The material discussed is only a part of the total work which has been done. Evaluations have been made and gas-lift designs run in dual completions and casing-flow installations with excellent success. The vertical-lift performance in rod and hydraulic-pump installations has been evaluated with good results, and even our approach to intermittent gas lift has been greatly improved by the knowledge gained from the work with the techniques. There is an uncounted amount of work still to be done to resolve all phases of vertical-lift performance to a true applied science.

For those whose interest is maximum rate rather than optimum efficiency, it should be pointed out that the study of every variable in the paper can be revised with increased production as the main objective.

A definite advantage to the techniques developed is their use of charted flowing gradients. This permits the techniques to be applied to any approach to flowing gradients so long as the approach can be resolved to a depth-pressure relationship.

It is the author's sincere belief that vertical-lift performance is the true field of petroleum production engineering and that it is a scientific field as important economically as the field of reservoir engineering. In comparison, it is virtually untouched. Though some may regard this paper as an oversimplification of the problem, they may also agree that some simplification would serve to promote improved practices in the evaluation of vertical-lift performance in producing wells.

NOMENCLATURE

P_{WH} = flowing wellhead pressure, psig
P_{BHS} = static bottom-hole pressure, psig
P_{BHF} = flowing bottom-hole pressure, psig
P.I. = Productivity Index in B/D of total produced liquid/psi drop in bottom-hole pressure
IPR = inflow performance relationship
D = reference depth of well

ACKNOWLEDGMENT

The author wishes to thank W. K. Woodward and B. A. Abercrombie of Axelson-Garrett for their contributions to the material contained in this paper.

REFERENCES

1. Gilbert, W. E.: *Drill. and Prod. Prac.*, API (1954).
2. Poettmann, Fred H. and Carpenter, Paul G.: *Drill. and Prod. Prac.*, API (1952).
3. *Handbook of Gas Lift*, Axelson-Garrett, Div. of U. S. Industries, Inc.

★★★

The Influence of Production Rate, Permeability Variation and Well Spacing on Solution-Gas-Drive Performance

G. J. HEUER, JR.
G. C. CLARK
JUNIOR MEMBERS AIME
J. N. DEW
MEMBER AIME

CONTINENTAL OIL CO.
PONCA CITY, OKLA.

ABSTRACT

The effect on well behavior of partial permeability barriers, changes in producing rates and well spacings have been calculated through use of a radial, unsteady-state, two-phase-flow mathematical model. This model allows for variations in permeabilities and porosities with distance from the wellbore. The numerical methods necessary to solve the problem require use of a high-speed digital computer, in this case an IBM 704.

In each instance, pressure and saturation gradients, gas-oil ratios and recoveries around a well producing by solution-gas drive have been calculated as a function of time and distance from the wellbore. Comparisons are made to show the effect of changes in producing rate and of varying permeability near the wellbore and out in the formation on the production and pressure history of the well. The effect of different well spacings on producing rate and ultimate recovery is considered. Although the mathematical description of the reservoir is simplified in comparison to an actual reservoir, the results do give some insight into the difficult problem of spacing and proration in a heterogeneous solution-gas-drive reservoir. Results show that for the cases considered spacing has little effect on ultimate recovery and that permeability barriers removed from the well decrease producing rate for a period of time but have only a small effect on ultimate production.

INTRODUCTION

The effect of spacing and producing rate on the production characteristics and ultimate recovery of a well producing by the solution-gas-drive mechanism have been topics of interest to the oil industry for many years and the subject of many hearings before state regulatory bodies. The problem is very complicated because of the difficulty of simulating in the laboratory a reservoir producing by the solution-gas-drive mechanism under anything like normal field conditions. This paper gives the initial results of a study aimed at determining the effect of these factors on production from reservoirs simulated by a mathematical model. Two-phase, unsteady-state equations are used to calculate pressures, saturations, and rates of oil and gas flow as a function of time and distance from the wellbore. The model is radial, and reservoir properties may be varied with distance from the wellbore. A decrease in permeability at a given distance results in a low-permeability ring concentric with the wellbore through which all the fluids from more distant portions of the reservoir must flow.

The current mathematical model allows for variation of permeability, porosity and saturations as a function of distance from the well. Any desired drainage radius for the well may be selected. Drainage radii of 745 and 1,053 ft, which correspond to 40- and 80-acre spacing, were chosen for the calculations which follow. A large amount of the input data has been held constant. No investigation was made into the effect of changes in fluid properties and relative permeability characteristics on oil and gas production behavior. Fluid properties and relative permeabilities are essentially those of the White Mesa portion of the Greater Aneth area in southeastern Utah. A recently concluded hearing before the Utah Oil and Gas Conservation Commission to determine spacing for the field aroused interest in the possible effect of permeability constrictions located some distance from the well on production and recovery. This interest stimulated the present study.

In this paper, no attempt has been made to simulate any field production characteristics exactly. Only the solution-gas-drive mechanism has been investigated, and production by liquid expansion has not been considered. This investigation is exploratory in nature but does give some insight into the problems of spacing and proration in a solution-gas-drive field having permeability variations.

THE MATHEMATICAL MODEL

The mathematical model is similar to that proposed by West, Garvin and Sheldon.[1] Approximately the same techniques have been used in arriving at a solution. The equations are nonlinear, partial differential equations which have been known for some time. The particular equations used for this study neglect the effects of capillary pressure and gravitational forces. The advent of modern digital computing equipment has made their solution practical. Basically, the method solves for pressure, saturations, and oil and gas flow rates as a function of distance and time. In our model, distance to the

Original manuscript received in Society of Petroleum Engineers office Aug. 6, 1960. Revised manuscript received Feb. 3, 1961. Paper presented at 35th Annual Fall Meeting of SPE, Oct. 2-5, 1960, in Denver.

Discussion of this and all following technical papers is invited. Discussion in writing (three copies) may be sent to the office of the *Journal of Petroleum Technology*. Any discussion offered after Dec. 31, 1961, should be in the form of a new paper. No discussion should exceed 10 per cent of the manuscript being discussed.

[1]West, W. J., Garvin, W. W. and Sheldon, J. W.: "Solution of the Equations of Unsteady-State, Two-Phase Flow in Oil Reservoirs", *Trans.*, AIME (1954) **201**, 217.

This page of *Petroleum Transactions, AIME* follows page 398. The intervening non-Transactions pages appeared in *Journal of Petroleum Technology*.

drainage radius is divided into not more than 50 cells which vary logarithmically in size, the smallest at the wellbore and the largest at the drainage radius. This allows the model to simulate radial flow. Either an oil flow rate or pressure boundary condition may be prescribed at the wellbore. Saturations, pressures and flow rates are calculated for each cell as a function of time according to the fluid characteristics, permeability and relative permeability characteristics prescribed. The process continues until the producing rate declines to some preselected economic limit.

RESERVOIR PROPERTIES

The reservoir simulated was a tight dolomitic limestone with wide and rapid variation in porosity, permeability and lithology, both horizontally and vertically. There is considerable evidence of natural fracturing in the area, and the average effective permeability from production characteristics appears to be higher than the average value taken from core analysis. The average water saturation based on oil-cut core data is 20 per cent of pore space. Initially, the reservoir pressure was 2,200 psi. Fluid analysis placed the bubble-point pressure at 1,640 psi. Wells for the most part are completed through the formation, perforated and given rather extensive acid jobs. Initial potentials after acidization frequently were over 1,000 B/D. Fluid properties used throughout the calculations are given in Figs. 1 and 2. Calculations were performed only from the bubble-point pressure to depletion conditions and do not consider production by liquid expansion from 2,200 psi to the bubble point. At bubble-point conditions, the oil had a solution gas-oil ratio of 690 scf/bbl and a viscosity of 0.748 cp.

The relative permeability curve resulting from averaging the results of measurements on numerous core samples is given in Fig. 3. Measurements were made by the "Penn State" or steady-state type of equipment. The curve shown in Fig. 3 was used in all calculations reported.

A basic value of 9-md air permeability was used for the formation. The effect of acidization around the wellbore was taken into account by increased values of permeability. The values of permeability around the well shown in Table 1 were used in all cases. An economic limit of 8 BOPD/well was used in all runs. The effect of constrictions around, but away from, the well was investigated by decreasing the permeability in one or more cells. For convenience, run numbers will be used in discussing the results. Table 1 gives data held constant in all runs. The cases or runs were designed to investigate the influence of five factors, and combinations thereof, on reservoir behavior and recovery: (1) the effect of a single permeability constriction; (2) the effect of two permeability constrictions; (3) the effect of drilling into a localized tight area; (4) the effect of reduced producing rate; and (5) the effect of spacing.

The effect of producing rate was studied by setting initial maximum-flow-rate boundary conditions of 100 and 200 BOPD so long as the well was capable of making its allowable, after which it declined at a sand-face-pressure boundary condition of 100 psi. The effect of spacing was investigated for two cases—radii of drainage corresponding to 40- and 80-acre spacing.

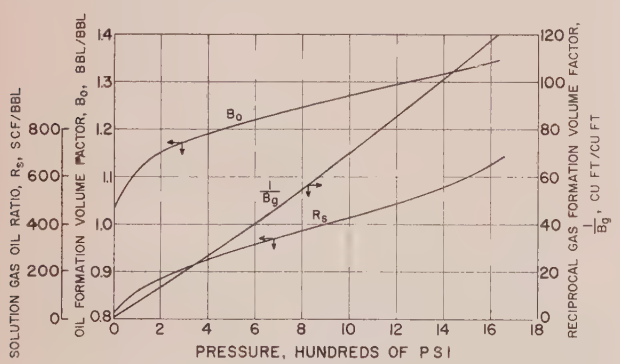
SOLUTION GAS OIL RATIO, R_s, SCF/BBL
OIL FORMATION VOLUME FACTOR, B_o, BBL/BBL
RECIPROCAL GAS FORMATION VOLUME FACTOR, $\frac{1}{B_g}$, CU FT/CU FT
B_o
$\frac{1}{B_g}$
R_s
PRESSURE, HUNDREDS OF PSI

FIG. 1—RESERVOIR FLUID PROPERTIES.

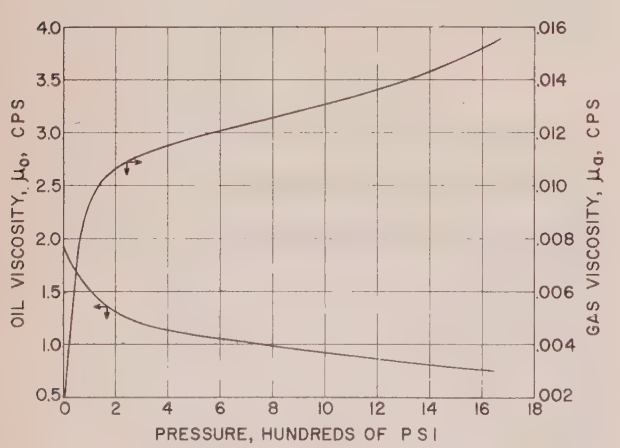

FIG. 2—RESERVOIR FLUID VISCOSITIES.

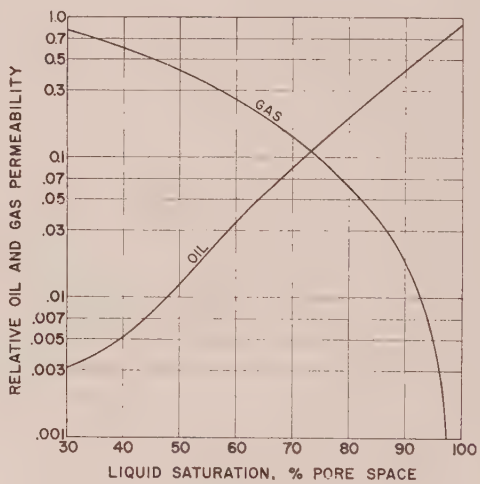

FIG. 3—RELATIVE OIL AND GAS PERMEABILITY.

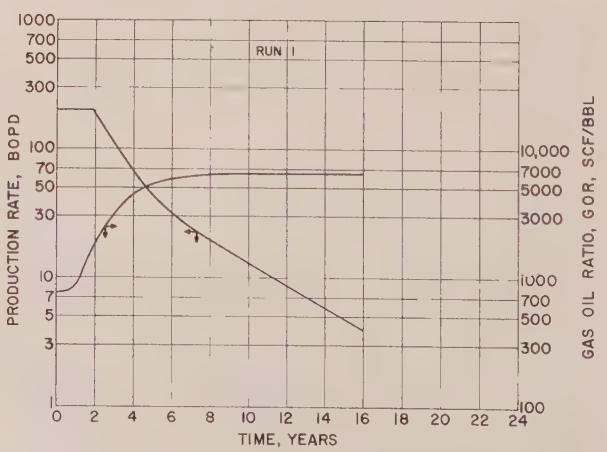

FIG. 4—PRODUCTION RATE DECLINE AND GAS-OIL RATIO FOR RUN 1. SPACING = 80 ACRES; PERMEABILITIES FROM TABLE 1; MAXIMUM FLOW RATE = 200 BOPD.

TABLE 1—CONSTANT RESERVOIR PROPERTIES

1. Formation Thickness = 42.9 ft
2. Original Oil Saturation = 80 per cent pore volume
3. Water Saturation = 20 per cent pore volume
4. Porosity = 11.26 per cent
5. Initial Oil in Place = 886,000 bbl for 40-acre spacing or 1,772,000 bbl for 80-acre spacing
6. Original Reservoir Pressure = 1,639 psi
7. Minimum Sand-Face Pressure = 100 psi
8. Well Radius = 0.3 ft
9. Acidization Effect Around the Wellbore:

Radius (ft)	Permeability (md)
0.3	
1.5	30
1.8	28
2.1	26
2.5	24
2.9	22
3.5	22
4.1	18
4.8	16
5.7	14
6.6	12
7.8	10

(Remainder 9 md Unless Specified)

10. Fluid Properties: Figs. 1 and 2
11. Relative Permeability Characteristics: Fig. 3

RESULTS

THE EFFECT OF A SINGLE PERMEABILITY CONSTRICTION

This effect was investigated in Runs 1, 2 and 3. All of these runs were made for 80-acre spacing at an initial flow rate of 200 BOPD. Run 1 had a uniform permeability of 9 md beyond the acidization zone around the wellbore. Run 2 contained a 1.5-md constriction from 395 to 548 ft, and in Run 3 the permeability of the constriction was decreased to 0.9 md. Results are given in Figs. 4 through 6.

Run 1 (Fig. 4) is the reference case for 80-acre spacing. Both the decline and gas-oil ratio curves are normal for a solution-gas-drive type of reservoir. The well is capable of making the allowed 200 BOPD for approximately 23 months. It should be noted that the GOR is always above the solution value of 690 scf/bbl. This is due to creation of a considerable free-gas saturation near the wellbore before the average reservoir oil saturation is noticeably decreased from its initial value. The maximum gas-oil ratio is around 6,400 scf/bbl. The well reaches an economic limit of 8 BOPD after 12.3 years and a cumulative production of 304,600 bbl, or 17.1 per cent of the initial oil in place.

In Run 2 (Fig. 5), the well starts to decline after producing at 200 BOPD for about 7.5 months. The producing rate declines to a minimum value of about 165 BOPD at 11 months. During this period, the majority of the production has come from inside the permeability constriction. The producing rate then increases continuously and reaches a maximum which is nearly equal to the original 200 BOPD after 17 months of production. From this point, the decline curve appears normal for a solution-gas-drive reservoir. The gas flow rate also fluctuates during the period in which the producing rate is varying, although it does not reach its maximum and minimum at the same time as the oil rate. The gas-oil ratio reaches a maximum after 9.5 months of production and declines to a minimum value of 1,020 scf/bbl at about 17 months. For this time on, behavior is more or less normal. The maximum gas-oil ratio is somewhat less than in the corresponding case without a permeability constriction. The economic limit is reached after 12.8 years, which is one-half year longer than the similar case without a partial barrier. Cumulative production at economic limit is 300,500 bbl, or approximately 98.6 per cent as much oil as without a partial barrier.

In Run 3 (Fig. 6), the same data were used as Run 2 except the permeability of the constriction was decreased to 0.9 md. The result is to magnify the effects which were obtained from Run 2. The well starts to decline after maintaining allowable about 6.5 months, or one month less than Run 2. The maximum and minimum in the production rate and gas-oil ratio are

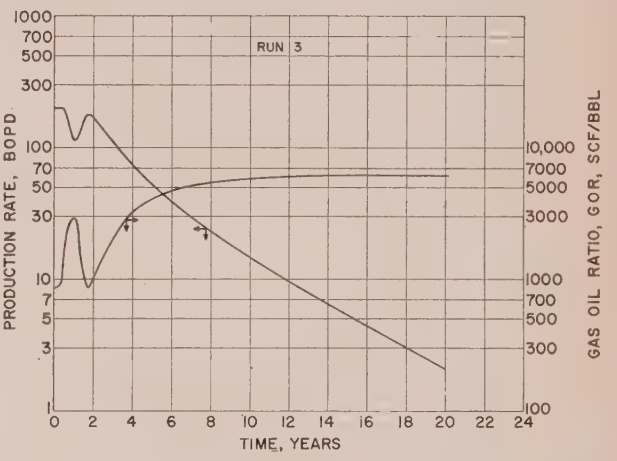

FIG. 6—PRODUCTION RATE DECLINE AND GAS-OIL RATIO FOR RUN 3. SPACING = 80 ACRES; PERMEABILITIES FROM TABLE 1, EXCEPT 0.9 MD FROM 395 TO 548 FT; MAXIMUM FLOW RATE = 200 BOPD.

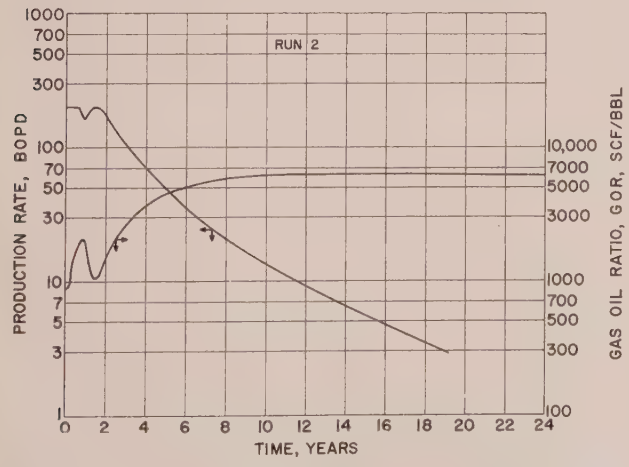

FIG. 5—PRODUCTION RATE DECLINE AND GAS-OIL RATIO FOR RUN 2. SPACING = 80 ACRES; PERMEABILITIES FROM TABLE 1, EXCEPT 1.5 MD FROM 395 TO 548 FT; MAXIMUM FLOW RATE = 200 BOPD.

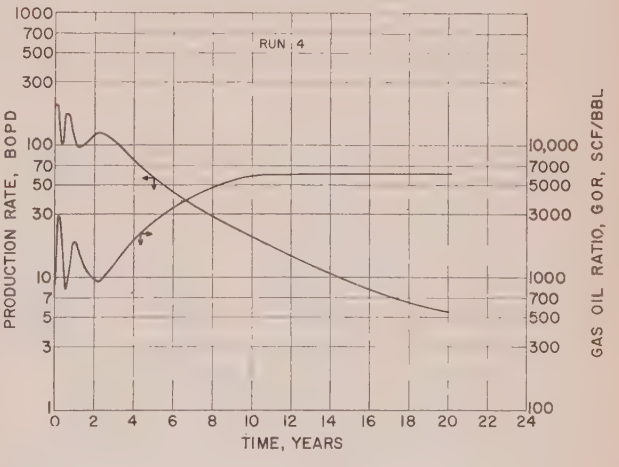

FIG. 7—PRODUCTION RATE DECLINE AND GAS-OIL RATIO FOR RUN 4. SPACING = 80 ACRES; PERMEABILITIES FROM TABLE 1, EXCEPT 0.9 MD FROM 175 TO 285 FT AND 0.9 MD FROM 395 TO 548 FT; MAXIMUM FLOW RATE = 200 BOPD.

more pronounced than those which occurred in Run 2, and they take place at about a 15 per cent later time. The cumulative oil production at the economic limit, which is reached after 13.3 years, is 299,800 bbl or 98.4 per cent as much oil as the case without a barrier.

THE EFFECT OF TWO PERMEABILITY CONSTRICTIONS

The effect of having two tight permeability zones around the well was investigated in Run 4 (Fig. 7). Restrictions of 0.9 md were located 175 to 285 ft and 395 to 548 ft from the wellbore. Initially, production comes from inside the first restriction, and the well goes on decline after about 0.2 years. The gas-oil ratio peaks before production rate reaches the first minimum. The second peaks in both gas-oil ratio and producing rates are broader due to the double restriction through which fluids must flow. The economic limit occurs in 16.2 years after a cumulative production of 287,000 bbl. This is 94.2 per cent as much oil as produced by the base case without any permeability restriction.

THE EFFECT OF DRILLING INTO A LOCALIZED TIGHT AREA

A permeability restriction of 0.9 md was placed around the wellbore in Run 5 from 7.8 to 548 ft. The remaining formation to 1,053 ft was at 9 md. The spacing was 80 acres and the maximum rate was 200 BOPD. Fig. 8 shows the rapid decline in production rate and the brief but sharp increase in gas-oil ratio. After the first two months, both rate and GOR remain fairly constant for a long period of time. After about 16 years, the gas-oil ratio starts to increase again and the rate starts to fall off more rapidly. Although not shown in the figure, the economic limit is reached in 27.5 years after a cumulative production of 249,000 bbl. This is 81.7 per cent as much oil as produced by the 80-acre case with uniform permeability of 9 md.

THE EFFECT OF REDUCED PRODUCING RATES

The effect of reduced producing rates may be seen by comparing Run 1 (Fig. 4) with Run 6 (Fig. 9) and Run 3 (Fig. 6) with Run 7 (Fig. 10). Run 6 is identical to Run 1 except that the production rate is held to a maximum of 100 BOPD. The well is capable of making its allowable for 5.8 years and reaches its economic limit of 8 B/D after 14.5 years, only 2.2 years longer than it took the 200-BOPD well. At this time, it has produced 304,300 bbl of oil as compared with the 304,600 bbl of oil produced by the 200-BOPD well in Run 1. From these two cases, cutting the allowable rate in half increases the length of time necessary to reach an economic limit, but it does not increase recovery.

Runs 3 (Fig. 6) and 7 (Fig. 10) both have a single 0.9-md restriction from 395 to 548 ft, and they are are similar except that the maximum rate is 200 BOPD in Run 3 and 100 BOPD in Run 7. This extends the economic limit from 14.3 to 16.5 years. Cumulative production for the 100-BOPD case is 300,300 bbl. The 200-BOPD case produced 299,800 bbl, or 500 bbl less than the 100-BOPD well. The maximums in gas-oil ratios in both cases are about the same, but the magnitude of the hump in GOR is decreased in the 100-BOPD case. The lower allowed production rate has suppressed the peak in the decline curve.

THE EFFECT OF SPACING

The effect of spacing on recovery may be seen by comparing Run 8 (Fig. 11) with Run 1 (Fig. 4) and Run 3 (Fig. 6) with Run 9 (Fig. 12). Run 8 is the 40-acre base case for a reservoir having a uniform permeability of 9 md beyond the zone affected by acidization. Maximum producing rate is 200 BOPD, and the well is capable of making this allowable for one year, after which the production rate declines more-or-less hyperbolically. The cumulative stock-tank oil pro-

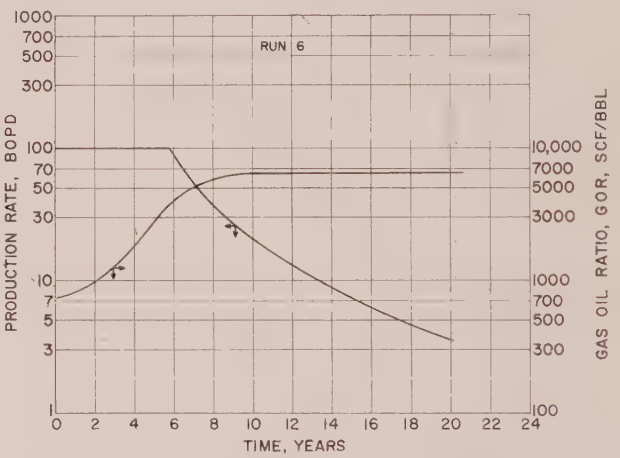

FIG. 9—PRODUCTION RATE DECLINE AND GAS-OIL RATIO FOR RUN 6. SPACING = 80 ACRES; PERMEABILITIES FROM TABLE 1; MAXIMUM FLOW RATE = 100 BOPD.

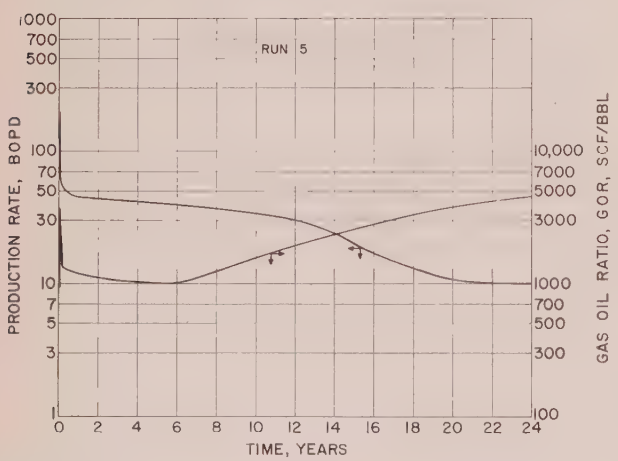

FIG. 8—PRODUCTION RATE DECLINE AND GAS-OIL RATIO FOR RUN 5. SPACING = 80 ACRES; PERMEABILITIES FROM TABLE 1, EXCEPT 0.9 MD FROM 7.8 TO 548 FT; MAXIMUM FLOW RATE = 200 BOPD.

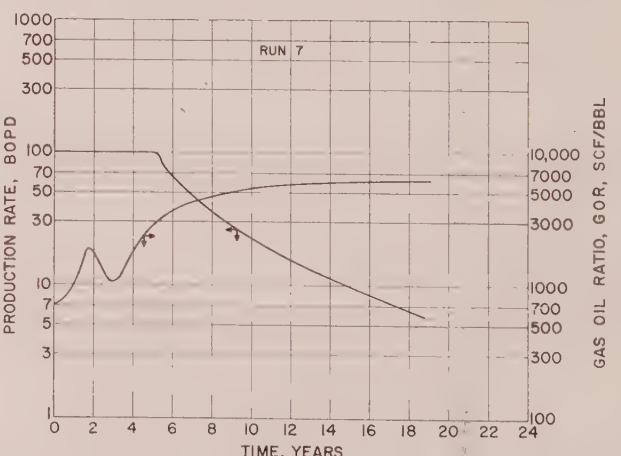

FIG. 10—PRODUCTION RATE DECLINE AND GAS-OIL RATIO FOR RUN 7. SPACING = 80 ACRES; PERMEABILITIES FROM TABLE 1, EXCEPT 0.9 MD FROM 395 TO 548 FT; MAXIMUM FLOW RATE = 100 BOPD.

duction at an 8-BOPD economic limit is 152,700 bbl after 6.0 years. Run 1 has already been discussed. It is the reference case for 80-acre spacing, and its characteristics are very similar to Run 8 except that the time scale is approximately doubled. It is interesting to note that the maximum gas-oil ratios in both cases are almost exactly the same. Here the well takes 12.3 years to reach an economic limit, or 2.05 times longer than the 40-acre case. Cumulative oil production at the economic limit is 304,600 bbl. At the same economic limit of 8 BOPD/well, the calculations indicate that one 80-acre well will produce 99.7 per cent as much oil as two 40-acre wells but will take 2.05 times longer to do it.

Run 3 (Fig. 6) with 80-acre spacing and Run 9 (Fig. 12) with 40-acre spacing each have an 0.9-md constriction from 395 to 548 ft from the wellbore and a maximum producing rate of 200 BOPD. Run 3 reached an economic limit in 13.3 years after a cumulative production of 299,800 bbl. The 40-acre well in Run 9 reaches its economic limit in 7.0 years after a cumulative production of 150,100 bbl. In the case of a single permeability restriction, one 80-acre well produces about 99.8 per cent as much oil as two 40-acre wells and requires 2.04 times longer to do it. It is interesting to note that presence of a barrier has no effect on comparisons between 40- and 80-acre spacing at the economic limit.

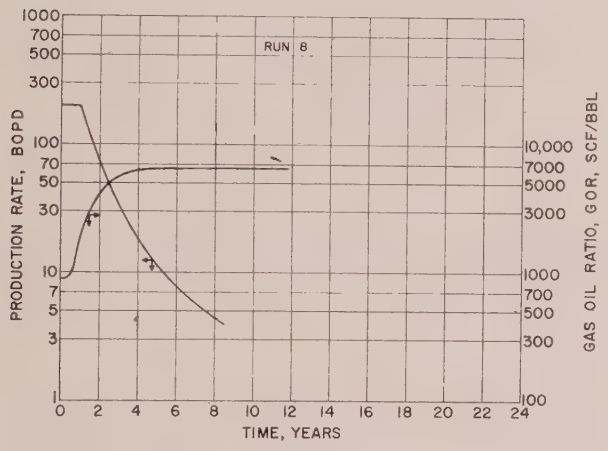

Fig. 11—Production Rate Decline and Gas-Oil Ratio for Run 8. Spacing = 40 Acres; Permeabilities from Table 1; Maximum Flow Rate = 200 BOPD.

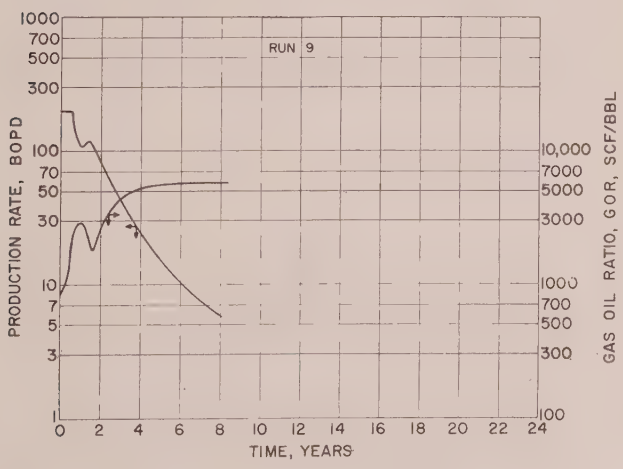

Fig. 12—Production Rate Decline and Gas-Oil Ratio for Run 9. Spacing = 40 Acres; Permeabilities from Table 1. Except 0.9 md from 395 to 548 ft; Maximum Flow Rate = 200 BOPD.

DISCUSSION

Some of the results from the various runs were unexpected and rather surprising. Of particular interest were the reversals in rate of decline and gas-oil ratio occasioned by presence of a permeability constriction

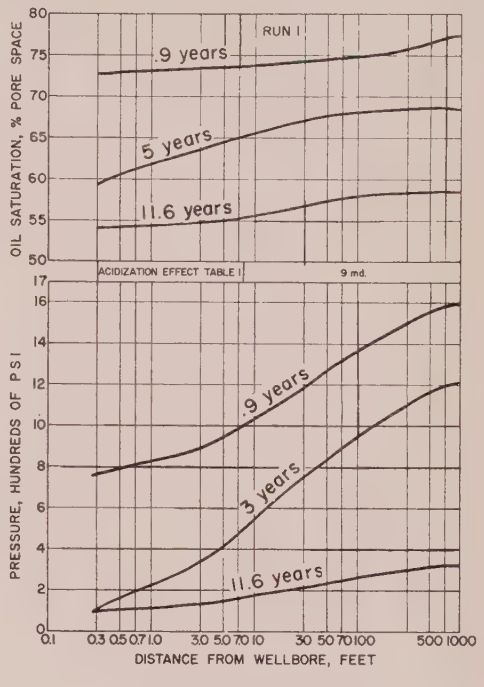

Fig. 13—Pressure and Oil Saturations from Run 1 as a Function of Distance from the Wellbore at Different Times.

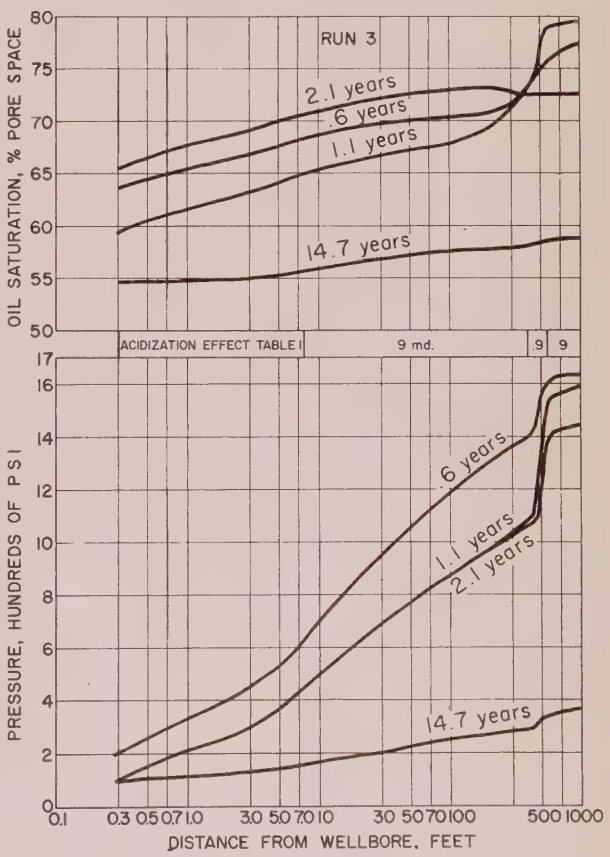

Fig. 14—Pressure and Oil Saturations from Run 3 as a Function of Distance from the Wellbore at Different Times.

surrounding the wellbore. Another interesting result was that a zone more than 100-ft wide having 10 per cent of the permeability of the remaining rock has little effect on cumulative recovery at economic limit.

The key to this behavior lies in changes in saturations and pressures with time throughout the reservoir. Fig. 13 shows the oil saturation and pressure profiles at three different times for Run 1, the case that had no permeability constriction. The results are more or less as would be expected. The curves closer than 7.8 ft from the wellbore are influenced by the acidization effect.

Fig. 14 portrays similar plots at four different times for Run 3, the case with the 0.9-md restriction. Inspection of the pressure curves shows a normal behavior at 0.6 year, which corresponds to the well going off the 200-BOPD allowable. The minimum in production rate occurs at 1.1 years. As oil flowing through the constriction starts to increase the production rate to a maximum at 1.9 years, the pressure between the well and the constriction remains essentially constant. After this, the pressure declines continuously. Approximate abandonment conditions are shown by the 14.7-year curve. A look at the oil saturations shows little drainage beyond the constriction at 0.6 year. At 1.1 years, saturations throughout the reservoir have decreased, and the region beyond the constriction is starting to drain. At 2.1 years, saturations inside the constriction are slightly higher than outside. This is a transient situation which smooths out to a normal decrease in oil saturation nearer the wellbore. Again, approximate abandonment conditions are shown by the 14.7-year curve.

Examination of the data shows that the following chain of events occurs due to the presence of a permeability constriction. Initially, most of the production comes from inside the constriction. Here pressures fall normally. This produces an increasing pressure difference across the zone of decreased permeability which increases the oil throughput. Oil flowing through the constriction moves toward the well, resaturating the formation as it goes. This resaturation of the reservoir with oil causes the permeability of the formation to oil to be increased, which results in less pressure drop per unit of oil flow. This produces a decrease in GOR before the oil bank reaches the wellbore. Arrival at the well causes a rapid increase in production rate. Thereafter, rate of production decline depends on the distance and magnitude of the constriction. For moderate restrictions, reversals in rate are produced by saturation increases between the well and the partial barrier.

It is felt that results of this study should be indicative of the behavior of solution gas-drive fields as far as the effects of spacing and proration on oil recovery at economic limit are concerned. Analyzing the possible effect of a multitude of permeability variations on production rate decline and GOR curves is more difficult. The result could be a large number of small fluctuations in decline and GOR which when combined in the wellbore might result in smooth curves similar to runs without variation. However, it is quite possible that some of the vagaries in actual decline curves are due to inhomogeneities out in the formation rather than changes at or in the wellbore.

On the basis of this work, it appears that permeability variation may tend to hold down gas-oil ratios. They may produce decline curves that seem to show evidence of reservoir energy sources other than the solution-gas-drive mechanism. Drilling into a tight area in Run 5 resulted in flat curves, portions of which appear to be the result of gravity drainage. The work reported here is exploratory in nature, and many more possibilities must be considered before direct application can be made to field conditions.

CONCLUSIONS

A mathematical model study of a solution-gas-drive reservoir has been made neglecting capillary forces and gravity. As a result, the following conclusions can be drawn for the cases considered.

1. Substantial permeability constriction, located at some distance from the well and about 100-ft thick, only slightly decreases the recovery at economic limit.

2. Development on 80-acre spacing produces substantially as much total oil recovery at economic limit as 40-acre development, but requires twice the time within the limited conditions which were studied.

3. Curtailment of production from 200 to 100 BOPD does not significantly alter recovery at economic limit, but increases time required to obtain this recovery.

4. Zones of decreased permeability at some distance from the wellbore can produce short-term increases in production rate and decreases in gas-oil ratio.

5. A restriction near the wellbore may produce decline and GOR curves that appear to show evidence of production mechanisms other than solution-gas drive.

ACKNOWLEDGMENTS

The authors wish to express their appreciation to John W. Sheldon of the Computer Usage Co. for development work on the program and to Continental Oil Co. for permission to publish this paper. ★★★

Simplified Analysis Aids in Optimizing Drilling Factors for Minimum Cost

H. W. R. WARDLAW
MEMBER AIME

BATAAFSE INTERNATIONALE PETROLEUM MAATSCHAPPIJ N.V.
THE HAGUE, THE NETHERLANDS

ABSTRACT

This paper shows how the cost of the drilling operation per 100-ft drilled can be related directly to bit weight, rotary speed and hydraulic horsepower variations. This enables optimum drilling conditions to be determined in a rapid and concise manner.

The paper also shows how data for such calculations can be obtained quickly and accurately by the "drill-off" method suggested by Lubinski.

Examples are given to illustrate the principles and methods used.

INTRODUCTION

The problem of drilling oil wells at lowest cost and hazard needs little introduction, since it has been with us virtually from the earliest days of our industry.

With better understanding of the effect of the various factors of bit weight, rotary speed and hydraulic jet action, however, the problem has recently taken on a more scientific aspect, and engineers or groups of engineers have been assigned to study many of the facets of this problem not immediately apparent to the general observer.

Moreover, the availability of better equipment and materials has enabled certain practices to be adopted which were hitherto impractical or uneconomic. This has paved the way for further efforts to reduce footage costs, and so on.

The improvements to be made in drilling technology and cost reduction are by no means exhausted, and we still frequently hear of new records being set and new materials and equipment becoming available.

Some of the analytical methods used by the author to assist in promoting faster and more economic methods of drilling, particularly in Venezuela, form the basis for this descriptive study.

STATEMENT OF THEORY AND DEFINITIONS

In a highly competitive industry, it is no longer permissible to regard penetration rate as the sole criterion for drilling efficiency. Every new technique, however spectacular, must nowadays be viewed in the cold light of whether it will eventually lead to lower cost per foot drilled.

Original manuscript received in Society of Petroleum Engineers office July 8, 1960. Revised manuscript received Feb. 6, 1961. Paper presented at 35th Annual Fall Meeting of SPE, Oct. 2-5, 1960, in Denver.

In the exposition which follows, therefore, actual drilling rates will play only a secondary role, and attention will be focused on the more important aspect of cost per foot drilled. Changes in drilling factors such as weight and rotary speed will be studied in the light of how they directly affect the cost of operations.

The advantage of this method is twofold—(1) cost increments are indicated directly; and (2) the relationships are, surprisingly enough, simpler than those relating to drilling rates.

To achieve these advantages, it is necessary to introduce a new unit of measurement which, although unfamiliar, is readily understood.

The unit in question will be referred to as the "actual drilling cost factor" and will be designated by the symbol h. The unit is defined as the number of rotating hours taken to penetrate 100 ft of formation. The unit can be obtained immediately from the actual drilling rate (r) in feet per hour; thus,

$$h = \frac{100}{r} \quad \ldots\ldots\ldots\ldots\ldots (1)$$

The new unit may also be converted rapidly into "on-bottom" drilling cost per foot (C) by multiplying by the rig-time cost (C_R) in (hundreds of) dollars per hour. Thus,

$$C = h\,(C_R) \quad \ldots\ldots\ldots\ldots\ldots (2)$$

This latter transformation is so easily effected that it may be convenient to use h as an international symbol for drilling cost, and to delay conversion to dollars, bolivars, pounds, etc, per foot until actually required (e.g., for fiscal reasons, etc.).

In actual operations, h was found to vary in a relatively simple manner with increases in bit weight.

The variation in h with rotary speed was found to be somewhat more complex. However, this also could be enormously simplified by introducing a further factor known as L or relative bit life. The factor L is also defined very simply by dividing 1,000 by the rotary speed (N) in revolutions per minute.

Thus,

$$L = \frac{1{,}000}{N} \quad \ldots\ldots\ldots\ldots\ldots (3)$$

The factor L is thus the number of hours taken to rotate the bit 60,000 times.

The actual bit life (t_o) in hours can be obtained from the relative bit life (L) by the following simple equation.

$$t_o = L\,(k) \quad \ldots\ldots\ldots\ldots\ldots (4)$$

In this case, k is a dimensionless factor, depending on the bit weight, formation, drilling fluid, etc.

It will be noted that h is expressed in hours per 100-ft drilled, and L is expressed in hours per 60,000 revolutions of the bit. Both units are obtained immediately by taking the reciprocal of the more familiar units of penetration rate and rotary rpm. The new units are, however, far more significant and simplify cost calculations considerably.

It will be noted that h refers to the number of hours actual drilling "on-bottom" required to drill 100-ft of formation. Needless to say, the cost of the bits and round-trips required also play a significant part in drilling economics.

Therefore, we shall introduce the following additional terms.

t_1 = time (in hours) taken to make a round-trip,
b = equivalent cost of the bit in hours of rig-time,
f = footage made by the bit in hundreds of feet, and
H = over-all cost of drilling in hours per 100 ft.

We may also state the following equivalence.

$$h = \frac{t_o}{f} \quad . \quad . \quad . \quad . \quad . \quad . \quad . \quad . \quad . \quad . \quad . \quad . \quad (5)$$

The general equation then becomes

$$H = \frac{t_o + t_1 + b}{f} \quad . \quad . \quad . \quad . \quad . \quad . \quad . \quad . \quad . \quad (6)$$

Or, expressed in more convenient form

$$H = h\left[1 + \frac{t_1 + b}{t_o}\right] \quad . \quad . \quad . \quad . \quad . \quad . \quad . \quad . \quad . \quad (7)$$

The engineer's problem, therefore, is largely one of minimizing H by manipulating drilling factors such as weight, rotary speed and bit hydraulics in such a way that h is kept as low as possible, within reasonable limits for the second term within the square brackets in Eq. 7.

RIG TECHNIQUES

The technique used for obtaining instantaneous drilling rates under various conditions is that proposed by Lubinski in 1958.[1] This method is often referred to as the "drill-off" method and utilizes the elastic properties of steel to determine the drilling rate from observed rate of change of drilling weight with the brake chained down.

Lubinski's formula is as follows.

$$r = L' \times \frac{1}{EA} \times R_w \quad . \quad . \quad . \quad . \quad . \quad . \quad . \quad . \quad (8)$$

where

r = the rate of penetration, feet per hour,
R_w = the rate with which the weight on the bit is decreasing, pounds per hour,
E = the Young's modulus of steel; E = 30×10^6 psi,
A = the cross-sectional area of drill-pipe wall, square inches, and
L' = the length of drill pipe, feet.

[1]References given at end of paper.

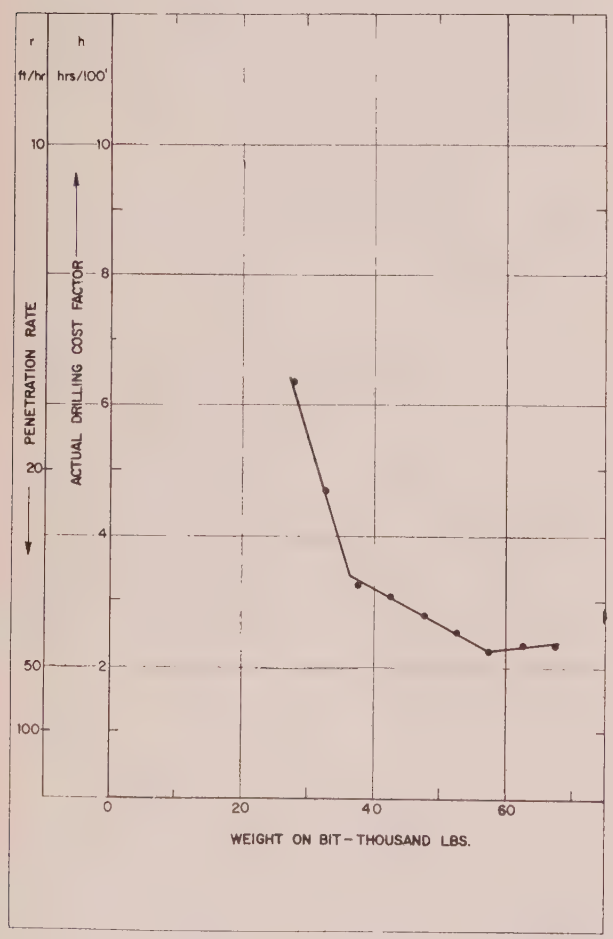

FIG. 1—COST VS BIT WEIGHT IN SANDY SHALE (ROTARY).

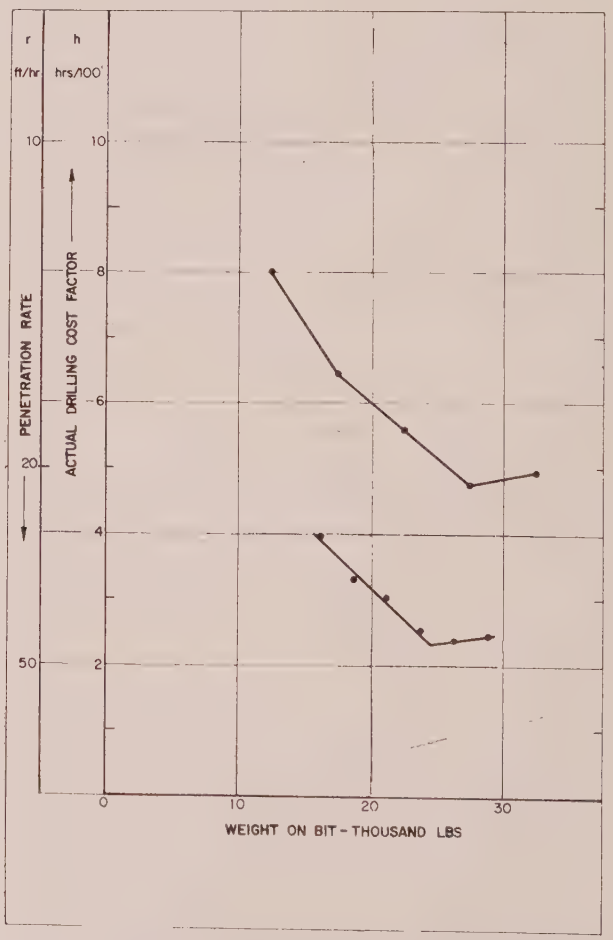

FIG. 2—COST VS BIT WEIGHT IN FRACTURED GRANITE (TURBODRILL).

This formula is easily modified as follows. From Eq. 1,

$$h = \frac{100 \times E \times A}{L' \times R_w} \quad \ldots\ldots\ldots \quad (9)$$

if t_2 is the time in seconds taken to drill off 5,000 lb:

$$R_w = \frac{5{,}000 \times 3{,}600}{t_2} \quad \ldots\ldots\ldots \quad (10)$$

Combining Eqs. 9 and 10,

$$h = t_2 \left[\frac{E \times A}{180 \times L' \times 10^2}\right] \quad \ldots\ldots\ldots \quad (11)$$

The quantity inside the bracket is rapidly and easily computed for the depth at which the measurements are taken, so that the value h is a direct multiple of the stop-watch reading. In the case of worn drill pipe, it may be desirable to use a correction factor to obtain the absolute true values. This factor can be computed by making a direct reading of the penetration rate and comparing it with that obtained from the drill-off formula. Thereafter, the drill-off method is preferable to direct readings because it enables a large volume of data to be obtained over a very short depth interval.

Replications are made by this method as far as is necessary to obtain consistent data, especially if the formation lacks homogeneity.

In sandy shales encountered in Venezuela, the drill-off method was found highly practical, even at rates as high as 120 ft/hour, and was the method used almost exclusively for the latest tests. For the higher penetration rates, a stop watch with 10-second sweep proved to be a valuable asset, although by no means essential.

TABLE 1—DATA OBTAINED FROM DRILL-OFF RUN.

Bit Weight (1,000 lb)	t_2	h
70-65	26	2.35
65-60	26	2.35
60-55	25	2.26
55-50	28	2.53
50-45	31	2.80
45-40	34	3.07
40-35	36	3.25
35-30	52	4.70
30-25	70	6.33

PRESENTATION OF RESULTS AND DATA

EFFECT OF WEIGHT-ON-BIT

Fig. 1 shows the results of a drill-off run using the method described in the preceding paragraph. Conditions for this run were as follows: hole size, 9⅝ in.; depth, 10,360 ft; drill collars, 630 ft; drill pipe, 9,730 ft; table speed, 130 to 135; bit hp (hydraulic), 434; formation, sandy shale; and drill-pipe size, 5-in. XH.

Data obtained are listed in Table 1.

Figures in the right-hand column are computed from Eq. 11, using $A = 5.275$ (sq in.) and $L' = 9{,}730$ (ft).

Inspection of Fig. 1 reveals three phases of response to drilling weight: Phase 1 (up to 36,500 lb); Phase 2 (36,500 to 57,500 lb); and Phase 3 (above 57,500 lb).

Replication revealed that the phases do not represent changes in formation but actual phenomena associated with ranges of weight-on-bit. Similar patterns were observed on the other runs made, although the limits occurred at different weights when drilling a different-type formation, or when the hydraulic conditions were changed.

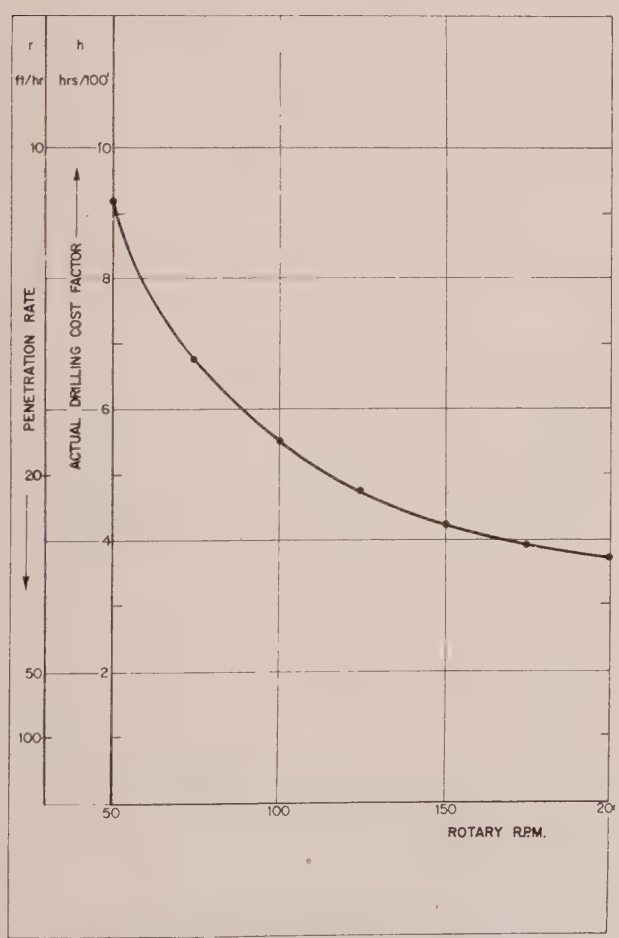

FIG. 3—COST VS ROTARY SPEED IN SANDY SHALE (ROTARY).

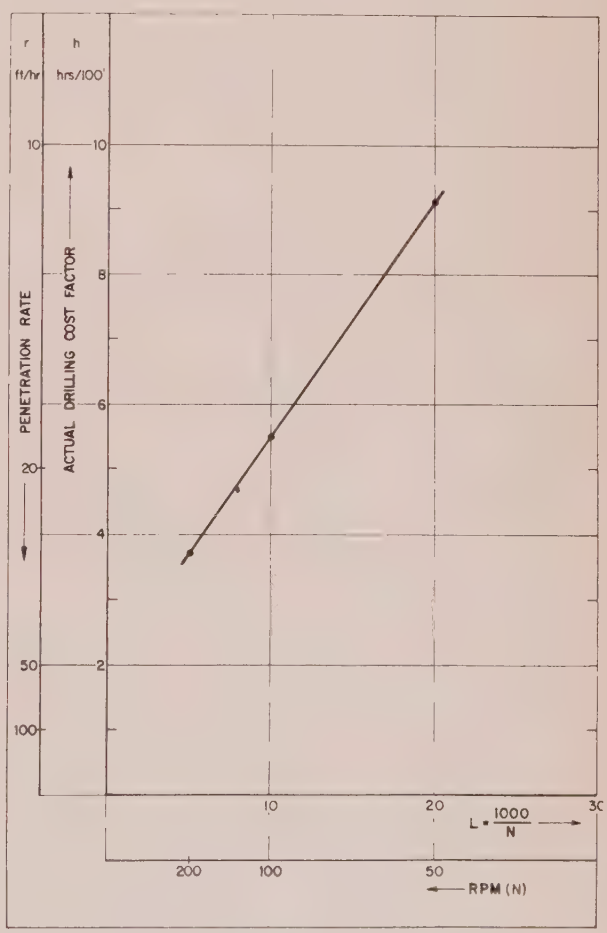

FIG. 4—COST VS RELATIVE BIT LIFE (INVERSE OF ROTARY SPEED).

Similar results were obtained during turbodrill runs. However, in this case the rotary speed was not kept constant but depended on weight and other factors controlled by the design of the turbine used. Fig. 2 shows the results of drill-off tests using a 7¼ in. OD turbine coupled to an 8½ in. insert-type bit for drilling granite. The lower figure is for the upper crust of the granite section, which was considerably fractured.

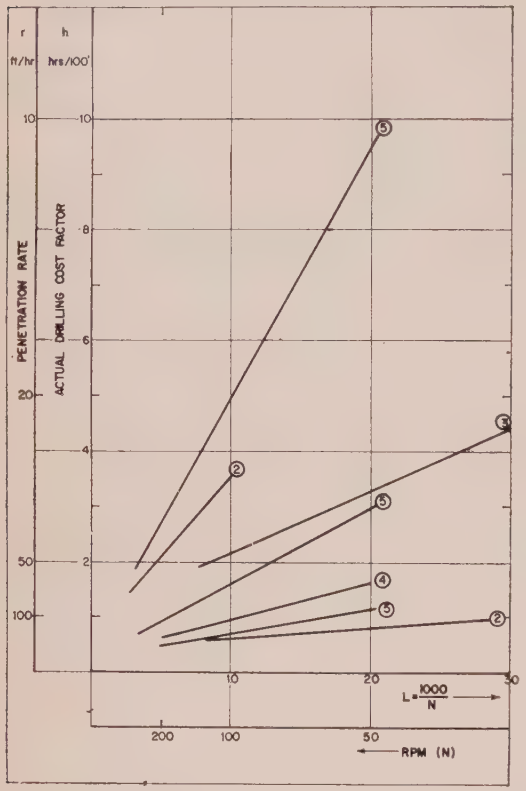

FIG. 5—COST VS RELATIVE BIT LIFE. (SEE LIST OF REFERENCES.)

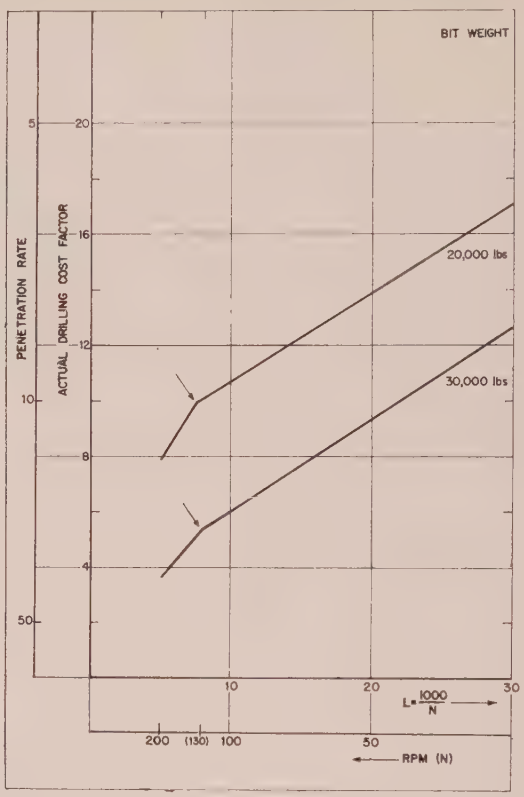

FIG. 7—COST VS RELATIVE BIT LIFE IN SANDY SHALE (ROTARY).

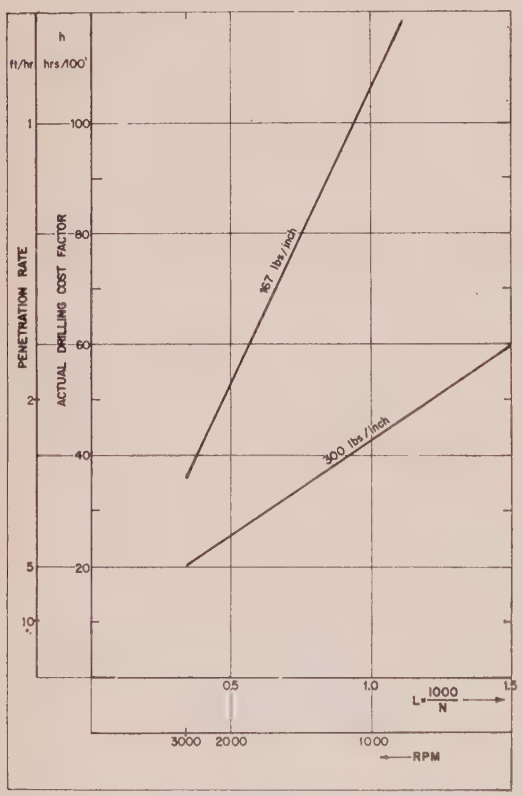

FIG 6—COST VS RELATIVE BIT LIFE (LABORATORY DRILLING IN GRANITE).

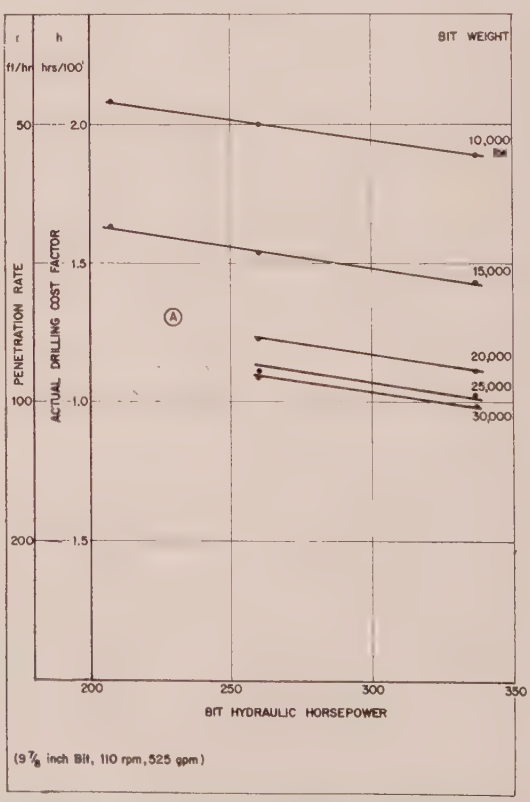

FIG. 8—COST VS BIT HYDRAULIC HORSEPOWER IN SHALE (ROTARY).

The drill-off method also allows accurate comparisons of response to drilling in the same formation at varying rotary speeds. Here again, replications may have to be made to ensure that the readings are representative, and the speed changed only after consistent results are obtained from several replications.

EFFECT OF ROTARY SPEED

Fig. 3 shows the results of drilling sandy shale at about 10,000 ft, with various rotary speeds but with constant weight of 30,000 lb on a 12¼-in. bit. The drilling cost h in hours per 100 ft is represented by a smooth curve decreasing at first rapidly and then slowly with increasing rpm.

If, however, the scale of rpm (N) is replaced by a scale of $L = 1{,}000/N$ as obtained by Eq. 3, the picture is considerably simplified. Fig. 4 illustrates this point. It will be noted that the results follow a straight-line relationship almost exactly.

An examination of published results shows that this is by no means an exceptional result. In fact, most of the data[2-5] studied by the author showed similar linearity of plot when examined using these ordinates. Fig. 5 shows a number of sets of data taken from the literature on this subject, which now show markedly linear relationship between these simple functions.

It is interesting to note that this straight-line relationship extends to higher speed ranges, as shown in Fig. 6, which shows results of drilling granite in the laboratory at high speeds, as indicated in published literature.[5]

Occasionally, the straight-line relationship may show

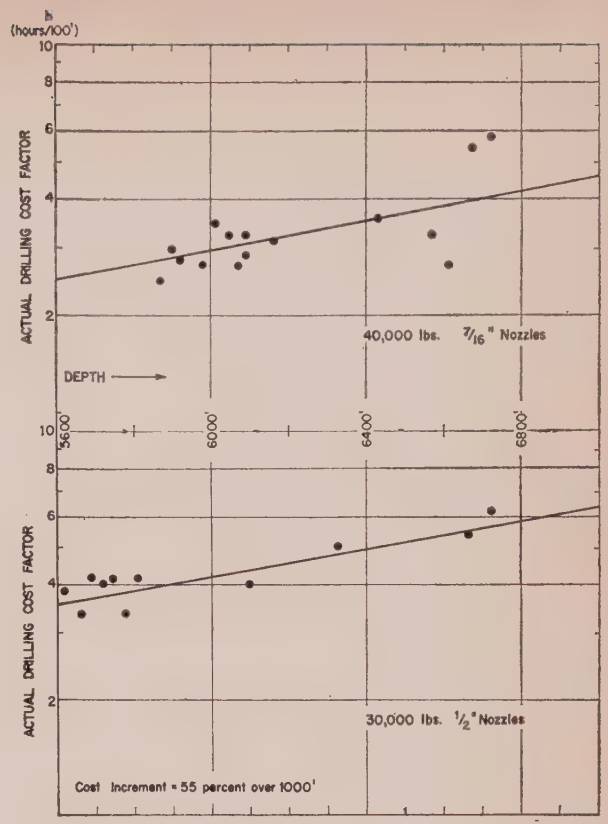

FIG. 10—COST VS WELL DEPTH IN SANDY SHALE (ROTARY).

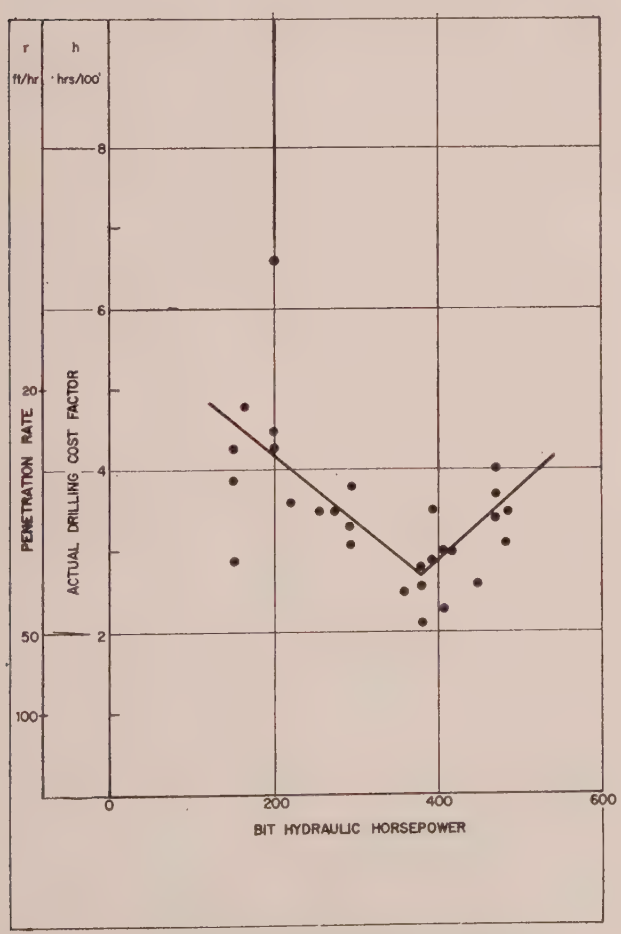

FIG. 9—COST VS BIT HYDRAULIC HORSEPOWER IN SANDY SHALE (ROTARY).

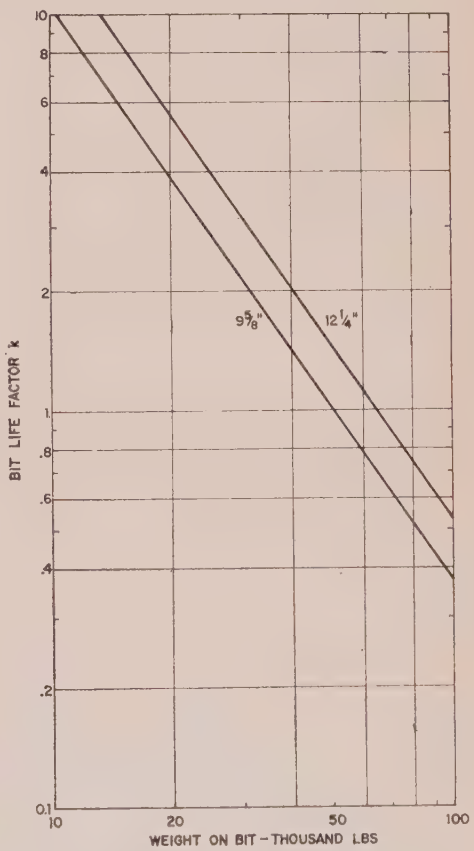

FIG. 11—BIT LIFE FACTOR VS BIT WEIGHT IN SANDY SHALE (ROTARY).

an abrupt change of slope as indicated in Fig. 7 which was prepared from our own data from Lake Maracaibo drilling. The change takes place at approximately 130 rpm and perhaps may indicate the point at which vacuum starts to occur beneath the formation chip.[6]

EFFECT OF HYDRAULIC HORSEPOWER

The effect of bit hydraulic horsepower on the drilling cost factor h also is relatively simple.

Fig. 8 shows the relationship for shale according to information given in the literature,[7] from which it will be noted that the cost factor is reduced by a fixed amount per unit of hydraulic horsepower, irrespective of weight. In the region of Point A, however, the bit is balled up and erratic values are indicated.

For Lake Maracaibo conditions, there was some indication that, for very high values of bit hydraulic horsepower, the penetration rate actually decreased; the cost factor, therefore, actually increased with hydraulic horsepower above a certain value. Fig. 9 illustrates this point. The data are taken from a field test in Lake Maracaibo concessions. Drilling is in Eocene sandy shale at approximately 6,000 ft, using 9⅝-in. diameter bit rotating at 85 to 120 rpm, with 40,000-lb weight-on-bit.

The explanation of this effect is probably that the higher horsepower creates excessive turbulence, which may tend to return some of the chips to a position below the teeth where they are re-ground.

EFFECT OF DEPTH

Both penetration rate and drilling cost factor were found to vary approximately logarithmically with depth. In some of the early tests in Venezuela, the drill-off method was not yet in use so that results covered a much wider interval of depth. In such cases a correction factor may be used, based on a logarithmic relationship such as shown in Fig. 10, so that all data could be related to a reference depth of, say, 6,000 ft. The slope of the line represents the percentage increment of cost per foot (over unit depth interval).

INFLUENCE OF BEARING AND TOOTH WEAR

As indicated in Eq. 7, the over-all cost factor H is made up of two parts, the second part being the actual drilling cost factor h times a term depending mainly on round-rip time and bit life.

Eqs. 3 and 4 show that the bit life in turn depends on: (1) the rotary speed used; and (2) the dimensionless factor k, which varies with bit weight, formation characteristics, drilling fluid, and so on.

To establish the value of k for various bit weights, an empirical log-log plot is necessary, based on bit life over a large number of bits and using Eqs. 3 and 4 for computation. The values of k for 9⅝ and 12¼-in. bits, for drilling sandy shale in Lake Maracaibo southern block at 10,000 ft, are shown in Fig. 11. It should be noted that this formation is not abrasive and that bits usually are pulled on account of bearing wear in this instance.

The method of estimation of bit life is similar to that suggested by Graham and Muench in a recent publication.[8] The value for the exponent s from this paper corresponding to the data shown in Fig. 11 would be 1.46, which is close to the value 1.5 suggested by these authors as an initial estimate.

The bit life in Lake Maracaibo drilling was also

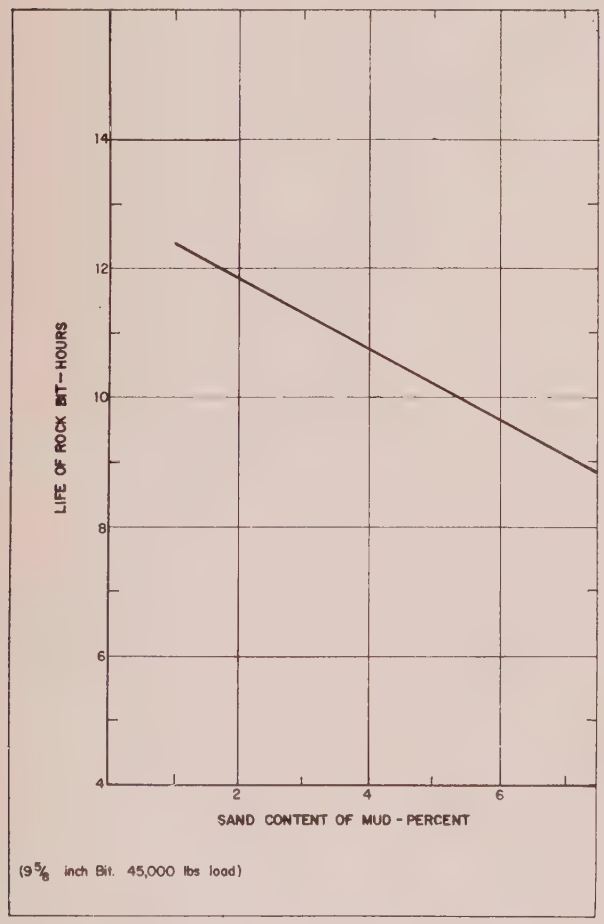

Fig. 12—Bit Life vs Sand Content.

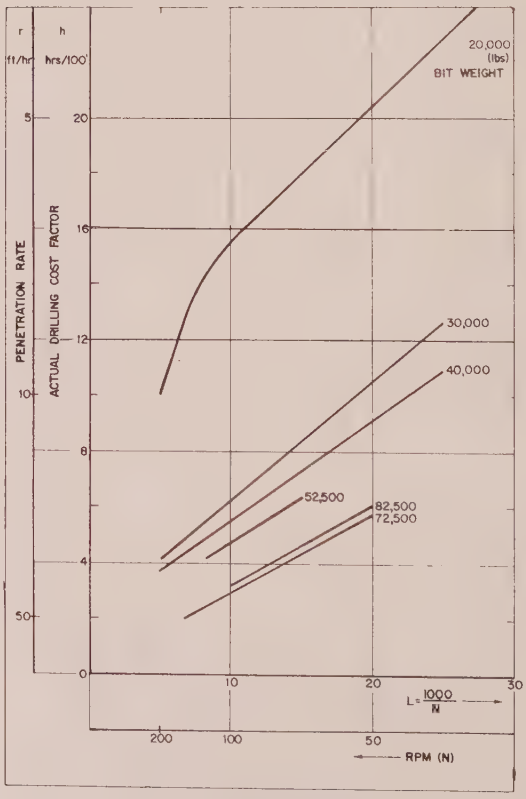

Fig. 13—Cost vs Relative Bit Life in Sandy Shale (Rotary).

found to vary appreciably with sand content of the mud, as shown in Fig. 12.

INFLUENCE OF ROUND-TRIP TIME

The round-trip time is also a component of Eq. 7. This in turn depends on depth, size of drill pipe, size and length of drill collars (depending also on bit weight), and design and capacity of the rig. Crew experience is also a relevant factor, together with the manipulative skill of the driller.

Round-trip time may also have to include time working on the pumps, so that it is important to use only the best grade of materials for pump parts.

EXAMPLE OF DRILLING-DATA INTERPRETATION

To illustrate how optimum drilling conditions may be established by the methods shown in the preceding paragraphs, an example will be taken from actual field measurement.

The results of the drill-off runs are shown in Fig. 13. In this case bit hydraulic horsepower was around 500, which was near-optimum for the 12¼-in. bit used. Sets of readings were taken at various bit weights as indicated. All sets showed near-straight-line correlation, except the 20,000-lb set which showed a characteristic droop.

If desired, the effect of the factors on cost of bits plus round-trips (per 100 ft) can be indicated by calculating the right-hand term inside the bracket of Eq. 7 and multiplying by h for a suitable set of points. This is shown in Fig. 14.

The over-all drilling cost (H) per 100 ft is given by repeating the process using the entire Eq. 7. Results are shown in Fig. 15. The inverse plot, using L rather than N as abscissa (Fig. 15), is preferred, especially where extrapolation is desired for rotary speeds outside the range actually tested (e.g., for turbodrill estimates). However, the same data can of course be plotted using a straight scale for rpm as abscissa (Fig. 16).

Lowest cost for convenient rotary operation is indicated as 5.1 hours/100 ft drilled, occurring at 72,500 lb and 150 rpm. Higher rotary speeds were impractical at this weight-on-bit.

Conversion to monetary value may be made immediately by using the equivalent of Eq. 2; e.g., at \$120/hour, the minimum cost would be \$1.20 × 5.1 equals \$6.12/ft.

CONCLUSIONS

1. By relating weight, rotary speed and hydraulic horsepower to cost in hours per 100 ft, definite advantages are gained in clarity and simplicity of results.

2. Lubinski's "drill-off" method proved entirely practical for collecting a large volume of data over a very short depth interval. This method may also be used for turbodrill runs.

3. Straight-line relationships were found between cost in hours per 100 ft drilled and weight-on-bit, over wide ranges of bit weight.

4. Straight-line relationships were found between cost in hours per 100-ft drilled and hours per 60,000 revolutions (inverse of rpm).

5. Straight-line relationships were found between cost in hours per 100-ft drilled and bit hydraulic horsepower.

6. By adding the cost of bits and round-trips per 100-ft drilled, the over-all cost in hours per 100-ft drilled can be easily related to bit weight and rotary speed.

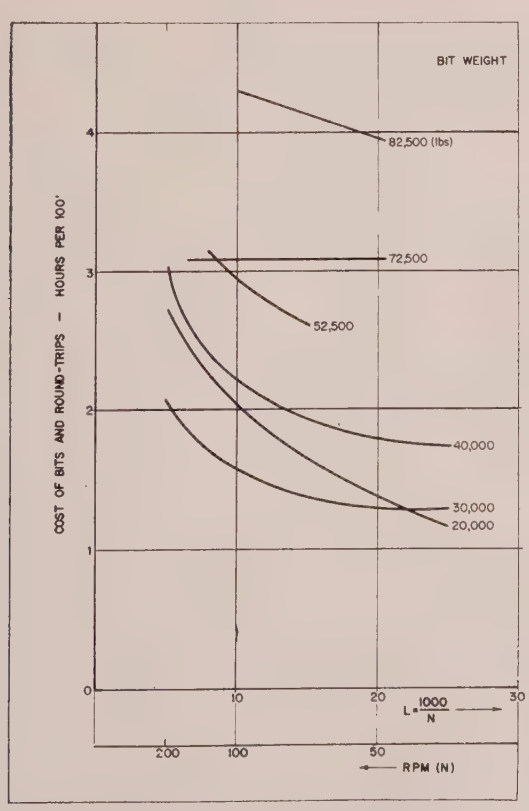

FIG. 14—COST OF BITS AND ROUND TRIPS IN SANDY SHALE (ROTARY).

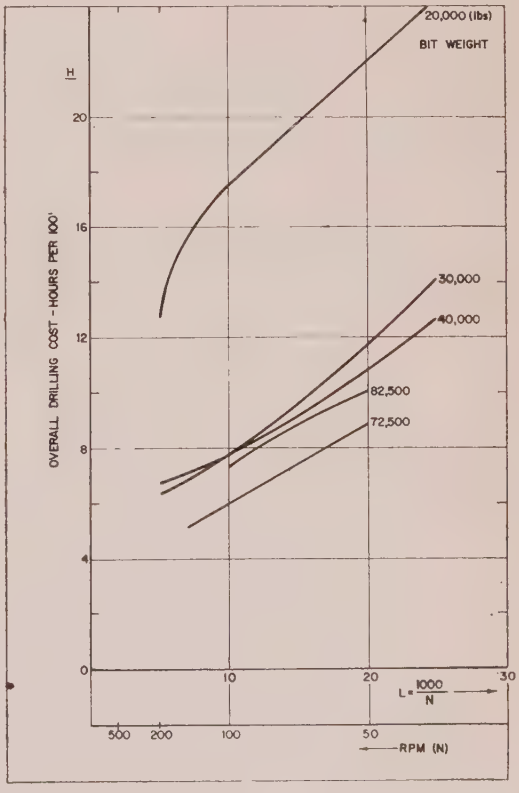

FIG. 15—OVER-ALL COST VS RELATIVE BIT LIFE IN SANDY SHALE (ROTARY).

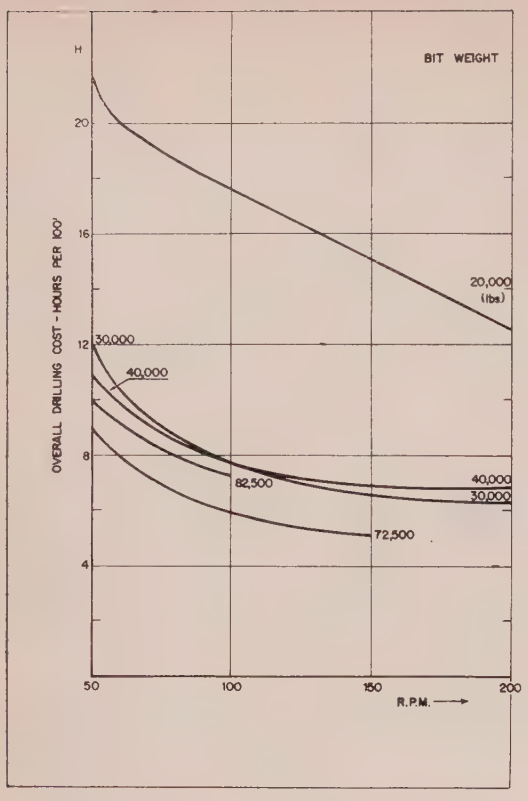

FIG. 16—OVER-ALL COST VS ROTARY SPEED IN SANDY SHALE (ROTARY).

This relationship allows direct choice of conditions for minimum cost.

ACKNOWLEDGMENTS

The author wishes to thank S. R. H. Johnson of Cia. Shell de Venezuela, who coordinated many of the tests described in this paper, and also the Drilling Dept. of Cia. Shell de Venezuela for their keen cooperation.

Thanks also are due to Cia. Shell de Venezuela and Bataafse Internationale Petroleum Mij. N. V., for permission to present this paper.

REFERENCES

1. Lubinski, Arthur: "Proposal for Further Tests," (Comment on work of AAODC Study Committee on Weight/Speed/Penetration), *Pet. Engr.* (Jan., 1958).
2. Outmans, H. D.: "The Effect of Some Drilling Variables on the Instantaneous Rate of Penetration", *Trans.*, AIME (1960) **219**, 137.
3. Eckel, J. E. and Rowley, D. S.: "The Effect of Speed on Penetration Rate", (Work of AAODC Study Committee on Weight/Speed/Penetration), *Pet. Engr.* (Jan., 1958).
4. Bielstein, W. J. and Cannon, George E.: "Factors Effecting the Rate of Penetration of Rock Bits", *Drill. and Prod. Prac.*, API (1951) 28.
5. Speer, John W.: "A Method for Determining Optimum Drilling Conditions", Paper No. 1242-G presented at SPE Drilling and Production Practices Symposium in Lafayette, La. (April 24, 1959).
6. Garnier, A. J. and van Lingen, N. H.: "Phenomena Affecting Drilling Rates at Depth", *Trans.*, AIME (1959) **216**, 232.
7. Payne, L. L.: "The Effect of Circulating Media and Nozzle Design on Rock Bit Performance", *Jour. Pet. Tech.* (Jan., 1952).
8. Graham, J. W. and Muench, N. L.: "Analytical Determination of Optimum Bit Weight and Rotary Speed Combinations", Paper No. 1349-G presented at 34th Annual Fall Meeting of SPE in Dallas (Oct. 4-7, 1959). ★★★

Theory of Formation Cutting Using the Sand Erosion Process

ROBERT WADE BROWN
JUNIOR MEMBER AIME
JACK L. LOPER*
ASSOCIATE MEMBER AIME

WESTCO, DIV. OF THE WESTERN CO.
DALLAS, TEX.

ABSTRACT

The process of sand erosion has been harnessed to perform a useful function—the directed perforating of oilfield tubular goods and formation rock. In this process the sand is carried by a liquid medium and the resulting slurry is forced through a nozzle at an extremely high velocity. Upon impingement against casing or formation, the fast-moving sand particles erode a perforation in the casing followed by cavity formation in the medium behind the casing. The many factors influencing the rate and extent of this penetration are inherently difficult to establish experimentally. Equations describing submerged jet behavior have been applied to these conditions. The following paper develops the equations for predicting the performance of the perforating jet.

INTRODUCTION

The cutting power of high-velocity sand has been well known in the petroleum industry for many years. Sand carried by a high-velocity gas stream causes severe erosion. This effect has been the cause of numerous production problems in certain areas.

It was logical to expect that this phenomenon would one day be adapted to useful industrial applications. Development of mobile, high-pressure, high-horsepower pumping equipment in the last decade has made this possible.

The sand erosion process involves pumping a fluid containing abrasive solids through a set of nozzles at a high differential pressure (2,000 to 4,000 psi). The pressure conversion into kinetic energy imparts high velocity to the sand particles which, upon impact with the formation face or casing wall, erode the material in an organized pattern.

This paper attempts to establish the effects of the various parameters and to predict the performance and limitations of the process. The following factors will be considered: nozzle differential pressure, perforation size, sand concentration, nozzle stand-off distance and back-pressure. In general, this discussion is presented along theoretical lines and is substantiated by field results and data where reliable field data exists.

Original manuscript received in Society of Petroleum Engineers office Aug. 23, 1960. Revised manuscript received Nov. 17, 1960. Paper presented at 35th Annual Fall Meeting of SPE, Oct. 2-5, 1960, in Denver.

*Now with Air Force Systems Command, Altus AFB, Okla.

THEORY

POWER EQUATIONS

The penetration rate of a high-velocity hydraulic jet is proportional to the power or energy of the jet at the point in quesion. The power of the submerged jet will decrease with distance (or penetration) into the cavity created by the jet. As the cavity is extended into the formation, the power of the jet diminishes to a value equal to the threshold cutting power of the particular formation which is defiined as the lowest power level at which the formation will be abraded by the jet. Obviously, when this point is reached, no further cutting of the formation can occur. It is assumed that this power level for a particular formation is a function of the hardness of that formation.

The following equation can be written for the hydraulic process of formation abrasion.

$$\frac{dL}{dt} = K_p(P_L - P_{th} - P_{losses}) \text{ . . ft/sec . (1)}$$

A diagram of the hydraulic jet, nozzle and formation cavity are shown in Fig. 1 for open-hole as well as cased conditions.

The power contained in the jet at a point L distance from the nozzle exit can be represented in the following manner.

$$P_L = \tfrac{1}{2}\, \overline{m}_L \overline{V}_L^2 \text{ . ft-lb}_f\text{/sec or hp . . (2)}$$

Because of diffusion of the jet with distance, the mass rate of flow m_L is proportioned to the initial mass rate at zero distance from the nozzle, $\overline{m}_o$, and the ratio of the nozzle diameter to the distance L[1]

$$\overline{m}_L = C_m \overline{m}_o \frac{D}{L} \text{ . . . lb}_m\text{/sec . . . (3)}$$

The velocity of the jet at distance L is proportional to the initial velocity of the jet at the nozzle discharge V_o and the ratio of the nozzle diameter to the distance L[1]

$$\overline{V}_L = C_v \overline{V}_o \frac{D}{L} \text{ . . . . . ft/sec . . (4)}$$

Substituting Eqs. 3 and 4 into Eq. 2 and eliminating $\overline{m}_L$ and $\overline{V}_L$, Eq. 2 becomes

$$P_L = \frac{C_m C_v^2 \overline{m}_o \overline{V}_o^2 D^3}{2g\, L^3} \text{. ft-lb}_f\text{/sec or hp . . (5)}$$

where C_m and C_v are empirical constants.

Substituting Eq. 5 into Eq. 1, the penetration rate ex-

[1]References given at end of paper.

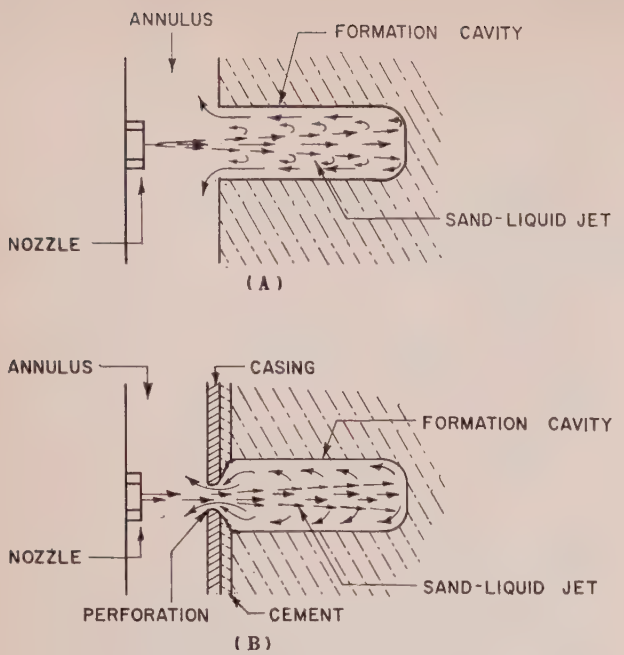

FIG. 1—SAND EROSION PROCESS FOR OPEN-HOLE (A) AND CASED (B) CONDITIONS.

pressed in energy terms becomes

$$\frac{dL}{dt} = K_p\left(\frac{C_m C_v^2 \overline{m}_o \overline{V}_o^2 D^3}{2gL^3} - P_{th} - P_{\text{losses}}\right) \quad \ldots\ldots \text{ ft/sec} \quad (6)$$

Eq. 6 indicates that the penetration rate into the formation is a function of distance L that the jet has already penetrated, the threshold cutting power of the formation, P_{th}, the differential pressure across the nozzle ($\overline{m}_o$ and $\overline{V}_o$ are both functions of the nozzle differential pressure, and the power losses occuring within the cavity.

Referring back to Eq. 5, the hydraulic power at a point L in the formation cavity can be expressed in terms of the nozzle differential pressure, Δp_o, cavity length L, nozzle diameter D and fluid density ρ.

By substitution of the following two expressions into Eq. 5,

$$\overline{m}_o = \rho A \overline{V}_o \text{ (by continuity)}$$

and

$$\overline{V}_o = \left(2g\,\frac{\Delta p}{\rho}\,144\right)^{\frac{1}{2}},$$

Eq. 5 becomes

$$P_L = \frac{BD^5(\Delta p_o)^{3/2}}{L^2\rho^{\frac{1}{2}}} \quad \ldots \text{ ft-lb}_f\text{/sec or hp} \quad (7)$$

where $B = 3\pi C_m C_v^2 (2g)^{\frac{1}{2}}$.

The hydraulic power equations developed in this section can be used for determining the maximum possible penetration, as a function of nozzle Δp_o, the penetration rate into the formation and the threshold power level of the particular formation, provided that at least two reliable tests points are available. In addition, if the hardness of this particular formation is known in relation to the hardnesses of other materials, then the same information can be predicted for these materials based upon the original data points.

This procedure was followed, but to simplify computation the equations were set up on a velocity basis.

VELOCITY EQUATIONS

The penetration rate dL/dt, of the high-velocity hydraulic jet is proportional to the velocity of the jet at the point in question V_L (distance L out into the formation) diminished by the threshold cutting velocity V_{th} of the particular formation. The threshold cutting velocity V_{th} is assumed to be a function of the abrasion hardness of the formation. The cutting rate and maximum cutting depth are further diminished by the restricted return flow through the perforation (cased condition) and effects of back-pressure. This loss is expressed as ΔV_p.

The following equation in velocity terms can be written for the hydraulic process of formation abrasion.

$$\frac{dL}{dt} = K_v'(V_L - V_{th} - \Delta V_p) \quad \ldots \text{ ft/sec} \quad (8)$$

where K_v' is a constant of proportionality to be determined from experimental data.

Experiments conducted by Forstall and Gaylord[1] on submerged jets indicate that the center line velocity of a submerged jet will diminish with distance according to the relationship of Eq. 4.

Substituting Eq. 4 into Eq. 8 and eliminating V_L,

$$\frac{dL}{dt} = K_v'\left(\frac{C_v\overline{V}_o D}{L} - V_{th} - \Delta V_p\right) \quad \ldots\ldots \text{ ft/sec} \quad (9)$$

Solving for dt,

$$dt = \frac{K_v L\,dL}{(C_v D\overline{V}_o - V_{th}L - \Delta V_p L)} \text{ seconds} \quad (10)$$

where K_v is reciprocal of K_v'.

Eq. 10 applies to cased conditions, that is, conditions where the "spent" fluid must re-enter the wellbore through a casing perforation. If the casing perforation area is sufficiently large, then the velocity loss of the jet due to the restriction caused by the perforation is reduced to a negligible amount, and conditions would approach that of open hole. See Fig. 6.

Tests performed by the authors indicate that a pressure differential exists across the casing perforation. Apparently then, a portion of the velocity of the jet is transformed into pressure within the cavity due to the flow restriction offered by the perforation. The larger the entry hole into the wellbore, the smaller the pressure rise in the formation cavity and, consequently, the smaller the velocity loss of the impinging jet. For example, a hydraulic jet of .180 in. in diameter normally forms a casing perforation of approximately .42-in. in diameter. If the perforation area is increased by some means (such as slotting of the casing) to an area equivalent to a diameter of ¾-in., then the velocity loss is reduced to about 44 per cent of the velocity reduction occurring with a diameter of .42-in. If the area of the casing perforation is increased to an equivalent diameter of 2.0-in., then the loss becomes essentially zero and it becomes equivalent to open-hole conditions. See Fig. 6.

For open-hole conditions, Eq. 10 becomes

$$dt = \frac{K_v L\,dL}{(C_v D\overline{V}_o - V_{th}L)} \text{ seconds} \quad \ldots \quad (11)$$

Integration of Eq. 9 yields the following equation for open-hole conditions.

$$t = K_v\left[\frac{C_v D\overline{V}_o}{V_{th}^2}\ln_e\left(\frac{C_v D\overline{V}_o}{C_v D\overline{V}_o - V_{th}L}\right) - \frac{L}{V_{th}}\right] \quad \ldots\ldots \text{ seconds} \quad \ldots\ldots \quad (12)$$

For cased conditions, this equation is

TABLE 1—TEST POINTS FOR GRANITE

	Point 1	Point 2	Point 3
Cutting Time (min)	95	3	18
Penetration (in.)	10.5	2.4	4.5
Nozzle Δp_o (psi)	3200	3200	2000

TABLE 2—MAXIMUM PENETRATIONS CALCULATED FOR GRANITE AS A FUNCTION OF NOZZLE DIFFERENTIAL PRESSURE.

Δp_o Nozzle (psi)	V_{th} (ft/sec)	L_{max} at $t = \infty$ (in.)
2000	41.5	14.6
2500	41.5	16.4
3000	41.5	17.9
3500	41.5	19.4
4000	41.5	20.7

$$t = k_v \left[\frac{C_v D \overline{V}_o}{(V_{th} + \Delta V_p)^2} \ln_e \left(\frac{C_v D \overline{V}_o}{C_v D \overline{V}_o - (V_{th} + \Delta V_p) L} \right) - \frac{L}{(V_{th} + \Delta V_p)} \right] \quad \text{seconds} \quad (12A)$$

(The constant of integration is evaluated based on the boundary conditions $L = 0$ when $t = 0$.)

It was necessary to determine the threshold cutting velocity V_{th} and the proportionality constant K_v. Test data obtained on granite were used to obtain these constants. Granite data were selected because the test conditions were most consistent and reproducible. The granite hardness was more easily established in relation to other materials and shows less variation in hardness. The granite was fairly homogeneous and completely impermeable. A granite test block was prepared to simulate open-hole conditions. The granite test points obtained are shown in Table 1.

Results for granite were $K_v = 4.7 \times 10^5$ and $V_{th} = 41.5$ ft/sec, based on International Critical Table (ICT)[2] scale of hardness equal to 19.

Based on this information, Table 2 shows the maximum penetrations calculated for granite as a function of nozzle differential pressure, Δp_o.

Eq. 12 was generalized for formations other than granite. This was done in the following manner. The property of hardness was assumed to be the chief criterion affecting the maximum penetration or penetration rate. (It was recognized that permeability and porosity of the formation would affect dL/dt, but this effect is included in various constants.) Since hardness is defined as resistance to penetration, hardness will vary inversely with the maximum penetration obtainable for a given power level and a given period of time. Expressed in equation form, $H \propto 1/L_{max}$. Also, the threshold cutting velocity is proportional to the reciprocal of the maximum penetration by Eq. 4, $V_{th} \propto 1/L_{max}$. Therefore, $V_{th} = cH$. The threshold cutting velocity varies directly with hardness.

Data from the ICT scale of abrasion hardness was used because a large number of different materials are available for comparison. A listing of some of these materials is given in Table 3. Using the relative hardness value of 19 for granite, the following equation is obtained.

$$V_{th} = 2.184H \quad \text{ft/sec} \quad (13)$$

When Eq. 13 is substituted into Eq. 12, eliminating V_{th}, the following general equation is obtained for open-hole conditions.

$$t = K_{vH} \left[\frac{C_v D \overline{V}_o}{4.77H^2} \ln_e \left\{ \frac{C_v D \overline{V}_o}{(C_v D \overline{V}_o - 2.184HL)} \right\} - \frac{L}{2.184H} \right] \quad \text{seconds} \quad (14)$$

The proportionality constant K_{vH} varies in the following manner for formations of different hardness.

$$K_{vH} = \left(\frac{V_{th}}{V_{th\ granite}} \right)^2 K_{v\ granite} \quad (15)$$

The numerical values for the proportionality constants are as follows.

$H = 19, K_{v19} = 4.700 \times 10^5$
$H = 18, K_{v18} = 4.215 \times 10^5$
$H = 17, K_{v17} = 3.756 \times 10^5$
$H = 14, K_{v14} = 2.555 \times 10^5$
$H = 11, K_{v11} = 1.572 \times 10^5$
$H = 8, K_{v8} = 0.8357 \times 10^5$
$H = 6, K_{v6} = 0.4680 \times 10^5$
$H = 3, K_{v3} = 0.1171 \times 10^5$.

To determine maximum penetration for open-hole conditions, the expression $C_v D \overline{V}_o - V_{th} L$ is set equal to zero in Eq. 12.

$$L_{max} = \frac{C_v D \overline{V}_o}{V_{th}} \quad \text{ft} \quad (16)$$

Table 3 lists the limiting maximum possible penetration in inches as a function of nozzle differential pressure and formation hardness on the ICT scale.

Fig. 2 is a time-peneration plot with open-hole conditions for parameters of hardness and nozzle differential pressures of 2,500 and 3,500 psi.

EFFECT OF BACK-PRESSURE AND CASING PERFORATION SIZE

For cased conditions, the perforation size (cross-sectional area) materially affect the performance obtained with the abrasion process. The larger the perforation area (jet diameter constant), the greater the penetration rate and extent of penetration which approach open-hole conditions as the maximum limit.

For cased conditions, the general time-penetration equation is

$$t = K_{vH} \left[\frac{C_v D \overline{V}_o}{(2.184H + \Delta V_p)^2} \ln_e \frac{C_v D \overline{V}_o}{C_v D \overline{V}_o - (2.184H + \Delta V_p) L} - \frac{L}{(2.184H + \Delta V_p)} \right] \quad \text{seconds} \quad (17)$$

TABLE 3—MAXIMUM PENETRATION IN INCHES (OPEN-HOLE AND $t = \infty$). BASED ON EQ. 16.

Material	H (ICT Scale)	V_{th} (ft/sec)	Nozzle Differential Pressure (psi) 2000	2500	3000	3500	4000
Basalt, Nephelite, Austin, Tex.	19	41.5	14.6	16.4	17.9	19.4	20.7
Quartzite, Roanoke, Va.	19	41.5	14.6	16.4	17.9	19.4	20.7
Granite Biotite, Barre, Vt.	19	41.5	14.6	16.4	17.9	19.4	20.7
Granite, Quartz Monzonite, Milford, N. H.	18	39.3	15.5	17.3	18.9	20.4	21.9
Schist, Muscovite. Charlottesville, Va.	17	37.1	16.4	18.3	20.0	21.7	23.2
Limestone, Siliceous, Coyote, Calif.	17	37.1	16.4	18.3	20.0	21.7	23.2
Sandstone, Ferruginous, Shreveport, La.	14	30.6	19.9	22.2	24.3	26.3	28.1
Limestone, Dolomite, Joliet, Ill.	14	30.6	19.9	22.2	24.3	26.3	28.1
Marble, Calcite, Ball Ground, Ga.	11	24.0	25.3	28.3	21.0	33.5	35.8
Marble, Siliceous, Texas, Maryland	8	17.5	34.7	38.8	42.5	45.9	49.1
Sandstone, Bituminous, Provo, Utah	6	13.1	46.4	51.8	56.8	61.4	65.6
Limestone, Bituminous, Ravia, Okla.	3	6.55	92.7	103.7	113.6	122.7	131.2

Penetration rate and maximum penetration are less for the cased condition than for the open-hole condition by the term ΔV_p in Eq. 17 which represents the loss in momentum across the perforation. For the maximum penetration, the factor $C_v D \overline{V}_o - (2.184H + \Delta V_p)L = 0$ must hold.

$$L_{max} = \frac{C_v D \overline{V}_o}{2.184H + \Delta V_p} \quad . \quad . \quad \text{ft} \quad . \quad . \quad . \quad (18)$$

Fluid cavity tests under cased conditions were run to determine the effects of perforation cross-sectional flow area and fluid back-pressure on performance. The test setup is shown in Fig. 3. The tests indicate that the pressure within the cavity and ΔV_p are increased as the nozzle differential pressure (or tool pressure) is increased. Conversely, as the casing perforation area is increased, the cavity pressure and ΔV_p are reduced. These relationships are shown in Figs. 4 and 5.

A correlation of pressure data was obtained for cavity lengths of 14 and 39 in. and for tool pressures ranging from 2,000 to 4,000 psi, as shown in Fig. 4, which indicates that the momentum loss at first increases, reaches a maximum of approximately 0.40 and then declines. These data are for a casing perforation diameter of 0.42 in.

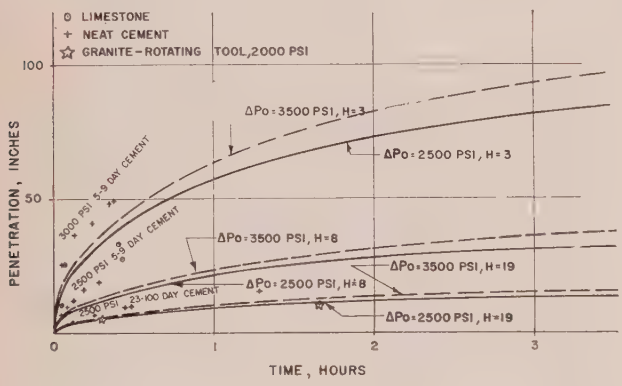
LIMESTONE
NEAT CEMENT
GRANITE – ROTATING TOOL, 2000 PSI
PENETRATION, INCHES
TIME, HOURS
ΔPo = 3500 PSI, H = 3
ΔPo = 2500 PSI, H = 3
ΔPo = 3500 PSI, H = 8
ΔPo = 2500 PSI, H = 8
ΔPo = 3500 PSI, H = 19
ΔPo = 2500 PSI, H = 19
3000 PSI 5-9 DAY CEMENT
2500 PSI 5-9 DAY CEMENT
2000 PSI 23-100 DAY CEMENT

FIG. 2—TIME-PENETRATION CURVES.

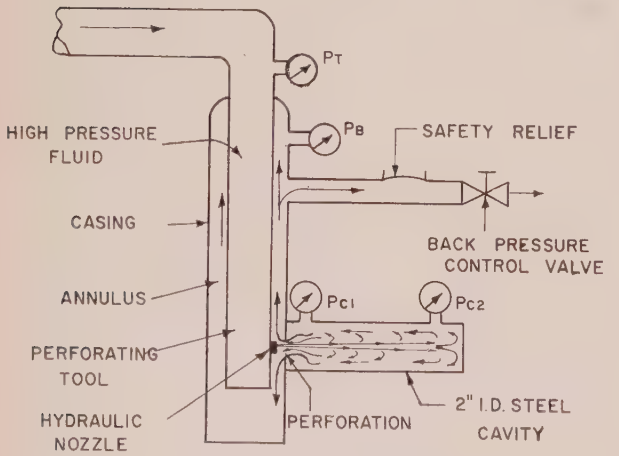

PC = CAVITY PRESSURE
PB = ANNULUS BACK PRESSURE
PT = TOOL PRESSURE
FLUID = CLEAR WATER (NO SAND)

FIG. 3—HYDRAULIC BACK-PRESSURE TESTS.

Fig. 5 shows the relationship between ΔV_p and nozzle Δp_o for casing perforation diameters of 0.42, 0.50 and 0.75 in. and for back-pressures of 0, 500 and 1,000 psi. This indicates that back-pressure has less effect on ΔV_p losses as the perforation area increases. Also, for any perforation size the momentum or velocity loss tends to stabilize at some maximum value as back-pressure is increased.

Perforation cross-sectional area is of more significance in obtaining improved performance than is back-pressure, as indicated in Fig. 5. In actual perforating operations, if the tool is allowed to move, a slotting of the casing is produced which tends toward open-hole conditions, with the subsequent increase in maximum penetration and reduction of cavity pressure. The smallest perforation diameter produced, using a hydraulic nozzle of 0.180-in. ID, is 0.360 in. This is based on the experimental fact that a jet impinging on a flat plate (normal to it) will produce a jet area of at least four times the nozzle area.[3] There is always some perforation area growth with time (even when the tool position is fixed) until equilibrium is reached. Tests indicate that this final equilibrium diameter is slightly less than 0.5 in. for a nozzle diameter of 0.180 in.

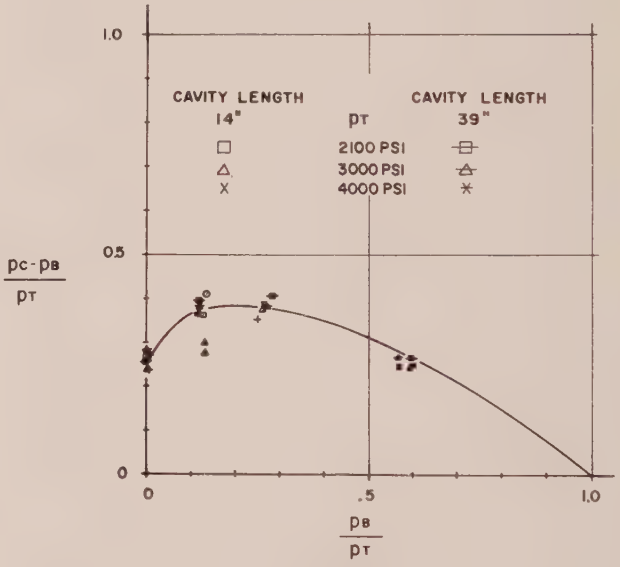

FIG. 4—BACK-PRESSURE CAVITY TESTS. CAVITY DIAMETER = 2.0 IN., AND PERFORATION DIAMETER = .42 IN.

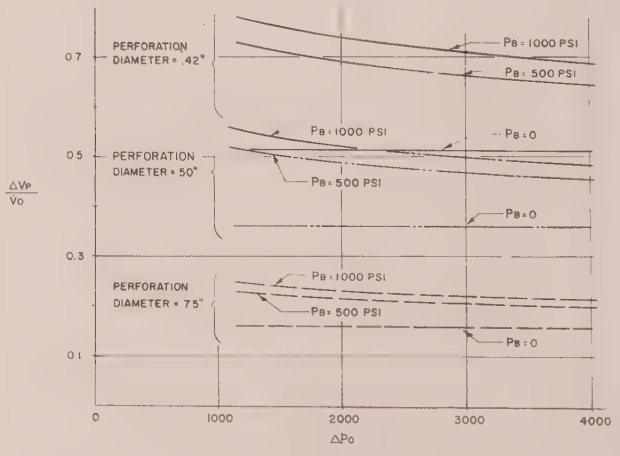

FIG. 5—JET VELOCITY LOSS DUE TO BACK-PRESSURE AND PERFORATION SIZE.

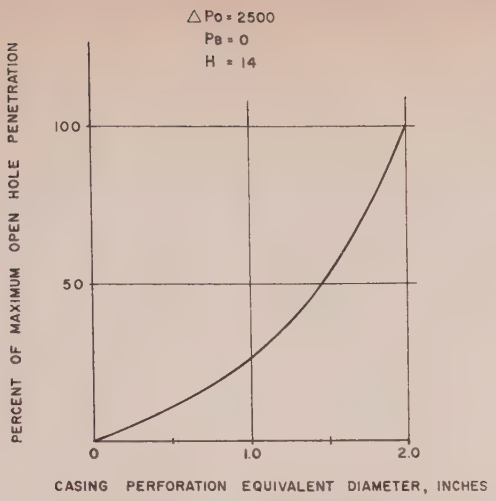

FIG. 6—EFFECT OF CASING PERFORATION SIZE ON PENETRATION.

Fig. 6 shows the relationship between maximum penetration and casing perforation area. Maximum possible penetration in any medium increases rapidly with increase in area until open-hole conditions are reached at approximately 2.0-in. equivalent diameter. The diameter at which open-hole conditions are reached will vary somewhat with the type of material being penetrated.

EFFECT OF HYDRAULIC JET STAND-OFF

Hydraulic jet stand-off is defined as the distance in the annular space between the hydraulic nozzle exit ($L = 0$) and the casing wall or, for open-hole conditions, the formation wall. The data of Forstall and Gaylord[1] indicates that, for a distance up to approximately six nozzle diameters, no loss of either power or velocity occurs in the jet stream. For a nozzle diameter of 0.180 in., this distance is approximately 1.1 in. Beyond this point, the jet power diminishes according to the relationship

$$\frac{P_L}{P_o} = \frac{C_v^2 C_m}{\left(\frac{L}{D}\right)^3} \quad \ldots\ldots\ldots\ldots \quad (19)$$

Thus, it is seen from Eq. 19 that the hydraulic power in the jet decays rapidly with distance according to $(L/D)^3$.

The jet velocity decays according to Eq. 4. There is essentially no loss in jet velocity until the L/D exceeds 6.4.[1]

These relationships for power and velocity are plotted in Fig. 7. It is obvious from Fig. 7 that for the sake of maximum cutting performance minimum stand-off distances should be used. However, use of minimum stand-off points up the necessity for tool protection from jet back-splash. A compromise must be made between designs to provide adequate abrasion protection for the tool and performance to maintain maximum cutting ability.

EFFECT OF SAND CONCENTRATION

It is known from experience that even minute quantities of sand will provide exceptional cutting ability when a high velocity is imparted to the grain. Experience has indicated further that an optimum sand concentration does exist above which it is not desirable to go, from an economic as well as a performance standpoint. Information from tests and numerous field jobs

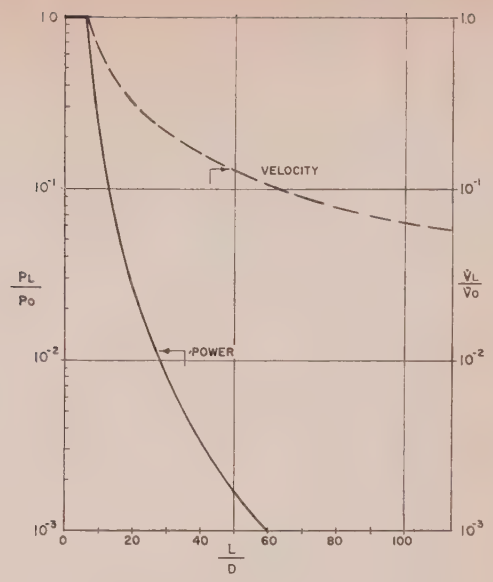

FIG. 7—EFFECT OF HYDRAULIC JET STAND-OFF VS POWER LOSSES AND VELOCITY LOSSES.

indicates this optimum falls in the range of 0.75 to 2.0 lb/gal. The reasoning developed in the following paragraph is an attempt to develop a theory describing relative abrasion performance as a function of sand concentration.

The abrasion or cutting ability of the sand is dependent upon the momentum of the individual sand grains. Momentum at a given point in the jet is a product of sand mass and sand velocity at that point. The mass can be effectively increased until the sand particles collide with one another at the extremity of the formation cavity. It is assumed that the minimum distance that the sand grains must be separated in order to keep the grains from colliding is approximately one-half of a sand grain diameter. This corresponds to a maximum sand concentration of 4 lb/gal. This assumption is based on the fact that sand grains, after contacting the formation, must move radially at least one-half of a diameter in order to clear the area for the impact of the next grain. If a particular sand grain is not clear of the area, then the following grain will collide with it, and energy will be dissipated in fracturing the individual grain. However, in actual practice it is necessary that a distance greater than one-half a sand grain diameter be allowed because the grain motion after contacting the formation will be delayed by initial impact, direction and velocity change, friction and abrading along the cavity wall. It follows as a result of this reasoning that the sand concentration should be adjusted to maintain, on the average, distances between grains greater than the minimum theoretical distance in order to compensate for this effect. Considering all of these factors, the optimum sand concentration approximates 1.0 to 2.0 lb/gal.

EFFECT OF COMMUNICATION

All theory in this paper has been developed on the premise that the formation material does not fracture or communicate during the perforating operation and that it has essentially zero permeability. For the purpose of this discussion, the term communication refers to any condition whereby the fluid is permitted to re-enter the wellbore through channels other than the casing perforation. If the formation fractures or takes fluid so

that all the perforating fluid does not return into the wellbore through the perforation, the penetration performance of the jet is substantially increased. The amount of increase in penetration depends upon the amount of fluid lost to the formation. Surface test data are plotted in Fig. 2, showing the increase which results under partial or fully communicating conditions.[4] These data also indicate the variation in penetration with hardness and Δp_o for the cement targets.

CONCLUSIONS

The following conclusions can be drawn from the analysis developed in the previous sections. The maximum possible penetration and penetration rate is strongly influenced by the power or energy supplied to the jet, the formation hardness and perforation size. Factors which affect the performance, but not as significantly as those just noted, are nozzle stand-off distance, casing back-pressure and sand concentration. Nozzle stand-off distance and sand concentration, although important, are placed in this secondary category because any detrimental effect attributed to them can be controlled by proper tool design and proper operating technique. Casing back-pressure is a factor which is not easily controlled because it is a function of well depth, casing-tubing size and reservoir pressure. Tests indicate that its effect approaches a constant value as the magnitude of the back-pressure is increased.

The type of fluid is considered to have negligible effect except insofar as its properties influence its sand-carrying ability in the annulus and as its flow losses in the tubing affect the surface treating pressure.

It has been established that a threshold cutting velocity exists for each material. The criterion for determining these values is assumed to be abrasion hardness. There is a maximum possible penetration corresponding to infinite pumping time for each material. This maximum penetration increases for any particular material with increase in the differential pressure (or energy) supplied to the jet. The maximum possible peneration is also strongly affected by the size or area of the casing perforation or formation cavity for open-hole completions. Greatest penetration is obtained for a given nozzle Δp_o and formation material under open-hole conditions. Open-hole conditions afford the least resistance to penetration and the smallest pressure build-up (velocity loss) in the cavity. The minimum equilibrium casing perforation area severely limits the maximum penetration. It is advantageous to increase the perforation size by slotting the casing. This slotting effect can be accomplished by increasing the treating pressure, thereby stretching the tubing, or by a slight radial movement of the tubing at the surface. As the perforation area increases, conditions rapidly approach open-hole conditions as far as maximum penetration is concerned.

Optimum pumping time cannot be recommended based solely on the information developed in this paper. Factors of an operational nature (such as number of perforations to be made at one time, formation depth, type of formation, tubing and casing size, etc.) influence the pumping time.

However, the following general recommendations can be made. The maximum nozzle Δp_o consistent with safe practice should be used. The tool should be designed for stand-off distances of six nozzle diameters or less, consistent with reasonable tool wear. Sand ratios in the range from 1 to 2 lb/gal should be used. Also, if conditions allow it, the casing should be slotted or a relief perforation formed to improve penetration characteristics.

NOMENCLATURE

C_m = empirical constant ($C_m = 5.2$), dimensionless
C_v = empirical constant ($C_v = 6.4$), dimensionless
D = nozzle diameter, in., ft
$\frac{dL}{dt}$ = instantaneous peneration rate, ft/sec, ft/hr
g = conversion constant, $lb_m - ft/lb_f - sec^2$
H = relative abrasion hardness of material measured on ICT scale, dimensionless
K_p = constant of proportionality for power equation, $1/lb_f$
K_v = constant of proportionality for velocity equation, dimensionless
K_v' = reciprocal of K_v
L = distance measured along jet axis, in., ft
$\overline{m}_L$ = average fluid mass rate of the jet at distance L from the nozzle, lb_m/sec
$\overline{m}_o$ = average fluid mass rate of the jet at nozzle discharge ($L = 0$), lb_m/sec
P_L = power level of the hydraulic jet at distance L, ft-lb_f/sec, hp
P_{losses} = hydraulic losses caused by casing perforation restriction, back-pressure and formation pressure, ft-lb_f/sec, hp
P_o = power level of jet at nozzle discharge ($L = 0$), ft-lb_f/sec, hp
P_{th} = threshold cutting power of the particular formation, ft-lb_f/sec, hp
Δp_o = pressure differential across nozzle, ($L = 0$), psi
p_b = annular static back-pressure, psi
p_c = cavity static pressure, psi
p_t = static pressure in tool, psi
R = sand-fluid ratio, lb_m/gal
ρ = sand-slurry density, lb_m/cu ft
S. G. = specific gravity, dimensionless
t = time, seconds, hours
$\overline{V}_L$ = average fluid velocity of the jet at L distance, ft/sec
$\overline{V}_o$ = average fluid velocity of the jet at nozzle distance ($L = 0$), ft/sec
V_{th} = threshold cutting velocity for a particular material, ft/sec
ΔV_p = velocity loss of jet resulting from flow through perforation, ft/sec

ACKNOWLEDGMENT

The authors wish to express their appreciation to the management of Westco, Div. of The Western Co., for permission to publish the paper.

REFERENCES

1. Forstall, W. and Gaylord, E. W.: "Momentum and Mass Transfer in a Submerged Water Jet", *Jour. of Appl. Mech.* (June, 1955) 161.
2. "Resistance to Abrasion Table", *International Critical Tables* (1927) **2**, 49.
3. Daugherty, R. L.: *Hydraulics*, McGraw-Hill Publishing Co., N. Y. (1937) 314.
4. Brown, Robert Wade and Loper, Jack L.: "A New Completion Technique — Sand Erosion", API Paper No. 906-5-N presented at the API Spring Meeting of Southwestern Dist., Div. of Production, Dallas (March 2-4, 1960). ★★★

Investigation of Abrasive-Laden-Fluid Method For Perforation and Fracture Initiation

FORREST C. PITTMAN, HALLIBURTON CO.
DON W. HARRIMAN, DUNCAN, OKLA.
JAMES C. ST. JOHN, JUNIOR MEMBER AIME, BAKERSFIELD, CALIF.

ABSTRACT

This paper mentions briefly the history of hydraulic jetting as applied to perforating and fracture initiation. It points out the advantages of hydraulic perforation and undercutting as an aid for creating a fracture at the point desired rather than depending upon the weakest point in the formation for breakdown.

It describes early experimental work with jet nozzles in search of better nozzle materials. The effect of splash-back damage and its subsequent influence on jet body and tool design during this work is discussed.

A series of cutting-rate curves for jets cutting steel and steel-cement-formation combinations is presented to show the effect of hydrostatic head and the point of diminishing returns with respect to cutting time.

There is a series of photographs showing various types of rock formation in which perforation and undercutting tests were made. These stones were drilled and the casing cemented in place as in an actual well. The casing was perforated and circularly cut as if preparing for a fracturing job.

The conclusion reached in the paper is that hydraulic jetting with sand-laden fluid can be used for perforating and undercutting casing, cement and formation rock for the intended purpose of inducing the formation to fracture at a desired point.

INTRODUCTION

Hydraulic jetting as a means of cleaning a formation during acidizing has been used for many years. The acid-jet gun was used to clean formation and for drilling cement from casing with acid. This tool was dropped to a seating ring installed on the tubing and could be retrieved by reverse circulation or wire line. In this process, the fluids were directed against the formation to clean and penetrate beyond the mud-damaged area. After the development of the hydraulic fracturing process, interest in jetting the formation with abrasive-laden fluid was renewed. The cutting action of abrasive fluid on pumping equipment, which is a well known problem, has been utilized to perforate and undercut casing, tubing and formation. In this process, surface areas are provided in the formation on which the fracturing pressures may work to produce a fracture at the location desired.

Original manuscript received in Society of Petroleum Engineers office Aug. 24, 1960. Revised manuscript received April 13, 1961. Paper presented at 31st Annual California Regional Fall Meeting of SPE, Oct. 20-21, 1960, in Pasadena, Calif.

EQUIPMENT

The tools used consist of bodies containing two, three or four jets in a single horizontal plane equally spaced around the circumference. The body is threaded to the end of a string of tubing and run into the well. In addition, an expendable tool is available that may be left in the hole after perforating and produced through until necessary to remove the tubing. The bottom of each tool is equipped with a ball-type back-pressure valve. The ball can be reversed to the surface and recovered. This allows reverse circulation so that loose sand which accumulated below the tool while jetting may be removed before the fracturing job. The present jetting tools are of such length that, when screwed together, the jets fall on 12-in. spacing.

ANALYSIS OF THE PROBLEM

Early work with nozzles indicated that hardened steel was not a suitable material for jets and that more durable material would be required. Ceramics were tried and found to be superior to steel but still too short-lived for most applications. Tungsten carbide, which was tried and found to be the best material available, is now being used for jet nozzles. Analysis of the problems presented by this process indicated that the following information was needed.

1. The effect of submergence on a jet stream and the effect of submergence on the cutting rate of a jet stream.
2. The cutting rate and depth of a jet stream in steel.
3. The cutting rate in various formations and point of diminishing returns.
4. Size of hole or slot cut in a pipe by a given jet.
5. Fluids and sands used.
6. The flow of various weight fluids through the jet nozzle and the discharge coefficients.
7. The type cut formed in the formation by the jet stream.
8. The stretch and contraction of tubing due to temperature and pressure.

The cutting effect of a jet stream on a target in the atmosphere is rapid and spectacular as most of the

impact of the solid particles and fluid is expended in the removal of material from the target. On the other hand, a submerged jet stream has a much slower cutting rate because it must do work by displacing the surrounding fluid before reaching the target. Since all jetting in a well would be performed under submerged conditions, it was concluded that experimental work should be done likewise so that the data could be applied to actual field jobs.

The theoretical energy per unit of time or power available in the jet stream at the exit of the jet nozzle may be expressed as

$$\text{Power} = QWh \quad . \quad . \quad . \quad . \quad . \quad . \quad . \quad . \quad . \quad (1)$$

where Q = flow rate of the sand-fluid mixture, cu ft/sec,
W = specific weight of the sand-fluid mixture, lb/cu ft, and
h = drop in pressure head across the jet nozzle, ft.

Setting

$$W = Ws + Wf$$

where Ws = the weight of sand/cu ft of sand-fluid mixture and
Wf = the weight of fluid/cu ft of sand-fluid mixture,

Eq. 1 can written as

$$\text{Power} = Q\,(Ws + Wf)\,h. \quad . \quad . \quad . \quad . \quad . \quad . \quad (2)$$

Assuming that, in the process of cutting casing, cement and formation rock, the energy in the jet stream due to the presence of the fluid is negligible and that the entrained sand has the same velocity as the fluid, this equation can be reduced to

$$\text{Power} = Q\,Ws\,h \quad , \quad . \quad . \quad . \quad . \quad . \quad . \quad . \quad . \quad (3)$$

which is an expression of the power due to the presence of the sand only in the jet stream.

The flow rate Q can be expressed as

$$Q = VA \quad . \quad . \quad . \quad . \quad . \quad . \quad . \quad . \quad . \quad . \quad . \quad (4)$$

where V = velocity of jet stream in ft/sec, and
A = area of nozzle orifice in sq ft.

Substituting $V = \sqrt{2gh}$ for V in Eq. 4 gives

$$Q = A\sqrt{2gh} \quad . \quad . \quad . \quad . \quad . \quad . \quad . \quad . \quad . \quad . \quad (5)$$

Substituting Eq. 5 in Eq. 3 gives the expression,

$$\text{Power} = A\sqrt{2gh}\,Wsh \text{ or } WsA\sqrt{2g}\,(h)^{3/2} \quad . \quad . \quad . \quad . \quad . \quad . \quad . \quad . \quad . \quad . \quad . \quad (6)$$

Since the head h can be expressed as

$$h = \frac{P}{W} \quad . \quad . \quad . \quad . \quad . \quad . \quad . \quad . \quad . \quad . \quad . \quad . \quad (7)$$

where P = the pressure drop in lb/sq ft, and
W = specific weight of the sand-fluid mixture, lb/cu ft,

Eq. 6 can be written as

$$\text{Power} = WsA\sqrt{2g}\left(\frac{P}{W}\right)^{3/2} \quad . \quad . \quad . \quad . \quad . \quad . \quad (8)$$

It thus is seen that the theoretical power varies with the 3/2 power of the pressure drop across the jet nozzle for constant values of A, Ws and W. Therefore, increasing the pressure drop across the jet nozzle from 1,000 to 2,000 psi increases the cutting power of the sand-fluid stream by 2.83 times, since $2^{3/2} = 2.83$.

PROCEDURE

The first data were taken during the perforation of steel plates at various pressure drops and stand-off distances using gelled water containing 1 lb of 20-40 Ottawa sand per gallon of water. Stand-off, as used herein, means the distance between the discharge end of nozzle and target. Fig. 1 shows the cutting-rate curves for three pressure ranges at various stand-off distances for one minute's cutting time. It was found that for practical reasons a stand-off distance between ½ and 1 in. should be maintained, but to do so is at the expense of the cutting rate. Starting with the 1-in. mark on the 1,000-psi curve, each increase of 1-in. stand-off decreases the cutting rate about 20 per cent; at the 6-in. mark, cutting virtually ceases. This has been confirmed many times in cutting hard formations as well as steel.

The 2,000-psi curve also shows a rapid decrease in cutting rate as the stand-off distance increases to a distance of approximately 8.5 in. (curve extrapolated), at which point cutting also virtually ceases. Fig. 1 also shows that the penetration rate in the steel plate at the ½-in. stand-off mark increased from .16-in./min at 1,000 psi to .39 in./min at 2,000 psi, or by a factor of 2.44 times when the pressure drop was doubled. As was pointed out earlier, increasing the pressure drop from 1,000 to 2,000 psi increased the power of the sand-laden jet stream by 2.83 times. Therefore, it is ad-

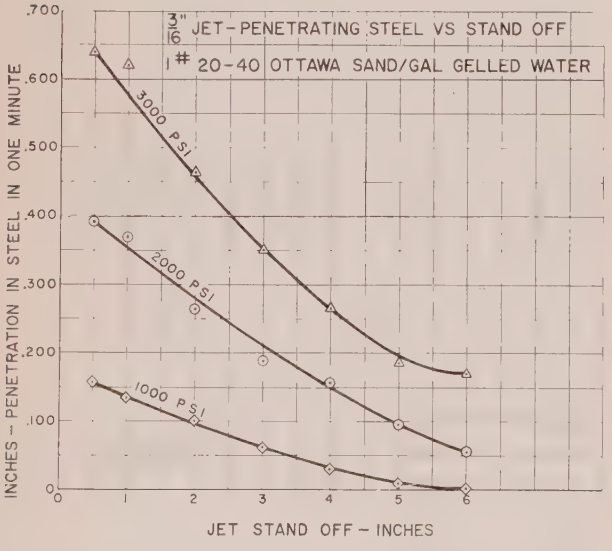

FIG. 1—CUTTING-RATE CURVES FOR THREE PRESSURE RANGES AT VARIOUS STAND-OFF DISTANCES FOR ONE MINUTE'S CUTTING TIME.

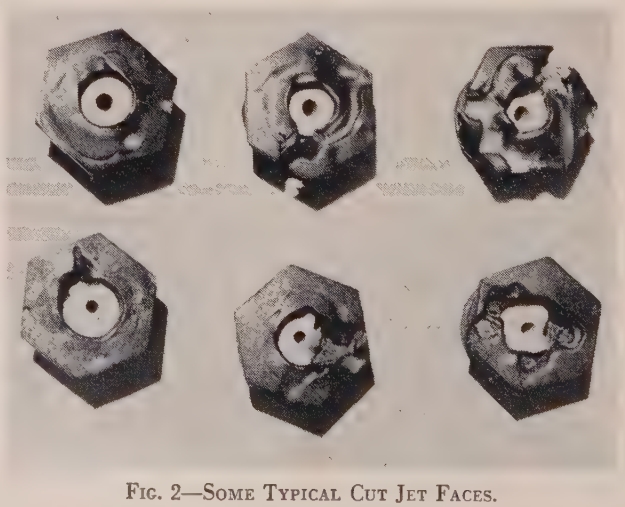

FIG. 2—SOME TYPICAL CUT JET FACES.

vantageous to jet with as high a differential pressure as can economically be obtained.

During this work, the damage due to splash-back from the target to the jet face became apparent, and corrective measures were necessary. The jet faces and tool body were being cut away almost as rapidly as the target. In fact, a tool body containing the jet could be destroyed in a few minutes. The first protection devised was a large thick hex-head on the jet nozzle to absorb the splash-back. This method proved feasible, for it protected the tool body and lasted as long as the jet itself. The next step was to increase the distance between the jet and target by reducing the OD of the tool itself. This was done at the expense of a faster cutting rate; however, it did increase jet life considerably. It was found that the jet should not be run closer than three jet diameters from the target; otherwise, severe splash-back cutting would occur. For this reason we suggest running a tubing centralizer above the tool so that each jet will have an equal stand-off. Fig. 2 shows typical, cut jet faces.

The effect of depth of submergence on the cutting rate was considered and experiments were run on Berea sandstone targets submerged 60-, 1,000- and 2,000-ft deep in the test well. Each target was perforated with the same diesel oil-sand mixture, jet and pressure conditions except for depth of submergence. A plot of these cuts (Fig. 3) shows that all have virtually the same cutting rate. Identical tests conducted with water and sand on targets submerged 2 ft show slightly less cutting rate. For a given pressure, water has a lower head than oil; therefore, a lower velocity and less cutting power are available at the target. Indications are that the depth of cut in a given time at a given pressure drop across the nozzle is independent of the depth of submergence or hydrostatic pressure so long as the jet stream cannot cavitate and draw air or communicate as through a

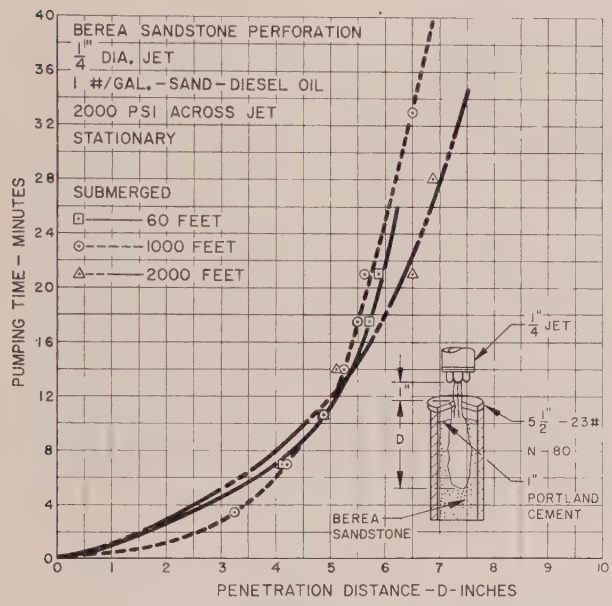

Fig. 3—Effect of Depth of Submergence on Cutting Rate.

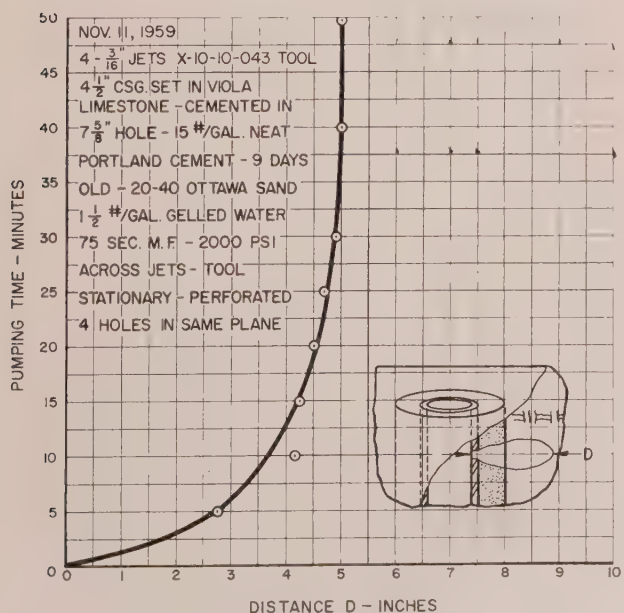
NOV. 11, 1959
4 - 3/16" JETS X-10-10-043 TOOL
4 1/2" CSG. SET IN VIOLA LIMESTONE - CEMENTED IN
7 5/8" HOLE - 15 #/GAL. NEAT PORTLAND CEMENT - 9 DAYS
OLD - 20-40 OTTAWA SAND
1 1/2 #/GAL. GELLED WATER
75 SEC. M.F. - 2000 PSI ACROSS JETS - TOOL STATIONARY - PERFORATED 4 HOLES IN SAME PLANE
D
PUMPING TIME - MINUTES
DISTANCE D - INCHES

Fig. 4—Cutting-Rate Curve.

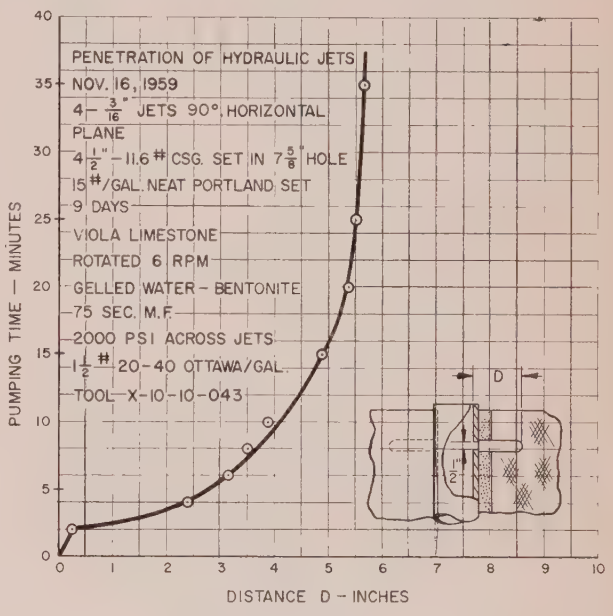
PENETRATION OF HYDRAULIC JETS
NOV. 16, 1959
4 - 3/16" JETS 90° HORIZONTAL PLANE
4 1/2" - 11.6 # CSG. SET IN 7 5/8" HOLE
15 #/GAL. NEAT PORTLAND SET 9 DAYS
VIOLA LIMESTONE
ROTATED 6 RPM
GELLED WATER - BENTONITE
75 SEC. M.F.
2000 PSI ACROSS JETS
1 1/2 # 20-40 OTTAWA/GAL.
TOOL - X-10-10-043
D
1 1/2"
PUMPING TIME - MINUTES
DISTANCE D - INCHES

Fig. 5—Cutting-Rate Curve.

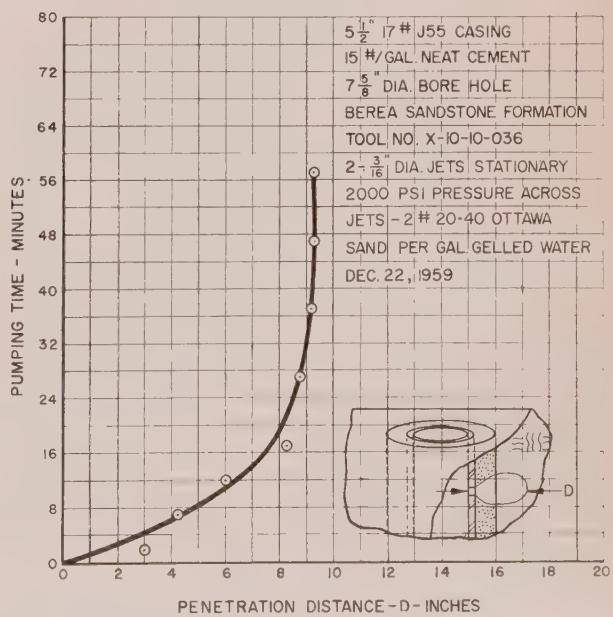
5 1/2" 17 # J55 CASING
15 #/GAL. NEAT CEMENT
7 5/8" DIA. BORE HOLE
BEREA SANDSTONE FORMATION
TOOL NO. X-10-10-036
2 - 3/16" DIA. JETS STATIONARY
2000 PSI PRESSURE ACROSS JETS - 2 # 20-40 OTTAWA SAND PER GAL. GELLED WATER
DEC. 22, 1959
D
PUMPING TIME - MINUTES
PENETRATION DISTANCE - D - INCHES

Fig. 6—Cutting-Rate Curve.

crack or into a very porous formation that will take fluid easily.

An analysis of the cutting-rate curves (Figs. 4 through 8) shows that, after about 20 to 25 minutes' pumping time, a maximum of penetration (or point of diminishing returns) has been reached and further pumping is not profitable. This has been proved by a number of experiments based on the cutting of steel. Tests show that penetration is deeper in soft formations than in hard ones, but there still remains a limit reached even in clear water where it can be observed.

The size hole produced in a pipe by a given jet while perforating is a function of pumping time. In a normal pumping time of 20 to 25 minutes at a stand-off of ¾ to 1½ in., the hole produced in the target is approximately three times the diameter of the jet used. A longer pumping time enlarges the hole without materially increasing the depth of penetration because the fluid entering the perforation must return to the wellbore through the same perforation, thus eroding the circumference and enlarging the diameter of the perforation. In perforating a Berea sandstone target with a ¼-in. jet, for instance, a ¾-in. diameter hole was produced in 21 minutes' pumping time and a 1⅛-in. diameter hole in 33 minutes (Fig. 9).

The width of a circumferential cut in steel pipe is approximately 2½ times the jet diameter, irrespective of pumping time. For instance, a 13⅜-in. casing cemented inside 20-in. casing was cut off in 3 hours and 20 minutes by rotating two 3/16-in. diameter jets, using 1 lb 20-40 Ottawa/gal at 3,000-psi differential, and the width of the cut in both pipes was barely ½ in. The reason is that a path has been cut for the return fluid and the interference of back-flow is decreased. A circular cut penetrates deeper than a straight perforation; however, it takes slightly more time because of the removal of more material. This is shown by comparing Fig. 6 with Fig. 8. The curve in Fig. 6 has reached its maximum penetration, and further pumping will not

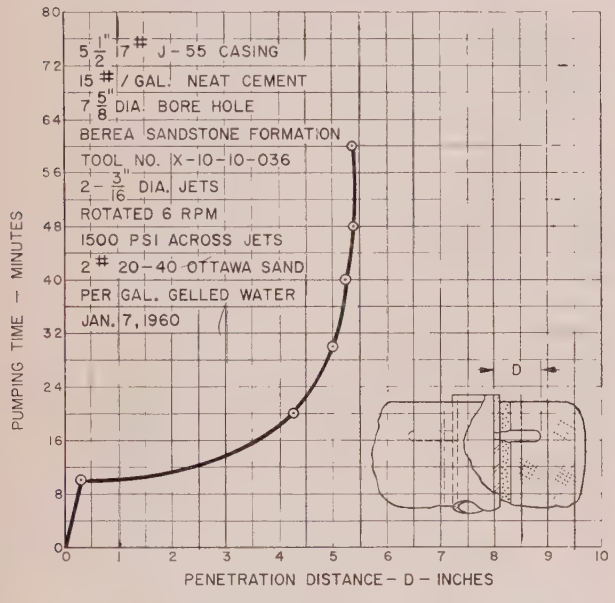

FIG. 7—CUTTING-RATE CURVE.

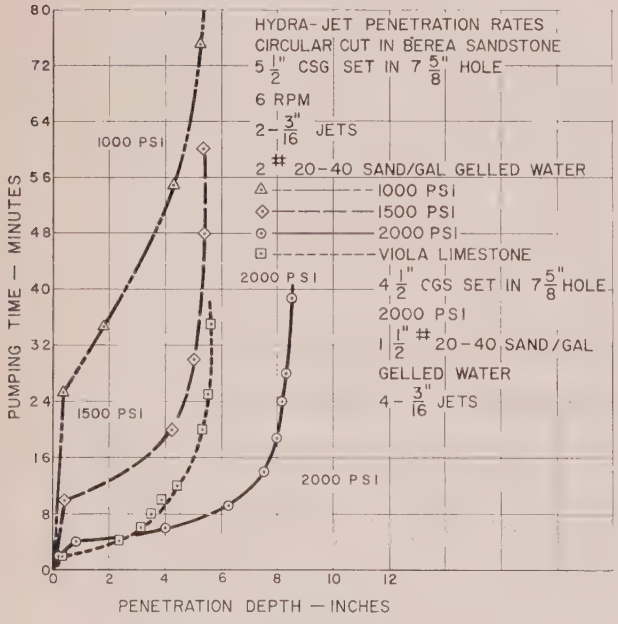

FIG. 8—CUTTING-RATE CURVE.

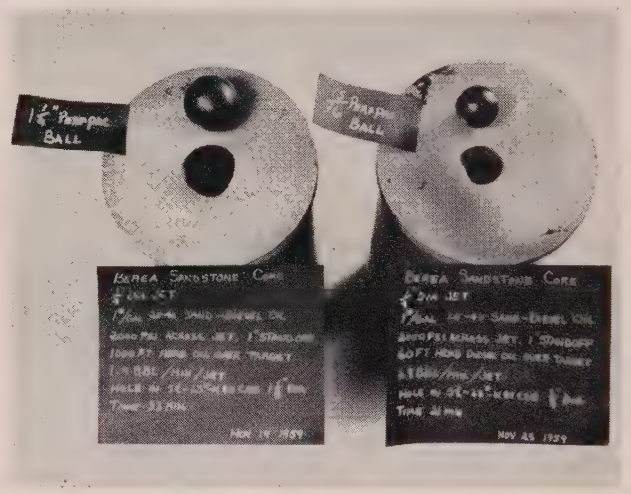

FIG. 9.

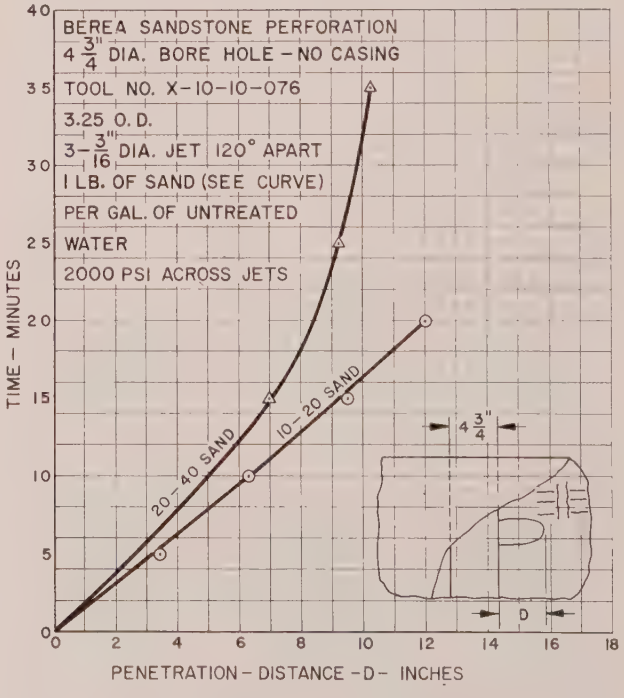

FIG. 10—RELATIVE CUTTING RATES, 10-20 MESH SUBANGULAR SAND VS 20-40 MESH OTTAWA SAND.

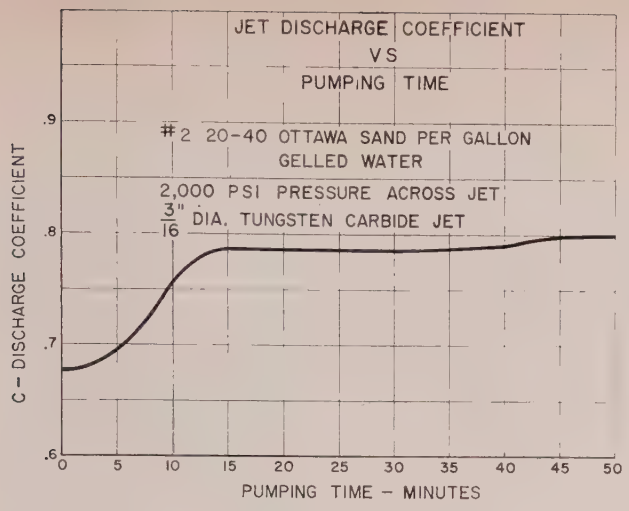

FIG. 11—COEFFICIENT CHANGE VS PUMPING TIME.

increase the depth while the corresponding curve in Fig. 8 has not yet reached its maximum penetration. It has been learned that a deeper penetration may be made by perforating in a position for three or four minutes, then rotating the tubing a few degrees and re-perforating a new hole beside the first one. This provides a return path for the fluid.

Any type fluid, gelled or ungelled, may be used for jetting. However, it is desirable that it be compatible with the formation and formation fluids on which it is to be used. Gelled fluids are generally used to circulate sand from a hole where the fluid velocity up the annulus is too low for ungelled fluid to carry the sand. Most any type of sand may be used; however, the round-grain 20-40 Ottawa sand has been the most popular to date because it is the sand used in most fracturing jobs and is available. Recent tests indicate that the cutting rate of a 10-20 subangular sand cuts approximately 25 per cent faster and further than the 20-40 Ottawa. Fig. 10 shows the relative cutting rates. The increase in cutting rate of the 10-20 over the 20-40 appears due to the greater mass of each grain having greater momentum to expend against the target.

The flow of fluid through an orifice is a function of the cross-sectional area, velocity and coefficient of discharge.

$$Q = AVC_D \quad . \quad . \quad . \quad . \quad . \quad . \quad . \quad . \quad . \quad . \quad (9)$$

where Q = cu ft of fluid/sec,
A = area of orifice in sq ft, and
V = velocity in ft/sec.

$$C_D = \frac{\text{actual flow}}{\text{theoretical flow}}, \quad . \quad . \quad . \quad . \quad . \quad . \quad . \quad (10)$$

and

$$V = \sqrt{2gh} \quad . \quad . \quad . \quad . \quad . \quad . \quad . \quad . \quad . \quad . \quad (11)$$

where g = acceleration due to gravity, and
h = head of height of column of fluid.

$$h = \frac{P \times 144}{\rho \times 7.48}. \quad . \quad . \quad . \quad . \quad . \quad . \quad . \quad . \quad (12)$$

where P = pressure drop across nozzle, psi,
ρ = density of fluid, lb/gal.

Eq. 12 shows that, for a given pressure, a lightweight fluid has a higher head h than a heavier fluid. For this reason, oil has a greater velocity through the jet than water and should cut faster.

The carbide nozzles used now have a sharp entrance.

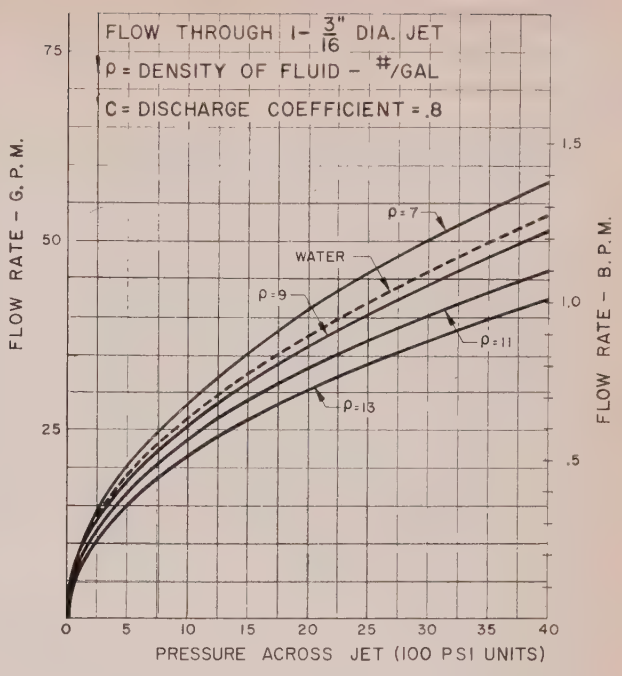

FIG. 12—DISCHARGE THROUGH 3/16-IN. JET NOZZLE FOR VARIOUS DENSITIES OF FLUID VS PRESSURE.

A rounded entrance of the proper shape would be more desirable, but the sharp-edged nozzles are used for economic and availability reasons. It was found that the sharp-entrance nozzle would wear down rapidly to the proper shape after a few minutes' running time. Fig. 11 shows the coefficient change vs pumping time. The discharge coefficient of this sharp-edge jet nozzle at the beginning was .69, rapidly improved to .79 and, later, to .80. The highest coefficient reached was .88. Fig. 12 shows the discharge through a 3/16-in. jet nozzle for various densities of fluid vs pressure. These data were computed using a discharge coefficient of 0.8. To more easily compute the flow through a jet nozzle, a simplified formula was worked out as follows.

$$Q \text{ gal/min} = 69D^2\sqrt{\frac{P}{\rho}} \quad . \quad . \quad . \quad . \quad . \quad . \quad . \quad (13)$$

where P = pressure, psi
ρ = density, lb/gal, and
D = diameter of jet, in.

The types of cuts in formations are shown by the photographs of Figs. 13 through 16. Perforations through the pipe into the cement and formation are generally potato-shaped behind the pipe and round in cross section. The diameter of the washed-out area is generally about one quarter the depth of the cut. Longer pumping time beyond a normal 20 to 25 minutes does not materially increase the depth of cut, but does enlarge the cross-sectional area. If the cement behind the pipe is softer than the formation, it will be cut away faster than the formation and the hole produced will have a stepped conical shape. Fig 14 shows a typical open-hole perforation in Berea sandstone.

The circular cuts shown in Figs 13 and 15 are typical and reach deeper than a fluid-cut perforation. The circular cut provides a flow path for the returning fluid so that it does not interfere with the jet stream to produce severe turbulence, which cuts a wider slot if present, as in a perforation. It should be noticed that the outer edge of a circular cut terminates in a rather sharp ending rather than a rounded end as in a perfo-

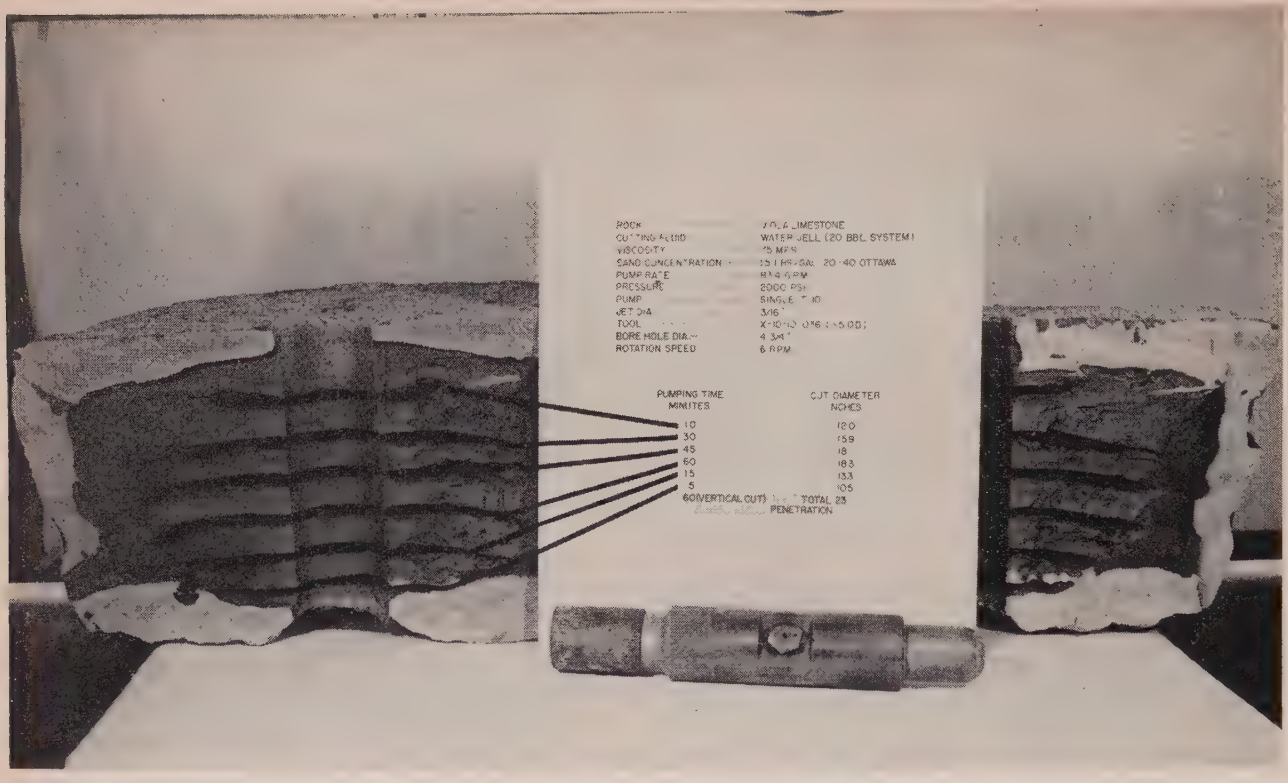

FIG. 13—TYPES OF CUTS IN FORMATIONS BY HYDRAULIC JET PENETRATION.

ration. The larger area produced provides an excellent working area on which fracturing pressure may bear to lift the formation and form a fracture at the sharp notch at the outer edge of cut.

Figs 15 and 16 show a piece of casing cemented in Viola limestone formation. Both perforations and circular cuts were made under simulated well conditions of submergence. On completion of the tests, a vertical cut was made by reciprocating the jetting tool in order to part the stone from within. The cement sheath was not fractured, nor was the casing disturbed, prior to its removal from the stone with a hammer.

The motion of a string of tubing due to changes of temperature, pump pulsations and stretch due to pressure must be recognized and allowed for in placing the jetting tool at the desired location. In shallow wells, this has not been a problem; however, in the deeper ones, corrections for a change in length should be made. A collar locator and a mechanical tubing holddown have been developed so that a jetting tool may be accurately located and held in place during a job. By anchoring the tubing just above the jetting tool, any stretch or change of length due to pressure or temperature will

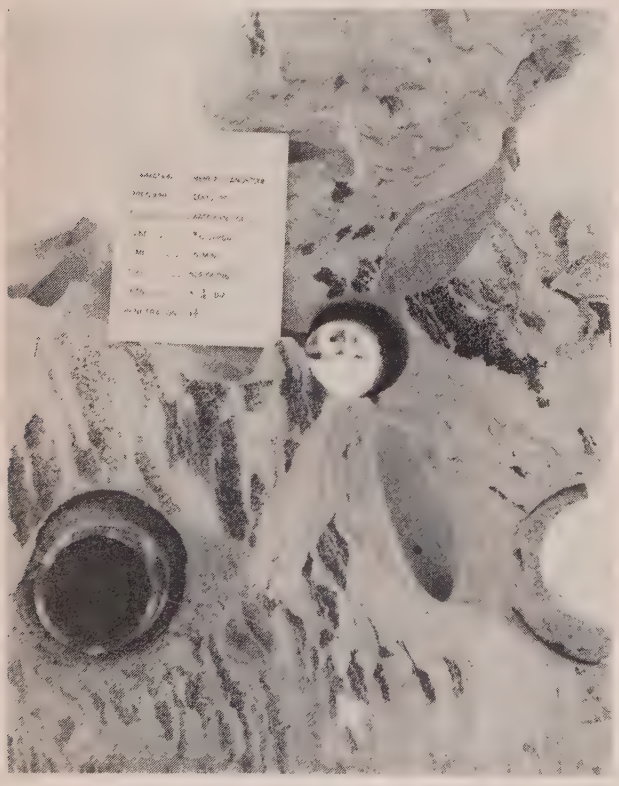

FIG 14—TYPES OF CUTS IN FORMATIONS BY HYDRAULIC JET PENETRATION.

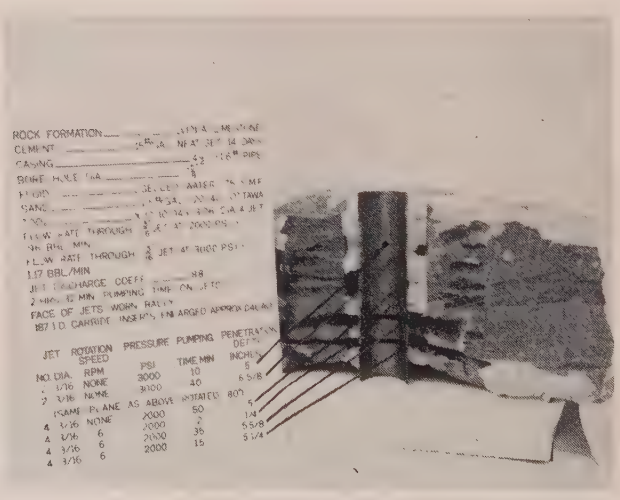

FIG. 15—TYPES OF CUTS IN FORMATIONS BY HYDRAULIC JET PENETRATION.

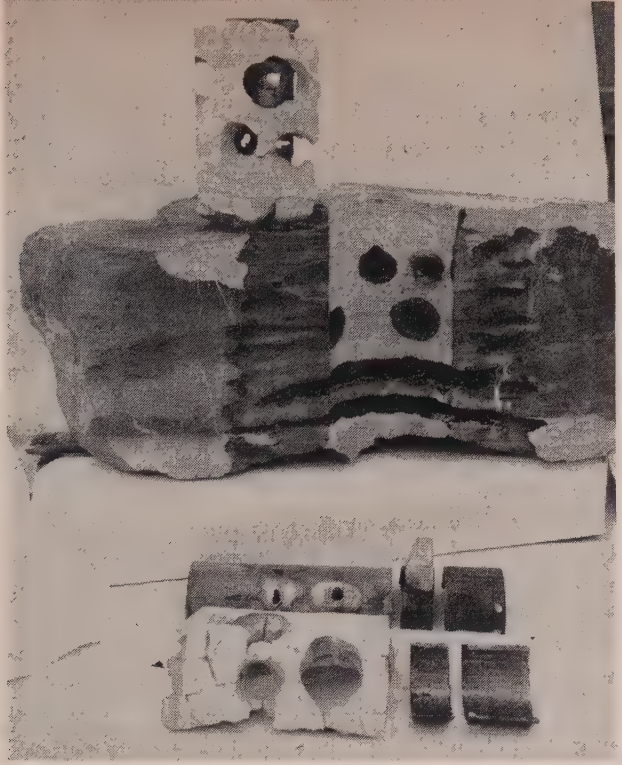

FIG. 16—TYPES OF CUTS IN FORMATIONS BY HYDRAULIC JET PENETRATION.

be reflected at the surface and will show up as a change in weight on the weight indicator. The collar locator is operated by turning the tubing to the right and lifting. This in turn moves two fingers outward to engage the pipe wall; and, as the tubing moves upward, the fingers engage the collars and stop movement. The increase in weight on the indicator shows that a collar has been found. Lowering the tubing releases the fingers and resets the tool so that it is ready for another collar.

The mechanical holddown operates by rotating the tubing to the right and lowering. Lifting the tubing unsets the slips and resets the tool, making it ready for immediate re-use. The top end of the holddown is equipped with bearings which allow free rotation of the jetting tool. It has a full 2-in. opening through the mandrel and will fit all weights of a given casing size.

Field experience up to this time has successfully handled such situations as perforating in 2⅞-in. tubing where other means of perforating had failed. Additionally, combination strings of casing cemented together have been perforated or cut-off to establish communication with the formation. In many cases where the circular cut was made through the casing into the formation, wells have been made into better wells because the fracture produced was located at the point of initiation desired rather than depending upon the weakest place in the formation for breakdown.

CONCLUSIONS

The development of this process has shown that oil-well casing, cement sheath and formation can be perforated or undercut in a relatively short time—that there is a point of diminishing returns beyond which a longer pumping time will not produce appreciably deeper penetration. The depth of penetration is determined by the pressure drop across the nozzle, the size of sand grain, the hardness of the target being cut and the pumping time.

ACKNOWLEDGMENT

The authors wish to express their appreciation to Halliburton Co. for permission to prepare and publish this paper. Appreciation also is extended to those in this organization who offered suggestions for the preparation of this paper. ★★★

Experimental Stress Analysis of Tool Joints

JOHN F. GORMLEY | REED ROLLER BIT CO. HOUSTON, TEX.

INTRODUCTION

Drill pipe, and the connections used to join the pipe together, have had a long history of development and improvement. With the growing use of high tensile-strength pipe, the rotary shouldered connections used to join the lengths of drill pipe have become more critical. Fatigue-type failures of rotary-shouldered connections, or tool joints, have become a cause of much conern to operators and manufacturers.

Most fatigue tests on tool joints have been made on the basis of bending moment applied vs number of cycles, rather than on the basis of stress vs cycles. A desire to learn more about the nature of stress in a tool joint due to bending caused a rather intensive experimental study to determine what actually happens to cause fatigue failure. It was known that a tool joint with insufficient make-up torque was subject to early fatigue failure. Therefore, the establishment of the relationship between make-up torque and allowable bending moment would enable a testing engineer to better correlate the results of various tests.

The problem of calculating the stress in a tool joint due to an applied bending moment was complicated by: the effect of unknown stress concentrations; the applicability of the well known formula $S = Mc/I$; and the question of whether to use the combined cross section of the pin and box in calculating the moment of inertia I.

TEST EQUIPMENT

The test equipment consisted of the following.

1. A lathe modified to act as a fatigue machine for full-size tool joint or drill-collar specimens.

2. An adapter plate bolted to the headstock of the lathe and into which a short adapter was screwed.

3. Tool-joint pins on sections of drill collars bucked into the adapter.

4. A hydraulic load cylinder which rested on the bed of the lathe and applied bending moments to the joints.

5. Paper-backed strain gauges (FAP-12-12, ⅛-in. gauge length and A-5-1, ½-in. gauge length).

6. Eastman 910 contact cement for bonding gauges to joint and Epoxylite 222 waterproofing.

7. A 12-position switchbox, SR-4 bridge balancing unit connected to an SR-4 strain indicator to read the gauge output.

8. A four-channel Sanborn recorder, Model 150, was used as the readout instrument for part of the testing.

The fatigue machine was well suited as a loading device. Because of the long lever arm available, the change of moment with distance was small; consequently, the vertical shear stress was small, less than 300 psi. Some difficulty was experienced with the hydraulic load cylinder at high bending moments due to leakage. The strain gauge equipment was simple and quite reliable.

A 4½-in. extra hole (E. H.) joint with "as machined" threads and shoulders and a 2⅞-in. internal flush (I. F.) joint with copper-plated threads and shoulders were selected for testing because of their common usage in the field. In addition, the 4½-in. E. H. was suitable because it had an inside diameter large enough to permit the insertion and accurate positioning of strain gauges without using special jigs, while the 2⅞-in. I. F. joint required much lower bending loads to cause separation of the shoulders of the joint when made up to the recommended torque. The joints were made to standard API specifications, except for very small bevels on the box and pin shoulders and cylindrical stress-relief grooves added to the pins. Larger bevels would have

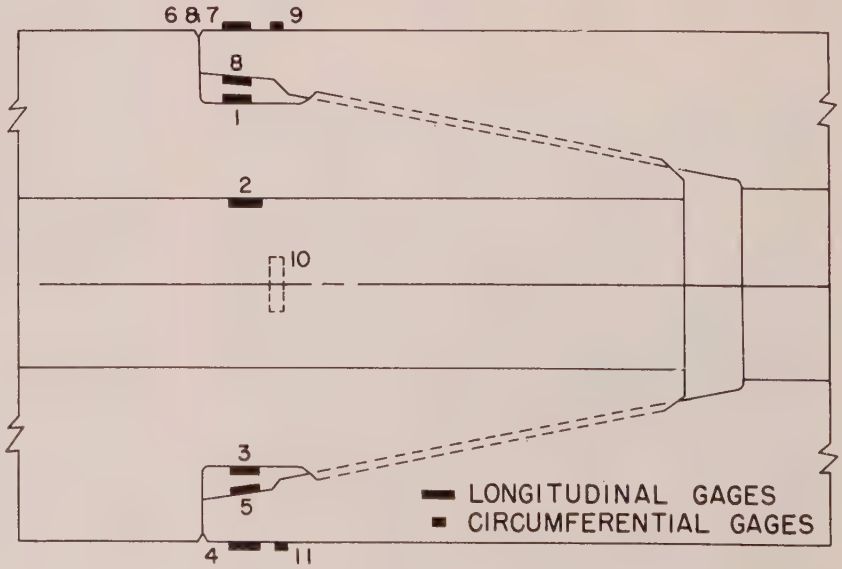

FIG. 1—LOCATION OF STRAIN GAUGES ON 4½-IN. E. H. TOOL JOINT.

Original manuscript received in Society of Petroleum Engineers office Aug. 16, 1960. Revised manuscript received Feb. 13, 1961. Paper presented at 35th Annual Fall Meeting of SPE, Oct. 2-5, 1960, in Denver.

changed the stresses at the surface to less representative values of the stresses throughout the cross section.

Fig. 1 shows the location of the strain gauges on the 4½-in. E. H. joint.

TEST PROCEDURE

A 60 per cent zinc-base grease was applied liberally to the threads and shoulders of the pin and box. The tool-joint pin was screwed into the adapter box hand-tight, and zero readings were taken on all strain gauges. The joint was then screwed together to some higher torque value. New strain readings were taken on all gauges, the difference in the readings being the strain due to torque alone. The joint was then rotated so that the strain gauges would record the maximum and minimum strains resulting from the bending moment. From this new reference position, the strain readings of successive bending loads were recorded, the procedure being repeated at increased bending loads until perceptible shoulder separation occurred. The complete procedure was then repeated at successively higher make-up torques.

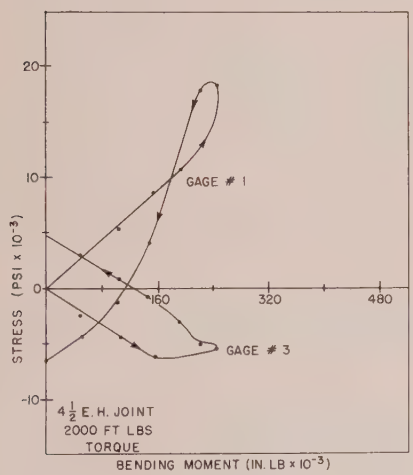

FIG. 2—BENDING MOMENT-STRESS CURVE. GAUGES WERE LOCATED IN STRESS-RELIEF GROOVE OF PIN, 180° APART.

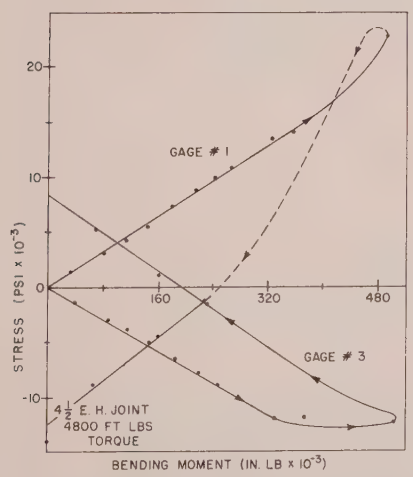

FIG. 3—BENDING MOMENT-STRESS CURVE. GAUGES WERE LOCATED IN STRESS RELIEF GROOVE OF PIN, 180° APART.

DEFINITIONS

The calculation of proper make-up torque for various bending loads on tool joints has been made on the assumption that the stress due to bending follows the flexure formula of

$$S = Mc/I \quad . \quad . \quad . \quad . \quad . \quad . \quad (1)$$

and the average stress in the pin or box due to the make-up torque was calculated on the basis of a modified screw-jack formula[1]

$$T = SA(P/2\pi + f [Rt/\cos\ \theta + Rs]) \quad . \quad . \quad (2)$$

The bending strain is assumed to be linear with stress according to

$$S_1 = \frac{E}{1 - \mu^2}(\varepsilon_1 + \mu\varepsilon_2). \quad . \quad (3)$$

The minimum recommended make-up torque was then found by equating the stress in the box due to bending, to the stress induced by the make-up torque.

In an effort to verify the results of this analysis, it was discovered that an unanticipated phase occurred during the bending of a pair of tool joints. There was a phase of bending during which the shoulders of the pin and box had no perceptible separation, yet the stress in the pin and box due to bending was no longer linear. Therefore, it is believed that a tool joint actually has three zones or phases during bending. These zones are the following.

1. *Solid body bending* (i.e., no relative slippage between the threads or shoulders). The threaded portions of the pin and box bend as a solid body. This zone is the safest from the standpoint of fatigue damage.

2. *Slippage zone.* Shoulders have no perceptible separation, yet stresses increase in a nonlinear manner. Relative axial motion occurs between the threads of the pin and box. This is a danger zone and may cause worn threads and early fatigue failure.

3. *Shoulder separation.* The pin loses much of the strengthening effect of the box shoulder. The joint would leak fluid if in service.

Throughout this discussion, a fully torqued tool joint is understood to be a pin and box made up with sufficient shoulder compression to cause single body bending of the threaded portion of the pin and box.

It was felt that the bending loads would induce a uniaxial stress situa-

[1]References given at end of paper.

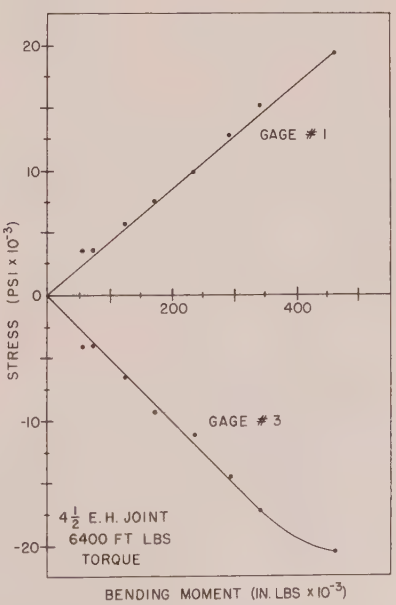

FIG. 4—BENDING MOMENT-STRESS CURVE. GAUGES WERE LOCATED IN STRESS-RELIEF GROOVE OF PIN, 180° APART.

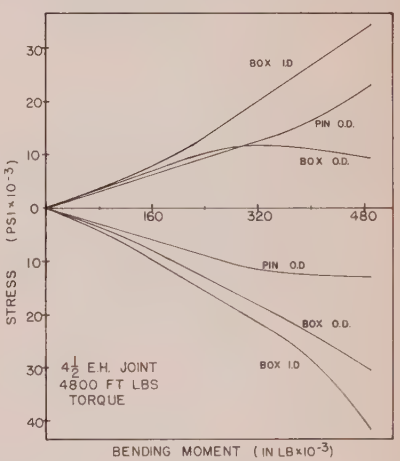

FIG. 5—BENDING MOMENT-STRESS CURVE MEASURED AT VARIOUS POINTS ACROSS THE STRESS-RELIEF GROOVE OF THE PIN AND THE COUNTERBORE OF THE BOX.

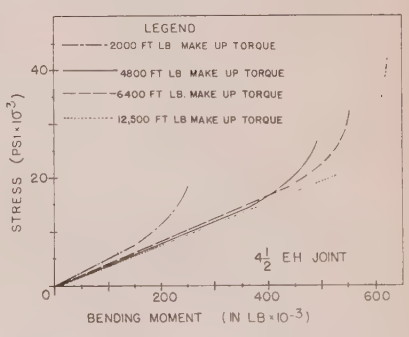
LEGEND
2000 FT LB MAKE UP TORQUE
4800 FT LB MAKE UP TORQUE
6400 FT LB MAKE UP TORQUE
12,500 FT LB MAKE UP TORQUE
4½ E.H JOINT
STRESS (PSI x 10⁻³)
BENDING MOMENT (IN LB x 10⁻³)

FIG. 6—BENDING MOMENT-STRESS CURVE FOR 4½-IN. E. H. JOINT. STRESS WAS MEASURED IN STRESS-RELIEF GROOVE OF THE PIN.

tion. This situation was checked and found to be true on the box OD; therefore, it was assumed to be true elsewhere. The stress situation due to the torque is triaxial, even in the box counterbore.

INTERPRETATION OF RESULTS

Fig. 2 shows the bending moment-stress curve on a 4½ in. E. H. tool joint. The make-up torque (2,000 ft-lb) was low, so the shoulders of the pin and box separated at a relatively low bending moment. The stress on the tension side of the pin increased linearly with bending moment to approximately 160,000 in.-lb. Above this moment, the tensile stress increased in an increasing nonlinear manner, while the compression side of the pin remained at a constant stress value. Figs. 3 and 4 are similar to Fig. 2, but show bending moment stress linearity with higher bending moments because of the higher make-up torques.

Fig. 5 shows a more complete picture of the bending stress across a pin and box. The tension stress of the pin increases linearly, as does the box stress to about 280,000 in.-lb moment. Above this moment, the pin stress increases more rapidly, while the box tension becomes constant and then falls off. This indicates that equilibrium is maintained by shifting the transfer of the bending moment from the contact shoulders to the threaded sections. The reverse side of the joint shows the opposite effect. The compression side of the pin refuses to carry a higher stress, which transfers additional stress into the compression side of the box. This slippage zone occurs before the shoulders of the pin and box have appreciable separation. Even though the shoulders have not separated enough to leak, this slippage between the pin and box may be accompanied by a shift of the neutral axis, but this has not been determined. This effect is possibly caused by the bending tension on one side of the pin, increasing the make-up torque tension and reducing the box make-up compression. Just the opposite situation holds true on the other side of the joint.

Fig. 6 shows the bending moment-stress curves in the pin for various make-up torques. It is evident that the bending stress is lower at high

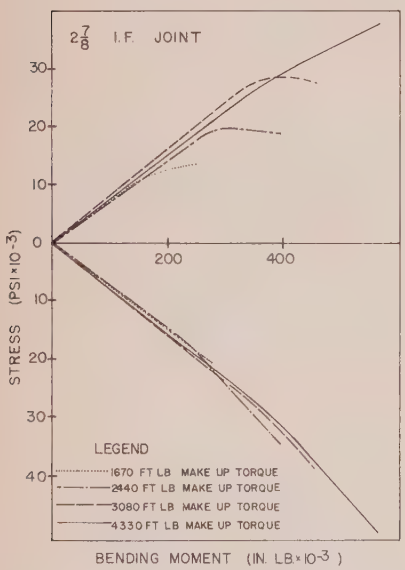
2⅞ I.F. JOINT
STRESS (PSI×10-3)
BENDING MOMENT (IN. LB×10-3)
LEGEND
1670 FT LB MAKE UP TORQUE
2440 FT LB MAKE UP TORQUE
3080 FT LB MAKE UP TORQUE
4330 FT LB MAKE UP TORQUE

Fig. 7—Bending Moment-Stress Curve for 2⅞-in. I. F. Joint. Stress Was Measured on the Box OD Near the Shoulder.

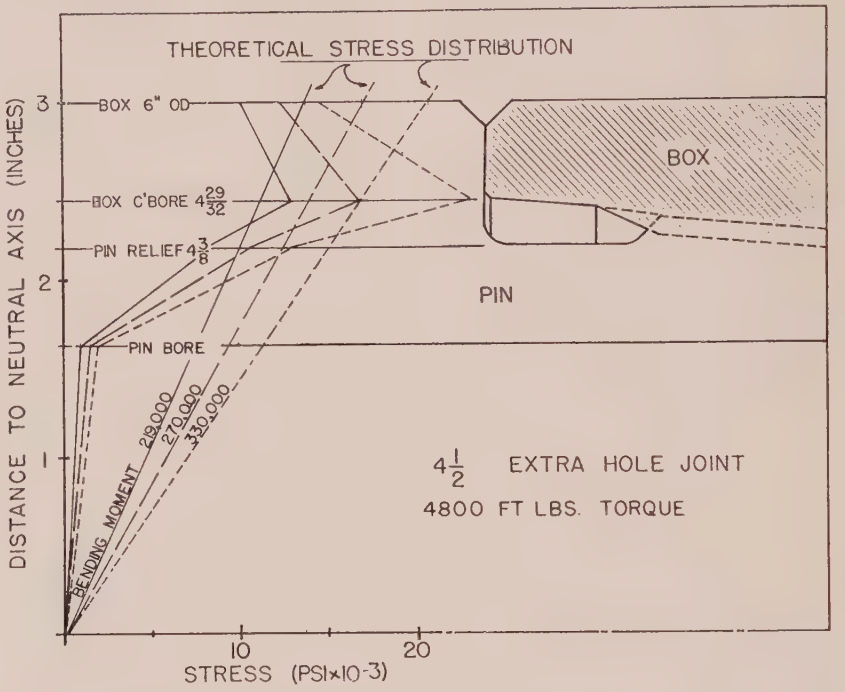

Fig. 8—Theoretical vs Actual Bending Stress Distribution on 4½-in. E. H. Joint. Actual Stress Was Measured on Surfaces of Joint.

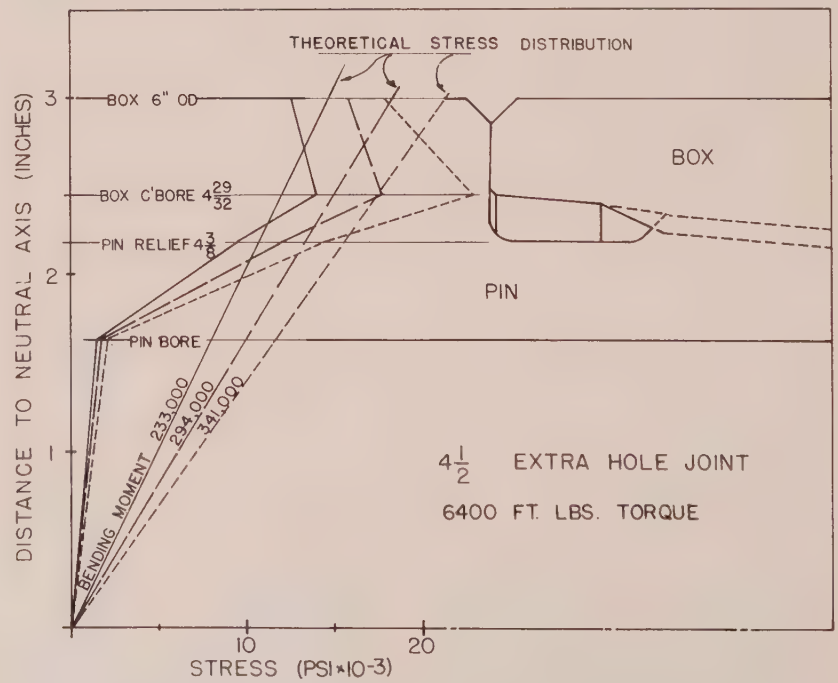

Fig. 9—Theoretical vs Actual Bending Stress Distribution on 4½-in. E. H. Joint. Actual Stress Was Measured on Surfaces of Joint.

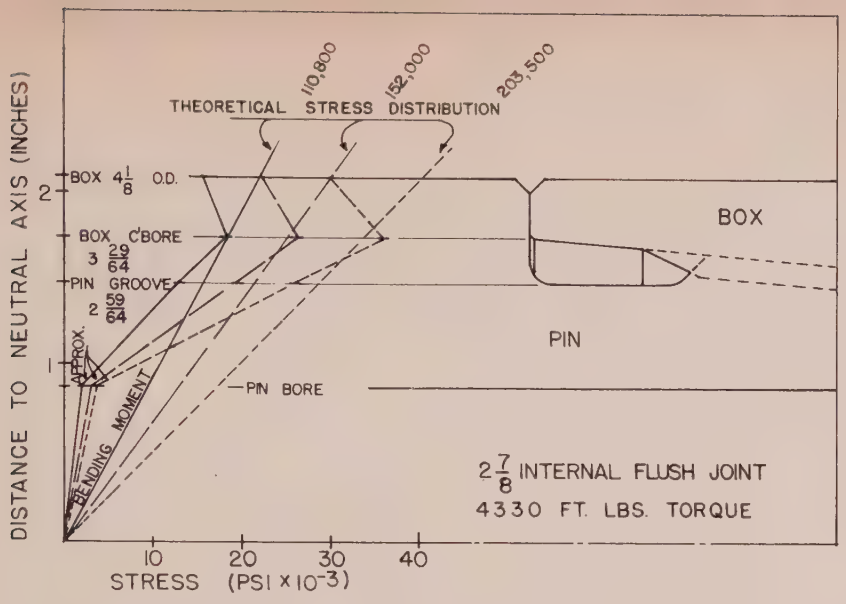

FIG. 10—THEORETICAL VS ACTUAL STRESS DISTRIBUTION MEASURED ON SURFACES OF PIN AND BOX OF 2⅞-IN. I. F. JOINT.

make-up torques compared to low torques. Fig. 7 shows similar-type curves on the 2⅞-in. I. F. joint with the stress measured on the box OD. The box tension levels off at higher moments because the tension is superimposed on the compressive stress resulting from make-up, and this observed tension is actually due to a reduction of the existing compression. An interesting note is that the bending tension on the box OD is somewhat greater than the make-up compression. This is possibly due to a shifting of the neutral axis, hence a varying moment of inertia.

Inspection of Figs. 8, 9, and 10 reveals that the stress distribution across the stress-relief groove of the pin and the counterbore of the box must be fairly complex. For equilibrium to exist, the theoretical bending stress in the pin and box, integrated over the area, must equal the actual stress over this section integrated over this area. From comparison of the actual stress at the surfaces of the pin and box to the theoretical stresses, one concludes that the bending stress on the inside of the cross section is greater than the surface stress. This is somewhat unusual but might be expected from the irregular nature of the composite beam.

Efforts were made to predict the point of incipient slippage in correlation with the make-up torque, and the stress due to the make-up. The closest correlation is shown in Fig. 11. The curve for the 2⅞-in. I. F. joint has the same general shape as the curve for the 4½-in. E. H. joint, but obviously some factor is missing. A fairly linear relationship between make-up torque and maximum safe bending load does exist in the lower torque ranges. As make-up torque increases, the ability of the joint to carry higher bending loads increases more slowly. The increase in static pin tension at the higher torque does slightly lower the allowable alternating stress, but the reduction in the actual bending stress does more than offset the reduction of the allowable alternating stress. Fig. 13 shows that a high mean stress (or average stress), even above the yield point, can be applied but that the material may last 10-million cycles if the alternating stress — the stress amplitude — is small.

Figs. 2, 3 and 4 all show the linearity of stress vs bending moment until slippage occurs. Before slippage, the stress can be calculated from a modification of Eq. 1.

$$S = M\,Kc/I \quad . \quad . \quad . \quad . \quad . \quad (4)$$

where K does not depend on the absolute value of c but is a stress concentration factor caused by the geometry of the joint. The agreement in K values between the two joints tested is fairly good, usually within 10 per cent of the average value.

Table 1 gives the K values for the tool joints tested. Each value was taken from an average of several readings at various torques. It is believed that these values of K apply to other sizes and types of joints.

A qualitative picture of the stress distribution of a made-up tool joint is shown in Fig. 12.

CONCLUSIONS

1. The stresses in a tool joint due to bending are linear up to some point at which the stress in the tension side of the pin increases in an increasing, nonlinear manner. This increase of stress raises the likelihood of fatigue failures.

2. This transition zone occurs at some point at which the friction between the pin and box due to make-up torque is insufficient to transmit the bending loads, yet there is no perceptible separation of the shoulders.

3. The higher the make-up torque, the larger the bending moment at which the stress becomes nonlinear.

4. Due to the complicated stress flow in the pin, the stress due to

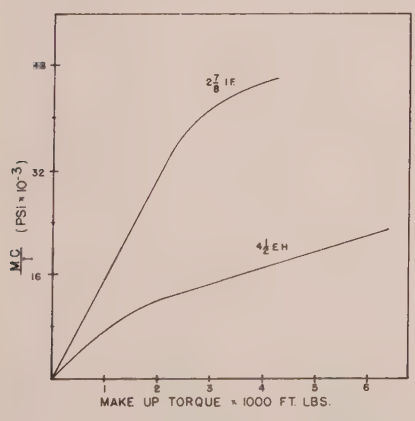

FIG. 11—MAKE-UP TORQUE VS THEORETICAL STRESS AT THE POINT OF INCIPIENT SLIPPAGE DUE TO BENDING FOR TWO DIFFERENT-SIZE JOINTS.

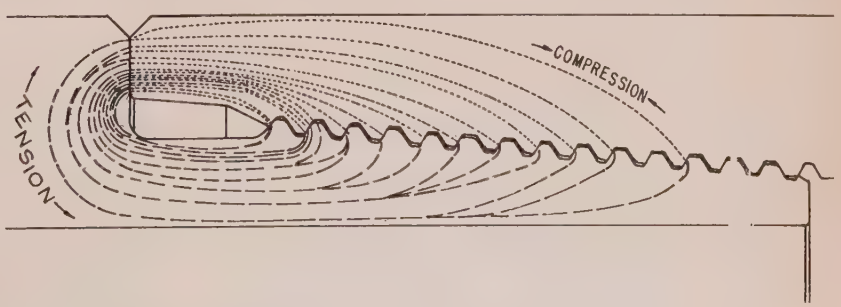

FIG. 12—A QUALITATIVE PICTURE OF THE STRESS DISTRIBUTION IN A MADE-UP TOOL JOINT.

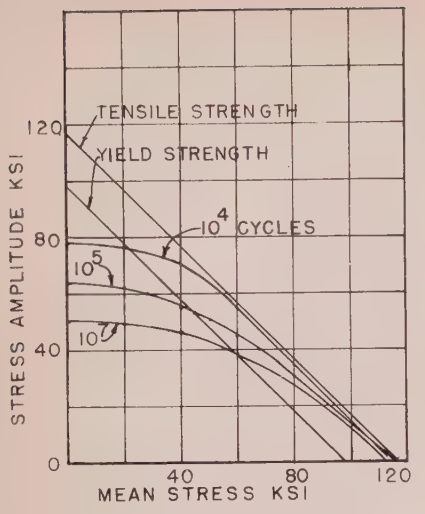

FIG. 13—EFFECT OF ALTERNATING STRESSES AND STEADY STRESS ON FATIGUE LIMIT.

bending cannot be calculated from $S = Mc/I$, but it is equal to $S = MKc/I$ until slippage occurs. K is a geometry factor which depends upon the point at which the stress is measured.

5. The distribution of make-up stress in a cross section of the tool-joint pin is very irregular. Eq. 2 gives the average stress due to the torque,

TABLE 1—K VALUES FOR TESTED TOOL JOINTS

Joint	Location: Pin OD*	Box ID	Box OD
4½ E. H.	1.01	1.35	.90
2⅞ I. F.	.93	1.13	.78
Average	.97	1.24	.84

*Stress-Relief Groove.

but the maximum stress can be several times that value. This is a static stress and is not as damaging in fatigue as an alternating stress.

6. It appears that the suggested field-practice torque range is correct, but that the high side of the torque range is safer from an operating standpoint than the lower end of the torque range.

NOMENCLATURE

S = stress at any point, psi
M = bending moment, in.-lb
c = distance from neutral axis to fibers, in.
I = moment of inertia, in.^{4}
T = applied torque, in.-lb
A = area of pin or box, in.^{2} (measured ⅝-in. from shoulder)
P = thread pitch = 1/number of threads/in.
π = 3.1416, radians
f = coefficient of friction between mating surfaces, dimensionless
Rt = mean thread radius, in.
Rs = mean shoulder radius, in.
θ = one-half the included thread angle, degrees
ε = unit strain, in./in.
E = Young's modulus = 30×10^6 psi
μ = Poisson's ratio (dimensionless) = .28

ACKNOWLEDGMENTS

The author extends thanks to the management of Reed Roller Bit Co. for the opportunity to publish this paper, and W. M. Koch, R. J. Kotch and Mrs. Lee Barker for their constructive criticism.

REFERENCES

1. Farr, A. P.: "Torque Requirements for Rotary Shouldered Connections", presented at the ASME Pet. Mech. Eng. Conf. in Tulsa (Sept. 22-25, 1957).
2. Grover, H. J., Gordon, S. A. and Jackson, L. R.: "Fatigue of Metals and Structures", U. S. Government Printing Office publication NAVAER 00-25-534 (1954). ★★★

Some Effects of Size Distribution on Particle Bridging in Lost Circulation and Filtration Tests

CARL GATLIN
MEMBER AIME
CHARLES E. NEMIR*
JUNIOR MEMBER AIME

THE U. OF TEXAS
AUSTIN, TEX.

INTRODUCTION

A common cure of lost circulation is the introduction of granular bridging agents into the mud system. Many materials, such as ground nut shells, are used for this purpose. If the trouble causing void (fracture, fissure, vug, etc.) is not too large, the granular agent forms a "bridge" across or within the opening. Successively smaller particles in the mud stream then accumulate on and/or within this bridge until normal filtration is finally established. The efficiency of many bridging agents has been studied in the laboratory using various slot testers.[1,2]

Many investigators have remarked that a granular bridging material should have the proper particle size distribution. With the exception of the broad range specified in the patent of Goins and Nash,[3] there is apparently no definition as to what this distribution should be.

A bridge may be initiated when several particles of lost circulation material lodge against each other in a fracture or other void. Smaller particles then may bridge the openings between the larger, previously bridged particles. This process continues until the voids become quite small and the problem becomes one of filtration. It would seem logical that an optimum particle size distribution exists, i.e., one containing the proper quantity of properly sized material to fill the successively smaller voids of the bridge.

The filtration characteristics of drilling fluids may be subject to a similar analysis. It has been clearly demonstrated by many workers that the filtration behavior of various muds can be altered by particle size control.[4-8] Slusser, *et al*,[7] divided filtration into three periods and showed that particle sizes affecting a given period did not necessarily affect other portions of the filtration curve.

An analagous problem is the proper sizing of gravel, liner slots and screen sizes in various sand-exclusion problems. Here the situation is reversed in that a proper "void" size, rather than the size of the bridging agent, is sought. The classic work of Coberly[9] forms the quantitative basis for most sand-exclusion processes. It is interesting to note that, in general, Coberly's work has been overlooked by most drilling-mud researchers.

Other investigators have made various studies of the effect of particle size distribution on drilling-mud properties. As a part of their studies, Fancher and Oliphant reported 30-minute filtration loss of a variety of mixtures of particle sizes.[10] Gates and Bowie noted an effect of particle size distribution on filtration, as well as on other physical properties.[4]

MAXIMUM DENSITY THEORY

A maximum density mixture has been mentioned as the possible solution for both lost circulation and mud filtration problems.[11] Furnas[12] derived mathematically a method for obtaining maximum density of beds of packed solids, having either a given number of component sizes or a continuous gradation of sizes. This work was verified experimentally by Anderegg.[13] For mixtures having a continuous grading of sizes, the interval between sizes is taken as successive screen sizes of interval $\sqrt{2}$. The ratio of the quantity of each size and the next smaller size is given by the equation

$$r = \frac{1}{\phi^{n/m}}$$

where r = the quantity ratio between successive sizes of interval $\sqrt{2}$,

ϕ = the porosity of a bed composed of material of one screen size,

n = one less than the number of component sizes obtained from the ordinate of Fig. 1, and

m = one less than the number of screens used, i.e., the number of size intervals of ratio $\sqrt{2}$.

Fig. 1, number of size intervals of ratio $\sqrt{2}$ taken from Furnas' paper, gives the value of $n + 1$ for any given values of ϕ and K, where K is the ratio of the diameter of the smallest particles to the diameter of the largest particles. Measurement by weight assumes, of course, constant density for all particle sizes. Choosing the quantity of the smallest particle size as a unit weight, the required weights of the successively larger intervals are then r, r^2, r^3, . . . , $(r)^m$. Thus, the grading curve of a maximum density mixture represents a geometric progression of ratio r.

Original manuscript received in Society of Petroleum Engineers office Nov. 10, 1960. Revised manuscript received, March 23, 1961.

*Currently with Texaco, Inc., Sweetwater, Tex.

[1]References given at end of paper.

Discussion of this and all following technical papers is invited. Discussion in writing (three copies) may be sent to the office of the *Journal of Petroleum Technology*. Any discussion offered after Dec. 31, 1961, should be in the form of a new paper. No discussion should exceed 10 per cent of the manuscript being discussed.

This page of *Petroleum Transactions, AIME* follows page 500. The intervening non-Transactions pages appeared in *Journal of Petroleum Technology*.

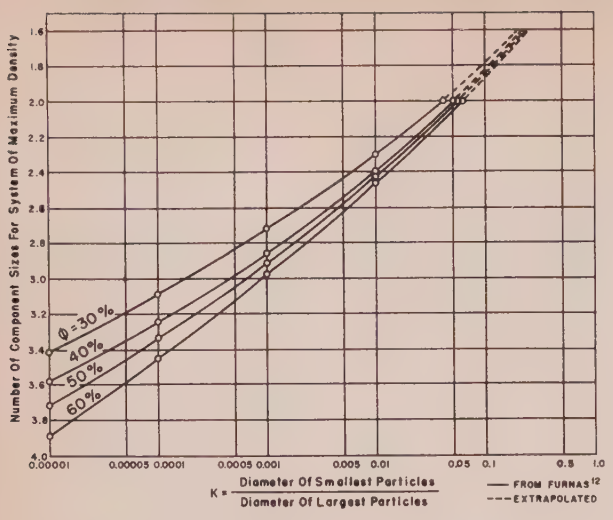

FIG. 1—RELATION BETWEEN SIZE RATIO AND NUMBER OF COMPONENT SIZES FOR SYSTEMS OF MAXIMUM DENSITY.

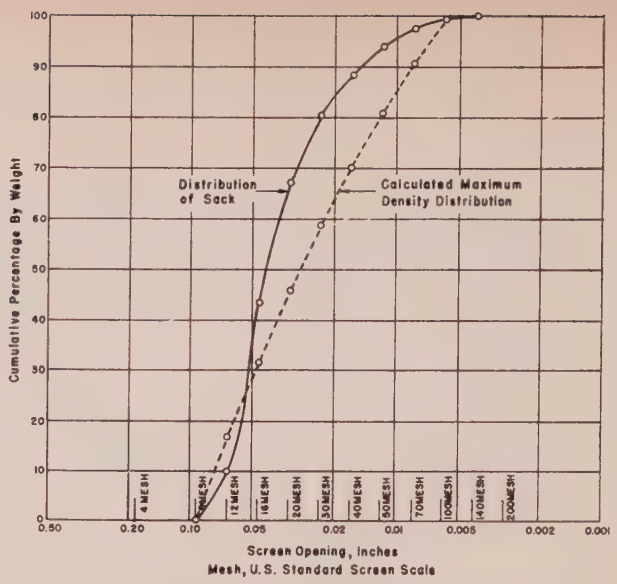

FIG. 2—PARTICLE SIZE DISTRIBUTION OF RANDOM NUT-SHELL SACK.

The purpose of this study was the preliminary application of the Furnas theory to some particle bridging features of lost circulation and mud filtration.

LOST CIRCULATION TESTS

These tests were conducted with a wedge-shaped slot tester, as described elsewhere.[2] The slot used had an entrance width of 0.50 in., tapering to about 0.06 in. at the exit.

A 50-lb, randomly selected sack of medium-sized crushed walnut shells was screened using United States Standard sieves; the sizes of successive sieves vary by $\sqrt{2}$. The particle size distribution of this sample is shown in Fig. 2. It is realized, of course, that not all sacks will necessarily have this distribution. The maximum density distribution of particle sizes then was calculated by Furnas' method, using $\phi = 0.50$; this distribution curve also appears in Fig. 2.

A nut shell sample having its original particle size distribution was thoroughly mixed into a 16-gal sample of mud in a concentration of 20 lb/bbl. Likewise, a quantity of particles was combined to give the calculated maximum density distribution. This was mixed into an identical portion of mud in the same concentration of 20 lb/bbl.

Each sample was pumped through the tester at about 8 gal/min until bridging occurred, or until the entire sample was expended. A stable bridge occurred when fluid did not pass the slot at 225-psi differential. Results of these tests are shown in Table 1, Runs 1 through 12. It is clear that the maximum density mixture consistently bridged the slot, while that from the original sack did not.

An additional quantity of the largest particles (12 mesh) then was added to the standard sample so that it contained the same amount of the largest size as did the maximum density sample. Runs 13 through 15 were made with this mixture. In Run 13 a stable bridge formed; however, Runs 14 and 15 were unsuccessful. These three tests suggest that, while the quantity of large particles is important in initiating the bridge, a proper distribution of successively smaller sizes supplements the "seal".

FILTRATION TESTS

Standard API equipment was used for the filtration tests against filter paper. Other tests substituted a 2¾-in. diameter by 2-in.-thick sandstone core for the filter paper. The cores used were quite uniform and had permeabilities of 600 to 800 md.

The fractionated aquagel samples obtained by Jessen and Mungan[14] were used in this investigation. Their nomenclature will be used for each size range as listed in Table 2, taken from their paper. Muds having maximum density, as well as standard particle size distributions were prepared as defined by the following. These will be referred to by number.

MUD

1. 6.1 per cent by weight of particles having the original size distribution of Sizes B through M.

2. 6.1 per cent by weight of the calculated maximum density distribution of Sizes B through M plus 4.23 gm of particle Size M. The extra quantity of Size M was required to furnish viscosity.

3. 4.0 per cent by weight of Size M only.

4. 6.1 per cent by weight of particles having the original distribution of Sizes H through M.

TABLE 1—RESULTS OF WEDGE-SHAPED SLOT TESTS

Run No.	Nut Shell Sample	Time for Stable Bridge (sec)	Volume of Mud Pumped Through (gal)	Remarks
1	Random Sack	—	16	No bridge formed and no pressure held on system after test.
2	" "	—	16	"
3	" "	—	16	"
4	" "	—	16	"
5	Maximum Density	43	3	System held 130 psi after test.
6	" "	95	4	"
7	" "	105	5	"
8	" "	10	0	"
9	" "	70	4.5	"
10	" "	70	4.5	"
11	" "	120	8	"
12	" "	135	8	"
13	Added 150 grams of 12-mesh size to random sack sample	45	2	System held 125 psi pressure after test
14	" "	—	16	System held 55 psi pressure after test
15	" "	—	16	15-psi pressure bled-off in 30 sec

TABLE 2--SIZE DISTRIBUTION OF AQUAGEL (AFTER JESSEN AND MUNGAN)[14]

Fraction	Size Range (microns)	Cumulative Per Cent by Weight
B	40	3.76
C	40 — 20	5.56
D	20 — 10	8.41
E	10 — 4	10.81
F	4 — 2	12.91
G	2 — 1	15.91
H	1 — 0.4	20.42
I	0.4 — 0.3	29.42
K	0.3 — 0.15	41.43
L	0.15 — 0.05	62.46
M	0.05	99.99

TABLE 3—PROPERTIES OF MUD SAMPLES

Sample	Plastic Viscosity	Initial Gel Strength (lb/100 ft²)	10-min Gel Strength (lb/100 ft²)
1	25 cp	10	24
2	11.5	5	17
3	6	4	15
4	20	7	26
5	11	2	4

5. 6.1 per cent by weight of the calculated maximum density distribution of Sizes H through M.

After mixing, the flow properties of the mud samples were measured with a Fann V-G meter and are given in Table 3.

A standard filtration test was run and repeated using Sample 1. Using the same procedure, filtration tests were run on Samples 2 and 3. Sample 3 flowed freely through the filter paper without depositing a filter cake. Filtration curves were drawn for Samples 1 and 2 and are shown in Fig. 3. Since the curves become linear, for convenience only the first portion of each curve is shown.

A series of filtration tests then were performed using sandstone cores as the filter septum. Results of these tests are given in Fig. 4.

DISCUSSION OF FILTRATION STUDY

FILTER PRESS TESTS

Two things are immediately apparent from Fig. 3. First, the spurt loss of mud Sample 2 is less than that of Sample 1. A second difference is the steeper slope observed for the filtration of mud Sample 2. Since Sample 2 was composed of the calculated maximum density distribution of particle sizes, except for Size M, this result does not agree with the maximum density idea. This verifies prior work showing that the straight-line portion of filtration is controlled by the highly-hydratable small sizes,[8] which evidently cannot be treated

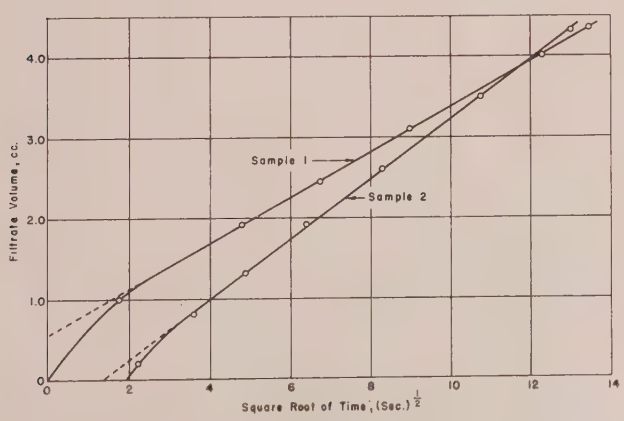

FIG. 3—FILTRATION CURVES OF SAMPLES 1 AND 2 ON FILTER PRESS.

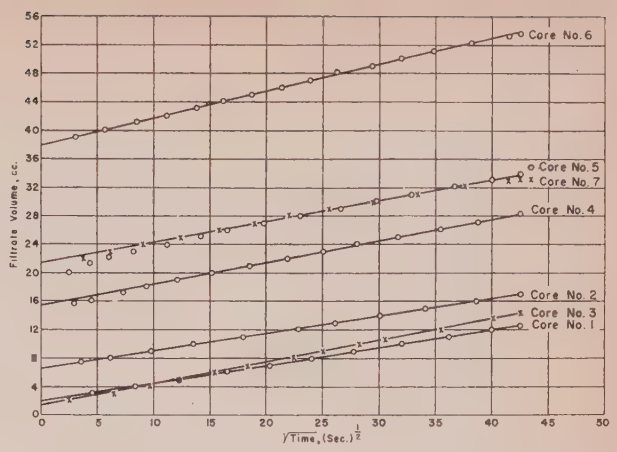

FIG. 4—FILTRATION OF MUD THROUGH SANDSTONE CORES.

as inert particles. It appears, however, that the larger sizes (which control the spurt loss) may be treated as inert particles since the maximum density mixture exhibited a reduced spurt loss on filter paper. This confirms the lost circulation results, since lost circulation is little more than a "large-scale spurt".

CORE SAMPLE TESTS

A close similarity between the curve shapes was noted in all of the core sample tests (Fig. 4). The main difference is the spurt loss, which shifts the curves vertically.

In Fig. 4, the spurt loss through Cores 1, 2 and 3 ranges from approximately 2 to 7 cc. These tests were conducted with Muds 1 and 2, containing the full range of particle sizes from B to M. Mud 2 (maximum density sample) was used on Core No. 3, and it is seen that filtration through this core had a slightly smaller spurt loss than that of mud Sample 1 through Cores 1 and 2, but had a steeper slope and, hence, a larger 30-minute water loss. This is in qualitative agreement with the previously discussed results from the filter-press experiments; however, the spurt loss difference is quite small. Slight variations in pore entry sizes of the cores may obscure the effect. The filtration tests of Samples 4 and 5 against the cores show a high spurt loss, ranging from about 15 to 38 cc. This was from two to six times as high as the spurt loss obtained from the mud samples containing the larger particles. Note from Fig. 4, however, that all the curves have substantially the same slope once bridging occurs. There was no significant difference between the filtration characteristics of mud Samples 4 and 5. Therefore, the increased spurt loss was essentially due to the deletion of the large particle sizes with a negligible contribution from the maximum density effect.

Permeability measurements were made on the core samples before and after the tests. In all cases the bulk (75 per cent or more) of formation damage occurred in the first 0.25 cm, as expected. In general, for a given particle size range, the damage depth was less for the maximum density mixture. The data were, however, scattered and inconclusive.[15]

SPECULATIONS

In rotary drilling, the selection of a drilling fluid often involves a considerable compromise between hole conditioning and penetration rate. Much penetration-

rate reduction has been attributed to the "chip hold-down" forces which accompany low-water-loss, high-solid-content, high-viscosity, etc., muds, even in "impermeable rocks". These forces are a consequence of a high pressure difference, or more correctly, a high pressure gradient across the hole bottom, i.e., the element being drilled.[16-18] It also is well known that beneath bit filtration is something quite different from that measured by the API test.[19] Because of the continual bit action beneath bit, filtration is better described by some early portion of the filtration curve. A high spurt mud will clearly result in a reduced pressure gradient across bottom, thereby facilitating cutting removal. The use of clear water is an example.

Deletion of "large" particles from colloidal drilling muds results in high spurt muds. Once bridging occurs, however, the behavior is apparently normal. Thus, it appears possible to construct a mud which can satisfy hole-conditioning requirements with less sacrifice of drilling rate. While this is somewhat conjectural, the principle seems sound, although it is realized that continual maintenance of such a mud may be difficult.

Many other possibilities exist for application of the Furnas theory. The selection of aggregate for gravel packs and, possibly, the sizing of particles for filtration control in other wellbore fluids are typical examples. The Furnas approach can even be applied to the packing of unconsolidated cores for laboratory purposes.

Because of the limited testing performed, the following conclusions are necessarily restricted to the few systems studied. The results are, however, sufficiently promising to encourage further work.

CONCLUSIONS

1. A maximum density distribution of nut-shell particle sizes is more efficient in bridging and sealing a wedge-shaped slot than the distribution found in a randomly selected sack.

2. A maximum density distribution of the "large" particles in commercial bentonite reduces the initial surge or "spurt loss" of a bentonite mud in the standard filter press test.

3. The maximum density theory, which is based on inert particles, apparently does not hold for the linear portion of the filtration curve of a bentonite mud.

ACKNOWLEDGMENT

The authors express their thanks to Necmettin Mungan for the use of his clay samples.

REFERENCES

1. Howard, G. C. and Scott, P. P., Jr.: "An Analysis and the Control of Lost Circulation", *Trans.*, AIME (1951) **192**, 171.
2. Green, B. Q.: "Which Lost-Circulation Materials to Use and How to Use Them", Parts I and II, *Oil and Gas Jour.* (March, 1959) **57.**
3. Goins, W. C., Jr. and Nash, Fred, Jr.: "Method of and Composition for Recovering Circulation of Drilling Fluids in Wells", U. S. Patent No. 2,815,079 (Dec. 3, 1957).
4. Gates, G. L. and Bowie, C. P.: "Correlation of Certain Properties of Oil-Well Drilling-Mud Fluids with Particle Size Distribution", RI 3645, USBM (May, 1942).
5. Nowak, T. J. and Krueger, R. F.: "The Effect of Mud Filtrate and Mud Particles Upon the Permeability of Cores", *Drill. and Prod. Prac.*, API (1951) 164.
6. Krueger, R. F. and Vogel, L. C.: "Damage to Sandstone Cores by Particles from Drilling Muds", *Drill and Prod. Prac.*, API (1954) 158.
7. Slusser, M. L., Glenn, E. E. and Huitt, J. L.: "Fractures Affecting Well Productivity: I. Drilling Fluid Filtration", *Trans.*, AIME (1957) **210**, 126.
8. Glenn, E. E. and Slusser, M. L.: "Factors Affecting Well Productivity: II. Drilling Fluid Particle Invasion Into Porous Media", *Trans.*, AIME (1957) **210**, 132.
9. Coberly, C. J.: "Selection of Screen Openings for Unconsolidated Sands", *Drill. and Prod. Prac.*, API (1937) 189.
10. Fancher, G. H. and Oliphant, S. C.: "The Effect of Particle Size on the Physical Properties of a Gulf Coast Drilling Mud", *Proc.*, Third World Pet. Cong. (1951) Section II.
11. Gatlin, C.: *Petroleum Engineering: Drilling and Well Completions*, Prentice-Hall, Inc., N. J. (1960).
12. Furnas, C. C.: "Mathematical Relations for Beds of Broken Solids of Maximum Density", *Ind. and Eng. Chem.* (Sept., 1931) **23**, 1052.
13. Anderegg, F. O.: "The Application of Mathematical Formulae to Mortars", *Ind. and Eng. Chem.* (Sept., 1931) **23**, 1058.
14. Jessen, F. W. and Mungan, N.: "The Effect of Particle Size Distribution and Exchange Cation on Gel Properties of Fractionated Bentonite Suspensions", *Trans.*, AIME (1959) **216**, 455.
15. Nemir, Charles E.: "The Effect of Particle Size Distribution on Granular Lost Circulation Materials and on Drilling Mud Filtration", MS Thesis, U. of Texas (1960).
16. Cunningham, R. A. and Eenink, J. G.: "Laboratory Study of Effect of Overburden, Formation and Mud Column", (1959) **216**, 455.
17. Handin, John: "Discussion" (of Ref. 16) *Trans.*, AIME (1959) **216**, 15.
18. Garnier, A. J. and van Lingen, N. H.: "Phenomena Affecting Drilling Rates at Depth", *Trans.*, AIME (1959) **216**, 232.
19. Ferguson, C. K. and Klotz, J. A.: "Filtration from Mud During Drilling", *Trans.*, AIME (1954) **201**, 29. ★★★

Effect of Reservoir Environment on Water-Oil Displacements

J. R. KYTE
V. O. NAUMANN
MEMBERS AIME
C. C. MATTAX

JERSEY PRODUCTION RESEARCH CO.
TULSA, OKLA.

ABSTRACT

Imbibition and waterflooding tests at reservoir conditions show that conventional tests at room conditions sometimes lead to recovery estimates that are too low. Core samples which are of intermediate wettability at normal test conditions may be strongly water-wet at reservoir conditions. This was found to be true for samples from two of three reservoirs investigated.

For the other reservoir, less difference was observed between the wettability of samples at normal test conditions and at reservoir conditions. Samples which became more water-wet at reservoir temperature and pressure also water flooded more efficiently at reservoir conditions. These results show that core analysis tests on intermediate wettability samples should be performed at reservoir conditions to obtain representative data.

INTRODUCTION

Throughout the oil industry, core analysis tests normally are performed using refined oils and at room temperature and pressure. This procedure has always been subject to question because the possibility is generally recognized that the reservoir environment may influence displacement behavior. Burkhardt, *et al*,[1] have performed waterflood tests at reservoir conditions on East Texas cores. They found little difference between results obtained at reservoir conditions and results of conventional flooding tests at room conditions. As they pointed out, however, this situation might not be general since they obtained data on only one rock and crude-oil system.

This paper presents data which demonstrate that it is sometimes necessary to perform core analysis tests in a simulated reservoir environment to properly represent the reservoir wettability and displacement characteristics. The work is specifically concerned with reservoirs which were thought to be of intermediate wettability on the basis of conventional test results at room conditions, i.e., core samples imbibed only small amounts of either oil or water and exhibited no decided preferential wettability characteristics. Tests were performed on cores from three such reservoirs to determine their behavior in the reservoir environment.

Original manuscript received in Society of Petroleum Engineers office Oct. 17, 1960. Revised manuscript received March 22, 1961. Paper presented at the Middle East Regional Meeting of SPE March 27-29, 1961, in Dhahran, Saudi Arabia and the Seventh Annual Rocky Mountain Regional Meeting of SPE May 25-26, 1961, in Farmington, N. M.

[1]References given at end of paper.

EXPERIMENTAL

Imbibition and waterflood tests were used to demonstrate the effect of reservoir environment on reservoir rock wettability and displacement characteristics. Results of tests performed at reservoir conditions were compared with results from conventional tests. Imbibition tests were performed on samples from all three reservoirs. Waterflood tests were performed on samples from only one reservoir.

Fluid properties for the three reservoirs studied are shown in Table 1. Tests at reservoir conditions were performed using bottom-hole crude oil at reservoir temperature and pressure. The aqueous phase used in these tests was a synthetic brine approximating the reservoir brine composition. Conventional tests were performed at room conditions with refined oils and synthetic reservoir brine. The oil-to-water viscosity ratios were adjusted to the reservoir values.

The cores used in all the tests were taken from the reservoirs using either brine alone or a bentonite-carboxymethylcellulose mud without additives as coring fluids. Previous tests show that these fluids have no significant effect on the wettability of reservoir rock samples.[2] The cores were preserved in brine at the wellsite to prevent wettability changes during shipment and storage. Wellsite imbibition tests have been performed on fresh samples from several reservoirs (including Reservoir A) and compared with later laboratory imbibition tests on samples preserved in brine. The comparison showed that the wettability of the preserved cores was the same as that of fresh, surfaced cores at the wellsite.[2]

IMBIBITION TESTS

Conventional imbibition tests were performed on preserved cores using the apparatus and procedures described by Bobek, *et al*.[2]

A sketch of the apparatus for imbibition tests at reservoir conditions is shown in Fig. 1. The preserved samples were first centrifuged to expel excess water and then placed in a stainless-steel container which served

TABLE 1—FLUID PROPERTIES AT RESERVOIR CONDITIONS

	Reservoir A	Reservoir B	Reservoir C
Temperature (°F)	206	160	194
Pressure (psia)	2,600	2,630	2,920
Crude-Oil Bubble Point (psia)	1,830	307	314
Crude-Oil Viscosity (cp)	0.75	5.7	2.36
Brine Viscosity (cp)	0.39	0.52	0.34
Brine Salinity (ppm)*	235,000	170,000	42,000

*Total dissolved solids expressed as equivalent parts of NaCl.

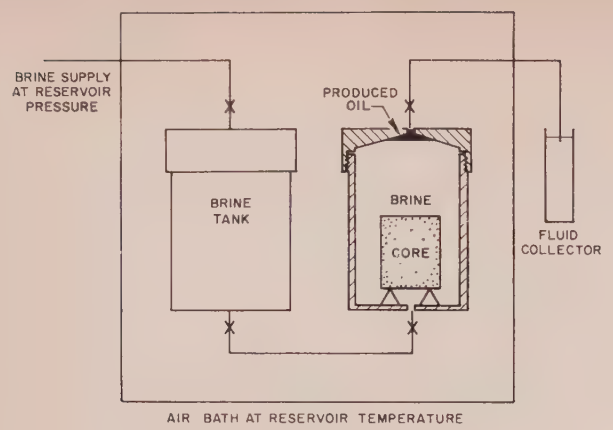

FIG. 1—APPARATUS FOR IMBIBITION TESTS.

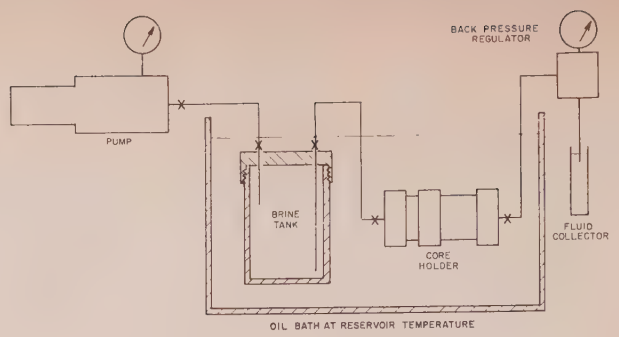

FIG. 2—APPARATUS FOR WATERFLOOD TESTS.

as the imbibition cell (Fig. 1). Then this cell was evacuated to remove the air, and bottom-hole crude oil under high pressure was flashed into it. By maintaining the pressure on the crude oil above the bubble point, it was possible to fill the cell and saturate the samples with bottom-hole crude oil with no free gas present. While the system was at reservoir pressure but still at room temperature, excess oil surrounding the samples was rapidly displaced by brine at reservoir pressure. The system was then heated to reservoir temperature. Reservoir pressure was continually maintained on the brine supply which was connected to the bottom of the imbibition cell. Periodically, oil displaced by water imbibition was flushed from the top of the imbibition cell and measured.

When imbibition ceased, the pressure on the system was gradually reduced. Oil produced from the core samples during this pressure reduction was measured in the same way imbibition oil production was measured. Then, after cooling, the core samples were extracted to determine final fluid saturations. With this information, together with produced oil measurements and knowledge of the oil shrinkage characteristics, it was possible to calculate the quantity of water imbibed during the test.

WATERFLOOD TESTS

A conventional waterflood test was first performed on the sample at room temperature and pressure using refined oils. Then a flood was performed on the same sample with crude at reservoir conditions. The apparatus for waterflood tests at reservoir conditions is shown in Fig. 2. The flooding cell is very similar to the conventional Hassler sleeve-type cell, although it is of heavier construction than normal to withstand higher pressures.

After the conventional water flood, the preserved sample was flushed with bottom-hole crude oil at reservoir temperature and pressure, and then water flooded at reservoir conditions. After this flood, the sample was cooled, de-pressured and extracted to determine final fluid saturations. From these data and the fluid production during the tests, it was possible to calculate fluid saturations at any particular stage of either the conventional flooding test or the test at reservoir conditions.

Waterflood tests also were performed on a preserved aquifer sample from Reservoir A. The aquifer cores initially contain no crude oil and are strongly water-wet. Two flooding tests were performed on the aquifer sample. First a test was performed at reservoir conditions using bottom-hole crude. Then, after cooling and de-pressuring the sample to simulate surfacing operations, a conventional waterflood test was performed at room conditions with a refined oil. The purpose of these tests was to find out if core surfacing could change the wettability of a sample from strongly water-wet to the intermediate wettability exhibited by preserved oil-zone cores.

RESULTS

IMBIBITION TESTS

The imbibition test data summarized in Table 2 show that rock samples from two of the three reservoirs which have intermediate wettability characteristics at surface conditions became strongly water-wet at reservoir conditions. This means that core analysis tests on such samples should be performed at reservoir conditions to represent the true reservoir wettability. It also means that there probably are more strongly water-wet reservoirs and fewer intermediate wettability reservoirs than previously believed.

At room conditions, samples from all three reservoirs imbibe only from 3 to 8 per cent pore volume of water.

TABLE 2—WATER IMBIBITION AT RESERVOIR CONDITIONS

Sample No.	Rock Type	Permeability (md)	Porosity (per cent)	Water Saturation (per cent V_p)		Water Imbibed (per cent V_p)
				Initial	Final	
Reservoir A						
1	Dolomite	175	15.3	10	52	42
2	Limestone	127	15.2	15	70	55
3	Limestone	63	12.9	16	69	53
						Average 50 (8)*
Reservoir B						
1	Sandstone	3000**	28.1	6	72	66
2	Sandstone	3000**	25.4	7	74	67
						Average 67 (7)
Reservoir C						
1	Dolomite	9.3	6.3	35	52	17
2	Dolomite	11.8	6.1	35	45	10
3	Limestone	0.3	9.7	40	51	11
						Average 13 (3)

*Numbers in parentheses indicate average amount of water imbibed by preserved samples at room conditions.
**Not measured. Estimated on the basis of previous measurements on other samples.

On this basis, these reservoirs would be classified as slightly water-wet.[2] Actually, rock samples from Reservoir B also imbibe about 6 per cent pore volume of oil at room conditions, so that this reservoir appeared to be dual-wet (imbibes both oil and water). At reservoir conditions, samples from Reservoirs A and B imbibed about 50 and 67 per cent pore volume of water, respectively. Thus, these two reservoirs must now be classified as strongly water-wet. In the case of Reservoir C, a relatively small increase in water imbibition was observed at reservoir conditions. On this basis, Reservoir C is still believed to be slightly water-wet. However, the possibility cannot be ruled out that this reservoir is also strongly water-wet and that wettability changes may occur during surfacing of the cores which cannot be reversed by subjecting the cores to the reservoir environment.

WATERFLOOD TESTS

Results of waterflood tests on preserved samples from the oil zone of Reservoir A are summarized in Table 3. Oil saturations in per cent of pore volume are compared for tests at room and reservoir conditions after the injection of one pore volume of water. In field practice, water floods seldom are carried beyond this quantity of injected water. Oil recoveries in per cent of original oil in place also are compared at this same flooding stage. Tests on five samples at room conditions showed an average recovery of 39 per cent of the original oil in place. The average recovery for the same samples at reservoir conditions was 55 per cent of the original oil in place. The difference between these two numbers represents a drastic change in oil-reserve estimates for Reservoir A.

The curves in Fig. 3 also demonstrate the marked difference between flooding behavior at normal test conditions and at reservoir conditions for a typical oil-zone sample from Reservoir A. The flooding curve for the conventional test is representative of fresh or preserved slightly water-wet surfaced cores. Water breakthrough occurs early in the flood, and oil displacement efficiency is poor. In the test at reservoir conditions, much more oil is recovered at water breakthrough, and residual oil saturations are much lower after breakthrough. This latter behavior is representative of strongly water-wet cores and implies that the samples are strongly water-wet at reservoir conditions. From the figure, it is obvious that estimates of waterflood oil recovery for this reservoir will be much greater on the basis of tests at reservoir conditions than on the basis of conventional test results.

Waterflooding curves for the aquifer sample are shown in Fig. 4. The test at reservoir conditions shows efficient oil displacement and gives results similar to those usually obtained in conventional tests on these strongly water-wet cores. However, after simulated surfacing of the sample, the conventional waterflood test shows poor oil displacement efficiency and is typical

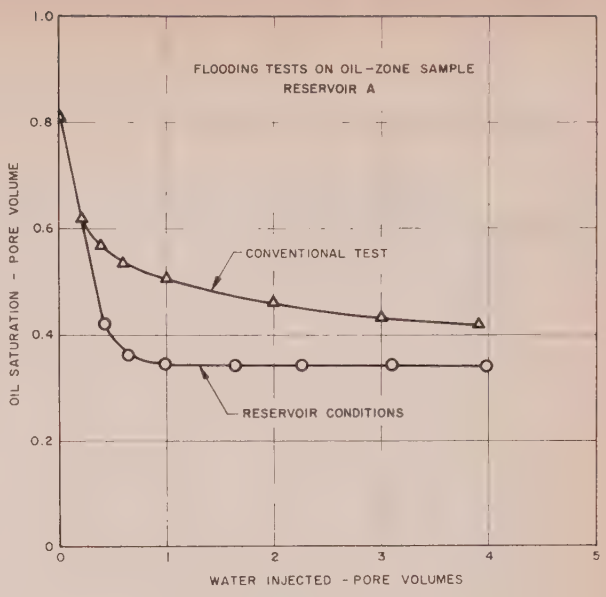

FIG. 3—EFFECT OF RESERVOIR ENVIRONMENT ON WATERFLOOD TEST RESULTS.

of surfaced slightly water-wet, oil-zone cores. These results, together with results obtained on the oil-zone cores, leave little doubt that Reservoir A is strongly water-wet but that surfaced cores will be slightly water-wet.

The present work demonstrates that rock samples that have intermediate wettability characteristics at surface conditions may become strongly water-wet in the reservoir environment. It should be pointed out that the three reservoirs studied are high-temperature and high-pressure reservoirs. For low-temperature, pressure-depleted reservoirs, there is much less difference between the environment in the reservoir and at the surface. In such case, it is reasonable to expect that pronounced differences in wettability between reservoir and surface conditions would be less likely.

Individual effects of temperature, pressure and fluid composition on rock wettability were not studied. Thus, the reason why cores from Reservoirs A and B become less water-wet when they are surfaced cannot be attributed to a definite factor. However, it is known that reservoir rocks can become less water-wet by adsorbing certain crude-oil components on the walls of the rock pores.[2,3] It is reasonable to assume that, in many instances, the preferential adsorption of such material will decrease with temperature and possibly with the pressure of the system. Thus, a rock which is strongly water-wet at reservoir conditions may become slightly water-wet at surface conditions because of increased adsorption of oil-wetting components at the lower temperature and pressure. If the adsorption is reversible, these rocks may again become strongly water-wet if their initial reservoir environment is re-established. This

TABLE 3—WATERFLOOD TESTS ON PRESERVED SAMPLES FROM RESERVOIR A (OIL-ZONE CORES)

Core No.	Core Type	Permeability (md)	Oil Saturation (Per Cent V_p)*				Recovery at 1 V_p* Per Cent OOIP	
			Room		Reservoir			
			Initial	1 V_p*	Initial	1 V_p*	Room	Reservoir
4	Limestone	44	84	50	83	37	41	55
5	Limestone	429	89	58	87	43	35	51
6	Limestone	148	84	57	93	40	32	57
7	Limestone	11	79	41	83	35	48	58
8	Dolomite	145	90	57	92	45	37	51
	Average		85	53	88	40	39	55

*1 V_p = Flooding stage at which one pore volume of water has been injected.

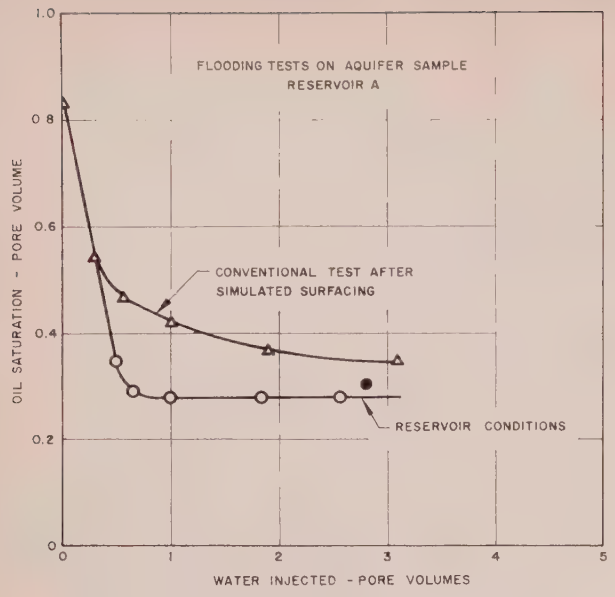

FIG. 4—EFFECT OF CORE SURFACING ON WATERFLOOD TEST RESULTS.

is a possible explanation of the behavior of rock samples from Reservoirs A and B.

CONCLUSIONS

The present work is concerned with reservoirs which were thought to be of intermediate wettability on the basis of conventional tests. Consequently, the results should not be construed as a recommendation to perform all core analysis tests under reservoir conditions. Core samples that are strongly water-wet in conventional tests may show no significant changes in wettability when subjected to the reservoir environment.

With regard to core samples that exhibit intermediate wettability characteristics in conventional core analysis tests, the following conclusions can be drawn from the present work.

1. The reservoir environment can be an important factor in water-oil displacements. Core samples which were of intermediate wettability at surface conditions were found to be more strongly water-wet and to water flood more efficiently at reservoir conditions. This points out the need for performing core analysis tests on such samples at reservoir conditions.

2. Since rock samples tend to be more water-wet at reservoir conditions than at surface conditions, certain reservoirs now thought to be of intermediate wettability may, in fact, be strongly water-wet.

3. More research is needed to isolate the individual effects of temperature, pressure and fluid composition on the wettability and displacement behavior of reservoir rocks.

REFERENCES

1. Burkhardt, J. A., Ward, M. B. and McLean, R. H.: "Effect of Core Surfacing and Mud Filtrate Flushing on Reliability of Core Analysis Conducted on Fresh Cores", Paper No. 1139-G presented at 33rd Annual Fall Meeting of SPE (Oct. 5-8, 1958), Houston.
2. Bobek, J. E., Mattax, C. C. and Denekas, M. O.: "Reservoir Rock Wettability — Its Significance and Evaluation", *Trans.*, AIME (1958) **213**, 155.
3. Denekas, M. O., Mattax, C. C. and Davis, G. T.: "Effects of Crude Oil Components on Rock Wettability", *Trans.*, AIME (1959) **216**, 330. ★★★

Propping Fractures with Aluminum Particles

L. R. KERN
MEMBER AIME
T. K. PERKINS
JUNIOR MEMBER AIME
R. E. WYANT
MEMBER AIME

THE ATLANTIC REFINING CO.
DALLAS, TEX.

ABSTRACT

This paper presents information on the use of a new propping agent (malleable aluminum particles) which has been used successfully for producing high-conductivity fractures.

The conductivity of a packed fracture depends on the width of the fracture as well as the permeability of the propping material. It is significant that the flow capacity of a propped crack is often increased many fold by propping the crack with a sparse distribution of particles. However, the flow capacity of a sparsely propped crack can be limited by two phenomena: (1) crushing of the propping particles, and (2) embedment of the propping particles in the formation walls.

Malleable aluminum particles exhibit interesting properties which tend to overcome these limitations. As high loads are applied to the particles they will deform slightly, rather than shattering. The deformation results in a greater bearing area against the formation wall. This reduces the stress on the particle and reduces particle penetration into the formation.

The behavior of aluminum particles under load and the bearing capacities of serveral formation rocks have been measured in the laboratory. By properly using these data, as explained in this paper, the flow capacities of aluminum-propped cracks can be calculated for a variety of conditions.

Aluminum particles have been used successfully in the field to prop fractures. Where high-conductivity fractures were needed, the aluminum-propped fractures have given greater well stimulation than could have been expected for conventional fracturing processes.

INTRODUCTION

The purpose of a hydraulic fracture treatment is to create a *conductive* channel from the wellbore out into the oil or gas formation. The word conductive is emphasized because we believe that the fracture conductivity (flow capacity) is one of the most important factors influencing fracturing results.

Previous papers[2,6,10,11] have pointed out the additional well stimulation that can sometimes be achieved by increasing fracture conductivity. Several years ago, we investigated in some detail the effect of fracture conductivity on productivity increases to be expeced from vertical fractures. Both electrical analog and theoretical studies of unsteady-state flow behavior were made. A discussion of the electrical analog equipment and some of the results of the study were given in a previous paper[2] by Dyes, Kemp and Caudle. Further details were given recently by McGuire and Sikora.[5]

Fig. 1 shows the remarkable influence of relative fracture flow capacity and length on well stimulation. Briefly, the study indicates the following.

1. High-permeability formations require high-conductivity cracks for best results.

2. The longer the crack, the higher the fracture conductivity required for best results.

3. If the conductivity of the crack is very large compared to the formation (i.e., flow is not being limited by crack conductivity), then the longer the fracture, the better will be the results.

Judging from recently published articles,[1,3,4] there is current interest in methods for obtaining high fracture conductivities. Hence, we would like to present in this paper a discussion of a new fracture propping process (use of aluminum particles[12]) which we have used successfully to obtain highly conductive fractures.

There are several factors which influence the conductivity of a propped crack. Conventional fracturing techniques frequently result in a crack completely packed with fracturing sand. For such conditions, the crack conductivity is the product of the width of the packed fracture and the permeability of the propping material. It is significant that a large increase in conductivity sometimes can be obtained by propping with particles which are distributed sparsely (less than a

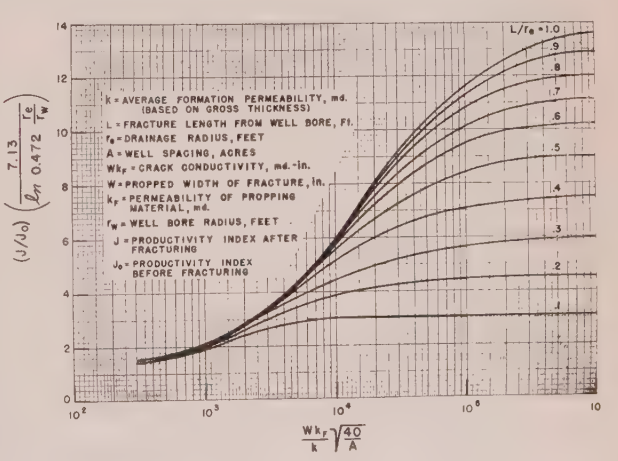

FIG. 1—INCREASE IN PRODUCTIVITY FROM FRACTURING.

Original manuscript received in Society of Petroleum Engineers office Aug. 18, 1960. Revised manuscript received March 27, 1961. Paper presented at 35th Annual Fall Meeting of SPE, Oct. 2-5, 1960, in Denver.

[2]References given at end of paper.

fully packed, single layer). Although the final width of the crack may be less for the sparse distribution, the fluid can flow much more easily around the sparsely distributed propping particles than it could through a full pack of particles.

An important factor that must be considered in all cases is the effect of load on the final conductivity. As the fracturing fluid leaks off after a fracturing job, the walls of the formation tend to close back together and are literally held apart by the propping material.

This results in a large pressure or stress on the propping material. Three things may happen which would reduce the crack conductivity.

1. The propping material itself may shatter, giving a lower conductivity.

2. The particles may not shatter, but they may sink into the formation wall to some extent, allowing the crack to become narrower and therefore less conductive.

3. Particles may become closely packed together (for example, concentrating because of fluid leak-off) and, thus, appreciably interfere with fluid flow.

Malleable aluminum particles exhibit interesting properties which tend to overcome propping limitations. As high loads are applied to sparsely placed particles, they will deform slightly rather than shatter. The deformation results in a greater bearing area against the formation wall. This reduces the average stress under the particle and, therefore, reduces particle penetration into the formation. In general, aluminum has sufficient strength to permit propping with a sparse array of particles, and this leads to very high conductivities. These points will be discussed further in this paper.

BEHAVIOR OF ALUMINUM PARTICLES UNDER LOAD

First consider the behavior of aluminum particles under load. (Later, we will combine this information with rock bearing capacity data to estimate conductivities of propped fractures.)

Aluminum particles used are available in several sizes and are nearly spherical. Experiments have shown, however, that with sufficient deformation between parallel plates, the particles will yield to form nearly uniform cylinders or disks. *The remainder of this paper will deal with particles which have deformed to the cylindrical shape (deformed thickness $\leq$ 0.5 unmashed diameter).*

If the mass of aluminum present per unit area is known, then the average stress under each resulting disk is easily calculated by Eq. 1.

$$S = \frac{\text{Force/Particle}}{\text{Bearing Area/Particle}} = \frac{\left(\frac{\sigma}{N}\right)}{\left(\frac{M}{T\rho}\right)} = \frac{\sigma T \rho}{MN} \quad \ldots\ldots\ldots\ldots (1)$$

where S = average stress under each particle (psi),
σ = average stress applied by the fracture face (psi),
T = thickness of the disk (in.),
ρ = particle density = 0.098 lb/in.^{3} for aluminum,
M = average mass per particle (lb), and
N = number of particles per unit area of fracture face (No./in.^{2}).

The average mass per particle for several size ranges is shown on Fig. 2.

There are two reasons why the average stress on the aluminum disk will not be constant as the particle deforms. First, the compressive strength of aluminum increases as the strain increases because of work hardening.[8] Second, as the diameter of the cylinder becomes large compared with its thickness, friction between the ductile material and the bearing plate will cause considerable distortion of the yielding material. The increased distortion increases the resistance to deformation. Nadai,[8] for instance, discusses data showing the distortion of ductile metal when compressed between hard parallel plates. It would appear reasonable that the ratio of diameter to thickness of the disk would be a measure of the distortion and strain hardening—hence, this $\left(\frac{D}{T}\right)$ ratio should be a measure of the average stress that the aluminum disk can support; i.e., strength should correlate with $\left(\frac{D}{T}\right)$.

Several sizes of aluminum particles have been pressed between cemented tungsten-carbide plates. The maximum stresses that the particles could support are plotted vs the resultant $\left(\frac{D}{T}\right)$ ratio on Fig. 3. This figure shows that the data can be represented approximately by a straight line. Combining the straight-line equation with Eq. 1 yields Eq. 2.

$$S = \frac{\sigma T \rho}{MN} = a\left(\frac{D}{T}\right).$$

But,

$$\frac{\pi D^2}{4} T\rho = M.$$

Therefore,

$$S = \frac{\sigma T \rho}{MN} = a\left(\frac{D}{T}\right) = a\frac{\sqrt{\frac{4M}{\pi T\rho}}}{T} = a\sqrt{\frac{4M}{\pi \rho T^3}} \quad \ldots\ldots\ldots\ldots (2)$$

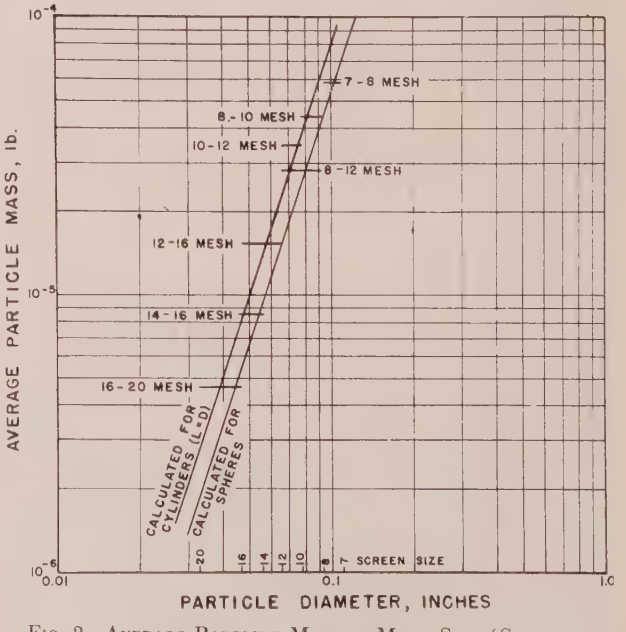

FIG. 2—AVERAGE PARTICLE MASS VS MESH SIZE (SCREENED ALUMINUM PARTICLES).

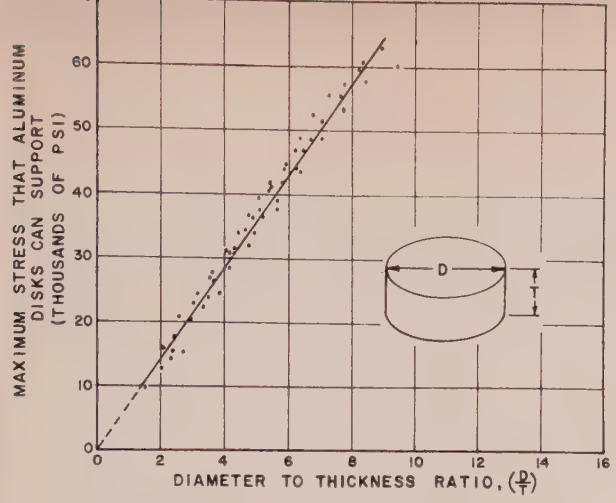

FIG. 3—EFFECTIVE COMPRESSIVE STRENGTH OF ALUMINUM DISKS.

where a = an empirically determined constant.

It is convenient to re-arrange Eq. 2 so that T can be represented explicitly. Eq. 3 results from this re-arrangement.

$$\frac{\sigma T \rho}{MN} = a\sqrt{\frac{4M}{\pi \rho T^3}},$$

$$T = a'\left(\frac{M^3N^2}{\sigma^2}\right)^{1/5} \quad \ldots\ldots\ldots \quad (3)$$

where a, a' = constants.

A re-plot of the aluminum deformation data $\left(T \text{ vs} \frac{M^3N^2}{\sigma^2}\right)$ is shown in Fig. 4. This figure gives a convenient graphical method for estimating the thickness of aluminum disks resulting from mashing of particles between parallel plates. The dashed lines on this figure show early deformation behavior before disk shapes have been completely achieved.

PENETRATION INTO FORMATION ROCKS

Now let us see what will happen when disk-shaped particles are pressed into formation rocks. Fig. 5 shows a sketch of equipment which was used to press cylindrical steel dies into rocks. The dies were made from ⅛-, 3/16- and ¼-in. diameter hardened tool steel. Relative movement of a die into a rock sample was transmitted through a yoke to a dial gauge. The penetration into the rock was measured to the nearest hundred-thousandth of an inch. The equipment initially was calibrated by pressing the die between cemented tungsten-carbide blocks to measure the elastic strain of the equipment. This elastic strain was subtracted from later dial-gauge readings to give actual rock penetrations. Short-term penetration data for several rock samples are shown on Fig. 6. It is interesting to note that, for a given rock, the ratio of penetration to diameter of the die was a unique function of the average stress under the die. This is similar to results reported by Terzaghi[9] for formation-bearing capacities of various types of soil. The effect of time on depth of penetration has not yet been fully evaluated.

CONDUCTIVITIES OF ALUMINUM-PROPPED CRACKS

Now that we have discussed the behavior of aluminum particles under load and the amount of penetration into fracture walls, we are in a position to devise an engineering method for estimating conductivities of cracks propped with aluminum particles.

In a typical treatment, the aluminum particles are mixed with a suspending fluid and pumped into the fracture. After injection has stopped, the fluid continues to leak off, thus allowing the formation walls to come back together. As the walls come together, they first touch the particles, gripping them in place. Then, as the walls continue to close, the particles are mashed into disks. At the same time, the disks are pushed into the formation walls for some distance. If the job is properly designed, there will still be an open conductive channel when all the formation stress has been applied to the particles. Fig. 7 is a sketch showing a crack propped open with aluminum particles.

Estimation of the conductivity obtained by aluminum propping requires four steps.

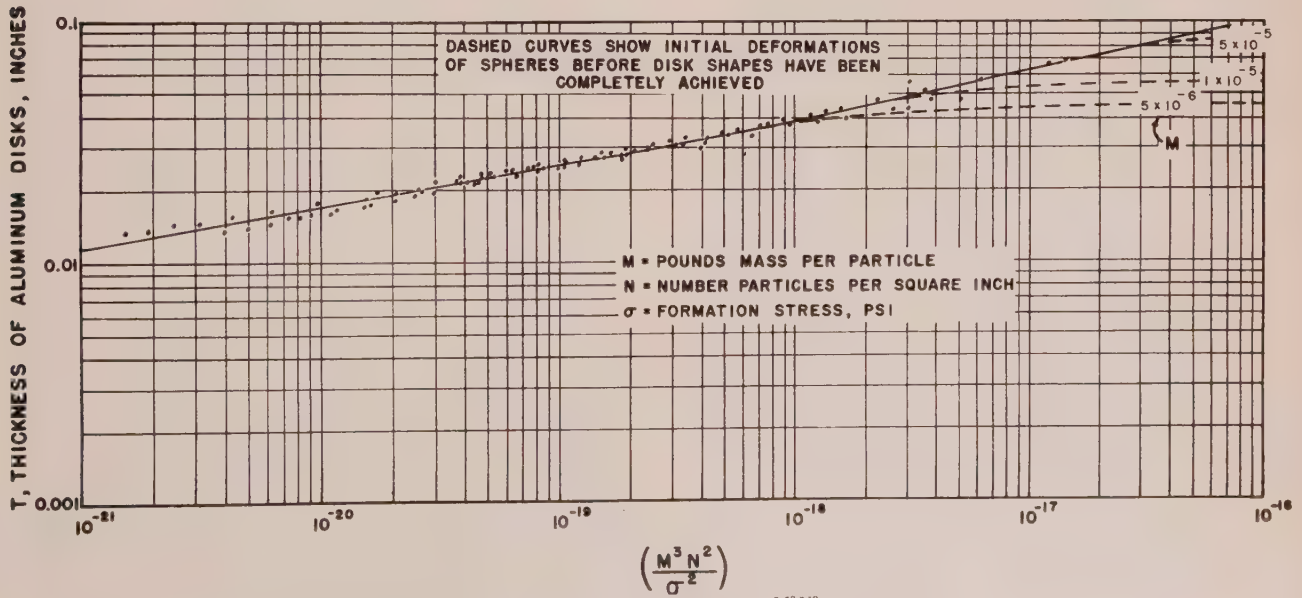
T, THICKNESS OF ALUMINUM DISKS, INCHES
DASHED CURVES SHOW INITIAL DEFORMATIONS OF SPHERES BEFORE DISK SHAPES HAVE BEEN COMPLETELY ACHIEVED
5 x 10^-5
1 x 10^-5
5 x 10^-6
M
M = POUNDS MASS PER PARTICLE
N = NUMBER PARTICLES PER SQUARE INCH
σ = FORMATION STRESS, PSI
(M^3N^2/σ^2)

FIG. 4—THICKNESS OF ALUMINUM DISKS VS $\frac{M^3N^2}{\sigma^2}$ PARAMETER.

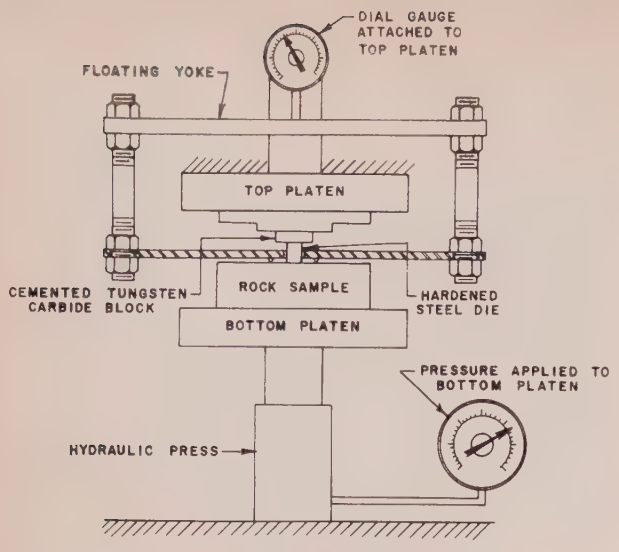

FIG 5—SKETCH OF EQUIPMENT USED TO OBTAIN PENETRATION DATA.

1. Determine the number of particles per square inch of fracture face.

2. Determine the thickness of the resulting aluminum disks.

3. Determine the penetration into the formation walls.

4. Calculate the conductivity resulting from the propped width. (The propped width, of course, is equal to the total thickness of the aluminum disks minus the penetration into both formation walls.)

Consider these steps in more detail. The concentration of aluminum in suspending fluid and the amount of leak-off determine the number of particles per unit area of propped fracture face. When leak-off is low, the number of particles per square inch can be calculated from Eq. 4.

$$\frac{\text{(No. of Particles) (Mass per Particle)}}{\text{(Volume of Crack When Particles are Gripped)}} = \text{Concentration of Particles.}$$

$$\frac{NM\ (231 \text{ cu in./gal})}{d_{max}} = \frac{\text{pounds of aluminum}}{\text{total gallons}},$$

$$N = \frac{C\, d_{max}}{231\, M}. \quad . \quad . \quad . \quad . \quad (4)$$

where N = number of particles per square inch of propped fracture,

C = concentration of aluminum (lb/gal),

d_{max} = maximum diameter of unmashed aluminum particles (in.), and

M = average mass per aluminum particle (lb).

The average thickness of the resulting aluminum disks can be determined from Fig. 4.

The penetration into the formation wall can be determined from laboratory data similar to that shown in Fig. 6. The average stress under each aluminum particle can be calculated by Eq. 1. The penetration into one fracture face is then determined from Eq. 5.

$$\delta = \left(\frac{\delta}{D}\right)(D).$$

For cylinders, $\frac{\pi D^3}{4} T\rho = M.$

Therefore,

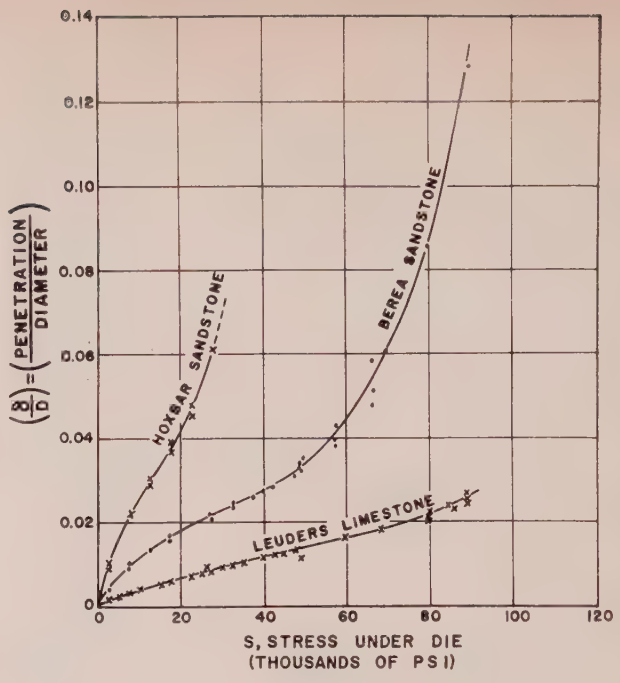

FIG. 6—PENETRATION DATA FOR CIRCULAR DIES.

$$\delta = \left(\frac{\delta}{D}\right)(D) = \left(\frac{\delta}{D}\right)\sqrt{\frac{4M}{\pi T\rho}}$$

$$= 3.60\left(\frac{\delta}{D}\right)\sqrt{\frac{M}{T}}. \quad . \quad . \quad . \quad . \quad . \quad . \quad . \quad . \quad (5)$$

where δ = penetration into one fracture face (in.), and

$\frac{\delta}{D}$ = dimensionless penetration evaluated at the calculated stress. (See Fig. 6.)

The conductivity of the propped crack can now be calculated from Eq. 6. (See Appendix for derivation.)

$$k_f W = \frac{c(T - 2\delta)^3\left(1 - \frac{NM}{0.098\, T}\right)^3}{\left[\left(1 - \frac{NM}{0.098\, T}\right) + 5.65(T - 2\delta)N\sqrt{\frac{M}{T}}\right]^2}$$

$$. \quad . \quad . \quad . \quad . \quad . \quad . \quad . \quad . \quad . \quad (6)$$

where $k_f W$ = propped crack conductivity (md-in.), and c evaluated from Fig. 8.

In this equation, the propped width is recognized as equal to the thickness of the aluminum disks minus the total penetration into both formation faces. This equation also takes into account the resistance to flow caused by the presence of the aluminum particles in the propped crack.

Fig. 9 shows a sketch of equipment used to measure conductivity of sparsely propped cracks. Plates of formation rock were set in metal rings with a low-melting alloy. With the propping material in place between the plates, the desired formation stress was applied with a hydraulic press. Mineral oil was then pumped through a central inlet tube in the top plate. Crack conductivities were calculated from the steady-state radial flow equation using pressure-drop and flow-rate data. The range covered experimentally was 7 to 20 mesh particle sizes and stresses from 1,000 to 12,000 psi.

Conductivities calculated from Eq. 6 are compared with some typical experimentally measured conductivi-

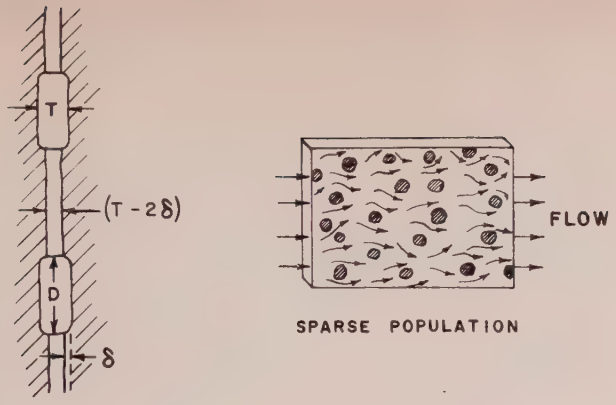

FIG. 7—SKETCH OF AN ALUMINUM-PROPPED CRACK.

ties in Fig. 10. The agreement appears to be satisfactory for design purposes. We believe that Eq. 6 can be used with confidence for estimating crack conductivities for a variety of conditions.

FIELD TESTS

Aluminum pellets have been used in the field many times as a propping material for fractures. Information about two of the treatments is discussed in following paragraphs.

One of the wells treated was completed with 5 ft of perforations in the Maquoketa formation at 3,438 ft. The well previously had been treated with 2,000 gal of acid and previously was fractured with 5,000 lb of 20-40 mesh sand in 5,000 gal of heavy oil. These previous treatments had resulted in an improvement in productivity. The well later was re-fractured with 17,500 lb of 20-40 sand in 20,000 gal of oil followed by 500 lb of 8-12 mesh aluminum carried in 5,000 gal of gelled fracturing oil. The average pump rate was about 32 bbl/min. The re-fracture job resulted in a sustained threefold increase in productivity. For a similar re-fracture treatment without aluminum propping particles, we would have expected no more than a 60 or 70 per cent sustained increase in productivity.

It may appear surprising that such a small quantity of aluminum could have been expected to contribute to the success of the job. At the injected concentration, however, the aluminum would have propped a vertical fracture 100-ft high extending 150 to 200 ft from two sides of the wellbore (30,000 to 40,000 sq ft of fracture area). The resulting crack conductivity would have been about 1.4×10^5 md-in. The effect of such a fracture on productivity can be estimated from Fig. 1.

For this particular well, the formation permeability was about 10 md and the drainage area was 40 acres. Hence, with aluminum propping,

$$\frac{Wk_f}{k}\sqrt{\frac{40}{A}} = \frac{1.4 \times 10^5}{10}\sqrt{\frac{40}{40}} = 1.4 \times 10^4,$$

and

$$\frac{L}{r_e} = \frac{150}{660} \text{ to } \frac{200}{660} = 0.23 \text{ to } 0.3.$$

Fig. 1 shows that the expected P.I. ratio after fracturing with aluminum was about 4.3 to 4.7. (The term $\frac{7.13}{\ln 0.472\, r_e/r_w}$ is unity for this example.)

For 20-40 mesh sand (permeability = 1.4×10^5 md)

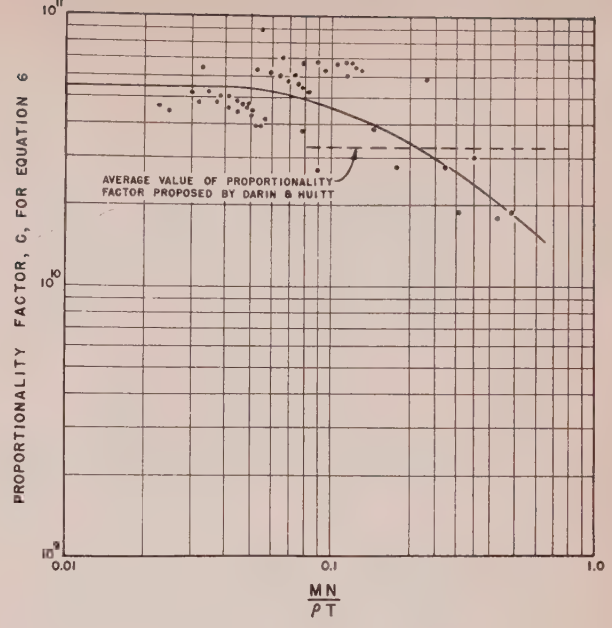

FIG. 8—PROPORTIONALITY FACTOR c TO BE USED IN KOZENY-CARMAN EQUATION (EQ. 6).

and a ⅛-in. crack, $\frac{Wk_f}{k}\sqrt{\frac{40}{A}}$ would have been about 1.8×10^3. For the same length of fracture, the expected P.I. ratio with sand would have been about 2.5.

The previous fracture job resulted in about a 1.5 increase in productivity. Hence, the second fracture job with aluminum should have resulted in about $\left(\frac{4.3}{1.5}\right)$ to $\left(\frac{4.7}{1.5}\right)$, or about a threefold improvement. With a 20-40 mesh sand alone, the improvement would have been about $\left(\frac{2.5}{1.5}\right)$, or about 60 or 70 per cent increase.

In another recent trial of aluminum propping, the treated well was completed with a total perforated interval of 30 ft in the Wilcox formation at about 7,100 ft. The well had not been acidized or fractured previously. The well was fractured with 13,000 lb of 40-60 mesh sand carried at ½ lb/gal in an emulsion fluid. This was followed with 4,500 lb of 12-16 mesh aluminum carried in 2,500 gal of emulsion. Pump rates during the treatment were about 5½ bbl/min. The treatment resulted in a five- to sixfold improvement in productivity. This is about two to three times the improvement that would have been expected if the aluminum had not been used.

We have sometimes used sand in conjunction with aluminum for two reasons.

1. A desired well stimulation sometimes can be achieved at a lower cost by using sand ahead of the aluminum rather than using aluminum alone.

2. In other cases, this combination will offer a margin of safety. If the aluminum does not perform as expected (e.g., if the particles do not enter the fracture, if the particles sink into the formation farther than expected, or if there is an inadvertent overflush of the particles), then the well stimulation will be at least as great as for a conventional fracturing process. If the aluminum behaves as desired, the sand will not interfere unduly with the increased stimulation.

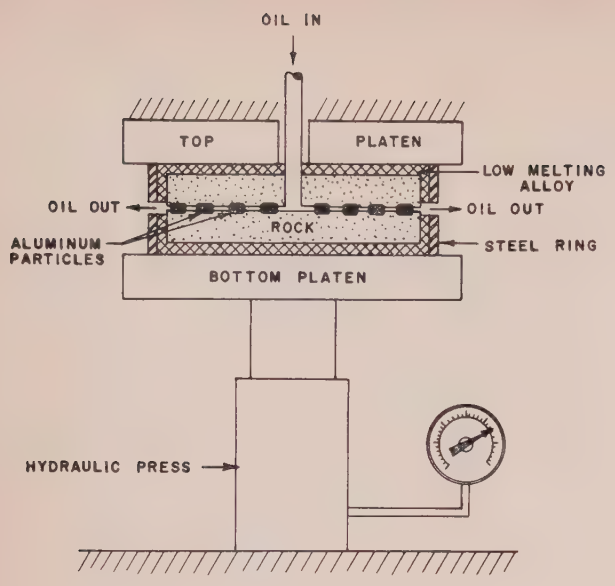

FIG. 9—SKETCH OF EQUIPMENT FOR MEASURING CONDUCTIVITIES OF SPARSELY PROPPED CRACKS.

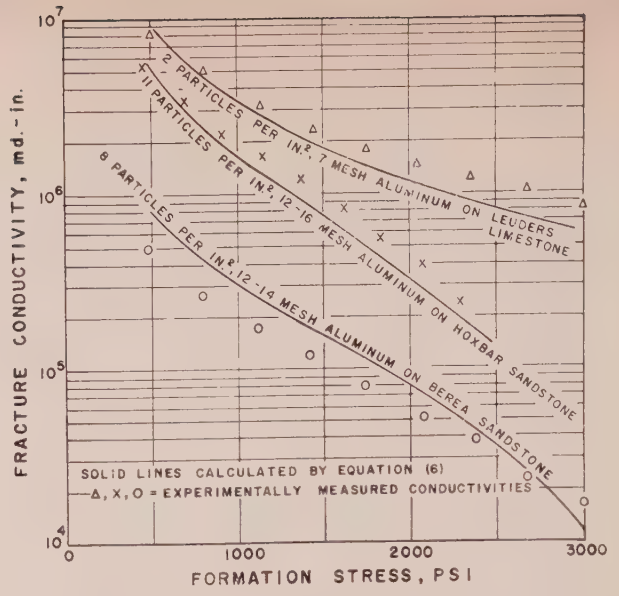
FRACTURE CONDUCTIVITY, md.-in.
2 PARTICLES PER IN.², 7 MESH ALUMINUM ON LEUDERS LIMESTONE
4-11 PARTICLES PER IN.², 12-16 MESH ALUMINUM ON HOXBAR SANDSTONE
8 PARTICLES PER IN.², 12-14 MESH ALUMINUM ON BEREA SANDSTONE
SOLID LINES CALCULATED BY EQUATION (6)
Δ, X, O = EXPERIMENTALLY MEASURED CONDUCTIVITIES
FORMATION STRESS, PSI

FIG. 10—COMPARISON OF CALCULATED AND EXPERIMENTAL CONDUCTIVITIES FOR CRACKS SPARSELY PROPPED WITH ALUMINUM.

SUMMARY AND CONCLUSIONS

This study has shown that high fracture conductivities can be obtained by propping cracks with malleable aluminum particles.

An engineering method has been devised for estimating crack conductivities under a variety of conditions. Calculated conductivities have been compared with experimentally measured conductivities and found to be in good agreement.

Aluminum particles have been used many times in field treatments. Where high-conductivity fractures were needed, the aluminum-propped fractures have given greater well stimulation than could have been expected for conventional fracturing processes.

NOMENCLATURE

a, a', c' = constants
A = well spacing, acres
c = a proportionality factor in the Kozeny-Carman equation (Eq. 6) (See Fig. 8.)
C = concentration of aluminum, lb/gal
d_{max} = maximum diameter of uncrushed aluminum particles, in.
D = diameter of crushed aluminum disks, in.
J = productivity index after fracturing
J_o = productivity index before fracturing
k = permeability, md
k_fW = propped crack conductivity, md-in.
L = length of vertical fracture from wellbore, ft
M = average mass of an aluminum particle, lb
N = number of particles per unit area of fracture face, No./in.^{2}
r_e = well drainage radius, ft
r_w = wellbore radius, ft
s = total surface area exposed per volume of propping material contained between fracture faces, in.$^{-1}$
S = average stress under a crushed aluminum disk, psi
T = thickness of aluminum disks, in.
W = propped width of fracture
δ = penetration of an aluminum disk into a formation wall, in.
ρ = density of aluminum = 0.098 lb/in.^{3}
σ = average stress applied by the fracture face, psi
ϕ = fraction porosity of a propped creck

REFERENCES

1. Darin, S. R. and Huitt, J. L.: "Effect of a Partial Monolayer of Propping Agent on Fracture Flow Capacity", *Trans.*, AIME (1960) **219**, 31.
2. Dyes, A. B., Kemp, C. E. and Caudle, B. H.: "Effect of Fractures on Sweep-out Pattern", *Trans.*, AIME (1958) **213**, 245.
3. Huitt, J. L. and McGlothlin, B. B.: "The Propping of Fractures in Formations Susceptible to Propping Sand Embedment", Paper No. 801-34B presented at Spring Meeting of Pacific Coast Dist., API, Los Angeles (May, 1958).
4. Huitt, J. L. and McGlothlin, B. B.: "The Propping of Fractures in Formations in which Propping Sand Crushes", Paper No. 875-13-E, API (May, 1959).
5. McGuire, W. J. and Sikora, V. J.: "The Effect of Vertical Fractures on Well Productivity", *Trans.*, AIME (1960) **219**, 401.
6. Morrisson, T. E. and Henderson, J. H.: "Gravity Drainage of Oil Into Large Horizontal Fractures", *Trans.*, AIME (1960) **219**, 7.
7. Muskat, M.: *Physical Principles of Oil Production*, First Ed., McGraw-Hill Book Co., Inc., N. Y. (1949) 246.
8. Nadai, A.: *Theory of Flow and Fracture of Solids*. Vol. I, Second Ed., McGraw-Hill Book Co., Inc., N. Y. (1950) 340-343.
9. Terzaghi, K.: *Theoretical Soil Mechanics*, John Wiley and Sons, Inc., N. Y. (1943).
10. van Poollen, H. K.: "Productivity vs. Permeability Damage in Hydraulically Produced Fractures", Paper 906-2-G presented at Spring Meeting of API in Dallas (March, 1957).
11. van Poollen, H. K., Tinsley, J. H. and Saunders, C. D.: "Hydraulic Fracturing—Fracture Flow Capacity vs Well Productivity", *Trans.*, AIME (1958) **213**, 91.
12. U. S. Patent No. 2,950,247.

APPENDIX

DERIVATION OF THE CONDUCTIVITY EQUATION

In a recent paper[1] the Kozeny-Carman equation was used to estimate the effect of porosity on the conductivities of sparsely propped cracks. A similar approach has been used to estimate conductivities of aluminum-propped cracks. Eq. A-1 gives the Kozeny-Carman equation shown by Darin and Huitt to be suitable for sparsely propped cracks.

$$k = \frac{\phi^3}{c's^2(1-\phi)^2} \quad \text{. . . . . (A-1)}$$

where

k = permeability,

ϕ = fraction porosity,

c' = an empirical constant, and

s = $\dfrac{\text{total surface area exposed}}{\text{(volume of propping material contained between fracture faces)}}$.

For the case of aluminum propping, we can write Eq. A-2.

$$\phi = 1 - \frac{N\pi D^2}{4} = 1 - \frac{NM}{T\rho} \quad \text{. . . . (A-2)}$$

The total surface area per unit volume of propping material contained between fracture faces is given by Eq. A-3.

$$s = \frac{2\left(1 - \dfrac{\pi D^2 N}{4}\right) + \pi DN(T - 2\delta)}{\dfrac{\pi D^2}{4} N(T - 2\delta)},$$

$$s = \frac{2\left(1 - \dfrac{NM}{\rho T}\right) + (T - 2\delta)\pi N\sqrt{\dfrac{4M}{\pi\rho T}}}{\dfrac{NM}{\rho T}(T - 2\delta)} \quad \text{. . . . . (A-3)}$$

Multiplying both sides of Eq. A-1 by the propped width $(T - 2\delta)$ and then substituting in Eq. A-2 and A-3 yields Eq. A-4.

$$kW = \frac{c'(T - 2\delta)^3\left(1 - \dfrac{NM}{T\rho}\right)^3}{\left[2\left(1 - \dfrac{NM}{T\rho}\right) + (T - 2\delta)N\pi\sqrt{\dfrac{4M}{\pi T\rho}}\right]^2} \quad \text{. . . . . (A-4)}$$

Equation A-4 can be simplified somewhat as shown by Eq A-5. (Note that Eq. A-5 is the same as the final Eq 6 given in the text of this paper.)

$$(k_f W)_{\text{md in.}} = \frac{c(T - 2\delta)^3\left(1 - \dfrac{NM}{0.098\,T}\right)^3}{\left[\left(1 - \dfrac{NM}{0.098\,T}\right) + 5.65(T - 2\delta)N\sqrt{\dfrac{M}{T}}\right]^2} \quad \text{. . . . . (A-5)}$$

If T and δ are held constant and M is allowed to approach zero, the equation reduces to that giving the conductivity of an open crack. Therefore, as the concentration of solid material in the crack approaches zero, c approaches 5.48×10^{10} (see Muskat[2]). Fig. 8 shows experimentally determined values of c at various concentrations of solid material in the crack. Fig. 8 also shows an average value for the constant proposed by Darin and Huitt[1] for similar conditions. ★★★

Natural Gas Hydrates at Pressures to 10,000 psia

HARRY O. McLEOD, JR.
JOHN M. CAMPBELL
MEMBER AIME

THE U. OF OKLAHOMA
NORMAN, OKLA.

ABSTRACT

This paper presents the results of the data obtained in the first stage of a long-range study at high pressures of the system, vapor-hydrate-water rich liquid-hydrocarbon rich liquid. The data presented are for the three-phase systems in which no hydrocarbon liquid exists. Tests were performed on 10 gases at pressures from 1,000 to 10,000 psia. One of these was substantially pure methane, and the remainder were binary mixtures of methane with ethane, propane, iso-butane and normal butane.

Several conclusions may be drawn from the data.

1. Contrary to previous extrapolations, the hydrocarbon mixtures tested form straight lines in the range of 6,000 to 10,000 psia which are parallel to the curves for pure methane, when the log of pressure is plotted vs hydrate formation temperature.

2. The hydrate formation temperature may be predicted accurately at pressures from 6,000 to 10,000 psia by using a modified form of the Clapeyron equation. The total hydrate curve may be predicted by using the vapor-solid equilibrium constants of Carson and Katz[1] to 4,000 psia and joining the two segments with a smooth continuous curve between 4,000 and 6,000 psia.

3. The use of gas specific gravity as a parameter in hydrate correlations is unsatisfactory at elevated pressures.

4. The hydrate crystal lattice is pressure sensitive at elevated pressures.

INTRODUCTION

Prior to 1950 many studies had been made of the hydrate forming conditions for typical natural gases to pressures of 4,000 psia.[3-6,10,13,14] Most of these attempted to correlate the log of system pressure vs hydrate formation temperature, with gas specific gravity as a parameter. One of the more promising correlations was made by Katz, *et al*,[1] which utilized vapor-solid equilibrium constants. The only published data above 4,000 psia are those of Kobayashi and Katz[7] for pure methane to a pressure of 11,240 psia. In the intervening years, most published charts for the high-pressure range have represented nothing more than extrapolations of the low-pressure data, with the methane line serving as a general guide. The reliability of these charts has become increasingly doubtful (and critical) in our present technology as we handle more high-pressure systems.

The portion of our high-pressure hydrate research program reported here was designed to: (1) investigate the reliability of existing charts; (2) obtain actual data on gas mixtures to 10,000 psia; and (3) develop a simple hydrate correlation that was more reliable than those which simply used specific gravity as a parameter.

Binary mixtures of methane and ethane, propane normal butane, or iso-butane were injected into a high-pressure visual cell containing an excess of distilled water. Hydrates were formed and then melted to observe the decomposition temperature of the hydrates at pressures from 1,000 to 10,000 psia.

EQUIPMENT

The equipment consisted of a Jerguson 10,000-lb high-pressure visual cell, a 10,000-lb high-pressure blind cell and a Ruska 25,000-lb pressure mercury pump. The visual cell was placed in a constant-temperature water bath controlled by a refrigeration unit and an electric filament heater. A Beckman GC-2 gas chromatograph was used in analyzing the gas mixtures after each run was completed.

EXPERIMENTAL PROCEDURE

After evacuating the gas system, the heavier hydrocarbon was injected into the high-pressure mixing cell to that pressure necessary to give the desired composition. This cell then was pressured to 1,100 to 1,200 psia by methane from a high-pressure cylinder. The mixing cell holding the gas contained a steel flapper plate and was shaken intermittently over a period of 15 minutes. After mixing, the valve to the high-pressure visual cell containing excess distilled water was opened, and the gas mixture was allowed to flow into the cell.

The temperature in the water bath was lowered 10° to 15°F below the estimated hydrate decomposition point. As a first check, the temperature was increased at a rate of 1°F every six minutes to find the approximate point of decomposition. It was again lowered 1.5° to 5°F to form hydrates. The temperature was raised to within 1° of the estimated decomposition point and then increased 0.2°F every 10 to 15 minutes until the hydrates decomposed. This procedure was repeated at various pressures to obtain 7 to 13 points for each mixture between 1,000 and 10,000 psia. After completion of the hydrate decomposition tests, the gas mixture composition was analyzed with a calibrated gas chromatograph. These gas analyses have an estimated error of ± .1 per cent.

Original manuscript received in Society of Petroleum Engineers office Aug. 5, 1960. Revised manuscript received April 8, 1961. Paper presented at 35th Annual Fall Meeting of SPE, Oct. 2-5, 1960, in Denver.

[1]References given at end of paper.

EXPERIMENTAL RESULTS

Data were obtained on the gases shown in Table 1. Table 2 summarizes the experimental data which have permissable errors of ± 0.2°F and ± 50 psia, based on the temperature measurements and the accuracy of the 25,000-psig Heise gauge.

Up to 4,000 psia, our data generally confirmed earlier published results except for the methane-n butane system. Except for this system, an increase in specific gravity was accompanied by a corresponding increase in hydrate decomposition temperature for each binary system.

As shown in Figs. 1 through 3, this general pattern held for all systems through methane-iso butane at pressures to 10,000 psia. However, the methane-n butane system reversed this trend. As shown in Fig. 4, the two methane-n butane mixtures generally followed the pure methane curve and actually crossed it. This would indicate that normal butane had little effect on hydrate formation and may have acted as an inhibitor to some slight degree as pressure increased.

Figs. 1 through 4 show that the data above 6,000 psia may be accurately represented by straight lines, which are substantially parallel.

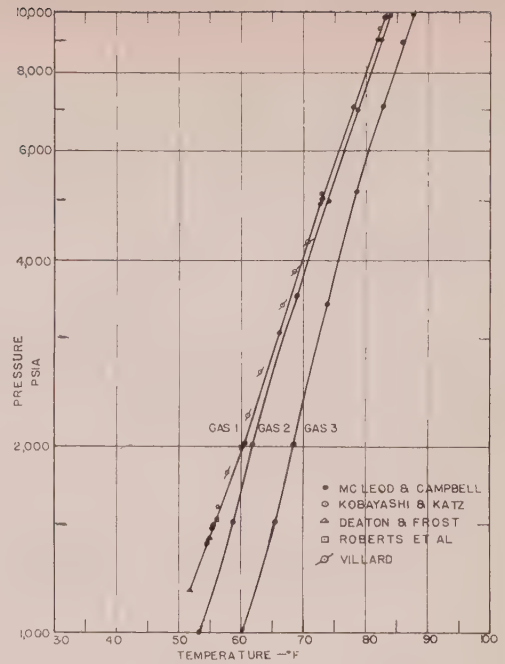

FIG. 1—HYDRATE EQUILIBRIUM CURVES, METHANE-ETHANE.

INTERPRETATION OF DATA

Figs. 1 through 4 contradict earlier extrapolated charts which indicated that the hydrate equilibrium curves for natural gas would intersect the methane curve at pressures higher than those reported. Several deductions are possible from the pattern of curves shown in Figs. 1 through 4.

The behavior of the methane-n butane mixtures is likely affected to some degree by the pressure sensitivity of the hydrate crystal lattice,[2,12] wherein the lattice is either deformed or assumes a different structure from that proposed for low-pressure hydrates. If this is true, the pressure would have to be higher to compress the larger butane molecule within the voids and stabilize this lattice.

Although as yet we have insufficient data to substantiate it, we suspect that the nature of the hydrate curves obtained has some significance with regard to both hydrate composition and pressure sensitivity of the lattice. At pressures of 4,000 psia and above, the vapor-solid equilibrium constant for methane is approximately equal to one ($K = 1.0$). We deduce from our data that $K = 1.0$ above 6,000 psia (in the region of straight lines parallel to the pure methane curve) for each of the mixtures studied. If this is true, the composition of the hydrate is the same as the gas being tested (on a dry basis). If this is a reasonable assumption, as we believe, it means that there is further evidence suggesting lattice deformation.

Recent notable works by von Stackelberg, Pauling, Claussen, van der Waals and others indicate that all gas hydrates crystallize in one cubic structure, or in a combination of two cubic structures, in which the gas molecules are "trapped" in cavities formed by a framework composed of water molecules linked together by hydrogen bands. One type consists of 46 water molecules enclosing two types of cavities. One class of cavity is formed of a pentagonal dodecahedral with the formula $H_{40}O_{20}$. The other, larger oblate cavities are caused by bridges between these dodecahedra formed by the remaining six water molecules. Methane, ethane and hydrogen sulfide can enter the smaller cavities, which are nearly spherical, while propane and heavier may enter only the larger ones. This accounts for the relative nonstability of propane hydrates and points out why

TABLE 1—GAS COMPOSITIONS TESTED

Gas Number	Mol Per Cent Composition C_1	C_2	C_3	i-C_4	n-C_4	Specific Gravity Gas
(1)	100.0	—	—	—	—	0.552
(2)	94.6	5.4	—	—	—	0.578
(3)	80.9	19.1	—	—	—	0.643
(4)	96.5	—	3.5	—	—	0.586
(5)	94.5	—	5.5	—	—	0.605
(6)	97.4	—	—	—	2.6	0.591
(7)	94.7	—	—	—	5.3	0.628
(8)	98.6	—	—	1.4	—	0.571
(9)	95.4	—	—	4.6	—	0.619
(10)*	90.6	6.6	1.8	0.5	0.5	0.607

*Pseudo-percentage of each component so that their total equals 100. The relative quantity of each component has been preserved.

TABLE 2—SUMMARY OF EXPERIMENTAL DATA

Gas No. 1		Gas No. 2		Gas No. 3		Gas No. 4		Gas No. 5		Gas No. 6		Gas No. 7		Gas No. 8		Gas No. 9		Gas No. 10	
psia	°F	psia	°F	psia	°F	psia	°F	psia	°F	psia	°F	psia	°F	psia	°F	psia	°F	psia	°F
1395	54.5	9925	83.9	9945	87.6	1005	63.2	1075	67.9	1115	53.3	1545	57.8	6915	80.3	975	70.0	1965	68.8
1495	55.6	9025	82.4	8985	85.9	9060	67.0	1075	67.4	1805	58.2	3465	66.7	5005	76.4	975	69.2	4015	75.8
1465	55.3	6995	78.6	7055	82.7	10005	88.3	5015	81.3	5015	72.5	4955	71.5	4875	76.0	2015	74.0	5995	80.3
1395	54.6	4995	74.1	5165	78.5	5005	78.7	7015	85.2	9565	82.2	6995	76.6	3055	71.7	2025	75.0	7565	83.3
2025	60.5	3515	68.8	3405	73.8	3025	74.2	9025	89.2	1515	55.7	8935	80.4	7125	80.1	3375	77.0	9115	85.8
3065	66.0	2015	61.7	2015	68.3	7015	83.1	3425	77.6	1315	54.6	9925	82.2	985	59.8	5015	81.2	2935	72.8
5040	73.0	1515	58.6	1515	65.4	9035	86.9	2015	73.5	835	48.9	2605	62.8	9025	84.1	7015	84.9	4895	77.8
7060	78.0	1005	53.2	1015	60.2	2015	70.4					2015	60.2			9185	89.3		
9050	81.9					1515	68.2					1545	57.9			7115	85.9		
9875	83.2					1005	63.5					1260	56.2			3455	77.3		
												1015	53.9			2025	74.3		
																1535	71.9		
																1115	70.6		

larger molecules do not form hydrates at all. The lattice is only stabilized by the presence of gas in the voids. It further follows that the formula for the resultant hydrate will depend on the number of cavities filled, which in turn is a function of the formation mechanism and the system. Based on our data, however, we hypothesize that this lattice is pressure sensitive (distorts), which in turn disturbs the normal size distribution of molecules in the lattice.

CORRELATION OF DATA

An attempt to correlate our data using specific gravity as a parameter was completely unsatisfactory. The use of equilibrium constants above 6,000 psia showed no promise since $K = 1$ was a good approximation.

Below 4,000 psia, it was found that the equilibrium values previously published[1] gave satisfactory results. It appeared that above 6,000 psia a Clapeyron-type equation might have application because of the constant slope of the lines. When applied to hydrate formation, this latter equation would be applied in the following manner.

Equilibrium Condition 1 — The partial molar free energy of a component in one phase is equal to its partial molar free energy in the other phase.

$$\overline{F}_i^{\alpha} = \overline{F}_i^{\beta} \quad . \quad . \quad . \quad . \quad . \quad . \quad . \quad . \quad . \quad . \quad . \quad (1)$$

Equilibrium Condition 2 — For univariant equilibria,

$$\overline{F}_i^{\alpha} + d\overline{F}_i^{\alpha} = \overline{F}_i^{\beta} + d\overline{F}_i^{\beta} \quad . \quad . \quad . \quad . \quad . \quad . \quad (2)$$

for $T + dT$, $P + dP$.

Using these two conditions and combining with

$$d\overline{F}_i = \overline{V}_i dP - \overline{S}_i dT, \quad . \quad . \quad . \quad . \quad . \quad . \quad . \quad . \quad (3)$$

it follows that

$$\overline{V}_i^{\alpha} dP - \overline{S}_i^{\alpha} dT = \overline{V}_i^{\beta} dP - \overline{S}_i^{\beta} dT \quad . \quad . \quad (4)$$

and

$$\frac{dP}{dT} = \frac{\overline{S}_i^{\alpha} - \overline{S}_i^{\beta}}{\overline{V}_i^{\alpha} - \overline{V}_i^{\beta}} = \frac{\overline{H}_i^{\alpha} - \overline{H}_i^{\beta}}{T(\overline{V}_i^{\alpha} - \overline{V}_i^{\beta})} = \frac{\Delta\overline{H}_i}{T\Delta\overline{V}_i} \quad (5)$$

For three components — 1, 2 and 3 — which can represent methane, ethane and water,

$$\frac{dP}{dT} = \frac{\Delta\overline{H}_1}{T\Delta\overline{V}_1} = \frac{\Delta\overline{H}_2}{T\Delta\overline{V}_2} = \frac{\Delta\overline{H}_3}{T\Delta\overline{V}_3} \quad . \quad . \quad . \quad . \quad . \quad . \quad (6)$$

where the subscripts designate the changes accompanying each component in the phase change.

This equation is equivalent to

$$T\frac{dP}{dT} = \frac{n_1\Delta\overline{H}_1 + n_2\Delta\overline{H}_2 + h_3\Delta\overline{H}_3}{n_1\Delta\overline{V}_1 + n_2\Delta\overline{V}_2 + n_3\Delta\overline{V}_3} \quad . \quad . \quad . \quad . \quad . \quad (7)$$

Dividing numerator and denominator by n_t (total number of moles reacting),

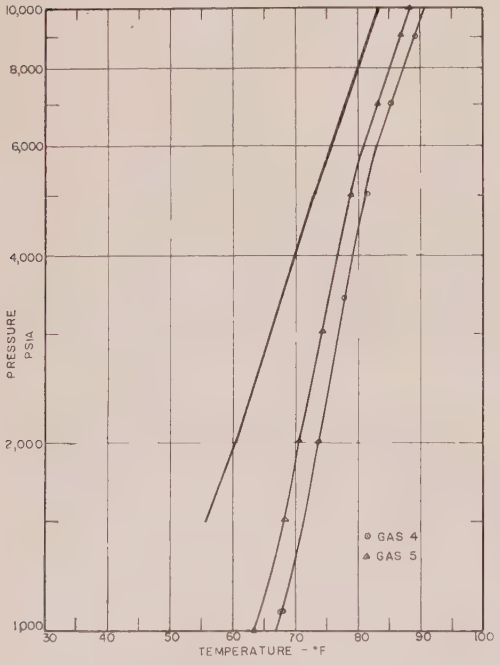

Fig. 2—Hydrate Equilibrium Curves, Methane-Propane.

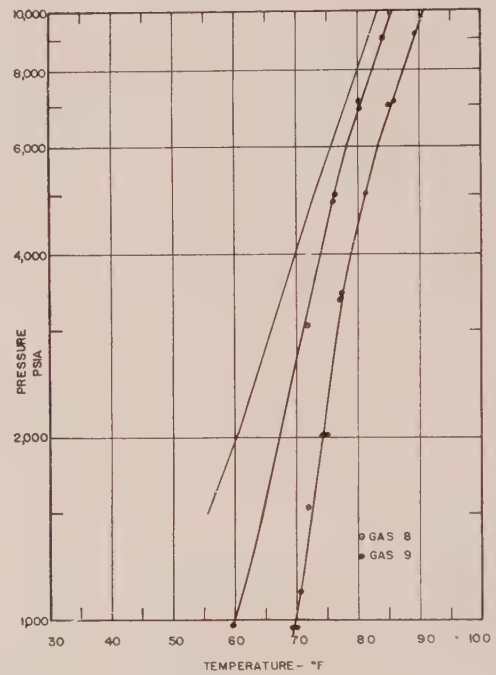

Fig. 3—Hydrate Equilibrium Curves, Methane-iso Butane.

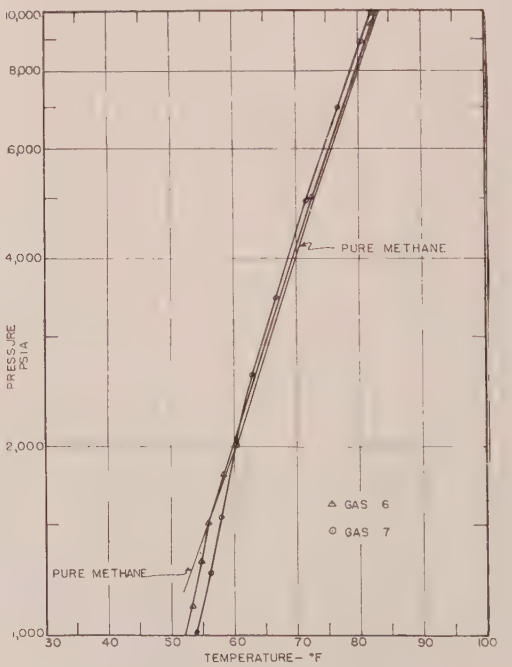

Fig. 4—Hydrate Equilibrium Curves, Methane-normal Butane.

$$T\frac{dP}{dT} = \frac{X_1\Delta\bar{H}_1 + X_2\Delta\bar{H}_2 + X_3\Delta\bar{H}_3}{X_1\Delta\bar{V}_1 + X_2\Delta\bar{V}_2 + X_3\Delta\bar{V}_3} = \frac{\Delta H_{-t}}{\Delta V_{-t}} = \frac{\Delta H_t}{\Delta V_t} \quad \ldots\ldots\ldots\ldots\ldots (8)$$

where

$\frac{dP}{dT}$ = slope of the hydrate equilibrium curve at a given temperature,
ΔH = latent heat of phase transformation,
T = absolute temperature at which the phase change occurs,
ΔV = the volume change accompanying the phase change,
F = free energy,
S = entropy,
H = enthalpy, and

superscripts α and β refer to different phases.

The term ΔV applies only to the gas and water tied up in any hydrate formed. Therefore, it is the volume occupied by that gas and liquid in their initial gaseous and liquid states, respectively, minus the volume of the hydrate. The initial volume of the gas involved is the dominant factor and may be used for ΔV without significant error.

Applying the gas law $PV = ZRT$, Eq. 8 becomes

$$\frac{dP}{dT} = \frac{P\Delta H}{ZRT^2} \quad \ldots\ldots\ldots\ldots (9)$$

On re-arrangement this becomes

$$\frac{d\ln P}{dT} = \frac{\Delta H}{ZRT^2} \quad \ldots\ldots\ldots\ldots (10)$$

If H, Z and R are combined to form one factor C, then

$$\frac{d\ln P}{dT} = \frac{C}{T^2} \quad \ldots\ldots\ldots\ldots (11)$$

where $\frac{d\ln P}{dT}$ is the slope of the equilibrium curve as plotted on semilog paper. This slope, which can be represented by m, is constant for all the mixtures tested between 6,000 and 10,000 psia. Eq. 4 then may be modified to read

$$C = mT^2 \quad \ldots\ldots\ldots\ldots (12)$$

The assumption that ΔV is equal to the volume of the reacting gas in the vapor phase may seem to be an over-simplification when one considers the higher pressures encountered. It can be shown that the inclusion of the smaller volume change would yield essentially the same final result.

The average slope m calculated from the data was 0.066, or

$$C = 0.066T^2 \quad \ldots\ldots\ldots\ldots (13)$$

A factor C then was calculated for each component tested by assuming that the law of ideal solutions was applicable; i.e., the mol fraction of each component times its C yielded a partial C, found from Eq. 12. This was used to find the C values shown in Table 3.

In the determination of C values, it is not essential that the actual slope n be known exactly because it cancels out in the calculation. The method shown, however, does assume that the hydrate formation curves are parallel. Therefore, it would apply only in the region where this condition is essentially met.

The values shown in Table 3 actually do not vary markedly between 6,000 and 10,000 psia. The total range is less than 3 per cent of the absolute values. Consequently, an average value of the components heavier than methane could be used with little loss in accuracy. The numbers are shown as calculated from the data without regard for the number of figures that might be significant.

TABLE 3—SUMMARY OF C VALUES FOR HYDRATE FORMATION PREDICTION

Pressure (psia)	C Values				
	C_1	C_2	C_3	i-C_4	n-C_4
6000	18,933	20,806	28,382	30,696	17,340
7000	19,096	20,848	28,709	30,913	17,358
8000	19,246	20,932	28,764	30,935	17,491
9000	19,367	21,094	29,182	31,109	17,868
10,000	19,489	21,105	29,200	30,935	17,868

The following is an example calculation.

Composition of mixture: methane, 80.9 per cent
ethane, 19.1 per cent
Pressure: 6,000 psia
Temperature of phase change: 540.5°R

From Eq. 13,

$$(C_{methane}) = (0.066)\ (540.5)^2 = 19{,}281.$$

Since

$$(0.809)\ (C_{methane}) + (0.191)\ (C_{ethane}) = 19{,}281,$$

then

$$C_{ethane} = \frac{19{,}281 - (0.809)\ (18{,}933)}{0.191} = 20{,}806.$$

The C values shown for methane were calculated from the curve for pure methane. The temperatures were taken from the lines drawn.

The values tabulated in Table 3 may be used to predict the hydrate formation temperature for any gas above 6,000 psia once the composition is known. The procedure is as follows.

1. Express the gas composition in terms only of the relative quantities of methane through normal butane present. All heavier components are ignored. This is done by rationing the relative quantities of these components so that their total percentage equals 100, as shown in Table 4.

2. At the pressure involved, multiply the pseudo-

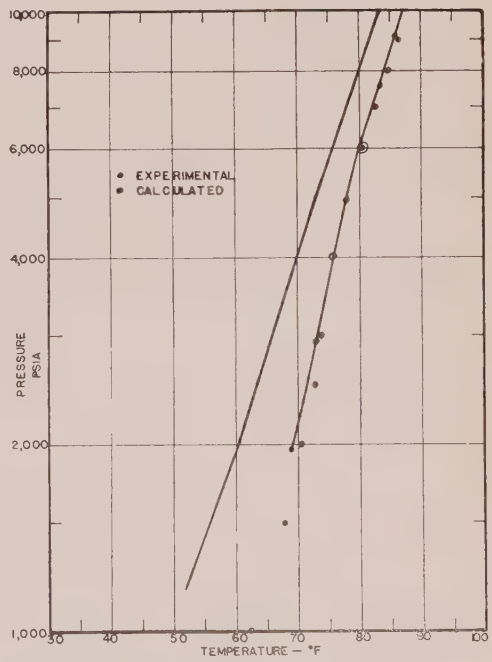

FIG. 5—HYDRATE EQUILIBRIUM CURVE, NATURAL GAS.

TABLE 4—SAMPLE HYDRATE FORMATION CALCULATION, NATURAL GAS NO. 10

Gas Composition (mol per cent)	Pressure (psia) 6000 C Val.	6000 Part. C Val.	7000 C Val.	7000 Part. C Val.	8000 C Val.	8000 Part. C Val.	9000 C Val.	9000 Part. C Val.
C_1 .906	18,933	17,153	19,096	17,301	19,246	17,437	19,367	17,547
C_2 .066	20,806	1,373	20,848	1,376	20,932	1,382	21,094	1,392
C_3 .018	28,382	511	28,709	517	28,764	518	29,182	525
i-C_4 .005	30,696	153	30,913	155	30,935	155	31,109	156
n-C_4 .005	17,340	87	17,358	87	17,491	87	17,868	89
Pseudo—C Values		19,277		19,436		19,579		19,709
Hydrate Formation Temperature* (Eq. 6)		80.4°F		82.7°F		84.7°F		86.4°F

*Calculated points are plotted on Fig. 5.

percentage of each component by its C value. Interpolation between the pressures shown is permissible.

3. Add up the partial C values for each component to determine total C.

4. Calculate the hydrate formation temperature from Eq. 13.

An example of this procedure is shown for Gas No. 10 in Table 4. Fig. 5 compares the calculated points and the experimental curve for the same gas. The error does not exceed 1°F.

The method developed by Katz[1] using vapor-solid equilibrium constants may be used up to 4,000 psia. The curve thus developed then can be joined to the points predicted from 6,000 to 10,000 psia. The points calculated using this method are also shown in Fig. 5.

Many more natural-gas and binary-gas mixture data for hydrate formation will have to be evaluated to determine if the correlation presented is sufficiently accurate in the range of 6,000 to 10,000 psia. The effect of other components such as CO_2, N_2, H_2S and the hydrocarbons heavier than butane must be evaluated at these pressures.

CONCLUSIONS

On the basis of the limited data available, the proposed correlation offers the first reliable method of predicting hydrate formation conditions at pressures exceeding 4,000 to 6,000 psia. Although the data rigorously apply only to a system without a hydrocarbon liquid phase, they have application in production operations where such liquid is present. Use of the predicted temperature in field operations is satisfactory and slightly conservative, for the liquid phase "depresses" the dew point slightly. Although liquids are usually present in a field system, they are not necessarily distributed in any quantity throughout it. For example, after closing in a well the liquids gravitate downward and there is little present in the upper wellbore where hydrates usually form. Therefore, the inherent limitations of the experimental system do not destroy the applicability of the results in many field installations.

The data and therefore the results, are subject to obvious limitations, but they serve as a better guide for future investigations than do available published data.

ACKNOWLEDGMENT

The work reported here was supported partially by a grant from Sunray Mid-Continent Oil Co. and partially by a graduate fellowship from Socony Mobil Oil Co. The authors thank them for their support.

REFERENCES

1. Carson, D. B. and Katz, D. L.: "Natural Gas Hydrates", *Trans.*, AIME (1942) **146,** 150.
2. Claussen, W. F.: "Suggested Structures of Water on Inert Gas Hydrates", *Jour. Chem. Phys.* (1951) **19,** 259, 622, 1425.
3. Deaton, W. M. and Frost, E. M., Jr.: *Gas Hydrates and Their Relation to the Operation of Natural Gas Pipe Lines,* Monograph 8, USBM (1946).
4. Frost, E. M., Jr. and Deaton, W. M.: "Gas Hydrates Compositions and Equilibrium Data", *Oil and Gas Jour.* (1946) **45,** No. 12, 170.
5. Hammerschmidt, E. G.: "Formation of Gas Hydrates in Natural Gas Transmission Lines", *Ind. Eng. Chem.* (1934) **26,** 851.
6. Katz, D. L.: "Prediction of Conditions for Hydrate Formation in Natural Gases", *Trans.*, AIME (1945) **160,** 140.
7. Kobayashi, R. and Katz, D. L.: "Methane Hydrates at High Pressure", *Trans.*, AIME (1949) **186,** 66.
8. Moore, W. J.: *Physical Chemistry,* Prentice-Hall, Inc., Englewood Cliffs, N. J. (1958) 106.
9. Parent, J. D.: *The Storage of Natural Gas as Hydrate,* Research Bull. 1, Inst. Gas Tech. (1948).
10. Roberts, O. L., Brownscombe, E. R. and Howe, L. S.: "Hydrates of Methane and Ethane", *Oil and Gas Jour.* (1940) **39,** No. 30, 37.
11. Scauzillo, F. R., Baker, O. and Swerdloff, W.: "Hydrate Formation on Two-Phase Hydrocarbon Systems", paper presented at Gas Hydrate Control Conf., U. of Oklahoma (1953).
12. von Stackelberg, M. and Muller, H. G.: "On the Structure of Gas Hydrates", *Jour. Chem. Phys.* (1951) **19,** 1319.
13. Unruh, C. H. and Katz, D. L.: "Gas Hydrates of Carbon Dioxide-Methane Mixtures", *Trans.*, AIME (1949) **186,** 83.
14. Wilcox, W. I., Carson, D. B. and Katz, D. L.: "Natural Gas Hydrates", *Ind. Eng. Chem.* (1941) **33,** 662.
15. van der Waals, J. H. and Platteeuw, J. C.: "Clathrate Solutions", *Advances in Chemical Physics,* **II,** Interscience Publishers, Inc., N. Y. (1959). ★★★

Wellbore Pressure Surges Produced by Pipe Movement

J. A. BURKHARDT
JUNIOR MEMBER AIME

HUMBLE OIL & REFINING CO.
HOUSTON, TEX.

ABSTRACT

Field measurements and theoretical studies have been made of pressure surges—momentary variations in fluid pressure—produced by movement of pipe in mud-filled boreholes. Pressure measurements were recorded by five pressure gauges located at various positions in the borehole. An important positive pressure peak was found to occur as the casing moved with maximum velocity. Important negative peaks were found as the casing was lifted from the slips and as brakes were applied to stop pipe movement. A rigorously formulated theory has successfully predicted the sequence and magnitudes of these positive and negative surges and has established a basis for understanding how they occur.

Both the measurements and theory indicate that the most important pressure surge is usually due to viscous drag of the flowing mud. The theory of viscous-drag pressure surges has been approximated by simplified graphs and calculation procedures to facilitate ready use in field operations. Comparison of measured results with those predicted by the simplified theory shows that the magnitude of this surge can be predicted accurately.

INTRODUCTION

It is widely recognized that raising or lowering pipe in a fluid-filled borehole produces momentary variations in fluid pressure, commonly called pressure surges. Both negative (or "swabbing") surges and positive (or "fracturing") surges may occur. In 1934, Cannon[1] measured the negative surges and showed that they could be large enough to cause flow of formation fluids into the wellbore and, in extreme cases, lead to blowout conditions. Later, Goins[2] measured the positive surges associated with lowering pipe. His results and subsequent field operations strikingly demonstrated that pressure surges could be an important factor in some cases of lost returns. In addition, although the evidence is less clear than in the case of blowouts and lost returns, other investigators[3,4] feel that pressure surges probably play a part in many instances of minor gas cutting, salt-water flow and other hole trouble.

The importance of pressure surges in drilling operations led naturally to attempts to explain the physical causes, nature and magnitude of the surges. Cardwell[5] was the first to publish a theory which allowed the quantitative prediction of momentary pressure variations. He assumed that the drilling fluid was a 300-cp Newtonian fluid in turbulent flow. Most field muds have a considerably lower viscosity and are generally believed to be Bingham plastic in nature.[6] However, Cardwell's results were useful because they were presented in a form convenient for field use and, in some cases, gave a reasonably accurate predicted value for the maximum pressure surge.

Subsequently, Ormsby[7] published a more comprehensive theory of pressure surges. He discussed both laminar and turbulent flow and considered the theory of mud-bypass devices for reducing pressure surges. As a consequence of his more rigorous approach, his results were more accurate but more complex and difficult to use. Further, both Ormsby and Cardwell considered only the pressure surge arising from viscous drag of the moving mud.

Clark[3,8] later published idealized graphs of surges and presented equations for predicting their magnitudes. In addition to pressure variations arising from viscous drag, he considered those caused by inertial effects. His theory was in this respect more complete than those of Cardwell and Ormsby, although he did not discuss pressures due to breaking of the gel. Furthermore, his equations, while not exceptionally complicated, were too complex for ready use at a drilling location.

One difficulty common to all three theories is that none was tested rigorously by direct comparison with measured pressure surges. Their accuracy, therefore, could, not be demonstrated. Further, the two theories based on most realistic assumptions (Ormsby and Clark) required the solution of one or more rather complex algebraic equations.

The research described in this paper was undertaken to supplement that described and to overcome some of the difficulties noted. It seemed obvious that a fully satisfactory study of pressure surges should encompass three main phases.

1. A valid theory useful in all field situations must be developed. This theory must be based upon realistic assumptions, must be formulated rigorously and should lead to clear concepts whereby the nature of pressure surges can be easily understood.

2. The theory, however complex and involved, ultimately must be presented in simplified form for convenient field use. This may involve extensive machine computations and the use of figures and empirical equations.

3. The accuracy of the simplified equations must be established by comparing measured pressure surges with those predicted by the theory. These must agree both in their characteristic nature and in magnitude. This means that careful measurements of surges occurring in actual field operations must be made.

Original manuscript received in Society of Petroleum Engineers office July 21, 1960. Revised manuscript received March 5, 1961. Paper presented at 35th Annual Fall Meeting of SPE, Oct. 2-5, 1960. in Denver.

[1]References given at end of paper.

THEORETICAL DESCRIPTION OF PRESSURE-SURGE GENERATION

A qualitative understanding of pressure surges is perhaps best achieved by first examining an experimental measurement. Fig. 1 shows the several positive and negative pressure fluctuations produced when a single joint of casing was lowered into a mud-filled borehole. The casing-running operations were customary: (1) the casing was lifted a foot or so from the slips; (2) the added joint was lowered smoothly; (3) it was braked to a stop; and (4) it was set in the slips.

The immediate cause of all pressure surges observed during this operation was the natural resistance of the mud column to motion. Movement of the mud column is related directly to motion of the displacing pipe string. In understanding how the pressure variations arise, it is necessary to consider the velocity and acceleration of the pipe string.

Fig. 2 shows the pipe velocities and accelerations measured during the same time interval that the pressures in Fig. 1 were observed. Certain corresponding features are immediately apparent. A large positive pressure surge (b) in Fig. 1 occurred at the maximum pipe velocity (B) in Fig. 2, suggesting that viscous drag of the flowing mud is an important factor in producing some pressure surges. One or more negative pressure peaks (c) occurred as the pipe string was suddenly decelerated (C) by application of the brakes. This indicates that inertial effects can also cause pressure surges. Another negative pressure surge (a) invariably occurred as the casing was lifted from the slips (A). The theoretical analysis to follow shows that this might be due either to breaking of the mud gel or to inertial effects.

In summary, a preliminary comparison of Figs. 1 and 2 reveals that each individual pressure peak in the surge pattern may be due to one or more of three effects — viscous drag, inertia and breaking of mud gel. An adequate theory must explain and correctly predict the magnitudes of each of these effects. The following paragraphs consider the theoretical aspects of the three proposed mechanisms.

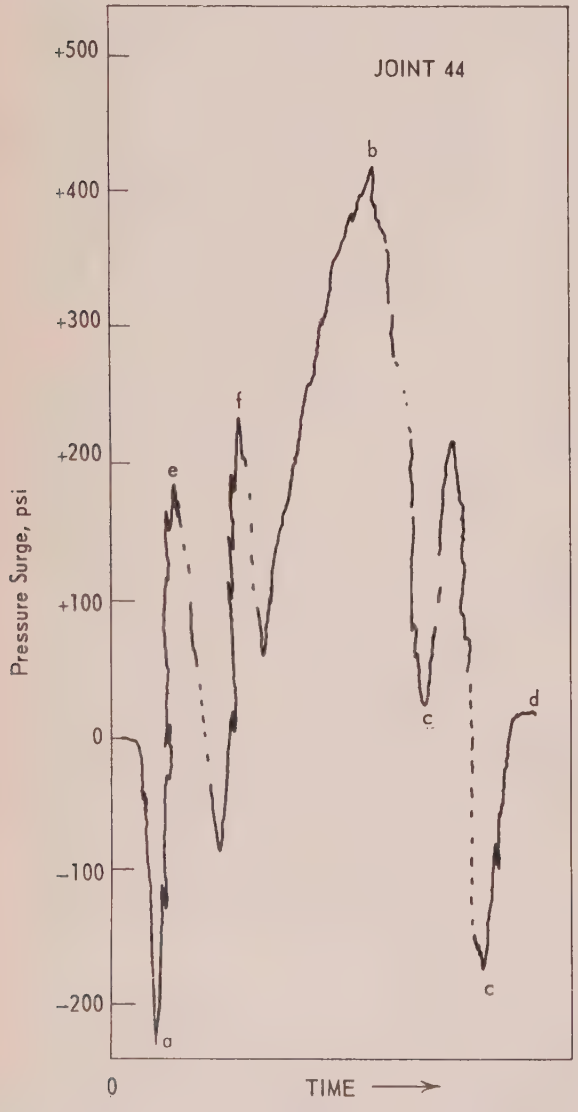

FIG. 1—TYPICAL PRESSURE-SURGE PATTERN MEASURED AS A JOINT OF CASING WAS LOWERED INTO THE WELLBORE.

PRESSURE GENERATED BY BREAKING THE MUD GEL

An expression for the pressure required to break the mud gel and start circulation has been given by Melrose, *et al.*[9] The important parameters are the hole diameter D_h, the outside and inside pipe diameters D_p and D_i, the length of pipe L in the hole and the mud gel strength ζ.

Inside the pipe,

$$P = \frac{4L\zeta}{D_i} \quad \ldots\ldots\ldots\ldots\ldots\ldots \quad (1)$$

In the annulus,

$$P = \frac{4L\zeta}{D_h - D_p} \quad \ldots\ldots\ldots\ldots\ldots\ldots \quad (2)$$

Once the pressure required to break the gel is exceeded and the pipe begins to move, this mechanism is no longer important. Any subsequent pressure surges which occur must be explained by such effects as the inertia and viscous drag of the mud.

PRESSURE GENERATED BY INERTIA OF THE MUD COLUMN

The inertial-pressure-surge component is due to the tendency of the mud column to resist a change in motion, as described by Newton's laws of motion. Following Clark,[3] the inertial-pressure-surge component is expressed for the following.

For closed pipe strings,

$$P = \frac{L\rho a_p D^2_p}{g(D^2_h - D^2_p)} \quad \ldots\ldots\ldots\ldots\ldots\ldots \quad (3)$$

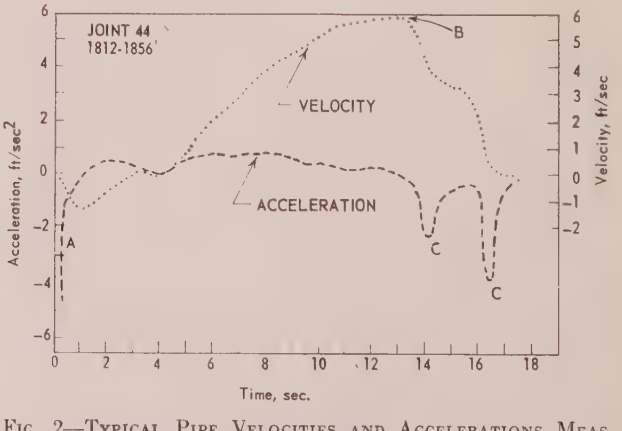

FIG. 2—TYPICAL PIPE VELOCITIES AND ACCELERATIONS MEASURED AS A JOINT OF CASING WAS LOWERED INTO THE WELLBORE.

For open pipe strings,

$$P = \frac{L\rho a_p\ (D^2_p - D^2_s)}{g(D^2_h - D^2_p + D^2_s)} \quad \ldots\ldots\ (4)$$

where a_p = pipe acceleration,
ρ = mud density, and
g = acceleration of gravity.

PRESSURE GENERATED BY VISCOUS DRAG OF THE MUD COLUMN

The theoretical treatments of the pressure-surge components arising from inertial effects and gel breaking are relatively straightforward. However, the theoretical treatment of the pressure-surge component due to viscous drag is considerably more difficult. Various limitations of the theories of Cardwell,[5] Ormsby[7] and Clark[3,8] have been noted. The theory presented here supplements previous work by the utilization of recent advances of the technology of mud flow in annuli and pipes and by a more rigorous inclusion of the effects of the moving pipe walls on the mud flow in the annulus. Since the moving pipe walls greatly influence the mud velocity in the annulus (and, hence, the pressure surge), the procedure for calculating the pressure surge follows a description of the effect of the moving pipe walls on the annulus mud velocity.

The principal mathematical difficulty in describing viscous-drag pressure surges is the effect of the moving pipe walls on the annular mud velocity. The moving pipe walls transport mud in the direction of motion of the pipe, and at the same time the volume of the pipe displaces mud in an opposite direction to the pipe's motion. The "effective" mud velocity that produces pressure surges is a combination of the mud velocity due to the pipe displacing mud and due to the tendency of the pipe walls to transport mud. The mud velocity due to the pipe displacing the mud is simply related to the cross-sectional area of the pipe and of the annulus and the velocity of the pipe. However, the component of mud velocity arising from the moving pipe walls is not a simple relationship. The procedure for arriving at the value of this velocity component is: (1) theoretically describe the velocity profile of the mud due to the moving pipe; and then (2) integrate the velocity profile to obtain a component of the effective mud velocity due to the moving pipe walls. The following paragraphs outline the considerations used in describing the velocity profile and integrating it to obtain a usable resultant component of mud velocity.

The velocity profile depends upon several factors—the nature of the fluid (whether Bingham or Newtonian), the geometry (annular of parallel plates), the type of flow (laminar or turbulent) and the pipe velocity. These will be considered in turn.

Beck[6] has shown that most drilling muds can be approximated as Bingham plastics. Melrose[9] has shown that the movement of Bingham and Newtonian fluids in a fixed annulus can be accurately approximated by flow between fixed parallel plates, provided the ratio D_p/D_h is 0.5 or greater. These two findings indicate that the velocity profile of a drilling mud in an annulus should be quite similar to the profile of a Bingham fluid between parallel plates.

The effect of type of flow remains to be considered. For turbulent flow of Newtonian fluids, the effects of a moving surface on the velocity profile has been measured by Laufer[10] and caculated by Pai.[11] Although the drilling mud is believed to be Bingham rather than Newtonian in nature, the velocity profiles of either fluid in turbulent flow should be similar. In developing the theory reported here, the method of Pai was used to calculate velocity profiles due to the moving surface when the annular mud flow was turbulent. Classical methods were used to calculate velocity profiles due to the moving pipe wall when the mud flow was laminar.

The velocity profiles for a number of different annular geometries were calculated. An average velocity of the mud resulting from the moving pipe wall was obtained by integration of the velocity profile. Fig. 3 shows the results of the integration in a form suitable for convenient use. Here, the component V_{ms} of effective mud velocity due to the moving pipe wall is related to pipe velocity V_p by a proportionality constant K.

$$V_{ms} = -K V_p \quad \ldots\ldots\ (5)$$

The value of the constant K depends upon the ratio of pipe and hole diameters according to the curves shown in Fig 3. Since the mud "clinging" to the pipe must, in effect, displace an equal volume of mud in the opposite direction of the pipe's velocity to maintain a volumetric balance of mud and volume of the hole, V_{ms} is in opposition to V_p; hence, the negative sign occurs in Eq. 5.

In drilling and completing operations, the pressure surges result from pipe string being moved into or out of a borehole. These pipe strings are either open to mud flow in the pipe bore or closed so that no mud flows in the pipe bore. The component of mud velocity due to the moving pipe wall, V_{ms}, is the same whether the pipe string is open or closed.

Viscous-Drag Pressure Surges with Closed Pipe String

The theoretical descriptions of viscous-drag surges in open and closed pipe strings are qualitatively similar. The equations differ somewhat in form and concept, however, and it therefore is desirable to discuss the two situations separately. In this section, closed pipe strings are considered. Closed pipe strings are pipe strings that do not allow mud to flow from the annulus into the pipe bore, and they are typified by casing strings with float shoes.

Determination of the Effective Annular Mud Velocity. In addition to the component of effective velocity due to mud clinging to the inner moving annular wall (Eq. 5), there is a component V_{da} due to volumetric mud flow produced by the displacing pipe. This is determined from the relative cross-sectional areas of the annulus and the closed pipe.

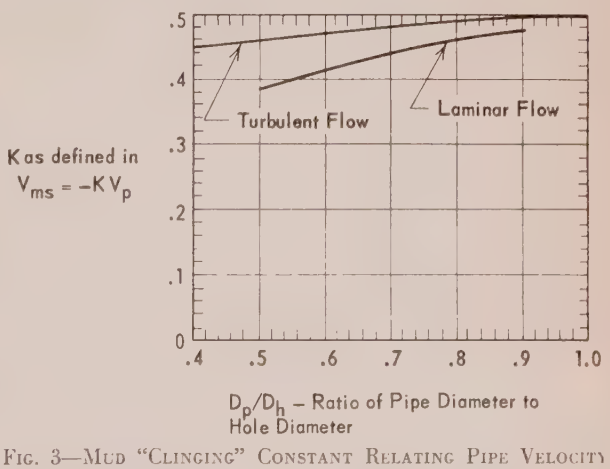

FIG. 3—MUD "CLINGING" CONSTANT RELATING PIPE VELOCITY TO THE COMPONENT OF ANNULAR MUD VELOCITY DUE TO MOVING PIPE WALLS AS A FUNCTION OF RATIO OF ANNULAR DIAMETERS.

$$V_{da} = -\frac{D_p^2}{D_h^2 - D_p^2} V_p \left[\frac{\text{ft}}{\text{min}}\right] \quad . \quad . \quad . \quad . \quad . \quad (6)$$

The average effective annular mud velocity V_{ae} is the sum of Eqs. 5 and 6.

$$V_{ae} = -\left(\frac{D_p^2}{D_h^2 - D_p^2} + K\right) V_p \left[\frac{\text{ft}}{\text{min}}\right] \quad . \quad . \quad (7)$$

The average effective annular mud velocity is the mud velocity which produces the viscous drag component of surge pressure, and its frame of reference is the wellbore wall. The following section describes the procedure for obtaining the numerical value of pressure surge from this average effective annular mud velocity, V_{ae}.

Pressure Generated Due to the Mud Flow in an Annulus. The pressure gradients associated with the flow of Bingham plastics in pipes and annuli have been described by Melrose, *et al.*[9] A computational procedure adapted from that of Melrose was used to calculate the pressure gradients generated by viscous drag of a mud column. Since these calculations are fully covered in the literature,[9,12,13] only the essential information for using the procedure will be described.

A dimensionless quantity, fluid conductance γ, relates the viscous-drag pressure gradients of Bingham plastics to those of Newtonian fluids. Fig. 4 is a graph of the fluid conductance for pipes and annuli as a function of another dimensionless quantity called the plasticity S. The plasticity for an annulus is defined to be

$$S = 2394 \frac{(D_h - D_p)\tau_o}{\mu_p V_{ae}} \quad . \quad . \quad . \quad . \quad . \quad . \quad . \quad (8)$$

Here, τ_o and μ_p are the mud yield point and plastic viscosity. The calculation of the plasticity from Eq. 8 leads directly to the determination of conductance γ from Fig. 4.

A modified friction factor-Reynolds number chart for use with Bingham plastics is shown in Fig. 5. The Reynolds number for annular flow of Bingham plastics is defined by

$$R_e = 15.44 \frac{(D_h - D_p) V_{ae} \rho}{\mu_p} \quad . \quad . \quad . \quad . \quad . \quad . \quad (9)$$

From Fig. 5, a value of the friction factor f is obtained, knowing the numerical values of fluid conductance (γ) and Reynolds number (R_e). And with this friction factor f, the pressure surge generated by the average effective mud velocity in the annulus resulting from the movement of *closed* pipe in the borehole is given by the conventional Fanning equation

$$\frac{\Delta P}{L} = \frac{f V_{ae}^2 \rho}{9.282 \times 10^4 (D_h - D_p)} \left(\frac{\text{psi}}{\text{ft}}\right) \quad . \quad . \quad . \quad (10)$$

In those situations where the hole or pipe geometry changes, the contribution to the pressure gradients for each particular geometry should be calculated. The total pressure is the sum of the separate components.

Viscous-Drag Pressure Surges with Open Pipe Strings

For purposes of discussion, open pipe strings are defined as those which have openings connecting the annulus and pipe bore at the bottom of the string, such as a bit on drill pipe or a fill-up shoe on a casing string.

To determine the effective annular mud velocity that generates the viscous-drag pressure-surge component, a statement must be made about how the additional mud flow path of the pipe bore is related to the annular mud flow path. The criterion used to describe

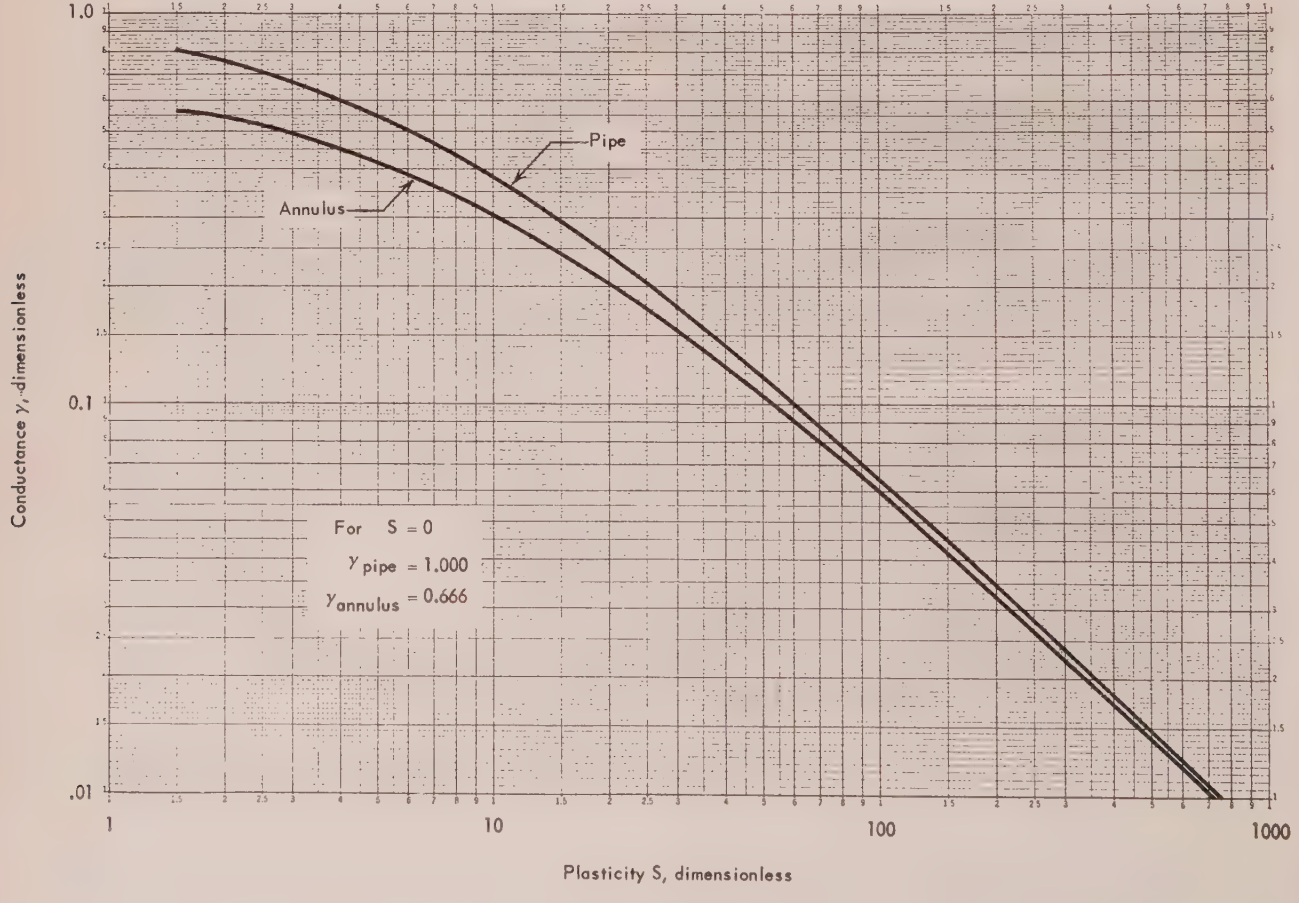

FIG. 4—FLUID CONDUCTANCE OF PIPES AND ANNULI AS A FUNCTION OF PLASTICITY.

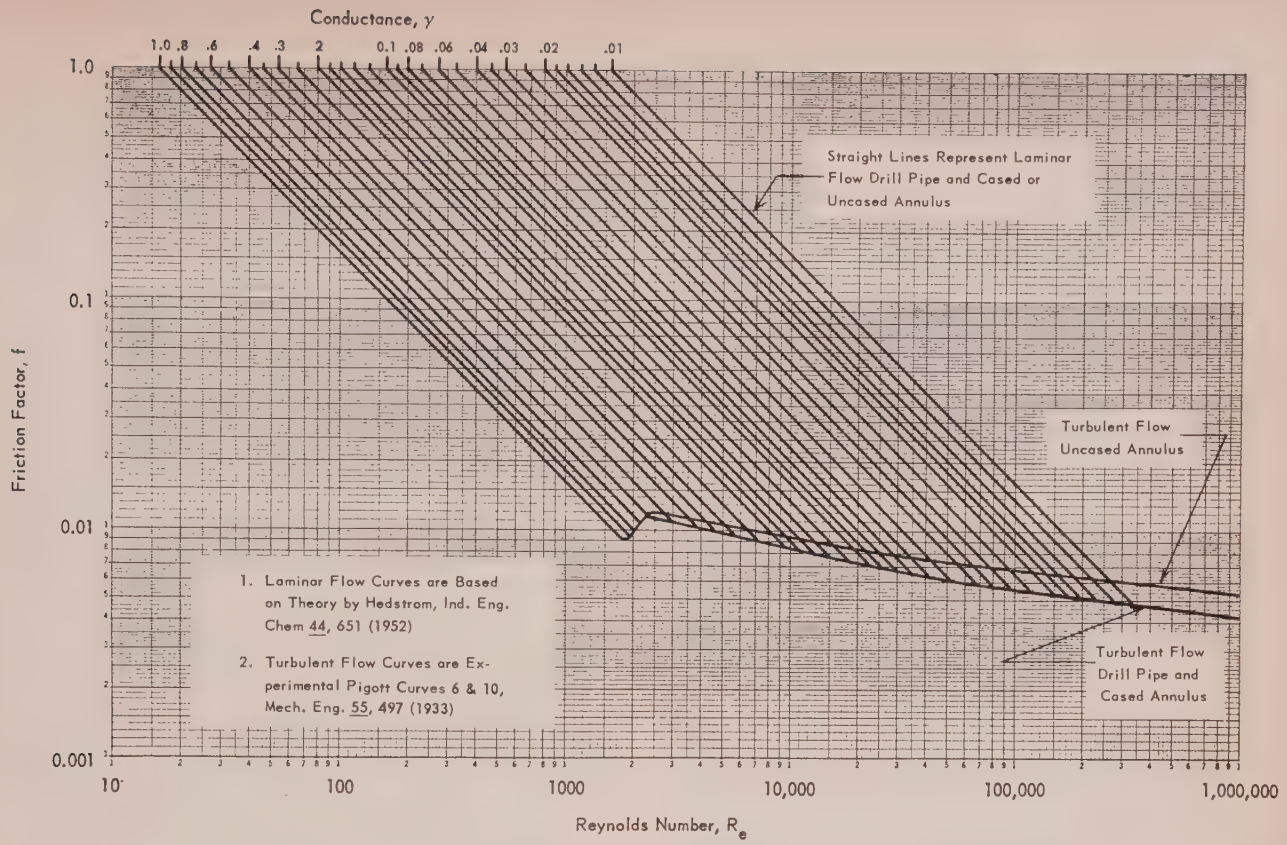
Conductance, γ
1.0 .8 .6 .4 .3 .2 0.1 .08 .06 .04 .03 .02 .01
Friction Factor, f
1.0
0.1
0.01
0.001
Straight Lines Represent Laminar Flow Drill Pipe and Cased or Uncased Annulus
Turbulent Flow Uncased Annulus
Turbulent Flow Drill Pipe and Cased Annulus
1. Laminar Flow Curves are Based on Theory by Hedstrom, Ind. Eng. Chem 44, 651 (1952)
2. Turbulent Flow Curves are Experimental Pigott Curves 6 & 10, Mech. Eng. 55, 497 (1933)
10
100
1000
10,000
100,000
1,000,000
Reynolds Number, R_e

FIG. 5—MODIFIED FRICTION FACTOR-REYNOLDS NUMBER DIAGRAM FOR USE WITH BINGHAM PLASTICS.

a relationship between these two parallel flow paths was that the total pressure surge generated in the pipe bore must equal the total pressure surge generated in the annulus.

$$P_b = P_a \quad . \quad . \quad . \quad . \quad . \quad . \quad . \quad . \quad . \quad . \quad . \quad . \quad (11)$$

This equal pressure condition is obtained by partitioning the mud flow between the two paths in various ratios until equal pressures are generated in both flow paths. This final pressure should be identical to that which actually occurs; thus, it is the surge pressure.

The complexity of the calculations of viscous-drag pressure surges for various geometries of the annulus and pipe bore, plus the trial-and-error procedure of partitioning the mud between the two flow paths, requires the use of a high-speed computing machine. These computational complexities are minimized by an approximate procedure presented in a later section.

Effective Mud Velocities for Pressure-Surge Generation. As before, the effective average annulus mud velocity is the sum of components due to mud displacement and moving pipe wall. Thus,

$$V_{ae} = -\left(\frac{-576\ q_a}{\pi(D_h^2 - D_p^2)} + KV_p\right)\left[\frac{\text{ft}}{\text{min}}\right]. \quad (12)$$

where q_a is the volumetric mud flow in the annulus measured with respect to the fixed wall. The effective average velocity of the mud in the pipe bore with respect to the walls of the pipe bore is

$$V_{be} = \frac{576\ \{q_b\}}{\pi D_i^2}\left[\frac{\text{ft}}{\text{min}}\right], \quad . \quad . \quad . \quad . \quad . \quad . \quad . \quad . \quad (13)$$

and the pressure in the pipe bore is generated by the relative flow $\{q_b\}$ of the mud and pipe walls, irrespective of which is considered to be moving.

Pressure Generated in the Annulus and Pipe Bore. The pressure generated in the annulus of open pipe strings is computed in the same way as outlined for *closed* pipe except V_{ae} is defined by Eq. 12. The pressure generated in the pipe *bore* uses the same procedures as outlined for the annulus. The changed geometry causes Eqs. 8, 9 and 10 to become:

$$S = \frac{2394\ (D_i)\ \tau_o}{\mu_p V_{be}}; \quad . \quad . \quad . \quad . \quad . \quad . \quad . \quad . \quad (14)$$

$$R_e = \frac{15.44\ (D_i)\ V_{be}\ \rho}{\mu_p}; \quad . \quad . \quad . \quad . \quad . \quad . \quad . \quad (15)$$

and

$$\frac{\Delta P}{L} = \frac{f V_{be}^2 \rho}{9.282 \times 10^4\ D_i}\left(\frac{\text{psi}}{\text{ft}}\right). \quad . \quad . \quad . \quad . \quad . \quad (16)$$

For each change in diameter of the pipe bore and the annulus, the pressure gradient will be different and the pressure generated in each of the flow paths will be the sum of the contributions from each change of diameter.

In developing the theory and graphs described herein, the process of partitioning the mud flow, computing the pressures, repartitioning the flow, etc., was continued until the pressure generated in the annulus was within 5 psi of that generated in the pipe bore. When this condition was met, the pressure generated in either path was considered to be identical to the pressure surge.

The constants appearing in Eqs. 5 through 16 are pooled conversion factors to make the equations numerically correct when the dimensions of the parameters are those listed in the table of nomenclature of the symbols.

QUALITATIVE COMPARISON OF PREDICTED AND OBSERVED SURGES

The pipe velocity and accelerations depicted in Fig. 2 were used to calculate a surge pattern from the theoretical treatment of the surge components associated with the inertial and viscous-drag effects. The com-

puted pattern is shown in Fig. 6. A comparison of the computed pattern in Fig. 6 with the measured patterns in Fig. 1 clearly demonstrates the similarity of the computed and measured surge patterns.

SUMMARY OF THEORETICAL ASPECTS OF PRESSURE-SURGE GENERATION

A theoretical treatment of surge pressure generation has been formulated in terms of quantities that can be measured: pipe velocity, pipe acceleration, mud properties, hole size and pipe-string size. The theory predicts a surge pattern from pipe velocity and acceleration that is similar in detail with the measured surge patterns.

The last requirement of the theory, that it quantitatively predict the magnitude of the major peaks and valleys of the measured surge patterns, will be demonstrated following the discussion of field measurements of pressure surges.

FIELD MEASUREMENTS OF PRESSURE SURGE

It has been noted previously that measured surge pressures were qualitatively in agreement with those predicted. This section of the report will present field data that will permit a quantitative evaluation of the theory.

DESCRIPTION OF PROCEDURE

A 9⅝-in., 40-lb/ft casing string was set and cemented at 2,100 ft in a field well to form a "wellbore" of uniform diameter into which a smaller casing string was lowered. This second string consisted of 48 joints of 7-in., 23-lb/ft casing equipped with a differential fill-up collar. Normal casing handling procedures were followed. Measurements of (1) instantaneous mud pressure as a function of time, (2) position of the casing as a function of time and (3) mud properties were made during the running of the casing string.

Pressure Measurements

Five subsurface pressure gauges were used to record instantaneous mud pressure. Two gauges were placed at the bottom of the hole, two at the bottom of the casing string and one inside the moving string above the fill-up collar. Since the average running time for a joint of casing was less than 20 seconds, the pressure fluctuations recorded on the gauge charts were examined by microscopic techniques.

A comparison of the pressures measured by two different types of subsurface gauges located adjacent to each other was used to estimate the precision of the pressure measurements. It was found that the two gauges at the bottom of the hole and the two at the bottom of the moving pipe all recorded approximately the same values for pressure surges. The pressure data presented in this report are the average of the four readings. Characteristics of the gauges in measuring transient pressures were such that the deviations of the measurements were generally less than 10 per cent, with extreme differences of 30 per cent occasionally observed.

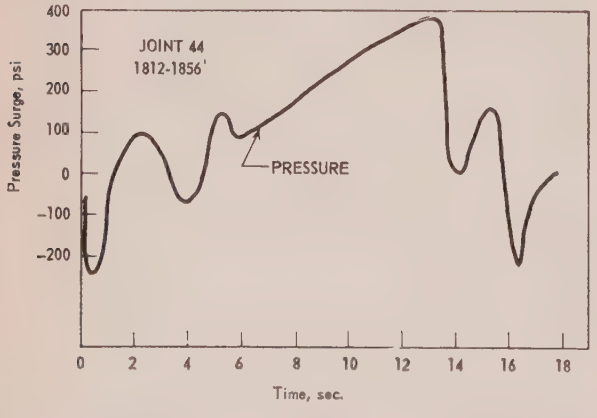

FIG. 6—THEORETICAL PRESSURE-SURGE PATTERN COMPUTED FROM PIPE VELOCITY AND ACCELERATION OCCURRING AS A CASING JOINT IS LOWERED.

Pipe-Movement Measurements

Movement of the casing string as a function of time was measured by three procedures.

1. A telephoto movie camera photographed marks at one-foot intervals on the casing string as the casing was being lowered into the hole. The pipe velocity was obtained by determining its position as a function of time.

2. A rig runner pointer was also photographed with a second movie camera and the pipe velocity computed.

3. The last device used to measure the pipe movement was a DC voltage generator driven by a rig runner line. The voltage output of the generator was proportional to the speed of the rig runner line and was recorded with a strip-chart recorder.

Acceleration of the pipe was obtained by numerical differentiation of data obtained by each of these three measurements.

The three measurements of pipe velocity were generally in good agreement. The two camera devices correlated within 2 per cent deviation at velocities of 1 ft/sec or greater. The recorder deviated 3 to 5 per cent from the camera in the velocity range of 1 ft/sec or greater. Fig. 2 is a typical pipe-string velocity and acceleration chart measured as an added joint of casing was lowered into the hole.

Mud Property Measurements

Properties of the mud were measured at various times during the casing running operation. Table 1 is a listing of the measured mud properties. A constant-speed rotary viscometer was used to measure the initial and three-minute gel strengths, ξ_o and ξ_3, the plastic viscosity μ_p and the yield point τ_o. The Marsh funnel viscosity, the compressibility and the density ρ were measured, as was the API filtration rate.

Differential Fill-Up Collar

Measurements were made with the differential fill-up collar operative, as well as closed and inoperative. This permitted an evaluation of the utility of such a device and, more important, provided data to check the theory of pressure surges for both open and closed pipe strings.

RESULTS AND COMPARISON WITH THEORY

This research was undertaken to describe pressure surges qualitatively as well as quantitatively. It previously has been noted that certain pressure peaks occurred at maximum pipe velocity or acceleration. The pipe motion, of course, was related to pipe handling operations on the rig floor.

The theoretical predictions were compared to the measured surge patterns at four characteristic points—(1) the maximum value of the first negative peak, (2) the maximum value of the first negative braking peak, (3) the maximum value of the second negative braking peak and (4) the maximum value of the major positive peak.

TABLE 1—MUD PROPERTIES DURING PRESSURE SURGE MEASUREMENTS

Time of Day	Gel Strength lb/100 ft² Initial	Gel Strength lb/100 ft² 3-Min	Plastic Viscosity (cp)	Yield Point (lb/100 ft²)	Mud Wt. (lb/gal)	Filtration Rate (cc/30 min API)	Compressibility (per cent)	Funnel Viscosity (seconds)
8:45 AM	11	22	14	6	10.8	—	0	—
8:55	9	32	12	7	10.9	12.5	0	41
9:10	—	—	—	—	10.75	—	—	—
9:25	9	36	12	8	10.85	—	—	43
9:35	9	38	12	8	10.85	—	—	—
10:00	9	41	12	8	10.85	—	—	—
3.00 PM	—	—	13.2	6	—	12.3	—	—
4:30	10	28	14	6	—	—	—	—
4:50	12	38	12.5	6.5	10.9	—	—	—

An experimental difficulty produced a minor limitation to the verification of the theory. As it was designed to do, the automatic fill-up collar closed the pipe string during the negative surges, preventing an evaluation of the negative surge for an open pipe string. Therefore, the negative pressure surges obtained while the fill-up collar was operating were not used. The comparisons of negative surges were limited to the measurements made while the differential fill-up collar was permanently closed and inoperative. Comparisons of the positive viscous-drag surges measured with the fill-up device operative are presented in a later section of the report.

Negative Surges Due to Lifting Pipe String Off Slips

Measured values of the initial negative surge peakes were compared to computed values that arise from inertial and gel-breaking effects. The velocity component is of little interest at this particular instant, for the velocity of the mud is essentially zero (Fig. 2). Table 2 lists the measured surges and the computed inertial and gel-breaking surge pressures. The gel strength of the mud was taken to be the measured average three-minute strength ξ_3 of 32.9 lb/100 ft² as three minutes was the approximate time involved in adding a new casing joint.

The results in Table 2 show that this negative surge peak could arise from either the gel-breaking pressure or the inertial pressure, depending upon the value of the acceleration and the gel strength of the mud in particular cases.

Negative Surges Due to Braking the Pipe

A comparison of the measured and predicted surges which result from applying the brakes to stop the downward travel of the pipe is shown in Table 3. The predicted surge was obtained by computing the positive value of the surge due to the velocity of the pipe and subtracting the negative surge due to pipe deceleration. Considering the errors involved in the measured value of surge pressure and in the determination of pipe acceleration, the agreement is reasonably good on the first deceleration surge and better on the second. The average deviation between measured and calculated values is 36 psi/1,000 ft of pipe (a discrepancy of 36 per cent) for the first deceleration surge and 18 psi/1,000 ft of pipe (a discrepancy of 18 per cent) for the second.

TABLE 2—COMPARISON OF MEASURED AND COMPUTED SURGE OCCURRING AS THE PIPE IS LIFTED FROM THE SLIPS

Joint No.	Avg. Pipe Depth (ft)	First Negative Surge, in psi/1,000 ft of Pipe: Measured	Calculated as Due to: Acceleration of Mud (Eq. 4)	Calculated as Due to: Breaking of Gel (Eq. 2)
38	1576	61	59	60
29	1617	76	63	60
40	1660	67	59	60
41	1704	87	99	60
42	1747	102	107	60
43	1791	109	160	60
44	1834	127	117	60
45	1878	36	—	60
46	1920	122	195	60
47	1964	102	138	60
48	2008	81	130	60

Positive Surges Due to Pipe Velocity

The maximum values of the observed positive surges were compared to the viscous-drag surges computed when the instantaneous pipe velocity was a maximum. This comparison for the closed pipe string is shown in Table 4.

Agreement between measured and calculated values is excellent, the difference being in every case less than the experimental error in measuring pressure and instantaneous pipe velocity. The actual difference between measured and predicted values averaged 32 psi, a discrepancy of about 13 per cent. In planning field operations, it is important that these large surges can be predicted accurately.

Summary of Comparisons

The comparisons listed in Tables 2, 3 and 4 confirm the theory as a quantitative means of predicting pressure surges. Although several large deviations are present in the comparisons, the deviations are generally well within the experimental accuracy. Agreement is especially good in the case of viscous-drag pressures, which are the largest and therefore most important pressure peaks of the pressure-surge pattern.

FIELD UTILIZATION OF THEORY FOR PRESSURE-SURGE PREDICTIONS

Previous sections of this paper emphasize the theoretical description of surge pressure patterns and how this theory corresponds to the observed surges. In this section, the application of the theory to the control of pressure surges in field operations will be discussed. Effective field use requires the development of a simple,

TABLE 3—COMPARISON OF MEASURED AND COMPUTED PRESSURE SURGES DUE TO A VISCOUS DRAG AND INERTIAL SURGE COMPONENTS OCCURRING AS THE PIPE IS BRAKED TO A STOP

Joint No.	Avg. Pipe Depth (ft)	First Pipe Deceleration Surge in psi/1,000 ft of pipe: Measured	First Pipe Deceleration Surge in psi/1,000 ft of pipe: Calculated	Second Pipe Deceleration Surge in psi/1,000 ft of pipe: Measured	Second Pipe Deceleration Surge in psi/1,000 ft of pipe: Calculated
38	1576	—	—	− 60	− 63
39	1617	−149	−153	—	—
40	1660	−146	−225	—	—
41	1704	—	—	− 86	− 86
42	1747	− 94	− 92	− 74	− 78
43	1791	− 54	−110	−108	− 77
44	1834	+ 1	+ 36	−122	− 98
45	1878	− 48	−111	−154	−149
46	1920	− 61	− 59	—	—
47	1964	—	—	− 86	− 91
48	2008	−159	−109	− 86	−147

TABLE 4—COMPARISON OF MEASURED AND COMPUTED PRESSURE SURGE DUE TO VISCOUS-DRAG SURGE COMPONENT OCCURRING AS THE PIPE IS LOWERED INTO THE WELLBORE

Joint No.	Avg. Pipe Depth (ft)	Maximum Positive Pressure Surge in psi/1,000 ft of pipe	
		Measured	Calculated
38	1576	254	287
39	1617	230	295
40	1660	241	311
41	1704	241	260
42	1747	257	319
43	1791	250	279
44	1834	233	260
45	1878	226	246
46	1920	218	246
47	1964	229	222
48	2008	226	216

straightforward procedure for accurately computing the pressure surges which may occur.

The simplifications necessary are (1) the determination of which of the pressure peaks are largest and, hence, most important and (2) a simple method of computing these largest peaks—be they positive or negative.

IDENTIFICATION OF IMPORTANT SURGES

The characteristically largest pressure surges were identified from field observations of the various positive and negative surge peaks occurring as added joints of casing were lowered into the hole. Fig. 7 is a compilation of the maximum surge values. The data from Joints 38 through 48 measured with the fill-up device closed and inoperative (closed pipe) clearly show that the largest surge is a positive one. Table 4 shows this positive peak to be associated with the viscous drag of the mud that occurs at maximum pipe velocity.

The data measured with the differential fill-up device operative, Joints 4 through 37 in Fig. 7, show the measured negative surges to be somewhat greater than the corresponding positive surges. But as previously stated, the differential fill-up collar in its normal operating condition closed the casing string during the negative surges and *opened* the casing to mud flow during the positive surges. The casing string, when running Joints 4 through 37, thus appeared to be a closed pipe for negative surges and an open pipe for positive surges. In many assemblies, such as drill strings, the bore of the pipe would be opened to flow during both surges.

To gain an insight into the surges occurring in this

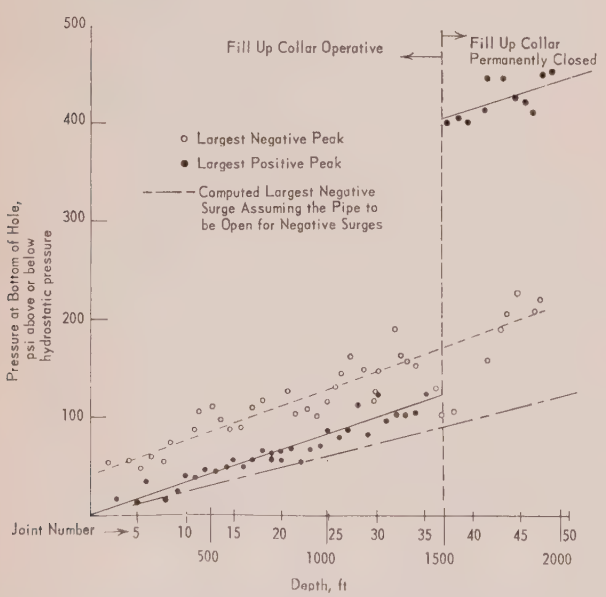

FIG. 7—LARGEST MEASURED POSITIVE AND NEGATIVE PRESSURE SURGES AS A FUNCTION OF DEPTH.

open-pipe case, the inertial and gel-breaking pressures were calculated with Eq. 4 and with Eq. 2, respectively. These computed negative surges were less than the measured positive surges. (See Fig. 7.)

For field use in controlling pressure surges, it is thus normally sufficient to consider only the major pressure peak arising from the viscous drag of the mud at maximum pipe velocity. The computational procedure previously described for the viscous-drag component of surge pressure generation is complex. A straightforward procedure for estimating this surge pressure is presented in the following section.

APPROXIMATE PROCEDURE FOR COMPUTING VISCOUS-DRAG PRESSURE SURGES

The approximate procedure for computing viscous-drag components of pressure surges is a simplification of the theory given in a previous section. The central idea of the simplification is to fit approximate equations to theoretical results computed for specific conditions and to state these approximate equations in terms of pipe velocity, mud properties, hole size and pipe geometry. Using a high-speed computer, over 500 combinations of pipe and hole sizes and mud properties were used to evaluate the approximate equations for the conditions most often encountered in field operations.

Fig 8 is a typical graph showing computed pressure surge vs instantaneous pipe velocity. Also shown in Fig. 8 are the two approximate equations used to fit the computed curves. In the laminar flow region, the curve can be approximated by an equation of the form

$$P_s = \psi V_p + \Gamma \text{ [psi/1,000 ft of pipe]} \quad . \quad . \quad (17)$$

For the turbulent flow region,

$$P_s = \theta V_p^{1.8} \text{ [psi/1,000 ft of pipe]} \quad . \quad . \quad . \quad (18)$$

The curve-fitting parameters, ψ, Γ and θ were evaluated for a range of mud properties, hole sizes and pipe-string geometries. The dependence of these three parameters upon the several variables was found to differ for open and closed pipe strings. These two cases, therefore, are discussed separately.

Closed Pipe

For a closed pipe string, Eqs. 17 and 18 were found to be expressible as the following.

For laminar flow—closed pipe,

$$P_s = B\mu_p V_p + \tau_o/0.3(D_h - D_e) \text{ [psi/1,000 ft of pipe]} \quad . \quad . \quad . \quad . \quad . \quad (19)$$

For turbulent flow—closed pipe,

$$P_s = A\,\mu_p^{0.21}\,\rho^{0.806}\,V_p^{1.8} \text{ [psi/1,000 ft pipe]} \quad (20)$$

In these equations, the pipe velocity and mud properties, μ_p, τ_o and ρ, appear directly. The remaining parameters, B, D_e and A, are associated with pipe and hole geometries.

The numerical values of A and B evolved by curve fitting are plotted in Figs. 9 and 10 as a function of hole size for various pipe strings. The nominal casing sizes represent all weights of casing and standard couplings. The drill pipe strings are 3½-in. full hole with 4⅝-in. tool joints, and 5-in. extra hole with 6¼-in OD tool joints. Each drill string had sufficient drill collars to place 40,000 lb on the bit in 12-lb/gal mud.

Next, it was desirable to study the effect of different tool joint sizes, casing-protector bushings size and number as well as size of drill collars upon the constants A and B. Using the computer, pressure surges were calculated using a number of different drill strings with nominal 3½- or 5-in. pipe but with various drill-collar sizes

and lengths, various tool joints, etc. If the clearances $(D_h - D_{tj})$, $(D_h - D_{dc})$ and $(D_h - D_b)$ were always greater than 1 in. and if the length of the drill collars did not exceed that required to place 80,000 lb on the bit in 12-lb/gal mud, then the maximum variation in A or B from the tabulated values was less than 8 per cent at a depth of 12,000 ft. Thus, the numerical values of A and B as tabulated may be used with confidence for the drill strings and casing strings most often used in the field.

The parameter D_e is an empirically determined effective outer diameter of the pipe string. For casing strings, it was found that this empirical value was nearly identical to the average diameter of the pipe and collars.

$$D_e = \frac{D_p + D_c}{2} \text{[in.]} \quad . \quad . \quad . \quad . \quad . \quad . \quad . \quad . \quad . \quad (21)$$

Because of the larger clearance, however, D_e of *drill* strings turned out to be quite insensitive to usual variations in drill strings of a specific nominal size Fig. 11 is a graph of $(D_h - D_e)$ vs D_h for 3½- and 5-in. nominal drill strings.

Open Pipe

The approximation is completed by modifying Eqs. 19 and 20 for *closed* pipe string to cover *open* pipe strings. The modification is as follows.

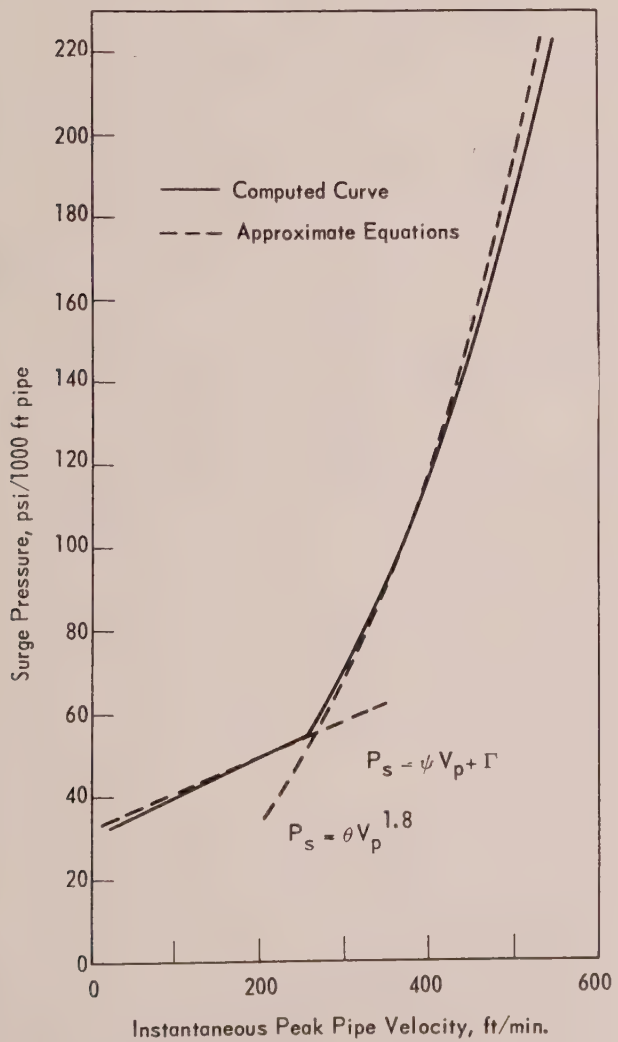

FIG. 8—RIGOROUS AND APPROXIMATE THEORETICAL RELATIONSHIP BETWEEN VISCOUS-DRAG PRESSURE SURGE AND PIPE VELOCITY.

For laminar flow—open pipe,

$$P_s = \beta B \mu_p V_p + \tau_o / 0.3 (D_h - D_e)$$
[psi/1,000 ft of pipe] . . . . . (22)

For turbulent flow—open pipe,

$$P_s = \alpha A \mu_p^{0.21} q^{0.806} V_p^{1.8}$$
[psi/1,000 ft of pipe] . . . . . (23)

where the coefficients of the openings, α and β, are used to adjust the closed-pipe equations for open pipe. The values of α and β are plotted in Figs. 12 and 13 as a function of hole sizes for various nominal casing and drill-pipe sizes. A 1½-in. orifice was assumed to represent all fill-up devices used on casing strings. For drill-pipe strings, three-nozzle jet bits whose nozzles varied in sizes from ¼ to 9/16 in. were used as orifices. In general, the sizes of the jet nozzles were found not to affect appreciably the calculated surge. The α and β plotted for drill pipe were obtained from calculations using ⅜- or 7/16-in. diameter jet bit nozzles as orifices.

Calculations of cases with the same mud and pipe geometry showed that the mud flow regime in the annulus of open pipe may be laminar but may shift to

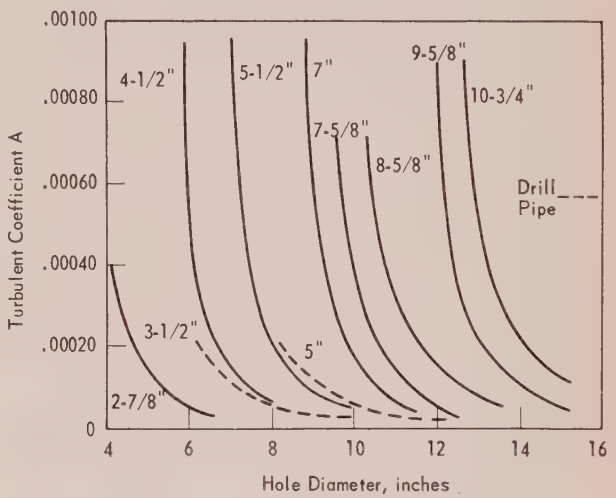

FIG. 9—TURBULENT FLOW GEOMETRY COEFFICIENT A AS A FUNCTION OF WELLBORE SIZE AND NOMINAL PIPE-STRING SIZE.

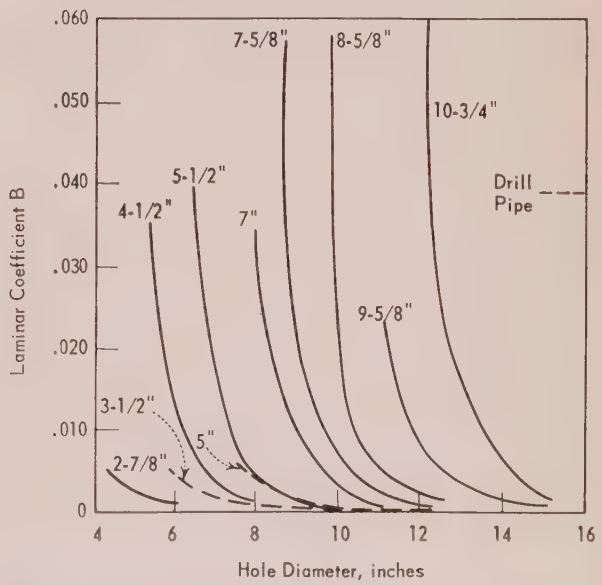

FIG. 10—LAMINAR FLOW GEOMETRY COEFFICIENT B AS A FUNCTION OF WELLBORE SIZE AND NOMINAL PIPE-STRING SIZE.

turbulent when the pipe string is closed, even though the pipe velocity is decreased simultaneously from an average maximum value of 420 ft/min to 340 ft/min. Thus, the utilization of the pipe velocity as an *a priori* basis for determining the flow regime of the mud is not valid. To find the actual surge pressure, both the laminar and turbulent flow equations should be evaluated at the same velocity. From the graphical representation of the approximate equations in Fig. 8, the larger of the two values correctly describes the flow regime and the surge pressure.

The equations for laminar flow, Eqs. 19 and 22, were evolved assuming the mud to be an ideal Bingham plastic. Actually, the mud which is displaced by the moving pipe has a fairly well developed gel strength. Kruyt[14] has shown that this is due to the thixotropic character of the clay suspension. Because the gel was allowed to develop approximately three minutes between casing movement, in the calculations described herein, the three-minute gel strength ξ_3 has been used in lieu of τ_o.

Comparison of Approximate Surge-Pressure Predictions with Measurements

The maximum values of positive pressure surge measured with the casing *open* and *closed* are compared in Fig. 14 with the value of surge pressure predicted by the approximate equations. The comparison of the predictions with the measurements are excellent for both open and closed pipe strings. Deviations between the two values of pressure surges are within the experimental precision of the measurements.

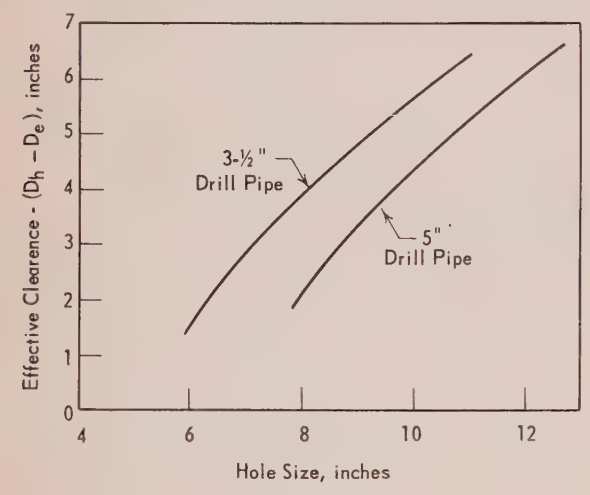

FIG. 11—EFFECTIVE ANNULAR CLEARANCE ($D_h - D_e$) AS A FUNCTION OF WELLBORE SIZE AND NOMINAL DRILL-PIPE SIZE.

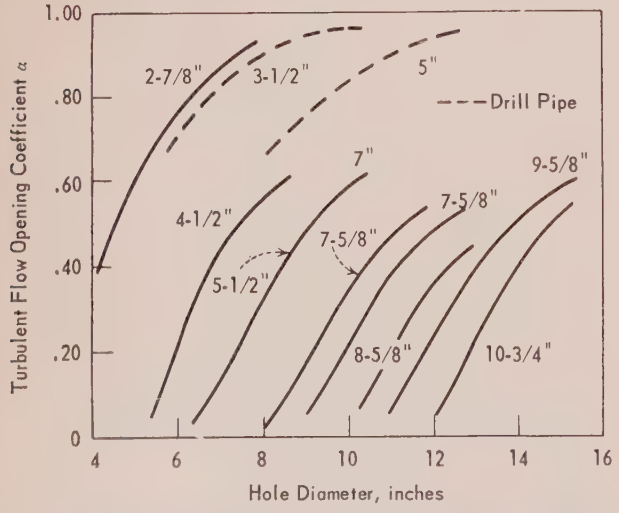

FIG. 12—TURBULENT FLOW OPENING COEFFICIENT α AS A FUNCTION OF WELLBORE SIZE AND NOMINAL PIPE-STRING SIZE.

CONCLUSIONS

1. A quantitative, theoretical description of surge pressures generated by pipe movement in a mud-filled wellbore has been developed and verified by experimentation.

2. The theory correctly predicts the existence and magnitude of various positive and negative peaks due to gel breaking, inertia and viscous drag of the mud.

3. When running drill pipe, or casing without fill-up devices, the surge due to viscous drag is usually largest and, therefore, most important.

4. Simple, approximate equations were developed to predict the viscous-drag surge, and the predictions were found to be within experimental accuracy.

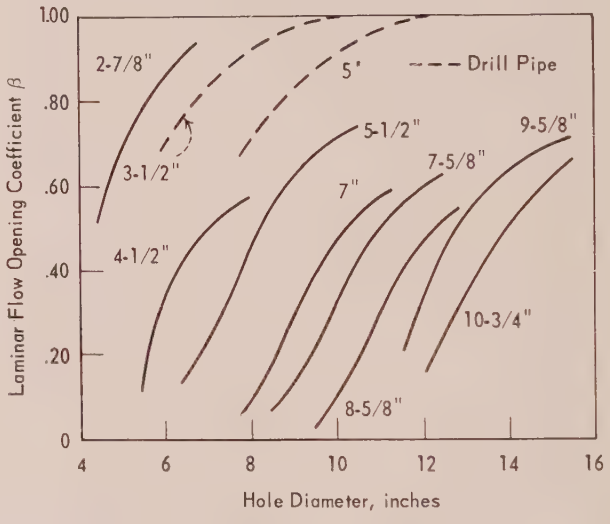

FIG. 13—LAMINAR FLOW OPENING COEFFICIENT β AS A FUNCTION OF WELLBORE SIZE AND NOMINAL PIPE-STRING SIZE.

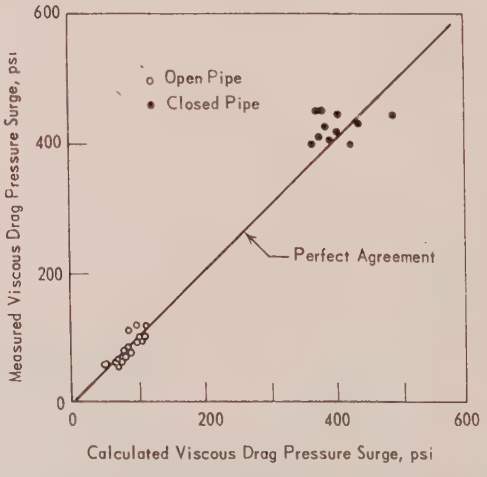
Measured Viscous Drag Pressure Surge, psi
Calculated Viscous Drag Pressure Surge, psi
o Open Pipe
• Closed Pipe
Perfect Agreement

FIG. 14—COMPARISON OF APPROXIMATE PREDICTED PRESSURE SURGE WITH MEASURED PRESSURE SURGE FOR OPEN AND CLOSED PIPE STRING.

NOMENCLATURE

A = empirical geometry coefficient, turbulent flow
a_p = acceleration of pipe, ft/sec^2
B = empirical geometry coefficient, laminar flow
D_i = inside diameter of pipe, in.
D_h = inside diameter of hole, in.
D_p = outside diameter of pipe, in.
D_c = outside diameter of casing coupling, in.
D_{tj} = outside diameter of tool joint, in.
D_{dc} = outside diameter of drill collar, in.
D_b = outside diameter of rubber casing-protector bushings, in.
D_e = empirical effective pipe string outside diameter, in.
f = friction factor
g = acceleration of gravity, ft/sec^2
L = length of pipe section, ft
P = pressure, psi
P_a = annulus pressure, psi
P_b = pipe bore pressure, psi
P_s = pressure surge, psi/1,000 ft of pipe
$\frac{\Delta P}{L}$ = pressure gradient, psi/ft
q_a = mud flow in annulus measured with respect to the fixed wall of the hole, ft^3/min
$\{q_b\}$ = mud flow in pipe bore measured with respect to pipe walls, ft^3/min
R_e = Reynolds number
S = plasticity
V_{ae} = effective annulus mud velocity, ft/min
V_{be} = effective pipe-bore mud velocity, ft/min
V_{da} = annulus component of mud velocity due to displacement, ft/min
V_{ms} = annulus component of mud velocity due to moving surface, ft/min
V_p = velocity of pipe, ft/min
α = empirical opening coefficient, turbulent flow
β = empirical opening coefficient, laminar flow
γ = fluid conductance
ρ = mud weight, lb/gal
τ_o = yield point, lb/100 ft^2
μ_p = plastic viscosity, cp
ξ = gel strength, lb/100 ft^2
ξ_o = initial gel strength, lb/100 ft^2
ξ_3 = three-minute gel strength, lb/100 ft^2

ACKNOWLEDGMENTS

The author expresses his gratitude and indebtedness to R. J. Blackwell, G. W. Binkley, J. E. Eckel and J. A. Rickard for their contributions to many phases of the work described in this paper. The help and cooperation extended by field and engineering personnel of the Humble Oil & Refining Co. are also gratefully acknowledged.

REFERENCES

1. Cannon, George E.: "Changes in Hydrostatic Pressure Due to Withdrawing Drill Pipe from the Hole", *Drill. and Prod. Prac., API* (1934) 42.
2. Goins, W. C., Jr., Weichert, J. P., Burba, J. L., Jr., Dawson, D. D., Jr. and Teplitz, A. J.: "Down-the-Hole Pressure Surges and Their Effect on Loss of Circulation", *Drill. and Prod. Prac.*, API (1951) 125.
3. Clark, E. H., Jr.: "Bottom-Hole Pressure Surges While Running Pipe", ASME Paper No. 54-PET-22 presented at the Pet. Mech. Eng. Conf., Los Angeles, Calif. (Sept., 1954); also published in *Pet. Eng.* (1955) **27,** B-68.
4. Eckel, J. E.: *Oil and Gas Jour.* (1959) **57,** No. 13, 96.
5. Cardwell, W. T., Jr.: "Pressure Changes in Drilling Wells Caused by Pipe Movement", *Drill. and Prod. Prac.*, API (1953) 97.
6. Beck, R. W., Nuss, W. F. and Dunn, T. H.: "Flow Properties of Drilling Muds", *Drill. and Prod. Prac.*, API (1947) 9.
7. Ormsby, George S.: "Calculation and Control of Mud Pressures in Drilling and Completion Operations", *Drill. and Prod. Prac.*, API (1954) 44.
8. Clark, E. H., Jr.: "A Graphic View of Pressure Surges and Lost Circulation", *Drill. and Prod. Prac.*, API (1956) 424.
9. Melrose, J. C., Savins, J. G., Foster, W. R. and Parrish, E. R.: "A Practical Utilization of the Theory of Bingham Plastic Flow in Stationary Pipes and Annuli", *Trans.*, AIME (1958) **213,** 316.
10. Laufer, J.: *Jour. of Aero. Sci.* (1950) **17,** 277.
11. Pai, S. I.: *Jour. of Appl. Mech.* (1953) **20,** 109.
12. Piggott, R. J. S.: *Mech. Eng.* (1933) **55,** 497.
13. Hedstrom, B. O. A.: *Ind. Eng. Chem.* (1952) **44,** 651.
14. Kruyt, H. R.: *Colloid Science,* **1,** Elsevier Publishing Co., Amsterdam, 364. ★★★

Laboratory Studies of Oil Recovery by Steam Injection

B. T. WILLMAN
MEMBER AIME
V. V. VALLEROY
G. W. RUNBERG
A. J. CORNELIUS
L. W. POWERS
JUNIOR MEMBERS AIME

JERSEY PRODUCTION RESEARCH CO.
TULSA, OKLA.

ABSTRACT

This paper reports the results of an investigation into the use of steam as a recovery agent.

High oil recoveries by steam, as much as 100 per cent greater than by water flood, were demonstrated in laboratory linear cores. The principal mechanisms responsible for the additional oil have been identified as (1) thermal expansion of the oil, (2) viscosity reduction and (3) steam distillation. Although the first two also enhance recovery by hot water flood, they are effective with steam injection at lower volumes of produced fluids. Steam-zone residual oil saturation is independent of initial saturation. Recovery by steam is greater for lighter oils because they contain a greater fraction of steam-distillable components.

Equations for the steam-zone advance in a radial homogeneous system are presented; these show the effect of reservoir parameters. The displacement in the hot liquid region moving ahead of the steam front can be estimated by a calculative procedure which is suggested. The method which takes account of the temperature gradient is applicable also to a regular hot water flood.

INTRODUCTION

Considerable industry interest in the application of heat to petroleum reservoirs as a means of increasing oil recovery has been evident in the past few years. Three thermal methods which have attracted interest are (1) the injection of saturated steam, (2) the injection of hot water and (3) the injection of air into a formation to support combustion within the reservoir. Much has been published in recent years on underground burning, and there have been several papers on hot water injection.[3-6,10] Although there are several early reports[1,2] on steam injection, no recent experimental studies have been published on this recovery method.

In our early thermal methods research, a marked improvement was found in oil recovery by steam injection compared with recovery by water injection in the same system. An investigation subsequently was undertaken to obtain quantitative information from which to evaluate steam injection as an oil recovery method. In addition, it was desired to investigate the recovery mechanism of hot water as compared with that of "cold" water and steam injection. An understanding of the mechanisms by which these processes operate would generally define favorable field conditions for their successful application. This paper reports the results of the laboratory study and suggests calculative approaches to estimate the field behavior of the steam-injection process.

EXPERIMENTAL METHOD

EQUIPMENT

A schematic diagram of the equipment used for the displacement tests is shown in Fig. 1. Essentially, it consisted of a core with suitable means for recording temperatures, a feed system for injecting steam or cold or hot water, and a receiving train for condensing, cooling and measuring produced fluids.

For the steam experiments, air-free saturated steam was piped from the boiler to the core face in insulated lines that were provided with steam traps and bleeds to remove any condensate formed in the lines due to heat losses. A 12-in. section of the line immediately ahead of

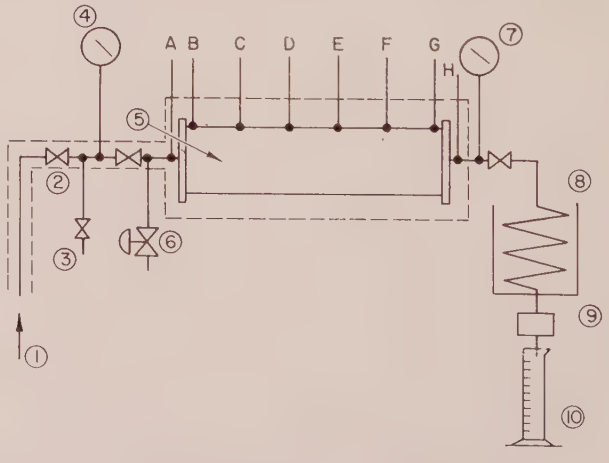

FIG. 1—SCHEMATIC DIAGRAM OF TEST CORE, SHOWING: (A THROUGH H) THERMOCOUPLES, (1) AIR-FREE SATURATED STEAM, (2) INSULATION, (3) BLEED ON INLET LINE, (4) INLET PRESSURE GAUGE, (5) CORE HOLDER, (6) AUTOMATIC BLEED AT CORE INLET, (7) OUTLET PRESSURE GAUGE, (8) CONDENSER ASSEMBLY, (9) BACK-PRESSURE REGULATOR AND (10) COLLECTION GRADUATE.

Original manuscript received in Society of Petroleum Engineers office July 14, 1960. Revised manuscript received June 1, 1961. Paper presented at 35th Annual Fall Meeting of SPE, Oct. 2-5, 1960, in Denver.

[3]References given at end of paper.

Discussion of this and all following technical papers is invited. Discussion in writing (three copies) may be sent to the office of the *Journal of Petroleum Technology*. Any discussion offered after Dec. 31, 1961, should be in the form of a new paper. No discussion should exceed 10 per cent of the manuscript being discussed.

This page of *Petroleum Transactions, AIME* follows page 603. The intervening non-Transactions pages appeared in *Journal of Petroleum Technology*.

the core was wrapped with heating tape and maintained a few degrees above saturated steam temperature to prevent steam condensation between the last bleed and the core face.

For the hot-water runs, a heat exchanger was employed for heating distilled water to input temperature. In these tests, the core pressure was maintained sufficiently high to insure an all-liquid system at the operating temperature.

A Bausch and Lomb single-scale refractometer was used to obtain the composition of produced white oils, and either a pycnometer or an API hydrometer was used to measure the gravities of the produced crude samples. In most of the viscous oil experiments, after condensate breakthrough the oil was produced in the form of an emulsion. These emulsions were broken by centrifuging or through the use of chemicals or heat. Emulsions also often were produced while water flooding the viscous oils. The steam-produced emulsions, however, were somewhat harder to break.

TEST CORES

Cylindrical cores of several sizes and mounted in various containers were used for the experiments. Test core properties, dimensions and mountings are summarized in Table 1. All core mountings were insulated to reduce heat losses to the ambient air.

Cores 1 through 8 were used for the recovery of Primol and four different crude oils. Core 9 was used exclusively for the white-oil tests, Core 10 with both white and crude oils, and Cores 11 and 12 for crude-oil displacements with high-pressure steam.

TEST OILS

Properties of the test oils are shown in Table 2. Besides the crude oils, special white-oil mixtures were made up to specified distillation qualities. Primol was rendered entirely nondistillable at steam test conditions by heating it to 450°F and bubbling nitrogen through it to strip off any light components that might be present. White-oil blends then were made up from this nondistillable Primol and Napoleum, a naptha which is almost entirely steam-distillable at steam test conditions. When checked by actual steam distillation (90-psig steam), the distillates consisted of 100 per cent Napoleum and the residuum of a 97 per cent Primol-3 per cent Napoleum mixture regardless of whether the initial oil was a 50-50 or a 75-25 blend. In this report, we have treated the light component, Napoleum, as being 100 per cent steam-distillable at steam test conditions.

EXPERIMENTAL RESULTS

The laboratory experiments fall naturally into three separate groups. The short core tests (Tables 3 and 4) demonstrated the greater recovery by steam injection and established that the laboratory residual oil saturation after steam drive is essentially independent of the initial water and oil saturations. The second group of tests consists of those which were used to determine the mechanisms responsible for the higher recoveries by hot water injection and steam. These are presented in Tables 5 and 6, except for two special tests which are reported during the discussion of the data. The third grouping is comprised of four runs in Table 7 to check steam-drive behavior with high pressure (800-psig) steam. Comparative tests were kept on the same basis by conducting displacement tests on the same core wherever possible. Except for the two special tests, wherever a steam displacement followed a hot water flood, the cores were allowed to cool to ambient temperature before starting steam injection.

In all of the experiments performed, it was observed that recovery by injection of hot water was always greater than for cold water and that steam-drive recoveries always exceeded both. All three kinds of dis-

TABLE 1—TEST CORE PROPERTIES

Core No.	Core	Mounting Seal Used	Length (cm)	Area (cm^2)	ϕ (per cent)	Permeability (md) Air	Water	Oil*	Average** Interstitial Water (% PV)
1	Synthetic (Glass Beads)	Glass	61.7	45.6	34.0	440	428	385	11.0
2	Bartlesville A	Alum.	11.09	20.42	23.9	149	126	115	37.3
3	Torpedo A	Alum.	30.04	45.24	29.6	3035	3030	2430	16.9
4	Warner A	Rubb.	17.3	19.95	24.3	463	372	305	20.8
5	Warner B	Rubb.	16.85	19.95	24.9	542	464	309	17.5
6	Warner C	Rubb.	16.92	19.95	24.0	396	344	253	19.5
7	Weiler A	Rubb.	22.45	19.95	21.0	197	188	165	25.2
8	Weiler B	Rubb.	15.72	19.95	19.3	121	116	108	26.4
9	Torpedo	Lead	91.4	182.4	26.2	—	856	600	26.0
10	Torpedo	Lead	91.4	182.4	27.0	—	1500	1300	18.5
11	Torpedo	Sand	104.0	182.4	26.0	—	581	575	22.3
12	Torpedo	Sand	104.0	182.4	26.5	—	1064	—	17.8

*Permeability to oil measured in the presence of interstitial water.

**Test cores reduced to interstitial water by flushing with viscous oil. For Cores 9 through 12, the average connate waters are ± 1.8, 1.1, 2.3 and 0.9 per cent pore volume, respectively, for the maximum variations between tests in the same core.

TABLE 2—TEST OILS, WHITE-OIL AND CRUDE-OIL PROPERTIES

Oil	API 60°	Viscosity at 80°F (cp)	Specific Gravity 80°F	Average Molecular Weight*	Initial Boiling Point* (°F)	50 Per Cent Boiling Point* (°F)	Refractive Index at 74°F	Per Cent Distilled** 89-psig Steam	Per Cent Distilled** 800-psig Steam
Primol		138	0.884	420	620	827	1.4800		
Napoleum		1.2	0.780	140	310	340	1.4330		
25 Per Cent Distillable (25% Napoleum: 75% Primol)		22.5	0.855				1.4690		
50 Per Cent Distillable (50% Napoleum: 50% Primol)		5.4	0.827				1.4590		
Crude A	21.0	330	.928						
" B	12.2	6500	.978					15.9	33.0
" C	34.7	8.0	.844					49.8	—
" D	37.0	5.4	.832					55.0	72.6
" E	19.1	420	.939					32.0	—

*Data on Primol were obtained from distillation data supplied by the Chemicals Research Div., Esso Research and Engineering Co. Data on Napoleum were supplied by the Deep Rock Oil Co.

**The volume percentage of the crude which was carried over at water-oil ratios greater than 500:1 during steam distillation with saturated steam in a pressurized flask.

placements actually occur, however, during a steam flood. Immediately ahead of the advancing steam zone, there is a zone of hot condensate which acts as a hot water flood, and this is preceded in a sufficiently long core by a region of cooled condensate which is a cold water drive. To study then what happens during such a process, it becomes necessary first to examine the reasons for improved recovery by hot water drive.

HOT WATERFLOOD RECOVERY AND MECHANISMS

It would appear that the phenomena of viscosity reduction and thermal expansion of the oil are responsible for the improved recoveries in hot water drives. To investigate these phenomena, some preliminary tests were made in test cores composed of Bartlesville sandstone. The data of Table 3 show that the recovery of Primol by steam injection was 67 per cent of the oil initially in place. Recovery by water flood of Primol was 46.8 per cent of that initially in place. To check the effect of viscosity reduction, a water flood was run at room temperature with oil having the same viscosity as that of Primol (4.7 cp) at steam temperature (325°F). The recovery of the low-viscosity oil by water flood at room temperature was 52.1 per cent of that initially in place, thus indicating the effect of viscosity reduction.

The influence of thermal expansion on the recovery process was next considered. Primol expands approximately 5 per cent upon heating from room temperature to 212°F, and about 10 per cent upon heating from room temperature to 325°F. These values, when applied to the residual oil after water flood, would indicate that 3 per cent additional oil would be recovered by expansion or swelling at 212°F, and 5 per cent at 325°F. Based on viscosity reduction and oil expansion, the recovery by water flood at 212°F was predicted as 55 per cent of that initially in place (52 per cent plus 3 per cent). An experimental water flood of a Bartlesville core containing Primol preheated to 212°F gave a recovery of 55.5 per cent of the initial hydrocarbon in place, which is in good agreement with the predicted recovery.

The effects of these two mechanisms can be also seen through inspection of the hot and cold waterflood curves of Figs. 2 and 3. Terminal recoveries (at 500:1 water-oil ratios) by hot water flood were 5 per cent and 2 per cent greater for the nondistillable and 50-50 blend, respectively. The improved performance, however, is much more noticeable in the early stages of the tests, i.e., from 0.1 to 4 pore volumes (PV) in Fig. 2 and 0.2 to 2 PV in Fig. 3.

The reason for the more efficient displacements of the distillable oil by either hot or cold water is apparent in Table 8 which shows the significantly lower oil-water viscosity ratios for the 50-50 mixture.

In Table 8, one sees also that the viscosity ratio for the 50 per cent distillable oil is only slightly changed, from 5.4 to 4.1, during the hot water flood. Accordingly, the history of the hot water flood is quite similar to that of the cold water flood conducted entirely at a viscosity ratio of 5.4. On the other hand, in the case of the nondistillable oil, the marked improvement in viscosity ratio (from an initial 138 to 16) allows the hot water flood to show a great improvement in flooding efficiency, particularly at low throughputs.

The comparison of Figs. 2 and 3 suggests that hot water injection, as compared with cold water injection, has its main advantage with heavier oils where viscosity reduction would result in considerably improved recoveries at economical field throughputs. It should be recog-

TABLE 3—OIL RECOVERIES BY STEAM INJECTION AND WATER FLOODING INTO SHORT CORES CONTAINING OIL AND CONNATE WATER

Test No.	Core No.	Core	Oil in Place	% OOIP Recovered By: Reference Water Flood	Steam Injection
1	1	Glass Beads	Primol	62.4	80.4
2	2	Bartlesville SS	Primol	46.8	67.0
3	3	Torpedo SS	Primol	60.0	73.1
4	3	" "	Crude B	—	77.1
5	3	" "	" A	—	75.8
6	4	Warner SS, A	" E	36.6	82.2
7	5	" " , B	" E	—	82.8
8	6	" " , C	" E	39.3	85.3

TABLE 4—OIL RECOVERIES BY STEAM INJECTION INTO SHORT CORES CONTAINING OIL AND MOBILE WATER

Test No.	Core	Core No.	Oil in Place	% OOIP Recovered By: Gas Drive	WF at 80°	Steam Drive	Cum. Recovery Per Cent OOIP
6A	Warner	4	Crude E	—	36.6	45.3	81.9
8A	Warner	6	" "	—	39.3	44.5	83.8
9	Weiler SS	7	Crude D	20.5*	43.6	17.1	81.2
10	" "	7	" "	20.1*	—	61.6	81.7
11	" "	8	" "	48.2	9.4	23.5	81.1
12	" "	8	" "	23.7*	—	59.0	82.7

*Gas injection terminated to simulate field recovery by solution-gas drive.

TABLE 5—OIL RECOVERIES BY STEAM INJECTION INTO TORPEDO CORES CONTAINING OIL AND CONNATE WATER

Test No.	Core No.	Oil	Viscosity at 80°F	Oil Recovery as Per Cent OOIP By: WF at 80°	Hot WF (330°F)	Steam Drive
13	9	Nondist. white oil	138	49.5	54.8	59.0
15	9	25% dist. white oil	22.5	—	54.8	76.0
16	9	50% dist. white oil	5.4	56.0	58.0	83.9
18	9	Crude B	6500	—	—	73.8
19	10	Crude B	6500	45.0	59.8	—
20	9	Crude C	8.2	60.0	67.0	91.8

TABLE 6—OIL RECOVERY BY STEAM INJECTION INTO TORPEDO CORES CONTAINING WATERFLOOD RESIDUAL OIL AND MOBILE WATER

Test No.	Core No.	Oil	Per Cent OOIP Recovered By: Cold WF	Hot WF (330°F)	Steam Injection	Cum. Oil Recovery Per Cent OOIP
13A	9	Nondistill.	49.5	—	8.4	57.9
14	9	Nondistill.	—	54.8	3.1	57.9
15A	9	25% Distill.	—	54.8	20.7	75.5
16A	9	50% Distill.	—	58.0	25.1	83.1
20A	9	Crude C	—	67.0	24.7	91.7
21	10	Crude B	—	59.8	11.2	71.0

TABLE 7—OIL RECOVERY BY 800- AND 84-PSIG STEAM INJECTION IN TORPEDO CORES CONTAINING CRUDE OIL AND CONNATE WATER

No. Test	Core No.	Oil	Per Cent OOIP Recovered By: 520°F Hot WF	520°F (800-psig) Steam Drive	330°F Hot WF	330°F (84-psig) Steam Drive
22	11	Crude D			68.7	91.9
23	11	" D	71.0	97.6		
24	12	" B			66.0	77.6
25	12	" B	68.7	84.0		

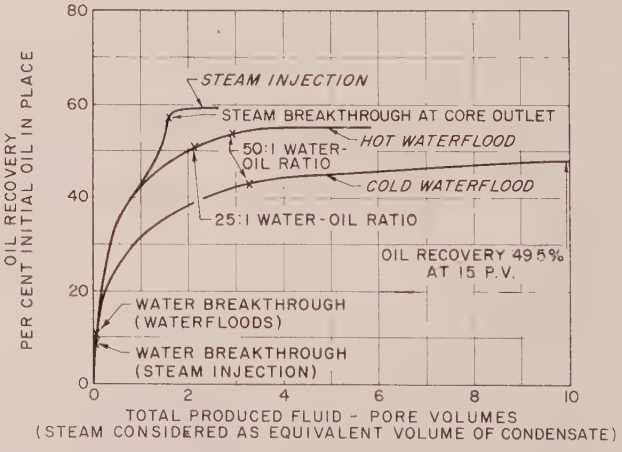

FIG. 2—OIL RECOVERIES BY STEAM INJECTION, HOT WATER FLOOD AND COLD WATER FLOOD, IN CORE 9 INITIALLY CONTAINING NONDISTILLABLE WHITE OIL AND CONNATE WATER.

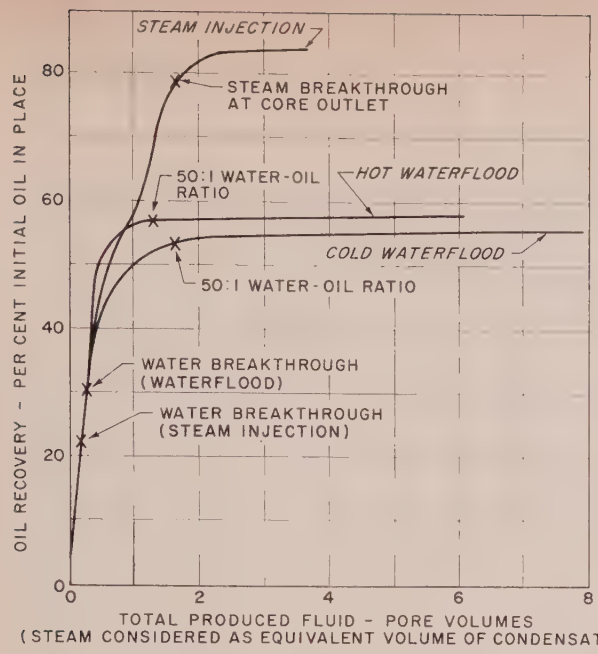

FIG. 3—OIL RECOVERIES BY STEAM INJECTION, HOT WATER FLOOD AND COLD WATER FLOOD IN CORE 9, INITIALLY CONTAINING 50 PER CENT DISTILLABLE WHITE OIL AND CONNATE WATER.

nized, though, that the highest economical field, water-oil producing ratio in the case of hot water will be less than for cold water flooding because the per-barrel costs of hot injection water will be greater. Thus, a 50:1 economical water-oil ratio cut-off on a cold water flood might, for example, correspond to an economical cut-off ratio on a hot water flood of 25:1. In the case of the nondistillable oil, the cold waterflood recovery at 50:1 was 43.0 per cent of the oil in place, while the hot waterflood recovery at 25:1 was 51.0 per cent of the oil in place. In the hot water flood, an extra 2.6 per cent of the initial oil in place was recovered during the time in which the producing water-oil ratio rose from 25:1 to 50:1. This extra oil could be nonrecoverable in the field since it might not be economical to continue the hot water flood beyond a 25:1 water-oil ratio.

The same general observations on cold and hot water injection drawn from the white-oil tests apply also to similar tests with Crudes B and C. The initial viscosities of the Crude C (8.2 cp) and the 50-50 white-oil blend (5.4 cp) are about the same; consequently, their floods are quite comparable. As would be expected, the very viscous Crude B (6,500 cp) is influenced relatively much more by the higher-temperature flood than the nondistillable white oil (138 cp).

To predict the ultimate recovery from a hot water-flooded core, we suggest this procedure: (1) in a regular laboratory cold water flood, determine the recovery for the viscosity ratio that would exist at hot-water injection temperature; and then (2) add to this value the additional recovery by thermal swelling of the waterflood residual oil.

STEAM-DRIVE RECOVERIES

A number of core-oil systems were considered in the investigation of oil recovery by steam injection. For the short core tests reported in Tables 3 and 4, eight separate cores were used with five different oils. Further data on steam recoveries were obtained on the large Torpedo cores employed in the mechanism tests. Without exception, the results demonstrate that oil recoveries by steam drive are greater than for cold or hot (same temperature as steam) water injection into the same system.

TABLE 8—OIL VISCOSITY-TO-WATER VISCOSITY RATIOS FOR NONDISTILLABLE AND 50 PER CENT DISTILLABLE OILS DURING COLD AND HOT WATER FLOODS

Water Flood	Oil	μ_w cp at 80°F	μ_w cp at 330°F	μ_o cp at 80°F	μ_o cp at 330°F	μ_o/μ_w at 80°F	μ_o/μ_w* at 330°F
Cold (80°F)	Nondist.	1.0	—	138	—	138	—
Hot (330°F)	Nondist.	—	0.15	—	2.4	—	16
Cold (80°F)	50% Dist.	1.0	—	5.4	—	5.4	—
Hot (330°F)	50% Dist.	—	0.15	—	0.62	—	4.1

*It should be recognized that the viscosity ratio at the beginning of a hot water flood is that of the cold water flood. The ratio decreases to that shown as the core is heated by the injected 330°F hot water.

Recoveries of 75 to 85 per cent of the initial oil in place are reported in Table 3 for steam floods of cores containing crude and connate water. A similar flood of Crude C (Table 5) gave approximately 92 per cent recovery. For systems where reference water floods (80°F) were performed, oil recoveries by steam were from 20 to more than 100 per cent greater than for the water floods. The results of the mechanism experiments display, in like fashion, the superiority of steam in achieving high ultimate recoveries from cores.

Following some of the cold and hot water floods, steam was injected into the watered-out cores containing waterflood residual oil and mobile water. In the case of the hot water floods, the core was cooled prior to steam injection. Results of these tests are presented in Tables 4 and 6. In all cases, extra oil was recovered by steam injection. Furthermore, the combined hot or cold waterflood recovery plus steam-injection recovery agreed, within experimental error, with the recoveries obtained by steam injection into the core initially saturated with oil and connate water. The analyses of the produced oil indicated that the composition was very similar to the case of the cores containing mobile and connate water. The combination of these observations indicates that the residual oil saturation following steam injection is independent of the initial state of the test core, i.e., whether the core contains a high oil saturation with connate water or a relatively low saturation from a preceding hot or cold water flood.

STEAM-DRIVE RECOVERY MECHANISMS

Since a hot water flood effectively is a part of a steam drive, the thermal phenomena connected with the former are, likewise, associated with the latter. The still better recoveries that result from steam injection are then the result of several other mechanisms, the principal one being steam distillation. Some small additional benefit also occurs, as will be shown, from solvent extraction and gas-drive effects.

VISCOSITY REDUCTION AND THERMAL SWELLING

The effect of these mechanisms is even more evident with steam than with hot water when the oil recoveries are plotted vs produced fluids, as in Figs. 2 through 5. Since steam was considered as the equivalent volume of condensate in making these drawings, the effect of lowered viscosity and swollen oil is observed much earlier in the produced fluid history because the heating value for a pore volume of steam (as condensate) is four to five times greater than that of the equivalent volume of hot water.

STEAM DISTILLATION

Steam distillation is defined as the vaporization of a portion of the residual oil left by the hot-condensate

water flood moving ahead of the steam zone. The distillable portions of the oil are the light components, which possess a high vapor pressure as compared with the heavy ends. The mixture of steam and oil vapor resulting from the distillation is pushed ahead until a cooler portion of the rock is encountered and both the oil and water vapor are condensed.

The effect of steam distillation can readily be seen by a comparison of the recoveries of the three white-oil blends shown in Table 5. It will be recalled that these test white oils were blends of nondistillable oil and an essentially completely steam-distillable oil, with 330°F saturated steam. The oil recovery by steam injection increased from 59.0 per cent of the initial oil in place in the case of the nondistillable oil to 76.0 per cent with the 25 per cent distillable oil, and to 83.9 per cent in the case of the 50 per cent distillable oil. Most, but not all, of this recovery was due to steam distillation because a change in the distillation property was the principal parameter varied among the three test oils.

GAS-DRIVE AND SOLVENT-EXTRACTION EFFECTS

In the steamed-out region of a core, the steam moves as a vapor, but with an increasing fraction condensing to supply the external heat losses. In effect, then, in the steam zone a simultaneous gas-water drive of a hot-watered-out core is taking place. The effect of this action was demonstrated after a 330°F hot water flood of the nondistillable oil. This flood recovered 54 per cent of the oil in place at a terminal water-oil ratio of 1000:1. With the core still hot, 330°F nitrogen was injected in alternate slugs with 330°F water. The purpose of the nitrogen was to simulate steam as a gas and produce a three-phase flow in the core. Recovery from the watered-out core by alternate hot water-nitrogen slugs was an additional 3.0 per cent of the initial oil in place.

The quantitative effects of the mechanisms discussed so far are not sufficient to account for all of the observed steam-recovery improvements. This is shown in Table 9 which tabulates the predicted and actual recoveries.

In the case of the nondistillable oil, the agreement between the observed and predicted values is considered to lie within the range of experimental accuracy and reproducibility. We feel, accordingly, that the gas-drive effects are entirely responsible for the improved recovery by steam injection over hot-water injection recovery with the nondistillable oil.

For the distillable oils, we believe that recovery is

TABLE 9—ACTUAL STEAM RECOVERIES COMPARED TO PREDICTED RECOVERIES WITHOUT SOLVENT EXTRACTION

	Recovery—Per Cent of Oil in Place		
	Non-distillable	25 Per Cent Distillable	50 Per Cent Distillable
1. Hot Waterflood Recovery (Table 5) (includes viscosity reduction and swelling)	54.8	54.8	58.0
2. Extra Recovery Due to Gas-Drive Effects	3.0	3.0	3.0
3. Extra Recovery Due to Distillation*	—	10.5	19.5
4. Predicted Recovery Based on Above Mechanisms	57.8	68.3	80.5
5. Actual Recovery by Steam (Table 5)	59.0	76.0	83.9
6. Unexplained Recovery (Line 5 minus Line 4)	1.2	7.7	3.4

*(Per cent of oil which is steam-distillable) × [100 − (Line 1 + Line 2)]

aided by solvent extraction of the original oil in the core just ahead of the steam zone where liquid water and oil are enriched in light components by the condensed products of the steam distillation. The lighter hydrocarbons will mix with the oil, reducing its viscosity and resulting in a lower hot waterflood residual than is represented by the original oil at steam temperature. As the steam zone advances, a greater and greater percentage of the oil saturation immediately ahead of the steam zone will be composed of light hydrocarbons. The lighter ends remaining in the hot waterflood residual oil will subsequently be moved ahead again by distillation as the steam zone advances.

The effect of the steam distillation and light oil-bank build-up on the produced oil analyses is apparent in Fig. 6. It can be seen that the light oil bank exists as a liquid in the core, since the produced fluids get richer in the light components before steam breakthrough at the producing end of the test core.

The quantitative effect of solvent extraction is not so easily demonstrated as the other mechanisms, but it almost surely aids recovery. Assuming that it does and if these light ends were withdrawn as vapors before condensation, no solvent extraction would result. Therefore, even with a distillable oil, observed recovery should

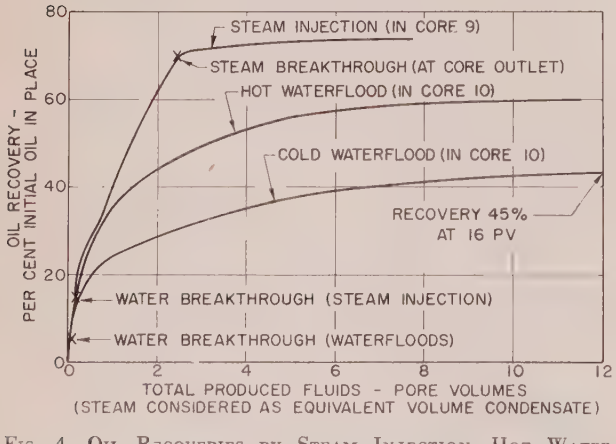

FIG. 4—OIL RECOVERIES BY STEAM INJECTION, HOT WATER FLOOD AND COLD WATER FLOOD, IN CORES INITIALLY CONTAINING CRUDE B AND CONNATE WATER.

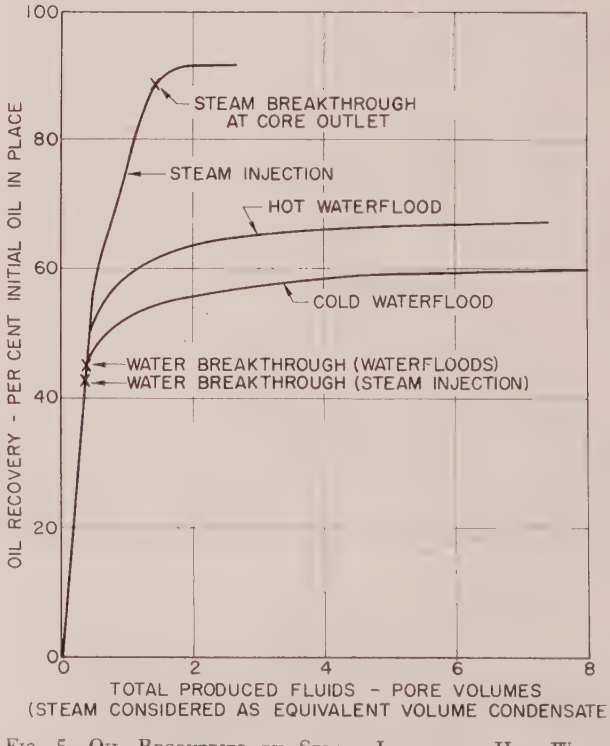

FIG. 5—OIL RECOVERIES BY STEAM INJECTION, HOT WATER FLOOD AND COLD WATER FLOOD IN CORE 9, INITIALLY CONTAINING CRUDE C AND CONNATE WATER.

check within experimental accuracy and reproducibility with predicted recovery based only on the other mechanisms.

Such an experiment was performed in Torpedo Core 10 with the 50 per cent distillable oil. This core, while similar to Core 9 in which most of the comparative tests were performed, had slightly better waterflood recovery characteristics; consequently, Core 10 data should not be compared with Core 9 data except with respect to mechanisms. In this test, the 330°F hot water flood was immediately followed by the injection of 330°F steam. Neither the steam nor the light hydrocarbon vapor resulting from steam distillation was condensed because the core was already at steam temperature. Although in principle some mass transfer of light ends from gas to liquid phases could have occurred, no liquid light-hydrocarbon bank was formed. Recovery of the hot water flood was 64 per cent, and subsequent steam injection into the hot core resulted in an added 19 per cent hydrocarbon volume recovery. Table 10 presents an analysis for this experiment similar to Table 9. The difference in predicted and observed recovery lies within the experimental accuracy.

This experiment confirms that the steam distillation and gas-drive effects are sufficient to explain the greater recovery of a distillable oil by steam injection than by hot water injection when the distillation products are not allowed to condense to form a light-hydrocarbon bank. We believe that the unexplained recoveries shown in Table 9 for the 25 and 50 per cent distillable oils are due to solvent extraction by light-hydrocarbon vapors as they condense ahead of the steam zone and dissolve in the residual oil. The apparent recovery by solvent extraction is larger for the 25 per cent distillable blend (7.7 per cent) than for the 50 per cent distillable blend (3.4 per cent). We have no clear explanation for this. Solvent extraction is also supported by a comparison of the analyses of the oil produced by steam injection into hot and cooled cores after hot water flooding. The oil produced during steam injection into the hot core following the hot water flood was almost entirely Napoleum (97 per cent). This was not the case in the experiment in which steam was injected in cool Torpedo Core 9 containing hot-waterflood residual (50 per cent distillable) oil. With the cool core, a liquid hydrocarbon bank forms (Fig. 6), which shows that the produced oil at various stages of the experiment contained from 50 to 97 per cent Napoleum.

HIGH-PRESSURE STEAM RECOVERY

Several further tests were performed to determine whether the same mechanisms responsible for high recovery by low-pressure steam would also apply to high-pressure steam. Four displacements were conducted to compare recoveries by 800-psig (520° F) with 84-psig (327°F) steam. A light (37° API) and a heavy (12.2° API) crude oil were used for these tests, and a resume of their viscosity and thermal-swelling characteristics is given in Table 11.

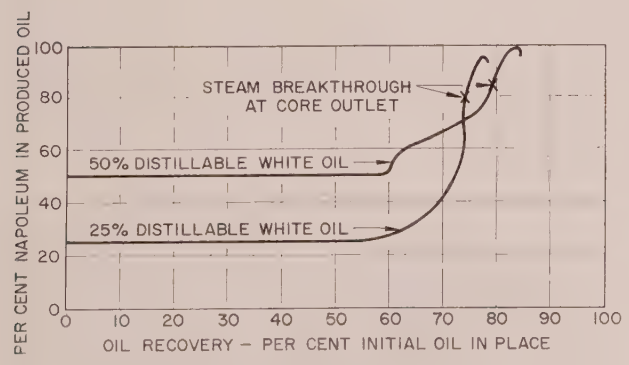

FIG. 6—COMPOSITION OF THE OIL PRODUCED DURING STEAM INJECTION INTO CORE 9, INITIALLY CONTAINING THE TWO STEAM-DISTILLABLE WHITE OILS AND CONNATE WATER.

Greater recoveries were obtained with high-pressure steam for both oils, and these values are given in Line 4 of Table 12 which is a tabular analysis of the recovery mechanisms. The improved recoveries for the light and heavy crudes appear to be the result primarily of the increased temperature associated with the high-pressure steam. The fraction of the crudes distillable at the elevated temperatures was 72.6 per cent for Crude D and 33 per cent for Crude B. This represents a substantial increase from the corresponding values of 55 and 16 per cent with 327°F steam.

Steam at both high and low pressures recovered more oil than accounted for after including the benefits of viscosity reduction, thermal swelling and steam distillation. The unaccounted-for recovery is from 5 to 6 per cent and is attributed to gas-drive and solvent-extraction effects. The differences are reasonably consistent for both steam pressures and are approximately equal to the values assigned to these same mechanisms in the white-oil mechanism studies.

CORE THERMAL BEHAVIOR

The rate of steam-front advance and the heat requirements depend upon heat losses and the heat storage capacity of the test core. Table 13 summarizes the weights, heat capacities and thermal conductivities of Cores 9 and 10.

During the experiments, temperatures were measured at various positions on the core axis and used to determine the thermal behavior of the core. Temperature profiles measured in Core 9 during a hot water flood and during steam injection are shown in Figs. 7 and 8. The heat capacity of the sandstone in Core 9 was 54

TABLE 10—PREDICTION FOR STEAM INJECTION IMMEDIATELY FOLLOWING A HOT WATER FLOOD

Torpedo Core 10 with 50 Per Cent Distillable White Oil	Per Cent Hydrocarbon Volume
1. Hot Waterflood Recovery	64.0
2. Extra Recovery Due to Gas-Drive Effects	3.0
3. Recovery Due to Distillation*	16.5
4. Predicted Recovery Based on 1, 2, and 3	83.5
5. Actual Observed Recovery	83.0

*0.50 × [100 − (64.0 + 3.0)] + 16.5.

TABLE 11—EFFECT OF TEMPERATURE ON OIL VISCOSITY, OIL-WATER VISCOSITY RATIO AND OIL SWELLING

Temp. °F	Oil Viscosity (cp)		Oil-Water Viscosity Ratio		Swelling Per Cent Increase
	Crude D	Crude B	Crude D	Crude B	
80	5.4	6500	6.0	7200	0
327	.35	7.0	2.0	40	10
520	.14	0.5	1.5	5	18

TABLE 12—EVALUATION OF MECHANISMS CONTRIBUTING TO STEAM RECOVERY

	Recovery Per Cent Initial Oil in Place			
	Core 11 Crude D		Core 12 Crude B	
Steam Injection Pressure (psig)	(520°F) 800	(327°F) 84	(520°F) 800	(327°F) 84
1. Hot Waterflood Recovery (includes viscosity reduction and swelling)	71.0	68.7	68.7	66.0
1a. Recovery Due to Gas Drive	3.0	3.0	3.0	3.0
2. Extra Recovery Due to Steam Distillation	18.9[a]	15.6[b]	9.3[c]	4.9[d]
3. Predicted Recovery Based on 1, 1a and 2	92.9	87.3	81.0	73.9
4. Actual Recovery by Steam	97.6	91.9	84.0	77.6
5. Recovery Improvements Due to Solvent-Extraction Effects	4.7	4.6	3.0	3.7

[a](0.26 × 0.726) [b](0.283 × 0.55) [c](0.283 × 0.33) [d](0.31 × 0.159)

per cent of the total heat capacity of the system including the lead, steel and fiber-glass insulation. Experiments were run with a 40-psi pressure drop across the core which initially contained connate water and 25 per cent distillable oil. The temperature profiles show the more rapid heating which occurred during steam injection and demonstrate that steeper temperature profiles are present in the case of steam injection because steam can lose heat at constant temperature as it condenses. The volumes of fluid produced during the tests as a function of time are shown in Fig. 9.

The rate of steam-front advance is different in the laboratory than it is in the field because of different confining materials, exploitation times and geometry. Equations are set forth in the remainder of the paper which may be used to predict the steam-zone growth and oil-production history for field conditions.

METHOD FOR ESTIMATING STEAM-DRIVE PERFORMANCE

The steam recovery process may be visualized as consisting of three distinct floods. A water flood at reservoir temperature is followed by a hot water flood at temperatures varying from reservoir to steam temperature. These are followed by the steam-drive proper, which recovers additional oil mainly by the mechanism of steam distillation and partially through solvent-extraction and gas-drive effects. The following procedure is suggested to estimate heat requirements and oil recovery for a steam drive.

STEAM FRONTAL ADVANCE

The position of the steam front during a steam flood in a radial homogeneous system (see Fig. 10) may be approximated from energy balance considerations. A solution to a basic energy balance has been published in a paper by Marx and Langenheim.[8] Another approximation to a radial field system for a constant injection rate is given by

$$R_{st}^2 = \frac{14.6\ i_{st} h_{fg}}{K\ (T_{st} - T_r)} \sqrt{\frac{\alpha}{\pi}} \left[\frac{\sqrt{t}}{2} - \frac{h}{8} \sqrt{\frac{\pi}{\alpha}} \frac{(\rho c_p)_r}{(\rho c_p)_{OB}} \ln \left(\frac{4}{h} \sqrt{\frac{\alpha}{\pi}} \frac{(\rho c_p)_{OB}}{(\rho c_p)_r} \sqrt{t} + 1 \right) \right] \quad . \quad . \quad (1)$$

Fig. 11, which is a graphical representation of Eq. 1, may be used to quickly determine R_{st}^2. Eq. 1 may be extended to include a variable rate by a superposition method as described by Ramey.[9]

Still another solution of interest is that in which the steam injection rate increases with time to satisfy heat losses, resulting in a constant volumetric rate of steaming out the reservoir; i.e., $\pi R_{st}^2 = Ct$. For this case, the steam injection rate required is given by

$$i_{st} = \frac{C(T_{st} - T_r)}{14.6\ h_{fg}} \left[h(\rho c_p)_r + 4K \sqrt{\frac{t}{\pi \alpha}} \right] . \quad . \quad (2)$$

Both Eqs. 1 and 2 describe minimum steam-zone radii because sensible heat is neglected. However, radial conduction (which is also neglected) would partly reduce the conservatism of the estimate of steam-zone size.

The major variables affecting the advance of the steam zone are formation thickness (h), steam injection rate (i_{st}) and steam injection pressure, which affects the ratio $h_{fg}/(T_{st} - T_r)$. Consideration of their relative effects suggests that thick, relatively shallow and highly permeable reservoirs would offer the most promise for the steam process.

TABLE 13—THERMAL CONDUCTIVITIES AND HEAT CAPACITIES OF CORES 9 AND 10

	Cores 9 and 10 Avg. Wt. (lb)	Conductivity, Btu/hr (ft²) (°F/ft)	Specific Heats (Btu/lb)
Fiber-Glass Insulation	3	.021	.31
Dry Sandstone	68	1.00	.225
Steel Mounting	93	26	.117
Lead Seal	48	19	.031

HOT WATERFLOOD TEMPERATURE DISTRIBUTION

An approximate expression for the temperature profile ahead of the steam zone may be obtained by writing

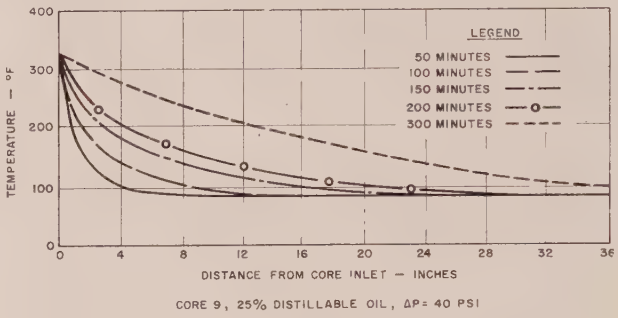

FIG. 7—TEMPERATURE PROFILES DURING HOT-WATER INJECTION.

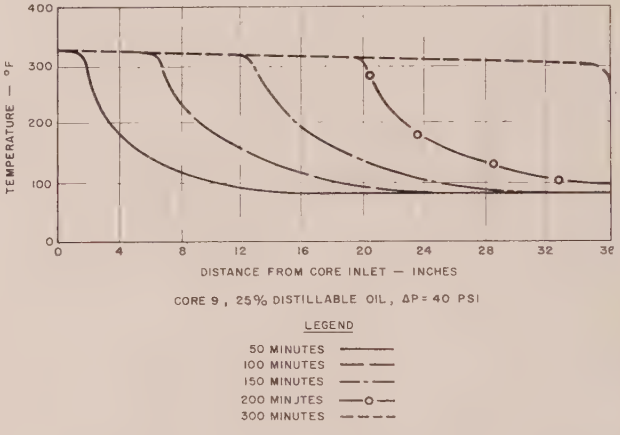

FIG. 8—TEMPERATURE PROFILES DURING STEAM INJECTION.

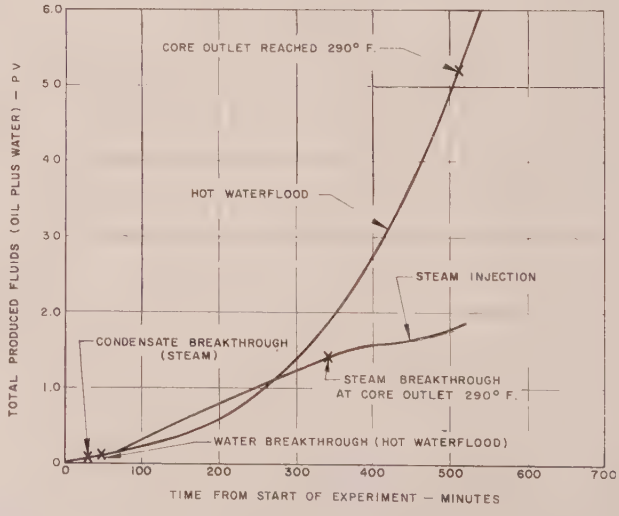
TOTAL PRODUCED FLUIDS (OIL PLUS WATER) — PV
CORE OUTLET REACHED 290° F.
HOT WATERFLOOD
STEAM INJECTION
CONDENSATE BREAKTHROUGH (STEAM)
STEAM BREAKTHROUGH AT CORE OUTLET 290° F.
WATER BREAKTHROUGH (HOT WATERFLOOD)
TIME FROM START OF EXPERIMENT — MINUTES
CORE 9, 25% DISTILLABLE OIL, ΔP = 40 PSI

FIG. 9—PRODUCED FLUID VS TIME.

an energy balance for an idealized system which assumes that the hot-water region is all at steam temperature (see Fig. 10). The radius of the hot-water zone R_{hw} may be calculated by using $[(h_g)_{T_{st}} - (h_f)_{T_r}]$ instead of h_{fg} in Eq. 1. An average (ρc_p) is assumed for the combined steam and hot-water zone.

It appears reasonable to further modify the idealized-step temperature profile by a straight line connecting T_{st} at R_{st}^2 with $\frac{(T_{st} + T_r)}{2}$ at R_{hw}^2, as shown in Fig. 12, because this results in the same energy stored in the hot-water zone as was the case when the hot-water region was considered to be all at steam temperature. Further, heat losses from the hot-water zone will be similar because the lower average temperature in the hot-water region offsets the larger surface area across which conductive losses occur.

RECOVERY PREDICTION METHOD

The saturation distribution in the waterflood region may be calculated by use of Eq. 3, which is the Buckley-Leverett[7,10] equation applied to a radial system.

$$\left[\frac{\partial(R^2)}{\partial t}\right]_{s=c} = \frac{Q}{13.43\,\phi h}\left(\frac{\partial f_w}{\partial S_w}\right)_{s=c} \quad . \quad . \quad . \quad . \quad (3)$$

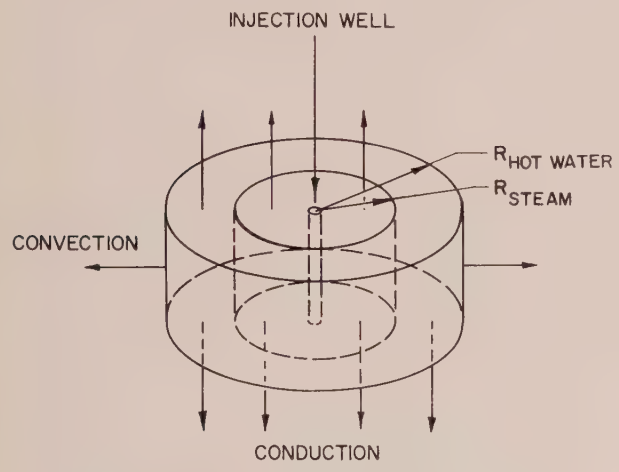

FIG. 10—STEAM INJECTION INTO A RADIAL SYSTEM.

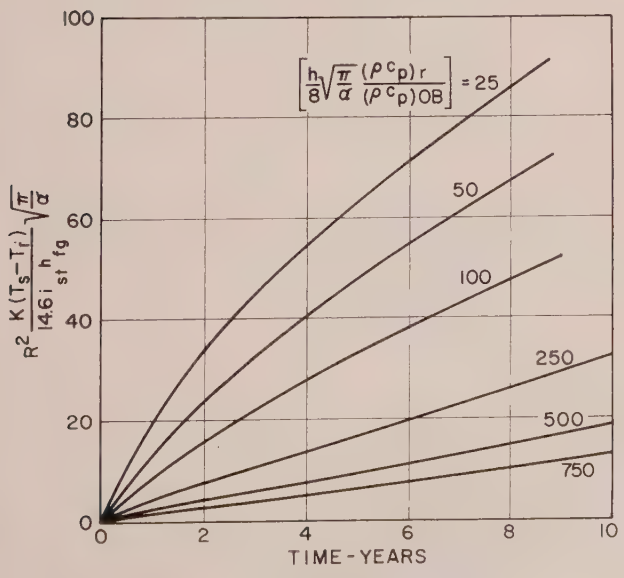

FIG. 11—VARIATION OF R^2 WITH TIME AND RESERVOIR PARAMETERS.

For the steam process, both Q and $\left(\frac{\partial f_w}{\partial S_w}\right)_{s=c}$ are functions of temperature which, in turn, is a function of time. Accordingly, the general solution to the equation is

$$\left(R^2\right)_{s=c} = \frac{1}{13.43\,\phi h}\int_0^t Q\left(\frac{\partial f_w}{\partial S_w}\right)_{s=c} dt \quad . \quad (4)$$

Eq. 4 can most conveniently be solved by a graphical integration technique. The straight-line temperature distribution (T vs R^2) in the hot waterflood region is approximated by small constant-temperature steps, shown in Fig. 12. The position of these steps with time is calculated as described earlier in conjunction with Eq. 1 and plotted as in Fig. 13. The values of Q and $\left(\frac{\partial f_w}{\partial S_w}\right)_{s=c}$ are next calculated for each isothermal step. The calculation of $\left(\frac{\partial f_w}{\partial S_w}\right)_{s=c}$ is straightforward because only the viscosity ratio changes as a function of temperature. To determine the effective volumetric flow rate (Q), it is necessary to consider both the variation of the water's density with temperature and the rate at which the steam zone is expanding and displacing water. The rate at which the steam volume is displacing water is determined by differentiating Eq. 1 with respect to time (analytically or by measuring the slope on Fig. 11) and multiplying by $\pi\phi h\,(S_{st} - \Delta S_o)$. This rate is added to the injection rate (i_{st}). This combined rate is then multiplied by the ratio of the density of water at reservoir temperature to the density of water at the temperature of the isothermal region. Mathematically,

$$Q_T = \frac{(\rho_w)_{T_r}}{(\rho_w)_T}\left[i_{st} + 13.43\,\phi h\,(S_{st} - \Delta S_o)\frac{\partial R^2_{st}}{\partial t}\right] \quad . \quad . \quad . \quad . \quad . \quad . \quad . \quad . \quad . \quad . \quad . \quad . \quad (5)$$

These values are substituted in Eq. 4, which then can be solved by a graphical technique illustrated in the Appendix.

This calculational method assumes that the fractional flow of water across the steam-zone boundary is equivalent to the fractional flow of water across an isothermal hot-water boundary at steam temperature, which is a good assumption for a viscous oil. The effects of viscosity reduction as a result of steam distillation, which are neglected in the development, would tend to increase the calculated recovery.

The oil recovery may be predicted by using the saturation distribution previously calculated for the

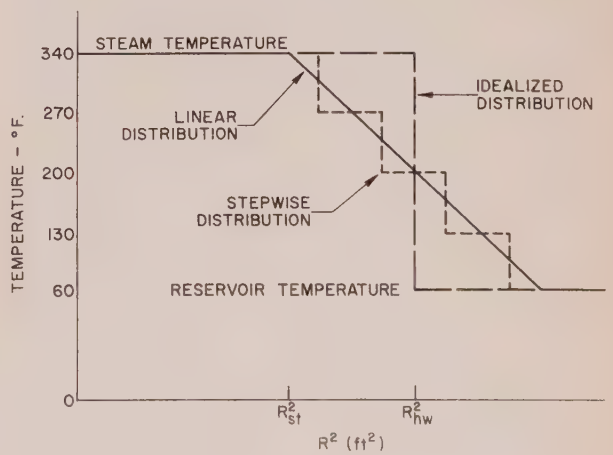

FIG. 12—TEMPERATURE DISTRIBUTION IN HOT-WATER ZONE.

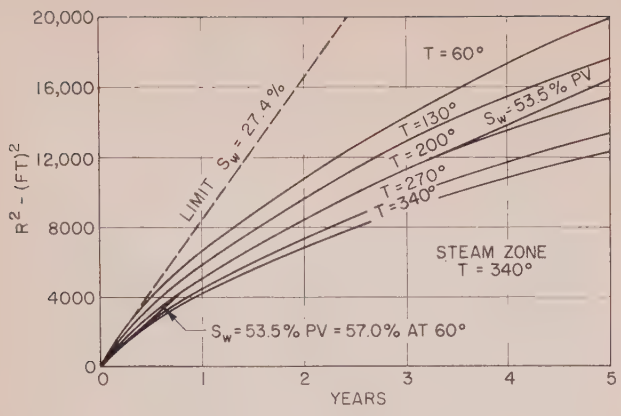

FIG. 13—RESERVOIR TEMPERATURE DISTRIBUTION VS TIME.

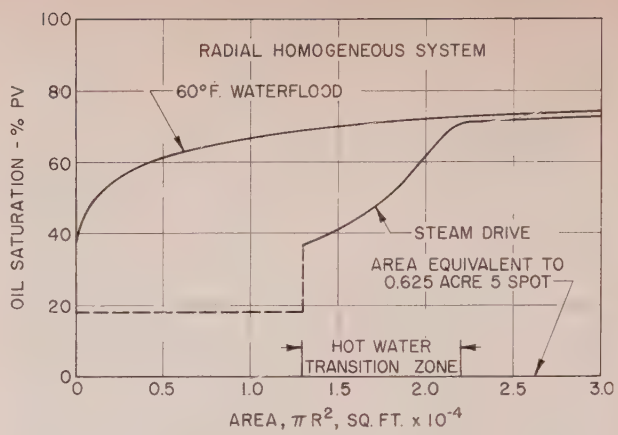

FIG. 14—SATURATION DISTRIBUTION AFTER ONE YEAR OF INJECTION.

waterflood region and assuming that the saturation in the steam-swept region is at a residual value determined by laboratory tests. Details are illustrated in the Appendix.

CONCLUSIONS

1. Laboratory tests show that both hot-water injection and steam injection recover more oil than an ordinary water flood.

2. The mechanisms for increased recovery by hot-water injection are viscosity reduction and thermal swelling of the oil.

3. Hot water flooding is most attractive with viscous oils because the water-oil viscosity ratio is significantly reduced at elevated temperature compared to ordinary water flood. With low-viscosity oils, the water-oil viscosity ratio is not greatly different at high temperatures compared to reservoir temperature, and recovery benefits accrue largely due to swelling of the residual oil.

4. Steam injection results in significantly greater recovery of crude oils than does a hot water flood because steam distillation and related gas-drive and solvent-extraction effects are added to viscosity reduction and swelling as recovery mechanisms. Appreciable amounts of even low-gravity crude oils are steam-distillable. With high-gravity crudes, steam distillation is particularly effective and results in high recovery, even though the viscosity-reduction mechanism does not contribute greatly to increased recovery.

5. As a result of steam distillation, the oil produced shortly ahead of steam breakthrough has a higher gravity than the initial oil in place; similarly, steam residual oil will be lower in gravity than the initial crude because it has been steam-stripped of light ends.

6. The residual oil left after steam injection is essentially independent of the starting oil saturation.

7. High-pressure (and temperature) saturated steam is more effective at recovering oil than is low-pressure steam because all the recovery mechanisms are enhanced at high temperature. However, the gain in recovery with high-pressure steam is not so great percentagewise as is the extra heat required to heat the reservoir to high temperature.

8. Because steam has a much higher heat content per unit mass than does hot water at the same temperature, the mass of water required as steam to accomplish a fixed amount of reservoir heating is much less than if the water were injected as liquid. Further, temperature profiles in the rock are sharper with steam than with hot water.

9. The heat requirements for exploiting a reservoir are virtually independent of the amount of oil in place. To minimize heat requirements, exploitation times should be short (high injection rates or small patterns) and formations should be thick. Good oil recovery per barrel of injected steam will depend upon a high initial oil saturation per unit of reservoir heated. Because interbedded shales will absorb heat but do not contain oil, a high percentage of net sand in the formation is desirable.

NOMENCLATURE

i_{st} = steam injection rate (B/D as condensate)
h_{fg} = latent heat of steam at injection pressure (Btu/lb)
h_f = enthalpy of saturated water (Btu/lb)
h_g = enthalpy of saturated steam (Btu/lb)
t = time (hr)
R = radius at time t (ft)
h = sand thickness (ft)
ρ = density (lb/cu ft)
c_p = specific heat (Btu/lb °F)
T = temperature (°F)
K = thermal conductivity (Btu/hr ft °F)
α = thermal diffusivity (sq ft/hr)
C = constant = $\pi R^2/t$
Q = effective water injection rate (B/D)
ϕ = porosity
f_w = fractional flow of water = $\dfrac{1}{1 + \dfrac{k_o}{k_w} \cdot \dfrac{\mu_w}{\mu_o}}$
S = saturation
S_{or} = residual oil saturation
ΔS_o = $(S_{or})_{HWF} - (S_{or})_{st}$
μ = viscosity (cp)
k = permeability (md)

SUBSCRIPTS

st = steam
r = reservoir
OB = overburden
w = water
HWF = hot water flood
i = initial
cw = connate water
sz = steam zone

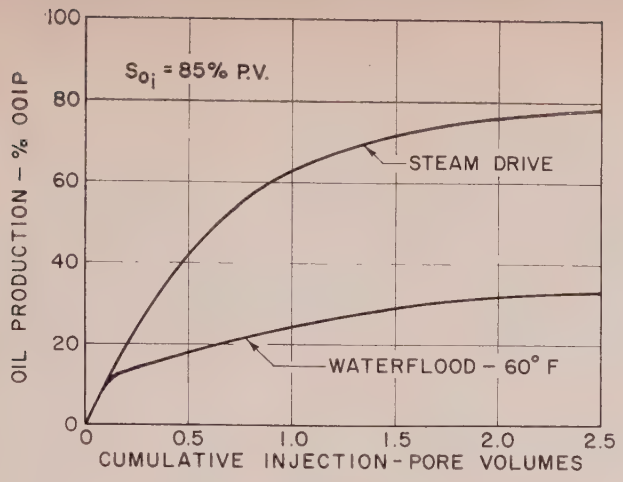

FIG. 15—OIL RECOVERY PREDICTION, RADIAL HOMOGENEOUS SYSTEM.

ACKNOWLEDGMENTS

The authors gratefully acknowledge the contributions of E. F. Johnson and L. K. Shallenberger to this study and express appreciation to the management of the Jersey Production Research Co. for permission to publish the results of this research.

REFERENCES

1. Stovall, S. L.: *Oil Weekly* (Aug. 13, 1934) **74,** No. 9, 17.
2. Tucker, M.: *Oil and Gas Jour.* (Jan. 28, 1937) **35,** 176.
3. "Warm Water Drive May Bring Big Pay-Off", *Oil and Gas Jour.* (June 11, 1956) **43,** No. 58, 80.
4. Breston, J. N. and Pearman, B. R.: *Prod. Monthly* (Nov., 1953) **18,** No. 1, 15.
5. Van Heiningen, J. and Schwarz, N.: *Proc.*, Fourth World Pet. Cong., Rome (June 6-15, 1955) **11,** 299.
6. Lauwerier, H. A.: *Appl. Scien. Res.* (1955) **A5,** 145.
7. Buckley, S. E. and Leverett, M. C.: *Trans.*, AIME (1941) **146,** 107.
8. Marx, J. W. and Langenheim, R. H.: *Trans.*, AIME (1959) **216,** 312.
9. Ramey, H. J., Jr.: *Trans.*, AIME (1959) **216,** 364.
10. Jordan, J. K., Rayne, J. R. and Marshall, S. W., III: "A Calculation Procedure for Estimating the Production History During Hot Water Injection in Linear Reservoirs", presented at the 20th Tech. Conf. on Pet. Prod., The Pennsylvania State U, University Park, Pa. (May 9-10, 1957).

APPENDIX

PREDICTED RECOVERY FOR STEAM PROCESS — EXAMPLE

To illustrate the method of prediction, the following example is given for a radial system having the same area as a 0.625-acre five-spot. Assumed reservoir and fluid parameters are presented as follows: $S_{oi} = 0.85$; $S_{cw} = 0.15$; $T_r = 60°F$; $i_{st} = 54$ B/D (as condensate); $T_{st} = 340°F$; μ_o at $60° = 900$ cp; μ_o/μ_w at $340° = 16.8$; μ_o/μ_w at $60° = 900$; $\phi = 0.23$; $(S_{st})_{sz} = 0.50V_p$ – linear core data; and $(S_{or})_{sz} = 0.18\ V_p$ – linear core data.

The temperature distribution was approximated by five isothermal planes between initial reservoir temperature at 60°F and steam temperature at 340°F (Fig. 12). The position of these planes as a function of time is shown in Fig. 13. The effect of the expanding steam zone on the average flow rate was determined using Eq. 5. This effect was found to be approximately constant after one year of steam injection and averaged 3.75 B/D. The effective injection rate uncorrected for density change in the hot-liquid region was assumed to be 57.75 B/D. $\frac{\partial f_w}{\partial S_w}$ as a function of saturation was then calculated for the five isothermal planes. These values then were used with Eq. 4 in a modified Buckley-Leverett type of calculation.

The velocity of the first temperature step at zero time defines the limiting condition between the cold and hot waterflood regions. All cylinders of constant saturation which initially flow faster than the leading edge of the hot-water transition zone are handled by conventional[7] waterflood treatment. Those saturations satisfying this condition will not be affected by the hot water-and-steam flood behind it, except for the small increase in flow rate as a result of steam-zone expansion.

It is necessary to graphically integrate Eq. 4 to determine the position of all oil saturations less than this limiting condition. An example for $S_w = 53.5$ per cent is shown in Fig. 13. In a given isothermal region, these cylinders of saturation will have a constant speed (since Q and $\frac{\partial f_w}{\partial S_w}$ are assumed constant). Since the temperature discontinuities are continually slowing down, they intersect these cylinders of constant saturation. At the intersection point with the discontinuity, the values of $\left(\frac{\partial f_w}{\partial S_w}\right)_{s=c}$ and Q used in the calculation are changed to correspond to the new temperature plane. This results in a smaller slope of the saturation curve as shown in Fig. 13. The saturation values obtained by this method are then corrected for thermal shrinkage back to initial reservoir temperature in each isothermal region.

The saturation distribution at the end of one year of steam injection calculated by this procedure is shown in Fig. 14. The dotted line indicates the average saturation in the steam zone based on linear core data. The saturation distribution resulting from a 60° water flood at the same input rate is also shown. Fig. 15 shows the calculated production histories for the steam flood and a 60°F water flood for the same homogeneous reservoir.

★★★

Determining Areal Permeability Distribution by Calculations

W. D. KRUGER
JUNIOR MEMBER AIME

HUMBLE OIL & REFINING CO.
HOUSTON, TEX.

ABSTRACT

Methods for analyzing flooding or cycling projects by means of two-dimensional flow calculations are presented in the literature. The use of these methods allows the determination of optimum operating conditions for such projects and provides information on pattern efficiencies, relative flow rates, pressure distributions and floodout histories. The accuracy of such analyses depends on the basic reservoir data employed, especially the absolute permeability distribution in the reservoir; however, absolute permeability data normally are determined from well flow tests and/or core measurements and are so limited in quantity and quality that they do not adequately describe the reservoir flow properties.

A calculation procedure is presented for determining the areal permeability distribution in the reservoir. Use of the procedure allows verification of the basic reservoir data through the matching of past reservoir conditions, thereby providing proper data for reliable predictions of future operations. The calculation procedure is a numerical technique based on a mathematical model of the reservoir and is designed for solution by means of an electronic digital computer.

Results from field application of this procedure are presented. Permeability distributions from measured data are compared to those calculated to indicate the need for the analysis. Comparisons of field-measured and calculated pressure distributions are given to establish the validity of the calculation procedure.

The conclusions of this paper are (1) use of the calculation provides data that allow a match of past reservoir conditions and thus reliable prediction of future operations; and (2) the procedure should, where applicable, be used to provide adequate reservoir data for use in two-dimensional flow calculations and related reservoir analyses.

INTRODUCTION

One means of providing more precise engineering control over reservoir operations during all stages of depletion is to develop some type of model to simulate the reservoir, using information developed from the behavior of the prototype to predict the performance of the actual reservoir. The use of mathematical rather than physical models for this purpose has been gaining in importance recently because of the application and availability of electronic computers. Mathematical models avoid instrumentation difficulties and allow easier handling of large-scale problems. At present, analyses employing two-dimensional models are common, and thought is being given to the use of models in three dimensions. The use of multi-dimensional models is necessary to show not only what is occurring in the reservoir, but also where in the reservoir the phenomena of interest are taking place.

Methods for analyzing flooding or cycling projects by means of two-dimensional numerical models are presented in the literature.[1-3] The use of these methods allows the determination of optimum operating conditions for such projects and provides information on pattern efficiencies, relative flow rates, pressure distributions and floodout histories. The applicability of numerical models and the results of using such analyses have been presented through field examples.[4,5] The references indicated here discuss fully the data necessary to build the mathematical reservoir model and the way the model is used to study or predict the future performance of the reservoir.

The accuracy of the analysis of such projects depends on the basic reservoir data employed in the construction of the model. In order to be sure the model represents the reservoir, it must be used to match some known set of reservoir conditions, i.e., to match past reservoir performance. The accuracy of the model is directly dependent upon the absolute permeability distribution in the reservoir; however, absolute permeability data are normally determined from well flow tests and/or core measurements, and are so limited in quantity and quality that they do not adequately describe the reservoir flow properties. There is always the need for better data and for verification of existing data.

The purpose of this paper is to show the use of the mathematical model to match past performance in flooding or cycling projects, the use of numerical techniques to adjust the basic absolute permeability data if necessary so that a match is obtained, and in this way to generate the effective areal permeability distribution of the reservoir. A review of the basic concepts of the numerical model will be given, followed by a discussion of the data-adjusting technique for matching past performance. Two field examples will be cited to show

Original manuscript received in Society of Petroleum Engineers office Aug. 23, 1960. Revised manuscript received May 22, 1961. Paper presented at 35th Annual Fall Meeting of SPE, Oct. 2-5, 1960, in Denver.

[1]References given at end of paper.

the application of these methods to actual reservoir problems.

THE MATHEMATICAL MODEL

The problem of representing the reservoir with an appropriate two-dimensional numerical model has been discussed fully in the literature;[2] however, a review of the mechanics of a model is in order here to provide the background necessary for complete understanding of the work presented in this paper.

One requirement of the model is that an adequate description of the reservoir mechanism be formulated into a basic differential equation describing the process. Normally, in flooding or cycling calculations, it is assumed that a distinct interface is formed at the flood front and a single fluid (either the displacing or native fluid, respectively) is flowing in the regions behind or ahead of the front. In addition, both the native and the displacing fluids are assumed to be incompressible, and the effects of gravity are neglected. These assumptions allow the use of Laplace's equation modified to handle variable coefficients as the basic equation, which is as follows.

$$\frac{\partial}{\partial x}\left(\frac{kh}{\mu}\frac{\partial p}{\partial x}\right)+\frac{\partial}{\partial y}\left(\frac{kh}{\mu}\frac{\partial p}{\partial y}\right)=0 \quad . \quad . \quad . \quad . \quad (1)$$

where x and y are the space co-ordinates of the model.

Solution of this two-dimensional equation for the reservoir pressure distribution can be achieved by various numerical means which employ finite-difference equations; the method used in connection with the work of this paper is the alternating-direction implicit procedure.[1] Such a solution requires an integration net which can be conveniently formed by superimposing a grid network over a scaled map of the reservoir, as illustrated in Fig. 1 taken from the literature.[2] Values for pressure at each point of the grid result from the solution of the equation for any particular set of conditions.

The grid or integration net is also used as the base for defining the physical characteristics of the reservoir. From the best data available, isopachous and isopermeability maps are drawn from which values of reservoir thickness and absolute permeability can be assigned to each grid point. In addition, values of viscosity of the reservoir fluid can be assigned to each grid point to reflect the distribution of this flow characteristic. Reservoir boundaries can be formed by assigning zero permeability to all grid points outside the region of flow. The effects of sinks or sources of flow in the model caused by wells, natural water influx, or other phenomena can be handled by assigning the proper flow rates to those grid points at the proper location. In solving Eq. 1, the permeability, thickness and viscosity data are used as kh/μ factors averaged in the direction of both space dimensions of the model so as to apply at the midpoints of the grid.

In analyzing a set of operating conditions, the data peculiar to those conditions are used to build the model, and Eq. 1 is solved for the resulting reservoir pressure distribution. With these values for pressure, the component velocities at any position in the model can be determined by interpolation of values calculated at the grid points by the following pair of equations.

$$v_x=\left[\frac{k}{\mu\phi}\frac{\Delta p}{\Delta x}\right]_x \; ; \; v_y=\left[\frac{k}{\mu\phi}\frac{\Delta p}{\Delta y}\right]_y \quad . \quad . \quad . \quad . \quad (2)$$

where the subscripts x and y denote directions along the axes of the grid system.

The position of any front can then be tracked for a series of time steps using the velocities and arbitrary time increments. The calculations for new pressures and corresponding velocities and front movements are repeated each time an operating situation warrants a change in the model (such as shutting-in wells) until the study of the set of conditions is complete. The large volume of calculations necessary for such an analysis demands the use of a large-scale electronic computer.

CALCULATION PROCEDURE

In all reservoir analyses, it is desirable to use the calculation procedure to be employed for predicting future performance to make a study of past history in order to be assured of the validity of the calculation procedure and of the reservoir data. This is also true of the mathematical model, discussed in the previous sections, which is to be used to study future operations of flooding and cycling projects. In this case, the match of past history is made to verify the use of proper data in the model, since Eq. 1 and its solution are known to be valid.

Since the solution of Eq. 1 for pressure values is the key to the entire analysis, a determination of the validity of the model can be made by comparing calculated to field-measured pressures at some time in the past. Indeed, if the model truly represents the reservoir, pressures calculated using conditions representative of *any* time in the past should equal field-measured pressures throughout the reservoir at that time. Such tests are made using the best-known values for the reservoir conditions, which include well flow rates and field-measured pressures for the time in question, along with permeability, thickness and viscosity data. In this case, field-measured pressure values are assigned to each point in the grid in the same fashion as the other data by reading from an isobaric map.

If the two sets of pressures — calculated and actual — do not agree, the question then arises as to which of the data in the numerical model are incorrect. Normally the field-measured pressures used for comparison should prove reliable, as should the values for flow rates. The least reliable data are usually thought to be those used in the kh/μ factors, primarily because of the uncertainty of the permeability values. Core analyses and/or well flow tests are generally used to determine permeability distributions, giving sparse, spotty and doubful information which is difficult to interpret and to apply to reservoir studies. It should normally be expected that adjustments to these data will be necessary to properly characterize the reservoir.

The model can be adjusted to provide a pressure match at the given time by changing the kh/μ factors to the proper values — namely, those which truly represent the reservoir. A relation for adjusting the kh/μ values is as follows.

$$\left[\frac{kh}{\mu}\right]_{i,j}^{n+1}=\left[\left(\frac{kh}{\mu}\right)\left(\frac{\alpha_c}{\alpha_a}\right)\right]_{i,j}^{n} \quad . \quad . \quad . \quad . \quad . \quad . \quad . \quad (3)$$

$$\alpha=|p_{i+1,j}-p_{i,j}|+|p_{i-1,j}-p_{i,j}|+|p_{i,j+1}-p_{i,j}|+|p_{i,j-1}-p_{i,j}| \; .$$

Here, (α_c/α_a) is the adjustment parameter at each grid point, i and j are location counters in the grid system, n is the iteration counter, and c and a denote calculated and actual values, respectively. This relation

is not rigorous; rather, it is an iterative numerical technique based on the simple premise that, if the calculated pressure gradient at a point is in some proportion to the actual gradient, the actual kh/μ value at the point is in the same proportion to the assumed kh/μ value, and corrections can be made accordingly. The proportions do not strictly hold since the flow is in two dimensions and all points of the grid are interrelated; however, the adjustments will yield the proper values by iteration.

The procedure consists of initially calculating pressures using original kh/μ data and adjusting these values by means of actual and calculated pressure differences. The corrected values are then used to recalculate pressures, and the actual and recalculated pressure differences are used to further refine the kh/μ values. The latter step is repeated until the desired pressure match is obtained. Normally, three or four adjustments are sufficient. It was noted previously that the kh/μ values are averaged to the midpoints of the grid for use in solving for pressures; the adjustments are made on data at the grid points, with each new set of corrected values averaged to the midpoints prior to the pressure solution.

Similar results can be achieved with other combinations of pressure differences in the parameter α; however, the relation for α given earlier is recommended since it provides for rapid and proper handling of the conditions at all points, including the sinks and sources. It is recommended that $\frac{\alpha_c}{\alpha_a}$ be limited in value to $0.2 \leqslant \frac{\alpha_c}{\alpha_a} \leqslant 5.0$ for any step to avoid the factor at any point tending to become unstable or oscillatory during the corrections. Notice that the relation for α is independent of the method used for solving for pressure; thus, this technique may be coupled with any means of solving Eq. 1.

The corrections made to the kh/μ factors may be thought of as affecting the permeability, thickness and/or viscosity data; but it is considered that thicknesses and viscosities can normally be defined reliably and that permeabilities are the least dependable and, thus, subject to the corrections. The final permeability distribution can be calculated from the final set of kh/μ factors since the values for thickness and viscosity are known. However, should there be reason to believe that either thickness or viscosity data are the least reliable, a similar procedure can be used to determine these values.

Although this discussion has been along the lines of adjustments, with an initial set of permeabilities representing the best-known data being required, it should be noted that the correction procedure holds for any reasonable initial assumption for permeabilities, even for a constant value over the reservoir. Thus, the requirement for good initial permeability data for flooding and cycling analyses can be greatly relaxed, and the need for core and well testing for permeability determination can be reduced or eliminated in these cases.

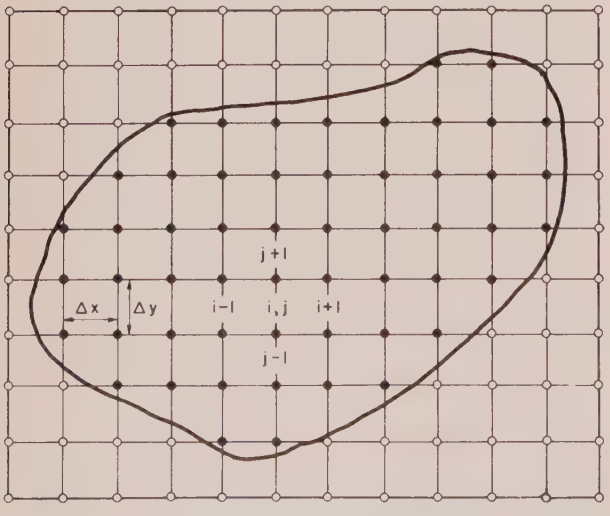

FIG. 1—TYPICAL NUMERICAL MODEL.

FIELD EXAMPLES

In the following discussion the results obtained from the use of the permeability calculation procedure for two reservoirs being analyzed for floods are given, along with illustrations comparing the initial permeability distributions derived from the best available test data to those distributions determined by calculations. The variation between the distributions for each case indicates the need for better permeability data and the need to verify the model to be used in a study. Also, illustrations of the pressure matches obtained through the use of the calculated permeabilities are presented to show the validity of the calculation procedure.

CASE I

Analysis in this case was for a limestone reservoir that had been producing about 10 years. Both water and gas-injection projects were being conducted to maintain pressure, but a study was undertaken to find the optimum injection program for full-scale flooding of the reservoir.

The field engineers associated with this project had made exhaustive studies of the operating mechanism of the reservoir under the existing gas and water injection. Production gas- and water-oil ratios had been resolved to reservoir gas and water saturations at various times and at the location of wells through relative permeability curves and the proper volume factors. Thus, "saturation contours" over the reservoir could be plotted for the various times. Fluid volumes determined by planimetering the saturation contours and isopachous maps were balanced against known injection volumes of gas and water as a check on the saturation plots. This also served as a check on the relative permeability curves used to derive the saturation data. From these plots,

FIG. 2—FIELD-MEASURED ISOPERMS, CASE I.

the positions of the gas and water banks with time were known; in addition, the saturation values at any point in the reservoir, not just at wells, could be determined.

Data on absolute permeability were available for 25 wells from core tests, and bottom-hole pressures were available at the desired time from pressure surveys on 66 standing or 48-hour shut-in wells. For both sets of data, the test wells were located in all parts of the field. Standard contouring methods were used to relate these data to all points in the field, giving the plots of field-measured isoperms and isobars shown in Figs. 2 and 4.

Because of this work, considerably more than normal information was available for this reservoir; consequently, more than the normal data was used in building and checking the model. At the time in the past chosen for the match, field-measured pressures, injection and production rates, and the saturations at all points were known, so that the effects of two-phase flow, varying fluid viscosities and gas compressibility could be accounted for at that particular time. Since the water and gas banks were in separate areas of the reservoir and the effects of capillary pressure and gravity were neglected, the kh/μ factor of Eq. 1 for this case could be replaced by the factor for two-phase flow,

$$kh\left(\frac{k_{ro}}{\mu_o}+\frac{k_{r2}}{\mu_2}\frac{B_{gstd}}{B_g}\right).$$

The subscript 2 refers to either water or gas, depending on which is flowing with the oil at any point. The value of B_{gstd} was determined at the volume-weighted field-measured reservoir pressure, and gas volumes at the various known pressures could be made relative to this standard pressure through the ratio of volume factors. Thus, if gas was flowing at a grid point, the proper value of B_g was used in the two-phase flow factor to correct the gas volume for the field-measured pressure at that point. If water was flowing at a point, B_g was set equal to B_{gstd}, since water and oil were assumed incompressible with no volume correction needed. In this manner, all known reservoir flow conditions would be properly accounted for when the calculated pressures equalled actual field pressures.

When the numerical model representing the chosen time of the past had been assembled, the pressure distribution of the reservoir was calculated. These pressures failed to match known pressures, so the permeability-adjustment technique described previously was employed. After two adjustments of the model, a pressure match considered to be satisfactory was obtained. The adjustments were applied to the entire flow factors given previously; however, the corrected absolute permeabilities for each grid point could be derived since all other parameters of the flow factors were known. Here, permeabilities were considered to be the data most poorly defined and most subject to change. Viscosities and volume factors were based on known pressures at each point; relative permeabilities and reservoir thicknesses were previously checked by the volumetric balances used to derive the saturation plots.

An illustration of the original permeability data assembled from core tests is given in Fig. 2. These data were adjusted to achieve the desired pressure match, resulting in the permeability distribution shown in Fig. 3. Close comparison of these two plots indicates the great difference in the two sets of data, not only in the shape and position of the isoperms, but also in the magnitude of the values. It is obvious that these two sets of permeabilities would not produce the same result if used for predicting future operations; the calculated values must be used based on the match of past performance. The large difference between the measured and calculated values clearly demonstrates the necessity of verifying the model to be used in a study. It is interesting to note that subsequent analysis of the original data in the light of calculated permeabilities by field personnel resulted in logical agreement with the calculated values in all areas.

The comparison of calculated to field-measured pressures from the final match is given in Fig. 4. It can be seen that good agreement was obtained in all areas, with the possible exception of that in the upper right of the plot where it is believed better results could have been obtained with subsequent permeability adjustments. It should be noted that calculated pressures are based on an undefined level, with both positive and negative values, as a result of the numerical procedure used for the solution of Eq. 1. However, all calculations made with these values use pressure gradients so that the level or sign of the pressures is not important. But in comparing the values for the match, these peculiarities should be kept in mind. No one isobar of the calculated pressures can be said to correspond to an isobar of known pressures, since the two sets are contoured on a different basis. Here again, pressure gradients are the important thing and must be used for comparison, although the over-all shape of the isobars from each set should be the same.

FIG. 3—CALCULATED ISOPERMS, CASE I.

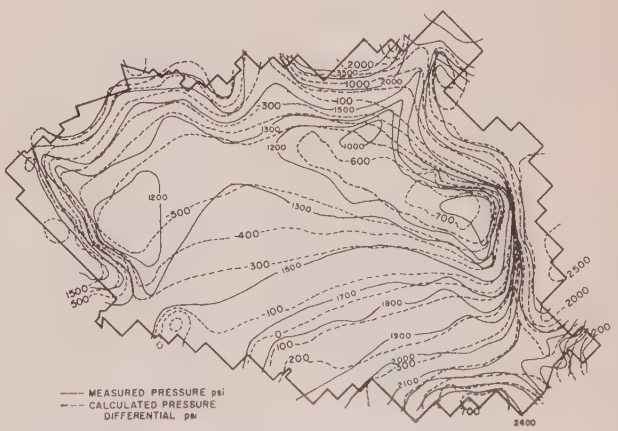

FIG. 4—FIELD-MEASURED AND CALCULATED ISOBARS, CASE I.

CASE II

The analysis in this case was for a sandstone reservoir operating under a strong natural water drive augmented by the re-injection of all produced water. A study was made to determine future production through various operating conditions with continuation of the present drive.

In this case also there were considerable data available. Field engineers associated with the project had made volumetric balances on separate portions of the reservoir to determine the source and strength of the natural water drive in each portion.

Values of absolute permeability were obtained for 29 cored wells, and some 400 well flow tests and bottomhole pressures were available from surveys in 100 key standing wells at various times in the past. Again in each case these control wells were located throughout the entire area of study, and the data were related to all points by standard contouring methods. In addition, good data were available for thickness, viscosity and porosity.

Also, the position of the edge of the water influx had been tracked throughout the reservoir history by the watering-out of various wells.

The mathematical model was assembled from the best-known field data with the flow factors of Eq. 1 represented by kh/μ. Since water and oil with almost equal mobilities were the only fluids flowing in this very efficient water drive, the situation met the necessary conditions of Eq. 1. Again, the effects of capillary pressure and gravity were considered negligible.

It was deemed necessary to test the model for its representation of the reservoir before using it for extensive study of future operations. Using the best known data, with flow conditions representing known producing, injecting and natural-water influx rates for a particular time of the past, pressures were calculated in an attempt to match known reservoir pressures. When the two sets of pressures failed to agree, the permeability calculation outlined previously was used until the desired match was achieved. All corrections to the kh/μ factors were assumed to apply to the permeability values.

An illustration of a part of the measured permeability distribution as known from core and field tests is presented in Fig. 5. It can be seen that these data were sparse, that wide areas of the reservoir had essentially no control and that values in these regions were derived solely by interpolation. From such a picture, which is by no means rare, the need for better data is apparent as is the necessity for determining the adequacy of the model.

A portion of the permeability distribution derived by calculations is shown in Fig. 6. Over-all, this plot presents a more comprehensive picture insofar as coverage of the reservoir permeabilities is concerned. Comparison of this drawing with Fig. 5 indicates the variations between the two, especially in the distributions, although the magnitudes of the permeabilities were in fair agreement.

A comparison of the final pressure match obtained by permeability calculations is shown in Fig. 7, where calculated and field-measured pressures are given. Examination of this comparison reveals that the shape of the isobars agree quite well in all areas, as do the magnitudes of the pressure gradients. It should be remembered that, as discussed for Case I, the calculated pressures are on an undefined level and that isobars from the two systems cannot be compared directly. The close

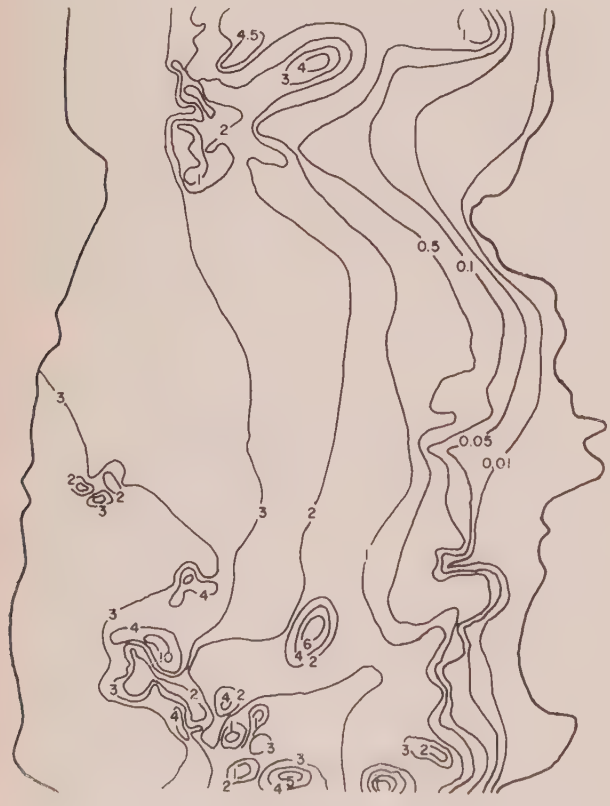

FIG. 5—FIELD-MEASURED ISOPERMS, CASE II.

FIG. 6—CALCULATED ISOPERMS, CASE II.

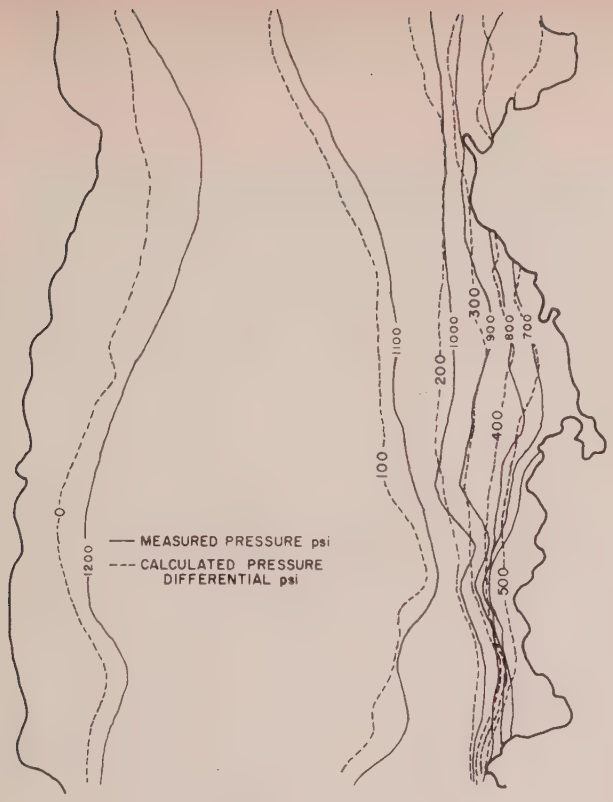

FIG. 7—FIELD-MEASURED AND CALCULATED ISOBARS, CASE II.

agreement of this match indicates that the permeability calculations were proper.

With the model thus apparently proven, additional checks were made to test its validity. Using the permeabilities calculated as shown in Fig. 6, with flow data representing reservoir conditions at a time eight years previous to that of the first match, a second pressure match was attempted. Pressures were calculated in the normal fashion and compared to known reservoir pressures for this second time. Agreement comparable to that of the first pressure match was obtained in this case also. Thus, the calculated permeabilities were found to be valid with changing time and reservoir conditions.

Movement of a front through the reservoir depends on $k/\mu\phi$ factors, not kh/μ, as shown by Eq. 2. A match of past history using frontal advance as the criterion thus proves the calculated permeabilities independently of thicknesses and also verifies any porosity data employed in the model. Consequently, calculations of the frontal advance over eight years of past reservoir history were performed by the analysis procedure outlined previously in the discussion of the model. Again, good agreement was achieved between calculated and field-measured results, indicating a third time the validity of the model and the calculated permeabilities.

CONCLUSIONS

From the results cited in this report, it is obvious that there is a definite need to prove the validity of any numerical model that is to be used for predicting reservoir operations. The use of the permeability calculation technique presented provides data that will allow a match of past reservoir conditions and, thus, reliable predictions of future performance. This procedure should be used where applicable to provide adequate reservoir data for use in two-dimensional flow calculations and related reservoir analyses.

ACKNOWLEDGMENTS

The author wishes to thank those engineers of the Humble Oil & Refining Co. whose work on various reservoir studies provided the background data necessary for the development of the results given in this paper. Special appreciation is due R. E. Lohec, J. R. Vague and G. C. Kunkel for the maps from which the field illustrations given here were taken.

REFERENCES

1. Peaceman, D. W. and Rachford, H. H., Jr.: "The Numerical Solution of Parabolic and Elliptic Differential Equations", *Jour. Soc. Ind. Appl. Math.* (1953) **3,** 28.
2. McCarty, D. G. and Barfield, E. C.: "The Use of High-Speed Computers for Predicting Floodout Patterns", *Trans.*, AIME (1958) **213,** 139.
3. Douglas, Jim, Jr., Peaceman, D. W. and Rachford, H. H., Jr.: "A Method for Calculating Multi-Dimensional Immiscible Displacement", *Trans.*, AIME (1959) **216,** 297.
4. Elkins, Lincoln F.: "Fosterton Field—An Unusual Problem of Bottom-Water Coning and Volumetric Water Invasion Efficiency", *Trans.*, AIME (1959) **216,** 130.
5. Barfield, E. C., Jordan, J. K. and Moore, W. D.: "An Analysis of Large-Scale Flooding in the Fractured Spraberry Trend Area Reservoir", *Jour. Pet. Tech.* (April, 1959) **XI,** No. 4, 15. ★★★

Equilibrium Ratios of Water in the Water-Triethylene Glycol-Natural Gas System

FRANK R. SCAUZILLO | SOCONY MOBIL OIL CO., INC. DALLAS, TEX.

ABSTRACT

Equilibrium data which should be useful in the design and/or evaluation of glycol dehydration units were prepared from an analysis of various published data and the correlation of these data by the use of the thermodynamic equilibrium ratio. The equilibrium ratios of water are used to solve the glycol absorber problem; such solutions are necessary to define the number of trays and the glycol circulation rate needed to meet drying requirements.

Activity coefficients were obtained which relate directly to the equilibrium ratios of water in the water-TEG-natural gas system. These activity coefficients have been used to calculate the equilibrium dew points for aqueous TEG concentrations of 60 to 99.9 weight per cent for the temperature range of 40° to 120°F. They also provide a means of calculating equilibrium ratios for water in the water-TEG-natural gas system; this applies to any desired TEG concentration and to the temperature range from 40° to 120°F.

INTRODUCTION

During the last several years, the drying of natural gas with aqueous triethylene-glycol (TEG) solutions has become very prominent. Most users of TEG as a drying agent have been satisfied with the performance of TEG solutions at the conditions used; however, there always has been some discussion of the drying ability of TEG solutions at conditions not commonly encountered such as temperatures below 50° or 60°F, but more particularly temperatures above 100°F, and pressures above 1,000 psia. Today, when higher wellhead temperatures such as 120°F are more commonly encountered many are skeptical of TEG's ability to dry sufficiently well to provide dew points around 32°F, which is generally the maximum tolerable when attempting to dry a gas to contract specifications of 7 lb/MMscf.

These views probably have evolved to some extent from the days when suppliers would not guarantee dew-point depressions in excess of 65° to 75°F. Also, the feelings about TEG drying may have arisen from the lack of information about the equilibrium relation of water in the drying operations.

Porter and Reid[1] have reported equilibrium data for a 95 per cent TEG solution, while Townsend[2] reported equilibrium data for 95, 98 and 100 per cent TEG solutions. Townsend also presented a calculational method which obtains activity coefficients in the liquid phase and, subsequently, the equilibrium water content of a saturated gas over glycol from published[3] atmospheric dew points. Wise, Puck and Failey[4] presented activity data for the water-TEG system at atmospheric pressure.

In the past, the equilibrium ratios published for water in a 95 per cent by weight aqueous TEG solution have been used indiscriminately by many for all concentrations of TEG encountered in gas drying operations. Since essentially all such gas operations require the use of more concentrated TEG solutions, a study was undertaken to correlate the existing equilibrium data for aqueous TEG and gas systems and to provide some means of calculating the equilibrium ratio of water in the natural gas-water-TEG system where TEG concentrations were other than 95 per cent. The data presented herein consider only the equilibrium drying ability of the TEG solutions and do not consider the effect of temperature and pressure on the tray efficiency of contactors. In other words, this paper is concerned primarily with the development of the equilibrium relationship between water in the dried natural gas and the water in the lean TEG entering the top tray of the absorber.

BASIC EQUILIBRIUM RELATIONS

A relationship which relates the K value of water in the natural gas-water-TEG system to the vapor pressure of water at the system temperature, the total pressure of the system and the activities of the liquid and gas phases has been evaluated.

It is well known that, for any component of a mixture at equilibrium between a gas phase and a liquid phase,

$$f_v = f_L \text{ and } \gamma_v\, y\, f_v^\circ = \gamma_L\, x\, f_L^\circ \quad , \quad . \quad . \quad (1)$$

$$\frac{y}{x} = \frac{\gamma_L\, f_L^\circ}{\gamma_v\, f_v^\circ}, \quad . \quad . \quad . \quad . \quad . \quad . \quad . \quad . \quad . \quad . \quad (2)$$

and

$$\frac{y}{x} = \frac{\gamma_L\, f'\, e^{\frac{V(p-p')}{RT}}}{\gamma_v v p} \quad . \quad . \quad . \quad . \quad . \quad . \quad . \quad . \quad . \quad (3)$$

At the vapor pressure of water p', f' is essentially equal to the vapor pressure, and

$$\frac{yp}{xp'} = \frac{\gamma_L\, e^{\frac{V(p-p')}{RT}}}{\gamma_v v} \quad . \quad . \quad . \quad . \quad . \quad . \quad . \quad . \quad . \quad (4)$$

Original manuscript received in Society of Petroleum Engineers office July 13, 1960. Revised manuscript received March 10, 1961. Paper presented at 35th Annual Fall Meeting of SPE, Oct. 2-5, 1960, in Denver

[1]References given at end of paper.

To solve Eq. 4, as it applies to the water-TEG system, a knowledge of the activity coefficients of water in both phases is required. This type of information for the natural gas-water-TEG system is not easy to come by experimentally. The problem deals with the determination of small amounts of water in the vapor phase, and any absolute error in the water determination can conceivably result in a large error on a percentage basis. It seems practical, then, to devise some manner of calculating the equilibrium for water in the subject system. The vapor phase in equilibrium with a glycol solution contains essentially no TEG, and the liquid phase contains very little methane or natural gas. Therefore, it appears that the activity of water in either phase can be obtained independently of the other phase.

NON-IDEALITY OF WATER IN THE VAPOR PHASE

In the vapor phase, TEG is normally present in amounts up to 1 lb/MMscf. This is a pretty well-accepted maximum for glycol units operating with a good mist eliminator. Assuming all of the glycol lost overhead is in a true solution in the gas phase, this amounts to a concentration of approximately 2.5×10^{-6} mol fraction TEG; for all practical considerations, the TEG can be thought of as nonexistent in this phase. This then leads to the natural gas-water system for which there is sufficient information to define the behavior of water in the vapor phase.

Considering the right side of Eq. 4 as it applies to the natural gas-water system, all of the terms except the activity coefficients γ_L and γ_v are explicit functions of the contact temperature and pressure, while the activity coefficients are primarily functions of concentration. Since the water concentrations usually dealt with fall in the range of approximately 7 to 120 lb/MMscf (the mol fractions being approximately 0.000147 to 0.00252), the systems are essentially at infinite dilution and the activity coefficient of water in the vapor phase can be taken as a constant value at any given temperature and pressure normally encountered. Therefore, Eq. 4 can be rewritten as

$$\frac{yp}{xp'} = \frac{\gamma_L}{C} \quad . \quad . \quad . \quad . \quad . \quad . \quad . \quad . \quad . \quad . \quad . \quad . \quad (5)$$

where C is an empirical constant and equal to $\dfrac{\gamma_v v}{e^{\frac{V(p-p')}{RT}}}$.

This eliminates evaluating the fugacity coefficient as a separate variable. The value of C then can be evaluated from existing data on the natural gas-water system, such as the data of McCarthy, Boyd and Reid.[5]

In the natural gas-water system, the liquid phase will follow ideal behavior because the mol fraction of methane in the liquid is very small even at high pressures and $\gamma_L \approx 1.0$. The value of x (mol fraction of water) can be assigned a value of 1.0 for all practical considerations. The only information then needed to evaluate C is the water content of the water-saturated gas, the total pressure and the vapor pressure of water at the temperature of interest.

$$C = \frac{p'}{yp}, \quad . \quad . \quad . \quad . \quad . \quad . \quad . \quad . \quad . \quad . \quad . \quad . \quad (6)$$

and

$$C = \frac{47500\ p'}{Wp} \quad . \quad . \quad . \quad . \quad . \quad . \quad . \quad . \quad . \quad . \quad (7)$$

where W is the water content of the gas in lb/MMscf.

If Eq. 6 is substituted into Eq. 5, the resulting equation can be used to determine the activity of the water in the aqueous phase from experimental data.

$$a_L = \gamma_L x = \frac{y_e}{y} \quad . \quad . \quad . \quad . \quad . \quad . \quad . \quad . \quad . \quad . \quad . \quad (8)$$

where a_L is then the ratio of the concentration of water in the dry gas to the concentration of water when gas is saturated at the same pressure and temperature.

ACTIVITY OF WATER IN THE LIQUID PHASE

The data used to evaluate the activity of water in aqueous TEG solutions were taken from the experiments of Townsend[2] and of Wise, Puck and Failey.[4]

Townsend experimentally obtained the concentration of water in the vapor phase of a natural gas in equilibrium with 95 and 98 weight per cent TEG glycol solutions and approximately 100 per cent TEG. The glycol concentrations were reported accurate to 0.5 weight per cent. Since 100 per cent TEG normally contains about 0.3 weight per cent water, it was decided to treat the 100 per cent glycol as a 99.5 per cent solution in this evaluation.

Table 1 presents the experimental data of Townsend and the equilibrium data calculated therefrom with Eqs. 7 and 8. The temperatures investigated were 70°, 80° and 90°F over the pressure range of approximately 500 to 2,500 psia. The data for all three temperatures were averaged for each pressure level used in the experiments, and the results are tabulated in Table 2. These data reveal that the activity of water in glycol solutions is essentially independent of the system pressure. There were insufficient data to evaluate any temperature effect on activity.

Wise, *et al*, investigated the activities of aqueous TEG solutions at atmospheric pressure and 70°, 80° and 90°F. The highest TEG concentration reported was 96.8 per cent. The activities reported then were used to determine the more useful variable, the activity coefficient. The activity coefficients for water in TEG concentrations greater than 96.8 per cent were evaluated with the aid of the binary Van Laar equations; namely,

$$\log \gamma_1 = \frac{A}{\left(1 + \frac{Ax_1}{Bx_2}\right)^2}, \quad . \quad . \quad . \quad . \quad . \quad . \quad . \quad (9)$$

and

$$\log \gamma_2 = \frac{B}{\left(1 + \frac{Bx_2}{Ax_1}\right)^2} \quad . \quad . \quad . \quad . \quad . \quad . \quad . \quad (10)$$

where $A = \log \gamma_1$ at $x_1 = 0$ and $B = \log \gamma_2$ at $x_1 = 1.0$. Values of A and B were estimated from the activity coefficients of water and TEG calculated from the experimental data of Wise, *et al*. The best agreement with the experimental data was obtained for $A = -0.405$ and $B = -0.356$. The average deviation of the experimental data from the calculated data thus obtained was about 0.3 per cent for water and 4 per cent for TEG. Fig. 1 presents the calculated curve for water. The plotted points are the activity coefficients calculated from the experimental data of Wise, *et al*, and Townsend. Table 3 summarizes the activity coefficients and activities of water at 80°F. These data are considered as representative of the temperature range from 40° to 120°F since the effect of temperature in this range is negligible.

The effect of temperature on the activity coefficient of

TABLE 1—VAPOR-LIQUID EQUILIBRIA DATA FOR NATURAL GAS-AQUEOUS TRIETHYLENE GLYCOL SYSTEMS

Glycol Concentration (Wt. %)	Temp. (°F)	Pressure (psia)	p' (psia)	W (lb/MMscf)	W_g* (lb/MMscf)	Mol Fraction Water	C	γ_L/C	γ_L	a_L
99.5	70	2545	0.3631	14.0	1.32	0.0391	0.484	4.98	2.41	0.0943
		2035		15.5	0.32	0.0392	0.547	0.964	0.528	0.0207
		1555		18.5	0	0.0393	0.599	0	0	0
		1090		23.5	0.87	0.0396	0.673	1.39	0.935	0.0370
		515		42.0	0.73	0.0399	0.798	0.546	0.436	0.0174
	80	2515	0.5069	19.2	1.22	0.0391	0.499	3.25	1.62	0.0635
		1540		25.0	0.93	0.0393	0.626	1.515	0.949	0.0373
		540		54.0	2.10	0.0399	0.828	1.18	0.977	0.0390
	90	2565	0.6982	24.7	0.60	0.0391	0.522	1.19	0.621	0.0243
		1540		34.0	1.25	0.0393	0.633	1.48	0.936	0.0368
		565		73.0	1.05	0.0399	0.803	0.448	0.359	0.0143
98	70	2545	0.3631	14.0	1.05	0.1405	0.484	1.10	0.538	0.0750
		2085		15.1	1.00	0.1410	0.548	0.857	0.469	0.0662
		1555		18.5	2.75	0.1412	0.599	1.76	1.055	0.149
		1015		24.7	2.50	0.1420	0.688	1.04	0.716	0.102
		505		42.0	2.70	0.1434	0.813	0.551	0.448	0.0643
	80	2515	0.5069	19.2	0.87	0.1405	0.499	0.646	0.322	0.0452
		2015		21.5	1.20	0.1410	0.557	0.711	0.396	0.0558
		1535		25.0	0.90	0.1412	0.628	0.407	0.256	0.0361
		990		34.0	1.73	0.1420	0.715	0.502	0.359	0.0510
		455		62.0	4.35	0.1434	0.855	0.572	0.489	0.0701
	90	2536	0.6982	24.9	2.27	0.1405	0.524	1.24	0.650	0.0913
		2055		28.0	3.33	0.1410	0.576	1.47	0.847	0.119
		1565		34.0	2.00	0.1412	0.622	0.669	0.416	0.0587
		1005		47.0	2.05	0.1420	0.701	0.438	0.307	0.0436
		575		72.0	4.17	0.1434	0.800	0.504	0.403	0.0578
95	70	2535	0.3631	13.9	2.35	0.294	0.490	1.18	0.578	0.169
		2040		15.2	3.10	0.295	0.557	1.24	0.691	0.204
		1600		18.5	2.17	0.296	0.582	0.68	0.396	0.117
		1015		24.7	3.60	0.298	0.688	0.712	0.490	0.146
		435		48.0	6.45	0.300	0.825	0.544	0.449	0.135
	80	2525	0.5069	19.3	1.85	0.294	0.494	0.66	0.326	0.096
		2095		21.0	2.80	0.295	0.548	0.825	0.452	0.133
		1515		26.0	3.50	0.296	0.612	0.744	0.455	0.134
		1015		34.0	4.12	0.298	0.699	0.582	0.407	0.121
		485		59.0	7.85	0.300	0.842	0.532	0.448	0.134

*Data of Townsend (Ref. 2). Above data for 99.5 per cent TEG was reported by Townsend as approximately 100 per cent.

a component in a solution of two completely miscible liquids is approximated by the following equation.

$$\Delta \ln \gamma = \frac{\overline{H} - H}{R}\left(\frac{1}{T_2} \quad \frac{1}{T_1}\right) \ldots \quad (11)$$

where $\overline{H} - H$ is the average differential heat of solution for the component in question for the temperatures considered. Table 4 is a tabulation of enthalpy data for the water-TEG binary system compiled from the Union Carbide Co.[3] heat-capacity data on TEG solutions. The partial enthalpy of water was obtained by applying the method of intercepts to the solution heats calculated from the heat-capacity data.

The differential heat of solution was found to be positive in the temperature range from 40° to 120°F; as such, the activity coefficient of water will decrease as the temperature increases. The change in activity coefficient is about 3 per cent/40°F. Since drying at the higher temperatures is of primary concern, the data of Fig. 3 and Table 3 can be applied conservatively at temperatures around 120°F without fear of any detrimental temperature effects.

APPLICATIONS

EQUILIBRIUM RATIOS FOR WATER IN THE WATER-TEG-NATURAL GAS SYSTEM

The vapor-liquid equilibrium ratios for water in this basic system have been calculated and are suggested as the values to be used in all dehydration calculations involving TEG. The K values for the system, 98 weight per cent TEG-natural gas, are plotted in Fig. 2. These values have been calculated from the water-content data of natural gases after McCarthy, Boyd and Reid,[5] and the activity coefficient at 80°F for water in a 98 weight per cent aqueous solution of TEG by solving Eq. 5 for y/x or K.

TABLE 2—ACTIVITY AND ACTIVITY COEFFICIENTS FOR WATER IN THE NATURAL GAS-AQUEOUS TRIETHYLENE GLYCOL SOLUTIONS IN TEMPERATURE RANGE FROM 70° TO 90°F*

Pressure (psia)	95 Wt % TEG		98 Wt % TEG		99.5 Wt % TEG	
	γ_L	a_L	γ_L	a_L	γ_L	a_L
500	0.448	0.134	0.447	0.0641	0.591	0.0236
1000	0.448	0.134	0.461	0.0655	0.935	0.0370
1500	0.426	0.126	0.576	0.0813	0.628	0.0247
2000	0.572	0.169	0.571	0.0805	0.528	0.0207
2500	0.452	0.136	0.502	0.0705	1.550	0.0606
Average	0.469	0.140	0.511	0.0724	0.846	0.0333

*From data of Townsend (Ref. 2).

The data of Fig. 2 present the K values of water in the 98 per cent solution over the temperature range from 40° to 120°F and over the pressure range from 14.7 to 2,500 psia. These data are considered accurate through this temperature range because the effect of temperature on the activity of the water phase in the range is small. A relationship which relates K for any concentration to the K for 98 per cent TEG is given and allows the user to correct the plotted values to any desired concentration with the use of the activity coefficients of water found in Fig. 1 and Table 3.

The values of K were found to decrease linearly as the pressure increased to about 200 psia. Thereafter, the incremental changes in the K value became smaller

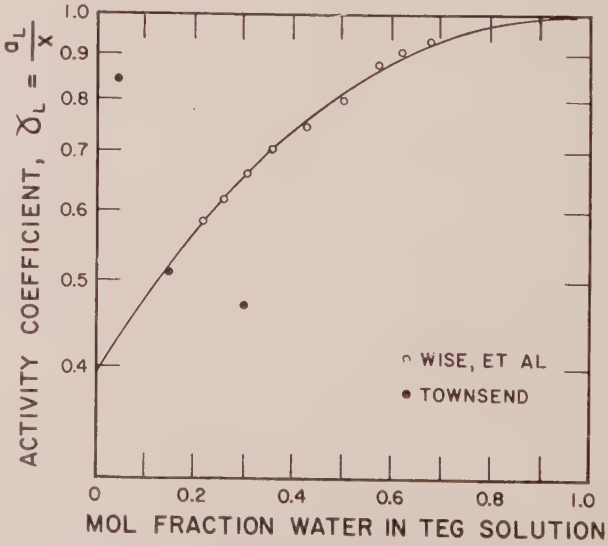

FIG. 1—ACTIVITY COEFFICIENTS OF WATER IN TRIETHYLENE-GLYCOL SOLUTIONS AT 80°F.

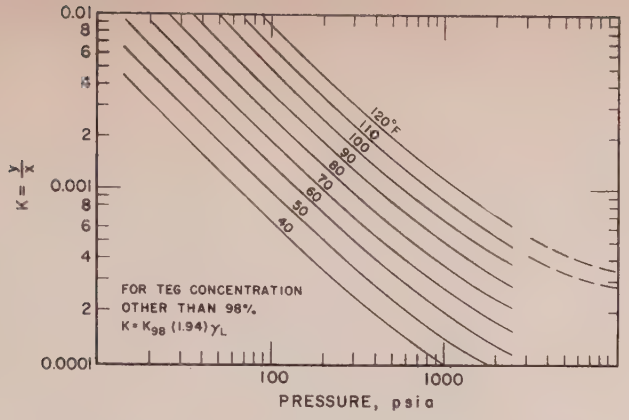

FIG. 2—VAPOR-LIQUID EQUILIBRIUM RATIO FOR WATER IN 98 WEIGHT PER CENT TRIETHYLENE-GLYCOL SOLUTIONS.

as the pressure increased, and K neared a limiting value as the pressure approached 10,000 psia. The latter is inherent in the way the K values were calculated because equilibrium water contents over glycol solutions were related directly to the water content of a gas over pure water, and the water content of a gas over water tends to approach a limiting value as pressures around 10,000 psia are reached.

The equilibrium ratios for water in the water-TEG-natural gas system also can be evaluated directly from the water content of the saturated gas at the temperature and pressure of interest and the activity coefficient of the water in the glycol solution. The data of Townsend reveal that the ratio of the water content of the gas over a glycol solution to the water content of the saturated gas is essentially constant for any given glycol concentration and is equal to the activity of the water in the glycol solution, or $W_g = Wa_L$. Then,

$$K = \frac{y}{x} = (2.105)\ (10^{-5})\ (W)\ (\gamma_L) \quad . \quad (12)$$

The equilibrium ratios presented herein have been based on the water content of natural gases as presented by McCarthy, *et al.*[5] Eq. 12 enables one to evaluate K from any source of water-content data he might choose. If the water-content data of McCarthy, *et al,* is used, the K's obtained from Eq. 12 will be consistent with K's evaluated from Fig. 1.

A sample dehydration calculation which explains the use of the water equilibrium ratio is presented in the Appendix. This problem solves for the circulation rate of lean glycol when given the inlet temperature and pressure, the lean glycol concentration, tray efficiency and the number of trays in the contactor. The problem can be amended to solve for any one of these variables as the unknown.

TABLE 3—ACTIVITY OF WATER IN AQUEOUS TRIETHYLENE GLYCOL SOLUTIONS AT 80°F

Mol Fraction Water	TEG (Wt %)	γ_L	a_L
0.02	99.76	0.410	0.0082
0.05	99.37	0.434	0.0217
0.10	98.68	0.475	0.0475
0.15	97.93	0.520	0.0780
0.20	97.08	0.565	0.113
0.30	95.1	0.654	0.196
0.40	92.6	0.738	0.295
0.50	89.3	0.815	0.408
0.60	84.7	0.880	0.528
0.70	78.1	0.935	0.656
0.80	67.5	0.970	0.776
0.90	48.0	0.990	0.891
1.00	0	1.000	1.000

TABLE 4—ENTHALPY DATA FOR AQUEOUS TRIETHYLENE GLYCOL SOLUTIONS

Mol Fraction Water	40°F		86°F		122°F	
	H_s	$\overline{H_1}$	H_s	$\overline{H_1}$	H_s	$\overline{H_1}$
0	577.2	254	4018	1550	6858	2840
0.01	573.8	253	3995	1514	6820	2841
0.02	570.5	241	3968	1462	6772	2720
0.05	560.2	221	3888	1368	6652	2505
0.10	541.2	204	3754	1282	6430	2320
0.20	502.3	187	3473	1192	5952	2120
0.30	461	177	3183	1147	5445	2000
0.40	418	169	2887	1098	4929	1910
0.50	374	163	2590	1067	4400	1840
0.60	330	158	2285	1042	3887	1785
0.70	284	154	1975	1022	3350	1735
0.80	238	150	1655	1002	2796	1695
0.90	192	147	1323	988	2230	1655
0.95	168	145	1150	980	1940	1638
0.98	154	144	1042	975	1780	1623
1.00	144	144	972	972	1620	1620

H_s = enthalpy of solution, Btu/mol solution.
$\overline{H_1}$ = partial enthalpy water, Btu/mol water.
Enthalpy datum = 32°F.

WATER-VAPOR DEW POINTS WITH TEG SOLUTIONS

The equilibrium dew points available with glycol concentrations of 60 to 99.9 per cent by weight in the temperature range 40° to 120°F are presented in Fig. 3. These have been obtained by calculating the water content of the gas at the dew point as equal to the product of the activity and the water content of the gas saturated with water at the contact temperature and pressure. The dew-point temperature then was taken directly from the water-content chart of McCarthy, *et al,*[5] by entering the chart with the water concentration at the dew point and the contact pressure.

The temperature of contact affects the dew point such that the dew-point depression, or the difference in the contact temperature and the dew-point temperature, at a temperature of 40°F is approximately 75 per cent of the dew-point depression theoretically possible at 120°F.

Pressure was found to have no effect on the equilibrium dew point. The dew points of Fig. 3 represent data calculated over the pressure range from 14.7 to 2,500 psia. These dew points for any given contact temperature were found to agree within 1°F throughout this range of pressures.

Data such as shown in Fig. 3 have limited application in the design of glycol units. One bit of information obtained from it is the minimum glycol concentration which can be used to obtain a certain dew point. For example, if a 32°F dew point at a contact temperature of 100°F is desired, the lowest lean glycol concentration which will suffice is approximately 97 per cent TEG. If it is assumed the desired dew point will be about 20°F above the equilibrium dew point (quite often expressed as an approach to equilibrium of 20°F), the lean glycol concentration should be one which gives a dew point of 32 minus 20, or 12°F. This sets the desired lean glycol concentration at approximately 98.5 per cent TEG.

Another application of Fig. 3 is to use the glycol concentration shown as the average concentration in the dehydrator. Then the dew point obtained in this manner will approximate the dew point which is obtained in the actual operation. Nothing has been said about rates, and this information cannot be obtained without performing the more detailed analysis illustrated in the Appendix.

During the last several years, the gas engineer has become more aware of the fact that dew-point depressions in excess of 100°F are needed and that depressions of this magnitude are possible only if the lean glycol is stripped to very small water concentrations. At a contact temperature of 120°F and using a lean glycol concentration of 99.7 per cent TEG, a dew-point de-

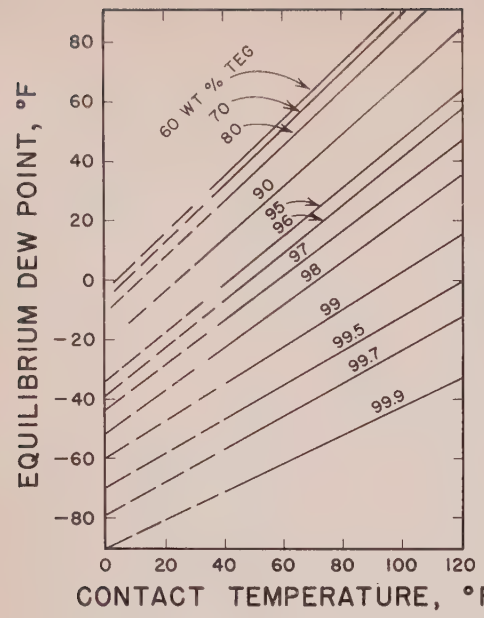

FIG. 3—WATER-VAPOR DEW POINTS OBTAINED BY DRYING NATURAL GAS WITH TRIETHYLENE-GLYCOL SOLUTIONS.

pression of 133°F is theoretically possible. However, the theoretical dew point (based on the concentration of the incoming lean glycol) is never obtained in field operations due to the enriching of the glycol with water on the top tray and the inefficiency of the gas-liquid contact in the absorber. The approach to equilibrium dew point is often 20°F or less, and this approach can always be improved by increasing the circulation rate or by adding more trays. In the problem in the Appendix, an 18°F approach to equilibrium is obtained. The dew point of the dried gas is 28°F, and the theoretical dew point for the stated conditions is 10°F. At the same circulation rate with an extra tray added, the dew point of the dried gas will be approximately 22°F to give a 12°F approach to equilibrium. If the circulation were approximately doubled, and with five trays, the approach to equilibrium would be approximately 10°F.

Consider drying a natural gas at 600 psia and 120°F. In an average four-tray contactor, a 100°F dew-point depression could be made by circulating approximately 20 gal of 99.7 per cent TEG/lb of water in the inlet gas. Increasing the number of trays by two to a six-tray unit at the same conditions, a 120°F dew-point depression would be possible at only one-third of the same circulation rate. The point to remember is that drying to meet some requirements at higher temperatures can be done, although an extra tray or two may be required as well as more complete regeneration of the glycol. More complete regeneration of glycol is being accomplished by the use of stripping gas as part of the regeneration system.

In years past, the rule of thumb was 3 gal of glycol circulated/lb of water in the wet gas. This rule probably does very well at temperatures below 90°F and pressures above 600 psia, but it is not a recommended practice. The absorber-type analysis such as presented in the Appendix should be used to properly define drying needs.

CONCLUSIONS

The application of the data presented herein should permit (1) a more accurate estimate of the dew point of a dried natural gas, (2) a more critical look at dehydrator performance and (3) a more accurate prediction of rate and tray requirements.

NOMENCLATURE

a_L = activity of water in liquid phase
A = absorption factor for water
A_c = absorption factor for methane
f' = fugacity of pure liquid water at its vapor pressure, psia
f° = fugacity of pure component in standard state taken as temperature and pressure of systems, psia
f_L = fugacity of liquid water at system conditions, psia
f_v = fugacity of water vapor at system conditions, psia
$\overline{H}$ = partial enthalpy, Btu/mol
H = enthalpy of pure component, Btu/mol
K = equilibrium ratio of water
K_c = equilibrium ratio of methane
L_n = rich glycol rate, mol rich solution/mol inlet gas
L_o = lean glycol rate, mol lean solution/mol inlet gas
p' = vapor pressure of water at system temperature, psia
p = system pressure, psia
R = gas constant = $10.71 \frac{\text{(psia) (cu ft)}}{\text{(lb mol) (°R)}}$ = $1.99 \frac{\text{Btu}}{\text{(lb mol) (°R)}}$
T = absolute temperature, °R
V = molal volume of water, cu ft/mol
V_{n+1} = inlet gas, mol
W = water content of water-saturated gas, lb/MMscf
W_g = water content of gas over glycol solution, lb/MMscf
x, x_1 = mol fraction of water in the liquid phase
x_o = mol fraction of water in lean glycol
y = mol fraction of water in water-saturated gas
y_g = mol fraction of water in the vapor phase over glycol solution
y_{n+1} = mol fraction of water in wet inlet gas
y_1 = mol fraction of water in dry outlet gas
y_o = mol fraction of water in outlet gas in equilibrium with lean glycol
γ_1, γ_L = activity coefficient of water in liquid phase
γ_v = activity coefficient of water in vapor phase
ν = fugacity coefficient of pure water at temperature and pressure of system.

ACKNOWLEDGMENT

The author wishes to thank the Socony Mobil Oil Co. for permission to publish these data and to thank E. B. Elfrink, Ovid Baker and Will Swerdloff of the Socony Mobil Oil Co. for their critical reviews of this paper.

REFERENCES

1. Porter, J. A. and Reid, L. S.: *Trans.*, AIME (1950) **189**, 235.
2. Townsend, F. M.: "Equilibrium Water Contents of Natural

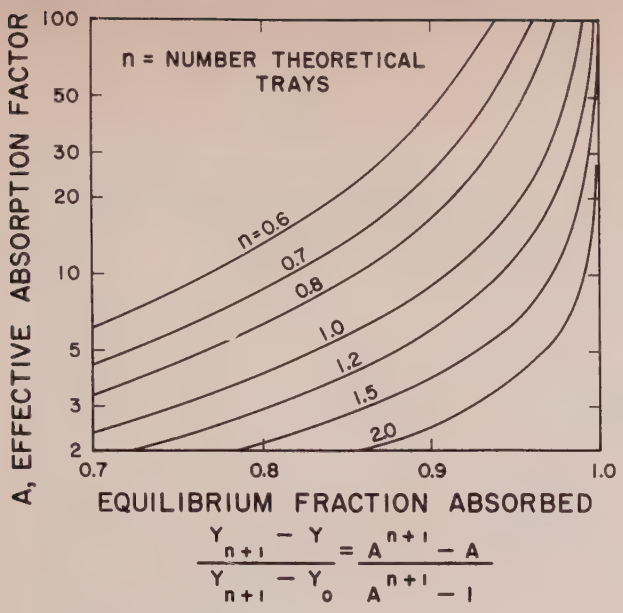

FIG. 4—KREMSER-BROWN ABSORPTION FACTOR FOR ABSORBERS.

Gas Dehydrated by Aqueous Diethylene and Triethylene Glycol Solutions at Various Temperatures and Pressures", PhD dissertation, The U. of Oklahoma (1955).

3. Union Carbide Co.: *Gas Treating Chemicals.*
4. Wise, H., Puck, T. T. and Failey, C. F.: *Jour. Phys. Chem.* (1950) **54,** 734.
5. McCarty, E. L., Boyd, W. L. and Reid, L. S.: *Trans.*, AIME (1950) **189,** 241.

APPENDIX

SAMPLE DEHYDRATION CALCULATIONS

Calculate the circulation rate of 98.6 weight per cent TEG solution required to dry 1 MMscf/D of gas at 800 psia and 100°F so as to make a dry gas containing 7 lb/MMscf. The contactor has five trays.

COMPUTATION OF *K*

K from water content of natural gas and the activity coefficient of water in the 98.6 weight per cent solution can be calculated by either of the following methods.

Method 1

$$K = \frac{y}{x} = (2.105)\ (10^{-5})\ (W)\ (\gamma_L) \quad . \quad (24)$$

where W = water content of saturated gas = 72 lb/MMscf.

γ_L = activity coefficient of water = 0.481 (Fig. 1) and $(2.105)\ 10^{-5}$ is a constant converting water concentration from lb/MMscf to mol fraction.

$K = (2.105)\ (10^{-5})\ (72)\ (0.481) = 0.000728.$

Method 2

K from Fig. 2 and γ_L

$K_{98.6} = (K_{98})\ (1.94)\ (\gamma_L)$

$= (0.00079)\ (1.94)\ (0.481) = 0.000728.$

CIRCULATION RATE

y_{n+1} = mol fraction water in wet gas $(72)\ (2.105)10^{-5} = 0.001515.$

y_1 = mol fraction water in dry gas $(7)\ (2.105)\ 10^{-5} = 0.000147.$

y_o = mol fraction water in dry gas at equilibrium ($y_o = Kx_o$)

TABLE 5—APPROXIMATE EQUILIBRIUM RATIOS FOR METHANE IN TRIETHYLENE GLYCOL SOLUTIONS*

PSIA	50°F	80°F	120°F
100	150	152	150
150	126	126	122
200	111	110	106
250	100	99	96
300	94	91	87
400	82	79	76
500	72	70	66
600	66	62	58
700	60	57	54
800	53	51	48
900	49	48	44
1000	44	43	39
1500	34	33	29
2000	32	31	27

*Calculated from data given in Ref. 1.

$= (0.000728)\ (0.106) = 0.0000772.$

$\frac{y_{n+1} - y_1}{y_{n+1} - y_o}$ = equilibrium fraction to be absorbed

$= \frac{0.001515 - 0.000147}{0.001515 - 0.0000772}$

$= 0.951.$

Past experience has indicated trays in glycol units to be approximately 25 per cent efficient. Then assume 25 per cent efficiency for each tray and *n*, the number of theoretical trays, = 5(.25) = 1.25 theoretical trays. Refer to Fig. 4 and find the absorption factor $A = 10.6$ for 1.25 trays and an absorbed fraction = 0.951.

Then the circulation rate of rich glycol,

$L_n = (A)\ (V_{n+1})\ (K)$

$= (10.6)\ (1.0)\ (0.000728)$

$= 0.00772$ mol rich glycol/mol inlet gas

A_c = absorption factor of methane or natural gas

$= \frac{L_n}{K_c V_{n+1}} = \frac{0.00772}{50(1)} = 0.000154,$

where K_c is equilibrium ratio of methane in glycol solutions (Table 5).

Since the gas phase consists mainly of methane (C_1), the absorption factor will approximate the moles of natural gas absorbed when using 1 mol of gas as basis, or

moles C_1 absorbed = 0.000154 mol/mol inlet gas;

moles water absorbed = 0.001515 − 0.000147 = 0.001368 mol/mol inlet gas.

Then the circulation rate of lean glycol,

$L_o = L_n$ − (mol C_1 absorbed + mol water absorbed)

$= 0.00772 - (0.000154 + 0.001368)$

$= 0.0062$ mol lean glycol/mol inlet gas.

Molecular weight (MW) of lean glycol = mol fraction water (MW water) + mol fraction TEG (MW TEG)

$= 0.106\ (18) + 0.894\ (150)$

$= 136.$

Density of lean glycol = 9.3 lb/gal.

Therefore,

$$L_o = 0.0062 \left(\frac{\text{mol lean glycol}}{\text{mol inlet gas}}\right)\left(\frac{2637 \text{ mol gas}}{\text{MMscf gas}}\right)\left(\frac{136 \text{ gal TEG}}{9.3 \text{ mol TEG}}\right)$$

$= 239$ gal/MMscf

$= 0.166$ gal/min / MMscf/D

$= 3.32$ gal/lb water in inlet gas. ★★★

Use of Oxygen Scavengers To Control External Corrosion of Oil-String Casing

F. W. SCHREMP
J. F. CHITTUM
CALIFORNIA RESEARCH CORP.
LA HABRA, CALIF.

T. S. ARCZYNSKI
STANDARD OIL CO. OF CALIF.
LA HABRA, CALIF.

ABSTRACT

This paper describes a laboratory study of causes of external casing corrosion and the test work that led to the use of oxygen scavengers to prevent this attack. External casing failures are classified as water-line, casing-casing, collar and body failures. A corrosion mechanism based on principles of differential oxygen availability is developed that is consistent with facts known about each kind of failure. The field use of oxygen scavengers is depicted as a direct result of the laboratory study.

A part of the paper is devoted to reporting on the field use of hydrazine to control external casing corrosion. Results of field measurements made over a period of several years are presented as evidence of the effectiveness of the hydrazine treatment. The first conclusion reached is that the use of hydrazine materially reduces the cathodic protection requirements for treated wells. This result is interpreted to mean that a reduction is taking place in the amount of corrosion on the casing. Results indicate also that hydrazine shows its greatest usefulness within the first 12 to 18 months after a well is completed when pitting corrosion is likely to be most active.

INTRODUCTION

According to surveys sponsored by the National Association of Corrosion Engineers,[1] the cost of repairing casing leaks caused by external corrosion may exceed $4 million per year. In addition, well damage and lost production resulting from casing leaks probably costs the petroleum industry an additional $5 to $6 million per year.

Concern about the cost of external casing corrosion led to an extensive laboratory study of factors causing this external corrosion and to the development of a new approach to its prevention. This paper presents a discussion of various causes of external casing corrosion, details of laboratory studies and the results of the field use of an oxygen scavenger in well cementing fluids to prevent the external corrosion of oil-string casing.

Measurements on test wells over a period of several years show that cathodic-protection current requirements are greatly reduced when hydrazine is used in cementing mud. Reduction of current requirements can be interpreted to mean that removal of oxygen by hydrazine has greatly suppressed corrosion cells on the external surface of the casing and thereby, has reduced corrosion.

To date, hydrazine has been used by the Standard Oil Co. of California in more than 200 well completions.

KINDS OF CASING FAILURES

A survey of a large number of casing leaks disclosed four types of external casing failures — water-line, casing-casing, collar and body failures. These types are identified largely by their location on the casing. Water-line failures are found just below the surface of water or mud in the casing annulus. Casing-casing failures occur on the oil string just below the shoe of the surface string. Collar failures are found in the threaded ends of casing joints where they are screwed into casing collars. Body failures may occur at any point on the body of a casing joint. Examples of each kind of failure have some of the general characteristics that are shown in Fig. 1.

Water-line failures usually result in the circumferential severance of an oil-string casing. The corrosive action causing a water-line failure usually is sharply defined and is limited to a short length of the casing. Casing-casing failures usually are accompanied by pitting corrosion distributed around the oil-string casing for distances up to 100-ft below the shoe of the surface string. Casing-casing failures may also sever the casing. Collar failures seem to start on the first thread at the bottom of recesses between collar and casing joint. Corrosion proceeds across the threads by what appears to be a normal pitting mechanism. Both casing and collar are severely attacked. Body failures are the result of highly localized pitting at any point on a casing wall. Besides the pit that perforates a casing, a large number of other pits usually are found along one side of the casing joint. The pits occasionally are filled with corrosion products consisting largely of oxides and sulfides.[2] Frequently, the mill scale is largely intact on the rest of the casing.

Examination of a casing failure does not always reveal the cause of the failure. Frequently, the necessary details are destroyed when the failure occurs. For example, formation water flowing through a perforation at high velocity may enlarge the hole and destroy any remaining evidence of the cause of the failure. One way to obtain undistorted information about a failure is to study the nature of other pits on the casing in the vicinity of the failure. A study of such pits frequently suggests that they are characteristic of an attack resulting from the differential availability of molecular oxygen.

Original manuscript received in Society of Petroleum Engineers office Aug. 24, 1960. Revised manuscript received April 28, 1961. Paper presented at 31st Annual California Regional Meeting of SPE, Oct. 20-21, 1960, in Pasadena, Calif.

[1]References given at end of paper.

CONDITIONS LEADING TO EACH TYPE OF CASING CORROSION

WATER-LINE ATTACK

Water-line attack is found in wells with open casing annuli. Air diffuses into the casing annulus and makes oxygen available for the cathode reaction,

$$\frac{1}{2}O_2 + H_2O + 2e^- = 2OH^- \quad . \quad . \quad . \quad . \quad . \quad . \quad (1)$$

This reaction occurs at the fluid-air interface. Just below the interface the fluid is deficient in oxygen, but the metal lattice is exposed so metallic iron takes part in the anode reaction,

$$Fe = Fe^{++} + 2e^- \quad . \quad . \quad (2)$$

Occurrence of these reactions at the fluid-air interface will result in corrosive attack on the casing just below the fluid-air interface. Prolonged reaction at a constant interface level will result in a severed casing, as shown in Fig. 1(A).

Other chemical reactions also take place during the process of casing corrosion. These reactions, as shown by Eqs. 3 and 4, also help maintain the potential of the corrosion cell.

$$Fe^{++} + 2OH^- = Fe(OH)_2 \quad . \quad (3)$$

$$3\,Fe(OH)_2 + \frac{1}{2}O_2 = Fe_3O_4 + 3H_2O \quad . \quad . \quad . \quad . \quad . \quad . \quad . \quad . \quad . \quad . \quad (4)$$

Removal of ferrous ions from solution near the fluid-air interface causes the attack to continue and be concentrated near this interface, as shown in Fig. 2(A). This corrosion mechanism is identical to that first given by Evans[3,4] in formulating his principle of "differential aeration" as the cause of pitting.

CASING-CASING CORROSION

Casing-casing corrosion occurs when oil and surface casing strings are in contact with two different muds. Such an occurrence is possible when the surface string is imperfectly cemented. The difference in mud composition may be either in oxygen content or pH, or both. If the oil string is in contact with a mud of lower pH than the surface string, or with mud having a lower oxygen concentration than the surface string, the oil string will behave as an anode. The reaction of Eq. 2 will be concentrated on the oil string near the shoe of the surface string, and iron will be removed most rapidly from the casing surface at any susceptible points on the metallic lattice. The cathode reaction of Eq. 1 will occur on the surface string. The complete corrosion cell with current lines in solution is illustrated in Fig. 2(B).

COLLAR FAILURE

Collar failure may be caused solely by improper joint make-up. The original leak in this case would be enlarged by erosion-corrosion while formation water flows through it. Improper joint make-up includes joints not torqued sufficiently to make a tight joint, and galled threads resulting from damaged threads, or failure to use lubricant.

Failure due to corrosion also may occur in the recess between the threaded portion of the casing joint and the end of the collar. The mechanism of such a failure is illustrated in Fig. 2(C). Differential availability of oxygen in the recess may set up the condition in which the anode reaction (Eq. 2) can take place on the exposed thread. The cathode reaction of Eq. 1 could occur on the mill-scale-coated casing adjacent to the recess. The potential of this cell could be maintained by the reactions of Eqs. 3 and 4. Current in this cell can be expected to produce rapid attack on the exposed threads.

BODY CORROSION

Body corrosion apparently occurs when differential conditions produce a corrosion cell along the body of a casing joint. The tendency for pitting to occur along one side of a casing joint suggests the possibility of mill-scale damage being the cause of increased corrosion susceptibility. Usually, the rest of the varnish and mill-scale coating on the surface of the joint is undamaged. Mill-scale damage of this kind along one side of a casing string can occur as the casing is run into a well. The removal of mill scale exposes the metallic lattice directly to the cementing mud. Under these conditions, the anode reaction of Eq. 2 takes place on the exposed iron. The small anode and large cathode areas cause highly localized corrosive attack.

Localized corrosive attack also may be created when formation waters free from oxygen seep into the mud and make contact with the casing at small areas. The points of contact with the formation water will be anodic to the rest of the

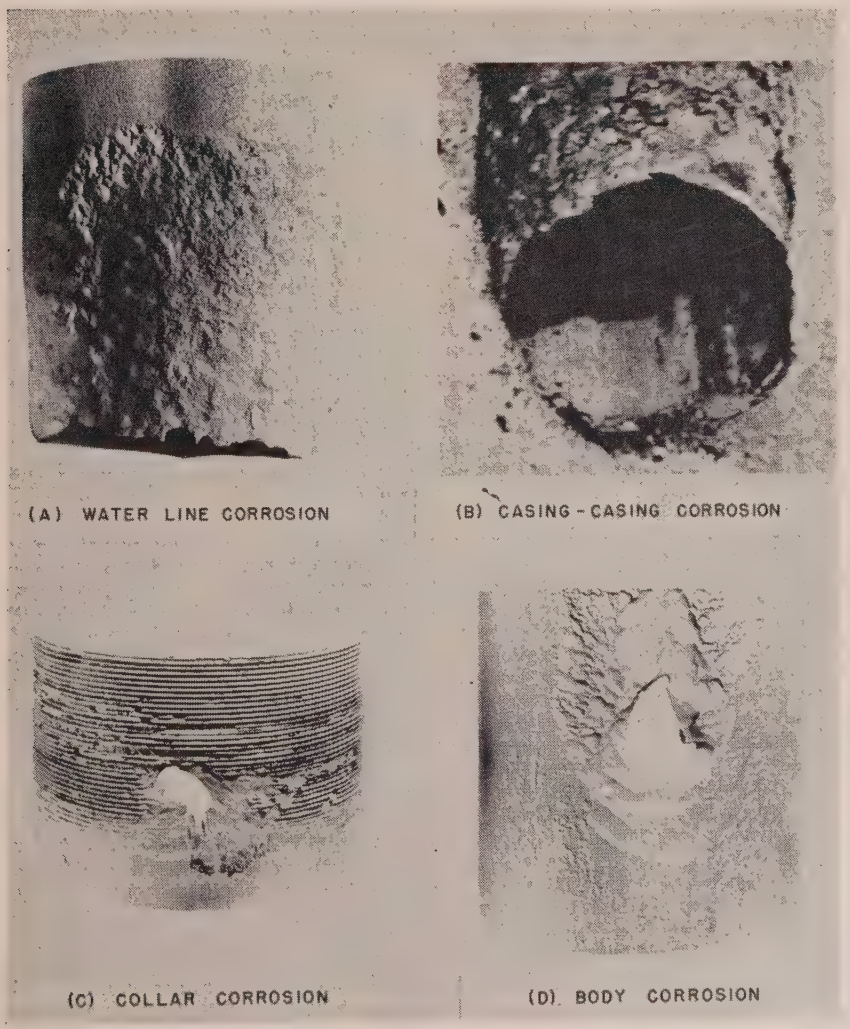

FIG. 1—EXAMPLES OF THE VARIOUS TYPES OF CASING CORROSION.

casing. Furthermore, colonies of bacteria in a pit on a casing may localize corrosive action.[5] The metal surface covered by corrosion products from which bacteria have removed oxygen may be anodic to the surrounding casing surface. Both of these conditions will cause pitting corrosion. Two kinds of body corrosion are illustrated in Fig. 2(D).

CAUSES OF CASING CORROSION

The various kinds of casing corrosion were studied in the laboratory by devising experiments to simulate each kind of corrosion. Both potential and current measurements were made as a function of time in an effort to follow the effects of the various conditions that were changed during the study.

WATER-LINE CORROSION

A laboratory study was carried out to determine the magnitude of the potentials that could be built up to cause water-line corrosion. A water sample was collected from a casing annulus and adjusted to anaerobic conditions comparable to those in the casing annulus. Potentials (referred to saturated calomel electrode) of a small iron electrode were measured at different levels below the surface of the water sample. In the test apparatus, an iron electrode was sealed with insulating material into a hole through the wall of an iron tube so that the potentials of this electrode could be measured separately as the tube was moved up and down in the water. Atmospheres of air, nitrogen and oil-air were used successively above the water during the study. Fig. 3 shows that there was a 90-mv difference in the first 5 to 10 mm below the surface of the water sample as a result of differential oxygen concentration. Nitrogen atmosphere and the oil layer prevented the formation of the oxygen concentration cell.

A study of the current obtainable from a water-line corrosion cell and the nature of the anode was carried out in apparatus shown in Fig. 4. Six steel rods ¼-in. in diameter and 3-feet long were centered in ¾-in. glass tubes with rubber stoppers. The first of three steel rods—A, B and C—were each cut in two pieces and reconnected by means of short pieces of plastic rod. Wires were attached to the top and bottom ends of the

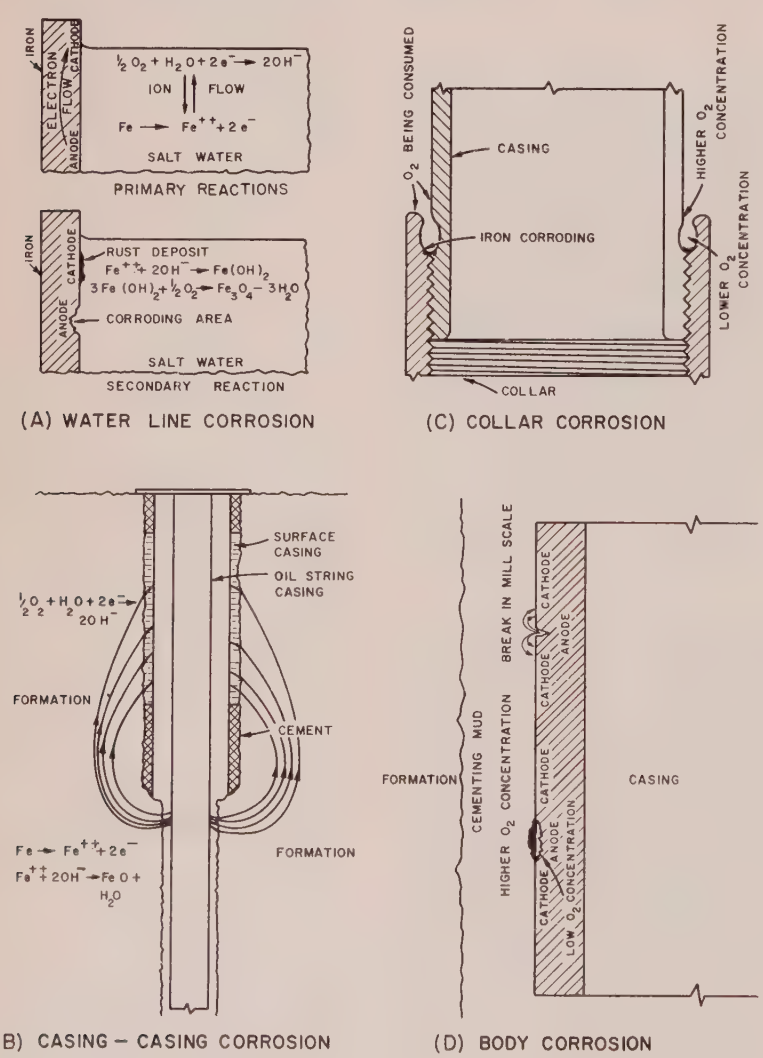

FIG. 2—MECHANISMS OF THE VARIOUS TYPES OF CASING CORROSION.

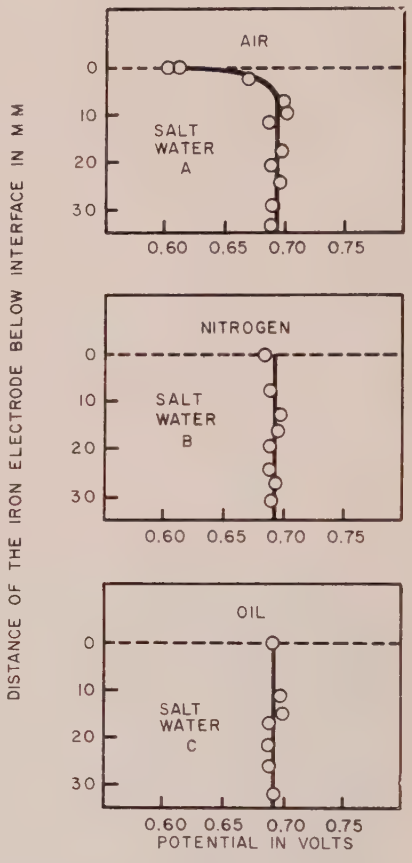

FIG. 3—EFFECT OF IMMERSION DEPTH ON POTENTIAL OF WATER-LINE CORROSION CELL.

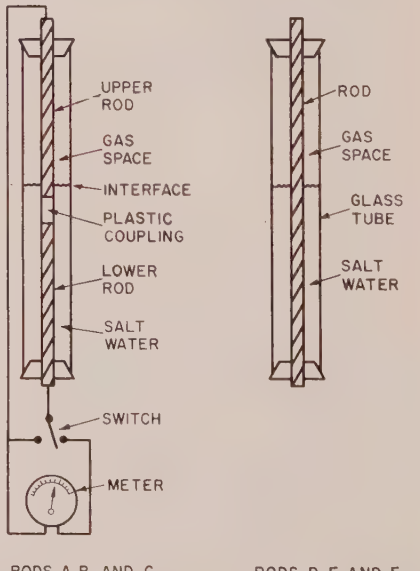

FIG. 4—ARRANGEMENT OF TEST RODS USED TO MEASURE THE CURRENT CAPACITY OF WATER-LINE CORROSION CELLS.

three re-assembled rods. Each pair of wires was connected outside the glass tube to complete the cell. On occasion, these wires were disconnected and reconnected to an ammeter to measure the current flowing between the two sections of each rod. The remaining three rods—D, E and F—were left intact. The glass tubes were mounted in a vertical position, and formation water was poured in each tube so that the lower half of each rod was submerged. Fluid in the tubes containing the plastic-separated rods was adjusted so that the top of the plastic coupling was ½-in. below the water-air interface.

Rod A was allowed to stand for 60 days in formation water with the water surface open to the air. Rod B was allowed to stand for 10 days, and then a small amount of oil was poured on top of the water for the remaining 50 days of the test. Rod C was treated similarly to Rod B except that the oil contained 1 per cent of an oil-soluble corrosion inhibitor. The three unbroken rods—D, E and F—also were permitted to stand partially submerged in the formation water for the 60-day test. During this period air was maintained above the water line on Rod D, an oil-air interface was maintained above the water line on Rod E and nitrogen gas was maintained above the water on Rod F.

Results of current measurements are shown in Fig. 5 for each of the three separated rods. Fig. 6 shows the appearance of all six rods after the 60-day test. The current produced in such a corrosion cell will flow for as long a time as the differential oxygen concentration exists.

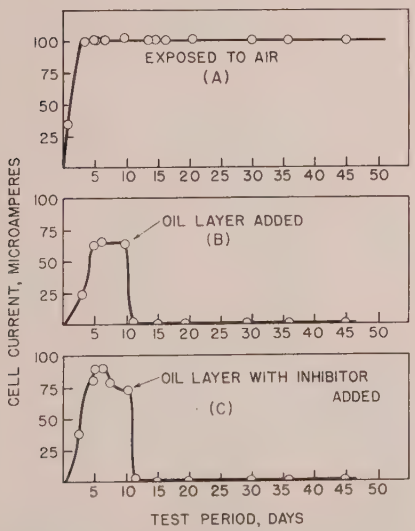

Fig. 5—Effect of Oil Layer on Water-Line Corrosion-Cell Current.

The anodic action is sharply localized on the iron below the liquid surface. Action of the water-line corrosion cell can be minimized by placing a refined oil layer on the water surface or by removal of oxygen from the gas space above the liquid surface.

CASING-CASING CORROSION

The potentials of casing-casing corrosion cells were next studied. Muds of different pH and different molecular oxygen concentrations were obtained, and the potentials of iron electrodes against a saturated calomel electrode were measured in these muds. Results of these measurements are shown in Fig. 7. Iron became more cathodic with increasing pH of the muds. Between pH 9.0 and pH 13.0, an iron potential was shown to be more anodic as the oxygen concentration in the mud was decreased.

The nature of the current density on an oil-string casing was studied using a model in which the oil string and the surface string were separate electrodes. The current was found to be quite concentrated along the length of oil string immediately below the shoe of the surface string. Decrease in current density below this point was found to behave according to accepted principles of potential theory.

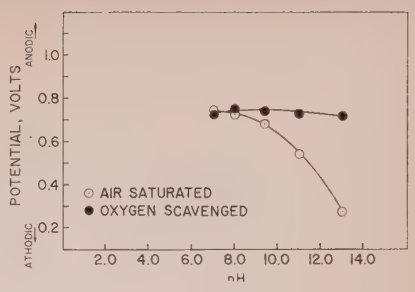

Fig. 7—Effect of pH on the Potential of Iron in Air-Saturated and Oxygen-Scavenged Drilling Mud at 150°F.

An additional study was carried out with the apparatus shown in Fig. 8. The cathode was made out of three short sections of iron pipe welded together concentrically, and the anode was made of a small iron coupon. Welded areas of the cathode were coated with plastic to eliminate galvanic couples at the weld joints. The area of the cathode was about 330 sq in. The area of the anode was 2 sq in. The cathode was placed in mud at a pH of 12.1, the anode in mud at a pH of 8.5. The two electrodes then were shorted together for

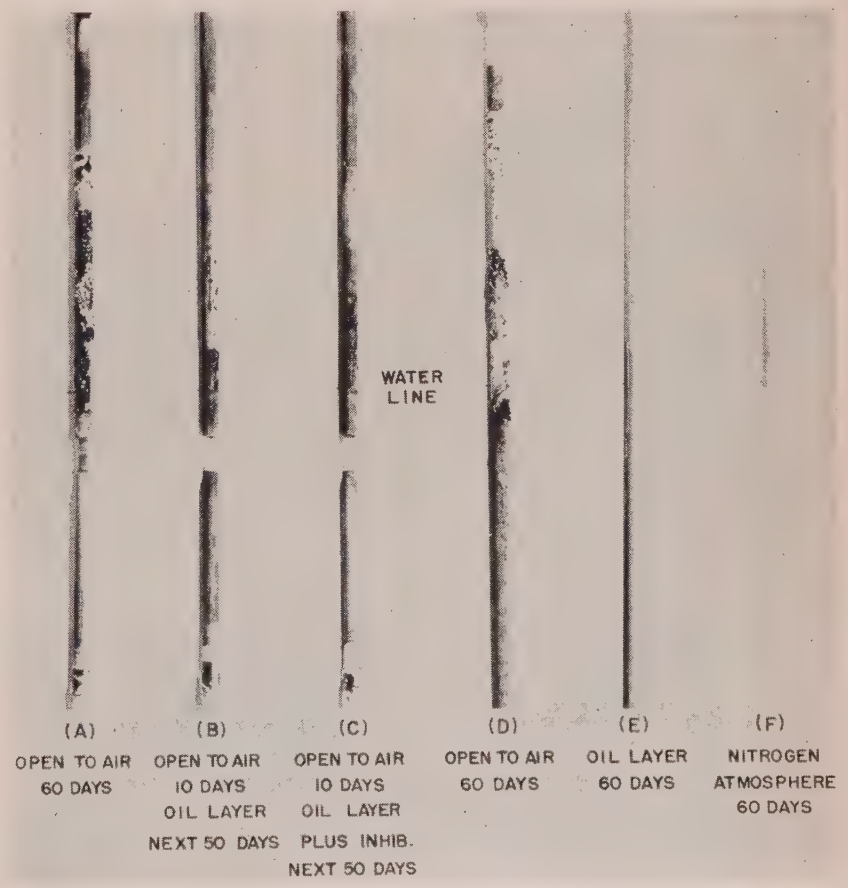
WATER LINE
(A) OPEN TO AIR 60 DAYS
(B) OPEN TO AIR 10 DAYS OIL LAYER NEXT 50 DAYS
(C) OPEN TO AIR 10 DAYS OIL LAYER PLUS INHIB. NEXT 50 DAYS
(D) OPEN TO AIR 60 DAYS
(E) OIL LAYER 60 DAYS
(F) NITROGEN ATMOSPHERE 60 DAYS

Fig 6—Appearance of Test Rods After 60 Days of Partial Submersion in Formation Salt Water.

several days. The results of measurements are shown in Table 1.

The results of these tests show that corrosion cells with potentials of 0.2 to 0.6 v might be expected between two casings in contact with aerated muds of different pH. The current-producing capacity of such cells is substantial. During tests on casing models, the current from an oil string that is anodic was shown to be concentrated at the surface area where casing-casing corrosion has been found to be severe in the field. It further was found that the potential of a casing becomes more anodic as the oxygen concentration decreases.

TABLE 1—WEIGHT LOSS OF ANODE IN SHORTED CASING-CASING CORROSION CELLS IN 12-DAY TEST

Cathode			Anode			Weight Loss (gm)	
Sol.	pH	Init. Poten. (v) (−)	Sol.	pH	Init. Poten. (v) (−)	Cal.	Meas.
Mud	12.1	0.170	Mud	8.5	0.760	0.090	0.117

COLLAR CORROSION

The potential of a collar-corrosion cell was measured in mud utilizing the recess between a joint of 9¼-in. casing and a casing collar. A ring made from 0.005-in. diameter iron wire was placed in the bottom of the recess, and its potential was measured with respect to another iron-wire ring outside of the recess. The arrangement of wires in this apparatus is shown in Fig. 9(A). The iron wires were protected from contact with either the casing or the collar by means of heavy cotton cloth. The measured potentials of the two iron wires are compared in Table 2. The current-carrying capacity of the collar corrosion cell is given also in Table 2.

Test results indicated that a potential of about 0.2 v might be expected from the collar corrosion cell. The current-producing capacity of such a cell is substantial and can be expected to produce current so long as the differential oxygen concentration exists. Observations also indicated that the anode was located so that the corrosion would be concentrated on the first exposed thread of the joint.

BODY CORROSION

A corrosion cell consisting of bare iron and mill scale was studied first. Electrodes of mill scale and mill-scale-coated iron were prepared in an electric furnace at 1,800°F. The potentials of the bare-iron and mill-scale electrodes were measured againt a saturated calomel electrode in muds of various pH's. Results of these measurements are shown in Table 3.

Other electrodes of mill-scale-coated iron were assembled with sand-blasted iron electrodes in sealed jars, as shown in Fig. 9(B). The muds placed in these jars were given various treatments to introduce or remove molecular oxygen. Electrical currents produced by these cells were measured with a zero-resistance milliameter and are given in Table 4.

The results of tests on mill-scale electrodes showed that potentials of 0.2 to 0.3 v can be produced by a bare iron-mill scale corrosion cell. The current-producing capacity of this cell is sufficient to last indefinitely when molecular oxygen is available, and for weeks even if molecular oxygen is not available. Ultimately, as was observed at the end of several years, the current flow stops when sources of oxygen are depleted.

The effect of formation water on body corrosion was studied next. This study was undertaken because of the severity of corrosion in some oil fields where high-pressure formation fluids were believed to aggravate external casing corrosion. In laboratory tests, penetration of high-pressure formation water into cementing mud was found to follow vertical paths in the mud and was thought possibly to account for pitting along one side of a casing joint.

Iron electrode potentials measured in typical formation waters of pH's 6.5 to 8.0 are shown in Table 5. These potentials are compared with potentials of the same iron electrodes in high-pH aerated muds. The corrosion capacity expressed as coupon weight loss for the anode of a cell made from these electrodes also is given. The tests again showed that potentials of the corrosion cells made by the formation water-mud con-

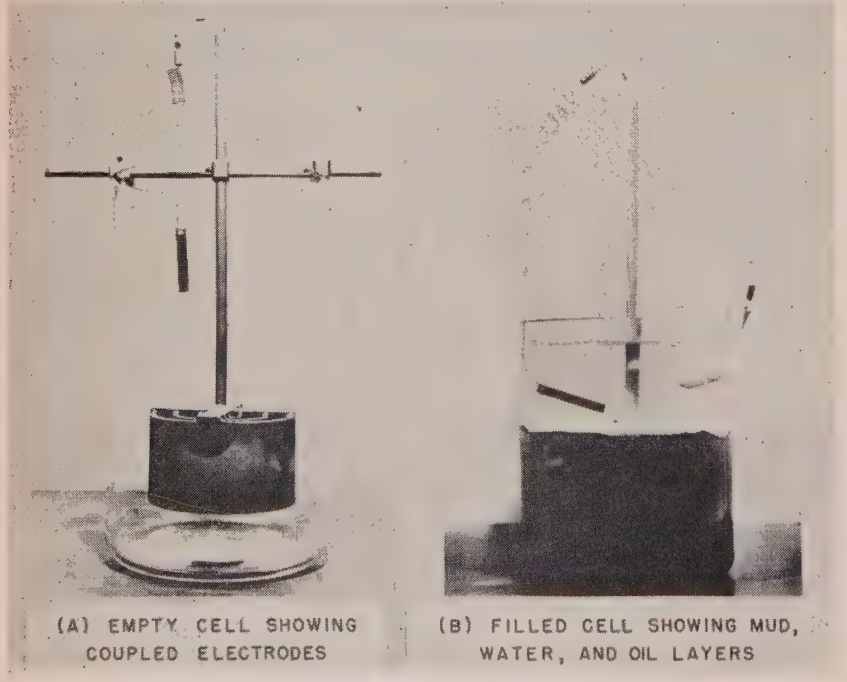

(A) EMPTY CELL SHOWING COUPLED ELECTRODES

(B) FILLED CELL SHOWING MUD, WATER, AND OIL LAYERS

FIG. 8—CORROSION CELL FOR STUDY OF ELECTROLYTIC CAPACITY OF IRON IN DIFFERENT FLUIDS

TABLE 2—CORROSION POTENTIALS AND CURRENTS MEASURED IN RECESS BETWEEN CASING JOINT AND CASING COLLAR

Sol.	pH	Potential of Iron Wires (v) (−) Recessed	Potential of Iron Wires (v) (−) Exposed	Current (μamps) at End of 3-Min. Between Wires Shorted Through 10-ohm Resistor
Mud	12.0	0.622	0.352	2.00
Mud	10.5	0.680	0.650	0.65

TABLE 3 — POTENTIALS OF MILL-SCALE AND IRON ELECTRODES IN AN ALKALINE DRILLING MUD PURGED WITH NITROGEN

Time (mos.)	Mill-Scale Iron Elec. Poten. (v) (−)	Sand-Blasted Iron Elec. Poten. (v) (−)	Poten. Diff. (v)
Start	0.272	0.540	0.268
1	0.284	0.513	0.229
2	0.310	0.503	0.193
3	0.329	0.483	0.154
4	0.338	0.470	0.132

TABLE 4—CURRENT MEASURED BETWEEN MILL-SCALE AND IRON ELECTRODES IN ALKALINE DRILLING MUD PURGED WITH NITROGEN

Time (mos.)	Current (milliamps) Shorted Electrodes	Current (milliamps) Unshorted* Electrodes
Start	0.055	0.030
1	0.045	0.090
2	0.040	0.070
3	0.001	0.105
4	0.065	0.107

*Instantaneous reading.

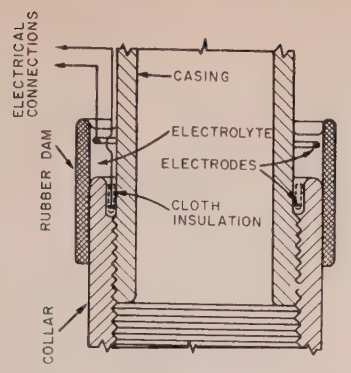

(A)
SETUP USED TO MEASURE THE POTENTIAL OF CASING COLLAR CORROSION CELLS

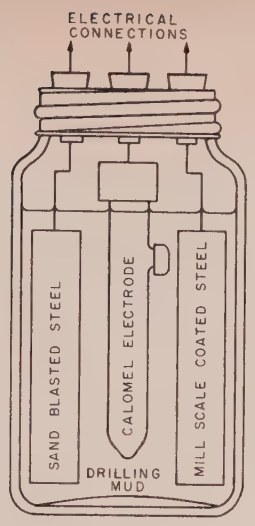

(B)
SETUP USED TO STUDY THE BEHAVIOR OF BRIGHT STEEL, MILL SCALE CORROSION CELLS.

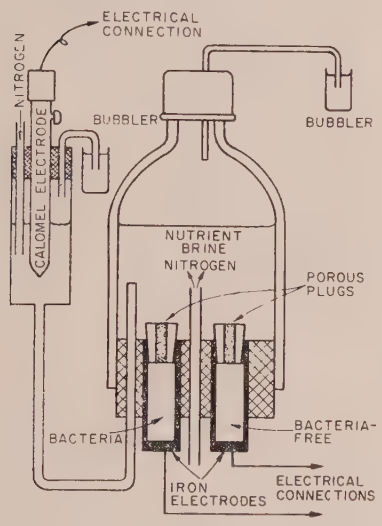

(C)
CELL USED TO STUDY THE EFFECT OF SULFATE REDUCING BACTERIA ON THE CORROSION OF STEEL.

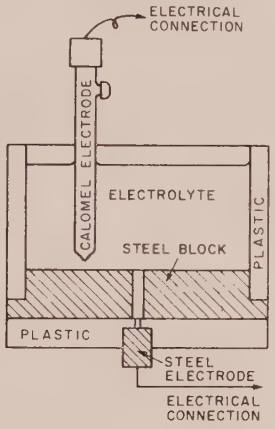

(D)
CELL USED TO STUDY THE EFFECT OF PIT DIAMETER ON THE CORROSIVITY OF STEEL.

FIG. 9—VARIOUS LABORATORY SET-UPS USED TO STUDY THE PROCESSES OF EXTERNAL CASING CORROSION.

tacts on the casing are reduced to a low value when molecular oxygen is removed from the mud.

The effect of sulfate-reducing bacteria was investigated as a promoter of body corrosion. The study was carried out because iron sulfides frequently are found in pits on oilstring casing.[2] Conventional cementing mud was considered too alkaline to support appreciable growth of sulfate reducers or to allow metal contamination with these bacteria. Therefore, artificial iron pits were used which were not precontaminated with sulfate-reducing bacteria, and solutions were used which might be present in a pit filled with nearly neutral iron oxide and sulfide corrosion products. The object of the study was to discover if sulfate-reducing bacteria could grow in a casing pit and could make the iron more anodic on this area. A general mechanism for corrosion by sulfate-reducing bacteria was not tested.

Electrode potentials were measured for iron covered with colonies of sulfate-reducing bacteria. The apparatus used to carry out the study is shown in Fig. 9(C). Pieces of iron were sand-blasted and placed in the apparatus under anaerobic conditions. Nutrient solutions were prepared containing sulfate-reducing bacteria. The cultures then were incubated at 90°F inside the test apparatus. Potentials of the iron electrodes referred to saturated calomel electrodes were measured as a function of time and are shown in Table 6. These potentials are compared also with potentials of iron in aerated brine but without bacteria. The increased current density that is possible at an iron anode promoted by a local colony of sulfate-reducing bacteria was estimated to be appreciable. Current densities, however, were not measured because of the difficulty in determining the area of the bacterial activity.

TABLE 6—POTENTIALS OF IRON ELECTRODES IN BRINE SHOWING DIFFERENCES PRODUCED BY GROWTH OF SULFATE-REDUCING BACTERIA

Time (days)	pH of Brine	Potential of Iron (v) (−)	
		Bact. Growing	No Bact. Growing
Start	7.0	0.769	0.769
1	7.0	0.771	0.749
2	7.0	0.768	0.743
3	7.0	0.766	0.736
Start	8.0	0.762	0.736
1	8.0	0.774	0.768
2	8.0	0.770	0.757
3	8.0	0.765	0.748

GROWTH OF CORROSION PIT

The effect of pit diameter on pitting activity was studied because of the frequent occurrence of localized external attack on casings. The study was confined to determining the influence of pit diameter on the potential that might develop at the bottom of a corrosion pit. The apparatus used in the experiments is shown in Fig. 9(D). To represent pits, a number of holes of different diameters were made in ½-in.-thick carbon steel blocks. An iron electrode was sealed across the bottom of each hole, and each of these electrodes was insulated from the steel block by means of a plastic plate. An aerated polyphosphate solution, sometimes used for wash water in oilwell cementing operations, was used in the test cell. The solution filled all of the holes and covered the top of the test block to a depth of ⅜ in. The potential of each iron electrode was measured against a saturated calomel electrode over a period of many days.

As shown in Fig. 10, the potential at the bottom of each hole became more cathodic with increase in hole diameter at the end of the test. The

TABLE 5—WEIGHT LOSS OF ANODES IN SHORTED CORROSION CELLS IN 14-DAY TEST

Cathode			Anode			Weight Loss (gm)	
Sol.	pH	Init. Poten. (v) (−)	Sol.	pH	Init. Poten. (v) (−)	Calc.	Meas.
Mud A	12.0	0.237	FW**	7.1	0.771	0.137	0.120
Mud B	12.3	0.372	FW	7.3	0.737	0.135	0.139
Mud A*	12.3	0.531	FW	7.2	0.717	0.125	0.132

*Treated with corrision inhibitor.
**FW = Formation Water.

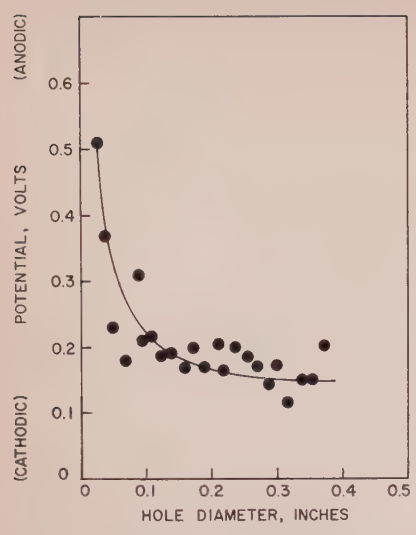

FIG. 10—EFFECT OF PIT DIAMETER ON THE ANODIC CHARACTER OF CORROSION PITS.

results of this test indicate that differential aeration pits tend to become sharper as they progress into the iron.

SECONDARY FACTORS IN CASING CORROSION

The causes of corrosion previously discussed describe the necessary and sufficient conditions for developing the highly localized character of casing corrosion. However, other factors also may be involved in the corrosion rate when the anodic areas are small. Three of these factors may have a significant effect on the life of some casings because they tend to accelerate the pitting processes by flow of gross positive current out from large areas of the casing.

An experiment was considered necessary to demonstrate this acceleration of pitting by outward flow of positive current from a casing surface. Therefore, a prototype casing coated with mill scale was built, with a small isolated area of metal left exposed. Positive currents of varying strengths from an external cathode were used to increase the average anode current density on the casing surface when it was immersed in mud. Current densities then were measured for positive currents leaving the exposed area. When the ratio of mill-scale-covered area to exposed area was 60:1, all applied external currents that created an average current density above 2.5 milliamp/sq ft resulted in a greater than-average discharge current density from the exposed area of the casing. When the ratio of mill-scale-covered area to exposed area was 1,000:1, a greater-than-average discharge current density occurred when the average applied current density exceeded 1.2 milliamp/sq ft.

FLOW LINE CURRENT

A positive current of sufficient strength flowing into a well from attached flow lines, as shown before, tends to accelerate pitting corrosion at almost any place on the casing. The effect is similar to one where the cathode of the corrosion cell is made much larger because the surface flow lines become a part of the casing cathodic area. Current lines to some degree follow the classic potential theory lines through the ground when no highly localized anodic areas exist. If highly localized anodic areas do exist, however, the current density at these areas may be increased, and pitting may tend to be more severe.

INTERFERENCE CURRENTS

A positive current from a cathodic-protection anode may flow underground first to an unprotected casing and then return to a protected casing if the unprotected casing is in the electrical field of the protected well. Current flowing in this path is called interference current. Uniform return of the interference current from the unprotected casing may be expected if there are no localized anodic areas on the unprotected casing. If there are localized anode areas, interference current will accelerate pitting corrosion on the unprotected casing.

SELF-POTENTIAL CURRENTS

Self-potential currents flowing in wellbores have been suggested as a primary source of casing corrosion for several years.[6] However, the experiment described herein suggests that self-potential currents are only secondary factors. The positive current flowing on a casing from a point opposite a shale bed and leaving the casing at a point opposite a sand formation containing brine usually is discharged uniformly over the casing surface. If anodic areas are highly localized, then a positive self-potential current of sufficient magnitude would tend to leave the anodic areas at greater-than-average current density. Self-potential in this case has the effect of increasing the potential of the local corrosion cells.

FLOWING FORMATION WATER

Body corrosion may be accelerated if formation water flows behind the casing from one formation to another. Flow of formation water will increase the chance of water contact with the casing surface. Current in the corrosion cells that is set up at the formation water-mud boundary is increased by the movement of the water. The current-producing capacity of this cell will be greater than in the static system, and the current will last a longer time. The accelerative corrosion effects of the flowing formation water are not produced, however, if oxygen is absent from the water and if oxygen is also removed from the mud surrounding the casing.

LABORATORY STUDY OF OXYGEN SCAVENGERS

The four kinds of casing corrosion discussed in this paper were seen to be largely the result of differential oxygen concentration attack. Therefore, oxygen scavengers were investigated in the laboratory as a means of controlling the external corrosion of oil-string casing.

Laboratory investigations showed that water-soluble reducing agents, such as ferrous chloride, ferrous hydroxide, powdered iron, stannous chloride and hydrazine, react with dissolved oxygen in alkaline drilling muds. These investigations also showed that the potential of iron in such treated mud shifts in the anodic direction as oxygen is consumed. Complete removal of the dissolved oxygen resulted in virtual cessation of corrosion.

Standard API tests of drilling-fluid properties showed that the use of ferrous chloride or stannous chloride adversely affected the physical properties of some test fluids and that mud reconditioning frequently would be necessary if these oxygen scavengers are used. Similar tests with hydrazine showed no adverse effects. Table 7 compares the physical properties of a typical alkaline-emulsion drilling fluid before and after the addition of 1.5 lb/bbl of 35 per cent hydrazine-water solution. Table 7 shows that the addition of 1.5 lb/bbl of hydrazine had no adverse effect on the drilling-fluid properties. The amount of hydrazine used in this test is estimated to be about 100 times the amount needed to consume the oxygen dissolved in typical air-saturated drilling fluid.

TABLE 7—EFFECT OF HYDRAZINE ON THE PHYSICAL PROPERTIES OF A TYPICAL ALKALINE DRILLING FLUID

Fluid Property	Before Treatment	After Treatment
Weight, lb/cu ft	78	78
Marsh Viscosity $\left(\frac{1{,}500\ cc}{1\ qt}\right)$, sec.	45	45
Gel Strength (10 min)	0.0 & 1.5	0.0 & 1.5
Water Loss (30 min; 100 psi), ml	1.2	1.2
Filter Cake (API), in.	1/32	1/32
pH	12	12
Temperature, °F	135	135

Standard tests also were made to study the effect of hydrazine on the physical properties of set cement. Results of the tests are shown in Table 8.

Differences noted in the tensile and compressive strengths of treated and untreated cements are not considered to be significant. The spread of data for multiple tests was greater than the difference in the averages shown in Table 8. Apparently, hydrazine has no adverse effect on the physical properties of oilwell cement.

Electrochemical cells were set up to study the effect of hydrazine on the potential of J-55 steel electrodes in treated and untreated alkaline drilling-fluid samples. The objective of the study was to find out if the potential of iron could be shifted sufficiently far in the anodic direction to prevent corrosion attack on the test coupons. Potentials were measured for several months, and results of the tests are shown in Table 9.

Table 9 shows that the initial potential of sand-blasted J-55 steel in untreated drilling fluid was about 390 mv (538 to 146 mv) more anodic (negative) than the mill-scale-coated J-55 steel. This indicates that the bare steel was corroding because of the bare steel-mill scale couple existing in the oxygen-saturated mud. Such a couple can produce rapid pitting corrosion if the area of bare steel is small compared to the surrounding area of mill scale. The table shows also that the potentials of both the bare steel and mill-scale-coated steel are shifted in the anodic direction by the consumption of available oxygen. In the untreated mud, oxygen consumption is accomplished by the corrosion reaction shown by Eqs. 1 through 4. In the hydrazine-treated mud, oxygen reacts with the hydrazine and is converted to water.

$$N_2H_4 + O_2 = N_2 + 2H_2O \quad . \quad (5)$$

Potential shifts in the anodic direction indicate a reduction in the general corrosion tendency, while the disappearance of potential differences between the bare steel and the mill-scale indicates the disappearance of the tendency for pitting corrosion.

This reaction shows that hydrazine can have no deleterious effect on the drilling mud because its reaction products are only water and nitrogen gas. Hydrazine is an alkaline material and will have a slight tendency to raise the pH of some treated muds.

The next section of the paper describes results of field tests with hydrazine injected into the mud used in cementing several wells.

HYDRAZINE FIELD TESTS

Hydrazine was injected into the drilling fluid left behind each casing in four test wells in two Southern California oil fields. Three untreated wells also were selected in the same field for comparison purposes. Treated and untreated test wells in each field were selected because of the similarity in depth, casing size, method of completion and kind of mud used to drill and complete each well. Information about the test wells is given in Table 10.

Hydrazine effectiveness can be estimated from the difference in the cathodic currents needed to protect treated and untreated wells. Consumption of available oxygen reduces corrosion and reduces the amount of cathodic current needed to protect a well. Comparison of current requirements for treated and untreated wells, therefore, should be an indirect measure of hydrazine effectiveness. Cathodic current requirements during these tests were measured by the "null" potential method that was first proposed by Pearson[7] in 1942.

A series of direct currents of increasing strengths was applied to each test casing, and the potential of each casing was measured between the wellhead and a remote reference electrode (Cu, $CuSO_4$ half cell) for each current immediately after the current was interrupted. Cathodic current requirements then were estimated from the intersection of the straight-line portions of the potential vs log-current curves plotted from this null-potential data. Representative curves are shown in Fig. 11.

Fig. 11 shows that a current of 36 amps would be needed to protect untreated Well B-1. Fig. 11 also shows that hydrazine-treated Well B-5 required only a current of 17 amps for protection. Current requirements were determined for both wells approximately three years after each was completed. The lower current required to protect Well B-5 is attributed to oxygen scavenging by the hydrazine used to treat the well.

Current requirements were determined for each test well at various times over a four-year period. Results of the determinations are presented in Table 11 and plotted as current-vs-time curves in Figs. 12 and 13.

In Fig. 12 the assumption is made that the initial current requirements for Wells A-1 and A-2 are approximately 25 amps. This value was chosen because it is typical of current requirements measured for wells in the area.

Fig. 12 shows a marked reduction in current required during the first year for both the untreated and treated wells. The current-requirement reduction in the untreated well is attributed to partial oxygen consumption by corrosion. The much greater and more rapid reduction in current requirements in the treated well is attributed to the action of the hydrazine. It also will be noted that after the first year the current required to protect the treated well was

TABLE 8—EFFECT OF HYDRAZINE ON THE PHYSICAL PROPERTIES OF CLASS E OILWELL CEMENT*

Strength Property	Untreated		Hydrazine-Treated	
	1-Day	7-Day	1-Day	7-Day
Avg. Tensile (psi)	316	425	290	465
Avg. Compress. (psi)	3506	7361	2627	6031

*40-per cent slurry cured at 160°F.

TABLE 9—EFFECT OF HYDRAZINE ON THE POTENTIALS* OF SAND-BLASTED AND MILL-SCALE-COATED J-55 STEEL IN AN ALKALINE-EMULSION DRILLING FLUID

Hydrazine (lb/bbl)	Potential (— mv)** Initial		Final	
	SB	M-S	SB	M-S
0	538	146	525	513
0.2	577	363	619	620
1.0	575	462	643	652

*Potentials are referred to saturated calomel scale; add 80-mv to convert to Cu, $CuSO_4$ scale.

**SB = Sand Blasted, M-S = Mill-Scale.

TABLE 10—PERTINENT INFORMATION ABOUT THE TEST WELLS

Well No.	Well Depth (ft)	Hydrazine Treated	Kind of Drilling Mud
Field A			
A-1	10,100	No	High pH Oil Emul.
A-2	10,658	Yes	High pH Oil Emul.
Field B			
B-1	14,260	No	High pH Oil Emul.
B-2	13,950	No	High pH Oil Emul.
B-3	13,350	Yes	High pH Oil Emul.
B-4	14,195	Yes	High pH Oil Emul.
B-4*	13,947	Yes	High pH Oil Emul.
B-5	13,955	Yes	High pH Oil Emul.

*Well B-4 was re-drilled and recompleted.

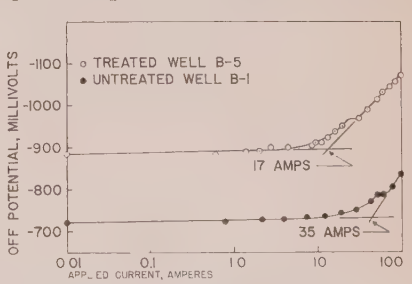

FIG. 11—EFFECT OF HYDRAZINE ON CATHODIC-PROTECTION CURRENT REQUIREMENTS.

TABLE 11—CURRENT REQUIRED TO PROTECT THE TEST WELLS

Well No.	Time from Completion (years)	Cathodic Current (amps)
Field A		
A-1	1.5	15½
	4.6	16
A-2	0.95	7½
	4.1	10
Field B		
B-1	2.0	35
	3.0	36
	4.8	20
B-2	0.98	28
	2.3	27½
	4.0	23
B-3	0.46	25
	0.79	23
	3.5	15
B-4	0.26	32
	0.59	28
Re-drill	1.8	15
B-5	0.19	20
	0.60	18
	2.9	17

TABLE 12 — HYDRAZINE REQUIREMENTS FOR VARIOUS VOLUMES OF DRILLING MUD

Drilling Mud (bbl)	Approx. Well Depth (ft)	35% Hydrazine	
		Gal	Lb
Up to 100	Up to 4000	6	48
100-200	4000- 6000	12	96
200-300	6000- 8000	18	144
300-500	8000-12000	30	240

nearly 45 per cent less than for the untreated well. Undoubtedly less corrosion took place on the outside of the casing in the treated well than on the casing of the untreated well during the first three to four years after completion.

Fig. 13 shows the effectiveness of hydrazine in another oil field. In each instance, the current required to protect a treated well rapidly decreased during the first year after completion and either continued a downward trend or leveled off during the next one to two years. There is no indication of an increase in current, which presumably could indicate depletion of the hydrazine and an influx of oxygen. Fig. 13 also shows that current requirements for the two untreated wells (B-1 and B-2) decreased with time, but at a much slower rate than in the treated wells. Hydrazine apparently makes its greatest contribution to the prevention of external casing failure during the first 12 to 18 months after a well is completed. This is a particularly important period because it is during this period that differential oxygen concentration

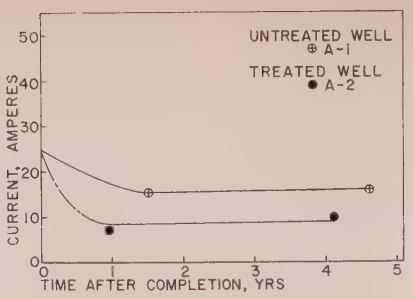

FIG. 12—EFFECT OF HYDRAZINE ON THE CORROSIVITY OF TEST WELLS IN FIELD A.

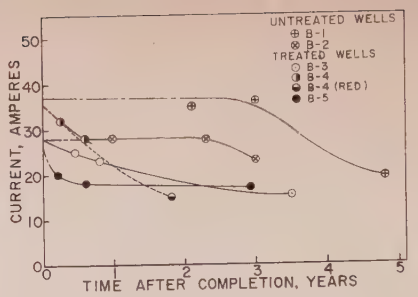

FIG. 13—EFFECT OF HYDRAZINE ON THE CORROSIVITY OF TEST WELLS IN FIELD B.

cells can cause the greatest amount of damage through pitting corrosion attack.

The favorable results from the laboratory and field tests showed that the use of hydrazine in the cementing mud was an effective, inexpensive and easily applied method for controlling external casing corrosion. The material has been used in over 200 wells of Standard Oil Co. of California.

CONCLUSIONS

1. External casing corrosion can be classified into four major types: water-line, casing-casing, collar and body. A mechanism for each type of external corrosion can be developed from principles of differential aeration.

2. Casing leaks are caused by highly localized corrosion attack.

3. The use of oxygen scavengers to control the corrosion attack is based on corrosion mechanisms developed from the principles of differential aeration. Laboratory tests show that hydrazine is a convenient and effective oxygen scavenger for use in oil wells.

4. Field tests of hydrazine show that the use of hydrazine in cementing mud materially reduces cathodic-protection current requirements for treated wells. This reduction in current requirements is interpreted to indicate substantial consumption of oxygen around the oil-string casing and consequent reduction in external corrosion.

5. Hydrazine appears to have particular usefulness for removing oxygen during the first 12 to 18 months after well treatment. Hence, a significant amount of corrosion can be prevented early in the life of a well when differential oxygen concentration cells are most active and able to cause pitting corrosion at a high rate.

6. Test results do not show any significant reduction in hydrazine effectiveness even after use in wells for three to four years. It is possible that a major part of the effectiveness may last the life of the treated well.

ACKNOWLEDGMENT

The authors wish to express their appreciation to R. V. Scott of Standard Oil Co. of California, Western Operations, Inc., for his cooperation and assistance in carrying out the field evaluation of hydrazine.

REFERENCES

1. Battle, J. L.: *Corrosion* (1957) **13**, 62.
2. Greathouse, W. D., Lehman, J. J., Landers, J. E. and Sudbury, J. D.: "Field Evaluation of Cathodic Protection of Casings", *Trans.*, AIME (1959) **216**, 354.
3. Evans, U. R.: *Jour. Inst. Metals* (1923) **30**, 239.
4. Evans, U. R.: *An Introduction to Metallic Corrosion*, Arnold Press (1951).
5. Doig, K. and Wachter, A.: *Corrosion* (1951) **7**, 213.
6. de Witte, L. and Radd, F. J.: "Corrosion of Oil Well Casing by Earth Currents", *Trans.*, AIME (1955) **204**, 66.
7. Pearson, J. M.: *Trans.*, Electrochem. Soc. (1942) **81**, 485. ★★★

The Linear Displacement of Oil from Porous Media by Enriched Gas

H. J. WELGE
E. F. JOHNSON
S. P. EWING, JR.
F. H. BRINKMAN
MEMBERS AIME

JERSEY PRODUCTION RESEARCH CO.
TULSA, OKLA.

ABSTRACT

This paper presents a method for predicting the manner in which oil will be displaced from a porous body by enriched gas. The calculations apply to a gas rich enough to give a partially, but not a completely, miscible displacement. The method — a three-component, two-phase analysis — takes into account condensation of some of the intermediate hydrocarbons from the injected gas into the oil, as well as enhanced volatility of heavier hydrocarbons at elevated pressures and temperatures. The condensation swells the oil and decreases its viscosity, thus aiding in its recovery.

The calculations have been extended to apply to actual crude oil-natural gas systems by arranging the components into three groups according to their volatility. As an approximation, each group is then treated as a single component in the analysis. The influence of an angle of dip for an inclined displacement is also taken into account.

The recovery predictions are corroborated by experiments which used both consolidated sand cores and unconsolidated glass beads. In some of these tests, actual live crude oil was displaced by a multicomponent gas typical of enriched gases used in oil fields.

INTRODUCTION

This paper presents a method for predicting the amount of oil that can be displaced from a homogeneous, linear, porous body at various stages during the injection of enriched, or "wet", gas. The porous body can be in either a horizontal or an inclined position. This type of displacement is sometimes known as "condensing gas drive".[1-4] The method is developed especially for the case in which the injected gas is enriched enough to be partially, but not completely, miscible with the reservoir oil. The need for a calculative procedure for this type of operation is emphasized by the number of field projects where completely miscible drives are not practical, but where near-miscible conditions are feasible.

The factors taken into account in the predictive calculations include: (1) the condensation of gas components into the oil, with a resulting increase in oil volume; (2) the lowering of oil viscosity by the addition of lighter ends from the gas; (3) the increase in oil volatility at high temperatures and pressures; and (4) the physical displacement of the oil by the gas.

The techniques developed in the paper can be extended to other nonequilibrium displacement processes. Other such processes that we have analyzed include a displacement by lean gas which stripped intermediates from the oil, and a water flood in which the water contained in solution a substance somewhat soluble in the oil.

ANALYSIS OF ENRICHED-GAS DRIVE

GENERAL PRINCIPLES

Our method for predicting the amount of oil that can be displaced by an enriched gas uses an analogy between a three-component and a multicomponent system.[2] The predictive method is based on these assumptions: (1) constant, or nearly constant, pressure; (2) complete equilibrium by diffusion perpendicular to the main direction of flow, but no significant mixing along the direction of flow; (3) constant injection velocity; and (4) flow in a linear porous body.

The composition of a liquid or a vapor with respect to three components can be plotted on a three-component, or ternary, diagram like that in Fig. 1. Let Point A represent the composition of the oil originally in place. In this case, Oil A is undersaturated with gas. If Point A lay on the equilibrium Curve BF, the oil would be saturated. In the extreme case where the original oil contained no intermediates or dissolved gas, Point A would lie at the lower left-hand corner of the ternary diagram.

In a displacement of Oil A by Gas D, there will be a progressive change in the composition of the oil phase as more and more gas is brought into equilibrium with the oil. The end result of this progressive change is an oil having the composition represented by Point F. This oil is richer in intermediate hydrocarbon and methane than the original oil and, therefore, has a greater forma-

Original manuscript received in Society of Petroleum Engineers office July 11, 1960. Revised manuscript received June 19, 1961. Paper presented at 35th Annual Fall Meeting of SPE, Oct. 2-5, 1960, in Denver.

[1]References given at end of paper.

Discussion of this and all following technical papers is invited. Discussion in writing (three copies) may be sent to the office of the *Journal of Petroleum Technology*. Any discussion offered after Dec. 31, 1961, should be in the form of a new paper. No discussion should exceed 10 per cent of the manuscript being discussed.

This page of *Petroleum Transactions, AIME* follows page 711. The intervening non-Transactions pages appeared in *Journal of Petroleum Technology*.

tion volume factor and a lower viscosity than the original oil.

BC is the particular tie line, or line connecting liquid and vapor compositions in equilibrium, that will pass through Point A if extended (Fig. 1). EF is the particular tie line that will pass through Point D.

The actual displacement process is visualized as follows (later in the paper, the conclusions given are verified both mathematically and experimentally). As wet gas enters a porous body originally saturated with liquid, various gas saturations form at different positions along the porous body. As injection continues, gas moves farther downstream. With a constant rate of injection each gas saturation moves at a constant velocity, with the lower saturations moving fastest — indicating gas fingering into the oil. Because of the constant-velocity condition, a saturation profile in terms of distance need be established for only one time; as injection continues, the profile for any other time can readily be derived by simply stretching the original profile. Further explanation and justification of this simplifying principle will be found in Appendix B.

Fig. 2 shows a typical saturation profile resulting from wet-gas injection. This profile has been divided into various regions, I through V, to illustrate both the phase behavior and the process by which the gas physically displaces the oil. The liquids and vapors present at various points in Fig. 2 have compositions shown in Fig. 1. For example, in Fig. 2, the original oil (A) has

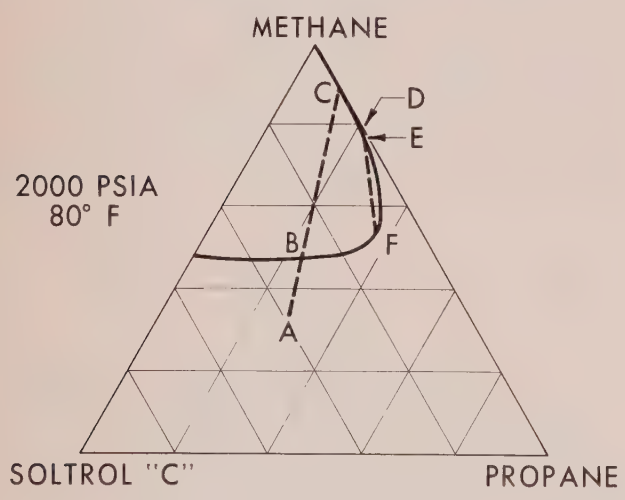

FIG. 1—PHASE DIAGRAM FOR THREE-COMPONENT SYSTEM.

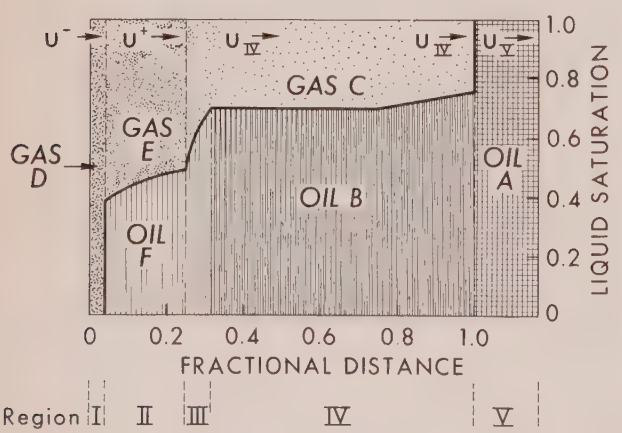

FIG. 2—LIQUID DISTRIBUTION IN WET-GAS DRIVE.

the composition represented by Point A in Fig. 1. Oil A is present in the downstream part of the porous body, ahead of the farthest point of gas penetration (Region V). After contact with the advancing gas (Region IV, Fig. 2), the oil composition is changed to that of Point B in Fig. 1. The oil gradually becomes enriched by the wet gas in Region III, and the fully enriched liquid represented by Point F in Fig. 1 is found near the point of enriched-gas injection in Region II of Fig. 2. If the heaviest component (or components) in the enriched liquid has appreciable volatility, the liquid phase will be completely evaporated near the inlet end of the porous body. Thus, a region (Region I) that contains only injected Gas D will be formed.

STARTING DATA AND EQUATIONS USED

In addition to the equilibrium information given in the ternary diagram just described, the following starting data are needed to predict the performance of a wet-gas drive.

1. Densities of the liquids and gases existing in equilibrium, whose compositions are shown on the ternary diagram. Liquid and gas densities were estimated by the methods of Standing[5] and Maxwell,[6] respectively.

2. Viscosities of the liquids and gases existing in equilibrium. These viscosities were estimated by the methods of Beal[7] and Maxwell,[6] respectively. For check purposes, a few liquid viscosities were measured by the standard rolling-ball technique.

3. Relative permeabilities to gas and to liquid as a function of saturation. The k_{rg}/k_{ro} ratios for the porous media used are shown in Fig. 3.

4. Absolute permeability and hydrocarbon-occupied porosity.

5. Composition of the gas to be injected and the rate of gas injection.

6. Average dip angle, if any, and average cross-sectional area of the porous body exposed to flow.

7. Operating temperature and average operating pressure.

The equations used (see Appendix A for their development) have the form of a material balance. This balance states: the mass of any one of the three components (Component 1, 2, or 3) that enters a thin slice of the porous body in a short time interval, less the mass of that component leaving the section, is equal to the mass accumulated within the section.

The material-balance equations are of two types.

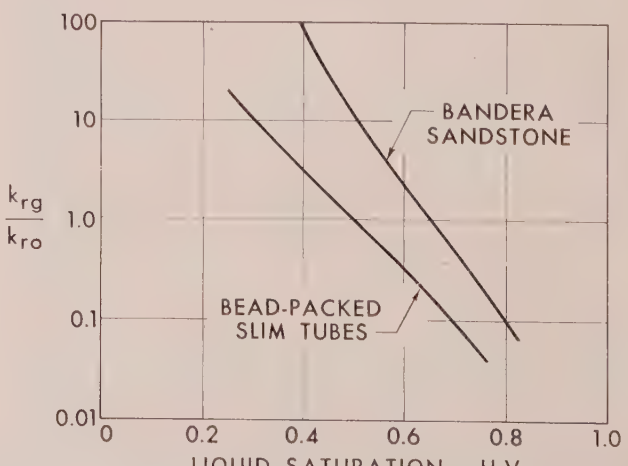

FIG. 3—RELATIVE PERMEABILITY OF POROUS MEDIA USED.

They are ordinary algebraic equations if they are applied to the motion of a discontinuity, such as the boundary between Regions I and II in Fig. 2. They are partial differential equations if they are applied to flow within a region, such as Region III in Fig. 2, in which the concentrations change gradually.

The key relations needed to construct a plot of saturation against distance, like that shown in Fig. 2, are those giving the velocities with which saturations move. In regions (such as Regions II or IV) in which the concentrations do not change, the velocity will be given by

$$\left(\frac{dx}{dt}\right)_{S_o} = u\frac{df}{dS_o} \quad \ldots\ldots\ldots (1)$$

Eq. 1 has been derived previously.[3] In Region III, where the gas and the oil are changing in concentration, the velocity is given by

$$\left(\frac{dx}{dt}\right)_{S_o} = u\frac{f+\varepsilon}{S_o+\varepsilon} \quad \ldots\ldots\ldots (2)$$

Both Eqs. 1 and 2 follow from material-balance considerations. Eq. 2 is derived in Appendix A.

Since any particular saturation moves at a constant velocity, its position at any time will be the product of this velocity and the time at which its position is desired. The time scale starts at the start of the wet-gas injection.

In predicting the performance of a wet-gas displacement, we first calculate the velocities with which liquid saturations move in Regions II, III and IV (Fig. 2), in that order.* Then we obtain the time of arrival of each saturation at the outflow face of the porous body. This time is directly proportional to the cumulative volume of gas injected.

Finally, for any one of these arrival times, we can calculate the mass of Component 3 (which represents stock-tank oil) left in the porous body. In principle, this calculation is carried out by integrating under a saturation profile like that shown in Fig. 2. Account must, of course, be taken of the different oil concentrations in the various regions shown in Fig. 2. If the oil has some volatility, the relatively small amount of it present in the gas space should also be taken into account. The mass of the residual oil is expressed as a fraction of the mass of Component 3 originally present in the porous body.

The fraction of the stock-tank oil *recovered* at any of the afore-mentioned times will, of course, be the complement of the fraction of residual oil. Further details on this calculation are illustrated in the sample calculation given in Appendix C.

EXPERIMENTAL WORK TO TEST THE ANALYSIS

Slim models of Bandera sandstone and of glass beads were used in the displacement work. Displacement tests using a strictly three-component system (methane, propane and Soltrol "C", Fig. 1) were carried out in the sandstone models. Tests using a multicomponent system in which an enriched gas displaced a saturated crude oil were carried out in the glass-bead models. The required relative permeability data, shown in Fig. 3, were

*To determine the saturation at the start of each region, we use the following equations found in Appendix A. For Region II, we use Eqs. 6, 8, and 9; for Region III, we set equal the velocities given by Eqs. 1 and 2 above; for Regions IV and V, refer to section beginning under the heading "Calculations in Region IV", Appendix A.

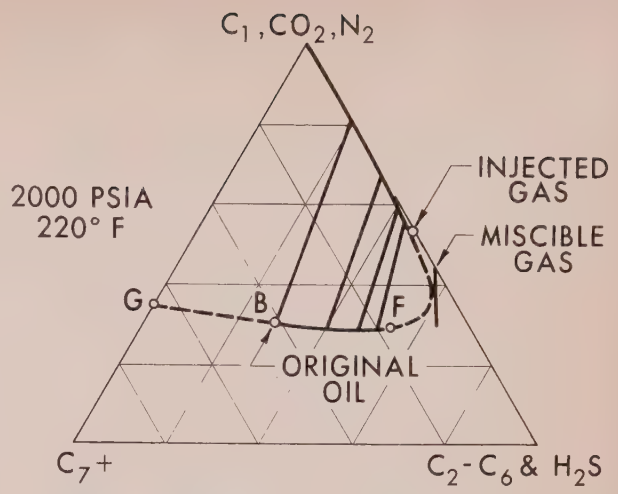

FIG. 4—PHASE DIAGRAM FOR CRUDE-OIL SYSTEM.

obtained for each model by displacing oil with an insoluble gas (gas drive).

The Bandera sandstone models, which were 2 in. in diameter and about 18 ft in length, were confined in low-melting alloy cast inside a steel pipe. They had a permeability of about 10 md. Connate water was established by displacing water from the core with a viscous refined oil. The oil was then displaced with Soltrol "C", a close-cut refined oil approximating n-$C_{12}H_{26}$ in composition and physical properties.

In the work done with unconsolidated glass beads, the beads were packed in stainless-steel tubes about ¼ in. in diameter and 20 ft in length. The bead packs had permeability ranging from 4 to 25 darcies. Each tube was coiled inside an oven to maintain the proper reservoir temperature. For inclined displacement, the tube was wound in a helix of constant pitch, and the helix was placed inside a larger heated tube set upright.

Crude oil-natural gas systems can be described by arranging their components in three groups. The following grouping, shown in the ternary diagram of Fig. 4, was found best with the crude oil-gas system used: Component 1 — N_2, C_1, CO_2; Component 2 — C_2-C_6 and H_2S; and Component 3 — C_{7+}.

The diagram in Fig. 4 was arrived at by analyzing samples of liquid and of coexisting vapor produced in an actual horizontal displacement from a slim tube. We have also found, however, that tests in a PVT cell may possibly be used to establish the ternary diagram. Reservoir oil is placed in the cell with gas having the composition of the enriched gas that is to be injected into the porous body. The fluids are then brought into equilibrium and analyzed.

The reservoir crude had a saturation pressure of about 2,000 psia. The actual compositions (mol fractions) of this crude oil, of the gas in equilibrium with it and of the injected gas are shown in Table 1.

RESULTS

The experimental results with both Bandera sandstone and glass beads confirm the theoretical predictions. Satisfactory confirmation is shown for multicomponent as well as for three-component systems, and for inclined as well as for horizontal systems. The results, together with the predictions, are shown in Figs. 5 and 6. In these figures, gas throughput is expressed in terms of the

TABLE 1—MEASURED COMPOSITIONS (MOL FRACTIONS) OF CRUDE OIL, EQUILIBRIUM GAS AND INJECTED GAS IN PVT CELL TESTS

Component	Crude Oil**	Equilibrium Gas	Injected Gas
N_2	0.0036	—	—
C_1	0.2422	0.733	0.430
CO_2	0.0549	0.079	0.117
C_2	0.0939	0.113	0.180
H_2S	0.0126	—	0.012
C_3	0.0635	0.056	0.161
iC_4	0.0130	—	—
nC_4	0.0422	0.013	0.062
iC_5	0.0105	—	—
nC_5	0.0264	0.006	0.038
C_6	0.0266	—	—
C_{7+}*	0.4106	—	—
	1.0000	1.000	1.000

Specific gravity of C_{7+} = 0.875; Molecular weight of C_{7+} = 248.
**Stock-tank gravity of crude oil was about 36° API.

hydrocarbon-occupied pore space in the porous body, that is, in terms of hydrocarbon volumes (HV).

Various arrangements were tried as alternatives for the grouping proposed in the preceding section on experimental work. For example, we tried the following grouping: Component 1 — N_2, C_1, CO_2; Component 2 — C_2-C_5 and H_2S; and Component 3 — C_6^+. It will be seen that this arrangement differs from the preceding one in that the hexane is considered part of Component 3 instead of part of Component 2. With this change, the predicted oil recoveries shown by the lower curve in Fig. 6 were slightly increased. For example, at 1.4 HV of wet-gas injection, the recovery was increased by about 0.02 units on the vertical scale, i.e., from 0.80 to 0.82.

Other trial arrangements of components included grouping ethane with Component 1 instead of with Component 2 and grouping carbon dioxide with Component 2 instead of with Component 1. In no case did a change in the grouping raise or lower the recovery curve by more than 0.05 units on the vertical scale of Fig. 6.

The method of calculation has been programed for the IBM 650 computer. The solution of a wet-gas displacement problem requires about an hour's time on this medium-speed machine.

CONCLUSIONS

An analysis for predicting recovery of oil by wet-gas injection into homogeneous, linear, porous bodies has been developed and tested. The method, a three-component analysis, fully takes into account a number of mechanisms by which wet gas displaces oil. These mechanisms include: (1) condensation of some of the gas into the oil, with a resulting increase in volume; (2) reduction of oil viscosity by the addition of lighter ends; (3) increase in oil volatility, particularly at high temperatures and pressures; and (4) physical displacement of the oil by the gas.

The accuracy of the prediction method has been proved by laboratory experiments, some of which used actual crude oil. Experimental recovery from both consolidated sandstone and slim, bead-packed tubes agreed well with that predicted.

NOMENCLATURE*

A = cross-sectional area of hydrocarbon-occupied pores, sq cm

$a_j = m_{oj} - m_{gj}$, gm/cc

$a'_j = \frac{d}{dC}(m_{oj} - m_{gj})$, gm/cc

$B = S_o\, m_{o1} + (1 - S_o)\, m_{g1}$, gm/cc

C = parameter denoting the concentration of Component 3 in liquid phase. C is given by (mol fraction of Component 3 in liquid free of intermediates) less (mol fraction of Component 3 in enriched liquid)

D = determinant

$F = f\, m_{o1} + (1 - f)\, m_{g1}$, gm/cc

f = fraction of liquid flow in total flow

$$= \frac{k_{ro}\,\mu_g}{k_{ro}\,\mu_g + K_{rg}\,\mu_o} + \frac{k\,(\rho_o - \rho_g)\,g \sin\theta/\phi}{\mu_o/k_{ro} + \mu_g/k_{rg}} \times \frac{1}{u}$$

$f_s = df/dS_o$ (in the immediately preceding expression, the quantities that need derivatives are k_{ro} and k_{rg})

G_i = accumulated gas injected (hydrocarbon volumes) = $t\,\bar{u}/L$

L = length of porous body, cm

M = average molecular weight of component in the injected gas

*For other symbol definitions, see AIME Symbols List in *Trans.*, AIME (1956) **207**, 363.

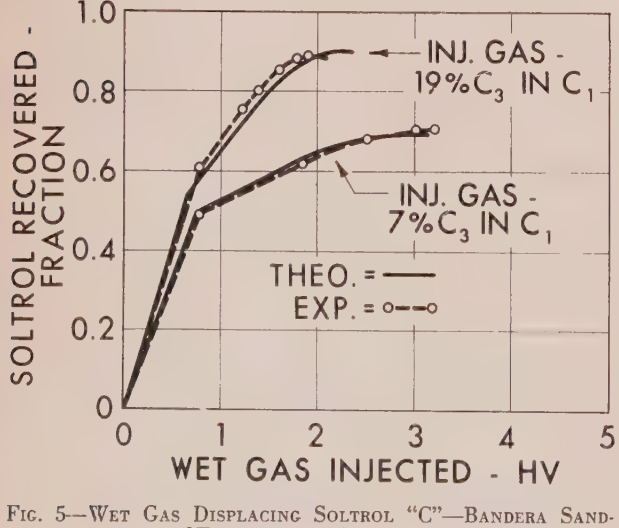

FIG. 5—WET GAS DISPLACING SOLTROL "C"—BANDERA SANDSTONE, 80°F, 2,000 PSIA, HORIZONTAL DRIVE.

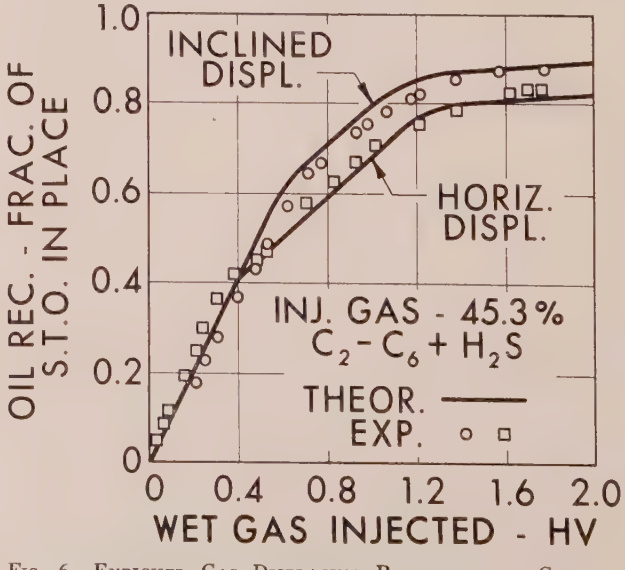

FIG. 6—ENRICHED GAS DISPLACING RECONSTITUTED CRUDE—BEAD-PACKED TUBES, 2,000 PSIA, 220°F.

m_{gj} = mass of Component j per unit volume of gas = (mass fraction of Component j in the gas phase) × (gas density), gm/cc

m_{oj} = mass of Component j per unit volume of liquid = (mass fraction of Component j in the liquid phase) × (liquid density), gm/cc

Res = amount of Component 3 remaining in porous body, gm

S_o = liquid saturation

t = time after start of gas injection, sec

u = volumetric flow per unit cross section of hydrocarbon pore space, cm/sec

X = distance from inlet end along porous body, cm

y^-_1, y^-_2 = mol fraction of Component 1 or Component 2 in the injected gas

z^- = supercompressibility of injected gas

$\alpha_1 = m^+_{o2} m^+_{g3} - m^+_{o3} m^+_{g2}$, $(gm/cc)^2$

$\alpha_2 = m^+_{o1} m^+_{g3} - m^+_{o3} m^+_{g1}$, $(gm/cc)^2$

$\gamma_3 = \dfrac{m_{g3}}{m_{o3} - m_{g3}}$

$\varepsilon = D\,[a_j, m'_{gj}, m_{gj}]/D\,[a_j, a'_j, m_{gj}]$

$\zeta = \dfrac{f + \varepsilon}{S_o + \varepsilon}$, cm/sec

$\eta = -D\,[a_j, a'_j, m'_{gj}]/D\,[a_j, a_j', m_{gj}]$

θ = angle of dip of porous body, degrees of arc

$\sigma = y\dfrac{S_o - f}{S_o + \varepsilon}$

ϕ = hydrocarbon-occupied porosity

SUBSCRIPTS

a, b = pertaining to the discontinuity at farthest point of gas penetration for case a or base b

$C, C + \Delta C$ = pertaining to the concentration C or $C + \Delta C$

e = pertaining to the discontinuity at the point where liquid is first encountered by the injection gas (i. e., the evaporation front)

j = pertaining to any one of the three components: light ends (1), intermediates (2) and heavy ends (3)

S = derivative with respect to S_o

1, 2, 3 = pertaining to Component 1, 2 or 3; or pertaining to the start, 1, or to the end, 2, of a step in Region III

I, II, III, IV, V = pertaining to Regions I, II, III, IV or V

SUPERSCRIPTS

$'$ = ordinary derivative

$-$ = pertaining to the upstream side of the first discontinuity encountered by the injected gas

$+$ = pertaining to the downstream side of the first discontinuity

ACKNOWLEDGMENTS

The authors wish to acknowledge the contributions of A. T. Clothier and W. P. Banks, who developed the experimental methods for determining the ternary diagram for the multicomponent system, and of S. D. Yoelin, who programed and carried out the calculations on the automatic computer.

REFERENCES

1. Stone, H. L. and Crump, J. S.: "Recovery of Oil by Condensing Gas Drive", *Trans.*, AIME (1956) **207,** 105.
2. Slobod, R. L. and Koch, H. A., Jr.: "High Pressure Gas Injection Mechanism of Recovery Increase", *Drill. and Prod. Prac.*, API (1953) 82.
3. Clark, N. J., Schultz, W. P. and Shearin, H. M.: "New Injection Method Affords Total Oil Recovery", *Pet. Eng.* (Oct., 1956) B45.
4. Arnold, C. W., Stone, H. L. and Luffel, D. L.: "Displacement of Oil by Rich Gas Banks", *Trans.*, AIME (1960) **219,** 305.
5. Standing, M. B.: *Oil Field Hydrocarbon Systems,* Reinhold Publishing Corp., N. Y. (1952) 33.
6. Maxwell, J. B.: *Data Book on Hydrocarbons,* D. Van Nostrand Co., Inc., Princeton, N. J. (1950).
7. Beal, C.: "Viscosity of Air, Water, Natural Gas, Crude Oil, and Its Associated Gases at Oil Field Temperatures and Pressures", *Trans.*, AIME (1946) **165,** 94.
8. Buckley, S. E. and Leverett, M. C.: "Mechanism of Fluid Displacement in Sands", *Trans.*, AIME (1942) **146,** 107.
9. Welge, H. J.: "A Simplified Method for Computing Oil Recovery by Gas or Water Drive", *Trans.*, AIME (1952) **195,** 91.
10. Miller, F. H.: *Partial Differential Equations,* John Wiley & Sons, Inc., N. Y., 127.
11. Johnson, E. F. and Welge, H. J.: "An Analysis of the Linear Displacement of Oil by Gas-Driven Solvent", Paper No. 906-G presented at 32nd Annual Fall Meeting of SPE in Dallas (Oct. 6-9, 1957).
12. Hall, H. N. and Geffen, T. M.: "A Laboratory Study of Solvent Flooding", *Trans.*, AIME (1957) **210,** 48.

APPENDIX A

DERIVATION OF EQUATIONS AND OUTLINE OF CALCULATION PROCEDURE

EXISTENCE OF A REGION (II) OF CONSTANT COMPOSITION

Three material-balance equations must be written at the boundary between Regions I and II (Fig. 2), or the "evaporation front"—one equation each for Components 1, 2 and 3. These algebraic equations are:

$$\left(\frac{dX}{dt}\right)_e [S_o^+ m_{oj}^+ + (1 - S_o^+)\, m_{gj}^+ - m_{gj}^-] = u^+ [f^+ m_{oj}^+ + (1 - f^+)\, m_{gj}^+] - u^- m_{gj}^- \quad . \quad . \quad (3)$$

The symbols used are defined in detail in the Nomenclature. It should be noted that the subscript j may be either 1, 2, or 3. Each of the quantities m_{o1}^+, m_{o2}^+, m_{o3}^+, m_{g1}^+, m_{g2}^+, and m_{g3}^+ can be expressed in terms of a single concentration C^+, which is related to the mol fraction of Component No. 3 in the liquid phase (see Nomenclature).

The three equations (Eq. 3) contain, explicitly, three unknowns: $\left(\dfrac{dX}{dt}\right)_e$, S_o^+ and u^+. In addition, they contain implicitly the unknown C^+. Hence, one more equation is needed. This equation must be developed by assuming either that the concentrations do change or that they do not change just downstream from the front. The first of these two possibilities is ruled out in the discussion contained in the next three paragraphs.

If the first region containing some liquid (Region II in Fig. 2) is a region in which the concentration changes, the velocity of the saturation near the front

will be given by the following equation (which will be derived later in this appendix in the section "Continuity Equations—Region III").

$$\left(\frac{dX}{dt}\right)_{so} = u^{+}\frac{f+\varepsilon}{S_o+\varepsilon} \quad \ldots\ldots\ldots\ldots (2)$$

Combination of Eq. 2 with Eq. 3 for $j = 3$ (note that $m_{g3}^{-} = 0$, since no heavy ends are injected) gives the result

$$\frac{f+\gamma_3}{S_o+\gamma_3} = \frac{f+\varepsilon}{S_o+\varepsilon} \quad \ldots\ldots\ldots\ldots (4)$$

In Eq. 4, γ_3 and ε are different functions of concentration and are, in general, not equal. Thus, the only saturation values that satisfy Eq. 4 are $S_o = 0$ (and, hence, $k_{ro} = 0$ and $f = 0$) and $S_o = f$. These two cases can easily be ruled out because, in either case, Eq. 2 would require that this first liquid saturation travel with the same velocity as that of the gas stream itself, in the manner of a miscible type of displacement. This type is impossible for the range of concentrations considered for the injected gas. Thus, there will be a region (II) with a uniform (and somewhat enriched) composition.

DISCONTINUITY EQUATIONS APPLYING AT THE BOUNDARY BETWEEN REGIONS I AND II, AND RELATIONS NEEDED WITHIN REGION II

If the concentrations do not change, at least for some finite distance into Region II, the saturations there should move with velocities given by Buckley and Leverett.[8]

$$\left(\frac{dX}{dt}\right)_{so} = u\frac{df^{+}}{dS_o} \quad \ldots\ldots\ldots\ldots (1)$$

This relation will serve as the fourth relation needed, in connection with Eq. 3, to evaluate conditions at the evaporation front, or the boundary between Regions I and II.

The constant concentration C^{+} in Region II may now be obtained by first writing the three equations (Eq. 3) in determinant form, viewing the unknowns as $\left(\frac{dX}{dt}\right)_o$, u^{+} and u^{-}. The following expression for $\left(\frac{dX}{dt}\right)_o$ can now be obtained.

$$\left(\frac{dX}{dt}\right)_o = \frac{(0)}{D\,[S_o^{+}(m_{oj}^{+} - m_{gj}^{+}) + m_{gj}^{+} - m_{gj}^{-}, m_{gj}^{-}, f^{+}(m_{oj}^{+} - m_{gj}^{+}) + m_{gj}^{+}} \quad \ldots\ldots\ldots\ldots (5)$$

Since the velocity of the evaporation front is not zero, this relation requires that the denominator be zero. Setting this determinant equal to zero and noting that

$$m_{g1}^{-} = y_1^{-}\frac{P}{z^{-}RT}M_1,$$

$$m_{g2}^{-} = y_2^{-}\frac{P}{z^{-}RT}M_2$$

and

$$y_1^{-} = 1 - y_2^{-}, \quad \ldots\ldots\ldots\ldots (5a)$$

we obtain

$$y_2^{-} = \frac{M_1\alpha_1}{M_1\alpha_1 + M_2\alpha_2} \quad \ldots\ldots\ldots\ldots (6)$$

α_1 and α_2 are functions of C^{+}. Since y_2^{-} (the mol fraction of Component 2 in the injected gas) is given as starting data, Eq. 6 is solved by trial and error for C^{+}. Eq. 6 is equivalent to the requirement that the tie line passing through oil of composition C^{+}, if extended, passes also through the gas composition y_2^{-} (Point D, Fig. 1). However, we will use Eq. 6 to get more accuracy than can conveniently be obtained using a ternary diagram.

To find the liquid saturation just downstream from the evaporation front, we use Eq. 3, written for Component 3 (heavy ends).

$$\left(\frac{dX}{dt}\right)_o = u^{-}\frac{f^{+}+\gamma_3}{S_o+\gamma_3}. \quad \ldots\ldots\ldots\ldots (7)$$

Combining Eq. 7 with Eq. 1 gives

$$f_g^{*} = \frac{f^{+}+\gamma_3}{S_o+\gamma_3} \quad \ldots\ldots\ldots\ldots (8)$$

Eq. 8 can be solved for the liquid saturation by trial and error if the gas drive is horizontal. If it is inclined, f_g and f contain u^{+}. In this event, another equation must be used in conjunction with Eq. 8 to obtain S^{+} and u^{+} by trial and error. The other equation needed is obtained from Eq. 3, written for Component 1. Combining this Eq. 3 with Eq. 1 to eliminate $\frac{dx}{dt}$ gives

$$\frac{u^{-}}{u^{+}} = m_{g1}^{+} - (S_o^{+}f_g^{*} - f^{+})(m_{o1}^{+} - m_{g1}^{+}) - f_g^{*}(m_{g1}^{+} - m_{g1}^{-})/m_{g1}^{-} \quad \ldots\ldots\ldots\ldots (9)$$

To review, the four equations needed to this point are Eqs. 6, 8, 9 and 1, in that order.

Since the compositions of the liquid and gas do not change in Region II, the value obtained for u^{+} will remain constant until Region III is encountered. The velocity (or position at a given time) of any saturation in Region II is then given by Eq. 1.

CONTINUITY EQUATIONS—REGION III

Partial differential equations are required to arrive at the behavior in the region of the porous body in which condensation is occurring (Region III in Fig. 2). These describe material balances over a thin slice of the porous body. They may be written

$$\frac{\partial}{\partial t}[S_o m_{oj} + (1 - S_o)\,m_{gj}] = -\frac{\partial}{\partial X}\left\{u\,[fm_{oj} + (1-f)\,m_{gj}]\right\}, \quad \ldots\ldots (10)$$

where the subscript j may be 1 (light ends), 2 (intermediates) or 3 (heavy ends). Expanding and re-arranging Eq. 10 gives

$$\left[\frac{\partial S_o}{\partial t} + u\frac{\partial f}{\partial X}\right]a_j + \underline{\frac{\partial C}{\partial t}}\left[S_o a'_j + m'_{gj}\right] + \underline{\frac{\partial u}{\partial X}}\left[fa_j + m_{gj}\right] = -u\frac{\partial C}{\partial X}\left[fa_j' + m_{gj}'\right]. \quad (11)$$

Using these three equations, one can determine for specified values of concentration C the velocity of its motion $\left(\frac{dX}{dt}\right)_o$, the stream velocity u and the liquid saturation S_o. Solutions for the two underlined quantities, in terms of the other quantities present, can now be written. These solutions are developed with the aid of third-order determinants and take the form

$$\frac{\frac{\partial C}{\partial t}}{\frac{\partial C}{\partial X}} = \left(\frac{\partial X}{\partial t}\right)_C = u\frac{f+\varepsilon}{S_o+\varepsilon} - u\zeta, \quad \ldots\ldots (2)$$

and

$$\frac{\frac{\partial u}{\partial X}}{\frac{\partial C}{\partial X}} = \left(\frac{\partial u}{\partial C}\right)_t = u\,\eta\,\frac{S_o - f}{S_o + \varepsilon} = u\,\sigma\,. \quad . \quad (12)$$

The third equation obtainable from Eqs. 10 or 11 serves to solve for liquid saturations at various concentrations in Region III. Here one bears in mind that solutions of a particular wet-gas problem at various times of injection are all similar, except for stretching. (See Appendix B.) This means that a particular concentration will accompany a particular saturation. Accordingly in Eq. 10, both $S_o m_{oj} + (1 - S_o)\, m_{gj}$ and u $[f m_{oj} + (1 - f)\, m_{gj}]$ are functions of C only. Thus, a concentration C and a saturation S_o will move together with a velocity that can be obtained from Eq. 2, and also from the development of Eq. 10 as written for Component 1. (This velocity is obtained from Eq. 10 by the Lagrange method.) Since the same velocity is obtained by these two methods, we find

$$\left(\frac{\partial X}{\partial t}\right)_{S_o} = \left(\frac{\partial X}{\partial t}\right)_C = \frac{(u\zeta)_C + (u\zeta)_{C+\Delta C}}{2} = \frac{(uF)_{C+\Delta C} - (uF)_C}{B_{C+\Delta C} - B_C}\,. \quad . \quad . \quad . \quad . \quad . \quad (13)$$

Eqs. 13, 12 and 2 can be used to obtain the changes in S_o, u and X accompanying prescribed steps in C throughout Region III (Fig. 2). The integration with respect to change in C continues until C and the concentration of intermediates in the liquid are reduced to correspond to that represented by Point B in Fig. 1.

In addition, Eq. 2 must be used to define the initial saturation of Region III, which is the saturation at the boundary between Regions II and III. This saturation is common to both of these regions; hence, its velocity near the boundary between Regions II and III is the same in both regions. Thus, for this particular boundary saturation, we set Eq. 1 equal to Eq. 2. The resulting expression can then be solved for the saturation by trial and error.

CALCULATIONS IN REGION IV

Region IV, like Region II, is a section of the porous body in which the concentrations do not change. In Region II the liquid is enriched and has a composition corresponding to that of Point F in Fig. 1; in Region IV the liquid is leaner in intermediates and has a composition corresponding to that of Point B in Fig. 1.

A gas "bank" forms the boundary between Regions IV and V (Fig. 2). The pertinent material-balance relations at the gas bank are as follows.

$$\left(\frac{dX}{dt}\right)_b \left\{ (m_{oj})_V - [S_o\, m_{oj} + (1 - S_o)\, m_{gj}]_{IV} \right\} = (u\, m_{oj})_V - u_{IV}\,[f\, m_{oj} + (1 - f)\, m_{gj}]_{IV} \quad . \quad . \quad . \quad . \quad . \quad . \quad . \quad . \quad . \quad . \quad . \quad . \quad . \quad . \quad . \quad (14)$$

From this point on, there will be somewhat different methods of solution, depending on the kind of oil originally present in the porous body.

Undersaturated Oil

An undersaturated oil was displaced in the work the results of which are shown in Fig. 5. This oil was a completely "dead" oil consisting of Soltrol "C" only.

The velocity of the gas bank and the change in stream velocity (u) caused by gas dissolving at the bank can be determined from Eqs. 14. Two Eqs. 14 are written, one for Component 1 and one for Component 3. For original gas-free oil, $(m_{o1})_V = 0$. Also, Component 3 is not appreciably volatile in the absence of an intermediate hydrocarbon 2, which has been stripped from the gas in Region III, so that $(m_{g3})_{IV} = 0$. For these conditions, second-order determinants can be used to reduce Eqs. 14 to

$$\left(\frac{dX}{dt}\right)_b = \xi = u_{IV}\,\frac{f_{IV} + \psi_{IV}}{(S_o)_{IV} + \psi_{IV}} \quad . \quad . \quad . \quad (15)$$

where $\psi_{IV} = \dfrac{(m_{g1})_{IV}}{(m_{o1})_{IV} - (m_{g1})_{IV}}$.

$$\frac{u_V}{u_{IV}} = \frac{\xi}{u_{IV}}(1 - \psi_V) + \psi_V \quad . \quad . \quad . \quad . \quad . \quad . \quad (16)$$

where $\psi_V = -\dfrac{(m_{o3})_{IV}}{(m_{o3})_V}\,\psi_{IV}$.

For this case, the saturation needed in Eq. 15 turns out to be the saturation present at the end of Region III, and this saturation is constant throughout Region IV. This point is developed more fully in the following discussion of saturated oil.

Saturated Oil

The crude-oil experiments and calculations were based on the displacement of a reconstituted crude, saturated with gas under a pressure fairly typical of enriched-gas drives (2,000 psi). Two cases arose here, one for a slightly enriched injected gas (Case *a*), the other for a richer gas (Case *b*). To distinguish between Case *a* and Case *b*, one computes by trial and error the apparent saturation at the point of farthest gas penetration, using the equation[9]

$$\frac{df}{dS_o} = \frac{1 - f}{1 - S_o} \quad . \quad . \quad . \quad . \quad . \quad . \quad . \quad . \quad . \quad . \quad (17)$$

If the saturation at the boundary between Regions III and IV is lower than that given by Eq. 17 (Case *a*), Eq. 17 is used to determine the saturation at the gas bank. The velocity of the bank will be given by

$$\left(\frac{dX}{dt}\right)_a = u\,\frac{df}{dS_o}\,. \quad . \quad . \quad . \quad . \quad . \quad . \quad . \quad . \quad . \quad (18)$$

In this event (Case *a*), there will be a constant liquid saturation through the upstream end of Region IV and an increasing liquid saturation near the downstream end of Region IV. This is the case illustrated in Fig. 2.

When rich-enough gas is injected, or when very lean oil is displaced, or both (Case *b*), the excess condensation of intermediates will build up the liquid saturation at the boundary between Regions III and IV until it is *higher* than the saturation given by Eq. 17. In this case, the latter saturation must not be used because the former saturation will be present throughout all of Region IV. The velocity of the gas bank in this case (Case *b*) can be obtained by noting that $(m_{oj})_V = (m_{oj})_{IV}$ and, thus, that $u_V = u_{IV}$ since there is no condensation or evaporation between Regions IV and V. Eq. 14 written for any component now reduces to

$$\left(\frac{dX}{dt}\right)_b = u\left[\frac{1 - f}{1 - S_o}\right]_{IV}\,. \quad . \quad . \quad . \quad . \quad . \quad . \quad . \quad (19)$$

which gives the velocity of the gas bank.

GAS THROUGHPUT

The velocity of a saturation in Region II (or in Region IV) is given by the relation derived by Buckley and Leverett.[8]

$$\left(\frac{dX}{dt}\right)_s = u\,\frac{df}{dS_o} = u\,f_s \quad . \quad . \quad . \quad . \quad . \quad . \quad . \quad (1)$$

If we define $G_i = u\,t/L$, Eq. 1 becomes, for $X = L$,

$$G_i = \frac{u^-}{(u\ f_s)_{II}} \text{ or } \frac{u^-}{(u\ f_s)_{IV}} \quad . \quad . \quad . \quad . \quad . \quad . \quad (20)$$

This gives the hydrocarbon volumes of gas injection required to cause a particular saturation to reach the outflow face.

In like manner, when a particular saturation (or its associated concentration) in Region III reaches the outflow face, we have

$$G_i = u^- \left[\frac{S_o + \varepsilon}{u\ (f + \varepsilon)}\right]_{III} \quad . \quad . \quad . \quad . \quad . \quad . \quad . \quad (21)$$

FRACTIONAL OIL RECOVERY AND OVER-ALL MATERIAL BALANCE

The mass of residual stock-tank oil (Component 3), which is the oil that has not been produced, can now be calculated by integration from the information in a sketch such as Fig. 2.

For example, where exploitation has progressed far enough so that only Regions I and II remain inside the porous body, the integration gives the result,

$$Res_{II} = Au^+ t \Big\{ [(S_o f_s - f)_{II} - (S_o f_s - f)_e] (m_{o3} - m_{g3})_{II} + [(f_s)_{II} - (f_s)_e] (m_{g3})_{II} \Big\} \quad . \quad . \quad . \quad . \quad . \quad . \quad . \quad . \quad . \quad (22)$$

When the porous body contains Region III as well as Regions I and II, the additional residual oil contained in Region III is obtained by digital integration.

$$Res_{III} = A\ t \int [S_o\ (m_{o3} - m_{g3}) + m_{g3}]\ d\ (u\zeta) \quad (23)$$

To obtain the residual oil at first breakthrough of free gas, one must add the residual oil left in Regions II, III and IV.

For Case *a*, illustrated in Fig. 2, the saturation will be constant through part of Region IV, called Region IV A, but will rise in Region IV B. For this case, the residual oil in Region IV will be

$$Res_{IV} = A\ t \Big\{ [S_o\ (m_{o3} - m_{g3}) + m_{g3}]\ u\ [f_s - \zeta] \Big\}_{IVA} + A\ t\ u_{IV}\ (m_{o3} - m_{g3})_{IV} [(S_o f_s - f)_a - (S_o f_s - f)_{IVA}] + A\ t\ u_{IV}\ (m_{g3})_{IV}\ [(f_s)_a - (f_s)_{IVA}]. \quad (24)$$

The integrated residual oil can also be used to arrive at an over-all balance for any component, if one remembers that the amount of that component left in the porous body equals that originally present, plus that injected and minus the amount produced. This type of material balance will detect most of the possible errors in derivation, programing or calculation.

APPENDIX B

DERIVATION OF STRETCHING PRINCIPLE

A saturation profile during wet-gas injection undergoes simple "stretching" with time. The stretching principle can be justified either with the aid of diagrams (Fig. 7 and 8) or by mathematical development.

Fig. 7 shows two porous bodies, different only in that one of them is twice the length of the other. If each receives the same amount of wet-gas injection, their saturation profiles will be identical (as shown in Fig. 7). Suppose now that the length scale in Fig. 7(a) be modified to that in Fig. 8(a). In Fig. 8(a and b), the saturations are plotted on a scale such that the length in each case is unit length. On this basis, all the saturations will have moved twice as far in Case 8(a) as in Case 8(b). Also, since porous body (a) has half the pore volume of (b), it will have received twice as many hydrocarbon volumes of gas injection. It will now be noted from Fig. 8 that injection of twice as much gas causes a saturation to advance twice as far along the porous body. In other words, the distribution "stretches" in proportion to the time of injection, as mentioned before.

The mathematical justification depends on two facts. (1) The partial differential equations used are first order, and they contain the independent variables X and t in the derivatives only. (2) The boundary conditions are uniform; that is, the gas injected at $X = 0$ has the same composition at all times, and the oil in place originally (at $t = 0$) has the same composition at all positions.

The three equations (Eq. 10) may be written in the form,

$$\frac{\partial B_j\ (S_o, C)}{\partial t} + \frac{\partial F_j\ (u, S_o, C)}{\partial X} = Q_j = 0. \quad . \quad . \quad . \quad . \quad . \quad . \quad . \quad . \quad . \quad . \quad . \quad . \quad (10a)$$

Suppose, as a test, we set $S_o = S_o\ (C)$ and $u = u\ (C)$; that is, both are functions of concentration only. These latter relations imply that there will be a particular saturation and a particular velocity which will move or stretch along with a particular concentration.

Expansion of Eq. (10a) now gives

$$\frac{\partial B_j}{\partial C}\frac{\partial C}{\partial t} + \frac{\partial F_j}{\partial C}\frac{\partial C}{\partial X} = Q_j = 0. \quad . \quad . \quad . \quad (10b)$$

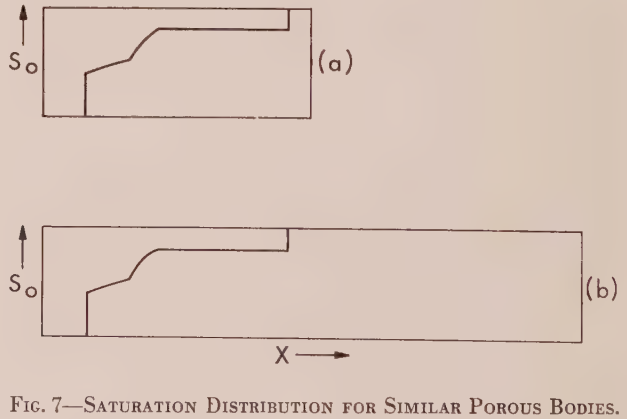

FIG. 7—SATURATION DISTRIBUTION FOR SIMILAR POROUS BODIES.

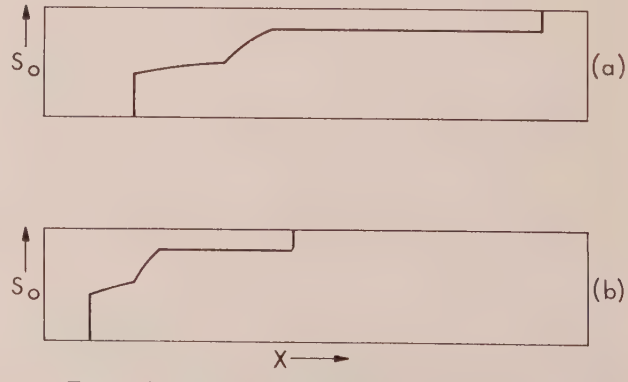

FIG. 8—REPLOTTED SATURATION DISTRIBUTION FOR SIMILAR POROUS BODIES.

Further, for simplicity set $\frac{\partial C}{\partial t} = p$ and $\frac{\partial C}{\partial X} = q$ in Eq. 10b. Then for three such first-order equations (Eq. 10b) to be mathematically consistent with each other requires[10]

$$\frac{\partial (Q_1, Q_2)}{\partial (t, p)} + \frac{\partial (Q_1, Q_2)}{\partial (X, q)} = 0,$$

$$\frac{\partial (Q_2, Q_3)}{\partial (t, p)} + \frac{\partial (Q_2, Q_3)}{\partial (X, q)} = 0,$$

and

$$\frac{\partial (Q_1, Q_3)}{\partial (t, p)} + \frac{\partial (Q_1, Q_3)}{\partial (X, q)} = 0. \quad . \quad . \quad . \quad . \quad . \quad (26)$$

Inasmuch as X and t do not explicitly occur in Eqs. 10a or 10b, all the Jacobians in Eq. 26 vanish and the consistency conditions are satisfied.

APPENDIX C

SAMPLE CALCULATION

The sample calculation presented here is for horizontal displacement of a live crude oil from a slim, bead-packed tube. The results of this calculation are shown as the lower recovery curve in Fig. 6. A horizontal displacement was chosen for simplicity; if the displacement were inclined, the calculations would be somewhat more complex (as explained in the text of the paper).

STARTING DATA

$m_{o1} = 0.019 + 0.0768C$
$m_{o2} = -0.0468 + 0.517C$
$m_{o3} = 0.874 - 1.09C$
$\rho_o = 0.8462 - 0.4962C$ (Sum of above three lines).

$m_{g1} = 0.0758 + 0.0094C$
$m_{g2} = -0.0597 + 0.385C$
$m_{g3} = -0.00744 + 0.03C$
$\rho_g = 0.00866 + 0.4244C$ (Sum of above three lines).

Minimum value of C corresponding to the concentration of original oil in place = 0.248. (To obtain this number, refer to Fig. 4. The mol fraction of Component 3 (C_{7+}) in the oil having the composition represented by Point G of Fig. 4 is 0.6586. Similarly, the mol fraction represented by Point B is 0.4106. Thus, the value of the concentration parameter C for the latter oil is 0.6586 − 0.4106 = 0.248.)

$y^-_2 = 0.453$ (see Table 1). ($y^-_2 = 1 - y^-_1 = 1 - 0.430 - 0.117$).

$M_1 = 21.99$ (weighted average molecular weight of C_1 and CO_2 in injected gas, Table 1). That is, $M_1 = (16 \times 0.430 + 44 \times 0.117)/(0.430 + 0.117)$.

$M_2 = 42.49$. This value is the weighted average molecular weight of the C_2-C_5 and H_2S fraction in the injected gas (Table 1). If the injected gas contained any C_6, the amount of C_6 would be included in computing the average molecular weight.

$P/RT = 0.00439$ gm mol/cc = 2,000 psia/(14.7 × 82.07 × 377.1°K).

Supercompressibility factor (z^-) for injected gas = 0.67.

$u^- = 0.0286$ cm/sec (average velocity of injected gas in hydrocarbon-occupied pore space), or 3.38 ft/hr.

$$\frac{k_{rg}}{k_{ro}} = \left[0.7369 \, \frac{1.1054 - S_o}{S_o - 0.03849} \right]^3 \text{(see Fig. 3)}.$$

$$\mu_g = \frac{0.01447}{0.758 - C}, \text{ cp.}$$

$$\mu_o = 1.4545 - 2.025\,C, \text{ cp.}$$

SAMPLE CALCULATIONS FOR EVAPORATION FRONT

By trial and error in Eq. 6, $C^+ = 0.496$. This value of C^+ corresponds to the mol fraction of Component 3 in the enriched liquid, whose composition is represented by Point F (Fig. 4). The tie line passing through Point F passes through the composition of the injected gas. For this value of C^+, $\gamma_3 = 0.02283$ and $\mu_o/\mu_g = 8.15$.

Now trial and error using Eq. 8 gives $S_o^+ = 0.2652$. This liquid saturation will be the first encountered by the entering gas (compare with left side of Fig. 2). For this saturation, k_{rg}/k_{ro} is computed to be 20.36; $d/dS_o\,[k_{rg}/k_{ro}] = -342.1$; $f = 0.00599$; and $f_s = 0.1000$.

Calculation of u^+, using Eq. 9, requires knowledge of m^-_{g1}, the mass of Component 1 per cubic centimeter of injected gas. According to Eq. 5a, $M^-_{g1} = 0.07885$ gm/cc. Now, use of Eq. 9 gives $u^+ = 0.02792$ cm/sec.

From Eq. 1, the velocity of the evaporation front is

$$\left(\frac{dX}{dt}\right)_s = 0.00279 \text{ cm/sec},$$

or about 1/10 the average stream velocity u^+.

Since the injected gas contains no heavy ends, their recovery will be complete when the evaporation front reaches the end of the bead-packed tube. The hydrocarbon volumes of injected gas needed to reach this recovery will be

$$\frac{u^-}{u^+}\left(\frac{dS_o}{df}\right)_s = u^- \Big/ \left(\frac{dX}{dt}\right)_s \quad . \quad . \quad . \quad . \quad . \quad . \quad (27)$$

For the case of the evaporation front, the hydrocarbon volumes will be 10.24.

CONDITIONS AT THE REGION II-REGION III BOUNDARY

The liquid saturation at this boundary is obtained by using the equation resulting from equating Eqs. 2 and 1.

$$\frac{df}{dS_o} = \frac{f + \varepsilon}{S + \varepsilon}.$$

The value of ε needed here (i.e., for $C = 0.496$) is calculated to be 0.8516, and the value of S_o obtained by trial and error is 0.4400. The corresponding values for f and f_s (u_o/u_g is still 8.15) are 0.0631 and 0.708, respectively.

CALCULATIONS FOR REGION II

Saturations lying between 0.4400 and 0.2652 lie inside Region II. Therefore, one can choose a number of saturations in this range, compute velocities of their motion by Eq. 1, and use Eq. 27 to calculate the amounts of gas injection needed to make them travel to the outflow face of the porous body. Using a method previously published,[9] one can also compute by integrating the fraction of the stock-tank oil that will be left in Region II for any of these amounts of gas injection.

To do this last, one uses Eq. 22 and bears in mind that, according to Eq. 1, the time needed for a saturation in Region II to reach the outflow face at $X = L$ will be

$$t = \frac{L}{u^+ (f_s)_{II}}. \quad . \quad . \quad . \quad . \quad . \quad . \quad . \quad . \quad . \quad . \quad (1a)$$

Substituting Eq. 1a into Eq. 22 and noting that the stock-tank oil originally in place is $AL\,(m_{o3})_{IV}$, the fraction of residual stock-tank oil will be

$$\frac{1}{(m_{o3})_{IV}\ (f_s)_{II}}\Big\{[(S_o f_s - f)_{II} - (S_o f_s - f)_e]$$
$$(m_{o3} - m_{g3})_{II} + [(f_s)_{II} - (f_s)_e]\,(m_{g3})_{II}\Big\}.$$

The fraction of stock-tank oil recovered will, of course, be the complement of this last expression. The results of a few typical calculations inside Region II are shown in Table 2.

CALCULATIONS FOR THE INTERIOR OF REGION III

We express Eqs. 12 and 13 in digital form, covering a finite but small step in C, ΔC.

$$\frac{\Delta u}{\Delta C} = \frac{u_2 - u_1}{C_2 - C_1} = \frac{u_2\,\sigma_2 + u_1\,\sigma_1}{2},$$

or

$$u_2 = u_1 \frac{2 + \sigma_1\,\Delta C}{2 - \sigma_2\,\Delta C} \quad \ldots\ldots\ldots \quad (12a)$$

$$\frac{u_1\,\zeta_1 + u_2\,\zeta_2}{2} = \frac{u_2 F_2 - u_1 F_1}{B_2 - B_1} \quad \ldots\ldots \quad (13a)$$

Here, subscripts 1 and 2 do not refer to components but, rather, to conditions at C and at $C + \Delta C$, respectively. The component to be used is Component 1.

Substituting the value for u_2 given in Eq. 12a into Eq. 13a gives

$$\frac{\zeta_1 + \zeta_2 \dfrac{2 + \sigma_1\,\Delta C}{2 - \sigma_2\,\Delta C}}{2} = \frac{\dfrac{2 + \sigma_1\,\Delta C}{2 - \sigma_2\,\Delta C} F_2 - F_1}{B_2 - B_1}$$

$$\ldots\ldots\ldots\ldots\ldots\ldots \quad (28)$$

Assigning, arbitrarily, $\Delta C = -0.0464$, or $C_2 = C_1 - 0.0464 = 0.496 - 0.0464 = 0.4496$, $(S_o)_2$ is calculated by trial and error from Eq. 28. Two functions of C, ε and η, are needed at C_1 and at C_2. Their values at these two concentrations are shown in Table 3. The result of the trial-and-error calculation for $(S_o)_2$ is 0.5900. u_2 can now be calculated from Eq. 12a.

$$u_2 = 0.02792 \times 1.00343 = 0.02801 \text{ cm/sec.}$$

Also, the velocity with which $(S_o)_2$ or C_2 moves is

$$\left(\frac{dX}{dt}\right)_{C_2} = u_2\,\zeta_2 = 0.02132 \text{ cm/sec.}$$

The hydrocarbon volume of gas injection required to cause a given C in Region III to reach the outflow face is given by $u^-/(u\,\zeta)$. The residual oil, and hence the recovery, is computed by integrating under a plot of saturation against X. Account should also be taken of a small amount of Component 3 in the vapor.

C is now reduced in further steps, and the calculations are repeated until the value of C reaches 0.248. This is the value at the boundary between Region III and Region IV. The results are summarized in Table 4. The results from the last two columns of Table 4 will also be found plotted as the lower curve of Fig. 6.

TABLE 2—RESULTS OF SOME TYPICAL CALCULATIONS INSIDE REGION II

S_o	$\left(\frac{dX}{dt}\right)_{S_o}$ (cm/sec)	Injected Gas (HV)	Recovery (fraction)
.2652	0.00279	10.24	1.000
.3052	0.00465	6.152	0.9333
.3652	0.00925	3.092	0.8696
.4052	0.01407	2.033	0.8386
.4400	0.01977	1.447*	0.8156*

*Plotted in the bottom curve of Fig. 6.

TABLE 3—VALUES OF ε AND η AT C

C	ε	η
0.4960	0.8516	−0.2783
0.4496	1.0043	−0.2819

TABLE 4—RESULTS OF SOME TYPICAL CALCULATIONS INSIDE REGION III

C	μ_o/μ_g	S_o	$\left(\frac{dX}{dt}\right)_{S_o}$ (cm/sec)	Injected Gas (HV)	Recovery (fraction)
0.4960	8.15	0.4400	0.01977	1.447	0.8156
0.4496	11.59	0.5900	0.02132	1.342	0.8057
0.4072	15.28	0.6500	0.02236	1.279	0.7950
0.3480	21.25	0.7109	0.02347	1.219	0.7800
0.3147	25.04	0.7367	0.02397	1.193	0.7718
0.2480	33.57	0.7804	0.02478	1.154	0.7560

μ_o/μ_g increases as the concentration of intermediates decreases. At the same time, the velocity with which a saturation advances rises as the liquid saturation increases. The values of cumulative gas injection decrease because the higher saturations in Region III arrive sooner at the outflow face.

THE DOWNSTREAM GAS BANK

The gas-bank saturation that would have been obtained in a displacement with equilibrium gas was $S_o = 0.7208$. Hence, this sample problem turned out to be of the type called Case *b* (discovered in the section of Appendix A entitled "Saturated Oil"). The actual velocity of the bank was computed by Eq. 19 for $S_o = 0.7804$ and $\mu_o/\mu_g = 33.57$ (see last row of Table 4). Thus, $\left(\frac{dX}{dt}\right)_b = 0.0683$ cm/sec, and the cumulative gas injection will be $u^-/\left(\frac{dX}{dt}\right)_b = 0.419$.

A plot of liquid saturation vs position for this sample problem looks fairly similar to Fig. 2. Distances moved by the various saturations will, of course, be proportional to the values of dX/dt given in Tables 2 and 4.

The results just given were computed by a medium-speed computing machine and checked with a desk calculator. They satisfied the requirements of an over-all material balance for each component. ★★★

Induced Nuclear Reaction Logging

W. A. HOYER
MEMBER AIME

HUMBLE OIL & REFINING CO.
HOUSTON, TEX.

ABSTRACT

A pulsed high-energy neturon-induced spectral logging tool has been built and field-tested. The reaction of deuterium on tritium is used to generate pulses of 14-Mev neutrons. By detecting only the prompt gamma rays produced by neutron inelastic reactions in the formation, the presence and relative abundance of carbon, oxygen, calcium, silicon and other important elements may be ascertained from a gamma-ray spectrum. Gamma-ray spectra obtained in a shallow test well and in experimental field use show that it is possible to identify formations and their contained fluids.

INTRODUCTION

The penetrating gamma rays from naturally occurring radioactive elements in subsurface formations have been used for a number of years in well logging as a means of characterizing and distinguishing strata.[1] Still another nuclear logging method which has been employed for some years consists of the bombardment of strata with neutrons and the measurement of the number of gamma rays produced by neutron capture reactions involving elements in subsurface strata.[2] Since one of the principal elements entering into capture reactions is hydrogen, the latter procedure essentially results in a hydrogen log, whether the hydrogen be in combined form in either oil or water; thus, the log gives an indirect measure of porosity. These methods, with various refinements, have been developed to such an extent that they have become routine procedures in formation evaluation.

Neither gamma-ray logging nor conventional neutron logging, however, yields sufficient information to permit unequivocal identification of the mineralogic composition of formations, and neither method gives information which may be used for the positive identification of hydrocarbons in strata. Accordingly, a number of efforts have been made in recent years to gain additional information from nuclear logs. Brannon and Osoba[3] have shown that it is possible to identify naturally occurring radioactive elements in subsurface formations by spectral analysis of gamma rays emanating from these elements. Such an identification is of value in the characterization of strata. A simplified form of spectral analysis of gamma radiation resulting from neutron capture reactions between elements in earth materials and bombarding neutrons has been used with some success under favorable conditions to differentiate between petroleum and water.[4] This method relies upon the relatively high energy of gamma radiation from neutron capture by chlorine and, in effect, furnishes a chlorine log. In areas in which interstitial water is of sufficiently high salinity, this log can give valuable information on water saturation and, thus, indirectly on hydrocarbon saturation. Still another approach to obtaining more information by nuclear techniques is "activation logging", in which certain elements yield short-lived radioactive isotopes on neutron activation and, thus, can be detected by gamma-ray spectral analysis.[5]

From the standpoint of determining by nuclear logging methods the mineralogic composition of strata and the presence or absence of hydrocarbons, it is essential that information be obtained on the presence and relative amounts of several elements such as carbon, oxygen, hydrogen, calcium, silica and others. Some elements, such as hydrogen, chlorine and sulfur, can be determined by spectral analysis of gamma radiation resulting from neutron capture reactions.[6,7] Others — carbon and oxygen, for example — do not enter readily into capture reactions but do yield gamma rays of characteristic energies from inelastic scattering reactions with high-energy neutrons.[8,9] Accordingly, the latter reactions are of particular interest as a means of identifying hydrocarbons in subsurface strata.

Several years ago it was recognized that information requisite to the identification of subsurface strata and of contained fluids could be obtained by pulsed operation of a subsurface neutron generator and associated gamma-ray detector. It was contemplated that pulsed operation would be effective in discriminating in time that gamma radiation which results predominantly from inelastic scattering reactions from that gamma radiation arising from neutron capture reactions. Accordingly, research was continued and construction of such a device was initiated. Although many problems were encountered, they were solved successfully. The following sections describe the tool which has evolved, its performance and the results which have been obtained with it to date.

THEORY OF OPERATION OF NEUTRON-INDUCED GAMMA-RAY SPECTRAL LOGGING TOOL

THEORY OF INDUCED NUCLEAR REACTIONS

Of fundamental importance is the fact that an element, when bombarded with neutrons, emits gamma radiation of energy characteristic of that element. In theory, therefore, an element may be identified by

Original manuscript received in Society of Petroleum Engineers office Nov. 23, 1960. Revised manuscript received July 5, 1961. Paper presented at SPE Formation Evaluation Symposium, Nov. 21-22, 1960, in Houston.

[1]References given at end of paper.

analysis of the energy spectrum of the neutron-induced gamma radiation.

Of the various interactions which can occur between neutrons and nuclei of elements, two are of particular interest — neutron capture reactions and inelastic scattering reactions.

In neutron capture reactions a low-energy neutron is captured by a nucleus, and the nucleus then emits a gamma ray of characteristic energy in order that it may become energetically stable. In the case of some nuclei, multiple gamma rays are emitted. Even in this case, however, the energies of the gamma rays are characteristic of the isotope. An essential feature of the neutron capture reaction is that a neutron may be captured only when it has very low energy.

In an inelastic scattering reaction a high-energy neutron penetrates the nucleus of an element and, after a very short period of time (approximately 10^{-8} second), is emitted by the nucleus at a lower energy. The nucleus, which is left with the energy that was lost by the neutron, then promptly (10^{-7} second) emits a gamma ray to become energetically stable. The energy of the emitted gamma ray is characteristic of the element. Unlike the neutron capture reaction, the inelastic scattering reaction requires neutrons of *high* energy.

Different elements have different propensities for entering into neutron interactions, whether these interactions be neutron capture or inelastic scattering. A measure of this propensity is the cross section expressed in barns, which are units of 10^{-24} sq cm. The larger the cross section, the greater is the probability of interaction.

Table 1 lists cross sections of various elements of interest for both neutron capture and inelastic scattering reactions. It is apparent from Table 1 that some elements, such as carbon and oxygen, have extremely low cross sections for capture reactions and that the probability of detecting these elements by means of gamma radiation from neutron capture reactions is extremely low. On the other hand, the probability that these elements can be detected and measured quantitatively by utilization of gamma radiation from inelastic scattering reactions is high.

DISCRIMINATION BETWEEN GAMMA RADIATION FROM NEUTRON CAPTURE AND FROM INELASTIC SCATTERING REACTIONS

When a steady flux of high-energy neutrons is allowed to impinge upon earth materials, both capture reactions and inelastic scattering reactions result. Some of the high-energy neutrons react immediately (within approximately 10^{-8} second) to produce inelastic scattering reactions; others suffer loss of energy by collision and eventually are reduced in velocity until their energies are sufficiently low to enable them to be captured. The process by which fast neutrons lose sufficient energy to enable them to be captured generally requires 10^{-6} to 10^{-3} second, and it is this fact which may be exploited in discriminating gamma radiation from inelastic scattering reactions from that gamma radiation which is produced by capture reactions.

The method of discrimination is dependent upon pulsing of the neutron flux and of the gamma-ray detector, and the principle involved is illustrated schematically in Fig. 1. This figure is a plot of neutron flux, both at the neutron generator and at a point within a formation opposite the generator, as a function of time. High-energy neutrons emanate from the pulsed neutron source in bursts of about 5 microseconds' duration. Some of these reach the formation opposite the generator without loss of energy and enter into inelastic scattering reactions. Others, as shown in the figure, lose energy by collision so that the flux of low-energy neutrons within the formation begins to build up during the duration of the pulse, reaches a maximum and then decays. The time interval between pulses can be chosen to allow almost complete decay of low-energy neutrons from preceding pulses. In brief, then, the gamma rays produced during the duration of the pulses are predominantly from inelastic scattering reactions, while those produced during the interpulse intervals are entirely from capture reactions.

By gating the gamma-ray detector so that it operates only during the operating interval of the neutron generator, it is possible to discriminate against gamma rays from capture reactions; by operating the detector during interpulse intervals, it is possible to discriminate completely against gamma radiation from inelastic scattering

TABLE 1—CROSS SECTIONS FOR CAPTURE AND INELASTIC NEUTRON REACTIONS

Inelastic Neutron Cross Section (barn)*	Element	Capture Neutron Cross Section (barn)
0.07	Calcium	0.43
.353	Carbon	0.0042
?	Chlorine	31.6
0	Hydrogen	0.330
0.859	Iron	2.53
0.485	Magnesium	0.06
0.104	Oxygen	0.0002
0.13	Silicon	0.13
?	Sodium	0.505
0.173	Sulfur	0.49

*The inelastic cross sections listed are for a threshold, minimum neutron energy. This results in a relatively large cross section for iron and magnesium, which have a low threshold energy, and an approximately correct cross section for carbon and oxygen.

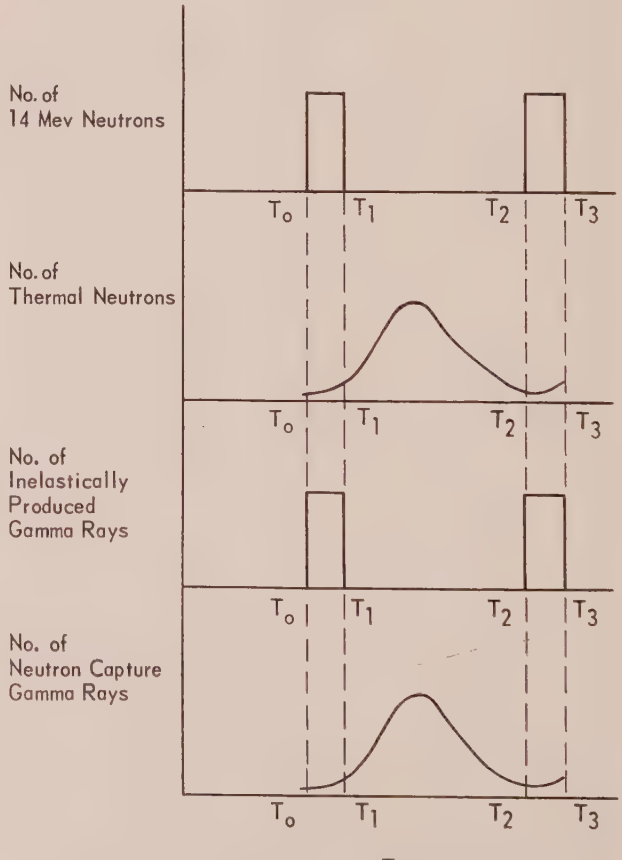

FIG. 1—TIMING OF LOGGING TOOL.

reactions. This is the principle upon which the logging tool has been built; although the tool has been operated to date with the objective of measuring gamma radiation from inelastic scattering reactions, it is apparent that by minor adjustment it can operate equally well to detect only gamma radiation from neutron capture reactions.

GENERAL DESCRIPTION OF THE LOGGING TOOL

The logging tool that has been built is shown diagramatically in Fig. 2. It has a pulsed 14-Mev neutron generator, a pulsed or gated scintillation gamma-ray detector and an intervening shield. Electrical pulses from the gamma-ray detector, proportional in voltage to the energy of the gamma rays impinging on the detector, are transmitted to the surface where they are recorded and where the energy spectrum is analyzed.

PHYSICAL DESCRIPTION

The logging sonde is composed of two sections of 4½-in. OD, 4-in. ID high-yield steel. The section which houses the gamma-ray detector is 6-ft long; the section containing the neutron generator is 7-ft long. These two sections, together with the nose plug and the cable head, make the tool when assembled about 15-ft long. The total weight of the tool is approximately 300 lb.

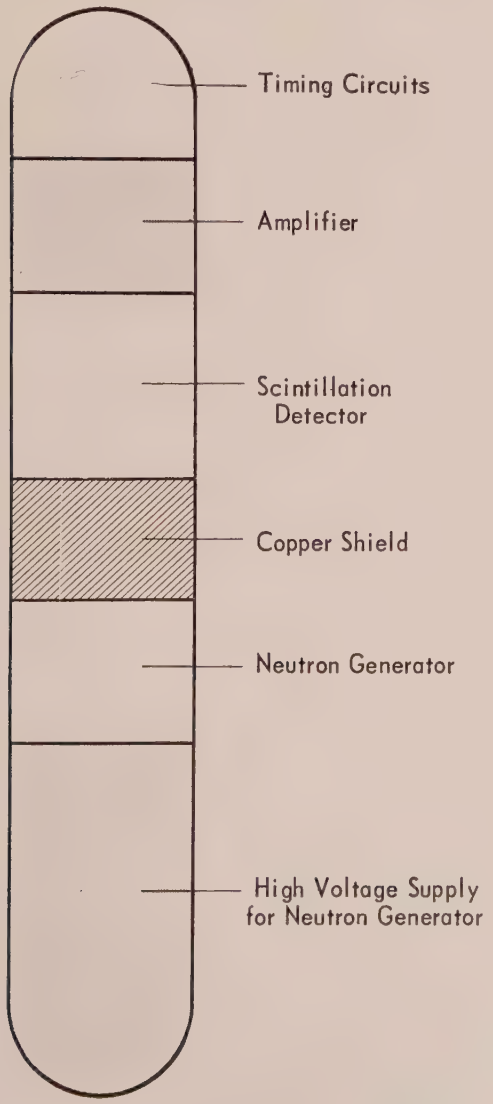

Fig. 2—Schematic Diagram of Logging Tool.

The shield separating the two sections of the logging tool is constructed of solid copper and is 7-in. long. A small hole traverses the shield diagonally and serves as a conduit through which interconnecting cables are fed.

The sonde is run on 7/16-in. armored, single-conductor cable of the type ordinarily used in a number of logging operations.

ELECTRICAL DESCRIPTION

The logging tool is powered by 400-cycle alternating current. The voltage at the tool is 260 v. Because the gamma-ray analysis is done at the surface, the cable must transmit signal pulses of about 4 microseconds' duration to the surface, as well as 400-cycle power to the logging tool.

A block diagram of the circuits of the logging tool is shown in Fig. 3. The light lines indicate the path of the 400-cycle power, the medium lines the path of the gate pulses and the heavy lines the path of the signals from the tool.

It is necessary to delay the gating of the photomultiplier to coincide with the peak production of neutrons, since the 100,000-v supply has an inherent 3-microsecond delay.

The filter between the linear amplifier and the cable is a high pass filter, so that the signals are passed but the power is not. Stated another way, the filter is so designed that the signals see the low impedance of the cable and are transmitted on it, while the impedance to the 400-cycle power is very high; hence, only a very small 400-cycle current flows between the amplifier output and the power cable.

The logging tool may be pulsed at repetition rates up to 5,000 or more pulses/sec with a neutron production of about 10^4 neutrons/pulse. To date, the tool has usually been operated at a pulse repetition rate of 1,000 pulses/sec. At this repetition rate the total electrical load of the logging tool is about 200 w.

NEUTRON GENERATION

The generation of neutrons usually follows as a result of certain nuclear reactions;[10] generally, a particle is bombarded into the nucleus of an atom and the result is a new type of atom, accompanied by neutron emission. There are many reactions which result in neutron generation, but most of these are impractical for use; for a reaction to be practical as a borehole neutron generator, the following requirements must be fulfilled.

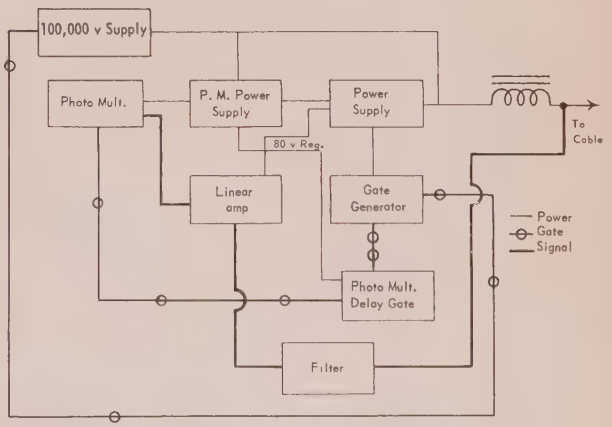

Fig. 3—Block Diagram of Logging Tool.

1. This reaction should proceed at reasonably low bombarding energies. There is not room in a logging sonde to generate and handle voltages much larger than 100-kv.

2. The reaction should produce neutrons having energies of 7 Mev or more.

3. The reaction should have a large cross section so that there is prolific neutron production.

4. The reaction should preferably produce monoenergetic neutrons.

5. The reaction should use materials which are both readily available and relatively inexpensive.

A reaction which best fulfills all of these requirements is the bombardment of tritium with deuterium. This results in production of a helium atom and in the emission of a 14-Mev neutron. This reaction will begin at deuterium energies as low as 50 kev, but since the cross section for the reaction is a maximum at 110 kev, the optimum production is attained at the latter energy.

The neutron generator is simply a device which supplies a controllable number of deuterium ions to a region of high electric field. The high electric field accelerates the ions to 100-kv energy onto a target containing tritium from which neutrons are generated. The neutrons are generated in pulses of about 4 microseconds' duration. The high voltage that operates the neutron generator is produced by a specially designed transformer. The transformer generates pulses of 100-kv magnitude and of about 4 microseconds' duration. The 100-kv transformer and its associated circuitry comprise the main portion of the lower half of the logging tool.

SURFACE EQUIPMENT

Surface equipment used in conjunction with the logging tool consists of filters for the 400-cycle power, means of extracting the signals received from the tool, an amplifier for the signals and a means of recording and displaying the gamma-ray spectra. Particular care has been taken in the design and construction of the surface equipment in order to achieve a high signal-to-noise ratio.

In the recording and display of gamma-ray spectra, it has been the practice to date to hold the tool stationary at each depth of interest while sufficient signals are accumulated to constitute a spectrum. The display of the gamma-ray spectrum may employ relative numbers of gamma rays (as in the case of photographic techniques[3]) or absolute numbers (as accomplished by a multichannel analyzer). Both photographic techniques and multichannel-analyzer methods have been used. At present, an analyzer is employed that counts the number of gamma rays in 200 consecutive small-energy intervals. The multichannel analyzer prints the number of gamma rays in each energy interval and can plot a complete spectrum.

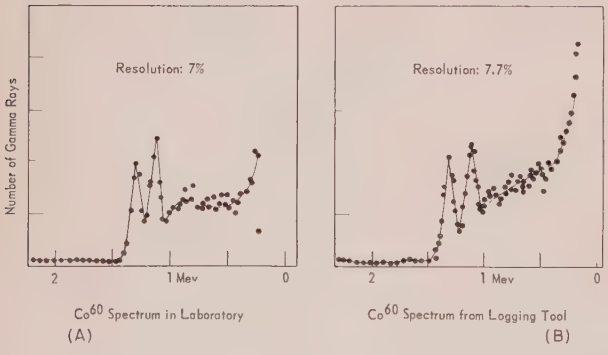

FIG. 4—Co^{60} SPECTRUM (A) IN LABORATORY AND (B) FROM LOGGING TOOL.

PERFORMANCE AND RESULTS

GAMMA-RAY RESOLUTION

The ability of gamma-ray spectra to portray accurately the elemental composition of strata is partially determined by the ability of the equipment to display accurately the gamma-ray spectrum. A measure of this ability is the resolution. The resolution of gamma rays is defined as the ratio of the width of a gamma-ray peak at half the peak height to the energy of the gamma ray. The resolution of gamma rays is about 7 per cent in the laboratory under ideal conditions. The question arises as to what effects pulsing of the photomultiplier, use of a long logging cable and filtering of signals have on the resolution of gamma rays. Fig. 4 shows the total of these effects by comparison, under nearly the same conditions, of the resolution of the two Co^{60} gamma rays in the laboratory and through the logging system. It is seen that the resolution through the logging system is approximately 8 per cent and, consequently, that the loss of resolution in the logging system is at most only about 1 per cent.

The gamma rays produced in the formation from neutron inelastic scattering must traverse some distance in the formation before being detected. Previous work[3] has shown that it is possible, despite some loss of resolution due to degradation of radiation in the formation, to determine quantitatively the relative abundance of elements by use of gamma-ray spectra.

Still another factor affects the resolution of gamma-ray spectra—the background effect of one gamma ray on the other. Fig. 5 shows spectra obtained in a test well in which large-diameter casing was filled with 100 per cent oil and 100 per cent water, respectively. The characteristic oxygen gamma rays obtained from the water have higher energy than those of carbon. There is no interaction when either of these gamma rays is present singly, but Fig. 6 shows that there is an effect of the oxygen background on the resolution of carbon. Fig. 6 is a spectrum of an oil-saturated sand obtained in a well in the Gulf Coast area. The carbon is discernible, but not nearly so clearly as in Fig. 5. Thus, the

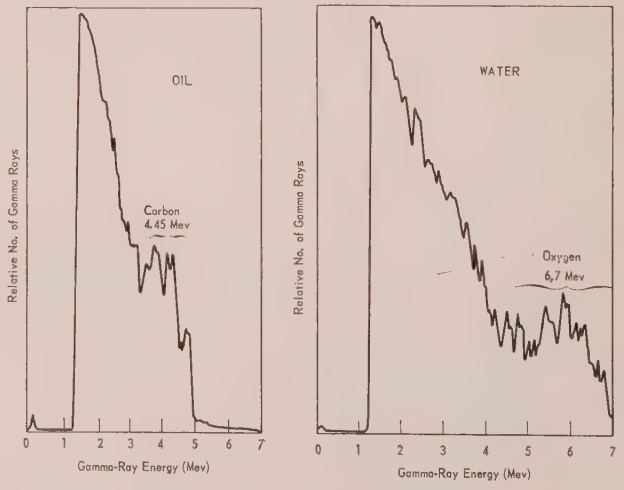

FIG. 5—GAMMA-RAY SPECTRA OF OIL AND WATER.

presence of the characteristic gamma rays of formation elements is discernible when all the gamma rays from formation elements are present, but not so clearly as in ideal laboratory spectra.

IDENTIFICATION OF FORMATION FLUIDS

Spectra from a known oil sand and from a known salt-water sand, both obtained in a cased well in the Gulf Coast area, are shown in Fig. 7. At first glance, there is not a great deal of difference discernible between these, but there is enough information in the spectra to distinguish between oil and water in the sand. Data of Fig. 8, taken from Fig. 7, show the amplitudes of the four gamma-ray peaks at 5, 4.5, 4 and 3.5 Mev. A comparison of the curves of Fig. 8 for oil and for water sands shows that the relative heights of the carbon gamma rays of 4.5, 4 and 3.5 Mev, compared to the oxygen gamma ray of 5 Mev, clearly distinguish oil from water. In effect, the comparison of carbon and oxygen peak heights is a means of normalizing the effect of the oxygen background on the carbon gamma-ray peaks in a spectrum and makes possible the estimation of the relative amounts of oil and water in a formation.

Plots similar to Fig. 8 have been used as the criterion for determining whether or not a sand contains oil during the course of field-testing the logging method. In one field test of a shallow sand, a plot similar to Fig. 8 indicated petroleum; a production test of the zone showed that it produced gas. It is evident, therefore, that the logging method is sufficiently sensitive to the presence of carbon that it will even give indication of the presence of gas.

It is apparent that, in addition to the carbon which is present as a constituent of petroleum, some carbon may be present as a component of the rock matrix of subsurface strata. To investigate the ability of the logging method to distinguish between water and oil in such cases, the plots of Fig. 9 were obtained in water-saturated and in oil-saturated limestone in a test well. The limestone had about 40 per cent porosity. Here again the carbon content shows a difference between oil and water, even though carbon was present as a major-constituent element of the calcium-carbonate matrix.

RESUME OF FIELD RESULTS

Results obtained in the field with this logging method have been extremely gratifying. The principle usage to date has been in diagnosing productive possibilities of sands behind casing in workover operations. The correlation of predictions made from data obtained by this

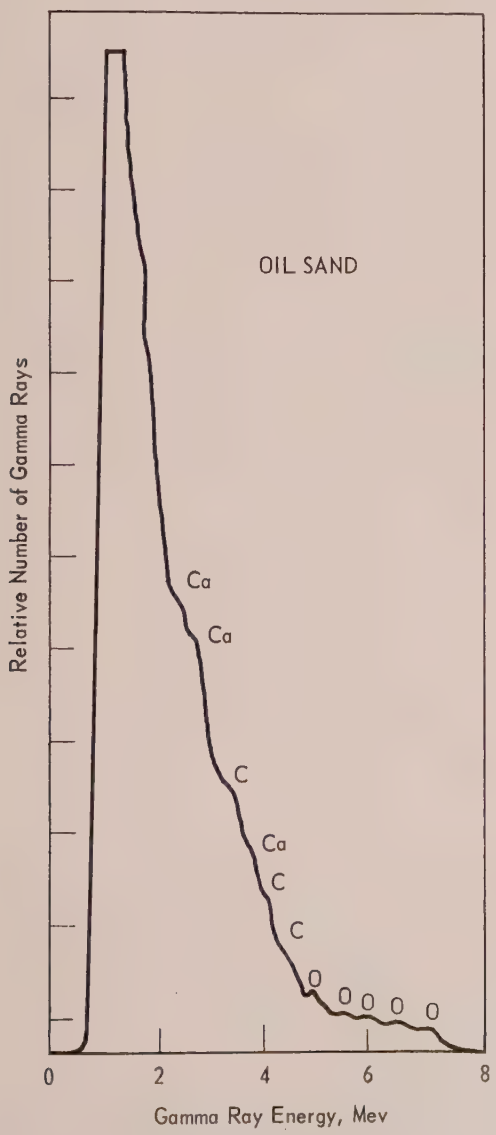

Fig. 6—Gamma-Ray Spectra of an Oil Sand.

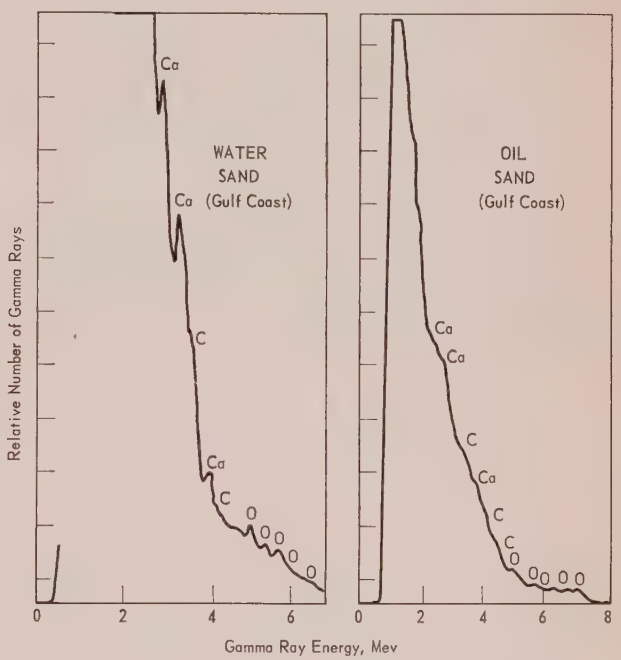

Fig. 7—Gamma-Ray Spectra of an Oil Sand and a Water Sand from the Same Well.

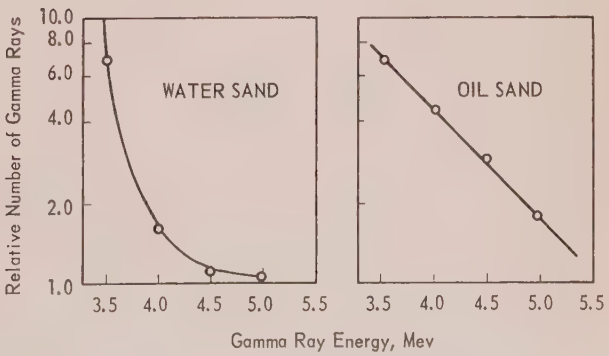

Fig. 8—Comparison of the Gamma-Ray Spectra of Fig. 7.

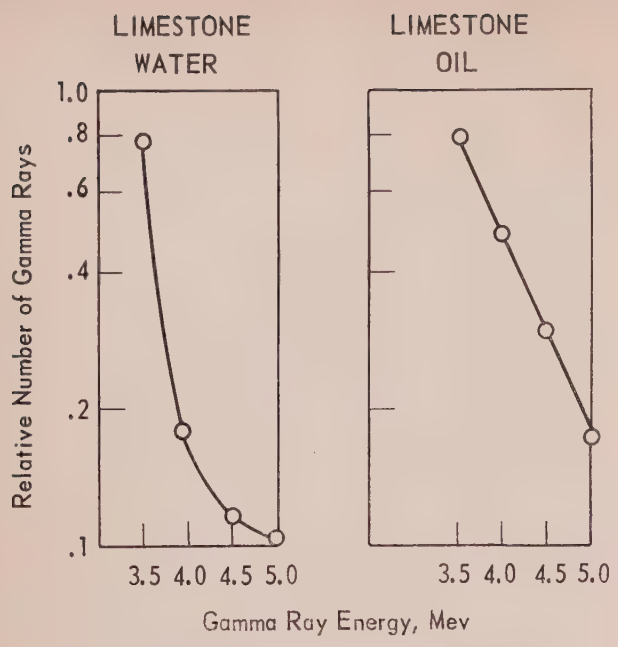

FIG. 9—COMPARISON OF THE GAMMA-RAY SPECTRA OF AN OIL LIMESTONE AND WATER LIMESTONE.

method with results of formation or production tests has been excellent, even though a number of runs have been made in areas and in zones in which sand conditions are far from ideal. Further, the tool has been operated successfully where casing has been filled with oil, salt water or fresh water.

To date, the tool has been allowed to remain stationary opposite zones of interest while spectral information is recorded. However, this has been dictated more by the desire to obtain definitive spectral information than by any innate characteristics of the tool which might prevent it from being used in a continuous logging system.

Field experience has demonstrated that both logging tool and surface equipment are capable of routine operation. In particular, experience with the neutron generator and its associated high-voltage supply has shown that these units are rugged, reliable and capable of sustained operation under well conditions.

ACKNOWLEDGMENTS

The author wishes to acknowledge the contributions to the research of the following people: R. C. Rumble and D. H. Britton for assistance in the design and construction of the logging system; H. R. Brannon, Jr., N. L. Muench, J. S. Osoba, J. A. Rickard and Milton Williams for the theoretical foundation of this work and the functional design; and J. D. Ball, and others, of Geophysics Research for the design and construction of many components of the logging system.

REFERENCES

1. Howell, L. G. and Frosch, Alex: "Gamma-Ray Well Logging", *Geophysics* (1939) **4**, No. 2, 106.
2. Pontecorvo, Bruno: "Neutron Well Logging—A New Geological Method Based on Nuclear Physics", *Oil and Gas Jour.* (1941) **40**, No. 18, 32.
3. Brannon, H. R., Jr. and Osoba, J. S.: "Spectral Gamma Ray Logging", *Trans.*, AIME (1956) **207**, 30.
6. Muench, N. L. and Osoba, J. S.: "Identification of Earth *Pet. Eng.* (1959) **31**, No. 3, B-102.
5. Youmans, A., Hopkinson, E. C. and Stewart, R. M.: "(D. T.) Neutron Activation Logging", Paper 1304-G presented at 34th Annual Fall Meeting of SPE in Dallas (Oct. 4-9, 1959).
6. Muench, N. L. and Osoba, J. S.: "Identification of Earth Materials by Induced Gamma-Ray Spectral Analysis", *Trans.*, AIME (1957) **210**, 89.
7. Baker, P. E.: "Neutron Capture Gamma-Ray Spectra of Earth Formations", *Trans.*, AIME (1957) **210**, 97.
8. Caldwell, R. L. and Sippel, R. F.: "New Developments in Radioactive Well Logging Research", *Bull.*, AAPG (1958) **42**, No. 1, 159.
9. Tittman, J. and Nelligan, W. B.: "Laboratory Studies of a Pulsed Neutron-Source Technique in Well Logging", *Trans.*, AIME (1960) **219**, 375.
10. Marion, J. B. and Fowler, J. L.: *Neutron Physics*, Interscience Publishers, N. Y. (1960) Part I, 1-133. ★★★

A Simple Method for Correcting Spot Pressure Readings

F. BRONS
MEMBER AIME
W. C. MILLER
JUNIOR MEMBER AIME

SHELL OIL CO.
LOS ANGELES, CALIF.
FARMINGTON, N. M.

ABSTRACT

Pressure information for use in material-balance calculations is obtained, where possible, from pressure build-up surveys in shut-in wells. Using proper extrapolation methods, static pressures are obtained which, by averaging, give the field static pressure.

Often, particularly in fields with a large number of wells, only spot pressure readings are available. A graphical method is presented here which enables the determination of the corrections which must be applied to the spot readings to give an estimate of the static pressure. Although the static pressures thus obtained are not so reliable as those from build-up surveys, they are more nearly correct than the spot readings themselves for use in material-balance calculations.

INTRODUCTION

The average static pressure in a bounded reservoir is determined from a number of individual-well pressure measurements. Where pressure build-up curves are available, extrapolation methods such as described in Ref. 3 may be used to determine the static pressure in the drainage area of each individual well.

The possibility of using pressure build-up curves presupposes that each well being surveyed is closed in during a certain period and that, during this time, a pressure recorder is left suspended in the hole. For surveys in fields with a large number of wells, this is usually not feasible for economic and other reasons. Either a large number of pressure recorders would have to be used simultaneously or, using a limited number of recorders, the time interval needed to complete a field-wide survey would be too long. The data obtained for this incomplete coverage are insufficient to permit reliable averaging of the few calculated static pressures over the entire reservoir.

In many such cases another type of pressure information is available, i.e., spot pressure readings. During this type of pressure survey all wells are closed-in simultaneously and, after a reasonable shut-in time (e.g., three days), pressure readings are taken by running the recorder in and out of each successive well. These surveys, which are less expensive, are often taken at regular intervals, say once or twice a year. In fact, such surveys are required by the state regulatory bodies in many portions of the United States.

These spot readings are normally lower than the static (fully built-up) pressure due to the relatively short shut-in time. No direct means of extrapolating such a reading to the static pressure is available because no pressure build-up record is obtainable. Consequently, these data are inferior to pressure build-up information as a basis for estimating the stabilized reservoir pressure in the drainage area of a specific well. For the common case where abundant spot readings but only a few pressure build-up surveys are available, our studies suggest that it may be possible to design a program which will combine the two types of information and provide an estimate of the average reservoir pressure that is more reliable than that obtainable solely from either set of data.

Fig. 1 illustrates graphically the information obtained by a pressure build-up curve as compared to a single spot reading. The shut-in pressure is plotted, according to common procedure, vs the logarithm of $\frac{t + \Delta t}{\Delta t}$ where t is the past production time and Δt the shut-in time. The point marked with a cross is the final pressure read in either case. The straight-line portion of the build-up curve extrapolated to $\frac{t + \Delta t}{\Delta t} = 1$ (i.e., infinite shut-in time) gives a point marked p^*. The actual static pressure at the time the well was shut-in is marked by p_s. The illustration shows that, even if a build-up curve is available and can be extrapolated, a correction

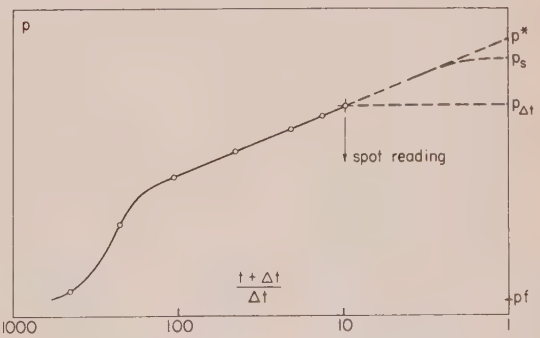

FIG. 1—ILLUSTRATION OF THE RELATION BETWEEN EXTRAPOLATED PRESSURE (p^*), SPOT PRESSURE ($p_{\Delta t}$) AND STATIC PRESSURE (p_s).

Original manuscript received in Society of Petroleum Engineers office Aug 10, 1960. Revised manuscript received May 16, 1961. Paper presented at 31st Annual California Regional Meeting of SPE, Oct. 20-21, 1960, in Pasadena, Calif.
[1]References given at end of paper.

$p^* - p_s$ is needed to arrive at the true static pressure p_s. Methods such as described in Refs. 1, 2 and 3 must be applied to calculate this correction, which is usually in a downward direction. On the other hand, if only a spot reading $p_{\Delta t}$ is available, an upward correction $p_s - p_{\Delta t}$ must be applied. In the following, a simple method is presented by which the correction to be applied to each spot reading is read from a graph. Although the static pressures thus obtained are generally not so reliable as those from pressure build-up surveys, they are more nearly correct than the spot readings themselves for use in material-balance equations.

DESCRIPTION OF METHOD

The method is based on two basic equations. The first relates the flowing (producing) pressure p_f in a well and the static pressure p_s in the area drained by this well by

$$p_s - p_f = \frac{q\mu B}{4\pi kh} \ln \frac{4A}{\gamma\, C_A\, r_w^2} \quad . \quad . \quad . \quad . \quad . \quad (1)$$

Eq. 1 is valid only after a sufficiently long period of regular production to allow equilibrium conditions to have been reached. A list of symbols is given in Table 1, but some of the properties need further classification. The wellbore radius r_w is the "effective" wellbore radius in which any positive or negative skin effect is incorporated according to $r_w = \bar{r}_w\, e^{-S}$, where $\bar{r}_w$ is the physical well radius and S is the well known skin factor. C_A is the shape factor, its value depending on the shape of the drainage area and the position of the well within this area. In Fig. 2, a list of shape factors is given for a number of configurations, as derived from Ref. 3. For a circular area with a well in the center, the shape factor is equal to $C_A = \dfrac{4\ \pi e^{3/2}}{\gamma} = 31.6$ which, inserted in Eq. 1, gives the better known equation for the radial case.

$$p_s - p_f = \frac{q\mu B}{4\pi k\ h}\left(\ln \frac{r_e^2}{r_w^2} - \frac{3}{2}\right) \quad . \quad . \quad . \quad (1a)$$

The second equation to be used relates the pressure $p_{\Delta t}$ reached after a shut-in time Δt to the flowing (producing) pressure p_f by

$$p_{\Delta t} - p_f = \frac{q\mu B}{4\pi\ k\ h} \ln \frac{4\ k\ \Delta t}{\gamma\phi\mu\ c r_w^2} \quad . \quad . \quad . \quad (2)$$

This equation is only valid during a certain period of the shut-in time, occurring after the effect of after-production has disappeared and before either the closed-in time becomes of the same order of magnitude as the previous production time or before the drainage boundaries noticeably affect the shape of the build-up curve.

TABLE 1—SYMBOL DEFINITIONS, UNITS AS USED IN EQ. 5, AND VALUES USED IN CONSTRUCTING SAMPLE GRAPHS IN FIG. 3

Meaning of Symbols	Units	Value Used In Fig. 3
q = Stabilized rate of production prior to shut-in	B/D	Measured
h = Formation thickness	ft	Petrophysical data
ϕ = Porosity	fraction	(0.1)
A = Drainage area	acres	(40)
c = Fluid compressibility	psi^{-1}	(3×10^{-4})
r_w = Effective wellbore radius	ft	(.4) Estimated
B = Oil formation volume factor	fraction	(1.33)
C_A = Shape factor (depends on shape of drainage area and position of well)		(31.6)
p_s = Static formation pressure	psi	To be determined
p_f = Producing bottom-hole pressure	psi	Estimated
Δt = Shut-in time	hours	(72)
$p_{\Delta t}$ = Bottom-hole pressure after well has been shut-in for Δt hours	psi	Measured
γ = Exponential of Euler's constant		(1.781)
LN = Natural logarithm		
log = ^{10}logarithm		

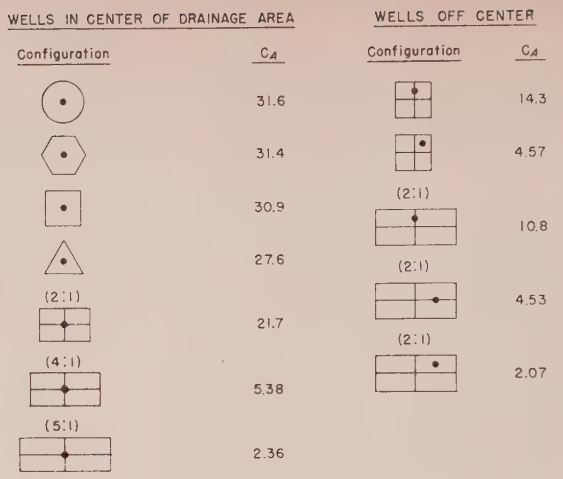

FIG. 2—SHAPE FACTORS (C_A) FOR A NUMBER OF DRAINAGE CONFIGURATIONS.

This implies that Eq. 2 is valid for the straight-line part of the curve expressing $p_{\Delta t}$ as a function of $\ln\Delta t$. In practice, for shut-in times Δt of the order of three to several days, Eq. 2 may be used. Before application of this method, the validity of this assumption in the field being studied must be checked by an analysis of some pressure build-up curves.

The pressure correction $p_s - p_{\Delta t}$, which when added to the spot reading gives the static pressure, is found by subtracting Eq. 2 from Eq. 1.

$$\text{Correction} = p_s - p_{\Delta t} = \frac{q\mu B}{4\ \pi\ kh} \ln \frac{\phi\mu\ cA}{C_A\ k\Delta t} \quad . \quad . \quad . \quad . \quad . \quad . \quad . \quad . \quad . \quad . \quad . \quad (3)$$

If the permeability is reasonably uniform throughout the field, then according to Eq. 3 the correction is roughly proportional to q/h, i.e., the preceding production rate per unit sand thickness. By an extension of this concept, other methods in which the average of all the spot pressure readings are corrected by a factor proportional to the average q/h can be devised, but they will not be discussed here. The method presented here, although of general applicability, is especially useful for the case where large variations of the permeability occur throughout the field. It is based on the elimination of the mobility ratio k/u from Eqs. 1 and 3, which leads by normal algebraic methods (which are not repeated here) to the equation

$$\ln \frac{q}{h} = \ln (p_s - p_f) + \ln \frac{4\pi\phi\ cA}{C_A\ aB} - \ln\Delta t - a\,\frac{p_s - p_{\Delta t}}{p_s - p_f} \quad . \quad . \quad . \quad . \quad (4)$$

with $a = \ln \dfrac{4A}{\gamma C_A\ r_w^2}$.

In conventional U. S. engineering units and using the ^{10}log instead of the natural log, Eq. 4 becomes

$$\log q/h = \log (p_s - p_f) + G - \log \Delta t - a\,\frac{p_s - p_{\Delta t}}{p_s - p_f} \quad . \quad . \quad . \quad (5)$$

where $G = \log \dfrac{10^6\phi\ cA}{C_A\ aB}$ and $a = \log \dfrac{10^5\ A}{C_A\ r_w^2}$.

Graphs based on Eq. 5 can be constructed for any given average situation, from which the correction $p_s - p_{\Delta t}$ to be applied to the spot reading $p_{\Delta t}$ is read for given values of $p_{\Delta t}$, p_f and q/h.

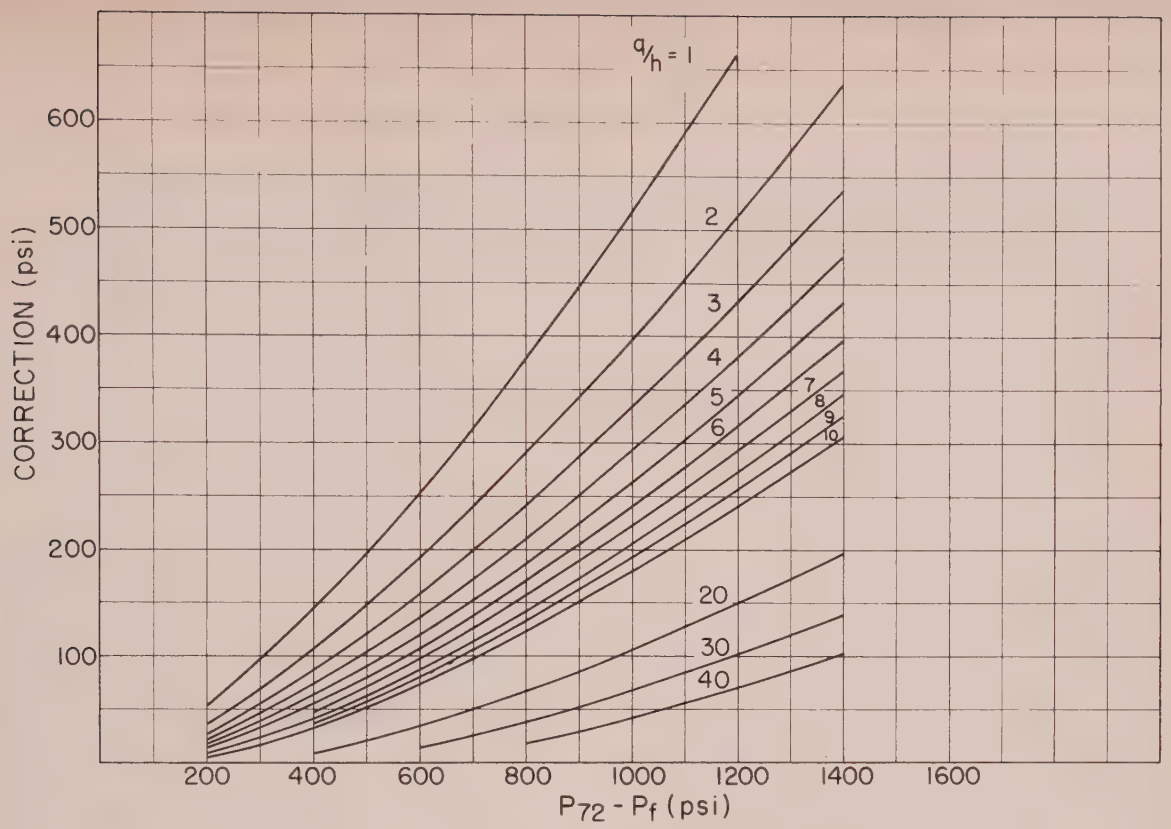

FIG. 3—SAMPLE GRAPHS FOR CORRECTING SPOT READINGS ($p_{\Delta t}$) TO STATIC PRESSURES (p_s) BASED ON EQ. 5 AND USING VALUES AS GIVEN IN TABLE 1.

In utilizing this method, it is necessary to estimate two important factors — the effective wellbore radius and the producing pressure. The method is most applicable in dealing with fields in which sufficient pressure build-up curves are available to ascertain that the completion practices used result in similar, effective wellbore radii for most of the wells in the field. In a field with wells suffering from serious wellbore damage where, as a consequence, it is possible to have widely varying wellbore radii, the accuracy of the method would be reduced. In most flowing wells, the producing pressure can be determined with sufficient accuracy from routine surface measurements of tubing and casing pressure. In pumping wells, fluid-level measurements and/or knowledge that most of the wells are "pumped off" while producing are generally available.

A list of symbols, together with the units as used in Eq. 5, is given in Table 1. The last column shows the values used in the construction of the sample graphs in Fig. 3.

APPLICATION

The procedure of estimating the static pressure from a spot reading after 72 hours shut-in, for a situation characterized by the sample graphs, can best be explained by an example.

Given: $p_{\Delta t} = 800$ psi ($\Delta t = 72$ hours),
$p_f = 200$ psi (estimated),
$q = 120$ B/D (average prior to shut-in), and
$h = 40$ ft.

From $p_{\Delta t} - p_f = 600$ psi and $q/h = 3$ B/D/ft, read from Fig. 3:

Correction $= p_s - p_{\Delta t} = 160$ psi and $p_s = 960$ psi.

To interpret a spot reading taken after a shut-in period Δt which differs from 72 hours, the same graph can be used. In such a case, enter the graph with $\frac{q}{h} \times \frac{\Delta t}{72}$, rather than q/h.

During the stage in the life of a field where the average static pressure is above bubble point but where the flowing-well pressures are below it, the shut-in times Δt should be long enough to ascertain that the spot reading $p_{\Delta t}$ has reached bubble point. A correction which, applied to a spot reading below bubble point, would give a static pressure above bubble point cannot be trusted because of the sudden change in fluid compressibility which occurs in passing the bubble point. However, for many situations, this method is adaptable to the case of two-phase flow of oil and gas by the inclusion of the proper total mobility and compressibility values in the manner proposed by Perrine[5] in his discussion of pressure build-up analysis.

REFERENCES

1. Miller, C. C., Dyes, A. B. and Hutchinson, C. A., Jr.: "Estimation of Permeability and Reservoir Pressure from Bottom Hole Pressure Build-up Characteristics", *Trans.*, AIME (1950) **189,** 91.
2. Horner, D. R.: "Pressure Buildup in Wells", *Proc.*, Third World Pet. Cong. (1951) **Sect. II,** 503.
3. Matthews, C. S., Brons, F. and Hazebroek, P.: "A Method for Determination of Average Pressure in a Bounded Reservoir", *Trans.*, AIME (1954) **201,** 182.
4. van Everdingen, A. L.: "The Skin Effect and Its Influence on the Productive Capacity of a Well", *Trans.*, AIME (1953) **198,** 171.
5. Perrine, R. L.: "Analysis of Pressure Build-up Curves", *Drill. and Prod. Prac.*, API (1956) 482. ★★★

Effect of Bank Size on Oil Recovery in the High-Pressure Gas-Driven LPG-Bank Process

J. W. LACEY
MEMBER AIME
J. E. FARIS
F. H. BRINKMAN
MEMBER AIME

JERSEY PRODUCTION RESEARCH CO.
TULSA, OKLA.

ABSTRACT

This paper presents an analysis of the high-pressure, gas-driven LPG-slug process, based on fluid flow tests in areal models. Two types of tests were made. One series was made in low-pressure models which permitted observation of fluid movement. Three completely miscible analog fluids were used. A second series of tests was made in high-pressure models using methane, propane and a light refined oil saturated with methane at room temperature and 1,550 psig. Under the test conditions of room temperature and a pressure level of 1,550 psig, the phase diagram for the fluids used is similar to those for many of the field systems where the process is considered for use. A method for using these laboratory data to calculate field performance of the process is outlined.

As a result of this work, it is concluded that small banks of LPG (5 per cent HV or less) are not effective in increasing oil recovery in horizontal reservoirs. Instead, where small banks are used, the driving gas quickly penetrates the LPG bank because of fingering and channeling; and from this point on, the process behaves essentially as an immiscible gas-injection project. The validity of this conclusion was substantiated by: (1) laboratory studies of the effect of rate, model size and mobility ratio on miscible displacement in areal models; and (2) calculation of field recovery, which compared closely with actual field recovery.

INTRODUCTION

Field applications and pilot tests of the gas-driven, LPG-bank, oil-recovery process are on the increase.[1-4] Most of these tests are employing small banks (2½ to 5 per cent hydrocarbon volume) of LPG, which is miscible with both the driving gas and the oil in place, in an effort to attain an effective yet economical miscible displacement of oil by gas. The expectation of miscible displacement with small banks is based on the concepts that: (1) lengths of solvent-oil mixed zones, measured during miscible displacements in long slim cores, are representative of those that will occur in the field; and (2) areal sweep efficiencies[5] measured in electrolytic model studies are applicable to miscible displacement in reservoirs.

Original manuscript received in Society of Petroleum Engineers office Aug. 2, 1960. Revised manuscript received April 3, 1961. Paper presented at 35th Annual Fall Meeting of SPE, Oct. 2-5, 1960, in Denver.
[1]References given at end of paper.

Our experimental evidence indicates that the mixed-zone lengths and sweep efficiencies mentioned are not applicable to miscible displacement in reservoirs. In this paper we present an evaluation of the gas-driven, LPG-bank oil-recovery process based on fluid flow experiments in areal models. These results are used to predict the performance of a field pilot test of this process, and the results are compared with the actual test results.

THE EFFECTIVENESS OF LPG BANKS

The effectiveness of LPG banks of various sizes in accomplishing miscible displacement of oil by gas was determined by displacement tests in a model representing one-quarter of a confined five-spot pattern. The model, 12 × 12 × ¼ in. in size, was packed uniformly with glass beads. It was operated at a pressure of 1,550 psig and at room temperature; the fluids used were methane, propane and refined oil saturated with methane at 1,550 psig. The saturated oil had a viscosity of 1.2 cp at room temperature.

The results of these tests are shown in Fig. 1, where recovery is plotted as a function of the volume of fluid injected for: (1) an immiscible-gas drive with an oil-to-gas viscosity ratio of 85; (2) three sizes of LPG banks; and (3) two completely miscible displacements with mobility ratios of 85:1 and 10:1. (The miscible displacement data plotted are the averages of several tests.) The results show that a 2½ per cent bank of LPG does not increase oil recovery over that obtained by immiscible-gas drive. The 7 and 17 per cent banks are, respectively, about 30 and 50 per cent effective (with reference to the $M = 85$ miscible-displacement curve) in increasing oil recovery at the point where 2½ hydrocarbon volumes (HV) of fluid have been injected. The percentage effectiveness of the banks at a given volume of fluid injected is defined as

$$\frac{\text{Recovery by Bank} - \text{Recovery by Gas Drive}}{\text{Recovery by Miscible Flooding} - \text{Recovery by Gas Drive}} \times 100.$$

We conclude from these results that banks of LPG smaller than about 5 per cent HV in an individual stratum will cause from little to no increase in oil recovery.

This finding was substantiated by work in low-pressure models, which permitted visual observation of fluid movements. In these tests, three completely miscible fluids having the same viscosity ratios as those used in

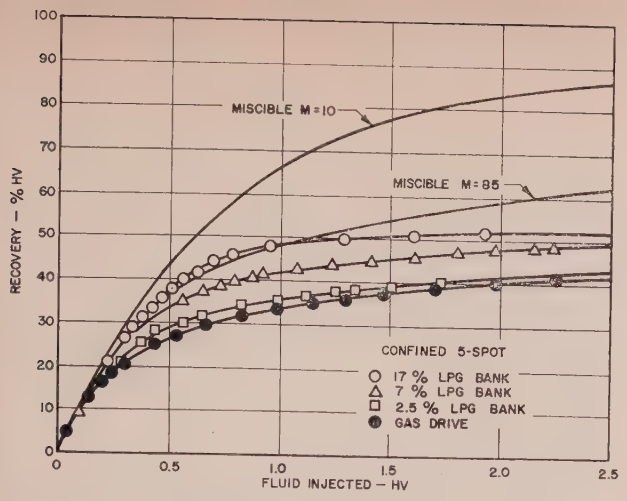

FIG. 1—HIGH-PRESSURE GAS-DRIVEN PROPANE-BANK EFFICIENCY.

the bank efficiency tests just discussed were used. Banks of dyed fluid representing LPG banks were injected to displace clear fluid representing oil and followed by clear fluid representing gas. Transmitted light was used to observe and photograph how and when the solvent bank was breached by the driving fluid. It was found that a bank as small as 5 per cent HV was penetrated early in the displacement. Therefore, an LPG bank of this size could not be very effective in maintaining a miscible displacement of oil by gas. These results are in sharp contrast with those obtained in electrolytic model studies[5] and tests in slim cores.

EXTENSION TO RESERVOIR SYSTEMS

To check the applicability of these results to larger systems, we made a study of miscible displacement in low-pressure models of various sizes representing one-quarter of a five-spot. Again, these models were packed uniformly with glass beads, and equal-density fluids (Dow Corning fluids and Halocarbons) were used. These results were later compared with those from high-pressure tests using fluids having unequal densities (propane and oil). The sides of the low-pressure models were Lucite plates, which together with the use of dyed fluids permitted visual observation of fluid movement. From these observations, we estimated the amount of mixing by diffusion and dispersion in some tests.

LOW-PRESSURE MODELS

In our low-pressure models, we studied how miscible displacement efficiency is affected by (1) mobility ratio, (2) flow rate, (3) model size and (4) well-spacing to model-thickness ratio.

The results of this work are shown in Table 1. They show that mobility ratio was the only variable that had any measurable influence on over-all miscible displacement efficiency. All tests at a given mobility ratio, in three different-sized models and at a variety of injection rates, fall on one curve. These recovery curves for the mobility ratios of 1, 10 and 41 are plotted on Fig. 2. Since recovery by miscible displacement from these areal models is not a function of rate or model size, it follows that molecular diffusion and/or dispersion are not important in this no-gravity system.

It was necessary to consider additional factors before extending these findings to our bank efficiency tests. For example, it is possible that, even though diffusion is not important for straight miscible displacement, allowances must be made when small banks are

TABLE 1—VOLUMETRIC OIL RECOVERY FOR FIVE-SPOT MODELS

Model Size (in.)	Rate** (in./day)	Oil Recovery (per cent HV) Breakthrough	1 HV	2 HV	5 HV
	Mobility Ratio* = 1				
36 × 36 × 9/16	260	69.2	—	—	—
	180	67.3	—	—	—
	20	69.8	—	—	—
18 × 18 × 5/16	360	68.0	—	—	—
	360	67.8	—	—	—
	40	69.0	—	—	—
	20	67.3	—	—	—
9 × 9 × 1/8	720	71.5	—	—	—
	80	70.0	—	—	—
	20	71.1	—	—	—
9 × 9 × 1/2	20	70.0	—	—	—
9 × 9 × 3	20	68.0	—	—	—
	Mobility Ratio* = 10				
36 × 36 × 9/16	20	33.0	68.0	82.0	—
	20	31.6	68.0	—	—
18 × 18 × 5/16	180	26.8	70.5	—	—
	40	28.0	69.0	83.0	99.5
	20	34.5	68.5	—	—
	20	31.0	65.5	81.5	—
9 × 9 × 1/8	290	33.0	65.5	81.0	97.0
	80	31.0	—	—	—
	80	31.9	—	—	—
	80	31.4	68.0	84.0	99.5
	20	34.3	—	—	—
	20	36.4	66.5	84.0	—
	2	40.7	—	—	—
	2	38.1	69.5	85.0	—
9 × 9 × 1/2	20	34.0	65.0	82.0	—
9 × 9 × 3	20	35.0	69.0	84.0	—
	Mobility Ratio* = 41				
36 × 36 × 9/16	20	23.9	59.0	—	—
	20	20.7	53.0	—	—
	1	31.2	60.0	—	—
18 × 18 × 5/16	40	16.6	54.0	67.0	77.0
	20	22.2	56.0	67.0	76.0
	2	25 3	54.5	66.5	—
	2	24.8	—	—	—
9 × 9 × 1/8	80	18.6	57.5	68.0	75.5
	20	20.7	—	—	—
	20	26.1	57.5	68.0	75.5
	3	22.4	50.0	—	—
9 × 9 × 1/2	20	22.0	55.0	69.0	—
9 × 9 × 3	20	18.0	55.0	72.0	—

*Mobility Ratio = Viscosity displaced phase/viscosity displacing phase.
**Rate = Length of diagonal of model, in inches/time in days to inject 1 HV.

used. Furthermore, gravitational forces were present in our bank efficiency tests. These factors were handled as follows.

GRAVITY EFFECTS

The ratio of gravitational forces to viscous forces in our bank efficiency tests where actual reservoir fluids were used was greater than in most pilot tests of this process. To determine if these gravitational forces influenced our results, we miscibly displaced 1.0-cp oil by liquid propane from a confined five-spot model at the same rate as our bank tests. We compared the results of this test with those from tests where equal-density fluids were used (see Fig. 3) and found that the recovery curve where gravitational forces were present was almost identical to those where gravitational forces were zero. This indicates that conclusions from our tests using equal-density fluids are applicable to reservoirs where gravity vertical to the bedding plane is a minor term.

DIFFUSION AND/OR DISPERSION

We used our 1:1 mobility-ratio miscible displacements in the 18- × 18- × 5/16-in. model to estimate the amount of mixing due to the combination of dispersion and diffusion. The use of dye in the injection fluid allowed us to obtain this estimate by comparing the volumetric recovery with the areal coverage at breakthrough of injection fluid. A comparison of these values for experiments made at different rates is shown in Table 2.

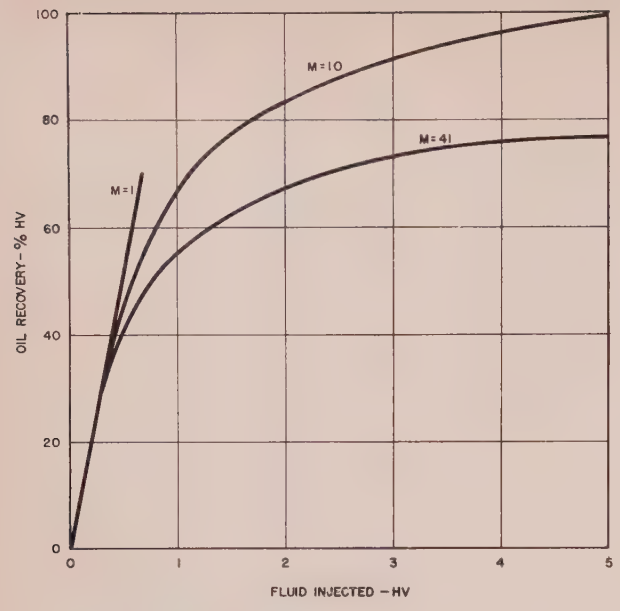

FIG. 2—EFFECT OF MOBILITY RATIO ON OIL RECOVERY BY MISCIBLE FLUID DISPLACEMENT—CONFINED FIVE-SPOT.

A difference of about 2 per cent was found for all tests. We assumed that this difference was due to mixing by diffusion and dispersion. This amount of mixing is greater than would be the case by these mechanisms in the field. Therefore, we discounted the bank sizes in our laboratory tests. In our bank tests there were two mixed zones (oil-propane and gas-propane); however, tests with analog fluids showed bank penetration much before breakthrough. We considered that these effects were compensating and discounted our propane banks by 2 per cent HV; that is, we said a 5 per cent bank in our model would act like a 3 per cent bank in a reservoir, a 10 per cent bank would act like an 8 per cent bank, etc.

There are little data in the literature which can be compared with the data just mentioned. Most of the areal miscible-displacement work have been reported on the basis of areal coverage which is not comparable with volumetric recovery. In general, it can be said that the data in this report are in good agreement with those reported by Habermann.[6]

We believe that the lack of sensitivity of miscible displacement efficiency to rate and model size strongly indicates that fluid flow tests in areal models are much more representative of how this process will behave in a reservoir than are electrolytic model studies and slim-tube tests. The latter tests have the following limitations.

1. Electrolytic model studies do not permit fingers to form whereas, in miscible fluid-flow experiments, fingering is the predominant feature for adverse-mobility-ratio miscible displacement.

2. Ample experimental and theoretical work has been published which shows that, for linear models, the length of a mixed zone formed during miscible displacement increases with core diameter.

Lacey, *et al*,[7] observed that increasing the core diameter from 2 to 6 in. caused a drastic increase in the length of the mixed zone. This observation is substantiated by Perrine's[8] theoretical study on instability. His conclusion was that, although the dispersion process may stabilize the laboratory flood because disturbances are limited to short "wave lengths", it need not stabilize field floods because of the larger cross section of reservoirs.

TABLE 2—AREAL COVERAGE VS VOLUMETRIC OIL RECOVERY, $\mu_o/\mu_s = 1.0$

Model Size (in.)	Rate (in./day)	Volumetric Recovery (% PV)	Areal Coverage (%)
18 × 18 × 5/16	360	68.0	69.8
	360	67.8	68.9
	40	69.0	69.8
	20	67.3	69.8

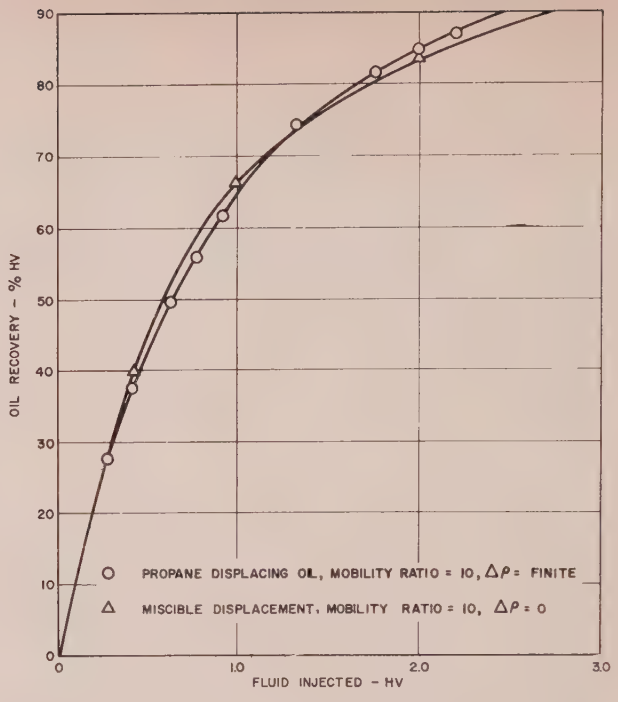
OIL RECOVERY - % HV
FLUID INJECTED - HV
PROPANE DISPLACING OIL, MOBILITY RATIO = 10, ΔP = FINITE
MISCIBLE DISPLACEMENT, MOBILITY RATIO = 10, ΔP = 0

FIG. 3—GRAVITY HAS MINOR EFFECT ON LABORATORY TESTS.

Offeringa and van der Poel[9] concluded from the application of scaling concepts to miscible displacements that the short, stabilized mixed zones observed in long slim cores will not occur in the field, where the diameter is much larger and where lateral diffusion cannot make itself felt over such a large distance in the time available. Blackwell, *et al*,[10] verified this explanation in work with models of different widths. They found that their narrowest model produced a stabilized mixed zone. However, they observed that the prototype of this narrow model is not typical of any reservoir of practical dimensions. They noted that, in models representing wider and more realistic prototypes, diffusion did not produce a stabilized zone and the displacement remained independent of rate. They concluded that this latter behavior is more typical of reservoir performance.

All of this work shows that zones measured in slim cores should not be extrapolated to reservoirs.

CALCULATION OF FIELD BEHAVIOR

An evaluation of a process based on laboratory tests must be compatible with the results of full-scale field tests. Unfortunately, no full-scale field test of the LPG miscible-slug process is far enough along for the results to be conclusive. However, pilot tests have been completed. For most of the tests reported on, the test pattern was a single, unconfined five-spot consisting of one injection and four production wells. To compare laboratory test results with this type of pilot test, three factors must be considered: (1) pattern or sweep efficiency, (2) effect of bank size on oil recovery, and (3) reservoir stratification. The recommended approach

to analysis of these factors is described below. The data obtained from calculations and experiments in such an analysis are also discussed.

PATTERN EFFICIENCY

A model study should be made to measure the pattern efficiency of the unconfined five-spot pattern for both miscible and immiscible fluid displacement. The model should be geometrically similar to the pilot test area of interest.[10] The model should permit observation of the swept area, and the ratio of the volume of injected fluid to produced fluid in the pilot test should be reproduced. Mobility ratios and the ratio of viscous to gravitational forces in the field should be reproduced insofar as possible.

To determine the relative efficiencies of the confined and unconfined five-spot pattern, we ran displacement tests in models packed uniformly with glass beads and having the dimensions shown on Fig. 4. Here again the models permitted visual observation of fluid movement. The volume of fluid injected was equal to the volume produced from the single producing well for all of this work. Both miscible and immiscible fluid displacement were investigated to bracket the oil-recovery performance between these two extremes.

Miscible Displacements

We ran miscible displacement tests in these models using fluids of equal density and having a viscosity ratio (displaced fluid/displacing fluid) of 85. The results of these tests, given in Fig. 5, show that the unconfined five-spot is about 1.4 times as efficient as the confined five-spot. Photographs made of the unconfined model after injection of about 3 HV of solvent reveal that only a small amount of solvent had gone outside the five-spot area, as shown in Fig. 6 (alongside the same results for immiscible displacement in Fig. 7), and that much of the improvement in displacement efficiency was due to increased areal sweep within the five-spot area. These findings are consistent with those of Paulsell.[11]

Immiscible Tests

For the immiscible-fluid displacement tests, we displaced 1.5- and 4.8-cp oil from glass-bead-packed models with 0.018-cp nitrogen. We also displaced 1.5-cp oil with nitrogen from confined and unconfined five-spot models of consolidated Bartlesville sandstone. This material has a gas-oil relative permeability curve which is similar to that of many reservoir rocks. These results are shown in Figs. 7, 8, 9 and 10. In all cases it was found that roughly twice as much oil was recovered from the unconfined five-spot pattern. A photograph, shown on Fig. 7, made of the unconfined five-spot bead-packed model during the displacement of 1.5-cp oil (after injection of 3.0 HV of nitrogen) explains why more oil is recovered from the unconfined pattern. It shows that the area swept by gas is over twice as large as the confined pattern and that much of the recovered oil came from outside the five-spot pattern. Therefore, high recovery from an unconfined pattern is not necessarily representative of any confined pattern. Data are not available in the literature for comparison with these results; however, the high recovery efficiency of the unconfined pattern is consistent with the work of Dalton.[12]

These findings show that pilot-test oil recoveries from unconfined, inverted five-spot patterns, where the volume of produced fluid is equal to the volume injected, are

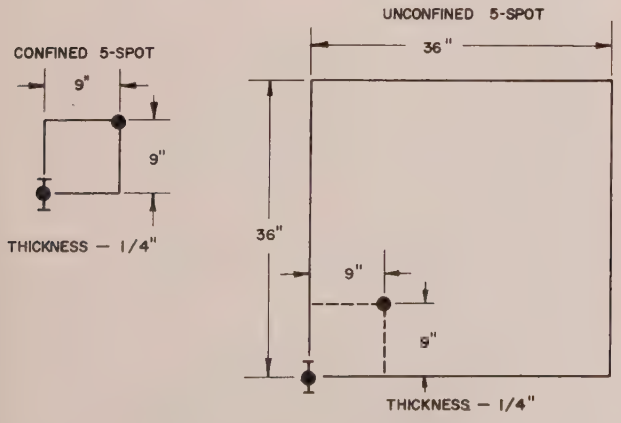

FIG. 4—MODEL DIMENSIONS.

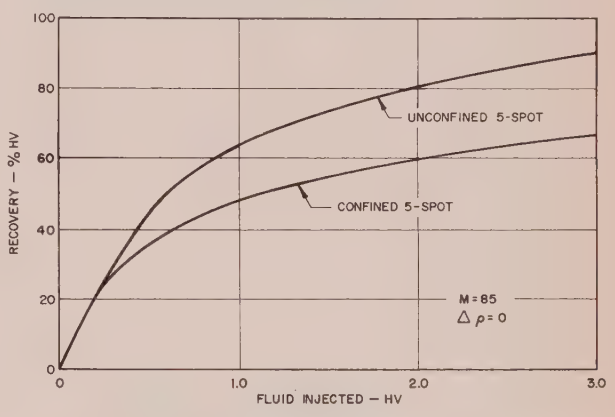

FIG. 5—EFFECT OF PATTERN ON MISCIBLE-DISPLACEMENT BEHAVIOR.

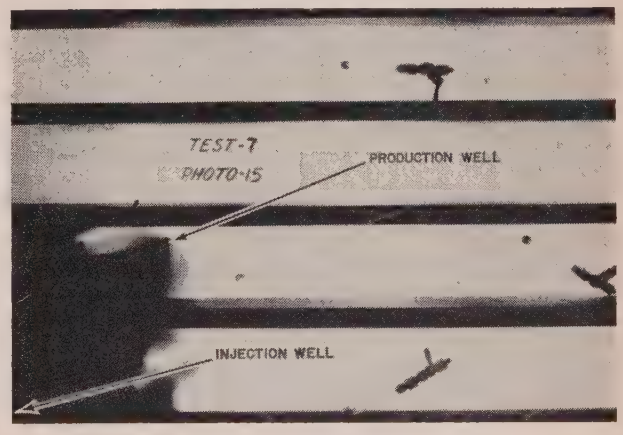

FIG. 6—AREAL SWEEP BY MISCIBLE FLUID DISPLACEMENT.

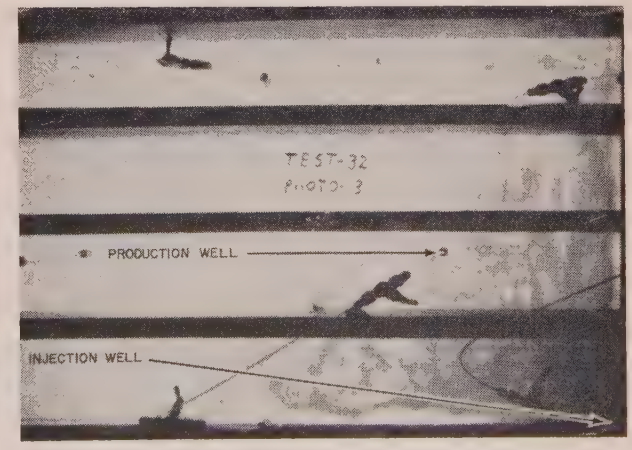

FIG. 7—AREAL SWEEP BY IMMISCIBLE FLUID DISPLACEMENT.

very optimistic and should not be directly extrapolated to predict performance of full-scale applications.

EFFECT OF LPG BANK SIZE ON OIL RECOVERY

A model study should be made to measure the extent to which the LPG bank used in the field will increase recovery over that which can be achieved by immiscible-gas drive. This should be done for a range of bank sizes because stratification in the field will probably cause variation in the bank size injected in each layer of the reservoir.

RESERVOIR STRATIFICATION

Using the model data herein and core-analysis data from the pilot test area, the recovery from the pilot test can be calculated. This will involve two considerations: (1) an analysis of the stratification in the test area, and (2) a conventional calculation of flooding in a noncommunicating stratified system.

Analysis of Stratification in Test Area

This is very important for processes in which the injectivity increases greatly during the life of the process. In other words, prediction of performance is very sensitive to the degree of stratification. We propose a statistical method using core data (both porosity and permeability) from the pilot wells to divide lithologic intervals of interest in each well into zones such that the *correlation index* for each well is nearly a maximum. The correlation index is defined as

$$Y = \frac{a\,\alpha_B^2}{\alpha_W^2 + a\,\alpha_B^2}$$

where α_W^2 = the variance within a zone,
α_B^2 = the variance component between zones, and
a = the weighting coefficient for α_B^2.

Estimates of these quantities are obtained, using the analysis of variance technique,[13] by the following relationships.

$$\alpha_W^2 = \sum_{i=1}^{I} \sum_{j=1}^{J_i} (X_{ij} - \overline{X}_{i\cdot})^2/Q - I$$

and

$$\alpha_W^2 + a\,\alpha_B^2 = \sum_{i=1}^{I} \sum_{j=1}^{J_i} (\overline{X}_{i\cdot} - \overline{X})^2/I - 1,$$

where Q = the total number of data,
I = the number of zones,
J_i = the number of data in the ith zone,
$\overline{X}_{ij}$ = the measurement of the reservoir property (e.g., permeability),
$\overline{X}_{i\cdot}$ = the mean of the measurements of the ith zone, and
$\overline{X}$ = the mean for all measurements in one well.

This approach allows the formation to be broken into zones such that (1) there is minimum variation within zones, and (2) there is maximum variation between zones.

We assume that within each zone there is a random distribution of properties so that each zone will behave as a homogeneous unit having properties equal to the average properties of the zone. Since it is required that these zones correlate from well to well, it will sometimes be necessary to use a single-well zonation, which gives something less than a maximum correlation index. We believe the statistical method outlined will give the best estimate of reservoir stratification. An alternate and common method of obtaining reservoir zonation is to use a fractional capacity-fractional thickness curve. This approach essentially assumes the worst possible stratification — that is, complete segregation of the permeability ranges. It is also possible that a reservoir could be so heterogeneous it would act as a homogeneous system. Actual reservoirs are undoubtedly between these extremes.

Conventional Calculation of Flooding in a Noncommunicating Stratified System

To calculate recovery for the field, use k_g/k_o data for the field plus recovery, injectivity and bank efficiencies from models as outlined by the following.

1. Use field k_g/k_o data to calculate recovery for each zone by gas drive only.

2. Use model data to calculate recovery for each zone by miscible flooding.

3. Calculate the bank size in each zone and use bank efficiencies from models to interpolate a recovery curve for each zone between the two extremes (in 1 and 2).

4. Sum up recovery from all zones using a method similar to that used by Justen, *et al.*[1]

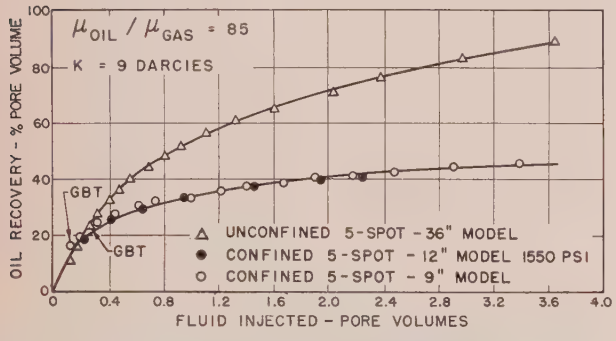
μOIL / μGAS = 85
K = 9 DARCIES
GBT
GBT
UNCONFINED 5-SPOT - 36" MODEL
CONFINED 5-SPOT - 12" MODEL 1550 PSI
CONFINED 5-SPOT - 9" MODEL
OIL RECOVERY - % PORE VOLUME
FLUID INJECTED - PORE VOLUMES

FIG. 8—GAS-DRIVE PATTERN EFFICIENCY FOR GLASS-BEAD MODELS.

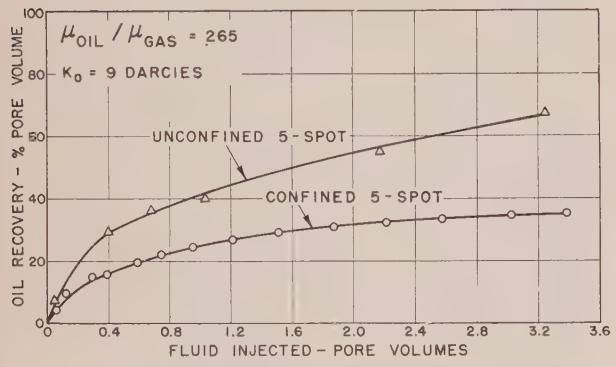

FIG. 9—GAS-DRIVE PATTERN EFFICIENCY FOR GLASS-BEAD MODELS.

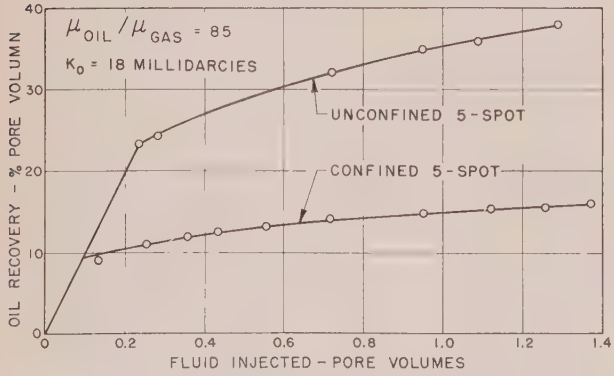

FIG. 10—GAS-DRIVE PATTERN EFFICIENCY FOR BARTLESVILLE SANDSTONE.

APPLICATION TO THE PEMBINA PILOT TEST

At the present time, only a few pattern tests of the miscible-slug process have been completed. Available data on most of these are limited. However, a pilot test, which was carefully controlled and on which extensive data were collected and complete results were published,[1] is that run by Mobil Oil, Ltd. in the Pembina field of Alberta, Canada. This was a 10-acre inverted five-spot with one input well and four producers. An LPG bank equal to 7 per cent of the hydrocarbon volume of the 10-md-plus sand was injected. We have used the method proposed in this paper to analyze the performance of this pilot. Results are given in following paragraphs.

We concluded from this analysis that no layer of the reservoir received a large-enough bank of LPG to allow a substantial improvement over a gas drive. Instead, the process behaved essentially as a gas-injection project, resulting in recovery of oil from a much larger area than the pilot area, as shown by our immiscible displacements from unconfined five-spot patterns (Fig. 7).

The oil recovery from this pilot test was calculated for two assumptions regarding reservoir thickness — (1) that hydraulic fracturing had opened a thin sand about 4-ft below the perforated interval, and (2) that no sand below the perforated interval was open to production. In both cases, all sand having permeability in excess of 0.1 md was included. Using the statistical zonation technique previously described, the reservoir was divided into four layers in the first case and three in the second. Relative permeability data (k_g/k_o) from two sources[14,15] were used in these calculations.

These calculations and the actual field results are compared on Figs. 11 and 12. There is excellent agreement between the calculated and actual results. Also shown are calculated recovery curves for a confined five-spot pattern. These are the recovery curves which would be expected for a full-scale field application.

These comparisons show that evaluation of the process, based on flow tests in areal models and the described calculative method, is compatible with field behavior. They also show the hazards of direct extrapolation of unconfined pilot-test results, since more oil was recovered from the pilot test than would be expected from any confined pattern.

CONCLUSIONS

1. From the results of our evaluation of the LPG-slug process, we conclude that small LPG banks of the order of 5 per cent HV or less are not effective in increasing oil recovery from horizontal reservoirs. This conclusion will not necessarily apply if the mobility ratio or its adverse effects are reduced in some manner. Further, it does not apply if the process is used in a dipping reservoir where gravity forces can suppress fingering and channeling.

2. In our opinion, an evaluation of the bank efficiency in reservoir applications should be made on the basis of fluid flow tests in areal models in preference to electrolytic model studies and fluid flow tests in long slim cores.

3. The calculated recovery curve for the Pembina pilot test, using our model data and calculation method, closely matches the actual recovery curve.

ACKNOWLEDGMENTS

The authors wish to express their appreciation to the management of the Jersey Production Research Co. for permission to publish this paper. J. D. Testerman's contribution of the statistical zonation technique and H. H. Jacks' and M. C. Miller's help in obtaining the experimental data are gratefully acknowledged.

REFERENCES

1. Justen, J. J., Hoenmans, P. J., Groeneveld, H., Connally, C. A. and Mason, W. L.: "The Pembina Miscible Displacement Pilot and Analysis of Its Performance", *Trans.*, AIME (1960) **219**, 38.
2. Brinkley, T. W.: "Review of Bisti LPG Pilot Test, Bisti Pool, San Juan County, New Mexico", presented at SPE Mid-Continent Local Section Reservoir Study Group (May 17, 1960).
3. Sturdivant, W. C., Jr.: "Field Performance of a Pilot Propane Injection Project", *Jour. Pet. Tech.* (May, 1959) **XI**, No. 5, 27.
4. Marrs, D. G.: "Miscible Drive in Parks Field", *Jour. Pet. Tech.* (May, 1958) **X**, No. 5, 20.
5. Aronofsky, J. S. and Ramey, H. J., Jr.: "Mobility Ratio—Its Influence on Injection or Production Histories in Five-Spot Water Flood", *Trans.*, AIME (1956) **207**, 205.
6. Habermann, B.: "The Efficiency of Miscible Displacement as a Function of Mobility Ratio", *Trans.*, AIME (1960) **219**, 264.
7. Lacey, J. W., Draper, A. L. and Binder, G. G., Jr.: "Miscible Fluid Displacement in Porous Media", *Trans.*, AIME (1958) **213**, 76.

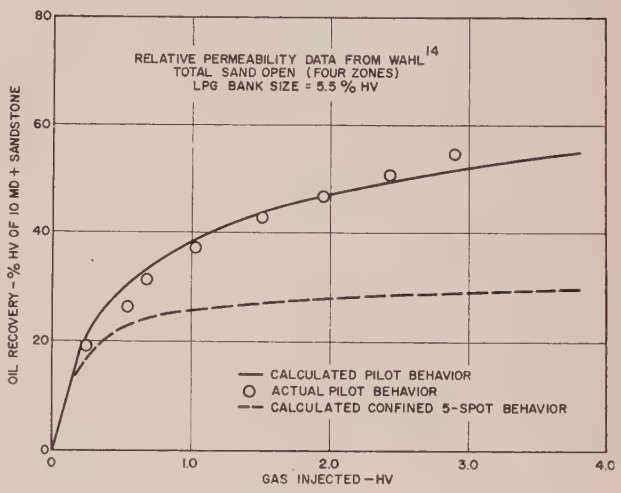

FIG. 11—FIELD RECOVERY—TOTAL SAND.

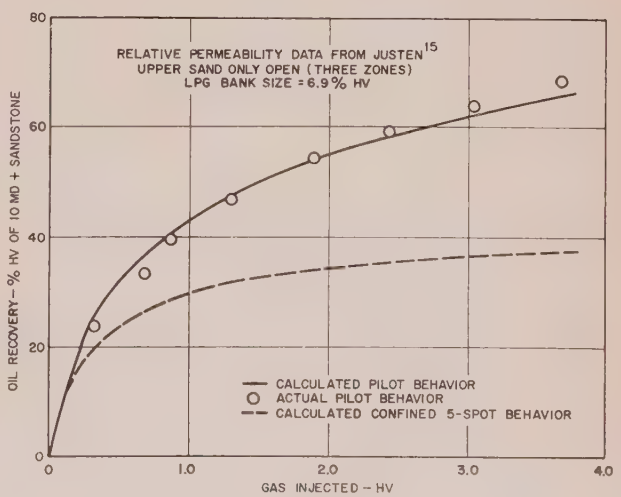

FIG. 12—FIELD RECOVERY—UPPER SAND ONLY.

8. Perrine, R. L.: "Conditional Instability in Miscible Liquid-Liquid Displacement", Preprint No. 42 presented at the AIChE-SPE Joint Symposium on Miscible Fluid Displacement in San Francisco (Dec. 6-9, 1959). See also: "Stability Theory and Its Use to Optimize Solvent Recovery of Oil", *Soc. Pet. Eng. Jour.* (March, 1961) 9; and "The Development of Stability Theory for Miscible Liquid-Liquid Displacement", *Soc. Pet. Eng. Jour.* (March, 1961) 17.
9. Offeringa, J. and van der Poel, C.: "Displacement of Oil from Porous Media by Miscible Liquids", *Trans.*, AIME (1954) **201,** 310.
10. Blackwell, R. J., Rayne, J. R. and Terry, W. M.: "Factors Influencing the Efficiency of Miscible Displacement", *Trans.*, AIME (1959) **217,** 1.
11. Paulsell, B. L.: "Areal Sweep Performance of Five-Spot Pilot Floods", Master's thesis, Pennsylvania State U. (1958).
12. Dalton, R. L., Jr., Rapoport, L. A. and Carpenter, C. W., Jr.: "Laboratory Studies of Pilot Water Floods", *Trans.*, AIME (1960) **219,** 24.
13. Davies, O. L.: *Statistical Methods in Research and Production* (1958) 103.
14. Wahl, J.: "An Engineering Analysis of Methods for Increased Oil Reserves, Cardium Reservoir, Buck Creek, Wolf Creek-Buck Lake Area of the Pembina Field, Alberta, Canada", James A. Lewis, Inc. (March, 1959).
15. Justen, J. J., *et al:* "An Analysis of Primary Depletion, Cardium Sand Reservoir, Pembina Field, Alberta, Canada", Reservoir Working Subcommittee of Pembina Operators Committee (June, 1956).

DISCUSSION

C. A. CONNALLY
MEMBER AIME

SOCONY MOBIL OIL CO., INC.
DALLAS, TEX.

The type of performance reported for miscible displacements with unfavorable mobility ratios and with small miscible banks in miniature models is not unexpected. Viscous fingering is the predominant factor controlling such displacements for short distances. There is little opportunity, in such small models, for dispersion and diffusion to provide a significant blended zone between displaced and displacing fluids and to reduce the viscosity gradient before the fingers of displacing fluid reach the outlet well or penetrate the thin banks of miscible fluid.

Weinaug and Ling[1] and Slobod and Lestz[2] have demonstrated that reducing the viscosity gradient, with blended zones of only a few inches in length, results in a drastic decrease in viscous fingering. Blended zones of a number of feet in length, resulting in a marked decrease in viscosity gradient, could be expected to be formed during displacement over distances between wells in actual reservoirs.

Therefore, it is surprising that the authors would suggest application of their model results to field reservoirs, in a manner implying that the experiments were properly scaled. There was no scaling of the most important factor in the experiments, viscosity gradient.

In studying areal-sweep behavior in small models of unconfined five-spot patterns, the authors found a substantial difference between the areal-sweep results of miscible and immiscible displacement. From the picture in Fig. 7 of the subject paper, it is evident that there is a large variation in fluid saturation throughout the area swept by immiscible displacement. Fluid mobility depends upon saturation, and areal-sweep behavior depends upon fluid mobility. In field-scale patterns the zone of saturation gradient, varying from original saturation to residual saturation of displaced fluid, is expected to occupy a much smaller fraction of the pattern than in the miniature model. Therefore, the model would not provide the same areal sweep as would be obtained on a field scale with immiscible displacement.

In application of the model results to the Pembina pilot test, it was necessary to account for the effects of permeability stratification on the pilot performance. The "zonation" approach in the subject paper averaged correlatable zones over the entire area between pilot producing wells. This averaging technique eliminates much of the actual difference in reservoir properties between the injection well and individual production wells and inherently assumes that each producer will exhibit the same performance. Flow between the injection well and an individual producer is influenced primarily by the characteristics of the flow path between them. It is obvious from the actual results of the pilot test[3] that there were large differences in the performance history of each of the producers. Helium tracer tests,[3] conducted in the pilot area, resulted in evidence of at least 7 to 10 separate zones of different transmission characteristics between the injector and each producer. The "zonation" technique correlated only three or four separate zones for the entire pilot area. Over-all performance of water floods in Pembina indicates that a more detailed zonation is necessary in this reservoir.

It is concluded that the authors have not correctly evaluated any of the individual factors—microscopic displacement, areal sweep, or permeability stratification—which affected oil recovery in the Pembina pilot. By underestimating displacement efficiency and overestimating volumetric sweep, they have arrived at an oil-recovery estimate that matches over-all pilot oil recovery. However, their analysis does not agree with many important details of the pilot test which provide a true insight to its performance.

The successful performance of the Parks field miscible flood,[4] which utilized a 4 per cent bank of LPG, disproves the authors' conclusion concerning the ineffectiveness of LPG banks of less than 5 per cent of the hydrocarbon volume. Further, the arguments that viscous fingering will predominate in the performance of miscible floods in the field are refuted by the successful performance of the University Block 31 high-pressure-gas miscible flood.[5]

REFERENCES

1. Weinaug, C. F. and Ling: U. S. Patent No. 2,867,277 (June 6, 1959).
2. Slobod, R. L. and Lestz, S. J.: "Use of a Graded Viscosity Zone to Reduce Fingering in Miscible Phase Displacements", *Prod. Monthly* (Aug., 1960) 12.

3. Justen, J. J., Hoenmans, P. J. and Groeneveld, H.: "The Pembina Miscible Displacement Pilot and Analysis of Its Performance", *Trans.*, AIME (1960) **219**, 38.
4. Marrs, D. G.: "Field Results of Miscible-Displacement Program Using Liquid Propane Driven by Gas, Parks Field Unit, Midland County, Texas", *Jour. Pet. Tech.* (April, 1961) 327.
5. Herbeck, E. F. and Blanton, J. P.: "Ten Years of Miscible Displacement in Block 31 Field", *Jour. Pet. Tech.* (June, 1961) 543.

DISCUSSION

A. L. BENHAM
W. B. GOGARTY
JUNIOR MEMBERS AIME
F. H. POETTMANN
MEMBER AIME

THE OHIO OIL CO.
LITTLETON, COLO.

The authors of this paper present experimental data obtained on small-scale three-dimensional models. The assumption is made throughout the paper that results based on this data can be scaled to full-size reservoirs. The justification for this assumption is based on the successful prediction of the recovery obtained in the Pembina pilot flood. However, there are other methods of calculation which also successfully predict the recovery obtained in this particular pilot. For example, a calculation method based on a different concept was performed at our laboratory and the results were in agreement with the pilot flood recovery. These recoveries have also been calculated and reported in the literature using results obtained in slim-core models and aerial sweep efficiencies obtained in electrolytic model studies.

This paper represents a good example of the misunderstanding existing in the oil industry with respect to the application of small-scale laboratory results to a large field. The authors have ignored scaling laws which may be deduced from a study of the basic mechanisms involved in a miscible-flood process and have naively contended that results obtained in a model 1 ft on a side could be directly applied to a segment of a field which is 330 ft on a side. Scaling laws applicable to miscible fluid displacement have been developed using inspectional analysis as reported by Geertsma, Croes and Schwarz.[1] It is quite possible that some of the scaling rules listed in this paper are unnecessary for real application.

At this time, however, there is no real evidence in the literature which would allow the authors to ignore any of the scaling rules for a study of the miscible-slug process.

The authors present results in the section entitled, "Low-Pressure Models", to show the effect of mobility ratio, flow rate, model size and well spacing to model thickness ratio for a simple miscible displacement of one fluid by a second. They conclude that recovery by miscible displacement is not a function of rate or model size. Experimental errors involved in making their determination would completely mask the sort of effects anticipated for the dependency of model size. The authors state that flow rate does not affect recovery, while an examination of their Table 1 shows a definite trend towards increased recoveries at breakthrough with decreased injection rates. Furthermore, their studies of the effects of these variables were performed in a low-pressure model and did not include studies of the miscible-slug process. Therefore, these studies do not reveal the effect of the variables studied upon the process of interest, the miscible-slug process.

The conclusion that molecular diffusion and dispersion are not important in a no-gravity system was based on results of a micible displacement in a low-pressure model in which a miscible slug was not used. These results give no information as to the effect of diffusion or dispersion on the bank in a full-size reservoir. Data obtained in our laboratory have shown that the coefficient of diffusion is a function of the absolute viscosity of the displacing and displaced fluids, lower absolute viscosity fluids having the larger values of diffusion coefficient. In the systems measured thus far, diffusion coefficients have been observed to vary by a factor of 30. Gases have much lower viscosities than liquids. Therefore, the diffusion between the contact of the gas and LPG bank in a field displacement may be much larger than heretofore suspected. Hence, the observation by the authors of the diffusion and dispersion in low-pressure models where fluids of high absolute viscosity were used is probably misleading. Also, the flow rate through the high permeable medium in the authors' experiments has probably made the mixing by diffusion insignificant. The point is made that the mobility ratio is the only factor which is significantly influencing the recovery. However, since a completely miscible fluid displacement was used (no slug), the recovery should not be a strong function of the molecular diffusion or dispersion.

The authors chose to ignore scaling their models for the effects of diffusion and dispersion. This undoubtedly led them into serious difficulties in an area to which they apparently gave little or no consideration. The fluids used in the studies made of the effect of slug size were refined oil equivalent to dodecane, a slug consisting of propane, and gas consisting of pure methane. Phase calculations may be made which show that, if as little as 3 per cent dodecane is present with propane and methane, an immiscible displacement will result. Studies of mixing-zone lengths in slim tubes have shown that the mixing-zone length due to diffusion and dispersion is as long as the distance traveled by the front during the early period of the displacement. Applying this result to the models used in this study, we would note that the mixing zones would extend across the slug from the gas to the oil and miscibility could not have been maintained over a very long distance because of the unscaled diffusion and dispersion effects. These effects would not be present to this same

[1]Geertsma, J., Croes, G. A. and Schwarz, N.: "Theory of Dimensionally Scaled Models of Petroleum Reservoirs", *Trans.*, AIME (1956) **207**, 118.

magnitude in full field application of the process where the initial thickness of the slug may be a few hundred feet.

In the "Introduction," the authors state that their experimental evidence indicates that the mixed zone length and sweep efficiencies obtained in slim-core models and electrolytic models are not applicable to miscible displacement in reservoirs. However, many of the conclusions arrived at from a study of data obtained in the models used by the authors could have been obtained from a study of the results obtained in a slim tube. For example, their results which indicate that recoveries are very low for the injection of small slugs would also be obtained in a slim core which is only 1-ft long. However, the use of a slim core which is 10-ft long or longer would show that the result obtained in the first foot is not directly applicable to that to be obtained through a sweep of 10 ft of core. It is difficult to understand how the authors could believe that the same sort of scale-up problems would not exist in their small three-dimensional models.

DISCUSSION

F. F. CRAIG, JR.
R. C. KOELLER
MEMBERS AIME

PAN AMERICAN PETROLEUM CORP.
TULSA, OKLA.

This paper presents the results of a series of flow tests which lead the authors to conclude that "small LPG banks of the order of 5 per cent HV or less are not effective in increasing oil recovery from horizontal reservoirs". The purpose of this discussion is to show that the experiments performed do not provide a valid test of this conclusion.

The key tests cited to support the above conclusion are those in which oil was displaced from a glass-bead-packed five-spot quadrant with various-sized banks of propane followed by gas. The implication is made that these were scaled model experiments.

The results presented in Fig. 1 are not data from scaled experiments. They are misleading in that they do not reflect the fact that miscible-displacement efficiency (recovery from swept portion of system) is 100 per cent, regardless of rock flow properties, whereas immiscible-displacement efficiency depends upon the relative permeability characteristics. The data in Fig. 1 indicate that a miscible-slug drive has only a slightly better oil-recovery efficiency than a conventional gas drive. This applies to the glass-bead-packed apparatus from which the data were derived. This comparison cannot be extended to a reservoir system. Numerous published data have shown that the oil-displacement efficiency from glass beads by gas injection is very nearly as high as that by solvent injection. In reservoir systems the oil-displacement efficiency by gas drive can be as much as fivefold smaller than that by solvent injection. Thus, in a reservoir system the contrast in oil-displacement efficiency between miscible slug and conventional gas drives could be as much as a factor of five greater than that inferred from Fig. 1.

The work of Blackwell, *et al* (authors' Ref. 10) underscores the need for dispersion scaling in miscible-displacement model tests in which gravity segregation and fingering are manifest. Instead of adhering to the constraints imposed by dispersion scaling, the authors performed a series of independent tests from which they concluded that flow rate, a prime factor in dispersion scaling, was not a factor in their bank experiments. This was the series of miscible displacements with equal-density fluids in five different-sized models at three levels of mobility ratio. Of course with no density difference between the fluids, it would be expected that the rate effects would be minimized. But still, the authors overlooked a statistical tool which can be used to determine if there is indeed no effect of rate in the data of Table 1, as they concluded.

To apply the statistical test, a second-degree polynomial was fitted by least squares to various sets of the data in Table 1 to express breakthrough oil recovery vs flow rate. Correlation coefficients were then calculated to express closeness of fit between the polynomials and the data. The probability that there is a correlation can be determined from the correlation coefficient, the number of data points in the set and the degree of the fitted polynomial, using available tables.[1] For the entire set of $M = 10$ data, it was determined that there is a probability of 0.998 that the recovery at breakthrough can be correlated with, and is thus dependent upon, rate. The probability that there is a correlation of breakthrough recovery with rate in the $M = 10$ data from the $9 \times 9 \times \frac{1}{8}$-in. model is 0.999; for the entire set of the $M = 41$ data, the probability of such a correlation is 0.995. No other sets of data given in the paper, particularly those for unfavorable mobility ratios, contain enough points to make a similar analysis. We conclude from this analysis that the breakthrough recoveries given in Table 1 are affected by rate. Moreover, the polynomials fitted through the three sets of data analyzed showed increasing recovery at breakthrough with decreasing flow rate. For example, the polynomial fit to the $M = 41$ data indicates that the recovery at breakthrough increases from 18.3 to 26.6 per cent as the flow rate decreases from 80 to 1 in./day. This trend is consistent with conclusions of Blackwell, *et al*, regarding the effects of dispersion due to molecular diffusion and convective mixing in laboratory tests.

In conclusion, there is no indication that the authors' tests were scaled experiments. The recovery data for which flow rates were given (Table 1) show a dependence upon rate. Since the LPG-bank tests, as well as the confined and unconfined five-spot tests, were conducted at unspecified flow rates with fluids of finite density difference, there is a question about the applicability of these results to reservoir conditions.

[1]Volk, W.: *Applied Statistics for Engineers*, McGraw-Hill Book Co., Inc., N. Y. (1958) 231.

Authors' Reply to C. A. Connally, F. F. Craig, Jr., R. C. Koeller, A. L. Benham, W. B. Gogarty and F. H. Poettmann

The discussions of the gentlemen above will be replied to individually, and then a few general statements will be made.

REPLY TO C. A. CONNALLY

Connally suggests that the graded-viscosity-bank work of Weinaug and Ling and Slobod and Lestz indicates that viscous fingering will not be a severe problem in the field. This conclusion does not at all follow from their work. In laboratory tests by Slobod and Lestz, relatively large graded banks (ranging from 0.15 to 0.30 PV in size) were used to combat the fingering in a miscible displacement where the mobility ratio was only slightly adverse ($\mu_o/\mu_s = 3$). In the Weinaug and Ling work, a 0.06 PV graded bank was used to combat fingering in a miscible displacement where the mobility ratio was also only slightly adverse ($\mu_o/\mu_s = 2.7$). Under these test conditions, representing only slightly adverse mobility ratios, there is virtually no tendency for solvent to finger anyway. Furthermore, there has been no work, by these authors or others to show that the bank size requirements can be reduced and still achieve the same oil-recovery performance in larger, geometrically similar models.

Connally further claims that for immiscible displacement the length of the zone of saturation gradient becomes relatively smaller in larger systems. Since we injected the nonwetting fluid at stabilized rates, this comment is not applicable to our work because it would be contrary to the generally accepted Buckley-Leverett theory.

It is suggested by Connally that the zonation technique used in our paper was inadequate, and results of helium tracer tests are cited to back up this claim. We made a detailed study of these tracer results. Very significantly, material-balance calculations showed that only about 25 per cent of the injected helium appeared at the production wells. This is strong evidence that a large fraction of the injected gas went outside the test pattern as was indicated by our model study. Furthermore, careful examination shows that stratification could not possibly account for the helium-concentration profiles observed at the production wells. Channels resulting from viscous fingering could account for the observed behavior.

Finally, Connally cites the performance of the Parks and Block 31 fields to disprove our conclusion concerning the ineffectiveness of small LPG banks. The Parks project has only recovered about 18 per cent of the predicted recovery by this process, and eight out of 32 production wells have suffered LPG breakthrough. In light of these facts, labeling the Parks test as a successful project is premature. In the Block 31 test, a straight miscible displacement is being achieved by injecting dry gas at high pressures. In this project the mobility ratio is much lower than generally encountered in the LPG-slug process (10 rather than 80 to 100). Therefore, we would expect fingering and channeling to be much less of a problem. This test is also in a relatively early stage (about 20 per cent of the oil in place has been produced), and results are not conclusive at this time. However, it should be noted that, of the six wells that have had gas breakthrough, three occurred after producing only about one-half of the predicted amount of oil and three occurred as predicted.

REPLY TO F. F. CRAIG, JR. AND R. C. KOELLER

Craig and Koeller state that Fig. 1 is misleading because it does not show that miscible-displacement efficiency is 100 per cent in the swept portion. We also know that miscible-displacement efficiency is essentially 100 per cent in the swept area. What the miscible-displacement curves on Fig. 1 show is that in areal models miscible displacement contacts only a fraction of the model and the size of this fraction is a function of the mobility ratio. If the mobility ratio of a miscible displacement is sufficiently adverse, the recovery curve will fall below that for an immiscible gas drive of oil.

Craig and Koeller note that the data in our Table 1 do show an effect of rate on *breakthrough* recovery. However, if the entire recovery curves for these experiments are compared (see Fig. 2 of the paper), there is no significant difference in them. This comparison is more significant than a comparison of breakthrough recoveries.

REPLY TO A. L. BENHAM, W. B. GOGARTY AND F. H. POETTMANN

Benham, Gogarty and Poettmann object to our application of conclusions from miscible-displacement experiments (two-fluid systems) to the miscible-slug process (three-fluid system). The effects of variables such as rate and model size should be essentially the same for both types of displacement.

Benham, *et al,* imply that the fluid system used in the laboratory tests was such that a miscible fluid displacement could occur only over a very narrow range of compositions. This is very misleading because essentially the same calculations and conclusions can be made for many crude oil-propane-methane systems (including Pembina crude). In fact, a comparison of the ternary phase diagram for the laboratory fluid system with phase diagrams for fluids similar to Pembina field fluids shows that the two-phase region for the laboratory fluids is slightly smaller than for the crude-oil system. Therefore, the laboratory fluid system is more favorable to the miscible-slug process than the field fluids.

Benham, *et al,* state that many of our conclusions could have been arrived at by a study of miscible displacement in slim cores 1- and 10-ft long. This is in error. We would have found, for example, that displacement efficiency in *slim cores* is rate-sensitive and that, therefore, dispersion and diffusion are important. This is not the case in areal models. We would find that, to scale up from a 1-ft long model to a 10-ft long model, we would also have to increase the diameter of the model by a factor of 10 and would run at different rates in the two models to scale dispersion and diffusion. This also is not the case in areal models.

GENERAL COMMENTS

The gentlemen who discussed this paper have expressed strong doubts as to whether various factors have been adequately scaled and about the calculation

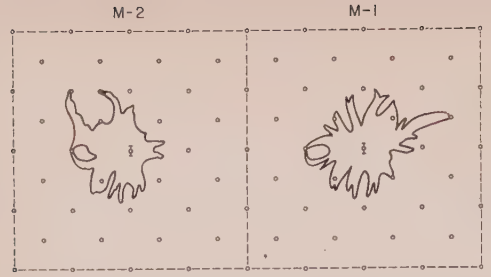
M-2
M-1
BREAK THROUGH PATTERN AFTER INJECTION OF 1.0 PER CENT HV OF SOLVENT (10 MD PLUS SANDSTONE)
BREAK THROUGH PATTERN AFTER INJECTION OF 1.6 PER CENT HV OF SOLVENT (10 MD PLUS SANDSTONE)

FIG. 1—PEMBINA FIELD—MISCIBLE DISPLACEMENT IN TWO 2,560-ACRE 41-SPOT PATTERNS.

procedure used to apply results from glass-bead models to the Pembina field. Certainly not all factors were exactly scaled and there were approximations in the calculation procedure. However, what counts is whether the important factors were *sufficiently* scaled that conclusions concerning field performance are correct. The *most important conclusion* from this study was that small banks will be ineffective due to fingering and channeling.

Since this paper was written, Mobil Oil, Ltd. has started injection of a small solvent bank in two large patterns in the Pembina field. The early performance of these floods is shown in Fig. 1. While the shape of the solvent front as shown is schematic, the wells shown to have experienced LPG breakthrough have actually broken through. After the injection of only 1.6 per cent HV of solvent in Pattern M-1, LPG breakthrough occurred at six wells, with one breakthrough well being about 0.8 mile from the injection well. After injection of only about 1.0 per cent HV of solvent in Pattern M-2, LPG breakthrough occurred in five wells, with one being about 0.7 mile from the injection well. This is ample evidence that fingering and channeling far in excess of stratification are proving to be a serious problem.

Other field information is now becoming available

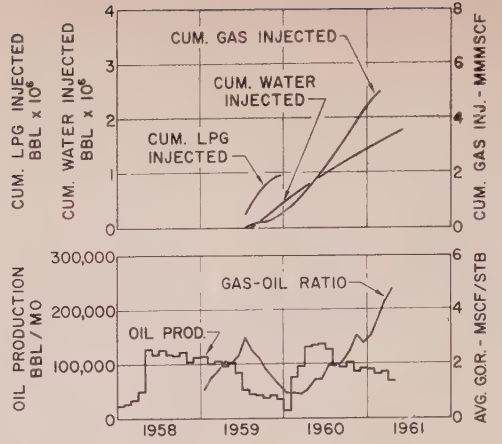

FIG. 2—MISCIBLE FLOODING AT BISTI.

which supports this conclusion—for example, the full-scale miscible-slug project in the Bisti field in New Mexico. This project was also started as the result of a pilot test in a single, unconfined five-spot pattern. Here also, oil recovery from the pilot test was reported to be about 50 per cent of the oil in place in the pattern. Production and injection data from the New Mexico Oil Conservation Commission are plotted on Fig. 2. These figures are totals for what is called the "central unit". A 4 per cent HV LPG bank was injected into ten 160-acre five-spots. These patterns were surrounded by gas- and water-injection wells to confine the area. Due to this complication, the interpretation of Fig. 2 is difficult. However, since only a small fraction (about 20 per cent) of the gas injected went into confining wells and only a small volume of water (8 per cent HV) was injected, the GOR behavior and oil-production-rate behavior are mostly due to the miscible patterns. Of course, some of the oil produced is due to the water flood. While no attempt has been made to analyze these data in detail, it is readily apparent that the injection of a 4 per cent bank of LPG had only a very transient effect on the GOR behavior and oil-production rate for the full-scale project. ★★★

Improved Bentonite Cements Through Partial Acceleration

H. J. BEACH | GULF OIL CORP. HOUSTON, TEX.

ABSTRACT

This paper describes the properties and uses of cementitious mixtures containing 10 to 20 per cent bentonite and 2 per cent or more sodium chloride. Salt additions improve bentonite cement by increasing early strength and stabilizing viscosity without changing thickening time. The volume yield of cement is increased 20 per cent or more without lowered early strength. The unique properties of salt in this type of system make savings of more than 10 per cent possible where light-weight, low-strength cementitious material is adequate to fill behind pipe. The density range of these mixtures is 12 to 13 lb/gal and the filtration rates are medium-low, aiding the placement of long columns in primary cementing. Where available, sea water is an ideal salt source in preparing these slurries.

INTRODUCTION

Accelerators increase the rate of cement hydration. In speeding reaction with water, they can affect cement performance by reducing thickening time and increasing early strength after set. Accelerators that cause both effects can be considered "total", and those which produce only one effect can be called "partial".

Materials that act conversely to accelerators are retarders, and they also can be total or partial. Partial retarders make high-temperature cementing possible by prolonging thickening time while impairing early strength only slightly.

Most known accelerators are total. A useful partial accelerator would increase strength without altering thickening time. This report concerns material combinations in which a normally total accelerator exerts unique partial properties. Utilizing these limited effects improves bentonite cement.

SEPARATE EFFECTS OF SODIUM CHLORIDE AND BENTONITE ON CEMENT

Sodium chloride and calcium chloride are commonly used in cement, and at low concentrations their effects are similar. Ludwig[1] studied sodium chloride in API Class A and Class E cements.[2] Figs. 1 and 2 summarize his data taken at 140°F on slurry pumpability and early strength.

Normal water-to-cement ratios are 0.46 and 0.40, respectively, for Class A and Class E cements. At saturation the salt content is 12 to 14 per cent of the weight of cement solids. The illustrations, therefore, cover the range of salt solubility in the mixing water.

The data show that sodium chloride is a total accelerator of the Class E cement studied over the range of solubility. It is total in Class A cement to 6 per cent. Above this concentration salt becomes a retarder—partial from 6 to 10 per cent and total above. These results are general for different brands of Class A cement, although the shift from acceleration to retardation may occur at different salt concentrations for different temperatures. The results are specific for the Class E brand studied. In discussing his data, the investigator emphasized that different Class E cements might respond erratically to salt, depending on the brand chosen.

Morgan and Dumbauld[3] describe the properties of bentonite cement in a paper that is a standard reference in using these systems. Bentonite functions in cement as an enabling agent; each bentonite addition equal to 1 per cent of the weight of dry cement makes possible the further addition of 4.5 per cent water.[4] Thus, 10 per cent bentonite in Class A cement, normally slurried neat with 46 per cent water, enables the slurry to contain another 45 per cent before settling. Water is one of the lightest and cheapest cement extenders; it reduces density and cost. Bentonite cements produce uniform slurries having low susceptibility to solids separation. After set, they offer low resistance to perforation.

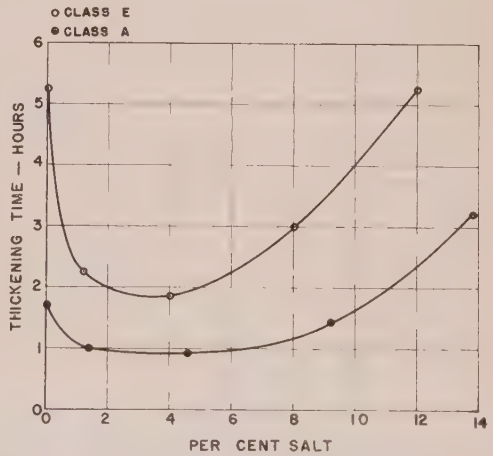

FIG. 1—EFFECTS OF SODIUM CHLORIDE ON CEMENT THICKENING TIME AT 140°F.

Original manuscript received in Society of Petroleum Engineers office March 8, 1961. Revised manuscript received July 25, 1961. Paper presented at Third Biennial Permian Basin Oil Recovery Conference of SPE, May 4-5, 1961, in Midland, Tex.

[1]References given at end of paper.

Discussion of this and all following technical papers is invited. Discussion in writing (three copies) may be sent to the office of the *Journal of Petroleum Technology*. Any discussion offered after Dec. 31, 1961, should be in the form of a new paper. No discussion should exceed 10 per cent of the manuscript being discussed.

This page of *Petroleum Transactions, AIME* follows page 816. The intervening non-Transactions pages appeared in *Journal of Petroleum Technology*.

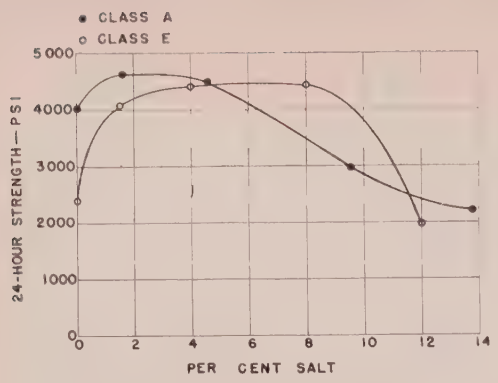

FIG. 2—EFFECTS OF SODIUM CHLORIDE ON CEMENT STRENGTH AT 140°F.

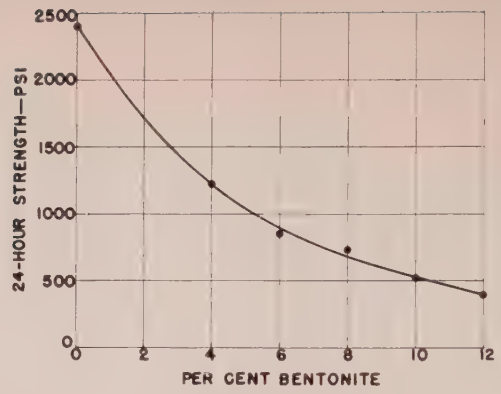

FIG. 3—EFFECTS OF BENTONITE ON CEMENT STRENGTH AT 110°F.

These advantages result from a compromise with strength supported by classic demonstrations of Farris[5] showing the strength of neat cement to be many times that required to support casing. This compromise has received mixed acceptance, varying from regard of bentonite cements as fill material to reliance on them for competent seals between casing and pay formations. In most cases these slurries are followed by a few hundred cubic feet of neat cement for added strength around the lower end of casing.

Bentonite, in adding sodium ions to cement, accelerates it. Partial evidence of this comes from observed thickening-time decreases resulting from additions. But bentonite can be considered a total accelerator although the effect on strength is obscured by the dilution of accompanying water.

As bentonite and water are added to a cement slurry, the strength developed after set declines uniformly as shown in Fig. 3. At some concentration, the strength of the mixture falls below a minimum value acceptable to the user; this is the practical limit of adulteration. A widely accepted limit for this is 500 psi after 24 hours' aging at low temperature (100° to 120°F). This strength limitation is recognized, although individual opinion may set it higher or lower. Thus, a slurry containing 10 per cent bentonite and 90 per cent water has about the limit of adulteration possible before falling below the 500-psi strength specification. This dilution in sacrificing surplus strength reduces density to 13.2 lb/gal, a 2.5-lb/gal reduction from neat Class A cement containing 46 per cent water.

Bentonite additions thicken, accelerate and severely restrict admixed cements unless they are co-additive with a dispersing and retarding agent. Calcium lignosulfonate universally serves this dual purpose. Strength tests at 100°F on bentonite cements containing varied amounts of this retarder would produce a family of curves similar to that of Fig. 3. All members would fall under the base curve shown and would lie below minimum strength specification at the 10 per cent bentonite, 90 per cent water composition. However, retarded compositions in practice are used at higher temperatures that would increase strengths to or above the minimum. Therefore, Fig. 3 is simply representative of the strength decline occurring with bentonite additions. A minimum strength specification sets a maximum bentonite content.

Bentonite intensifies high-temperature-induced retrogression of cement strength. This strength loss during prolonged aging at extremely high temperature is inherent in all cements; when it further weakens a material at a low basic strength level, the only remedy is to restrict permanent placement of bentonite cements to safe temperatures. The work of Carter and Smith[6] suggests the safe maximum to be about 230°F. However, this leaves a wide range for advantageous application of bentonite cements.

COMBINED EFFECTS OF SODIUM CHLORIDE AND BENTONITE ON CEMENT

The effects on 24-hour strength of varied concentrations of sodium chloride were studied for bentonite additions of 12, 16 and 20 per cent to API Class A cement. The water contents were adjusted so that the slurries contained 46 per cent by weight of the cement and additional 4.5 per cent quantities for each 1 per cent bentonite. Following this formula, the 16 per cent slurries contained 16 gm of bentonite and 118 gm of water/100 gm of cement.

Fig. 4 shows the results for the 16 and 20 per cent compositions that contained 0.2 per cent calcium lignosulfonate. Test specimens were cured at 110°F under 1,600-psi pressure. Sodium-chloride additions from 0.5 to 5.0 per cent nearly doubled the 24-hour strengths. Above 5 per cent, the strengths decreased with approach toward saturation. Spot checks at saturation showed strength had fallen below the base values for slurries containing no salt.

Standard API consistometer tests were conducted on the 16 per cent retarded bentonite-cement slurry at several sodium-chloride concentrations over the range of accelerated strength shown in Fig. 4. The tests simulated the setting of casing at 3,000 ft where the bottom-hole static temperature is 125°F, circulating temperature is 97°F, and the bottom-hole pressure is 2,000 psi. All mixtures contained 0.2 per cent calcium lignosulfonate, the usual retarder requirement when conventional bentonite cements are used under these conditions.

Fig. 5 shows the results of these tests. Except for a very slight drop at low concentrations, there is no change in thickening time until 5 per cent sodium chloride is exceeded. The stability of thickening times between the 2.0 and 5.0 per cent salt additions are especially significant; these are virtually identical with the time obtained for the mixture containing no salt.

The combined results from the strength and thickening-time tests indicate sodium chloride to be a partial accelerator of bentonite cement in concentrations ranging from about 0.5 to 5.0 per cent. Strengths are substantially increased without change in fluidity. Based

on the bentonite parameter, similar results were obtained for 12 and 20 per cent slurries, retarded and nonretarded.

The effects of sodium chloride on viscosity 15 and 45 minutes after initial mixing are shown in Fig. 6 for the 16 per cent bentonite cement. The values were taken during thickening-time tests and fix the general effect of sodium chloride as viscosity reduction. At salt contents between 2 and 4 per cent, the reduction persists over a considerable portion of the time required to position cement in oilwell operations. This is a departure from the slurry behavior of non-salt bentonite cement. The data show a 10-poise viscosity rise between readings for the mixture containing no sodium chloride, with smaller increases as the salt content rises. Although a further water addition will reduce an initial viscosity in the lower range, a salt increase to 2 per cent is necessary to stabilize it. The optimum salt concentration lies between 2 and 3 per cent. Viscosity stability permits lower pump pressure with faster displacement.

Bentonite reduces the filtration rate of cement; calcium lignosulfonate, when co-additive, further reduces it. A mixture of API Class A cement containing 16 per cent bentonite, 0.6 per cent calcium lignosulfonate and 2.0 per cent sodium chloride had an API fluid loss of 140 cc under a pressure differential of 1,000 psi. Based on filter-cake thickness, this is equivalent to a 70-cc loss from neat cement. Differences in filter-cake thicknesses from slurries of different compositions but equal water losses are functions of the water-to-solids ratios. These amounts of filtrate can be described as medium-low. They probably are low enough to aid the placement of a long cement column against a high-porosity formation where neat, high-filtration-rate cement builds thick filter cake that chokes the annulus. Bentonite cements containing sodium chloride can also be treated with the new fluid-loss additive described by Stout and Wahl[7] to produce slurries with exceptionally low filtrate rates. This new additive can be used with or as a substitute for the normal lignin dispersant.

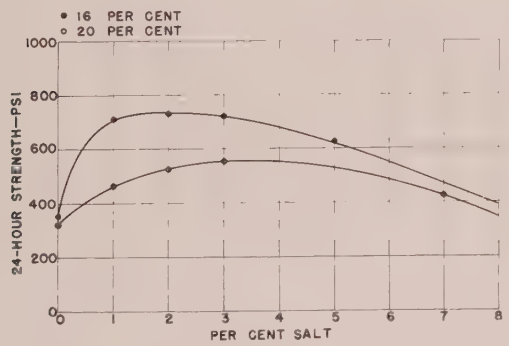

Fig. 4—Effects of Salt on Strength of Bentonite Cement at 110°F.

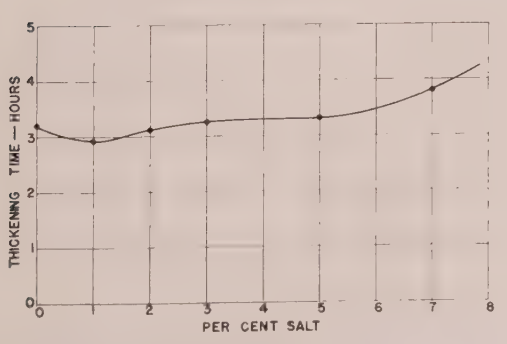

Fig. 5—Effects of Salt on Thickening Time of 16 Per Cent Bentonite Cement at 3,000 ft.

APPLICATION

The savings using the improved slurries described average 10 per cent of the cost of non-saline bentonite cements of lower volume yield, higher density and equal strength. The saving results from a slurry volume increase sufficiently large to overcompensate for the added cost of extra bentonite and salt. However, as bentonite contents are increased beyond 16 per cent, the additional saving is less in proportion to slurry volume increase. For example, assuming a price of $1.00/sack of Class A cement, 1 cu ft of non-saline, 10 per cent bentonite cement containing 0.2 per cent dispersant costs $0.94; an equal volume of 16 per cent saline slurry of equal strength costs $0.84, and the 20 per cent slurry costs $0.80. The diminished saving results from pricing policies on bentonite followed by cement service companies. The saving between 16 and 20 per cent is subjected to other diminished returns not shown in this cost comparison. At the higher bentonite content, strengths are lower and more dispersant is usually required to control thickening time. For these reasons it is recommended that slurries improved by the partial acceleration of sodium chloride contain 16 per cent bentonite.

API Class C cements, where available, provide the most economical application of the principles of partial acceleration. Only one brand of this class has been used extensively, making more general usage subject to further laboratory testing.

The data used to demonstrate the partial acceleration by sodium chloride were taken with mixtures that contained 4.5 parts extra water for each part bentonite by weight. This would be the optimum ratio if salt were not present. For slurries based on Class A cement containing 2 to 3 per cent sodium chloride, a more satisfactory ratio is 4.3:1. In Class C cement with the same salt range, bentonite additions enable a ratio of 5.0:1. Table 1 shows the compositions, densities and volumes of these slurries. The densities range from 12.1 to 12.6 lb/gal.

The viscosity effect of sodium chloride on bentonite cement is principally a reduction in yield point. This alters the appearance of the slurries when they are field-mixed. There is little visual evidence that bentonite is present, and there is a strong tendency to adjust controls to decrease their water contents to produce slurries that have the look of non-saline bentonite cement. This should be countered by relying on con-

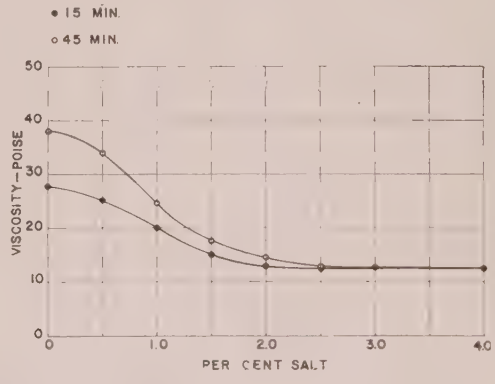

Fig. 6—Viscosity Effects of Sodium Chloride in 16 Per Cent Bentonite Slurries.

tinuous density measurements. In spite of a watery appearance, slurries in the composition ranges suggested show no tendency to settle. The reduction in yield point has the advantage of speeding mixing. In a recent application, 1.2 Mcf of slurry were mixed in less than nine minutes.

Sodium chloride can be used to control viscosity. When higher concentrations of dispersant are required for higher temperatures, the slurries become very thin if the salt content is held at 3.0 per cent. Viscosities can be restored to more desirable values by decreasing the accelerator within the optimum range. Table 2 reflects the adjustments. Shown are 16 per cent slurries which were prepared in various brands of Class A and in one brand of Class C cement with water contents as defined previously. The principal data contained are thickening times obtained from tests which simulated the setting of casing at various depths. These tests were conducted according to API *RP 10B*, which fixed standard temperatures for each test depth. The static formation temperature associated with 10,000 ft is 230°F, the limiting temperature chosen earlier for permanent bentonite-cement placement. Naturally, these slurries can be used at greater depths so long as the restricting temperature is not exceeded.

In recommendations, practice has been to require three hours' pumpability of these slurries in tests which simulate conditions of use where the job size ranges from 1 to 2 Mcf. Jobs larger than 2 Mcf thus far have received recommendations on an individual basis.

Generally, bentonite used in cement must be high in quality and free of enriching additives which can produce unexpected deleterious effects. Specifically, it should pass specifications set both in API *Standard 10A*.[2] Quality becomes increasingly important as the bentonite content of a slurry is increased.

Sea water contains about 3 per cent sodium chloride and many lesser constituents. Where readily available, it is the natural mixing water for bentonite cement. Tests yield similar results, with respect to partial acceleration, when sea water is used to prepare bentonite cement and when optimum salt is added to slurries prepared in fresh water.

FIELD USE

Sixteen-per cent bentonite cements made from both Class A and Class C materials have been used to set casing in 39 wells in West Texas. The prime reasons for use were to achieve lower cost and to prevent loss of cement to thief zones. Field reports indicate satisfactory results. Only one job experienced lost circulation during cementing. The same compositions have been successfully used for cementing casing in five wells in the Hobbs, N.M., and Kermit, Tex., areas. Use of this light-weight slurry has reduced loss of cement to thief zones and has resulted in an appreciable reduction of cementing costs.

Sixteen-per cent Class C slurries were used in two wells in the Texas Panhandle. In the first well, 7-in. casing was set at 11,440 ft using 870 cu ft of bentonite cement with a 200-sack neat tailout. A 3,000-ft interval was covered, and the later well completion indicated a good job. In the second job, 5½-in. casing was set at 8,804 ft using 1,070 cu ft of bentonite slurry with a 100-sack tailout. Circulation was lost during the job and later completion indicated communications.

This cement has been applied to about 25 jobs of surface casing in Mississippi, primarily to obtain reduced cementing costs. Large slurry volumes have featured these jobs partly due to hole washout. The improved slurries have been regarded primarily for fill in this area and usually have been followed with enough neat cement to give a 200-ft tailout.

TABLE 1—COMPOSITION AND PHYSICAL PROPERTIES OF BENTONITE CEMENTS CONTAINING SALTS

Class Cement	Per Cent Bentonite	Per Cent Water	Density (lb/gal)	Sack (cu ft/sack)
A	16	115	12.62	2.32
A	20	132	12.30	2.59
C	16	136	12.10	2.67

TABLE 2—THICKENING TIMES OF 16 PER CENT BENTONITE CEMENT

Class Cement	Per Cent Salt	Per Cent Calcium Lignosulfonate	API Casing-Setting Depth (ft)	Time to 100 Poise (minutes)
A	3.0	0.20	6,000	115
A	3.0	0.40	6,000	208
A	3.0	0.40	8,000	118
A	2.5	0.60	8,000	324
C	3.0	0.20	3,000	197
C	3.0	0.40	6,000	193
A	2.5	0.80	10,000	188
A	2.0	1.00	12,000	180+

CONCLUSION

1. Sodium chloride increases the strength of bentonite cement in concentrations from 0.5 to 5.0 per cent based on the weight of cement solids. In the range from 2 to 5 per cent, it has no effect on thickening time.

2. Sodium chloride in the optimum 2 to 3 per cent concentration stabilizes slurry viscosity at low values for extended periods prior to initial set.

3. The partial acceleration effects of sodium chloride can be utilized in API Class A and Class C cements to increase slurry specific volumes sufficiently to effect savings of 10 per cent or more compared to other light-weight mixtures of equal strength and higher density.

4. Cements containing sodium chloride and 16 per cent bentonite have medium-low fluid losses. These are further reduced by calcium lignosulfonate and compatible water-loss additives.

5. These compositions have performed successfully in a wide variety of applications.

ACKNOWLEDGMENT

The author expresses his appreciation to the management of Gulf Oil Corp., Domestic Production Dept., for permission to prepare and publish this paper.

REFERENCES

1. Ludwig, N. C.: "Effects of Sodium Chloride on the Setting Properties of Oil-Well Cements", *Drill. and Prod. Prac.*, API (1951) 20.
2. "Specification for Oil-Well Cements and Cement Additives", *STD 10A*, API, Seventh Ed. (Jan., 1961).
3. Morgan, B. E. and Dumbauld, G. K.: "A Modified Low-Strength Cement", *Trans.*, AIME (1951) **192**, 165.
4. "Recommended Practice for Testing Oil-Well Cements and Cement Additives", *RP 10B*, API, Ninth Ed. (Jan., 1960).
5. Farris, R. F.: "Method for Determining Minimum Waiting-on-Cement Time", *Trans.*, AIME (1946) **165**, 175.
6. Carter, Greg and Smith, D. K.: "Properties of Cementing Compositions at Elevated Temperatures and Pressures", *Trans.*, AIME (1958) **213**, 20.
7. Stout, C. M. and Wahl, W. W.: "A New Organic Fluid-Loss-Control Additive for Oilwell Cements", *Jour. Petr. Tech.* (Sept., 1960) **XII**, No. 9, 20. ★★★

Analysis of Gravity Drainage

H. N. HALL
ASSOCIATE MEMBER AIME

PAN AMERICAN PETROLEUM CORP.
TULSA, OKLA.

ABSTRACT

Various factors must be considered in an engineering evaluation of gravity-drainage reservoirs. Among these are: (1) the effect of producing rate on total oil recovery; (2) the effect upon well productivity and ultimate recovery of the pressure level maintained during the producing life of the reservoir; (3) the economic advantage of full or partial pressure maintenance; and (4) estimate of the rate of gas production and injection and the possible purchase of gas under conditions of full pressure maintenance to ascertain compressor facilities needed. All of these factors can be evaluated only when a reliable method is employed for determining reservoir performance in gravity-drainage reservoirs.

The purpose of this paper is to present a general method for calculating the performance of a gravity-drainage reservoir. This method is applicable for conditions of complete pressure maintenance, partial pressure maintenance and normal pressure depletion. Provisions are made to take into account variations throughout the reservoir of reservoir configuration, changes in permeability and fluid composition.

Based on the method presented in this paper, an IBM 650 computer program has been developed. The past performance of an actual gravity-drainage reservoir producing under conditions of declining pressure and no gas injection was duplicated using this program.

INTRODUCTION

In tilted reservoirs the production of oil is influenced by drainage of oil from upstructure to downstructure locations. When this downstructure drainage of oil is sufficient to cause effective segregation of the gas and oil in a reservoir, the reservoir is usually classified as a segregation drive or gravity-drainage reservoir. (Discussion will be restricted to gravity-drainage reservoirs which have no encroachment of edge water.) The important feature in gravity-drainage reservoirs is the density difference between reservoir oil and gas. These phases tend to segregate in the reservoir with the result that in the gas cap the oil saturation is maintained at a higher level by drainage of oil from the gas-cap area. Oil can be produced from the oil zone at a low gas-oil ratio and reservoir energy is thereby conserved.

The standard material balance in not adequate for predicting gravity-drainage reservoir performance because it does not take into account the difference in saturation above and below the gas-oil contact. Several authors[1-4] have presented methods for calculating the performance of gravity-drainage reservoirs in which reservoir pressure is maintained constant by gas injection into the gas cap. Using some simplifying assumptions, these methods can be employed with a desk calculator to give acceptable results. The problem of predicting the performance of gravity-drainage reservoirs under the conditions of declining reservoir pressure is many time more complex than that of constant pressure. Therefore, attempts to develop a method suitable for desk calculation have required excessively simplified assumptions. In the past several years, high-speed digital computers have become more widely available for reservoir engineering problems. These computers are well suited to problems such as the prediction of the performance of gravity-drainage reservoirs with pressure decline. Many of the simplifying assumptions necessary for hand computation can be eliminated so that a realistic approach to the gravity-drainage process can be made.

CONCEPTUAL PICTURE OF OIL MOVEMENT IN GRAVITY-DRAINAGE RESERVOIRS

Before attempting to develop an analytical treatment for conditions occuring in a gravity-drainage reservoir, a concept should be formed concerning the movement of fluids in the reservoir as oil is produced.

A review of the literature[1-4] shows that it is customary to classify gravity-drainage operations into two categories—(1) with complete pressure maintenance, and (2) with declining pressure. The same line of reasoning will be followed in presenting the concept of the movement of fluids in the reservoir because it is easier to visualize the movement of fluids under conditions of complete pressure maintenance. After discussing complete pressure maintenance, an analogy will be made between that and the case of declining pressure. It should be kept in mind throughout that the final aim for the problem of solving gravity-drainage performance with digital computers will be to develop a general program for any kind of gravity-drainage reservoir.

COMPLETE PRESSURE MAINTENANCE

One feature which is generally common in gravity-drainage reservoirs is a gas cap located at the top of the structure. This is shown in Fig. 1(a). Fig. 1(b) shows oil saturations that might occur through the reservoir. In the gas cap, oil saturation is lower than

Original manuscript received in Society of Petroleum Engineers office July 18, 1960. Revised manuscript received July 5, 1961. Paper presented at 35th Annual Fall Meeting of SPE, Oct. 2-5, 1960, in Denver.

[1]References given at end of paper.

in the oil column. The oil column and gas cap are separated by the gas-oil contact (a zone in which oil saturation changes rapidly with distance). Under the condition of complete pressure maintenance, sufficient gas is injected into the gas cap to maintain a constant gas-cap pressure. As a result, no gas saturation develops in the oil column, and all of the oil produced comes from the downward movement of the gas-oil contact.

Fig. 2 illustrates reservoir conditions after the reservoir has been produced for some time.*

As a result of production of oil from the oil column, oil drains downstructure, and the gas-oil contact moves from Position A to a new Position B. The movement of the oil as it drains downstructure is governed by the pressure gradient that develops in the oil column. Fig. 2(c) shows a static pressure distribution as a solid line and the flowing pressure distribution as a dashed line. Under the conditions of constant producing rate, the pressure gradient will assume a "stable" value after a certain period of production. At that time all of the oil produced comes from the frontal-type displacement. Until the "stable" pressure gradient is achieved, part of the oil produced comes from expansion of the oil column in going from the initial pressure distribution to the "stable" conditions.

The liquid saturation distribution, average liquid saturation above the gas-oil contact and the rate of advance of the gas-oil contact can be determined for a uniform reservoir in a manner described by Shreve, *et al.*[2] This method is based on determining the oil flow rate (at a stated total flow rate) for any given gas saturation. For a given value of total flow rate (e), the value of oil flow at various saturations is determined by means of Eq. 1.

$$e_o = -6.33\,(k_{ro})\frac{kA}{\mu_o}\left\{\frac{1}{(k_{ro})\frac{kA}{\mu_o}+(k_{rg})\frac{kA}{\mu_g}}\left[(K_{rg})\frac{kA}{\mu_g}(\alpha_g-\alpha_o)-\frac{e}{6.33}\right]\right\} \quad . \quad . \quad . \quad (1)$$

The curve in Fig. 3 shows the variation of oil flow rate with gas saturation for a total flow rate equal to $(e_o)_1$. The average saturation above the gas-oil contact is obtained by drawing a line from the point of zero gas flow [i.e., from $(e_o)_1$ and S_{gc}] tangent to the curve, and finding its intersection with the abscissa. The average gas saturation found in this manner is labelled as (A) in Fig. 3. The rate of advance of the gas-oil contact (Point B) is obtained by measuring the slope of the tangent line and then using this value for $\left(\frac{\partial e_o}{\partial S_g}\right)$ in the following Eq. 2.

$$\left(\frac{\partial L}{\partial t}\right)_{S_g} = -\frac{\left(\frac{\partial e_o}{\partial S_g}\right)}{A\phi} \quad . \quad . \quad . \quad . \quad . \quad . \quad . \quad . \quad . \quad (2)$$

For a reservoir having constant dip, cross-sectional area and thickness, with uniform rock and fluid properties, and having the oil production confined to the area below the gas-oil contact, constant-pressure gravity-drainage performance can be calculated using Eqs. 1 and 2. A method similar to this was described by Stewart, *et al.*[1] In an attempt to compensate for variations in reservoir properties throughout the reservoir, Stewart made adjustments in the equations for the variation of fluid and rock properties at different positions of the gas-oil contact during the life of the reservoir. New values for the average gas saturation above the gas-oil contact were calculated at different positions in the reservoir. The proper position of the gas-oil contact at a certain time was obtained by adjusting its position so that the change in oil content behind the front was equal to the oil produced.

In most reservoirs, variations in reservoir configuration, producing rate with time, and fluid properties and rock properties with structure are common rather than the exception. As a result, the method outlined by Stewart is inadequate, except qualitatively to determine the relative importance of gravity in a particular reservoir.

Welch and Shreve[2] and Essley, *et al*,[3] have presented methods which provide for variations in reservoir properties. In contrast to the idea of using the average saturation above the gas-oil contact as determined in Fig. 3, they used the rate of advance of various

*Wells completed through the gas-oil contact can either be produced to an economical gas-oil ratio limit or shut-in as the gas-oil contact reaches them. This factor will be determined by local conditions and completion practices.

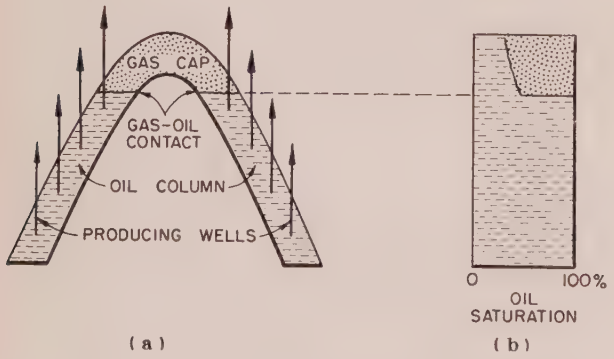

FIG. 1—CROSS SECTION OF TYPICAL GRAVITY-DRAINAGE RESERVOIR.

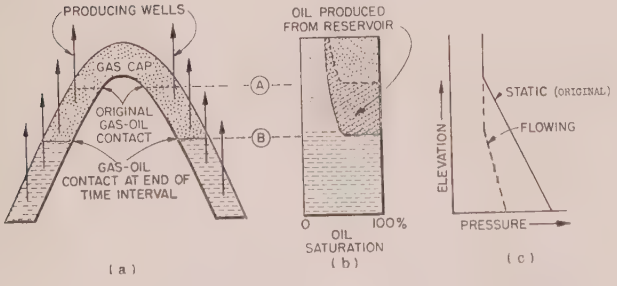

FIG. 2—CONSTANT-PRESSURE GRAVITY-DRAINAGE RESERVOIR.

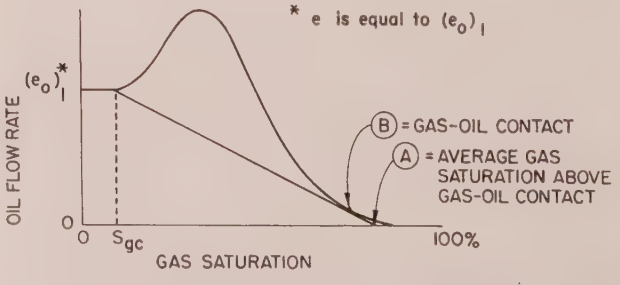

FIG. 3—OIL FLOW RATE VS GAS SATURATION.

saturations above the gas-oil contact. Welch and Shreve divide the reservoir into a series of assumed isotropic segments, of different volumes and properties, and determine the location of all saturation in these blocks to arrive at an average saturation above the gas-oil contact. Essley, *et al,* use average properties for the depth interval studied in each individual time-step calculation, find the saturation distribution with these average properties and then get the average saturation above the gas-oil contact. In all developments presented to date, the reservoir pressure is considered constant; therefore, no variation in fluid properties with time occurs. As a consequence, the value of total flow rate at the gas-oil contact (*e* in Eq. 1) is the sum of all producing rates below the gas-oil contact.

DECLINING PRESSURE

Declining gas-cap pressure occurs because either no gas is injected into the gas cap or the amount injected is insufficient to maintain pressure. As soon as the pressure declines to the bubble point at some position in the oil column below the gas-oil contact, gas will come out of solution and tend to migrate in the reservoir. If the pressure gradient in the oil column is exactly equal to the hydrostatic gradient of the gas, gas that is evolved would not move up or down. It seems highly unlikely that this condition would ever occur at all points in the oil column. Even though it did occur at the one particular time, the flowing pressure gradients will continually change with time so that free gas would eventually migrate either up or downstructure. Fig. 4 illustrates a reservoir produced under conditions of declining pressure to a point where free gas exists at all points throughout the oil column.

The conditions depicted are for a flowing pressure gradient in the oil column which will allow migration of free gas into the gas cap. In a sense, then, this is a 'built-in" partial pressure-maintenance system because part of the free gas, instead of being produced, will migrate into the gas cap. The condition of oil flow downdip and gas flow updip is herein called "counter-flow." Under the conditions where the "gravity reference rate"* is exceeded, the pressure gradients at the gas-oil contact will be such that free gas would tend to migrate downdip into the oil column.

The total oil produced during the time interval the gas-oil contact moves from A to B in Fig. 4 comes from a combination of drainage from above the gas-oil contact, frontal displacement at the gas-oil contact and a decrease in oil content in the oil column. Under normal processes where gravity drainage is not effective, oil production causes a decrease in the oil saturation in the oil column. In reservoirs having conditions favorable for gravity drainage, the oil saturation in the oil column throughout the life of the reservoir remains at a high level as a result of drainage. Consequently, oil can be produced at a low gas-oil ratio. In the event that the amount of drainage occuring is not a significant part of the total production, much of the oil is produced by pressure depletion which decreases the oil content of the oil column, resulting in a constantly increasing gas-oil ratio.

The movement of the gas-oil contact and the displacement efficiency for specified reservoir oil and gas flow rates can be determined by the method described by Welch and Shreve.[2] In the case of constant-pressure operations, the displacement efficiency is specified by the oil-production rate below the gas-oil contact since efficiency of displacement at the gas-oil contact is determined by the total flow rate at that point. In the case of declining pressure, the conditions of flow at the gas-oil contact are not directly related to oil production below the gas-oil contact. This problem represents a major difficulty in solving declining-pressure gravity drainage performance. The over-all problem of gravity drainage with declining pressure is to relate the amount of oil drainage from the upstructure locations to the total production from the reservoir. Therefore, the problem of predicting declining-pressure gravity-drainage performance can be determined only when the movement of oil and gas throughout the reservoir and the movement of gas-oil contact are incorporated as an integral part of the solution.

Based on the concepts which have been discussed, a method will be presented for calculating the performance of gravity-drainage reservoirs with or without pressure maintenance. The following sections contain the assumptions used in developing the prediction method, the details of the method of solution and results of calculations made to predict the performance of an actual gravity-drainage reservoir produced with declining pressure.

*The "gravity reference rate" is defined as the rate at which oil will drain downdip with a pressure gradient equal to the density difference between the oil and gas phases.

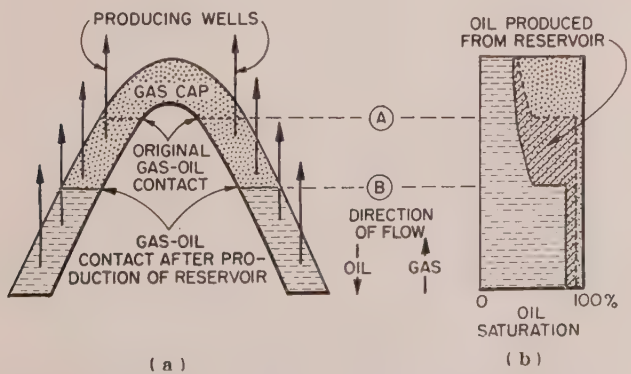

FIG. 4—DECLINING-PRESSURE GRAVITY-DRAINAGE RESERVOIR.

DEVELOPMENT OF THEORY

ASSUMPTIONS

The following assumptions were used in developing the method for calculating the performance of gravity-drainage reservoirs.

1. The flow of oil and gas is parallel to the dip of the reservoir.

2. The flow of oil at the gas-oil contact is always downdip.

3. A gas cap exists at the start of calculations.

4. The effect of capillary pressure can be neglected in calculating oil and gas flow rates above and below the gas-oil contact.

5. Connate water does not flow.

6. There is no water influx.

7. There is no variation of pressure with position in the gas cap.

8. The reservoir can be represented by a series of horizontal blocks, in which average values of pres-

sure and saturation in the block are satisfactory approximations of actual values at the average level of the block. In addition, fluid and rock properties and reservoir properties are constant within the block.

DESCRIPTION OF RESERVOIR GEOMETRY

Fig. 5 shows a three-dimensional view of a segment of the "average" reservoir.

Fig. 6(a) shows a vertical cross section of this segment and illustrates how fluids could be distributed throughout.

Because of the tendency of fluids to seek their own level, the gas-oil contact is assumed to be horizontal. It is assumed that there will be no change in pressure with distance in the gas cap; therefore, the pressure at all points on the gas-oil contact will be constant. Since all flow is assumed parallel to the dip of the structure, lines of equal pressure will be horizontal. Therefore, for the purpose of mathematically expressing the flow of oil and gas, the reservoir will be divided into horizontal sections similar to that shown in Fig. 6(b). The width of an individual block is considered constant and the three-dimensional view of the reservoir will be a series of parallelepipeds.

Although the reservoir characteristics and fluid properties are assumed uniform within a given block, variations may occur between blocks.

In developing equations for the flow of fluids in the reservoir, the geometric model which is divided into horizontal blocks will be separated into three regions as shown in Fig. 6(b). The reason for this breakdown is as follows.

Zone I (All Blocks Above the Block Containing the Gas-Oil Contact)

In this region the potential force causing oil flow will always equal the head of the oil column since, according to Assumption 7, there is no difference in pressure with position in the gas cap. Therefore, an equation describing a material balance of the oil can be solved directly to determine the change in saturation during a given time interval. This equation takes into account the flow of oil in and out of the block and the oil production from the block.

Zone III (The Blocks Below the Block Containing the Gas-Oil Contact)

For blocks in this region, it is necessary to relate the change in saturation and pressure with time. In this region material balances for both the oil and gas must be written because two unknowns (pressure and saturation in the block) are involved. These equations

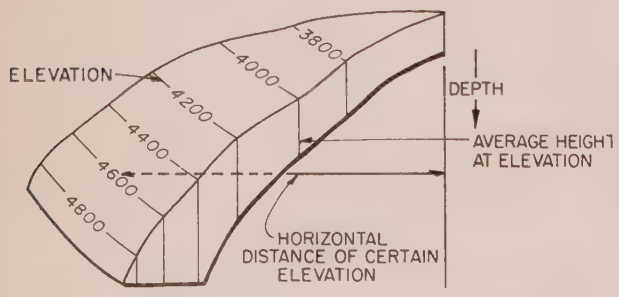

FIG. 5—SECTION OF GRAVITY-DRAINAGE RESERVOIR.

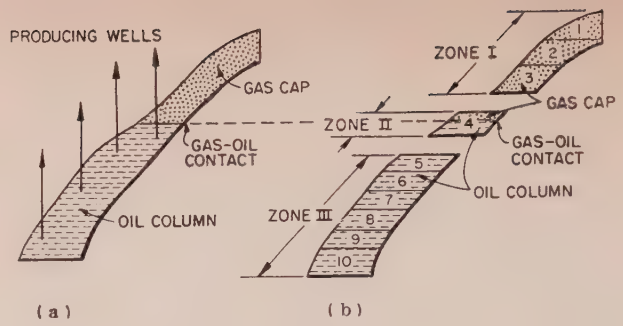

FIG. 6—RESERVOIR MODEL.

must take into account the flow of oil and gas in and out, and the production of both phases from that block.

These three zones (I, II and III) will be tied together by the flow of oil and gas occurring at the zone boundaries.

MOVEMENT OF THE GAS-OIL CONTACT

One of the most sensitive factors in predicting gravity-drainage performance is that of describing the movement of the gas-oil contact. Although this contact (the zone where the changes in gas saturation with distance are the greatest) has a finite length, it is assumed to have zero length as an expedient to mathematical handling. This assumption is justified by the fact that the actual oil volume included within this zone is very small compared with the oil in place in the reservoir. Only when the correct value for the rate of advance or movement of the gas-oil contact is used will the saturations and flow conditions above and below the gas-oil contact satisfy the necessary mathematical equations, i.e., the equations of continuity and Darcy's law.

Based on the assumption that oil flow at the gas-oil contact will always be downdip, the amount of free gas flowing across the gas-oil contact and its direction of flow will determine the efficiency of displacement occuring and the proper procedure to be used in predicting movement of the boundary. The following conditions of gas flow can occur: (1) no flow of free gas (i.e., the gas saturation is less than the critical gas saturation); (2) free gas flow downdip; and (3) free gas flow updip into the gas cap. The procedure for calculating the rate of advance of the gas-oil contact for any situation in these three categories is given by Welch and Shreve.[3]

DEVELOPMENT OF IBM 650 PROGRAM FOR DETERMINING PERFORMANCE OF GRAVITY-DRAINAGE RESERVOIRS

The prediction of the performance of gravity-drainage reservoirs must take into account the flow of oil and gas at all points throughout the reservoir while simultaneously satisfying the equation of continuity. Because the equations relating the flow of oil and gas and the equation of continuity are nonlinear partial differential equations,[6] an analytical solution is impossible. Therefore, an iterative-type process is used to determine the variation of pressure and saturation with time at any point in the reservoir. The numerical expressions consist of material-balance equations (gas and oil) for each block in the reservoir and Darcy's law to

describe the flow of oil and gas into and out of the individual blocks. These equations involve unknown values of pressure and saturation at the end of one time interval in the future; hence, numerous iterative processes are used to determine the change of these factors as a function of time and position.

SOLUTION OF EQUATIONS GOVERNING FLOW OF OIL AND GAS WITHIN THE RESERVOIR

Fig. 7 is a flow diagram showing the sequence of operations involved in obtaining saturations and pressures throughout the reservoir. The solution of these equations is dependent on the value of $(e_{of})_{t+1}$, the reservoir oil flow rate immediately below the gas-oil contact at the end of the time interval chosen. A discussion of how to determine the correct value for this variable will be given in the next section.

Calculations for Blocks in Zone I

The gas saturations in the various blocks in Zone I are determined by Eq. 4 of the Appendix. A value of the change in gas-cap pressure during the future time interval considered is estimated to account for the shrinkage of oil and the amount of gas evolved during this time interval. This estimated value is improved by an iterative process. When the calculations for Zones I and II are completed, the value for change in gas-cap pressure used to calculate saturations will be a good approximation of the actual change in pressure. This iteration will be discussed at the end of the section dealing with calculations for Zone II.

Calculations for the Block in Zone II

The calculations performed for Zone II, the block containing the gas-oil contact, consist of determining (1) the movement of the gas-oil contact during the interval, (2) the average saturations above and below the gas-oil contact at the end of the time interval, (3) the gas-cap pressure and (4) the pressure in the top or first block in Zone III at the end of the time interval.

The determination of these factors involves estimates based on extrapolations of calculated results from prior time intervals. By use of numerous interrelated iterative processes, the estimated values of each of the unknown factors are refined. The process used to determine these factors is as follows.

Step 1—Using an estimated value of $(S_{of})_{t+1}$ the gas saturation in Zone II below the gas-oil contact at the end of the time interval considered and the estimated value of $(e_{of})_{t+1}$, the distance moved by the gas-oil contact during the time interval (t to $t+1$) is calculated.

Step 2—Calculate the gas saturation in Zone II above the gas-oil contact. This is calculated from Eq. 7 (in the Appendix) and the positions of the gas-oil contact.

Step 3—Knowing the gas saturation above the gas-oil contact in Zone II and the gas saturation in Zone I, the value of $(p_{gc})_{t+1}$ is determined using a material balance on the gas in the gas cap (Eq. 8 in the Appendix).

Step 4—A simultaneous solution of Eqs. 9 and 12 (in the Appendix), material balances on the oil and gas phase in Zone II below the gas-oil contact, deter-

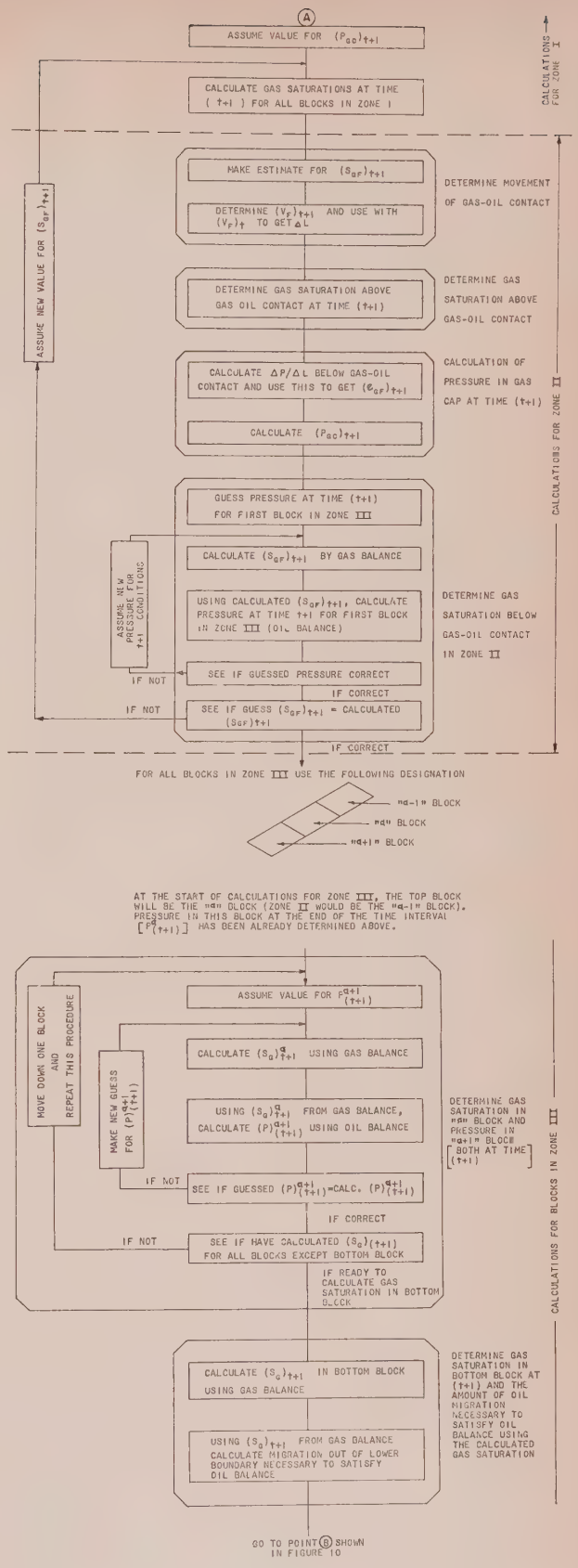
A
ASSUME VALUE FOR $(P_{gc})_{t+1}$
CALCULATE GAS SATURATIONS AT TIME (t+1) FOR ALL BLOCKS IN ZONE I
CALCULATIONS FOR ZONE I
MAKE ESTIMATE FOR $(S_{gf})_{t+1}$
DETERMINE $(V_f)_{t+1}$ AND USE WITH $(V_f)_t$ TO GET ΔL
DETERMINE MOVEMENT OF GAS-OIL CONTACT
ASSUME NEW VALUE FOR $(S_{gf})_{t+1}$
DETERMINE GAS SATURATION ABOVE GAS OIL CONTACT AT TIME (t+1)
DETERMINE GAS SATURATION ABOVE GAS-OIL CONTACT
CALCULATE $\Delta P/\Delta L$ BELOW GAS-OIL CONTACT AND USE THIS TO GET $(e_{gf})_{t+1}$
CALCULATE $(P_{gc})_{t+1}$
CALCULATION OF PRESSURE IN GAS CAP AT TIME (t+1)
CALCULATIONS FOR ZONE II
GUESS PRESSURE AT TIME (t+1) FOR FIRST BLOCK IN ZONE III
CALCULATE $(S_{gf})_{t+1}$ BY GAS BALANCE
ASSUME NEW PRESSURE FOR t+1 CONDITIONS
USING CALCULATED $(S_{gf})_{t+1}$, CALCULATE PRESSURE AT TIME t+1 FOR FIRST BLOCK IN ZONE III (OIL BALANCE)
DETERMINE GAS SATURATION BELOW GAS-OIL CONTACT IN ZONE II
IF NOT
SEE IF GUESSED PRESSURE CORRECT
IF CORRECT
IF NOT
SEE IF GUESS $(S_{gf})_{t+1}$ = CALCULATED $(S_{gf})_{t+1}$
IF CORRECT
FOR ALL BLOCKS IN ZONE III USE THE FOLLOWING DESIGNATION
"q-1" BLOCK
"q" BLOCK
"q+1" BLOCK
AT THE START OF CALCULATIONS FOR ZONE III, THE TOP BLOCK WILL BE THE "q" BLOCK (ZONE II WOULD BE THE "q-1" BLOCK). PRESSURE IN THIS BLOCK AT THE END OF THE TIME INTERVAL $[P^q_{(t+1)}]$ HAS BEEN ALREADY DETERMINED ABOVE.
ASSUME VALUE FOR $P^{q+1}_{(t+1)}$
CALCULATE $(S_o)^{q+1}_{t+1}$ USING GAS BALANCE
MOVE DOWN ONE BLOCK AND REPEAT THIS PROCEDURE
MAKE NEW GUESS FOR $(P)^{q+1}_{(t+1)}$
USING $(S_o)^{q+1}_{t+1}$ FROM GAS BALANCE, CALCULATE $(P)^{q+1}_{(t+1)}$ USING OIL BALANCE
DETERMINE GAS SATURATION IN "q" BLOCK AND PRESSURE IN "q+1" BLOCK [BOTH AT TIME (t+1)]
IF NOT
SEE IF GUESSED $(P)^{q+1}_{(t+1)}$=CALC. $(P)^{q+1}_{(t+1)}$
IF CORRECT
IF NOT
SEE IF HAVE CALCULATED $(S_o)_{(t+1)}$ FOR ALL BLOCKS EXCEPT BOTTOM BLOCK
IF READY TO CALCULATE GAS SATURATION IN BOTTOM BLOCK
CALCULATIONS FOR BLOCKS IN ZONE III
CALCULATE $(S_o)_{t+1}$ IN BOTTOM BLOCK USING GAS BALANCE
USING $(S_o)_{t+1}$ FROM GAS BALANCE CALCULATE MIGRATION OUT OF LOWER BOUNDARY NECESSARY TO SATISFY OIL BALANCE
DETERMINE GAS SATURATION IN BOTTOM BLOCK AT (t+1) AND THE AMOUNT OF OIL MIGRATION NECESSARY TO SATISFY OIL BALANCE USING THE CALCULATED GAS SATURATION
GO TO POINT B SHOWN IN FIGURE 10

FIG. 7—FLOW DIAGRAM FOR DETERMINING SATURATION AND PRESSURE THROUGHOUT THE RESERVOIR AT END OF TIME INTERVAL (SOLUTION DEPENDENT ON OIL FLOW RATE AT GAS-OIL CONTACT).

mines the value for $(S_{of})_{t+1}$ and the pressure in the first block of Zone III. The method of solution of these equations (described in the Appendix) is an iterative-type process which converges to a consistent solution based on an estimated value of $(e_{of})_{t+1}$.

The actual solution in Step 4 involves not only Eqs. 9 and 12, but also, for each refined value of $(S_{of})_{t+1}$ used, Steps 1 through 3 are repeated.

Therefore, at the end of the calculations for Zone II, the values determined are only a function of the estimated value of $(e_{of})_{t+1}$.

Calculations for Blocks in Zone III

Starting at the top block in Zone III (for which the value of pressure at the end of the time interval has been determined by calculations from Zone II), the value of the gas saturation at time $(t + 1)$ is determined by Eq. 13 of the Appendix (a material balance on the gas content of the block). The solution of this equation is dependent on the value of the pressure in the next lower block; therefore, an iterative process like that used to determine $(S_{of})_{t+1}$ is used. The value of this assumed pressure in the next block is determined from Eq. 16 of the Appendix (a material balance on the oil) using the value of gas saturation calculated from the gas balance. Iteration is continued until the guessed and calculated values of pressure in the next lower block agree.

The process just described is continued on down through Zone III until the gas saturation in the next to the bottom block is determined by iterating on the pressure in the bottom block. At this point, a slightly different procedure is followed in determining the gas saturation in the bottom block.

Eq. 13 is used in all blocks in Zone III to determine the gas saturation. For the bottom block, this equation must be altered slightly to take into account the boundary conditions of no flow at the bottom of the reservoir. By eliminating these terms describing the flow of oil and gas at the lower boundary from Eq. 13, the gas saturation in the bottom block can be obtained, since the pressure and flow of oil and gas into the block are known from the block above. Instead of solving the oil balance on this block to determine the pressure in the next block, the material balance is re-arranged to determine the amount of oil which would migrate over the lower boundary of the reservoir. (The significance of the term representing a migration over the lower boundary will be discussed in the section which follows.) This material balance is given by Eq. 17 of the Appendix.

DETERMINATION OF PROPER VALUE OF OIL FLOW RATE AT THE GAS-OIL CONTACT

In the previous section, the procedure is outlined for determining the saturations and pressures throughout the reservoir based on an assumed value of $(e_{of})_{t+1}$, the value of the oil flow rate at the gas-oil contact at reservoir conditions at time $(t + 1)$. For any assumed value of $(e_{of})_{t+1}$, unique values of saturation and pressure can be calculated throughout the reservoir at the end of the time interval. Since there can be only one correct value of $(e_{of})_{t+1}$, the choice of the proper one is determined by the last item discussed in the previous section, i.e., the calculated amount of oil migrating over the bottom boundary of the reservoir. Unless the amount of oil migrating over the bottom boundary is zero, the value of $(e_{of})_{t+1}$ assumed is not correct. Fig. 8 shows the iteration process involved in determining the value of $(e_{of})_{t+1}$ to be used to give the proper distribution of saturation and pressure throughout the reservoir at the end of the time step.

GENERALIZATIONS IN IBM PROGRAM FOR SPECIFIC CASES

The procedure just outlined and shown in Figs. 7 and 8 is for the most general case, that is, for declining pressure where both pressure and saturation vary with time. The IBM program that has been written in accordance with this diagram contains short-cuts to simplify calculation procedures for the case of constant-pressure operations where there is no gas saturation developed below the gas-oil contact. As an example, in calculating the gas saturation below the block containing the gas-oil contact, a check is first made to determine whether the pressure at the end of the time step is above the saturation pressure of the fluid in that block. If it is, the procedure of guessing the pressure in the next lower block is eliminated and a material balance on the oil can be written to give the pressure at the end of the time interval in the next block. There will be no gas saturation in the block in question because the liquid would be undersaturated. This same line of reasoning can also be applied to calculations for the block containing the gas-oil contact, since the liquid phase immediately below the gas-oil contact can be undersaturated.

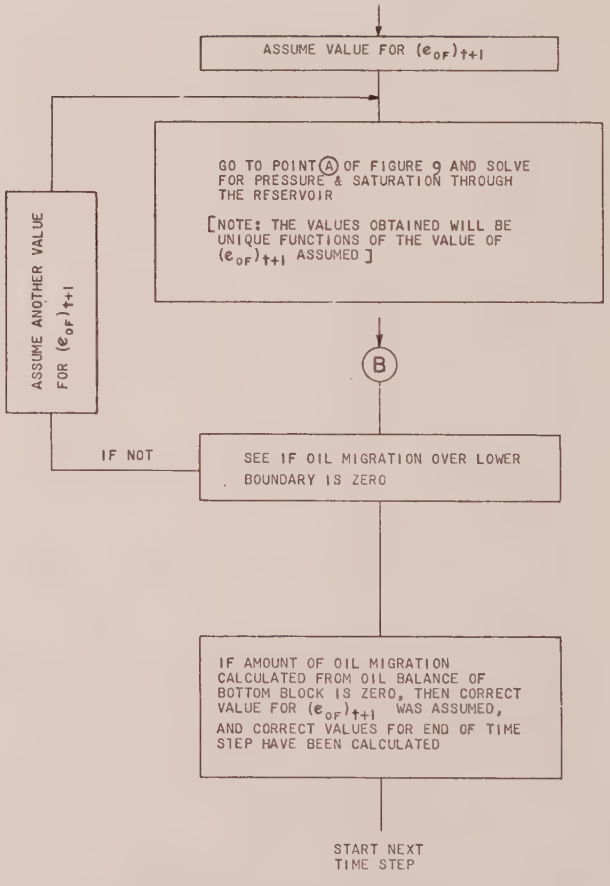

FIG. 8—FLOW DIAGRAM FOR DETERMINING CORRECT VALUE OF OIL FLOW RATE (AT END OF TIME INTERVAL) AT GAS-OIL CONTACT.

APPLICATION OF THEORY TO ACTUAL RESERVOIR PREDICTIONS

To determine the applicability of the method developed for predicting the performance of gravity-drainage reservoirs, the IBM 650 program written using this theory was used to calculate the performance of an actual reservoir. The reservoir chosen was a volumetric gravity-drainage reservoir that has been produced without gas injection. The field is located in East Texas and is a dome-type structure overlying a deep salt plug, with production from the Woodbine sand.

FLUID PROPERTIES

Fluid properties vary widely through the reservoir. At the crest of the structure, the saturation pressure of the oil is 2,100 psia compared to 1,880 psia for fluid found at the bottom. The oil viscosity variation is perhaps the most important factor to be considered since it varies from 2 cp at the crest to 16 cp at the bottom of the reservoir. Solution gas-oil ratios vary from 400 scf/bbl for the 2,100-psia saturation-pressure fluid to 300 scf/bbl at the saturation pressure of 1,880 psia. This variation in fluid properties was taken into account in the IBM calculations by specifying different saturation pressures for the fluid in each block throughout the reservoir. All fluid properties were then calculated as a function of the saturation pressure to give the proper variation from the crest to the bottom of the structure.

RESERVOIR CONFIGURATION

A geometrical model of the reservoir was constructed from elevation and isopach maps. A segment of this model was divided into 10 parallelepipeds of equal pore volume. Average values of height and width of each unit were then obtained to be used to describe the flow of fluids between the blocks.

RESERVOIR ROCK PROPERTIES

For the calculations performed on this reservoir, a constant value of 3 darcies was used for the absolute permeability throughout the reservoir. Relative permeability relationships were also considered constant throughout the reservoir. Although the data for this particular reservoir indicated that rock properties should be considered constant through the reservoir, variations of both absolute and relative permeability can be handled by the IBM program.

PRODUCTION RATES FROM INDIVIDUAL BLOCKS

The total production rate from this reservoir was allocated on the bases of a constant rate per well and of wells having equal spacing throughout the field. In determining the production from individual blocks, it was necessary to allocate the production from a well into the blocks penetrated by that well. Normally, a well's production had to be allocated to two or more blocks. The allocation of production was based on a fraction of the total flow capacity in each block penetrated by the well. Once the contribution of each well was made to the various blocks involved, the total production from that block was summed. These values were used for the production from the blocks in the calculation.

The primary factor determining production rate of this reservoir was proration. In other reservoirs the rate may be strongly influenced by the productivity of the wells. In this event, separate calculations must be made at the end of each time step to determine the rate at which the reservoir can be produced, and the pressure at the elevation level and permeability to oil and gas at a given time will be the governing factors determining well productivity.

RESULTS OF DECLINING-PRESSURE GRAVITY-DRAINAGE CALCULATIONS

Fig. 9 shows a comparison of actual and calculated performance of this gravity-drainage reservoir. Calculations were made for the first 13.5 years of the reservoir's performance. At the end of this period, the actual field pressure had dropped to 1,595 psia from an initial value of 1,990 psia. Although the over-all pressure drop during this period is satisfactorily matched by the calculation procedure, there is a discrepancy occurring from the middle of 1944 to the middle of 1949. The calculated pressure declines in a gradual manner, while field data indicate a rapid decrease during the first part of 1944 and an increase in pressure in the latter part of 1949. Throughout this interval the calculated reservoir pressure is nearly 50-psi higher than field data. The calculated rate of pressure decline throughout this period is approximately the same except for the periods during the early part of 1944 and late 1950. Despite this discrepancy it is considered that the reservoir pressure is adequately predicted by the calculation procedure employed.

Fig. 9 also shows a comparision between field and calculated gas-oil ratios. These values are in good agreement and show that during this period the gas-oil ratio has been practically constant, with a tendency to show a sharper increase during the last 1½ years of production. The fact that the gas-oil ratio is essentially constant during this period demonstrates the effectiveness of gravity drainage in this reservoir. After the production of 144 million bbl of oil (a recovery of 14 per cent of the original oil in place), the gas-oil ratio is only slightly higher than the original solution gas-oil ratio.

CONCLUSION

Reservoir performance of an actual gravity-drainage field producing without any gas injection was duplicated with the IBM program developed using the method presented in this paper.

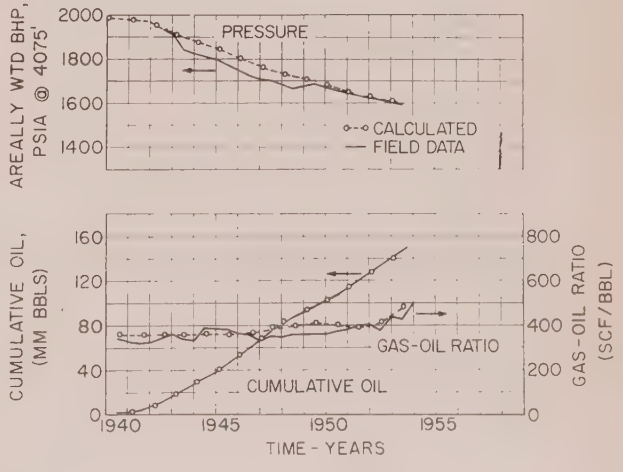

FIG. 9—PRODUCTION HISTORY.

NOMENCLATURE

A = cross-sectional area (perpendicular to the dip of the formation) for the flow of fluids, sq ft

B_o = oil formation volume factor, (bbl at reservoir temperature and pressure) /(bbl at 60° F and 14.7 psi)

B_g = gas formation volume factor, (cu ft of gas at reservoir temperature)/(cu ft of gas at 60°F and 14.7 psi)

e = total influx rate, cu ft/day at reservoir temperature and pressure

e_o = oil influx rate, cu ft/day at reservoir temperature and pressure

e_g = gas influx rate, cu ft/day at reservoir temperature and pressure

e_{of} = oil flow rate at gas-oil contact, cu ft/day at reservoir temperature and pressure

e_{gf} = gas flow rate at gas-oil contact, cu ft/day at reservoir temperature and pressure

F = elevation difference between points in the reservoir (used to determine the gravity gradient between blocks), ft

G = gas in place in the gas cap, cu ft at 60°F and 14.7 psi

h = fraction of the oil-producing rate in Zone II occuring above the gas-oil contact

k = absolute permeability, darcies

k_{ro} = relative permeability to oil

k_{rg} = relative permeability to gas

L = distance along formation parallel to dip of reservoir, ft

L' = distance from top of block (in the block containing the gas-oil contact) to the gas-oil contact, ft

ΔL = movement of gas-oil contact during interval, ft

M = 6.33 × absolute permeability × cross-sectional area, darcies × sq ft

p = pressure, psi

p_c = capillary pressure, psi

p_{gc} = gas-cap pressure, psi

p_{bf} = average pressure in Zone II below the gas-oil contact, psi

q_o = oil producing rate, cu ft (measured at 60°F and 14.7 psi)

R = producing gas-oil ratio, cu ft/cu ft (measured at 60°F and 14.7 psi)

R_s = solution gas-oil ratio (gas solubility in oil), cu ft/cu ft (measured at 60°F and 14.7 psi)

S_{cw} = connate-water saturation

S_g = gas saturation

S_{gc} = critical gas saturation

S_{gf} = gas saturation in the oil column immediately below gas-oil contact

$V\phi$ = total pore space, cu ft

T = temperature, °R

Δt = time interval, days

Z = gas compressibility factor

$$\psi^{a,a-1} = \frac{\text{(effective oil permeability)}}{\text{(length} \times \text{oil viscosity)}},$$

$$= \left[\frac{(k_{ro}^{\,a})_t \ (k_{ro}^{\,a-1})_t}{(k_{ro}^{\,a})_t \ (L^{a-1}) + (k_{ro}^{\,a-1})_t \ (L_a)}\right] \cdot \left[\frac{1}{(\mu_o^{\,a-1})_t}\right],$$

1/ft × cp

$$\Omega^{a,a-1} = \frac{\text{(effective gas permeability)}}{\text{(length} \times \text{gas viscosity)}},$$

$$= \left[\frac{(k_{rg}^{\,a})_t \ (k_{rg}^{\,a-1})_t}{(k_{rg}^{\,a})_t \ (L^{a-1}) + (k_{rg}^{\,a-1})_t \ (L^a)}\right] \cdot \left[\frac{1}{(\mu_g^{\,a-1})_t}\right],$$

1/ft × cp

ρ_o = density of oil, lb/cu ft

ρ_g = density of gas, lb/cu ft

α = gravity gradient due to difference in gas and liquid density, psi/ft (Note: Distance measured along line parallel to dip.)

α_o = gravity gradient due to oil density, same as α

α_g = gravity gradient due to gas density, same as α

$$\gamma = \text{conversion factor} = \left(\frac{1}{14.7}\right)\left(\frac{460}{460+T}\right)\left(\frac{1}{Z}\right)$$

μ_o = oil viscosity, cp

μ_g = gas viscosity, cp

ϕ = porosity

SUBSCRIPTS AND SUPERSCRIPTS

(a) = properties of Block "a"

$(a)_t$ = properties of Block "a" at time t

$(a)_{t+1}$ = properties of Block "a" at time $(t+1)$

$(a)_{t+\frac{1}{2}}$ = average properties of Block "a" during the time interval from (t) to $(t+1)$

$(a,a-1)$ = average properties of Blocks "a" and "a−1"

REFERENCES

1. Stewart, F. M., Garthwaite, D. L. and Krebil, F. K.: "Pressure Maintenance by Inert Gas Injection with High Relief Elk Basin Field", *Trans.*, AIME (1955) **204**, 49.
2. Shreve, D. R. and Welch, L. W., Jr.: "Gas Drive and Gravity Drainage Analysis of Pressure Maintenance Operations", *Trans.*, AIME (1956) **207**, 136.
3. Essley, P. L., Jr., Hancock, G. L. and Jones, K. E.: "Gravity Drainage Concepts in a Steeply Dipping Reservoir", Paper 1029-G presented at SPE Prod. and Reservoir Eng. Conf. held in Tulsa (March, 1958).
4. Kirby, J. E., Jr. Stamm, H. E., III and Schmitz, L. B.: "Calculation of the Depletion History and Future Performance of a Gas-Cap-Drive Reservoir", *Trans.*, AIME (1957) **210**, 218.
5. Terwilliger, P. L., Wilsey, L. E., Hall, H. N., Bridges, P. M. and Morse, R. A.: "An Experimental and Theoretical Investigation of Gravity Drainage Performance", *Trans.*, AIME (1951) **192**, 285.
6. Muskat, M.: *Physical Principles of Oil Production*, McGraw-Hill Book Co., Inc., N. Y. (1949).

APPENDIX

DEVELOPMENT OF EQUATIONS

EQUATIONS FOR BLOCKS IN ZONE I

Fig. 10 represents a typical block and the adjacent blocks in Zone I. Eq. 1 is a form of Darcy's law and describes the flow of oil (at reservoir conditions) into the "a" block during the time interval Δt, i.e., from times t to $t+1$.

$$(e_o^{\,a,a-1})_{t+\frac{1}{2}} = (M^{a,a-1})(\psi^{a,a-1})\left[\frac{(p^{a-1}-p^a)_t + (p^{a-1}-p^a)_{t+1}}{2} + (F^{a,a-1})(\rho_o^{\,a,a-1})\right] \quad . \quad (1)$$

Since it is assumed that there is no change of pressure with distance in the gas cap, Eq. 1 becomes

$$(e_o^{\,a,a-1}) = (M^{a,a-1})(\psi^{a,a-1})(F^{a,a-1})(\rho_o^{\,a,a-1}) \quad . \quad (2)$$

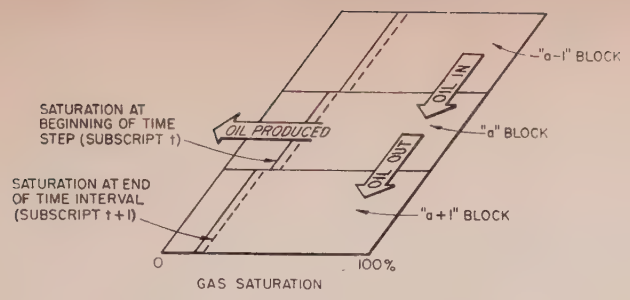

FIG. 10—TYPICAL BLOCK IN ZONE I.

A similar equation can be written to describe the flow of oil between the "a" and "a-1" block.

$$(e_o^{a,a+1}) = (M^{a,a+1})(\psi^{a,a+1})(F^{a,a+1})(\rho_o^{a,a+1}). \quad . \quad (3)$$

Using Eqs. 2 and 3, a material balance (Eq. 4) on the oil can be written to calculate the gas saturation at the end of the time interval.

$$(S_g^a)_{t+1} = (B_o^a)_{t+1}\left\{\frac{(S_g^a)_t}{(B_o^a)_t} + (1-S_{cw}^a)\left[\frac{1}{(B_o^a)_{t+1}} - \frac{1}{(B_o^a)_t}\right] + \frac{\Delta t}{(V\phi^a)}\left[\frac{2(M^{a,a+1})(\psi^{a,a+1})(F^{a,a+1})(\rho_o^{a,a+1})}{(B_o^{a,a+1})_t + (B_o^{a,a+1})_{t+1}} - \frac{2(M^{a,a-1})(\psi^{a,a-1})(F^{a,a-1})(\rho_o^{a,a-1})}{(B_o^{a,a-1})_t + (B_o^{a,a-1})_{t+1}} + (q_o^a)_t\right]\right\} \quad (4)$$

The rate of advance of the gas-oil contact is not completely defined by fixing $(e_{of})_{t+1}$. In addition, the gas saturation existing at the end of the time interval at the front of the displacement front, $(S_{gf})_{t+1}$, must be specified. This is, unfortunately, a variable which can be calculated only when the rate of advance at time $(t+1)$ has been determined. Therefore, an iterative process must be used to determine the proper relationship for gas saturation existing ahead of the gas-oil contact at the end of the time interval for the particular value of $(e_{of})_{t+1}$ chosen. This iterative process is outlined with the necessary equations as follows.

1. On the basis of the change in saturation with time from the previous time step, an estimate is made for $(S_{gf})_{t+1}$.

2. The pressure gradient below the gas-oil contact can be determined from the following equation.

$$\left(\frac{\partial p}{\partial L}\right) = \frac{(F^{a,a+1})(\rho_o^{a,a+1})}{(L^{a,a+1})} - \frac{(e_{of})_{t+1}(\mu_o^a)_{t+1}}{6.33(k)\ (A_{gf})(k_{ro})s_{gf}} \quad . \quad (5)$$

3. $\partial p/\partial L$ is used in Eq. 6 to determine the volume of free gas flowing past the gas-oil contact at reservoir conditions.

$$(e_{gf})_{t+1} = \frac{6.33kA(k_{rg})_{s_{gf}}}{(\mu_g^a)_{t+1}}\left[-\left(\frac{\partial p}{\partial L}\right) + \frac{(F^{a,a+1})\ (\rho_g^{a,a+1})}{(L^{a,a+1})}\right] \quad . \quad (6)$$

4. The rate of advance of the gas-oil contact is determined in the manner outlined by Welch and Shreve.[2] The proper value is dependent on the values of $(S_{gf})_{t+1}$, $(e_{gf})_{t+1}$ and $(e_{of})_{t+1}$.

5. By using Eq. 7, the gas saturation above the gas-oil contact in Zone II is determined when the position of the gas-oil contact is known at time $(t+1)$.

$$(S_g^a)_{t+1} = (B_o^a)_{t+1}\left\{(1-S_{cw}^a)\left[\frac{1}{(B_o^a)_{t+1}} - \frac{1}{(B_o^a)_t}\right] + \frac{L'(S_g^a)_t}{(L'+\Delta L)\ (B_o^a)_t} + \frac{(\Delta L)\ (S_{gf})_t}{(L'+\Delta L)\ (B_o^a)_t} + \frac{(L^a)\Delta t}{(L'+\Delta L)\ (V\phi^a)}\left[h(q_o^a)_t + \frac{(e_{of})_t + (e_{of})_{t+1}}{(B_o^a)_t + (B_o^a)_{t+1}} - \frac{(e_o^{a,a-1})_t + (e_o^{a,a-1})_{t+1}}{(B_o^a)_t + (B_o^a)_{t+1}}\right]\right\}. \quad . \quad (7)$$

(Note: The superscript a is used in Eq. 7 to denote the gas saturation in Zone II above the gas-oil contact. The gas saturation below the gas-oil contact is (S_{gf}).

6. The next step is to determine the pressure in the gas cap at time $(t+1)$.

$$(p_{gc})_{t+1} = \frac{(G)_{t+1}}{(\gamma^a)_{t+1}\sum_{\substack{\text{Zone III}\\ \text{top of}\\ \text{reservoir}}}(V\phi^a)^*(S_g^a)_{t+1}} \quad . \quad (8)$$

7. Knowing the gas-cap pressure at the end of the time interval, calculations can be made to determine the gas saturation below the gas-oil contact. Because both $(S_{gf})_{t+1}$ and the pressure gradient at the boundary between this block and the next block downstructure are known, material balances on both oil and gas must be written. A gas balance on the area below the gas-oil contact at time $(t+1)$ yields the following expression for $(S_{gf})_{t+1}$.

$$(S_{gf})_{t+1} = \frac{1}{\left[(p_{gf})_{t+1}(\gamma_{gf})_{t+1} - \frac{(R_s^a)_{t+1}}{(B_o^a)_{t+1}}\right]}\left((1-S_{cw}^a)\left[\frac{(R_s^a)_t}{(B_o^a)_t} - \frac{(R_s^a)_{t+1}}{(B_o^a)_{t+1}}\right] + (S_{gf})_t\left[(p_{gf})_t(\gamma_{gf})_t - \frac{(R_s^a)_t}{(B_o^a)_t}\right] + \frac{(L^a)\Delta t}{(L'+\Delta L)\ (V\phi^a)}\left\{\frac{(e_{of})_t + (e_{of})_{t+1}}{2}\left[\frac{(R_s^a)_t + (R_s^a)_{t+1}}{(B_o^a)_t + (B_o^a)_{t+1}}\right] - \frac{(e_o^{a,a+1})_t + (e_o^{a,a+1})_{t+1}}{2}\left[\frac{(R_s^a)_t + (R_s^a)_{t+1}}{(B_o^a)_t + (B_o^a)_{t+1}}\right] + \left[\frac{(e_{gf})_t(\rho_{gf})_t(\gamma_{gf})_t + (e_{gf})_{t+1}(p_{gf})_{t+1}(\gamma_{gf})_{t+1}}{2}\right] - \left[\frac{(e_g^{a,a+1})_t(p^{a,a+1})_t(\gamma^{a,a+1})_t + (e_g^{a,a+1})_{t+1}(p^{a,a+1})_{t+1}(\gamma^{a,a+1})_{t+1}}{2}\right] - (1-h)\ (q_o^a)_t\left[\frac{(R^a)_t + (R^a)_{t+1}}{2}\right]\right\}\right). \quad . \quad (9)$$

where

$$(e_g^{a,a+1})_{t+1} = (M'^{a,a+1})(\Omega'^{a,a+1})[(p_{gf})_{t+1} - (p^{a+1})_{t+1} + (F'^{a,a+1})\ (\rho_g^{a,a+1})] \quad . \quad (10)$$

and

$$(e_o^{a,a+1})_{t+1} = (M'^{a,a+1})\ (\psi'^{a,a+1})(p_{gf})_{t+1} - (p^{a+1})_{t+1} + (F'^{a,a+1})\ (\rho_o^{a,a+1})] \quad . \quad (11)$$

The primed value of M, Ω, ψ and F are used to indicate that these relationships depend on the position of the gas-oil contact. In order that $(e_g^{a,a+1})_{t+1}$ and $(e_o^{a,a+1})_{t+1}$ can be determined, the pressure in the block below, $(p^{a+1})_{t+1}$ will be established and used to calculate the values above so that $(S_{gf})_{t+1}$ can be determined from Eq. 9. This value of $(S_{gf})_{t+1}$ will be used in an oil material balance to calculate $(p^{a+1})_{t+1}$. When the guessed and calculated values of $(p^{a+1})_{t+1}$ agree within ac-

*For Zone II, multiply $(V\phi^a)$ by $\frac{(L'+\Delta L)}{(L^a)}$.

ceptable limits, the value of gas-cap pressure and the saturations above and below the gas-oil contact at time $(t+1)$ are correct for the rate of advance of the gas cap used during the period. The equation for calculating $(p^{a+1})_{t+1}$ from the oil balance is

$$(p^{a,t+1})_{t+1} = \frac{(B_o^a)_t + (B_o^a)_{t+1}}{(M'^{a,a+1})\ (\psi'^{a,a+1})}\left\{\frac{(M'^{a,a+1})\ (\psi'^{a,a+1})}{(B_o^a)_t + (B_o^a)_{t+1}}\right.$$
$$[(p_{bf})_{t+1} - (F'^{a,a+1})\ (\rho_o^{a,a+1})] + \left[\frac{(e_o^{a,a+1})_t}{(B_o^a)_t + (B_o^a)_{t+1}}\right.$$
$$+ (1-h)\ (q_o^a)_t - \frac{(e_{of})_t + (e_{of})_{t+1}}{(B_o^a)_t + (B_o^a)_{t+1}}\Big] +$$
$$\frac{(V\phi^a)\ (L' + \Delta L)}{(L^a)\ (\Delta t)}\left[\frac{(1 - S_{cw}^a) - (S_{gf})_{t+1}}{(B_o^a)_{t+1}} - \right.$$
$$\left.\left.\frac{(1 - S_{cw}^a) - (S_{gf})_t}{(B_o^a)_t}\right]\right\} \quad . \quad . \quad . \quad . \quad . \quad . \quad . \quad . \quad (12)$$

8. The only uncertainty at this point is that of whether the value of $(S_{gf})_{t+1}$ used to estimate the rate of advance of the gas-oil contact in Step 1 is the same as the value calculated in Step 7. If it is not within a specified limit, then another value of $(S_{gf})_{t+1}$ should be used and all calculations described in Steps 1 through 7 should be repeated.

EQUATIONS FOR BLOCKS IN ZONE III

Eq. 13 describes a material balance on the gas content of the "a" block.

$$(S_g^a)_{t+1} = \frac{1}{\left[(p^a)_{t+1}\ (\gamma^a)_{t+1} - \dfrac{(R_s^a)_{t+1}}{(B_o^a)_{t+1}}\right]}\left(\right.(1 - S_{cw}^a)$$
$$\left[\frac{(R_s^a)_t}{(B_o^a)_t} - \frac{(R_s^a)_{t+1}}{(B_o^a)_{t+1}}\right] + (S_g^a)_t\ [(\rho^a)_t\ (\gamma^a)_t - \frac{(R_s^a)_t}{(B_o^a)_t}$$
$$+ \frac{\Delta t}{(V\phi^a)}\left\{\left[\frac{(e_o^{a,a-1})_t + (e_o^{a,a-1})_{t+1}}{2}\right]\right.$$
$$\left[\frac{(R_s^{a-1})_t + (R_s^{a-1})_{t+1}}{(B_o^{a-1})_t + (B_o^{a-1})_{t+1}}\right] - \left[\frac{(e_o^{a,a+1})_t + (e_o^{a,a-1})_{t+1}}{2}\right]$$
$$\left[\frac{(R_s^a)_t + (R_s^a)_{t+1}}{(B_o^a)_t + (B_o^a)_{t+1}}\right] +$$
$$\left[\frac{(e_g^{a,a-1})_t\ (p^{a,a-1})_t (\gamma^{a,a-1})_t + (e_g^{a,a-1})_{t+1} (p^{a,a-1})_{t+1}\ (\gamma^{a,a-1})_{t+1}}{2}\right]$$
$$- \left[\frac{(e_g^{a,a+1})_t\ (p^{a,a+1})_t (\gamma^{a,a+1})_t + (e_g^{a,a+1})_{t-1} (p^{a,a+1})_{t+1}\ (\gamma^{a,a+1})_{t+1}}{2}\right]$$
$$\left.\left.- (q_o^a)_t \left[\frac{(R^a)_t + (R^a)_{t+1}}{2}\right]\right\}\right). \quad . \quad . \quad . \quad . \quad (13)$$

Inspection of Eq. 13 shows that the value of $(S_g^a)_t$ can be solved provided values of $(e_g^{a,a+1})_{t+1}$ and $(e_o^{a,a+1})_{t+1}$ are known. Eqs. 14 and 15 can be used to calculate these factors. It should be noted that these equations are dependent on $(p^{a+1})_{t+1}$ which is not known.

$$(e_g^{a,a+1})_t = (M^{a,a+1})\ (\Omega^{a,a+1})\ [(p^a)_{t+1} - (p^{a+1})_{t+1}$$
$$+ (F^{a,a+1})\ (\rho_g^{a,a+1})] \quad . \quad . \quad . \quad . \quad (14)$$

$$(e_o^{a,a+1})_{t+1} = (M^{a,a+1})\ (\psi^{a,a+1})[(p^a)_{t+1} - (p^{a+1})_{t+1}$$
$$+ (F^{a,a+1})\ (\rho_o^{a,a+1})] \quad . \quad . \quad . \quad . \quad (15)$$

Like the calculations for $(S_{gf})_{t+1}$, a value is assumed for $(p^{a+1})_{t+1}$ and Eq. 13 is solved to obtain $(S_g^a)_{t+1}$. This value of $(S_g^a)_{t+1}$ is then used in Eq. 16 to determine the value of $(p^{a+1})_{t+1}$ in order that a balance on the oil content in Block "a" will be satisfied.

$$(p^{a+1})_{t+1} = \frac{(B_o^a)_t + (B_o^a)_{t+1}}{(M^{a,a+1})\ (\psi^{a,a+1})}\left\{\left[\frac{(M^{a,a+1})\ (\psi^{a,a+1})}{(B_o^a)_t + (B_o^a)_{t+1}}\right]\right.$$
$$\left[(p^a)_{t+1} - (F^{a,a+1})\ (\rho_o^{a,a+1})\right] + \left[\frac{(c_o^{a,a+1})_t}{(B_o^a)_t + (B_o^a)_{t+1}}\right.$$
$$+ (q_o^a)_t - \frac{(e_o^{a,a-1})_t + (e_o^{a,a-1})_{t+1}}{(B_o^{a-1})_t + (B_o^{a-1})_{t+1}}\Big] + \frac{(V\phi^a)}{\Delta t}$$
$$\left.\left[\frac{(1 - S_{cw}^a) - (S_g^a)_{t+1}}{(B_o^a)_{t+1}} - \frac{(1 - S_{cw}^a) - (S_g^a)_t}{(B_o^a)_t}\right]\right\}$$
$$. \quad . \quad . \quad . \quad . \quad . \quad . \quad . \quad . \quad . \quad . \quad . \quad . \quad . \quad . \quad . \quad . \quad (16)$$

When the value guessed for $(p^{a+1})_{t+1}$ agrees within specified limits of the values calculated, the value of $(S_g^a)_{t+1}$ is considered to be the correct value for the initial conditions known for this block.

Eqs. 13, 14, 15 and 16 can be used to determine gas saturation at time $(t+1)$ in all blocks in Zone III except the bottom block. In the bottom block, special provisions have to be made since there is no migration of oil or free gas across the bottom boundary of the reservoir. The oil balance on this block can be written to determine the oil flow across the "a", "a + 1" boundary which will be compatible with the value of $(p^a)_{t+1}$ and $(S_g^a)_{t+1}$ for the bottom block. This is the same approach used in developing Eq. 16 except, in the case of the bottom block, the average flow rate over the botton boundary $(e_o^{a,a+1})_{t+\frac{1}{2}}$, will be determined instead of evaluating $(p^a)_{t+1}$. The equation describing $(e_o^{a,a+1})_{t+\frac{1}{2}}$ is Eq. 17.

$$(e_o^{a,a+1})_{t+\frac{1}{2}} = [(B_o^a)_t + (B_o^a)_{t+1}]\left\{\frac{(V\phi^a)}{\Delta t}\right.$$
$$\left[\frac{(1 - S_{cw}^a) - (S_g^a)_t}{(B_o^a)_t} - \frac{(1 - S_{cw}^a) - (S_g^a)_{t+1}}{(B_o^a)_{t+1}}\right]$$
$$\left.+ \frac{(e_o^{a,a-1})_t + (e_o^{a,a-1})_{t+1}}{(B_o^{a-1})_t + (B_o^{a-1})_{t+1}} - (q_o')_t\right\} \quad . \quad . \quad (17)$$

If the value of $(e_o^{a,a+1})_{t+\frac{1}{2}}$ is not zero, the boundary condition of no flow across the bottom of the reservoir is not satisfied, the value of $(e_{of})_{t+1}$ originally estimated was incorrect, and another estimate must be made for this value. ★★★

Widths of Hydraulic Fractures

T. K. PERKINS
L. R. KERN
MEMBERS AIME

THE ATLANTIC REFINING CO.
DALLAS, TEX.

ABSTRACT

A study of fluid mechanics, rupture of brittle materials and the theory of elastic deformation of rocks shows that, for a given formation, crack width is essentially controlled by fluid pressure drop in the fracture. Operating conditions which cause high pressure drop along the crack (such as high injection rate and viscous fluids) will result in relatively wide cracks. Conversely, operating conditions which cause low pressure drop (low injection rates and thin fluids) will result in relatively narrow cracks.

Charts and equations have been derived which permit the estimation of fracture widths for a variety of flow conditions and for both horizontal and vertical fractures.

INTRODUCTION

There has been considerable speculation concerning the geometry of hydraulically created fractures in the earth's crust. One of the questions of practical importance is the width of fractures under dynamic conditions, i.e., while the fracture is being created and extended. Such width information could be used, for instance, to help estimate the area of a fracture generated under various conditions.[10] Also, there has been a recent trend toward the use of large propping particles.[13,15] Therefore is is desirable to know what factors can be varied in order to assure entry of the large particles into the fracture.

There has been some work on fracture widths reported in the literature. In particular, there have been several Russian publications dealing with this subject.[1,31,32] These papers have dealt principally with the elastic theory and the application of this theory to hydraulic fractures. These studies have not led to an engineering method for estimating fracture widths under dynamic conditions. A recent paper[3] has reviewed and summarized the Russian concepts.

An earlier paper[9] from our laboratories also discussed the application of the elastic theory to hydraulic fractures. This first approach, based largely on photoelastic studies, has proved to be too simplified to accurately describe the fracturing process. However, these early thoughts have served as a guide during the development of more exact concepts.

We would like to present in this paper our current concepts regarding fracture widths and some estimates of hydraulic fracture widths for several conditions. We believe that it is now possible to predict with fair accuracy the factors influencing fracture widths. Furthermore, the method of prediction has been reduced to a simple and convenient graphical or numerical calculation.

CRACKS IN A BRITTLE, ELASTIC MATERIAL

Many investigators[2,4,30] have shown that competent rocks behave elastically over some range of stresses. Of course, if the tensile stress imposed upon a rock exceeds some limiting value, then the rock will fail in tension. In similar manner, there are some limiting shear stresses that can be imposed upon rocks. Hubbert and Willis[11] have discussed the shear conditions which will lead to failure.

Under moderate stress conditions (such as those likely to be encountered when hydraulically fracturing) and when stresses are rapidly applied, relatively, most rocks will fail in a brittle manner. Hence, for this discussion of hydraulic fractures in the earth's crust, we assume the rocks behave as brittle, elastic materials.

Let us develop the discussion in the following way. (The following thoughts are applicable only to brittle materials.)

1. First we consider a brittle, elastic system. An energy balance will show the *minimum* pressure necessary to fracture rock, and from this pressure we calculate the *minimum* crack width resulting from extension of a hydraulic fracture.

2. Then we will show that, under ordinary fracturing conditions, fracture widths are *appreciably greater* than the minimum widths of extending fractures. In fact, we will find that crack width is *controlled* by fluid pressure drop in the fracture.

3. We will discuss pressure drops in fractures and resulting crack widths for various operating conditions and both vertical and horizontal fractures.

4. Finally, we will discuss the significance of these concepts, their relationship to fracturing pressures, etc.

First, consider minimum fracture extension pressures. We can shed some light on this question by considering the theory proposed by Griffith[7,8] to explain the rupture of brittle, elastic materials. Griffith recognized that solid materials exhibit a surface energy[6] (similar to surface tension in a liquid). The fundamental concept of the Griffith theory is that, when cracks spread without the application of external work (in the interior of an elastic medium which is stressed

Original manuscript received in Society of Petroleum Engineers office May 2, 1961. Revised manuscript received July 31, 1961. Paper to be presented at 36th Annual Fall Meeting of SPE, Oct. 8-11, 1961, in Dallas.

[10]References given at end of paper.

externally), the decrease in strain energy resulting from the elastic strain in the vicinity of the crack is balanced by the increase in surface energy.

A similar approach when external work is applied by the injection of fluid can be used to estimate hydraulic fracture widths in rocks under static conditions (when the fluid has stopped moving). Consider an infinite elastic medium containing a plane crack bounded by a circle—a penny-shaped crack. If fluid were injected into this pre-existing crack but at a pressure less than that necessary to extend the fracture in length, then the crack would be "inflated". For a perfectly elastic medium, the relationship between crack shape and pressure within the crack has been calculated by Sneddon.[22] Fig. 1 shows a conceptual sketch with some of the geometrical relationships predicted by the elastic theory.

Now let us suppose the pressure in the crack is increased until the crack is just ready to extend in radius. Let volume dV be injected at the fracture extension pressure P, and suppose this results in an increase in fracture radius dC. The amount of work done to pump the fluid into the fracture is clearly PdV. The amount of energy stored in the fracture system arises from (1) an increase in potential energy of the elastic medium and (2) an increase in the surface energy caused by the increase in fracture radius. To obtain the minimum fracture extension pressure, the work done is equated to the energy stored in the fracture system. By using this approach, Sack[21] has derived an equation which will give the minimum pressure necessary to extend a fracture in rock (Eq. 1).

$$(P_m - \sigma) = \sqrt{\frac{\pi \alpha E}{2(1-\nu^2)C}} \quad . \quad . \quad . \quad . \quad . \quad (1)$$

where P_m = minimum fracture extension pressure, psi,
σ = total earth stress perpendicular to the plane of the fracture, psi (total earth stress is defined as the sum of stress in rock matrix plus pore pressure, see Ref. 11),
α = specific surface energy of the rock, ft-lb/sq in.,
E = Young's modulus of the rock, psi,
ν = Poisson's ratio for the rock, and
C = fracture radius, ft.

This equation predicts that, for a given rock (i.e., fixed values of surface energy, Young's modulus and Poisson's ratio), the *minimum* fracture extension pressure (in excess of the earth stress) varies inversely as the square root of the fracture radius.

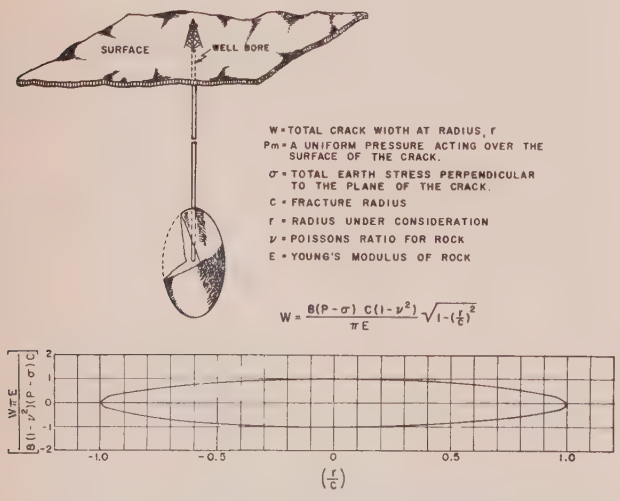

FIG. 1—SKETCH OF AN UNRESTRICTED FRACTURE WITH GEOMETRY PREDICTED BY THE ELASTIC THEORY.

EXPERIMENTAL VERIFICATION OF THE GRIFFITH-SNEDDON APPROACH

The Griffith-Sneddon approach to minimum fracture extension pressure can be verified experimentally. Sneddon has shown that the volume of a radially symmetrical crack with a uniform pressure P acting in the crack is given by Eq. 2.

$$V = \frac{16\,(1-\nu^2)\,C^3\,(P-\sigma)}{3\,E} \quad . \quad . \quad . \quad . \quad . \quad (2)$$

where V = volume of the crack.

Combining this with Eq. 1 to eliminate C yields Eq. 3.

$$(P-\sigma) = \left[\frac{2\pi^3\alpha^3E^2}{3(1-\nu^2)^2V}\right]^{1/5} \quad . \quad . \quad . \quad . \quad . \quad (3)$$

Hence, the fracture extension pressure should vary inversely as the fifth root of crack volume.

We have measured fracture extension pressure and crack volume for a Portland cement model. Fluid leak-off into the model could not be eliminated completely. However, it was minimized by using a fluid of low leak-off properties and a cement of low permeability. The volume of fluid leaking off was estimated and subtracted from the total volume injected to estimate the volume of fluid remaining in the crack. The model was arranged so that the pressure acting within the fracture could be measured.

Fig. 2 shows a sketch of the model and a plot of log P vs log V. A line with slope of " $-1/5$" is drawn through the data, thus verifying the relationship shown by Eq. 3.

MIMIMUM FRACTURE EXTENSION PRESSURES

To predict minimum fracture extension pressures for field cases, we must determine typical physical properties of rocks.

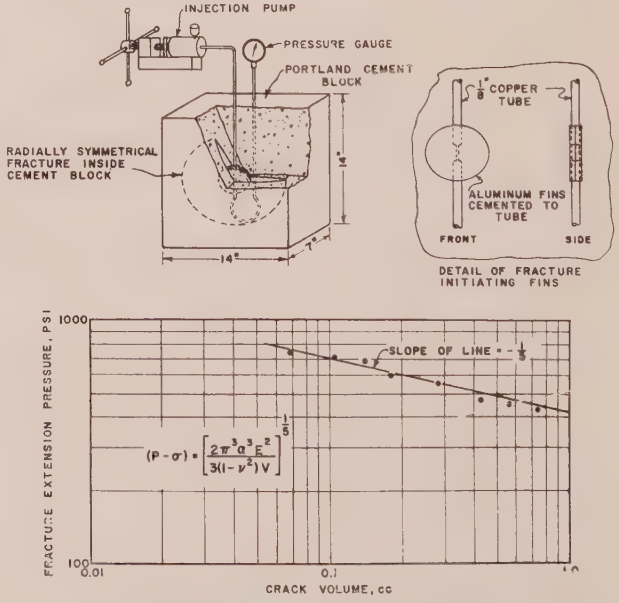

FIG. 2—SKETCH OF PORTLAND CEMENT MODEL AND THE CRACK PRESSURE-VOLUME RELATIONSHIP.

The values of Poisson's ratios for rocks reported in the literature[2,4,30] range from about 0.05 to 0.25. Since the minimum fracture extension pressure is not very sensitive to changes in Poisson's ratio, the use of an average value of 0.15 appears justified.

Young's moduli for rocks vary over a much broader range. Elastic moduli are influenced by the type of rock, porosity and average stress. Table 1 gives ranges of moduli that appear to be in agreement with most literature data.[2,4,30]

There is a paucity of surface energy data for rocks. The U.S. Bureau of Mines[26] has reported some of the best data. They report a value of 0.0265 ft-lb/sq in. for the surface energy of quartz crystals and 0.00613 ft-lb/sq in. for the surface energy of calcite crystals ($CaCO_3$).

The apparent surface energy during fracturing probably corresponds to the surface energy of the cementing material and quartz grains actually fractured. Because of the porous nature of rock, however, the *new surface* actually created during cleavage is less than 1 sq in./sq in. of fracture surface. Hence, the apparent surface energy during typical fracturing is estimated to be not more than 0.01 ft-lb/sq in. and perhaps much less.

The minimum pressures needed to extend an average fracture can now be estimated. Let us take a simplified case of an axially symmetrical fracture (a penny-shaped crack). Assume that the following properties are typical: $E = 4 \times 10^6$ psi, $\alpha = 0.01$ ft-lb/sq in. (or less) and $\nu = 0.15$.

The minimum fracture extension pressure can be calculated from Eq. 1, and the corresponding maximum crack width at the wellbore can be calculated from Eq. 4. Eq. 4 is derived by Sneddon[22] for the case of a penny-shaped crack.

$$W_m = \frac{8(P - \sigma)\ (1 - \nu^2)C}{\pi E} \quad . \quad . \quad . \quad . \quad . \quad . \quad (4)$$

where W_m = maximum crack width at the wellbore.

The calculated values are plotted vs the fracture radius on Fig. 3. These curves show that, for this condition of static fluid in a hydraulic fracture, the crack widths are very small.

FRACTURE WIDTHS UNDER DYNAMIC CONDITIONS

From the previous discussion it is clear that under static conditions (and assuming no fluid leak-off) fractures would be very narrow. If fluid were injected at reasonable pump rates into these narrow cracks, the injection pressures would have to be extremely large. However, the resulting high fluid pressures in the fracture would force the fracture walls farther apart. As the crack width increased, the pressure necessary to inject the fluid would decrease. In actuality, an equilibrium condition is reached. The resulting fracture width is controlled essentially by the fluid pressure drop in the fracture. The fluid pressure at the leading edge of the crack is nearly equal to the opposing earth stress. (The pressure in excess of the earth stress at the leading edge of the crack is usually negligible, as we have just seen in the previous section; therefore, it is taken as zero in the remainder of this paper.) This is shown conceptually on Fig. 4. (A similar sketch could be drawn for a horizontal fracture.) Operating conditions which lead to high pressure drop along the crack (such as high injection rates and viscous fluids) will result in relatively wide cracks. Conversely, operating conditions which lead to low pressure drop (low injection rates and thin fluids) will result in relatively narrow cracks.

Since crack widths are controlled by pressure drop in the crack, we must consider several controlling situations. In this paper, we will discuss the following cases.

1. Vertically oriented, vertically restricted fractures —includes crack widths resulting: (a) from Newtonian fluids flowing along the crack in laminar flow; (b) from Newtonian fluid flowing along the crack in turbulent flow; (c) from non-Newtonian fluids flowing along the crack in laminar flow; and (d) when a large amount of sand in the fracture restricts fluid flow and thereby increases pressure drop along the fracture.

2. Horizontally oriented, axially symmetrical fractures resulting from Newtonian fluids in laminar flow— includes: (a) fractures deep within the earth; and (b) very shallow fractures.

There are, of course, other conditions which could be considered. However, we believe that these cases will cover most situations and generally will show the behavior to be expected. (For instance, widths of *unrestricted* vertical fractures will be about the same as for horizontal fractures of the same size.)

TABLE 1—ESTIMATES OF YOUNG'S MODULI OF FORMATION ROCKS

Type of Rock	Probable Value of E (psi)
Porous, Unconsolidated to Lightly Consolidated (Friable) Sands	0.5 to 1.5 × 10^6
Medium-Hardness Sandstone	2 to 4 × 10^6
Hard, Dense Sandstone	5 to 7.5 × 10^6
Limestone and Dolomite	8 to 13 × 10^6

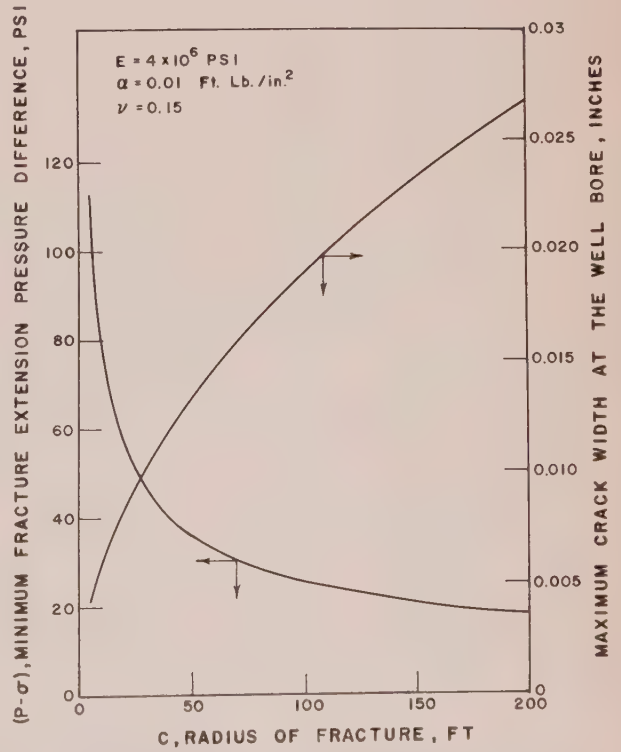

FIG. 3—MINIMUM FRACTURE EXTENSION PRESSURES AND MAXIMUM CRACK WIDTHS FOR A TYPICAL UNRESTRICTED FRACTURE.

VERTICAL FRACTURES

Within the earth there often are conditions which will cause vertical fractures to be limited in growth in a vertical direction. Zones with horizontal stress higher than in the pay zone are sometimes found above and below the pay zone and will, for instance, cause the vertically limiting effect. (High horizontal stresses are sometimes found in shale. Also, in limestone reservoirs, nonpermeable sections may have higher horizontal stresses than permeable sections after the reservoir pressure has been drawn down.) The fracture will grow until it reaches the bounding zone and then will be restricted in vertical growth. However, it will continue to extend laterally away from the wellbore as shown on Fig. 5. The fracture will penetrate up and down into the bounding zones until an equilibrium condition is reached. This equilibrium condition is similar to that of a lever at static equilibrium. The fracturing fluid exerts a pressure against the fracture face tending to open and extend the fracture. The high stresses at top and bottom tend to close the fracture. The fracture, therefore, will extend into the bounding zones until the opposing forces counter-balance one another. If these bounding zones are not thick enough or if pressure drop in the fracture gets high enough, then the fracture may crack through into other zones.

CRACK WIDTHS RESULTING FROM NEWTONIAN FLUIDS IN LAMINAR FLOW

Fortunately, it is rather easy to predict whether a Newtonian fluid will be in laminar or turbulent flow. In a classic work,[19] Reynolds discovered that turbulence would begin when the Reynolds' number (the ratio of viscous to inertial forces in the fluid) exceeded a certain value. In terms of fracturing conditions, the Reynolds' number can be reduced to (see Appendix A):

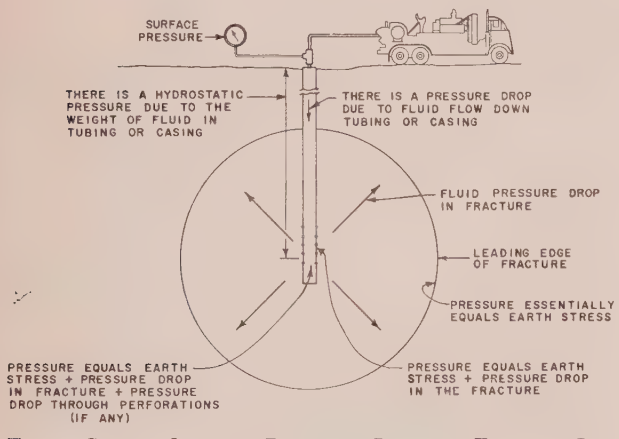
SURFACE PRESSURE
THERE IS A HYDROSTATIC PRESSURE DUE TO THE WEIGHT OF FLUID IN TUBING OR CASING
THERE IS A PRESSURE DROP DUE TO FLUID FLOW DOWN TUBING OR CASING
FLUID PRESSURE DROP IN FRACTURE
LEADING EDGE OF FRACTURE
PRESSURE ESSENTIALLY EQUALS EARTH STRESS
PRESSURE EQUALS EARTH STRESS + PRESSURE DROP IN FRACTURE + PRESSURE DROP THROUGH PERFORATIONS (IF ANY)
PRESSURE EQUALS EARTH STRESS + PRESSURE DROP IN THE FRACTURE

FIG. 4—SKETCH SHOWING PRESSURES DURING A FRACTURE JOB.

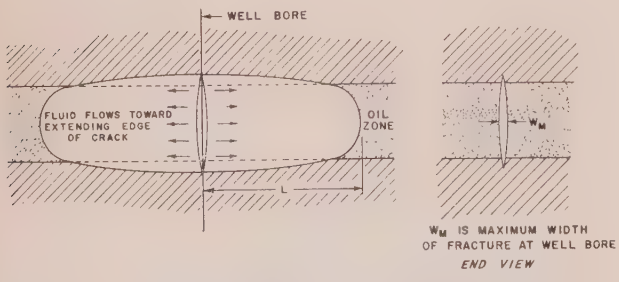

FIG. 5—SKETCH OF A RESTRICTED VERTICAL FRACTURE (NOT DRAWN TO SCALE).

$$N_{Re} = 7.81 \times 10^3 \frac{(Q)\ (Sp\ Gr)}{(H)\ (\mu)}$$

where N_{Re} = Reynolds' number,
Q = total injection rate, bbl/min,
$Sp\ Gr$ = specific gravity of fracturing fluid,
H = height of fracture, ft and
μ = viscosity of fracturing fluid, cp.

Then, when $(Q)\ (Sp\ Gr)/(H)\ (\mu)$ is less than about 0.32, the fluid within the crack will be in laminar flow. The crack width is then given by Eq. 5 (see Appendix A for derivation).

$$W = 0.38 \left[\frac{(Q)\ (\mu)\ (L)}{E}\right]^{1/4} \quad . \quad . \quad . \quad . \quad . \quad (5)$$

where W = maximum crack width at the wellbore, in.,
Q = total pump rate, bbl/min,
μ = effective fracturing fluid viscosity, cp,
L = length of a vertical fracture measured from the wellbore, ft, and
E = Young's modulus of formation rock, psi.

Using the range of values of Young's moduli from Table 1, Eq. 5 is presented in a convenient graphical manner as Fig. 6.

As an example, suppose conditions for a fracture job in a medium-hardness sandstone were as follows: Q = 30 bbl/min, μ = 4 cp, L = 500 ft, $Sp\ Gr$ = 0.9 and H = 40 ft.

$$\frac{Q\ (Sp\ Gr)}{H\mu} = \frac{(30)\,(0.9)}{(40)\,(4)} = 0.17.$$

(Therefore, fluid is in laminar flow and Fig. 6 can be used.)

$$Q\mu L = (30)\,(4)\,(500) = 6 \times 10^4.$$

Therefore, Fig. 6 shows that the maximum crack width at the wellbore would be about 0.13 to 0.15 in.

CRACK WIDTHS RESULTING FROM NEWTONIAN FLUIDS IN TURBULENT FLOW

If $(Q)(Sp\ Gr)/(H)(\mu)$ is greater than 0.32, then the fluid will be in turbulent flow within the fracture. For this case, the width is given by Eq. 6 (see Appendix B for derivation).

$$W = 0.6 \left[\frac{(Q)^2(Sp\ Gr)\,(L)}{(E)\,(H)}\right]^{1/4} \quad . \quad . \quad . \quad (6)$$

where $Sp\ Gr$ = specific gravity of fracturing fluid, and
H = height of a restricted, vertical fracture, ft.

Again using values of Young's moduli from Table 1, Eq. 6 can be shown graphically as Fig. 7. Let us consider the same example as before, except suppose that the viscosity of the fracturing fluid were 1 cp, Q = 30 bbl/min, μ = 1 cp, L = 500 ft, $Sp\ Gr$ = 0.9, and H = 40 ft.

$$\frac{Q(Sp\ Gr)}{H\mu} = \frac{(30)\,(0.9)}{(40)\,(1)} = 0.68.$$

Therefore, the fluid is in turbulent flow and Fig. 7 can be used.

$$\frac{Q^2(Sp\ Gr)L}{H} = \frac{(30)^2(0.9)\,(500)}{40} = 1.01 \times 10^4.$$

Fig. 7 shows that in this case the maximum crack width at the wellbore would be about 0.14 to 0.16 in.

CRACK WIDTHS RESULTING FROM NON-NEWTONIAN FLUIDS IN LAMINAR FLOW

If non-Newtonian fluids such as gelled oils or emul-

sions are used, then it is necessary to determine the fluids' flow properties before estimating crack width. Fann meter data should be plotted in a manner similar to the log-log plot shown on Fig. 13 in Appendix C. The equation of the straight-line portion is reduced to two constants, k' which is proportional to an intercept at a particular rotor speed, and n' which is proportional to the slope of the line. (Details for actually determining k' and n' from Fann data are given in Appendix C.) These two constants are then used in place of "viscosity".

Unfortunately, we have not been able to plot crack widths for non-Newtonian fluids in as simple a manner as Figs. 6 and 7. It has been necessary to include in the

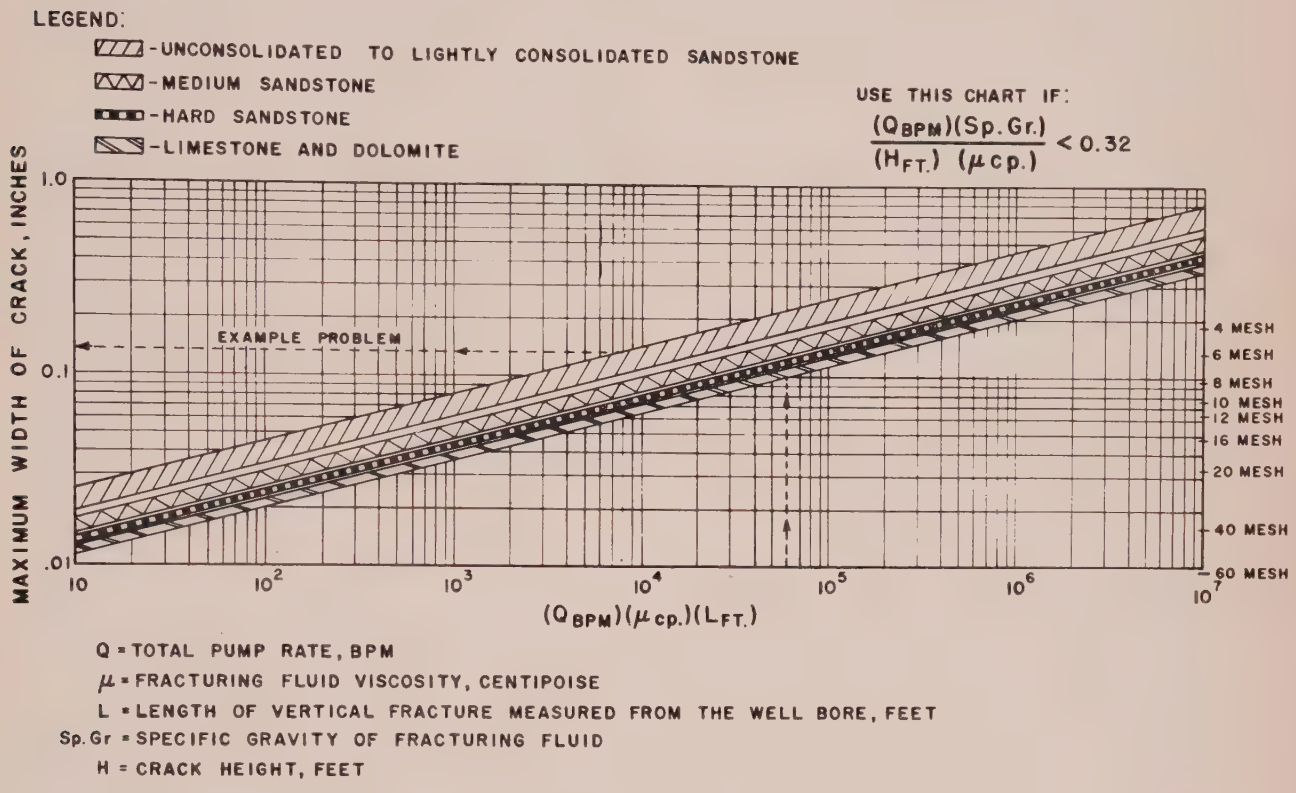

Q = TOTAL PUMP RATE, BPM

μ = FRACTURING FLUID VISCOSITY, CENTIPOISE

L = LENGTH OF VERTICAL FRACTURE MEASURED FROM THE WELL BORE, FEET

Sp.Gr = SPECIFIC GRAVITY OF FRACTURING FLUID

H = CRACK HEIGHT, FEET

FIG. 6—CRACK WIDTHS FOR RESTRICTED VERTICAL FRACTURES RESULTING FROM NEWTONIAN FLUIDS IN LAMINAR FLOW.

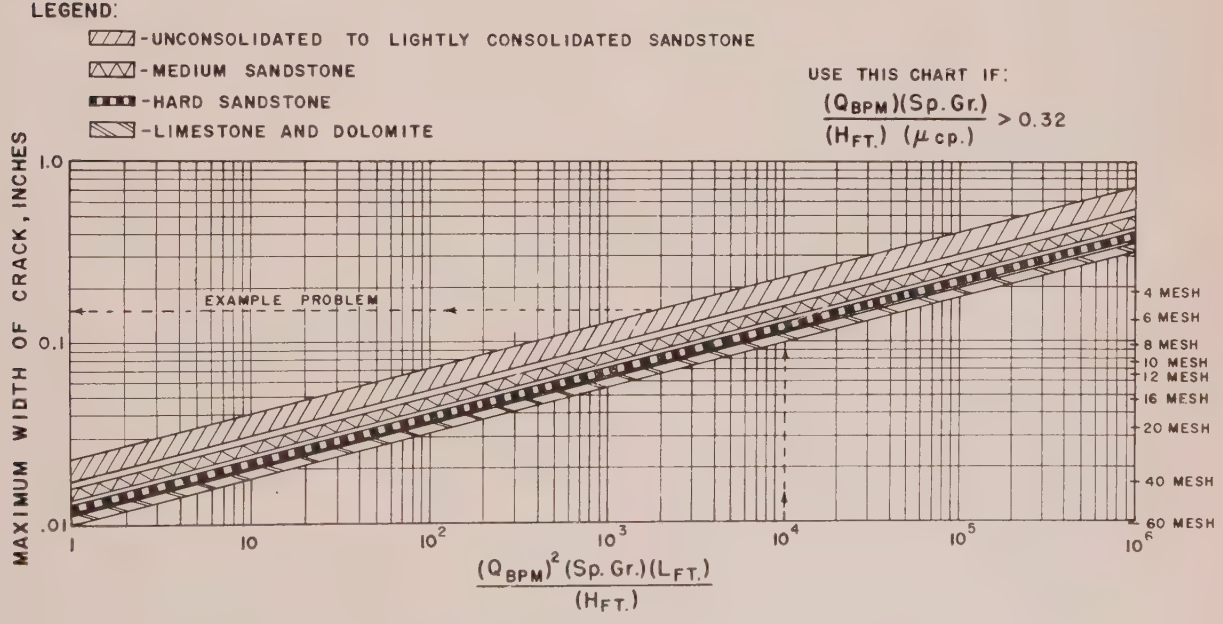

Q = TOTAL PUMP RATE, BPM

μ = FRACTURING FLUID VISCOSITY, CENTIPOISE

L = LENGTH OF VERTICAL FRACTURE MEASURED FROM THE WELL BORE, FEET

Sp.Gr = SPECIFIC GRAVITY OF FRACTURING FLUID

H = CRACK HEIGHT, FEET

FIG. 7—CRACK WIDTHS FOR RESTRICTED VERTICAL FRACTURES RESULTING FROM NEWTONIAN FLUIDS IN TURBULENT FLOW.

design chart Young's moduli of the formation rocks. Values of Young's moduli can again be estimated from Table 1. After the flow constants k' and n' are determined for the fluid and the Young's modulus of the rock has been estimated, crack widths can be estimated from Fig. 8. (See Appendix C for derivation.)

Suppose, for a given fracturing case, $k' = 4.69 \times 10^{-2}$ lb-sec$^{n'}$/sq ft, $n' = 0.654$,* $Q = 20$ bbl/min, $L = 100$ ft, $H = 30$ ft, and $E = 6 \times 10^6$ psi (estimated for hard sandstone from Table 1).

$$\frac{k'Q^{n'}L\,H^{1-n'}}{E} = \frac{(4.69 \times 10^{-2})(20)^{0.654}(100)(30)^{0.346}}{6 \times 10^6} = 1.8 \times 10^{-5}.$$

From Fig. 8, the maximum crack width at the wellbore is then estimated to be 0.2 in.

CRACK WIDTHS RESULTING WHEN SAND IN THE FRACTURE RESTRICTS FLUID FLOW

The crack widths estimated from Figs. 6, 7 and 8 apply when pure fluids are being pumped along a fracture. These estimated widths are also valid when there is a sparse distribution of propping agent suspended in the fluid (because a dilute suspension of solid material will not appreciably influence pressure drop along the crack). However, if a large amount of sand is injected as a propping agent, then its presence in the fracture will influence pressure drop and thereby influence crack width.

In field operations, sand is usually placed in the fracture such that one of the two following conditions will be obtained: (1) a great deal of sand settles to the bottom of the fracture; or (2) the sand is nearly uniformly suspended in the fracture and concentrated due to leak-off of the fracturing fluid.

*These particular values of k' and n' are for a very thick gelled fracturing oil.

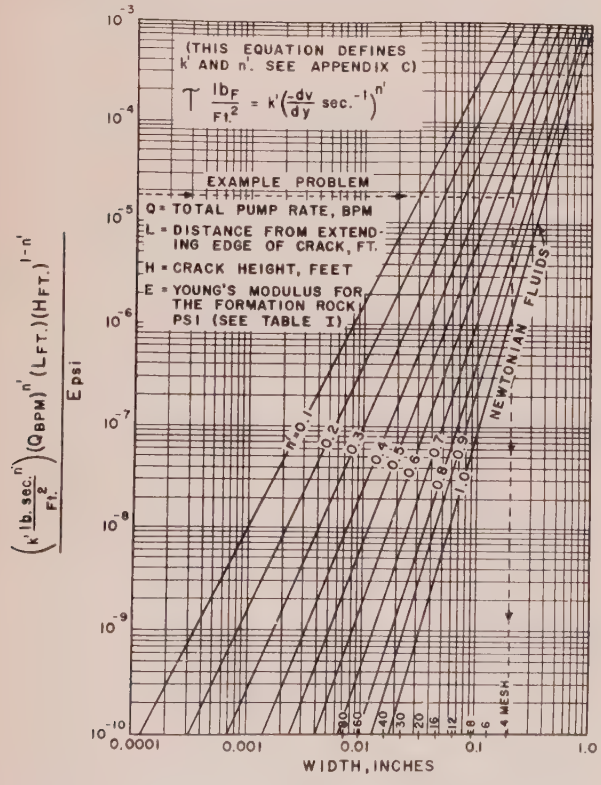

FIG. 8—CRACK WIDTHS FOR RESTRICTED VERTICAL FRACTURE RESULTING FROM NON-NEWTONIAN FLUIDS IN LAMINAR FLOW.

The conditions which lead to settling of sand in a fracture were discussed in a previous paper.[14] The crack width is not easily calculated for these conditions. We have studied a few cases and found that the crack widths were several times as wide as the predicted crack width without sand present. At the present time, we can only suggest that, for all cases when sand is present, crack width should be estimated in the manner described below where sand concentrates due to fluid leak-off but does not settle.

If the sand is suspended in a very viscous fluid, it will settle so slowly that a settled sand pack will not have time to form during the fracture treatment. However, during the treatment, the fracturing fluid can leak off into the porous formation, leaving a high concentration of sand suspended in the fracture. The viscosity of the concentrated sand *slurry* will be considerably greater than the viscosity of the pure fracturing fluid. Fig. 9 shows the ratio of the slurry viscosity to the pure fracturing fluid viscosity as a function of the volume fraction of solid material in the slurry.[24]

The crack width is easily estimated in the following way if the sand concentrates because of fluid leak-off.

1. The amount of fluid remaining in the fracture is estimated by the method proposed by Howard and Fast.[10] By knowing the amount of fluid in the fracture and the amount of sand in the fracture, the average slurry concentration can be calculated.

2. The average slurry viscosity can then be estimated from Fig. 9.

3. The crack width is then estimated from Figs. 6 and 7 using the average slurry viscosity and density rather than the viscosity and density of the pure fracturing fluid.

In the actual case, slurry properties vary from point to point in the fracture. Hence, the width calculated as just shown must be interpreted as only an approximate width.

HORIZONTAL FRACTURES

If a fracture is oriented horizontally, crack width may result from two types of rock movement. If the fracture is deep within the earth, crack width results principally from *compression* of rock in the vicinity of the fracture. However, if the fracture is very shallow, crack width may also result from flexing and lifting of the overburden. This is shown conceptually in Fig. 10. It is shown in Appendix D that compression of sur-

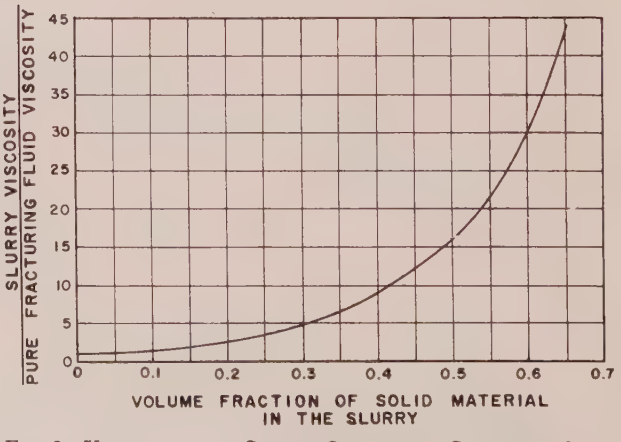

FIG. 9—VISCOSITY OF A SLURRY CONTAINING SUSPENDED SOLID MATERIAL COMPARED TO THE VISCOSITY OF THE BASIC FLUID.

rounding rock is the principal mechanism leading to crack width if the depth is greater than about three-fourths of the fracture radius. (Hence, this is the mechanism that controls during most fracture treatments.) For this condition, the width is given approximately by Eq. 7.

$$W(\text{in.}) = 0.22\left[\frac{Q(\text{bbl/min})\,\mu(\text{cp})\;C(\text{ft})}{\text{E(psi)}}\right]^{1/4} \quad . \quad . \quad (7)$$

where C = radius of the fracture, ft.

(In deriving this equation we have assumed a homogeneous medium. Actually, in the case of a horizontal fracture, the value of Young's modulus should be an effective average for the pay zone and the formations above and below it, since they are also compressed when the fracture is opened. However, for simplicity we have used the values of Young's moduli for the pay zones as shown in Table 1 in applying this equation.)

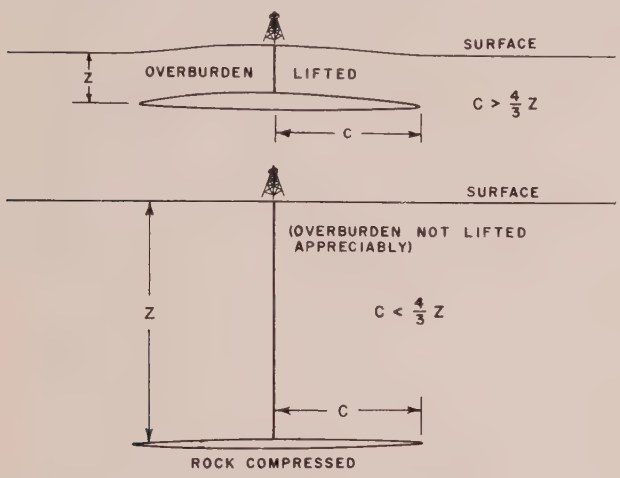

FIG. 10—SKETCH SHOWING A SHALLOW AND A DEEP HORIZONTAL FRACTURE.

Fig. 11 graphically shows the order of magnitude of crack width to expect in horizontal fractures (depth is greater than three-fourths of the fracture radius) if the fluid is in laminar flow. Laminar flow of the fluid at every point in a horizontal fracture is probably encountered only rarely in field operations. Hence, turbulent flow must also be considered before a generally applicable equation can be derived. However, the turbulent zone usually will not extend far from the wellbore; therefore, Fig. 11 is approximately correct in all cases.

Appendix D also shows an equation for estimating crack widths of shallow horizontal fractures (depth is less than three-fourths of the fracture radius).

If a large amount of suspended sand is injected into the fracture, then the width of the fracture can be estimated by using the viscosity of the sand slurry rather than the viscosity of the basic fracturing fluid.

CONSEQUENCES OF THESE WIDTH CONCEPTS

Now let us briefly discuss some of the consequences and significance of these width concepts. First, consider the relationship between crack width and fracturing pressure. Pressure drops along the fracture can be estimated from Eq. A-10 or D-4 (in Appendixes A and D, respectively) and crack width Eqs. 5, 6, or 7. For those fractures oriented vertically, pressure drops along the cracks will probably range from a few tens of pounds per square inch (for very tall cracks) to perhaps 1,000 psi (for thin zones). The higher pressures in thin zones increase the probability of cracking out of the pay zone into zones above and below.

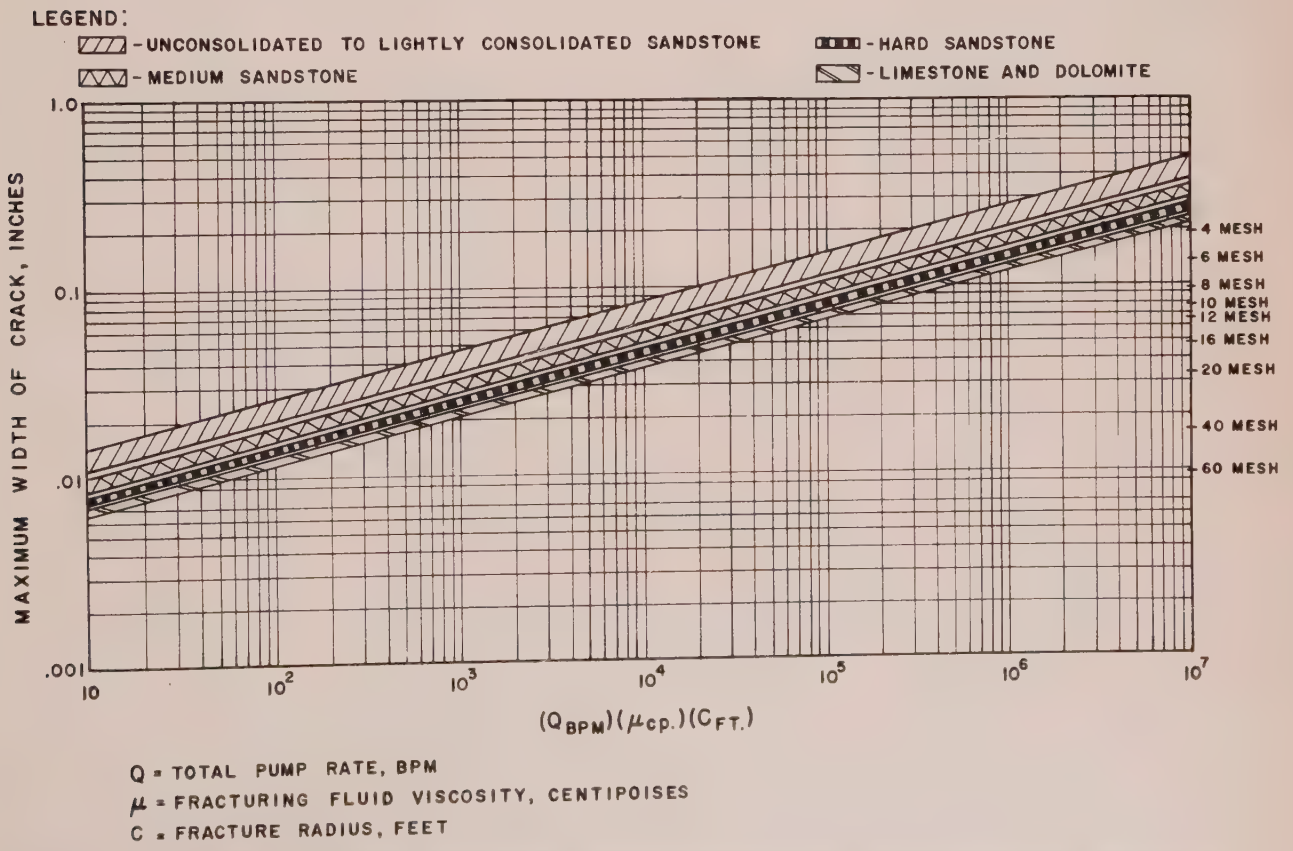

FIG. 11—APPROXIMATE CRACK WIDTHS FOR HORIZONTAL FRACTURES RESULTING FROM NEWTONIAN FLUIDS IN LAMINAR FLOW.

For horizontal fractures or unrestricted vertical fractures, pressure drops will be very high initially but quite low for large fractures.

Bottom-hole fracturing pressures will be equal to the sum of the total earth stress perpendicular to the plane of the crack and the pressure drop in the fracture. Hubbert and Willis[11] and Cleary[4] have discussed the factors influencing earth stresses.

Fig. 12 shows our estimates of the ranges of earth stresses (similar to estimates of Hubbert and Willis or Cleary) plus pressure drops for vertical and horizontal fractures (as discussed in this paper). This figure also shows some bottom-hole fracturing pressures calculated from actual field treatments. It is apparent that bottom-hole pressures for most of these fracturing treatments fell in the range predicted for vertical fractures. It is interesting to note that predicted pressures for vertical and horizontal fractures overlap at depths less than about 3,000 ft. Hence, at these shallow depths, fracture orientation cannot be determined by cursory inspection of the bottom-hole fracturing pressure gradient.

Another interesting consequence of these concepts is the behavior to be expected after pumping has ceased. Since the fracture extension pressure is nearly equal to the earth stress, the fracture will *continue to extend* after pumping has ceased. The crack will become narrower and longer until the minimum width (previously discussed) is reached or until formation walls grip the propping material. Of course, fluid will continue to leak-off over the whole fracture area and particularly near the extending edge of the fracture as the walls close. This limits the additional length obtained after pumping stops.

Finally, let us review the factors which influence crack width (see Eqs. 5, 6, and 7).

1. The thickness of pay zone should have no effect on pressure or width of horizontal fractures. For restricted vertical fractures, pressure drop along the fracture will be large for thin zones but small for thick zones. On the other hand, crack width at the wellbore is nearly independent of height of a vertical fracture (except in turbulent flow).

2. Depth of pay zone will generally have little effect on crack width (except that rock properties may vary with depth). For very shallow horizontal fractures, the width may be somewhat greater than normal because of lifting of the overburden. However, this should be of no significance in most normal fracturing operations.

3. Crack width is not particularly sensitive to rock properties. Young's moduli of rocks have a range of about ten- or twenty-fold. However, crack width is inversely proportional to the fourth root of Young's modulus; therefore, only about a twofold variation in crack width should be expected from this range of moduli.

4. Since the viscosity of a fracturing fluid (or effective viscosity if slurries are considered) can be varied over a very wide range, this factor will have an appreciable effect on crack width.

5. Pump rate will also influence width, but usually the range of pump rates is limited by the horsepower available.

6. Fracture width at the wellbore will also be influenced by length or radius of a fracture. As the *volume* of fluid in the fracture increases, the crack width will increase.

7. Crack width is strongly influenced by a large amount of solid propping material in the fracture. The solid material increases resistance to fluid flow and results in a wider crack.

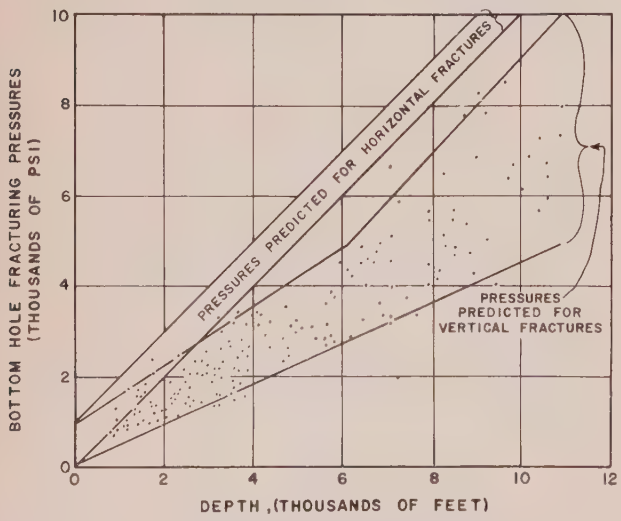

FIG. 12—THEORETICALLY PREDICTED BOTTOM-HOLE FRACTURING PRESSURES AND FIELD DATA.

NOMENCLATURE

C = fracture radius
D_e = equivalent diameter
E = Young's modulus of rock
f = friction factor
H = height of a vertical fracture
k' = a measure of the flow properties of a non-Newtonian fluid. It is determined as explained in Appendix C, $\left[\frac{(\text{lb})\,(\text{sec})^{n'}}{\text{sq ft}}\right]$
L = length of a vertical fracture (measured from the wellbore)
n' = a measure of the flow properties of a non-Newtonian fluid. It is determined as explained in Appendix C.
N_{Re} = Reynolds' number
P = pressure
P_{avg} = average fluid pressure in the fracture
P_m = minimum fracture extension pressure
P_w = fluid pressure at the wellbore
Q = total injection rate into a well
r = radius
r_w = radius of the wellbore
R_H = hydraulic radius
$Sp\ Gr$ = specific gravity of fracturing fluid
u = velocity
v = velocity
V = volume
W = crack width
W_a = average fracture width
W_m = maximum crack width at wellbore
x = distance
y = distance
Z = depth of fracture (measured from surface of ground)
α = specific surface energy of rock
$\beta = \frac{10^8 \text{ darcies}}{12 \text{ sq cm}}$ (a constant), see Eq. D-1
γ = a proportionality constant relating equiva-

lent diameter and hydraulic radius (see Eq. A-3)

δ_1 = upward deflection of an elastic plate clamped at the edge (see Eq. D-8)

δ_2 = downward deflection of an elastic medium (see Eq. D-9)

μ = viscosity of a fracturing fluid

ν = Poisson's ratio for rock

ρ = fluid density

σ = total earth stress perpendicular to the plane of the fracture

τ = shear stress

REFERENCES

1. Barenblatt, G. I.: "On Equilibrium Cracks Formed in Brittle Fracture", Soviet physics—*Doklady.*, (1960) **4.**
2. Birch, Francis: Editor, *Handbook of Physical Constants*, GSA Special Paper No. 36 (Jan. 31, 1942).
3. Khristianovitch, S. A. Zheltov, Y. P., Barenblatt, G. I. and Maximovich, G. K.: "Theoretical Principles of Hydraulic Fracturing of Oil Strata", *Proc.*, Fifth World Pet. Cong., N. Y. (1959) **Section II.**
4. Cleary, J. M.: "Hydraulic Fracture Theory, Parts I, II, III", Circulars 251, 252, 281, Illinois Geological Survey, Urbana, Ill. (1959).
5. Davies, S. J. and White, C. M.: *Proc.*, Roy. Soc. of London (1928) **119A,** 92.
6. Gilman, J. J.: "Direct Measurement of the Surface Energies of Crystals", *Jour. Appl. Phys.* (1960) **31,** 2208.
7. Griffith, A. A.: *Phil. Trans.* Roy. Soc of London, (1920) A, **221,** 163.
8. Griffith, A. A.: *Proc.*, Int. Cong. Appl. Mech. (1924) Delft, 55.
9. Harrison, Eugene, Kieschnick, W. F., Jr. and McGuire, W. J.: "The Mechanics of Formation Fracture Induction and Extension", *Trans.*, AIME (1954) **201,** 252.
10. Howard, G. C. and Fast, C. R.: "Optimum Fluid Char acteristics for Fracture Extension", *Drill. and Prod. Prac.*, API (1957) 261.
11. Hubbert, M. K. and Willis, D. G.: "Mechanics of Hydraulic Fracturing", *Trans.*, AIME (1957) **210,** 153.
12. Huitt, J. L.: "Fluid Flow in Simulated Fractures", *AIChE Jour.* (1956) **2,** 259.
13. Huitt, J. L. and McGlothlin, B. B.: "The Propping of Fractures in Formations in which Propping Sand Crushes", API Paper No. 875-13-E (May, 1959).
14. Kern, L. R., Perkins, T. K. and Wyant, R. E.: "The Mechanics of Sand Movement in Fracturing", *Trans.*, AIME (1959) **216,** 403.
15. Kern, L. R., Perkins, T. K. and Wyant, R. E.: "Propping Fractures with Aluminum Particles", *Jour Pet. Tech.* (June, 1961) 583.
16. Lamb, Horace: *Hydrodynamics*, Sixth Ed., Cambridge U. Press (1932).
17. Moody, L. F.: *Trans.*, ASME (1944) **66,** 671.
18. Perry, J. H.: Editor, *Chemical Engineers' Handbook*, Third Ed., McGraw Hill Book Co., Inc., N. Y. (1950) 378.
19. Reynolds, O.: "An Experimental Investigation of the Circumstances Which Determine Whether the Motion of Water Will Be Direct or Sinuous, and of the Law of Resistance in Parallel Channels", *Phil. Trans.* (1883) Roy. Soc. of London.
20. Rothfus, R. R., Archer, D. H., Klimas, I. C. and Sikchi, K. G.: "Simplified Flow Calculations for Tubes and Parallel Plates", *AIChE Jour.* (1957) **3,** 208.
21. Sack, R. A.: "Extension of Griffith's Theory of Rupture to Three Dimensions", *Proc.*, Phys. Soc. of London (1946) **58,** 729.
22. Sneddon, I. N.: "The Distribution of Stress in the Neighbourhood of a Crack in an Elastic Solid", *Proc.*, Roy. Soc. (1946) A, **187,** 229.
23. Sneddon, I. N. and Elliott, H. A.: "The Opening of a Griffith Crack Under Internal Pressure", *Quarterly of Appl. Math.* (1946) **4,** 262.
24. Steinour, H. H.: "Rate of Sedimentation — Nonflocculated Suspensions of Uniform Spheres", *Ind. Eng. Chem.* (1944) **36,** 618.
25. Timoshenko, S.: *Theory of Plates and Shells*, McGraw-Hill Book Co., Inc., N. Y. (1940) 60.
26. USBM Bulletin 402, U. S. Dept. Interior.
27. Walker, J. E., Whan, G. A. and Rothfus, R. R.: "Fluid Friction in Noncircular Ducts", *AIChE Jour.* (1957) **3,** 484.
28. Way, S.: "Bending of Circular Plates with Large Deflections", *Trans.*, AIME (1934) **56,** 627.
29. Weil, N. A. and Newmark, N. M.: "Large Deflections of Elliptical Plates", *Jour. Appl. Mech.* (1956) **23,** 21.
30. Wuerker, R. G.: "Annotated Tables of Strength and Elastic Properties of Rocks", Paper 663-G published as separate publication by SPE (1956).
31. Zheltov, Y. P. and Khristianovich, S. A.: "The Hydraulic Fracturing of an Oil-Producing Formation", *Izvest, Akad. Nauk USSR*, Otdel. Tekh. Nauk (1955) No. 5, 3.
32. Zheltov, Y. P.: "An Approximate Method of Calculating the Size of Fissures Produced by the Hydraulic Fracturing of a Formation", *Izvest. Akad. Nauk USSR*, Otdel. Tekh. Nauk (1957) No. 3, 180.

APPENDIX A

DERIVATION OF AN EQUATION GIVING VERTICAL CRACK WIDTHS RESULTING FROM NEWTONIAN FLUIDS IN LAMINAR FLOW

Widths of restricted, vertical cracks resulting from injection of Newtonian fluids can be estimated by making the following assumptions.

1. Assume that the fracture is vertical and of fixed height H (the height is independent of the distance from the wellbore).

2. Assume that the cross-sectional shape of the crack at any point is essentially elliptical and that the maximum width at that point is proportional to the difference between pressure and stress at that point. The equation of the ellipse is taken as Sneddon's equation for a two-dimensional system (Eq. A-10).

3. Assume that the pressure drop can be estimated by means of Fanning's equation in which the hydraulic radius for an ellipse has been substituted.

4. Assume that the fluid pressure at the extending edge of the crack is essentially equal to the total earth stress perpendicular to the plane of the fracture.

5. Assume there is no leak-off of the injected fluid. (By assuming the limiting condition of a total fluid leak-off rate large enough that the fracture is no longer extending, one can readily show that leak-off has little effect on crack width.)

The Fanning equation may be written as Eq. A-1.

$$\frac{dP}{dx} = \frac{2 f v^2 \rho}{D_e} \quad \ldots\ldots\ldots \quad (A\text{-}1)$$

where, for laminar flow,

$$f = \frac{16\mu}{D_e v \rho} \quad \ldots\ldots\ldots \quad (A\text{-}2)$$

For an ellipse of essentially zero eccentricity (eccentricity is the ratio of minor to major diameters), Perry[18] has shown

$$D_e = \gamma R_H = \gamma \left(\frac{W}{2.546} \right) \quad \ldots\ldots \quad (A\text{-}3)$$

where D_e = equivalent diameter,

γ = a proportionality constant,

R_H = hydraulic radius, and

W = minor diameter of the ellipse (equals maximum crack width).

Lamb[16] has shown for an ellipse of nearly zero eccentricity and for laminar flow

$$\frac{dP}{dx} = \frac{32Q\mu}{\pi H W^3} \quad \text{(A-4)}$$

Substituting Eqs. A-2, A-3 and A-8 into Eq. A-1 and equating to Eq. A-4 shows

$$\gamma = 3.6 \quad \text{(A-5)}$$

(This can be compared with γ for a circular pipe of 4 or γ for parallel plates of 3.26.)

We assume that $\gamma = 3.6$ is the value that should be used for all cases considered here, both laminar and turbulent. The Reynolds' number of the fluid flowing down the crack can now be written.

$$N_{Re} = \frac{D_e v \rho}{\mu} = \frac{(\gamma R_H)\left(\frac{\text{flow rate}}{\text{area}}\right)\rho}{\mu}$$

$$= \frac{\gamma\left(\frac{\text{area}}{\text{wetted perimeter}}\right)\left(\frac{\text{flow rate}}{\text{area}}\right)\rho}{\mu}$$

$$= \frac{3.6\left(\frac{\text{flow rate}}{2H}\right)\rho}{\mu}$$

$$= 7.81 \times 10^5 \frac{(Q)(Sp\ Gr)}{(H)(\mu)} \quad \text{(A-6)}$$

Fluid will be in laminar flow in the crack if Reynolds' number is less than about 2,500. (See, for instance, the data of Huitt[12] or Rothfus, *et al*[20].) Substitution of $N_{Re} < 2{,}500$ into Eq. A-6 shows that laminar flow will obtain if

$$\frac{(Q)(Sp\ Gr)}{(H)(\mu)} < 0.32.$$

In the laminar region, the friction factor is given by Eq. A-2. We can compare this friction-factor relationship for parallel plates with experimental data which have been reported in the literature. For smooth parallel plates, the data of Huitt,[12] Davies and White,[5] Rothfus, *et al*,[20] and Walker, *et al*,[27] are in agreement with each other. Furthermore, in the laminar region the experimental data are in exact agreement with this theoretical approach.

Substituting Eqs. A-2, A-3 and A-5 into Eq. A-1 yields Eq. A-7.

$$\frac{dP}{dx} = \frac{32\ (2.546)^2\ v\ \mu}{(3.6)^2\ W^2} \quad \text{(A-7)}$$

But we note that

$$v = \frac{2Q}{\pi W H} \quad \text{(A-8)}$$

Therefore,

$$\frac{dP}{dx} = \frac{64\ (2.546)^2\ Q\mu}{\pi\ (3.6)^2\ W^3 H} \quad \text{(A-9)}$$

For a fracture restricted at top and bottom, Sneddon[23] has shown

$$W_x = \frac{2\ (1 - \nu^2)\ (P_x - \sigma)\ H}{E} \quad \text{(A-10)}$$

If we assume that Q_x is constant (this neglects leak-off and accumulation in the crack), then substituting Eq. A-10 into Eq. A-9 gives Eq. A-11.

$$(P - \sigma)^3\, dP = \left[\frac{(8)(2.546)^2}{\pi\ (3.6)^2}\right]\left[\frac{\mu\, Q\, E^3}{H^4\ (1 - \nu^2)^3}\right] dx \quad \text{(A-11)}$$

By integrating and noting that $(P - \sigma) = 0$ at the leading edge of the crack, we can express the pressure as a function of the distance from the leading edge of the crack. By then substituting into Eq. A-10, the width is given as a function of the distance from the end of the crack. Assuming $\nu = 0.15$, we can therefore express the width in convenient units as

$$W(\text{in.}) = 0.38\left[\frac{Q(\text{bbl/min})\ \mu(\text{cp})\ L(\text{ft})}{E(\text{psi})}\right]^{1/4} \quad \text{(A-12)}$$

APPENDIX B

DERIVATION OF AN EQUATION GIVING VERTICAL CRACK WIDTHS RESULTING FROM NEWTONIAN FLUIDS IN TURBULENT FLOW

The basic assumptions for this case are the same as those listed in Appendix A. If Reynolds' number is greater than 2,500, we assume that

$$f = 0.0125 \quad \text{(B-1)}$$

The friction factor is influenced by the roughness of the walls; the $f = 0.0125$ value corresponds to a relative roughness[17] of about 0.02. The effect of relative roughness is clearly shown by the experiments of Huitt.[12]

Substituting Eqs. A-3, A-5, A-8, A-10 and B-1 into Eq. A-1 yields Eq. B-2.

$$(P - \sigma)^3\, dP = \left[\frac{(0.0125)(2.546)}{\pi^2\ (3.6)}\right]\left[\frac{\rho Q^2\, E^3}{(1 - \nu^2)^3\, H^5}\right] dx \quad \text{(B-2)}$$

By integrating, noting that $(P - \sigma) = 0$ at the leading edge of the crack and substituting into Eq. A-10, we obtain Eq. B-3 for maximum crack width at the wellbore.

$$W = 0.6\left[\frac{(Q)^2\ (Sp\ Gr)\ (L)}{(E)\ (H)}\right]^{1/4} \quad \text{(B-3)}$$

APPENDIX C

DERIVATION OF AN EQUATION GIVING VERTICAL CRACK WIDTHS RESULTING FROM NON-NEWTONIAN FLUIDS IN LAMINAR FLOW

The relationship between shear stress and shear rate for many non-Newtonian fluids (as well as Newtonian fluids) can be represented by Eq. C-1.

$$\tau = k'\left(\frac{du}{dy}\right)^{n'} \quad \text{(C-1)}$$

where τ = shear stress,

u = velocity = $f(y)$,

k', n' = constants, and

$\left(\frac{du}{dy}\right)$ = shear rate.

The shear behavior of most fracturing fluids, in fact, can be represented by this equation. The constants k' and n' can be evaluated with a Fann meter. Table 2 shows the relationship between shear rate in seconds^{-1} and rotor rpm for a Fann meter.

At each shear rate, the meter will indicate a scale reading which can be converted to shear stress in pounds per square feet by means of Eq. C-2.

$$\tau\ \text{lb/sq ft} = \frac{(\text{scale reading})(\text{spring constant})}{100}. \quad \text{(C-2)}$$

Shear stress should then be plotted vs shear rate on

log-log paper. Fig. 13 shows typical data for a thick fracturing oil which has been gelled varying amounts.

A straight line is drawn through each set of data points. (The points at low shear rate frequently deviate from the straight line and should not be used.) The constant n' is then determined from any two points on the straight lines, as indicated by Eq. C-3.

$$n' = \left[\frac{(\log)(\tau_2/\tau_1)}{(\log)\dfrac{(\text{shear rate})_2}{(\text{shear rate})_1}}\right] \quad . \quad . \quad . \quad . \quad . \quad (C\text{-}3)$$

Having n', the constant k' is determined at any point on the straight line by means of Eq. C-4.

$$k' = \frac{\tau}{(\text{shear rate})^{n'}} \quad . \quad . \quad . \quad . \quad . \quad . \quad . \quad (C\text{-}4)$$

Now let us derive an equation giving crack widths in terms of the constants k' and n'. Fig. 14 is a schematic representation of a fluid flowing in laminar flow between parallel plates. For steady, nonaccelerated flow, the force per unit height acting to the right on the fluid element of thickness y and length L may be equated to the force per unit height acting towards the left as shown by Eq. C-5.

$$y\,\Delta P = L\,\tau \quad . \quad . \quad . \quad . \quad . \quad . \quad . \quad . \quad . \quad (C\text{-}5)$$

Eq. C-1 may be substituted into Eq. C-5, and the equation can then be integrated by observing that the velocity is zero at the wall. Eq. C-6 gives the resulting velocity profile.

$$u = \left(\frac{n'}{n'+1}\right)\left(\frac{\Delta P}{k'L}\right)^{\frac{1}{n'}}\left[\left(\frac{W}{2}\right)^{\frac{n'+1}{n'}} - y^{\frac{n'+1}{n'}}\right] .$$

$$. \quad . \quad . \quad . \quad . \quad . \quad . \quad . \quad . \quad . \quad . \quad . \quad . \quad . \quad (C\text{-}6)$$

The total flow rate into the two sides of the fracture is given by Eq. C-7.

$$Q = 4\int_0^{w/2} H\,u\,dy$$

$$= 4\left(\frac{n'}{2n'+1}\right)\left(\frac{\Delta P}{k'L}\right)^{\frac{1}{n'}} H\left(\frac{W}{2}\right)^{\frac{2n'+1}{n'}} . \quad (C\text{-}7)$$

Re-arrangement of Eq. C-7 yields Equation C-8 explicit in the pressure gradient.

$$\left(-\frac{dP}{dx}\right) = 2k'Q^{n'}\left(\frac{2n'+1}{n'}\right)^{n'}\frac{1}{H^{n'}}\frac{1}{W^{2n'+1}} \quad . \quad . \quad (C\text{-}8)$$

Lamb[13] has shown that the pressure gradient when flowing Newtonian fluids in an elliptical conduit of essentially zero eccentricity is $\left(\frac{16}{3\pi}\right)$ times as great as the pressure gradient when flowing the same fluid between parallel plates under the same condition of height, maximum width and flow rate. If it is assumed that this same relationship holds approximately for non-Newtonian fluids, then Equation C-9 applies to essentially elliptical fractures.

$$\left(-\frac{dP}{dx}\right)_{\text{ellipse}} \approx \frac{16}{3\pi}2k'\left(\frac{2n'+1}{n'}\right)^{n'}\frac{1}{H^{n'}}\frac{Q^{n'}}{W^{2n'+1}}$$

$$. \quad . \quad . \quad . \quad . \quad . \quad . \quad . \quad . \quad . \quad . \quad . \quad . \quad . \quad (C\text{-}9)$$

TABLE 2

Speed of Rotor (rpm)	Rate of Shear (seconds^{-1})
600	959
300	479
200	320
100	160
6	9.6
3	4.8

By substituting in the Sneddon equation for the width of a two-dimensional elliptical crack (Eq. A-10) and by assuming that the flow rate is independent of x, Eq. C-9 can be integrated. Substitution of the resulting $(P - \sigma)$ into Eq. A-10 yields Eq. C-10.

$$W = \left[\frac{2(1-\nu^2)H}{E}\right]\left\{\frac{(2n'+2)\,\phi E^{2n'+1}Q^{n'}L}{[2(1-\nu^2)\,H]^{n'+1}}\right\}^{\frac{1}{2n'+2}}$$

$$. \quad . \quad . \quad . \quad . \quad . \quad . \quad . \quad . \quad . \quad . \quad . \quad . \quad . \quad (C\text{-}10)$$

where $\phi = \dfrac{32}{3\pi}k'\left(\dfrac{2n'+1}{n'}\right)^{n'}\dfrac{1}{H^{n'}}$.

Equation C-10 can be written with a more convenient set of units as shown by Eq. C-11.

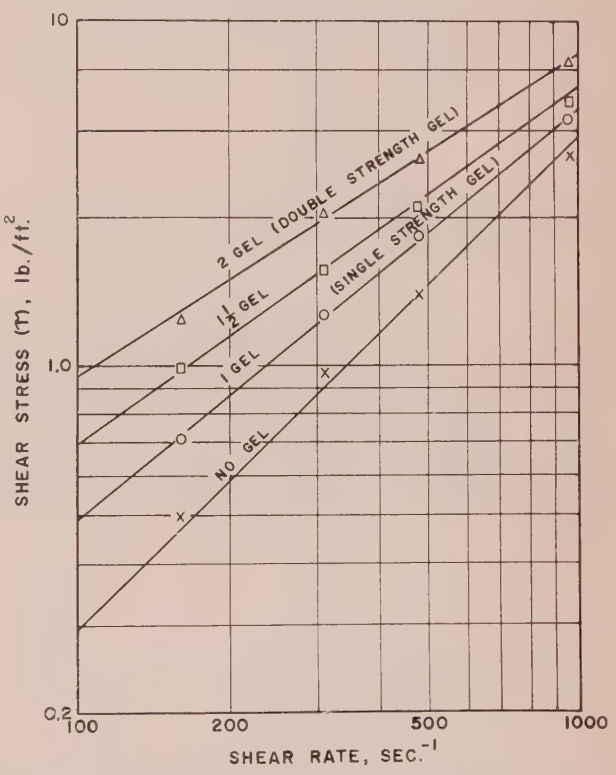

FIG. 13—FANN METER DATA FOR GELLED FRACTURING OIL.

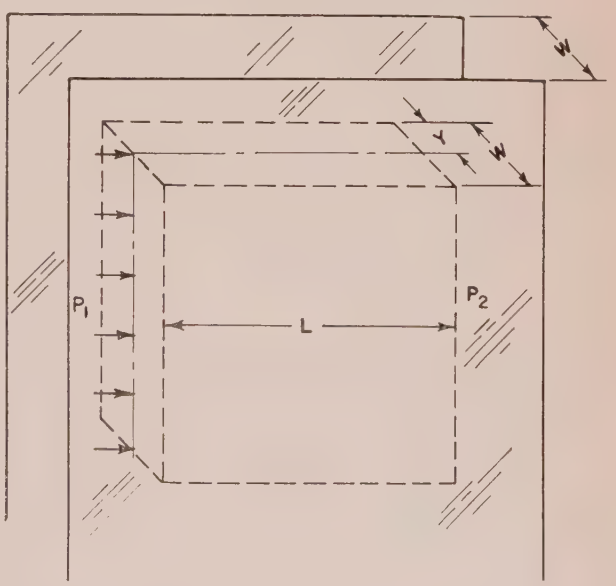

FIG. 14—LAMINAR FLOW OF FLUID BETWEEN PARALLEL PLATES.

$$W = 12\left[\left(\frac{2^{7}}{3\pi}\right)(n'+1)\left(\frac{2n'+1}{n'}\right)^{n'}\left(\frac{0.9775}{144}\right)\left(\frac{5.61}{60}\right)^{n'}\right]^{\frac{1}{2n'+2}}\left[\frac{Q^{n'}k'L\,H^{1}}{\mathrm{E}}\right]^{\frac{n'}{2n'+2}} \quad \text{(C-11)}$$

where W = maximum crack width at the wellbore, in.,
k' = a measure of the flow properties of a non-Newtonian fluid, (lb)(sec)$^{n'}$/sq ft,
n' = a measure of the flow properties of a non-Newtonian fluid,
Q = total injection rate, bbl/min,
L = length of a vertical fracture measured from the wellbore,
H = height of a vertical fracture, ft, and
E = Young's modulus of the formation rock, psi.

Eq. C-11 is plotted as Fig. 8.

APPENDIX D

DERIVATION OF AN EQUATION GIVING APPROXIMATE CRACK WIDTHS FOR HORIZONTAL FRACTURES

Let us derive an approximate relationship which will give the order of magnitude for horizontal crack widths if the fluid is in laminar flow. Assume that there is some average crack width in the fracture and that this average width can be used to get the approximate pressure distribution. Then for a radial system and fluid in laminar flow, the pressure distribution is given by Eq. D-1.

$$P = P_w - \frac{Q\mu \ln\frac{r}{r_w}}{2\pi\beta W_a^{3}} \quad \text{(D-1)}$$

where P = pressure at radius r,
P_w = pressure at the wellbore,
r_w = radius of the wellbore,
Q = total injection rate,
μ = viscosity of the fluid,
β = $10^{8}/12$ darcies /sq cm (a constant), and
W_a = average crack width.

The average pressure exerted over the fracture face is given by Eq. D-2.

$$P_{avg} = \frac{\pi r_w^{2} P_w + \int_{r_w}^{C} 2\pi r P\, dr}{\pi C^{2}} \quad \text{(D-2)}$$

Substituting Eq. D-1 into Eq. D-2 and integrating yields Eq. D-3.

$$P_{avg} = P_w - \frac{Q\mu}{\pi\beta W_a^{3}}\left[\frac{1}{2}\ln\frac{C}{r_w} + \frac{1}{4}\left(\frac{r_w}{C}\right)^{2} - \frac{1}{4}\right] \quad \text{(D-3)}$$

Sneddon[22] shows that, for a three-dimensional radially symmetrical crack, the width is given approximately by Eq. D-4.

$$W_{max} = \frac{8(1-\nu^{2})\,C\,(P_{avg}-\sigma)}{\pi \mathrm{E}} \quad \text{(D-4)}$$

Based on volume, the average width is related to maximum width by Eq. D-5.

$$\frac{\pi}{6}(2C)^{2} W_{max} = \pi C^{2} W_{avg},$$

$$W_{avg} = \frac{2}{3} W_{max}. \quad \text{(D-5)}$$

By noting that the pressure at the leading edge of the crack is equal to the earth stress, substitution of Eqs. D-1, D-3 and D-5 into Eq. D-4 yields Eq. D-6.

$$W_{max} = \left\{\frac{27(1-\nu^{2})\,C\,Q\mu\left[1-\left(\frac{r_w}{C}\right)^{2}\right]}{4\pi^{2}\mathrm{E}\beta}\right\}^{1/4} \quad \text{(D-6)}$$

The term $\left[1-\left(\frac{r_w}{C}\right)^{2}\right]$ may be assumed equal to unity for any practical size of fracture. Assuming $\nu = 0.15$, Eq. D-7 gives the approximate crack width at the wellbore with a more convenient set of units.

$$W(\text{in.}) = 0.22\left[\frac{Q(\text{bbl/min})\,\mu(\text{cp})\,C(\text{ft})}{\mathrm{E}(\text{psi})}\right]^{1/4} \quad \text{(D-7)}$$

This derivation assumes that the crack width results from compression of rock in the vicinity of the fracture. If the radius of the fracture is large compared to the depth, then it will be possible to lift the overburden as well as compress the rock near the fracture. Let us now consider crack widths if the overburden is lifted.

Again it is assumed that there is an average pressure acting in the fracture given by Eq. D-3. The deflection of an elastic plate which is clamped at the edges has been given by Timoshenko,[25] Way,[28] and Weil and Newmark.[29] If the center deflection of the plate is less than 40 per cent of the plate thickness, then the deflection is given by Eq. D-8.

$$\delta_1 = \frac{3(P_{avg}-\sigma)(1-\nu^{2})\,C^{4}\left[1-\left(\frac{r}{C}\right)^{2}\right]^{2}}{16\,\mathrm{E}\,Z^{3}} \quad \text{(D-8)}$$

where δ_1 = upward deflection of the plate at radius r, and
Z = thickness of the plate (or depth of the fracture).

The rock below the fracture is compressed slightly; the downward deflection is given approximately by Sneddon's equation, Eq. D-9.

$$\delta_2 = \frac{4(P_{avg}-\sigma)(1-\nu^{2})\,C}{\pi \mathrm{E}}\left[1-\left(\frac{r}{C}\right)^{2}\right]^{1/2} \quad \text{(D-9)}$$

The resulting maximum crack width at the wellbore is given by Eq. D-10.

$$W_{max} = \frac{(P_{avg}-\sigma)(1-\nu^{2})\,C}{\mathrm{E}}\left[\frac{4}{\pi} + \frac{3}{16}\left(\frac{C}{Z}\right)^{3}\right] \quad \text{(D-10)}$$

Based on volume, the average width can be related to maximum width as shown by Eq. D-11.

$$\frac{W_{avg}}{W_{max}} = \frac{\int_0^{C} 2\pi r\, W\, dr}{\pi C^{2} W_{max}} = \int_0^{C} 2\pi r \frac{(P_{avg}-\sigma)(1-\nu^{2})\,C}{\mathrm{E}}\left\{\frac{4}{\pi}\left[1-\left(\frac{r}{C}\right)^{2}\right]^{\frac{1}{2}} + \frac{3}{16}\left(\frac{C}{Z}\right)^{3}\left[1-\left(\frac{r}{C}\right)^{2}\right]^{2}\right\} dr \Big/ \pi C^{2}\frac{(P_{avg}-\sigma)(1-\nu^{2})\,C}{\mathrm{E}}$$

$$\left\{\frac{\pi}{4} + \frac{3}{16}\left(\frac{C}{Z}\right)^{3}\right\} = \frac{2\left[\frac{4}{3\pi} + \frac{1}{32}\left(\frac{C}{Z}\right)^{3}\right]}{\left[\frac{4}{\pi} + \frac{3}{16}\left(\frac{C}{Z}\right)^{3}\right]} \quad \text{(D-11)}$$

By noting that the pressure at the leading edge of the

crack is essentially equal to the earth stress, substitution of Eqs. D-1, D-3 and D-11 into Eq. D-10 yields Eq. D-12.

$$W_{max} = \left\{ \frac{(1-\nu^2)\, C\, Q\mu \left[1-\left(\frac{r_w}{C}\right)^2\right]\left[\frac{4}{\pi}+\frac{3}{16}\left(\frac{C}{Z}\right)^3\right]^4}{32\pi\, E\, \beta\left[\frac{4}{3\pi}+\frac{1}{32}\left(\frac{C}{Z}\right)^3\right]^3} \right\}^{1/4} \quad \text{. . . . . (D-12)}$$

This gives a crack width equal to that calculated for deep horizontal fractures (Eq. D-6) when $C/Z \approx 4/3$. Hence, Eq. D-12 is applicable if $C \geq 4/3\, Z$. Neglecting the term $\left[1-\left(\frac{r_w}{C}\right)^2\right]$, assuming $\nu = 0.15$ and simplifying units results in Eq. D-13.

$$W_{max}(\text{in.}) = 0.0765 \left\{ \frac{Q(\text{bbl/min})\, \mu(\text{cp})\, C(\text{ft})\left[\frac{4}{\pi}+\frac{3}{16}\left(\frac{C}{Z}\right)^3\right]^4}{E(\text{psi})\left[\frac{4}{3\pi}+\frac{1}{32}\left(\frac{C}{Z}\right)^3\right]^3} \right\}^{1/4} \quad \text{. . . . . (D-13)}$$

where $\frac{C}{Z} \geq \frac{4}{3}$. ★★★

Model Studies of Oil Displacement from Thin Sands by Vertical Water Influx from Adjacent Shales

J. E. BOBEK
P. T. BAIL
MEMBERS AIME

JERSEY PRODUCTION RESEARCH CO.
TULSA, OKLA.

ABSTRACT

In reservoirs containing soft shales interbedded with oil-producing sands, it is possible to have water movement from the shales into the sands during reservoir depletion.

This paper presents the results of scaled flow-model tests performed to investigate the efficiency of oil displacement by this vertical influx of water into oil-producing sands. In these model tests, the effects of rate of influx and rock wettability were considered.

Oil recoveries by shale-water influx and by water flooding were compared after 0.4 hydrocarbon volume of water entered the producing sand. This comparison was made for water-wet and oil-wet systems. In water-wet sand, shale-water influx produces slightly less oil than conventional water flooding; in oil-wet sand, shale-water influx produces about one-half as much oil as conventional water flooding. In another type of comparison, it was found that shale-water influx followed by water flooding recovers less oil than water flooding alone. This is true for both water-wet and oil-wet sands. A comparison of tests run at different rates of shale-water influx shows that oil recovery is insensitive to rate in water-wet sand; in oil-wet sand, oil recovery decreases with decreasing rate of influx.

INTRODUCTION

Localized subsidence of the earth's surface has accompanied the depletion of some oil reservoirs, particularly in California,[1,2] along the Texas Gulf Coast,[3,4] and in the Bolivar Coastal fields of Venezuela.[5] Subsidence occurs when fluid withdrawals reduce the pressure in the reservoir. The reasons for subsidence accompanying a reduction in reservoir pressure are not known with certainty.[1,6-9] However, there is considerable evidence that compaction of soft shale beds adjacent to producing oil sands can be a major cause of this subsidence.[3,6,10-12] When the shales compact, a limited amount of water moves from the shales into the producing sands. A schematic illustration of this oil-producing mechanism is shown in Fig. 1. As the pressure in the sand declines due to oil production, a predominantly vertical pressure gradient develops at the sand-shale boundary. This causes water to move from the shale into the sand as indicated by the solid arrows.

This paper reports the results of scaled flow-model tests to investigate the efficiency of oil displacement by the vertical influx of shale water into producing sands. The model tests were not performed with the aim of duplicating the recovery behavior of any specific reservoir. The primary purpose of the tests was to obtain a better understanding of oil displacement by shale-water influx. A knowledge of the oil- and water-production characteristics of even a simplified reservoir system should be of value to engineers estimating the performance of reservoirs where shale-water influx is occurring in conjunction with other production mechanisms. The following limitations and assumptions apply to the model work.

1. The sand of the prototype reservoir is homogeneous and horizontal.

2. The shale-water influx is uniformly distributed along the top and bottom of the sand member being studied.

3. No effects of edge-water drive or dissolved-gas drive that might accompany shale-water influx are considered.

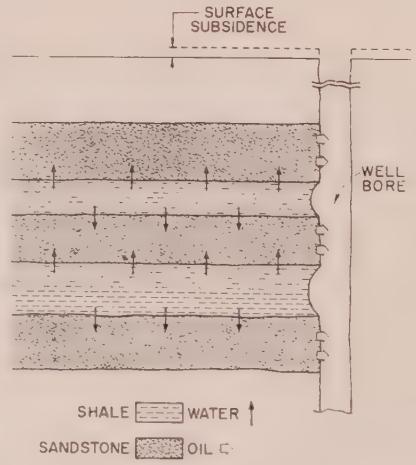

FIG. 1—SHALE CONSOLIDATION PRODUCING MECHANISM.

PROTOTYPE RESERVOIRS

Scaled-model tests were performed to study oil displacement from three prototype reservoir sections. The reservoir sections modeled consist of single sand layers out of a sequence of sand and shale layers, as illustrated in Fig. 1. Each prototype represents a homogeneous, high-permeability, unconsolidated sand layer. In the field, the prototype is oriented in such a manner that one end is at the radius of drainage of a producing well and the other end is pointed toward the producing well (Fig. 2).

The sand and fluid properties and the dimensions of the three prototypes are given in Table 1. The capillary pressure relationships for the three prototypes are presented in Figs. 3, 4 and 5. The oil-water per-

Original manuscript received in Society of Petroleum Engineers office Aug. 24, 1960. Revised manuscript received April 5, 1961. Paper presented at 31st Annual California Regional Meeting of SPE, Oct. 20-21, 1960, in Pasadena, Calif.

[1]References given at end of paper.

meability ratio curves for the prototypes are presented in Fig. 6. Prototype 1 is a strongly water-wet sand layer containing viscous crude oil. Prototype 2 is also strongly water-wet but has a narrower range of pore sizes (Figs. 3 and 4) and contains oil of lower viscosity than does Prototype 1. Prototype 3 is similar to Prototype 2 except that it is a strongly oil-wet sand layer.

SCALING CONDITIONS

The generalized scaling relationships proposed by Rapoport[13] were used in designing and operating the laboratory flow models to give results representative of field behavior. In using these relationships, the following scaling principles were applied. The geometry, boundary conditions, relative permeabilities and liquid viscosity ratio were the same for model and prototype. The ratio of gravitational gradient to capillary pressure gradient and the ratio of capillary pressure gradient to flowing pressure gradient were the same for model and prototype. The capillary pressure curves for model and prototype were similar in shape.

In the scaling where the slope of the capillary pressure curve is needed, imbibition capillary-pressure functions were used for the water-wet systems and drainage capillary-pressure functions were used for the oil-wet system. Drainage capillary-pressure functions were used in approximating the permeability of the prototypes for both water-wet and oil-wet systems.

MODEL DESCRIPTION

Two models were used—one for the water-wet studies and one for the oil-wet studies. The model for the water-wet studies consisted of a rectangular aluminum box packed with water-wet glass beads to simulate the sand member. A schematic longitudinal section of the model is presented in Fig. 7.

The bead pack was 210-cm long, 3.8-cm wide and 5.5-cm thick. The top and bottom of the model were each lined with 10 strongly water-wet alundum plates, having a permeability of 40 md. These plates were required to distribute the injected water uniformly over the entire length and width of the bead pack to simulate entry of shale water into the producing sand.

To insure the uniform injection of water along the length of the bead pack, a separate pump was used to supply water to each alundum plate. The outlet end of the model was tapered down to a very small cross-sectional area to minimize capillary end effects and the associated hold-up of water at the outlet face by increasing the pressure drop across the outlet.

The glass beads used were approximately 120 microns in diameter. They were treated with 10 per cent hydrochloric acid, repeatedly washed with distilled water and, finally, heated to 550°C to assure that they were strongly water-wet.

The model used in the oil-wet tests was similar in construction and geometry to the model used in water-wet tests. The oil-wet model was 152-cm long, 5-cm wide and 5-cm thick. The model was packed with 120-micron diameter beads that were preferentially oil-wet by "dri-filming".

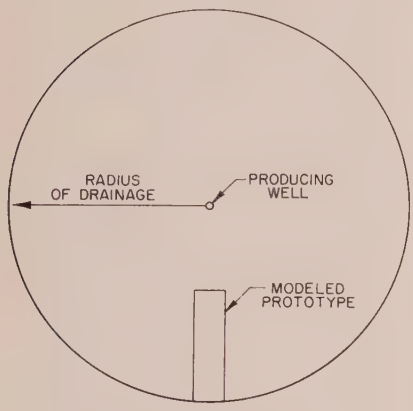

FIG. 2—PROTOTYPE ORIENTATION.

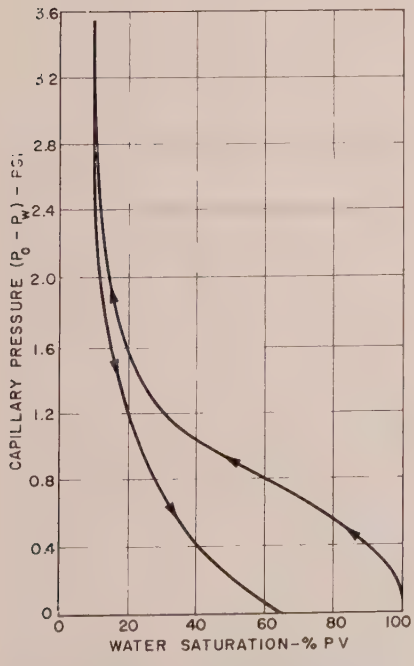

FIG. 3—DRAINAGE AND IMBIBITION CAPILLARY PRESSURE CURVES, WATER-WET PROTOTYPE 1.

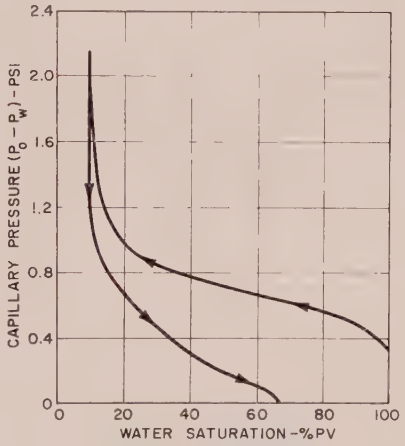

FIG. 4—DRAINAGE AND IMBIBITION CAPILLARY PRESSURE CURVES, WATER-WET PROTOTYPE 2.

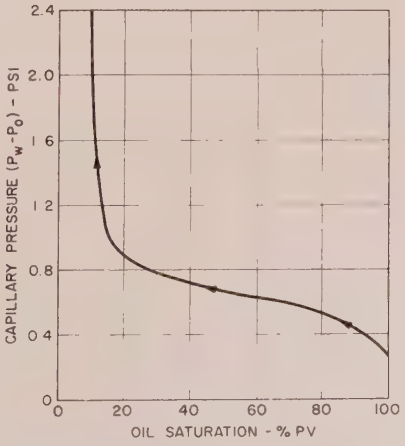

FIG. 5—DRAINAGE CAPILLARY PRESSURE CURVE, OIL-WET PROTOTYPE 3.

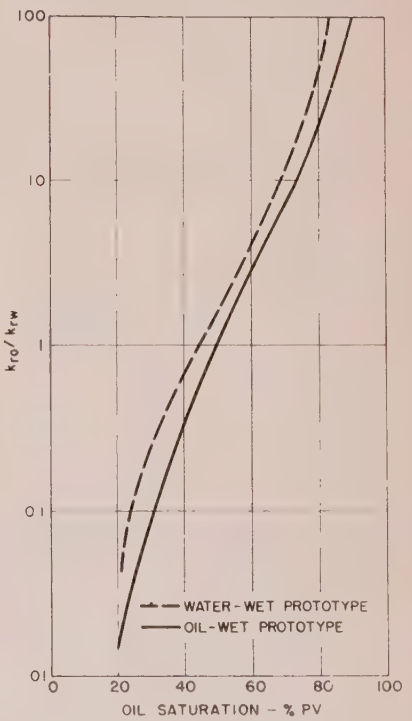

FIG. 6—k_{ro}/k_{rw} CURVES FOR PROTOTYPE RESERVOIRS.

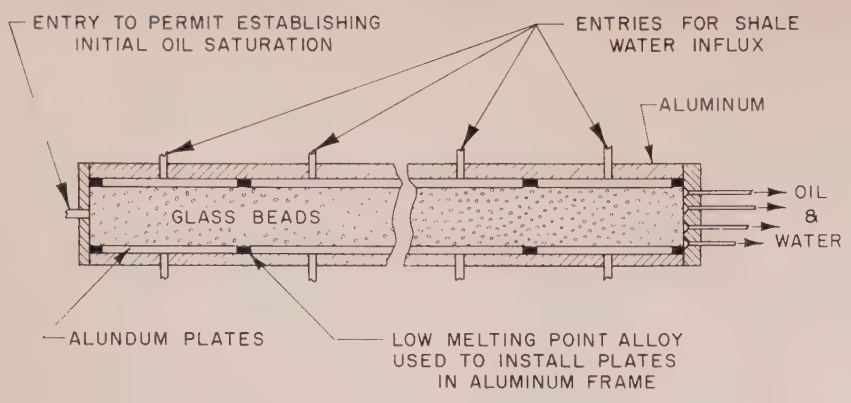
ENTRY TO PERMIT ESTABLISHING INITIAL OIL SATURATION
ENTRIES FOR SHALE WATER INFLUX
ALUMINUM
GLASS BEADS
OIL & WATER
ALUNDUM PLATES
LOW MELTING POINT ALLOY USED TO INSTALL PLATES IN ALUMINUM FRAME

FIG. 7—SCHEMATIC LONGITUDINAL SECTION OF WATER-WET MODEL.

The rates of water injection into the alundum plates required to simulate field rates of shale-water influx were of the order of .5 ml/day for each plate. A 20-piston positive-displacement pump was constructed to supply water at this low constant rate without pressure-pulsing. The 20 pistons were advanced by micrometer heads which were simultaneously driven through a gearing arrangement by a variable-speed DC motor. All equipment was contained in a thermostatically controlled room at a temperature of 25°C.

The fluids used in the water-wet studies consisted of mixtures of refined white oils and water solutions of potassium bromide. Bromide solutions were used to provide the required density differences between water and oil for gravity scaling. For the scaled experiment simulating Prototype 2, both the oil and water phases contained isopropyl alcohol to provide the required low interfacial tension (Table 1). For the experiments simulating Prototype 1, no alcohol was required to attain the desired interfacial tension. The fluids used for the oil-wet studies (Prototype 3) were distilled water and "Halocarbon 4-11-V", a low polymer of chlorotrifluoroethylene with a density of 1.86. Both fluids contained isopropyl alcohol to provide the required interfacial tension. Halocarbon was selected because of its high density and chemical stability.

PROCEDURES

SHALE-WATER INFLUX TESTS

Six model tests were performed to study oil recovery by shale-water influx. Two of the tests simulated water-wet Prototype 1, one test simulated water-wet Prototype 2 and three tests simulated oil-wet Prototype 3. A connate-water saturation of 8 per cent ± 1 per cent pore volume was established before each test in the water-wet model by oil-flushing an initially water-saturated model. The tests in the oil-wet model were performed with no connate water present. During the constant-rate shale-water influx tests, water was injected uniformly over the top and bottom of the bead layer through the 20 alundum plates. Both injected water and displaced oil then moved toward the outflow, or downstream, end of the model. No fluid was injected into the upstream end of the model, which represents the end of the prototype at the radius of drainage of a producing well (Fig. 2).

TABLE 1—MODEL AND PROTOTYPE CHARACTERISTICS

	Model 1	Prototype 1	Model 2	Prototype 2	Model 3	Prototype 3
Sand Properties						
Permeability, md	7,500	2,000	7,500	1,700	13,500	1,700
Porosity, per cent	37	34	37	35	39	35
Capillary-Pressure Function, psi	p_c	$P_c = 4.06\ p_c - 0.5$	p_c	$P_c = 9.4\ p_c - 0.15$	p_c	$P_c = 5.0\ p_c - 0.61$
Wettability*	WW	WW	WW	WW	OW	OW
Contact Angle (in wetting phase)	25-35	45-65	25-35	45-65	25-35	45-65
Fluid Properties (at Reservoir Conditions)						
Water Viscosity, cp	0.85	0.47	1.25	0.45	1.05	0.45
Oil Viscosity, cp	55.0	30.4	11.80	4.25	10.00	4.28
Oil-Water Viscosity Ratio	64.7	64.7	9.44	9.44	9.52	9.52
Water Density, gm/cc	1.19	0.99	1.27	0.99	0.99	0.99
Oil Density, gm/cc	0.87	0.93	0.84	0.81	1.86	0.81
Density Difference, gm/cc	0.32	0.06	0.43	0.18	0.87	0.18
Interfacial Tension, dynes/cm	50.7	30	10.6	30	20.0	30
Dimensions						
Length, meters	2.10	45	2.10	47	1.52	37
Thickness, meters	0.055	1.2	0.055	1.2	0.050	1.2

*WW = Water-Wet, OW = Oil-Wet.

In scaling the effect of gravity in the oil-wet prototype, it was more convenient to make the oil phase heavier than the water phase in the model by using Halocarbon as the oil phase. Thus, the direction of gravity-segregation effects in the model was opposite to that existing in the field. This means that the bottom of the model simulates the top of the sand layer in the field, and vice versa. However, the overall effect of gravity on oil and water production from the model is the same as if the water had been a dense phase instead of the oil.

WATER FLOODING FOLLOWING INFLUX

Tests were performed to investigate the efficiency of normal water flooding following limited shale-water influx into both oil-wet and water-wet models. For the oil-wet model, this was accomplished by stopping shale-water influx into the sides of the model after the injection of 0.4 hydrocarbon volume and commencing water injection at the upstream end of the model. This approach could not be used in the water-wet model because water, bypassing through the alundum plates that line both sides of the model, caused excessive water production. To avoid this difficulty, a linear flooding cell was used to investigate normal water flooding following limited shale-water influx for the water-wet system. The linear flooding cell contained the same size glass beads and was saturated with the same fluids used in the shale-water influx tests. The average initial oil saturation at the beginning of the linear test was the same as that existing at the end of the shale-water influx test. The initial oil saturation in the linear cell was established by simultaneous flow of oil and water through the cell until the desired equilibrium oil saturation was obtained. The linear cell was then water flooded. The results of this test should give a good indication of the behavior of a water flood following shale-water influx, even though the initial saturation distribution in the cell was not exactly the same as that existing at the end of shale-water influx.

REFERENCE WATER FLOODS

Linear floods of cells packed with the same glass beads used in the shale-water influx models were performed for comparison with the results obtained from the shale-water influx tests. Prior to the reference waterflood of the water-wet beads, an 8 per cent pore volume connate

water was established by flushing the water-saturated cell with oil. No connate water was present during the reference water flood of the oil-wet beads.

DISCUSSION OF RESULTS

EFFECT OF RATE

The results of the two scaled experiments performed to simulate water-wet Prototype 1 containing a high-viscosity oil are presented in Fig. 8. It will be noted that no significant difference in oil recovery was observed for rates of shale-water influx of 0.01 to 0.04 hydrocarbon volume/year. The small difference in oil recovery indicated between the two tests is within the range of experimental error.

The effect of rate on the oil recovery from oil-wet Prototype 3 for scaled field rates of 0.026, 0.06 and 0.16 hydrocarbon volume/year is illustrated in Fig. 9. The figure shows that the oil-displacement efficiency by shale-water influx decreases with decreasing rates of influx. However, the variation of displacement efficiency with rate is small. The rate of 0.16 hydrocarbon volume/year is above the rate of influx to be expected in most reservoirs. The reduction of oil recovery with a decrease in rate is believed to be caused by the adverse effects of capillary and gravity forces, both of which have a greater influence on oil displacement as the rate of influx decreases.

The recovery data for both the water-wet and oil-wet tests are expressed as per cent of hydrocarbon volume. In the water-wet tests, a hydrocarbon volume is equal to 92 per cent of a pore volume. In the oil-wet tests, a hydrocarbon volume is equal to 100 per cent of a pore volume because no connate water was present during the oil-wet tests.

COMPARISON WITH LINEAR WATER FLOODS

A comparison of oil recovery by shale-water influx to that by water flooding is given in Fig. 8 for water-wet Prototype 1. The recovery by shale-water influx is about 85 per cent as efficient as linear water flooding after 0.4 hydrocarbon volume of water influx. The comparison was made only up to 0.4 hydrocarbon volume of water injected because shale-water influx in the reservoir will normally be limited and probably will not exceed 0.4 hydrocarbon volume.

Oil recovery by shale-water influx in oil-wet Prototype 3 was found to be considerably less efficient than that by normal water flooding. Fig. 9 shows that the oil recovery by linear water flooding is over twice as great as that by the shale-water influx after a cumulative influx of 0.4 hydrocarbon volume.

WATER FLOODING FOLLOWING SHALE-WATER INFLUX

To obtain an estimate of the amount of oil that could be recovered by water flooding after shale-water influx, a composite curve of oil recovery by shale-water influx followed by linear water flooding for the water-wet Prototype 1 is given in Fig. 10. The figure shows that injection of 1.0 hydrocarbon volume of water following shale-water influx gives an additional 14 per cent hydrocarbon volume oil recovery. However, the oil recovery by shale-water influx followed by water flooding is still only 92 per cent of the recovery by linear water flooding alone at 1.4 hydrocarbon volumes of water injected.

Similar data for oil-wet Prototype 3 are given in Fig. 11. After influx of 0.4 hydrocarbon-volume shale water at a rate of 0.026 hydrocarbon volume/year, linear flooding with 1.0 hydrocarbon volume of water gave an additional oil recovery of 28 per cent hydrocarbon volume. The combined oil recovery from 0.4 hydrocarbon volume shale-water influx and 1.0 hydrocarbon volume of linear water flooding gave only 72 per cent as much oil recovery as would be obtained by linear water flooding alone at 1.4 hydrocarbon volumes of water injected.

EFFECT OF WETTABILITY

An exact comparison of the effect of wettability on oil recovery by shale-water influx cannot be made with the data collected in these studies. However, a run simulating water-wet Prototype 2 was made at a rate of water influx of 0.16 hydrocarbon volume/year, which is the same rate as one of the tests run for oil-wet Prototype 3. From Table 1 it can be seen that Prototypes 2 and 3 are similar. Thus, an indication of the effect of wettability can be obtained by comparing the results of these two tests. This is done in Fig. 12, which shows that the oil recovery from the oil-wet prototype is less than from the water-wet prototype, giving only 66 per cent as much recovery at 0.4 hydrocarbon volume shale-water influx.

CONCLUSIONS

1. For a water-wet porous medium containing high-viscosity oil, recovery was found to be independent of rate of shale-water influx over the range of rates studied. For an oil-wet porous medium containing medium-viscosity crude oil, recovery decreased with decreasing rate of shale-water influx.

2. A comparison of oil recoveries by shale-water and by normal water flooding when 0.4 hydrocarbon volume of water had entered the model showed that (a) shale-water influx into a water-wet porous medium produced slightly less high-viscosity oil than water flooding, and (b) shale-water influx into an oil-wet porous medium produced about one-half as much medium-viscosity oil as water flooding.

3. Injection of 1.4 hydrocarbon volumes of water during a normal water flood gave a higher oil recovery than did an influx of 0.4 hydrocarbon volume of shale water followed by injection of 1.0 hydrocarbon volume of water during normal water flooding. This is true for both water-wet and oil-wet systems.

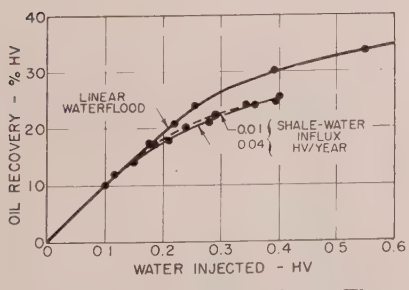

FIG. 8—EFFECT OF RATE OF SHALE-WATER INFLUX ON OIL RECOVERY, WATER-WET PROTOTYPE 1, (μ_o/μ_w = 64.7).

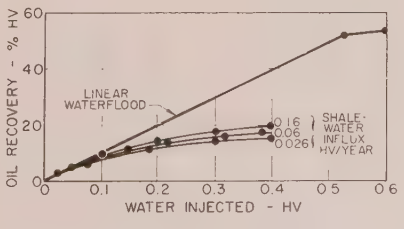

FIG. 9—EFFECT OF RATE OF SHALE-WATER INFLUX ON OIL RECOVERY, OIL-WET PROTOTYPE 3, (μ_o/μ_w = 9.5).

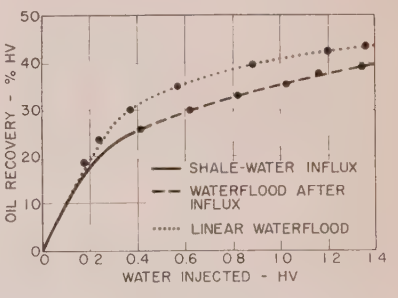

FIG. 10—OIL RECOVERY BY LINEAR WATER FLOODING AFTER SHALE-WATER INFLUX. WATER-WET PROTOTYPE 1, (μ_o/μ_w = 64.7).

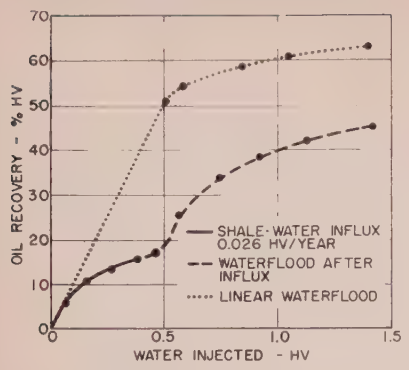

FIG. 11—OIL RECOVERY BY LINEAR WATER FLOODING AFTER SHALE-WATER INFLUX, OIL-WET PROTOTYPE 3, (μ_o/μ_w = 9.5).

4. In tests where shale-water influx displaced a medium-viscosity oil, the efficiency of oil displacement was greater from the water-wet model than from the oil-wet model.

ACKNOWLEDGMENT

The authors wish to thank the management of Jersey Production Research Co. for permission to publish this paper.

REFERENCES

1. Gilluly, J. and Grant, U. S.: "Subsidence in the Long Beach Harbor Area, California", *Bull.*, GSA (March, 1949) **60**, 461.
2. Berbower, R. F.: "Subsidence Problem in the Long Beach Harbor District", *Jour. of Waterways and Harbors Div.* (June, 1959) **85**, 43.
3. Pratt, W. E. and Johnson, D. W.: "Local Subsidence of the Goose Creek Oil Field", *Jour. of Geol.* (Oct., 1926) **34**, 577.
4. "A Mystery of the Oil Fields", *Oil Weekly* (Sept. 23, 1946) **123**, 28.
5. Kugler, H. G.: "Contribution to the Knowledge of Sedimentary Volcanism in Trinidad", *Inst. Pet. Tech., Jour.* (1933) **19**, 743.
6. Carpenter, C. B. and Spencer, G. B.: "Measurements of Compressibility of Consolidated Oil-Bearing Sandstones", RI 3540, USBM (Oct., 1940).
7. Poland, J. F. and Davis, G. H.: "Subsidence of the Land Surface in the Tulare-Wasco (Delano) and Los Banos-Kettleman City Area, San Joaquin Valley, California", *Trans.*, AGU (June, 1956) **37**, 287.
8. Botset, H. G. and Reed, D. W.: "Experiment on Compressibility of Sand", *Bull.*, AAPG (July, 1935) **19**, 1053.
9. Taylor, J. M.: "Pore Space Reduction in Sandstone", *Bull.*, AAPG (April, 1950) **34**, 701.
10. Hedberg, H. D.: "Gravitational Compaction of Clays and Shales", *Am. Jour. of Science* (April, 1936) **31**, 241.
11. Athy, L. F.: "Compaction and Oil Migration", *Bull.*, AAPG (Jan., 1930) **14**, 25.
12. Terzaghi, K.: *Theoretical Soil Mechanics*, John Wiley and Sons, Inc., N. Y. (1943) 265.
13. Rapoport, L. A.: "Scaling Laws for Use in Design and Operation of Water-Oil Flow Models", *Trans.*, AIME (1955) **204**, 143. ★★★

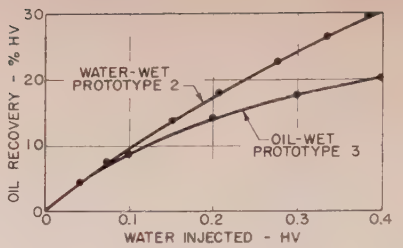

FIG. 12—EFFECT OF WETTABILITY ON OIL RECOVERY BY SHALE-WATER INFLUX. (FIELD RATE = 0.16 HYDROCARBON VOLUME/YEAR).

Further Discussion of Paper Published in
***Journal of Petroleum Technology*, March, 1961**

Fractures and Craters Produced in Sandstone by High-Velocity Projectiles

JOHN S. RINEHART
WILLIAM C. MAURER

COLORADO SCHOOL OF MINES
GOLDEN, COLO.

DISCUSSION

A. A. VENGHIATTIS
MEMBER AIME

LANE-WELLS CO.
HOUSTON, TEXAS

This paper is discussed not because of its intrinsic value but because it has been related by its authors to the oilwell gun perforators. It is well known that conditions almost ever present in oilwell perforations are the overburden and the presence of the casing.

Because of the lack of information in the paper on the dimensions or confinement of the target rocks, one is led to guess that they were not confined at all and, particularly, that no steel front plates were used on the impact face of the rocks to materialize the presence of the cemented casing.

This situation, plus the fact that small steel balls have been used as projectiles instead of actual bullets, makes the whole thing unapplicable to oilwell perforation.

When shooting is performed against target rocks confined (as shown on Fig. 1) in such a way as to give a fair image of the overburden applied to the formation to be perforated, as well as of the cemented casing, the following are found.

1. There is no cratering worthy of mention, even with bullets having 10 times higher impact energy per unit projected area than the steel balls mentioned in the article. This has been confirmed with sandstone as well as with other rocks (granite, limestone and chalk). See Figs. 2 and 3.

2. Penetrations vary closely as the logarithm of the impact velocity. On this matter I have established the relation

$$X = \frac{2.3\ a\delta\left(\frac{1 - \cos\alpha}{\alpha}\right)^n}{R\Delta}\log\ (1 + bRV^2),$$

which applies with a ± 10 per cent approximation to penetration in metals or rocks, with X being the total penetration, δ the density of the bullet, R its radius, V its impact velocity and 2α its ogive angle; n is an adaptation exponent and Δ the Brinell hardness in the use of metals with $\Delta = (P \times 10^{-7})^{0.88}$ cm/gm/sec in the case of rocks, P being their compressive strength. In the case of targets as shown on Fig. 1, the constants a and b have the following values.

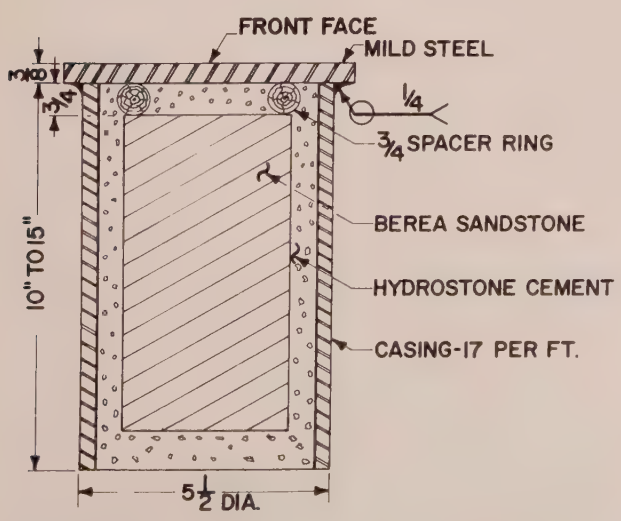

FIG. 1—TARGET ARRANGEMENT FOR PERFORATION TESTING.

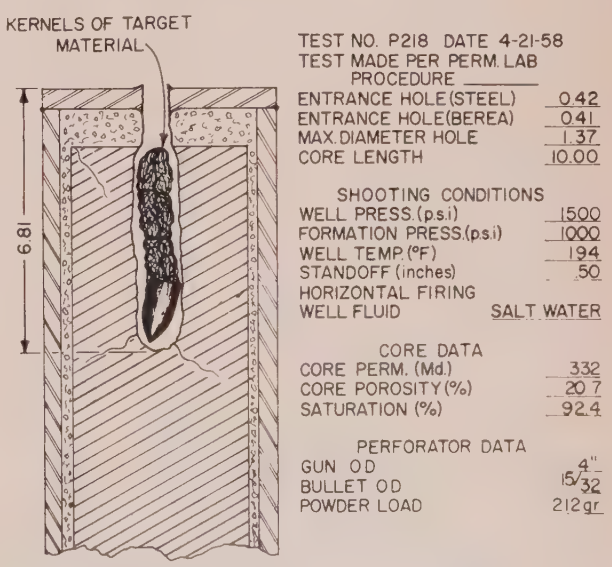

FIG. 2—BULLET PERFORATION OF SANDSTONE IN SALT-WATER ENVIRONMENT.

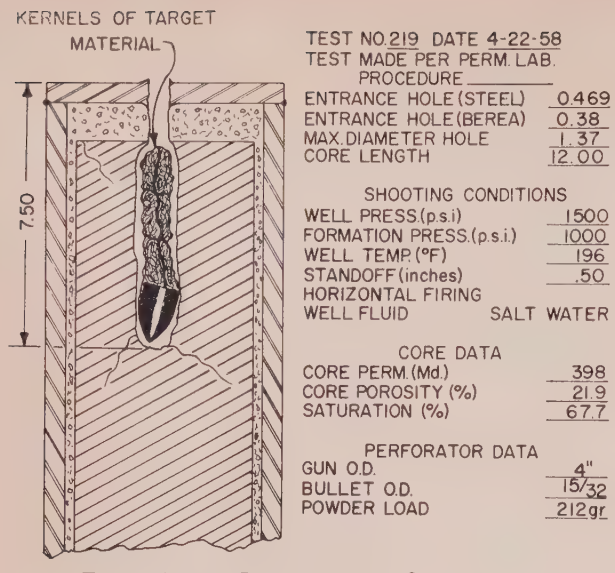

FIG. 3—BULLET PERFORATION OF SANDSTONE IN SALT-WATER ENVIRONMENT.

$$a = 2 \times 10^5 \text{ cm/gm/sec}$$
and $b = 10^{-4}$ cm/gm/sec,

with $n = 0.4$. These values apply as well to all-metallic targets.

3. No formation of step fractures as shown in Fig. 3 of the paper has ever been observed except in one unique case out of hundreds, where it is believed that a steel plate supporting the back of the target was at such a distance of the front face that a reflected pressure wave had interfered with the oncoming one.

A word also should be said about the presence of a fluid in most oilwell perforations. This affects appreciably the profile and the condition of the perforation as in favorizing, for example, the formation of a compact carrot of aggregated target material filling the perforation behind the bullet (Figs. 2 and 3).

This effect has never been observed in the absence of well fluid.

AUTHORS' REPLY TO A. A. VENGHIATTIS

The authors wish to thank A. A. Venghiattis for his interesting and informative discussion of the paper. The rock specimens used in the impact tests were unconfined, no attempt having been made to simulate oilwell perforations. The fractures which were observed below the cup of the crater have not been described in the literature, and the authors thought that they would be of interest to the oil industry. If these fractures can be produced in oilwell perforation work, the area of the passage-ways through which the oil can flow could be greatly increased. It may be possible to produce a free face to which the crater can form by such unique methods as using shaped charges and bullet perforators in conjunction with each other.

The sandstone used has tensile, compressive and shear strengths of 50, 2,780 and 300 psi, respectively — considerably lower than the Berea sandstone. In tests using sandstones of higher strengths, the number of fractures below the cup of the crater decreased. It is possible that, if the sandstone described in one paper had been used in Venghiattis' experiments instead of the Berea sandstone, the fractures would have been formed in the oilwell perforation tests. ★★★

The Calculation of Pressure Gradients In High-Rate Flowing Wells

P. B. BAXENDELL
MEMBER AIME
R. THOMAS*

CIA. SHELL DE VENEZUELA
MARACAIBO, VENEZUELA

ABSTRACT

Work on the calculation of vertical two-phase flow gradients by Cia. Shell de Venezuela has been based mainly on the "energy-loss" method proposed by Poettmann and Carpenter in 1952.

The "energy-loss-factor" correlation proposed by Poettmann and Carpenter was based on relatively low-rate flow data. This correlation proved inapplicable to high-rate flow conditions. In an attempt to establish a satisfactory correlation for high rates, a series of experiments was carried out at rates up to 5,000 B/D in Cia. Shell de Venezuela's La Paz field in Venezuela, using tubing strings fitted with electronic surface-recording pressure elements.

As a result of these experiments a correlation between energy-loss factor and mass flow rate was established which is believed to be applicable to a wide range of conduit sizes and crude types at high flow rates (e.g., above 900 B/D for 2⅞-in. OD tubing). It is anticipated that the resulting gradient calculations will have an accuracy of the order of ± 5 per cent.

At lower flow rates the energy-loss factor cannot be considered as constant for any mass rate of flow, but varies with the free gas in place and the mixture velocity. No satisfactory correlating parameter was obtained. As a practical compromise for low flow rates, a modification of the curve proposed by Poettmann and Carpenter was used. In practice this was found to give gradient accuracies of approximately ± 10 per cent down to flow rates as low as 300 B/D in 2⅞-in. tubing.

INTRODUCTION

Production operations in Cia. Shell de Venezuela's light- and medium-crude fields are principally concerned with high-rate flowing or gas-lift wells. Under these conditions the analysis of well performance, the selection of production strings and the design of gas-lift installations are vitally dependent on an accurate knowledge of the pressure gradients involved in vertical two-phase flow.

Initially, attempts were made to establish the gradients empirically as done by Gilbert,[1] but the results were not reliable due to scarcity of data over a full range of rates and gas-oil ratios. Several methods of calculation based on energy-balance considerations were attempted, but the computations were cumbersome and the results discouraging. In 1952 a paper was published by Poettmann and Carpenter[2] which proposed a new approach. Their method was also based on an energy-balance equation, but it was original in that no attempt was made to evaluate the various components making up the total energy losses. Instead, they proposed a form of analysis which assumed that all the significant energy losses for mutiphase flow could be correlated in a form similar to that of the Fanning equation for frictional losses in single-phase flow. They then derived an empirical relationship linking measurable field data with a factor which, when applied to the standard form of the Fanning equation, would enable the energy losses to be determined.

The basic method was applied in Venezuela to the problem of annular flow gradients in the La Paz and Mara fields[3]. This involved establishing a new energy-loss-factor correlation to cover high flow rates and, also, some adaptation of the method to permit mechanized calculation using punch-card machines. The final result was a set of gradient curves for La Paz and Mara conditions which proved to be surprisingly accurate.

With the encouraging results of the annular flow calculations, several attempts were made to obtain a corresponding set of curves for tubing flow. Here, unfortunately, little progress could be made. The original correlation of Poettmann and Carpenter was based on rather limited data derived from low-rate observations in 2⅜- and 2⅞-in. OD tubing. It did not cover the higher range of production rates, and extrapolation proved unsuccessful.

A new correlation covering high flow rates was required, but this proved to be extremely difficult to establish since tubing flow pressure measurements at high rates did not exist—due to the difficulty of running pressure bombs against high-velocity flow.

The necessity for reliable tubing flow data increased with the development of the new concessions in Lake Maracaibo, where high-rate tubing flow from depths of 10,500 ft became routine.

Thus, it was decided to set up a full-scale test to establish a reliable energy-loss factor for tubing flow conditions. A La Paz field light-oil producer with a potential of approximately 12,000 B/D on annular flow was chosen. To obtain full pressure gradients, a special tubing string was installed which was equipped with electronic surface-recording pressure measuring devices,

*Recently transferred by Shell to Indonesia.

[1]References given at end of paper.

Original manuscript received in Society of Petroleum Engineers office Jan. 16, 1961. Revised manuscript received Aug. 7, 1961. Paper presented by H. Duns, Cia. Shell de Venezuela, at Joint AIChE-SPE Symposium held Sept. 25-28, 1960, in Tulsa.

Discussion of this and all following technical papers is invited. Discussion in writing (three copies) may be sent to the office of the *Journal of Petroleum Technology*. Any discussion offered after Dec. 31, 1961, should be in the form of a new paper. No discussion should exceed 10 per cent of the manuscript being discussed.

This page of *Petroleum Transactions, AIME* follows page 956. The intervening non-Transactions pages appeared in *Journal of Petroleum Technology*.

located at intervals in the string. The production rate was varied by means of adjustable bottom-hole chokes, and by this means a set of gradients covering a wide range of flow rates was obtained for both 2⅞- and 3½-in. OD tubing.

This paper describes the analysis of the experimental results, the establishment of the energy-loss correlation and the accuracy of the resulting depth-pressure gradients.

THE GRADIENT EQUATION

From energy-balance considerations, Poettmann and Carpenter[2] derived the following relationship for the pressure gradient in vertical two-phase tubing flow.

$$144\frac{\Delta p}{\Delta h} = \overline{\rho} + \frac{fQ^2M^2}{7.413 \times \overline{\rho} \times D^5 \times 10^{10}} \quad . \quad . \quad (1)$$

where Δp = pressure difference (in psi) between any two points in the vertical conduit,

Δh = difference in height (in ft) between the two points,

$\overline{\rho}$ = integrated average density (in lb/cu ft) of the two-phase mixture between the two points,

Q = oil flow rate (in STB of oil/D),

M = total mass (in lb of the gas and oil associated with 1 bbl of tank oil),

D = inside diameter (in ft) of the pipe, and

f = dimensionless factor used as the correlating function for total energy loss due to irreversibilities of the fluid in flow.

Eq. 1 is the basic form employed in this paper.

To establish a correlation linking the energy-loss factor f with field data, Poettmann and Carpenter retained the analogy with single-phase flow and the Fanning equation by correlating f against the product of diameter, density and velocity, $D\rho v$, which corresponds to the numerator of the Reynolds number. The viscosity term, which forms the denominator of the Reynolds number, could not be evaluated for two-phase flow conditions and is ignored. This appeared to be a logical development, for as Poettmann and Carpenter point out: "The fact that viscosity is not one of the variables involved in the vertical multiphase flow is both fortunate and to be expected. This is because of the fact that the degree of turbulence is of such a magnitude that, of the total energy loss, W_f, that portion resulting from viscous shear is negligible". Various other workers in this field[4,5] have made the same observation.

In terms of field units, the $D\rho v$ term is equivalent to mass rate of flow divided by diameter or, in the terms already defined, QM/D.

THE LA PAZ EXPERIMENTS

FIELD INSTALLATION AND DATA

A packer was set in the casing at 6,250 ft just above the productive interval. The tubing string was latched into the packer and carried surface-recording Maihak pressure-transmitting elements spaced at approximately 1,000-ft intervals in the lower part of the string and 500-ft intervals in the upper part. The pressure elements were connected to the outside of the tubing on "limpet"-type gas-lift valve mandrels and, thus, offered no impedance to flow within the tubing. The well was produced on tubing flow against a constant tubinghead pressure, which was maintained by a back-pressure regulator. Different flow rates were obtained by means of retrievable bottom-hole chokes set in an Otis nipple immediately above the packer. This arrangement enabled the tubinghead pressure to be maintained at a constant value for all flow rates. Two separate installations were used, one employing 3½-in OD EU tubing, the other 2⅞-in.

The stability and repeatability of the pressure-recording elements under operating conditions were found to be excellent. Recalibration of the elements after their use in the 3½-in. tubing string indicated no change in the calibration constants—notwithstanding that, in the period after completion of the 3½-in. test and before recalibration, the instruments had been subjected to the buffeting turbulence of casing flow for some six months.

Since the recalibration was carried out in a different instrument shop, on a different tester, by different personnel and gave identical results to the first calibration, it is safe to assume that the stability of the instruments during the period of the actual test can be relied upon and that an accuracy of ± 1 per cent in the subsurface pressure readings can be expected.

The tubinghead pressure was read from a new manometer gauge, calibrated especially for the experiment and capable of ± 1-psi accuracy over the pressure range considered.

Special precautions were taken to ensure that the oil and gas gauging procedure was as accurate as possible. The GOR figures quoted are based on gas production from a single-stage 60-psig separator.

The well was always in gauge at the time that the pressure measurements were being taken.

The survey results from the test in 3½-in. and 2⅞-in. tubing are detailed in Tables 1 and 2, respectively, and examples of the gradient curves drawn from the results are shown in Fig. 1.

The maximum deviation of the observed points from the smooth curve was generally less than 2 per cent,

TABLE 1—DATA FROM 3½-in. OD TUBING FLOW EXPERIMENT

Prod. (B/D)	GOR (vol/vol)	THP (psia)	Maihak Pressures (in psia) at Depths Shown (ft)						
			488	993	1494	1998	4015	5018	5989
5082	129	165	290	400	500	615	1041	1250	1565
5051	129	167	290	404	498	615	1045	1238	1539
4931	128	167	290	403	493	609	1034	1228	1517
4780	124	165	275	380	472	605	1004	1206	1485
4321	129/130	164	269	365	447	558	941	1137	1401
4057	123	165	256	336	402	511	866	1079	1346
3799	122	165	250	330	—	493	850	1052	1313
3264	132	165	243	315	378	468	773	950	1168
3113	133	165	231	299	353	438	735	914	1144
2245	122	165	218	263	314	321(?)	593	744	945
1937	131	161/169	211	260	299	365	558	685	845
1346	122	165	192	227	252	299	454	558	719
956	128	165/167	195	225	240	295	445	505	640
176	135	159/169	185	215	227	265	373	473	569

TABLE 2—DATA FROM 2⅞-IN. OD TUBING FLOW EXPERIMENT

Prod. (B/D)	GOR (vol/vol)	THP (psia)	Maihak Pressures (in psia) at Depths Shown (ft)						
			516	1010	1998	3019	4007	5018	6001
3189	132	150	304	427	647	888	1125	1387	1618
3164	129	150	298	416	629	862	1093	1356	1580
3013	132	150	295	413	627	856	1083	1339	1563
2881	132	150	288	401	606	830	1046	1296	1517
2692	136	150	284	389	583	802	1010	1265	1471
2510	140	150	271	370	555	762	959	1186	1396
2025	135	147/159	250	328	473	654	822	1037	1219
1881	148	138/162	238	312	450	616	767	962	1139
1648	137	145/165	239	295	420	575	714	—	1056
1252	142	145/157	217	256	346	471	577	723	834
818	162	135/181	191/255	231/255	305	405	481	586	677

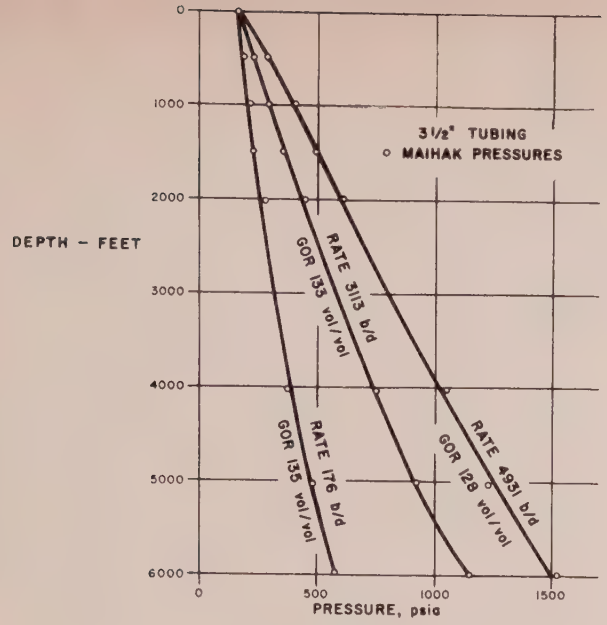

FIG. 1—EXAMPLES OF GRADIENT CURVES FOR THE LA PAZ WELL, 3½-IN. TUBING.

and the arithmetic mean deviation of all observed points from the smooth curves was 0.15 per cent.

LABORATORY DATA

From surface samples of oil and gas taken from the well immediately prior to the vertical flow experiments, a set of pressure-density curves was obtained for GOR's of 119.9, 131.5 and 141.1 vol/vol at temperatures of 140°, 160° and 180°F.

These curves formed the basis for the pressure-density calculations made in the analysis of the results.

A tabulation of the physical properties of the crude oil and gas from the well is given in Table 3.

TABLE 3—PHYSICAL PROPERTIES OF CRUDE OIL AND GAS, LA PAZ TEST WELL

Specific Gravity of Tank Oil	0.8548
Gravity of Separator Gas	0.8170 (Air = 1.0)
Separator Gas-Oil Ratio	130 vol/vol
Gravity of Tank Gas	1.270 (Air = 1.0)
Tank Gas-Oil Ratio	5 vol/vol
Average Flow-String Temperature	180°F
Viscosity of Oil at Atmospheric Pressure:	
200°F	1.87 cp
160°F	2.58 cp

ANALYSIS OF FIELD DATA

The first step in the analysis of the field data was to examine the individual depth-pressure traverses and attempt to fit them to the basic energy equation to determine the value of the energy-loss factor.

This was done by calculating depth-pressure traverses from the basic energy equation using the individual gauged production and an arbitrary spread of values for the energy-loss factor f. The theoretical curves were then superimposed on the actual curve recorded in the well, and the appropriate mean value of f selected together with limiting values of f to give ± 5 per cent accuracy over the measured pressure range.

The fit of the calculated curves to the observed data was generally excellent, particularly at the higher rates of flow.

The resulting values of f with ± 5 per cent upper and lower limits were then plotted against the QM/D parameter. The correlation is the excellent fit illustrated in Fig. 2. Both 2⅞ and 3½-in. OD tubing results apparently follow a single consistent trend.

ADDITIONAL SUPPORTING DATA

The correlation obtained in the plot of f vs QM/D was a far closer fit than had been anticipated. The closeness of this fit and the fact that the correlation showed no appreciable divergence with tubing size indicated that it might be generally applicable to two-phase flow conditions over a similar range of QM/D values in other sizes or types of conduit.

In an attempt to establish further supporting data, previous work on the subject of two-phase flow was re-examined.

ANNULAR FLOW

The analysis of the annular flow conditions in La Paz and Mara fields made in 1955[3] established a high-rate correlation for the energy-loss factor for the annulus between 2⅞-in. OD tubing and 7-in casing.

In this analysis it was not necessary to consider the problem of the equivalent diameter of the annular conduit. The diameter term in the energy equation, though unknown, was in fact constant because only one particular size of annulus was under consideration. The energy-loss correlation was drawn up with parameters of QM/D and f/D^5 where D, a composite term of true and equivalent diameters (discussed later), was unknown but constant and the term f/D^5 could be evaluated as a single unit from the field data.

The annular flow data, upon which the 1955 investigation was based, was recalculated using a standard form of equivalent hydraulic diameter to compare the results with the high-rate tubing flow correlation obtained in the La Paz experiments.

The equivalent diameter D_e is derived as follows.

$$D_e = 4 \times \frac{\text{Cross-sectional Area}}{\text{Wetted Perimeter}}$$

$$= D_c - D_t = 4 \times \frac{\pi/4\,(D_c^2 - D_t^2)}{\pi\,(D_c + D_t)}$$

where D_c = ID casing, and
D_t = OD tubing.

In Eq. 1, which is derived from a basic energy equation,[2] the term D^5 is in fact a compound of the square of the cross-sectional area and a hydraulic diameter.

In tubing flow, the diameter used for the calculation

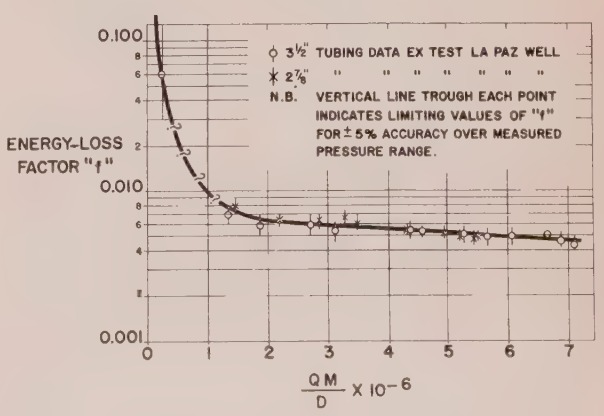

FIG. 2—COMPARISON OF f-VS-QM/D RELATIONSHIPS FOR 3½- AND 2⅞-IN. TUBING DATA, LA PAZ WELL.

of area is the same as the hydraulic diameter, thus raising no difficulties. However, for annular flow the term D^5 is equivalent to $(D_c^2 - D_t^2)(D_c - D_t)$.

Furthermore, in the correlating parameter QM/D, against which f is plotted for tubing flow, for annular flow this term becomes $QM/(D_c + D_t)$.

To compare the annular flow correlation of 1955 with that derived in the experiments in La Paz, the values of f/D^5 from the original data were multiplied by $(D_c^2 - D_t^2)^2 (D_c - D_t)$ to give a value for f, and the correponding values of QM were divided by $(D_c + D_t)$ to give a value for QM/D_e.

The resulting correlation is shown in Fig. 3. As can be seen, there is very close agreement between the two sets of data.

This close support is important in that it should now be possible to calculate vertical flowing gradients for an annular conduit of any size using the form of the equivalent hydraulic diameter stated previously. In the case of a small-sized outer conduit, the presence of tubing collars and upsets may cause additional restrictions to flow. However, in areas where little or no empirical data on annular flow exists, this method is good enough as a first approach.

HORIZONTAL PIPELINE FLOW

Earlier work in Venezuela had derived a friction-factor correlation for two-phase pipeline flow in 4- and 6-in. lines,[6] which has been used in the Mara-Maracaibo area with consistently accurate results at high rates of flow.

The analysis used in this derivation was basically similar to the energy-balance equation used for vertical flow and assumed that the energy losses could be correlated in a form similiar to the Fanning equation as was used in the analysis of the La Paz data. Consequently, the friction-factor values so derived are directly comparable with the energy-loss factor of the current investigation.

These flow-line friction factors were plotted against QM/D and superimposed on the tubing flow correlation (see Fig. 3). The flow-line data support the tubing flow correlation closely at high rates but diverge at values of QM/D less than 2.5×10^6, the point which was considered in the original flow-line analysis to be the lower limit of truly turbulent flow in flow lines.

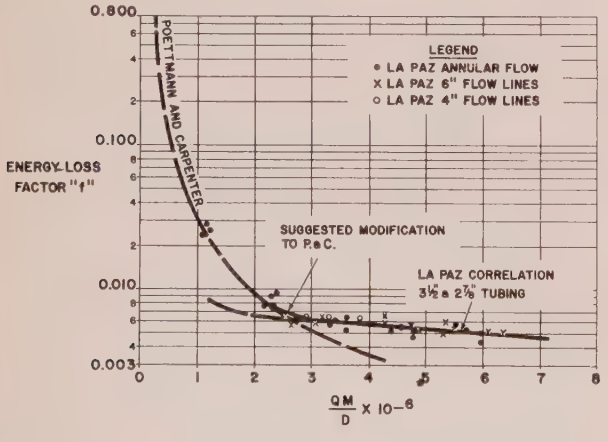

FIG. 3

TUBING FLOW DATA (POETTMANN AND CARPENTER)

The friction-factor correlation derived originally by Poettmann and Carpenter is the best average curve drawn through a group of widely scattered points calculated from 49 surveys. These surveys were taken mainly at low flow rates, less than 300 B/D, in tubing sizes of 2⅜- and 2⅞-in. OD.

At the low-rate end, there were no local data available to confirm the correlation, other than the extreme low-rate end of the La Paz annular flow correlation which appears conformable.

Above values of $D\rho v = 30$ (i.e., $QM/D = 2.0 \times 10^6$ approximately), the Poettmann and Carpenter correlation diverges from the general trend of the high-rate correlation established from the La Paz tubing data, the annular flow data and the flow-line data. The divergence probably has no significance as, above this value of QM/D, the Poettmann and Carpenter correlation was not strongly supported by their basic data. The low-rate correlation of Poettmann and Carpenter can be readily adjusted to fit smoothly into the high-rate correlation derived from the other data.

THE SIGNIFICANCE OF THE ENERGY-LOSS CORRELATION

The excellent agreement of the tubing flow, annular flow and pipeline correlations above a value of $QM/D = 3.0 \times 10^6$ indicates that at high flow rates the correlation of f against QM/D is well justified for practical purposes and that, given the correct PVT data, it should be possible to make computations of pressure changes in both vertical and horizontal* flow with an accuracy of $\pm$ 5 per cent.

At low flow rates (i.e., at values of QM/D less than 2.0 to 3.0×10^6), the different sets of empirical data diverge considerably.

As a hypothesis, it has been assumed that the flattened portion of the f correlation in Fig. 3 (i.e., at values of QM/D greater than 2.0 to 3.0×10^6) represents the truly turbulent phase of flow in which little or no gas slippage occurs; while below this point, the sharply rising portion of the curve represents slippage.

Since the energy loss by slippage will depend to some degree on the amount of free gas present and on the over-all velocity of the mixture, it can be expected that, for the same mass rate of flow under different conditions of pressure, the energy loss due to slippage and hence the energy-loss factor will not be constant.

The wide spread of f values for the same value of QM/D in the Poettmann and Carpenter correlation and the different correlation obtained from the La Paz data are then explicable by the variation in GOR's and pressure. These variations will result in variations of the percentage free gas in place and the mixture velocity.

Attempts were made to correlate f with a variety of parameters incorporating variables of percentage free gas and mixture velocity. Very few data are available at low rates, and the attempts to establish a satisfactory correlation with more complex parameters proved unsuccessful. It was decided to accept Poettmann

*Horizontal flow in this sense means the flow through lines in which differences in end elevations are small enough to be ignored and in which no appreciable variations in elevation occur along the route.

and Carpenter's correlation, somewhat modified as shown in Fig. 3 to fit smoothly in the well defined high-rate correlation derived from the La Paz data, and to calculate assuming a constant energy-loss factor for a given mass rate of flow.

It was considered that such an approximation would give adequately accurate results for normal field conditions in view of the original results of Poettmann and Carpenter.

To establish an independent check on the accuracy of gradient calculations at low rates, a set of gradient curves were calculated for Lake Maracaibo conditions using the modified Poettmann and Carpenter correlation just proposed. These curves were then checked against a total of 78 flowing bottom-hole pressure surveys made in Lake Maracaibo wells at flow rates between 300 and 1,600 B/D in 3½-in. OD tubing and between 500 and 1,250 B/D in 2⅞-in. OD tubing. It appears that an accuracy of ± 10 per cent is achievable under these conditions, which is reasonably satisfactory for gas-lift design or flowing-well analysis.

The accuracy obtained by using what is admittedly an approximation to the true energy-loss factor can be explained by the following points.

1. At high flow rates ($QM/D > 2.0 \times 10^6$) under all normal pressure conditions, the value of $\Delta p/\Delta h$ is vitally dependent on the value of f since the term $\frac{(f)(Q^2)(M^2)}{(7.413)(10^{10})(\bar{\rho})(D^5)}$ (see Eq. 1) assumes significant proportions with respect to $\bar{\rho}$.

2. At medium or low production rates (i.e., QM/D values lower than 2.0×10^{-6}), it appears that at high pressure the first term ($\bar{\rho}$) in the gradient equation is dominant. Consequently, under such conditions, deviations in the value of f are of less significance in the final value of $\Delta p/\Delta h$.

3. At low flow rates and low pressures, the term $\frac{(f)(Q^2)(M^2)}{(7.413)(10^{10})(\bar{\rho})(D^5)}$ again assumes significance in the calculation of the gradient. However, it is under such conditions that "heading" also begins to manifest itself in the long flow string of the producing well. The over-all gradient is then in fact fluctuating, and a high degree of accuracy in its estimation is not possible.

It should be realized, moreover, that the use of a more complex factor which is not related solely to the mass flow rate, but to such variables as the percentage free gas in place, would result in an extremely complex calculation requiring the derivation of separate values of f for each pressure increment. With the present field methods of oil and gas measurements, it is doubtful whether a higher accuracy could be obtained even with a more complex solution.

REVERSED CURVATURE

A further point of significance in connection with the question of calculated pressure gradients is that of the reversal of curvature of the calculated pressure-depth curves at low pressure—i.e., the condition occasionally arises where the calculated pressure traverse in the low-pressure range is concave downwards instead of concave upwards.

In the past[2,3] this reversal had been considered as an anomaly due solely to the inadequacies of the method of calculation. In the course of the La Paz experiments, however, this behavior was observed in the recorded traverses at high rates of flow in both 3½- and 2⅞-in. tubing (Fig. 1). To establish a check independent of the Maihak readings, a special test was carried out in another La Paz well. During a workover, six closely spaced retrievable gas-lift mandrels were run in the upper part of the tubing string. Dummy valves were inserted in each mandrel and the tubing plugged-off below the bottom mandrel with a retrievable Otis-S-plug. The well was produced on casing flow to a wellhead separator, thus ensuring a low casinghead pressure. The pressure at the level of each mandrel was obtained by pulling each dummy valve in turn and injecting gas at a very low rate down the tubing until the injection pressure stabilized.

The pressure at the open mandrel could thus be obtained from the observed tubinghead pressure, measured with a highly accurate gauge and corrected to allow for the weight of the gas column. The casinghead pressure was also read with a newly calibrated standard manometer. On completion of the test, the tubing plug was pulled and the pressure at the tubing shoe read with an Amerada bomb.

As shown in Fig. 4, the observed pressure-depth relationship was then compared with a calculated curve obtained from the energy-loss correlation shown in Fig. 3.

It can be seen that, although the calculated curve is not a perfect fit to the observed data, the deviation is small and the reversed curve is a better approximation to the actual conditions than that obtained by extrapolating the concave upwards section of the calculated curve.

It is concluded, therefore, that the calculated curves should be drawn with the reversed curvature inherent in the calculation and that no attempt should be made to extrapolate the lower part of the curve back over the low-pressure range.

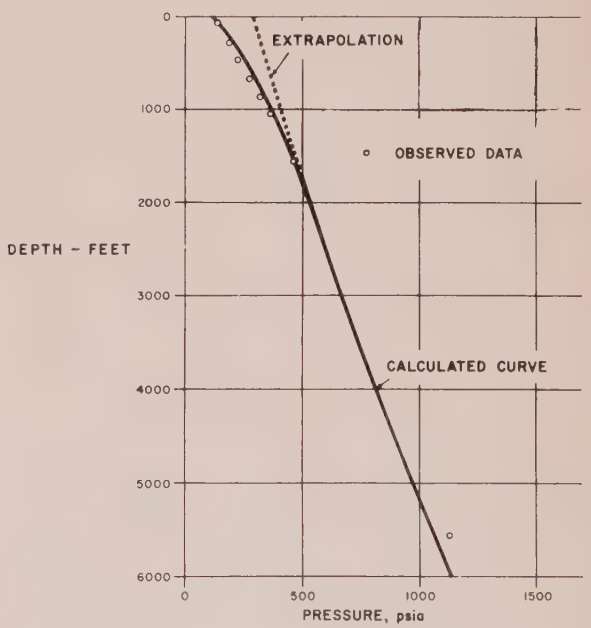

FIG. 4—OBSERVED PRESSURE-DEPTH RELATIONSHIP VS CALCULATED CURVE OBTAINED FROM THE ENERGY-LOSS CORRELATION OF FIG. 3, LA PAZ WELL.

CHECK DATA

The check data available at low rates of flow have been discussed and analyzed in the section entitled "The Significance of the Energy-Loss Correlation". These 78 readings represent the total low-rate data available for Lake Maracaibo conditions.

Very few data are available at the higher flow rates, the difficulty being, of course, that special equipment is required to obtain readings in tubing against high vertical flow rates. Some measurements have been taken using either a long string or sinker bars above the bombs or an anchoring device supporting the bomb which latches in a tubing-collar recess. While there are insufficient readings for any satisfactory statistical analysis, it would appear that an average accuracy of the order of $\pm$ 5 per cent can be expected at these higher rates.

ACKNOWLEDGMENT

The authors wish to thank Cia. Shell de Venezuela for permission to publish this paper and to express appreciation to their colleagues for help in accumulating and checking the field data.

REFERENCES

1. Gilbert, W. E.: "Flowing and Gas Lift Performance", *Drill. and Prod. Prac.*, API (1954).
2. Poettmann, F. H. and Carpenter, P. G.: "Hhe Multiphase Flow of Gas, Oil and Water Through Vertical Flow Strings, with Application to the Design of Gas Lift Installations", *Drill. and Prod.*, API (1952) 257.
3. Baxendell, P. B.: "Producing Wells on Casing Flow—An Analysis of Flowing Pressure Gradients", *Trans.*, AIME (1958) **213**, 202.
4. Moore, T. V. and Wilde, H. D.: "Experimental Measurements of Slippage in Flow Through Vertical Pipes", *Trans.*, AIME (1931) **92**, 296.
5. Moore, T. V. and Schilthuis, R. J.: "Calculation of Pressure Drops in Flowing Wells", *Trans.*, AIME (1933) **103**, 170.
6. Baxendell, P. B.: "Pipeline Flow of Oil and Gas Mixtures", *Proc.*, Fourth World Pet. Cong. (1955) Section II E. ★★★

Multiphase Flow of Water, Oil and Natural Gas Through Vertical Flow Strings

M. RASIN TEK
MEMBER AIME

THE U. OF MICHIGAN
ANN ARBOR, MICH.

ABSTRACT

A new method for correlating the data on multiphase flow through vertical pipe is presented.

The correlation is based on a "two-phase f factor" concept which was developed and successfully applied to horizontal multiphase flow by Bertuzzi, Tek and Poettmann. Field data previously published on several flowing and gas-lift wells have been used as the basis for the developed correlation.

The application of the method to actual two-phase flow problems indicate that this method is capable of predicting the pressure distribution in vertical multiphase flow strings well within the accuracy range usually desired for common engineering and design calculations.

A new working chart developed for calculation of two-phase pressure gradients and a graphical step-by-step procedure for the computation of pressure distribution are presented along with an example problem.

INTRODUCTION

Multiphase flow through vertical pipe is encountered in many engineering installations. In petroleum, chemical process, nuclear engineering and many other industries, problems associated with simultaneous flow of two or more phases through vertical pipe have been of interest for a long time. This interest has increased considerably during recent years due to applications to new processes in petroleum production and refining and to problems of steam generation and heat removal from nuclear reactors. One prominent example of vertical two-phase flow is provided by the gas-lift process where oil, water and gas flow simultaneously. If the pressure profile in a gas-lift well can be predicted within reasonable accuracy, it would be possible to get good estimates of the power required to lift the oil, the optimum depth, the pressure and the rate at which to inject gas. Furthermore, the effect of production rate and tubing sizes on these quantities can be evaluated before any design decision is made on the installation and operation of the flow string.

The majority of experimental work available in the literature deals with two-component systems where individual phase flow rates in and out of the pipe remain constant. The general problem of prediction of pressure drops in multiphase flow systems is very complicated. The co-existence of numerous flow patterns of widely different geometry and mechanism, conditions of surface instability and the nature of force fields acting upon the system are among the major difficulties commonly encountered. The classical approach of fluid dynamics which would be based upon the formulation and solution of Navier-Stokes equations has been found by many investigators completely devoid of any hope of success—not only because of inherent nonlinearities but also because of insurmountable analytical difficulties standing in the way of setting up the boundary conditions. The presence and effect of interfacial forces on multiphase flow systems further complicate the theoretical approach. For these reasons, many investigators choose to adopt semi-empirical if not purely empirical approaches in order to obtain solutions of engineering utility.

A prominent practical solution has been given by Poettmann and Carpenter[1] in the form of an empirical correlation. In their paper, total flowing densities of fluids and solubility effects of gas in oil have been taken into account for the correlation of field data covering a wide range of operating conditions for oil wells. They treated the gas, oil and water as a single phase of combined properties and correlated the multiphase friction factor as a function of the product (ρvd), i.e., density $\times$ velocity $\times$ diameter of the flow string. However, because the product (ρvd) is dimensional while the friction factor is dimensionless, the generality of their results is somewhat restricted. It seems that the omission of viscosity effect may be one of the reasons for the scatter of data as shown in their correlation chart.

The concepts of the "two-phase f factor" and the "two-phase Reynolds' number function" were recently developed and successfully applied to correlate horizontal multiphase flow by Bertuzzi, Tek and Poettmann.[2] Recently, two new methods of correlation by Tek and Chan[4] have been presented on simultaneous flow of liquid and gas through vertical pipe. These two methods of correlation and the working equations in field units necessary for their application are included in this paper. The extension of the concept of two-phase Reynolds' number function successfully developed for horizontal flow into vertical multiphase flow systems, development and evaluation of working charts permitting calculation of two-phase pressure gradients and

Original manuscript received in Society of Petroleum Engineers office Dec. 5, 1960. Revised manuscript received Sept. 5, 1961. Paper presented at Joint SPE-AIChE Symposium, Sept. 25-28, 1960, in Tulsa.

[1]References given at end of paper.

application of the results to actual engineering problems have been the main objectives of this work.

CORRELATION OF DATA ON MULTIPHASE FLOW

Field data available on vertical multiphase flow systems have been analyzed and computed by using the flow equation and the equation of the two-phase friction factor f'. The derivation of these equations are included in the Appendix.

The final equations giving the definition of the two-phase friction factor and permitting its calculation from field data are given as follows.[4]

$$f' = \frac{2g_c W_f D}{4v^2 \Delta h} \quad . \quad . \quad . \quad . \quad . \quad . \quad . \quad . \quad . \quad . \quad . \quad (1)$$

where W_f denotes lost work and v is the average velocity of both phases combined.

$$f' = \left[\frac{144}{M}\int_{P_1}^{P_2} V_m \, dP - \Delta h\right]\frac{7.413 \times 10^{10} D^5}{\overline{V}^2_m \, Q^2 \, \Delta h}. \quad (2)$$

where f' = the two-phase friction factor, dimensionless,
M = total lb mass of all phases associated/bbl of oil produced at the stock tank,
Δh = the height of the vertical flow string,
V_m = specific volume of all phases associated with each bbl of stock tank oil, cu ft/bbl,
$\overline{V}_m$ = integrated mean value of V_m,
Q = oil-production rate at the stock tank, B/D, and
D = pipe diameter ID.

To correlate the f' calculated with Eq. 2, a two-phase Reynolds' number function like the one in horizontal flow was defined as follows.

$$R_t = R_g{}^a \, R_l{}^b; \quad . \quad . \quad . \quad . \quad . \quad . \quad . \quad . \quad . \quad . \quad . \quad (3)$$

$$a = \frac{k}{1+k}; \quad . \quad . \quad . \quad . \quad . \quad . \quad . \quad . \quad . \quad . \quad . \quad (4)$$

$$b = \frac{1}{e^{0.1k}}; \quad . \quad . \quad . \quad . \quad . \quad . \quad . \quad . \quad . \quad . \quad . \quad (5)$$

and

$$R_t = (R_g)^{\frac{k}{1+k}} (R_l)^{e^{\frac{1}{0.1k}}} \quad . \quad . \quad . \quad . \quad . \quad . \quad . \quad . \quad . \quad . \quad (6)$$

where R_t = two-phase Reynolds' number function defined with Eq. 6, dimensionless,
R_g = Reynolds' number of gas phase,
R_l = Reynolds' number of liquid phase, and
k = mass ratio of gas to liquid, based on separator and stock-tank quantities.

The constants a and b have been so chosen that the two-phase Reynolds' number function will be reduced to the well-known single-phase Reynolds' number whenever k is equal to zero or infinity. When k approaches zero, there is no more gas phase due to the definition of k itself, and the two-phase Reynolds' number function approaches the Reynolds' number of single liquid phase.

$$\lim_{k\to 0} R_t = \lim_{k\to 0} (R_g)^{\frac{k}{1+k}} (R_l)^{e^{\frac{1}{0.1k}}} = R_g{}^{0} R_l{}^{e^{0}} = R_l$$

$$. \quad . \quad . \quad . \quad . \quad . \quad . \quad . \quad . \quad . \quad . \quad . \quad . \quad . \quad . \quad . \quad . \quad . \quad . \quad (7)$$

Similarly, when k approaches infinity, there is no more liquid phase and R_t approaches R_g.

$$\lim_{k\to\infty} R_t = \lim_{k\to\infty} R_g{}^{\frac{k}{1+k}} (R_l)^{e^{\frac{1}{0.1k}}} = R_g (R_l)^{\frac{1}{\infty}} = R_g$$

$$. \quad . \quad . \quad . \quad . \quad . \quad . \quad . \quad . \quad . \quad . \quad . \quad . \quad . \quad . \quad . \quad . \quad . \quad . \quad (8)$$

Field data of flowing wells and gas-lift wells from the U S. Bureau of Mines, Bartlesville, Okla., and data from the files of the Phillips Petroleum Co. have been published in Poettmann's paper. These data were believed to be taken from wells of clean tubing. These data were used as a basis for the new correlations discussed previously and are shown in Table 1. Among the data of 31 wells, the pressure differences range from 240 psia to 2,571 psia and the depth of wells range from 1,053 to 10,800 ft. It can be seen that the correlation developed should apply for a wide range of operating conditions.

TABLE 1—SUMMARY OF DATA

Well No.*	Oil (B/D)	Total GOR (ft³/bbl)	Total GLR (ft³/bbl)	WOR (bbl/bbl)	Gravity Oil (°API)	Gravity Water (spec.)	Gravity Gas	Tbng. Size (in.)	Tbng. Pres. (psia)	Well or Inj. Depth (ft) Δh	Pres. Diff. Obsvd. (psia) ΔP	Obsvd. $\Delta P/\Delta h$ (psi/ft)
					A. Flowing Oil Wells							
1	244.8	3640	—	—	50.8	—	0.680	2.5	2360	9592	1730	0.180
2	313.2	2151	—	—	47.6	—	0.742	2.5	1784	10683	2531	0.236
3	60.0	2250	—	—	44.4	—	0.796	2.5	1264	10800	2571	0.238
4	82.0	3393	—	—	54.0	—	0.752	2.0	1645	7450	1655	0.222
5	125.0	3393	—	—	54.0	—	0.752	2.0	1635	7350	1655	0.226
6	480.0	3393	—	—	54.0	—	0.752	2.0	1455	9620	1910	0.199
7	187.2	1019	—	—	38.8	—	0.9349	2.0	990	7850	2200	0.280
8	167.0	1245	—	—	42.0	—	0.8225	2.0	985	6550	1680	0.256
9	138.0	1245	—	—	42.0	—	0.8225	2.0	665	6570	1890	0.288
10	168.0	1747	—	—	42.6	—	0.8400	2.0	1261	7800	1880	0.241
11	259.2	1747	—	—	42.6	—	0.8400	2.0	1229	8070	1970	0.244
12	91.2	1747	—	—	42.6	—	0.8400	2.0	1221	8000	2030	0.234
13	60.0	906	—	—	36.2	—	0.8225	2.5	555	6500	1770	0.272
14	106.0	906	—	—	36.2	—	0.8225	2.5	455	6500	1180	0.182
15	131.0	3588	—	—	43.9	—	0.8287	2.0	1665	8480	1595	0.188
16	245.3	192	—	—	41.3	—	1.048	2.0	145	4410	1274	0.289
17	160.3	189	—	—	41.3	—	1.048	2.0	175	3000	908	0.303
18	392.4	230	—	—	41.3	—	1.048	2.0	105	4410	1124	0.255
					B. Gas-Lift Wells							
19	80.0	5110	741	5.90	35.5	1.150	0.625	2.0	107	2980	440	0.148
20	68.0	4776	451	9.06	35.5	1.150	0.625	2.0	155	2850	425	0.149
21	28.0	5321	405	12.14	35.5	1.150	0.625	2.0	110	2770	405	0.146
22	14.0	15875	434	35.60	36.0	1.076	0.650	2.0	105	3461	555	0.160
23	36.0	13243	607	20.83	35.5	1.150	0.625	2.0	170	3380	580	0.172
24	18.0	18333	1586	10.56	36.0	1.076	0.650	2.5	115	3376	273	0.081
25	10.6	40849	781	51.32	38.1	1.074	0.650	2.0	180	3222	455	0.141
26	21.0	15576	562	26.71	39.7	1.150	0.625	2.0	155	3222	485	0.151
27	5.2	34808	607	56.38	38.1	1.074	0.650	2.0	122	2780	355	0.128
28	53.0	2557	156	15.43	30.4	1.082	0.600	2.0	195	1053	240	0.228
29	52.0	2888	112	25.71	30.6	1.082	0.600	2.0	112	1248	342	0.274
30	38.6	8233	719	10.45	34.4	1.074	0.650	2.0	132	3657	456	0.125
31	49.1	8890	801	10.10	34.8	1.074	0.662	2.0	111	3646	464	0.127

*Wells 1 through 6, U. S. Bureau of Mines; Wells 7 through 31, Phillips Petroleum Co.

The correlation of f' as a function of $\left(R_g^{\frac{k}{1+k}} \times R_l^{e^{\frac{1}{0.1k}}}\right)$ is shown graphically in Fig. 1. It appears to be a family of almost parallel curves with k as parameter in the log-log plot. The depth of wells have been calculated with this correlation and are summarized in Table 2. As the calculated pressure difference per foot is compared with the observed one, the algebraic average deviation for the 31 wells is + 2.19 per cent and the standard deviation is 7.3 per cent from the algebraic average.

Fig. 2 shows a plot of all of the available data points with the gas-liquid mass ratios indicated at each point. It can be seen that the distribution and location of the points with nearly the same k values suggest a family of curves, each having a constant value of the parameter k. This is the basis for the chart given in Fig. 1.

It must be noted that the gas-to-liquid mass ratio k was based on separator gas and stock-tank liquid quantities, i.e., as both phases flow out of the vertical pipe. Actually, because the gas is constantly coming out of solution as both liquid and gas phases flow vertically upward through the production or gas-lift tubing, the in situ value of k must change from point to point. The use of terminal values of k is believed to result in the correlation in only an approximate characterization of the multiphase flow system. In vertical two- or three-phase flow systems in general, if data on pressure distribution down the pipe is available in addition to the terminal pressures, it appears that a more general correlation with better accuracy may be found by taking into account the variation of in-place k values.

Further analysis of data correlated and presented in Figs. 1 and 2 suggested that all of the curves of the family with different k values could be brought together by changing the form of the correlating Reynolds' number function. After an extensive study of several forms, it was found that the following model was able to correlate the data around a unique curve.

$$R_2 = \log\left[(R_g)^{\frac{k}{\alpha+k}}(R)^{\frac{1}{e^{\beta k}}}\right] - ck \quad . \quad . \quad . \quad . \quad (9)$$

where α, β and c are constants.

It was noted that the values of the constants α, β and c defined in Eq. 9 affect the distance between the curves shown in Fig. 1. Several choices of α, β and c had been tried and the correlation of f' as a function of R_2 (which is $\log\left[R_g^{\frac{k}{5+k}} R^{e^{\frac{1}{0.11k}}}\right] - 0.1\,k$) is shown in Fig. 3. The results of this correlation are summarized in Table 3. It shows an algebraic average deviation of + 0.67 per cent and a standard deviation from the algebraic average of 11.6 per cent. With more well test data, the model defined with Eq. 19 can be investigated again to get a better choice of α, β and c for a more precise correlation with R_2.

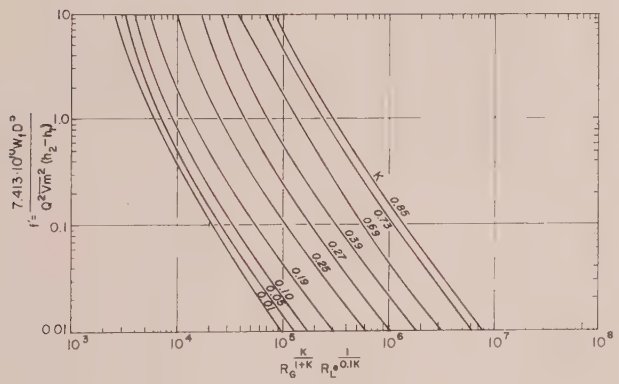

FIG. 1—CORRELATION OF VERTICAL TWO-PHASE FLOW OF R_1.

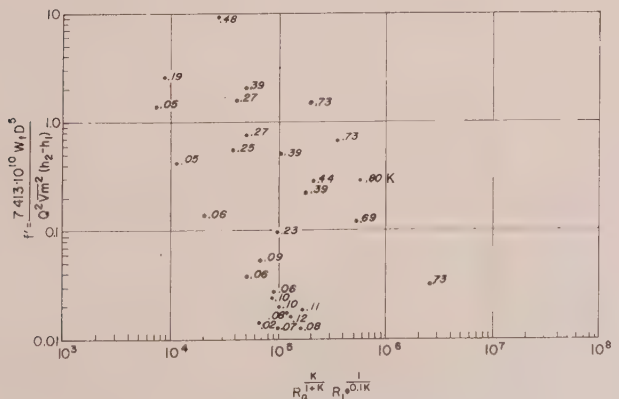

FIG. 2—TWO-PHASE f' FACTORS COMPUTED FROM DATA.

TABLE 2—SUMMARY OF RESULTS OF CORRELATION R_1

Well No.*	Gas-Liquid Mass Ratio K	Depth Calc. (ft) Δh_1	$\Delta P/\Delta h_1$ Calc. (psi/ft)	Deviation (psi/ft)	Deviation (per cent)
		A. Flowing Oil Wells			
1	0.6926	9589	0.1804	−0.0004	− 0.22
2	0.4388	11110	0.2278	+0.0082	+ 3.47
3	0.4836	10610	0.2423	−0.0043	− 1.81
4	0.7267	7460	0.2218	+0.0002	+ 0.09
5	0.7267	7688	0.2153	+0.0107	+ 4.73
6	0.7267	9601	0.1989	+0.0001	+ 0.05
7	0.2490	7860	0.2799	+0.0001	+ 0.04
8	0.2727	6563	0.2560	0.0000	0.00
9	0.2727	7624	0.2479	+0.0401	+13.92
10	0.3920	7809	0.2407	+0.0003	+ 0.12
11	0.3920	8050	0.2447	−0.0007	− 0.29
12	0.3920	8000	0.2538	+0.0002	+ 0.08
13	0.1919	6495	0.2725	−0.0005	− 0.18
14	0.1919	6498	0.1816	+0.0004	+ 0.22
15	0.8004	8270	0.1929	−0.0049	− 2.61
16	0.0534	4386	0.2905	−0.0015	− 0.52
17	0.0526	3178	0.2857	+0.0173	+ 5.71
18	0.0639	4227	0.2659	−0.0109	− 4.27
		B. Gas-Lift Wells			
19	0.1028	2898	0.1518	−0.0038	− 2.57
20	0.0654	2556	0.1663	−0.0173	−11.61
21	0.0556	2713	0.1493	−0.0033	− 2.26
22	0.0614	4014	0.1383	+0.0217	+13.56
23	0.0829	3983	0.1456	+0.0264	+15.35
24	0.2268	3383	0.0807	+0.0002	+ 0.25
25	0.1105	4075	0.1117	+0.0293	+20.78
26	0.0768	3527	0.1375	+0.0135	+ 8.94
27	0.0859	3378	0.1051	+0.0229	+17.89
28	0.0204	989	0.2426	−0.0146	− 6.40
29	0.0142	1247	0.2743	−0.0003	− 0.11
30	0.1028	3635	0.1254	−0.0004	− 0.32
31	0.1167	3509	0.1322	−0.0052	− 4.09

Algebraic average deviation + 2.2 per cent; standard deviation from algebraic average, σ, 7.3 per cent.

*Wells 1 through 6, U. S. Bureau of Mines; Wells 7 through 31, Phillips Petroleum Co.

CONCLUSIONS

Two new methods of correlation have been developed for prediction of pressure drops in multiphase flow through vertical pipe. The correlated dimensionless quantity is the two-phase friction factor f', based on multiphase mixture properties and defined by a Fanning-type equation on lost work. Two correlating dimensionless Reynolds' number functions were found to be almost equally effective in predicting data available in the literature. The first one R_1 is a product of single-phase Reynolds' numbers of both gas and liquid phases, each raised to power, function of the gas-liquid mass ratio. This correlation is a direct extension of one given by Bertuzzi, Tek and Poettmann for horizontal flow. On the basis of data available from 31 flowing and gas-lift wells, this correlation resulted in a bias of

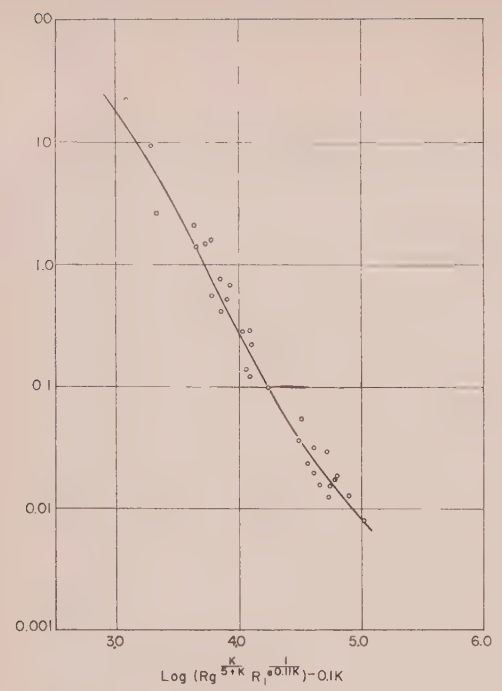

FIG. 3—CORRELATION OF f' WITH R_2.

+ 2.2 per cent and a standard deviation of 7.3 per cent. The second correlating Reynolds' number function R_2 was found to be a function of R_g, and R_l and k also. It resulted in bringing all of these data around one unique correlating curve with a substantially narrower range of spread. A statistical evaluation of the correlation by R_2, based on this field data, resulted in a bias of only + 0.67 per cent and a standard deviation of 11.6 per cent.

WORKING CHART FOR GRAPHICAL ESTIMATION OF PRESSURE GRADIENTS

Fig. 4 presents a working chart developed for estimating pressure gradients or pressure distributions for the design of gas-lift systems. The chart is based on the correlations of the data by the correlating variable R_2. It is based on the following equation derived from energy relationships expressed in field units.

$$\frac{(-\Delta P)}{\Delta H} = \frac{g}{g_c}\bar{\rho} + \frac{f'(QM)^2}{7.413 \times 10^{10}\bar{\rho}D^5} \quad . \quad . \quad . \quad (10)$$

where $(-\Delta P)/\Delta H$ = the pressure gradient, lb/sq ft/ft,
$\bar{\rho}$ = average density of multiphase mixture over the pressure increment ΔP, lb mass/cu ft,
f' = two-phase friction factor, dimensionless function of R_2, and
QM = total mass flow/day of all phases, lb mass/day.

Fig. 4 indicates that, once (QM) is computed starting from the proper point on QM axis by drawing a vertical line through the proper tubing diameter, a horizontal line through R_2 value and a vertical line through calculated average $\bar{\rho}$ value, one can readily determine $(\Delta P/\Delta h)$ in pounds per square foot per foot over the considered pressure or length increment.

This graphical procedure and the working equations necessary for the calculations are illustrated in the example problem given later. Fig. 5 represents the pressure distribution computed for the example problem.

TABLE 3—SUMMARY OF RESULTS CALCULATED WITH R_2

Well No.	Depth Calc. (ft) Δh_2	$\Delta P/\Delta h$ Calc. (psi/ft)	Deviation (psi/ft)	Deviation (per cent)
1	9064	0.1909	−0.0109	− 6.06
2	11176	0.2265	+0.0095	+ 4.03
3	11626	0.2211	+0.0169	+ 7.10
4	8227	0.2012	+0.0208	+ 9.37
5	8405	0.1969	+0.0291	+12.88
6	10290	0.1856	+0.0134	+ 6.73
7	7093	0.3102	−0.0302	−10.79
8	7006	0.2398	+0.0162	+ 6.33
9	8335	0.2268	+0.0612	+21.25
10	7961	0.2362	+0.0048	+ 1.99
11	8576	0.2297	+0.0143	+ 5.86
12	8436	0.2406	+0.0134	+ 5.28
13	7607	0.2327	+0.0393	+14.45
14	4990	0.2365	−0.0545	−29.95
15	8669	0.1840	+0.0040	+ 2.13
16	4112	0.3098	−0.0208	− 7.20
17	2998	0.3029	+0.0001	+ 0.03
18	3951	0.2845	−0.0295	−11.57
19	2542	0.1731	−0.0251	−16.96
20	2523	0.1685	−0.0195	−13.09
21	2777	0.1458	+0.0002	+ 0.14
22	3956	0.1403	+0.0197	+12.31
23	3596	0.1613	+0.0107	+ 6.22
24	3383	0.0807	+0.0002	+ 0.25
25	3663	0.1242	+0.0168	+11.91
26	3473	0.1396	+0.0114	+ 7.55
27	3325	0.1068	+0.0212	+16.56
28	1019	0.2355	−0.0075	− 3.29
29	1247	0.2743	−0.0003	− 0.11
30	3264	0.1397	−0.0147	−11.76
31	3022	0.1535	−0.0265	−20.87

Algebraic average deviation + 0.67 per cent; standard deviation from algebraic average, 11.6 per cent.

It must be noted that, in spite of the very large (500 psi) pressure increments which have been used, the graphical method predicts the bottom-hole pressure with an error of 7 per cent.

EXAMPLE PROBLEM

Well No. 3 in Table 1 indicates the following data: Q = 60 B/D; $S_{g/o}$ = 2,250; gravity of oil, 44.4° API; specific gravity of the gas, 0.796; tubing size, 2½ in. = 2.44 in. ID; tubing pressure, 1,264 psia wellhead; total depth = 10,880 ft; and μ_l = 1.48 cp.

It is desired to calculate the pressure profile for this well down the flow string and compare the predicted bottom-hole pressure with the observed one of 3,835 psia. The formation-volume-factor curve and solubility data are given in Figs. 6 and 7.

The reservoir temperature T = 189°F, and the average tubing temperature T_{av} = 75°F.

SOLUTION

The calculations given step-by-step in the following section are included to illustrate the use of working equations and application of the developed working chart.

1. Calculate gas-to-liquid mass ratio K. In all vertical multiphase flow problems where there exists substantial mutual solubility effects, the K ratio varies along the length of the flow string.

Take a reasonably small pressure drop:
$(-\Delta P_1)$ = 500 psi;
$P_0 = P_{top}$ = 1,264 psia;
$P_1 = P_0 + \Delta P$ = 1,264 + 500 = 1,764 psia;
$(P_{av})_1$ = 1,264 + 250 = 1,514 psia $(S_s)_1$ = 680 cu ft/bbl at $P = (P_{av})$ = 1,514 psia;
$S_{g/o}$ = 2,250 cu ft/bbl.

Knowing $(S_{g/o})$, G_G and G_o calculate:

$$k_1 = \frac{S_{g/o}G_G \times 0.0764}{351\ G_o + 62.4\ G_w V_w}$$

$(S_{g/o})_1$ at P_{av1} = 1,514 psia is 2,250 − (680 − 200) = 1,770 cu ft/STB;

$$G_o = \frac{141.5}{°\text{API} + 131.5} = \frac{141.5}{44.4 + 131.5} = \frac{141.5}{175.9}$$
$$= 0.805;$$

$$k_1 = \frac{1{,}770 \times 0.796 \times 0.0764}{351 \times 0.805} = 0.382.$$

2. Calculate $(R_L)_1$.

$$(R_L)_1 = \frac{W_{L_1} D}{\mu_{L_1}}$$

$$= \frac{Q[352\, G_o + S_{s1}\, G_g\, 0.0164 + 62.4 \times G_w V_w]}{86{,}400 \times \pi \frac{D^2}{4} \times 6.72 \times 10^{-4}} \frac{D}{\mu_{L_1}}$$

$$= \frac{Q}{\mu D} 352\, G_o + S_{s1}\, G_g\, 0.0764 + 62.4 \times G_w V_w \times \frac{4}{86{,}400 \times \pi \times 6.72 \times 10^{-4}}$$

$$= 2.29 \times 10^{-2} \frac{Q}{\mu_L D} \times [351\, G_o\, (S_s)_1\, G_G\, 0.0764 + 62.4 \times G_w V_w]$$

$$= 2.29 \times 10^{-2}(351 \times 0.805 + 680 \times 0.796 \times 0.0764) \times \frac{60 \times 12}{1.48 \times 2.44}$$

$$= 2.29 \times 10^{-2}(282 + 41.3)\frac{60 \times 12}{1.48 \times 2.44}$$

$$= 2.29 \times 10^{-2} \frac{323.3 \times 60 \times 12}{1.48 \times 2.44}.$$

$(R_L)_1 = 1{,}470.$

3. Calculate $(R_G)_1$.

$$(R_G)_1 = 1.71 \times 10^{-3} \frac{Q(S_{g/o})_1\, G_g}{\mu_g D}$$

$$= \frac{1.71 \times 10^{-3} \times 60 \times 1{,}770 \times 0.796 \times 12}{0.0222 \times 2.44}$$

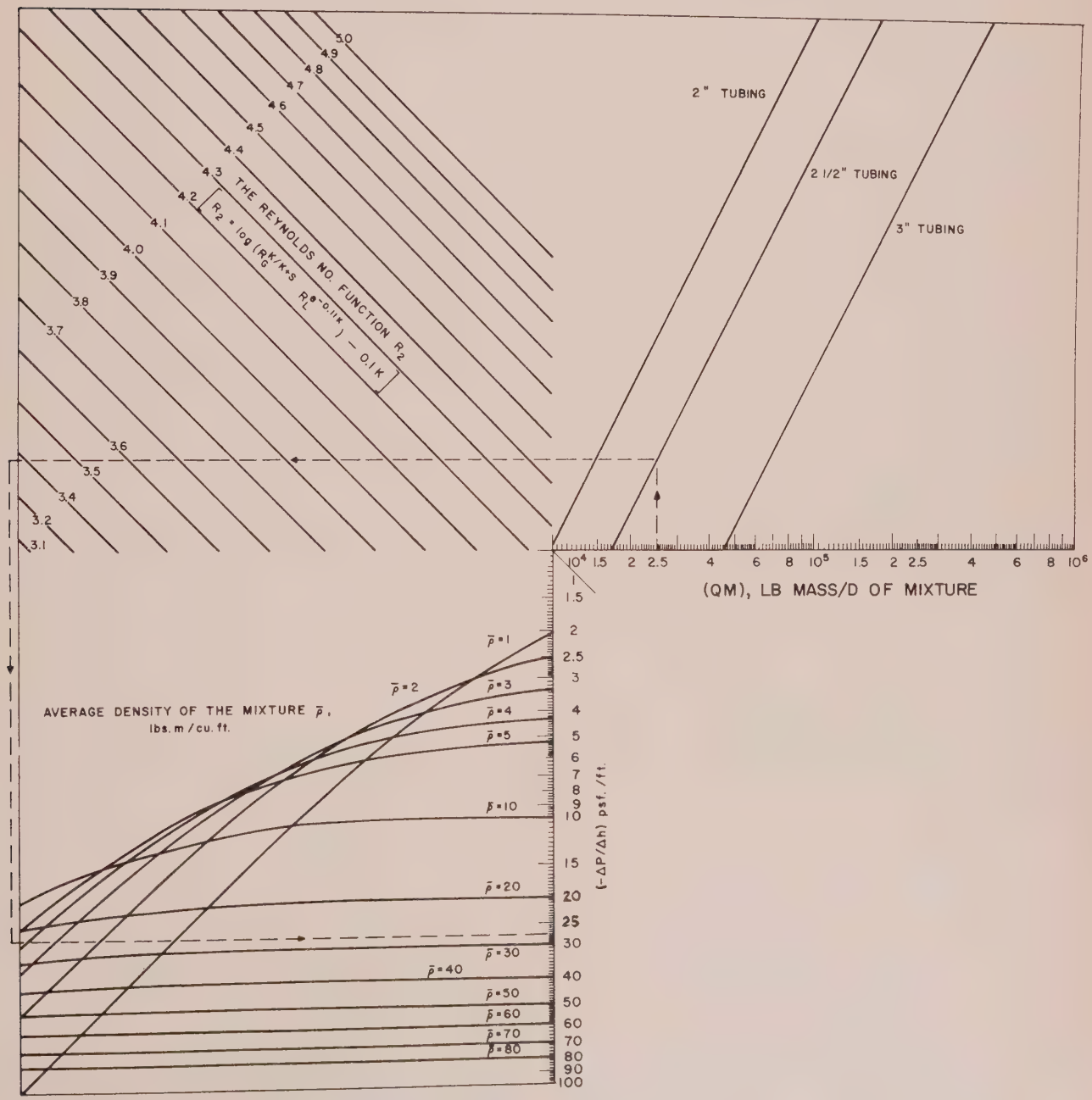

FIG. 4—WORKING CHART FOR GRAPHICAL DETERMINATION OF PRESSURE GRADIENT.

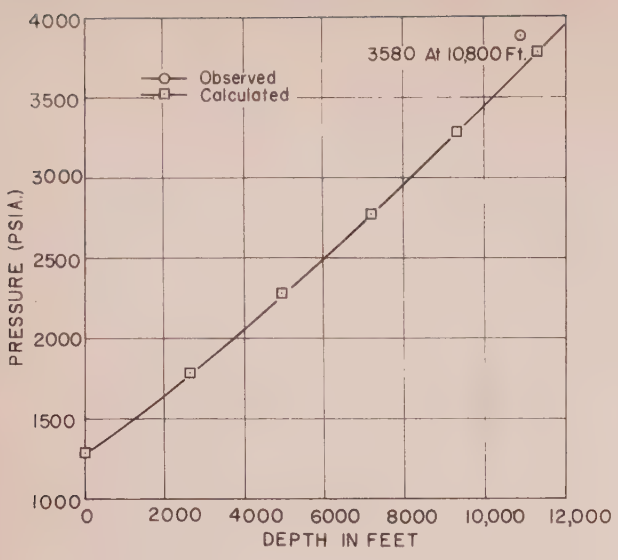

FIG. 5—PRESSURE PROFILE FOR EXAMPLE PROBLEM.

$= 3.19 \times 10^4$.

$(R_G)_1 = 31{,}900$.

4. Calculate $(R_2)_1 = \log\ (R_G^{k/k+5} R_L^{-0.11k}) - 0.1\ k$.

$$(R_2)_1 = \log\ [(31{,}900)^{0.382/5.382}\ (1{,}470)^{-0.11 \times 0.382}] - 0.1 \times 0.382$$

$$= \log\ [(31{,}900)^{0.071}\ (1{,}470)^{0.958}] - 0.0382$$

$$= \log\ (2.08 \times 1.08 \times 10^3) - 0.0382$$

$$= 3.352 - 0.0382$$

$(R_2)_1 = 3.314$.

5. Calculate $(\bar{\rho})_1$.

$$(\bar{\rho})_1 = \frac{M_1}{(\bar{V}_m)_1}.$$

$M_1 = 351\ G_o + 0.0764\ G_g (S_{g/o})_{ST} + 62.4\ G_w V_w$ (where ST denotes stock tank)

$= 351 \times 0.805 + 0.0764 \times 0.796 \times 2{,}250$

$= 282 + 107.8 = 419$ lb/bbl produced at stock tank.

$$(V_m) = 5.61\ F + \frac{P_a T_{av} Z}{P\ T_a} [(S_{g/o} - S_{s1})] + V_w;$$

at average pressure P_1,

$$(\bar{V}_m)_1 = 5.61 F + \frac{P_a T_{av} Z}{P_1 T_a} [(S_{g/o} - S_{s1})] + V_w;$$

$F_1 = 1.45$ at $(P_{av})_1 = 1{,}514$ psia.

${}_pP_{crit} = 668$ psia pseudocritical pressure.

${}_pT_{crit} = 425°$R absolute pseudocritical temperature from Eq. 3.

$${}_pP_r = \frac{1{,}513}{668} = 2.27.$$

$${}_pT_r = \frac{460 + 75}{425} = \frac{535}{425} = 1.26.$$

$Z_1 = 0.6$.

$$(\bar{V}_m)_1 = 5.61 \times 1.45 + \frac{14.65 \times 535 \times 0.6}{1{,}514 \times 520} \times [2{,}250 - 680]$$

$= 8.15 + 9.38$

$= 17.53$ total cu ft/bbl of stock-tank oil.

$$\bar{\rho}_1 = \frac{419}{17.53} = 22.2 \text{ lb mass/cu ft.}$$

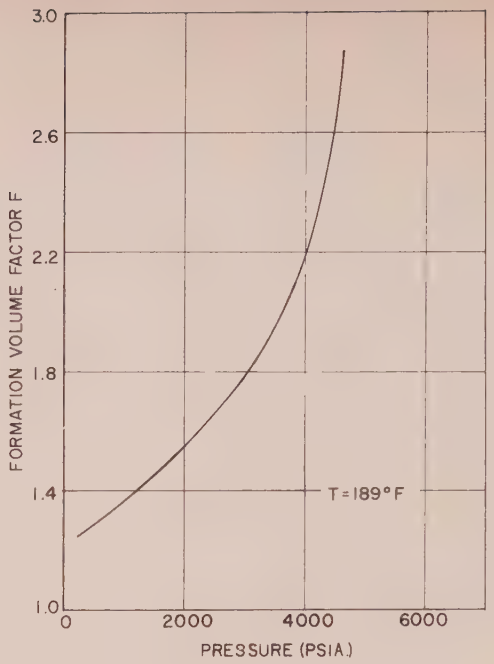

FIG. 6—FORMATION-VOLUME-FACTOR CURVE.

6. Calculate $(QM)_1 = 60 \times 419 = 2.514 \times 10^4$ lb mass total/day.

7. Calculate $(-\Delta P)/\Delta h$ from working chart (Fig. 4). First locate $QM = 2.514 \times 10^4$ on horizontal QM scale; then, go vertically up through the intersection with 2½-in. tubing line, horizontally to left through $R_2 = 3.314$ (interpolated) vertically down through $\bar{\rho} = 22.2$ (interpolated) and read on vertically down the scale $(\Delta P/\Delta h) = 27.5$ lb/sq ft/ft.

$\Delta P = 500$ psi or $500 \times 144 = 72{,}000$ lb/sq ft/ft.

$$(\Delta h)_1 = \frac{72{,}000}{27.5} = \underline{2{,}620 \text{ ft} \leftarrow}.$$

NOMENCLATURE

a = a function of gas-liquid mass ratio $a = k/(k+1)$, dimensionless

b = a function of gas-liquid mass ratio $b = e^{-0.1k}$, dimensionless

c = a universal constant, dimensionless

D = pipe or tubing diameter, ft ID

F = formation volume factor, dimensionless

f' = two-phase friction factor, dimensionless

G = specific gravity, dimensionless

$g_c = 32.17 \frac{\text{lb mass}}{\text{lb force}} \frac{\text{ft}}{\text{sec}^2}$

g = acceleration of gravity, ft/sec²

h = length of the vertical flow string, ft

k = gas-liquid mass ratio, lb mass of gas/lb of liquid,

M = lb mass of oil gas and water/STB oil

P = pressure, psia

P_a = base pressure = 14.65 psia

Q = oil-production rate STB/D

R_1 = two-phase Reynolds' number function, dimensionless

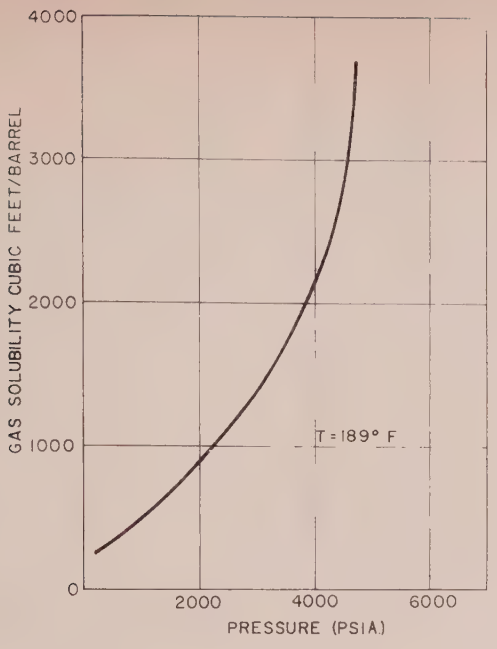

FIG. 7—SOLUBILITY CURVE.

R_2 = two-phase Reynolds' number function, dimensionless
$S_{g/o}$ = produced gas-liquid ratio, scf gas/STB oil
S_s = gas solubility, scf/STB oil
T_{av} = average temperature of the flow string, °R absolute
T_a = base temperature, = 520°R absolute
V = specific volume of gas-liquid mixture, cu ft/lb mass
V_m = specific volume of gas-liquid mixture in field units, cu ft/STB oil
$\overline{V}_m$ = integrated average value of V_m, cu ft/STB oil
V_w = water-oil ratio, cu ft of water/STB oil
v = average velocity of gas-liquid mixture, ft/sec
W = work, ft × lb force/lb mass
W_s = shaft work, ft × lb force/lb mass
Z = compressibility factor, dimensionless
α = a constant, dimensionless
β = a constant, dimensionless
Δ = difference
μ = viscosity, cp
ρ = density, lb mass/cu ft
$\overline{\rho}$ = pressure-integrated mean density, lb mass/cu ft

SUBSCRIPTS

1 = point upstream, down pipe
2 = point downstream, up pipe
o = oil
g = gas
l = liquid
w = water
f = friction
r = reduced condition

REFERENCES

1. Poettmann, F. H. and Carpenter, P. G.: "The Multiphase Flow of Gas, Oil and Water through Vertical Flow Strings", *Drill. and Prod. Prac.*, API (1952) 257.
2. Bertuzzi, A. F., Tek, M. R. and Poettmann, F. H.: "Simultaneous Flow of Liquid and Gas through Horizontal Pipes", *Trans.*, AIME (1956) **207**, 17.
3. Katz, D. L., *et al.*: *Handbook of Natural Gas Engineering*, McGraw-Hill Book Co., Inc., N. Y. (1959).
4. Tek, M. R. and Chan, W. J.: "Simultaneous Flow of Liquid and Gas Through Vertical Pipe", paper presented at AIChE Annual Meeting in San Francisco (Dec., 1959).

APPENDIX

DEVELOPMENT AND DERIVATION OF EQUATIONS USED FOR ANALYSIS OF DATA

It is known that the vertical simultaneous flow of liquid and gas may be treated as the flow of one phase with combined properties through the use of energy balances expressed in the well known flow equation.

$$\int_{P_1}^{P_2} V dP + \Delta h + \Delta\left[\frac{v^2}{2g_c}\right] + W_f + W_s = 0 \quad \ldots\ldots\ldots\ldots\ldots\ldots \text{(A-1)}$$

where V = specific volume of the fluid, in cu ft/lb mass,
P_1 = pressure of the fluid entering the vertical system under consideration, in lb/sq ft absolute,
P_2 = pressure of the fluid leaving the system, in lb/sq ft absolute,
Δh = height of the system, ft,
$\Delta\left[\frac{v^2}{2g_c}\right]$ = difference in kinetic energy of the flowing fluid, ft-lb force/lb mass,
W_f = irreversible energy losses due to slippage, liquid hang-up, friction and other effects in ft-lb force/lb mass, and
W_s = shaft work in ft-lb force/lb mass.

This equation states that the energy entering the system at Point 1 must equal the energy leaving the system at Point 2 plus the energy interchanged between the fluid and its surroundings.

Considering that the fluid flow is steady, work done by the fluid is zero and the change of kinetic energy is negligible, Eq. 1 may be simplified as

$$\int_{P_1}^{P_2} V dP + \Delta h + W_f = 0 \quad \ldots \text{(A-2)}$$

Defining a two-phase f' factor which is similar to the one in single-phase flow, then

$$f' = \frac{2g_c W_f D}{4\bar{v}^2 \Delta h} \quad \ldots\ldots\ldots\ldots \text{(A-3)}$$

where f' = two-phase f factor, dimensionless,
D = diameter of the flow string, ft, and
$\bar{v}$ = integrated average value of velocity between limits of P_1 and P_2 (assumed approximately constant), in ft/sec.

Combining Eqs. 2 and 3 to eliminate term W_f, one gets

$$\Delta h = \frac{\int_{P_2}^{P_1} V dP}{1 + \frac{4\bar{v}^2 f'}{2g_c D}} \quad \ldots\ldots\ldots\ldots \text{(A-4)}$$

If we arbitrarily define

$$\overline{V}_m = \frac{\int_{P_2}^{P_1} V_m dP}{P_1 - P_2},$$ let the following quantities be expressed with terms of units readily obtained from field data of oil wells, such as

$$\int_{P_2}^{P_1} V dP = \frac{1}{M}\int_{P_2}^{P_1} V_m dP,$$

and

$$\bar{v} = \frac{Q\bar{V}_m}{21{,}600\,\pi D^2}.$$

Eq. A-4 can be re-arranged to get two working equations to calculate Δh or f' as follows.

$$\Delta h = \frac{\frac{144}{M}\int_{P_2}^{P_1} V_m dP}{1 + \frac{f'Q^2\bar{V}_m^2}{7.413 \times 10^{10} D^5}} \quad \ldots\ldots \text{(A-5)}$$

$$f' = \left[\frac{144}{M}\int_{P_2}^{P_1} V_m dP - \Delta h\right]\frac{7.413 \times 10^{10} D^5}{\bar{V}_m^2 Q^2 \Delta h} \quad \ldots\ldots \text{(A-6)}$$

where P = pressure, in psi absolute,
M = total mass of fluid such as gas, oil and water in lb mass, associated with 1 STB of oil flowing into and out of the system,
V_m = volume of fluid at pressure P, in cu ft/STB oil,
$\bar{V}_m$ = the integrated average value of V_m between limits of P_1 and P_2 in cu ft/STB oil, and
Q = STB/D of oil produced.

The total mass M associated with 1 STB of oil can be calculated as

$$M = (5.61)(62.4)(G_o) + (0.0764)(G_g)(S_{g/o}) + (62.4)(G_w)(V_w) \quad \ldots\ldots \text{(A-7)}$$

where G_o = specific gravity of stock-tank oil,
G_g = specific gravity of natural gas (air = 1),
G_w = specific gravity of produced water,
$S_{g/o}$ = producing gas-oil ratio, in cu ft/STB oil, and
V_w = cu ft of water produced/STB oil.

In Poettmann's paper,[1] the process to calculate $\bar{V}_m$ is shown in detail along with tables of values of Z, $\int_{0.2}^{P_r} Z\,dP_r$ and $\int_{0.2}^{P_r} \frac{Z}{P_r} dP_r$ to facilitate the calculation of $\bar{V}_m$.

Since

$$\bar{V}_m = \frac{\int_{P_2}^{P_1} V_m dP}{P_1 - P_2}, \quad \ldots\ldots \text{(A-8)}$$

$$V_m = 5.61F + \frac{P_a T_{avg} Z}{P T_a}(S_{g/o} - S_s) + V_w. \quad \text{(A-9)}$$

where F = formation-volume factor of oil, which is a function of pressure P, in bbl of reservoir oil/STB oil
T_{avg} = arithmetic average temperature in the flow string, in °R,
P_a = base pressure at which gas is measured,
T_a = base temperature,
Z = compressibility factor of the gas at temperature T_{avg} and pressure P, and
S_s = solubility of gas in oil and is a function of P, in cu ft/bbl of oil

If the formation-volume factor and the solubility of the oil are linear functions of pressure over the range of pressure under consideration, V_m can be calculated analytically as follows.

$$V_m = 5.61\,n_f P + 5.61\,F_i + \frac{P_a T_{avg} Z}{T_a}\left[\frac{S_{g/o}}{P} - n_s - \frac{S_i}{P}\right] + V_w \quad \ldots\ldots \text{(A-10)}$$

where n_f = slope of formation-volume-factor curve,
F_i = intercept of formation-volume-factor curve,
n_s = slope of solubility curve, and
S_i = intercept of solubility curve.

By using Eq. A-10 and collecting common factors, then

$$\int_{P_2}^{P_1} V_m dP = 2.805\,n_f(P_1^2 - P_2^2) + (5.61\,F_i + V_w)(P_1 - P_2) + \frac{P_a T_{avg}}{T_a}\left[(S_{g/o} - S_i)\int_{P_2}^{P_1}\frac{Z}{P_r}dP_r - n_s\int_{P_2}^{P_1} Z_d P_r\right] \quad \ldots\ldots \text{(A-11)}$$

$$\int_{P_2}^{P_1}\frac{Z}{P}dP = \int_{P_2}^{P_1}\frac{Z}{P_r}dP_r = \int_{0.2}^{P_{r_1}}\frac{Z}{P_r}dP_r - \int_{0.2}^{P_{r_2}}\frac{Z}{P_r}dP_r \quad \ldots \text{(A-12)}$$

$$\int_{P_2}^{P_1} Z dP = P_c\int_{P_{r_2}}^{P_{r_1}} Z dP_r = P_c\left[\int_{0.2}^{P_{r_1}} Z dP_r - \int_{0.2}^{P_{r_2}} Z dP_r\right] \quad \ldots \text{(A-13)}$$

where $P_r = \frac{P}{P_c}$, and

P_c = pseudocritical pressure.

If the formation-volume-factor curve and the gas-solubility curve cannot be approximated with straight-line functions, graphical integration is recommended to calculate the term $\bar{V}_m$. ★★★

Simultaneous Flow of Gas and Liquid As Encountered in Well Tubing

N. C. J. ROS*
MEMBER AIME

KONINKLIJKE/SHELL LABORATORIUM
DELFT, THE NETHERLANDS

ABSTRACT

The paper deals with pressure gradients occurring in flowing and gas-lift wells, a knowledge of which can be applied to the determination of optimum flow-string dimensions and to the design of gas-lift installations. The study is based on a pressure-balance equation for the pressure gradient. It appears that a pressure-gradient correlation of general validity must essentially consist of two parts—one part being a correlation for liquid hold-up and the other part being one for wall friction. Dimensional analysis indicates that both liquid hold-up and wall friction are related to nine dimensionless groups. It is shown that in the field of interest only four groups are really important. On the basis of these four groups a restricted experimental program could be selected that nevertheless covered practically all conditions encountered in oil wells. This experimental program has been carried out in a laboratory installation. Three essentially different flow regimes were found. The pressure gradients in these regious are presented in the form of a set of correlations. Comparison of these correlations with a few available oilfield data showed excellent agreement.

INTRODUCTION

Prediction of the pressure drop in the flow string of a well is a widely known problem in oilfield practice.

Accurate data on the pressure gradient of a simultaneous flow of gas and liquid in a vertical pipe are especially useful for the determination of optimum flow-string dimensions. It is well known that with moderate gas and liquid flows such a vertical string acts as a "negative restriction". The pressure drop decreases (1) when the throughput through a given pipe increases, and (2) when at a given throughput the cross-sectional area is decreased. The reason is that, with increasing velocities, the flow becomes more agitated so that the gas slips relatively more slowly through the liquid. With the resulting increase in gas content in the string, the static head decreases. When the area becomes very small, however, the high velocities entail great wall friction, which causes an increase in pressure drop. For a given flow, therefore, minimal pressure drop is obtained by using a certain cross section. This means that, in principle, each well can be provided with an optimum flow string for minimum pressure drop and, hence, maximum possible production rate. The procedure for the selection of the optimum string has been discussed by Gilbert.[1] A necessary tool in the procedure, however, is accurate knowledge of the pressure gradient to be expected for various values of the governing variables.

Another application of pressure-gradient data lies in the field of gas-lift practice: they provide a means of determining the optimum gas-injection rate, optimum injection pressure and optimum injection depth.

Much work has already been done in the study of the pressure gradient of vertical gas-liquid flow. Poettmann and Carpenter[2] presented a pressure-gradient correlation based on measurements in wells. This correlation has been found to provide accurate predictions in high-pressure wells and in high-production wells for flow through both tubing and annuli.[2-5] However, when their method is checked on low pressure-low production wells or on wells with viscous crudes, serious discrepancies are found. As we shall see in the next section, this is due to the fact that their correlation factor, representing all irreversible energy losses, is given as a function of only one correlation group. Some important variables, such as gas-liquid ratio and liquid viscosity, are not incorporated in this group so that their specific effects are not accounted for.

To study also the mechanism of vertical gas-liquid flow outside the ranges covered by the Poettmann-Carpenter publication and extensions, a laboratory investigation has been carried out. This study is founded on a pressure-gradient equation that is based on a pressure balance. To reduce the number of test runs required, a dimensional analysis has been carried out, followed by a selection of relevant dimensionless groups. These groups guided a subsequent experimental study, and with their aid the experimental program could be minimized while still covering the majority of the situations encountered in oilfield practice.

In this paper the choice of a formula for the pressure gradient is discussed first. This is followed by a brief description of the experimental setup. Subsequently, the dimensional analysis is discussed and the relevant dimensionless groups are selected, resulting in the experimental program required. The general relationships of pressure gradient and liquid hold-up are then described; various flow patterns and a certain flow instability (so-called "heading") are discussed and a set of correlations is presented which shows a good agreement with the measurements and a few available field

Original manuscript received in Society of Petroleum Engineers office Feb. 8, 1961. Revised manuscript received Aug. 1, 1961. Paper presented at Joint AIChE-SPE Symposium, Sept. 25-28, 1960, in Tulsa.

*On temporary assignment with Shell Development Co., Houston, Tex.

[1]References given at end of paper.

data. It would seem that these correlations hold promise of general application in oilfield practice.

FORMULA FOR THE PRESSURE GRADIENT OF GAS-LIQUID FLOW

The two main methods for producing a formula for the pressure gradient of gas-liquid flow are (1) evaluation of an energy-balance equation between any two points of the flow string and (2) evaluation of a pressure-balance equation, again between any two points of the system under consideration.

The first method has been used by Poettmann and Carpenter.[2] Their resulting formula reads

$$\frac{dP}{dh} = \bar{\rho} + f_p \frac{Q^2M^2}{7.413 \times 10^{10} \bar{\rho} D^5} + \text{Acceleration Gradient}$$

where $\frac{dP}{dh}$ = pressure gradient (lb/sq ft/ft),

$\bar{\rho}$ = gas-liquid mixture density, which would occur when all energy losses were zero (no slip) (lb/cu ft),

QM = total mass flow (lb/day),

D = inside diameter of tubing (ft), and

f_p = dimensionless correlating function for the total energy loss (-).

For the flow in wells, all quantities occurring in the right-hand part of this equation are known except the value of f_p. This factor f_p represents all irreversible energy losses, mainly consisting of the slip losses between the phases and the energy losses due to wall friction. It has been defined using a modified Fanning-type friction equation and, therefore, will be most suitable for conditions where wall friction is dominant. This is borne out by the experiments carried out in high-potential wells, referred to earlier and reported by Baxendell and Thomas.[5] The high velocities occurring in these wells caused the slip losses to be slight, whereas the losses due to wall friction were substantial. Therefore, the resulting f_p-correlation could be presented as a single curve, with which it appeared to be possible to predict the entire flow-gradient relationship in the well with very high accuracy (errors below some 5 per cent).

The situation in low-potential wells appears to be very different, however. Here, the velocities in the flow string are low so that wall friction cannot help but be very small; consequently, the slip losses must be the main contribution to f_p. Whereas Poettmann and Carpenter in this range presented for f_p-correlation one single curve based on field data, controlled laboratory tests reported by Govier, *et al*,[6] resulted in a family of curves for f_p with the insitu gas-liquid ratio as parameter. This family of curves moreover appeared to depend on the diameter of the flow string,[7] whereas some influence of liquid viscosity is also likely to be present. Therefore, it is to be expected that a large number of f_p-curves will be required to cover the entire flowing and gas-lift field practice. This apparently is due to the fact that the mechanisms causing slip losses and wall friction are entirely different from each other. Therefore, correlation of slip losses using a typical friction equation cannot help but give undesirably complicated results when the full range has to be covered. Use of a pressure-balance equation, in which the influences of gas slip and wall friction are separately dealt with, would seem to be more appropriate. For this reason, a pressure-balance equation rather than an energy-balance equation has been chosen as a basis for further study.

In the case of single-phase flow, the pressure gradient is equal to the sum of static gradient, friction gradient and acceleration gradient.

$$\frac{dP}{dh} = \rho g + 4f\tfrac{1}{2}\rho v^2 \frac{1}{D} + \text{Acceleration Gradient}$$

where $\frac{dP}{dh}$ = pressure gradient ($ML^{-2}T^{-2}$),

ρ = density of the fluid (ML^{-3}),

g = gravity acceleration (LT^{-2}),

v = fluid velocity (LT^{-1}),

D = inside diameter of the pipe (L), and

f = friction factor (−).

This equation is identical to that of Poettmann and Carpenter when single-phase systems are considered. When applied to gas-liquid systems, the pressure-balance equation becomes very different, however. Also, then, we may split up the pressure gradient into three parts: $\frac{dP}{dh}$ = Static Gradient + Friction Gradient + Acceleration Gradient.

The "static gradient" supports the gas and liquid present in the vertical column. The effects of slip between the phases are thus incorporated in this gradient, and it therefore basically differs from the term $\bar{\rho}$ of the Poettmann and Carpenter equation, in which the slip losses are not included.

The static gradient is equal to

$$\varepsilon_l \rho_l g + \varepsilon_g \rho_g g$$

where ρ_l, ρ_g = density of liquid and gas, respectively (ML^{-3}), and

ε_l, ε_g = hold-up of liquid and gas, respectively (−).

The two terms represent the contributions of liquid and gas, respectively. The liquid term is equal to the static gradient of a nonflowing liquid column without gas, $\rho_l g$, times a correction factor ε_l that corrects for the fact that only part of the column is filled with liquid and the remainder with gas. This correction factor ε_l, the liquid hold-up, is thus defined as the volume of liquid actually present in a certain length of pipe, divided by the volume of that length of pipe. A similar expression holds for the gas term, being equal to the static gas gradient $\rho_g g$ times the gas hold-up $\varepsilon_g = 1 - \varepsilon_l$.

This expression for the static gradient presupposes that this gradient supports all the liquid and gas present in the column. This is usually true. In certain cases, however, a small part of the liquid is supported by the wall (see "Experimental Results") and cannot contribute to the static gradient. However, we may still use the same expression for the static gradient and adapt the value of ε_l, which then becomes a "pseudo liquid hold-up".

The "friction gradient" represents the drag of the flowing gas-liquid mixture on the wall of the pipe only. It will be dealt with in more detail in the "Correlations" section.

The "acceleration gradient" fortunately is so small that it may be neglected for flow in wells.[2,3]

Thus, the expression for the pressure gradient becomes as follows, when in addition it is divided by the constant factor $\rho_l g$ in order to obtain a convenient dimensionless expression.

$$G = \frac{1}{\rho_l g}\frac{dP}{dh} = \varepsilon_l + (1 - \varepsilon_l)\frac{\rho_g}{\rho_l} + \text{Friction Term} \quad \ldots\ldots\ldots\ldots\ldots\ldots\ldots\ldots (1)$$

where G = dimensionless pressure gradient.

In the large majority of field situations, as well as in any atmospheric test setup, the contribution of the gas hold-up term $(1 - \varepsilon_l)\rho_g/\rho_l$ is negligibly small. Then the equation reduces to

$$G = \varepsilon_l + \text{Friction Term}.$$

As discussed before, the behaviors of friction and of liquid hold-up (the latter depending on slip only) will be basically different. Therefore, for any pressure-gradient correlation to be of general validity, it is essential that such a correlation be split into two separate correlations—the first for liquid hold-up and the second for friction. Then, it will also be necessary to measure both hold-up and friction, or their sum, the total gradient. Accordingly, a test installation for measuring both hold-up and total pressure gradient has been used, as described in the next section.

TEST INSTALLATION (Fig. 1)

The measurements were carried out in a vertical flow string, consisting of an inflow section with a length between 30 and 45 m, a 10-m-long measuring section and a 2-m-long outflow section. The flows of gas and liquid, the temperature, and the pressure on the top of the column were kept constant manually or by means of controllers.

The measuring section being transparent, the flow could be observed either visually or by making films. Pressure-gradient measurements were carried out using

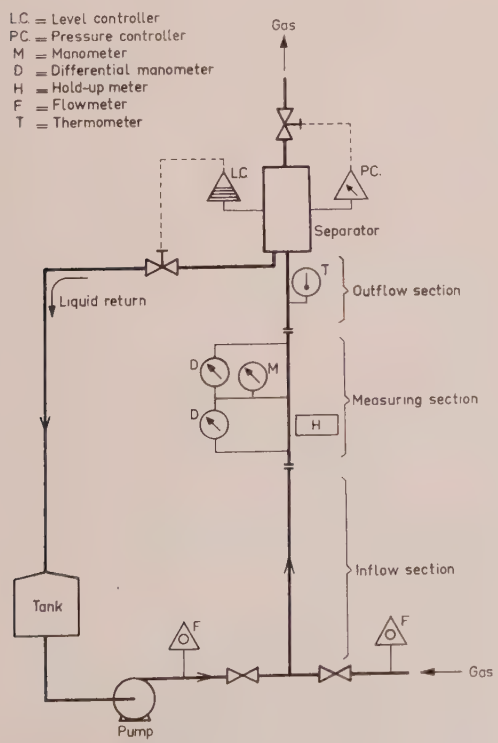

FIG. 1—SIMPLIFIED FLOW SHEET TEST SETUP.

differential manometers. The liquid hold-up, defined previously as the volume of liquid actually present in a short length of pipe divided by the volume of that length of pipe, was measured using a radioactive tracer technique. To that end, a small amount of radioactive cobalt naphthalate was dissolved in the liquid. The intensity of radiation from a pipe section, being proportional to the amount of liquid present and hence to the liquid hold-up, was measured by means of a scintillation counter.

Most of the measurements were carried out at atmospheric pressure using air as gas and liquid hydrocarbons or water as liquid. In a similar installation, a limited number of test runs was made at elevated pressures, using natural gas and gas-oil.

For any experimental flow study to be of value for wide ranges of conditions, data should be obtained for a great number of different flow situations. The number of test runs required, in fact, depends on the number of independent quantities that govern the flow mechanism in the pipe. Many of such quantities are present (viz., internal tubing diameter, liquid throughput, gas throughput, etc.). Since for the investigation of the influence of all quantities the number of test runs required would be far beyond anything that could reasonably be carried out, it is essential that a preliminary investigation be made to select those independent quantities which are actually of importance for the flow in wells. Such a study has been carried out and will be dealt with in the next two sections.

DIMENSIONAL ANALYSIS

The mechanism of any flow situation is governed by dimensionless groups, the number of which is three less than the number of independent quantities required to describe fully the boundary conditions (configuration), the relevant properties of the material and the interaction between material and boundary or surroundings. Use can be made of the observed fact that, in two-phase flow as in single-phase flow, the mechanism at any spot is independent of the way the fluids are supplied at the entrance or flow off at the outlet provided that the spot is not too close to the inlet or the outlet. Then, for this equilibrium flow of gas-liquid in a cylindrical pipe, the governing independent quantities at any spot are those shown in Table 1.

These 12 independent quantities determine the pressure gradient dP/dh. Application of the π-theorem[8] to all 13 variables results in 10 dimensionless groups. These groups may be chosen as shown in Table 2.

According to the theory of dimensionless numbers, the value of the dimensionless pressure gradient is fully determined by the values of the nine governing groups.

In this analysis, the pressure gradient has been chosen as the dependent quantity. Actually, however, we are only interested in the flow mechanism, by which we mean the geometrical and velocity distribution of gas

TABLE 1

Tube			Liquid	Gas
Internal Diameter	D (L)	Density	ρ_l	ρ_g (ML^{-3})
Wall Roughness	ε (L)	Viscosity	μ_l	μ_g ($ML^{-1}T^{-1}$)
Inclination	ϕ (-)	Superficial Velocity*	v_{sl}	v_{sg} (LT^{-1})

Interaction	
Surface Tension	σ (MT^{-2})
Wall Contact Angle	α (-)
Gravity Acceleration	g (LT^{-2})

*This measure of throughput equals the volume throughput at in situ conditions per unit of total cross-sectional area.

TABLE 2—DIMENSIONLESS GROUPS

Governing Groups:		
Diameter Influence Number	N_d	$= D\sqrt{(\rho_l g/\sigma)}$
Specific Wall Roughness	ε/D	
Inclination of the Pipe	ϕ	
Gas-Liquid Density Ratio	N_ρ	$= \rho_g/\rho_l$
Viscosity Influence Number Liquid	N_l	$= \mu_l \sqrt[4]{(g/\rho_l\sigma^3)}$
Viscosity Influence Number Gas	N_g	$= \mu_g \sqrt[4]{(g/\rho_l\sigma^3)}$
Velocity Influence Number Liquid	N	$= v_{sl}\sqrt{(\rho_l/g\sigma)}$
In Situ Gas-Liquid Velocity Ratio	R	$= v_{sg}/v_{sl}$
Wall Contact Angle	α	
Dependent Group:		
Dimensionless Pressure Gradient	G	$= (1/\rho_l g)\,(dP/dh)$.

and liquid in the pipe. This distribution in fact establishes the values of both the liquid hold-up and the wall friction—that of the liquid hold-up because it is a direct consequence of the space distribution of gas and liquid, and that of the wall friction because it exclusively depends on the shear stresses in the liquid phase. The shear stresses follow from the velocity gradients in the liquid, which in turn depend on the velocity distribution, i.e., on the flow mechanism. Thus, a known flow mechanism establishes the values of the liquid hold-up, the wall friction and, according to Eq. 1, the pressure gradient. Moreover, the flow mechanism reflects the type of flow, as well as the conditions for transition from one type into another and the regimes for each particular type of flow.

Regarding this, and the afore-mentioned analysis, it can thus be concluded that the flow mechanism, expressed in terms of liquid hold-up, wall friction and boundaries of flow regimes, must fully be determined by the values of the nine governing groups. Since the complexity of the problem excludes theoretical treatment, the relationship must be determined experimentally. Fortunately, it can be shown that only a few groups are of real importance for the flow in oil wells.

ELIMINATION OF IRRELEVANT GROUPS

INCLINATION ϕ

Most wells are vertical or nearly vertical, so that ϕ will be equal to 90° ± a few degrees (say a maximum of 8°). In this range any effect of ϕ-variation on the pressure gradient cannot be anything but very small. Thus, ϕ can be ignored in the field of interest.

WALL CONTACT ANGLE α

Visual observation of gas-liquid flow through vertical flow strings of oilfield dimensions shows that the wall is always wetted so that the wall contact angle α cannot have any influence and, hence, may be ignored.

VISCOSITY INFLUENCE NUMBER GAS N_g

The gas viscosity can influence the flow mechanism only in cases of high shear stresses, comprising high-velocity gradients in the gas. It now appears (see "Experimental Results") that, at the correspondingly high gas velocities, mist flow occurs where the gas phase is highly turbulent. Then, the influence of gas viscosity is negligible and, with it, that of the viscosity influence number of the gas N_g.

SPECIFIC WALL ROUGHNESS ε/D

Experiments with gas-liquid flow in horizontal pipes[9] showed that wall friction remains small when liquid flow is small. This holds for both smooth pipes and for pipes with roughness comparable with that of tubing. This will also hold for vertical pipes. For, in the low-velocity range, the pressure gradient will be determined mainly by what occurs in the pipe center where the flow is highly irregular and will not be significantly affected by small additional irregularities caused by wall roughness. In the high-velocity range, however, wall roughness may be a significant factor. Experiments will have to show what the influence actually is.

GAS-LIQUID DENSITY RATIO N_ρ

The physical influence of gas density ρ_g incorporated in the density ratio N_ρ on the flow mechanism consists of two parts: (1) the effect of $(\rho_l - \rho_g)$, governing the driving force of the slip between gas and liquid; and (2) the effect of $\frac{1}{2}\rho_g v_{sg}^2$, the kinetic head of the gas.

The value of $(\rho_l - \rho_g)$ is chiefly determined by ρ_l, since ρ_g is small, except for very high pressure (some thousands of pounds per square inch). In this range, however, the volumetric gas flow is very small, most gas being in solution and the remainder being highly compressed. It now appears (see later) that for the correspondingly low gas velocities the slip losses are very small, so that any effect of N_ρ will be of the second order and can be ignored.

The quantity $\frac{1}{2}\rho_g v_{sg}^2$ can only affect the flow mechanism if its value is comparable with the values of other relevant quantities, e.g., that derived from the static liquid gradient $\rho_l g D$. This condition only occurs for high values of v_{sg}, i.e., in the upper part of the flow string in the well. Experiments will have to decide whether incorporation of N_ρ as governing group is necessary for flow in wells and, if so, in what way.

The remaining groups —N_l (liquid viscosity), N_d (pipe diameter), R (velocity ratio) and N (liquid velocity)—will chiefly govern the flow mechanism. These groups may serve as variables in any experimental program and can be used for correlating purposes.

By this use of dimensional analysis, three independent quantities have been automatically accounted for—the surface tension, the liquid's density and the gravity acceleration. Whereas the latter two would not vary much anyway, the surface tension may vary by as much as a factor of 40 or more when water is produced instead of oil. Such a variation would have the same effect as that of a simultaneous change in diameter, liquid viscosity and liquid velocity, as can be seen from the shapes of the groups.

On the basis of the remaining four relevant groups, the following experimental program would seem to cover the field.

1. Variation of gas and liquid flows for liquids of various viscosities, all in a certain pipe. This covers N, R and N_l.

2. Variation of gas and liquid flows in pipes differing in diameter, for a limited number of liquids. This covers N_d, while it can be verified whether σ, ρ_l and g have been correctly incorporated in the governing groups.

3. A series of experiments with a rough and a smooth pipe would show whether the effect of ε/D were as small as anticipated.

4. Variation of the pressure level for a range of gas and liquid flows would show whether N_ρ had any effect.

Such a program has been carried out in the laboratory. It was extended by a series of experiments in annuli. Main data are shown in Table 3. The ranges cover the greater part of oilfield conditions. This pro-

gram required, notwithstanding the restrictions discussed, some 4,000 test runs, comprising some 20,000 data points for pressure gradient and liquid hold-up.

EXPERIMENTAL RESULTS

A typical example of the results obtained is presented in Fig. 2 for the flow of air and gas oil in an 8-cm pipe. The solid lines refer to the observed pressure gradient, the dotted lines to the liquid hold-up ε_l. Both have been plotted against the gas throughput for various values of the liquid throughput. The gradient is expressed in its dimensionless form, $G = (1/\rho_l g)(dP/dh)$. The throughputs are characterized by superficial velocities.

The lines originate from test runs in which the throughputs were varied in geometrical succession, with multiplying factors of $\sqrt{2}$ and 2 for the gas and liquid, respectively. The lines of Fig. 2 represent a set of curves derived from some 1,250 data obtained in some 250 test runs. Except in the heading region (see section entitled "Heading"), the standard deviation between measurements amounts to less than 5 per cent and that for the averaging curves to less than 3 per cent.

GENERAL PICTURE

As shown in Fig. 2, pressure gradient and hold-up depend strongly on the gas throughput.

At low gas throughput bubble flow prevails, the liquid phase then being continuous and the gas being dispersed in small bubbles. So long as the volume of the bubbles remains negligibly small, the liquid hold-up is equal to unity and the pressure gradient nearly equals the static gradient of gas-free liquid; thus, $G \approx 1$. Wall friction makes the gradient slightly higher at high liquid flow rates.

At greater gas throughputs, wall friction causes the picture for a low liquid flow rate to differ from that for a high one.

TABLE 3

Flow String			Liquid			
Type	D (cm)	D_t (cm)	Type	ρ_l (gm/cc)	σ (dyne/cm)	ν_l (centistokes)
Pipe	3.20	—	Gas oil	0.828	28.0	4.0
Pipe	3.20	—	Lubricating oil	0.886	30.0	18.0
Pipe	3.20	—	Lubricating oil	0.937	32.0	337
Pipe	8.02	—	Water	1.000	72.0	1.00
Pipe	8.02	—	Mineral spirit	0.780	24.5	1.23
Pipe	8.02	—	Gas oil	0.827	27.5	4.2
Pipe	8.02	—	Lubricating oil	0.852	28.1	6.6
Pipe	8.02	—	Lubricating oil	0.880	29.1	13.1
Pipe	8.02	—	Lubricating oil	0.902	30.1	25.5
Pipe	8.02	—	Lubricating oil	0.920	33.8	51.5
Pipe	8.02	—	Lubricating oil	0.933	33.1	290
Pipe	14.23	—	Gas oil	0.831	27.0	4.4
Pipe	14.23	—	Lubricating oil	0.878	29.0	16.0
Annulus	14.23	6.01	Gas oil	0.834	28.0	4.8
Annulus	14.23	8.99	Gas oil	0.837	28.0	4.9
Annulus	14.23	8.99	Lubricating oil	0.877	29.0	14.1

v_{sg} between 0 and 10,000 cm/sec.

v_{sl} between 0 and 320 cm/sec.

Considering low liquid rates ($v_{sl} < 40$ cm/sec), it is found that increased gas flow initially causes the number and size of the bubbles to increase. At a still greater gas flow they unite and form bullet-shaped gas plugs, which collapse at still higher gas throughputs. Then slugs, containing mainly gas, alternate with slugs containing mainly liquid. All through these regions, friction remains negligibly small and the pressure gradient G consequently equals the liquid hold-up which diminishes since, with increasing gas flow, there is more gas in the pipe. In a limited range ($v_{sl} < 5$ cm/sec, $30 < v_{sg} < 600$ cm/sec), the measured liquid hold-up is even greater than G. In this case a downward-flowing wall film is present between pipe wall and gas slugs. This liquid film is supported by the wall and therefore contributes nothing to the pressure gradient, but increases the observed liquid hold-up.

At still higher gas flows ($v_{sg} > 1{,}500$ cm/sec, still $v_{sl} < 40$ cm/sec), the flow pattern changes from slug flow to mist flow. There, the gas becomes the continuous phase with the liquid being transported mainly as droplets in the gas, and for a small part as a film along the wall. Wall friction makes its appearance,

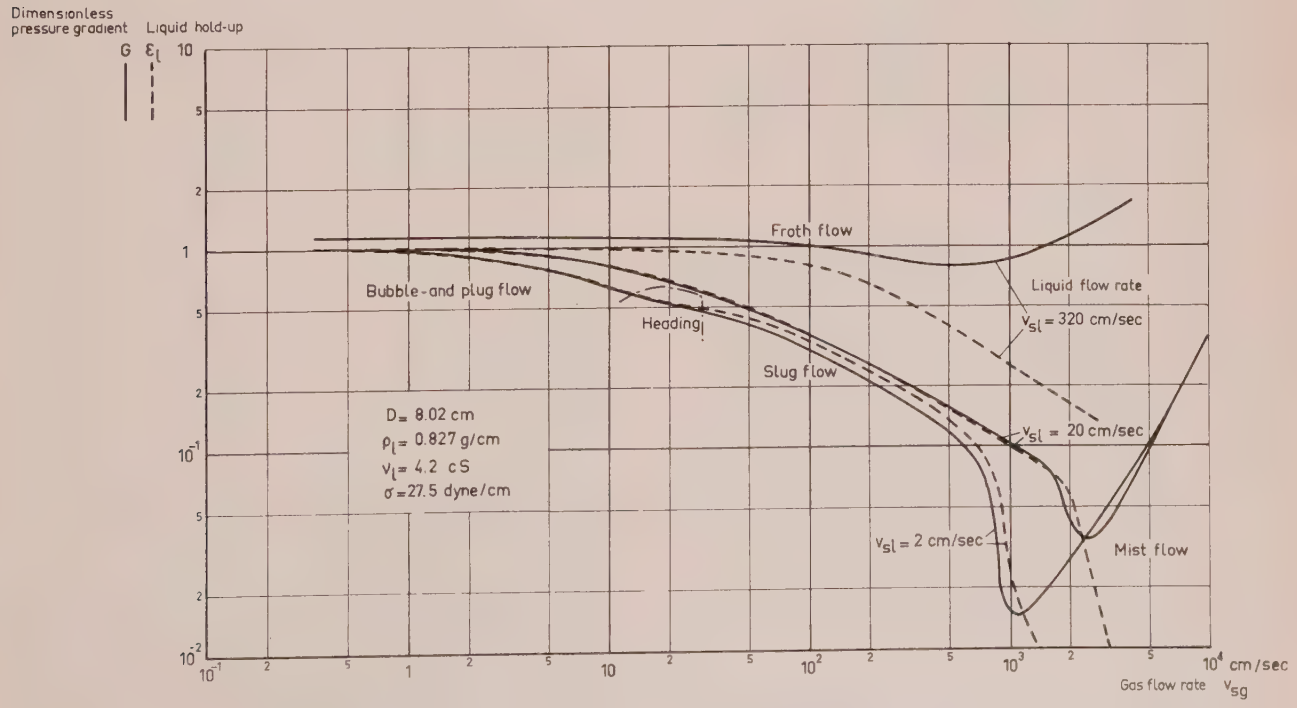

FIG. 2—PRESSURE GRADIENT AND LIQUID HOLD-UP AGAINST GAS FLOW AND LIQUID FLOW.

increases sharply with increasing gas flow rate, and far exceeds the ever-diminishing hold-up. Thus, the pressure gradient passes a minimum and rises sharply after that.

On increasing the liquid throughput, the picture gradually changes over to the situation of high liquid velocity ($v_{sl} > 160$ cm/sec), where the various flow patterns cannot clearly be discerned. When the gas flow increases from zero, no plug flow can be observed, but the flow becomes turbulent and frothy, with the gas dispersed in small bubbles. Only at high gas throughputs does any segregation take place, causing a rapidly repeating slug flow, gradually changing to mist flow at extremely high gas throughputs ($v_{sg} > 5{,}000$ cm/sec). Hold-up decreases only slowly, since with the high liquid velocity the volume of the gas in the pipe remains relatively small. The substantial friction, however, increases continuously so that the pressure gradient initially decreases slowly with increasing gas flow and, after reaching a flat minimum, rises sharply.

HEADING

In a limited range (in the case of Fig. 2 for $v_{sl} < 10$ cm/sec and $10 < v_{sg} < 30$ cm/sec), the flow in the test installation varies in a cyclic manner with a period of some tens of seconds, in spite of the fact that at the bottom of the inflow section the injection rates of both gas and liquid are strictly constant. This phenomenon closely resembles the "heading cycle" discussed by Gilbert.[1] According to Gilbert, cyclic gas accumulation at some spot with gas storage capacity causes a relaxation oscillation. In a well producing through the tubing, the volume of the casing-tubing annulus has this capacity. In the experimental setup, however, no distinct volume is present and the gas storage capacity presumably is provided by the volume of the gas bubbles in the tubing. The detailed mechanism, however, is rather complex and not well understood.

The heading intensity is greater the smaller the pipe and the lower the liquid viscosity. Greatest intensity was observed in a 3.2-cm pipe with gas oil. In this case the heading range was fairly wide and pressure fluctuations were so great as to make the accuracy of the pressure-gradient curves no better than 30 per cent. In less extreme cases, such as that of Fig. 2, accuracy in the heading range is estimated at 10 per cent.

FLOW REGIME DIAGRAM

The various flow patterns and heading phenomena just discussed only occur in limited zones. These zones can be presented in a diagram, in which the transitions between the various flow regimes are plotted as a function of gas throughput and liquid throughput. Such a diagram is presented in Fig. 3 for the flow of air and gas oil in the 8-cm pipe. The throughputs are characterized by the velocity numbers of gas and liquid, i.e, RN and N, respectively. The various lines actually represent the limits of the correlations (discussed later) and roughly agree with the transitions between adjoining flow patterns.

LIQUID VISCOSITY

The picture just given is broadly true for all situations examined. Liquid viscosity has no noticeable effect on the pressure gradient so long as it remains less than 6 centistokes. Higher viscosity, however, causes the pressure gradient to increase not only through increased friction when friction is of influence, but also at low liquid throughputs where the hold-up is decisive. Apparently, the slip between gas and liquid increases with increasing viscosity—in contrast to what might have been expected from the friction law of Stokes.[10] The velocity distribution in the liquid, as it is affected by the presence of the pipe wall, presumably is responsible, or perhaps the interaction between gas bubbles.

DIAMETER

Wall friction appears to decrease with increasing diameter, just as in the case of single-phase flow. In the high velocity ranges where the friction is dominant, the pressure gradient consequently decreases with increasing diameter. With small liquid throughputs, however, the pressure gradient will be affected only insofar as the hold-up is influenced. This is only the case at moderately high gas throughputs where increased diameter causes increased slip between gas and liquid, resulting in an increase in pressure gradient.

ANNULI

With annuli, a distinction between large and small liquid throughputs must again be made. With high liquid throughputs when wall friction is great, the hydraulic diameter (that is, the difference between internal casing and external tubing diameters) proves decisive, so that the pressure gradient increases with increasing tubing diameter for a given casing. When the liquid throughput is small, however, wall friction is small and the pressure gradient is nearly equal to the liquid hold-up. The latter appears to increase when the sum of the diameters of casing and tubing (i.e., the wetted perimeter) increases.

Collars on the tubing in annular flow appear to give so slight an increase in pressure gradient that it can safely be ignored in field practice.

WALL ROUGHNESS

Wall roughness slightly affects wall friction, but not hold-up. The effect is noticeable when the pipe is very rough ($\varepsilon/D \sim 10^{-2}$). Though with a roughness comparable to that of oilwell tubing ($\varepsilon/D < 10^{-3}$) the effect is very small, it nevertheless has been incorporated in the friction correlation (see "Correlations").

GAS DENSITY

As discussed in the section "Elimination of Irrelevant Groups", some effect of gas density may only be ex-

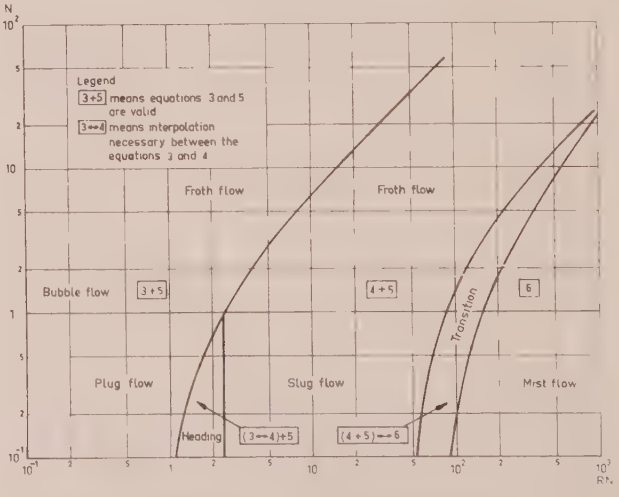

FIG. 3—REGIONS OF VALIDITY OF CORRELATIONS.

pected when the kinetic head of the gas, $\frac{1}{2}\rho_g v_{sg}^2$, is large. Then, the flow mechanism is affected, i.e., the geometrical distribution and velocity distribution of gas and liquid that governs both liquid hold-up and wall friction.

The effect of $\frac{1}{2}\rho_g v_{sg}^2$ was studied in a high-pressure setup, in which v_{sg}-values up to 2,500 cm/sec and gas densities up to 17 times atmospheric were realized. It appeared that both liquid hold-up and wall friction at high pressure were equal, within measuring accuracy, to those occurring under atmospheric conditions. The experiments covered all ranges, except the mist-flow range, corresponding to practically the entire range encountered in flowing and gas-lift wells. Thus, in these wells any effect of gas density ρ_g on the flow mechanism, i.e., hold-up and friction, may be ignored. This fact does not necessarily mean that the pressure gradient too will be independent of the gas density. According to Eq. 1, a contribution of gas density to the pressure gradient is present, viz., by means of the gas hold-up term $(1-\varepsilon_l)\ \rho_g/\rho_l$. Whereas the contribution of this term to the pressure gradient is negligibly small both for any experimental installation and for almost all field circumstances, in extreme cases some influence may occur, i.e., in those cases where gas density is very high and hold-up and friction are low (low v_{sl}, moderately high v_{sg}).

In the mist-flow range, however, the kinetic head of the gas will be substantial so that some influence of gas density is to be expected. No special tests at high gas density have been carried out in this range. However, certain indications have been found with atmospheric tests carried out at extremely high gas velocities ($v_{sg} > 6{,}000$ cm/sec). Here, the pressure gradient was high, resulting in a slight difference in absolute pressure of the successive subsections and, consequently, also in gas density. It appeared that the pressure gradient increased with increasing gas density. This fact indicates that in any well where mist flow occurs (viz., in wet-gas wells or in air-drilled wells with water-cut) the flow mechanism, and hence the pressure gradient, both must depend on the gas density.

INFLOW AND OUTFLOW

In the dimensional analysis carried out previously, equilibrium flow has been assumed. Regarding the great lengths of flow strings in field practice, this equilibrium flow will definitely occur in the field. In a test installation, however, some influence of inflow and/or outflow may occur.[11]

In the installation used, the pressure gradient at the outflow appeared to remain unchanged up to just before the outflow opening. Apparently, the outflow has no reaction on the mechanism of the flow just upstream. At the inflow side, however, the pressure gradient may be considerably greater than higher up for the same conditions, in particular at high flow rates. With the 8-cm pipe a ratio of up to 3:1 prevails for distances of 1 and 25 m from the bottom, respectively. The pressure gradient remains unchanged at distances L greater than 25 m, which corresponds to a relative inflow length L/D of 300. As in single-phase flow, the influence of pipe inflow length L on the flow mechanism will decrease with increasing relative inflow length L/D, in particular for those cases where wall friction is great and gas slip is small. However, for opposite situations with low wall friction and large gas slip, it is very likely that the inflow phenomenon will be influenced not only by L/D, but also by the inflow length L itself or, rather, by the "dimensionless inflow section length" $L\sqrt{(\rho_l g/\sigma)}$. Therefore, care was taken to ensure that in all runs the values of both L/D and $L\sqrt{(\rho_l g/\sigma)}$ exceeded those of the aforementioned experiments, so that the data presented are free from any inflow effect.

It should be mentioned that the critical values of L/D and $L\sqrt{(\rho_l g/\sigma)}$ ($\sim$300 and $\sim$ 13,000, respectively) are far higher than those for the majority of experimental installations reported in the literature. The data obtained in those setups, therefore, as a rule will not be free from inflow effects.

CORRELATIONS

From physical considerations and experimental evidence, the following can be concluded. The various flow regimes can be divided into three main regions—those with low, intermediate and high gas throughputs, respectively. Region I, where the liquid phase is the continuous one, covers bubble flow, plug flow and the lower part of the froth-flow regime. Region II, where the phases of liquid and gas alternate, covers slug flow and the remainder of the froth-flow regime. Region III covers the mist-flow range and is characterized by a continuous gas phase. As can be expected, the entirely different nature of these main regimes (continuous liquid, alternating phases and continuous gas) causes, according to the section on "Experimental Results", the behavior of both liquid hold-up and friction to be different; in principle, therefore, $3 \times 2 = 6$ different correlations are to be expected.

The flow mechanism in Regions I and II appeared to depend exclusively on the four main dimensionless groups, representing the throughputs of liquid and gas, the pipe diameter and the viscosity of the liquid. In Region III, however, the flow mechanism depends not only on the above four groups, but also on the density ratio or, rather, on the gas density. Thus, liquid hold-up, wall friction and boundaries of the regions will depend on the four or five governing dimensionless groups, respectively. By means of the experimental data, the following correlations were obtained for these quantities.

LIQUID HOLD-UP

As discussed earlier, ε_l signifies a "pseudo hold-up" representing that part of the measured liquid hold-up which contributes to the pressure gradient. All measured liquid hold-up data, therefore, have been corrected for the liquid film that is supported by the wall. (See also the sections "Formula for the Pressure Gradient of Gas-Liquid Flow" and "Experiental Results".) In practice this means that, for experiments with great liquid throughput where the influence of wall film can be ignored, the measured hold-up has been taken; while at low liquid throughput, where the friction is negligibly small, ε_l is equal to G.

The liquid hold-up ε_l is functionally related to the slip velocity v_s, which is the difference between real average gas and real average liquid velocities and is defined as follows.

$$v_s = \frac{v_{sg}}{1-\varepsilon_l} - \frac{v_{sl}}{\varepsilon_l}.$$

From this definition, the expression for ε_l follows.

$$\varepsilon_l = \frac{(v_s - v_{sg} - v_{sl}) + \sqrt{(v_s - v_{sg} - v_{sl})^2 + 4v_s v_{sl}}}{2v_s} \quad . \quad . \quad . \quad . \quad . \quad . \quad . \quad . \quad . \quad . \quad . \quad . \quad . \quad . \quad . \quad (2)$$

or, in dimensionless form,

$$\varepsilon_l = \tfrac{1}{2}\left[1 - (1+R)\frac{N}{S}\right] + \tfrac{1}{2}\sqrt{\left[1 - (1+R)\frac{N}{S}\right]^2 + 4\frac{N}{S}} \quad . \quad (2a)$$

where S = dimensionless slip velocity $= v_s\sqrt[4]{(\rho_l/g\sigma)}$.

For the sake of convenience, the slip velocity and not the liquid hold-up has been correlated with the governing groups. As pointed out three ranges must be discerned—that of low, that of intermediate and that of high gas throughput. The formula which covers the bubble-flow and part of the plug-flow and froth-flow regimes (Region I) reads as follows.

Slip Correlation I

$$S = F_1 + F_2 N + F'_3\left(\frac{RN}{1+N}\right)^2 . \quad . \quad . \quad . \quad (3)$$

In this equation, the dimensionless slip velocity S is related to the velocity numbers of liquid and gas, $N\left[= v_{sl}\sqrt[4]{(\rho_l/g\sigma)}\right]$ and $RN\left[= v_{sg}\sqrt[4]{(\rho_l/g\sigma)}\right]$, respectively. F_1 and F_2, given in Fig. 4, are dimensionless factors depending on the liquid's viscosity number only. F'_3 depends on both viscosity and diameter and is represented by

$$F'_3 = F_3 - \frac{F_4}{N_d} \quad . \quad . \quad . \quad . \quad . \quad . \quad . \quad . \quad . \quad . \quad (3a)$$

where both F_3 and F_4 are again factors depending on the liquid's viscosity number only (see Fig. 4). For flow in pipes, the diameter number N_d is based on the internal diameter of the pipe $[N_d = D\sqrt{(\rho_l g/\sigma)}]$. For flow in annuli, however, the diameter number is based on the sum of internal casing diameter D and external tubing diameter D_t (or, rather, on the wetted perimeter); thus, $N_d = (D + D_t)\sqrt{(\rho_l g/\sigma)}$.

The lower limit of the range of validity of Eq. 3 prevails for both RN and N zero. Then, S equals F_1 and ε_l equals unity. The upper limit of Eq. 3 coincides with the lower limit of the heading range in the experimental installation given by

$$RN < L_1 + L_2 N \quad . \quad . \quad . \quad . \quad . \quad . \quad . \quad . \quad . \quad . \quad . \quad (3b)$$

while the dimensionless factors L_1 and L_2, given in Fig. 5, depend on the diameter number.

Slip Correlation II

In the range of intermediate gas throughputs, covering the slug-flow and part of the froth-flow regimes (Region II), the correlation reads

$$S = (1 + F_5)\frac{(RN)^{0.982} + F'_6}{(1 + F_7 N)^2} . \quad . \quad . \quad . \quad . \quad (4)$$

As in the previous correlation, the F-factors in Eq. 4 become constants in specific field applications when viscosity and diameter are given. F_5 and F_7 again depend in fact on the liquid's viscosity number only (see Fig. 6); likewise, F_6 in the expression for F'_6, reading

$$F'_6 = F_8 N_d + F_6 . \quad . \quad . \quad . \quad . \quad . \quad . \quad . \quad . \quad . \quad . \quad (4a)$$

The factor F_8 seems to be a constant, but its value has not yet fully been established. Again, for flow in annuli the diameter influence number N_d should be based on $(D + D_t)$.

The lower limit of the range of validity of Eq. 4 coincides with the upper limit of Eq. 3 when liquid throughput is high. However, when heading occurs at low liquid throughput, the limit becomes equal to the upper limit of the heading range. This leads to the condition

$$RN > L_3 L_1 \quad . \quad . \quad . \quad . \quad . \quad . \quad . \quad . \quad . \quad . \quad . \quad (4b)$$

next to

$$RN > L_1 + L_2 N$$

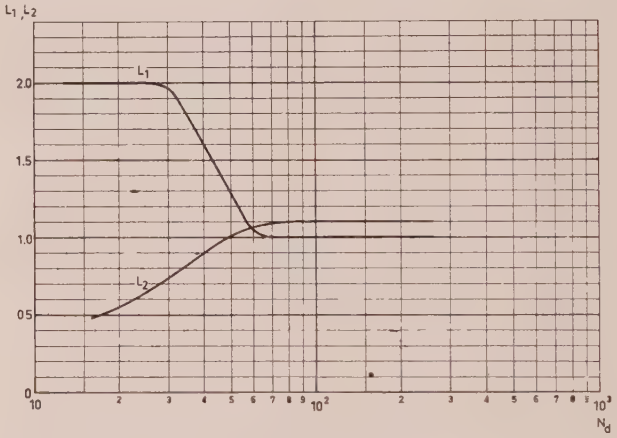

FIG. 5—L_1 AND L_2 AGAINST DIAMETER NUMBER N_d (N_d BASED ON $D + D_t$).

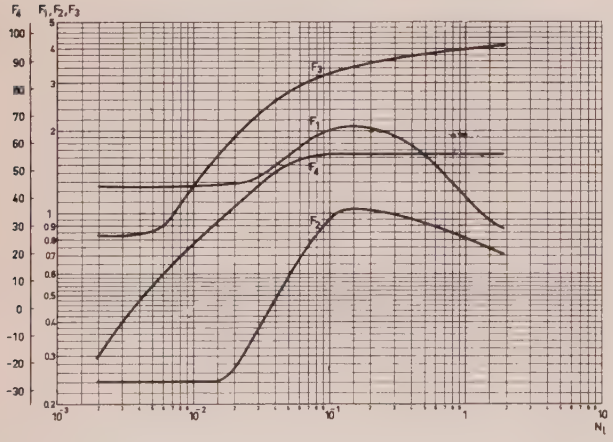

FIG. 4—F_1, F_2, F_3 AND F_4 AGAINST VISCOSITY NUMBER N_l.

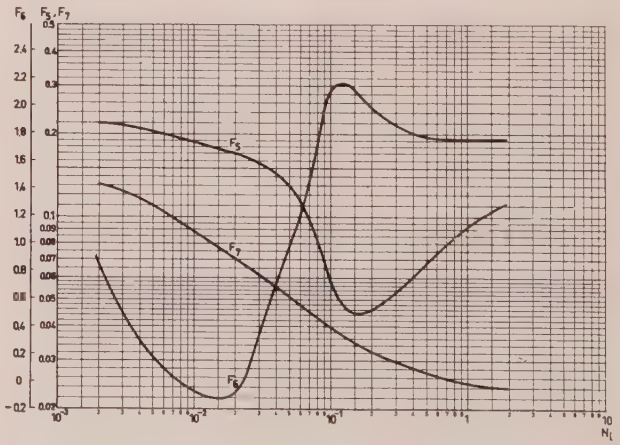

FIG. 6—F_5, F_6 AND F_7 AGAINST VISCOSITY NUMBER N_l.

in which the L-factors depend on the diamenter influence number (see Figs. 5 and 7) and on the viscosity number (see Fig. 8).

Eq. 4 covers the slug-flow and the remainder of the plug-flow and froth-flow regions up to the transition zone to mist flow. This upper limit is expressed by

$$RN < 50 + 36N \quad . \quad . \quad . \quad . \quad . \quad . \quad . \quad . \quad . \quad (4c)$$

Between the ranges of validity of Eqs. 3 and 4 a gap exists, enclosing the heading range of the experimental installation, viz., when

$$L_1 + L_2N < RN < L_3L_4.$$

No attempt has been made to derive a correlation for the slip velocity in this range because the measurements are not very accurate. It is thought, however, that the slip velocity can be approximated with reasonable accuracy by linear interpolation between the S-values of Eqs. 3 and 4 along the respective boundaries on the basis of the value of RN.

Hold-up Correlation III

For high gas throughputs outside the slug-flow range (that is, for $RN > 50 + 36N$), the gas phase becomes continuous, resulting in a high slip velocity and, consequently, a small ε_l-value. This small value can be approximated for mist-flow conditions (Region III) by $\varepsilon_l = \dfrac{20}{N_d^2}$. In contrast to the previous correlations, N_d is here based on the hydraulic diameter of the flow string; thus, for annuli $N_d = (D - D_t)\sqrt{(\rho_l g/\sigma)}$. For the high gas flow rates encountered in gas-condensate wells, the contribution of the hold-up to the total pressure gradient is very small.

WALL FRICTION

In the equation for the dimensionless pressure gradient

$$G = \frac{1}{\rho_l g}\frac{dP}{dh} = \varepsilon_l + (1 - \varepsilon_l)\frac{\rho_g}{\rho_l} + \text{Friction Term}, \quad . \quad . \quad . \quad . \quad . \quad . \quad . \quad . \quad . \quad . \quad . \quad . \quad . \quad (1)$$

the last term represents the wall friction. We may postulate that the friction is governed by a Fanning-type of friction law.

$$\text{Friction Gradient} = 4f_w\frac{\rho_l v_{sl}^2}{2D}\left(1 + \frac{v_{sg}}{v_{sl}}\right)$$

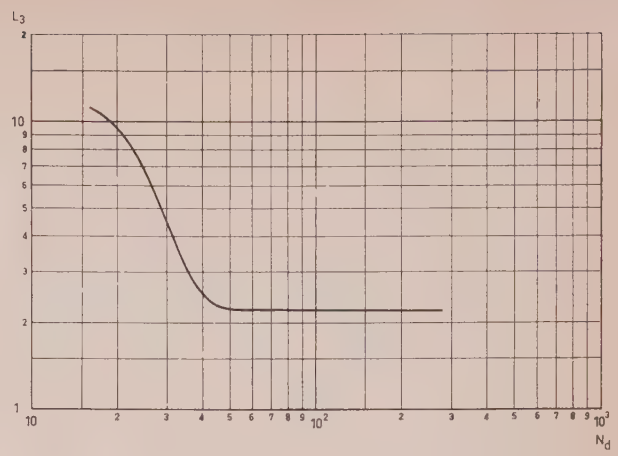

Fig. 7—L_3 Against Diameter Number N_d (N_d Based on $D + D_t$

Thus, when made dimensionless by dividing by $\rho_l g$, the last term in Eq. 1 becomes

$$\text{Friction Term} = 4f_w\frac{v_{sl}^2}{2gD}\left(1 + \frac{v_{sg}}{v_{sl}}\right) \quad . \quad . \quad (1a)$$

In this equation it has been assumed that the friction is caused by shear stress in the liquid phase. This assumption would seem reasonable for the Regions I and II where the liquid phase is more-or-less continuous. In Region III, however, the gas phase is continuous and friction originates from the drag of the gas on the pipe wall. Then, the friction law should be based on the gas phase.

$$\text{Friction Gradient} = 4f_w\frac{\rho_g v_{sg}^2}{2D}\left(1 + \frac{v_{sl}}{v_{sg}}\right).$$

Since in the mist-flow range v_{sl} is very small compared with v_{sg}, this equation when made dimensionless simplifies to

$$\text{Friction Term} = 4f_w\frac{\rho_g}{\rho_l}\frac{v_{sg}^2}{2gD} \quad . \quad . \quad . \quad . \quad . \quad (1b)$$

For given conditions of flow, the friction term (Eq. 1a or Eq. 1b) can be evaluated when the dimensionless friction factor f_w is given. On the basis of the experimental data, it appeared possible to derive one correlation for f_w which covers both Region I and Region II. This correlation reads as follows.

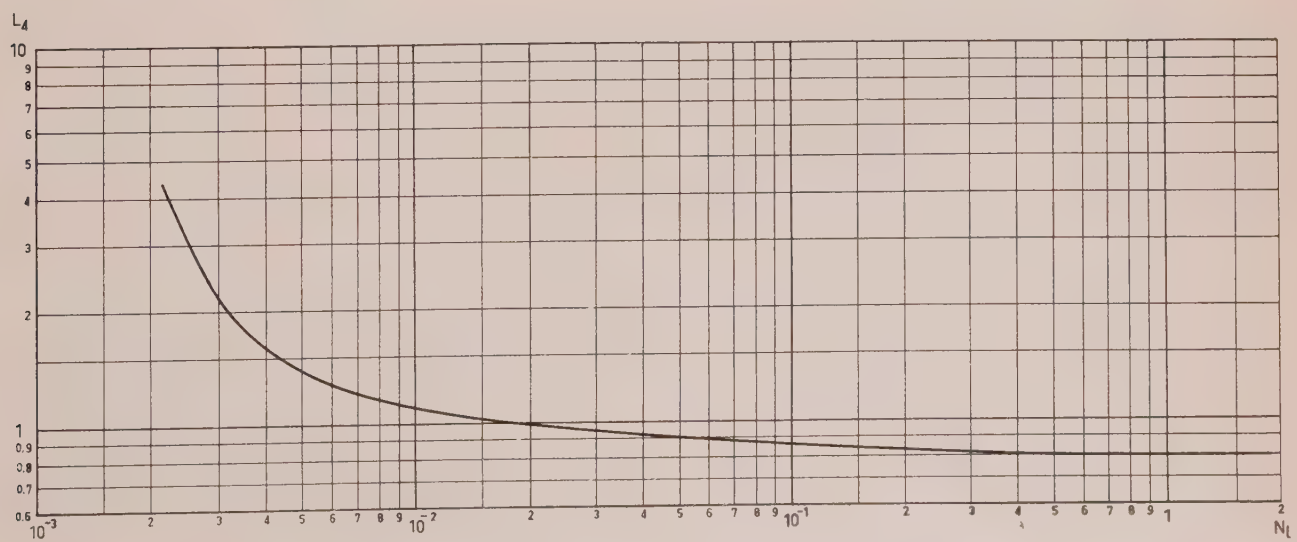

Fig. 8—L_4 Against Viscosity Number N_l.

Friction Correlation I-II

$$f_{tp} = f_1 \frac{f_2}{f_3} \quad . \quad . \quad . \quad . \quad . \quad . \quad . \quad . \quad . \quad . \quad . \quad . \quad (5)$$

where the following are true.

f_1 is given in Fig. 9 as a function of the Reynolds number of the liquid: $Re_l = \rho_l v_{sl} D/\mu_l$. As in Eq. 1a, D is the hydraulic diameter D_h of the flow string. Thus, for annuli $D_h = D - D_t$ and $N_d = (D - D_t)\sqrt{(\rho_l g/\sigma)}$. Fig. 9 is identical with the well known Moody diagram (see Ref. 12) valid for single-phase flow, except in the transition range between laminar and turbulent flow at $700 < Re_l < 3{,}000$. The effect of relative wall roughness ε/D, though a factor of secondary importance, is shown as well.

f_2 is a correction for the in situ gas-liquid ratio R and is given as a function of the group $f_1 RN_d^{2/3}$ in Fig. 10 (unbroken line). The value of f_2 is nearly equal to unity when R is small, but decreases sharply when R becomes high.

f_3 is a further correction of the second order for both liquid viscosity and in situ gas-liquid ratio and equals $1 + f_1\sqrt{R/50}$. For low-viscosity liquids, the value of f_1 is very small, so that f_3 then nearly equals unity. With increasing viscosity, f_1 increases and with it f_3. Its influence on the pressure gradient, however, is of importance only for viscosities higher than some 50 centistokes.

Eq. 5 is valid for all values of N encountered and for RN-values up to $RN = 50 + 36N$. The Friction Correlation I-II thus covers both the ranges of the Slip Correlations I and II, and the heading range as well.

Friction Correlation III

This correlation, covering the mist-flow range, Region III, reads

$$f_{tp} = f_1 \quad . \quad . \quad . \quad . \quad . \quad . \quad . \quad . \quad . \quad . \quad . \quad . \quad (6)$$

where f_1 is given in Fig. 9 as a function of the Reynolds number. As has already been mentioned, the friction term of Eq. 1b has been defined on the basis of a continuous gas phase. Accordingly, in Fig. 9 the Reynolds number of the gas phase must be taken as $Re_g = \rho_g v_{sg} D/\mu_g$. Again, in this expression as in Eq. 1b, D is the hydraulic diameter of the flow string.

The liquid film on the pipe wall is rippled, causing a high friction for the fast-moving gas. This friction can be accounted for by a fictitious wall roughness ε. For the low-pressure cases investigated, the value of ε appeared constant and equal to 0.032 cm.

Eq. 6 is valid in the mist-flow range, Region III, characterized by

$$RN > 75 + 84N^{3/4} \quad . \quad . \quad . \quad . \quad . \quad . \quad . \quad (6a)$$

for air-liquid systems at nearly atmospheric pressure and temperature. No data are available from systems at elevated pressures. It is thought, however, that a modest extrapolation of Eq. 6 to higher pressures is permissible.

A gap exists between the upper limit of the slug-flow region, Eq. 4c, and the lower boundary of the mist-flow region, Eq. 6a. The pressure gradient in this transition zone can be approximated by linear interpolation of the G-values along the respective boundaries on the basis of the value of RN.

In Fig. 3, the various boundaries are given for the flow of air and gas oil through the 8-cm pipe. The various correlations to be used have also been indicated.

ACCURACY

The accuracy of the correlations is reasonable. In the range of low gas throughputs, Region I, the standard deviation between measured G-values and those determinated from the correlations amounts to 3 per cent, which is equal to the measuring accuracy. In the range of intermediate gas flows, Region II, the standard devia-

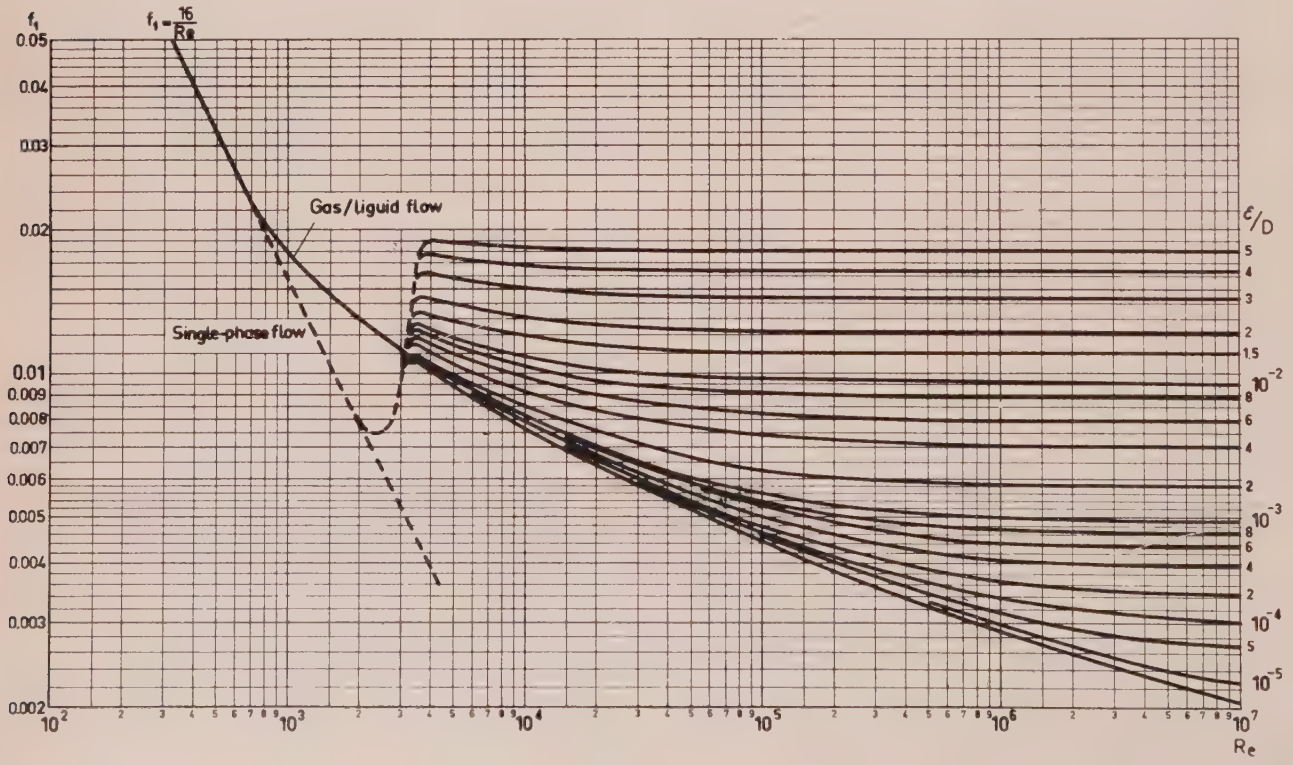

FIG. 9—f_1 AGAINST REYNOLDS NUMBER Re.

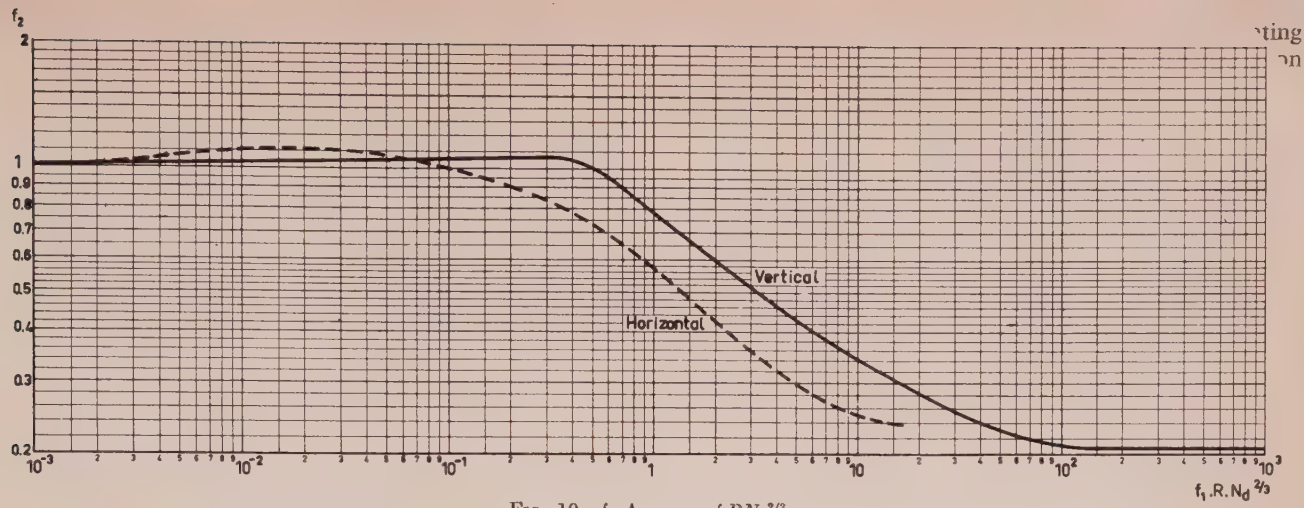

FIG. 10—f_2 AGAINST $f_1RN_d^{2/3}$.

tion of the discrepancies amounts to 8 per cent. This figure unfortunately is higher than that of the measuring accuracy, 3 per cent, but this is only to be expected in view of the unstable and pulsating character of the flow. For mist flow, Region III, the standard deviation amounts to some 10 per cent.

RANGES OF APPLICATION

Regions I and II, for which Slip Correlations I and II and the Friction Correlation I-II are valid with boundaries between

$$0 < RN < 50 + 36N,$$

cover almost the entire range encountered in flowing and gas-lift wells: (1) liquid viscosities between 1 and 300 centistokes; (2) gas-liquid ratios between 0 and 1,400 scf/bbl, assuming a wellhead pressure of 70 psig or higher; and (3) liquid flow rates between 0 and 2,400, 10,000 and 30,000 B/D through 1.66-, 3.5- and 6-in. tubing, casing or annuli.

Since no systematic deviations were found with the highest liquid flow rates or with the largest flow strings, extrapolation of these values for rate and size would seem permissible.

Region III, representing the type of flow encountered in gas-condensate wells, is covered by Hold-up Correlation III and Friction Correlation III. The corresponding range in wells depends on the gas velocity, which should be greater than about 30 ft/sec. It should be noted that both Region III correlations originate from experiments carried out at atmospheric conditions. Therefore, their application in high-pressure wells should be regarded as an approximation.

PRESSURE-GRADIENT CORRELATION FOR HORIZONTAL FLOW

It appeared that a modification of the correlations valid in Regions I and II may also be used for predicting the pressure gradient for gas-liquid flow in horizontal pipes. In establishing this fact, some 2,000 pressure-gradient measurements carried out by Hoogendoorn[9] for gas-liquid flow in horizontal pipes have been analyzed on the basis of Eq. 1. However, the contribution of hold-up to the pressure gradient is zero in a horizontal pipe, so that the corresponding hold-up term has been omitted. Moreover, for the cases investigated, the effect of acceleration was only slight so that the acceleration term was also ignored. The resulting formula then becomes identical to Eq. 1a.

$$G = 4f_w \frac{v_{sl}^2}{2gD}\left(1 + \frac{v_{sg}}{v_{sl}}\right).$$

The f_w-values obtained from Hoogendoorn's data were substituted in Eq. 5.

$$f_w = f_1 \frac{f_2}{f_3}$$

in which the values of f_1 and f_3 for the corresponding situations in a vertical pipe were substituted. As a result, a relationship for f_2 for horizontal flow was obtained (see Fig. 10, broken line). Comparison of Hoogendoorn's data with the obtained correlation appeared to be favorable for R-values below 50. The relative standard deviation of the value of G amounts to 11 per cent when G exceeds 0.15. For lower G-values, the standard deviation of the absolute discrepancies was determined to be 0.015.

DISCUSSION

In the section "Elimination of Irrelevant Groups", we have seen that with the use of dimensionless groups three independent quantities should automatically be accounted for, of which only the surface tension may vary appreciably. This has appeared to be correct. In the form given, the correlations predict the pressure gradient satisfactorily for both oil and water. If the values of ρ_l and σ of gas oil are applied to the flow of water, however, the discrepancy between measurements and correlations rises sharply.

The results presented by Baxendell and Thomas[5] have been compared with the correlations presented herein (see the Appendix). The agreement is excellent, showing that the set of correlations presented is at least valid for high-potential wells where the influence of slip is small. More data, however, will be required to establish the validity in other ranges.

Apart from the phenomena that limit the range of validity of the correlations presented, at least four more phenomena might cause a discrepancy between the pressure gradient in a well and that computed from the correlations—i.e., heading, flashing, slug length and water-cut.

The heading ranges in the field will probably differ from those encountered in the laboratory installation. In a well, interaction is to be expected between heading zone and adjoining zones. Moreover, in most cases the volume of the annulus will provide an extra gas-

capacity. Both factors will extend the heading Whether or not this will influence the pressure can only be decided by making tests in wells. ver, it should be noted that when heading occurs the liquid velocity is likely to be low. Such a low liquid velocity usually indicates that the flow string for maximum potential production (see "Introduction") will have a cross-sectional area smaller than that in use. Therefore, replacement of the existing flow string by a smaller-sized one may result in a considerable increase in production.

Both increase in production and decrease in cross-sectional area cause the superficial liquid velocity to increase. Its value is likely to become so great that the flow is outside the heading range, despite the fact that this range becomes increasingly extensive with decreasing pipe cross section.

As for flashing, the following can be remarked. The flow pattern in the test setup differs in one essential respect from that in a well. In the test setup, gas is injected through fairly large-sized nozzles so that big gas bubbles are to be expected. In a well, however, the gas originates from flashing so that, at least initially, the gas bubbles will be very small. Consequently, discrepancies between well and test setup are to be expected. Fortunately, these discrepancies will be of importance in a limited range only, namely for bubble flow. Some tests carried out in this range with dispersions of different fineness did not show any measurable influence of bubble-size distribution on the pressure gradient, so that the effect probably can be ignored altogether.

The longest gas slug observed in the experimental installation had a length of approximately 60 ft. In gas-lift wells, however, gas slugs of far greater length occur. This probably is due to interaction. Whereas the flows of gas and liquid at the bottom of our test setup were strictly constant, the flow through a certain cross section of the flow string in a well is fluctuating; viz., gas and liquid alternate in slug flow. The flow mechanism in the string above this cross section, therefore, cannot help but be different from the flow for comparable situations in the test setup. The resulting discrepancy may cause some difference in pressure gradient.

The investigation carried out dealt with gas-liquid systems with either oil or water as liquid. However, as soon as wells are encountered that produce oil and water as well as gas, some discrepancies are again to be expected. The difference in density of the two liquids in fact causes the lighter component (oil) to rise faster than the heavier one. Moreover, some emulsification is likely to take place, which has a bearing on the coalescense of gas bubbles and the formation of gas slugs and which may even yield a highly viscous pseudo-liquid. The degree of emulsification depends both on the flow variables and on the chemical composition of the components, a dependence which is likely to be extremely complex. Therefore, it is considered impractical to establish such relationships for the general case. For the approximation of the pressure gradient for this type of flow, it is recommended that linear interpolation be carried out between the pressure gradients which would occur for the same total throughputs in the cases of water-gas and oil-gas flows. This interpolation should be carried out on the basis of the percentage water-cut.

Finally, it can be remarked that the correlations presented are rather complicated. However, if one of the F-factors is omitted or its dependence on viscosity number is simplified, the discrepancy between measurements and correlations increases significantly. The complexity of the correlations makes their evaluation laborious. However, the computation of pressure against depth is laborious anyway, so that machine computation can be used with advantage. This has even been the case with the relatively simple correlation method of Poettmann and Carpenter.[3] Fortunately, with machine computation the intricacy of the formula to be evaluated is of little importance.

NOMENCLATURE

D = internal diameter of tubing or casing, L
D_h = hydraulic diameter = $D - D_t$, L
D_t = external diameter of tubing, L
G = dimensionless pressure gradient = $(1/\rho_l g)(dP/dh)$, —
L = length of inflow section, L
N = velocity influence number liquid = $v_{sl}\sqrt[4]{(\rho_l/g\sigma)}$, —
N_d = diameter influence number = $D_h\sqrt{(\rho_l g/\sigma)}$, —
N_g = viscosity influence number gas = $\mu_g\sqrt[4]{(g/\rho_l\sigma^3)}$, —
N_l = viscosity influence number liquid = $\mu_l\sqrt[4]{g/\rho_l\sigma^3)}$, —
N_ρ = gas-liquid density ratio = ρ_g/ρ_l, —
S = dimensionless slip velocity = $v_s\sqrt[4]{(\rho_l/g\sigma)}$, —
dP/dh = pressure gradient, $ML^{-2}T^{-2}$
R = in situ gas-liquid velocity ratio = v_{sg}/v_{sl}, —
f_p = dimensionless irreversible energy-loss factor, —
f = friction factor in single-phase flow, —
f_w = friction factor in gas-liquid flow, —
g = gravity acceleration, LT^{-2}
v = fluid velocity in single-phase flow, LT^{-1}
v_s = slip velocity = $v_{sg}/(1 - \varepsilon_l) - v_{sl}/\varepsilon_l$, LT^{-1}
v_{sg} = superficial gas velocity, LT^{-1}
v_{sl} = superficial liquid velocity, LT^{-1}
α = wall contact angle, —
ε = wall roughness, L
ε_l = liquid hold-up, —
ϕ = inclination of the pipe, —
μ_g = dynamic gas viscosity, $ML^{-1}T^{-1}$
μ_l = dynamic liquid viscosity, $ML^{-1}T^{-1}$
ν_g = kinematic gas viscosity = μ_g/ρ_g, L^2T^{-1}
ν_l = kinematic liquid viscosity = μ_l/ρ_l, L^2T^{-1}
ρ = fluid density in single-phase flow, ML^{-3}
ρ_g = gas density, ML^{-3}
ρ_l = liquid density, ML^{-3}
σ = surface tension, MT^{-2}

ACKNOWLEDGMENT

The author would like to express his gratitude to F. H. Poettmann for providing a valuable set of data and with whom he had an interesting discussion and correspondence, to J. J. M. van Oosterhout for carrying out most of the measurements and calculations, and to C. Stillebroer for fruitful discussions and other contributions to the production of this paper.

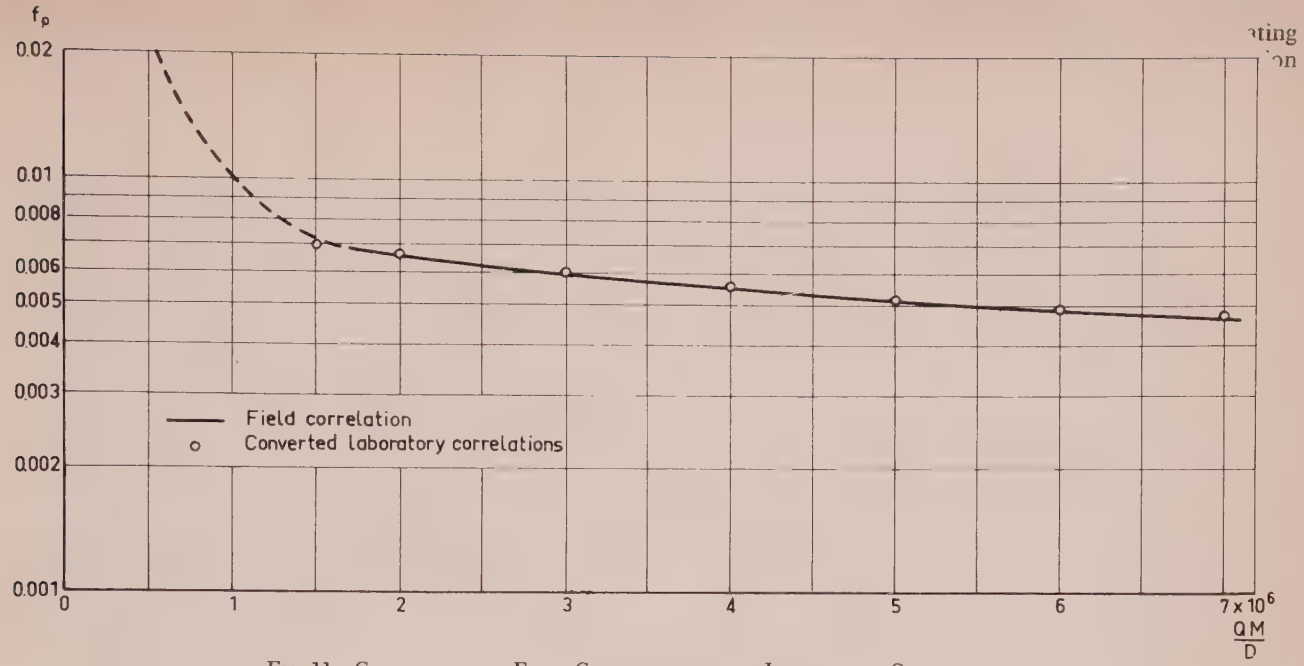

FIG. 11—COMPARISON OF FIELD CORRELATION WITH LABORATORY CORRELATIONS.

REFERENCES

1. Gilbert, W. E.: "Flowing and Gaslift Well Performance", *Drill. and Prod. Prac.*, API (1954) 126.
2. Poettmann, F. H. and Carpenter, P. G.: "Multiphase Flow of Gas, Oil and Water Through Vertical Flow Strings", *Drill. and Prod. Prac.*, API (1952) 257.
3. Baxendell, P. B.: "Producing Wells on Casing Flow", *Trans.*, AIME (1958), **213**, 202.
4. Benham, A. L. and Poettmann, F. H.: "Gas Lifting Through the Annulus of a Well", *Pet. Engr.* (July, 1959) 25B.
5. Baxendell, P. B. and Thomas, R.: "Calculation of Pressure Gradients in High-Rate Flowing Wells", *Jour. Pet. Tech.* (Oct., 1961) 1023.
6. Govier, G. W., Radford, B. A. and Dunn, J. S. C.: "The Upward Flow of Air-Water Mixtures I", *Can. Jour. of Chem. Eng.* (Aug., 1957) 58.
7. Govier, G. W. and Short, W. Leigh: "The Upward Flow of Air-Water Mixtures II", *Can. Jour. of Chem. Eng.* (Oct., 1958) 195.
8. Bridgman, P. W.: *Dimensional Analysis*, Yale U. Press, New Haven, Conn., Rev. Ed. (1948).
9. Hoogendoorn, C. J.: "Gas-Liquid Flow in Horizontal Pipes", *Chem. Eng. Science*, (1959) **9**, 205.
10. Daugherty, R. L. and Ingersoll, A. C.: *Fluid Mechanics with Engineering Application*, McGraw-Hill Book Co., N. Y. (1954).
11. Moore, T. V. and Wilde, H. D.: "Experimental Measurements of Slippage in Flow Through Vertical Pipes", *Trans.*, AIME (1931) **92**, 296.
12. Moody, L. F.: "Friction Factors in Pipe Flow", *Trans.*, ASME (1944) **66**, 671.

APPENDIX

A comparison has been made between the results of Baxendell and Thomas[5] and the set of correlations given in this paper. Baxendell and Thomas presented the relationship between f_p and QM/D for high-potential wells and high-rate flow lines, f_p being Poettmann and Carpenter's irreversible energy-loss factor and QM/D the correlating parameter (see Ref. 2). In the range of QM/D covered by Baxendell and Thomas, values of f_p were computed from our set of correlations for the prevailing conditions. To achieve this, our set of correlations was used to determine the pressure gradient, whose value in turn was substituted in Poettmann and Carpenter's energy-balance equation; thus, values for f_p were found. It appeared that for a given value of QM/D the computed values of f_p varied slightly with the percentage of free gas present. The slightly differing f_p-values have been averaged and the resulting figures plotted vs QM/D next to the f_p-QM/D relationship of Baxendall and Thomas. As shown in Fig. 11, the agreement is excellent. ★★★

The Effect of Horizontal Hydraulic Fracturing On Well Performance

J. H. HARTSOCK
J. E. WARREN
MEMBERS AIME

GULF RESEARCH & DEVELOPMENT CO.
PITTSBURGH, PA.

ABSTRACT

Because of the extensive utilization of hydraulic fracturing for the stimulation of low-productivity wells, the two related problems of fracture design and evaluation have become economically significant and, as a consequence, have motivated this investigation. The producing characteristics of horizontally fractured wells were studied to determine the fracture configuration that should be employed as the basis for the design of the treatment and to develop a method that can be used to establish the degree to which the design objectives have been achieved.

The equations which describe the steady-state flow of a single-phase fluid into, and through, a finite-capacity fracture were solved numerically for an idealized reservoir-fracture model. The numerical results were used to obtain an apparent skin effect for each combination of the parameters considered.

Based on the computed results, subject to the limitations implied by the assumptions that were made, the following general conclusions were drawn.

1. For a radius of drainage at least four times as large as the radius of the fracture, an apparent skin effect that is independent of the radius of drainage can be calculated.

2. The productivity of the hydraulically fractured system, relative to that of the unfractured well, can be determined from the apparent skin effect and can be used to establish design objectives.

3. In the evaluation of a fracture job, it is not possible to determine both the radius of the fracture and its flow capacity uniquely from the apparent skin effect; an independent determination of one of the quantities is necessary.

INTRODUCTION

Although hydraulic fracturing has been employed as a method for stimulating the productivity of literally hundreds of thousands of wells during the past 10 years, it is only in the last few years that improvements in fracture design[1-6] and fracturing technique[7] have combined to increase the probability of obtaining a successful treatment to such an extent that the mechanics of the method may be considered to be standardized. From an economic point of view, however, two related questions must be satisfactorily answered before hydraulic fracturing can be used in the most profitable manner. The two questions are the following.

1. For a particular well in a given formation, what are the optimum design specifications for the fracture treatment?

2. Have the design objectives been achieved by the fracture treatment?

The significance of these questions has been recognized, and some attempts to obtain answers have been made. Howard, *et al*,[8] endeavored to determine the optimum treatment, based on maximizing profits, for any given formation; unfortunately, this work was based on a crude method for approximating the productivity of a well. Carter and Tracy[9] utilized the same approximation to study the effect of fracturing on the behavior of a well producing by virtue of a solution-gas drive. Electrolytic models were used by van Poollen[10] to investigate the variation in productivity due to fracturing; however, only a limited number of results were presented. Later, from the same model results, van Poollen, *et al*,[11] attempted to justify an approximate expression for determining the productivity of a fractured well. It is quite apparent that there is a definite lack of the practical information necessary for specifying the optimum fracture configuration to be considered for design purposes.

The only detailed attempt to develop a procedure for evaluating the result of a given fracture treatment appears to be that of van Dam and Horner.[12] These authors described a technique for analyzing pressure build-down data, obtained immediately after fracturing, to determine the final fracture volume, the final fracture porosity, the fracture area, the fracture thickness and the in situ fluid loss of the fracturing fluid. While this approach should be useful whenever acceptable pressure measurements are available, it does not yield a value for the flow capacity of the fracture.

Since the problems of fracture design and evaluation are inversely related, it should be sufficient to study the effect of the fracture configuration on the performance of a well. The primary objective of this investigation is to evolve a technique for computing the desired solutions. The secondary objective is to analyze these computed results in order to prescribe a method for evaluating fracture treatments.

Because this study is exploratory in nature, its scope

Original manuscript received in Society of Petroleum Engineers office April 13, 1961. Revised manuscript received Sept. 12, 1961. Paper presented at Seventh Annual Rocky Mountain Regional Meeting of SPE, May 25-26, 1961, in Farmington, N. M.

[1]References given at end of paper.

must be kept within reasonable bounds. Therefore, only the steady-state flow of a single-phase fluid will be considered and only idealized horizontal fractures in idealized formations will be investigated.

THEORETICAL CONSIDERATIONS

To simplify the mathematical problem, the following physical assumptions are made.

1. The reservoir is horizontal and homogeneous; it has a uniform thickness h and anisotropic permeability with components k_r and k_z; it is completely penetrated by a well with a radius of r_w.

2. A single, horizontal, symmetrical fracture with a radius of r_f and a uniform flow capacity $(kh)_f$ is located at the mid-point of the reservoir; formation damage due to invasion by the fracturing fluid is negligible.

3. A single-phase, slightly compressible fluid is flowing from the reservoir to the well at a constant rate; there is no flow across the horizontal reservoir boundaries or the cylindrical surface at the well's radius of drainage, r_e; and, the only flow into the well itself is via the fracture, i.e., single-point entry.

4. At some critical radius r_c, flow is purely radial so that the pressure is constant over the cylindrical surface at r_c; the pressure distribution in the region between the well and the critical radius approaches a steady-state distribution after a sufficient period of production; and the flow between the critical radius and the radius of drainage is unaffected by the presence of the fracture.

5. The apparent skin-effect, due to the distortion of the flow pattern by the fracture, can be calculated from the steady-state pressure distribution; it can be used to interpret pressure build-up data if the theory for the infinite reservoir applies to at least a portion of the build-up curve (i.e., the effect of the fracture has disappeared and the effect of the drainage radius has not been felt so that the build-up curve is linear); and it can be employed in the interpretation of stabilized productivity indices (PI) measurements.

A cross-section of this idealized reservoir-fracture model is shown in Fig. 1.

At first glance, it may appear that the idealized model defined by these physical assumptions is so restricted that it has few practical applications. Fortunately, this is not the case. This model should be fairly realistic since it has been demonstrated that results from similar physical models were not particularly sensitive to deviations from idealizing assumptions. For example, Crawford and Landrum[13] indicated that either a fracture dip of as much as 15° from the horizontal or an ellipsoidal fracture with a major axis-minor axis ratio as great as two could be tolerated without introducing an appreciable error. Brons and Marting[14] showed that

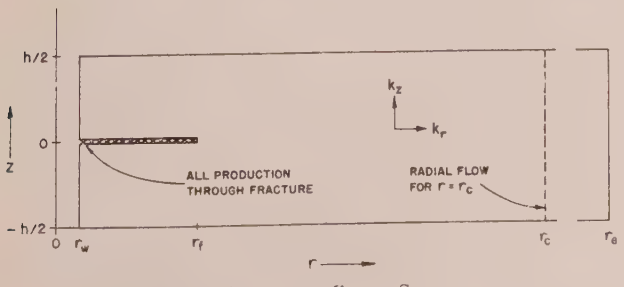

FIG. 1—IDEALIZED CROSS SECTION.

the apparent skin effect, due to a partially penetrating well, that was obtained from an unsteady-state solution could be approximated by that determined from the steady-state solution of Muskat;[15] theoretical results from Miller, *et al*,[16] and field results from van Everdingen[17] corroborated the applicability of the skin-effect concept in the analysis of pressure build-up data from stimulated wells.

The behavior equations for the idealized physical system are given in the Appendix. Although the mathematical problem is susceptible to formal solution in dual intergral- or infinite-series form, the numerical evaluation of the solution is eventually required; therefore, the problem was cast in finite-difference form and solved by numerical methods. The numerical technique —implicit alternating-direction method[18]—as well as other computational considerations, are discussed in the Appendix.

The computed solutions are characterized by the following three dimensionless parameters.

$$R_f = r_f/r_w;$$

$$H = \sqrt{k_r/k_z}\,\frac{h}{r_w}$$

$$\lambda = (kh)_f/r_w\sqrt{k_r k_z} \quad . \quad . \quad . \quad . \quad . \quad . \quad . \quad . \quad (1)$$

For each combination of these parameters, the apparent skin effect S is obtained by operating on the numerical solutions. According to definition,

$$S = \frac{2\pi(kh)_r}{q\mu\beta}\left[(\Delta p)_f - (\Delta p)_r\right] \quad . \quad . \quad . \quad . \quad (2)$$

If $H \leq 8R_f$, Eq. 2 can be evaluated numerically with a maximum error of approximately 1 per cent for $R_e = 4R_f$. Obviously, this condition imposes a restriction on the radius of drainage (i.e., $R_e \geq 4R_f$); consequently, the results from this study apply only if the fracture radius is less than 25 per cent of the drainage radius. The conditions on R_e is based on computational experiments, and it is a sufficient condition for all of the cases considered. The determination of the necessary condition for each particular combination of parameters is beyond the scope of this investigation.

The results obtained with a single fracture located at the mid-point of the formation can be generalized quite simply to include other geometries. The apparent skin effect for a fracture located at the top or bottom of the formation, S', is given by the following expression.

$$S'(H,\lambda,R_f) = S(2H,2\lambda,R_f) \quad . \quad . \quad . \quad . \quad . \quad (3)$$

If the formation is subdivided into N equal intervals and a fracture is placed at the mid-point of each interval, the apparent skin effect S_N is the following.

$$S_N(H,\lambda,R_f) = S(H/N,\lambda,R_f) \quad . \quad . \quad . \quad . \quad . \quad (4)$$

Two equations are necessary to provide essential information concerning reservoir behavior for the optimization of the fracture treatment. Generally, for a fixed pressure drawdown and a fixed average reservoir pressure,

$$q_f = \left(\frac{\ln r_e/r_w - .75}{\ln r_e/r_w - .75 + S}\right)q_r \quad . \quad . \quad . \quad . \quad (5)$$

To a limiting economic production rate q_{ec}, the difference in the ultimate recoveries that can be expected from the fractured and unfractured systems is related to the difference in the average reservoir pressures at abandonment, $(\bar{p}_r - \bar{p}_f)$.

$$(\bar{p}_r - \bar{p}_f) = \frac{-141.4\, q_{ec}\mu\beta}{(kh)_r} S \quad . \quad . \quad (6)$$

For evaluating a fracture treatment, the skin effect can be found by two methods. If a pressure build-up test is run after a well has been fractured and if an adequate linear segment is obtained when the shut-in pressure is plotted vs log $(t + \Delta t)/\Delta t$, the skin effect can be calculated as follows.

$$S = 1.15\left(\frac{p_{w1} - p_{wo}}{m} - \log_{10}\frac{\beta q}{m\phi c h r_w^2} + 1\right)$$
$$. \quad (7)$$

If stabilized productivity indices are measured just before fracturing, $(PI)_r$, and immediately after fracturing, $(PI)_f$, the skin effect can be determined from the following equation.

$$S = -(\ln r_e/r_w - .75)\left[1 - \frac{(PI)_r}{(PI)_f}\right] \quad . \quad (8)$$

For identical drawdowns, the ratio of the productivity indices can be replaced by the ratio of the production rates, q_r/q_f.

RESULTS AND DISCUSSION

Figs. 2 through 5 show the generalized results obtained by numerical computation; the apparent skin effect S is given as a function of the dimensionless parameters R_f, H and λ. The following ranges of the parameters are considered: $100 \leq R_f \leq 800$, $100 \leq H \leq 800$, and $200 \leq \lambda \leq 25{,}000$. The fracture-formation flow capacity ratio $(kh)_f/(kh)_r$ is equal to λ/H; therefore, the range of this ratio is $.25 \leq (kh)_f/(kh)_r \leq 250$.

It is significant that the generalized results indicates that it is possible to obtain a reduction in productivity, $S > 0$, if a fracture treatment is poorly designed. This possibility is particularly evident when H is large; i.e., the formation is very thick or extremely anisotropic, $k_r \gg k_z$. It is obvious that there is an infinite number of combinations of R_f, H and λ that will give the same value for S; in this sense, these results are not unique.

The relative effect of fracturing on productivity for typical field conditions is indicated in Fig 6; results obtained from two different approximations as well as those based on computation are shown. The approximation due to Howard, *et al*,[8] is

$$S \approx -(\ln r_f/r_w)\left[1 - (kh)_r/(kh)_f\right];$$

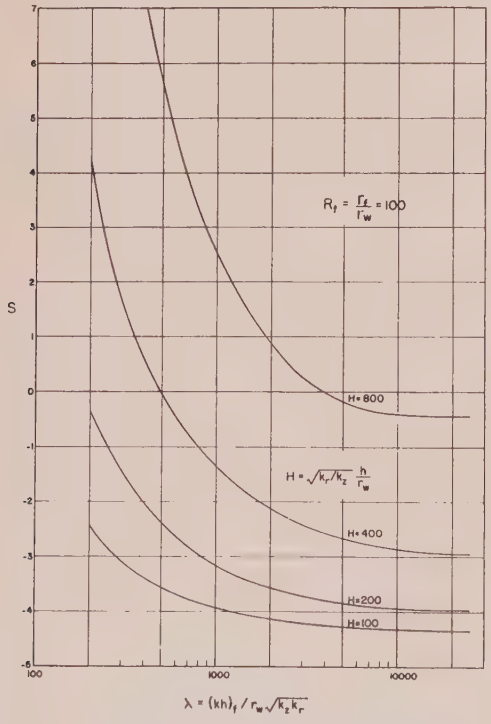

FIG. 2—COMPUTED RESULTS, $R_f = \frac{r_f}{r_w} = 100$.

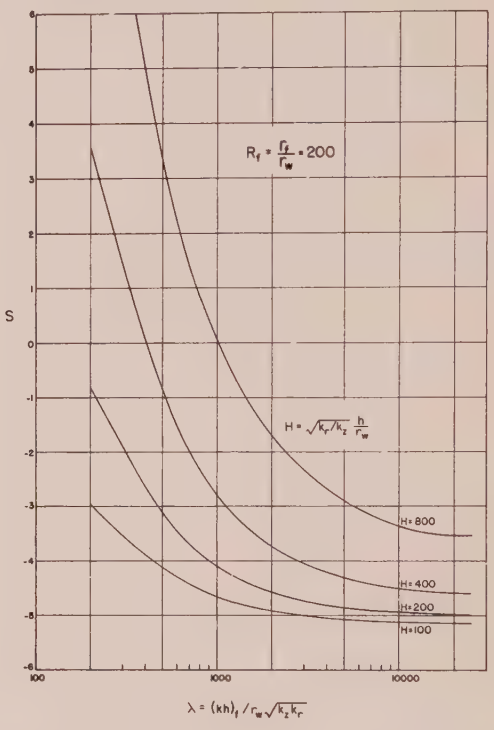

FIG. 3—COMPUTED RESULTS, $R_f = \frac{r_f}{r_w} = 200$.

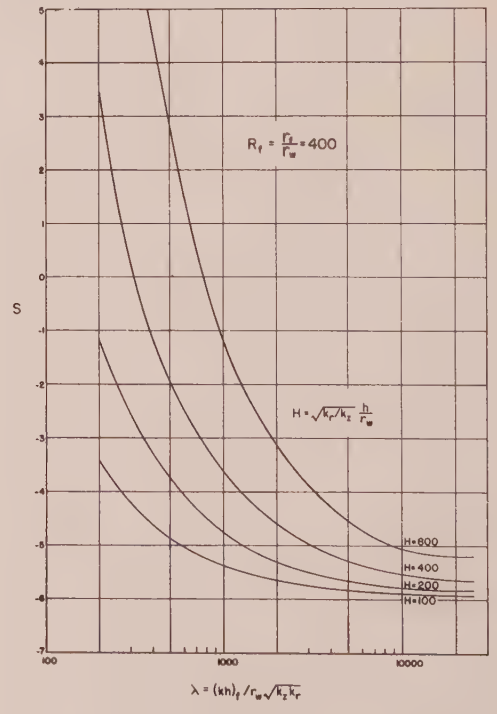

FIG. 4—COMPUTED RESULTS, $R_f = \frac{r_f}{r_w} = 400$.

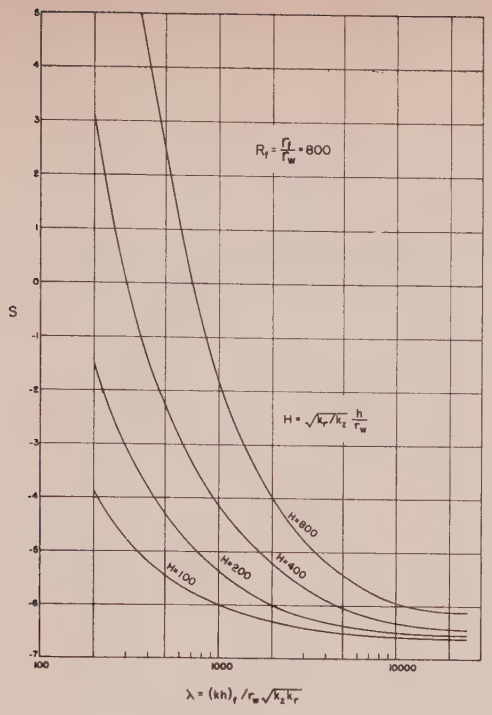

FIG. 5—COMPUTED RESULTS, $R_f = \frac{r_f}{r_w} = 800$.

and, from van Poollen, *et al*,[11]

$$S \approx -(\ln r_f/r_w) \Big/ \left[1 + (kh)_r/(kh)_f\right].$$

These two approximations converge if $(kh)_f \gg (kh)_r$; however, since neither of them contains the formation thickness explicitly, it is not surprising that they agree reasonably well with the computed results only for thin formations. For short fractures in thick formations, errors in excess of 100 per cent are possible if these approximations are used.

The effect of fracture location on productivity is demonstrated by the typical results presented in Fig. 7. As might be expected, the thicker formation is more sensitive to the position of the fracture, i.e., a relative productivity decrease of 24 per cent compared to a 7 per cent decrease for the thinner formation. In both cases, however, the productivity decrease per foot of deviation from the mid-point is approximately .5 per cent; since the probable error in fracture placement may be assumed to be independent of bed thickness, the effect of missing the mid-point of the formation appears to be insignificant. Curves similar to those shown can be used to determine the relative productivity change that can be expected when the fracture is deliberately placed at the top or bottom of the pay because of fluid segregation problems.

To illustrate the influence of multiple fractures on productivity, two cases are compared in Fig. 8. In one, a single 100-ft fracture is placed in the center of the formation; in the other, four 50-ft fractures are located at the mid-points of four equally thick subdivisions of the reservoir. The total surface areas are equal for both cases and the flow capacities of the fractures are constant. The results indicate that multiple fractures are more desirable when the $(kh)_f/(kh)_r$ is small and that a single fracture is more beneficial when the ratio is large. The ratio of flow capacities at which the two curves cross will increase as the thickness is increased,

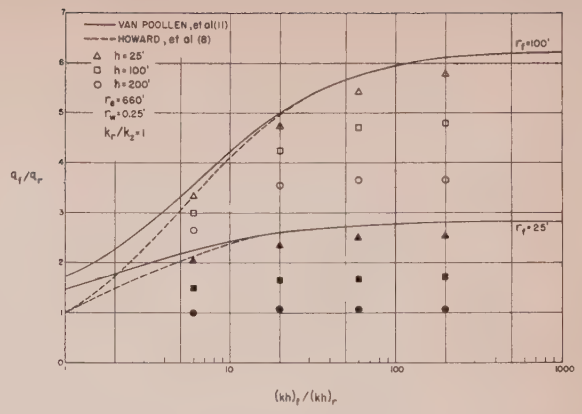

FIG. 6—COMPARISON WITH SIMPLIFIED THEORY SHOWING EFFECT OF FORMATION THICKNESS.

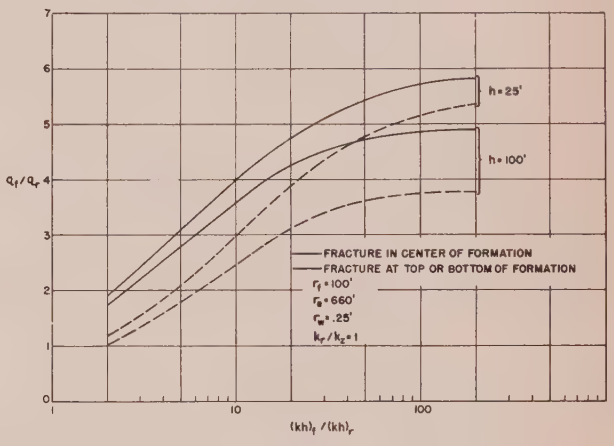

FIG. 7—EFFECT OF FRACTURE LOCATION.

and it will decrease as the radius of fracture is increased.

The manner in which the productivity is affected by the vertical permeability is shown in Fig. 9. The effect is quite substantial over the range of k_r/k_z considered. It must be borne in mind that the effective value of the ratio of the directional permeabilities probably is much greater than that determined from laboratory measurements on small core samples because of the presence of shale breaks and other permeability barriers in the reservoir. Unfortunately, little is known quantatively about the in situ anisotropy of reservoirs; a method for determining the ratio of horizontal and vertical permeabilities has been proposed,[19] but it has not been tested in the field.

PRACTICAL APPPLICATIONS

FRACTURE DESIGN

To use the computed results for determining the optimum objectives for the design of a fracture treatment, it is necessary to prepare a work curve similar to that shown in Fig. 10. If the well spacing, formation thickness, wellbore radius, horizontal permeability and vertical permeability are known, the work curve can be obtained from the data in Figs. 2 through 5 and Eq. 5 for a given fracture location. From imbedment, crushing and fluid-loss tests on core samples, practical limits on the flow capacity of the fracture can be determined and the fracturing costs can be fixed. Then, the production history of the well, PVT data and/or the formation characteristics can be used to predict performance from the time of fracturing for both the fractured

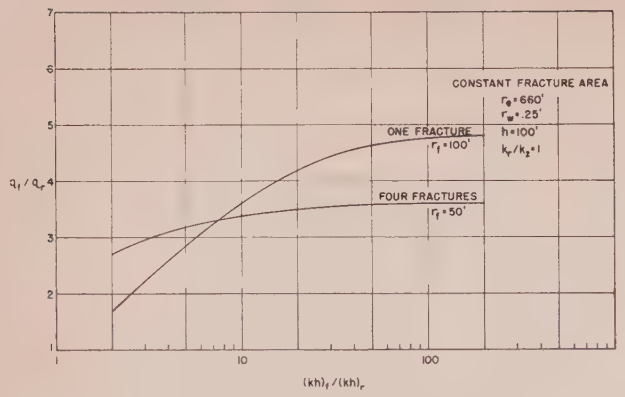

FIG. 8—EFFECT OF MULTIPLE FRACTURES.

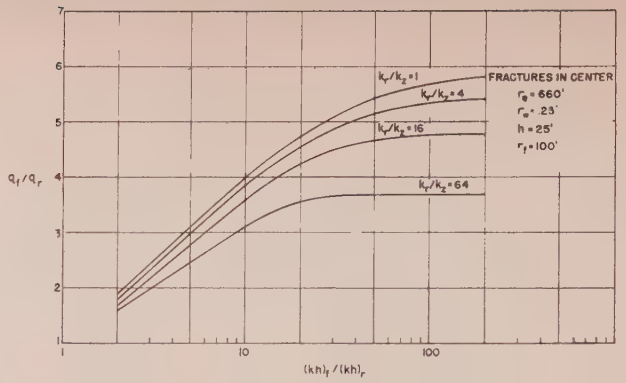

FIG. 9—EFFECT OF VERTICAL PERMEABILITY.

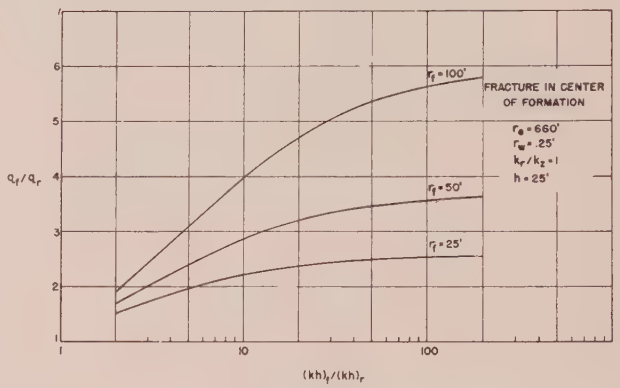

FIG. 10—WORK CURVE.

and unfractured cases. With this information in hand, an economic evaluation can be made to determine which fracture configuration will yield the maximum profit. For a detailed discussion of the economic comparison, see the paper by Howard, *et al.*[8]

If a particular well has a constant-percentage decline curve characterized by a decline factor D, there is a simple method for obtaining a lower limit on the value of q_f/q_r for a given treatment. For payout, the net income from the additional ultimate economic oil production due to fracturing, ΔQ, must equal the cost of the fracture; for the required value of ΔQ, the minimum value of q_f/q_r is given by the following expression.

$$(q_f/q_r)_{\min} = q_{ec}/(q_{ec} - D\Delta Q).$$

This limiting condition will serve to eliminate many possible treatments from further consideration.

The most uncertain quantity used in the preparation of the work curve is the vertical permeability. Since this parameter can have a marked effect on the productivity, it will affect the subsequent economic analysis significantly; therefore, it would be desirable to determine a reasonable value for each field or each distinct portion of a field. Fortunately, when the formation has been notched for the single-point entry of fluid, the wellbore conditions are ideal for determining the vertical permeability from pressure build-up data.[19] In lieu of this method, whole-core analysis can be used to evaluate the vertical permeability.

FRACTURE EVALUATION

To evaluate the fracture treatment, the apparent skin effect can be calculated from pressure build-up data (Eq. 7) or from the stabilized productivity indices (Eq. 8). Using the measured value for S and Eq. 5, q_f/q_r can be determined. If this value of the productivity ratio agrees with that which was the basis for the design of the fracture treatment, the design objectives probably have been achieved.

Because the productivity ratio is not a unique function of the flow capacity and the radius of the fracture, an independent source of information is required for a more complete comparision with the design objectives. The technique proposed by van Dam and Horner[12] can be used to estimate the radius of the fracture by analyzing pressure build-down data obtained immediately after fracturing. With this value for the fracture radius and the apparent skin effect, the flow capacity of the fracture can be estimated from Figs. 2 through 5. If agreement with the design objectives is observed, the method of design is probably valid for that particular formation. If agreement is lacking, the discrepancies between the observed and designed characteristics — together with the fracture thickness, fracture porosity and in situ fluid loss, determined according to van Dam and Horner—may be utilized to diagnose the deficiencies inherent in the treatment employed.

If consistently favorable evaluations of fracture treatments are obtained in a given formation, it is highly probable that the fractures conform to the idealized horizontal pattern that was assumed. The accumulation of results from design evaluations could help to settle the controversy concerning fracture orientation, i.e., horizontal or vertical.

SUMMARY AND CONCLUSIONS

The equations which describe the steady-state flow of a single-phase fluid into, and through, a finite-capacity fracture were solved numerically for an idealized reservoir-fracture model. The numerical results were used to obtain an apparent skin effect for each combination of the parameters considered.

The use of the apparent skin effect in the specification of design objectives for fracture treatments was discussed. A technique for evaluating the success of a given fracture treatment was outlined.

Based on the computed results, subject to the limitations imposed by the assumptions that were made, the following general conclusions were drawn.

1. For a radius of drainage at least four times as large as the radius of fracture, an apparent skin effect that is independent of the radius of drainage can be calculated.

2. The productivity of the fractured system, relative to that of the unfractured well, can be determined from the apparent skin effect and can be used to establish design objectives.

3. In the evaluation of a given fracture job, it is not possible to determine both the radius of the fracture and its flow capacity uniquely from the observed skin effect; and independent determination of one of the quantities is necessary.

NOMENCLATURE

A = flow resistance matrix composed of horizontal and vertical submatrices A_r and A_z, dimensionless
B = $F^{-1/2}\ AF^{-1/2}$, normalized flow resistance matrix composed of horizontal and vertical submatrices B_r and B_z, dimensionless
D = productivity decline factor, $(\text{days})^{-1}$
F = capacitance matrix, dimensionless
H = $\sqrt{k_r/k_z}\ h/r_w$, formation thickness, dimensionless
M = total number of acceleration parameters, dimensionless
N = number of fractures in a particular formation, dimensionless
PI = productivity index, STB/D/psi
ΔQ = additional oil production necessary for payout, STB
R = r/r_w, radial co-ordinate, dimensionless
S = apparent skin effect with fracture at midpoint of formation, dimensionless
S' = apparent skin effect with fracture at top or bottom of formation, dimensionless
S_N = apparent skin effect for N fractures, dimensionless
Z = $\sqrt{k_r/k_z}\ z/r_w$, vertical co-ordinate, dimensionless
b = element of B-matrix, dimensionless
c = liquid compressibility, $(\text{psi})^{-1}$
f = element of F-matrix, dimensionless
$\vec{g}$ = boundary-condition vector, dimensionless
h = formation thickness, ft
k = absolute permeability composed of horizontal and vertical components k_r and k_z, md
$(kh)_f$ = flow capacity of fracture, md-ft
$(kh)_r$ = radial flow capacity of formation, md-ft
m = slope of linear portion of pressure build-up curve, psi/cycle
n = iteration number, dimensionless
p = pressure, psi
Δp = $p_e - p_w$, pressure drawdown, psi
P_{w0} = flowing wellbore pressure at shut-in, psi
P_{w1} = built-up wellbore pressure one hour after shut-in, psi
$\bar{p}$ = volumetrically weighted average pressure, psi
q = production rate, STB/D
q_{ec} = limiting economic rate of production, STB/D
r = radial co-ordinate, ft
t = time of shut-in, hours
Δt = time after shut-in, hours
$\vec{w}$ = $F^{-1/2}\ \vec{g}$, normalized boundary-condition vector, dimensionless
$\vec{x}$ = dependent-variable vector, dimensionless
$\vec{y}$ = $F^{1/2}\ \vec{x}$, normalized dependent-variable vector, dimensionless
β = formation volume factor, reservoir bbl/STB
ε = stopping criterion, dimensionless
θ = $(p - p_w)/(p_e - p_w)$, normalized pressure, dimensionless
λ = $(kh)_f/r_w\sqrt{k_r k_z}$, flow capacity of fracture, dimensionless
μ = viscosity of liquid, cp
ρ = acceleration parameter, dimensionless
ρ^* = optimum acceleration parameter for single-parameter case, dimensionless
ϕ = porosity, dimensionless

SUBSCRIPTS

c = value at critical radius
e = value at radius of drainage
f = fractured system
i = dummy index
j = dummy index
r = radial component of unfractured system
w = value at wellbore radius
z = vertical component

REFERENCES

1. Howard, G. C. and Fast, C. R.: *Drill. and Prod. Prac.*, API (1957) 261.
2. Huitt, J. L. and McGlothlin, B. B.: *Drill. and Prod. Prac.*, API (1958) 115.
3. Huitt, J. L. and McGlothlin, B. B.: *Drill. and Prod. Prac.*, API (1959) 120.
4. Darin, S. R. and Huitt, J. L.: "Effect of a Partial Monolayer of Propping Agent on Fracture Flow Capacity", *Trans.*, AIME (1960) **219,** 31.
5. *Frac Guide* privately published by Dowell Div. of The Dow Chemical Co. (1959).
6. *Fracplan*, privately published by the Halliburton Co. (1960).
7. Huitt, J. L.: *Jour. Pet. Tech.* (March, 1960) **XII,** No. 3, 11.
8. Howard, G. C., Flickinger, D. H., Fast, C. R. and Evans, R. B.: *Drill. and Prod. Prac.*, API (1958) 91.
9. Carter, R. D. and Tracy, G. W.: *Trans.*, AIME (1960) **219,** 415.
10. van Poollen, H. K.: *Drill. and Prod. Prac.*, API (1957) 103.
11. van Poollen, H. K., Tinsley, J. M. and Saunders, C. D.: *Trans.*, AIME (1958) **213,** 91.
12. van Dam, J. and Horner, D. R.: "Interpretation of Pressure Build Down after a Sandfrac Treatment", Paper 982-G presented at Second Annual Meeting of Venezuelan Sections of SPE in Caracas (Nov. 6-9, 1957).
13. Crawford, P. B. and Landrum, B. L.: *World Oil*, (1956) **142,** No. 6, 196.
14. Brons, F. and Marting, V. E.: *Jour. Pet. Tech.*, (Feb., 1961) 172.
15. Muskat, M: *Physical Priniciples of Oil Production*, McGraw-Hill Book Co., Inc., N. Y. (1949) 211.
16. Miller, C. C., Dyes, A. B. and Hutchinson, C. A.: *Trans.*, AIME (1950) **189,** 91.
17. van Everdingen, A. F.: *Trans.*, AIME (1953) **198,** 171.
18. Peaceman, D. W. and Rachford, H. H.: *Jour. Soc. Ind. and Appl. Math.*, (1955) **3,** 28.
19. Hartsock, J. H. and Warren, J. E.: "A Method for the Determination of Vertical Permeability", Gulf Research and Development Co., to be published.
20. Wachspress, E. L. and Habetler, G. J.: *Jour. Soc. Ind. and Appl. Math.*, (1960) **8,** 403.
21. Varga, R. S. and Price, H. S.: "Recent Numerical Experiments Comparing the IAD and the SOR Methods", Paper presented at AEC Symposium on Matrix Problems held in Gatlinburg, Tenn. (April 24-28, 1961).

APPENDIX

BEHAVIOR EQUATIONS

The equation that describes the pressure distribution in the assumed model is the following.

$$\frac{\partial^2 p}{\partial r^2} + \frac{1}{r}\frac{\partial p}{\partial r} + \frac{k_z}{k_r}\frac{\partial^2 p}{\partial z^2} = 0 \quad \ldots\ldots \quad (A\text{-}1)$$

The boundary conditions imposed by the physical assumptions are as follows.

$$p = p_w \text{ for } r = r_w,\ z = 0;$$

$$\frac{\partial p}{\partial r} = 0 \text{ for } r = r_w,\ 0 < z \leq h/2;$$

$$\frac{\partial^2 p}{\partial r^2} + \frac{1}{r}\frac{\partial p}{\partial r} + \frac{k_z}{(kh)_f}\left(\frac{\partial p}{\partial z}\right)_{z=0} = 0 \text{ for } z = 0,\ r_w < r < r_f;$$

$$\frac{\partial p}{\partial z} = 0 \text{ for } z = 0,\ r_f < r \leq r_e;$$

$$p = p_e \text{ for } r = r_e,\ 0 \leq z \leq h/2;$$

and

$$\frac{\partial p}{\partial z} = 0 \text{ for } z = h/2,\ r_w \leq r \leq r_e.$$

After normalizing the dependent variable and making the equation dimensionless, Eq. A-1 and the boundary conditions can be written as follows.

$$\frac{\partial^2 \theta}{\partial R^2} + \frac{1}{R}\frac{\partial \theta}{\partial R} + \frac{\partial^2 \theta}{\partial Z^2} = 0. \quad \ldots\ldots \quad (A\text{-}2)$$

$$\theta = 0 \text{ for } R = 1,\ Z = 0;$$

$$\frac{\partial \theta}{\partial R} = 0 \text{ for } R = 1,\ 0 < Z \leq H/2;$$

$$\frac{\partial^2 \theta}{\partial R^2} + \frac{1}{R}\frac{\partial \theta}{\partial R} + \frac{1}{\lambda}\left(\frac{\partial \theta}{\partial Z}\right)_{z=0} = 0 \text{ for } Z = 0,\ 1 < R < R_f;$$

$$\frac{\partial \theta}{\partial Z} = 0, \text{ for } Z = 0,\ R_f < R \leq R_e;$$

$$\theta = 1, \text{ for } R = R_e,\ 0 \leq Z \leq H/2;$$

and

$$\frac{\partial \theta}{\partial Z} = 0, \text{ for } Z = H/2,\ 1 \leq R \leq R_e.$$

METHOD OF SOLUTION

If the region of interest is covered with a nonuniform mesh, if Eq. A-2 is approximated by a five-point finite-difference equation and if the boundary conditions are imposed in finite-difference form, the problem is reduced to obtaining a solution to a system of simultaneous linear equations. The problem can be expressed in the following matrix form.

$$\vec{Ax} = \vec{g} \quad \ldots\ldots \quad (A\text{-}3)$$

A is a Stieltjes matrix which is poorly conditioned; therefore, it should be normalized to improve the rate of convergence of the iterative method of solution that is to be used.[20] If F is a diagonal matrix with elements which correspond to the volume assigned to each mesh-point and if $\vec{y} = F^{1/2}\vec{x}$, Eq. A-3 can be written as follows.

$$F^{-1/2} A F^{-1/2} \vec{y} = F^{1/2}\vec{g} \quad \ldots\ldots \quad (A\text{-}4)$$

Or,

$$B\vec{y} = \vec{w}. \quad \ldots\ldots \quad (A\text{-}5)$$

The matrix B can be split into two tridiagonal submatrices (i.e., $B = B_r + B_z$), and the implicit alternating-direction technique developed by Peaceman and Rachford[18] can be used. Their method is described by the following pair of equations.

$$(B_r + \rho_n I)\vec{y}^{*(n)} = (\rho_n I - B_z)\vec{y}^{(n)} + \vec{w};$$

$$(B_z + \rho_n I)\vec{y}^{(n+1)} = (\rho_n I - B_r)\vec{y}^{*(n)} + \vec{w}. \quad (A\text{-}6)$$

The acceleration parameters ρ_n can be estimated in the following indicated manner.[21]

$$\rho_1 = \max_i \left[\sum_j |b_{i,j}|\right]/\sqrt{2};$$

$$\rho_n = \rho_{n-1}/2;\ 1 < n \leq M \quad \ldots\ldots \quad (A\text{-}7)$$

where M = total number of parameters.

A total of 22 parameters were used to adequately span the spectrum of eigenvalues; after each cycle of 22 iterations, the ρ's were re-introduced in order. The total number of parameters, M, was determined by demanding that M be the smallest integer that satisfies the following inequality.

$$M \geq [1.445 \ln (\rho_1/\rho^*) + .500] \quad \ldots \quad (A\text{-}8)$$

where ρ^* = optimum single acceleration parameter experimentally determined for a similar problem.

A criterion for stopping the iterative procedure must be specified. For this problem, computation was halted when the following condition was met.

$$\max_{i,j}\left\{\frac{y_{i,j}^{(n)} - y_{i,j}^{(n-22)}}{y_{i,j}^{(n)}}\right\} < \varepsilon \quad \ldots\ldots \quad (A\text{-}9)$$

The maximum value used for ε was 10^{-4}.

COMPUTATIONAL CONSIDERATIONS

The nonuniform mesh finally used to obtain the indicated results was determined by digital experimentation. Using 80 mesh points in the R-direction and 10 in the Z-direction, the maximum error in the calculated flow rate (or in S) was estimated to be 1 per cent by extrapolation.

For fixed values of R_f, H and λ, the critical radius R_e was determined by computing the flow rate at R_e from the gradient in the R-direction only and comparing this result with the computed flow rate out of the fracture. When the two rates agree, the flow at R_e is essentially radial. For $R_e \geq 4R_f$, the two rates agree to at least three significant figures for all of the cases considered.

The apparent skin effect was calculated from Eq. 2 of the text by utilizing the following relationships.

$$(\Delta p)_r = \frac{q\mu\beta}{2\pi(kh)_r} 1n\, R_e;$$

and

$$q = \frac{2\pi(kh)_r (\Delta p)_f}{\mu\beta} R_e \left(\frac{\partial \theta}{\partial R}\right)_{R=R_e} \quad \ldots \quad (A\text{-}10)$$

Consequently,

$$S = -\left[1n\, R_e - 1/R_e\left(\frac{\partial \theta}{\partial R}\right)_{R=R_e}\right] \quad \ldots \quad (A\text{-}11)$$

Solutions to the normalized problem with $\varepsilon < 10^{-4}$ and 1,040 mesh points, guaranteeing an error of less than 1 per cent were obtained on an IBM 704 computer; the computer time required for each case was about 45 minutes. Under the same conditions, an IBM 7090 required only 7.5 minutes/case. ★★★

Further Discussion of Paper Published in *Journal of Petroleum Technology*, March, 1961

The Significance of Particle Shape in Formation Resistivity Factor-Porosity Relationships

E. R. ATKINS, JR.
MEMBER AIME
G. H. SMITH

UNION OIL CO OF CALIFORNIA
BREA, CALIF.

DISCUSSION

G. H. F. GARDNER
MEMBER AIME

GULF RESEARCH & DEVELOPMENT CO.
PITTSBURGH, PA.

Atkins and Smith maintain that the equation

$$1/F = a\phi^m, \quad . \quad . \quad . \quad . \quad . \quad . \quad . \quad . \quad . \quad . \quad (1)$$

or a pair of such equations, represents a basic relationship between formation factor and porosity, and they attempt to attach physical significance to the parameters a and m. Their argument uses the boundary condition $F = 1.0$ when $\phi = 100$ per cent.

It may be noted, however, that this is only one of two boundary conditions which must be satisfied when ϕ approaches 100 per cent. Maxwell's[1] equation for randomly dispersed spheres is

$$F = (3 - \phi)/2\phi, \quad . \quad . \quad . \quad . \quad . \quad . \quad . \quad . \quad . \quad .(2)$$

and it is valid for ϕ close to unity. From this equation we obtain

$$\frac{dF}{d\phi} = -1.5 \text{ when } \phi = 1.0 \quad . \quad . \quad . \quad . \quad . \quad . \quad (3)$$

An examination of Rayleigh's[2] analysis will show that Eq. 3 is exactly true. Hence, this is a boundary condition of equal standing with that invoked by Atkins and Smith, but it is not satisfied in their theory.

Eq. 1 can be used to correlate any data, but this does not imply a basic significance. It is clear that the choice of a and m depends on the degree of precision demanded, the porosity range covered and the boundary conditions imposed. For example, the data of Wyllie and Gregory[3] for packings of spheres in the porosity range from 10 to 50 per cent give $a = .87$ and $m = 1.22$. Atkins and Smith suggest that the condition $a = 1$ and $m = 1.3$ is more meaningful, but this choice gives a 10 per cent divergence from the measured data at porosities near 40 per cent. It has the merit of satisfying one boundary condition, but it does not satisfy the other. In the porosity range from 10 to 25 per cent, however, it would be perfectly satisfactory for practical use.

All this is not to say that the effect of particle shape and cementation cannot be described. The data of Atkins and Smith on mud slurries will be useful in establishing such a theory.

[1]Maxwell, J. C.: *A Treatise on Electricity and Magnetism*, Second Ed., Slarendon Press (1881) **1**, 435.

[2]Lord Rayleigh: "On the Influence of Obstacles Arrayed in Rectangular Order Upon the Properties of a Medium", *Phil. Mag.* (1892) **34**, 481.

[3]Wyllie, M. R. J. and Gregory, A. R.: *Ind. and Eng. Chem.* (1955) **47**, 1379.

AUTHORS' REPLY TO G. H. F. GARDNER

The boundary conditions $F = 1.0$ and $\phi = 1.0$ (100 per cent) are dictated by the definition of F in the equation $1/F = a\phi^m$. These conditions have physical significance as the "limiting conditions" for the observed behavior in systems of dispersed particles. The other boundary conditions, cited by Gardner in his Eq. 3 as applying to this system, have no significance in the systems we studied.

Maxwell's equation (Eq. 2) cited in Gardner's comments was developed for and limited to a regular, rather than random, dispersion of spheres which are sufficiently removed from each other so that they do not interfere with current flow about their neighbors. These restrictions also apply to Rayleigh's analysis. The title of Rayleigh's paper cited by Gardner is "On the Influence of Obstacles Arrayed in Rectangular Order upon the Properties of a Medium". He is not discussing randomly dispersed spheres.

It might be inferred from Gardner's comments that Rayleigh specifically considered the differential equation (Gardner's Eq. 3). This is not the case. Mathematically, Gardner's Eq. 3 is exactly true for the system to which it applies, however, as both Rayleigh and Maxwell note that their equation for F in terms of ϕ is not for randomly dispersed spheres.

At the time we wrote our paper, we were aware of the work of Wyllie and Gregory as cited by Gardner. We cited their work in Ref. 5 of our paper. Our comment on page 287 of the paper about the validity of an m value of 1.3 for spheres with a porosity of 38 per cent remains as our answer to Gardner's question on this point. Our data, at 38 per cent porosity, show that the condition $a = 1$ and $m = 1.3$ holds for spheres near 40 per cent porosity. ★★★

Calculated Pressure Build-Up for a Low-Permeability Gas-Condensate Well

H. DYKSTRA*
MEMBER AIME

CALIFORNIA RESEARCH CORP.
LA HABRA, CALIF.

ABSTRACT

Calculated wellbore pressures were obtained for parameters of radius ratio and permeability. In all cases but two, after-production was allowed to occur for one day. The calculated pressure build-up data were compared with actual pressure build-up data from a condensate well. The paper discusses the comparison, gives reasons for, inability to match calculated and actual data, and presents conclusions derived from the comparison.

INTRODUCTION

Considerable information has been published on the decline in wellbore pressure for oil and gas fields resulting from production of fluids. Considerable information also has been published on pressure build-up for oil fields, but relatively little has been published for gas and condensate fields.

Perrine[1] summarized the equations derived for pressure build-up in oil wells and showed how the different methods could be applied. On the other hand, very little theoretical information has been published on pressure build-up in gas or gas-condensate wells.[2-4] Tracy,[2] by pointing out the similarity between the equation describing oil wellbore pressure decline and the equation describing gas wellbore pressure decline, showed how methods of pressure build-up analysis could be applied to a gas well.

In analyzing pressure build-up data for gas or gas-condensate wells, it would be very desirable to compare actual pressure build-up data with calculated pressure build-up data. Such a comparison would lead to a better feeling for the quantitative picture of gas-well build-up curves and would help to establish a degree of confidence in a given build-up curve. This paper discusses the comparison and presents conclusions made from it.

Calculated wellbore pressures are given for parameters of radius ratio and permeability. In all cases but two, after-production was allowed to occur for one day. The work was done in an attempt to evaluate the reserves of a gas-condensate field. As will be discussed later, it was not possible to make an evaluation.

METHOD OF CALCULATION

The method used for solving the depletion and pressure build-up behavior for a gas-condensate well was that developed by West, Garvin and Sheldon.[5] For the IBM 704 computer program used, it was assumed that liquid condensing out of solution would have only a minor effect on the flow behavior. Therefore, the field was treated as having single-phase flow, with the gas saturation S_g remaining constant at unity minus the connate-water saturation S_{wc}. As will be discussed later, this may not have been a good assumption. It also was assumed that oil production could be considered as equivalent gas production by using a conversion factor based on an analysis of the liquid produced. An outer boundary condition of no-flow was assumed.

BASIC DATA

The data required for the study were reservoir properties, fluid properties and production data. Reservoir properties included the following: thickness h, 179 ft; porosity, 0.194; connate-water saturation, 0.43; gas saturation, 0.57; permeabilities k, 1.0, 0.5, 0.25 and 0.15 md; radius ratios r_e/r_w, 800, 1,000 and 2,000; wellbore radius r_w, 5 in.; initial reservoir pressure P_i, 6,529 psia; and reservoir temperature, 272°F.

The selection of permeabilities was based on core-analysis data showing an average air permeability of about 2 md. With a relatively high connate-water saturation, the average effective gas permeability would be about one-half, or less, of the air permeability. The selection of radius ratios was based partly on the observed rapid decline in wellbore pressure during production and partly on the fact that the well was believed to be located in a relatively small fault block.

Reservoir fluid properties were obtained from a reservoir fluid study on a recombined sample of gas and condensate. Gas formation-volume factors were calculated from pressure-volume measurements made at reservoir temperature. Gas viscosities were calculated by the method of Carr, *et al*,[6] from an analysis of the recombined sample. These data are shown as a function of pressure in Table 1.

The production schedule from the gas-condensate

Original manuscript received in Society of Petroleum Engineers office June 6, 1961. Revised manuscript received Sept. 26, 1961.

*Now with Standard Oil Co. of California, Western Operations, Inc., San Francisco.

[1]References given at end of paper.

Discussion of this and all following technical papers is invited. Discussion in writing (three copies) may be sent to the office of the *Journal of Petroleum Technology*. Any discussion offered after Dec. 31, 1961, should be in the form of a new paper. No discussion should exceed 10 per cent of the manuscript being discussed.

This page of *Petroleum Transactions, AIME* follows page 1057. The intervening non-Transactions pages appeared in *Journal of Petroleum Technology*.

well consisted of two parts. For the first part, a short (10-day) production period was followed by a long (65-day) shut-in period. For the second part, the well was put back on a 50-day production period, which was followed by the shut-in period of interest. For purposes of the analysis in this paper, it was assumed that the reservoir was at static pressure at the end of the first shut-in period. The pressure would be less than the original pressure by an amount determined from material-balance calculation and from the assumed size of the reservoir.

Production-rate data for the 50-day period declined in a manner than could be described reasonably well by a quadratic equation. In addition, the computer program used a quadratic formula for interpolation between tabulated values of production and time. Therefore, a quadratic equation was fitted to the production-rate data such that the area under the rate curve was equal to the cumulative production. This procedure greatly simplified the work required to prepare production data for the computer. Production data derived from the quadratic equation are given in Table 2. We assumed that production rate declined to zero in one day to allow for after-production because the well was shut in at the surface. For two computed cases, the production was stopped immediately to simulate shutting-in the well at the wellbore face.

DISCUSSION OF RESULTS

As shown in Table 3, six computer runs were made to determine pressure decline and pressure build-up with after-production, and two runs were made to find pressure build-up without after-production.

TABLE 1—FORMATION-VOLUME FACTOR AND VISCOSITY OF GAS

Pressure (psia)	B_g (res bbl/Mcf)	μ_g (cp)
7000	0.658	0.0357
6500	.676	.0342
6000	.698	.0326
5500	.728	.0309
5000	.768	.0291
4500	.814	.0272
4000	.880	.0252
3500	.971	.0232
3000	1.103	.0212
2500	1.298	.0192
2000	1.633	.0172
1500	2.20	.0154
1000	3.40	.0139
500	6.98	.0127

TABLE 2—PRODUCTION DATA

Time (days)	Rate* (Mcf/D)
0	6556
10	5095
20	3960
30	3149
40	2658
50	2500
51	Shut-in

*Rate is that of gas plus liquid, with the liquid rate being given in equivalent Mcf.

TABLE 3—COMPUTER RUNS

r_e/r_w	P_i (psia)	k (md)	Curve No.
2000	6430	0.25	1
1000	6150	1.0	2
1000	6150	0.5	3
1000	6150	0.25	4*
1000	6150	0.25	5
1000	6150	0.15	6
800	5960	0.25	7*
800	5960	0.25	8

*No after-production.

The calculated wellbore pressure-decline curves for permeabilities of 0.5 md and less showed similar behavior, with a minimum occurring at three to four days and then followed by a rise. Three of these curves, along with the calculated curve for 1 md which did not have a minimum, are shown in Fig. 1.

A run also was tried at 0.10 md. For this run the calculated wellbore pressure tended to go below 500 psia, for which PVT and viscosity data were not available; this caused the computer to stop. Such a low wellbore pressure undoubtedly would be insufficient to allow gas and condensate to flow from the bottom of the well to the surface. Hence, we could conclude that the permeability of the formation was above 0.10 md.

Calculated wellbore pressure build-up curves showing the effect of permeability at a radius ratio of 1,000 are shown in Fig. 3. Calculated curves showing the effect of radius ratio for a permeability of 0.25 md, plus the calculated curves for no after-production, are shown in Fig. 2. Also shown in these two figures is the measured pressure build-up curve. The curves are plotted as P_w^2 vs

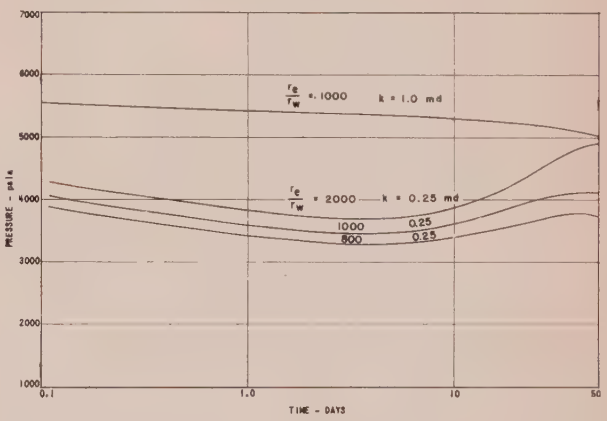

FIG. 1—PRODUCING WELLBORE PRESSURE VS TIME.

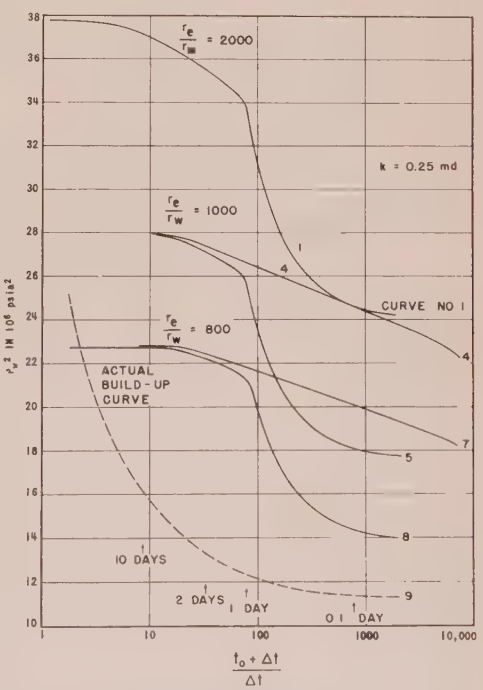

FIG. 2—PRESSURE BUILD-UP CURVES SHOWING EFFECT OF RADIUS RATIO.

$\frac{t_o + \Delta t}{\Delta t}$, in accordance with the procedure described by Tracy.[2]

From the calculated curves plotted in Figs. 2 and 3, one can see that the calculated wellbore pressure builds up much more rapidly than the measured wellbore pressure for all the parameters studied. The calculated pressure rapidly builds up in about one day (with the exception of the case with no after-production) to a point where the curves reverse in curvature. The pressure has about reached maximum build-up in from 2 to 20 days, with the longer times for the lower permeabilities.

As stated in the introduction, the purpose of the analysis was to attempt to evaluate reserves of a gas-condensate field. The runs made indicated that it was not possible to match the wellbore pressure at time of shut-in with a uniform permeability and reasonable size of the volume drained by a well. Furthermore, the amount of after-production was more than enough to fill up the wellbore to the maximum pressure reached during build-up. Therefore, no further attempts were made to match the actual build-up curve by varying the rate and amount of after-production. Consequently, no estimate of reserves could be made.

The curves shown in Figs. 2 and 3 show the effect of after-production. For permeabilities of 0.5 and 1.0 md, the straight-line portion is not obvious, having been masked as a result of after-production. The remaining curves do have a straight-line portion which can be used for pressure build-up analysis (as shown later). These results point out that it is almost imperative, if useful pressure build-up data are to be obtained, to shut-in gas wells at the top of the producing interval.

The difference between calculated and actual build-up in pressure can be explained with the aid of results published by Perrine[1] on pressure build-up analysis for oil wells. In Fig. II-4 of his paper, he has shown the

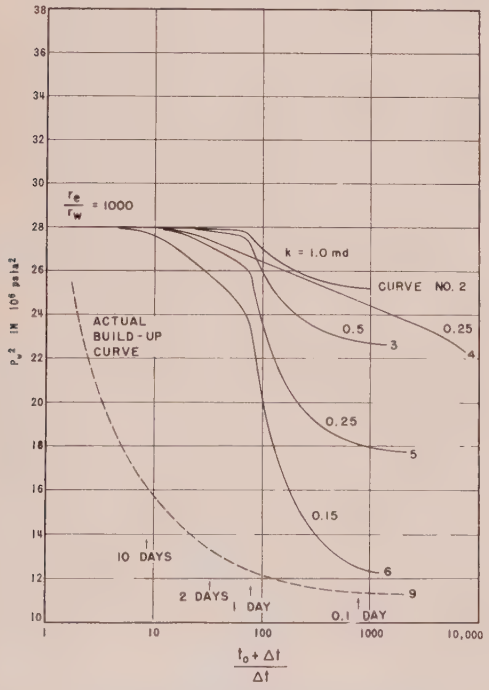

FIG. 3—PRESSURE BUILD-UP CURVES SHOWING EFFECT OF PERMEABILITY.

effect of shutting-in a well at the surface and the effect of permeability reduction around a wellbore. For a well shut-in at the surface, a certain amount of time is required before the pressure builds up to the straight-line portion of the curve. (Compare Curves 1 and 6 of Perrine's Fig. II-4.) For a permeability reduction around a wellbore, the effect is to delay pressure build-up still more (compare Curves 6 and 8). In fact, Perrine says the following.

"With very serious damage, afterproduction slows down the buildup in pressure at the well bore until interpretation is impossible. The straight-line portion of the curve is completed masked by a smooth transition from behavior dominated by wellbore conditions to behavior determined by conditions at the drainage radius."

Additional information has also been supplied by Pitzer, *et al*,[7] to show the advantages of bottom-hole shut-in tests.

This same reasoning applies equally well to pressure build-up for a gas well. Thus, we can conclude that the slow build-up of measured pressure is probably a result of after-production from a formation whose permeability is severely reduced around the wellbore. How far the reduction extends beyond the wellbore cannot be said.

Three reasons can be given for a reduction in gas permeability around the wellbore (1) drilling fluid filtrate invasion; (2) an increase in water saturation around the wellbore (some water is being produced); and (3) an increase in oil saturation around the wellbore. This last reason is a very probable one because the gas condensate is fairly rich. With the high drawdown, a considerable amount of oil could be deposited around the wellbore to lower the gas saturation and, hence, the gas permeability. Therefore, the assumption made earlier in this paper of treating the system as single-phase flow may not have been valid.

One other point can be brought out regarding the actual build-up curve. Even after 50 days the wellbore pressure is still building up. An explanation for this is based on a geologic interpretation that the fault block may extend into an aquifer. If this is so, then the outer boundary condition of no-flow would not apply. Therefore, the reservoir may eventually build up to a pressure close to the original pressure, thus making it impossible to determine reserves.

ANALYSIS OF PRESSURE BUILD-UP DATA

The calculated pressure build-up Curves 4 and 5 shown in Fig. 2 can be used to check the method described by Tracy.[2] For calculation of permeability k, the curves are replotted in Fig. 4 as P_{wo}^2 vs log time in hours. The calculation of k shown in Table 4 indicates a good check between actual k and calculated k.

The calculation of static reservoir pressure P_s (using Tracy's notation) given in Table 5 shows a reasonably good check with the actual static pressure of 5,297 psia.

CONCLUSIONS

1. The calculations indicated that it was not possible to match calculated wellbore pressure and actual wellbore pressure at time of shut-in with a uniform permeability and reasonable size of volume drained by the producing well.

2. Calculated pressure build-up data point out that

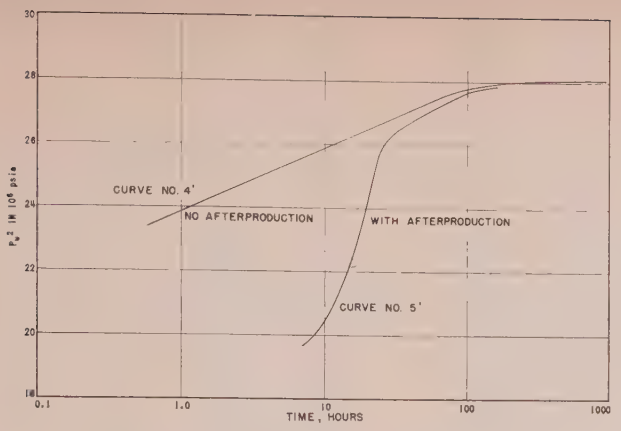

FIG. 4—PRESSURE BUILD-UP CURVES SHOWING EFFECT OF AFTER-PRODUCTION.

it is almost imperative, if useful pressure build-up data are to be obtained, to shut-in gas wells at the top of the producing interval.

3. Plotting P_w^2 vs time t and log $\frac{t_o + \Delta t}{\Delta t}$ is a satisfactory method for obtaining the effective permeability and the static reservoir pressure, respectively, where correct boundary conditions exist for application of this method.

NOMENCLATURE

P_w = wellbore pressure, psia
P^* = extrapolated pressure on plot of P_w^2 vs time
P_i = initial pressure, psia
r_e = outer radius of area being drained, cm
T = reservoir temperature, °R
t_o = time well was on production prior to shut-in, hours
Δt = time after well is shut in, hours
$Y\left(\frac{B\,r^2\phi\mu}{KtP_s}\right)$ = a function (see Ref. 2)

TABLE 4—CALCULATION OF PERMEABILITY k

Q = 2,500 Mcf/D. T = 272° + 460° = 732°R.
P_s = Static Pressure = 5,297 psia. H = 179 ft.
μ = 0.030 at 5,297 psia. Z = 1.06.

$$k = \frac{1{,}637 \times 2{,}500 \times 0.030 \times 732 \times 1.06}{m \times 179} = \frac{.532 \times 10^6}{m}$$

Slope m = 2.01 × 10^6 for no after-production (Curve 4', Fig. 3);
k = 0.265 md.
Slope m = 2.31 × 10^6 for no after-production (Curve 5', Fig. 3);
k = 0.23.

TABLE 5—CALCULATION OF STATIC RESERVOIR PRESSURE P_s

P_i = 6,150 psia P_i^2 = 37.82 × 10^6

	Curve 4	Curve 5
1. $(P^*)^2$	30.46 × 10^6	30.75 × 10^6
2. $P_i^2 - (P^*)^2$	7.36 × 10^6	7.07 × 10^6
3. Slope m	2.03 × 10^6	2.44 × 10^6
4. $\frac{P_i^2 - (P^*)^2}{m} = Y\left(\frac{Br^2\phi\mu}{kt\,P_s}\right)$	3.63	2.90
5. $\frac{Br^2\phi\mu}{kt\,P_s}$	0.086	0.102
6. $\frac{m}{2.303}\left(\frac{kt\,P_s}{Br^2\phi\mu}\right)$	10.25 × 10^6	10.39 × 10^6
7. $P_i^2 - 6$	27.57 × 10^6	27.43
8. P_s	5,250 psia	5,240 psia

Z = gas compressibility factor
ϕ = porosity, fractional
μ = viscosity, cp

REFERENCES

1. Perrine, R. L.: "Analysis of Pressure Build-up Curves", *Drill. and Prod. Prac.*, API (1956) 482.
2. Tracy, G. W.: "Why Gas Wells Have Low Productivity", *Oil and Gas Jour.* (Aug. 6, 1956) **54,** 84.
3. Tek, M. R., Grove, M. L. and Poettmann, F. H.: "Method for Predicting the Back-Pressure Behavior of Low-Permeability Gas Wells", *Trans.*, AIME (1957) **210,** 302.
4. Katz, D. L., *et al: Handbook of Natural Gas Engineering,* McGraw-Hill Book Co., N. Y. (1959) 445.
5. West, W. J., Garvin, W. W. and Sheldon, J. W.: "Solution of the Equations of Unsteady-State Two-Phase Flow in Oil Reservoirs", *Trans.*, AIME (1954) **201,** 217.
6. Carr, N. L., Kobayashi, R. and Burrows, D. B.: "Viscosity of Hydrocarbon Gases Under Pressure", *Trans.*, AIME (1954) **201,** 264.
7. Pitzer, S. C., Rice, J. D. and Thomas, C. E.: "A Comparison of Theoretical Pressure Build-up Curves with Field Curves Obtained from Bottom-Hole Shut-in Tests", *Trans.*, AIME (1959) **216,** 416. ★★★

Calculation of Differential Gas Liberation and Shrinkage

C. F. WEINAUG
MEMBER AIME

U. OF KANSAS
LAWRENCE, KANS.

INTRODUCTION

In recent years, several methods have been proposed for correlation of physical properties and behavior of hydrocarbon systems. These correlations were found to be unsatisfactory for predicting differential gas liberation and shrinkage data now obtained experimentally. To achieve the desired accuracy, methods were developed to adjust the correlations with two experimental pieces of data.

The required data are the saturation pressure at reservoir temperature and the specific volume or density at these conditions. The saturation pressure is used to adjust the vapor-liquid equilibrium-ratio correlations. The density measurement is used to determine the apparent density of liquid methane. With these adjustments, differential gas liberation and shrinkage are predicted within the experimental error.

EQUILIBRIUM RATIOS

Equilibrium ratios published by the National Gas Assn. of America[4] were used as a basis for the calculation. The convergence pressure for the sample was determined by using a hypothetical binary system, with methane as one component and the remainder of the system lumped together to form the other component. For the critical temperature of the heavy constituent, the weight average of the critical temperatures of the ethane and heavier components was used. The correlation of pseudo-critical temperature, density and molecular weight of Matthews, Roland and Katz[1] was used in this calculation for the hexane and heavier fractions. Points for the critical properties of methane and the hypothetical heavy constituent were placed on a chart of the critical loci of hydrocarbon systems.[4] A critical loci for the hypothetical binary system was drawn, and the critical pressure of this system was determined at the reservoir temperature. This critical pressure became the convergence pressure for which equilibrium ratios were read from the NGAA[4] charts.

The NGAA equilibrium constants for C_6 through C_9 were used for the C_6 through C_9 fractions since they were separated on the bases of normal paraffin boiling points. The correlation of Hoffman, Crump and Hocott[5] was used to estimate the equilibrium constant for the C_{10+} fraction.

The NGAA equilibrium-ratio charts are based primarily on paraffin systems and have to be corrected for the presence of naphthenes and aromatics. The correlations in the literature proved too unsatisfactory for determining these corrections. Experimental data, the saturation pressure, is used with the correlation of Soloman[2] to make this adjustment. The correction factors of Soloman were cross-plotted so that the factors for ethane and heavier components were made a function of the factor for methane.

$$a_{2+} = 0.7927\, a_1 + 0.1646 \quad . \quad . \quad . \quad . \quad . \quad . \quad . \quad . \quad . \quad (1)$$

where a_1 = correction coefficient for for methane NGAA equilibrium ratio, and
a_{2+} = correction coefficient for ethane and heavier NGAA equilibrium ratios.

This equation and the equation for the bubble point are solved simultaneously for the correction coefficients. The bubble-point equation is

$$\Sigma\, a_n K_n X_n = 1.0 \quad . \quad . \quad . \quad . \quad (2)$$

The equilibrium constant for the saturation pressure at reservoir temperature is used.

This procedure not only corrects for the relative volatility between components, but also assures that the results will be directly related to the experimental saturation pressure.

METHANE DENSITY

After determining a set of equilibrium ratios, the apparent density of condensed methane at 60°F and 14.7 psia was estimated. This was found to be necessary because the correlations of Standing[3] were found to be unsatisfactory. The law of additive volumes was employed to make this calculation.

$$\frac{x_1 M_1}{\rho_1} + \sum_{2}^{n} \frac{x_n M_n}{\rho_n} = \frac{\sum_{1}^{n} x_n M_n}{\rho} \quad . \quad (3)$$

where x = mole fraction,
M = molecular weight,
ρ = density, and the subscripts refer to components.

The specific volume, at reservoir saturation pressure and temperature, was corrected to 60°F and 14.7 psia. This value was substituted into Eq. 3, and the apparent liquid density for methane at 60°F and 14.7 psia was computed. This apparent density was assumed to apply for all other mixtures formed during the liberation of gas.

CALCULATIONS

The saturated reservoir fluid then was flashed to the first pressure below the saturation pressure. In most cases, this pressure corresponded to the one chosen by the laboratory. The normal flash-vaporization equations were used to compute the moles and compositions of the resulting liquid. The law of additive

Original manuscript received in Society of Petroleum Engineers office March 27, 1961. Revised manuscript received Sept. 18, 1961. Paper presented at 32nd Annual California Regional Meeting of SPE, Nov. 2-3, 1961, in Bakersfield, Calif.

[4]References given at end of paper.

TABLE 1—COMPARISON OF EXPERIMENTAL AND COMPUTED RESULTS

Press. (psig)	Shrinkage Exper.	Shrinkage Calc.	Solution GOR Exper.	Solution GOR Calc.
	Sample 1			
2,360	1.0000	1.0000	0	0
2,150	0.9801	0.9822	45	40
1,950	0.9624	0.9659	84	77
1,750	0.9458	0.9497	122	114
1,550	0.9289	0.9338	158	150
1,350	0.9141	0.9182	192	185
1,150	0.8986	0.9031	228	219
950	0.8840	0.8879	263	253
750	0.8695	0.8721	295	288
550	0.8545	0.8563	329	322
207	0.8242	0.8295	396	380
0	0.8025	0.7741	441	462
	Sample 2			
880	1.000	1.0000	0	0
800	0.996	0.9938	10	11
700	0.989	0.9858	22	25
600	0.983	0.9775	35	40
500	0.975	0.9685	51	55
400	0.966	0.9592	68	71
300	0.956	0.9486	88	88
200	0.940	0.9352	112	110
100	0.910	0.9113	151	144
0	0.817	0.7906	215	276
	Sample 3			
760	1.0000	1.0000	0	0
500	0.9763	0.9831	46	36
300	0.9604	0.9618	87	79
110	0.9385	0.9349	133	130
0	0.9005	0.8658	199	226
	Sample 4			
2,150	1.000	1.0000	0	0
2,000	0.995	0.9946	20	15
1,800	0.988	0.9866	42	36
1,600	0.981	0.9782	64	59
1,400	0.974	0.9699	85	81
1,200	0.967	0.9622	106	101
800	0.952	0.9468	150	142
500	0.940	0.9349	179	173
200	0.929	0.9227	213	206
0	0.889	0.9113	243	233
	Sample 5			
2,915	1.000	1.0000	0	0
2,700	0.982	0.9789	46	45
2,500	0.963	0.9607	87	85
2,300	0.947	0.9439	126	121
2,100	0.931	0.9282	163	156
1,700	0.900	0.8973	231	223
1,500	0.886	0.8819	264	257
1,300	0.873	0.8170	297	289
1,100	0.859	0.8523	330	321
900	0.844	0.8379	361	352
700	0.829	0.8236	391	383
500	0.815	0.8091	421	414
0	0.764	0.7145	519	556
	Sample 6			
2,710	1.0000	1.0000	0	0
2,500	0.9813	0.9872	39	28
2,300	0.9611	0.9674	81	69
2,100	0.9430	0.9449	120	116
1,900	0.9252	0.9239	158	159
1,700	0.9083	0.9073	193	194
1,500	0.8900	0.8918	228	226
1,300	0.8753	0.8766	263	258
1,100	0.8607	0.8615	296	290
900	0.8418	0.8461	330	322
700	0.8256	0.8296	362	355
500	0.8104	0.8122	396	391
185	0.7745	0.7762	463	460
0	0.7210	0.6769	549	589
	Sample 7			
2,055	1.0000	1.0000	0	0
1,840	0.9824	0.9838	41	39
1,600	0.9638	0.9658	82	82
1,400	0.9480	0.9512	119	116
1,200	0.9352	0.9370	150	150
1,000	0.9221	0.9230	183	183
800	0.9086	0.9091	218	215
600	0.8943	0.8949	252	248
400	0.8792	0.8800	284	282
200	0.8612	0.8625	324	320
0	0.8230	0.7914	387	421
	Sample 8			
2,720	1.0000	1.0000	0	0
2,400	0.9234	0.9218	147	138
2,100	0.8660	0.8681	255	236
1,800	0.8171	0.8200	351	325
1,500	0.7741	0.7746	431	409
1,200	0.7342	0.7365	509	481
900	0.6970	0.6996	580	550
600	0.6599	0.6595	654	625
300	0.6135	0.6123	736	712
0	0.4846	0.4055	905	994
	Sample 9			
1,540	1.0000	1.0000	0	0
1,400	0.9820	0.9843	36	30
1,200	0.9615	0.9608	81	76
1,000	0.9405	0.9365	128	123
800	0.9195	0.9127	176	168
600	0.8960	0.8882	225	215
400	0.8697	0.8621	280	265
200	0.8323	0.8282	349	327
0	0.7190	0.6687	502	549
	Sample 10			
1,165	1.0000	1.0000	0	0
1,100	0.9940	0.9936	21	19
800	0.9865	0.9862	45	40
600	0.9807	0.9787	64	62
400	0.9740	0.9714	86	84
200	0.9640	0.9635	119	107
0	0.9535	0.9525	154	137
	Sample 11			
2,390	1.0000	1.0000	0	0
2,100	0.9692	0.9693	68	72
1,800	0.9398	0.9402	139	140
1,500	0.9088	0.9137	210	202
1,200	0.8792	0.8864	279	264
900	0.8504	0.8577	347	330
600	0.8200	0.8255	420	402
300	0.7839	0.7878	503	484
0	0.6410	0.6254	713	743
	Sample 12			
1,570	1.0000	1.0000	0	0
1,300	0.9707	0.9718	67	56
1,000	0.9395	0.9382	133	122
700	0.9082	0.9048	197	187
400	0.8722	0.8686	267	257
150	0.8261	0.8256	352	336
0	0.7730	0.7055	438	503
	Sample 13			
815	1.0000	1.0000	—	—
745	0.9948	0.9943	—	—
700	0.9913	0.9905	—	—
650	0.9866	0.9865	—	—
600	0.9824	0.9819	—	—
550	0.9784	0.9773	—	—
500	0.9744	0.9726	—	—
400	0.9640	0.9628	—	—
300	0.9533	0.9514	—	—
200	0.9376	0.9365	—	—
100	0.9146	0.9091	—	—
0	0.8550	0.7638	—	—
	Sample 14			
1,700	1.000	1.0000	0	0
1,500	0.984	0.9847	33	34
1,300	0.971	0.9696	67	67
1,100	0.957	0.9545	102	102
900	0.943	0.9390	140	138
700	0.929	0.9228	176	176
500	0.914	0.9055	215	217
300	0.896	0.8881	256	257
100	0.872	0.8633	310	311
0	0.854	0.8082	345	398

volumes then was employed to find the density of this liquid at 60°F and 14.7 psia. This density then was corrected to reservoir temperature and the pressure of the determination by using the correction curves presented by Standing.[3] From the corrected density, composition and pound-moles of liquid, the volume of the liquid was determined. This volume, divided by the volume of 1 lb-mol original liquid at saturated pressure and reservoir temperature, is the computed shrinkage.

The gas-oil ratio was computed with the following equation.

$$R = \frac{(379.4)(5.61)V}{\overline{V}_{sR}} \quad . \quad (4)$$

where R = gas-oil ratio, cu ft/bbl,
V = total pound-mols of vapor formed/pound-mol of saturated reservoir liquid, and
$\overline{V}_{sR}$ = volume of 1 lb-mol of saturated reservoir liquid, cu ft/lb-mol.

The process then was repeated at lower pressures until 14.7 psia was reached.

RESULTS

Table 1 shows the results of the computations for 14 subsurface oil samples. The agreement between the experimental and calculated values is believed to be within the experimental error. Shrinkage and gas-oil ratios were computed for several other samples where the results did not agree with the experimental values. When a detailed check of the laboratory data was made for some of these samples, it was found that (due to experimental difficulties) rather large adjustments were required to obtain the reported values. Therefore, these cases were not reported in Table 1. Agreement was not obtained on two other samples studied. The saturation pressure was almost equal to the convergence pressure in each of these cases, and the reliability of the correlations is poor at these conditions. Thus, this method should not be used unless the convergence pressure is 2,000-psi above the saturation pressure. It should be noted that agreement could not be obtained for any samples at the 0-psi check point. However, more recent data indicate that the 0-psi data are in error since checks are now being obtained. All the samples tested by the laboratory during the last year have shown similar results.

CONCLUSIONS

A computation method using limited laboratory data has been developed which will predict the experimental values for differential gas liberation and shrinkage within the experimental error for most subsurface oil samples.

ACKNOWLEDGMENT

This investigation was supported by Humble Oil & Refining Co. Appreciation is expressed to members of Humble's staff for their suggestions and assistance.

REFERENCES

1. Matthews, T. A., Roland, C. H. and Katz, D. L.: *Proc.*, NGAA (1942) 41; *Pet. Refiner*, 2116: (5811942).
2. Soloman, Ernest: *Chem. Eng. Prog.* (1952) Symposium Series 48, No. 3, 93.
3. Standing, M. B. and Katz, D. L.: *Trans.*, AIME (1942) **146**, 159.
4. *Equilibrium Ratio Data Book*, NGAA, Tulsa, Okla. (1957).
5. Hoffman, A. E., Crump, J. S. and Hocott, C. R.: *Trans.*, AIME (1953) **198**, 1.

★★★

The Effect of Coil Design on the Performance of the Induction Log

W. C. DUESTERHOEFT, JR.
APPLIED RESEARCH ASSOCIATES OF TEXAS
AUSTIN, TEX.

RALPH E. HARTLINE
MEMBER AIME
LANE-WELLS CO.
TULSA, OKLA.

H. SANDOE THOMSEN
TWR COMPUTERS CO.
CANOGA PARK, CALIF

ABSTRACT

The attenuation and phase shift which formations produce in the electromagnetic field of an induction-type electrical well-logging instrument are great enough to substantially affect the response of the tool to formation conductivity under normal logging conditions. The application of the general equations for the propagation of an electromagnetic field in a conductive medium to the transmitter-receiver coil pair of an induction-logging-tool coil system gives an expression for the response which properly takes the propagation effects into account.

A comparison of a calculation of this type with the response computed from the commonly used geometric factor concept, which does not include the propagation effect, leads to a factor G_o representing the ratio of the responses computed by the two methods. The value of G_o decreases not only with increasing formation conductivity, but also with increasing transmitter-to-detector coil spacing. For a single coil pair with a 40-in. spacing, the value of G_o is 0.972 in a 20-millimho/m formation. The value is reduced to 0.915 and 0.812 for conductivities of 200 and 1,000 millimhos/m. As a result, the basic signal generated by the induction-logging coil system is not linearly related to formation conductivity as expected from the geometric factor concept. A uniform conductivity scale can be obtained only by adding a suitable nonlinear element to the recording system. The addition of auxiliary coils, having spacings less than the main-coil span, to achieve focusing results in an even greater departure of the basic signal from linearity with conductivity.

The solution of the field equations near the interface between two formations of different conductivity gives the curve shape on an induction logging tool in crossing the interface. The addition of auxiliary coils to achieve focusing can add anomalous character to the curve shape in crossing the interface, which might be mistaken for lithological detail.

Preliminary calculations which include the propagation effects in the determination of the conductivity correction for thin beds lead to correction factors which are substantially smaller than those obtained from geometric factor considerations. It is apparent that thin-bed corrections derived from geometric factor calculations are of doubtful validity.

Original manuscript received in Society of Petroleum Engineers office Aug. 2, 1960. Revised manuscript received Sept. 5, 1961. Paper presented at 35th Annual Fall Meeting of SPE, Oct. 2-5, 1960, in Denver.

INTRODUCTION

Although the electromagnetic induction type of electrical well log has been used for a number of years and has gained general acceptance in quantitative well-log interpretation, no technically complete investigation of the mechanism and of its operation has been published. The studies which have been presented are based upon the premise that neither the shape nor the intensity of the induction field of the logging tool is in any way affected by the electrical characteristics of the formation.

From the inception of induction logging it has been recognized that under some formation conditions the performance of the instrument could be expected to be substantially different from that predicted by the simplified analysis. This anomalous performance has been called "skin effect" since it is the result of the same phenomenon which causes high-frequency alternating currents to flow only near the surface of metallic conductors. In the range of conductivities encountered in the sediments, the formation actually does not exhibit the sharply defined conducting "skin" shown by metals. The gradual modification of the distribution of the currents in the formation, produced by the induction field of the logging tool, is the direct result of phenomena associated with the propagation of the electromagnetic field through the formation. Therefore, it can be much more appropriately described as the "propagation effect". One purpose of this paper is to review the results of a solution of the equations for the performance of a single transmitter-receiver coil pair induction-logging system which takes into account the propagation effect, showing the manner in which the tool performance established by this analysis differs from that derived from the less comprehensive analyses currently in use.

PRINCIPLE OF OPERATION OF THE INDUCTION LOGGING INSTRUMENT

The high-frequency alternating current which is maintained at a constant value in the transmitter coil

of the induction logging instrument sets up an electromagnetic field which extends into the formation surrounding the instrument. The periodically changing electromagnetic flux of this field induces secondary currents of the same frequency in the conducting formation surrounding the transmitter coil. In effect, the conductive formation surrounding the coil serves as a single-turn secondary circuit which is inductively coupled to the transmitter coil. The current induced in this secondary field, the formation, flows in the entire volume of conducting formation surrounding the logging tool. For mathematical analysis as well as illustrative convenience, however, the current induced in the formation is considered as being broken up into separate, closed, circular loops of formation surrounding the transmitter coil. In a completely homogeneous formation these elemental conductive paths are toroidal in shape and have axial symmetry with the borehole. The density of the current induced in each of these elemental paths depends upon the position of the path with respect to the transmitter coil and upon the conductivity of the formation within the path.

Fig. 1 shows only three of these elemental loops in different positions with respect to the transmitter and receiver coils. An alternating current I_3, for example, is induced in the elemental loop a_3 by the electromagnetic field from the transmitter coil traveling over a path from T to a_3.

The high-frequency currents which are induced in these elemental toroids of conductive formation produce their own electromagnetic fields. These secondary fields travel through the formation in the same manner as the primary field. The portion of the field traveling over a path from the elemental loop a_1 to the receiver coil R induces a voltage in the receiver circuit. The full signal developed in the receiver coil is the sum of the voltage contributions of all of the toroidal currents flowing in the formation.

All other factors being equal, the total voltage induced in the receiver coil depends upon the intensity of the currents in the elemental toroids and, thus, upon the conductivity of the formation. The recorded response of the induction curve can be calibrated in terms of the properly weighted average of the conductivities of the elements of the formation within the sensible field of investigation of its coil system.

IMPLICATIONS OF THE GEOMETRIC FACTOR METHOD OF COMPUTING THE INDUCTION LOG RESPONSE

All of the currents and voltages involved in the formation and in the receiver circuit are alternating with the frequency of the transmitter current. Therefore, it is necessary in a proper quantitative evaluation of the received signal to take into account not only the amplitude, but also the phase relationships of all the elements which contribute to the signal.

One of the early papers presenting an analysis of the performance of the induction type of electric log was that of Doll.[1] This study developed the geometric factor concept. This analysis led to the conclusion that the contribution of any elementary toroid of formation to the conductivity response of the tool depended only upon the geometric position of the element with respect to the transmitter and receiver coils and the conductivity of the material comprising the toroidal element. This geometric factor concept has been useful in the qualitative evaluation of induction log performance, but it has failed to provide results which are sufficiently accurate for quantitative use. The analysis is inadequate since it considers that the electromagnetic field from the transmitter coil is moving through the formation instantaneously and that the energy lost to the formation by the circulating currents induced by the field is not extracted from the energy of the field. In effect, the electromagnetic fields of the transmitter and each one of the elementary toroids are considered to be acting independently of each other with no interaction among them. The signals developed in the receiver coil (calculated for each toroidal element acting alone) are considered as being directly additive and, hence, all in the same phase to produce the response of the tool.

In effect, the geometric factor concept considers each toroidal element as standing alone in free space. Under this condition the electromagnetic wave travels from the transmitter coil to the element and then to the receiver at a velocity of 186,000 miles/sec, or approxi-

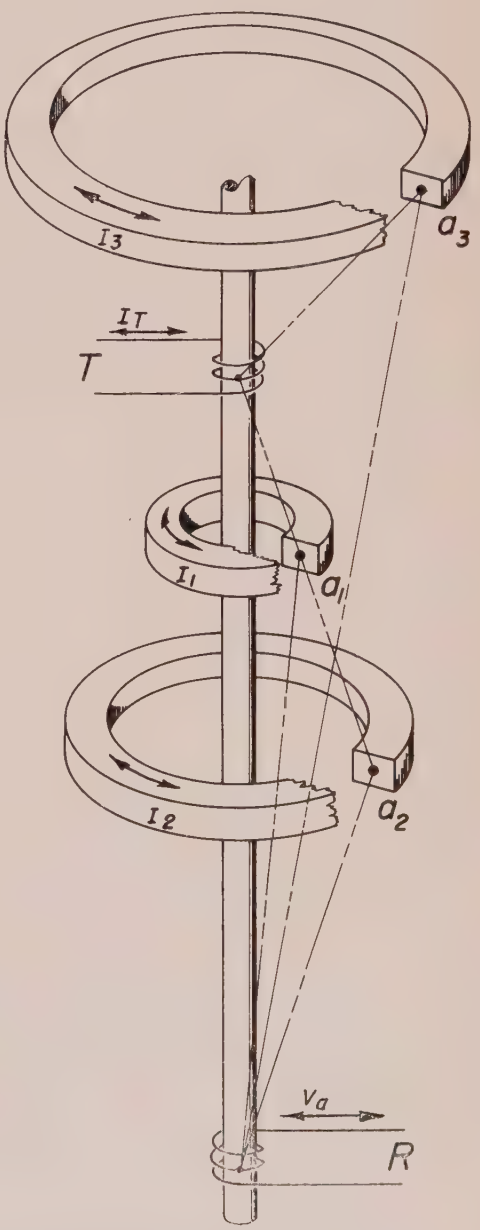

FIG. 1— PRINCIPLE OF OPERATION OF THE INDUCTION LOG.

[1]References given at end of paper.

mately 1 billion (10^9) ft/sec. Further, the transmission of the signal is accomplished without attenuation or loss of energy by the wave. Induction logging systems commonly employ a 20,000-cps alternating current. Each wave, representing 360° of phase change, is therefore 50,000-ft long. This means than one degree of phase change occurs in each 140 ft of wave travel. Under this concept, therefore, there is no attenuation of the wave during its travel and the phase change within the field of investigation of the tool is negligible. It is only under this condition that the results derived from the geometric factor concept are valid.

EFFECT OF THE FORMATION ON THE ELECTROMAGNETIC FIELD

It easily can be shown that the velocity of an electromagnetic wave in sedimentary formations, as encountered in well logging, is substantially lower than that in free space. In a formation having a conductivity of 1 mho/m, a 20,000-cps electromagnetic wave has a velocity of approximately 1.5 million (1.5×10^6) ft/sec. This is only 0.15 per cent of the velocity in free space. This reduction in the velocity of propagation is the result of the reaction of the counter electromagnetic fields developed by the currents induced in the formation upon the electromagnetic field of the primary advancing wave. This reaction has the additional effect of reducing the amplitude of the advancing wave by approximately one-half in each 8 ft of wave travel. The reduction of the velocity of the wave reduces the wave length to approximately 73 ft. This means that the phase of the wave changes approximately 5°/ft of wave travel. It is apparent that attenuation and phase changes of these magnitudes can be expected to cause the electromagnetic field, and the resultant signals produced in the induction logging tool, to be substantially different from those predicted from an analysis based upon the "free space" performance of the field. A correct analysis of the performance of the induction log must properly account for the attenuation of the electromagnetic wave and for the changes in its phase within the sensible field of the logging tool.

APPLICATION OF WAVE EQUATIONS TO THE FIELD OF A SINGLE TRANSMITTER-RECEIVER COIL PAIR

A theoretical treatment of the electromagnetic-field equations for the induction log has led to a solution for the complete signal developed in the receiver coil of a transmitter-receiver coil pair. This solution, developed by one of the authors,[2] is based upon a rigorous solution of the Maxwell equations for the propagation of an electromagnetic wave in a homogeneous, moderately conductive medium. The solution has been extended to include the performance of the transmitter-receiver coil pair in thin, uniformly conductive, noninvaded beds and in very thick invaded beds.

One object of this paper is to demonstrate the manner in which the results of these mathematical analyses can be applied to establish the quantitative response of practical multicoil-pair induction-logging tools under actual formation conditions.

The expression for the voltage V_a, developed in the receiver coil of a transmitter-receiver coil pair when operating in a homogeneous conductive formation of infinite extent, is shown to be

$$V_a = j \frac{\omega\mu A_T N_T A_R N_R I_T}{2\pi} \frac{(1 + \gamma L)}{L^3} e^{-\gamma L} \quad . \quad . \quad (1)$$

where j = the complex operator $\sqrt{-1}$,

$\mu = 4\pi \times 10^{-7}$ (rationalized MKS units) = the permeability of free space and may be taken as the permeability of the sediments with small error,

A_T, A_R = area of cross section of the transmitter and receiver coils (sq m),

$N_T N_R$ = number of turns on the transmitter and receiver coils,

I_T = transmitter current (amp), and

L = distance between the transmitter and receiver coils (m).

$$\gamma^2 = j\omega\mu(\sigma + j\omega\varepsilon). \quad . \quad . \quad . \quad . \quad . \quad . \quad . \quad . \quad . \quad (2)$$

where σ = conductivity of the formation (mho/m), and

ε = dielectric constant of the formation, approximately 10^{-10} (rationalized MKS units).

For normal sediments σ is very large compared to $\omega\varepsilon$ so that the $j\omega\varepsilon$ term may be neglected. Eq. 2 reduces to

$$\gamma^2 = j\omega\mu\sigma \quad . \quad . \quad . \quad . \quad . \quad . \quad . \quad . \quad . \quad . \quad . \quad (2a)$$

The voltage developed in the receiver coil, as shown by Eq. 1, is a complex quantity. It can be rationalized, separating the real and imaginary portions, by expanding in a power series. An intermediate step in this development puts the equation in the form

$$V_a = j \frac{K}{L^3}\left[1 - \frac{(\gamma L)^2}{2} + \frac{(\gamma L)^3}{3} - \frac{(\gamma L)^4}{8} + \cdots + \frac{(n-1)(\gamma L)^n(-1)^{n-1}}{n!} \quad . \quad . \quad . \quad . \quad (3)$$

where

$$K = \frac{\omega\mu A_T N_T A_R N_R I_T}{2\pi} \quad . \quad . \quad . \quad . \quad . \quad . \quad . \quad . \quad . \quad (4)$$

This form of the equation is especially interesting because the separate terms can be identified as a particular component of the receiver-coil signal.

THE MUTUAL-INDUCTANCE COMPONENT OF INDUCTION LOG RESPONSE

The first term of the equation

$$V_m = j \frac{K}{L^3} \quad . \quad . \quad . \quad . \quad . \quad . \quad . \quad . \quad . \quad . \quad . \quad . \quad (3a)$$

represents the mutual-inductance voltage generated in the receiver coil by direct induction from the current in the transmitter coil. This is the only voltage that would appear in the receiver circuit if the tool were operating in a completely nonconducting medium because γ becomes zero when σ is zero, and Eq. 3 for the total voltage reduces to Eq. 3a. The imaginary operator j indicates that this signal is in quadrature phase with the transmitter current. In actual logging instruments, the auxiliary or focusing coils of the system often are designed to reduce the mutual inductance between the transmitter and receiver circuit to a small value.

THE "GEOMETRIC FACTOR" COMPONENT

The second term of the equation

$$V_{gf} = -j \frac{K}{L^3} \frac{(\gamma L)^2}{2},$$

by substituting for γ from Eq. 2a, becomes

$$\frac{K\omega\mu}{2L}\sigma \quad . \quad . \quad . \quad . \quad . \quad . \quad . \quad . \quad . \quad . \quad . \quad . \quad (3b)$$

This equation represents the signal that would be de-

veloped in the receiver circuit if the electromagnetic wave experienced no attenuation or phase shift in passing through the formation. This portion of the signal does not contain the operator j and, hence, is in phase with the current in the transmitter coil. In fact, this signal is identical with the signal calculated by the geometric factor method. It should be noted that its magnitude is proportional to the formation conductivity. It is this signal which has given the induction log the reputation of having a response which is strictly proportional to formation conductivity.

MODIFICATION OF INDUCTION LOG RESPONSE BY PROPAGATION EFFECTS

The remaining portion of Eq. 3 thus represents the perturbation of induction log signal from that of the simple geometric concept, which arises as a result of the attenuation and phase shift of the primary and secondary electromagnetic waves in passing through the formation. It is this portion of the signal that is responsible for the propagation effects shown by the induction log. It will be shown that the propagation effect always reduces the signal to be recorded by the conductivity curve to a value lower than that obtained from a geometric factor calculation.

METHOD OF CALIBRATION OF THE INDUCTION LOG

Induction logging tools are commonly calibrated by suspending them in air to establish the zero conductivity position and then adjusting the conductivity response to some predetermined value when the tool is surrounded by a conducting-loop calibrating device. The conductance of the loop is calculated to develop a voltage in the receiver coil equal to that of an infinite homogeneous formation of a standard conductivity. In this single-conductive-loop method of calibration, the electromagnetic wave travels through a nonconductive medium (air) over both its primary path from the transmitter coil to the loop and its secondary path from the conductive loop to the receiver coil. Since the electromagnetic wave travels entirely in free space, this method of calibration does not include the attenuation and phase shift that would occur in the equivalent formation. This calibration procedure, therefore, gives a signal which corresponds to that expected from the geometric factor concept and does not inherently include the propagation effect. Logging-service companies have not described their calibrating procedures and the manner in which the propagation effect is taken into account.

In the following presentation it will be assumed that the logging tool is calibrated in accordance with this geometric factor concept. This is done for simplicity in demonstrating the manner in which propagation effects influence the log response. It is not implied that this is the recommended calibration procedure nor the procedure used by well-logging companies.

The voltage developed by the conductive calibrating loop, equivalent to a formation of conductivity σ_c, will be given by the portion of the equation shown by Eq. 3b. That is,

$$V_c = V_{gf} = \frac{K\omega\mu}{2L}\sigma_c \quad . \quad . \quad . \quad . \quad . \quad . \quad . \quad . \quad . \quad (4)$$

The calibration constant C_c of the logging system is defined as the number which when multiplied by the receiver circuit voltage gives the apparent formation conductivity; that is,

$$\sigma_a = C_c V_a \quad . \quad . \quad . \quad . \quad . \quad . \quad . \quad . \quad . \quad . \quad . \quad . \quad (5)$$

Under the "no propagation effect" conditions of the conductive-loop calibration, the conductivity recorded by the tool (as expressed by Eq. 4) will be equal to the formation conductivity assigned to the calibrating loop (σ_c) provided that the sensitivity of the recording circuit is adjusted so that

$$C_c = \frac{2L}{K\omega\mu} \quad . \quad . \quad . \quad . \quad . \quad . \quad . \quad . \quad . \quad . \quad . \quad . \quad (6)$$

RELATIVE RESPONSE UNDER ACTUAL FORMATION CONDITIONS

The apparent conductivity σ_a recorded by an induction coil pair, calibrated on the basis of the conductive loop in an infinite homogeneous formation of conductivity σ, can be obtained from Eq. 5 with appropriate values of V_a and C_c taken from Eqs. 3 and 6.

$$\sigma_a = C_c V_a = j\frac{2}{L^2\omega\mu}\left[1 - \frac{(\gamma L)^2}{2} + \frac{(\gamma L)^3}{3} + \ldots\right]$$
$$. \quad . \quad . \quad . \quad . \quad . \quad . \quad . \quad . \quad . \quad . \quad . \quad . \quad . \quad . \quad (7)$$

Continuing with the separation of the real and the imaginary portions of this equation, and converting the equation from the series to the trigonometric form, leads to

$$\sigma_a = \frac{2}{L^2\omega\mu}\left[\left\{(1+\Delta)\sin\Delta - \Delta\cos\Delta\right\} + j\left\{(1+\Delta)\cos\Delta + \Delta\sin\Delta\right\}\right] e^{-\Delta}$$
$$. \quad . \quad . \quad . \quad . \quad . \quad . \quad . \quad . \quad . \quad . \quad . \quad . \quad . \quad . \quad (8)$$

where

$$\Delta^2 = \frac{L^2\omega\mu}{2}\sigma \quad . \quad . \quad . \quad . \quad . \quad . \quad . \quad . \quad . \quad . \quad . \quad . \quad (9)$$

A factor G_o can be defined to be the fraction of the true formation conductivity that is actually recorded by an induction log calibrated under these conditions.

$$G_o = \frac{\sigma_a}{\sigma} \quad . \quad . \quad . \quad . \quad . \quad . \quad . \quad . \quad . \quad . \quad . \quad . \quad . \quad (10)$$

Dividing both sides of Eq. 8 by σ,

$$G_o = \frac{\sigma_a}{\sigma} = \frac{1}{\Delta^2}\left[\left\{(1+\Delta)\sin\Delta - \Delta\cos\Delta\right\} + j\left\{(1+\Delta)\cos\Delta + \Delta\sin\Delta\right\}\right] e^{-\Delta}$$
$$. \quad . \quad . \quad . \quad . \quad . \quad . \quad . \quad . \quad . \quad . \quad . \quad . \quad . \quad . \quad (11)$$

The imaginary portion of this quantity, representing the portion of the induction log signal at quadrature with the transmitter coil current, is rejected by the phase-sensitive detector of the recording circuit. The remaining real portion of G_o thus gives the conductivity response of an induction logging tool calibrated on the basis of the geometric factor concept in terms of its fraction of the true formation conductivity.

The value of the real part of G_o has been calculated for values of Δ of interest in induction logging. The results are shown in Fig. 2. If the propagation effect were not active, the recorded conductivity would be equal to the formation conductivity and G_o would be equal to unity for all values of conductivity. The effect of attenuation and phase shift in the formation is shown by the deviation of the value of G_o from unity. Due to propagation effects, the relative response of the induction log falls off rapidly with increasing values of the dimensionless parameter Δ. Thus, it is apparent that the perturbations of the induction log response as a result of the propagation effect increase not only with

increasing formation conductivity, but also with increasing transmitter-receiver coil spacing.

For a given induction logging instrument, the coil spacing and operating frequency are fixed so that the value of Δ varies only with the formation conductivity. The solid curve of Fig. 3 shows the variation of G_o with formation conductivity for a single transmitter-receiver coil pair spaced at 40 in. The operating frequency is 20,000 cps. At 20 millimhos/m (50 ohm-m), the conductivity recorded by an instrument calibrated without taking the propagation effect into acount is 97.2 per cent of the true formation conductivity. The response falls to 91.5 per cent in a 200-millimho/m (5 ohm-m) formation, and at 1,000 millimhos/m (1 ohm-m) the response is only 81.2 per cent of the actual conductivity.

It is thus apparent that, as a result of the propagation effect, the response of the induction log departs from linearity with formation conductivity. The conductivity curve can be only approximately recorded on a uniformly divided scale of the conductivity track unless some instrumental provision is made to correct for this nonlinearity of response.

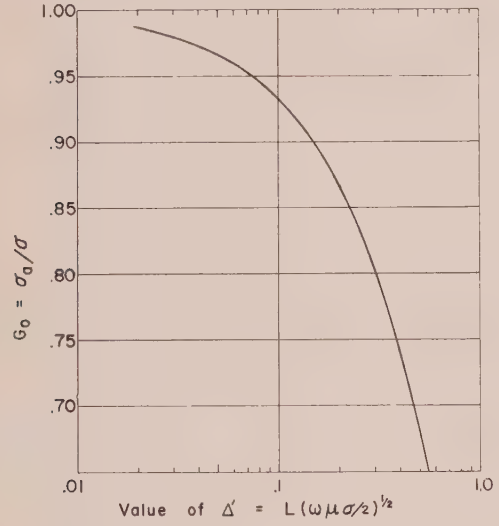

FIG. 2—EVALUATION OF G_o FOR A SINGLE TRANSMITTER-RECEIVER COIL PAIR.

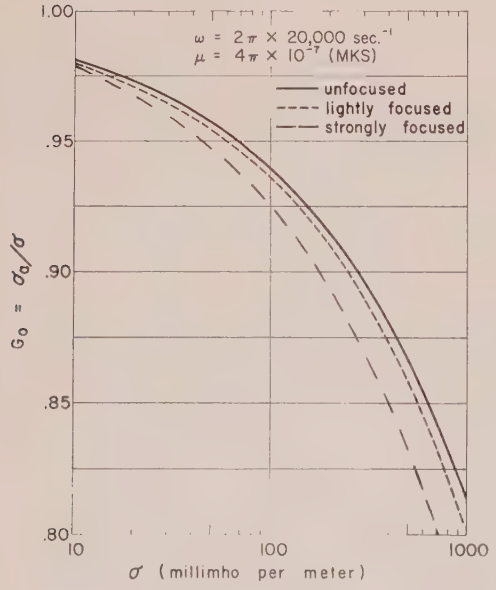

FIG. 3—G_o FOR A 40-IN. LOGGING TOOL.

APPLICATION OF METHOD TO MULTIPAIR COIL SYSTEMS

Practical induction logging instruments employ multicoil systems[4] to achieve a more satisfactory pattern for their field of investigation. This is done by adding auxiliary or focusing coils, connected in series with the coils of the main pair. In this way signals which are generated in the auxiliary receiver coils through the action of induction from the main and auxiliary transmitter coils can be made to add or subtract from the basic signal of the tool produced by the main-coil pair. The same form of calculation made for the single-coil pair can apply to any combination of auxiliary coils by simply adding, with due regard to magnitude and phase, the signals calculated for each possible transmitter-receiver coil pair of the complete coil system.

EFFECT OF AUXILIARY COILS IN FOCUSING

Fig. 4 illustrates a simple four-coil, symmetrical-form, focused induction-logging tool. Auxiliary transmitter and receiver coils are mounted at equal distances outside the main receiver and transmitter coils, respectively. The auxiliary coils are wound with a smaller number of turns of wire than the main coil. The auxiliary coils usually are connected to the main coils so that their directions of winding are in opposite sense. Thus, signals developed in the receiver circuit through the action of any main-auxiliary coil pair are in the opposite direction and, hence, subtract from the signal developed by the main-coil pair. The composite signal in the receiver circuit of the coil system illustrated is the algebraic sum of the four signals developed by each separate transmitter-receiver coil pair.

$$V_a]_{tool} = V_a]_{TR} + V_a]_{tR} + V_a]_{Tr} + V_a]_{tr} \quad . \quad (12)$$

The subscripts identify the particular transmitter-receiver coil combination through which the voltage component is developed. The calculating procedure for

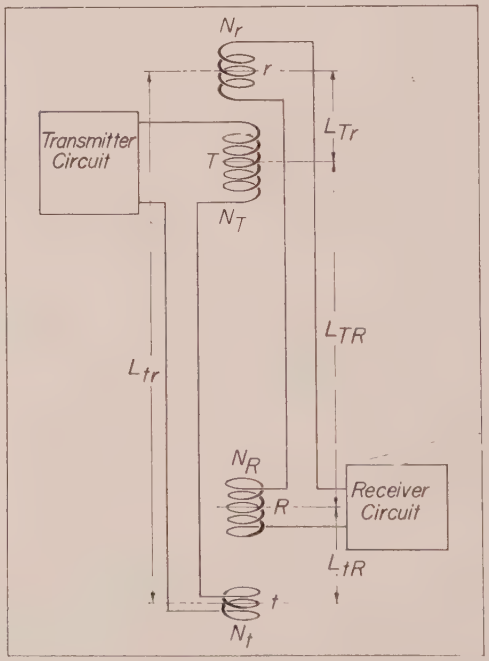

FIG. 4—COIL ARRANGEMENT FOR TWO-COIL-PAIR SYSTEM.

the voltage components generated by the separate coil pairs can be made to have the algebraic sign to properly combine in this summation by employing a uniform sign convention for each individual calculation. The reverse winding of any coil can be accounted for by assigning a negative sign to the number of turns on all coils wound in a direction opposite to that of the main transmitter coil.

THE CALIBRATION FACTOR FOR MULTIPAIR COIL SYSTEMS

The voltage signal developed in the receiver circuit can be converted to the apparent conductivity of the formation by multiplying it by a suitable calibration factor.

$$\sigma_a = C_c]_{tool}\, V_a]_{tool} \quad . \quad . \quad . \quad . \quad . \quad . \quad . \quad . \quad . \quad (13)$$

For the purpose of illustrating tool performance, it is convenient to base the calibration on the geometric factor concept just as was done in the previous consideration of a single coil pair. Under the geometric concept, the voltage expected to be developed by a single coil pair was shown in Eq. 3b to be

$$V_{gf} = \frac{K\omega\mu}{2L}\sigma = \frac{\omega^2\mu^2 A_T A_R I_T}{4\pi}\frac{N_T N_R}{L_{TR}}\sigma \quad . \quad . \quad (3b)$$

If all of the coils of the tool have the same area of cross section, the first fraction on the right-hand side of the equation will be a constant for each of the coil pairs. The magnitude of the voltage is then proportional to the variable portion of the expression represented by the second fraction. Insofar as the addition of the magnitudes of the components of the signal voltage is concerned, therefore, this fraction can serve as a weighting factor W.

$$W_{TR} = \frac{N_T N_R}{L_{TR}} \quad . \quad . \quad . \quad . \quad . \quad . \quad . \quad . \quad . \quad . \quad (14)$$

By applying Eq. 3b to the separate components of Eq. 12 it can be shown that the calibration factor for the complete tool becomes

$$C_c]_{tool} = \frac{4\pi}{\omega^2\mu^2 A_T A_R I_T\left[\frac{N_T N_R}{L_{TR}} + \frac{N_T N_r}{L_{Tr}} + \frac{N_t N_R}{L_{tR}} + \frac{N_t N_r}{L_{tr}}\right]} \quad . \quad . \quad . \quad . \quad . \quad . \quad . \quad . \quad . \quad . \quad . \quad (15)$$

RELATIVE RESPONSES OF MULTIPAIR COIL SYSTEMS

Following the definition of G_o given in Eq. 10 for a single coil pair, the apparent conductivity recorded by a tool (calibrated in this way) in a formation having a true conductivity σ can be defined as

$$\sigma_a]_{tool} = G_o]_{tool}\,\sigma; \quad . \quad . \quad . \quad . \quad . \quad . \quad . \quad . \quad . \quad (16)$$

combining this with Eq. 13 gives

$$\sigma_a]_{tool} = G_o]_{tool}\,\sigma = C_c]_{tool}\, V_a]_{tool}, \quad . \quad . \quad . \quad (17)$$

so that

$$G_o]_{tool} = C_c]_{tool}\left\{V_a]_{TR} + V_a]_{Tr} + V_a]_{tR} + V_a]_{tr}\right\} \quad . \quad . \quad . \quad . \quad . \quad . \quad . \quad . \quad . \quad . \quad . \quad . \quad . \quad . \quad (18)$$

On the basis of the definition of the calibration constant for a single coil pair represented by Eq. 5, we may write

$$G_o]_{tool} = \frac{C_c]_{tool}}{\sigma}\left\{\frac{\sigma_a]_{TR}}{C_c]_{TR}} + \frac{\sigma_a]_{Tr}}{C_c]_{Tr}} + \frac{\sigma_a]_{tR}}{C_c]_{tR}} + \frac{\sigma_a]_{tr}}{C_c]_{tr}}\right\} \quad . \quad . \quad . \quad . \quad . \quad . \quad . \quad . \quad . \quad . \quad . \quad . \quad . \quad . \quad (19)$$

Each one of the several calibration constants has the form

$$C_c = \frac{4\pi}{\omega^2\mu^2 A_T A_R I_T}\frac{1}{W_{TR}}.$$

The first fraction on the right of the equation is a factor common to all of the constants and, therefore, cancels out. Since by definition

$$G_o]_{TR} = \frac{\sigma_a]_{TR}}{\sigma},$$

Eq. 19 can be reduced to the form

$$G_o]_{tool} = \frac{W_{TR}\times G_o]_{TR} + W_{Tr}\times G_o]_{Tr} + W_{tR}\times G_o]_{tR} + W_{tr}\times G_o]_{tr}}{W_{TR} + W_{Tr} + W_{tR} + W_{tr}} \quad . \quad . \quad . \quad . \quad . \quad . \quad . \quad . \quad . \quad . \quad . \quad . \quad . \quad . \quad (20)$$

Therefore, the effective value of G_o for the composite tool is the weighted average of all of the G_o values for the separate transmitter-receiver coil pairs which contribute to the receiver signal. The quantity $N_T N_R/L_{TR}$ for each coil is used as the weighting factor.

COMPARISON OF RESULTS—"GEOMETRIC FACTOR" VS "PROPAGATION EFFECT" METHODS OF CALCULATION

The separate portions of the right-hand side of Eq. 18 are the voltages developed by separate coil pairs. All are multiplied by the calibration constant for the tool. Each product, therefore, is in the conductivity units for which the tool is calibrated and can be considered as the specific contribution of each coil pair to the over-all conductivity response recorded by the tool. That is,

$$\sigma_a]_{tool} = \sigma]_{TR} + \sigma]_{Tr} + \sigma]_{tR} + \sigma]_{tr} \quad . \quad . \quad . \quad . \quad . \quad (21)$$

where the notation $\sigma]_{TR}$ identifies the component of the signal contributed by the coil pair TR expressed in conductivity units of the calibration of the tool. Taken in this sense, each component must be considered as having the algebraic sign of the voltage signal from which it was derived. The response of the same tool, computed on the basis of the geometric factor concept, may be expressed in a similar manner.

$$\sigma_{gf}]_{tool} = \sigma_{gf}]_{TR} + \sigma_{gf}]_{Tr} + \sigma_{gf}]_{tR} + \sigma_{gf}]_{tr} \equiv \sigma \; . \; . \quad (22)$$

In this analysis the calibration constant is chosen so that the apparent conductivity calculated on the basis of the geometric factor concept is identically equal to the formation conductivity shown by the identity at the right of the equation. The factor G_o (defined by Eq. 10) relates the ratio of the response calculated on the basis which includes the propagation effect to the true conductivity of the medium. Because of the identity between the true conductivity and that calculated on the basis of the geometric factor,

$$\sigma_a = G_o\,\sigma \equiv G_o\,\sigma_{gf}.$$

Eq. 21 may be rewritten in the form

$$\sigma_a]_{tool} = G_o]_{TR}\,\sigma_{gf}]_{TR} + G_o]_{Tr}\,\sigma_{gf}]_{Tr} + G_o]_{tR}\,\sigma_{gf}]_{tR} + G_o]_{tr}\,\sigma_{gf}]_{tr} \quad . \quad . \quad . \quad (21a)$$

Comparing this equation term-for-term with Eq. 22 makes it apparent that the performance of the induction log, calculated on the basis of the geometric factor concept (Eq. 22), may be corrected to account for the propagation effect (as shown in Eq. 21) by multiplying the signal contributed by each coil pair (expressed in conductivity units) by the value of G_o appropriate to the coil-pair spacing and the conductivity of the formation involved.

ILLUSTRATIVE EXAMPLES

The results of the computation of the conductivity response of two different coil systems of the four-coil symmetrical type shown in Fig. 4 for an infinite medium of uniform conductivity are shown in Tables 1 and 2.

Both tools have the same main-coil spacing and the same number of main-coil turns. One coil system has its auxiliary coils spaced at approximately 11 in. outside the main coils, while the other uses a 25-in. spacing. In both cases the number of turns on the auxiliary coils have been calculated to provide approximately zero mutual inductance between the transmitter and receiver circuits, as required to provide minimum response to conductive material near the axis of the coil system.[3] The mutual-inductance condition makes the number of turns greater on the more widely spaced auxiliary coils. This increases the relative weight of the negative signal developed between the combinations of these coils with the oppositely wound main-coil pairs. As a result, the coil system having the greatest auxiliary-coil spacing has a substantially greater degree of focusing than that of the shorter-spaced auxiliary-coil pair. The calculations are based upon the use of a calibration constant determined by the geometric factor concept. Therefore, the geometric factor calculation of necessity gives a conductivity equal to the true conductivity of the formation. This is, of course, the value that the tool would be expected to read if the geometric factor analysis were valid.

Lightly Focused Tool

The results of the calculations for the coil system with the 11-in. auxiliary-coil spacing, operating in a material of 500 millimhos/m, are shown in Table 1. The calculation based upon geometric factor considerations gives an expected response from the main-coil pair alone of 539.6 millimhos/m. This increased response for the main-coil pair is necessary since the two coil pairs formed by combinations of main and auxiliary coils give subtractive signals (due to the reverse winding of the auxiliary coils) of 19.84 millimhos/m each. The positive contribution of the remaining coil pair, made up of the two auxiliary coils, is almost negligible because of the small number of turns on each coil and the large distance between them. The sum of the contributions of all of the coil pairs, calculated by the geometric factor procedure, must equal 500 millimhos/m because of the way the calibration constant is defined.

As a result of the propagation phenomena, the actual contribution of each coil pair to the total response is reduced to the fraction G_o of the response calculated from the geometric factor method. The main-coil pair contributes the fraction $G_o = 0.866$ of the signal shown by the geometric factor calculation. Thus, the main-coil contribution is actually only 467.33 millimhos/m. The subtractive signals, since they are produced by coil pairs of shorter spacing, have larger G_o values. Thus, the subtractive signals produced by the shorter-spaced coil pairs are not reduced by the propagation effect in as great a proportion as the main-coil signal. The net signal recorded by the focused tool, therefore, will be relatively smaller than for an unfocused tool. In this example the conductivity actually recorded by the composite tool is 429.1 millimhos/m. This is 85.8 per cent of the true conductivity. In a 500-millimho/m formation, this focused tool operates with an effective value of G_o equal to 0.858. This reduction from the value of 0.866 for the main-coil pair amounts to an increase in the influence of the propagation effect by the application of focusing to the tool. The effective value of G_o for this tool over the full conductivity range is shown in the dotted curve of Fig. 3.

Strongly Focused Tool in a Moderate-Conductivity Formation

The results of calculations on the more highly focused coil system are shown in Table 2. In this coil system the relative signal magnitude of the subtractive signals calculated by the geometric factor method is increased due to the greater weight given these components by the increased number of turns on the auxiliary coils. The particular method of calibration used takes this into account and makes the sum of signal components 500 millimhos/m as required for the geometric factor procedure. The main-coil pair develops a signal which is equivalent to 811.2 millimhos/m. This is necessary because each one of the main auxiliary coil pairs develops a subtractive signal equivalent to 158.3 millimhos/m.

The fraction G_o of the geometric factor response which the main coil develops when propagation effects are taken into account is dependent on the coil-pair spacing and the formation conductivity; thus it remains the same for the main-coil pair in both the lightly and the heavily focused tool. However, the values of G_o for coil pairs involving the auxiliary coils are decreased due to the increased spacing of the auxiliary coils in the more heavily focused tool. The net signal developed in the receiver coil system, taking propagation effects into account, is 416.63 millimhos/m, which is 83.3 per cent of the value calculated from the geometric

TABLE 1—CONTRIBUTION OF SIGNALS OF SEPARATE COIL PAIRS OF A LIGHTLY FOCUSED FOUR-COIL INDUCTION LOGGING TOOL TO THE TOTAL TOOL RESPONSE

Main Coils: Spacing (L_{TR}) = 40 in.; Turns (N_T, N_R) = 500.
Auxiliary Coils: Spacing (L_{Tr}, L_{tR}) = 11 in.; Turns (N_t, N_r) = 5.
Formation Conductivity = 500 millimhos/m.

Coil Pairs		Weight $\frac{N_T N_R}{L_{TR}}$		Calculated Conductivity		
Transmitter T	Receiver R		Relative Weight	G_o	By Geometric Factor	With Propagation Effect
Main	Main	9842.5	1.0792	.8660	539.60	467.33
Main	Auxil.	—361.9	—.0397	.9635	—19.84	—19.12
Auxil.	Main	—361.9	—.0397	.9635	—19.84	—19.12
Auxil.	Auxil.	0.6	.0002	.7950	.04	.03
Complete Tool		9119.3	1.0000	.8582	500.00	429.12

TABLE 2—CONTRIBUTION OF SIGNALS OF SEPARATE COIL PAIRS OF A HIGHLY FOCUSED FOUR-COIL INDUCTION LOGGING TOOL TO THE TOTAL TOOL RESPONSE

Main Coils: Spacing (L_{TR}) = 40 in., Turns (N_T, N_R) = 500.
Auxiliary Coils: Spacing (L_{Tr}, L_{tR}) = 25 in., Turns (N_t, N_r) = 61.

Coil Pairs		Weight $\frac{N_T N_R}{L_{TR}}$		Formation Conductivity (Millimhos/m)					
				500			1,000		
Transmitter T	Receiver R		Relative Weight	G_o	Calc. By Geometric Factor	Cond. With Propagation Effect	G_o	Calc. By Geometric Factor	Cond. With Propagation Effect
Main	Main	6250.0	1.622	.8660	811.2	702.86	.8124	1622.4	1318.10
Main	Auxil.	—1220.0	—.317	.9161	—158.3	—145.01	.8817	—316.6	—279.13
Auxil.	Main	—1220.0	—.317	.9161	—158.3	—145.01	.8817	—316.6	—279.13
Auxil.	Auxil.	41.3	.012	.7019	5.4	3.79	.600	10.7	6.42
Complete Tool		3851.34	1.000	.8333	500.0	416.63	.7663	1000.0	766.25

factor concept. Thus, the effective value of G_o for the complete coil system is 0.833. The lower value of G_o is a direct result of the greater degree of focusing in the second tool.

Strongly Focused Tool in a High-Conductivity Formation

The results of a third calculation are shown in the last three columns of Table 2. They apply to the more highly focused tool operating in a homogeneous material of 1,000 millimhos/m. In the geometric factor calculation, the contribution of each coil pair is strictly dependent upon its geometry and is directly proportional to the formation conductivity. Thus, the values computed on this basis are exactly double those obtained for the same tool in the 500-millimho/m material. In considering the propagation effect, however, each one of the signals is reduced to a lower fraction than for the 500-millimho/m material because both the attenuation and phase shift of the electromagnetic wave are increased. By increasing the conductivity to 1,000 millimhos/m, the G_o for the main-coil pair is reduced from 0.866 to 0.8124. The auxiliary-main coil pairs have spacings less than the main-coil pair so that the increase in conductivity does not reduce the G_o for these coil pairs as much as for the main-coil pair. As a result, the conductivity signal for the composite tool drops at a more rapid rate with increasing conductivity than for the main-coil pair. With propagation effects taken into account, the conductivity signal developed by this tool in a 1,000-millimho/m formation is 76.6 per cent of that value.

The variation of the effective value of G_o for the composite coil system of this more highly focused tool is shown in the dashed curve of Fig. 3. It is apparent that, in coil systems of this type in which the auxiliary-coil pairs effective in focusing have a shorter spacing than the main-coil pair, the value of $G_o]_{tool}$ decreases with increasing degrees of focusing.

EFFECT OF PROPAGATION PHENOMENON ON LINEARITY OF CONDUCTIVITY RESPONSE

It is evident that all induction logging tools calibrated without taking the propagation effect into account will record an apparent conductivity which is lower than the true conductivity. Further, the plots of the relative response of the several coil arrangements shown in Fig. 3 emphasize the fact that the actual response of induction-log coil systems is not linear with conductivity and that the departure from linearity increases with increasing degrees of focusing. The apparent conductivity becomes a smaller fraction G_o of the true conductivity as the formation conductivity increases. Therefore, any attempt to correct for this loss of signal due to the propagation effect by a simple increase in the gain of the recording circuit can result in only a partial correction. This becomes apparent from Eq. 17, which may be rewritten

$$\sigma = \frac{C_c]_{tool}}{G_o]_{tool}} V_a]_{tool}.$$

The true formation conductivity σ cannot be strictly proportional to the voltage developed in the receiver system of the tool, $V_a]_{tool}$, unless the calibration factor $C_c]_{tool}$, and hence the gain of the recording circuit of the tool, is made to vary in precisely the same proportion with formation conductivity as the G_o value for the tool. To accomplish this, a suitable nonlinear element must be added to the recorder circuit. In modern induction-logging equipment, a correction of this type is commonly applied to make the amplitude of the conductivity curve a linear function of the formation conductivity.

FIELD EQUATIONS NEAR A PLANE CONDUCTIVITY INTERFACE

The field equations for a single transmitter-receiver pair have been solved for the case of the approach of a plane interface between two conductive formations by the use of the Hankel type of integral transforms following the method of Sommerfield.[2]

COIL PAIR IN HIGHER-CONDUCTIVITY FORMATION

When the coil pair is situated in the formation having the higher conductivity σ_2 with the axis of the tool perpendicular to the plane interface between the two formations, the apparent conductivity recorded by the coil pair has been calculated as

$$\sigma_a(\text{tool in } \sigma_2) = \sigma_a]_{\sigma_2} - \frac{Lg_1}{2l_2} \frac{\sigma_2 - \sigma_1}{\sigma_2} . \quad [32]^* \quad . \quad (23)$$

where l_2 = the distance through σ_2 from the center of the coil pair to the interface with σ_1,

$\sigma_a]_{\sigma_2}$ = the apparent conductivity that would be recorded in an infinite formation of conductivity σ_2 as established by the preceding analysis, and

g_1 = the solution of an integral equation which is a function of the formation conductivities and the distance l_2. The form of the relationship is shown in Fig. 6 of Ref. 2.

The first term of the right-hand side of the equation represents the response of the coil pair in an infinite formation of conductivity σ_2. The approach of the coil pair to the interface of the formation with a lower conductivity will cause the apparent conductivity recorded to become lower. The negative term on the right-hand side of the equation, therefore, represents the amount of lowering of the apparent conductivity recorded by the coil pair due to the approach of the adjacent low-conductivity formation.

COIL PAIR IN LOWER-CONDUCTIVITY FORMATION

For the case of a coil pair situated in the lower-conductivity formation, the equation for the apparent conductivity has been found to have a similar form.

$$\sigma_a(\text{tool in } \sigma_1) = \sigma_a]_{\sigma_1} + \frac{LG_1}{2l_1} \frac{\sigma_2 - \sigma_1}{\sigma_1} . \quad [28] \quad . \quad (24)$$

where l_1 = the distance through σ_1 to the interface with σ_2, and

G_1 = the solution of an integral equation which is a function of the formation conductivities and the distance from the center of the coils in σ_1 to the interface (the form of the relationship is shown in Fig. 5 of Ref. 2).

In this case the first term of the right-hand side of the equation represents the response of the coil pair in an infinite formation of conductivity σ_1. The second term represents the increase in the apparent conductivity due to the higher-conductivity formation beyond the interface.

*The number in brackets is the equation number in Ref. 2 in which the development of the equation is presented.

The integral equations, represented by the factors g_1 and G_1, were programed for solution by a digital computer. Using Eqs. 23 and 24 in conjunction with suitable values of g_1 or G_1, the response of a single coil pair in passing through a plane interface was programed for computer evaluation.

APPLICATION TO A MULTIPAIR COIL SYSTEM

The computational procedure for the response in the receiver circuit of a single transmitter-receiver pair can be applied to the calculation of the response of a complete logging tool. The response of each coil pair, expressed as an apparent conductivity, is computed separately using Eq. 23 or Eq. 24, whichever is appropriate. For a particular position of the composite tool, each coil-pair calculation uses a different value of l_1 (or l_2), the distance from the center of that particular coil pair as it sits in the coil assembly to the interface. The signal for the composite tool in a specific position is the weighted average of the apparent conductivities computed for each coil pair at its particular position with respect to the interface. The weighting factors, used in the calculation of the tool performance in a homogeneous conductive material given by Eq. 14, also apply to this case.

Eq. 23 or Eq. 24 applies only when the coil pair is wholly within the high- or the low-conductivity formation. The limiting condition for each equation thus occurs when the nearer coil of the pair rests at the interface, that is, when l_2 or l_1 becomes equal to one-half the distance L between the coils of the pair. The response of each coil pair over the intervening interval in crossing the interface has been computed by linearly interpolating between the limiting value for the response given by Eq. 23 and that given by Eq. 24.

The computational program for the response of a composite logging tool approaching and crossing a plane interface has been made in such a way that the properly weighted response of each coil pair is separately recorded. This means that the contribution of each coil pair to the over-all response of the tool is computed and recorded in the conductivity units of the calibration of the tool. Therefore, it is possible to plot not only the shape of the curve recorded by the composite tool in crossing the interface, but also the curve shape of the component signals developed by each one of its transmitter-receiver coil pairs.

THE CONTROL OF CURVE SHAPE BY AUXILIARY COILS

The manner in which the use of auxiliary coils affect the shape of the response of an induction logging tool in crossing the plane interface between two formations of different conductivity is shown in Fig. 5. The figure shows the shape of the response curves for each one of the transmitter-receiver coil pairs and for the complete coil system of the more highly focused coil system in logging upward from a formation having a conductivity of 100 millimhos/m into one of 1,000 millimhos/m. The solid curves illustrate the response calculated on the basis of Eqs. 23 and 24 and, thus, include propagation effects. The dashed curves are the response calculated on the basis of the geometric factor concept alone. The depth reference point for the curves of all the coil pairs is the center of the coil system.

The signal produced by the main-coil pair is shown by the curve $\sigma_a]_{TR}$. The signals developed by the auxiliary coils in combination with a main coil are shown by the two curves $\sigma_a]_{Tr}$ and $\sigma_a]_{tR}$ in the separate section at the extreme right of the figure. They are plotted as negative conductivities because of their reverse direction with respect to the signal produced by the main-coil pair. The sum of these two negative signals is shown by the curve $\sigma_a]_{Tr} + \sigma_a]_{tR}$ at the right side of the main part of the figure. The signal developed by the combination of the auxiliary transmitter coil and the auxiliary receiver coil, a small signal having a relative weight of 0.012 (Table 2), is shown by the curve $\sigma_a]_{tr}$.

The complete signal developed in the receiver circuit of the coil system is the sum of the four separate signals described previously. It is shown by the heaviest solid curve of the plot—$\sigma_a]_{tool}$. The several curves clearly illustrate the manner in which focusing, accomplished by adding the auxiliary coils, sharpens the response of the tool in crossing the conductivity interfaces.

The main-coil pair, because of its large coil span, has a relatively large field of investigation. This field extends not only laterally into the formation, but also above and below the tool. The steepest break in the conductivity curve of a coil pair is developed as the interface passes between its coils. The long, gradual sweep of the main-coil-pair curve on each side of the sharp break is due to the change in the portion of the signal which the coil receives from the formation on the opposite side of the interface as the pair approaches and as it moves away from the interface. Since the leading auxiliary-coil pair approaches the interface just in advance of the main-coil pair, the size of the signal it develops increases or decreases as a result of changes in conductivity of the formations in advance of the tool in the same way as the signal produced by the main-coil pair.

However, due to the reverse connection of the auxiliary coil, the voltage (and, hence, the conductivity response) developed by the leading coil pair is in the reverse sense and subtracts from that of the main pair. Therefore, an increase in the signal of the main-coil pair upon approaching a higher-conductivity formation is accompanied by an increase in the subtractive component supplied by the leading auxiliary-coil pair. In this way the leading auxiliary coil acts in such a way as to compensate, at least in part, for changes in the signal in the main-coil circuit which arise from changes in the conductivity of the formation in advance of the tool. In a similar way the trailing auxiliary-coil pair develops a signal which, at least in part, compensates for changes in the main-coil signal which are due to changes in the conductivity of the formation from which the tool is receding.

SPURIOUS DETAIL ADDED TO CONDUCTIVITY CURVE BY AUXILIARY COILS

The compensation which auxiliary coils provide for the contribution of formations above and below the main-coil span can only be approximated. Often, this method of focusing adds spurious detail to the conductivity curve which might easily be misinterpreted as lithological changes. In Fig. 5, the "peaks" which appear in the conductivity curve above and below the interface are examples of distortion resulting from the action of the auxiliary coils.

In logging upward toward the high-conductivity formation, the conductivity curve recorded by the coil system $\sigma_a]_{tool}$ starts to increase slowly in the expected way about 100-in. below the interface. The compensating action of the leading auxiliary coil then comes into play to diminish the effect of the approaching high-

conductivity formation. From 50- to 20-in. below the interface, the contribution $\sigma_a]_{Tr}$ of this coil pair is increasing at its greatest rate. Actually, its rate of increase over this interval is greater than that of the main-coil pair for which it is to supply compensation. As a result, the leading auxiliary-coil pair is subtracting signals at too great a rate, so that the over-all conductivity recorded by the coil system through this interval actually decreases as the tool moves toward the higher-conductivity material. The reversal of direction of the conductivity curve over this short interval causes the peak developed approximately 35-in. below the interface. In a similar way, the signal $\sigma_a]_{tR}$ developed by the trailing auxiliary coil supplies a negative signal above the interface which increases more rapidly than the signal from the main-coil pair decreases. This causes a reversal of the conductivity curve which results in the conductivity peak developed at approximately 35-in. above the interface.

The effect of the leading and trailing auxiliary-coil pairs in the lightly focused coil system is so slight that the shape of its response across an interface is essentially the same as that of the main-coil pair—$\sigma_a]_{TR}$—shown in Fig. 5. It does not develop the peaks shown by the conductivity curve of the more highly focused coil system.

THE FOCUSING EFFECT OF THE PROPAGATION PHENOMENA

The shapes of the conductivity curves, computed solely on the basis of geometric factor considerations, are shown by the dashed curves of Fig. 5 for the main-coil pair, $\sigma_{gf}]_{TR}$, and for the complete tool, $\sigma_{gf}]_{tool}$. Although both of these curves have the same general shape as the corresponding solid curves which include propagation effects, there are some very significant quantitative differences. The attenuation introduced by the propagation effect reduces the distance at which conductive material produces a measurable response on the conductivity curve. This is illustrated by the solid (propagation-effect) curves which reach substantially a constant value beyond 100 in. from the interface, while the dashed curves (based upon geometric factor calculations) continue to change for a substantially greater distance from the interface. This is equivalent to improving the focusing of the coil system insofar as vertical resolution is concerned.

The improvement in the interface response resulting from the operation of propagation effects is shown quantitatively in Table 3 for an unfocused single-coil pair and for the more highly focused of the four-coil systems previously described. The example used in the table is for the coil system on the 100-millimho/m side of the interface with a 1,000-millimho/m material as shown in the lower section of Fig. 5.

The second and third columns of the table apply to the performance of a single coil pair. It is apparent that the approach to the interface actually produces a much less-drastic change in the response of the coil pair when propagation effects are taken into account than would be expected on the basis of the geometric factor

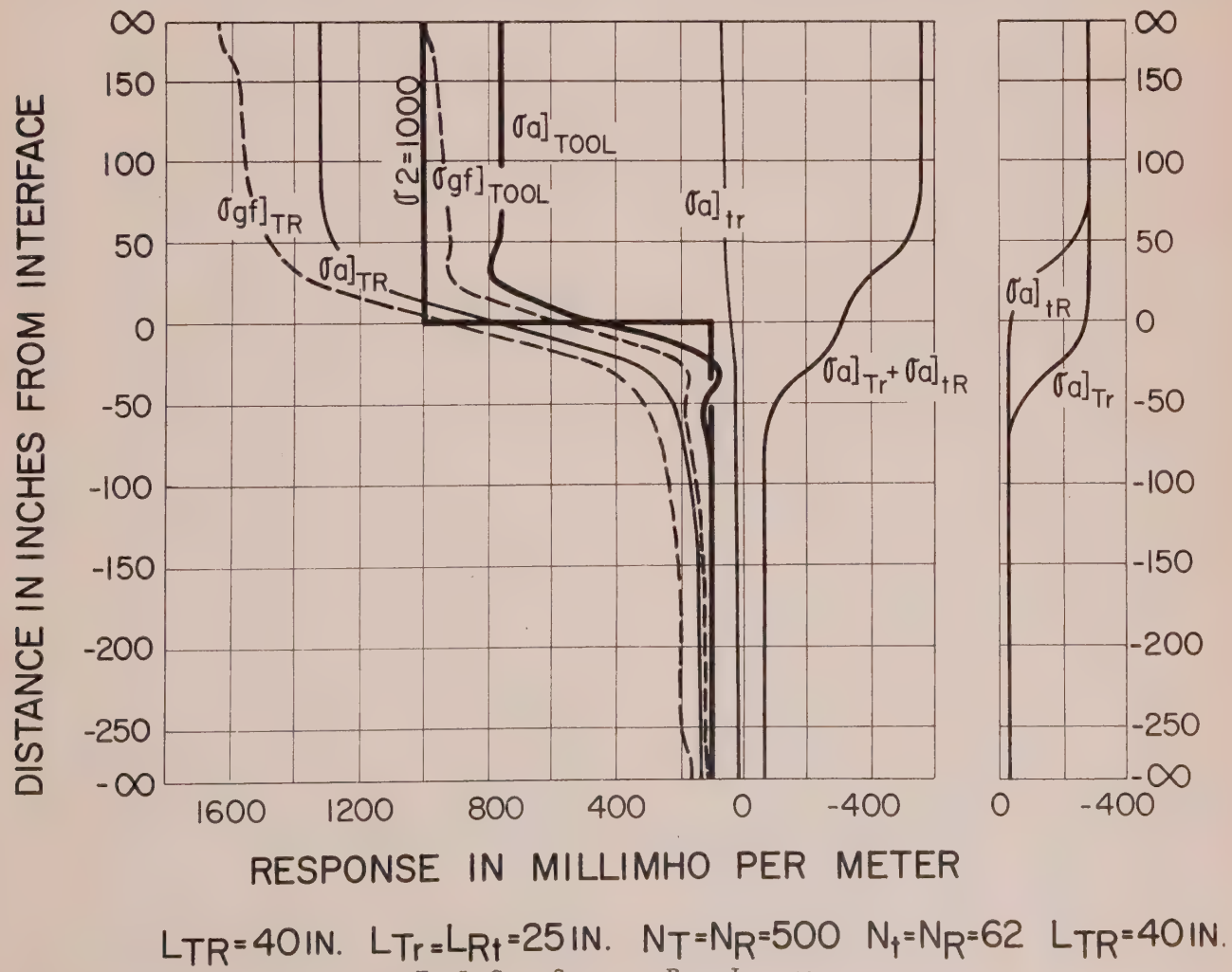

FIG. 5—CURVE SHAPE AT A PLANE INTERFACE.

concept. From the geometric factor calculation, a 45 per cent change in the response is expected when the tool reaches 100 in. from the interface. Due to propagation effects, this percentage of change actually does not occur until the center of the coil pair is less than 50 in. from the interface.

The response of the more highly focused four-coil system is shown in the last two columns of the table. On the basis of the geometric factor calculation, the change from the conductivity recorded at a very great distance from the interface reaches 54 per cent at 100 in. from the interface. When propagation effects are taken into account, the coil system can be brought to less than 30 in. from the interface before a change this great is actually encountered. The small change shown in the range from 40 to 30 in. is the result of the peak developed by the relatively high degree of focusing employed.

A paradoxical result of this type of focusing is made apparent in Table 3. On the basis of geometric factor calculations, the addition of the auxiliary coils increases (rather than decreases) the effect of material on the opposite side of the interfaces at the larger distances from the interface. This can be seen by comparing the second column for the single-coil pair with the fourth column for the four-coil system. The percentage change on approaching the interface is greater for the focused, four-coil system up to a distance of approximately 55 in. from the interface. The smaller change occurs in the focused system only for the shorter distances. This anomalous condition arises from the fact that the geometric factor calculations include the contribution of formations at relatively great distances from the coil system. At the greater distances from the focused coil system, the contributions of the 25-in.-spaced auxiliary-coil pairs fail to fully cancel the signal developed by the 40-in. main-coil pair. As the distance increases, the response of the tool is controlled to an increasingly greater extent by the overriding field of the main-coil pair.

The principle effect which the inclusion of propagation phenomena produces in the response of a coil pair is the marked decrease in the contribution of conductive materials at great distances. This means that the sensible field of the main-coil pair does not extend as far beyond that of the auxiliary pairs as would be expected from geometric factor considerations. This is made apparent by comparing the single-coil pair with the four-coil system as shown by the third and fifth columns of the table. When propagation effects are considered, there is little difference in the percentage change of the reading on approaching the interface up to approximately 60 in. For shorter distances from the interface, the four-coil system shows substantially smaller changes than the single-coil pair.

The negative change in response occurring at 400 in. from the interface in the calculation including propagation effects is the result of portions of the approaching conductive formation which are sufficiently far from the interface that the electromagnetic field, in moving outward to that portion of the formation from the transmitter and then back to the receiver system, experiences 180° of phase shift with respect to the transmitter current. The signal from these remote portions of the formation is opposite in phase to that produced by the nearby conductive material and, thus, records as a negative signal—in effect, a negative conductivity. At 400 in. from the interface with the high-conductivity material, the magnitude of this negative signal is greater than the positive signal received from the lower-conductivity material immediately surrounding the coil system.

TABLE 3—IMPROVEMENT IN SHARPNESS OF INTERFACE RESPONSE RESULTING FROM ACTION OF PROPAGATION EFFECTS—(TOOL IN σ_1, 100 MILLIMHOS/M; ADJACENT BED σ_2, 1,000 MILLIMHOS/M)

Distance from Center of Coil System to Interface (in.)	Percentage Change of Reading from Conductivity Recorded at a Great Distance from Interface			
	Unfocused Tool (L_{TR} = 40 in., $N_T = N_R$ = 500)		More Highly Focused Tool (L_{TR} = 40 in. $L_{Tr} = L_{tR}$ = 25 in.; $N_T = N_R$ = 500 $N_t = N_r$ = 61)	
	Geometric Factor Calculation	With Propagation Effect	Geometric Factor Calculation	With Propagation Effect
600	+ 7.5	+ .04	+ 9.4	+ .05
400	11.3	− .26	14.0	− .34
200	22.5	+ .17	27.9	+ .10
100	45.0	8.70	54.0	9.20
80	56.0	15.50	66.0	15.60
60	75.0	29.00	81.0	24.60
50	90.0	41.40	86.0	25.40
40	112.0	61.00	73.0	5.30
30	150.0	96.00	76.0	2.40
20	225.0	170.00	138.0	63.00

FIELD EQUATIONS NEAR A THIN FORMATION

The solution of the field equations for the case of two parallel interfaces enclosing a material having a conductivity different from that on either side is particularly important since it forms the basis for the calculation of thin-bed corrections for the induction log. The general solution has been worked out following the method used for the single-interface problem. The solution has additional terms which arise from the electromagnetic wave reflections which occur each time the wave crosses an interface. Each order of reflection involves the evaluation of an additional integral equation. In general, the contribution of these components decreases rapidly with increasing order of reflection. To the present, only a limited number of calculations of an exploratory character have been made. Nevertheless, it is apparent that the disparity of the results from those determined from geometric factor considerations is even greater than for the single-interface case.

The effect of propagation phenomena on the thin-bed response of the more highly focused of the two example coil systems is shown in Table 4. The table gives the multiplying correction factor to convert the apparent conductivity recorded by the coil system at the center of the bed to the conductivity that would have been recorded were the bed of infinite thickness. The table illustrates the response of the tool both in a low-conductivity object bed with higher-conductivity side beds and in a high-conductivity bed with lower-conductivity side beds. In each case, the values of the factors are nearer unity when propagation effects are taken into account than for the calculation based upon geometric factor considerations only. For the less-conductive bed, the geometric factor calculation suggests a correcting factor averaging approximately × 0.40 over beds ranging from 6 to 16 ft in thickness. When propagation effects are taken into account, the correcting factor lies generally above × 0.70.

CONCLUSIONS

The attenuation and phase shift produced by the conductive formation in the electromagnetic field of the induction-logging coil system reduce the response

TABLE 4—IMPROVEMENT OF THIN-BED RESPONSE RESULTING FROM ACTION OF PROPAGATION EFFECTS (MORE HIGHLY FOCUSED TOOL: $L_{TR} = 40$ in., $N_T = N_R = 500$; $L_{Tr} = L_{tR} = 25$ in., $N_t = N_r = 61$)

	Multiplying Correction Factor to Convert Apparent Thin-Bed Conductivity to That of Very Thick Formation.			
	$\sigma_1 = 100$ $\sigma_2 = 1{,}000$ (millimhos/m)		$\sigma_1 = 1{,}000$ $\sigma_2 = 100$ (millimhos/m)	
Bed Thickness (ft)	Geometric Factor Only	With Propagation Effect	Geometric Factor Only	With Propagation Effect
16	.47	.83	1.13	.99
14	.41	.72	1.16	1.00
12	.38	.67	1.19	1.00
10	.37	.68	1.21	.99
8	.40	.83	1.18	.96
7	.42	.99	1.16	.93
6	.40	.95	1.18	.93
5	.33	.66	1.25	.98
4	.23	.36	1.49	1.14
3	.16	.22	2.03	1.53

of the tool to portions of the formation at the greater distances to values substantially lower than those predicted from geometric factor considerations. Thus, the actual field of investigation of the induction log is smaller than established by geometric factor calculations. The use of computational procedures which include propagation effects is necessary to avoid overly pessimistic pictures of the curve shape, interface resolution and thin-bed corrections for the induction log.

The quantitative performance of any multipair coil system cannot be calculated—either by geometric-factor or propagation-effect methods—unless the position, size and turns ratio of each coil is known. Therefore, it is apparent that this information should be supplied on each log heading for log users who wish to verify existing performance charts or to prepare their own interpretational procedures.

ACKNOWLEDGMENTS

The assistance of Eugene Usdin of Southwestern Computing Service, Tulsa, Okla., in putting the equations in a form suitable for computer evaluation and in programing the procedure for computer computation is gratefully acknowledged. The authors express their appreciation to the Lane-Wells Co., under whose sponsorship the work was done, for permission to publish this paper.

REFERENCES

1. Doll, H. G.: "Introduction to Induction Logging and Application to Logging of Wells Drilled with Oil-Base Mud", *Trans.*, AIME (1949) **186**, 148.
2. Duesterhoeft, W. C., Jr.: "Propagation Effects in Induction Logging", *Geophysics* (April, 1961) **26**, No. 2, 192.
3. Doll, H. G.: U. S. Patent Nos. 2,582,314 and 2,582,315.

DISCUSSION

J. H. MORAN | *SCHLUMBERGER WELL SURVEYING CORP. RIDGEFIELD, CONN.*

This paper deals with an important aspect of induction logging—skin or propagation effect. In fact, it seems to imply that interpretation of induction logs is still in the stage where the geometrical factor only is considered. This is far from being true today.

We have in the past made studies similar to those described in this paper. Some results for the 5FF40 sonde were published by Dumanoir, Tixier and Martin in an appendix to their paper.[1] (Also see Ref. 2.) We also have made similar studies for the 6FF40 and for many other coil arrangements. Our studies have been made for the cases of homogeneous media, two media of different conductivity separated by a plane interface, thin beds and thick invaded beds.

The formulas and numerical results of the paper are in agreement with those we have obtained. However, we cannot agree with some of the qualitative deductions based on these results.

The most significant point on which we differ with the authors is the relation between "focusing" and skin effect that they emphasize. Their conclusion that more "strongly focused" sondes exhibit a larger skin effect is at variance with our conclusions, which have been based on many studies. The authors seem to realize that their conclusion is only valid if the auxiliary coils, introduced to achieve focusing, have a shorter spacing than the main pair. This is correct. If the auxiliary coils have a greater spacing than the main pair, then the skin effect is reduced and by suitable design can be effectively eliminated. Such a design is also a "focused" sonde.

To illustrate these remarks refer to Fig. D-1, where G_o as defined in the paper has been plotted for the 5FF40 and the 6FF40 sondes along with the three sondes considered in the paper. It is seen that, relative to the unfocused sonde, the 6FF40 has more skin effect while the 5FF40 has less skin effect. However, both are "focused" sondes with the same main-pair spacing. Therefore, on the basis of this comparison and numerous others that could be made, we reject the implication of the paper that strong focusing and large skin effect tend to accompany one another. This conclusion is supported only by results for three specific sonde designs. Our studies of dozens of designs show that the real art of sonde design lies in achieving "strong focusing" and small skin effect, and that this combination can be realized. We might also remark that the spurious detail at a bed boundary noted by the authors is due to their particular sonde designs, and sondes without this objectionable feature can and have been designed.

It is important to remark here that the large skin effect shown in Fig. D-1 for the 6FF40 coil system does not represent the final response of the field tool. The nonlinear coil response due to skin effect is corrected in the field equipment by a compensating circuit. Thus, the readings recorded on the 6FF40 log do not require corrections for skin effect for thick beds to which Fig. D-1 applies. Corrections will be needed only where the beds are highly conductive *and* deeply invaded, or too thin.

[1]References given at end of Discussion.

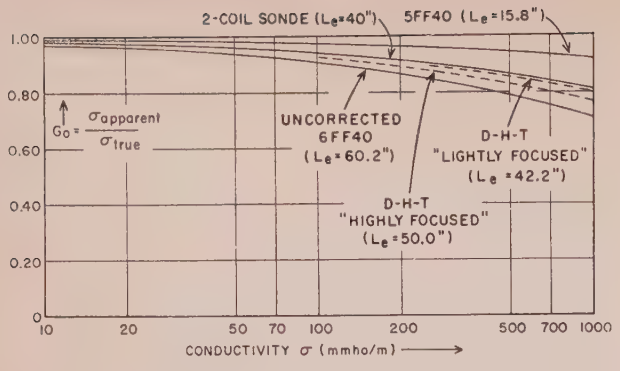

FIG. D-1—"G_o" PLOTTED FOR THE 5FF40 AND 6FF40 SONDES, ALONG WITH THE THREE SONDES NOTED IN THE TEXT OF THE PAPER.

With regard to a relation between skin effect and sonde design, in the course of our studies we have arrived at a somewhat more specific statement. To understand this statement, "an effective spacing" L_e of a multipair sonde is defined as follows.

$$L_e = \frac{\Sigma\,(N_T\,N_R)_i}{\Sigma\left(\frac{N_T\,N_R}{L}\right)_i}$$

where $(N_T\,N_R)_i$ is the product of the number of transmitter-coil turns by the number of receiver-coil turns for a particular coil pair (the ith pair), and where $(N_T\,N_R/L)_i$ is the turns product divided by the spacing of the ith pair. Both quantities are summed over all coil pairs, and the sums are divided to obtain the effective spacing L_e.

In Fig. D-1, the corresponding value of L_e has been shown on each curve. It is seen that the skin effect increases as L_e increases. Thus, the effective spacing L_e is a parameter which permits a quick assessment of the amount of skin effect for any given coil design.

The design of an induction logging sonde is a very complex problem. Such variables as geometrical factor, skin effect, hole size, caves, bed thickness and invasion diameter must all be taken into account in arriving at the most suitable instrument. This is not made clear in the paper.

REFERENCES

1. Dumanoir, J. L., Tixier, M. P. and Martin, Maurice: "Interpretation of the Induction-Electrical Log in Fresh Mud", *Trans.*, AIME (1957) **210**, 202.
2. Kunz, K. S. and Moran, J. H.: "Basic Electromagnetic Theory of Induction Logging", Abstracted *Geophysics* (Dec., 1958) 1077.

AUTHORS' REPLY TO J. H. MORAN

It is true that Ref. 1 cited by Moran brought up the question of the influence of the so-called "skin effect" on the response of the induction log (in Fig. 18a) by illustrating the large reduction in the correction for relatively thick beds. However, that paper gave no theoretical discussion of this propagation phenomena, nor did it suggest a computational procedure by which the reader could verify the results. The reference to the abstract of a second paper is inappropriate since this paper was not presented as scheduled in 1958 and, as far as we are aware, has not yet been published.

Insofar as information available to the log user is concerned, understanding the performance of the induction log really is not far beyond the state in which geometric factor considerations alone are used. As far as we are aware, there is no previously published analysis of the basic principles of the induction log which takes propagation effects into account and which explains the principles involved in the placement of auxiliary coils to achieve focusing.

The need for this type of information to assist the dedicated log analyst in studying the factors influencing the conductivity curve recorded by the induction log was strongly emphasized in a paper by DeWitte and Lowitz.[1] Many of the advances in well-log interpretation have been made by the log analysts of the industry. We believe that this can best be encouraged by a full exposition of the principles involved in the operation of logging tools. It was with this view that the work described in this paper, and the more basic analysis described in Ref. 2, was initiated. Technical information is of little value to the log user so long as it is confined to the service companies' confidential files.

The concept of equivalent length, introduced in the comment as a measure of the influence of propagation effects, is misleading. It involves purely arithmetic considerations, being the turns weighted-average separation of the transmitter-receiver pairs for the complete coil system. It follows the quantity we call G_e in a general way because G_e for a composite coil system is, in part, a function of the coil spans and turns.

This paper has emphasized the need for full data on coil spacings and turns in the calculation of the performance of a focused induction log. It is difficult to compare our results with those of the coil systems referred to in the comments by code symbols. Lacking details on the coil-system designs, only general observations can be made. It seems almost axiomatic that the objective in the design of any logging tool — intended to be interpreted in terms of the resistivity of the deep, uninvaded portion of the formation — should be to obtain maximum depth of its zone of investigation. Focusing the induction log to achieve thin-bed resolution should not be done at the expense of its depth of investigation.

We question the objective in the focusing of the tool cited as having auxiliary coils at greater spacings than the main-coil pair. It is implied that this is the case for the coil system coded as 5FF40. The radial characteristic of this tool has been published in a paper by Tixier, *et al.*[2] Fig. 1 of that paper gives its effective geometric factor for the formation *outside* of a radius of 50 in. to be only 0.25 $(1 - G_{(r)})$. This is almost identical to the radial response of a single-coil-pair, unfocused system having a 20-in. span. In contrast, a 40-in. unfocused pair has an effective geometric factor in excess of 0.45 for the formation beyond this radius. This figure can be increased at the same time the thin-bed response is *improved* by employing the type of focusing we describe.

The second coil system cited has the bed thickness

[1]References given at end of "Authors' Reply".

and radial response of an advantageously focused, 40-in. coil system. We question the propriety of classing the 5FF40 as a 40-in. coil system in making the comparison of its G_o with that of a 40-in. tool, as is done in Fig. D-1. Actually, the curve indicated for the tool is in the position that would be occupied by a 20-in. basic span tool. If the equivalent length of 15.8 in. indicated for the tool is significant, it also supports our speculation.

We are aware that induction-logging coil systems can be designed which do not develop the spurious "peaks" at each side of a high-conductivity contrast interface. It is pointed out that the lightly focused coil system does not develop this curve shape. The more heavily focused system was illustrated for the specific purpose of demonstrating how these peaks, so commonly displayed by the present generation of logging tools, are attributes of the tool focusing system and not of lithological details in the formation under examination.

REFERENCES

1. deWitte, A. J. and Lowitz, David A.: "Theory of the Induction Log", Paper presented at Symposium of Society of Professional Well Log Analysts (May 18-19, 1961) in Dallas.
2. Tixier, M. P., Alger, R. P. and Tanguy, D. R.: "New Developments in Induction and Sonic Logging", *Trans.*, AIME (1960) **219**, 362.

★★★

Unsteady-State Gas Flow into Gas Wells

R. V. SMITH
MEMBER AIME

PHILLIPS PETROLEUM CO.
BARTLESVILLE, OKLA.

ABSTRACT

The theory for unsteady radial flow of gas, as simplified by Aronofsky and Jenkins, has been reviewed and compared with actual well performance. This study indicated that the theory should be modified by the introduction of an empirical "rate of flow" function "$Y_{(q)}$". The expansion of the theory on the flow of gas to include a $Y_{(q)}$ term bridges the gap between the theory of unsteady-state flow of gas and actual gas-well behavior. Apparently, the $Y_{(q)}$ term is a function only of the rate of flow for a given well. The completion factor or skin effect is associated with the $Y_{(q)}$ function in such a manner that at least two or more sets of drawdown or pressure build-up tests are needed to separate the $Y_{(q)}$ function and the completion factor. Since the $Y_{(q)}$ function used in this report represents an energy loss dependent on rate of flow near the wellbore of a gas well which is in addition to the loss required by Darcy's law, the $Y_{(q)}$ function is related to the exponent of the back-pressure curve for a gas well.

Techniques and equations are presented which permit the estimation of stabilized and "short-time" deliverabilities.

INTRODUCTION

The published theory of radial unsteady-state flow of gas through porous media may be divided into papers[1-3] which use Darcy's law as a premise and other papers[4-7,16-19] which recognize that Darcy's law may not hold for flow into gas wells. Miller[8] compared theory based on Darcy's law with actual gas-well behavior and concluded that flow into gas wells deviates from Darcy's law. Houpeurt[4,5] in a thorough investigation of flow into gas wells concluded that the flow rate into a gas well is proportional to the difference between the squares of upstream and downstream pressures elevated to a power between 1.0 and 0.5. Houpeurt also concluded that the deviation from Darcy's law is caused by irreversible, kinetic energy exchange between the flowing gas and the porous media. Tek[9] presented a complete evaluation of the flow problem in gas wells. Several investigators state that the inclusion of gas compressibility into flow equations based on Darcy's law does not begin to explain the flow problems suggested by gas-well behavior.

For many years, natural-gas engineers have realized that gas wells by actual test exhibit behavior which cannot be explained entirely by Darcy's law. Many tests on gas wells have indicated that a value of 0.85 for the exponent in the back-pressure equation is a fair average for many wells. However, Darcy's law either for steady or unsteady-state conditions indicates that the exponent should be 1.0. The purpose of this paper has been to examine this deviation from Darcy's law and to present a reasonable mathematical means of evaluating the deviation.

The method presented in this paper combines previous theory with an empirical function to provide a description of gas-well behavior. All equations in this report are for constant terminal-rate-of-flow conditions. While present methods of testing wells usually are not based on this concept, they are believed to approach the constant terminal-rate conditions closely in many tests. However, several gas wells were tested by holding the rates of flow constant in order to approach more closely the constant terminal rate of flow; the results confirm the concepts presented in this paper.

REVIEW OF THEORY FOR UNSTEADY-STATE FLOW OF GAS

The basic partial differential equation for the flow of natural gas has been given in technical literature; the equation for a cylindrical reservoir with the well in the center is

$$\frac{\partial^2(P/P_o)^2}{\partial r^2} + \frac{1}{r}\frac{\partial(P/P_o)^2}{\partial r} = \frac{2\phi\mu}{KP_o}\frac{\partial(P/P_o)}{\partial t} \quad . \quad . \quad (1)$$

According to Aronofsky and Jenkins,[1] Eq. 1 is based on the following assumptions.

1. The top, bottom and outer curved surfaces are impermeable.
2. The permeability to gas is constant and independent of pressure.
3. The density of the gas is proportional to pressure.
4. The flow follows Darcy's law.
5. The viscosity of the gas is constant.
6. Gravitational forces are negligible.

Eq. 1 is nonlinear, and the only analytical solution[10] known is for a one-dimensional semi-infinite medium. However, numerical solutions for Eq. 1 have been published[2,3] which were reviewed by Aronofsky and Jenkins.[1] They concluded that the numerical solutions for Eq.

Original manuscript received in Society of Petroleum Engineers office July 5, 1960. Revised manuscript received Sept. 21, 1961. Paper presented at 35th Annual Fall Meeting of SPE, Oct. 2-5, 1960, in Denver.

[1]References given at end of paper.

1 could be represented very closely by the solutions for transient liquid flow. A brief review of the conclusions of Aronofsky and Jenkins[1] is presented in Appendix C. Also, Appendix C shows how the solution for transient liquid flow may be used to arrive at the following approximate equation for transient flow of gas in a radial system.

$$P_{(\tau)} - 4\theta = \frac{2\,[(1 - \overline{Q}\theta)^2 - (P_w/P_e)^2]}{\overline{Q}} \quad . \quad . \quad (2)$$

where $P_{(\tau)}$ is the "cumulative pressure drop for a unit rate of flow" function described by van Everdingen and Hurst.[11] Table 4 includes values and equations for calculating the $P_{(\tau)}$ function.

Eq. 2 does not represent a solution to Eq. 1, but it is a close approximation to the numerical solutions.[2,3] The numerical solutions given in Ref. 3, for seven values of the dimensionless flow ratio $\overline{Q}$ from 0.005 to 0.5, show only a small variation from Eq. 2. The value of 0.5 for $\overline{Q}$ corresponds to an actual flow rate of 54 Mscf of gas/24 hours/ft of sand for an initial pressure, viscosity and permeability of 450 psia, 0.012 cp and 10 md, respectively. Aronofsky called attention to the small variation of the numerical solutions with $\overline{Q}$ from that indicated by Eq. 2.

When the dimensionless time ratio θ increases until it is larger than 0.3 and the effective radius of drainage has become stabilized, Eq. 2 becomes

$$\ln\left(0.472\frac{r_\tau}{r_w}\right) = \frac{2\,[(1 - \overline{Q}\,\theta)^2 - (P_w/P_e)^2]}{\overline{Q}} \quad . \quad . \quad . \quad . \quad . \quad . \quad . \quad . \quad . \quad . \quad . \quad . \quad . \quad (3)$$

At this time, the well may be said to have become stabilized.

For short periods of flow which start with the well shut-in, when the fraction of the gas reserve removed from the reservoir ($\overline{Q}\theta$) during the flow is less than 0.001, and when the dimensionless time ratio θ is small, Eq. 2 becomes, for all practicable purposes,

$$P_{(\tau)} = \frac{2\,[1 - (P_w/P_e)^2]}{\overline{Q}} \quad . \quad . \quad . \quad . \quad . \quad . \quad . \quad . \quad (4)$$

In regard to the $P_{(\tau)}$ function, van Everdingen and Hurst[11] state that, for dimensionless time ratios (referred to the well radius) larger than 100, the $P_{(\tau)}$ may be approximated by

$$P_{(\tau)} = \tfrac{1}{2}\,(\ln \tau + 0.809) \quad . \quad . \quad . \quad . \quad . \quad . \quad . \quad . \quad (5)$$

Substituting for $P_{(\tau)}$ from Eq. 5 into Eq. 4, the result is

$$\tfrac{1}{2}\,(\ln \tau + 0.809) = \frac{2\,[1 - (P_w/P_e)^2]}{\overline{Q}} \quad . \quad . \quad . \quad . \quad (6)$$

where

$$\tau = \frac{KP_e t}{\phi \mu r_w^2}.$$

Time in seconds, the pressure term and $\overline{Q}$ are the only variables in Eq. 6 for a well and a given initial pressure. Consequently, a plot of drawdown data for gas wells should result in a straight-line relationship between the pressure term and the logarithm of time. This straight-line relationship permits the direct calculation of the dimensionless flow ratio $\overline{Q}$ from the slope by means of the following derived from Eq. 6.

$$\overline{Q} = 1.737\,m \quad . \quad . \quad . \quad . \quad . \quad . \quad . \quad . \quad . \quad . \quad . \quad . \quad (7)$$

Determinations of $\overline{Q}$ by means of Eq. 6 are dependent only on measurements of pressure and time, provided the rate of flow is constant.

Permeability may be calculated from $\overline{Q}$ by the definition of $\overline{Q}$ given in the Nomenclature, which requires the estimation of the viscosity of the gas and the net productive thickness of the reservoir at the well. Permeabilities calculated in this manner should be the average permeability of the reservoir out to the extent of the radius of drainage for the particular time period under consideration. However, these permeabilities do not include the effect of the drilling and completion of the well on the reservoir near the wellbore.

COMPARISON WITH EXPERIMENTAL RESULTS

Special tests were conducted on gas wells in low-permeability reservoirs to study unsteady-state behavior and to test the theory just outlined. Several wells were tested by actually keeping the rate of flow constant in order to approach more closely the constant terminal rate of flow. These wells were tested according to the isochronal-performance method described by Cullender,[14] which requires that the well be shut-in after each flow, and the sand-face pressure being permitted to build up to almost the stabilized reservoir pressure before the well is started flowing. The performance curves for these wells, as indicated by the equation

$$Q = C\,(P_f^2 - P_s^2)^n, \quad . \quad . \quad . \quad . \quad . \quad . \quad . \quad . \quad . \quad . \quad (8)$$

had values of n that ranged from 0.696 to 0.948. Isochronal-performance and back-pressure[15] curves for gas wells are known by experience to have exponents (values of n) that vary from 0.5 to 1.0. Even though the theory outlined previously predicts an exponent of 1.0, it was decided to test the theory step-by-step and, if possible, determine why exponents other than 1.0 are observed in gas-well performance studies. Each set of drawdown data for each well was used to calculate the permeability of the reservoir rock around the well. Fig. 1 illustrates a typical set of drawdown data from Well A. Permeabilities for different rates of flow for five of the wells tested are given in the third column of Table 1.

Although there is some variation in the permeabilities for each well—and there may be a systematic variation with rate of flow—the agreement between the separate determinations is believed to be good. The consistency of the permeabilities for each well, despite the variation in rate of flow, indicates that Darcy's law is applicable to the flow of gas in reservoirs at least to the

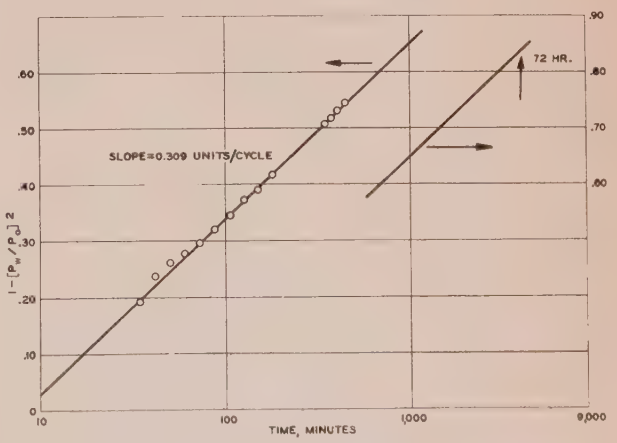

FIG. 1—DRAWDOWN DATA FROM WELL A.

TABLE 1—PERMEABILITIES, COMPLETION FACTORS AND $Y_{(q)}$ VALUES CALCULATED FROM DRAWDOWN DATA ON FIVE GAS WELLS (180-MINUTE PERIODS OF FLOW)

Well	Rate of Flow (Mcf/D)	Permeability (Darcy)	S	$Y_{(q)}$
A	67.8	0.000,47	−3.397	0.173
	120.4	.000,56		.266
	239.8	.000,57		.541
	309.3	.000,59		.695
B	1,946	0.018,2	−4.420	0.305
	3,911	.019,2		.585
	4,956	.019,5		.730
C	817	0.010,8	−5.065	0.536
	1,531	.011,8		.912
	1,804	.011,2		1.127
D	1,112	0.011,4	−4.437	0.330
	1,898	.010,4		.600
	2,642	.010,5		.830
E	1,619	0.022,4	−4.894	0.778
	2,793	.022,0		1.358
	3,664	.024,6		1.601

extent involved in the calculation of permeability from the slope of the drawdown curves for the particular rates of flow. It is not known whether larger variations in rate of flow would cause a variation in the calculated permeability.

The average permeability for each of the five wells from the third column of Table 1 was substituted into Eq. 6 along with the approximate time, the wellbore radius, effective porosity, viscosity and rates of flow, to calculate the isochronal-performance curve which is labeled as "Eq. 6" in Figs. 2 through 6. Actual data points from rates of flow and pressures taken during testing also are shown on Figs. 2 through 6, as circles. The agreement between the measured isochronal data and that calculated by means of Eq. 6 is very poor. In addition, the value of n (the exponent in Eq. 8) is 1.000 for the isochronal-performance curves calculated by means of Eq. 6. Although Eq. 6 indicates that $[1 - (P_w/P_e)^2]$ forms a straight-line relationship with the logarithm of time which is confirmed by experimental data, it must be concluded that Eq. 6 is inadequate for computing the behavior of gas wells.

The first obvious deficiency in Eq. 6 is that it does not contain the "skin effect" or completion factor S as defined by van Everdingen[12] and Hurst.[13] If completion factor term S is added to the left side of Eq. 6 and values of S are taken as given in Table 1, a new set of isochronal-performance curves may be calculated for the five wells listed in Table 1. The results of including S are the curves labeled as "Eq. $6 + S$" in Figs. 2 through 6. Again, the calculated performance curve has an exponent n of 1.000. However, the position of the curve from Eq. 6 with completion effect added is considerably different from that of the curve from Eq. 6, but it does not adequately represent the experimental data for the wells indicated by circles in Figs. 2 through 6. The positions of the curves labeled "Eq. $6 + S$" could be changed by changing the value of the completion factor S and could even be made to fall on any of the experimental points by adjusting the value of S. However, such calculated performance curves would have an exponent of 1.000. Therefore, such curves would not be representative of actual data taken on wells because an exponent of 1.000 is rarely observed in isochronal-performance curves from test data.

A review of the literature[4,5,9,16–19] suggested that a non-Darcy effect which is rate-dependent may cause the difference between Eq. 6 with the completion factor and actual well-test data. This effect must be rate-dependent in order to make Eq. 6 give performance curves with an exponent less than unity.

If $\overline{Q}$ is computed as outlined and substituted into Eq. 6 with time- and pressure-factor values from the straight-line portion of the drawdown curve, apparent values of $[\ln (KP_e/\phi\mu r_w^2)]$ may be computed. The re-

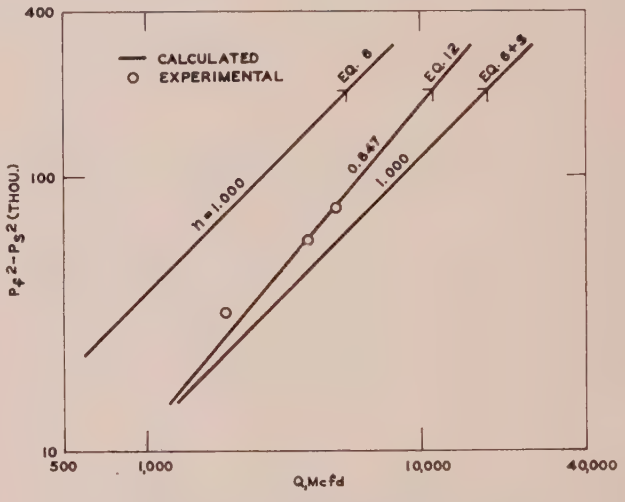

FIG. 3—EXPERIMENTAL AND CALCULATED ISOCHRONAL CURVES FOR WELL B.

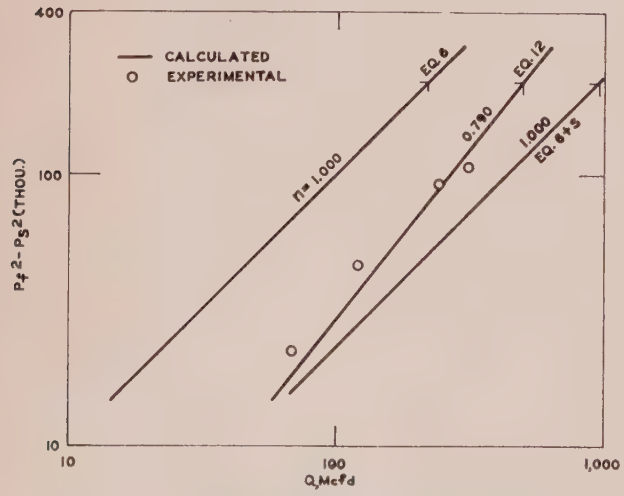

FIG. 2—EXPERIMENTAL AND CALCULATED ISOCHRONAL CURVES FOR WELL A.

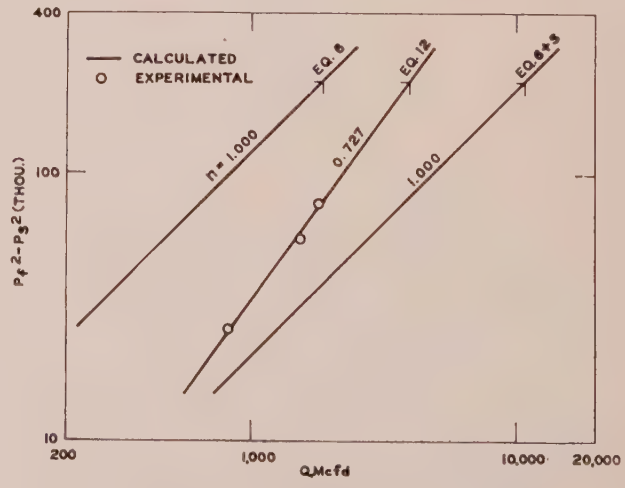

FIG. 4—EXPERIMENTAL AND CALCULATED ISOCHRONAL CURVES FOR WELL C.

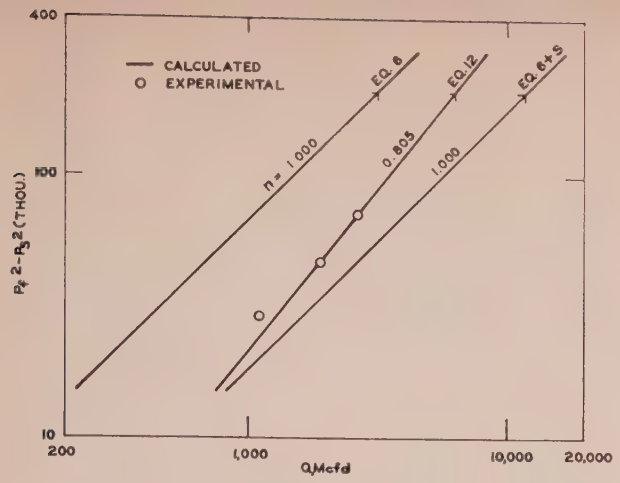

FIG. 5—EXPERIMENTAL AND CALCULATED ISOCHRONAL CURVES FOR WELL D.

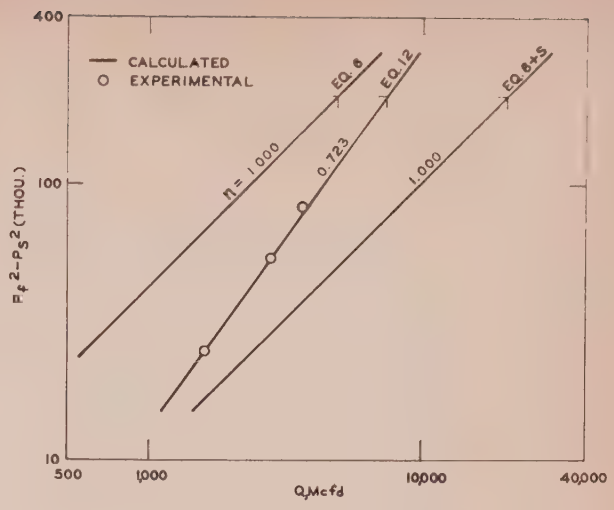

FIG. 6—EXPERIMENTAL AND CALCULATED ISOCHRONAL CURVES FOR WELL E.

sults of such calculations for Well C are given in the last column of Table 2. These results are not constant, and they show a progressive change with rate of flow. An examination of the [ln $(KP_o/\phi\mu r_w^2)$] values in Table 2 and similar computations shows that these values vary with the rate of flow. As mentioned previously, it is believed that Eq. 6 should contain the completion factor S. However, there is nothing in the literature that would indicate that the completion factor S would vary with the rate of flow for a given well. Neither permeability, porosity and wellbore radius would be expected to vary with rate of flow. The pressure at stabilized shut-in conditions in the reservoir would decrease very slightly, but the decrease during a short-time test would be so small that it would be impossible to measure in a commercial reservoir. The compressibility and viscosity of the gas flowing to a well would vary with the pressure drop for various rates of flow, but it is believed that their variations would not account for the wide range in apparent values of [ln $(KP_o/\phi\mu r_w^2)$] listed in the last column of Table 2 and similar results obtained on other gas wells.

A variation in the apparent value of [ln $(KP_o/\phi\mu r_w^2)$] with rate of flow was observed in the results of the tests on all the gas wells tested. If the flow of gas followed Darcy's law from the radius of drainage to the wellbore, there would be no variation with rate of flow for the term in brackets. This suggested that observed variation is related to the exponent in Eq. 8, the back-pressure relationship, because the exponent would have a value of unity (or very close thereto) if the flow of gas followed Darcy's law.

It is then concluded that Eqs. 2, 3, 4 and 6 should be modified by adding the completion factor S and a rate-of-flow dependent term which has been designated $Y_{(q)}$. The addition of the $Y_{(q)}$ function is merely an empirical method for adjusting theory to conform with actual gas-well behavior.

If completion factor S and the $Y_{(q)}$ function are added to the $P_{(\tau)}$ term in Eqs. 2, 3, 4 and 6, the resultant equations are

$$P_{(\tau)} - 4\theta + S + Y_{(q)} = \frac{2[(1-\overline{Q}\theta)^2 - (P_w/P_o)^2]}{\overline{Q}}, \quad \ldots\ldots\ldots\ldots\ldots\ldots\ldots (9)$$

$$\ln\left(0.472\frac{r_r}{r_w}\right) + S + Y_{(q)} = \frac{2[(1-\overline{Q}\theta)^2 - (P_w/P_o)^2]}{\overline{Q}}, \quad \ldots\ldots\ldots\ldots\ldots\ldots\ldots (10)$$

$$P_{(\tau)} + S + Y_{(q)} = \frac{2[1-(P_w/P_o)^2]}{\overline{Q}}, \quad \ldots\ldots (11)$$

and

$$\tfrac{1}{2}(\ln\tau + 0.809) + S + Y_{(q)} = \frac{2[1-(P_w/P_o)^2]}{\overline{Q}} \quad \ldots\ldots\ldots\ldots\ldots\ldots\ldots (12)$$

TABLE 2—APPARENT VALUES OF [ln $(KP_o/\phi\mu r_w^2)$] FOR THREE RATES OF FLOW FROM WELL C (180-MINUTE PERIODS OF FLOW)

Well	Rate of Flow (Mcf/D)	$\overline{Q}$	Apparent Values of ln $(KP_o/\phi\mu r_w^2)$
C	817	0.148	−6.914
	1,531	.254	−6.090
	1,804	.316	−5.712

CALCULATION OF $Y_{(q)}$ VALUES

While $Y_{(q)}$ is similar to the completion factor in many respects, it probably represents a variable deviation from Darcy's law which is related to the rate of flow. It is then reasonable to expect that, as the rate of flow approached zero, $Y_{(q)}$ would approach zero. This relationship is illustrated in Fig. 7 where values of [ln $(KP_o/\phi\mu r_w^2) + 2S + 2Y_{(q)}$] are plotted against $\overline{Q}$, the dimensionless rate-of-flow ratio. Extrapolation of the established relationship to where $\overline{Q} = 0$ permits the determination of the value of [ln $(KP_o/\phi\mu r_w^2) + 2S$] which was − 7.95 for the test data illustrated in Fig. 7. The calculated values of $Y_{(q)}$ corresponding to the three rates of flow for Well C in Table 2 are 0.518, 0.930 and 1.119, respectively, while values read from the straight line on Fig. 7 are 0.536, 0.912 and 1.127, respectively (Table 1). Values of $Y_{(q)}$ were calculated in a similar manner for the other four wells and are given in Table 1. Similar calculations may be made for other gas wells if data are available for two or more rates of flow.

CALCULATION OF COMPLETION FACTOR OR SKIN EFFECT

By means of Fig. 7, the following was determined for Well C at $\overline{Q} = 0$.

$$\ln(KP_o/\phi\mu r_w^2) + 2S = -7.95,$$

or

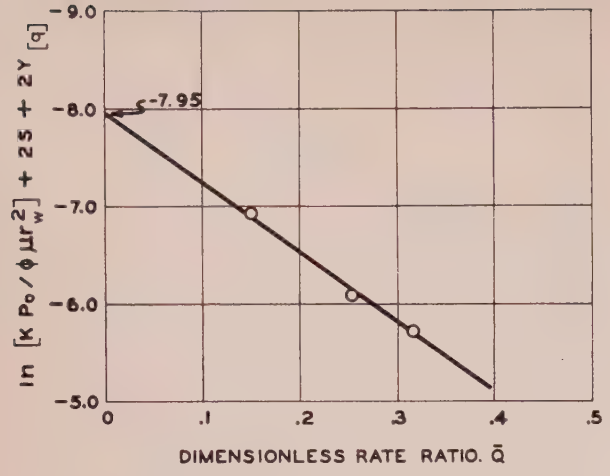

FIG. 7—DETERMINATION OF $Y_{(q)}$ VALUES FOR WELL C.

$$\ln (KP_o e^{2S}/\phi\mu r_w^2) = -7.95.$$

If the values of K, P_o, ϕ and μ are known, the completion factor may be calculated for the well. K = 0.011,3 darcy; P_o = 32.1 atm; ϕ = 0.07; and μ = 0.012 cp. Then,

$$r_s = r_w/e^s = 1{,}106 \text{ cm, or } 36.3 \text{ ft.}$$

If the value of r_w/e^s is defined as the effective radius of the wellbore, S can be arbitrarily assumed to be zero. However, if the drilled radius of the wellbore (6.98 cm, or 0.229 ft) is substituted into this expression, the completion factor or skin effect S is determined to be −5.065 (Table 1).

As Well C has been treated with a large quantity of acid, it probably is more realistic to consider a large, negative completion factor as an enlargement of the wellbore rather than as an increase in the permeability of the reservoir near the wellbore. Probably, the effect actually is a combination of both an increase in permeability and an enlargement of the wellbore.

A well, on which the drilling and completion have neither damaged nor improved the permeability around the wellbore, would have a completion factor of zero. A negative completion factor indicates an improvement in the productive capacity of the well, while a positive completion factor indicates a damaged productive capacity. The productive capacity of Well C had been improved considerably by the net effect of drilling and completion, which included treatment with acid.

If the values of S, $Y_{(q)}$ and permeability from Table 1—along with effective porosity, viscosity and the drilled wellbore radius—are substituted into Eq. 12, isochronal-performance curves may be calculated for the wells listed in Table 1. Three-hour isochronal-performance curves were calculated in this manner and are labeled as "Eq. 12" on Figs. 2 through 6. Each of the performance curves calculated by means of Eq. 12 has an exponent for the back-pressure equation of less than unity. Also, each calculated curve represents very closely the actual experimental data taken on each well. Therefore, it is concluded that the theory of unsteady-state gas flow derived from the work of Aronofsky and Jenkins can be made to fit actual well data by the addition of the completion factor and a $Y_{(q)}$ function which is dependent on the rate of flow.

SIGNIFICANCE OF THE $Y_{(q)}$ FUNCTION

Although the $Y_{(q)}$ function is an empirical factor added to various equations to make them agree with actual data taken during the testing of gas wells, certain observations can be made regarding the implied nature of the $Y_{(q)}$ function as it is used in this report. As $Y_{(q)}$ has been associated in a particular way in this report with the completion factor S, it represents an additional energy loss near the wellbore for the flow of gases. Since isochronal back-pressure curves of short time duration have the same exponents as those of longer duration, the pressure drop represented by $Y_{(q)}$ is established very quickly after a well is started producing. The experimental data reported by Cullender[14] indicated that $Y_{(q)}$ is not a variable with respect to time. Data presented in Appendix A also support this conclusion.

The $Y_{(q)}$ function is not contradictory to the ideas proposed by Houpeurt[5] or those of Katz and others.[17–19] Houpeurt states that the kinetic energy losses in gas flow are concentrated in a "deviation zone" near the wellbore and that flow in the zone can be assumed to be in a steady state. Katz and others have postulated a zone of turbulent flow near the wellbore of gas wells.

ESTIMATION OF DELIVERABILITY

After a gas reservoir has been discovered and before the wells are connected to a pipeline, the correct estimation of the change in delivery capacity with time caused by unsteady-state effects for the wells is essential to the determination of the number of wells required for a given obligation to deliver gas. Actual determination of stabilized delivery capacity for wells in low-permeability reservoirs before connection to a pipeline can be extremely wasteful of gas.

Since deliverability is a factor in determining the allowable for a well in several gas fields, it is often necessary to estimate the deliverability of a well before incurring the expense of connecting the well to a pipeline. Deliverability, as usually defined by state regulatory bodies, is the daily rate of flow which would exist at the end of a 72-hour flow period, following a 72-hour shut-in period, if the well at that time were producing against a pipeline pressure equal to the deliverability standard pressure.

In deliverability tests it usually is necessary to convert the test rate of flow to the deliverability at 72 hours with a formula established by the regulatory body in which deliverability is related to the test rate, the shut-in pressure, working pressure, the deliverability standard pressure and the exponent in the back-pressure curve. In each case the exponent is given by the rules of the regulatory body.

If a three- or six-hour, three-point isochronal test is run on the well, the $Y_{(q)}$ function and the completion factor can then be calculated for the well by means of Eq. 12. A working pressure at 72 hours can be calculated from the experimental data taken over a short period of time by means of Eq. 12 or, more simply, by extrapolation of the relationship between $[1 - (P_w/P_o)^2]$ and the logarithm of time to 72 hours. The estimated working pressure and the rate of flow can be used to compute a deliverability at 72 hours.

A working pressure at stabilization can be calculated from short-time test data by means of Eqs. 12 and 10. Appropriate test data—permeability, porosity and viscosity—are substituted into Eq. 12 and the value of $[\ln 1/r_w + S + Y_{(q)}]$ is determined since all the other

terms in Eq. 12 are known. This value can be substituted into Eq. 10. If the radius of drainage can be estimated and if $(\bar{Q}\theta)$ is small with respect to 1.0, a value of (P_w/P_o) can be calculated for the constant rate of flow at stabilization. If desired, this "performance point" can be used with the definition of deliverability to calculate a stabilized deliverability for the well.

In connection with the estimation of deliverability, it is interesting to note that the relationship between the ½-, 3- and 72-hour isochronal-performance curves can be derived (see Appendix A) for wells in reservoirs with low permeability from Eq. 12. This relationship, as an approximation, is

$$\frac{[P_f^2 - P_{s(72h)}^2] - [P_f^2 - P_{s(3h)}^2]}{[P_f^2 - P_{s(3h)}^2] - [P_f^2 - P_{s(1/2h)}^2]} = 1.77 \quad . \quad . \quad (13)$$

The symbols in Eq. 13 have been changed to conform with those used by Cullender[14] for the isochronal tests, and the subscripts in parentheses have been added to indicate times at which the pressures were taken. The relationship in Eq. 13 has been compared with the actual performance of 509 gas wells in the Guymon and Texas Hugoton fields, with results as shown in Col. 2 of Table 3.

PRESSURE BUILD-UP IN GAS WELLS

Eq. 12 may be used to derive the pressure build-up relationship for gas wells by following the procedures used by van Everdingen[12] and Hurst[13] for oil wells. At time t (seconds), the difference between the squares of the initial pressure and the flowing pressure is

$$P_o^2 - P_{w(t)}^2 = \frac{qP_b\mu}{2\pi Kh}\left[\ln\frac{KP_o}{\phi\mu r_w^2} + \ln t + 0.809 + 2S + 2Y_{(q)}\right] . \quad . \quad (14)$$

At time Δt after the well has been shut in at time t, the difference is

$$P_o^2 - P_{w(\Delta t)}^2 = \frac{qP_b\mu}{2\pi Kh}\left[\ln\frac{t+\Delta t}{\Delta t}\right] \quad . \quad . \quad . \quad (15)$$

By subtracting Eq. 15 from Eq. 14, the result is

$$P_{w(\Delta t)}^2 - P_{w(t)}^2 = \frac{qP_b\mu}{2\pi Kh}\left[\ln\frac{KP_o}{\phi\mu r_w^2} + \ln t - \ln\frac{t+\Delta t}{\Delta t} + 0.809 + 2S + 2Y_{(q)}\right] \quad . \quad . \quad (16)$$

where subscript Δt indicates the square of the pressure at the well at time Δt after the well is shut in, and subscript t indicates the flowing pressure at the well at the time the well was shut in. For values of Δt that are small compared to t, Eq. 16 becomes

$$P_{w(\Delta t)}^2 - P_{w(t)}^2 = \frac{qP_b\mu}{2\pi Kh}\left[\ln\frac{KP_o}{\phi\mu r_w^2} + \ln\Delta t + 0.809 + 2S + 2Y_{(q)}\right] . \quad (17)$$

The determination of the permeability from pressure build-up data requires a selection of the proper time variable. If Δt is small compared to t, the square of pressure at the sand face in the well may be plotted against the logarithm of Δt. Otherwise, the square of pressure must be plotted against the logarithm of either $(t + \Delta t)/\Delta t$ or $\Delta t/(t + \Delta t)$. The permeability of the reservoir rock out to the radius of drainage of the well, but not including the immediate vicinity of the wellbore, may be computed from the slope of the pressure build-up curve by the following.

$$K = 248.78\frac{qP_b\mu}{\pi hm'} , \quad . \quad . \quad . \quad . \quad . \quad . \quad . \quad . \quad (18)$$

or

$$K = 1.632\frac{QT_f\mu}{Hm'} . \quad . \quad . \quad . \quad . \quad . \quad . \quad . \quad . \quad (19)$$

Common gas-engineering units, which are given in the Nomenclature, are used in Eq. 19.

As both $Y_{(q)}$ and the completion factor are involved in pressure build-up Eqs. 14, 16 and 17, any determination of the completion factor or skin effect for a gas well requires pressure build-up data for at least two tests starting with different rates of flow before the well is shut in. Theory indicates that data on permeability, completion factor and $Y_{(q)}$ from pressure build-up tests should be identical with those from pressure drawdown tests.

TABLE 3—AGREEMENT BETWEEN CALCULATED AND ACTUAL 72-HOUR PERFORMANCE FOR 509 WELLS IN THE GUYMON (OKLA.) AND HUGOTON (TEX.) FIELD

Ratio of Actual to Calculated 72-Hour Performance	Number of Wells	
	Col. 1	Col. 2
More than 1.35	15	10
1.35-1.30	3	5
1.30-1.25	4	4
1.25-1.20	8	5
1.20-1.15	14	10
1.15-1.10	36	28
1.10-1.05	55	44
1.05-1.00	63	48
1.00- .95	69	61
.95- .90	61	69
.90- .85	51	56
.85- .80	40	48
.80- .75	24	31
Less than .75	66	90
	509	509

Col. 1 = Number of wells having the indicated ratio of the actual performance to the 72-hour performance calculated from the one- and three-hour isochronal curves.

Col. 2 = Number of wells having the indicated ratio of the actual performance to the 72-hour performance calculated from the one-half- and three-hour isochronal curves.

CONCLUSIONS AND SUMMARY

1. The expansion of published theory on the flow of gas to include a $Y_{(q)}$ term bridges the gap between the theory of unsteady-state flow of gas and actual gas-well behavior.
2. The $Y_{(q)}$ term apparently is a function only of rate of flow for a given well.
3. The completion factor or skin effect for a gas well is associated with the $Y_{(q)}$ function in such a manner that at least two or more sets of drawdown or pressure build-up tests are needed to separate completion factor and the $Y_{(q)}$ function. These tests must be conducted at different rates of flow.
4. The exponent of the back-pressure curve for a gas well is related to the $Y_{(q)}$ function.
5. Techniques and equations are presented which permit the estimation of stabilized and short-time deliverabilities.

ACKNOWLEDGMENT

This paper is presented by permission of the Phillips Petroleum Co.

NOMENCLATURE*

C = coefficient in back-pressure equation

*In general, units used in this report are those of the darcy, but in Eqs. 8, 13, and 19 units are those used in natural-gas engineering. In several equations, pressures appear as a ratio permitting the use of pressure in psia.

h = effective formation thickness, cm

H = effective formation thickness, ft

K = permeability, darcy

m = slope of drawdown curve, units of $[1 - (P_w/P_o)^2]$/cycle

m' = slope of pressure build-up curve, units of P^2 (psia^2)/cycle

n = exponent in back-pressure equation

P = pressure within reservoir, atm

P_b = standard pressure base, atm

P_f = stabilized shut-in pressure at the sand face, psia, in Eqs. 8 and 13

P_s = flowing pressure at the sand face, psia, in Eqs. 8 and 13

P_o = pressure at stabilized shut-in conditions in the reservoir, atm

P_w = pressure at the well in the reservoir, atm (P_w varies with time)

$P_{(\tau)}$ = function defined by van Everdingen and Hurst[11]

q = production rate into well, standard cc/sec at reservoir temperature

Q = production rate, Mcf/24 hours (14.65 psia and 60°F)

$\overline{Q} = \dfrac{2\,q\,P_b\,\mu}{\pi\,P_o^{\,2}\,Kh}$ = dimensionless flow-rate ratio for gas

r_r = reservoir radius, cm

r_w = well radius, cm

r_e = effective radius of the well, cm

S = completion factor or skin effect, dimensionless (van Everdingen and Hurst skin effect)

t = time, seconds

T_f = reservoir temperature, °F absolute

$Y_{(q)}$ = function related to rate of flow

μ = viscosity, cp

ϕ = effective porosity, fraction (available for containing gas)

$\tau = \dfrac{K\,P_o\,t}{\phi\mu r_w^{\,2}}$ = dimensionless time ratio for gas referred to well radius

$\theta = \frac{1}{2}\tau\left(\dfrac{r_w}{r_r}\right)^2$ = dimensionless time ratio for gas referred to reservoir radius

ln = natural logarithm

SUBSCRIPTS

$\frac{1}{2}h, 3h, 72h$ (Eq. 13) = sand-face pressures at the well for times of ½, 3 and 72 hours, respectively.

REFERENCES

1. Aronofsky, J. S. and Jenkins, R.: "A Simplified Analysis of Unsteady Radial Gas Flow", *Trans.*, AIME (1954) **201**, 149.
2. Jenkins, R. and Aronofsky, J. S.: "Unsteady Radial Flow of Gas Through Porous Media", *Jour. Appl. Mech.*, ASME (June, 1953) **20.**
3. Bruce, G. H., Peaceman, D. W. Rachford, H. H., Jr. and Rice, J. D.: "Calculation of Unsteady-state Gas Flow Through Porous Media", *Trans.*, AIME (1953) **198**, 79.
4. Houpeurt, A.: "Etude Analogigue de l'Ecoulement Radial Circulaire Transitoire des Gaz Dans Les Milieux Poreau", *Revue de l'Institute Francais du Petrole et Anales des Combustibles Liquids* (1953) **8**, No. 4, 5.
5. Houpeurt, A.: "On the Flow of Gases in Porous Media", *Institut Francais du Petrole* (May, 1959) Ref. 3341.
6. Tek, M. R., Grove, M. L. and Poettmann, F. H.: "Method for Predicting the Back-Pressure Behavior of Low Permeability Natural Gas Wells", *Trans.*, AIME (1957) **210**, 302.
7. Poettmann, F. H. and Schilson, R. E.: "Calculation of the Stabilized Performance Coefficient of Low Permeability Gas Wells", *Trans.*, AIME (1959) **216**, 240.
8. Miller, J. S.: "How Does Theoretical Gas Well Performance Compare with Field Data?", *World Oil* (Oct., 1957) **145**, No. 5, 222.
9. Tek, M. R.: "Developments in Natural Gas Reservoir Engineering", *Pet. Eng.* (March, 1959) **31**, No. 3, B-47.
10. Kidder, R. E.: "Unsteady Flow of Gas Through a Semi-Infinite Porous Medium," *Jour. Appl. Mech.* (Sept., 1957) **24**, 329.
11. van Everdingen, A. F. and Hurst, W.: "The Application of the LaPlace Transformation to Flow Problems in Reservoirs", *Trans.*, AIME (1949) **186**, 305.
12. van Everdingen, A. F.: "The Skin Effect and Its Influence on the Productive Capacity of a Well", *Trans.*, AIME (1953) **198**, 171.
13. Hurst, William: "Establishment of the Skin Effect and Its Impediment to Fluid Flow into a Well Bore", *Pet. Eng.* (Oct., 1953) **25**, B-6.
14. Cullender, M. H.: The Isochronal Performance Method of Determining the Flow Characteristics of Gas Wells", *Trans.*, AIME (1955) **204**, 137.
15. Rawlins, E. L. and Schellhardt, M. A.: "Back-Pressure Data on Natural Gas Wells and Their Application to Production Practices", *Monograph 7*, USBM (1935) 210.
16. Tek, M. R.: "Development of a Generalized Darcy Equation", *Trans.*, AIME (1957) **210**, 357.
17. Elenbaas, J. R. and Katz, D. L.: "A Radial Turbulent Flow Formula", *Trans.*, AIME (1948) **174**, 25.
18. Cornell, D. and Katz, D. L.: "Flow of Gases through Consolidated Porous Media", *Ind. Eng. Chem.* (1953) **45**, 2145.
19. Cornell, D. and Katz, D. L.: "Pressure Gradients in Natural Gas Reservoirs", *Trans.*, AIME (1953) **198**, 61.

APPENDIX A

RELATIONSHIP BETWEEN ISOCHRONAL-PERFORMANCE CURVES

The position of the 72-hour isochronal-performance curve may be calculated from the one-half- and the three-hour curves by means of Eq. 13 in the text. The general equation derived as follows is more useful because it permits the calculation of any isochronal-performance curve when the positions of two curves are known.

$$\tfrac{1}{2}\,(\ln\tau + 0.809) + S + Y_{(q)} = \frac{2\,[1 - (P_w/P_o)^2]}{\overline{Q}} \qquad (12)$$

where

$$\tau = \frac{KP_o t}{\phi\mu r_w^{\,2}}$$

and

$$\overline{Q} = \frac{2qP_b\mu}{\pi P_o^2 Kh};$$

by letting

$$A = \frac{KP_o \exp 2S \exp 0.809 \exp 2Y_{(q)}}{\phi\mu r_w^2},$$

the result for t_1 is

$$\tfrac{1}{2} \ln A + \tfrac{1}{2} \ln t_1 = \frac{2[1 - (P_{w1}/P_o)^2]}{\overline{Q}} \quad . \quad . \quad (20)$$

If $t_1 < t_2 < t_3$, by substituting t_2 into Eq. 20 and subtracting Eq. 20 from the result, the relationship is

$$\tfrac{1}{2} \ln t_2/t_1 = \frac{2[(P_{w1}/P_o)^2 - (P_{w2}/P_o)^2]}{\overline{Q}} \quad . \quad (21)$$

If the equivalent relationship for t_2 and t_3 is divided by Eq. 21, the general relationship between isochronal curves is found for a constant rate of flow to be

$$\frac{\ln t_3/t_2}{\ln t_2/t_1} = \frac{(P_{w2})^2 - (P_{w3})^2}{(P_{w1})^2 - (P_{w2})^2},$$

or

$$\frac{\log t_3/t_2}{\log t_2/t_1} = \frac{[P_f^2 - P_s^2{}_{t_3}] - [P_f^2 - P_s^2{}_{t_2}]}{[P_f^2 - P_s^2{}_{t_2}] - [P_f - P_s^2{}_{t_1}]}. \quad . \quad . \quad . \quad (22)$$

where time is any convenient unit and pressures are pounds per square inch absolute. Eq. 22 is the general form of Eq. 13 in the text, and it gives the relationship between isochronal-performance curves for a well before stabilization.

Eq. 22 has been checked against the actual performance of 509 gas wells in the Guymon (Okla.) and Hugoton (Tex.) gas field. The results are given in Table 3 where Col. 1 is the number of wells having the indicated ratio of the actual performance to the 72-hour performance calculated from the one- and three-hour isochronal curves. Col. 2 is the number of wells having the indicated ratio calculated from the one-half- and three-hour isochronal curves. Where the ratio of the actual to the calculated performance is more than 1.00, the distribution of errors according to the number of wells is considered normal. At ratios less than 1.00, however, there are too many wells for the distribution to be normal. Changes in permeability of the reservoir rock away from the well would cause variations on either side of a ratio of 1.00, but water entry into the well after the test was started would damage the performance of the well.

Many of the 509 wells on which this performance study was made are subject to water problems. Actually, the performance ratio given in Table 3 has been used, along with other information, to decide whether or not the performance of a well could be improved by the installation of tubing or other equipment to remove water from the well. This is believed to be one of the more important applications of Eq. 22.

APPENDIX B

RELATIONSHIP BETWEEN PERFORMANCE COEFFICIENTS AT VARIOUS TIMES BEFORE STABILIZATION

At a constant rate of flow Q, the following relationships hold for isochronal back-pressure curves for a gas well.

$$Q = C_1[P_f^2 - P_s^2{}_{t_1}]^n, P_f^2 - P_s^2{}_{t_1} = [Q/C_1]^{1/n};$$

$$Q = C_2[P_f^2 - P_s^2{}_{t_2}]^n, P_f^2 - P_s^2{}_{t_2} = [Q/C_2]^{1/n};$$

$$Q = C_3[P_f^2 - P_s^2{}_{t_3}], P_f^2 - P_s^2{}_{t_2} = [Q/C_3]^{1/n}.$$

By substituting thse expressions into Eq. 22, the result is the following relationship for performance coefficients which applies before the well reaches stabilization.

$$\frac{\log t_3/t_2}{\log t_2/t_1} = \frac{[1/C_3]^{1/n} - [1/C_2]^{1/n}}{[1/C_2]^{1/n} - [1/C_1]^{1/n}}. \quad . \quad . \quad . \quad . \quad (23)$$

APPENDIX C

DEVELOPMENT OF EQS. 2 AND 3

Aronofsky and Jenkins[1] have defined a quantity, $\ln (r_d/r_w)$, which represents a type of correlative function. It was related to the steady-state formula for radial gas flow by their Eq. 2, which is

$$\ln (r_d/r_w) = \frac{\pi KhP_o^2}{qP_b\mu}\left[\left(\frac{P_a}{P_o}\right)^2 - \left(\frac{P_w}{P_o}\right)^2\right]^* \quad . \quad (24)$$

where P_a = bulk average pressure in reservoir, atm.

Aronofsky and Jenkins[1] stated that the effective drainage radius r_d must be allowed to take on any value required to force the steady-state portion of Eq. 24 to represent the transient solution.

Since

$$\overline{Q} = \frac{2qP_b\mu}{\pi P_o^2 Kh} \text{ and } P_a = P_o(1 - \overline{Q}\theta),$$

Eq. 24 may be rewritten as follows.

$$\ln (r_d/r_w) = \frac{2}{\overline{Q}}[(1 - \overline{Q}\theta)^2 - (P_w/P_o)^2] \quad . \quad (25)$$

The effective radius of drainage for a liquid system has been given in Eq. 8 of Aronofsky and Jenkins,[1] in terms of the van Everdingen and Hurst[11] $P_{(\tau)}$ function, as

$$\ln (r_d/r_w) = P_{(\tau)} - 2\tau (r_w/r_r)^2 \quad . \quad . \quad . \quad . \quad (26)$$

Since

$$\theta = \frac{\tau}{2}(r_w/r_r)^2,$$

Eq. 26 may be rewritten as

$$\ln (r_d/r_w) = P_{(\tau)} - 4\theta \quad . \quad . \quad . \quad . \quad . \quad . \quad . \quad (27)$$

The numerical solutions of Eq. 1 published by Bruce, Peaceman, Rachford and Rice[3] may be substituted into Eq. 25 to calculate values of $\ln (r_d/r_w)$ for various values of dimensionless time θ and various rates of gas flow $\overline{Q}$. Also, values of $\ln (r_d/r_w)$ for liquid systems may be calculated from Eq. 26 and values of $P_{(\tau)}$ function given by van Everdingen and Hurst.[11]

After a study of the numerical solutions for Eq. 1 published by Bruce, Peaceman, Rachford and Rice,[3] Aronofsky and Jenkins concluded the following.

1. The numerical solutions of gas flow for various rates almost coincide with the solution for transient liquid flow in a radial system.

2. The quantity $\ln (r_d/r_w)$ represents a type of correlation function that correlates well pressure P_w and time θ for both transient gas flow and transient liquid flow for all constant-rate uses studied up to a maximum gas rate $\overline{Q}$ of at least 0.5. It appears that this correlation is reasonably good over the entire time range for $(r_r/r_w) = 200$ and that a similar correlation can be made for any other reservoir radius where r_r is much larger than r_w.

*Symbols have been changed to agree with those in the nomenclature.

TABLE 4—THE VAN EVERDINGEN AND HURST $P_{(\tau)}$ FUNCTION (REF. 11)

τ	$P_{(\tau)}$	τ	$P_{(\tau)}$
0.01	0.112	10	1.651
.1	.315	15	1.829
.2	.424	20	1.960
.5	.616	25	2.067
1.0	.802	30	2.147
2.0	1.020	40	2.282
3.0	1.169	50	2.388
4.0	1.275	60	2.476
5.0	1.362	80	2.615
7.0	1.500	100	2.723

For $\tau > 100$

$$P_{(\tau)} = \tfrac{1}{2}(\ln \tau + 0.809)$$

For τ Extremely Large

$$P_{(\tau)} = \tfrac{1}{2}\left(\frac{r_w}{r_e}\right)^2 + 2\tau\left(\frac{r_w}{r_e}\right)^2 - \tfrac{3}{4} \cdot \cdot \cdot \left(\frac{r_w}{r_e}\right)$$

Values of $P_{(\tau)}$ taken from the tabulation and computed from the equations in Table 4 were used to determine a series of values of ln (r_d/r_w) for $(r_d/r_w) = 200$. These values of ln (r_d/r_w) are represented by the solid line of Fig. 8. Data presented by Bruce, Peaceman, Rachford and Rice[3] were substituted into Eq. 25 to calculate corresponding values of ln (r_d/r_w) for radial gas flow at rates of 0.5 and 0.005 for $\overline{Q}$. These values of ln (r_d/r_w) for gas flow are represented on Fig. 8 by the plotted points. For rates of flow between 0.5 and 0.005, see Fig. 4 of Ref. 1. An examination of Fig. 8 in this paper and Fig. 4 of Ref. 1 shows that the numerical solutions for gas flow almost coincide with the solution for transient liquid flow in a radial system. In this connection, Kidder[20] states that the numerous worked examples of heat-conduction problems become immediately applicable as approximate solutions to the corresponding problems in the flow of gases in porous media. Therefore, an approximate equation for transient gas flow in a radial system may be obtained

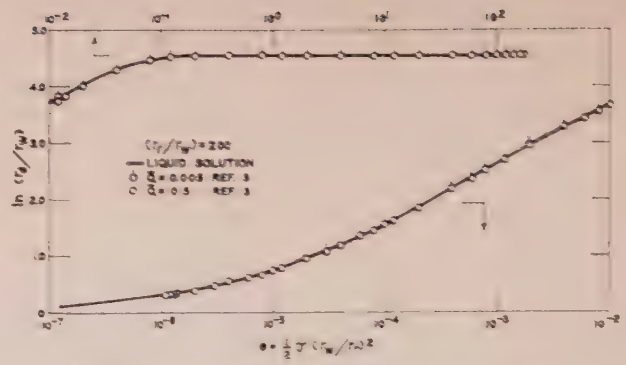

FIG. 8—EFFECTIVE RADIUS OF DRAINAGE AND TIME FOR GAS AND LIQUID SYSTEMS.

by eliminating the quantity ln (r_d/r_w) between Eq. 25 and Eq. 27. The result is

$$P_{(\tau)} - 4\theta = \frac{2[(1 - \overline{Q}\theta)^2 - (P_w/P_e)^2]}{\overline{Q}} \quad . \quad . \quad . \quad (2)$$

which is Eq. 2 in the text.

According to Aronofsky and Jenkins,[1] Eq. 25 becomes

$$P_w/P_e = \left[(1 - \overline{Q}\theta)^2 - \frac{\overline{Q}}{2}\ln\left(0.472\frac{r_e}{r_w}\right)\right]^{1/2} \quad . \quad . \quad . \quad (28)$$

when θ is larger than 0.3 and when the effective radius of drainage has become stabilized at approximately $0.472\ r_e$. Eq. 28 may be re-arranged to become

$$\ln\left(0.472\frac{r_e}{r_w}\right) = \frac{2[(1 - \overline{Q}\theta)^2 - (P_w/P_e)^2]}{\overline{Q}} \quad . \quad . \quad (3)$$

which is Eq. 3 in the text. ★★★

Large-Scale Laboratory Investigation of Sand Consolidation Techniques

WAYNE F. HOWER
MEMBER AIME
WILLIAM BROWN

THE HALLIBURTON CO.
DUNCAN, OKLA.

ABSTRACT

Large-scale sand consolidation tests were conducted in an effort to determine the reasons for the successes and failures of this method of sand control. Several different consolidating materials were used in treating both clean and bentonitic sands that were packed in a chamber having a capacity of 3.3 cu ft. The results were essentially the same for all of the different consolidating materials. The data show that low-viscosity consolidating materials pumped at a relatively slow rate gave the best results.

Where the formation has produced sand, the treating fluids can compress the formation, thus permitting the channeling of fluids to another horizon. Pressure-packing these zones before attempting to consolidate is recommended. Sands containing more than 4 per cent of water-swelling clays are not good candidates for consolidation. It is indicated that loose sand, particularly when it is bentonitic, can be fractured during the placement of the treating fluids.

INTRODUCTION

Sand production in oil and gas wells has plagued the industry for many years, and numerous cures for this problem have been suggested. Most methods have been successful to a certain degree, but the great variety of well conditions that exist in the different areas has magnified the problem and limited the successful use of the various systems. Four review papers[1-4] present a wealth of information concerning the degrees of success that have been obtained by the different sand-control methods. The bridging of sand grains by the use of gravel packs and screens has been quite successful. However, these methods do not leave the casing clear for all types of multiple completions, and the cure does not last for the production life of the well in some instances.

The control of loose sands by sand consolidation with resins has never been as successful as desired. It has always been hoped that such a treatment would eliminate all sand problems for the life of the well, but initial applications, starting in the middle 1940's, were only moderately successful. Lott, *et al*,[3] reported a success ratio of approximately 50 per cent and made the following conclusions.

> The highest percentage of successes were obtained where:
>
> a. Consolidation of a zone was made at the time of *initial completion* or *prior to the production of sand.*
>
> b. The interval treated was less than 12 ft in length.
>
> c. Between 30 and 50 gal plastic/ft of producing interval was displaced through the perforations.

REASONS FOR SAND CONSOLIDATION FAILURES

Our own experiences in the field of sand consolidation point toward the following conditions as the major reasons for the failure of sand consolidation attempts.

1. Mud-plugged perforations and mud invasion of the formation.

2. Sand in the casing covering all or part of the perforations. This sand could be either formation sand or one of the coarser sands used as propping agents in hydraulic fracturing.

3. Holes in the casing.

4. Channels behind the casing.

5. Attempting to treat too long a perforated section.

6. Too high a percentage of water-swelling clays in the formation.

7. Formations that have produced sand.

Recent attempts were made to treat perforated sections ranging from 10 to 30 ft, in wells that have produced sand, by using a straddle packer that was raised and lowered through the perforations as the consolidating material was being pumped. In most instances, the pressure required to pump fluid into the formation varied considerably as the tool was raised and lowered. This suggested the possibility that significant differences in permeability were present or that only part of the formation had produced sand.

There were times when a sudden break in pressure indicated that a fracture was being formed. Research conducted several years ago concerning the problem of the control of water in air and gas drilling indicated that shale sections could be fractured quite easily. In addition, it was determined that it was easier to pump fluids into shale bodies by fracturing the shale itself, or the interface between the shale and sand, than to pump into a fluid-saturated formation. Formations that produce sand are usually adjacent to shale bodies and frequently have shale streaks of various thicknesses interbedded in the sand. Therefore, where shale is exposed to fluid pressure it

Original manuscript received in Society of Petroleum Engineers office July 6, 1961. Revised manuscript received Oct. 23, 1961. Paper presented at 36th Annual Fall Meeting of SPE, Oct. 8-11, 1961, in Dallas.

Discussion of this and all following technical papers is invited. Discussion in writing (three copies) may be sent to the office of the *Journal of Petroleum Technology*. Any discussion offered after Dec. 31, 1961, should be in the form of a new paper. No discussion should exceed 10 per cent of the manuscript being discussed.

[1]References given at end of paper.

This page of *Petroleum Transactions, AIME* follows page 1159. The intervening non-Transactions pages appeared in *Journal of Petroleum Technology*.

is reasonable to assume that the consolidating material can enter the shale instead of the sand horizon. We can now add to our list an eighth possible reason for sand consolidation failures.

8. Perforating into shale bodies.

Knowing the reason for a failure is important, but it is more important to be able to do something about it. Some of the listed troubles can be alleviated if the well owner will more carefully complete and prepare the well for treatment. An analysis of a representative formation sample is helpful in determining if the sand can be treated. The presence of water-swelling clays, such as montmorillonite and illite, have a tremendous influence on the retained permeability after consolidating. Significant quantities of these clays can cause very low permeabilities or even plugging as the result of the sand consolidation attempt.

TEST METHODS

Laboratory methods of testing sand consolidating systems have been quite varied. Most methods have been confined to small samples in tubes that are usually less than 2 in. in diameter and 6-in. long. Materials and/or treating techniques can be partially screened by these small-scale systems, but many questions concerning field applications still are left unanswered.

In an effort to gain further insight in the field of sand consolidation, we decided to greatly enlarge the size of the testing equipment. We particularly wished to obtain knowledge of what takes place in the formation adjacent to the perforation as the treating fluids are being injected. It is at this point that a hard and permeable consolidation must be obtained for the treatment to be a success.

We also hoped that the work would lead to a better understanding of the reasons for the successes and failures of past applications, and to suggestions for improving the techniques of placing the consolidating materials. The purpose of this paper is to present the findings of such an investigation.

LARGE-SCALE TEST EQUIPMENT

The equipment designed for this research project is much larger than that ordinarily used in sand consolidation testing.

Several separate phases were investigated in the 91 tests conducted with this equipment and it was determined that most of these phases and the effects that they caused are interdependent. The major phases included the viscosity of the consolidating materials, the fluid injection rates, the amount of oil used to displace the consolidating materials and the effects of these materials in fine, coarse and bentonitic sands. Both one- and two-stage treatments were performed using one and two perforations.

The interpretation of the results obtained in this research is based on physical data and the appearance of the consolidations. Pictures were made of almost every trial, and several of these illustrations are included in this discussion. However, many observations that were difficult to record in notes and pictures frequently exerted an influence on many of the conclusions noted in this paper.

Fig. 1 is a picture of the test equipment. The tanks on the left were used to hold the treating solutions. A variable-speed 3-hp motor was used to power a pump that was capable of developing 200-psi pressure. Maximum flow rates of 11 gal/min were obtained in some tests. The test chamber on the right of the illustration was made of 10-gauge steel on the sides and ¼-in. steel on the top and bottom. Reinforcing ribs were placed at the top for added strength. Fig. 2 shows the chamber's dimensions and its capacity. The perforation is ½ in. in diameter and was made in a section of 7-in. casing with a jet charge. The two-perforation system, where two ½-in. bushings were used as outlets, is shown in Fig. 3. A divider was used here to confine the treating chemicals to the side of the chamber they entered.

MATERIALS USED

The clean sand used as the basic sand in these tests had the following sieve analysis.

U. S. Sieve No.	Cumulative Per Cent Retained
40	0.1
60	2.55
80	29.94
100	42.71
120	73.31
140	88.81
170	95.74
200	98.60
325	99.99
Pan	100.00

In some trials, this sand was mixed with an untreated drilling-mud bentonite to simulate a bentonitic formation sand. The clean sand normally was packed using fresh water, but a synthetic brine was employed when bentonite was added to the sand. The brine had the following analysis: specific gravity at 67° F, 1.049; pH, 6.5; total dissolved solids, 72,700 ppm; calcium, 1,400 ppm; magnesium, 100 ppm; chloride, 44,000 ppm; sulfate, 200 ppm; bicarbonate, 100 ppm; and iron, 30 ppm.

FIG. 1—LARGE-SCALE EQUIPMENT USED IN TESTS—CHEMICAL STORAGE TANKS SHOWN ON LEFT AND TEST CHAMBER ON RIGHT.

In other trials, the clean sand (usually referred to as fine sand) was mixed in equal weights with 40-60 Ottawa sand to form what we called coarse sand.

Three basic consolidating systems were investigated in these tests. An inorganic consolidating agent, two different phenolic resins and a urea resin were tested. A great deal of comparative work was done, and essentially the same results were obtained with all consolidating systems. All of these methods are identical in one essential phase; i.e., the consolidating material is placed in the sand and then over-displaced with a specified volume of oil to develop an effective permeability in the consolidation.

A majority of the research used the inorganic binder and one of the phenolic resin systems. The inorganic binder proved to be uniquely valuable in that it caused the sand to be consolidated within a few seconds after it entered the test chamber. Any condition of sand-body deformation or fracturing was literally 'frozen" in place by this type of treatment, which thus permitted us

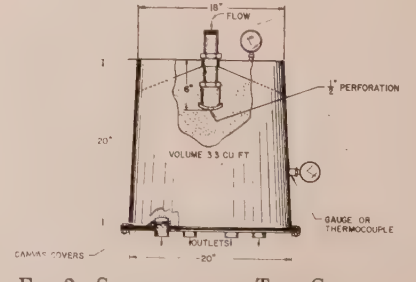

FIG. 2—SKETCH OF THE TEST CHAMBER.

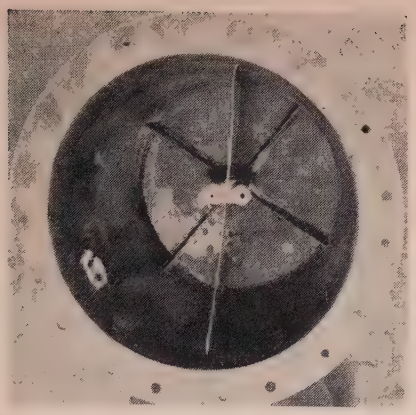

FIG. 3—THE TEST CHAMBER WITH TWO PERFORATIONS AND A METAL DIVIDER IN PLACE.

to observe the actual condition of the sand while it was being treated.

Unless otherwise stated, the inorganic binder is the system reported in this paper. The phenolic and urea resins required several hours to harden, whereas any sand-body deformation cause by fluid injection had usually returned to its original condition by this time.

The excess sand was washed away with water to reveal the consolidated pattern. The consolidation then was examined for visual effects, a procedure which included splitting it in two sections. In most cases, portions of the consoliation were removed and used to determine air permeabilities and compressive strengths. Fig. 4 shows the standard points or stations from which these portions were taken.

Views A, B and C of Fig. 5 picture a consolidation using one perforation. Fig. 5(A) shows the consolidation in the chamber, looking from the bottom of the consolidation directly toward the perforation. Fig. 5(B) is a side view of the consolidation, and Fig. 5(C) is a cross-section view after the consolidation was split in half.

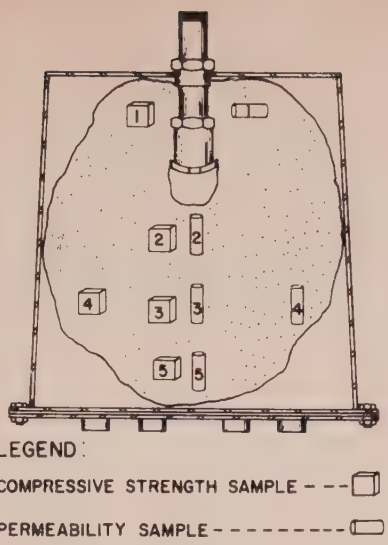

FIG. 4—STANDARD STATIONS IN CONSOLIDATION PATTERN WHERE SAMPLES WERE TAKEN FOR PERMEABILITY AND COMPRESSIVE-STRENGTH DETERMINATION.

TREATING PROCEDURE

The following treating procedure, which closely approaches a typical field application, was observed.

1. The sand was packed in the chamber. The permeability of the unconsolidated sand usually varied between 9.5 to 10.5 darcies.

2. A 5-gal diesel oil preflush was used for most of the tests, but the volume was varied between 2.5 to 25 gal. A water-wetting, emulsion-breaking surfactant was used in the oil in most of the trials.

3. The consolidating material was pumped, with 1 gal of consolidating material being used for most of the tests. Where a two-stage treatment was planned, this volume was reduced to 0.5 gal for each stage.

4. Where necessary, a setting chemical was pumped to harden the consolidating material.

Where the phenolic resin systems were used, the chamber and its contents were preheated to the desired testing temperature, usually 120° to 130°F. The treating solutions were maintained at atmospheric temperature when pumped into the chamber. After treatment, the outlets were plugged and the entire chamber was placed in a thermostatically controlled water bath until the resin was properly cured.

VISCOSITY OF THE CONSOLIDATING MATERIAL

Table 1 lists data using two basic fluid-injection rates. In all cases, 1 gal of consolidating material was used and this was displaced with 5 gal of diesel oil. The Table 1 data, plus many other observations, point to certain conclusions.

There was always more permeability below the perforation (Station 2) than at the sides of the consolidation. This is logical because the 5 gal of displacing oil would have a tendency to flow from the perforation to the outlets. Therefore, any

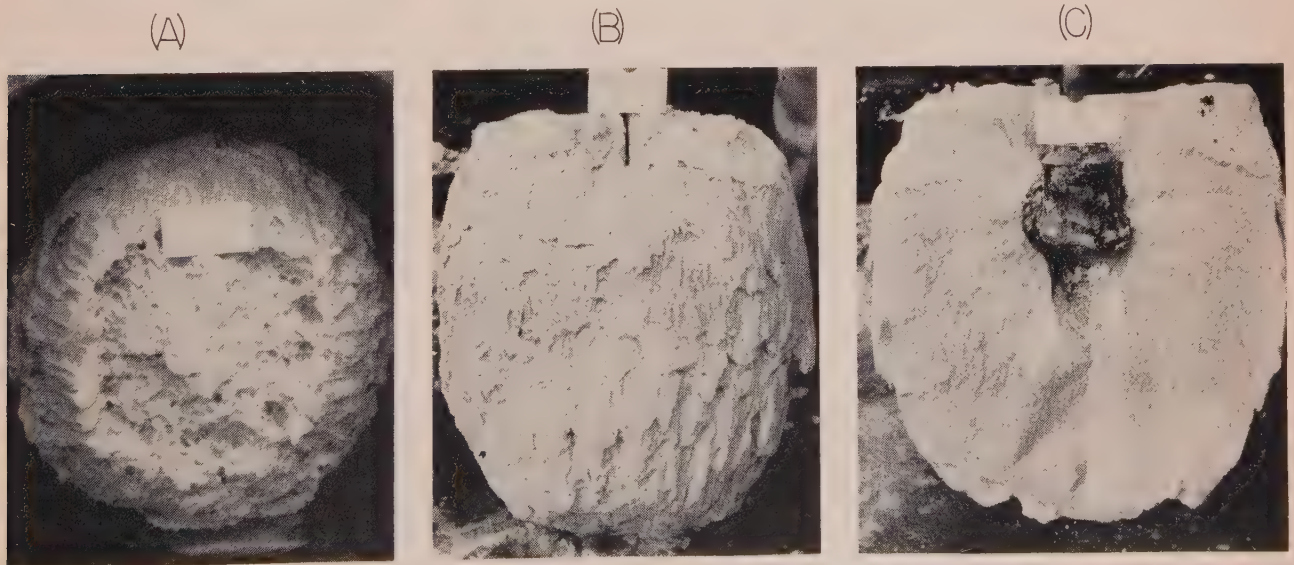

FIG. 5—TYPICAL CONSOLIDATION USING LOW-VISCOSITY CONSOLIDATING MATERIAL, SHOWING—(A) BOTTOM OF CONSOLIDATION IN TEST CHAMBER, LOOKING DIRECTLY TOWARD PERFORATION OUTLET; (B) SIDE VIEW OF CONSOLIDATION REMOVED FROM TEST CHAMBER; AND (C) CONSOLIDATION SPLIT IN HALF TO SHOW CROSS-SECTION VIEW (NOTE CAVITY BELOW PERFORATION, FORMED DURING CONSOLIDATION TREATMENT).

mechanical-washing action of the oil in removing the consolidating material from the sand grains would be more pronounced at this point.

Generally speaking, the retained permeability increased and the compressive strength of the consolidation decreased as viscosity decreased. Increasing the velocity of the displacing oil showed a greater tendency to remove the consolidating material from the sand grains.

A high-viscosity consolidating material caused fracturing of the sand at high injection rates. This was particularly true for low-permeability sands and for those that contain bentonite. Here, the displacing oil frequently broke through and formed channels instead of evenly displacing the consolidating material. This effect is shown in Fig. 6 where a high-viscosity consolidating material was used; several void or unconsolidated areas are easily detected. The net result would be a very poor or inadequate consolidation near the perforation, with the well producing sand either immediately or shortly after treatment. Fig. 6 is quite different from the consolidation obtained in Fig. 5 where a low-viscosity consolidating material was used.

Additional work with a phenolic resin having a viscosity of 6 to 11 cp confirmed the afore-mentioned findings. Penetration of the resin into the sand was excellent, but the resin showed a greater tendency to be removed from the sand by the displacing oil.

The ideal viscosity for the consolidating material appears to be a compromise. A low-viscosity fluid is desirable for obtaining good penetration of the sand, to minimize channeling and for optimum permeability retention. When a low-viscosity consolidating material was used, we found the average permeability retention to be approximately 60 per cent at Station 2 and approximately 35 per cent at Station 1. However, the very low-viscosity materials showed a greater tendency to be completely removed from the sand grains by the displacing oil.

The ideal consolidating material would have a viscosity of approximately 1 cp and would exhibit the ability to stick very tightly to the sand grains during the oil-displacing step. Recent research has indicated that such a condition is being approached—where a 6- to 11-cp resin can be made to adhere quite effectively to the sand grains by first wetting the grains with a specific chemical. However, until this new procedure is proved under a variety of field conditions, it is felt that a viscosity of 6 to 25 cp at the formation treating temperature is optimum for the various consolidating materials.

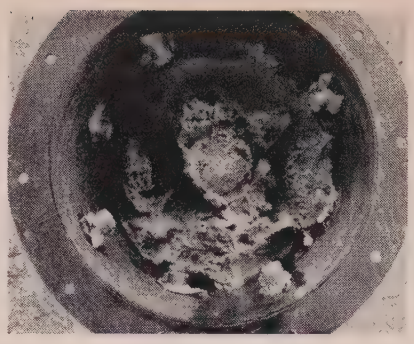

FIG. 6—CONSOLIDATION OBTAINED USING A HIGH-VISCOSITY CONSOLIDATING MATERIAL. COMPARE WITH FIG. 5 FOR SIZE OF CONSOLIDATION, AND NOTE THE MANY AREAS WHERE NO CONSOLIDATION WAS OBTAINED.

INJECTION RATE

The exact injection rate of the treating chemicals, in gallons per perforation per minute, is difficult to determine in a field application. An average rate can be calculated quickly but many feel that all perforations do not accept fluids at the same rate.

In this work, it was quite easy to treat the sand at different injection rates and to observe the results. Table 2 reports such a study. In each trial, we used the fine sand, 1 gal of consolidating material having a viscosity of 20 to 26 cp and 5 gal of displacing oil. The injection rates are expressed in gallons per perforation per minute.

It is interesting to note that the volume of consolidation and the retained permeability of the sand do not materially increase at injection rates above 2.2 gal/perforation/min. However, the strength of the consolidation below the perforation was not as good at the higher injection rates.

There is a notation in Table 2 concerning "cavity area". Fig. 5(C) clearly shows a cavity immediately below the perforation. This is not a washed-out or unconsolidated area; rather, it is a void space formed by the compression or packing of the entire sand body. Every effort was made to pack the sand the same for every trial, but it was not always possible to accomplish this effect. Therefore, some variation in the tightness of the sand pack and in the size of the cavity development is to be expected. However, we believe that the size of the cavity, and the new area so exposed, is somewhat proportional to the injection rate.

Table 3 follows the work reported in Table 2, but the sand contained 2 per cent bentonite. All other conditions were identical.

The volume of the consolidation and the cavity beneath the perforation increased rapidly as the injection rate increased. At the highest injection rate, there was no consolidation within 4 in. of the cavity and none of the consolidation was in contact with any part of the inlet pipe. Under such conditions, the perforation would produce sand in a well. Fig. 7 is a picture of the consolidation obtained with the 5-gal/min injection rate.

In the fine sand, the higher injection rates tended to move the consolidation out farther from the perforation in the same direction as the flow of fluids. The lower injection rates gave patterns that had more consolidation above and around the pipe, thus providing good control of the sand at and around the perforation. These effects were more noticeable for the sands containing 2- and 4-per cent bentonite. Channeling and by-passing were also more evident in the bentonitic sands, particularly at the 4-per cent bentonite concentration at the higher injection rates.

Fig. 8 illustrates a phenomenon that has been noticed several times. In this case, sand leaked out of the chamber during the diesel-oil preflush and reduced the tightness of the sand pack. The phenolic resin (9-cp viscosity) was pumped at the rate of 3.5 gal/min, and the direction of the main flow of fluids can be easily detected. This picture of the consolidation (Fig. 8), after it was split in half, shows a cavity plus a round section of weakly consolidated sand in the left side of the right section.

TABLE 1

Viscosity of Consolidating Material (cp)	Injection Rate (gal/min)	Permeability (md)		Compressive Strength (psi)		Volume of Consolidation (cu ft)
		Station 1	Station 2	Station 1	Station 2	
20-26	0.7	4341	5001	520	340	1.02
60-70	0.5	2256	3003	1080	840	0.85
20-26	3.76	3641	6228	540	400	1.38
33-39	3.75	3629	4999	600	350	1.28
60-70	3.5	4142	5098	490	380	1.26

TABLE 2—FLOW-RATE STUDY USING FINE SAND

Injection Rate (gal/perf./min)	Volume of Consolidation (cu ft)	Station 2 Perm. (md)	Station 2 Compressive Strength (psi)	Cavity Area Below Perforation (sq in.)	Condition of Set Below Perforation
0.7	1.02	4162	520	Nil	Good
2.2	1.34	6516	415	7	Good
6.0	1.37	6878	320	38.5	Poor for 2 in.
7.2	1.40	6531	320	19.7	Poor for 3 in.

TABLE 3—FLOW-RATE STUDY IN SAND CONTAINING 2 PER CENT BENTONITE

Injection Rate (gal/perf./min)	Volume of Consolidation (cu ft)	Station 2 Perm. (md)	Station 2 Compressive Strength (psi)	Cavity Area Below Perforation (sq in.)	Condition of Set Below Perforation
0.52	0.75	949	725	None	Good
1.25	1.28	1428	610	7.1	Fair
5.00	1.64	Not Deter.	*	78.5	Not set for 4 in.

*Not determined, but the set was good in the main body of the consolidation.

TABLE 4—VARYING VOLUME OF DISPLACEMENT OIL

Displ. Oil Vol. (gal)	Stat. 2 Perm. (md)	Consol. Vol. (cu ft)	Consol. Cond. Below Perf.
2.5	4301	0.93	Hard
5	5064	1.37	Good
15	6228	1.38	Not set for 1 in.
25	5464*	1.40	Not set for 4½ in.

*Taken at side of Station 2 because the sand was not consolidated at that point.

We believe that the sand here was fluidized by the treating fluids as they flowed into the chamber from the perforation. The sand remained fluidized during the 5-gal diesel-oil afterflush and then settled into place after injection was stopped. The same effect has been noticed in a tight sand pack at an injection rate of 4.75 gal/min.

It is our belief that a high injection rate has little value, and the previous discussion suggests several drawbacks to the high rate. It is difficult to suggest an optimum injection rate for field applications because all we base it on is an average rate for the number of perforations believed to be accepting fluid.

Since most sanding formations contain some water-swelling clays, we feel that the injection rate should be held as low as possible. For most wells, the range of 0.5 to 1.5 gal/min/perforation is believed to be an optimum rate and has proven to be quite successful in a number of field applications. Such a recommendation creates a problem in treating 1- to 2-ft sections where a pump rate of 2 to 12 gal/min may not be possible under some well conditions. However, conditions have existed where one to three perforations have been treated successfully in newly perforated formations using the 6- to 9-cp consolidating material. A total injection rate approaching 20 gal/min was used. These successes emphasize the importance of using a low-viscosity consolidating material and treating the formation before it has produced sand.

DISPLACEMENT OIL PUMPED AFTER THE CONSOLIDATING MATERIAL

The displacement oil plays a major role in the development of permeability in a resin-treated formation. Table 4 shows the effect of the volume of oil pumped after the consolidating material through one perforation. For all of the trials, 1 gal of consolidating material (20- to 26-cp viscosity) was pumped at an average rate of 5 gal/min into the fine sand.

It is quite obvious that the larger volumes of oil washed all of the consolidating material from the sand grains adjacent to the perforation. Fig. 9, the test where 15 gal of displacing oil was used, illustrates this effect. This actually may be an advantage if a good consolidation is obtained around the casing at the perforation. The unconsolidated sand would be removed with the first fluid production from the formation, leaving a void space behind the casing to provide a larger drainage area. Many successfully consolidated formations have produced relatively small amounts of sand immediately after treatment, and this could be the source of that sand. However, if the well is treated at a high injection rate and/or with a high-viscosity fluid, in addition to a large volume of displacing oil, there is a good possibility that no consolidation will be obtained at or near the perforation and casing.

A 5-gal overflush of oil per perforation appears to be satisfactory. In field applications, we must assume that the flow of fluids into the perforations will not be equal, and there is a good possibility that too much oil will enter some of the perforations. Improved field results have been obtained where the volume of

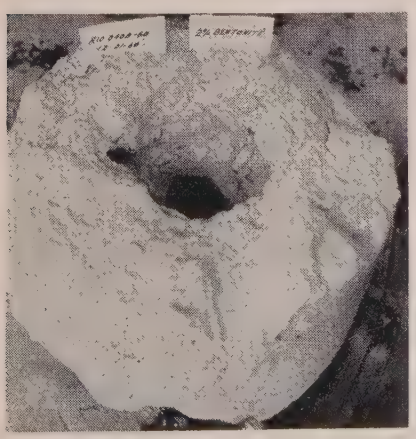

FIG. 7—CONSOLIDATION MADE IN SAND CONTAINING 2 PER CENT BENTONITE AT INJECTION RATE OF 5 GAL/MIN—NO CONSOLIDATION AT OR AROUND PERFORATION.

FIG. 8—SPLIT CONSOLIDATION MADE IN TEST CHAMBER AFTER SOME SAND HAD LEAKED FROM ONE SIDE AT GASKET. NOTE OBLONG BULGING PORTION OF CONSOLIDATION SAND AT RIGHT. THIS SAND BECAME FLUIDIZED DURING FLUID INJECTION AND WAS VASTLY DIFFERENT IN TEXTURE FROM MAIN BODY OF CONSOLIDATION.

displacing oil has been held in the range of 2 to 4 gal/perforation. The results were not as good as desired even then, however, and two-stage treatments have been used sucessfully in an effort to consolidate behind every perforation.

Laboratory research and many large-scale trials indicate that a new method of placement may alleviate some of the problems encountered in the displacement of the consolidating material. A dispersion is made of the consolidating material in oil. As the dispersion is pumped into the formation, alternate slugs of consolidating material and oil enter the flow channels. This provides a continuous placement-and-displacement process that should minimize the effect of mechanically washing consolidating material from the sand grains by the displacing oil.

CAVITY DEVELOPMENT

It has been mentioned previously that the entire sand body can be compressed and deformed as fluids are pumped into the formation. This would be particularly true where the formation has produced sand. Fig. 5(C) shows a definite cavity, and Tables 2 and 3 mention this cavity development. Several tests were performed in an effort to determine how the cavities were formed. This work, along with the information in Tables 2 and 3, shows that the higher pump rates contribute to the formation of cavities. A high-viscosity preflush oil or consolidating material also tends to form the larger cavities.

Fig. 10 shows a consolidation obtained using two perforations. The larger consolidation on the left was obtained in sand containing 2 per cent bentonite, while the one on the right came from the fine sand. One gallon of consolidating material (20- to 26-cp viscosity) was used to make the consolidations, and it was pumped at a total rate of 3.6 gal/min. The ratio of the two cavity areas is approximately 5:1, with the larger cavity being in the bentonitic sand. The volume of consolidation in the bentonitic sand is 76 per cent greater than in the fine sand. The larger cavity in the bentonitic sand provided a greater cross-sectional area for the flow of fluids; thus, more consolidating material entered this sand, in spite of the fact that its permeability was significantly lower. This run was duplicated, with essentially the same results being obtained.

If the volume of consolidating material should be reduced to ½ gal, then the consolidation volume ratios will be reversed. It appears that most of the cavity is formed by the higher-viscosity consolidating material, and ½ gal would not be enough fluid to develop the cavity and treat the sand. Fig. 11 illustrates the effect of treating a formation that has produced a little sand; 10 lb of sand were omitted in the final packing of the test chamber, which then was treated with ½ gal of consolidating material. The fine sand evidently packed faster as it developed the larger cavity. Fig. 8 also illustrates cavity development when the sand is not packed tightly.

The treatment of different-permeability sands using two perforations in the test chamber has been mentioned previously. Fig. 12 illustrates the consolidation patterns obtained in coarse and fine sands. The results were as expected, with the coarse sand on the left of Fig. 12 being the larger consolidation. The consolidation volume ratio of the coarse sand to fine sand is 4.1:1. The large cavity in the coarse sand undoubtedly influenced the flow of consolidating material to form the resulting larger consolidation.

Similar sands were placed on both sides of the chamber in several trials. Where the fine sand was located on each side of the chamber, consolidations of equal volume were obtained. When the sand on each side contained 2 per cent bentonite, the consolidations were different in size. The volume of one consolidation was 2.4 times greater than the other one, and the area of the cavity in the larger consolidation was 2.9 times larger than that in the smaller consolidation.

Thus, cavity development greatly influences the distribution of treating fluids. However, we have not been able to influence the place or perforation where a cavity will form. Once a cavity starts to develop at a perforation, we believe that the increased flow of fluid will cause the cavity to enlarge rather rapidly until that portion of the sand body cannot be compressed further. The greater area developed by the cavity as it grows will also be a factor in how large it will become.

Theoretically, cavity development behind the casing could be exten-

FIG. 9—VOID LEFT BELOW PERFORATION WHEN UNCONSOLIDATED SAND WAS WASHED OUT—15 GAL OF DISPLACING OIL HAD WASHED ALL CONSOLIDATING MATERIAL FROM SAND GRAINS, LEAVING SOME OF THE SAND UNCONSOLIDATED.

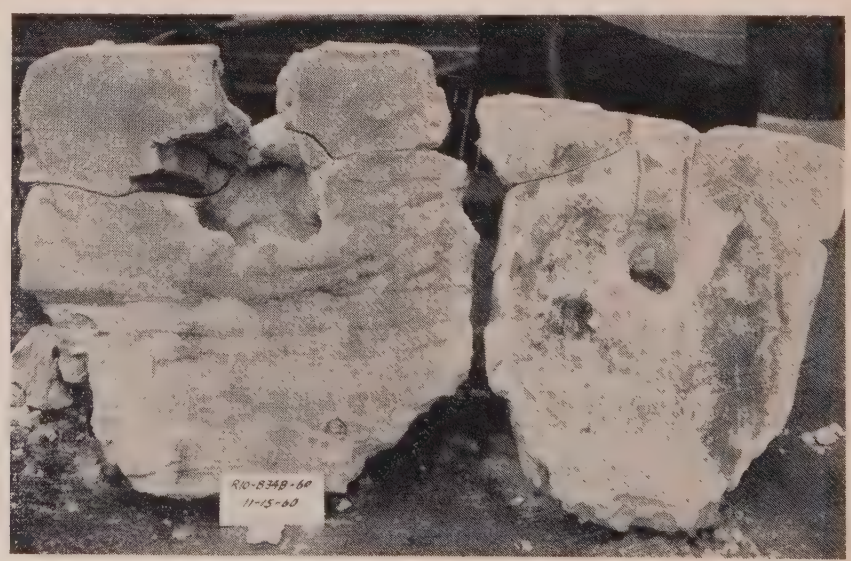

FIG. 10—CONSOLIDATIONS OBTAINED WITH TWO-PERFORATION SYSTEM WITH METAL DIVIDER REMOVED—CLEAN SAND AT RIGHT, AND 2 PER CENT BENTONITIC SAND AT LEFT. LARGER CAVITY ON LEFT INFLUENCED FLUID FLOW AND CAUSED THIS SAND TO HAVE THE LARGER VOLUME OF CONSOLIDATION.

cent as large as the clean fine sand. This ratio varies slightly for the different consolidating materials, but it continues in the same direction.

TWO-STAGE TREATMENTS

Two-stage consolidation treatments have been used extensively in many field applications in an effort to consolidate all parts of the formation. Several two-stage treatments were performed in the large-scale equipment using both the one- and two-perforation systems. Both stages used ½ gal of consolidating material. In every case, we found that the second-stage fluids fractured the consolidation formed by the first-stage treatment.

Fig. 14 shows the cavity below the perforation and several fractures in the upper part of the consolidation. Fig. 15 depicts a more striking result. The general ball-type configuration of this consolidation was formed during the first stage; the protruding belt around the ball, which is perpendicular to the flow of fluids, is the consolidation formed by the second stage. The position of the fracture is quite obvious in this illustration.

Fig. 16 shows the results of a two-stage treatment in fine sand (on left) and in coarse sand (right). Four distinct fractures can be seen to radiate from the cavity in the fine sand. In addition, the outline of the first-stage consolidation can be seen at the extremities of the lower two fractures. Additional consolidated sand at the top of the consolidation was broken off during removal from the test chamber.

Two fractures in the coarse sand produced a small band of consolidated sand near the top of the consolidation. The permeability of all consolidations were determined, particularly adjacent to the cavities. In almost every instance, these permeabilities were essentially the same as those obtained in one-stage treatments. It appears that the consolidation fractured either during the injection of oil between stages or at the start of the second-stage injection of consolidating material.

We have always been somewhat concerned that permeability might be severely reduced as a result of two-stage treatments, but the findings here indicate that this reduction is not so acute as we first had feared. A survey of successful two-stage field jobs has shown that, in many applications, the second-stage entered the formation at a lower pressure than the first stage. We now believe that this pressure difference is due mainly to the first-stage consolidation being fractured.

FRACTURING OF LOOSE SANDS

As mentioned previously, we were able to fracture loose sands with high injection rates, particularly when the viscosity of the fluids was high and the sands were bentonitic. The addition of colloidal material, which acts as a low-fluid-loss additive, to the fluids made it much easier to develop a fracture. A cavity was formed first, and then a fracture occured perpendicular to the flow of fluids—similar to the fracture described in Fig. 15. Observations made in these tests have convinced all observers that it is quite easy to fracture loose sand formations.

SAND IN THE PERFORATIONS

There were several instances where the fine sand became lodged in the perforation proper in the test chamber. This sand, although it contained no clays, limited the flow of fluids into the test chamber to a very small fraction of the normal rate. The chamber was vibrated briefly to cause this sand to settle out of the perforation, which immediately restored fluid flow to the normal injection rate. This flow restriction was not so severe when 40-60 Ottawa sand was present in the perforation, but it was still quite noticeable. In field applications, it is very important that the perforations in the casing and cement be clear of sand. If not, they will not accept an appreciable quantity of consolidating material and the perforations either will be-

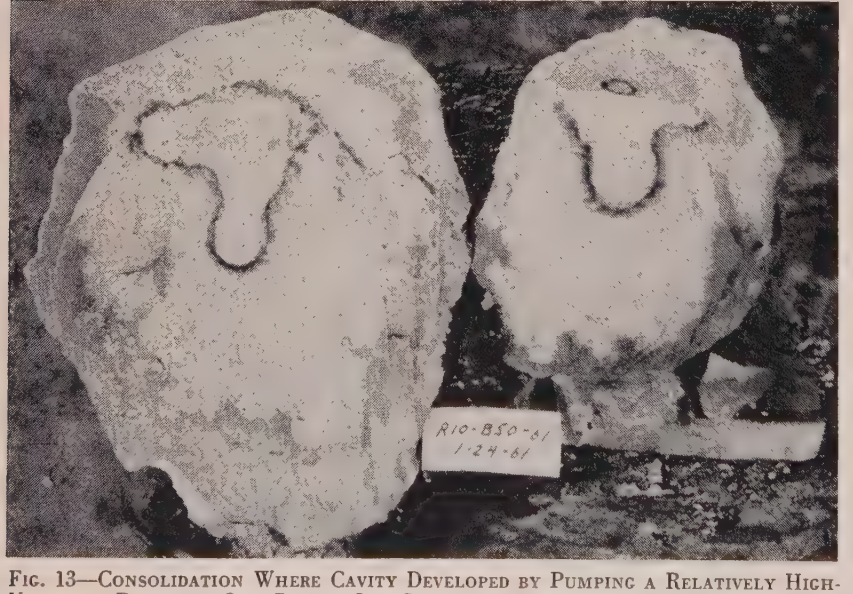

FIG. 13—CONSOLIDATION WHERE CAVITY DEVELOPED BY PUMPING A RELATIVELY HIGH-VISCOSITY PREFLUSH OIL, DIESEL OIL CONTAINING 40-60 OTTAWA SAND AND THEN CONSOLIDATING MATERIAL—CONSOLIDATED 40-60 SAND OUTLINED IN BLACK AND PERFORATION OUTLET SHOWN AS BLACK CIRCLE.

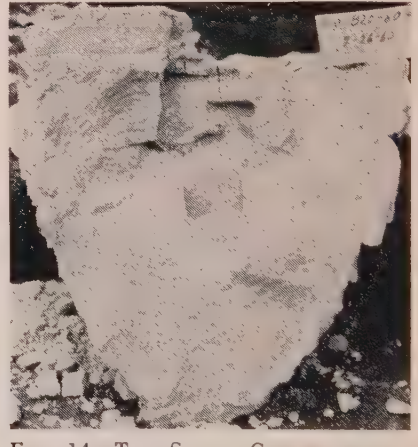

FIG. 14—TWO-STAGE CONSOLIDATION SHOWING FRACTURES CAUSED BY SECOND STAGE.

FIG. 15—TWO-STAGE CONSOLIDATION —SECOND STAGE FORMED BELT AROUND FIRST-STAGE CONSOLIDATION BY DEVELOPING FRACTURE PERPENDICULAR TO FLOW OF FLUIDS.

FIG. 16—TWO-STAGE CONSOLIDATION IN TWO-PERFORATION SYSTEM USING FINE SAND (LEFT) AND COARSE SAND (RIGHT). FOUR FRACTURES RADIATE FROM CAVITY IN FINE SAND TO EXTREMITIES OF FIRST-STAGE CONSOLIDATION. MOST OF SECOND-STAGE TREATMENT ENTERED FINE SAND THROUGH FRACTURES, IN PREFERENCE TO HIGHER-PERMEABILITY COARSE SAND.

come plugged with set consolidating material or they will continue to produce sand. One well was consolidated successfully to produce sand-free oil for more than two years. It suddenly started to produce sand, and at least two discs of set resin ½-in. in diameter and 3/16-in. thick were recovered with the sand.

SUMMARY

Sand consolidation is one of the most difficult chemical treatments to accomplish successfully in the oil-producing industry. The past history of sand consolidation has not been too encouraging, but the success ratio of this method of sand control will be increased if the well owner will more carefully prepare the wells to be treated. We feel that the following suggestions are important to the proper selection, preparation and treatment of a well by sand consolidation.

1. The well preferably should be perforated in a fluid that contains no solids. Perforating should be done from a log to avoid nonproductive sections, particularly shale bodies.

2. Both the wellbore and the perforations must be clean of all solid materials. Although this recommendation is not original, it still is a very important step in any type of sand-control work.

3. The chances of obtaining a successful consolidation are reduced materially when the formation contains more than 4 per cent of water-swelling clays.

4. Do not perforate long sections for sand consolidation. In most instances, 2- to 8-ft segments are preferred.

5. A sand consolidation treatment has the best chance of success in formations that have not produced any sand.

6. Where the formation has produced sand, it should be pressure-packed to a sand-out with a selected pack sand. All of the sand should be reversed from the casing before consolidation is attempted. If the formation is not pressure-packed, the possibility of a successful consolidation is quite low.

7. The consolidating material should have a low viscosity. A viscosity of 6 to 25 cp at the time the fluid enters the formation is preferred. This relatively wide viscosity range is used to cover the variances in different types of consolidating materials.

8. The consolidating material and all related fluids should be pumped at a relatively low rate. An injection rate of 0.5 to 1.5 gal/perforation/min is believed to be optimum and should reduce the possibility of causing fractures to occur.

9. The volume of displacing oil following the consolidating material into the formation should be limited to 2 to 4 gal/perforation.

A survey of our past field work shows that most of the sand consolidation failures occured in wells that did not meet a majority of these conditions. Where most of the conditions have been observed, the success ratio has been decidedly improved. If all the conditions could be followed, we believe that the success ratio of sand consolidation applications would greatly increase.

Complying with all of these suggestions will limit the number of wells that can be treated with a consolidating material for sand control. Ultimately, however, such a limitation will prove advantageous because this method of sand control will be more effective and will not be wasted in wells where it has no chance of succeeding.

ACKNOWLEDGMENT

The authors wish to thank Lloyd Crowell and several members in the Chemical Laboratory and the Mechanical Research and Development sections of Halliburton Co. for their help in conducting these tests.

REFERENCES

1. Tausch, G. H. and Corley, C. B.: "Sand Exclusion in Oil and Gas Wells", Paper presented at Spring Meeting of API in Houston (1958).
2. Desjardins, P. E.: "Thirty Years of Sand Control Experience", Paper presented at Spring Meeting of API in New Orleans (1959).
3. Lott, L. D., Viney, Ralph and Abbott, S. J.: "Survey of Sand Control", Paper preesnted at Spring Meeting of API in Houston (1954).
4. Garten, J. P.: "An Investigation of the Production Characteristics of Wells Completed with Gravel Screen Liners", Paper 683-G presented at California Regional Meeting of SPE in Los Angeles (1956). ★★★

Characteristics of the Delaware Formation

RALPH E. JENKINS
MEMBER AIME

CORE LABORATORIES, INC.
DALLAS, TEX.

ABSTRACT

The Bell Canyon member of the Delaware Mountain group has yielded quite a large number of fields in which completion and production problems have been numerous and complex. Reserves are difficult to estimate due to the problem of evaluating the formation water saturation, and the feasibility of water flooding is questionable.

Extensive laboratory investigations were undertaken to determine if normally measured rock and contained fluids properties could account for many of the peculiar characteristics of the formation. A statistical study of routine core-analysis data was made. Capillary-pressure data were obtained by several techniques. Fresh-water and brine permeabilities were measured and relative permeabilities of oil, water and gas were determined. Some qualitative wettability tests were performed, and the petrography of a few thin sections was studied. The results of this work are presented, with typical or average data shown for each test. The permeability-to-water characteristic of the Delaware was found to be abnormally poor. Correlations of laboratory and field performance data indicate high water saturations in much of the formation. Pore geometry is highly uniform.

INTRODUCTION

The Delaware formation has undergone extensive exploration and development in the past few years. This has resulted in the discovery of quite a number of fields—producing oil for the most part. A large percentage of the productive wells have produced water along with the oil. Often there is no apparent pattern for the percentage of water cut experienced. In several instances vertical displacments of over 200 ft have been established between communicating wells in which the formation appears to be about the same, yet the structurally high wells yield a much higher water cut than the lower wells. Drill-stem tests have contributed little to well completion because they nearly always show small amounts of water (usually mud filtrate), regardless of what is produced later in the life of the well. Other formation evaluation methods have had no more than limited success in indicating ultimate productivity. Consequently, predicting the type of fluid productivity of Delaware wells has been very difficult.

Hydraulic fracture treatments are almost universal, and unstimulated Delaware wells have not exhibited the productivity that normally would be expected of wells with the specific permeabilities encountered. Some operators have indicated that their Delaware wells need frequent restimulation.

The uncertainty of reservoir water saturations reported for the Delaware has made difficult the task of evaluating oil in place in the reservoirs and estimating primary recovery. The unreliability of this data also will cause feasibility studies for water flooding or other secondary-recovery methods to be problematical.

Several opinions have been voiced to explain why the Delaware performs as it does. Chronically poor well completions, dynamic water and tilted water tables, capillary inequilibria, peculiar relative permeability characteristics and oil-wetness are among the suggested reasons. The dual purpose of this paper is (1) to describe the principal rock characteristics, and (2) to present an evaluation of those characteristics so that approaches can be made to explain the irrational behavior of wells completed in the Delaware.

STUDY OF ROUTINE CORE-ANALYSIS DATA

A statistical study of routine core-analysis data has been made to relate fundamental rock properties and characteristics of the formation to well productivity. For the most part, well production data were obtained from operators and augmented by production data from commercial information services. Only data which were available in detail and which were considered to be accurate were used. The core data used were obtained on samples from the perforated or open interval only and, thus, may not always represent the total productive interval in a well.

All the core-analysis data included in this study are from the Bell Canyon member of the Delaware and were obtained by "plug-type" techniques, as opposed to whole-core or full-diameter techniques. Porosity values were obtained by the summation-of-fluids technique, permeability values are air permeabilities corrected for slippage to an equivalent liquid permeability, and the oil and water contents were determined by means of a high-temperature downdraft retort. All the procedures used are discussed at length in Ref. 1.

The core-analysis data were sorted

Original manuscript received in Society of Petroleum Engineers office March 22, 1961. Revised manuscript received Sept. 15, 1961. Paper presented at Third Biennial Permian Basin Oil Recovery Conference of SPE, May 4-5, 1961, in Midland, Tex.

according to the percentage of water cut in the total liquid production from each specific well. The assignment of symbols used for each water-cut group is shown in Table 1. The curves designated by "G" represent formation from wells classified as gas wells. The representation of data is outlined in Table 2. The water-cut value used for a well was established after an initial well-stabilization period, usually two to three months.

The data were processed with high-speed punched-card equipment. Virtually all combinations of the simple factors available for study and several mathematical combinations were plotted. Only a few of the plots revealed intelligible patterns. As expected, the correlations of water cut with subsea depth were unusable, even on an individual field basis.

A correlation of permeability and porosity is shown in Fig. 1. The average deviation for all the water-cut-group curves was found to be about ± 1.2 porosity per cent.

All data from the perforated intervals of wells included in this study were used, regardless of the permeability. However, of the 26 oil-producing wells studied with average permeability values of 5 md or less, only three wells were continued on production for as long as six months. Thus, 5 md was taken to be the minimum productive permeability for oil wells in this study. In general, the permeability of gas-productive intervals was found to be lower than that for oil-productive intervals. No attempt has been made to establish a lower limit of permeability for a gas-productive formation.

The permeability-porosity correlation is rather good. The average data would lead to the conclusion that a porosity cut-off point for the Delaware would be on the order of 20 per cent, an abnormally high value. When the average deviation of the individual points from the average lines is considered, the cut-off point would be below 19 per cent; about 5 per cent of the porosity values near the 5-md permeability value were 16 per cent or less. Thus, 16-per cent porosity is considered to be a reasonable minimum porosity for an economically oil-productive formation.

The square root of permeability (in millidarcies) times porosity (per cent) is shown in Fig. 2 as a function of total water saturation. No physical significance is assigned to the factor $\sqrt{K\phi}$ in this study. It was found to be a convenient factor that allowed a relatively logical resolution of the water-cut parameter. Line G and Lines O through W are averages for each respective group. The shaded areas related to Lines O and W represent the area for each group into which 95 per cent of its samples fell. Similar bands relate to the other average lines, P through S, but were omitted for the sake of clarity.

The separation of the bands related to Groups O and W in Fig. 2 should be used with caution because the bands related to the intermediate water cuts badly overlap the two bands shown. Where the $\sqrt{K\phi} = 9$ value is used as the lower limit for productive characteristics, a core-analysis total-water-saturation value of 52 per cent of pore space can be used as the limit of water saturation for an economically oil-productive formation. Formations with core-analysis water saturations less than 45 per cent of pore space can safely be interpreted as having water cuts which are low enough for economically feasible production.

The relationship of residual oil saturation to permeability and percentage of water cut is shown in Fig. 3. The bands related to Groups O and W again represent 95 per cent of the samples in each group. A definite criterion for interpreting the fluid productivity of a Delaware core is seen in Fig. 3. The band representing the data for Group O above 5-md permeability shows a minimum residual-oil value of 12 per cent. The average lines representing the intermediate water-cut groups lie very close to the Group O line, and their associated bands almost exactly coincide with the O band. It is obvious, then, that core samples with residual oil saturations less than 12 per cent of pore space nearly always represent formations which will have water cuts too high to be economically productive.

The band related to Group W in Fig. 3 is asymmetric to the average line through it. This is caused by the high density of points to the left of the average line and near the line on the right side. The density of the points diminishes as the residual-oil value increases. The deep invasion of the W band into the O-band area, when 95 per cent of the data are considered, is one of the reasons that the performance of Delaware wells is difficult to predict from core analysis alone. The left side of the band has a very sharp cut-off, a condition which is considered normal. This condition is undoubtedly influenced by the general practice

TABLE 1—WATER-CUT IDENTIFICATION AND SAMPLE DISTRIBUTION

Group	Per Cent Water Cut	No. Samples
O	0-5	596
P	5-25	885
Q	25-50	683
R	50-75	491
S	75-90	487
W	Over 90	395
G = Gas Productive		298

TABLE 2—SAMPLE DISTRIBUTION

Area (County)	No. Samples	Per Cent of Samples
Lea	376	9.8
Eddy	294	7.7
Culberson	346	9.0
Reeves	1,092	28.5
Loving	1,206	31.4
Ward	521	13.6

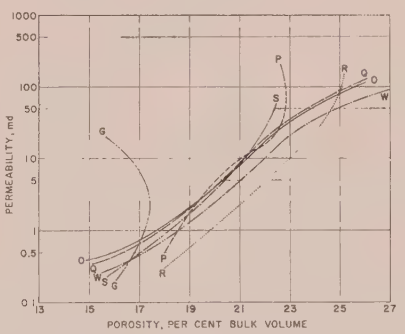

FIG. 1—POROSITY-PERMEABILITY CORRELATION.

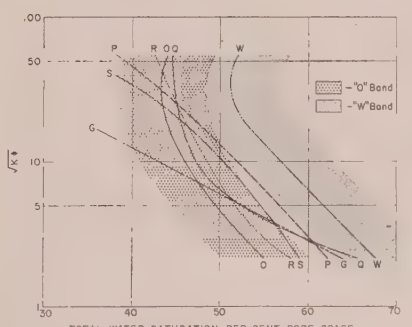

FIG. 2—CORRELATION OF $\sqrt{K\phi}$ VS TOTAL WATER SATURATION.

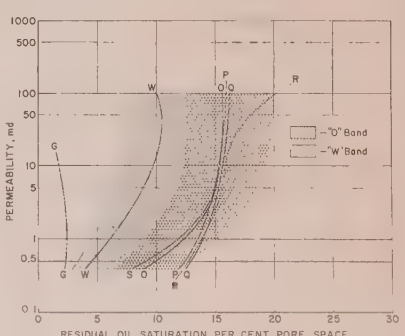

FIG. 3—RESIDUAL OIL-PERMEABILITY CORRELATION.

of not analyzing core samples which appear, from visual and fluoroscopic examination, to be unproductive or water-productive. If the W band were altered to include only the best 75 per cent of the data, the left boundary of the band would remain virtually unaltered; whereas, when only data above the 5-md permeability limit are considered, the right boundary would move to the left to a residual-oil-saturation value of approximately 14 per cent.

The residual oil saturations in the gas-productive formation are considered normal for gas-productive sands. Since they are distinctly lower than saturations associated with a formation that exhibits high water cut, distinguishing between the two conditions seldom is difficult.

ADDITIONAL CORE TESTING

PETROGRAPHIC EXAMINATIONS

The Bell Canyon member of the Delaware is strongly characterized by the exceptionally well-sorted, fine-grained quartz contained throughout virtually the entire basin. The feldspar content is higher than that normally encountered in sandstone, with the crystals being remarkably preserved. Most of the samples analyzed show no more than slight disintegration of the feldspars. The cementing material is calcareous, and the porosity in the productive intervals appears to be controlled principally by the amount of cementing material present.

Further, the Bell Canyon typically contains fine laminations of sands and shales. However, in the productive intervals (such as those shown in Fig. 4, from 4,945 to 4,949 ft and from 4,951 to 4,957 ft), the formation usually is virtually free of shale material and generally contains only trace amounts of clay-sized minerals. Maximum clay-sized mineral contents have been observed to be 5 per cent. It should be noted that clay-sized minerals are not necessarily true clays. The true clays were not identified in this study, but they are believed to be principally of the illite types since the formation is of Permian age.[2] The brine and fresh-water permeability characteristics (to be discussed later) tend to confirm this premise because only a small amount of additional permeability damage occurred when the formation was contacted with fresh water rather than with brine.

The formation is quite isotropic in the productive intervals, as evidenced by the similarity between horizontal and vertical permeabilities. The values reported in Fig. 4 for each sample were measured on the same cube-shaped sample. The permeabilities shown in Fig. 4 have been corrected for slippage to an equivalent liquid permeability.

Petrographic data obtained from 10 of the thin sections studied are presented in Table 3. No calcium sulfate was observed in any of the samples tested, although small quantities of it were expected. Muscovite, biotite, zircon and a few other minerals were observed in minor quantities.

[2]References given at end of paper.

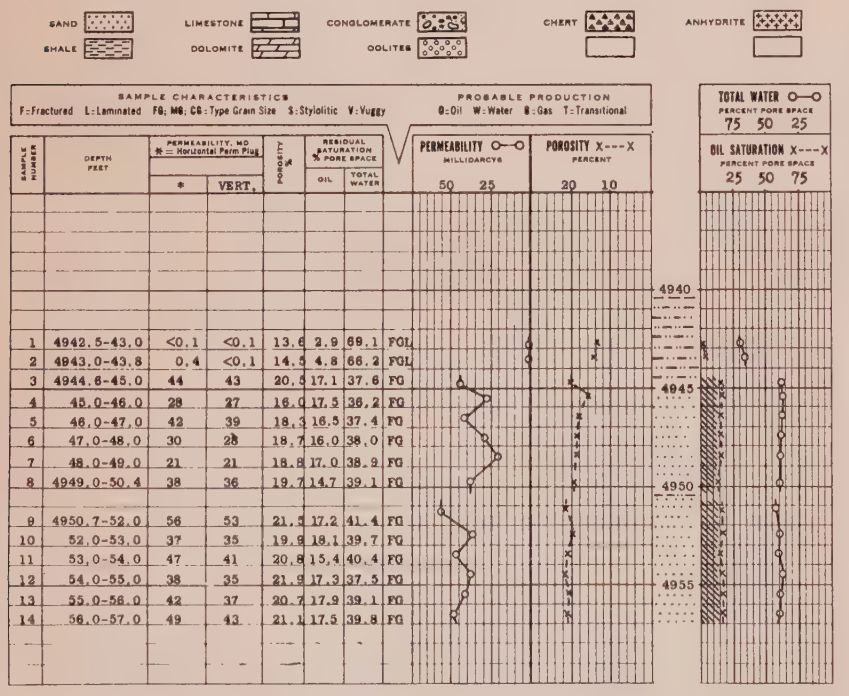

FIG. 4—COREGRAPH OF THE DELAWARE SAND SECTION.

QUALITATIVE WETTABILITY TESTS

Reports have been made that the Delaware formation is oil-wet, in spite of the fact that visual inspection of the core material and routine core-analysis data showed no evidence of oil-wetness and in spite of the fact that the oil produced from the Delaware is not at all typical of oil produced from reservoirs reputed to be oil-wet. To evaluate the wetting characteristics, 25 fresh samples representing all areas of the basin were subjected to imbibition tests. Thirteen samples were evacuated under refined oil and saturated with the oil; then they were place in imbibition cells filled with water. The samples imbibed water so rapidly, displacing the oil, that the imbibition rate could not be established. The remaining 12 fresh samples were evacuated under water and, thus, saturated with water. When placed in imbibition cells filled with refined oil, not one sample imbibed oil.

Although wettability characteristics often are difficult to define and evaluate, the definite results of these imbibition tests are taken as proof that the Delaware is water-wet.

CAPILLARY PRESSURE

Capillary-pressure tests were performed on 150 samples from various locations in the Delaware basin. Tests were made with the porous-plate (or restored-state),[3] the centrifuge[4] and the mercury-injection[5] methods. Complete capillary-pressure curves were defined on 20 samples by the restored-state method and on 61 samples by the mercury-injection method. Single end-point tests were performed on 69 samples with the centrifuge method. All the tests were performed on extracted samples with water as the wetting phase. Soltrol was used as the nonwetting phase in the centrifuge tests.

Typical complete curves by the restored-state method are shown in Fig. 5 and typical curves by the mercury-injection method are shown in Fig. 6. Capillary-pressure data confirm the uniform sorting and the uniform pore-size characteristic observed in the thin-section studies. The curves are remarkably flat for such fine-grained material, and the bends of the curves are unusually

TABLE 3—PETROGRAPHIC DATA, DELAWARE BASIN

Sample	Porosity Range (% Bulk Vol.)	Median Grain Diam. (mm)	Sorting Coef.	Composition (per cent) Quartz	Felds.	Calcite Cement	Clay-Size Minerals
			East Central				
A	10-15	.06	1.28	50	30	15	Minor
B	10-15	.06	1.20	55	25	15	Minor
C	15-20	.07	1.30	55	25	10	5
D	15-20	.07	1.32	60	30	10	5
E	20-25	.06	1.34	60	30	5	Minor
			North Central				
F	20-25	.06	1.18	65	20	10	5
G	20-25	.06	1.34	70	15	5	5
H	25	.06	1.28	60	20	10	5
I	>25	.06	1.34	65	20	10	Minor
J	>25	.07	1.32	65	20	5	5

narrow. The displacement pressures for 21 of the samples are shown plotted vs permeability in Fig. 7.[6] The restored-state data were used directly, but the mercury-injection pressure values were reduced by a factor of five to obtain pressure values equivalent to an air-brine system.[5] The radius of the largest pores for each sample was calculated from the pressure displacement equation.

$$P_D = \frac{2 \cos \theta}{R} \quad . \quad . \quad . \quad . \quad (1)$$

The water-solid contact angle is assumed to be zero, and the surface tension of water is taken to be 70 dynes/cm. The diameter of the largest pores for each sample so calculated varied from about .004 mm at 1-md permeability to about .02 mm at 100 md. This is consistent with the observations made in the thin-section studies. It would also be the order of magnitude expected from rhombohedral packing of the size grains observed in the samples.

The end-point wetting-phase saturations obtained by all three methods are shown in Fig. 8. The final pressures developed in the mercury-injection and centrifuge systems have been converted to equivalent pressures in an air-brine system[4,5] and are shown in Fig. 8. The final pressure used in the air-brine system is also shown.

In view of the 175-psi pressure difference involved, the mercury-injection and centrifuge data above 10-md permeability are in reasonable agreement. As expected, the restored-state end-point saturations are much higher than the others, due to the relatively low capillary pressures at which they were established. These data show that immobile water saturations in the Delaware can vary generally from 15 to 45 per cent of pore space, depending upon permeability and position.

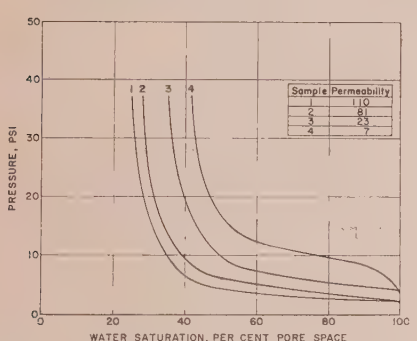

FIG. 5—CAPILLARY PRESSURE CURVES, RESTORED-STATE METHOD.

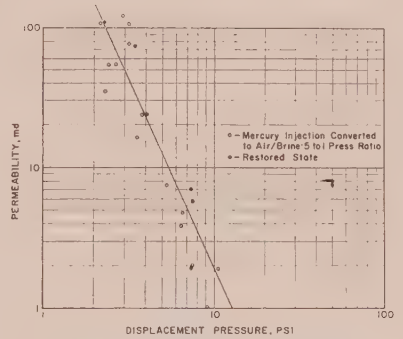
PERMEABILITY, md
DISPLACEMENT PRESSURE, PSI
o- Mercury Injection Converted to Air/Brine 5 to 1 Press Ratio
o- Restored State

FIG. 7—DISPLACEMENT PRESSURE VS PERMEABILITY.

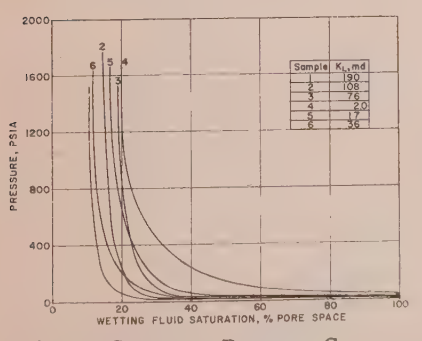

FIG. 6—CAPILLARY PRESSURE CURVES, MERCURY-INJECTION METHOD.

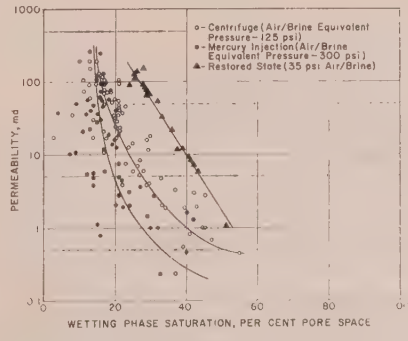
PERMEABILITY, md
WETTING PHASE SATURATION, PER CENT PORE SPACE
o- Centrifuge (Air/Brine Equivalent Pressure-125 psi)
o- Mercury Injection (Air/Brine Equivalent Pressure-300 psi)
▲- Restored State (35 psi Air/Brine)

FIG. 8—WETTING-PHASE SATURATION VS PERMEABILITY, THREE METHODS.

RELATIVE PERMEABILITY

Gas-Oil

Gas-oil relative permeability tests were performed on several samples from the east-central and north-central portions of the basin, using the unsteady-state method.[7] The tests were performed on extracted samples. To restore the samples, they were saturated with a refined oil, and then a portion of the oil was displaced with gas at relatively high rates. The gas-oil relative permeability characteristics were then calculated, by the Welge method,[8] as a function of the saturations. The curves for three of the samples, varying in permeability from 5.7 to 110 md, are shown in Fig. 9. The gas-oil relative permeabilities are considered to be normal for a sandstone and do not indicate abnormal pore geometry.

Oil-Water

The oil-water relative permeability tests also were performed on several extracted samples using an unsteady-state method. The prepared samples were saturated with brine and then desaturated to "irreducible" water saturations with conventional restored-state techniques. The voided pores were resaturated with a refined oil of 17-cp viscosity, except for one sample in which 60-cp oil was used. Oil permeabilities were measured at the irreducible brine saturations, and then the oil was displaced with brine. Brine permeabilities at residual oil saturations were noted particularly. Relative permeability characteristics as a function of saturations were calculated by the Welge method.[8] The curves for six samples, varying from 6.6- to 125-md permeability, are shown in Figs. 10

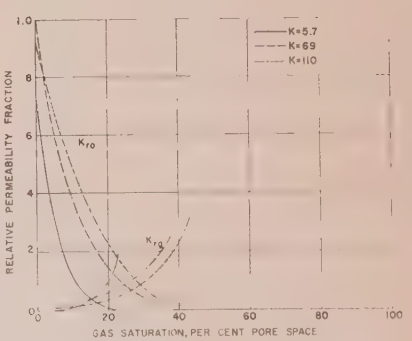

FIG. 9—GAS-OIL RELATIVE PERMEABILITY.

through 14. Note the variation of the vertical scale in these figures.

The oil-water relative permeability characteristics of these Delaware samples are quite peculiar. Only one sample tested, shown in Fig. 12, exhibits characteristics that are near normal. In all other samples tested, the permeability—with two phases flowing or with just water flowing—is unusually low. In many instances the permeability is only 10 per cent of the values normally encountered. This condition exists even though the permeability to oil with irreducible water present is normal and is close in value to the slippage-corrected air permeability. The oil-water relative permeability characteristics observed in the laboratory appear to be consistent with field production experience in that the Delaware wells are not so productive as they should be in view of the specific permeability and reservoir energy characteristics of the formation.

Of all the core-analysis tests performed, the oil-water relative permeability tests were the only ones that were difficult to accomplish. The flood fronts built up in the samples were quite flat and the end of a test was virtually at hand when water breakthrough occurred. It was difficult to measure a desirable number of oil and water flow rates while both phases were flowing. One sample was analyzed using 60-cp oil (Fig. 14) to optimize the experiment, but the results were about the same as when 17-cp oil was used. This condition is caused by the favorable uniform-pore-size characteristic of the formation.

OTHER PERMEABILITY TESTS

The sensitivity of Delaware samples to fresh water was examined by testing the permeability of samples to both a synthetic brine and fresh water. The brine used for these tests had 40,000 ppm NaCl and 10,000 ppm $CaCl_2$, the principal components of natural Delaware waters. The samples were saturated with brine and the permeability to the brine was measured. The brine permeability value for each sample, as initially measured, was only 21 to 25 per cent of the equivalent slippage-corrected air permeability. The brine permeability declined rather rapidly for each sample as additional pore volumes of brine were put through the sample. After the samples were allowed to remain static for several hours, the initial brine permeabilities were almost completely recovered. The samples tested recovered much of their initial permeability after being static for only two hours. This is shown in Fig. 15.

Subsequent to the brine permeability tests, the samples were leached of brine and were saturated with fresh water. Some of the samples were damaged during the handling processes and, hence, were lost for testing purposes. The permeabilities to water of the remaining samples were measured. The fresh-water permeabilities were somewhat lower than the brine permeabilities. The ratio of liquid permeabilities of each sample to its slippage-corrected air permeability is plotted against the slippage-corrected air permeability in Fig. 16. Also shown are the ratios of specific brine permeabilities, of permeabilities to brine at residual oil saturation, and of permeabilities to oil at irreducible water saturation to their respective slippage-corrected air permeabilities.

When fresh-water permeabilities are lower than brine permeabilities, the conclusion usually drawn is that the formation has swelling clays present. In this case, however, the brine permeabilities are so low that the additional loss in permeability to fresh water is not particularly significant. If the brine itself were to cause the formation clays to swell, the permeabilities to oil which were measured with irreducible water (brine) present would be much lower than they are; the 25 to 50 per cent pore brine saturations present in these tests certainly represent enough water to have caused considerable clay swelling. It is believed that some mechanism other than clay swelling must be found to explain this abnormally low permeability to a water phase found in the Delaware formation.

One possible explanation of the low water permeabilities is that there are mobile solid fines which are water-wet and which stay in the water phase. When the water phase is flowing, these fines can flow into the necks of pores where they can block part of the permeability. On the other hand, when the water phase is immobile and only oil is flowing, the fines which remain in the water phase do not move and,

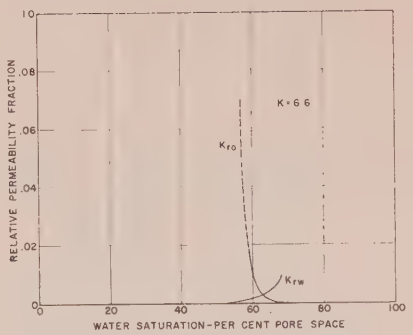

FIG. 10—WATER-OIL RELATIVE PERMEABILITY.

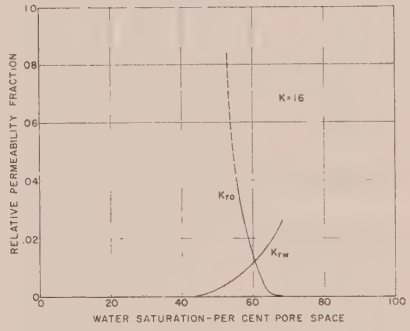

FIG. 11—WATER-OIL RELATIVE PERMEABILITY.

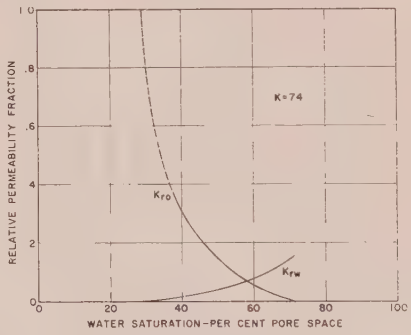

FIG. 12—WATER-OIL RELATIVE PERMEABILITY.

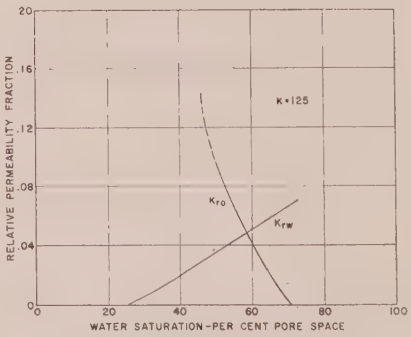

FIG. 13—WATER-OIL RELATIVE PERMEABILITY.

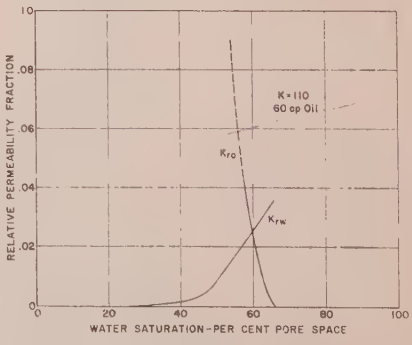

FIG. 14—WATER-OIL RELATIVE PERMEABILITY.

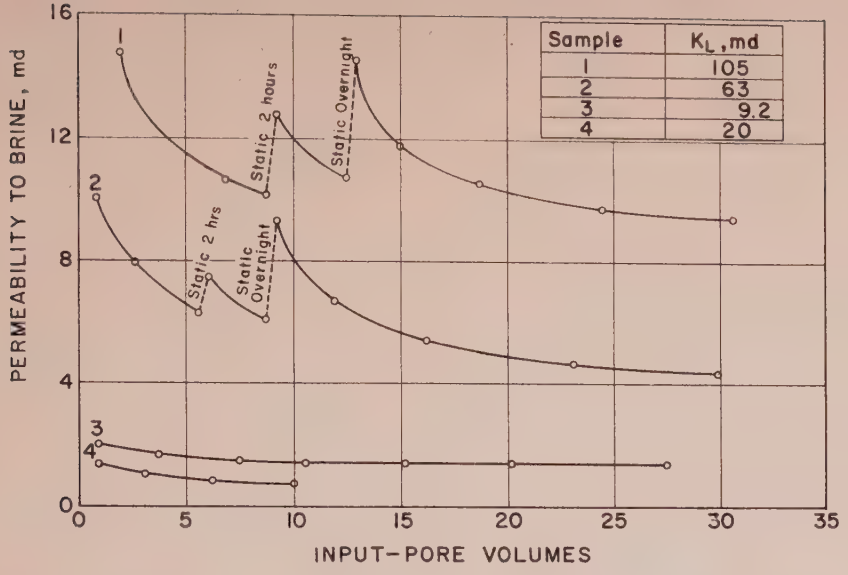

FIG. 15—PERMEABILITY TO BRINE AS A FUNCTION OF PORE VOLUME THROUGHPUT.

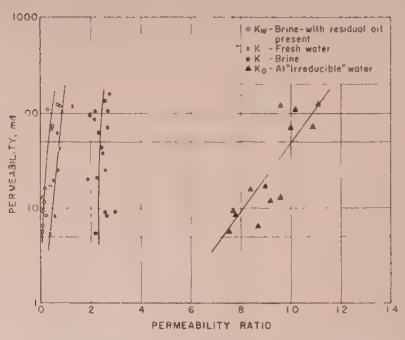

FIG. 16—RATIO OF PERMEABILITY TO LIQUID VS PERMEABILITY TO AIR, SLIPPAGE CORRECTED.

hence, cannot block the necks of the pores to reduce the permeability.

Such a mechanism has been examined by Bertness[9] and by Jones and Neil.[10] Their findings show that the mobile fines or clay-sized particle-movement concept is very plausible for explaining permeability plugging. They show that permeability damage is nearly always restricted to permeability to the wetting phase and that the permeability is recoverable. The Jones and Neil work was performed on samples which did not exhibit dispersion of the mobile solid fines in brine. Bertness indicates experience with sands which did exhibit dispersion of the fines in both brine and fresh water. The latter case appears to describe the Delaware water-phase permeability characteristics.

CONSIDERATIONS OF LABORATORY DATA AND FIELD PERFORMANCES

PRODUCTIVE CAPACITY

A detailed study of the performance of Delaware wells is beyond the scope of this paper. Statistical correlations of theoretical and actual productive indices, and their relationships to water cut, have not been attempted. Such a study should be of great interest. Several operators, when questioned about the performance of their Delaware wells, have indicated that: (1) the productive indices for wells with very low or no water cut are much better than those for wells with intermediate or high water cut; and (2) the higher water-cut wells decline more rapidly than low or no water-cut wells and, thus, must be re-stimulated relatively often to be kept economically productive. Shutting-in a well for a few weeks has restored productivity in at least one case. This field performance information is compatible with the laboratory permeability data. It is believed that the productivity peculiarities of the Delaware are definitely associated with the low water-phase permeabilities measured in the laboratory.

Pressure declines in Delaware-formation oil reservoirs indicate that solution-gas drive accounts for nearly all of the reservoirs' energy. There appears to be only a small amount of evidence of water movement into the reservoirs, and the operators questioned have stated that the evidence is inconclusive. Lack of definite evidence of a natural water drive in a formation so uniformly deposited as the Delaware, and with its fairly good permeability, is somewhat unusual. Low permeability to the water phase probably is one of the reasons for this.

WATER SATURATIONS

Establishing water saturations in the Delaware is perhaps the most difficult task related to analyzing Delaware production, and it is a problem for which there is no easy solution.

If the formation water is immobile in the productive zones, the water saturations can be expected to be between 20 and 45 per cent of pore space. This would make the oil-in-place reserve estimates very favorable. Many contend that this is the case even though water may be produced. Poor well completions and production of water from sources outside the completed intervals are cited as explanations—explanations which we reject here. Perhaps it is possible, but certainly improbable, that these reasons could account for the fact that so many completions and recompletions have failed. A more plausible explanation would be that variations in well and lease equipment and in completion design have combined with irregular production schedules to influence the erratic water-cut patterns experienced in many fields.

On the other hand, if there is mobile water in the formation, it appears from the relative permeability data that the formation's water saturation will nearly always be in excess of 40 per cent of pore space—and often in excess of 60 per cent of pore space. The large percentage of wells which are producing water to some degree is strong evidence that mobile water is present in much of the formation.

FEASIBILITY OF WATER FLOODING

The feasibility of water flooding Delaware formation reservoirs is another problem being considered by many operators at this time. The presence of water production in most fields is causing concern—and it should. This does not mean that it will be economically unfeasible to water flood Delaware reservoirs but, rather, that the engineering work will have to be done carefully and thoroughly. For example, extensive water flooding has been carried out in the Bartlesville formation, which has been notable for its water-cut oil production.

The economic feasibility of water flooding any particular Delaware reservoir obviously would have to be based on consideration of numerous factors peculiar to the property. However, it is possible to generalize somewhat. The pore geometry is very favorable for flooding, and the

residual oil after flooding should not be high. On the other hand, injectivity may be a problem. Also, the high water saturations could severely limit the amount of recoverable oil and will require that more water be injected per barrel of oil recovered.

CONCLUSIONS

1. The productive Delaware formation is a highly uniform sand with very fine grains and pores.

2. A formation with permeability less than 5 md is considered to be unproductive.

3. Core-analysis residual oil saturations should be greater than 12 per cent of pore space for the water cut to be within economic limits. When core-analysis total water saturations are below 45 per cent of pore space, the water cut should be within economic limits.

4. The permeability-to-water characteristics are abnormally poor. In turn, this influences the permeability to oil while water is mobile. The permeability to oil when water is immobile is normal. The gas-oil relative permeability characteristics are normal.

5. Mobile fines in the water phase may account for the low permeability to the water phase.

6. The large percentage of wells producing some degree of water-cut oil strongly indicates that much of the formation has high water saturations.

7. Pore geometry is favorable for water flooding. Low permeability to water may cause injectivity problems. High water saturations will influence the efficiency and economics of a flood.

REFERENCES

1. "API Recommended Practice for Core Analysis Procedure", *RP-40*, API (Aug., 1960).
2. Grim, Ralph E.: *Clay Mineralogy*, McGraw-Hill Book Co., Inc. (1953) 356.
3. Rose, W. and Bruce, W. A.: "Evaluation of Capillary Character in Petroleum Reservoir Rock", *Trans.*, AIME (1949) **186,** 127.
4. Slobod, R. L., Chambers, A. and Prehn, W. L.: "Use of Centrifuge for Determining Connate Water, Residual Oil, and Capillary Pressure Curves of Small Core Samples", *Trans.*, AIME (1951) **192,** 127.
5. Purcell, W. R.: "Capillary Pressure —Their Measurement Using Mercury and the Calculation of Permeability Therefrom", *Trans.*, AIME (1949) **186,** 39.
6. Clark, J. R.: Unpublished work, TXL Oil Corp.
7. Owens, W. W., Parrish, D. R. and Lamoreaux, W. E.: "An Evaluation of a Gas Drive Method for Determining Relative Permeability Relationships", *Trans.*, AIME (1956) **207,** 275.
8. Welge, H. J.: "A Simplified Method for Computing Oil Recovery by Gas or Water Drive", *Trans.*, AIME (1952) **195,** 91.
9. Bertness, T. A.: "Observations of Water Damage to Oil Productivity", *Drill. and Prod. Prac.*, API (1953) 287.
10. Jones, F. O. and Neil, J. D.: "The Effect of Clay Blocking and Low Permeability on Formation Testing", Paper 1515-G presented at 35th Annual SPE Fall Meeting in Denver (Oct. 2-5, 1960). ★★★

PART II

PETROLEUM TRANSACTIONS

Papers Reprinted from

SOCIETY OF PETROLEUM ENGINEERS JOURNAL

Experiments on Mixing During Miscible Displacement in Porous Media

WILLIAM E. BRIGHAM
JUNIOR MEMBER AIME
PHILIP W. REED
JOHN N. DEW
MEMBERS AIME

CONTINENTAL OIL CO.
PONCA CITY, OKLA.

ABSTRACT

The paper describes experiments on miscible displacement in various porous media and the results of these experiments. Both glass bead packs and natural cores were used. Bead diameters varied from 0.044 to 0.47 mm, and pack lengths varied from 83 to 678 cm. Natural cores used were Berea and Torpedo sandstone.

By taking samples as small as 0.5 cc and using refractive index for analysis, the data on breakthrough curves could be plotted to within ±0.5 per cent. To plot the data correctly on error function paper, a parameter $(V_P - V)/\sqrt{V}$ was used which allowed for the predicted growth of the front as it moved past the observer.

The change in the amount of mixing (length of mixed zone) was studied by varying velocity, length of travel, bead size, viscosity ratio and pack diameter. When the displaced material was less viscous than the displacing material (favorable viscosity ratio), these changes were adequately predicted by theory. When natural cores were used, rather than glass beads, the amount of mixing was greatly increased — also qualitatively predicted by theory.

In experiments with favorable viscosity ratios in which the ratio was varied from 0.175 to 0.998, it was found that the rate of mixing was changed by a factor of 5.7. Thus, the rate of mixing is strongly affected by viscosity ratio, even when the theoretical error function relationship for mixing is valid.

Experiments using fluids with viscosity ratios near 1.0 showed that the instability effects of even a slightly unfavorable viscosity ratio (1.002) caused disproportionately more elongated breakthrough curves than found with a favorable viscosity ratio (.998). When the viscosity ratio was as high as 5.71 these instability effects were much more pronounced, as evidenced by the shape of the breakthrough curve. The displacements at viscosity ratios above 1.0 no longer followed the theoretical error function curve.

It was found that at reservoir rates in natural reservoir materials the rate of mixing (as measured by the dispersion coefficient K) was considerably higher than in glass bead packs. The higher mixing rate is caused by the inhomogeneity of reservoir rock as compared to glass beads. The amount of inhomogeneity is expressed in terms of a mixing coefficient a.

Data on length of mixed zone vs velocity showed that there exists a velocity at which the zone length is a minimum. At this velocity, diffusional mixing contributes only a small fraction of the total mixing.

INTRODUCTION

Data have been taken on the amount of mixing between two miscible fluids during the displacement of one fluid by another using various systems of porous media and various fluids. The porous media were packs of relatively uniform spherical glass beads (which form an ideal medium for flow studies) and consolidated sandstone cores. The effects of displacing rate, bead size, length of travel, diameter of bead pack and viscosity ratio were investigated.

EQUIPMENT AND EXPERIMENTAL PROCEDURE

The glass beads were packed in Lucite tubes which had an inside diameter of 3.19 cm and a wall thickness of 0.64 cm, except for those packs used to study diameter effects. Porous stainless steel discs were set in the ends of the tube to contain the beads. Minnesota Mining and Manufacturing Co. "Superbrite" beads were used. The consolidated cores were mounted in Lucite tubes, which had been heated to the softening point and bonded to the cores using external pressure. Data on the bead packs and cores are given in Table 1. The prefix numbers on the bead packs (107, 113 and 117) are the Minnesota Mining and Manufacturing code numbers for the particular bead size used.

Fluid movement at any desired rate was obtained by a Zenith gear-type pump driven through a variable

Original manuscript received in Society of Petroleum Engineers Office Nov. 30, 1959. Revised manuscript received Oct. 13, 1960. Paper presented at AIChE-SPE Joint Symposium, Dec. 6-9, 1959, in San Francisco.

speed transmission. The bead packs (or cores) were mounted vertically with the displacing oil injected at the bottom. Oils of matched density were used. Oil compositions are given in Table 1. The diffusion coefficient of these fluids was found experimentally to be 3.2×10^{-6} cm^2/sec. The proportion of each oil in the effluent was determined from refractive index (R.I.) measurements since one oil was mainly Soltrol (an isoparaffinic oil with a low R.I.) and the other was mainly commercial kerosene with a high R.I. For convenience in identification and visual observation of the fluid displacement, one of the pair of oils was dyed red with a dye which did not change the refractive index.

In preparation for a run, a pack was saturated with oil to be displaced. The oil-saturated pack was inverted, the header filled with displacing oil and the tubing carrying displacing oil was connected. The pack was re-inverted so that the inlet was at the bottom, the outlet header was emptied and the run started immediately. In this way, an exact material balance could be made on the effluent. The effluent was caught in a graduate until the approximate arrival of the mixed zone. Incremental samples of suitable size were then taken as the effluent accumulated in the header. Samples were taken with a hypodermic syringe so that each sample emptied the header; thus, each sample was exactly representative of the oil passing the end of the pack during the small time interval of that sample. The refractive index was measured and the proportions of displacing and displaced oil determined from an experimental calibration curve. By taking samples as small as 0.50 cc, the data on breakthrough curves could be plotted within ±0.5 per cent.

EXPERIMENTAL RESULTS

EFFECT OF LENGTH OF TRAVEL

Taylor's[1] theory of displacement in capillary tubes, Scheidegger's[2] statistical theory of porous media, Keulemans'[3] "eddy diffusion" theory and Frankel's[4] "stagnant pockets" theory all predict that longitudinal dispersion will be governed by the following equation.

$$\frac{\partial C}{\partial t} = K \frac{\partial^2 C}{\partial x_1^2} \quad \ldots\ldots\ldots\ldots\ldots (1)$$

Eq. 1 is identical in form to the well known diffusion equation; however, the rate of dispersion or mixing of the flood front is governed by a dispersion coefficient *(K)* rather than the Fick diffusion coefficient *(D)*, as in the diffusion equation. Also, since the flood front is moving through the porous medium, the space variable used is the distance from the midpoint of the flood front (x_1) rather than the distance from the inlet end of the porous medium (x). The variables x and x_1 are simply related as follows:

$$x_1 = x - ut = x - \frac{L}{T}t \quad \ldots\ldots\ldots\ldots (2)$$

The solution of Eq. 1 with appropriate boundary conditions is well known in the following form.

$$C = 1/2 \left[1 - \text{erf}\left(\frac{x_1}{2\sqrt{Kt}}\right)\right] \quad \ldots\ldots (3)$$

where

$$\text{erf}(\xi) = \frac{2}{\sqrt{\pi}} \int_0^{\xi} e^{-\xi^2} d\xi .$$

Eq. 3 defines the well known "S" shaped curve of the error function integral, and a plot of this equation is a straight line on arithmetic probability co-ordinate paper.

The argument of the error function in Eq. 3 $(x_1/2\sqrt{Kt})$ indicates that at a constant rate of flow and with a constant dispersion coefficient the spread of the mixed zone will be proportional to the square root of the distance traveled. It is of interest to determine the validity of this "square root law"; however, first it is necessary to change

[1]References given at end of paper.

TABLE 1 – POROUS MEDIA AND FLUIDS

Pack or Core No.	Length (cm)	Diameter (cm)	Pore Vol. (cc)	Porosity (per cent)	Permeability (darcies)	Avg. Bead Dia. (mm)
117-1	83.2	3.19	221	33.2	0.65	.044
113-1	83.3	3.19	230	34.6	7.1	.100
107-1	83.5	3.19	215	32.2	115	.470
113-2	167.2	3.20	500	37.1	7	.100
113-3	83.4	14.00	4615	36.0	7	.120
113-4	83.5	1.30	47	37.0	7	.100
113-6	678	3.19	1946	35.8	7	.100
B-1	82.2	7.60	725	20.0	0.300	Berea Sandstone .042 (Calculated)
T-1	82.2	4.88	346	22.5	0.258	Torpedo Sandstone .036 (Calculated)

Oils for Favorable Viscosity Ratio Runs:

Displaced Oil – 89.4 vol. per cent Soltrol, 10.6 per cent Carbon Tetrachloride
Density 0.840 gm/cc, Viscosity 1.25 cp at 25°C.

Displacing Oil – 50 vol. per cent Mineral Oil, 50 vol. per cent Kerosene
Density 0.840 gm/cc, Viscosity 7.14 cp at 25°C.

Oils for Runs at Approximately Equal Viscosity Ratios:

Clear Oil – 94.9 vol. per cent Soltrol, 5.1 per cent Carbon Tetrachloride
Density 0.795 gm/cc, Viscosity 1.296 cp at 25°C.

Red Oil – 94.8 vol. per cent Kerosene, 5.2 per cent Heptane
Density 0.795 gm/cc, Viscosity 1.299 cp at 25°C.

the equation variables somewhat. Eq. 3 defines the concentration profile in the porous medium at a given time, while the experimental data give the concentration at a given point as the constantly growing mixed zone moves past the observer. The following substitutions can be made:

$$x_1 = L\left(\frac{V_p - V}{V_p}\right) \quad \ldots\ldots\ldots\ldots \quad (4)$$

$$t = T\left(\frac{V}{V_p}\right) \quad \text{or} \quad t = \frac{x}{u} \quad \ldots\ldots\ldots \quad (5)$$

Thus, the argument of the error function becomes,

$$\frac{x_1}{2\sqrt{Kt}} = \frac{L(V_p - V)}{2\sqrt{TKV_p V}} = \frac{L}{2\sqrt{KTV_p}}(U) \quad \ldots\ldots \quad (6)$$

where

$$U = \frac{V_p - V}{\sqrt{V}} \ .$$

The error function parameter U serves two purposes. First, it accounts for the predicted growth of the mixed zone as it passes an observer stationed at a fixed point. Second, with displacements varying only in length of travel, plots of U vs concentration should fall on the same line if the "square root law" holds.

As a test of the square root law, runs were made at approximately the same rate (5.2 to 6.3 $\times 10^{-3}$ cm/sec) at a viscosity ratio of 0.175. Three bead packs of 3.19-cm ID were used – Pack Nos. 113-1, 2 and 6. The lengths of these packs were 83.3, 167.2 and 678 cm, respectively. The results of these runs are plotted in Fig. 1. As can be seen, the data fall on a straight line in the concentration range of 5 to 80 per cent displacing fluid. This shows that the theoretical equation for the composition profile (the error function) is valid over most of the concentration range, although at high concentrations the profile is somewhat longer than predicted. Further, since all the data fall on the *same* straight line, the square root law is also valid.

It appears appropriate at this point to define the relationship between the error function parameter U and the rate of growth of the mixed zone which is

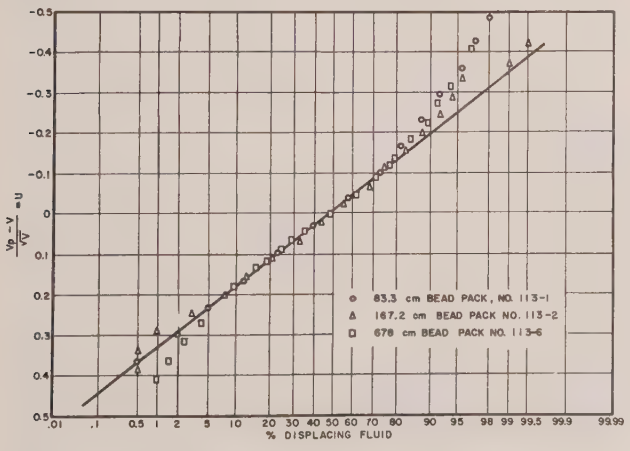

FIG. 1 – EFFECT OF LENGTH OF TRAVEL ON ERROR FUNCTION PLOT.

characterized by the dispersion coefficient K. Taylor[1] has shown that K can be related to the length of the transition zone between any two specified compositions. For instance, if x_{10} is defined as the distance to the point of 10 per cent displacing fluid and x_{90} is the distance to the point of 90 per cent displacing fluid, the length of transition zone so defined is $x_{90} - x_{10}$, and the dispersion coefficient is defined as follows.

$$K = \frac{1}{t}\left[\frac{x_{90} - x_{10}}{3.625}\right]^2 \quad \ldots\ldots\ldots \quad (7)$$

However, for our purposes it is necessary to relate the dispersion coefficient K to the error function parameter U. The following method is used. The best straight line is drawn through the data points. Values of U are read from this line at the 10 per cent (U_{10}) and 90 per cent (U_{90}) concentration values. The dispersion coefficient is then defined as follows.

$$K = \frac{1}{V_P T}\left[\frac{L\,(U_{90} - U_{10})}{3.625}\right]^2 \quad \ldots\ldots \quad (8)$$

Eq. 8 is identical to Eq. 7, as can be shown by substituting Eqs. 5 and 6 into Eq. 7. If a person prefers to use other concentration values, such as 20 and 80 per cent, the form of the equations would be the same as Eqs. 7 and 8, but a different constant would be necessary (e.g., 2.380 for 20 and 80 per cent concentrations). These constants can be obtained from any standard table of error integrals.

EFFECT OF VISCOSITY RATIO

Data were run in the 113-1 bead pack at viscosity ratios of 0.175, 0.998, 1.002 and 5.71 at a constant velocity ($\cong 6.0 \times 10^{-3}$ cm/sec). The effluent composition curves are shown in Figs. 2 and 2A. In Fig. 2 only the 5.71 and 0.998 viscosity ratio data are shown due to crowding of the other curves near 1.0 pore volume injected. In Fig. 2A the central portion of the effluent composition plot of Fig. 2 has been greatly expanded, and the data at 0.175 and 1.002 viscosity ratios have also been included. Of course, on this expanded plot only a small portion of the 5.71 viscosity ratio curve can be seen.

Fig. 2 best shows the marked difference when the viscosity ratio of 0.998 (a favorable viscosity ratio) is compared to a ratio of 5.71 (an unfavorable viscosity ratio). The favorable ratio curve is the typical "S" shaped curve of the error function, as defined by Eq. 3. The unfavorable viscosity curve is greatly extended, no longer follows the theoretical "S" shaped curve and exhibits a number of bumps and irregularities in composition. The irregularities are caused when "fingers" of displacing fluid run ahead of the bulk of the flood front. These fingers could be easily observed since the displacing fluid was dyed red; also, they have been reported visually by Blackwell, *et al.*[5]

In Fig. 3, the data of Fig. 2A have been plotted

on probability co-ordinates. The most noticeable phenomenon is that increasing the viscosity ratio also increases the value of $U_{90} - U_{10}$ and, thus, increases K and the rate of dispersion. For instance, compare the data at viscosity ratios of 0.175 and 0.998. Both of these are favorable ratios and both follow the theoretical error function of Eq. 3. But, it is evident that the change in viscosity ratio caused an increase in mixing rate (shown through $U_{90} - U_{10}$). This phenomenon has not been adequately studied to date, so no generalization can be made about the effect of viscosity ratio on mixing rate. But this points out the need to view with care data from different authors who may be using different viscosity ratios.

Another important effect of viscosity ratio is found by comparing the 0.998 data with the 1.002 data. The instability effects of only a slightly unfavorable viscosity ratio (1.002) cause a disproportionately large change in the effluent concentration curve. Also, along with a greater amount of mixing, the unfavorable viscosity ratio data no longer plot a straight line on the probability co-ordinates of Fig. 3. The 5.71 viscosity ratio data are not plotted on Fig. 3, but these data exhibit even more curvature. So Eq. 3 cannot be considered valid for displacements at a viscosity ratio greater than unity.

EFFECT OF PACK DIAMETER

Displacements were run in 14.00-cm (113-3), 3.19-cm (113-1) and 1.30-cm (113-4) packs to determine the effect of over-all pack diameter. The beads used in all three packs were 0.100-mm average diameter, and the viscosity ratio used was 0.175. As can be seen in Fig. 4, the 3.19 and 14.00-cm packs show almost identical breakthrough curves; but, the 1.30-cm pack definitely exhibits more dispersion. There are two possible reasons for the greater mixing found in the small-diameter pack. One reason can be deduced from the nature of the mixing theories in porous media.[2, 3, 4] All these theories assume a cross section large enough that boundary or wall effects are negligible, and it is likely that this assumption is not valid in the 1.30-cm pack. Another reason for greater dispersion may

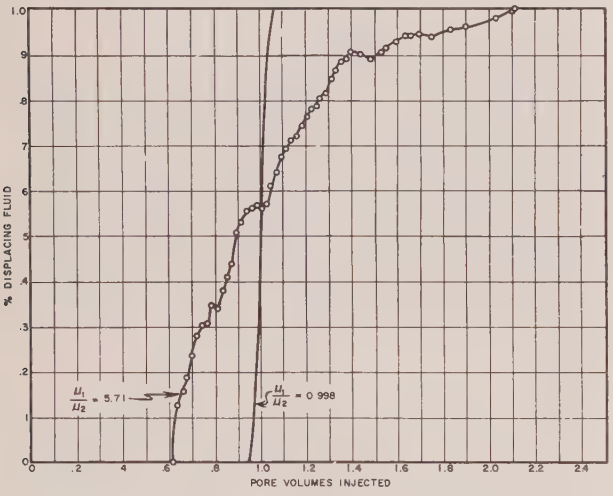

FIG. 2 – EFFECT OF VISCOSITY RATIO ON EFFLUENT CONCENTRATION CURVE, BEAD PACK NO. 113-1.

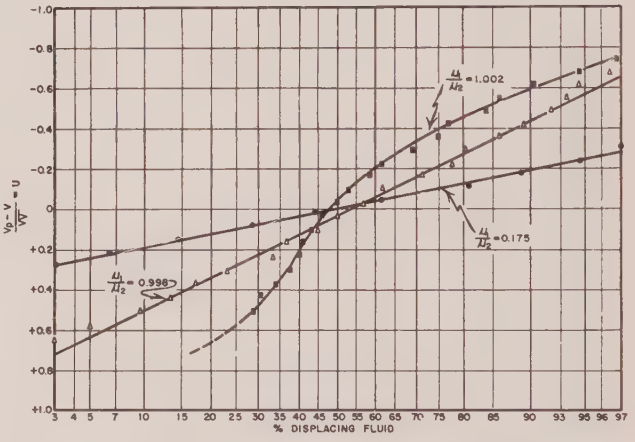

FIG. 3 – EFFECT OF VISCOSITY RATIO ON ERROR FUNCTION PLOT, BEAD PACK NO. 113-1.

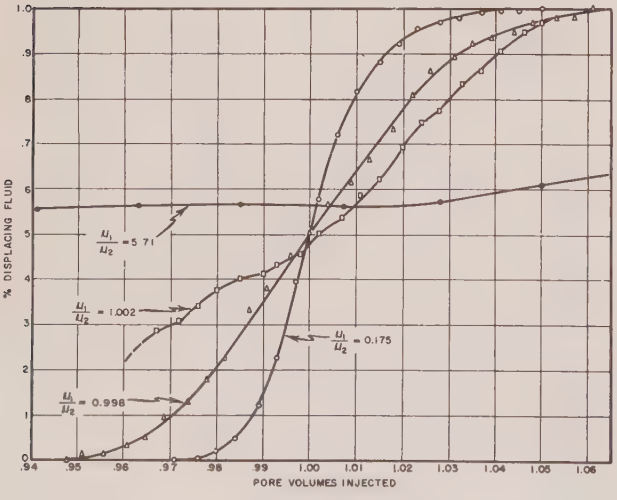

FIG. 2A – EFFECT OF VISCOSITY RATIO ON EFFLUENT CONCENTRATION CURVE, BEAD PACK NO. 113-1.

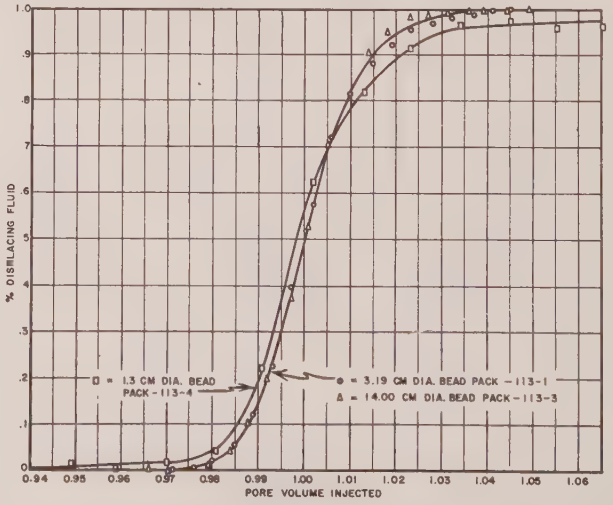

FIG. 4 – EFFECT OF BEAD PACK DIAMETER ON EFFLUENT COMPOSITION CURVE.

be the difficulty in achieving uniform packing in a small tubing; but, whatever the reason, the data of Fig. 4 emphasize the need for viewing with caution any data acquired from small-diameter packs (less than approximately 3-cm diameter).

EFFECT OF FLOW VELOCITY

Keulemans[3] has suggested that one source of dispersion at higher flow rates is due to the separation and rejoining of channels of flow in the porous medium and has termed this "eddy diffusion". If one considers a particular porous medium, the amount of dispersion introduced with each centimeter of distance traveled is the same, regardless of the velocity of flow through that medium. The dispersion is entirely due to the amount of separation and rejoining that is inherent in the medium itself. However, the dispersion coefficient (K) is a measure of the *rate* of dispersion, not the amount, and thus would be proportional to velocity. Also, when considering two similar porous media differing only in size of flow channels and particles, the amount of dispersion is directly proportional to particle size. So, for Keulemans' "eddy diffusion",

$$E = \lambda \, u\bar{r} \quad \ldots \quad (9)$$

where λ is a term which expresses the amount of irregularity of packing and, thus, the amount of eddy diffusion characteristic of the particular porous medium. It is often desirable to express variables in dimensionless form, and Eq. 9 suggests the following form.

$$\frac{K}{D} \sim \frac{\bar{r}u}{D} \quad \ldots \quad (10)$$

Taylor's capillary tube theory and Frankel's "stagnant pockets" theory both reduce to the following proportionality,

$$K \sim \frac{(\bar{r}u)^2}{D} \quad \ldots \quad (11)$$

which, again in dimensionless form, becomes

$$\frac{K}{D} \sim \left(\frac{\bar{r}u}{D}\right)^2 \quad \ldots \quad (12)$$

By referring to Expressions 10 and 12, it would appear reasonable to plot $\bar{r}u/D$ vs K/D, both for the purpose of correlation of data and to test the validity of these theories. Accordingly, a plot of all the data has been made in Fig. 5 using K/D and $\bar{r}u/D$ as co-ordinates, as done by Blackwell, *et al.*[5] A log-log co-ordinate system is preferable here because of the wide range of variables covered and because $\bar{r}u/D$ is expressed as a power function in the above proportionalities.

EFFECT OF FLOW VELOCITY – LOW FLOW RATES

To understand the amount of mixing which occurs at low velocity, one should consider the limiting case where velocity is zero. At non-flow conditions, the only case of mixing should be ordinary molecular (Fick) diffusion, and the dispersion coefficient K will be constant. In Fig. 5, the data on 0.100-mm beads approaches this condition at a value of $\bar{r}u/D$ of about 0.2. Thus, at low rates the equation for the dispersion coefficient in glass bead packs becomes

$$\frac{K}{D} = 0.7 \quad \ldots \quad (13)$$

Blackwell, *et al*[5] and Carman[6] have also found this relationship at low flow rates for spherical glass bead packs. The number 0.7 should not be considered a universal constant, for diffusion in a porous medium is directly analogous to the electrical resistivity of the medium. Thus, K/D is related to the formation factor F and porosity ϕ, and a more exact equation at low rates is

$$\frac{K}{D} = \frac{1}{F\phi} \quad \ldots \quad (14)$$

The term $1/F\phi$ will commonly vary between 0.15 and 0.7, depending on the lithology of the porous medium.[7]

EFFECT OF FLOW VELOCITY – HIGH FLOW RATES

At high flow rates, as stated, Keulemans' theory predicts that the term K/D is proportional to $\bar{r}u/D$ to the first power. The other theories predict a second power dependence. The data of Fig. 5 show that none of these theories is exact but, rather, that the result lies somewhere between them. The exponent was found experimentally to be 1.24, 1.20 and 1.19 in the 0.470-mm beads, 0.100-mm beads and the Berea core, respectively. These data compare closely with the 1.17 power reported by Blackwell, *et al*,[5] and the 1.20 power shown by Aronofsky and Heller[8] on data reported by von Rosenburg.[9]

From these data it appears that, for glass bead packs and fairly homogeneous sandstone, a reasonable value to use for the exponent is 1.20. Thus, we get the empirical equation

$$\frac{K}{D} = a\left(\frac{\bar{r}u}{D}\right)^{1.20} \quad \ldots \quad (15)$$

The exponent (1.20) may not be a constant, valid for all porous media, since it has only been tested for bead packs and sandstone. It lies between the 1.00 and 2.00 limits of the mixing theories, so it

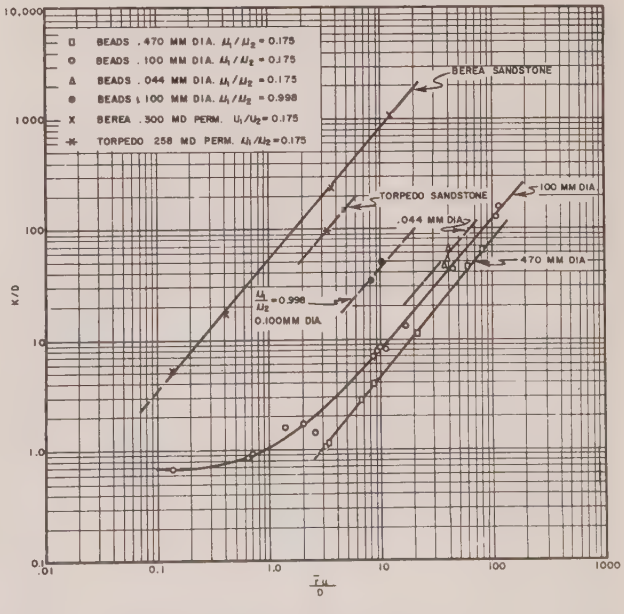

FIG. 5 – EFFECT OF RATE AND TYPE OF POROUS MEDIUM ON DISPERSION RATE.

appears that both eddy diffusion of Keulemans' model and statistical dispersion of either the Scheidegger or Frankel type play a part in determining the rate of mixing. Also, since the result is close to the first power, eddy diffusion must be the dominant factor in these media.

Eq. 14 for low rates can be combined with Eq. 15 for high rates to give a single equation expressing the dispersion coefficient as a function of velocity and lithology. Thus, we get

$$\frac{K}{D} = \frac{1}{F\phi} + a\left(\frac{\bar{r}u}{D}\right)^{1.20} \quad \ldots\ldots\ldots\ldots (16)$$

It will be noted that no attempt has been made to give an exact numerical value for the mixing coefficient (a) in these equations. The reason is that a is not a constant, as implied in other work[5] but, rather, varies widely depending on the geometry of the porous medium and the viscosity ratio of the flowing fluids. A further discussion on the effect of porous medium type on a is found in the next section, and a comparison of a values has been made in Table 2. The authors feel that, with more experimental evidence, the mixing coefficient (a) could be used with success to characterize porous media, for a is a measure of the inhomogeneity of a medium in a dynamic situation, while the present pore size distribution techniques are based on non-flow measurements.

Upon studying Eq. 16, one observes an interesting relationship between the dispersion coefficient K and the molecular diffusion coefficient D. At high flow rates with all other variables held constant, K is inversely proportional to $D^{0.2}$; this means that, if the fluids had a larger diffusion coefficient, the amount of mixing would be slightly less. No attempt has been made to study this possibility here, but the data of Handy[10] at least qualitatively substantiate that mixing rate is decreased somewhat when using a fluid with a greater diffusion coefficient.

EFFECT OF POROUS-MEDIUM TYPE

Keulemans' eddy diffusion term includes the coefficient λ which expressed the inhomogeneity of the flow channels. Let us assume we have two porous media which are geometrically similar with different particle sizes, such as two identically packed bead packs differing only in diameter of beads. These packs would have identical values for λ according to Keulemans' theory. Scheidegger's theory contains a dispersivity term a which from its definition would also be constant under the afore-mentioned conditions, and Frankel's stagnant pockets theory gives the same result. However, in practice, λ (and, thus, a and a) has experimentally been found to increase with finer particles. Klinkenberg and Sjenitzer[11] report values of λ increasing from one to eight as particle diameters drop from 1.0 to .05 mm. The data of Fig. 5 and Table 2 on 0.470, 0.100 and .044-mm beads also point out this trend, for the values of a increase as the bead diameters decrease.

Why then is a not constant? Keulemans suggested that this increase with small particles is due partially to the difficulty in packing smaller particles uniformly and partially to the greater variation in particle size usually found with finer particles. That is, the larger a is caused by more inhomogeneity in the porous medium. The data reported here from glass bead packs corroborates this theory, for the small beads have a greater variation in particle size than the large beads.

Also, we can compare the values for a reported here to those cited by Blackwell[5] and Klinkenberg.[11] The a values found in this paper are considerably smaller than found by these two authors. Part of this difference is caused by viscosity ratio (explained earlier), but even the 0.998 viscosity ratio data give less mixing than reported by Blackwell and Klinkenberg. Again, this is caused by the narrow particle-size range of these beads — that is, by the more homogeneous porous media.

To plot the Berea and Torpedo sand data on Fig. 5 for comparison with the bead pack data, an assumption must be made on average particle radius to be used for these natural porous media. The following equations were used to calculate average pore radii and particle radii.

$$\bar{r}_p \cong \sqrt{\frac{8k\ r^2}{\phi}} \times 10^{-4} \quad \ldots\ldots\ldots\ldots (17)$$

$$\bar{r} \cong 3\bar{r}_p \quad \ldots\ldots\ldots\ldots (18)$$

where

$r \cong 2.0$

Using these equations, the average sand-grain radii calculated 2.1×10^{-3} cm for the Berea sandstone and 1.8×10^{-3} cm for the Torpedo sandstone. These average grain radii are, of course, not exact, but they are close enough to show without doubt the tremendously increased importance of the a term (the inhomogeneities) in naturally occurring porous media when the data are compared in Fig. 5 to the homogeneous bead pack. Handy's[10] data obtained from a Boise consolidated sandstone show the same results. In Table 2, the a values for the bead pack data and the natural core data may be easily compared.

To more readily see the effect of inhomogeneities on rate of mixing at reservoir rates, let us consider a displacement at 3.0×10^{-4} cm/sec (0.85 ft/day). In the .100-mm glass bead pack, the dispersion rate was controlled almost entirely by molecular diffusion. But, in the Berea core used in this study, the dispersion rate was 9.2 times as great as in the glass bead pack because natural sandstone is more

TABLE 2 – EFFECT OF VISCOSITY RATIO AND POROUS MEDIUM ON a, FOR $K/D = a\,(\bar{r}u/D)^{1.20}$

Porous Medium	Viscosity Ratio	a
.044-mm Beads	.175	0.69
.100-mm Beads	.175	0.49
.100-mm Beads	.998	2.78
.470-mm Beads	.175	0.30
Torpedo Sandstone	.175	23.2
Berea Sandstone	.175	53

heterogeneous. This result is reflected directly in the values for α found in Table 2.

EFFECT OF VELOCITY ON ZONE LENGTH

It is of considerable interest to know the effect of velocity on the length of the mixed zone. Consider Eqs. 7 and 16. We can substitute $\frac{LV}{uV_p}$ for t in Eq. 7, and then solve these equations simultaneously for $x_{90} - x_{10}$ as a function of velocity. The result is

$$\left(\frac{x_{90}-x_{10}}{3.625}\right)^2 = \frac{1}{F\phi}\frac{DLV}{uV_p} + \alpha\left(\frac{\bar{r}u}{D}\right)^{1.20}\left(\frac{DLV}{uV_p}\right) \quad \ldots\ldots\ldots\ldots\ldots\ldots\ldots\ldots (19)$$

A glance at Eq. 19 will show that there exists a velocity at which the mixed zone length is a minimum. Eq. 19 can be differentiated with respect to velocity and set equal to zero to solve for this velocity.

$$u = \frac{D}{\bar{r}}\left(\frac{1}{.2aF\phi}\right)^{1/1.20} \quad \ldots\ldots\ldots\ldots (20)$$

Using the data for the 113-1 bead pack (0.70 for $1/F\phi$ and 0.49 for a), the velocity for minimum mixing is found from Eq. 20 to be 3.3×10^{-3} cm/sec. Fig. 6 shows the data on velocity and zone length for this pack along with the calculated minimum.

Another method of fixing this "minimum" velocity is to draw a 45° line on Fig. 5 tangent to the curve. The point of tangency corresponds to the minimum point. By this procedure it is apparent that this velocity will be lower as the porous medium becomes more heterogeneous. For instance, assuming $1/F\phi$ equals 0.50 for the Berea sandstone and a equals 53, the velocity for minimum mixing in Berea is calculated to be 1.2×10^{-4} cm/sec. Also, it can be seen from the K/D value that only about 20 per cent of the total dispersion coefficient is caused by diffusion at the "minimum mixing" velocity.

SUMMARY AND CONCLUSIONS

This investigation has found that the viscosity ratio during displacement greatly affects dispersion rate in the following ways.

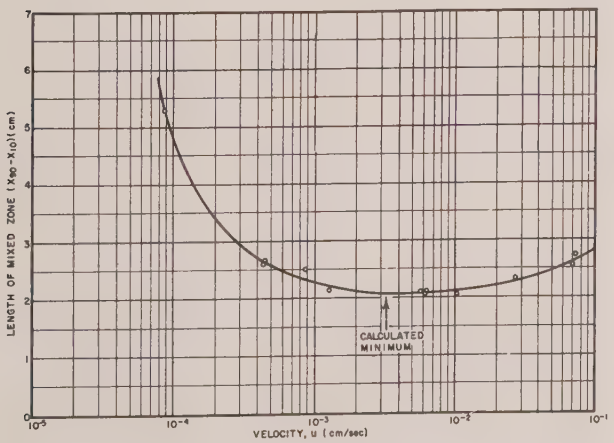

FIG. 6—EFFECT OF VELOCITY ON ZONE LENGTH, BEAD PACK NO. 113-1, VISCOSITY RATIO 0.175.

1. When a favorable viscosity ratio was changed by a factor of 5.7 (0.175 to 0.998), the dispersion coefficient was also changed by a factor of 5.7. Although this seems to suggest a linear relationship, there are not enough data available to substantiate such a conclusion. This should be investigated further.

2. When changing only slightly from a favorable (0.998) to an unfavorable (1.002) viscosity ratio, the mixing rate was disproportionately increased and the predicted error function curve was no longer valid.

3. When the viscosity ratio was 5.71, the effluent concentration curve was greatly extended, and there was both visual and analytical evidence of distinct "fingers" of displacing fluid running ahead of the average displacement front.

4. At viscosity ratios above 1.0, the theoretical error function curve no longer was valid.

The following conclusions can be drawn for displacements at a favorable viscosity ratio (viscosity ratio $\leq$ 1.0).

1. The "square root law", which concludes that the amount of mixing is proportional to the square root of the distance traveled, is valid.

2. Diameter of the pack can be an important variable, and data from small-diameter packs should be treated with caution. Data obtained using .100-mm diameter beads were consistent for packs 3.2 cm in diameter and larger.

3. At very low rates of flow, the dispersion coefficient K is directly proportional to the Fick diffusion coefficient, as expected.

$$\frac{K}{D} = \frac{1}{F\phi} .$$

4. At high rates of flow, the dispersion coefficient is characterized by the following relation for sandstones and glass bead packs.

$$\frac{K}{D} = a\left(\frac{\bar{r}u}{D}\right)^{1.20} .$$

5. a in this equation is not a constant but, rather, is a function of the viscosity ratio of the flowing fluids and the inhomogeneity of the porous medium.

6. In natural sandstones at reservoir rates, the dispersion coefficient K is proportional to $(u)^{1.20}$, as in the above equation, and the rate of dispersion is considerably higher than found in glass bead packs.

7. The length of the mixed zone is a function of velocity. The zone length increases at very low flow rates and very high flow rates, and there exists a velocity at which the zone length is a minimum. At this velocity, diffusion contributes only a small fraction of the total dispersion coefficient.

NOMENCLATURE

C = concentration (cc/cc)
t = time (seconds)
x_1 = distance from midpoint of flood front (cm)
K = dispersion coefficient (cm^2/sec)

D = Fick diffusion coefficient (cm^2/sec)
x = distance from inlet end of porous medium (cm)
u = average pore velocity (cm/sec) $u = L/T$
L = length of porous medium (cm)
T = time required to inject or produce one pore volume of fluid (seconds)
V_p = pore volume of porous medium (cc)
V = volume of fluid recovered at time of sample (cc)
U = error function parameter $(V_p - V)/\sqrt{V}$
$\bar{r}$ = average radius of glass beads or sand grains (cm)
E = Keulemans' eddy diffusion coefficient (cm^2/sec)
λ = Keulemans' packing coefficient
F = formation resistivity factor
ϕ = fractional porosity
a = mixing coefficient
a = Scheidegger's dispersivity
$\bar{r}_p$ = average pore radius (cm)
k = permeability (darcies)
Viscosity Ratio = the ratio of the displaced phase viscosity to the displacing phase viscosity

ACKNOWLEDGMENTS

The authors wish to express their appreciation to the management of Continental Oil Co. for permission to publish this paper, to Byron Dyche and Wilbur Hullet for performing many of the experiments, and to Stanley Frankel for his helpful comments and suggestions.

REFERENCES

1. Taylor, G. I.: "Dispersion of Soluble Matter in Solvent Flowing Slowly Through a Tube", *Proc.*, Royal Society (1953) Vol. 219, 186.
2. Scheidegger, A. E.: "Statistical Hydrodynamics in Porous Media", *Jour. Appl. Phys.* (1954) Vol. 25, No. 8, 994.
3. Keulemans, A. I. M.: *Gas Chromatography*, Reinhold Press, N. Y. (1957).
4. Frankel, Stanley: "Mixing of Fluid Flowing in a Porous Medium", Conference on Theory of Fluid Flow in Porous Media, U. of Oklahoma (March 23-24, 1959).
5. Blackwell, R. J., Terry, W. M. and Rayne, J. R.: "Factors Influencing the Efficiency of Miscible Displacement", *Trans.*, AIME (1959) Vol. 216, 1.
6. Carman, P. C.: *Flow of Gases Through Porous Media*, Reinhold Press, N. Y. (1956).
7. Pirson, S. J.: *Oil Reservoir Engineering*, McGraw-Hill Book Co., Inc., N. Y. (1958).
8. Aronofsky, J. S. and Heller, J. P.: "Diffusion Model to Explain Mixing of Flowing Miscible Fluids in Porous Media", *Trans.*, AIME (1957) Vol. 210, 345.
9. von Rosenburg, D. U.: "Mechanics of Steady-State Single-Phase Fluid Displacement from Porous Media", *AIChE Jour.* (March, 1956) Vol. 2, No. 1, 55.
10. Handy, L. L.: "An Evaluation of Diffusion Effects in Miscible Displacement", *Trans.*, AIME (1959) Vol. 216, 61.
11. Klinkenberg, A. and Sjenitzer, F.: *Chem. Engrg. Science* (1956) Vol. 5, 528.

***

Stability Theory and Its Use to Optimize Solvent Recovery of Oil

RICHARD L. PERRINE
MEMBER AIME

U. OF CALIFORNIA AT LOS ANGELES
LOS ANGELES, CALIF.

ABSTRACT

This paper shows how stability theory can be used to optimize solvent recovery of oil. Application of the theory leads to definition of the limiting conditions required for stable displacement to occur. One of these conditions is that the size of a solvent "slug" must at least equal a prescribed minimum. The criteria to be satisfied are miscibility and stability. Stability implies that no viscous fingering will occur and that mixing will be caused only by a dispersion process. Miscibility implies that complete recovery will be obtained from the swept regions. Thus, for any specified set of reservoir conditions, an optimum use of solvent is defined.

INTRODUCTION

The early outlook for solvent flooding as a means to increase oil recovery was very favorable. Some laboratory results indicated that a "slug" containing perhaps 2 to 3 per cent of a hydrocarbon pore volume could be successful. However, other data suggested as much as 30 per cent would be required. The difference is of considerable economic importance. A theoretical explanation for these divergent results has been advanced by the author.[1,2] Stability theory defines conditions for two distinct flow regimes. In stable displacement, solvent and oil become mixed by a dispersion process, and the solvent requirement is small. On the other hand, unstable displacement can degenerate into viscous fingering. The practical result is a considerable increase in the extent of mixing and, thus, in the solvent required.

The present paper shows how to use stability theory to optimize solvent recovery of oil. Oil is usually considered to be displaced by a small amount, or a slug, of solvent. Gas in turn follows solvent. Any fingering will permit contact of nearly solvent-free gas and oil, leading to immiscibility and reduced recovery. Thus, our optimum is defined by two restrictions — stable flow and miscibility. Although an immiscible solvent process could prove more profitable than any miscible process, such processes lie outside the selected definition of an optimum. The usefulness of computations based on the present work will depend on the validity of the general theory. Because the important idealizations required tend to minimize the predicted solvent requirement, the results should state correctly the limiting conditions required. Therefore, theoretical calculations should have practical value.

This paper first reviews several principles that result from stability theory. The following section describes use of these ideas in relatively simple systems which symmetry makes appear one-dimensional. Of particular importance is the step-by-step design of a stable minimum-solvent slug. The use of stability theory in cases of multi-dimensional displacement is discussed and, finally, suggestions are given for simplified practical application of the theoretical results.

PRINCIPLES OF STABILITY THEORY

The use of perturbation methods to derive stability conditions has been shown by the author.[1] The discussion is presented in terms of the fractional concentration of solvent in the single hydrocarbon phase. Quite generally, any disturbance can be represented as a Fourier series, of which only the least stable term need be considered. Denoting this term at time $t = 0$ by c_n,

$$c_n = \tilde{c}_n \cos \alpha x L^{-1} \cos \beta y L^{-1} \cos n\pi z L^{-1} \quad \ldots\ldots (1)$$

The initial growth of this least stable term is calculated according to

$$\exp(-\gamma t) \quad \ldots\ldots (2)$$

where

$$\gamma = L^{-2}\left[\alpha^2 D_1 + (\beta^2 + n^2\pi^2) D_3\right] + u_0 \delta^{-2}\left[\alpha n\pi \frac{\partial \bar{c}}{\partial x} - (\alpha^2 + \beta^2)\frac{\partial \bar{c}}{\partial z}\right] g_3 + u_0 \delta^{-2}\left[\alpha n\pi \frac{\partial \bar{c}}{\partial z} - (\beta^2 + n^2\pi^2)\frac{\partial \bar{c}}{\partial x}\right] g_1 \quad \ldots\ldots (3)$$

Original manuscript received in Society of Petroleum Engineers office May 23, 1960. Revised manuscript received Oct. 27, 1960.

[1] References given at end of paper.

and the functions are defined by

$$g_1 = \frac{d \ln \mu}{dc} + \frac{k}{\bar{\mu}} \frac{d\rho}{dc} \frac{g \sin \theta}{\phi u_0}$$

$$g_3 = \frac{k}{\bar{\mu}} \frac{d\rho}{dc} \frac{g \cos \theta}{\phi u_0}$$

$$\delta^{-2} = (\alpha^2 + \beta^2 + n^2\pi^2)^{-1} \ldots\ldots\ldots (4)$$

The least stable term has the highest growth rate, yet stability requires that no growth occur. This means that the stability coefficient γ must be zero or positive, and Eq. 3 shows how this requirement restricts displacement conditions.

The derivation assumed flow in the x-direction within a reservoir of large x and y dimensions and limited thickness L in the z-direction. D_1 is the axial and D_3 the lateral dispersion coefficient.[3-5] The constant, stable volumetric flow rate per unit of cross-sectional area and per unit of porosity is u_0. Flow symmetry maintains solvent concentration $\bar{c}$ for stable flow independent of y. Viscosity $\bar{\mu}$ is for a fluid mixture of solvent concentration $\bar{c}$. From Eq. 1, α, β and n are Fourier expansion parameters depending on the initial disturbance. Other symbols are k for permeability, ϕ for porosity, ρ for density, g for the acceleration of gravity and θ for the dip angle of the formation. For downward tilt in the direction of flow, θ is negative.

Consider what happens as solvent moves through a reservoir displacing oil. Dispersion will cause mixing and a gradual transition from oil to solvent. Values of γ will vary within the solvent bank depending on the relative importance of gravity, viscosity and dispersion. So long as any part of the system is unstable, viscous fingers can grow to dominate flood behavior. The problem is to keep the most negative value of γ zero, forcing all others to be positive. No real system is simple. However, several useful generalizations can be derived and are presented in the following discussions.

THE PRINCIPLE OF GRAVITY STABILIZATION

The most important stabilizing mechanism is gravity segregation. The function g_1 in Eq. 4 is positive when gravity is dominant, but it becomes negative when gravity is subordinate to viscous forces. Thus, it measures the relative importance of gravity. This assumes "normal" solvent-oil density, viscosity and displacement conditions. Gravity stabilization can be achieved by controlling rate.

THE MINIMUM-SLUG-SIZE PRINCIPLE

The stability limit is marked by $\gamma = 0$. This same condition defines the minimum solvent slug for stable displacement. Take the simple example in which concentration is independent of z and make the assumption that α is negligible. Inserting these conditions together with $\gamma = 0$ and re-arranging terms in Eq. 3,

$$\frac{\partial \bar{c}^*}{\partial x} = \frac{(\beta^2 + n^2\pi^2)D_3}{u_0 L^2 g_1} \ldots\ldots\ldots (5)$$

The asterisk indicates a critical, or limiting, relationship. Stability results whenever either one of the following occurs.

1. g_1 is positive and (a) the concentration gradient has any negative value or (b) the concentration gradient has a positive value no larger than that indicated by Eq. 5.

2. g_1 is negative and (a) the concentration gradient has any positive value or (b) the concentration gradient has a negative value no larger in magnitude (no more negative) than indicated by Eq. 5.

While a solvent slug should be kept small, at high rates stability and an abrupt change from oil to solvent may be incompatible.[6] Maximum gradients for a given rate will depend on system properties.

SOURCES OF REQUIRED DATA

Most information required to apply Eqs. 3 through 5 is readily obtained. Although the dispersion coefficients D_1 and D_3 are new parameters, measurement techniques have been developed.[3,7-9] These coefficients characterize the mixing capability of a porous medium in much the same way that permeability denotes flow capacity. Because at very low rates the lateral dispersion process will reduce to molecular diffusion, these coefficients must be measured under appropriate experimental conditions.

The remaining new parameters arise from the Fourier series representation of possible disturbances in solvent concentration. They are denoted by the letters α, β and n. As shown by Eq. 1, these parameters reflect the scale, or "wave length", of disturbances propagated as a result of inhomogeneity in reservoir properties. The principal cause would be permeability inhomogeneity. Means for proper determination of α, β and n will require research into the variation characteristic of porous media. Such studies have yet to be made.

From theory,[1] however, together with even cursory observation of natural oil-reservoir rocks, we can draw several useful conclusions. The first is that very frequently α, and perhaps also β, can be neglected. The most important quantity is n. It must be an integer and must be greater than or equal to one. Thus, conservative practice would dictate the values $\alpha = 0$, $\beta = 0$ and $n = 1$ when estimates must be used.

Before assuming that this crude approach will always be necessary, consider possible sources of information. What we require is a measure of the greatest distance between successive extreme values of permeability characteristic of the formation. In the vertical direction, for example, suppose that permeability maxima occur (at most) each L' units apart. Then, it is reasonable to expect the fundamental component of a resulting disturbance to be periodic with the approximate interval L'. That is, we expect that it will contain as its long wave-length Fourier component of appreciable amplitude a term with $n \approx 2L/L'$. One source of such characteristic maxima might be well logs that have been properly interpreted. Certainly this should be true for n because it is characteristic of vertical variation. It is fortunate that precise values of α

and β would seem to be much less important.

USE OF STABILITY THEORY WITH LINEAR FLOW

Symmetry makes it possible to treat many reservoir problems and laboratory core flood problems as if the flow were one-dimensional. For this reason we will discuss in some detail an example long-core flood. The discussion shows how stability theory can be used to optimize solvent recovery of oil. It leads to results applicable to a variety of practical problems. Later discussion will cover the more complex multi-dimensional cases.

STABILITY IN A LONG-CORE FLOOD

The fluid and rock properties to be used in example calculations are given in Table 1. Density and viscosity depend on the composition of the single hydrocarbon phase. The relationships are conveniently given as empirical equations. Fractional solvent concentration is $\bar{c}$, while fractional concentration of dissolved gas is denoted by $\bar{c}_g$. By difference, the remaining material is oil. Values for the dispersion coefficients based on experiment are given in Table 1. Other materials and other flow conditions could require different values.

As an example problem, we consider flow through a long, square-cut core about 2 in. on a side and positioned with a 10° dip. The core has been flooded with solvent for 40 days at a frontal advance rate of about 1 ft/day. The flood is also assumed to have been started by an abrupt change to solvent, as shown by the input curve in Fig. 1 (Curve A). If flow is linear and stable so that no fingering occurs, concentrations will be uniform across any section of the core. Thus, it is convenient to picture the result by means of a solvent concentration profile, as if solvent could be separately observed within the system. For this case, the concentration profile should look like Curve B in Fig. 1 after traveling 40 ft. This profile is defined by the equation,

$$\bar{c} = \tfrac{1}{2}\,\mathrm{erfc}\left[\frac{x - u_0 t}{2\sqrt{D_1 t}}\right] \qquad (6)$$

in which a negligible term has been dropped.[1]

The first question to be answered is whether or not such a flood should be stable. Using solvent concentration data from Fig. 1, dimensionless stability coefficient values such as those from Eq. 3

TABLE 1 – PROPERTIES FOR EXAMPLE CALCULATIONS

Linear Flow

t for $\bar{c} = 3.46 \times 10^6$	seconds ($t \approx 40$ days)
D_1	$= 0.375\ u_0$ cm^2/sec
D_3	$= 0.0375\ u_0$ cm^2/sec
u_0	$= 3.47 \times 10^{-4}$ cm/sec ($u_0 \approx 1$ ft/day)
L	= 5 cm ($L \approx 2$ in.)
k	= 0.87 darcies
μ	$= 10 \exp(-3\bar{c} - 6.3\bar{c}_g)$ cp
ρ_g	$= (8 - 2.9\bar{c} - 7.3\bar{c}_g) \times 10^{-4}$ atm/cm
θ	$= -10^0$
ϕ	= 0.25

Two-Dimensional Flow

As Above Except:

t	$= 1.38 \times 10^8$ sec ($t \approx 1{,}600$ days)
L	= 305 cm ($L \approx 10$ ft)

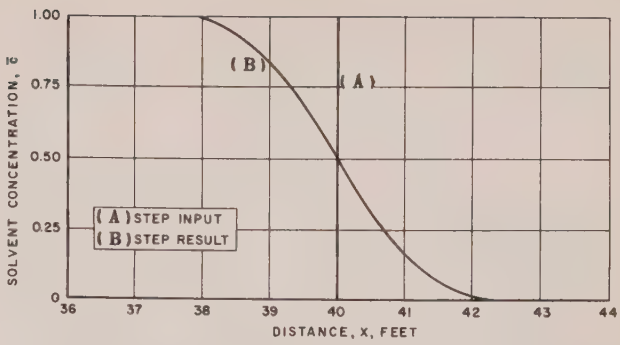

FIG. 1 – CONCENTRATION PROFILE, LONG-CORE EXAMPLE.

are plotted in Fig. 2 for three different, long wavelength disturbances. Instability is indicated over a considerable concentration range in each case, as shown by negative values of the coefficient γ. The results imply a substantial space region within which such disturbances can grow. Because natural core properties always are such as to initiate small disturbances, it is doubtful that displacement could have occurred as shown by Fig. 1. A more likely sequence would be initial instability followed by viscous fingering and, finally, a larger mixing zone than that shown.

GRAVITY STABILIZED MINIMUM SOLVENT SLUG

The hypothetical core flood just described can be modified to make use of gravity stabilization. Suppose conditions are maintained such that the function g_1 (Eq. 4) is positive. Then by Eq. 5, the concentration gradient can be made as steep as we like. To see what is required to accomplish this, Fig. 3 shows g_1 as a function of concentration $\bar{c}$ for possible flood rates u_0.

Since gravity stabilization requires that g_1 be positive for all $\bar{c}$, the limiting value is obtained at $\bar{c} = 0$ where fluid viscosity is greatest and the response to gravity is least. Thus, a critical rate for gravity stabilization is defined by setting $g_1 = 0$ and maximizing $\bar{\mu}$. The result is

$$u_g^* = -\frac{k}{\bar{\mu}}\frac{d\rho}{dc}\left[\frac{d\ \ln\ \mu}{dc}\right]^{-1}\frac{g\ \sin\ \theta}{\phi} \qquad (7)$$

For the example data, u_g^* (Curve 4 of Fig. 3) corresponds to 0.017 ft/day. At or below this very low rate, complete gravity stabilization is possible with no reliance on dispersion. The rate is low enough for the dispersion mechanism to become molecular diffusion, but a result similar to Curve B of Fig. 1 would be obtained.

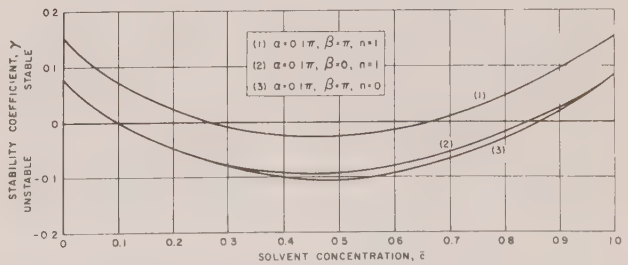

FIG. 2 – EXAMPLE STABILITY COEFFICIENTS (γ) FOR LONG-CORE FLOOD.

An elementary treatment of this kind of problem considers the entire mixing zone as a kind of "interface" region. This suggests as a condition for stability

$$u = -k \frac{\Delta(\rho g)}{\Delta\mu} \frac{\sin\theta}{\phi} \quad \ldots\ldots\ldots\ldots\ldots\ldots (8)$$

where Δ represents total change in the quantity across the interface. Eq. 8 is the limiting finite-difference form of Eq. 7 and represents a kind of average behavior through the interface. Used with the example data, Eq. 8 suggests a limiting rate of 0.053 ft/day. Unfortunately, correct use of Eq. 8 requires that mixing-zone thickness be negligible. Because a mixed region forms almost immediately, only the more restrictive Eq. 7 is appropriate.

FORMATION OF A MINIMUM-SOLVENT SLUG

The preceding discussion showed how gravity could be used to stabilize displacement. Because such low flow rates are required, the process is unlikely to prove practical. The present section will show how to form a slug containing minimum solvent, yet in such a manner that flow will be stable at some pre-selected rate. The results apply to linear flow. To do this requires a somewhat novel approach – the use of a gradual change in properties of the injected fluid rather than an abrupt change from one fluid to another.[6] In addition, it is necessary to consider the complete problem in which gas displaces solvent, which in turn recovers oil. Thus, the complete definitions of viscosity and density in Table 1 are required. The symbol $\bar{c}_g$ is used for fractional gas concentration.

The principles are as follows. Flow behavior is single-phase and the mixing mechanism is dispersion provided (1) all fluid compositions remain in the miscible region, and (2) stability conditions are satisfied. Formation of a solvent slug which will satisfy these criteria involves three steps: (1) finding the maximum rates of change of solvent concentration consistent with stability for the specified conditions and, thus, the way in which solvent-oil and gas-solvent transition zones are to be injected; (2) finding how much pure solvent must be injected between transition zones to make certain that dispersion mixing does not lead to immiscibility; and (3) finding out how much the rate can be increased as the solvent slug travels and stability criteria become less restrictive. These steps are illustrated by an example.

Step 1

The first step is to establish maximum concentration gradients consistent with stability. This can be done by applying Eq. 5 separately to solvent-oil and gas-solvent transition zones. The results specify just what the "shape" of the injected concentration profile must be. We use the core and fluid properties in Table 1 and a displacement rate of 1 ft/day. To obtain the required data, note the following equivalence.

$$\frac{\partial \bar{c}^*}{\partial x} = -\frac{1}{u_0} \frac{\partial \bar{c}^*}{\partial t} \quad \ldots\ldots\ldots\ldots\ldots\ldots\ldots\ldots (9)$$

which, combined with Eq. 5, gives on integration

$$t^* = -\frac{}{\bar{c}_i{}^*} \int^{\bar{c}^*} \frac{L^2 g_1 d\bar{c}}{(\beta^2 + n^2\pi^2) D_3} + t_i{}^* \quad \ldots\ldots (10)$$

If a concentration $\bar{c}_i^*$ is being injected at the initial time t_i^*, Eq. 10 tells what concentration $\bar{c}^*$ must be injected at any subsequent time t^* to keep the solvent slug stable but as small as possible.

Eq. 10 is used first to construct the leading transition zone by which solvent is to displace oil. The conservative values $\beta = 0$ and $n = 1$ can be used for the perturbation properties. Eq. 4 defines the function g_1 which depends on both density and viscosity. To compute these functions, note that $\bar{c}_g = 0$ at this leading part of the transition zone. It is convenient to measure time t^* relative to a time $t_i^* = 0$ for which $\bar{c}_i^* = 0$. In this way we arrive at the solvent-oil injection profile $\bar{c}_a^*$ shown in Fig. 4 as a function of time. A backward time scale is used, listing time after start of injection. Thus, the profile appears the same as it would if we were able to observe it within the core.

Construction of the trailing transition zone where gas displaces solvent is handled similarly. In this case $\bar{c}_g = 1 - \bar{c}$, a condition which denotes no oil present. Thus, the function g_1 has different numerical values at the trailing edge. Using Eq. 10 once again but with the new data, the shape of the gas-solvent transition zone $\bar{c}_c^*$ is as shown in Fig. 5. A convenient starting point for the calculation is $\bar{c}_i^* = 1$ at $t_i^* = 0$.

The curve calculated from Eq. 10 at the trailing edge of the slug gives the same t^* value for two different concentrations. This occurs because the permissible gradient becomes infinite at a concentration just below $\bar{c}_c^* = 0.8$. When solvent concentrations fall below this point, the mixture becomes gravity stabilized. Solvent is minimized by abrupt termination of the slug, following the solid curve. The dashed extension giving double values in Fig. 5 merely shows what the limiting behavior would be if the gas-solvent positions in the system were reversed.

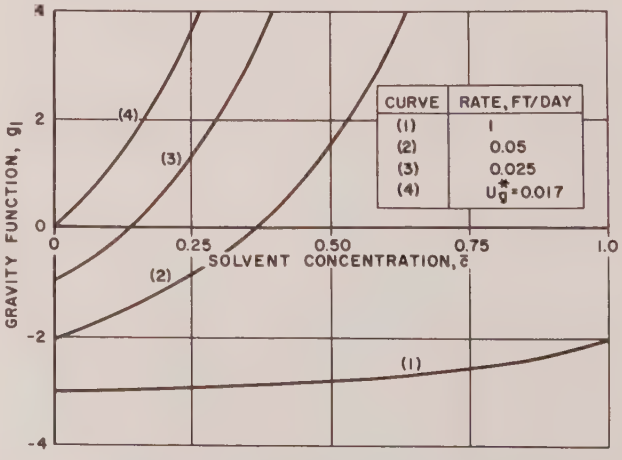

FIG. 3 – GRAVITY FUNCTION (g_1) FOR LONG-CORE FLOOD.

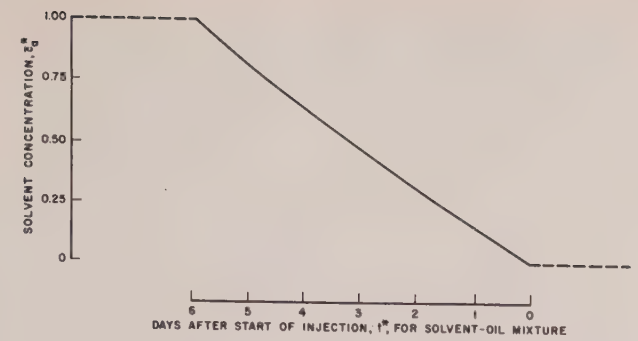

FIG. 4 — STABLE SOLVENT-OIL TRANSITION ZONE, LONG-CORE FLOOD.

Step 2

The second step is to find a way to form a slug that includes the stable transition zones, and that will not separate into two fluid phases at some later stage. The method is trial-and-error solution of a dispersion problem. Phase behavior is assumed to be known as a function of $\bar{c}$ and $\bar{c}_g$. (Note that the flow equations were written in terms of volume fractions, not mole fractions).

We start by visualizing the two transition zones separated by an unknown amount of gas- and oil-free solvent. The transition zones are shaped as noted under Step 1. These zones are conveniently labelled as $\bar{c}_a^*$ for the solvent-oil transition, $\bar{c}_b^*$ for plain solvent and $\bar{c}_c^*$ for the final gas-solvent transition. Each $\bar{c}^*$ will be a function $\bar{c}^*(\tau)$ of time τ. The time t_1 required to inject the solvent-oil transition zone $\bar{c}_a^*$ is known (Fig. 4), as is the time difference $t_3 - t_2$ for the final gas-solvent transition $\bar{c}_c^*$ (Fig. 5). The problem is to find the unknown time interval $t_2 - t_1$, during which plain solvent must be injected to prevent two-phase behavior at some later time.

When these fractions of the total solvent requirement are put together into a single injection program, the solvent concentration at any later time t and a distance x into the system will be given by

$$\bar{c}(x,t) = \int_0^{t_1} \bar{c}_a^*(\tau) F(\tau)\, d\tau + \int_{t_2}^{t_3} \bar{c}_c^*(\tau - t_2) F(\tau)\, d\tau + \tfrac{1}{2}\operatorname{erfc}\left[\frac{x - u_0(t-t_1)}{2\sqrt{D_1(t-t_1)}}\right] - \tfrac{1}{2}\operatorname{erfc}\left[\frac{x - u_0(t-t_2)}{2\sqrt{D_1(t-t_2)}}\right] \quad \ldots\ldots(11)$$

Negligible terms have been dropped from Eq. 11. The functions $\bar{c}_a^*(\tau)$ and $\bar{c}_c^*(\tau - t_2)$ are the transition zones as shown in Figs. 4 and 5. These are given implicitly by Eq. 10 as indicated under Step 1. The time variable τ is a dummy integration variable, and the function $F(\tau)$ is

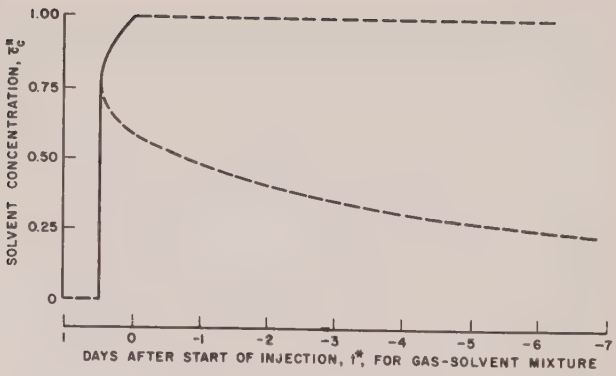

FIG. 5 — STABLE GAS-SOLVENT TRANSITION ZONE, LONG-CORE FLOOD.

$$F(\tau) = \left\{\frac{[x + u_0(t-\tau)]}{4\sqrt{\pi D_1}\,(t-\tau)^{3/2}}\right\} \exp\left\{-\left[\frac{x - u_0(t-\tau)}{2\sqrt{D_1(t-\tau)}}\right]^2\right\} \quad \ldots\ldots(12)$$

In a similar way, gas concentration is given by the following equation.

$$\bar{c}_g(x,t) = \tfrac{1}{2}\operatorname{erfc}\left[\frac{x - u_0(t-t_2)}{2\sqrt{D_1(t-t_2)}}\right] - \int_{t_2}^{t_3} \bar{c}_c^*(\tau - t_2) F(\tau)\, d\tau \quad \ldots\ldots(13)$$

Oil can be obtained by difference because the sum of all fractional concentrations must be one.

Starting with any reasonable estimate for the time t_2, trial-and-error procedures will lead to a solution. For example, let t be the time required for the flood to progress through the entire system. Using a trial value of t_2, compute $\bar{c}$ and $\bar{c}_g$ for a number of positions x. If all $\bar{c}$ and $\bar{c}_g$ values correspond to a single fluid phase, the trial t_2 overestimated the amount of solvent needed. A smaller t_2 should then be used. On the other hand, the data could indicate that two fluid phases would be present at some point in the system. This shows a need for more solvent and a larger value of t_2. The final time difference that proves satisfactory, $t_2 - t_1$, will indicate the shortest time for which plain solvent can be injected between leading and trailing transition zones while maintaining single-phase behavior throughout displacement. The result, $t_2 - t_1 = 0$, can be a correct answer for this problem and often may be a useful starting value for t_2.

Phase behavior for the example system is indicated by the data in Table 2. These data lead to the injection profile of Fig. 6 (Part A) that will remain both stable and in a single fluid phase while traveling 40 ft through the example long-core system. This profile contains less than 8 per cent of a pore volume of solvent. The appearance of the

profile after traveling 40 ft is shown by Part B of Fig. 6. Just a trace of oil in the gas-solvent transition region is enough to reach the miscibility limit. Everywhere except at the single indicated point the mixture is safely within the single-phase region, even though no region of pure solvent remains.

Step 3

The final step is to see how much, if any, flow rate can be increased with time. As the flood progresses, dispersion spreads out the solvent bank. Smaller concentration gradients should permit higher rates. The appropriate generalization of Eq. 7 for the critical rate becomes the minimum positive value of

$$u^* = \left\{ \frac{k}{\bar{\mu}} \frac{g \sin\theta}{\phi} \left[\frac{\partial \rho}{\partial \bar{c}} \frac{\partial \bar{c}}{\partial x} + \frac{\partial \rho}{\partial \bar{c}_g} \frac{\partial \bar{c}_g}{\partial x} \right] \right\} \left\{ \frac{D_3}{u^* L^2} \left[\beta^2 + n^2 \pi^2 \right] - \left[\frac{\partial \ln \mu}{\partial \bar{c}} \frac{\partial \bar{c}}{\partial x} + \frac{\partial \ln \mu}{\partial \bar{c}_g} \frac{\partial \bar{c}_g}{\partial x} \right] \right\}^{-1} \quad \ldots\ldots (14)$$

Eq. 14 includes the assumption that $\alpha = 0$ and is valid for one-dimensional flow. It allows for the effect of dispersion in stabilization, which is an addition to Eq. 7, and also allows for a three-component fluid.

The function u^* from Eq. 14 for the slug profile of Fig. 6 at 40 ft is plotted in Fig. 7. Because u^* is a limit function, Eq. 14 gives the limiting rates (from a possibly large range of rates as shown in Fig. 7) for which the displacement is stable. Thus, the shaded areas represent rates for which the corresponding part of the profile of Fig. 6 (Part B) is stable. As shown in Figs. 6 and 7, the critical rate is determined near the leading edge of the solvent bank. This is the smallest positive value of u^* obtained from Eq. 14, as shown by the data in Fig. 7. Negative rates calculated from Eq. 14 have no meaning. For the example data, the critical rate is about 2 ft/day, and a gradual increase in rate throughout the displacement is possible.

TABLE 2 – LIMITING COMPOSITIONS FOR MISCIBILITY, EXAMPLE THREE-COMPONENT SYSTEM

If $\bar{c}_g$ Is	$\bar{c}$ Must Be ≥	$(1-\bar{c}-\bar{c}_g)$ Must Be ≤
1.00	0	0
0.97	0.0291	0.0009
0.94	0.0582	0.0018
0.92	0.0774	0.0026
0.90	0.0966	0.0034
0.89	0.1062	0.0038
0.88	0.1157	0.0043
0.87	0.1251	0.0049
0.86	0.1344	0.0056
0.85	0.1435	0.0065
0.84	0.1524	0.0076
0.83	0.1611	0.0089
0.82	0.1695	0.0105
0.81	0.1777	0.0123
0.80	0.1854	0.0146

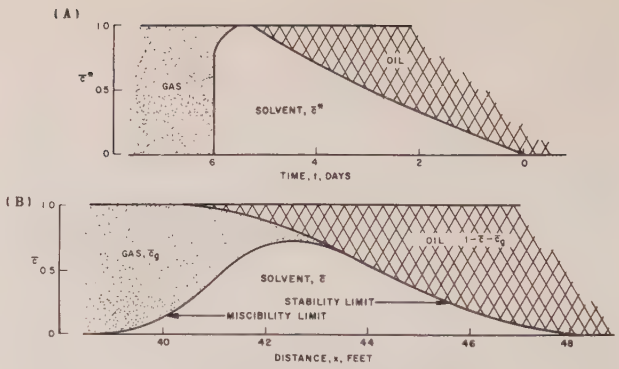

FIG. 6 – (A) MINIMUM SLUG INJECTION PROFILE AND (B) RESULTING PROFILE AT 40 FT, LONG-CORE FLOOD.

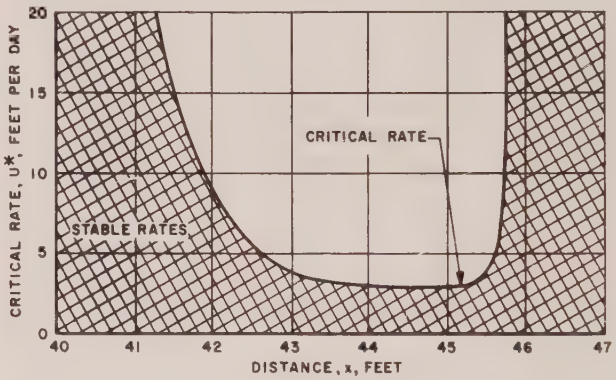

FIG. 7 – CRITICAL RATES FOR THE PROFILE OF FIG. 6 (PART B).

USE OF STABILITY THEORY WITH TWO-DIMENSIONAL FLOW

A mathematical solution to the problem of two-dimensional, stable displacement behavior has been obtained[1] for a set of reasonable assumptions. The present section of this paper shows an example result which makes use of this solution. The example reservoir is linear, 10-ft thick and has a 10° dip. The flood rate is 1 ft/day. Other properties are given in Table 1. While profiles are useful in depicting one-dimensional flow behavior, two-dimensional flow is best illustrated as a solvent concentration "wave". Any cross section through the wave then gives a concentration profile. If fingering did not occur, therefore, the advancing solvent can be pictured as the wave shown in Fig. 8. Fig. 8 is an oblique view illustrating the shape of the wave after it travels 1,600 ft. Concentration is plotted along the vertical axis. The positive x-direction is to the right and the positive z-direction into the page; thus, the view is the same as if the reservoir were tipped on its side. For clarity, z-distances are also magnified relative to x-distances. Concentration profiles parallel to the direction of flow are given for distances of 0, 2.5, 5, 7.5 and 10 ft above the lower reservoir boundary.

Similar calculations reveal that, at the short distance of 100 ft, lateral dispersion has had almost no effect at all. The effect gradually increases, until at 6,400 ft the solvent wave is completely

smeared out in the (vertical) z-direction. As shown in Fig. 8, some segregation persists at 1,600 ft. The regions stable to a $\cos \pi y \cos \pi z$ disturbance are cross-hatched in Fig. 8. These exclude large regions of intermediate concentration with high concentration gradients in the x-direction. The steepest gradients in the z-direction occur near the center of the system. Here the stabilizing influence of gravity is felt most strongly, and the thickness of the unstable region is reduced to a minimum.

It is unlikely that displacement could occur without fingering when unstable regions persist as shown by Fig. 8. The perturbation considered has a wave length of 2 ft. This is equivalent to considering the example 10-ft section of reservoir as if it were made up from a stack of similar 2-ft thick sections. Within this stack, similar inhomogeneities would be (at most) 2-ft apart. Although each geologic formation must have its own pattern of variability, such values would seem to be reasonable for many natural oil-reservoir rocks. We conclude that, for stability and for maximum efficiency, the flood described above should have been conducted under more restrictive conditions. A relatively high oil viscosity of 10 cp was included in the assumptions for this example, however. A more suitable reservoir would contain lower viscosity oil. For example, with 2-cp oil and no change in the other properties, displacement would be stable except during an early period of high concentration gradients. Provided initial problems could be overcome, efficient displacement would become practical.

SIMPLIFIED METHODS FOR USE OF THEORETICAL RESULTS

The principles outlined in the preceding sections can be applied to any reservoir problem, no matter how complex the flow pattern may be. A more exact theory could have been developed by starting from a more detailed mathematical picture of flow within an imperfect system. This would add complexity, however, and does not at present appear justified. Economics will usually dictate just how detailed a useful theory should be. For some purposes it would seem that even simpler methods than those presented could be adopted; therefore, we will discuss several useful simplifications.

EQUIVALENT LINEAR SYSTEM

Whatever the detailed pattern of a field-scale flood, a useful approximation is as an equivalent rectangular system in which flow is linear. That is, rows of injection wells and production wells are replaced by lines drawn to connect members of a row across the system. The distance between injection and production lines drawn in this way then is chosen to represent the path length along which dispersion mixing will occur. Thus, the mathematical problem is reduced in crude fashion by one dimension, and the methods presented herein become applicable. Growth of the transition zone during stable flow is related approximately to the square root of the distance traveled. Thus, to minimize solvent requirement, a single slug should be made to travel the entire length of a long and narrow system.

EXTENDED "RECTANGULAR" SLUG

Although the concept of the injection of a solvent gradient is sound, many practical problems are involved. These may make further consideration of abrupt injection of solvent worthwhile. Fingering is almost certain to follow such an abrupt change and

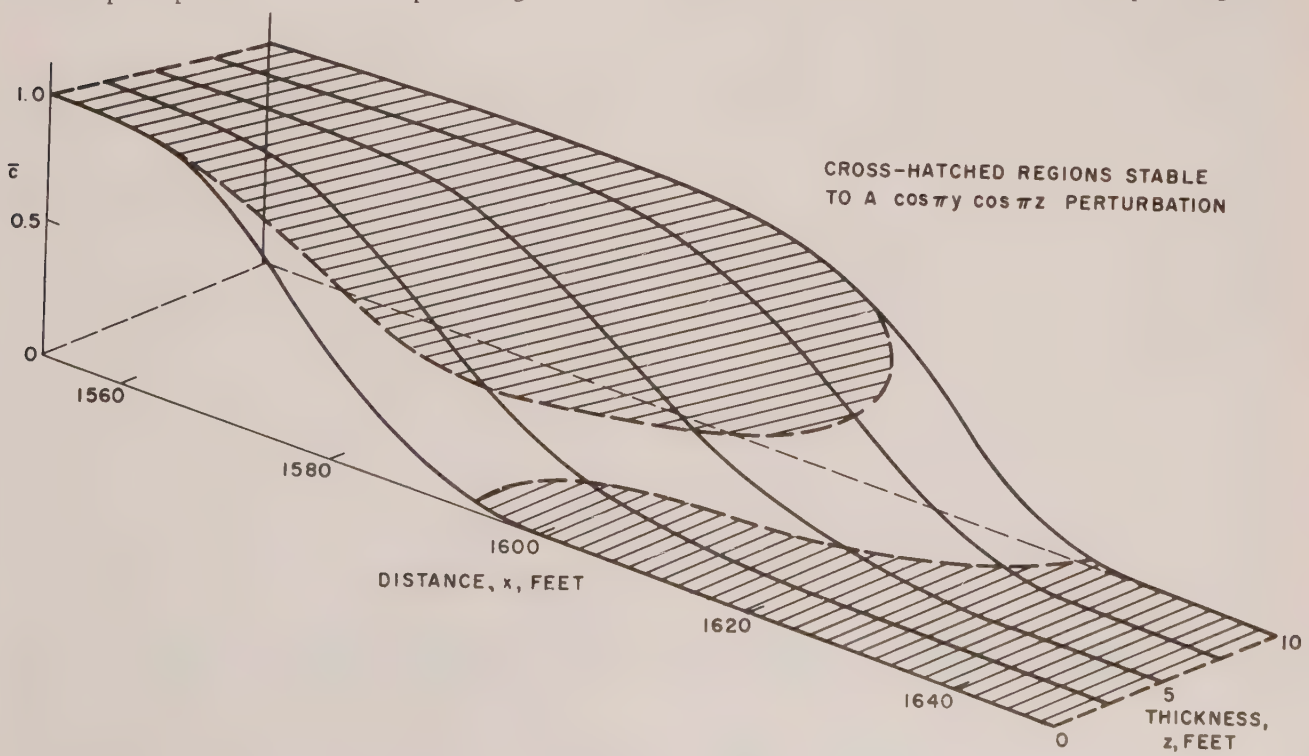

FIG. 8 — CONCENTRATION PROFILES AT 1,600 FT, TWO-DIMENSIONAL EXAMPLE.

will increase the solvent requirement. The question is, how much should such an excess be?

The first step toward a useful approximate answer is to compute the time required to inject a minimum-solvent transition zone, as given by Eq. 10. In place of the gradient, however, plain solvent is to be injected for the same total length of time. Thus, the solvent injection profile becomes rectangular in shape and contains a solvent excess that depends in an appropriate way on the degree of instability. This makes a reasonable allowance for instability. Miscibility calculations for a rectangular slug with stable flow become particularly simple. If fingering ensues, however, the computed results could be in serious error. The excess solvent injected because of instability will be lost. A proper way to approximate the extended slug requirement is as follows.

Step 1

When the injected concentration profile is rectangular in shape and dispersion is the mixing mechanism, solvent and gas concentration equations reduce to

$$\bar{c} = \tfrac{1}{2}\,\mathrm{erfc}\left[\frac{x-u_0 t}{2\sqrt{D_1 t}}\right] - \tfrac{1}{2}\,\mathrm{erfc}\left[\frac{x-u_0(t-t')}{2\sqrt{D_1 (t-t')}}\right] \quad \ldots\ldots\ldots (15)$$

$$\bar{c}_g = \tfrac{1}{2}\,\mathrm{erfc}\left[\frac{x-u_0(t-t')}{2\sqrt{D_1 (t-t')}}\right] \quad \ldots\ldots\ldots (16)$$

The first step is to compute $\bar{c}$ and $\bar{c}_g$ using Eqs. 15 and 16 for various positions x within the transition zone. The time t' is the time for which plain solvent is assumed to have been injected. Trial-and-error procedures are used to find the smallest time t' for which all portions of the solvent slug will remain miscible until it has reached the end of the system.

Step 2

Compute from Eq. 10 the total time required to inject a stable solvent-oil transition zone. Repeat the computation to find the time to inject a gas-solvent transition zone. The function g_1 will differ for the two computations.

Step 3

Take one-half the sum of the transition-zone times from Step 2 and add this to the minimum time t' found under Step 1. The total is the estimated time during which solvent alone should be injected to form an extended rectangular slug. It includes an allowance for instability.

GRAVITY SEGREGATION

The two-dimensional result in Fig. 8 shows the behavior of a stable concentration wave after it has traveled a substantial distance. During earlier stages, a large amount of "extra" solvent appears necessary because of gravity segregation. For the example data at a distance of 6,400 ft, however, the profile proved nearly uniform in cross section. In addition, it was spread out in the direction of flow little more than it would have been had true one-dimensional flow and dispersion prevailed.

We conclude that no allowance for gravity segregation is required when a solvent bank is to travel as much as 1,000 times the bed thickness. In such cases the problem can be reduced to one dimension. This does not apply to shorter, thicker systems for which solvent may tend to override the oil. These require detailed study.

CONCLUSIONS

A theory of stability in miscible displacement of oil by a solvent has been presented. Application of the theory leads to the definition of limiting conditions for stable miscible displacement, such as a minimum slug size. The criteria that must be satisfied are miscibility and stability. Stability means that no viscous fingering will occur and that mixing will be caused only by dispersion. Miscibility means that complete recovery in the swept regions will be obtained. Thus, for any specified set of reservoir conditions an optimum use of solvent is defined.

ACKNOWLEDGMENT

This paper is an outgrowth of a paper[2] presented in 1959 at the AIChE-SPE Joint Symposium in San Francisco. The author prepared the Symposium paper while associated with the California Research Corp., La Habra, Calif.

REFERENCES

1. Perrine, R. L.: "The Development of Stability Theory for Miscible Liquid-Liquid Displacement", *Soc. Pet. Eng. Jour.* (March, 1961) 17.
2. Perrine, R. L.: "Conditional Instability in Miscible Liquid-Liquid Displacement", Preprint No. 42 presented at the AIChE-SPE Joint Symposium in San Francisco (Dec. 6-9, 1959).
3. Blackwell, R. J.: "Laboratory Studies of Microscopic Dispersion Phenomena in Porous Media", Preprint No. 29 presented at the AIChE-SPE Joint Symposium in San Francisco (Dec. 6-9, 1959).
4. de Jong, G. de Josselin: *Trans.*, Am. Geophys. Union (Feb., 1958) Vol. 39, 67.
5. Saffman, P. G.: *Jour. Fluid Mech.* (Oct. 1959) Vol. 6, 321.
6. Weinaug, C. F. and Ling, D.: U. S. Patent No. 2,867,277 (Jan. 6, 1959).
7. von Rosenberg, D. U.: *AIChE Jour.* (March, 1956) Vol. 2, 55.
8. Day, P. R.: *Trans.*, Am. Geophys. Union (1956) Vol. 37, 595.
9. Blackwell, R. J., Rayne, J. R. and Terry, W. M.: "Factors Influencing the Efficiency of Miscible Displacement", *Trans.*, AIME (1959) Vol. 216, 1. ***

The Development of Stability Theory for Miscible Liquid-Liquid Displacement

RICHARD L. PERRINE
MEMBER AIME

U. OF CALIFORNIA AT LOS ANGELES
LOS ANGELES, CALIF.

ABSTRACT

A stability theory is developed for miscible liquid-liquid displacement within a porous medium. In the usual case considered, a high-density high-viscosity "oil" is displaced downdip by a low-density low-viscosity "solvent". Perturbation methods are used to find the conditions under which the spreading mechanism changes from the stable dispersion process to unstable viscous fingering. We find that instability is conditional, that there is a dependence on the shape of a disturbance leading to a "diameter" effect and that very difficult experimental scaling problems may result. A useful consequence is the definition of a minimum "slug size" for stable miscible displacement. This should make possible optimum use of the solvent process for oil recovery. The results may apply to many situations in which one fluid displaces another of somewhat different fluid properties within a porous medium.

INTRODUCTION

The process of miscible liquid-liquid displacement looked very favorable when it first received serious consideration as a means to increase petroleum recovery. Some early laboratory results were interpreted to mean that only a small "slug" of solvent was needed, perhaps 2 to 3 per cent of a hydrocarbon pore volume. This "slug" could recover the oil in an entire reservoir provided the fluids remained miscible.[1,2] Only a slow growth of the "mixing zone", or gradual transition from oil to solvent, should occur. This would follow naturally from mixing by a dispersion mechanism such as that described by Scheidegger.[3] And, indeed, laboratory cores have shown this kind of behavior provided solvent viscosity was at least as great as that of the oil.[2,4-6] The same kind of behavior has also been observed with solvent viscosity lower than that of the oil after the distance traversed became large. Not all laboratory results have been this favorable, however.[7-9] Mixing zone growth may become proportional to the distance traveled rather than the square root of this quantity. Such behavior accompanies high rates in short systems of large diameter, provided the viscosity ratio is adverse. If this more rapid spreading were to persist in a reservoir, the solvent requirement for miscible "slug" displacement could exceed 30 per cent of a pore volume. There is considerable economic importance in the difference between 3 and 30 per cent solvent.

A logical conclusion is that two different kinds of flow behavior are possible, with each kind leading to a different result. One kind gives efficient displacement, the other does not. In the efficient case, the solvent bank spreads out only by the mechanism we have termed dispersion. Under these conditions, displacement is as near piston-like as possible. In the second kind of flow, found only with adverse viscosity ratios, viscous fingering occurs. That is, permeability variations cause a small finger of low-viscosity solvent-rich fluid to move ahead of its average position within the mixing zone. This creates a path of low resistance to flow, and an even greater amount of solvent-rich fluid follows. Thus, the process is autocatalytic. Once started, the fingering mechanism rapidly becomes dominant.

The question to be answered is this. Under what conditions will each of these two different kinds of flow occur? In particular, what conditions denote the transition from dispersion to viscous fingering as the solvent spreading mechanism? The answer may tell us whether or not the desirable, near piston-like miscible displacement process is practical. An answer to this problem can be obtained from theory by the use of perturbation methods. The procedure is as follows. We first formulate a mathematical representation of the system. Then a small disturbance (or perturbation) in solvent concentration profile is introduced and observed to see what happens. Unstable flow is indicated when a small disturbance will grow larger. This will lead to eventual viscous fingering. If on the other hand the disturbance dies out, the displacement is stable. In this latter case, with dispersion as the spreading mechanism, near piston-like displacement is possible.

Thus, this paper presents the development of a stability theory for miscible liquid-liquid displace-

Original manuscript received in Society of Petroleum Engineers office May 23, 1960. Revised manuscript received Oct. 27, 1960.

[1]References given at end of paper.

ment. The problem differs from immiscible displacement theory[10] in that no interface between fluids is involved. The results are important because they state the limiting conditions required for efficient, stable miscible displacement of oil by a solvent. Thus, they determine a minimum "slug" size. The results are optimistic to the extent that only small disturbances in an otherwise ideal system are considered. A less ideal system could only lead to less favorable results such as the requirement of additional solvent. When the required conditions prove impractical, the reservoir is not suited to the miscible "slug" process. An alternative recovery method should then be used.

APPLICATION OF PERTURBATION METHODS

Mathematical description of stable miscible displacement involves two transport mechanisms – flow, and what we will term "hydrodynamic dispersion".[3,11-16] While such concepts as flow and diffusion are well understood, dispersion is relatively new. Thus, a brief description is included. The reader is urged to consult the references for thorough, rigorous development.

We consider a system that is semi-infinite in the x-direction, infinite in the y-direction, and bounded at $z' = 0$ and $z' = L$ in the z-direction. The x-axis is rotated to a negative angle θ below the horizontal. Flow is one-dimensional in the positive x-direction, and the respective dispersion coefficients are assumed constant. Fluid density is a linear function of solvent concentration, while viscosity dependence is exponential. Although not necessary, these assumptions give simplicity with little loss in generality. The fluids are assumed incompressible, and the system homogeneous in its properties.

We will use the following notation, where primes indicate actual variables and unprimed quantities their dimensionless equivalents.

$$x = x'/L - u_0 t'/L, \quad x_s = x'/L, \quad y = y'/L$$

$$z = z'/L, \quad t = u_0 t'/L, \quad u = u'/u_0,$$

$$v = v'/u_0, \quad w = w'/u_0, \quad p = kp'/Lu_0\mu_0\phi,$$

$$D_1 = D_1'/Lu_0, \quad D_3 = D_2'/Lu_0 = D_3'/Lu_0$$

$$\eta_q = \frac{\partial \eta}{\partial q}, \text{ etc.}$$

The space co-ordinates, thus, are x, y and z, and t is the time. The linear displacement velocity for stable displacement is u_0, while μ_0 is the fluid viscosity at zero concentration and c is the fractional solvent concentration. Velocities in the x, y and z directions are u, v and w. These velocities are volumetric flow rates per unit cross-sectional area and per unit porosity. P is pressure, k permeability, ρ density, g the acceleration of gravity and ϕ porosity. Dispersion coefficients are denoted by D, and letter subscripts are used to denote partial derivatives.

To help visualize the way in which fluid moves through porous rock, it is convenient to think of the fluid as if it existed in many separate fluid "elements", each bounded by an imaginary surface. Thus, it is possible to discuss the motion of a single element much as if it moved independently of all others. Thinking this way and recognizing that porous materials are homogeneous only in a gross sense, at any time some elements will be moving faster than others. The relative speed will vary with local pore geometry. Thus, of many possible paths leading downstream, some will prove to be much faster on the average than others. An element entering a fast path will travel further in a given period of time than the average of all such elements. But there must also be some slower than average paths. The net result is that a cloud of fluid elements starting out together will become spread out, or dispersed, both in the direction of flow and to the side. A few will end up far downstream, a few will move very little and most will travel at nearly the average rate. This spreading is what is termed dispersion.

The several theoretical treatments of dispersion that have been given[3,11-16] lead to a common result: to a good approximation, the dispersion process is mathematically described by the diffusion equation with constant dispersion coefficients (units of a diffusion coefficient). Dispersion coefficients in the direction of flow (axial) and at right angles (lateral) may differ substantially.[15-17] At some low rate, the dispersion process necessarily reduces to molecular diffusion. Thus, the description of stable miscible displacement requires a diffusion-type equation for solvent continuity, an equation for continuity of velocity and Darcy's law for the equations of motion. In terms of the stationary dimensionless co-ordinates (x_s), these become

$$c_t - D_1 c_{xx} - D_3 c_{yy} - D_3 c_{zz} + uc_x + vc_y + wc_z = 0 \quad \text{.....(1.1)}$$

$$u_x + v_y + w_z = 0 \quad \text{.....(1.2)}$$

$$u + (\mu_0/\mu)p_x + (k\rho g \sin\theta)/u_0\mu\phi = 0 \quad \text{..... (1.3)}$$

$$v + (\mu_0/\mu)p_y = 0 \quad \text{..... (1.4)}$$

$$w + (\mu_0/\mu)p_z + (k\rho g \cos\theta)/u_0\mu\phi = 0 \quad \text{..... (1.5)}$$

DEVELOPMENT OF PERTURBATION EQUATIONS

There are two kinds of displacement – stable and unstable – so that we are led to ask the following question. Which kind of flow is more likely to occur, and under what conditions? Mathematically, the problem can be stated this way. Suppose there is a quantity $\bar{c}$ which represents solvent concentration for stable flow. It is a solution of Eqs. 1.1 through 1.5. Suppose also that the actual sol-

vent concentration c differs just slightly from the barred quantity. Will c then change toward $\bar{c}$ or away from it?

This problem can be pictured for a hypothetical system by drawing contours along which concentration remains constant. Fig. 1 shows such a visualization for a two-dimensional system. Initially, all contours parallel the z-axis in an ideal system, as shown in Part A. This corresponds to stable behavior. A more natural kind of behavior is shown in Part B of Fig. 1. Rather than being straight, the contours contain small disturbances, or perturbations, such as would result from the normal variation of properties within a real system. When instability occurs, any small disturbances (as in Part B) may grow and acquire a finger-like shape. This result is what is shown in Part C.

Thus, the dependent variables in a real system (including small perturbations) are denoted by a set of equations of the form given by Eq. 2.[18]

$$\eta = \bar{\eta} + \epsilon\eta^{(1)} + \epsilon^2\eta^{(2)} + \cdots,$$

$$\eta = c,\ u,\ v,\ w,\ p \qquad \ldots\ldots\ldots\ldots\ldots\ldots\ldots\ldots (2.0)$$

Each barred quantity represents a stable displacement result, such as is shown in Part A of Fig. 1. These are solutions of Eq. 1.1 through 1.5. The remainder of Eq. 2 represents the perturbation. If Eq. 2 is also to be a solution of the equations of Eq. 1 with an arbitrary small ϵ, after substitution the coefficients of ϵ^n must vanish separately for each n. Thus, from the coefficients of $\epsilon^1 = \epsilon$, we obtain the first-order perturbation equations.

$$c_t^{(1)} - D_1 c_{xx}^{(1)} - D_3 c_{yy}^{(1)} - D_3 c_{zz}^{(1)} + \bar{u}c_x^{(1)} + \bar{v}c_y^{(1)} + \bar{w}c_z^{(1)} + \bar{c}_x u^{(1)} + \bar{c}_y v^{(1)} + \bar{c}_z w^{(1)} = 0 \qquad \ldots\ldots\ldots\ldots\ldots (3.1)$$

$$u_x^{(1)} + v_y^{(1)} + w_z^{(1)} = 0 \qquad \ldots\ldots\ldots\ldots (3.2)$$

$$u^{(1)} + \frac{\mu_0}{\bar{\mu}} p_x^{(1)} + \left[\frac{kg}{\bar{\mu}u_0}\frac{d\rho}{dc}\frac{\sin\theta}{\phi} + \bar{u}\frac{d\ln\mu}{dc}\right] c^{(1)} = 0 \qquad \ldots\ldots\ldots\ldots\ldots (3.3)$$

$$v^{(1)} + \frac{\mu_0}{\bar{\mu}} p_y^{(1)} + \left[\bar{v}\frac{d\ln\mu}{dc}\right] c^{(1)} = 0 \qquad \ldots\ldots\ldots\ldots\ldots\ldots\ldots\ldots\ldots\ldots\ldots\ldots (3.4)$$

$$w^{(1)} + \frac{\mu_0}{\bar{\mu}} p_z^{(1)} + \left[\frac{kg}{\bar{\mu}u_0}\frac{d\rho}{dc}\frac{\cos\theta}{\phi} + \bar{w}\frac{d\ln\mu}{dc}\right] c^{(1)} = 0 \qquad \ldots\ldots\ldots\ldots\ldots (3.5)$$

The dispersion coefficients D_1 and D_3 are considered to be unaffected by the perturbation. This is not strictly correct because they depend on the displacement velocity. For cases of interest, however, flux by dispersion is a small fraction of the total. We considerably simplify the problem by this neglect of a second-order effect.

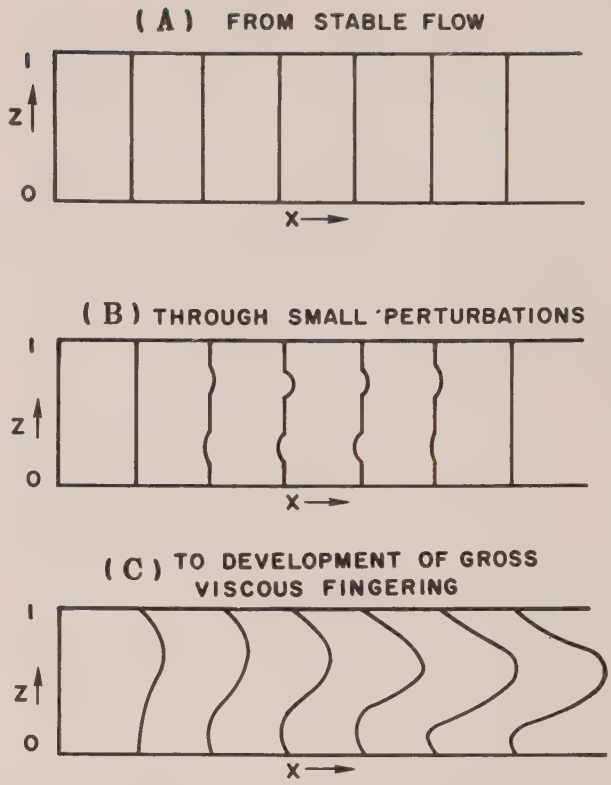

FIG. 1 – GROWTH OF FINGERING AS SHOWN BY CONTOURS.

So long as discussion is restricted to the first-order theory, the superscripts (1) for the perturbation variables can be dropped. The bar is retained to designate the properties of the stable displacement. At this point, we also make use of several assumed properties of the linear stable flow: $\bar{u} = 1$, $\bar{v} = \bar{w} = 0$, $\bar{c}_y = 0$. Transforming to moving space co-ordinates $x = x_s - t$, we obtain as the perturbation equations

$$c_t - D_1 c_{xx} - D_3 c_{yy} - D_3 c_{zz} + \bar{c}_x u + \bar{c}_z w = 0 \qquad \ldots\ldots\ldots\ldots\ldots\ldots (4.1)$$

$$u_x + v_y + w_z = 0 \qquad \ldots\ldots\ldots\ldots\ldots\ldots (4.2)$$

$$u + (\mu_0/\bar{\mu})p_x + g_1 c = 0 \qquad \ldots\ldots\ldots\ldots (4.3)$$

$$v + (\mu_0/\bar{\mu})p_y = 0 \qquad \ldots\ldots\ldots\ldots\ldots\ldots (4.4)$$

$$w + (\mu_0/\bar{\mu})p_z + g_3 c = 0 \qquad \ldots\ldots\ldots\ldots (4.5)$$

where the functions g (of $\bar{c}$) are defined by

$$g_1 = \frac{d\ln\mu}{dc} + \frac{kg}{\bar{\mu}u_0}\frac{d\rho}{dc}\frac{\sin\theta}{\phi} \qquad \ldots\ldots\ldots (5.1)$$

$$g_3 = \frac{kg}{\bar{\mu}u_0}\frac{d\rho}{dc}\frac{\cos\theta}{\phi} \qquad \ldots\ldots\ldots\ldots\ldots (5.2)$$

Because the set of equations of Eq. 4 are linear, an arbitrary initial perturbation is readily expressed as the sum of its Fourier components. This assumes that conditions of convergence and differentiability

are met. The equations of Eq. 4 describe the deviation of a small perturbation from stable behavior. Higher-order perturbation theory can be applied for larger disturbances by also considering variables with superscripts of two or higher.

SOLUTION OF THE PERTURBATION EQUATIONS

Linearity of the equations of Eq. 4 also means that the solution for an arbitrary perturbation will be the sum of solutions for the individual Fourier components. Thus, we need only study separately the behavior of particular complex Fourier terms. One such follows.

$$\eta = \tilde{\eta} \exp\,[if(x,y,z,t)],$$

$$\eta = c, u, v, w, p \quad \ldots\ldots\ldots\ldots\ldots\ldots\ldots\ldots (6.0)$$

where

$$f(x,y,z,0) = \alpha x + \beta y + n\pi z \ldots\ldots\ldots (7.0)$$

It is understood that the physical quantities represented by Eq. 6 are real. Substituting in the equations of Eq. 4 from Eq. 6,

$$\left[if_t - iD_1 f_{xx} - iD_3 f_{yy} - iD_3 f_{zz} + D_1 f_x^2 + D_3 f_y^2 + D_3 f_z^2 \right] \tilde{c} + \bar{c}_x \tilde{u} + \bar{c}_z \tilde{w} = 0$$

$$\ldots\ldots\ldots\ldots\ldots\ldots\ldots\ldots\ldots\ldots\ldots\ldots\ldots\ldots (8.1)$$

$$if_x \tilde{u} + if_y \tilde{v} + if_z \tilde{w} = 0 \ldots\ldots\ldots\ldots (8.2)$$

$$g_1 \tilde{c} + \tilde{u} + i(\mu_0/\bar{\mu}) f_x \tilde{p} = 0 \ldots\ldots\ldots (8.3)$$

$$\tilde{v} + i(\mu_0/\bar{\mu})\, f_y \tilde{p} = 0 \ldots\ldots\ldots\ldots\ldots (8.4)$$

$$g_3 \tilde{c} + \tilde{w} + i(\mu_0/\bar{\mu})\, f_z \tilde{p} = 0 \ldots\ldots\ldots (8.5)$$

In matrix notation, these equations are of the form, $A\tilde{y} = 0$, which requires either that the column vector $\tilde{y}$ is zero or that $|A| = 0$. Thus, we obtain

$$\{[if_t - iD_1 f_{xx} - iD_3 f_{yy} - iD_3 f_{zz} + D_1 f_x^2 + D_3 f_y^2 + D_3 f_z^2][f_x^2 + f_y^2 + f_z^2]\} + Ef_x^2 + Ff_x f_z + Gf_z^2 + (E+G) f_y^2 = 0$$

$$\ldots\ldots\ldots\ldots\ldots\ldots\ldots\ldots\ldots\ldots\ldots\ldots\ldots\ldots (9.0)$$

where the functions E, F and G are defined as

$$E = -\, g_3 \bar{c}_z \ldots\ldots\ldots\ldots\ldots\ldots\ldots\ldots\ldots (10.1)$$

$$F = g_3 \bar{c}_x + g_1 \bar{c}_z \ldots\ldots\ldots\ldots\ldots\ldots (10.2)$$

$$G = -\, g_1 \bar{c}_x \ldots\ldots\ldots\ldots\ldots\ldots\ldots\ldots\ldots (10.3)$$

The solution $f(x,y,z,t)$ to Eq. 9 must satisfy the initial condition, Eq. 7, and also the boundary conditions

$$\left.\begin{array}{l} \text{Real } c_z = 0 \\ \text{Real } w = 0 \end{array}\right\} \quad z = 0,\ z = 1 \ldots\ldots (11.0)$$

To solve Eq. 9, we assume that the function can be expanded as a Taylor series. This requires that the complex variable f be an analytic function. If f is also to satisfy Eq. 7,

$$f(x,y,z,t) = \alpha x + \beta y + n\pi z + f_t^\circ t + (2!)^{-1}[f_{tt}^\circ t^2 + 2f_{xt}^\circ (x-x_o)t + 2f_{yt}^\circ (y-y_o)t + 2f_{zt}^\circ (z-z_o)t] + \cdots$$

$$\ldots\ldots\ldots\ldots\ldots\ldots\ldots\ldots\ldots\ldots\ldots\ldots\ldots\ldots (12.0)$$

The superscripts o indicate that the coefficients are to be evaluated at the point $(x_o, y_o, z_o, 0)$. We can similarly expand the known functions E, F and G of the stable solution. For example,

$$E = E^\circ + E_x^\circ (x-x_o) + E_z^\circ (z-z_o) + E_t^\circ t + (2!)^{-1}[E_{xx}^\circ (x-x_o)^2 + E_{zz}^\circ (z-z_o)^2 + E_{tt}^\circ t^2 + 2E_{xz}^\circ (x-x_o)(z-z_o) + 2E_{xt}^\circ (x-x_o)t + 2E_{zt}^\circ (z-z_o)t] + \cdots \ldots (13.0)$$

After taking the indicated derivatives, the results are substituted in Eq. 9. For f to be a solution, the coefficients of each term in $(x-x_o)$, $(x-x_o)t$, t^2, etc., must vanish. This leads to an infinite sequence of algebraic equations. In terms of the functions,

$$\delta^{-2} = (\alpha^2 + \beta^2 + n^2\pi^2)^{-1} \ldots\ldots\ldots (14.1)$$

$$H^\circ(x,z,t) = (\alpha^2 + \beta^2)E^\circ + \alpha n\pi F^\circ + (\beta^2 + n^2\pi^2)G^\circ \ldots\ldots (14.2)$$

$$H_x^\circ = (\alpha^2 + \beta^2)E_x^\circ + \alpha n\pi F_x^\circ + (\beta^2 + n^2\pi^2)G_x^\circ, \text{ etc.} \ldots\ldots (14.3)$$

The first of these equations are

$$if_t^\circ = -\,\alpha^2 D_1 - (\beta^2 + n^2\pi^2) D_3 - \delta^{-2} H^\circ \ldots\ldots\ldots\ldots (15.1)$$

$$if_{xt}^\circ = -\,\delta^{-2} H_x^\circ \ldots\ldots\ldots\ldots\ldots (15.2)$$

$$if_{yt}^\circ = 0 \ldots\ldots\ldots\ldots\ldots\ldots\ldots (15.3)$$

$$if_{zt}^\circ = -\,\delta^{-2} H_z^\circ \ldots\ldots\ldots\ldots\ldots (15.4)$$

$$if_{tt}^\circ = -\,\delta^{-2}(H_t^\circ + D_1 H_{xx}^\circ + D_3 H_{zz}^\circ) - i\delta^{-2}\{H_x^\circ [2\alpha D_1 + \delta^{-2}(2\alpha E^\circ + n\pi F^\circ) - \delta^{-4}(2\alpha H^\circ)] + H_z^\circ [2n\pi D_3 + \delta^{-2}(\alpha F^\circ + 2n\pi G^\circ) - \delta^{-4}(2n\pi H^\circ)]\} \ldots\ldots\ldots (15.5)$$

$$if_{xxt}^\circ = -\,\delta^{-2} H_{xx}^\circ \ldots\ldots\ldots\ldots\ldots (15.6)$$

$$if^{\circ}_{yyt} = 0 \quad \ldots\ldots(15.7)$$

$$if^{\circ}_{zzt} = -\delta^{-2}H^{\circ}_{zz} \quad \ldots\ldots(15.8)$$

Before proceeding further, it is worthwhile to note several facts. First, if perturbation growth requires that the higher-order theory be considered, these higher-order terms will contribute a higher growth rate. For example, if a term in the first-order solution grows initially at the rate exp (bt), there will be a corresponding part of the second-order solution initially proportional to exp ($2bt$). Thus, any growth implies rapid growth, and it is sufficient to follow the behavior of the system for a short time. The behavior must be known at every position, however. Because we know the functions H for every position (x_o, y_o, z_o), the results are conveniently expressed as the family of particular solutions $f(x_o,y_o,z_o,t)$. The Taylor series then simplifies to a series in time t only, from which we need at most a few terms.

$$f(x_o,y_o,z_o,t) = \alpha x_o + \beta y_o + n\pi z_o + f^{\circ}_t t + (2!)^{-1}f^{\circ}_{ttt}t^2 + (3!)^{-1}f^{\circ}_{ttt}t^3 + \cdots \quad \ldots\ldots(16.0)$$

The first two coefficients of t are given by Eqs. 15.1 and 15.5.

Thus, the first-order perturbation solution can be expressed in the following form, as for concentration.

$$c = \tilde{c} \exp(i\alpha x + i\beta y + in\pi z + i\gamma_I t) \exp(-\gamma_R t) \quad \ldots\ldots(17.0)$$

in which the "phase shift" coefficient γ_I is given by

$$\gamma_I = \text{Real}\left[\sum_{m=1}^{\infty} (m!)^{-1}f^{\circ}_{mt}t^{m-1}\right] \quad \ldots(18.1)$$

and the "stability" coefficient γ_R is given by

$$i\gamma_R = \text{Imaginary}\left[\sum_{m=1}^{\infty} (m!)^{-1}f^{\circ}_{mt}t^{m-1}\right] \quad \ldots\ldots(18.2)$$

In terms of the function values given in Eqs. 15.1 and 15.5, these are

$$\gamma_I = -\tfrac{1}{2}t\delta^{-2}\{H^{\circ}_x[2\alpha D_1 + (2\alpha E^{\circ} + n\pi F^{\circ})\delta^{-2} - 2\alpha H^{\circ}\delta^{-4}] + H^{\circ}_z[2n\pi D_3 + (\alpha F^{\circ} + 2n\pi G^{\circ})\delta^{-2} - 2n\pi H^{\circ}\delta^{-4}]\} + \cdots \quad \ldots\ldots(19.1)$$

$$\gamma_R = [\alpha^2 D_1 + (\beta^2 + n^2\pi^2)D_3 + \delta^{-2}H^{\circ}] + \tfrac{1}{2}t\delta^{-2}[H^{\circ}_t + D_1 H^{\circ}_{xx} + D_3 H^{\circ}_{zz}] + \cdots \quad \ldots\ldots(19.2)$$

The parameters α, β and n characterize the initial perturbation, as do the functions E°, F° and G° the initial state of the corresponding stable displacement.

We wish to find from Eq. 17 the conditions under which the perturbation becomes smaller in time. Because $\tilde{c}$ is constant and the complex exponential is limited in magnitude to one, stability does not depend on them at all. The important factor in determining growth is the exponential term that remains and which, in turn, depends on the stability coefficient γ_R. For stability to be assured, each such coefficient of time in the Fourier series must be positive. This will guarantee that each term grows smaller with time. If so much as a single value of γ_R were negative, a small disturbance could grow at an exponential rate and eventually lead to viscous fingering. This means that only the least stable term of the original, complete Fourier series need be considered. If this one term with minimum γ_R grows smaller, all other terms will do the same.

A study of the functions involved will show that stability can arise from several sources. For example, gravitational forces can offset viscous forces under some conditions and provide gravity stabilization. In other cases gravity may not be quite sufficient, but the additional effect of dispersion may keep γ_R positive. This second case is dispersion stabilization. Stability is determined by the interplay of forces so that behavior changes with different displacement conditions. However, even the most general problem can be reduced to determining the sign of the coefficient of time in an exponent.

To repeat the reasoning we have followed, suppose we are given an arbitrary initial disturbance. A complete description of flow behavior would require solution of nonlinear partial differential equations in which coefficients (such as the flow rate) depend on the solvent concentration answer. In fact, for some conditions we may even be uncertain as to what equations will eventually be required to describe the behavior. But before it can die out, any disturbance must first become small enough for our linearized theory to apply. Giving this small disturbance a Fourier series representation, any unstable terms with negative γ would grow rather than die out, although there would be deviations from the predicted growth for moderately large amplitudes. The limiting conditions for stable miscible displacement can be specified after consideration of all possible modes of disturbance.

It is possible to have borderline instability without viscous fingering. If growth is slow enough, a return to stable displacement is possible before any macroscopic fingers are formed. Substantial growth will accelerate divergence, however. Perhaps the true condition for prevention of viscous fingering in a natural system is that the disturbance must die out before it travels past a second perturbation source. However fingering is defined, it is experimentally easy to show that, once formed, fingers cause a radically different displacement mechanism.[6] This less efficient mechanism is like immiscible displacement with no interfacial ten-

sion[7,8] so that, given enough solvent, almost all oil can be recovered.

SOLUTION FOR STABLE DISPLACEMENT

The perturbation parameters γ_I and γ_R defined in the preceding section are functions of the stable behavior $\bar{c}$ through their dependence on the functions E°, F°, G° and H°. Thus, we anticipate that any criteria for stability will depend strongly on the appropriate kind of stable behavior. To interpret the result implicit in Eq. 17 will require a reasonably general form of the solution $\bar{c}$ for stable behavior.

In most cases of stable displacement, gravity will be very important. Coupled with the effect of dispersion, gravity must prevent viscous fingering. The flow will then be very nearly parallel and there will be a nearly horizontal "mixing zone" between the solvent and the displaced fluid. This will be broadened from an "interface" by the effects of dispersion. Thus, in the mathematical description we assume parallel flow, or flow in the x-direction only. Dispersion occurs in both x and z directions, with the behavior independent of y position.

Any boundary condition that may be suggested for the inlet end of the system, $x=-t$, can be questioned. We select one which in the absence of dispersion would result in a horizontal interface, stationary in a moving co-ordinate system. Thus the equation to be solved and its boundary conditions are

$$\bar{c}_t - D_1 \bar{c}_{xx} - D_3 \bar{c}_{zz} = 0 \quad \text{.....(20.1)}$$

$$\bar{c}(x,z,0) = 0, \quad x > 0;$$

$$\lim_{x \to \infty} \bar{c}(x,z,t) = 0 \quad \text{.....(20.2)}$$

$$\bar{c}_z(x,0,t) = \bar{c}_z(x,1,t) = 0 \quad \text{.....(20.3)}$$

For $0 \leq t \leq -\cot\theta$:

$$\lim_{x \to -t} \bar{c}(x, z>h, t) = 1;$$

$$\lim_{x \to -t} \bar{c}(x, z<h, t) = 0 \quad \text{.....(20.4)}$$

while, for $t \geq -\cot\theta$:

$$\lim_{x \to -t} \bar{c}(x,z,t) = 1 \quad \text{.....(20.5)}$$

where

$$h = 1 + t \tan\theta, \quad -\pi/2 \leq \theta < 0 \quad \text{.....(20.6)}$$

The time t is the time for which displacement at the constant linear velocity u_o has been maintained.

Disregarding the effects of dispersion, these equations describe the kind of behavior illustrated in Fig. 2(A) for a time $t < -\cot\theta$. A similar description is given by Fig. 2(B) for times $t > -\cot\theta$. For the special case where $\theta = -\pi/2$, the system reduces to a one-dimensional problem with step-function input.

This boundary value problem can be solved by construction of an image system that implicitly

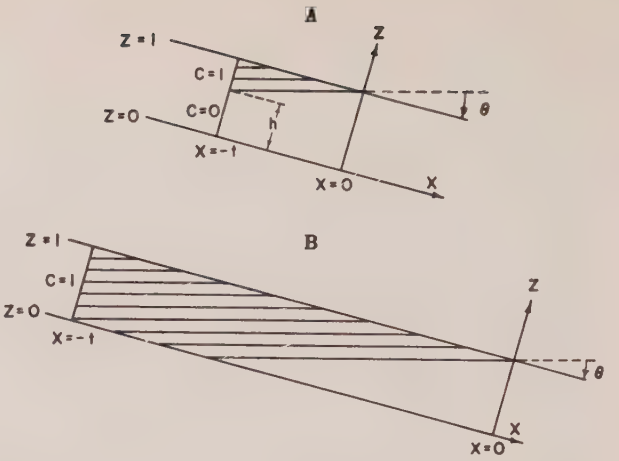

FIG. 2 — STABLE DISPLACEMENT SOLUTION WITH NO DISPERSION — (A) $t < -\cot\theta$, (B) $t > -\cot\theta$. SHADED AREA REPRESENTS SOLVENT.

makes use of the Green's function for the solution[19] and separation of variables. We construct an "extended" system of mirror images of the real system. This implies the extended definition of gravity g and dip angle θ in the equations of Eq. 1 as the following anti-periodic functions.

$$g(z) = g, \quad \theta(z) = \theta, \quad 0 < z < 1 \quad \text{.....(21.1)}$$

$$g(z) = -g, \theta(z) = -\theta, 1 < z < 2 \quad \text{.....(21.2)}$$

$$g(z) = g(z + 2n), \quad \theta(z) = \theta(z + 2n);$$

$$n = \pm 1, 2, \ldots \quad \text{.....(21.3)}$$

A new boundary condition for Eq. 20.1 then replaces Eq. 20.4 so that, for $0 \leq t \leq -\cot\theta$,

$$\lim_{x \to -t} \begin{cases} \bar{c}(x, h<z<2-h, t) = 1 \\ \bar{c}(x, -h<z<h, t) = 0 \\ \bar{c}(x,z,t) = \bar{c}(x, z+2n, t); \\ n = \pm 1, 2, \ldots \end{cases}$$

$$\quad \text{.....(21.4)}$$

The remaining equations apply as before. The extended system is such that its solution automatically satisfies the conditions contained in Eq. 20.3. Summing the point-source contributions throughout the extended system and solvent "reflected" from the $x = -t$ boundary, we obtain as the stable solution

$$\bar{c}(x,z,t) = {}_1\int^0 Z(z,t,\phi) \exp(-\omega^2) \frac{\partial\omega}{\partial\phi} d\phi$$

$$+ \tfrac{1}{2} \operatorname{erfc} [(x - \cot\theta)/2\sqrt{D_1(t + \cot\theta)}]$$

$$+ \exp[(x+t)/D_1] \; {}_1\int^0 Z(z,t,\phi) \exp(-\lambda^2) \frac{\partial\lambda}{\partial\phi} d\phi$$

$$+ \tfrac{1}{2} \exp[(x + t)/D_1] \operatorname{erfc} [(x + 2t$$

$$+ \cot\theta)/2\sqrt{D_1(t + \cot\theta)}] \quad \text{..... (22.1)}$$

where

$$\omega(\phi) = [x - (1-\phi)\cot\theta]/2\sqrt{D_1[t + (1-\phi)\cot\theta]}$$

.....(22.2)

$$\lambda(\phi) = [x+2t+(1-\phi)\cot\theta]/2\sqrt{D_1[t+(1-\phi)\cot\theta]}$$

.....(22.3)

$$Z(z,t,\phi) = \sum_m (4\pi)^{-1/2}\left\{ \operatorname{erf}\left[\frac{2m + 2 - \phi - z}{2\sqrt{D_3[t+(1-\phi)\cot\theta]}}\right] - \operatorname{erf}\left[\frac{2m + \phi - z}{2\sqrt{D_3\ [t+(1-\phi)ctn\theta]}}\right]\right\};$$

$$m = -\infty, \ldots -1, 0, 1, \cdots, +\infty$$

.....(22.4)

When $\theta = -\pi/2$, we obtain the important special case corresponding to injection of a step-function, for which the solution reduces to[20]

$$\bar{c}(x,t) = \tfrac{1}{2}\operatorname{erfc}\left[\frac{x}{2\sqrt{D_1\ t}}\right] + \tfrac{1}{2}\exp\left[\frac{x+t}{D_1}\right]\ \operatorname{erfc}\left[\frac{x+2t}{2\sqrt{D_1\ t}}\right]$$

..... (22.5)

This result can be obtained directly by use of the Laplace transform and arises naturally for a vertical displacement. However, it also applies when the injection rate is high enough for viscous forces to be dominant with any angle θ. In this latter case, dispersion must be the stabilizing mechanism, which may severely restrict the range of applicability.

PROPERTIES OF THE PERTURBATION SOLUTION

At this point it is convenient to note some of the properties of the perturbation solution and their relation to the real initial perturbation. Suppose that we had started with the real disturbance,

$$c(x,y,z,0) = 2\cos\alpha x\cos\beta y\cos n\pi z$$

.....(23.0)

This gives eight complex exponential terms including all combinations of wave numbers $(\pm\alpha, \pm\beta, \pm n\pi)$. The properties of γ_R are such that

$$\gamma_R(+\alpha, \pm\beta, +n\pi) = \gamma_R(-\alpha, \pm\beta, -n\pi)$$

.....(24.1)

$$\gamma_R(+\alpha, \pm\beta, -n\pi) = \gamma_R(-\alpha, \pm\beta, +n\pi)$$

.....(24.2)

Similarly, we can show that for γ_I,

$$\gamma_I(+\alpha\ \pm\beta, +n\pi) = -\gamma_I(-\alpha, \pm\beta, -n\pi)$$

.....(24.3)

$$\gamma_I(+\alpha, \pm\beta, -n\pi) = -\gamma_I(-\alpha, \pm\beta, +n\pi)$$

.....(24.4)

Thus, the complex exponentials resulting from Eq. 23 recombine into two families of cosine terms, in general with different damping and phase shift.

$$c_1 = \cos\beta y\cos[\alpha x+n\pi z+\gamma_I(\alpha,n\pi)t]\exp[-\gamma_R(\alpha,n\pi)t]$$

.....(25.1)

$$c_2 = \cos\beta y\cos[\alpha x-n\pi z+\gamma_I(\alpha,-n\pi)t]\exp[-\gamma_R(\alpha,-n\pi)t]$$

.....(25.2)

The extended system described under "Solution for Stable Displacement" is also useful for studying boundary conditions on the perturbation. Take an initial perturbation from the c_1 family, $\cos\beta y\cos(\alpha x+n\pi z)$. The part of this disturbance lying within the real system, $0 < z < 1$, has as its mirror image in the right-hand adjacent strip $1 < z < 2$ a member of the c_2 family, given by Eq. 25.2. That is, for any point z_1 and its geometrical image $z_2 = 2-z_1$,

$$\begin{aligned}\cos(\alpha x-n\pi z_2) &= \cos[\alpha x-n\pi(2-z_1)]\\ &= \cos(\alpha x+n\pi z_1-2n\pi)\\ &= \cos(\alpha x+n\pi z_1)\end{aligned}$$

.....(26.0)

But the stable solution for $\bar{c}$ (Eq. 22) has similar image properties as a consequence of the anti-periodicity of the extended system. These are reflected in the functions E°, F°, G° and H°. Thus we can show that, when an $(\alpha, -n\pi)$ perturbation and the corresponding stable solution from the $1<z<2$ strip are mapped into the $0 < z < 1$ strip by reflection, the result is identical to that for an $(\alpha, n\pi)$ perturbation. This requires that the behavior of the superimposed systems remain the same for all time. We always have members of both families in any real solution; thus, perturbation flux into the boundary from the right is always equal in magnitude but oppositely directed to that from the left. This argument is readily extended to any other "boundary" z = integer in the extended system; in this sense, the boundary conditions of Eq. 11 are satisfied.

Thus, the solution to the perturbation problem consists of two families of perturbation waves given by the equations of Eq. 25. Considered in the extended system, these satisfy the first-order perturbation equations of Eq. 3 and the initial and boundary conditions. The effect of a boundary is to reflect the wave back into the system, with an image of the original in the extended anti-periodic system as the source of the reflection.

SUMMARY OF THEORETICAL RESULTS

We have shown in the preceding sections that there are two families of mathematical solutions for the equations describing growth of an initially small disturbance. Each solution contains an exponential factor, $\exp(-\gamma_R t)$. The coefficient of time γ_R depends on the appropriate stable displacement behavior $\bar{c}$ and also on the parameters α, β and n of the real initial perturbation term, $\cos\alpha x$

cos βy cos $n\pi z$. For a displacement to be stable, the coefficient γ_R in each such exponent must be positive. Thus, it is sufficient to consider the particular term with minimum γ_R. No doubt the most important part of this particular term is the time-independent element, which determines the initial behavior of the disturbance. This is given by

$$\gamma_R = [\alpha^2 D_1 + (\beta^2 + n^2\pi^2)D_3 + \delta^{-2}H^\circ] \quad \ldots\ldots(27.0)$$

a special case of Eq. 19.2 for which the terms are defined by Eqs. 6, 7 and 14. The functions used are to be evaluated at any point of interest (x_o, y_o, z_o) and at the initial time with respect to perturbation behavior, $t = 0$.

In terms of the stability coefficient γ_R, we can define a surface of neutral stability on which such a coefficient vanishes. When present, this surface divides the system into two parts – an exterior region where all γ_R are positive, and an interior region of higher concentration gradients within which at least one γ_R is negative. Thus, given an appropriate perturbation source, unstable fingers can grow from the interior region to dominate displacement behavior. For true stability, this interior region must be absent, in which case the surface $\gamma_R = 0$ does not exist. With time, the enclosed unstable concentration range will shrink. This leads to the first of several important generalizations.

CONDITIONAL INSTABILITY

The first term in γ_R is a positive constant representing the stabilizing effect of dispersion. All other terms depend on concentration gradients which must eventually become very small. This means that the only instability observed is a conditional instability–one which will disappear after a sufficiently long time.

"WAVE LENGTH" DEPENDENCE

The numbers α, β and n characterize the initial disturbance as the sum of a series of sinusoidal concentration waves. One effect of the constant term in γ_R is to make long "wave lengths" the least stable modes. Thus, stability is determined by the "fundamental" Fourier mode of an arbitrary initial perturbation, a term with small α, β and n. Provided the smallest of these numbers are large enough, the particular perturbation can be stable even though displacement is not stable in the general sense.

"DIAMETER" EFFECT

Wave-length dependence is most important in laboratory-size systems. In laboratory cores, the longest wave length (which determines stability) is likely to reflect the size of the system rather than characteristics of the formation material. The importance of dispersion as a stabilizing mechanism is enhanced many-fold by such a reduction in maximum wave length. This is shown when dimensions are introduced into Eq. 27 and the first terms acquire an inverse proportionality to L^2, with L the width of the system. Experimental results showing the indicated "diameter" effect have been obtained.[9]

GRAVITY STABILIZATION

We assume a normal case in which a low-density low-viscosity solvent displaces oil downdip. The function g_1 (from the equations of Eq. 5) then becomes positive when gravity is dominant, and negative when gravity is subordinate to viscous forces. The second function of the pair g_3 is always negative. If we consider a case in which both α and n are positive and g_1 is positive, gravity effectively stabilizes the mode. This can be shown through the defining equations (Eqs. 5, 10 and 14).

Gravity dominance will not always lead to stability, however, as can be shown for some combinations of parameters. In particular, gravity dominance naturally leads toward instability when the less-dense fluid displaces updip.

MINIMUM SLUG SIZE

The condition for neutral stability, $\gamma_R = 0$, also defines the minimum size of a solvent "slug" for stable displacement of oil. As an example, consider the simplified case for which the stable flow is one-dimensional, $\bar{c}_z = 0$, and α for the perturbation is negligible. This latter corresponds to a perturbation extending almost indefinitely in the direction of flow, as could follow if it neither grew nor died out. With all other properties specified, we wish to define the maximum permissible solvent concentration gradient, $\bar{c}_x^*$. In magnitude this is given by

$$|\bar{c}_x^*| = |(\delta^2 D_3)(g_1)^{-1}| \quad \ldots\ldots(28.0)$$

Maximum gradients occur at injection before any dispersion has occurred. Thus, Eq. 28 defines the steepest solvent concentration profile consistent with stability that can be injected under the prescribed conditions.

Optimum use of solvent requires the smallest "mixing zones" possible. This implies the construction of a stable solvent slug by: (1) formation of a transition zone from oil to solvent, such as would be defined by Eq. 28 for example; (2) addition of enough pure solvent to prevent later immiscibility as a result of dispersion mixing; and, finally, (3) formation of a second transition zone from solvent to gas. This final transition requires re-application of Eq. 28. The total quantity of solvent required can be obtained by integration over such a contour, thus defining a minimum slug size.

SCALING OF LABORATORY EXPERIMENTS

Scaling rules for laboratory miscible displacement experiments have been presented by previous authors.[6,21] Stability phenomena impose additional requirements that must be met if a laboratory flood is to represent particular reservoir conditions. For stable displacement, only the dispersion and flow relationships between systems need be scaled. We expect a similar simplification for a high degree of instability. Unpublished experimental data tend to verify this view. Near the limits of stability, however, both the degree and source of instability must be matched in scaled experiments.

Inclusion of the very difficult requirement of scaled perturbation sources is a condition which may well make exact scaling impossible.

ACKNOWLEDGMENT

This paper is an outgrowth of "Conditional Instability in Miscible Liquid-Liquid Displacement", presented at the AIChE-SPE Joint Symposium on Fundamental Concepts of Miscible Fluid Displacement: Part II; Fifty-Second Annual Meeting, San Francisco, December 6-9, 1959. The author prepared the Symposium paper while associated with the California Research Corporation, La Habra, Calif.

REFERENCES

1. Hall, H. N. and Geffen, T. M.: "Laboratory Study of Solvent Flooding", *Trans.*, AIME (1957) Vol. 210, 48.
2. Koch, H. A., Jr. and Slobod, R. L.: "Miscible Slug Process", *Trans.*, AIME (1957) Vol. 210, 40.
3. Scheidegger, A. E.: "Theory of Flow of Miscible Phases in Porous Media", presented at International Union of Geodesy and Geophysics in Toronto (Sept., 1957); *Jour. Appl. Phys.* (1954) *25*, 994; *The Physics of Flow Through Porous Media*, U. of Toronto Press (1957).
4. von Rosenberg, D. U.: *AIChE Jour.* (1956) Vol. 2, 55.
5. Day, P. R.: *Trans.*, Am. Geophys. Union (1956) Vol. 37, 595.
6. Blackwell, R. J., Rayne, J. R. and Terry, W. M.: "Factors Influencing the Efficiency of Miscible Displacement", *Trans.*, AIME (1959) Vol. 216, 1.
7. Everett, J. P., Gooch, F. W., Jr. and Calhoun, J. C., Jr.: "Liquid-Liquid Displacement in Porous Media as Affected by the Liquid-Liquid Viscosity Ratio and Liquid-Liquid Miscibility", *Trans.*, AIME (1950) Vol. 189, 215.
8. Griffith, J. D. and Nielsen, R. F.: "Some Studies on Miscible Fluid Displacement", *Bull. No. 68*, Mineral Ind. Exper. Stat., Pennsylvania State U., 71.
9. Lacy, J. W., Draper, A. L. and Binder, G. G.: "Miscible Fluid Displacement in Porous Media", *Trans.*, AIME (1958) Vol. 213, 76.
10. Chuoke, R. L., van Meurs, P. and van der Poel, C.: "The Instability of Slow, Immiscible, Viscous Liquid-Liquid Displacements in Permeable Media", *Trans.*, AIME (1959) Vol. 216, 188.
11. Baron, T.: *Chem. Eng. Prog.* (1952) Vol. 48, 118.
12. McHenry, K. W. and Wilhelm, R. H.: *AIChE Jour.* (1957) Vol. 3, 83.
13. Beran, M. J.: *Jour. Chem. Phys.* (1957) Vol. 27, 270.
14. Rifai, M. N. E., *et al: Dispersion Phenomena in Laminar Flow Through Porous Media*, San. Eng. Res. Lab., U. of California, Berkeley, Report I. E. R., Series 93, Issue 2 (1956).
15. de Jong, G. de Josselin: *Trans.*, Am., Geophys. Union (1958) Vol. 39, 67.
16. Saffman, P. G.: *Jour. Fluid Mech.* (1959) Vol. 6, 321.
17. Blackwell, R. J.: "Laboratory Studies of Microscopic Dispersion Phenomena in Porous Media", Preprint 29 presented at AIChE-SPE Joint Symposium in San Francisco (Dec. 6-9, 1959).
18. Lin, C. C.: *The Theory of Hydrodynamic Stability*, Cambridge U. Press (1955).
19. Sneddon, I.: *Elements of Partial Differential Equations*, McGraw-Hill Book Co., Inc., N. Y. (1957).
20. Aronofsky, J. S. and Heller, J. P.: "Diffusion Model to Explain Mixing of Flowing Miscible Fluids in Porous Media", *Trans.*, AIME (1957) Vol. 210, 345.
21. Offeringa, J. and van der Poel, C.: "Displacement of Oil from Porous Media by Miscible Liquids", *Trans.*, AIME (1954) Vol. 201, 310.

***

Effect of Oil Production Rate on Performance of Wells Producing from More Than One Horizon

W. TEMPELAAR-LIETZ
MEMBER AIME

SHELL OIL CO.
LOS ANGELES, CALIF.

ABSTRACT

The performance of a two-horizon depletion-type reservoir produced through combination wells is analyzed. By introducing some simplifying approximations, it has been possible to obtain formulas which are easy to handle. Only ordinary differential equations are used, and the development of the analysis can be followed without difficulty by the non-specialist. A rigorous analysis has been made of this problem. It has been found that the approximations introduced in the simplified analysis are fully justified and that errors seldom will be more than 2 per cent.

The report shows the effect of the rate of withdrawal upon the relative depletion of the two horizons. Numerical examples are given.

INTRODUCTION

In its simplest form an oil reservoir consists of a continuous, homogeneous body of porous and permeable rock, enclosed at the top and the bottom by impermeable material. The flow of fluid through such a reservoir has been the subject of numerous papers, and the mathematical analysis of well performance, pressure build-up, etc., has reached a high degree of refinement. One of the basic assumptions introduced into these analyses is the homogeneity of the reservoir. In non-homogeneous reservoirs, these computations still can be carried out satisfactorily, provided small irregularities in the physical properties of the rock are distributed in a random fashion.

The flow equations are derived as solutions of the continuity equation, and their solutions are dependent upon the assumption of many constant factors in the reservoir: permeability to oil, compressibility of the reservoir fluid, viscosity saturation, etc. When these are assumed to be constant, the continuity equation can be solved rigorously. When these assumptions do not hold and corrections are introduced, it becomes very difficult and often impossible to solve analytically.

The present analysis is concerned with production from a two-layer depletion-type reservoir in which the layers have different permeabilities. Instead of using the continuity equation, results were derived from some simple physical ideas. In a single-layer reservoir in which the oil is at a pressure above the bubble point, the rate of production often has been assumed to be directly proportional to the pressure drawdown. In the simplified analysis it has also been assumed that the drop in average reservoir pressure is directly proportional with the cumulative withdrawal. These considerations in the past have been the basis of the analysis of reservoir performance and have been applied to a variety of problems, often with marked success. In the problem under investigation these relationships are shown to be compatible with the equation of continuity, but the approach has the advantage of leading to ordinary differential equations in which changes in constants can be introduced without making the analytical solution impossible.

It has the additional advantage that it can be understood more readily by the large group of engineers who are not reservoir specialists. For that reason, detailed steps in the mathematical developments have been shown in full.

SCOPE OF ANALYSIS

The analysis in this paper has been applied to a two-layer depletion-type reservoir in which both horizons are produced simultaneously in the same well. Because of the difference in permeability, it is obvious that the depletion of the two zones will proceed at different rates. For various problems it may be of interest to know the degree of depletion of the two zones at any arbitrary time and to in-

Paper originally published in 1953 as Shell Oil Co. report. At that time a search of the literature revealed no mathematical analysis of the production from a multiple-zone reservoir as herein described. Since then, the report has been referenced in later studies on related subjects.

At the 34th Annual Fall Meeting of SPE in Dallas in 1960, the paper by C. S. Matthews, *et al* (page 43 of this issue of *Soc. Pet. Eng. Jour.*) was presented. A portion of that paper is devoted to a rather detailed analysis of the report, and it was felt that publication of the 1953 report might be desirable.

Consequently, the author submitted this paper—essentially in its original 1953 form — for presentation at the Regional SPE Meeting in Pasadena, Calif. on Oct. 22-23, 1959. Subsequent constructive comments by the Society's Transactions Editorial Committee are gratefully acknowledged and have led to modification of the text to its present form.

vestigate the possibility of affecting this relative depletion by operating practices. One of the main factors under control of the operator is the rate of withdrawal, and the effect of various rates upon the distribution of depletions is demonstrated. In the development of the analysis, some basic assumptions have been introduced which now will be discussed.

BASIC ASSUMPTIONS

The following assumptions have been made.

1. Each of the two layers producing simultaneously in one well has an equal (unit) thickness. The reasoning followed in the computations should not change when layers of different thicknesses are assumed.

2. The two layers have the same initial reservoir pressure.

3. The P-V-T data of the fluids in the two reservoirs are equal.

4. The well under consideration is one in a regular drainage pattern, and surrounding wells are producing at comparable rates.

5. The structure is flat, and gravity effects can be ignored so that radial flow formulas can be applied.

6. The reservoir is the depletion type.

7. The present analysis is mainly concerned with the period in which the producing GOR is equal or close to the original solution GOR, up to the time that free gas starts moving; and, experience has shown that during that period the relationship between pressure and cumulative production can be approximated closely by a straight line. In this analysis, it has been assumed that such a straight-line relationship does exist.

8. Although the permeabilities of the two layers may differ widely, it often is found that the porosities show a random scattering. It has been assumed for this analysis that the average porosities of the layers are equal.

This assumption will lead to a simplification of the formulas. For the case of different porosities, adjustments in the analysis easily can be made.

9. The instantaneous rate of production is directly proportionate with the difference between the average pressure of the reservoir and the producing pressure in the well. This assumption will be discussed in detail in the Appendix.

10. The drainage reservoirs of the individual wells are approximated by circles with radii equal to one-half the distance between the wells.

MATHEMATICAL ANALYSIS

Let it be assumed that a well is producing from two zones simultaneously, and let the two zones be referred to as Zone I and Zone II.

The recovery per psi pressure drop for each of the zones will be represented by A barrels (Assumptions 7 and 8).

The proportionality factor according to Assumption 9 will be referred to as the productivity index and will be represented by i_1 for Zone I and i_2 for Zone II. The nature of these i-values will be discussed further in the Appendix.

The instantaneous rate of production from the two zones combined will be denoted by q B/D, and in this analysis it has been assumed that this rate is constant throughout the period under consideration.

The original reservoir pressure is represented by P_o; and at a time t the average reservoir pressure in Zone I will be $\bar{p}_1$; the average pressure in Zone II will be represented by $\bar{p}_2$, and the back pressure in the producing well by p_w, all expressed in pounds per square inch.

At that time the cumulative production from Zone I will be equal to

$$Q_1 = A(P_o - \bar{p}_1).$$

Similarly, for Zone II,

$$Q_2 = A(P_o - \bar{p}_2).$$

Therefore, the cumulative recovery from both zones at time t can be represented by

$$Q = Q_1 + Q_2 = 2AP_o - A(\bar{p}_1 + \bar{p}_2).$$

Since it has been assumed that the well has produced at a constant rate of q B/D,

$$2AP_o - A(\bar{p}_1 + \bar{p}_2) = qt. \quad \ldots\ldots\ldots\ldots \quad (1)$$

The rate of production from Zone I at the time t will be equal to

$$\frac{dQ_1}{dt} = i_1(\bar{p}_1 - p_w),$$

and because of Assumptions 6 and 8

$$\frac{dQ_1}{dt} = i_1(\bar{p}_1 - p_w) = -A\frac{d\bar{p}_1}{dt} \quad \ldots\ldots\ldots\ldots \quad (2)$$

Similarly, for Zone II,

$$\frac{dQ_2}{dt} = i_2(\bar{p}_2 - p_w) = -A\frac{d\bar{p}_2}{dt} \quad \ldots\ldots\ldots\ldots \quad (3)$$

Therefore,

$$\frac{dQ_1}{dt} + \frac{dQ_2}{dt} = \frac{dQ}{dt} = q,$$

or

$$i_1\bar{p}_1 + i_2\bar{p}_2 - (i_1 + i_2)p_w = q,$$

so that

$$p_w = \frac{i_1\bar{p}_1 + i_2\bar{p}_2 - q}{i_1 + i_2}. \quad \ldots\ldots\ldots\ldots \quad (4)$$

Substituting Eq. 4 in Eq. 2,

$$-A\frac{d\bar{p}_1}{dt} = i_1\bar{p}_1 - \frac{i_1}{i_1 + i_2}(i_1\bar{p}_1 + i_2\bar{p}_2 - q) \ldots\ldots \quad (5)$$

From Eq. 1,

$$2P_o - (\bar{p}_1 + \bar{p}_2) = \frac{q}{A}t,$$

or

$$\bar{p}_2 = 2P_o - \bar{p}_1 - \frac{q}{A}t. \quad \ldots\ldots\ldots\ldots \quad (6)$$

Substituting Eq. 6 in Eq. 5,

$$-A\frac{d\bar{p}_1}{dt} = i_1\bar{p}_1 - \frac{i_1^2}{i_1+i_2}\bar{p}_1 - \frac{i_1 i_2}{i_1+i_2}(2P_o - \bar{p}_1 - \frac{q}{A}t) + \frac{i_1}{i_1+i_2}q,$$

or

$$\frac{dp_1}{dt} + \frac{2\,i_1\,i_2}{A\,(i_1+i_2)}p_1 + \frac{q\,i_1\,i_2}{A^2(i_1+i_2)}t + \frac{q\,i_1 - 2\,i_1\,i_2\,P_o}{A\,(i_1+i_2)} = 0 \quad \ldots\ldots\ldots\ldots \quad (7)$$

Let

$$\frac{2\,i_1\,i_2}{A\,(i_1+i_2)} = C_1$$

$$\frac{q\,i_1\,i_2}{A^2\,(i_1+i_2)} = C_2$$

$$\frac{q\,i_1 - 2\,i_1\,i_2\,P_o}{A\,(i_1+i_2)} = C_3$$

Then,

$$\frac{d\bar{p}_1}{dt} + C_1\,\bar{p}_1 + C_2 t + C_3 = 0. \quad \ldots\ldots\ldots \quad (8)$$

This equation is linear and can be solved as follows. Assume $\bar{p}_1 = uv$.

Then, $$\frac{d\bar{p}_1}{dt} = u\frac{dv}{dt} + v\frac{du}{dt}. \quad \ldots\ldots\ldots\ldots \quad (9)$$

Substituting Eq. 9 in Eq. 8,

$$u\frac{dv}{dt} + v\frac{du}{dt} + C_1 uv + C_2\,t + C_3 = 0,$$

or

$$u\left(\frac{dv}{dt} + C_1 v\right) + \left(v\frac{du}{dt} + C_2 t + C_3\right) = 0. \quad \ldots \quad (10)$$

One now can assume one relationship between u and v.

$$u\left(\frac{dv}{dt} + C_1 v\right) = 0. \quad \ldots\ldots\ldots\ldots \quad (11)$$

Eq. 10 now can be written

$$v\frac{du}{dt} + C_2 t + C_3 = 0. \quad \ldots\ldots\ldots \quad (12)$$

From Eq. 11,

$$\frac{dv}{dt} = -C_1 v$$

$$v = e^{-C_1 t} \quad \ldots\ldots\ldots\ldots \quad (13)$$

Substitution of Eq. 13 into Eq. 12 gives

$$e^{-C_1 t}\frac{du}{dt} + C_2 t + C_3 = 0,$$

or

$$\frac{du}{dt} = -C_2 t\, e^{C_1 t} - C_3\, e^{C_1 t},$$

so that

$$u = -\frac{C_2}{C_1^2}(C_1 t - 1)\, e^{C_1 t} - \frac{C_3}{C_1}\, e^{C_1 t} + C_4, \quad (14)$$

in which C_4 = constant of integration.

With $\bar{p}_1 = uv$ and $v = e^{-C_1 t}$ Eq. 14 can be transformed to

$$\bar{p}_1 = -\frac{C_2}{C_1^2}(C_1 t - 1) - \frac{C_3}{C_1} + C_4 e^{C_1 t}. \quad \ldots \quad (15)$$

For $t = o$ is $\bar{p}_1 = P_o$ or

$$C_4 = P_o - \frac{C_2}{C_1^2} + \frac{C_3}{C_1}.$$

Substituting the values for C_1, C_2 and C_3,

$$C_4 = \frac{q\,(i_1 - i_2)}{4\,i_1\,i_2}. \quad \ldots\ldots\ldots\ldots \quad (16)$$

Substituting the value of p_1 in Eq. 6,

$$\bar{p}_2 = 2\,P_o - \bar{p}_1 - \frac{q}{A}t$$

using the proper values,

$$\bar{p}_2 = P_o - \frac{qt}{2A} + \frac{q(i_1 - i_2)}{4\,i_1\,i_2}\left[1 - e^{\frac{-2\,i_1\,i_2\,t}{A(i_1+i_2)}}\right]. \quad (17)$$

Eq. 17 gives the value of the average pressure in Zone II = $\bar{p}_2$ at any given time t, and substitution of this value into Eq. 6 gives the corresponding value for $\bar{p}_1$.

$$\bar{p}_1 = P_o - \frac{qt}{2A} - \frac{q(i_1 - i_2)}{4\,i_1\,i_2}\left[1 - e^{\frac{-2\,i_1\,i_2\,t}{A(i_1+i_2)}}\right].$$

NUMERICAL EXAMPLES

To illustrate the theory, numerical examples have been worked out. The following basic data were used. Porosity of reservoir rock = 0.200; water saturation S_w = 0.300; oil saturation S_o = 0.700; compressibility of water $C_w = 2.5 \times 10^{-6}$ vol/vol/psi; and compressibility of oil $C_o = 10 \times 10^{-6}$ vol/vol/psi.

Therefore, effective compressibility referred to oil $= C_o + \frac{S_w}{S_o} \times S_w = 11.09 \times 10^{-6}$ vol/vol/psi.

In the first example it is assumed that the original reservoir pressure was P_o = 6,000 psi while the bubble point of the oil was P_b = 3,000 psi. Further assumptions include: zonal thickness h = 100 ft;

drainage radius r_b = 500 ft; well radius r_w = 0.25 ft; permeability Zone I k_1 = 100 md; and permeability Zone II k_2 = 10 md.

Considering the period in which the reservoir pressure is still above 3,000 psi, Fig. 1 was constructed. For this plot, the value of 11.09×10^{-6} vol/vol/psi was used. It will be observed that, while in the early stages the rate of production from Zone I represents the bulk of the well's production, gradually the production from Zone II increases while that from Zone I decreases.

After having produced about 30,000 bbl from the well, each zone is contributing half the production of the well. It also will be observed that from that time the lines run practically parallel. Theoretically, the lines should come together after an infinite time. At the time Zone I reaches the bubble point, it will have produced a cumulative production of 65,000 bbl. If the well had been producing at a rate of 100 B/D, Zone II would have produced about 63,000 bbl, while at a rate of 500 B/D this recovery would be only 55,000 bbl.

To demonstrate the effect of changes in one of the controlling factors, an expansion factor of 50×10^{-6} vol/vol/psi has been used. From about 100 P-V-T analyses carried out by Shell, this figure represents a good average value for the expansion of oil in the first period after it passes the bubble point.

Fig. 2, therefore, represents the performance of an oil reservoir that has the same properties as the one considered in the first case, with the exception that the oil has a bubble point equal to the original reservoir pressure. Again considering the time that 65,000 bbl have been withdrawn from Zone I (maximum expansion oil of Case 1) it now will be seen that, if the well had been producing at a rate of 500 B/D, Zone II would have produced 27,000 bbl or less than half of Zone I (Point Z of Fig. 2).

No corrections have been made for the gradual change in relative permeability because both are changing downward and the magnitude of these changes for 100 and 10 md may affect the difference in depletion one way or the other. In those cases where relative permeability data are available, corrections in the permeability can be made if considered necessary.

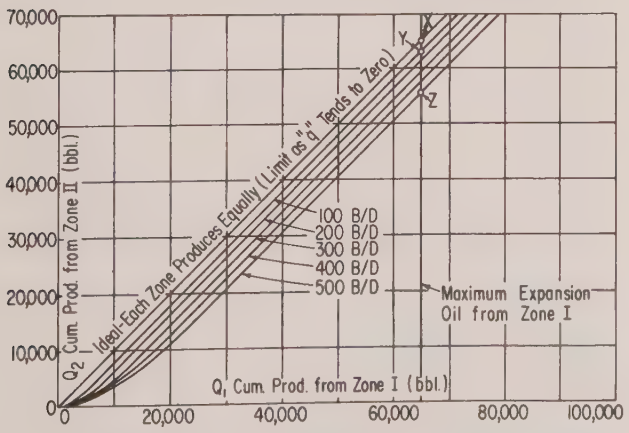

FIG. 1 – CUMULATIVE PRODUCTION FROM ZONE II VS CUMULATIVE PRODUCTION FROM ZONE I. A = 21.7 BBL/PSI; i_1 = 5.17 B/D-PSI; i_2 = .517 B/D-PSI.

GENERAL REMARKS

The analysis carried out in this paper essentially is based on steady-state flow. As such, it should find application in depletion-type reservoirs, i.e., in reservoirs with closed boundaries and in which no edge water encroaches. To verify the validity of this approach for the problem under consideration in which the relative rates of production from the two zones are controlled by continuously changing pressure conditions, the same problem has been solved rigorously. It has been found that, with the exception of the first few hours of production, errors of less than 2 per cent are introduced by the steady-state approach.

CONCLUSIONS

1. An analysis has been made of the performance of a depletion-type reservoir consisting of two horizons of different permeabilities, producing through wells penetrating both horizons.

2. It has been found that simple formulas, based on steady-state conditions, lead to answers that are within a few per cent from the results of computations based upon transient conditions.

3. It is demonstrated that the relative depletion of the two horizons can be affected to a large extent by adjusting the rate of production from the well.

NOMENCLATURE

A = recovery in bbl per psi pressure drop for each zone

c_w = compressibility of water, vol/vol/psi

c_o = compressibility of oil, vol/vol/psi

f = porosity of reservoir rock, fraction of bulk volume

b = zonal thickness, ft

i_1 = productivity index Zone I

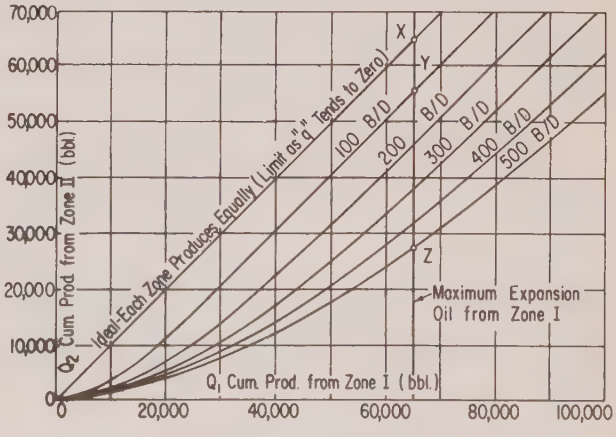

FIG. 2 – CUMULATIVE PRODUCTION FROM ZONE II VS CUMULATIVE PRODUCTION FROM ZONE I. A = 108.5 BBL/PSI; i_1 = 5.17 B/D-PSI; i_2 = .517 B/D-PSI.

i_2 = productivity index Zone II
k = permeability, md
k_1 = permeability, Zone I, md
k_2 = permeability, Zone II, md
P_o = original reservoir pressure, psi
P_b = bubble point of oil, psi
$\bar{p}_1$ = average reservoir pressure Zone I, psi
$\bar{p}_2$ = average reservoir pressure Zone II, psi
p_w = pressure in production well, psi
Q = cumulative production from well, bbl
Q_1 = cumulative production Zone I, bbl
Q_2 = cumulative production Zone II, bbl
q = rate of production of well, B/D
r_b = drainage radius, ft
r_w = radius borehole, ft
S_w = water saturation, fraction of porosity
S_o = oil saturation, fraction of porosity
t = time
ρ = viscosity of fluid
μ = density of fluid

ACKNOWLEDGMENT

The author wishes to express his appreciation to the Shell Oil Co. for permission to publish this paper.

APPENDIX

In the preceding analysis, some assumptions have been made which call for further investigation. In the development of the formulas, it has been assumed that the productivity-indexes i_1 and i_2 can be considered as constant multiplication factors.

It will be shown first that, if the flow pattern at any time can be considered as one of steady state, this assumption is justified.

Under steady-state conditions the pressures throughout the drainage-area are falling equally; i.e., $\frac{dp}{dt}$ is not a function of position.

The density of the fluid can be expressed as

$$\rho = \rho_o e^{-c(P_o - p)} \quad \ldots\ldots\ldots\ldots\ldots\ldots \quad (18)$$

for $p < P_o$. The initial pressure and density will be taken for the reference state (P_o, ρ_o). The compressibility c is assumed constant and sufficiently small for the approximation:

$$\rho = \rho_o [1 - c(P_o - p)]. \quad \ldots\ldots\ldots\ldots\ldots \quad (19)$$

In the steady state, the mass rate at the wellbore face can be expressed by close approximation as

$$m = r_b^2 \, bf \left(\frac{dp}{dt}\right), \quad \ldots\ldots\ldots\ldots\ldots\ldots \quad (20)$$

in which r_b = boundary radius, in this case the drainage radius of the well, f = porosity of the rock and b = thickness of the zone. From Eq. 19 one finds

$$\frac{d\rho}{dt} = \rho_o c \frac{dp}{dt}.$$

Therefore,

$$m = \pi r_b^2 bf \left(c\rho_o \frac{dp}{dt}\right),$$

or

$$\frac{m}{\rho_o} = q = \pi r_b^2 bfc \frac{dp}{dt}, \quad \ldots\ldots\ldots\ldots\ldots \quad (21)$$

in which q is now expressed as a volume rate and equal to the rate in volumes of original oil per unit time.

The rate past some circular boundary of arbitrary radius r will be

$$q_r = q \frac{(r_b^2 - r^2)}{r_b^2}. \quad \ldots\ldots\ldots\ldots \quad (22)$$

The rate of production past a radius r can be expressed, according to Darcy's law, as

$$q_r = \frac{q(r_b^2 - r^2)}{r_b^2} = 2\pi rh \frac{k}{\mu} \left(\frac{\partial p}{\partial r}\right) \quad \ldots\ldots\ldots \quad (23)$$

in which k is permeability and μ is viscosity, so that

$$\frac{\partial P}{\partial r} = \frac{q\mu}{2\pi kh} \cdot \frac{1}{r}\left(1 - \frac{r^2}{r_b^2}\right),$$

By integration the following expression is obtained for P_r.

$$P_r = \frac{q\mu}{2\pi kh}\left(\ln r - \frac{r^2}{2r_b^2}\right) + C, \quad \ldots\ldots\ldots \quad (24)$$

for $r = r_w$, $P_r = P_w$.

$$P_w = \frac{q\mu}{2\pi kh}\left(\ln r_w - \frac{r_w^2}{2r_b^2}\right) + C. \quad \ldots\ldots\ldots \quad (25)$$

Subtracting Eq. 25 from Eq. 24,

$$P_r - P_w = \frac{q\mu}{2\pi kh}\left(\ln \frac{r}{r_w} - \frac{r^2 - r_w^2}{2r_b^2}\right). \quad \ldots\ldots \quad (26)$$

Introducing a volume average pressure $\bar{P}_r$ for any radius r defined by

$$\bar{P}_r = \frac{1}{V_r} \int_{r_w}^{r} P_r \, dV, \quad \ldots\ldots\ldots \quad (27)$$

in which V_r is the volume of the drainage area from the wellbore to the radius r, the following equation can be written.

$$\bar{P}_r = \frac{1}{\pi(r^2 - r_w^2)bf}\left\{\frac{q\mu}{2\pi kh}\int_{r_w}^{r}\left(\ln \frac{r}{r_w} - \frac{r^2 - r_w^2}{2r_b^2}\right)(2\pi rhf\,dr) + \int_{r_w}^{r} P_w (2\pi rhf\,dr)\right\} \quad \ldots\ldots\ldots\ldots \quad (28)$$

or

$$\bar{P}_r = p_w + \frac{q\mu}{2\pi kh}\left\{\frac{r^2}{r^2 - r_w^2}\ln \frac{r}{r_w} - \frac{1}{2} - \frac{r^2 - r_w^2}{4r_b^2}\right\}. \quad (29)$$

Substituting $r = r_b$ and realizing that under normal conditions $r_w^2 \ll r_b^2$, this formula can be written with close approximation as

$$\bar{P}_r = p_w + \frac{q\mu}{2\pi kh}\left(\ln \frac{r_b}{r_w} - \frac{3}{4}\right), \quad \ldots\ldots\ldots \quad (30)$$

Comparing

$$\bar{P}_{r_b} - P_w = \frac{q\mu}{2\pi kh}\left\{\ln \frac{r_b}{r_w} - \frac{3}{4}\right\}, \quad \ldots \quad (31)$$

with Eq. 26,

$$P_{r_b} - P_w = \frac{q\mu}{2\pi kh}\left\{\ln\frac{r_b}{r_w} - \frac{1}{2}\right\}, \quad \ldots\ldots\ldots \quad (32)$$

it appears that the difference between using $\overline{P}_{r_b}$ and P_{r_b} when substituting normal values for $\frac{r_b}{r_w}$ is of secondary importance.

Eq. 31 may now be written

$$q = i(\overline{P}_{r_b} - p_w), \quad \ldots\ldots\ldots\ldots\ldots \quad (33)$$

in which

$$i = \frac{2\pi kh}{\mu(\ln\frac{r_b}{r_w} - \frac{3}{4})}. \quad \ldots\ldots\ldots\ldots\ldots \quad (34)$$

It appears that the value of i is not a function of time and, therefore, is constant for the reservoir so long as k and μ do not change.

The mass in the reservoir at any time t can be derived from Eq. 19.

$$\int_{r_w}^{r_b} \rho dV = \rho_o \int_{r_w}^{r_b} dV - C\ \rho_o P_o \int_{r_w}^{r_b} dV +$$

$$C\ \rho_o \int_{r_w}^{r_b} P_r\, dV. \quad \ldots\ldots\ldots\ldots\ldots \quad (35)$$

Using the definition of Eq. 27 for P_r, Eq. 35 can be rewritten. Let m represent the mass in the reservoir at time t and m_o the original mass; then,

$$m = m_o - C\rho_o P_o V_{r_b} + C\rho_o \overline{P}_{r_b} V_{r_b},$$

or

$$\frac{m_o - m}{\rho_o} = C\, V_{r_b}\, (P_o - \overline{P}_{r_b}),$$

and with

$$V_{r_b} = \pi bf\,(r_b^2 - r_w^2) - Q = C\pi bf\,(r_b^2 - r_w^2)\,(P_o - P_{r_b}),$$

$$Q = A(P_o - \overline{P}_{r_b})$$

in which Q = cumulative production in volumes of original reservoir oil and A is a constant. $\overline{P}_{r_b}$ is the same pressure appearing in Eq. 33.

Hence, if we can assume that, if the formulas developed for steady-state conditions can be applied to the problem under consideration, the following main equations can be written.

$$Q = A(P_o - \overline{P})$$

$$q = \frac{dQ}{dt} = i\,(\overline{P} - p_w)$$

These equations are essentially the same as those used in the main body of the report.

***

Linear Water Flood with Gravity and Capillary Effects

S. A. HOVANESSIAN
MEMBER AIME
F. J. FAYERS*
JUNIOR MEMBER AIME

CALIFORNIA RESEARCH CORP.
LA HABRA, CALIF.

ABSTRACT

The one-dimensional displacement equation for a homogeneous porous medium, including the effects of gravity and capillary forces, has been solved by a numerical method. A finite-difference scheme is developed for obtaining saturation, pressure and fractional flow profiles in waterflood recovery problems. From the numerical examples given, it is concluded that the gravitational forces have a pronounced effect on the saturation profiles and the pressure distribution curves of the system.

INTRODUCTION

Within the past 20 years, a number of papers have appeared in the literature dealing with the quantitative treatment of waterflood recovery problems. In their celebrated paper, Buckley and Leverett[1] described a method for calculating saturation profiles when the effects of capillary pressure and gravity are excluded. Terwilliger, *et al*,[2] included the effect of gravity in their theoretical and experimental investigation of oil recovery problems and obtained close correlation between experiment and theory. Welge[3] described a simplified method for obtaining the average saturation and the oil recovery from an oil reservoir. The effect of gravity can be included in this calculation.

More recently (1958) Douglas, *et al*,[4] presented a method for calculating saturation profiles which includes the effect of capillary pressure. The authors start with the one-dimensional displacement equation (which is nonlinear in the derivative) and, by a change of variable, transform this equation to a semi-linear partial differential equation. This equation is then solved by a finite-difference method on a high-speed digital computer. Fayers and Sheldon[5] obtained the solution of the one-dimensional displacement equation by directly replacing the differential equation by a finite-difference equation. The effects of capillary pressure and gravity were included in their solution. Here, since the movement of the foot of the saturation front is governed by a separate equation, the elapsed time in attaining a particular saturation profile cannot be obtained. The results of these two papers indicate that the inclusion of capillary forces eliminates the triple-valued Buckley-Leverett saturation profiles.

In the present paper, the one-dimensional displacement equation for a homogeneous permeable medium, including the effects of capillary and gravity forces, is solved.

The method of solution resembles that described in the paper by Douglas, *et al*, since it involves a similar transformation of variable. However, it extends their work in that the effect of gravity is included and, in addition, pressure profiles may be calculated. Also, the functions of saturation [$k_{ro}(S)$, $k_{rw}(S)$ and $P_c(S)$] required are entered in tabular form rather than as low-order polynomials. This simplifies data preparation and permits the use of a greater range of function types.

Unlike the method of Fayers and Sheldon, the corresponding elapsed time required for the development of each saturation profile is calculated and, also, saturation profiles may be calculated after breakthrough.

THEORETICAL CONSIDERATIONS

The dimensionless form of the one-dimensional displacement equation for a homogeneous porous medium as obtained from Darcy's law and material balance relations can be written as follows.[5]

$$\frac{\partial S}{\partial T} + \frac{dG(S)}{dS}\frac{\partial S}{\partial X} + N_c \frac{\partial}{\partial X}\left[C(S)\frac{\partial S}{\partial X}\right] = 0 \quad \ldots\ldots\ldots\ldots\ldots (1)$$

where S = water saturation,

T = dimensionless time = $\frac{qt}{L\phi}$,

$G(S)$ = gravity function = $F_w(1 - N_G k_{ro})$,

F_w = fractional water flow = $\left(1 + \frac{k_{ro}}{k_{rw}}\frac{\mu_w}{\mu_o}\right)^{-1}$,

N_G = gravity constant = $[(\rho_w - \rho_o) gk \sin \theta]/\mu_o q$,

X = dimensionless distance = x/L,

Original manuscript received in Society of Petroleum Engineers office June 6, 1960. Revised manuscript received Oct. 14, 1960.

[1]References given at end of paper.

*Now with English Electric Co., Atomic Power Div., Leicester, England.

N_c = capillary pressure constant = $\frac{k\bar{p}_c}{\mu_o q L}$,

$C(S)$ = capillary function = $F_w k_{ro} \frac{dP_c}{dS}$,

$p_c = p_w - p_o$, and

f_w = actual fractional water flow = $G(S) - N_c C(S) \frac{\partial S}{\partial X}$.

The solution of Eq. 1 will give the values of saturation S as a function of time T and position X. This equation is a second-order nonlinear partial differential equation and it cannot be solved by the present classical techniques. However, it is possible to remove the "nonlinearity in the derivative" from the equation by introducing the following transformation.[4,6]

$$r(S) = \frac{1}{Z}\int_{S_i}^{S} C(S)\,dS \qquad \ldots\ldots\ldots\ldots\ldots\ldots (2)$$

where $Z = \int_{S_i}^{1-S_{or}} C(S)\,dS$,

S_i = initial water saturation, and

S_{or} = residual water saturation.

The introduction of transformation Eq. 2 into Eq. 1 yields

$$\frac{1}{C(r)}\frac{\partial r}{\partial T} + \frac{1}{Z}\frac{dG(r)}{dr}\frac{\partial r}{\partial X} + N_c \frac{\partial^2 r}{\partial X^2} = 0 \qquad \ldots\ldots\ldots\ldots\ldots\ldots (3)$$

In Eq. 3, the capillary pressure and gravity functions are both expressed as functions of the transformed variable r. This equation is nonlinear but not in the derivative.

The partial differential equation (Eq. 3) can be approximated by the finite-difference equation,[7,8]

$$-\frac{r_n - r_n'}{\Delta T} = A(r_n^*)\left[\frac{\bar{r}_{n+1} - \bar{r}_{n-1}}{2\Delta X}\right] + B(r_n^*)\left[\frac{\bar{r}_{n+1} - 2\bar{r}_n + \bar{r}_{n-1}}{(\Delta X)^2}\right] \qquad \ldots\ldots\ldots\ldots\ldots\ldots (4)$$

The space subscript is n. Primed and unprimed quantities denote, respectively, values at the beginning and end of the time step ΔT. Also,

$$r_n^* = r_n' + \left(\frac{\partial r_n}{\partial T}\right)' a\Delta T \qquad \ldots\ldots\ldots\ldots\ldots\ldots (5)$$

$$\bar{r}_n = a r_n + (1-a) r_n' \qquad \ldots\ldots\ldots\ldots\ldots\ldots (6)$$

where a = time centering parameter, $0 < a \leqslant 1$ (usually set at 0.5) and

$$A(r^*) = \frac{C(r^*)}{Z}\frac{dG(r^*)}{dr^*} \quad \text{and} \quad B(r^*) = N_c\, C(r^*)$$

Using Eq. 4 to approximate $(\partial r_n/\partial T)'$ in Eq. 5, Eqs. 4 and 5 combine to give

$$a\Delta T\left[\frac{B(r_n^*)}{(\Delta X)^2} - \frac{A(r_n^*)}{2\Delta X}\right]\bar{r}_{n-1} - \left[\frac{2B(r_n^*)\,a\Delta T}{(\Delta X)^2} - 1\right]\bar{r}_n + a\Delta T\left[\frac{B(r_n^*)}{(\Delta X)^2} + \frac{A(r_n^*)}{2\Delta X}\right]\bar{r}_{n+1} = r_n' \qquad \ldots\ldots\ldots\ldots\ldots\ldots (7)$$

Denoting the coefficients of $\bar{r}_{n-1}, \bar{r}_n$ and $\bar{r}_{n+1}$ by a_n, b_n and c_n, respectively, and setting $d_n = r_n'$, we can write Eq. 7 as

$$a_n \bar{r}_{n-1} + b_n \bar{r}_n + c_n \bar{r}_{n+1} = d_n, \quad n = 1, \cdots, n \qquad \ldots\ldots\ldots\ldots\ldots\ldots (8)$$

The boundary conditions are fixed as follows: (1) the fractional flow of water f_w is always unity at the inflow boundary; and (2) the saturation at the outflow boundary must build up to a value S_{out} before water will flow out of the system, thereafter being calculated.

The solution of the finite-difference equations (Eq. 8), together with Eq. 6, will give the values of r as a function of time T and distance X. These values are in turn transformed back to saturation values by means of Eq. 2. Since the numerical procedure involves a great number of algebraic calculations, an electronic digital computer was used for obtaining solutions. Equations also are written for obtaining the fractional water flow and the pressure distribution across the system.

DISCUSSION OF RESULTS

Saturation, fractional-flow and pressure-distribution curves are obtained for oil-wet and for water-wet systems, with angle of inclination and injection flow rate as parameters. The relative permeability and capillary pressure data of the two systems are the same as given in Ref. 5.

Figs. 1 through 3 illustrate the effect of gravity

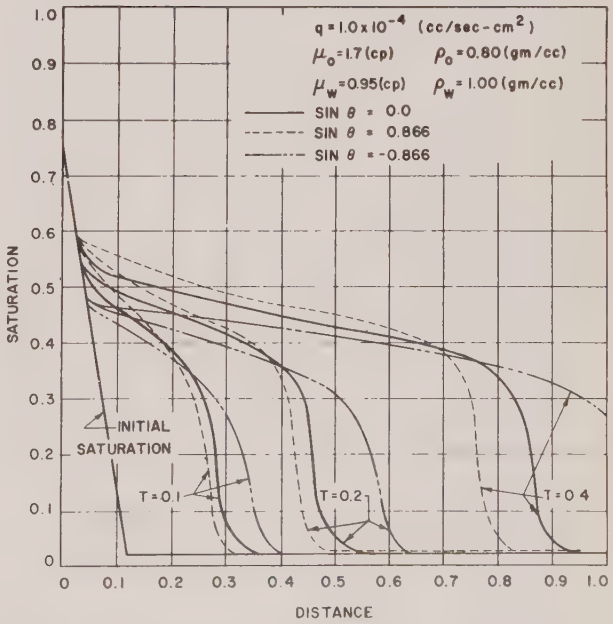

FIG. 1 – SATURATION VS DISTANCE, OIL-WET SYSTEM.

on the saturation, pressure and fractional flow profiles of an oil-wet system. From Fig. 1 it is noted that, for a constant injection rate $q = 10^{-4}$, the saturation profiles move slower for an upward angle of inclination ($\theta = 60°$) than for a horizontal or declined system. The areas under the saturation curves for the same value of T are equal, since T represents the pore volume of water injected. The initial saturation line starts from maximum saturation ($1-S_{or}$) at the input face and drops to a value slightly greater than the connate-water saturation and maintains this value for the remainder of the system.* Fig. 2 gives pressure distribution curves for the same system. It may be seen from this figure that the greatest pressure drop occurs for an inclination angle of +60°. Note the slight dip in the pressure curves at a distance of about 0.4 and 0.8 for T = 0.2 and 0.4, respectively, corresponding to the position of the saturation fronts at the times indicated (Fig. 1). Note also that almost no pressure drop occurs for a dipping angle of 60° below the horizontal, indicating that the pressure difference required to maintain the specified flow rate is approximately offset by gravity forces. Fig. 3 gives the actual fractional flow-vs-saturation curves for the cases illustrated by the previous figures. From Fig. 3, using Welge's method of calculation, we observe that the breakthrough saturation increases as the dip angle increases (from −60° below horizontal to +60° above). This is intuitively reasonable because, in general, the greater the slope of the test section, the greater the tendency for the injected water to accumulate and, thus, to increase the water saturation rather than to move the saturation front forward.

*The finite-difference scheme employed requires that all saturation values be at least slightly greater than the connate-water saturation. This can be seen from Eq. 4, which represents the rate of change of $s(r \approx$ saturation). This rate depends on the values of $A(r^*_n)$ and $B(r^*_n)$ which, in turn, depend on the value of r at the beginning of the time step and, hence, are zero for connate-water saturation.

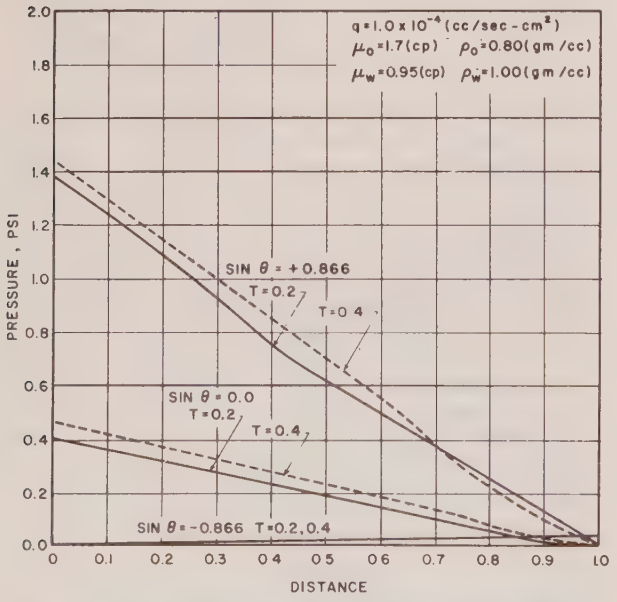
q = 1.0 x 10⁻⁴ (cc/sec - cm²)
μo = 1.7 (cp) ρo = 0.80 (gm/cc)
μw = 0.95 (cp) ρw = 1.00 (gm/cc)
SIN θ = +0.866
T = 0.2
T = 0.4
SIN θ = 0.0
T = 0.2
T = 0.4
SIN θ = -0.866 T = 0.2, 0.4
PRESSURE, PSI
DISTANCE

FIG. 2 — PRESSURE VS DISTANCE, OIL-WET SYSTEM.

Figs. 4 and 5 give the saturation and pressure profiles for a horizontal section at two flow rates. Comparison of Figs. 4 and 1 reveals that, as the flow rate increases, the breakthrough saturation increases. This effect has also been observed by Perkins[9] in his experimental investigations. Fig. 5 represents the pressure distribution across the test section for the same input conditions illustrated in Fig. 4. Observe that the greatest pressure drop occurs for the highest flow rate, and note the dips on the two pressure curves corresponding to the flow rate of $q = 10^{-2}$. It may be observed (Fig. 4) that these dips occur at the location of the saturation front at the times indicated.

Figs. 6 and 7 represent the saturation and pres-

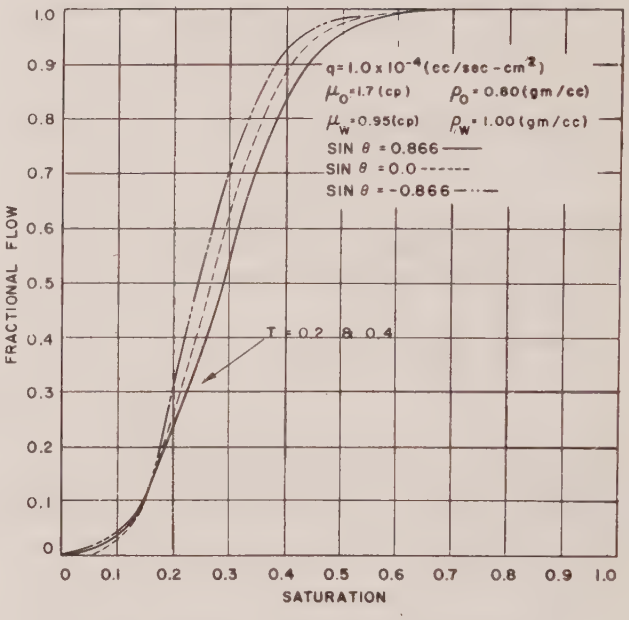

FIG. 3 — FRACTIONAL FLOW VS SATURATION, OIL-WET SYSTEM.

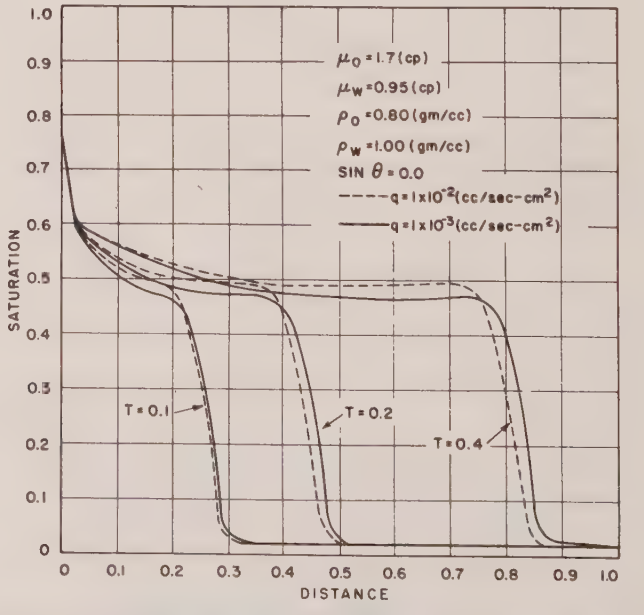

FIG. 4 — SATURATION VS DISTANCE, OIL-WET SYSTEM.

sure profiles for a water-wet system. From Fig. 6 it is noted that the saturation profile for the higher flow rate (dashed line) is steeper than that of the lower flow rate. Comparing Figs. 6 and 4, note that the saturation distribution lines of the former have a greater slope than those of the latter. This comes mainly from the capillary pressure curve because the capillary pressure curves of water-wet and oil-wet systems differ greatly, while the relative permeability curves of the two systems have substantially the same shape. Fig. 7 represents the pressure distribution across the system. Here again, the higher pressure drop occurs in the case of higher flow rate, and the dips in the pressure curves correspond to the location of saturation fronts. The effects of gravity forces were investigated for water-wet systems and no significant change was observed in the saturation, pressure or fractional-flow profiles.

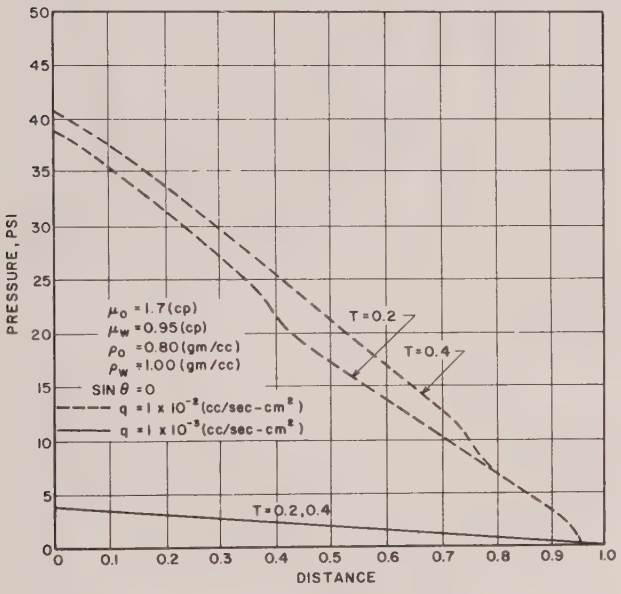

FIG. 5 — PRESSURE VS DISTANCE, OIL-WET SYSTEM.

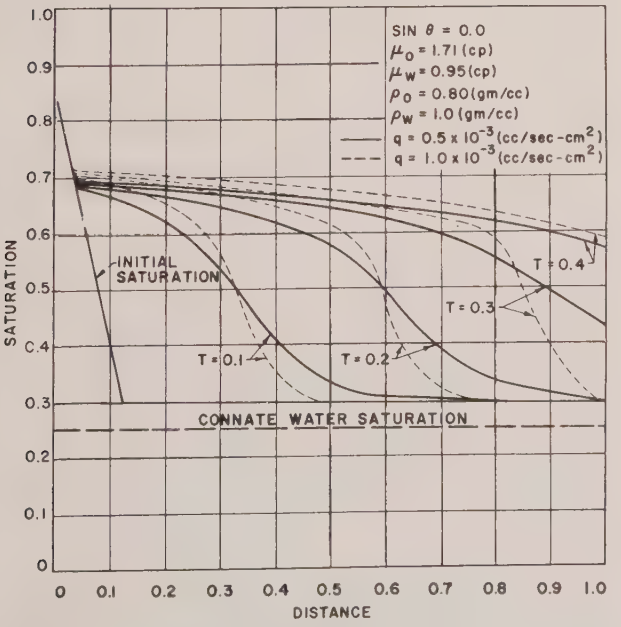

FIG. 6 — SATURATION VS DISTANCE, WATER-WET SYSTEM.

In obtaining these solutions, ΔX was set at 0.04 and ΔT was set at 0.01. The material balance error, using these space and time increments, was less than 1 per cent.

CONCLUSIONS

From the results of this study, the following conclusions can be made.

1. The inclusion of capillarity eliminates the triple-valued Buckley-Leverett saturation profiles.
2. The inclusion of gravity significantly affects the rate of movement of saturation profiles for a certain range of injection flow rates.
3. Gravity forces have a pronounced effect on pressure distribution curves for a certain range of injection flow rates.
4. Injection flow rates have a pronounced effect on saturation profiles and pressure distribution curves.
5. The initial saturation distribution had little effect on the computed results [$S(X)$, $P(X)$, $f_w(X)$] when the initial water in place was small compared to the water in place at the time under consideration.

NOMENCLATURE

a = centering parameter
$C(S)$ = capillary function
F_w = fractional water flow
f_w = actual fractional water flow
$G(S)$ = gravity function
g = gravitational constant (cm/sec^2)
k_o, k_w = permeability to oil and water (darcy)
k_{ro}, k_{rw} = relative permeability to oil and water
k = absolute permeability (darcy)
L = length of system (cm)
N_c = capillary pressure constant

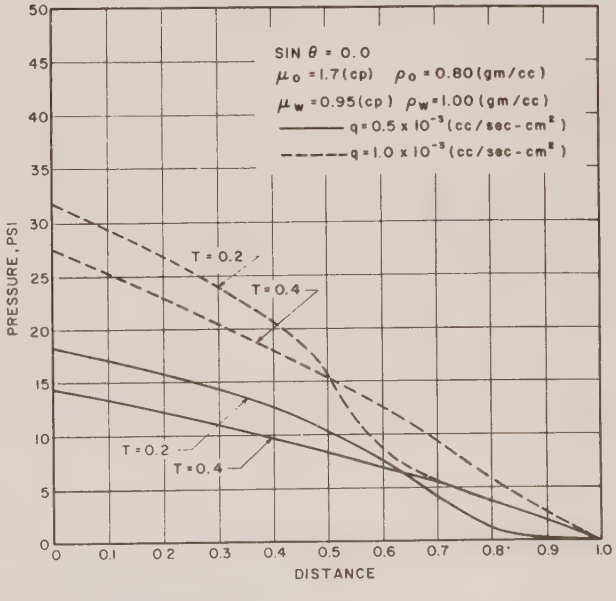

FIG. 7 — PRESSURE VS DISTANCE, WATER-WET SYSTEM.

N_g = gravity constant

P_o, P_w = pressure in oil and water phases (dyne/cm^2)

$\bar{p}_c$ = capillary pressure normalization constant (dyne/cm^2)

P_c = dimensionless capillary pressure

q_o, q_w = volumetric oil and water flow rates (cc/cm^2)/(sec)

$r(S)$ = transformed variable

S = water saturation

S_i = initial water saturation

S_{or} = residual oil saturation

S_{out} = saturation at the outflow boundary

t = time (sec)

T = dimensionless time (pore volume of water injected)

x = distance (cm)

X = dimensionless distance

Z = constant of transformation $= \int_{S_i}^{1-S_{or}} C(S)\,dS$

μ_o, μ_w = viscosity of oil and water (cp)

θ = angle of inclination

ϕ = porosity

ρ_o, ρ_w = density of oil and water (gm/cc)

REFERENCES

1. Buckley, L. E. and Leverett, M. C.: "Mechanism of Fluid Displacement in Sands", *Trans.*, AIME (1942) Vol. 46, 107.
2. Terwilliger, P. L., Wilsey, L. E., Hall, H. N., Bridges, P. M. and Morse, R. A.: "An Experimental and Theoretical Investigation of Gravity Drainage Performance", *Trans.*, AIME (1951) Vol. 192, 258.
3. Welge, H. J.: "Simplified Method for Computing Oil Recovery by Gas or Water Drive", *Trans.*, AIME (1952) Vol. 195, 91.
4. Douglas, Jim, Jr., Blair, P. M. and Wagner, R. J.: "Calculation of Linear Waterflood Behavior Including the Effects of Capillary Pressure", *Trans.*, AIME (1958) Vol. 213, 96.
5. Fayers, F. J. and Sheldon, J. W.: "The Effect of Capillary Pressure and Gravity on Two-Phase Fluid Flow in a Porous Medium", *Trans.*, AIME (1959) Vol. 216, 147.
6. Carslaw, H. S. and Jaeger, J. E.: *Conduction of Heat in Solids*, Oxford U. Press (1959) 10.
7. Richtmyer, R. D.: *Difference Methods for Initial Value Problems*, Interscience Publishers, Inc., N. Y. (1957).
8. Kunz, K. S.: *Numerical Analysis*, McGraw-Hill Book Co., Inc., N. Y. (1957).
9. Perkins, F. M.: "An Investigation of the Role of Capillary Forces in Laboratory Water Floods", *Trans.*, AIME (1957) Vol. 210, 409.

***

Thermal Conductivities of Porous Rocks Filled with Stagnant Fluid

D. KUNII — U. OF TOKYO, TOKYO, JAPAN

J. M. SMITH — NORTHWESTERN U., EVANSTON, ILL.

ABSTRACT

Effective thermal conductivities of sandstones filled with stagnant fluids were measured using a steady-state technique. Data were obtained for seven sandstone samples, taken from four different locations and ranging in permeability from 18 to 590 md. The measurements with gases (helium, nitrogen, air and carbon dioxide) covered a pressure range from 0.039 psia to 400 psig. Data were taken for four liquids – n-heptane, methyl alcohol, 79.8 weight per cent glycerol-water solution and pure water at atmospheric pressure.

The experimental results were used to evaluate the theoretical equations for predicting stagnant conductivities developed earlier.[4] The low-pressure measurements permitted evaluation of the consolidation parameter $h_p D_p/k_s$ (necessary to utilize the theory) for the various types of sandstones. Using these characteristic values, the theoretical equations correlated well with the experimental conductivity data for the several fluids and rock samples.

INTRODUCTION

An aspect of heat transfer in solid-fluid systems of considerable current interest is the effective thermal conductivity of porous media. The stimulus for study of the subject arises from the need for sound procedures for designing thermal methods of petroleum production. The general system occurs when there exists a flow of fluid through the pores of the solid material. However, a logical starting point in developing a theory for predicting the effective thermal conductivity in the general system is to attack the special case when the porous solid is filled with stagnant fluid. Since the flow rates anticipated in thermal production processes are very low, such stagnant conductivities k_e° are also of practical significance.

Original manuscript received in Society of Petroleum Engineers Office Aug. 2, 1960. Revised manuscript received Nov. 4, 1960. Paper presented at Joint AIChE-SPE Symposium, Sept. 22-25, 1960, in Tulsa.

[4]References given at end of paper.

Kunii and Smith[4] recently reviewed the existing data for stagnant conductivities and proposed a theory for heat transfer in porous rocks. This leads to equations for predicting the stagnant conductivity as a function of the properties of the fluid and solid phases. The existing experimental information[1-3,5,7,8] covered a range of porosities and agreed well with the theory. However, the available data were insufficient to examine critically the effects of two important properties on k_e° – the thermal conductivity of the fluid and the pressure. The objectives of the present study are twofold: (1) to measure the effect on k_e° of (a) the pressure for gases, and (b) the thermal conductivity of the fluid k_g for both gases and liquids; and (2) to determine for rocks of different porosities and permeabilities the apparent solid conductivity k_s and the consolidation parameter $h_p D_p/k_s$ required in applying the theoretical equations.

Measurements extrapolated to zero pressure are helpful in evaluating k_s and the consolidation parameter. However, the extrapolations must be based upon data obtained at low pressures because in small pores the molecular conductivity of the fluid may be unusually depressed. This occurs when the mean free path of the molecules is of the same order of magnitude as the pore diameter, that is, in small-diameter pores at low pressures. The phenomenon has been studied recently by Schotte[6] in beds of unconsolidated fine particles. With particles in the size range of 45 to 200 microns, a significant reduction of k_g with pressure was found even at absolute pressures greater than 1 atm. In the sandstones employed in the present investigation, pore diameters lower than those experienced by Schotte are likely, so that the effect would presumably be greater.

SCOPE OF MEASUREMENTS

Stagnant conductivities were measured for four types of sandstones using a total of seven samples. The characteristics of the samples, including porosity and permeability values, are given in Table

1.

Four gases were employed, data being obtained with nitrogen, helium and carbon dioxide at pressures above atmospheric; all sub-atmospheric data were determined using air. To provide a reasonably wide range of fluid thermal conductivity, measurements also were made using four fluids – normal heptane, methyl alcohol, a solution of 79.8 weight per cent glycerol and 20.2 weight per cent water, and pure water. The range of k_g values obtained with these seven fluids is approximately 0.01 to 0.36 Btu/(hr ft °F).

The mean temperatures existing in the rock samples during the runs are given in Table 2 for each fluid.

EXPERIMENTAL

The apparatus for measuring the stagnant conductivity is shown in Fig. 1. The test section consisted of two cylindrical cores, each 1 in. in diameter and about 1 3/8 in. in length. To reduce longitudinal heat transfer, one additional core sample of the same dimensions was used on each end of the test section. The conductivity was determined in the radial direction of the cylindrical cores, that is, in the direction parallel to the plane of the sandstone formation.

To introduce a radial temperature gradient, an electric heater was made by winding 30-gauge nichrome wire around a flexible rod. This rod was inserted into holes 0.093 in. in diameter drilled through the central axis of the core samples. The power input in the test section was determined with a Weston Wattmeter (Model #432) with an accuracy of 0.5 w. The measurement was made by attaching electrical leads to the heater wire across the length of the test section (approximately 2 3/4 in.) Fine sand was used between the test cores and the inner wall surface to adjust the position of the cores, as illustrated in Fig. 1. Cooling water was passed through a jacket surrounding the sample when runs were made with gases.

Copper-constantan thermocouples (30 B. and S. gauge) were used to measure the radial temperature gradient. The thermocouples were inserted in holes drilled in the end surface of the separate core sample as illustrated in Fig. 1. The holes, 0.027 in. in diameter, were drilled to a depth of 0.17 in. Three or four thermocouples were used across each of several radii, and their radial location was measured carefully to the nearest 0.1 mm.

For runs made with gases as the stagnant fluid, the temperatures were measured using a recorder with an expected accuracy of 0.5°F. The fluid was alternately added and evacuated from the test section several times before making thermal measurements. Fluid pressures on the sample at atmospheric pressure and above were measured with a mercury manometer or a Heisse gauge. Sub-atmospheric pressures were determined with a vacuum gauge.

A somewhat different procedure was employed with liquids. The solid cores, dried completely with an infra-red lamp, were first placed in a container half-filled with the required liquid. The remaining gas in the pores of the core was removed with a vacuum pump. Upon removal from the container, the samples were covered with scotch tape to prevent evaporation of fluid. Then, as quickly as possible, the thermocouples were inserted. The

TABLE 1 – POROUS ROCK SAMPLES USED

Boise Sandstone from Idaho Outcrop

Yellowish gray, medium-grained, argillaceous sandstone; micaceous, feldspathic, "pepper and salt" appearance; massive.
BO-1: porosity 0.248, permeability 590 md
BO-2: porosity 0.256

Bartlesville Sandstone from an Oklahoma Outcrop

Moderate yellowish brown, fine-grained, argillaceous sandstone; minor muscovite flakes, altered iron minerals, massive.
BA-2: porosity 0.203, permeability 28 md
BA-5: porosity 0.220

Berea Sandstone from Ohio Outcrop

Very light gray, fine-grained, clean, well sorted sandstone; massive.
BE-1: porosity 0.189, permeability 170 md
BE-2: porosity 0.185

Rangely (Colorado) Reservoir Rock

Olive gray, fine-grained, clean, well compacted sandstone.
RA: porosity 0.117, permeability 18 md

TABLE 2 – RANGE OF MEAN TEMPERATURES OF SANDSTONE SAMPLES DURING RUNS

	°F
Carbon Dioxide	140 to 200
Nitrogen	140 to 190
Helium	90 to 100
Normal Heptane	110 to 140
Methyl Alcohol	90 to 110
Glycerol*	130 to 160
Water	100 to 140

*79.8 wt. per cent glycerol and 20.2 wt. per cent water

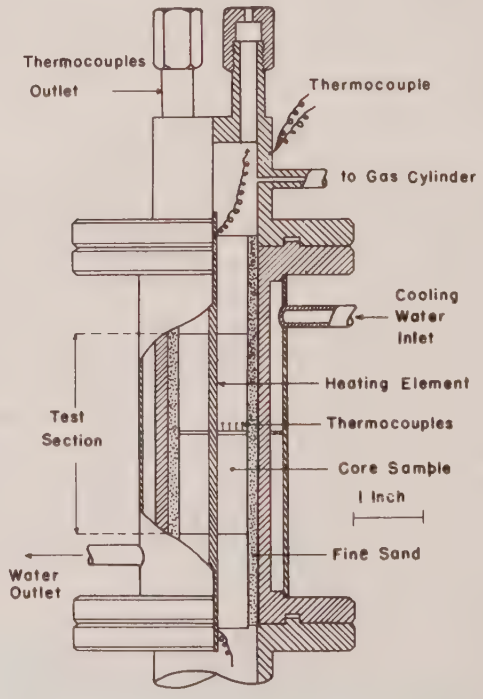

FIG. 1 – EXPERIMENTAL APPARATUS FOR GASES.

test element was then placed in a container filled with the required liquid. The entire unit was inserted in an ice-water, constant-temperature bath. Temperatures were determined for the runs with liquids using a precision portable potentiometer.

EVALUATION OF EXPERIMENTAL PROCEDURE

If longitudinal heat transfer in the core samples is negligible, the stagnant conductivity can be calculated from the measured radial temperature profile by the expression,

$$k^{\circ}_e = -\frac{Q}{2\pi L}\frac{d(\ln r)}{dT} \quad \cdots\cdots\cdots (1)$$

Typical measurements for several fluids in Core Sample BE-1 are shown in Fig. 2. Within the precision of the data, a straight line relationship is observed. This suggests, according to Eq. 1, that the variation of k°_e with temperature across the radius of the sample is not sufficient to be measured by the experimental procedure used. Hence, a single mean value for k°_e is calculated from Eq. 1 using the slope of the line obtained from plots similar to those illustrated in Fig. 2.

To test the assumption of negligible longitudinal heat transfer, several preliminary measurements were made using Sample BA-5 with air. First, radial temperature profiles were observed and compared at the three contact surfaces (the ends of the cylindrical core samples) of the four core samples mounted in the apparatus (Fig. 1). These results indicated that approximately 0.4 per cent of the total energy input from the heater flowed out in the longitudinal direction.

As the energy input from the heater decreases, a point is ultimately reached when longitudinal heat losses will be significant. Preliminary measurements indicated that this energy level was about 10 w. All the runs were made at values of Q greater than this limiting value.

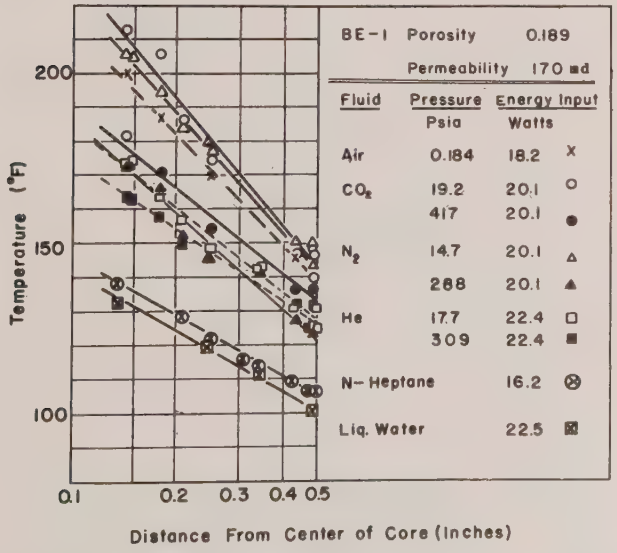

FIG. 2 – EXAMPLES-TEMPERATURE DISTRIBUTION IN CORE SAMPLE.

To test further the significance of longitudinal heat transfer, measurements were carried out when the ends of the apparatus were maintained at different temperatures with nichrome wire heaters. The energy input to the central heater was maintained at 15 w, leading to a mean core temperature of about 150°F. Under these conditions, varying the temperature of the ends of the apparatus from 70° to 200° F did not affect the stagnant conductivity.

From these preliminary tests it appeared that the equipment was satisfactory for measuring reasonably accurate values of k°_e. Considering errors in energy input, temperature and position measurements, and errors in applying Eq. 1, it is believed that the maximum uncertainty was less than 10 per cent.

RESULTS

EFFECT OF PRESSURE ON k°_e

The data showing the effect of pressure on k°_e for gases are plotted in Figs. 5 and 6 for pressures greater than 1 atm. Fig. 5 demonstrates that different core samples from the same sandstone formation (Bartlesville sandstone) do not exhibit significant differences in stagnant conductivity. On the other hand, the thermal conductivity of the gas is a significant factor; i.e., the results for helium are appreciably higher than those for nitrogen and carbon dioxide. In Fig. 6, data are plotted for three different types of sandstones, and here large differences are observed.

The small increase in k°_e with pressure at high pressures, shown in Figs. 3 and 4, is probably due to the small increase in the normal thermal conductivity of the gas with pressure. However, the more rapid change in k°_e with pressure at low values of P must be the result of another factor because the normal thermal conductivity is essentially constant at these pressures. This effect is more pronounced at sub-atmospheric pressures as demonstrated by the curves in Fig. 5 for air. The decrease in k°_e with pressure is most pronounced for the sample with the lowest porosity, Rangely sandstone (RA). This suggests that the fluid conductivity is being reduced by the small-diameter pores in the core samples. Schotte[6] has adapted equations based upon kinetic theory to show the effect of pressure on the apparent value of k_g in packed beds of fine particles (45 to 200 microns). One of his equations can be reduced to the following form to illustrate the effect of pressure P and pore size b.

$$k_g = \frac{k^*_g}{1 + C\,(T/pb)} \quad \cdots\cdots\cdots\cdots (2)$$

Here, k^*_g is the normal thermal conductivity of the gas. For a given core sample at a fixed temperature, Eq. 2 indicates that k_g approaches the normal conductivity as P approaches a large value and that k_g approaches zero as P tends toward zero. This suggests that the stagnant thermal conductivity of the core (k°_e) would approach a constant value, equal to the contribution of the solid phase, as the pressure approaches zero. The S-shaped

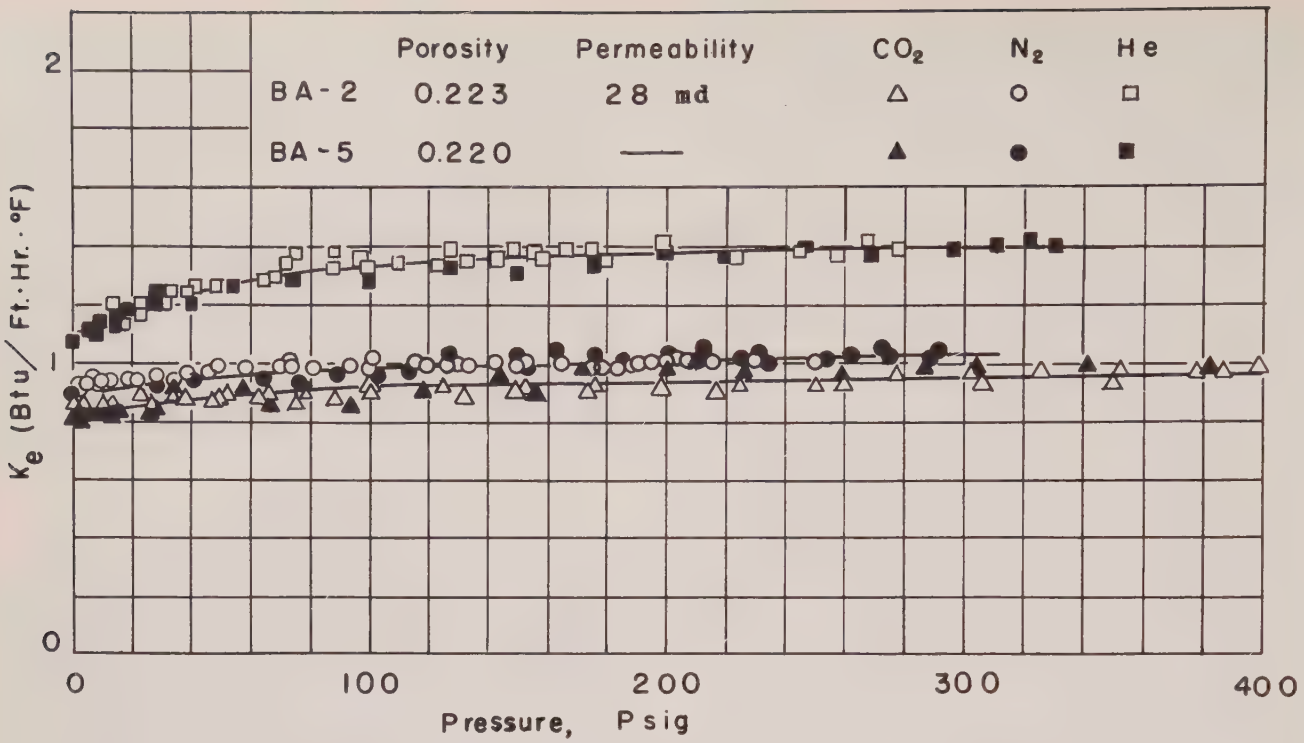

FIG. 3 – STAGNANT CONDUCTIVITIES OF BARTLESVILLE SANDSTONE.

behavior of the curves in Fig. 5 is in agreement with this reasoning. The significant conclusion here is that the solid contribution to the stagnant conductivity $(k^o_e)_o$ cannot be obtained by extrapolating to $P = 0$ data at above atmospheric pressure, such as shown in Figs. 3 and 4. Rather, measurements must be made under vacuum conditions to obtain $(k^o_e)_o$ by extrapolation. The values of this parameter, as determined from Fig. 5 for the four types of sandstone, are given in Table 3.

EVALUATION OF CONSOLIDATION PARAMETER

In Ref. 4, the following equation was proposed to predict the stagnant conductivity of porous rocks (radiation negligible).

$$\frac{k^o_e}{k_s} = \phi'\left(\frac{k_g}{k_s}\right) + \frac{(1-\phi')\left(1+\frac{\phi'}{\phi}a\right)}{1+\frac{\phi'/\phi}{\frac{1}{a}\left(\frac{k_g}{k_s}\right)+\frac{D_p b_p}{k_s}}} \quad \ldots \quad (3)$$

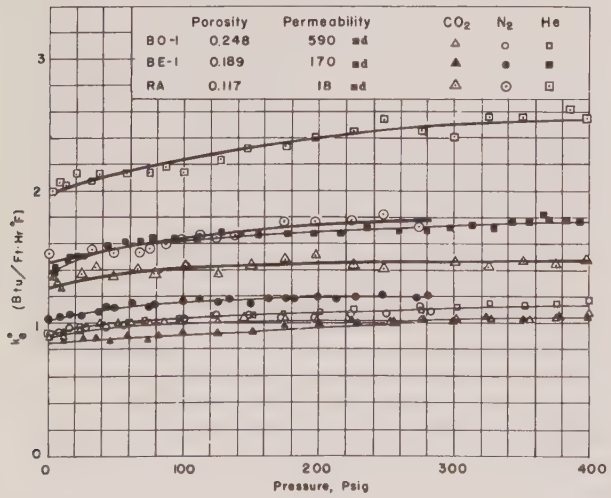

FIG. 4 – STAGNANT CONDUCTIVITIES OF SANDSTONES.

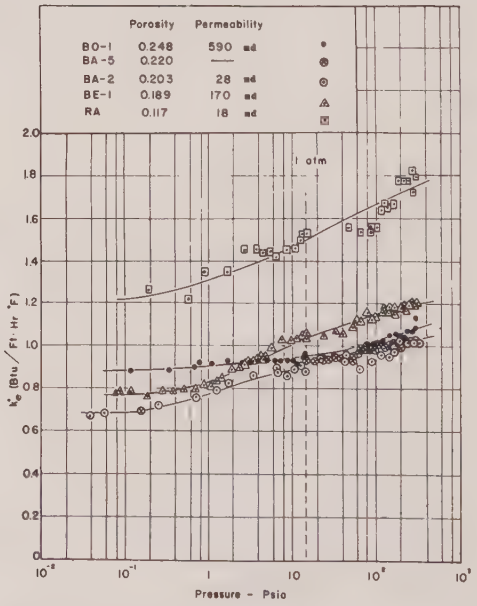

FIG. 5 – EFFECT OF PRESSURE ON STAGNANT CONDUCTIVITIES OF SANDSTONE DATA TAKEN BELOW ATMOSPHERIC WITH AIR AND DATA TAKEN ABOVE ATMOSPHERIC WITH NITROGEN.

The objective here is to use this expression and the experimental values of $(k^o_e)_o$ in Table 3 to determine the relationship between the apparent thermal conductivity of the solid phase k_s and the consolidation parameter $h_p D_p/k_s$. Both are characteristic properties of the sandstone sample. This is accomplished by considering Eq. 3 at zero pressure where k_g approaches zero. From the equations in Ref. 4, the following limiting results are readily obtained.

$$\lim_{k_g \to 0} \left(\frac{1}{a} \frac{k_g}{k_s} \right) = 0 \quad \ldots\ldots\ldots\ldots (4)$$

and

$$\lim_{k_g \to 0} a = 0 \quad \ldots\ldots\ldots\ldots (5)$$

The value of ϕ, the void fraction of the original bed of unconsolidated particles prior to consolidation, is suggested in Ref. 4 to be 0.476. This is the maximum void fraction in a uniform arrangement of spherical particles in contact. Using this result and Eqs. 4 and 5, the general expression (Eq. 3) for k^o_e/k_s reduces at zero pressure to the form,

$$(k^o_e)_o/k_s = \frac{1 - \phi'}{1 + \frac{\phi'}{\phi} \Big/ \left(\frac{D_p h_p}{k_s} \right)} \quad \ldots\ldots (6)$$

This equation provides a relationship between k_s and $D_p h_p/k_s$. If k_s were known, $D_p h_p/k_s$ could be determined from $(k^o_e)_o$ and Eq. 6. However, k_s is not necessarily the thermal conductivity of the pure solid phase (for example, quartz for sandstone cores). It may differ from this due to the non-uniform geometry of the solid phase and due to impurities between the grains of solid particles and the cementing material holding the grains together.

This problem is avoided by utilizing the experimental data for the effect of k_g on k^o_e, along with Eq. 6, to ascertain separate values for k_s and $D_p h_p/k_s$. The experimental data for the several fluids and sandstone samples are shown in Figs. 6 through 8. The curves on the figures represent Eq. 3 plotted for certain values of k_s and $D_p h_p/k_s$. These specific values were obtained in the following way.

1. Sets of consistent numbers for k_s and $D_p h_p/k_s$ were first determined from Eq. 6.

2. The most appropriate set was then obtained for each type of sandstone by comparison with the experimental data in Figs. 6 through 8.

Figs. 6 and 7 include calculated curves for three sets of k_s and $h_p D_p/k_s$, designated on the curves by the numerical value for k_s. These results indicate that it is not possible to determine k_s more closely than approximately ± 0.2 Btu/(hr ft °F).

TABLE 3 – THERMAL PROPERTIES OF SANDSTONE

Sandstone Sample	$(k^o_e)_o$ Btu/ft hr °F	k_s Btu/ft hr °F	$\frac{D_p h_p}{k_s}$
BO	0.88	1.8	0.965
BA	0.69	3.2	0.159
BE	0.77	4.6	0.103
RA	1.22	4.6	0.105

The values of the two parameters so evaluated are shown in the last two columns of Table 3.

It is interesting to note that these parameters are essentially the same for the BE and RA sandstones. The difference in stagnant conductivity between the two types of rock must be due primarily to the difference in porosities. Visual examination of the Boise (BO) sandstone suggests that it has a markedly different structure from the other types. It seems to be well consolidated with somewhat larger pore diameters than those associated with the other sandstones. This micaceous and feldspathic structure is probably responsible for the low value of k_s (Table 3) determined for the Boise sample.

CORRELATION AND PREDICTION OF STAGNANT CONDUCTIVITIES

For Eq. 3 to be a useful prediction method for k^o_e, it is necessary that values of k_s and $D_p h_p/k_s$ be available. At present these values cannot be obtained except by experimental means. Until data such as that shown in Table 3 are available for a large variety of rock samples, the method is not valuable for prediction purposes. However, the agreement in Figs. 6 through 8 between experimental

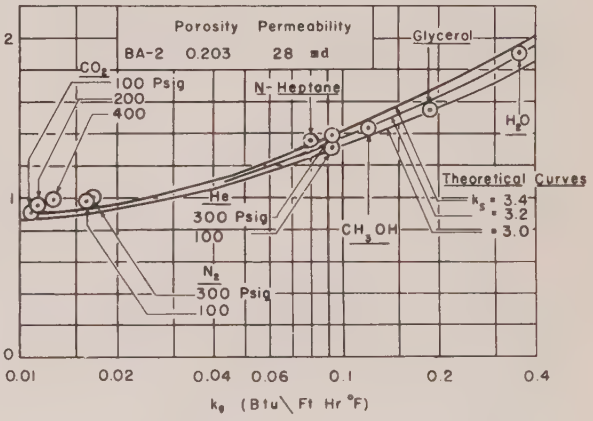

FIG. 6 – STAGNANT CONDUCTIVITIES VS CONDUCTIVITIES OF FLUIDS, BARTLESVILLE SANDSTONE.

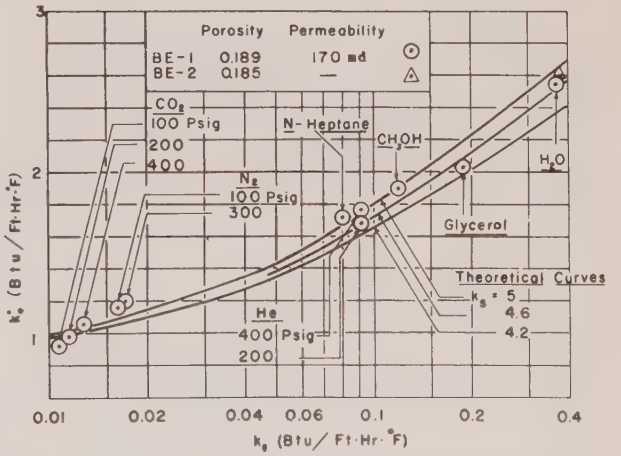

FIG. 7 – STAGNANT CONDUCTIVITIES VS CONDUCTIVITIES OF FLUIDS, BEREA SANDSTONE.

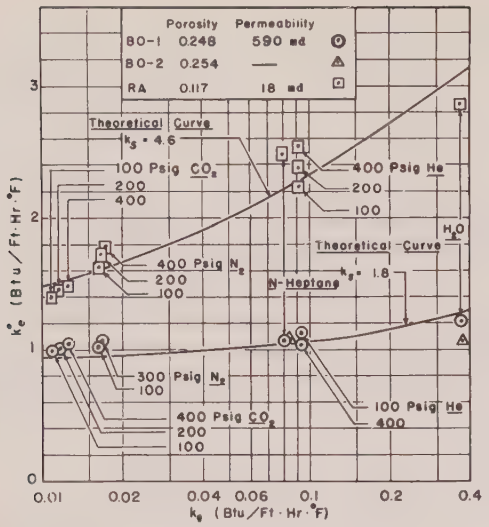

FIG. 8 — STAGNANT CONDUCTIVITIES VS CONDUCTIVITIES OF FLUIDS, BOISE AND RANGELY SANDSTONES.

data and Eq. 3 suggests that the procedure correctly accounts for the effects of properties of the rock and fluid, such as void fraction and fluid conductivity k_g. Hence Eq. 3 is useful now as a means of predicting the effect of these properties on k_e and requires no experimental data for this use. The method is also valuable for correlating experimental k_e information.

Of the data in the literature, only that of Zierfuss and Vliet[8] included information on the effect of different fluid conductivities. Their conductivity results for air and liquid water showed increases in k^o_e with k_g of the same magnitude as indicated in Figs. 6 through 8. Data were presented for only these two fluids with known thermal conductivities, and no information was given at low pressures. Hence, it was not possible to evaluate $(k^o_e)_o$ and make a quantitative analysis of their results according to Eq. 3.

NOMENCLATURE

b = distance over which conduction takes place (i.e., pore diameter), ft
C = constant, (psi)(ft)(1/°R)
$D_p h_p / k_s$ = dimensionless consolidation parameter for expressing the heat transfer in the solid phase (see Ref. 4)
k^o_e = stagnant conductivity, Btu/(ft)(hr)(°F)
$(k^o_e)_o$ = asymptotic value of stagnant conductivity corresponding to zero thermal conductivity of gas phase (i.e., zero pressure), Btu/(ft)(hr)(°F)
k_g = apparent thermal conductivity of gas, Btu/(ft)(hr)(°F)
k^*_g = normal thermal conductivity of gas, Btu/(ft)(hr)(°F)
k_s = apparent thermal conductivity of solid phase, Btu/(ft)(hr)(°F)
L = length of test section, ft (approximately 2 3/4 in.)
p = absolute pressure, lb/sq ft
r = radial distance, measured from center of core, ft
Q = energy input in the test section, Btu/hr
T = absolute temperature, °R
a = ratio of effective thickness of the fluid film adjacent to the contact surface of two solid particles in the original packed bed (prediction of ϕ is described in Ref. 4)
ϕ = void fraction of original packed bed of unconsolidated particles
ϕ' = porosity of sandstone
$\frac{d \ln r}{d T}$ = slope of temperature vs radial distance line plotted as $\ln r$ vs T (Fig. 2), °R^{-1}

ACKNOWLEDGMENT

The authors wish to express their appreciation for the financial assistance of the California Research Corp., Petroleum Research Fund (American Chemical Society) and the Socony-Mobil Oil Co. J. P. Mason assisted in some of the experimental work.

REFERENCES

1. Asaad, T.: Ph.D. Thesis, U. of California, Berkeley (June, 1955).
2. Birch, F. and Clark, H.: *Am. Jour. Sci.* (1940) Vol. 238, 529.
3. Clark, H.: *Trans.*, Am. Geophys. Union (1940) 543.
4. Kunii, D. and Smith, J. M.: *AIChE Jour.* (1960) Vol. 6, 71.
5. Niven, C. D.: *Can. Jour. Research* (1940) Vol. 18, 132.
6. Schotte, W.: *AIChE Jour.* (1960) Vol. 6, 63.
7. Somerton, W. H.: "A Laboratory Study of Rock Breakage by Rotary Drilling", *Trans.*, AIME (1958) Vol. 213, 375.
8. Zierfuss, H. and Vliet, G.: *Bull.*, AAPG (1958) Vol. 40, No. 10, 2475.

***

A Study of the Behavior of Bounded Reservoirs Composed of Stratified Layers

H. C. LEFKOVITS
P. HAZEBROEK
E. E. ALLEN
C. S. MATTHEWS
MEMBER AIME

SHELL DEVELOPMENT CO.
HOUSTON, TEX.

ABSTRACT

A rigorous study was made of the behavior of reservoirs composed of horizontal layers, unconnected except at the well and filled with a compressible fluid. The report is presented in two parts. Part I deals with the practical implications of the results obtained; Part II contains the mathematical derivation of the solution. The main portion of Part I is concerned with application of the results to reservoirs composed of two layers. Relative rates of depletion of the layers are studied, and it is shown that differential depletion between layers exists in the transient stage of the reservoir, which generally is of an order of magnitude longer than the transient stage in a single-layer reservoir. In the transient stage, the more permeable layer is depleted faster than the less permeable. However, the reservoir approaches a steady-state situation where both layers contribute equally to production. Theoretical build-up curves from such reservoirs are presented, and the influence of a skin effect and flow into casing and tubing are also evaluated. The build-up curves are predicted to have, first, the familiar logarithmic straight-line section and, subsequently, a rising and flattened section. The results found are compared with an extension of an approximate theory, and it is found that this simplified theory is applicable over most of the life of the reservoir. Extensions to reservoirs containing more than two layers are indicated, and examples of the performance and build-up curves for three-layered reservoirs are presented. The theoretical results on build-up curves were applied to field examples of such reservoirs, and satisfactory results were obtained. From the build-up curve, the permeability-thickness product, the wellbore damage and the static pressure are obtained. However, it apparently is not possible to determine the properties of the individual layers from the combined build-up curve.

Original manuscript received in Society of Petroleum Engineers office July 9, 1959. Revised manuscript received March 2, 1960. Paper presented at 34th Annual Fall Meeting of SPE, Oct. 4-7, 1959, in Dallas.

PART I — PRACTICAL APPLICATIONS

INTRODUCTION

A large number of reservoirs have been found where the producing formation is composed of two or more layers of differing physical characteristics, such as permeability and porosity, and where also the thicknesses of the layers differ. Since in general a differential depletion should exist between the layers of such reservoirs, it would be advantageous to know the amount of the differential depletion under a given production history. It also would be valuable to know the pressure behavior, because it could be undesirable to produce a reservoir in such a manner that the pressure in one of the layers would have fallen below the bubble point of the oil at a time when another layer might still be virtually undepleted.

The determination of static pressures in shut-in wells with slow build-up is another feature of importance in layered reservoirs. If the behavior of the reservoir differs appreciably from the predicted behavior of a single-layer reservoir, the type of analysis for build-up curves suggested for single-layer reservoirs is not applicable.

Several authors have treated the problem of finding the pressure and production characteristics of multilayer reservoirs. Horner[1] treated the problem of n layers in an infinite field, the layers being connected only at the well. Tempelaar-Lietz[2] has presented an approximate treatment of the characteristics of a bounded reservoir composed of two layers of different permeabilities and equal thicknesses. Horner gave no information on differential depletion between layers, and the treatment of Tempelaar-Lietz was not applicable for prediction of pressure build-up behavior. In addition, it was thought that a more rigorous treatment than the one by Tempelaar-Lietz would be valuable in determining the range of validity of this solution. The present study, therefore, was made of a bounded reservoir composed of two or more layers,

[1]References given at end of paper.

these layers being unconnected except at the well.

BASIC ASSUMPTIONS

The reservoir to be studied is shown in Fig. 1. Each layer of the reservoir is assumed to be homogeneous and isotropic, and filled with a fluid of small and constant compressibility c. The permeability k, oil-filled porosity ϕ and thickness h of each layer are designated by the corresponding symbol with the subscript 1, 2, ..., n, depending on which layer is referenced. The viscosity of the oil is assumed to be constant and is denoted by μ. The reservoir is initially at a uniform pressure p_o; and at all times $t > 0$, the fluid is produced in such a manner that the production rate q_T, measured at initial reservoir conditions, is held constant.

Under these assumptions, the pressure at any point must satisfy the well known equation for flow of a fluid of small but constant compressibility given in Part II. The solution of this equation for the proper boundary conditions is obtained with the aid of the Laplace transform.

DISCUSSION OF RESULTS

FLOWING-WELL PERFORMANCE

For all but very small times, the solution to the differential equation leads to the following results:

$$p_i - p_w(t) = \frac{q_T}{2\pi}\left[\frac{2t}{\sum_{j=1}^{n} h_j \phi_j r_e^2 c} + \frac{\sum_{j=1}^{n} \frac{\phi_j^2 h_j \mu}{k_j}\left(\ln\frac{r_e}{r_w} - \frac{3}{4}\right)}{\left(\sum_{j=1}^{n} \phi_j h_j\right)^2}\right] + Y(t) \quad \ldots\ldots\ldots\ldots\ldots\ldots\ldots\ldots (1)$$

and

$$q_j(t) = q_T \frac{\phi_j h_j}{\sum_{j=1}^{n} \phi_j h_j} + Z_j(t) \quad , \quad \ldots\ldots\ldots\ldots\ldots\ldots\ldots\ldots (2)$$

where $Y(t)$ and $Z_j(t)$ are transients which approach zero with increasing time. Both of these functions are directly proportional to q_T.

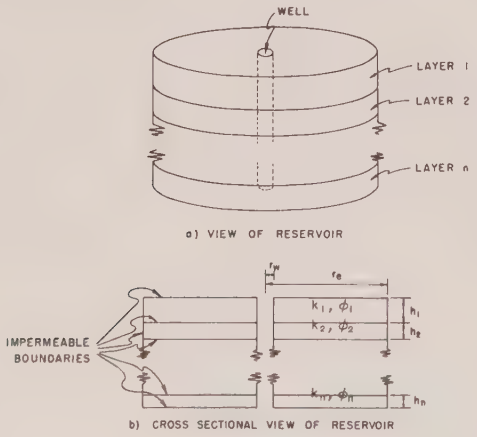

FIG. 1 – THE RESERVOIR.

For the case of two layers, these equations can be rewritten as

$$\frac{p_i - p_w(t)}{q_T \mu / 4\pi \bar{k} \bar{h}} = 4\frac{r_w^2}{r_e^2}\, t_D + 2\left(\ln\frac{r_e}{r_w} - \frac{3}{4}\right)\frac{\left(1 + \frac{k_2 b_2}{k_1 b_1}\right)\left\{\left(\frac{b_1\phi_1}{b_2\phi_2}\right)^2 + \frac{b_1 k_1}{b_2 k_2}\right\}}{\left(1 + \frac{b_1\phi_1}{b_2\phi_2}\right)^2} + \frac{Y(t)}{q_T \mu / 4\pi \bar{k} \bar{h}} \quad \ldots\ldots\ldots\ldots\ldots\ldots (3)$$

and

$$q_1(t) = q_T \frac{\phi_1 b_1}{\phi_1 b_1 + \phi_2 b_2} + Z_1(t) \quad , \quad \ldots\ldots\ldots\ldots\ldots\ldots (4)$$

where $\bar{k} = (k_1 b_1 + k_2 b_2)/(b_1 + b_2)$,

$\bar{\phi} = (\phi_1 b_1 + \phi_2 b_2)/(b_1 + b_2)$,

$\bar{h} = b_1 + b_2$,

$t_D = \bar{k} t / \bar{\phi} \mu c r_w^2$.

For early times at which the influence of the boundary has not been felt, the expression

$$\frac{p_i - p_w(t)}{q_T \mu / 4\pi \bar{k} \bar{h}} = \ln t - \ln \gamma - \frac{k_1 b_1 \ln \frac{\phi_1 \mu c r_w^2}{4k_1} + k_2 b_2 \ln \frac{\phi_2 \mu c r_w^2}{4k_2}}{k_1 b_1 + k_2 b_2} \quad \ldots\ldots (5)$$

gives the correct pressure behavior at the well, γ denoting Euler's constant. The lower limit of the time range of validity of this equation is small enough to include most times of practical interest.

From Eqs. 3 and 4 it can be seen that a steady state is finally attained in the reservoir, during which the rate of change of the well pressure with respect to time (i.e., dp_w/dt) is constant. Furthermore, at this time the production rate from each layer becomes constant, and it then follows that the pressure everywhere within the reservoir varies linearly with time.

Solutions for two sample cases for two sets of parameters are presented in Figs. 2 and 3. The curves labeled I correspond to the parameters

$$\frac{k_1}{k_2} = 10 \quad , \qquad \frac{\phi_1}{\phi_2} = 1 \quad ,$$

$$\frac{b_1}{b_2} = 1 \quad , \qquad \frac{r_e}{r_w} = 2{,}000 \quad ;$$

whereas, the curves labeled II correspond to the parameters

$$\frac{k_1}{k_2} = 1.25 \quad , \qquad \frac{\phi_1}{\phi_2} = 1 \quad ,$$

$$\frac{b_1}{b_2} = 1 \quad , \qquad \frac{r_e}{r_w} = 2{,}000 \quad ;$$

Fig. 2 shows the pressure behavior at the well. Eq. 5 was used in calculating this behavior for $t_D < 10^6$. During this first period, the pressure decreases logarithmically with time. Physically, this

time range corresponds to the time during which the well has not detectably influenced the pressure at the outer drainage boundary. Hence, the pressure decline at the well is identical to the decline of a well draining an infinite reservoir. The time at which the influence of the drainage boundary is first detected at the well is characterized by the break of the pressure curve away from the straight-line portion of the curve. Now the reservoir produces as if it were composed of one bounded layer and one infinite layer because the influence of the boundary has been reflected only in the more permeable layer. After some time, the less permeable layer also feels its boundary. From then on, the reservoir behaves as a fully bounded reservoir. Steady state, where the relation between p_w and t would be a straight line if plotted on a linear scale, is reached some time thereafter. The dotted lines in Fig. 2 are the approximations given by the method of Tempelaar-Lietz and will be discussed in a later section.

The magnitude of the time necessary to reach steady state in a two-layer reservoir can be compared with the corresponding time for a single-layer reservoir. Matthews and Brons[3] have shown that for a cylindrical reservoir steady state is reached at a dimensionless time

$$\frac{kt}{\phi\mu c r_e^2} \simeq 0.3 \ ,$$

If $r_e/r_w = 2{,}000$, then steady state is reached at

$$\frac{kt}{\phi\mu c r_w^2} \simeq 1.2 \times 10^6$$

In a two-layer reservoir, the dimensionless time needed to reach steady state varies with the properties of the two layers; the average of the cases studied in this report is about

$$\frac{\bar{k}t}{\bar{\phi}\mu c r_w^2} \simeq 8 \times 10^7 \ .$$

Hence, the time needed to reach steady state is of the order of 50 times as great as the corresponding time for a single-layer reservoir. The reason for

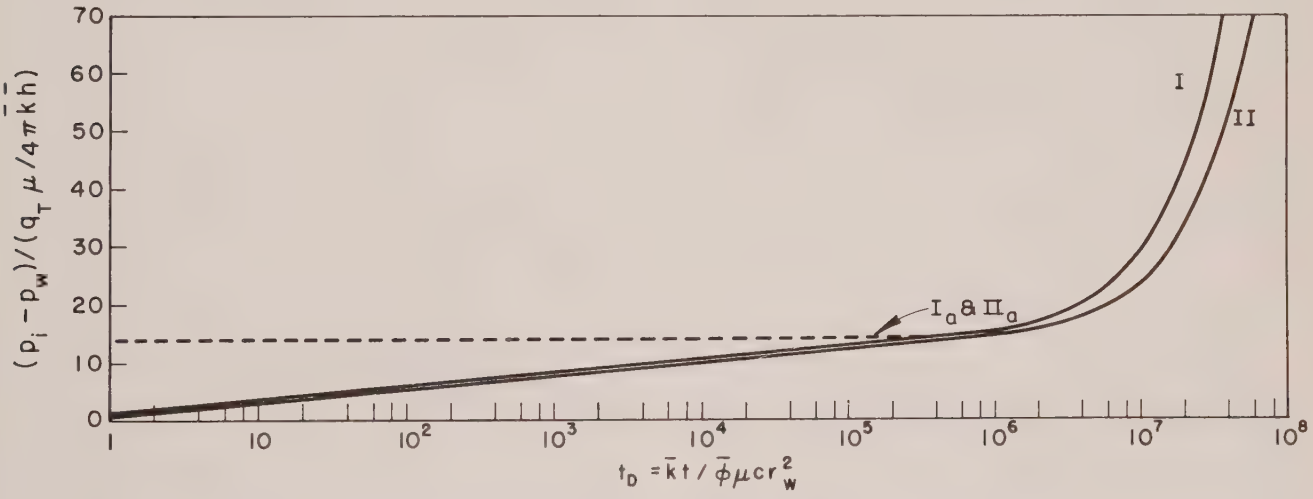

FIG. 2 – WELL PRESSURE-DECLINE CURVES FOR TWO-LAYER RESERVOIRS.

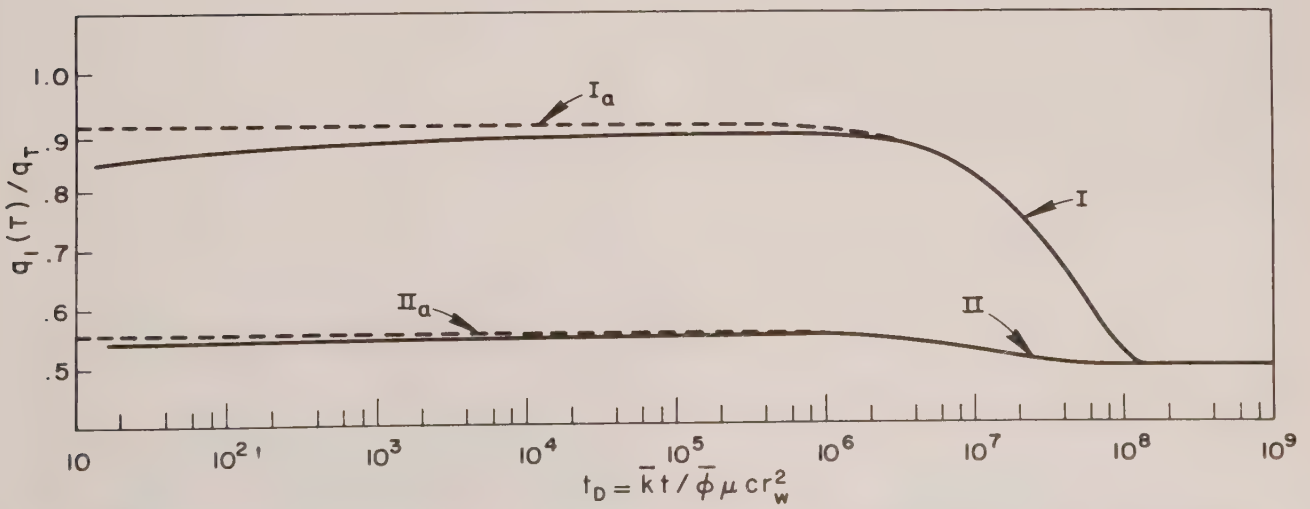

FIG. 3 – FRACTIONAL PRODUCTION RATES FROM THE MORE PERMEABLE LAYER OF TWO 2-LAYER RESERVOIRS.

this lies mainly in the changing rates of production from the layers in the multilayer case.

The behavior of the production rate for these two cases is shown in Fig. 3, in each instance for the more permeable layer. The ordinate in the graph is $q_1(t)/q_T$, the fractional production rate from this layer. The dotted lines again are the approximations of Tempelaar-Lietz. The fractional production rate from the other layer $q_2(t)/q_T$ can be obtained from the relation

$$\frac{q_2(t)}{q_T} = 1 - \frac{q_1(t)}{q_T}.$$

At early times, the production rate from the more permeable layer is increasing; it approaches asymptotically the value $q_1(t)/q_T = k_1h_1/(k_1h_1 + k_2h_2)$, which behavior corresponds to the case of a well draining an infinite reservoir. After the initial increase, the production rate begins to decrease, a phenomenon which corresponds to the physical fact that the influence of the boundary in the more permeable layer has been reflected on the behavior of the reservoir. At some later time, the effect of the boundary is also felt in the less permeable layer; subsequent to this time, the curves are seen to approach asymptotically a constant value, this value being $q_1(t)/q_T = h_1\phi_1/(h_1\phi_1 + h_2\phi_2)$. This value is the fractional production rate of Layer 1 at steady state.

The ratio $h_1\phi_1/(h_1\phi_1 + h_2\phi_2)$ is equal to the ratio of the oil-filled volume of Layer 1 to the oil-filled volume of the entire reservoir; hence, at steady state, each layer produces at a fractional rate equal to the fraction of oil-filled volume it contains.

With regard to fractional depletion between the layers, if each layer always produced at a fractional rate proportional to the oil-filled volume it contains, there would be no differential depletion. Hence, during production of a reservoir, differential depletion takes place previous to the time when steady state is reached.

The total production rate q_T from the reservoir is an important factor in the differential depletion of the reservoir. The time required to reach steady state is essentially independent of q_T, but the cumulative production from each layer is directly proportional to q_T. If $Q_1(t)$ and $Q_2(t)$ denote the cumulative production at the time t from Layers 1 and 2, respectively,

$$\frac{Q_1(t)}{h_1} = \int_0^t \frac{q_1(t)}{h_1}\,dt,$$

$$\frac{Q_2(t)}{h_2} = \int_0^t \frac{q_2(t)}{h_2}\,dt.$$

Also, the differential depletion $\Delta D(t)$ per unit thickness is then defined as

$$\Delta D(t) = \left| \frac{Q_1(t)}{h_1} - \frac{Q_2(t)}{h_2} \right|.$$

But we can also write

$$\frac{Q_j(t)}{h_j} = q_T \int_0^t \frac{q_j(t)}{h_j q_T}\,dt, \qquad j = 1, 2,$$

so that

$$\Delta D(t) = q_T \left| \int_0^t \frac{q_1(t)}{h_1 q_T}\,dt - \int_0^t \frac{q_2(t)}{h_2 q_T}\,dt \right| \quad . \quad . \quad . \quad (6)$$

Since the ratios $q_1(t)/q_T$ and $q_2(t)/q_T$ are independent of q_T, the differential depletion is directly proportional to q_T. For example, if the maximum differential depletion in a reservoir produced at a rate q_T is ΔD and if the reservoir had been produced at a rate 2 q_T, the maximum differential depletion would have been $2\Delta D$.

The results from another sample case are presented in Figs. 4 and 5. The properties of the layers are $k_1/k_2 = 4$, $h_1/h_2 = 0.05$ and $\phi_1/\phi_2 = 2$. The results are presented for four different values of r_e/r_w — r_e/r_w = 2,000, 1,000, 100 and 10. Fig. 4 shows the well pressure behavior as a function of production time; the straight-line portion again corresponds to the time range when the influence of the boundary has not been felt at the well, and the deviation from this straight line corresponds to the influence of the boundary.

The times at which the pressure-decline curves deviate from the straight-line portion increase with with the dimensions of the reservoir. This is because the time required (t_r) for the pressure disturbance caused by the opening of the well to reach a certain point (r) away from the well increases with the distance of the point from the well. A good approximation is given by $t_r \propto r^2$.

Fig. 5 shows the fractional production rate from the more permeable layer for several ratios r_e/r_w for the properties just mentioned.

THEORETICAL PRESSURE BUILD-UP CURVES

Since the behavior of the reservoir is described by linear differential equations, the behavior during build-up can be obtained by superposition. Fig. 6 shows a typical theoretical pressure build-up curve obtained from a two-layer reservoir. As in a single-layer reservoir, there is an initial straight-line section, AB. After the straight-line portion, the build-up curve levels off (BC), this leveling off corresponding in a single-layer reservoir to the pressure's having almost reached its average pressure. However, in a multilayer reservoir the pressure again rises (CD) and then finally levels off at the average pressure (DE). The rise in CD is due to the repressuring of the more depleted, permeable layer by the less depleted, less permeable layer.

Several other examples of pressure build-up curves are presented in Figs. 7 through 10, the parameters for each reservoir being indicated on the same page as the graph. Figs. 7 and 8 present pressure build-up curves, plotted both against Δt, the shut-in time and against $\Delta t/(t + \Delta t)$. Figs. 7 and 8 are at a closed-in time when the reservoir is still in the stage where the influence of the boundary has not

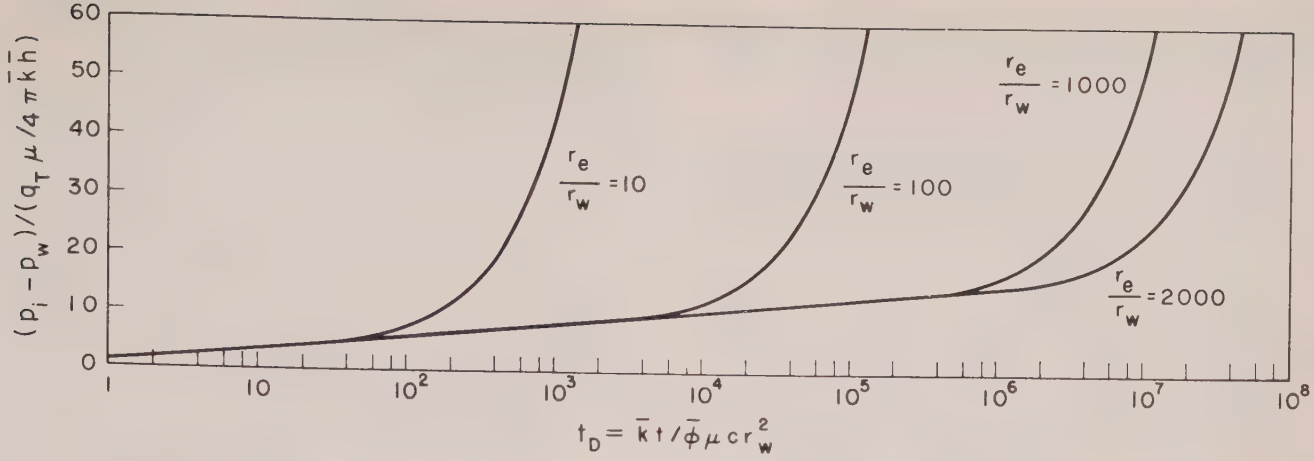

FIG. 4 – WELL PRESSURE-DECLINE CURVES FOR A TWO-LAYER RESERVOIR FOR DIFFERENT RATIOS OF r_e/r_w.

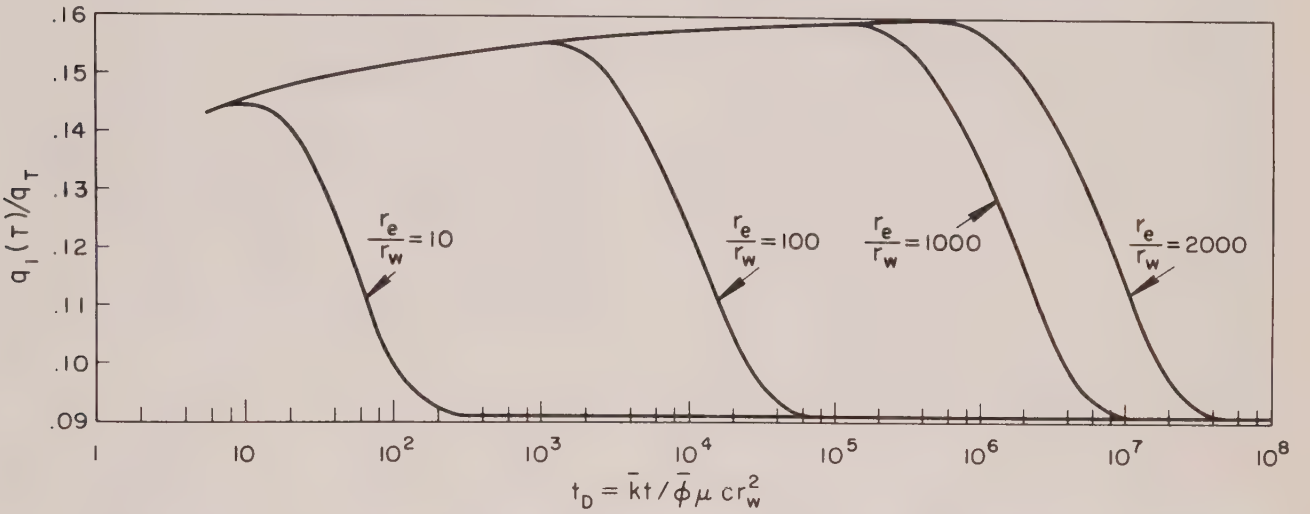

FIG. 5 – FRACTIONAL PRODUCTION RATES FROM MORE PERMEABLE LAYER OF A TWO-LAYER RESERVOIR FOR DIFFERENT RATIOS OF r_e/r_w.

been felt during production. Fig. 9 is a build-up curve for the same reservoir at a closed-in time when the influence of the boundary has been felt. From these curves, it can be seen that the entire portion CDE (as in Fig. 6) expands greatly in vertical scale with increasing production time.

The magnitude of the pressure rise during the portion CDE of the pressure build-up curve depends on the contrast of the properties of the layers. If the two layers are nearly equal in permeability, the pressure rise in this portion will be small (see Fig. 10), whereas if the two layers differ widely in properties, the pressure rise will be considerable (see Fig. 9).

For equivalent information, a well in a multilayer reservoir must remain shut in longer than a well in a single-layer reservoir, the ratio of required shut-in times being roughly equal to the ratio of the times needed to attain steady state in the two reservoirs. It was seen that this latter ratio is large (of the order of 50); it then follows that wells producing from multilayer reservoirs may have to remain shut in for considerable times to provide useful pressure build-up data.

A reason for the difference in type of pressure build-up curves obtained from two-layer and single-layer reservoirs is that in a two-layer reservoir flow occurs from one layer to the other during build-up. There is differential depletion between the layers, the more permeable layer having been depleted more than the less permeable layer; when the well is shut in, there must be flow from the

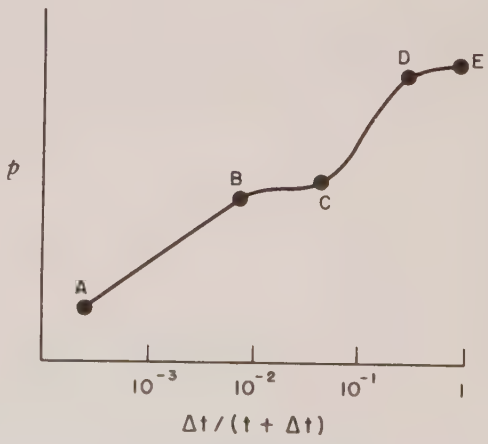

FIG. 6 – THEORETICAL PRESSURE BUILD-UP CURVE FOR TWO-LAYER RESERVOIR.

less permeable layer to the more permeable layer for the pressure to stabilize over the entire reservoir.

SKIN EFFECT

In the study of skin effects, the skin factor S_j in each layer was defined by means of the equations

$$S_j = \frac{p_{fj} - p_w}{q_j(t)\mu/2\pi k_j h_j}, \quad j = 1, 2, \ldots, n \quad . \quad (7)$$

where p_{fj} denotes the formation pressure in the jth layer.

The mathematical analysis of the problem showed that the effect of the skin could be represented by a fictitious well radius in each layer. Eqs. 1 and 2 were modified to include these characteristics.

The effect of introducing a fictitious well radius can best be illustrated for the case of a single-layer reservoir producing at a constant rate. As shown in Fig. 11, the skin will cause a discontinuity in the pressure at the well. The behavior of the pressure in the vicinity of the well is logarithmic; if the curve is extrapolated logarithmically (the dotted line in Fig. 11), there exists a point r^*_w such that $p(r^*_w) = p_w$. Then r^*_w can be considered the fictitious well radius representing the skin. The relation between r_w and r^*_w is given by

$$r^*_w = r_w e^{-S} \quad . \quad (8)$$

Several curves showing the influence of skin effects are presented in Figs. 12 and 13. The characteristics of the reservoir studied are

$$\frac{k_1}{k_2} = 10 \quad , \qquad \frac{\phi_1}{\phi_2} = 1 \quad ,$$

$$\frac{h_1}{h_2} = 10 \quad , \qquad \frac{r_e}{r_w} = 2{,}000 \quad .$$

In each graph, Curve a refers to the case where no skin was present in either layer (i.e., $S_1 = 0$ and $S_2 = 0$); Curve b refers to the case where the skin effects were taken to be $S_1 = 10$ and $S_2 = 1$; and Curve c refers to the case where the skin effects were taken to be $S_1 = 1$ and $S_2 = 10$.

A comparison shows that for Case b there was less differential depletion than for Case a, where the reservoir had no skin, and that for Case c there was more differential depletion than for Case a. These facts are readily explained; if a high resistance to flow is placed in the more permeable layer, it will tend to equalize the flow from the layers and, thus, will reduce differential depletion.

Pressure build-up curves for these cases and for cases with no skin have the same sort of shape. However, the effect of the skin on pressure build-up curves is different for multilayer and single-layer reservoirs. For a reservoir composed of a single layer, the effect vanishes after a short interval of shut-in time; on the other hand, in a multilayer reservoir the effect of the skin is present

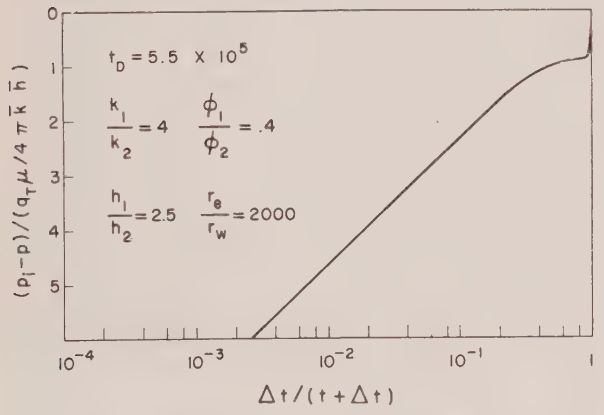

FIG. 7 — PRESSURE BUILD-UP CURVE WITH $\Delta t/(t+\Delta t)$ AS ABSCISSA.

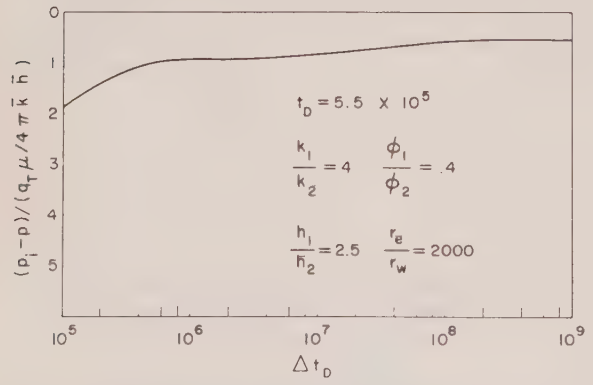

FIG. 8 — PRESSURE BUILD-UP CURVE WITH Δt AS ABSCISSA.

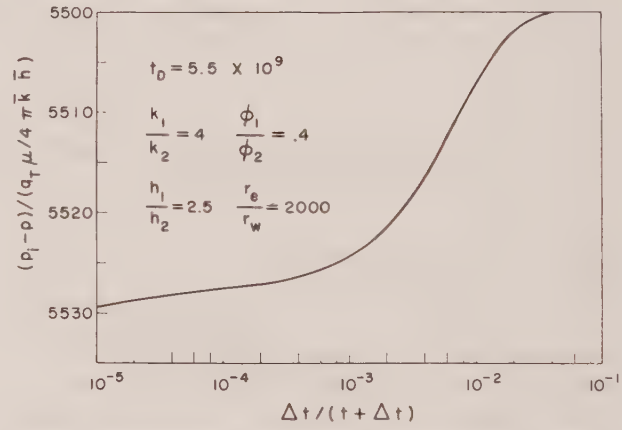

FIG. 9 — PRESSURE BUILD-UP CURVE WITH $\Delta t/(t+\Delta t)$ ABSCISSA.

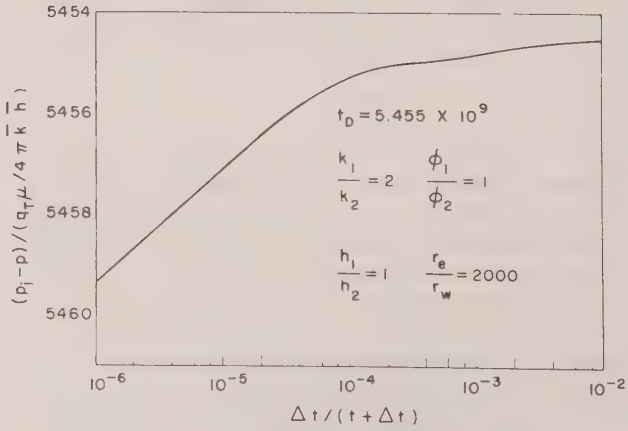

FIG. 10 — PRESSURE BUILD-UP CURVE.

during the entire range of shut-in time. This is true because, at the time the well is closed in, differential depletion exists between the layers; during shut-in, flow must then occur from one layer to another through the wellbore, and the skin acts as a resistance to that flow. Hence, the influence of the skin is felt during the entire pressure build-up.

FLOW INTO CASING AND TUBING DURING BUILD-UP

To evaluate this effect, it was assumed that the flow from the formation did not drop discontinuously to zero at the instant the well was closed in, but that the flow decreased in an exponential fashion; that is,

$$q_c(\Delta t) = q_T e^{-a\Delta t}, \quad \ldots\ldots\ldots \quad (9)$$

as discussed by van Everdingen[4] for the single-layer case.

Results show that after-production deforms the straight-line portion of the pressure build-up curve in the same fashion that it influences the curve for a single-layer reservoir. Fig. 14 shows a build-up

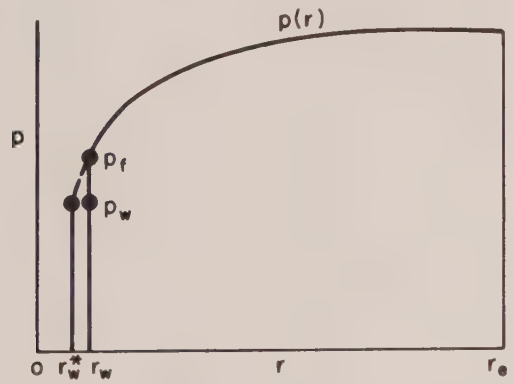

FIG. 11 – FICTITIOUS WELL RADIUS TO REPRESENT SKIN EFFECT.

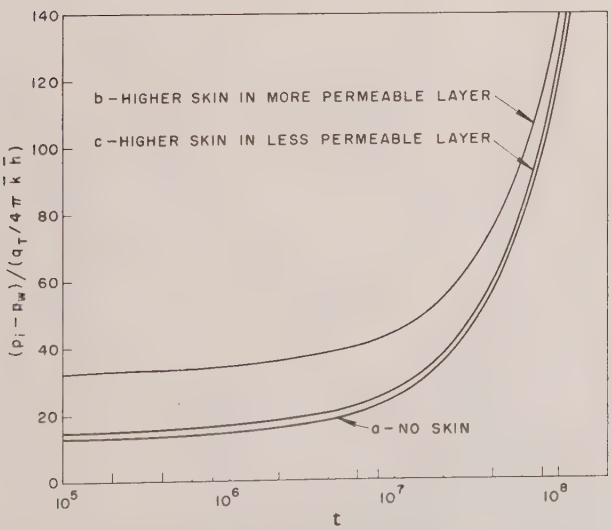

FIG. 12 – PRESSURE-DECLINE CURVES SHOWING INFLUENCE OF SKIN EFFECT.

curve both with and without after-flow. The two curves overlap for all shut-in times for which the flow due to after-production is essentially zero.

EXTENSION TO THREE-LAYER RESERVOIRS

Several examples of three-layer reservoirs were studied; results show that, qualitatively, their behavior is like that of a two-layer reservoir. Differential depletion exists between layers, the differential depletion being directly proportional to the total production rate. The shape of the pressure build-up curves is the same as that for two-layer reservoirs. Figs. 15 and 16 give examples of results obtained for three-layer reservoirs.

COMPARISON OF RESULTS WITH THE TEMPELAAR-LIETZ THEORY

The previously mentioned work of Tempelaar-Lietz presents an approximate theory of the behavior of a two-layer reservoir where the layers had different permeabilities, equal thicknesses and equal porosities. The simplifying assumption made by Tempelaar-Lietz in his treatment was that the production rate from each layer was proportional to the difference between average pressure in that layer and the well pressure, the constant of proportionality being a function of the parameters associated with that layer.

The theory presented by Tempelaar-Lietz easily can be extended to include differences between the layers in thicknesses and porosities, as well as in well radii. The formulas obtained from this treatment are given at the end of this section.

The results obtained by the Tempelaar-Lietz theory were compared with the exact solutions obtained in this study. It was found that the Tempelaar-Lietz solutions are very good approximations to the true solutions for pressure decline and rate behavior for all but early production times. To be more exact, the Tempelaar-Lietz solutions do not express the true behavior for early times (when the reservoir can be considered to behave like an infinite reservoir) and for times shortly thereafter. After the influence of the boundary is felt, the Tempelaar-Lietz solutions become applicable with good approximation. A comparison of results is presented in Figs. 2 and 3, where both the true and approximate solutions are presented for one example. The approximate solutions are labeled with the subscript *a*.

The Tempelaar-Lietz pressure-decline equation cannot be used as an approximation to the pressure build-up curves because the pressure values are needed at times at which the Tempelaar-Lietz solution is inapplicable. However, the portion CDE in Fig. 6 can be described by the Tempelaar-Lietz equation, and the method for finding average pressures described later will make use of this fact.

The generalization of the Tempelaar-Lietz theory to the case of unequal properties of the layers gives the following formulas.

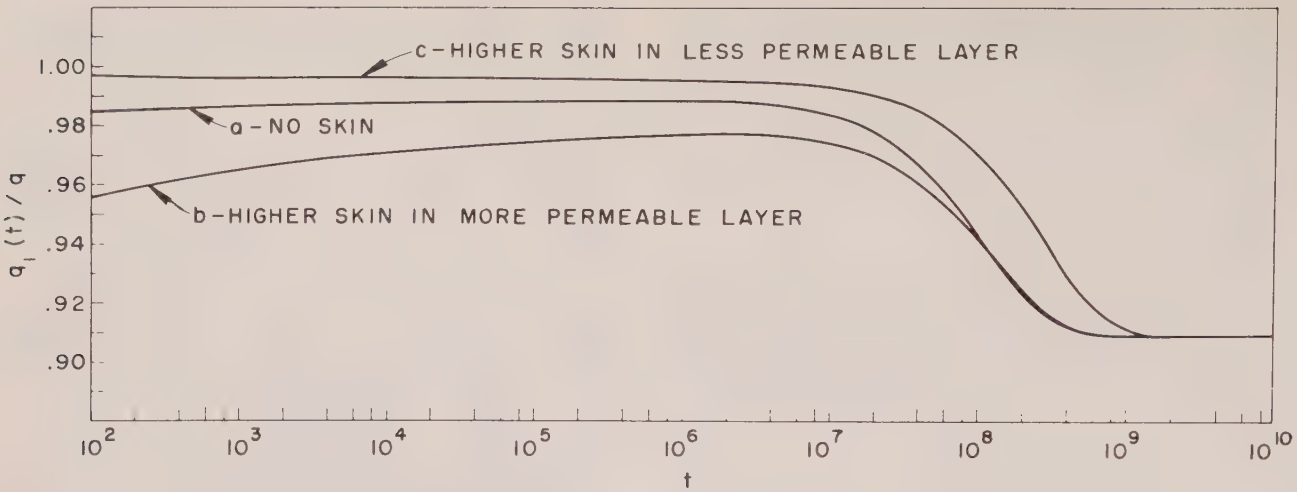

FIG. 13 – FRACTIONAL PRODUCTION RATES SHOWING INFLUENCE OF SKIN EFFECT.

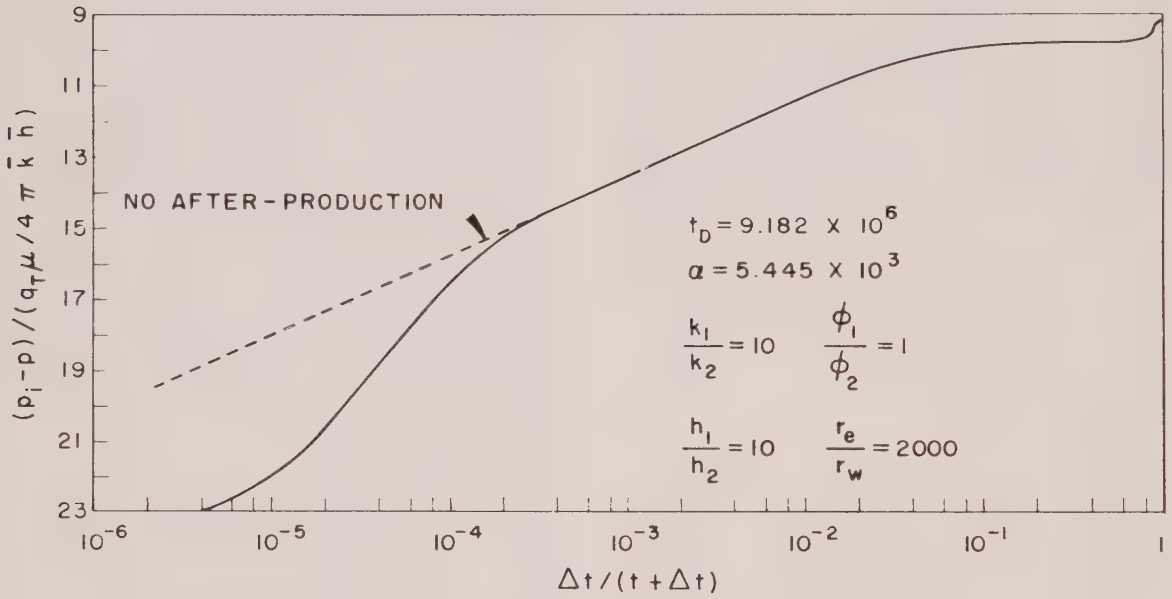
NO AFTER-PRODUCTION
$t_D = 9.182 \times 10^6$
$\alpha = 5.445 \times 10^3$
$\frac{k_1}{k_2} = 10$ $\frac{\phi_1}{\phi_2} = 1$
$\frac{h_1}{h_2} = 10$ $\frac{r_e}{r_w} = 2000$
$(p_i - p)/(q_T \mu / 4\pi \bar{k} \bar{h})$
9 11 13 15 17 19 21 23
10^{-6} 10^{-5} 10^{-4} 10^{-3} 10^{-2} 10^{-1} 1
$\Delta t/(t+\Delta t)$

FIG. 14 – PRESSURE BUILD-UP CURVE SHOWING EFFECT OF AFTER-PRODUCTION.

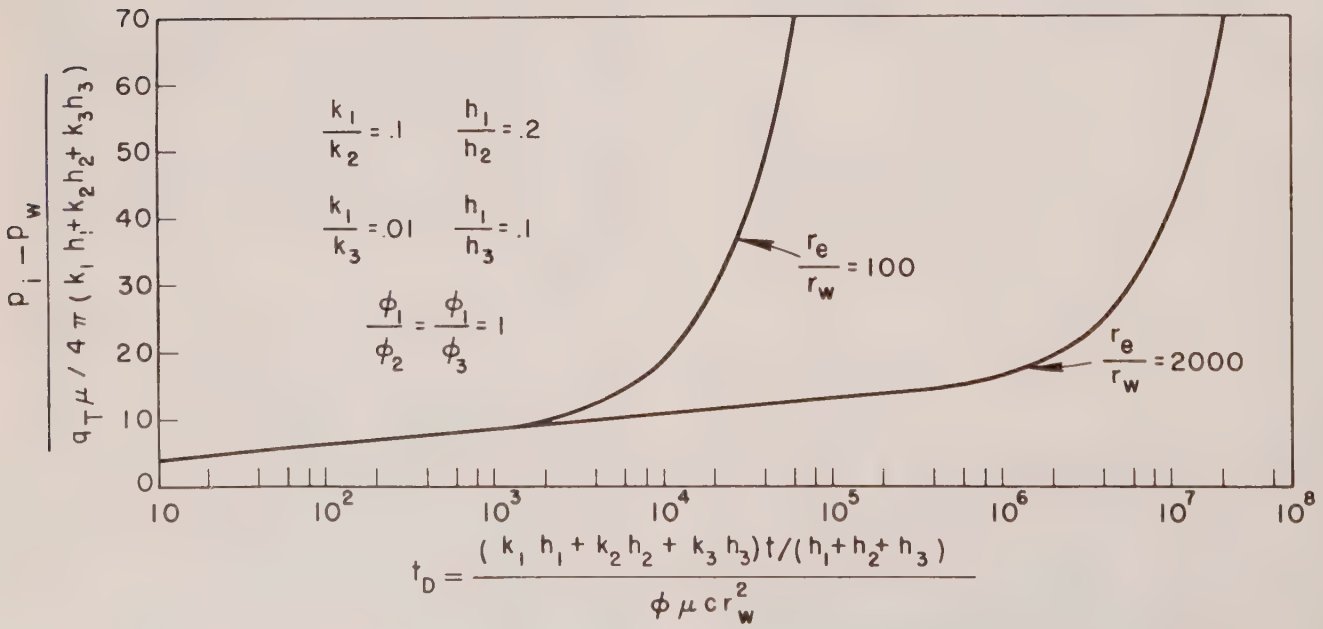
$\frac{p_i - p_w}{q_T \mu / 4\pi (k_1 h_1 + k_2 h_2 + k_3 h_3)}$
70 60 50 40 30 20 10 0
$\frac{k_1}{k_2} = .1$ $\frac{h_1}{h_2} = .2$
$\frac{k_1}{k_3} = .01$ $\frac{h_1}{h_3} = .1$
$\frac{\phi_1}{\phi_2} = \frac{\phi_1}{\phi_3} = 1$
$\frac{r_e}{r_w} = 100$
$\frac{r_e}{r_w} = 2000$
10 10^2 10^3 10^4 10^5 10^6 10^7 10^8
$t_D = \frac{(k_1 h_1 + k_2 h_2 + k_3 h_3) t/(h_1 + h_2 + h_3)}{\phi \mu c r_w^2}$

FIG. 15 – PRESSURE-DECLINE CURVES (3 LAYERS).

$$p_i - p_w(t) = \frac{q_T t}{A_1 + A_2} + \frac{q_T}{i_1 + i_2} + \frac{q_T (i_1 A_2 - i_2 A_1)^2}{i_1 i_2 (i_1 + i_2)(A_1 + A_2)^2} \times \left[1 - \exp\left(-\frac{i_1 i_2 (A_1 + A_2)}{(i_1 + i_2) A_1 A_2}\, t\right)\right] \quad \ldots\ldots\ldots\ldots\ldots\ldots\ldots\ldots (10)$$

$$p_i - \bar{p}_1(t) = \frac{q_T t}{A_1 + A_2} + \frac{q_T A_2 (A_2 i_1 - A_1 i_2)}{(A_1 + A_2)^2 i_1 i_2} \times \left[1 - \exp\left(-\frac{i_1 i_2 (A_1 + A_2)}{(i_1 + i_2) A_1 A_2}\, t\right)\right] \quad \ldots\ldots\ldots\ldots\ldots\ldots\ldots\ldots (11)$$

$$p_i - \bar{p}_2(t) = \frac{q_T t}{A_1 + A_2} - \frac{q_T A_1 (A_2 i_1 - A_1 i_2)}{(A_1 + A_2)^2 i_1 i_2} \times \left[1 - \exp\left(-\frac{i_1 i_2 (A_1 + A_2)}{(i_1 + i_2) A_1 A_2}\, t\right)\right] \quad \ldots\ldots\ldots\ldots\ldots\ldots\ldots\ldots (12)$$

Also,

$$Q_j(t) = A_j [p_i - \bar{p}_j(t)]$$

$$q_1(t) = q_T \left[\frac{A_1}{A_1 + A_2} - \frac{A_2 i_1 - A_1 i_2}{A_1 (i_1 + i_2)} \exp\left(-\frac{i_1 i_2 (A_1 + A_2)}{(i_1 + i_2) A_1 A_2}\, t\right)\right] ; \ldots\ldots (13)$$

and $q_2(t)$ can be obtained from $q_2(t) = q_T - q_1(t)$. In these equations, A_j is the recovery per unit pressure drop of Layer j and i_j is the productivity index of Layer j, as defined by

$$A_j = c\phi_j \pi r_e^2 h_j \quad , \ldots\ldots\ldots\ldots (14)$$

$$i_j = \frac{2\pi k_j h_j}{\mu \left(\ln \frac{r_e}{r_w} - \frac{3}{4}\right)} \ldots\ldots\ldots\ldots (15)$$

APPLICATIONS

RELATIVE DEPLETION BETWEEN LAYERS

One application of the results of this study lies in the prediction of relative depletion between layers as a function of withdrawal rate.

If the rate of withdrawal q is not constant, the solutions for varying rate can be built up by appropriate superposition. The following example should make this clear.

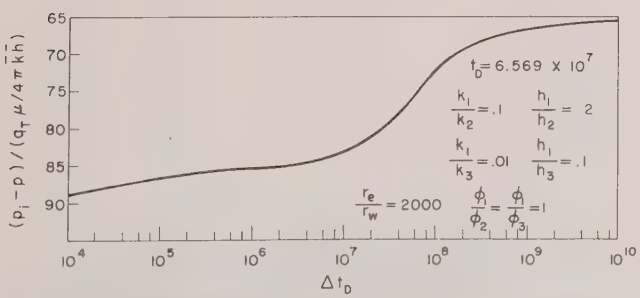

FIG. 16—PRESSURE BUILD-UP CURVE (3 LAYERS).

Example

Let a well which penetrates two layers be produced at a rate of 100 B/D for 30 days, shut in one day, then produced at a rate of 50 B/D. Find the differential depletion between layers at the end of 60 days. The physical constants of the reservoir are as follow: $k_1 = 0.05$ darcy, $k_2 = 0.005$ darcy, $h_1 = 25$ ft, $h_2 = 75$ ft, $c = 10^{-5}$ psi^{-1}, $\mu = 0.5$ cp, $\phi = 0.2$, $r_e = 500$ ft and $r_w = 1/4$ ft; t' denotes production time in days.

Then

$$A_1 = \frac{c\phi\pi r_e^2 h_1}{5.615} = 6.99 \text{ bbl/psi},$$

$$A_2 = 20.97 \text{ bbl/psi},$$

$$i_1 = \frac{2\pi k_1 h_1}{\mu\left(\ln \frac{r_e}{r_w} - \frac{3}{4}\right)} \times \frac{1}{1.84} \times 30.48 \times \frac{1}{14.7} = 2.583 \text{ B/D} \times \text{psi},$$

$$i_2 = 0.775 \text{ B/D} \times \text{psi},$$

and

$$p_i - \bar{p}_1 = \frac{qt'}{27.96} + 0.652\, q(1 - e^{-0.1137\, t'}).$$

For the production schedule outlined, we have at the end of 60 days,

$$p_i - \bar{p}_1 = \frac{100(60)}{27.96} + 0.652(100)\,[1 - e^{-0.1137(60)}] - \frac{100(60-30)}{27.96} - 0.652(100)[1 - e^{-0.1137(60-30)}] + \frac{50(60-31)}{27.96} + 0.652(50)[1 - e^{-0.1137(60-31)}]$$

$$= 192 \text{ psi}.$$

$$p_i - \bar{p}_2 = \frac{100(30) + 50(29)}{20.97} - \frac{6.99}{20.97}(192)$$

$$= 148 \text{ psi}.$$

$Q_1 = 6.99(192) = 1{,}342$ bbl or 53.6 bbl/ft sand,
$Q_2 = 20.97(148) = 3{,}103$ bbl or 41.4 bbl/ft sand.

For a rate of 300 B/D, the corresponding pressures at the same cumulative total production are

$$p_i - \bar{p}_1 = 319 \text{ psi},$$
$$p_i - \bar{p}_2 = 106 \text{ psi},$$

and the cumulative production per ft,

$$Q_1/h_1 = 89.1 \text{ bbl/ft sand},$$
$$Q_2/h_2 = 29.6 \text{ bbl/ft sand}.$$

The effect of rate on the differential depletion thus is emphasized. These equations can also be used to calculate how near the average pressures in each layer approach one another during shut-in. The effect of a skin in each layer is taken into account by changing r_w in each layer according to the manner of Eq. 8.

PRESSURE BUILD-UP FOR MULTILAYER CASES

As shown previously, the pressure build-up curves for multilayer cases have a "tail" which gives an essentially different shape to the build-up curve from that obtained for one-layer reservoirs. The method for obtaining the average pressure in

the drainage area of wells in such cases thus must be different from that for more homogeneous cases. The initial section of such a build-up curve is linear on a plot of pressure vs log $[\Delta t/(t + \Delta t)]$ as shown in Fig. 6 where Δt is the shut-in time. Next a slight flattening may occur, then a rise and, after a long time, a final flattening. In the initial straight-line portion, a value for $(k_1 b_1 + k_2 b_2)$ can be obtained from the slope by using

$$k_1 b_1 + k_2 b_2 = \frac{q'_T \mu / 4\pi}{\text{slope, psi}} \times (14.7)\,(2.303) \quad ,$$

where q_T is the total production rate measured at reservoir conditions at the time of shut-in.

The applicable equation for the section of the build-up curve subsequent to the straight-line section, provided the well has been producing long enough before shut-in, is

$$p_w(\Delta t, t) = \bar{p} - be^{C\Delta t} \quad , \quad \ldots\ldots\ldots \quad (16)$$

where b and C are constants. Thus, a plot of log $(\bar{p} - p)$ vs Δt should give a straight line. One method of determining $\bar{p}$ is to assume a value for $\bar{p}$, make this type of plot, and see whether or not a straight line is obtained. If not, a new value of $\bar{p}$ is assumed and the plotting is repeated. Fig. 17 shows a series of these plots for different assumed values of $\bar{p}$. The correct value is seen to be about 2,750 psi because the lines on either side curve away from each other.

It has been found that types of reservoirs other than multilayer reservoirs also show this same exponential behavior during build-up. Fig. 18 is a build-up curve from a fractured dolomite reservoir, the dotted line being the extrapolation to the average pressure determined by the plot in Fig. 19. In Fig. 20 a build-up curve from a hydrafracked reservoir is presented, the average pressure having been determined with the aid of Fig. 21. Fig. 22

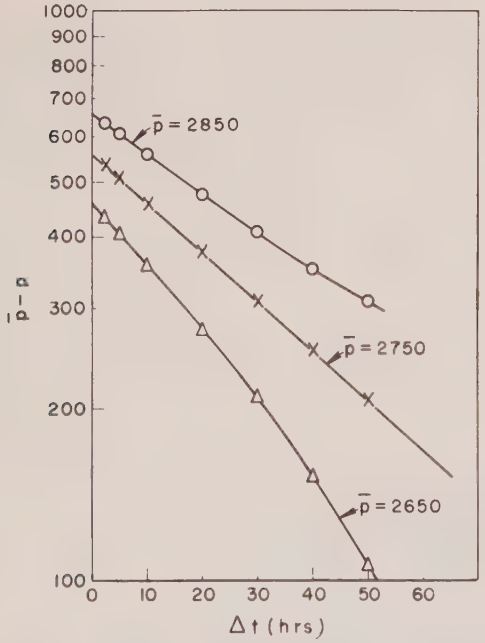

FIG. 17 – PLOT FOR DETERMINATION OF $\bar{p}$.

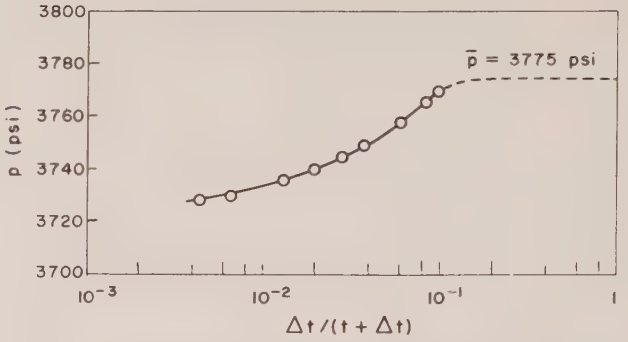

FIG. 18 – PRESSURE BUILD-UP CURVE, WILLISTON BASIN FIELD (FRACTURED DOLOMITE RESERVOIR) JUNE, 1953.

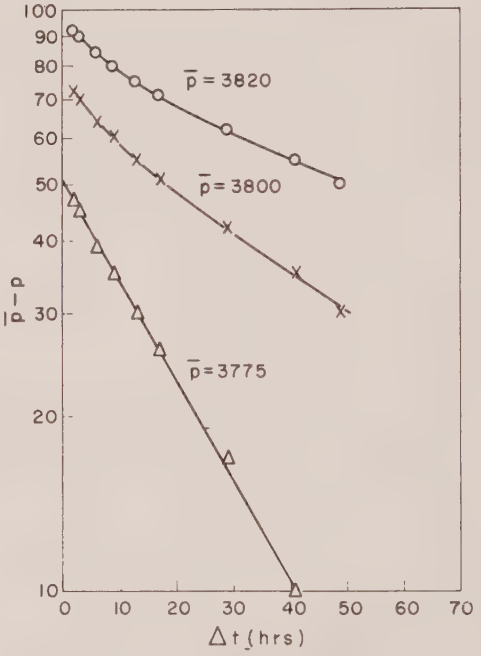

FIG. 19 – WILLISTON BASIN FIELD (FRACTURED DOLOMITE RESERVOIR) JUNE, 1953.

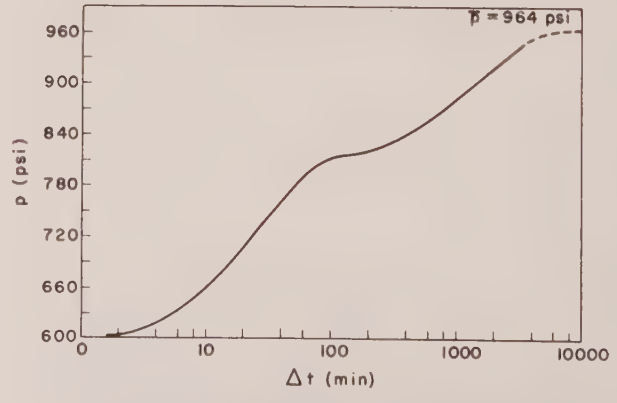

FIG. 20 – PRESSURE BUILD-UP CURVE, SOUTH TEXAS FIELD (HYDRAFRACKED RESERVOIR) OCT. 24 TO OCT. 27, 1952.

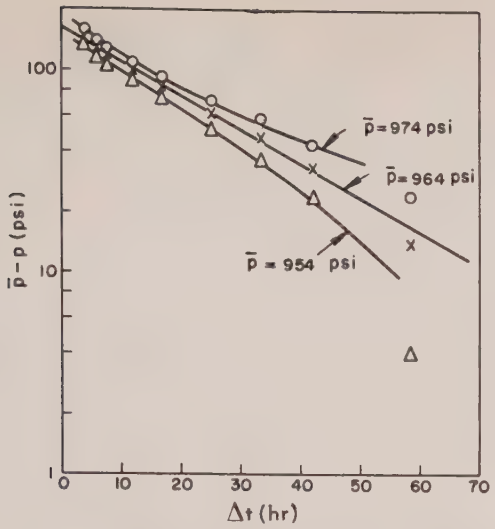

FIG. 21 — SOUTH TEXAS FIELD (HYDRA-FRACKED RESERVOIR) OCT. 24 TO OCT. 27, 1952.

is a build-up curve from a multilayer* reservoir in California. The exponential-rise type of build-up appears applicable to all three types of reservoirs.

CONCLUSIONS

The present investigation has shown that the simple formulas developed by Tempelaar-Lietz and generalized in this report can be used successfully for predicting differential depletion between layers of a multilayer reservoir except at very early times. The simpler formulas can also be used to predict pressure decline at the well. A method for determination of average pressures of these reservoirs is presented. This method can be applied to multilayer reservoirs and appears to be applicable to reservoirs of other types which have the same type of build-up behavior.

PART II — MATHEMATICAL DERIVATION

ASSUMPTIONS AND BASIC EQUATIONS

We assume that the reservoir to be studied is a bounded, horizontal cylindrical disk, with a completely penetrating well at its center, that its thickness is small enough that the forces of gravity can be neglected and that it is bounded above, below and on the outside by impermeable boundaries. The reservoir is divided horizontally into n parallel layers which are separated throughout the reservoir by impermeable boundaries through which no fluid can flow. The radius of the wellbore at the jth layer is denoted by $r_{w,j}$ and the exterior radius of the jth layer by $r_{e,j}$. Each layer is assumed to be homogeneous, isotropic, and filled with a fluid of small and constant compressibility c_j and constant viscosity μ_j ($j = 1, 2, \ldots, n$). For each

*For reservoirs composed of more than two layers, the applicable equation for build-up is of the type of Eq. 16, but it should contain $n - 1$ exponential terms if the reservoir contains n layers. Practically, however, it has been found that good results generally can be obtained by using only one exponential.

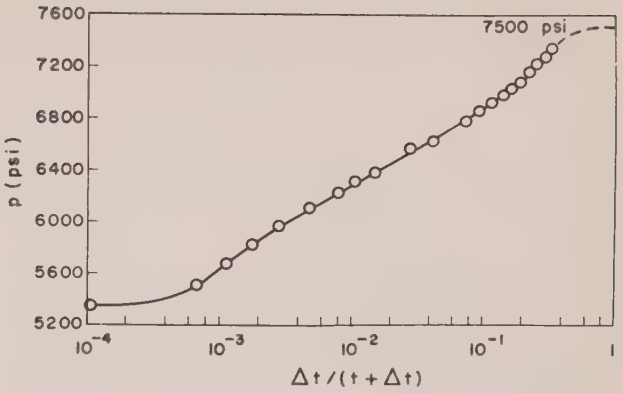

FIG. 22 — CALIFORNIA FIELD, PRESSURE BUILD-UP (MULTILAYER RESERVOIR) MAY, 1952.

layer, k_j denotes its permeability, ϕ_j its porosity and h_j its thickness. The reservoir is initially at a uniform pressure p_i; and, at all times $t > 0$, the fluid is withdrawn through the wellbore in such a manner that the total production rate q, measured at initial reservoir conditions, is held constant.

For simplicity of notation we let

$$\eta_j = \frac{k_j}{\phi_j \mu_j c_j}$$

$$\alpha_j = \frac{r_{w,j}}{\sqrt{\eta_j}}$$

$$\beta_j = \frac{h_j k_j}{\mu_j}$$

$$\gamma_j = \frac{r_{e,j}}{\sqrt{\eta_j}}$$

$$j = 1, 2, \ldots, n$$

and define the pressure drops $P_j(r,t)$ by

$$P_j(r,t) = p_i - p_j(r,t) \qquad j = 1, 2, \ldots, n$$

where $p_j(r,t)$ denotes the pressure in the jth layer at a radial distance r and time t. Then, $P_j(r,t)$ must satisfy the equation

$$\frac{1}{r}\frac{\partial}{\partial r}\left(r\frac{\partial P_j}{\partial r}\right) = \frac{1}{\eta_j}\frac{\partial P_j}{\partial t} \qquad j = 1, 2, \ldots, n, \quad \ldots\ldots\ldots\ldots\ldots\ldots\ldots\ldots (1)$$

This system of equations must be solved subject to the following initial and boundary conditions.

1. At $t = 0$, the pressure drop in each layer is zero; i.e.,

$$P_j(r,0) = 0 \qquad j = 1, 2, \ldots, n. \quad \ldots (2)$$

2. There is no flow across the outer boundaries, so that

$$\frac{\partial P_j}{\partial r} = 0 \qquad \text{at } r = r_{e,j},\ j = 1, 2, \ldots, n. \quad \ldots (3)$$

3. The pressures in all layers at the well are equal and, hence, the pressure drops are also equal; i.e.,

$$P_j(r,t) = P_w(t) \text{ at } r = r_{w,j},\ j = 1, 2, \ldots, n. \quad (4)$$

the function $P_w(t)$ being independent of j.

4. The total production rate from all the layers

is constant and equal to q.

$$\sum_{i=1}^{n} q_j(t) = -2\pi \sum_{i=1}^{n} \beta_j \left(r \frac{\partial P_j}{\partial r} \right)_{r=r_{w,j}} = q \quad . \quad (5)$$

where $q_j(t)$ denotes the rate of flow from the jth layer into the well at time t.

THE TRANSFORMED EQUATIONS AND THEIR SOLUTION

Let $\bar{X}(z) = L[X(t)]$ denote the Laplace transform of $X(t)$ where z is the complex variable $x + iy$. Applying this transform to both sides of the Eqs. 1 and using Eq. 2, we obtain the system

$$\frac{1}{r} \frac{\partial}{\partial r} \left(r \frac{\partial \bar{P}_j}{\partial r} \right) - \frac{z}{n_j} \bar{P}_j = 0 \qquad j = 1, 2, \ldots, n$$

. . . . . (6)

which must be solved subject to the boundary conditions

$$\frac{\partial \bar{P}_j}{\partial r} = 0 \quad \text{at } r = r_{e,j}, \qquad j = 1, 2, \ldots, n$$

. . . . . (7)

$$\bar{P}_j(r,z) = \bar{P}_w(z), \text{ at } r = r_{w,j}, \; j = 1, 2, \ldots, n$$

. . . . . (8)

$$\sum_{i=1}^{n} \beta_j \left(r \frac{\partial \bar{P}_j}{\partial r} \right)_{r=r_{w,j}} = -\frac{q}{2\pi z} \quad . \quad . \quad . \quad (9)$$

Eq. 6 has general solutions of the form

$$\bar{P}_j(r,z) = A_j K_o \left(r\sqrt{\frac{z}{n_j}} \right) + B_j I_o \left(r\sqrt{\frac{z}{n_j}} \right)$$

and A_j and B_j are constants to be determined from Eqs. 7, 8 and 9. These conditions lead to the set of equations

$$\left.\begin{aligned} A_j K_1(\gamma_j\sqrt{z}) &= B_j I_1(\gamma_j\sqrt{z}) \\ A_j K_0(a_j\sqrt{z}) + B_j I_0(a_j\sqrt{z}) &= \bar{P}_w(z) \\ \Sigma\, \beta_j a_j [A_j K_1(a_j\sqrt{z}) - B_j I_1(a_j\sqrt{z})] &= \frac{q}{2\pi z^{3/2}} \end{aligned}\right\} \quad (10)$$

Letting

$$\psi_{0j}(z) = K_0(a_j\sqrt{z})I_1(\gamma_j\sqrt{z}) + I_0(a_j\sqrt{z})K_1(\gamma_j\sqrt{z}),$$

$$\psi_{1j}(z) = K_1(a_j\sqrt{z})I_1(\gamma_j\sqrt{z}) - I_1(a_j\sqrt{z})K_1(\gamma_j\sqrt{z}),$$

we obtain by simple manipulation

$$\bar{P}_w(z) = \frac{q}{2\pi z^{3/2}} \frac{1}{\sum_{j=1}^{n} \beta_j a_j \frac{\psi_{1j}(z)}{\psi_{0j}(z)}} \quad . \quad . \quad . \quad (11)$$

and also

$$\bar{P}_j(r,z) = \frac{K_0\left(\frac{r}{r_{w,j}} a_j\sqrt{z}\right) I_1(\gamma_j\sqrt{z}) + I_0\left(\frac{r}{r_{w,j}} a_j\sqrt{z}\right) K_0(\gamma_j\sqrt{z})}{\psi_{0j}(z)} \bar{P}_w(z),$$

. . . . . (12)

$$\bar{q}_j(z) = 2\pi\beta_j a_j \sqrt{z} \frac{\psi_{1j}(z)}{\psi_{0j}(z)} \bar{P}_w(z) \quad . \quad . \quad . \quad . \quad . \quad (13)$$

INVERSION OF THE SOLUTIONS

In this section, we derive expressions for the inverses of the functions of Eqs. 11, 12 and 13 suitable for numerical calculations at large times.

Letting

$$F(z) = \sqrt{z} \sum_{j=1}^{n} \beta_j a_j \frac{\psi_{1j}(z)}{\psi_{0j}(z)},$$

so that

$$\bar{P}_w(z) = \frac{q}{2\pi z} \frac{1}{F(z)},$$

we first note that $\sqrt{z}\psi_{1j}(z)/\psi_{0j}(z)$ is a meromorphic function and that, therefore, the functions $\bar{P}_w(z)$, $\bar{P}_j(r,z)$ and $\bar{q}_j(z)$ are also meromorphic functions. From the stability of the physical system, it also can be deduced that these functions do not have poles with positive real part.

Expanding $1/F(z)$ about $z = 0$, we obtain

$$F(z) = \frac{2}{\sum_j \beta_j \gamma_j^2} \frac{1}{z} + \frac{\sum_j \beta_j \gamma_j^4 \left(\ln \frac{r_{ej}}{r_{wj}} - \frac{3}{4} \right)}{\left(\sum_j \beta_j \gamma_j^2 \right)^2} + 0(z),$$

so that

$$P_w(t) = \frac{q}{2\pi} \left[\frac{2t}{\sum_j \beta_j \gamma_j^2} + \frac{\sum_j \beta_j \gamma_j^4 \left(\ln \frac{r_{ej}}{r_{wj}} - \frac{3}{4} \right)}{\left(\sum_j \beta_j \gamma_j^2 \right)^2} \right] + Y(t) \quad , \quad . \quad . \quad . \quad . \quad . \quad . \quad . \quad . \quad . \quad . \quad . \quad (14)$$

where $Y(t)$ represents the contribution of the other poles of $\bar{P}_w(z)$. These poles are the non-vanishing roots of $F(z) = 0$. If we let $z = s^2$, this equation can be written

$$\sum_{j=1}^{n} \beta_j a_j \frac{K_1(a_j s)I_1(\gamma_j s) - I_1(a_j s)K_1(\gamma_j s)}{K_0(a_j s)I_1(\gamma_j s) + I_0(a_j s)K_1(\gamma_j s)} = 0. \quad (15)$$

It can be shown that the roots of this equation are conjugate complex and lie on the imaginary s axis.

Letting z_k, $k = 1, 2, \ldots$ denote the non-zero roots of $F(z) = 0$ and letting $\sqrt{z} = ix$, $z_k = -x_k^2$ so that the x_k are roots of

$$G(x) = \sum_{j=1}^{n} \beta_j a_j \frac{Y_1(a_j x)J_1(\gamma_j x) - J_1(a_j x)Y_1(\gamma_j x)}{Y_0(a_j x)J_1(\gamma_j x) - J_0(a_j x)Y_1(\gamma_j x)} = 0, \quad (16)$$

we have

$$Y(t) = \frac{q}{\pi} \sum_{k=1}^{\infty} \frac{e^{-x_k^2 t}}{x_k^2 G'(x_k)} \quad . \quad . \quad . \quad . \quad . \quad . \quad . \quad . \quad (17)$$

Evaluating this expression with the aid of the eigenvalue Eq. 16, we obtain

$$Y(t) = -\frac{\pi q}{4} \sum_{k=1}^{\infty} \frac{e^{-x_k^2 t}}{\sum_{j=1}^{n} \beta_j \frac{1 - \frac{\pi^2}{4} a_j^2 x_k^2 \left(\phi_{0,jk}^2 + \phi_{1,jk}^2\right)}{\phi_{0,jk}^2}} \quad \ldots\ldots\ldots\ldots\ldots\ldots\ldots\ldots\ldots\ldots (18)$$

where

$$\phi_{0,jk} = Y_0(a_j x_k)\, J_1(\gamma_j x_k) - J_0(a_j x_k)\, Y_1(\gamma_j x_k)$$

$$\phi_{1,jk} = Y_1(a_j x_k) J_1(\gamma_j x_k) - J_1(a_j x_k)\, Y_1(\gamma_j x_k) .$$

This expression for $Y(t)$ is correct for all values of t. In the calculations performed, it was found that the times for which the solution was evaluated were large enough that only the smaller roots x_k were needed to evaluate $Y(t)$.

For such values of t, Eqs. 16 and 18 were simplified to

$$G(x) = \sum_{j=1}^{n} \frac{\beta_j J_1(\gamma_j x)}{\frac{2}{\pi} J_1(\gamma_j x) \ln \frac{\gamma}{2} a_j x - Y_1(\gamma_j x)} = 0 \quad (19)$$

and

$$Y(t) =$$

$$-\frac{\pi q}{4} \sum_{k=1}^{\infty} \frac{e^{-x_k^2 t}}{\sum_j \beta_j \frac{1 - J_1^2(\gamma_j x_k)}{\left[\frac{2}{\pi} J_1(\gamma_j x_k) \ln \frac{\gamma}{2} a_j x_k - Y_1(\gamma_j x_k)\right]^2}} \quad \ldots\ldots\ldots\ldots\ldots\ldots\ldots\ldots\ldots\ldots (20)$$

respectively. The accuracy of the approximations checks in each case calculated.

If we assume that the first root of Eq. 19 is small, further approximations can be made for the calculation of this root. For the case of two layers, Eq. 19 then becomes

$$\sum_{j=1}^{2} \frac{1}{\beta_j} \left(\ln \frac{\gamma_j}{a_j} - \frac{\frac{1}{\gamma_j x} + \frac{1}{4} \gamma_j x}{\frac{1}{2} \gamma_j x - \frac{1}{16} \gamma_j^3 x^3} \right) = 0 .$$

From this, the smallest root x_1 can be approximated by

$$x_1^2 \simeq \frac{2\left(\gamma_1^2 \beta_1 + \gamma_2^2 \beta_2\right)}{\gamma_1^2 \gamma_2^2 \left[\beta_2 \left(\ln \frac{\gamma_1}{a_1} - \frac{3}{4}\right) + \beta_1 \left(\ln \frac{\gamma_2}{a_2} - \frac{3}{4}\right)\right]} . \quad \ldots\ldots\ldots\ldots\ldots\ldots\ldots (21)$$

It is interesting to note that this expression coincides with the exponent obtained in the simplified theory of Tempelaar-Lietz for two layers.

The transform of the production rate from the jth layer is given by

$$\overline{q_j}(z) = \frac{q}{z} \frac{\beta_j a_j \frac{\psi_{1j}(z)}{\psi_{0j}(z)}}{\sum_{j=1}^{n} \beta_j a_j \frac{\psi_{1j}(z)}{\psi_{0j}(z)}} .$$

By a procedure similar to the one used in obtaining $P_w(t)$, we obtain

$$\frac{q_j(t)}{q} = \frac{\beta_j \gamma_j^2}{\sum_j \beta_j \gamma_j^2} + Z_j(t) \quad , \ldots\ldots\ldots\ldots (22)$$

where

$$Z_j(t) =$$

$$-\frac{\pi^2}{2} \beta_j \sum_{k=1}^{\infty} \frac{a_j x_k \frac{\phi_{1,jk}}{\phi_{0,jk}} e^{-x_k^2 t}}{\sum_{j=1}^{n} \beta_j \frac{1 - \frac{\pi^2}{4} a_j^2 x_k^2 \left(\phi_{0,jk}^2 + \phi_{1,jk}^2\right)}{\phi_{0,jk}^2}} . \quad \ldots\ldots\ldots\ldots\ldots\ldots\ldots\ldots (23)$$

The x_k are the non-vanishing roots of Eq. 16.

Again for large values of t, a simplified expression for Eq. 23 can be constructed. This is

$$Z_j(t) =$$

$$\pi \beta_j \sum_{k=1}^{\infty} \frac{\frac{J_1(\gamma_j x_k)}{\frac{2}{\pi} J_1(\gamma_j x_k) \ln \frac{\gamma}{2} a_j x_k - Y_1(\gamma_j x_k)}}{\sum_j \beta_j \frac{1 - J_1^2(\gamma_j x_k)}{\left(\frac{2}{\pi} J_1(\gamma_j x_k) \ln \frac{\gamma}{2} a_j x_k - Y_1(\gamma_j x_k)\right)^2}} e^{-x_k^2 t} \quad \ldots\ldots\ldots\ldots\ldots\ldots\ldots\ldots\ldots\ldots (24)$$

A similar treatment gives the solution $P_j(r,t)$.

THE PRESSURE AT SMALL TIMES

The use of the solutions derived in the preceding section is not convenient for small times, since too many terms in the expressions for $Y(t)$ and $Z_j(t)$ are required. However, since it is known that a bounded reservoir behaves as an infinite reservoir during its early life, the solutions corresponding to infinite and bounded reservoirs must coincide for all times smaller than the time at which the influence of the boundary is said to be felt upon the behavior of the reservoir.

The actual procedure used in the calculation of the results obtained in this paper was, first, to evaluate the solution corresponding to an infinite field, and, then, to evaluate the solution corresponding to the bounded reservoir, using enough terms in the series for the transient parts of the solutions to obtain a significant time range where the two solutions would overlap.

The solution to the problem of finding the well pressure in an infinite field composed of n horizontal layers has been solved by Horner.* The equations to be solved are the same as for the bounded reservoir, but the boundary equation in Eq. 3 must be replaced by the condition

$$P_j(r,t) \to 0 \quad \text{as } r \to \infty,\ t \geq 0,$$
$$j = 1, 2, \ldots, n. \quad \ldots\ldots\ldots\ldots (25)$$

The solution for $P_w(t)$ can be written

*The authors gratefully acknowledge this contribution which has only been published within the Shell companies.

$$P_w(t) = \frac{q}{4\pi \sum_{j=1}^{n} \beta_j} \left(\ln \gamma t - \frac{\sum_{j=1}^{n} \beta_j \ln \frac{\gamma^2 a_j^2}{4}}{\sum_{j=1}^{n} \beta_j} + J(t) \right), \quad \ldots\ldots\ldots\ldots\ldots\ldots\ldots\ldots (26)$$

where

$$J(t) = \int_0^\infty \frac{e^{-ut}}{u} \left\{ 1 - \frac{4 \sum_j \beta_j}{\pi^2} \right.$$

$$\left. \frac{\sum_{j=1}^{n} \frac{\beta_j}{J_{0j}^2 + Y_{0j}^2}}{u \left[\left(\sum_{j=1}^{n} a_j \beta_j \frac{J_{0j} J_{1j} + Y_{0j} Y_{1j}}{J_{0j}^2 + Y_{0j}^2} \right)^2 + \frac{4}{\pi^2 u} \left(\sum_{j=1}^{n} \frac{\beta_j}{J_{0j}^2 + Y_{0j}^2} \right)^2 \right]} \right\} du$$

$\ldots\ldots\ldots\ldots\ldots\ldots\ldots\ldots\ldots\ldots\ldots\ldots (27)$

The following abbreviations have been used.

$$J_{0j} = J_0(a_j \sqrt{u}) ,$$
$$J_{1j} = J_1(a_j \sqrt{u}) ,$$
$$Y_{0j} = Y_0(a_j \sqrt{u}) ,$$
$$Y_{1j} = Y_1(a_j \sqrt{u}) .$$

The integral in the form given in Eq. 27 is quite intractable for numerical calculations. For the case of $n = 2$ (that is, when the reservoir is composed of only two layers), however, approximations can be obtained which make a numerical analysis possible.

Introducing approximations for the Bessel functions for small values of u, we can show that

$$-J(t) = \frac{\beta_1 \beta_2 \ln^2(\alpha_1^2/\alpha_2^2)}{(\beta_1 + \beta_2)^2} \int_0^\infty \frac{e^{-ut}\, du}{u[(\ln u - A)^2 + \pi^2]} ,$$

$\ldots\ldots\ldots\ldots\ldots\ldots\ldots\ldots\ldots\ldots\ldots\ldots (28)$

where

$$A = -\frac{\beta_1 \ln \frac{\gamma^2}{4} \alpha_2^2 + \beta_2 \ln \frac{\gamma^2}{4} \alpha_1^2}{\beta_1 + \beta_2} .$$

Now if we let $\tau = te^A$, the integral in Eq. 28 is transformed into the integral

$$\phi(\tau) = \int_0^\infty \frac{e^{-u\tau}\, du}{u(\ln^2 u + \pi^2)} .$$

This integral must be evaluated to calculate $J(t)$.

From the table of Laplace transforms of McLachlan, Humbert and Poli[5] it can be found that

$$\phi(\tau) = e^\tau - \int_0^\infty \frac{\tau^u du}{\Gamma(u+1)} .$$

This last integral can be further transformed as follows.

$$\int_0^\infty \frac{\tau^u\, du}{\Gamma(u+1)} = \sum_{n=0}^{\infty} \int_n^{n+1} \frac{\tau^u\, du}{\Gamma(u+1)} =$$

$$\sum_{n=0}^{\infty} \int_0^1 \frac{\tau^{u+n} du}{\Gamma(u+n+1)} = \int_0^1 F(\tau, u)\, du ,$$

where

$$F(\tau, u) = \sum_{n=0}^{\infty} \frac{\tau^{n+u}}{\Gamma(u+n+1)} .$$

This function $F(\tau,u)$ satisfied the differential equation

$$\frac{dF}{d\tau} - F = \frac{\tau^{u-1}}{\Gamma(u)}$$

with the condition $F(0,u) = 0$. Solving this equation we find that

$$F(\tau, u) = \frac{e^\tau}{\Gamma(u)} \int_0^\tau e^{-v} v^{u-1} dv = e^\tau \left(1 - \frac{Q(u,\tau)}{\Gamma(u)} \right) ,$$

where

$$Q(u,\tau) = \int_\tau^\infty e^{-v} v^{u-1} dv$$

is an incomplete gamma function. Then, upon substitution of these results,

$$\phi(\tau) = e^\tau \int_0^1 \frac{Q(u,\tau)}{\Gamma(u)} du . \quad \ldots\ldots\ldots (29)$$

This expression is used to calculate $\phi(\tau)$ for values of $\tau \leq 10$. For values of $\tau > 10$, an asymptotic expression is used for $Q(u,\tau)$ which gives rise to the equation

$$\phi(\tau) \simeq \int_0^1 \frac{dv}{\tau^v \Gamma(1-v)} + \frac{1-\tau}{\tau^2} \int_0^1 \frac{v\, dv}{\tau^v \Gamma(1-v)} +$$

$$\frac{1}{\tau^2} \int_0^1 \frac{v^2\, dv}{\tau^v \Gamma(1-v)} . \quad (30)$$

It is found that the magnitude of the last two terms decreases rapidly with increasing values of τ.

An upper limit for $\phi(\tau)$ can be obtained in the following manner.

$$\phi(\tau) < \int_0^1 \frac{dv}{\tau^v} < \int_0^\infty \frac{dv}{\tau^v} = \frac{1}{\ln \tau} .$$

This upper limit gives a good approximation for $\phi(\tau)$ for large values of τ.

The values of $\phi(\tau)$ obtained are given in Table 1.

TABLE 1 – VALUES OF $\phi(\tau)$

τ	$\phi(\tau)$	τ	$\phi(\tau)$
1	0.452	1×10^4	0.1003
2	0.392	2×10^4	0.0939
3	0.359	4×10^4	0.0883
4	0.337	1×10^5	0.0818
6	0.308	2×10^5	0.0775
1×10	0.2765	4×10^5	0.0736
2×10	0.2398	1×10^6	0.0690
4×10	0.2100	2×10^6	0.0659
1×10^2	0.1792	4×10^6	0.0631
2×10^2	0.1608	1×10^7	0.0597
4×10^2	0.1456		
1×10^3	0.1291		
2×10^3	0.1189		
4×10^3	0.1101		

THE PRODUCTION RATE AT SMALL TIMES

The production rate at small times is obtained from the solution for an infinite reservoir evaluated in the case of two layers. The Laplace transform of the fraction production rate from the first layer is

$$\frac{\bar{q}_1(z)}{q} = \frac{1}{z} \frac{\beta_1 a_1 \dfrac{K_1(a_1\sqrt{z})}{K_0(a_1\sqrt{z})}}{\beta_1 a_1 \dfrac{K_1(a_1\sqrt{z})}{K_0(a_1\sqrt{z})} + \beta_2 a_2 \dfrac{K_1(a_2\sqrt{z})}{K_0(a_2\sqrt{z})}} \quad \ldots\ldots\ldots\ldots\ldots\ldots\ldots\ldots (31)$$

The corresponding solution is

$$\frac{q_1(t)}{q} = \frac{1}{2\pi i} \int_{\beta-i^\infty}^{\beta+i^\infty} \frac{\bar{q}_1(z)}{q} e^{zt}\, dz ,$$

the path of integration passing to the right of the origin. Replacing the Bessel functions by the approximations

$$K_0(a_j\sqrt{z}) \simeq -\ln\frac{\gamma}{2}\, a_j\sqrt{z} ,$$

$$K_1(a_j\sqrt{z}) \simeq \frac{1}{a_j\sqrt{z}} ,$$

and neglecting quantities of the order a^2_j, it can be shown that

$$\frac{q_1(t)}{q} =$$

$$\frac{1}{2\pi i} \int_{\beta-i^\infty}^{\beta+i^\infty} \frac{\beta_1 \ln\frac{\gamma}{2} a_2\sqrt{z}}{\beta_1 \ln\frac{\gamma}{2} a_2\sqrt{z} + \beta_2 \ln\frac{\gamma}{2} a_1\sqrt{z}} \cdot \frac{e^{zt}}{z}\, dz,$$

or

$$\frac{q_1(t)}{q} = \frac{1}{2\pi i} \int_{\beta-i^\infty}^{\beta+i^\infty} \left[\frac{\beta_1}{\beta_1+\beta_2} \frac{1}{z} + \frac{\beta_1\beta_2}{(\beta_1+\beta_2)^2} \ln\frac{a_2^2}{a_1^2} \frac{1}{z(\ln z - A)} \right] e^{zt}\, dz ,$$

$$\ldots\ldots\ldots\ldots\ldots\ldots\ldots\ldots (32)$$

where A is defined as before. The first term in the integrand yields the constant $\beta_1/(\beta_1+\beta_2)$. The integral

$$\frac{1}{2\pi i} \int_{\beta-i^\infty}^{\beta+i^\infty} \frac{e^{zt}\, dz}{z(\ln z - A)} \quad \ldots\ldots\ldots (33)$$

is evaluated as follows. According to Doetsch,[6]

$$\frac{1}{z(\ln z - A)} \quad \ldots\ldots\ldots\ldots\ldots (34)$$

is the Laplace transform of

$$\int_0^\infty \frac{r^u}{\Gamma(u+1)}\, du \qquad (r = te^A) \quad \ldots\ldots (35)$$

The function Eq. 34 has a pole at $z = e^A$ which, however, does not contribute to the integral Eq. 33. This contribution, therefore, must be subtracted, yielding

$$\frac{1}{2\pi i} \int_{\beta-i^\infty}^{\beta+i^\infty} \frac{e^{zt}\, dz}{z(\ln z - A)} \int_0^\infty \frac{r^u\, du}{\Gamma(1+u)} - e^r = -\phi(r).$$

We can then write

$$\frac{q_1(t)}{q} = \frac{\beta_1}{\beta_1+\beta_2} - \frac{\beta_1\beta_2 \ln\dfrac{a_2^2}{a_1^2}}{(\beta_1+\beta_2)^2} \phi(r) \quad \ldots (36)$$

It can be noted that values of $\phi(r)$ have already been calculated for evaluation of the pressures.

The effects of the transient terms in the infinite solutions are both proportional to $\phi(r)$; but, whereas this effect is negligible in the pressure equation for all but very small times, the effect of this term on the rate solution is in general of considerable magnitude.

INCLUSION OF THE SKIN EFFECT

The skin factor S_j of the jth layer is defined by the equation*

$$S_j = \frac{P_w - P_{fj}}{q_j(t)\,\mu_j/2\pi k_j b_j} \quad \ldots\ldots\ldots (37)$$

The equations to be solved are the same in the presence of a skin as without one, except that the boundary condition (that the pressures at the well are the same in all layers) must be restated to say that the pressures inside the wellbore are the same in all layers. This can be stated as

$$\frac{S_j q_j(t)\mu_j}{2\pi k_j b_j} + P_{fj}(t) = P_w(t) \qquad j = 1, 2, \ldots, n$$

$$\ldots\ldots\ldots\ldots\ldots\ldots\ldots (38)$$

where $P_w(t)$ is independent of j.

The method of analysis used to solve this problem is identical to the method outlined for solving the equations without the skin; the equations are similar, and only some extra terms containing S_j are present.

The transform of $P_w(t)$ can be obtained as

$$\bar{P}_w(z) = \frac{q}{2\pi z} \frac{1}{\sqrt{z}\sum_j \beta_j a_j \dfrac{\psi_{1j}(z)}{\psi_j(z)}} , \quad \ldots (39)$$

where

$$\psi_j(z) = a_j S_j \sqrt{z}\, \psi_{1j}(z) + \psi_{0j}(z) ,$$

and $\psi_{0j}(z)$ and $\psi_{1j}(z)$ have the same meaning as as before. Similarly

$$\bar{q}_j(z) = 2\pi\beta_j a_j \sqrt{z} \frac{\psi_{1j}(z)}{\psi_j(z)} \bar{P}_w(z) . \quad \ldots (40)$$

The functions $\bar{P}_w(z)$ and $\bar{q}_j(z)$ are again meromorphic functions of z, and the inversion proceeds in the same manner as before. Then,

*Where P_{fj} denotes the pressure drop at the well in the formation in Layer j.

$$P_w(t) = \frac{q}{2\pi}\left[\frac{2t}{\sum_{j=1}^{n}\beta_j\gamma_j^2} + \frac{\sum_{j=1}^{n}\beta_j\gamma_j^4\left(\ln\frac{\beta_j}{\alpha_j} - \frac{3}{4} + S_j\right)}{\left(\sum_{j=1}^{n}\gamma_j\beta_j^2\right)^2}\right] + Y_s(t) \quad (41)$$

where $Y_s(t)$ represents the transient solution.

With the same approximations as before and in the time range of validity of these approximations, the skin factors S_j always appear in such a fashion that they can be completely absorbed by replacing α_j by α_j^*, which is defined by

$$\alpha_j^* = \alpha_j e^{-S_j} \quad (42)$$

The solution for the infinite reservoir with skins was found by a method similar to the one used by Horner; it was concluded that again, in the time range of validity of the approximations taken when no skin was present, the presence of the skin factors in the equations could be absorbed into the quantities α_j in the manner of Eq. 42.

Hence, it can be concluded that, for times of practical importance, the effect of a skin with skin factor S_j in each one of the layers can be described completely by assigning a fictitious well radius $r_{w,j}^*$ to each layer, the relation between the true well radius $r_{w,j}$ and $r_{w,j}^*$ being given by

$$r_{w,j}^* = r_{w,j}e^{-S_j} \quad (43)$$

NOMENCLATURE

A_j = recovery/unit pressure drop of Layer j (Eq. 14)

h_j = thickness of jth layer, cm

$\bar{h}$ = $h_1 + h_2$, total thickness, cm

i_j = productivity index of Layer j (Eq. 15)

k_j = permeability of jth layer, darcy

$\bar{k}$ = $(k_1h_1 + k_2h_2)/(h_1 + h_2)$, weighted mean of permeabilities, darcy

$p_j(r,t)$ = pressure in the jth layer at position r and time t, atm

$p_w(t)$ = pressure at the well at time t, atm

$\bar{p}_j(t)$ = average pressure in the jth layer at time t

p^* = pressure obtained by straight-line extrapolation of first linear portion of p_w vs $\ln[\Delta t/(t + \Delta t)]$

p_{fj} = pressure in the formation of Layer j at the well

$P_j(r,t)$ = pressure drop in the jth layer at position r and time t

$P_w(t)$ = pressure drop function at the well

q_T = total production rate from multilayer reservoir in cc/sec, measured at initial reservoir conditions

q_T' = total production rate in cc/sec measured at average reservoir conditions

$q_j(t)$ = production rate from jth layer at time t, in cc/sec, measured at initial reservoir conditions

$q_j(\Delta t,t)$ = flow rate out of jth layer at shut-in time Δt for a well closed in at production time t

$q_c(\Delta t)$ = production rate during after-production at dimensionless shut-in time Δt

$Q_j(t)$ = cumulative production from Layer j at time t, in cc, measured at initial reservoir conditions

r_w^* = fictitious well radius to represent skin effect, cm

S_j = skin factor of jth layer, dimensionless

t' = production time, days

t_r = time at which the pressure disturbance reaches the point r, sec

$Y(t)$ = transient solution in well-pressure equation

$Z_j(t)$ = transient solution in rate equation for jth layer

α = loading constant (dimensionless) with respect to T

$\Delta D(t)$ = differential depletion per unit thickness at time t between the layers of a two-layer reservoir

Δt = shut-in time, sec

Δt_D = dimensionless shut-in time = $\bar{k}\Delta t/\bar{\phi}\mu c r_w^2$

ϕ_j = oil-filled porosity of the jth layer, dimensionless

$\bar{\phi}$ = $(\phi_1h_1 + \phi_2h_2)/(h_1 + h_2)$ weighted mean of porosities

γ = Euler's constant, $\ln\gamma = 0.5772$

REFERENCES

1. Horner, D. R.: "Pressure Behavior in a Well Producing from a Number of Different Horizons", Shell Oil Co. Report.
2. Tempelaar-Lietz, W.: "The Effect of the Rate of Oil Production upon the Performance of Wells Producing from More than One Horizon", *Soc. Pet. Eng. Jour.* (March, 1961) 26.
3. Matthews, C. S., Brons, F. and Hazebrook, P.: "A Method for Determination of Average Pressure in a Bounded Reservoir", *Trans.*, AIME (1954) Vol. 201, 182.
4. van Everdingen, A. F.: "The Skin Effect and Its Influence on the Productive Capacity of a Well", *Trans.*, AIME (1953) Vol. 198, 171.
5. McLachlan, N. W., Humbert, P. and Poli, L.: "Supplement au Formulaire pour le Calcul Symbolique", *Memorial pour les Sciences Mathématiques* (1950) CXIII.
6. Doetsch, G.: *Tabellen zur Laplace – Transformation und Anleitung zum Gebrauch*, Springer-Verlag (1947) Berlin und Göttingen.

***

Effect of Viscosity on Relative Permeability

J. DOWNIE
F. E. CRANE

GULF RESEARCH & DEVELOPMENT CO.
PITTSBURGH, PA.

INTRODUCTION

The general application of Darcy's law to natural rocks has already been challenged in the literature.[1] The evidence shows that the permeability as calculated from the Darcy equation can be a function of the pressure drop and the salt concentration of the water phase. Most explanations for aberrant behavior involve clays and their properties and have been qualitatively satisfactory. Recently, however, Odeh[2] revived the theoretical views of Yuster.[3] Since Yuster's concept implies a fundamental error in using Darcy's relationship for two-phase flow, and not merely that conditions may limit its use, Odeh's experimental support arouses considerable interest. However, Odeh's work as presented is thought to to be inadequate. He has omitted important information about his materials and procedures; therefore, acceptance of his conclusions should be withheld.

Since a clay effect is possible, Odeh should have been allowed space to present a more detailed account of the rocks which he used and the precautions which he took to avoid confounding the effects of clay and fluid circulation. In addition, it follows from Odeh's discussion that the oil relative permeability should increase as the viscosity ratio increases. Odeh presents data corroborating this deduction. It also follows that the oil relative permeability should decrease as the viscosity ratio of oil to water decreases. However, our results show that a high relative permeability, when once attained by using a viscous oil, may be maintained when that oil is replaced by an oil of much lower viscosity.

Original manuscript received in Society of Petroleum Engineers office Sept. 27, 1960. Revised manuscript received Nov. 30, 1960.

[1]References given at end of paper.

EXPERIMENTAL PROCEDURE

The results are shown in Fig. 1 and were obtained as follows. Sandstone cores, 3-in. long × 1-in. in diameter and which contained clays, were saturated with

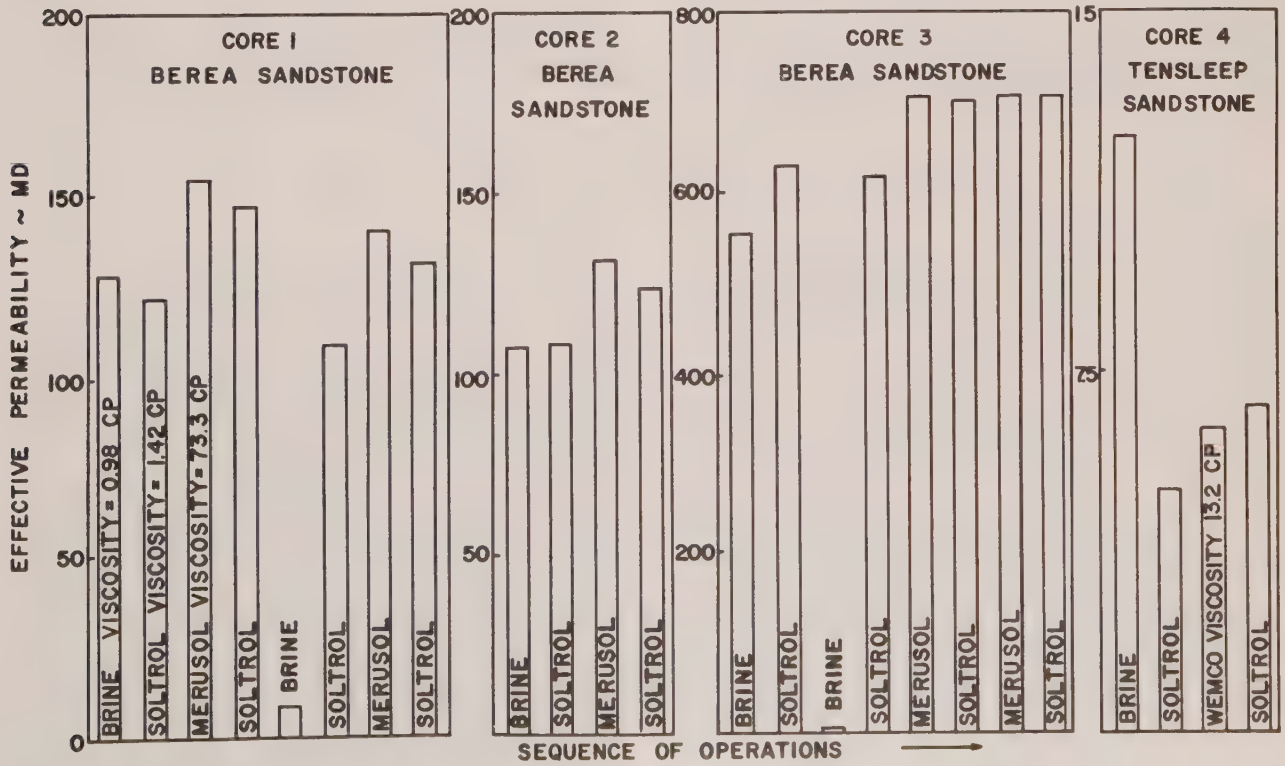

FIG. 1 — EFFECTIVE PERMEABILITY RELATED TO THE SEQUENCE OF OPERATIONS.

brine (50g. NaCl/l. solution), and the permeabilities were measured in a slightly modified Penn State apparatus. Each core was flooded with the lowest-viscosity oil (i.e., Soltrol having a viscosity of 1.42 cp), and the oil permeability was measured with the residual brine stationary. This was the saturation region which Odeh found produced the greatest effect. The low-viscosity oil was then displaced by higher-viscosity oils – either Wemco (viscosity = 13.2 cp) or Merusol (viscosity = 73.3 cp) – and the effective permeability to oil was again measured. The low-viscosity Soltrol was again introduced into the core so as to displace the Merusol miscibly, and the effective permeability was measured. The fluids followed one another in the order shown in Fig. 1.

CONCLUSIONS

We conclude that oil viscosity can influence the effective permeability of some natural rocks to oil. However, when once attained, such an increase is not necessarily lost on replacing the high-viscosity oil with one of low viscosity – an observation strongly at variance with Odeh's analysis but qualitatively explicable in terms of the movement of colloid particles at oil-water interfaces.

REFERENCES

1. von Engelhardt, W. and Tunn, W. L. M.: "The Flow of Fluids Through Sandstones," Illinois State Geological Survey, Circular 194 (1955). Translated by P. A. Witherspoon from *Heidelberger Beiträge zur Mineralogie und Petrographie* (1954) Vol. 2, Parts 1 and 2, 12.
2. Odeh, A. S.: "Effect of Viscosity Ratio on Relative Permeability", *Trans.*, AIME (1959) Vol. 216, 346.
3. Yuster, S. T.: "Theoretical Considerations of Multiphase Flow in Idealized Capillary Systems", *Proc.*, Third World Pet. Congress, The Hague (1951) 11, 437.

DISCUSSION

A. S. ODEH
MEMBER AIME

MOBIL OIL CO. DE VENEZUELA
CARACAS, VENEZUELA

It is gratifying to see that Downie and Crane, on the basis of experimental results, concluded that "oil viscosity can influence the effective permeability of some natural rocks to oil". The authors also suggest that once the influence is attained it is not lost, which is at strong variance with Odeh's analysis.[1]

In examining the authors' results, Odeh does not see such a strong variance; in fact, he detects support. Admittedly, in Cores 1, 2 and 3 the effective permeability to Soltrol was higher in the second cycle than in the first, but it was still lower than the effective permeability to Merusol, the more viscous oil. This is in line with Odeh's analysis.[1] The writer has no explanation for Core 4.

As far as the effect of clay on Odeh's work, Table 1[1] indicates that the corrected air permeabilities checked with the liquid permeabilities, thus implying a negligible clay effect if any.

AUTHORS' REPLY TO A. S. ODEH

Odeh[1] omitted to describe what would seem an obvious and necessary extension of his investigation of the relationship between relative permeability and viscosity ratio. If Odeh's analysis is correct, the relative permeability to oil must increase when the viscosity ratio increases and must decrease again by the same amount when the viscosity ratio is returned to its original value.

However, our results indicate that this is not necessarily so. We presented a group of results (Fig. 1) which provide examples of slight decreases in effective permeability (Cores 1 and 2), no change in effective permeability (Core 3) and an increase in effective permeability (Core 4) when a more-viscous oil is replaced by a less-viscous oil.

Our contention, which is in danger of misrepresentation by Odeh, is that the increase in permeability is *not necessarily* lost on replacing the high-viscosity oil with one of low viscosity. This is at variance with Odeh's analysis. Support by selection, as employed by Odeh in his discussion of our paper, seems an approach of contestable validity.

The effect of the presence of clay particles on the permeability of a rock is still incompletely understood. The identity of air and liquid permeabilities is open to various interpretations until the liquid is more fully described. For example, if the liquid used were distilled water the implication would be that clays were absent or inert and, if the liquid were a concentrated $CaCl_2$ solution, that clays might or might not be present. However, at this stage in our knowledge of clays, there is no implication that clays (if present) would not affect the relative permeability to oil. ***

[1] Odeh, A. S.: "Effect of Viscosity Ratio on Relative Permeability", *Trans.*, AIME (1959) Vol. 216, 346.

An Imbibition Model—Its Application to Flow Behavior and the Prediction of Oil Recovery

J. NAAR
JUNIOR MEMBER AIME
J. H. HENDERSON
MEMBER AIME

GULF RESEARCH & DEVELOPMENT CO.
PITTSBURGH, PA.

INTRODUCTION

The displacement of a wetting fluid from a porous medium by a non-wetting fluid (drainage) is now reasonably well understood. A complete explanation has yet to be found for the analogous case of a wetting fluid being spontaneously imbibed and the non-wetting phase displaced (imbibition). During the displacement of oil or gas by water in a water-wet sand, the porous medium ordinarily imbibes water. The amount of oil recovered, the cost of recovery and the production history seem then to be controlled mainly by pore geometry. The influence of pore geometry is reflected in drainage and imbibition capillary-pressure curves and relative permeability curves. Relative permeability curves for a particular consolidated sand show that at any given saturation the permeability to oil during imbibition is smaller than during drainage.[1,2] Low imbibition permeabilities suggest that the non-wetting phase, oil or gas, is gradually trapped by the advancing water.

This paper describes a mathematical image (model) of consolidated porous rock based on the concept of the trapping of the non-wetting phase during the imbibition process. The following items have been derived from the model.

1. A direct relation between the relative permeability characteristics during imbibition and those observed during drainage.
2. A theoretical limit for the fractional amount of oil or gas recoverable by imbibition.
3. An expression for the resistivity index which can be used in connection with the formula for wetting-phase relative permeability to check the consistency of the model.
4. The limits of flow performance for a given rock dictated by complete wetting by either oil or water.
5. The factors controlling oil recovery by imbibition in the presence of free gas.

Original manuscript received in Society of Petroleum Engineers office July 13, 1960. Revised manuscript received Jan. 20, 1961. Paper presented at 35th Annual Fall Meeting of SPE, Oct. 2-5, 1960, in Denver.

[1]References given at end of paper.

The complexity of a porous medium is such that drastic simplifications must be introduced to obtain a model amenable to mathematical treatment. Many parameters have been introduced by others in "progressing" from the parallel-capillary model to the randomly interconnected capillary models independently proposed by Wyllie and Gardner[3] and Marshall[4]. To these a further complication must be added since an imbibition model must trap part of the non-wetting phase during imbibition of the wetting phase. Like so many of the previously introduced complications, this fluid-block was introduced to make the model performance fit the observed imbibition flow behavior.

THE IMBIBITION MODEL

ASSUMPTIONS

The following assumptions are common to many two-phase models previously described.

1. The wetting characteristics of the medium are clearly defined.
2. When two fluids co-exist in the medium, the wetting phase will fill the smaller pores and the non-wetting fluid the bigger ones.
3. The pores have a circular cross section.
4. Apparent pore radii are related to the capillary pressure (drainage) by

$$P_c = \frac{2\gamma}{r} \quad \ldots\ldots \quad (1)$$

5. The size distribution of the pores defined in Assumption 1 can be derived from the drainage capillary-pressure curve.

A model valid for the imbibition process must meet the following additional requirements.

1. When the medium has been desaturated to its irreducible wetting-phase saturation S_{wi}, the relative permeability to the non-wetting phase must be the same whether computed for the drainage process or for the imbibition process.
2. A mechanism must be provided for the wetting phase to by-pass pores full of non-wetting fluid.
3. Valid results must be given when other properties of the medium are computed.

DESCRIPTION

The imbibition model is a combination of Wyllie and Gardner's[3] and Marshall's[4] representation of a porous medium, with additional provisions to allow the invading fluid to by-pass and block pores full of non-wetting phase.

The random interconnection of pores, characteristic of a porous material, is created by slicing the model normal to the capillaries as shown in Fig. 1. Two parts (1 and 2) thus are created with exposed Faces A and B, which are rejoined to form one element of the model after a random rotation of Parts 1 and 2 about the axis of the capillaries. A fluid particle entering the element through a capillary of Part 1 is dispersed through pores of Part 2 at the contact of A and B.

The ratio ϕ of void area to total area in Faces A and B is taken equal to the porosity of the real medium. This is justified by the fact that, in an isotropic porous medium, space and surface porosity are equal. The irreducible wetting-phase saturation is assumed to be part of the solid matrix, and the porosity ϕ is replaced by an effective porosity ϕ^* equal to $\phi\,(1 - S_{wi})$.

The effective pore-size distribution of the model is defined by the drainage capillary-pressure curve of the real medium. To this point the model is like that described by Wyllie and Gardner

The blocking of the non-wetting phase during imbibition can be readily visualized for a real medium. Access to a large pore such as that of Fig. 1 (a) may be controlled by small pores. When all the adjoining small pores are filled with the wetting phase, the non-wetting fluid occupying the large pore cannot escape by any simple mechanism involving viscous flow. Forms of mass transfer such as diffusion of gas through the wetting phase are excluded from consideration. The blocking mechanism which occurs in the real medium cannot be duplicated in a single element of the model such as shown in Fig. 1 (b). A further difficulty arises when two identical elements are placed in series (Fig. 1c). The permeability of the resulting element is not equal to that of the individual components, as in the case of a real medium.

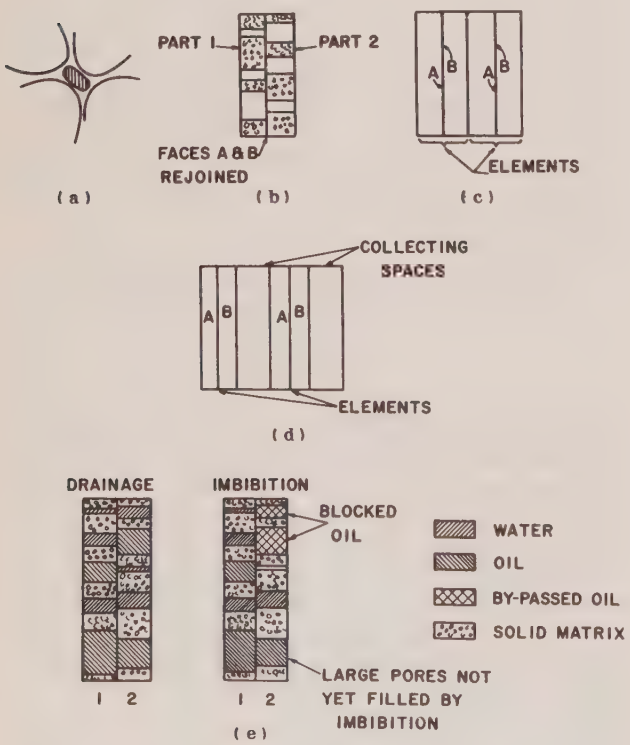

FIG. 1 – SCHEMATIC DIAGRAM OF MODEL COMPONENTS, THEIR SATURATIONS DURING DRAINAGE AND IMBIBITION.

To overcome the latter deficiency and to satisfy the blocking requirement, an artificial space is introduced at the end of each element which will be called the "collecting space" (see Fig. 1d). The collecting space does not represent a physical reality but is used only to meet the model requirements specified earlier in the paper.

The collecting space introduces the fluids, leaving Part 2 of any element into the proper capillaries of Part 1 of the following element. Thus, all the elements are in the same condition. In addition, the collecting space acts as a valve to trap the non-wetting phase in the manner explained as follows.

During the drainage process, when the capillary pressure becomes sufficiently large that the non-wetting phase invades capillaries with radius r, all larger capillaries are desaturated and there is no by-passing of blocking of the fluids. During the imbibition process, the collecting space allows *all the capillaries of Part 1* of any element to be saturated by the imbibed fluid while *only those capillaries of Part 2 which abut against larger ones* are permitted to saturate. Thus, the wetting-fluid saturations of Parts 1 and 2 will differ during imbibition. The wetting-phase saturation of Part 1 will be the same during drainage and imbibition, whereas that of Part 2 will be lower during imbibition because of the by-passed non-wetting phase. Fig. 1(e) compares a model saturation distribution which results from drainage with that which results from imbibition to the same capillary pressure.

The relative permeabilities at any stage of the imbibition procees can now be derived from the model by determining the area available to flow for each of the phases occupying the medium. (The expression for $k_{rw(imb)}$ and $k_{rnw(imb)}$ are developed in the Appendix, and $k_{rw(dr)}$ is shown to be a lower limiting value of $k_{rw(imb)}$.)

MODEL CHARACTERISTICS

RELATIONSHIP BETWEEN DRAINAGE AND IMBIBITION SATURATION

The relationship between the drainage and imbibition saturation for equal values of k_{rnw} which is established by the model is given by Eq. 25 *.

*The development of the formulas expressing the capillary-pressure and relative permeability behavior of the imbibition model may be found in the Appendix.

$$S^*_{w,imb} = S^*_{w,dr} - \frac{1}{2} S^{*2}_{w,dr} \quad \text{---------- (25)}$$

The family of curves of Fig. 2 shows the imbibition saturation vs the drainage saturation with the S_{wi} value as a defining parameter. The imbibition model is linked to any prototype whose fluid distribution is controlled by capillary forces by making the model capillary-pressure curve the same as that of the prototype.

MAXIMUM OIL RECOVERY

The maximum quantity of oil recoverable by ideal imbibition conforming to model requirement is equal to 50 per cent of the oil initially in place. This value is determined by making $S^*_{w,dr} = 1$ in Eq. 25.

DRAINAGE AFTER IMBIBITION

Let the medium reach a saturation S_{imb} through an imbibition process. The pores with radius r_n to r_j are filled by the wetting fluid, except for those pores where the non-wetting phase is blocked. Assume that at this point the process is reversed and that desaturation begins. The biggest pores filled with wetting fluid, which are the pores with radius r_j are emptied first. At this stage, the fluid distribution in all the pores with radii r_{j+1} to r_n has not been modified and is exactly the same as it was before the wetting fluid was imbibed into pores with radius r_j; the permeabilities after desaturation and before imbibition are the same. This description of desaturation after imbibition is independent of r_j and the relative permeability curves which describe desaturation after imbibition are the same as those governing the imbibition process. The behavior taught by the model conforms to the observed stability of relative permeability curves after a cycle of oil displacing water and water displacing oil.[5,6]

RESISTIVITY INDEX

The resistivity index can be shown to be given by

$$I = S_{imb}^{-(1+\epsilon)} \quad \text{---------- (2)}$$

where ϵ is a function of S_{imb}, smaller than or equal to one. The formula for the resistivity index can be used to check the consistency of the model. ϵ can be computed from experimental measurements of I and introduced into the computation of relative permeability to the wetting phase. These computed values, in turn, can be checked against experimental results.

MODEL APPLICATION

IMBIBITION RELATIVE PERMEABILITY

Although the assumptions necessary to build the model are too sweeping and arbitrary for the results to be rigorously applicable to real reservoir rock, the agreement between measured and predicted relative permeability is surprisingly good. Fig. 3 (a, b and c) shows three sets of measured curves from different sources[5,7] with the corresponding computed values. Here, the agreement is excellent. In general, as the rock characteristics shift toward those of unconsolidated sands (i.e., toward high permeability and low S_{wi} values), the conformance between predicted and observed behavior becomes poorer. From the experience acquired in checking the model predictions against available data, the agreement seems to be generally good for consolidated sands characterized by S_{wi} values in excess of 15 per cent.

Fig. 2 shows the model definition of the water saturation for an idealized porous medium which has undergone imbibition (water invasion) from the irreducible water saturation. It is a graphical picture of the solution of Eq. 25. The S_{wi} value designating each curve is the parameter used to characterize the pore geometry. Hence, if one can measure or otherwise estimate S_{wi}, one can define in a few minutes the corresponding imbibition oil or gas relative permeability curve.

The practice of working wholly from the S_{wi} value of a sand is acceptable only in the absence of any measured flow data. When gas relative permeability curves are available it is recommended that they be used to define the imbibition k_{ro} curve from Fig. 3. Use of measured gas relative permeability data compensates, at least in part, for the deviation of the actual pore-size distribution from the distribution which is assumed when working from S_{wi} values alone.

It is interesting to note that, if the relation between $S^*_{w,imb}$ and $S^*_{w,dr}$ given by Eq. 25 is accepted, the equation for the non-wetting drainage relative permeability (Eq. 32 of Ref. 3) may be transformed into an approximation for the imbibition relative permeability. Thus,

$$k_{rg\,(imbibition)} = \left(\frac{0.5 - S^*_{w,imb}}{0.5}\right)\left(1 - S^{*2}_{w,imb}\right) \quad \text{---------- (3)}$$

RECOVERABLE OIL.

It is evident that the model value of 0.5 for the fractional recovery of oil in place results from the assumptions of random pore interconnection and of trapped non-wetting phase. These assumptions are substantiated by the fact that they lead to predictions agreeing closely with observations made on many consolidated media.

The development of both drainage and imbibition models is based on the premise that the equilibrium saturations, at which the effective permeabilities become (approach) zero, depend on the pore-size distribution. Since the assumed interconnections in the models are certainly oversimplified, the behavior of a reservoir sand having a particular S_{wi} value might depart from that predicted by the model. This will be particularly true near the equilibrium satu-

rations when the extremes in the pore sizes dominate the behavior of the fluid. Thus, as an imbibition or drainage process approaches the limiting values, one expects and observes differences between model and sand behavior.

It is difficult to assess the agreement between the residual oil saturation predicted by the model and that which actually occurs. Rough estimates of oil recoverable by water flood quite commonly match the 50 per cent figure predicted by the model.[8] Nevertheless, firm field or laboratory evidence based on data which meet model requirements are hard to find. Much of this difficulty stems from the infrequency with which reliable S_{wi} values are reported. The curves of Fig. 3 show the good agreement which would obviously result were steady-state relative permeability tests used to estimate residuals. In such tests, the saturation changes are induced in a gradual stepwise manner so the condition for an imbibition saturation distribution are favorable. In a flood on a small test plug made at a high pressure gradient, the conditions favorable for imbibition are doubtful and poorer agreement between observed and predicted values is expected.

The laboratory data of several investigators 9-12 who used widely divergent displacement techniques and the locus of S_{or} predicted by the model are plotted on Fig. 4 as S_{wi} vs S_{or}. The obvious scatter of the data seems to confirm rather than condemn the usefulness of the model prediction. The plotted data include tests by Welge [10] and Stahl [9] which were made under complete capillary control, flood tests on both sands and limestones and flood tests on cores containing free-gas saturation induced by

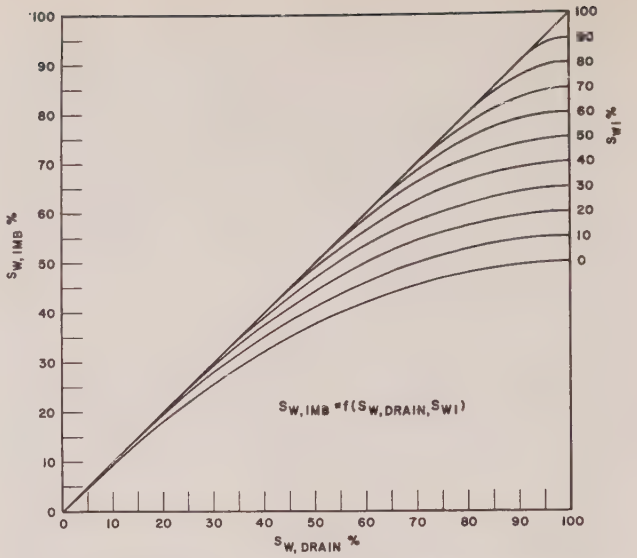

FIG. 2–MODEL RELATIONSHIP BETWEEN DRAINAGE AND IMBIBITION SATURATIONS AS A FUNCTION OF S_{wi}.

both external and internal gas drives. The predicted curve is about as good a "fit" as could be expected. Welge cautioned that his data could not be reproduced to better than 10 per cent V_p. Where flood tests were conducted on cores containing free gas, the plotted S_{or} values on Fig. 4 are values of "one minus the final water saturation achieved".

It may be worth emphasizing that the percentage of oil recovery predicted by the model is the oil recoverable by idealized imbibition into a completely water-wet system. Departure of the surface wetting from the ideal water-wet condition may change the

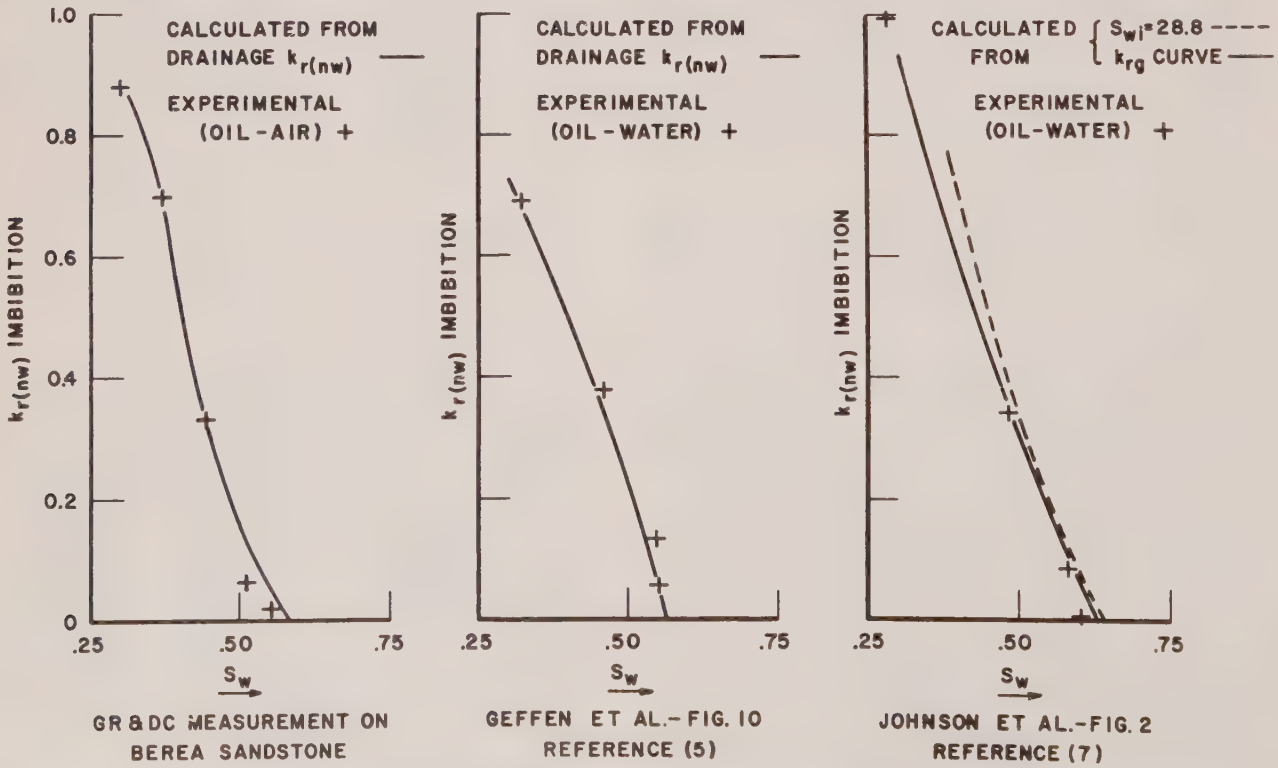
CALCULATED FROM DRAINAGE $k_{r(nw)}$
EXPERIMENTAL (OIL-AIR) +
$k_{r(nw)}$ IMBIBITION
S_w
GR & DC MEASUREMENT ON BEREA SANDSTONE
CALCULATED FROM DRAINAGE $k_{r(nw)}$
EXPERIMENTAL (OIL-WATER) +
GEFFEN ET AL.-FIG. 10 REFERENCE (5)
CALCULATED FROM S_{wi}=28.8 ---- k_{rg} CURVE
EXPERIMENTAL (OIL-WATER) +
JOHNSON ET AL.-FIG. 2 REFERENCE (7)

FIG. 3 – COMPARISON OF CALCULATED AND OBSERVED IMBIBITION RELATIVE PERMEABILITY FOR THE NON-WETTING PHASE.

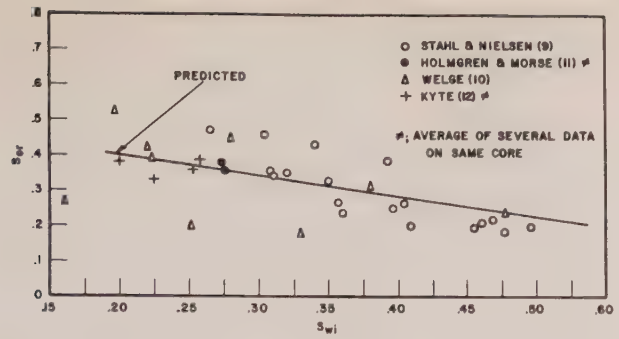

FIG. 4—RESIDUAL OIL SATURATION (S_{or}) AS A FUNCTION OF IRREDUCIBLE WATER SATURATION (S_{wi}); S_{or} PREDICTED COMPARED TO THAT OBSERVED.

recoverable oil even from a sand whose pore geometry conforms to model requirements. Departure of the real distribution of pore sizes from the idealized distribution of the model will also cause the observed permeability to approach a zero value at a different limiting saturation.

LIMITS ON THE ROLE OF WETTABILITY

The water relative permeability for the imbibition cycle departs only slightly from that of the wetting phase during drainage. The drainage k_{rw} curve is shown in the Appendix to be the lower limit of k_{rw} of an imbibition process. Although little work has been done as yet on the behavior of the wetting phase, the imbibition k_{rw} curve derived from the model lies very close to the drainage k_{rw} curve. The conformance between measured drainage and imbibition k_{rw} is so good that it seems justifiable for present needs to use the much simpler drainage curves for the wetting phase. Experimental evidence of the similarity between drainage and imbibition k_{rw} curves is shown in Refs. 2, 5 and 7.

If this suggestion is adopted, it is easy to construct k_{ro}/k_{rw} curves for a consolidated sand having a known S_{wi} value. The curves can be constructed for both drainage 3,13 and imbibition processes. If water invades the sand, its limiting behavior when completely water-wet must be characterized by the imbibition k_{ro}/k_{rw} curves of Fig. 5. These are labelled water-wet to signify the limiting flow behavior expected during imbibition of water. Were the sand completely oil-wet, water invasion would be a drainage process and the limiting curves labelled "oil-wet" would apply. Thus, for a consolidated oil sand subjected to a water flood, the curves of Fig. 5 define the limits between which flow behavior can be influenced by wettability. Similar curves for other S_{wi} values readily can be constructed which show clearly the increased sensitivity of water-oil flow behavior on wettability as the S_{wi} values increase.

The limiting ratio curves are shown for two sands characterized by different S_{wi} values; S_{wi} = 0.30 and 0.15, respectively. If the sand having an S_{wi}

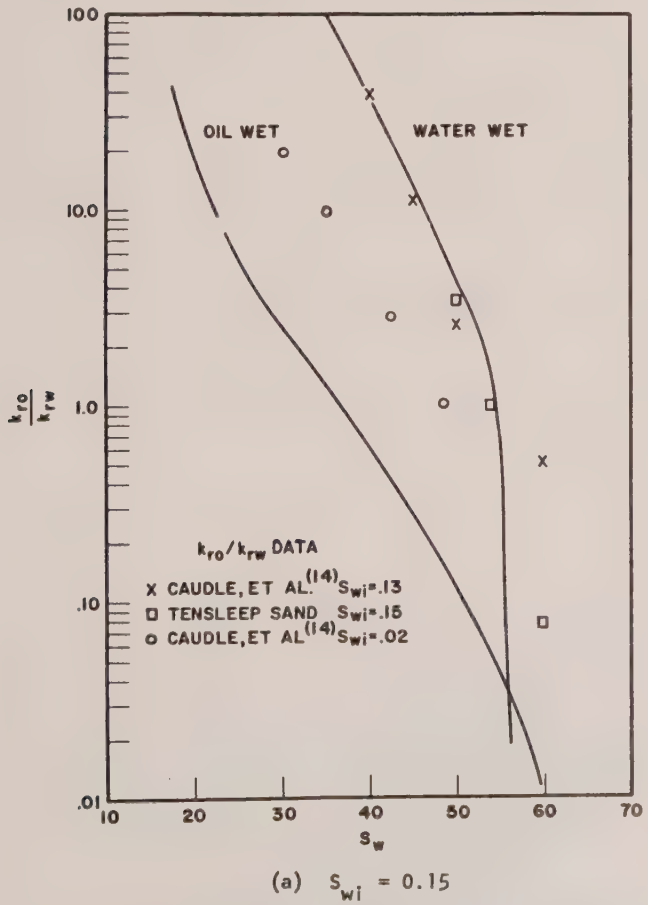

(a) S_{wi} = 0.15

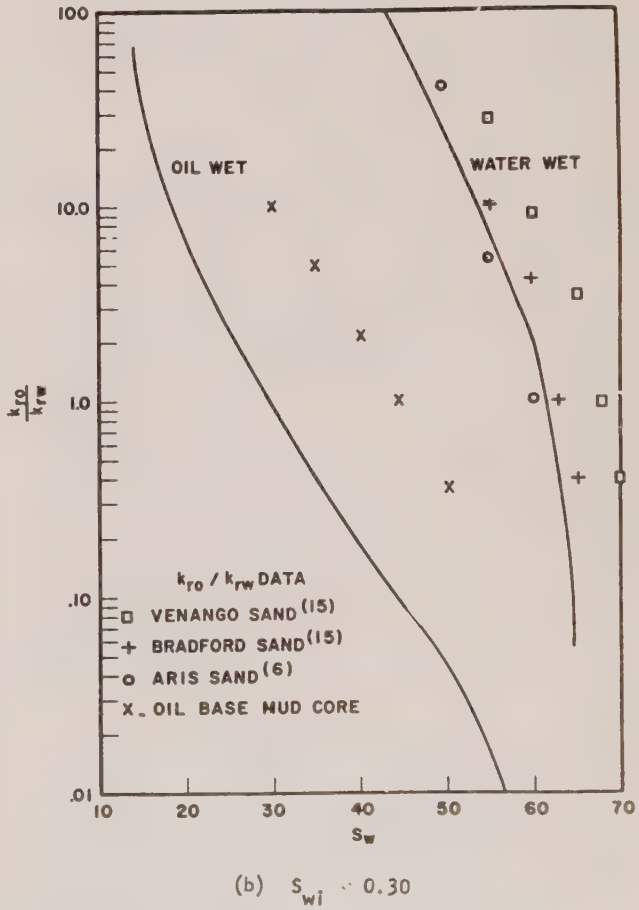

(b) S_{wi} = 0.30

FIG. 5—LIMITING RELATIVE PERMEABILITY RATIOS.

value of 0.30 were to change from a water-wet condition to a completely oil-wet condition, the k_{ro}/k_{rw} ratio and the 50 per cent saturation value would decrease to 1/600 of its water-wet value. In contrast, a sand characterized by an S_{wi} value of 0.15 would experience a much less-marked change in flow behavior due to a like change in wettability. At 50% saturation, the k_{ro}/k_{rw} ratio would decrease to only 1/30 of the water-wet value.

A point of interest lies in the interpretation of flooding tests which may have been conducted on test plugs of intermediate wettability. Oil residuals shown by flood tests on plugs which had been made partially oil-wet by mud filtrate or surface handling may be erroneously low, as shown by Fig. 5(a). However, the same conditions in a test plug of low permeability (Fig. 5b) might indicate an erroneously high residual oil saturation. A more detailed picture of the effect of wettability is shown in Fig. 6. A marked difference is evident between the oil relative permeability curves measured on oil-base mud cores before and after extraction. For comparison, the limiting oil-wet and water-wet behavior predicted by model theory is also shown. Note how the interpretation of the intercept, $k_{ro} = 0$, as a residual oil can be misleading when the condition of the rock surface is uncertain.

It is conceivable that the practical use of the imbibition model to estimate recoverable oil may lie in the limiting ratio curves. By the use of these, the effective residual oil saturation would not be decided by the ultimate saturation achievable but by the permeability ratio beyond which further oil recovery becomes unattractive.

EVIDENCE OF RESERVOIR WETTABILITY

A search of company files and the industrial literature has failed to uncover an example of oil-water k_{ro}/k_{rw} curves which lie near the oil-wet limits. The experimental data plotted on Fig. 5 show some of the correlations.[6,14,15] Although the S_{wi} values of the test sands were rarely known exactly, the approximate values assigned are certainly close to those for which the correlating model curves are shown. Even the Bradford sand, so often described as oil-wet, yields k_{ro}/k_{rw} curves very near the water-wet limit. A few data gathered by Caudle, *et al*,[14] suggests a sand of appreciable intermediate wettability. However, the S_{wi} values reported for this sand was only 1.8 per cent V_p, an unseemly low value for the other properties. Some oil-water relative permeability data for high-permeability cores, which were badly contaminated with oil-base mud filtrate, fall midway between the oil-wet and water-wet limiting curves.

OIL RECOVERY IN THE PRESENCE OF FREE-GAS SATURATION

If one extends the model behavior to a three-phase system under the conditions that water is the dominant wetting phase with respect to oil and oil with respect to gas, then the fluid distributions

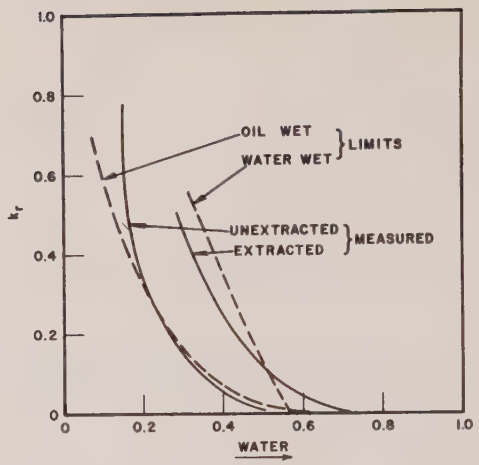

FIG. 6 – OIL RELATIVE PERMEABILITY ON OIL-BASE CORE. LIMITS DERIVED FROM S_{wi} VALUE COMPARED TO EXPERIMENTAL CURVES MEASURED BEFORE AND AFTER EXTRACTION, $K_o = 147$ MD – $S_{wi} = 0.15$.

resulting from water imbibition will again depend on relative pore sizes. The residual saturations can be predicted by reasoning similar to that developed in the Appendix for two-phase imbibition.

The maximum water saturation will be

$$(S_{w,\,imb})_{max.} = 0.5 + \frac{S_{wi}}{2} \qquad (4)$$

The residual oil saturation will be

$$S_{or} = \frac{1}{2}\left(1 - S_{wi}\right)\left(\frac{S_{oi}}{1 - S_{wi}}\right)^2 \qquad (5)$$

where S_{oi} is the initial oil saturation.

The residual gas saturation fills the remainder of the space or

$$S_{gr} = \frac{1 - S_{wi}}{2}\left[1 - \left(\frac{S_{oi}}{1 - S_{wi}}\right)^2\right] \qquad (6)$$

The fractional oil recovery in terms of the initial gas saturation S_{gi} is

$$\frac{N_p}{N} = \frac{1}{2} + \frac{S_{gi}}{2\left(1 - S_{wi}\right)} \qquad (7)$$

Based on such a model, the group $S_{gi}/(1-S_{wi})$ governs the recovery of oil by water imbibition into water-wet sands containing a free-gas saturation. On Fig. 7(a) the fractional oil recovered is plotted vs the parameter $S_{gi}/(1-S_{wi})$. Some control of oil recovery by this functional group is indicated by the Holmgren[11] and Morse data which is compared to the curve predicted by Eq. 12. Data from the Kyte[12] paper show no such correlation on this type of plot.

RESIDUAL GAS SATURATION

When the model predictions of final saturations

are checked against observed residual gas saturations, the agreement is good only if long times for imbibition are prohibited.

The gas residual after a prolonged time for imbibition will be considerably lower than that predicted. The present interpretation of this apparent discrepancy is that, if imbibition tests on plugs were conducted at high pressures (where diffusional effects are relatively small), the residual gas saturation would have been considerably higher. The paper by Gardner, Messmer and Woodside[1] reported the possibility that significant quantities of trapped gas may escape by diffusion at low pressures. Before a final decision can be reached regarding the true meaning of an experimental or computed residual gas saturation, this uncertainty must be resolved.

Fig. 7(b) shows residual gas saturations computed by Eq. 11 compared with observed values from flood tests in the presence of free gas.[11,12] Data from the Kyte paper [12] are plotted only for tests in which mobile gas was initially present. The data from the Holmgren paper [11] reflect the presence of trapped gas, i.e., gas which was already immobilized when the water flood started.

CONCLUSIONS

A mathematical image(model) has been proposed to describe the behavior of a porous medium when imbibing a wetting liquid. This model is based on the concept that the non-wetting phase is gradually blocked during imbibition.

A theoretical relationship between behavior exhibited during drainage and imbibition has been obtained from the model. This relationship has been applied to show that the relative permeability characteristics during imbibition can be determined directly from those observed during drainage, or from the drainage capillary-pressure curve.

Application of this model in conjunction with its predecessors for the drainage process suggests the following.

1. The degree of oil or water wetness has less influence on the flow behavior in sand as its permeability increases, (S_{wi} decreases).

2. In lieu of measured oil-water relative permeability curves, the limiting oil relative permeability curve can be determined from a measured or estimated S_{wi} value. The preferred situation would be to have a measured k_{rg} curve from which to define the k_{ro} limits.

3. A practical limit on the oil recoverable by water flood in consolidated rock will be one-half that originally present.

4. The gas volume trapped by water invasion of a gas-oil complex may be estimated.

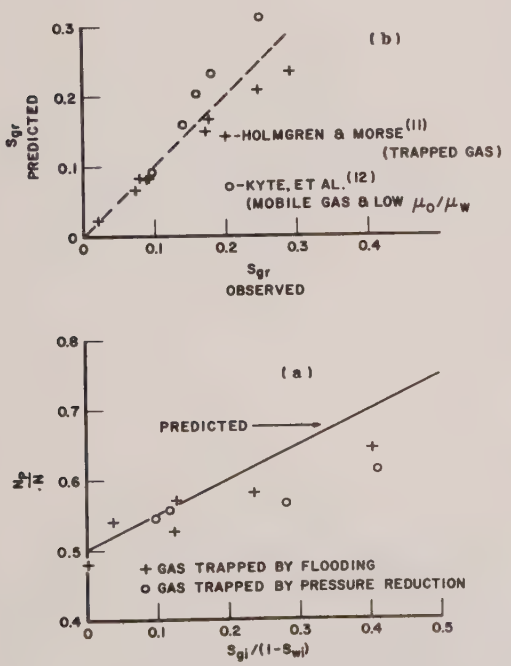

FIG. 7 – OIL RECOVERY BY WATER FLOOD WITH A FREE-GAS SATURATION. (a) FRACTIONAL OIL RECOVERED VS $[S_{gi}/(1-S_{wi})]$. (b) OBSERVED VS PREDICTED RESIDUAL GAS SATURATIONS.

NOMENCLATURE

I = resistivity index
k = permeability
N = total pore volume
N_p = pore volume produced
P_c = capillary pressure
R_o = fluid resistivity
S_w = wetting-phase saturation
S_{wi} = irreducible wetting-phase saturation
S_{nw} = non-wetting phase saturation
S_w^* = reduced wetting-phase saturation, equal to $\dfrac{S_w - S_{wi}}{1 - S_{wi}}$
S_{nw}^* = reduced non-wetting phase saturation equal to $\dfrac{S_{nw}}{1 - S_{wi}}$
f = factor indicating the overlap of pores
k_w = relative permeability to the wetting phase
k_{nw} = relative permeability to the non-wetting phase
r = pore radius
γ = surface tension
ϕ = porosity
ϕ^* = reduced porosity, equal to $(1 - S_{wi})\phi$
F = a function of the wetting-phase saturation such that $F > S_{imb}$

Subscripts

dr = drainage
imb = imbibition

REFERENCES

1. Gardner, G. H. F., Messmer, J. H. and Woodside, W.: "Effective Porosity and Gas Relative Permeability", *Proc.*, Conf. on Theory of Fluid Flow in Porous Media (March 23-24, 1960) U. of Oklahoma, Norman, Okla.
2. Osoba, J. S., Richardson, J. G., Kerver, J. K., Hafford, J. A. and Blair, P. M.: "Laboratory Measurements of Relative Permeability", *Trans.*, AIME (1951) Vol. 192, 47.

3. Wyllie, M. R. J. and Gardner, G. H. F.: "The Generalized Kozeny-Carman Equation", *World Oil* (March, April, 1958) Vol. 146, No. 4 and 5.

4. Marshall, T. J.: "A Relation Between Permeability and Size Distribution of Pores", *Jour. of Soil Sci.* (1958) Vol. 9, No. 1.

5. Geffen, T. M., Owens, W. W., Parrish, D. R. and Morse, R. A.: "Experimental Investigations of Factors Affecting Laboratory Relative Permeability Measurements", *Trans.*, AIME (1951) Vol. 192, 99.

6. Sandberg, C. R., Gournay, L. S. and Sippel, R. F.: "The Effect of Fluid Flow Rate and Viscosity on Oil-Water Relative Permeabilities", *Trans.*, AIME (1958) Vol. 213, 36.

7. Johnson, E. F., Bossler, D. P. and Naumann, V. O.: "Calculation of Relative Permeability from Displacement Experiments", *Trans.*, AIME (1959) Vol. 216, 370.

8. Geffen, T. M. and Roberts, G.: "Fluid Injection for Oil Recovery", *Oil and Gas Jour.* (Aug., 25, 1958) Vol. 56, 86.

9. Stahl, C. D. and Nielsen, R. F.: "Residual Water and Residual Oil by Capillary Pressure Technique", *Proc.*, 13th Tech. Conf. on Pet. Prod. (Oct., 1959); M. I. Bulletin No. 54. The Pennsylvania State U., University Park, Pa.

10. Welge, H. J.: "Displacement of Oil from Porous Media by Water or Gas", *Trans.*, AIME (1949) Vol. 179, 133.

11. Holmgren, C. R. and Morse, R. A.: "Effect of Free Gas Saturation on Oil Recovery by Water Flooding", *Trans.*, AIME (1951) Vol. 192, 135.

12. Kyte, J. R., Stanclift, R. J., Jr., Stephan, S. C., Jr. and Rapoport, L. A.: "Mechanism of Water Flooding in Presence of Free Gas", *Trans.*, AIME (1956) Vol. 207, 215.

13. Corey, A. T.: "The Interrelationship Between Gas and Oil Relative Permeabilities", *Prod. Monthly* (Nov., 1954) Vol. 19, No. 1, 38.

14. Caudle, B. H., Brownscombe, E. R. and Slobod, R. L.: "Further Developments in the Laboratory Determination of Relative Permeability", *Trans.*, AIME (1951) Vol. 192, 145.

15. Henderson, J. H. and Yuster, S. T.: "Relative Permeability Studies", *Prod. Monthly* (Jan., 1948) Vol. 12, No. 3, 13.

16. Lanchon, M.: "Etude du Deplacement Spontane d' un Fluide par un Autre dans un Milieux Poreux (Imbibition)", *Revue de l'Institut Francais du Petrole* (Sept.-Oct., 1960) Vol. XV, No. 9-10.

APPENDIX

THE COMPUTATION OF FLOW CHARACTERISTICS

PERMEABILITY

The method presented here for the computation of permeability closely parallels Marshall's[4] treatment of the problem for the drainage process. It provides a foundation for the application of the model to the imbibition process.

When the Faces A and B of the capillaric model described in the body of the paper are rejoined at random, a series of necks of different shapes and sizes are created which will govern the flow through the medium. The flow through a mean area of these necks can be considered as the flow through a circular pipe with an equivalent cross section. In computing the mean area, the following assumptions are made.

1. When the fit of one pore to the next is perfect (the perimeters do not cross), the cross-sectional area of a neck is taken to be that of the smaller pore.

2. The necks are of circular section.

3. The effective flow path is not increased by imperfect alignment of the necks.

The widening of the flow path within pores is neglected and the resulting error is considered to be compensated by those introduced by assumptions 2 and 3. To determine the equivalent area of flow, consider the pores as composed of n classes of equal total pore area, each class having pores of one size only with radii $r_1 > r_2 > r_3 > \ldots > r_n$. If $\phi^* a$ is the total area available to flow, the area of each class is $\phi^* a/n$. When the Faces A and B are rejoined at random, the area occupied by each class of pores on Face A will be in contact with equal areas of all classes of pores on Face B.

Let f be a factor expressing the partial abutment of a pore class against the solid matrix. Thus, when two pores with radii r_i and r_j abut against each other ($r_i > r_j$), the area of the neck open to flow will be $f\pi r_j^2$. The total area of flow through necks with area $f\pi r^2_j$ is composed of:

1. j areas $f(\phi^* a/n^2)$ of A with pore radii bigger than or equal to r_j abutting against pores of B with radii r_j.

2. $(j-1)$ areas $f(\phi^* a/n^2)$ of B with pore radii bigger than r_j abutting against pores of A with radii r_j.

The total area of flow a_f is then equal to

$$a_f = \left(\frac{f\phi^* a}{n^2}\right)(2j-1) \qquad (8)$$

For the whole medium, the area of flow is obtained by summing Eq. 8 from $j = 1$ to $j = n$. It can be shown that, when a fluid with viscosity μ flows under a pressure gradient P through x_1 capillaries with radius r_1, x_2 capillaries, with radii r_2, x_n capillaries with radius r_n, such that $x_1 r^2_1 = x_2 r^2_2 = \ldots = x_n r^2_n$, the flow per unit area is proportional to the arithmetic average of the component areas. Then one can write for the flow per average unit neck area,

$$\frac{Q}{a} = \frac{P}{8\mu}\,\phi^*\,\frac{f^2}{n^2}\sum_{i=1}^{i=n}(2i-1)\,r^2_i \qquad (9)$$

The permeability is then given by

$$K = \frac{\phi f^2}{8n^2}\sum_{i=1}^{i=n}(2i-1)\,r^2_i \qquad (10)$$

RELATIVE PERMEABILITY (DRAINAGE)

This formula can be applied to compute the relative permeability to one phase by considering the pores filled with the other phase as part of the solid matrix. When the pores r_1 to r_{j-1} are filled with non-wetting fluid, k_{rnw} is given by

$$k_{rnw} = \frac{1}{K}\,\frac{\phi^* S^*_{nw} f^2}{8(j-1)}\sum_{i=1}^{i=j-1}(2i-1)\,r^2_i \qquad (11)$$

and k_{rw} by

$$k_{rw} = \frac{1}{K} \frac{\phi^* S_w^{*} f^2}{8(n-j+1)^2} \cdot \sum_{i=j}^{i=n} \left[2i-(2j-1)\right] r_i^2 \quad \text{---------- (12)}$$

If f is taken equal to $\phi^* S_{nw}^*$ in Eq. 11 or to $\phi^* S_w^*$ in Eq. 12, the formulas become

$$k_{rnw} = \frac{1}{K} \frac{\phi^{*3} S_{nw}^{*3}}{8(j-1)^2} \sum_{i=1}^{i=j-1} (2i-1) r_i^2 \quad \text{----- (13)}$$

and

$$k_{rw} = \frac{1}{K} \frac{\phi^{*3}}{8} \frac{S_w^{*3}}{(n-j+1)^2} \sum_{i=j}^{i=n} \left[2i-(2j-1)\right] r_i^2 \quad \text{---------- (14)}$$

RELATIONSHIP BETWEEN DRAINAGE AND IMBIBITION SATURATIONS

Consider the medium at irreducible saturation and let the capillary pressure be decreased to

$$P_{c,n} = \frac{2\gamma}{r_n} \quad \text{---------- (15)}$$

At this pressure, all the pores with radius r_n of Part 2 abut against pores of Part 1 with radii bigger than or equal to r_n, and the saturation of Part 2 is the same as that of Part 1.

$$S_{w,2} = S_{w,imb} = S_{wi} + \Delta S_w \quad \text{---------- (16)}$$

where ΔS_w is equal to $(1 - S_{wi})/n$

At the same time, the saturation of Part 1 will be

$$S_{w,1} = S_{w,dr} = S_{wi} + \Delta S_w \quad \text{---------- (17)}$$

The next step is to decrease $P_{c,n}$ to $P_{c,n-1}$. The area of the class with radius r_{n-1} of Part 2 which will abut against pores of Part 1 with radii bigger than or equal to r_{n-1} is $[(n-1)/n]\,\Delta S_w$. These pores will be filled with wetting fluid, while the pores with area $(1/n)\Delta S_w$ which abut against pores with radii r_n will be by-passed. Then, for Part 2,

$$S_{w,imb} = S_{wi} + \Delta S_w + (1 - \frac{1}{n})\,\Delta S_w \quad \text{----- (18)}$$

and for Part 1,

$$S_{w,dr} = S_{wi} + 2\Delta S_w \quad \text{---------- (19)}$$

This process can be continued until pores with radius r_j are filled. The saturation of Part 2 will be

$$S_{w,imb} = S_{wi} + \Delta S_w \left[1 + \sum_{i=1}^{i=n-j} (1 - \frac{i}{n})\right] \quad \text{---- (20)}$$

and the saturation of Part 1,

$$S_{w,dr} = S_{wi} + (n-j)\,\Delta S_w \quad \text{---------- (21)}$$

When the number n of classes of pores goes to infinity, Eq. 20 takes an integral form. Writing $j = an$, $\frac{i}{n} = x$ and $\frac{1}{n} = dx$ gives, after integration,

$$S_{w,imb} = S_{wi} + \frac{1 - S_{wi}}{2}(1 - a^2) \quad \text{--------- (22)}$$

The saturation of Part 1 is computed in the same way and is found to be

$$S_{w,dr} = S_{wi} + (1 - S_{wi})(1 - a) \quad \text{---------- (23)}$$

Elimination of a and introduction of

$$S_{w,imb}^* = \frac{S_{w,imb} - S_{wi}}{1 - S_{wi}} \quad \text{---------- (24)}$$

gives

$$S_{w,imb}^* = S_{w,dr}^* - \frac{1}{2} S_{w,dr}^{*\,2} \quad \text{---------- (25)}$$

RELATIVE PERMEABILITY (IMBIBITION)

The mechanics of imbibition will be examined hereafter to derive formulas analogous to drainage Eqs. 13 and 14 for the imbibition process.

The permeability to one phase was computed by assuming that the pores full of the other phase are part of the solid matrix. During the imbibition cycle, a certain number of pores of Part 2, full of non-wetting fluid, are by-passed and abut against pores of Part 1 which are full of wetting fluid. The by-passed pores do not contribute to the flow of the non-wetting phase, and for the computation of non-wetting relative permeability Part 2 can then be assumed to have the same saturation as Part 1. This means that the medium is assumed to be at the saturation of Part 1 or, in other words, that it arrived at its present state through a drainage cycle. However, its permeability to the non-wetting phase corresponds to the true saturation of Part 2. These remarks are valid whether the drainage relative permeability to the non-wetting phase is computed or measured and provide a way of relating imbibition properties to drainage ones. If the permeability is computed, its value is given by Eq. 13.

$$k_{rnw} = \frac{1}{K} \frac{\phi^{*3} S_{nw}^{*3}}{8(j-1)^2} \sum_{i=1}^{i=j-1} (2i-1) r_i^2 \quad \text{----- (13)}$$

The permeability to the wetting phase is estimated as follows. If Part 2 of the slice had the same saturation as Part 1, k_{rw} would be given by:

$$k_{rw} = \frac{1}{K} \frac{\phi^* S_w^{*} f^2}{8(n-j+1)^2} \cdot \sum_{i=j}^{i=n} \left[2i-(2j-1)\right] r_i^2 \quad \text{---------- (12)}$$

As a certain number of pores of Part 2 are blocked and do not participate in the flow, the expression for k_{rw} changes. The number of areas is reduced to $1 + 2 + 3 + \ldots + (n - j + 1) = \frac{1}{2}[(n - j + 1)(n - j + 2)]$, and their flow characteristics are distributed as follows:

One area has necks with cross-sectional area $f\pi r_j^2$;

Two areas have necks with cross-sectional areas $f\pi r_{j+1}^2$; and

$n - j + 1$ areas have necks with cross-sectional areas $f\pi r_n^2$.

The value of k_{rw} is then

$$k_{rw,imb} = \frac{1}{K} \frac{f^2 \phi^* S^*_{w,imb}}{8\frac{1}{2}(n-j+1)(n-j+2)} \sum_{i=j}^{i=n} \left[i-(j-1)\right] r_i \quad \text{---------- (26)}$$

The value of f which was taken equal to $\phi^* S^*_w$ in the drainage process must be re-evaluated. Indeed, since the wetting-phase saturation of Part 1 is greater than that of Part 2, the probability of having a common area of overlap for pores full of wetting liquid is greater than if Part 1 had the same saturation as Part 2. Therefore, f must be written

$$f = \phi^* F^* \quad \text{---------- (27)}$$

where F^* is a function of $S^*_{w,imb}$ such that

$$F^* \geq S^*_{w,imb} \quad \text{---------- (28)}$$

and $k_{rw,imb}$ is given by

$$k_{rw,imb} = \frac{1}{K} \frac{1}{8} \frac{\phi^{*3} F^{*2} S^*_{w,imb}}{\frac{1}{2}(n-j+1)(n-j+2)} \sum_{i=j}^{i=n} \left[i-(j-1)\right] r_i^2 \quad \text{---------- (29)}$$

For n going to infinity, k_{rw} takes the following integral form

$$k_{rw,imb} = \frac{\phi^{*3}\gamma^2}{K} S^*_{w,imb} \left(\frac{F^*}{S^*_{w,imb}}\right)^2 \int_0^{S^*_{w,imb}} \frac{S^*_{w,imb} - S^*}{P_c^2} dS^* \quad \text{---(30)}$$

The relationship between $k_{rw,imb}$ and $k_{rw,dr}$ follows from the observation that the permeability to the wetting phase, on drainage, is given by

$$k_{rw,dr} = \frac{\phi^{*3}\gamma^2}{K} S^*_{w,dr} \int_0^{S^*_{w,dr}} \frac{S^*_{w,dr} - S^*}{P_c^2} dS^* \quad \text{---(31)}$$

and that for $S^*_{w,imb} = S^*_{w,dr}$

$$k_{rw,imb} = k_{rw,dr} \left(\frac{F^*}{S^*_{w,imb}}\right)^2 \quad \text{------- (32)}$$

From the definition of F^*, the factor $F^*/S^*_{w,imb}$ is greater than or equal to one and

$$k_{rw,imb} \geq k_{rw,dr} \quad \text{---------- (33)}$$

$k_{w,dr}$ is then lower limit of $k_{w,imb}$.

The value of F^* cannot be deduced from theoretical arguments only, and experiments are required to determine the error made by writing $k_{w,imb} = k_{w,dr}$ ***

Microbial Flora in a Number of Oilfield Water-Injection Systems

V. CARLSON*
E. O. BENNETT
U. OF HOUSTON
J. A. ROWE, JR.**
MEMBER AIME
GULF OIL CORP.
HOUSTON, TEX.

ABSTRACT

This report concerns the microbial flora found throughout the surface facilities of six water-injection systems in Texas and Oklahoma. Each system is described in detail and water quality data are presented when available.

Pseudomonads and sulfate-reducers (Desulfovibrio) were the predominate organisms found in the systems. The genera Sphaerotilus, Bacillus, Achromobacter, Micrococcus, Clostridium, Flavobacterium, and Sarcina were also isolated in significant numbers. Molds, iron bacteria, sulfur bacteria and soil bacteria were found less frequently in the systems.

It is concluded that a complex microbiological flora exists in oilfield water-injection systems. A tendency for waters to deteriorate in passage through solid bed filters is also noted.

INTRODUCTION

The injection of water into a subsurface formation is often accompanied by numerous problems, the origin and nature of which are only partially understood. During the past few years, investigators have indicated that bacteria are involved in some of these problems even though very little specific information is available concerning this matter.

It is surprising that investigators working on microbiological problems in water injection have never made a complete study of the flora of these systems. The logical course to pursue is that of identifying the microbial flora and then examining each organism individually and in combination with others to determine if they produce a particular problem.

The objective of the present investigation is to identify the microbial flora in water-injection systems. In addition, the quality of the water in most of the systems was determined and some observations made on the extent to which passage through surface-handling facilities affects water quality.

The information derived from this study can serve as a foundation for additional basic investigations.

Original manuscript received in Society of Petroleum Engineers office Aug. 25, 1960. Revised manuscript received Jan. 9, 1961. Paper presented at 35th Annual Fall Meeting of SPE, Oct. 2-5, 1960, in Denver.

*Now attending the U. of Texas Medical School in Galveston.
**Now associated with Magna Chemicals, Kilgore, Tex.

EXPERIMENTAL PROCEDURE

The microbial flora of six water-injection systems were studied at 50 sampling points. These systems are experiencing problems which may be attributable to micro-organisms, and two were being treated with antimicrobial agents at the time of this study.

The samples were obtained by inoculating 1.0 ml of the water onto the different media at the sampling point. The media used for primary isolation included nutrient agar, Strokes agar, M-10-E medium and semi-solid thioglycollate medium.

The cultures were returned to the laboratory, incubated at 30°C until growth occured; then, pure cultures were obtained from individual colonies. The pure cultures were identified according to standard bacteriological procedures. Those organisms not fitting identification criteria exactly, even though exhibiting close similarities to known species, are listed as unidentified organisms.

Membrane filters were used to make water-quality tests at intervals before and after collection of the microbiological samples. The filter discs were 47 mm in diameter with a 0.45-micron particle-size retention, and the tests were done under closed conditions at 20 psi. Membrane flow rates are plotted as increasing filtrate volumes, and the total solids contents are given when available.

An effort was made to sample at each place in a system where a change in environment occurred. In this manner, the effect of passage through filters, tanks, hay sections, etc., on the microbial flora and water quality could be observed.

RESULTS

SYSTEM A

This waterflood system (Fig. 1) is about four years old and daily pumps approximately 110,000 bbl of oil-free sour water from a 3,700-ft deep reef. The

water passes through two sets of flue gas scrubbers which lower the hydrogen-sulfide content from 250 to 20 to 30 ppm. Chlorine is added to remove the residual hydrogen sulfide, and this treatment results in the formation of some colloidal sulfur which cannot be removed efficiently by the anthrafilt filter. The supply water is treated with an organic corrosion inhibitor. There is no perceptible change in quality after passage through a maximum of 11 miles of distribution lines.

Chemical analysis of the supply water gave the following information; pH, 6.85; sodium, 776 ppm; calcium, 870 ppm; magnesium, 212 ppm; bicarbonate, 403 ppm; chloride, 2128 ppm; sulfate, 1350 ppm; and hydrogen sulfide, 250 ppm.

The system also handles several thousand barrels of produced brine per day in two recycling stations. The ratio of recycled brine to supply water is currently less than 1:7. The brine is sometimes produced sour, expecially in the older parts of the flood, but it is generally considered to be sulfide-free in the native state. The injection wells yield appreciable amounts of iron sulfide when they are backwashed.

Table 1 shows that the microbial flora in this system is quite extensive. In general, the same organisms were found in the oil-contaminated brine recycle systems as in the oil-free supply water, however, there was less variety in the latter system, Pseudomonads and sulfate-reducers were prevalent in the recycling systems and at the injection wells.

The membrane data obtained from the supply water portion of the system may be found in Fig. 2. The water is of good quality through the first scrubber; however, it deteriorates during passage through the second scrubber. The filtered water has a high initial flow rate, which falls off rapidly to a value below that of Curve C. Further deterioration is evident at the injection well.

The membrane data (Fig. 3) on the brine recycle system shows that the water is of poor quality and that coalescing, separation and bed filtration are of very little benefit. Undoubtedly, appreciable quantities of insoluble materials are removed, but the solid filter cake which develops on the membrane disc (and probably at the wellbore) is highly resistant to the passage of water. The poor quality of water in the recycle systems is due primarily to hydrocarbons; however, bacteria and scale deposition may be responsible for the deterioration noted as the water passes through both systems.

A core taken from an injection well in this system was cut to 1 in. diameter X 1 in. long, mounted in plastic and placed in a stainless-steel flow cell. The cell was connected to the discharge header so that water flowed through the core under a pressure

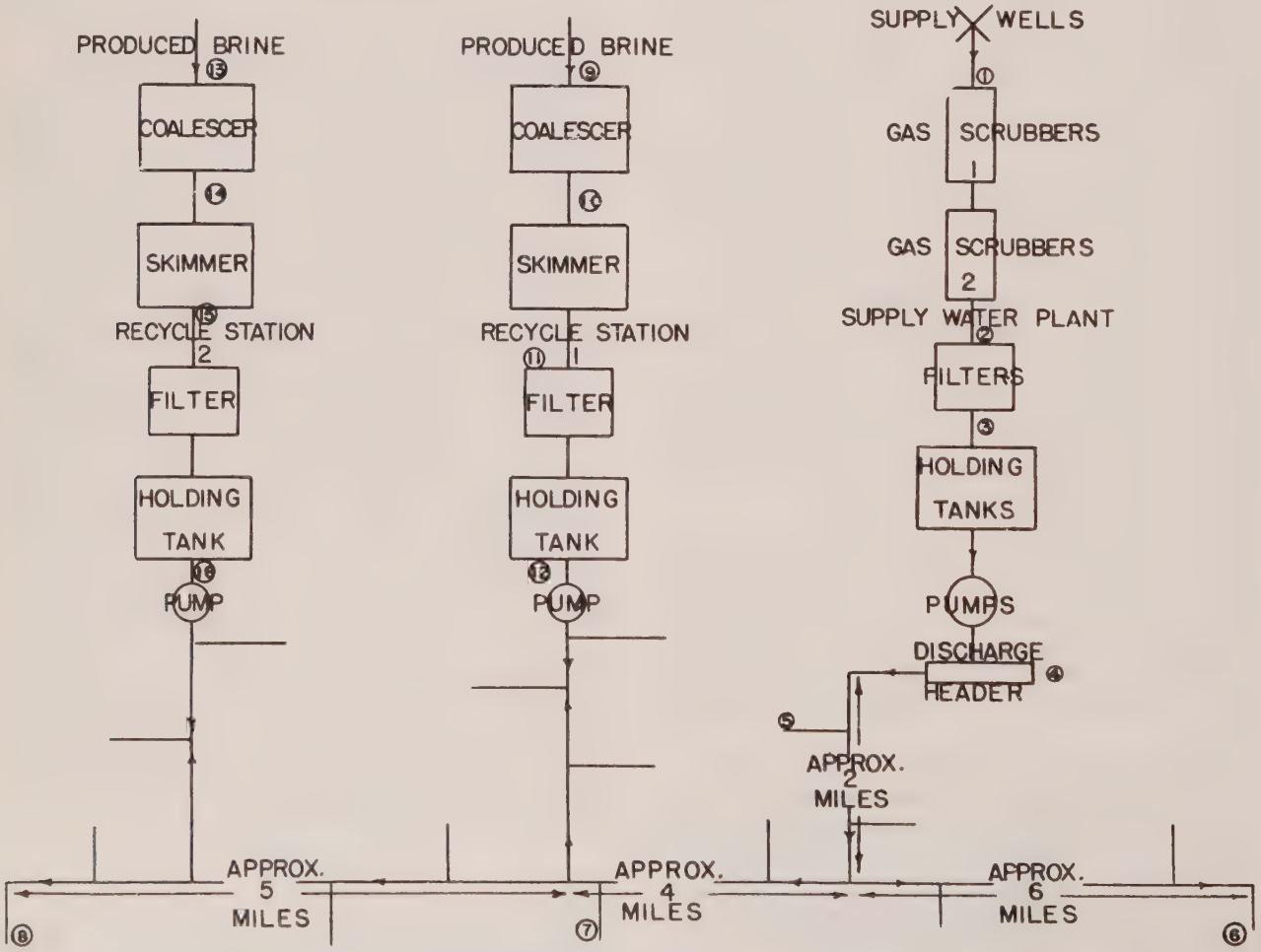

FIG. 1 – SYSTEM A.

TABLE 1 – MICROBIAL FLORA OF SYSTEM A

Site 1–Gas Scrubber No. 1 Inlet
- Alginomonas spp.
- Pseudomonas putida
- Achromobacter spp.
- Desulfovibrio desulfuricans

Site 2–Gas Scrubber No. 2 Outlet
- Beggiatoa spp.
- Bacillus mascerans
- Pseudomonas oleovorans
- Desulfovibrio desulfuricans

Site 3–Filter Outlet
- Vitreoscilla spp.
- Leptothrix spp.
- Pseudomonas boreopolis

Site 4–Discharge Header (Core Outlet)
- Sarcina auriantica
- Proteus spp.
- Achromobacter spp.

Site 5–Injection Well
- Escherichia freundii
- Pseudomonas spp.
- Desulfovibrio desulfuricans

Site 6–Injection Well
- Nocardia spp.
- Thiobacillus spp.
- Pseudomonas fluorescens
- Sphaerotilus natans

Site 7–Injection Well
- Cellulomonas aurogena
- Thiobacillus spp.
- Desulfovibrio desulfuricans

Site 8–Injection Well
- Pseudomonas striata
- Bacillus mascerans
- Pseudomonas boreopolis
- Desulfovibrio desulfuricans

Site 9–Coalescer Inlet (Station 1)
- Thiobacillus spp.
- Thiobacillus spp.
- Alginomonas nonfermentans
- Mycoplana dimorpha
- Desulfovibrio desulfuricans

Site 10–Coalescer Outlet
- Micrococcus flavus
- Achromobacter liquefaciens
- Desulfovibrio desulfuricans

Site 11–Filter Inlet
- Sarcina lutea
- Micrococcus varians
- Desulfovibrio desulfuricans

Site 12–Holding Tank Outlet
- Mycoplana dimorpha
- Bacillus cereus
- Pseudomonas ovalis
- Sphaerotilus natans
- Desulfovibrio desulfuricans

Site 13–Coalescer Inlet (Station 2)
- Corynebacterium spp.
- Nocardia opaca
- Proteus rettgeri
- Sarcina auriantica
- Bacillus cereus
- Desulfovibrio desulfuricans

Site 14–Coalescer Outlet
- Micrococcus conglomeratus
- Pseudomonas ovalis
- Pseudomonas arvilla
- Desulfovibrio desulfuricans

Site 15–Skimmer Outlet
- Bacillus cereus
- Thiobacillus nevellus
- Vitreoscilla spp.
- Leptothrix spp.
- Desulfovibrio desulfuricans

Site 16–Holding Tank Outlet
- Aerobacter aerogenes
- Escherichia coli
- Thiobacillus spp.
- Pseudomonas aeruginosa
- Pseudomonas fluorescens
- Pseudomonas putida
- Desulfovibrio desulfuricans

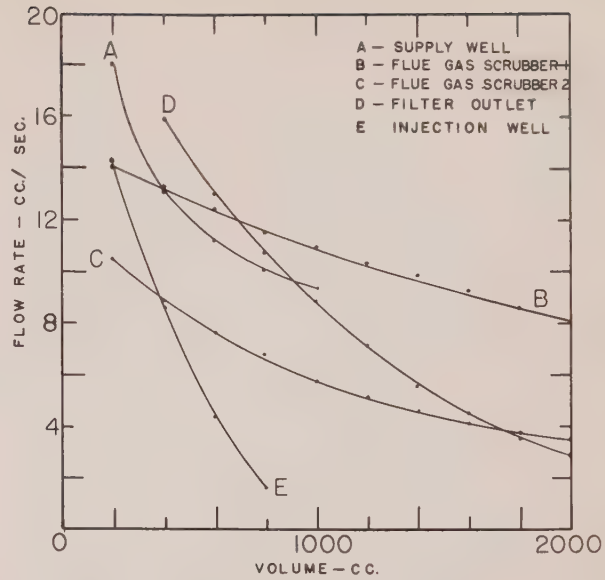

FIG. 2 – SYSTEM A – SUPPLY WATER.

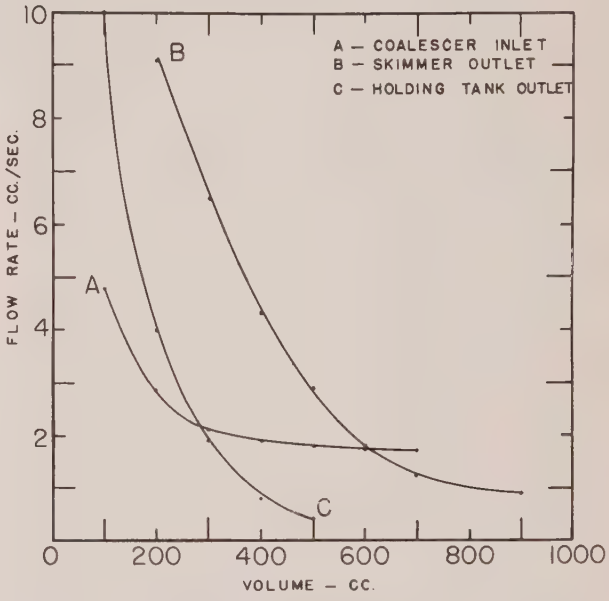

FIG. 3 – SYSTEM A – BRINE RECYCLE STATION 2.

of 700 psi. Based on the Darcy equation, the core showed an initial permeability of 96 md, 40 md after eight hours, and 37 md after 16 hours, indicating that the permeability declined slowly following an initial rapid decline. This permeability stability at a fairly high figure correlates with the general lack of injection problems in portions of this system. Injection problems will probably increase as the production of brine increases unless more efficient oil removal is accomplished.

SYSTEM B

This waterflood system (Fig. 4) is two years old and daily pumps approximately 90,000 bbl of water (temperature, 58° to 60° F) from alluvial beds adjacent to the Arkansas River. The water is pumped through a coated line to three injection stations, and at two of these stations it is mixed with produced brine. There is bare steel in the section containing produced brine, and black water has been observed in this section and in the injection wells. The system was under treatment with a quaternary amine bactericide at the time the microbiological study was made. Chemical analysis of the water gave the results shown in Table 2.

Table 3 shows that pseudomonads were the predominant organisms in the system. The bactericide was doing an excellent job of reducing the variety of flora coming from the supply wells since only one organism was isolated from the treated water.

The sulfate-reducers were found primarily in the brine portion of the system, but they may be working upstream since they were isolated at Site 3. The supply wells contain bare steel, and it is possible that they may start producing black water in the future when the sulfate-reducers reach this point.

Appreciable quantities of iron oxide have built up in the pump bowls and transfer lines in the

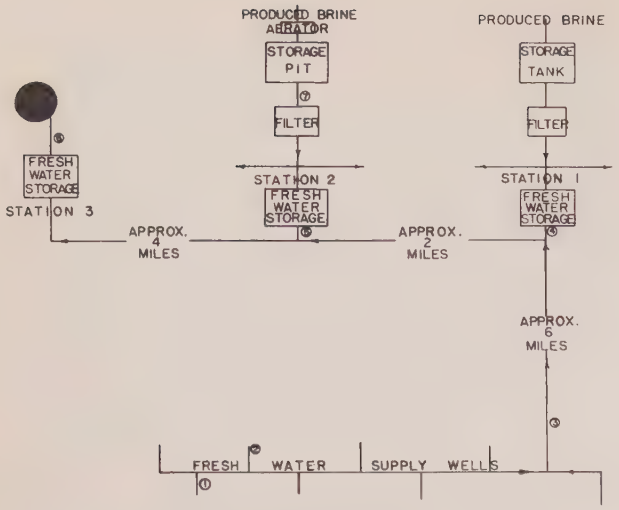

FIG. 4 – SYSTEM B.

fresh-water portion of this system. These deposits were believed by some to be caused primarily by iron bacteria (Gallionella), while others thought they were due to the presence of oxygen in the system. Gallionella disc counts have been as high as 20,000/ml at various points in the system. Oxygen levels periodically ran in excess of 1 ppm, and considerable effort has been made to reduce air entry in the supply wells.

A study was made to compare Gallionella counts, dissolved-oxygen content and suspended iron during six-months treatment with an organic sulfur biocide and three months without treatment. The oxygen level was reduced to less than 0.05 ppm, and the total iron available for oxidation was 3 to 4 ppm. The results showed that there was no significant increase in suspended iron coincident with an increase in Gallionella to a point too numerous to count.

Fig. 5 exhibits the membrane data accumulated during the biocide treatment at sampling points at both ends of the system. The sample taken in January was just prior to initiating treatment. Water quality improved markedly through June and has continued to improve since discontinuing biocide treatment.

Fig. 5 also gives an analysis of the solids retained on the filter disc. The acid-soluble portion is represented as Fe (hydroxide and/or sulfide) and Ca (carbonate and/or sulfate). That portion insoluble in acid but ignitable is reported as "organic".

The brine is passed through a graphilter filter prior to mixing with fresh water, since it is considerably poorer in quality than the fresh water. This practice results in a water of fair quality being

TABLE 2–CHEMICAL ANALYSIS OF WATER FOR SYSTEM B

	Fresh Water	Brine (Average Val.)
pH	7.20	6.60
Sodium	238 ppm	23,257 ppm
Calcium	118 ppm	3,565 ppm
Magnesium	25 ppm	902 ppm
Bicarbonate	171 ppm	363 ppm
Chloride	518 ppm	44,591 ppm
Sulfate	43 ppm	32 ppm

TABLE 3 – MICROBIAL FLORA OF SYSTEM B

Site 1 – Treated Supply Well
- Aerobacter aerogenes

Site 2 – Untreated Supply Well
- Sphaerotilus natans
- Pseudomonas putida
- Pseudomonas fluorescens
- Pseudomonas boreopolis
- Aerobacter aerogenes

Site 3 – Composite Supply Water
- Desulfovibrio desulfuricans

Site 4 – Inlet to Fresh-Water Storage Tank, Station 1
- Desulfovibrio desulfuricans
- Cytophaga rubra
- Flavobacterium ferrugineum
- Pseudomonas fluorescens
- Pseudomonas putida

Site 5 – Inlet to Fresh-Water Storage Tank, Station 2
- Sphaerotilus natans
- Pseudomonas aeruginosa
- Pseudomonas boreopolis

Site 6 – Injection Pump Inlet, Station 3
- Alginomonas nonfermentans

Site 7 – Produced Brine, Above Filter, Station 2
- Desulfovibrio desulfuricans
- Sphaerotilus natans
- Pseudomonas fluorescens

furnished to the injection wells. Fig. 6 shows that the filter is doing a good job of total solids removal, but membrane plugging persists. This suggests that only the large particles are removed.

SYSTEM C

This pressure-maintenance system (Fig. 7) is about four years old and daily injects 250 to 1,000 bbl of brine produced from wells about 7,300-ft

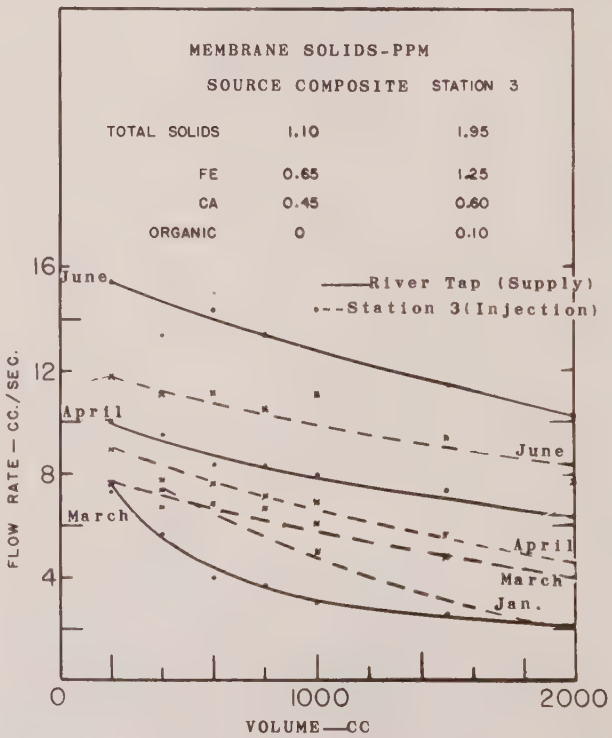

FIG. 5 – SYSTEM B – FRESH WATER.

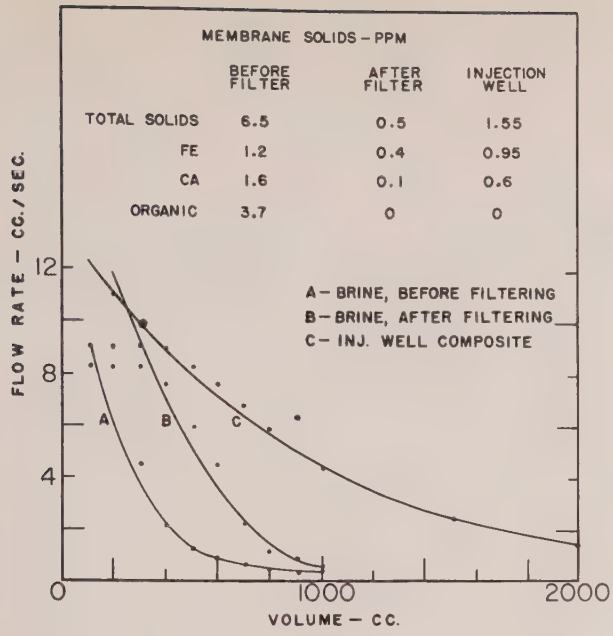

FIG. 6 – SYSTEM B – PRODUCED BRINE.

deep. The temperature of the brine varies from 75° to 100°F, and it contains a considerable amount of entrained oil in the form of an inverse emulsion. The injection well has plugged severely and does not respond satisfactorily to acidification. A blend of corrosion inhibitor, scale preventive and surfactant is added to the water. Chemical analysis of the composite water gave the following information: pH, 6.2; sodium, 20,423 ppm; calcium, 1,120 ppm; magnesium, 249 ppm; bicarbonate, 268 ppm; chloride, 34,042 ppm; and sulfate, 24 ppm.

Table 4 shows that this system is extensively contaminated with bacteria and that most of the organisms were encountered around the skimmer tank and injection well. This system, like the others, contains pseudomonads and sulfate-reducers but, unlike the other systems, also contains a number of molds.

The membrane data (Fig. 8) show that the ultimate plugging time of the water was not materially improved by passage through the conditioner and that an appreciable quantity of nonferrous acid-soluble material (mostly calcium carbonate) is present. The organic matter does not include oil, which was found to be 20-ppm above and 10-ppm below the conditioner.

A core flow test was made at sample Point 6 (Fig. 7) with a 1-in. plug of Berea sandstone at 100 psi. The initial permeability was 64 md, which was reduced to 4.2 md after one hour, and 1.9 md after five hours. The permeability of the core was increased to 8 md after treatment with acid and organic solvents with and without surfactants.

The data suggest that bacteria and suspended solids are responsible for the plugging problems encountered in this field.

SYSTEM D

This waterflood system (Fig. 9) has been in operation for about eight years and daily injects approximately 3,500 bbl of produced brine and 6,500 bbl of fresh water. The temperature of the produced brine varies from 75° to 100°F, and the fresh water from 50° to 60°F. An aldehyde bactericide is added to the water because the system has developed several problems such as plugged wells, black water and corroded meters. Table 5 shows the chemical analysis of the waters.

Table 6 shows that the system is contaminated with Sphaerotilus and sulfate-reducers, which may account for the black water. Only one organism was isolated from the fresh water, and the variety of flora is not great throughout the system.

Membrane data (Fig. 10) show that mixing good-quality fresh water with the brine produces a composite water with rapid-plugging tendencies. The standard graphilter-pack filter (minimum particle size 1/16 in.)

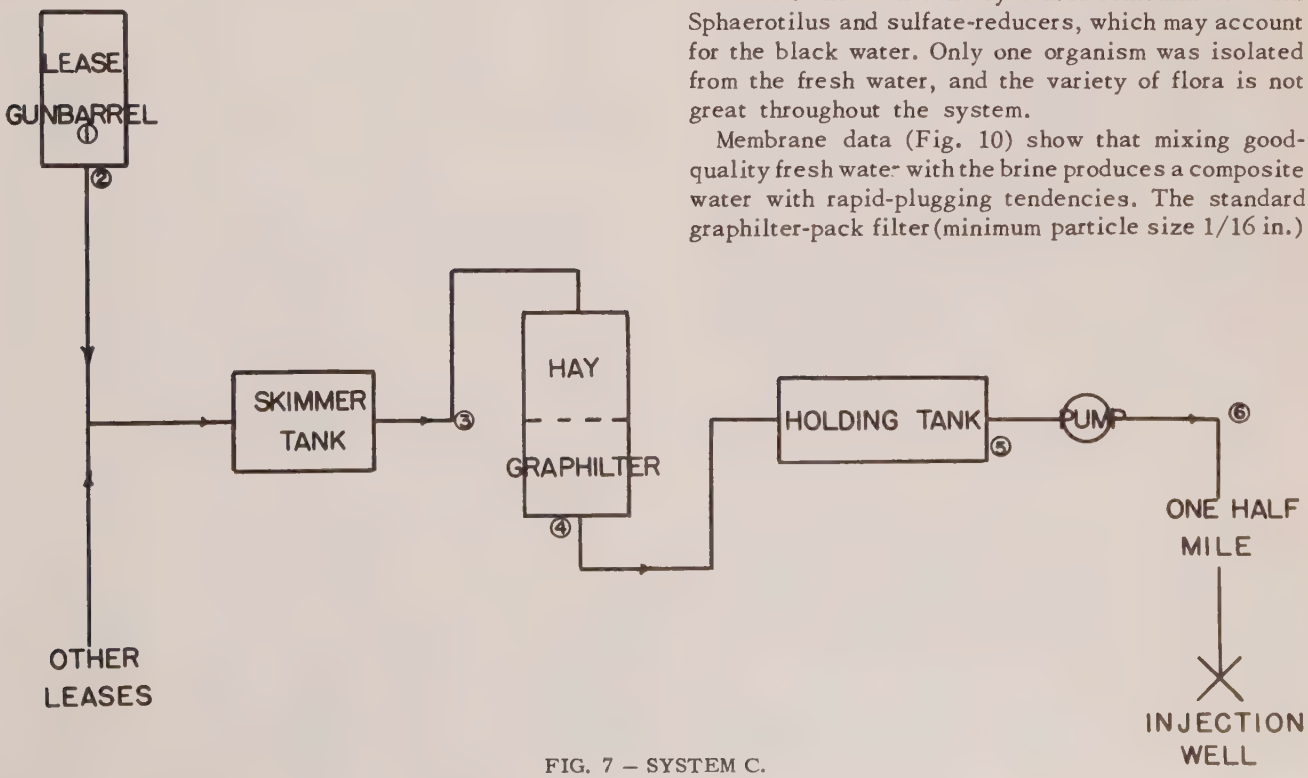

FIG. 7 – SYSTEM C.

TABLE 4 – MICROBIAL FLORA OF SYSTEM C

Site 1–Clear Water 4-Ft Off Bottom of Gunbarrel

Pseudomonas aeruginosa
Bacillus megaterium
Corynebacterium poinsettiae
Unidentified organism

Site 2–Sediment 2 to 3 In. Off Bottom of Gunbarrel

Micrococcus agilis
Sphaerotilus natans
Pseudomonas putida
Pseudomonas oleovorans
Bacillus sphaericus
Desulfovibrio desulfuricans
Two unidentified organisms

Site 3–Centrifugal-Pump Discharge Between Skimmer Tank and Conditioner

Achromobacter stenohalis
Pseudomonas oleovorans
Pseudomonas putida
Pseudomonas fluorescens
Mycobacterium marinum
Micrococcus halodenitrificans
Penicillium notatum
Penicillium spp.
Mucor spp.
Asperfillis spp.
Monilia spp.
Rhizopus spp.
Desulfovibrio desulfuricans
Three unidentified organisms

Site 4–Line From Bottom of Filter

Bacillus cereus
Desulfovibrio desulfuricans
Two unidentified organisms

Site 5–Discharge Line From Bottom of Horizontal Holding Tank

Bacillus cereus
Bacillus cereus, var. mycoides
Desulfovibrio desulfuricans
Two unidentified organisms

Site 6–Line Between Horizontal Holding Tank and Injection Well

Micrococcus varians
Micrococcus flavus
Sarcina flava
Sarcina lutea
Pseudomonas fluorescens
Pseudomonas putida
Pseudomonas oleovorans
Alcaligenes metalcaligenes
Cytophaga rubra
Desulfovibrio desulfuricans
Two unidentified organisms

produces an unusually good water which undergoes extreme deterioration by the time it reaches the injection well. The problems encountered in this system may be of microbiological origin since entrained oil does not appear to be the major source of trouble.

SYSTEM E

This pressure-maintenance system (Fig. 11) has been in operation for about five years and daily injects between 30,000 to 60,000 bbl of sour water obtained from the same reef as in System A. A semipolar organic corrosion inhibitor is added (25 ppm) continuously at the supply wells, and the water is then pumped through an 18-in. bare-steel line to the injection plant where it is filtered through 12 parallel anthrafilt filters (0.6 to 0.8 mm). Chemical analysis of the water gave the same results as in System A. It was also noted that the sulfate and sulfide content of the water remains unchanged throughout the system.

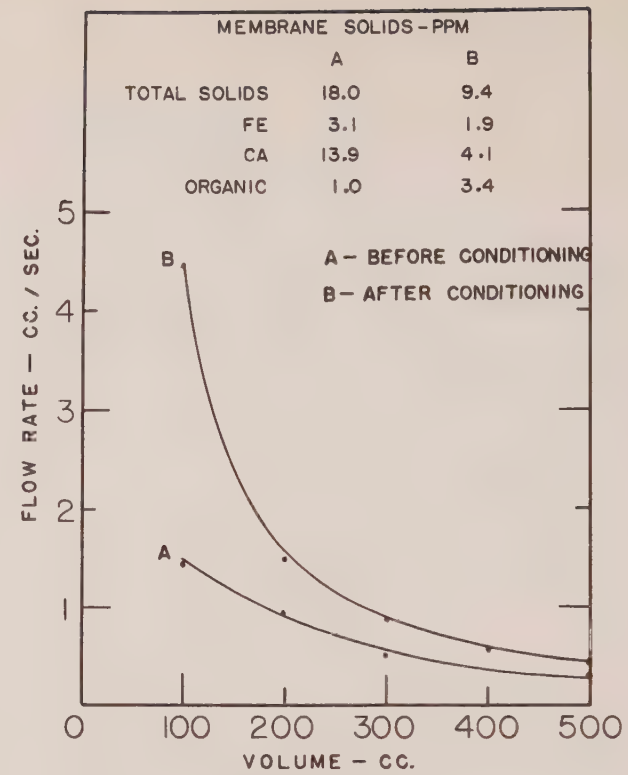

FIG. 8 – SYSTEM C – PRODUCED BRINE.

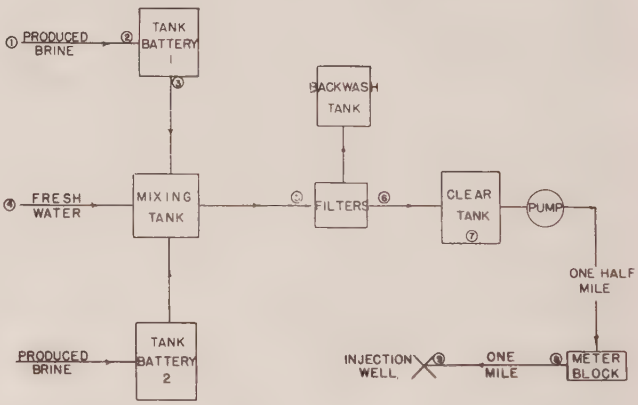

FIG. 9 – SYSTEM D.

Table 7 shows that Desulfovibrio, Sphaerotilus and Flavobacterium species were prevalent throughout the system. Bacteriological analysis four months prior to this study also indicated that the system was extensively contaminated with sulfate-reducers.

Membrane filter analysis shows that the filters (Fig. 12) are effectively removing solids which consist predominantly of iron sulfide. The water undoubtedly deteriorates before it reaches the injection

TABLE 5–CHEMICAL ANALYSIS OF SYSTEM D WATERS

	Composite Fresh Water	Brine
pH	7.4	6.8
Sodium	191 ppm	15,876 ppm
Calcium	39 ppm	2,555 ppm
Magnesium	19 ppm	604 ppm
Bicarbonate	232 ppm	220 ppm
Chloride	11 ppm	30,645 ppm
Sulfate	11 ppm	10 ppm

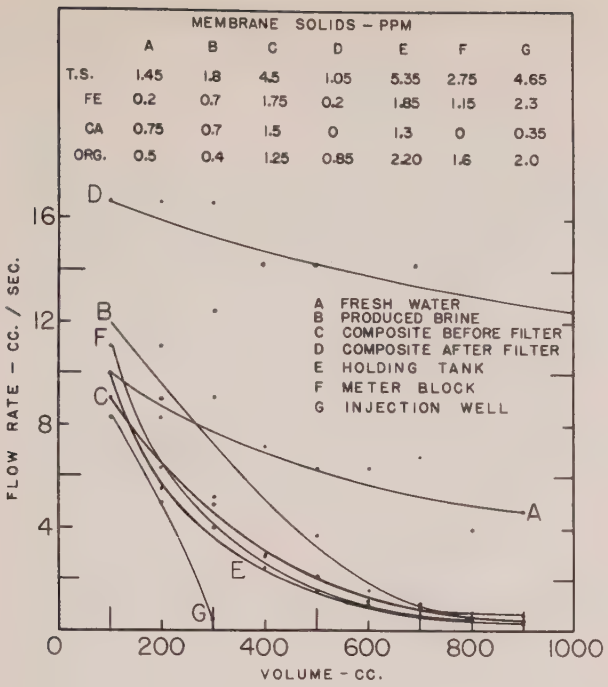

FIG. 10 – SYSTEM D.

wells, but no injection problems have been encountered in the porous dolomitic reservoir.

SYSTEM F

This salt-water-disposal system (Fig. 13) has been in operation for 10 years and daily injects approximately 3,000 bbl of produced brine obtained from wells that are about 7,000 ft deep. Several years ago it was suspected that entrained oil was plugging the injection well. Temporary benefit was obtained by acidizing the well, and treatment with a nonionic surfactant was helpful for several months but eventually ceased to be effective. A kerosene wash was installed at that time, which increased intervals between backwashing and/or acidizing considerably. The well is having no injectivity injectivity difficulties at the current rate of water input, and for this reason the system is not under chemical treatment. Chemical analysis of the water gave the following results: pH, 7.1; Calcium, 1,935 ppm; Magnesium, 165 ppm; Barium, 108 ppm; Strontium, 91 ppm; Bicarbonate, 188 ppm; Chloride, 55,000 ppm; and Sulfate, 3 ppm.

The system is not experiencing any trouble that can be attributed to bacteria even though Table 8 shows that it is heavily contaminated with microorganisms. Desulfovibrio species were found in every sample taken from the system, but black water

TABLE 6 – MICROBIAL FLORA OF SYSTEM D

Site 1–Producing Well Untreated	Site 6–Composite Water Below Filter
Micrococcus lutea	Desulfovibrio desulfuricans
Bacillus megaterium	Sphaerotilus natans
Arthrobacter ureafaciens	Arthrobacter spp.
Arthrobacter citreus	
Bacillus cereus	
Site 2–Producing Well, Treated	Site 7–Composite Water at Clear Tank
Sphaerotilus natans	Desulfovibrio desulfuricans
Sarcina ureae	Sphaerotilus natans
Micrococcus flavus	Proteus vulgaris
Unidentified yeast	Proteus rettgeri
Site 3–Tank Battery No. 1	Site 8–Composite Water, Meter Block
Desulfovibrio desulfuricans	Desulfovibrio desulfuricans
Sphaerotilus natans	Alginomonas nonfermentans
Unidentified yeast	Achromobacter liquefaciens
Site 4–Fresh-Water Supply Well	Site 9–Backflow at Injection Well
Achromobacter xerosis	Desulfovibrio desulfuricans
Site 5–Composite Water Before Filter	Achromobacter liquefaciens
Desulfovibrio desulfuricans	Clostridium histolyticum
Sphaerotilus natans	

has never been a problem. The very low sulfate (SO_4) content of the brine may account for this observation.

Curve A of Fig. 14 shows that one of the lease gunbarrels produces a fair-quality brine. The composite brine is less filterable, but it is improved by the kerosene-wash treatment. Passage through the open pit and sand filter results in a very poor-quality water going to the injection well.

DISCUSSION

Table 9 shows that Desulfovibrio, Pseudomonas, Sphaerotilus and Bacillus were the most predominant genera found in the systems. These organisms have been found previously in injection systems, and they have been implicated in hydrogen-sulfide production, metal corrosion, slime formation, hydrocarbon oxidation and plugging problems.[1-4]

It is interesting to note that pseudomonads and sulfate-reducers (Desulfovibrio) were isolated from all systems. These organisms are often found together where microbiological problems are encountered in the petroleum industry. They have been repeatedly observed in waterflood systems, in the soil surrounding pipelines and in deteriorated petroleum products.[5-7]

Several investigators have suggested that there is an interrelationship between pseudomonads and

[1]References given at end of paper.

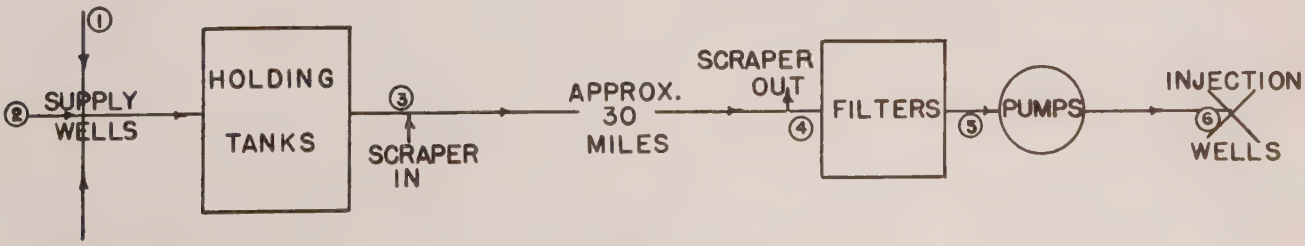

FIG. 11 – SYSTEM E.

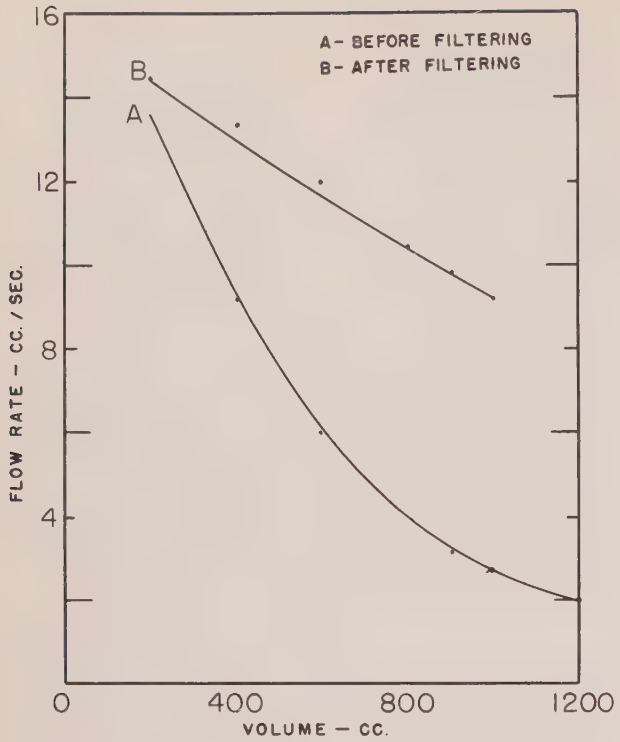

FIG. 12 – SYSTEM E – SUPPLY WATER.

sulfate-reducers [8,9]. The pseudomonads may oxidize the hydrocarbons and feed the sulfate-reducers, and the latter organisms may protect the pseudomonads from antimicrobial agents.

There is no relationship between the age of the system and the type of flora encountered. The predominant flora of the newer systems is not significicantly different from that of the older systems, and the number of different species isolated per sample cannot be related to age of the system.

No specific differences in the microbial flora of treated and untreated systems could be detected Fewer species (per sample) were isolated from the systems under treatment with antimicrobial agents,

TABLE 7 – MICROBIAL FLORA OF SYSTEM E

Site 1– Supply Wellhead (Treated Water)	
	Desulfovibrio desulfuricans
	Sphaerotilus natans
	Flavobacterium rhenanum
	Unidentified organism
Site 2– Supply Wellhead (Untreated Water)	
	Desulfovibrio desulfuricans
	Sphaerotilus natans
	Achromobacter liquefaciens
	Two unidentified organisms
Site 3– Composite Water, 18-In. Line Near Scraper Inlet	
	Desulfovibrio desulfuricans
	Flavobacterium lutescens
	Micrococcus rubens
	Scopulariopsis brevicaulis
Site 4– Composite Water Before Entering Filter Pump Station	
	Desulfovibrio desulfuricans
	Sphaerotilus natans
	Flavobacterium arborescens
	Unidentified organism
Site 5– Composite Water Below Filter Station	
	Desulfovibrio desulfuricans
	Flavobacterium arborescens
	Pseudomonas aeruginosa
	Bacillus coagulans
Site 6– Composite Water, Southeast Section of Field Near Injection Well	
	Desulfovibrio desulfuricans
	Sphaerotilus natans
	Unidentified organism

and one system receiving a corrosion inhibitor contains the greatest variety of flora.

The nature of the injection water may influence the variety of organisms isolated from the systems. The greatest number of different species (per sample) were found in two systems handling produced brine containing appreciable quantities of entrained oil.

The membrane and solids data are of limited value if they cannot be related to the ability of the formation in question to take water. A water is of poor quality if it plugs a 0.45-micron disc to a rate of less than 2 ml/sec; at 1,000-ml throughput at 20 psi, however, it may not produce plugging problems. This depends on the permeability and porosity of the formation and the surface pressure. More work of the type reported on cores in Systems A and C is needed.

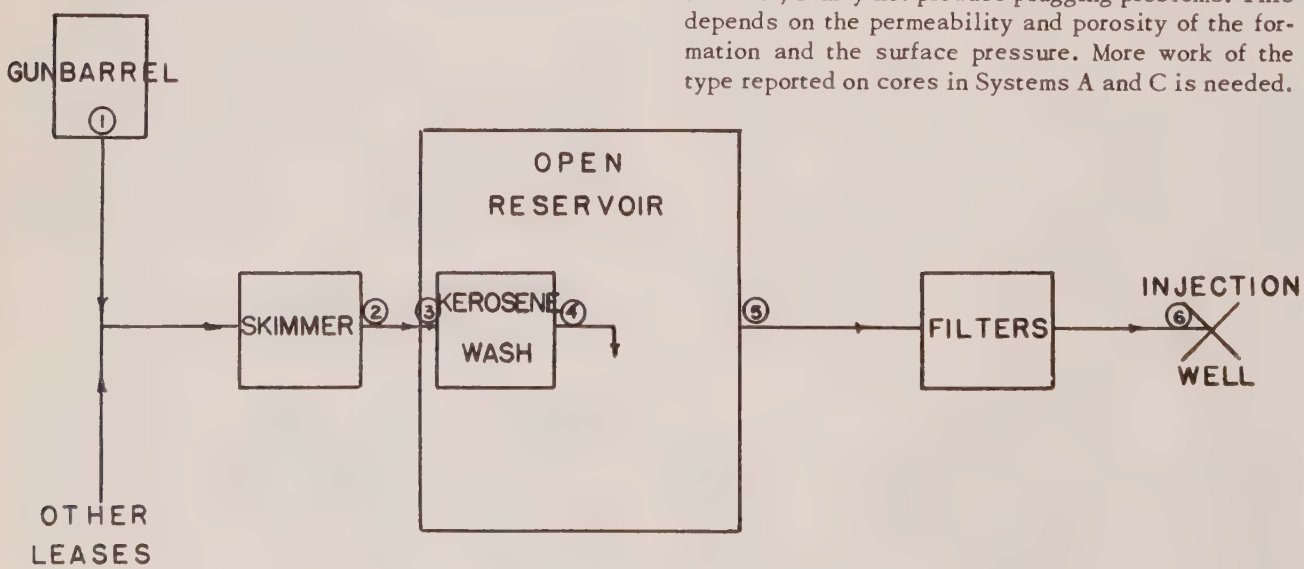

FIG. 13 – SYSTEM F.

With appropriate core flow data, it should be possible to predict much more accurately the anticipated injectivity into a formation of known capacity.

The problem of effective surface water handling continues to be largely unsolved in the systems studied. The membrane filter tests show that bed-type filters generally do not improve water quality. These filters remove considerable solids and prevent occasional slugs of oil from entering the formation, but they do not remove fine solids. In addition, the filters and other surface vessels are excellent environments for microbial growth. Diatomaceous earth filters remove solids more efficiently, but they usually represent a high initial investment and have a much lower flow rate per square foot of filter surface. Bare-screen type filters or strainers have application in installations where there are only traces of hydrocarbons.

There is a definite need for improvement in oilfield water-filtration equipment, but it may not be forthcoming until more definite water-quality standards are established by the operators.

TABLE 8 – MICROBIAL FLORA OF SYSTEM F

Site 1–Gunbarrel Produced Water, Bottom Level
- Pseudomonas putida
- Bacillus sphaericus
- Micrococcus lutea
- Desulfovibrio desulfuricans

Site 2–Produced Water At Oil-Skimmer Outlet
- Pseudomonas aeruginosa
- Arthrobacter simplex
- Arthrobacter ureafaciens
- Sarcina lutea
- Achromobacter iophagus
- Flavobacterium spp.
- Escherichia coli
- Desulfovibrio desulfuricans

Site 3–Kerosene-Wash Inlet
- Clostridium histolyticum
- Proteus inconstans
- Pseudomonas fluorescens
- Bacillus cereus
- Desulfovibrio desulfuricans

Site 4–Kerosene-Wash Outlet
- Clostridium tertium
- Pseudomonas fluorescens
- Desulfovibrio desulfuricans

Site 5–Open-Pit Outlet
- Pseudomonas fluorescens
- Pseudomonas putida
- Arthrobacter pascens
- Bacillus cereus
- Desulfovibrio desulfuricans

Site 6–Injection Well Below Filter
- Pseudomonas aeruginosa
- Pseudomonas boreopolis
- Bacillus megaterium
- Bacillus cereus
- Bacillus polymyxa
- Escherichia intermedia
- Proteus rettgeri
- Flavobacterium spp.
- Arthrobacter spp.
- Desulfovibrio desulfuricans

TABLE 9 – SUMMARY OF THE MICROBIAL FLORA OF ALL SYSTEMS

Genus	Per Cent Times Isolated From System						
	A	B	C	D	E	F	Average
Desulfovibrio spp.	81	42	83	66	100	100	78.6
Pseudomonas spp.	56	57	66	11	16	100	51.0
Sphaerotilus spp.	12	42	16	55	66	0	31.8
Bacillus spp.	31	0	66	11	16	66	31.6
Clostridium spp.	–	–	–	11	–	33	22.0
Micrococcus spp.	18	0	50	22	16	16	20.3
Flavobacterium spp.	0	14	0	0	66	33	18.8
Achromobacter spp.	18	0	16	33	16	16	16.5
Arthrobacter spp.	0	0	0	22	0	50	12.0
Sarcina spp.	18	0	16	11	0	16	10.1
Proteus spp.	12	0	0	11	0	33	9.3
Escherichia spp.	12	0	0	0	0	33	7.5
Alginomonas spp.	12	14	11	0	0	0	6.1
Aerobacter spp.	6	28	0	0	0	0	5.6
Yeast	0	0	0	33	0	0	5.5
Thiobacillus spp.	31	0	0	0	0	0	5.1
Cytophaga spp.	0	14	16	0	0	0	5.0
Scopulariopsis spp.	0	0	0	0	16	0	2.6
Penicillium spp.	0	0	16	0	0	0	2.6
Alcaligenes spp.	0	0	16	0	0	0	2.6
Aspergillis spp.	0	0	16	0	0	0	2.6
Corynebacterium spp.	6	0	16	0	0	0	3.6
Monilia spp.	0	0	16	0	0	0	2.6
Mucor spp.	0	0	16	0	0	0	2.6
Mycobacterium spp.	0	0	16	0	0	0	2.6
Rhizopus spp.	0	0	16	0	0	0	2.6
Leptothrix or Toxothrix spp.	12	0	0	0	0	0	2.0
Mycoplana spp.	12	0	0	0	0	0	2.0
Nocardia spp.	12	0	0	0	0	0	2.0
Vitreoscilla spp.	12	0	0	0	0	0	2.0
Beggiatoa spp.	6	0	0	0	0	0	1.0
Cellulomonas spp.	6	0	0	0	0	0	1.0

CONCLUSIONS

1. A wide variety of microbial flora is present in the six water-injection systems. Four genera constitute the major portion of the flora; however, other previously unreported organisms are also present.
2. Only one system appeared to be experiencing problems that may be due to micro-organisms.
3. Membrane data are of comparative interest but do not relate directly to well injectivity unless accompanied by core flow data on the formation in question.
4. Membrane filter tests on the systems show that bed filters do not usually improve water quality.

ACKNOWLEDGMENT

The authors express their appreciation to the management of Gulf Oil Corp., Domestic Production Dept., for permission to publish these data which were accumulated as a joint project between Gulf and the Biology Dept. of the U. of Houston. Thanks are also due W. L. McCann and L. C. Case of Gulf for their assistance in accumulating the membrane filter data.

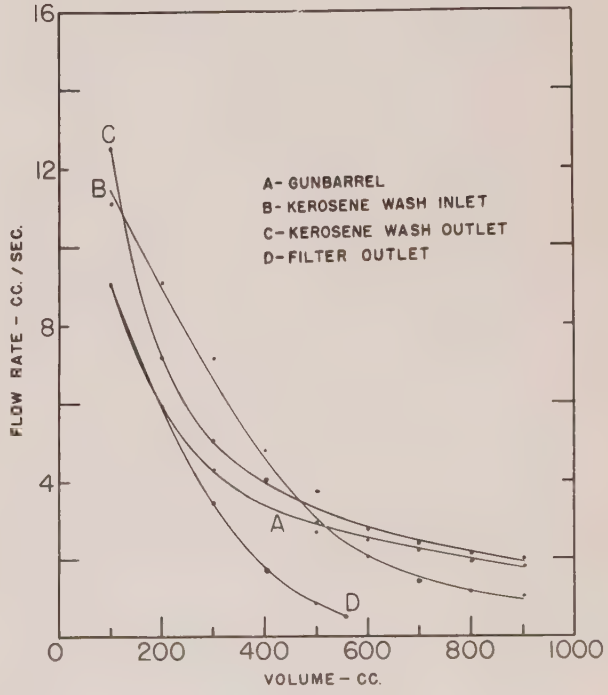

FIG. 14 – SYSTEM F.

REFERENCES

1. Plummer, F. B., Merkt, E. E., Power, H. H., Sawin, H. J. and Tapp, P.: "Effect of Certain Micro-Organisms on the Injection of Water into Sand", *Trans.*, AIME (1944) Vol. 155.
2. Allred, R. C.: "The Role of Microorganisms in Oil Field Water Flooding Operations—Bacterial Control on North Burbank Unit Water Flood, Osage County, Oklahoma", *Prod. Monthly* (1954) Vol. 18, 18.
3. Allen, F. H.: The Micro-Flora of Several West Texas Oil Field Brines and Their Relation to Corrosion", *Proc. and Trans.*, Texas Academy of Science (1944) Vol. 27, 219.
4. Lada, A.: "The Role of Microorganisms in Secondary Oil Recovery", *Proc.*, Chem. Specialties Manufacturers Assn. (1958) Vol. 55, 125.
5. Carlson, V. and Bennett, E. O.: "The Microbial Flora of Petroleum Flood Waters", *Bacteriological Proc.* (1960) 35.
6. Harris, J. O.: "Microbial Development in The Pipeline Ditch", Fifth Annual Appalachian Underground Corrosion Short Course, West Virginia U. (1960) 1.
7. Guynes, G. J. and Bennett, E. O.: "Bacterial Deterioration of Emulsion Oils. I. Relationship Between Aerobes and Sulfate-Reducing Bacteria in Deterioration", *Applied Microbiology* (1959) Vol. 7, 117.
8. Isenberg, D. L. and Bennett, E. O.: "Bacterial Deterioration of Emulsion Oils. II. Nature of the Relationship Between Aerobes and Sulfate-Reducing Bacteria", *Applied Microbiology* (1959) Vol. 7, 121.
9. Bennett, E. O. and Bauerle, R. H.: "The Sensitivities of Mixed Populations of Bacteria to Inhibitors", *Australian Jour. of Biol. Sciences* (1960) Vol. 13, 142.

***

Injection Rates—The Effect of Mobility Ratio, Area Swept, and Pattern

JOHN C. DEPPE
MEMBER AIME

THE ATLANTIC REFINING CO.
DALLAS, TEX.

ABSTRACT

A method is presented for calculating approximate injection rates in secondary recovery operations. The method can be applied to cases of unequal fluid mobilities, irregular well patterns and boundary patterns.

The steady-state pressure distributions for the four flood patterns reported by Muskat and for five additional patterns reveal that most of the difference in pressure between the injection and producing wells occurs in regions around the wells which can adequately be described as regions of radial flow. This leads to a method of calculating injectivity by approximating the flood pattern with radial flow elements (or a combination of radial- and linear-flow elements for some patterns such as the direct line drive). Irregular and boundary patterns can also be approximated by radial and linear elements.

Each of these elements can be described by radial- and linear-flow equations and the results combined as series flow resistances to give an approximate equation for the initial injection rate. The mobility ratio does not affect the initial rate; therefore, if the well pattern is one of those regular patterns for which theoretical rate equations have been derived for unity mobility ratio, the approximate initial rate equation can be improved by adjusting it to match the theoretical equation. The available theoretical rate equations are listed, including five new cases.

As the flood progresses, the injectivity changes because in general the flood front will divide the pattern into areas of different fluid mobilities. Simple shapes can be assumed for the flood front so that both areas can be divided into radial- and linear-flow elements.

Radial- and linear-flow equations are applied to these elements to account for the change in flow resistance behind the front.

To calculate injection rates after breakthrough, it is necessary to know the sweep efficiency at breakthrough. Areal sweep data are available in the literature for a number of patterns, and sufficiently accurate breakthrough sweep efficiency can be estimated from these data if it is not otherwise available.

Again, simple shapes for the flood front can be assumed after breakthrough, and injection rates can be calculated for the remainder of the flood. When areal sweep data are available, these data can be used to check the calculated injection rates after breakthrough.

Injection rates calculated by this approximate method compare favorably with available model data.

Original manuscript received in Society of Petroleum Engineers office March 11, 1960. Revised manuscript received Dec. 22, 1960. Paper presented at SPE Secondary Recovery Symposium, May 2-3, 1960, in Wichita Falls, Tex.

INTRODUCTION

When the fluid mobilities in the swept and unswept regions are equal, the injectivity will not change as the flood front advances; and for regular patterns it can be calculated by mathematical formulas.[1]

When the fluid mobilities in the swept and unswept regions are not equal, the injectivity will increase or decrease as the flood front advances. In this case, the injectivity has not been calculated by analytical means for any practical well pattern; and, furthermore, scale model[5] and analog[4,6] results have been published only for the five-spot pattern.

The main object of this paper is to present an approximate method for calculating injectivity for the case of unequal mobilities. The method can be applied to regular, irregular and boundary patterns.

Before the approximate method is discussed, the analytical formulas for equal mobilities will be summarized, and the analytical solution for radial flow with unequal mobilities will be used to show how the injectivity changes as the flood progresses.

EQUAL MOBILITIES, REGULAR PATTERNS

In a flooding operation the injectivity, the rate at which fluid can be injected per unit difference in pressure between injection and producing wells, depends on basic physical properties and, in addition, on three variables to be treated here—the area of the swept region, the fluid mobilities in the swept and unswept regions, and the well geometry (pattern,

[1]References given at end of paper.

spacing and wellbore radii).

When the fluid mobilities in the swept and unswept regions are the same, the injectivity of a given well array is independent of the first variable, the size and shape of the area swept, and is directly proportional to the single fluid mobility involved. The calculation of the injectivity thus reduces to the geometrical problem of treating the particular well pattern, well spacing and well radii.

For regular patterns, Muskat[1] has offered a method for finding analytical mathematical solutions and has worked out the formulas for special cases – the direct line drive, the staggered line drive, the five-spot and the seven-spot. Five more cases are presented here—the nine-spot with arbitrary corner-well to side-well producing ratios, a direct-line-drive boundary pattern, two five-spot boundary patterns and a nine-spot boundary pattern. These nine cases are listed in Table 1, which is thus a summary of the available results on injectivity of regular patterns with unity mobility ratio. The derivations of the five new cases are omitted because they follow the method of Muskat.

The five new cases can be used in the development of an approximate method for handling irregular patterns. The nine-spot will be used to show the extent of approximately radial flow even for large differences in corner-well and side-well rates. The four boundary cases can be used to aid in estimating the angle open to flow in irregular-boundary patterns.

RADIAL SYSTEM, UNEQUAL MOBILITIES

In each of the cases appearing in Table 1, the injectivity is independent of the area swept and depends on mobility only to the extent of simple proportionality. The only important variable is the

TABLE 1A – INJECTIVITIES FOR REGULAR PATTERNS WITH UNITY MOBILITY RATIO.

Solid line indicates symmetry pattern of infinite well network.
Dashed line indicates symmetry element of infinite well network.

Code: ○ Injection Wells, ● Producing Wells

DIRECT LINE DRIVE[1]

$$i = \frac{0.001538\,\lambda h \Delta P}{\log \frac{a}{r_w} + 0.682\,\frac{d}{a} - 0.798}$$

$$\frac{d}{a} \geq 1$$

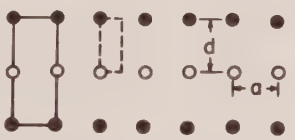

STAGGERED LINE DRIVE[1]

$$i = \frac{0.001538\,\lambda h \Delta P}{\log \frac{a}{r_w} + 0.682\,\frac{d}{a} - 0.798}$$

$$\frac{d}{a} \geq 1$$

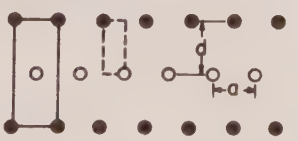

FIVE-SPOT[1]

$$i = \frac{0.001538\,\lambda h \Delta P}{\log \frac{d}{r_w} - 0.2688}$$

SEVEN-SPOT[1]

$$i = \frac{0.002051\,\lambda h \Delta P}{\log \frac{d}{r_w} - 0.2472}$$

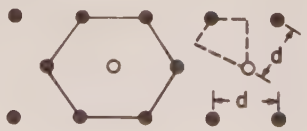

TABLE 1B – INJECTIVITIES FOR REGULAR PATTERNS WITH UNITY MOBILITY RATIO.

NINE-SPOT[2]

$$i = \frac{0.001538\,\lambda h \Delta P_{i,c}}{\frac{1+R}{2+R}\left[\log \frac{d}{r_w} - 0.1183\right]},$$

$$i = \frac{0.003076\,\lambda h \Delta P_{i,s}}{\frac{3+R}{2+R}\left[\log \frac{d}{r_w} - 0.1183\right] - \frac{0.301}{2+R}},$$

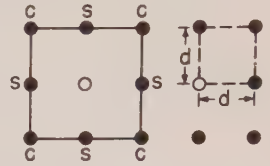

R = Ratio of producing rates of corner well (c) to side well (s),

$\Delta P_{i,c}$ = Difference in pressure between injection well and corner well (c),

$\Delta P_{i,s}$ = Difference in pressure between injection well and side well (s).

DIRECT LINE DRIVE BOUNDARY PATTERN[2]

$$i = \frac{0.003076\,\lambda h \Delta P_{i1',q1'}}{\frac{q_1 + 4q_1'}{q_1 + 2q_1'}\left[\log \frac{d}{r_w} + 0.166 + 0.400R\right] + \frac{1.368\,q_1(1+R)}{q_1 + 2q_1'}},$$

$$R = \frac{q_2}{q_1} = \frac{q_2'}{q_1'},$$

$\Delta P_{i1',q1'}$ = Difference in pressure between injection well i_1' and producing well q_1'.

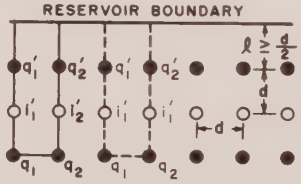

TABLE 1C – INJECTIVITIES FOR REGULAR PATTERNS WITH UNITY MOBILITY RATIO.

FIVE-SPOT BOUNDARY PATTERN[2]

$$i' = \frac{0.001538\,\lambda h \Delta P_{i',q'}}{\log \frac{d}{r_w} - 0.158 - 0.036\,\frac{q}{q'}},$$

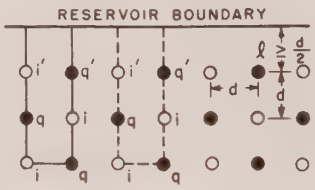

$\Delta P_{i',q'}$ = Difference in pressure between injection well i' and producing well q'

(Wells of outer row are alternating injection and producing wells.)

FIVE-SPOT BOUNDARY PATTERN[2]

$$i' = \frac{0.003076\,h\lambda\,(q_1 + q_2 + 2q_1' + 2q_2')\,\Delta P_{i',q_1'}}{2q_1'\left[(3+R)\{\log \frac{d}{r_w} + 0.815\} - 1.7216\right] + q_1(1+R)\{\log \frac{d}{r_w} - 0.098\}},$$

$$R = \frac{q_2}{q_1} = \frac{q_2'}{q_1'}$$

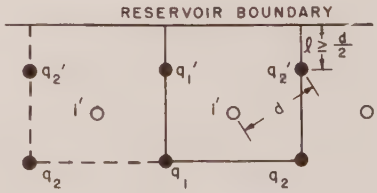

$\Delta P_{i',q'}$ = Difference in pressure between injection well i' and producing well q'.

(Wells of outer row are all producing wells.)

TABLE 1D – INJECTIVITIES FOR REGULAR PATTERNS WITH UNITY MOBILITY RATIO.

NINE-SPOT BOUNDARY PATTERN[2]

$$i' = \frac{0.003076\,\lambda h \Delta P_{i',s'}(2q_{s'} + 2q_{c'} + 3q_s + q_c)}{2q_{s'}\left[(2+R)\{\log\frac{d}{r_w} + 0.548\} - 1.49\right] + q_s\left[(3+R)\{\log\frac{d}{r_w} + 0.885\} - 0.577\right]},$$

$$i' = \frac{0.003076\,\lambda h \Delta P_{i',c'}(2q_{s'} + 2q_{c'} + 3q_s + q_c)}{2q_{s'}\left[(1+2R)\{\log\frac{d}{r_w} + 0.204\} + 0.362\right] + q_s\left[(3+R)\{\log\frac{d}{r_w} - 0.460\} + 0.124\right]},$$

$$R = \frac{q_c}{q_s} = \frac{q_{c'}}{q_{s'}}.$$

$\Delta P_{i',s'}$ = Difference in pressure between injection well i' and producing well s'.

$\Delta P_{i',c'}$ = Difference in pressure between injection well i' and producing well c'.

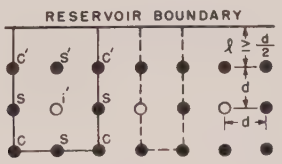

system geometry and, for these restricted conditions, analytical solutions are possible.

In this section another analytical solution is considered, this time made possible by geometrical simplicity. This solution illustrates the manner in which the other variables enter the problem, showing explicitly the variation of injectivity with position of the flood front for any mobility ratio.

Consider a radial system with a central injection well of radius r_w and imagine that fluid is produced uniformly from each point on a circle of radius r_e. Purely radial flow will result, and the front between injected and original fluids will be a circle whose radius will be called r_f. Simple radial-flow equations will apply in both the swept and unswept regions. In the unswept region, the production rate q will be given by

$$q = \frac{0.003076\,h\lambda_u(p_e - p_f)}{\log(r_e/r_f)}, \text{.....res B/D} \quad \ldots\ldots\ldots\ldots\ldots\ldots\ldots\ldots (1)$$

where h is the thickness (in feet), λ_u is the fluid mobility in the unswept region (millidarcies/centipoise), and p_e and p_f are the pressures at the outer boundary and at the front (psi). Similarly, in the swept region the injection rate i will be

$$i = \frac{0.003076\,h\lambda_s(p_f - p_w)}{\log(r_f/r_w)}, \text{....res B/D} \quad \ldots\ldots\ldots\ldots\ldots\ldots\ldots\ldots (2)$$

where λ_s is the mobility in the swept region and p_w is the pressure at the injection well.

For steady-state incompressible flow, the injection rate is equal to the production rate ($i = q$), and these two equations can be combined to eliminate p_f and give an expression for the injection rate in terms of the position of the front r_f which is valid for any mobility ratio.

$$i = \frac{0.003076\,h\lambda_u \Delta p}{\log\frac{r_e}{r_f} + \frac{1}{M}\log\frac{r_f}{r_w}}, \text{....res B/D} \quad \ldots\ldots\ldots\ldots\ldots\ldots\ldots\ldots (3)$$

where $\Delta p = p_e - p_w$ and $M = \lambda_s/\lambda_u$.

In most applications, it is convenient to express the variation in injectivity with the progress of the front in terms of the initial injectivity. In this case, that is, a relative injectivity I_r is defined as the ratio of the injectivity at any time (given by Eq. 3) to the initial injectivity (given by Eq. 3 with $r_f = r_w$).

$$I_r = \frac{\log\frac{r_e}{r_w}}{\log\frac{r_e}{r_f} + \frac{1}{M}\log\frac{r_f}{r_w}} \quad \ldots\ldots (3a)$$

The relative injectivity starts at unity when $r_f = r_w$ and ends at M when $r_f = r_e$ (corresponding to complete sweeping of the area and complete change of fluid mobility from λ_u to λ_s).

Curves calculated from this equation are plotted in Fig. 1 for mobility ratios of 5, 1 and 1/2, and for radius ratios r_e/r_w of 160 and 500. These ratios also appear in later comparisons of approximate

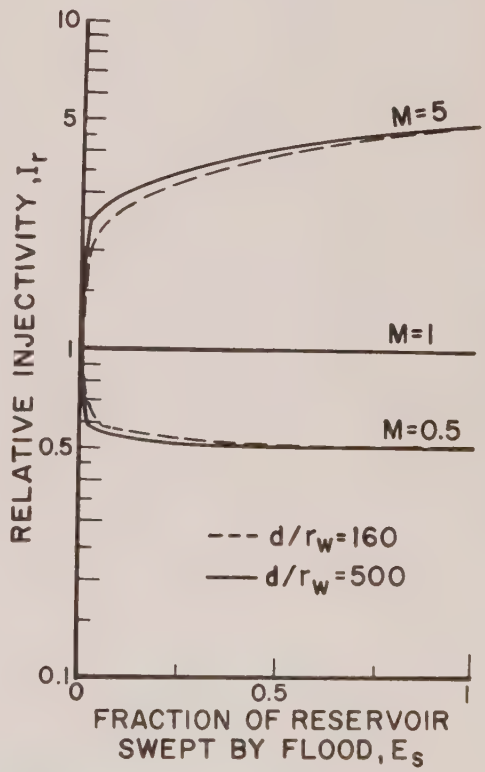

FIG. 1 – EFFECT OF MOBILITY RATIO ON RELATIVE INJECTIVITY DURING SWEEPOUT OF RADIAL FLOOD PATTERN. CALCULATED FROM EQ. 3a.

calculations and model results. The relative injectivity is plotted against fraction of area swept E_s, rather than against the position of the front. In this case, the relation is $r_f^2/r_e^2 = E_s$, for $r_w \ll r_e$.

The relative injectivity changes very rapidly during the early part of the flood, and then shows a gradual change during the remainder of the flood. This early, rapid change followed by a long period of slow change is typical of radial systems. In complex systems, the rapid change occurs while the flood front is moving out from the injection well in a near-radial manner.

In this simple example of complete radial flow, the period of gradual change extends to the end of the operation because breakthrough of the injected fluid into the producing circle occurs at complete sweep of the area. In a more complex system, with producing wells rather than the producing circle, a nose of injected fluid may reach a producing well before complete sweep of the area. After this breakthrough point, there again will be a more rapid change in the injectivity.

APPROXIMATE METHOD

REGULAR PATTERNS

Analytical equations of steady-state pressure distributions in complex flood patterns have been derived by Muskat[1] for the case of unity mobility ratio. An examination of these pressure distributions shows that most of the pressure difference between injection wells and producing wells occurs in areas around the wells which can adequately be described as regions of radial flow. In flood patterns as complex as the nine-spot pattern (see the Appendix), these regions of near-radial flow still occur around the injection and producing wells.

Porous, fluid-flow model studies[3] show that, even when the mobilities of the swept and unswept regions are different, the flood front moves out from the injection well in a radial manner during the early part of the flood.

These properties of flood systems suggest that the injectivity of any system can be simply and quickly approximated by dividing the pattern into segments of radial and linear flow and computing the total flow by combining the radial- and linear-flow equations which apply to individual segments.

In estimating injectivity by this approximate method, the volume of the pattern must be divided among the producing wells of the pattern. The volume assigned to each of the wells is then approximated by regions of radial and linear flow. The injectivity can be calculated by assuming that the flood front advances radially in the radial regions and linearly in the linear regions until breakthrough is approached. In this manner, injectivity prior to breakthrough of the swept region into a producing well can be estimated without the need of areal-sweepout data for the flood pattern.

As breakthrough is approached, a nose begins to grow at the flood front and streaks to the producing well during a short period of time when only a small part of the total-pattern volume is swept. As further production occurs, the finger opens up and the rate of flow from the swept region is nearly proportional to the angle this finger makes at the producing well. Prats, *et al*,[6] showed that it is the existing angle open to flow which controls the injectivity. For a given angle, the exact shape of the flood front after breakthrough has little effect on injectivity. If the flood front after breakthrough is approximated by a circle with a sector whose angle is proportional to the rate of flow from the swept region, the injectivity after breakthrough can be estimated from the same radial- and linear-flow segments used before breakthrough.

To illustrate this method of estimating injectivity, consider the five-spot pattern shown in Table 1. The symmetry element of the five-spot can be divided into two radial segments as shown in Fig. 2.

Applying the radial-flow equation to each of the two radial segments and combining gives for the *initial* injection rate

$$i = \frac{0.003076\, h\lambda_u (p_{wi} - p_{wp})}{\log \frac{r_{ei}}{r_{wi}} + \log \frac{r_{ep}}{r_{wp}}}, \text{..res B/D} \quad \ldots\ldots\ldots\ldots\ldots\ldots\ldots\ldots (4)$$

where h = net pay thickness, ft,
r_{ei} = radius of the radial segment around the injection well,
r_{ep} = radius of the radial segment around the producing well,
r_{wi} = effective wellbore radius of the injection well,
r_{wp} = effective wellbore radius of the producing well,
p_{wi} = pressure at injection well, psi,
p_{wp} = pressure at producing well, psi,
λ_u = mobility of the reservoir fluid, k_u/μ_u, md/cp, and
d = distance between injection and producing wells (see Fig. 2).

When the effective wellbore radii are equal and $r_{ei} = r_{ep}$, Eq. 4 becomes

$$i = \frac{0.001538\, h\lambda_u (p_{wi} - p_{wp})}{\log \frac{d}{r_w} - 0.249}, \text{..res B/D} \quad \ldots\ldots\ldots\ldots\ldots\ldots\ldots\ldots (5)$$

FIG. 2—DIVISION OF FIVE-SPOT PATTERN AREA INTO APPROXIMATING RADIAL-FLOW SECTORS FOR DERIVING APPROXIMATE EQUATION OF INJECTIVITY.

which agrees very closely with the exact equation for the five-spot pattern given in Table 1 (the only difference is between the constants 0.249 and 0.269). A still closer agreement could be obtained by approximating the pattern area with a linear-flow segment between two radial-flow segments.

On the assumption that the flood front moves out in a true radial manner, the injectivity while the front is between the injection well and the radial boundary r_{ei} is

$$R_6 = \frac{1}{M}\log\frac{r_f}{r_{wi}} + \log\frac{r_{ei}}{r_f} + \log\frac{r_{ep}}{r_{wp}}$$

$$\frac{i}{p_{wi}-p_{wp}} = \frac{0.003076\,h\lambda_u}{R_6}, \quad \text{res B/D-psi} \quad \ldots\ldots\ldots\ldots\ldots\ldots\ldots\ldots (6)$$

where M = mobility ratio λ_s/λ_u, and the relation between the radius of the flood front r_f, and the fraction of total area covered by the swept region E_s, is

$$r_f = d\sqrt{\frac{2E_s}{\pi}}, \quad \text{ft} \quad \ldots\ldots\ldots (7)$$

When the flood front is between the boundary r_{ep} and the producing well prior to breakthrough, the injectivity is

$$R_8 = \frac{1}{M}\log\frac{r_{ei}}{r_{wi}} + \frac{1}{M}\log\frac{r_{ep}}{r_f} + \log\frac{r_f}{r_{wp}}$$

$$\frac{i}{p_{wi}-p_{wp}} = \frac{0.003076\,h\lambda_u}{R_8}, \quad \text{res B/D-psi} \quad \ldots\ldots\ldots\ldots\ldots\ldots\ldots\ldots (8)$$

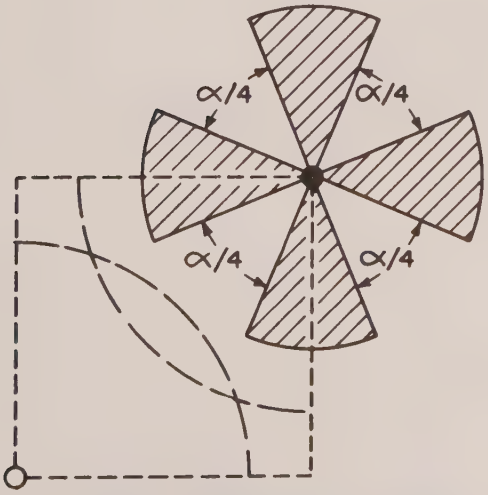

FIG. 3—ASSUMED SHAPE OF FLOOD FRONT AFTER BREAKTHROUGH OF THE SWEPT REGION INTO A PRODUCING WELL OF A FIVE-SPOT PATTERN.

where $r_f = d\sqrt{\frac{2(1-E_s)}{\pi}}$, ft . . . . (9)

After breakthrough, the flood front will be assumed to have the shape shown in Fig. 3.

The flow rate from each region is proportional to the mobility and to the angle open to flow from that region. This leads to the relation

$$\frac{\alpha}{2\pi} = \frac{f}{f+M(1-f)}, \quad \ldots\ldots (10)$$

where f is the fraction of the producing stream from the swept region, and α is the angle (in radians) open to flow from the swept region.

With values of α from Eq. 10 and data of areal sweep vs fractional flow from the swept region, the injectivity after breakthrough is

$$R_{11} = \log\frac{r_{ei}}{r_{wi}} + \log\frac{r_{ep}}{r_f} + \frac{2\pi f}{\alpha}\log\frac{r_f}{r_{wp}}$$

$$\frac{i}{p_{wi}-p_{wp}} = \frac{0.003076\,h\lambda_s}{R_{11}}, \quad \text{res B/D-psi} \quad \ldots\ldots (11)$$

where $r_f = d\sqrt{\frac{2(1-E_s)}{\pi(1-\frac{\alpha}{2\pi})}}$, ft . . . (12)

When areal sweep vs fractional flow from the swept region is not known, an approximation of injectivity after breakthrough can be obtained by assuming the radius r_f to be constant and equal to the value obtained from Eq. 9 or Eq. 12 using the breakthrough value of areal sweep E_s. With a fixed radius r_f, the angle α determined by Eq. 10 also establishes areal sweep as a function of fractional flow from the swept region. Patterns for which areal sweep data are available show no significant difference between the injectivity calculated using areal sweep data and the injectivity calculated by fixing the radius r_f at the breakthrough value of areal sweep.

The approximate relative injectivities for the five-spot pattern calculated from Eqs. 4, 6, 8, 10 and 11 are shown in Figs. 4 and 5 for comparison with experimental data reported by Aronofsky, *et al*,[4] and by Caudle, *et al*.[5] The agreement is good except for very low mobility ratios where the effects of by-passing, fingering, and saturation gradient across the front become more pronounced. For these calculations, the value of r_{ei} was taken equal to r_{ep} for mobility ratios for which breakthrough occurs at areal sweeps of more than 50 per cent of the total area. For mobility ratios in which breakthrough occurred prior to 50 per cent areal sweep, the value of r_{ei} was calculated from the per cent areal sweep

at breakthrough as $r_{ei} = d\sqrt{\frac{2E_s}{\pi}}$, and the value of r_{ep} was calculated as $r_{ep} = \sqrt{\frac{2d^2}{\pi} - r_{ei}^2}$.

IRREGULAR WELL SPACING OR UNEQUAL PRODUCING RATES

The injectivity of a flood pattern with irregular well spacing or unequal producing rates can be estimated in a manner similar to that described for the five-spot by distributing the drainage area of the pattern among the producing wells. The area assigned to each of the wells is then approximated by radial- and linear-flow segments, and the progress of the front is traced through these segments.

Dividing the area among the producing wells first involves dividing the total area into isolated or separate elements (corresponding to the division of the five-spot into symmetrical elements) and, then, dividing this isolated element among the producing wells in the element.

One method of dividing the total area into isolated elements for separate treatment is to use as dividing lines the lines joining all the producing wells which are supplied by one particular injection well. Fig. 6 shows an isolated element obtained in this way. The centrally located injection well supplies four producing wells. Lines are drawn connecting each of these producing wells with its two neighbors, and these lines form an irregular polygon which is taken as an isolated element of the total flood area.

To distribute this isolated element among the producing wells, a point is located on the line joining each pair of neighboring wells. This point divides the line between the wells in proportion to the total producing rates of the wells. In Fig. 6, for example, suppose that the total well rates have the following ratios: $q_1/q_2 = 1$, $q_2/q_3 = 5/4$, $q_3/q_4 = 8/9$, and $q_4/q_1 = 9/10$. Then four points are located as shown in Fig. 6, dividing the four sides of the irregular polygon into these ratios. Points are located at one-half the distance from Well 1 toward Well 2, five-ninths the distance from Well 2 toward Well 3, and so on.

Each of these individual well areas is now divided into radial segments, or possibly into radial and linear segments. The radius of the segment at the injection well, r_{ei}, can usually be taken as half the distance to the nearest producing well. A value of r_{ep} can then be calculated for each well so that the sum of the areas of the two radial sectors for each well is equal to the area assigned to that well.

The flood front is then traced through these sectors in a manner similar to that described for the five-spot. In the flood pattern of Fig. 6, for example, when the flood front is between the injection well and the radial boundary, r_{ei} (and prior to break-

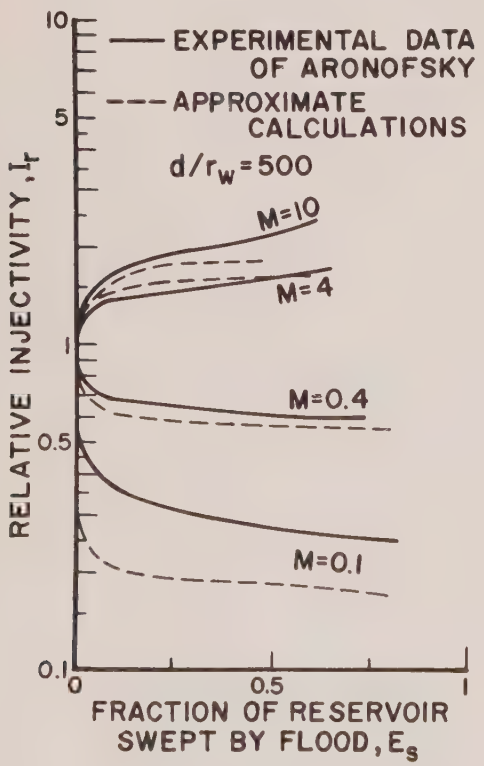

FIG. 4 — COMPARISON OF APPROXIMATE CALCULATIONS WITH EXPERIMENTAL INJECTIVITY OF ARONOFSKY FOR FIVE-SPOT PRODUCING PATTERNS.

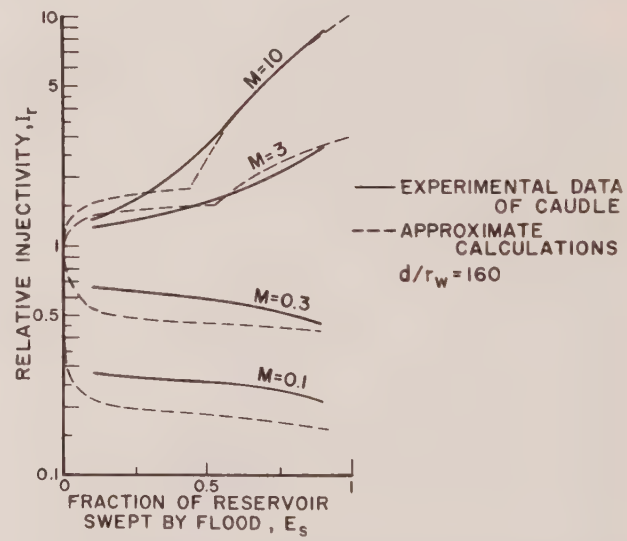

FIG. 5 — COMPARISON OF APPROXIMATE CALCULATIONS WITH EXPERIMENTAL INJECTIVITIES OF CAUDLE FOR FIVE-SPOT PRODUCING PATTERN.

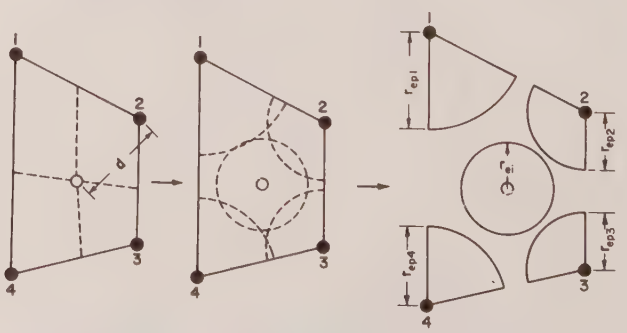

FIG. 6 — DIVISION OF IRREGULAR PATTERN INTO APPROXIMATING RADIAL-FLOW SECTORS FOR ESTIMATING INJECTIVITY.

through), the injectivity of the pattern referred to the difference in pressure between the injection well and producing Well 1) is

$$R_{13} = \frac{1}{M}\log\frac{r_f}{r_{wi}} + \log\frac{r_{ei}}{r_f} + \frac{q_1}{i}\log\frac{r_{ep1}}{r_{wp1}}$$

$$\frac{i}{p_i - p_{p1}} = \frac{0.003076\,h\lambda_u}{R_{13}}, \text{ res B/D-psi} \quad \ldots\ldots\ldots\ldots\ldots\ldots\ldots\ldots (13)$$

Referred to the difference in pressure between the injection well and producing Well j, the injectivity of the pattern during the same period of the flood is

$$R_{14} = \frac{1}{M}\log\frac{r_f}{r_{wi}} + \log\frac{r_{ei}}{r_f} + \frac{q_j}{i}\log\frac{r_{epj}}{r_{wpj}}$$

$$\frac{i}{p_i - p_{pj}} = \frac{0.003076\,h\lambda_u}{R_{14}}, \text{ res B/D-psi} \quad \ldots\ldots\ldots\ldots\ldots\ldots\ldots\ldots (14)$$

where

$i = \frac{1}{2\pi}\sum_{j=1}^{n}\theta_j q_j$, reservoir B/D,

n = number of producing wells in the pattern element ($n = 4$ in this example),

θ_j = vertex angle of the pattern boundary at producing Well j, radians,

q_j = total producing rate of Well j, reservoir B/D,

$r_f = \sqrt{\frac{E_s A_t}{\pi}}$, ft, and

A_t = total area of the isolated pattern element, sq ft.

When the flood front is between r_{ep} and the producing well, the injectivity is

$$R_{15} = \frac{1}{M}\log\frac{r_{ei}}{r_{wi}} + \frac{q_j}{i}\left[\frac{1}{M}\log\frac{r_{epj}}{r_{fj}} + \log\frac{r_{fj}}{r_{wpj}}\right]$$

$$\frac{i}{p_i - p_{pj}} = \frac{0.003076\,h\lambda_u}{R_{15}}, \text{ res B/D-psi} \quad \ldots\ldots\ldots\ldots\ldots\ldots\ldots\ldots (15)$$

where

$$r_{fj} = \sqrt{r_{epj}^2 - \frac{2q_j}{i}\left[E_s A_T - \pi r_{ei}^2\right]}, \text{ ft} \quad \ldots\ldots\ldots\ldots\ldots\ldots\ldots\ldots (16)$$

After breakthrough occurs, the injectivity is

$$R_{17} = \log\frac{r_{ei}}{r_{wi}} + \frac{q_j}{i}\left[\log\frac{r_{epj}}{r_{fj}} + \frac{2\pi f_j}{a_j}\log\frac{r_{fj}}{r_{wpj}}\right]$$

$$\frac{i}{p_i - p_{pj}} = \frac{0.003076\,h\lambda_s}{R_{17}}, \text{ res B/D-psi} \quad \ldots\ldots\ldots\ldots\ldots\ldots\ldots\ldots (17)$$

where the radius r_{fj} after breakthrough can be assumed to be constant and equal to the value obtained from Eq. 16 using the breakthrough value of areal sweep, E_s. The angle open to flow from the swept region, a_j, can be calculated with Eq. 10.

The isolated element of a producing pattern can also be distributed among the producing wells by using the differences in pressure between the injection well and the producing wells as the criteria for assigning the radial-flow sectors to each producing well. Eq. 14 can be written for each producing well and the resulting equations solved for the appropriate values of r_{epj} according to the differences in pressure desired between the injection well and the producing wells. One method of doing this is by a simple iterative scheme. Eq. 14 can be written for each producing well and the results combined to give the total injection rate for the pattern as

$$i = \frac{\frac{0.003076\,h\lambda_u}{2\pi}\sum_{j=1}^{J}\frac{\theta_j(p_i - p_{pj})}{\log\frac{r_{epj}}{r_{wj}}}}{1 + \frac{\log\frac{r_{ei}}{r_{wi}}}{2\pi}\sum_{j=1}^{J}\frac{\theta_j}{\log\frac{r_{epj}}{r_{wj}}}}, \text{ res B/D} \quad \ldots\ldots\ldots\ldots\ldots\ldots\ldots\ldots (14a)$$

We begin by guessing the ratio of producing rates for all neighboring producing wells and calculating a set of r_{epj}'s as before. From Eq. 14a an approximate total injectivity is calculated. Substituting this injectivity into Eq. 14 gives an approximate producing rate for each producing well. The ratios of these producing rates can be used to re-divide the pattern and calculate a better approximation of the total injection rate. The initial guess is based only on the ratio of producing rates for neighboring producing wells and not on absolute rates. When the theoretical equations or model data for initial injectivities are available for unity mobility ratio, the actual injection rate (rather than the rate calculated from Eq. 14a) is used with Eq. 14 to re-divide the pattern area.

For comparison with experimental model data, the injectivity of a nine-spot pattern was calculated for an adverse mobility ratio of 10:1, and corner wells and side wells producing at equal rates. Although the nine-spot pattern generally is not considered to be an irregular pattern, it represents a system in which the producing wells are not all equidistant from the injection well. The injectivity was calculated from Eqs. 10, 14, 15, 16 and 17 by approximating the pattern area using two different criteria for determining the radii of the radial-flow sectors—(1) producing rates of the producing wells, and (2) the initial injectivities from the theoretical equations in Table 1.

The approximate calculations for the nine-spot are shown in Fig. 7, together with porous-model results[7] for the same conditions. The calculated injectivities show very close agreement with the model data. The disagreement at early areal sweep could be accounted for by wellbore damage in construction of the model. The slight disagreement in the two sets of model data is probably due to inhomogeneity in the model and extent of wellbore damage at the two corner wells of the model shown in Fig. 7.

BOUNDARY PATTERNS

To estimate the injectivities of boundary patterns, the effect of flow from outside the normal well network must be taken into account. A study of the boundary patterns listed in Table 1 showed that the effect of the position of the boundary on the injectivity of the outer row of wells approaches a limiting value when the boundary is more than one-half the well spacing beyond the outer row of wells, and it has almost no effect on wells two or more rows in from the boundary. All wells except the outer row thus can be treated as interior wells, and an estimate of injectivity in boundary patterns can be made by calculating an effective drainage angle θ for the outer row of wells and then tracing the front advance as was done for the regular five-spot pattern. For example, if the five-spot pattern with all wells producing at the same rate were a boundary pattern as shown in Fig. 8, the injectivity of this boundary pattern could be estimated as follows.

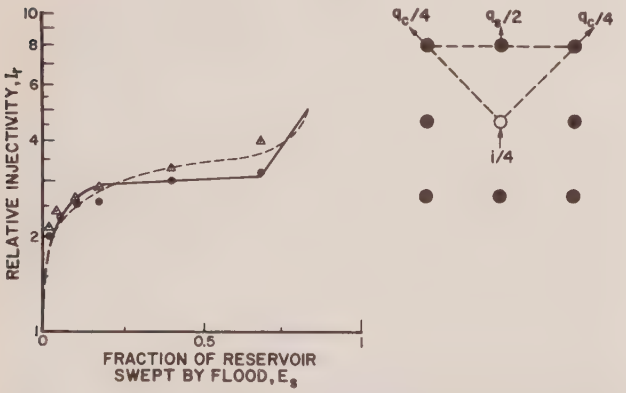

FIG. 7—COMPARISON FOR ESTIMATED INJECTIVITY WITH EXPERIMENTAL DATA BY CAUDLE FOR A NINE-SPOT PRODUCING PATTERN ($M=10$, $R=1$, AND $d/r_w=160$). CIRCLES AND TRIANGLES ARE EXPERIMENTAL INJECTIVITIES FOR THE TWO CORNER WELLS USED IN THE MODEL. DASHED LINE EQUALS CALCULATED INJECTIVITY WITH PATTERN AREA DIVIDED TO MAKE APPROXIMATE EQUATION MATCH THEORETICAL EQUATION AT $E_s=0$. SOLID LINE EQUALS CALCULATED INJECTIVITY WITH PATTERN AREA DIVIDED IN PROPORTION TO PRODUCING RATES.

The area of this pattern inside the well network can be approximated by radial-flow segments identical to those of Fig. 2. With these values of r_{ei} and r_{ep}, the assumed symmetry pattern is then represented by the radial sectors shown in Fig. 9.

Describing the flow in each sector by the radial-flow equation and combining gives an initial injectivity for this assumed-boundary symmetry element of

$$R_{18} = \log \frac{r_{ei}}{r_{wi}} + \frac{\pi q_b}{i\theta} \log \frac{r_{ep}}{r_{wp}}$$

$$\frac{i}{p_{wi} - p_{wpb}} = \frac{0.003076\, h\lambda_u}{R_{18}},$$

res B/D-psi

. . . . . (18)

where q_b = producing rate at the boundary well, reservoir B/D,

i = total injection rate of pattern, reservoir B/D, and

θ = effective drainage angle of boundary well, radians.

With all wells producing at the same rate, $q_b = (2/3)i$. With the injectivity by the approximate Eq. 18 set equal to the injectivity by the analytical equation in Table 1, the effective drainage angle θ can be calculated. For $d/r_w = 160$, the effective drainage angle θ in Fig. 9 is 2.05 radians. This effective drainage angle can be used in the radial flow equation, and the injectivity of this boundary pattern then can be estimated by tracing the front

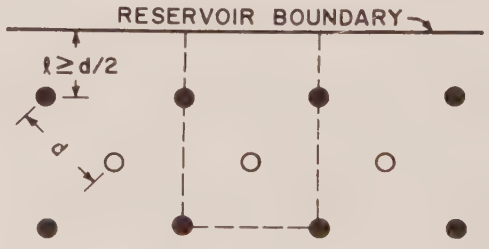

FIG. 8—BOUNDARY FIVE-SPOT PATTERN. DASHED LINE INDICATES ASSUMED SYMMETRY PATTERN.

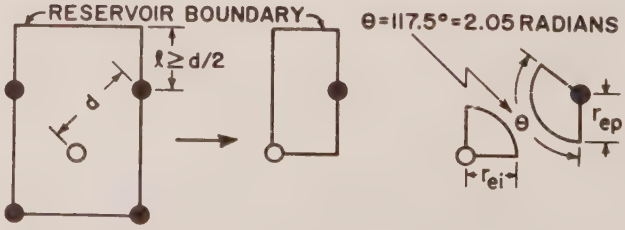

FIG. 9—DIVISION OF BOUNDARY FIVE-SPOT PATTERN INTO APPROXIMATING RADIAL SECTORS FOR ESTIMATING INJECTIVITY.

through these radial sectors in the same manner as was done for the interior five-spot pattern.

Based on the difference in pressure between the injection well and producing Well j, the injectivity of the five-spot boundary pattern of Fig. 9, prior to breakthrough and while the flood front is between the injection well and the boundary r_{ei}, is

$$R_{19} = \frac{1}{M}\log\frac{r_f}{r_{wi}} + \log\frac{r_{ei}}{r_f} + \frac{2\pi q_j}{i\theta_{jt}}\log\frac{r_{epj}}{r_{wj}}$$

$$\frac{i}{p_{wi}-p_{wj}} = \frac{0.003076\,h\lambda_u}{R_{19}}, \quad \text{res B/D-psi} \qquad \ldots\ldots\ldots\ldots\ldots\ldots\ldots\ldots (19)$$

where $r_f = \sqrt{\frac{E_s A}{\pi}}$, ft,

A = total area within the normal well network, sq ft, and

θ_{jt} = total angle open to radial flow at Well j, radians.

While the flood front is between the boundary r_{epj} and the producing Well j, the injectivity is

$$R_{20} = \frac{1}{M}\log\frac{r_{ei}}{r_{wi}} + \frac{2\pi q_j}{i\theta_{jt}}\left[\frac{1}{M}\log\frac{r_{epj}}{r_{fj}} + \log\frac{r_{fj}}{r_{wpj}}\right]$$

$$\frac{i}{p_{wi}-p_{wj}} = \frac{0.003076\,h\lambda_u}{R_{20}}, \quad \text{res B/D-psi} \qquad \ldots\ldots\ldots\ldots\ldots\ldots\ldots\ldots (20)$$

where

$$r_{fj} = \sqrt{r_{epj}^2 - \frac{2q_j}{i\theta_{jt}}\left[E_s A - \pi r_{ei}^2\right]}, \text{ ft} \qquad \ldots\ldots\ldots\ldots\ldots\ldots\ldots\ldots (21)$$

After breakthrough occurs, the injectivity is

$$R_{22} = \log\frac{r_{ei}}{r_{wi}} + \frac{2\pi q_j}{i\theta_{jt}}\left[\log\frac{r_{epj}}{r_{fj}} + \frac{f_j\theta_{jt}}{\alpha_j}\log\frac{r_{fj}}{r_{wj}}\right]$$

$$\frac{i}{p_{wi}-p_{wj}} = \frac{0.003076\,h\lambda_s}{R_{22}}, \text{ res B/D-psi} \qquad \ldots\ldots\ldots\ldots\ldots\ldots\ldots\ldots (22)$$

where

$$\frac{f_j\theta_{jt}}{\alpha_j} = f_j + M(1-f_j), \qquad \ldots\ldots (23)$$

and r_{fj} is assumed to remain constant after breakthrough and can be calculated from Eq. 21 using the value of E_s at the time breakthrough occurs at Well j.

Eqs. 19 to 23 are the general equations for estimating injectivity in complex well networks and reduce to the identical equations of the interior flood patterns given in previous sections for the five-spot infinite array and for the irregular interior patterns.

A comparison of the approximate injectivity of the boundary five-spot pattern of Fig. 9 with the injectivity of the interior five-spot pattern of Fig. 2 is shown in Fig. 10 for a mobility ratio of 10.

CONCLUSIONS

When the mobility of the fluid injected into a reservoir is different from the mobility of the reservoir fluid, the injectivity changes rapidly during the early part of the operation – and then only gradually until breakthrough occurs. Since most of the change in injectivity occurs during the early part of the flood while the flood front is nearly radial, reliable estimates of injectivity can be obtained by approximating the flood pattern with radial- and linear-flow segments.

Injectivity can be estimated after breakthrough by assuming that the flood front can be approximated by simple shapes and that the angle the swept region makes at the producing well is proportional to the rate of flow from the swept region. An estimate of breakthrough sweep efficiency is required to calculate injectivity after breakthrough.

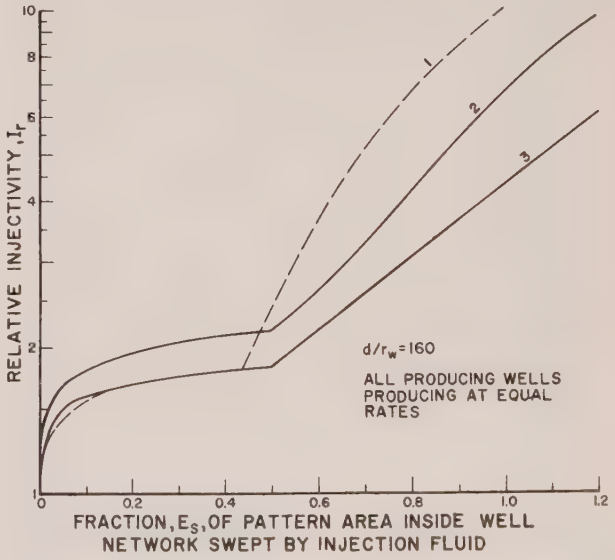

FIG. 10–COMPARISON OF RELATIVE INJECTIVITY OF (1) FIVE-SPOT INFINITE ARRAY WITH RELATIVE INJECTIVITY OF THE FIVE-SPOT BOUNDARY ARRAY OF FIG. 9 BASED ON (2) PRESSURE DIFFERENCE BETWEEN INJECTION WELL AND INTERIOR WELL AND (3) PRESSURE DIFFERENCE BETWEEN INJECTION WELL AND BOUNDARY WELL.

The approximate equations of injectivity can be applied to irregular interior patterns and to boundary patterns.

NOMENCLATURE

d = distance between injection and producing wells, ft
f = fraction of producing stream which is from the swept region
h = net pay thickness, ft
i = injection rate, reservoir B/D
k = specific permeability, md
p = pressure, psi
q = producing rate, reservoir B/D
r = radius, ft
E_s = fraction of reservoir swept by injection fluid
M = ratio of mobilities of swept region to unswept region
R = ratio of producing rates of corner well to side well for nine-spot producing pattern
α = angle open to flow from the swept region, radians
θ = vertex angle of pattern boundary at producing well, radians
λ = fluid mobility (k/μ), md/cp
μ = fluid viscosity, cp

SUBSCRIPTS

b = boundary well
e = external boundary
ei = external boundary of radial sector around injection well
ep = external boundary of radial sector around producing well
f = flood front
j = Well j
s = swept region
u = unswept region
w = well
wi = injection well
wp = producing well

ACKNOWLEDGMENT

The author wishes to express his appreciation to Francis Collins, The Atlantic Refining Co., for his assistance and suggestions in preparation of this paper.

REFERENCES

1. Muskat, M.: *Physical Principles of Oil Production*, McGraw-Hill Book Company, Inc., N. Y. (1949) 650.
2. Previously unpublished. A special case of the nine-spot equation was reported by Krutter, H.: "Nine-Spot Flooding Program", *Oil and Gas Jour.* (Aug., 1939) Vol. 38, 50.
3. Dyes, A. B., Caudle, B. H. and Erickson, R. A.: "Oil Production After Breakthrough — As Influenced by Mobility Ratio", *Trans.*, AIME (1954) Vol. 201, 81; also, original data on which this paper was based.
4. Aronofsky, J. S. and Ramey, H. J., Jr.: "Mobility Ratio — Its Influence on Injection or Production Histories in Five-Spot Water Flood", *Trans.*, AIME (1956) Vol. 207, 205.
5. Caudle, B. H. and Witte, M. D.: "Production Potential Changes During Sweep-Out in a Five-Spot System", *Trans.*, AIME (1959) Vol. 216, 446.
6. Prats, M., Matthews, C. S., Jewett, R. L. and Baker, J. D.: "Prediction of Injection Rate and Production History for Multifluid Five-Spot Floods", *Trans.*, AIME (1959) Vol. 216, 98.
7. Preliminary results from a model program now being

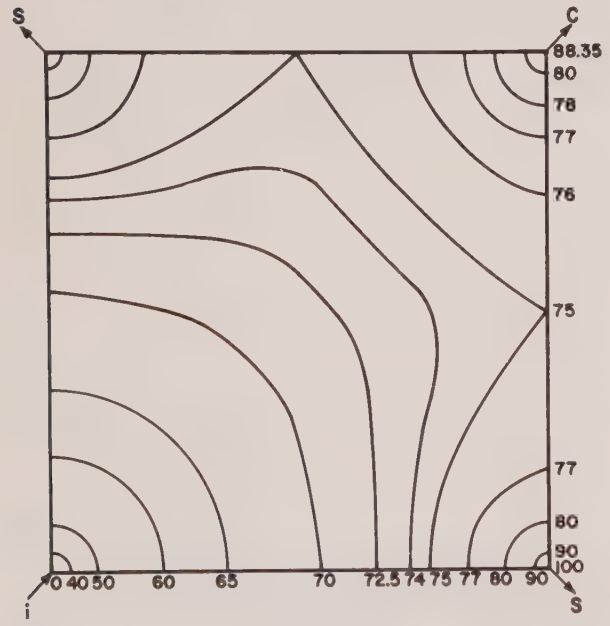

FIG. 11a—STEADY-STATE PRESSURE DISTRIBUTION IN NINE-SPOT PATTERN FOR UNITY MOBILITY RATIO AND CORNER-TO-SIDE PRODUCING RATIO = 0.5. (PER CENT OF TOTAL DIFFERENCE IN PRESSURE BETWEEN INJECTION WELL AND SIDE PRODUCING WELL.) d/r_w = 1,000.

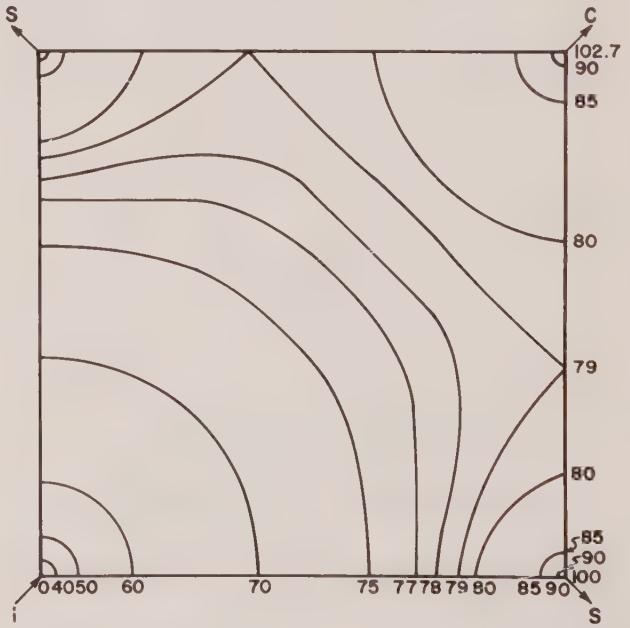

FIG. 11b—STEADY-STATE PRESSURE DISTRIBUTION IN NINE-SPOT PATTERN FOR UNITY MOBILITY RATIO AND CORNER-TO-SIDE PRODUCING RATIO = 1. (PER CENT OF TOTAL DIFFERENCE IN PRESSURE BETWEEN INJECTION WELL AND SIDE PRODUCING WELL.) d/r_w = 1,000.

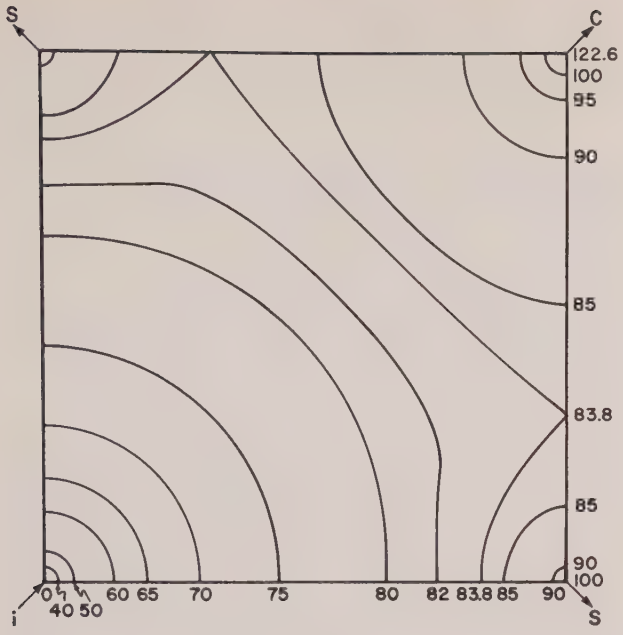

FIG. 11c—STEADY-STATE PRESSURE DISTRIBUTION IN NINE-SPOT PATTERN FOR UNITY MOBILITY RATIO AND CORNER-TO-SIDE PRODUCING RATIO = 2. (PER CENT OF TOTAL DIFFERENCE IN PRESSURE BETWEEN INJECTION WELL AND SIDE WELL.) $d/r_w = 1{,}000$.

carried on at the laboratory of The Atlantic Refining Co., Dallas.

8. Muskat, M.: "The Theory of Nine-Spot Flooding Networks", *Prod. Monthly* (March, 1948) 14.

APPENDIX

STEADY-STATE PRESSURE DISTRIBUTION IN THE NINE-SPOT PATTERN

The steady-state pressure distribution in the nine-spot pattern for unity mobility ratio was calculated after the method of Muskat[1,8] for ratios of corner-well to side-well production of 1/2, 1 and 2. For the infinite well array shown in Fig. 7, the steady-state pressure distribution is given by

$$H_k = \cosh \frac{\pi(y - kd)}{d} + \cos \frac{\pi x}{d}$$

$$H_k' = \cosh \frac{\pi(y - kd)}{d} - \cos \frac{\pi x}{d}$$

$$\frac{4\pi\lambda h p(x,y)}{i} = \frac{1}{2+R} \sum_{m=-\infty}^{m=+\infty} \ln \frac{H_{2m} H'_{2m+1}}{(H'_{2m})^2} + \frac{R}{2+R} \sum_{m=-\infty}^{m=+\infty} \ln \frac{H_{2m+1}}{H'_{2m}}, \quad \ldots\ldots\ldots\ldots\ldots\ldots\ldots\ldots (24)$$

where R = ratio of corner-well to side-well producing rates.

The calculated pressure distributions are shown in Fig. 11 as percentages of the total pressure difference between the injection well and the side well.

The singular point (discontinuity of pressure gradient) between the side well and the corner well was obtained by cross-plotting of the calculated pressure distribution and is only approximate. However, the large extent of the near-radial pressure distribution is readily apparent. In the case of R = 1 in Fig. 11, for example, more than 95 per cent of the pressure difference between the injection well and the corner well could adequately be described as radial. ***

Analysis of Gas-Cap or Dissolved-Gas Drive Reservoirs

H. L. STONE
A. O. GARDER, JR.
MEMBERS AIME

HUMBLE OIL & REFINING CO.
HOUSTON, TEX.

ABSTRACT

A numerical method of solving the partial differential equations which describe the one-dimensional displacement of oil by gas has been presented. Possible extension of the method to treat multidimensional flow is discussed, and the limitations of this extension are indicated. Using this method, it is possible to allow for the existence of a gas cap, the presence of any number of gas-injection or oil-production wells and the evolution of dissolved gas from the oil. It is also possible to allow for variation in the cross-sectional area, elevation, porosity and permeability of the reservoir. The influence of relative permeability and the force of gravity in the direction of flow upon the displacement is considered.

The influence of capillary pressure upon the flow and the effect of gravity in the direction perpendicular to flow are neglected. The physical properties of the fluids are considered to be functions of pressure only, and equilibrium between contiguous phases is assumed.

The numerical calculations can be readily carried out by the use of a digital computer. Several example analyses have been performed using the IBM 704 computer, and about one-third of an hour of computing time was required per case. Reservoir behavior predicted by use of this numerical method was compared to data obtained by other methods for three cases — complete pressure maintenance, dissolved-gas drive and gas-cap drive. The independent solutions to these problems were obtained by analytical solution, laboratory experiment and field data, respectively. Agreement of the numerical solution with data from these sources was good; this agreement establishes the convergence and accuracy of the numerical method.

INTRODUCTION

Most petroleum reservoirs can be produced by any one of several alternative programs. When a reservoir is produced by primary methods, production economics can be influenced by controlling the number and location of wells and the flow rate of each well. An even greater influence may be achieved by augmenting the recovery of oil obtainable by primary methods. This can be accomplished by injection of fluids such as water, natural or enriched gas or a bank of light liquid hydrocarbons. Selection of the most desirable operation requires a means of predicting the reservoir behavior which will result from each of the several alternative programs. The purpose of this paper is to present a mathematical method for predicting the behavior of reservoirs produced by gas-cap drive, dissolved-gas drive or pressure maintenance by gas injection.

The method described herein takes cognizance of phase changes caused by a decline or an increase (due to gas injection) in reservoir pressure, of the presence of a gas cap and of the effect of gravity on the flow of gas and oil. Relative permeability relationships are used to define the flow properties of the rock. Allowance is made for variation in cross-sectional area, elevation, permeability and porosity of the reservoir. Both the influence of capillary pressure upon the flow and pressure gradients in the gas cap are neglected. Whenever a liquid phase and a gas phase are in contact, they are assumed to be in equilibrium. The physical properties of the fluids are considered to be functions of pressure only. Therefore, if the method is to be used to predict the effects of a gas-injection program, mixtures of the injected gas and formation crude should have the same physical properties as mixtures of formation gas and crude.

The equations to be presented in this paper apply only to a one-dimensional case; therefore, they neglect the influence of gravity in the direction transverse to the flow. As is well known, this gravitational influence may lead to overriding of oil by gas. Consequently, this procedure as presented is most applicable to long, thin reservoirs for which gravity overriding is not important. On the other hand, the equations presented can be generalized to treat multidimensional flow and, hence, to consider gravity overriding, if desired. A word of caution on two points is advisable here, however. First, the authors have not demonstrated the accuracy of the numerical technique for multidimensional flow. Second, and more important, capillary pressure will often be of importance in multidimensional problems. Obviously, in such cases a generalization of the

Original manuscript received in Society of Petroleum Engineers office July 21, 1960. Revised manuscript received Jan. 3, 1961. Paper presented at 35th Annual Fall meeting of SPE, Oct. 2-5, 1961, in Denver.

present method would be inadequate.

These limitations of the present method are less restrictive than limitations on previously published methods of predicting gas-drive reservoir behavior.[1-9] For example, the method of Ref. 1 is restricted by the assumption that pressures and saturations are uniform throughout the reservoir, and the method of Ref. 2 is limited to dissolved-gas-drive reservoirs involving a single well. Ref. 3 through 8 are suitable only for complete pressure maintenance by gas injection. Ref. 9 presents a method capable of handling pressure decline, but the mathematical relations used are not rigorous, the method of computation is tedious and it does not provide a way of calculating pressure distribution throughout the reservoir.

The method presented in the paper differs from that of Ref. 9 by being based on solution of a more rigorous mathematical statement of the problem. This statement consists of two simultaneous partial differential equations and suitable boundary conditions. These equations are solved by a systematic approximation technique which has been adapted to solution by electronic computation. This relieves the engineer of most of the labor involved and makes feasible the completion of a reservoir analysis in approximately 20 minutes on an IBM 704 computer. The calculations provide complete pressure and saturation profiles at frequent time intervals, as well as gas-oil ratios and cumulative production data for each well.

Derivation of the differential equations stating the problem is presented first. This is followed by transformation of the equations into finite-difference equations. Finally, the convergence and accuracy of the method is evaluated by comparing computed results with results obtained from analytical solution, laboratory experiment and field observation.

THE DIFFERENTIAL SYSTEM

The fundamental equations used to define the reservoir behavior are the equations of continuity for gas and stock-tank oil and Darcy's law of flow for each phase. The continuity equation for gas allows for the presence of a distributed sink for fluid production of strength V_o for oil and V_g for gas. This equation is

$$-\frac{\partial}{\partial x}(u_g A\delta + u_o A B_o R_s) - V_o R_s - V_g = \phi A \frac{\partial}{\partial t}(S_g\delta + S_o B_o R_s) \quad \ldots\ldots\ldots\ldots \quad (1)$$

where δ = the standard cubic feet of gas per cubic feet of gas at reservoir conditions,
V_g = the rate of free-gas production per unit length of the reservoir, and
V_o = the rate of oil production per unit length of the reservoir.

Eq. 2 is the continuity equation for oil. In this expression, the volatility of the stock-tank oil has been neglected.

$$-\frac{\partial}{\partial x}(u_o A B_o) - V_o = \phi A \frac{\partial}{\partial t}(S_o B_o) \quad \ldots \quad (2)$$

Darcy's law of flow for each phase,

$$u_o = -\frac{kk_{ro}}{\mu_o}\left(\frac{\partial P}{\partial x} + \rho_o g \frac{\partial z}{\partial x}\right), \quad \ldots\ldots \quad (3)$$

and

$$u_g = -\frac{kk_{rg}}{\mu_g}\left(\frac{\partial P}{\partial x} + \rho_g g \frac{\partial z}{\partial x}\right), \quad \ldots\ldots \quad (4)$$

where z = the elevation of the reservoir above an arbitrary datum plane, and the equation,

$$S_o = 1 - S_{wc} - S_g, \quad \ldots\ldots\ldots\ldots \quad (5)$$

complete the statement of the differential problem except for boundary and initial conditions.

Eqs. 3, 4 and 5 may be used to eliminate u_o, u_g and S_o from Eqs. 1 and 2. This would result in two differential equations containing two dependent variables, S_g and P. These two equations may be solved simultaneously to obtain the desired solution. Instead of taking this approach, it is desirable first to combine Eqs. 1 and 2 to eliminate time derivatives of saturation and, then, to use the new equation and Eqs. 2, 3, 4 and 5 to define the problem. The advantage of doing this is that the new equation can be approximated by a difference equation having only pressures at an advanced time level as unknowns. This gives rise to a set of equations which can be solved to obtain a complete pressure distribution at the new time. These new pressures can be used in a difference approximation of Eq. 2 to yield saturations at the new time. Thus, the solution of the two equations is divided into two steps, solution of a pressure equation and solution of a saturation equation. The necessity of solving for pressures and saturations simultaneously is avoided by this procedure.

The desired combination of Eqs. 1 and 2 is effected by multiplying Eq. 1 by B_o, multiplying Eq. 2 by $(\delta - B_o R_s)$, replacing S_o by $(1 - S_{wc} - S_g)$, expanding the product derivatives on the right-hand side of the equation and replacing terms of the form

$$\frac{\partial C(P)}{\partial t} \text{ by } \frac{dC(P)}{dP}\frac{\partial P}{\partial t} = C'\frac{\partial P}{\partial t}.$$

Here C or $C(P)$ indicates a function of pressure only, and C' denotes $\frac{dC}{dP}$. Adding the resulting equations gives

[1] References given at end of paper.

$$- B_o \frac{\partial}{\partial x}(u_g A\delta + u_o A B_o R_s) - (\delta - B_o R_s) \cdot$$

$$\frac{\partial}{\partial x}(u_o A B_o) - B_o(V_o R_s + V_g) - (\delta - B_o R_s)V_o$$

$$= \phi A\{S_g[B_o(\delta - B_o R_s)' - B_o'(\delta - B_o R_s)] +$$

$$[1 - S_{wc}][B_o(B_o R_s)' + B_o'(\delta - B_o R_s)]\} \frac{\partial P}{\partial t} =$$

$$\phi A[D(P, S_g)] \frac{\partial P}{\partial t} , \quad \ldots\ldots\ldots\ldots\ldots (6)$$

where the function, $D(P, S_g)$ is defined by the last equality.

Next, u_o, u_g and S_o are eliminated from Eqs. 6 and 2 by use of Eqs. 3, 4 and 5, which results in the following equations.

$$B_o \frac{\partial}{\partial x}\left[\left(\frac{kk_{rg}A\delta}{\mu_g}\right)\left(\frac{\partial P}{\partial x} + \rho_g g \frac{\partial z}{\partial x}\right)\right. \cdot\cdot$$

$$\left.\left(\frac{kk_{ro}AB_o R_s}{\mu_o}\right)\left(\frac{\partial P}{\partial x} + \rho_c g \frac{\partial z}{\partial x}\right)\right] + (\delta - B_o R_s)$$

$$\cdot \frac{\partial}{\partial x}\left[\left(\frac{kk_{ro}AB_o}{\mu_o}\right)\left(\frac{\partial P}{\partial x} + \rho_o g \frac{\partial z}{\partial x}\right)\right] -$$

$$B_o(V_o R_s + V_g) - (\delta - B_o R_s)V_o = \phi AD \frac{\partial P}{\partial t}$$

$$\ldots\ldots\ldots\ldots\ldots\ldots\ldots\ldots (7)$$

and

$$\frac{\partial}{\partial x}\left[\left(\frac{kk_{ro}AB_o}{\mu_o}\right)\left(\frac{\partial P}{\partial x} + \rho_o g \frac{\partial z}{\partial a}\right)\right] - V_o =$$

$$\phi A\left[(1 - S_{wc} - S_g)B_o' \frac{\partial P}{\partial t} - B_o \frac{\partial S}{\partial t}\right] \quad \ldots (8)$$

All that is needed in addition to Eqs. 7 and 8 to define the reservoir behavior is a statement of suitable boundary and initial conditions.

The initial conditions in most gas-cap-drive situations are that the gas saturation throughout the reservoir is zero and that the pressure at the original gas-oil contact is specified. Since the reservoir fluids are initially at rest, the pressure gradient at any point in the reservoir is equal to the density of the oil times the elevation gradient at that point. This completely defines the initial pressure distribution in the reservoir. Stated symbolically, these initial conditions are

$$S_g = 0 \text{ for } 0 \leq x \leq X , \; t = 0 ;$$

$$P = P_o \text{ for } x = 0 , \; t = 0 ;$$

and

$$\frac{\partial P(x)}{\partial x} = - \rho_o(x) g \frac{\partial z}{\partial x} \text{ for } 0 \leq x \leq X , \; t = 0$$

where X = total length of the reservoir, and
P_o = initial gas-cap pressure.

The boundary condition at the original gas-oil contact is that the rate of gas entry at that point, i_g, is determined by the expansion of the gas-cap gas which has a volume V. The amount of gas in the gas cap at any pressure is $V\,\delta\,(P)$, and the rate at which gas enters the oil zone is $-V\,\delta' \frac{\partial P}{\partial t} = i_g$.

At any production-well location, it is desirable to specify the rate of stock-tank oil production q_o provided this rate does not exceed the productivity of the well. This oil rate is related to the gas-production rate through the relative permeabilities and fluid properties existing at that time at the location in question. The quantitative relationship is derived from material balances on the differential element Δx of the reservoir which contains a production well. A material balance on the oil phase yields

$$B_o A(u_o)_1 = q_o + B_o A(u_o)_2 .$$

where subscript 1 indicates conditions at $x - \Delta x/2$ and subscript 2 conditions at $x + \Delta x/2$.

The gas-phase material balance yields

$$\delta A(u_g)_1 = q_g + \delta A(u_g)_2 .$$

Darcy's law of flow is used to eliminate $(u_g)_1$, $(u_g)_2$, $(u_o)_1$ and $(u_o)_2$ from these equations; then the resulting equations are combined to eliminate

$$\left(\frac{\partial P}{\partial x}\right)_1 - \left(\frac{\partial P}{\partial x}\right)_2 .$$

Assuming $\left(\frac{\partial z}{\partial x}\right)_1 = \left(\frac{\partial z}{\partial x}\right)_2$, the result is

$$q_g = q_o \frac{\delta}{B_o} \frac{k_{rg}}{k_{ro}} \frac{\mu_o}{\mu_g} \quad \ldots\ldots\ldots\ldots (9)$$

If the well is located at the end of a reservoir, then $(u_o)_2 = (u_g)_2 = 0$. In this case, Eq. 10 is the result of this analysis and should be used in place of Eq. 9.

$$\frac{q_g}{q_o} = \frac{\delta k_{rg}\mu_o}{B_o k_{ro}\mu_g} + (\rho_o - \rho_g)\frac{kk_{rg}A\delta g}{q_o \mu_g} \frac{\partial z}{\partial x} . \quad (10)$$

Note that in both Eqs. 9 and 10 q_g represents only gas produced as free gas. A quantity of dissolved gas equal to $q_o R_s$ is also produced with the oil.

If the productivity of the well is less than the desired production rate, the boundary condition becomes one of constant pressure at the well. Since the one-dimensional analysis presented in this paper neglects the pressure drop due to radial flow around the well, the constant pressure employed in the calculations should be greater than the actual bottom-hole pressure to be maintained in the well. The difference in these two pressures should equal the pressure drop caused by radial flow into

the well and can be estimated from radial flow formulas.

At the reservoir boundaries, there must be no flow of either gas or oil. This is accomplished by setting $u_o = u_g = 0$.

At injection wells (if there are any), the rate of gas injection may be arbitrarily specified. The gas saturation at gas-injection wells and at the gas-cap contact is set equal to that saturation existing when the rock contains residual oil.

Specifying the boundary conditions completes the statement of the problem in differential form. The next step is to write suitable difference approximations to Eqs. 7 and 8.

THE DIFFERENCE SYSTEM

There exist many difference equations which under casual investigation appear to be valid analogues of Eqs. 7 and 8. Some of these provide adequate approximation, while others do not. Since there is no rigorous analysis to demonstrate that the solution of these analogues converges to that of the differential system, the final test must be experimental computing. Analysis of similar, but simpler, systems serves as a useful guide in selecting equations to be tested.

The set of difference approximations to Eqs. 7 and 8 presented in this section have been subjected to extensive testing, and the results are discussed in the following section. This testing has shown the set to be suitable for the prediction of reservoir behavior for gas-cap drive, dissolved-gas drive and pressure maintenance by gas injection. However, no claim is made that this is the only set of equations which will satisfactorily approximate Eqs. 7 and 8.

In writing finite-difference approximations to Eqs. 7 and 8, the distance axis is divided into J increments Δx in length, and the time scale is divided into increments Δt in length. The following definitions are used.

$x_j = j\Delta x$,
$X = J\Delta x$ = total length of reservoir,
$t_n = n\Delta t$, and
$P_{jn} = P(x_j, t_n)$, etc.

Derivatives of the form,

$$\frac{\partial}{\partial x}\left[C(P)E(S_g)\frac{\partial P}{\partial x}\right]$$

to be evaluated at x_j and t_{n+1} are replaced by terms of the form,

$$\frac{C_{j+\frac{1}{2},n}E_{j,n}\dfrac{(P_{j+1,n+1}-P_{j,n+1})}{\Delta x} - C_{j-\frac{1}{2},n}E_{j-1,n}\dfrac{(P_{j,n+1}-P_{j-1,n+1})}{\Delta x}}{\Delta x}$$

in arriving at difference approximations of Eqs. 7 and 8.

Attention is called to the fact that the coefficient E, which is a function of saturation only, is evaluated at the upstream end of the interval. That is, if the pressure difference involves points j and $j+1$, E is evaluated at point j. This is the upstream end of the interval since in the problem being considered flow is from point j to $j+1$. If E were evaluated at the midpoint of the interval, like $C\ (P)$, then the numerical procedure would not give solutions which converge to a true solution of the differential system. If the equations presented herein are generalized to treat multidimensional flow, care must be taken to evaluate the function E at the upstream end of the interval whenever it appears in approximations of distance derivatives. Otherwise, the extension of

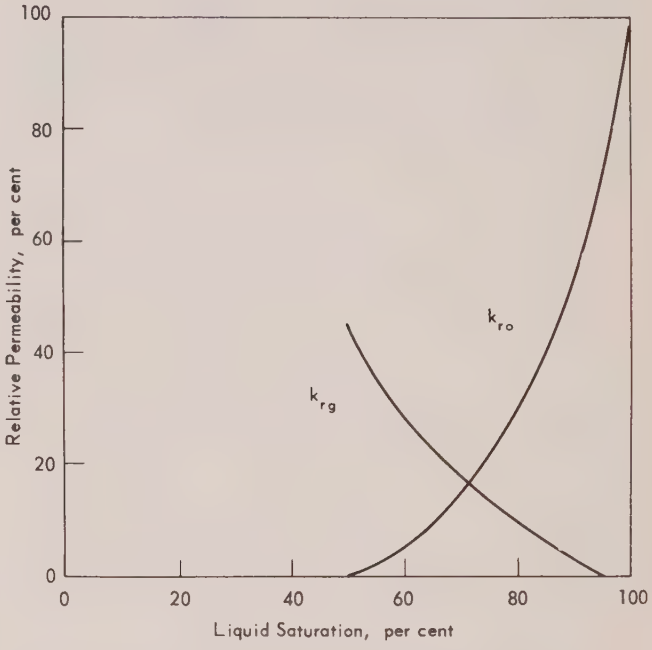

FIG. 1 – RELATIVE PERMEABILITY-SATURATION RELATION, PRESSURE MAINTENANCE.

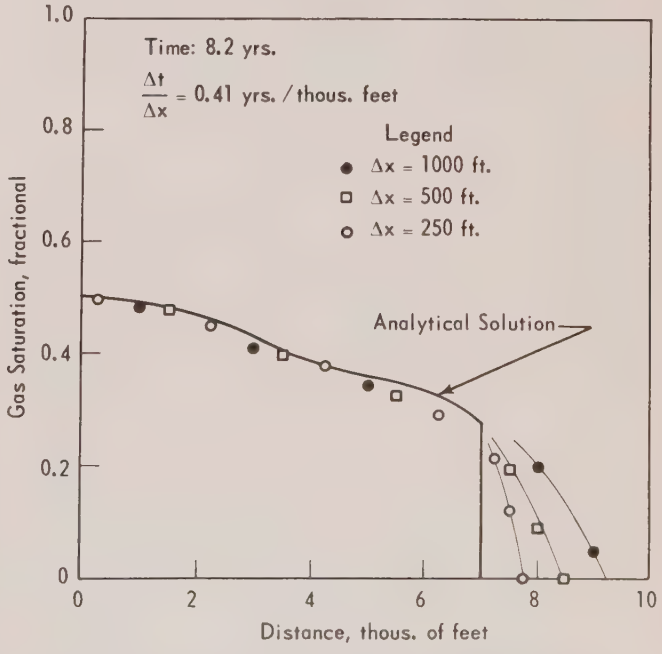

FIG. 2 – SATURATION PROFILE, PRESSURE MAINTENANCE.

the procedure to two or three dimensions is perfectly straight-forward.

Time derivatives such as $\left(\frac{\partial P}{\partial t}\right)_j$ are approximated as $\frac{P_{j,\,n+1} - P_{j,\,n}}{\Delta t}$. Production wells are approximated as distributed sinks of strength $\left(\frac{q_o}{\Delta x}\right)_{j,n}$ for oil and $\frac{q_o}{\Delta x}$ for gas. Injection wells are treated as sources of strength $\frac{i_g}{\Delta x}$. The inclusion of these source and sink terms satisfies the boundary conditions of specified rates at the wells.

In writing the difference equations, subscripts were dropped from B_o, R_s and S_g for simplicity. The approximation to Eq. 7 is implicit in pressures and is given by

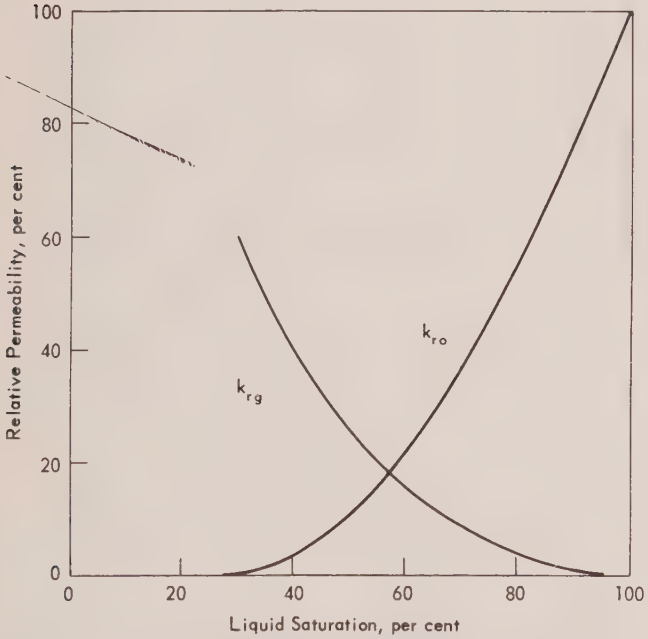

FIG. 3 — RELATIVE PERMEABILITY-SATURATION RELATION, DISSOLVED-GAS DRIVE.

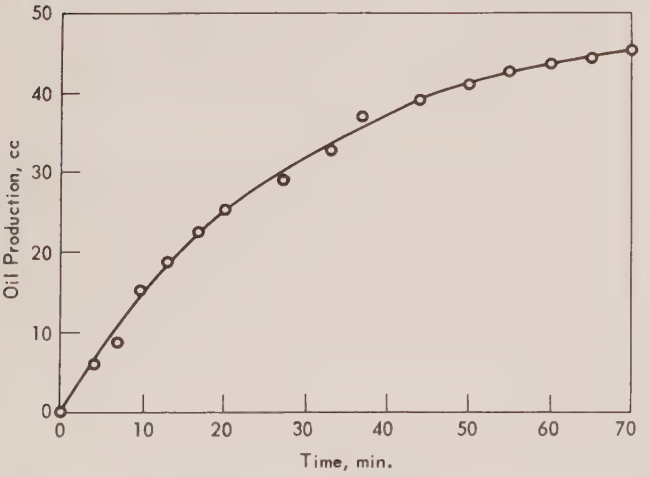

FIG. 4 — EXPERIMENTAL PRODUCTION HISTORY, USED AS BOUNDARY CONDITION TO COMPUTE BEHAVIOR OF DISSOLVED-GAS DRIVE.

$$
\begin{aligned}
&B_{j,n}\left\{(kk_{rg})_{j,n}\left(\frac{A\delta}{\mu_g}\right)_{j+\frac{1}{2},n}\right.\\
&\left[\frac{(P_{j+1,n+1}-P_{j,n+1})+(\rho_g g)_{j+\frac{1}{2},n}(z_{j+1}-z_j)}{(\Delta x)^2}\right]\\
&-(kk_{rg})_{j-1,n}\left(\frac{A\delta}{\mu_g}\right)_{j-\frac{1}{2},n}\\
&\left[\frac{(P_{j,n+1}-P_{j-1,n+1})+(\rho_g g)_{j-\frac{1}{2},n}(z_j-z_{j-1})}{(\Delta x)^2}\right]\\
&+(kk_{ro})_{j,n}\left(\frac{ABR}{\mu_o}\right)_{j+\frac{1}{2},n}\\
&\left[\frac{(P_{j+1,n+1}-P_{j,n+1})+(\rho_o g)_{j+\frac{1}{2},n}(z_{j+1}-z_j)}{(\Delta x)^2}\right]\\
&-(kk_{ro})_{j-1,n}\left(\frac{ABR}{\mu_o}\right)_{j-\frac{1}{2},n}\\
&\left.\left[\frac{(P_{j,n+1}-P_{j-1,n+1})+(\rho_o g)_{j-\frac{1}{2},n}(z_j-z_{j-1})}{(\Delta x)^2}\right]\right\}\\
&+(\delta-BR)_{j,n}\left\{(kk_{ro})_{j,n}\left(\frac{AB}{\mu_o}\right)_{j+\frac{1}{2},n}\right.\\
&\left[\frac{(P_{j+1,n+1}-P_{j,n+1})+(\rho_o g)_{j+\frac{1}{2},n}(z_{j+1}-z_j)}{(\Delta x)^2}\right]\\
&-(kk_{ro})_{j-1,n}\left(\frac{AB}{\mu_o}\right)_{j-\frac{1}{2},n}\\
&\left.\left[\frac{(P_{j,n+1}-P_{j-1,n+1})+(\rho_o g)_{j-\frac{1}{2},n}(z_j-z_{j-1})}{(\Delta x)^2}\right]\right\}\\
&+B_{j,n}\left(\frac{i_g}{\Delta x}\right)_{j,n}-B_{j,n}\left(\frac{q_oR+q_g}{\Delta x}\right)_{j,n}\\
&-(\delta-BR)_{j,n}\left(\frac{q_o}{\Delta x}\right)_{j,n}\\
&=(\phi A)_j D_{j,n}\frac{(P_{j,n+1}-P_{j,n})}{\Delta t}\quad\ldots\ldots\quad(11)
\end{aligned}
$$

where i_g, q_o, $q_g \geq 0$.

There are $(J + 1)$ grid points in the reservoir corresponding to $j = 0, 1, 2 \ldots J\text{-}1, J$. The reservoir may be divided into segments of length Δx, centered about grid points. Eq. 11 as applied to the point j represents a combination of the two material-balance equations for the segment centered on j. At the end points $j = 0$ and $j = J$, there exists only one-half of a segment; hence, the right-hand side of Eq. 11 should be divided by two when applying it to these points.

Maintaining the proper boundary conditions at the points $j = 0$ and $j = J$ also requires that $k_j = -1$ and k_J be set equal to zero in Eq. 11. The resulting form of the equation places a restriction on the pressure such that the rate of flow at these points is equal to that specified by the i_g, q_o, and q_g terms of Eq. 11. If no production or injection occurs at $j=J$, then $i_g = q_o = q_g = 0$ and the no-flow boundary conditions of $u_o = u_g = 0$ are satisfied. The boundary condition at the gas-cap contact is satisfied by setting i_g at $j = 0$ equal to

$$- V\delta' \frac{(P_{o,n+1} - P_{o,n})}{\Delta t}.$$

As stated earlier examination of Eq. 11 reveals that, if conditions of saturation and pressure are known at time level t_n, the only unknowns in Eq. 11 are pressures at time t_{n+1}. The equation may, therefore, be put in the form,

$$a_j P_{j-1,n+1} + b_j P_{j,n+1} + c_j P_{j+1,n+1} = d_j$$

where a_j, b_j, c_j and d_j are known constants for each point j. The equation for each point involves three unknowns, except for the first ($j=0$) and last ($j = J$) equations which contain only two. There are, altogether, J equations and J unknowns. This system of linear simultaneous equations can readily be solved by a method described in the literature[10] to yield a set of pressures at the new time level t_{n+1}. These new pressures are used in a difference approximation of Eq. 8 to find the new saturation at t_{n+1}. The approximation used for Eq. 8 is

$$(kk_{ro})_{j,n}\left(\frac{AB}{\mu_o}\right)_{j+\frac{1}{2},n}\left[\frac{(P_{j+1,n+1}-P_{j,n+1}) + (\rho_o g)_{j+\frac{1}{2},n}(z_{j+1}-z_j)}{(\Delta x)^2}\right]$$
$$- (kk_{ro})_{j-1,n}\left(\frac{AB}{\mu_o}\right)_{j-\frac{1}{2},n}\left[\frac{(P_{j,n+1}-P_{j-1,n+1}) + (\rho_o g)_{j-\frac{1}{2},n}(z_j-z_{j-1})}{(\Delta x)^2}\right]$$
$$- \left(\frac{q_o}{\Delta x}\right)_{j,n} = (\phi A)_j \left\{[(1 - S_{wc})B' - SB']_{j,n}\left[\frac{(P_{j,n+1}-P_{j,n})}{\Delta t}\right] - B_{j,n}\frac{(S_{j,n+1}-S_{j,n})}{\Delta t}\right\} \quad . . (12)$$

At $j = 0$, the original gas-oil contact, the gas saturation is held constant at a value corresponding to the residual oil saturation. At $j = J$, as for Eq. 11, it must be noted that $k_J = 0$ and that only one-half of a segment is present.

When the pressure at a well is specified rather than the flow rate, this pressure is first corrected to allow for the pressure drop due to radial flow into the well. Then this corrected pressure is used in lieu of Eq. 11 at the grid point corresponding to the well. Writing Eq. 11 for all points except those at which pressures are specified and combining this set of equations with the specified pressures results in a system of equations which can be solved to yield a complete pressure distribution at time level $n + 1$ (assuming pressures and saturations were known at time level n). Then Eq. 11 written for the points at which the pressure was arbitrarily specified will contain two unknowns, q_o and q_g, and can be combined with either Eq. 9 or Eq. 10, as appropriate, to yield q_o and q_g for the well.

Eq. 12 is solved explicitly for the saturation at time level $n + 1$. As with all explicit equations, there is an upper limit on the size of the time step that can be employed. This limit cannot be established precisely for the general case, but for the case of constant coefficients (i.e., the pressure-maintenance problem where fluid properties are considered invariant), this limit is given by

$$\Delta t \leq \left[\frac{\Delta x \phi}{(u_o + u_g) f_g'}\right]_{\text{minimum}}$$

The maximum value of $(u_o + u_g)$ is employed in this equation. The quantity f_g' is equal to $\frac{df_g}{dS_g}$ evaluated at the gas saturation existing at the gas front.

This limitation was derived from a heuristic stability analysis and verified by experimental computing for the case of pressure maintenance. While it was found that a slightly less stringent time-step limitation could be applied for gas-cap or dissolved-gas-drive calculations, this equation serves as a useful guide in selecting the time step.

MATERIAL BALANCE EQUATIONS

The difference equations presented in the preceding section are consistent with the conservation of matter. Thus, the amount of gas and oil should be conserved during the course of the calculations. It is advantageous to monitor the accuracy of the calculations by means of over-all material balances on both gas and oil, since such balances represent independent checks on the accuracy with which the difference equations are being solved. In this way, machine or other errors may be detected.

To compute an over-all material balance it is necessary to integrate to obtain both the quantity of oil and the quantity of gas present in the reservoir as a function of time. It also is necessary to integrate to obtain the cumulative production of gas and oil. The integrals are of an elementary form and will not be repeated here. However, it should be noted that, to make the material balance exact except for machine round-off error, these integrals must be evaluated by the trapezoidal rule.

EVALUATION OF THE METHOD

The method described in the preceding sections is intended for application to a wide variety of gas-drive problems including dissolved-gas drive, gas-cap drive, complete pressure maintenance and pressure-buildup operations. Therefore, in evaluating the validity of the method, it was desirable to solve a number of problems by the numerical method of calculation and to compare the answers to ones obtained by analytical methods, laboratory experiment or field data. Three problems were selected — complete pressure maintenance, dissolved-gas drive and gas-cap drive. In all three cases, gravity was an important factor in the recovery mechanism. The first problem, complete pressure maintenance, was solved analytically by the Buckley-Leverett technique. Laboratory data were obtained for a dissolved-gas-drive reservoir, and field data were available for a gas-cap-drive reservoir.

The numerical calculations were programed for the IBM 704 in machine language using the SHARE assembly program. The total machine storage requirement for input-output routines, program and data storage is approximately 7,000 words. If the reservoir is divided into 20 grid intervals, which is adequate for the problems described, the computations require six seconds per time step. About 200 time steps are required in a typical case, and this results in a total computing time of approximately 20 minutes per case. Increasing the number of grid intervals increases the number of time steps required, so that total computing time is proportional to the square of the number of intervals used.

COMPLETE PRESSURE MAINTENANCE

The results of complete pressure maintenance were computed for a hypothetical reservoir 10,000-ft long, 25,000 sq ft in cross-sectional area and with an angle of inclination of 6° from the horizontal direction. The reservoir was initially 75 per cent saturated with oil; the other 25 per cent saturation was connate water. Production was taken only from the bottom extremity of the reservoir, and gas was injected into the upper extremity at a rate of 500,000 scf/day. This rate of injection just balanced the total rate of production so that the pressure at the lower end of the reservoir was constant at 1,000 psig. Reservoir permeability was 1 darcy, and the porosity was 25 per cent. The relative permeability-saturation relationship for the reservoir matrix is shown in Fig. 1.

This problem was solved under the assumption that the pressure drop in the reservoir was small enough that the fluid properties could be treated as invariant. The fluid properties employed in the calculations were: oil viscosity, 0.5 cp; gas viscosity, 0.014 cp; oil density, 45.5 lb/cu ft; gas density, 0.5 lb/cu ft; oil formation volume factor, 0.8; gas solubility, 600 scf/STB; and gas expansion factor, 82.5 scf/reservoir cu ft.

The saturation profile after 8.2 years of injection, as calculated by the Buckley-Leverett[4,5] analytical technique, is shown as the solid curve in Fig. 2. Results of the numerical calculations are also shown in this figure. The open circles were computed with $\Delta x = 250$ ft, the squares with $\Delta x = 500$ ft and the solid circles with $\Delta x = 1{,}000$ ft. The ratio $\Delta t/\Delta x$ was equal to 0.41×10^{-3} years/ft in all three calculations. Behind the gas front, the data from all three numerical calculations give good agreement with the analytical solution, but at the front it is only fair for Δx equal to 500 or 1,000 ft. With Δx equal to 250 ft, the computed front is relatively accurate; further refinement of the size of Δx, while keeping $\Delta t/\Delta x$ constant, would further increase the accuracy.

Refinement of Δt while keeping Δx constant at 500 ft did not appreciably alter the solution shown in Fig. 2.

Application of the numerical technique to this problem constitutes a severe test of the method because of the saturation discontinuity which develops during the displacement. Nevertheless, the data given in Fig. 2 show that the approximate solution can be made to approach the analytical solution as closely as desired by refining the size of Δx.

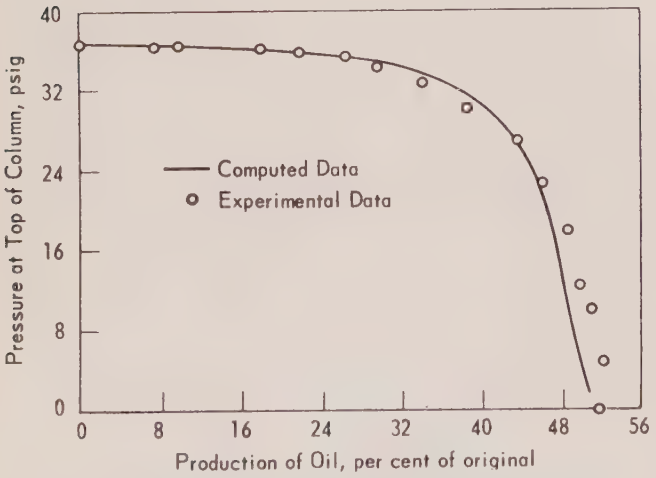

FIG. 5 — PRESSURE BEHAVIOR AT TOP OF COLUMN, DISSOLVED-GAS DRIVE.

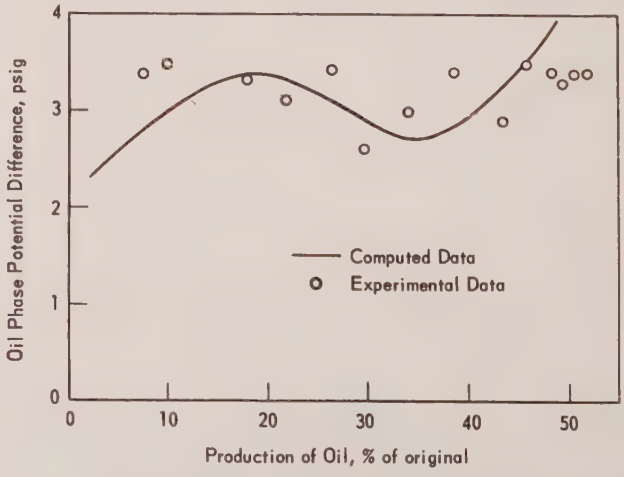

FIG. 6 — VARIATION OF THE DIFFERENCE IN OIL-PHASE POTENTIAL AT TOP AND BOTTOM OF COLUMN, DISSOLVED-GAS DRIVE.

TABLE 1 – PHYSICAL PROPERTIES OF FLUIDS FOR DISSOLVED-GAS-DRIVE SYSTEM, TEMPERATURE = 75°F

Pressure (psig)	Solubility*	Oil Formation Volume Factor	Expansibility of Gas**	Oil Viscosity (cp)	Gas Density (lb/cu ft)
0	0	1.000	1.00	1.55	0.115
5	6.26	0.991	–	–	–
10	11.73	0.980	1.70	1.31	0.198
15	17.48	0.967	–	–	–
20	23.58	0.950	2.43	1.11	0.280
25	30.32	0.930	–	–	–
30	38.00	0.908	3.17	0.93	0.364
35	47.62	0.882	–	–	–
40	62.06	0.854	3.94	0.76	0.450

*Cubic feet of gas at standard conditions per cubic foot of stock-tank oil.

**Cubic feet at standard conditions per cubic foot at reservoir conditions.

DISSOLVED-GAS DRIVE

Dissolved-gas-drive calculations were used to simulate the behavior of a laboratory model. This model consisted of a rectangular column packed with sand and mounted with the long dimension vertical. The dimensions of the model were 3/8 × 1/2 × 72 in. It was packed with 1/2 Wausau sand to a porosity of 44.1 per cent and a total permeability of 13.0 darcies. Relative permeability data for the sand are presented in Fig. 3. These data were determined experimentally by the displacement technique of Johnson, *et al.*[11]

The oil phase charged to the column was a light refined hydrocarbon (Bayol D) saturated with propane at a temperature of 75°F and a pressure of 36.64 psig. The experiment was conducted at a constant temperature of 75°F; some of the properties of the equilibrium phases of Bayol D-propane mixtures at this temperature are given in Table 1 as a function of pressure. These properties are the oil formation volume factor and viscosity, and the gas expansibility, solubility and density. The gas viscosity was constant at 0.008 cp. The oil density varied linearly from 47.5 lb/cu ft at a pressure of 0 psig to 45.0 lb/cu ft at a pressure of 40 psig. At the start of the experiment, the model was saturated with oil containing dissolved gas, there being no connate water present. Production of oil was initiated from the bottom of the column by reducing the back-pressure maintained at this point. The resulting cumulative production of stock-tank oil is shown in Fig. 4 as a function of elapsed time.

A material balance applied to the experimental data indicated that the oil and gas in the column after the initiation of production were not in complete equilibrium. This lack of equilibrium probably was caused by supersaturation of the liquid phase. The average degree of supersaturation during the early

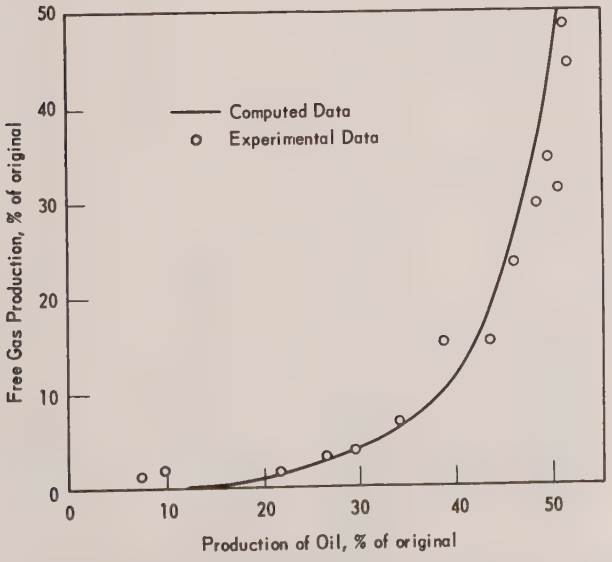

FIG. 7 – FREE-GAS PRODUCTION HISTORY, DISSOLVED-GAS DRIVE.

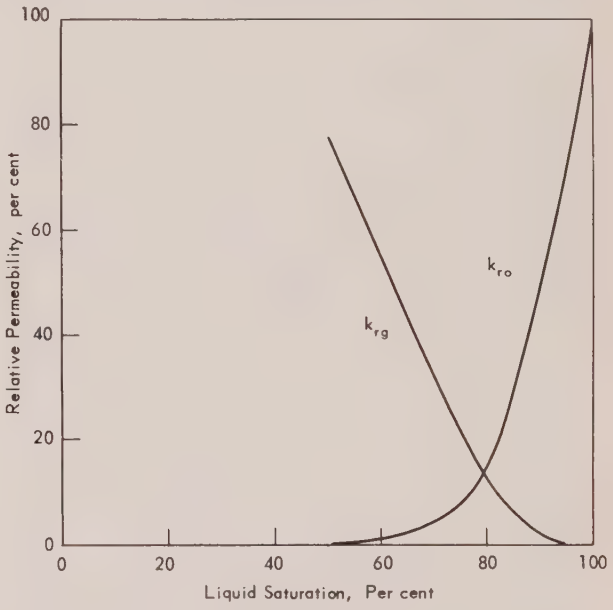

FIG. 8 – RELATIVE PERMEABILITY-SATURATION RELATION, GAS-CAP DRIVE.

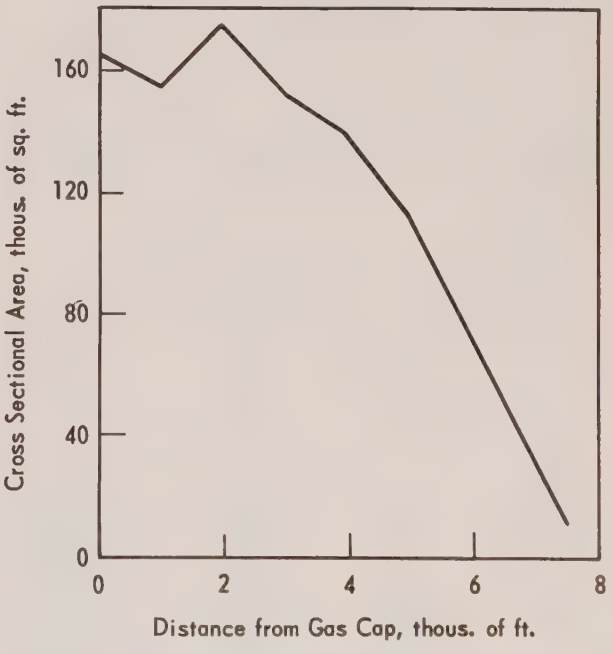

FIG. 9 – VARIATION OF CROSS-SECTIONAL AREA, GAS-CAP RESERVOIR.

TABLE 2 – PERTINENT RESERVOIR DATA – GAS-CAP DRIVE

Original and Saturation Pressure (psig)	2,700
Reservoir Temperature (°F)	181
Volume of Oil Zone (acre-ft)	20,986
Volume of Effective Gas Cap (acre-ft)	10,883
Formation Dip (ft/mile)	226
Average Permeability (md)	165
Average Porosity (per cent)	23
Average Connate-Water Content of Oil Zone (per cent)	28
Average Connate-Water Content of Gas Zone (per cent)	25
Original Oil in Place (STB)	19,840,000
Original Gas-Cap Gas in Place (Mscf)	13,969,000

part of the experiment was estimated to be slightly in excess of 1 psi. Inconsistencies in the material balance on gas of about 4 per cent prevented estimation of the degree of supersaturation late in the experiment.

In computing the behavior of this model, the rate of production of stock-tank oil at any time was derived from the data of Fig. 4. This rate schedule was entered into the calculations as the boundary condition at the production end of the model, and the resulting gas production and pressure behavior of the model was calculated by the previously described numerical technique.

Both the results of calculation and experiment are shown in Figs. 5, 6 and 7. In all three figures, the abscissa is the cumulative quantity of oil produced. The ordinate in Fig. 5 is the pressure at the top of the column; in Fig. 6 it is the difference in the oil-phase potential ($P + \rho_o g \Delta z$) measured at the top and bottom of the column, and in Fig. 7 it is the cumulative quantity of free (undissolved) gas produced. In these figures, the solid curves represent the calculated data; the open circles are data points which were experimentally measured.

The computed pressure behavior at the top of the column (Fig. 5) agrees quite well with that observed experimentally, especially early in the experiment. Agreement was not as good late in the experiment when the pressure was declining very rapidly, making it experimentally difficult to measure accurately the cumulative quantity of oil produced. Note, however, that the final cumulative oil recovery measured after the final blowdown to zero pressure agreed very well with the calculated ultimate recovery.

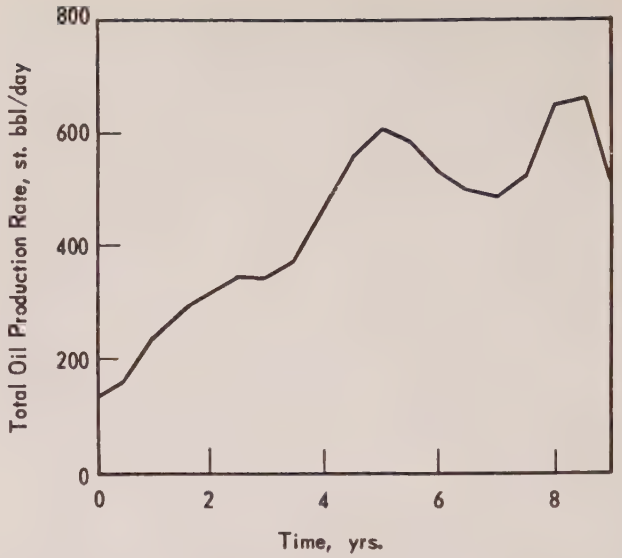

FIG. 10 – VARIATION OF TOTAL PRODUCTION RATE, GAS-CAP RESERVOIR.

The difference in oil-phase potential measured between the top and bottom of the column (Fig. 6) was relatively small, 2.5 to 3.5 psig, and the pressure difference was of course smaller, 0.6 to 1.6 psig. The experimental data exhibit appreciable scatter; but, even so, the average deviation of the experimental from the computed values is ± 12 per cent.

The data of Fig. 7 indicate that the first free-gas production occurred when about 15 per cent of the original oil had been produced. Thereafter, the agreement of the experimental and computed data is reasonably good. In fact, the comparisons shown on Figs. 5, 6 and 7 indicate that the computed and experimental reservoir behavior agree within the probable error of the experiment.

GAS-CAP DRIVE

Kirby, *et al,*[12] published a limited amount of production history for a gas-cap-drive reservoir in which there was no active water drive. Data for this reservoir are given in Table 2. Table 3 gives data on fluid properties as a function of pressure for the reservoir fluids. Relative permeability data for the reservoir are shown in Fig. 8. These

TABLE 3 – PHYSICAL PROPERTIES OF FLUIDS FOR GAS-CAP-DRIVE SYSTEM, TEMPERATURE = 181°F

Pressure (psig)	Solubility*	Oil Vol. Factor	Expansibility of Gas**	Oil Viscosity (cp)	Gas Viscosity (cp)	Oil Density (lb/cu ft)	Gas Density (lb/cu ft)
0	0	1.000	0.8	0.816	0.0117	50.3	0.03
300	17.0	0.930	17.0	0.664	0.0131	47.6	0.75
600	31.3	0.888	34.0	0.576	0.0145	46.5	1.48
900	42.8	0.865	51.5	0.515	0.0157	45.8	2.20
1200	51.0	0.845	69.3	0.470	0.0168	45.0	2.95
1500	63.0	0.823	87.2	0.435	0.0177	44.2	3.73
1800	75.5	0.802	106.5	0.407	0.0185	43.5	4.52
2100	88.5	0.782	126.0	0.383	0.0194	42.7	5.22
2400	102.8	0.760	144.0	0.360	0.0201	42.0	5.93
2700	119.0	0.738	159.0	0.338	0.0209	41.2	6.65

* Cubic feet of gas at standard conditions per cubic foot of stock-tank oil.

** Cubic feet at standard conditions per cubic foot at reservoir conditions.

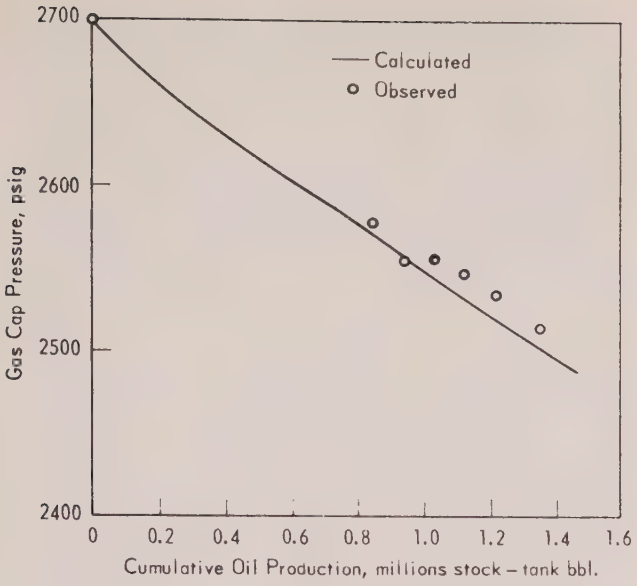

FIG. 11 – GAS-CAP PRESSURE, GAS-CAP DRIVE.

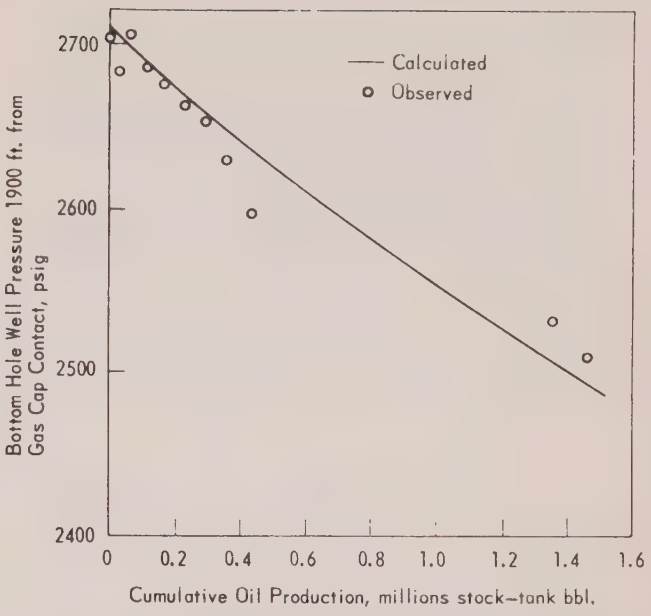

FIG. 12 – OIL-ZONE PRESSURE 1,900-FT FROM GAS-CAP CONTACT.

data were measured on cores taken from the field. Fig. 9 shows the variation of cross-sectional area with location in the reservoir, and Fig. 10 shows the oil-production schedule for the reservoir.

All of these data were employed in the numerical computation of the reservoir behavior. Producing wells were distributed throughout the reservoir as indicated by the field map given in the reference paper.

In Fig. 11 computed gas-cap pressures are compared to those observed in the field. The solid curve is computed, and the circles represent the field data. Agreement is quite good; the best curve through the experimental points would fall a little above the computed curve, with a maximum deviation of 15 psi.

For the production rates used in this reservoir, oil-zone pressures differ only slightly from the gas-cap pressure. This is illustrated in Fig. 12, which shows shut-in bottom-hole pressures for a well 1,900 ft from the gas cap as a function of total cumulative production. As in Fig. 11, the solid curve represents the computed data, and the circles are the observed data. The data presented in Fig. 12 were not presented *per se* by Kirby, *et al,* but were taken from their original worksheets. Kirby, *et al,* chose to present an average pressure of all the wells in the field, rather than the pressures for a single well. Also, they adjusted the observed pressures at all wells to a common elevation by subtracting the quantity $(\rho_o\ g\ \Delta\ z)$ from the observed pressures. Here $\Delta\ z$ is the difference in elevation between the well being observed and the reference elevation. The computed pressures in this figure are a little higher (15 psi or less) than the computed gas-cap pressure at corresponding amounts of production. As for the gas-cap pressures, the computed pressure data are in reasonably good agreement with the observed data.

CONCLUSIONS

A numerical method of solving the partial differential equations which describe the displacement of oil by gas has been presented. This method and the assumptions made in deriving it are described in the paper.

Results presented in the paper lead to the following conclusions.

1. Comparison of data computed by this method to the analytical solution for complete pressure maintenance demonstrates the convergence and accuracy of the numerical method.
2. Comparison of computed results to data obtained from a laboratory model produced by dissolved-gas drive shows the applicability of the method to this mode of production.
3. Finally, a comparison of predicted data with field data from a gas-cap-drive reservoir demonstrates its applicability to a field problem.

ACKNOWLEDGMENT

The assistance of J. R. Sheffield in providing the laboratory data on the dissolved-gas-drive model is gratefully acknowledged.

REFERENCES

1. Muskat, M. and Taylor, M. O.: "Effect of Reservoir Fluid and Rock Characteristics on Production Histories of Gas-Drive Reservoirs", *Trans.*, AIME (1946) Vol. 165, 78.
2. West, W. J., Garvin, W. W. and Sheldon, J. W.: "Solution of the Equations of Unsteady State Two-Phase Flow in Oil Reservoirs", *Trans.*, AIME (1954) Vol. 201, 217.
3. Muskat, M. and Meres: *Physics* (1936) Vol. 7, 346.
4. Buckley, S. E. and Leverett, M. C.: "Mechanism of Fluid Displacement in Sands", *Trans.*, AIME (1941) Vol. 146, 107.
5. Welge, H. J.: "Simplified Method for Computing Oil Recoveries by Gas or Water Drive", *Trans.*, AIME (1952) Vol. 195, 91.
6. Kern, L. R.: "Displacement Mechanism in Multi-Well Systems", *Trans.*, AIME (1952) Vol. 195, 39.

7. Shreve, D. R. and Welch, L. W., Jr.: "Gas Drive and Gravity Drainage Analysis for Pressure Maintenance Operations", *Trans.*, AIME (1956) Vol. 207, 137.
8. Terwilliger, P. L., Wilsey, L. E., Hall, H. N., Bridges, P. M. and Morse, R. A.: "Experimental and Theoretical Investigation of Gravity Drainage Performance", *Trans.*, AIME (1951) Vol. 192, 285.
9. Wooddy, L. D., Jr. and Moscrip, Robert, III: "Performance Calculations for Combination Drive Reservoirs", *Trans.*, AIME (1956) Vol. 207, 128.
10. Douglas, Jim, Jr.: *Jour. Assoc. of Computing Machinery* (1959) Vol. 6, No. 1, 48.
11. Johnson, E. F., Bossler, D. P. and Naumann, V. O.: "Calculation of Relative Permeability From Displacement Experiment", *Trans.*, AIME (1959) Vol. 216, 61.
12. Kirby, J. E., Jr., Stamm, H. E., III and Schnitz, L. B.: "Calculation of Depletion History and Future Performance of Gas-Cap Reservoir", *Trans.*, AIME (1957) Vol. 210, 218.

DISCUSSION

J. C. MARTIN
MEMBER AIME

CALIFORNIA RESEARCH CORP.
LA HABRA, CALIF.

The authors have considered a very difficult problem and one in which many questions remain to be answered. The partial differential equations are very complex, and the finite-difference method of solution has not been established rigorously. It is known that finite-difference methods can fail to approximate the true solutions of partial differential equations. Thus, there is reason to doubt the validity of the method from a mathematical viewpoint.

The results of reservoir analysis may lead to large capital investments and may be a prime factor in determining the amount of oil recovery. Thus, there is an economic incentive for the results of reservoir analysis to reflect the true nature of the reservoir. Misleading results can be worse than no results at all if they lead to poor investments and the waste of important national resources. Thus, there is a considerable justification for being very critical of the validity of new methods of reservoir analysis.

The method of analysis presented by the authors involves the solution by finite-difference approximations of two simultaneous partial differential equations containing the fluid pressure and one of the fluid saturations as dependent variables, and distance and time as the independent variables. Since two dependent variables can vary with distance and time, it seems reasonable to expect that the authors would present examples where the pressure and the saturations have considerable variations with both time and distance. Also, one would expect that numerical results would be shown to approach the results obtained by analytical methods as the increments in time and distance are reduced.

In the example of complete pressure maintenance, the numerical results do not appear to converge to the analytical solution of the partial differential equations. The analytical solution is contained in the well known paper by Buckley and Leverett.[1] It is maintained by some that the Buckley-Leverett solution is not the true analytical solution and that the multivalues given by Buckley and Leverett occur because they made a mathematical transformation which is not valid in the vicinity of the saturation discontinuity. Thus, there is some disagreement concerning the Buckley-Leverett solution. For this reason, it is discussed in the following paragraphs.

The Buckley-Leverett solution can be obtained by well established mathematical methods of the type employed in Ref. 2. The partial differential equation for the gas saturation is

$$\frac{\partial}{\partial x}\left[V(t)\,F(S_g) - \frac{\alpha g(\rho_o - \rho_g)}{\mu_o}\,G(S_g)\right] = -\phi\frac{\partial S_g}{\partial t} \quad \ldots\ldots\ldots\ldots\ldots\ldots\ldots\ldots (1)$$

where α = the dip angle,

$V(t)$ = a known function of time,

$$F(S_g) \equiv \frac{1}{1 + \frac{\mu_g}{\mu_o}\frac{k_o}{k_g}}, \text{ and}$$

$$G(S_g) \equiv k_o/k\ F(S_g).$$

Eq. 1 is a first-order partial differential equation of a type for which there is a well known method of obtaining solutions (see, for example, Chapter 4 of Ref. 3). The analytical solution of Eq. 1 is

$$x = F'(S_g)\int_o^t \frac{V(t)}{\phi}\,dt - \frac{\alpha g(\rho_o - \rho_g)}{\phi\mu_o}\,G't + \psi(S_g) \quad \ldots\ldots\ldots\ldots\ldots\ldots\ldots\ldots (2)$$

where $\psi(S_g)$ is the initial gas saturation. For the case considered by the authors where the initial gas saturation is zero, $\psi(S_g)$ is zero. That Eq. 2 satisfies Eq. 1 can be verified by direct substitution. Eq. 2 yields the same multivalue saturations profiles as obtained by Buckley-Leverett. Thus, the Buckley-Leverett solution is the true analytical solution, and it contains multivalued saturations. Furthermore, the analytical solution does not contain a discontinuity.

In formulating the partial differential equation, it is assumed that the saturations are continuous

[1]References given at end of Discussion.

functions of distance. The presence of a discontinuity violates this assumption and across the discontinuity the partial differential equation breaks down. If it is assumed that a discontinuity exists at a given point and a given time, continuity considerations yield the relation for the velocity of the discontinuity. Buckley-Leverett, followed by a number of investigators, have used the procedure of first determining the analytical solution and then eliminating the presence of multivalue saturations by employing discontinuities which satisfy conditions.

The results presented in Fig. 2 do not approximate the true analytical solution but appear to approximate the combination of the analytical solution and the discontinuity which satisfies material balance. The authors should explain why the results do not approach the true analytical solution since the finite-difference relations are represented as being approximations to the partial differential equations. Furthermore, in the vicinity of the discontinuity the numerical results are a very poor approximation to the combination of the analytical solution and the discontinuity. Thus, it is not clear that the finite-difference method would yield results that approach the solid line in Fig. 2 as the increments in time and distance approach zero.

The Buckley-Leverett flow considered by the authors is a very simple flow compared to what the partial differences can represent. There may be many discontinuities present in the porous media. They can arise within the body, and they can begin at the boundaries even after the flow has been in progress for some time. Since the authors have failed to present a completely satisfactory demonstration that their method yields the correct results for a very simple case, how can one be sure the method will be applicable in a very involved case which may arise in the analysis of a natural reservoir?

REFERENCES

1. Buckley, S. E. and Leverett, M. C.: "Mechanism of Fluid Displacement in Sands", *Trans.*, AIME (1941) Vol. 146, 107.
2. Martin, J. C.: "Some Mathematical Aspects of Two-Phase Flow With Applications to Flooding and Gravity Segregation Problems", paper presented at 1st Venezuelan Regional Meeting of AIME, Caracas (Nov., 1956); also *Prod. Monthly* (April, 1958).
3. Miller, F. H.: *Partial Differential Equations*, John Wiley & Sons, Inc., N. Y. (1941).

AUTHORS' REPLY TO J. C. MARTIN

Many of Martin's comments concern the example case of complete pressure maintenance. The analytical statement of this problem was formulated by Buckley and Leverett[1] as a first-order quasilinear hyperbolic differential equation. This class of differential equation often arises in simplified theories which ignore mechanisms of dissipation such as viscous stresses, heat conduction, ohmic loss or, as in the present case, capillary pressure. It is the rule, rather than the exception, that the physically meaningful solutions of these problems develop singularities (discontinuities) after a finite time.[2] Lax[3] notes that, while the classical solution of the differential equation cannot be continued after this time, it is possible to continue it in a generalized sense. This kind of generalization is dictated by the integral version of the conservation law. Lax refers to this generalized solution as a weak solution and gives a formal definition of it. It develops that these weak solutions are not determined uniquely by their initial values. Therefore, an additional principle is needed for developing a relevant subclass. In this aspect, the problem is similar to the solution of a quadratic equation. A unique answer cannot be obtained from the equation alone; additional information is necessary to reject the extraneous root.

With this background, we are prepared to consider Martin's comments. One of his objections is that, when the authors' numerical procedure is applied to the case of complete pressure maintenance, it does not approximate what he calls the "true analytical solution" of the differential equation. The solution to which he refers was given by Buckley and Leverett and contains multiple values of saturation at some locations in space. Obviously, this is not a physically significant solution of the problem and so must be rejected. The generalized solution which does occur in nature is formed by replacing the region of multiple-valued saturations by a saturation discontinuity so located that the resulting solution satisfies the law of conservation of mass. The authors selected the difference analogue of the differential equation with the objective of approximating the solution having physical significance.

The comparison of Fig. 2 gives a measure of the degree of achievement of this objective. Martin is critical of the accuracy of the approximation in the vicinity of the saturation discontinuity. He states, "... It is not clear that the finite-difference method would yield results that approach the solid line in Fig. 2 as the increments in time and distance approach zero". The authors take issue with this statement. For a perfect solution, the length of the region of the reservoir containing saturations between zero and the frontal saturation should be zero. The data of Fig. 2 show that when a distance increment of 1,000 ft was used in the numerical procedure, this region occupied 22 per cent of the reservoir (from 7,000 to 9,200 ft). For a distance increment of 500

ft, it occupied 14 per cent; for a distance increment of 250 ft, it occupied 8 per cent. Thus, halving the size of the distance increment while holding $\Delta t/\Delta x$ constant approximately doubles the slope of the saturation curve in the vicinity of the front. This experimental relationship of error to grid size is the same as predicted by an elemental truncation error analysis of the difference equations used. This analysis shows that the size of the error should be proportional to Δx. The authors feel that this evidence makes clear the convergence of the numerical method as the time and distance increments approach zero.

Martin's final criticism is that the testing of the procedure was not sufficient to verify its accuracy in "a very involved case which may arise in the analysis of a natural reservoir". While the testing of an experimental method is never complete, the validity of the present method has been demonstrated for a wide variety of conditions. To date, the authors have not encountered a case for which it fails. If evidence of such failure is obtained, the authors will welcome the information.

REFERENCES

1. Buckley, S. E. and Leverett, M. C.: "Mechanism of Fluid Displacement in Sands", *Trans.*, AIME (1941) Vol. 146, 107.
2. Douglas, Jim, Jr.: "On The Numerical Solution of a Non-Linear, First-Order Differential Equation", *Proc.* Rome Symposium organized by Provisional International Computation Centre, Libreria Eredi Virgilio Veschi, Rome (Jan. 28-30, 1959) 12.
3. Lax, P. D.: "Hyperbolic Systems of Conservation Laws II", *Communications on Pure and Applied Mathematics* (1955) Vol. X, 537-566.

***

Effect of Vertical Fractures on Reservoir Behavior—Incompressible Fluid Case

M. PRATS
MEMBER AIME

SHELL DEVELOPMENT CO.
HOUSTON, TEX.

ABSTRACT

The effect of a sand-filled vertical fracture of limited radial extent and finite capacity (fracture capacity is the product of the permeability and width of the fracture) on the flow behavior of a cylindrical reservoir producing an incompressible fluid through a centrally located well has been investigated mathematically. The shape of the lines of equal pressure near the fracture is essentially independent of the size of the reservoir, provided that the field radius is of the order of the fracture length or larger. For reasonable values of production rates and of fluid, reservoir and fracture properties, the total pressure drop between the end of the fracture and the well is generally negligible compared with the pressure drop in the reservoir.

With regard to production response, the effect of vertical fractures can be represented by the production response of an equivalent or effective well radius. For a high-capacity fracture, the effective well radius is a quarter of the total fracture length, decreasing with the fracture capacity.

When invasion effects are simulated by decreasing the width of the damaged zone with distance from the well, the effect of formation damage around a fracture on the production response is not so serious as indicated by the literature. This suggests that frac fluids with a conventional filter-loss response are better than high-spurt-loss frac fluids, provided the effective permeability of the damaged zone is the same.

INTRODUCTION

This paper considers the effect of the fracture capacity, as well as the formation damage which can result from fracture treatments, on the productive capacity of vertically fractured wells. Other publications, notably those of van Poollen,[1,2] consider these same effects.

In addition to providing more general results for vertical fractures than are available from the literature, the present paper gives the equivalent well radius of fractures having different lengths and capacities and, also, includes pressure distributions in and around the fractures.

The effect of a damaged zone around a fracture on the production response was not found to be so great as that reported by van Poollen.[2] This difference probably stems from the fact that we consider a damaged zone which is widest (but is still small) near the well and thins out toward the extremities of the fracture, whereas van Poollen considers a damaged zone having a uniform width for the entire fracture length.

Simple, but adequate, equations which describe the effect of these variables on production response are presented (in Appendixes A and B). Thus, results can easily be extended to values of the variables not specifically considered here.

IDEALIZATION AND DESCRIPTION OF THE FRACTURED SYSTEM

It is assumed that a horizontal oil-producing layer of constant thickness and of uniform porosity and permeability is bounded above and below by impermeable strata. The liquid is incompressible. It is assumed that, after the well is fractured, the cylindrical outer "boundary" is at a uniform potential, provided that it is not too near the fracture. The fracture system is represented by a single, plane, vertical fracture of limited radial extent, bounded by the impermeable matrix above and below the producing layer (reservoir).[3]

Fig. 1 indicates the general three-dimensional geometry of the fractured reservoir described above. If gravity effects are neglected, the flow behavior in the reservoir will be independent of the vertical position in the oil sand. This means that the flow behavior in the fractured reservoir can be described by the two-dimensional flow behavior shown in the horizontal cross section of the reservoir, Fig. 2.

PARAMETERS

The effect of a fracture on the pressure distribution in the fracture itself and in an otherwise undamaged (no skin) reservoir indicates that the pressure distribution is a function of three parameters.

Original manuscript received in Society of Petroleum Engineers office July 8, 1960. Revised manuscript received Nov. 23, 1960. Paper presented at 35th Annual Fall Meeting of SPE, Oct. 2-5, 1960, in Denver.

[1]References given at end of paper.

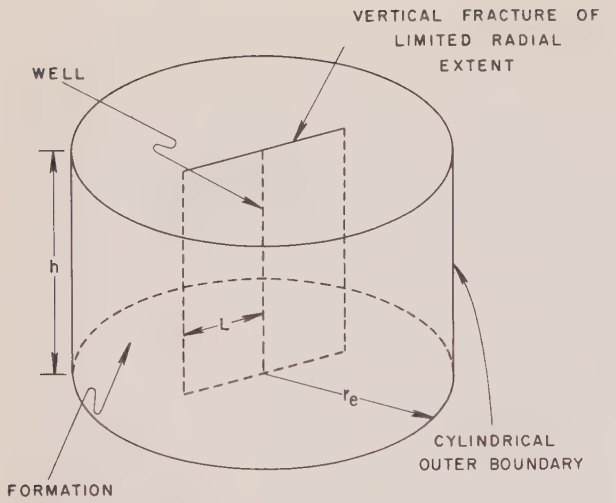

FIG. 1 – SCHEMATIC DIAGRAM OF FRACTURED SYSTEM.

The first of these can be described as the ratio of the ability of the formation to carry fluids into the fracture to the ability of the fracture to carry fluids into the well, and it is defined by

$$a = \frac{\pi\,(\text{formation permeability, } k)\,(\text{fracture length, } 2L)}{4\,(\text{fracture permeability, } k_f)\,(\text{fracture width, } w)},$$

or

$$a = \frac{\pi k\, 2L}{4 k_f w} \quad \ldots\ldots\ldots\ldots\ldots\ldots\ldots \quad (1)$$

The last two parameters describe only the geometry of the system, that is, the size of the wellbore and drainage radius relative to the extent of the fracture from the well axis (L). These parameters are denoted by r_{wD} and r_{eD}.*

Thus, for a given geometry, the effectiveness of the fracture is described by the relative capacity parameter a. For a very effective fracture – one having a great ability to carry fluids to the well – the relative capacity parameter is very small and approaches the limiting value of zero for infinite fracture permeability. Likewise, for a very ineffective fracture–one having a low capacity–the parameter a is relatively large, approaching infinity for the limiting case of no fracture.

Practical values of the parameter a appear to be less than 0.1 when the fracture permeability is the same as that of the sand used in the treatment. It is known, however, that fine particles from the reservoir, and in some cases other suspended solids in the fracturing fluid, will mix with the fracturing sand and will greatly reduce its permeability. In these cases, the values of the capacity parameter a could be much larger than 0.1.

When the formation is damaged as a result of fracture treatment, the permeability damage and the depth of the damaged zone (relative to the fracture length) are added parameters. In this case, well effects and pressure drops in the fracture have been neglected to simplify the presentation of results.

*All dimensionless distances are in terms of L, half the fracture length. For example, $r_{eD} = r_e/L$.

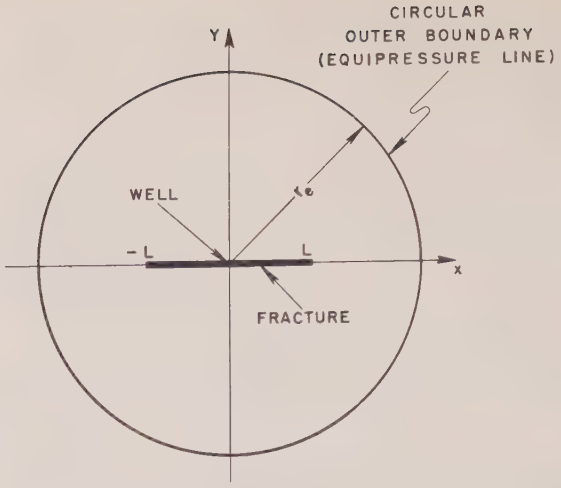

FIG. 2 – RESERVOIR CROSS SECTION.

RESULTS AND DISCUSSION

For formations with no skin, this study provides two types of information – one, such as the pressure distribution in and near the fracture, gives a general picture and understanding of the action of the fracture on the pressures behavior in the formation, and the other describes quantitatively the action of the fracture on such items as the magnitude of the pressure drop in the fracture and improvement in production rate.

For formations damaged as a result of the fracture, production rates are compared to those which would have been obtained without damage. These results will be treated separately at the end of this section.

PRESSURE DISTRIBUTION IN AND NEAR THE FRACTURE

The dimensionless pressure drop between the end of the fracture and any point in the fracture is essentially independent of the size of the reservoir, i.e., of the length parameter r_{eD}. However, this pressure drop is strongly dependent on the value of the relative capacity parameter a.

Fig. 3 shows the variation of this dimensionless pressure drop in the fracture with the dimensionless distance from the well. This dimensionless pressure drop is given by

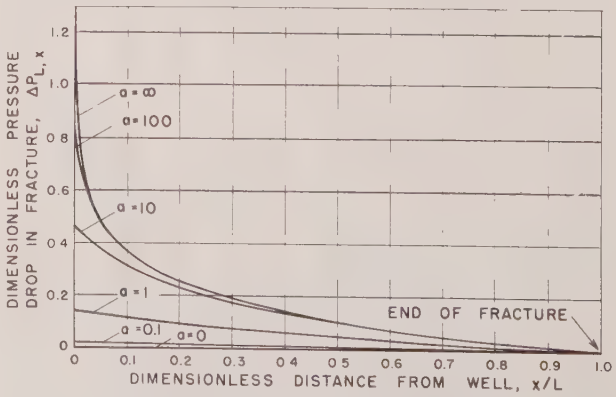

FIG. 3 – PRESSURE-DROP DISTRIBUTION IN FRACTURE.

$$\Delta P_{L,x} = \frac{kh}{q\mu}(p_L - p_x) \quad \ldots \ldots \ldots \quad (2)$$

In Eq. 2, $p_L - p_x$ is the pressure drop between the end of the fracture at $x = L$, in the co-ordinate system of Fig. 2, and any point in the fracture a distance x from the well axis.

The curves presented in Fig. 3 indicate that as the fracture becomes less important (increasing a), the dimensionless-pressure-drop distribution in the fracture approaches that corresponding to strictly radial flow into a well of zero radius.* On the other hand, as the ability of the fracture to carry fluids increases (decreasing a), the pressure variation in the fracture becomes smaller, as indicated by the small values of $\Delta P_{L,x}$. Thus, the pressure drop in the fracture is negligible unless the fracturing sand is contaminated with fine particles from the formation, either during the course of the fracture treatment or after the well is put on production.

It is interesting to note from Fig. 3 that, in general, the pressure gradients in the fracture at the well are finite even though the well has a zero radius. The only exception is for the limiting case of no fracture given by the curve for infinite a, for which case the pressure behaves as ln r near the well. Thus, for a given production rate, the effect of the fractures is to reduce the pressure gradients near a well.

Pressure distributions in the reservoir were determined for a few values of the capacity parameter a and for a value of the length parameter $r_{eD} = 2.40$. Values given at the outer boundary are numerically equal to $\Delta P_{e,o}$, which is discussed in the next section. These pressure distributions in the reservoir were obtained in a few hours by using relaxation methods,[6] except for values of a equal to zero and infinity, for which cases the shapes of the equipressure lines were known.

Figs. 5, 6 and 7 show the pressure distribution in the reservoir for $a = 0.1$, 1.0 and 10, respectively. The pressure distribution for the case of no pressure drop in the fracture ($a = 0$) is given by confocal ellipses, as shown in Fig. 4. For infinite a, the fracture is of no influence, and the equipressure lines are circles concentric with the well axis (Fig. 8). To give the pressure distribution for infinite a in a manner which could be compared with the curves in Figs. 4 through 7, that is, for $r_{eD} = 2.40$, the the equipressure lines in Fig. 8 were determined for a fictitious fracture length of 416 ft in a reservoir of 500-ft radius drained by a well of 1/4-ft radius. In Figs. 4 through 7, the value of the equipressure lines represents the dimensionless pressure drop between the equipressure lines and the well of zero radius. In Fig. 8, the value of the equipressure lines represents the dimensionless pressure drop between the equipressure lines and the well of 1/4-ft radius.

*The results of Fig. 3 indicate that the pressure distribution for $a \geq 100$ is very nearly the same as that for radial flow. Whenever the permeability of the fracture is the same as that of the reservoir, the fracture is trivial because it is not effective. This means that the pressure distribution for such an ineffectual fracture must be that associated with values of $a \geq 100$. However, for such fractures, the parameter a is given by $a = \pi L/2w$, so that the method used in this study to obtain the pressure distribution appears to be limited to cases where the length/width ratio of the fracture is larger than 130. This is not considered to be a practical limitation.

SPECIFIC PRODUCTIVITY INDEX

It has been found that the pressure drop between the outer boundary and a well of radius r_w can be be represented as the difference of the total pressure drop to a well of zero radius, with a correction term added to represent the pressure drop between the well of radius r_w and one of zero radius.

$$\Delta P_{e,w}(a, r_{eD}, r_{wD}) = \Delta P_{e,o}(a, r_{eD}) - \Delta P_{w,o}(a, r_{wD}) \quad \ldots \quad (3)$$

Here, $\Delta P_{e,o}$, the dimensionless pressure drop between the outer boundary and a well of zero radius, is a function of a and r_{eD} only; and $\Delta P_{w,o}$, the

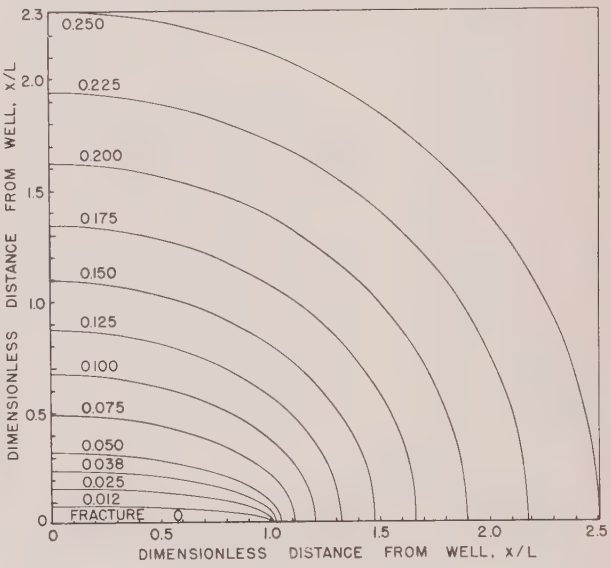

FIG. 4 – PRESSURE DISTRIBUTION AROUND FRACTURE. $a = 0$.

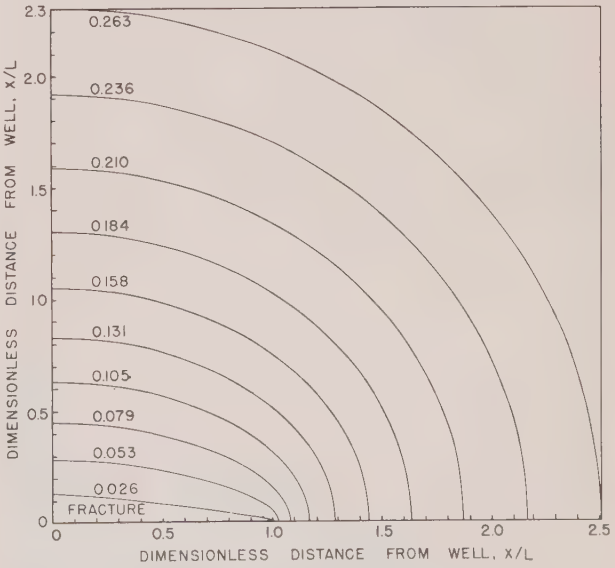

FIG. 5 – PRESSURE DISTRIBUTION AROUND FRACTURE. $a = 0.1$.

dimensionless pressure drop between a well of radius r_w and a well of zero radius, is a function of a and r_{wD} only. We note that the main contribution to the two terms in the right-hand side of Eq. 3 is in $\Delta P_{e,o}$, which is plotted in Fig. 9. It should be noted that $\Delta P_{e,o}$ is also the reciprocal of the specific productivity index SPI defined by

$$SPI = \frac{q\mu}{kh(p_e - p_o)} \; .$$

The term $\Delta P_{w,o}$ plotted in Fig. 10 is only a correction term which takes into account the effect of the well radius.

For values of r_{eD} larger than two, the curves of $\Delta P_{e,o}$ given in Fig. 9 can be represented very well by

$$\Delta P_{e,o}(a, r_{eD}) = \frac{1}{2\pi}\ln\frac{r_e}{r_w'} = \frac{1}{2\pi}\ln r_{eD} - \frac{1}{2\pi}\ln r_{wD}'(a) \quad \ldots\ldots (4)$$

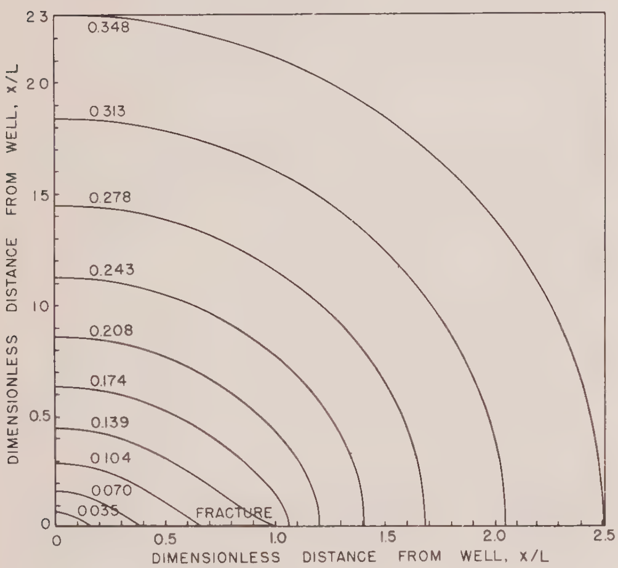

FIG. 6 – PRESSURE DISTRIBUTION AROUND FRACTURE. $a = 1.0$.

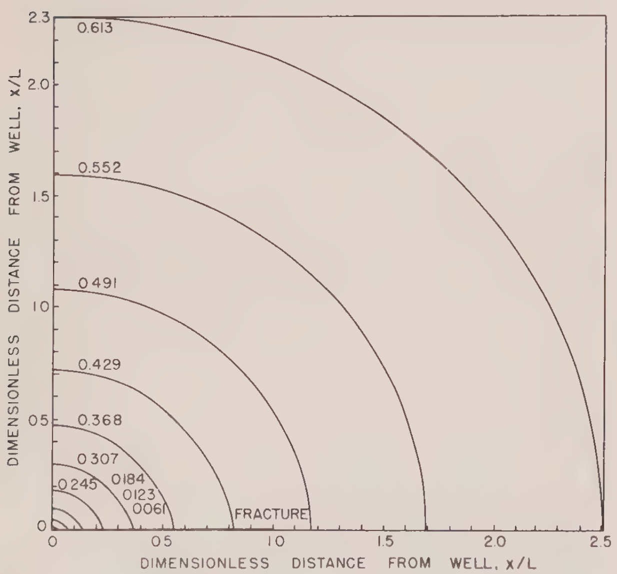

FIG. 7 – PRESSURE DISTRIBUTION AROUND FRACTURE. $a = 10$.

where $r_{wD}'(a) = r_w'/L$ is only a function of a. Values of the effective well radius $r_{wD}'(a)$ are given in Fig. 11, showing that for fractures of infinite capacity, the effective well radius is always equal to a quarter of the fracture length, $(2L)/4$. Smaller values of the effective well radius correspond to less effective fractures.

The well pressure used in the correction term $\Delta P_{w,o}$ given in Eq. 3 is approximated by the arithmetic average of the pressure along the fracture and the pressure along the normal to the fracture, with both these pressures being evaluated at a distance r from the center of the fracture. Fig. 10 shows the correction term $\Delta P_{w,o}$ obtained as described. We note that the correction term is unimportant for reasonably effective fractures ($a \leq 1$). Figs. 6, 7 and 8 indicate that averaging the well pressure in the manner described is quite adequate for $a \geq 1$.

MAGNITUDE OF THE PRESSURE DROP IN THE FRACTURE

It is common practice now to consider that the pressure drop in the fracture is small compared to the pressure drop in the field. In fact, it is generally

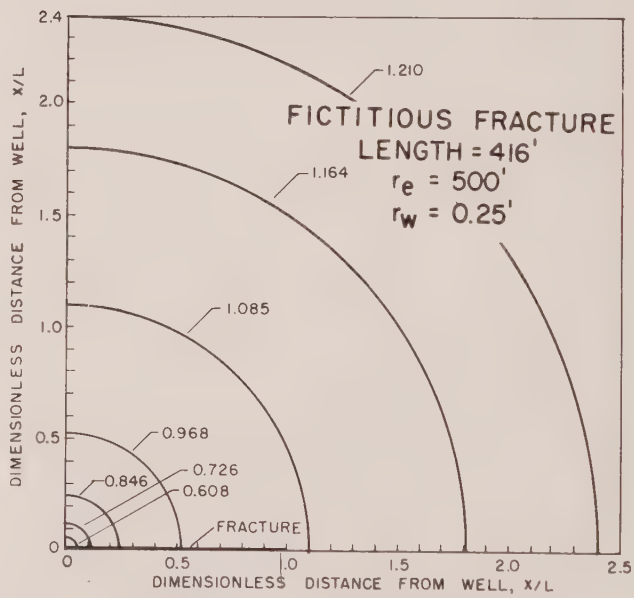

FIG. 8 – PRESSURE DISTRIBUTION AROUND FRACTURE. $a = \infty$.

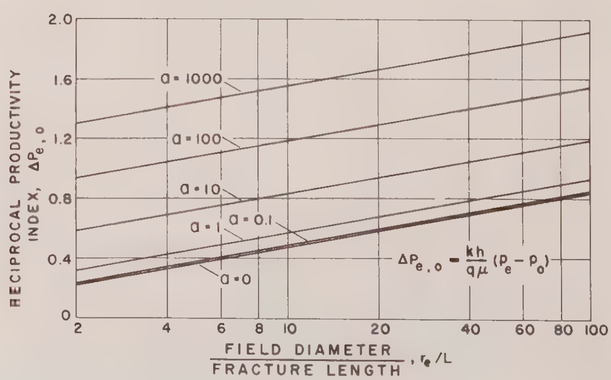

FIG. 9 – DIMENSIONLESS SPECIFIC PRODUCTIVITY INDEX.

assumed that there is no pressure drop in the fracture.[4,5] It is desirable to determine the conditions of fracture effectiveness and length that will permit neglecting the pressure drop in the fracture (say, less than 10 per cent of the pressure drop in the field). A plot of the ratio of pressure drop in the fracture to that in the field is given in Fig. 12 for for a well of zero radius. Consideration of the small correction terms for the well radius would only complicate the presentation of the results without changing their character. The ratio of the pressure drops plotted in Fig. 12 as a function of a and r_{eD} has been obtained from the results presented in Figs. 3 and 9. The results presented in Fig. 12 show that the pressure drop in the fracture is negligible (less than 10 per cent of the pressure drop in the field) for values of $a \leq 0.1$ and for fracture lengths smaller than the field radius. Since most of today's fractures probably satisfy these conditions, it appears that pressure drops in clean fractures can be considered negligible in most present cases.

However, the curves in Fig. 12 show that the ratio of the pressure drops is strongly dependent on the values of a and r_{eD}. Thus, for values of $a = 0.5$ and fractures as short as 1/40 of the field radius, the pressure drop in the fracture is between 10 and 30 per cent of the pressure drop in the field. This means, of course, that the pressure drop in fractures can become an appreciable fraction of the pressure drop in the field if the propping agent becomes contaminated with fine particles. Also, the present trend in using larger volumes of fracture treatment (as well as increasing the sand content) will probably result in larger values of a and smaller values of r_{eD}. It follows that appreciable pressure drops in the fracture may become more frequent in the future, even when the propping agent remains clean.

IMPROVEMENT IN PRODUCTION RATE

The improvement in production rate q_f/q is given by

$$\frac{q_f}{q} = \frac{\frac{1}{2\pi} \ln \frac{r_e}{r_w}}{\Delta P_{e,o}\,(a, r_{eD}) - \Delta P_{w,o}\,(a, r_{wD})} \quad . \quad . \quad . \quad (5)$$

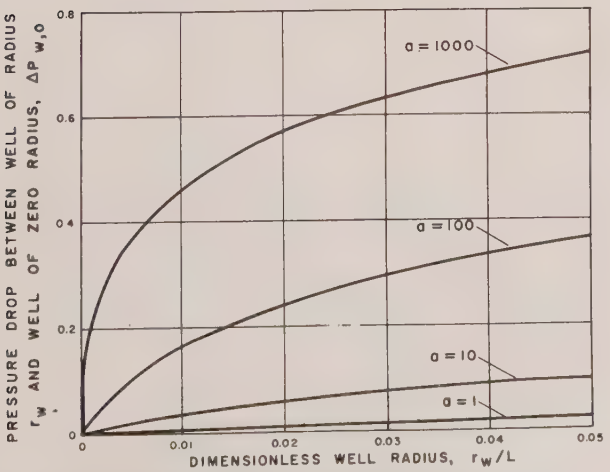

FIG. 10 – PRESSURE CORRECTION AT WELL.

As an example, the improvement in production rate is determined below for a well of 1/4-ft radius in the middle of a 200-ft fracture of infinite capacity ($a = 0$) and "draining" from a radius of 500 ft. Using the results of Figs. 9 and 10 in Eq. 5, we obtain

$$\frac{q_f}{q} = \frac{\frac{1}{2\pi} \ln 2000}{0.365\,(\text{from Fig. 9}) - 0\,(\text{from Fig. 10})} = 3.3.$$

Whenever the effect of the well radius is small, the improvement in production rate can be obtained most simply by using the effective well radius of the fracture in the formula

$$\frac{q_f}{q} \doteq \frac{\ln \frac{r_e}{r_w}}{\ln \frac{r_e}{r'_w}} \quad . \quad . \quad . \quad . \quad . \quad . \quad . \quad . \quad . \quad . \quad . \quad . \quad . \quad (6)$$

For the conditions described above ($a = 0$),

$$r'_w = \frac{2L}{4} = \frac{200}{4} = 50$$

from Fig. 9, and

$$\frac{q_f}{q} = \frac{\ln \frac{r_e}{r_w}}{\ln \frac{2r_e}{L}} = \frac{\ln \frac{r_e}{r_w}}{\ln 2 + \ln r_{eD}} = \frac{\ln 2000}{\ln 10} = 3.3 \ ,$$

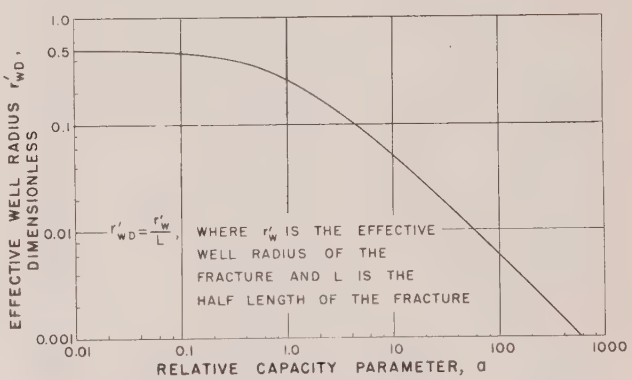

FIG. 11 – EFFECTIVE WELL RADIUS.

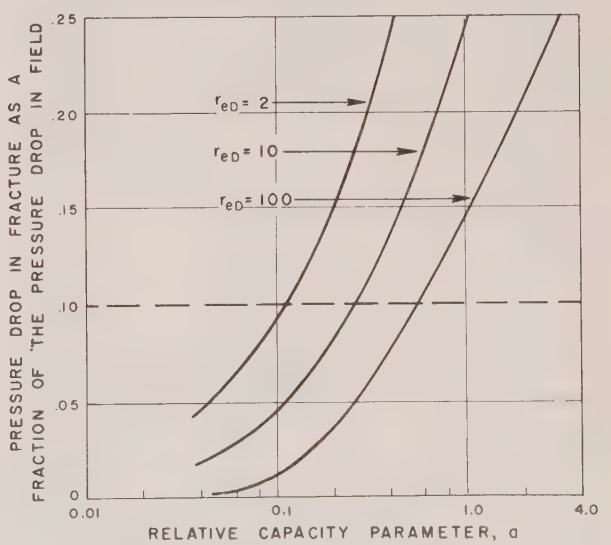

FIG. 12 – PRESSURE DROP IN FRACTURE.

as was also obtained by the more general method given by Eq. 5.

This means that the maximum increase in production rate per unit pressure drop for such conditions cannot be expected to be more than 3.3 times the rate obtained before fracturing, assuming that the well is not damaged before the fracture treatment.

Increases in the production rate (SPI) can generally be associated with increases in the effective radius of the well, as can also be obtained, say, by acid treatments. Whenever the formation is homogeneous and is not fractured during the acid treatment, the acid enters the formation radially, enlarging the well radius equally in all directions to a new effective well radius of value r'_w. The example given above suggests that, if a well is stimulated by acidizing the formation, the acid treatment must result in an effective radius of 50 ft before the improvement of production rate per unit pressure drop can match the improvement due to a single fracture of infinite capacity having a total length of 200 ft.

A similar interpretation can be placed on the other values of effective well radius associated with the values of the parameter a given in Fig. 9. These values of r'_{wD} indicate that, for large values of a, acidizing shows more promise than fracturing and that, for relatively small values of a, long fractures show more promise than acid treatment. For intermediate values of a, the relative merits of the two methods, according to the interpretation given, will largely depend on the size of the fracture and of the acid treatment.

Still another interpretation can be given to the effective well radius. It is interesting to note that, for a hypothetical case of an actual well radius of 100 ft (corresponding to a large number of distinct finite vertical fractures, each 200 ft in length, centered at the well axis), the maximum improvement in productivity index is 4.7 times the productivity index given by a well of 1/4-ft radius draining a field of 500-ft radius. Since the improvement due to a single fracture for the same conditions has been shown to be 3.3, this factor of 4.7 indicates that, after one long fracture is created, the additional gain by multiple radial fractures (assuming that it is possible to form such a system of fractures) will be small. This, in turn, suggests that one long fracture may be preferred to several shorter ones.

MAXIMUM PRODUCTION RATE FOR A GIVEN FRACTURE VOLUME

For a given fracture volume, an increase in the width results in a shorter fracture. These changes have opposite effects on the production rate, as can be determined from Fig. 9. This raises the question of which parameter values result in a maximum rate of production for a given fracture volume.

This question can be answered by finding the value of a at which q_f at constant fracture volume (constant ar_{eD}^2) has a maximum. The result is that, for a fracture of any volume and a production well of zero radius, the maximum production rate is obtained when a is about 1.25. Thus, from the definition of a, the optimum length-width ratio of any fracture is

$$\frac{2L}{w} = 1.59\,\frac{k_f}{k} \quad \ldots\ldots\ldots\ldots\ldots\ldots (7)$$

Thus, for a fracture volume of 6.4 cu ft/ft of net pay, when $k_f = 100$ darcies and $k = 0.01$ darcy, the optimum dimensions for this fracture volume are $w = 0.02$ and $2L = 320$ ft. Less reasonable values of w and $2L$ could be obtained with different (and yet practical) values of k and k_f.

If we could learn how to control the average separation between fracture faces, fracture treatments could be planned to give optimum results not only on the basis of fracture area alone, but also upon consideration of the length-width ratio of the fracture. These results are valid only in the area below and to the left of the line labeled $r_{eD} = 2$ in Fig. 13. Dashed curves have been extrapolated from $r_{eD} = 2$ to $r_{eD} = 1$,* but this portion of the curves cannot be used with confidence.

EFFECT OF SKIN ON PRODUCTION RATE

Results presented thus far consider no damage to the formation during the fracturing operations. This section will consider the possible loss of potential production due to a damaged zone around the fracture in a region of relatively low permeability, resulting, say, from the plugging of the formation by certain fluid-loss additives which may be used in fracturing treatments.[7]

To obtain an idea of the degree of impairment in production rate due to such a damaged zone, we consider only the case in which the fracture capacity is infinite ($a = 0$). Physically, the decrease in production rate with the damage depends on the flow resistance of the skin compared with that of the formation. It must be noted that the flow resistance depends on the flow pattern. In an unfractured well, this flow resistance is largest nearest the well because the fluids converge radially into the well over its relatively small surface area. Any damage to this zone of high resistance may thus result in drastic reductions in production rate. In a fractured well, the flow is distributed over the large surface area of the fracture, resulting in almost linear flow in the formation near the fracture and, consequently, a small flow resistance. In the latter case, damage to the formation near the fracture may not change the total flow resistance appreciably and, thus, could not be expected to reduce the production rate significantly. Details of the solution of this problem are found in Appendix B. A horizontal cross section of the reservoir-fracture-skin system is shown in Fig. 14.

The ratio of production rate after damage to undamaged production rate is

*For $r_{eD} = 1$, the fracture extends to the (pre-fracture) drainage radius of the field.

$$\frac{q_{fd}}{q_f} = \frac{1}{1 + \dfrac{\dfrac{4\,w_d}{\pi\,L}\left(\dfrac{k}{k_d} - 1\right)}{\ln \dfrac{2\,r_e}{L}}} \quad \ldots\ldots\ldots (8)$$

as developed in Appendix B.

Figs. 15 and 16 show the calculated ratio of production rate after damage to undamaged production rate for fracture lengths of 200 and 40 ft, respectively, in a reservoir of 500-ft radius. A permeability reduction of 99 per cent in a damaged zone of 1-in. average depth results in a reduction of only 4 and 13 per cent for the 200- and 40-ft fractures, respectively. Within this range of fracture length, permeability reduction and depth of damaged zone, the effect of the skin on the production rate is relatively unimportant. However, for a similar damaged zone, a reduction in permeability of 99.9 per cent results in a reduction in production rate of 32 and 58 per cent for the 200- and 40-ft fractures, respectively.

Fig. 15 also gives one of the data points of Ref. 2, which shows more production impairment than our results show. This difference is believed to result from the assumed shape of the damaged zone. In this paper, the skin is widest at the well and thins out toward the ends of the fracture. This simulates the damaged zone due to filtrate invasion which could be obtained with frac fluids having conventional filter-loss response (that is, the loss is proportional to the square root of the time). In Ref. 2, the width of the skin is taken to be constant over the extent of the fracture. This simulates the damaged zone due to filtrate invasion which could be obtained with frac fluids having an initial spurt loss and a small subsequent loss. In this latter case, the depth of the damaged zone and the degree of damage would be approximately uniform over the surface area of the fracture. On the basis of productivity impairment, the use of the frac fluid having a conventional filter-loss response is indicated.

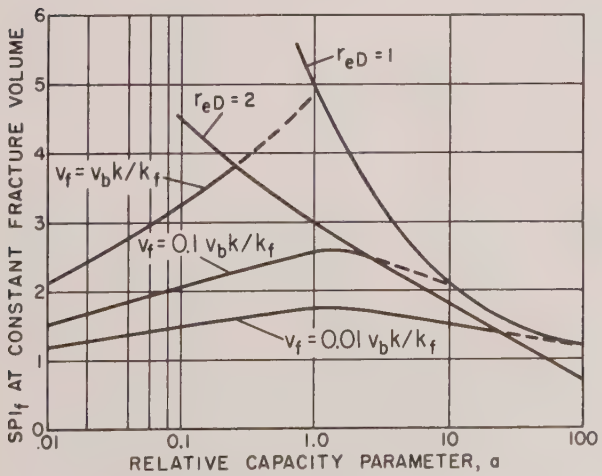

FIG. 13 – CURVES SHOWING THE OPTIMUM PRODUCTION RATE.

Results of a similar nature were also determined for unfractured wells surrounded by a damaged zone. Fig. 17 shows the calculated ratio of production rate after damage to undamaged production rate for an oil sand which has been in contact with fracturing fluids but which has not been fractured. Muskat's [8] equation (7.3.11) was re-arranged as

$$\frac{q_{fd}}{q_f} = \frac{1}{1 + \left(\dfrac{k}{k_d} - 1\right)\dfrac{\ln\left(1 + \dfrac{w_d}{r_w}\right)}{\ln \dfrac{r_e}{r_w}}} \quad \ldots\ldots (9)$$

to obtain these results. For the case of a well of 3-in. radius having a damaged zone 2-in. deep, a permeability reduction of only 90 per cent reduces the production rate by 37 per cent. Thus, we can conclude that the production rate from any sand section which fails to fracture will be reduced severely, especially if the sand section is separated from the fractured sections by shale breaks. This loss in potential production may be obscured by the increased productivity of the fractured sections.

CONCLUSIONS

Some general conclusions drawn or suggested by the results of this study are briefly discussed here. It must be kept in mind that these conclusions are valid only within the limitations of the idealizations used in this investigation. However, they serve at least as valuable guides in other situations.

A high-capacity vertical fracture has an effective well radius of one-fourth the fracture length. This equivalence can be used to advantage to show that the production rate resulting from a 200-ft, high-capacity fracture in a field of 500-ft radius drained by a well of 1/4-ft radius is 3.3 times the production rate before fracturing. Changing either the well or field radius or the fracture length by a factor of two results in production rates from 2.5 to 4.7 times the rate before fracturing. The order of magnitude of this improvement in production rate is believed to correspond to that obtained at semi-steady state in depletion-type reservoirs. The equivalent well radius for fractures of lower capacity is given in the paper.

The improvement in production rate due to a high-

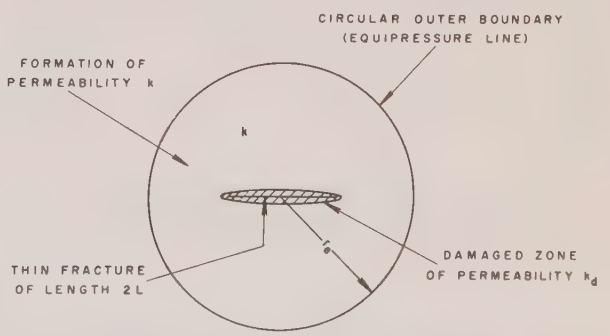

FIG. 14 – HORIZONTAL SECTION THROUGH A VERTICALLY FRACTURED RESERVOIR WITH A SKIN.

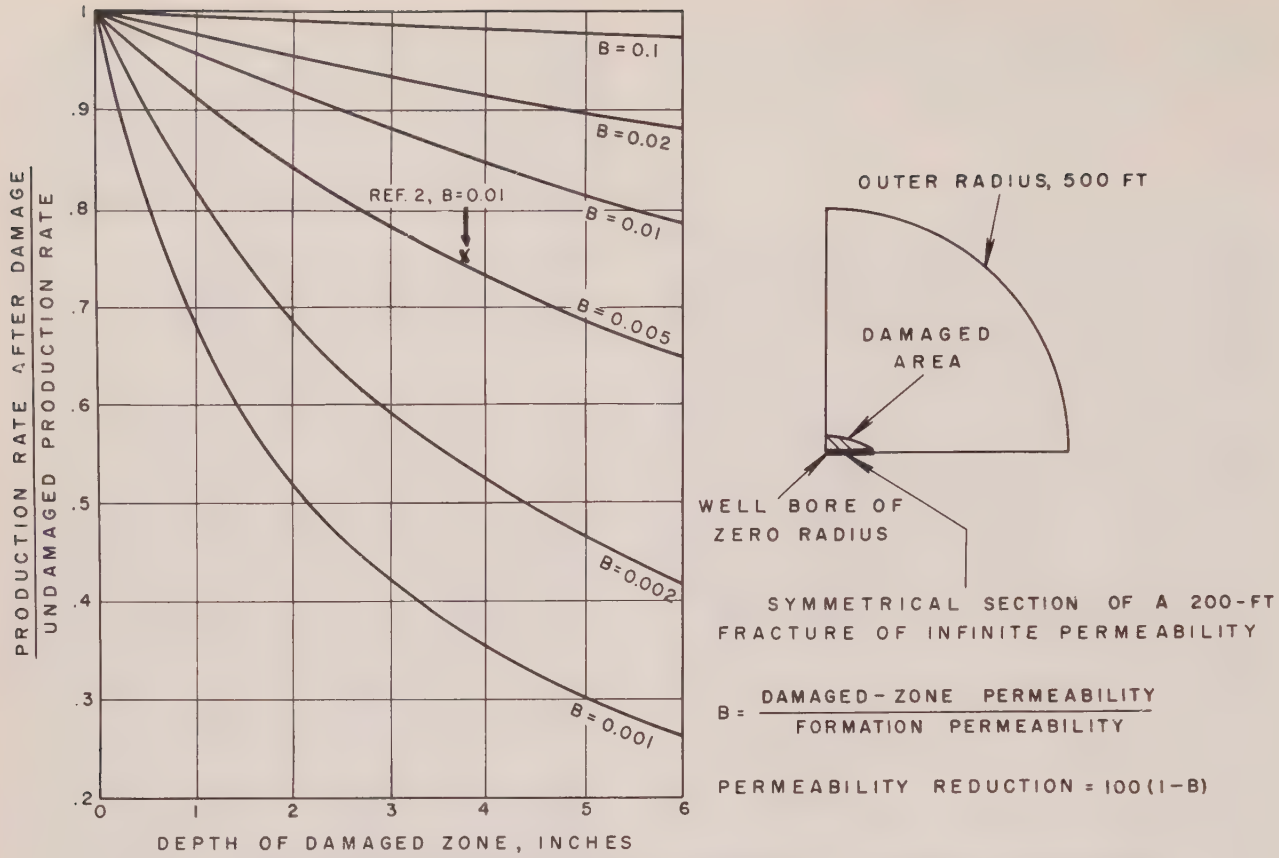
PRODUCTION RATE AFTER DAMAGE / UNDAMAGED PRODUCTION RATE
DEPTH OF DAMAGED ZONE, INCHES
B = 0.1
B = 0.02
REF. 2, B=0.01
B = 0.01
B = 0.005
B = 0.002
B = 0.001
OUTER RADIUS, 500 FT
DAMAGED AREA
WELL BORE OF ZERO RADIUS
SYMMETRICAL SECTION OF A 200-FT FRACTURE OF INFINITE PERMEABILITY
B = DAMAGED-ZONE PERMEABILITY / FORMATION PERMEABILITY
PERMEABILITY REDUCTION = 100(1-B)

FIG. 15 – LOSS OF PRODUCTION DUE TO DAMAGE AROUND A LONG VERTICAL FRACTURE.

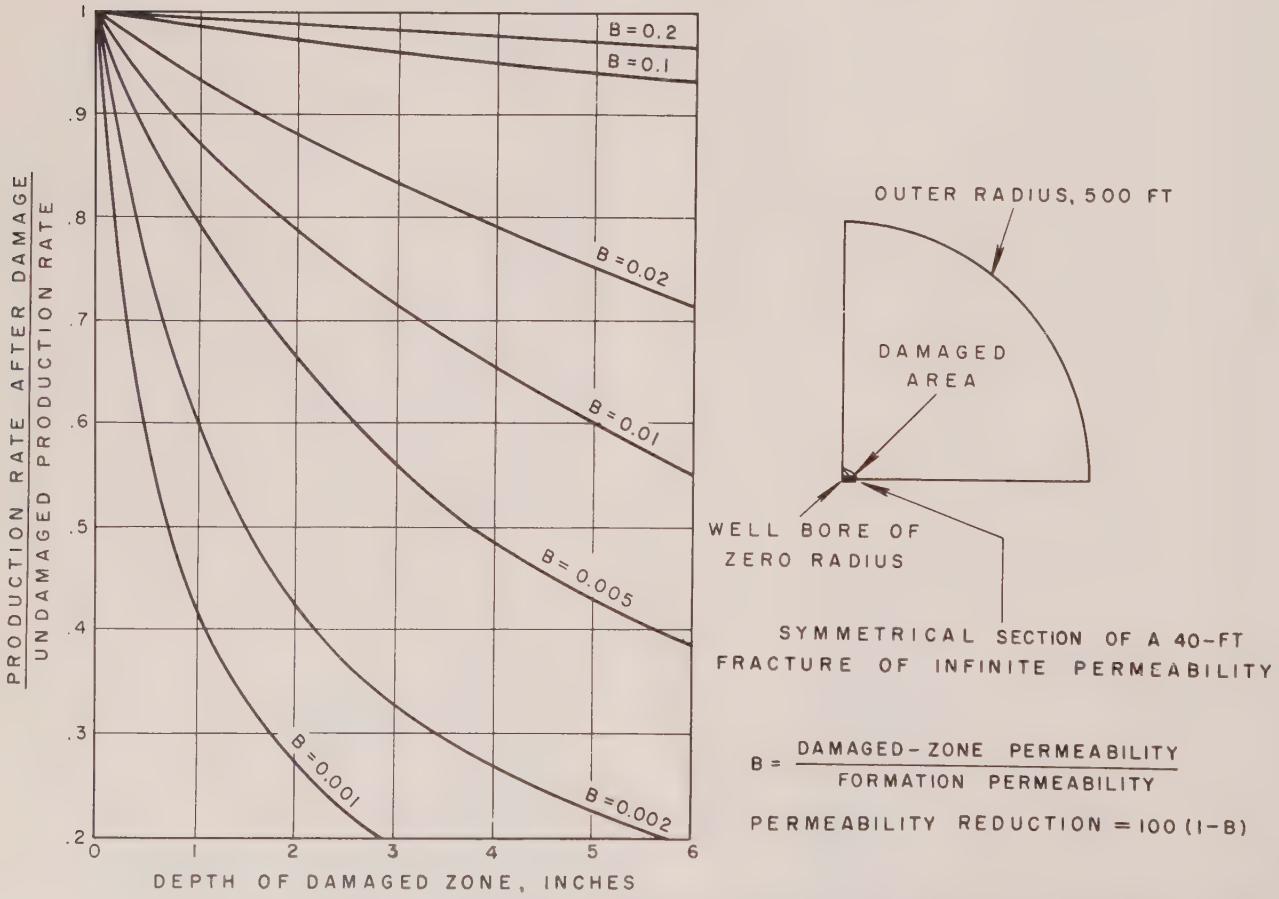
PRODUCTION RATE AFTER DAMAGE / UNDAMAGED PRODUCTION RATE
DEPTH OF DAMAGED ZONE, INCHES
B = 0.2
B = 0.1
B = 0.02
B = 0.01
B = 0.005
B = 0.002
B = 0.001
OUTER RADIUS, 500 FT
DAMAGED AREA
WELL BORE OF ZERO RADIUS
SYMMETRICAL SECTION OF A 40-FT FRACTURE OF INFINITE PERMEABILITY
B = DAMAGED-ZONE PERMEABILITY / FORMATION PERMEABILITY
PERMEABILITY REDUCTION = 100(1-B)

FIG. 16 – LOSS OF PRODUCTION DUE TO DAMAGE AROUND A SHORT VERTICAL FRACTURE.

capacity fracture is equal to the improvement in production rate due to an acid treatment which results in an effective well radius of one-fourth the fracture length. This suggests that fracturing is to be preferred to acidizing if the formation of long fractures appears probable. This conclusion is based on the premise that acid is injected radially into a homogeneous formation (no natural fractures exist) and that the formation is not fractured during the acid treatment.

The pressure drop in the fracture is small (less than 10 per cent of the pressure drop in the field) in most present cases, that is, for $a \leq 0.1$ and fracture lengths less than the field radius. However, pressure drops in the fracture of the order of 25 per cent (and more) of the pressure drop in the field may be expected for values of $a = 0.5$. Such values of a may be realized if fine particles mix with the propping agent or possibly if the present trend in using larger volumes of fracture treatment and sand content continues.

Extensive damage to the formation around a fracture (99 per cent permeability reduction for a depth of 1 in.) may not necessarily result in appreciably poorer production rate response (up to 13 per cent for $r_e/L = 5$). When the depth of the damaged zone is proportional to the filtrate invasion, the decrease in production rate resulting from a frac fluid with a conventional filter-loss response appears to be less than that resulting from a high-spurt-loss frac fluid. However, the production rate from any producing section which fails to fracture may be reduced appreciably (25 per cent for a 90-per-cent permeability reduction for a depth of 1 in. around a 3-in. well radius). Thus, in fracturing a long producing section, loss in potential production due to damaged zones in sections which fail to fracture may be obscured by the increased productivity of the fractured sections.

NOMENCLATURE

a = $(\pi/4)\ (2Lk/wk_f)$, dimensionless
h = net formation thickness, cm
k = effective formation permeability to oil, darcy
L = half the fracture length, ft
ln = logarithm to the base e
p = pressure, atm
q = production rate, cc/sec
r = distance from well axis, ft
r'_w = effective well radius of a fracture, ft
SPI = $q\mu/kh\Delta p$, dimensionless specific productivity index
V_f = volume of the fracture, cu ft
V_b = bulk volume of the formation, cu ft
w = average width of the fracture, ft
w_d = average depth of the damaged zone, ft
x = distance from well, ft

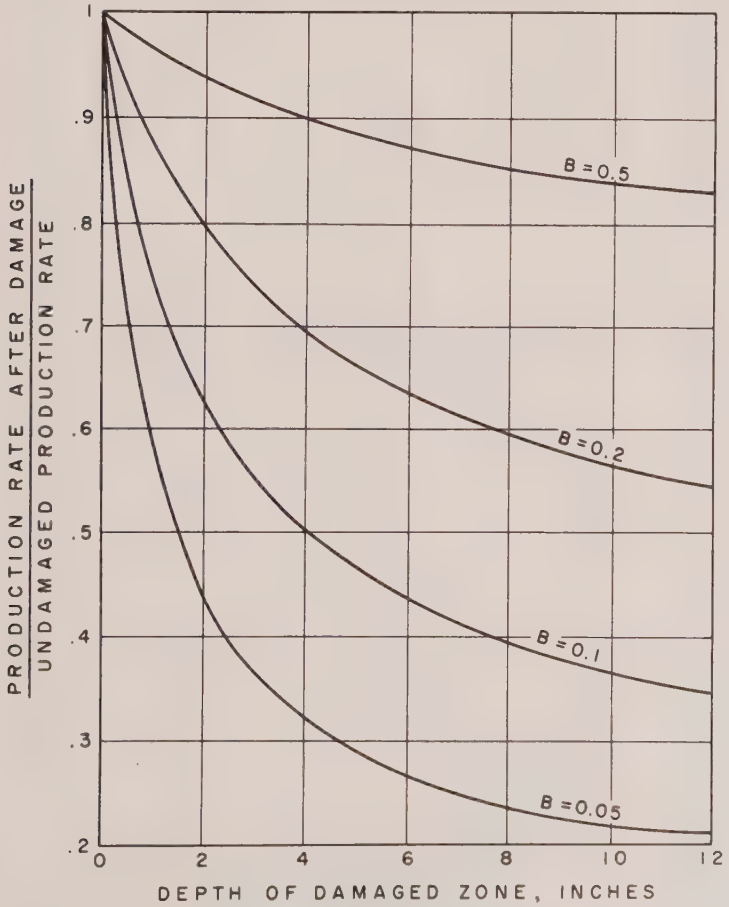

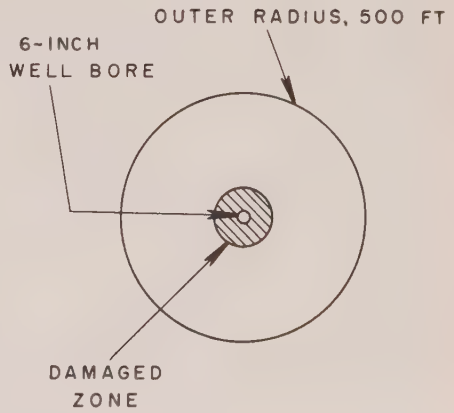

$$B = \frac{\text{DAMAGED-ZONE PERMEABILITY}}{\text{FORMATION PERMEABILITY}}$$

PERMEABILITY REDUCTION = 100(1−B)

FIG. 17—LOSS IN PRODUCTION DUE TO DAMAGE AROUND A WELLBORE.

$\Delta P_{i,j} = kh(p_i - p_j)/q\mu$, dimensionless

Δp = pressure drop between outer boundary and well, atm

$p_i - p_j$ = pressure drop between two points symbolized by i and j, atm

μ = viscosity of produced fluid, cp

SUBSCRIPTS

D = dimensionless, all distances are referred to L, one-half the fracture length

d = damaged

e = external boundary

f = fracture

L = end of fracture

O = well axis

w = wellbore

x = distance along fracture

REFERENCES

1. van Poollen, H. K., Tinsley, J. M. and Saunders, C. D.: "Hydraulic Fracturing: Fracture Flow Capacity vs Well Productivity", *Trans.*, AIME (1958) Vol. 213, 91.
2. van Poollen, H. K.: "Productivity vs Permeability Damage in Hydraulically Produced Fractures", *Drill. and Prod. Prac.*, API (1957) 103.
3. Hubbert, M. K. and Willis, D. G.: "Mechanics of Hydraulic Fracturing", *Trans.*, AIME (1957) Vol. 210, 167.
4. Crawford, P. B. and Collins, R. E.: "Estimated Effect of Vertical Fractures on Secondary Recovery", *Trans.*, AIME (1954) Vol. 198, 192.
5. Crawford, Paul B., Honeycutt, Baxter, Sanderlin, James and Ince, Henry: "How Do Vertical Fractures Affect a Cycling Program", *World Oil* (Oct., 1956) Vol. 143, 245.
6. Southwell, R. V.: *Relaxation Methods in Theoretical Physics*, The Clarendon Press, Oxford U., N. Y. (1946).
7. Allen, T. O. and Hough, E. W.: "Determination of Formation Damage from Fracturing Fluids by Laboratory Techniques", *Drill. and Prod. Prac.*, API (1957) 33.
8. Muskat, M.: *The Flow of Homogeneous Fluids through Porous Media*, McGraw-Hill Book Co., Inc., N. Y. (1937).
9. Prats, M., Stricker, W. R. and Matthews, C. S.: "Single-Fluid Five-Spot Floods in Dipping Reservoirs", *Trans.*, AIME (1955) Vol. 204, 160.

APPENDIX A

METHOD OF SOLUTION USED TO OBTAIN THE PRESSURE DISTRIBUTION IN A VERTICALLY FRACTURED SYSTEM

As a consequence of the assumptions made in the text with regard to the fluids and the formation, the pressure obeys Laplace's equation both in the fracture and in the reservoir. The detailed mathematical procedures used in solving Laplace's equation to obtain the pressure distribution in the formation and in the fracture are given herein, but it seems desirable to indicate first two pertinent points about the method of solution.

One of these points is that the circular outer boundary is replaced by an ellipse having an almost circular shape. The ratio of axes of the ellipses chosen depends on the fracture length but is in all cases greater than 0.88. It was actually shown that, for $r_{eD} \geq 2$, the use of the slightly elliptical boundary has a negligible effect on the value and shape of the interior equipressure lines given in Figs. 4 through 7.

The second point is that the reservoir is divided into two regions of different permeability, Regions I and II, as shown in Fig. 18. Region I represents the fracture of permeability k_f, and Region II represents the formation of permeability k.

Initially, Region I is represented by the interior of an ellipse with foci at $x = \pm L$. The circular outer boundary of radius r_e is replaced by an almost circular ellipse of equivalent radius, also having foci at $x = \pm L$. Region II, between the outer boundary and the inner ellipse, represents the formation proper. The pressure distribution in these two regions is then obtained by making use of conformal-mapping transformations and Fourier series. In the final stage of the method of solution, the minor axis of the inner ellipse is reduced to zero in such a way that the average width of the ellipse times its permeability corresponds to the fracture capacity. The inner ellipse of zero minor axis degenerates to the straight line with ends at $x = \pm L$ and, thus, represents the fracture shown in Fig. 2. This is the method used to obtain the pressure distribution for the fractured system shown in Fig. 2. A somewhat more detailed description follows.

The pressure in Regions I and II obeys Laplace's equation:

$$\nabla^2 p_1 = 0 \text{ in Region I} \quad , \quad . \quad . \quad . \quad . \quad . \quad . \quad . \quad . \quad . \quad (A\text{-}1)$$

$$\nabla^2 p_2 = 0 \text{ in Region II} \quad , \quad . \quad . \quad . \quad . \quad . \quad . \quad . \quad . \quad . \quad (A\text{-}2)$$

with refraction conditions

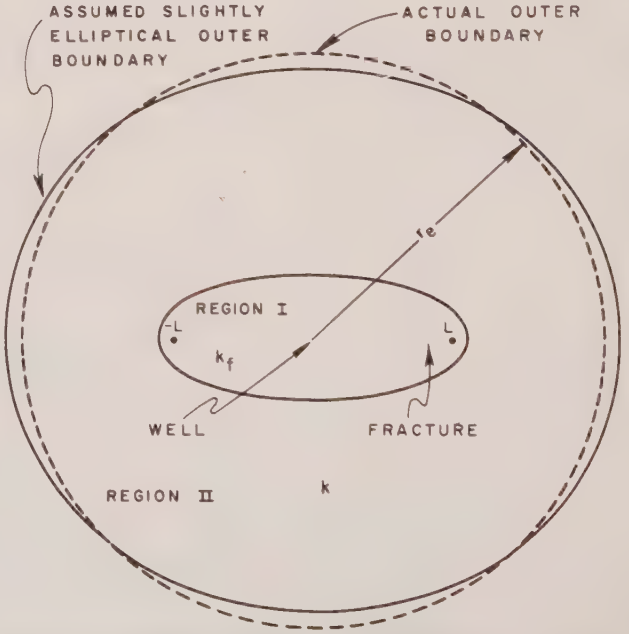

FIG. 18—AUXILIARY MODEL OF RESERVOIR SYSTEM.

$$\left.\begin{aligned} p_1 &= p_2 \,, \\ k_f \frac{\partial p_1}{\partial n} &= k \frac{\partial p_2}{\partial n} \end{aligned}\right\} \quad \ldots\ldots\ldots\ldots \text{(A-3)}$$

on the boundary of inner ellipse, where derivatives are taken normal to this boundary, and boundary conditions

$$\frac{\partial p_1}{\partial y} = 0 \quad \text{on} \quad y = 0,\ x \neq 0 \quad \ldots\ldots \text{(A-4)}$$

$$\frac{\partial p_2}{\partial y} = 0 \quad \text{on} \quad y = 0 \,. \quad \ldots\ldots\ldots \text{(A-5)}$$

$p_2 = c_o$ (a constant) on the outer boundary, and q/h is the production rate per unit thickness at the well located at $x = 0$, $y = 0$.

It is difficult to apply these conditions in a Cartesian co-ordinate system on elliptical curves; thus, the transformation $z = x + jy = L \cosh \zeta = L \cosh (\xi + j\eta)$ is used to map the two regions in the first quadrant of the reservoir shown in Fig. 18 into the rectangles shown in Fig. 19.

The pressure in the rectangular Regions I and II of Fig. 19 still obeys Laplace's equation and the refraction conditions at the common boundary between the two regions, represented now by $\xi = \xi_1$. The boundary conditions become

$$\frac{\partial p_1}{\partial \eta} = \frac{\partial p_2}{\partial \eta} = 0 \quad \text{on} \quad \eta = 0,\ \eta = \frac{\pi}{2} \quad \ldots \text{(A-6)}$$

and

$$\frac{\partial p_1}{\partial \xi} = 0 \quad \text{on} \quad \xi = 0 \quad \ldots\ldots \text{(A-7)}$$

because of symmetry, and

$$p_2 = c_o \quad \text{on} \quad \xi = \xi_e, \text{ where } \frac{L}{r_e} = 2e^{-\xi_e} \,. \quad \text{(A-8)}$$

q/h is the production rate per unit thickness at the well located at $\xi = 0$, $\eta = \pi/2$.

To decrease the likelihood of obtaining a slowly convergent series for the pressure distribution owing to the singular behavior of the production well (point sink) at D ($\xi = 0$, $\eta = \pi/2$) in Fig. 19, it was considered desirable to define reduced pressures by subtracting a solution having the same singular behavior at D and satisfying the boundary conditions but not the refraction conditions. Thus, the

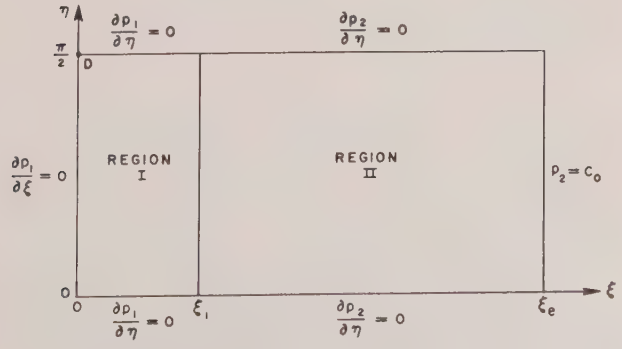

FIG. 19—RESERVOIR MAPPED IN ξ, η PLANE.

reduced pressures are

$$\phi_1 (\xi,\eta) = k_f p_1 (\xi,\eta) - p_s (\xi,\eta) \,. \quad \ldots \text{(A-9)}$$

$$\phi_2 (\xi,\eta) = k p_2 (\xi,\eta) - p_s (\xi,\eta) \quad \ldots \text{(A-10)}$$

where $p_s (\xi,\eta)$, the pressure distribution having the desired singular behavior at D and satisfying the boundary conditions, is given by

$$p_s (\xi,\eta) = -q_o \, Re \, \ln \operatorname{dn} \left(\frac{\zeta K}{2\xi_e} \,\middle|\, m \right) \,, \quad \text{(A-11)}$$

where q_o is the production rate in reduced units ($q_o = q\mu/2\pi h$), and dn is one of the Jacobian elliptic functions of parameter m. The parameter m is chosen such that

$$\frac{\pi}{4\xi_e} = \frac{K'(m)}{K(m)} \quad , \quad \ldots\ldots\ldots\ldots \text{(A-12)}$$

where $K'(m)$ and $K(m)$, related by $K'(1-m) = K(m)$, are the complete elliptic integrals of the first kind. Properties of these functions can be found in any standard text on the subject, and the method for obtaining this solution is given in Ref. 9.

The boundary condition at $\xi = \xi_e$ requires that

$$c_o = p_s (\xi_e,\eta) = \frac{-q_o}{4} \ln (1-m) \,;$$

but, although $p_s (\xi,\eta)$ satisfies all the boundary conditions of p_1 and p_2, it does not satisfy the refraction conditions. Therefore, the boundary and refraction conditions for the reduced pressures are

$$\frac{\partial \phi_1}{\partial \eta} = \frac{\partial \phi_2}{\partial \eta} = 0 \quad \text{on} \quad \eta = 0,\ \eta = \frac{\pi}{2} \,. \quad \text{(A-13)}$$

$$\frac{\partial \phi_1}{\partial \xi} = 0 \quad \text{on} \quad \xi = 0 \quad \ldots\ldots \text{(A-14)}$$

$$\phi_2 = 0 \quad \text{on} \quad \xi = \xi_e \quad \ldots \text{(A-15)}$$

$$\left.\begin{aligned} k\phi_1 &= k_f \phi_2 + (k_f - k) p_s \\ \frac{\partial \phi_1}{\partial \xi} &= \frac{\partial \phi_2}{\partial \xi} \end{aligned}\right\} \quad \text{on} \quad \xi = \xi_1 \,. \quad \text{(A-16)}$$

The use of Fourier series is particularly well suited to obtain the reduced pressure distributions ϕ_1 and ϕ_2. These are given by

$$\phi_1 (\xi,\eta) = \sum_{n=0}^{\infty} A_n \cos 2n\eta \cosh 2n\xi \,, \quad \text{(A-17)}$$

$$\phi_2 (\xi,\eta) = \sum_{n=0}^{\infty} B_n \cos 2n\eta \sinh 2n(\xi_e - \xi) \quad \ldots\ldots\ldots\ldots \text{(A-18)}$$

where these expressions satisfy all conditions except the refraction conditions. By making use of the refraction conditions given by Eq. A-16, it is possible to determine the constants A_n and B_n, so that

$$\phi_1(\xi,\eta) = -(k_f - k)\,\frac{q_o}{k}\left\{\xi_e + \frac{1}{4}\ln(1-m) + k\sum_{n=1}^{\infty}\frac{K_n(0)\cos 2n\eta\cosh 2n\xi}{[k + k_f \tanh 2n(\xi_e - \xi_1)\tanh 2n\xi_1]\cosh 2n\xi_1}\right\}$$

. . . . . (A-19)

and

$$\phi_2(\xi,\eta) = (k_f - k)q_o \cdot \sum_{n=1}^{\infty}\frac{K_n(0)\cos 2n\eta \sinh 2n(\xi_e - \xi)\tanh 2n\xi_1}{[k + k_f \tanh 2n(\xi_e - \xi_1)\tanh 2n\xi_1]\cosh 2n(\xi_e - \xi_1)},$$

. . . . . (A-20)

with

$$K_n(0) = \frac{(-1)^n}{n} - \frac{2}{n}\left[\frac{1}{1 + (-q_1)^n} - \frac{1 - (-1)^n}{1 - q_1^{2n}}\right]q_1^n,$$

. . . . . (A-21)

and where $q_1 = e^{-4\xi_e} = (L/2r_e)^4$ is very small.

From Eqs. A-9 and A-10, the pressure in the fracture (p_1) and in the formation (p_2) are given by

$$p_1(\xi,\eta) = \frac{1}{k_f}(p_s + \phi_1) = \frac{p_s(\xi,\eta)}{k_f} - \left(1 - \frac{k}{k_f}\right)\cdot \frac{q_o}{k}\left\{\xi_e + \frac{1}{4}\ln(1-m) + k\sum_{n=1}^{\infty}\frac{K_n(0)\cos 2n\eta\cosh 2n\xi}{[k + k_f \tanh 2n(\xi_e - \xi_1)\tanh 2n\xi_1]\cosh 2n\xi_1}\right\}$$

. . . . . (A-22)

and

$$p_2(\xi,\eta) = \frac{1}{k}(p_s + \phi_2) = \frac{p_s(\xi,\eta)}{k} + \left(\frac{k_f}{k} - 1\right)q_o \cdot \sum_{n=1}^{\infty}\frac{K_n(0)\cos 2n\eta \sinh 2n(\xi_e - \xi)\tanh 2n\xi_1}{[k + k_f \tanh 2n(\xi_e - \xi_1)\tanh 2n\xi_1]\cosh 2n(\xi_e - \xi_1)}$$

. . . . . (A-23)

These solutions given for the pressures in the formation and in the fracture are valid for any fracture of elliptical shape as shown in Fig. 18. In practice, however, the fracture is narrow and long and has a high permeability. For these conditions, the reservoir pressure $p(\xi,\eta)$ is given by

$$p(\xi,\eta) = \underset{\substack{\xi_1 \to 0 \\ k_f \to \infty \\ 2L\xi_1 k_f = Ca'}}{\text{Limit}} p_2(\xi,\eta;\ \xi_e, \xi_1, k, k_f) \quad \text{. (A-24)}$$

$$= \frac{p_s(\xi,\eta)}{k} + \frac{2q_o}{k}\sum_{n=1}^{\infty}\frac{n\cos 2n\eta \sinh 2n(\xi_e - \xi)}{(a + 2n\tanh 2n\xi_e)\cosh 2n\xi_e}K_n(0),$$

. . . . . (A-25)

where

$$a = \frac{2Lk}{Ca'}, \quad \text{. . . . . (A-26)}$$

and Ca' is the permeability of the fracture times its maximum width, the minor axis of the ellipse.

In a similar manner, the pressure in the narrow fracture can be found to be

$$p_f(\eta) = \frac{-q_o}{k}\left[\xi_e + \frac{1}{4}\ln(1-m) + a\sum_{n=1}^{\infty}\frac{\cos 2n\eta}{a + 2n\tanh 2n\xi_e}K_n(0)\right] \quad \text{(A-27)}$$

Although the fracture capacity Ca' has been defined above in terms of the maximum width of the fracture, it may be more reasonable to define a new fracture capacity Ca in terms of the average fracture width w. Since the average width of such a fracture is $\pi/4$ times its maximum width, it follows that the average capacity of the fracture Ca is given by

$$Ca = \frac{\pi}{4}Ca' \quad \text{. . . . . (A-28)}$$

and

$$a = \frac{\pi}{4}\frac{2Lk}{wk_f} \quad \text{. . . . . (A-29)}$$

Eqs. A-25, A-27 and A-29 were used for evaluating the results discussed in the text.

APPENDIX B

EFFECT OF A SKIN ON PRODUCTION RATE

Use is made of the methods discussed in Appendix A to investigate the effect of a skin on the production rate. For the case of infinite fracture capacity ($a = 0$), the entire fracture is at a uniform pressure equal to the well pressure. We shall call this fracture pressure p_f. The damaged zone around the fracture shown in Fig. 14 and the rest of the reservoir can be transformed into rectangular sections

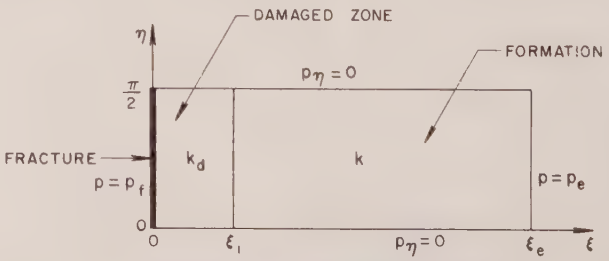

FIG. 20 — DAMAGED, FRACTURED RESERVOIR IN TRANSFORMED PLANE.

as shown in Fig. 20.

We note from Fig. 20 that the pressure distribution in ξ should be the same for all values of η; that is, the pressure distribution is only a function of ξ. This is because the pressure obeys Laplace's equation in both the ξ, η plane and in the x, y plane; therefore, the pressure distribution in the skin of permeability k_s is

$$p_d = b + c\,\xi \ ,$$

and the pressure distribution in the reservoir is

$$p = d + e\,\xi \ .$$

The constants b, c, d and e appearing in these equations are to be determined from the boundary conditions

$p_d = p_f$ at $\xi = 0$ (the fracture),

$p = p_e$ at $\xi = \xi_e$ (the outer boundary of the field),

and the refraction conditions

$$p_d = p$$

$$k_d \frac{dp_d}{d\xi} = k \frac{dp}{d\xi} \quad \text{on} \quad \xi = \xi_2$$ (the boundary between the skin and the formation).

The quantity ξ_1 is related to the average depth of the skin by

$$w_d = \frac{\pi}{4} L\xi_1$$

where $2L$ is the total length of the fracture. The quantity ξ_e is related to the average field radius r_e by

$$\xi_e = \ln \frac{2r_e}{L} \ .$$

The application of the boundary, refraction and Darcy equations leads to a production rate after damage given by

$$q_{fd} = \frac{2\pi kh}{\mu} \frac{(p_e - p_f)}{\ln \frac{2r_e}{L} + \left(\frac{k}{k_d} - 1\right)\frac{4w_d}{\pi L}} \ .$$

Before the formation is damaged, $k_d = k$, and the production rate is

$$q_f = \frac{2\pi kh}{\mu} \frac{(p_e - p_f)}{\ln \frac{2r_e}{L}} \ .$$

Thus, the ratio of damaged to undamaged production rate is given by

$$\frac{q_{fd}}{q_f} = \frac{1}{1 + \frac{\frac{4w_d}{\pi L}\left(\frac{k}{k_d} - 1\right)}{\ln \frac{2r_e}{L}}} \ .$$

DISCUSSION

F. E. CAMPION
MEMBER AIME

JERSEY PRODUCTION RESEARCH CORP.
TULSA, OKLA.

The results of Prats' analysis of flow behavior in vertical fractures are enlightening, particularly in regard to the effects of formation damage. The conclusions he has reached concerning the effects of damage to fractured wells appear valid within the framework of the assumptions set forth; however, further comments seem appropriate regarding the projection of these results to a physical prototype.

The author has demonstrated resourcefulness in the treatment and handling of this problem, but we feel that the conditions assumed for evaluation of fracture damage are optimistic. There are a number of conditions that could render his results less favorable. For this reason, a direct extrapolation of his conclusions to a practical field situation may be difficult if the situation does not comply with the assumptions prescribed for the mathematical model. Frac fluids that damage formation permeability may not necessarily reduce production-rate response, but it is not difficult to envision a situation where they could.

It appears from this study that the shape of the damaged zone surrounding the fracture is a critical factor in determining the fluid-flow behavior in the system and that much depends on the fluid-loss characteristics of the fracturing fluid. Since high spurt loss is not uncommon for frac fluids, less favorable production-rate response than that cited in the paper may occur as a result of the more uniform distribution of damage along the fracture length.

Considerations other than fluid-loss characteristics are also important in determining the suitability of fracturing fluids. The depth of formation damage may also be significant. Although depth of damage is limited, in many instances to 1 or 2 in., this is not consistent for all frac fluids. We have found wide variations in the depth as well as degree of damage and feel that assignment of representative values for either of these factors is restrictive.

The assumption of infinite fracture capacity

employed in the study may also limit the scope of the results. van Poollen[1] has shown that the effects of formation damage are compounded by reduced fracture capacity. Our experience shows that frac fluids which damage formation permeability may also reduce permeability of propping agents in the fracture. Although it has become common practice to neglect pressure drop in the fracture, this assumption is not wholly justified and conclusions based upon it tend to be optimistic.

Laboratory measurements of permeability damage by fracturing fluids can do much to aid in the selection of suitable frac fluids. Although these measurements may not be useful in a strict quantitative sense, they can serve as a basis for comparison of fracture fluids. Through such tests, the use of fluids which do extensive damage can be avoided and the risk of losing significant quantities of oil over a period of years can be minimized.

[1]van Poollen, H. K.: "Productivity versus Permeability Damage in Hydraulically Produced Fractures", *Drill. and Prod. Prac.*, API (1957) 103.

AUTHORS' REPLY TO S. E. CAMPION

Although the conditions assumed in the report for evaluating fracture damage may be optimistic in some cases, it is clear that the conditions assumed in the other published works on this subject,[2] namely that of a uniformly thick damaged zone, are definitely pessimistic. Even with the assumption of a uniformly thick damage zone over the entire fracture surface, results in Ref. 2 indicate that the main contribution to the production is derived from the portion of the fracture surface which is farther from the well. When one considers that the time of contact between the frac fluid and the fracture surface is longest nearest the well, it is almost certain that the extent of damage and the depth of the damaged zone would be smallest far from the well, regardless of the type and properties of the frac fluid used. Thus, it is entirely reasonable to anticipate that the contribution to production from the sections of the fracture surface farther from the well under conditions existing in the formation after a frac treatment would be larger than indicated in Ref. 2. This means that the results of Ref. 2 regarding the effect of a damage zone on loss of production are pessimistic.

It should be stressed that, although the general shape of the damaged zone can be surmised to thin out with increasing distance from the well, its exact shape in situ will probably never be determined. In fact, the shape of the damaged zone and the extent of damage will depend not only on the properties of the frac fluid, but also on those of the reservoir rock fluids as well as on the pressure, saturation and temperature conditions existing in the reservoir at the time of the fracture treatment. For example, a gas saturation increasing towards the well could result in a damaged zone which thins out away from the well. Thus, it cannot be said that the results presented in the paper are generally optimistic, although they might be in some cases. By contrast, the results of Ref. 2 are almost certainly pessimistic.

Although the paper does not consider the multiple effects of a damage zone and reduced fracture capacity, similar arguments suggest that the results presented for such conditions in the only other reference to the subject are also somewhat pessimistic. ★★★

Sand Concentration for Maximum Fracture Flow Capacity

ANTONIO ROMERO-JUÁREZ
MEMBER AIME

PETRÓLEOS MEXICANOS
MEXICO, D. F.

ABSTRACT

This paper is concerned with the effect of propping-agent concentration on flow capacity of a fracture in the case in which there is embedment of the propping agent. Previous published studies have shown definitely that there is a relationship between fracture flow capacity and propping-agent concentration, and it has been shown that the theoretical results are confirmed by laboratory experiments.

The problem of directly finding sand concentration for maximum flow capacity of a sand-propped fracture is solved, and formulas and charts are given to obtain this concentration under various conditions of effective overburden pressure, medium sand-grain diameter and rock properties. It is shown that, for the same effective overburden pressure and the same rock characteristics, optimum sand concentration in pounds per gallon does not depend on medium sand diameter. For conditions met in hydraulic fracturing operations, it is found that sand concentration in grains per square inch for maximum flow capacity varies within a wide range of values; this indicates the convenience of using data of fracturing pressure and rock characteristics for calculating sand concentration in order to achieve the best results in fracture treatments.

INTRODUCTION

It has been pointed out in the published literature[1] that one important factor controls the success of a hydraulic fracturing operation – the propping of the fracture. The main effect of the propping agent is to hold the fracture open by means of the reaction forces that oppose the pressure due to the overburden. It is assumed in this paper that the propping agent is sand, that the grains are spherical and uniform in size, and that this sand is distributed in a monolayer in the fracture.

The existence of a sand concentration value for maximum fracture flow capacity has been recognized since the publication of one of the first studies on the subject.[2] In the reference cited, flow capacity was assumed to be proportional to the cube of the fracture volume per square inch not filled by sand.

The obtained experimental curves relating to flow capacity and sand concentration had the same appearance as the curves obtained with the afore-mentioned assumption. Recent work[3] has shown that fracture permeability, in the case of a monolayer, can be calculated accurately by means of a modified Kozeny-Carman equation; thus, it can be shown that fracture permeability is a function of free volume in the fracture and of the rock and sand wet surfaces.

The flow capacity of a fracture is dependent on the permeability of the fracture and on the fracture width. If an excessive quantity of sand is present in the fracture, its width may be large but its permeability is low due to the greater flow resistance; too few grains of sand per square inch are present in the fracture, sand embedment in the rock is greater and the width becomes small enough to appreciably decrease the rate of flow. To determine optimum conditions of flow, therefore, it is necessary to know the dependence of fracture width on density or concentration of propping agent. This relation is given in a study[4] in which the approach to embedment is similar to the one made in a penetration hardness test of metal.

With the equations presented by Darin and Huitt,[3] the number of sand grains per square inch that results in maximum fracture capacity can be determined graphically by plotting fracture capacity vs sand concentration.

Since the relationship between fracture capacity and sand concentration may be considered known, one is led to formulate the analytical problem of directly determining sand concentration for maximum fracture flow capacity, in order to study the effect of the various quantities that come into the process.

The solution of this problem appears to be interesting both from the viewpoint of fluid mechanics and from the practical viewpoint of oil production in hydraulic fracturing treatments.

EQUATION FOR FRACTURE FLOW CAPACITY

It can be shown[3] that the fracture flow capacity of a monolayer is given by the following expression,

Original manuscript received in Society of Petroleum Engineers office April 13, 1960. Revised manuscript received April 10, 1961. Paper presented at 35th Annual Fall Meeting of SPE, Oct. 2-5, 1960, in Denver.

[1]References given at end of paper.

obtained by a modified Kozeny-Carman equation.

$$(KW_f) = 1.1 \times 10^{10} \frac{W_f}{S_p^2} \frac{\Phi_p^3}{(1-\Phi_p)^2}, \quad \ldots\ldots\ldots\ldots\ldots\ldots\ldots (1)$$

where (KW_f) = fracture capacity in md-ft, W_f = fracture width (in.) and ϕ_p = porosity of a partial monolayer, given by

$$\Phi_p = \frac{W_f - V_p}{W_f}, \quad \ldots\ldots\ldots\ldots\ldots\ldots\ldots (2)$$

where V_p = volume of sand between fracture faces per unit area of fracture surface.

Also in Eq. 1

$$S_p = \frac{A_w}{V_p}, \quad \ldots\ldots\ldots\ldots\ldots\ldots\ldots (3)$$

in which A_w is the total (rock and sand) wetted area (square inch per square inch) of fracture.

Now, substituting Eqs. 2 and 3 in Eq. 1,

$$(KW_f) = 1.1 \times 10^{10} \frac{W_f^3 \Phi_p^3}{A_w^2},$$

or

$$(KW_f) = \frac{1.1 \times 10^{10}}{A_w^2} (W_f - V_p)^3. \quad \ldots\ldots\ldots\ldots\ldots\ldots\ldots (4)$$

(Compare Dehlinger, *et al*,[2] Eqs. 7 and 8.)

From the geometry of the problem it also is readily found that

$$V_p = n\pi W_f \left(\frac{D^2}{4} - \frac{W_f^2}{12}\right) \quad \ldots\ldots\ldots\ldots\ldots\ldots\ldots (5)$$

and

$$A_w = 2 - \frac{n\pi}{2}(D^2 - W_f^2) + n\pi D W_f \quad \ldots\ldots\ldots\ldots\ldots\ldots\ldots (6)$$

if n = sand concentration = number of grains per square inch (one face of fracture) and D = mean sand-grain diameter.

Then, the equation for fracture capacity can be written in the following convenient form.

$$(KW_f) = \frac{1.1 \times 10^{10}}{A_w^2} \left[W_f - n\pi W_f \left(\frac{D^2}{4} - \frac{W_f^2}{12}\right)\right]^3 \quad \ldots\ldots\ldots\ldots\ldots\ldots\ldots (7)$$

FRACTURE WIDTH AND TREATING PRESSURE

The following relation is found[4] to adequately describe the embedment of a spherical sand grain in a formation.

$$\frac{d}{D} = B^{1/2} \left(\frac{L}{D^2}\right)^{\frac{m}{2}} \quad \ldots\ldots\ldots\ldots\ldots\ldots\ldots (8)$$

In this equation, d is the diameter of the impression made by the penetrating grain, L is the load in the grain, and B and m are two characteristic constants of the formation rock. Since embedment increases with B, this characteristic constant will be called "softness" of the rock; m could be called the "pseudo-rigidity". Eq. 8 is supported by experimental data.

From the problem's geometry,

$$W_f^2 = D^2 - d^2. \quad \ldots\ldots\ldots\ldots\ldots\ldots\ldots (9)$$

Combining Eqs. 8 and 9 and putting

$$L = \frac{P_e}{n},$$

P_e being the effective overburden pressure, the following equation results for fracture width.

$$W = D\left[1 - B\left(\frac{P_e}{nD^2}\right)^m\right]^{1/2}. \quad \ldots\ldots\ldots\ldots\ldots\ldots\ldots (10)$$

By means of Eqs. 6, 7 and 10, fracture capacity may be calculated as a function of concentration for different values of effective overburden pressure.

Figs. 1 and 2 show flow capacity vs sand concentration for two fractures propped with sand of different grain diameter. For Fig. 1, D = 0.025 in. (20–30 mesh), P_e = 600 psi, $B = 6.8 \times 10^{-5}$ and m = 0.92. For Fig. 2, D = 0.16 in. (4–6 mesh), P_e = 3,000 psi, $B = 4.2 \times 10^{-5}$ and m = 1.

Note that a large-diameter propping sand produces a fracture flow capacity of about two orders of magnitude greater than that obtained with a small (20–30 mesh) sand grain.

The following considerations are made in order to estimate the values of effective overburden pressure when a fracture is induced.

The effective overburden pressure is the difference between the confining pressure P_c, which tends to close the fracture, and the formation pressure P_f.

$$P_e = P_c - P_f. \quad \ldots\ldots\ldots\ldots\ldots\ldots\ldots (11)$$

There has been a great controversy over the determination of confining pressure P_c. According to most investigators,[5] P_c for horizontal fractures is equal to the overburden pressure P_{ob} corresponding to the weight of the overlaying rocks; therefore,

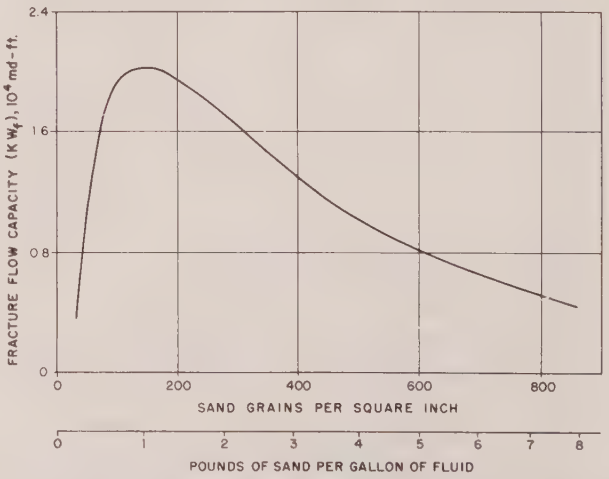

FIG. 1 – FRACTURE FLOW CAPACITY AS A FUNCTION OF SAND CONCENTRATION FOR 0.025-IN. MEAN SAND-GRAIN DIAMETER (20-30 MESH).

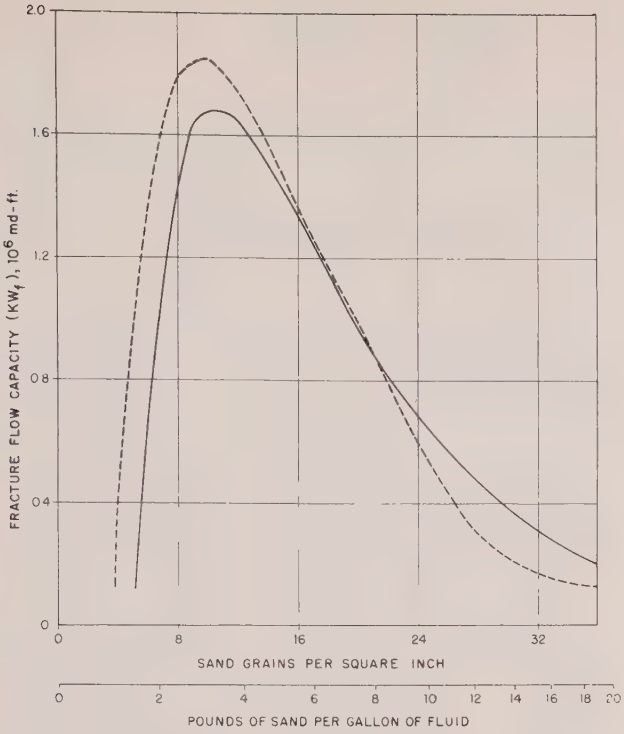

FIG. 2 – FRACTURE FLOW CAPACITY AS A FUNCTION OF SAND CONCENTRATION FOR 0.16-IN. MEAN SAND-GRAIN DIAMETER (4-6 MESH). DOTTED CURVE CALCULATED BY MEANS OF APPROXIMATE FORMULAS.

P_c is simply the product of the specific weight of the rock times the depth. For a fracture making its plane on an angle Φ with the horizontal, the confining pressure is

$$P_c = \frac{P_{ob}}{2}\left[\left(1+\frac{2\mu}{1-\mu}\right) + \left(1-\frac{2\mu}{1-\mu}\right)\cos 2\Phi\right], \quad \ldots\ldots\ldots\ldots\ldots\ldots\ldots\ldots (12)$$

μ being Poisson's ratio. It follows from Eq. 12 that, for a vertical fracture,

$$P_c = \frac{2\mu P_{ob}}{1-\mu} \quad \ldots\ldots\ldots\ldots (13)$$

Several authors[5] give field data on treating pressures. A rough estimation will be made here of the effective overburden pressure defined by Eq. 11. Rock densities are considered to range from 1.9 to 2.4 gm/cc; since hydrostatic pressure gradient (corresponding to 1-gm/cc density) is equal to 0.433 psi/ft, the following equations are correct to a rough approximation.

$$P_{ob} = 2.2 \times 0.43h$$

and

$$P_f = 0.43h$$

where h is the depth in feet and pressures are measured in pounds per square inch. Then, for horizontal fractures

$$P_e = (2.2-1)\,0.43h = 0.52h \quad \ldots\ldots (14)$$

Taking in Eq. 13 $\mu = 0.25$,

$$P_c = 0.67\,P_{ob},$$

or

$$P_c = 0.64h;$$

therefore, for vertical fractures,

$$P_e = 0.21h \quad \ldots\ldots\ldots\ldots\ldots\ldots (15)$$

SAND CONCENTRATION FOR MAXIMUM FLOW CAPACITY

The problem to be solved may be formulated in the following terms. Find the value of n for which (KW_f) has a maximum value, when P_e, D and B are given, where

$$(KW_f) = \frac{1.1\times 10^{10}}{A_w^2}\left[W_f - n\pi W_f\left(\frac{D^2}{4}-\frac{W_f^2}{12}\right)\right]^3 \quad \ldots\ldots\ldots\ldots\ldots\ldots (16)$$

and

$$A_w = 2 - \frac{n\pi}{2}(D^2-W_f^2) + n\pi D W_f \quad \ldots (17)$$

and where

$$W_f = D\left[1-B\left(\frac{P_e}{nD^2}\right)^m\right]^{1/2} \quad \ldots\ldots\ldots (18)$$

The condition for extreme values of (KW_f) is

$$\frac{d(KW_f)}{dn} = 0;$$

setting in Eq. 16

$$\Psi = W_f - n\pi W_f\left(\frac{D^2}{4}-\frac{W_f^2}{12}\right), \quad \ldots\ldots (19)$$

the condition becomes

$$3A_w\frac{d\Psi}{dn} - 2\Psi\frac{dA_w}{dn} = 0 \quad \ldots\ldots\ldots (20)$$

Let

$$x = \left(\frac{P_e}{nD^2}\right)^m \quad \ldots\ldots\ldots\ldots (21)$$

in Eq. 18; then,

$$W_f = D(1-Bx)^{1/2}.$$

Since by Eqs. 8 and 21 $(d/D)^2 = Bx$, the quantity Bx is a small fraction and is considered as such

in the following equations. Then this equation may be expressed as

$$W_f = D\left(1 - \frac{Bx}{2}\right), \quad \ldots\ldots\ldots\ldots (22)$$

To make the problem tractable, the calculation will be carried taking terms up to the first power of x. It can be shown that the results obtained keeping terms of the second degree in x are, for practical conditions, the same as obtained by the first approximation.

From Eqs. 19 and 22,

$$\Psi = D\left(1 - \frac{n\pi D^2}{6}\right) - \frac{DBx}{2} \quad \ldots\ldots (23)$$

and from Eqs. 17 and 22,

$$A_W = (2 + n\pi D^2) - n\pi D^2 Bx \quad \ldots\ldots (24)$$

By derivation, from Eqs. 23 and 24:

$$\frac{d\Psi}{dn} = -\frac{\pi D^3}{6} - \frac{DB}{2}\frac{dx}{dn}, \quad \ldots\ldots (25)$$

$$\frac{dA_W}{dn} = \pi D^2 - \pi D^2 Bx - n\pi D^2 B\frac{dx}{dn}; \quad \ldots (26)$$

but, from Eq. 21,

$$\frac{dx}{dn} = -\frac{mx}{n}; \quad \ldots\ldots\ldots\ldots (27)$$

then, substituting dx/dn in Eqs. 25 and 26,

$$\frac{d\Psi}{dn} = -\frac{\pi D^3}{6} + \frac{DBmx}{2n}, \quad \ldots\ldots (28)$$

$$\frac{dA_W}{dn} = \pi D^2 + \pi(m-1) D^2 Bx. \quad \ldots\ldots (29)$$

Since the second term in Eq. 29 is very small compared with the first,

$$\frac{dA_W}{dn} = \pi D^2 \quad \ldots\ldots\ldots\ldots (30)$$

Substituting Eqs. 23, 24, 28 and 30 in Eq. 20, the following equation is obtained, after some reductions.

$$\left(1 + \frac{\pi n D^2}{2}\right)\left(\frac{3Bm}{nD} + \pi DB\right)x = \pi D\left(3 + \frac{\pi n D^2}{6}\right),$$

or

$$\left(1 + \frac{\pi n D^2}{2}\right)\left(1 + \frac{\pi n D^2}{3m}\right)\frac{3mB}{nD}x = 3\pi D\left(1 + \frac{\pi n D^2}{18}\right),$$

from which

$$x = \frac{1 + \frac{\pi n D^2}{18}}{\left(1 + \frac{\pi n D^2}{2}\right)\left(1 + \frac{\pi n D^2}{3m}\right)}\frac{\pi n D^2}{mB} \quad \ldots\ldots (31)$$

By means of this formula and Eq. 21, optimum sand concentration for given values of P_e, B and m can be calculated easily.

Fig. 3 shows the variation of n with P_e for D = 0.025 in., $B = 7 \times 10^{-5}$ and for different values of m for maximum flow capacity, as determined by Eq. 31. Fig. 4 is a plot of Eq. 31 for D = 0.16 in., m = 1 and for different rock-softness values B.

Note the wide range of values of sand concentration, in grains per square inch, for maximum fracture flow capacity under different conditions of the effective pressure (therefore, under different kinds of fractures) and under different rock properties.

Fig. 2 also shows fracture capacity vs sand concentration as calculated using the approximations made, that is, by means of the equation

$$(KW_f) = 1.1 \times 10^{10}\frac{W_f^3 \Psi^3}{A_W^2}$$

and the approximate formulas

$$\Psi = D\left(1 - \frac{n\pi D^2}{6}\right) - \frac{DBx}{2}$$

and

$$A_W = (2 + n\pi D^2) - n\pi D^2 Bx.$$

This figure reveals that the approximation leads to practically the same results yielded by the exact

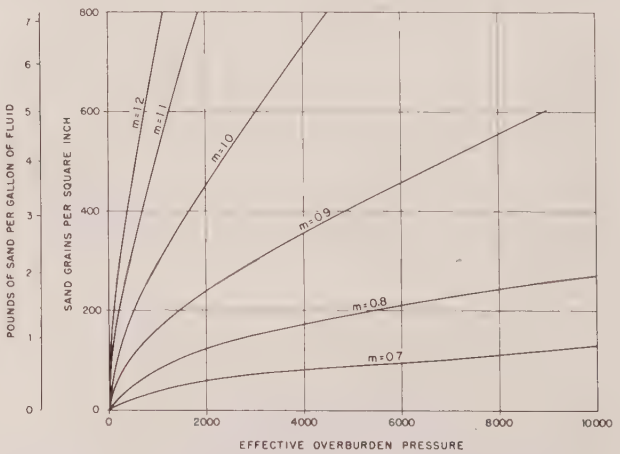

FIG. 3—SAND CONCENTRATION FOR MAXIMUM FLOW CAPACITY AS A FUNCTION OF OVERBURDEN PRESSURE FOR 0.025-IN. SAND-GRAIN DIAMETER (20-30 MESH) AND ROCK SOFTNESS $B = 7 \times 10^{-5}$.

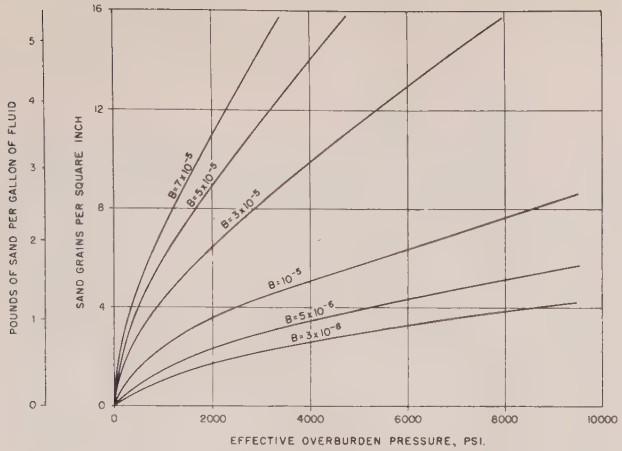

FIG. 4 – SAND CONCENTRATION FOR MAXIMUM FLOW CAPACITY AS A FUNCTION OF EFFECTIVE OVERBURDEN PRESSURE FOR 0.16-IN. SAND-GRAIN DIAMETER (4-6 MESH) AND FOR DIFFERENT ROCK SOFTNESSES.

relations. Particularly note that the concentration value corresponding to maximum fracture capacity is the same for both curves.

Fig. 5 shows fracture width vs concentration as calculated by

$$W_f = D\left[1 - B\left(\frac{P_e}{nD^2}\right)^m\right]^{1/2}$$

and by the approximate formula

$$W_f = D\left(1 - \frac{Bx}{2}\right).$$

Again, the approximation is shown to be satisfactory.

CONCENTRATION IN POUNDS OF SAND PER GALLON OF FLUID

Under the assumptions of no fluid leak-off through the fracture faces and of monolayer arrangement, the conversion of concentration from grains per square inch to pounds of sand per gallon of fluid can be made immediately.

If ρ is the specific weight of the sand material in pounds per cubic foot and n is the number of sand grains per square foot, the weight in pounds of a monolayer of 1 sq ft of fracture surface is

$$P = \frac{\pi D^3}{6}\rho n;$$

the corresponding void volume in cubic feet of propped fracture is

$$\Psi = W_f - V_p,$$

or

$$\Psi = W_f - n\pi W_f\left(\frac{D^2}{4} - \frac{W_f^2}{12}\right).$$

Then the concentration C in pounds of sand per cubic feet of fluid, measured in the fracture, is

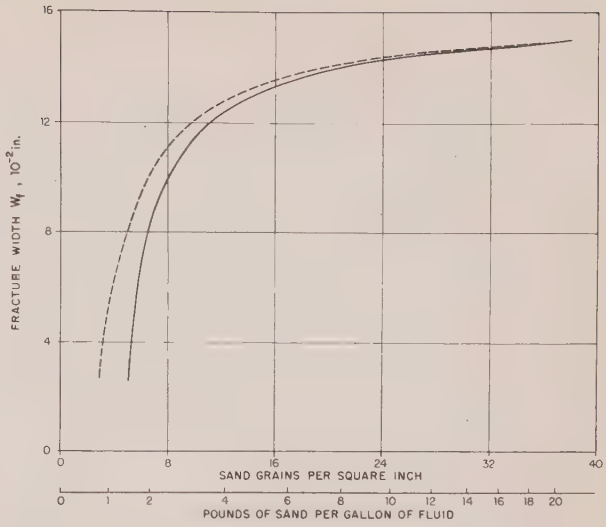

FIG. 5 – FRACTURE WIDTH AS A FUNCTION OF SAND CONCENTRATION FOR 0.16-IN. MEAN SAND-GRAIN DIAMETER (4-6 MESH), $m = 1$, $B = 4.2 \times 10^{-5}$ AND $P_e = 3{,}000$ PSI. DOTTED CURVE CALCULATED BY MEANS OF APPROXIMATE FORMULA.

$$C = \frac{P}{\Psi}$$

or

$$C = \frac{\pi\rho}{6}\,\frac{nD^2}{\frac{W_f}{D} - n\pi\frac{W_f}{D}\left(\frac{D^2}{4} - \frac{W_f^2}{12}\right)} \quad \ldots (32)$$

It is readily seen that the last expression contains n and D only in the product nD^2. Also, in Eq. 31 n and D appear only in the product nD^2; therefore, it is possible to write

$$nD^2 = f(P_e, B, m).$$

Thus by Eq. 32 it is concluded that C for maximum flow capacity does not depend on sand-grain diameter.

If during the time that sand is being pumped into the fracture its width is equal to the grain diameter, Eq. 32 becomes

$$C = \frac{\pi\rho}{6}\,\frac{nD^2}{1 - \frac{\pi}{6}nD^2}.$$

If D is expressed in inches and n in grains per square inch, the concentration in the fracture in pounds of sand per gallon of fluid is

$$C = \frac{\pi\rho}{6\times 7.481}\,\frac{nD^2}{1 - \frac{\pi}{6}nD^2}. \quad \ldots (33)$$

This is the formula used to calculate the con-

centration in pounds per gallon corresponding to a value of the density given in grains per square inch. The concentration in pounds of sand per gallon of fluid in the fracture, for the corresponding values of n shown in the scales of Figs. 1 through 5, is calculated by Eq. 33 with the value $\rho = 2.44$ gm/cc.

That C is independent of D can be checked by Figs. 3 and 4 for the values $B = 7 \times 10^{-5}$, $m = 1$, $P_e =$ 3,000 psi for instance, and the two grain diameters $D = 0.16$ and 0.025 in., respectively; in both cases, $nD^2 = 0.37$ and also in both cases $C = 4.9$ lb/gal.

When fracture width equals grain diameter of the propping agent, sand concentration in the fracture given by Eq. 33 will be equal to, in the absence of leak-off through fracture faces, the concentration measured at the surface.

Fluid leak-off through the fracture faces affect, of course, the concentration in a propping-sand operation; the fluid lost has the result of increasing the concentration within the fracture. In other words, the concentration measured in the fracture shown in Figs. 1 through 5 is greater than the concentration measured at the surface. Thus, concentration measured at the surface for maximum flow capacity, in the case of fluid leak-off, should be less than indicated in Figs. 3 and 4.

CONCLUSIONS

1. The problem of directly calculating sand concentration for maximum fracture flow capacity under various conditions is solved.

2. Sand concentration measured in the fracture in pounds of sand per gallon of fluid, for maximum flow capacity and for the same conditions of pressure and rock characteristics, is independent of medium-size grain diameter.

3. For conditions met in hydraulic fracturing treatments, it is convenient to determine sand concentration for maximum flow capacity, using data of treating and reservoir pressures and laboratory data of rock characteristics in order to obtain the best results from the fracturing operation.

NOMENCLATURE

(KW_f) = fracture capacity, md-ft

W_f = fracture width, in.

ϕ_p = porosity of a partial monolayer in fracture

V_p = volume of sand between fracture faces per unit area of fracture surface

A_w = total wetted area (sq in.) per unit area (sq in.) of fracture

$S_p = A_w/V_p$ (see definitions of A_w and V_p)

n = sand concentration, equal to number of grains per sq in. of fracture

D = mean sand-grain diameter, in.

d = diameter of the impression made by the grain in the rock, in.

L = load on the grain, lb

B = characteristic constant of the formation rock (softness)

m = characteristic constant of the formation rock (pseudo-rigidity)

P_e = effective overburden pressure, psi (confining pressure due to overburden minus formation pressure)

P_c = confining pressure due to overburden, psi

P_f = formation pressure, psi

P_{ob} = pressure corresponding to the weight of overlaying rocks, psi

h = depth, ft

μ = Poisson's ratio

Φ = angle of fracture plane with horizontal

Ψ = void volume in 1 sq ft of propped fracture

$x = (P_e/nD^2)^m$ = an auxiliary variable (see definitions of P_e, n and D).

P = weight of a sand monolayer in 1 sq ft of fracture, lb

ρ = specific weight of the sand material, lb/cu ft

C = sand concentration measured in the fracture, lb sand/gal (or cu ft, when specified) of fluid

ACKNOWLEDGMENTS

The author wishes to express his appreciation to José Colomo, assistant to the general director of Petróleos Mexicanos, and Alfonso Barnetche, production manager, for permission to publish this paper. The author also wishes to thank John F. Schnars, Camco de México, S.A., for revising the English manuscript of this paper.

REFERENCES

1. Huitt, J. L., McGlothlin, B. B., Jr. and McDonald, J. F.: "Evaluation and Selection of Fracture Propping Agents", *Pet. Eng.* (June, 1959) Vol. 31, No. 6, B-65.

2. Dehlinger, P., Browne, W. H. and Bundrant, C. O.: "Optimum Sand Concentrations in Well Treatments", *Trans.*, AIME (1954) Vol. 201, 273.

3. Darin, S. R. and Huitt, J. L.: "Effect of a Partial Monolayer of Propping Agent on Fracture Flow Capacity", *Trans.*, AIME (1960) Vol. 219, 31.

4. Huitt, J. L. and McGlothlin, B. B., Jr.: "The Propping of Fractures in Formations Susceptible to Propping Sand Embedment", *Drill. and Prod. Prac.* (1958).

5. Crittendon, B. C.: "The Mechanics of Design and Interpretation of Hydraulic Fracture Treatments", *Jour. Pet. Tech.* (Oct., 1959) Vol. XI, No. 10, 21.

★★★

A Potentiometric Study of the Effects of Mobility Ratio on Reservoir Flow Patterns

H. B. BRADLEY
MEMBER AIME
J. P. HELLER
A. S. ODEH
MEMBER AIME

SOCONY MOBIL OIL CO., INC.
DALLAS, TEX.

ABSTRACT

A potentiometric model technique is presented for determining the areal sweep efficiency of a five-spot well pattern, at and beyond breakthrough. A sharp interface between displaced and displacing fluids is assumed. Although the prototype system is referred to as a waterflood operation, obvious changes in the notation and computations will adapt the results to other displacement processes.

The results of the study include the following.

1. Areal sweep efficiencies for a five-spot well pattern, at and beyond breakthrough, for mobility ratios (displacing to displaced fluid) of 4:1, 2:1, 1:1 and 1:4.

2. Extension of potentiometric analysis to the investigation of the areal sweep efficiency beyond breakthrough in a five-spot pattern by the application of conformal mapping and conductive-solid models.

3. The use of layers of conductive fabric in representing mobility ratio changes in potentiometric models.

4. The development of a probe mechanism for probing conductive solids.

The results obtained by conductive-cloth models agree with earlier areal sweep efficiencies at breakthrough obtained by Aronofsky and Ramey [1] on the potentiometric analyzer using electrolytic-tank models. Results beyond breakthrough differ from those obtained by the X-Ray Shadowgraph technique. Data from this study show that, for mobility ratios greater than one, water cut rises rapidly as fluid is produced after breakthrough. However, for mobility ratios smaller than one, a large increase in area swept resulted with only a small increase in water cut.

INTRODUCTION

In calculating reservoir performance of waterflooding operations and other fluid-injection programs, it is necessary to estimate the areal sweep efficiency * before and after injected-fluid breakthrough into production wells. Influence of mobility ratio on oil-production history, before and after breakthrough for a five-spot well pattern, has been studied by X-Ray Shadowgraph techniques [2-5] and by gelatin models.[6] In none of these investigations was the transition zone controlled experimentally.

Steady-state analog techniques assume that a vertical and discrete interface exists between the displacing and displaced phase. Thus, when using a potentiometric analysis, it is assumed that no transition zone exists.

To determine the areal sweep efficiency beyond breakthrough for a five-spot well pattern using the potentiometric analyzer, four principal problems had to be resolved. These were the following.

1. The laborious method of representing changes in mobility ratio in electrolytic tanks by means of contoured wooden blocks.
2. Vaporization of the electrolyte solution during the study causing concentration changes and, thereby, variable conductivity.
3. The scale-limitation problem [7] that is accentuated by abrupt electrolyte depth changes.
4. A wellbore geometry problem.

EXPERIMENTAL EQUIPMENT AND PROCEDURES

CONDUCTIVE-SOLID MODEL

The theory, equipment and procedural techniques of the electrolytic-tank potentiometric model have been treated excellently by Lee [8] and by Muskat.[9] By the use of a conductive solid to represent the fluid conductivity of the porous media, the need for contouring wooden blocks to represent mobility ratio was eliminated. It was found that a carbon-black coated fabric, Uskon D-16,** could be employed as a fairly uniform conductive media. This material, when stacked in appropriate layers and pressed together, can be used to represent changes in mo-

Original manuscript received in Society of Petroleum Engineers office June 17, 1960. Revised manuscript received Feb. 8, 1961. Paper presented at 35th Annual Fall Meeting of SPE, Oct. 2—5, 1960, in Denver.

[1] References given at end of paper.

*Areal sweep efficiency is the area enclosed by the leading edge of the injected-fluid front divided by the portion of the reservoir area under consideration.

**United States Rubber Co.

bility. A new probing mechanism was necessary for use on dry-conductive solids. A photograph of a leaf-spring-type probe developed for this purpose is shown in Fig. 1. Two areal-sweep-efficiency runs, made on a developed, one-quarter five-spot well pattern at a 1:1 mobility ratio by two different investigators, checked the theoretical value closely (Table 1). Therefore, the dry-probing technique was considered reliable.

Conductive fabric eliminated the use of electrolyte solutions and their accompanying vaporization losses. Compensating for this advantage, it was found that the fabric was sensitive to changes in humidity; this problem was circumvented by providing a humidity-controlled atmosphere.

Since the thickness of the conductive fabric was 0.012 in., the erroneous deviation of flow lines caused by large variations in electrolyte depth was reduced materially.

TABLE 1–EFFECT OF MOBILITY RATIO ON AREAL SWEEP EFFICIENCY AT BREAKTHROUGH – DEVELOPED FIVE-SPOT WELL PATTERN

	Areal Sweep Efficiency – per cent				
	Potentiometric Analyzer				
Mobility Ratio M	Conductive Cloth-Uskon	Electrolytic Tank[1]	Fluid Mapper[13]	X-Ray[2,3] Shadowgraph	Analytical Calculation
∞:1	62.6[12]	62.5	–	–	–
10:1	–	64.5	52.7	51.0	–
4:1	66.4	65.8	62.0	54.0	45.0[14]
2:1	68.8	68.0	68.0	60.4	–
1:1	71.6–71.5*	70.0	71.7	69.8	71.5[15]–71.8**
1:4	82.2	88.5	78.0	87.0	–
1:10	–	94.5	82.0	100.0	–

*First value obtained on regular, one-quarter five-spot well pattern and second value obtained on transformed, one-quarter five-spot well pattern.

**Calculated by J. R. Milne from formula presented in Ref. 16.

BIPOLAR TRANSFORMATION

For two reasons, extension of the investigation to the problem of sweep-out after breakthrough was impractical using the regular, developed five-spot pattern. First, the fraction of current carried by the swept and unswept regions, and hence the rate at which the area of the unswept section is decreased, is dependent on the angle that the tip (Fig. 4) of the cloth is cut at the producing well. The tip is extremely small, making it difficult to preserve the analogy as far as geometry is concerned. The precise cutting and connecting of the cloth in the region of the producing well determines the outcome of the problem at succeeding points. Thus, in this situation, it was highly desirable to greatly enlarge the model or to adopt a different approach. Second, in attempting to advance the front after breakthrough, it becomes physically impossible to probe in the immediate vicinity of the producing well. A smaller probe spacing would help, but the number of readings and the solution time would increase proportionately. As a result, a method was devised which transformed the regular, developed-five-spot well pattern by means of analytic functions into another geometrical system in which the geometry of the critical region around the wells is more favorable for precise potential measurements. In essence, the injection and production sand faces of a one-quarter-developed five-spot well pattern were transformed by a bipolar co-ordinate system into a straight line; also, the diagonal between the wells was lengthened and the opposite diagonal was shortened (Fig. 2).

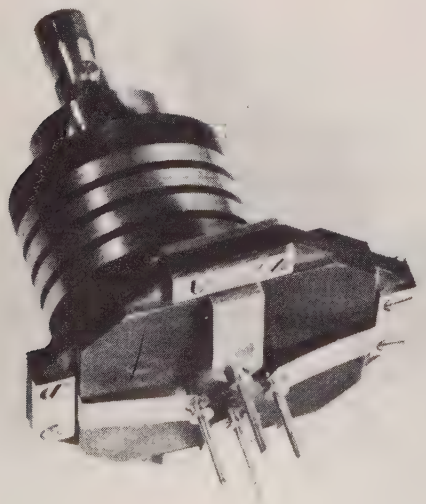

FIG. 1–CONDUCTIVE-SOLIDS PROBE.

The procedure used in the bipolar transformation method, using the case of 2:1 mobility ratio as an example, was as follows (Fig. 2).

1. Several transformed 16-in. one-quarter five-spot well patterns (hereafter referred to as the transformed five-spot) were cut out of a roll of Uskon D-16 cloth, some in the direction of the woof and others in the direction of the warp. A stainless-steel template of the transformed five-spot assured the cutting of uniform patterns.

2. Four layers of cloth were carefully stacked, alternating the woof and warp sheets, and pressed together. The model was then placed on a piece of ¼-in. plywood.

3. The cloth was cut 2-in. longer on each end than the proper boundaries of the transformed model; these strips were used as electrodes. The last 2 in. of the top of the top-most layer and the bottom of the bottom-most layer were painted with conductive silver paint. A piece of aluminum foil was placed over the silver paint and the entire assembly was drawn down tightly by means of a ¼-in. bakelite sheet and screws (Fig. 2). Connection to the DC power source is made through the aluminum foil.

4. Since the position of the front at breakthrough had been determined previously on a regular five-spot model, this front was converted to the transformed model and the two top sheets were cut accord-

ingly. The positions of the front near the wellbore after breakthrough were followed on the transformed five-spot, and the portion of the front near the opposite diagonals was followed on the regular five-spot. The portion of the front investigated on the transformed five-spot was converted back to the regular pattern to determine areal sweep efficiency.

5. The water cut was determined by a material balance calculation.

A 1:1 mobility ratio, one-quarter-developed five-spot was run to breakthrough on a transformed model to check its validity. The results are reported in Table 1. The results of the areal sweep efficiency obtained for the developed five-spot flood pattern beyond breakthrough for mobility ratios 4:1, 2:1, 1:1 and 1:4, run as outlined previously, are shown in Fig. 3. The interface positions for a mobility ratio of 1:4 are shown in Fig. 4. Fig. 5 presents the potentiometric model and detecting circuit diagrams. The circuitry is identical for the regular and transformed models.

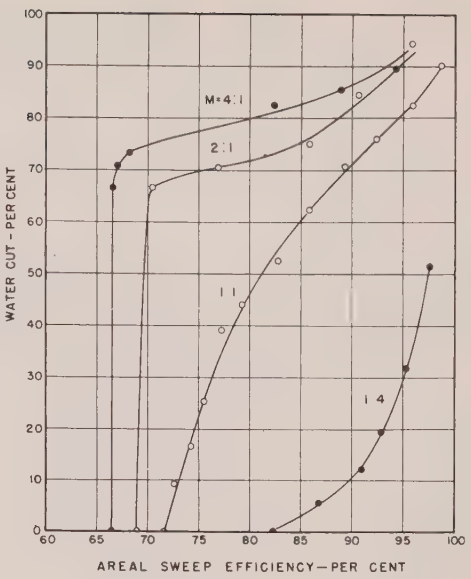

FIG. 3—WATER CUT VS AREAL SWEEP EFFICIENCY AFTER BREAKTHROUGH FOR VARIOUS MOBILITY RATIOS.

DISCUSSION

It is known that, when the mobility ratio is greater than one, the displacement front may develop fingers.[10,11] In any actual displacement in which the displacing phase is the more mobile, these nonuniformities of flow arise due to the shape instability of the interface between fluids. Thus, a small dimple or protrusion on the front causes the fluid velocity pattern to be altered. In the case of frontal instability, this change in flow pattern causes the ripple to grow larger. The rate at which such parasitic flow patterns develop evidently depends on the fluid mobility itself, as well as on the ratio of mobilities, the gradient of fluid mobility and the homogeneity of the formation.

The phenomenon has been observed in laboratory models of various geometries, but it is not yet known what effect it will have in reservoirs where the travel distance is so much greater. On the scale of an oil field, the fingered transition zone may in some cases still be treated as a thin interface separating the displaced from the displacing fluids.

In the potentiometric analogy, the instability due to the shape of the displacement front is not observed.

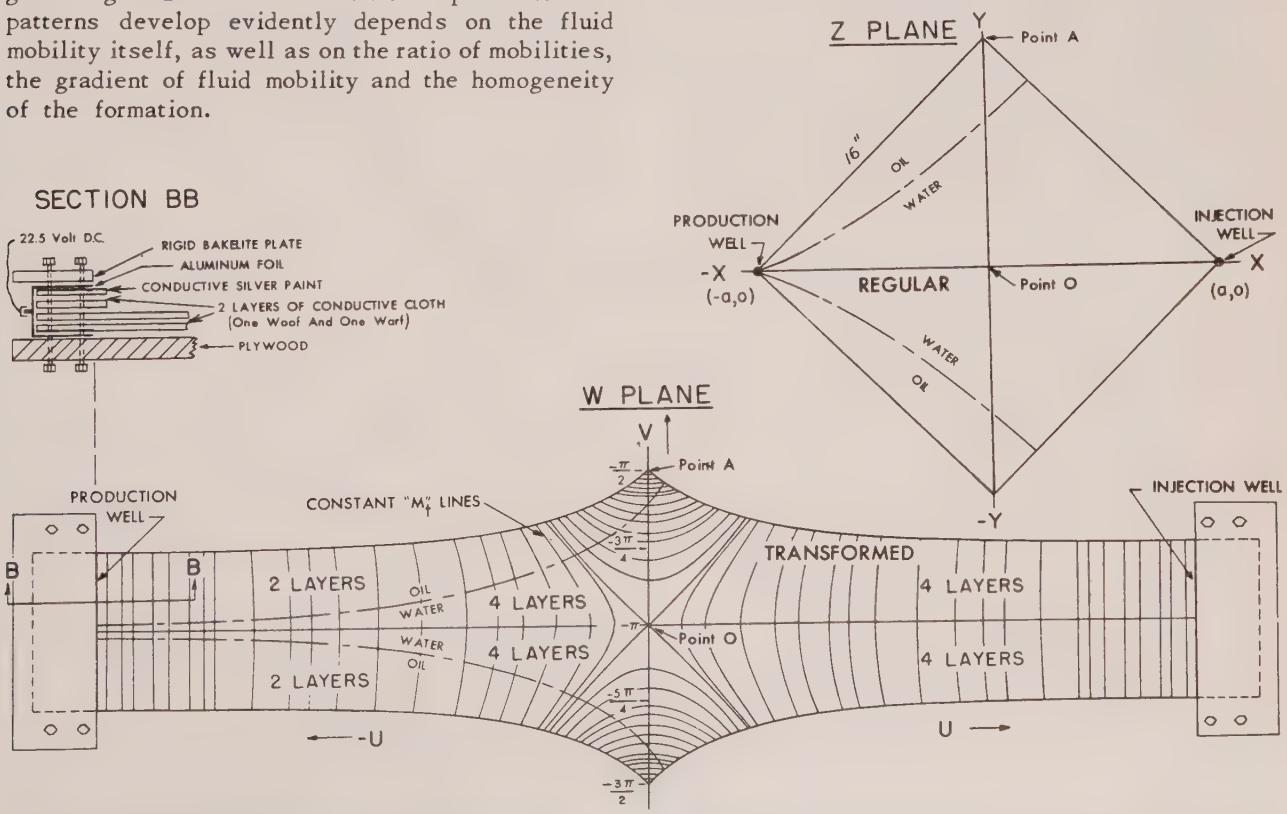

FIG. 2—RELATIONSHIP OF REGULAR AND TRANSFORMED DEVELOPED, ONE-QUARTER, FIVE-SPOT WELL PATTERN, 2:1 MOBILITY RATIO.

The limitation evidently arises from the fixed inter-electrode separation on the probe. The observed potential differences and calculated fluid-travel times are averaged automatically over this distance. Thus, flow inhomogeneities in the reservoir which are smaller than the scaled-up inter-electrode spacing are virtually disregarded by the potentiometric model.

The potentiometric method used in this work is open to several criticisms. A major objection is the use of step-wise approximation to the displacement, with the "front" being advanced incrementally on the basis of potential gradients in the model. It has not been shown mathematically that this process converges uniquely to the correct result. Similarly, it is not clear how dispersion at the front will affect the after-breakthrough production. The results presented are based on the assumption that the displacement behavior in the reservoir is not grossly affected by such phenomena at the front — that the width of the front remains negligible in comparison to the well spacing. It is hoped that these problems can be resolved by future work.

SUMMARY AND CONCLUSIONS

1. The utilization of conductive-solid materials in a potentiometric model was investigated. It was found that layers of conductive, carbon-black coated fabric (Uskon D-16) can be used to represent changes in mobility ratio from 4:1 to 1:4. Layers of conductive cloth also can be used to represent changes in permeability-thickness product of a reservoir. In addition, an infinite mobility ratio that has proved valuable in in-situ combustion studies can be represented by silver-painting the cloth behind the front.

2. A new type of probing mechanism was developed for use on conductive solids. To obtain consistent potential readings, it was necessary to maintain a uniform probe pressure on the conductive cloth. A combination helical- and leaf-spring-loaded probe mechanism was found to satisfy this requirement.

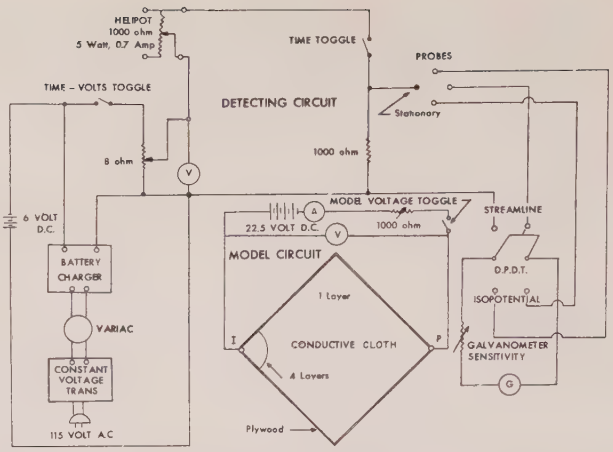

FIG. 5 — POTENTIOMETRIC MODEL AND DETECTING CIRCUIT DIAGRAMS.

3. A new technique was developed for using the potentiometric analyzer to determine areal sweep efficiency after water breakthrough. The physical impossibility of probing (to obtain the potential distribution) the model of a developed five-spot well pattern in the immediate vicinity of the wellbore was the main difficulty to be overcome. This was circumvented by employing a bipolar transformation system which changed the configuration of the regular, developed five-spot well pattern; in particular, the 90° curved face of the wellbore is converted to a straight line. Thus, it is possible to obtain the potential distribution in the area

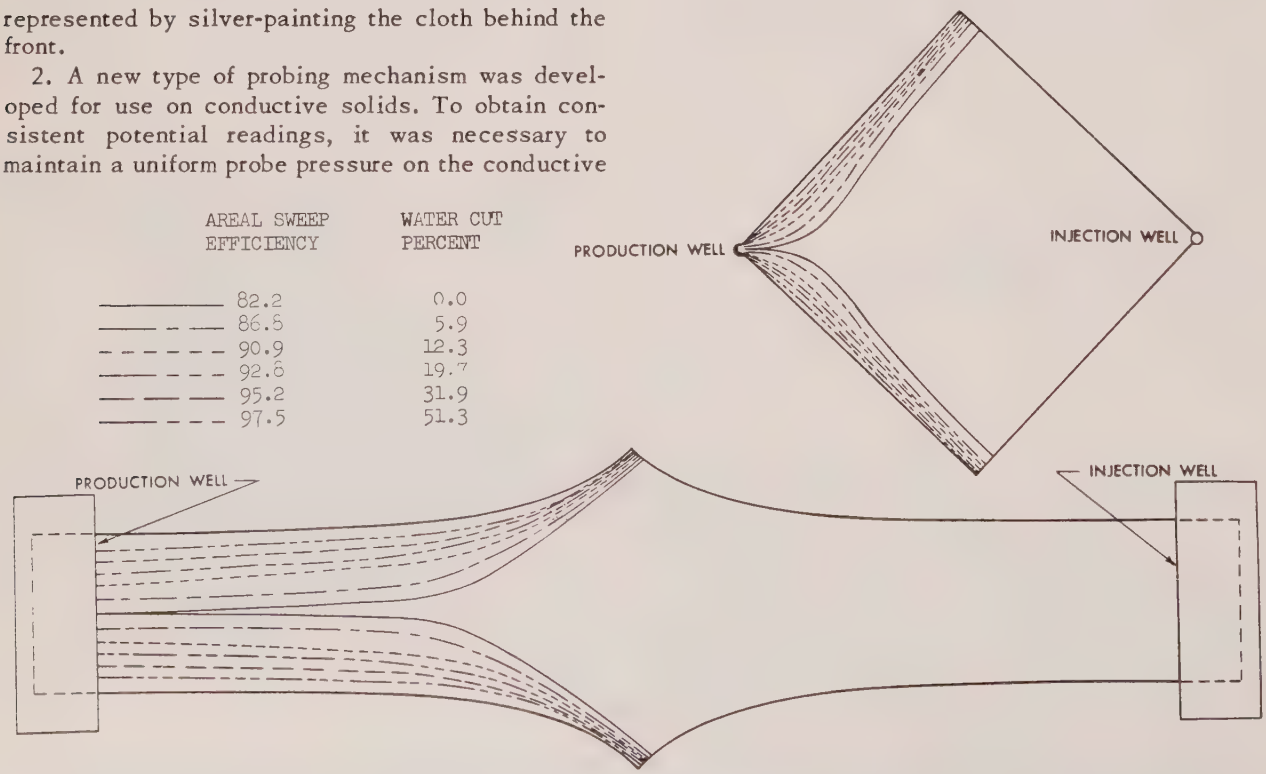

FIG. 4 — INTERFACE POSITIONS AFTER BREAKTHROUGH FOR DEVELOPED FIVE-SPOT WELL PATTERN, 1:4 MOBILITY RATIO.

adjacent to the wellbore on the transformed five-spot well pattern. All runs made employing the transformed well pattern gave reasonable and reproducible results.

4. The results of areal-sweep-efficiency runs at breakthrough for various mobility ratios are shown in Table 1. As the mobility ratio decreases below one, the area swept increases rapidly. This is contrasted to a small change in the area swept as the mobility ratio increases above one. There is good agreement of the data obtained by conductive-cloth models and by electrolytic-tank models (obtained by Aronofsky and Ramey[1]) on the potentiometric analyzer at mobility ratios greater than one.

5. The effect of mobility ratio on water cut and areal sweep efficiency after water breakthrough is shown in Fig. 3. For mobility ratios greater than one, the water cut increases rapidly, immediately after breakthrough, to more than 50 per cent of the produced fluid. It then increases more gradually with increasing production. For a mobility ratio smaller than one, however, large increases in area swept resulted, with only a small increase in water cut.

ACKNOWLEDGMENT

The authors wish to express their appreciation to Socony Mobil Oil Co., Inc. for permission to publish this paper. The suggestions made by P. P. Reichertz, G. W. Nabor and E. E. Moreland in reviewing the paper are gratefully acknowledged.

REFERENCES

1. Aronofsky, J. S. and Ramey, H. J., Jr.: "Mobility Ratio — Its Influence on Injection or Production Histories in Five-Spot Water Flood", *Trans.*, AIME (1956) Vol. 207, 205.
2. Dyes, A. B., Caudle, B. H. and Erickson, R. A.: "Oil Production After Breakthrough as Influenced by Mobility Ratio", *Trans.*, AIME (1954) Vol. 201, 81.
3. Craig, F. F., Jr., Geffen, T. M. and Morse, R. A.: "Oil Recovery Performance of Pattern Gas or Water Injection Operations from Model Tests", *Trans.*, AIME (1955) Vol. 204, 7.
4. Caudle, B. H., Erickson, R. A. and Slobod, R. L.: "The Encroachment of Injected Fluids Beyond the Normal Well Pattern", *Trans.*, AIME (1955) Vol. 204, 79.
5. Caudle, B. H. and Witte, M. D.: "Production Potential Changes During Sweep-out in a Five-Spot System", *Trans.*, AIME (1959) Vol. 216, 63.
6. Burton, M. B., Jr. and Crawford, P. D.: "Application of the Gelatin Model for Studying Mobility Ratio Effects", *Trans.*, AIME (1956) Vol. 207, 333.
7. Odeh, A. S., Bradley, H. B. and Heller, J. P.: "Scale Limitations in Potentiometric Model Construction", *Trans.*, AIME (1956) Vol. 207, 200.
8. Lee, B. D.: "Potentiometric-Model Studies of Fluid Flow in Petroleum Reservoirs", *Trans.*, AIME (1948) Vol. 174, 41.
9. Muskat, M.: "The Theory of Potentiometric Models", *Trans.*, AIME (1949) Vol. 179, 216.
10. Blackwell, R. J., Rayne, J. R. and Terry, W. M.: "Factors Influencing the Efficiency of Miscible Displacement", *Trans.*, AIME (1959) Vol. 216, 1.
11. Chuoke, R. L., van Meurs, P. and van der Poel, C.: "The Instability of Slow, Immiscible, Viscous Liquid-Liquid Displacements in Permeable Media", *Trans.*, AIME (1959) Vol. 216, 188.
12. Boston, Couch, Moss and White: Socony Mobil Field Research Laboratory, Dallas, Private Communication.
13. Cheek, R. E. and Menzie, D. E.: "Fluid Mapper Model Studies of Mobility Ratio", *Trans.*, AIME (1955) Vol. 204, 278.
14. Fay, C. H. and Prats, M.: "Application of Numerical Methods to Cycling and Flooding Problems", *Proc.*, Third World Pet. Cong., Section II (1951) 555.
15. Muskat, M.: *Physical Principles of Oil Production*, McGraw-Hill Book Co., Inc., N. Y. (1949) 659.
16. Prats, M., Strickler, W. R. and Matthews, C. S.: "Single-Fluid Five-Spot Floods in Dipping Reservoirs", *Trans.*, AIME (1955) Vol. 204, 160.

***

Nonequilibrium Gas Displacement Calculations

H. D. ATTRA
JUNIOR MEMBER AIME

HUMBLE OIL & REFINING CO.
HOUSTON, TEX.

ABSTRACT

The effects of phase behavior on reservoir economics is a function of both fluid composition and flow properties of the reservoir rock. In some operations such as gas injection into volatile crude-oil reservoirs, the stock-tank recovery derived from vaporization of the reservoir oil by the displacing gas can approach the recovery derived from the displacement mechanism. In other cases of gas-cycling reservoirs, the dry injected gas can effectively vaporize a retrograde liquid phase, allowing a substantial reduction in cycling pressure with no appreciable loss in recoverable liquids. Because of these effects, it is essential that phase behavior be considered in developing the economics of any secondary recovery program in which gas is the injected fluid.

The inclusion of phase behavior in conventional calculation procedures has been retarded because of the complexity of the calculation and the large volume of laboratory data required. However, by applying high-speed computers and new laboratory techniques, the phase-behavior displacement calculation has been developed to economically include this basic fundamental of gas displacement.

The calculation is performed by reducing the reservoir to a series of one-dimensional segments. Phase changes, saturation distributions and changing fluid properties are evaluated for each segment as a function of time. The relative volumes of equilibrium liquid and gas displaced from each segment are determined by a trial-and-error procedure to meet the requirements of phase equilibrium and two-phase flow. The produced fluids are flashed through conditions of surface separation approximating those in the field to obtain actual values for stock-tank liquid recovery and producing gas-oil ratios.

Based on the results of successful field studies, the technique appears to have application to reservoirs producing under a nonmiscible gas-displacement mechanism and should substantially increase the reliability of this type of analysis when phase behavior is an important factor.

Original manuscript received in Society of Petroleum Engineers office July 15, 1960. Revised manuscript received Jan. 25, 1961. Paper presented at 35th Annual Fall Meeting of SPE, Oct. 2-5, 1960, in Denver.

INTRODUCTION

Predicting reservoir performance under gas-injection operations involves three basic principles of reservoir engineering. First, a material balance exists between the displacing gas and the displaced reservoir fluid. Second, the oil and gas flow in relationship with the two-phase flow property of the reservoir rock; and third, phase equilibrium exists between the displacing gas and the native reservoir fluid. To illustrate these three principles, consider the one-dimensional reservoir shown in Fig. 1. The reservoir is divided into a series of segments representing a one-dimensional cross section between an injection area and a producing area. S_o represents the oil saturation, C_w represents the connate-water saturation and S_g represents the displacing gas saturation. The gas is moving into Segment 1 and the reservoir oil is being produced out of Segment N.

Consider the case when gas has just moved into Segment 1 and the displacing gas-oil contact is at position a-a'. The volume of oil pushed out of Segment 1 is a function only of mobility and the two-phase flow properties of the reservoir rock, that is, K_g/K_o and μ_o/μ_g. Behind the front if the injected gas is foreign to the reservoir oil (a nonequilibrium gas), there will either be vaporization of the oil into the gas or condensation of the gas into the oil. In either case the net result is a mass transfer and a re-distribution of composition and liquid and gas saturation.

If the displacement is at constant pressure and is continued, the gas moves into new segments, proceeding succesively into Segment 2, 3, etc. The total volume of oil produced from the reservoir

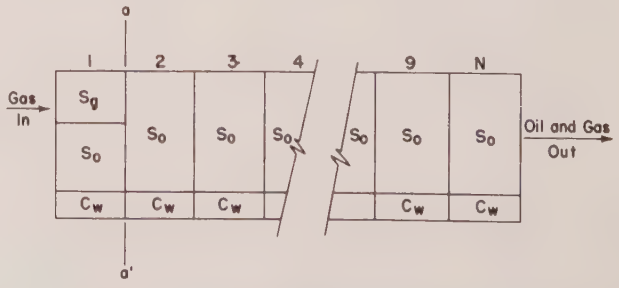

FIG. 1 — ONE-DIMENSIONAL REDUCTION OF RESERVOIR.

becomes a function of phase behavior behind the front and displacement at the front with the net result, "total fluid produced = total fluid injected ± phase changes".

In the past, conventional methods of analyses[1] have included only the concept of two-phase flow (K_g/K_o) (μ_o/μ_g) and a material balance. The third fundamental of phase behavior has been neglected because of the complexity of the calculation procedure and large volume of laboratory data required for an accurate prediction. These conventional calculations have been and will continue to be satisfactory for heavy-crude reservoirs being produced under dry-gas injection programs, gas-cap expansion, or any other form of an equilibrium or near-equilibrium displacement process. However, because of the increasing number of volatile oil reservoirs and rich-gas injection programs, it has been recognized that the undefined factor of phase behavior is operative in most gas-injection programs and contributes materially to liquid recovery by either (1) reducing liquid viscosity, (2) swelling the residual oil phase, or (3) vaporizing the reservoir oil.

BASIC CONSIDERATIONS AND RESTRICTIONS

By using high-speed computers and new laboratory techniques, the nonequilibrium gas displacement program was developed to include all three of the basic principles of a gas displacement process. The calculation is performed by reducing the reservoir to a series of one-dimensional segments as shown in Fig. 1. Values of gas saturation, composition of injected gas and native reservoir oil and gas, flow properties of the rock and pore volumes are entered for each segment. The displacing gas enters Segment 1 and fluid flows in one direction, either being produced in accordance with predictable field performance or being displaced into the next segment. One time step tracts the total fluid flow in all segments considering the phase changes, displacement mechanism and material balance ahead of the front, at the front and behind the front.

Earlier work[2] designed to calculate the effects of phase behavior on a gas displacement process has assumed the reservoir to be one cell with uniform compositions and phase properties throughout the entire reservoir. Preliminary work done in a model of this type (one segment) indicates complete loss of the compositional front and gross exaggeration of the effects of phase behavior. The principle employed in this earlier work assumes that phase equilibrium is reached simultaneously throughout the reservoir, which distorts the effects of either vaporization or condensation. The segment principle employed in the nonequilibrium calculation is for the purpose of more closely approximating the actual reservoir process of a nonequilibrium gas contacting reservoir oil as it moves through the reservoir and, by this repeated contact, becoming in equilibrium with it.

The nonequilibrium calculation is subject to four basic assumptions.

1. Capillary pressure and gravity are not considered.
2. The fluids *within each segment* are assumed to be in phase equilibrium at the end of each time step.
3. An average gas saturation is calculated for each segment and is assumed to represent the flow properties of the entire segment.
4. There is a constant pressure during any one time step; that is, declining reservoir pressure must be approximated by a series of constant-pressure steps.

It should be noted that some smearing of the compositional front is inherent in the segment principle used in this calculation; therefore, it is not considered applicable to a slug displacement process.

CALCULATION PROCEDURE

The nonequilibrium displacement analysis is quite complex, involving several interdependent trial-and-error solutions. Figs. 2 and 3 illustrate the basic principles used in the calculation procedure, with a listing of each of the major equations included in the Appendix.

Fig. 2 illustrates the mechanism for calculating the displacement process as the gas front moves into each segment. Bear in mind that the displacement mechanism is a function only of relative permeability and oil and gas viscosity and, as such, is affected by phase behavior only through changing viscosity. Referring to Fig. 2, the Buckley-Leverett displacement equations are solved to determine the displacing gas saturation in Segment 1 (Step 1). Based on this saturation the residual oil and gas behind the front are combined in proportion to their calculated volumes and are flashed at reservoir pressure and temperature to determine the phase

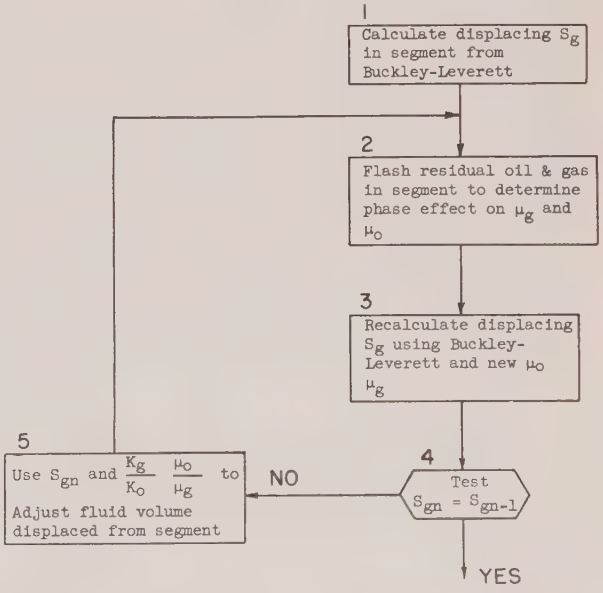
1
Calculate displacing S_g in segment from Buckley-Leverett
2
Flash residual oil & gas in segment to determine phase effect on μ_g and μ_o
3
Recalculate displacing S_g using Buckley-Leverett and new μ_o μ_g
4
Test $S_{gn} = S_{gn-1}$
NO
YES
5
Use S_{gn} and $\frac{K_g}{K_o}$ $\frac{\mu_o}{\mu_g}$ to Adjust fluid volume displaced from segment

FIG. 2—DISPLACEMENT.

[1]References given at end of paper.

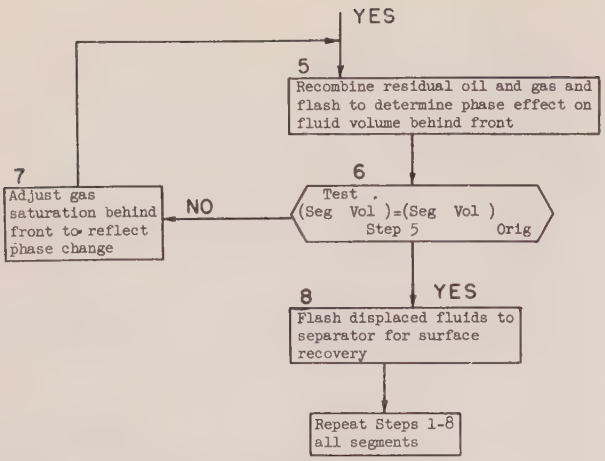

FIG. 3 – PHASE BEHAVIOR.

effects on oil and gas viscosity (Step 2). The new viscosities are used to recalculate the Buckley-Leverett displacement and evaluate a new value for displacing efficiency or gas saturation (Step 3). The test is made to compare the original value of displacing gas saturation with the current value (Step 4). If agreement is not obtained, the new gas saturation and new viscosities are used to adjust the volume of fluid *displaced from the segment* (Step 5). Steps 2 through 5 are repeated until the displacing gas saturation calculated on two successive trials agrees within a predetermined tolerance (0.1 per cent).

Referring back to Fig. 1, at the completion of Steps 1 through 5 the gas front is at *a-a'* in Segment 1; the volume of fluid displaced from the segment has been calculated considering phase effects on oil and gas viscosities.

Fig. 3 illustrates the basic mechanism for calculating phase behavior behind the front. The purpose here is to determine the re-distribution of fluid compositions and saturations to satisfy phase equilibrium. Once we satisfy the displacement mechanism, the volume of oil and gas behind the front is again combined and flashed at reservoir pressure and temperature to determine the re-distribution of composition. New fluid volumes are calculated and compared to the original segment volume (Step 6). If agreement is not obtained between the original and the calculated segment volume, the gas saturation behind the front is adjusted to reflect the phase exchange (Step 7). This procedure is continued until the calculated segment volume agrees with the original segment volume. When agreement is reached, the fluids produced from the segment are flashed through surface separation conditions to determine gas-oil ratio, surface recovery and producing composition (Step 8). The entire procedure is repeated for succeeding time steps as the gas front moves into Segments 2, 3, 4, etc. Steps 1 and 3 are omitted for all segments behind the front; i.e., displacement behind the gas front is dependent only on two-phase flow and phase behavior.

Again in review, Steps 1 through 4 satisfy the displacement process considering the effects of phase behavior only on mobility. Steps 5 through 8 evaluate phase behavior behind the front and its effect on oil and gas saturation. Full details of the equations used in the analysis are included in the Appendix.

LABORATORY DATA REQUIRED

The laboratory data requirements for the nonequilibrium gas displacement calculation are quite extensive in relationship to most high-pressure phase-behavior work. All of the data used in this calculation are required as a function of pressure, temperature and *composition.* Equilibrium vaporization constants (*K*-values) are the most important data used. These values are used to determine the mols and composition of the liquid and gas in each segment from which all volume data are calculated.

Because of equilibrium properties of the reservoir gas and liquid change through repeated contacts of the displacing gas and native reservoir fluid, it is necessary to use *K*-values that will reflect this change independent of pressure and temperature. For example, consider constant-pressure gas injection in a reservoir containing a volatile crude. The first gas injected may effectively vaporize a portion of the crude contacted. However, as the gas moves away from the injection well and contacts more oil, it eventually becomes saturated and a new over-all hydrocarbon system exists. If the pressure and temperature of the reservoir are constant, standard *K*-values would also be constant and would not adequately predict the changing phase properties of this new system.

To obtain *K*-values that would apply, reservoir liquid and displacing-gas samples were used in the laboratory to perform a series of constant-pressure contacting experiments. The original liquid was contacted by a volume of displacing gas and allowed to come to equilibrium. The resulting gas and liquid compositions were measured and used to calculate the *K*-values for that step ($k_i = y_i / x_i$). The equilibrium gas was removed, and the equilibrium liquid was again contacted by new volumes of original gas. This procedure was repeated until no further change was noted in the compositions. This process is analogous to the reservoir process occurring near the injection well. A second series of experiments was performed in the same manner as the first except that the displacing gas was repeatedly contacted by original reservoir fluid. This process is equivalent to the phase changes occurring at the gas front. The *K*-values obtained from the two processes were then plotted as a function of liquid composition to give a plot of *K* vs composition for a given pressure and temperature. If the reservoir study requires a declining pressure, the *K*-value data are obtained by the same procedure at both a high and low pressure and the two sets of curves are interpolated for *K*-values at any intermediate pressure. Fig. 4 illustrates a typical set of *K* vs composition data used in a case field study.

Liquid viscosity, molecular weights and gallons-

per-mol factors for the hydrocarbon components above C_5 were also obtained as a function of liquid composition. It was determined from laboratory experiments that the molecular weights and volume relationship of the heavy components were basically insensitive to pressure but underwent a definite change with changing composition. Fig. 5 illustrates the molecular weight and gallon-per-mol factor for the C+ fraction as a function of the mol fraction of C+ in the liquid.

Other basic data required for the calculation consists of relative permeability data (K_g/K_o), compositions of the reservoir liquid and gas, standard *K*-values at surface pressure and temperature (for separator flashes), and critical pressures and temperatures of the components. A complete table of gas-compressibility data (*Z* factors) is also required.

FIELD APPLICATIONS

Three field applications of the nonequilibrium gas calculations have been completed. One of these fields, a volatile-oil system with shrinkage of 1.7, had been produced under a dry-gas injection program for three years and recovery was substantially higher than expected. A match of observed performance could not be obtained using conventional displacement analyses and any reasonable value for relative oil and gas permeability. Fig. 6 illustrates the observed and calculated production curve of the reservoir. Shown on this chart is the cumulative stock-tank recovery vs producing gas-oil ratio. The curves are of the actual field performance (center curve), the calculated performance using the conventional Buckley-Leverett displacement (upper curve) and the calculated reservoir performance using the nonequilibrium displacement (lower curve). The same relative permeability data were used in both of the calculated cases.

There was good agreement between all curves up to 7 million bbl of cumulative production or to the point of gas breakthrough. The slight difference shown in the calculated (conventional and nonequilibrium) curves in this region is a result of phase behavior increasing the displacing-gas viscosity and, thereby, increasing the efficiency of the displacement mechanism. There is, however, a marked difference in the results of the two calculations during the production history following gas breakthrough. The nonequilibrium indicated a much lower producing gas-oil ratio and higher oil production than the conventional. This difference results solely from the phase reaction of gas behind the

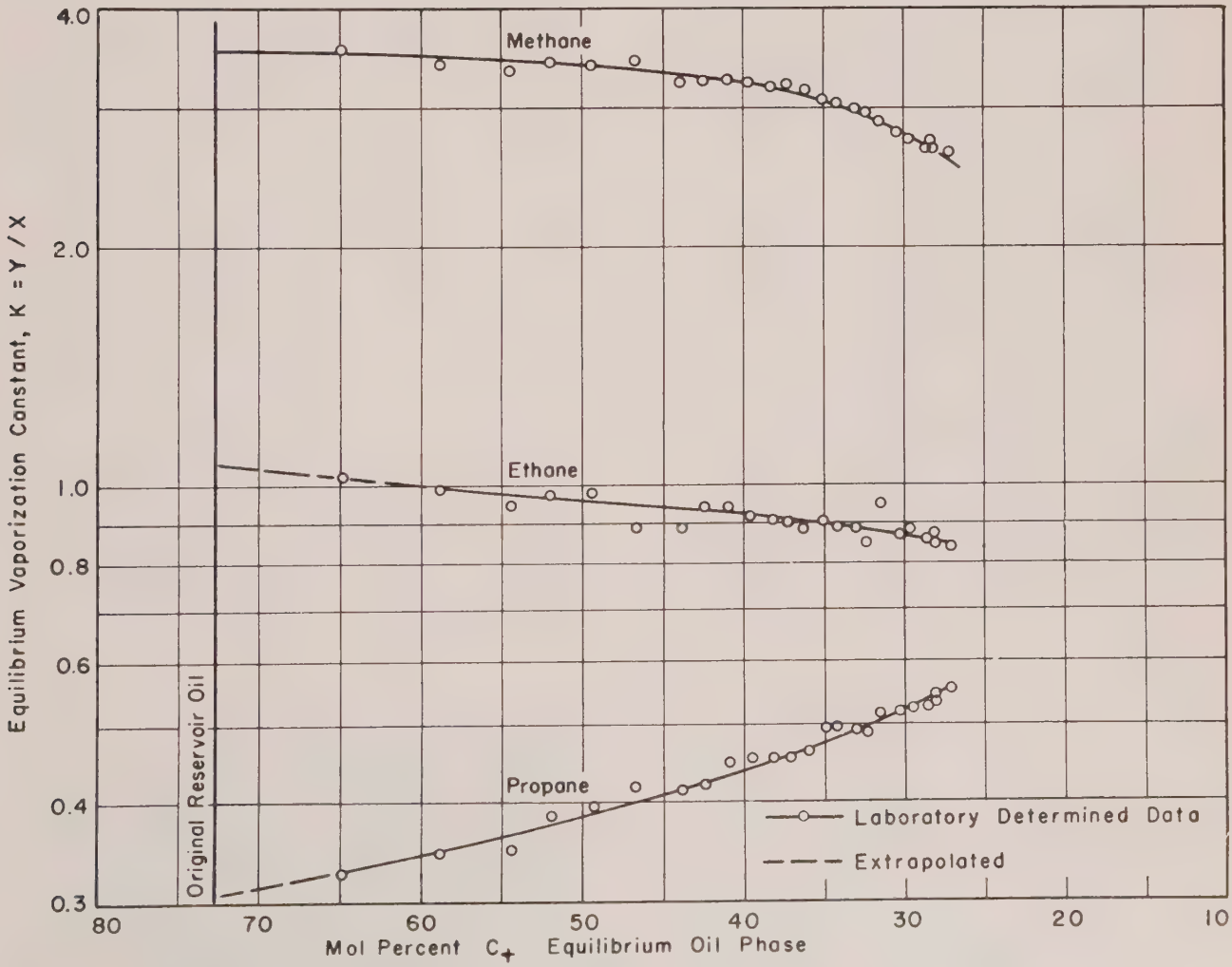

FIG. 4—TYPICAL *K*-VALUE SYSTEM WITH CONSTANT PRESSURE AND TEMPERATURE.

front vaporizing the oil at reservoir conditions and condensing it out in the separators. The field has continued to follow the prediction of the nonequilibrium calculation, indicating that the recovery mechanism is being accurately simulated with the principles used.

Table 1 is a more detailed comparison of the observed field production history with the calculated results using nonequilibrium gas displacement. The reservoir was divided into 10 segments for the study so that the observed and calculated performance is presented for each segment and for the field as a whole. Note that there is excellent agreement for Segments 1 through 9, both at the end of one year of injection and at the end of three years. The discrepancy in Segment 10 of some 200,000 STB at the end of the first year is the result of fillup. The reservoir was actually being repressured during the first year while the calculation was performed for a constant pressure. The 200,000-bbl difference between observed and calculated figures is directly attributable to fillup and remained stable over the three year match of history. Table 2 illustrates the change in oil composition, resulting from the injected gas repeatedly contacting the reservoir oil. Both analyses are at the same reservoir pressure and temperature, with the difference in composition resulting from the injected gas vaporizing the intermediate (C_2 to C_6) components out of the reservoir oil. The original oil composition was 52 per cent methane and 23 per cent C_{7+} components. After three years of injection, the oil composition had changed to 44 per cent methane and 49 per cent C_{7+}. The API gravity of the produced crude had changed from 50° to 37° API.

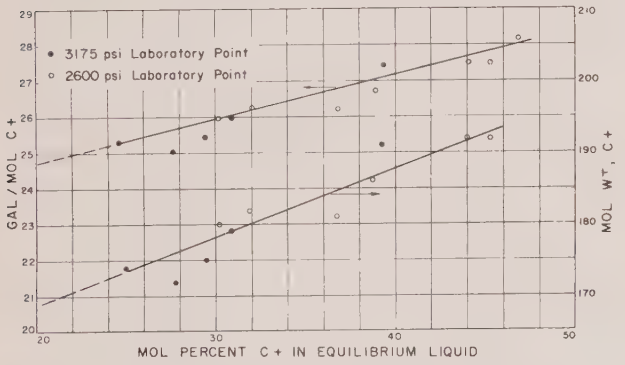

FIG. 5—EFFECT OF FLUID COMPOSITION ON PHYSICAL PROPERTIES OF THE HEAVY COMPONENT.

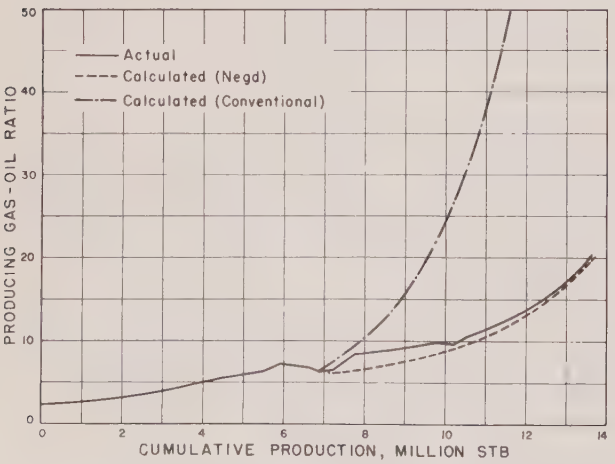

FIG. 6—FIELD PERFORMANCE OF DRY-GAS-INJECTION PROGRAM.

TABLE 1 – COMPARISON OF CALCULATED AND OBSERVED FIELD PERFORMANCE

Segment	Separator Gas-Oil Ratio		Cumulative Oil Production	
	Calculated	Observed	Calculated	Observed
		1.0 Year		
1	114,000	No Data	–	–
2	46,000	No Data	–	–
3	30,000	No Data	–	–
4	24,000	No Data	21,000	14,000
5	20,000	No Data	61,000	56,000
6	17,000	23,000	52,000	75,000
7	15,000	17,000	104,000	95,000
8	13,000	13,000	695,000	666,000
9	10,000	10,000	560,000	562,000
10	5,000	5,000	663,000	448,000
Total	10,200	10,000	2,157,000	1,916,000
		3 Years		
1	244,000	No Data	–	–
2	114,000	No Data	–	–
3	62,000	No Data	–	–
4	40,000	No Data	24,000	15,000
5	30,000	No Data	70,000	60,000
6	25,000	No Data	52,000	70,000
7	22,000	23,000	143,000	125,000
8	21,000	20,000	1,068,000	1,058,000
9	18,000	16,000	1,156,000	1,200,000
10	11,000	10,000	1,203,000	1,010,000
Total	16,000	15,000	3,718,000	3,544,000

TABLE 2 – EFFECT OF GAS INJECTION ON RESERVOIR OIL COMPOSITION, CONSTANT PRESSURE

Component	Mol Per Cent	
	Original	After 3 Years Injection
C_1	52.0	44.0
C_2	6.3	4.9
C_3	5.3	1.5
C_4	6.5	0.2
C_5	3.6	0.1
C_6	3.4	0.1
C_{7+}	22.9	49.2
	100.0	100.0
API Gravity	50	37

CONCLUSIONS

Based on the field studies performed to date, four basic conclusions have been reached.

1. Fluid compositional data obtained from the nonequilibrium calculation are essential in designing surface separation and plant facilities. It was found that, because of phase behavior, produced oil and gas compositions undergo marked changes during the producing history of an injection program, necessitating periodic changes in separator conditions for maximum stock-tank recovery.

2. The net effect of phase behavior in all calculations performed is to give substantially improved recovery and lower gas-oil ratios than would have been predicted by conventional methods of analysis.

3. In the case of volatile oils being produced by dry-gas injection, recovery derived from phase behavior equaled that of the displacement mechanism. Although there are no rules of thumb relating to the volatility at which phase behavior becomes important, it is felt that dry-gas injection for an oil shrinkage of 1.5 or greater justifies a nonequilibrium-type analysis. Considering a heavy crude, the non-equilibrium displacement analysis is considered necessary only for injected-gas compositions of 15 per cent or more intermediates (C_2 to C_6).

4. The basic assumptions and limitations discussed earlier do not appear to seriously restrict the application of this analysis to field studies. In fact, a substantially improved analysis should result for reservoirs in which phase behavior is an important factor.

NOMENCLATURE

v = volume of fluid at reservoir conditions
f_g = fraction of total flow that is gas
K_o = relative permeability to oil, fraction
K_g = relative permeability to gas, fraction
p = reservoir pressure, psia
V = mols of gas per mol of total fluid
S_g = average gas saturation in segment, fraction
T = reservoir temperature, °R
x = composition of oil, mol fraction
y = composition of gas, mol fraction
z = composite fluid composition, mol fraction
Z = gas compressibility
μ_o = oil viscosity, cp
μ_g = gas viscosity, cp
$\bar{\mu}$ = average viscosity
K = equilibrium vaporization ratio
m = mols of fluid
MWT = molecular weight
R_{wf} = bottom-hole flowing gas-oil ratio

SUBSCRIPTS

c = critical constants
s = segment number
l = liquid

REFERENCES

1. Buckley, S. E. and Leverett, M. C.: "Mechanism of Fluid Displacement in Sands", *Trans.*, AIME (1942) Vol. 146, 107.
2. Jacoby, R. H. and Berry, V. J., Jr.: "A Method for Predicting Pressure Maintenance Performance for Reservoirs Producing Volatile Crude Oil", *Trans.*, AIME (1958) Vol. 213, 59.
3. Kunz, K. S.: *Numerical Analysis*, McGraw Hill Book Publishing Co., Inc., N.Y. (1957).
4. Beal, Carlton: "The Viscosity of Air, Water, Natural Gas, Crude Oil and Its Associated Gases at Oil Field Temperatures and Pressures", *Trans.*, AIME (1946) Vol. 165, 94.
5. Standing, M. B.: *Volumetric and Phase Behavior of Oil Field Hydrocarbon Systems*, Chapter 4.

APPENDIX

BASIC EQUATIONS UTILIZED

EQUILIBRIUM FLASH

Equilibrium flash =

$$\frac{z}{V + (1/K - 1)} = 0 \quad \ldots\ldots\ldots\ldots (1)$$

$$\frac{z}{V(K-1) + 1} = x \quad \ldots\ldots\ldots\ldots (2)$$

$$\frac{zK}{V(K-1) + 1} = y \quad \ldots\ldots\ldots\ldots (3)$$

Eq. 1 is used to calculate V the mols of gas per mol of fluid, for all reservoir and surface flashes. The equation is solved using the Neutonian[3] iteration technique. Eqs. 2 and 3 are used to calculate the molar composition of equilibrium gas and liquid resulting from each flash.

CALCULATION OF PHYSICAL PROPERTIES OF OIL AND GAS

The following data are calculated as a function of composition for both the gas and oil following every flash calculation.

Gas

1. Gas Compressibility (Z):
   Pseudo-reduced temperature = $\Sigma y(p_c)/p$.
   Pseudo-reduced temperature = $\Sigma y(T_c)/T$.
   Z is evaluated from a table of standard compressibility vs reduced temperature and pressure.
2. Gas Viscosity (μ_g):
   The determination of gas viscosity is based on the procedure and curves outlined in Fig. 6 of Ref. 4, which relates gas viscosity at a given pressure and temperature as a function of gas density. Two curves are used in the nonequilibrium gas displacement calculation to bracket the range of reservoir pressure. All values of viscosity are determined by interpolating between the two curves.
3. Gas Volume (v_g):
   $v_g = ZRTm_g/p$.

Liquid

1. Volume Per Mol (v_l):
   (a) *Laboratory Data* — A laboratory curve of mol per cubic centimeter vs mol fraction of the "plus component" in the liquid is used to calculate liquid volume at reservoir conditions. The laboratory-data curves are at two pressures which bracket the range of interest so that any value can be obtained by a linear interpolation. These basic data are obtained during the K-value determination.

(b) *Published data* — Apparent liquid density

$$= \frac{\Sigma[(MWT)\,(x)]}{\Sigma[(\text{gal/mol})\,(x)]} \quad .$$

The calculated liquid density is corrected for reservoir pressure and temperature using the procedure outlined in Ref. 5.

This corrected density is then used to calculate a correct volume per mol for liquid using the following procedure.

$$v_l = \frac{\Sigma\,[(MWT)\,(x)]}{\text{corrected liquid density}} \quad .$$

2. Liquid Viscosity:

These data are obtained from two laboratory-determined curves of viscosity vs the mol fraction of plus component in the liquid for two pressures which bracket the pressure range of interest.

DISPLACEMENT AND TWO-PHASE FLOW

$$\frac{df_g}{dS_g} = \frac{\left[\left(\frac{\bar{\mu}_g}{\bar{\mu}_o}\right)\left(\frac{K_o}{K_g}\right)\right]\left[\frac{d\,(\ln K_o/K_g)}{d\,(S_g)}\right]}{1 + \left[\left(\frac{\bar{\mu}_g}{\bar{\mu}_o}\right)\left(\frac{K_o}{K_g}\right)\right]^2} \quad . \quad . \quad . \quad (4)$$

$$f_g = \frac{1}{1 + \left[\left(\frac{K_o}{K_g}\right)\left(\frac{\bar{\mu}_g}{\bar{\mu}_o}\right)\right]} \quad . \quad . \quad . \quad . \quad . \quad . \quad . \quad (5)$$

$$\frac{df_g}{dS_g} = \frac{f_g}{S_g} \quad . \quad . \quad . \quad . \quad . \quad . \quad . \quad . \quad . \quad . \quad . \quad . \quad . \quad (6)$$

Eqs. 4 and 5 (Buckley-Leverett displacement) are solved simultaneously for a value of S_g at the displacing-gas front that will satisfy Eq. 6. The Neutonian iteration technique[3] is used for this solution. These equations are used to determine the volume of fluid displaced *from the segment which is being invaded by the front.*

$$\left(\frac{K_g}{K_o}\right)\left(\frac{\mu_o}{\mu_g}\right) = R_{wf} \quad . \quad . \quad . \quad . \quad . \quad . \quad . \quad . \quad . \quad . \quad . \quad (7)$$

Eq. 7 is used to determine the relative volume of oil and gas flowing in each segment *behind and ahead of the front.*

FLUID COMPOSITIONS (z_s)

The composition and volumes of fluid in each segment at the beginning of one displacement step is derived from four sources, as indicated by Eq. 8.

$$z_s = \frac{\left[\begin{array}{l}(\text{mol of disp. gas})_{s-1}\,(y)_{s-1} \\ + (\text{mol of resid. gas})_s\,(y)_s \\ + (\text{mol of disp. liq.})_{s-1}\,(x)_{s-1} \\ + (\text{mol of resid. liq.})_s\,(x)_s\end{array}\right]}{\Sigma(\text{mol of disp. liq. and gas} + \text{resid. liq. and gas})} \quad . \quad (8)$$

***

Multiple Liquid Phases in a Natural-Gas System

LOWELL STROUD
WILL E. DEVANEY
JOHN E. MILLER

U. S. BUREAU OF MINES
HELIUM RESEARCH CENTER
AMARILLO, TEX.

ABSTRACT

During a recent phase study of a natural gas, two stable equilibrium liquid phases were observed at temperatures below –200°F and pressures above 200 psi. This paper reviews the published literature on the occurrence of multiple equilibrium liquid phases and presents analytical data for the vapor and two equilibrium liquid phases of the liquefied natural gas at five experimental conditions. In addition, data for 30 conditions of two-phase equilibria are included.

INTRODUCTION

The low-temperature phase behavior of gases, most of which contained helium, has been investigated in the laboratories of the Helium Activity for many years. Since 1952, experimental studies of these systems have been continuous as part of the research program at Amarillo, Tex. Because of their value to private industries interested in participating in the Helium Conservation Program, several "Open File" reports containing phase equilibria data for helium-bearing natural gases have already been released by the Helium Activity. A paper containing information on the general phase behavior, operating criteria and extensive vapor-liquid data for two helium-containing systems was recently published.[2] Additional publications presenting experimental data on the phase relationships of various gas systems are now in process and will be available in the near future.

PREVIOUS EXPERIMENTAL WORK

Although the formation of multiple liquids has been reported for various systems, to our knowledge this paper is the only substantiated evidence of a vapor-liquid-liquid equilibria in a naturally occurring gas. In 1940, Vink, Ames, and others[13] reported the presence of two liquid phases in a hydrocarbon system consisting of mixtures of crude oils, solvents and natural gas. Eilerts and co-workers[7] published data on the recombined fluids from a gas-condensate well. This condensed gas, containing approximately 76 per cent methane and 24 per cent ethane-plus, exhibited two distinct liquid phases. Weinaug and Bradley[14] observed "unusual" phase behavior in a reservoir mixture. These workers postulated that the anomalous phase behavior was due to the "imminent formation of a second liquid phase". Botkin, Reamer, Sage and Lacey[1] studied two California crude oils that exhibited multiple phases. Kohn and Kurata[10] recently reported two equilibrium liquid phases in the methane-hydrogen sulfide system. Roof and Crawford[11] and Eakin, *et al*,[6] also have reported experiments with binary systems that formed two stable equilibrium liquid phases.

APPARATUS AND PROCEDURE

A U. S. Bureau of Mines Phase Equilibrium Apparatus was used in conducting this study. The apparatus and procedures employed in its operation have been previously described[3] and will not be repeated in detail in this report. Briefly, the apparatus consists of a windowed cell which can be maintained within ±0.5°F for temperatures between room temperature and –320°F. Pressure within the cell can be maintained within 0.1 per cent of gauge reading up to 800 psig.

Equilibrium vapor and liquid samples are obtained in special containers[4] for analysis by a mass spectrometer. Although the accuracy of the analyzer is about ±0.1 mol per cent, the reproducibility of the phase-equilibrium apparatus is considered relatively poor. Values reported from methane and nitrogen are considered accurate to ±1.0 and ±0.6 mol per cent. Data for ethane-plus in the vapor are accurate within 0.2 mol per cent; liquid-phase data for this aggregate component are accurate within 1.5 mol per cent. For helium in the vapor phase, the analytical data are accurate within 0.2 mol per cent; liquid-phase analyses for this component were obtained by the charcoal adsorption method described by Frost[8] and are accurate within 0.006 mol per cent.

All of these references to the accuracy of reported values are conservative estimates based upon a statistical treatment of reproducibility data obtained with the apparatus.

Original manuscript received in Society of Petroleum Engineers office Feb. 24, 1961. Revised manuscript received June 20, 1961.

[2]References given at end of paper.

MATERIALS

The natural gas from which dual liquid phases were produced was obtained from the inlet gas line to the Navajo helium plant at Shiprock, N.M. At the time of sample collection in 1958, the plant was supplied with the helium-bearing natural gas from Pan American Petroleum Corp. Wells 13 and 17, located in the Hogback field of San Juan County, N.M.

Composition of the gas is shown in Table 1. Carbon dioxide, present to the extent of 2.2 mol per cent, and traces of moisture were removed from the gas before experimentation; therefore, the data of Table 1 are on a CO_2- and water-free basis. For reporting convenience, the gas is considered as one of only six components – methane, ethane, propane, butanes-plus, nitrogen (including argon) and helium.

The composition of Hogback gas differs greatly from most helium-bearing natural gases. Methane concentration in Hogback is less than that of nitrogen and is only about half that in the natural gases supplied to other Bureau of Mines plants. The nitrogen content is twice that in the gas processed at the Amarillo, Tex., and Keyes, Okla., plants and is more than three times that in the gas supplying the Exell, Tex. helium plant. Even more unusual is the high helium content of Hogback gas – more than three times that in Amarillo or Keyes gases, and seven times that in Exell gas.

EXPERIMENTAL RESULTS

VAPOR-LIQUID DATA

Results of mass spectrometer analyses of two-phase equilibria in Hogback gas are shown in Tables 2 and 3.

As an illustration of general phase behavior, the 400-psia data are plotted in Fig. 1.

It should be emphasized that the data shown in Tables 2 and 3 and Fig. 1 apply only to two-phase vapor-liquid equilibria in Hogback gas. At lower temperatures and at pressures above 200 psi, two stable liquid phases formed; data for these conditions are treated separately in the following section of this paper. Fig. 1 does not show a maximum value for nitrogen in the vapor – a common char-

TABLE 1 – COMPOSITION OF HOGBACK GAS (MOL PER CENT)

Component	12-Component Analysis	6-Component Analysis
Methane	32.9	32.9
Ethane	3.3	3.3
Propane	1.8	1.8
Butane	.9	
Isobutane	.7	2.6
Pentane	.3	
Isopentane	.4	
Cyclopentane	.0	
Hexanes-plus	.3	
Nitrogen	51.8	52.4
Argon	.6	
Helium	7.0	7.0
Total	100.0	100.0

TABLE 2 – VAPOR PHASE, HOGBACK GAS (MOL PER CENT)

Press. (psia)	Temperature (°F)	Methane	Ethane	Propane	Butanes-plus	Nitrogen	Helium
100	–100	34.5	3.0	1.0	0.0	54.3	7.3
	–125	33.7	2.8	.3	.1	52.9	9.6
	–150	34.2	2.0	.1	.0	55.8	7.8
	–175	33.9	1.0	.1	.1	56.8	8.0
	–200	34.4	.4	.0	.1	57.0	8.0
	–225	32.0	.1	.0	.0	59.8	8.0
	–250	20.1	.1	.0	.0	70.0	9.8
200	–100	34.5	2.7	.6	.1	54.7	7.4
	–125	34.7	2.2	.1	.1	55.8	7.1
	–150	34.4	1.5	.1	.0	56.2	8.0
	–175	34.9	.7	.0	.1	56.4	8.0
	–200	32.2	.2	.0	.1	59.3	8.2
	–225	23.4	Tr.	.0	.0	66.7	9.9
300	–100	34.5	2.4	.5	.1	55.0	7.4
	–125	34.3	2.0	.2	.0	55.9	7.6
	–150	34.2	1.2	Tr.	.0	57.0	7.5
	–175	32.7	.5	Tr.	.0	58.3	8.4
	–200	29.5	.1	.0	.0	61.9	8.4
	–225	17.5	.1	.0	.0	71.2	11.3
400	–100	34.6	2.3	.4	.0	55.2	7.5
	–125	34.4	1.7	.1	.1	56.7	7.2
	–150	33.6	1.0	.1	.0	57.1	8.2
	–175	32.2	.4	.0	.0	58.7	8.6
	–200	26.3	.1	.0	.0	65.3	8.2
	–225	13.5	.1	.0	.0	71.6	14.8
500	–100	34.6	2.2	.4	.0	55.5	7.3
	–125	34.2	1.5	.2	.0	56.7	7.4
	–150	33.3	.9	.1	.0	57.5	8.2
	–175	30.9	.4	Tr.	.0	59.6	9.1
	–200	24.6	.1	.0	.0	64.9	10.4

Tr. is less than 0.05 mol per cent.

TABLE 3 – LIQUID PHASE, HOGBACK GAS (MOL PER CENT)

Press. (psia)	Temperature (°F)	Methane	Ethane	Propane	Butanes-plus	Nitrogen	Helium
100	–100	4.8	8.2	27.1	57.6	2.4	.016
	–125	5.2	16.1	33.9	44.5	.2	.005
	–150	7.6	22.9	30.3	39.1	.1	.007
	–175	11.9	28.2	27.5	32.3	.1	.005
	–200	22.2	35.4	19.0	21.2	2.2	.002
	–225	37.2	25.3	15.6	19.4	2.3	.002
	–250	53.4	13.2	10.3	15.5	7.5	.005
200	–100	9.9	15.2	28.4	43.8	2.9	.018
	–125	11.6	22.3	27.9	35.8	2.6	.012
	–150	17.1	22.9	21.9	35.5	2.6	.008
	–175	21.6	27.3	22.3	27.4	1.4	.009
	–200	36.8	24.7	15.9	18.7	3.8	.005
	–225	59.2	13.4	8.1	8.8	10.5	.015
300	–100	12.0	17.7	26.7	40.6	3.1	.017
	–125	15.2	23.4	6.1	34.3	1.0	.030
	–150	20.1	27.2	23.3	27.3	2.0	.023
	–175	31.1	25.4	18.6	21.5	3.4	.020
	–200	48.7	18.1	11.6	14.0	7.5	.020
	–225	58.2	9.1	5.3	6.0	21.4	.038
400	–100	17.0	20.0	21.2	35.4	6.3	.029
	–125	20.1	23.5	23.0	29.1	4.3	.058
	–150	24.2	24.1	20.1	27.7	3.9	.063
	–175	37.4	21.9	15.8	19.2	5.6	.032
	–200	54.9	13.8	8.4	9.2	13.6	.043
	–225	50.8	6.3	3.8	5.5	33.4	.142
500	–100	18.8	19.3	23.0	33.7	5.1	.043
	–125	21.6	20.1	20.0	33.0	5.4	.082
	–150	31.1	24.0	13.7	22.7	8.5	.066
	–175	42.8	19.7	13.5	15.5	8.4	.048
	–200	54.2	11.1	6.9	7.4	20.3	.114

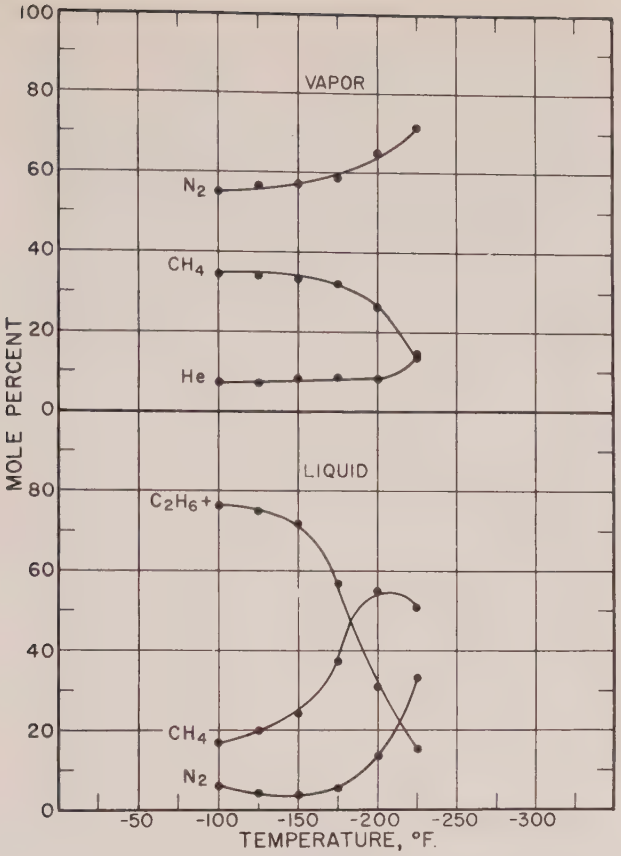

FIG. 1 – VAPOR-LIQUID DATA, HOGBACK GAS, 400 PSIA.

acteristic for nitrogen in natural-gas phase relationship data – because colder temperatures which would have been required to produce it resulted in the formation of two liquids. A maximum concentration of methane in the liquid was reached before the anomalous phase behavior occurred and is shown in the figure. It is also noted that the helium content of the vapor phase increases sharply at temperatures below –200°F.

VAPOR-LIQUID-LIQUID DATA

At 500 psia and –250°F, it was observed that two stable equilibrium liquid phases were present. Runs at 200, 300 and 400 psia and –250°F, and 500 psia and –225°F also produced the anomalous phase behavior. Samples of the vapor and both liquid phases were taken at these five conditions. The analytical results are presented in Table 4, and a photograph showing two equilibrium liquid phases

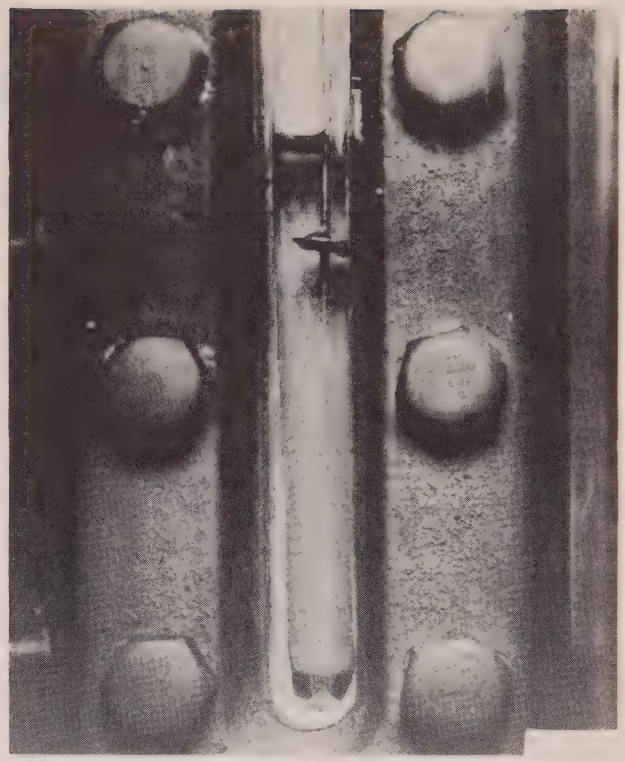

FIG. 2 – TWO EQUILIBRIUM LIQUID PHASES IN HOGBACK GAS AT 400 PSIA AND -250°F.

in Hogback gas at 400 psia and –250° F is shown in Fig. 2.

What appears to be a white material on the window of the cell is actually a deposit of finely divided metal from a stirrer blade that had contacted the inside surface of the window during operation of the apparatus prior to the present study.

The experimental apparatus was not designed to permit direct sampling of two discrete liquid phases; however, by sampling the lower liquid and then carefully draining the cell until only the upper liquid remained, fairly representative samples of the upper liquid were obtained. The limitations of this sampling technique were recognized but it was considered worthwhile to obtain samples of the upper liquid, even though the analytical data might not represent true equilibrium conditions. Vink[13] and co-workers encountered a similar problem; they had to void the vapor and upper liquid phases in order to sample a lower liquid phase.

Although the data contained in Table 4 are too few for significant representation by plotting, they

TABLE 4 – VAPOR-LIQUID-LIQUID COMPOSITIONS, HOGBACK GAS (MOL PER CENT)

	200 psia – 250 °F			300 psia – 250 °F			400 psia – 250 °F			500 psia – 250 °F			500 psia – 225 °F		
Component	Vapor	Upper Liquid	Lower Liquid	Vapor	Upper Liquid	Lower Liquid	Vapor	Upper Liquid	Lower Liquid	Vapor	Upper Liquid	Lower Liquid	Vapor	Upper Liquid	Lower Liquid
Methane	7.6	50.7	50.9	7.6	41.7	28.8	5.3	39.0	25.9	4.4	38.4	34.2	12.1	43.7	41.0
Ethane	Trace*	12.5	13.3	0.0	3.7	12.4	0.0	3.5	13.9	Trace	5.1	13.8	0.1	4.5	12.4
Ethane-plus	Trace	31.7	33.5	Trace	7.3	45.8	0.0	6.6	52.1	0.1	14.1	54.1	0.2	10.3	43.5
Nitrogen	75.7	17.5	15.5	69.5	50.6	15.4	57.5	53.9	11.8	48.8	46.9	11.6	67.9	45.7	15.4
Helium	16.7	.046	.011	22.8	.149	.040	37.1	.389	.034	46.8	.511	.055	19.9	.383	.058

* Trace indicates less than 0.05 mol per cent.

do reveal the following.

1. At 200 psia and –250°F, the compositions of the two liquid phases are almost identical except for their helium contents. The upper liquid contained about four times the helium concentration in the lower liquid.

2. With respect to the 300 and 400 psia data at –250°F, the corresponding liquid phases at each pressure, except for helium content, are fairly similar in composition. The chief difference in the vapor phases at these two conditions is a helium content of 37.1 mol per cent at 400 psia, compared to 22.8 mol per cent at 300 psia. This difference in the partial pressure of helium may account for the increased helium concentration in the upper liquid at the higher pressure. The helium contents of the lower liquids at both pressures are about the same.

3. Comparison of the 400 and 500 psia data at –250°F shows the chief difference to be in the vapor phases, where the helium content at 500 psia is 46.8 mol per cent compared to 37.1 mol per cent at 400 psia. The helium content of the upper liquid at 500 psia is .511 compared to .389 mol per cent at the lower pressure.

4. The ratio of helium content in the upper liquid to that in the lower liquid is approximately four at both 200 and 300 psia and –250°F; at 400 and 500 psia this ratio is about 10 and may be a reflection of the increased partial pressure of helium due to increasing helium concentration in the vapor phase. The concentration of helium in the lower liquids increases about fourfold between 200 and 300 psia and then remains essentially constant at the higher pressures.

5. Comparison of the 500 psia data at –225° and –250°F shows the effect of reduced temperature at constant pressure. Considerably less methane and nitrogen content in the vapor phase at the colder temperature result because of the increase in the per cent of the feed gas that is condensed. As a consequence, the helium content of the vapor phase more than doubled, increasing from 19.9 mol per cent at –225°F to 46.8 per cent at –250°F; the composition of the two liquid phases, except for ethane-plus, does not change markedly as a result of the lower temperature. The helium content of the upper liquid phase increased from .383 mol per cent at –225°F to .511 at –250°F, while the helium content of the lower liquid remained essentially unchanged.

DISCUSSION AND CONCLUSIONS

The limited vapor-liquid-liquid data obtained in this study are too meager for adequate interpretation. The sampling technique which had to be employed for the upper liquid phase probably introduced errors which prevent the analytical data from being exactly representative of equilibrium conditions. For this reason no emphasis has been placed on determining equilibrium vaporization constants, *K*, for the various components. Nevertheless, the unusual phase behavior of Hogback gas merits some discussion.

The anomalous behavior of Hogback gas probably is not a retrograde phenomenon. The only apparent requirements for the formation of the two liquid phases were that the temperature be colder than about –200° or –225°F and the pressure be higher than about 200 psi.

Glasstone[9] points out that two partially miscible liquids may, upon saturation with each other, become a conjugate solution wherein the two liquid systems are in equilibrium with each other. As the temperature is raised, the composition of the two layers approach each other (note data for 200 psia and –250°F in Table 4). The mutual solubilities of the two liquids increase with increasing temperature, and finally a point is reached where the two liquids become identical in composition. The temperature at which this occurs is known either as the critical solution temperature (D. O. Masson, 1891) or the consolute temperature (W. D. Bancroft, 1894) of the system.

Although the critical solution temperature of Hogback gas was not determined precisely, visual observations during the tests indicated it to be between –200° and –225°F. The minimum pressure required to obtain two liquid phases appeared to be about 200 psi. Data shown in Table 4 for this pressure and –250°F show a similarity in composition between both liquids, indicating proximity to critical solution conditions.

During the summer of 1959, water flooding of the Hogback wells occurred and the wells were reworked and extended to lower depths. Samples taken after these modifications show compositions radically different from that used in this study. This has precluded any further study of the unusual behavior exhibited by the original gas, but gas from the Pan American Corp. Navajo C-1 well, now supplying the Bureau of Mines helium plant at Shiprock, is known to exhibit multiple condensed phases. A phase study of this system has been scheduled for next year.

In an effort to produce a two-liquid system, a synthetic mixture containing nitrogen, methane, ethane and helium, in concentrations equivalent to their values in Hogback gas, was prepared. Several experiments with this mixture, including all those that resulted in two liquid phases in Hogback gas, plus additional runs at temperatures as low as –320°F, failed to produce two liquids. It might be concluded, therefore, that hydrocarbons heavier than ethane in Hogback gas were responsible for the two-liquid phase formation in that system. The presence of a nonparaffinic hydrocarbon compound has been suggested recently as a cause of the unusual phase behavior in Hogback gas. As a part of the future study of Pan American Navajo C-1 gas, analyses for benzene and other nonparaffinic hydrocarbons will be made.

REFERENCES

1. Botkin, D. F., Reamer, H. H., Sage, B. H., and Lacey, W. N.: *Fundamental Research on Occurrence and Recovery of Petroleum,* API (1943) 62; (1944) 42.
2. Brandt, L. W., Stroud, L. and Miller, J. E.: *Jour. Chem. Eng. Data* (1961) Vol. 6, No. 1, 6.
3. Brandt, L. W. and Stroud, L: *Ind. Eng. Chem.* (1958)

Vol. 50, 849.

4. Brandt, L. W.: *Chem. Anal.* (1956) Vol. 45, 106.
5. Brown, G. G., Katz, D. L., Oberfell, G. G. and Alden, R. C.: *Natural Gasoline and the Volatile Hydrocarbons,* NGAA, Mid-West Printing Co., Tulsa, Okla. (1948) Section 1.
6. Eakin, B. E., Ellington, R. T. and Gami, D. C.: *Inst. Gas Tech. Bull.* (1955) 26.
7. Eilerts, C. K., Barr, V. L., Mullens, M. B. and Hanna, B.: *Pet. Eng.* (1948) Vol. 19, No. 5, 154.
8. Frost, E. M., Jr.: RI 3899, USBM (1946).
9. Glasstone, S.: *Textbook of Physical Chemistry.* Second Ed., D. Van Nostrand, N. Y. (1946) 721-26.
10. Kohn, J. P. and Kurata, F.: *AIChE Jour.* (1958) No. 4, 211.
11. Roof, J. G. and Crawford, N. W.: *Jour. Phys. Chem.* (1958) Vol. 62, 1138-39.
12. Standing, M. B.: *Volumetric and Phase Behavior of Oil Field Hydrocarbon System,* Reinhold Publishing Co., N.Y. (1952).
13. Vink, D. J., Ames, A. M., David, R. A. and Katz, D. L.; *Oil and Gas Jour.* (1940) No. 39, 34.
14. Weinaug, C. F. and Bradley, H. B.: "Phase Behavior of A Natural Hydrocarbon System", *Trans.,* AIME (1951) Vol. 192, 233.

***

The Calculated Performance of Solution-Gas-Drive Reservoirs

J. S. LEVINE*
M. PRATS
MEMBERS AIME

SHELL DEVELOPMENT CO.
HOUSTON, TEX.

ABSTRACT

Several methods are available for calculating the performance of solution-gas-drive reservoirs from the PVT properties of the oil and from the relative permeability and other properties of the formation. These methods require a number of simplifying assumptions. The present method of computation has made use of a high-speed computer to solve simultaneously the nonlinear partial differential equations that describe two-phase flow by solution-gas drive in order to calculate the performance of a reservoir. Some of the results obtained by the nonlinear partial differential equation solution are compared with those obtained with an approximate method, which has been called the semisteady-state solution. The pressure and saturation profiles from the wellbore to outer boundary calculated by the two methods are compared for one constant-terminal-rate case and two constant-terminal-pressure cases. The agreement in these profiles, as well as in the values of average reservoir pressure and cumulative recovery, leads to the conclusion that, for most engineering calculations, the semisteady-state method will give a reasonable approximation to the numerical solution of the differential equations describing solution-gas drive.

An unfavorable (as regards ultimate oil production) set of relative permeability curves was used in the calculations in the belief that the effect of the parameters which were studied would be emphasized to a greater degree. Furthermore, the reservoir was assumed to be completely homogeneous, *and these results should not be considered applicable to any other type of reservoir. Gravity effects are not considered.*

The absolute permeability was varied from 25 to 0.5 md. At an economic limit of 2 B/D, the recovery for a 25-md reservoir is about 1.8 times as great as that for a 0.5-md reservoir. The effect of permeability on the producing gas-oil ratio is minor. Once PVT properties of the oil and the relative permeability properties of the reservoir are fixed, the producing gas-oil ratio is found to be a function of the fraction of oil recovered.

Well spacings of 10, 40 and 80 acres were considered. For the assumed homogeneous-reservoir properties, the effect of spacing on recovery at an economic limit of 2 B/D was very slight.

Certain dimensionless groups can be used to extend the results to other fields having different permeabilities, spacings, reservoir thicknesses, well radii and porosities, so long as the PVT and relative permeability properties are similar to those used in this paper.

INTRODUCTION

An important aspect of reservoir engineering is the prediction of the performance of the reservoir based on the limited information normally available early in the life of a field. Usually, soon after a field has been discovered, it is necessary to decide upon the spacing to be employed and the production program to be used for most efficient utilization of reservoir energy. Where these decisions have not been dictated by legal or political considerations, they have frequently been based on experience factors which indicate that two fields with similar characteristics will probably have similar performances. To the extent that the industry has been successful in economically exploiting oil reservoirs, this rule-of-thumb method has been found to have merit.

A large amount of theory has been developed with which it is possible to predict the performance of a reservoir by using certain known properties of the oil and the formation. Because of the difficulties of the mathematics involved for a drainage area having square or rectangular boundaries, the problem usually has been simplified and idealized by assuming each drainage area to have radial symmetry and the field to be represented by a number of these drainage areas. Muskat[1] was one of the first to formulate the theory for two-phase flow and to solve the equations for a few cases by numerical integration, using the relatively slow means of computing available at that time. His equations describing

Original manuscript received in Society of Petroleum Engineers office July 21, 1960. Revised manuscript received April 3, 1961. Paper presented at 35th Annual Fall Meeting of SPE, Oct. 2-5, 1960, in Denver.

*Present address: Shell Oil Co., Denver.

[1]References given at end of paper.

multiphase flow in the presence of gravity are called "exact" equations in this paper, even though it is recognized they require gross assumptions regarding phase behavior and relative permeability concepts. Muskat later[2] simplified the two nonlinear, second-order differential equations to one nonlinear, first-order differential equation giving an approximation that could be solved easily by numerical methods. This gave a means of determining the pressure and saturation of the reservoir at the external boundary and of calculating an "average" performance of the reservoir. Calculations showing the effect of reservoir fluid and rock characteristics on production histories were made by Muskat and Taylor[3] in 1946. In 1955, Arps and Roberts[4] used the simplified equation of Muskat to calculate the performance of solution-gas-drive reservoirs for a large number of different relative permeability ratios and solution-gas-oil ratios. The curves presented in their paper gave a rapid means of determining the relation between recovery and average pressure in a reservoir if the average k_g/k_o, solution gas-oil ratio and oil gravity were known.

The development of the very high-speed computer with large storage capacity made possible a numerical solution of the "exact" equations for unsteady-state two-phase flow. West, Garvin and Sheldon[5] were the first ones to do this by replacing the derivatives by finite differences. Their method was programed for the IBM 701 computer, and the results for one set of conditions were presented for both a radial and a linear flow system. The present report will show the results obtained by a variation of the West method used with a program written for the IBM 704 computer. Some details of this method will be discussed later. In addition, the results of the exact method (that is, the computational results of the finite-difference equations representing the exact equations of Ref. 1) will also be compared with the semisteady-state results for three cases.

PURPOSE OF THE WORK

This work was undertaken for three primary purposes: (1) to compare the solution-gas-drive results obtained by the exact method with those obtained by an approximate method in order to determine whether the latter is suitable for engineering purposes; (2) to compare a constant-terminal-rate with a constant-terminal-pressure method of production; and (3) to determine the effect of absolute permeability and spacing on the recovery at economic limit from homogeneous solution-gas-drive reservoirs.

These objectives have been reached only to the extent that a single set of PVT and relative permeability data has been used. In a sense, therefore, the work to be discussed is exploratory, and the objectives will not be attained entirely until other cases are considered.

RESERVOIR CHARACTERISTICS AND ASSUMPTIONS

The PVT properties of the oil and gas are shown in Fig. 1. Fig. 2 gives the gas and oil relative permeability relationship. It is apparent to one acquainted with various types of relative permeability curves that the ones shown are "unfavorable"; that is, they will result in a low ultimate oil production. These curves were chosen intentionally, with the idea that such relative permeability data might emphasize the effect of the various parameters.

It was assumed that the reservoir was at the bubble-point pressure and had the following additional characteristics: $\phi = 0.139$, $S_{wc} = 0.177$, $h = 23.5$ ft, $r_w = 1/3$ ft and $p_b = 2{,}060$ psig.

Three different external boundary distances were used – 372, 745 and 1,053 ft – corresponding to an equivalent circular area of 10, 40 and 80 acres, respectively. The reservoir was assumed to be horizontal, *completely homogeneous and not to be affected by gravity.* Vertical differences in pressure due to hydrostatic gradient were neglected. The relative permeability values indicated by Fig. 2 were assumed to be independent of the absolute permeability of the formation. At the critical gas saturation of 2 per cent (corresponding to a total liquid saturation of 98 per cent), the relative permeability to gas was taken to be zero. There was no free gas initially in the reservoir.

Throughout this report, the term "economic limit" will refer to an arbitrarily chosen minimum production rate of 2 BOPD. Thus, the oil recovery at

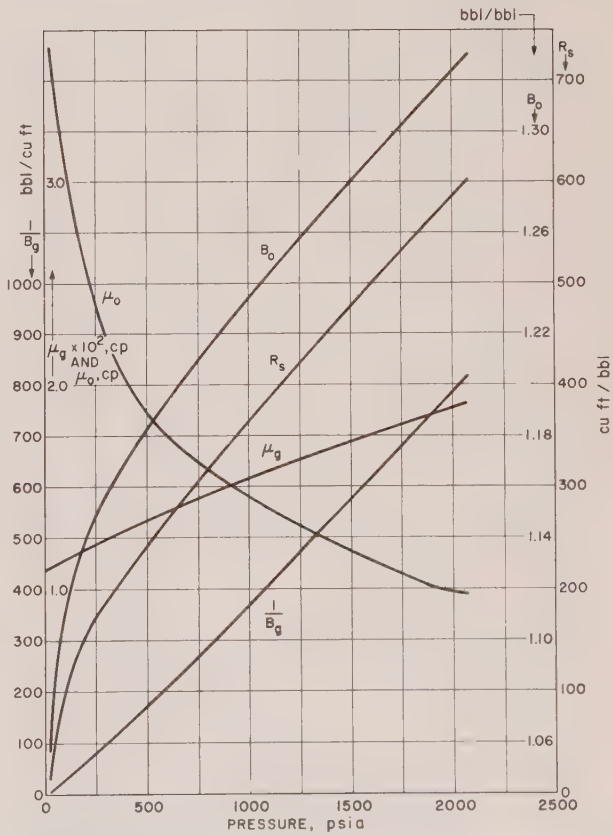

FIG. 1 – PVT PROPERTIES OF THE OIL AND GAS.

economic limit will mean the cumulative recovery when the production rate has reached 2 B/D. This cumulative recovery will be expressed either in barrels or as a per cent of the initial oil in place.

The program for solution of the exact equations on the IBM 704 allows one to specify either the wellbore rate or pressure as a function of time. In addition, one other condition must be specified, namely, the minimum pressure to which the producing well can go. For all the calculations of this report, the minimum well pressure was assumed to be 50 psig. In those cases where the specified rate could be maintained long enough to obtain a cumulative recovery of at least 3 per cent of the initial oil in place, the problem has been called a "constant-terminal-rate" case. Where the specified rate could not be maintained for this amount of production, the problem has been called a "constant-terminal-pressure" case. Obviously, all problems automatically became constant-terminal-pressure cases when the wellbore pressure reached 50 psig.

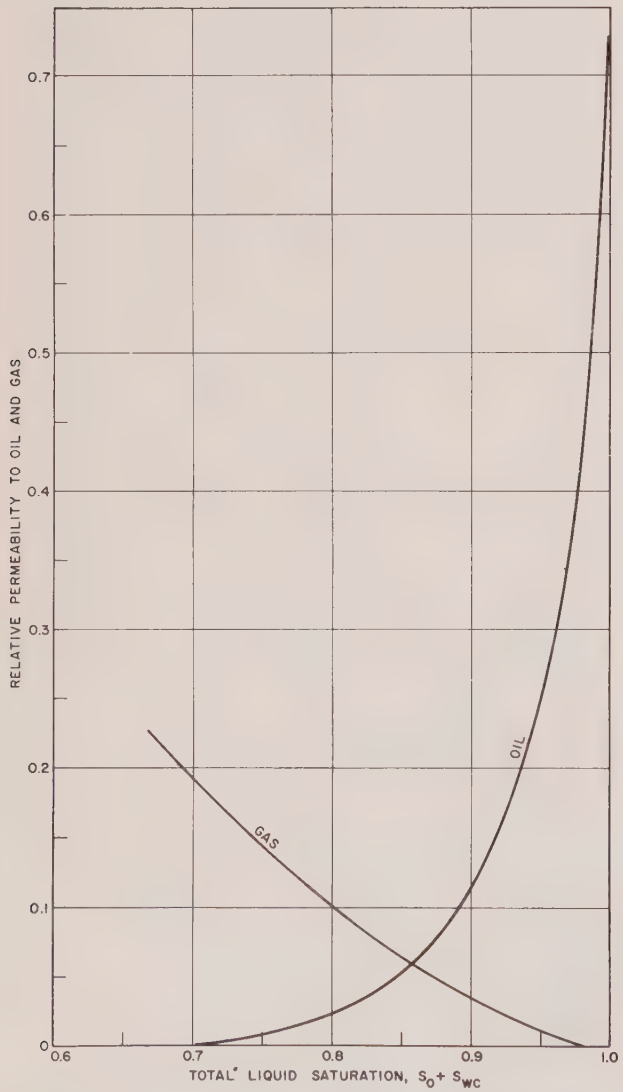

FIG. 2 — GAS AND OIL RELATIVE PERMEABILITY PROPERTIES OF THE RESERVOIR.

METHODS OF SOLUTION

The preceding section discussed the properties of the reservoir rock and the crude in it, as well as the shape and orientation of the reservoir itself. It also mentioned that gravity effects were neglected. Two different things are meant by this: (1) buoyancy effects resulting from density difference were not considered; and (2) the effect of the varying hydrostatic head on the pressure at the various elevations throughout the thickness of the formation was neglected. If this last effect were not neglected, then at any fixed distance from the well the pressure would be lowest at the top of the formation and more gas would be evolved at the top of the formation than at any point directly below it. This would necessitate determining the pressure and saturation not only as a function of the distance from the well, but also as a function of the vertical position within the reservoir. This cannot be done with available methods. In neglecting both gravity effects, in fact, we are essentially considering an infinitesimally thin reservoir. Of course, results based on this thin-reservoir concept are applied later to practical cases where variations in hydrostatic head may be as large as 100 psi (and higher), but usually are less. Also, when a nominal back-pressure of, say 50 psig is put on a formation, the actual back-pressure will depend on the position along the producing interval. These nominal back-pressures are usually referred to the midpoint of the producing interval. Although not strictly so, the numerical results based on the thin-reservoir concept will refer to the horizontal plane through the midpoint of the producing interval. The pressure and saturation are then only a function of the distance from the well, and the system of differential equations describing solution-gas-drive reservoirs can be written as

$$\frac{1}{r}\frac{\partial}{\partial r}\left(rk\frac{k_{ro}}{B_o\mu_o}\frac{\partial p}{\partial r}\right) = -\phi\frac{\partial}{\partial t}\left(\frac{S_o}{B_o}\right), \quad \ldots \quad (1)$$

$$\frac{1}{r}\frac{\partial}{\partial r}\left[r\left(\frac{k_{ro}R_s}{\mu_o B_o} + \frac{k_{rg}}{B_g\mu_g}\right)k\frac{\partial p}{\partial r}\right] = -\phi\frac{\partial}{\partial t}\left(\frac{1 - S_{wc} - S_o}{B_g} + \frac{S_o R_s}{B_o}\right) \quad \ldots \quad (2)$$

At the outer boundary, both pressure and saturation gradients vanish, whereas at the well the production rate or the pressure can be specified. In addition, the initial pressure and saturation distribution are specified.

This system of differential equations and its associated conditions have been solved by two different methods, both numerical. In one method, Eqs. 1 and 2 are represented by finite-difference equations after the substitution

$$\alpha = \ln\frac{r_w}{r} \quad \ldots \quad (3)$$

has been made. The range of a is divided into M equal increments, as shown schematically in Fig. 3. ($M = 30$ for most of the calculations in this report.) The pressures are obtained at the midpoint of the cells, whereas the saturations are obtained at the cell boundaries. Whenever saturations are needed at the midpoints of the cells, these are obtained from the arithmetic average of the saturations at the adjoining cell interfaces. The resultant equations are, in general,

$$\left[(q_o)_{2m+2}-(q_o)_{2m}\right]_{t+\tau/2}+\frac{2\pi h\phi r_e^2 e^{2a_{2m+1}}\sinh\Delta a}{5.615(\tau/2)}\cdot\left[\left(\frac{S_o}{B_o}\right)_{t+\tau/2}-\left(\frac{S_o}{B_o}\right)_t\right]_{2m+1}=0 \quad . . . . (4)$$

$$\left[(q_g+R_sq_o)_{2m+2}-(q_g+R_sq_o)_{2m}\right]_{t+\tau/2}+\frac{2\pi h\phi r_e^2 e^{2a_{2m+1}}\sinh\Delta a}{5.615(\tau/2)}\left[\left(\frac{S_{oi}-S_o}{B_g}+\frac{R_sS_o}{B_o}\right)_{t+\tau/2}-\left(\frac{S_{oi}-S_o}{B_g}+\frac{R_sS_o}{B_o}\right)_t\right]_{2m+1}=0 \quad . . . . (5)$$

$$(q_o)_{2m+2,t+\tau/2}=\left\{\left[\frac{(1.127\times10^{-3})2\pi khbk_{ro}}{\mu_oB_o\Delta a}\right]_{2m+2}\cdot(p_{2m+3}-p_{2m+1})\right\}_{t+\tau/2} \quad . . . . . (6)$$

$$(q_g)_{2m+2,t+\tau/2}=\left\{\left[\frac{(1.127\times10^{-3})2\pi khbk_{rg}}{\mu_gB_g\Delta a}\right]_{2m+2}\cdot(p_{2m+3}-p_{2m+1})\right\}_{t+\tau/2} \quad . . . . . (7)$$

These equations are modified near the inner and outer boundaries to incorporate the proper boundary conditions and are then solved on an IBM 704, by procedures similar to those reported by West, Garvin and Sheldon,[5] to give pressure and saturations at the time increment $\tau/2$. The pressures and saturations corresponding to the end of the time step are obtained from those at the beginning and midpoint of the time step by linear extrapolation.

The program is designed to double the time interval of each succeeding time step, providing this gives convergence. There are also provisions for reducing the time interval to any level required to give a convergent series of iterations. A maximum time interval could also be specified. About 40 time steps were usually required to complete a problem.

It should be pointed out that significant cumulative errors can result from approximating the derivatives by finite differences. However, cumulative material balances run at each time step indicated small errors, with representative errors at the end of the run being 1 bbl of oil and 800 cu ft of gas.

The factor 5.615 appearing in Eqs. 4 and 5 and the factor 1.127×10^{-3} appearing in Eqs. 6 and 7 result from the fact that input data for the problem are expressed in practical engineering units. That is, data required for the system of Eqs. 4 through 7 are given in units of barrels per day, feet, centipoise, millidarcies and pounds per square inch. In fact, except in the basic Eqs. 1 and 2, practical units are used throughout this report.

It was stated earlier in this report that one of the purposes of the work was to compare the numerical solution of Eqs. 1 and 2 with the solution obtained by an approximate method which will be called the semisteady-state solution. The present authors wish to point out that the basic derivation of the approximate method was undertaken many years ago by A. F. van Everdingen, E. H. Timmerman and G. Stewart of Shell Oil Co., but the results have never been publicly circulated. More recently, the Koninklijke/Shell Laboratorium, The Netherlands, have used the assumptions proposed by van Everdingen, Timmerman and Stewart to derive an equation which could be integrated very simply on a medium-speed computer.

The approximation proposed by van Everdingen, *et al,* consisted in assuming that, at any one instant of time, both the rate of decline of stock oil in place and the total gas-oil ratio are everywhere constant. With the assumption that the rate of decline of stock oil in place is everywhere constant, the right-hand side of Eq. 1 becomes equal to the production rate divided by the reservoir pore volume. Workers at the Koninklijke/Shell Laboratorium have pointed out that the resultant expression can be integrated directly to give

$$\int_{p_D}^{p_{De}}\left[\frac{k_{ro}(S_{TL})}{\mu_oB_o}\right]dp=\frac{887q_o}{4\pi khbp_b}\left[\left(\frac{r_D^2-r_{De}^2}{r_{De}^2}\right)-2\ln\frac{r_D}{r_{De}}\right] \quad . . . (8)$$

when the integrand is evaluated at constant GOR conditions. The pressure and saturation relationship which results in a constant total GOR everywhere is the same as given by Muskat,[2] and is called the differential material balance. Results of

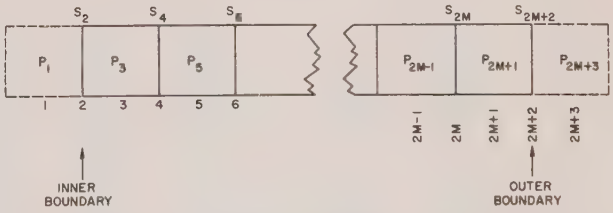

FIG. 3—SPACE POSITIONS AT WHICH PRESSURES AND SATURATIONS ARE CALCULATED IN THE EXACT SOLUTION.

this single integration of Eq. 8 will yield pressures and saturations as a function of r_D, and further manipulation of the results will yield production-history curves.

NUMERICAL RESULTS

COMPARISON OF THE EXACT AND APPROXIMATE METHODS

One of the purposes of this study was to compare results obtained by the exact and the approximate (or semisteady-state) methods of solution, discussed previously. For this comparison, three cases were calculated by the exact method on the IBM 704, and some of the same data were used to obtain a solution by the approximate method. Table 1 shows the results for a constant-terminal-rate case in a reservoir with 40-acre spacing and 25-md permeability. The external boundary pressures and production rates used were the same as those calculated by the IBM 704, and the pressure and saturation distribution, average pressure and per cent recovery were calculated for several periods in the production history. It can be seen that the results agree quite well. The average reservoir pressures are always within a few pounds per square inch, although this result is not surprising since the outer boundary pressures were assumed to be the same and the average pressure is always nearly equal to the outer boundary pressure. The recoveries are also in very good agreement by both methods. The biggest difference is in the producing gas-oil ratios, which are too low by the approximate method when the reservoir is producing at the assumed constant rate and too high when the rate can no longer be maintained and the problem becomes essentially a constant-terminal-pressure case. In every case, the constant gas-oil ratio used for the approximate method is that obtained from the differential material balance for the pressure and saturation at the outer boundary. This present case and the other two to be discussed later all indicate that, later in the life of a field, the actual gas-oil ratio is more favorable (lower) than would be anticipated from the differential material balance at the same average reservoir pressure. The higher gas-oil ratios are the result of the lower oil saturations calculated by the approximate method than those obtained by the exact method. This can be seen in Fig. 4, which shows the pressure and

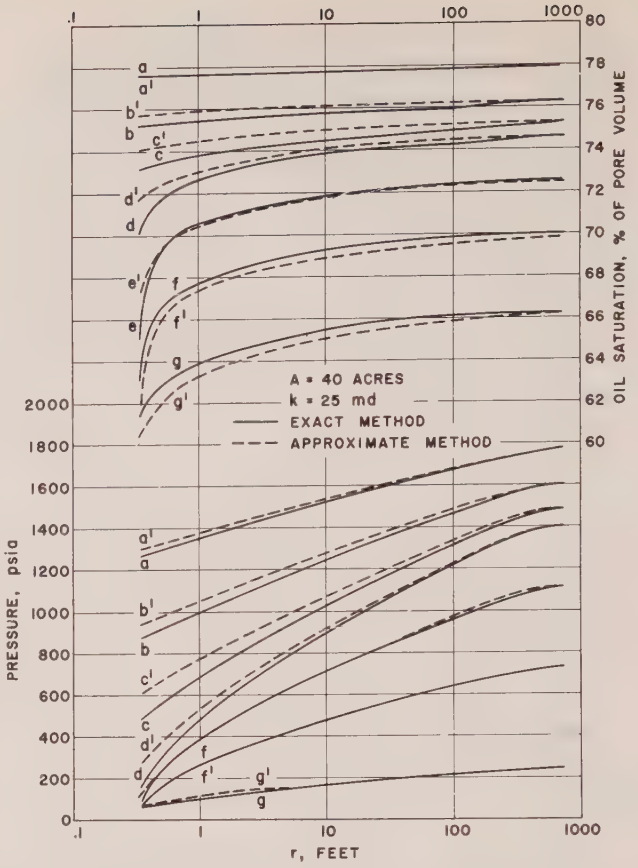

FIG. 4—PRESSURE AND SATURATION PROFILES FOR A CONSTANT-TERMINAL-RATE CASE.

saturation distributions throughout the reservoir obtained by both methods. It is evident that in this case the semisteady-state method gives too high a pressure near the wellbore and, therefore, a somewhat higher pressure distribution throughout the reservoir at any given instant. For the corresponding times, the oil saturations throughout the reservoir are first slightly higher by the approximate method and then slightly lower. However, as indicated in Table 1 and Fig. 4, the general results obtained by the two methods are in reasonable agreement. It should be pointed out that the use of a log scale to plot the radial distances for the pressure and saturation distributions shown in Fig. 4 (also Figs. 5 and 6) essentially overemphasizes that portion near the producing well, which comprises a very small percentage of the drainage

TABLE 1 – COMPARISON OF THE EXACT AND APPROXIMATE METHODS FOR THE SAME PRODUCTION RATE AND EXTERNAL BOUNDARY PRESSURE

Curves (Fig. 4)	p_e (psia)	q_o (B/D)	$\bar{p}$ (psia)		N_{pD} (per cent)		R (cu ft/bbl)		p_w (psia)	
			Exact	Approx.	Exact	Approx.	Exact	Approx.	Exact	Approx.
a–a′	1,770	50.0	1,751	1,751	3.34	3.36	2,340	2,350	1,273	1,304
b–b′	1,605	50.0	1,581	1,581	4.28	4.23	4,570	4,150	865	940
c–c′	1,485	50.0	1,453	1,457	4.75	4.67	6,610	5,840	480	610
d–d′	1,400	50.0	1,368	1,368	4.99	4.92	7,680	7,320	153	277
e–e′	1,115	26.8	1,086	1,088	5.64	5.62	12,790	13,150	65	119
f–f′	730	10.1*	711	712	6.24	6.26	21,110	23,130	65	65
g–g′	240	1.14**	233	235	6.83	6.91	27,730	30,210	65	65

*q_o = 9.71 B/D by the approximate method.

**q_o = 1.02 B/D by the approximate method.

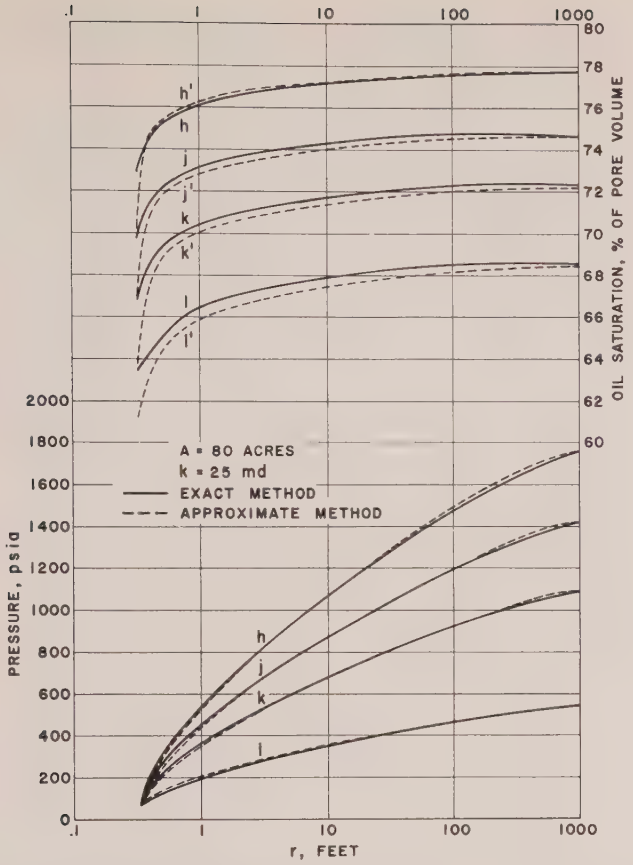

FIG. 5—PRESSURE AND SATURATION PROFILES FOR A CONSTANT-TERMINAL-PRESSURE CASE, k = 25 MD.

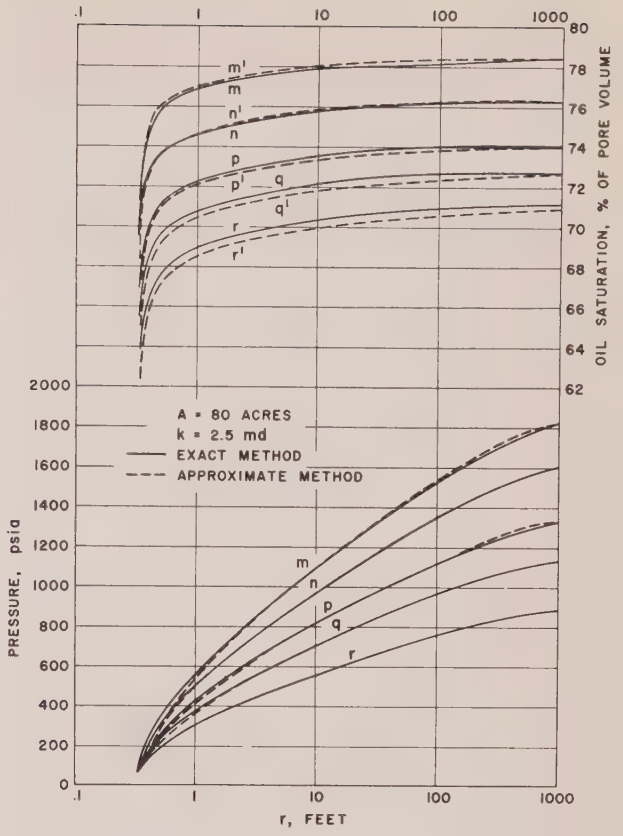

FIG. 6—PRESSURE AND SATURATION PROFILES FOR A CONSTANT-TERMINAL-PRESSURE CASE, k = 2.5 MD.

volume.

Table 2 gives a comparison of the results for two constant-terminal-pressure cases for reservoirs of 80-acre spacing and of 25-md and 2.5-md permeability, respectively. In both cases, the approximate solutions were calculated by using the same external boundary pressures as were obtained by the exact method, as well as the same constant terminal pressure of 65 psia. Shown in the table are the average reservoir pressures, gas-oil ratios, per cent recoveries and production rates. As in the case discussed previously, agreement of the various values is very good. The largest discrepancy of about 10 per cent is in the production rate calculated for the 25-md reservoir at a value of p_e = 1,757 psia. As the outer boundary pressures decrease, however, the production rates agree more closely. For the 2.5-md case, the agreement is good in all instances. The pressure and saturation distributions for these two cases are shown in Figs. 5 and 6, respectively. The pressure distributions in both cases are almost identical but, of course, were assumed to be the same at the inner and outer boundaries. The slight differences in saturation distributions are the result of the assumptions made for the semisteady-state method.

Fig. 7 shows a typical set of curves of gas-oil ratio as a function of radius for the 2.5-md reser-

TABLE 2 – COMPARISON OF THE EXACT AND APPROXIMATE METHODS FOR THE SAME EXTERNAL BOUNDARY PRESSURE AND CONSTANT TERMINAL PRESSURE

(Curves)	p_e (psia)	p_w (psia)	$\bar{p}$ (psia)		N_{pD} (per cent)		R (cu ft/bbl)		q_o (B/D)	
			Exact	Approx.	Exact	Approx.	Exact	Approx.	Exact	Approx.
			A = 80 Acres, k = 25 md (Fig. 5)							
h–h′	1,757	65	1,708	1,712	3.21	3.24	2,600	2,470	108.8	119.4
j–j′	1,413	65	1,377	1,378	4.78	4.82	6,350	7,110	53.3	52.4
k–k′	1,077	65	1,054	1,050	5.57	5.66	12,830	14,000	24.6	23.7
l–l′	529	65	519	517	6.38	6.53	24,280	27,850	5.12	4.71
			A = 80 Acres, k = 2.5 md (Fig. 6)							
m–m′	1,825	65	1,778	1,779	2.78	2.75	1,940	1,840	13.0	14.3
n–n′	1,610	65	1,567	1,569	4.12	4.06	4,090	4,090	7.88	8.37
p–p′	1,330	65	1,297	1,296	5.03	5.06	8,130	8,610	4.32	4.33
q–q′	1,135	65	1,112	1,107	5.49	5.55	11,620	12,730	2.82	2.72
r–r′	890	65	871	868	5.92	6.01	17,090	18,920	1.54	1.46

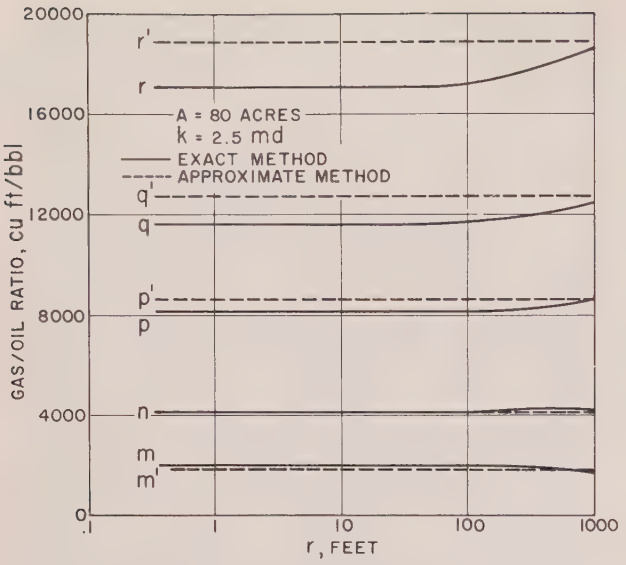

FIG. 7—GAS-OIL RATIO PROFILES FOR A CONSTANT-TERMINAL-PRESSURE CASE, k = 2.5 MD.

voir. The curves are for the same instant as the corresponding curves in Fig. 6. It is perhaps surprising that, although initially the gas-oil ratio at the wellbore is higher than at the outer boundary, this situation soon reverses, and during much of the producing life, the gas-oil ratio is less at the producing well than at the boundary. This was true in all the cases calculated by the exact method. The maximum variation in gas-oil ratio from outer boundary to wellbore was found to be about 10 per cent, so the assumption of a constant gas-oil ratio used in the approximate method of solution is not too radical. It should be emphasized that these results were obtained for a particular set of PVT and relative permeability data and may not be applicable if the PVT properties are drastically changed.

EFFECTS OF PERMEABILITY AND SPACING

Some of the results obtained by the exact method of solution on the IBM 704 are shown in Table 3. It can be seen that the effect of spacing on the economic recovery becomes greater as the permeability decreases. For permeabilities of 25 and 2.5 md, the recovery efficiency is decreased from 6.75 to 6.64 per cent and from 5.80 to 5.74 per cent, respectively (slightly over 1 per cent of the total), when the spacing is increased from 10 to 80 acres. However, for a permeability of 0.5 md the recovery efficiency is decreased from 3.85 to 3.53 per cent (about 7 per cent of the total) for the same increase in spacing. The effect of permeability on the economic recovery is much more pronounced. At the economic limit of 2 B/D, the per cent recovery for a 25-md reservoir is about 1.8 times as great as that for a 0.5-md reservoir. This difference in recovery for different permeabilities is, except for spacing effects, entirely the result of having to stop production when a minimum is reached; it should not be construed as a difference in the production mechanism. The calculated values indicate that the maximum production for the same spacing,

TABLE 3 – SOME RESULTS OF CALCULATIONS OBTAINED BY THE EXACT METHOD OF SOLUTION ON THE IBM 704.

Spacing (acres)	k (md)	Method of Production: Constant Terminal Rate	Method of Production: Constant Terminal Pressure	Oil Recovery per Spacing Unit at Economic Limit (bbl)	Time to Economic Limit (days)	N_{pD} (%)
10	25.0	x		10,600	410	6.75
40	25.0	x		42,200	1,680	6.73
80	25.0	x		84,100	3,360	6.71
80	25.0		x	83,200	2,680	6.64
10	2.50		x	9,100	1,030	5.80
80	2.50		x	72,000	8,600	5.74
10	0.50		x	6,030	1,560	3.85
80	0.50		x	44,200	14,300	3.53

without regard to economic rates, would be independent of the absolute permeability. This trend can be seen in Fig. 8, where the production rate has been plotted against per cent cumulative oil produced for reservoirs of 25-, 2.5- and 0.5-md permeabilities. If the production had been continued to very low rates (<0.1 B/D), all the curves would have come together at about the same recovery efficiency of around 7.3 per cent. It is evident that, if the economic limit of production had been raised to about 5.5 B/D, no oil would have been produced from the 0.5-md reservoir because its maximum production rate at initial reservoir pressure was only 5.3 B/D.

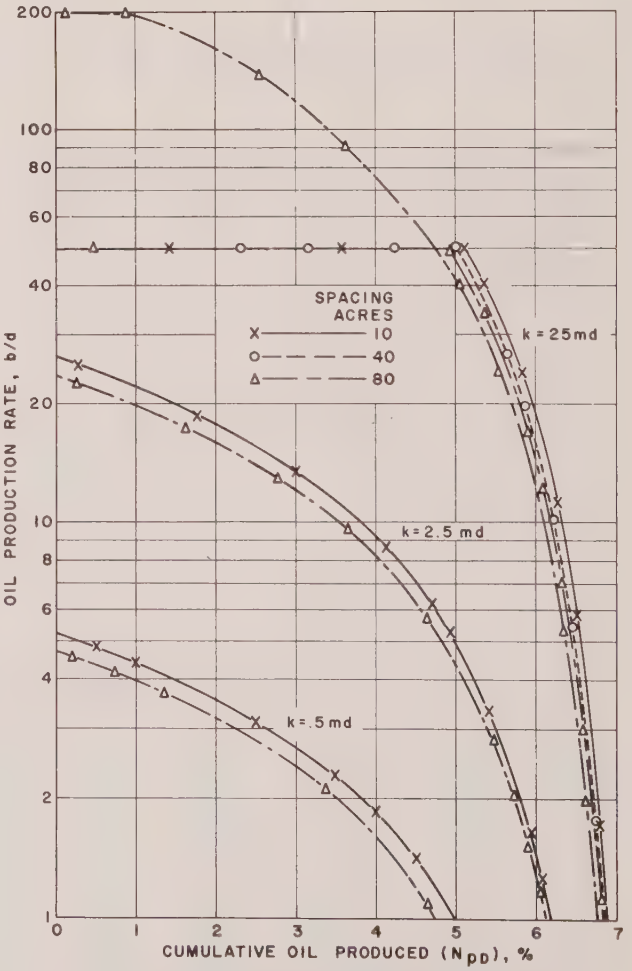

FIG. 8 – OIL-PRODUCTION RATE AS A FUNCTION OF CUMULATIVE OIL PRODUCED.

Fig. 8 also shows that, for a constant terminal pressure and at a given permeability, the closer-spaced wells will produce at a higher rate than the wider-spaced wells at the same per cent recovery. This means that the closer the spacing, the faster a well will drain a given fraction of oil from its drainage area. The time required to reach the economic limit is also shown in Table 3. It can be seen that, for a given permeability, the time is approximately proportional to the spacing. Based on the associated cumulative production and rate performance, one could choose a spacing to optimize profits.

Only one case was run in which the effect of rate of production on the economic recovery was indicated. Fig. 8 shows the curve of rate vs per cent cumulative oil produced for a well which initially produced at a constant terminal rate of 200 B/D, which was four times greater than the constant 50-B/D production of the other wells for the 25-md reservoir. After approximately 1 per cent of the initial stock tank oil in place had been produced at 200 B/D, the well pressure reached the limiting 50-psig value; thereafter, the well produced as a constant-terminal-pressure case. It can be seen that at the economic limit the production from this well was 6.64 per cent, compared to 6.71 per cent from an identical well whose initial rate was one-fourth as great. However, Table 3 shows that the time to reach economic limit was 2,680 days, compared to 3,360 days. Thus, if the well produces at approximately the maximum attainable rate at all times, the operating life is decreased about 25 per cent, while the economic recovery is decreased only about 1 per cent of the total recovery.

Fig. 9 shows a plot of the average recovery efficiency at the economic limit as a function of permeability. This curve shows that a formation having a *kh* product of about 5 md-ft (0.215 md × 23.5 ft) would not be able to produce any oil at a rate of 2 B/D. Similarly, extension of the curve to higher permeabilities would indicate that, no matter how great the permeability, the maximum recovery efficiency would be about 7.3 per cent at the economic limit. (This recovery efficiency compares with a value of 7.32 per cent obtained by differential material balance at a pressure of 50 psig.) Shown also in Fig. 9 is the average gas-recovery efficiency (defined as standard cubic feet of produced gas divided by standard cubic feet of gas initially in place) as a function of oil-recovery efficiency. For the 0.5-md reservoir about 10 per cent of the original gas has been produced at the economic limit, while for the 25-md reservoir about 68 per cent of the original gas has been produced. In any economic evaluation, this difference in produced gas must be considered.

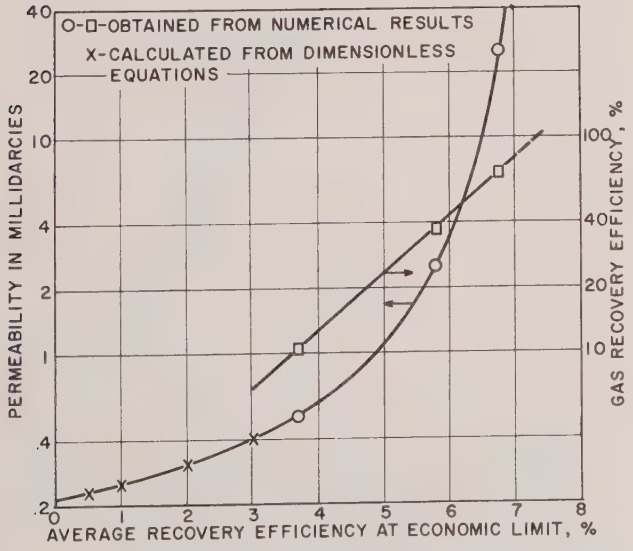
O-□-OBTAINED FROM NUMERICAL RESULTS
X-CALCULATED FROM DIMENSIONLESS EQUATIONS
PERMEABILITY IN MILLIDARCIES
GAS RECOVERY EFFICIENCY, %
AVERAGE RECOVERY EFFICIENCY AT ECONOMIC LIMIT, %

FIG. 9 – RELATIONSHIP BETWEEN OIL-RECOVERY EFFICIENCY, GAS-RECOVERY EFFICIENCY AND PERMEABILITY.

GAS-OIL RATIO AND CUMULATIVE OIL PRODUCED

Fig. 10 is a plot of the producing gas-oil ratio for various per cent recoveries for all the runs listed in Table 3. No attempt has been made to distinguish between the various cases, but it is obvious that at the same recovery the effects of permeability and spacing on the producing gas-oil ratio are minor. Thus, once the PVT properties of the oil and the relative permeability properties of the reservoir are fixed, the producing gas-oil ratio will be essentially independent of the spacing and of the absolute permeability. The peak occurs at a recovery of about 6.75 per cent and starts to decline after that in the normal way.

EXTENSION OF RESULTS BY DIMENSIONLESS GROUPS

It was emphasized earlier that the results obtained in this study were for a particular set of fluid and reservoir properties. Therefore, it will be of interest to determine whether the range of applicability of the results can be extended by the use of some dimensionless groups pertinent to depletion-type reservoirs.

The theory of dimensionally scaled models of petroleum reservoirs has been adequately discussed in papers by Rapoport[6] and Geertsma, *et al.*[7] Proper

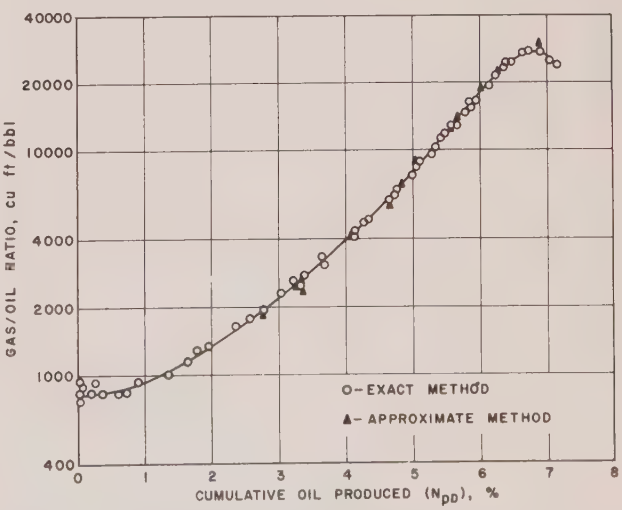

FIG. 10 – PRODUCING GAS-OIL RATIO AS A FUNCTION OF CUMULATIVE OIL PRODUCED.

dimensionless expressions for the time, oil-production rate and cumulative oil production can be written as follows.

$$t_D = \frac{1.266(10^{-2})\,(p_i - p_w)\,kt}{\mu_{ob}\phi(r_e^2 - r_w^2)} \quad , \quad . \quad . \quad . \quad . \quad . \quad (9)$$

$$q_{oD} = \frac{141.2\,\mu_{ob}q_o}{kh(p_i - p_w)} \quad , \quad . \quad . \quad . \quad . \quad . \quad . \quad . \quad . \quad . \quad . \quad (10)$$

$$N_{pD} = \frac{B_{oi}}{S_{oi}} \int_o^{t_D} q_{oD}\,dt_D. \quad . \quad . \quad . \quad . \quad . \quad . \quad . \quad . \quad . \quad (11)$$

These equations* have been used to calculate the values of the dimensionless quantities for all the problems discussed in this report. Fig. 11 shows a plot of dimensionless rate as a function of dimensionless time. The parameters that have been varied are the permeability, which ranged from 0.5 to 25 md, and the external radius, which ranged from 372 to 1,053 ft. It can be seen that the points lie essentially along two curves which can be classified according to whether the problem approximated a constant-terminal-pressure case (lower curve) or a constant-terminal-rate case (upper curve). It was mentioned earlier that, although only one problem was actually a constant-terminal-pressure case, several others approximated it in that the producing well pressure dropped to the minimum permissible value in a relatively short time after oil production started. The duration of this transient effect for those problems intended as constant-terminal-rate cases determined whether the points fell closer to the upper or to the lower curve of Fig. 11. Thus, it might be said that the constant-terminal-pressure curve is a limiting curve giving the maximum dimensionless rate at any dimensionless time, and that all rates less than this maximum will produce a series of dimensionless curves which must fall above the limiting curve. Those runs which behaved as constant-terminal-rate cases did so until a dimensionless time of about 50 was reached.

For constant-terminal-rate cases, the dimensionless rates determined from Eq. 10 will vary with the wellbore pressure. For constant-terminal-pressure cases, the dimensionless rates will vary proportionally to the actual production rate, while the pressure drop has the highest possible value. Because the pressure drop is the highest possible, the dimensionless production rate for the constant-terminal-pressure case is less than that for the constant-terminal-rate case.

The curves of Fig. 11 give a means of determining the oil-producing rate at any time for other permeabilities, spacings, sand thicknesses, well radii and porosities. One need calculate only the values of real time and rate from the dimensionless values, using Eqs. 9 and 10. Thus, the results of this report can be extended to other reservoirs having similar PVT and relative permeability characteristics.

Fig. 12 is a plot of dimensionless cumulative oil production as a function of dimensionless oil rate. Here again, there is a spread in a portion of the curve, depending on whether the early production was at constant terminal pressure or at constant

*Great care should be exercised in using Eqs. 9 and 10 to extend results to other systems having properties different from those used in this report.

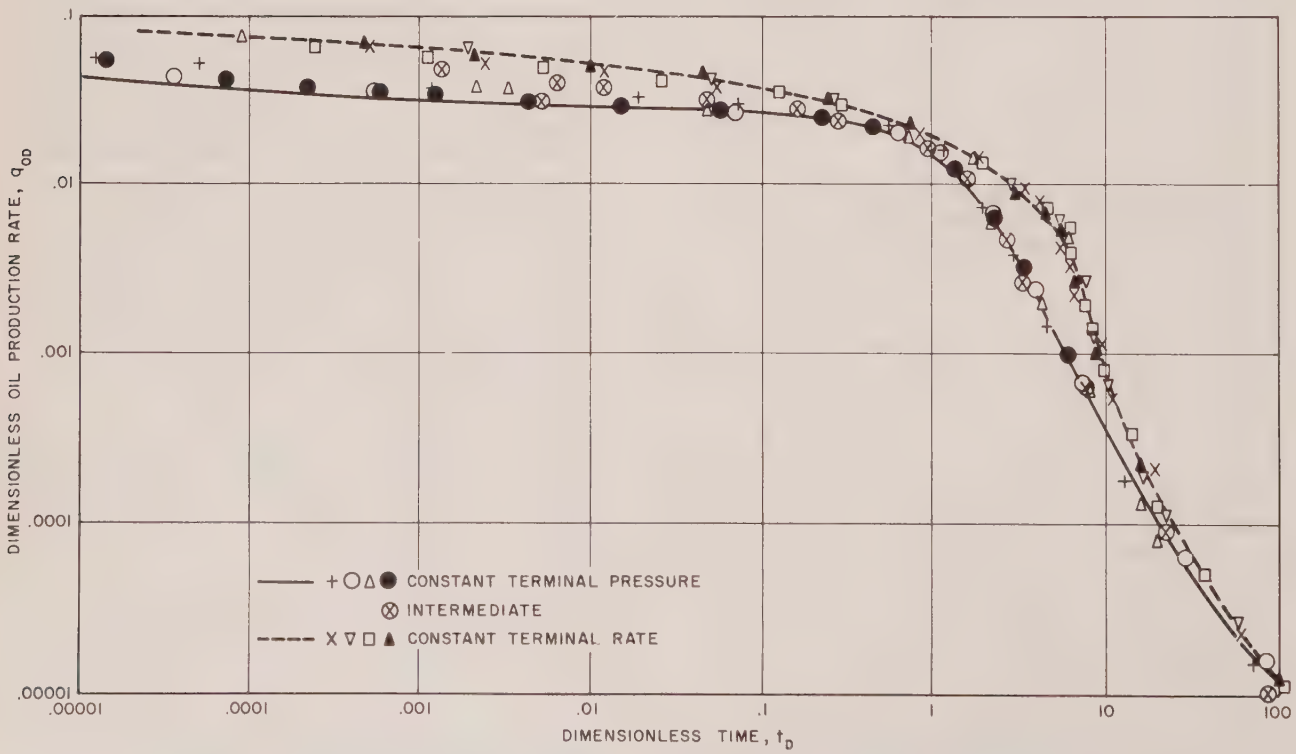

FIG. 11 – DIMENSIONLESS OIL RATE AS A FUNCTION OF DIMENSIONLESS TIME.

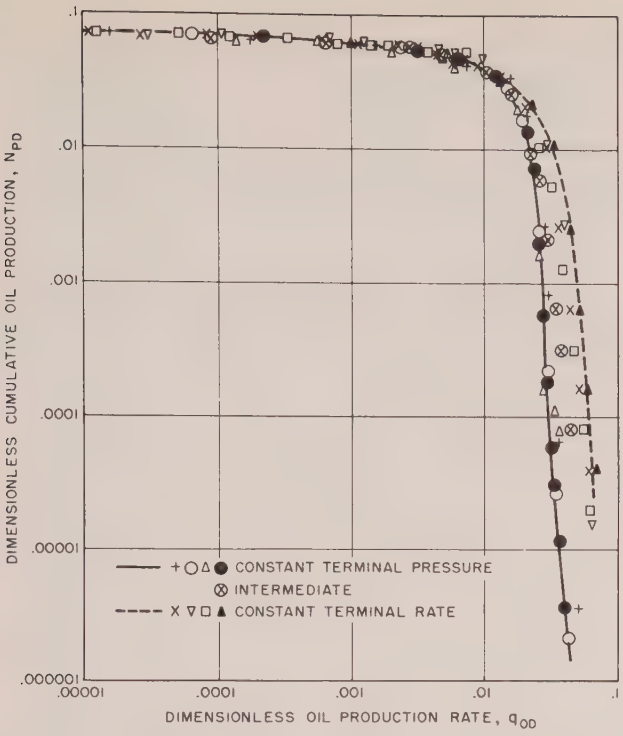

FIG. 12 — DIMENSIONLESS CUMULATIVE OIL PRODUCTION AS A FUNCTION OF DIMENSIONLESS OIL RATE.

terminal rate. For dimensionless rates below a value of 0.01, the cumulative production is independent of initial rate. The use of Figs. 11 and 12, therefore, allows one to determine the producing rate and cumulative production at any time in the life of a well.

CONCLUSIONS

Based on the results discussed previously for a completely homogeneous reservoir and for the range of conditions as given, the following conclusions can be made.

1. The methods described in this report provide a useful means for calculating the performance of solution-gas-drive reservoirs. To solve the exact equations governing two-phase flow, a high-speed computing machine with large storage capacity is required. By comparison, the semisteady-state method does not require such high-speed computers and can be calculated by means of an IBM 650 or equivalent. For the ranges covered in this report, it has been shown that for engineering calculations the semisteady-state method will give a satisfactory approximation to the correct solution.

2. At an arbitrarily chosen economic limit of 2 B/D, the per cent recovery for a 25-md reservoir is 1.8 times as great as that for a 0.5-md reservoir. This is not the result of a difference in production mechanism but, rather, is the result of arbitrarily cutting off production when a minimum rate is reached. The lower this economic rate, the more nearly will the recovery be independent of permeability.

3. Producing gas-oil ratio is essentially independent of both spacing and permeability at the same value of fractional recovery.

4. The effect of well spacing on recovery at an economic limit of 2 B/D is not significant for permeabilities above 2.5 md (corresponding to a $kh \approx$ 60 md-ft). For a 0.5-md permeability ($\approx$ 12 md-ft), the recovery is decreased about 7 per cent for a change in spacing from 10 to 80 acres.

5. For the PVT and relative permeability properties given in this report, certain dimensionless groups can be used to extend a given set of results to other fields having different permeabilities, spacings, reservoir thicknesses, well radii and porosities. The effect of whether early production is at constant terminal rate or constant terminal pressure is important; however, for dimensionless rates less than 0.01, the cumulative dimensionless production is independent of initial rate.

NOMENCLATURE

A = area, acres
a = $\ln r_w/r$
B_g = gas formation volume factor, bbl/cu ft
B_o = oil formation volume factor, bbl/bbl
B_{oi} = initial oil formation volume factor
ϕ = porosity, fraction
h = thickness of reservoir, ft
k = absolute permeability, md
k_{rg} = relative permeability to gas, fraction
k_{ro} = relative permeability to oil, fraction
M = total number of cells into which reservoir is divided
m = cell number
N = initial oil in place, bbl
N_p = cumulative oil produced, bbl
N_{pD} = cumulative oil produced, fraction or per cent, $= N_p/N$
p = pressure, psi
p_D = pressure, dimensionless, $= p/p_b$
$\bar{p}$ = average pressure, psi
p_b = bubble-point pressure, psi
p_i = initial pressure, psi
p_e = pressure at external boundary, psi
p_w = pressure at wellbore, psi
q_o = oil-production rate, B/D
q_{oD} = oil-production rate, dimensionless
r = radius, ft
r_D = radius, dimensionless, $= r/r_w$
r_e = external boundary radius, ft
r_{De} = external boundary radius, dimensionless, $= r_e/r_w$
r_w = well radius, ft
R = producing gas-oil ratio, cu ft/bbl
R_s = solution gas-oil ratio, cu ft/bbl
S_g = gas saturation, fraction
S_o = oil saturation, fraction
S_{oi} = initial oil saturation, fraction

S_{TL} = total liquid saturation, fraction

S_{wc} = critical water saturation, fraction

t = time, days

t_D = time, dimensionless

τ = time increment, days

μ_g = gas viscosity, cp

μ_o = oil viscosity, cp

μ_{ob} = oil viscosity at bubble point, cp

REFERENCES

1. Muskat, M. and Meres, M. W.: "The Flow of Heterogeneous Fluids Through Porous Media", *Physics* (1936) Vol. 7, 346.
2. Muskat, M.: "The Production Histories of Oil Producing Gas-Drive Reservoirs", *Jour. Appl. Phys.* (1945) Vol. 16, 147.
3. Muskat, M. and Taylor, M. O.: "Effect of Reservoir Fluid and Rock Characteristics on Production Histories of Gas-Drive Reservoirs", *Trans.*, AIME (1946) Vol. 165, 78.
4. Arps, J. J. and Roberts, T. G.: "The Effect of the Relative Permeability Ratio, the Oil Gravity, and the Solution Gas-Oil Ratio on the Primary Recovery from a Depletion Type Reservoir", *Trans.*, AIME (1955) Vol. 204, 120.
5. West, W. J., Garvin, W. W. and Sheldon, J. W.: "Solution of the Equations of Unsteady State Two-Phase Flow in Oil Reservoirs", *Trans.*, AIME (1954) Vol. 201, 217.
6. Rapoport, L. A.: "Scaling Laws for Use in Design and Operation of Water-Oil Flow Models", *Trans.*, AIME (1955) Vol. 204, 143.
7. Geertsma, J., Croes, G. A. and Schwarz, N.: "Theory of Dimensionally Scaled Models of Petroleum Reservoirs", *Trans.*, AIME (1956) Vol. 207, 118. ***

Flow in Heterogeneous Porous Media

J. E. WARREN
H. S. PRICE
MEMBERS AIME

GULF RESEARCH & DEVELOPMENT CO.
PITTSBURGH, PA.

ABSTRACT

Techniques for studying the performance characteristics of heterogeneous reservoirs have been developed. The effect of permeability variation on both the steady-state and the transient flow of a single fluid has been investigated. Limited comparisons with field and laboratory data have been made.

The physical models studied consist of random three-dimensional arrays of homogeneous porous blocks. The permeabilities of the individual elements are assigned according to a specific distribution function; uniform anisotropy is introduced by varying the relative dimensions of the blocks. A particular model is perturbed simply by re-arranging its elements at random. The behavior of a physical model is determined by digitally solving its numerical analogue.

Based on computational experiments, subject to the restrictions implied by the assumptions that were made, the following general conclusions have been drawn.

1. The most probable behavior of a heterogeneous system approaches that of a homogeneous system with a permeability equal to the geometric mean of the individual permeabilities.

2. The effects of flow geometry and anisotropy on the most probable value of the effective permeability of a heterogeneous medium are finite but not significant.

3. The permeability determined from a pressure build-up curve for a heterogeneous reservoir gives a reasonable value for the effective permeability of the drainage area.

4. A qualitative measure of the degree of heterogeneity and its spatial configuration are obtained from a comparative study of core analysis and pressure build-up data.

It has been indicated that these conclusions are predicated on the assumption that the core analysis and the pressure build-up data represent true reservoir characteristics. Common sources of error in these data have been discussed.

Original manuscript received in Society of Petroleum Engineers office Sept. 2, 1960. Revised manuscript received April 17, 1961. Paper presented at 35th Annual Fall Meeting of SPE, Oct. 2-5, 1960, in Denver.

INTRODUCTION

One of the most significant problems of reservoir engineering is that of determining the nature and the disposition of the heterogeneities that inevitably occur in petroliferous formations. It is with this problem that this paper is concerned.

Extensive research, both theoretical and experimental, has provided reasonable descriptions of the physical processes that are associated with primary and secondary recovery mechanisms. Similar progress in the field of numerical analysis and the evolution of truly high-speed digital computers have made it feasible to calculate the behavior of these mechanisms under almost any environmental conditions. It appears to be logical, then, to conclude that the mechanistic performance of any reservoir can be predicted with some confidence. Unfortunately, a necessary condition for the validity of this conclusion is that the formation be adequately described in a macroscopic sense. This condition cannot be satisfied in general; therefore, a frustrating situation currently exists – it is possible to compute the effect of reservoir heterogeneity on behavior, but it is not possible to specify the heterogeneity itself. In many cases, the predicted behavior of a project is so completely dominated by irregularities in the formation's physical properties that the gratuitous assumption of a particular form for the variation can reduce the solution of the problem to a mere tautological exercise.

While all porous media are microscopically heterogeneous, only macroscopic fluctuations need be considered since the fundamental concepts of reservoir mechanics are based on macroscopic quantities. For the simplest case in which only one physical property varies from point to point, the degree of heterogeneity that is apparent depends on three distinct factors, i.e., the nature of the property's variation (frequency distribution), its disposition (spatial distribution) and the inherent stability of the mechanism being studied. Consequently, any attempt to devise an unambiguous scale of heterogeneity must take these factors into account.

Since this investigation is intended to be exploratory, it will be restricted to single-phase flow because of the simplification implied; both steady-state and unsteady-state behavior will be considered. Furthermore, to keep the number of parameters

within reasonable limits, only variations in the absolute permeability will be permitted.

Although the problem under consideration deals with the effects of permeability variations on flow through porous media, analogous problems exist whenever potentials are involved, e.g., thermal conduction, electrical conduction, molecular diffusion, electrostatics and magnetostatics. Historically, Maxwell[1] first evaluated the conductivity of a composite medium which was comprised of a uniform matrix with random, spherical inclusions of a different material; Rayleigh[2] extended this work by obtaining exact series solutions for ideal geometries. More recently, Odelevskii[3] and Brown[4] proposed general methods for determining the effective conductivity of two-component systems; Brown's paper included a useful bibliography for the subject. An attempt to extend the theory to systems containing more than two components was made by Korneenko,[5] but his results applied to rather specific geometries. None of these analogous investigations suggested a plausible approach to the subject problem.

The first real attempt to study heterogeneous permeability was apparently that reported by Law;[6] he used the log-normal distribution function to represent permeability variations. Useful limits for the effective permeability of a heterogeneous medium were suggested by Cardwell and Parsons;[7] they correctly indicated the effect of weighing the samples. Muskat[8] considered the effect of stratification on cycling operations; log-normal, exponential and linear permeability distributions were discussed. The influence of stratification, with no cross-flow between layers, on waterflood performance was indicated by Stiles[9] and Dykstra and Parsons.[10] McCarty and Barfield[11] proposed a method for including lateral permeability variations in the computation of flood patterns. Houpert[12] studied permeabilities that could be expressed as analytic functions of position; Albert, *et al*,[13] derived general expressions for the transient behavior of reservoirs that had arbitrary permeability distributions and presented some numerical results. The effects of heterogeneity on miscible displacement were reported by Blackwell, *et al*;[14] Mamedov[15] and Douglas, *et al*;[16] considered immiscible displacement with crossflow between layers of different permeability by analytic and numerical methods, respectively. The transient behavior of a reservoir composed of noncommunicating layers was investigated by Lefkovits, *et al*;[17] both depletion and build-up performance were analyzed. An excellent discussion of the problem of reservoir heterogeneity was presented by Hutchinson;[18] a comprehensive bibliography for the subject was contained in this publication. Despite a large number of reported studies, in addition to those cited here, none of them indicated a reasonably systematic method for investigating the role played by heterogeneity in the performance of a reservoir.

The objectives of this project can be stated quite simply as follows: to study the effect of the disposition of heterogeneous permeabilities on single-phase flow when the nature of the heterogeneity is known, i.e., the frequency distribution is given; and to determine if it is possible to infer the presence and the probable configuration of the heterogeneity from data obtained by conventional well tests and core measurements.

The achievement of these objectives, even in a qualitative sense, should help to diminish some of the uncertainty usually associated with the information required to predict reservoir performance.

PHYSICAL PROBLEM

The existence of heterogeneous reservoir permeabilities has always been admitted, but the extent and the significance of these irregularities have been disputed. Vertical permeability variations have generally been assumed because they can be justified by the nature of depositional processes. On the other hand, lateral variations have largely been ignored despite the fact that sedimentation is rarely uniform even over reservoir distances. Probably a lack of information has contributed to the perpetuation of such inconsistent reasoning.

The sources of useful information for describing petroleum reservoirs are severely limited. Geologically, some knowledge of structure, sedimentation and composition may be available. Continuity, net pay, porosity and fluid saturations may be estimated from appropriate well logs. From core analysis, permeability, porosity, pay thickness and fluid saturations may be obtained; the permeability of the formation and completion damage may be calculated from pressure build-up data. Injectivity and productivity tests may be used to evaluate the flow capacity of the formation and, if profiles are recorded, to obtain a crude indication of the vertical variation in flow capacity immediately adjacent to the wellbore. Since this study is concerned with changes in permeability, only data from core analysis and build-up tests will be assumed to be acceptable.

Although the sample size, based on the cored interval, is infinitesimal when compared to the reservoir itself, it is essential to assume that the sample is volumetrically representative; then, the nature of the heterogeneity can be estimated from core data. The permeability determined from a build-up test represents an effective average over the drainage area of the well; therefore, it can be assumed that this value is a measure, albeit an indirect one, of the disposition of the heterogeneity. To achieve the objectives of this investigation, the core analysis data must be operated upon in such a manner that all spatial distributions of heterogeneous permeabilities, allowing for both vertical and lateral variations, may be considered. Then, a distribution corresponding to the one reflected by the value of the build-up permeability must be found. If the selected distribution can be used to synthesize a build-up curve that matches the measured one, the spatial configuration has a reasonable probability of being qualitatively correct. Agreement must be

[1]References given at end of paper.

considered to be only qualitative since uniqueness cannot be generally assumed.

To put the problem in a form that is amenable to mathematical formulation, it is assumed that the reservoir can be simulated by a three-dimensional ensemble of uniform, homogeneous, porous blocks in which the permeability of each element corresponds to that of one of the core samples; this model is an extension of the analog and analytic models used by Fatt[19] and Rose[20] to study the microscopic flow behavior of porous media. Since it has been assumed that the core samples are volumetrically representative, uniform weighting is implied; so, the original frequency distribution must persist in the model and the total number of blocks must be some multiple of the number of core samples. To compensate for our ignorance, a mechanism for randomly re-arranging a fixed number of elements in a given geometry must also be included to permit a statistically significant number of permutations to be considered.

This physical model indicates the three factors that apparently control heterogeneous behavior and must be examined, i.e., the permeability distribution as inferred from core data, the flow geometry and the number of elements. The first factor includes the effect of the distribution function, the range of permeabilities and the class interval; the second reflects the drainage area, formation thickness and well penetration; and the third is actually a measure of the degree of heterogeneity that is present. The importance of the first two factors is evident, and no amplification is necessary. The significance of the last factor becomes apparent when the limits are considered. Because of uniform weighting, the minimum number of elements is equal to the number of core samples; for the minimum case, there is a high probability that any rearrangement of the elements will produce a meaningful effect since there is virtually no redundancy, or entropy, present. As the number of elements is increased, the effect of rearrangement decreases until the system tends to behave homogeneously as the number becomes very large. Thus, it is obvious, in passing from the truly heterogeneous case to the homogeneously heterogeneous one, that the probable behavior of the proposed model should approach some limit while the possible behavior limits remain invariant; i.e., the maximum and minimum permeabilities are unchanged.

The generality of the results obtained through the use of this model will depend on the validity of the assumptions involved in its development; therefore, the principal assumptions should be explicitly stated. They are the following.

1. A true distribution function for reservoir permeability can be obtained from core analysis information.
2. The weighted average permeability of the drainage can be determined from pressure build-up data.
3. Random spatial distributions of permeabilities may exist in reservoirs; i.e., vertical and lateral variations may be of the same order of magnitude.
4. A heterogeneous reservoir can be adequately simulated by some particular array of uniform porous elements which have the same permeability-distribution function as the reservoir itself.

The first two assumptions are quite broad and will be discussed further in a subsequent section. The last two assumptions are not particularly restrictive; Assumption 3 is certainly true for some cases, and Assumption 4 only requires that a sufficient number of elements be used.

MATHEMATICAL PROBLEM

The mathematical problem was divided into three parts. The first part consisted of generating random arrangements of the individual elements of the physical model; the second required that the behavior equations for the physical model be solved; and the last involved the determination of the effective permeability of the physical system.

ORDERING

Random spatial distributions were generated by determining a set of N values of permeability from the specified distribution function, or reading in the N values directly, assigning a random number to each of the N permeabilities, ordering the permeabilities according to the magnitudes of the assigned random numbers and establishing a one-to-one correspondence between the ordered permeabilities and the mesh points of the physical model. Random numbers were generated by the method of Taussky and Todd.[21]

$$X_{n+1} = \rho X_n \ (\text{MOD } 2^{36}) \quad . \quad . \quad . \quad . \quad . \quad (1)$$

where

$$X_1 = 1,$$
$$\rho = 5^{13}.$$

The chosen value of ρ gave a sequence with a period approximately equal to 2×10^{10}. By retaining the first random number for any case, it was possible to reproduce the distribution if required.

BEHAVIOR EQUATIONS

The behavior equations for the physical model were solved by numerical methods. To establish these discrete approximations, the physical model was constrained to be a rectangular parallelopiped composed of homogeneous volume elements with dimensions of Δx, Δy and Δz. A mesh point was placed at the center of each element to define a three-dimensional rectangular mesh within the model. The mesh spacing was uniform in each direction so that the co-ordinates of the mesh points were $i\Delta x$, $j\Delta y$ and $k\Delta z$, respectively; $1 \leq i \leq p$, $1 \leq j \leq q$, $1 \leq k \leq r$ and $p \cdot q \cdot r = N$, the total number of elements.

The behavior equation that was approximated was the following.

$$\text{div} \left[K \ \text{grad} \ p \right] = \phi \mu c \ \frac{\partial p}{\partial t} \quad . \quad . \quad . \quad (2)$$

The conditions imposed on the solutions were the usual ones of pressure and flux continuity at the internal boundaries. The continuous time-discrete space approximation of Eq. 2 was based on the seven-point formula.

$$\Delta_x (K\Delta_x p)_{i,j,k} + \Delta_y (K\Delta_y p)_{i,j,k} + \Delta_z (K\Delta_z p)_{i,j,k} = d_{i,j,k} \left(\frac{dp}{dt}\right)_{i,j,k} \quad \ldots\ldots\ldots\ldots\ldots\ldots (3)$$

where

$$\Delta_x(K\Delta_x p) = \left[a_{i+1,j,k} (p_{i+1,j,k} - p_{i,j,k}) + a_{i-1,j,k} (p_{i-1,j,k} - p_{i,j,k})\right]$$

$$a_{i+1,j,k} = \frac{1}{(\Delta x)^2} \left[\frac{K_{i+1,j,k} K_{i,j,k}}{K_{i+1,j,k} + K_{i,j,k}}\right]$$

$$d_{i,j,k} = \frac{1}{2} \mu c \phi_{i,j,k}.$$

For the steady-state case, Eq. 3 was solved with $d_{i,j,k} \equiv 0$ and the following boundary conditions. Quasi-linear flow between opposing faces,

$$p_{o,j,k} = 1.0$$
$$p_{p+1,j,k} = 0$$
$$K_{o,j,k} = K_{p+1,j,k} = \infty$$
$$K_{i,o,k} = K_{i,q+1,k} = K_{i,j,o} = K_{i,j,r+1} = 0 \quad \ldots\ldots\ldots\ldots\ldots\ldots (4)$$

Quasi-radial flow into a well located at

$$x = i_o \Delta x \text{ and } y = j_o \Delta y \; (2 \le i_o \le p-1, 2 \le j_o \le q-1),$$
$$P_{o,j,k} = P_{p+1,j,k} = P_{i,o,k} = P_{i,q+1,k} = 1.0$$
$$P_{i_o,j_o,k} = 0; \quad 1 \le r' \le k \le r'' \le r$$
$$K_{o,j,k} = K_{p+1,j,k} = K_{i,o,k} + K_{i,q+1,k} = \infty$$
$$K_{i,j,o} = K_{i,j,r+1} = 0 \quad \ldots\ldots\ldots (5)$$

where r' and r'' denote the limits on a partially penetrating well. The solution was uniquely determined by the N simultaneous equations together with one of the boundary conditions. This determinate set was expressed in matrix form, shown later, and was solved by the procedure described in Appendix A, the modified Chebyshev semi-iterative method.[22]

$$A\bar{x} = \bar{g} \quad \ldots\ldots\ldots\ldots (6)$$

For the transient behavior, $d_{i,j,k} \neq 0$, only one case was considered, i.e., quasi-radial flow from a bounded reservoir into a well at $(i_o \Delta x, j_o \Delta y)$. The imposed conditions, required for a constant rate of production followed by a shut-in period, were the following.

$$p_{i,j,k} = 1.0; \quad t = 0$$

$$\left(\frac{\Delta x \Delta y \Delta z}{\mu}\right) \sum_{k=r'}^{r''} \left[\Delta_x (K\Delta_x p)_{i_o,j_o,k} + \Delta_y (K\Delta_y p)_{i_o,j_o,k}\right] = \begin{cases} q; & 0 < t \le t_s \\ 0; & t > t_s \end{cases}$$

$$K_{o,j,k} = K_{p+1,j,k} = K_{i,o,k} = K_{i,q+1,k} = K_{i,j,o} = K_{i,j,q+1} = 0 \quad \ldots\ldots\ldots (7)$$

A well-set problem was determined by Eq. 3 and the conditions given by Eq. 7. To make the numerical solution compatible with that used for the steady-state case, the boundary condition at the well was approximated according to the method suggested by Douglas, *et al*;[16] in this manner, the wellbore pressure for any time period was treated as a constant that was completely determined by the past history; e.g.,

$$p(t)_{i_o,j_o,k} = \gamma; \; t_o < t \le t_1 \quad \ldots (8)$$

where

$$\gamma = p(t_o)_{i_o,j_o,k} \left(1 - \frac{q - q'}{2q}\right)$$

$$q' = \left(\frac{\Delta x \Delta y \Delta z}{\mu}\right) \sum_{k=r'}^{r''} \left[\Delta_x (K\Delta_x p)_{i_o,j_o,k} + \Delta_y (K\Delta_y p)_{i_o,j_o,k}\right]; \quad t = t_o.$$

The set of simultaneous differential equations was solved by the Crank-Nickolson method,[23] described in Appendix B; the matrix form of these equations was that which follows.

$$D \frac{d\bar{x}}{dt} = -A\bar{x} + \bar{g} \quad \ldots\ldots (9)$$

PERMEABILITY DETERMINATION

After the steady-state pressure distribution was calculated, the effective permeability of the heterogeneous system was determined from the general equation for flow between two equipotential surfaces. For the two surfaces S_1 and S_2 maintained at potentials of unity and zero, respectively,

$$K_n = \frac{1}{\Gamma} \int_{S_1} K \left(\frac{\partial p}{\partial n}\right) dS \quad \ldots\ldots (10)$$

where $\Gamma = \int S_1 \left(\frac{\partial p}{\partial n}\right) dS$, for a homogeneous medium with the same geometry. The discrete approximation used to evaluate Eq. 10 was the following.

$$K_n = \frac{1}{\Gamma'} \sum_{k=1}^{r} \sum_{j=1}^{q} \left[K_{1,j,k} (1 - p_{1,j,k})\right] \quad \ldots (11)$$

In the quasi-linear case, Γ' was obtained directly since it involved only the area-length ratio.

$$\Gamma' = \frac{q r}{2 p} \quad \ldots\ldots\ldots\ldots (12)$$

When flow was quasi-radial, Γ' was determined by solving a homogeneous case with the same geometry.

$$\Gamma' = \sum_{k=1}^{r} \sum_{j=1}^{q} (1 - p_{1,j,k}) \quad \ldots\ldots (13)$$

To determine the effective permeability during transient flow, a pressure build-up test was simulated. The well was produced at a constant rate for a time period equal to t_s; then, for $t > t_s$, the well was shut in and the build-up history was recorded. Conventional analysis was applied to the build-up data; the wellbore pressure was plotted against log $(t - t_s/t)$, the slope of the straight-line segment was measured and the effective permeability was calculated with the following equation.

$$K_{BU} = \frac{162.5\, q \mu}{s h} \quad \ldots\ldots\ldots (14)$$

where s = slope of linear portion (psi/cycle) and
$h = r\Delta z$ = formation thickness (ft).

EXPERIMENTAL COMPUTATION

To permit an orderly investigation of the behavior of the proposed model, a distributation function $P(K)$ had to be specified; for our purposes, $P(K)$ was the probability that a given permeability value was less than or equal to K. Several distribution functions were considered; they were the log-normal exponential, skewed log-normal, linear and discontinuous. The equations and characteristics of these functions were tabulated as Table 1. The frequency, or probability density, functions which correspond to these distribution functions were sketched in Fig. 1, i.e., the derivative of $P(K)$ with respect to K or ln K. The discontinuous case was not included since its frequency function was simply a pair of delta-functions.

For computational purposes, it was necessary that the continuous distribution function be replaced with a discrete one. This was accomplished by stipulating the number of elements in the model, N, the number of class intervals, M, and the ratio of the maximum and minimum permeabilities to be included in the discrete version, R; then, the parameters and limits were obtained from the continuous form; e.g.,

$$P(K_{min}) < \frac{1}{2N} \quad \text{and} \quad P(K_{max}) > \frac{2N-1}{2N}.$$

After the approximate distribution was calculated, it was characterized by a number of statistical measures; they were the following.

$$K_A = \text{arithmetic mean} = \frac{1}{n} \sum_{1}^{n} K_i$$

$$K_H = \text{harmonic mean} = n \Big/ \sum_{1}^{n} (1/K_i)$$

$$K_G = \text{geometric mean} = \left[\prod_{i}^{n} K_i\right]^{1/n}$$

$$K_M = \text{median}; \quad P(K_M) = 1/2$$

$$K_m = \text{mode}; \quad P(K_m) = \text{maximum}.$$

Of these quantities, only the first three were determinate for all distributions.

Because of the Monte Carlo-type of model chosen, it was necessary to interpret the results probabilistically. For each combination of distribution function — N, M, R and geometry — a series of effective permeabilities K_n were generated as the elements of the model were randomly re-arranged. According to the central-limit theorem, these K_n's should have asymptotically formed a normal distribution; this was verified by the data shown in Fig. 2. Furthermore, by virtue of the law of large numbers, the true values for the "most probable" permeability and the standard deviation should have been approached as $n \to \infty$. Since only a finite number of runs were possible, it was obvious that a method for estimating the necessary parameters was needed.

Based on the assumption that the sample analyzed was representative of the population, a maximum-likelihood estimate for the "expected" permeability was obtained from the following equations.[24]

$$\hat{K} = \frac{1}{m} \sum_{1}^{m} K_n \quad \ldots\ldots\ldots (15)$$

Using this estimate for the most probable value, expected value or arithmetic mean of the K_n – distribution, the standard deviation of the sample was determined.

TABLE 1 – FUNDAMENTAL AND COMPOSITE DISTRIBUTIONS

FUNDAMENTAL DISTRIBUTIONS

Type	Distribution Function, $P(K)$	Range	Argument, $\eta(K)$	Frequency Function, $\frac{dP(K)}{d\eta(K)}$	K_A	K_G	K_H	K_m
Log-Normal	$\frac{1}{2}\left[1+\text{ERF}\left(\frac{\ln K/K_M}{\sqrt{2}\,S\ln a}\right)\right]$	$0<\frac{K}{K_M}<\infty$	$\ln(K/K_M)$	$\frac{\exp\left[-\frac{1}{2}\left(\frac{\ln K/K_M}{S\ln a}\right)^2\right]}{\sqrt{2\pi}\,S\ln a}$	$K_M\exp\left[\frac{1}{2}(S\ln a)^2\right]$	K_M	$K_M\exp\left[-\frac{1}{2}(S\ln a)^2\right]$	K_M
Exponential	$\frac{1}{2}\left[1+\frac{2}{b}(\ln K/K_M)\right]$	$e^{-b/2}<\frac{K}{K_M}<e^{b/2}$	$\ln(K/K_M)$	$1/b$	$\frac{2K_M}{b}\sinh\frac{b}{2}$	K_M	$\frac{bK_M}{2}\,\text{cosech}\,\frac{b}{2}$	--
Skewed Log-Normal	$\frac{1}{2}\left[1+\text{erf}\left(\frac{\ln K/K_M}{\sqrt{2}\,S\ln a}\right)\right]$	$0<\frac{K}{K_M}<\infty$	K/K_M	$\frac{\exp\left[-\frac{1}{2}\left(\frac{\ln K/K_M}{S\ln a}\right)^2\right]}{(K/K_M)\sqrt{2\pi}\,S\ln a}$	$K_M\exp\left[\frac{1}{2}(S\ln a)^2\right]$	K_M	$K_M\exp\left[-\frac{1}{2}(S\ln a)^2\right]$	$K_M\exp\left[-(S\ln a)^2\right]$
Linear	$\frac{1}{2}\left[1+\frac{2}{b'}(K/K_M-1)\right]$	$1-\frac{b'}{2}<\frac{K}{K_M}<1+\frac{b'}{2}$	K/K_M	$1/b'$	K_M	--	$b'/\ln\left(\frac{2+b'}{2-b'}\right)$	--
Discontinuous	$\psi U(K-K_1)$ $+(1-\psi)\,U(K-K_2)$	$0<K<\infty$	K	$\psi U'(K-K_1)$ $+(1-\psi)\,U'(K-K_2)$	ψK_1 $+(1-\psi)\,K_2$	$K_1^{\psi}K_2^{1-\psi}$	$\frac{K_1K_2}{K_1+\psi(K_2-K_1)}$	--

COMPOSITE DISTRIBUTIONS

Type	No. of Elements, N'	No. of Classes, M'	Range, R'	Median, K_M'	K_A	K_G	K_H
Log-Normal	432	27	2	1.000	.527	.298	.107
	432	27	8	.707			
	432	27	32	.250			
	432	27	128	.0442			
Log-Normal	864	27	128	1.000	.964	.707	.519
	864	27	128	.500			
Log-Normal	864	27	2	1.000	.957	.841	.709
	864	27	128	.707			

Type	No. of Elements, N'	No. of Classes, M'	Range, R'	Median, K_M'	K_A	K_G	K_H
Exponential	432	27	2	1.000	32.5	.149	.0308
	432	27	8	.250			
	432	27	32	.0162			
	432	27	128	.125			
Exponential	864	27	32	1.000	1.022	.500	.248
	864	27	32	.250			
Exponential	864	27	2	1.000	20.1	.250	.0498
	864	27	128	.0625			

$$\sigma = \left[\sum_{i}^{m} (\hat{K} - K_n)^2 / (m-1) \right]^{1/2} \quad \ldots \quad (16)$$

A maximum-likelihood estimate of the population's standard deviation was calculated from σ and m.

$$\hat{\sigma} = \sigma / \zeta(m) \quad \ldots \quad (17)$$

where

m	2	3	4	5	6	8	10	∞
ζ(m)	.798	.886	.921	.940	.951	.965	.973	1.000

Confidence limits were assigned to K by utilizing the well known "Student" τ-distribution together with the standard deviation of the sample; i.e., there was a probability of $1-\epsilon$ that the true mean value was contained in the interval $\hat{K} - \Delta\hat{K} < \hat{K} < \hat{K} + \Delta\hat{K}$.

$$\Delta\hat{K} = \sigma\tau(\epsilon, m)/\sqrt{m} \quad \ldots \quad (18)$$

The variation of $\Delta\hat{K}$ with the number of runs was illustrated by Fig. 3.

The computational process was halted by placing the following restrictions on the number of runs m.

$$3 \leq m \leq m^* \leq m_{max} \quad \ldots \quad (19)$$

$$\text{where } \frac{\sigma(m^*)}{K(m^*)} \leq .01$$

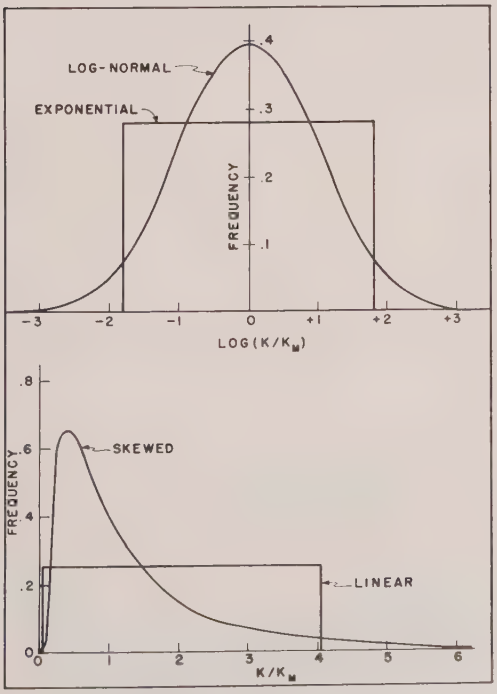

FIG. 1 – FREQUENCY FUNCTIONS.

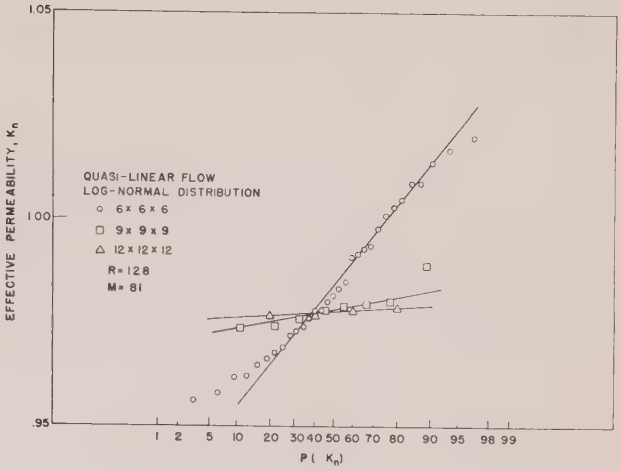

FIG. 2 – DISTRIBUTION OF EFFECTIVE PERMEABILITIES.

$$m_{max} \approx 0 \left[\frac{5 \times 10^4}{N \ln N} \right].$$

The value of m^* was chosen to guarantee that $\Delta\hat{K}/\hat{K} < .10$ for $m^* \geq 3$ with a confidence level of .995.

It was previously postulated that the standard deviation for the $\hat{K}$ associated with a given distribution function was a function of the redundancy, or entropy, of the system. The relative redundancy θ was defined in the following manner.

$$\theta = 1 - (1 - 1/\prod_{1}^{k} n_i!)/(1 - 1/N!) \quad \ldots \quad (20)$$

where $n_1 + n_2 + \ldots + n_k = N$, and

n_i = number of elements in the ith class.

The parameter θ was taken to be a measure of the

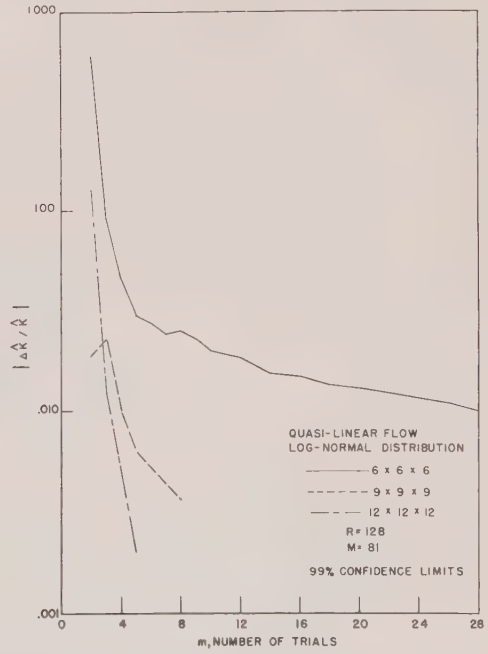

FIG. 3 – COVERGENCE OF CONFIDENCE LIMITS.

scale of heterogeneity; for a homogeneous case, θ was equal to zero. For the other extreme, $k = N$, θ was equal to unity.

For the transient cases, only a single run was made for each combination of distribution function — N, M, R and geometry — since the time required for computation was quite large. After the effective permeability was determined from the build-up data, K_{BU}, a relative measure of the degree of heterogenity λ was assigned to that particular spatial configuration for a particular distribution function by means of the following equation.

$$\lambda = 1 - \frac{(K_A - K_{BU})(K_{BU} - K_H)}{(K_A - \hat{K})(\hat{K} - K_H)} \quad . \quad . \quad (21)$$

The values for K_A and K_H were obtained from the original distribution function; $\hat{K}$ was determined from steady-state calculations; and K_{BU} was based on transient behavior. The form of λ was such that it gave the correct limiting results; i.e., complete heterogeneity was indicated when the system was ordered in either parallel or series, and homogeneous heterogeneity was assigned when the system was completely disordered.

DISCUSSION OF RESULTS

STEADY STATE

The first step in the investigation was designed to determine if there was a single permeability value that could be used to characterize a heterogeneous medium with a given distribution function. The first distribution function that was studied was the log-normal — sometimes called the Gibrat, Kapteyn or Galton-McAlister distribution. This was considered to be the most natural distribution since reasonable physical models for its genesis have been suggested;[25] Law[6] introduced it for describing permeability distributions. A series of computational experiments were performed on a cubic model composed of cubic elements with quasi-linear flow between opposing faces. The ranges for the parameters were $27 \leq N \leq 1{,}728$, $2 \leq R \leq 128$ and $3 \leq M \leq 81$; and, the median permeability was assigned a unit value. The results of these experiments are presented as Fig. 4; the expected permeability $\hat{K}$ with its 99 per cent confidence limits is plotted as a function of (S ln a) the effective deviation for the distribution. For this case, the median, mode and geometric mean are all equal to unity; obviously, unity is the best estimate for the expected value so this result is ambiguous.

The exponential distribution was considered next. Although no mechanistic basis for this distribution has been hypothesized, its existence has been observed quite frequently. Since the discrete form of this distribution has no mode, it serves to eliminate some of the uncertainty that resulted from the previous experiment. Under the same conditions used in the log-normal case, the results obtained are those shown in Fig. 5; clearly, the median or the geometric mean gives the best value for the expected permeability.

In an attempt to decide between the median and the geometric mean, a series of runs (using the same conditions on N, R and M as the previous two cases) were made with the skewed log-normal, linear and composite distributions described in Table 1. The results (Fig. 6) show that the geometric mean is to be preferred as an estimate of $\hat{K}$ since it is always determinate while the median is not. The data presented in Fig. 7 (based on the discontinuous distribution with $8 < R < 1{,}000$) verify the choice of the geometric mean because the median

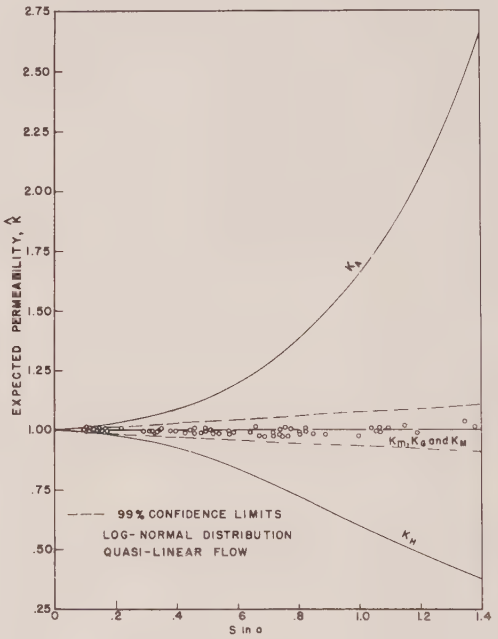

FIG. 4 — THE EXPECTED VALUE OF EFFECTIVE PERMEABILITY.

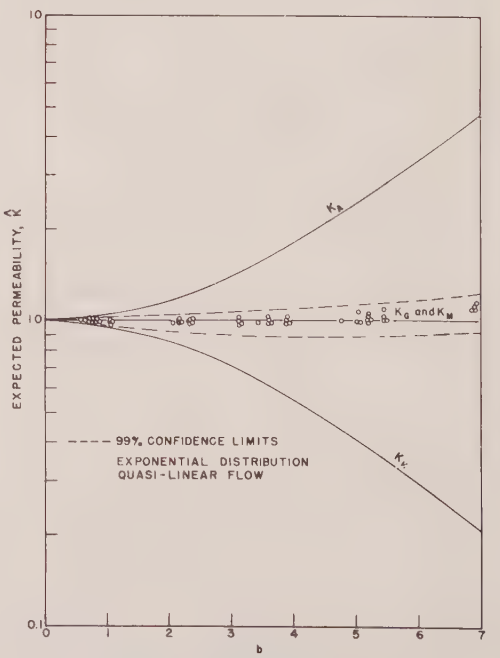

FIG. 5 — THE EXPECTED VALUE OF EFFECTIVE PERMEABILITY.

is not physically meaningful. The results shown agree qualitatively with those obtained by Asaad[23] from his thermal conductivity experiments.

Figs. 8 and 9 result from a comparison between the expected permeability from quasi-linear flow and that from quasi-radial flow in the cubic model for log-normal and exponential distributions, respectively. These curves indicate that the expected permeability values are essentially independent of geometry. As a result, the importance of the connection between the geometric mean and $\hat{K}$ is established. Since $\hat{K}$ is a maximum-likelihood estimate, the maximum-likelihood value for a single-valued function of permeability, $f(K)$, is known to be $f(\hat{K})$; therefore, when the porosity and water saturation from core analysis are correlated with permeability, the best estimates are those values that correspond with $\hat{K}$. Consequently, the geometric mean can be used to determine applicable values for other reservoir parameters.

When the cubic elements are replaced by ones in which $\Delta x = \Delta y \neq \Delta z$, it is possible to examine the influence of anisotropy since a change in the element geometry is equivalent to a change in the ratio of the vertical and horizontal permeabilities; i.e., $(\Delta x/\Delta z)^2 = K_v/K_h$. The experimental results (Fig. 10) reveal a finite but not particularly significant effect; the apparent increase in permeability with increased values of K_v/K_h is due to cross-flow. The combined effects of anisotropy and

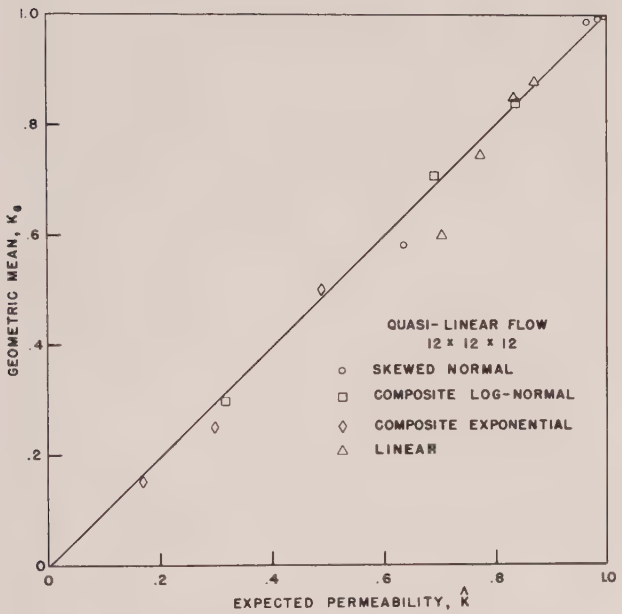

FIG. 6 – PERMEABILITY CORRELATION.

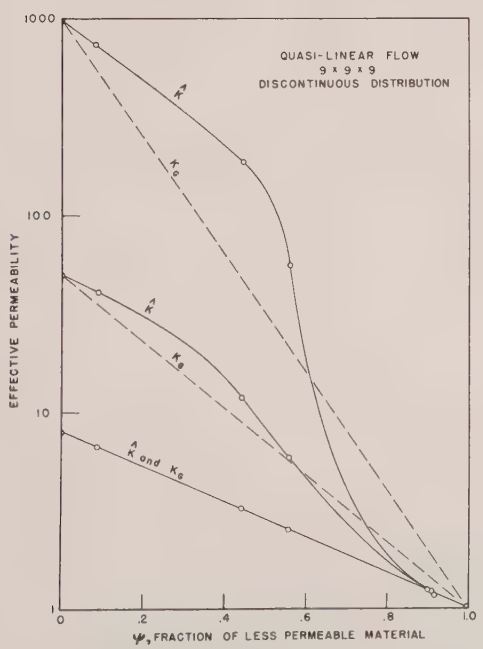

FIG. 7 – PERMEABILITY OF TWO-COMPONENT SYSTEM.

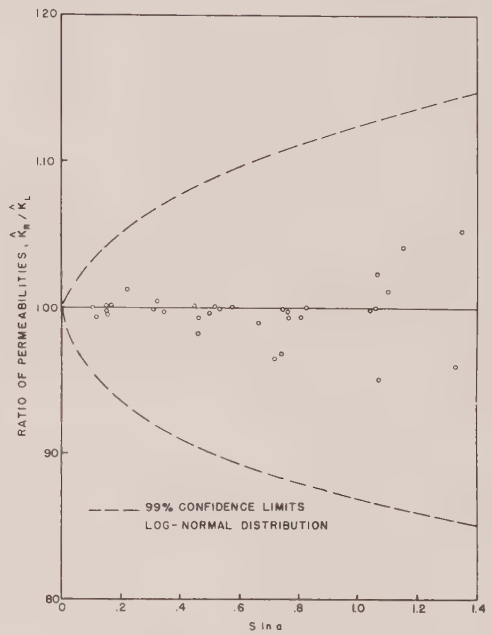

FIG. 8 – EFFECT OF GEOMETRY.

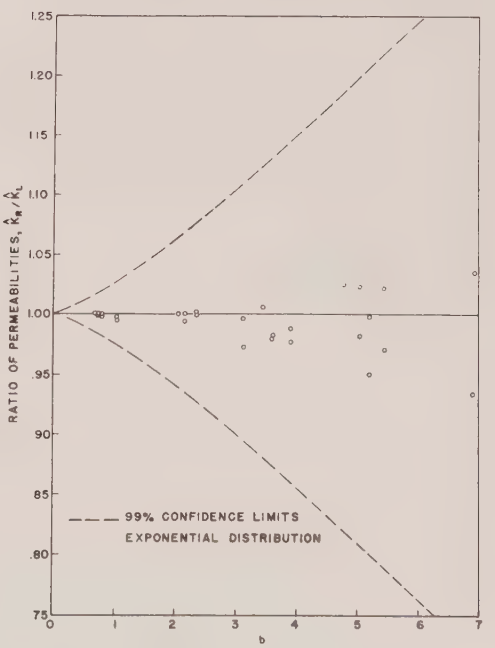

FIG. 9 – EFFECT OF GEOMETRY.

partial penetration on quasi-radial flow are illustrated in Fig. 11.

The basic difference between linear and radial flow is emphasized by the data shown in Fig. 12; i.e., $\hat{\sigma}_R/\hat{\sigma}_L > 1$. For linear flow, uniform volumetric weighting is roughly equivalent to uniform weighting on the basis of flow resistance; for radial flow, this is not true so the absolute position, as well as the relative position, of the different elements is more important.[7] As the range of permeabilities increases, $\hat{\sigma}_R/\hat{\sigma}_L$ decreases because the linear system is more sensitive to distortions in the flow pattern.

The postulated relationship between the relative redundance and the standard deviation was tested by a series of calculations based on the exponential distribution. For this case, Eq. 20 reduces to the following.

$$\theta = 1 - \left\{ 1 - 1/\left[\left(\frac{N}{M} \right)! \right]^M \right\} / (1 - 1/N!) \quad \ldots\ldots\ldots\ldots\ldots\ldots\ldots\ldots (22)$$

The variation of $\hat{\sigma}$ with N/M was determined for quasi-linear flow, and the results are presented in Fig. 13. The correlation is reasonably good and indicates that $\hat{\sigma}$ and the redundancy θ are related; therefore, either can be used as a measure of the scale of heterogeneity.

Although a thorough investigation of the computational errors associated with the solution of an elliptic equation in a heterogeneous medium was beyond the scope of this paper, a cursory examination was conducted. Using a fixed spatial distribution of permeability, the mesh size was successively decreased and the effects of truncation and round-off errors on $\hat{K}$ and $\hat{\sigma}$ were estimated. The calculated value of $\hat{K}$ is essentially dependent on the truncation errors, while the value of $\hat{\sigma}$ is much more sensitive to round-off errors; for the worst possible cases, the errors in $\hat{K}$ and/or $\hat{\sigma}$ are approximately 10 per cent.

TRANSIENT

The objective of this portion of the study was to determine if the permeability calculated from pressure build-up data was a reasonable measure of the effective permeability in the drainage region of a well completed in a heterogeneous reservoir.

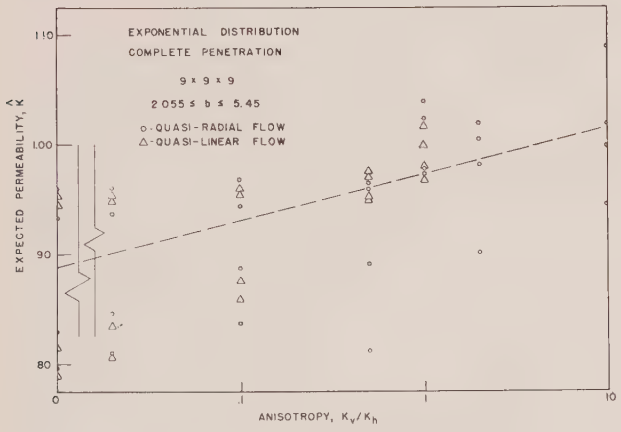

FIG. 10 – EFFECT OF ANISOTROPY.

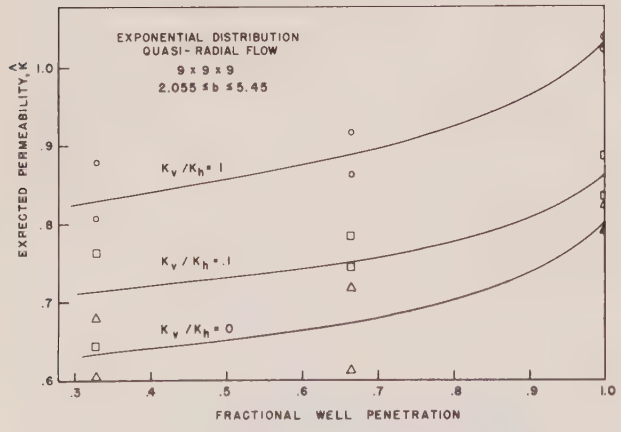

FIG. 11 – EFFECT OF WELL PENETRATION.

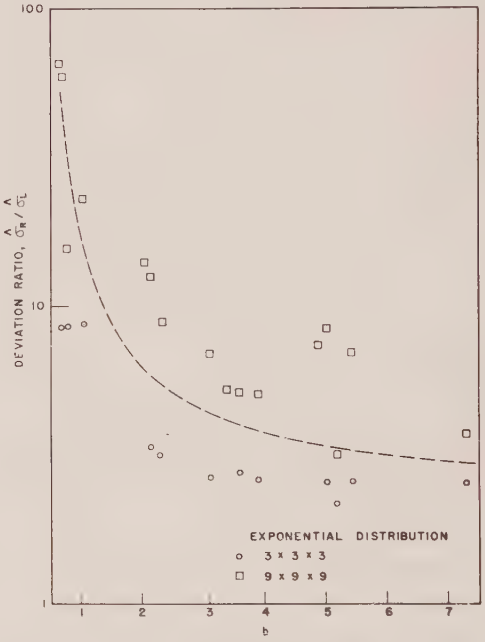

FIG. 12 – EFFECT OF GEOMETRY ON DEVIATION.

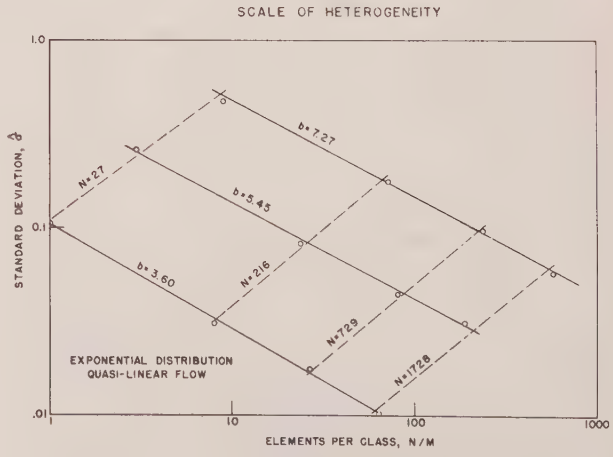

FIG. 13 – SCALE OF HETEROGENEITY.

A 27- × 3- × 27-in. model was used to simulate a closed, heterogeneous reservoir; the distribution function for the permeability elements was the log-normal; and the ranges of the parameters were $3 \leq M \leq 81$, $8 \leq R \leq 128$ and $0 \leq K_v/K_h \leq 1$. For a particular random arrangement of the elements, a build-up curve was synthesized and the build-up permeability K_{BU} was calculated. Then, using the same random arrangement, the effective steady-state permeability K_{SS} was computed for quasi-radial flow between the outer boundary and the well.

Since uniform mesh spacing was used and the well was represented by a line sink, the synthesized build-up curves were not particularly accurate immediately after shut-in. However, for reasonably large shut-in times, the computed build-up curves tended to approach the expected type asymptotically. Two typical build-up curves are shown in Fig. 14 to illustrate this behavior.

The permeability ratio K_{BU}/K_{SS} that indicated the quality of the estimate based on build-up data was determined for a number of cases — both isotropic and anisotropic. These results are presented in Fig. 15; the data show that K_{BU} is a reasonable measure of the effective permeability of the drainage region. No attempt was made to determine an expected value for the build-up permeability since the computer time necessary for such a determination would have been excessive.

The relative degree of heterogeneity, defined by Eq. 20, was determined for the isotropic cases; the results are those in Fig. 16. Apparently, the degree of heterogeneity is greater for small values of (S ln a). This is rather misleading since λ is a relative measure; as the arithmetic and harmonic values converge, (S ln a) decreases and the value of λ becomes much more sensitive to errors in both the computed data and the graphical determination of the slope of the linear segment of the build-up curve. Consequently, the usefulness of λ is considered quite limited.

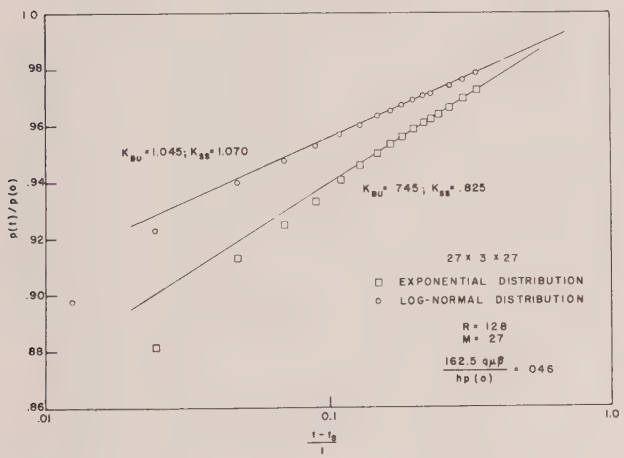

FIG. 14 — SYNTHESIZED BUILD-UP CURVES.

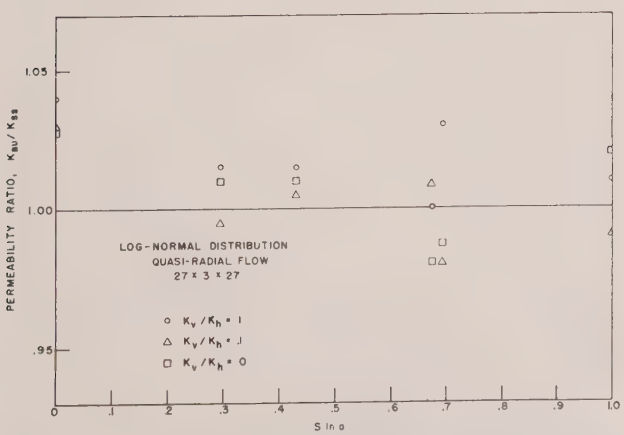

FIG. 15 — COMPARISON OF BUILD-UP AND STEADY-STATE PERMEABILITIES.

LABORATORY EXPERIMENT

Some time ago, the model studies section of the Reservoir Mechanics Div., Gulf Research & Development Co., began to investigate the possibility of studying the effect of reservoir heterogeneities on recovery processes by means of scaled models. Under the supervision of J. H. Henderson, W. T. Rouleau constructed a 10- × 10- × 10-in. model composed of randomly arranged, uniform, cubic elements with different permeabilities. The individual cubes were formed by packing sand into a mold according to the techniques developed by J. Naar; when the packing was completed, the mold was completely immersed in molten wax. After they were cooled, the cubes were arranged in a cubical container in locations determined with the aid of a table of random numbers. The wax was removed by heating and extracting with heptane; after the wax was removed, the container was vibrated to attempt to insure that no by-passing would occur. Finally, the effective air permeability of the system was determined to have been 60.5 darcies. The permeability distribution used was that shown in Fig. 17; it was approximately an exponential distribution with N = 1,000, M = 10 and R = 19.7. The arithmetic, geometric and harmonic means were 70.2, 47.0 and 29.5, respectively.

The experimental model was numerically simulated, and the effective permeability was calculated to have been 46.3 darcies for the conditions of the

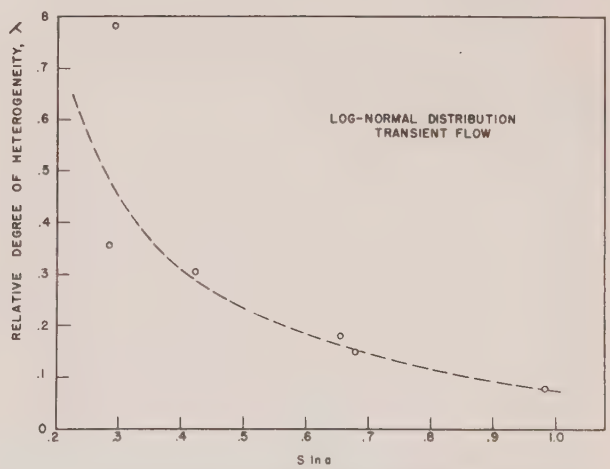

FIG. 16 — RELATIVE DEGREE OF HETEROGENEITY.

experiment. Then, still using the experimental arrangement of permeability elements, the permeabilities between the other two pairs of opposing faces were determined to have been 46.1 and 45.8; these results indicated that the model was large enough to have appeared homogeneously heterogeneous. The elements of the model were successively re-arranged at random for 10 additional runs; the expected values $\hat{K}$ and $\hat{\sigma}$ were 46.6 and .84, respectively; the most probable value for the effective permeability was, again, virtually identical to the geometric mean.

The lack of agreement between the computed permeability and the experimental value indicates that either the experimental permeability measurements, for the individual elements or the entire array, were grossly in error or that by-passing occurred in the model. In any event, the difficulties associated with attempts to model heterogeneities physically are apparent;* the same type of uncertainty that exists in the reservoir problem is still present in the model; i.e., given a permeability distribution and an effective permeability measurement, can a probable spatial distribution be found that is compatible with all the data? In this case, it is obvious that the probable configuration would not have agreed with that which was used in the construction of the model.

FIELD DATA

To illustrate the use of the developed techniques, core analysis data and pressure build-up information from a wildcat well were evaluated for indications of heterogeneity. The well was cored over the entire gross-pay interval of 150 ft, core recovery was 93 per cent and the permeability data from 160 samples gave the distribution shown in Fig. 18. The well was produced (open-hole completion) for about a month at an average rate slightly in excess of 100 STB/D; then, a pressure build-up test was conducted. The data from this test are plotted in Fig. 19.

The permeabilities form a distribution that is approximately exponential (b = 9.35). It is characterized by the following quantities: K_A = 148 md, K_G = 20 md, K_H = 1.05 md, K_M = 17.2 md, M = 160, and R = 11,700. From the analysis of the build-up data, the effective permeability was calculated; i.e., K_{BU} = 5.72 md.

A 16- × 10- × 10-in. model was used to determine the expected permeability value for quasi-linear flow. The results for five different permeability orderings and N/M = 10 were the following: $\hat{K}$ = 20.5 md; $\hat{\sigma}$ = 1.22 md; 18.6 < $\hat{K}$ < 22.8, confidence level = 99 per cent.

*An electrical analogue of the packed sand model was constructed by the model studies section. As might be expected, the effective conductivity of this three-dimensional, resistance network agreed with the computed result and differed from that measured on the packed sand model.

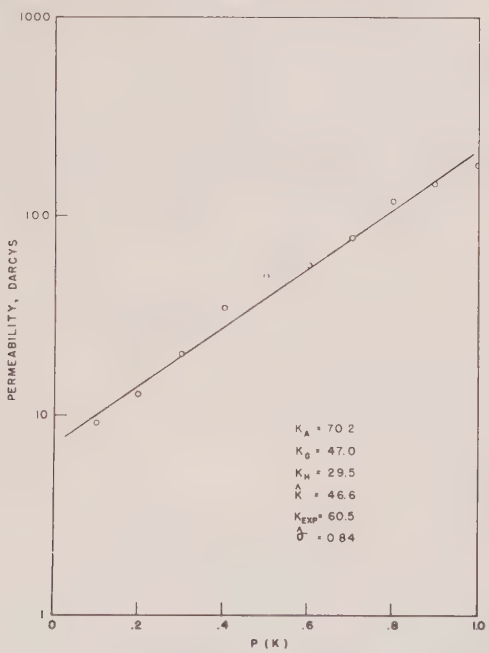

FIG. 17 – PERMEABILITY DISTRIBUTION FOR LABORATORY EXPERIMENT.

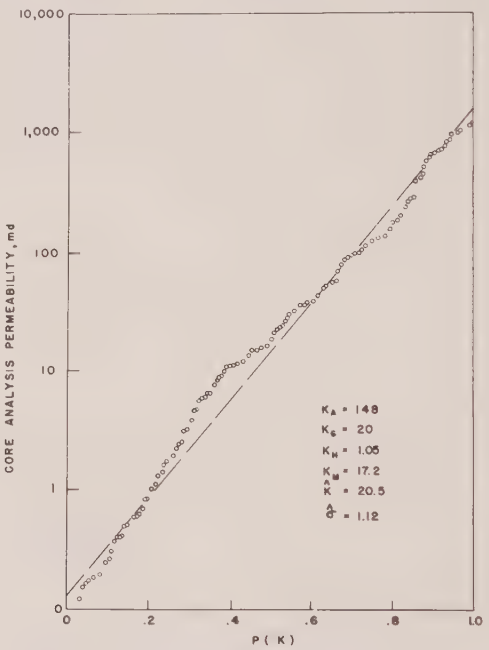

FIG. 18 – FIELD DATA.

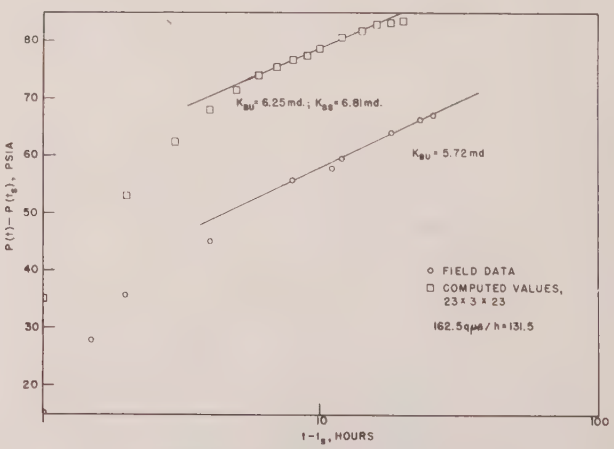

FIG. 19 – SYNTHESIS OF FIELD BUILD-UP CURVE.

The relative degree of heterogeneity λ was found to have been .733, a fairly high value; since the build-up permeability was less than the expected value, it was apparent that the permeabilities were arrayed in a manner more similar to a series system than a parallel one.

Based on the relationship between σ_R and σ_L (e.g., Fig. 12), it was conjectured that a radial model with $N/M = 10$ would probably yield a steady-state permeability reasonably close to the field build-up permeability within 10 trials. For $\Delta x = \Delta y = 57.5$ ft and $\Delta z = 50.0$ ft, a 23- × 3- × 23-in. model simulated an isotropic reservoir with a drainage area of 40 acres and a thickness of 150 ft.

After testing only two random arrangements of the elements in the model, an ordering was found which gave an effective steady-state permeability K_{SS} of 6.81 md. Using that same ordering, the transient behavior of the model was computed; the resulting build-up curve is indicated by Fig. 19. The permeability determined from the synthesized build-up curve was 6.25 md. This value is within 10 per cent of the field build-up permeability.

The outlined method for evaluating reservoir heterogeneity from core and build-up data gives maximum-likelihood estimates for the expected permeability value $\hat{K}$ and the standard deviation $\hat{\sigma}$. In addition, the relative degree of heterogeneity λ, an indirect measure of the scale of heterogeneity N/M or Δx, and an approximate spatial permeability distribution are determined. Although most of these measures are only qualitative and the permeability configuration is certainly not unique, this type of approach appears to be reasonable. Some ambiguity is present in the suggested model since the mesh spacing is affected by the anisotropy of the system as well as by the number of elements. Before quantitative results can be expected, an independent method for determining the effective anisotropy of the formation must be developed.

SUMMARY, CONCLUSIONS AND RECOMMENDATIONS

The objectives of this investigation were to study the effect of the disposition of heterogeneous permeabilities on single-phase flow for a known permeability-distribution function and to attempt to infer the presence and probable configuration of heterogeneities from core analysis and pressure build-up data. These objectives were achieved in a qualitative sense under the restrictive assumption that both the core data and the build-up information represented valid measures of the reservoir properties.

Physical models consisting of random three-dimensional arrays of homogeneous porous blocks were studied. The permeabilities of the individual elements were assigned according to a specific distribution function; uniform anisotropy was introduced by varying the relative dimensions of the porous blocks. A particular model was perturbed by simply re-arranging its elements at random; the effect of these perturbations on the behavior of the physical model was determined by digitally solving its numerical analogue.

Steady-state flow in quasi-linear and quasi-radial systems was considered; for these cases, the results were interpreted statistically. Transient flow in a quasi-radial geometry was studied by synthesizing pressure build-up curves and using conventional analysis. A comparison of the computed behavior of a known system with laboratory data was made; agreement was not obtained. The application of the developed techniques to the evaluation of field data was illustrated; a permeability ordering was found such that the field build-up curve was approximately reproduced.

Based on computational experiments, subject to the limitations implied by the assumptions that were made, the following general conclusions are inferred.

1. The most probable behavior of a heterogeneous system with single-phase flow approaches that of a homogeneous system having a permeability equal to the geometric mean of the individual permeabilities.

2. The effects of flow geometry and anisotropy on the most probable value for the effective permeability of a heterogeneous medium are finite but not significant.

3. The permeability determined from a pressure build-up test of a heterogeneous reservoir gives a reasonable value for the effective permeability within the drainage area.

4. Qualitative measures of the degree and the scale of the heterogeneity and its spatial configuration are obtainable if core analysis and pressure build-up data are available.

Since this investigation is exploratory in nature, it leaves many questions unanswered; as an example, no attempt was made to extend the study on a field-wide basis. In retrospect, there were many areas in which obvious improvements could have been made; e.g., the use of a fixed mesh for computational purposes and a superimposed variable mesh for locating the permeability elements and varying their size would have minimized the effects of truncation and round-off errors. Despite these deficiencies, it is felt that this work represents the first consistent and logical attempt to treat the basic problem of describing heterogeneous reservoirs.

It was indicated that the validity of the conclusions drawn from the numerical experiments depended on the assumption that the core analysis and the pressure build-up data represented true reservoir characteristics. Unfortunately, this is a weak assumption since it is known that the required information generally contains various types of errors; however, it is apparent that many of the errors are avoidable.

In obtaining core analysis data to describe a reservoir, it is recognized that two principal types of errors occur – those related to sampling methods and those due to testing techniques. The most probable errors are the result of coring an insufficient number of wells, incompletely coring the entire

productive interval, recovering only part of the core from friable or poorly consolidated sections, selecting core samples only from those sections that appear promising, choosing test samples from irregular limestones and fractured sandstones that are macroscopically heterogeneous, changing the properties of the cores by extracting, drying and/or ageing the samples, masking the effects of clays by using samples that do not contain connate water, failing to apply the Klinkenberg correction to gas permeabilities and neglecting to correct the values measured on low-permeability samples for the effect of rock compressibility. All of these errors with the exception of those due to partial core recovery and incomplete sampling, cause the measured permeabilities to be greater than the true values.

The errors associated with permeability determinations from build-up tests are less obvious. The most probable errors result from selecting the incorrect portion of the build-up curve – caused by a lack of stabilization prior to shut-in, an insufficient shut-in period, after-flow or phase re-distribution in the well – and failing to consider the effect of multiphase flow on the behavior equations. Errors from these sources cause the calculated permeabilities to be lower than the true permeabilities.

It is evident that the errors in core analysis and build-up data combine to indicate a higher degree of heterogeneity than that which actually exists in the reservoir. Furthermore, results based on these erroneous data tend to imply that the spatial permeability distribution is of the series type rather than parallel.

NOMENCLATURE

A = Stieltjes permeability matrix, dimensionless

$\tilde{B}$ = normalized Jacobi iteration matrix, dimensionless

D = diagonal capacitance matrix, 1/T

K = absolute permeability, L^2

$\hat{K}$ = most probable value of effective permeability, L^2

K_n = effective permeability of heterogeneous medium, L^2

K_A = arithmetic mean permeability, L^2

K_{BU} = build-up permeability, L^2

K_G = Geometric mean permeability, L^2

K_H = harmonic mean permeability, L^2

K_M = median permeability, L^2

K_m = mode of permeabilities, L^2

K_{SS} = steady-state permeability, L^2

K_v/K_h = anisotropy, ratio of vertical and horizontal permeabilities, dimensionless

M = number of classes in discrete distribution, dimensionless

N = number of elements, or mesh points; in model, dimensionless

$P(K)$ = probability that a permeability is less than or equal to K, dimensionless

R = ratio of maximum and minimum permeabilities for discrete distribution, dimensionless

S = standard deviation for log-normal distribution, dimensionless

a = measure of class interval for log-normal distribution K_n/K_{n-1}, dimensionless

b = characteristic parameter for exponential distribution, dimensionless

c = liquid compressibility, LT^2/M

$\bar{g}$ = boundary condition vector, M/LT^2

h = formation thickness, L

m = number of runs, dimensionless

p = pressure, M/LT^2

q = production rate, L^3/T

s = slope of linear portion of build-up curve, M/LT^2 (cycle)

t = time, T

t_s = time of shut-in, T

x,y,z = rectangular co-ordinates, L

$\Delta x, \Delta y, \Delta z$ = difference operators, 1/L

δ = permissible error in pressure, M/LT^2

ϵ = probability that a maximum-likelihood estimate will fall outside the confidence interval, dimensionless

ζ = correlation factor for maximum-likelihood estimate of standard deviation, dimensionless

θ = relative redundancy, dimensionless

λ = relative degree of heterogeneity, dimensionless

μ = viscosity, M/LT

$\rho(\tilde{B})$ = spectral radius of matrix B, dimensionless

σ = standard deviation for effective permeabilities, L^2

$\hat{\sigma}$ = most probable standard deviation for effective permeabilities, L^2

ϕ = porosity, dimensionless

ω = acceleration parameter for iterative process, dimensionless

ψ = fraction of less permeable material in discontinuous distribution

SUPERSCRIPTS

– = vector

T = transpose of a matrix

m = order of iteration

SUBSCRIPTS

R = quasi-radial

L = quasi-linear

h = horizontal

i,j,k = dummy indices

n = order of perturbation

v = vertical

ACKNOWLEDGMENT

The authors wish to acknowledge the exceptional cooperation extended by the computational analysis section of the Gulf Research & Development Co. during the performance of the numerical experiments.

REFERENCES

1. Maxwell, C.: *Electricity and Magnetism*, The Clarendon Press, Oxford (1892).
2. Rayleigh, J. W.: *Philosophical Magazine* (1892) Vol. 34, 481.
3. Odelevskii, V. I.: *Jour. Tech. Phys. (USSR)* (1951) Vol. 21, Nos. 6 and 11.
4. Brown, W. F.: *Jour. Chem. Phys.* (1955) Vol. 23, 1514.
5. Korneenko, I. A.: *Jour. Tech. Phys. (USSR)* (1960) Vol. 30, No. 1.
6. Law, J.: "Statistical Approach to the Interstitial Heterogeneity of Sand Reservoirs", *Trans.*, AIME (1944) Vol. 155, 202.
7. Cardwell, W. T. and Parsons, R. L.: "Average Permeabilities of Heterogeneous Oil Sands", *Trans.*, AIME (1945) Vol. 160, 34.
8. Muskat, M.: "Effect of Permeability Stratification in Cycling Operations", *Trans.*, AIME (1948) Vol. 179, 313.
9. Stiles, W. E.: "Use of Permeability Distribution in Water-flood Calculations", *Trans.*, AIME (1949) Vol. 186, 9.
10. Dykstra, H. and Parsons, R. L.: "The Prediction of Oil Recovery by Water Flood", *Secondary Recovery of Oil in the United States*, API, The Lord Baltimore Press (1950).
11. McCarty, D. G. and Barfield, E. C.: "The Use of High Speed Computers for Predicting Flood-Out Patterns", *Trans.*, AIME (1958) Vol. 213, 139.
12. Houpert, A.: *Revue de l'Institute Francais du Petrole* (1959) Vol. XIV, 549.
13. Albert, P., Jaisson, J. and Marion, H: *Revue de l'Institute Francais du Petrole* (1959) Vol. XIV, 560.
14. Blackwell, R. J., Rayne, J. R. and Terry, W. M.: "Factors Influencing the Efficiency of Miscible Displacement", *Trans.*, AIME (1959) Vol. 216, 1.
15. Mamedov, G. A.: *Oil and Gas (USSR)* (1959) Vol. 2, No. 4.
16. Douglas, J., Jr., Peaceman, D. W. and Rachford, H. H., Jr.: "A Method for Calculating Multi-Dimensional Immiscible Displacement", *Trans.*, AIME (1959) Vol. 216, 297.
17. Lefkovits, H. C., Hazebroek, P., Allen, E. E. and Mathews, C. S.: "A Study of the Behavior of Bounded Reservoirs Composed of Stratified Layers", *Soc. Pet. Eng. Jour.* (March, 1961) 43.
18. Hutchinson, C. A.: *Pet. Eng.* (1959) Vol. 31, No. 10, B-19.
19. Fatt, I.: "The Network Model of Porous Media: I. Capillary Pressure Characteristics", *Trans.*, AIME (1956) Vol. 207, 144.
20. Rose, W.: "Studies of Water Flood Performance: III. Use of Network Models", Illinois State Geological Survey, Circular 237, Urbana, Ill. (1957).
21. Taussky, O. and Todd, J.: "Generation of Pseudo-Random Numbers", *Symposium on Monte Carlo Methods*, John Wiley & Sons, Inc. N. Y. (1956).
22. Varga, R. S. and Golub, G. H.: *Chebyshev Semi-Iterative, Successive Overrelaxation Iterative Methods*, Computing Center, Case Institute of Technology, Cleveland, Ohio (1960).
23. Crank, J. and Nicholson, P.: *Proc.*, Cambridge Phil. Soc. (1957) Vol. 43, 50.
24. Bennett, C. A. and Franklin, N. L.: *Statistical Analysis in Chemistry and the Chemical Industry*, John Wiley & Sons, Inc., N. Y. (1954).
25. Aithchison, J. and Brown, J. A. C.: *The Lognormal Distribution*, University Press, Cambridge (1957).
26. Asaad, Y.: "A Study of Thermal Conductivity of Fluid Bearing Porous Rocks", Thesis, U. of California (1955).
27. Pitzer, S. C., Rice, J. D. and Thomas, C. E.: "A Comparison of Theoretical Pressure Build-Up Curves with Field Curves Obtained from Bottom-Hole Shut-In Tests", *Trans.*, AIME (1959) Vol. 216, 416.
28. Varga, R. S.: "Iterative Numerical Analysis", Computation and Data Processing Center, U. of Pittsburgh, Pittsburgh, Pa. (1959).
29. Garabedian, P. R.: *Mathematical Tables and Aids to Computation* (1956) Vol. 10, 183.
30. Varga, R. S.: "Orderings of the Successive Overrelaxation Scheme", Westinghouse Atomic Power Div. Report T-788, Pittsburgh, Pa. (1958).
31. Lieberstein, H. M.: "Overrelaxation for Non-Linear Ellystic Partial Differential Problems", Army Math. Research Center Report 20, Madison, Wisc. (1959).
32. Varga, R. S.: "Factorization and Normalized Iterative Methods", *Boundary Value Problems in Differential Equations*, U. of Wisconsin Press, Madison, Wisc. (1959).
33. Cuthill, E. H. and Varga, R. S.: *Jour. of Assn. for Computing Machinery* (1959) Vol. 6, 236.

APPENDIX A

STEADY-STATE SOLUTION

In matrix notation, the equation to be solved has the following form.

$$A\bar{x} = \bar{g} \qquad \ldots\ldots\ldots \text{(A-1)}$$

Because of the nature of the physical problem, the use of a rectangular mesh and the method employed to derive the difference equation, A is a two-cyclic, $N \times N$ Stieltjes matrix.[28] $\bar{x}$ is the unknown vector representing the potential distribution; $\bar{g}$ is a known vector whose entries are determined only by the boundary conditions.

After a suitable permutation of indices, the matrix may be partitioned as shown in Fig. 20.*

The co-ordinates x, y and z corresponding to a particular point are given by $i\Delta x$, $j\Delta y$ and $k\Delta z$, respectively; the total number of mesh points in each direction is p, q and r; and the total number of points N is equal to $p \cdot q \cdot r$. For the simple line method that is to be used, the nonsingular, diagonal submatrices, $A_{j,j}$, are $p \times p$ tridiagonal for $1 \leq j \leq \beta$ where $\beta = q \cdot r$. When either q or r is even, $\alpha = \frac{1}{2}$

*The treatment described is an abridgement of the detailed approach given by Varga.[22]

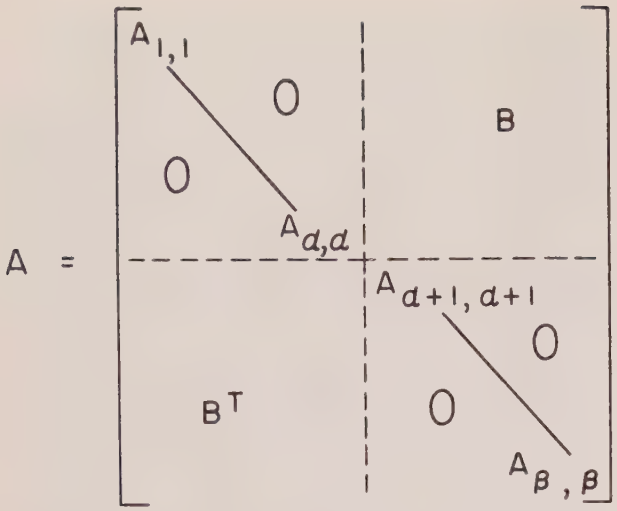

FIG. 20

$(q \cdot r)$; and $\alpha = \frac{1}{2}(q \cdot r + 1)$ when both q and r are odd. This type of partitioning is equivalent to block interation[28] over a complete horizontal line of mesh points in the x-direction.

Let C be the positive diagonal matrix composed of the nonsingular, diagonal blocks $A_{j,j}$ of the Stieltjes matrix A; then, the usual splitting and normalization procedures allow Eq. A-1 to be written as follows.

$$\bar{y} = \tilde{B}\,\bar{y} + \bar{h} \quad \ldots\ldots\ldots\ldots \quad \text{(A-2)}$$

where

$$\bar{y} \equiv C^{1/2}\,\bar{x}$$

$$\bar{h} \equiv C^{-1/2}\,\bar{g}$$

$$\tilde{B} \equiv I - C^{-1/2} A C^{-1/2}$$

The matrix $\tilde{B}$ is symmetric, non-negative, irreducible and convergent; therefore, the modified Chebyshev semi-iterative method can be used to solve Eq. A-2. This technique is defined by the following pair of equations.

$$Y_{\alpha+j}^{(2m+1)} = \omega_{2m+1}\left\{\sum_{k=1}^{\alpha} \tilde{B}_{\alpha+j,k}\, Y_k^{(2m)} + H_{\alpha+j} - Y_{\alpha+j}^{(2m-1)}\right\} + Y_{\alpha+j}^{(2m-1)};$$

$$1 \le j \le \beta - \alpha\ ;$$

$$Y_j^{(2m+2)} = \omega_{2m+2}\left\{\sum_{k=1}^{\beta-\alpha} \tilde{B}_{j,\alpha+k}\, Y_{\alpha+k}^{(2m+1)} + H_j - Y_j^{(2m)}\right\} + Y_j^{(2m)};$$

$$1 \le j \le \alpha,\ m \ge 0 \quad \ldots\ldots \quad \text{(A-3)}$$

where the vector components $Y_j^{(0)}$, $1 \le j \le \alpha$, are given or guessed and the superscripts refer to the order of the iteration.

The acceleration parameters are calculated by means of a recursion relationship.

$$\omega_{i+1} = \frac{1}{1 - \left[\dfrac{\rho^2(\tilde{B})\,\omega_i}{4}\right]}\ ;\ i > 2 \ \ldots \quad \text{(A-4)}$$

where

$$\omega_1 = 1 \text{ and } \omega_2 = \frac{2}{2 - \rho^2(\tilde{B})}.$$

In this equation, $\rho(\tilde{B})$ is the spectral radius of $\tilde{B}$, i.e., the absolute value of the largest eigenvalue. Because of similarity, $\rho(\tilde{B}) = \rho(B)$ where $B = 1 - C^{-1}A$. In all calculations, $\rho(B)$ was based on experimental estimates; however, a good min-max approximation is given in Ref. 28. It was observed experimentally that $\rho(B)$ was fairly insensitive to the entries in the matrix A while it was very sensitive to the geometry. In fact, correlating $\rho(B)$ with the fraction of non-zero entries in the vector $\bar{g}$ for the homogeneous case permitted the $\rho(B)$'s for the heterogeneous case to be adequately estimated. Similar observations concerning the effect of perturbations on the spectral radii of matrices have been reported in the literature.[29-31]

The norm used for halting the iterative procedure was the following.

$$\max_i \left|Y_i^{(m+1)} - Y_i^{(m)}\right| < (2-\omega)\,\delta;\ 1 \le i \le N$$

$$\ldots\ldots\ldots\ldots\ldots\ldots \quad \text{(A-5)}$$

where δ = desired accuracy and

$$\omega = \frac{2}{1 + \sqrt{1 - \rho^2(B)}}.$$

The initial guess for all cases was $Y_j^{(0)} = 0.0$, $1 \le i \le N$; δ was fixed at .0001 for all runs to guarantee at least four significant figures of accuracy.

For a 9- × 9- × 9-in. model with flow over two opposing faces, the required time of computation was 105 seconds on the IBM 704. With a fixed δ, the total volume of computation varied with N ln N.

APPENDIX B

TRANSIENT SOLUTION

Using matrix notation, the equation to be solved is the continuous time-discrete space form that follows.

$$D\frac{d\bar{x}}{dt} = -A\bar{x} + \bar{g} \quad \ldots\ldots \quad \text{(B-1)}$$

D is a positive diagonal $N \times N$ matrix; A is a two-cyclic $N \times N$ Stieltjes matrix; $\bar{x}$ is the vector of unknown potentials; and $\bar{g}$ is a known vector with time independent components determined by the boundary conditions.

The solution to Eq. B-1 can be obtained in the conventional manner.

$$\bar{x}(t) = A^{-1}\bar{g} + \exp\left[-(t-t_o)\ D^{-1}A\right]\left[\bar{x}\ (t_o) - A^{-1}\bar{g}\right] \quad \ldots\ldots \quad \text{(B-2)}$$

Expanding the exponential in the Crank-Nicholson[23] form leads to an implicit approximation[28] for the solution to Eq. B-1.

$$\left[A+\frac{2D}{\Delta t}\right]\bar{x}(t_o+\Delta t) = -\left[A-\frac{2D}{\Delta t}\right]\bar{x}(t_o) + 2\bar{g} \quad \ldots\ldots\ldots\ldots\ldots\ldots \quad \text{(B-3)}$$

where $\Delta t = t - t_o$.

Some computation can be saved if Eq. B-3 is written in the following form.

$$\left[A+\frac{2D}{\Delta t}\right]\bar{x}(t) = -\bar{Q}(t_o) + \frac{4D}{\Delta t}\bar{x}(t_o) + 2\bar{g}(t_o) \quad \ldots\ldots\ldots\ldots\ldots\ldots \quad \text{(B-4)}$$

where

$$\bar{Q}(t_o) \equiv \left[A+\frac{2D}{\Delta t}\right]\bar{x}(t_o).$$

Since $\left[A+\frac{2D}{\Delta t}\right]$ is symmetric and positive definite, a regular splitting[32] would be

$$\left[A+\frac{2D}{\Delta t}\right] = B - C \quad \ldots\ldots\ldots\ldots \quad \text{(B-5)}$$

B is tridiagonal, and C has zero diagonal entries with no more than six non-zero entries per row. Because B is symmetric and positive definite, there are unique matrices[33] R and T such that the following factorization exists.

$$B = RT^{T}TR \quad \ldots\ldots\ldots\ldots \quad \text{(B-6)}$$

R is a diagonal matrix and T is an upper triangular matrix with unit diagonal entries.

Eq. B-4 can now be written as follows.

$$T^{T}T\bar{y}(t_o+\Delta t) - (R^{-1}CR^{-1})\bar{y}(t_o+\Delta t) = -R^{-1}\bar{Q}(t_o) + \frac{4}{\Delta t}(R^{-1}DR^{-1})\bar{y}(t_o) + 2R^{-1}\bar{g} \quad \ldots\ldots\ldots\ldots\ldots\ldots \quad \text{(B-7)}$$

where

$$\bar{y}(t) \equiv R\bar{x}(t)$$

$$R^{-1}\bar{Q}(t_o) = T^{T}T\bar{y}(t_o) - (R^{-1}CR^{-1})\bar{y}(t_o).$$

If $\bar{y}(t_o)$ is known, $\bar{y}(t_o+\Delta t)$ can be obtained by solving the simultaneous equations represented by Eq. B-7. This was accomplished by using the single line version of the modified Chebyshev semi-iterative method described in Appendix A.

Using a 27- × 3- × 27-in. model and $\delta = .0001$ in Eq. A-5, the number of iterations per time step varied between four and seven depending on the well penetration. On the average, the computer time required to complete one time step was 30 seconds; therefore, the calculation of the depletion and build-up required about 30 minutes per case.

***

Pressure Drop in a Composite Reservoir

T. L. LOUCKS
JUNIOR MEMBER AIME
THE PENNSYLVANIA STATE U.
UNIVERSITY PARK, PA.

E. T. GUERRERO
MEMBER AIME
THE U. OF TULSA
TULSA, OKLA.

ABSTRACT

Pressure drop characteristics in a system composed of two adjacent concentric regions of different permeability were studied. The differential equations for continuity of mass flow in the two regions were solved using the Laplace transformation and the necessary boundary conditions to give the pressure distribution in the composite reservoir. the resulting equation for pressure drop at the inner boundary was evaluated for a variety of composite reservoirs and compared with the results for a uniform reservoir. From this study it was found that under certain conditions the permeability in both zones, as well as the size of the inner zone, can be determined from the pressure drop curve.

INTRODUCTION

The theory for the pressure distribution and pressure build-up behavior of a well producing a single, slightly compressible fluid from infinite and finite homogeneous reservoirs was presented by Horner[1] and Miller, Dyes and Hutchinson.[2] Extensions on this original work to provide improved and extended interpretations and better agreement between theory and observed results have been made by Matthews, *et al*,[3] van Everdingen,[4] Gladfelter, *et al*,[5] Stegemeier and Matthews,[6] Hurst and Guerrero,[7] and Perrine.[8] More recently Lefkovits, *et al*,[9] studied pressure build-up behavior in bounded reservoirs composed of stratified layers.

Houpeurt[10] has suggested various approaches to the general problem of variable permeability and porosity but presented no analytic solutions for particular permeability variations. Albert, Jaisson and Marion[11] studied the finite composite reservoir and presented numerical solutions to the unsteady-state case and an analytical solution valid only for large times. They also studied the so-called pseudo-steady state for several examples of radial permeability variations. Very similar examples have been treated in the unsteady state with application to pressure build-up by Loucks in an unpublished manuscript.

More recently Hurst[12] has presented the complete point-sink solution (valid for all times) for the infinite composite reservoir. He applied these solutions to interference between oil fields along with an even more elegant application of his explicit solution to the material-balance equation including water influx. Mortada[13] approaches the same application by avoiding the point-source limitation but gives the solution for the aquifer region which is valid only for large times. Hopkinson, Natanson and Temple[14] have treated both the finite and infinite composite reservoir obtaining the pressure distribution for the inner zone valid for large times.

This paper presents a theoretical study of the pressure distribution in an infinite composite reservoir composed of two adjacent concentric regions of different permeability. The object was to determine the manner in which pressure drop at the inner boundary of a composite reservoir depends upon time, the permeability of each zone and the size of the inner zone. Expressions for the pressure distribution in both zones are developed which take into account the radius of the sink and are valid for small times as well as large times. It was felt that an understanding of the pressure drop behavior in various composite reservoirs would be of assistance in the interpretation of some pressure build-up curves which do not behave according to the theory derived for uniform systems.

Often the region surrounding the wellbore is either more permeable or less permeable than the reservoir because of the various drilling and completion practices. The effects of reduced permeability due to drilling-fluid invasion and of increased permeability due to fracturing or acidizing need to be more carefully defined. Therefore, an equation for the pressure drop in a composite reservoir was developed, and the effects of both the permeability in each zone and the size of the inner zone were studied.

STATEMENT AND SOLUTION OF PROBLEM

BOUNDARY CONDITIONS AND ASSUMPTIONS

The physical system studied was a composite

Original manuscript received in Society of Petroleum Engineers office Feb. 9, 1961. Revised manuscript received June 22, 1961. Paper used for partial fulfillment of the requirements for a Master's degree in petroleum engineering at The U. of Tulsa.

[1]References given at end of paper.

reservoir made up of two adjacent concentric regions of different permeabilities (Fig. 1). The reservoir was assumed to extend infinitely in the radial direction and to be bounded on the top and bottom by impervious planes. The inner zone (Zone 1) was assumed to be uniform and to have an average permeability k_1. The outer zone (Zone 2) was also assumed uniform and its permeability was k_2.

Initially, the reservoir was assumed to have zero pressure drop throughout both zones. Then the reservoir was produced through the inner boundary at a constant rate. The requirements at the intermediate boundary were that the pressures a small distance on each side of the interface remain equal for all times and that the flow rate from the outer zone always be equal to the flow rate into the inner zone.

By imposing these conditions on two general solutions of the diffusivity equation, an expression for the pressure distribution was developed for each zone using the theory of Laplace transforms. These equations define the pressure at all points in the reservoir for all times. The expression for pressure distribution in the inner zone was then specialized to give the relation between the pressure drop at the inner boundary and the length of time the constant rate had been imposed.

DERIVATION OF EQUATIONS

The equations which express the continuity of mass flow through each of the zones are

$$\frac{1}{r_D}\frac{\partial}{\partial r_D}\left[r_D\frac{\partial P_1}{\partial r_D}\right] = \frac{1}{\gamma_1}\frac{\partial P_1}{\partial t_D} \quad \ldots\ldots (1)$$

and

$$\frac{1}{r_D}\frac{\partial}{\partial r_D}\left[r_D\frac{\partial P_2}{\partial r_D}\right] = \frac{1}{\gamma_2}\frac{\partial P_2}{\partial t_D} \quad \ldots\ldots (2)$$

where γ_1 is the dimensionless constant which gives the permeability in Zone 1 when multiplied by $\bar{k}$ an arbitrary reference permeability, γ_2 is similarly defined to give the permeability in Zone 2, r_D is the dimensionless radial distance ($r_D = r/r_w$), t_D is the dimensionless time ($t_D = \bar{k}t/\phi\mu c r_w^2$), and P is the pressure drop in atmospheres ($P = p_e - p$).

The general solution of the equations resulting from taking the Laplace transformation of Eqs. 1 and 2 with respect to time has been shown to be[15-17]

$$\bar{P}_1(s) = AI_0(q_1 r_D) + BK_0(q_1 r_D) \quad \ldots\ldots (3)$$

$$\bar{P}_2(s) = CI_0(q_2 r_D) + DK_0(q_2 r_D) \quad \ldots\ldots (4)$$

where $\bar{P}(s)$ is the Laplace transformation of the pressure drop, s is the Laplace operator, $q_1 = \sqrt{s}/\sqrt{\gamma_1}$, and $q_2 = \sqrt{s}/\sqrt{\gamma_2}$.

The boundary conditions (transformed) are

$$r_D\frac{\partial \bar{P}_1(s)}{\partial r_D} = -\xi/\gamma_1 s \text{ at } r_D = 1,$$

$$\bar{P}_2(s) = 0 \text{ at } r_D = \infty,$$

$$\bar{P}_1(s) = \bar{P}_2(s) \text{ at } r_D = a,$$

and

$$\gamma_1\frac{\partial \bar{P}_1(s)}{\partial r_D} = \gamma_2\frac{\partial \bar{P}_2(s)}{\partial r_D} \text{ at } r_D = a.$$

The equations resulting from the imposition of the four boundary conditions can easily be shown to be

$$AI_1(q_1) - BK_1(q_1) = -\xi/\gamma_1 q_1 s,$$

$$C = 0,$$

$$AI_0(aq_1) + BK_0(aq_1) = DK_0(aq_2),$$

and

$$AI_1(aq_1) - BK_1(aq_1) = -\frac{1}{\gamma}K_1(aq_2)$$

where $\gamma = \sqrt{\gamma_1}/\sqrt{\gamma_2}$.

From these equations the values of the constants in Eqs. 3 and 4 are found to be

$$A = \left[\xi/\Delta\gamma_1 q_1 s\right]\left[\gamma K_0(aq_2)K_1(aq_1) - K_0(aq_1)K_1(aq_2)\right], \quad \ldots\ldots (5)$$

$$B = \left[\xi/\Delta\gamma_1 q_1 s\right]\left[I_0(aq_1)K_1(aq_2) + \gamma K_0(aq_2)I_1(aq_1)\right], \quad \ldots\ldots (6)$$

$$D = \left[\xi\gamma/\Delta\gamma_1 q_1 s\right]\left[I_0(aq_1)K_1(aq_1) + K_0(aq_1)I_1(aq_1)\right], \quad \ldots\ldots (7)$$

where

$$\Delta = \gamma K_0(aq_2)\left[I_1(aq_1)K_1(q_1) - I_1(q_1)K_1(aq_1)\right] + K_1(aq_2)\left[I_1(q_1)K_0(aq_1) + I_0(aq_1)K_1(q_1)\right] \quad \ldots\ldots (8)$$

With these constants thus evaluated and substituted into Eqs. 3 and 4, the transformed solutions for pressure distribution are completed. These equations will now be inverted by the Bromwich – Wagner integral.[17]

Pressure Drop in Zone 1

The expression for pressure drop in the inner

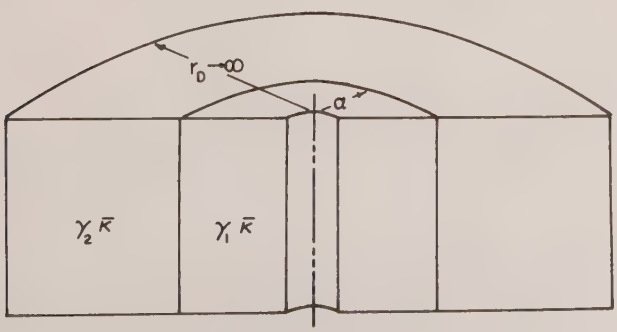

FIG. 1 – PHYSICAL SYSTEM STUDIED.

zone is given by

$$P_1(r_D, t_D) = L^{-1}\left\{\bar{P}_1(s)\right\} = \frac{1}{2\pi i} \lim_{R\to\infty} \int_{\nu-iR}^{\nu+iR} e^{st_D}\bar{P}_1(s)ds \quad \ldots\ldots\ldots\ldots (9)$$

Since for $t_D = 0$ the integrand is equal to zero,[18] this can also be written

$$P_1(r_D, t_D) = \frac{-1}{2\pi i} \lim_{R\to\infty} \int_{\nu-iR}^{\nu+iR} (1 - e^{st_D})\bar{P}_1(s)ds \quad \ldots\ldots\ldots\ldots\ldots\ldots (10)$$

Since the denominator (Δ) of $\bar{P}_1(s)$ has a branch point at $s = 0$, the contour of Fig. 2 is used. The contribution of the small circle around the origin is zero,[18] and the integral in Eq. 10 can be replaced by the negative values of the integrals along CD and EF.[19,20,17] Thus,

$$P_1(r_D, t_D) = \frac{1}{2\pi i}\left[\int_{-\infty}^{0} (1 - e^{st_D})\bar{P}_1(s)ds + \int_{0}^{-\infty} (1 - e^{st_D})\bar{P}_1(s)ds\right] \quad \ldots\ldots (11)$$

In the first integral $\int(1)$ along CD, let $s = \gamma_1 e^{i\pi}\omega^2$ to get

$$\int(1) = \frac{2i\xi}{\gamma_1}\int_0^{\infty} \frac{(1 - e^{-\gamma_1\omega^2 t_D})}{\omega^2}\,\frac{(\Lambda + i\lambda)}{(\Phi + i\psi)}\,d\omega \quad . \quad (12)$$

where

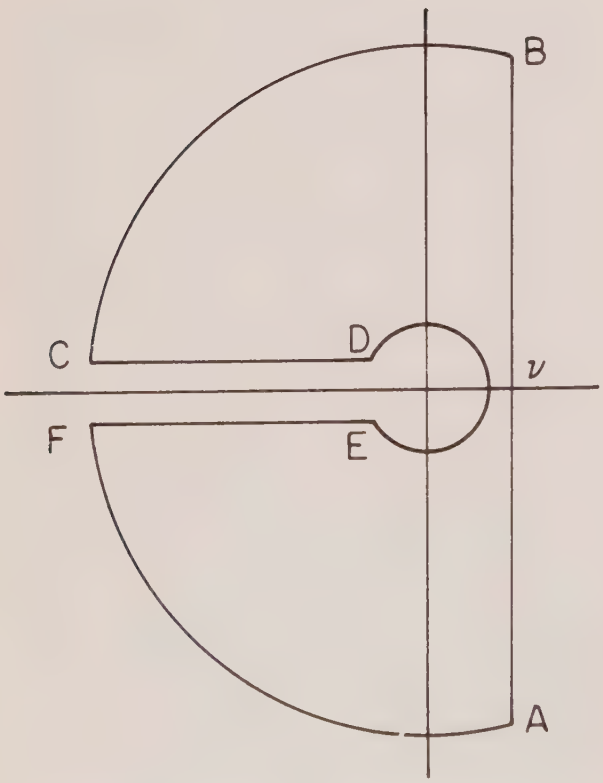

FIG. 2 – CONTOUR USED FOR INVERSION.

$$\Phi = \gamma Y_0(\gamma a\omega)\left[J_1(a\omega)Y_1(\omega) - J_1(\omega)Y_1(a\omega)\right] + Y_1(\gamma a\omega)\left[J_1(\omega)Y_0(a\omega) - J_0(a\omega)Y_1(\omega)\right];$$

$$\psi = \gamma J_0(\gamma a\omega)\left[J_1(a\omega)Y_1(\omega) - J_1(\omega)Y_1(a\omega)\right] + J_1(\gamma a\omega)\left[J_1(\omega)Y_0(\gamma a\omega) - J_0(\gamma a\omega)Y_1(\omega)\right];$$

$$\Lambda = aJ_0(\omega r_D) - mY_0(\omega r_D);$$

$$\lambda = bJ_0(\omega r_D) - nY_0(\omega r_D);$$

$$a = \gamma J_0(\gamma a\omega)Y_1(a\omega) - J_1(\gamma a\omega)Y_0(a\omega);$$

$$b = Y_0(a\omega)Y_1(\gamma a\omega) - \gamma Y_0(\gamma a\omega)Y_1(a\omega);$$

$$m = \gamma J_0(\gamma a\omega)J_1(a\omega) - J_0(a\omega)J_1(\gamma a\omega);$$

$$n = J_0(a\omega)Y_1(\gamma a\omega) - \gamma J_1(a\omega)Y_0(\gamma a\omega) \quad . \quad (13)$$

Multiplying numerator and denominator by $\Phi - i\psi$, the complex conjugate of the denominator, gives

$$\int(1) = \frac{2i\xi}{\gamma_1}\int_0^{\infty} \frac{(1 - e^{-\gamma_1\omega^2 t_D})}{\omega^2}\,\frac{\left[\Phi\Lambda + \lambda\psi + i(\Phi\lambda - \Lambda\psi)\right]}{(\Phi^2 + \psi^2)}\,d\omega \quad . \quad . \quad . \quad (14)$$

Next returning to the second integral $\int(2)$ in Eq. 11, let $s = \gamma_1 e^{-i\pi}\omega^2$ along EF and rationalize the denominator to get

$$\int(2) = \frac{2i\xi}{\gamma_1}\int_0^{\infty} \frac{(1 - e^{-\gamma_1\omega^2 t_D})}{\omega^2}\,\frac{[\Phi\Lambda + \lambda\psi - i(\Phi\lambda - \Lambda\psi)]}{(\Phi^2 + \psi^2)}\,d\omega \quad . \quad . \quad . \quad . \quad (15)$$

Adding $\int(1)$ and $\int(2)$ and recalling Eq. 11, it follows that

$$P_1(r_D, t_D) = \frac{2\xi}{\pi\gamma_1}\int_0^{\infty} \frac{(1 - e^{-\gamma_1\omega^2 t_D})}{\omega^2}\,\frac{[\Phi\Lambda + \lambda\psi]}{(\Phi^2 + \psi^2)}\,d\omega. \quad . \quad . \quad . \quad . \quad . \quad . \quad . \quad (16)$$

Pressure Drop in Zone 2

The expression for pressure drop in the outer zone is found in a manner similar to that used for Zone 1 to be

$$P_2(r_D, t_D) = \frac{4\gamma\xi}{\pi^2\gamma_1 a}\int_0^{\infty} \frac{(1 - e^{-\gamma_1\omega^2 t_D})}{\omega^3}\,\frac{[\psi Y_0(\gamma\omega r_D) - \Phi J_0(\gamma\omega r_D)]}{(\Phi^2 + \psi^2)}\,d\omega \quad . \quad (17)$$

Pressure Drop at the Inner Boundary

An expression for the pressure drop at the inner boundary is found by setting $r_D = 1$ in Eq. 16. By expanding the numerator and combining terms, it

is found that the bracketed expression reduces to simply

$$\Phi\Lambda + \psi\lambda = 8/\pi^3\omega^3\alpha^2.$$

Thus, the pressure drop at the inner boundary is given by

$$P(t_D) = \frac{16\,\xi}{\pi^4\gamma_1\,\alpha^2} \int_0^\infty \frac{(1 - e^{-\gamma_1\omega^2 t_D})}{\omega^5(\Phi^2 + \psi^2)}\,d\omega \quad . \quad (18)$$

Pressure Build-Up

Let δ be defined as that value of ω such that neither of the two expressions $\gamma\alpha\omega$ and $\gamma\omega$ is greater than .02. Then if Eq. 18 is broken up into two parts,

$$P(t_D) = \frac{16\,\xi}{\pi^4\gamma_1\alpha^2} \int_0^\delta (1 - e^{-\gamma_1\omega^2 t_D})\,f(\omega)d\omega$$

$$+ \frac{16\,\xi}{\pi^4\gamma_1\,\alpha^2} \int_\delta^\infty (1 - e^{-\gamma_1\omega^2 t_D})\,f(\omega)d\omega,$$

where

$$f(\omega) = 1/[\omega^5(\Phi^2 + \psi^2)],$$

the approximations for Bessel functions of small argument can be used in the first integral to give

$$\Phi = -4/(\pi^2\gamma\omega^2\alpha),$$
$$\psi = \gamma/(\pi\alpha).$$

Since ω is small, the value of ψ^2 is negligible compared to Φ^2, and the first term in the $P(t_D)$ equation reduces to

$$\frac{\xi}{\gamma_2} \int_0^\delta \frac{(1 - e^{-\gamma_1\omega^2 t_D})}{\omega}\,d\omega.$$

It has been shown[15] that this is equivalent to

$$\frac{\xi}{2\gamma_2}\,[C - Ei(-\gamma_1\delta^2 t_D) + \log(\gamma_1\delta^2 t_D)].$$

Using this, the expression for pressure drop at the inner boundary becomes

$$P(t_D) = \frac{\xi}{2\gamma_2}\,[C - Ei(-\gamma_1\delta^2 t_D) + \log(\gamma_1\delta^2 t_D)]$$

$$+ \frac{16\,\xi}{\pi^4\gamma_1\alpha^2} \int_\delta^\infty (1 - e^{-\gamma_1\omega^2 t_D})\,f(\omega)d\omega$$

. . . . . (19)

For large time, say $\gamma_1\delta^2 t_D > 8$, both the exponential integral and $e^{-\gamma_1\omega^2 t_D}$ become negligible and Eq. 19 reduces to the form

$$P(t_D) = C_2\xi + \frac{\xi}{2\gamma_2}\log(t_D) \quad . \quad . \quad . \quad . \quad . \quad . \quad (20)$$

where C_2 is independent of time and is given by

$$C_2 = \frac{16}{\pi^4\gamma_1\alpha^2} \int_\delta^\infty f(\omega)d\omega + \frac{1}{2\gamma_2}\,[C + \log(\gamma_1\delta^2)].$$

Since $P(t_D) = p_e - p(t_D)$,

$$p(t_D) = p_e - C_2\xi - \frac{\xi}{2\gamma_2}\log(t_D) \quad . \quad . \quad . \quad . \quad (21)$$

By superimposing three expressions for pressure as given in Eq. 21 in order to simulate the pressure build-up test procedure, we arrive at the following pressure build-up equation.

$$p(\Delta t) = p_e - \frac{q\mu}{4\pi hk_2}\log\left[\frac{t(q) + \Delta t}{\Delta t}\right] \quad . \quad . \quad . \quad (22)$$

where $t(q)$ is the time during which the reservoir was produced at the constant flow rate (q) before it was shut in, and Δt is the shut-in time. Thus, we have found that the pressure build-up equation given by Horner[1] is valid in the composite reservoir with the restriction on time that $t_D > 8/\gamma_1\delta^2$. We have also proved that the permeability in the log coefficient is that of the outer zone in the region distant from the well.

RESULTS

The pressure drop at the inner boundary of several composite reservoirs is presented in Figs. 3, 4, 5 and 6. The curves were obtained by using Eq. 19 for $\xi = 1$ with the modification that for $\gamma_1\delta^2 t_D < 1$, the term

$$[C - Ei(-\gamma_1\delta^2 t_D) + \log(\gamma_1\delta^2 t_D)]$$

was found to be best computed using the series

$$\sum_{n=1}^{\infty} [(-1)^{n+1}\,(\gamma_1\delta^2 t_D)^n/n!n].$$

At this point the reason for setting $k_1 = \gamma_1\,\bar{k}$ and $k_2 = \gamma_2\bar{k}$ becomes apparent. By arbitrarily setting

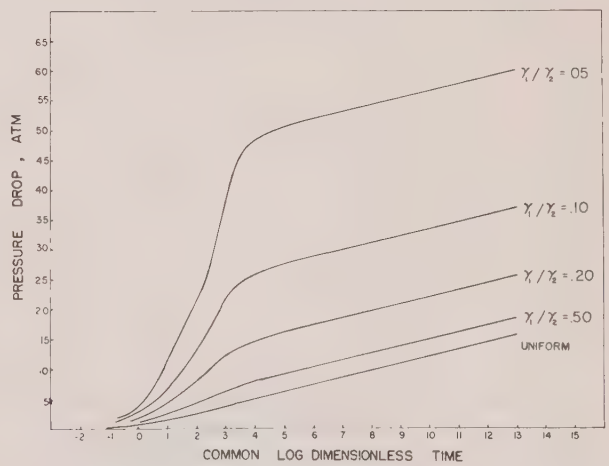

FIG. 3 – PRESSURE DROP AT THE INNER BOUNDARY AS A FUNCTION OF DIMENSIONLESS TIME FOR COMPOSITE RESERVOIRS IN WHICH THE RATIO OF THE PERMEABILITY OF THE INNER ZONE TO THAT OF THE OUTER (γ_1/γ_2) IS LESS THAN UNITY. THE RADIUS OF THE INNER ZONE IS 40 r_w.

$k_2 = \bar{k}$ ($\gamma_2 = 1$), the dimensionless time term t_D becomes equivalent to the corresponding t_D used by Hurst and van Everdingen[10] for a uniform reservoir with permeability k_2. Thus, $\gamma_1 = k_1/\bar{k} = k_1/k_2$ becomes the ratio of the permeabilities in the two zones. This enables us to compare the pressure drop behavior of a homogeneous reservoir of permeability k_2 with the behavior of the same system modified by an inner zone of radius αr_w which has a permeability equal to $\gamma_1 k_2$. However, it should be realized that this particular selection was completely arbitrary and the user of the basic equations is free to make his own selection for the purpose at hand.

Fig. 3 shows the pressure drop $P(t_D)$ as a function of dimensionless time t_D for a reservoir of permeability k_2 in which the inner zone of radius 40 r_w is less permeable. The ratio of the permeabilities is given by the parameter γ_1/γ_2.

Fig. 4 shows $P(t_D)$ vs t_D for the same reservoir except the inner zone has a radius of 250 r_w and the permeability in this zone is greater than that in the rest of the reservoir.

Figs. 5 and 6 show the effect of the radius of the inner zone. Fig. 5 is for an inner zone with 1/10 the permeability of the rest of the reservoir. Fig. 6 is for an inner zone with a permeability four times greater than the reservoir.

Fig. 7 shows the pressure drop curve for the cases in which the radius of the inner zone was taken to be very large.

DISCUSSION OF RESULTS

It should be remembered in the interpretation of these curves that they are all calculated for the same flow rate ($\xi = q\mu/4\pi hk_2 = 1$). For this reason

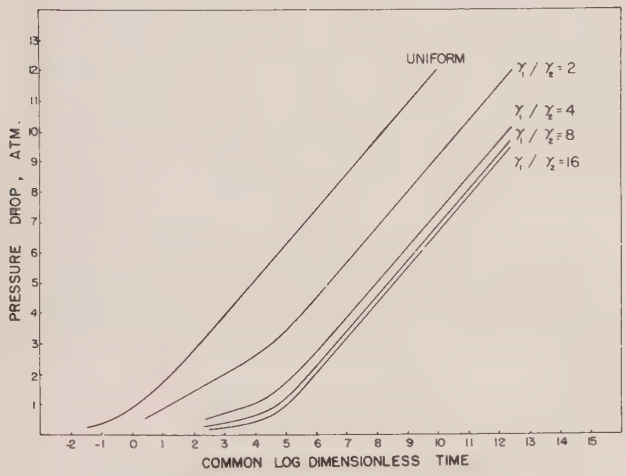

FIG. 4 – PRESSURE DROP AT THE INNER BOUNDARY AS A FUNCTION OF DIMENSIONLESS TIME FOR COMPOSITE RESERVOIRS IN WHICH THE RATIO OF THE PERMEABILITY OF THE INNER ZONE TO THAT OF THE OUTER (γ_1/γ_2) IS GREATER THAN UNITY. THE RADIUS OF THE INNER ZONE IS 250 r_w.

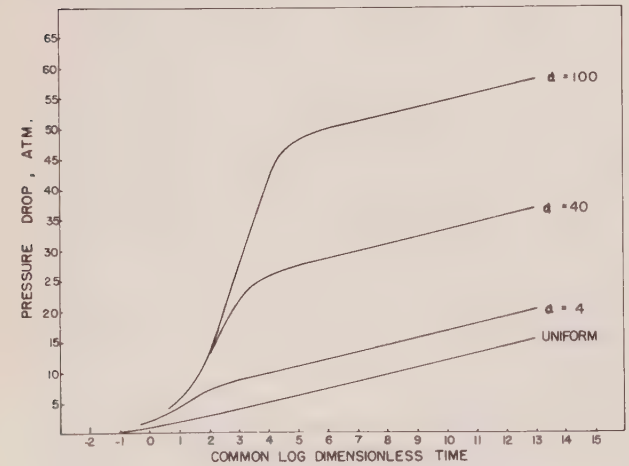

FIG. 5 – PRESSURE DROP AT THE INNER BOUNDARY AS A FUNCTION OF DIMENSIONLESS TIME FOR COMPOSITE RESERVOIRS IN WHICH THE RATIO OF THE PERMEABILITY OF THE INNER ZONE TO THAT OF THE OUTER (γ_1/γ_2) IS 1/10. THE SIZE OF THE INNER ZONE IS αr_w.

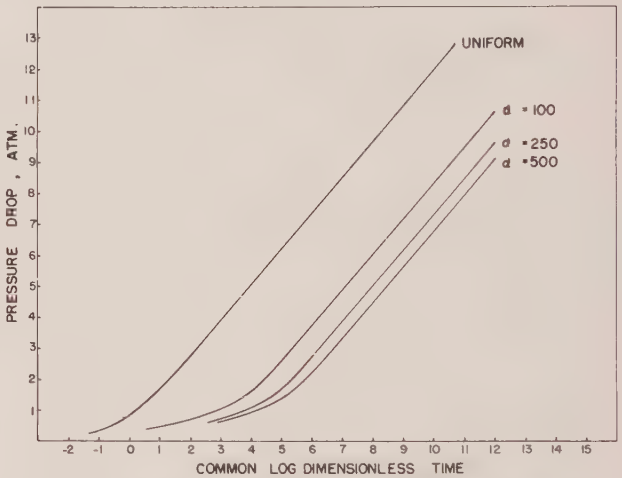

FIG. 6 – PRESSURE DROP AT THE INNER BOUNDARY AS A FUNCTION OF DIMENSIONLESS TIME FOR COMPOSITE RESERVOIRS IN WHICH THE RATIO OF THE PERMEABILITY OF THE INNER ZONE TO THAT OF THE OUTER (γ_1/γ_2) IS FOUR. THE SIZE OF THE INNER ZONE IS αr_w.

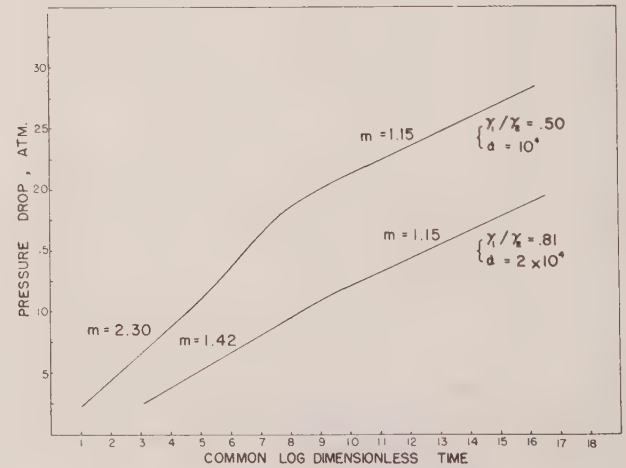

FIG. 7 – PRESSURE DROP AT THE INNER BOUNDARY AS A FUNCTION OF DIMENSIONLESS TIME FOR TWO COMPOSITE RESERVOIRS WITH LARGE INNER ZONES. THE RATIO OF THE PERMEABILITY OF THE INNER ZONE TO THAT OF THE OUTER IS GIVEN BY (γ_1/γ_2), AND THE SIZE OF THE INNER ZONE IS αr_w.

some of the pressure drop values are very large. In practice, the flow rate would necessarily be less for an increase in the resistance around the well. However, changing the value of q for the purpose of presentation would also change the slope of the linear portion of each curve. It was felt that the graphs served better in their present form to point out the important fact that the linear portion for large time yields the permeability of the outer zone regardless of the condition of the inner zone. This can also be seen from Eq. 22. The slope of the pressure build-up curve for large time is given by the coefficent of the log term. For a given q, μ and h, it is dependent only upon k_2, the permeability of the outer zone.

The time for which Eq. 22 becomes valid was found in the calculations to be when the term $1 - e^{-\gamma_1 \delta^2 t_D}$ could be approximated by $\gamma_1 \delta^2 t_D$. This is valid for $\gamma_1 \delta^2 t_D \leqq .01$. Recalling the definition of δ, the following equations can easily be developed.

$$t_D' = 25\ \alpha^2/\gamma_1 \quad (\gamma<1);$$

$$t_D' = 25\ \alpha^2/\gamma_2 \quad (\gamma>1) \quad \ldots\ldots\ldots \quad (23)$$

where t_D' is the value of dimensionless time at which the linear portion of the pressure drop curve for large time begins. This is the time at which the so-called large time solution becomes valid.

As an example for comparison purposes, the conversion between t_D and t in minutes for a particular reservoir ($\phi = .20$, $\mu = 1$ cp, $c = 10^{-5}$/psi, $r_w = .25$ ft and $k_2 = 100$ md) is $t(\text{min}) = 2.84 \times 10^{-4} t_D$. For this reservoir if $\gamma_1/\gamma_2 = 4$ and $\alpha = 250$, then t' is found to be 7.4 hours. It is of interest that this value of t' is valid for any $\gamma_1/\gamma_2 > 1$ since we have taken $\gamma_2 = 1$ and γ_1 does not enter the expression for t_D' in Eq. 23. For $\gamma_1/\gamma_2 < 1$, however, t_D' depends not only on α but also on the ratio γ_1/γ_2. Of course, the effect of the number α^2 usually far outweighs that due to the γ_1/γ_2 ratio.

The limiting case in which $\alpha \to \infty$ is of interest. One would expect that the resulting pressure drop curve would have the slope $m = q\mu/4\pi bk_1$ where $k_1 = \gamma_1 k_2$. Therefore, if some intermediate value of α were taken so that two linear portions developed, we would expect the inverse ratio of the resulting slopes to equal the ratio of the permeabilities of the two zones. This possibility was explored by taking a relatively large value of α. As seen in Fig. 7, the resulting pressure drop curves had two linear portions. The ratio of the slope of the first linear portion to that of the second was indeed found to equal γ_2/γ_1. It was also of interest to check the time at which the second linear portion began. It was found to agree with that predicted by Eq. 23. This indicates the possibility of detecting permeability changes of this type from the pressure build-up curve. After determining the permeability of each zone by the Horner method, then the appropriate form of Eq. 23 can be selected. This equation then affords a method of calculating the size of the inner zone from the knowledge of the time at which the second linear portion begins. However, in the cases shown, the radius of the inner zone had to be very large before the earlier linear portion was able to form. For smaller α, as in Figs. 3 through 6, there is no obvious rule as to the behavior of the early portion of the curves. In these cases we are unable to determine either the permeability or the size of the inner zone. However, the early portion of the curve is usually distorted for reasons not considered in this study (after-flow, etc.).

Figs. 3 through 6 provide qualitative information for those faced with the task of interpreting pressure build-up or pressure drop curves. By studying the effects of the known reservoir nonuniformities presented in these figures, one can learn to recognize the characteristics of such phenomena. This familiarity with nonuniformities should assist the engineer in selecting the proper build-up portion for determining the permeability of the reservoir.

CONCLUSIONS

From the study of pressure drop in composite reservoirs, the following conclusions have been reached. For a composite reservoir with a large inner zone, the pressure drop curve has two linear portions. The permeability of each zone can be determined from the slope of the corresponding linear portion using the Horner method. The size of the inner zone can be determined by selecting the time at which the second linear portion begins. For a composite reservoir with a small inner zone, the first linear portion does not always form, and only qualitative information from the shape of the curve is available for the inner zone. Regardless of the condition of the reservoir near the wellbore, the permeability of the outer reservoir can be determined in the usual manner. However, the time at which the linear portion should begin is delayed by the presence of a zone of different permeability near the well.

NOMENCLATURE

a = see Eq. 13
b = see Eq. 13
C = Euler's constant, .5772157...
h = thickness of the reservoir, cm
I_0 = modified Bessel function of the first kind, zero order
I_1 = modified Bessel function of the first kind, first order
J_0 = Bessel function of the first kind, zero order
J_1 = Bessel function of the first kind, first order
K_0 = modified Bessel function of the second kind, zero order
K_1 = modified Bessel function of the second kind, first order
$\bar{k}$ = arbitrary reference permeability, darcies
m = see Eq. 13

n = see Eq. 13

P = pressure drop = $p_e - p$, atm

p = pressure, atm

p_e = original reservoir pressure, atm

$\bar{P}$ = Laplace transformation of P

$P(t_D)$ = pressure drop at the inner boundary, atm

$p(\Delta t)$ = pressure build-up, atm

q = volumetric flow rate, cc/sec

$q_1 = \sqrt{s}/\sqrt{\gamma_1}$

$q_2 = \sqrt{s}/\sqrt{\gamma_2}$

r = radial distance, cm

a = dimensionless radius of the inner zone, $(r_D = r/r_w)$

s = complex Laplace operator

t_D = dimensionless time, $(t_D = \bar{k}t/\Phi\mu c r_w^2)$

$t(q)$ = time that q has been imposed, seconds

Δt = shut-in time, seconds

$\omega = \sqrt{\rho}/\sqrt{\gamma_1}$ where ρ is the radial distance in the s-plane

Y_0 = Bessel function of the second kind, zero order

Y_1 = Bessel function of the second kind, first order

$\gamma = \sqrt{\gamma_1}/\sqrt{\gamma_2}$

γ_1 = defined by $k_1 = \gamma_1 \bar{k}$

γ_2 = defined by $k_2 = \gamma_2 \bar{k}$

δ = that value of ω such that neither of the two expressions $\gamma\omega a$ and ωa is greater than .02

Δ = see Eq. 8

Λ = see Eq. 13

λ = see Eq. 13

μ = viscosity, cp

$\xi = q\mu/2\pi h\bar{k}$

Φ = see Eq. 13

ϕ = porosity

ψ = see Eq. 13

log = natural logarithm

REFERENCES

1. Horner, D. R.: "Pressure Build-Up in Wells", *Proc.*, Third World Pet. Cong. (1951) Sect. 11, 503.
2. Miller, C. C., Dyes, A. B. and Hutchinson, C. A., Jr.: "Estimation of Permeability and Reservoir Pressure from Bottom Hole Pressure Build-Up Characteristics", *Trans.*, AIME (1950) Vol. 189, 91.
3. Matthews, C. S., Brons, F. and Hazebroek, P.: "A Method for Determination of Average Pressure in a Bounded Reservoir", *Trans.*, AIME (1954) Vol. 201, 182.
4. van Everdingen, A. F.: "The Skin Effect and Its Influence on the Productive Capacity of a Well", *Trans.*, AIME (1953) Vol. 198, 171.
5. Gladfelter, R. E., Tracy, C. W. and Wilsey, L. F.: "Selecting Wells Which Will Respond to Production-Stimulation Treatments", *Drill and Prod. Prac.*, API (1955) 117.
6. Stegemeier, G. L. and Matthews, C. S.: "A Study of Anomalous Pressure Buildup Behavior", *Trans.*, AIME (1958) Vol. 213, 44.
7. Hurst, L. L. and Guerrero, E. T.: "Calculating Static Bottom-Hole Pressures", *Oil and Gas Jour.* (Sept. 29, 1958).
8. Perrine, R. L.: "Analysis of Pressure Build-Up Curves", *Drill. and Prod. Prac.*, API (1956) 482.
9. Lefkovits, H. C., Hazebroek, P., Allen, E. E. and Matthews, C. S.: "A Study of the Behavior of Bounded Reservoirs Composed of Stratified Layers", *Soc. Pet. Eng. Jour.* (March, 1961) 43.
10. Houpeurt, A.: "Possibilites De Resolution Analytique Des Problemes D'Ecoulements Liquides Dans Des Milieux Poreux A Caracteristiques Varies", *Revue De L'Institut Francais Du Petrole* (1959) Vol. XIV No. 4-5, 549.
11. Albert, Jaisson and Marion: "Etude De L'Ecoulement Radial Circulaire Dans Un Milieu Ferme Heterogene", *Revue De L'Institut Francais Du Petrole* (1959) Vol. XIV No. 4-5, 561.
12. Hurst, W.: "Interference Between Oil Fields", *Trans.*, AIME (1960) Vol. 219, 175.
13. Mortada, M.: "Oilfield Interference in Aquifers of Non-Uniform Properties", *Trans.*, AIME (1960) Vol. 219, 412.
14. Hopkinson, J. L., Natanson, S. G. and Temple, A. P.: Effects of Reservoir Heterogeneity on Performance", paper 1581-G presented at 35th Annual Fall Meeting of SPE in Denver (Oct. 2-5, 1960).
15. Hurst, W. and van Everdingen, A. F.: "The Application of the Laplace Transformation to Flow Problems in Reservoirs", *Trans.*, AIME (1949) Vol. 186, 305.
16. Hildebrand, F.: *Advanced Calculus for Engineers*, Prentice-Hall, Inc., Englewood Cliffs, N. J. (1949).
17. Scott, E. J.: *Transform Calculus*, Harper and Bros., N. Y. (1955).
18. Loucks, T. L.: "A Study of Pressure Build-Up in a System Composed of Two Adjacent Concentric Regions of Different Permeabilities", Master's thesis, The U. of Tulsa (1960).
19. Carslaw, H. S. and Jaeger, J. C.: *Conduction of Heat in Solids*, Clarendon Press, Oxford (1959).
20. Carslaw, H. S. and Jaeger, J. C.: *Operational Methods in Applied Mathematics*, University Press, Oxford (1953).

***

Stresses Caused by Bit Loading at the Center of the Hole

J. B. CHEATHAM, JR.
MEMBER AIME

J. C. WILHOIT, JR.

SHELL DEVELOPMENT CO.

RICE U.
HOUSTON, TEX.

ABSTRACT

Although an oil well is a long cylindrical hole with an irregular bottom, it appears likely that the nature of the stress concentration at the bottom of the hole can be ascertained from an analysis of the stresses around a short cylindrical cavity with rounded corners and smooth bottom. Such a cavity is studied primarily because it leads more readily to a solution to the problem by the use of stress functions. In this paper the stress distribution around a short cylindrical cavity subjected to bit loading, overburden and drilling-fluid pressures is determined by means of an analytical solution which approximately satisfies the boundary conditions of the problem. From this solution the stresses at the corner of the hole are calculated to be about 35 per cent lower than comparable results obtained by photoelastic and relaxation analyses. This difference is apparently due to the large radius of curvature at the corner of the cavity in the present analysis. Since good agreement is obtained between the results of this analysis and the stresses calculated for a similar loading on a semi-infinite elastic solid, it is concluded that the bit action in the region near the center of the hole is not appreciably affected by the presence of the sides of the hole.

INTRODUCTION

Much has been written concerning drilling "under down-hole conditions" and pertaining to the stress distribution in the rock at the bottom of an oil well.[1-5] For example, it is known that identical rocks can be drilled more rapidly at the surface than under subsurface conditions of pressure and stress.[6] Information on the behavior of rocks under loading can be obtained from triaxial test data.[7-9] From such tests it is found that rocks exhibit brittle failure when the confining pressure and pore pressure are equal, but the mode of failure may change to ductile as the difference between the confining pressure and the pore pressure is increased. Brittle failure implies that there is very little permanent deformation before fracture, whereas ductile failure indicates that permanent deformation takes place before fracture. Some rocks are ductile at differential pressures of 5,000 psi, but other rocks are brittle even at differential pressures of more than 50,000 psi.

Cuttings embedded in mud at the bottom of the hole may act as a plastic mass which the bit teeth must penetrate in order to attack the virgin rock below.[10] During drilling, the mud pressure acts as the confining pressure, and in many cases the difference between the mud pressure and the formation pore pressure is sufficiently low so that the rock most likely fails in a brittle manner. Very little penetration by the bit teeth may be required for brittle failure of the rock. For these brittle materials, the elastic stress distribution is of practical interest in determining the possible effects of a given loading on failure. The penetration of bit teeth into ductile or plastic rock has been analyzed previously[11,12] and will not be considered further in the present work.

During actual drilling, many teeth act at various points over an irregular hole bottom. In the present analysis a solution is obtained for an idealized problem of determining the elastic stress distribution caused by only one tooth acting alone at the center of a smooth hole bottom. It obviously is not proposed that any driller should put a special one-tooth bit on bottom, but it is hoped that extensions of the simpler problems can eventually lead to a better understanding of more complex actual drilling phenomena.

To obtain a solution by the use of stress functions, a short cylindrical cavity with rounded corners and smooth bottom is studied. The solution to this problem should give an insight into the nature of the stress concentration at the bottom of an oil well which is in reality a long cylindrical hole with an irregular bottom. After selection of the proper curvilinear co-ordinate system, the stress functions are expressed as series of Legendre polynomials. The coefficient of each term in the series is then determined to satisfy the boundary conditions at a finite number of discrete points on the boundary of the cavity with least square error. Results are compared with bottom-hole stresses obtained by photoelastic and relaxation analyses.

Original manuscript received in Society of Petroleum Engineers office July 21, 1960. Revised manuscript received Jan. 26, 1961. Paper presented at the 35th Annual Fall Meeting of SPE, Oct. 2-5, 1960, in Denver.

[1] References given at end of paper.

STATEMENT OF THE PROBLEM

Consider a homogeneous, isotropic, impermeable elastic body containing a cylindrical cavity; it is desired that the stresses and displacements in the region exterior to the cavity be determined when the distribution of forces acting on the surface of the cavity are prescribed.

The displacement equation of equilibrium is given by[13]

$$G(\nabla^2 + \frac{1}{1-2\nu} \nabla \text{ div}) \bar{\rho} + \bar{F} = 0 \quad . \quad . \quad . \quad . \quad (1)$$

where the displacement vector is expressed as

$$\bar{\rho} = iu + jv + kw$$

and the body force vector is denoted by

$$\bar{F} = iF_x + jF_y + kF_z.$$

The general solution of Eq. 1 for axisymmetric loading in the absence of body forces is given by the sum of the following displacement fields.[14]

$$\bar{\rho} = \frac{1}{2G} \text{ grad } \phi.$$

$$\bar{\rho} = \frac{1}{2G} [\text{grad } z\psi - 4(1-\nu)\, k\psi] \quad . \quad . \quad . \quad . \quad . \quad . \quad (2)$$

where

$$\nabla^2\phi = 0$$

and

$$\nabla^2\psi = 0.$$

These harmonic functions, ϕ and ψ, are referred to as the Boussinesq-Papkovich stress functions. The displacements in general axisymmetric orthogonal curvilinear co-ordinates defined by Eq. 2 and the associated stress fields are given by Sternberg, Eubanks and Sadowsky.[14] The problem therefore becomes one of determining harmonic functions which, when used as Boussinesq-Papkovich stress functions, satisfy the desired boundary conditions.

CO-ORDINATE TRANSFORMATION FOR A CYLINDRICAL CAVITY

The transformation which is used in this analysis is given by[1]

$$Z = \zeta - \frac{n}{\zeta^3} \quad . \quad . \quad . \quad . \quad . \quad . \quad . \quad . \quad . \quad . \quad . \quad . \quad . \quad (3)$$

where $Z = z + ir$ and $\zeta = ae^{i\beta}$. In this equation, $n^{1/4}$ has dimensions of length. With $n = 1/6$, the figure described by $\alpha = 1$ and $\gamma =$ constant is an approximation to a square in the r-z plane. The cylindrical co-ordinates (r, γ, z) are related to the curvilinear co-ordinates (α, β, γ) by the following equations obtained by taking real and imaginary parts of Eq. 3.

$$r = a \sin\beta + \frac{n}{a^3} \sin 3\beta,$$

$$z = a \cos\beta - \frac{n}{a^3} \cos 3\beta,$$

$$\gamma = \gamma \quad . \quad . \quad . \quad . \quad . \quad . \quad . \quad . \quad . \quad . \quad . \quad . \quad . \quad . \quad . \quad . \quad . \quad . \quad (4)$$

Since $x = r \cos\gamma$ and $y = r \sin\gamma$, the required co-ordinate transformations are

$$x = (a \sin\beta + \frac{n}{a^3} \sin\beta) \cos\gamma,$$

$$y = (a \sin\beta + \frac{n}{a^3} \sin 3\beta) \cos\gamma,$$

$$z = a \cos\beta - \frac{n}{a^3} \cos 3\beta \quad . \quad . \quad . \quad . \quad . \quad . \quad . \quad (5)$$

where $n = 1/6$. Co-ordinate surfaces for the α, β, γ curvilinear co-ordinate system are shown in Fig. 1, and one quadrant of the γ = constant plane is depicted in Fig. 2 where R and θ are spherical co-ordinates.

SOLUTION BY POLYNOMIALS

To satisfy arbitrary boundary conditions, it is desirable to obtain separated solutions of Laplace's equation of the form

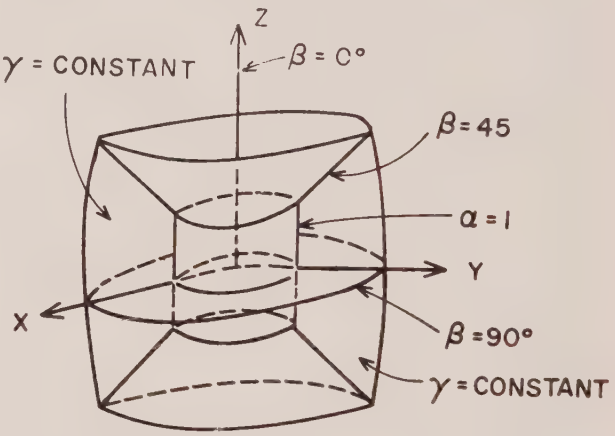

FIG. 1 – CURVILINEAR CO-ORDINATE SURFACES.

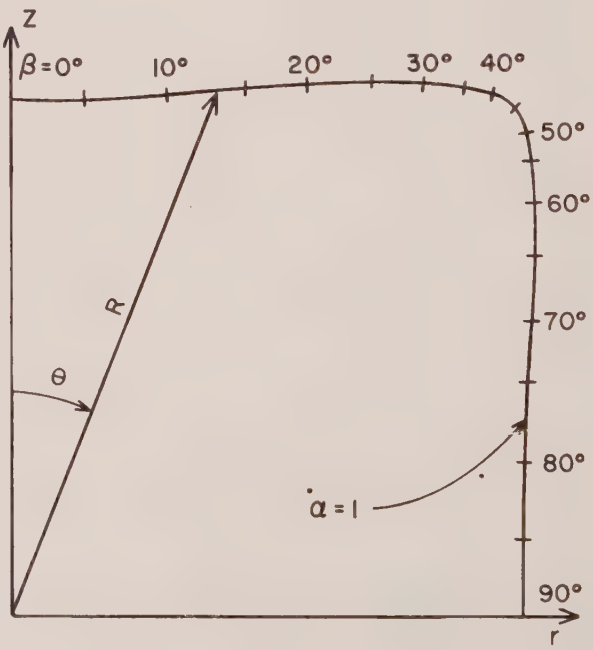

FIG. 2 – ONE QUADRANT OF γ = CONSTANT PLANE.

$$\Phi(\alpha, \beta) = X_1(\alpha)\, X_2(\beta).$$

However, certain relations must exist between the scale factors of a co-ordinate system in order for it to be possible to express solutions of Laplace's equation in the separated form given by this equation.[15] The scale factors of the co-ordinate system defined by Eqs. 5 do not satisfy these requirements; therefore, it is necessary to seek harmonic functions in another manner.[1]

Solutions of Laplace's equation can be obtained in the form of polynomials generated by spherical harmonics.[1,16] External spherical harmonics are given by the expression

$$\Phi_n = R^{-n-1}\ P_n\ (\cos\theta) \quad \ldots\ldots\ldots\ (6)$$

where R, θ and γ are spherical co-ordinates, and P_n $(\cos\theta)$ is the Legendre polynomial of order n, where

$$P_n(\cos\theta) = \frac{(2n)!}{2^n (n!)^2}\ \cos^n\theta - \frac{n(n-1)}{2(2n-1)}\ \cos^{n-2}\theta + \frac{n(n-1)(n-2)(n-3)}{2\cdot 4\,(2n-1)(2n-3)}\ \cos^{n-4}\theta + \ldots .$$

Spherical co-ordinates R and θ are related to the cylindrical co-ordinates r and z by the equations

$$R = (r^2 + z^2)^{1/2},$$

$$\cos\theta = \frac{z}{(r^2 + z^2)^{1/2}}.$$

Substitution of Eqs. 4 into these equations yields the following relations between spherical co-ordinates and the curvilinear co-ordinates α and β.

$$R = \left[\left(\alpha^2 + \frac{n^2}{\alpha^6}\right) - \frac{2n}{\alpha^2}\ \cos 4\beta\right]^{1/2},$$

$$\cos\theta = \frac{\alpha\cos\beta - \frac{n}{\alpha^3}\cos 3\beta}{\left[\left(\alpha^2+\frac{n^2}{\alpha^6}\right) - \frac{2n}{\alpha^2}\cos 4\beta\right]^{1/2}} \quad \ldots\ (7)$$

Harmonic functions in terms of α and β are obtained by substitution of Eqs. 7 into Eq. 6; thus,

$$\Phi_n = \Phi_n(\alpha, \beta) \quad \ldots\ldots\ldots\ (8a)$$

or

$$\Phi_0 = \frac{1}{R} = \left[\left(\alpha^2 + \frac{n^2}{\alpha^6}\right) - \frac{2n}{\alpha^2}\ \cos 4\beta\right]^{-1/2},$$

$$\Phi_1 = \frac{\cos\theta}{R^2} = \frac{\alpha\cos\beta - \frac{n}{\alpha^3}\cos 3\beta}{\left[\left(\alpha^2+\frac{n^2}{\alpha^6}\right) - \frac{2n}{\alpha^2}\cos 4\beta\right]^{3/2}} \quad . (8b)$$

Each of these functions defines a particular displacement field and the corresponding stress field when used as a Boussinesq-Papkovich stress function. By superposition, the solution in terms of polynomials can be represented by

$$\phi = \sum_n^N a_n\, \Phi_n,$$

$$\psi = \sum_n^N b_n\, \Phi_n \quad \ldots\ldots\ldots\ (9)$$

where a_n and b_n are coefficients to be determined to satisfy the boundary conditions. The stresses and displacements are calculated by substitution into the equations given in Appendix A.

Arbitrary boundary conditions cannot necessarily be fitted exactly by the use of Eqs. 8 and 9, but a satisfactory fit can be obtained at a large number of points on the boundary by the method of least squares. By this method the sum of the squares of the deviations of the calculated values from the stipulated boundary conditions is minimized.

The problem for which a solution is sought is illustrated by Fig. 3. In the formation around an oil well the overburden stress increases approximately 1 psi/ft of depth, while inside the borehole the fluid pressure increases about ½ psi/ft. The boundary conditions of the problem are given by

Overburden Pressure = 2,000 psi,
Pressure Inside Cavity = 1,000 psi,
Bit Loading Over Center Part of Hole,

or

$$\left.\begin{aligned} \sigma_\alpha &= \sigma_\beta = \sigma_\gamma = -2{,}000 \text{ psi} \\ \tau_{\alpha\beta} &= 0 \end{aligned}\right\} @\ \infty$$

and

$$\left.\begin{aligned} \sigma_\alpha &= -1{,}000 \text{ psi (except under bit)} \\ \tau_{\alpha\beta} &= 0 \end{aligned}\right\} @\ \alpha = 1.$$

The solution of this problem, denoted by "A" in Fig. 4, is obtained by superposition of: B, a hydrostatic compressive stress of 2,000 psi; C, a tensile stress of 1,000 psi acting on the cavity wall; and D, the simulated bit load.

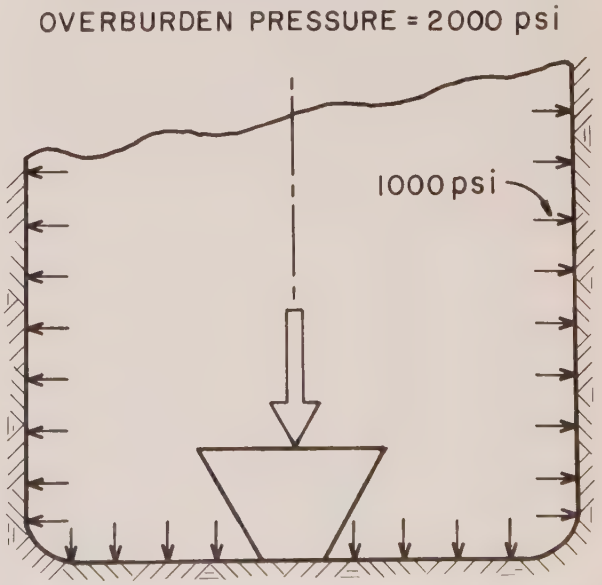

FIG. 3 – ILLUSTRATION OF BOUNDARY CONDITIONS OF PROBLEM.

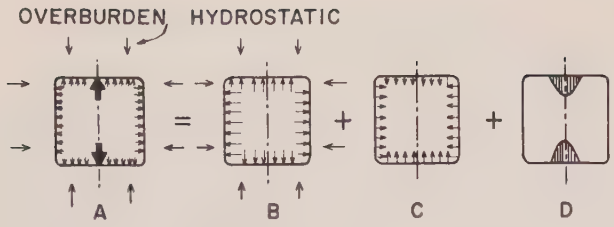

FIG. 4 – SUPERPOSITION OF SOLUTIONS.

The hydrostatic stress distribution is given by the following.

$$\sigma_\alpha = \sigma_\beta = \sigma_\gamma = -2{,}000 \text{ psi},$$
$$\tau_{\alpha\beta} = 0.$$

Solution [C + D] is found by use of the Boussinesq-Papkovich polynomial solutions given by Eqs. 9. The coefficients a_n and b_n in Table 1 are determined from a least-square fit to the boundary conditions of Part C for $\alpha = 1$ and $8° < \beta < 172°$. The loading for Part D is obtained from this solution and is not actually an imposed boundary condition.

The load distribution under the bit tooth given by this solution is shown in Fig. 5. The total load represented by this distribution is equivalent to 200,000 lb in an 8 3/4-in. diameter hole. This load represents about twice the maximum load normally applied to present-day bits, but the magnitude of this simulated bit load could be decreased by allowing the load to act over a smaller area or by superposing concentrated tensile loads along the z axis. The boundary conditions are satisfied within ± 8 per cent for the normal stress and within ± 1 per cent for the shearing stress by use of the least-square method at 2° increments on the boundary. Stresses are plotted in Fig. 6 for $\alpha = 1$ and $\alpha = 1.5$, and the stresses under the bit are shown in Fig. 7. The stresses along the z axis are shown in Fig. 8.

Stresses in a semi-infinite body under approximately the same loading as shown in Fig. 5 are calculated from the equations given in Appendix B and plotted in Fig. 9. Comparing the stress distribution shown in Fig. 9 with that of Fig. 8, it can be seen that the results are in remarkably good agreement.

TABLE 1

n	a_n	n	b_n
0	1432	1	-1231
2	1203	3	-1210
4	911	5	- 810
6	515	7	- 415
8	262	9	- 245
10	175	11	- 184
12	124	13	- 108
14	63	15	- 46
16	26	17	- 25
18	15	19	- 15
20	9.6	21	- 7.3
22	4.6	23	- 3.5
24	1.6	25	- 1.26
26	0.030	27	- 0.068

$a_n = 0$, $(n = 1, 3, 5, \ldots)$,

$b_n = 0$, $(n = 0, 2, 4, \ldots)$.

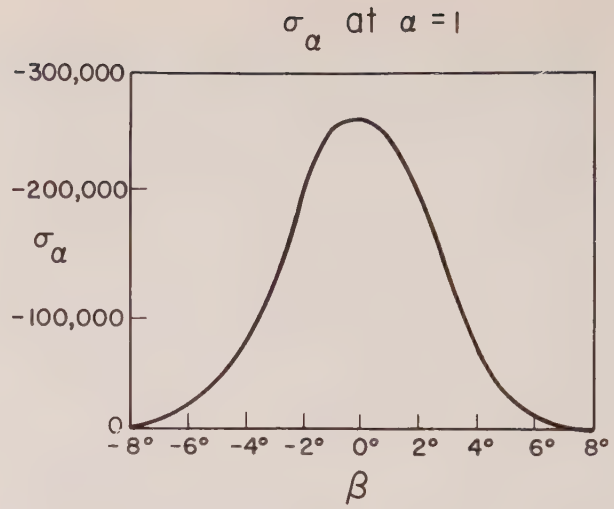

FIG. 5 – LOAD DISTRIBUTION AT CENTER OF HOLE.

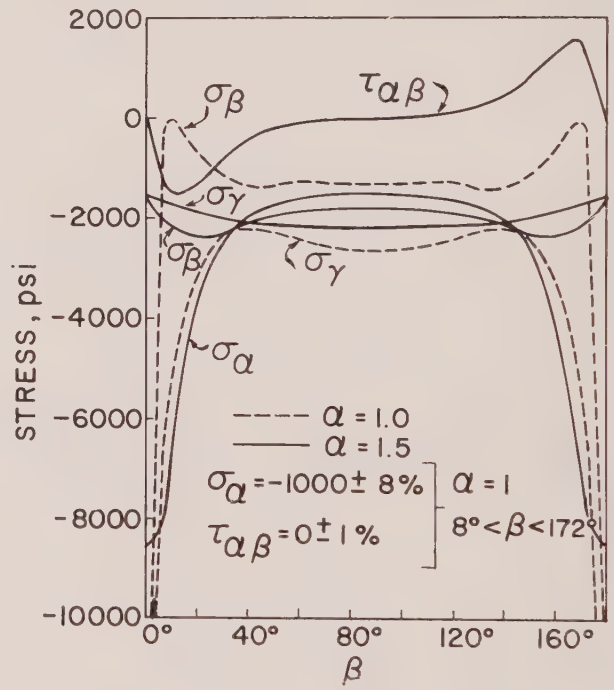

FIG. 6 – STRESSES AROUND CAVITY.

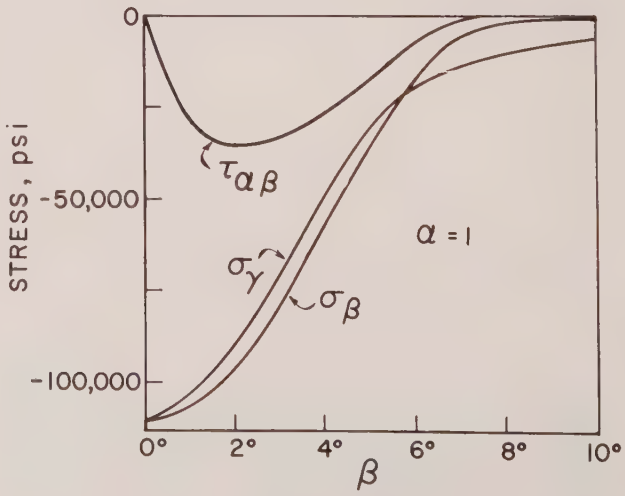

FIG. 7 – STRESSES NEAR CENTER OF HOLE BOTTOM.

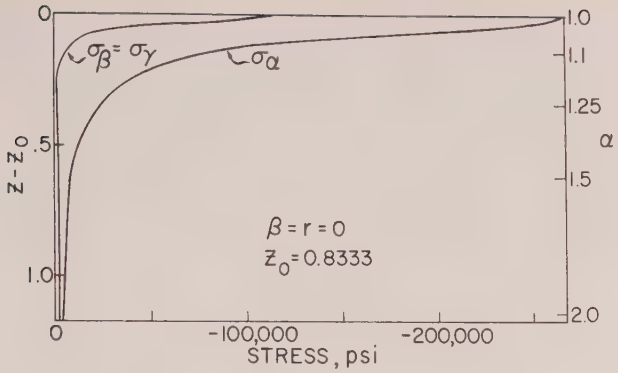

FIG. 8 – STRESSES ALONG z-AXIS.

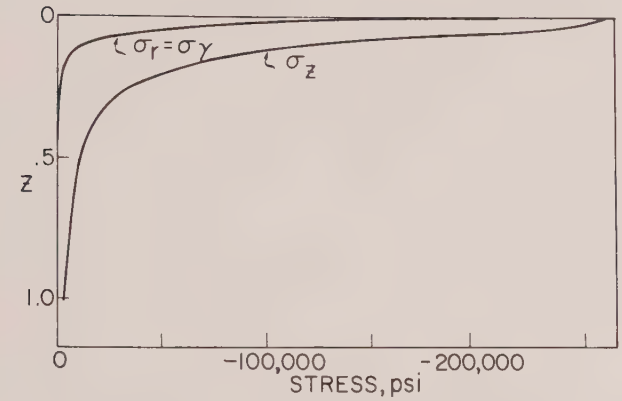

FIG. 9 – STRESSES ALONG z-AXIS FOR SEMI-INFINITE BODY WITH LOADING SHOWN IN FIG. 5.

A direct comparison of the results obtained by the present analysis cannot be made with the works of Whitworth[2] and Galle[3] since the hole configurations are different, the values of Poisson's ratio are not the same and the loading differs in the three analyses. However, qualitative comparisons can be made by neglecting the influence of Poisson's ratio and by superposing a concentrated load obtained from Boussinesq's solution[15] with the results of the other two authors. If it is assumed that the effect of the concentrated load can be effected by the Boussinesq solution, disregarding the corner,[17] the stresses at the corner of an 8 3/4-in. hole produced by a concentrated load of 200,000 lb acting at the center are

$$\sigma_r = \frac{P(1-2\nu)}{2\pi r^2} = 650 \text{ psi},$$

$$\sigma_\gamma = -\sigma_r = -650 \text{ psi}.$$

Superposition of a hydrostatic stress of –2,000 psi and the Boussinesq solution with the negative of Whitworth's solution gives

Overburden Stress = –2,000 psi,

Stress at Boundary of Hole Due to Fluid Pressure = –1,000 psi;

and at the corner of the hole the stresses are

$$\sigma_r = -2{,}000 + 650 - 1{,}000 = -2{,}350 \text{ psi},$$

$$\sigma_\gamma = -2{,}000 - 650 - 1{,}000 = -3{,}650 \text{ psi}.$$

Galle's solution, when multiplied by 10 and superposed with a hydrostatic loading of –1,000 psi and added to the Boussinesq solution, gives the same boundary conditions; and the stresses at the corner of the hole are

$$\sigma_r = -1{,}600 - 1{,}000 + 650 = -1{,}950 \text{ psi},$$

$$\sigma_\gamma = -1{,}900 - 1{,}000 - 650 = -3{,}550 \text{ psi}.$$

These results are tabulated in Table 2.

CONCLUSIONS

Larger values for the stresses at the corner of the hole were obtained by photoelasticity and relaxation analyses than were found by the stress-function calculations presented here. It appears likely that this difference is due largely to the much sharper corners used in the previous work. It is of interest to note that the ratios of the magnitude of the hoop stress to that of the radial stress is in rather good agreement for all three analyses.

From the good agreement between the results for the loading at the center of the hole and a similar loading on a semi-infinite solid, it can be concluded that the presence of the sides of the hole has little effect upon the stresses beneath a bit tooth acting near the center of the hole. It is hoped that extensions of this study to analyses of the effects of bit tooth loading near the corner of the hole and to combinations of several teeth acting at various points on the bottom of the hole will aid in better understanding of the mechanics of oilwell drilling.

NOMENCLATURE

$\bar{F}$ = body force vector

F_x, F_y, F_z = components of body force vector

G = shear modulus

h_1 = curvilinear co-ordinate scale factor

i, j, k = unit vectors along x, y and z axes, respectively

P_n = Legendre polynomial of order n

R, θ, γ = spherical co-ordinates

r, z, γ = cylindrical co-ordinates

u, v, w = displacements along x, y and z axes, respectively

$Z = z + ir$

α, β, γ = curvilinear co-ordinates

σ_α = normal stress

$\tau_{\alpha\beta}$ = shearing stress

TABLE 2 – STRESSES AT THE CORNER OF THE HOLE

Stress Function	Galle (Photoelastic)	Whitworth (Relaxation)
$\sigma_\beta = -1{,}400$ psi	$\sigma_r = -1{,}950$ psi	$\sigma_r = -2{,}350$ psi
$\sigma_\gamma = -2{,}200$ psi	$\sigma_\gamma = -3{,}550$ psi	$\sigma_\gamma = -3{,}650$ psi
$\frac{\sigma_\gamma}{\sigma_\beta} = 1.57$	$\frac{\sigma_\gamma}{\sigma_r} = 1.82$	$\frac{\sigma_\gamma}{\sigma_r} = 1.55$

ν = Poisson's ratio

$\overline{\rho}$ = displacement vector

ϕ, ψ, Φ = stress functions

∇ = gradient operator

∇^2 = Laplacian operator

REFERENCES

1. Cheatham, J. B., Jr.: "The Use of Boussinesq-Papkovich Stress Functions to Determine the Stresses Around the Bottom of a Cylindrical Cavity", PhD thesis, Rice U. (1960).
2. Whitworth, B. J.: "The Stresses in the Rock Formation near the Bottom of a Hole Due to Overburden and Drill Fluid Pressures", Master's thesis, Rice U. (1956).
3. Word, H. S., Jr.: "Photoelastic Analysis of the Stresses Around the Bottom of a Cylindrical Bore Hole Due to Overburden and Fluid Column Pressures", Master's thesis, Rice U. (1958).
4. Galle, E. M.: "Photoelastic Analysis of the Stresses Near the Bottom of a Cylindrical Cavity Due to Non-Symmetrical Loading", Master's thesis, Rice U. (1959).
5. Durelli, A. J. and Deily, F. H.: "Bottom-Hole Stresses in a Well Bore", Paper 1095-G presented at 33rd Annual Fall Meeting of SPE in Houston, Tex. (Oct., 1958).
6. Cunningham, R. A.: "The Effect of Hydrostatic Stress on the Drilling Rates of Rock Formations", Master's thesis, Rice U. (1955).
7. Handin, J. W.: "Experimental Deformation of Rocks and Minerals", *Colorado School of Mines Quart.* (1957) Vol. 52, 74.
8. Bredthauer, R. O.: "Strength Characteristics of Rock Samples Under Hydrostatic Pressure", *Trans.*, ASME (May, 1957) Vol. 79, No. 4, 695.
9. Robinson, L. H., Jr.: "The Effect of Pore and Confining Pressure on the Failure Process in Sedimentary Rock", *Colorado School of Mines Quart.* (1959) Vol. 54, 179.
10. Garnier, A. J. and van Lingen, N. H.: "Phenomena Affecting Drilling Rates at Depth", *Trans.*, AIME (1959) Vol. 216, 232.
11. Cheatham, J. B., Jr.: "An Analytical Study of Rock Penetration by a Single Bit Tooth", Eighth Annual Drill. and Blast. Sym., The U. of Minnesota (Oct., 1958).
12. Outmans, H. D.: "The Effect of Some Drilling Variables on the Instantaneous Rate of Penetration", *Trans.*, AIME (1960) Vol. 219, 137.
13. Eubanks, R. A. and Sternberg, E.: "On the Completeness of the Boussinesq-Papkovich Stress Functions", *Jour. Rational Mech. and Analysis* (1956) Vol. 5, 735.
14. Sternberg, E., Eubanks, R. A. and Sadowsky, M. A.: "On the Stress-Function Approaches of Boussinesq and Timpe to the Axisymmetric Problem of Elasticity Theory", *Jour. Appl. Phys.* (Sept., 1951) Vol. 22, 1121.
15. Morse, R. M. and Feshbach, H.: *Methods of Theoretical Physics*, Part I, McGraw-Hill Book Publishing Co., Inc., N. Y. (1953).
16. Timoshenko, S. and Goodier, J. N.: *Theory of Elasticity*, Second Ed., McGraw-Hill Book Publishing Co., Inc., N. Y. (1951).
17. Unpublished Photoelastic Data, Rice U.

APPENDIX A

DISPLACEMENT AND STRESS FIELDS DEFINED BY THE BOUSSINESQ-PAPKOVICH STRESS FUNCTIONS

The displacement and stress fields for the Boussinesq-Papkovich stress functions can be calculated from the following equations after Sternberg, Eubanks and Sadowsky.[14]

For axisymmetric orthogonal curvilinear coordinates defined by the transforms

$$x = r(\alpha, \beta) \cos \gamma,$$
$$y = r(\alpha, \beta) \sin \gamma,$$
$$z = z(\alpha, \beta), \quad \ldots\ldots\ldots\ldots\ldots \text{(A-1)}$$

the scale factors are*

$$h_1 = \left(r_\alpha^2 + z_\alpha^2\right)^{-1/2},$$
$$h_2 = \left(r_\beta^2 + z_\beta^2\right)^{-1/2},$$
$$h_3 = \frac{1}{|r|}, \quad \ldots\ldots\ldots\ldots\ldots \text{(A-2)}$$

and Laplace's equation becomes

$$\frac{\partial}{\partial \alpha}\left(\frac{r h_1}{h_2}\phi_\alpha\right) + \frac{\partial}{\partial \beta}\left(\frac{r h_2}{h_1}\phi_\beta\right) = 0. \quad \ldots \text{(A-3)}$$

From the displacement fields for the Boussinesq-Papkovich functions (Eqs. 2), the displacements become

$$u_\alpha = \frac{h_1 \phi_\alpha}{2G},$$
$$u_\beta = \frac{h_2 \phi_\beta}{2G}, \quad \ldots\ldots\ldots\ldots \text{(A-4)}$$

and

$$u_\alpha = \frac{h_1}{2G}\left[z\psi_\alpha - (3-4\nu) z_\alpha \psi\right],$$
$$u_\beta = \frac{h_2}{2G}\left[z\psi_\beta - (3-4\nu) z_\beta \psi\right], \quad \ldots\ldots \text{(A-5)}$$

and the associated stresses in curvilinear coordinates are

$$\sigma_\alpha = h_1^2 \phi_{\alpha\alpha} + h_1 \frac{\partial h_1}{\partial \alpha}\phi_\alpha - \frac{h_2^2}{h_1}\frac{\partial h_1}{\partial \beta}\phi_\beta,$$
$$\sigma_\beta = h_2^2 \phi_{\beta\beta} + h_2 \frac{\partial h_2}{\partial \beta}\phi_\beta - \frac{h_1^2}{h_2}\frac{\partial h_2}{\partial \alpha}\phi_\alpha,$$
$$\sigma_\gamma = \frac{h_1^2 r_\alpha}{r}\phi_\alpha + \frac{h_2^2 r_\beta}{r}\phi_\beta,$$
$$\tau_{\alpha\beta} = h_1 h_2 \phi_{\alpha\beta} + h_2 \frac{\partial h_1}{\partial \beta}\phi_\alpha + h_1 \frac{\partial h_2}{\partial \alpha}\phi_\beta,$$
$$\ldots\ldots\ldots\ldots\ldots\ldots\ldots\ldots \text{(A-6)}$$

*Subscripts to functions originally without subscripts denote differentiation, $r_\alpha = \frac{\partial r}{\partial \alpha}$ and $\phi_\beta = \frac{\partial \phi}{\partial \beta}$.

and

$$\sigma_\alpha = b_1^2 z \psi_{\alpha\alpha} + \left(b_1 \frac{\partial b_1}{\partial \alpha} z - 2 b_1^2 z_\alpha \right) - \frac{b_2^2}{b_1} \frac{\partial b_1}{\partial \beta} z \psi_\beta + (2\nu)(b_1^2 z_\alpha \psi_\alpha - b_2^2 z_\beta \psi_\beta),$$

$$\sigma_\beta = b_2^2 z \psi_{\beta\beta} + \left(b_2 \frac{\partial b_2}{\partial \beta} z - 2 b_2^2 z_\beta \right) - \frac{b_1^2}{b_2} \frac{\partial b_2}{\partial \alpha} z \psi_\alpha + (2\nu)(b_2^2 z_\beta \psi_\beta - b_1^2 z_\alpha \psi_\alpha),$$

$$\sigma_\gamma = \frac{z}{r} (b_1^2 r_\alpha \psi_\alpha + b_2^2 r_\beta \psi_\beta) - (2\nu)(b_1^2 z_\alpha \psi_\alpha + b_2^2 z_\beta \psi_\beta),$$

$$\tau_{\alpha\beta} = b_1 b_2 z \psi_{\alpha\beta} + z \left(b_1 \frac{\partial b_2}{\partial \alpha} \psi_\beta + b_2 \frac{\partial b_1}{\partial \beta} \psi_\alpha \right) - (1 - 2\nu) b_1 b_2 (z_\alpha \psi_\beta + z_\beta \psi_\alpha). \quad \text{(A-7)}$$

APPENDIX B

STRESSES UNDER LOAD DISTRIBUTED OVER PART OF THE BOUNDARY OF A SEMI-INFINITE SOLID

The stresses produced by a uniform pressure q acting over a circular area of radius a are given by the following equations (see Timoshenko and Goodier[16]).

$$\sigma_z = q \left[-1 + \frac{z^3}{(a^2 + z^2)^{3/2}} \right],$$

$$\sigma_r = \sigma_\gamma = \frac{q}{2} \left[-(1 + z\nu) + \frac{2(1 + \nu) z}{\sqrt{a^2 + z^2}} - \left(\frac{z}{\sqrt{a^2 + z^2}} \right)^3 \right].$$

The loading shown in Fig. 5 is approximated by constant values of a and q over 2° increments, and the resulting stresses are plotted in Fig. 9. ★★★

A Numerical Solution to the Unsteady-State Partial-Water-Drive Reservoir Performance Problem

WALTER L. HENSON
MEMBER AIME
PAUL L. WEARDEN
JOHN D. RICE
MEMBER AIME

SUN OIL CO.
BEAUMONT, TEX.

DALLAS, TEX.

ABSTRACT

Solutions to the unsteady-state partial water-drive reservoir performance problem can be obtained through the use of analogue computers or high-speed electronic digital computers. The solutions that have previously been resolved for use on digital computers, however, demand a knowledge of the aquifer parameters. Generally, the analogue computers now in use do not require this knowledge.

A solution is presented herein where the aquifer performance, expressed in terms of difference equations, is related to the reservoir performance as expressed by the modified Schilthuis material-balance equation. A numerical procedure for a medium-sized digital computer also is presented in which a solution to the set of equations defining the aquifer and reservoir performance is obtained and the aquifer parameters (permeability and sand thickness) are automatically optimized while simultaneously matching the known pressure behavior. Predicted pressure behavior can be calculated using rates from any assumed future production practice. The procedure provides an output format which presents the cumulative, incremental and average rate of natural water influx, the per cent gas-cap expansion, the calculated reservoir pressure, the measured reservoir pressure, and the difference between the measured and calculated pressures.

Results of a test problem are presented in comparison with results obtained by the Bruce Analyzer, Ohio Oil Co.'s Pace General Purpose Analogue Computer, and Sun Oil Co.'s Single-Pool Electronic Reservoir Analyzer. These results indicate that unsteady-state reservoir performance for a single-pool system can be adequately simulated by a numerical method employing a digital computer and that the special-purpose analogue computer can be supplanted by this method.

INTRODUCTION

The numerical approach to the unsteady-state partial water-drive reservoir performance problem heretofore has been limited in that solutions have been resolved only for certain fixed parameters. Also, prior to the advent of high-speed electronic digital computers in the last few years, calculations were so tedious and time-consuming that they ordinarily were neglected, or some other means of obtaining the solutions were used.

The analogue approach had been used for obtaining solutions to the transmission-of-heat problem and, consequently, means were developed for applying the electrical analogue to the unsteady-state reservoir performance problem. Bruce submitted a paper for AIME publication in Sept. 1942, in which he described an electronic device (now called the Bruce Analyzer) for analyzing the water-drive performance of any reservoir, based on either steady or unsteady-state flow characteristics.[1]

Sun Oil Co. adopted the analogue approach in 1949 and now has two special-purpose high-speed electronic reservoir analyzers in use.[2,3] Two main features of Sun's analyzers are (1) the high repetitive rate of reproducing the entire history of reservoir performance cyclically a number of times per second, and (2) the elimination of the necessity of knowing the properties of the associated aquifer. Since the advent of larger and faster digital computers, the possibility of incorporating this second feature into a numerical approach appeared feasible.

Previous work has been done and material published covering the application of numerical methods to the behavior of the pressure with respect to time at any point in an associated aquifer.[4] However, the aquifer parameters must be known from some source. The material presented in Ref. 4 has been used to a great degree in developing the numerical method described herein.

DIFFERENTIAL EQUATION AND BOUNDARY CONDITIONS

The problem of simulating the performance of a reservoir and the associated aquifer is to determine the characteristics of the aquifer such that the

Original manuscript received in Society of Petroleum Engineers office Nov. 7, 1960. Revised manuscript received May 2, 1961.

[1]References given at end of paper.

simultaneous solution of the material-balance equation for the reservoir and the differential equation of the aquifer will produce a pressure decline matching the field-measured pressure-decline curve.

The differential equation describing a radial aquifer, $r_w \leq r \leq r_R$, with variable permeability (K) and sand thickness (h) is

$$\frac{r}{\phi\mu ch}\frac{\partial}{\partial r}\left(Khr\frac{\partial P}{\partial r}\right)=r^2\frac{\partial P}{\partial t} \quad . \quad . \quad . \quad . \quad . \quad (1)$$

Then if the variable changes

$$r = r_R e^{-u}$$

and

$$Z = \frac{P_o - P}{P_o - P_m}$$

are made, Eq. 1 becomes

$$\frac{\partial}{\partial u}\left(Kh\frac{\partial Z}{\partial u}\right)=r_R^2\phi\mu che^{-2u}\frac{\partial Z}{\partial t}, \quad . \quad . \quad . \quad . \quad (2)$$

$$0 \leq u \leq \ln\frac{r_R}{r_w}$$

which is the general expression in dimensionless radial distance and pressure for any point within the aquifer.

The boundary conditions imposed on Eq. 2 are as follows.

At the outer boundary of the aquifer, $u = 0$ and radial flow is zero. This condition is satisfied if

$$\left[Kh\frac{\partial Z}{\partial u}\right]_{u=0}=0 \quad . \quad . \quad . \quad . \quad . \quad . \quad . \quad . \quad . \quad (3)$$

At the inner boundary of the aquifer or the original oil-water contact, a rate of influx (in reservoir volumes per unit of time) occurs across r_w. Thus,

$$\frac{\partial I(t)}{\partial t}=\left[\frac{-2\pi Kh}{\mu}\left(\frac{\partial P}{\partial u}\right)\right]_{u=\ln\frac{r_R}{r_w}},$$

or

$$\frac{\partial I(t)}{\partial t}=\left[\frac{2\pi Kh(P_o-P_m)}{\mu}\left(\frac{\partial Z}{\partial u}\right)\right]_{u=\ln\frac{r_R}{r_w}}.$$

But remembering that the influx is also equivalent to the difference between the voidage from the reservoir and its expansion, then

$$\frac{\partial V(t)}{\partial t}-\frac{\partial E(t)}{\partial t}=\frac{\partial I(t)}{\partial t}.$$

Then the inner boundary condition is

$$\frac{\partial V(t)}{\partial t}-\frac{\partial E(t)}{\partial t}=\left[\frac{2(P_o-P_m)\pi Kh}{\mu}\left(\frac{\partial Z}{\partial u}\right)\right]_{u=\ln\frac{r_R}{r_w}}$$

. . . . . (4)

NUMERICAL APPROXIMATION TO DIFFERENTIAL EQUATIONS

The system defined by Eq. 2 and the boundary condition (Eqs. 3 and 4) can be expressed in terms of a system of difference equations which are algebraic functions that can be solved numerically and whose solution converges to the solution of the solution of the system defined by Eqs. 2, 3 and 4.

To write such a set of equations, a distance grid is set up by considering Z as a function of u and t at the points $(i + \frac{1}{2})\,\Delta u$, $n\Delta t$ where $i = 0, 1, 2, \ldots, j$ and $n = 0, 1, 2, \ldots$. The terms of Eq. 2 are approximated by the following difference relationships.

$$\frac{\partial}{\partial u}\left(Kh\frac{\partial Z}{\partial u}\right)_{i+\frac{1}{2},n+\frac{1}{2}}\approx$$

$$\frac{1}{2(\Delta u)^2}\Big[(Kh)_{i+1}(Z_{i+\frac{3}{2},n+1}-Z_{i+\frac{1}{2},n+1})$$

$$-(Kh)_i(Z_{i+\frac{1}{2},n+1}-Z_{i-\frac{1}{2},n+1})$$

$$+(Kh)_{i+1}(Z_{i+\frac{3}{2},n}-Z_{i+\frac{1}{2},n})$$

$$-(Kh)_i(Z_{i+\frac{1}{2},n}-Z_{i-\frac{1}{2},n})\Big]. \quad . \quad . \quad . \quad . \quad (5)$$

$$\left(\frac{\partial Z}{\partial t}\right)_{i+\frac{1}{2},n+\frac{1}{2}}\approx$$

$$\frac{Z_{i+\frac{1}{2},n+1}-Z_{i+\frac{1}{2},n}}{\Delta t} \quad . \quad . \quad . \quad . \quad . \quad . \quad . \quad . \quad (6)$$

Substituting Eqs. 5 and 6 into Eq. 2 yields

$$\frac{\Delta t}{2(\Delta u)^2}\Big[(Kh)_{i+1}(Z_{i+\frac{3}{2},n+1}-Z_{i+\frac{1}{2},n+1})$$

$$-(Kh)_i(Z_{i+\frac{1}{2},n+1}-Z_{i-\frac{1}{2},n+1})$$

$$+(Kh)_{i+1}(Z_{i+\frac{3}{2},n}-Z_{i+\frac{1}{2},n})$$

$$-(Kh)_i(Z_{i+\frac{1}{2},n}-Z_{i-\frac{1}{2},n})\Big]$$

$$=r_R^2\phi\mu ch_{i+\frac{1}{2}}e^{-2i\Delta u}(Z_{i+\frac{1}{2},n+1}-Z_{i+\frac{1}{2},n}) \quad . \quad (7)$$

which is the general expression for any point within the aquifer.

The boundary condition defined by Eq. 3 (the outer boundary) is satisfied if either the permeability (K) or thickness (h) is zero. For convenience, let the permeability K be zero. Thus,

$$K_o=0 \quad . \quad (8)$$

Eq. 4 is approximated in difference form at the point $u_{j+\frac{1}{2},\ n+\frac{1}{2}}$. Thus,

$$\left(\frac{\partial Z}{\partial u}\right)_{j+\frac{1}{2},n+\frac{1}{2}}\approx$$

$$\frac{Z_{j+\frac{1}{2},n+1}-Z_{j-\frac{1}{2},n+1}+Z_{j+\frac{1}{2},n}-Z_{j-\frac{1}{2},n}}{2\Delta u},$$

$$\left(\frac{\partial V(t)}{\partial t}\right)_{j+\frac{1}{2},n+\frac{1}{2}}\approx\frac{V(t)_{n+1}-V(t)_n}{\Delta t},$$

and

$$\left(\frac{\partial E(t)}{\partial t}\right)_{j+\frac{1}{2},n+\frac{1}{2}}\approx\frac{E(t)_{n+1}-E(t)_n}{\Delta t}.$$

Substituting these approximations into Eq. 4 yields

$$V(t)_{n+1}-V(t)_n-E(t)_{n+1}+E(t)_n=$$

$$\frac{(P_o-P_m)\pi\Delta t}{\mu\Delta u}(Kh)_j$$

$$(Z_{j+\frac{1}{2},n+1}-Z_{j-\frac{1}{2},n+1}+Z_{j+\frac{1}{2},n}-Z_{j-\frac{1}{2},n}) \quad . \quad (9)$$

The left-hand member of Eq. 9 can be expressed in terms of the modified Schilthuis material balance.

It is remembered that, during a given time interval,

Δ Voidage $-$ Δ Expansion $=$ Δ Influx.

Now expressing this equation in terms of cumulative oil (Δn), gas (Δg) and water (Z) production with their respective compressibility factors, the expansion of the interstitial water (W) and the original in-place oil (N) and free-gas (G) values, we have for the time period between n and $n+1$

$$\left[\Delta nU_z+(\Delta g-\Delta nr_o)V_z+Z\left[1-(P_o-Z(P_o-P_m))c_w\right]\right]_{n+1}$$

$$-\left[\Delta nU_z+(\Delta g-\Delta nr_o)V_z+Z\left[1-(P_o-Z(P_o-P_m))c_w\right]\right]_n$$

$$-\left[N(U_z-U_o)+G(V_z-V_o)+Wc_wZ(P_o-P_m)\right]_{n+1}$$

$$+\left[N(U_z-U_o)+G(V_z-V_o)+Wc_wZ(P_o-P_m)\right]_n=\Delta\text{ Influx},$$

where U and V are the compressibility factors for the oil and gas, respectively, and are expressed as a function of the dimensionless pressure Z and where r_o is the original solution GOR.

Thus, Eq. 9 expressed in terms of the modified Schilthuis material balance becomes

$$\left[\Delta nU_z+(\Delta g-\Delta nr_o)V_z+Z\left[1-(P_o-Z(P_o-P_m))c_w\right]\right.$$

$$\left.-N(U_z-U_o)-G(V_z-V_o)-Wc_wZ(P_o-P_m)\right]_{n+1}$$

$$-\left[\Delta nU_z+(\Delta g-\Delta nr_o)V_z+Z\left[1-(P_o-Z(P_o-P_m))c_w\right]\right.$$

$$\left.-N(U_z-U_o)-G(V_z-V_o)-Wc_wZ(P_o-P_m)\right]_n$$

$$=\frac{(P_o-P_m)\Delta t\,\pi}{\mu\Delta u}(Kh)_j$$

$$(Z_{j+\frac{1}{2},n+1}-Z_{j-\frac{1}{2},n+1}+Z_{j+\frac{1}{2},n}-Z_{j-\frac{1}{2},n})$$

. . . . . (10)

The system defined by Eq. 7, 8 and 10 can be expressed in the following form if terms are rearranged.

$$B_oZ_{\frac{1}{2},n+1}+C_oZ_{\frac{3}{2},n+1}=D_{o,n}$$

$$A_1Z_{\frac{1}{2},n+1}+B_1Z_{\frac{3}{2},n+1}+C_1Z_{\frac{5}{2},n+1}=D_{1,n}$$

$$A_iZ_{i-\frac{1}{2},n+1}+B_iZ_{i+\frac{1}{2},n+1}+C_iZ_{i+\frac{3}{2},n+1}=D_{i,n}$$

$$A_jZ_{j-\frac{1}{2},n+1}+B_jZ_{j+\frac{1}{2},n+1}=D_{j,n}$$

. . . . . (11)

where for any value of $i \neq j$ and $n = 0,1,2, \ldots,$

$$A_i = \frac{I\Delta t}{(\Delta u)^2}(Kh)_i$$

$$B_i = -\frac{I\Delta t}{(\Delta u)^2}\left((Kh)_{i+1} + (Kh)_i\right) - Jr_R^2 \phi uch_{i+\frac{1}{2}} e^{-2i\Delta u}.$$

$$C_i = \frac{I\Delta t}{(\Delta u)^2}(Kh)_{i+1} = A_{i+1},$$

$$D_{i,n} = -Jr_R^2 \phi uch_{i+\frac{1}{2}} e^{-2i\Delta u} Z_{i+\frac{1}{2},n} + \frac{I\Delta t}{(\Delta u)^2}(Kh)_i (Z_{i+\frac{1}{2},n} - Z_{i-\frac{1}{2},n}) - \frac{I\Delta t}{(\Delta u)^2}(Kh)_{i+1}(Z_{i+\frac{3}{2},n} - Z_{i+\frac{1}{2},n}),$$

and for $i = j$ (the inner boundary) and $n = 0,1,2, \ldots.$

$$A_j = \frac{L\Delta t}{\mu \Delta u}(Kh)_j,$$

$$B_j = -\frac{L\Delta t}{\mu \Delta u}(Kh)_j = -A_j,$$

$$D_{j,n} = \frac{M}{P_o - P_m}\left[(NU_z + GV_z)_{n+1} - (NU_z + GV_z)_n + Wc_w(P_o - P_m)(Z_{j+\frac{1}{2},n+1} - Z_{j+\frac{1}{2},n}) - \left[\Delta n U_z + (\Delta g - \Delta n r_o)V_z + Z\left\{1 - (P_o - Z_{j+\frac{1}{2}}(P_o - P_m))c_w\right\}\right]_{n+1} + \left[\Delta n U_z + (\Delta g - \Delta n r_o)V_z + Z\left\{1 - (P_o - Z_{j+\frac{1}{2}}(P_o - P_m))c_w\right\}\right]_n\right] + \frac{L\Delta t}{\mu \Delta u}(Kh)_j (Z_{j+\frac{1}{2},n} - Z_{j-\frac{1}{2},n}).$$

It should be noted that $h_{i+\frac{1}{2}}$ is the average formation thickness of the segment lying between i and $i+1$. In B_i, thus $h_{i+\frac{1}{2}}$ is equivalent to the value of h in the term $(Kh)_{i+1}$. The constants I, J, L and M are unit conversion constants for converting practical oilfield units to the demanded "cgs" system. Thus,

$$I = 1.3167 \times 10^6,$$

$$J = 4.1626 \times 10^5,$$

$$L = 8.2733 \times 10^6,$$

and

$$M = 2.3372 \times 10^6,$$

SOLUTION TO THE SYSTEM OF DIFFERENCE EQUATIONS

The system of equations as defined by Eq. 11 now contains coefficients which can be determined through use of practical oilfield units. Also notice that the system of equations is of the form of a tridiagonal matrix which is readily adaptable to machine computations. Gaussian elimination can be used to obtain the solution to the system of equations.[5] Referring to Eq. 11, let

$$B_o' = B_o$$

$$B_i' = B_i - A_i/C_{i-1}', \qquad 1 \leq i \leq j \quad \ldots\ldots \quad (12)$$

$$C_i' = C_i/B_i, \qquad 0 \leq i \leq j-1 \quad \ldots \quad (13)$$

and

$$D_{o,n+1}' = (D_{o,n})/B_o'$$

$$D_{i,n+1}' = (D_{i,n} - A_i D_{i-1,n+1}')/B_i', \qquad 1 \leq i \leq j \quad \ldots\ldots\ldots \quad (14)$$

The solution is

$$Z_{j+\frac{1}{2},n+1} = D_{j,n+1}' \quad \ldots\ldots\ldots \quad (15)$$

$$Z_{i+\frac{1}{2},n+1} = D_{i,n+1}' - C_i' Z_{i+\frac{3}{2},n+1}, \qquad 0 \leq i \leq j-1 \quad \ldots\ldots\ldots \quad (16)$$

Then in machine computations, B', C', and D' are calculated in order of increasing i (the forward solution), and z is calculated in order of decreasing i (the backward solution). The solutions to Eq. 12 and 13 are independent of time and remain fixed for a given set of aquifer parameter values, but Eqs. 14, 15 and 16 have to be solved at the end of every time period (n). Thus, a part of the forward solution need be performed only once for a complete history with a given set of aquifer parameters.

In applying this scheme to Eq. 11, an iterative

process is required at the end of the forward solution before the backward solution is performed. If the definition of $D_{j,n}$ is referred to, it can be seen that voidage and expansion terms are indicated involving U_z and V_z at the end of time period $(n+1)$. As can be seen from Eqs. 14 and 15, $D_{j,n}$ is required for calculating $Z_{j+\frac{1}{2},n+1}$, the dimensionless pressure of the reservoir at time $(n+1)$. This necessitates the use of an iterative process in which the difference between an assumed value of $Z_{j+\frac{1}{2},n+1}$ in $D_{j,n}$ and the value of $Z_{j+\frac{1}{2},n+1}$ as determined from Eq. 15 satisfies a specified criterion.

An iteration that will accomplish the required covergence can be performed by first assuming a starting value of $Z_{j+\frac{1}{2},n+1}$ from the equation,

$$Z_{j+\frac{1}{2},n+1} = 2Z_{j+\frac{1}{2},n} - Z_{j+\frac{1}{2},n-1} \quad \ldots \ldots \quad (17)$$

Using the value of $Z_{j+\frac{1}{2},n+1}$ (designated as Z_1) thus determined, $D_{j,n+1}$ (designated as D_1') is calculated using Eqs. 14 and 15. The second assumed value of $Z_{j+\frac{1}{2},n+1}$ (designated as Z_2) is obtained by averaging Z_1 and D_1'. The resultant Z_2 is used to calculate a second value of $D'_{j,n+1}$ (designated D_2'). These four values define two points on a rectangular co-ordinate system in which Z is the independent variable and D' is the dependent variable. A third value of $Z_{j+\frac{1}{2},n+1}$ (designated as Z'') is obtained from the equation

$$Z'' = \frac{Z_1 D_2' - Z_2 D_1'}{D_2' - D_1' - Z_2 + Z_1} \quad \ldots \ldots \quad (18)$$

Using Z'', a third value of $D'_{j,n+1}$ (designated as D'') is calculated from Eq. 14. Then if Z'' agrees with D'' within a specified accuracy, the backward solution is obtained by solving Eq. 16 in decreasing order of i. If the criterion is not satisfied, then Z'' is inserted into Eq. 18 for Z_2 and D'' for D_2' and Z''' is resolved holding Z_1 and D_1' fixed. Z''' is used in Eq. 14 to determine D'''. If Z''' and D''' do not satisfy the criterion, the process is repeated. Ordinarily, satisfactory convergence can be obtained with less than 10 iterations.

MACHINE PROCEDURE FOR OPTIMIZING AQUIFER PARAMETERS

A method, which is readily adaptable to machine computations, has been described in which the pressure distribution in the aquifer and the pressure within the reservoir can be calculated with a given set of production figures, fluid and gas compressibility factors, and aquifer parameters. If the assumed values of the aquifer parameters are incorrect, then the calculated reservoir pressures as provided by this method would not match the actual measured reservoir pressures.

Then the problem of designing a procedure for a medium-sized digital computer, in addition to being centered around inverting the matrix defined by Eq. 11 and the iterative process at the inner boundary, is primarily concerned with devising a means of varying the aquifer parameters (permeability K and formation thickness h) for each aquifer segment such that the proper values can be chosen. The criterion for measuring the goodness of the K and h values is the degree to which the calculated reservoir pressures match the actual measured reservoir pressures. Then, for a given set of K's and h's, the performance can be calculated and the deviation from measured pressures can be expressed by $\sum_{n=1}^{n} d_n^2$. The value of h for the inner aquifer can be varied, a history calculated and a second Σd^2 obtained. In the same manner, a third Σd^2 can be obtained. Thus, three values of h and corresponding Σd^2 are obtained. Treating Σd^2 as the dependent variable, a second-order polynomial can be fitted to these points and an improved value of h can be obtained by finding the minimum of this polynomial. This optimized value is then substituted for the original h, and the remaining K's and h's are optimized sequentially in the same manner until the outer boundary is reached. Then the entire calculation from inner to outer boundary is repeated until the goodness of fit is not improved or no change is indicated in the K and h values. At this point, the aquifer is adequately defined.

The sequence of calculations performed by a medium-sized computer to accomplish the foregoing adheres to the following procedure.

1. Perform calculations with data in which results are completely independent of time or the aquifer parameters K and h.

2. Perform calculations for determining the coefficients of Eq. 11 using an assumed set of K's and h's.

3. Calculate B''s, C''s and partial D''s. Thus, that part of the forward solution to the matrix inversion which is independent of time is calculated and does not need to be repeated for a given set of K's and h's.

4. Solve Eq. 15 for a given time (n) using the iterative process described previously. This completes the forward solution to the matrix inversion and yields as a result the dimensionless reservoir pressure $Z_{j+\frac{1}{2}}$.

5. Before performing the backward solution to the matrix inversion, $Z_{j+\frac{1}{2}}$ is converted to pressure in pounds per square inch and compared to the measured pressure. The difference (d) is determined, squared, added to the previous Σd^2 and stored.

6. The backward solution is next performed by solving Eq. 16 and yields as a result the dimensionless pressure for each aquifer segment. These values are stored for use in the calculation of the D_i's of Eq. 11 for the next time step.

7. The time (n) is increased by one, and Steps 4, 5 and 6 are repeated. This repetition is continued until a history has been calculated.

8. With the completion of a history, the Σd^2 formed in Step 5 (designated Σd_o^2) is stored along

with the value of h used for the inner or jth aquifer segment (designated as object parameter zero, or $O.P._0$).

9. The value of h for the inner or jth segment is modified and, using the previously assumed values of K's and h's for the remaining aquifer segments, Steps 2 through 7 are repeated.

10. The Σd^2 formed in Step 5, now designated as Σd_1^2, is stored along with the modified value of h from Step 9, now designated as $O.P._1$.

11. The value of h is again modified and steps 2 through 7 are again repeated.

12. The Σd^2 formed in Step 5, now designated as Σd_2^2, is stored along with the corresponding value of h ($O.P._2$).

13. With the completion of Step 12, three sets of of values (Σd_0^2, $O.P._0$; Σd_1^2, $O.P._1$; Σd_2^2, $O.P._2$) are formed. A second-order polynomial with the $O.P.$ being the independent variable is fit through these points.

14. Having obtained the polynomial, the first derivative is obtained and set equal to zero, and the optimum value of the $O.P.$ is obtained.

15. This optimum value is used as another modified value of h ($O.P._3$). Another history is calculated (Steps 2 through 7) and the resulting Σd^2 is stored with the extrapolated value of h as (Σd_3^2, $O.P._3$).

16. $O.P._0$, $O.P._1$, $O.P._2$ and $O.P._3$ are compared, and the one having the lowest value of Σd^2 is inserted as the best value of h into the set of K's and h's for the aquifer segments. The Σd^2's and corresponding $O.P.$'s are typed out along with the set of K's and h's.

17. Next, the K of the (j-1)th segment is chosen as the object parameter and Steps 2 through 16 are repeated.

18. The h of the (j-1)th segment next is chosen as the object parameter and Steps 2 through 16 are repeated.

19. This process is repeated using K's and h's alternately as the object parameter and moving out to the next aquifer segment after each pair until the outer segment is reached.

20. After the K and h of the outer segment is optimized, another complete history is calculated. In calculating this history, results other than pressures are obtained. The cumulative expansion of the interstitial or bottom water, the cumulative water influx, incremental water influx, water-influx rate (all in practical units), gas-cap expansion as a per cent of original gas-cap volume, the calculated reservoir pressures, the difference between the calculated and measured reservoir pressures and, after the last time period, the Σd^2 and the standard pressure deviation in pounds per square inch are typed out.

21. After the type-out, calculations are again started at the inner boundary, and Steps 2 through 20 are repeated. If the values of K and h do not change, the aquifer is considered to be adequately defined. If the values of K and h do change, calculations are again started at the inner boundary with another repetition of Steps 2 through 20. This process is repeated until there is no change in the values of K and h.

Predictions have not been mentioned in the preceding outline. However, in Step 20, with given production information, predictions are automatically made after the history calculations. The type-out format is the same with the exception that there are no measured pressures and, therefore, no pressure difference. Each time Step 20 is reached, therefore, a type-out is obtained containing both history and predictions.

NOMENCLATURE

Z = dimensionless pressure function defined by $Z = \frac{P_o - P}{P_o - P_m}$, where P_o is the original pressure in psi, P is the pressure at a given time, and P_m is the lowest pressure that is expected to be encountered[4]

i = number of the boundary separating the aquifer segments. $i = j$ at the inner boundary or boundary between the oil zone and the inner aquifer segment (the original oil-water contact). The value of i varies from zero at the outer boundary to a value of 5 at inner boundary for a five-segment aquifer and to a value of 10 for a 10-segment aquifer.

n = number designating a particular time period

Δt = time period in days. All Δt's must be equal in length. Δt is obtained by taking the total time in question (history plus predictions) in days and dividing by the number of time periods (n) desired.

Δu = dimensionless length of an aquifer segment. Δu is a logrithmic function defined by the $\ln\left(\frac{r_R}{r_w}\right)$ divided by the number of desired aquifer segments.

r_R = radius of the aquifer, ft

r_w = radius of the reservoir, ft

ϕ = fractional porosity of the reservoir. For practical purposes, it is assumed that the reservoir formation porosity also prevails in the aquifer formation

μ = viscosity of salt water at the prevailing pressure and temperature, cp

c = compressibility of salt water, psi^{-1}. If rock compressibility is a factor, it is included in this term

c_w = compressibility of salt water only, psi^{-1}

K_{i+1} = average permeability, darcies, of the aquifer segment lying between i and $i+1$

h_{i+1} = average thickness of the aquifer segment, ft, lying between i and $i + 1$

N = original in-place oil, STB

G = original gas-cap volume, Mcf

W = original interstitial or bottom-water volume, bbl

Δn = cumulative oil production at the end of a given time period, STB

Δg = cumulative gas production at the end of a given time period, Mcf

Z = cumulative water production at the end of a given time period, bbl

r_o = original solution GOR, Mcf/STB

U_z = two-phase formation volume factor for oil, defined as the reservoir space occupied by 1 STB of oil and the solution gas originally associated with it at any given pressure Z, reservoir bbl/STB

V_z = formation volume factor for gas, defined as the reservoir space occupied by 1 Mcf of gas at any given pressure defined by Z, reservoir bbl/Mcf

REFERENCES

1. Bruce, W. A.: "An Electrical Device for Analyzing Oil Reservoir Behavior", *Trans.*, AIME (1943) Vol. 151, 112.
2. Patterson, O. L., Montague, K. E. and Wiess, Byron, Jr.: "High-Speed Electronic Reservoir Analyzer", *Drill. and Prod. Prac.*, API (1951) 47.
3. Patterson, O. L., Dutton, Granville and Ellis, H. E.: "The Determination of the Water Injection Program for the Delhi Field by means of the Automatic Multipool Analyzer", *Trans.*, AIME (1956) Vol. 207, 73.
4. Rachford, H. H., Jr., Taylor, R. D., Douglas, Jim, Jr. and Dyke, P. M.: "Applications of Numerical Methods to Predict Recovery from Thin Oil Columns", *Trans.*, AIME (1958) Vol. 213, 193.
5. Bruce, G. H., Peaceman, D. W., Rachford, H. H., Jr. and Rice, J. D.: "Calculations of Unsteady-State Gas Flow through Porous Media", *Trans.*, AIME (1953) Vol. 198, 79.
6. Balch, Sinclair and Dutton, Granville: "Report on the Electronic Analysis of the Main Conroe Sand", Sun Oil Co., Production Dept., Gulf Coast Div. (Aug., 1950).
7. Summary of Testimony Presented by Humble Oil & Refining Co., at Railroad Commission of Texas MER Hearing on the Main Conroe Sand (Dec. 14, 1949).
8. Miller, G. B. and Harley, R. K.: "Technical Report No. 58-3R, Analysis of Reservoirs by Analog Computation", The Ohio Oil Co., Denver Research Center (Feb., 1958).

APPENDIX

TEST PROBLEM – MAIN CONROE RESERVOIR, CONROE FIELD, TEX.

The Main Conroe reservoir was chosen as a test problem because: (1) reliable data were available; (2) the producing mechanism is a combination gas-cap and water-drive system; and (3) the results obtained from the calculations can be compared with those obtained from Sun's Single-Pool Electronic Reservoir Analyzer, the Bruce Reservoir Analyzer and Ohio Oil Co.'s Pace General Purpose Analogue Computer.[6-8]

BASIC ASSUMPTIONS AND DATA

The basic assumptions used in the Conroe analysis are listed in Table 1.

TABLE 1 – BASIC ASSUMPTIONS USED FOR TEST PROBLEM ANALYSIS, MAIN CONROE RESERVOIR CONROE FIELD, TEX.

Original In-Place Oil	801,440,000 STB
Original Gas-Cap Volume	336,980,000 Mcf
Original Solution Gas-Oil Ratio	600 cu ft/STB
Original Oil Formation Volume Factor	1.2050 res bbl/STB
Original Gas Formation Volume Factor	1.1870 res bbl/Mcf
Interstitial Water	20,000,000 bbl
Original Pressure at Datum	2,180 psia
Average Gross Sand Thickness	200 ft
Sand Porosity (ϕ)	.28
Reservoir Radius r_w (as cal. for radial case)	6,600 ft
Aquifer Radius r_R ($r_R/r_w = 40$)	264,000 ft
Permeability (K)	265 md
Water Compressibility	3.4×10^{-6} psi^{-1}
Water Compressibility plus Formation Compressibility (C)	6.8×10^{-6} psi^{-1}
Water Viscosity (μ)	.38 cp
Time Increment (Δt)	182.5 days

The original pressure as indicated by measured pressures on Fig. 1 was 2,250 psia. However, the analyses performed on both Sun's single-pool analyzer and Ohio Oil Co.'s analogue computer indicated that the original pressure should be 2,180 psia. Therefore, for this analysis the original pressure of 2,180 psia was used.

The analysis performed by the Ohio Oil Co. encompassed the Conroe performance only through Jan. 1, 1952. Thus, the history involved in this analysis goes only to Jan. 1, 1952. Then for the convenience of calculations, initial production was assumed to have occurred on Jan. 1, 1932, and a time increment or period of 182.5 days (six months) was used. The production and pressure statistics based on time intervals of 182.5 days are presented in Table 2. The pressures, as presented in Table 2, are interpolated values obtained by plotting the measured pressures and using straight-line interpolation between pressure points. The measured pressures are plotted on Figs. 1 and 2. The PVT data are presented in Table 3 where both U and V are expressed as functions of pressure (pounds per square inch absolute) and the dimensionless pressure function Z.

APPROACH

The actual analysis was performed in two parts. The first part was designed to test the predictive powers of the numerical method. Thus, a part of the past performance was used as "history" and the remaining portion was used as "future". In this way a match to the history could be obtained, predictions made using the actual production, and then a comparison of the predicted pressures and the measured pressures could be made. The division of the performance into history and future was the same as that in the analysis performed by Ohio Oil Co. on the Pace General Purpose Analogue Computer. Time previous to Jan. 1, 1943, was used as history, and subsequent time through Jan. 1, 1952, was used as future. Thus, the predicted pressures not only could be compared with measured pressures, but they also could be compared with the predictions made by Ohio. The aim of the second part of the

TABLE 2 – MAIN CONROE RESERVOIR PRODUCTION AND PRESSURE STATISTICS

Date	Press. (psia)	Cum. Oil Prod. (STB)	Cum. Water Prod. (bbl)	Cum. Water Inj. (bbl)	Net Cum. Water Prod. (bbl)	Cum. Gas Prod. (Mcf)
1-1-32	2180	0	0	0	0	0
7-1-32	2177	1,341,096	0	0	0	3,332,412
1-1-33	2170	2,681,691	0	0	0	6,412,824
7-1-33	2148	9,784,770	0	0	0	14,900,678
1-1-34	2125	23,440,301	0	0	0	24,295,374
7-1-34	2110	32,325,186	0	0	0	30,585,954
1-1-35	2103	39,819,896	71,470	0	71,470	35,940,966
7-1-35	2105	47,414,017	143,243	0	143,243	41,313,677
1-1-36	2096	54,185,666	188,180	0	188,180	46,221,132
7-1-36	2089	61,129,694	346,001	0	346,001	50,923,634
1-1-37	2086	67,378,129	621,511	0	621,511	54,994,547
7-1-37	2071	74,007,965	1,237,936	0	1,237,936	59,843,930
1-1-38	2070	80,288,085	1,955,796	0	1,955,796	64,227,103
7-1-38	2077	85,420,752	2,540,916	0	2,540,916	67,579,098
1-1-39	2081	89,939,817	3,075,559	0	3,075,559	70,413,230
7-1-39	2084	94,079,034	3,637,095	0	3,637,095	72,842,724
1-1-40	2088	97,807,353	4,233,114	0	4,233,114	75,044,349
7-1-40	2088	101,842,090	5,316,796	0	5,316,796	77,298,214
1-1-41	2086	105,976,912	6,667,947	0	6,667,947	79,689,996
7-1-41	2083	110,693,569	8,243,152	0	8,243,152	82,349,469
1-1-42	2075	116,325,407	10,303,045	0	10,303,045	85,469,153
7-1-42	2067	121,994,709	12,259,760	0	12,259,760	88,685,435
1-1-43	2058	128,616,349	14,457,438	0	14,457,438	92,402,515
7-1-43	2048	136,611,380	17,423,141	0	17,423,141	96,737,481
1-1-44	2029	147,542,601	21,984,941	0	21,984,941	102,403,644
7-1-44	2005	158,657,723	27,417,511	0	27,417,511	108,565,599
1-1-45	2003	169,849,367	32,471,516	0	32,471,516	115,162,979
7-1-45	1988	180,887,165	37,984,397	0	37,984,397	121,797,080
1-1-46	1976	190,411,918	43,371,194	425,740	42,945,454	128,037,651
7-1-46	1963	199,922,874	49,642,250	1,726,335	47,915,915	134,159,643
1-1-47	1952	210,459,721	56,024,549	3,162,063	52,862,486	141,180,021
7-1-47	1944	220,774,533	62,864,018	4,808,602	58,055,416	147,509,416
1-1-48	1936	231,740,016	71,001,152	6,804,763	64,196,389	154,771,643
7-1-48	1917	242,437,265	80,637,545	9,150,546	71,486,999	161,803,778
1-1-49	1918	251,569,049	89,510,757	11,423,390	78,087,367	167,936,891
7-1-49	1919	257,592,185	96,020,745	13,179,242	82,841,503	171,741,098
1-1-50	1926	262,732,935	103,025,693	14,909,110	88,116,583	175,136,593
7-1-50	1924	267,885,501	110,850,275	16,636,036	94,214,239	178,653,325
1-1-51	1920	274,225,279	120,710,305	18,929,656	101,780,649	183,040,036
7-1-51	1903	280,900,564	131,513,601	21,179,343	110,334,258	187,932,039
1-1-52	1900	287,877,554	142,354,003	23,522,371	118,831,632	193,361,197

analysis was to obtain an over-all match of the history through Jan. 1, 1952. These results then could be compared with those obtained by the Bruce Analyzer and Sun's single-pool analyzer.

RESULTS

The results of the first part of the analysis are indicated on Table 4. On Fig. 1 are presented the history pressure match with predictions as calculated the numerical method, the history pressure match and predictions made by the Ohio analogue computer and the actual measured pressures through Jan. 1, 1952. Table 5 is a comparison of the two matches.

The results obtained by the numerical method are very favorable when compared to that of the Ohio Oil Co.'s analogue computer. Notice that, even though the predictions calculated by the numerical method are consistently high (the maximum pressure difference of 19.8 psi is attained on July 1, 1948), the character of the predicted pressure decline is similar to that of the measured pressure decline; at the end of the predictions (Jan. 1, 1952, nine years of predictions), the calculated pressure is only 13.6-psi high.

The second part of the Conroe analysis was performed by matching the history through Jan. 1, 1952. The results obtained from the performance calculations are indicated on Table 4a. The calculated pressures are shown on Fig. 2 along with the measured pressures, the pressure match obtained by Sun's single-pool analyzer, and the pressure

TABLE 3 – MAIN CONROE RESERVOIR FLUID PVT DATA

Pressure (psia)	Z^*	V (res bbl/Mcf)	U (res bbl/Mcf)
2180	0	1.1870	1.2050
2164	.039474	1.1970	1.2080
2115	.17105	1.2260	1.2180
2065	.30263	1.2560	1.2290
2015	.43421	1.2890	1.2400
1965	.56579	1.3220	1.2530
1915	.69737	1.3580	1.2660
1865	.82895	1.3950	1.2800
1815	.96053	1.4350	1.2950
1765	1.0921	1.4750	1.3100
1715	1.2237	1.5170	1.3270
1665	1.3553	1.5650	1.3460
1615	1.4868	1.6220	1.3660

*$Z = \frac{P_o - P}{P_o - P_m}$ where P_m is the lowest pressure value expected to be encountered (P_m = 1,800 psia).

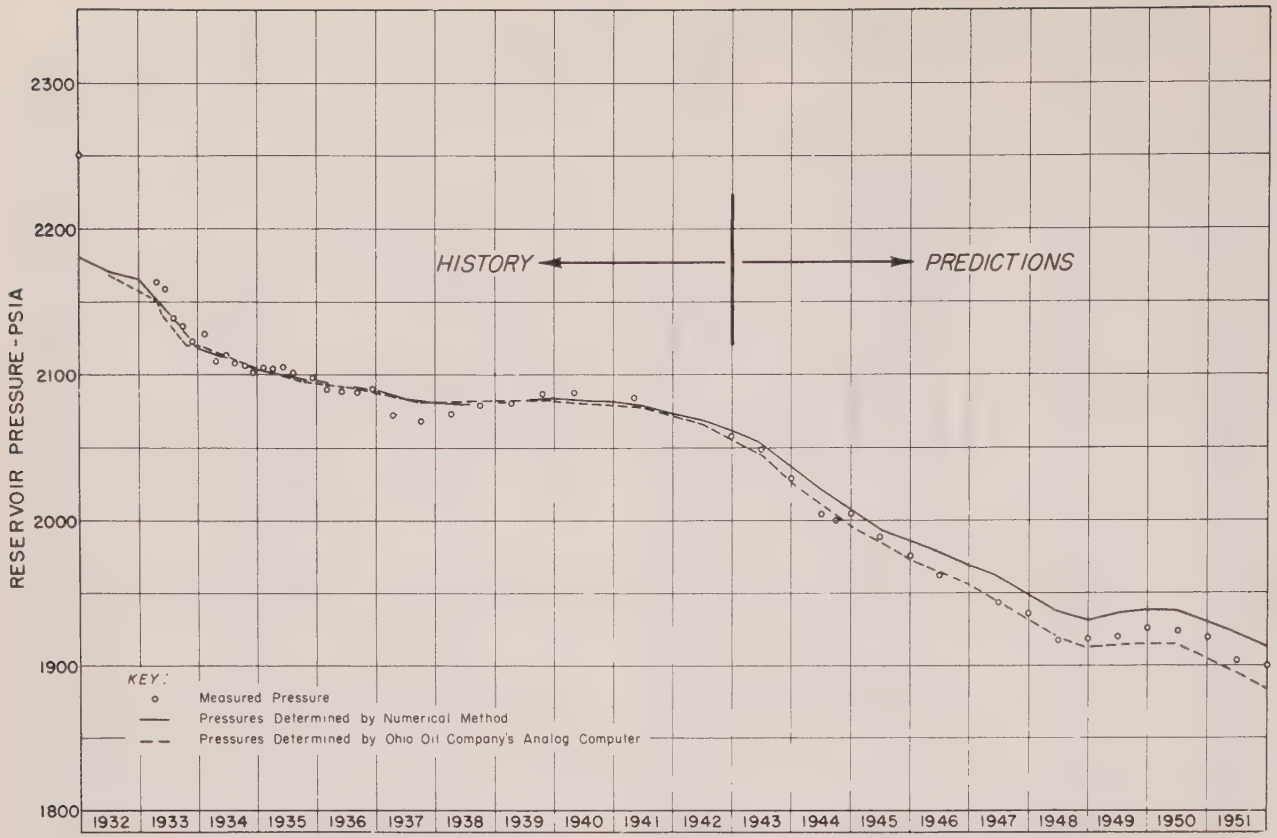

FIG. 1 – MAIN CONROE RESERVOIR PRESSURE DECLINE, CONROE FIELD, TEX.

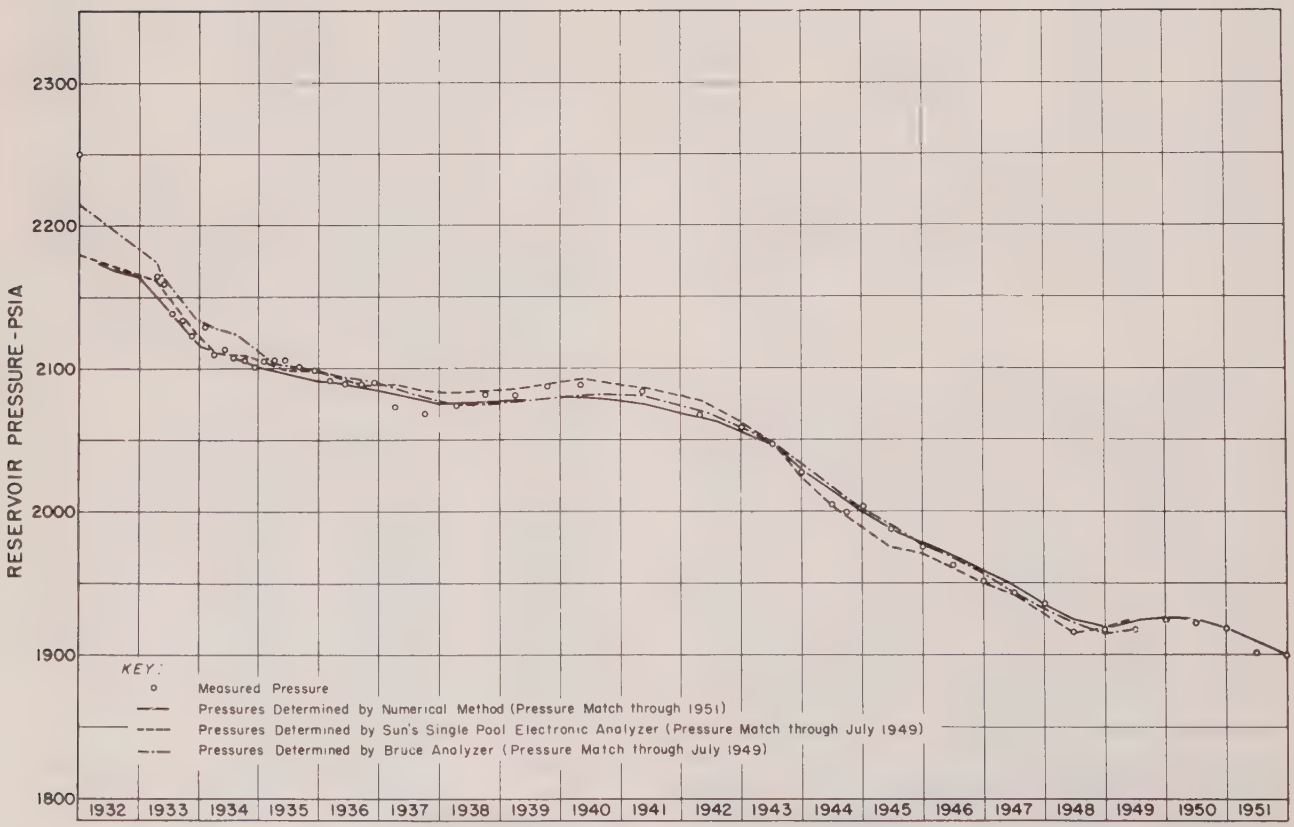
RESERVOIR PRESSURE - PSIA
2300
2200
2100
2000
1900
1800
KEY:
Measured Pressure
Pressures Determined by Numerical Method (Pressure Match through 1951)
Pressures Determined by Sun's Single Pool Electronic Analyzer (Pressure Match through July 1949)
Pressures Determined by Bruce Analyzer (Pressure Match through July 1949)
1932 1933 1934 1935 1936 1937 1938 1939 1940 1941 1942 1943 1944 1945 1946 1947 1948 1949 1950 1951

FIG. 2 – MAIN CONROE RESERVOIR PRESSURE DECLINE, CONROE FIELD, TEX.

match obtained by the Bruce Analyzer. The matches obtained by both Sun's analyzer and the Bruce Analyzer go only through July, 1949. Table 6 is a comparison of the three matches.

Notice that the match obtained by the Bruce Analyzer (Fig. 2) indicates an original pressure of 2,215 psi. Then the figures quoted in Table 6 for the Bruce Analyzer do not pertain to the match previous to April 20, 1933. The character of the pressure decline, as determined by the numerical Method, is similar in nature to that of the measured pressures and matches the pressure at the end of history, Jan. 1, 1952. Comparatively speaking, the results as determined by the numerical method are in excellent agreement with those as obtained by analogue devices.

TIME REQUIREMENTS

Heretofore, the time requirements for a numerical solution to the unsteady-state reservoir performance problem was considered to be prohibitive due to the number of b and K combinations in a 10-segment aquifer that would have to be tried before a "fit" or "match" to the known pressure decline could be obtained. However, the procedure resolved for optimizing the aquifer parameters reduced the time requirements to within the realm of practicality for a medium-size drum computer. In essence, the analysis of the performance of a reservoir requires (1) the loading of data and the program on the computer memory drum, (2) going through the manual portion of the procedure, (3) putting the computer on the automatic mode of calculations and (4) returning after approximately 24 to 36 hours of unattended computer operation to find the final results typed out.

The computing time requirements for a given problem (using the Bendix G-15 digital computer) can be roughly determined by the fact that an average of approximately 40 seconds is required for all the calculations about one history point or time period. Then if 10 aquifer segments are to be used, a total of 60 histories will be calculated in optimizing the

TABLE 4 – MAIN CONROE RESERVOIR PERFORMANCE CALCULATION RESULTS

Date	Cum. Exp. Interst. Water (bbl)	Cum. Influx (10^6 res bbl)	Inc. Influx (10^6 res bbl)	Influx Rate (res B/D)	Gas-Cap Exp. (% of Orig. Vol.)	Calc. Press. (psia)	Meas. Press. (psia)	Press. Diff.
1-1-32	0	0	0	0	100.00	2180.0	2180	0
7-1-32	603	1.409	1.409	7721	99.70	2171.1	2177	−5.9
1-1-33	972	3.961	2.552	13983	99.26	2165.7	2170	−4.3
7-1-33	2585	9.599	5.638	30894	99.08	2142.0	2148	−6.0
1-1-34	4195	19.286	9.687	53080	99.85	2118.3	2125	−6.7
7-1-34	4711	28.543	9.257	50723	99.93	2110.7	2110	.7
1-1-35	5099	36.743	8.200	44933	99.95	2105.0	2103	2.0
7-1-35	5493	44.980	8.237	45135	99.99	2099.2	2105	−5.8
1-1-36	5744	52.994	8.014	43911	99.92	2095.5	2096	− .5
7-1-36	6016	60.848	7.854	43036	99.95	2091.5	2089	2.5
1-1-37	6153	68.430	7.582	41544	99.95	2089.5	2086	3.5
7-1-37	6531	76.216	7.787	42666	99.96	2084.0	2071	13.0
1-1-38	6755	84.189	7.973	43687	99.94	2080.7	2070	10.7
7-1-38	6754	91.406	7.217	39546	99.86	2080.7	2077	3.7
1-1-39	6699	97.927	6.521	35731	99.78	2081.5	2081	.5
7-1-39	6619	103.920	5.992	32835	99.73	2082.7	2084	−1.3
1-1-40	6535	109.480	5.558	30456	99.68	2083.9	2088	−4.1
7-1-40	6590	115.000	5.526	30277	99.77	2083.1	2088	−4.9
1-1-41	6700	120.730	5.726	31376	99.88	2081.5	2086	−4.5
7-1-41	6911	126.760	6.027	33026	100.09	2078.4	2083	−4.6
1-1-42	7277	133.460	6.701	36718	100.45	2073.0	2075	−2.0
7-1-42	7570	140.590	7.127	39052	100.73	2068.7	2067	1.7
1-1-43	8012	148.250	7.662	41981	101.15	2062.2	2058	4.2
Unweighted Σd^2 = 596.95			Standard Deviation = ±5.21 psi				Weighted Σd^2 = 240.69	
				Predictions				
7-1-43	8647	157.060	8.813	48288	101.79	2052.8		
1-1-44	9756	167.970	10.910	59779	102.94	2036.5		
7-1-44	10804	180.790	12.825	70272	103.93	2021.1		
1-1-45	11724	194.510	13.713	75142	104.71	2007.6		
7-1-45	12589	209.000	14.490	79395	105.41	1994.9		
1-1-46	13132	223.510	14.512	79519	105.68	1986.9		
7-1-46	13671	237.920	14.410	78957	105.99	1979.0		
1-1-47	14382	253.030	15.116	82829	106.35	1968.5		
7-1-47	14906	268.450	15.411	84445	106.73	1960.8		
1-1-48	15747	284.620	16.173	88620	107.21	1948.4		
7-1-48	16537	301.840	17.219	94348	107.67	1936.8		
1-1-49	16931	318.670	16.831	92227	107.77	1931.0		
7-1-49	16562	333.290	14.618	80097	107.40	1936.4		
1-1-50	16408	346.300	13.009	71282	107.17	1938.7		
7-1-50	16439	359.280	12.984	71147	107.05	1938.3		
1-1-51	16926	373.080	13.803	75630	107.26	1931.1		
7-1-51	17500	388.070	14.986	82116	107.44	1922.7		
1-1-52	18117	403.750	15.682	85926	107.54	1913.6		

TABLE 4a – MAIN CONROE RESERVOIR PERFORMANCE CALCULATION RESULTS

Date	Cum. Exp. Interst. Water (bbl)	Cum. Influx (10^6 res bbl)	Inc. Influx (10^6 res bbl)	Influx Rate (res B/D)	Gas-Cap Exp. (% of Orig. Vol.)	Calc. Press. (psia)	Meas. Press. (psia)	Press. Diff.
1-1-32	0	0	0	0	100.00	2180.0	2180	0
7-1-32	621	1.327	1.327	7272	99.71	2170.9	2177	–6.1
1-1-33	1012	3.764	2.437	13354	99.29	2165.1	2170	–4.9
7-1-33	2674	9.142	5.378	29469	99.14	2140.7	2148	–7.3
1-1-34	4359	18.416	9.273	50813	99.97	2115.9	2125	–9.1
7-1-34	4920	27.427	9.011	49376	100.08	2107.6	2110	–2.4
1-1-35	5328	35.514	8.088	44315	100.12	2101.6	2103	–1.4
7-1-35	5740	43.655	8.141	44607	100.17	2095.6	2105	–9.4
1-1-36	6005	51.593	7.938	43496	100.11	2091.7	2096	–4.3
7-1-36	6286	59.392	7.799	42733	100.15	2087.6	2089	–1.4
1-1-37	6432	66.931	7.539	41308	100.16	2085.4	2086	– .6
7-1-37	6820	74.660	7.729	42352	100.18	2079.7	2071	8.7
1-1-38	7057	82.563	7.903	43305	100.17	2076.2	2070	6.2
7-1-38	7060	89.766	7.203	39468	100.08	2076.2	2077	– .8
1-1-39	7004	96.299	6.533	35798	100.00	2077.0	2081	–4.0
7-1-39	6921	102.310	6.013	32948	99.96	2078.2	2084	–5.8
1-1-40	6835	107.890	5.579	30569	99.91	2079.5	2088	–8.5
7-1-40	6891	113.410	5.524	30266	100.00	2078.7	2088	–9.3
1-1-41	7006	119.110	5.698	31219	100.11	2077.0	2086	–9.0
7-1-41	7226	125.080	5.972	32723	100.33	2073.7	2083	–9.3
1-1-42	7609	131.690	6.611	36224	100.70	2068.1	2075	–6.9
7-1-42	7919	138.720	7.025	38491	101.00	2063.5	2067	–3.5
1-1-43	8381	146.270	7.547	41353	101.43	2056.7	2058	–1.3
7-1-43	9045	154.920	8.651	47401	102.10	2047.0	2048	–1.0
1-1-44	10197	165.560	10.648	58343	103.29	2030.0	2029	1.0
7-1-44	11297	178.080	12.513	68566	104.33	2013.9	2005	8.9
1-1-45	12265	191.520	13.439	73638	105.15	1999.6	2003	–3.4
7-1-45	13174	205.750	14.230	77970	105.89	1986.3	1988	–1.7
1-1-46	13754	220.060	14.311	78419	106.19	1977.7	1976	1.7
7-1-46	14322	234.310	14.250	78082	106.53	1969.4	1963	6.4
1-1-47	15066	249.240	14.936	81842	106.91	1958.4	1952	6.4
7-1-47	15620	264.490	15.245	83536	107.33	1950.3	1944	6.3
1-1-48	16496	280.470	15.985	87587	107.84	1937.4	1936	1.4
7-1-48	17325	297.470	16.997	93136	108.33	1925.2	1917	8.2
1-1-49	17748	314.150	16.680	91397	108.46	1919.0	1918	1.0
7-1-49	17385	328.780	14.625	80136	108.09	1924.3	1919	5.3
1-1-50	17224	341.850	13.076	71652	107.85	1926.7	1926	.7
7-1-50	17257	354.850	12.994	71198	107.74	1926.2	1924	2.2
1-1-51	17758	368.570	13.727	75215	107.96	1918.9	1920	–1.1
7-1-51	18359	383.410	14.834	81280	108.17	1910.0	1903	7.0
1-1-52	19008	398.920	15.511	84989	108.29	1900.5	1900	.5

Unweighted Σd^2 = 1240.64 Standard Deviation = ± 5.57 psi Weighted Σd^2 = 764.19

TABLE 5 – COMPARISON OF HISTORY PRESSURE MATCH AND PREDICTIONS, NUMERICAL METHOD VS OHIO OIL CO.'S ANALOGUE COMPUTER

	History Standard Deviation	Maximum Pressure Difference
Numerical Method	±5.21 psi	19.8 psi
Ohio's Analogue Computer	±6.63 psi	17.0 psi

TABLE 6 – COMPARISON OF PRESSURE MATCHES

	Standard Deviation	Maximum Pressure Difference
Numerical Method	±5.57 psi	9.4 psi
Sun's Single-Pool Electronic Reservoir Analyzer	±5.86 psi	17 psi
Bruce Analyzer	±8.34 psi	17 psi

aquifer parameters for one pass from the inner to the outer boundary of the aquifer. If all 40 points as provided for in the program are used in this history, then a total of 2,400 history points will be calculated, requiring a total of approximately 26 hours to attain one history type-out on the automatic mode of operation. (Each time the outer boundary is reached, a complete history and predictions are typed out.) Most problems would not need over five passes through the aquifer parameters; thus, a maximum time requirement normally would be in the neighborhood of 100 to 130 hours. This is an exaggerated number, and in most cases much less computing time would be required.

***

Mechanism of Alcohol Displacement of Oil from Porous Media

J. J. TABER
MEMBER AIME
I. S. K. KAMATH
JUNIOR MEMBER AIME
RONALD L. REED
MEMBER AIME

GULF RESEARCH & DEVELOPMENT CO.
PITTSBURGH, PA.

ABSTRACT

Alcohol floods of consolidated sandstone cores have shown the process to be strongly dependent on the phase behavior of the particular alcohol-oil-water system used. This means that in many cases the mechanism does not conform to the idea of a piston-like displacement. Instead, it is found that by changing the alcohol it is possible to change the relative velocities of the oil and water and, in fact, the entire mechanism of the process.

The effects of rate, viscosity, initial saturation, distance travelled and hysteresis of relative permeability on the alcohol flooding mechanism are discussed.

INTRODUCTION

Reasons for interest in the use of alcohol to miscibly displace oil and water from a porous medium appear in the existing literature.[1-7] The mechanism of the displacement has been considered and the apparent implications formulated into a theory which presumably would enable one to predict the essential features of the process.[6] Unfortunately, most of the reported experiments have been performed with unconsolidated or artificially consolidated sands. With these systems some of the noteworthy facets of the process are obscured and resulting data appear uncertain.

It is the purpose of this paper to show how the use of consolidated sandstones has led to revision of the mechanism and, hence, the theory of alcohol flooding.

The practical result is increased pessimism toward the possibilities of commercial application of the simplest form of the alcohol-slug process. However, elucidation of the mechanism has made it possible to define the essential characteristics of a system of slugs which will behave in a nearly piston-like fashion and, thus, yield the best possible result.

Original manuscript received in Society of Petroleum Engineers office July 19, 1960. Revised manuscript received Feb. 20, 1961. Paper presented at 35th Annual Fall Meeting of SPE, Oct. 2–5, 1960, in Denver.

[1] References given at end of paper.

EQUILIBRIUM PHASE BEHAVIOR

Fig. 1 is a diagram of the ternary system isopropyl alcohol (IPA)-Soltrol-calcium chloride brine.* Brine was used to prevent plugging of the core and calcium chloride was used because sodium-chloride brine exhibits a solid phase with Soltrol and IPA.

If alcohol is added in increments to the immiscible mixture of water and oil represented by Point A, the path followed by the successively equilibrated samples will be on the Line ABC and pass from the immiscible region to the miscible region by crossing the binodal curve at B. Consider the intersection D of this path with the tie Line EF. The quantity of oleic phase is proportional to the Segment ED and the quantity of the aqueous phase is proportional to DF. Compositions of the two phases are specified by Points E and F. It is clear that in the case shown the oleic phase is diminishing and entirely disappears when miscibility is achieved. Such will

* In all equilibrium diagrams, the binodal curve compositions are read at the outside edge of the curve. The co-ordinates represent volume per cent in all cases.

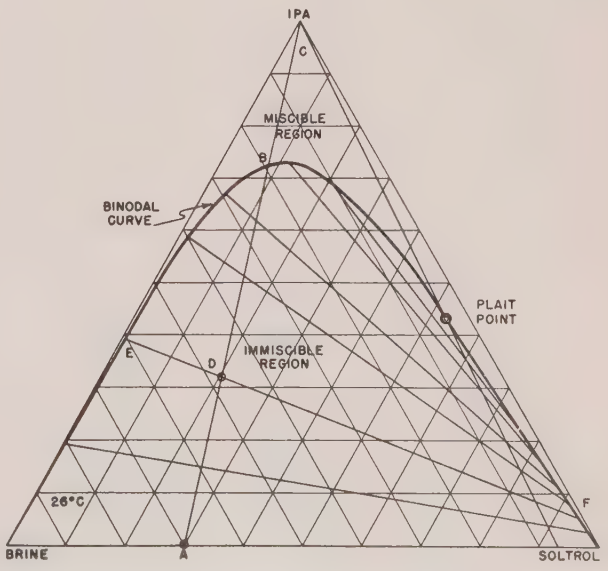

FIG. 1 – EQUILIBRIUM PHASE DIAGRAM, IPA-SOLTROL-2 PER CENT $CaCl_2$ BRINE.

be the case for any path lying entirely to the left of the line joining the Point C to the plait point.

Fig. 2 is a similar diagram for tertiary butyl alcohol (TBA). In this case the plait point is to the left of the binodal peak and the same Path AC will result in disappearance of the aqueous phase when miscibility is achieved. Again, so long as the actual path followed in a real flooding situation lies entirely to the right of the line passing through the plait point and Point C, the phase behavior will be of this nature. Following the Path AC, it happens (because of the change in slope of the tie lines) that first the oil phase diminishes; then, it increases until at miscibility the aqueous phase entirely disappears.

For the oil-water distributions studied, it turns out that TBA leads to preferential disappearance of the aqueous phase whereas IPA leads to preferential disappearance of the oleic phase. This is not always the case. If a higher molecular-weight oil such as Drakeol 6 is used with TBA and water, the plait point shifts to the right of the binodal peak.

Fig. 3 is a diagram for the system IPA-Drakeol 6-calcium chloride brine. In this case the binodal peak is much higher than it is for Soltrol, but the location of the plait point is nearly the same. The shift of the binodal curve toward the 100 per cent co-ordinate lines is characteristic of increase in molecular weight. It will be shown later that this is of practical importance and imposes a severe limitation on the usefulness of the alcohol process.

It is now obvious that an essential first step in any investigation of alcohol flooding is to determine the phase diagram complete with tie lines and plait point for the exact system in question.

DESCRIPTION OF THE PROCESS

Consider a core saturated with water and oil. If the oil saturation is sufficiently above residual, flooding with alcohol will initially produce 100 per cent oil. If the oil saturation is at or below residual (i.e., discontinuous), initial production will be 100 per cent water. In any event, the initial pure fluid production is followed by a stabilized bank of constant water-oil ratio. If the alcohol used has its plait point on the right side (i.e., toward 100 per cent oil) of the binodal peak, the stabilized bank is followed by a decrease in oil saturation concomitant with alcohol breakthrough.* This decrease in saturation renders the oil residual (and, hence, discontinuous), makes it vulnerable to solution in the advancing alcohol and complete miscibility is ultimately achieved. If the alcohol used has its plait point on the left side of the binodal peak, the stabilized bank is followed by a continual increase in oil saturation until complete miscibility is attained. In the latter case, the oil phase remains continuous throughout and residual oil is not encountered. In all the foregoing circumstances, all of the oil and water are removed from the core when sufficient alcohol has been injected. For this reason it has been thought that the idea of a "piston-like" displacement adequately describes the process. However, it turns out that use of alcohols with basic differences in their equilibrium-phase characteristics leads (with the same oil) to substantially different flowing water-oil ratios in the stabilized bank. This makes it obvious that the piston-like displacement assumption cannot account for all the data. It follows that the nature of the alcohol and oil must be taken into consideration.

When residual oil is achieved in the transition zone, oil ganglia are deposited at a constant rate. Thus, an oil-enriched aqueous phase flows past these ganglia and gradually extracts them to miscibility. An element of fluid which just achieved

*Henceforth, the two-phase region between the rear of the stabilized bank (first appearance of alcohol) and the miscible front will be referred to as the "transition zone". Each phase in the transition zone will, in general, contain all components.

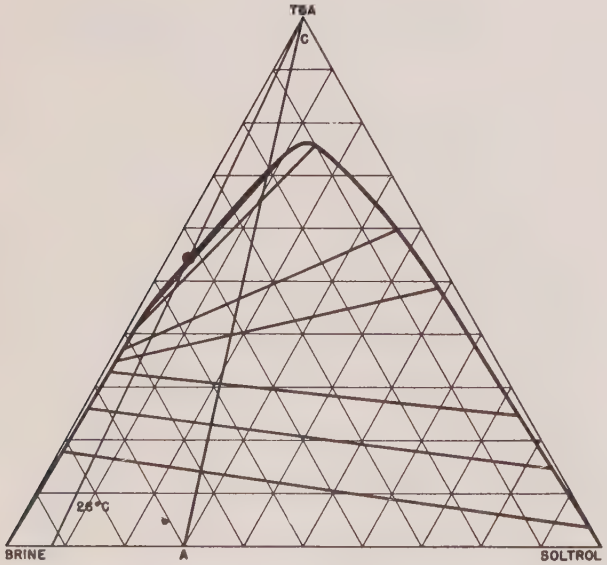

FIG. 2 – EQUILIBRIUM PHASE DIAGRAM, TBA-SOLTROL-2 PER CENT $CaCl_2$ BRINE.

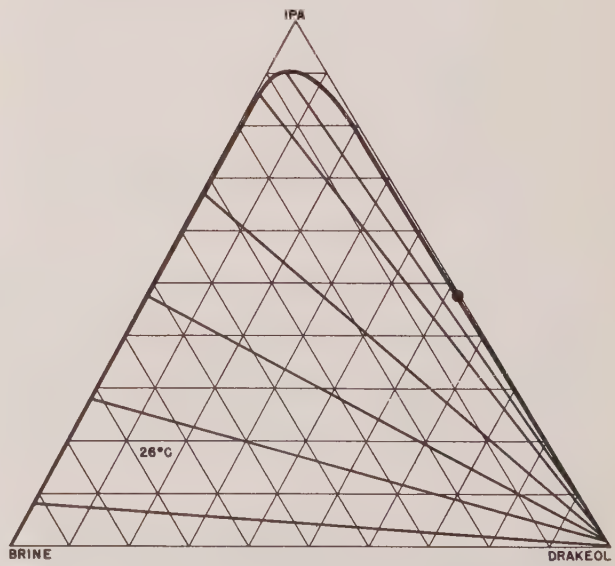

FIG. 3 – EQUILIBRIUM PHASE DIAGRAM, IPA-DRAKEOL 6–2 PER CENT $CaCl_2$ BRINE.

miscibility tends to undergo a subsequent decrease in water and oil concentrations and increase in alcohol concentration as a result of miscible mixing. However, this element of fluid must sweep over stationary ganglia (containing alcohol and some water) and possibly some genuine irreducible water, which tends to increase the water and oil concentrations. Inspection of the phase diagram shows that such an increase can only be very minute, or else it will result in re-deposition of residual oil. The net effect is that the total percentages of oil, water and alcohol remain at an almost constant value over a very long interval extending from the transition-zone well into the miscible region. In view of the foregoing, the production history does not give a direct account of the condition within the core. Thus, the early part of the production of completely miscible fluid was still part of the transition zone when inside the core; i.e., it was sweeping over residual oil ganglia when produced. This part of the produced miscible region can be distinguished from the remainder by the flatness of the concentration distributions in oil, water and alcohol.

Since the residual oil mechanism dominates the process at the expense of miscible mixing, one can no longer expect to interpret this kind of alcohol flooding in terms of simple miscible displacement at an adverse mobility ratio.

The distance which a given length of alcohol slug will move before losing miscibility is strongly affected by this mechanism. It means that the spreading alcohol-water front rapidly encounters the long smeared-out tail of the alcohol-oil-water distribution, resulting in early phase breakdown.

ALCOHOL FLOODING EXPERIMENTS

EQUIPMENT AND MATERIALS

The apparatus consisted of a collection of long consolidated cores molded in plastic, two constant-rate positive-displacement pumps with variable-speed transmissions, a multi-range pressure recorder and an automatic fraction collector and timer. Injection pressures were continuously recorded and effluent fractions were collected at equal time intervals.

Porous media used consisted of various lengths of Berea and Torpedo cores, as described in Table 1.

Fluids used were distilled water, calcuim-chloride brine, Soltrol, Drakeol 6, isopropanol and tertiary butanol. Their properties and sources are given in Table 2. All liquids were de-aerated before use.

SATURATION OF THE CORES

Initial saturation of the cores was performed by evacuating and admitting de-aerated oil or water to the core until full. For all cores, saturations at any stage were determined by material balance based on volumes of fluids in and out. In the case of Berea-A, these figures were checked by total weight differences. High oil saturations (i.e., irreducible water to an oil flood) were achieved by flowing 3 to 5 pore volumes (PV) of oil through the water-saturated core until water production ceased. Residual oil

TABLE 1 – SANDSTONE PROPERTIES

No.	Core Name	Length cm	Length ft	Area of Cross Section (cm^2)	Diameter or Width cm	Diameter or Width in.	Pore Volume (ml)	Porosity (%)	k_o (md)	k_w (md)	$k_{calc.}$ (md)	Source
1	Berea-A	83.0	2.73	5.99	2.58 × 2.32*	1.02 × .915	100	20.1	130	153	123	Ohio
2	Torpedo	173	5.68	18.23	4.82	1.90	675	21.4	394	378	338	Wyo.
3	Berea B-1	67.3	2.21	20.27	5.08	2.00	278**	20.3**		610	515	Ohio
4	Berea B-2	70.3	2.31	20.27	5.08	2.00	291**	20.3**				Ohio
5	Berea B-3	90.2	2.96	20.27	5.08	2.00	373**	20.3**				Ohio
6	Berea B-123	228	7.47	20.27	5.08	2.00	938	20.3		550	625	Ohio
7	Berea B-23	161	5.27	20.27	5.08	2.00	663**	20.3**		700	595	Ohio
8	Berea B-13	158	5.19	20.27	5.08	2.00	651**	20.3**				Ohio

* Berea-A had an approximately square cross section.
** Calculated from No. 6.

TABLE 2 – PROPERTIES OF TEST LIQUIDS

No.	Liquid	Purity (per cent)	Density, 77°F (gm/ml)	Viscosity, 77°F (cp)	Refractive Index (79°F)	Source
1	Distilled Water	Pure	.9970	.8937	1.3327	--
2	2% $CaCl_2$ Brine	Pure	1.0195	1.081	1.3367	--
3	Isopropanol	98 – 99	.7883	2.073	1.3747	Enjay Co., N. Y.
4	Tertiary Butyl Alcohol	99	.7878	4.440	1.3843	Eastman Organic Chem., Rochester 3, N. Y.
5	Soltrol*	–	.7591	1.405	1.4210	Phillips Pet. Co., Bartlesville, Okla.
6	Drakeol 6*	–	.8355	13.37	1.4593	Pennsylvania Ref. Co., Butler, Pa.

*Highly refined, narrow cut of paraffin hydrocarbons.

saturations were obtained by water flooding the core at this stage. On completion of all alcohol flooding experiments, cores were thoroughly flushed with alcohol to remove all of the oil and water. The alcohol was miscibly displaced with water and the sequence repeated to achieve the desired saturation. The special high and low oil saturations used for the runs with Berea-A were obtained by air flooding until the desired low water (or oil) saturation was achieved as determined by the core weight. The core was then evacuated, and de-aerated water (or oil) was injected into the core until the weight became consistent. Saturations of all the cores for the various runs are listed in Table 3.

INJECTION AND COLLECTION OF FLUIDS

Experiments T-7 and T-14 were carried out at rates corresponding to a calculated linear velocity of 1.25 ft/day. All other runs were performed at rates of 19 ft/day.

In view of the importance to data interpretation of the total pressure drop across the core, care was exercised to ensure that termination of injection of one fluid and initiation of injection of a different fluid were accomplished at the same inlet pressure. The flow rate was then adjusted to the desired value.

Produced fluids were collected in 10-ml centrifuge tubes, using an automatic fraction collector.

As one would expect, it frequently happened that a suspension of oleic phase in aqueous phase was produced during efflux of the transition zone. It also occasionally happened that three or four layers appeared in a single fraction of the transition zone. In all such cases, the samples were thoroughly shaken and then centrifuged to produce two clear, stable phases prior to making final readings and analyses.

ANALYTICAL METHODS

A complete analysis of the produced fluids was performed for most of the flow experiments. The technique involved is well described elsewhere.[5,7]

RESULTS

The production history of a continuous alcohol flood can be naturally divided into four principal parts.[6] Pure oil or water production is followed by the stabilized bank, the transition zone and, finally, the miscible region. These zones are labelled in Fig. 4.

One of the noteworthy features of alcohol flooding consolidated sandstone cores is the constancy and reproducibility of the flowing water-oil ratio in the stabilized bank. The data are far better than result from unconsolidated sands of about the same length,[7] and perhaps even superior to data obtained from unconsolidated sands over 10 times as long.[6]

TABLE 3 – ALCOHOL FLOODING EXPERIMENTS ON CONSOLIDATED SANDSTONES

Run No.	Core	Initial Saturation (per cent) S_o	S_w	Rate (ft/day)	System*	Fract. Flow of Oil in Stab. Bank f_o (%)	Break-through of Stab. Bank V (ml)	Alcohol Break-through (ml)	Oil Recovery (ml) Pure Oil	Oil in Oleic Phase	Oil in Aqueous Phase	Oleic Phase after Alcohol Break-through	Oil in Miscible Region	End of Two-Phase Flow (ml)	Slug Size (ml)	Vol. Inj. to Slug Break-down (ml)
T-1	Torpedo	58.0	42.0	19	ISB	30	172	443	244	22.2	22.5	24.6	103	720	∞	–
T-7	Torpedo	57.2	42.8	1.25	ISB	30	150	508	241	11.6	14.0	12.3	122	611	∞	–
T-5S	Torpedo	36.8	63.2	19	ISB	29	112	446	96.0	18.2	19.6	20.3	116	670	∞	–
T-6	Torpedo	58.0	42.0	19	ISB	29	156	449	233	13.5	2.5	11.2	–	541	190	453
T-4	Torpedo	56.8	43.2	19	ISB	30	154	436	228	0.7	–	0.7	–	–	139	405
T-2	Torpedo	57.8	42.2	19	ISB	29	156	423	197	1.4	–	1.4	–	–	96	267
T-3	Torpedo	56.2	43.8	19	ISB	–	151	389	161	0.7	–	0.7	–	482	47	150
T-5	Torpedo	57.0	43.0	19	SB	–	–	–	136	–	–	–	–	–	0	–
T-14	Torpedo	65.0	35.0	1.25	IDB	19	165	435	209	42.8	129	45.1	58	2600	∞	–
T-10	Torpedo	57.5	42.5	19	TSB	43	195	478	311	48.6	1	189	26.8	796	∞	–
T-13	Torpedo	57.0	43.0	19	TSB	44	203	446	274	11.1	0.8	11.5	–	668	96	324
T-11	Torpedo	57.0	43.0	19	TSB	–	200	434	219	1.3	0	1.3	–	504	47.0	200
B-4	Berea	28.0	72.0	19	ISW	34	55.3	57.9	2.1	3.9	2.9	4.1	19.0	99	∞	–
B-2	Berea	33.0	67.0	19	ISW	34	22.4	61.7	13.2	5.7	4.5	6.1	9.7	112	∞	–
B-1	Berea	57.0	43.0	19	ISW	34	33.3	53.9	34.8	6.7	3.3	7.0	12.2	111	∞	–
B-3	Berea	80.0	20.0	19	ISW	–	63.8	63.8	59.4	7.3	3.2	7.6	10.1	91.1	∞	–
B-3B	Berea	57.6	42.4	19	ISW	34	28.9	44.7	22.1	5.6	1.6	6.4	28.3	93.1	∞	–
B-4B	Berea	55.0	45.0	19	ISW	–	30.6	45.3	30.5	6.1	2.7	6.3	15.7	–	42	69
B-2B	Berea	58.0	42.0	19	ISW	–	27.7	53.3	33.5	3.2	0.1	3.3	21.2	90.3	28	60
B-1B	Berea	55.0	45.0	19	ISW	–	27.0	60.6	16.2	0	0	0	–	68	14	39
2A	Berea-B1	37.9	62.1	19	ISB	32	48.5	183	46.8	13.4	5.8	14.5	39.6	287	∞	–
3A	Berea-B23	37.1	62.9	19	ISB	35	139	468	126	16.8	18.9	18.8	83.3	667	∞	–
1A	Berea-B123	37.8	62.2	19	ISB	36	209	638	157	46.9	13.5	50.5	137.6	839	∞	–

* I = Isopropyl alcohol, T = tertiary butyl alcohol, S = Soltrol, D = Drakeol-6, B = 2 per cent $CaCl_2$ brine, W = distilled water.

Results will be presented in two parts. The first part includes information derived from continuous alcohol injection and bears directly on the process mechanism. The second part treats alcohol slugs, these being more pertinent to process application. Reference will be made to Table 3 and Figs. 4 through 15.

CONTINUOUS ALCOHOL INJECTION

Initial Oil Saturation

Figs. 4 and 5 show production histories for continuous alcohol floods on the 6-ft Torpedo sandstone core at high initial oil saturation (S_o = 58 per cent) and residual oil saturation (S_o = 36 per cent). The curves shown represent total water, oil and alcohol concentrations, and f_w is the fraction of water or aqueous phase in the two-phase effluent. In both cases, the average fractional flow of oil in the stabilized bank is close to 30 per cent. Runs B-1 and B-2 show a similar result on a 2-ft Berea core, wherein initial oil saturations of 57 and 33 per cent both gave average stabilized-bank fractional oil flows of about 34 per cent. Evidently, the flowing water-oil ratio during production of the stabilized bank is independent of initial saturation. The initial oil saturation was artificially reduced (see "Saturation of Cores") to 28 per cent for Run B-4 to see if the stabilized-bank characteristics remained independent of initial saturation even well below a normal waterflooding residual. Unfortunately, the core was not sufficiently long to form a good bank, but the producing fractional flow of oil did achieve 34 per cent at one point.

It was found that the oil remaining behind in alcohol solution was about the same for Runs B-1, B-2 and B-3 on the short Berea core, i.e., 15.5, 14.1 and 13.3 per cent PV. This means that for a given system a fairly constant quantity of oil is lost to the alcohol phase. Oil recoveries obtained on the short Berea core are plotted as a function of initial saturation in Fig. 6. The curve drawn through these points corresponds to the theoretical recovery calculated on the basis of a constant oil saturation of 14.3 per cent being lost to the alcohol phase and, thus, represents maximum possible oil recovery using continuous alcohol injection. When the oil saturation is reduced below residual initially, the quantity of oil in alcohol solution is greatly increased (19 per cent PV for Run B-4) since it is more difficult for the oil phase to achieve continuity before being dissolved in the alcohol. The point which does not fall on the curve indicates this change. Presumably, a longer core would show less

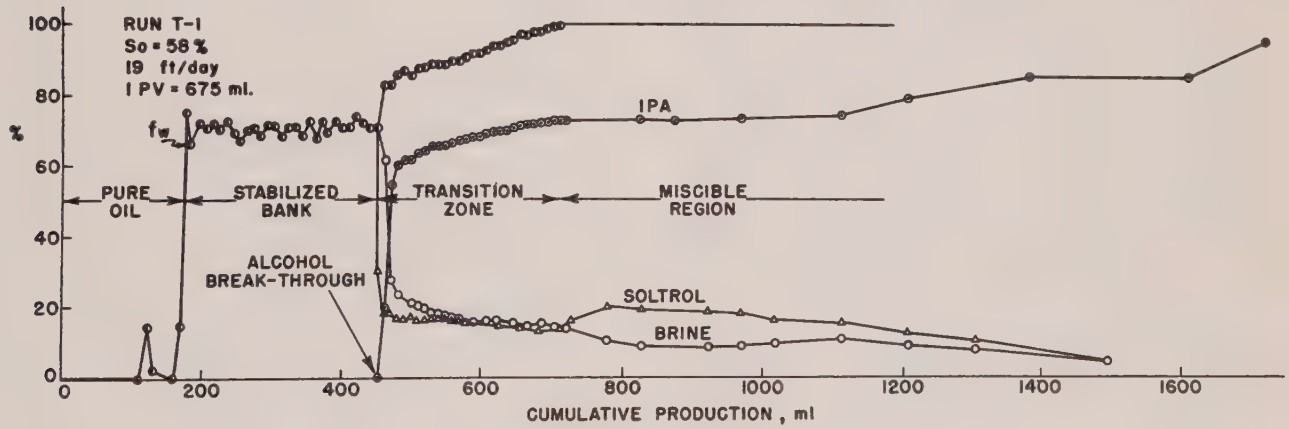

FIG. 4 – PRODUCTION HISTORY FOR CONTINUOUS IPA INJECTION.

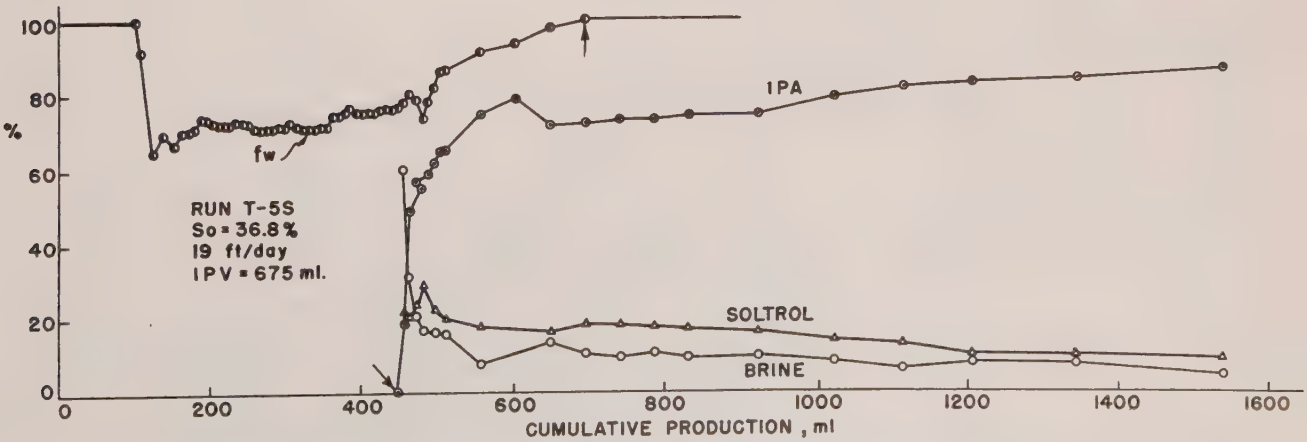

FIG. 5 – PRODUCTION HISTORY FOR CONTINUOUS IPA INJECTION; EFFECT OF INITIAL OIL SATURATION.

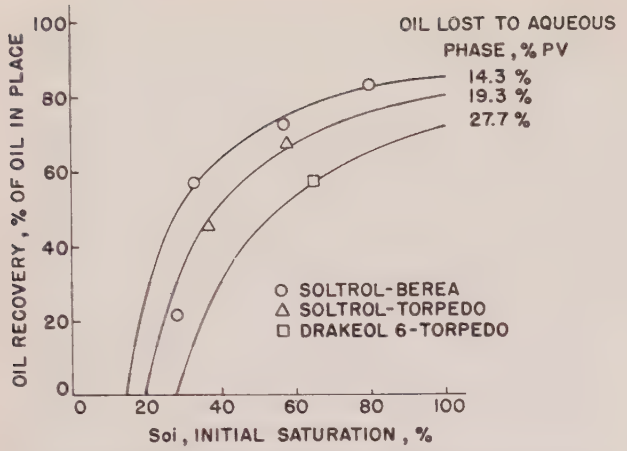

FIG. 6 – MAXIMUM POSSIBLE RECOVERY UNDER CONTINUOUS IPA INJECTION.

of an effect. The other curves in Fig. 6 show similar results for the Torpedo core.

Rate

Run T-7 and Fig. 7 illustrate a reduction in rate to 1.25 ft/day. In comparison to Run T-1 and Fig. 4, breakthrough of the stabilized bank is earlier and commences at a higher fractional flow of water. The change in breakthrough time is a result of the high initial f_w value which in turn results from the greater time required to stabilize at the lower rate. Pure oil recovery is the same (62.1 per cent) at both rates, the higher initial f_w being compensated by a later alcohol breakthrough in the low-rate case. Total usable oil recovery is a little higher at the high rate in view of a larger oil-phase volume in the transition zone. The fact that a low rate yields a short transition zone with a high oil concentration is simply a result of the increased contact time between residual oil and aqueous-phase extract.

Another view of occurrences in the transition zone as influenced by rate is given by the observation that the point at which the system passes into the miscible region shifts toward the plait point. It has been speculated that a sufficiently small rate would permit the system to achieve miscibility exactly at the plait point.[7]

Molecular Weight and Viscosity

Drakeol 6 is a white oil having a viscosity (25°C) of 13.37 cp. It was used with IPA to assess the effect of a heavy oil on the critical parameters. The production history appears in Fig. 8 and corresponds to Run T-14. The fractional flow of oil in the stabilized bank has changed from 30 to about 20 per cent. This shift to a higher water-oil ratio in the stabilized bank (i.e., 2.33 to 4) is just the reverse of the trend previously reported for an unconsolidated sand.[6] The transition zone has stretched from .17 to 3.22 PV. Reference to the phase diagram of Fig. 3 shows why this happens. The binodal curve is so close to the alcohol-oil axis that, from the plait point all the way to the binodal peak, only a very minute concentration of water is required to maintain separate phases wherever the system attempts to pass into the miscible region. Because of this, the system does not move into the miscible region until the binodal peak has almost been reached. The long path of the transition zone along the inside of the binodal curve further emphasizes the importance of the residual oil mechanism in dominating the process. With this heavy oil, the nature of the phase diagram tends to maintain the initially higher (than Soltrol) residual oil saturation for a long time. The transition zone teeters on the verge of miscibility, but cannot achieve it until better than 3 PV have swept through.

It is noteworthy that the recovery of oil is most seriously affected by the increase in viscosity and molecular weight. Not only has pure oil recovery been reduced from 62.1 to 47.7 per cent, recovery in the transition zone has been spread over a time interval 18.8 times that of Soltrol. If this run had been made at residual oil, the maximum possible oil recovery using continuous alcohol injection would probably have been only about 20 per cent of the oil in place. The implication is strong that, without a buffer between a heavy oil and an alcohol

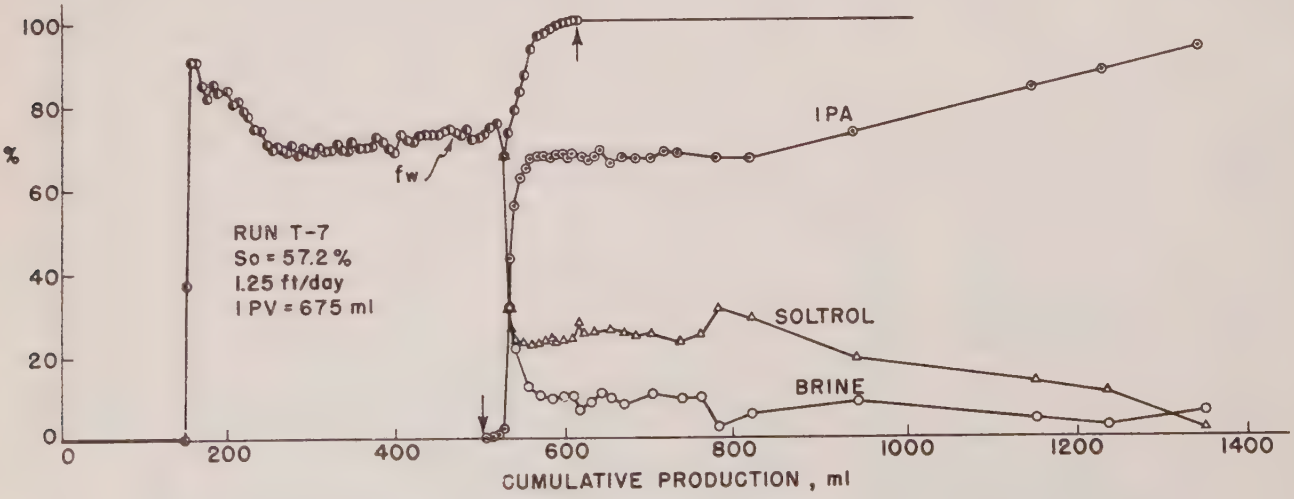

FIG. 7 – PRODUCTION HISTORY FOR CONTINUOUS IPA INJECTION; EFFECT OF RATE.

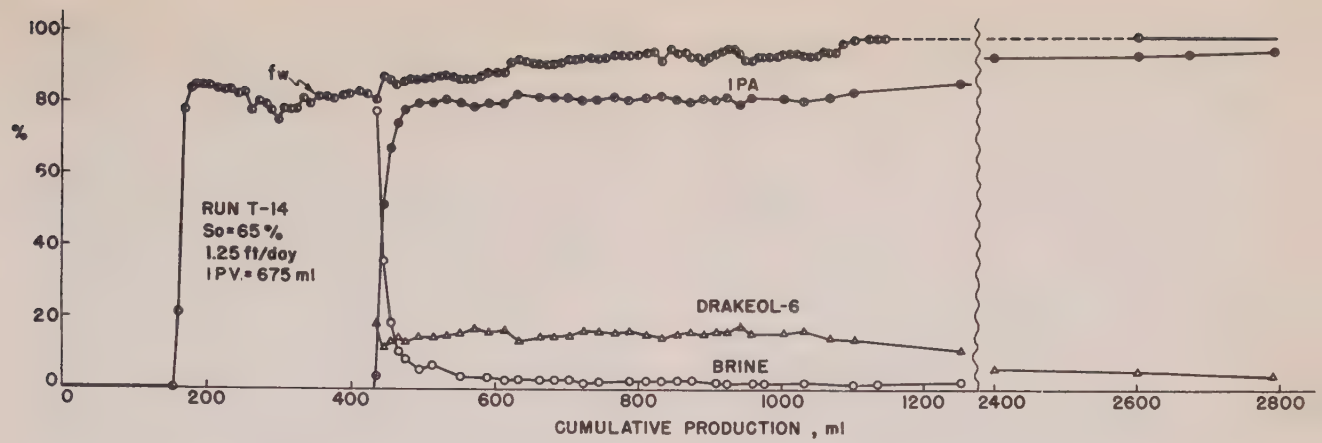

FIG. 8 – PRODUCTION HISTORY FOR CONTINUOUS IPA INJECTION; EFFECT OF VISCOSITY AND MOLECULAR WEIGHT.

slug, results can be dismal indeed.

Distance Travelled

Three Berea cores (Berea-B) were fastened together to form three different path lengths for experiments using continuous IPA injection to displace residual Soltrol (see Runs 1-A, 2-A and 3-A). There were definite variations in the properties of these cores, so that perfect correlations with distance could not be expected.

The principal result is that the oil recovery (all oil in oleic phase) expressed as per cent of oil initially in place was found to be independent of distance travelled, i.e., 56.1 and 57.3 per cent. Since the volumetric oil recovery is proportional to distance travelled, the oil remaining behind is also proportional to the distance travelled. The adverse consequences of this have been established and it can now be seen that no improvement can be expected with increased distances traversed. Apparently, the rate of extraction of residual oil ganglia is always less than the rate at which they are deposited. This seems reasonable in view of the diffusional nature of the extraction process.

The length of the transition zone is graphed in Fig. 9 along with the length of the stabilized bank. Linearity of these graphs is what one should expect in view of the previous discussion.

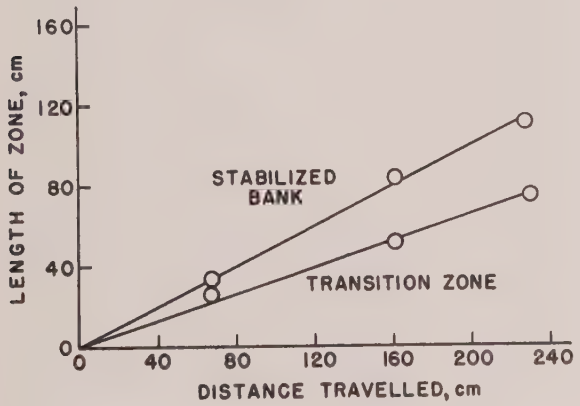

FIG. 9 – GROWTH OF STABILIZED BANK AND TRANSITION ZONE.

Plait Point

So far, all results have pertained to systems which pass through residual oil in the transition zone. Fig. 10 (Run T-10) gives the production history for the system TBA-Soltrol-2 per cent calcium

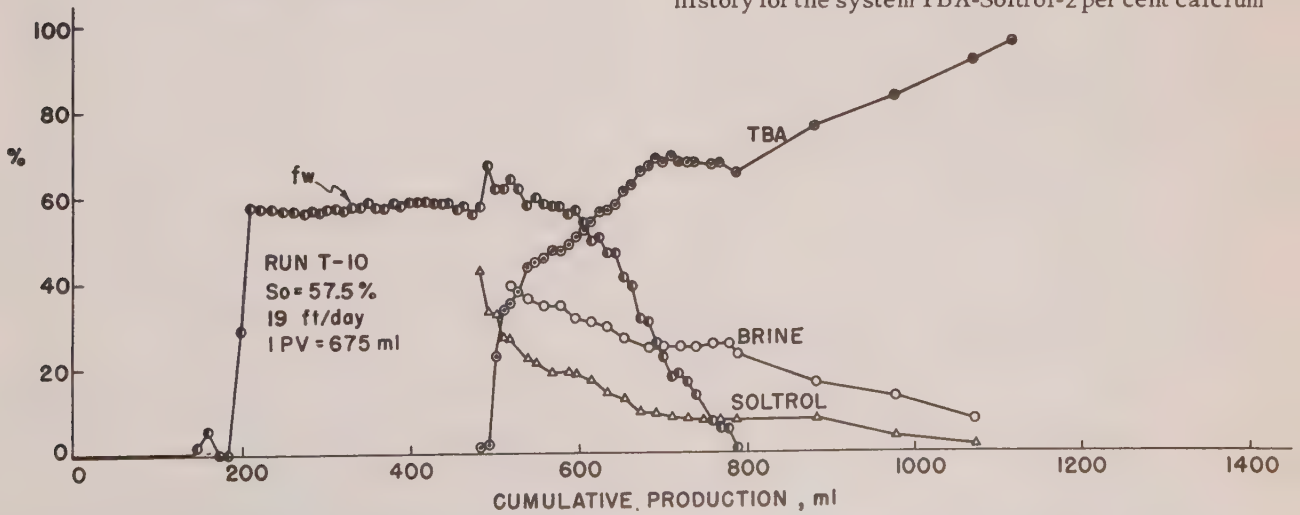

FIG. 10 – PRODUCTION HISTORY FOR CONTINUOUS TBA INJECTION; EFFECT OF PLAIT POINT.

chloride brine which does not pass through residual oil (see "Equilibrium Phase Behavior"). In contrast with Fig. 4, it can be seen that the end of the stabilized bank is followed by a continual increase in oil saturation through the transition zone to the point of complete miscibility. The fractional flow of oil in the stabilized bank is substantially different from what it is in the case of IPA, having shifted from 30 to about 43 per cent. In this case, both phases undergo miscible displacement and the process more nearly conforms to the idea of piston-like behavior. In view of the change in stabilized-bank fractional flow, it follows that alcohol floods that pass through residual oil are not piston-like. We will return to this point later.

Another significant difference is exhibited by the concentration distributions after miscibility is achieved. It can be seen that the water and oil concentrations decrease and the alcohol concentration increases more nearly as one would expect to see in consequence of miscible mixing.

It is interesting to note that the change in slope of tie lines (Fig. 2) is reflected in the production history (Fig. 10) by a temporary increase in f_w just after alcohol breakthrough.

OIL SATURATION IN THE CORE

Three 4-in. segments were cut from the production end of the long Torpedo core, carefully faced, provided with O-ring grooves and fastened back in place. A standard alcohol flood on a high oil saturation was then initiated. As soon as the produced stabilized bank reached f_w = 70 per cent, the core segments were simultaneously detached from the remainder of the core without stopping alcohol injection.

Each of the three core segments then was equipped with end flanges, and all oil and water removed using alcohol floods. Two cores were flooded with IPA and one with TBA. Produced fluids were analyzed for water, oil and alcohol content using mass spectrography. Pore volumes of the core segments were then determined. Results are shown in Table 4.

Thus, when IPA displaced Soltrol from the Torpedo core at a stabilized-bank fractional flow of oil of 30 per cent, the oil saturation in the core in the stabilized bank was in the vicinity of 45 per cent. Errors in the analysis tend to give low values of S_w.

ALCOHOL SLUGS

Experimental determination of the distance an alcohol slug moves before deteriorating into two phases is not easy. If the slug successfully traverses the core, one can only say the distance to breakdown is greater than the core length. If it breaks down just prior to emerging, then one is not certain of the data because part of the mixing at the front of the slug is absent in view of alcohol breakthrough having already taken place. Any attempt to patch together two experiments corresponding to separate studies of mixing at the front and mixing at the rear is quite difficult in view of the flatness of the concentration distributions peculiar to the residual oil mechanism. This can be seen more specifically by reference to Fig. 4 where the alcohol concentration is still very low at more than 1.6 PV. Thus, in this case it is not possible to decide where the advancing alcohol-water front would encounter a sufficiently low alcohol concentration to cause breakdown.

In the following, these problems were avoided by allowing the slug to break down well inside the core. The location of breakdown (i.e., pore volume injected when breakdown occurred) was determined by one or more of the several means described.

TABLE 4 – OIL SATURATIONS FOR THREE CORE SEGMENTS

Core Location	S_o (Per Cent PV)
(IPA) At Producing End	44.4
(TBA) Toward Injection End	45.7
(IPA) Between the Above Cores	45.1

Determination of Slug Breakdown

Total pressure drop across the core gives one indication of slug breakdown. Fig. 11 shows this by comparison with the pressure history for continuous alcohol injection. The two curves decline at about the same rate after the onset of two-phase production. When slug breakdown occurs, residual oil is generated within the core and tends to increase the pressure drop in view of the decreased effective permeability to the aqueous phase. The net effect is a marked decrease in the rate of pressure decline. Location of the breakdown point was facilitated by use of a semilog plot of the pressure decline.

Another indication of breakdown is given by the production history. The produced fluids in Fig. 11 have just reached the stabilized-bank fractional flow when breakdown occurs. At slug breakdown, the change in boundary condition at the rear of the transition zone causes an instantaneous and rapid rise in the fractional flow of water. The small additional quantity of oil that is produced after slug breakdown represents the excess of the oil saturation over residual in the stabilized bank.

A third limit on the location of slug breakdown is imposed by the alcohol flood that always follows a slug experiment. When the alcohol-water front reaches the region where residual oil commences, the pressure drop increases in view of the onset of two-phase flow (creation of a stabilized bank) where previously there was single-phase flow.

Distance Travelled

The length of core traversed at slug breakdown is graphed as a function of slug size in Fig. 12. Corresponding data appear in Table 3 for Runs T-2 to T-6 and B-1 to B-4. In this figure, slug size and distance are merely the corresponding fluid volumes divided by $A\phi$. From Fig. 12, it can be seen that the slug requirement is increasing more rapidly than

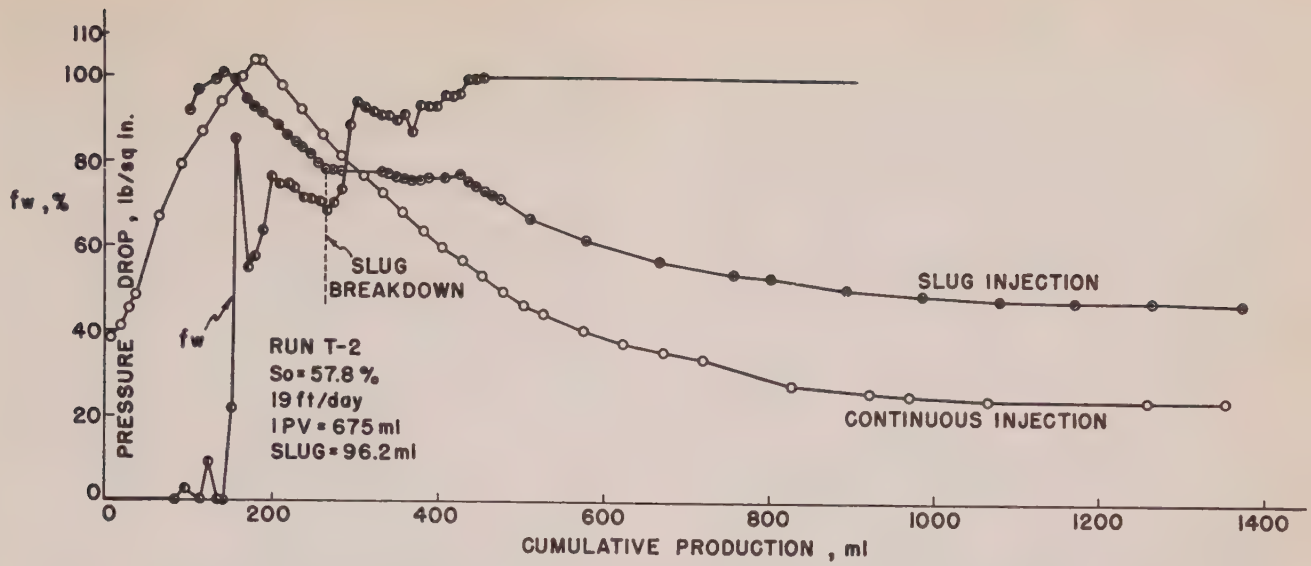

FIG. 11 – EFFECT OF SLUG BREAKDOWN ON PRESSURE AND PRODUCTION HISTORIES, IPA-SOLTROL.

the distance travelled. This is in sharp contrast to the square-root dependence usually observed under conditions of favorable mixing.[13] Such an adverse result is a consequence of viscous fingering at the rear of the slug superimposed on the linear deposition of residual oil (see "Description of the Process" and "Continuous Alcohol Injection – Distance Travelled").

Two points are given for the TBA-Soltrol system. For any given slug size, these data show that TBA will travel a greater distance than IPA before slug breakdown. The reason for this is indicated by the more rapid decline of the water and oil concentrations after miscibility is achieved in the produced fluids. (See "Continuous Alcohol Injection – Plait Point" and Fig. 10.) Nevertheless, the trend shown by these data indicates that the dependence on distance with the TBA process is no more favorable than with IPA. If the TBA-Soltrol system is controlled by miscible mixing at an adverse mobility ratio, then there is hope for improvement via dissipation of viscous fingering when sufficiently great distances have been traversed.[14] However, insufficient work has been done on continuous injection of TBA to be certain of this analogy.

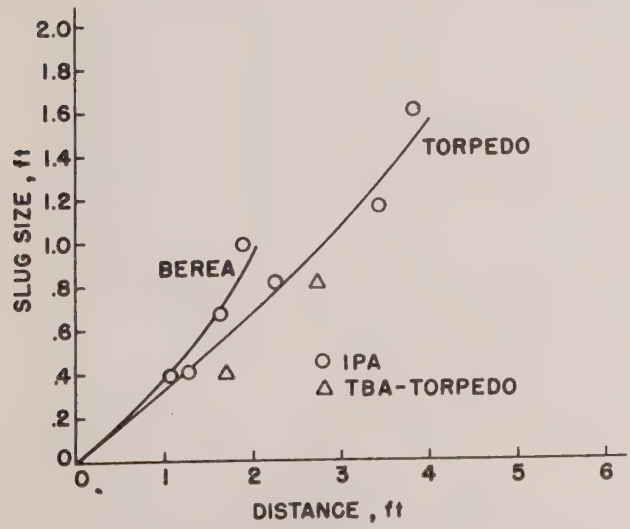

FIG. 12 – DISTANCE TO BREAKDOWN OF ALCOHOL SLUGS.

Oil Recovery

Oil recovered by the various-sized alcohol slugs is shown in Fig. 13. Data can be found in Runs T-1 to T-6, Table 3. The point at zero slug size corresponds to a water flood, and the highest points were obtained by making the oil recoveries from continuous alcohol injection correspond to the slug sizes obtained by double logarithmic extrapolation of the data in Fig. 12 to the total core length. Notice that the oil recovered using TBA slugs is much greater than that derived from corresponding IPA slugs. This would be expected in view of the more favorable displacement mechanism realized by TBA.

THEORY

In view of the experimental evidence, it is necessary to treat two cases. These are distinguished by the manner in which the oleic phase behaves

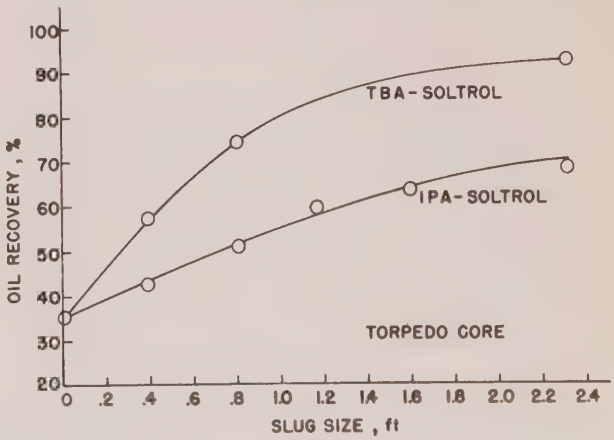

FIG. 13 – OIL RECOVERED BY ALCOHOL SLUGS.

as miscibility is approached.

PLAIT POINT LEFT OF BINODAL PEAK

The simplest approximation to this case has been treated in detail by Gatlin and Slobod using an analogy to combustion.[6] A more general approach was made earlier by Gardner and Warren,[8] who included the capillary pressure gradient and found the same result to hold. It turns out that the oil saturation in the stabilized bank is related to the mobility ratio by

$$\frac{1 - S_o}{S_o} = \frac{k_w}{k_o} \cdot \frac{\mu_o}{\mu_w} = \frac{q_w}{q_o} \cdot \quad \ldots\ldots\ldots\ldots\ldots\ldots\ldots\ldots\ldots\ldots (1)$$

Therefore, for any solution $S_o = S_{ob}$, the bank saturation equals the fractional flow and the relative phase velocity is unity. Further, the fraction of a pore volume produced at breakthrough of the stabilized bank is given by

$$V = \frac{S_{wb} - S_{wi}}{S_{wb}} \quad \ldots\ldots\ldots\ldots (2)$$

in the case of a high initial oil saturation (irreducible water to an oil flood), and

$$V = \frac{S_{ob} - S_{or}}{S_{ob}} \quad \ldots\ldots\ldots\ldots (3)$$

in the case of residual oil.

In the Appendix, it is pointed out that equivalent forms of Eqs. 2 and 3 are, respectively,

$$V = \frac{S_{wb} - S_{wi}}{f_w}, \quad \ldots\ldots\ldots\ldots (4)$$

and

$$V = \frac{S_{ob} - S_{or}}{f_o} \quad \ldots\ldots\ldots\ldots (5)$$

We accept these results so long as they are applied to systems with the plait point to the left of the binodal peak. In the application that has been made of them,[6] this was not the case.

Application of this model requires a choice of relative permeability data. The Penn State method is preferred as obviously representative of phenomena occurring in the stabilized bank. It has been shown (see "Results – Initial Oil Saturation") that the stabilized-bank fractional flow (and, hence, the oil saturation in the bank) is independent of initial oil saturation. Since formation of the bank is an imbibition or drainage process according to whether the core was initially at irreducible water or residual oil, respectively, it follows that the correct relative permeability curve must be hysteresis-free, i.e., the imbibition curve.[11]

Fig. 14 shows relative permeability data from a Torpedo sandstone core similar to that used in the alcohol experiments. Its absolute permeability was higher than the average for the long core (500 vs 350 md), but the residual oil was almost the same (37 vs 36.8 per cent). These data are graphed again in Fig. 15 for Soltrol, and the curve $(1 - S_o)/S_o$ is superimposed. In the case of TBA-Soltrol, the intersection with the imbibition curve should give the flowing water-oil ratio in the stabilized bank. From the graph it can be seen that this value is 1.42, as compared with an average of 1.38 from experiment. Note that, if the drainage curve had been used instead, the result would have been 2.10, which is completely out of the question.

From Eq. 4, breakthrough is obtained at 0.276 PV, whereas from Fig. 10 it can be seen that breakthrough actually occurred (using the half-height) at about 195 ml, or 0.289 PV. If the earliest experimental breakthrough is used, agreement is exact.

Thus, it is established that behavior of the system TBA-Soltrol-brine is close to piston-like and the correct relative permeability curve is the Penn State imbibition curve. We generalize on this result in view of the discussion of "Equilibrium Phase Behavior" and claim that all ternary systems with plait points to the left of the binodal peak will behave in this fashion.

PLAIT POINT RIGHT OF BINODAL PEAK

The essential feature of this case is the boundary condition required at the rear of the stabilized bank; i.e., residual oil at a saturation S_{or}* is being left behind at a constant rate and dissolved in the aqueous

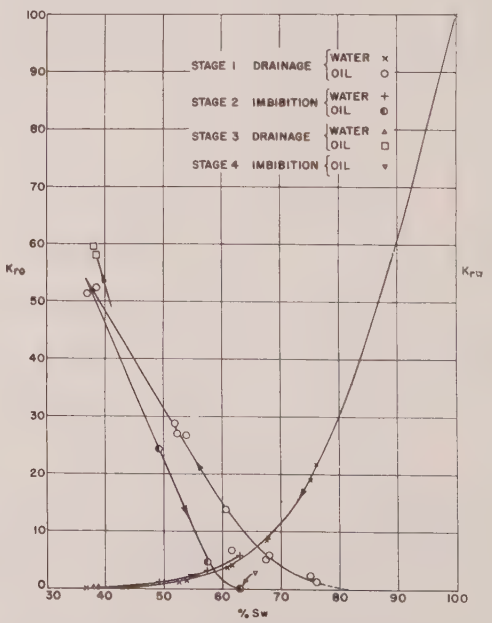

FIG. 14 – RELATIVE PERMEABILITY CURVES FOR TORPEDO SANDSTONE.

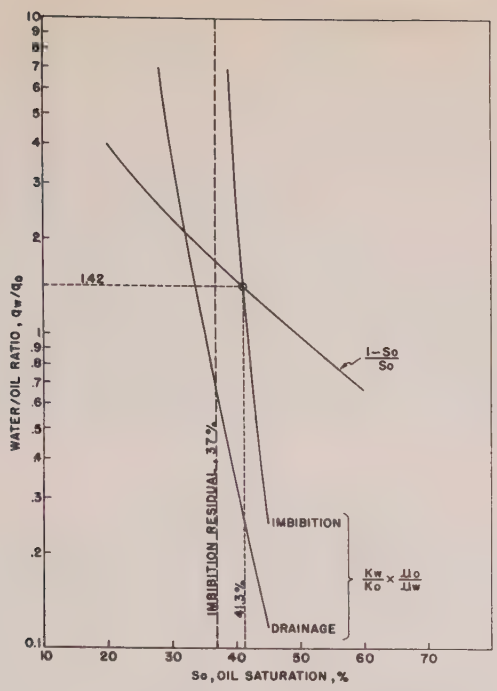

FIG. 15 – GRAPHICAL DETERMINATION OF S_{ob} FOR TBA-SOLTROL-BRINE.

phase. It is interesting to observe that this makes the analogy to combustion[12] more precise because there too an oil residual remains behind, except that it is consumed by oxidation instead of solution.

Under assumptions otherwise the same as used in deriving Eqs. 1 through 5, it is shown in the Appendix that the oil saturation in the stabilized bank is related to the mobility ratio by

$$\frac{1 - S_o}{S_o - S_{or}^*} = \frac{k_w}{k_o} \cdot \frac{\mu_o}{\mu_w} = \frac{q_w}{q_o} \quad \ldots\ldots\ldots\ldots\ldots\ldots\ldots\ldots (6)$$

For this relation, the solution $S_o = S_{ob}$ will no longer equal the fractional flow in the bank and there will be a definite flow of one phase relative to the other. In fact, the relative velocity is given by $v_{wb}/v_{ob} = S_{ob}/(S_{ob} - S_{or}^*)$, and the fractional flow is $f_{ob} = (S_o - S_{or}^*) / (1 - S_{or}^*)$. The relative velocity is different from unity and the fractional flow is different from S_{ob} whenever $S_{or}^* > 0$.

Further, it is shown that, when the oil saturation is initially residual, the fraction of a pore volume produced at breakthrough of the stabilized bank is given by

$$V = (1 - S_{or}^*) \left(\frac{S_{ob} - S_{or}}{S_{ob} - S_{or}^*} \right) \quad \ldots\ldots\ldots\ldots\ldots\ldots (7)$$

When the core is initially at irreducible water, then

$$V = (1 - S_{or}^*) \left(\frac{S_{wb} - S_{wi}}{S_{wb}} \right) \quad \ldots\ldots\ldots\ldots\ldots\ldots (8)$$

Again, it can be shown that equivalent forms of Eqs. 7 and 8 are given, respectively, by Eqs. 4 and 5.

Fig. 16 shows the imbibition k_w/k_o curves for Soltrol and Drakeol 6, together with graphs of the the function $(1-S_o) / (S_o - S_{or}^*)$ as a parameter.

To illustrate the method, consider Run T-1 for IPA-Soltrol-Brine, initially at a high oil saturation of 58 per cent; i.e., $S_{wi} = 42$ per cent. From experiment, $q_w/q_o = 2.33$ and intersects the Soltrol curve at an oil saturation of $S_{ob} = 40.4$ per cent. Using these figures and Eq. 6, the average residual oil saturation S_{or}^* can be calculated and equals 14.8 per cent. The graphical interpretation of this calculation is also given in the figure. From Eq. 8, the corresponding theoretical breakthrough is 0.252 PV vs an experimental value of 0.250.

It can be seen that the oil saturation in the bank of 40.4 per cent does not equal the fractional flow of oil which is 30 per cent. Further, the relative water-oil velocity is not unity; rather, it is 1.54.

In contrast to the piston-like case, one does not achieve prediction of both S_{ob} and q_w/q_o, in view of the additional parameter S_{or}^*. This situation is no worse than it is in combustion, where one cannot yet predict on purely theoretical grounds the fraction of oil which is burned. Nevertheless, it seemed desirable to obtain a completely independent check of the theory, and this was done by actually measuring S_{ob} (see "Results – Oil Saturation in the Core"). The result was 40.4 per cent calculated vs 45.1 experimental. We regard this as substantial evidence of the validity of the residual oil mechanism. For Run T-55 with the core initially at residual oil, V calculated Eq. 5 is 0.12 and experimental is

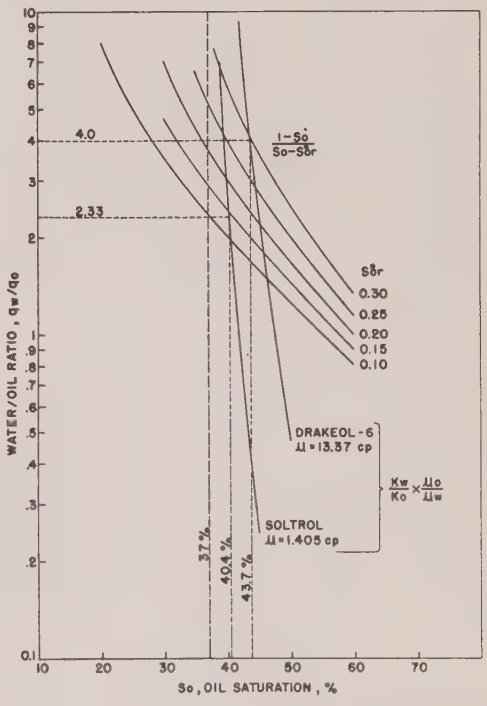

FIG. 16 – GRAPHICAL DETERMINATION OF S_{ob} FOR IPA-SOLTROL-BRINE AND IPA-DRAKEOL 6–BRINE.

0.166. Agreement here is not good, but the reason is that the oil saturation in the bank is so close to residual that the numerator of Eq. 5 is very sensitive. Further, f_w in the stabilized bank is not as constant as one would like for rigorous application of the derived formula for V.

Run T-7, corresponding to a high initial saturation but a rate of only 1.25 ft/day, gives the comparison 0.222 experimental vs 0.240 theoretical. Again agreement is not very good, although better than before. In this case, it appears that the slow-rate process does not stabilize so rapidly as does the fast-rate process, and this is reflected in the strong variation of f_w with V in the early production of the stabilized bank (see Fig. 7). Eq. 4 can be corrected for this by observing that changes in f_w do not affect S_{wb} much in view of the steepness of the q_w/q_o curve (Fig. 16). Therefore, considering f_w as a function of V, a correction of $\int f_w\,(V)dV$ evaluated over the region enclosed by the actual production curve and the line $f_w = 0.7$ can be introduced. When this is done, the calculated breakthrough time becomes 0.225, which is very close to the experimental value of 0.222.

The experiment with Drakeol 6 (Run T-14) was designed to test the viscosity dependence of Eq. 4. Unfortunately, it was not possible to use the high rate because of pressure limitations on the core. Therefore, the low rate was used and one would then expect V to be in excess of the experimental value just as it was for Soltrol at the slow rate. This is exactly what happened, and the comparison using Eq. 4 is 0.266 theoretical vs 0.240 experimental. Again, a correction for deviation from f_w = constant will improve the agreement. Thus, the result is consistent and all trends are in the right direction, but a quantitative check on the viscosity dependence was not achieved because of the rate effect. From Fig. 16 it can be seen that, for Drakeol 6, S_{ob} = 43.7 per cent and $S_{or}{}^*$ = 29.5 per cent. Thus, increasing the viscosity and molecular weight has increased the oil saturation in the stabilized bank from 40.4 to 43.7 per cent, but the flowing water-oil ratio has changed from 2.33 to about 4. Further, $S_{or}{}^*$ has increased from 14.8 to 29.5 per cent. Note also the great difference between the saturation in the core (43.7 per cent) and the fractional flow (20 per cent).

Thus, it is established that behavior of the system IPA-Soltrol-brine is not piston-like but, rather, conforms to a residual oil mechanism wherein the stabilized-bank saturations are determined using the Penn State imbibition relative permeability curve. Further, IPA Drakeol 6-brine is similar in character. Again, we generalize on these results and claim that all ternary systems with plait points to the right of the binodal peak will behave in this fashion.

CONCLUSIONS

Over the ranges of the variables studied, linear alcohol floods can be expected to conform to the following conclusions.

Two different kinds of alcohol displacements exist. In one of these, the oleic phase dominates as miscibility is approached and, therefore, remains continuous throughout the flood. Systems of this kind are characterized by a plait point lying to the left (toward 100 per cent brine) of the binodal peak. An example of this system is TBA-Soltrol-brine. In the other of these, the aqueous phase dominates as miscibility is approached; therefore, the oleic phase passes through a residual state before miscibility is achieved. Systems of this kind are characterized by a plait point lying to the right (toward 100 per cent oil) of the binodal peak. Examples of this system are IPA-Soltrol-brine and IPA-Drakeol 6-brine.

PLAIT POINT TO THE LEFT

1. The flowing water-oil ratio and the volume produced to breakthrough of the stabilized bank can be determined using the Penn State imbibition relative permeability curve, together with the boundary condition imposed by piston-like displacement.

2. In otherwise equivalent systems, a TBA slug will travel a greater distance and recover more oil before breaking down than an IPA slug of the same size. However, for the distances studied, the curve relating slug size to distance travelled has about the same slope for both alcohols.

PLAIT POINT TO THE RIGHT

1. The flowing water-oil ratio, the breakthrough volume and the oil saturation in the core can be related using the Penn State imbibition relative permeability curve, together with the boundary condition corresponding to the continual deposition of a constant saturation $S_{or}{}^*$ of residual oil.

2. The fractional flow of oil in the stabilized bank is independent of initial oil saturation. The quantity of oil permanently lost to the aqueous phase is independent of initial oil saturation and is a constant fraction of the pore volume swept by the alcohol front. Volumetric oil recovery for continuous alcohol injection is proportional to the pore volume swept by the alcohol front. Thus, maximum possible oil recovery can be measured.

3. Increasing the rate of advance causes more rapid stabilization, lengthens the transition zone, decreases the oil concentration in the transition zone and does not affect pure oil recovery. Decreasing the rate shifts the place where miscibility is achieved toward the plait point.

4. Increasing the oil molecular weight and viscosity makes the binodal curve less favorable, stretches out the transition zone and, thus, reduces pure oil recovery. For ordinary consolidated sandstones, increasing the viscosity decreases the fractional flow of oil in the stabilized bank.

5. Slug size varies as the distance travelled to breakdown to a power of at least unity and, therefore, is very unfavorable.

FINAL REMARKS

APPLIED ASPECTS

Most of the work herein has involved IPA since it is the least expensive, reasonably pure, readily available alcohol having a favorable phase diagram with light oils. It now appears that, if there is any hope for the alcohol slug process, it lies with systems having plait points to the left of the binodal peak. These systems can be obtained in practice by inserting an appropriate intermediate slug between the reservoir fluids and the alcohol. The economic success of such a system of slugs will rest on whether viscous fingering does, or can be caused to, disappear within reasonable distances.

COMPARISON WITH EARLIER WORK

The question arises as to how it can be that Gatlin and Slobod[6] obtained agreement between their experimental work with IPA and a theory which appears to be inadequate. The reasons lie in the nature of unconsolidated sand packs of the kind used. For such systems, both residual oil and irreducible water to an oil flood are very low, thus tending to obscure the features that distinguish piston-like displacement from the residual oil mechanism. In the 20-40 mesh sand used by Gatlin and Slobod, S_{or}* would be so small that its effect on the flowing water-oil ratio could not be detected. This results in apparent agreement with piston-like displacement.

A somewhat more difficult point is raised by their result that increasing viscosity decreases the flowing water-oil ratio in the stabilized bank, whereas in the foregoing the reverse was found to be true. At least part of the reason for the apparent discrepancy lies in the fact that the relation between drainage and imbibition relative permeabilities is quite different for unconsolidated sands than it is for consolidated media.

IRREDUCIBLE WATER

One may well ask about the role played by irreducible water under alcohol displacements. If the lead of Caudle and Dyes[15] is followed, it would be necessary to delete this quantity from the saturation available for brine flow in the stabilized bank. The analogy is between the miscible displacement of water by alcohol during an alcohol flood and the displacement of water by water during gas-water injection subsequent to a miscible-slug process.

However, in the case of TBA, the deletion of any water saturation greater than about 1 to 2 per cent gives an incorrect f_w using the imbibition curve. It is a remarkable coincidence that, if a capillary pressure value of irreducible water is introduced and the drainage curve is used, then the correct value of f_w is obtained. However, the breakthrough time is off by a large factor. Therefore, we conclude that, at least for a TBA-Soltrol flood on the Torpedo core and presumably any alcohol flood where the aqueous phase disappears at miscibility, it is incorrect to delete more than a few per cent in water saturation.

One may still ask if irreducible water should be deleted for an IPA flood. Here the situation is not so clear-cut since f_w and V are unaffected. Deletion of a fixed water saturation, in this case, merely changes S_{or}* in a compensating way. However, such a procedure results in a value of S_{or}* for the Drakeol 6 flood that is in excess of the total oil left behind according to experiment.

Some clarification of the precise role of irreducible water saturation under a miscible displacement seems desirable.

NOMENCLATURE

A = area of core cross-section, sq ft
L = length of core, ft
S = phase saturation, dimensionless
V = pore volumes injected to breakthrough of stabilized bank, dimensionless
f = fractional flow, dimensionless
k = relative permeability, dimensionless
q = flow rate, cu ft/hr
t = time to breakthrough of stabilized bank, hours
v = phase velocity or frontal velocity, ft/hr
μ = viscosity, cp
ϕ = porosity, dimensionless

SUBSCRIPTS AND SUPERSCRIPTS

b = stabilized bank
i = irreducible
o = oil
r = residual
w = water
* = transition zone

ACKNOWLEDGMENTS

The authors would like to express appreciation to J. E. Warren and J. H. Henderson for their participation in numerous informative discussions, to W. K. Meyer, William Ometz and N. H. Harrison for assisting with experiments, to J. Downie and F. E. Crane for making the relative permeability measurements, and to P. Raimondi for permitting us to use and ultimately destroy his best Torpedo core.

REFERENCES

1. Morse, R. A.: "Miscible Phase Displacement", German Patent No. 849,534 (July, 1952).
2. Paulsell, W. G.: "The Effect of a Mutually Miscible Intermediate Phase on Immiscible Fluid Displacement in a Porous Medium", Master's thesis, U. of Oklahoma (1953).
3. Sievert, J. A., Dew, J. N. and Conley, F. R.: "The Deterioration of Miscible Zones in Porous Media", *Trans.*, AIME (1958) Vol. 213, 228.
4. Slobod, R. L.: "A Review of Methods Used to Increase Oil Recovery", *Prod. Monthly* (Feb., 1958) Vol. 22, No. 4, 24.
5. Gatlin, C.: "The Miscible Displacement of Oil and Water from Porous Media by Various Alcohols",

PhD thesis. The Pennsylvania State U. (1959).

6. Gatlin, C. and Slobod, R. L.: "The Alcohol Slug Process for Increasing Oil Recovery", *Trans.*, AIME (1960) Vol. 219, 46.
7. Kamath, I. S. K.: "Transfer and Movement of Materials during the Recovery of Oil and Water from a Porous Medium by an Alcohol", PHD thesis, The Pennsylvania State U. (1960).
8. Gardner, G. H. F. and Warren, J. E.: "Effect of Initial Water Saturation on the Production of Oil by Miscible Displacement", Unpublished file note, Gulf Research & Development Co. (March 31, 1958).
9. Corey, A. T.: "The Interrelation between Gas and Oil Relative Permeabilities", *Prod. Monthly* (Nov., 1954) Vol. 19, 38-41.
10. Morse, R. A., Terwilliger, P. L. and Yuster, S. T.: "Relative Permeability Measurements on Small Core Samples", Tech Paper No. 124, The Penn State College Mineral Ind. Exp. Station (1947).
11. Geffen, T. M., Owens, W. W., Parrish, D. R. and Morse, R. A.: "Experimental Investigation of Factors Affecting Laboratory Relative Permeability Measurements", *Trans.*, AIME (1951) Vol. 192, 99.
12. Wilson, L. A., Wygal, R. J., Reed, D. W., Gergins, R. L. and Henderson, J. H.: "Fluid Dynamics During an Underground Combustion Process", *Trans.*, AIME (1958) Vol. 213, 146.
13. Raimondi, P., Gardner, G. H. F. and Petrick, C. B.: "Effect of Pore Structure and Molecular Diffusion on the Mixing of Miscible Liquids Flowing in Porous Media", Presented at AIChE Meeting, San Francisco (Dec., 1959); *AIChE Jour.*, in press.
14. Perrine, R. L.: "Conditional Instability In Miscible Liquid-Liquid Displacement", Preprint 42, Part II, presented at AIChE-SPE Joint Symposium in San Francisco (Dec. 6-9, 1959).
15. Caudle, B. H. and Dyes, A. B.: "Improving Miscible Displacement by Gas-Water Injection", *Trans.*, AIME (1958) Vol. 213, 281.

APPENDIX

Core saturations will be idealized according to the scheme of Fig. 17. Initially, the core is either at S_{or} (solid line) or S_{wi} (dashed line). The front of the stabilized bank is advancing at a rate v and the rear at a different rate v^*. An "average" or "effective" residual oil saturation S_{or}^* is being left behind and dissolved in the miscible region. The total flux is $q/A\phi$. All frontal velocities and phase velocities are assumed constant, the fluids are incompressible and the capillary pressure gradient is neglected.

WATER-OIL RATIO AND BANK SATURATION

In the stabilized bank,

$$q = q_{wb} + q_{ob}$$

where

$$q_{wb} = v_{wb} \; A \; \phi \; S_{wb}$$

and

$$q_{ob} = v_{ob} \; A \; \phi \; S_{ob} = v^* A \; \phi \; (S_{ob} - S_{or}^*) .$$

Therefore,

$$q = v_{wb} \; A \; \phi \; S_{wb} + v^* A \; \phi \; (S_{ob} - S_{or}^*) ,$$

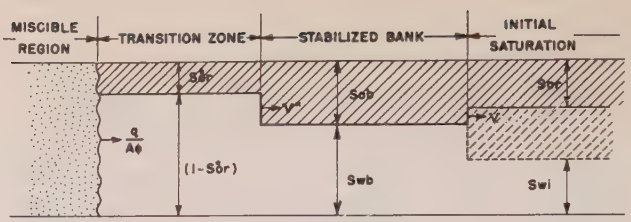

FIG. 17—IDEALIZED SATURATION SCHEME.

and

$$\frac{q_{wb}}{q_{ob}} = \frac{(q/v^* A \; \phi) - (S_{ob} - S_{or}^*)}{S_{ob} - S_{or}^*} \quad \ldots\ldots\ldots\ldots\ldots\ldots\ldots\ldots\ldots\ldots (A\text{-}1)$$

In the transition zone,

$$q = q_w^* + q_o^*$$

where

$$q_w^* = v_w^* \; A \; \phi \; (1 - S_{or}^*)$$

and

$$q_o^* = 0$$

as oil here is residual and effectively immobile. Therefore,

$$q = v_w^* \; A \; \phi \; (1 - S_{or}^*) = v^* \; A \; \phi \; (1 - S_{or}^*) ,$$

since the only flowing phase in the transition zone is the aqueous phase and its velocity v_w^* equals the frontal velocity v^*.

Thus,

$$\frac{q}{A \; \phi \; v^*} = 1 - S_{or}^* \quad \ldots\ldots\ldots\ldots\ldots\ldots\ldots\ldots\ldots\ldots (A\text{-}2)$$

From Eqs. 1 and 2, we have

$$\frac{q_{wb}}{q_{ob}} = \frac{1 - S_{ob}}{S_{ob} - S_{or}^*} = \frac{k_w}{k_o} \cdot \frac{\mu_o}{\mu_w} .$$

Since this is a relation to be solved for $S_o = S_{ob}$, we drop the subscript b and write

$$\frac{q_w}{q_o} = \frac{1 - S_o}{S_o - S_{or}^*} = \frac{k_w}{k_o} \cdot \frac{\mu_o}{\mu_w} \quad \ldots\ldots\ldots\ldots\ldots\ldots\ldots\ldots\ldots\ldots (A\text{-}3)$$

Note that the initial core saturation does not enter the calculation, so the result must be the same for both S_{or} and S_{wi}. Further, the fractional flow of oil f_{ob} is related to the oil saturation in the bank S_{ob} by

$$f_{ob} = \frac{q_{ob}}{q_{ob} + q_{wb}} = \frac{1}{1 + (q_{wb}/q_{ob})} = \frac{S_{ob} - S_{or}^*}{1 - S_{or}^*} ; \quad (A\text{-}4)$$

and the relative phase velocity is given by

$$\frac{v_{wb}}{v_{ob}} = \frac{q_{wb}}{q_{ob}} \cdot \frac{S_{ob}}{S_{wb}} = \frac{1 - S_{ob}}{S_{ob} - S_{or}^*} \cdot \frac{S_{ob}}{S_{wb}} = \frac{S_{ob}}{S_{ob} - S_{or}^*} \quad \ldots\ldots\ldots\ldots\ldots\ldots\ldots \text{(A-5)}$$

All of these results (Eqs. A-3, A-4 and A-5) reduce to the piston-like formulas when $S_{or}^* = 0$.

BREAKTHROUGH

This calculation depends on the initial core saturation, and commences with the core at irreducible water to an oil flood. Thus, in Fig. 17, the dashed line and S_{wi} are used.

Since initial production is virtually 100 per cent oil, the rate at which water enters the stabilized bank from the front is $v\ A\ \phi\ S_{wi}$. Since $v_w^* = v^*$, no water leaves the rear of the stabilized bank. Therefore, the entering water must equal the accumulation in the bank, which is $(v - v^*)\ A\ \phi\ S_{wb}$. Thus,

$$v\ S_{wi} = (v - v^*)\ S_{wb}$$

or

$$\frac{v^*}{v} = \frac{S_{wb} - S_{wi}}{S_{wb}}.$$

However, $v = L/t$ and $v^* = (q/A\ \phi)/(1 - S_{or}^*)$ from Eq. A-2. Therefore,

$$\frac{v^*}{v} = \frac{q\ t}{L\ A\ \phi} \cdot \frac{1}{(1 - S_{or}^*)} = \frac{S_{wb} - S_{wi}}{S_{wb}}.$$

Since $q\ t/L\ A\ \phi$ equals the pore volumes of alcohol injected to breakthrough V, we have

$$V = (1 - S_{or}^*) \left(\frac{S_{wb} - S_{wi}}{S_{wb}} \right) \quad \ldots \text{(A-6)}$$

If this result is combined with Eq. A-3, an equivalent expression for V results; namely,

$$V = \frac{S_{wb} - S_{wi}}{f_w} \quad \ldots\ldots\ldots \text{(A-7)}$$

When the core is initially at residual oil, Fig. 17 is interpreted using the solid line and S_{or}.

Since residual oil will not flow under a water flood, initial production is all water. The rate at which oil enters the stabilized bank, therefore, is $v\ A\ \phi\ S_{or}$, and the rate at which oil is leaving the rear of the stabilized bank is $v^*\ A\ \phi\ S_{or}^*$. Accumulation in the bank amounts to $(v - v^*)\ A\ \phi\ S_{ob}$ and, therefore,

$$v\ S_{or} = v^*\ S_{or}^* + (v - v^*)\ S_{ob}.$$

Proceeding as before, we have

$$V = (1 - S_{or}^*) \left(\frac{S_{ob} - S_{or}}{S_{ob} - S_{or}^*} \right) \quad \ldots \text{(A-8)}$$

If this result is combined with Eq. A-3, then

$$V = \frac{S_{ob} - S_{or}}{f_o} \quad \ldots\ldots\ldots \text{(A-9)}$$

Note that, when $S_{or}^* = 0$, Eqs. A-6 through A-9 reduce to the piston-like formulas.

How well Eqs. A-7 and A-9 agree with experiment will depend on how rapidly the system stabilizes, since it is implicit that the stabilized bank begins to form at S_{ob} and residual oil is left behind at S_{or} the instant alcohol injection commences.

***

DISCUSSION

CARL GATLIN
MEMBER AIME

THE U. OF TEXAS
AUSTIN, TEX.

The authors are to be complimented for their thorough and painstaking study of isopropyl and tertiary butyl-alcohol displacements in consolidated porous media. This work has cast further light on the mixing or extraction phenomena occurring in the transition zone when oil and water are displaced by alcohol. Since these results disagree in some respects with our previous work,[5,6] it is my desire to examine these differences in some detail and to offer alternate explanations or possibilities for consideration.

Two principal differences in the experimental systems exist. The Gulf Research group used consolidated cores, while our work utilized an unconsolidated sand pack (50-200 mesh). This led, of course, to wide differences of residual oil, ours being much lower. The second difference was in the core lengths, 2.2 to 7.5 ft for the Gulf work vs 100 ft in our study. We could not use tertiary butyl alcohol because of its high freezing point and were, hence, unaware of the favorable location of its plait point in the Soltrol-water system. We did, however,

recognize the unfavorable extraction preferences of IPA for water, and it was this line of reasoning which led us to the combination-slug experiments reported in our paper.

The main disagreement between the Gulf analysis and our results lies in whether one uses the simplified piston displacement scheme (Eqs. 2 and 3[6] or the "leaky" piston scheme described in the Appendix of the authors' paper. These lead to considerably different stabilized-bank saturations and flowing ratios, as is pointed out. The Gulf group attributes the agreement between our experimental results (IPA) and the piston "theory" with the inherently low value of S_{or}^* in unconsolidated packs. They are, however, unable to explain with complete satisfaction our data showing that increasing oil viscosity decreased water-oil ratio in the stabilized bank, a result completely opposite to theirs.

I suggest that at least two alternate possibilities exist. The cores used in the Gulf work were shorter than the transition zone in all IPA runs. To me this prohibits anything other than a simple extraction process from occurring. To prove definitely that the piston concept is invalid will, in my opinion, require experimental data on systems appreciably longer than the transition zones. In our one run using the viscous oil, the mixing zone had an apparent length of about 40 ft, based on effluent history.

A second possibility which now concerns me is that our system behaved as though it were oil-wet. As reported in the original work,[5] repeated contacts with IPA seemed to cause a steady increase in residual oil saturation. This, plus other evidence, indicated that our system became increasingly oil-wet with time.

In view of the Gulf results, I wonder if the system wettability (or more specifically the relative locations of water and oil within the pores) plays a role in the extraction efficiency and transition-zone behavior which may be as important as plait point location. This assumption is actually made by the authors; otherwise, the TBA system would "leak" a residual water saturation S_{wr}^* into the miscible region. It seems possible that this could explain some aspects of the disagreement.

The postulation that plait point location, i.e., left or right side, completely alters the gross displacement mechanism is not completely clear to me. It seems that this approach could lead to the conclusion that only systems having the plait point in the center (horizontal tie lines) could be treated in the piston manner. I realize, of course, that the stated distinction is the presumed continuity of the aqueous phase as opposed to the discontinuous ganglia of residual oil. I would appreciate some further clarification of this point.

I wonder if the authors have any additional data on longer systems which they might wish to report. I am also curious to know if they have experimented at all with combination slugs in their consolidated cores.

AUTHORS' REPLY TO CARL GATLIN

We are pleased to receive Gatlin's pertinent comments and will attempt to answer all of them in the order presented.

OIL VISCOSITY

There are two effects of increasing oil viscosity. One is to shift the q_w/q_o vs S_o curves to the right; the other is to render the phase behavior more unfavorable (via concomitant increase in molecular weight) by enlarging the immiscible region.

If the viscosity could be increased without changing the phase behavior, the effect would always be to reduce the water-oil ratio, independent of consolidation considerations. This is illustrated in Fig. 16 by noting for any fixed value of S_{or}^* (including $S_{or}^* = 0$) the intersections of the $(1-S_o)/(S_o-S_{or}^*)$ curves with the two q_w/q_o curves corresponding to different viscosities. The identical result holds when the relative permeability curves are measured on unconsolidated sands.

If the phase behavior could be made more unfavorable without changing the viscosity, the effect would always be to increase the water-oil ratio, independent of consolidation considerations. The reason for this is that an enlarged immiscible region implies an increased value for S_{or}^*. The effect can be seen in Fig. 16 by noting, for increasing values of S_{or}^*, the intersections of the $(1-S_o)/(S_o-S_{or}^*)$ curves with a single q_w/q_o curve (viscosity fixed).

Thus, for a given core, whether increase in viscosity results in a decrease or increase in water-oil ratio simply depends on which of these two effects dominates. In our particular consolidated systems, the phase behavior dominated. In the unconsolidated system of Gatlin and Slobod, with its inherently low values of S_{or}^*, viscous effects dominated. Both results are correct and both are described by the "leaky piston" scheme.

It should be noted that the drainage relative permeability curve used by Gatlin and Slobod is very close to being correct, even though one is dealing with an imbibition process. The reason for this is that the high rates used permit viscous forces to completely dominate the low capillary forces which obtain in their unconsolidated sand.[1] Thus, the invading water channels through the oil phase acting like a nonwetting phase. If the rates could be sufficiently reduced it would be found necessary to use an imbibition relative permeability curve lying above (in the sense of Fig. 14) the drainage curve.[2] Thus, one can expect the water-

[1]References given at end of paper.

oil ratio in the stabilized bank of an alcohol flood of an unconsolidated sand to depend on rate at very low rates, whereas this should not be the case with consolidated cores. However, as remarked in the following section entitled "Plait Point", a rate dependence at low rates may be introduced via equilbrium considerations even in a consolidated system.

CORE LENGTH

Since writing the subject paper, we have conducted IPA and TBA alcohol floods on consolidated Berea cores 2-, 6-, 12-, 18-, 25- and 50-ft long.* We have been unable to find any reason for changing any of our conclusions as a result of these experiments. For the IPA runs, the produced oil percentage varied from 33 to 35 per cent. For the TBA runs it ranged from 44 to 48 per cent. As before, these values obtained independent of initial saturation. A difference of 9 to 15 per cent was consistently found.

In all experiments, except that employing a highly viscous oil, the transition zone was much shorter than the core. For the Torpedo core, the transition zones were about one-third the core length. This can be seen in Figs. 4, 5, 7 and 10 as well as in Table 3. In the longer Berea cores just mentioned, the comparison of lengths was even more favorable.

WETTABILITY

If a core were completely oil-wet and prepared in such a way that there could be no question that oil constituted the wetting phase and water the nonwetting phase, then everything should be exactly reversed. A TBA flood should leak residual water ganglia which could be labelled S_{wr}*, whereas an IPA flood should be close to piston-like. Clearly, then, both plait-point location and wettability must be taken into account when predicting system behavior.

All of the subject paper refers to systems which are water-wet. If wettability changes, there is a corresponding change in relative permeability; hence, the water-oil ratio from the stabilized bank should change. We have never observed this nor have we observed any significant change in residual oil saturation under numerous floods spanning more than a year. However, we do not allow oil to remain in contact with a core for extended periods of time. Idle cores are always alcohol or brine saturated.

PLAIT POINT

We return now to the completely water-wet case. Since a TBA flood causes the aqueous phase to preferentially diminish as miscibility is approached (Fig. 12) whereas an IPA flood causes the oleic phase to diminish (Fig. 4) and since these floods proceed with different water-oil ratios in the stabilized banks, one must conclude that plait-point location does indeed alter the gross displacement mechanism.

Let the plait point lie to the left of the binodal peak. It was stated that the displacement was close to piston-like. The words "close to" were used advisedly since there is room for a few per cent of water (S_{wi}*) to remain behind. S_{wi}* then becomes a measure of piston-like behavior. The question of importance is whether the displacement becomes more nearly piston-like (smaller S_{wi}*) as the intersection of the composition path and the phase boundary approaches the plait point. We have established that a decrease in rate causes this intersection to move toward the plait point. This means that phase equilibrium is not established within the core except, possibly, at exceedingly low rates. If the rate is low, but still feasible according to field flooding standards, then there is the distinct possibility that in a given core there still exists water-filled channels sufficiently minute that alcohol does not diffuse into them in the time allowed by the advancing front. If so, these channels can be cut off by an interface and diffusion rendered even more ineffective. This "cut-off" water saturation represents our concept of S_{wi}*. Its magnitude should depend on the sandstone, fluid system, rate (at very low rates) and should always be substantially less than the laboratory-determined connate-water saturation.

A special TBA experiment was conducted to accurately determine S_{wi}* on an 18-ft Berea sandstone. Precautions were taken to reduce S_{wi} to a sufficiently low value prior to alcohol flooding that effectively no water was produced with the initial oil bank, thus establishing a very accurate value for stabilized bank breakthrough. The result was S_{wi}* = 5.2 per cent under a flooding rate of 12 ft/day. (Equations used to determine S_{wi}* and S_{or}* appear in the next section.)

In summary, plait-point location does affect the the gross flooding characteristics and true piston-like displacement is difficult to achieve in view of its apparent dependence on the existence of phase equilibrium.

CALCULATIONS OF S_{or}* AND S_{wi}*

In the absence of relative permeability data, these quantities can be determined by observing that the unknown bank saturations can be eliminated from the appropriate pairs of equations either given in the subject paper or similar to them. Thus from Eqs. 6 and 7 it follows that (plait point right)

$$S_{or}^* = \frac{q_o}{q_w}(S_{or} + V - 1) + S_{or} = 1 - V + \frac{1}{f_w}\left[V - (1 - S_{or})\right] \quad \ldots\ldots (9)$$

and from Eqs. 6 and 8

$$S_{or}^* = 1 - V - S_{wi}\left(1 + \frac{q_o}{q_w}\right) = 1 - V - \frac{S_{wi}}{f_w}. \quad \ldots\ldots\ldots\ldots\ldots (10)$$

*These cores were not from the same batch as those reported in the paper.

Similarly, when water is left behind at a saturation S_{wi}^* (plait point left),

$$V = (1 - S_{wi}^*) \left(\frac{S_{wb} - S_{wi}}{S_{wb} - S_{wi}^*} \right), \quad \ldots \quad (11)$$

or

$$V = (1 - S_{wi}^*) \left(\frac{S_{ob} - S_{or}}{S_{ob}} \right), \quad \ldots \quad (12)$$

and

$$\frac{q_w}{q_o} = \frac{S_{wb} - S_{wi}^*}{S_{ob}}, \quad \ldots \quad (13)$$

yield

$$S_{wi}^* = \frac{q_w}{q_o} (S_{wi} + V - 1) + S_{wi} = 1 - V + \frac{1}{f_o} \left[V - (1 - S_{wi}) \right], \quad \ldots \quad (14)$$

and

$$S_{wi}^* = 1 - V - S_{or} \left(1 + \frac{q_w}{q_o} \right) = 1 - V - \frac{S_{or}}{f_o}. \quad \ldots \quad (15)$$

Using these equations, it was found that 14.5 per cent $\leq S_{or}^* \leq$ 17.8 per cent for the first seven IPA Torpedo runs in Table 3. For the 25-ft Berea core with IPA it was found that 10.5 per cent $\leq S_{or}^* \leq$ 14.0 per cent. With regard to three TBA-Torpedo runs, 4.6 per cent $\leq S_{wi}^* \leq$ 8.8 per cent; and for TBA-25 ft Berea it was determined that $0 \leq S_{wi}^* \leq$ 5.2 per cent.

COMBINATION SLUGS

We have at this writing carried out numerous experiments using combination slugs of various kinds. These experiments have brought to light new facets of miscible displacement which we hope to discuss at another time. However, for water-wet systems we find that the behavior in all cases studied conforms to what would be predicted on the basis of plait-point considerations.

REFERENCES

1. Moore, T. F. and Slobod, R. L.: "The Effect of Viscosity and Capillarity on the Displacement of Oil by Water", *Prod. Monthly* (Aug., 1956) Vol. 20, No. 10, 20.
2. Naar, J. and Wygal, R. J.: "Structure and Properties of Unconsolidated Aggregates", Submitted for publication to *Trans.*, Faraday Soc.

***

Further Discussion of Paper Published in
Society of Petroleum Engineers Journal, March, 1961

Experiments on Mixing During Miscible Displacement In Porous Media

WILLIAM E. BRIGHAM
JUNIOR MEMBER AIME
PHILIP W. REED
JOHN N. DEW
MEMBERS AIME

CONTINENTAL OIL CO.
PONCA CITY, OKLA.

(*Published on Page 1*)

DISCUSSION

J. P. HELLER

SOCONY MOBIL OIL CO., INC.
DALLAS, TEX.

The purpose of this discussion is to comment briefly on one of the points raised in the paper. The topic is that referred to in the Conclusion 2, in which the authors note a "disproportionate increase in mixing rate" as they proceed from a displacement performed at viscosity ratio 0.998 to one at 1.002. The recovery curve of this displacement, Fig. 2A, shows a quite noticeable difference between the two runs in which displaced and displacing liquids were interchanged. This difference is ascribed by the authors to the change in viscosity ratio between the two experiments.

This interpretation of the experimental results must certainly be based on rather precise measurements of the fluid viscosities or, at least, of the ratio of their viscosities. The ordinary Ostwald viscometer, employed in the usual way, is only just able to distinguish between liquids whose viscosities differ by two or three parts per thousand. The experimental refinements which then must have been necessary to measure with any precision a viscosity ratio of 1.002 would be worthy of mention. Indeed, one would have expected the authors to devote at least a paragraph to the display of this technique. For the same reason – to emphasize that the details of such unusually critical experimental work should be reported and discussed in the literature – I would have liked to see some comment by the authors on the requirements for temperature control during both the viscosity measurements and the displacement experiments. The temperature coefficient of viscosity of Soltrol C at room temperature has been measured in this laboratory at about – 1.9%/1°C. How much did the coefficients for the fluid mixtures used in the experiment differ from this and from each other? Even if the two fluids were identical in this respect, it would appear that a temperature difference of .1°C between them in the flow system would produce a viscosity contrast equal to that imposed by their composition.

Reference to the experimental solutions of these problems would render Conclusion 2 more credible. Published theoretical work on the stability problem contains no indication of such extreme sensitivity to the viscosity ratio in the immediate neighborhood of unity. On the contrary, perturbation calculations such as those made by Chuoke[1] and Perrine[2] lead to initial finger growth rates proportional to the first power of the viscosity difference. The later instability growth calculated by Scheidegger,[3] using the assumption of zero pressure gradient perpendicular to the average flow, is also simply proportional to the viscosity difference.

The conflict regarding the sensitivity of the dependence of instability growth or mixing rate on the viscosity contrast needs explicit recognition in the literature. In particular, it would seem that the experimental work reported here should be supported by a more detailed description of the viscosity controls. Further discussion of possible alternative interpretations of the data would also be in order. For instance, is it possible that the unconsolidated bead pack used changed its characteristics between the runs (due, perhaps, to the handling and inverting involved in the injection of the front)? Or, are the data points of Fig. 2A averages from several runs performed in a series in which the two liquids alternated as displaced and displacing fluids?

To summarize, it seems to me that the relationship asserted by Conclusion 2 in the paper needs the support of more detailed experimental evidence.

REFERENCES

1. Chouke, R. L., van Meurs, P. and van der Poel, C.: "The Instability of Slow Immiscible Viscous Liquid-Liquid Displacements in Porous Media", *Trans.*, AIME (1959) Vol. 216, 188.

2. Perrine, R. L.: "The Development of Stability Theory for Miscible Liquid-Liquid Displacement", *Soc. Pet. Eng. Jour.* (March, 1961) 17.

3. Scheidegger, A.: "On The Stability of Displacement Fronts in Porous Media", *Can. Jour. Phys.* (1960) Vol. 38, 153.

AUTHORS' REPLY TO J. P. HELLER

We (like Heller) at first were somewhat surprised at the "disproportionate increase in mixing rate" found at a viscosity ratio only slightly greater than 1.00. We had tried to prepare two mixtures having essentially the same viscosity and felt that the slight differences would have little effect. Upon observing the displacements, however, we found that the fluids were acting alternately as favorable- and unfavorable-ratio displacements. Repeat runs in the same bead pack (labelled 113-1 in our original text) duplicated the results. We also made runs in another bead pack (107-1) with the same results.

We then more carefully checked the viscosities of the oils. The values of 1.296 and 1.299 reported were the result of averaging several readings. There was, of course, a slight variation from one reading to the next, but the results consistently showed the clear oil to have a slightly lower viscosity than the red oil. We recognize that the reported value of this viscosity ratio (0.998 or 1.002) may not be exact, but this is not the important point. The point is that only a slightly unfavorable viscosity ratio will cause the theoretical error-function equation to be incorrect. This effect was mentioned by von Rosenburg,[1] but no data were presented. It can also be seen in the data of Koch and Slobod[2] in their Fig. 4, although no mention of it was made in their text. Fluid viscosities of 0.899 and 0.895 cp were used by Koch and Slobod.

We were asked to comment on our "experimental refinements". Our Ostwald viscometer readings are regularly reproducible within 0.2 to 0.3 seconds in a total time range of 400 to 500 seconds. This good reproducibility is due to the viscometer being in a water bath at 77°F (25°C) – the same temperature as the room. Thus, there is little tendency for the fluids to change temperature due to heat loss or gain. The viscometer may not be calibrated to this degree of accuracy; but one must remember that, in determining a viscosity ratio near unity, it is not the *accuracy* of the instrument that is important but, rather, the *precision* of the instrument – that is, its reproducibility.

An *abrupt* change of about 0.2°F in one fluid would cause the viscosity ratio to change from 1.002 to 1.000, as suggested by Heller; but what is there to cause such a discontinuity of temperature within the medium? Any changes in temperature would occur throughout the bead pack; thus, the variable to consider is the difference in the viscosity indices.

The viscosity indices of the two oils are quite close, being –0.91 per cent/°F for the red oil and –0.95 per cent/°F for the white oil. It requires a temperature change of 5°F to change the viscosity ratio from 1.002 to 1.000. The air temperature in our laboratory, measured using a thermistor, shows about a 1/4°F oscillation with an over-all drift of about 1/2°F during a normal working day. We would expect the flow-system temperature to vary much less than this, but even a 1/2°F variation is considerably less than the required 5°F. Experimental evidence is the best indication of whether an unwanted viscosity-ratio inversion took place due to temperature effects. If such had occurred, the data would have shown it.

Now, what of the theoretical work mentioned by Heller? These theories all deal only with the beginning of an unstable displacement. They would not be expected to give a correct answer on growth rate after an appreciable growth of the perturbations. Rigorous theoretical treatment of an unstable displacement is well-nigh impossible. This was clearly expressed by Scheidegger[3] who, in referring to his own work as well as that of Chuoke and Perrine, stated the following. "The problem of fingering is an extremely involved one, owing to the complexity of the phenomenon. To treat it theoretically, drastic simplifications have to be made." So, it is not surprising that these theories are not quantitative with regard to viscosity.

We should also mention the theories for a viscosity ratio less than unity – the stable case. As we said in our text, all of these theories correctly predict the error-function *form* of the favorable displacement. However, experimental evidence shows that the dispersion rate is a function of the viscosity ratio, even for this stable case. This viscosity ratio dependence is *not* correctly predicted by the error-function theories.

However, we have been by-passing the most important point. One set of theories is for the unstable case (viscosity ratio > 1.000), and the other set is for the stable case (viscosity ratio < 1.000). Our data compare these cases at slightly above and below 1.000. No theory makes this comparison, nor can one be expected to because at 1.000 there is an abrupt change in the basic displacement mechanism. This very change is the cause of the "disproportionate increase" when ranging in viscosity ratio from below 1.000 to above 1.000.

REFERENCES

1. von Rosenburg, D. V.: "Mechanics of Steady-State, Single-Phase Fluid Displacement from Porous Media", *AIChE Jour.* (March, 1956) Vol. 2, No. 1, 55.

2. Koch, H. A., Jr. and Slobod, R. L.: "Miscible Slug Process", *Trans.*, AIME (1957) Vol. 210, 40.

3. Scheidegger, A. E.: "General Spectral Theory for the Onset of Instabilities in Displacement Processes in Porous Media", Paper No. 1551-G presented at the 35th Annual Fall Meeting of SPE in Denver, Colo. (Oct. 2-5, 1960). ★★★

A Study of Flow in Stratified Reservoirs by Use Of the Thermal Analogy

CHARLES H. PICKERING*
N. T. COTMAN*
JUNIOR MEMBER AIME
PAUL B. CRAWFORD
MEMBER AIME

TEXAS PETROLEUM RESEARCH COMMITTEE
A. AND M. DIV.
COLLEGE STATION, TEX.

ABSTRACT

A heat-conduction model has been developed to study the flow of fluids in a stratified oil reservoir which is being subjected to unsteady-state depletion. To simulate stratification, plates of different metals were joined together so that cross flow could occur between strata.

A description of the model, plate construction and necessary instruments is included. The data indicate that stratified oil reservoirs experiencing cross flow may be treated as a single, homogeneous, producing sand having properties intermediate between those of the layers making up the system. A technique for averaging core-analysis data to arrive at the proper average value of rock permeability and porosity is presented.

INTRODUCTION

Although oil has been produced from reservoirs for 100 years and reservoir injection processes have been undertaken for 40 years, the industry is still inadequately informed on the problem of reservoir inhomogeneities.

Stratification is perhaps the best-known type of reservoir heterogeneity. Uren[1] discussed the possible significance of this nonuniformity in his 1927 paper on the theoretical aspects of water flooding. Since this time the problem of vertical permeability variations has been the subject of much discussion and numerous papers.

Levorsen[2] simply describes the origin of layered beds in his *Geology of Petroleum.* Some beds are field-wide and may be traced from well to well, while others apparently pinch-out and become discontinuous. In addition, the physical characteristics of a layer may vary from place to place. For these reasons, a stratified system is not easily defined.

In calculations involving oil reservoirs in which permeabilities vary, methods presently used contain many simplifying assumptions. The reservoir frequently is considered as consisting of permeable layers, each of uniform vertical and lateral permeability and each behaving as if separated from adjacent layers by thin impermeable layers. Other assumptions frequently made in reservoir calculations are steady-state flow conditions, unit mobility ratio, linear geometry, average or homogeneous porosity, and negligible capillary-pressure and gravity effects.

Muskat[3] has developed solutions to the stratification problem for mobility ratios other than unity for both linear and exponential permeability distributions. He assumes lateral uniformity and continuity of all productive strata and does not consider porosity.

This study will take into account transient effects, cross flow and varying porosity, as well as the variations in permeability, by means of a heat analogy.

Muskat[5] has shown the similarity of the equations which describe the flow of fluids in a porous medium to the flow of heat through a solid. Landrum, *et al,*[6] made an analogy between the flow of fluid in an unsymmetrical reservoir and the conduction of heat in a similarly shaped metal plate. This analogy is summarized briefly as follows. If fluid is produced from an oil reservoir above the bubble point, the resulting pressure distribution will be identical to the temperature which would result in a metal or heat-conducting plate if heat were similarly removed. This means that a study of heat flow in stratified thermal models will behave like fluid flow in stratified oil reservoirs. For mathematical correspondencies, see Ref. 6.

The fluid mobility k/μ is proportional to the thermal conductivity, and the porosity-times-compressibility product is proportional to the density times specific heat of the thermal plate.

EXPERIMENTAL EQUIPMENT AND PROCEDURE

The stratified reservoir model used in this study is illustrated schematically in Fig. 1. A Leeds and Northrup Speedomax Type G temperature recorder

Original manuscript received in Society of Petroleum Engineers office June 19, 1961. Revised manuscript received Oct. 3, 1961.

*Pickering is currently employed by Continental Oil Co. and Cotman is now serving in the armed forces.

[1]References given at end of paper.

was used in conjunction with sixteen 36-gauge copper-constantan thermocouples to measure and record temperature distribution in both uniform and stratified thermal models. This instrument records a temperature every two seconds.

The thermocouples were spaced laterally along both sides of the plate in such a manner as to give the temperature distribution throughout the plate. The change in temperature with time at various points in a linear copper-Wood's metal plate is shown in Fig. 2. The parameter $\bar{X}$ is the ratio of the distance of a point measured from the end away from the source, to the length of the plate. Thus, the curve for $\bar{X} = .9$ shows the change in temperature at a point close to the source, while that for $\bar{X} = 0.0$ designates temperature data taken at the exterior boundary of the plate.

The linear plates were rectangular, 1-ft long, 4-in. wide and of varying thicknesses. The metals used were chosen according to their thermal properties so that studies could be made of the effects of large changes in strata permeability and porosity.

In the construction of the copper-lead plate, a plaster mold was used. The copper plate was placed into the mold and heated. One 12- × 4-in. side was covered with a thin layer of 50:50 lead-tin solder.

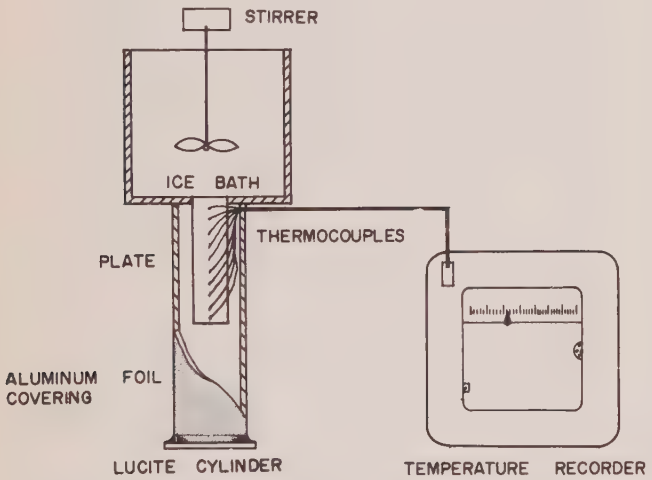

FIG. 1 — SKETCH OF CONSTANT-PRESSURE MODEL.

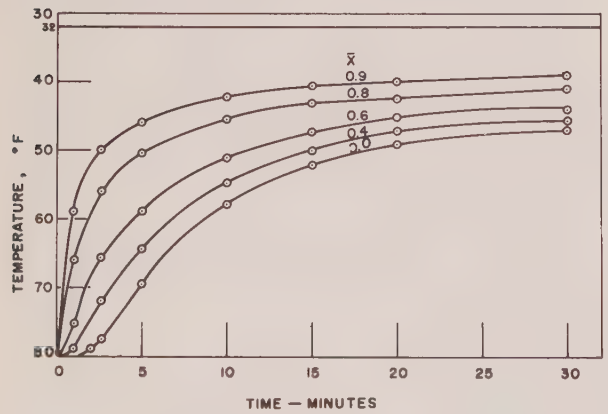

FIG. 2 — THE CHANGE IN TEMPERATURE WITH TIME IN A STRATIFIED, LINEAR, COPPER-WOOD'S METAL PLATE.

Molten lead then was poured onto this surface and allowed to cool. A good bond was achieved in this manner. Wood's metal was bonded to brass and copper in much the same way, except that the brass and copper surfaces were prepared by use of soldering paste and Wood's metal rather than solder. The aluminum-Wood's metal plate was more difficult to construct because the Wood's metal would not adhere to the aluminum. The problem was solved by drilling four 1/8-in. holes through the aluminum plate in a rectangular pattern. The molten Wood's metal was then poured onto the plate, filling the holes. Upon cooling the plates were found to be closely bound together. One three-layered plate was constructed by bonding Wood's metal to the copper side of a previously built copper-lead plate. Finally, a layer of Wood's metal was added to the lead side to make a four-layered plate. Other three-layered plates included a layer of rubber sandwiched between two metals held together by machine screws.

The plates were mounted with one end in contact with a mixture of ice and water in an ice bath, as shown in Fig. 1. The temperature of this end was maintained constant by directing a vigorous flow over the plate edge by means of a stirrer. This technique simulates reservoir depletion with a constant pressure maintained at the producing sand face.

The plate was surrounded by a Lucite cylinder, which in turn was wrapped with aluminum foil to retard heat gain through radiation. A vacuum pump was used to reduce convection effects.

After the recorder was activated and all points on the model had attained the same temperature, a run was commenced by suddenly introducing ice and water into the bath, which corresponds to an instantaneous drop in reservoir pressure at one end of a linear reservoir. Since the recorder registered a temperature every two seconds, a temperature at each of the 16 thermocouples was recorded once every 32 seconds.

Runs were made on six plates consisting of one metal only (simulating uniform homogeneous reservoirs), on four bimetallic plates, on one three-layered plate and on one four-layered plate. For the multilayered system, the plates were in direct contact, representing a reservoir with no barriers to flow between strata. In addition, one plate consisting of layers of aluminum, rubber and steel, and two consisting of layers of brass, rubber and steel were investigated. These latter studies correspond to depletion when the permeabilities differ by about 500:1 (see Table 1).

The temperature-distribution data obtained from the runs were plotted as dimensionless groups in the manner of Carslaw and Jaeger.[7] The equations presented by these authors considered heat losses to be nonexistent and were not applicable in this study. Corrections were made for heat gains through radiation and for resistence to heat flow caused by "skin" effects which would apply to that area of the plate in contact with the ice water.[8]

The temperature distribution at some real time would plot as a curve which would correspond to a dimensionless time. Knowing the real time and length of the plate, effective diffusivity was calculated easily. From correlations involving this parameter, the behavior of the flow of heat in the stratified system used is elucidated. By analogy, the flow of fluids in layered systems can then be inferred.

To better evaluate the multilayered systems, runs were made on the individual metal plates. These data are compared to calculated diffusivities in Fig. 3 and Table 1. With the exception of steel, the experimental data were slightly higher than the calculated diffusivities. Since the handbook diffusivity data are also experimental, it is felt that the measurements made in this study are valid.

The results taken from four bimetallic plates are shown in Fig. 4. All four show that the diffusivities decrease with time during the early production period. This may be explained on the assumption that, initially, the larger portion of the heat removed from the model comes from the more-conductive plate. The less-conductive plate is also losing heat, but at a lower rate. The combined heat flow would then indicate a higher-than-average diffusivity. As the temperature wave moves toward the outer boundary, the diffusivity decreases until a substantially steady-state condition is achieved. The diffusivity of a system depends on the diffusivities of its single-layer components, as shown by the positions of the copper-lead and copper-Wood's metal lines. The slopes of the two lines differ but little, while the effective diffusivity is lowered considerably due to the low conductivity of Wood's metal compared to that of lead.

The thickness of the plates also causes a shifting of the curves as seen in Fig. 5. The copper-lead plate was converted to a three-layered system by bonding a layer of Wood's metal on the lead side of the plate. The results show a downward shifting of the curve, as well as a reduction in its slope. Another layer of Wood's metal, attached to the copper, further lowered and flattened the curve. This curve could be considered as having negligible slope, indicating a constant diffusivity after a fairly short period of time.

Having the measured diffusivities of several layered systems, it was desired to find a satisfactory method for calculating the diffusivities of the same systems. In doing so, two methods were used, both of which are weighted diffusivities as follows.

$$\bar{\eta} = \frac{\sum_{n=1}^{n} k_n b_n}{\sum_{n=1}^{n} (C_n \rho)_n b_n} \qquad \ldots\ldots\ldots\ldots (1)$$

TABLE 1 — PHYSICAL PROPERTIES OF SOME METALS, ALLOYS AND RUBBER

Material	Specific* Heat	Density,* lb/ft	Conductivity, Btu/(hr)(sq ft)(° F/ft)		Diffusivity, sq ft/hr	
			Tables**	Experimental	Calculated	Experimental
Aluminum	0.22	168.5	117	120	3.15	3.23
Brass	0.094	534.4	56	61	1.12	1.22
Copper	0.0921	555	224	229	4.38	4.49
Lead	0.0316	687	20	23	0.92	1.08
Stainless Steel	0.107	488	16	8.6	0.31	0.165
Wood's Metal	0.0352	659.23	7.7*	8.9	0.334	0.389
Rubber			0.109		0.0043	

*From Ref. 11.
**From Refs. 9 and 10.

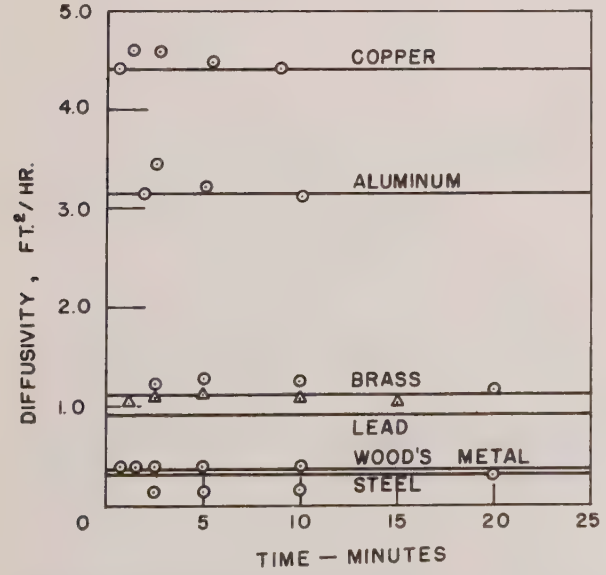

FIG. 3—COMPARISON OF CALCULATED AND EXPERIMENTAL DIFFUSIVITIES FOR VARIOUS METAL PLATES.

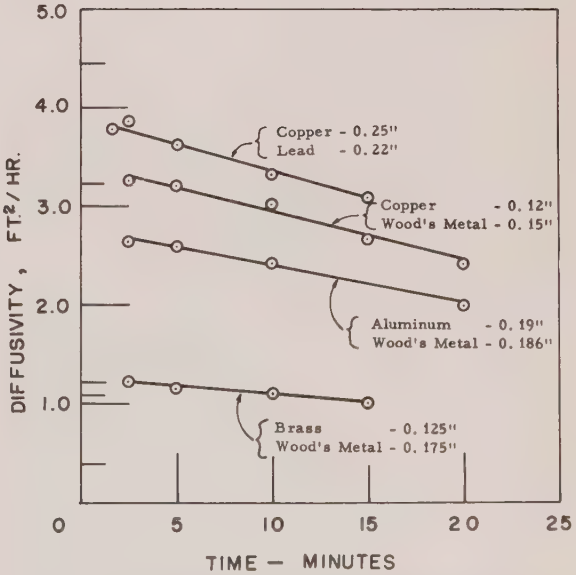

FIG. 4 — EFFECTIVE THERMAL DIFFUSIVITIES OF BIMETALLIC PLATES.

$$\bar{\eta}' = \frac{\sum_{n=1}^{n} a_n h_n}{\sum_{n=1}^{n} h_n} \quad \ldots\ldots\ldots\ldots \quad (2)$$

where k_n = conductivity of the nth layer or k/μ from core analyses,

h_n = thickness of the nth layer or thickness having permeability k from core analysis,

C_m = specific heat,

ρ = density,

ρC_m = density-specific heat product equivalent to product of rock porosity and fluid compressibility,

η_n = diffusivity of the nth layer in thermal or fluid-flow units, and

$\bar{\eta}, \bar{\eta}'$ = effective diffusivity in either system.

Based on analytical studies, Eq. 1 should be expected to provide a fairly good correlation of the experimental data.

The values calculated for the plates used are shown in Table 2 and are compared to the diffusivities obtained experimentally. The values used for measured diffusivities were obtained by computing the area under the curves, such as Fig. 5, and dividing by the total time elapsed. These values are in close agreement with diffusivities calculated by Eq. 1, with the exception of the brass-Wood's metal plate.

TABLE 2 — COMPARISON OF CALCULATED AND EXPERIMENTAL DIFFUSIVITIES

Plate	Effective Diffusivity $\bar{\alpha}$, (sq ft/hr) $\frac{\sum_{n=1}^{n} k_n h_n}{\sum_{n=1}^{n} (C_m\rho)_n h_n}$	$\frac{\sum_{n=1}^{n} a_n h_n}{\sum_{n=1}^{n} h_n}$	Experimental (Average)
Aluminum-Wood's Metal	2.17	1.83	2.24
Brass-Wood's Metal	0.89	0.73	1.07
Copper-Lead	3.54	2.88	3.51
Copper-Wood's Metal	2.98	2.20	2.97
Copper-Lead-Wood's Metal	3.17	2.45	3.20
Wood's Metal-Copper-Lead-Wood's Metal	3.11	2.37	3.08

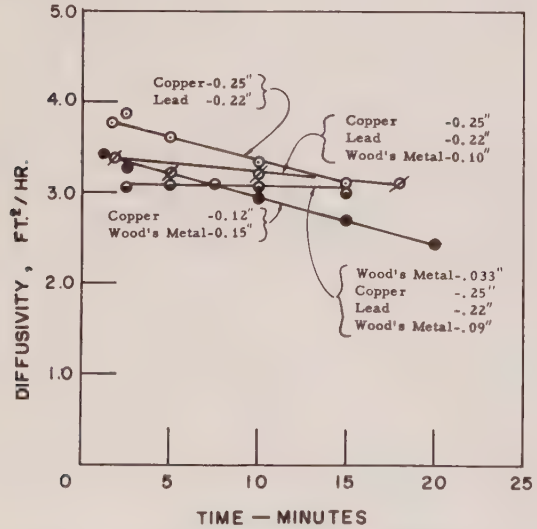

FIG. 5 — THE CHANGE IN DIFFUSIVITY WITH TIME OF MULTILAYERED, LINEAR METAL PLATES.

Further confirmation of the equation was obtained by studying a stratified model composed of 0.104 in. of rubber between two 1/8-in. copper plates. The thickness of the rubber layer was increased to 0.208, 0.312, 0.392 and 0.56 in. for successive runs. This resulted in ratios of total rubber thickness to total copper thickness of 0.416, 0.832, 1.248, 1.568 and 2.240, respectively. Experimentally determined values of the rubber used in this experiment indicated a heat capacity of 0.6 that of copper and a diffusivity of about 0.002 that of copper. Comparison of the calculated and the effective diffusivity values of the stratified models are shown in Table 3. The effective and calculated values agree quite well.

These results are plotted as ratios of effective to calculated diffusivity vs dimensionless time in Figs. 6 and 7. These plots then may be used for correcting a calculated diffusivity of some system to its effective diffusivity at any time within the range of dimensionless times studied. Experimentally, the two-layered systems showed a greater change in diffusivity with time than the multilayered plates studied, as indicated by the slopes of the lines. Mirror-image conditions should be kept in mind when building and operating the model.

DISCUSSION

The application of the results of Eq. 1 may best be illustrated by scaling the models to a hypothetical oil reservoir operated at pressures above the bubble point, and computing the cumulative fluid influx by the Hurst-van Everdingen equation.[4]

$$Q(t_m) = 2A\sqrt{\frac{\bar{\phi}\,C\,\bar{K}}{\pi\,\mu}}\left\{(P_o - P(t_1))\sqrt{t_m} + [P(t_1) - P(t_2)]\sqrt{t_m - t_1}\right\} + \ldots\ldots + \ldots\ldots\ldots\ldots\ldots\ldots\ldots\ldots \quad (3)$$

where Q = cumulative fluid influx,

A = cross-sectional area perpendicular to the direction of flow,

C = compressibility of fluid,

$\bar{\phi}$ = weighted porosity,

TABLE 3 — COMPARISON OF EXPERIMENTALLY OBTAINED DIFFUSIVITIES WITH THOSE CALCULATED BY PROPOSED EQUATION

Rubber-Copper Thickness Ratio	Effective Diffusivity Calculated by Proposed Eq.	Effective Diffusivity from Experimental Data		
		$\bar{t}=0.195$	$\bar{t}=0.391$	$\bar{t}=0.782$
.416	3.52	3.26	3.19	3.14
.832	2.94	2.92	3.02	2.95
1.248	2.52	2.36	2.69	2.52
1.568	2.27	2.24	2.24	2.30
2.240	1.88	—	1.79	1.96

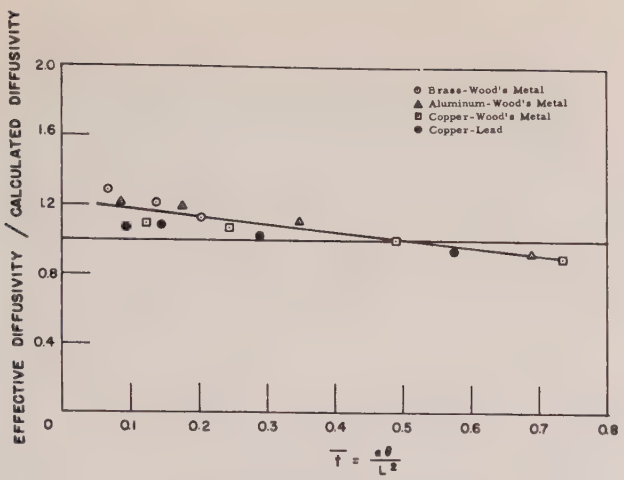

FIG. 6 — CHANGE IN DIFFUSIVITY WITH TIME FOR BIMETALLIC PLATES.

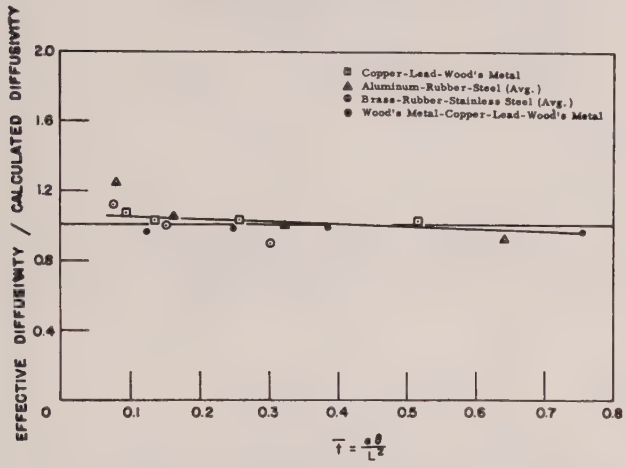

FIG. 7—THE CHANGE IN DIFFUSIVITY WITH TIME FOR MULTILAYERED PLATES.

P_o = initial reservoir pressure,
P = pressure,
$\overline{K}$ = weighted permeability,
μ = viscosity,
t_m = total period of time under consideration, and
t = time.

Because this equation is applicable to unsteady-state flow in infinite linear systems, a time will be chosen such that the pressure wave has not yet reached the outer boundary of the reservoir. The equation must be simplified for these calculations due to the manner in which the data were obtained. The sudden application of ice water to the edge of the plate is analogous to a sudden pressure drop at the inner boundary of a linear reservoir. It was not possible to lower the temperature in a step-wise manner with the method and equipment devised. Instead of a step-wise solution, therefore, a single pressure drop over one period of time will be used.

Then, by introducing the reservoir diffusivity analog $\eta = k/C\mu\phi t$ into the equation, it reduces to

$$Q = 2AC\,\phi\Delta P\sqrt{\frac{\eta\,\theta}{\pi}} \quad \ldots\ldots\ldots\ldots \quad (4)$$

The dimensions of the model will be expanded to reservoir size by using a horizontal scale of 1 in.: 1,000 ft and a vertical scale of 1 in.: 100 ft. The cross-sectional area, numerically, then will be 400,000 times the thickness of the model. The fluid was assigned a compressibility of 5.0×10^{-6} vol/vol/psi and a viscosity of 0.4 cp. The rock and fluid properties then were related to the thermal properties by setting the conductivity, in Btu's per (hour)(square feet)(degrees Fahrenheit per feet), equal to permeability in millidarcies and by setting the specific heat-density term equal to $C\mu\phi(10)^6$. The porosity is the only quantity which varies in the latter group of terms since each layer is assumed to contain the same fluid.

For the purpose of this analogy, a reservoir time of 5,000 hours was chosen. Since no pressure change has been felt at the outer boundary of the reservoir during this time, the system may be considered infinite.

The copper plate is then analogous to a reservoir 12,000-ft long, 4,000-ft wide and 25-ft thick, with a porosity of 25.5 per cent, a permeability of 229 md and the fluid properties previously mentioned. The initial reservoir pressure is considered to be well above the bubble point.

The lead plate will represent a reservoir having the same horizontal dimensions and a pay thickness of 22 ft. Its porosity is 10.9 per cent and its permeability 23 md. The fluid properties and initial reservoir pressure will be the same as those in the copper-plate analogy.

To calculate the cumulative influx of fluid, a pressure drop of 100 psi was introduced suddenly at the interior boundary of each individual reservoir. The fluid produced from the reservoir simulated by copper would then be

$$\frac{(2)(250(4000)(5\times10^{-5})(255)}{5.61}\sqrt{\frac{(0.33)(3600)(5000)}{\pi}}\,(100)$$

$$= 62{,}600 \text{ bbl.}$$

Similarly, the reservoir simulated by lead had a cumulative fluid influx of 11,320 bbl at the end of 5,000 hours. Assuming that the two reservoirs were separated by a thin impermeable layer, the total fluid produced would be the sum of the two, or 73,920 bbl.

In calculating the fluid influx for this system without the impermeable layer between the reservoirs, an average weighted porosity was used. The diffusivity was calculated by Eq. 1 and converted to a reservoir diffusivity analog. With all the other factors remaining the same, the cumulative fluid influx was 76,400 bbl. This is an increase of 2,480 bbl, or 3.25 per cent, over the total cumulative production of the two layers calculated individually. This increase could be attributed to the presence of a cross flow between the two reservoirs.

A third layer, represented by Wood's metal, had thermal properties proportional to a permeability of

8.9 md, a porosity of 11.5 per cent and a diffusivity of 0.028 sq ft/sec. Its thickness is 12 ft and the other dimensions, as well as its fluid properties, are the same as for the copper and lead layers. Using the same pressure differential for the same 5,000 hours, this reservoir would produce 3,930 bbl. When combined with the other two reservoirs to form a three-layered system susceptible to cross flow, the cumulative production from the system would be 84,200 bbl. In comparison, the sum of the cumulative production from each layer would be 77,850 bbl. According to these calculations then, an increase in production of 6,350 bbl, or 8.2 per cent, is realized when the pays are not isolated by impermeable layers.

Several other hypothetical stratified systems have been analyzed, and all have shown a higher cumulative fluid influx for the stratified systems where cross flow prevailed.

Cross flow is apparent in the thermal model by the absence of a marked difference between the temperature distributions in the various plates of a given system. When plotted after the manner of Carslaw and Jaeger,[7] the data points taken all fell on the same dimensionless time line, regardless of the material from which the data were taken.

It seems reasonable then to consider the higher values, obtained using a common diffusivity, to be values which compensate for a cross flow.

The effects of having a material of low conductivity between plates of relatively high conductivity are illustrated in Fig. 8. The diffusivity measured on the aluminum side of the plate is high initially, falls rather rapidly and then begins leveling off as the steady-state condition is approached. The stainless-steel-side data indicate little change, if any, during the course of the run.

The steep slope of the aluminum curve at low dimensionless times is due to a changing rate of cross flow induced by the large initial temperature differential between the rubber and aluminum. The steel, compared to aluminum, is itself fairly low in conductivity and experiences a rather small differential across its thickness.

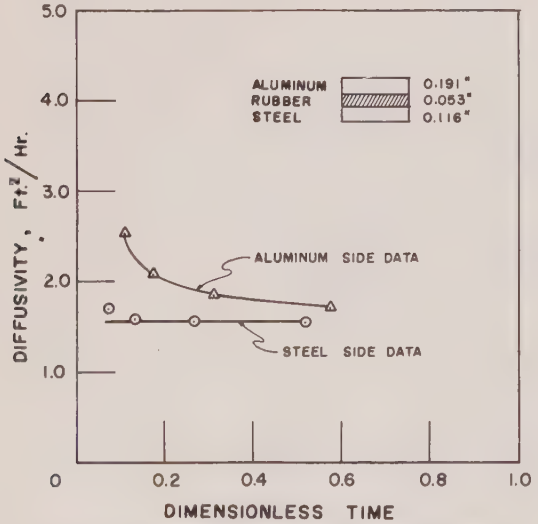

FIG. 8 — EFFECT OF A LAYER OF LOW CONDUCTIVITY ON EFFECTIVE THERMAL DIFFUSIVITY.

From mathematical model studies of layered systems, one finds that the rate of drainage may be expected to achieve a pseudo-steady state. The time required, rate of depletion and approach to steady state depends on the ratios of porosities, permeabilities, layer thicknesses and lengths.

To determine the effect of the thickness of the low-conductive layer on the performance of the system, runs were made on a brass, rubber and steel plate. The rubber thickness was increased from 0.009 in. in the first set of runs to 0.106 in. in the second set of runs. These results are illustrated in Fig. 9(A and B). The data taken from the thin-layer system gave results similar to those obtained in two-layered systems but with a definite temperature differential across the rubber, i.e., a brass-rubber and a steel-rubber plate, but with the rubber acting as if it were higher in conductivity than it is.

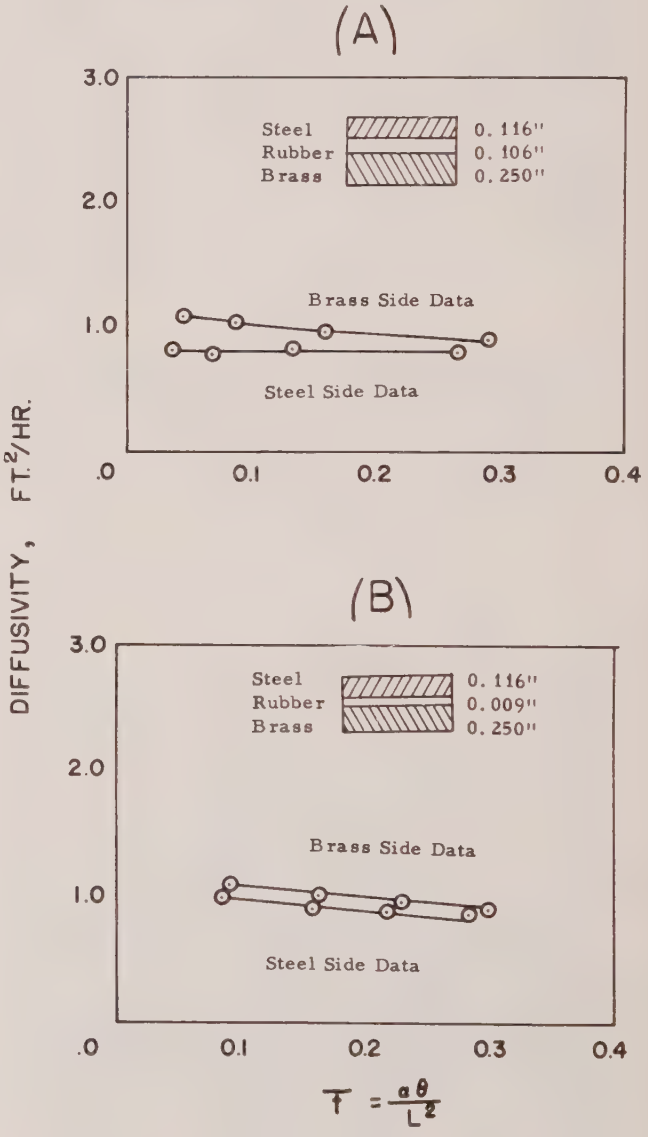

FIG. 9 — THE EFFECT OF VARYING THE THICKNESS OF A LOW-CONDUCTIVE MATERIAL BETWEEN TWO METALS ON DIFFUSIVITY.

The 0.106-in. rubber layer caused a higher initial diffusivity difference between the plates. These results are similar to those obtained with the aluminum-rubber-steel system.

In Fig. 10(A and B) the temperature differential across the thickness of the plate is plotted, in dimensionless form, with time. The maximum difference is shown at early times close to the source. Peaks are indicated at $\bar{X}$ values of 0.8 and 0.6, while none are discernible at distances farther than this from the source.

The effect of the thicker rubber layer is fairly obvious at early times. If the system were to be considered as a stratified pay with a maximum terminal-pressure differential of 200 psi, the peak at 0.165 dimensionless pressure would correspond to a pressure differential of 33 psi across the width of the sand. This differential would be felt at a distance of 200 ft from the pressure sink if the system were considered to be 1,000-ft long. At the same point and at the same time, the differential would be 10 psi in the thin-layer system. This difference is less pronounced at later times.

Using the same analogy at later times, the differential across the thick tight zone would be 7- to 12-psi while across the thin tight zone the maximum differential would be 11-psi near the source and 2- to 6-psi elsewhere.

CONCLUSIONS

Experimental confirmation has been obtained of the utility of an average permeability, porosity and compressibility for layered or stratified reservoirs in which cross flow occurs. This proper value is obtained by Eq. 5

$$\bar{\eta} = \frac{\sum_{n=1}^{n} k_n h_n}{\sum_{n=1}^{n} (C_n \phi)_n h_n} \quad \ldots\ldots\ldots\ldots \quad (5)$$

A knowledge of the proper method of weighting core-analysis data has considerable application. In its simplest application in petroleum reservoir equations involving transient pressure where rock compressibility is neglected and the rock is filled with a single fluid of constant compressibility, the proper single value of permeability to use in a stratified pay is indicated to be given by the sum of the permeabilities at each 1-ft interval divided by the total pay thickness in feet. If data are available at irregular spacing, then the proper value of k is given by $(\Sigma k h) \div \Sigma h$. The proper value of porosity to be used in the transient equation is equal to $(\Sigma \phi h)/(\Sigma h)$.

Using these definitions, a layered reservoir with cross flow can be considered as a uniform homogeneous reservoir of the same thickness and length if the permeability-porosity ratio is represented by $(\Sigma k h)/\Sigma \phi h$.

It should be clearly emphasized that this recommendation applies when the reservoir approaches pseudo-steady state because the effective value of k will be larger during the early transient period.

In their simplest application, these findings indicate that a first estimate of the proper value of permeability and porosity may be obtained quite easily by preparing a table listing the permeability and porosity at each 1-ft interval. Sum each column and divide by the total pay thickness to obtain the average permeability and porosity. This practice has been almost universal and may represent a first approximation.

In reality, an oil-water interface usually exists and the connate water varies from foot to foot. Since this is true, it should be recognized that the *effective* compressibilities are different at each 1-ft interval. For this case, the proper porosity-compressibility product is obtained from $(\Sigma c \phi h)/(\Sigma h)$, where the compressibility c at each 1-ft interval represents the properly weighted value for the particular rock properties, porosity, connate water and oil. Although this calculation takes longer, it yields a better answer for the best single

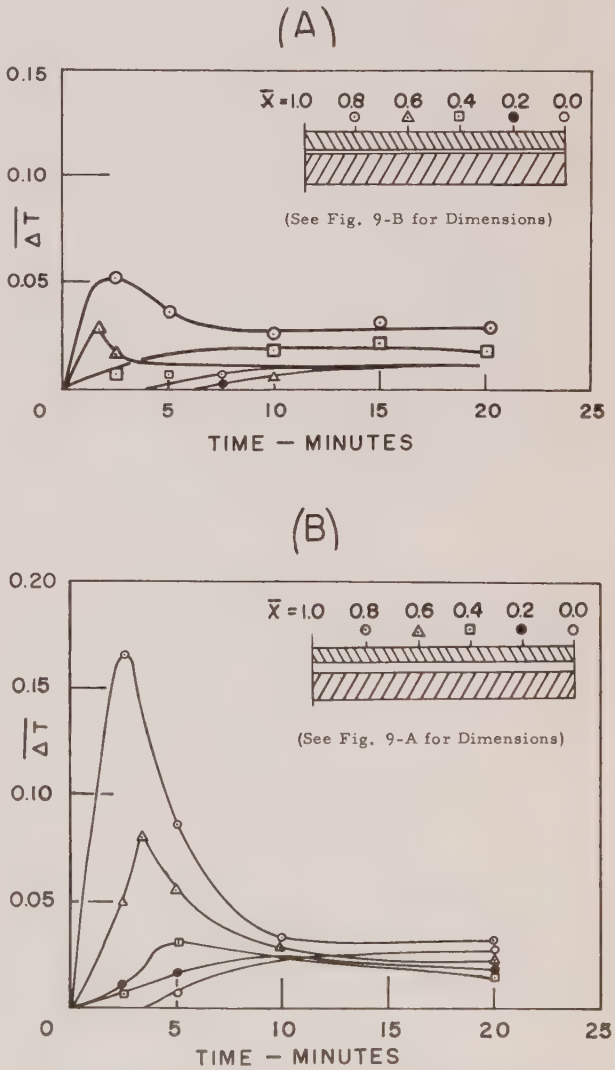

FIG. 10 — THE CHANGE IN TEMPERATURE DIFFERENTIAL ACROSS A LAYERED SYSTEM.

numbers to be used to represent the effective properties of the pay.

ACKNOWLEDGMENTS

The work reported here is part of that done on the Texas Petroleum Research Committee project entitled, "Studies of Fractured and Heterogeneous Reservoirs". Appreciation is expressed to TPRC for permission to publish the results.

REFERENCES

1. Uren, Lester C.: "Increasing Oil Recovery by Flooding", *National Petroleum News* (Aug. 3, 1927) 50.
2. Levorsen, A. I.: *Geology of Petroleum*, W. H. Freeman and Co., San Francisco (1956) 59.
3. Muskat, M.: "The Effect of Permeability Stratifications in Complete Water-Drive Systems", *Trans.*, AIME (1950) Vol. 189, 349.
4. Hurst, W. and van Everdingen, A. F.: "Application of the Laplace Transformation to Flow Problems in Reservoirs", *Trans.*, AIME (1949) Vol. 186, 305.
5. Muskat, M.: *The Flow of Homogeneous Fluids Through Porous Media*, McGraw-Hill Book Co., Inc., N. Y. (1937) 139.
6. Landrum, B. L. and Crawford, P. B.: "A New Experimental Model for Studying Transient Phenomena", *Trans.*, AIME (1959) Vol. 216, 33.
7. Carslaw, H. S. and Jaeger, J. C.: *Conduction of Heat in Solids*, Oxford U. Press (1947) 7.
8. Bowman, C. H. and Crawford, P. B.: "A Mathematical Study of Unsteady-State, Single-Phase Flow in Petroleum Reservoirs", Unpublished report, TPRC.
9. *International Critical Tables* (1929).
10. McAdams, W. H.: *Heat Transmission*, Second Ed., McGraw-Hill Book Co., Inc., N. Y. (1942).
11. *Handbook of Chemistry and Physics*, 24th Ed., Chemical Rubber Publishing Co.

★★★

Pressure Studies in Bounded Reservoirs

S. A. HOVANESSIAN
MEMBER AIME

CALIFORNIA RESEARCH CORP.
LA HABRA, CALIF.

ABSTRACT

Analytical solutions are obtained for calculating the pressure distribution in rectangular fields due to injection and/or producing wells located anywhere within the field. The field is assumed to be homogeneous with either constant pressure or no-flow boundaries. These solutions are extended to include the calculation of average reservoir pressure and permeability from pressure build-up curves. Numerical examples are given to illustrate the application of equations to practical problems.

INTRODUCTION

Pressure distribution analyses are of considerable importance in the field of reservoir mechanics. A number of papers dealing with this subject have appeared in the petroleum literature. Perrine[1] in 1956 presented a summary of the methods available for pressure build-up calculations and discussed the applicability of each in some detail. More recently (1958), Hazebroek, *et al,*[2] discussed a theoretical method for obtaining pressure distribution in a radial field. Also in 1958, Nisle[3] gave a theoretical solution of the pressure distribution in a field extending to infinity with a partially penetrating line source at the origin.

Mathews, *et al,*[4] applied the method of images to existing solutions for pressure distribution in radial fields and obtained expressions for calculating pressures in bounded reservoirs. However, a literature survey revealed that a general analytical solution for the pressure distribution in a rectangular field, with injection and/or production wells located anywhere within the field, was not available. Such a solution could be used to approximate the pressure distribution in a field the shape of which is nearly rectangular. Furthermore, it could be applied to pressure calculations pertaining to a single well taken from a system of wells which were drilled in a rectangular pattern. In this case the boundaries of the well drainage area are considered to be the perpendicular bisectors of the lines joining the well and its nearest neighbors.

Original manuscript received in Society of Petroleum Engineers office April 20, 1961. Revised manuscript received July 14, 1961. Paper presented at 36th Annual Fall Meeting of SPE, Oct. 8-11, 1961, in Dallas.

[1]References given at end of paper.

The basic problem considered in this paper consists of a rectangular field with either constant-pressure or no-flow boundaries and with either an injection or production well located anywhere within the field. The physical properties of the rock and fluids present are considered to be constant. Analytical expressions are obtained for the pressure distribution within the field during the production or injection periods. These expressions, which are infinite series, can be used to evaluate pressure at any point within the field as a function of time and position. For fields containing more than one well (production and/or injection), the solutions for each well acting independently are superposed. That is, at any point in the field, the pressures due to each injection or production well acting alone can be algebraically added to give the pressure resulting from all wells acting simultaneously. Evaluation of the series solutions given in this paper is readily accomplished by means of an electronic digital computer; and, in most cases, sufficient accuracy is obtained by setting the upper limits of summation at 20.

These solutions are extended to include the calculation of average reservoir pressure and permeability from build-up data. A number of numerical examples are given to illustrate application of the solutions to actual field problems.

ANALYTICAL SOLUTIONS

The partial differential equation representing the pressure distribution in a homogeneous rectangular field (see Fig. 1), having a single source or sink of strength Q, can be written*

$$\frac{\partial^2 p}{\partial x^2} + \frac{\partial^2 p}{\partial y^2} = \alpha \frac{\partial p}{\partial t} + \beta Q(l,q) \quad . \quad . \quad . \quad . \quad (1)$$

where

$$\alpha = 157.952 \frac{\phi c \mu}{k} \text{ and } \beta = 886.905 \frac{B_o \mu}{k},$$

x, y = space co-ordinates, ft,
(l, q) = location of source or sink, ft,
p = pressure at (x, y), psi,
ϕ = porosity, fractional,

*This equation is the same as the two-dimensional flow equation with a source (see Ref. 5).

c = compressibility of fluids plus rock structure, psi^{-1},
μ = viscosity, cp,
k = permeability, md,
t = time, days,
B_o = oil formation volume factor, reservoir bbl/STB, and
Q = specific production (+) or injection (–) rate, STB/D-ft of thickness.

Although Eq. 1 is for a homogeneous field with single-phase flow, by using "average" field properties,[6] the solutions of this equation can be applied to multiphase-flow systems.

Since Eq. 1 is a *linear* partial differential equation, the principle of superposition of solutions applies. Consequently, if there are two or more production and/or injection wells, the pressures due to each well acting independently can be added algebraically to give the resultant pressure.

CASE I – CONSTANT PRESSURE BOUNDARIES (CPB)

The solution of Eq. 1, subject to the constant pressure boundary condition and an initial constant pressure distribution of P_o, is given by the equation (see Appendix),

$$p(x,y,t) = P_0 - \frac{4\beta Q}{\pi^2 ab} \sum_{n=1}^{\infty} \sum_{m=1}^{\infty} \frac{1}{(m^2/a^2 + n^2/b^2)} \left\{1-\exp\left[-\frac{\pi^2}{\alpha}\left(\frac{m^2}{a^2}+\frac{n^2}{b^2}\right)t\right]\right\} \sin\frac{m\pi l}{a} \sin\frac{n\pi q}{b} \sin\frac{m\pi x}{a} \sin\frac{n\pi y}{b} \quad \ldots\ldots\ldots\ldots\ldots\ldots\ldots\ldots (2)$$

where P_o = uniform initial pressure distribution, psi,
m, n = summation indices, integers, and
a, b = dimensions of the rectangular section, ft.

The infinite series of Eq. 2 represents the pressure distribution as a function of location (x, y) and time (t). Note that the exponential expression within the brackets of Eq. 2 is the time-dependent part of each term. For large values of time t, this expression will go to zero and the steady-state solution will result. The series converges rapidly, except at the location of the source or sink, where it diverges to infinity.

Fig. 2 depicts the pressure distribution in a square field with an injection well at the center and an initial pressure distribution P_o of zero. This figure is obtained by evaluating Eq. 2 along lines of constant ordinate. Note that the pressures increase as one moves toward the injection well and that the rate of pressure change increases similarly. Note also that the pressures at the boundaries remain constant at zero, in accord with the boundary conditions.

CASE II – NO-FLOW BOUNDARIES (NFB)

The solution of Eq. 1, subject to the no-flow boundary condition and an initial constant pressure distribution of P_o, is as follows (see Appendix).

$$p(x,y,t) = P_0 - \frac{\beta Q}{ab}\left[\frac{t}{\alpha} + 2\sum_{m=1}^{\infty} \frac{1}{\pi^2(m^2/a^2)}\left\{1-\exp\left[-\frac{\pi^2}{\alpha}\left(\frac{m^2}{a^2}\right)t\right]\right\}\cos\frac{m\pi l}{a}\cos\frac{m\pi x}{a} + 2\sum_{n=1}^{\infty} \frac{1}{\pi^2(n^2/b^2)}\left\{1-\exp\left[-\frac{\pi^2}{\alpha}\left(\frac{n^2}{b^2}\right)t\right]\right\}\cos\frac{n\pi q}{b}\cos\frac{n\pi y}{b} + 4\sum_{n=1}^{\infty}\sum_{m=1}^{\infty} \frac{1}{\pi^2(m^2/a^2 + n^2/b^2)}\left\{1-\exp\left[-\frac{\pi^2}{\alpha}\left(\frac{m^2}{a^2}+\frac{n^2}{b^2}\right)t\right]\right\}\cos\frac{m\pi l}{a}\cos\frac{n\pi q}{b}\cos\frac{m\pi x}{a}\cos\frac{n\pi y}{b}\right] \quad \ldots\ldots\ldots\ldots\ldots\ldots\ldots\ldots (3)$$

Except at the location of the line source (where it diverges to infinity), Eq. 3 can be used to evaluate the pressure for any specified location at any given time. The series converges at a reasonable rate, and good approximations to the pressure can be obtained by setting the upper limits of the summation to 20.

Inspection of Eq. 3 shows that (in accord with the assumed initial condition) $p(x, y, t)$ equals P_o when t is zero. It can also be seen that the term t/α increases with time while all other terms get smaller and smaller. Consequently, no steady-state condition is ever reached because the pressure at any location must always increase with time so long as constant injection rate is maintained. It is interesting to note that in Eqs. 2 and 3 the exponential expressions depend on time but not on location, whereas the trigonometric expressions depend on location but not on time.

Fig. 3 depicts the pressure distribution in a square field with an injection well at the center and an initial pressure distribution P_o of zero. Since there is no flow across the outer boundary, pressures in the field increase with time. After an initial transient period, a semisteady-state period is encountered whereby with increasing time the curves maintain the same shape but move upward along the pressure axis. Note that the slope of all curves at the boundaries is zero, in accord with the no-flow boundary condition.

BUILD-UP ANALYSIS

The solutions given in the previous section express the pressure distribution in the reservoir during the periods of production or injection. Once the production or injection terminates, they no longer express the pressure behavior of the system. To utilize these solutions after the termination of production or injection, we resort to the convolution integral,[7] and assume a period of constant production T prior to a shut-in period of t_s. The following results.

$$\Delta p = p(T + t_s) - p(t_s) \quad \ldots\ldots (4)$$

where $\Delta p = P_o - p_s(t_s)$,
p_s = pressure after shut-in, psi,
p = flowing pressure as given by Eqs. 2 and 3, psi,
t_s = build-up time, days, and
T = production or injection time prior to shut-in, days.

If the well drainage area is square ($a = b$), the following dimensionless quantities[8] may be defined.

$$\overline{\Delta p} = 0.001127 \frac{k\Delta p}{Q\mu B_o} \quad \ldots\ldots (5)$$

$$\left.\begin{aligned} \overline{t} &= 0.006331 \frac{kt_s}{\varphi c\mu a^2} \\ \overline{T} &= 0.006331 \frac{kT}{\varphi c\mu a^2} \end{aligned}\right\} \quad \ldots\ldots (6)$$

Furthermore, if the pressure history of a well can be suitably expressed by either Eq. 2 or 3, then Eq. 4 may be evaluated in terms of these dimensionless quantities. Fig. 4 summarizes the results of a number of such evaluations for a square section with either an off-center or a centrally located well. The boundaries of the section are either at constant pressure or have no flow. In these calculations a point corresponding to a wellbore radius of 3-in. was used. It was observed, however, that varying this radius from 3 to 10 in. had no significant effect on the evaluation of Δp.

Fig. 4 includes the dimensionless pressure-vs-time plots for a production well located at $l = q = \frac{a}{4}$. It is noted that the slope of these curves and the curves of centrally located wells are the same. It is further observed that the curve of NFB case is higher than that of a centrally located well. This will result in lower pressures during the build-up period. This is reasonable because during the production period the effect of boundaries is greater at the well (compared to centrally located wells), resulting in lower flowing pressures at the time of shut-in. This, in turn, results in lower build-up

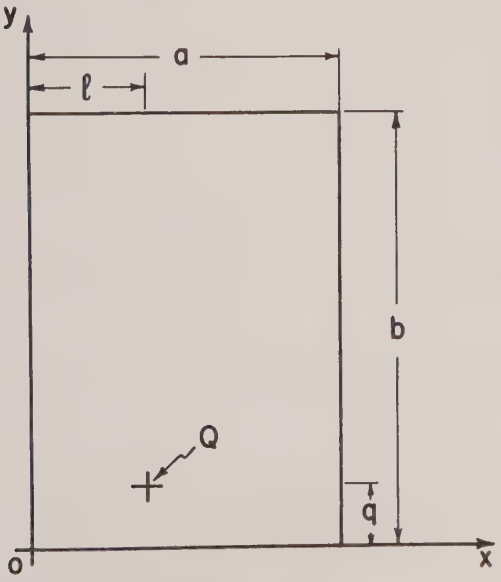

FIG. 1 – RECTANGULAR FIELD.

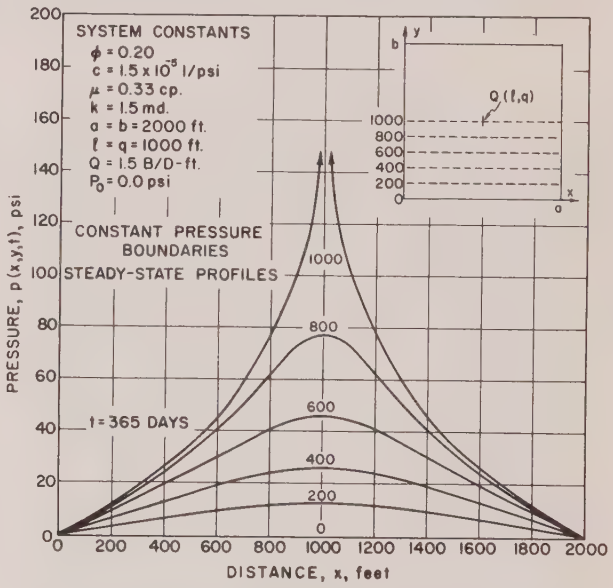

FIG. 2–PRESSURE DISTRIBUTION FOR FIELDS WITH CONSTANT PRESSURE BOUNDARIES.

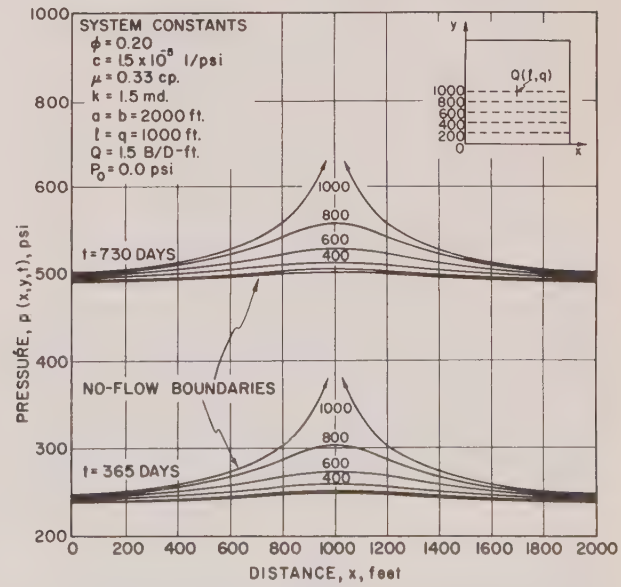

FIG. 3–PRESSURE DISTRIBUTION FOR FIELDS WITH NO-FLOW BOUNDARIES.

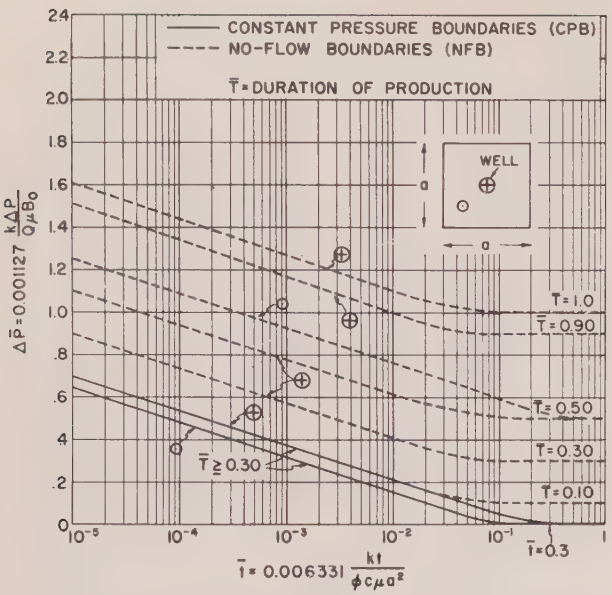

FIG. 4 – DIMENSIONLESS PRESSURE BUILD-UP CURVES.

pressures. The curve of CPB case of Fig. 4 is lower than that of a centrally located production well. This will result in higher build-up pressures. This is also reasonable since during the production period the constant pressure boundaries (at the original field pressure) are closer to the producing well, resulting in higher flowing pressures at the time of shut-in. This higher flowing pressure will result in higher pressures during the build-up period.

For $\bar{t} \leq 0.02$, observe that all curves of Fig. 4 have the same constant slope; this slope is

$$\frac{\Delta(\overline{\Delta p})}{\Delta(\log \bar{t})} = -0.1675 \quad \ldots\ldots\ldots \quad (7)$$

Since in practice the actual pressure against time is plotted on a semilogarithmic scale, we equate this slope (with proper conversion factors) to that of Eq. 7.

$$0.1675 = 0.001127 \frac{k}{Q\mu B_o}\left[\frac{\Delta p}{\Delta(\log t_s)}\right]_{\text{FIELD}} \quad \ldots\ldots\ldots\ldots\ldots\ldots \quad (8)$$

From Eq. 8 the effective permeability k is

$$k = 148.62 \frac{Q\mu B_o}{\left[\Delta p/\Delta(\log t_s)\right]_{\text{FIELD}}} \quad \ldots \quad (9)$$

With the aid of Fig. 4 and Eqs. 5, 6 and 9,* a number of calculations can be made utilizing the pressure build-up curves of practical field cases. A summary of possible calculations is given in Table 1. To illustrate the application of the method, a numerical example is worked out for each case. In all of the following examples the field is assumed to be square with a production well at the center.

*Comparing Eq. 9 above and Eq. 6 of Ref. 8, one notes a discrepancy of about 10 per cent. This is due to the effect of boundaries and also the fact that in the curves of the reference a steady-state condition is assumed prior to shut-in. This is equivalent to setting $P(T + t_s) = P(T)$ in Eq. 4.

TABLE 1 – SUMMARY OF POSSIBLE CALCULATIONS FOR FOUR CASES

	Case 1	Case 2	Case 3	Case 4
GIVEN:	P_o, k, ϕ, c μ, Q, B_o, a	Build-up Curves μ, Q, B_o	Build-up Curves ϕ, c, μ, Q, B_o, a	Complete Build-up Curves ϕ, c, μ, Q, B_o
FIND:	Build-up Curves	k	k, Field Pressure	k, a

CASE 1

Given: P_o = 3,500 psi, k = 1.5 md, ϕ = 0.20, c = 1.5×10^{-5} psi^{-1}, μ = 0.33 cp, Q = 1.0 STB/D-ft, B_o = 1.5 reservoir bbl/STB and a = 2,000 ft. Assume steady state before shut-in for CPB and a production time of 365 days for NFB.

Find: the pressure build-up curves.

The production time of NFB, from Eq. 6, corresponds to $\bar{T} = 0.88$. Suppose we want to obtain build-up pressures at 10^{-2}, 10^{-1}, 1, ... days. From Eq. 6, $t_s = 10^{-2}$ days corresponds to

$$\bar{t} = 0.006331 \frac{1.5 \times 10^{-2}}{0.20 \times 1.5 \times 10^{-5} \times 0.33 \times (2{,}000)^2}$$

$$= 2.4 \times 10^{-5}.$$

From Fig. 4 this value corresponds to

$\overline{\Delta p} = 0.63$ CPB

and

$\overline{\Delta p} = 1.42$ NFB.

Using Eq. 5, Δp corresponding to the above will be

Δp = 185 psi CPB

and

Δp = 415 psi NFB,

or the actual pressures are

p_s = 3,500 – 185 = 3,315 psi CPB,

and

p_s = 3,500 – 415 = 3,085 psi NFB.

The values of pressures can be obtained in a similar manner for the rest of the t_s values. A plot of the build-up curve is shown on Fig. 5.

CASE 2

Given: μ = 0.33 cp, Q = 1.0 STB/D-ft, B_o = 1.5 reservoir bbl/STB and the pressure build-up curves of Fig. 5.

Find: the effective permeability k.

The slope of the build-up curves of Fig. 5, taking the section between $t = 10^{-1}$ and 1, is

$$\left[\frac{\Delta p}{\Delta(\log t_s)}\right]_{\text{FIELD}} = \frac{3{,}408 - 3{,}360}{0 - (-1)} = 48.$$

From Eq. 9 we have

$$k = 148.62 \frac{1.0 \times 0.33 \times 1.5}{48} = 1.53 \text{ md.}$$

CASE 3

Given: ϕ = 0.20, c = 1.5×10^{-5} psi^{-1}, a = 2,000 ft

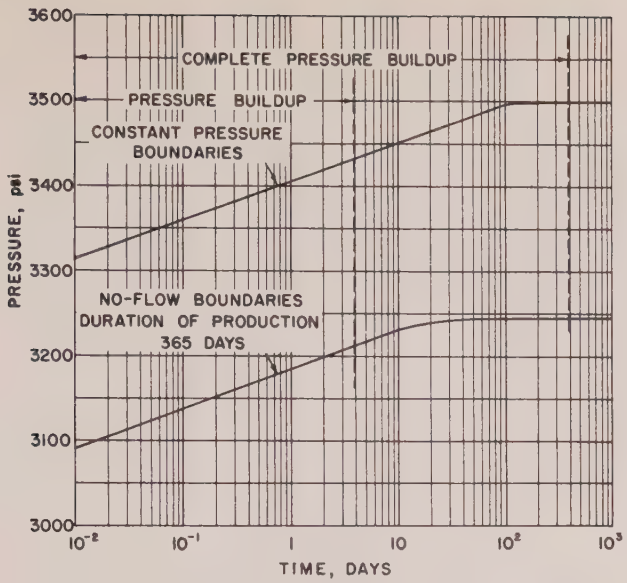

FIG. 5 – PRESSURE BUILD-UP CURVES OF THE FIELD PROBLEM.

and the data of Case 2.

Find: the effective permeability k and field pressure p.

The value of k is obtained by the procedure given in Case 2. Let us obtain the values of pressure at time $t = 10^{-1}$ days from Fig. 5.

p_1 = 3,360 psi CPB,

and

p_2 = 3,137 psi NFB.

The dimensionless time corresponding to this $t = 10^{-1}$, using the value of k calculated in Case 2, is

$$\bar{t} = 0.006331 \frac{1.53 \times 10^{-1}}{0.20 \times 1.5 \times 10^{-5} \times 0.33 \times (2{,}000)^2}$$

$$= 2.42 \times 10^{-4}.$$

From Fig. 4 this corresponds to $\overline{\Delta p}$ of 0.47 for CPB and $\overline{\Delta p}$ of 0.37 for NFB. Note that these $\overline{\Delta p}$ values are the differences of $\overline{\Delta p}$ values corresponding to $\bar{t} = 2.42 \times 10^{-4}$ and the $\overline{\Delta p}$ value of steady- or semisteady-state condition on the same curve. From Fig. 4 the steady-state $\overline{\Delta p}$ for CPB is zero, while for NFB it ranges between 0.10 and 1.0 depending on the duration of production. Using these Δp values from Eq. 5, the average stabilized field pressures are

$$p = 3{,}360 + \frac{0.47 \times 1.0 \times 0.33 \times 1.5}{1.53 \times 0.001127}$$

$$= 3{,}496 \text{ psi CPB},$$

and

$$p = 3{,}137 + \frac{0.37 \times 1.0 \times 0.33 \times 1.5}{1.53 \times 0.001127}$$

$$= 3{,}244 \text{ psi NFB}.$$

CASE 4

Given: $\phi = 0.20$, $c = 1.5 \times 10^{-5}$ psi^{-1}, $\mu = 0.33$ cp, $Q = 1.0$ STB/D-ft, $B_o = 1.5$ reservoir bbl/STB and the complete pressure build-up curves of Fig. 5.

Find: the average permeability k and the dimension a of the square field.

The average permeability k is obtained as in Case 2. From Fig. 5, the pressure increase from $t_s = 10^{-1}$ (transient period) to $t_s = 4 \times 10^2$ (steady-state period) is found to be

$\Delta p = 3{,}496 - 3{,}358 = 138$ psi or $\overline{\Delta p} = 0.485$ for CPB,

and

$\Delta p = 3{,}244 - 3{,}126 = 118$ psi or $\overline{\Delta p} = 0.360$ for NFB.

In Fig. 4, these values of Δp are seen to correspond to

$\bar{t} = 2.4 \times 10^{-4}$ for CPB,

and

$\bar{t} = 2.0 \times 10^{-4}$ for NFB.

Solving Eq. 6 for a and using $t_s = 10^{-1}$, we obtain $a = 2{,}200$ ft for NFB and $a = 2{,}000$ ft for CPB. The difference in the a values computed here is due principally to errors introduced when reading the graphs.

SUMMARY

Analytical solutions are obtained for calculating the pressure distribution in rectangular fields due to injection and/or production wells located anywhere within the fields. Boundaries of the field are assumed to be either at constant pressure or have no-flow. Properties of the field and of the fluids present are considered to be constant. The solutions are extended to include the calculation of average reservoir pressure and permeability from pressure build-up curves.

It is observed that, in most of the literature on pressure distribution analysis, the well is located at the center of the field. The solutions given in this paper are perfectly general and apply to fields with either off-center or centrally located wells. The analysis presented in this paper can also be used for well-interference problems.

NOMENCLATURE

a, b = sides of the rectangular section, ft
B_o = oil formation volume factor, reservoir bbl/STB
c = compressibility of rock and fluids present, psi^{-1}
CPB = constant pressure boundaries
k = effective field permeability, md
l, q = location of source or sink Q, ft
m, n = summation indices, integers
NFB = no-flow boundaries
P_o = initial pressure throughout the field, psi
p_s = pressure after shut-in, psi
p = pressure at location (x, y), psi
Δp = pressure during build-up, psi
$\overline{\Delta p}$ = dimensionless pressure, Eq. 5
Q = specific production (+) or injection (–), STB/D/ft of thickness
t = time, days
$\bar{t}$ = dimensionless time, Eq. 6
t_s = build-up time, days
T = duration of production or injection prior to

shut-in, days

$\bar{T}$ = dimensionless, duration of production or injection prior to shut-in, Eq. 6

x, y = space co-ordinates, ft

$a = 157.952 \frac{\phi c \mu}{k}$

$\beta = 886.905 \frac{B_o \mu}{k}$

ϕ = porosity, fraction

μ = viscosity, cp

ACKNOWLEDGMENT

Portions of the work presented in this paper were performed for the Arabian American Oil Co. The author is grateful to their management for permission to publish the paper. The general assistance of W. H. Schlieman, with Aramco, in the pressure build-up section of the paper is also appreciated.

REFERENCES

1. Perrine, R. L.: "Analysis of Pressure-Buildup Curves", *Drill. and Prod. Prac.* (1956) 482.
2. Hazebroek, P., Rainbow, H. and Matthews, C. S.: "Pressure Fall-Off in Water Injection Wells", *Trans.*, AIME (1958) Vol. 213, 250.
3. Nisle, R. G.: "The Effect of Partial Penetration on Pressure Buildup in Oil Wells", *Trans.*, AIME (1958) Vol. 213, 85.
4. Matthews, C. S., Brons, F. and Hazebroek, P.: "A Method for Determination of Average Pressure in a Bounded Reservoir", *Trans.*, AIME (1954) Vol. 201, 182.
5. Muskat, M.: *Physical Principles of Oil Production*, McGraw-Hill Book Co., Inc., N. Y. (1949) 188.
6. Martin, J. C.: "Simplified Equations of Flow in Gas Drive Reservoirs and the Theoretical Foundation of Multiphase Pressure Buildup Analysis", *Trans.*, AIME (1959) Vol. 216, 309.
7. Thomson, W. T.: *Laplace Transformation*, Prentice Hall, Inc., N. Y. (1960) 38.
8. Miller, C. C., Dyes, A. B. and Hutchinson, C. A.: "The Estimation of Permeability and Reservoir Pressure from Bottom Hole Pressure Buildup Characteristics", *Trans.*, AIME (1950) Vol. 189, 91.
9. Sneddon, I. N.: *Fourier Transforms*, McGraw-Hill Book Co., Inc., N. Y. (1951) 202.

APPENDIX

We define the symbols T' and Q' as follows.

$$T' = \frac{t}{\alpha}, \quad Q' = \beta Q.$$

Using these symbols in Eq. 1 and representing the point source Q by the Dirac delta function (δ),[9] we have

$$\frac{\partial^2 p}{\partial x^2} + \frac{\partial^2 p}{\partial y^2} = \frac{\partial p}{\partial T'} + Q'\delta(x-l)\delta(y-q). \quad (10)$$

The boundary and initial conditions of Eq. 10 are

$$p(0,y,T') = p(a,y,T') = 0, \quad 0 \leq y \leq b;$$

$$p(x,0,T') = p(x,b,T') = 0, \quad 0 \leq x \leq a;$$

$$p(x,y,0) = P_0(x,y), \text{ for all } x \text{ and } y.$$

Multiplying both sides of Eq. 10 by

$$\sin \frac{m\pi x}{a} \sin \frac{n\pi y}{b}$$

and integrating between the limits indicated, we have

$$\int_0^b \int_0^a \left(\frac{\partial^2 p}{\partial x^2} + \frac{\partial^2 p}{\partial y^2}\right) \sin \frac{m\pi x}{a} \sin \frac{n\pi y}{b}\, dxdy =$$

$$\int_0^b \int_0^a \frac{\partial p}{\partial T'} \sin \frac{m\pi x}{a} \sin \frac{n\pi y}{b}\, dxdy + Q'$$

$$\int_0^b \int_0^a \delta(x-l)\delta(y-q) \sin \frac{m\pi x}{a} \sin \frac{n\pi y}{b}\, dxdy$$

. . . . . .(11)

Applying the finite Fourier sine transform [9]

$$\bar{p}_s(m,n,T') = \int_0^b \int_0^a p(x,y,T') \sin \frac{m\pi x}{a} \sin \frac{n\pi y}{b}\, dxdy \quad . . . . .(12)$$

to Eq. 11 and utilizing the given boundary conditions, we have

$$-\pi^2 \left(\frac{m^2}{a^2} + \frac{n^2}{b^2}\right) \bar{p}_s(m,n,T') = \frac{d}{dT'} \bar{p}_s$$

$$(m,n,T') + Q' \sin \frac{m\pi l}{a} \sin \frac{n\pi q}{b} \quad . .(13)$$

The solution of Eq. 13 subject to the given initial condition can be written

$$\bar{p}_s(m,n,T') = \left[- \frac{Q' \sin m\pi l/a \sin n\pi q/b}{\pi^2 (m^2/a^2 + n^2/b^2)} \right.$$

$$\left. + \int_0^b \int_0^a P_0(x,y) \sin \frac{m\pi x}{a} \sin \frac{n\pi y}{b}\, dxdy \right]$$

$$\times \exp \left[-\pi^2 \left(\frac{m^2}{a^2} + \frac{n^2}{b^2}\right) T' \right]$$

$$+ \frac{Q' \sin m\pi l/a \sin n\pi q/b}{\pi^2 (m^2/a^2 + n^2/b^2)} \quad . . . . .(14)$$

The inverse of this transformed equation can be obtained from the Fourier Integral theorem. This transformation, subject to a constant initial pressure distribution P_o, results in Eq. 2.

The NFB solution, given by Eq. 3, is obtained by using the following boundary and initial conditions:

$$\frac{\partial}{\partial x} p(0,y,T') = \frac{\partial}{\partial x} p(a,y,T') = 0, \quad 0 \leq y \leq b;$$

$$\frac{\partial}{\partial y} p(x,0,T') = \frac{\partial}{\partial y} p(x,b,T') = 0, \quad 0 \leq x \leq a;$$

$$p(x,y,0) = P_0(x,y), \quad \text{for all } x \text{ and } y$$

and the Fourier cosine transform. This procedure is similar to the one given above. ***

Deflocculation of Fractionated Montmorillonite By Sodium Polyphosphates

F. W. JESSEN
MEMBER AIME
FARUK H. TURAN

THE U. OF TEXAS
AUSTIN, TEX.

ABSTRACT

The gel strength and viscosity of two different suspensions of fractionated montmorillonite clay were measured by using a Stormer viscosimeter and Fann V-G meter. The amount of sodium polyphosphate (sodium hexametaphosphate, sodium tetraphosphate and sodium acid pyrophosphate) adsorbed by the clay particles was determined.

A relationship seems to exist between the amount of polyphosphate adsorbed and the nature of the surface, edge or plate, assumed to be the principal sites for selective adsorption. Reduction in viscosity and gel strength was found to be directly related to the adsorption. Both chemical bonding and physical adsorption seem involved in deflocculation. Some indication of the axial ratios of particles of .1- to .04-micron average size is possible through study of the adsorption mechanism.

INTRODUCTION AND PURPOSE

A knowledge of surface areas of clay particles in a suspension and a precise determination of phosphate adsorption should provide a basis for a better understanding of reduction in viscosity and gel strength caused by molecularly dehydrated phosphates.

The purpose of this investigation was to study the adsorption of sodium polyphosphates on suspensions of fractionated sodium montmorillonite.

Although there is considerable uncertainty regarding details of the structure of montmorillonite, a generally accepted one is that suggested by Hofmann, Endell and Wilm.[1] The structure shown in Fig. 1 is an idealized one, and Marshall[2] has postulated that it is possible for several isomorphous replacements to occur. Thus, aluminum may replace silicon, in which case an exchangeable cation would go along with the aluminum to neutralize what would otherwise be a net negative charge on the structure.

Original manuscript received in Society of Petroleum Engineers office May 27, 1960. Revised manuscript received Sept. 18, 1961.

[1]References given at end of paper.

There is disagreement among various investigators as to the particle size and shape of montmorillonite clays. Marshall[2] reported the following results for the mean lateral dimensions of a Putnam clay (montmorillonite) — 3,730 A°* for particles having average diameters ranging from 500 to 1,000 A°, and 750 A° for those with an average diameter less than 200 A°. The latter particles were estimated at 50 A° in thickness, which would correspond to a stack of five unit cell layers. On the other hand, Shaw[3] has interpreted micrographs as indicating that particles of montmorillonite are readily broken down to the individual cell layers by dispersion in water. Brindley[4] and Mering[5] indicate the ultimate particles to be of the order of 300 A° in mean lateral dimension. Van Olphen[6] suggested the thickness of particles at four to five unit cell layers. It was suggested also that this number tends to become smaller with increasing dilution. Recently, Kahn and Lewis[7] determined the size of sodium montmorillonite particles in aqueous suspension from electro-optical bi-refringence decay curves. The

*Angstrom unit.

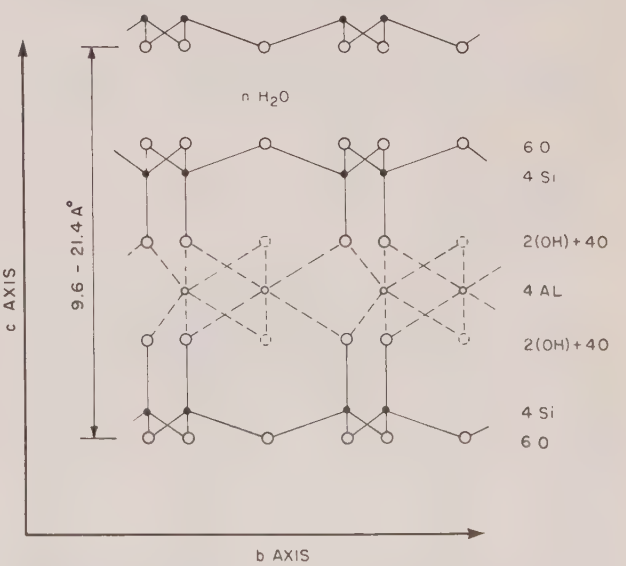

FIG. 1 — MONTMORILLONITE STRUCTURE SUGGESTED BY HOFMANN, ENDELL AND WILM (REF. 1).

results were interpreted in terms of the diameter of an oblate spheroid, the lateral dimension of the smallest particle being 5,000 A°. Melrose[8] concluded that, although numerous electron micrographs of montmorillonite clay have been published, in none of these can any particles of definite outline be identified or measured.

LABORATORY INVESTIGATION

Viscosity measurements were obtained with the Stormer and Fann V-G instruments, the latter also serving to give the gel strength. A standard API filter press was used to obtain samples of filtrate from the suspension, which were further clarified by filtering through Whatman analytical-grade filter paper.

A Lumerton photoelectric colorimeter (Model 400-A) was used in the colorimetric determination of phosphate. Known concentrations of sodium acid phosphate (NaH_2PO_4) representing 0.125, 0.250, 0.625, 1.250, 2.500 and 5.000 ppm of phosphorus were used for calibration. In the determination of phosphate in each filtrate sample, three different readings were made. In no instance was the variation in individual determinations of the percentage transmission greater than 1 per cent in the range of 90 per cent transmission, while a 4 per cent variation was found in the range of 50 per cent transmission. Dilution of the filtrate was controlled so that determinations were made with 85 to 95 per cent transmittance, assuring an accuracy of 1 per cent in the phosphorus determination.

Two clay suspensions were prepared using fractionated portions of a Wyoming bentonite studied by Jessen and Mungan.[9] The average particle diameter of one fraction (designated *M*) was 0.04 micron, while the other fraction (designated *L*) has an average particle size of 0.10 micron.

Quantities equivalent to 0.10, 0.25, 0.50, 1.00, 2.00 and 4.00 lb/bbl (1 lb/bbl = 2.8525 gm/liter) of sodium hexametaphosphate were added to the clay suspensions. The suspensions were stirred thoroughly for 30 minutes, and the Stormer viscosity, the plastic viscosity and the yield point were determined.

The filtrate was diluted with water and sulfuric acid added. The sample was allowed to boil in an Erlenmeyer flask for at least two hours to convert the metaphosphate to orthophosphate.[10] An aliquot was used in the colorimetric determination of phosphate, and the amount of the meta-, tetra-, and pyrophosphate adsorbed by the clay particles was calculated by subtracting the amount in the filtrate from the original quantity present.

The results are presented in Tables 1 through 6 to show the amount of sodium hexametaphosphate, sodium tetraphosphate and sodium acid pyrophosphate adsorbed vs the change in yield point and the reduction in plastic viscosity and Stormer viscosity.

Tables 7 through 12 present the extent of adsorption of sodium hexametaphosphate on the clay particles calculated on the basis of varying axial ratios *(c:b:a)*.

RESULTS AND DISCUSSION

The interaction of polyphosphates with montmorillonite has been studied by Van Olphen,[11] whose

TABLE 1 — 6 PER CENT SUSPENSION OF M FRACTION TREATED WITH SODIUM HEXAMETAPHOSPHATE

Amount Added (lb/bbl)	Amount Adsorbed (lb/bbl)	Stormer Viscosity (cp)	Plastic Viscosity (cp)	Yield Point (lb/100 ft²)
0.	–	46	32	50
0.10	0.075	20	26	20
0.25	0.182	15	22	12
0.50	0.325	13	20	10
1.00	0.556	10	20	7
2.00	0.890	10	20	6
4.00	1.120	14	22	11

TABLE 2 — 7 PER CENT SUSPENSION OF L FRACTION TREATED WITH SODIUM HEXAMETAPHOSPHATE

Amount Added (lb/bbl)	Amount Adsorbed (lb/bbl)	Stormer Viscosity (cp)	Plastic Viscosity (cp)	Yield Point (lb/100 ft²)
0.	–	57.0	38	65
0.10	0.078	34.0	28	29
0.25	0.196	23.0	26	19
0.50	0.320	18.0	25	12
1.00	0.566	17.5	24	10
2.00	0.900	14.5	22	9
4.00	1.160	14.0	21	7

TABLE 3 — 6 PER CENT SUSPENSION OF M FRACTION TREATED WITH SODIUM TETRAPHOSPHATE

Amount Added (lb/bbl)	Amount Adsorbed (lb/bbl)	Stormer Viscosity (cp)	Plastic Viscosity (cp)	Yield Point (lb/100 ft²)
0.	–	46	33	51
0.10	0.078	26	30	20
0.25	0.179	18	24	17
0.50	0.331	14	22	11
1.00	0.617	11	20	6
2.00	1.000	11	20	6
4.00	1.292	14	22	11

TABLE 4 — 7 PER CENT SUSPENSION OF L FRACTION TREATED WITH SODIUM TETRAPHOSPHATE

Amount Added (lb/bbl)	Amount Adsorbed (lb/bbl)	Stormer Viscosity (cp)	Plastic Viscosity (cp)	Yield Point (lb/100 ft²)
0	–	57	38	65
0.10	0.078	36	31	31
0.25	0.182	23	28	21
0.50	0.345	20	26	15
1.00	0.612	15	24	10
2.00	1.110	13	22	7
4.00	1.780	11	20	5

TABLE 5 — 6 PER CENT SUSPENSION OF M FRACTION TREATED WITH SODIUM ACID PYROPHOSPHATE

Amount Added (lb/bbl)	Amount Adsorbed (lb/bbl)	Stormer Viscosity (cp)	Plastic Viscosity (cp)	Yield Point (lb/100 ft²)
0	–	46	31	50
0.10	0.082	20	26	19
0.25	0.195	18	23	13
0.50	0.350	14	22	10
1.00	0.690	13	22	9
2.00	1.176	13	22	8
4.00	1.776	18	25	11

findings favored physicochemical adsorption as an explanation for deflocculation.

Sodium polyphosphates are linear polymeric structures composed of linked phosphorus-oxygen tetrahedra, with the general formula $Na_{n+2}P_nO_{3n+1}$. Single-bond radii for tetrahedral coordination are P = .35 and O = 1.49 A°.[12] Using a P-O length of 1.84 A°, the base of a PO_4 tetrahedron is calculated to be 15 sq A°.[13] To compute the coverage of any specific clay surface with phosphate molecules, the axial distance (*c*, *b* and *a*) must be known. Melrose[8] has suggested lateral dimensions (*b* and *a*) in the ratio of 1:2 to 3:4 for clay particles. The thickness *c* of the smallest clay particles is not known exactly, but minimum values from 10 to 50 A° have been suggested in the literature. These values define a particle of one to five unit cells in thickness. Assuming that fraction *M* with average particle diameter of 0.04 micron (400 A°) is composed of particles five-unit-cells thick, the axial lengths are arrived at as follows.

Volume of Particle = $V = (\pi/6)d^3 = (3.14/6)(400)^3$

$= 33.75 \times 10^6$ cu A°.

Lateral Area $= (b \times a) = V/c = (33.75 \times 10^6)/50$

$= 67.5 \times 10^4$ sq A°.

Therefore,

for *b:a* = 1:2, *b* = 580 A° and *a* = 1,160 A°, giving *c:b:a* ≅ 1:10:20;

and

for *b:a* = 3:4, *b* = 710 A° and *a* = 950 A°, giving *c:b:a* ≅ 1:14:19.

In the first case, a mean lateral dimension of (580 + 1,160)/2 = 870 A° is indicated; and in the second case, (710 + 950)/2 = 830 A°. The axial ratios obtained here may be assumed to apply to particles of fractions with greater average sizes as well. Should particles be assumed to be of a single unit cell layer as postulated by Shaw,[3] resulting axial ratios (*c:b:a*) of 1:130:170 or 1:100:200 will be obtained, and the mean lateral dimension is 1,650 A°. Similarly for the *L* fraction which has an average particle size of 0.10 micron, computations show 140 × 1,400 × 2,800 A° for the 1:10:20 ratios, 120 × 1,680 × 2,280 A° for 1:14:19 ratios, and 35 × 3,500 × 7,000 A° for the 1:100:200 ratios of *c:b:a*. Mean lateral dimensions range from 2,000 to 5,200 A°, while the indicated thickness varies from 3 to 14 unit cell layers. All of these derived particle dimensions fall within the range of sizes reported by most investigators. It is apparent that a rather wide variation in adsorption might exist if the assumption is made that the principal action of polyphosphate molecules is on the broken edges.

A compilation of the data is presented in Tables 7 through 12. The coverage on any clay surface was calculated from the amount of clay fraction treated, corresponding to a definite number of particles with the afore-mentioned postulated dimensions, and the surface area of the polyphosphate adsorbed. Specifically, consider 6 per cent *M* fraction treated with 0.10-lb/bbl polyphosphate (Table 2).

Using as a basis 100 cc of suspension

$c \times b \times a = 50 \times 500 \times 1{,}000$ A°,

$$\text{No. Clay Particles} = \frac{\text{Vol. of Clay}}{\text{Vol. of Particles}}$$

$$= \frac{(60/2.3) \times 10^{24}}{33.75 \times 10^6}$$

$$= 7.75 \times 10^{17}.$$

$$\text{No. Polyphosphate Tetrahedra} = \frac{(0.075)(2.8525)}{102} \times 6.02 \times 10^{23} = 12.5 \times 10^{20},$$

where 2.8525 is conversion factor from pounds per barrel to grams per liter.

Total Area of Polyphosphate = $12.5 \times 10^{20} \times 15$

$= 18.8 \times 10^{21}$ sq A°.

TABLE 6 — 7 PER CENT SUSPENSION OF *L* FRACTION TREATED WITH SODIUM ACID PYROPHOSPHATE

Amount Added (lb/bbl)	Amount Adsorbed (lb/bbl)	Stormer Viscosity (cp)	Plastic Viscosity (cp)	Yield Point (lb/100 ft²)
0	–	57	38	65
0.10	.083	35	30	30
0.25	.194	22	28	19
0.50	.333	18	25	11
1.00	.667	13	22	8
2.00	1.166	10	20	6
4.00	1.776	12	21	7

TABLE 7 — NUMBER OF MOLECULAR LAYERS OF SODIUM HEXAMETAPHOSPHATE ON THE SURFACES OF 7 PER CENT *L* FRACTION WITH THE AXIAL RATIOS OF 1:14:19

Amount Added (lb/bbl)	Amount Adsorbed		Number of Layers on the Surfaces of				
	lb/bbl	%	100 Faces A_1 (*bc*)	010 Faces A_2 (*ac*)	001 Faces A_3 (*ab*)	$A_1 + A_2$	$A_1 + A_2 + A_3$
0.10	0.078	78.0	0.760	0.575	0.036	0.328	0.032
0.25	0.194	77.7	1.900	1.435	0.090	0.818	0.081
0.50	0.320	64.0	3.130	2.370	0.148	1.350	0.133
1.00	0.570	57.0	5.600	4.220	0.264	2.410	0.238
2.00	0.900	45.0	8.820	6.670	0.417	3.800	0.375
4.00	1.160	21.0	11.450	8.600	0.537	4.900	4.830

Surface Area $(ab) = 2 \times a \times b = 2\ (500)\ (1000)$

$= 10^6$ sq A°.

Total Surface Area $(ab) = (7.75 \times 10^{17})\ (10^6)$

$= 7.75 \times 10^{23}$ sq A°.

$$\text{Coverage} = \frac{18.8 \times 10^{21}}{7.75 \times 10^{23}} \cong 0.02.$$

For clay particles of 100-millimicron average size (*L* fraction), reduction in viscosity and yield point was obtained with all the polyphosphates employed at about equal concentrations. From Tables 7, 8 and 9, single-layer coverage by sodium hexametaphosphate adsorption on the edges of the *L*-fraction particles is found at 0.24, 0.27, and 0.13 lb/bbl for corresponding particle dimensions having axial ratios of 1:14:19, 1:10:20 and 1:100:200, respectively. For the *M*-fraction particles, 0.52, 0.57 and 0.27 lb/bbl of sodium hexametaphosphate are required to cover the edges of particles with like axial ratios (Tables 10, 11 and 12). Substantially complete deflocculation of the clay is observed with coverage of the edges, as evidenced by the destruction of gel properties and the low viscosity values.

The experiments of Michaels[13] showed that the most likely site for adsorption of polyphosphates by kaolinite is the exposed edge of the gibbsite layer of a fractured sheet. Should the adsorption of polyphosphates on montmorillonite occur in the same manner, some degree of selectivity may be expected, particularly if direct chemical bonding takes place. It follows, therefore, that sharp changes in viscosity and gel properties would result because the neutralization of positively charged sites by attraction of anions would substantially reduce edge-to-face, as well as edge-to-edge, configurational positions.

Van Olphen[11] found the order of magnitude of adsorption of sodium hexametaphosphate to be about 14 m. eq.*/100 gm of unfractionated sodium montmorillonite. This corresponds to 0.35 lb/bbl of 7 per cent clay suspension.

*Abbreviation m. eq. is milliequivalent.

TABLE 8 — NUMBER OF MOLECULAR LAYERS OF SODIUM HEXAMETAPHOSPHATE ON THE SURFACES OF 7 PER CENT *L* FRACTION WITH THE AXIAL RATIOS OF 1:10:20

Amount Added	Amount Adsorbed		Number of Layers on the Surfaces of				
			100 Faces	010 Faces	001 Faces		
(lb/bbl)	lb/bbl	%	A_1 (*bc*)	A_2 (*ac*)	A_3 (*ab*)	$A_1 + A_2$	$A_1 + A_2 + A_3$
0.10	0.078	78.0	0.884	0.442	0.0442	0.295	0.038
0.25	0.194	77.7	2.210	1.105	0.0111	0.737	0.097
0.50	0.320	64.0	3.650	1.825	0.1835	1.215	0.160
1.00	0.570	57.0	6.500	3.250	0.3250	2.160	0.284
2.00	0.900	45.0	10.200	5.100	0.5100	3.400	0.448
4.00	1.160	21.0	13.200	6.600	0.6600	4.400	0.575

TABLE 9 — NUMBER OF MOLECULAR LAYERS OF SODIUM HEXAMETAPHOSPHATE ON THE SURFACES OF 7 PER CENT *L* FRACTION WITH THE AXIAL RATIOS OF 1:100:200

Amount Added	Amount Adsorbed		Number of Layers on the Surfaces of				
			100 Faces	010 Faces	001 Faces		
(lb/bbl)	lb/bbl	%	A_1 (*bc*)	A_2 (*ac*)	A_3 (*ab*)	$A_1 + A_2$	$A_1 + A_2 + A_3$
0.10	0.078	78.0	1.900	0.950	0.010	0.633	0.001
0.25	0.194	77.7	4.750	2.375	0.024	1.580	0.024
0.50	0.320	64.0	7.850	3.925	0.040	2.610	0.040
1.00	0.570	57.0	10.400	5.200	0.052	4.660	0.051
2.00	0.900	45.0	22.000	11.000	0.111	7.330	0.110
4.00	1.160	21.0	28.500	14.250	0.143	9.470	0.142

TABLE 10 — NUMBER OF MOLECULAR LAYERS OF SODIUM HEXAMETAPHOSPHATE ON THE SURFACES OF 6 PER CENT *M* FRACTION WITH THE AXIAL RATIOS OF 1:14:19

Amount Added	Amount Adsorbed		Number of Layers on the Surfaces of				
			100 Faces	010 Faces	001 Faces		
(lb/bbl)	lb/bbl	%	A_1 (*bc*)	A_2 (*ac*)	A_3 (*ab*)	$A_1 + A_2$	$A_1 + A_2 + A_3$
0.10	.075	75.0	0.345	0.258	0.018	0.148	0.016
0.25	0.183	73.0	0.812	0.608	0.043	0.348	0.038
0.50	0.325	65.0	1.440	1.080	1.077	0.620	0.068
1.00	0.556	55.6	2.470	1.850	0.132	1.060	0.117
2.00	0.890	44.5	3.960	2.970	0.210	1.700	0.187
4.00	1.120	28.0	4.980	3.730	0.264	2.140	0.235

The amounts of sodium hexametaphosphate required to cover the broken edges for the 6 per cent *M*-fraction and 7 per cent *L*-fraction clays are 0.27 and 0.57 lb/bbl, respectively, when the assumed particle axial ratio is 1:10:20. The average of the two values is 0.42 lb/bbl. If the axial ratio of clay particles is taken to be 1:14:19, an average of 0.38 lb/bbl of sodium hexametaphosphate should be adsorbed. This latter value is in good agreement with the value found by Van Olphen and gives support to the postulated specificity of adsorption on the edge surfaces. With axial ratios of 1:100:200, and correspondingly less broken edge surface, average adsorption for the two fractions is computed to be 0.20 lb/bbl.

Now, if the action be chemisorption, the phosphate tetrahedra would be attached to the aluminum by replacing the hydroxyl ions on the edges. There are two hydroxyl ions for each aluminum atom, the distance between the latter being 2.6 A° (Fig. 1). There are two aluminum atoms and four hydroxyl ions for every 7.8 A° unit repeating section; this, multiplied by the unit thickness of 14 A°, is 109.2 sq A°. Hence, the area can be covered completely by 109.2/15 = 7.3 phosphate tetrahedra. On the other hand, since there are only four replaceable hydroxyl ions in this same area, an area of only 60 sq A° may be assumed to be covered; or, in other words, only 55 per cent of the area may thus be occupied. In the latter case, the amount of sodium hexametaphosphate required to replace all hydroxyl ions on the edges is 0.14, 0.15 and 0.07 lb/bbl for the 7 per cent *L* fraction, and 0.28, 0.31 and 0.15 lb/bbl for the 6 per cent *M* fraction (as before, considering axial ratios of 1:14:19, 1:10:20 and 1:100:200, respectively).

If the principal selectivity of polyphosphate ions is by chemical bonding, then approximately 60 per cent reduction in the yield point of the *L*-fraction material is attained when this phase is reached; in the case of the *M*-fraction clay, greater edge surface area allows for more such direct bonding, and 80 per cent of the reduction in yield point may be attributed to such action. The data show that deflocculation results with complete coverage of the broken edges, and no further reduction in yield point is obtained regardless of the amount of polyphosphate further added. For axial ratios of 1:100:200, saturation of the edge surface is complete when the corresponding reduction in yield point is 60 per cent. Since substantial quantities of polyphosphates still are adsorbed, this may be interpreted to mean one of the following: (1) adsorption takes place on the plate (flat) surfaces — even though in these experiments with an excess of chemical, coverage of the .001 surface (*ab*) is computed to be only .143 molecular layers; (2) multimolecular layers are adsorbed on the edge surfaces; or (3) the configuration for the 1:100:200 axial ratio is rather improbable.

Sharper decreases in viscosity and gel strength are noted with sodium acid pyrophosphate. This may be due to comparatively better coverage of the edge sites since less interference may be occasioned in the attachment of the relatively smaller pyrophosphate.

SUMMARY

The adsorption of sodium hexametaphosphate, sodium acid pyrophosphate and sodium tetraphosphate on fractionated clay suspensions — primarily sodium montmorillonite — has been determined.

TABLE 11 — NUMBER OF MOLECULAR LAYERS OF SODIUM HEXAMETAPHOSPHATE ON THE SURFACES OF 6 PER CENT M FRACTION WITH THE AXIAL RATIOS OF 1:10:20

Amount Added (lb/bbl)	Amount Adsorbed		Number of Layers on the Surfaces of				
	lb/bbl	%	100 Faces A_1 (*bc*)	010 Faces A_2 (*ac*)	001 Faces A_3 (*ab*)	$A_1 + A_2$	$A_1 + A_2 + A_3$
0.10	.075	75.0	0.408	0.204	0.020	0.136	0.018
0.25	0.183	73.0	0.960	0.480	0.048	0.320	0.042
0.50	0.325	65.0	1.710	0.855	0.086	0.570	0.074
1.00	0.556	55.6	2.920	1.460	0.146	0.975	0.128
2.00	0.890	44.5	4.680	2.340	0.234	1.560	0.204
4.00	1.120	28.0	5.900	2.295	0.295	1.965	0.257

TABLE 12 — NUMBER OF MOLECULAR LAYERS OF SODIUM HEXAMETAPHOSPHATE ON THE SURFACES OF 6 PER CENT M FRACTION WITH THE AXIAL RATIOS OF 1:100:200

Amount Added (lb/bbl)	Amount Adsorbed		Number of Layers on the Surfaces of				
	lb/bbl	%	100 Faces A_1 (*bc*)	010 Faces A_2 (*ac*)	001 Faces A_3 (*ab*)	$A_1 + A_2$	$A_1 + A_2 + A_3$
0.10	.075	75.0	0.885	0.443	0.004	0.295	0.004
0.25	0.183	73.0	2.080	1.040	0.010	0.695	0.010
0.50	0.325	65.0	3.710	1.855	0.019	1.235	0.018
1.00	0.556	55.6	6.320	3.160	0.032	2.110	0.031
2.00	0.890	44.5	10.150	5.075	0.051	3.380	0.050
4.00	1.120	28.0	12.800	6.400	0.064	4.270	0.063

Reduction in viscosity and gel strength was found to be directly related to the adsorption of polyphosphates. Adsorption of each polyphosphate indicates the same general mechanism of deflocculation. Most of the adsorption, (55 to 80 per cent) is believed to be chemical-bonding in nature and appears to be confined principally to the edge surfaces. Although some adsorption undoubtedly occurs on the flat surfaces, the evidence shows that such adsorption probably plays a minor role in effecting changes in the gel strength.

Axial ratios of 1:15:20 are indicated for sodium-montmorillonite particles ranging from 0.1 to 0.04-micron average size. A 3:4 ratio of lateral dimensions appears correct.

REFERENCES

1. Hofmann, U., Endell, K. and Wilm, D.: "Kinstallstruktur und Ouellung von Montmorillonit", *Z. Krist.* (1933) Vol. 86A, 340.
2. Marshall, C. E.: "Layer Lattices and Base Exchange Clays", *Z. Krist.* (1935) Vol. 91A, 433.
3. Shaw, B. T.: "The Nature of Colloidal Clay as Revealed by the Electron Microscope", *Jour. Phy. Chem.* (1942) Vol. 46, 1032.
4. Brindley, G. W.: *X-Ray Identification and Crystal Structures of Clay Minerals,* The Mineralogical Soc., London (1951).
5. Mering, J.: "The Hydration of Montmorillonite", *Trans.,* Faraday Soc. (1946) Vol. 42B, 205.
6. Van Olphen, H.: "Interlayer Forces in Bentonite", *Proc. of the Second National Conference on Clays and Clay Minerals,* Pub. 327, Nat. Acad. Sci. Nat. Res. Council (1954) 418.
7. Kahn, A. and Lewis, D. R.: "The Size of Sodium Montmorillonite Particles in Suspension from Electro-Optical Birefringence Studies", *Jour. Phy. Chem.* (1954) Vol. 58, 801.
8. Melrose, J. C.: "The Thermodynamic Basis of Light Scattering Theory and Light Scattering Evidence for the Particle Size of Montmorillonite Clay", PhD dissertation, Stanford U. (1958).
9. Mungan, N. and Jessen, F. W.: "The Effect of Particle Size Distribution and Exchange Cation on Gel Properties of Fractionated Aquagel Suspensions", *Trans.,* AIME (1959) Vol. 216, 455.
10. Scott, W. W.: *Standard Methods of Chemical Analysis,* D. Van Nostrand Co., N. Y. (1939) Vol. 2, 2501.
11. Van Olphen, H.: "Stabilization of Montmorillonite Sols by Chemical Treatment: Part II, Effect of Polymetaphosphates, Sodium Metasilicate, Oxalate, Citrate, and Orthophosphate on Na and Ca Montmorillonite Sols", *Rec. Trav. Chem. Pays Bas. 69* (1950) 1313.
12. Van Wazer, J. R.: *Phosphorus and Its Compounds,* Interscience Publishers Inc., N. Y. (1958) Vol. 1, 27, 887.
13. Michaels, Alan S.: "Deflocculation of Kaolinite by Alkali Polyphosphates", *Ind. Eng. and Chem.* (1958) Vol. 50, No. 6, 951.

***

< 0.1 and for ω/ω_c
ly independent of
ese limits there
ht, therefore,
erpretation
al should
ctice,
ces

Velocity-Log Interpretation: The Effect of Rock Bulk Compressibility

J. GEERTSMA *
MEMBER AIME

KONINKLIJKE/SHELL LABORATORIUM
RIJSWIJK, THE NETHERLANDS

ABSTRACT

The relationship between porosity and the speed of propagation of acoustic waves in fluid-saturated porous rocks as measured by the Sonic log and by ultrasonic techniques is analyzed. Biot's continuum theory[1] is used to explain the difference in acoustic wave propagation between a dry and a liquid-saturated porous material. The porosity is a variable in this theory. However, the acoustic wave propagation in the dry rock depends too on porosity, and this dependence is not predicted by the theory. Frequently in dry sandstones, a nearly linear relationship between reciprocal acoustic wave velocity and porosity is observed in the low-porosity range. The physics behind this behavior is outlined. An empirical relationship of the form, $1/V \approx A + B\,\phi$, applies accordingly for many porous dry rocks, provided the porosity is the only variable. The presence of a liquid in the pores changes the value of B, and this change is found to be in agreement with the Biot theory.

The time-average relation introduced some years ago[2] results in an equation of the same type — $1/V = \phi/V_f + (1-\phi)/V_r$ — but is not based on a sound physical picture. Still, this relation sometimes predicts approximately correct A and B values.

Carbonate rocks with their complicated pore structures sometimes show a different relationship between wave velocity and porosity, unfavorable for log interpretation. Examples are presented. The simultaneous presence of calcite, dolomite and anhydrite, with their different grain densities and matrix compressibilities, complicates acoustic-log interpretation in carbonate rocks still further.

Other complicating effects of acoustic-log interpretation are discussed. They are related to the influence of shale streaks and natural fractures on the average wave velocity observed by the logging tool and to the effect of adsorption phenomena on wave propagation in unstressed rocks particularly in sandstones.

Original manuscript received in Society of Petroleum Engineers office July 11, 1960. Revised manuscript received July 6, 1961. Paper presented at 35th Annual Fall Meeting of SPE, Oct. 2-5, 1960, in Denver.

*Presently on temporary assignment with Shell Development Co., Houston, Texas.

[1]References given at end of paper.

INTRODUCTION

The velocity of propagation of sound waves in porous sediments as a function of depth is a quantity frequently measured. Velocity loggers of various design may be used, for which velocity is defined as the distance between a wave generator and a wave detector (one-receiver system) or the distance between two wave detectors (two-receiver system), divided by the shortest time required for a vibrational pulse to cross this distance. Velocity loggers are used to assist in seismic prospecting, to differentiate between the various types of sedimentary rock layers, and also to determine rock porosity and pore fluid content. This paper is especially concerned with the relation between velocity and porosity and the effect of the pore fluid.

Most velocity-log interpretation in terms of porosity is based on a formula advocated by Wyllie, *et al*,[2] suggested earlier by Hughes and Jones,[3] and known as the "time-average relation". This formula applies for a model consisting of a layered system of parallel alternating slices of a solid and a liquid, crossed by the wave path perpendicular to the interfaces. This must be an unsuitable model for the derivation of wave propagation properties of liquid-saturated porous media. It suggests that only rock matrix and fluid properties influence the wave velocity. The surprising fact, nevertheless, is that applications of this formula to clean sandstones under specific conditions (sufficient effective stress) results in porosity predictions which are close to reality.

Other authors, such as Gassmann,[4] White and Sengbush,[5] Brandt,[6] and Hicks and Berry,[7] make use of more realistic models to arrive at a wave velocity formula for porous sediments. Their models consist of various liquid-saturated packings of frictionless spherical grains and are, therefore, also highly idealized. A number of experimental results obtained in the laboratory can be better explained with these model theories than by the time-average relation. A study of a general character, not depending *a priori* on a special model of the porous structure, was still lacking.

Reduction in vis
found to be direc
polyphosphates
indicates the
tion. Most
believed
appear
surf
o

T THEORY

the speed of propagation
o-component system, one
vidual deformations. In a
stem, these are the de-
me and that of the fluid.
ional study by Zwikker
pagation in elastic porous
hree-dimensional general
t [1] showed that the determination of the relationship between the deformations of solid and fluid is a problem which can be solved by the classical theory of mechanics.

If a porous solid is deformed, its pore volume in general also changes. If this pore volume contains fluid, this fluid can change in volume owing to its own compressibility. As the fluid compressibility in most cases will be different from that of the pore volume, the fluid will try to flow through the porous medium under the influence of an induced pressure gradient. A continuity equation applied to this case describes the balance between fluid displacement and change in fluid volume. The equations of motion of solid and fluid and the equations of state (the stress-strain relation of both components), together with the equation of continuity, are sufficient for the determination of the dynamic behavior of the porous system, provided the effect of temperature changes due to dissipation of energy as heat can be neglected.

Applying this procedure to assumed isotropic and elastic porous media and further assuming that relative motion between rock grains and fluid takes place according to Darcy's law, one arrives at a set of equations that describe the behavior of dilatational waves (providing these waves are of a length greater than that of the largest grain dimension).

$$\nabla^2 (He - K\zeta) = \frac{\partial^2}{\partial t^2} (\rho e - \rho_l \zeta),$$

$$\nabla^2 (Ke - L\zeta) = \frac{\partial^2}{\partial t^2} (\rho_l e - \rho_c \zeta) - \frac{\mu}{k} \frac{\partial \zeta}{\partial t}. \quad (1)$$

In this set of simultaneous differential equations, e represents the absolute dilatation of the porous solid, and ζ the "relative dilatation" between solid and fluid. The proper definition of ζ is

$$\zeta = \phi (e - \epsilon),$$

where ϕ represents the porosity and ϵ is the absolute dilatation of the fluid. Three densities appear in these equations: ρ is the total or bulk density of the system; ρ_l is that of the pore liquid; and ρ_c can be written in the form

$$\rho_c = \kappa \frac{\rho_l}{\phi} \quad \ldots\ldots\ldots\ldots\ldots\ldots \quad (2)$$

where κ represents a mass-coupling factor which must have a numerical value ≥ 1; $\kappa = 1$ means that there is no mass-coupling. Zwikker and Kosten[8] obtained a theoretical value of $\kappa = 3$ for a system of randomly oriented pores. We will consider κ as an unknown material property. A method for the experimental evaluation of the mass-coupling factor will be published soon. μ/k is the mobility of the pore fluid, H, K and L are elastic deformation properties representing combined functions of the individual deformation properties of the components of the system and the porosity.

The nature of the constants H, K and L can be analyzed with the use of a more detailed theory relating stress and strain in a fluid-saturated porous medium. In 1951, Gassmann[9] outlined the fundamentals of this theory. Further studies on this subject have been published by Geertsma[10] and by Biot and Willis.[11] Applying these published results to define H, K and L, we find (for derivation see Geertsma and Smit[12])

$$H = \frac{(1 - \beta)^2}{(1 - \phi - \beta)c_r + \phi c_l} + \left(\frac{\beta}{c_r} + \frac{4}{3} G_b\right), \quad (3)$$

$$K = \frac{1 - \beta}{(1 - \phi - \beta)c_r + \phi c_l}, \quad \ldots\ldots \quad (4)$$

and

$$L = \frac{1}{(1 - \phi - \beta)c_r + \phi c_l} \quad \ldots\ldots\ldots \quad (5)$$

where

$\beta = c_r/c_b$,
c_r = compressibility of rock matrix,
c_b = compressibility of the rock bulk material,
c_l = compressibility of the pore fluid, and
G_b = the shear modulus of the rock bulk material.

The differential Eqs. 1 predict the existence of two plane dilatational waves with very different properties. Only the wave "of the first kind" is a true wave. The wave "of the second kind" obeys an equation which has more the character of a diffusion equation and is, thus, highly attenuated and only observable in the immediate neighborhood of the wave source.* For the interpretation of the velocity log, only the wave of the first kind has to be considered. The exact solution for the wave velocity of the wave of the first kind is easily arrived at but is impractical for engineering purposes. Geertsma and Smit[12] derived a suitable approximate solution which reads

*Patterson[13] reported rates of propagation which are very likely those of the wave of the second kind. Tchekaliuk[14] reported some preliminary work on the theory of the wave of the second kind.

$$V^2 = \frac{V_\infty^4 + V_0^4\left(\frac{\omega_c}{\omega}\right)^2}{V_\infty^2 + V_0^2\left(\frac{\omega_c}{\omega}\right)^2}, \quad \ldots\ldots\ldots \quad (6)$$

where

$$V_0^2 = \frac{H}{\rho}, \quad \ldots\ldots\ldots\ldots\ldots \quad (7)$$

$$V_\infty^2 = \frac{L\rho + H\rho_c - 2K\rho_l}{\rho\rho_c - \rho_l^2}, \quad \ldots\ldots\ldots \quad (8)$$

and

$$\frac{\omega}{\omega_c} = \frac{k\rho\omega}{\mu}\left(\frac{\rho\rho_c - \rho_l^2}{\rho^2}\right)^* \quad \ldots\ldots\ldots \quad (9)$$

V_0 represents the theoretical wave velocity at zero frequency, V_∞ is the wave velocity for infinitely large frequency and ω is the frequency. Substitution of Eqs. 3, 4 and 5 into Eqs. 7 and 8 leads to

$$V_0^2 = \left[\left(\frac{\beta}{c_r} + \frac{4}{3}G_b\right) + \frac{(1-\beta)^2}{(1-\phi-\beta)c_r + \phi c_l}\right]\frac{1}{\rho}. \quad \ldots\ldots\ldots\ldots\ldots\ldots\ldots\ldots\ldots\ldots \quad (7a)$$

which, by taking an average value of Poisson's ratio $\nu_b = 1/5$, reduces to

$$V_0^2 = \left[2\frac{\beta}{c_r} + \frac{(1-\beta)^2}{(1-\phi-\beta)c_r + \phi c_l}\right]\frac{1}{\rho} \quad \ldots\ldots \quad (7b)$$

And in the same way,

$$V_\infty^2 = \left[\left(\frac{\beta}{c_r} + \frac{4}{3}G_b\right) + \frac{\beta\phi/\kappa\rho_l + (1-\beta)(1-\beta-2\phi/\kappa)}{(1-\phi-\beta)c_r + \phi c_l}\right]\frac{1}{\rho\left(1-\frac{\rho_l}{\rho}\frac{\phi}{\kappa}\right)} \quad \ldots\ldots\ldots\ldots\ldots\ldots\ldots\ldots\ldots\ldots \quad (8a)$$

THE INFLUENCE OF FREQUENCY

It is thus predicted that the wave velocity depends on frequency, and we have to know the extent of this dependence in practice. Since the differential Eqs. 1 are valid only so long as Darcy's flow law is valid, the applicability of solution Eq. 6 is restricted to small values of ω/ω_c. The high-frequency range has also been investigated by Biot, but it appears that in this range neither the value of V_∞ nor the general picture of the frequency dependence of wave velocity is altered.

*The ratio ω/ω_c, the frequency number, may be considered as the Reynolds number of the vibrating motion. It represents the ratio of inertia and viscous forces.

Eq. 6 predicts that for $\omega/\omega_c < 0.1$ and for $\omega/\omega_c > 5$ the wave velocity is nearly independent of frequency. In the range between these limits there is a notable dispersion. At first sight, therefore, one should conclude that, for an easy interpretation of wave velocity, the frequency of the signal should not be chosen in the "transition zone". In practice, however, this depends on the numerical differences which can be expected between V_0 and V_∞.

The location of the transition zone is indicated in Fig. 1. Here, for the case of water-saturated sandstone, ω has been plotted against porosity with permeability as a parameter. Water viscosity was taken to be $\mu = 1$ *cp*, while for the densities of solid and liquid the values 2.5 and 1.0 gm/cc were taken, respectively. The formulas for the constant-permeability curves follow from Eq. 9. Assuming $\kappa = 3$, one finds for the lower limit of the transition zone

$$\omega_{low} = 10^{-3}\left(\frac{1 - 0.6\,\phi}{3 - 2.2\,\phi}\right)\frac{\phi}{k},$$

while

$$\omega_{high} = 50\,\omega_{low}$$

represents the upper limit of the transition zone. Only the curves for the lower limits are given in the figure for four values of the permeability. Though there is no theoretical relationship between porosity and permeability, we shall use a rough empirical correlation between the two quantities obtained from data collected by Muskat.[15] If this

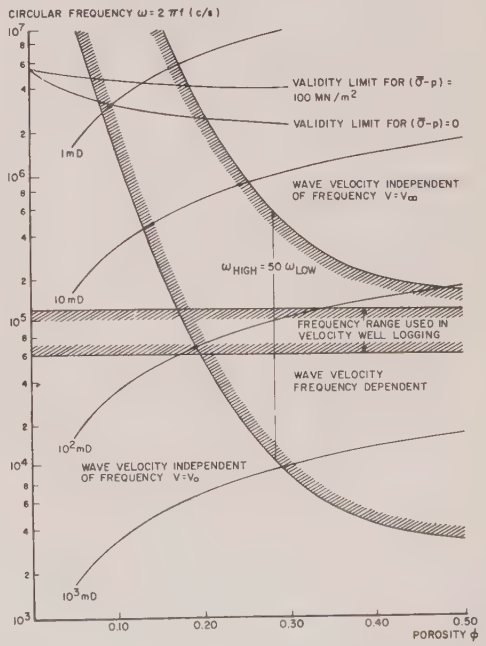

FIG. 1 – GRAPH INDICATING REGION WHERE WAVE VELOCITY IS FREQUENCY-DEPENDENT FOR WATER-SATURATED SANDSTONES (MASS-COUPLING FACTOR $\kappa = 3$).

correlation is applied, the frequency-dependent region can be roughly evaluated. This is represented by the L-shaped section in the figure. The frequency region used in practice in acoustic-logging techniques lies (see Stripling[16]) between 10 and 20 kc/sec. This region is also indicated in Fig. 1. It is seen that the frequency-dependent region is not completely avoided, but for porosities below 20 per cent the velocity approaches V_0, even for low liquid viscosities such as that of water.

On the other hand, laboratory experiments with ultrasonic devices will measure the approximate value of V_∞. A theoretical evaluation of the ratio V_∞/V_0 reveals that, when the mass-coupling factor κ approaches ∞, the frequency dependence disappears and $V_\infty = V_0$. In practice κ is not infinite, yet a numerical study of the ratio V_∞/V_0 for sedimentary rocks reveals that the difference between V_∞ and V_0 using reasonable values for κ will in general be smaller than 10 per cent. A more precise determination of the differences between V_∞ and V_0 can be given only after a correlation between β and ϕ has been discussed. In most cases the actual differences are not large, although they are not entirely negligible if one compares sonic and ultrasonic data.

Fig. 1 also indicates the limit of validity of the continuum theory. This limit is given by the condition that the wave length should be much larger than the grain diameter. It is assumed here that for sandstones the limiting wave length is 0.5 cm. This condition leads (using data presented later on) to the limiting curves in the upper part of the figure. The conclusion can be drawn from these curves that the Biot theory is applicable up to frequencies far in the ultrasonic region.

INFLUENCE OF THE BULK DEFORMATION PROPERTIES

Eq. 7 will be used from now on for the interpretation of acoustic wave velocities in saturated sediments. It gives the effect of the properties of rock matrix, rock bulk material and pore fluid on the wave velocity. Solid and liquid densities, porosity and compressibilities of solid matrix and liquid occurring in this equation can be considered as true and mutually independent constants. These same variables (though indirectly) appear in the time-average relation. In the present equation, however, the elastic properties of the rock bulk material (expressed by β) play a dominant role.

The first term in the velocity equation in general provides by far the largest contribution to the velocity value and is a direct function of the rock bulk elastic-deformation properties c_b and ν_b. An exception is found for suspensions, where one has to insert $\beta = 0$; accordingly, for this case the wave velocity depends only on porosity (or, rather, concentration) and the densities and compressibilities of the individual phases.

There are sufficient indications that the rock bulk compressibility is a function of porosity, pore-size distribution, composition of the cementing material, type of sedimentary rock and effective stress.

DEFORMATION THEORIES BASED ON MODELS OF THE BULK MATERIAL

The theory of Biot and its further development thus presents only a partial solution for the problem of acoustic-wave-velocity interpretation in terms of porosity. It predicts only the difference in acoustic wave velocity in dry and in fluid-saturated porous media. For further progress, basic knowledge on rock bulk compressibility is required. Many attempts to evaluate this property of sedimentary rocks on a theoretical basis can be found in the literature. Various models of porous structures have been analyzed for this purpose. Adams and Williamson[17] as early as 1923 suggested two simple theoretical models for an investigation of the influence of pores on rock bulk compressibility in the low-porosity range.

1. The unit element of the structure is a solid sphere with a central spherical cavity.

2. The unit element is a solid sphere with a narrow spherical shell-shaped cavity, separating a solid central sphere from an outer spherical shell comprising the remaining solid material.

We carried out the necessary calculations for these models using the classical theory of elasticity and found that, in the case of the spherical pores,

$$c_b = \frac{M + \phi}{M(1 - \phi)}\, c_r,$$

or

$$\left(\frac{1}{\beta} - 1\right) = \left(\frac{M + 1}{M}\right)\frac{\phi}{1-\phi}. \quad \ldots\ldots\ldots \quad (10)$$

M is only a function of Poisson's ratio of the matrix material,

$$M = \frac{2(1 - 2\nu)}{(1 + \nu)} \approx 1.$$

This result means that $(1/\beta - 1)$ is, roughly, directly proportional to ϕ in the low-porosity range. It can be shown that, for any model of a solid with sufficiently isolated holes distributed at random, a relationship of the form

$$(1/\beta - 1) \propto \frac{\phi}{1 - \phi} \quad \ldots\ldots\ldots \quad (10a)$$

holds. Using van der Knaap's[18] definition of pore compressibility

$$c_p = (1/\beta - 1)\, c_r/\phi,$$

this implies that

$$c_p \propto \frac{1}{1 - \phi}, \quad \ldots\ldots\ldots \quad (11)$$

or a nearly constant pore compressibility in the low-porosity range.

Conversely, for the model with the shell-shaped pores (shell crack at one-half the outer radius of the unit sphere), one obtains

$$c_b = \frac{8M + 1}{7M} c_r ,$$

or

$$\left(\frac{1}{\beta} - 1\right) = \left(\frac{M + 1}{7M}\right).$$

So here, $\left(\frac{1}{\beta} - 1\right)$ is independent of porosity. This may possibly be a suitable model for a rock containing microcracks. A model whose deformation characteristics agree in some important aspects with those of granular sediments is a packing of spheres. Several types of packing are possible, and different quantitative results are consequently obtained by various authors. Apart from this dependence of deformation characteristics on packing, there is the problem that an exact calculation of the bulk deformation properties of packings of spheres is complicated. Most investigators avoid some of the complications by assuming that the spheres of the model deform without friction at the contact points. This means that at the grain contacts only normal forces are taken into account. Only Mindlin[19] has considered the additional influence of friction.

Two characteristic deformation properties of packings of spheres are the following.

1. The elastic "constants" of an array of spheres are pressure-dependent. Calculations show that the bulk compressibility of such models is invariably proportional to $(\bar{\sigma} - p)^{-1/3}$.

2. The porosity of packings of uniform spheres varies roughly between 25 and 45 per cent, but from deformation studies of different uniform packings one cannot obtain a clear picture of how the compressibility of a uniform sphere packing depends on porosity. Brandt[6] did some interesting work on packings built up from spheres of various diameters. In this way the porosity could be varied more-or-less gradually. He found that the pore compressibility of nonuniform sphere packings should be nearly independent of porosity, as in the case of a solid with isolated holes.

We conclude from this analysis that for many porous sediments, other variables kept constant, a relationship of the form of Eq. 11 possibly exists between pore compressibility and porosity.

Introducing a constant C in Eq. 11, we can write

$$c_b = c_r + \phi c_p = c_r + \frac{C\phi}{1 - \phi}. \quad \ldots\ldots (12)$$

The dilatational wave velocity in the dry rock depends on this rock bulk compressibility.

$$V^2 = \frac{f(\nu_b)}{c_b \rho_r (1-\phi)} = \frac{f(\nu_b)}{\rho_r (1-\phi)\left[c_r + \frac{C\phi}{1-\phi}\right]}.$$

Assuming as a first approximation that Poisson's ratio is independent of porosity, we realize that $f(\nu_b)/\rho_r c_r = V_r^2$, the matrix wave velocity. So

$$1/V = 1/V_r \sqrt{1 + \left(\frac{C}{c_r} - 1\right)\phi} ,$$

which for small porosity values can be further approximated as

$$1/V \approx 1/V_r \left[1 + \frac{1}{2}\left(\frac{C}{c_r} - 1\right)\phi\right] .$$

This equation is of the form

$$1/V = A + B\phi, \quad \ldots\ldots\ldots\ldots (13)$$

and the additional information is that $A = 1/V_r$ in this approximation. The coefficient B depends strongly on the value of the pore compressibility, but it has nothing to do with the presence of a fluid in the pores. Substitution of Eq. 12 in Eq. 7a for the case of a liquid in the pores does not change the approximate result Eq. 13 very much. To a first approximation, only A and B obtain a different value.

EXPERIMENTAL DATA

CLEAN SANDSTONES

In Fig. 2, rock compressibility data calculated from velocity measurements for a number of dry sandstones at atmospheric pressure have been collected. They are derived from measurements by Wyllie, *et al*,[2] data collected by Wuerker[20] and a number of experiments carried out in our

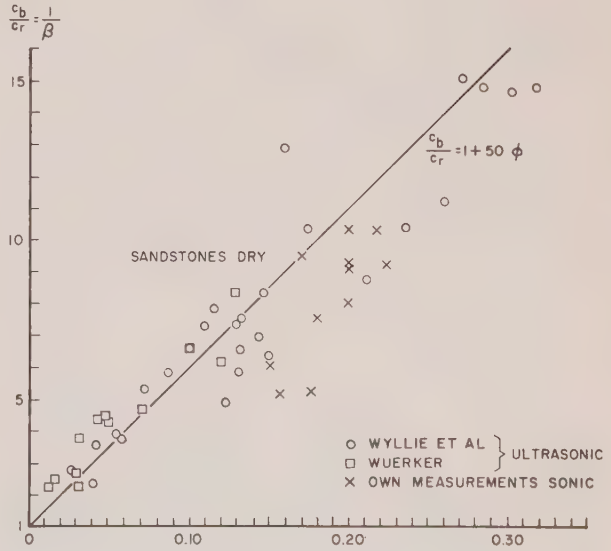

FIG. 2 – c_b/c_r AS A FUNCTION OF POROSITY FOR DRY SANDSTONES ACCORDING TO DYNAMIC MEASUREMENTS (ATMOSPHERIC PRESSURE).

laboratory. In this figure, $1/\beta = (c_b/c_r)$ is plotted against the porosity. Results roughly suggest a nearly linear relationship

$$(1/\beta - 1) = 50\,\phi \quad . \quad . \quad . \quad . \quad . \quad . \quad . \quad . \quad . \quad . \quad (10b)$$

A relationship of the form of Eq. 10a would be more satisfactory from a theoretical point of view, but would be less convenient to handle while it hardly gives a better result for low porosities. Thus, for these sandstones, the pore compressibility is indeed nearly independent of porosity, in agreement with the foregoing theoretical considerations.

For the dependence of β on effective stress, we can use van der Knaap's[18] empirical relationship for the bulk compressibility of sandstones, based upon an observed pore compressibility

$$c_p = \frac{c_r}{\phi}\left(\frac{1}{\beta} - 1\right) \approx 3.5 \times 10^{-3}\ (\bar{\sigma} - p)^{-2/3} \text{ sq m/MN.}^*$$

If it is assumed that $c_r = 0.25 \times 10^{-4}$ sq m/MN, this leads to

$$\left(\frac{1}{\beta} - 1\right) \approx 140\ \phi\ (\bar{\sigma} - p)^{-2/3} . \quad . \quad . \quad . \quad . \quad . \quad (14)$$

Eq. 14 cannot be the general relationship, since it predicts an infinitely large bulk compressibility at $(\bar{\sigma} - p) = 0$. This is only true for loose sand. A closer look at van der Knaap's results, which are reproduced here in Fig. 3, shows that the straight line between log c_p and log $(\bar{\sigma} - p)$ breaks down somewhere below $(\bar{\sigma} - p) = 2$ or 3 MN/sq m. At low effective stress values, the curve bends down to a horizontal asymptote; the pore compressibility for $(\bar{\sigma} - p) = 0$. Additional experimental work has confirmed this, and in Fig. 4 the final result is indicated. This result suggests that for consolidated clean sandstones an empirical relationship of the form

$$\left(\frac{1}{\beta} - 1\right) = \frac{\phi}{c_r}\left[b\ (\bar{\sigma} - p) + (a\ c_r)^{-n}\right]^{-\frac{1}{n}} . \quad . \quad (15)$$

will be the best average expression for the bulk compressibility. If we take $a = 50$, $n = 3/2$ and $b = 5{,}000$ (MN/sq m)$^{1/2}$, one obtains Eq. 10b for $(\bar{\sigma} - p) = 0$, while Eq. 14 is approached for large values of $(\bar{\sigma} - p)$, since

$$5{,}000^{-2/3} = 3.5 \times 10^{-3}.$$

The coefficients a, b and n will depend on grain cementing material, pore configuration, etc., but at any given stress level there is a linear relation between the porosity and $(1/\beta - 1)$.

Combination of Eq. 15 with the general theory just outlined permits a more precise determination of the ratio V_∞/V_0 in sandstones. This ratio is plotted in Fig. 5 for an average value of the mass-coupling factor $\kappa = 3$ and for water-saturated sandstones at different values of $(\bar{\sigma} - p)$ and ϕ. It is seen that the ratio V_∞/V_0 is in general lower than 1.05.

It is now possible to calculate the velocity of plane dilatational waves as a function of porosity at zero effective stress in water-saturated sandstones according to Eq. 8a. The results are given in Fig. 6 where V_∞ has been plotted for $\kappa = 3$. These theoretical results are compared with the ultrasonic measurements reported by Wyllie, *et al*,[2]

*1 sq m/MN (square meters per meganewton) = 6.89×10^{-3} psi^{-1}

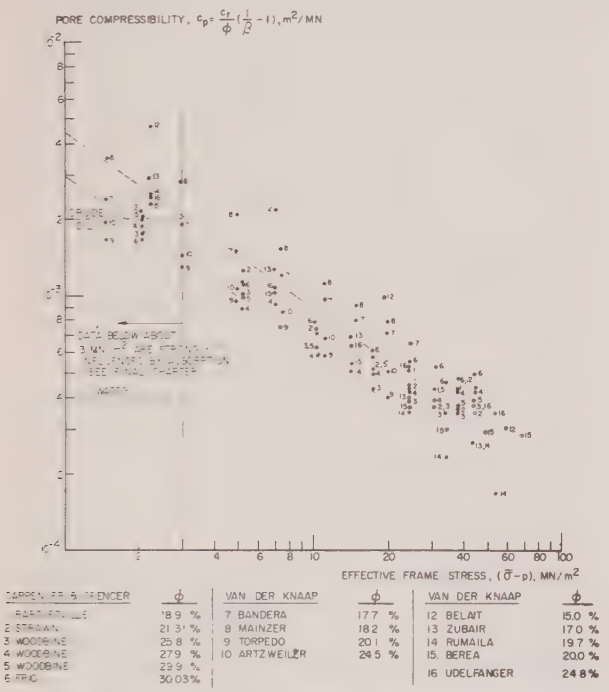
PORE COMPRESSIBILITY, $c_p = \frac{c_r}{\phi}(\frac{1}{\beta} - 1)$, m²/MN
EFFECTIVE FRAME STRESS, $(\bar{\sigma} - p)$, MN/m²
DATA BELOW ABOUT 3 MN/m² ARE STRONGLY INFLUENCED BY MICROFRACTURES
SEE ORIGINAL PAPER
VAN DER KNAAP
7 BANDERA 17.7 %
8 MAINZER 18.2 %
9 TORPEDO 20.1 %
10 ARTZWEILER 24.5 %
VAN DER KNAAP
12 BELAIT 15.0 %
13 ZUBAIR 17.0 %
14 RUMAILA 19.7 %
15. BEREA 20.0 %
16 UDELFANGER 24.8%

FIG. 3 — PORE COMPRESSIBILITY DATA OF SANDSTONES (ACCORDING TO VAN DER KNAAP IN REF. 18); 1 MEGANEWTON/SQ M = 145.04 PSI.

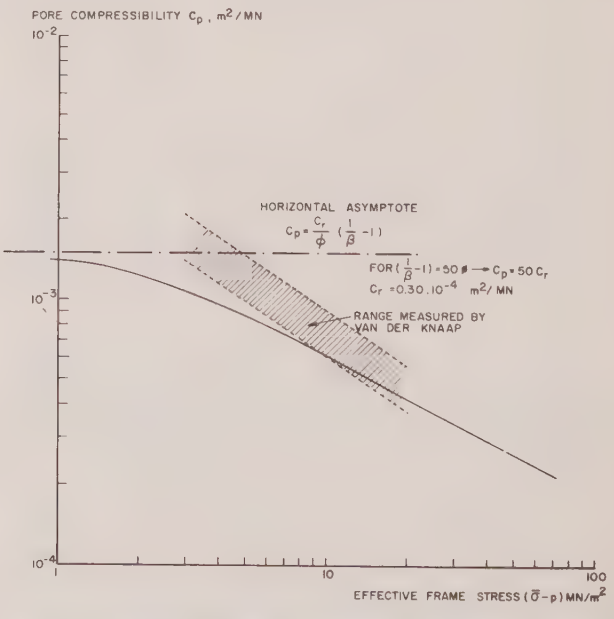
PORE COMPRESSIBILITY c_p, m²/MN
HORIZONTAL ASYMPTOTE
$c_p = \frac{c_r}{\phi}(\frac{1}{\beta} - 1)$
FOR $(\frac{1}{\beta} - 1) = 50\,\phi \rightarrow c_p = 50\,c_r$
$c_r = 0.30 \cdot 10^{-4}$ m²/MN
RANGE MEASURED BY VAN DER KNAAP
EFFECTIVE FRAME STRESS $(\bar{\sigma} - p)$ MN/m²

FIG. 4 — GENERAL RELATIONSHIP BETWEEN PORE COMPRESSIBILITY AND EFFECTIVE STRESS FOR CLEAN SANDSTONES (DRY).

and it is seen that the agreement is good over the whole porosity range.

Next, V_∞ and V_0 in water-saturated sandstones can be calculated as a function of both porosity and effective stress. Results are plotted in Fig. 7. In this figure the time-average relation is also indicated. A single curve is obtained for the time average relation since it is independent of effective stress. It is seen that, although the difference between the results of the two theories is considerable for moderate porosity values at very low and high effective stresses, for the stresses prevailing at average reservoir depths the time-average relation may predict more-or-less accurate porosity values.

Eq. 15 also explains the entirely different velocity data obtained by Hicks and Berry[7] and by Wyllie, *et al.*[2] The measurements by Hicks and Berry were carried out in water-saturated sandstones at an effective stress of about 42 MN/sq m. In Wyllie's measurements, the effective stress was zero. Fig.8 demonstrates that velocity predictions with Eq. 15 for $(\bar{\sigma} - p) = 50$ MN/sq m agree very well with Hicks and Berry's results, while those predicted for $(\bar{\sigma} - p) = 0$ fit in quite well with Wyllie's data (as was already shown in Fig. 6). Fig. 6 shows that the presence of water in the pores straightens

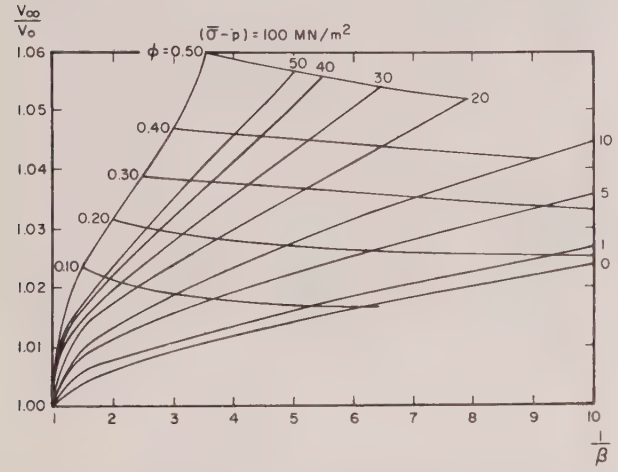

FIG. 5 – THE RATIO V_∞/V_0 FOR WATER-SATURATED SANDSTONES USING THE EMPIRICAL RELATION, EQ. 15.

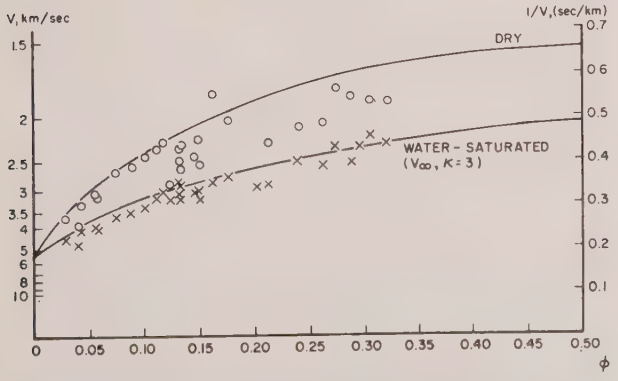

FIG. 6 – COMPARISON BETWEEN MEASURED AND CALCULATED ULTRASONIC PLANE DILATATIONAL WAVE VELOCITIES IN AIR-DRY AND WATER-SATURATED SANDSTONES (MEASURED DATA ACCORDING TO WYLLIE, *ET AL*).

the curves of $1/V$ against ϕ, and an approximate relationship of the form

$$1/V = A + B\phi$$

applies over a larger porosity range in the water-saturated situation. More detailed information on

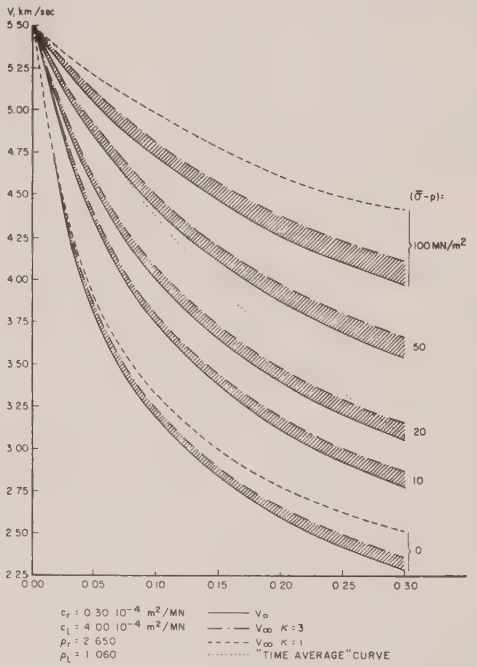

FIG. 7 – COMPARISON OF PLANE DILATATIONAL WAVE VELOCITIES IN WATER-SATURATED SANDSTONES AS PREDICTED BY THE TIME-AVERAGE RELATION AND BY PRESENT THEORY.

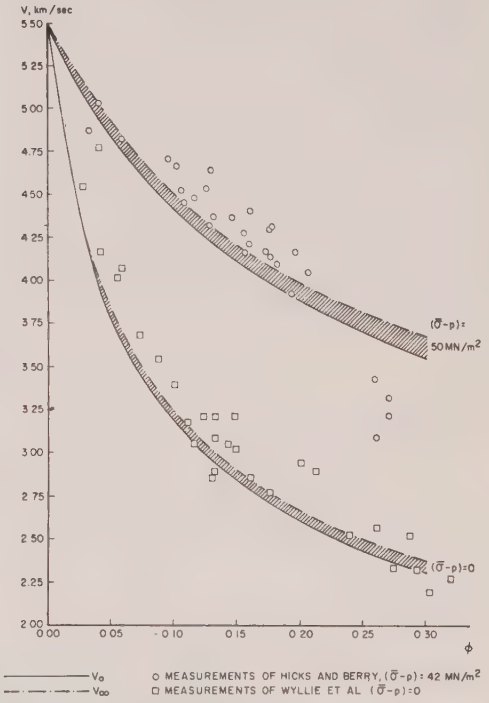

FIG. 8 – COMPARISON BETWEEN MEASURED AND CALCULATED ULTRASONIC PLANE DILATATIONAL WAVE VELOCITIES IN WATER-SATURATED SANDSTONES FOR DIFFERENT LEVELS OF EFFECTIVE STRESS.

TABLE 1 — SOME AVERAGE VALUES FOR MATRIX DENSITIES, MATRIX COMPRESSIBILITIES AND WAVE VELOCITIES FOR CALCITE, DOLOMITE AND ANHYDRITE

	Grain Density ρ_r	Matrix Compressibility $c_r \times 10^{-4}$ m²/MN	Plane Dilatational Acoustic Wave Velocity (m/sec)
Calcite	2.70 – 2.76	0.135	6400
Dolomite	2.81 – 2.86	0.100	7200
Anhydrite	2.96 – 3.00	0.135	6000

the difference between the acoustic wave velocity in dry and in water-saturated sandstones is given in Fig. 9. Here, the ratio $\frac{V_0 - V_{dry}}{V_0}$ is plotted against the porosity, in which it is assumed that $(1/\beta - 1) = C\phi$ and C is taken as a variable. Low C-values apply to tight rocks or rocks under high confining pressure. For V_0 the case of water in the pores is considered ($\rho_l = 1.00$ and $c_l = 4.00 \times 10^{-4}$ sq m/MN). It is seen that for low C-values the effect of water in the pores becomes small and that the difference $V_0 - V_{dry}$ can even be negative, that is, the water in the pores lowers the wave velocity. It is concluded that acoustic velocity data are able to differentiate between gas or liquid in the pores in soft formations only.

CARBONATE ROCKS

The different origin of carbonate porosity, together with the mixed presence of calcite and dolomite sometimes contaminated with anhydrite inclusions, suggests *a priori* that acoustic-log interpretation in carbonate rocks in terms of porosity will be more complicated than in sandstones.

Calcite, dolomite and anhydrite have different matrix densities and matrix compressibilities. Some average values are collected in Table 1.

Therefore, from the beginning we will make a subdivision in calcite and dolomite and exclude the (in general, nonporous) anhydrites. We determined ultrasonic wave velocities in a series of carbonate rock samples of which van der Knaap[18] has reported the pore compressibilities. We will refer to this series as Series A. In Ref. 18 van der Knaap showed that for these carbonates the pore compressibility was strongly influenced by the porosity. At a given stress level, c_p increases with decreasing porosity, particularly in the low-porosity range. If our theoretical conditions are correct, this predicts a quite different relationship between acoustic wave velocity and porosity than observed for sandstones, at least in this low-porosity range. Because van der Knaap's core material was partly calcite and partly dolomite, the velocity data had to be subdivided necessarily according to the type of carbonate. Unfortunately, this also resulted in a subdivision of the porosity range — the calcites were predominantly low porous, the dolomites showed higher porosity figures (9 to 17 per cent). In agreement with the pore compressibility data, the wave velocities varied considerably with effective stress. In Fig. 10, therefore, reciprocal wave velocities in the calcites are plotted as a function of porosity for the arbitrary stress level of 50 MN/sq m (about 500 atm). In Fig. 11 the corresponding data for the dolomites are shown. In neither plot can a linear relationship between $1/V$ and ϕ be detected; the reciprocal velocity varies rapidly in the low-porosity range and slowly at higher porosity. This is exactly what should be expected on the basis of the pore compressibility behavior.

Not all carbonates are alike, however. Also plotted in Figs. 10 and 11 are data obtained from dry cores of another carbonate reservoir, determined at the same effective stress of 50 MN/sq m. Again calcites are separated from the dolomites. This series, indicated by B, does show a nearly linear relationship and thus behaves similarly to many sandstones. A comparison between Curves A and B in the same figures further reveals that wave velocities in Series A for a given porosity are invariably lower. Accordingly, Formation A has

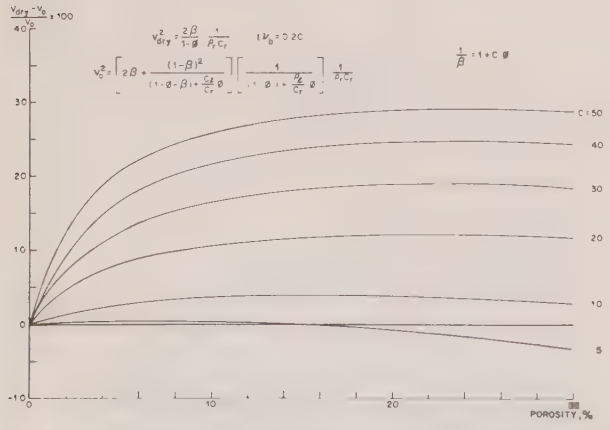

FIG. 9 — EFFECT OF THE PRESENCE OF WATER ON ACOUSTIC WAVE VELOCITY ACCORDING TO BIOT'S THEORY.

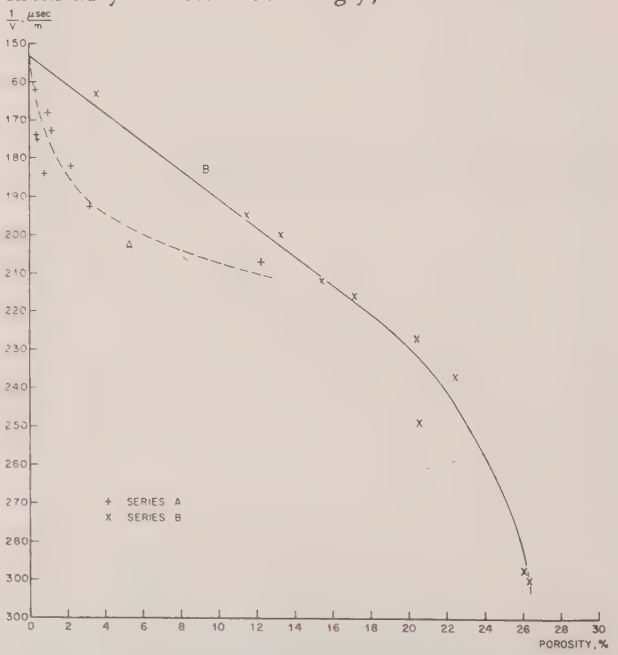

FIG. 10 — ULTRASONIC WAVE VELOCITY IN CALCITES AT 500 ATM (DRY CORES).

to show the largest pore compressibilities. Additional pore compressibilities measured by van der Knaap for Series B are reproduced in Fig. 12. Comparison between these data and the data pertaining to Series A reproduced in van der Knaap's publication[18] reveals that, indeed, Series A has by far the larger pore compressibilities, particularly in the low-porosity range. It is also apparent from Fig. 12 that in Series B the pore compressibility is independent of porosity, in agreement with the linear relationship between $1/V$ and ϕ.

In Fig. 13, finally, acoustic velocity data of various calcites are compared. Sonic-log data obtained in a typical calcite section in an Austrian well at an average depth of 1,400 m are compared with ultrasonic wave velocities in the calcite Series B just mentioned, at a corresponding effective stress of 150 atm. The agreement is satisfactory. In addition, some ultrasonic velocity measurements in West European calcite-outcrops are included. These data also seem to agree with the other data. For the sake of completeness, the time-average relation assuming the presence of water in the pores is also given. This line fits the data as well. It must be noted, however, that the laboratory measurements were taken on dry cores. Again we are forced to conclude that the time-average relation, although untenable from a physical point of view, can by a lucky coincidence give correct results.

INFLUENCE OF SHALE LAYERS AND HORIZONTAL FRACTURES ON EFFECTIVE VERTICAL STRESS

We have seen that a decrease in bulk compressibility with increasing effective stress is a property of most sedimentary rocks. It causes an over-all gradual increase in elastic wave velocity with depth. At the same time, any stress discontinuity in the neighborhood of the borehole must affect wave velocity. Such discontinuous wave velocities might easily be interpreted as porosity variations if one were not aware of the effective-stress effect. Three examples are given as follows.

1. So long as the fluid contact in the pores is continuous in a downward direction, the gradient of the effective vertical stress is fairly low. Impermeable shale layers, however, may sustain a considerable fluid pressure difference at both sides of the permeability barrier. Even if this impermeable

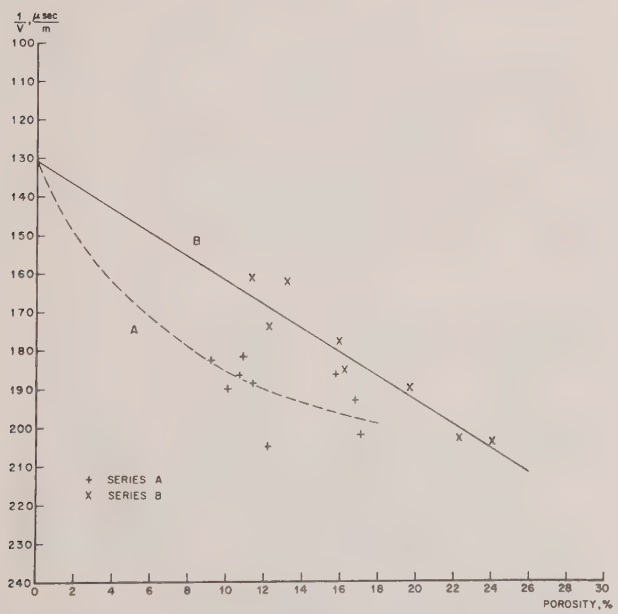

FIG. 11 – ULTRASONIC WAVE VELOCITIES IN DOLOMITES AT 500 ATM (DRY CORES).

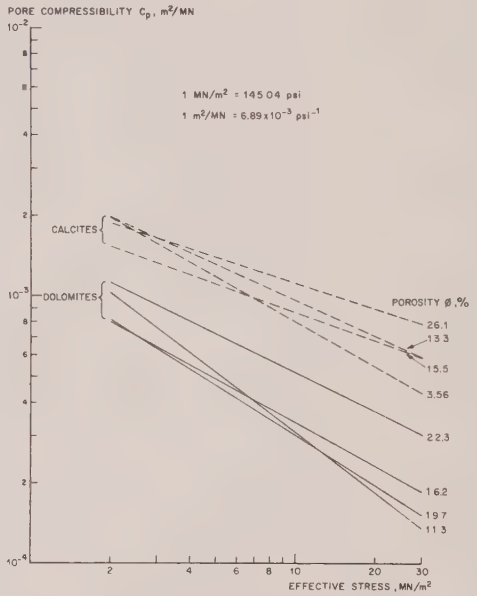

FIG. 12 – PORE COMPRESSIBILITIES OF SOME CARBONATE ROCK SAMPLES, SERIES B (MEASUREMENTS BY VAN DER KNAAP).

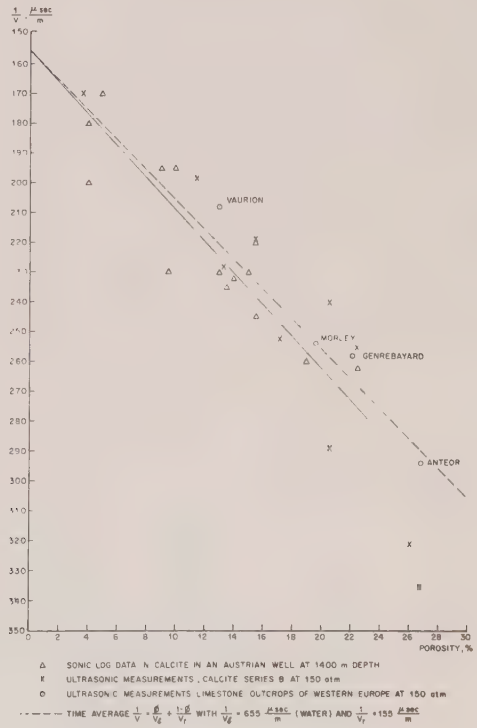
1/V, μsec/m
VAURION
MORLEY
GENREBAYARD
ANTEOR
POROSITY, %
SONIC LOG DATA IN CALCITE IN AN AUSTRIAN WELL AT 1400 m DEPTH
ULTRASONIC MEASUREMENTS, CALCITE SERIES B AT 150 atm
ULTRASONIC MEASUREMENTS LIMESTONE OUTCROPS OF WESTERN EUROPE AT 150 atm
TIME AVERAGE 1/V = ø/V_f + (1-ø)/V_r WITH 1/V_f = 655 μsec/m (WATER) AND 1/V_r = 155 μsec/m

FIG. 13 – COMPARISON OF DATA.

barrier separates two parts of the same porous sediment, the wave velocity in these parts may be different owing to different effective-stress conditions.

2. Shale layers may disturb the vertical stress distribution in yet another way. Zheltov and Khristianovich,[21] in a detailed study, showed that a considerable re-distribution of vertical effective stress may be caused by plastic clay formations of little strength. A plastic stress distribution around the well will result in a stress relief of the sediments immediately below the clay layer, while the rocks lying above the clay form a dome and experience an increased effective stress. If the layer below the clay is a producing formation, the low wave velocity found at the top of this formation might easily be interpreted as a high porosity. That such plastic stress conditions in clays around the well are real has been shown by Hicks.[22] Using a multi-receiver velocity-logging system, he found that the wave velocity in a clay layer increased with increasing receiver-transmitter spacing. The larger this distance, the deeper the penetration of the sound waves. This showed that there was a considerable pressure relief in the clay near the borehole. A further consequence, not mentioned by Hicks, is that this stress relief makes itself felt immediately below the shale layer. The distance over which it is felt outside the clay depends on the extent of the plastic zone in the clay, and this in turn depends on the deformation properties and strength characteristics of the clay and on the depth of the layer.

3. The same effect, but still more pronounced, may occur if a horizontal or nearly horizontal natural fracture intersects the wellbore. In the fracture, only the fluid pressure is available to sustain the vertical load of the overburden. This causes stress concentrations around the fracture, the formation directly above the fracture experiences an increased effective stress and the formation immediately below the fracture is relieved.

The resulting stress pattern leads to a reduction in velocity in the formation below the fracture which is greater than the increase in velocity in the formation above the fracture. The average result, "seen" by the log is a velocity reduction.

PHYSICAL INTERACTION OF PORE FLUID AND POROUS SKELETON

van der Knaap[18] and others have noted that the nature of the fluid, and also the amount of fluid present in the pores, may have a remarkable effect on the elastic properties of sedimentary rocks. This behavior results in experimental data on samples, particularly at atmospheric pressure, that are completely different from the theoretically predicted results, and one can easily misinterpret the observed wave velocities.

This will be illustrated with some examples. The resonance frequency (being directly proportional to wave velocity) of porous rods was measured for both torsional and longitudinal vibrations. The cylindrical samples were examined both air-dry and saturated with different liquids at atmospheric pressure and under frame pressure. In the latter case, the sample was covered by a very thin rubber jacket, placed in a pressure vessel and pressurized on the outside by means of hydrogen.

At atmospheric pressure the resonance frequencies of sintered porous material show a small decrease upon saturation with fluid. This is in agreement with the theory previously outlined. By contrast, corresponding measurements on sandstones show quite different results in this respect. This is illustrated by the data collected in Table 2. The figures in this table give reasonance frequencies for a number of sandstones and sintered porous structures saturated with various liquids. In the case of sandstones, only the addition of heptane and sym-tetrachloroethane results in a small decrease in resonance frequency. For sintered materials, all liquids show this effect. However, saturating the sandstone samples with water clearly results in a much greater drop in resonance frequency. Saturating the samples with oils gave rise to a considerable increase in resonance frequency, compared with that of the dry samples. One easily arrives at the conclusion that the wave velocity should make a clear distinction between oil-bearing and water-bearing formations. These facts cannot be explained by the Biot theory. The experiments also showed that the attenuation of elastic waves in water- and oil-saturated sandstones, as derived from the resonance tests, is considerably

TABLE 2 — RESONANCE FREQUENCIES OF WET AND DRY POROUS SYSTEMS AT ATMOSPHERIC PRESSURE

Porous System	ϕ (per cent)	k (darcies)	Resonance Frequency, Dry System*		Resonance Frequency, Wet System									
					Heptane		Sym-tetra-chloroethane		Transformer Oil		Middle East Crude		Water	
			l	t	l	t	l	t	l	t	l	t	l	t
Rumaila Ss	20	–	12900	8600	12550	8450	11250	9000	13350	8600	14450	8950	9180	7000
Zubair Ss	17	–	11600	8750	11200	8550	11550	8700	13550	8950	14100	9550	7600	5600
Berea Ss	24	0.24	12150	8750	11450	8300	11200	8200	14000	9400	14300	9075	7400	5800
Sintered Glass	36	39.5	10300	7150	9900	7200	–	–	9600	6650	–	–	9850	6750
Si Carbide	26	1.9	22400	14600	21700	14100	–	–	21600	14000	–	–	21400	13950
Carborundum	31	14.3	31700	20500	31000	20100	30400	19500	30800	19800	–	–	30000	18500

Heptane : $\rho = 0.68$, $\mu = 0.40$ cp
Sym-tetrachloroethane: $\rho = 1.50$, $\mu = 0.76$ cp
Transformer Oil : $\mu = 25$ cp
Middle East Crude : $\mu = 71.5$ cp

* l = longitudinal waves, t = torsional waves.

higher than predicted by the Biot theory. This derivation is omitted here but can be found in a paper by Geertsma and Smit.[12]

The observed anomalous behavior very probably is due to adsorption of the pore fluids and seems to be most important in an analysis of the physical behavior of the so-called weathered layer. The reason why there is no need to explain these experimental results in the present study is that these adsorption effects do not show up in the practice of velocity logging. This was concluded from a series of experiments which showed that these anomalous effects become almost unnoticeable and that results are always in line with what should be expected from Biot's theory provided a sufficiently large effective stress is applied to the skeleton.*

Except in the shallow depth range, the effective stress around the borehole is sufficiently high to eliminate adsorption effects. We were careful not to include data influenced by such adsorption phenomena in the present study. The interesting effects of adsorption and its influence on the mechanical properties of porous rocks are still subjects of investigation.

CONCLUSIONS

This investigation of the relationship between the speed of propagation of elastic waves in liquid-saturated porous rocks and porosity leads to a number of conclusions.

1. Unfortunately, the time-average relation now in use for deriving porosity values from the acoustic log is based on a wrong physical picture. However, in many sandstones and carbonates it predicts, independently of the fluid content of the pore space, about the correct trend of the relationship between acoustic travel time and porosity at depths between 1,000 and 3,000 m, if for the wave velocity of the liquid in that equation the velocity in water is taken.

2. The Biot theory explains the difference in acoustic wave velocity in dry and liquid-saturated porous media under reservoir conditions of effective stress. This difference is usually rather small in deeply buried well-cemented reservoir rocks. Differentiation between liquids and gas with the Sonic log is possible only in near-surface rocks, preferably consisting of loose particles.

3. In the dry rock frequently a nearly linear relationship between reciprocal acoustic wave velocity and porosity is observed, corresponding with a pore compressibility which is independent of porosity. The basic relationship between the deformation properties of the rock bulk material and the acoustic wave velocity is shown to be equal to that in nonporous solids.

4. Carbonate rocks sometimes show a rather peculiar relationship between pore compressibility and porosity, as has been reported earlier. This corresponds with an equally peculiar relationship between acoustic wave velocity and porosity.

5. The interpretation of the acoustic log in carbonate rocks is furthermore complicated by the presence of both calcite and dolomite, which have different matrix velocities.

6. Both compressibilities and acoustic wave velocities are nearly always strongly pressure-dependent. Therefore, porosity-velocity correlations must always be carried out at corresponding stress conditions.

7. The acoustic wave velocity in liquid-saturated porous sediments is somewhat frequency-dependent. The effect of frequency results in minor numerical differences (less than 5 per cent) between sonic- and ultrasonic-wave velocity data.

8. The fact that acoustic wave velocity is a function of effective stress renders the Sonic log sensitive to discontinuities in the vertical effective stress distribution around the borehole. Such stress discontinuities may result from impermeable barriers between permeable layers and plastic stress conditions in clay layers around the borehole; they also may be caused by natural fractures. Velocity variations resulting from these phenomena can easily be misinterpreted as being due to porosity variations.

9. The results of wave propagation experiments in sedimentary rocks under low or zero effective stress often are influenced by adsorption of the pore fluid on the grain surfaces. In that case, they are of no value for the interpretation of what the Sonic log "sees" at depth.

NOMENCLATURE

c_b = rock bulk compressibility, $m^{-1} L t^2$

c_l = liquid (fluid) compressibility, $m^{-1} L t^2$

c_p = pore compressibility, $m^{-1} L t^2$

c_r = rock matrix compressibility, $m^{-1} L t^2$

e = absolute dilatation of rock bulk material

G_b = shear modulus of rock bulk material = $\frac{3(1-2\nu)}{2c_b(1+\nu)}$, $m L^{-1} t^{-2}$

H, K, L = deformation constants occurring in Biot's theory, $m L^{-1} t^{-2}$

k = permeability, L^2

p = hydrostatic pore tension, $m L^{-1} t^{-2}$

t = time, t

V = acoustic wave velocity (real part), $L t^{-1}$

V_0 = acoustic wave velocity for zero frequency, $L t^{-1}$

V_∞ = acoustic wave velocity for infinite high frequency, $L t^{-1}$

$\beta = c_r/c_b$

ϵ = absolute dilatation of pore fluid

ζ = relative dilatation between solid and fluid = $\phi(e-\epsilon)$

κ = mass-coupling factor ≥ 1

μ = fluid viscosity, $m L^{-1} t^{-1}$

*Adsorption effects also disappear if the frequency is chosen in the higher ultrasonic region above about 1 megacycle/second.

ν_b = Poisson's ratio of rock bulk material

ρ = total or bulk density, m L^{-3}

ρ_l = fluid density, m L^{-3}

$\rho_c = \kappa \frac{\rho_l}{\phi}$, m L^{-3}

$\bar{\sigma}$ = external hydrostatic pressure, m L^{-1} t^{-2}

ϕ = porosity

ω = angular frequency, t^{-1}

ω_c = characteristic angular frequency = $\frac{\mu}{k\rho} \frac{\rho^2}{\rho\rho_c - \rho_l^2}$, t^{-1}

ACKNOWLEDGMENTS

The author wishes to express his thanks to W. van der Knaap for his kind cooperation, to D. C. Smit who made so many preliminary calculations and to J. van Steveninck who carried out the dynamic measurements.

REFERENCES

1. Biot, M. A.: "Theory of Propagation of Elastic Waves in a Fluid-Saturated Porous Solid", *Jour. Acoust. Soc. Amer.* (1956) Vol. 28, 168.
2. Wyllie, M. R. J., *et al*: "Elastic Wave Velocities in Heterogeneous and Porous Media", *Geophysics* (1956) Vol. 21, 41.
3. Hughes, D. S. and Jones, H. J.: "Variation of Elastic Moduli of Igneous Rocks with Pressure and Temperature", *Bull.*, GSA (Aug., 1950) Vol. 61, 843.
4. Gassmann, F.: "Elastic Waves Through a Packing of Spheres", *Geophysics* (1951) Vol. 16, 673.
5. White, J. E. and Sengbush, R. L.: "Velocity Measurements in Near-Surface Formations", *Geophysics* (1953) Vol. 18, 54.
6. Brandt, H.: "A Study of the Speed of Sound in Porous Granular Media", *Jour. Appl. Mech.* (1955) Vol. 22, 479.
7. Hicks, W. G. and Berry, J. E.: "Fluid Saturation of Rocks from Velocity Logs", *Geophysics* (1956) Vol. 21, 739.
8. Zwikker, C. and Kosten, C. W.: *Sound-Absorbing Materials*, Elsevier Publishing Co., Inc., N. Y. (1949).
9. Gassmann, F.: "Ueber die Elastizität poröser Medien", *Vierteljahrschrift der Naturforschenden Gesellschaft*, Zürich (1951) Vol. 96, 1.
10. Geertsma, J.: "The Effect of Fluid Pressure Decline on Volumetric Changes of Porous Rocks", *Trans.*, AIME (1957) Vol. 210, 331.
11. Biot, M. A. and Willis, D. G.: "The Elastic Coefficients of the Theory of Consolidation", *Jour. Appl. Mech.* (1957) Vol. 24, 594.
12. Geertsma, J. and Smit, D. C.: "Some Aspects of Elastic Wave Propagation in Fluid-Saturated Porous Solids", *Geophysics* (1961) Vol. 26, 169.
13. Patterson, N. R.: "Seismic Wave Propagation in Porous Granular Media", *Geophysics* (1959) Vol. 21, 691.
14. Tchekaliuk, E. B.: "The Velocity of Propagation of Elastic Deformations in a Porous Medium", (in Russian) *Neft. Chosiastwo* (1947) No. 11, 29.
15. Muskat, M.: *Physical Principles of Oil Production*, McGraw-Hill Book Co., Inc., N. Y. (1949) 172-173.
16. Stripling, A. A.: "Velocity Log Characteristics", *Trans.*, AIME (1958) Vol. 213, 207.
17. Adams, S. H. and Williamson, E. D.: "The Compressibility of Minerals and Rocks at High Pressures", *Jour. of the Franklin Inst.* (1923) Vol. 195, 475.
18. van der Knaap, W.: "Nonlinear Behavior of Elastic Porous Media", *Trans.*, AIME (1959) Vol. 216, 179.
19. Mindlin, R. D.: "Mechanics of Granular Media", *Proc.*, Second U. S. Nat. Cong. of Appl. Mech. (1954) Ann Arbor, Mich.
20. Wuerker, R. G.: "Annotated Tables of Strength and Elastic Properties of Rocks", AIME Paper 663-G published separately (1957).
21. Zheltov, Yu. P. and Khristianovich, S. A.: "The Hydraulic Fracturing of an Oil-Producing Formation", (in Russian) *Izvest. Akad. Nauk SSSR*, Otdel. Tekh. Nauk (1955) No. 5, 3; English translation, Assoc. Tech. Services, Inc., RJ-472.
22. Hicks, W. G.: "Lateral Velocity Variations Near Bore Holes", *Geophysics* (1959) Vol. 24, 45.

DISCUSSION

V. S. TUMAN
MEMBER AIME

U. OF ILLINOIS
URBANA, ILL.

Geertsma's analytical work is very interesting, but we wonder if the idealized average stress $\bar{\sigma}$ that he has used in his study can be justified for the wellbore conditions.

As he has mentioned, there will be stress relief at the wellbore, but these will appear in the shales as well as in the porous formations. Abnormal or residual stresses, not related to the overburden pressure, exists in the folded formations and in the vicinity of salt plugs. The temperature gradient between the wellbore and formation, due to mud circulation, will impose another set of stresses not related to the overburden pressure.

In permeable beds, a hydrostatic pressure gradient of several hundred pounds will also exist between the mud column and the formation fluid. Therefore, a "variable effective stress" exists, which increases radially from the wellbore.

In such circumstances, due to the stress envelope, sonic beams entering the formation with angles smaller than the critical angle are continuously refracted; following a curved path, they finally arrive back at the wellbore.

Such beams with a curved path, with some specific assumptions, arrive at the wellbore before the refracted beams with critical angle. The beams

with the curved path are affected by the vertical and horizontal effective stresses. Since the horizontal stresses differ considerably from the vertical stresses, we wonder if an average stress $\bar{\sigma} = \frac{\sigma_1 + \sigma_2 + \sigma_3}{3}$ can be applied under the wellbore conditions.

According to Topping,* for a semi-infinite elastic solid where lateral deformations have been prevented, the radial stress relief is given as

$$\sigma_r = -\rho_f z \frac{a^2}{r^2} + \rho_z \left(\frac{\nu}{1-\nu}\right)\left(\frac{a^2}{r^2} - 1\right)$$

where

a = radius of the well,
ρ_f = mud density,
ρ = bulk density of formation,
z = depth of the formation,
ν = Poisson's ratio, and
r = radial distance from the wellbore.

Notice that at the equilibrium condition the horizontal stress is given by $\sigma_r = \frac{\sigma_2}{3}$ when $\nu = 0.25$, or the radial stress in one-third of the vertical stress.

The velocity of sonic propagation is probably a function of the effective stress in the direction of propagation. This we believe is illustrated by two experiments performed by Wyllie, *et al* (Figs. 2 and 3).**

Wyllie and co-workers observed that, when a circumferential pressure was applied to the sample, the velocity of sonic propagation along the axis was less than when similar pressure was applied hydrostatically, or along the axis only. However, Wyllie offers a different explanation.

Since the Topping relation is purely theoretical, some further experiments along the lines of those performed by Wyllie and his colleagues would be extremely useful.

With this question in mind, we wonder if one should solve the differential equation of the wave propagation in terms of bulk compressibility, or whether it should be confined to the effective strains in the direction of propagation. We are inclined to think that the latter choice is more desirable.

* Topping, A. D. and Miles, A. J.: "Stresses Around a Deep Well", *Trans.*, AIME (1949) Vol. 179, 186.

** Wyllie, M. R. J., *et al:* "An Experimental Investigation of Factors Affecting Elastic Wave Velocities in Porous Media", *Geophysics* (1958) Vol. 23, 459.

AUTHOR'S REPLY TO V. S. TUMAN

Under field conditions in not too shallow intervals, laboratory tests indicate that the speed of propagation of plane dilatational elastic waves is indeed a function of the effective stress in the direction of propagation only. This is another consequence of the nonlinear elastic behavior of porous sedimentary rocks. These rocks, even when isotropic in the unstressed state, become anisotropic under nonuniform stress conditions.

Some years ago, Wyllie, *et al,*** reported some comparative measurements of ultrasonic elastic-wave velocities under various stress conditions, i.e., uniform, axial and circumferential pressure exerted on a jacketed cylindrical sandstone sample. Such measurements are required for translating laboratory experiments under, say, uniform pressure into data pertaining to field conditions. Wyllie reported results for extreme stress conditions, the

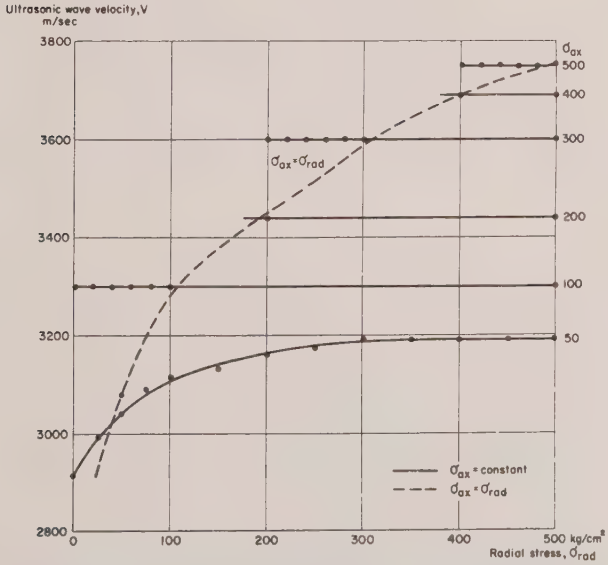

FIG. D-1 – VARIATIONS IN ULTRASONIC AXIAL WAVE VELOCITY UNDER TRIAXIAL STRESS CONDITIONS – MAINZER SANDSTONE, POROSITY 18 PER CENT.

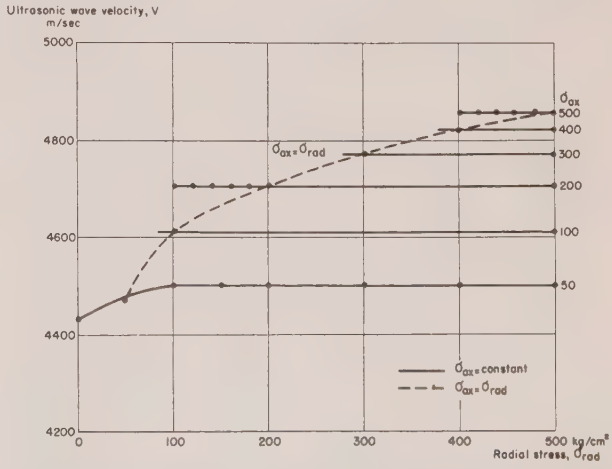

FIG. D-2 – VARIATIONS IN ULTRASONIC WAVE VELOCITY UNDER TRIAXIAL STRESS CONDITIONS – SAHARA SANDSTONE, POROSITY 8 PER CENT.

case of axial stress without circumferential stress and the effect of circumferential stress without any axial stress.

To study the effect of nonuniform stress on elastic wave velocity in more detail, we performed a series of experiments with jacketed samples in a triaxial loading apparatus. Both axial and circumferential pressures could be varied systematically. The wave velocity was always measured in the axial direction. Results obtained on two sandstone samples — a Mainzer outcrop sample of 18 per cent porosity and a Sahara reservoir core sample of 8 per cent porosity — are shown in Figs. D-1 and D-2, respectively. Families of curves showing ultrasonic wave velocity vs radial stress are shown for various axial stresses. The curves for uniform pressure ($\sigma_{ax} = \sigma_{rad}$), constructed by connecting points of equal axial and circumferential pressure are also shown. Raising the circumferential pressure above the axial pressure does not harm the samples. If the circumferential pressure is reduced considerably below the axial pressure, however, the sample may be crushed, and we stayed within safe limits in exerting this latter type of loading. Our results are more comprehensive than the curves reported by Wyllie, *et al.* Above 100 atm, the radial stress has no influence at all on the wave velocity. This follows from the fact that all experimental points for $\sigma_{ax} \geqslant 100$ atm are on horizontal lines.

For lower axial loadings, the circumferential stress influences the axial wave velocity to some extent. This effect is larger for the Mainzer sandstone than for the Sahara core. In practice, these results show that, as far as the acoustic log is concerned, it is primarily the vertical stress that governs the velocity and not the mean hydrostatic stress. Therefore, we agree with Tuman that in a more refined theory we must take these anisotropic effects into account. However, the present paper was meant to outline only the basic principles.

***

Additional Thermal Data for Porous Rocks--Thermal Expansion and Heat of Reaction

W. H. SOMERTON
MEMBER AIME
M. A. SELIM

THE U. OF CALIFORNIA
BERKELEY, CALIF.

ABSTRACT

Thermal expansions and heats of reaction of three typical sandstones were measured in the temperature range of 25° to 1,000°C. The significance of these data in subsurface heat-transfer calculations is discussed.

Linear thermal expansions were measured both parallel and perpendicular to the bedding planes. Volume expansions are reported as the perpendicular expansion plus two times the parallel expansion. Expansion behavior of the sandstones was found to be controlled by the expansion characteristics of the quartz content. Differential expansion of the quartz grains and other minerals included in the sandstones caused permanent deformation of the heated samples after they were cooled to room temperature. Structural damage resulting from heating is probably an important cause of the reduction of thermal conductivity of heated samples.

Measurements of heats of reaction were based on the known heat required for α-β quartz inversion. Thermal reactions, which probably include dehydroxylation of clay minerals and decomposition of carbonate minerals contained within the samples, were found to require more than one-fourth of the amount of heat necessary to raise the temperature of the rock alone. In shales and limestones, the reaction heat could be substantially greater than that required from specific heat considerations alone.

INTRODUCTION

In earlier work,[1-3] methods of measuring thermal properties were developed and thermal data for several sedimentary-rock types were reported. Data included thermal conductivity, specific heat and thermal diffusivity. In addition, calculations of heat transfer in subsurface formations may require data on the thermal-expansion characteristics of rock and the heats of reaction of mineral constituents.

Thermal expansion of rocks is relatively small in magnitude and, from the standpoint of change in bulk density, has only minor effects on heat-transfer characteristics. Thermal-expansion behavior, however, may have significant effects on the structure of rocks. Differential expansion of different minerals and along different crystallographic axes may result in structural damage which could effectively reduce the thermal conductivity of the rock.

Many mineral constituents of sedimentary rocks undergo phase or related changes when heated to sufficiently high temperatures. Although some of these reactions (such as the α-β quartz inversion) are reversible and the heat absorbed is returned to the system upon cooling, many of the major reactions are irreversible. Through certain temperature ranges, the additional heat energy required to complete the reactions may be nearly as great as that necessary to raise the temperature of the rock in the absence of thermal reactions. If the heat requirements for these reactions are not considered, serious errors in heat-transfer calculations may result.

Thermal-expansion and thermal-reaction data have been obtained for three typical sandstones. Methods of measurement and results obtained are reported and discussed in the following.

THERMAL EXPANSION OF SANDSTONES

The linear expansions of three outcrop sandstones (Bandera, Berea and Boise) have been measured in the temperature range of 25° to 1,000° C. Expansion measurements were made in the directions parallel and perpendicular to the bedding.

The differential expansion apparatus used is that described by Mitoff and Pask.[4] The test sample is heated in an electric furnace with a temperature rise of 6°C/minute. The lengthening of the samples upon heating is compared with the small and known expansion of a fused silica rod. The change in length is transmitted to an X-Y recorder by means of a Statham transducer. A maximum error of ± 1.5 per cent has been obtained with this apparatus

Original manuscript received in Society of Petroleum Engineers office Aug. 30, 1960. Revised manuscript received Sept. 27, 1961. Paper presented at 31st Annual California Regional Meeting of SPE, Oct. 21-22, 1960, in Pasadena, Calif.

[1]References given at end of paper.

for materials of known linear expansion. Upon reaching maximum temperature, the sample is cooled at approximately the same rate and the contraction is recorded. The final length of the sample is measured to test the reliability of the final recorded value.

The linear expansions of Berea sandstone both parallel and perpendicular to the bedding are compared in Fig. 1 with the expansion of quartz perpendicular and parallel to *C*-axis.[5] The most important features of Fig. 1 are: (1) the close agreement between the heating curves for Berea sandstone and the curve for quartz perpendicular to the *C*-axis; and (2) the lack of agreement of the Berea heating curves with the curve for quartz parallel to the *C*-axis. Discontinuities in the curves at 575°C are attributed to the α-β inversion of quartz. The cooling curves for Berea deviate considerably from the heating curves, the samples being permanently elongated at the conclusion of the test.

Linear expansions of the three sandstones perpendicular to the bedding are compared with the expansion of quartz in Fig. 2. Curves for expansion parallel to the bedding and cooling curves are not shown for Bandera and Boise because of their close similarity to the Berea curves. All sandstone samples showed permanent elongation upon cooling. The volume expansions shown in Fig. 3 were calculated as the sum of the perpendicular linear expansion and two times the parallel expansion.[5]

Interpretation of thermal expansion data is as follows.

1. The quartz contents of the three sandstones ranged from about 50 per cent for Boise to 90 per cent for Berea, and yet the linear thermal expansions of the three sandstones were nearly the same and about equal to that for quartz. The presence of quartz, probably above some minimum amount, appears to control the expansion behavior of sandstones.

2. Expansion of quartz in the direction perpendicular to the *C*-axis has a predominating effect on the expansion characteristics of the sandstones. Since the amounts of expansion of the sandstones in the directions parallel and perpendicular to the bedding were approximately the same, random orientation of the quartz crystals would be expected.

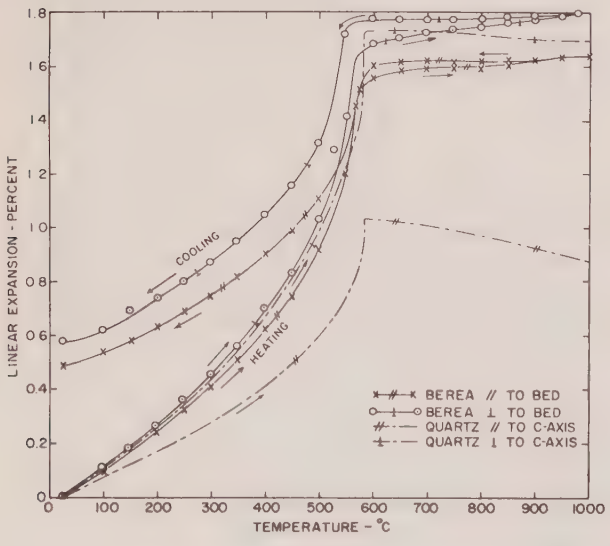

FIG. 1 – LINEAR EXPANSION OF BEREA SANDSTONE AND QUARTZ.

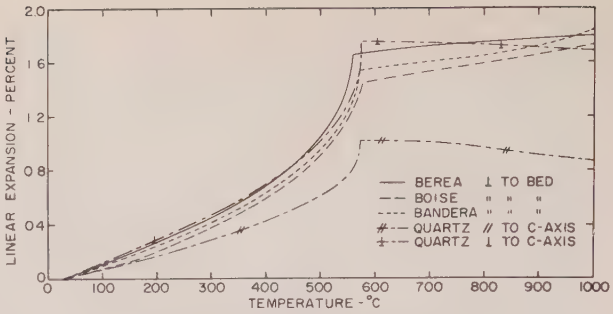

FIG. 2 – LINEAR EXPANSION OF SANDSTONES PERPENDICULAR TO BEDDING.

3. Permanent elongation of the samples after cooling resulted from deformation within the sample, due primarily to the differential expansion of the quartz grains. At temperatures above that for α-β quartz inversion, where the coefficient of expansion for quartz becomes negative, the role of other mineral constituents becomes important in determining expansion and deformation characteristics of the sandstones.

THERMAL REACTIONS

In measuring thermal diffusivities of rocks by the unsteady-state method,[2] anomalies were observed to occur in the differential temperature records. Similar to differential thermal analyses (DTA), these temperature anomalies may be correlated with thermal reactions which occur in certain of the mineral constituents. The most consistent reaction is the inversion of quartz from the α- to β-phase at 573°C. The amount of heat needed to complete this inversion is known to be 4.825 calories/gm.[6] The phase change is reversible, and an equivalent amount of heat is liberated upon cooling.

Other typical thermal reactions which may occur are summarized in Table 1. Most of these reactions occur over a broad temperature range and require substantially larger amounts of heat than the quartz

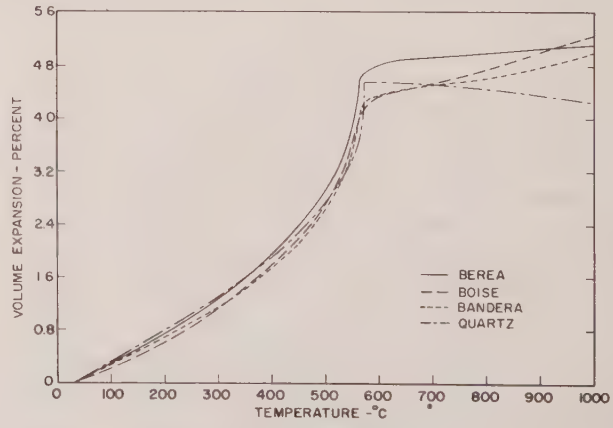

FIG. 3 – VOLUME EXPANSION OF SANDSTONES.

TABLE 1 — HEATS OF REACTION FOR SEVERAL MINERALS[7]

Temp. Range (°C)	Mineral	Heat of Reaction (Calories/gm)	Reaction
25-220	Ca-Montmorillonite	127	Desorption
25-220	Mg-Montmorillonite	135	Desorption
400-695	Mg-Illite	64	Decomposition
455-642	Kaolinite	253	Decomposition
554-723	Ca-Montmorillonite	67	Decomposition
573	Quartz	4.82	α-β Inversion
700-830	Calcium Carbonate	465	Decomposition
790-950	Mg-Illite	15	Decomposition
816-908	Ca-Montmorillonite	26	Decomposition

inversion. These reactions are normally irreversible or are only reversible under special conditions. Differential temperature records for the three sandstones shown in Fig. 4 demonstrate this point. The dashed lines show the quartz inversion starting at approximately 575° C, followed by several other temperature anomalies. The solid lines show the thermal behavior of the same sandstone samples on a repeat run. The reversible quartz reaction is the only important anomaly remaining.

The purpose of the present investigation was to estimate the magnitude of heat required to satisfy the thermal reactions and to compare this with the heat required to raise the temperature of the rock excluding thermal reactions. The known heat of reaction for quartz inversion and the known quartz content of Berea sandstone were used for standardization purposes.

The apparatus used to evaluate thermal reactions is the same as that described earlier for thermal diffusivity measurements.[3] In the earlier work, cylindrical core samples were mounted in an electric furnace and heated at a constant rate of temperature rise. At temperatures where thermal reactions were known to occur, temperature was held constant until the reaction was completed. The edge temperature of the sample and edge-to-center differential temperatures were measured with thermocouples and traced on a recorder chart. It was shown [3] that, for these conditions, thermal diffusivity is inversely proportional to the differential temperature; i.e.,

$$D_t = a^2 b/4\,\Delta T \quad \ldots\ldots\ldots\ldots \quad (1)$$

where D_t is thermal diffusivity ($D_t \equiv a$ in Refs. 1 through 3), a is the distance between center and edge thermocouples, b is the heating rate and ΔT is the temperature differential.

In the present case, differential thermocouples were located at distances r/a = 1.0, 0.8, 0.6, 0.4 and 0.2 from the center of the sample. The rate of temperature rise at the sample edge was maintained constant, and temperature differentials between the center of the sample and the several r/a locations were recorded. Fig. 5 shows the thermocouple responses caused by the α-β quartz inversion. Physically, the reaction is explained as follows. When the outer surface of the core reaches reaction temperature (573°C), part of the heat supply is used to promote the reaction. The normal temperature gradient in the sample is disturbed and a slight decrease in the differential temperature is noted for the first thermocouple. As the reaction reaches and then passes the first thermocouple, a sharp increase in the temperature differential for this couple occurs. The edge temperature continues to increase at the constant input rate; but less heat reaches the unreacted portion of the sample because of the large amount of heat consumed by the reaction,

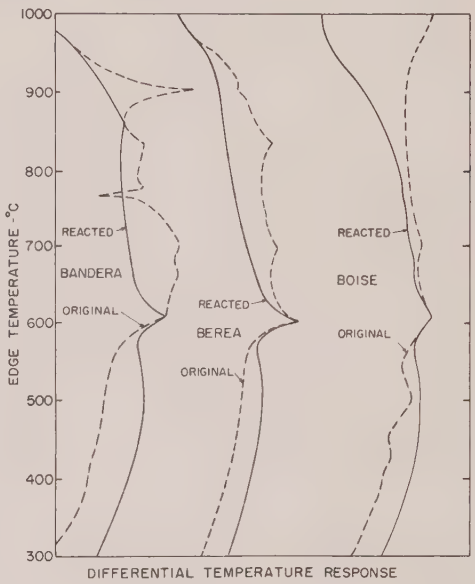

FIG. 4 — THERMAL BEHAVIOR OF SANDSTONES.

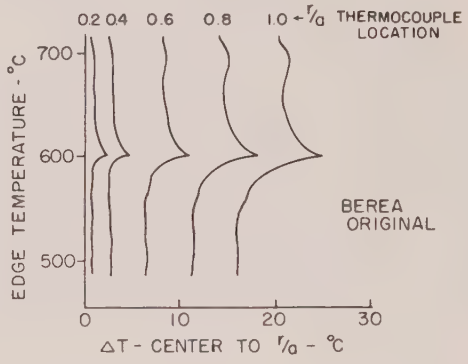

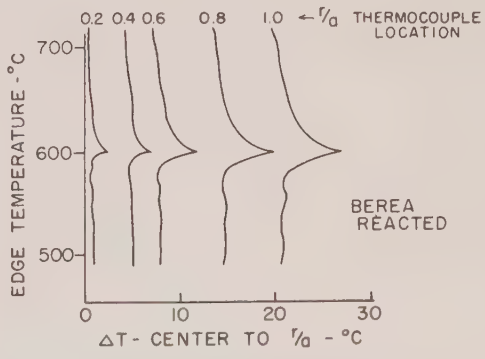

FIG. 5 — TEMPERATURE DIFFERENTIALS FOR QUARTZ INVERSION.

and the rise in center temperature lags. Thus, a sharp temperature discontinuity must exist at the reaction front. Similar response is noted as the reaction proceeds past each interior thermocouple. All curves show a maximum value when the reaction reaches the center thermocouple. The temperature differentials then decrease to re-establish the original temperature gradient in the sample.

If the supply of heat to the system is constant, a heat balance may be written as

$$\left(D_t C_p \frac{\delta T}{\delta r}\right)_\alpha - \left(D_t C_p \frac{\delta T}{\delta r}\right)_\beta = H_R \frac{\delta R}{\delta \theta} \quad . \quad . \quad . \quad (2)$$

where C_p is heat capacity, $\delta T/\delta r$ is temperature gradient, H_R is heat of reaction, $\delta R/\delta \theta$ is the rate of movement of the reaction through the sample and α and β refer to the unreacted and reacted zones, respectively. Since the change of D_t within the temperature range of the reaction is small, the assumption of constant heat supply is valid and Eq. 2 should apply to the present system. However, attempts to confirm the equation with experimental data from Fig. 5 failed. Many more thermocouples would be needed to establish reliable values of the temperature gradient ahead of and behind the reaction front, and the rate of movement of the reaction.

Resort was made to an empirical method to obtain useful information from the experimental data. The method, which is used in quantitative interpretation of DTA data,[7] involves the correlation of areas of the anomalies on the differential temperature-vs-edge temperature curves with heats of reaction. In Fig. 5 the areas between an estimated base line and the anomalies were measured for each thermocouple location. These areas were then plotted against calculated heats of reaction for a volume of unit length of sandstone contained within each thermocouple radius and the center of the sample. A reasonably good straight-line relation resulted, as shown in Fig. 6. A value of 1 calorie/unit of anomaly was used in determining the heats of unknown reactions.

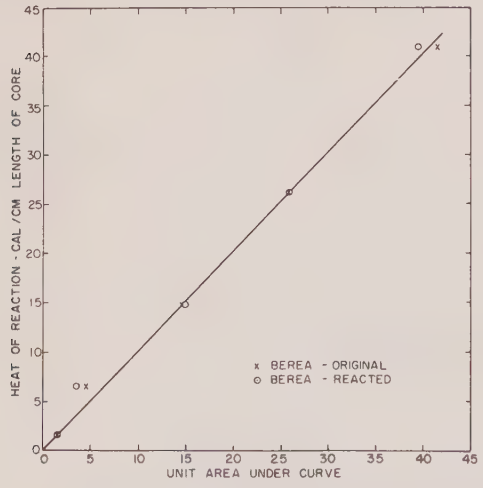

FIG. 6 — AREA-HEAT OF REACTION CORRELATION.

TABLE 2 — EXPERIMENTAL HEATS OF REACTION

Sample	Temp. Range (°C)	Heat of Reaction (Calories/gm rock)	Equiv. Heat (Calories/gm rock)
Bandera	577-615	2.9	11
	615-735	21.	34
	735-750	−0.9	4
	750-825	5.6	22
	825-920	7.9	27
		Σ 36.5	Σ 98
Berea	565-600	4.3	9
	600-725	10.	34
	725-840	14.	33
	840-925	8.7	25
		Σ 37.0	Σ 101
Boise	565-620	2.6	14
	620-725	3.9	28
	725-975	—	71

In analyzing the data of Fig. 4, the only known reactions were the α-β quartz inversions. Differences in the original and reacted curves below 573°C are due primarily to the reduction in thermal conductivities of the reacted samples. This is probably caused by the loss of free and combined water and structural damage of the cores by differential thermal expansion during the initial heating run. Reactions above 573°C include, in addition to quartz inversion, dehydroxylation of clay minerals and decomposition of calcium carbonate. It was not considered practical to attempt to separate specific mineral reactions because the purpose of the work was only to evaluate the additional heat requirements due to thermal reactions. Breaks in the curves were used to establish temperature ranges of the important reaction zones as shown in Table 2. Areas between the original and reacted curves of Fig. 4 were measured, and heats of reaction were calculated from the correlation factor and bulk densities of the samples.

In Table 2, the heats of reaction are shown and compared with the amount of heat required to raise the temperature of the rock without thermal reactions. The reaction heat is 27 per cent of the total heat requirements for both Bandera and Berea sandstones. A similar analysis was not made for Boise sandstone because of the difficulty of explaining the large thermal reaction above 725°C. This same behavior persisted in tests on several other samples of Boise.

SUMMARY AND APPLICATIONS

The results of these tests, made at atmospheric pressure on oven-dried sandstone samples, typify behavior at just one set of limiting conditions. Before such data can be applied directly to subsurface calculations, the effects of a wider range of conditions relating liquid saturation and overburden pressure needed to be investigated.

Differential thermal expansion of the mineral constituents of rocks will undoubtedly lead to structural damage under subsurface heating conditions. The magnitudes of effects on mechanical

and flow properties are unknown, but these currently are being investigated in this laboratory. It is possible that cores taken from high-temperature reservoirs may be altered by cooling as well as by the release of overburden and pore pressure.

Thermal reactions involving the release of adsorbed and combined water and the liberation of such gases as carbon dioxide will be different under subsurface conditions of liquid saturation and pressure than the same reactions observed on oven-dried cores at atmospheric pressure. Temperatures of reaction will be higher and the heats of reaction may be different. Brindley and Nakahira[8] report that the starting temperature of the endothermic kaolinite reaction is raised by 100°C under a water-vapor pressure of 6 atm. Further laboratory investigation will be necessary to evaluate these effects.

NOMENCLATURE

D_t = thermal diffusivity (≡ α in Refs. 1 through 3)

a = distance between center and edge thermocouples

b = heating rate

ΔT = temperature differential

r = radius of core sample

C_p = heat capacity

$\frac{\partial T}{\partial r}$ = temperature gradient

H_R = heat of reaction

$\frac{\partial R}{\partial \theta}$ = rate of reaction movement through the sample

θ = time

α, β = unreacted and reacted zones, respectively

REFERENCES

1. Somerton, W. H.: "Some Thermal Characteristics of Porous Rocks", *Trans.*, AIME (1958) Vol. 213, 61.
2. Somerton, W. H. and Boozer, G. D.: "Thermal Characteristics of Porous Rocks at Elevated Temperatures", *Trans.*, AIME (1960) Vol. 219, 77.
3. Somerton, W. H. and Boozer, G. D.: "A Method of Measuring Thermal Diffusivities at Elevated Temperatures", *AIChE Jour.* (1961) Vol. 7, 87.
4. Mitoff, S. P. and Pask, J. A.: "A Recording Differential Expansion Apparatus", *Am. Ceram. Soc. Bull.* (1956) Vol. 35, No. 10, 402.
5. Birch, F., Shairer, J. F. and Spicer, H.: editors, *Handbook of Physical Constants*, GSA (1942) 35.
6. Kelley, K. K.: "Contributions to the Data on Theoretical Metallurgy", Bull. 584, USBM (1960).
7. Barshad, I.: "Temperature and Heat of Reaction Calibration of the Differential Thermal Analysis Apparatus", *Am. Mineralogist* (1952) Vol. 37, 667.
8. Brindley, G. W. and Nakahira, M.: "Kinetics of Dehydroxylation of Kaolinite and Halloysite", *Jour. Am. Ceram. Soc.* (1957) Vol. 40, No. 10, 346.

★★★

Three-Phase Imbibition Relative Permeability

J. NAAR*
JUNIOR MEMBER AIME
R. J. WYGAL

GULF RESEARCH & DEVELOPMENT CO.
PITTSBURGH, PA.

ABSTRACT

An equation for three-phase (water, oil, gas) imbibition oil permeability is developed, assuming the water to be the dominant wetting fluid. Oil isoperms are obtained for consolidated sandstones characterized by $1/P_c^2 = CS^*$. The evolution of an oil-gas system imbibing water from S_{wi} to $(S_{w,imb})_{max}$ is shown to proceed along a line of constant oil saturation with increasing oil permeability and decreasing gas saturation. When the gas saturation cannot be reduced further, the system evolves along a line of constant S_g with decreasing oil saturation and permeability. The initial gas saturation is shown to reduce markedly the effect of complete wetting by either oil or water on flow performance.

INTRODUCTION

Imbibition oil isoperms are required for performance prediction when a well is producing water, oil and gas. This situation occurs in multiphase displacements such as underground combustion, steam injection and the water flooding of highly depleted reservoirs.

In a recent paper,[1] a model was presented for the prediction of two-phase imbibition characteristics. This paper extends the imbibition model to the case of three phases by assuming that the water is the dominant wetting fluid.

The following results were obtained from the model: (1) an analytical expression of oil isoperms; (2) oil isoperms as functions of reduced water, oil and gas saturations, valid for all sandstones having a capillary pressure curve which can be approximated by $1/P_c^2 = CS^*$; and (3) evaluation of the three-phase flow performance as dictated by complete wetting by either oil or water.

The agreement between predicted and observed oil recovery in the presence of a gas phase, reported in Ref. 1, is a partial support for the present development. However, experimental data are not available at this time to check fully the model predictions. Perhaps this paper will stimulate the collection of such data.

Original manuscript received in Society of Petroleum Engineers Office May 3, 1961. Revised manuscript received Sept. 27, 1961.

*Present address: Olin Mathieson Chemical Corp., New Haven, Conn.

[1]References given at end of paper.

THEORETICAL

The imbibition model of a porous medium has been described previously, and the reader is referred to the paper of Naar and Henderson[1] for details. In brief, the model is formed by the random interconnection of straight capillaries, with a provision for the blocking of the non-wetting phase by the invading wetting fluid.

The following expressions were derived from the model.

1. The amount of oil blocked by the invading water is

$$S_{ob} = (1 - S_{wi}) \int_0^{1-a} x\,dx \quad \ldots\ldots\ldots (1)$$

where a is defined by

$$a = \frac{1 - S_w}{1 - S_{wi}} .$$

2. The imbibition relative permeability to the wetting phase is

$$k_{rw,imb} = \frac{\phi^{*3}\gamma^2}{k} S^*_{w,imb} \int_0^{S^*_{w,imb}} \frac{S^*_{w,imb} - S^*}{P_c^2}\, dS^* \quad \ldots\ldots\ldots\ldots\ldots\ldots (18)$$

The permeability k is written

$$k = \phi^{*3}\gamma^2 \int_0^1 \frac{1 - S^*}{P_c^2}\, dS^* \quad \ldots\ldots (14)$$

3. Imbibition relative permeability to the nonwetting phase — for the nonwetting fluid during an imbibition process, the relative permeability at a given wetting-phase saturation $S^*_{w,imb}$ is equal to the drainage relative permeability at a saturation $S^*_{w,drain}$ defined by the relationship

$$S^*_{w,imb} = S^*_{w,drain} - \frac{1}{2} S^{*2}_{w,drain} \quad \ldots (19)$$

Relative Permeability to Water

If oil and gas are considered equivalent to a single nonwetting phase, the system can be treated as having only two phases; the relative permeability to water is then equal to the wetting-phase permeability during drainage. If only the capillary pressure curve is known, the relative permeability to water can be computed from Eq. 18.

Relative Permeability to Gas

To compute the relative permeability to gas, the system may again be treated as a two-phase system with water and oil forming the single wetting phase. The permeability to gas is then computed as explained in Ref. 1.

Relative Permeability to Oil

The permeability to oil is more complex to compute. The mechanics of the displacement are described as follows and the analytical details are given in the Appendix.

When the water invades the porous medium and occupies the pores of radius r which were initially full of oil, part of the oil in this size class of pores is blocked and the rest invades pores full of gas. In turn, part of the gas phase is blocked and the remainder is pushed out. The effects of these movements are twofold.

1. Because a certain volume of oil is trapped, the oil permeability tends to decrease.
2. Because a certain volume of oil moves from small pores into larger ones, the permeability tends to increase.

The relative permeability to oil, therefore, is a balance between these two tendencies, and it is possible to observe an increase in oil permeability at constant oil saturation.

After the oil invades all the size classes of gas-filled pores, the oil saturation and the oil relative permeability decrease when the water saturation increases.

The permeability to oil at any stage of the imbibition process is computed by assuming that the oil phase is wetting with respect to the gas. The water saturation plus the blocked oil saturation form a fictitious, irreducible wetting-phase saturation.

For consolidated sandstones having a capillary pressure curve approximated by the equation $1/P_c^2 = CS^*$, $k_{ro,imb}$ is given by

$$k_{ro,\,imb} = S_{of}^{*3}\,(S_{of}^{*} + 3S_{fw}^{*}) \quad \ldots\ldots (16)$$

where S^*_{of} and S^*_{fw} are defined by

$$S_{of}^{*} = \frac{S_o - S_{ob}}{1 - S_{wi}} \quad \ldots\ldots\ldots\ldots (20)$$

and

$$S_{fw}^{*} = \frac{(S_w - S_{wi}) + S_{ob}}{1 - S_{wi}} \quad \ldots\ldots\ldots (21)$$

Oil isoperms for consolidated sandstones are shown on a trilinear plot in Fig. 1 as functions of the reduced water, oil and gas saturations. The displacement mechanism proposed indicates that at the beginning of the imbibition process the water saturation S^*_w will increase at the expense of the gas saturation at *constant oil saturation* until no more gas is trapped. At this point the water saturation will increase at the expense of the oil saturation at *constant gas saturation.* In a trilinear diagram, therefore, the path describing the evolution of an oil-gas system is formed by two straight lines. By following the dotted lines from a point on the $S^*_w = 0$ axis to the locus of the intersection of these lines, the history of any element during imbibition may be traced.

LIMITS OF WATER-OIL BEHAVIOR DICTATED BY WETTABILITY

The influence of wetting on oil-water flow behavior has been examined in Ref. 1. The geometry of the porous medium, represented by S_{wi}, was shown to be important in assessing this influence. When gas is present as the third phase, the model and the assumed imbibition mechanism teach the following.

1. The total oil recovery* will exceed the 50 per cent limit of the two-phase system and is given by

$$N_p/N = \frac{1}{2} + \frac{S_{gi}}{2(1 - S_{wi})}.$$

2. For equal values of the oil recovery, the value of k_o/k_w is not a function of S_{wi} but is a function of the wettability and of the initial gas saturation. This dependence is shown in Fig. 3 where (k_o/k_w) water-wet/(k_o/k_w) oil-wet is plotted

* See Eq. 7 of Ref. 1.

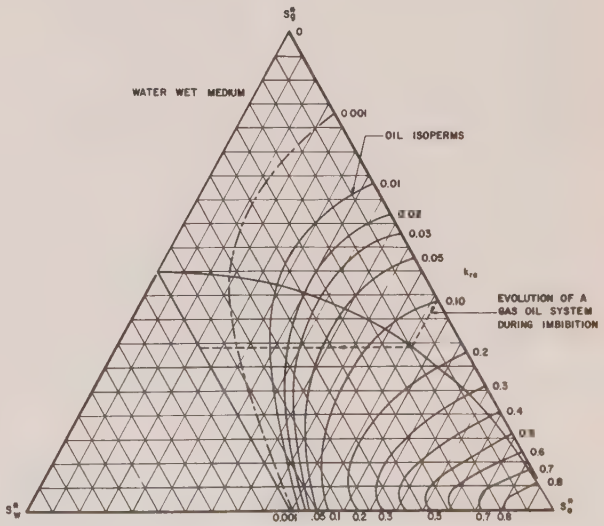

FIG. 1 – THREE-PHASE IMBIBITION.

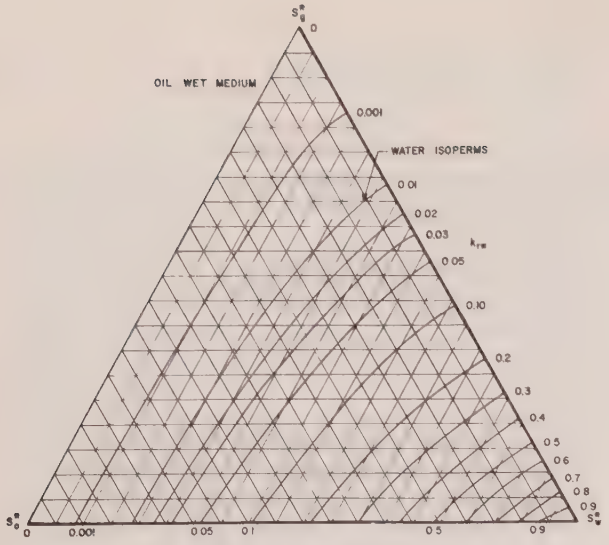

FIG. 2 – THREE-PHASE DRAINAGE.

vs S_{gi} for $N_p/N = .40$. This ratio decreases rapidly when S_{gi} increases. From the standpoint of oil recovery and flowing water-oil ratio, the higher the initial gas saturation, the less significant the wettability of the medium becomes. The values of k_o/k_w for an oil-wet medium and for increasing water saturation were computed from Eqs. 23 and 24 of Ref. 1. The water isoperms for that case are shown in Fig. 2.

3. The water saturation at a given recovery is a function of S_{wi} and the initial gas saturation. This can be seen in Fig. 3 where (S_w) water-wet/(S_w) oil-wet is plotted against S_{gi} for $S_{wi} = .15$ and $S_{wi} = .30$. This ratio increases with S_{gi} and its rate of increase is an increasing function of S_{wi}. The physical significance of this increase is immediately evident — water must be imbibed in sufficient quantity to displace the gas phase before the oil phase can be expelled.

The proposed displacement mechanism applies to a small elemental volume (ΔV) of porous rock. The gross production behavior then can have the appearance of an initial gas production followed by an oil bank. This type of apparent behavior was observed by Kyte, *et al.*[3]

The observation that, during imbibition, the gas phase is produced first was also made in this laboratory. We are indebted to J. J. Taber for the curves of Fig. 4 which show the imbibition history of a Berea core. The agreement between observed and predicted final gas and oil recoveries reported in Ref. 1 further supports this theory. It is also felt that, while experimental oil isoperms are not available at this time, the success of the predictions of relative permeability and oil recovery in two-phase flow are strong points in favor of the present development.

CONCLUSIONS

A mechanism to describe three-phase water imbibition has been proposed and applied to a theoretical model of a consolidated porous medium.

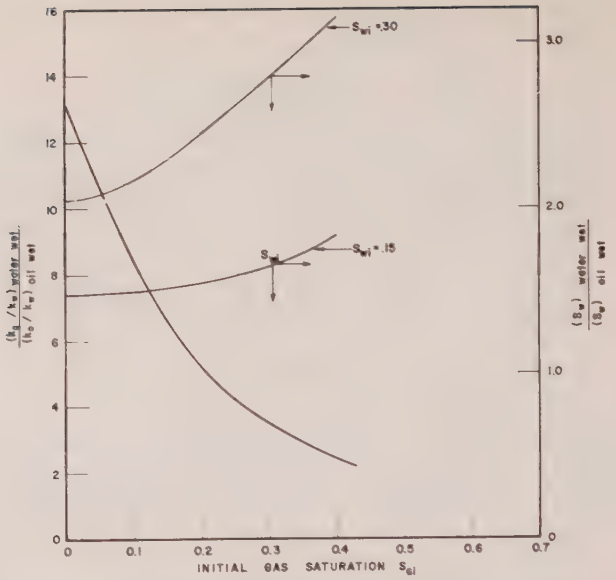

FIG. 3 – INFLUENCE OF WETTABILITY ON FLOWING OIL-WATER RATIO AND WATER SATURATION AT 40 PER CENT RECOVERY.

A formula has been derived for the imbibition oil permeability and has been used to compute oil isoperms for consolidated sandstones.

The gas phase has been shown to decrease the influence of wettability and to be important in determining the amount of water required to effect a given oil recovery.

NOMENCLATURE

C = constant
P_c = capillary pressure
S = saturation
N = total pore volume
N_p = pore volume produced
a = ratio of the pore volume full of nonwetting fluid to the total pore volume
k = permeability
r = pore radius
ϕ = porosity
γ = interfacial tension

SUBSCRIPTS

$drain$ = drainage
imb = imbibition
g = gas
o = oil
ob = oil blocked
of = oil flowing
r = relative
w = water
wi = water irreducible
fw = fictitious water irreducible

SUPERSCRIPTS

* indicates a reduced value of saturation or porosity; i.e., $S^*_w = \dfrac{S_w - S_{wi}}{1 - S_{wi}}$ (see Appendix)

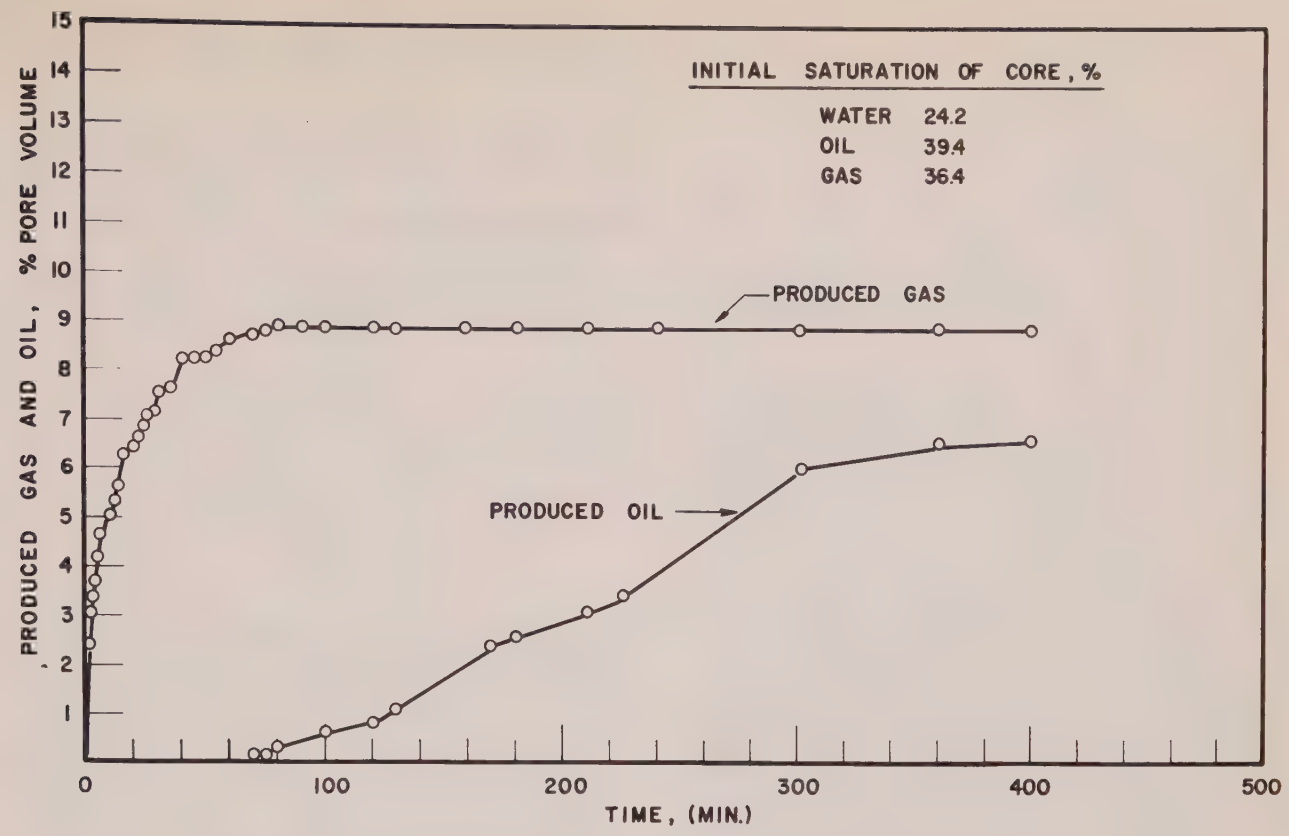

FIG. 4 – IMBIBITION OF WATER INTO A BEREA CORE CONTAINING WATER, OIL AND GAS.

REFERENCES

1. Naar, J. and Henderson, J. H.: "An Imbibition Model; Its Application to Flow Behavior and the Prediction of Oil Recovery", *Soc. Pet. Eng. Jour.* (June, 1961) 61.
2. Wyllie, M. R. J. and Gardner, G. H. F.: "The Generalized Kozeny-Carman Equation", *World Oil* (March and April, 1958).
3. Kyte, J. R., Stanclift, R. J., Jr., Stephan, S. C., Jr. and Rapoport, L. A.: "Mechanism of Water Flooding in Presence of Free Gas", *Trans.*, AIME (1956) Vol. 207, 215.

APPENDIX

The fictitious, irreducible wetting saturation which is needed to compute oil isoperms requires the definition of new symbols to avoid confusion. The final results, however, are expressed in terms of the reduced saturations S^*_o, S^*_w and S^*_g. The new symbols are the following.

1. Oil blocked by the invading water,

$$S_{ob} = (1-S_{wi}) \int_0^{\frac{S_w - S_{wi}}{1-S_{wi}}} x\,dx \quad \ldots \quad (1)$$

2. Oil saturation free to move,

$$S_{of} = S_o - S_{ob} \quad \ldots \quad (2)$$

3. Fictitious, irreducible water saturation,

$$S_{fw} = S_w + S_{ob} \quad \ldots \quad (3)$$

4. Reduced saturations (with respect to S_{wi}),

$$S^* = \frac{S - S_{wi}}{1 - S_{wi}} \quad \ldots \quad (4)$$

$$S^*_{of} = \frac{S_{of}}{1 - S_{wi}} \quad \ldots \quad (5)$$

$$S^*_o = \frac{S_o}{1 - S_{wi}} \quad \ldots \quad (6)$$

$$S^*_{fw} = \frac{S_{fw} - S_{wi}}{1 - S_{wi}} \quad \ldots \quad (7)$$

5. Reduced saturations (with respect to S_{fw}),

$$S^{**} = \frac{S - S_{fw}}{1 - S_{fw}} \quad \ldots \quad (8)$$

$$S^{**}_{of} = \frac{S_{of}}{1 - S_{fw}} \quad \ldots \quad (9)$$

From Eqs. 7 and 8 and from Eqs. 7 and 9, the following relationships are obtained between S^* and S^{**}, S^*_{of} and S^{**}_{of}.

$$S^{**} = \frac{S^* - S^*_{fw}}{1 - S^*_{fw}} \quad \ldots\ldots\ldots\ldots (10)$$

$$S^{**}_{of} = \frac{S^*_{of}}{1 - S^*_{fw}} \quad \ldots\ldots\ldots\ldots (11)$$

In addition, S^*_{ob} is given by

$$S^*_{ob} = \frac{1}{2} S^{*2}_{fw} \quad \ldots\ldots\ldots\ldots (12)$$

COMPUTATION OF THE OIL PERMEABILITY

Consider the medium at irreducible water saturation S_{wi}, oil saturation S_o and gas saturation S_g and let the water invade the medium to reach the value S_w. A part of the oil is blocked by the water, (S_{ob}); however, the gas phase is unable to distinguish between the water phase and the blocked oil. Only the oil free to flow contributes to the oil permeability; for all practical purposes, the water and the trapped oil can be considered as immobile and equivalent to a fictitious, irreducible wetting-phase saturation. The permeability to oil, therefore, will be that of a medium having an irreducible wetting-phase saturation equal to $S_w + S_{ob}$ and a wetting-phase saturation free to flow equal to $S_o - S_{ob}$. It is equal to

$$k_{o,imb} = \left[\phi (1 - S_{fw})\right]^3 \gamma^2 \times S^{**}_{of} \int_0^{S^{**}_{of}} \frac{S^{**}_{of} - S^{**}}{P_c^2} dS^{**} \quad . (13)$$

(See Ref. 1, Eq. 30.) The relative permeability to oil is obtained by dividing $k_{o,imb}$ by k, which is given by

$$k = \phi^3 (1 - S_{wi})^3 \gamma^2 \int_0^1 \frac{1 - S^*}{P_c^2} dS^* \quad . (14)$$

Then $k_{ro,imb}$ is written,

$$k_{ro,imb} = \frac{(1 - S_{fw})^3}{1 - S_{wi}} \times S^{**}_{of} \frac{\int_0^{S^*_{of}} \frac{S^{**}_{of} - S^{**}}{P_c^2} dS^{**}}{\int_0^1 \frac{1 - S^*}{P_c^2} dS^*} \quad . (15)$$

Oil isoperms can be calculated from Eq. 15 for any consolidated porous rock.

For consolidated sandstones, the capillary pressure curve can be fitted by

$$\frac{1}{P_c^2} = CS^* \quad \ldots\ldots\ldots\ldots (16)$$

Replacing in Eq. 15 and integrating gives

$$k_{ro,imb} = S^{*3}_{of} (S^*_{of} + 3 S^*_{fw}) \quad . . (17)$$

At the beginning of an imbibition process, $S_{fw} = 0$, $S^*_{ob} = 0$ and $k_{ro,imb} = S^{*4}_o$. This value is in agreement with the results of Wyllie and Gardner (Eq. 31 of Ref. 2). ***

Correlation of Surface and Interfacial Tension of Light Hydrocarbons in the Critical Region

E. W. HOUGH* MEMBER AIME
G. L. STEGEMEIER JUNIOR MEMBER AIME

THE U. OF TEXAS AUSTIN, TEX.
SHELL DEVELOPMENT CO. HOUSTON, TEX.

ABSTRACT

Empirical equations for surface tension of propane and normal butane as functions of reduced temperature are obtained from experimental data. Another correlation relating surface tension to enthalpy of vaporization is given for these two compounds. In addition, new parachor numbers are calculated for the normal paraffin hydrocarbons. These numbers are utilized for the calculation of interfacial tension of two-component systems as functions of pressure and temperature, using a modified form of Weinaug-Katz equation. The experimental data for two binary systems are approximated by the correlation. From these results it is found that the interfacial tension in the high-pressure region remains extremely low at large pressure decrements below the critical pressure. Thus, it appears that condensate systems may have flow characteristics almost like single-phase conditions even though the pressure is within the two-phase region.

Experimental data have shown that interfacial tension divided by density difference approaches zero as the critical pressure is approached. A calculation of wetting-phase saturations indicates that the saturation gradient at the two-phase contact becomes increasingly abrupt as the critical pressure is approached.

DISCUSSION

Prediction of the surface and interfacial tension of the light hydrocarbons and of two-component hydrocarbon mixtures at various temperatures and pressures may be made if other physical properties are known. Extensive experimental work on single-component and binary systems[1] is the basis for the correlations outlined in this paper.

Original manuscript received in Society of Petroleum Engineers office June 12, 1961. Revised manuscript received Sept. 29, 1961. Acknowledgment is made with thanks to API Grant-in-Aid 45, to the Shell Oil Co. for a fellowship which supported one of us, and to The U. of Texas which purchased much of the equipment used on a special grant.

*Now head of Petroleum Engineering Dept. at Mississippi State U.

[1]References given at end of paper.

Interfacial tension is defined as the specific surface-free energy between two phases of unlike fractional composition, while surface tension is defined as the specific surface-free energy between two phases of the same fractional composition. The usual definitions relating interfacial tension to a liquid-liquid interface and surface tension to a gas-liquid interface are not clearly defined when the critical region is included, and there is no sharp distinction between a gas and a liquid phase.

Interfacial tension is probably the most important single force that makes one-half to one-third of the total oil actually in place in a reservoir rock unrecoverable by conventional gas-drive or waterflood methods. A rough estimate of this figure for the United States is 100 billion bbl. Interfacial tension presently is used by petroleum engineers in the estimation of saturation gradients at the gas-oil contact and at the oil-water contact. The data in this paper should prove useful for estimates of reserves involving gas-oil contacts. Relative permeability undoubtedly is influenced by interfacial tension, for sufficiently small values. These data should be useful in determining how small the values are. In addition, these data should eventually add to our fundamental knowledge of surfaces. At the critical point, all surface excesses approach zero and the thickness becomes very large.

SINGLE-COMPONENT SYSTEMS

It has been observed[1] that the following relationships are good approximations to the physical properties of propane and n-butane.

For propane, $\Delta\rho = 0.80\,(1-T/T_c)^{0.326}$, $\gamma = 49.5\,(1-T/T_c)^{1.20}$, $\gamma/\Delta\rho = 61.9\,(1-T/T_c)^{0.874}$, and $\gamma = 112.5\,\Delta\rho^{3.68}$.

For n-butane, $\Delta\rho = 0.86\,(1-T/T_c)^{0.333}$, $\gamma = 52.5\,(1-T/T_c)^{1.22}$, $\gamma/\Delta\rho = 61.0\,(1-T/T_c)^{0.887}$ and $\gamma = 91.2\,\Delta\rho^{3.66}$.

Guggenheim's[2] values for these constants, not specifically for hydrocarbons, are $\Delta\rho = C'(1-T/T_c)^{1/3}$, $\gamma = C''(1-T/T_c)^{11/9}$, $\gamma/\Delta\rho = C'''(1-T/T_c)^{8/9}$, and $\gamma = C\Delta\rho^{11/3}$.

The symbols and units are

$\Delta\rho$ = difference in density of the liquid and vapor phases, gm/cc,
γ = surface tension, dynes/cm,
T = absolute temperature, °R or °K,
T_c = critical temperature (absolute), °R or °K, and
C', C'', C''' = constants.

The exponents for propane and n-butane are taken from log-log plots. The last equation may be recognized as the surface tension-density difference relationship leading to Sugden's parachor,[3] with the exponent "3/11" rather than "1/4". That is,

$$P = MC^{3/11} = \frac{M\gamma^{3/11}}{\Delta\rho}$$

where P = parachor, and
M = molecular weight.

From this modified equation, new values of parachor were calculated for some of the normal paraffin hydrocarbons. Surface-tension and density-difference data for methane, ethane, n-decane and n-eicosane were taken from Rossini,[4] for n-pentane from Sage and Lacey[5] and from Katz,[6] and for propane and n-butane from Sage and Lacey and from experimental work.[1] The values are shown in Table 1. Because the parachor is (ideally) independent of temperature, the values of surface tension and density difference were selected at the temperature at which the best data were obtainable or at the temperature at which the vapor density is negligible if this latter data were not available. Fig. 1 shows a regular increase in the parachor with an increase in molecular size from 3 to 20 carbon atoms. Methane and ethane appear to diverge slightly from this pattern. Some of this divergence is probably caused by the measurement of surface tension against air rather than its own vapor, and by the neglect of the vapor density.

A correlation suggested by Magaril[7] relates the enthalpy of vaporization at constant pressure to the surface tension. Tables 2 and 3 and Figs. 2 and 3 express this relation for propane and for n-butane. The straight-line relationship on log-log paper appears to deviate slightly as the critical point is approached.

TABLE 1 — PARACHOR OF NORMAL PARAFFIN HYDROCARBONS

Compound	Carbon Atoms	Temp. (°F)	Density Diff. (gm/cc)	Surf. or Intf. Tens. (dynes/cm)	Parachor
Methane	1	-256	0.4218[R]	13.7[R]	77.9
Ethane	2	-238	0.620[R]	26.34[R]	118.0
Propane	3	100	0.443[S]	5.47 5.45[K]	158.1 158
n-Butane	4	120	0.532[S]	9.27 9.20	200.5 200
n-Pentane	5	100	0.603[S]	14.0[K]	246
n-Decane	10	68	0.730[R]	23.92[R]	463
n-Eicosane	20	100	0.7754[R]	27.2[R]	899

R=Rossini (Ref. 4); S=Sage and Lacey (Ref. 5); and K=Katz (Ref. 6).

TABLE 2 — ENTHALPY OF VAPORIZATION AT CONSTANT PRESSURE — PROPANE

Temperature (°F)	Enthalpy of Vaporization* (calories/gm-mol)	Surface Tension** (dynes/cm)
100	3271	5.48
130	2878	3.66
160	2366	1.97
190	1660	0.58

*Sage and Lacey (Ref. 5).
**Current paper.

TWO-COMPONENT SYSTEMS

Prediction of interfacial tension in two-component systems is much more difficult than in the single-component systems because of the added composition variable. The correlation suggested by Weinaug and Katz[8] has been used with the new exponent and slightly modified for use with molal volumes rather than specific gravity. The relation is

$$\gamma = \left\{\frac{1}{62.43}\left[P_1\left(x_1/V_x - y_1/V_y\right) + P_2\left(x_2/V_x - y_2/V_y\right)\right]\right\}^k$$

where γ = interfacial tension, dynes/cm,
P_1 = parachor of the first component,
P_2 = parachor of the second component,

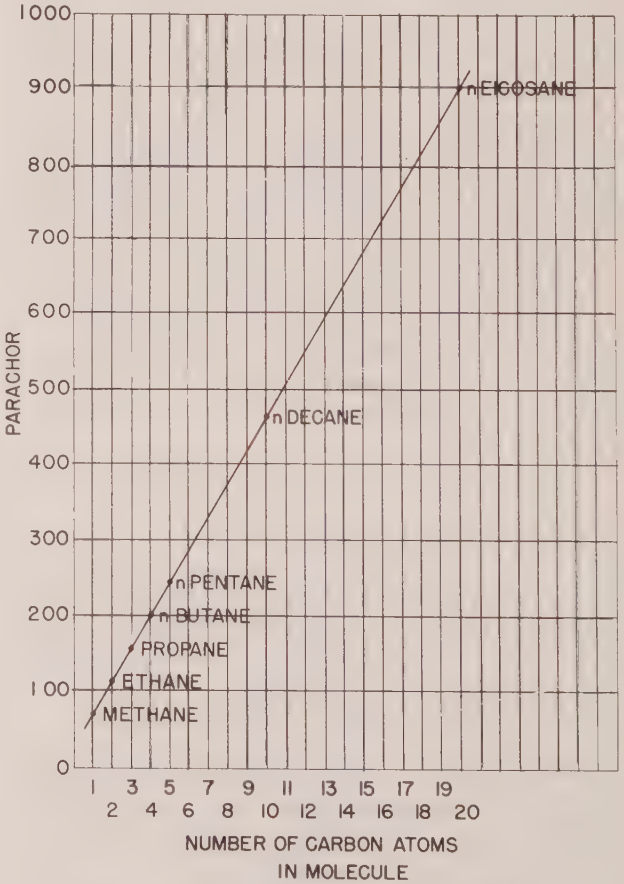

FIG. 1 — PARACHOR, NORMAL PARAFFIN HYDROCARBONS.

TABLE 3 — ENTHALPY OF VAPORIZATION AT CONSTANT PRESSURE — NORMAL BUTANE

Temperature (°F)	Enthalpy of Vaporization* (calories/gm-mol)	Surface Tension** (dynes/cm)
100	4816	10.49
130	4566	8.67
160	4266	6.88
190	3912	5.14
220	3498	3.48
250	2980	2.02
280	2307	0.80

*Sage and Lacey (Ref. 5).
**Current paper.

x_1, x_2 = mol fraction in the liquid phase,
y_1, y_2 = mol fraction in the vapor phase,
V_x, V_y = molal volume, cu ft/lb mol, and
k = new exponent of the parachor relation = 11/3.

The modified values of the parachor together with the new exponent are used in this equation to predict values of interfacial tension determined experimentally[1] on the methane-normal pentane system and on the methane-normal decane system. These experimental data are summarized on the pressure-temperature plots in Figs. 4 and 5. The boundaries of this region are the vapor-pressure curves for the pure components and the line of critical loci of the various intermediate mixtures. Superposed on these diagrams are the lines of constant interfacial tension. The known data for these iso-interfacial tension lines are the surface-tension data of the pure compounds and the experimental data by the authors, which include a very limited range in comparison to the complete two-phase region. Since the properties of the liquid and the gas at the critical point are identical, the line of critical loci is also the line of zero interfacial tension; hence, the subsequent iso-interfacial tension lines must roughly parallel this boundary. These data and assumptions allow extrapolation and interpolation to all points within the two-phase region. It is evident from these plots that the interfacial tension of a binary mixture in the temperature range in which the critical pressure is high increases much more slowly with a decrease in pressure than either of the pure components. In the case of the methane-normal pentane system, a pressure drop of 450 psi from the critical pressure is required at 100°F before the interfacial tension reaches 1 dyne/cm. The same increase for the pure components occurs with a pressure drop of about 120 psi. In the methane-normal decane system the effect is even more pronounced, the pressure drop at 100°F being 1,040 psi for a comparable increase in interfacial tension. These facts suggest that interfacial forces may be negligible, as far as flow conditions

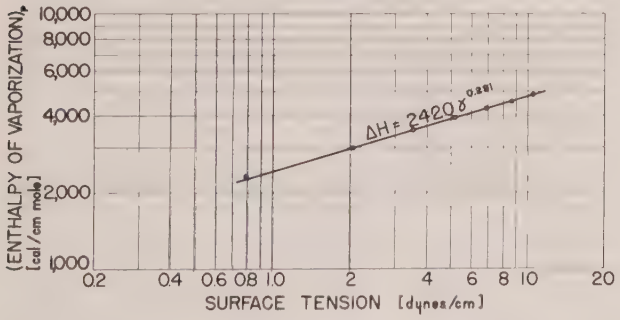

FIG. 2 — ENTHALPY OF VAPORIZATION, PROPANE.

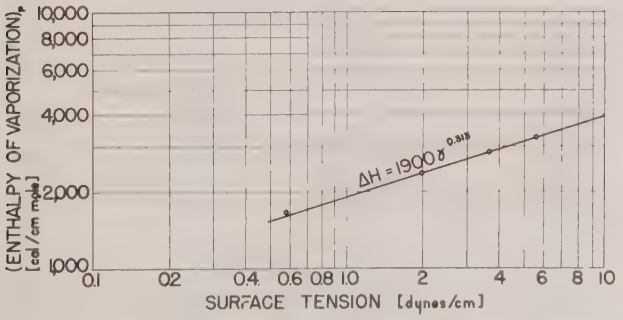

FIG. 3 — ENTHALPY OF VAPORIZATION, NORMAL BUTANE.

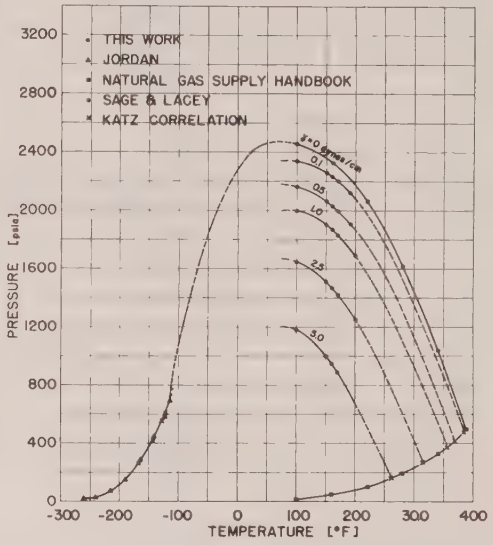

FIG. 4 — METHANE-NORMAL PENTANE.

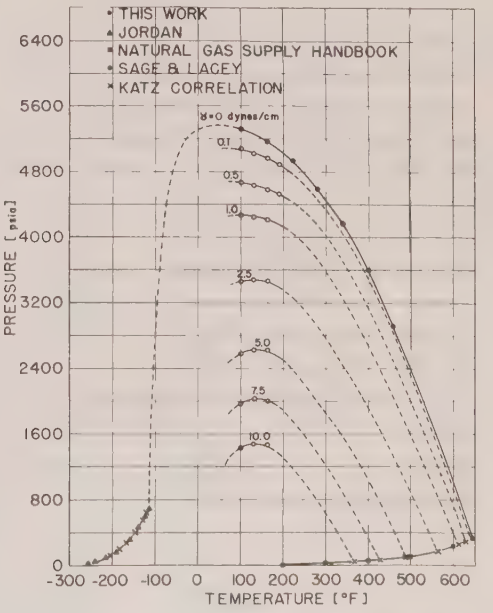

FIG. 5 — METHANE-NORMAL DECANE.

are concerned, for a condensate reservoir for an appreciable portion of the two-phase region.

Prediction of these experimental results from the modified equation of Weinaug and Katz was attempted with the PVT data of Sage and Lacey. A summary of these calculations is given in Table 4.

The equation for binary systems may be generalized to multicomponents systems as follows.

$$\gamma = \left\{ \frac{1}{62.43} \left[P_1 \left(\frac{x_1}{V_x} - \frac{y_1}{V_y} \right) + P_2 \left(\frac{x_2}{V_x} - \frac{y_2}{V_y} \right) + P_n \left(\frac{x_n}{V_x} \frac{y_n}{V_y} \right) \right] \right\}^{11/3} .$$

This calculation requires a knowledge of the composition of both phases and the molal volume or density of each phase. In the absence of density data, reduced temperature calculations may be used as an approximation to the density. The parachor numbers for each compound of the normal paraffin hydrocarbons from methane to n-eicosane are shown in Fig. 1.

SURFACE EXCESS

Excess concentration of methane at the liquid surface for the two-component systems may be approximated from the equation given by Rice.[9]

$$\Gamma_1 = -\rho_N \left(\frac{\partial \gamma}{\partial p} \right)_T$$

where Γ_1 = excess of methane in the surface, mol/sq cm,
ρ_N = density of methane, mol/cc,
p = pressure, dynes/sq cm, and
T = temperature, °R or °K.

It must be noted that this equation was derived with the assumption of a zero surface excess of the other (heavier) component.

Calculation of surface excess from experimental values is obtained by using the slope of isotherms of interfacial tension plotted against pressure for both two-component systems. If pressure is expressed in pounds per square inch, interfacial tension in dynes per centimeter and specific volume in cubic feet per pound-mole, a conversion factor must be used in the modified equation.

$$\Gamma_1 = - \frac{14.013 \times 10^{16}}{V_1} \left(\frac{\partial \gamma}{\partial p} \right)_t .$$

For example, methane-normal pentane at 100°F and 1,500 psia,

$$\left(\frac{\partial \gamma}{\partial p} \right)_t = -0.00506 \frac{\text{dynes/cm}}{\text{psi}} ,$$

V_1 = 3.50 cu ft/lb mol (methane), and

$\Gamma_1 = 2.03 \times 10^{14}$ mol methane/sq cm.

Results of surface-excess calculations are given in Tables 5 and 6. As the pressure approaches zero, the value of the density term in the surface-excess equation approaches zero and the isothermal change in interfacial tension with pressure remains finite; hence, the surface excess as the pressure approaches zero also approaches zero. See Figs. 6 and 7. As the pressure approaches the critical point of the mixture, the density of methane remains finite; but, according to experimental results, the change in interfacial tension with pressure approaches zero. Therefore, the surface excess again approaches zero as the critical pressure is approached. For intermediate values of pressure, the density term is positive and the slope was found to be negative; hence, the surface excess is positive between zero and the critical pressure, and has at least one

TABLE 4 — INTERFACIAL TENSION CORRELATION
(Weinaug and Katz[6])

Components	Temperature (°F)	Pressure (psia)	Interfacial Tension (dynes/cm) Exper.	Calc.
Methane and n-Pentane	100	600	9.02	9.30
		1250	4.59	4.78
		1750	2.01	2.09
		2250	0.27	0.21
	220	600	4.62*	5.02
		1250	1.98*	2.14
		2000	0.07*	0.05
	340	800	0.37*	0.37
Methane and n-Decane	100	1250	11.3	11.8
		2000	7.35	7.02
		3500	2.40	1.84
		5000	0.16	0.09
	280	1000	9.13*	9.30
		3000	2.31*	2.32
		4500	0.06*	0.02
	460	1000	3.3*	3.95
		2750	0.3*	0.10

*Extrapolated

TABLE 5 — SURFACE EXCESS OF METHANE IN THE METHANE-NORMAL PENTANE SYSTEM
(MOLECULES × 10^{-14}/SQ CM)

Pressure (psia)	Temperature (°F) 100	150	160	170	200
2250	1.38	0.72	0.57	0.42	–
2000	1.90	1.34	1.25	1.17	–
1750	2.09	1.53	1.40	1.36	0.99
1500	2.03	1.50	1.40	1.33	1.03
1250	1.92	1.46	1.35	1.27	0.98
1000	1.66	1.26	1.16	1.08	0.90
800	1.40	1.07	0.98	0.93	0.76
600	1.17	0.82	0.78	0.74	0.60

TABLE 6 — SURFACE EXCESS OF METHANE, METHANE-NORMAL DECANE (MOLECULES × 10^{-14}/SQ CM)

Pressure (psia)	Temperature (°F) 100	130	160
5000	0.98	0.86	0.69
4500	1.42	1.39	1.33
4000	1.74	1.56	1.57
3500	2.03	1.93	1.83
3000	2.34	2.21	2.12
2750	2.45	2.38	2.20
2500	2.54	2.41	2.22
2250	2.54	2.30	2.13
2000	2.44	2.12	1.96
1750	2.29	2.04	1.88
1500	2.00	1.79	1.67
1250	1.66	1.50	1.40

maximum point at some intermediate pressure.

The occurrence of a maximum, followed by decreasing values of surface excess, is attributed to the increased value of the surface excess of the heavier component. This value is probably small in the low-pressure region, but it becomes large as the pressure becomes large. Thus, it is reasonable to assume that the decrease in the "surface excess", as calculated, is the result of the surface excess of the heavier component's becoming significantly large. The maximum value of the calculated surface excess of the methane-normal pentane system (or the methane-normal decane system) might be associated with the attainment of a monolayer of methane on a solid surface, since extrapolation of these values for the various isotherms gives fairly good agreement of values of surface density[10] of a monolayer of methane on a solid surface at –297°F.

It appears that surface excess might be useful as a correlating device for interfacial tension, since its values appear to be much more constant for the various systems than interfacial tension itself. For instance, a plot of surface excess divided by density difference appears to give nearly a straight line when plotted against pressure and might possibly yield a finite value at the critical pressure, although in the case of the methane-normal pentane system the value appeared to approach zero very near the critical point.

Experimental data[1] have shown that not only the interfacial tension, but also the interfacial tension

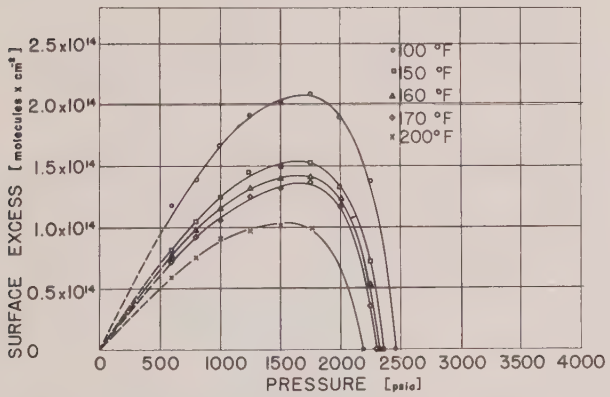

FIG. 6 – SURFACE EXCESS, METHANE-NORMAL PENTANE.

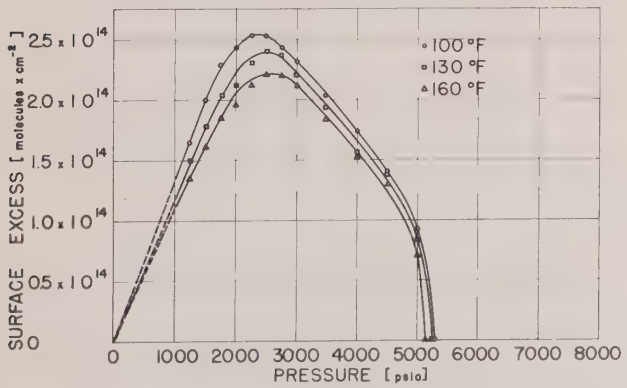

FIG. 7 – SURFACE EXCESS, METHANE-NORMAL DECANE.

divided by density difference approaches zero as the critical point is approached. The significance of the latter is emphasized by a calculation of wetting-phase saturation of porous media from interfacial-tension data. Plotting saturation gradient vs height, one obtains a very sharp gas-liquid contact as the critical point is approached.[1] This sharp liquid-gas saturation gradient may be a contributing factor to the nonequilibrium conditions found in oil reservoirs by Cupps, Lipstate and Fry.[11]

SUMMARY

A considerable amount of data has been accumulated on the surface tension of propane and normal butane, especially near their critical temperatures. In addition, the binary systems — methane-normal pentane and methane-normal decane — have been investigated throughout a wide pressure and temperature range, particularly in the region near the critical points. All these data point to the regularity of the pressure and temperature functions of surface and interfacial tension. Of most interest in the data, however, is the persistence of low interfacial tensions with relatively large changes in pressure in the region about the critical points. The importance of this fact to the petroleum engineer lies in its relationship to liquid saturations and flow behavior in an oil reservoir.

A means of predicting interfacial tension for hydrocarbon mixtures from composition and volumetric data appears to fit experimental results very well. Other correlating devices such as reduced temperature relations, enthalpy of vaporization relations, and surface-excess calculations give promise of relating the surface phenomena to better known physical phenomena.

REFERENCES

1. Stegemeier, G. L.: "Interfacial Tension of Synthetic Condensate Systems", PhD dissertation, The U. of Texas (1959).
2. Guggenheim, E. A.: *Thermodynamics*, Third Ed., North Holland Publishing Co., Amsterdam (1957); also, Interscience Publishers, Inc., N. Y.
3. Sugden, Samuel: *The Parachor and Valency*, George Routledge and Sons, Ltd., London (1930).
4. Rossini, F. D., *et al: Selected Values of Physical and Thermodynamic Properties of Hydrocarbons and Related Compounds*, Carnegie Press, Pittsburgh (1953).
5. Sage; B. H. and Lacey, W. N.: *Thermodynamic Properties of the Lighter Paraffin Hydrocarbons and Nitrogen*, API, N. Y. (1950).
6. Katz, D. L.: *Bull. No. 114*, The A & M College of Texas (1949) 38.
7. Magaril, R. Z.: *Zhurnal Fizicheskoi Khimii* (1955) Vol. 29, 1301.
8. Weinaug, C. F. and Katz, D. L.: *Ind. and Eng. Chem.* (1943) Vol. 25, 239.
9. Rice, O. K.: *Jour. Chem. Phys.* (1947) Vol. 15, 333.
10. Livingston, H. K.: *Jour. Colloidal Sci.* (1949) Vol. 4, 447.
11. Cupps, C. Q., Lipstate, P. H. and Fry, J.: *World Oil* (1951) Vol. 133, 192.

★★★

An Approximate Method for Computing Nonsteady-State Flow of Gases in Porous Media

L. G. JONES
JUNIOR MEMBER AIME

SOCONY MOBIL OIL CO., INC.
DALLAS, TEX.

ABSTRACT

An approximate method of calculation is developed in this paper which allows duplication of radial unsteady-state gas flow computer results where Darcy's law applies, such as those reported by Aronofsky and Jenkins and Bruce, Peaceman, Rachford, and Rice. Moreover, the new calculation method can be used to obtain results for radial unsteady-state gas flow obeying the quadratic flow law proposed by Duwez and Green.

Means are discussed for predicting well behavior at single or superimposed flow rates in finite or infinite reservoirs, determining reservoir rock properties from well-test data, reproducing and interpreting back-pressure test data, and determining the radial extent and reserves of gas reservoirs from well-test data. Example calculations are presented for gas flow following both Darcy's law and the quadratic flow law.

INTRODUCTION

Since the publishing of U. S. Bureau of Mines *Monograph 7*,[1] most gas-well testing methods have been based on the equation $q = \gamma (p_f^2 - p_w^2)^{\alpha}$, where q = production rate, p_f and p_w are formation pressure and sandface pressure, respectively, and γ and α are constants to be obtained from test data. These methods, used for predicting both deliverability and "open-flow" capacity of gas wells, have been useful and accurate in many cases but unsatisfactory in others. Even at best, however, they do not supply information about the formation or lead to an understanding of nonsteady-state gas flow in porous media.

Many theoretically based studies[2-4] of gas flow obeying Darcy's law have been made.* Since the partial differential equations which result from combining Darcy's flow law with the continuity equation are nonlinear, most of the published research consists of either numerical solutions or analytical solutions for linear approximating equations. Such solutions have been of limited value in field work due to their unhandy form and their failure to correlate most field data.

There is evidence[5,6] which indicates that Darcy's law is inadequate to describe gas flow at some flow rates of practical interest. A quadratic flow law,[5] which reduces to Darcy's law at low rates, is more successful in accounting for experimentally observed behavior. This flow law has been applied successfully to a few hypothetical reservoir cases in work which has recently been published.[10] However, these numerical solutions of the equations involved have been successful only on a special analog computer. Routine applications to field cases would be awkward and have not been attempted.

The present paper describes an approximate method for computing nonsteady-state gas flow solutions which has been completely successful in predicting the results for both Darcy flow and quadratic flow obtained by elaborate numerical methods. The new calculation method allows determination of the observable variables in gas-well testing at constant rates. It is similar to the scheme of using a succession of steady states suggested by Muskat[7] in that it makes use of steady-state and material-balance equations. It also is similar to the work of Aronofsky and Jenkins[2] in that the new method includes Aronofsky and Jenkins' stabilized flow equation as a special case. It improves upon both of these calculation schemes in that it accurately describes all portions of reservoir history and suggests means of determining reservoir rock properties from well-test data.

This paper deals only with production from a reservoir, in which case the rate is defined as being negative. The reservoir studied here is a homogeneous, disk-shaped porous body of uniform thickness, with all boundaries sealed except the inner radial boundary of the well.

Original manuscript received in Society of Petroleum Engineers office July 17, 1961. Revised manuscript received Nov. 27, 1961. Paper presented at 36th Annual Fall Meeting of SPE, Oct. 8-11, 1961, in Dallas.

[1] References given at end of paper.

* These are examples, there are many others.

THE CALCULATION METHOD

ASSUMPTIONS AND DEFINITIONS

The method is based upon the following assumptions and definitions.

1. The drainage radius r_d is defined from integration of the radial flow equation until this equation indicates that $r_d = r_e$, the radius of the outer extremity drained by a well, after which r_d is defined as being equal to r_e.

2. All production is assumed to have come from within the drainage area bounded by r_d as defined herein, and all of the reservoir energy is assumed to be provided by expansion of the reservoir gas.

3. It is assumed that the average pressure p_{ave} within the drainage area occurs at a characteristic radius r_{ave}, which can be described by the relation $r_{ave}/r_d = C$, where C can be uniquely determined as a function of r_d/r_e.

4. The "early transient period" is defined as that period during which $r_d < r_e$. The "post early transient period" is defined as that period during which $r_d = r_e$.

DARCY FLOW

The radial flow formula for gas flow obeying Darcy's law may be written as

$$-\ln r_D = \frac{\pi k h M p_i^2}{\mu W z_{ave} R T} (p_D^2 - p_{wD}^2),$$

or

$$\ln r_D = \frac{1}{W_D z_{ave}} (p_D^2 - p_{wD}^2), \quad . \quad . \quad . \quad . \quad . \quad (1)$$

where W_D = dimensionless mass flow rate, $\frac{-W\mu RT}{\pi k h M p_i^2}$,

r_D = dimensionless radius, r/r_w,

p_D = dimensionless pressure, p/p_i,

k = permeability,

h = net pay thickness,

M = molecular weight,

W = mass flow rate, ρq,

μ = viscosity,

z_{ave} = average compressibility factor,

R = gas constant,

T = absolute temperature,

p_{wD} = dimensionless well pressure,

p_i = initial pressure,

q = volumetric flow rate which is defined as being negative for production,

ρ = density, and

r_w = well radius.

Early Transient Period

During the early transient period the pressure at the drainage radius is defined as being equal to the shut-in or initial pressure p_i. The drainage radius for this case is then defined by the equation

$$\ln r_{dD} = \frac{1}{W_D z_{ave}} (p_{iD}^2 - p_{wD}^2) \quad . \quad . \quad . \quad . \quad (2)$$

where r_{dD} = dimensionless drainage radius and p_{iD} = dimensionless initial pressure.

Since

$$C = r_{ave}/r_d,$$

$$r_d = r_{dD} r_w$$

and

$$r_{ave} = r_{aveD} r_w,$$

$$C = r_{aveD}/r_{dD}$$

or

$$r_{aveD} = C r_{dD} \quad . \quad . \quad . \quad . \quad . \quad . \quad . \quad . \quad . \quad . \quad . \quad . \quad . \quad (3)$$

By definition, p_{ave} occurs at r_{ave} and

$$\ln r_{aveD} = \frac{1}{W_D z_{ave}} (p_{aveD}^2 - p_{wD}^2)$$

$$= \ln C r_{dD} = \ln C + \ln r_{dD}, \quad . \quad . \quad . \quad . \quad (4)$$

where p_{aveD} is dimensionless average pressure.

The average pressure decline, Δp_{ave}, within r_{dD} is defined as $p_i - p_{ave}$. This pressure decline must account for total production G_m, in moles, so that

$$\Delta p_{ave} = \frac{z_{ave} G_m R T}{h \phi \pi (r_d^2 - r_w^2)}, \quad . \quad . \quad . \quad . \quad . \quad . \quad . \quad . \quad . \quad (5)$$

where ϕ is the porosity of the reservoir. One may note the relationship between production and r_d. If Δp_{ave} is constant, G_m is approximately proportional to r_d^2. This indicates that r_d increases very rapidly upon initiation of flow, and very slowly after r_d becomes large.

Another bit of information can be gained at this point by adding the negative of Eq. 2 to Eq. 4. The sum of these is

$$\ln\left(\frac{r_{aveD}}{r_{dD}}\right) = \ln C = \frac{-1}{W_D z_{ave}} (1 - p_{aveD}^2) \quad . \quad (6)$$

It may be seen from this equation that, if C is constant for a constant-rate case during the early transient period, p_{aveD} and p_{ave} must also be constant.

Numerical digital-computer solutions for unsteady-

state flow, similar to those of Aronofsky and Jenkins[2] or Bruce, Peaceman, Rachford and Rice,[3] were used for determination of the C values. In this case the results were obtained by using a central-differencing scheme to numerically solve the equation.

$$\frac{\partial^2 p_D{}^2}{\partial u^2} = e^{2u} \frac{\partial p_D}{\partial t_D}$$

where $u = \ln r_D$ and $t_D = \frac{kp_i t}{\phi \mu r_w{}^2}$. Only boundary conditions, values of p_w and production G_m must be known to determine C.

C values for the early transient period can be calculated by using Eqs. 2, 4 and 5 in the following manner.

Step 1 — Calculate r_{dD} using Eq. 2.

Step 2 — Using r_{dD} from Step 1, calculate Δp_{ave} using Eq. 5. Then $p_{ave} = p_i - \Delta p_{ave}$.

Step 3 — Using p_{ave} from Step 2, calculate C using Eq. 4.

Fig. 1 shows values of C calculated from various computer runs. Rate is given in dimensionless terms for reasons explained in the Appendix. It is apparent that C is a function of r_{dD}/r_{eD} only. Two points are appreciably distant from the curve. One of these is for a dimensionless rate of .001, which is so low that digital round-off errors are appreciable. The other is for an r_{dD} value of around 10. Since $C = r_{aveD}/r_{dD}$ it is apparent that, if $C < 1$, r_{aveD} will be < 1 when $r_{dD} = 1$. Since this is physically impossible, the correlation obviously cannot work for extremely small values of r_{dD}. This situation is not of practical importance, however, since it would prevail for only a few seconds in a well test.

Post Early Transient Period

During this period $r_d = r_e$, and p_e, the pressure at the outer boundary, declines. For this situation,

$$\ln r_{aveD} = \ln C r_{eD} = \ln C + \ln r_{eD} = \frac{1}{W_D z_{ave}} (p_{aveD}{}^2 - p_{wD}{}^2) \quad . \quad . \quad . \quad (7)$$

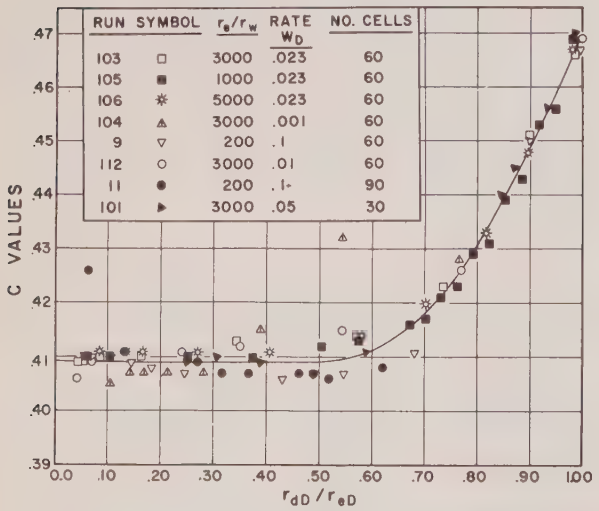

FIG. 1 — C VALUES FOR SELECTED COMPUTER RUNS.

and

$$\Delta p_{ave} = \frac{z_{ave} G_m RT}{h\phi\pi (r_e{}^2 - r_w{}^2)} \cong \frac{z_{ave} G_m RT}{h\phi\pi r_e{}^2} \quad . \quad (8)$$

C values for the post early transient period can be calculated by using Eq. 8 to calculate p_{ave} and by using this in Eq. 7 to determine C. Some calculated values for C in the post early transient period are presented in Table 1. In the table, G_D is dimensionless cumulative production and is the ratio of total production to total moles initially present in the reservoir. Values vary within the range .4486 to .4758. The variation is probably due to a relaxing of the convergence limits in the digital runs. It is believed that a C value of .470 will adequately represent the entire post early transient period. This compares with a value of .472 found by Aronofsky and Jenkins.[2] The difference is of no consequence and is due to the normal variations in digital solutions.

Calculation Procedures

If C, the gas properties and the reservoir constants are known, reservoir performance at constant flow rates can be predicted by using Eqs. 2, 3, 4 and 5 for early transient periods, and Eqs. 7 and 8 for post early transient periods.

For the early transient period, the calculation procedure is as follows.

Step 1 — Assume a value of p_w.

Step 2 — Calculate r_d using Eq. 2.

Step 3 — Calculate r_{dD}/r_{eD}; read C from Fig. 1.

Step 4 — Using C from Step 3, calculate r_{ave} using Eq. 3.

Step 5 — Using r_{ave} from Step 4, calculate p_{ave} using Eq. 4. Then $\Delta p_{ave} = p_i - p_{ave}$.

Step 6 — Using Δp_{ave} from Step 5 and r_d from Step 2, calculate G_m using Eq. 5.

For the post early transient period, the procedure is the following.

Step 1 — Assume a value of p_w.

Step 2 — Using $C = .470$ and p_w from Step 1, calculate p_{ave} using Eq. 7. Then $\Delta p_{ave} = p_i - p_{ave}$.

Step 3 — Using Δp_{ave} from Step 2, calculate G_m using Eq. 8.

TABLE 1

G_D	C	G_D	C
Run 103		Run 105	
.008568	.4692	.008994	.4517
.009486	.4613	.01470	.4695
.009742	.4657	.01964	.4486
.01257	.4573	.03394	.4734
.01470	.4638		
.01753	.4569	Run 106	
.01966	.4633	.009459	.4723
.03240	.4595	.01802	.4758
.05832	.4579	.03037	.4698
.08369	.4635	.05991	.4659
.12285	.4611		
.14298	.4751		

QUADRATIC FLOW

To adequately describe gas flow at moderate or high rates, it is necessary to add another term to Darcy's flow law,[5]

$$\frac{-dp}{dr} = \frac{\mu}{k}\frac{q}{A} + \rho\beta\left(\frac{q}{A}\right)^2 \quad \ldots\ldots\ldots\ldots \quad (9)$$

where β is a parameter to be determined experimentally by a laboratory procedure somewhat similar to that for determining permeability. Multiplying this by ρ gives

$$\frac{-\rho\, dp}{dr} = \frac{\mu\rho}{k}\frac{q}{A} + \frac{\beta\,\rho^2 q^2}{A^2},$$

which equals

$$\frac{\mu}{k}\frac{W}{2\pi rh} + \frac{\beta W^2}{4\pi^2 r^2 h^2} \quad \ldots\ldots\ldots\ldots \quad (10)$$

Substituting $r_D = r/r_w$ and $\rho = \frac{pM}{z_{ave}RT}$ into Eq. 10 and rearranging gives

$$\frac{-M\pi}{z_{ave}RT}\frac{dp^2}{dr_D} = \frac{\mu}{k}\frac{W}{r_D h} + \frac{\beta W^2}{2\pi r_D{}^2 r_w h^2} \quad \ldots(11)$$

If

$$L = \frac{-\pi M}{z_{ave}RT},$$

$$Y = \frac{W\mu}{kh}$$

and

$$J = \frac{\beta W^2}{2\pi r_w h^2}, \quad \ldots\ldots\ldots\ldots \quad (12)$$

then

$$L\frac{dp^2}{dr_D} = \frac{Y}{r_D} + \frac{J}{r_D{}^2} \quad \ldots\ldots\ldots\ldots \quad (13)$$

Rearranging variables and integrating yields

$$p^2 - p^2{}_w = \frac{Y}{L}\ln r_D - \frac{J}{L}\left(\frac{1}{r_D} - 1\right) \quad \ldots \quad (14)$$

If r_D is assumed to be large, making $\frac{1}{r_D}$ negligible in comparison to -1, Eq. 14 becomes

$$p^2 - p_w{}^2 = \frac{Y}{L}\ln r_D + \frac{J}{L} \quad \ldots\ldots\ldots \quad (15)$$

An analysis of Eq. 10 shows that it is possible to use the quadratic equation without resorting to computer solutions for determination of C values. C values determined from solutions to unsteady-state Darcy flow equations can be used for quadratic flow due to the fact that the quadratic term in the quadratic flow equation is of importance only in the region near the wellbore. For the moment let us consider W as the mass flow rate at any radial location in the reservoir. Since W is at its maximum value near the wellbore and since cross-sectional area perpendicular to flow (A) varies with the distance from the wellbore, the term $\frac{\beta W^2}{4\pi^2 r^2 h^2}$ is negligible except near the wellbore. It follows, then, that a pressure profile for quadratic flow in the portion of a reservoir away from the immediate vicinity of the wellbore is nearly identical to that for Darcy flow at the same flow rate, even when there is considerable deviation from Darcy flow near the wellbore. Since C is determined from material-balance considerations, since the region near the wellbore contributes a negligible amount of mass to the total flow after the first few seconds of reservoir life and since deviation from darcy flow occurs only near the wellbore, C values determined from studies of Darcy flow can be used for quadratic flow calculations.

Calculation Procedures

For the early transient period Eq. 15 becomes

$$\ln r_{dD} = \frac{p_i{}^2 - p_w{}^2 - \frac{J}{L}}{Y/L} \quad \ldots\ldots\ldots \quad (16)$$

As before, p_{ave} occurs at r_{aveD}, which is again defined as Cr_{dD} so that

$$\ln r_{aveD} = \ln Cr_{dD} = \frac{p_{ave}{}^2 - p_w{}^2 - \frac{J}{L}}{Y/L} \quad . (17)$$

Eq. 5 again applies for material-balance purposes. For the post early transient period,

$$\ln r_{aveD} = \ln Cr_{eD} = \frac{p_{ave}{}^2 - p_w{}^2 - \frac{J}{L}}{Y/L} \quad . (18)$$

The calculation procedures for quadratic flow are entirely analogous to those for Darcy flow. One item of theoretical importance arises from neglecting the term $1/r_D$ in Eq. 14. For small values of r_D the term $1/r_D$ can have an appreciable value. In such a case, the use of Eq. 15 would not be justified. For most practical situations, however, the use of Eq. 15 will not cause appreciable error because r_{dD} will be large for any time period of practical interest.

SUPERPOSITION

Data on flowing gas wells usually are reported in the form of back-pressure tests. For tests of short duration, the back-pressure test consists of single-point readings of well pressures for superimposed rates. Therefore, any effort to reproduce test data must include the effects of superposition in the calculation procedure.

Only the shut-in well pressure, top- and bottom-hole pressures at the end of a flow period, flow rates, gas gravity, reservoir temperature, formation thickness and duration of flow are reported for back-pressure tests. It is necessary, therefore, to determine values for k, β, ϕ and r_w by trial and error. When the trial values allow reproduction of the test results, it will be assumed that they are correct. It is believed that the values will be relatively correct if, and only if, the number of data points equals or exceeds the number of constants to be determined.

Superposition effects are calculated in the following manner.

1. In their order of occurrence, label each of the rates imposed upon the well by a number. The first rate is Rate 1, the second is Rate 2, etc.

2. Calculate the Δ rates which compose a total rate n by the equations,

$$\Delta \text{ rate } n = \text{rate } n - \text{rate } n-1 \quad \ldots\ldots\ldots (19)$$

and

$$\text{rate } n = \sum_{1}^{n} \Delta \text{ rate } n. \quad \ldots\ldots\ldots (20)$$

Thus, Rate 1 = Δ Rate 1, Rate 2 = Δ Rate 1 + Δ Rate 2 = Rate 1 + Rate 2 − Rate 1, etc.

3. Calculate the production associated with each Δ rate n at any time t by multiplying Δ rate n by the duration of time during which Δ rate n has been in effect.

4. Using the Darcy flow equations, calculate $p_i^2 - p_w^2$ for each Δ rate at every data point. A data point is defined as a point in time where rate, duration of rate and p_w are known.

5. For each rate, calculate the effect of the quadratic term $\frac{J}{L}$ in Eq. 15.

6. Add the individual $p_i^2 - p_w^2$ values to the quadratic effect to obtain the total pressure drop at any data point.

RESERVOIR EXTENT TEST

An analysis of the C values shown in Fig. 1 suggests that a method for determining the extent of a reservoir during the early transient period can be developed. r_{dD} and C can be determined by using Eqs. 16, 17 and 5. If C is greater than the minimum value of .409 (it is no longer constant), then r_{dD}/r_{eD} can be read from Fig. 1. Mathematically, $r_{dD}/r_{eD} = f$ where f is the value read from Fig. 1, and

$$r_{eD} = \frac{r_{dD}}{f} \quad \ldots\ldots\ldots\ldots\ldots (21)$$

If $C = .409$, f can have any value from 0 to approximately .5. To determine the extent of a reservoir, therefore, it is necessary to run a test at least until C is greater than .409. In actual practice it would be advisable to run the test until C was considerably above .409 to make sure that the change was not due to the random deviations expected in any attempted calculation of reservoir performance.

For quadratic flow, the steps in performing this calculation are as follows.

1. Calculate r_{dD} using Eq. 16.

2. Using r_{dD} from Step 1 and G_m from test data, calculate Δp_{ave} using Eq. 5, and p_{ave} from $\Delta p_{ave} = p_i - p_{ave}$.

3. From Eq. 17,

$$\ln C + \ln r_{dD} = \frac{p_{ave}^2 - p_w^2 - \frac{J}{L}}{Y/L}.$$

Calculate C using this equation, p_{ave} from Step 2 and r_{dD} from Step 1.

4. From Fig. 1 read f, r_{dD}/r_{eD} for C calculated in Step 3. Then calculate r_{eD} using Eq. 21.

DISCUSSION

To use the new calculation method, the engineer must know permeability, porosity, well radius, reservoir thickness, gas properties, outer drainage perimeter and β. Although permeability, porosity, well radius and β could be determined by other means, it is felt that better results will be obtained if they are calculated from well-test data.

The well tests can be run at any time during a reservoir's life if the reservoir is previously allowed to build up to a static pressure. However, one of the primary advantages of the new method is that it allows predictions of reservoir performance before the reservoir pressure has declined; therefore, to gain the fullest benefits from well tests, they should be made as early as possible.

After the engineer has obtained the necessary data, the new method provides for him a way to calculate the total production associated with any well pressure when the well is being produced at a constant rate. This is accomplished without iteration and without calculating production for any well pressure other than the one of interest.

It is realized that the necessity of determining k, β, ϕ and r_w by trial and error limits the usefulness of the new method at present. However, development of digital computer programs to perform the lengthy trial-and-error calculations should result in use of the new method for routine field calculations.

No rules have been given for determining the averaged values of z and μ to be used in a given calculation. It is felt that z_{ave} and μ should correspond with p_{ave}, but the use of values corresponding with p_i during the "early transient period" or p_e during the "post early transient period" probably will not cause appreciable error.

The analysis justifying the use of C values determined from Darcy flow studies for quadratic flow calculations should also apply for z and μ when they are variable functions of pressure. To use C values determined from Darcy flow studies for another type of flow, it is necessary that the pressure profile in the reservoir away from the immediate vicinity of the wellbore for the flow in question be almost identical to that for Darcy flow. This is true for variable z and μ because most of the pressure drop, and thus most of the deviation from Darcy flow, occurs near the wellbore.

NOMENCLATURE

A = area cross-sectional to flow
$C = r_{ave}/r_d = r_{aveD}/r_{dD}$
$f = r_{dD}/r_{eD}$
G_D = dimensionless cumulative production
G_m = cumulative production, mol
G_m total = total number of moles in the reservoir
Gp = cumulative production, Mscf
h = net reservoir thickness
$J = \dfrac{\beta W^2}{2\pi r_w h^2}$
k = permeability
$L = \dfrac{-\pi M}{z_{ave} RT}$
M = gram molecular weight
N = flow rate in gm mol/sec/cm of reservoir thickness
p = pressure
p_{ave} = average pressure
P_D = dimensionless pressure
p_e = pressure at the outer drainage radius
p_f = formation pressure
p_i = initial pressure
p_{iD} = dimensionless initial pressure = 1
p_w = well pressure
p_{wD} = dimensionless well pressure
Δp_{ave} = average pressure drop
Δp_{aveD} = dimensionless average pressure drop
q = volumetric flow rate
R = gas constant
r = radius
r_{ave} = radius at which p_{ave} occurs
r_{aveD} = dimensionless radius at which p_{ave} occurs
r_D = dimensionless radius
r_d = drainage radius
r_{dD} = dimensionless drainage radius
r_e = outer drainage radius
r_{eD} = dimensionless outer drainage radius
r_w = well radius
r_{wD} = dimensionless well radius = 1
T = absolute temperature
t = time
t_D = dimensionless time
$u = \ln r_D$
W = mass flow rate
W_D = dimensionless mass flow rate
$\bar{W}_D$ = average dimensionless mass flow rate
$Y = W\mu/kh$
z = compressibility factor
z_{ave} = average compressibility factor
γ, a = back-pressure-test constants
β = unnamed empirical constant
ϕ = porosity
ρ = density
μ = viscosity

ACKNOWLEDGMENT

Acknowledgment is made to Socony Mobil Oil Co., Inc., for permission to publish this paper. The author is also indebted to G. C. Wallick, who provided the digital computer results, and to W. D. Simpson and W. B. Lanier for their aid in this study.

REFERENCES

1. Shellhardt, M. A. and Rawlins, E. L.: "Back-Pressure Data on Natural Gas Wells and Their Application to Production Practices", *Monograph* 7, USBM.
2. Aronofsky, J. S. and Jenkins, R.: "A Simplified Analysis of Unsteady Radial Gas Flow", *Trans.*, AIME (1954) Vol. 201, 149.
3. Bruce, G., Peaceman, D., Rachford, H. and Rice, J.: "Calculation of Unsteady-State Gas Flow Through Porous Media", *Trans.*, AIME (1953) Vol. 198, 79.
4. MacRoberts, D. T.: "Effects of Transient Conditions in Gas Reservoirs", *Trans.*, AIME (1949) Vol. 186, 36.
5. Green, L. and Duwez, P.: "Fluid Flow through Porous Metals", *Jour. Appl. Mech.* (1951) Vol. 18, 39.
6. Cornell, D. and Katz, D. L.: "Flow of Gases Through Consolidated Porous Media", *Ind. Eng. Chem.* (1953) Vol. 45, 2145.
7. Muskat, M.: *The Flow of Homogeneous Fluids Through Porous Media*, McGraw-Hill Book Co., Inc., N. Y. (1937).
8. Baumel, J. K. and Breitung, C. A.: "Back-Pressure Test for Natural Gas Wells, State of Texas", Railroad Commission of Texas (July 31, 1950).
9. Cornell, D. and Katz, D. L.: "Pressure Gradients in Natural Gas Reservoirs", *Trans.*, AIME (1953) Vol. 198, 61.
10. Jones, L. G. and Skinner, W. C.: "Analog Solutions to Unsteady State Radial Gas Flow Problems", *Proc.*, Third International Conference on Analog Computation, Opatija, Yugoslavia (Sept. 4-9, 1961) in press.

APPENDIX

DIMENSIONLESS VARIABLES

The computer solutions used for determining C values are provided in dimensionless form. The dimensionless terms are dimensionless pressure, dimensionless rate, dimensionless time

$$t_D = \frac{k p_i t}{\phi \mu r_w^2}, \quad \ldots\ldots\ldots\ldots\ldots \quad (22)$$

and dimensionless cumulative production

$$G_D = G_m/G_m \text{ Total}, \quad \ldots\ldots\ldots\ldots (23)$$

where G_m total is total moles of gas initially present in the reservoir. From Eq. 2,

$$r_{dD} = \exp \frac{(1 - p_{wD}^2)}{z_{ave} W_D} \quad \ldots\ldots\ldots (24)$$

and

$$r_{dD}^2 = \exp \frac{2\ (1 - p_{wD}^2)}{z_{ave} W_D} \quad \ldots\ldots\ldots (25)$$

Total number of moles is as follows.

$$G_m \text{ Total} = \frac{P_i \phi \pi\ (r_e^2 - r_w^2) h}{z_{ave} RT} \quad \ldots\ldots (26)$$

If r_w^2 is assumed negligible in this equation (this is valid for almost all practical problems involving well behavior) and in Eq. 5,

$$G_D = G_m/G_m \text{ Total} = \frac{\Delta p_{ave} \phi \pi r_d^2 h}{z_{ave} RT} \Big/ \frac{p_i \phi \pi r_e^2 h}{z_{ave} RT}$$

$$= \frac{\Delta p_{ave} r_d^2}{p_i\ r_e^2} \quad \ldots\ldots\ldots\ldots (27)$$

and

$$G_D = \Delta p_{aveD} \frac{r_{dD}^2}{r_{eD}^2} \quad \ldots\ldots\ldots\ldots (28)$$

where Δp_{aveD} is dimensionless average pressure drop. Also, since

$$\Delta p_{ave} = p_i - p_{ave},$$

then

$$\Delta p_{aveD} = 1 - p_{aveD}. \quad \ldots\ldots\ldots\ldots (29)$$

Thus,

$$G_D = (1 - p_{aveD}) \frac{r_{dD}^2}{r_{eD}^2} \quad \ldots\ldots\ldots (30)$$

and

$$p_{aveD} = 1 - \frac{G_D r_{eD}^2}{r_{dD}^2} \quad \ldots\ldots\ldots (31)$$

From Eq. 6,

$$\ln C = \frac{p_{aveD}^2 - 1}{z_{ave} W_D}.$$

Substitution of Eq. 31 into this gives

$$\ln C = \frac{\left(1 - \frac{G_D r_{eD}^2}{r_{dD}^2}\right)^2 - 1.}{z_{ave} W_D} \quad \ldots\ldots (32)$$

Further substitution of Eq. 25 into Eq. 32 produces

$$\ln C = \frac{1}{z_{ave} W_D} \left[\left(1 - \frac{G_D r_{eD}^2}{\exp \frac{2(1 - p_{wD}^2)}{z_{ave} W_D}} \right)^2 - 1 \right], \quad \ldots\ldots\ldots\ldots (33)$$

or

$$C = \exp \frac{1}{z_{ave} W_D} \left[\left(1 - \frac{G_D r_{eD}^2}{\exp \frac{2(1 - p_{wD}^2)}{z_{ave} W_D}} \right)^2 - 1 \right]. \quad \ldots\ldots\ldots\ldots (34)$$

For the post early transient period, in dimensionless terms,

$$\ln C r_{eD} = \frac{1}{z_{ave} W_D} (p_{aveD}^2 - p_{wD}^2),$$

and

$$\Delta p_{aveD} = \frac{G_D r_{eD}^2}{r_{dD}^2} = \frac{G_D r_{eD}^2}{r_{eD}^2} = G_D,$$

or

$$p_{aveD} = 1 - G_D. \quad \ldots\ldots\ldots\ldots (35)$$

Therefore,

$$\ln C = \frac{1}{z_{ave} W_D} \left[(1 - G_D)^2 - p_{wD}^2 \right] - \ln r_{eD}, \quad \ldots\ldots\ldots\ldots (36)$$

or

$$C = \exp \left\{ \frac{1}{z_{ave} W_D} \left[(1 - G_D)^2 - p_{wD}^2 \right] - \ln r_{eD} \right\} \quad \ldots\ldots\ldots\ldots (37)$$

CALCULATIONS

DARCY FLOW — CONSTANT-RATE CASE

To illustrate the use of the calculation method for a constant-rate case, let $k = .3$ darcies, $r_{eD} = 1{,}000$, $r_w = 15.25$ cm, $p_i = 136$ atm, $z_{ave} = 1$, $\mu = .016$ cp, $T = 332°K$, $M = 20.86$ gm/gm mol, $\phi = .20$, $R = 82.06$ cc atm/gm mol °K, $h = 304.8$ cm, and $W = -5848.1$ gm/sec = 20,300 Mscf/D.

From Eq. 2,

$$\ln r_{dD} = \frac{(\pi)(.3)(20.86)(136)^2(304.8)}{(5848.1)(.016)(82.06)(332)}(1-p_{wD}^2)$$

$$= 43.478\,(1-p_{wD}^2);$$

from Eq. 4,

$$\ln r_{aveD} = 43.478\,(p_{aveD}^2 - p_{wD}^2);$$

and from Eq. 5,

$$\Delta p_{ave} = \frac{(1)(82.06)(332)\,G_m}{(304.8)(.2)(\pi)(r_d^2 - r_w^2)}$$

$$\cong 142.257\,\frac{G_m}{r_d^2}.$$

Also,

$$G_m \cong \Delta p_{ave} r_d^2/142.257.$$

For the first point let $p_w = 126.5$ atm. Table 2 shows calculations using this value. The dimensionless drainage radius is 351.4. Therefore, $r_{dD}/r_{eD} = .3514$. C is then read from the curve in Fig. 1 as .409. $r_{aveD} = .409\,r_{dD} = 143.72$, and $\ln r_{aveD} = 4.968$. Dimensionless average pressure is calculated as .98967, dimensionless average pressure drop as .01033 and average pressure drop as 1.40488 atm. $r_d = 15.25$, $r_{dD} = 5358.85$, and $r_{dD}^2 = 28.7173 \times 10^6$. G_m is then calculated as 283,601 gm mol production. Time t is then calculated by the equation

$$t = \frac{G_m M}{W} \qquad \ldots\ldots\ldots\ldots\ldots\ldots \quad (38)$$

= 1011.6 seconds, or 16.86 minutes.

For the next point let $p_w = 125.0$ atm. Calculated by the same process used for Point 1, $G_m = 1{,}536{,}110$ mol and $t = 5479.2$ seconds.

For the next point let $p_w = 120.0$ atm. Since $\ln r_{dD}$ is greater than ln 1,000, the reservoir is in the post early transient stage of production. For this situation Eqs. 7 and 8 are used for calculation purposes. G_m is then calculated as 9,071,192, and t as 32,356.1.

DARCY FLOW — CONSTANT-PRESSURE CASE

The calculation method can be used to calculate a constant-well-pressure case (pressure at the sand face remains constant) by treating it as a series of constant-rate cases. It is assumed that the pressure profile at a given rate is accurately described by C values determined from constant-rate studies. The procedure consists of assuming a series of decreasing rates, calculating the production associated with each rate and dividing the difference in production between two successive rate values by an average of these two rates to obtain the elapsed time between the occurrence of the two rates. Since this is essentially a numerical integration procedure, errors will occur. The magnitude of the error should depend upon the size of the time step and should disappear as the number of time steps used approaches infinity.

The constant-pressure case presented here is calculated in dimensionless terms. This is done so that it can be conveniently compared with digital computer results for the same problem.

The basic equation for use in the early transient period is Eq. 33, which can be written as

$$1 + z_{ave} W_D \ln C = \left[1 - G_D r_{eD}^2 \Big/ \exp\frac{2(1-p_{wD}^2)}{z_{ave} W_D}\right]^2.$$

From this is obtained

$$1 - G_D r_{eD}^2 \Big/ \exp\frac{2(1-p_{wD}^2)}{z_{ave}\,W_D} = \sqrt{1 + z_{ave} W_D \ln C},$$

and

$$G_D = \frac{1 - \sqrt{1 + z_{ave} W_D \ln C}}{r_{eD}^2 / \exp\dfrac{2(1-p_{wD}^2)}{z_{ave}\,W_D}} \qquad \ldots\ldots\ldots \quad (39)$$

The corresponding equation for the post early tran-

TABLE 2

Point	p_w	p_{wD}	p_{wD}^2	$1-p_{wD}^2$	$\ln r_{dD}$	r_{dD}	r_{dD}/r_{eD}	C	r_{aveD}
1	126.5	.930147	.865173	.134827	5.8620	351.4	.3514	.409	143.72
2	125.0	.91912	.844782	.155218	6.7486	852.8	.8528	.4395	374.81
3	120.0	.88235	.778542	.221458	9.6286*	1000	1.000	.470	470.00

Point	$\ln r_{aveD}$	p_{aveD}^2	p_{aveD}	Δp_{aveD}	Δp_{ave}	r_d	$r_d^2/10^6$	G_m	t
1	4.9680	.97944	.98967	.01033	1.40488	5358.85	28.7173	283601	1011.6
2	5.9264	.98109	.99050	.00950	1.2920	13005.2	169.1352	1536110	5479.2
3	6.1528	.92006	.95920	.04080	5.5488	15250.0	232.5625	9071192	32356.1

*Since this value is larger than ln 1,000, the reservoir is in the post early transient stage of production.

sient period is Eq. 36, which can be arranged as

$$(\ln C + \ln r_{eD})\, z_{ave} W_D + p_{wD}^2 = (1 - G_D)^2,$$

which yields

$$G_D = 1 - \sqrt{z_{ave} W_D\, (\ln C + \ln r_{eD}) + p_{wD}^2}\,. \quad (40)$$

For calculation purposes, let $p_{wD} = .1$, $r_{eD} = 1{,}000$, $\ln r_{eD} = 6.908$, and $z_{ave} = 1.0$.

During the early transient portion of the calculation, r_{dD}/r_{eD} can be calculated by the equation

$$r_{dD}/r_{eD} = \exp \frac{1 - p_{wD}^2}{z_{ave} W_D} \Big/ r_{eD} \quad (41)$$

(see Eq. 24), and C can be read from Fig. 1. The dimensionless time interval Δt_D associated with a production interval is calculated by the equation

$$\Delta t_D = \frac{\Delta G_D (r_{eD}^2 - r_{wD}^2)}{\bar{W}_D} \cong \frac{\Delta G_D \times 10^6}{\bar{W}_D} \quad (42)$$

where

$$\bar{W}_D = \frac{W_D \text{ at start of interval} + W_D \text{ at end of interval}}{2} \quad (43)$$

To calculate the first time step, it is necessary to assume an average rate. If the first rate chosen is high enough, this assumption produces a small and constant error which is of importance for only the first few time steps.

Tables 3 and 4 show early transient and post early transient calculations, respectively, for the constant-well-pressure case. Fig. 2 is a graph of these values of rate and production vs time, along with values from a digital computer solution to the same problem. Except for t_D values of less than 100, agreement seems quite good, especially when the approximate nature of both calculations is considered.

Values of t_D less than 100 correspond to small r_{dD} values and, consequently, to very small values of time. As explained earlier, there is a loss of accuracy at small values of r_{dD}. For this reason

TABLE 3 — CONSTANT-WELL-PRESSURE CASE, EARLY TRANSIENT

(1) W_D	(2) $\frac{(1-P_{wD}^2)}{W_D}$	(3) $\frac{r_{dD}}{r_{eD}}$	(4) C	(5) $W_D \ln C$	(6) $\sqrt{1+W_D \ln C}$	(7) 1-(6)	(8) $2[\ln r_{eD} - (2)]$	(9) $e^{2(8)}$	(10) G_D	(11) ΔG_D	(12) $\bar{W}_D$	(13) $\Delta t_D/10^6$	(14) t_D
.80	1.238	.00342	.409	-.715	.534	.464	11.340	8.39×10^4	$.553\times10^{-5}$	$.553\times10^{-5}$	1.0*	$.553\times10^{-5}$	5.53
.70	1.414	.00412	.409	-.626	.611	.389	10.988	5.90×10^4	$.659\times10^{-5}$	$.106\times10^{-5}$	.75	$.141\times10^{-5}$	6.94
.60	1.650	.00522	.409	-.536	.680	.320	10.516	3.68×10^4	$.869\times10^{-5}$	$.210\times10^{-5}$	.65	$.323\times10^{-5}$	10.2
.50	1.980	.00725	.409	-.447	.743	.257	9.856	1.902×10^4	$.135\times10^{-4}$	$.482\times10^{-5}$	.55	$.876\times10^{-5}$	18.9
.40	2.475	.0119	.409	-.358	.801	.199	8.866	7.07×10^3	$.281\times10^{-4}$	$.146\times10^{-4}$	.45	$.324\times10^{-4}$	51.3
.35	2.829	.0169	.409	-.313	.828	.172	8.158	3.48×10^3	$.494\times10^{-4}$	$.213\times10^{-4}$	.375	$.568\times10^{-4}$	108
.30	3.300	.0270	.409	-.268	.855	.145	7.216	1.355×10^3	$.107\times10^{-3}$	$.576\times10^{-4}$	.325	$.1772\times10^{-3}$	285
.28	3.536	.034	.409	-.250	.866	.134	6.744	8.47×10^2	$.158\times10^{-3}$	$.51\times10^{-4}$	.29	$.1759\times10^{-3}$	461
.26	3.808	.045	.409	-.232	.876	.124	6.200	492	$.252\times10^{-3}$	$.94\times10^{-4}$	.27	$.3481\times10^{-3}$	809
.24	4.125	.062	.409	-.215	.886	.114	5.566	261	$.437\times10^{-3}$	$.185\times10^{-3}$	.25	$.740\times10^{-3}$	1550
.22	4.50	.090	.409	-.197	.896	.104	4.816	123.1	$.845\times10^{-3}$	$.408\times10^{-3}$	.23	$.1779\times10^{-2}$	3320
.20	4.95	.142	.409	-.179	.905	.095	3.916	50.2	$.189\times10^{-2}$	$.1045\times10^{-3}$	.21	$.4976\times10^{-2}$	8300
.18	5.50	.245	.409	-.161	.915	.085	2.816	16.7	$.509\times10^{-2}$	$.320\times10^{-2}$	.19	$.1684\times10^{-1}$	25140
.16	6.188	.485	.409	-.143	.926	.074	1.440	4.22	$.177\times10^{-1}$	$.126\times10^{-1}$	.17	$.7418\times10^{-1}$	99320
.15	6.60	.735	.422	-.1296	.9329	.0671	.616	1.85	$.363\times10^{-1}$	$.186\times10^{-1}$	.155	.1198	219100
.1433	6.908	1.0	.470	-.1082	.9443	.0557	0	1	$.557\times10^{-1}$	$.194\times10^{-1}$	.14665	.1325	351600

*Assumed.

TABLE 4 — POST EARLY TRANSIENT

(1) W_D	(2)* $z_{ave} W_D(\ln C + \ln r_{eD}) + p_{wD}^2$	(3) $\sqrt{(2)}$	(4) G_D	(5) ΔG_D	(6) $\bar{W}_D$	(7) $\Delta t_D/10^6$	(8) t_D
.14	.87142	.9335	.0665	.0108	.14165	.0762	427800
.13	.80989	.9000	.1000	.0335	.135	.2481	675900
.12	.74836	.8651	.1349	.0349	.125	.2792	955100
.11	.68683	.8288	.1712	.0363	.115	.3157	1271000
.10	.62530	.7908	.2092	.0380	.105	.3619	1633000
.09	.56377	.7508	.2492	.0400	.095	.4211	2054000
.08	.50724	.7087	.2913	.0421	.085	.4953	2549000
.07	.44071	.6639	.3361	.0448	.075	.5973	3146000
.06	.37918	.6158	.3842	.0481	.065	.7400	3886000
.05	.31765	.5636	.4364	.0522	.055	.9491	4835000
.04	.25612	.5061	.4939	.0575	.045	1.2778	6113000
.03	.19459	.4411	.5589	.0650	.035	1.8571	7970000
.02	.13306	.3648	.6352	.0763	.025	3.0520	11020000
.01	.07153	.2675	.7325	.0973	.015	6.4867	17510000

*$C = .470$; $\ln C = -.755$; $\ln r_{eD} = 6.908$; and $\ln C + \ln r_{eD} = 6.153$.

no values were computed for W_D values greater than .80. Fortunately, the production at this point is so small that higher rates can be neglected with little effect on the over-all calculation. This necessarily will be true in all cases involving a constant well pressure.

QUADRATIC FLOW — CONSTANT-RATE CASE

To illustrate a quadratic flow calculation, the same case that was presented for Darcy flow, with the addition of $\beta = -.648$ atm sec^2/gm, is recalculated using quadratic flow equations.

From Eq. 12,

$$Y/L = \frac{W\mu z_{ave}RT}{kh\pi M}$$

$$= \frac{+(5848.1)(.061)(82.06)(1)(332)}{(.3)(304.8)(\pi)(20.86)}$$

$$= 425.414,$$

and

$$J/L = \frac{\beta W^2 z_{ave}RT}{2\pi^2 r_w h^2 M}$$

$$= \frac{+(.648)(5848.1)^2(1)(82.06)(332)}{2(\pi)^2(15.25)(304.8)^2(20.86)}$$

$$= 1035.0.$$

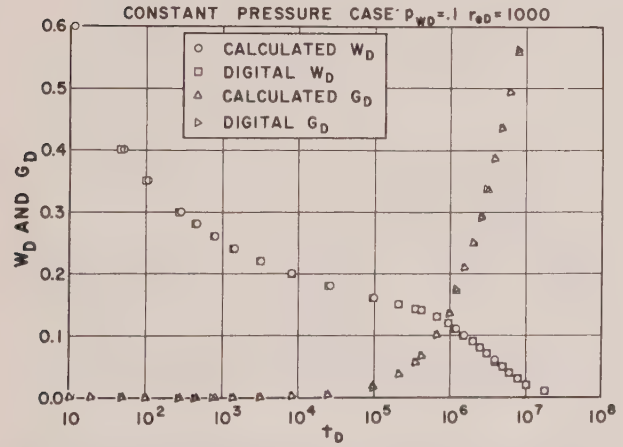

FIG. 2 — COMPARISON OF HAND-CALCULATED VALUES OF W_D AND G_D WITH COMPUTER VALUES — DARCY FLOW (CONSTANT-PRESSURE CASE p_{WD} = .1, r_{eD} = 1,000).

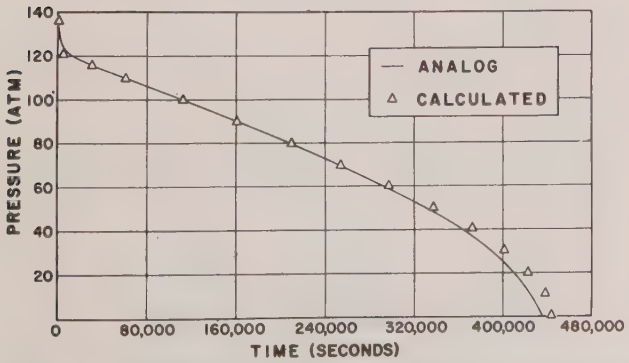

FIG. 3 — COMPARISON OF ANALOG AND CALCULATED VALUES OF p_w VS TIME — QUADRATIC FLOW.

Eq. 16 then becomes

$$\ln r_{dD} = \frac{p_i^2 - p_w^2 - 1035.0}{425.414}.$$

As before, Eq. 5 becomes

$$\Delta p_{ave} \cong 142.257\ G_m/r_d^2$$

or

$$G_m \cong \Delta p_{ave} r_d^2/142.257;$$

and, from Eq. 38,

$$t = G_m\ (20.86)\ /\ 5848.1.$$

Fig. 3 shows a comparison of calculated values of p_w vs t for this case with values computed on an analog.[10] The agreement is very good considering the problems associated with analog computations. The observable deviation in values at very small values of time is due to the inability of the x-y plotter to follow the analog computations at the particular time scale used to obtain this figure. The deviation at large values of time is probably due to analog drift.

Fig. 4 shows a comparison of the calculated values of p_w vs t for Darcy and quadratic flow given in Tables 2 and 5, respectively. As would be expected, a lower well pressure is indicated at a given time for quadratic flow.

QUADRATIC FLOW — CONSTANT-PRESSURE CASE

A constant-pressure case involving quadratic flow can be calculated in a manner analogous to that used for Darcy flow. The basic equations to be used here are Eqs. 16, 17 (or 18), and 5. After ΔG_m, the production during an interval, is determined, the elapsed time during the interval is calculated by the equation

$$\Delta t = \frac{M\Delta G_m}{\bar{W}} \quad \ldots\ldots\ldots\ldots \quad (44)$$

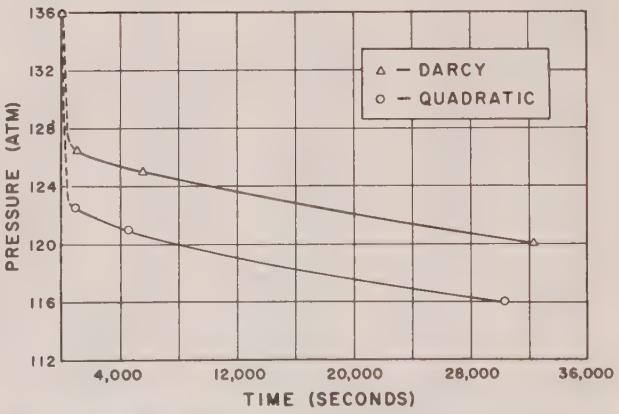

FIG. 4 — COMPARISON OF CALCULATED VALUES OF p_w VS TIME FOR DARCY AND QUADRATIC FLOW.

where

$$\bar{W} = \frac{W \text{ at start of interval} + W \text{ at end of interval}}{2} \quad \ldots\ldots\ldots\ldots\ldots\ldots\ldots\ldots (45)$$

SUPERPOSITION

An actual field case is used to illustrate application of the method when superimposed flow rates are involved. The data used here are those of Baumel and Breitung.[8] These data also were used by Cornell and Katz[9] in a paper in which they developed a graphical calculation procedure and attempted to correlate the data.

As a first trial, let $\phi = .20375$, $k = .10125$ darcies, $\beta = -2.7652$ atm sec^2/gm, and $r_w = .22969$ ft = 7.0009 cm.

These values were obtained by a computer method which is not described here. It is recommended that the engineer does not try to perform a trial-and-error procedure to determine ϕ, k, β and r_w unless he has access to a digital computer.

The test data include: $h = 21$ ft; $p_i = 3{,}127$ psia (24-hour shut-in pressure) = 212.721 atm; $q_1 = 3{,}710$ Mscf/D for 180 minutes, $p_w = 3{,}087$ psia; $q_2 = 5{,}980$ Mscf/D for 200 minutes, $p_w = 3{,}059$ psia; $q_3 = 8{,}191$ Mscf/D for 180 minutes, $p_w = 3{,}035$ psia; $q_4 = 14{,}290$ Mscf/D for 190 minutes, $p_w = 2{,}942$ psia; $T = 370°$K; $M = 20.3$ (gas gravity = 0.700); $\mu = 0.021$ cp (average value); $z_{ave} = 0.87$; and casing diameter = 5.5 in.

The equations to be used are Eqs. 2, 3, 4, 5, 6, 16, 19 and 20. In Eq. 16, Y/L and J/L will be rewritten as $-N\,\frac{\mu z_{ave} RT}{\pi k}$ and $-N^2\,\frac{\beta z_{ave} RTM}{2\pi^2 r_w}$, respectively. N is negative and equals W/Mh, which is rate in gram moles per second per centimeter of reservoir thickness. Therefore,

$$Y/L = \frac{-N\,(.021)\,(.87)\,(82.06)\,(370)}{(.10125)\,(3.1416)} = -1{,}743.9N$$

and

$$J/L = -N^2\,\frac{(-2.7652)\,(.87)\,(82.06)\,(370)\,(20.3)}{2(3.1416)^2\,(7.0009)} = 10{,}729.8N^2.$$

r_{eD} is unknown, but for a 12-hour test it is doubtful if r_{dD}/r_{eD} would much exceed .50. If r_{dD}/r_{eD} is less than .5, C is constant. Therefore, it will be assumed that C and ln$C$ have constant values of .410 and −.8915, respectively.

From Eq. 6,

$$p_{ave}^2 = p_i^2 + (Y/L) \ln C.$$

Since it has been assumed that C is a constant, p_{ave} is constant at a constant flow rate. It follows, therefore, that there is a constant Δp_{ave} associated with each Δ rate.

Before proceeding, it is necessary to calculate rates, Δ rates, production associated with the Δ rates, values of J/L and Y/L associated with the rates and Δ rates, respectively, and Δp_{ave} associated with each Δ rate. Now recall that

$$\Delta p_{ave} = \frac{z_{ave} G_m RT}{h\phi\,\pi\, r_{dD}^2\, r_w^2}$$

and that

$$\ln r_{aveD} = \ln C r_{dD} = \frac{-\pi k}{N \mu z_{ave} RT}\,(p_{ave}^2 - p_w^2) = \frac{p_{ave}^2 - p_w^2}{Y/L}.$$

Also,

$$r_{dD} = \sqrt{\frac{z_{ave} G_m RT}{h\phi\,\pi\,\Delta p_{ave}\, r_w^2}}$$

so that

$$(Y/L) \ln C \sqrt{\frac{z_{ave} G_m RT}{h\phi\,\pi\,\Delta p_{ave}\, r_w^2}} = p_{ave}^2 - p_w^2,$$

or

$$p_w^2 = p_{ave}^2 - 1/2\; Y/L \ln \frac{z_{ave} G_m RTC^2}{h\phi\,\pi\,\Delta p_{ave}\, r_w^2}.$$

TABLE 5 — QUADRATIC FLOW CALCULATIONS

Point	p_w	p_w^2	$p_i^2 - p_w^{2*}$	$p_i^2 - 1035 - p_w^2$	lnr_{dD}	r_{dD}	r_{dD}/r_{eD}	C	r_{aveD}
1	122.5	15006.3	3489.7	2454.7	5.7702	320.6	.3206	.409	131.13
2	121.0	14641.0	3855.0	2820.0	6.6288	756.5	.7565	.424	320.76
3	116.0	13456.0	5040.0	4005.0	9.41***	1000	1.0000	.470	470.00

Point	lnr_{aveD}	p_{ave}^2	p_{ave}	Δp_{ave}	r_d	$r_d^2/10^6$	G_m	t
1	4.87615	18115.7	134.595**	1.405	4889.15	23.90379	236086	842.1
2	5.77073	18131.0	134.652	1.348	11536.63	133.0938	1261168	4498.5
3	6.1528	17108.5	130.800	5.200	15250.0	232.5625	8500976	30322.1

*$p_i^2 = 136^2 = 18{,}496$.

**This is identical to the value for Darcy flow with $p_w = 126.5$.

***Greater than ln 1,000; therefore, post early transient stage.

TABLE 6 — RATES, Δ RATES AND ASSOCIATED VALUES

Data Point	Rate (Mscf/D)	N	ΔN	N^2	J/L
1	3710	−.08013	−.08013	.0064208	68.894
2	5980	−.12916	−.04903	.0166823	178.998
3	8191	−.17691	−.04775	.0312971	335.812
4	14290	−.30864	−.13173	.0952586	1022.106

ΔN	Data Points (G_p) 1	2	3	4	Y/L	$(Y/L)\ln C$, or $p_{ave}^2 - p_i^{2*}$	p_{ave}^2	p_{ave} (atm)	Δp_{ave} (atm)
−.08013	464	979	1443	1932	139.739	− 124.6	45125.6	212.428	.293
−.04903	0	315	599	899	85.503	− 76.2	45174.0	212.542	.179
−.04775	0	0	277	569	83.271	− 74.2	45176.0	212.546	.175
−.13173	0	0	0	804	229.724	−204.8	45045.4	212.239	.482

*$p_i^2 = 45{,}250.2$.

Since

$$G_m = \frac{Gp\,(453.6)\,(10^3)}{380.15}$$

where Gp is production in thousands of standard cubic feet, the equation becomes

$$p_w^2 = p_{ave}^2 - 1/2\ Y/L\ \ln \frac{z_{ave} GpRTC^2 (453.6 \times 10^3)}{h\phi\,\pi\,\Delta p_{ave}\, r_w^2\,(380.15)}$$

$$= p_{ave}^2 - 1/2\ Y/L$$

$$\ln \frac{.87\ Gp\ (82.06)\ (370)\ (.41)^2\ (453.6 \times 10^3)}{640\,(.20375)(3.14159)(\Delta p_{ave})(7.0009)^2(380.15)}$$

$$= p_{ave}^2 - 1/2\ Y/L\ \ln 263.878\ \frac{Gp}{\Delta p_{ave}}.$$

Thus, from Darcy flow equations, $p_i^2 - p_w^2$ terms associated with each Δ rate at each data point are calculated by the equation

$$p_i^2 - p_w^2 = p_i^2 - p_{ave}^2 + 1/2\ Y/L\ \ln 263.878\ \frac{Gp}{\Delta p_{ave}}.$$

The sum of these and the J/L term at a point gives the total $p_i^2 - p_w^2$ for the point, from which can be obtained the well pressure.

Calculations leading to the determination of p_w values are presented in Tables 6 and 7. Considering all factors, agreement between calculated values of p_w and field values is quite good. Maximum deviation of a calculated value from the reported value is 3.4 psi for the third data point, which is well within experimental error. The third data point proved difficult to fit. If the pressure at this point was lower than reported, or the rate higher, an excellent fit could be obtained.

Difficulties in matching reported data might occur in cases where reported pressures and rates are inaccurate, where the formation has been damaged with accompanying loss of permeability, when the time consumed in changing chokes is great enough to allow considerable pressure change, or if major variations from radial geometry are present.

RESERVOIR EXTENT TEST

For this example assume that the reservoir treated in the quadratic flow constant-rate case is being tested. In the present case the production data are known and r_{eD} is the unknown which is to be determined. Let p_w = 121 atm, G_m = 1,261,168 gm mol, W = −5,848.1 gm/sec, and t = 4,489.5 seconds.

This is a reverse calculation of the second point in Table 5. Y/L again equals 425.414 and J/L = 1,035.0. From Eq. 16,

$$\ln r_{dD} = \frac{p_i^2 - p_w^2 - 1035.0}{425.414}$$

$$= \frac{3855.0 - 1035.0}{425.414} = 6.6288.$$

TABLE 7 — DETERMINATION OF p_w VALUES

Δ Rate	$p_i^2 - p_{ave}^2$	1/2(Y/L)	$\frac{263.878}{\Delta p_{ave}}$
1	124.6	69.870	900.68
2	76.2	42.752	147.418
3	74.2	41.636	150.787
4	204.8	114.862	547.46

(1) Gp	(2) $Gp(263.878)/\Delta p_{ave}$	(3) ln(2)	(4) 1/2(Y/L)ln(2)	$p_i^2 - p_w^2$
		Δ Rate 1		
464	417916	12.9431	904.33	1028.9
979	881766	13.6898	956.51	1081.1
1443	1299681	14.0776	983.60	1108.2
1932	1740114	14.3696	1004.00	1128.6
		Δ Rate 2		
315	464367	13.0485	557.85	634.0
599	883034	13.6916	585.34	661.5
899	1325288	14.0972	602.68	678.9
		Δ Rate 3		
277	417680	12.9425	538.87	613.1
569	857978	13.6624	568.85	643.0
		Δ Rate 4		
804	440158	12.9950	1492.63	1697.4

Data Point	Reported p_w (psia)	Δ Rates and Associated $p_i^2 - p_w^2$ Values 1	2	3	4	J/L	$p_i^2 - p_w^2$ Total	p_w (atm)	p_w (psi)
1	3087	1028.9	0	0	0	68.9	1097.8	210.125	3088.8
2	3059	1081.1	634.0	0	0	179.0	1894.1	108.221	3060.8
3	3035	1108.2	661.5	613.1	0	335.8	2718.6	206.232	3031.6
4	2942	1128.6	678.9	643.0	1697.4	1022.1	5170.0	200.200	2942.9

Thus,

$$r_{dD} = e^{6.6288} = 756.5,$$

$$r_d = 15.25\ (756.5) = 11{,}536.63$$

and

$$r_d^2/10^6 = 133.0938.$$

From Eq. 5,

$$\Delta p_{ave} \cong 142.257\ \frac{G_m}{r_d^2}$$

$$= \frac{142.257\ (1261168)}{133093800} = 1.348 \text{ atm},$$

and

$$p_{ave} = 136 - 1.348 = 134.652 \text{ atm}.$$

From Eq. 17,

$$\ln C = \frac{p_{ave}^2 - p_w^2 - J/L}{Y/L} - \ln r_{dD}$$

$$= \frac{18131.0 - 14641.0 - 1035.0}{425.414} - 6.6288$$

$$= -.8580,$$

and

$$C = e^{-.8580} = .4240.$$

From Fig. 1,

$$r_{dD}/r_{eD} = .7565,$$

and

$$r_{eD} = r_{dD}/.7565 = 756.5/.7565 = 1{,}000.$$

Also,

$$r_e = r_{eD} r_w = 15.25\ (1000) = 15{,}250 \text{ cm} = 500 \text{ ft}.$$

***

An Approximate Method for Determining Areal Sweep Efficiency and Flow Capacity in Formations with Anisotropic Permeability

M. MORTADA
MEMBER AIME
G. W. NABOR
JUNIOR MEMBER AIME

SOCONY MOBIL OIL CO., INC.
DALLAS, TEX.

ABSTRACT

The effects of anisotropic or directional permeability on the areal sweep efficiency and the flow capacity are examined. The paper points out the importance of taking directional permeability into consideration in planning a flood. It analyzes the two-dimensional flow pattern associated with the skewed line drive for a unit mobility ratio. The direct and staggered line drives are treated as special cases of the skewed line drive.

Analytical expressions are developed for the areal sweep efficiency at breakthrough and the flow capacity. They are related to the spacing between like wells, the distance between a row of injectors and the nearest row of producers, and the degree of skewness of the line drive. The latter quantity is defined such that it is equal to zero for the direct line drive and equals one-half for the staggered line drive. The areal sweep efficiency and the flow capacity depend also on the orientation of the flood pattern with respect to the principal axis of anisotropy.

The paper provides a simple method for determining the areal sweep efficiency and the flow capacity for a formation in which the permeability in the bedding plane is anisotropic.

INTRODUCTION

Directional or anisotropic permeability is manifested by the ability of the formation to conduct fluids more readily along certain preferred directions. This situation occurs in many producing formations[1-4] and is usually attributed to depositional features in which the sand grains are oriented in a preferred direction. In some cases it results from the formation of a major and a minor fracture system.[4]

Directional permeability should be taken into account in many phases of the production and exploration activities. Recognizing its existence in the formation of interest and planning accordingly can lead to increased recovery and substantial savings. For instance, the areal sweep efficiency in a water flood depends to a great extent on the orientation of the flood pattern with respect to the principal axis of permeability. Anisotropic[5] permeability is specified by the directions of its three principal axes and the permeability along each axis. The principal axes of permeability are mutually perpendicular.

This paper deals with the areal sweep efficiency at breakthrough and the flow capacity for formations with anisotropic permeability. The flood pattern considered consists of alternate rows of injecting and producing wells. The rows of wells are parallel and form a developed, skewed line drive which is illustrated in Fig. 1. The staggered and direct line drives are treated as special cases of the skewed line drive.

PRELIMINARY CONSIDERATIONS

The formations considered in this paper are assumed to be of uniform thickness and porosity. The permeability is uniformly anisotropic, with each principal axis of permeability maintaining

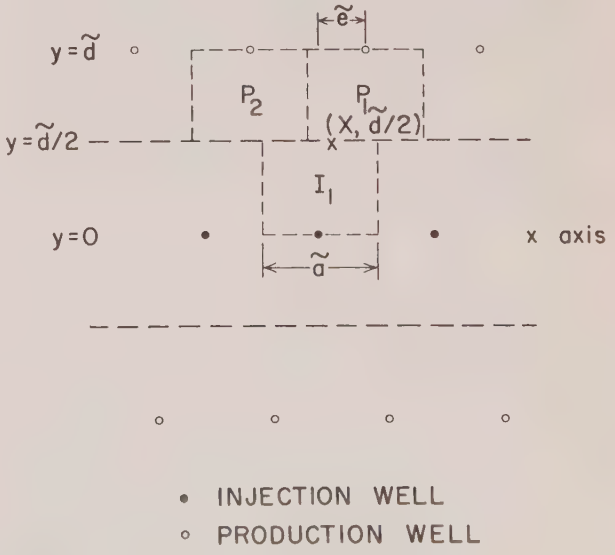

FIG. 1 – THE DEVELOPED SKEWED LINE DRIVE.

Original manuscript received in Society of Petroleum Engineers office Feb. 3, 1961. Revised manuscript received Oct. 12, 1961.

[1]References given at end of paper.

the same direction and magnitude at every point in the formation. Two of the principal axes lie in the bedding plane, and the third axis is perpendicular to it. Thus, neglecting gravity forces reduces the study to a two-dimensional flow problem. It is further assumed that the mobility of the fluids is the same ahead and behind the front.

TWO-DIMENSIONAL FLOW EQUATIONS

The flow velocities in anisotropic permeability systems can be described by Eqs. 1. In these equations the major and minor axes of permeability (η, ζ) serve as the co-ordinate system.

$$v_\eta = -\frac{k_\eta}{\mu\phi}\frac{\delta p}{\delta \eta} = -\frac{\delta \Psi}{\delta \zeta}$$

$$v_\zeta = -\frac{k_\zeta}{\mu\phi}\frac{\delta p}{\delta \zeta} = \frac{\delta \Psi}{\delta \eta} \quad \ldots\ldots\ldots (1)$$

k_η and k_ζ are the permeabilities along the major and minor axes of permeability, v_η and v_ζ are the microscopic flow velocities along these axes, p is the pressure distribution, Ψ is the stream function, ϕ is the porosity and μ is the fluid viscosity. The flow velocities in another co-ordinate system (l,m) which forms an angle θ with (η,ζ) are given by Eqs. 2.

$$v_l = -\frac{k_\eta \cos^2\theta + k_\zeta \sin^2\theta}{\mu\phi}\frac{\delta p}{\delta l} - \frac{k_\zeta \sin\theta\cos\theta - k_\eta \sin\theta\cos\theta}{\mu\phi}\frac{\delta p}{\delta m}$$

$$v_m = -\frac{k_\eta \sin^2\theta + k_\zeta \cos^2\theta}{\mu\phi}\frac{\delta p}{\delta m} - \frac{k_\zeta \sin\theta\cos\theta - k_\eta \sin\theta\cos\theta}{\mu\phi}\frac{\delta p}{\delta l} \quad \ldots (2)$$

Eqs. 2 show that isotropic permeability is a special case in which the permeabilities along the principal axes are equal. For isotropic permeability, Eqs. 2 become $v_l = -\frac{k}{\mu\phi}\frac{\partial p}{\partial l}$, $v_m = -\frac{k}{\mu\phi}\frac{\partial p}{\partial m}$, regardless of the choice of the co-ordinate system.

The flow of incompressible liquids in a formation that is uniformly anisotropic is described by the differential equations:

$$\frac{k_\eta}{\mu\phi}\frac{\delta^2 p}{\delta \eta^2} + \frac{k_\zeta}{\mu\phi}\frac{\delta^2 p}{\delta \zeta^2} = 0$$

$$\frac{k_\eta}{\mu\phi}\frac{\delta^2 \Psi}{\delta \eta^2} + \frac{k_\zeta}{\mu\phi}\frac{\delta^2 \Psi}{\delta \zeta^2} = 0$$

$$\frac{\delta F}{\delta t} - \frac{k_\eta}{\mu\phi}\frac{\delta p}{\delta \eta}\frac{\delta F}{\delta \eta} - \frac{k_\zeta}{\mu\phi}\frac{\delta p}{\delta \zeta}\frac{\delta F}{\delta \zeta} = 0 \quad \ldots\ldots (3)$$

$F(\eta,\zeta,t) = 0$ gives the position of the flood front as a function of time.[6]

For the explicit solution of these differential equations, it is necessary to specify the pressure or the influx (stream function) on the boundary of the region of interest, the initial position of the flood front and the location of injection and production wells. The solution of these equations is simplified by introducing the transformation[6] $\tilde{x} = \eta/\sqrt{k_\eta}$, $\tilde{y} = \zeta/\sqrt{k_\zeta}$ and applying it to the differential equations and the boundary conditions. The resulting equations,

$$v_{\tilde{x}} = -\frac{\sqrt{k_\eta k_\zeta}}{\mu\phi}\frac{\delta p}{\delta \tilde{x}} = -\frac{\delta \Psi}{\delta \tilde{y}}$$

$$v_{\tilde{y}} = -\frac{\sqrt{k_\eta k_\zeta}}{\mu\phi}\frac{\delta p}{\delta \tilde{y}} = \frac{\delta \Psi}{\delta \tilde{x}}$$

$$\frac{\delta^2 p}{\delta \tilde{x}^2} + \frac{\delta^2 p}{\delta \tilde{y}^2} = 0$$

$$\frac{\delta^2 \Psi}{\delta \tilde{x}^2} + \frac{\delta^2 \Psi}{\delta \tilde{y}^2} = 0$$

$$\frac{\delta F}{\delta t} - \frac{1}{\mu\phi}\frac{\delta p}{\delta \tilde{x}}\frac{\delta F}{\delta \tilde{x}} - \frac{1}{\mu\phi}\frac{\delta p}{\delta \tilde{y}}\frac{\delta F}{\delta \tilde{y}} = 0 \quad \ldots\ldots (4)$$

describe the pressure distribution, the stream function and the flood advance in an isotropic system with permeability equal to $\sqrt{k_\eta\, k_\zeta}$. The porosity and fluid viscosity are equal to those in the original system, and the geometry is related to the geometry of the original system by the transformation cited previously. The solution of Eqs. 4, accomplished either by analytical methods or by using a potentiometric analyzer, yields the areal sweep efficiency and the flow capacity for the new isotropic and the original anisotropic systems. This results because the areal sweep efficiency and the flow capacity are preserved in the transformation.

ANALYSIS OF THE FLOOD PATTERN — AND RESULTS

In analyzing the flood pattern it is useful to examine the pressure distribution due to an infinite array of point sources of strength q, with spacing a and forming an angle θ with the major axis of permeability. The infinite array upon transformation remains a straight line, but with spacing

$$\tilde{a} = a\sqrt{\frac{\cos^2\theta}{k_\eta} + \frac{\sin^2\theta}{k_\zeta}}$$

and forms an angle

$$\tilde{\theta} = \tan^{-1}\left(\sqrt{k_\eta/k_\zeta}\,\tan\theta\right)$$

with the x axis. The pressure distribution in the new system is given by[6]

$$p_{(\tilde{x},\tilde{y})} = \frac{\mu q}{4\pi h\sqrt{k_\eta\, k_\zeta}} \cdot \ln\left\{\begin{matrix}\cosh\left(\frac{2\pi}{\tilde{a}}\right)(\tilde{y}\ \cos\tilde{\theta}-\tilde{x}\ \sin\tilde{\theta}) \\ -\cos\left(\frac{2\pi}{\tilde{a}}\right)(\tilde{x}\ \cos\tilde{\theta}+\tilde{y}\ \sin\tilde{\theta})\end{matrix}\right\} \quad . \quad . \quad (5)$$

Eq. 5 points out two important features. First, at a distance from the array $\geq 0.6\tilde{a}$, the isobars can be approximated by straight lines parallel to the array. This is because the cosine term on the right-hand side of Eq. 5 becomes negligible with respect to the hyberbolic cosine. Also, at a distance $\geq 0.6\tilde{a}$, the pressure gradient becomes normal to the array and approximately equals

$$\left(\mu q/2\tilde{a}h\sqrt{k_\eta\, k_\zeta}\right) .$$

Second, the isobars are essentially concentric circles inside the circular regions with center at the point sources and radius $\leq 0.05\tilde{a}$.

AREAL SWEEP EFFICIENCY

To complete the flood pattern, let d be the distance in the original anisotropic system between one array of injectors and the closest array of producers. The corresponding distance in the transformed system is

$$\tilde{d} = d\Big/\sqrt{k_\zeta \cos^2\theta + k_\eta \sin^2\theta}$$

and

$$\left(\tilde{d}/\tilde{a}\right) = \left(d/a\right)\left[\sqrt{k_\eta\, k_\zeta}\Big/\left(k_\zeta \cos^2\theta + k_\eta \sin^2\theta\right)\right] .$$

For the same spacing (d/a) in the anisotropic system, $(\tilde{d}/\tilde{a})$ increases as θ decreases and reaches a maximum of

$$\left(\tilde{d}/\tilde{a}\right) = \left(d/a\right)\sqrt{k_\eta/k_\zeta}$$

at $\theta = 0$. Therefore, it usually is advantageous to arrange the arrays of like wells parallel to the major permeability axis. This arrangement results in maximum $(\tilde{d}/\tilde{a})$ and, hence, in larger areal sweep efficiency. In the remainder of this paper, it will be assumed that one array of wells in the transformed system either falls on the $\tilde{x}$ axis or that the coordinates in the transformed system have been rotated on angle $\tilde{\theta}$ to accomplish this purpose. This assumption causes no loss of generality; it only simplifies the analysis. Let x and y refer to the co-ordinate system after rotation. The pressure distribution, in the infinite strip bounded by the lines $y = 0$ and $y = \tilde{d}/2$ in Fig. 1, is equal to that due to the x-axis array plus the contributions of each pair of arrays equidistant from the x-axis. For $(\tilde{d}/\tilde{a}) \geq 1.2$, the contribution of each of these pairs to the pressure distribution in the strip of interest is for all practical purposes independent of x. Thus,[6]

$$p_{(x,y)} \simeq \frac{q\mu}{4\pi h\sqrt{k_\eta\, k_\zeta}} \cdot \left\{\ln\left[\cosh\frac{2\pi y}{\tilde{a}} - \cos\frac{2\pi x}{\tilde{a}}\right] + \sum_1^\infty (-1)^m \ln\frac{4\left[\cosh\frac{2\pi(m\tilde{d}-y)}{\tilde{a}}\right]\left[\cosh\frac{2\pi(m\tilde{d}+y)}{\tilde{a}}\right]}{\epsilon^{\left(\frac{4\pi m\tilde{d}}{\tilde{a}}\right)}}\right\} . \quad (6)$$

Further, since $y \leq 0.5\ \tilde{d}$, Eq. 6 becomes

$$p_{(x,y)} \simeq \frac{q\mu}{4\pi h\sqrt{k_\eta\, k_\zeta}} \cdot \ln\left[\cosh\frac{2\pi y}{\tilde{a}} - \cos\frac{2\pi x}{\tilde{a}}\right] . \quad (7)$$

Similarly, the potential distribution in the infinite strip bounded by the lines $y = \tilde{d}/2$ and $y = \tilde{d}$ is given by

$$p_{(x,y)} \simeq \frac{q\mu}{4\pi h\sqrt{k_\eta\, k_\zeta}} \cdot \ln\left[\cosh\frac{2\pi(\tilde{d}-y)}{\tilde{a}} - \cos\frac{2\pi(x-\tilde{e})}{\tilde{a}}\right] \quad . \quad . \quad . \quad . \quad . \quad . \quad . \quad . \quad . \quad . \quad . \quad . \quad . \quad . \quad . \quad . \quad . \quad . \quad . \quad (8)$$

$(\tilde{e}/\tilde{a})$ is a measure of the skewness of the transformed flood pattern, and equals zero for the direct line drive and 0.5 for the staggered line drive. Note that $(\tilde{d}/\tilde{a}) \geq 1.2$ is not a severe restriction and is usually fulfilled for any pronounced degree of anisotropy $[(k_\eta/k_\zeta) > 5]$ when the rows of wells lie in the direction of the major axis of permeability.

Using the pressure equation given, the stream function and time of travel along a streamline may be found. From these, the areal sweep efficiency at breakthrough is found to be

$$E_b \simeq \frac{1}{(\pi/2)(\tilde{d}/\tilde{a})} \cdot \ln\left[\frac{\cosh(\pi/2)(\tilde{d}/\tilde{a})}{\cos(\pi/2)(\tilde{e}/\tilde{a})}\right] \quad . \quad . \quad . \quad (9)$$

Details of the analysis are derived in Appendices A and B. Eq. 9 provides a simple expression for evaluating the areal sweep efficiency provided $(\tilde{d}/\tilde{a}) \geq 1.2$. In the foregoing analysis the initial position of the front was assumed to be at the center of the well instead of an ellipse with major and minor axes of $r_w/\sqrt{k\,\zeta}$ and $r_w/\sqrt{k_\eta}$, respectively. This approximation can introduce some error in the areal sweep efficiency and is currently under study.

FLOW CAPACITY

In analyzing the flow capacity, the geometry and size of the sources and sinks must be taken into account. This is true because the pressure gradient in the neighborhood of the sources and sinks is very large; consequently, an appreciable part of the resistance to flow occurs in these regions. Therefore, a more detailed examination of the pressure distribution in the neighborhood of the transformed well is necessary.

The analysis is greatly simplified by noticing that: (1) the isobars are essentially concentric circles inside a circular region the center of which is the point source and the radius of which is .05 $\tilde{a}$; and (2) cylindrical sources or sinks are transformed into elliptical cylinders, and the isobars due to an elliptical source or sink at a distance larger than seven times the focal distance $\tilde{f}$ of the ellipse are circles for all practical purposes, provided the sources do not interfere with each other.

Hence, the isobars are circular in a portion of the transformed reservoir, provided $(7\tilde{f}) \leq (0.05\ \tilde{a})$. For normal well spacings and well radii, this criterion is usually satisfied. Choosing a radius $\tilde{r}_m$ such that $(7\tilde{f}) < \tilde{r}_m < (0.05\ \tilde{a})$ and using this radius as a fictitious boundary, the pressure drop is found through the main body of the reservoir to $\tilde{r}_m$, and from $\tilde{r}_m$ to the transformed source or sink. These pressure drops are added and the final flow capacity equation follows.

$$q = \frac{h/\mu\sqrt{k_\eta\, k_\zeta}\ (p_{iw}-p_{pw})}{\left(\frac{\tilde{d}}{2\tilde{a}}\right)+\left(\frac{1}{\pi}\right)\ln\left[\frac{\tilde{a}}{(r_w)_{eff}}\right]-\left(\frac{\ln 2\pi}{\pi}\right)} \quad \ldots\ldots (10)$$

where q is the rate of flow at reservoir conditions, and

$$(r_w)_{eff} = \left(\frac{r_w}{2}\right)\left(\frac{1}{\sqrt{k_\eta}}+\frac{1}{\sqrt{k_\zeta}}\right) \quad \ldots\ldots (11)$$

PRACTICAL EXAMPLES

Shown in Fig. 2 are three proposed patterns for water flooding a reservoir which exhibits a large degree of permeability anisotropy,

$$(k_\eta/k_\zeta) = 144\ .$$

In these three cases, the rows of wells were oriented along the major axis of permeability; i.e., the angle θ = zero. Hence,

$$(\tilde{d}/\tilde{a}) = (d/a)\sqrt{k_\eta/k_\zeta}$$

or

$$(\tilde{d}/\tilde{a}) = 12\,(d/a)\ ,$$

and

$$(\tilde{e}/\tilde{a}) = (e/a)\ .$$

The spacing ratios $(\tilde{d}/\tilde{a})$ for Patterns A, B and C are 4.8, 4.8 and 2.4, respectively, satisfying the $(\tilde{d}/\tilde{a}) \geq 1.2$ requirement. The patterns were evaluated using Eqs. 9 and 10 and, also, by studying the transformed system potentiometrically. The streamlines and flood fronts obtained from the potentiometric model were back-transformed to the original reservoir co-ordinate system. The maps obtained for Patterns A, B and C are given in Figs. 3, 4 and 5, respectively. The four fronts shown correspond to times of 0.25 t_b, 0.50 t_b, 0.75 t_b and 1.00 t_b, where t_b = initial breakthrough time. These fronts, plus the streamlines shown as dashed lines on the pattern, indicate the advantage gained by orienting the rows of wells along the major permeability axis. The injected fluid spreads out rapidly along the major permeability axis and, thereafter, advances quite uniformly toward the row of producers, with high areal sweep efficiency resulting.

The results obtained using Eqs. 9 and 10 are presented in Table 1. These results agreed with

TABLE 1 — RESULTS FOR FLOOD PATTERNS OF FIG. 2

	Pattern A	Pattern B	Pattern C
a, miles	$\sqrt{1.25}$	$\sqrt{1.25}$	$\sqrt{1.25}$
d, miles	$0.4\sqrt{1.25}$	$0.4\sqrt{1.25}$	$0.2\sqrt{1.25}$
e, miles	$0.3\sqrt{1.25}$	$0.2\sqrt{1.25}$	$0.4\sqrt{1.25}$
$(\tilde{d}/\tilde{a})$	4.8	4.8	2.4
$(\tilde{e}/\tilde{a})$	0.3	0.2	0.4
E_b, Calculated	0.922	0.915	0.872
E_b, Pot. Analyses	0.912	0.914	0.863
C	4.7741	4.7741	3.5741

$$q = 1.127\left(\frac{h\sqrt{k_\eta\, k_\zeta}}{\mu}\right)\left(\frac{p_{iw}-p_{pw}}{C-(1/\pi)\ln r_w}\right)$$

Quantity	Units
q	reservoir B/D
h	ft
k_η, k_ζ	darcies
p_{iw}, p_{pw}	psig
μ	cp
r_w	in.

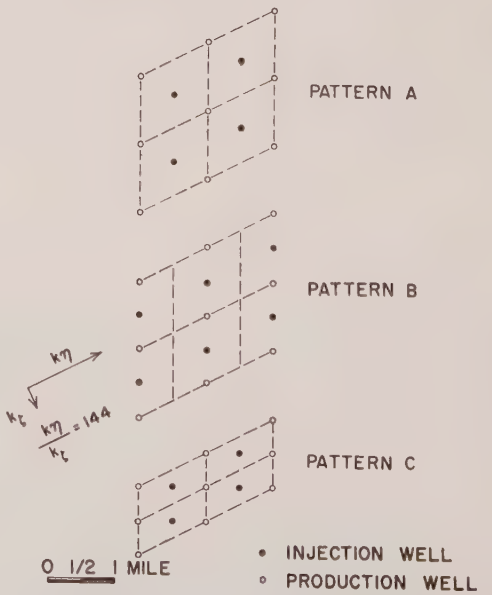

FIG. 2 — PROPOSED FLOODING PATTERNS.

the potentiometric results within 2 per cent for the flow capacity and within 1 per cent for the areal sweep efficiency. The flow-capacity equation presented in the table is a reduction of Eq. 10 to a form suitable for these particular patterns and to the use of engineering units.

The potentiometric model cannot be used to obtain the constant C appearing in the flow-capacity equation of Table 1 because it is not practical to use an electrode which is an exact analog of the transformed well. However, by using a circular electrode scaled to the radius $\tilde{r}_m$, mentioned previously, it is possible to compare measured potential drops with calculated values — using, for example, Eq. C-14 (Appendix C) modified appropriately to apply to the electrical model system.

COMPARISON WITH OTHER METHODS OF ANALYSIS

The direct and staggered line drives are special cases of the skewed line drive. Areal sweep efficiencies for these cases have been reported in the literature.[6,7] In Fig. 5, values computed from the analysis developed in this paper are compared with values given in Refs. 6 and 7. For a spacing ratio $(\tilde{d}/\tilde{a}) = 1.2$, the lower limit specified in this paper, values for the staggered line drive agree within 1 areal-sweep-efficiency per cent. The agreement for the direct line drive is even better, and both cases improve as $(\tilde{d}/\tilde{a})$ increases. Since these cases represent the extremes of skewness, the analytical method of this paper should be suitable for intermediate values.

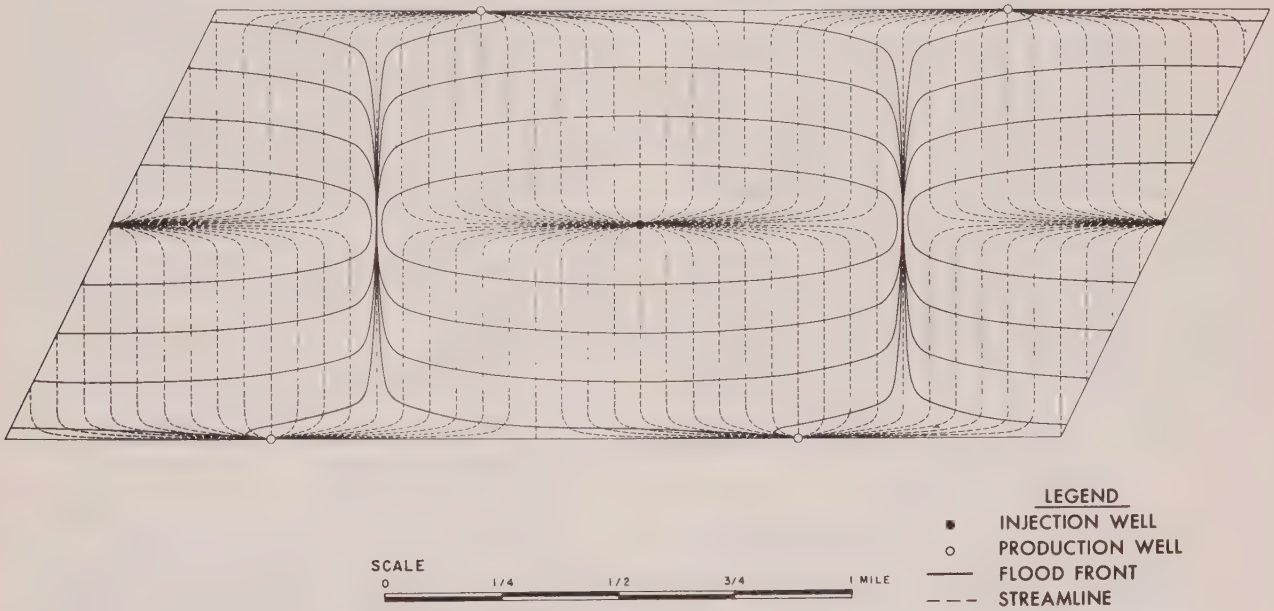

FIG. 3 — FLOOD-FRONT ADVANCE AND AREAL SWEEP EFFICIENCY FOR PATTERN A; CALCULATED E = 92.2 PER CENT, EXPERIMENTAL E = 91.2 PER CENT.

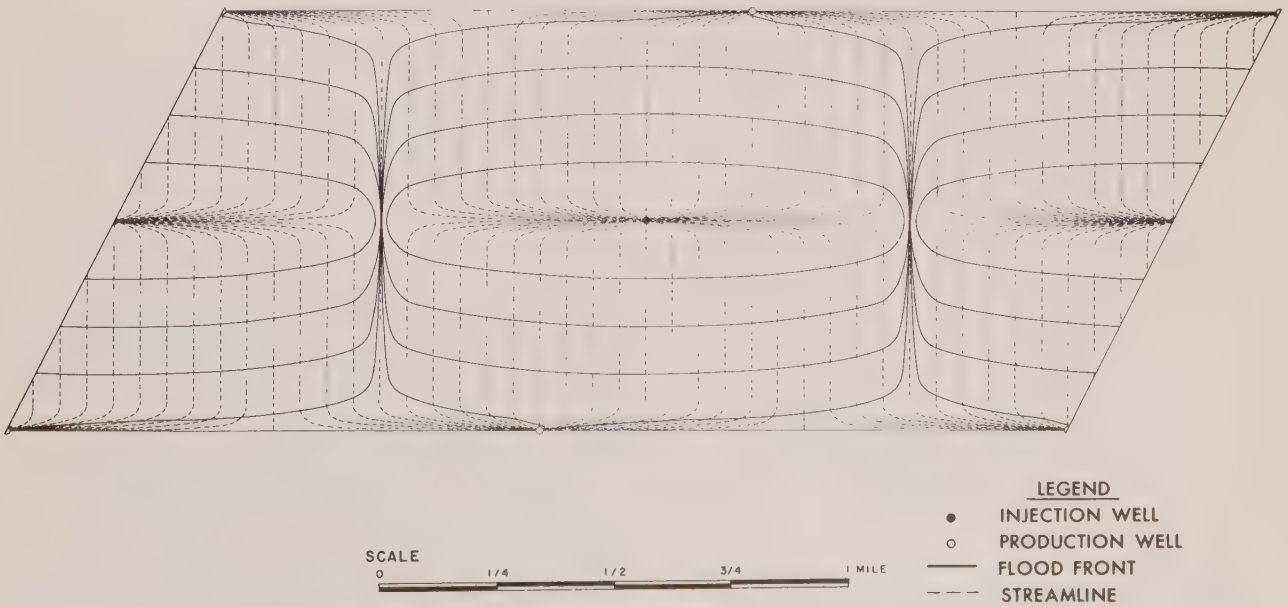

FIG. 4 — FLOOD-FRONT ADVANCE AND AREAL SWEEP EFFICIENCY FOR PATTERN B; CALCULATED E = 91.5 PER CENT, EXPERIMENTAL E = 91.4 PER CENT.

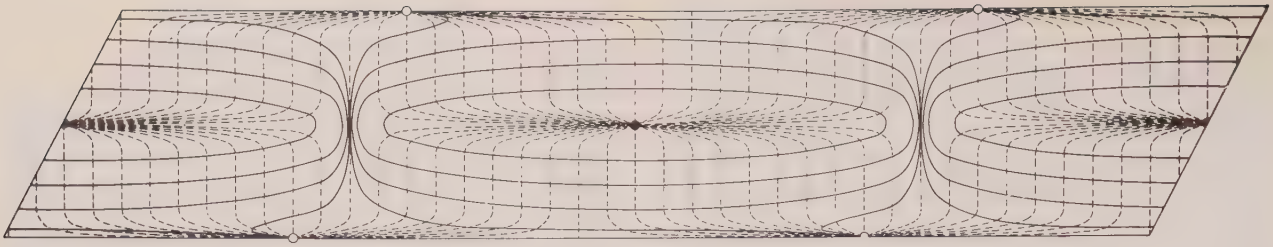

FIG. 5 – FLOOD-FRONT ADVANCE AND AREAL SWEEP EFFICIENCY FOR PATTERN C; CALCULATED E = 87.2 PER CENT, EXPERIMENTAL E = 86.3 PER CENT.

CONCLUSIONS

The following conclusions have been made.

1. This method of analysis provides a simple technique for evaluating the areal sweep efficiency at breakthrough and the flow capacity associated with flooding a formation with anisotropic permeability, using a developed, skewed line drive. The skewed line drive must be considered because a direct or staggered line drive may yield, upon transformation, a skewed line drive.

2. In anisotropic formations, rows of wells should be oriented along the major axis at permeability as nearly as possible to obtain larger sweep. In fields which are already developed, this can lead to a skewed line drive.

NOMENCLATURE

C = constant
E = areal sweep efficiency
I_1 = injection-well pattern element
K = ratio associated with major axis-minor axis permeabilities
P_1, P_2 = production-well pattern element
S = stream function cosine
X = stream function co-ordinate
Z = functional notation
a = well spacing within rows
b = major axis of ellipse
c = minor axis of ellipse
d = spacing between rows of wells
e = skewness of a pattern
f = focal distance of an ellipse
h = thickness
k = permeability
l = general distance co-ordinate
m = general distance co-ordinate
n = index
p = pressure
q = flow rate, reservoir conditions
r = radius
t = travel time
v = velocity
x = distance co-ordinate (transformed system)
y = distance co-ordinate (transformed system)
Ψ = stream function
η = distance co-ordinate (original system)
ζ = distance co-ordinate (original system)
θ = angle
μ = viscosity
ϕ = porosity

SUBSCRIPTS

b = breakthrough
iw = injection well
m = index
pw = production well
s = streamline index
w = well
x, y = x, y co-ordinate system
η, ζ = η, ζ co-ordinate system; axes oriented along major and minor axes of permeability, respectively

SUPERSCRIPTS

~ = transformed co-ordinate system *

*Note: (η, ζ) transforms to $(\tilde{x}, \tilde{y})$; $(\tilde{x}, \tilde{y})$ rotates to (x, y). Quantities unchanged upon rotation from $(\tilde{x}, \tilde{y})$ to (x, y) continue to carry superscript ~.

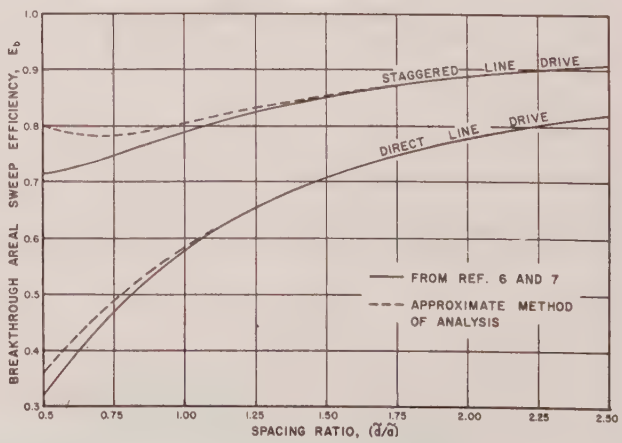

FIG. 6 – AREAL-SWEEP-EFFICIENCY COMPARISONS.

ACKNOWLEDGMENT

The authors express their appreciation to the management of Socony Mobil Oil Co., Inc., for permission to publish this paper. Thanks also are due F. R. Scauzillo and C. E. Rahn, who performed the potentiometric analyses.

REFERENCES

1. Johnson, W. E., *et al:* "Directional Permeability Measurements and Their Significance", *Prod. Monthly* (Nov., 1948) Vol. 13, 17.
2. Griffiths, J. C.: "Directional Permeability and Dimensional Orientation in Bradford Sand", *Prod. Monthly* (June, 1950) Vol. 14, 26.
3. Johnson, W. E., *et al:* "Directional Permeability Measurements on Oil Sandstones From Various States", *Prod. Monthly* (Feb., 1951) Vol. 15, 11.
4. Barfield, E. C., Jordan, J. K. and Moore, W. D.: "An Analysis of Large-Scale Flooding in the Fractured Spraberry Trend Area Reservoir", *Jour. Pet. Tech.* (April, 1959) Vol. XI, No. 4, 15.
5. Scheidegger, A. E.: *The Physics of Flow Through Porous Media*, The Macmillan Co., N. Y. (1957).
6. Muskat, M.: *The Flow of Homogeneous Fluids Through Porous Media*, J. E. Edwards, Inc., N. Y. (1946).
7. Prats, M.: "The Breakthrough Sweep Efficiency of the Staggered Line Drive", *Trans.*, AIME (1956) Vol. 207, 361.

APPENDIX A

THE POTENTIAL, STREAM-FUNCTION AND TRAVEL-TIME EQUATIONS

The equation presented in the main body of the the paper for the pressure distribution in the strip of reservoir $-\infty < x < +\infty$, $-(\tilde{d}/2) \leq y \leq (\tilde{d}/2)$ is

$$p = \frac{q\mu}{4\pi h\tilde{k}} \cdot \ln\left[\cosh\left(\frac{2\pi y}{\tilde{a}}\right) - \cos\left(\frac{2\pi x}{\tilde{a}}\right)\right] \quad \text{(A-1)}$$

where

$$\tilde{k} = \sqrt{k_\eta k_\zeta} \quad \text{(A-2)}$$

and q is flow rate at reservoir conditions (negative for injection).

The stream function is given by

$$\Psi = -\left(\frac{q}{4\pi h}\right) \cdot \arccos\left[\frac{\cosh\left(\frac{2\pi y}{\tilde{a}}\right)\cos\left(\frac{2\pi x}{\tilde{a}}\right) - 1}{\cosh\left(\frac{2\pi y}{\tilde{a}}\right) - \cos\left(\frac{2\pi x}{\tilde{a}}\right)}\right] \quad \text{(A-3)}$$

Letting

$$S = \cos\left(\frac{4\pi h\Psi}{-q}\right), \quad \text{(A-4)}$$

it follows immediately that

$$S = \frac{\cos\left(\frac{2\pi x}{\tilde{a}}\right) - \left[1/\cosh\left(\frac{2\pi y}{\tilde{a}}\right)\right]}{1 - \left[\cos\left(\frac{2\pi x}{\tilde{a}}\right)/\cosh\left(\frac{2\pi y}{\tilde{a}}\right)\right]} \quad \text{(A-5)}$$

The time of travel* along a streamline s from the point $(x, y) = (0,0)$ to the point x, y is given by

$$\tilde{t}_s = \int_{0,0}^{x,y} \frac{ds}{\left(\sqrt{v_x^2 + v_y^2}\right)_s} \quad \text{(A-6a)}$$

$$\tilde{t}_s = \int_0^x \frac{dx}{(v_x)_s}, \quad v_x \neq 0 \quad \text{(A-6b)}$$

$$\tilde{t}_s = \int_0^y \frac{dy}{(v_y)_s}, \quad v_y \neq 0 \quad \text{(A-6c)}$$

where the velocity component v_x or v_y is to be evaluated along s.

$$v_x = -\frac{\tilde{k}}{\mu\phi}\frac{\delta p}{\delta x} \quad \text{(A-7a)}$$

$$v_x = \left(\frac{q}{4\pi h\phi}\right)\left(\frac{2\pi}{\tilde{a}}\right)\left[\frac{-\sin\left(\frac{2\pi x}{\tilde{a}}\right)}{\cosh\left(\frac{2\pi y}{\tilde{a}}\right) - \cos\left(\frac{2\pi x}{\tilde{a}}\right)}\right] \quad \text{(A-7b)}$$

To evaluate v_x along a particular streamline s, Eq. A-5 may be used to give

$$\cosh\left(\frac{2\pi y}{\tilde{a}}\right) - \cos\left(\frac{2\pi x}{\tilde{a}}\right) = \frac{\sin^2\left(\frac{2\pi x}{\tilde{a}}\right)}{\cos\left(\frac{2\pi x}{\tilde{a}}\right) - S} \quad \text{(A-8)}$$

Substituting in Eqs. A-7b and A-6b gives

$$\tilde{t}_s = \frac{(\tilde{a}/2\pi)}{-(q/4\pi h\phi)} \cdot \int_0^x \frac{\sin\left(\frac{2\pi x}{\tilde{a}}\right)}{\cos\left(\frac{2\pi x}{\tilde{a}}\right) - S}\, dx \quad \text{(A-9)}$$

*The variable transformations used make x, y and $\tilde{a}$ dimensionless. Hence, formally v_x and v_y have the dimensions (L^2/t), and t has dimensions (t/L^2). This creates no problem in the analysis; the conversion to proper units will be shown later.

$$\tilde{t}_s = -\left(\frac{\phi\tilde{a}^2 h}{\pi q}\right)\cdot \ln\left[\frac{1-S}{\cos\left(\frac{2\pi x}{\tilde{a}}\right)-S}\right] \quad \ldots \text{(A-10a)}$$

Similar treatment of Eq. A-6c results in

$$\tilde{t}_s = -\left(\frac{\phi\tilde{a}^2 h}{\pi q}\right)\cdot \ln\left[\frac{\cosh\left(\frac{2\pi y}{\tilde{a}}\right)+S}{1+S}\right] \quad \ldots \text{(A-10b)}$$

These may also be further manipulated to give

$$\tilde{t}_s = -\left(\frac{\phi\tilde{a}^2 h}{\pi q}\right)\cdot \ln\left[\frac{\cosh\left(\frac{2\pi y}{\tilde{a}}\right)+1}{\cos\left(\frac{2\pi x}{\tilde{a}}\right)+1}\right] \quad \ldots \text{(A-10c)}$$

$$\tilde{t}_s = -\left(\frac{2\phi\tilde{a}^2 h}{\pi q}\right)\cdot \ln\left[\frac{\cosh\left(\frac{\pi y}{\tilde{a}}\right)}{\cos\left(\frac{\pi x}{\tilde{a}}\right)}\right] \quad \ldots \text{(A-10d)}$$

The negative sign preceding the equations of Eq. A-10 is proper when q is an injection rate, i.e., when q has a negative value. If the derivation has been carried out for a row of production wells, the direction of integration would have been from (x, y) toward $(0, 0)$, with a positive sign preceding the final Eq. A-10.

It should be noted that the equations are appropriate only in the region

$$|x| \le (\tilde{a}/2), |y| \le (\tilde{d}/\tilde{2}).$$

APPENDIX B

THE AREAL-SWEEP-EFFICIENCY EQUATION

The generalized line drive is characterized by three distance parameters: $\tilde{a}$, the spacing within rows between like wells; $\tilde{d}$, the spacing between rows of unlike wells; and $\tilde{e}$, the displacement or skewness in the x direction of unlike wells. Since the choice of positive x direction is arbitrary, $\tilde{e}$ may always be taken as positive, ranging from zero for the direct line drive to a maximum value $(\tilde{a}/2)$ for the staggered line drive.

The breakthrough time for the streamline which passes through the point $(X, \tilde{d}/2)$ will be the sum of times in Regions I_1 and P_1 (see Fig. 1). Eq. A-10 may be used to find the time in each region, providing consideration is given in Region P_1 to (1) the displacement $\tilde{e}$, and (2) the change in sign of the rate q.

Using the absolute value of q,

$$(\tilde{t}_x)_{I_1} = \left(\frac{2\phi\tilde{a}^2 h}{\pi q}\right)\cdot \ln\left[\frac{\cosh\left(\frac{\pi\tilde{d}}{2\tilde{a}}\right)}{\cos\left(\frac{\pi X}{\tilde{a}}\right)}\right] \quad \ldots \text{(B-1a)}$$

$$(\tilde{t}_x)_{P_1} = \left(\frac{2\phi\tilde{a}^2 h}{\pi q}\right)\cdot \ln\left[\frac{\cosh\left(\frac{\pi\tilde{d}}{2\tilde{a}}\right)}{\cos\left(\frac{\pi(X-\tilde{e})}{\tilde{a}}\right)}\right] \quad \ldots \text{(B-1b)}$$

$$\tilde{t}_x = (\tilde{t}_x)_{I_1} + (\tilde{t}_x)_{P_1} \quad \ldots \text{(B-2)}$$

$$\tilde{t}_x = \left(\frac{2\phi\tilde{a}^2 h}{\pi q}\right)\cdot \ln\left[\frac{\cosh^2\left(\frac{\pi\tilde{d}}{2\tilde{a}}\right)}{\cos\left(\frac{\pi X}{\tilde{a}}\right)\cos\left(\frac{\pi(X-\tilde{e})}{\tilde{a}}\right)}\right] \quad \ldots \text{(B-3)}$$

To find the point $(X, \tilde{d}/2)$ which yields the initial or minimum breakthrough time, Eq. B-3 is differentiated with respect to X.

$$\frac{dt}{dX} = Z(X)\sin\left(\frac{\pi(2X-\tilde{e})}{\tilde{a}}\right) \quad \ldots \text{(B-4)}$$

where $Z(X)$ is positive and finite for

$$[\tilde{e}-(\tilde{a}/2)] < X < (\tilde{a}/2),$$

the range of X common to Regions I_1 and P_1. If the derivative is set equal to zero,

$$\frac{\pi(2X-\tilde{e})}{\tilde{a}} = 0, \pm\pi, \text{ etc.} \quad \ldots \text{(B-5a)}$$

$$X = \left(\frac{\tilde{e}}{2}\right), \left(\frac{\tilde{e}+\tilde{a}}{2}\right), \left(\frac{\tilde{e}-\tilde{a}}{2}\right), \text{ etc.} \quad \ldots \text{(B-5b)}$$

The only value falling in the X range common to Regions I_1 and P_1 is

$$X = \left(\frac{\tilde{e}}{2}\right) \quad \ldots \text{(B-5c)}$$

By differentiating Eq. B-4 a second time, it can be shown that $X = (\tilde{e}/2)$ gives a minimum time of travel between the injector and producer.

A similar treatment of the travel-time equation for streamlines lying in Regions I_1 and P_2 will show a second minimum at $X = (\tilde{e} - \tilde{a})/2$. Travel time, however, is longer for this second minimum; thus, the actual minimum travel time occurs along the streamline passing through the point $(x, y) = (\tilde{e}/2, \tilde{d}/2)$. This is the time of initial breakthrough. In effect, each injection well displaces fluid toward two different production wells and has a different time of breakthrough to each producer. When $\tilde{e} = (\tilde{a}/2)$, the special case of the staggered line drive holds, and the times of breakthrough to the two producers are equal.

Substituting Eq. B-5c in Eq. B-3 and using the even nature of the cosine function, the time of

initial breakthrough is given by

$$\tilde{t}_b = \left(\frac{4\phi\tilde{a}^2 h}{\pi q}\right) \cdot \ln\left[\frac{\cosh\ (\pi/2)(\tilde{d}/\tilde{a})}{\cos\ (\pi/2)(\tilde{e}/\tilde{a})}\right] \quad . \quad . \quad (B\text{-}6)$$

The areal sweep efficiency is given by

$$E_b = \frac{q\tilde{t}_b}{(2\tilde{d}\tilde{a})h\phi} \quad . \quad . \quad . \quad . \quad . \quad . \quad . \quad . \quad . \quad . \quad . \quad (B\text{-}7a)$$

$$E_b = \frac{1}{(\pi/2)(\tilde{d}/\tilde{a})} \cdot \ln\left[\frac{\cosh\ (\pi/2)(\tilde{d}/\tilde{a})}{\cos\ (\pi/2)(\tilde{e}/\tilde{a})}\right] . \quad . \quad (B\text{-}7b)$$

To complete the working equations, introduce

$$K = \sqrt{k_\eta/k_\zeta} \quad . \quad . \quad . \quad . \quad . \quad . \quad . \quad . \quad . \quad . \quad . \quad (B\text{-}8)$$

Then,

$$\left(\frac{\tilde{d}}{\tilde{a}}\right) = \left(\frac{d}{a}\right)\left[\frac{K}{(K^2-1)\sin^2\theta+1}\right] . \quad . \quad . \quad . \quad . \quad . \quad (B\text{-}9)$$

$$\left(\frac{\tilde{e}}{\tilde{a}}\right)' = \left(\frac{e}{a}\right) + \left(\frac{d}{a}\right)\left[\frac{(K^2-1)\tan\theta}{(K\tan\theta)^2+1}\right] . \quad . \quad . \quad . \quad (B\text{-}10)$$

$(e/a)'$ is not necessarily within the range of 0 to 0.5. To find $(\tilde{e}/\tilde{a})$, apply the following where n is an integer. If

$$n \le (\tilde{e}/\tilde{a})' \le (n + 0.5),$$

then

$$(\tilde{e}/\tilde{a}) = (\tilde{e}/\tilde{a})' - n \quad . \quad . \quad . \quad . \quad . \quad . \quad . \quad . \quad . \quad . \quad (B\text{-}11a)$$

If

$$(n-0.5) \le (\tilde{e}/\tilde{a})' \le n,$$

then

$$(\tilde{e}/\tilde{a}) = n - (\tilde{e}/\tilde{a})' \quad . \quad . \quad . \quad . \quad . \quad . \quad . \quad . \quad . \quad . \quad (B\text{-}11b)$$

Breakthrough time in the original reservoir system will be related to $\tilde{t}_b$ by

$$t_b = \tilde{k}\tilde{t}_b \quad . \quad . \quad . \quad . \quad . \quad . \quad . \quad . \quad . \quad . \quad . \quad . \quad . \quad (B\text{-}12a)$$

which may also be written as

$$t_b = \left(\frac{4\phi a^2 h}{\pi q}\right)\left[\frac{(K^2-1)\sin^2\theta+1}{K}\right] \cdot \ln\left[\frac{\cosh\ (\pi/2)(\tilde{d}/\tilde{a})}{\cos\ (\pi/2)(\tilde{e}/\tilde{a})}\right] . \quad . \quad . \quad . \quad . \quad . \quad (B\text{-}12b)$$

Areal sweep efficiency will be unchanged from that found for the transformed system.

APPENDIX C

THE FLOW-CAPACITY EQUATION

The flow-capacity equation is developed by considering pressure drops in three regions: (1) from the transformed-injector wellbore surface (an ellipse) to the fictitious circular surface at $\tilde{r}_m$, (2) from this surface through the main body of the transformed reservoir to the isobaric surface located midway between the row of injectors and the row of producers, and (3) from this surface to the transformed production well (also an ellipse). The term $\tilde{r}_m$, introduced only as an aid in the formal treatment, disappears in the final form of the equation.

THE WELLBORE REGION

A well centered at the point (0,0) in the original (η, ζ) system of co-ordinates may be described by the equation

$$\eta_w^2 + \zeta_w^2 = r_w^2 \quad . \quad . \quad . \quad . \quad . \quad . \quad . \quad . \quad . \quad . \quad . \quad . \quad (C\text{-}1)$$

In the $\tilde{x}$, $\tilde{y}$ co-ordinate system,

$$\tilde{x}_w^2 = \eta_w^2/k_\eta \quad . \quad . \quad . \quad . \quad . \quad . \quad . \quad . \quad . \quad . \quad . \quad . \quad (C\text{-}2a)$$

$$\tilde{y}_w^2 = \zeta_w^2/k_\zeta \quad . \quad . \quad . \quad . \quad . \quad . \quad . \quad . \quad . \quad . \quad . \quad . \quad (C\text{-}2b)$$

Substituting, the equation describing the transformed well is obtained.

$$\frac{\tilde{x}_w^2}{(r_w/\sqrt{k_\eta})^2} + \frac{\tilde{y}_w^2}{(r_w/\sqrt{k_\zeta})^2} = 1 \quad . \quad . \quad . \quad . \quad . \quad (C\text{-}3)$$

This is the equation for an ellipse having semi-major and semi-minor axes $\tilde{b}_w$ and $\tilde{c}_w$ given by

$$\tilde{b}_w = r_w/\sqrt{k_\zeta} \quad . \quad . \quad . \quad . \quad . \quad . \quad . \quad . \quad . \quad . \quad . \quad . \quad (C\text{-}4a)$$

$$\tilde{c}_w = r_w/\sqrt{k_\eta} \quad . \quad . \quad . \quad . \quad . \quad . \quad . \quad . \quad . \quad . \quad . \quad . \quad (C\text{-}4b)$$

The axes of the ellipse are oriented in the ζ and η directions.

The transformed system has an equivalent isotropic permeability $\tilde{k} = \sqrt{k_\eta\, k_\zeta}$. Pressure and flow equations are available for isotropic permeability systems in which an elliptical source or sink is located in an infinite reservoir. These may be applied in the immediate vicinity of the transformed well without serious error. Muskat[6] points out that the isobars for such a system are confocal ellipses. The focal distance is determined by

$$\tilde{f}^2 = \tilde{b}^2 - \tilde{c}^2 \quad . \quad . \quad . \quad . \quad . \quad . \quad . \quad . \quad . \quad . \quad . \quad . \quad (C\text{-}5a)$$

or, since one isobar must coincide with the transformed well surface,

$$\tilde{f}^2 = \tilde{b}_w^{\,2} - \tilde{c}_w^{\,2} \quad \ldots\ldots\ldots\ldots \quad (C\text{-}5b)$$

$$\tilde{f}^2 = r_w^2\left(\frac{1}{k_\zeta} - \frac{1}{k_\eta}\right) \quad \ldots\ldots\ldots \quad (C\text{-}5c)$$

As confocal ellipses successively further removed from the wellbore are considered, it is clear that $\tilde{b}$ and $\tilde{c}$ approach the same value because $\tilde{f}$ is fixed. Stated differently, the isobars become circular in form as distance from the wellbore increases. This is typical of the pressure distribution due to any localized source; at distances sufficiently removed from it, the particular geometric form of the source no longer influences the pressure distribution.

The flow equation for the system described is

$$q = \frac{2\pi h\tilde{k}(p_m - p_w)}{\mu \ln\left(\frac{\tilde{b}_m + \tilde{c}_m}{\tilde{b}_w + \tilde{c}_w}\right)} \quad \ldots\ldots\ldots \quad (C\text{-}6)$$

where m refers to any general isobar (an ellipse) outside the transformed wellbore. At sufficiently great distances,

$$\tilde{b}_m \simeq \tilde{r}_m \simeq \tilde{c}_m \quad \ldots\ldots\ldots\ldots \quad (C\text{-}7)$$

Eqs. C-4, C-6 and C-7 may be combined to give

$$q = \frac{2\pi h\tilde{k}(p_{\tilde{r}_m} - p_w)}{\mu \ln\left[\tilde{r}_m/(r_w)_{eff}\right]} \quad \ldots\ldots\ldots \quad (C\text{-}8)$$

where $(r_w)_{eff}$ is an effective well radius given by

$$(r_w)_{eff} = \left(\frac{r_w}{2}\right)\left(\frac{1}{\sqrt{k_\zeta}} + \frac{1}{\sqrt{k_\eta}}\right) \quad \ldots \quad (C\text{-}9)$$

THE MAIN RESERVOIR REGION

It previously has been shown that, essentially, an isobar exists along the line $y = (\tilde{d}/2)$, for $(\tilde{d}/\tilde{a}) \geq 1.2$; i.e., the pressure is independent of x. This pressure $p_{(\tilde{d}/2)}$ is obtained from Eq. A-1 by neglecting the cosine term

$$p_{(\tilde{d}/2)} = \left(\frac{q\mu}{4\pi h\tilde{k}}\right) \cdot \ln\left[\cosh\left(\frac{\pi\tilde{d}}{\tilde{a}}\right)\right] \quad \ldots\ldots \quad (C\text{-}10)$$

For $(\tilde{d}/\tilde{a}) \geq 1.2$, it follows that

$$\ln\left[\cosh\left(\frac{\pi\tilde{d}}{\tilde{a}}\right)\right] \simeq \left(\frac{\pi\tilde{d}}{\tilde{a}}\right) - \ln 2 \quad \ldots\ldots \quad (C\text{-}11)$$

so

$$p_{(\tilde{d}/2)} \simeq \frac{q\mu}{4\pi h\tilde{k}}\left[\left(\frac{\pi\tilde{d}}{\tilde{a}}\right) - \ln 2\right] \quad \ldots\ldots \quad (C\text{-}12)$$

For sufficiently small values of $\tilde{r}_m$, compared to $\tilde{a}$, the hyperbolic cosine and cosine terms appearing in Eq. A-1 may be expanded in series. Only the first term of the expansion is significant, so

$$p_{\tilde{r}_m} \simeq \left(\frac{q\mu}{4\pi h\tilde{k}}\right)\left[2\ln\left(\frac{2\pi\tilde{r}_m}{\tilde{a}}\right) - \ln 2\right] \quad \ldots \quad (C\text{-}13)$$

Thus,

$$(p_{(\tilde{d}/2)} - p_{\tilde{r}_m}) = \left(\frac{q\mu}{4\pi h\tilde{k}}\right) \cdot\left[\left(\frac{\pi\tilde{d}}{\tilde{a}}\right) - 2\ln\left(\frac{2\pi\tilde{r}_m}{\tilde{a}}\right)\right] \quad \ldots \quad (C\text{-}14)$$

THE FINAL FLOW-CAPACITY EQUATION

Eqs. C-8 and C-14 may be combined to eliminate $p_{\tilde{r}m}$ and $\tilde{r}_m$.

$$(p_{(\tilde{d}/2)} - p_w) = \left(\frac{q\mu}{4\pi h\tilde{k}}\right) \cdot\left\{\left(\frac{\pi\tilde{d}}{\tilde{a}}\right) + 2\left[\ln\left(\frac{\tilde{a}}{(r_w)_{eff}}\right) - \ln 2\pi\right]\right\} \quad \ldots\ldots\ldots\ldots \quad (C\text{-}15)$$

This is the pressure drop between $y = (\tilde{d}/2)$ and a production well, considering q to be positive. The total pressure drop between an injection well and production well will be twice this.

$$(p_{iw} - p_{pw}) = 2(p_{(\tilde{d}/2)} - p_{pw}) \quad \ldots\ldots \quad (C\text{-}16)$$

Using Eq. C-16,

$$q = \frac{(h\tilde{k}/\mu)(p_{iw} - p_{pw})}{\left(\frac{\tilde{d}/\tilde{a}}{2}\right) + \left(\frac{1}{\pi}\right)\ln\left(\frac{\tilde{a}}{(r_w)_{eff}}\right) - \left(\frac{\ln 2\pi}{\pi}\right)} \quad \ldots\ldots\ldots\ldots \quad (C\text{-}17)$$

It may be noted also that

$$\left(\frac{\tilde{a}}{(r_w)_{eff}}\right) = \left(\frac{a}{r_w}\right)\left(\frac{2}{1+K}\right)\sqrt{(K^2-1)\sin^2\theta + 1} \quad \ldots\ldots\ldots\ldots \quad (C\text{-}18)$$

***

Study of Gas Reservoirs Subject to Water Drive on Electronic Differential Analyzer

H. D. YOO

D. L. KATZ
M. R. TEK
MEMBERS AIME

U. OF MICHIGAN
ANN ARBOR, MICH.

ABSTRACT

The behavior of gas-storage reservoirs subject to water drive is investigated through analog simulation on an electronic differential analyzer. The simulation technique developed on an LM-10 computer permits the prediction of reservoir volume or pressure resulting from the movement of water in the surrounding aquifer.

The method developed on the analog computer consists of setting up an appropriate transfer-function circuit and feeding the arbitrary time-varying boundary conditions as an input signal. The input may be specified as gas reservoir pressure, pore volume or the water flux.

Several cases studied include an isolated gas reservoir on a limited aquifer, interference among three reservoirs adjacent to a common aquifer and the growth of gas-storage volume on an aquifer.

It is concluded that the method developed on an electronic differential analyzer provides an excellent technique to simulate and investigate the behavior of gas reservoirs subject to water drive. The agreement between the reservoir performance as predicted from the simulation technique and as measured from actual field data is found to be better than the range usually encountered in predicting water-drive behavior.

INTRODUCTION

It is generally known that some gas-storage reservoirs are located on top of blanket sands of large extent, saturated with brine called aquifers.

Because the volume of the body of water associated with aquifers is usually very large and water is compressible, the cyclic pressure variations encountered in normal storage service inevitably cause unsteady, compressible flow conditions in the adjacent aquifers.

The solution to radial diffusivity equation for a limited aquifer for constant terminal conditions has been known[1] since the early 1930's. The solution for the constant terminal conditions for an infinite aquifer was published in 1949.[2]

The problem of handling the unsteady flow of water through a porous medium with time-varying boundary conditions has been studied by many investigators through the use of graphical,[3] digital[4] computing techniques or on an R-C type of electrical analog called a reservoir analyzer.[5] The digital computer performs a series of arithmetic calculations to superimpose the solutions of constant terminal conditions, while the R-C type of analyzer permits the simulation of the continuous medium by means of "lumped-cell" electrical resistance and capacitance elements based on finite-difference approximations. The graphical method is based on the convolution integral solution of the partial differential equation.

The purpose of the present study was to simulate the behavior of an aquifer on a general-purpose, electronic differential analyzer to obtain the influx of water or the change in pressure at the reservoir continuously and quickly. The use of the electronic differential analyzer was based on well known solutions for the constant terminal conditions already available in the literature.[2,6-8]

THEORETICAL DEVELOPMENT

MODEL.

The gas reservoir *(R)* is described in relation to an aquifer in Fig. 1. The permeability and porosity of an aquifer sand, the viscosity of the brine, and the compressibility of the brine and the formation are assumed to be constant. It further is assumed that the blanket sand is not thick enough to give appreciable vertical pressure distribution. The model in consideration is circular with radial geometry. The aquifer radius can be of limited or infinite extent. The gas-water interface is assumed to be fully segregated, and the displacement of the gas by

Original manuscript received in Society of Petroleum Engineers office Aug. 15, 1960. Revised manuscript received Oct. 4, 1961. Paper presented at SPE Gas Technology Symposium, April 21-22, 1961, in Tyler, Tex.

[1]References given at end of paper.

water or water by gas is considered to be pistonlike.

DIFFERENTIAL EQUATION

For the model described, the flow of the brine through the porous medium can be described by the following differential equation.

$$\frac{\partial^2 P}{\partial r^2} + \frac{1}{r}\frac{\partial P}{\partial r} = \frac{c\phi\mu}{k}\frac{\partial P}{\partial \theta'} \quad \ldots\ldots\ldots (1)$$

or in dimensionless form,

$$\frac{\partial^2 P}{\partial r_D^2} + \frac{1}{r_D}\frac{\partial P}{\partial r_D} = \frac{\partial P}{\partial t_D} \quad \ldots\ldots\ldots (2)$$

where

$$t_D = \frac{k\theta'}{c\phi\mu r_g^2},$$

and

$$r_D = \frac{r}{r_g}.$$

BOUNDARY CONDITIONS

The two basic cases encountered in most reservoir-engineering studies are constant-terminal-pressure and constant-terminal-rate cases. If the pressure is specified at the reservoir boundary, the problem may be referred to as terminal-pressure case. On the other hand, if the rate is specified one would have the terminal-rate case. In gas storage, a variable-pressure case often applies; for this case, the pressure at the aquifer boundary is specified as a function of time.

For the pressure case, the mathematical statements of the boundary conditions are

$$P[1, t_D] = G[t_D],$$

$$P[\infty, t_D] = O,$$

$$P[r_D, O] = O.$$

With these boundary conditions, the Laplace transform of the solution to Eq. 2 is given in the following.

$$Q_{tD}[s] = g[s]\left\{\frac{s \cdot K_1[\sqrt{s}]}{s^{3/2} \cdot K_o[\sqrt{s}]}\right\}$$

$$= g[s]\left\{s \cdot f_1[s]\right\}. \quad \ldots\ldots\ldots (3)$$

where $Q_{tD}(s)$ is the Laplace transform of the cumulative water-flux function, and $g(s)$ is the Laplace transform of the pressure function $G(t_D)$. It can be shown that Eq. 3 may be presented in the following form

$$Q_{tD} = \int_o^{t_D}\left(\frac{\partial P}{\partial r_D}\right)_{r_D=1} dt_D = \int_o^{t_D}\frac{dG}{d\tau}\cdot Q'_{tD}[t_D - \tau]d\tau$$

$$\ldots\ldots\ldots (4)$$

where Q'_{tD} is the constant-pressure-case cumulative-flux function.

Eq. 3 can be rewritten to take the form

$$\frac{Q_{tD}[s]}{g[s]} = s \cdot f_1[s]. \quad \ldots\ldots\ldots (5)$$

Eq. 5 becomes a useful equation on an electronic differential analyzer and is called a simulation equation for terminal-pressure case. Once the $Q_{tD}(t_D)$ function is found, the cumulative water flux or the reservoir volume change from the initial reservoir pore volume can be calculated by the following equation.

$$\bar{W} = [2\pi r_g' h]\frac{k}{\mu}\int_o^{\theta}\left(\frac{\partial P}{\partial r}\right)_{r_g} d\theta$$

$$= 2\pi r_g'^2 h c' \phi Q_{tD}. \quad \ldots\ldots\ldots (6)$$

Instead of specifying the reservoir pressure, one may specify the rate or flux at the reservoir boundary, with the following boundary conditions.

$$\frac{\partial P}{\partial r_D}[1, t_D] = -E[t_D]$$

$$P[\infty, t_D] = O$$

$$P[r_D, O] = O.$$

The Laplace transform of the pressure-change function at the distance of r_D can be shown to be

$$P_{tD}[r_D, s] = \{e[s]\}\left\{\frac{s \cdot K_o[r_D\sqrt{s}]}{s^{3/2} \cdot K_1[\sqrt{s}]}\right\}$$

$$= e[s]\left\{s \cdot f_1'[r_D, s]\right\}. \quad \ldots\ldots (7)$$

The terminal-rate case corresponding to Eqs. 4 and 5 of the terminal-pressure case is given as

$$P_{tD}[r_D, t_D] = \int_o^{t_D}\frac{dE}{d\tau}\cdot P'_{tD}[t_D - \tau]d\tau \quad \ldots (8)$$

where P'_{tD} is the constant-rate-case pressure-change function, and

$$\frac{P_{tD}[r_D, s]}{e[s]} = s \cdot f_1'[r_D, s] \quad \ldots\ldots (9)$$

The actual pressure change is then

$$P[r, \theta'] = \left(\frac{\mu}{2\pi k h}\right) \cdot P_{tD}[r_D, t_D]. \quad \ldots (10)$$

As shown in Eqs. 6 and 10, the problem of finding the pressure change or the reservoir pore-volume change narrows down to finding Q_{tD} and P_{tD}.

The terms $f_1(s)$ and $f_1'(r_D, s)$ are the Laplace transforms of the constant terminal-pressure-case cumulative-flux function and the constant terminal-

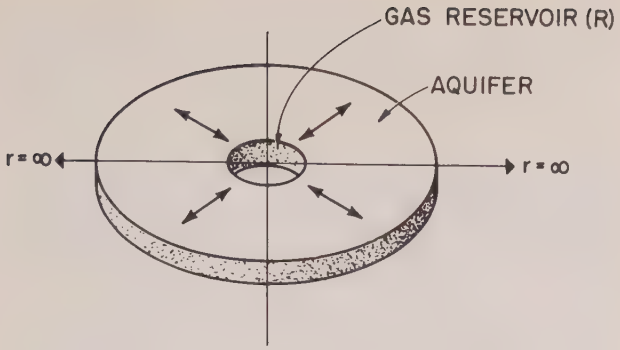

FIG. 1 — RADIAL FLOW MODEL.

rate-case pressure-change function, respectively. Eqs. 5 and 9 are used as the working equations of the analog simulation. This analog simulation is equivalent to the computation of the superposition or convolution integral expressed in Eq. 4 or Eq. 8.

Unfortunately, the rate data are not available, but in most any case the volume-variation data are available. From the definition of rate,

$$e[s] = L\left\{\frac{d[V_g - V_o]}{dt_D}\right\} = s\cdot[V_g - V_o][s] - O.$$

Substituting this equation into Eq. 9, one can obtain

$$\frac{P_{tD}[r_D, s]}{[V_g - V_o][s]} = s^2 f_1'[r_D, s] \cdot \cdot \cdot \cdot \cdot \cdot (11)$$

Eq. 11 is the analog simulation equation for the volume case.

ANALOG SIMULATION

The essential feature of analog simulation on an electronic differential analyzer is to obtain the desired reservoir performance as an output by feeding in the boundary condition as an input signal. The known information may be the arbitrary reservoir pressure schedule, the reservoir pore-volume variation, or the water flux. A block diagram representing the sequence of analog simulation is shown on Fig. 2.

The term $f_1(s)$ in Eq. 5 represents the Laplace transform of cumulative-flux function of the constant-terminal-pressure case or the unit step response for the variable-pressure case. Therefore, $sf_1(s)$ can be approximated from the solution of the constant-terminal-pressure case. Since the initial value of the cumulative-flux function is zero, from the well known property of the Laplace transform rule of a derivative, $sf_1(s)$ can be expressed better in the following form.

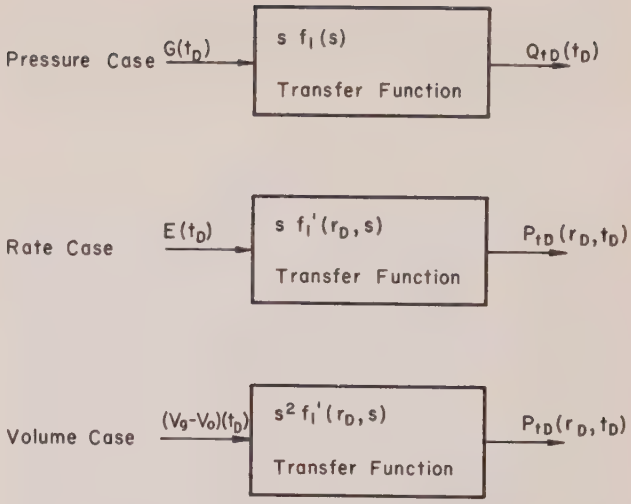

FIG. 3 — INPUT-OUTPUT RELATIONSHIPS FOR THE DIFFERENT RESERVOIR-TERMINAL CONDITIONS.

$$L\left\{\frac{dQ'_{tD}}{dt_D}\right\} = sf_1[s] - O.$$

This relationship can be used to approximate $sf_1(s)$ from $\left(\frac{dQ'_{tD}}{dt_D}\right)$ or directly from Q'_{tD}. When $sf_1(s)$ is known, the Eq. 5 can be simulated on an electronic differential analyzer. Eq. 5 may be interpreted in terms of system transfer function since the transfer function is the expression that establishes the relationship of the input and output variables of a system as an operator equation. When constant pressure is fed in, the output becomes the constant-pressure-case solution. Once the constant-pressure response check is made for a linear system, in general, the arbitrary pressure response can be obtained with the same circuit by simply feeding in the proper pressure variation.[10,11]

The terminal-rate case or volume case can be handled by the identical technique on the basis of Eq. 9 or Eq. 11 instead of Eq. 5.

The three different cases of the reservoir terminal conditions are represented in Fig. 3.

When a constant-terminal-case solution is avail-

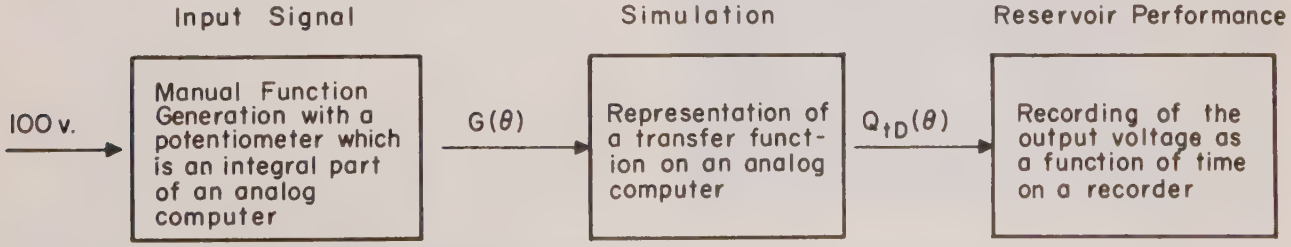
Input Signal
Simulation
Reservoir Performance
100 v.
Manual Function Generation with a potentiometer which is an integral part of an analog computer
G(θ)
Representation of a transfer function on an analog computer
QtD(θ)
Recording of the output voltage as a function of time on a recorder

FIG. 2 — OVER-ALL BLOCK DIAGRAM OF THE ANALOG SIMULATION ARRANGEMENT.

able, one can find the proper transfer function which can be set up on an electronic differential analyzer. The desired solution can then be obtained as an output, which can be recorded as a function of time.

EQUIPMENT

For the studies presented in this paper, the Sterling model LM 10 electronic differential analyzer was used. The LM 10 electronic differential analyzer is a small computer equipped with 10 high-gain DC amplifiers and 10 ten-turn precision helipots. The function $G(t_D)$ is generated manually with a 10-turn precision helipot. The potentiometer setting is changed as a function of time to give the desired voltage by means of a vernier dial. The output is recorded by using a two-channel Brush recorder. Fig. 4 shows a photograph of the actual equipment set-up.

APPLICATIONS

To demonstrate the application of the theory, a few typical problems are chosen.

PRESSURE CASE FOR AN AQUIFER OF LIMITED EXTENT

As a first illustration and proof of the method, an aquifer of $r_D = 10$ is chosen. The $r_D = 10$ is a ratio of the size of the aquifer to that of the gas bubble. For this aquifer size, three different checks or comparisons are made against theoretical or digitally computed values. These checks are (1) the unit-step-response check with that of van Everdingen and Hurst[2] table, (2) the application to the actual Field A to check with the digital computer solution and (3) the comparison of the response for sinusoidal-pressure-variation case with that of a mathematical solution.

The first step toward analog simulation is to obtain the transfer function based on the previous knowledge of unit impulse response. The unit step response for $r_D = 10$ is already expressed in an equation form, rather than in a tabular form. This unit-step response solution for the pressure case has been reported for a limited aquifer as follows.[2]

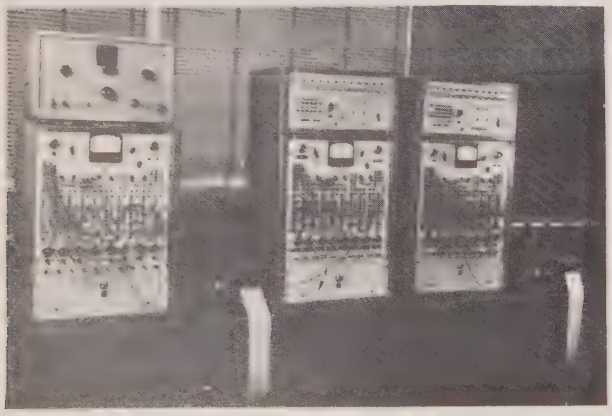

FIG. 4 — ELECTRONIC DIFFERENTIAL ANALYZERS ARRANGED FOR PRESSURE CASE WITH A FAULT IN THE AQUIFER.

$$Q'_{tD} = \frac{r_D^2 - 1}{2} - 2\sum_{a_1, a_2, \cdots}^{\infty} \frac{\left(e^{-a_n^2 tD}\right)\left[J_1^2(a_n r_D)\right]}{\left[J_o^2(a_n) - J_1^2(a_n r_D)\right] a_n^2}.$$

Since the series converges very rapidly for $r_D = 10$, the first term alone gives a good approximation, and the flux function for the constant-terminal-pressure case for the aquifer size of $r_D = 10$ can be written as

$$\begin{aligned} Q'_{tD} &= 49.5 - 47.3e^{-0.0122t_D} \\ &= 49.5 - 47.3e^{-0.0122a\theta} \quad . \quad . \quad . \quad . \quad (12) \end{aligned}$$

where a is a constant relating the actual time in months to the dimensionless time t_D; or,

$$t_D = \frac{k\theta'}{c\phi\mu r_g^2} = a\theta ,$$

and a has a unit of 1/month. It is necessary to change the dimensionless time to the actual time because the machine is running in the actual time, but in a much-condensed scale. For example, one month of actual reservoir time is one second of machine running time if the machine-time constant K is one. In Eq. 12, it is important to note that Q'_{tD} is dimensionless while Q_{tD} in Eq. 6 has a dimension of pressure in pounds per square inch. Upon taking the Laplace transform with respect to θ and multiplying by s, Eq. 12 gives

$$sf_1[s] = \left[49.5 - \frac{47.3s}{s + 0.0122a}\right].$$

By rearranging, this equation can be written as follows.

$$sf_1[s] = 2.2\left[1 + \frac{21.5}{1 + \dfrac{s}{0.0122a}}\right] \quad . \quad . \quad . \quad (13)$$

Based on Eq. 13, an LM 10 circuit diagram for $r_D = 10$ to get cumulative-flux function is obtained as shown in Fig. 5.

By feeding in a constant voltage at Potentiometer

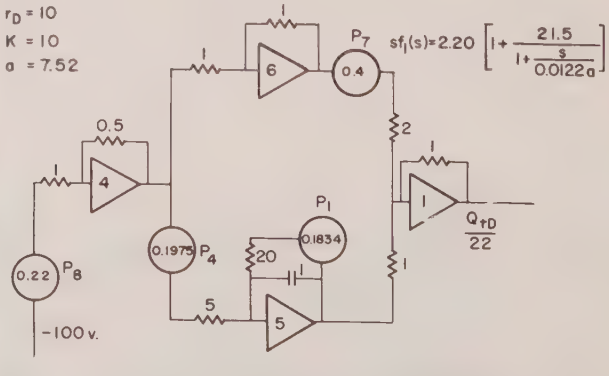

FIG. 5 — LM 10 (ELECTRONIC DIFFERENTIAL ANALYZER) CIRCUIT DIAGRAM FOR $r_D = 10$ TO GET CUMULATIVE-FLUX FUNCTION.

No. 8, which is equivalent to having a constant reservoir pressure, the response is obtained. The response is the cumulative-flux function at constant-pressure case, and the analog result is compared with theoretical values[2] in Fig. 6. The comparison in Fig. 6 shows good agreement, and the unit-step-response check is essentially a calibration operation. It is possible to calibrate the response by readjusting the potentiometer settings.

Since the circuit has been established by the unit-step-response check, the same circuit can be used for any pressure variations by simply generating the specified pressure variation with Potentiometer No. 8. Fig. 7 shows the generated pressure input and the function to be generated for the actual Field A. For this pressure variation, the response is obtained and compared with the results of digital computations[4] in Fig. 8. The reservoir volume is plotted against time.

To secure further proof of the developed method, the case of sinusoidal input pressure was studied. Table 1 shows the comparison of the analog results with theoretical solution,[12] for annual sinusoidal pressure variation.

$$G = 50 \sin\left(\frac{\pi}{6}\theta\right) = 50 \sin[0.0697\ t_D] \text{ psi.}$$

With the aid of the circuit given in Fig. 5, the various effects of practical interest are studied. These include the effect of permeability on water-return ability for a limited aquifer, the effect of aquifer size on water-return ability and the effect of phase shift in the pressure cycle on water-return ability. Figs. 9, 10 and 11 show the results of this study.

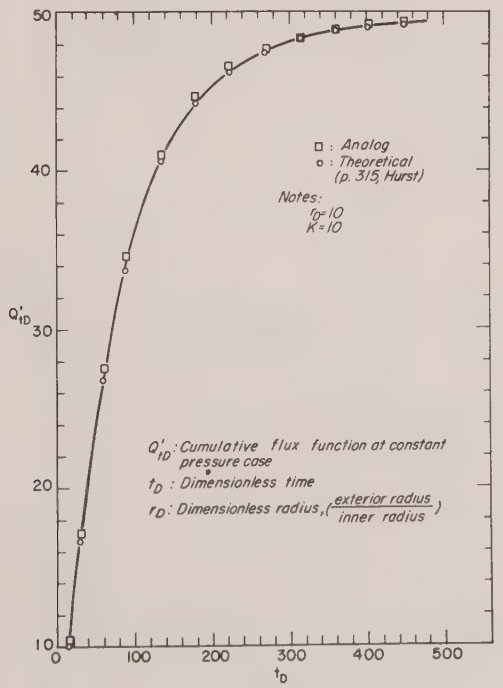

FIG. 6 — COMPARISON OF THE ANALOG RESULT WITH THEORETICAL VALUE TO A CONSTANT-PRESSURE CASE, r_D = 10.

TABLE 1 — COMPARISON OF ANALOG RESULTS WITH THEORETICAL CUMULATIVE-FLUX FUNCTION FOR SINUSOIDAL PRESSURE VARIATION (t_D = 7.52 θ).

θ (month)	Q_{tD} (psi), theoretical	Q_{tD} (psi) Analog Result
6	633 (efflux)	617
12	−267 (influx)	−275
24	−356.5	−348
36	−386.5	−374
48	−396.2	−396
60	−399.4	−400
120	−401	–

INTERFERENCE AMONG TWO OR MORE FIELDS SITUATED ON A COMMON AQUIFER

The first study of interference among the oil fields was made on an electrical reservoir analyzer to study the East Texas field.[13] But the first mathematical interference study was made by Mortada.[8] The application of Mortada's method to gas-storage problems was made by Coats.[14]

The basic idea of this theory stems from the fact that the original partial differential equation describing the liquid flow through a porous medium is linear and homogeneous.

The pressure drop at a field can be broken down into the contributions attributed by the flux of each individual neighboring field, as well as by its own flux, because the water flux can only be caused at the expense of the pressure change. The particular example studied in this work was concerned with

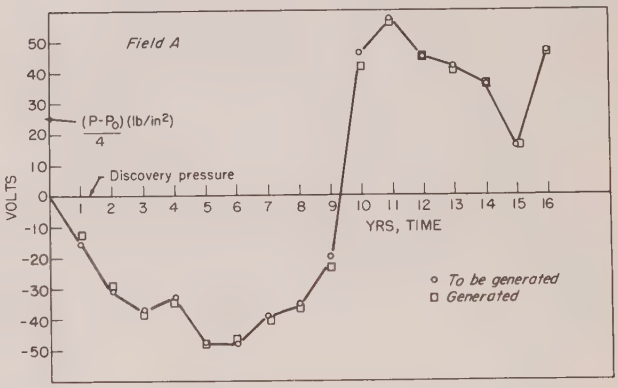

FIG. 7—SPECIFIED PRESSURE VARIATION IN FIELD A AND THE GENERATED FUNCTION.

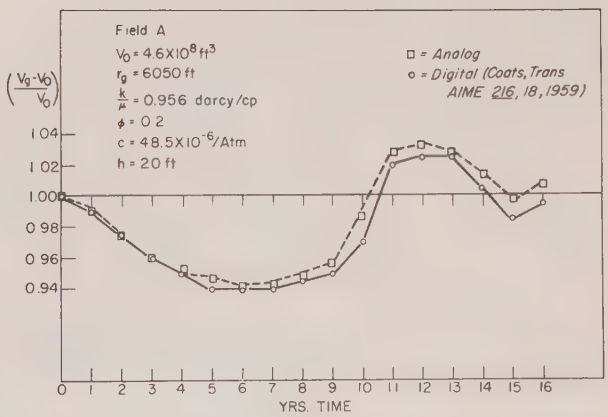

FIG. 8 — COMPARISON OF ANALOG RESULTS WITH DIGITAL RESULTS FOR FIELD A (r_D = 10).

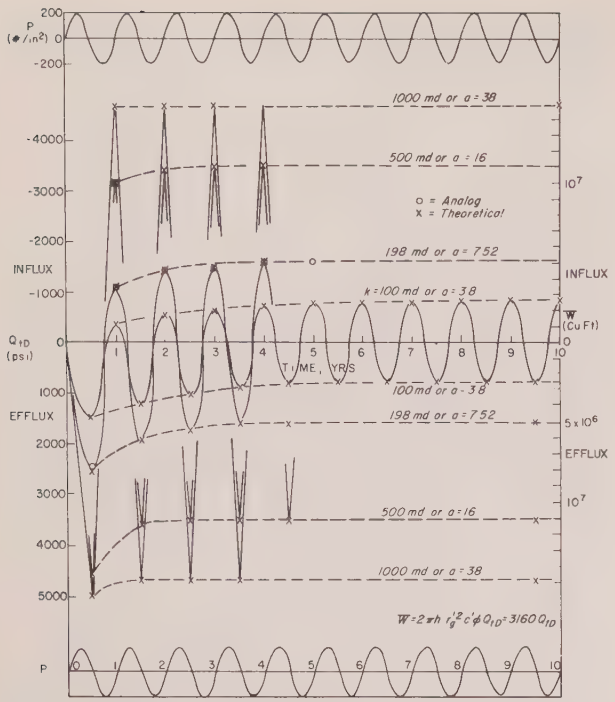

FIG. 9 — EFFECT OF PERMEABILITY ON WATER-RETURN ABILITY FOR LIMITED AQUIFER (r_D = 10).

three fields breathing on a common aquifer.

Fields C and D were discovered in Dec., 1944, while Field A was discovered in Sept., 1941. The approximate geometry is sketched in Fig. 12. The radii of the three fields were approximated from the contour maps to be 1.43 to 1.55 miles. The analog-predicted volume variation of Field A considering the interference of Fields C and D is shown in Fig. 12 along with actual data. Coats [14] studied Field A as an isolated field sitting on a limited aquifer. The circuits used for the study are shown in Figs. 13 and 14.

MOVING BOUNDARY PROBLEMS

The problems treated thus far were fixed boundary problems. The gas-field radius has been considered to be stationary or constant. However, in aquifer storage operations, the gas-bubble radius grows from zero to a large value during a certain period of time before a well developed and stabilized gas bubble is established.

The rigorous analytical solutions applicable to aquifer gas-storage problems are just about hopeless because of analytical difficulties introduced by the moving boundaries. An approximate solution has been derived for a growing disk model of a finite aquifer thickness.

$$P_g = P_{og} + \frac{1}{4c\phi\pi^{3/2}\,h^3}\int_o^{t_D}\frac{\left(\frac{dV_g}{d\tau}\right)}{[t_D-\tau]^{3/2}}\left(1 + 2e^{-\frac{1}{[t_D-\tau]}} + 2e^{-\frac{4}{[t_D-\tau]}} + \ldots\right)d\tau \quad . \quad (14)$$

Eq. 14 has the form of Eq. 8, for which analog simulation method is developed. If one defines the unit-volume step response for the pressure-change function as P''_{tD}, Eq. 14 can be written

$$P_g = P_{og} + \frac{1}{4c\phi\pi^{3/2}\,h^3}\int_o^{t_D}\left(\frac{dV_g}{d\tau}\right)\cdot P''_{tD}[t_D-\tau]\,d\tau. \quad . \quad (15)$$

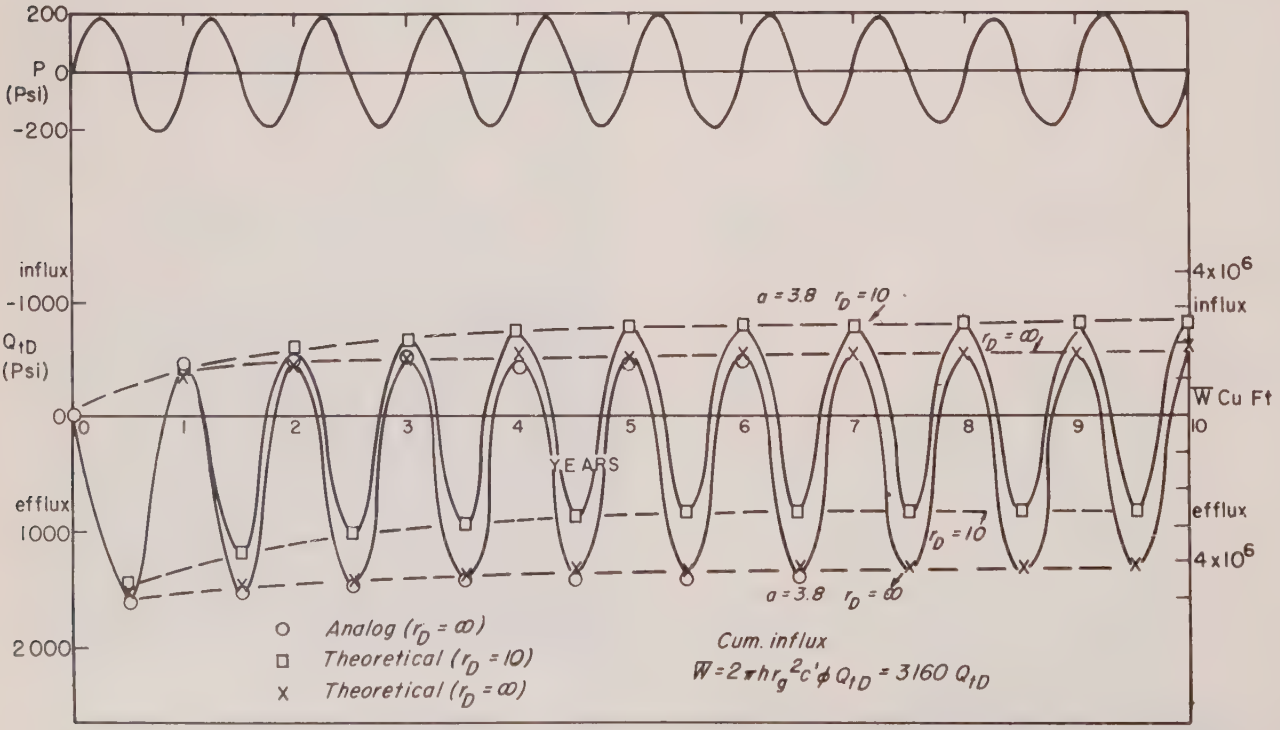

FIG. 10 — EFFECT OF AQUIFER SIZE ON WATER-RETURN ABILITY.

The unit-volume step response P''_{tD} is computed and is given in Table 2.

In obtaining the pressure-case solution from the rate- or volume-case solution, the developed analog method is used.

A circuit to get pressure-change function, using the volume as input for the growing disk model of a finite aquifer thickness, is given in Fig. 15. Some

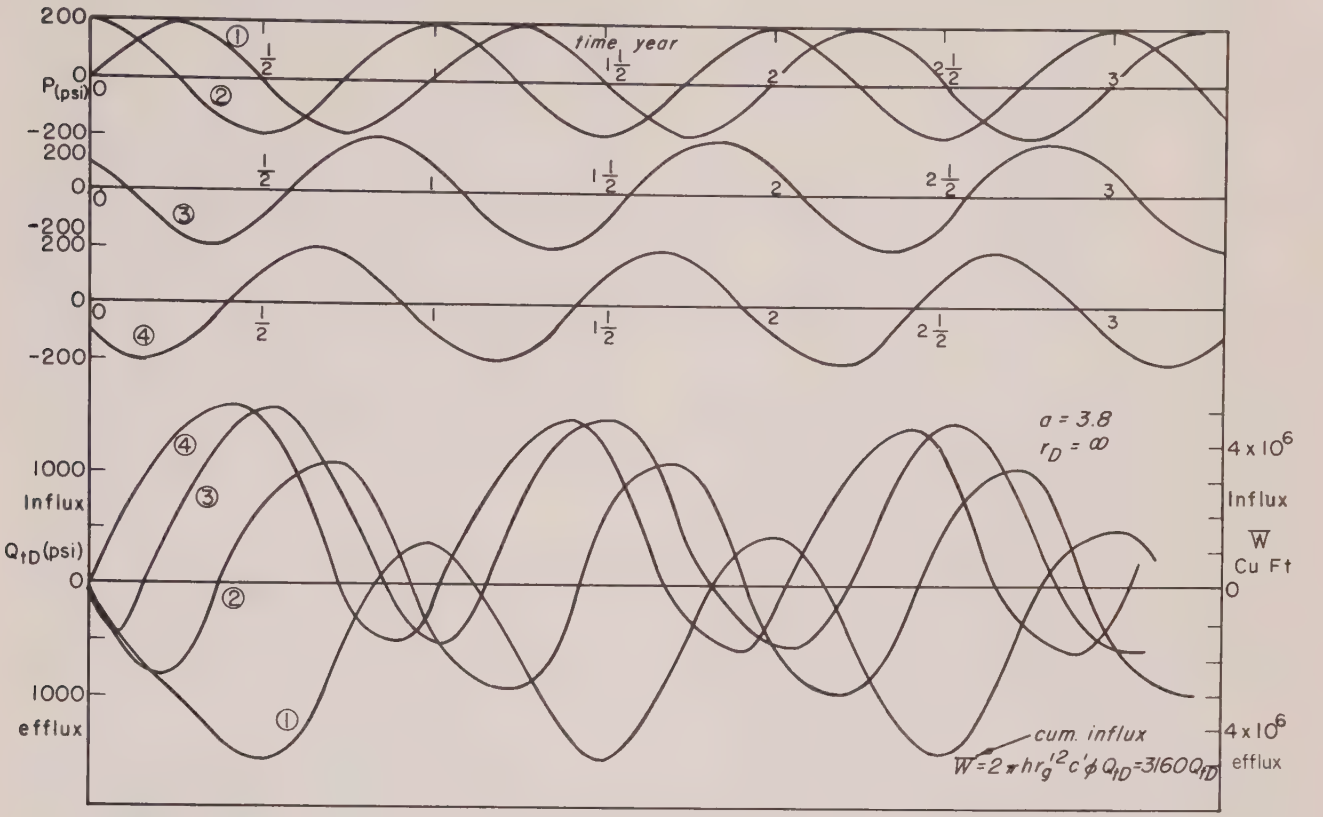

FIG. 11 — EFFECT OF PHASE SHIFT IN PRESSURE CYCLE ON WATER-RETURN ABILITY.

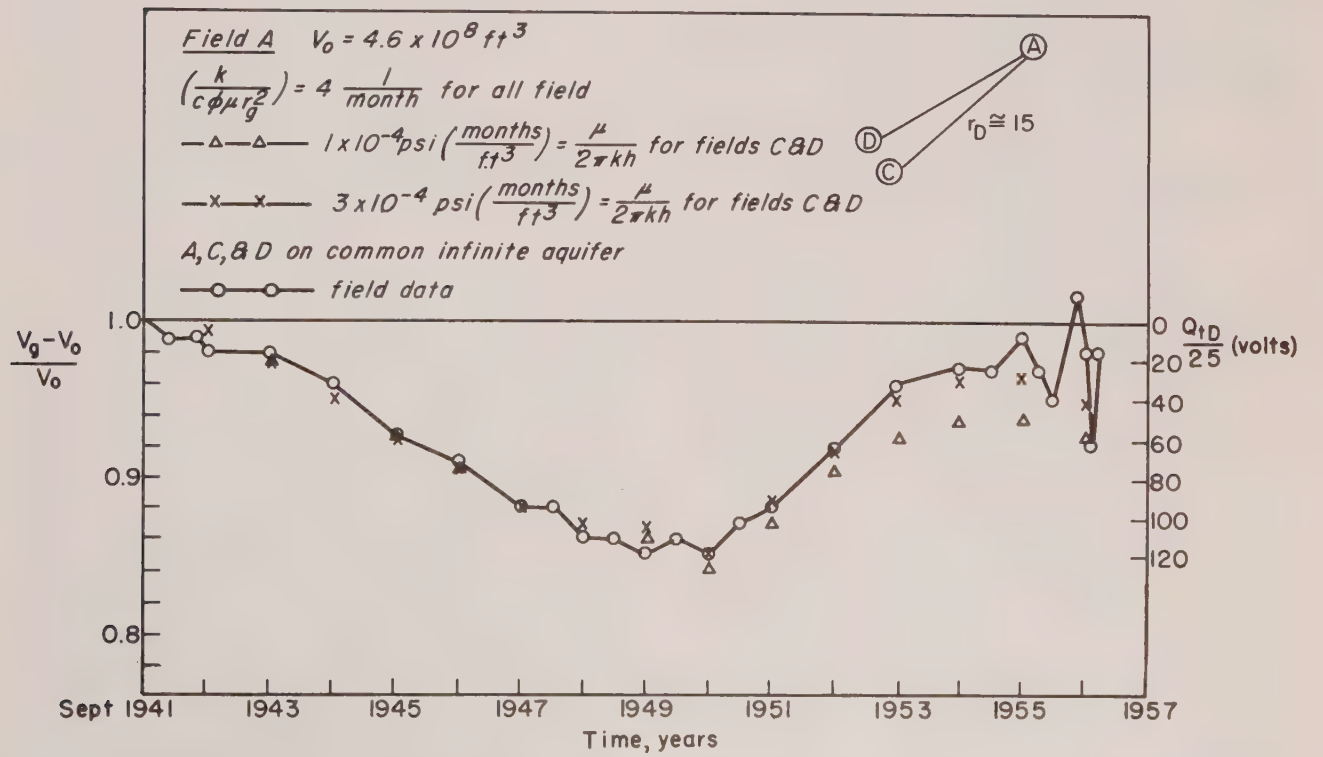
Field A $V_o = 4.6 \times 10^8$ ft^3
$\left(\frac{k}{c\phi\mu r_g^2}\right) = 4 \frac{1}{\text{month}}$ for all field
1×10^{-4} psi $\left(\frac{\text{months}}{\text{ft}^3}\right) = \frac{\mu}{2\pi kh}$ for fields C&D
3×10^{-4} psi $\left(\frac{\text{months}}{\text{ft}^3}\right) = \frac{\mu}{2\pi kh}$ for fields C&D
A, C, & D on common infinite aquifer
field data
$r_D \cong 15$
$\frac{V_g - V_o}{V_o}$
$\frac{Q_{tD}}{25}$ (volts)
Sept 1941
Time, years

FIG. 12—RESERVOIR-PORE-VOLUME VARIATION FOR FIELD A CONSIDERING THE INTERFERENCE OF FIELDS C AND D.

TABLE 2 — UNIT-VOLUME STEP RESPONSE TO GET PRESSURE-CHANGE FUNCTION FOR GROWING DISK OF FINITE AQUIFER THICKNESS.

t_D	P''_{tD} (Eq. 14)	P''_{tD} (Analog Check)
0.1	31.6	–
0.5	3.59	–
1.0	1.773	–
5.0	0.354	–
10	0.1772	–
50	0.03545	–
100	0.01773	–
200	0.00877	–
500	0.003545	0.0037
800	0.00218	–
1000	0.001815	0.00185
1300	0.00138	–
2000	0.00104	0.00105
3000	0.000782	0.0008
4000	0.000647	–

corrections have been made to the potentiometer settings of P_5 and P_7. With $P_5 = 0.1952$ and $P_7 = 0.1338$, the unit step response for the constant-volume case is checked by the analog method and is added to Table 2 for comparison. With the same circuit of Fig. 15, the constant-pressure-case solution is obtained. In doing this, the input (volume variation) is manually controlled in such a manner that the output pressure-change function would be a constant at all times. The constant-pressure-case solution thus obtained for the growing disk model is shown in Fig. 16. The Q''_{tD} in Fig. 16 is the quantity defined earlier as Q'_{tD}, and upon multiplying Q''_{tD} by a constant, the volume of the gas bubble can be obtained. The linearity of the curve at the large time portion particularly must be noted.

Suppose one can assume that the average value of the gas-bubble radius times the pressure gradient at the gas-water interface is a constant, or

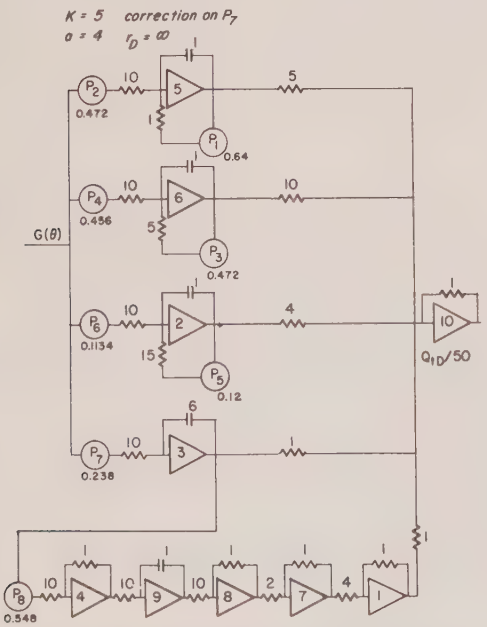

FIG. 13 — LM 10 CIRCUIT DIAGRAM TO GET CUMULATIVE-FLUX FUNCTION FOR INFINITE AQUIFER.

$$r_g \left(\frac{\partial P'}{\partial Z} \right)_{Z=0} \cong C_1 \quad \ldots\ldots\ldots\ldots (16)$$

Again assuming linear-system response and the gas-cap shape to be parabolic, the following relationship is derived.

$$V_g = A_1 \, S_1^{4/3} \quad \ldots\ldots\ldots\ldots (17)$$

where S_1 is the time integral of pressure. This equation demands that a plot of $Q''^{3/4}_{tD}$ vs t_D is a straight line (Fig. 16). This equation also says that a plot of V_g vs S_1 gives a straight line on log-log paper. Fig. 17 shows this plot for Field B. The slope of the curve in this case should be 4/3, theoretically, or 1.333; instead, the slope is found to be 1.37 from the actual data correlation. It gives a remarkable correlation, however, when the small time data are excluded.

Once the correlation curve or the performance

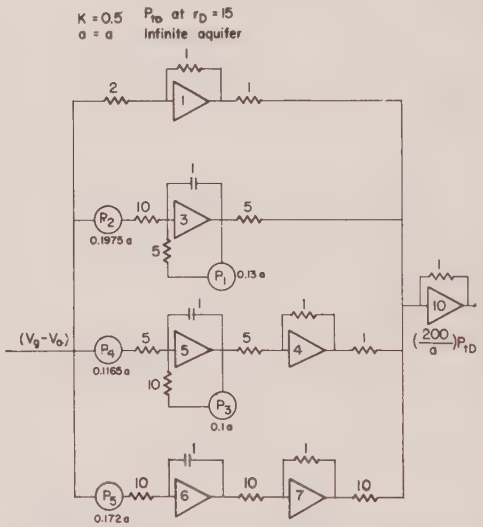

FIG. 14 — LM 10 CIRCUIT DIAGRAM TO GET PRESSURE-CHANGE FUNCTION AT $r_D = 15$.

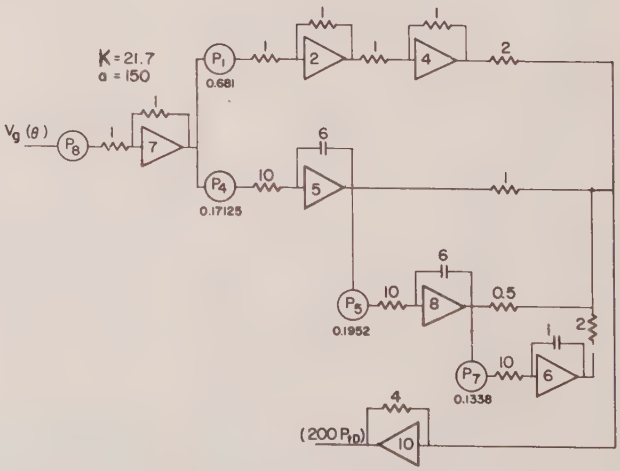

FIG.15—LM 10 CIRCUIT DIAGRAM TO GET PRESSURE-CHANGE FUNCTION USING VOLUME AS INPUT FOR GROWING DISK MODEL OF FINITE AQUIFER THICKNESS.

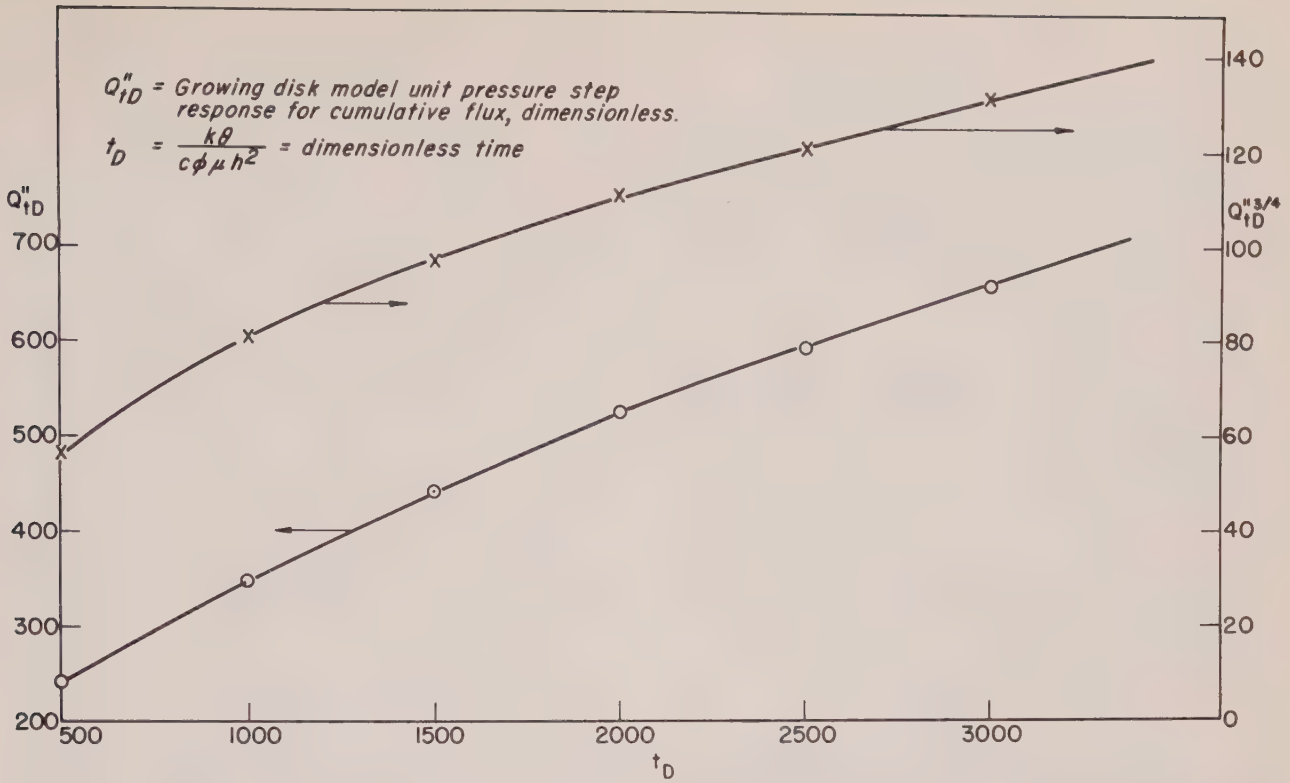

FIG. 16 — CONSTANT-PRESSURE-CASE SOLUTION TO GROWING DISK MODEL OF FINITE AQUIFER THICKNESS.

curve is established, as shown in Fig. 17, the future predictions can easily be made based on this curve. By knowing the gas injection-production schedule from the 30th week, the predictions of the pore-volume variation and the pressure variation are made using Fig. 17; and the predicted results are plotted along with the actual data in Figs. 18 and 19, respectively. The volume variation is predicted within 4 per cent error. This small error is magnified for the pressure prediction, giving as high an error as 50 psi when the reservoir pressure is over 1,000 psia.

OTHER APPLICATIONS

The use of an electronic differential analyzer is not limited to these examples, but can be extended to other reservoir-engineering problems. With slight modifications, the present method can be employed for oilfield problems. Recently, Hurst[16] has published a new chart to handle the oilfield pressure decline for constant oil-production-rate case. The arbitrary oil production can be handled using the new Hurst chart [16] by setting up a transfer function on an electronic differential analyzer.

A careful study reveals that there is an alternate method which does not necessitate the new chart. The usual constant-rate-case solution can be used to handle the arbitrary oil-production-rate case in simulating an aquifer-oilfield system on an electronic differential analyzer.

For an undersaturated oil field, the aquifer water flux can be incorporated with the material-balance equation in the following manner.

$$\text{Cumulative Water Flux} = (AN_p - BP)$$

where A and B are constants and N_p is the cumulative oil production. The simulation of this equation to obtain the pressure decline from the oil-production data is shown in Fig. 20. In Fig. 20, the circuit that goes in the block representation is the same as that of volume case. The extension of this idea can be applied to saturated oil reservoirs, considering the gas liberated from solution.

The method can also be applied to oilfield interference studies. A general circuit for oilfield interference studies is given in Fig. 21.

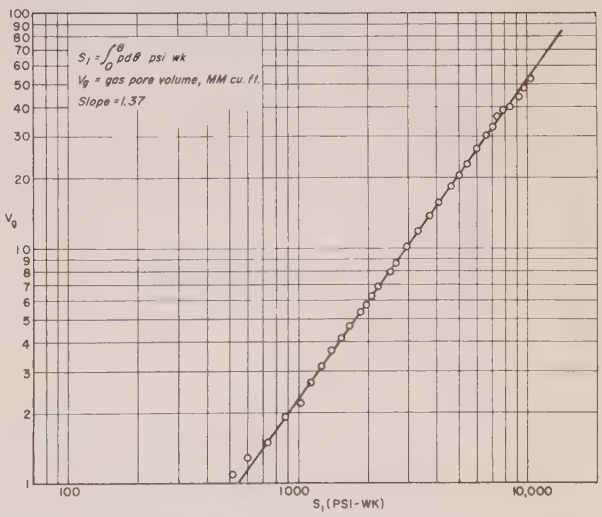

FIG. 17 — AQUIFER GAS-STORAGE PERFORMANCE CURVE FOR FIELD B.

CONCLUSIONS

The following general conclusions can be drawn from the study.

1. The developed, analog simulation method of an aquifer on an electronic differential analyzer is an excellent method to study the transient behavior of an underground gas-storage reservoir. It operates continuously, quickly and economically. The accuracy is well within the range usually required for typical gas-storage operations.

2. Because of the difficulties involved in the mathematical formulation of the actual problems, and the large number of reservoir variables, there is no reason why one should resort to an *a priori* model concept based on a series of assumptions. The model study can only be a guide to select a reasonable unit-step-response curve of a reservoir system.

3. The developed analog simulation method can be applied to any other physical linear system to analyze its transient behavior.

NOMENCLATURE

a = constant relating $t_D = a\theta$ or $\left(\frac{k}{c\phi\mu r^2_g}\right)$, 1/month

a_n = roots of characteristic equation[2]

c = sum of aquifer water and formation compressibility, vol/vol/atm

c' = sum of aquifer water and formation compressibility, vol/vol/psi

$e(s)$ = Laplace transform of E

E = rate function

$f_1(s)$ = Laplace transform of cumulative-flux function for constant-pressure case

$f'_1(s)$ = Laplace transform of pressure-change function of constant-rate case

g = Laplace transform of G

G = pressure function

h = aquifer water-sand thickness, ft

J_0, J_1 = Bessel functions of the first kind, of zero and first order, respectively

k = permeability, darcies

K = computer time constant

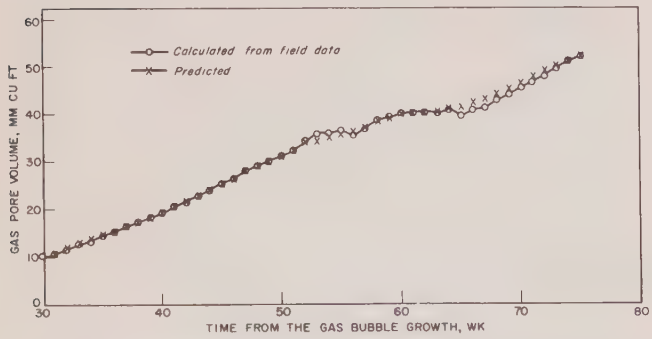

FIG. 18 — COMPARISON BETWEEN FIELD B DATA AND PREDICTED PORE VOLUME.

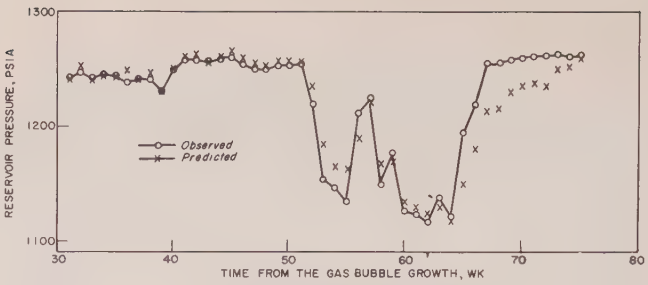

FIG. 19 — COMPARISON BETWEEN OBSERVED AND PREDICTED PRESSURES FOR FIELD B.

K_0, K_1 = Bessel function of second kind of zero and first order, respectively

L = Laplace transform

P = pressure

P_g = pressure at the gas field

P'_{tD} = dimensionless pressure-change function for constant-terminal-rate case tabulated in the literature[2,6-8]

P_{tD} = pressure-change function with arbitrary terminal rate, cu ft/month

P''_{tD} = growing-disk-model, unit-volume step response for pressure change, dimensionless

$\left(\frac{\partial P'}{\partial Z}\right)_{z=0}$ = vertical pressure gradient at $z = 0$ for unit-step pressure, atm/ft

Q'_{tD} = dimensionless cumulative-flux function for constant-pressure case, tabulated in the literature[2,6,7]

Q_{tD} = cumulative-flux function with arbitrary pressure, psi

Q''_{tD} = growing-disk-model, unit-pressure step response for cumulative flux, dimenless

r = radius of aquifer, cm

r' = radius of aquifer, ft

r_g = gas-field radius

r_D = r/r_g, dimensionless radius

s = Laplace transform variable

S_1 = time integral of pressure, psi/week

t_D = dimensionless time (see also a)

V_g = reservoir pore volume, MMcf

V_o = initial reservoir pore volume, MMcf

W = cumulative water flux, cu ft

Z = Cartesian co-ordinate

μ = viscosity of water, cp

θ = time, month

θ' = time, second

τ = a time variable

ϕ = fractional void space or porosity

ACKNOWLEDGMENT

The authors wish to acknowledge the financial assistance and the support provided by the Michigan Gas Assn. through their fellowship program at the U. of Michigan. Valuable assistance, advice and

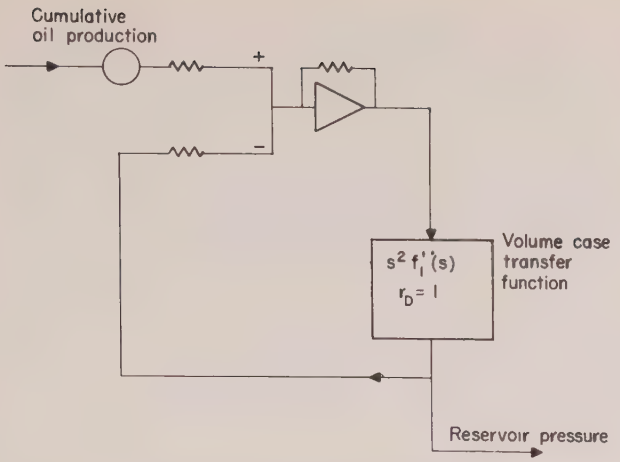

FIG. 20 — UNDERSATURATED OILFIELD PRESSURE DECLINE FROM OIL-PRODUCTION DATA

constructive criticism were generously provided by D. T. Greenwood of the Aeronautical and Astronautical Engineering Dept.

REFERENCES

1. Muskat, M.: *The Flow of Homogeneous Fluids Through Porous Media*, J. W. Edwards, Inc., Ann Arbor, Mich. (1946).
2. van Everdingen, A. F. and Hurst, W.: "The Application of the Laplace Transformation to Flow Problems in Reservoirs", *Trans.*, AIME (1949) Vol. 186, 305.
3. Yoo, H. D., Katz, D. L., White, R. R. and Tek, M. R.: "Methods for Predicting the Volume Variations of Gas or Oil Reservoirs Association with Active Water Drive", *Pet. Eng.* (Sept., 1959).
4. Katz, D. L., Tek, M. R. and Coats, K. H.: "The Effect of Unsteady-State Aquifer Motion on the Size of an Adjacent Gas Storage Reservoir", *Trans.*, AIME (1959) Vol. 216, 18.
5. Bruce, W. A.: "Electronic Computer's Magic Talents Speed Improved Production Technology", *Oil and Gas Jour.* (June 3, 1957).
6. Chatas, A. T.: "A Practical Treatment of Nonsteady-State Flow Problems in Reservoir Systems", *Pet. Eng.* (May, 1953).
7. Katz, D. L., *et al: Handbook of Natural Gas Engineering*, McGraw-Hill Book Co., Inc., N. Y. (1959).
8. Mortada, Mohamed: "A Practical Method for Treating Oil Field Interference in Water-drive Reservoirs", *Trans.*, AIME (1955) Vol. 204, 217.
9. Churchill, R. V.: *Modern Operational Mathematics in Engineering*, McGraw-Hill Book Co., Inc., N.Y. (1944).
10. Gardner, M. F. and Barnes, J. L.: *Transient in Linear Systems 1*, John Wiley & Sons, Inc., N. Y. (1948).
11. Josephs, H. J. and Radley, W. G.: *Heavisides Electric Circuit Theory*, Chemical Publishing Co., N. Y. (1946).
12. Yoo, H. D., Katz, D. L. and Tek, M. R.: "Simulation of Gas Storage Reservoir on Electronic Differential Analyzer", Paper presented at Summer Gas Storage Research Conf., U. of Michigan (1959).
13. Rumble, R. C., Spain, H. H. and Stamm, H. E., III: "A Reservoir Analyzer Study of the Woodbine Basin", *Trans.*, AIME (1951) Vol. 192, 331.
14. Coats, K. H.: *Prediction of Gas Storage Reservoir Behavior*, PhD thesis, U. of Michigan (April, 1959).
15. Carslaw, H. S. and Jaeger, J. C.: *Conduction of Heat in Solids*, Oxford at the Clarendon Press (1947).
16. Hurst, W.: "The Simplification of the Material Balance Formulas by the Laplace Transformation", *Trans.*, AIME (1948) Vol. 213, 292.

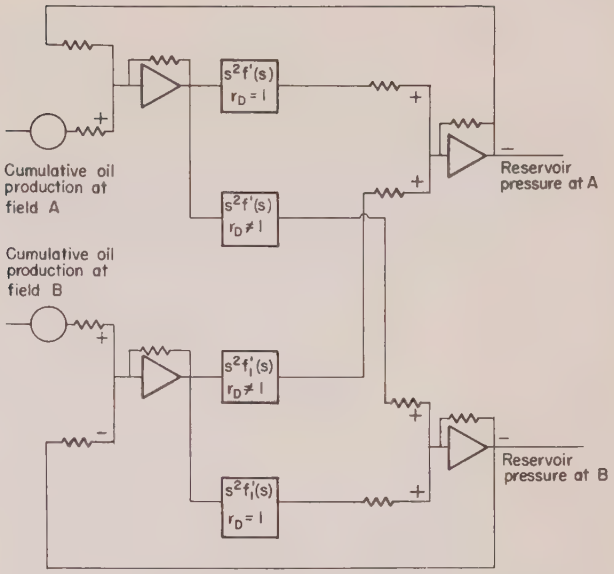

$f_1'(s)$: Laplace transform of the pressure change function for constant terminal rate case solution.

FIG. 21 — INTERFERENCE BETWEEN UNDERSATURATED OIL FIELDS.

★★★

Further Discussion of Paper Published in

***Society of Petroleum Engineers Journal*, March, 1961**

The Development of Stability Theory for Miscible Liquid-Liquid Displacement

RICHARD L. PERRINE
MEMBER AIME

U. OF CALIFORNIA AT LOS ANGELES
LOS ANGELES, CALIF.

(Published on Page 17)

DISCUSSION

H. D. OUTMANS
MEMBER AIME

UNION OIL CO. OF CALIFORNIA
BREA, CALIF.

The author applies the theory of hydrodynamic stability to fluid flow in porous media and concludes that the displacement of miscible liquids is stable if the stability coefficient, as defined by Eq. 19.2 or Eq. 27.0, is positive. The conclusion is invalid, however, since it is based on a faulty argument.

To demonstrate this, the reader is referred to Eqs. 4.1 through 4.5 of the paper which describe, in differential form, the first-order disturbances c, u, v, w and p. In these same equations, $\bar{c}_x$, $\bar{c}_z$, g_1, g_3 and $\bar{\mu}$ are functions of the stable concentration $\bar{c}$. This concentration $\bar{c}$ is known and depends on x, z and t (the author assumes $\bar{c}_y = 0$). It follows that $\bar{c}_x$, $\bar{c}_z$, g_1, g_3 and $\bar{\mu}$ are also functions of x, z and t. With this in mind, we turn to Eqs. 8.1 through 8.5 which were derived from Eqs. 4.1 through 4.5 by substituting Eq. 6.0. The significance of this substitution is that the author thereby limits the solutions of Eqs. 4.1 through 4.5 to equations of the form of Eq. 6.0. Eqs. 8.1 through 8.5 represent an infinite linear system with five unknowns: $\tilde{c}$, $\tilde{u}$, $\tilde{v}$, $\tilde{w}$ and $\tilde{p}$. The coefficients $\bar{c}_x$, $\bar{c}_z$, g_1, g_3 and $\bar{\mu}$ in this system are known at each point and at each instant; the coefficients containing derivatives of f are unknown. If this infinite linear system in $\tilde{c}$, $\tilde{u}$, $\tilde{v}$, $\tilde{w}$ and $\tilde{p}$ is to have a nontrivial solution, then it is indeed necessary (as the author states) that the determinant of the coefficient matrix of Eqs. 8.1 through 8.5, i.e., $|A|$, be equal to zero.

This condition, however, is not sufficient. A nontrivial solution exists if, and only if, the rank of the coefficient matrix of the entire infinite system is smaller than five. In other words, all minors of order five must vanish and only if all the coefficients in Eqs. 8.1 through 8.5 are constant is this equivalent to the condition $|A| = 0$. Constant coefficients means that g_1, g_3 and $\bar{\mu}$, for instance, are constant; and, since they depend on $\bar{c}$ it follows that $\bar{c}$ must be constant. We conclude that the condition $|A| = 0$, on which the author bases his calculations, is necessary and sufficient for a nontrivial solution only if the concentration $\bar{c}$ is constant. In other words, *the author does not investigate the stability of a miscible displacement but, rather, only the stability of the flow of a homogeneous liquid.*

Using the initial condition and the fact that the coefficients are constant, we find

$$f_x = \alpha,\ f_y = \beta,\ f_z = n\,\pi,\ E = F = G = 0.$$

Substituting this in Eq. 9.0, the latter becomes

$$if_t = -\alpha^2 D_1 - (\beta^2 + n^2\,\pi^2) D_3 .$$

This may be integrated

$$f = \alpha x + \beta y + n\,\pi z + i\{\alpha^2 D_1 + (\beta^2 + n^2\,\pi^2) D_3\}\,t,$$

and the stability coefficient

$$\gamma_R = \alpha^2 D_1 + (\beta^2 + n^2\,\pi^2) D_3 .$$

In this last equation, D_1 and D_3 are positive and the conclusion is that the motion of a homogeneous liquid is stable for all disturbances of the form

$$\eta = \tilde{\eta} \exp i\,(\alpha x + \beta y + n\,\pi z) .$$

It is perhaps well to point out that at $t = 0$ these disturbances do not satisfy the initial condition of Eq. 11.0, which states

$$w = 0 \text{ for } z = 0 \text{ and } z = 1.$$

Therefore, they are unsuitable for investigating the stability in a porous medium bounded in the z direction by parallel planes (although it would be simple to satisfy Eq. 11.0 for w by placing the boundaries at $z = \pm \frac{1}{2}$, which would result in nonzero values of c_z at the boundaries and violate the other part of

Eq. 11.0).

The general conclusion is that the author has not succeeded in establishing a stability criterion for miscible displacement. The reason for this is to be found in Eqs. 6.0 and 7.0. By assuming that Eqs. 4.1 through 4.5 could be satisfied by Eq. 6.0, he automatically excluded the possibility that the concentration $\bar{c}$ varies, and by Eq. 7.0 he excluded flow between parallel z-boundaries from his investigation.

If in any future attempt to find stability criteria for miscible displacement in porous media it should be necessary to solve Eqs. 4.1 through 4.5, then more general solutions than Eq. 6.0 will have to be postulated and initial disturbances should be introduced compatible with the boundary conditions.

AUTHOR'S REPLY TO H. D. OUTMANS

Outmans has suggested, quite correctly, that the author's paper[1] contains an error. To see what is involved requires that one consider both the purpose of the study and the methods that are used.

The comments by Outmans suggest that the Fourier series terms (Eq. 6) are not compatible with the required boundary conditions. Any real disturbance will satisfy flow equations and proper boundary conditions. The existence of such a disturbance is postulated. Single Fourier terms represent only part of the disturbance and, singly, need not satisfy such conditions. As a very simple example, consider $(c_1 \sin \pi z + c_3 \sin 3 \pi z)$. For $c_1 = -3c_3$, the condition that the z-direction concentration gradient must vanish at the boundaries is satisfied by the sum, although not satisfied by either single term. Corresponding sine velocity terms vanish identically at the boundaries as required. It should have been made clear in the original paper that the Fourier representation of any real disturbance may include such relationships.

We conclude that any real concentration perturbation can be described by a Fourier series in the space variables x, y and z, with Fourier coefficients that will depend only on time. It is important to note that the first-order perturbation equations (Eqs. 4.2 through 4.5) contain time only as a parameter. Thus, for a particular Fourier mode for which the spatial variation of concentration is known, the set of four equations (Eqs. 4.2 through 4.5) can be solved for the quantities u, v, w and p. The solutions contain a parametric time-dependence. In terms of the pressure function corresponding to the Fourier mode, the set reduces to a linear, second-order, elliptic, partial differential equation in canonical form. The remaining Eq. 4.1 can be solved to give the time-dependence for the Fourier coefficient once u and w are determined. Eq. 4.1 for the particular mode can be made linear and first-order in the time-dependent Fourier coefficient, with the space variables as parameters. This approach can be applied to inhomogeneous flow systems and is the subject of current research effort.

Most unfortunately, the nature of the pressure equation is such that simple solutions for interesting systems do not result from the approach just described. Thus, recourse has been made to other methods. Outmans has pointed out a flaw in the arguments used in one such attempt. However, useful results can be achieved in a way which satisfies the conditions of rank noted by Outmans.

Assuming only that the stable flow is well-behaved, the coefficients in the first-order perturbation Eqs. 4.1 through 4.5 of the original paper can be expanded as a Taylor series about the position (x_o, y_o, z_o), and about a time defined as $t = 0$. As an example, the coefficient g_1 in Eq. 4.3 becomes

$$g_1(x,y,z,t) = g_1^o + \left[\frac{\partial g_1}{\partial x}\right]^o (x - x_o) + \left[\frac{\partial g_1}{\partial y}\right]^o (y - y_o) + \left[\frac{\partial g_1}{\partial z}\right]^o (z - z_o) + \left[\frac{\partial g_1}{\partial t}\right]^o t + \ldots$$

The superscripts o indicate evaluation of the functions at $(x_o, y_o, z_o, 0)$. System properties with a well-behaved flow may change rapidly, but never infinitely rapid. Thus, within a sufficiently small space region surrounding (x_o, y_o, z_o) and for small-enough times t, one can neglect all but the leading constant term in the series.

Using standard methods of solution, results are obtained that are valid within this limited region and which should be compared with those from the original paper. One finds that the quantity γ_I in Eq. 19.1 disappears and that only the first, time-independent term of γ_R remains in Eq. 19.2. Thus, the final result applied to the solution of engineering problems,[1] Eq. 27, is unchanged. This treatment amounts to a complete linearization of the stability problem and can be extended to inhomogeneous systems. The method leads to a prediction of the initial growth of a disturbance in the space region immediately surrounding a point of interest (x_o, y_o, z_o). Thus, while the results are limited, which is typical of perturbation theory, they are sufficient to satisfy the purpose for which the original development was intended. ***

[1] Perrine, R. L.: "Stability Theory and Its Use to Optimize Solvent Recovery of Oil", *Soc. Pet. Eng. Jour.* (March, 1961) 9.

INDEX

Petroleum Transactions, Volume 222

(This volume is divided into two parts: Part I reprinted from JOURNAL OF PETROLEUM TECHNOLOGY *and Part II reprinted from* SOCIETY OF PETROLEUM ENGINEERS JOURNAL. *Page numbers are repeated in the two parts. When using this Index, the reader must keep this in mind in order to find papers quickly. The abbreviations for the two publications used here, JPT and SPEJ, are not the recommended abbreviations for use in formal reference listings. Instead, "Jour. Pet. Tech." and "Soc. Pet. Eng. Jour." are preferred.)*

A

ABRASIVE JETTING: investigation of method for perforation and fracture initiation, JPT May, 489

theory of formation cutting using the sand erosion process, JPT May, 483

ACCELERATORS: in improved bentonite cements, JPT Sept., 923

ACOUSTIC VELOCITY LOGGING: effect of rock bulk compressibility on interpretation, SPEJ Dec., 235; discussion, 246

ALCOHOL: mechanism of displacing oil from porous media, SPEJ Sept., 195; discussion, 209

ALLEN, E. E., et al: *A Study of the Behavior of Bounded Reservoirs Composed of Stratified Layers*, SPEJ Mar., 43

ALUMINUM PARTICLES: propping agent in formation fractures, JPT June, 583

ANISOTROPIC RESERVOIRS: approximate method for determining areal sweep efficiency and flow capacity, SPEJ Dec., 277

influence of production rate, permeability variation and well spacing on solution-gas-drive performance, JPT May, 469

ARCZYNSKI, T. S., et al: *Use of Oxygen Scavengers to Control External Corrosion of Oil-String Casing*, JPT July, 703

AREAL PERMEABILITY DISTRIBUTION: determining by calculations, JPT July, 691

AREAL SWEEP EFFICIENCY: approximate method for determining in formations with anisotropic permeability, SPEJ Dec., 277

ATKINS, E. R., JR. and SMITH, G. H.: *The Significance of Particle Shape in Formation Resistivity Factor-Porosity Relationships*, JPT Mar., 285; discussion, Oct., 1057

ATTRA, H. D.: *Nonequilibrium Gas Displacement Calculations*. SPEJ Sept., 130

ATTRA, H. D., et al: *Application of Optimizing Techniques for Studying Field Producing Operations*, JPT Jan., 82

B

BAIL, P. T. and BOBEK, J. E.: *Model Studies of Oil Displacement from Thin Sands by Vertical Water Influx from Adjacent Shales*, JPT Sept., 950

BAXENDELL, P. B. and THOMAS, R.: *The Calculation of Pressure Gradients in High-Rate Flowing Wells*, JPT Oct., 1023

BEACH, H. J.: *Improved Bentonite Cements Through Partial Acceleration*, JPT Sept., 923

BENHAM, A. L., et al: *Discussion on Effect of Bank Size on Oil Recovery in the High-Pressure Gas-Driven LPG-Bank Process*, JPT Aug., 813

BENNETT, E. O., et al: *Microbial Flora in a Number of Oilfield Water-Injection Systems*, SPEJ June, 71

BENTONITE CEMENTS: improved through partial acceleration, JPT Sept., 923

BITS: hydraulic horsepower and weight on, simplified analysis aids in optimizing for minimum cost, JPT May, 475

laboratory drilling performance of full-scale rock type, JPT Jan., 71

stresses caused by loading at center of hole, SPEJ Sept., 177

BLACK, W. M., et al: *Application of Optimizing Techniques for Studying Field Producing Operations*, JPT Jan., 82

BLENKARN, K. A., et al: *The Use of Alternating Flow to Characterize Porous Media Having Storage Pores*, JPT Apr., 383

BOBEK, J. E. and BAIL, P. T.: *Model Studies of Oil Displacement from Thin Sands by Vertical Water Influx from Adjacent Shales*, JPT Sept., 950

BOREHOLES: rotary, maximum permissible dog-legs, JPT Feb., 175

BOTTOM-WATER DRIVES: scale-model study of, JPT Jan., 90

BOUNDARY CONDITIONS: fixed: in study of behavior of bounded reservoirs composed of stratified layers, SPEJ Mar., 43

BOUNDED RESERVOIRS: pressure studies in, SPEJ Dec., 223

BRADLEY, H. B., et al: *A Potentiometric Study of the Effects of Mobility Ratio on Reservoir Flow Patterns*, SPEJ Sept., 125

BRIGHAM, W. E., et al: *Experiments on Mixing During Miscible Displacement in Porous Media*, SPEJ Mar., 1; discussion, Sept., 213

BRINKMAN, F. H., et al: *Effect of Bank Size on Oil Recovery in the High-Pressure Gas-Driven LPG-Bank Process*, JPT Aug., 806; discussion, 812, 813, 814

BRINKMAN, F. H., et al: *The Linear Displacement of Oil from Porous Media by Enriched Gas*, JPT Aug., 787

BRONS, F. and MARTING, V. E.: *The Effect of Restricted Fluid Entry on Well Productivity*, JPT Feb., 172

BRONS, F. and MILLER, W. C.: *A Simple Method for Correcting Spot Pressure Readings*, JPT Aug., 803

BROWN, R. W. and LOPER, J. L.: *Theory of Formation Cutting Using the Sand Erosion Process*, JPT May, 483

BROWN, W. and HOWER, W. F.: *Large-Scale Laboratory Investigation of Sand Consolidation Techniques*, JPT Dec., 1221

BUCKLEY-LEVERETT THEORY: use in nonequilibrium gas displacement calculations, SPEJ Sept., 130

BUILD-UP CURVES: use in study of behavior of bounded reservoirs composed of stratified layers, SPEJ Mar., 43

BUILD-UP PRESSURE: in oil wells, use of spot pressure readings, JPT Aug., 803

BUREAU OF MINES: phase equilibrium apparatus, use in studying multiple liquid phases in a natural gas, SPEJ Sept., 137

BURKHARDT, J. A.: *Wellbore Pressure Surges Produced by Pipe Movement*, JPT June, 595

C

CAMPBELL, J. M. and MCLEOD, H. O., JR.: *Natural Gas Hydrates at Pressures of 10,000 psia*, JPT June, 590

CAMPION, F. E.: *Discussion on Effect of Vertical Fractures on Reservoir Behavior — Incompressible Fluid Case*, SPEJ June, 117

CAPACITY: of fracture filled with a partial sand monolayer, SPEJ Sept., 119

CAPILLARY PRESSURE: effect on linear water flood with gravity, SPEJ Mar., 32

CARLSON, V., et al: *Microbial Flora in a Number of Oilfield Water-Injection Systems*, SPEJ June, 71

CASING: cementation of, a sonic method for analyzing the quality, JPT Feb., 165

oil-string, use of oxygen scavengers to control external corrosion, JPT July, 703

CELLAR OIL: laboratory model study, JPT Apr., 377

CEMENTATION OF CASING: sonic method for analyzing the quality, JPT Feb., 165

CEMENT: improved bentonite type through partial acceleration, JPT Sept., 923

improved compositions for wells with extreme temperatures, JPT Mar., 277

CHEATHAM, J. B., JR. and WILHOIT, J. C., JR.: *Stresses Caused by Bit Loading at the Center of the Hole*, SPEJ Sept., 177

CHITTUM, J. F., et al: *Use of Oxygen Scavengers to Control External Corrosion of Oil-String Casing*, JPT July, 703

CLAPEYRON-TYPE EQUATION: for predicting hydrate formation temperature, JPT June, 590

CLARK, G. C., et al: *The Influence of Production Rate, Permeability Variation and Well Spacing on Solution-Gas-Drive Performance*, JPT May, 469

CLAY: properties of: deflocculation of fractionated montmorillonite by sodium polyphosphates, SPEJ Dec., 229

COFFER, H. F., et al: *Hydraulic Fracture—Field Test to Determine Areal Extent and Orientation*, JPT Apr., 371

COMPOSITE RESERVOIR: pressure drop in, SPEJ Sept., 170

COMPRESSIBILITY: rock bulk: effect on velocity-log interpretation, SPEJ Dec., 235; discussion, 246

COMPUTERS: IBM 650: used to calculate performance of solution-gas-drive reservoirs, SPEJ Sept., 142

program for analysis of gravity drainage, JPT Sept., 927

IBM 704: use in calculation of pressure build-up for a low-permeability gas-condensate well, JPT Nov., 1131

use in determining influence of production rate, permeability variation and well spacing on solution-gas-drive performance, JPT May, 469

LM-10: study of gas reservoirs subject to water drive on electronic differential analyzer, SPEJ Dec., 287

CONDENSATES: calculated pressure build-up for a low-permeability well, JPT Nov., 1131

CONDUCTIVITY: thermal: of porous rocks filled with stagnant fluid, SPEJ Mar., 37

CONNALLY, C. A.: *Discussion on Effect of Bank Size on Oil Recovery in the High-Pressure Gas-Driven LPG-Bank Process*, JPT Aug., 812

CORE ANALYSIS: of Delaware Sand, JPT Dec., 1230

electrodeless system for measuring electric logging parameters on cores and mud samples, JPT Mar., 292

in studying the effect of reservoir environment on water-oil displacements, JPT June, 595

CORNELIUS, A. J., et al: *Laboratory Studies of Oil Recovery by Steam Injection*, JPT July, 681

CORRELATIONS: of surface and interfacial tension of light hydrocarbons in critical region, SPEJ Dec., 259

CORROSION: of oil-string casing, use of oxygen scavengers to control, JPT July, 703

COST: minimum, simplified analysis aids in drilling factors for, JPT May, 475

COTMAN, N. T., et al: *A Study of Flow in Stratified Reservoirs by Use of the Thermal Analogy*, SPEJ Dec., 215

CRAIG, F. F., JR., et al: *A Scale-Model Study of Bottom-Water Drives*, JPT Jan., 90

CRAIG, F. F., JR. and KOELLER, R. C.: *Discussion on Effect of Bank Size on Oil Recovery in the High-Pressure Gas-Driven LPG-Bank Process*, JPT Aug., 814

CRANE, F. E. and DOWNIE, J.: *Effect of Viscosity on Relative Permeability*, SPEJ June, 59

CRATER FORMATION: produced in sandstone by high-velocity projectiles, JPT Mar., 273; discussion, JPT Sept., 955

CRAWFORD, P. B.., et al: *A Study of Flow in Stratified Reservoirs by Use of the Thermal Analogy*, SPEJ Dec., 215

CRITICAL REGION: correlation of surface and interfacial tension of light hydrocarbons in, SPEJ Dec., 259

D

DEFLOCCULATION: of fractionated montmorillonite by sodium polyphosphates, SPEJ Dec., 229

DEILY, F. H., et al: *Laboratory Drilling Performance of the Full-Scale Rock Bit*, JPT Jan., 71; discussion, 80

DELAWARE SAND PROPERTIES: core analysis, capillary pressure, and waterflood feasibility data, JPT Dec., 1230

DEPLETION PERFORMANCE: effect of oil production rate of wells producing from more than one horizon, SPEJ Mar., 26

DEPPE, J. C.: *Injection Rates—the Effect of Mobility Ratio, Area Swept and Pattern*, SPEJ June, 81

DESIGN: of coil: effect on performance of induction log, JPT Nov., 1137; discussion, 1148

DEVANEY, W. E., et al: *Multiple Liquid Phases in a Natural-Gas System*, SPEJ Sept., 137

DEW, J. N., et al: *Experiments on Mixing During Miscible Displacement in Porous Media*, SPEJ Mar., 1; discussion, Sept., 213

The Influence of Production Rate, Permeability Variation and Well Spacing on Solution-Gas-Drive Performance, JPT May, 469

DISPLACEMENT MECHANISM: *See also* Miscible Displacement

nonequilibrium gas: calculations of, SPEJ Sept., 130

oil by alcohol from porous media, SPEJ Sept., 195; discussion, 209

oil by gas, analysis of, SPEJ June, 92; discussion, 102

DISPLACEMENT OF OIL: from thin sands by vertical water influx from adjacent shales, JPT Sept., 950

by water: effect of reservoir environment, JPT June, 579

DISSOLVED-GAS DRIVE: *See* Solution-Gas Drive

DOG-LEGS: maximum permissible in rotary boreholes, JPT Feb., 175

DOWNIE, J. and CRANE, F. E.: *Effect of Viscosity on Relative Permeability*, SPEJ June, 59

DRILLING: experimental stress analysis of tool joints, JPT May, 496

improved compositions for cementing wells with extreme temperatures, JPT Mar., 277

laboratory performance of the full-scale rock bit, JPT Jan., 71

maximum permissible dog-legs in rotary boreholes, JPT Feb., 175

simplified analysis aids in optimizing factors for minimum cost, JPT May, 475

stresses caused by bit-loading at center of hole, SPEJ Sept., 177

wellbore pressure surges produced by pipe movement, JPT June, 595

DRILLING FLUIDS: some effects of size distribution on particle bridging in lost circulation and filtration tests, JPT June, 575

DUESTERHOEFT, W. C., JR., et al: *The Effect of Coil Design on the Performance of the Induction Log*, JPT Nov., 1137; discussion, 1148

DYKSTRA, H.: *Calculated Pressure Build-Up for a Low-Permeability Gas-Condensate Well*, JPT Nov., 1131

E

EFFICIENCY: mechanical, of a rock bit, JPT Jan., 71; discussion, 80

ENERGY: consumption of: rotary drilling with rock bits, JPT Jan., 71; discussion, 80

ENRICHED-GAS DRIVE: linear displacement of oil from porous media, JPT Aug., 787

EQUILIBRIUM RATIOS: of water in the water-triethylene glycol-natural gas system, JPT July, 697

use in calculation of differential gas liberation and shrinkage, JPT Nov., 1135

EQUIPMENT: test: for large-scale investigation of sand consolidation techniques, JPT Dec., 1221

EVALUATION: of vertical-lift performance in producing wells, JPT Apr., 390

EWING, S. P. JR., et al: *The Linear Displacement of Oil from Porous Media by Enriched Gas*, JPT Aug., 787

F

FARIS, J. E., et al: *Effect of Bank Size on Oil Recovery in the High-Pressure Gas-Driven LPG-Bank Process*, JPT Aug., 806; discussions, 812, 813, 814

FATT, I.: *An Electrodeless System for Measuring Electric Logging Parameters on Cores and Mud Samples*, JPT Mar., 292

FAYERS, F. J. and HOVANESSIAN, S. A.: *Linear Water Flood with Gravity and Capillary Effects*, SPEJ Mar., 32

FILTRATION TESTS: effects of size distribution on particle bridging, JPT June, 575

FLORA: microbial: found in oilfield water-injection systems, SPEJ June, 71

FLOW CAPACITY: approximate method for determining in formations with anisotropic permeability, SPEJ Dec., 277

FLOW STABILITY: development of theory for miscible liquid-liquid displacement. SPEJ Mar., 17

use to optimize solvent-oil recovery, SPEJ Mar., 9

FLUID FLOW: alternating: use to characterize porous media having storage pores, JPT Apr., 383

gas: unsteady state into gas wells, JPT Nov., 1151

nonsteady state in porous media, approximate method for computing, SPEJ Dec., 264

in heterogeneous porous media, SPEJ Sept., 153

imbibition model: application of, SPEJ June, 61

incompressible: effect of vertical fractures on reservoir behavior, SPEJ June, 105; discussion, 117

of gas and liquid simultaneously as encountered in well tubing, JPT Oct., 1037

maximum capacity of fracture, effect of propping agent concentration, SPEJ Sept., 119

multiphase: of water, oil and natural gas through vertical flow strings, JPT Oct., 1029

restricted entry, effect on well productivity, JPT Feb., 172

study in stratified reservoirs by use of thermal analogy, SPEJ Dec., 215

three-phase imbibition relative permeability, SPEJ Dec., 254

two dimensional analyses: determining areal permeability distribution, JPT July, 691

two-phase pressure gradient calculations, JPT Oct., 1023

FLUID MECHANICS: in study of widths of hydraulic fractures, JPT Sept., 937

FORMATION CUTTING: theory using the sand erosion process, JPT May, 483

FORMATION EVALUATION: induced nuclear reaction logging, JPT Aug., 797

FORMATION FRACTURES: investigation of abrasive-laden-fluid method for initiation of, JPT May, 489

produced in sandstone by high-velocity projectiles, JPT Mar., 273; discussion, JPT Sept., 955

propping with aluminum particles, JPT June, 583

sand concentration for maximum fracture flow capacity, SPEJ Sept., 119

vertical: effect on reservoir behavior, incompressible fluid case, SPEJ June, 105; discussion, 117

FORMATION FRACTURING: hydraulic: field test to determine areal extent and orientation, JPT Apr., 371

horizontal: effect on well performance, JPT Oct., 1050

width of, JPT Sept., 937

FRACTURED RESERVOIRS: *See* Formation Fractures

FORMATION RESISTIVITY FACTOR: porosity relationships, significance of particle shape, JPT Mar., 285

FRACTURED RESERVOIRS OR FRACTURING: *See* Formation Fractures and Formation Fracturing

G

GARDER, A. O., JR. and STONE, H. L.: *Analysis of Gas-Cap or Dissolved-Gas Drive Reservoirs*, SPEJ June, 92; discussion, 102

GARDNER, G. H. F.: *Discussion on the Significance of Particle Shape in Formation Resistivity Factor-Porosity Relationships*, JPT Oct., 1050

GAS: *See also* Natural Gas

constant-pressure porosimeter, JPT Jan., 87

differential liberation of: calculation method, JPT Nov., 1135

nonequilibrium: displacement calculations for, SPEJ Sept., 130

nonsteady-state flow in porous media, approximate method for computing, SPEJ Dec., 264

unsteady-state flow into gas wells, JPT Nov., 1151

GAS-CAP DRIVE: reservoir analysis of, SPEJ June, 92; discussion, 102

GAS CONDENSATES: *See* Condensates

GAS LIFT: evaluation of vertical-lift performance in producing wells, JPT Apr., 390

multiphase flow of water, oil and natural gas through vertical flow strings, JPT Oct., 1029

simultaneous flow of gas and liquid as encountered in well tubing, JPT Oct., 1037

well performance, pressure losses in flow strings, JPT Oct., 1023

GAS RESERVOIRS: subject to water drive, study on electronic differential analyzer, SPEJ Dec., 287

GASKELL, M. H. and LINDLEY, D. C.: *Cellar Oil*, JPT Apr., 377

GATLIN, C.: *Discussion on Mechanism of Alcohol Displacement of Oil from Porous Media*, SPEJ Sept., 209

GATLIN, C. and NEMIR, C. E.: *Some Effects of Size Distribution on Particle Bridging in Lost Circulation and Filtration Tests*, JPT June, 575

GEERSTMA, J.: *Velocity-Log Interpretation: The Effect of Rock Bulk Compressibility*, SPEJ Dec., 235; discussion, 246

GLYCOL DEHYDRATION: equilibrium ratios of water in the water-triethylene glycol-natural gas system, JPT July, 697

GOGARTY, W. B., et al: *Discussion on Effect of Bank Size on Oil Recovery in the High-Pressure Gas-Driven LPG-Bank Process*, JPT Aug., 813

GOODMAN DIAGRAM: evaluating permissible dog-legs in rotary boreholes, JPT Feb., 175

GORMLEY, J. F.: *Experimental Stress Analysis of Tool Joints*, JPT May, 496

GRAVITY: effect on linear water flood with capillary effects, SPEJ Mar., 32

GRAVITY DRAINAGE: analysis of, JPT Sept., 927

GROSMANGIN, M., et al: *A Sonic Method for Analyzing the Quality of Cementation of Borehole Casings*, JPT Feb., 165

GUERRERO, E. T. and LOUCKS, T. L.: *Pressure Drop in a Composite Reservoir*, SPEJ Sept., 170

H

HALL, H. N.: *Analysis of Gravity Drainage*, JPT Sept., 927

HARRIMAN, D. W., et al: *Investigation of Abrasive-Laden-Fluid Method for Perforation and Fracture Initiation*, JPT May, 489

HARTLINE, R. E., et al: *The Effect of Coil Design on the Performance of the Induction Log*, JPT Nov., 1137: discussion, 1148

HARTSOCK, J. H. and WARREN, J. E.: *The Effect of Horizontal Hydraulic Fracturing on Well Performance*, JPT Oct., 1050

HAZEBROEK, P., et al: *A Study of the Behavior of Bounded Reservoirs Composed of Stratified Layers*, SPEJ Mar., 43

HEAT OF REACTION: of sandstone, SPEJ Dec., 249

HEAT TRANSFER: character of porous rocks filled with stagnant fluid, SPEJ Mar., 37

in porous rocks, SPEJ Dec., 249

HEIM, A. H.: *Constant-Pressure Gas Porosimeter*, JPT Jan., 87

HELLER, J. P.: *Discussion on Experiments on Mixing During Miscible Displacement in Porous Media*, SPEJ Sept., 213

HELLER, J. P., et al: *A Potentiometric Study of the Effects Mobility Ratio on Reservoir Flow Patterns*, SPEJ Sept., 125

HENDERSON, J. H. and NAAR, J.: *An Imbibition Model—Its Application to Flow Behavior and the Prediction of Oil Recovery*, SPEJ June, 61

HENLEY, D. H., et al: *A Scale-Model Study of Bottom-Water Drives*, JPT Jan., 90

HENSON, W. L., et al: *A Numerical Solution to the Unsteady-State Partial-Water-Drive Reservoir Performance Problem*, SPEJ Sept., 184

HEUER, G. J., JR., et al: *The Influence of Production Rate, Permeability Variation and Well Spacing on Solution-Gas-Drive Performance*, JPT May, 469

HOUGH, E. W. and STEGEMEIER, G. L.: *Correlation of Surface and Interfacial Tension of Light Hydrocarbons in the Critical Region*, SPEJ Dec., 259

HOVANESSIAN, S. A.: *Pressure Studies in Bounded Reservoirs*, SPEJ Dec., 223

HOVANESSIAN, S. A. and FAYERS, F. J.: *Linear Water Flood with Gravity and Capillary Effects*, SPEJ Mar., 32

HOWE, R. J., et al: *Laboratory Drilling Performance of the Full-Scale Rock Bit*, JPT Jan., 71; discussion, 80

HOWER, W. F. and BROWN, W.: *Large-Scale Laboratory Investigation of Sand Consolidation Techniques*, JPT Dec., 1221

HOYER, W. A.: *Induced Nuclear Reaction Logging*, JPT Aug., 797

HYDRATES: of natural gas at pressures to 10,000 psia, JPT June, 590

HYDRAULIC JETTING: *See* Abrasive jetting

HYDRAZINE: field evaluation as a casing corrosion preventive, JPT July, 703

I

IMBIBITION: three-phase relative permeability, SPEJ Dec., 254

IMBIBITION TESTS: effect of reservoir environment on water-oil displacement, JPT June, 579

INDUCTION LOG: effect of coil design on performance, JPT Nov., 1137; dicussion, 1148

INJECTION: *See* Water Flooding

INJECTION RATE: effect of mobility ratio, area swept, and pattern, SPEJ June, 81

INTERFACIAL TENSION: correlation of light hydrocarbons in critical region, SPEJ Dec., 259

J

JENKINS, R. E.: *Characteristics of the Delaware Formation*, JPT Dec., 1230

JESSEN, F. W. and TURAN, F. H.: *Deflocculation of Fractionated Montmorillonite by Sodium Polyphosphates*, SPEJ Dec., 229

JOHNSON, E. F., et al: *The Linear Displacement of Oil from Porous Media by Enriched Gas*, JPT Aug., 787

JONES, L. G.: *An Approximate Method for Computing Non-steady-State Flow of Gases in Porous Media*, SPEJ Dec., 264

K

KAMATH, I. S. K., et al: *Mechanism of Alcohol Displacement of Oil from Porous Media*, SPEJ Sept., 195; discussion, 209

KATZ, D. L., et al: *Study of Gas Reservoirs Subject to Water Drive on Electronic Differential Analyzer*, SPEJ Dec., 287

KERN, L. R. and PERKINS, T. K.: *Widths of Hydraulic Fractures*, JPT Sept., 937

KERN, L. R., et al: *Propping Fractures with Aluminum Particles*, JPT June, 583

KOELLER, R. C. and CRAIG, F. F., JR.: *Discussion on Effect of Bank Size on Oil Recovery in the High-Pressure Gas-Driven LPG-Bank Process*, JPT Aug., 814

KOKESH, F. P. et al: *A Sonic Method for Analyzing the Quality of Cementation of Borehole Casings*, JPT Feb., 165

KOZENY-CARMEN EQUATION: estimating conductivities of aluminum propped fractures, JPT June, 583

KRUGER, W. D.: *Determining Areal Permeability Distribution by Calculations*, JPT July, 691

KUNII, D. and SMITH, J. M.: *Thermal Conductivities of Porous Rocks Filled with Stagnant Fluid*, SPEJ Mar., 37

KYTE, J. R. et al: *Effect of Reservoir Environment on Water-Oil Displacements*, JPT June, 579

L

LABORATORY STUDIES: of bottom-water drives by scaled model, JPT Jan., 90

drilling performance of the full-scale rock bit, JPT Jan., 71; discussion, 80

of oil recovery by steam injection, JPT July, 681

of sand consolidation techniques, JPT Dec., 1221

LACEY, J. W. et al: *Effect of Bank Size on Oil Recovery in the High-Pressure Gas-Driven LPG-Bank Process*, JPT Aug., 806; discussions, 812, 813, 814

LEFKOVITS, H. C., et al: *A Study of the Behavior of Bounded Reservoirs Composed of Stratified Layers*, SPEJ Mar., 43

LEVINE, J. S. and PRATS, M.: *The Calculated Performance of Solution-Gas-Drive Reservoirs*, SPEJ Sept., 142

LINDLEY, D. C. and GASKELL, M. H.: *Cellar Oil*, JPT Apr., 377

LINEAR DISPLACEMENT: of oil from porous media by enriched gas, JPT Aug., 787

LINEAR PROGRAMING: application of optimizing techniques for studying field producing operations, JPT Jan., 82

LIQUIDS: multiple phases in a natural-gas system, SPEJ Sept., 137

LOGGING: *See* Well logging

LOPER, J. L. and BROWN, R. W.: *Theory of Formation Cutting Using the Sand Erosion Process*, JPT May, 483

LOST CIRCULATION TESTS: effects of size distribution on particle bridging, JPT June, 575

LOUCKS, T. L. and GUERRERO, E. T.: *Pressure Drop in a Composite Reservoir*, SPEJ Sept., 170

LPG INJECTION: high-pressure gas-driven bank process, effect of bank size on oil recovery, JPT Aug., 806; discussions, 812, 813, 814

LUBINSKI, A.: *Maximum Permissible Dog-Legs in Rotary Boreholes*, JPT Feb., 175

LUBINSKI, A., et al: *The Use of Alternating Flow to Characterize Porous Media Having Storage Pores*, JPT Apr., 383

M

MAJANI, P., et al: *A Sonic Method for Analyzing the Quality of Cementation of Borehole Casings*, JPT Feb., 165

MARTIN, J. C.: *Discussion on Analysis of Gas-Cap or Dissolved-Gas Drive Reservoirs*, SPEJ June, 102

MARTING, V. E. and BRONS, F.: *The Effect of Restricted Fluid Entry on Well Productivity*, JPT Feb., 172

MATTAX, C. C. et al: *Effect of Reservoir Environment on Water-Oil Displacements*, JPT June, 579

MATTHEWS, C. S., et al: *A Study of the Behavior of Bounded Reservoirs Composed of Stratified Layers*, SPEJ Mar., 43

MAURER, W. C. and RINEHART, J. S.: *Fractures and Craters Produced in Sandstone by High-Velocity Projectiles*, JPT Mar., 273; discussion JPT Sept., 955

MAXIMUM DENSITY THEORY: in lost circulation and filtration problems, JPT June, 575

MCAFEE, R. V.: *The Evaluation of Vertical Lift Performance in Producing Wells*, JPT Apr., 390

MCLEOD, H. O., JR. and CAMPBELL, J. M.: *Natural Gas Hydrates at Pressures to 10,000 psia*, JPT June, 590

MICROBIAL FLORA: in oilfield water-injection systems, SPEJ June, 71

MILLER, J. E., et al: *Multiple Liquid Phases in a Natural-Gas System*, SPEJ Sept., 137

MILLER, W. C. and BRONS, F.: *A Simple Method for Correcting Spot Pressure Readings*, JPT Aug., 803

MISCIBLE DISPLACEMENT: effect of bank size on oil recovery in the high-pressure gas-driven LPG-bank process, JPT Aug., 806; discussions, 812, 813, 814
experiments on mixing in porous media, SPEJ Mar., 1; discussion, Sept., 213
liquid-liquid: development of stability theory, SPEJ Mar., 17
oil by alcohol from porous media, SPEJ Sept., 195; discussion, 209
partial: of oil from porous media by enriched gas, JPT Aug., 787
use of stability theory to optimize, SPEJ Mar., 9
MIXING: experiments on, during miscible displacement in porous media, SPEJ Mar., 1; discussion, Sept., 213
MOBILITY RATIO: effect on injection rates in multifluid floods, SPEJ June, 81
potentiometric study of effects on reservoir flow patterns, SPEJ Sept., 125
use in scale-model study of bottom-water drives, JPT Jan., 90
MODELS: flow, sand-pack; scaled: study of bottom-water drives, JPT Jan., 90
heat conduction: study of flow in stratified reservoir, SPEJ Dec., 215
imbibition: application to flow behavior and the prediction of oil recovery, SPEJ June, 61
potentiometric, conductive cloth: study of the effects of mobility ratio on reservoir flow patterns, SPEJ Sept., 125
scaled: laboratory study of water flooding cellar oil, JPT Apr., 377
studies of oil displacement from thin sands by vertical water influx from adjacent shales, JPT Sept., 950
theoretical: of consolidated porous medium, three-phase relative permeability, SPEJ Dec., 254
three dimensional: used to study flow in heterogenous porous media, SPEJ Sept., 153
MONTMORILLONITE: fractionated: deflocculation by sodium pholphosphates, SPEJ Dec., 229
MORAN, J. H.: *Discussion on The Effect of Coil Design on the Performance of the Induction Log*, JPT Nov., 1148
MORTADA, M. and NABOR, G. W.: *An Approximate Method for Determining Areal Sweep Efficiency and Flow Capacity in Formation with Anisotropic Permeability*, SPEJ Dec., 277
MUD LOGGING: electrodeless system for measuring electric logging parameters on cores and mud samples, JPT Mar., 292
MULTIPLE ZONES: effect of oil production rate on performance of producing wells, SPEJ Mar., 26

N

NAAR, J. and HENDERSON, J. H.: *An Imbibition Model—Its Application to Flow Behavior and the Prediction of Oil Recovery*, SPEJ June, 61
NAAR, J. and WYGAL, R. J.: *Three-Phase Imbibition Relative Permeability*, SPEJ Dec., 254
NABOR, G. W. and MORTADA, M.: *An Approximate Method for Determining Areal Sweep Efficiency and Flow Capacity in Formation with Anisotropic Permeability*, SPEJ Dec., 277
NATURAL GAS: hydrates at pressures to 10,000 psia, JPT June, 590
multiphase flow with water and oil through vertical flow strings, JPT Oct., 1029
multiple liquid phases in, SPEJ Sept., 137
NAUMANN, V. O., et al: *Effect of Reservoir Environment on Water-Oil Displacements*, JPT June, 579
NEMIR, C. E. and GATLIN, C.: *Some Effects of Size Distribution on Particle Bridging in Lost Circulation and Filtration Tests*, JPT June, 575
NEWTONIAN FLUIDS: in study of widths of hydraulic fractures, JPT Sept., 937
NUMERICAL SOLUTION: linear water flood with gravity and capillary effects, SPEJ Mar., 32
to unsteady-state partial-water-drive reservoir-performance problem, SPEJ Sept., 184

O

ODEH, A. S.: *Discussion on Effect of Viscosity on Relative Permeability*, SPEJ June, 59
ODEH, A. S., et al: *A Potentiometric Study of the Effects of Mobility Ratio on Reservoir Flow Patterns*, SPEJ Sept., 125
OIL FIELDS: water injection system: microbial flora found therein, SPEJ June, 71
OIL PRODUCTION: effect of rate on performance of wells producing from more than one horizon, SPEJ Mar., 26
OIL RECOVERY: of cellar oil, JPT Apr., 377
effect of bank size in high-pressure gas-driven LPG-bank process, JPT Aug., 806; discussions, 812, 813, 814
prediction by an imbibition model, SPEJ June, 61
by steam injection, laboratory studies of, JPT July, 681
OPERATIONS RESEARCH: application of optimizing techniques for studying field producing operations, JPT Jan., 82
OPTIMIZING TECHNIQUES: application to study of field producing operations, JPT Jan., 82
ORGANISMS: found in oilfield water-injection systems, SPEJ June, 71
ORIENTATION: of hydraulic fractures, field test to determine, JPT Apr., 371
OSTROOT, G. W. and WALKER, W. A.: *Improved Compositions for Cementing Wells with Extreme Temperatures*, JPT Mar., 277
OUTMANS, H. D.: *Discussion on Stability Theory and Its Use To Optimize Solvent Recovery of Oil*, SPEJ Dec., 298
OWENS, W. W. et al: *A Scale-Model Study of Bottom-Water Drives*, JPT Jan., 90
OXYGEN SCAVENGERS: use to control external corrosion of oil-string casing, JPT July, 703

P

PARTICLE SHAPE: significance in formation resistivity factor-porosity relationships, JPT Mar., 285
PARTICLE SIZE DISTRIBUTION: effects of bridging in lost circulation and filtration tests, JPT June, 575
PERFORATING: investigation of abrasive-laden-fluid method, JPT May, 489
PERFORMANCE PREDICTIONS: calculated: solution gas-drive reservoirs, SPEJ Sept., 142
effect of vertical fractures, incompressible fluid case, SPEJ June, 105; discussion, 117
of gravity drainage reservoirs, JPT Sept., 927
in heterogeneous porous media, SPEJ Sept., 153
partial water-drive reservoir: a numerical solution to unsteady-state problem, SPEJ Sept., 184
PERKINS, T. K. and KERN, L. R.: *Widths of Hydraulic Fractures*, JPT Sept., 937
PERKINS, T. K., et al: *Propping Fractures with Aluminum Particles*, JPT June, 583
PERMEABILITY: anisotropic: approximate method for determining areal sweep efficiency and flow capacity in formations with, SPEJ Dec., 277
areal variation of: determining by calculations, JPT July, 691
of Delaware sand: characteristics of, JPT Dec., 1230
from pressure build-up curves: studies in bounded reservoirs, SPEJ Dec., 223
low: in gas-condensate well, calculated pressure build-up for, JPT Nov., 1131
relative: effect of viscosity on, SPEJ June, 59
imbibition in consolidated rock, SPEJ June, 61
three-phase imbibition, SPEJ Dec., 254
stratified: study of the behavior of bounded reservoirs, SPEJ Mar., 43

study of flow by use of thermal analogy, SPEJ Dec., 215
two concentric regions: pressure drop in a composite reservoir, SPEJ Sept., 170
variation in: influence on solution-gas-drive performance, JPT May, 469

PERRINE, R. L.: *Stability Theory and Its Use to Optimize Solvent Recovery of Oil*, SPEJ Mar., 9
The Development of Stability Theory for Miscible Liquid-Liquid Displacement, SPEJ Mar., 17; discussion, SPEJ Dec., 298

PHASE BEHAVIOR: equilibrium ratios of water in the water-triethylene glycol-natural gas system, JPT July, 697
multiple liquid phases in a natural-gas system, SPEJ Sept., 137
natural gas hydrates at pressures to 10,000 psia, JPT June, 590
nonequilibrium gas displacement calculations, SPEJ Sept., 130

PICKERING, C. H. et al: *A Study of Flow in Stratified Reservoirs by Use of the Thermal Analogy*, SPEJ Dec., 215

PIPE MOVEMENT: wellbore pressure surges produced by, JPT June, 595

PITTMAN, F. C. et al: *Investigation of Abrasive-Laden-Fluid Method For Perforation and Fracture Initiation*, JPT May, 489

POETTMANN, F. H., et al: *Discussion on Effect of Bank Size on Oil Recovery in the High-Pressure Gas-Driven LPG-Bank Process*, JPT Aug., 813

POLYPHOSPHATES: sodium, deflocculation of fractionated montmorillonite by, SPEJ Dec., 229

POPHAM, J. L., et al: *Hydraulic Fracture—Field Test to Determine Areal Extent and Orientation*, JPT Apr., 371

POROSIMETER: constant-pressure gas type, JPT Jan., 87

POROSITY: significance of particle shape in formation resistivity factor relationships, JPT Mar., 285

POROSTRICTION: use to characterize porous media having storage pores, JPT Apr., 383

POROUS MEDIA: approximate method for computing non-steady-state flow of gases, SPEJ Dec., 264
determining areal permeability distribution by calculations, JPT July, 691
effect of rock bulk compressibility on velocity-log interpretation, SPEJ Dec., 235; discussion, 246
experiments on mixing during miscible displacement, SPEJ Mar., 1; discussion, Sept., 213
heterogeneous, flow in, SPEJ Sept., 153
linear displacement of oil by enriched gas, JPT Aug., 787
mechanism of alcohol displacement of oil, SPEJ Sept., 195: discussion, 209
storage pores, use of alternating flow to characterize, JPT Apr., 383
thermal conductivities of rocks filled with stagnant fluid, SPEJ Mar., 37
thermal expansion and heat of reaction data for, SPEJ Dec., 249
three-phase imbibition relative permeability, SPEJ Dec., 254

POWERS, L. W. et al: *Laboratory Studies of Oil Recovery by Steam Injection*, JPT July, 681

PRATS, M.: *Effect of Vertical Fractures on Reservoir Behavior —Incompressible Fluid Case*, SPEJ June, 105; discussion, 117

PRATS, M. and LEVINE, J. S.: *The Calculated Performance of Solution-Gas-Drive Reservoirs*, SPEJ Sept., 142

PRESSURE BEHAVIOR: simple method for correcting spot pressure readings, JPT Aug., 803

PRESSURE BUILD-UP ANALYSES: calculated: for a low-permeability gas-condensate well, JPT Nov., 1131

PRESSURE DISTRIBUTIONS: steady state: in nine-spot pattern for single fluid injection, SPEJ June, 81
studies in bounded reservoirs, SPEJ Dec., 223

PRESSURE DROP: in a composite reservoir, SPEJ Sept., 170

PRESSURE GRADIENTS: in high-rate flowing and gas-lift wells, calculation of, JPT Oct., 1023
in multiphase flow of water, oil and natural gas through vertical flow strings, JPT Oct., 1029
in simultaneous flow of gas and liquid as encountered in well tubing, JPT Oct., 1037

PRESSURE MAINTENANCE: *See* Water Flooding

PRESSURE SURGES: produced in wellbore by pipe movement, JPT June, 595

PRICE, H. S. and WARREN, J. E.: *Flow in Heterogeneous Porous Media*, SPEJ Sept., 153

PRODUCTION: oil: effect of rate on performance of wells producing from more than one horizon, SPEJ Mar., 26

PRODUCTION OPERATIONS: application of optimizing techniques, JPT Jan., 82
evaluation of vertical-lift in wells, JPT Apr., 390

PRODUCTION PRACTICE: improved compositions for cementing wells with extreme temperatures, JPT Mar., 277

PRODUCTIVITY: effect of horizontal hydraulic fracturing on well performance, JPT Oct., 1050

PROJECTILES: high velocity, fractures and craters produced in sandstones by, JPT Mar., 273; discussion, JPT Sept., 955

PROPPING AGENT: aluminum particles used in formation fractures, JPT June, 583
concentration for maximum fracture flow capacity, SPEJ Sept., 119

PSEUDO SKIN FACTORS: in studies of the effect of restricted fluid entry on well productivity, JPT Feb., 172

R

REED, P. W. et al: *Experiments on Mixing During Miscible Displacement in Porous Media*, SPEJ Mar., 1; discussion, Sept., 213

REED, R. L., et al: *Mechanism of Alcohol Displacement of Oil from Porous Media*, SPEJ Sept., 195; discussion, 209

RELATIVE PERMEABILITY: effect of viscosity on, SPEJ June, 59
imbibition in consolidated rock, SPEJ June, 61
three-phase imbibition, SPEJ Dec., 254

RESERVOIR ANALYSIS: effect of vertical fractures, in compressible fluid case, SPEJ June, 105; discussion, 117

RESERVOIR ENVIRONMENT: effect on water-oil displacements, JPT June, 579

RESERVOIR PRESSURE: static, estimated from spot pressure measurements, JPT Aug., 803
studies in bounded reservoirs, SPEJ Dec., 223

RESERVOIR ROCK: *See also* Porous Media
porosity measurement by constant-pressure gas porosimeter, JPT Jan., 87

RESERVOIRS: composite: pressure drop in, SPEJ Sept., 170
stratified: a study of the behavior of bounded reservoirs, SPEJ Mar., 43

RESISTIVITY FACTOR: *See* Formation Resistivity Factor

REYNOLDS, J. J., et al: *Hydraulic Fracture—Field Test to Determine Areal Extent and Orientation*, JPT Apr., 371

RICE, J. D., et al: *A Numerical Solution to the Unsteady-State Partial-Water-Drive Reservoir Performance Problem*, SPEJ Sept., 184

RINEHART, J. S. and MAURER, W. C.: *Fractures and Craters Produced in Sandstone by High-Velocity Projectiles*, JPT Mar., 273; discussion, JPT Sept., 955

ROMERO-JUAREZ, A.: *Sand Concentration for Maximum Fracture Flow Capacity*, SPEJ Sept., 119

ROS, N. C. J.: *Simultaneous Flow of Gas and Liquid As Encountered in Well Tubing*, JPT Oct., 1037

ROWE, J. A., JR., et al: *Microbial Flora in a Number of Oilfield Water-Injection Systems*, SPEJ June, 71

ROWLEY, D. S., et al: *Laboratory Drilling Performance of the Full-Scale Rock Bit*, JPT Jan., 71; discussion, 80

RUNBERG, G. W., et al: *Laboratory Studies of Oil Recovery by Steam Injection*, JPT July, 681

S

St. John, J. C., et al: *Investigation of Abrasive-Laden-Fluid Method For Perforation and Fracture Initiation*, JPT May, 489

Sand consolidation: large-scale laboratory investigation of techniques, JPT Dec., 1221

Sand erosion process: theory of formation cutting using, JPT May, 483

Scaling: use in study of bottom-water drives, JPT Jan., 90

Scauzillo, F. R.: *Equilibrium Ratios of Water in the Water-Triethylene Glycol-Natural Gas System*, JPT July, 697

Schremp, F. W., et al: *Use of Oxygen Scavengers To Control External Corrosion of Oil-String Casing*, JPT July, 703

Scott, J. B., et al: *Hydraulic Fracture—Field Test to Determine Areal Extent and Orientation*, JPT Apr., 371

Secondary recovery: *See also* Miscible Displacement, Thermal Recovery of Oil, and Water Flooding
use of stability theory in solvent-oil recovery, SPEJ Mar., 9

Selim, M. A. and Somerton, W. H.: *Additional Thermal Data for Porous Rocks—Thermal Expansion and Heat of Reaction*, SPEJ Dec., 249

Shrinkage: oil: calculation of, JPT Nov., 1135

Simon, R.: *Discussion on Laboratory Drilling Performance of the Full-Scaled Rock Bit*, JPT Jan., 80

Skin effect: pseudo, in studies of the effect of restricted fluid entry on well productivity, JPT Feb., 172

Slug process: *See* Miscible Displacement

Smith, G. H. and Atkins, E. R., Jr.: *The Significance of Particle Shape in Formation Resistivity Factor-Porosity Relationships*, JPT Mar., 285; discussion, Oct., 1057

Smith, J. M. and Kunii, D.: *Thermal Conductivities of Porous Rocks Filled with Stagnant Fluid*, SPEJ Mar., 37

Smith, R. V.: *Unsteady-State Gas Flow into Gas Wells*, JPT Nov., 1151

Sodium chloride: as partial acceleration in improved bentonite cements, JPT Sept., 923

Solution-gas drive: calculated performance of reservoirs, SPEJ Sept., 142
influence of production rate, permeability variation and well spacing on performance, JPT May, 469
reservoir analysis of, SPEJ June, 92

Solvent flooding: development of stability theory for miscible liquid-liquid displacement, SPEJ Mar., 17
use to optimize recovery of oil, SPEJ Mar., 9

Somerton, W. M. and Selim, M. A.: *Additional Thermal Data for Porous Rocks—Thermal Expansion and Heat of Reaction*, SPEJ Dec., 249

Sonic method: for analyzing the quality of cementation of borehole casings, JPT Feb., 165

Stability theory: development for miscible liquid-liquid displacement, SPEJ Mar., 17
use to optimize solvent recovery of oil, SPEJ Mar., 9

Steam injection: *See* Thermal Recovery of Oil

Stegemeier, G. L. and Hough, E. W.: *Correlation of Surface and Interfacial Tension of Light Hydrocarbons in the Critical Region*, SPEJ Dec., 259

Stewart, C. R., et al: *The Use of Alternating Flow to Characterize Porous Media Having Storage Pores*, JPT Apr., 383

Stone, H. L. and Garder, A. O., Jr.: *Analysis of Gas-Cap or Dissolved-Gas Drive Reservoirs*, SPEJ June, 92; discussion, 102

Storage: pore: use of alternating flow to characterize porous media having, JPT Apr., 383

Stratification: *See* Permeability, stratified

Stress analysis: experimental, of tool joints, JPT May, 496

Stresses: caused by bit loading at center of hole, SPEJ Sept., 177

Stroud, L., et al: *Multiple Liquid Phases in a Natural-Gas System*, SPEJ Sept., 137

Surface tension: correlation of light hydrocarbons in critical region, SPEJ Dec., 259

Sweep efficiency: area (pattern): five-spot potentiometric study of effects of mobility ratio, SPEJ Sept., 125
bottom water-drive reservoirs, scaled-model study, JPT Jan., 90

T

Taber, J. J., et al: *Mechanism of Alcohol Displacement of Oil from Porous Media*, SPEJ Sept., 195; discussion, 209

Tek, M. R.: *Multiphase Flow of Water, Oil and Natural Gas Through Vertical Flow Strings*, JPT Oct., 1029

Tek, M. R., et al: *Study of Gas Reservoirs Subject to Water Drive on Electronic Differential Analyzer*, SPEJ Dec., 287

Tempelaar-Lietz, W.: *Effect of Oil Production Rate on Performance of Wells Producing from More Than One Horizon*, SPEJ Mar., 26

Thermal analogy: use in study of flow in stratified reservoirs, SPEJ Dec., 215

Thermal properties: conductivities of porous rocks filled with stagnant fluid, SPEJ Mar., 37
expansion of sandstone, SPEJ Dec., 249

Thermal recovery of oil: laboratory studies of oil recovery by steam injection, JPT July, 681

Thomas, R. and Baxendell, P. B.: *The Calculation of Pressure Gradients in High-Rate Flowing Wells*, JPT Oct., 1023

Thomsen, H. S., et al: *The Effect of Coil Design on the Performance of the Induction Log*, JPT Nov., 1137; discussion, 1148

Tool joints: experimental stress analysis of, JPT May, 496

Tuman, V. S.: *Discussion on Velocity-Log Interpretation: The Effect of Rock Bulk Compressibility*, SPEJ Dec., 246

Turan, F. H. and Jessen, F. W.: *Deflocculation of Fractionated Montmorillonite by Sodium Polyphosphates*, SPEJ Dec., 229

V

Valleroy, V. V., et al: *Laboratory Studies of Oil Recovery by Steam Injection*, JPT July, 681

Velocity: high: of projectiles, fractures and craters produced in sandstone by, JPT Mar., 273

Velocity logging: *See also* Acoustic Velocity Logging

Venghiattis, A. A.: *Discussion on Fractures and Craters Produced in Sandstone by High-Velocity Projectiles*, JPT Sept., 955

Viscosity: oil: effect on relative permeability, SPEJ June, 59

Viscosity ratio: in experiments on mixing during miscible displacement in porous media, SPEJ Mar., 1; discussion, Sept., 213

W

Walker, W. A. and Ostroot, G. W.: *Improved Compositions for Cementing Wells with Extreme Temperatures*, JPT Mar., 277

Wardlaw, H. W. R.: *Simplified Analysis Aids in Optimizing Drilling Factors for Minimum Cost*, JPT May, 475

Warren, J. E. and Hartsock, J. H.: *The Effect of Horizontal Hydraulic Fracturing on Well Performance*, JPT Oct., 1050

Warren, J. E. and Price, H. S.: *Flow in Heterogeneous Porous Media*, SPEJ Sept., 153

Water: equilibrium ratios in water-triethylene glycol-natural gas system, JPT July, 697
multiphase flow with oil and natural gas through vertical flow strings, JPT Oct., 1029
See also Water Influx

Water drive: bottom: model test results and performance predictions, JPT Jan., 90
of gas reservoirs, study on electronic differential analyzer, SPEJ Dec., 287
partial: a numerical solution to the unsteady-state reservoir performance problem, SPEJ Sept., 184

Water flooding: approximate equations for predicting injection rates in multifluid floods, SPEJ June, 81
of cellar oil, JPT Apr., 377
feasibility of Delaware formation, JPT Dec., 1230
linear: with gravity and capillary effects, SPEJ Mar., 32

microbial flora found in oilfield water-injection systems, SPEJ June, 71
oil recovery by imbibition, SPEJ June, 61
WATERFLOOD TESTS: effect of reservoir environment on water-oil displacement, JPT June, 579
WATER INFLUX: vertical: from adjacent shales, model studies of oil displacement from thin sands by, JPT Sept., 950
WATER-OIL DISPLACEMENT: effect of reservoir environment, JPT June, 579
WEARDEN, P. L., et al: *A Numerical Solution to the Unsteady-State Partial-Water-Drive Reservoir Performance Problem,* SPEJ Sept., 184
WEINAUG, C. F.: *Calculation of Differential Gas Liberation and Shrinkage,* JPT Nov., 1135
WELGE, H. J., et al: *The Linear Displacement of Oil from Porous Media by Enriched Gas.,* JPT Aug., 787
WELLBORE PRESSURE SURGES: produced by pipe movement, JPT June, 595
WELL COMPLETION: *See also* Well Stimulation
improved compositions for cementing wells with extreme temperatures, JPT Mar., 277
wellbore pressure surges produced by pipe movement, JPT June, 595
WELL LOGGING: effect of coil design on performance of induction log, JPT Nov., 1137; discussion, 1148
electrodeless system for measuring electric logging parameters on cores and mud samples, JPT Mar., 292
induced nuclear reaction logging, JPT Aug., 797
interpretation, significance of particle shape in formation resistivity factor-porosity relationships, JPT Mar., 285
WELL PATTERN: effect on injection rates in multifluid floods, SPEJ June, 81
potentiometric study of effects of mobility ratio, SPEJ Sept., 125
WELL PERFORMANCE: calculated pressure build-up for a low permeability gas-condensate well, JPT Nov., 1131
unsteady-state gas flow, JPT Nov., 1151
flowing and gas lift: evaluation of, JPT Apr., 390
WELL PRODUCTIVITY: effect of restricted fluid entry, JPT Feb., 172
WELL SPACING: influence on solution-gas-drive performance, JPT May, 469
WELL STIMULATION: effect of horizontal hydraulic fracturing on well performance, JPT Oct., 1050
field test to determine areal extent and orientation of hydraulic fractures, JPT Apr., 371
WELL TUBING: simultaneous flow of gas and liquid, JPT Oct., 1037
WETTABILITY: effect of reservoir environment on water-oil displacement, JPT June, 595
WILHOIT, J. C., JR. and CHEATHAM, J. B. JR.: *Stresses Caused by Bit Loading at the Center of the Hole,* SPEJ Sept., 177
WILLMAN, B. T., et al: *Laboratory Studies of Oil Recovery by Steam Injection,* JPT July, 681
WISE, W. B., et al: *Application of Optimizing Techniques for Studying Field Producing Operations,* JPT Jan., 82
WYANT, R. E., et al: *Propping Fractures with Aluminum Particles,* JPT June, 583
WYGAL, R. J. and NAAR, J.: *Three-Phase Imbibition Relative Permeability,* SPEJ Dec., 254

Y

"*Y*" FUNCTION: empirical "rate of flow" term in unsteady-state gas flow into gas wells, JPT Nov., 1151
YOO, H. D., et al: *Study of Gas Reservoirs Subject to Water Drive on Electronic Differential Analyzer,* SPEJ Dec., 277

Available Papers Not Published by the Society of Petroleum Engineers

The Society receives many papers during the year which are not selected for publication by the Transactions Editorial Committee or General Editorial Committee. Frequently, copies of these papers may help engineers in their work; therefore, the Society has asked permission of authors to list them. Authors choosing to list their papers here have agreed to fill a limited number of requests for their manuscripts; consequently, their addresses are given.

1594-G *Well Spacing Performance, Relative Permeabilities, and Acidization Effects in a Limestone Reservoir,* by L. W. Folmar, J. M. Williams, E. K. Stevenson, Texaco, Inc., P. O. Box 2420, Tulsa 2, Okla.

1625-G *Performance of Five-Spot Waterfloods in Stratified Reservoirs Using Streamlines,* by R. V. Higgins and A. J. Leighton, U. S. Dept. of the Interior, 1429 U. S. Appraisers Bldg., San Francisco 11, Calif.

1644-G *Modern Logging Programs and Interpretation Methods,* by R. P. Alger, Schlumberger Well Surveying Corp., 5000 Gulf Freeway, Houston, Tex.

1656-G *A New Method for the Estimation of Primary Oil Reserves,* by George Thodos and W. F. Stevens, Dept. of Chemical Engineering, Northwestern U., Evanston, Ill.

1659-G *A Rapid Method of Calculating Reserves of Water Drive Reservoirs by Material Balance,* by L. T. Stanley, Pure Oil Co., Research Center, Crystal Lake, Ill.

SPE-1 *Reserve Evaluation and the Independent Oilman,* by Earl A. Nichols, 212 Meadows Bldg., Dallas, Tex.

SPE-5 *Trends and Projections in Soviet Energy Output and Demand, 1947-72,* by Demitri B. Shimkin, U. of Illinois, Urbana, Ill.

SPE-17 *A Note on Plotting Pressure Build-Up Data,* by Kenneth E. Gray, Texas U., Dept. of Petroleum Engineering, Austin 12, Tex.

SPE-21 *AccuRay Measurement and Control of Sand Concentration During Fracturing Jobs,* by Leon R. Cort and Charles O. Badgett, Industrial Nucleonics, 650 Ackerman Rd., Columbus 2, Ohio.

SPE-27 *Gas Sales Contracts and Allied Problems,* by John G. Thorp, The Atlantic Refining Co., Box 2819, Dallas 21, Tex.

SPE-28 *A Method of Predicting the Future Performance of a Gas Reservoir Using a Digital Computer,* by Forrest A. Garb, H. J. Gruy and Associates, Inc., Southland Center, Dallas 1, Tex.

SPE-35 *Fuel Interchangeability—Measuring Its Extent in U. S. Energy Markets,* by W. Gibson Jaworek, The Ohio Oil Co., Findlay, Ohio; and John J. Schanz, Jr., Penn State U.

SPE-66 *Carbonated Waterflood Results—Texas and Oklahoma,* by R. J. Christensen, Oil Recovery Corp., Beacon Bldg., Tulsa 3, Okla.

SPE-71 *The Role of Acid Reaction Rates in Planning Acidizing Treatments,* by A. R. Hendrickson, R. B. Rosene, Dowell Div. of the Dow Chemical Co., P. O. Box 536, Tulsa, Okla.; and D. R. Wieland, U. of Tulsa.

SPE-72 *Pressure Distribution in Systems with Continuously Varying Permeability,* by T. L. Loucks, 2846 East 38th, Tulsa, Okla.

SPE-78 *Planning a Successful Accident Prevention Program,* by Charles Homewood, Arabian American Oil Co., Dhahran, Saudi Arabia.

SPE-88 *The Use of an Asymptotic Series in Determining Average Pressure in Steady-State Radial Gas Flow,* by C. D. Stahl and T. Loucks, Dept. of Petroleum and Natural Gas, Penn State U., University Park, Pa.

SPE-116 *The Determination of Miscibility Pressures,* by Phillippe Defrenne, Charles Marle, J. Pacsirszky, Institut Francais du Petrole, 1-4, Avenue de Bois Preau, Rueil-Malmaison, France; and Maurice Jeantet, S. N. Repal, Alger.

SPE-181 *An Analysis of "Single-Point Entry" Well Completions and Control of Fracture Plane,* by Roscoe C. Clark, Jr., and B. J. Bucy, Westco Research, P. O. Box 186, Fort Worth 1, Tex.

SPE-194 *Production Performance of Displacement Processes in Stratified Formations,* by W. A. Roper, A. Brown and T. S. Teasdale, Texaco, P. O. Box 425, Bellaire, Tex.

3 8198 309 334 041
THE UNIVERSITY OF ILLINOIS AT CHICAGO

THIS BOOK IS FOR USE
ONLY IN THE LIBRARY
IT DOES NOT CIRCULATE